

Ninth International
Conference on

Flow Dynamics

September **19-21, 2012**

Hotel Metropolitan Sendai, Japan

Proceedings

Preface

We appreciate for your participation in the Ninth International Conference on Flow Dynamics ICFD2012, Sendai, Japan.

"Flow Dynamics" is a comprehensive scientific field which deals with the flow and transport phenomena concerning to quantum wave, air, any fluid, any material, energy and information. Through the past eight conferences on Flow Dynamics held in Sendai, "Flow Dynamics" has become a major academic discipline deeply related to various difficult issues that the human society is currently facing, such as the global environment, the depletion of energy resources, and future lives on our planet.

One and a half year after the earthquake and tsunami struck followed by the accident of nuclear power plants in Tohoku area, we are on our way of recuperating and recovering from the after-effects of the disaster. The landscape of City of Sendai looks pretty decent now and no major effect of damage is noticeable. Many people who lived close to the sea shore and lost their houses by tsunami are now busy in relocating and/or rebuilding their houses.

We are pleased to hold "Ninth International Conference on Flow Dynamics ICFD2012, aiming to explore new science horizon and cutting edge technologies of Flow Dynamics, and providing young researchers with unique opportunities of experience and self-development in this very attractive and competitive field. We believe that this conference will give us a great opportunity to discuss what we have learned from the disastrous effects, and what we can do to transform our society living in harmony with the mother nature.

The Conference is comprised of 1 General Session, 10 Organized Sessions and 5 Planned Sessions. The number of presentation and participants are more than 400 and 650, respectively. We are glad to see the number of presenters is increasing every year.

This is the last ICFD which is supported by the Global COE Program "World Center of Education and Research for Trans-disciplinary Flow Dynamics" (the GCOE). ICFD2013 in the next year shall be held in November in Sendai, being coordinated by the Institute of Fluid Science (IFS), Tohoku University, an affiliated body of the GCOE. We appreciate so much for your cooperation and support to the activities of the GCOE in the past. We wish you give the same supports to IFS from now on.

On behalf of the organizing committee of the Ninth International Conference on Flow Dynamics, I wish you enjoy successful discussions and exchanges of information, and also renewing old friendships with the people from all over the world.

Dr. Shigenao Maruyama
Professor, Tohoku University
Program Leader, Tohoku University Global COE Program
"World Center of Education and Research for Trans-disciplinary Flow Dynamics"

Ninth International Conference on Flow Dynamics

Organized and Sponsored by:

- Tohoku University Global COE Program, "World Center of Education and Research for Trans-disciplinary Flow Dynamics"
- Institute of Fluid Science, Tohoku University

In cooperation with:

- Combustion Society of Japan
- The Japan Society of Applied Electromagnetics and Mechanics
- The Japan Society of Applied Physics
- Japanese Society of Biorheology
- The Japan Society for Computational Engineering and Science
- The Japan Society of Fluid Mechanics
- Japan Society of Maintenology
- Japan Society of Maintenology, Tohoku / Hokkaido Branch
- The Japan Society of Mechanical Engineers
- JSME Fluids Engineering Division
- The Japan Society for Multiphase Flow
- Aoba Foundation for the Promotion on Engineering
- Fluid Sciences Foundation

SCOPE:

One year has passed since the last Great East Japan Earthquake struck Tohoku area on March 11, 2011. Severe damages caused by the earthquake and tsunami, and the consequential disaster by the crippled Fukushima Dai-ichi Nuclear Power Plant, still leave some areas of Tohoku, as being overwhelmed and uninhabitable. Although the situation in Sendai now is perfectly normal as well as its radiation level is, we are still in a stage of preparation for the stabilized cooling of the nuclear power plant.

We appreciate the great support and help provided by the people of the world, our lives in Sendai have returned quickly to a stable and ordinary state. Actually for the last Eighth ICFD held in November 2011, contrary to our pessimistic forecast, six hundred (600) people, including over two hundred (200) from abroad, gathered together in Sendai. We are proud of what we have done in the past for the extension of the boundary of Flow Dynamics, and we will keep going for the future of Flow Dynamics and pursue finding out solutions for improved welfare of the people of the world.

Flow Dynamics is a comprehensive scientific field which deals with various flows and transport phenomena, ranging from nano-scale flows such as behavior of electrons, atoms, molecules and ions to gigantic scale flows such as solar radiation, air and water flows on the globe, volcanic activities, typhoon, tsunami etc. Theoretically, such phenomena are well covered by Newtonian, molecular and quantum dynamics.

The Ninth International Conference on Flow Dynamics (ICFD2012), in the annual series, which is supported by Tohoku University Global COE Program "World Center of Education and Research for Trans-disciplinary Flow Dynamics" will be held on September 19th through 21st, 2012 at Hotel Metropolitan Sendai, Sendai, Japan. The objectives of this conference are not only to explore new horizon by discussing matters in the most advanced academic fields, or exchanging information in cutting edge technologies in Flow Dynamics, but also to provide young researchers and students with unique opportunities of being educated and self-development through their proactive participation to the conference.

We cordially invite you scholars, researchers, engineers, educationists, students and planners, exploring and studying in the relevant research and development fields of bio-, nano-, material, energy, environmental, planetary and earth sciences and technologies, particularly in

the academic field of mechanical engineering, aerospace engineering, nuclear science and engineering, physics, medical science and engineering, chemistry, chemical engineering and so on, to join the conference.

CONFERENCE COMMITTEE:

Executive Committee Members:

Shigenao Maruyama (ICFD2012 Chair, Tohoku University)
Shigeru Obayashi (AFI/TFI-2012 Chair, Tohoku University)
Toshiyuki Takagi (CEO of ICFD2012, Tohoku University)
Toshiyuki Hayase (IFS Director, Tohoku University)

International Scientific Committee Members:

Chair: Shigenao Maruyama (Tohoku University)

Australia

Masud Behnia (The University of Sydney)
Gary Rosengarten (The University of New South Wales)

Canada

Javad Mostaghimi (University of Toronto)

China

XinGang Liang (Tsinghua University)
Xing Zhang (Tsinghua University)

France

Patrick Bourgin (ECL)
Jean-Yves Cavaille (INSA de Lyon)
Philippe Kapsa (ECL)

Germany

Serge A. Shapiro (Freie University Berlin)

India

Subhash C. Mishra (Indian Institute of Technology Guwahati)

Italy

Gian Piero Celata (ENEA)

Japan

Keisuke Asai (Tohoku University)
Yu Fukunishi (Tohoku University)
Masato Furukawa (Kyushu University)
Toshiyuki Hayase (Tohoku University)
Nobuhide Kasagi (The University of Tokyo)
Chisachi Kato (The University of Tokyo)
Yoichiro Matsumoto (The University of Tokyo)
Junichiro Mizusaki (Tohoku University)
Kazuhiro Nakahashi (Tohoku University)
Masami Nakano (Tohoku University)
Tomohide Niimi (Nagoya University)
Hideya Nishiyama (Tohoku University)
Masaki Sano (The University of Tokyo)
Akihiro Sasoh (Nagoya University)
Masaaki Sato (Tohoku University)
Toshiyuki Takagi (Tohoku University)

Michio Tokuyama (Tohoku University)
Takashi Yabe (Tokyo Institute of Technology)
Satoru Yamamoto (Tohoku University)

Korea

Joon-Hyun Lee (KETEP)
Joon Sik Lee (Seoul National University)
Hyung Jin Sung (Korea Advanced Institute of Science and Technology)

Russia

Mikhail Ivanov (Institute of Theoretical and Applied Mechanics SB RAS)
Oleg P. Solonenko (Institute of Theoretical and Applied Mechanics SB RAS)
Alexander Vasiliev (Moscow State University)

Sweden

Fredrik Lundell (KTH)

Switzerland

Bastien Chopard (University of Geneva)
Dimos Poulikakos (ETH Zurich)

Taiwan

Wu-Shung Fu (National Chiao Tung University)

UK

Yiannis Ventikos (University of Oxford)

USA

Louis N. Cattafesta III (University of Florida)
Yiguang Ju (Princeton University)
Ishwar K. Puri (Virginia Tech)
Kozo Saito (Kentucky University)
John P. Sullivan (Purdue University)
Rongia Tao (Temple University)
Satish Udpa (Michigan State University)

Organizing Committee Members:

Chair: Shigenao Maruyama (Tohoku University)
Koji Amezawa, Hideyuki Aoki, Keisuke Asai, Shinji Ebara, Yu Fukunishi, Hidetoshi Hashizume, Nozomu Hatakeyama, Yuka Iga, Jun Ishimoto, Takatoshi Ito, Sumio Kitajima, Tetsuya Kodama, Atsuki Komiya, Kaoru Maruta, Goro Masuya, Hiroyuki Miki, Hideo Miura, Masami Nakano, Hideya Nishiyama, Taku Ohara, Katsuhide Ohira, Makoto Ohta, Seiji Samukawa, Kazuhisa Sato, Takehiko Sato, Keisuke Sawada, Atsuhiko Shirai, Yuriko Takeshima, Takashi Tokumasu, Michio Tokuyama, Tetsuya Uchimoto, Yutaka Watanabe, Satoru Yamamoto, Shigeru Yonemura, Noritaka Yusa

Administrative Staff

Naoko Azumi, Ardian Gojani, Natsuko Hatakeyama, Mizuho Ito, Yuko Makita, Hisanori Masuda, Tomomi Nagayoshi, Fumio Saito, Takashi Sasabe, Yuko Sasaki, Yuko Shimokawara, Ryoko Suzuki, Masashi Takeyama, Naoto Wada, Pengfei Wang, Shejuan Xie

Plenary Lectures



Green Aircraft Concepts and Enabling Technology Research at NASA

Richard A. Wahls (NASA Langley Research Center, USA)
(9:20-10:10, September 19, at SENDAI (EAST))



HEAT —A Weighty Compressive Fluid

Zeng-Yuan Guo (Tsinghua University, China)
(10:15-11:05, September 19, at SENDAI (EAST))



Data Assimilation: Challenge for Big Data through Numerical Simulation

Tomoyuki Higuchi (The Institute of Statistical Mathematics, Japan)
(11:10-12:00, September 19, at SENDAI (EAST))

Sessions

General Session:

- GS1: General Session

Organized Sessions:

- OS1: Heat and Mass Transfer Issues in Materials
Organizer: P. Bourgin (INSA-Lyon)
- OS2: Geometric and Probabilistic Methods in Flow Dynamics
Organizer: S. Ross (Virginia Tech)
- OS3: Hybrid Rockets: A Quest for Next-Generation Environmentally-Compatible Space Transportation
Organizers: T. Shimada (JAXA), K. Sawada (Tohoku University)
- OS4: Green Aviation: Prospects for Environmentally – Compatible Air Transportation
Organizers: S. Obayashi, K. Asai (Tohoku University), S. Watanabe (JAXA)
- OS5: Advanced Control of Smart Fluids and Fluid Flows
Organizers: M. Nakano, Y. Fukunishi (Tohoku University)
- OS6: Multiphase Science and Ultra Clean Technology
Organizer: J. Ishimoto (Tohoku University)
- OS7: Blood Flow for Medical Equipment
Organizers: T. Nakayama, M. Ohta (Tohoku University)
- OS8: Membrane Micro Channel for Health Care
Organizers: N. Tomita, M. Ohta (Tohoku University)
- OS10: Thermal-Fluid Flows and Plasma Physics
Organizers: W. S. Fu, C. Y. Chen (National Chiao Tung University)
- OS11: The Eighth International Students/Young Birds Seminar on Multi-Scale Flow
Organizer: H. Nagashima (Tohoku University)
Co-organizers: S. Eita, S. Uramoto (Tohoku University)
Supervisors: K. Sato, Y. Iga, A. Komiya (Tohoku University)

Planned Sessions:

- PS1: IFS Collaborative Research Forum (AFI/TFI-2012)
Organizers: S. Obayashi, H. Takana (Tohoku University)

- PS2: Transdisciplinary Fluid Integration (AFI/TFI-2012)
Organizers: S. Obayashi, S. Jeong (Tohoku University)

- PS3: Functional Plasma Flow Dynamics and its Innovative Applications
Organizers: H. Nishiyama (Tohoku University), Y. Okuno, K. Yasuoka (Tokyo Institute of Technology), M. Tanaka (Osaka University), Y. Tanaka (Kanazawa University) , H. Takana (Tohoku University)

- PS4: Advanced Physical Stimuli and Biological Responses of Cells
Organizers: T. Sato (Tohoku University), T. Ohashi (Hokkaido University)

- PS5: 6th Functionality DEsign of the COntact Dynamics: (DECO2012)
Organizers: T. Takagi, H. Miki (Tohoku University), J. Fontaine (ECL)

Special Session:

- Liaison Office Session

General Information

Registration:

8:00 - , Wednesday, September 19

The conference registration desk is located in the lobby, 4th floor in the morning. It will be moved to 3rd floor in the afternoon.

7:45 - , Thursday, September 20

The conference registration desk is located in the lobby, 3rd floor.

7:50 - , Friday, September 21

The conference registration desk is located in the lobby, 3rd floor.

Opening: (at SENDAI (EAST))

9:00 - , Wednesday, September 19

Students/Young Birds Friendship Night: (at SAKURA HALL, Tohoku University)

19:00 – 20:30, Wednesday, September 19

All students and young researchers can attend to Students/Young Birds Friendship Night.

Banquet: (at SENDAI)

18:30 – 21:00, Thursday, September 20

Internet access corner

All conference attendees may use internet for free. Free Ethernet access will be possible during the conference at 3rd floor. Standard wired hubs (with RJ45 sockets) will be provided for networking.

Coffee service:

Coffee is served in the lobby, 3rd floor.

ICFD2012 Secretariat:

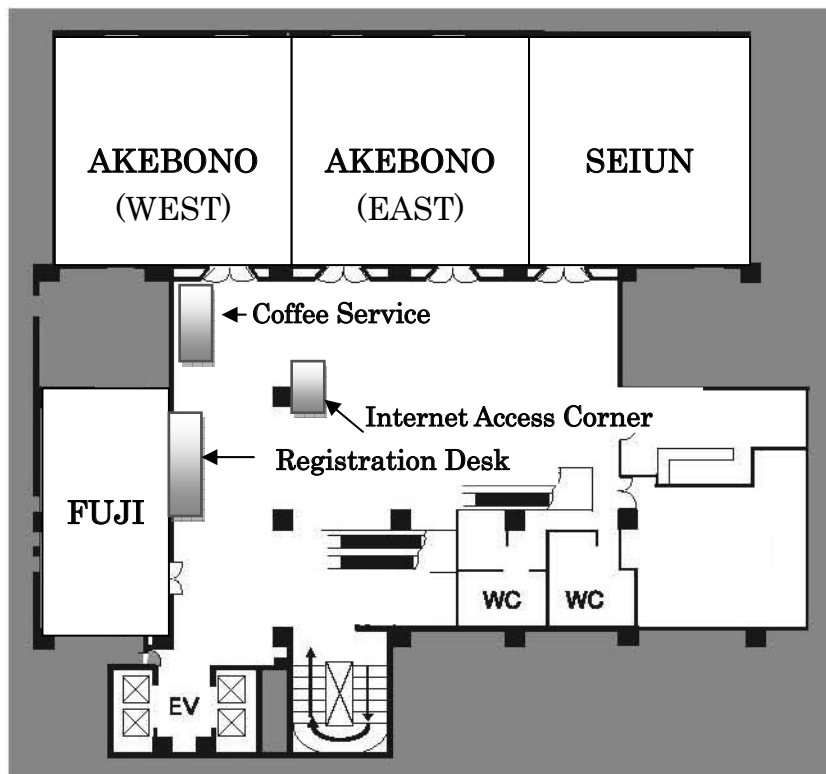
COE Building, Institute of Fluid Science, Tohoku University

2-1-1, Katahira, Aoba, Sendai, 980-8577, Japan

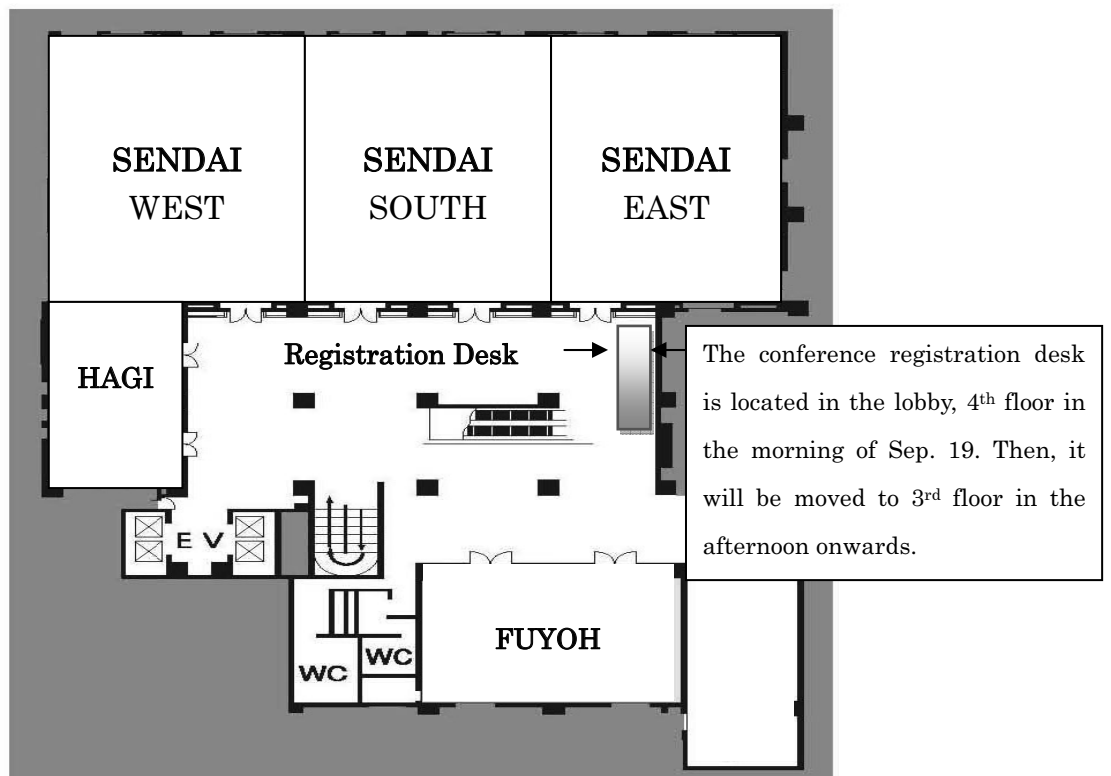
Phone&Fax: +81-22-217-5301

E-mail: icfd2012@gcoe.ifs.tohoku.ac.jp

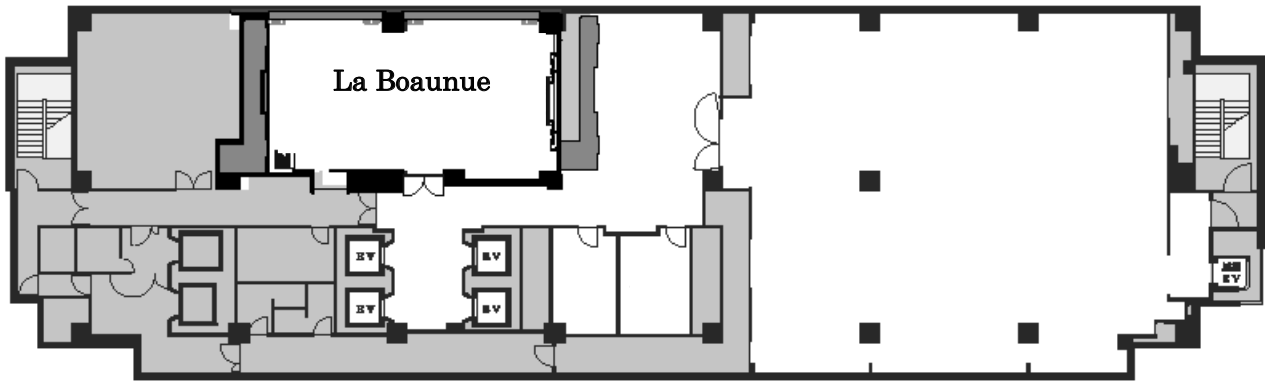
3rd floor (AKEBONO, SEIUN, FUJI)



4th floor (SENDAI, FUYOH, HAGI)



21st floor (La Boanue)



9th ICFD (2012) Time Table

Wednesday, September 19, 2012

ROOM	AKEBONO (WEST)	AKEBONO (EAST)	SEIUIN	FUJI	FUYOH	HAGI	ROOM
Floor	3rd Floor				4th Floor		Floor
8:00							8:00
9:00	9:00-9:20 Opening Address @ SENDAI (EAST)						9:00
9:20	9:20-10:10 Plenary Lecture @ SENDAI (EAST) "Green Aircraft Concepts and Enabling Technology Research at NASA" Richard A. Wahls (NASA, USA)						9:20
10:15	10:15-11:05 Plenary Lecture @ SENDAI (EAST) "HEAT - A Weighty Compressive Fluid" Zeng-Yuan Guo (Tsinghua University, China)						10:15
11:10	11:10-12:00 Plenary Lecture @ SENDAI (EAST) "Data Assimilation: Challenge for Big Data through Numerical Simulation" Tomoyuki Higuchi (The Institute of Statistical Mathematics, Japan)						11:10
12:00							12:00
13:00	OS11 13:00-13:05 Opening Session 1 - Award Session- 13:05-(14:08) OS11-1 - OS11-21 <i>Short Oral Presentation</i> (14:10-16:10) OS11-1 - OS11-21 <i>Poster Presentation</i>	OS7 13:00-13:30 OS7-1 Aike Qiao (Invited) 13:30-13:45 OS7-2 Yuriko Hatakeyama 13:45-14:00 OS7-3 Shigeki Kato 14:00-14:15 OS7-4 Tatsuki Okuno 14:15-14:30 OS7-5 Muneichi Shibata	OS1 13:00-13:45 OS1-1 Mhamed Boutaous (Invited) 13:45-14:30 OS1-2 Subhash C. Mishra (Invited)	PS4 13:00-13:05 Opening Takehiko Sato 13:05-13:45 PS4-1 Gyoo-Cheon Kim (Plenary Talk) 13:45-14:30 PS4-2 Christopher Jacobs (Plenary Talk)	OS10: Session I 13:00-13:30 OS10-1 Chi-Chuan Wang (Invited) 13:30-13:45 OS10-2 Sohey Nozawa 13:45-14:00 OS10-3 San-Yih Lin 14:00-14:15 OS10-4 Mohammad Naziffard 14:15-14:30 OS10-5 Yao-Hsien Liu	GS1: Combustion 13:00-13:20 GS1-1 Nickolay A. Lutsenko 13:20-13:40 GS1-2 Jingxiang Xu 13:40-14:00 GS1-3 Masud Behnia 14:00-14:20 GS1-4 Xing Li	13:00
14:30							14:30
14:40		OS7 14:40-15:10 OS7-6 Guy Courbebaisse (Invited) 15:10-15:25 OS7-7 Kenichi Kono 15:25-15:40 OS7-8 Yujie Li 15:40-15:55 OS7-9 Mingzi Zhang 15:55-16:10 OS7-10 Hitomi Anzai	OS1 14:40-15:10 OS1-3 Bing-Yang Cao 15:10-15:40 OS1-4 Palanisamy Muthukumar 15:40-16:10 OS1-5 B. Satya Sekhar	PS4 14:40-15:10 PS4-3 Tetsuji Shimizu (Invited) 15:10-15:40 PS4-4 Sunao Katsuki (Invited) 15:40-16:10 PS4-5 Kenichi Funamoto (Invited)	OS10: Session II 14:40-15:10 OS10-6 Xueming Shao (Invited) 15:10-15:25 OS10-7 Yao-Hsien Liu 15:25-15:40 OS10-8 Tzu-Chieh Lin 15:40-15:55 OS10-9 Kuen-Rung Huang 15:55-16:10 OS10-10 Yun Huang	PS2 14:40-14:50 Opening 14:50-15:10 TFI-1 Shigeru Obayashi 15:10-15:30 TFI-2 Yuriko Takeshima 15:30-15:50 TFI-3 Mingyu Sun 15:50-16:10 TFI-4 Toshiyuki Hayase	14:40
16:10							16:10
16:20	GS1: Numerical Simulation 1 16:20-16:40 GS1-5 Wakana Iwakami Nakano 16:40-17:00 GS1-6 Takashi Furusawa 17:00-17:20 GS1-7 Yuzuru Yatagai 17:20-17:40 GS1-8 Ryu Komatsu	GS1: Jets 16:20-16:40 GS1-9 Sivakumar Deivandren 16:40-17:00 GS1-10 Nannan Wu 17:00-17:20 GS1-11 Masayuki Takahashi 17:20-17:40 GS1-12 Tomoaki Watanabe 17:40-18:00 GS1-13 Jerry Min Chen	OS1 16:30-17:00 OS1-6 Subhash C. Mishra (Invited) 17:00-17:30 OS1-7 Subhash C. Mishra (Invited)	PS4 16:20-16:50 PS4-6 Masaru Tanaka (Invited) 16:50-17:20 PS4-7 Susumu Kudo (Invited) 17:20-17:50 PS4-8 Kimiko Yamamoto (Invited)	OS10: Session III 16:20-16:50 OS10-11 Wu Shung Fu (Invited) 16:50-17:05 OS10-12 Chien-Yuh Yang 17:05-17:20 OS10-13 Ming-Chang Lu 17:20-17:35 OS10-14 Shang-Hao Huang 17:35-17:50 OS10-15 Rong-Jer Lai	PS2 16:20-16:40 TFI-5 Seiji Samukawa 16:40-17:00 TFI-6 Kaoru Maruta 17:00-17:20 TFI-7 Jun Ishimoto	16:20
17:50							17:50

Thursday, September 20, 2012

ROOM	AKEBONO (WEST)	AKEBONO (EAST)	SEIUN	FUJI
Floor	3rd Floor			
8:00				OS8 8:00-8:20 OS8-1 Makiko Suwa (Invited) 8:20-8:40 OS8-2 Yuri Mukai (Invited) 8:40-9:00 OS8-3 Noriko Tomita (Invited)
9:00	OS11: Session 2 9:00-(10:00) OS11-22 - OS11-42 <i>Short Oral Presentation</i> (10:00-12:00) OS11-22 - OS11-42 <i>Poster Presentation</i>	GS1: General Fluid Flow 1 9:00-9:20 GS1-14 Cheng-Hsiung Kuo 9:20-9:40 GS1-15 Yasufumi Konishi 9:40-10:00 GS1-16 Hideyuki Tanno 10:00-10:30 GS1-17 Sung Jin Kim (Invited)	OS1 9:00-9:30 OS1-8 Ishwar K. Puri (Invited) 9:30-10:00 OS1-9 Philippe Vergne 10:00-10:30 OS1-10 Xin-Gang Liang (Invited)	PS4 9:00-9:30 PS4-9 Takuji Ishikawa (Invited) 9:30-10:00 PS4-10 Masayoshi Nishiyama (Invited) 10:00-10:30 PS4-11 Takayuki Ohta (Invited)
10:30				
10:40		GS1: General Fluid Flow 2 10:40-11:00 GS1-18 Jeongmin Ahn 11:00-11:20 GS1-19 Daiju Numata 11:20-11:40 GS1-20 Mehdi Baneshi (Invited) 11:40-12:00 GS1-21 Szu-Yung Chen 12:00-12:20 GS1-22 Takuya Kitamura	OS2 10:40-11:40 OS2-1 George Haller (Invited) 11:40-12:10 OS2-2 Ronald Peikert	PS4 10:40-11:10 PS4-12 Kazuaki Nagayama (Invited) 11:10-11:40 PS4-13 Shinji Deguchi (Invited) 11:40-12:10 PS4-14 Takeru Naiki (Invited)
12:10				
13:10	OS11: Session 3 13:00-(13:30) OS11-43 - OS11-53 <i>Short Oral Presentation</i> (13:30-14:40) OS11-43 - OS11-53 <i>Poster Presentation</i>	OS3: Scaling Issues 13:10-13:50 OS3-1 Arif Karabeyoglu (Invited) 13:50-14:05 OS3-2 Chidambaram Palani Kumar 14:05-14:20 OS3-3 Rajiv Kumar 14:20-14:35 OS3-4 Harunori Nagata	OS2 13:10-13:40 OS2-3 Gary Froyland 13:40-14:10 OS2-4 Plyush Grover 14:10-14:40 OS2-5 Marko Budišić	PS4 13:10-13:40 PS4-15 Jong-Shinn Wu (Invited) 13:40-14:10 PS4-16 Toshiro Ohashi (Invited) 14:10-14:40 PS4-17 Takehiko Sato (Invited)
14:40				
14:50	GS1: Numerical Simulation and Theory 14:50-15:20 GS1-23 Mikhail Ivanov (Invited) 15:20-15:40 GS1-24 Chih-Hua Chang 15:40-16:00 GS1-25 X-W. Sun 16:00-16:20 GS1-26 Hiroyuki Nishikawa	OS3: Fuel Development 14:50-15:30 OS3-5 Paul Joseph (Invited) 15:30-15:45 OS3-6 Gaurav Marothia 15:45-16:00 OS3-7 Rajiv Kumar 16:00-16:15 OS3-8 Yutaka Wada	OS2 14:50-15:20 OS2-6 Kayo Ide 15:20-15:50 OS2-7 Ana M Mancho 15:50-16:20 OS2-8 Irina I. Rypina	PS4 14:50-15:05 PS4-18 Daisuke Yoshino 15:05-15:20 PS4-19 Taiki Shigematsu 15:20-15:35 PS4-20 Lin Yuan 15:35-15:50 PS4-21 Takashi Oshibe 15:50- Closing Toshiro Ohashi
16:20				
16:30	GS1: Numerical Simulation 2 16:30-16:50 GS1-27 Shejuan Xie 16:50-17:10 GS1-28 Xinrong Su 17:10-17:30 GS1-29 Satoshi Miyake 17:30-17:50 GS1-30 Daiki Terakado	OS3: CFD1 16:30-17:10 OS3-9 Yen-Sen Chen (Invited) 17:10-17:25 OS3-10 Takaya Koda 17:25-17:40 OS3-11 Mikiro Motoe 17:40-17:55 OS3-12 Tzu-Hao Chou	OS2 16:30-17:00 OS2-9 Makoto Iima 17:00-17:30 OS2-10 Scott David Kelly 17:30-17:45 <i>Discussion</i>	GS1: Measurement 1 16:30-16:50 GS1-31 Suk Ho Chung 16:50-17:10 GS1-32 K. S. N. Abhinav Kumar 17:10-17:30 GS1-33 Linsheng Liu 17:30-17:50 GS1-34 Shota Fujii
18:00	18:00-18:30 Liaison Office Session @SENDAI (WEST) "ICFD - Past and Future"			
18:30	18:30-21:00 Banquet @SENDAI			
21:00				

SENDAI (WEST)	FUYOH	HAGI	La Boaune	ROOM
4th Floor			21st Floor	Floor
				9:00
PS1 9:00-10:30 CRF-1 - CRF-27 <i>Short Oral Presentation</i>	OS10: Session IV 9:00-9:30 OS10-16 Ching-Yao Chen (Invited) 9:30-9:45 OS10-17 Masanari Fujimura 9:45-10:00 OS10-18 Tomohiro Ujije 10:00-10:15 OS10-19 Kuo-Long Pan 10:15-10:30 OS10-20 ChungGang Li	PS3 9:00-9:10 Opening Hideya Nishiyama Session 1: Plasma Flow Control 9:10-9:40 PS3-1 Igor V. Adamovich (Invited) 9:40-10:00 PS3-2 Tomoyuki Murakami 10:00-10:20 PS3-3 Masaya Shigeta		10:30
PS1 10:40-12:10 CRF-28 - CRF-B1 <i>Short Oral Presentation</i>	OS10: Session V 10:40-10:55 OS10-21 Arđan B. Gođani 10:55-11:10 OS10-22 Hongbing Xiong 11:10-11:25 OS10-23 Fu-Li Li 11:25-11:40 OS10-24 Kazui Fukumoto 11:40-11:55 OS10-25 Ya-Ju Lin 11:55-12:10 OS10-26 Ranjeep Repaka	PS3: Session 2: Thermal Plasma Flow Material Process 10:40-11:10 PS3-4 Oleg P. Solonenko (Invited) 11:10-11:30 PS3-5 Yasutaka Ando 11:30-11:50 PS3-6 Takayuki Watanabe 11:50-12:10 PS3-7 Yasunori Tanaka		10:40
PS1 12:10-13:10 <i>Lunch and Poster Session</i>				12:10
PS1 13:10-14:40 CRF-53 - CRF-79 <i>Short Oral Presentation</i>	OS10: Session VI 13:10-13:25 OS10-27 Jong-Shinn Wu 13:25-13:40 OS10-28 Yan-Hom Li 13:40-13:55 OS10-29 Shotai Takagi 13:55-14:10 OS10-30 Fei-Bin Hsiao 14:10-14:25 OS10-31 Jurji Noda 14:25-14:40 OS10-32 Khaled Suleiman Mohammed AL-Mashrafi	PS3: Session 3: Arc 13:40-14:10 PS3-8 Milan Hrabovsky (Invited) 14:10-14:30 PS3-9 Jiri Jenista		13:10
PS1 The 1st Young Researcher Overseas Visits Program Research Forum 14:50-15:05 Kenichi Funamoto 15:05-15:20 Hisashi Nakamura 15:20-15:35 Tetsuya Uchimoto 15:35-16:20 <i>Poster Session</i>	OSS 14:50-15:10 OSS-1 Adam Edstrand 15:10-15:30 OSS-2 Gennady Alekseev 15:30-15:50 OSS-3 Nobuo Namura 15:50-16:10 OSS-4 Liu Aiming	PS3: Session 4: Arc, Welding 14:50-15:10 PS3-10 Shinichi Tashiro 15:10-15:30 PS3-11 Yoshihiro Tsujimura 15:30-15:50 PS3-12 Manabu Tanaka	OS10: Session VII 14:50-15:05 OS10-33 Yu-Sheng Huang 15:05-15:20 OS10-34 Yuki Ishii 15:20-15:35 OS10-35 Ming-Chung Lo 15:35-15:50 OS10-36 Wei Hsiang Wang 15:50-16:05 OS10-37 Yu-Chih Lai	14:50
PS1 Fluids Science Research Award Lecture 16:30-17:50	OSS 16:30-16:50 OSS-5 Kenta Watanabe 16:50-17:10 OSS-6 Konosuke Matsumoto 17:10-17:30 OSS-7 Hajime Okawa 17:30-17:50 OSS-8 Mikael A. Langthjem	PS3: Session 5: Reactive Flow, Environmental Process 16:30-16:50 PS3-13 Meng-Hua Hu 16:50-17:10 PS3-14 He-Ping Li 17:10-17:30 PS3-15 Nozomi Takeuchi 17:30-17:50 PS3-16 Hidemasa Takana 17:50-17:55 Closing Hideya Nishiyama	Liaison Office Session 16:30-17:45 Present Status and Future Plan of Liaison Office Activities	16:30
18:00-18:30 Liaison Office Session @SENDAI (WEST) "ICFD - Past and Future"				18:00
18:30-21:00 Banquet @SENDAI				18:30
				21:00

Friday, September 21, 2012

ROOM	AKEBONO (WEST)	AKEBONO (EAST)	SEIUN	FUJI	FUYOH	HAGI	ROOM
Floor	3rd Floor			4th Floor			Floor
8:00				OS8 8:00-8:30 OS8-4 Mohammad M. Mohammad (Invited) 8:30-9:00 OS8-5 Hitomi Mimuro (Invited)			
9:00	OS11: Session 4 9:00-(9:45) OS11-54 - OS11-66 <i>Short Oral Presentation</i> (9:45-11:45) OS11-54 - OS11-66 <i>Poster Presentation</i>	OS3: Instability Issues 9:00-9:40 OS3-13 Mario Kobald (Invited) 9:40-9:55 OS3-14 Takakazu Morita 9:55-10:10 OS3-15 Yuki Funami 10:10-10:25 OS3-16 Po-Jul Chang	OS2 9:00-9:30 OS2-11 Shane D. Ross 9:30-10:00 OS2-12 Kevin A. Mitchell 10:00-10:30 OS2-13 Takashi Sakajo	OS7 9:00-9:15 OS7-11 Subhash C. Mishra (Invited) 9:15-9:30 OS7-12 Miklós Zrinyi (Invited) 9:30-9:45 OS7-13 Futoshi Mori 9:45-10:00 OS7-14 Yasutomo Shimizu 10:00-10:30 OS7-15 Toshio Nakayama (Invited)	OS5 9:00-9:30 OS5-9 Louis Cattafesta (Invited) 9:30-9:50 OS5-10 Kazuo Matsuura 9:50-10:10 OS5-11 Jinhao Qiu 10:10-10:30 OS5-12 Shashank Khurana	OS4 9:00-9:30 OS4-1 Jinsoo Cho (Invited) 9:30-10:00 OS4-2 Takeshi Ohnuki (Invited) 10:00-10:30 OS4-3 Matthew Wilkinson (Invited)	9:00
10:30							10:30
10:40		OS3: CFD2 10:40-11:20 OS3-17 Changjin Lee (Invited) 11:20-11:35 OS3-18 Yorimoto Tokiwa 11:35-11:50 OS3-19 Nobuyuki Tsuboi 11:50-12:05 OS3-20 Jhe-Wei Lin	OS2 10:40-11:10 OS2-14 Guy Metcalfe 11:10-11:40 OS2-15 Lennaert van Veen 11:40-12:10 OS2-16 Tomohiro Yanao	GS1: Numerical Simulation 3 10:40-11:00 GS1-35 Chenguang Lai 11:00-11:20 GS1-36 Ryota Ibuki 11:20-11:40 GS1-37 Jing Wang 11:40-12:00 GS1-38 Kai Chen	OS5 10:40-11:10 OS5-13 Subhash C. Mishra (Invited) 11:10-11:40 OS5-14 Alexander Vasiliev (Invited) 11:40-12:00 OS5-15 Ming-Wen Wang	OS4 10:40-11:10 OS4-4 John Sullivan (Invited) 11:10-11:30 OS4-5 Masaya Oshimizu 11:30-11:50 OS4-6 Kohei Kuwamori 11:50-12:10 OS4-7 Hideaki Ogawa	10:40
12:10							12:10
13:10	OS11: Session 5 13:00-(13:45) OS11-67 - OS11-80 <i>Short Oral Presentation</i> (13:45-15:45) OS11-67 - OS11-80 <i>Poster Presentation</i>	OS3: Innovative Systems 13:10-13:50 OS3-21 Luigi T. DeLuca (Invited) 13:50-14:05 OS3-22 Shigeru Aso 14:05-14:20 OS3-23 Gary Cheng 14:20-14:35 OS3-24 Toru Shimada	OS2 13:10-13:40 OS2-17 Susumu Goto 13:40-14:10 OS2-18 John Mahoney 14:10-14:25 Closing	OS6 13:10-13:55 OS6-1 Jin-Goo Park (Invited) 13:55-14:40 OS6-2 Seiji Samukawa (Invited)	OS5 13:10-13:40 OS5-16 Rongjia Tao (Invited) 13:40-14:00 OS5-17 Katsufumi Tanaka 14:00-14:20 OS5-18 Sota Inomata 14:20-14:40 OS5-19 Roman Brizitskii	OS4 13:10-13:40 OS4-8 Akihiro Sasoh (Invited) 13:40-14:00 OS4-9 Takamasa Kikuchi 14:00-14:20 OS4-10 Takahiro Ukai 14:20-14:40 OS4-11 Takaya Uchida	13:10
14:40							14:40
14:50		OS3: R&D Activities 14:50-15:30 OS3-25 Jan-Erik Ranningen (Invited) 15:30-15:45 OS3-26 Koki Kitagawa 15:45-16:15 <i>WRAPUP</i>	PS5 14:50-15:10 PS5-1 Zahrul Fuadi (Invited) 15:10-15:25 PS5-2 Masanori Iwaki 15:25-15:40 PS5-3 Pengfei Wang	14:50-15:30 OS6-3 Takeshi Hattori (Invited) 15:30-16:00 OS6-4 Masao Watanabe (Invited) 16:00-16:20 OS6-5 Ahmed Busnaina (Invited)	OS5 14:50-15:20 OS5-20 Weihua Li (Invited) 15:20-15:40 OS5-21 Michihiro Shinozaki 15:40-16:00 OS5-22 Chun-Liang Lai	OS4 14:50-15:20 OS4-12 Yoshikazu Makino (Invited) 15:20-15:40 OS4-13 Keita Morimoto 15:40-16:00 OS4-14 Yoshinori Andoh 16:00-16:20 OS4-15 Tomoki Taira	14:50
16:20							16:20
16:30	GS1: Turbulence 16:30-16:50 GS1-39 Arpiruk Hokpunna 16:50-17:10 GS1-40 Debasish Biswas 17:10-17:30 GS1-41 Kosuke Hiruta 17:30-17:50 GS1-42 Shuang Xia	OS3: Forum 16:30-18:00 Toward International Collaborations - What Can Be Started Now? -	PS5 15:40-16:05 PS5-4 Michel Belin (Invited) 16:05-16:20 PS5-5 Hiroyuki Miki 16:30-16:50 PS5-6 Minoru Goto (Invited) 16:50-17:10 PS5-7 Ryoichi Hombo (Invited) 17:10-17:35 PS5-8 Philippe Kapsa (Invited) 17:35-18:30 <i>Panel Discussion</i>	OS6 16:30-16:48 OS6-6 Fredrik Lundell (ISC Invited) 16:48-17:06 OS6-7 Bong-Kyun Kang 17:06-17:24 OS6-8 Min-Su Kim 17:24-17:42 OS6-9 Naoya Ochiai 17:42-18:00 OS6-10 Ken Uzawa	GS1: Measurement 2 16:30-16:50 GS1-43 Markus Pastuhoff 16:50-17:10 GS1-44 Hidemasa Fujita 17:10-17:30 GS1-45 Tomohiro Kameya 17:30-17:50 GS1-46 Ardian B. Gojani	GS1: Micro Flow & Bio Flow 16:30-16:50 GS1-47 Thien X. Dinh 16:50-17:10 GS1-48 Toshiya Kainuma 17:10-17:30 GS1-49 Hari Krishna Chilukoti 17:30-17:50 GS1-50 Taiki Kamada	16:30
18:00							18:00

Ninth International Conference on Flow Dynamics

Program

Plenary Lectures

SENDAI (EAST)

September 19, 2012

Chair: Keisuke Asai (Tohoku University, Japan)

9:20-10:10 **Green Aircraft Concepts and Enabling Technology Research at
NASA** 72
Richard A. Wahls (NASA, USA)

Chair: Shigenao Maruyama (Tohoku University, Japan)

10:15-11:05 **HEAT — A Weighty Compressive Fluid** 74
Zeng-Yuan Guo (Tsinghua University, China)

Chair: Shigeru Obayashi (Tohoku University, Japan)

11:10-12:00 **Data Assimilation: Challenge for Big Data through Numerical
Simulation** 76
Tomoyuki Higuchi (The Institute of Statistical Mathematics,
Japan)

GS1: General Session

HAGI

September 19, 2012

Combustion

Chair: Suk Ho Chung (King Abdullah University of Science and Technology, Kingdom of Saudi Arabia)

- | | | |
|----------------------|--|----|
| GS1-1
13:00-13:20 | On Numerical Modeling of Heterogeneous Combustion in Porous Media under Free Convection
<u>Nickolay A. Lutsenko</u> (Far Eastern Federal University / FEB RAS, Russia) | 80 |
| GS1-2
13:20-13:40 | Investigation of Dopant Effects on Sintering Process in Solid Oxide Fuel Cell Anode Based on Molecular Dynamics Simulation
<u>Jingxiang Xu</u> , Ryota Sakanoi, Takeshi Ishikawa, Yuji Higuchi, Nobuki Ozawa, Tomomi Shimazaki, Kazuhisa Sato, Toshiyuki Hashida and Momoji Kubo (Tohoku University, Japan) | 82 |
| GS1-3
13:40-14:00 | Sizing of Stirling Engine as the Prime Mover of a Coal Mine CHP System
Mehdi Aghaei Meybodi, <u>Masud Behnia</u> (The University of Sydney, Australia) | 84 |
| GS1-4
14:00-14:20 | Experimental and Numerical Investigation on Ignition and Combustion Characteristics of CH₄/O₂/CO₂ Mixture Using a Micro Flow Reactor with a Controlled Temperature Profile
<u>Xing Li</u> (Tohoku University, Japan / Beijing Jiaotong University, China), Li Jia (Beijing Jiaotong University, China), Takakazu Onishi, Takuya Tezuka, Susumu Hasegawa and Kaoru Maruta (Tohoku University, Japan) | 86 |

AKEBONO (WEST)

September 19, 2012

Numerical Simulation 1

Chair: M. S. Ivanov (Khristianovich Institute of Theoretical and Applied Mechanics, Russia)

- | | | |
|----------------------|--|----|
| GS1-5
16:20-16:40 | Error Analysis for the Volume Penalization Method with Continuous Mask Functions
<u>Wakana Iwakami Nakano</u> , Nozomu Hatakeyama and Yuji Hattori (Tohoku University, Japan) | 88 |
| GS1-6
16:40-17:00 | Numerical Study of Particle Formation in Supercritical-fluid Flows of Hydrothermal Synthesis
<u>Takashi Furusawa</u> , Satoru Yamamoto (Tohoku University, Japan) | 90 |
| GS1-7
17:00-17:20 | Error Analysis of Volume Penalization Method for Two-Dimensional Navier-Stokes Equations
<u>Yuzuru Yatagai</u> , Wakana Iwakami Nakano and Yuji Hattori (Tohoku University, Japan) | 92 |
| GS1-8
17:20-17:40 | A Study of Volume Penalization Method for Direct Numerical Simulation of Aeroacoustic Sound
<u>Ryu Komatsu</u> , Wakana Iwakami Nakano and Yuji Hattori (Tohoku University, Japan) | 94 |

AKEBONO (EAST)

September 19, 2012

Jets

Chair: Cheng-Hsiung Kuo (National Chung Hsing University, Taiwan)

GS1-9 16:20-16:40	Effect of Orifice Shape on Liquid Jet Breakup <u>Sivakumar Deivandren</u> (Indian Institute of Science, India)	96
GS1-10 16:40-17:00	Analysis of Flow Characteristics of Turbulent Plane Jets Based on Velocity and Scalar Fields Using DNS <u>Nannan Wu</u> , Yasuhiko Sakai, Kouji Nagata (Nagoya University, Japan), Hiroki Suzuki (Nagoya Institute of Technology, Japan), Osamu Terashima (Nagoya University, Japan) and Toshiyuki Hayase (Tohoku University, Japan)	98
GS1-11 17:00-17:20	Supersonic Flight of Beam Riding Vehicle Sustained by Actively Controlled Laser <u>Masayuki Takahashi</u> , Naofumi Ohnishi (Tohoku University, Japan)	100
GS1-12 17:20-17:40	Numerical Simulation of a Reactive Liquid Jet by Combination of DNS and PDF Method <u>Tomoaki Watanabe</u> , Yasuhiko Sakai, Kouji Nagata, Osamu Terashima, Yasumasa Ito (Nagoya University, Japan) and Toshiyuki Hayase (Tohoku University, Japan)	102
GS1-13 17:40-18:00	Micromixing of Fluids within Droplets Generated on Centrifugal Microfluidics <u>Jerry Min Chen</u> , Yu-Jen Chen and Lung-Sheng Tseng (National Chung Hsing University, Taiwan)	104

AKEBONO (EAST)

September 20, 2012

General Fluid Flow 1

Chair: Chih-Hua Chang (Ling-Tung University, Taiwan)

GS1-14 9:00-9:20	Flow Induced Acceleration in Vertical Axis Wind Turbine System Chien-Chang Chen, <u>Cheng-Hsiung Kuo</u> (National Chung Hsing University, Taiwan)	106
GS1-15 9:20-9:40	Region of the Negative Magnus Force on Rotating Sphere <u>Yasufumi Konishi</u> , Tatsuo Itami, Hiroyuki Okuizumi, Tomoyuki Ohno and Shigeru Obayashi (Tohoku University, Japan)	108
GS1-16 9:40-10:00	Free-Flight Test Techniques Based on Ground Test Facilities <u>Hideyuki Tanno</u> , Tomoyuki Komuro, Kazuo Sato and Katsuhiro Itoh (Japan Aerospace Exploration Agency, Japan)	110
GS1-17 10:00-10:30	Heat Transfer Enhancement Using 2-Phase Flow Oscillation (<i>Invited</i>) <u>Sung Jin Kim</u> , Young Jik Youn (Korea Advanced Institute of Science and Technology, Korea)	112

General Fluid Flow 2

Chair: Sung Jin Kim (Korea Advanced Institute of Science and Technology, Korea)

- GS1-18 **Thermal Transpiration Based Pumping and Power Generation Devices** 114
10:40-11:00 Kang Wang, Pingying Zeng, Jeongmin Ahn (Syracuse University, USA) and Paul D. Ronney (University of Southern California, USA)
- GS1-19 **Passive Control of the Free-Stream Turbulence Intensity of the Mars Wind Tunnel by the Turbulence Screen** 116
11:00-11:20 Daiju Numata, Takaaki Tsuchiya and Keisuke Asai (Tohoku University, Japan)
- GS1-20 **Numerical Temperature Analysis of Optimized TiO₂ Pigmented Coatings under Sendai Climate Conditions (*Invited*)** 118
11:20-11:40 Mehdi Baneshi (Shiraz University, Iran), Hiroki Gonome and Shigenao Maruyama (Tohoku University, Japan)
- GS1-21 **Numerical Analysis of Swimming Patterns and Energy-Saving Mechanism in Fish School** 120
11:40-12:00 Szu-Yung Chen, Jing-Tang Yang (National Taiwan University, Taiwan)
- GS1-22 **Experimental Study on Low Mach Number Grid Turbulence Modulated by a Spherical Shock Wave** 122
12:00-12:20 Takuya Kitamura, Tatsuya Harasaki, Kouji Nagata, Yasuhiko Sakai, Akihiro Sasoh and Osamu Terashima (Nagoya University, Japan)

AKEBONO (WEST)

September 20, 2012

Numerical Simulation and Theory

Chair: Srinivas Karkenahalli (The University of Sydney, Australia)

- GS1-23 **Solving the Nonlinear Kinetic Boltzmann Equation on GPGPU (*Invited*)** 124
14:50-15:20 Evgeniy Malkov, Sergey Poleshkin and Mikhail Ivanov (Khristianovich Institute of Theoretical and Applied Mechanics, Russia)
- GS1-24 **Establishment Length for a Fully Developed Solitary Wave in Viscous Fluid** 126
15:20-15:40 Chih-Hua Chang (Ling-Tung University, Taiwan), Keh-Han Wang (University of Houston, USA)
- GS1-25 **The Shear-thinning Effect in Core-annular Flow Stability of Power-law Fluid** 128
15:40-16:00 X.-W. Sun (Commercial Aircraft Cooperation of China, LTD., China), J. Peng and K. -Q. Zhu (Tsinghua University, China)
- GS1-26 **Time Series Analysis of Flow Instability in a Natural Convection Loop** 130
16:00-16:20 Hiroyuki Nishikawa, Shigeki Okino and Fujio Suda (Tokai University, Japan)

Numerical Simulation 2

Chair: Wakana Iwakami Nakano (Tohoku University, Japan)

- GS1-27 **Sizing of Pipe Wall Thinning Using Pulsed Eddy Current Testing Method
Based on Inversion Analysis** 132
16:30-16:50 Shejuan Xie (Tohoku University, Japan), Zhenmao Chen (Xi'an Jiaotong
University, China), Toshiyuki Takagi and Tetsuya Uchimoto (Tohoku
University, Japan)
- GS1-28 **A Simple Method for Three Dimensional Characteristic Boundary Conditions
with Cell-centered Solver** 134
16:50-17:10 Xinrong Su, Satoru Yamamoto (Tohoku University, Japan) and Kazuhiro
Nakahashi (Japan Aerospace Exploration Agency, Japan)
- GS1-29 **Numerical Simulation of Unsteady 3-D Condensate Flows through Three-Stage
Stator-Rotor Blade Rows** 136
17:10-17:30 Satoshi Miyake, Takashi Furusawa and Satoru Yamamoto (Tohoku University,
Japan)
- GS1-30 **Statistical Properties of Two-Dimensional Decaying Weakly Compressible
Turbulence** 138
17:30-17:50 Daiki Terakado, Yuji Hattori (Tohoku University, Japan)

FUJI

September 20, 2012

Measurement 1

Chair: Ardian B. Gojani (Tohoku University, Japan)

- GS1-31 **Study on Flame Stabilization in Curved Wall Jet Burner with Time Resolved
OH-PLIF and PIV** 140
16:30-16:50 Alaa Dawood, Morkous Shoukry Mansour and Suk Ho Chung (King Abdullah
University of Science and Technology, Kingdom of Saudi Arabia)
- GS1-32 **Deflection and Orientation Measurement of Moving Delta Wing Using
Photogrammetry** 142
16:50-17:10 K. S. N. Abhinav Kumar, Tatsuya Hara, Takahiro Ito, Daiju Numata and
Keisuke Asai (Tohoku University, Japan)
- GS1-33 **A Novel Approach of Microwaves on Remote and Nondestructive Detection of
both Gradual and Abrupt Wall Thinning inside a Metal Pipe** 144
17:10-17:30 Linsheng Liu, Kota Sasaki, Noritaka Yusa and Hidetoshi Hashizume (Tohoku
University, Japan)
- GS1-34 **Development of Ultrafast Time Response Pressure-Sensitive Paint for
Visualization of Shock Wave Phenomena** 146
17:30-17:50 Shota Fujii, Daiju Numata, Hiroki Nagai and Keisuke Asai (Tohoku
University, Japan)

FUJI

September 21, 2012

Numerical Simulation 3

Chair: Hideyuki Tanno (Japan Aerospace Exploration Agency, Japan)

- GS1-35 **The Influence of Air Inlet of Indoor Substation on Cooling and Ventilation Effect** 148
10:40-11:00 Chenguang Lai, Yuting Zhou, Haibin Xing and Limin Fu (Chongqing University of Technology, China)
- GS1-36 **CFD Designing on Air Flow Circulation with Branching Perforating Duct and Fan System** 150
11:00-11:20 Ryuta Ibuki (Miyagi University, Japan) , Masud Behnia (The University of Sydney, Australia)
- GS1-37 **Effect of Shape of Shield on Sensitivity of Remote Field Eddy Current Testing for Inspecting Flaw of Large Diameter Tube** 152
11:20-11:40 Jing Wang (Tohoku University, Japan / East China University of Science and Technology, China), Noritaka Yusa (Tohoku University, Japan), Hongliang Pan (East China University of Science and Technology, China) and Hidetoshi Hashizume (Tohoku University, Japan)
- GS1-38 **Kinetomass Model for Wake Flow Simulation of Wind Turbine** 154
11:40-12:00 Kai Chen, Mengxuan and Xing Zhang (Tsinghua University, China)

AKEBONO (WEST)

September 21, 2012

Turbulence

Chair: Chenguang Lai (Chongqing University of Technology, China)

- GS1-39 **Flow Separation Control by Vortex-cell** 156
16:30-16:50 Arpiruk Hokpunna (King Mongkut's University, Thailand)
- GS1-40 **Studies on Flow Transition Under Simulated Low Pressure Turbine Conditions Based on a High Order LES Model** 158
16:50-17:10 Debasish Biswas, Tomohiko Jimbo (Toshiba Research and Development Center, Japan)
- GS1-41 **Turbulent Boundary Layer Influenced by Cylinder Wake in a Freestream** 160
17:10-17:30 Kosuke Hiruta, Kouji Nagata, Yasuhiko Sakai, Osamu Terashima and Yasumasa Ito (Nagoya University, Japan)
- GS1-42 **Direct Numerical Simulation on the Effects of Free-stream Turbulence on the Growth of Turbulent Boundary Layer** 162
17:30-17:50 Shuang Xia, Kousuke Hiruta, Kouji Nagata, Yasuhiko Sakai (Nagoya University, Japan), Hiroki Suzuki (Nagoya Institute of Technology, Japan), Osamu Terashima (Nagoya University, Japan) and Toshiyuki Hayase (Tohoku University, Japan)

FUYOH

September 21, 2012

Measurement 2

Chair: Mehdi Baneshi (Shirazu University, Iran)

- GS1-43 **Modal Analysis of Pressure Sensitive Paint Data** 164
16:30-16:50 Markus Pastuhoff (KTH Royal Institute of Technology, Sweden), Daisuke Yorita (Tohoku University, Japan), Nils Tillmark, P. Henrik Alfredsson (KTH Royal Institute of Technology, Sweden) and Keisuke Asai (Tohoku University, Japan)
- GS1-44 **Propagation Process of Streamer Discharge in Water** 166
16:50-17:10 Hidemasa Fujita (Tohoku University, Japan), Seiji Kanazawa (Oita University, Japan), Kiyonobu Ohtani, Atsuki Komiya and Takehiko Sato (Tohoku University, Japan)
- GS1-45 **Combined Pressure – and Temperature-Sensitive Paint Using Porphyrins and Quantum Dots** 168
17:10-17:30 Tomohiro Kameya, Yu Matsuda (Nagoya University, Japan), Yasuhiro Egami (Aichi Institute of Technology, Japan), Hiroki Yamaguchi and Tomohide Niimi (Nagoya University, Japan)
- GS1-46 **Quantitative Evaluation of Flow Visualization** 170
17:30-17:50 Ardian B. Gojani, Shigeru Obayashi (Tohoku University, Japan)

HAGI

September 21, 2012

Micro Flow & Bio Flow

Chair: Ryuta Ibuki (Miyagi University, Japan)

- GS1-47 **A Realizable Microelectromechanical–System-Based Triple-Axis Fluidic Gyroscope Sensor** 172
16:30-16:50 Thien X. Dinh, Yoshifumi Ogami (Ritsumeikan University, Japan)
- GS1-48 **Kinematic Analysis on Unique Jump of Springtail** 174
16:50-17:10 Toshiya Kainuma, Seiichi Sudo (Akita Prefectural University, Japan), Atsushi Shirai and Toshiyuki Hayase (Tohoku University, Japan)
- GS1-49 **Molecular Dynamics Study on Effect of Chain Length on Liquid-Vapor Interfacial Properties of Alkanes** 176
17:10-17:30 Hari Krishna Chilukoti, Gota Kikugawa and Taku Ohara (Tohoku University, Japan)
- GS1-50 **Ignition Characteristics of Lower Alkane Fuels in a Micro Flow Reactor with a Controlled Temperature Profile** 178
17:30-17:50 Taiki Kamada, Takuya Tezuka, Susumu Hasegawa and Kaoru Maruta (Tohoku University, Japan)

OS1: Heat and Mass Transfer Issues in Materials

SEIUN

September 19, 2012

OS1-1 13:00-13:45	Interactions Between Process and Structure in Polymer Materials: Case of Non-Isothermal Crystallization Kinetics During Processing (<i>Invited</i>) <u>Mhamed Boutaous</u> , Patrick Bourgin and Matthieu Zinet (INSA de Lyon, France)	182
OS1-2 13:45-14:30	Thermal Estimation of Properties and Location of Tumor in a 2-D Biological Tissue using Surface Temperature Profile (<i>Invited</i>) <u>Subhash C. Mishra</u> , Koushik Das, Mohit Ganguly and Pranab Goswami (Indian Institute of Technology Guwahati, India)	184
14:30-14:40	BREAK	
OS1-3 14:40-15:10	Flows of Polymer Melts through Nanopores: Experiments and Modelling <u>Bing-Yang Cao</u> , Guo-Jie Hu (Tsinghua University, China)	186
OS1-4 15:10-15:40	Three Dimensional Numerical Investigation of Hydrogen-Absorption Process in Metal Hydride Container P. Suresh, B. Satya Sekhar, <u>Palanisamy Muthukumar</u> and Subhash C. Mishra (Indian Institute of Technology Guwahati, India)	188
OS1-5 15:40-16:10	Thermal Modelling of A Double-Stage Metal Hydride Based Heat Transformer <u>B. Satya Sekhar</u> , Palanisamy Muthukumar (Indian Institute of Technology Guwahati, India)	190
16:10-16:30	BREAK	
OS1-6 16:30-17:00	Comparative Analysis of Transient Heat Conduction in a Planar Medium Using Smoothed Particle Hydrodynamics, Finite Volume Method and Lattice Boltzmann Method (<i>Invited</i>) <u>Subhash C. Mishra</u> , Harsh Sahai (Indian Institute of Technology Guwahati, India)	192
OS1-7 17:00-17:30	Analysis of Rayleigh-Bénard Convection with and without Volumetric Radiation (<i>Invited</i>) <u>Subhash C. Mishra</u> , Adnan Akhtar and Anshul Garg (Indian Institute of Technology Guwahati, India)	194

SEIUN

September 20, 2012

OS1-8 9:00-9:30	Thermal Rectification in Nanoscale Fluid-Solid Systems (<i>Invited</i>) <u>Ishwar K. Puri</u> (Virginia Tech, USA), Sohail Murad (University of Illinois at Chicago, USA)	196
--------------------	---	-----

OS1-9 9:30-10:00	Heat and Mass Transfer in Confined Lubricated Films <u>Philippe Vergne</u> , Nicolas Fillot (INSA-Lyon, France), Wassim Habchi (Lebanese American University, Lebanon), Vincent Bruyere and Thomas Doki-Thonon (INSA-Lyon, France)	198
OS1-10 10:00-10:30	Entransy, Entransy Dissipation and Entransy Loss for Analyses of Heat Transfer and Thermodynamics (<i>Invited</i>) <u>Xin-Gang Liang</u> (Tsinghua University, China)	200

OS2: Geometric and Probabilistic Methods in Flow Dynamics

SEIUN

September 20, 2012

OS2-1 10:40-11:40	Geodesic Detection of Transport Barriers in 2D Turbulence (<i>Invited</i>) <u>George Haller</u> , Mohammad Farazmand (ETH Zürich, Switzerland)	204
OS2-2 11:40-12:10	Ridge Surface Methods for the Visualization of Lagrangian Coherent Structures <u>Ronald Peikert</u> , Benjamin Schindler and Robert Carnecky (ETH Zurich, Switzerland)	206
12:10-13:10	LUNCH	
OS2-3 13:10-13:40	An Analytic Framework for Finite-Time Coherent Sets in Time-Dependent Flows <u>Gary Froyland</u> (University of New South Wales, Australia)	208
OS2-4 13:40-14:10	Topological Chaos and Braiding of Almost-cyclic Sets <u>Piyush Grover</u> (Mitsubishi Electric Research Laboratories, USA), Shane D. Ross, Mark A. Stremler and Pankaj Kumar (Virginia Tech, USA)	210
OS2-5 14:10-14:40	Identifying Coherence in Flows Using Lagrangian Averages <u>Marko Budišić</u> , Igor Mezić (University of California - Santa Barbara, USA)	212
14:40-14:50	BREAK	
OS2-6 14:50-15:20	Lagrangian Data Assimilation in Geophysical Flows <u>Kayo Ide</u> (University of Maryland, USA)	214
OS2-7 15:20-15:50	On the Performance of Lagrangian Descriptors in 2D and 3D Flows <u>Ana M Mancho</u> (CSIS, Spain), Jazabel Curbelo (CSIC, Spain / Universidad Autónoma de Madrid, Spain), Stephen Wiggins (University of Bristol, UK) and Carolina Mendoza (Universidad Politécnica de Madrid, Spain)	216
OS2-8 15:50-16:20	Short-Term Dispersal of Fukushima-Derived Radionuclides off Japan: Modeling Efforts and Model-Data Intercomparison <u>Irina I. Rypina</u> , Steven R. Jayne, Ken O. Buesseler, Sashiko Yoshida (Woods Hole Oceanographic Institution, USA), Elizabeth M. Douglass (Stennis Space Center, USA) and Alison M. Macdonald (Woods Hole Oceanographic Institution, USA)	218
16:20-16:30	BREAK	
OS2-9 16:30-17:00	Bifurcation Structures in Flapping Flight Problems <u>Makoto Iima</u> (Hiroshima University, Japan)	220

OS2-10 17:00-17:30	Symmetries and Constraints in Aquatic Propulsion via Vortex Shedding <u>Scott David Kelly</u> , Phanindra Tallapragada (University of North Carolina at Charlotte, USA)	222
17:30-17:45	Discussion	
 <u>SEIUN</u> <u>September 21, 2012</u>		
OS2-11 9:00-9:30	Atmospheric Coherent Structures and Biological Invasions <u>Shane D. Ross</u> , David G. Schmale III, Binbin Lin, Amir E. BozorgMagham, Aaron J. Prussin II, Shibabrat Naik (Virginia Tech, USA) and Phanindra Tallapragada (University of North Carolina at Charlotte, USA)	224
OS2-12 9:30-10:00	Invariant Manifolds and the Geometry of Front Propagation in Fluid Flows <u>Kevin A. Mitchell</u> , John R. Mahoney (University of California, USA)	226
OS2-13 10:00-10:30	Classification of Streamline Topologies for Structurally Stable Vortex Flows in Multiply Connected Domains <u>Takashi Sakajo</u> , Tomoo Yokoyama (Hokkaido University, Japan / JST CREST, Japan)	228
10:30-10:40	BREAK	
OS2-14 10:40-11:10	Bubbles and Flux: Scalar Transport Around Coherent Structures in Laminar Flow <u>Guy Metcalfe</u> (CSIRO Materials Science & Engineering, Australia), Marc Horner (ANSYS Inc., USA) and J. M. Ottino (Northwestern University, USA)	230
OS2-15 11:10-11:40	Global Bifurcations and the Onset of Turbulence in Shear Flows <u>Lennaert van Veen</u> (University of Ontario Institute of Technology, Canada), Genta Kawahara (Osaka University, Japan)	232
OS2-16 11:40-12:10	Intramolecular Energy Flow and the Mechanisms for Collective Motions of Complex Molecular Systems <u>Tomohiro Yanao</u> , Yurie Oka (Waseda University, Japan) and Wang Sang Koon (California Institute of Technology, USA)	234
12:10-13:10	LUNCH	
OS2-17 13:10-13:40	Coherent Structures in Homogeneous Turbulence Sustained by Steady Force <u>Susumu Goto</u> , Tatsuya Yasuda and Genta Kawahara (Osaka University, Japan)	236
OS2-18 13:40-14:10	Front Propagation in Fluid Flows: Structure, Transport and Invariant Barriers <u>John Mahoney</u> , Kevin Mitchell (University of California, USA)	238
14:10-14:25	Closing	

OS3: Hybrid Rockets: A Quest for Next-Generation Environmentally-Compatible Space Transportation

AKEBONO (EAST)

September 20, 2012

【Scaling Issues】

Chair: Shigeru Aso (Kyushu University, Japan)

- | | | |
|----------------------|--|-----|
| OS3-1
13:10-13:50 | Scalable Regression Rate Expressions for Hybrid Rockets (<i>Invited</i>)
<u>Arif Karabeyoglu</u> (Space Propulsion Group Inc., USA) | 242 |
| OS3-2
13:50-14:05 | Scaling in Hybrid Rocket Motors
<u>Chidambaram Palani Kumar</u> , Amit Kumar (Indian Institute of Technology Madras, India) | 244 |
| OS3-3
14:05-14:20 | Enhancement of Regression Rate using a Bluff Body in Hybrid Fuels
<u>Rajiv Kumar</u> , Periyapatna Ananthpadmanabiah Ramakrishna (Indian Institute of Technology Madras, India) | 246 |
| OS3-4
14:20-14:35 | Scale Effect between 2500 and 5000N Thrust Class CAMUI-type Hybrid Rocket Motors
<u>Harunori Nagata</u> , Tsuyoshi Totani, Masashi Wakita (Hokkaido University, Japan) and Tsutomu Uematsu (Camuispaceworks Co. Ltd., Japan) | 248 |

【Fuel Development】

Chair: Koki Kitagawa (Japan Aerospace Exploration Agency, Japan)

- | | | |
|----------------------|--|-----|
| OS3-5
14:50-15:30 | Reactive and Additive Routes to Novel Polymer-based Fuels for Hybrid Propulsion (<i>Invited</i>)
<u>Paul Joseph</u> (University of Ulster, UK), Koki Kitagawa (Japan Aerospace Exploration Agency, Japan), Vasily Novozhilov (University of Ulster, UK) and Toru Shimada (Japan Aerospace Exploration Agency, Japan) | 250 |
| OS3-6
15:30-15:45 | Enhancement of Regression Rate in HTPB Based Hybrid Rocket using Recrystallized AP and Pyral
<u>Gaurav Marothia</u> , Periyapatna A. Ramakrishna (Indian Institute of Technology Madras, India) | 252 |
| OS3-7
15:45-16:00 | Improving the Mechanical Properties of Paraffin Based Hybrid Fuels
Hiteshwar Brahma, <u>Rajiv Kumar</u> and Periyapatna A. Ramakrishna (Indian Institute of Technology Madras, India) | 254 |
| OS3-8
16:00-16:15 | Development of Lab Scale Hybrid Rocket Motor using Low Melting Point Thermoplastics
<u>Yutaka Wada</u> , Yo Kawabata, Ryuichi Kato (Akita University, Japan), Nobuji Kato (Katazen Corporation, Japan) and Keiichi Hori (Japan Aerospace Exploration Agency, Japan) | 256 |

【CFD 1】

Chair: Harunori Nagata (Hokkaido University, Japan)

- OS3-9
16:30-17:10 **Sounding Rocket Development with Hybrid Combustion Technology** 258
(Invited)
Yen-Sen Chen (National Space Organization, Taiwan), Tzu-Hao Chou, Jong-Shinn Wu (National Chiao Tung University, Taiwan) and Gary Cheng (University of Alabama in Birmingham, USA)
- OS3-10
17:10-17:25 **Computation of Swirling Flowfield Coupled with Fuel Surface Regression in Combustion Chamber for Hybrid Rocket Engine** 260
Takaya Koda, Yousuke Ogino and Keisuke Sawada (Tohoku University, Japan)
- OS3-11
17:25-17:40 **Improvement of Two-Equation Turbulence Model with Anisotropic Eddy-Viscosity for Swirl-Injected Hybrid Rocket Research** 262
Mikiro Motoe (The University of Tokyo, Japan), Toru Shimada (Japan Aerospace Exploration Agency, Japan)
- OS3-12
17:40-17:55 **Numerical Investigation of Flow Characteristics Past a Mixing Enhancer in a Single-Port Hybrid Combustion Chamber** 264
Tzu-Hao Chou, Jong-Shinn Wu (National Chiao Tung University, Taiwan), Yen-Sen Chen (National Space Organization, Taiwan) and Gary Cheng (University of Alabama, USA)

AKEBONO (EAST)September 21, 2012**【Instability Issues】**

Chair: Yutaka Wada (Akita University, Japan)

- OS3-13
9:00-9:40 **Injection Effects on Hybrid Rocket Combustion Instability** *(Invited)* 266
Mario Kobald (DLR, Germany / DGLR student group, Germany), Tobias Willerding, Alexander Schindler (DGLR student group, Germany), Helmut Ciezki (DLR, Germany) and Stefan Schlechtriem (DLR, Germany / University of Stuttgart, Germany)
- OS3-14
9:40-9:55 **Low-Frequency Oscillatory Combustion in Hybrid Rocket Motors** 268
Takakazu Morita (Tokai University, Japan), Saburo Yuasa (Tokyo Metropolitan University, Japan), Koki Kitagawa, Toru Shimada (Japan Aerospace Exploration Agency, Japan) and Shigeru Yamaguchi (Tokai University, Japan)
- OS3-15
9:55-10:10 **Validation of Integral Method for Numerical Prediction of Hybrid Rocket Internal Ballistics** 270
Yuki Funami (The University of Tokyo, Japan), Toru Shimada (Japan Aerospace Exploration Agency, Japan)
- OS3-16
10:10-10:25 **Local and Spontaneous Regression Rate Measurement of Hybrid Rocket Using Ultrasonic's** 272
Po-Jul Chang (The University of Tokyo, Japan), Yutaka Wada (Akita University, Japan), Toshiyuki Katsumi, Keiichi Hori (Japan Aerospace Exploration Agency, Japan), Hideo Nakayama (Ihi Aerospace Co., Ltd., Japan) and Motoyasu Kimura (Nof Corporation, Japan)

【CFD 2】

Chair: Keisuke Sawada (Tohoku University, Japan)

- OS3-17 **Internal Flow Characteristics in Combustor of Hybrid Rocket Engine** 274
10:40-11:20 *(Invited)*
Khim Oo Mon (Konkuk University, Korea), Heeseok Koo (Seoul National University, Korea) and Changjin Lee (Konkuk University, Korea)
- OS3-18 **Numerical Analysis of the Inside Flow of Ramjet Engine** 276
11:20-11:35 Yorimoto Tokiwa, Ichiro Nakagawa (Tokai University, Japan)
- OS3-19 **Three-dimensional Numerical Simulation on Unsteady Compressible** 278
11:35-11:50 **Flow using Preconditioning Method in Hybrid Rocket Engine: Effects of**
Preconditioning Schemes
Nobuyuki Tsuboi (Kyushu Institute of Technology, Japan), Katsuyoshi Fukiba (Shizuoka University, Japan) and Toru Shimada (Japan Aerospace Exploration Agency, Japan)
- OS3-20 **Numerical and Experimental Study of Venturi Flow Meters for Nitrous** 280
11:50-12:05 **Oxide**
K. -M. Chuang, Jhe-Wei Lin, Jong-Shinn Wu (National Chiao Tung University, Taiwan), Gary Cheng (University of Alabama, USA) and Yensen Chen (National Space Organization, Taiwan)

【Innovative Systems】

Chair: Nobuyuki Tsuboi (Kyushu Institute of Technology, Japan)

- OS3-21 **Hybrid Rocket Propulsion: State of the Art and Perspectives for Space** 282
13:10-13:50 **Activities Applications** *(Invited)*
Luigi T. DeLuca, Pietro Tadini (Politecnico di Milano, Italy), Carmen Pardini and Luciano Anselmo (ISTI-CNR, Italy)
- OS3-22 **Development of Hybrid Rocket Engines with Multi-Section Swirl** 284
13:50-14:05 **Injection Method for Higher Regression Rate and Combustion Efficiency**
Shigeru Aso, Yasuhiro Tani, Yoshihide Hirata, Sho Ohyama, Kentaro Araki, Kengo Ohe (Kyushu University, Japan) and Toru Shimada (Japan Aerospace Exploration Agency, Japan)
- OS3-23 **Numerical Investigation of a Dual Vortical Flow Hybrid Rocket Motor** 286
14:05-14:20 Yen-Sen Chen, Bill Wu (National Space Organization, Taiwan), Tzu-Hao Chou, Jong-Shinn Wu (National Chiao Tung University, Taiwan) and Gary Cheng (University of Alabama in Birmingham, USA)
- OS3-24 **Status Summary of FY 2011 Hybrid Rocket Research Working Group** 288
14:20-14:35 Toru Shimada (Japan Aerospace Exploration Agency, Japan)

【R&D Activities】

Chair: Toru Shimada (Japan Aerospace Exploration Agency, Japan)

- OS3-25 **Nammo Hybrid and Monopropellant Rocket Propulsion Work, an** 290
14:50-15:30 **Overview** *(Invited)*
Jan-Erik Rønningen (Nammo Raufoss, Norway)

OS3-26
15:30-15:45

Development Plan of Hybrid Rocket Test Engine Facility in Hybrid Rocket Research Working Group

292

Koki Kitagawa, Toru Shimada, Keiichi Hori, Toshiaki Takemae, Noriko Shiraishi, Toshio Tomizawa, Naohiro Suzuki, Tsuyoshi Yagishita (Japan Aerospace Exploration Agency, Japan), Nobuyuki Oshima, Harunori Nagata, Masashi Wakita (Hokkaido University, Japan), Keisuke Sawada, Hiroki Nagai (Tohoku University, Japan), Yutaka Wada (Akita University, Japan), Saburo Yuasa, Takashi Sakurai, Masahiro Kanazaki (Tokyo Metropolitan University, Japan), Ichiro Nakagawa, Takakazu Morita (Tokai University, Japan), Masaki Nakamiya (Kyoto University, Japan), Shigeru Aso, Yasuhiro Tani (Kyushu University, Japan) and Nobuyuki Tsuboi (Kyushu Institute of Technology, Japan)

【WRAPUP】

15:45-16:15

【Forum】

Chair: Toru Shimada & Keisuke Sawada

16:30-18:00

Toward International Collaborations – What Can Be Started Now? –

**OS4: Green Aviation: Prospects for Environmentally
– Compatible Air Transportation**

HAGI

September 21, 2012

Chair: Shigeru Obayashi (Tohoku University, Japan)

OS4-1 **Green Aviation Activities in Korea with UAV Platform Case Studies** 296
9:00-9:30 *(Invited)*
Jinsoo Cho (Hanyang University, Korea)

OS4-2 **JAXA's Environment Conscious Aircraft Technology Program Initiative** 298
9:30-10:00 *(Invited)*
Takeshi Ohnuki (Japan Aerospace Exploration Agency, Japan)

OS4-3 **A Meshless and Matrix-free Approach to Aerodynamic Modeling** 300
10:00-10:30 *(Invited)*
Matthew Wilkinson, Andrew J. Meade (William Marsh Rice University, USA)

Chair: Keisuke Asai (Tohoku University, Japan)

OS4-4 **Wall Shear Stress Measurement** *(Invited)* 302
10:40-11:10 Ebenezer Gnanamanickam, John Sullivan (Purdue University, USA)

OS4-5 **Evaluation of Four-Engines Configuration for Near-Future Fuel Efficient** 304
11:10-11:30 **Transonic Transports with Geared Turbo Fan Engines**
Masaya Oshimizu, Shinkyu Jeong, Shigeru Obayashi (Tohoku University, Japan), Daisuke Sasaki (Kanazawa Institute of Technology, Japan) and Kazuhiro Nakahashi (Japan Aerospace Exploration Agency, Japan)

OS4-6 **Wind Tunnel Tests on Aerodynamic Performance of Clustered Linear** 306
11:30-11:50 **Aerospoke Nozzles**
Kohei Kuwamori, Goro Masuya (Tohoku University, Japan), Hidemi Takahashi, Sadatake Tomioka, Noboru Sakuranaka and Takeo Tomita (Japan Aerospace Exploration Agency, Japan)

OS4-7 **Effects of Leading-Edge Truncation and Stunting on Drag and Efficiency** 308
11:50-12:10 **of Busemann Intakes for Axisymmetric Scramjet Engines**
Hideaki Ogawa, Russell R. Boyce (The University of Queensland, Australia) and Sannu Mölder (Ryerson University, Canada)

12:10-13:10 LUNCH

Chair: Shigeya Watanabe (Japan Aerospace Exploration Agency, Japan)

OS4-8 **Sabot Separation Schemes in the Rectangular Aeroballistic Range** 310
13:10-13:40 *(Invited)*
Akihiro Sasoh, Kakuei Suzuki, Takahiro Imaizumi and Atsushi Toyoda (Nagoya University, Japan)

OS4-9 **One Experimental Technique of Detecting the Trajectory of a Free-flight** 312
13:40-14:00 **Projectile Launched by a Ballistic Range**
Takamasa Kikuchi, Takahiro Ukai, Kiyonobu Ohtani and Shigeru Obayashi (Tohoku University, Japan)

OS4-10 14:00-14:20	Near-Field Pressure Measurement of a Projectile Flying up to Mach Number 2.0 <u>Takahiro Ukai</u> , Takamasa Kikuchi, Kiyonobu Ohtani, Takaya Uchida, Yuta Saito and Shigeru Obayashi (Tohoku University, Japan)	314
OS4-11 14:20-14:40	Attitude Measurement of a Projectile by Flash X-ray Stereography <u>Takaya Uchida</u> , Takahiro Ukai, Kiyonobu Ohtani and Shigeru Obayashi (Tohoku University, Japan)	316
Chair: Shigeru Obayashi (Tohoku University, Japan)		
OS4-12 14:50-15:20	Near-field Pressure Signature Measurement of D-SEND#1 Models <i>(Invited)</i> <u>Yoshikazu Makino</u> , Masayoshi Noguchi (Japan Aerospace Exploration Agency, Japan)	318
OS4-13 15:20-15:40	Investigation of Micro-scale Phenomenon of Clear Air Turbulence by High Accuracy Meteorological Analysis <u>Keita Morimoto</u> (Tohoku University, Japan), Hamaki Inokuchi (Japan Aerospace Exploration Agency, Japan), Soshi Kawai (Institute of Space and Astronautical Science, Japan), Koji Shimoyama, Shinkyu Jeong and Shigeru Obayashi (Tohoku University, Japan)	320
OS4-14 15:40-16:00	Study on Aerodynamic Optimization Using Compressible Euler Solver on Block-Structured Cartesian Mesh <u>Yoshinori Andoh</u> , Shinkyu Jeong and Shigeru Obayashi (Tohoku University, Japan)	322
OS4-15 16:00-16:20	GUI Tool for Creation of Aircraft Configuration <u>Tomoki Taira</u> , Shinkyu Jeong, Shigeru Obayashi (Tohoku University, Japan), Daisuke Sasaki (Kanazawa Institute of Technology, Japan) and Kazuhiro Nakahashi (Japan Aerospace Exploration Agency, Japan)	324

OS5: Advanced Control of Smart Fluids and Fluid Flows

FUYOH

September 20, 2012

Chair: Seiichiro Izawa (Tohoku University, Japan)

- OS5-1 **Wandering Correction of a Wing Tip Vortex Velocity Field via Deconvolution** 328
14:50-15:10 Adam Edstrand, Eric Deem and Louis Cattafesta (Florida State University, USA)
- OS5-2 **Multiparametric Control Problems for Boussinesq Equations** 330
15:10-15:30 Gennady Alekseev, Dmitry Tereshko (Institute of Applied Mathematics FEB RAS, Russia)
- OS5-3 **Verification of CFD Analysis for Vortex Generators on a Super Critical Infinite-Wing** 332
15:30-15:50 Nobuo Namura, Shinkyu Jeong and Shigeru Obayashi (Tohoku University, Japan)
- OS5-4 **Study on Drag Reduction of a Ship due to a Drainage Slit** 334
15:50-16:10 Liu Aiming (Wuhan University of Technology, China)

Chair: Kazuo Matsuura (Ehime University, Japan)

- OS5-5 **Statistical Properties of Disturbances in a Transitional Channel Flow** 336
16:30-16:50 Kenta Watanabe (Shinshu University, Japan), Syunsuke Akaoka (Nagano Automation, Japan), Masaharu Matsubara (Shinshu University, Japan) and Kvik Mathias (KTH Royal Institute of Technology, Sweden)
- OS5-6 **Experimental Study of Linear Disturbance in a Turbulent Boundary Layer** 338
16:50-17:10 Konosuke Matsumoto, Taiki Mishiba, Yasuyuki Sendai and Masaharu Matsubara (Shinshu University, Japan)
- OS5-7 **The Effect of Actuator Length-Scale on Excited Waves** 340
17:10-17:30 Hajime Okawa, Masaya Shigeta, Seiichiro Izawa and Yu Fukunishi (Tohoku University, Japan)
- OS5-8 **Jet Flow-sound Interaction in a Modified Hole Tone System with a Tail Pipe** 342
17:30-17:50 Mikael A. Langthjem (Yamagata University, Japan), Masami Nakano (Tohoku University, Japan)

FUYOH

September 21, 2012

Chair: Masaharu Matsubara (Shinshu University, Japan)

- OS5-9 **An Experimental Investigation of Wing-Tip Vortex Attenuation via Circulation Control (*Invited*)** 344
9:00-9:30 Adam Edstrand, Eric Deem and Louis Cattafesta (Florida State University, USA)
- OS5-10 **Flow Structures under Passive Control in a Hole-Tone System** 346
9:30-9:50 Kazuo Matsuura (Ehime University, Japan), Masami Nakano (Tohoku University, Japan)

OS5-11 9:50-10:10	Increased Lift Airfoil of Vibration Flow Control Technology Dawei Li, <u>Jinhao Qiu</u> , Rui Nie and Hongli Ji (Nanjing University of Aeronautics & Astronautics, China)	348
OS5-12 10:10-10:30	Parallel Hypersonic Flow Field Simulation around a Spiked Body using Hydraulic Analogy <u>Shashank Khurana</u> , Kojiro Suzuki (The University of Tokyo, Japan) and Ethirajan Rathakrishnan (Indian Institute of Technology Kanpur, India)	350
Chair: Rongjia Tao (Temple University, USA)		
OS5-13 10:40-11:10	Design and Simulation of Low Voltage Cascade Electroosmotic Pump (<i>Invited</i>) Ujjal Barman, <u>Subhash C. Mishra</u> (Indian Institute of Technology Guwahati, India) and Ashis K. Sen (Indian Institute of Technology Madras, India)	352
OS5-14 11:10-11:40	Various Quantum Ground States of Low – Dimensional Nickel - Based Nitrates (<i>Invited</i>) Olga Volkova, Igor Morozov, Viktor Shutov and <u>Alexander Vasiliev</u> (Moscow State University, Russia)	354
OS5-15 11:40-12:00	A Microfluidic Device Demonstrated by Two-color Fluorescence MPIV <u>Ming-Wen Wang</u> (Oriental Institute of Technology, Taiwan)	356
Chair: Weihua Li (University of Wollongong, Australia)		
OS5-16 13:10-13:40	Suppressing Turbulence in Flows of Liquid Suspensions with Electromagnetic Fields (<i>Invited</i>) <u>Rongjia Tao</u> (Temple University, USA)	358
OS5-17 13:40-14:00	Electro-Rheological Properties of Nano-Suspensions based on Titanium Dioxide Nano-Particles <u>Katsufumi Tanaka</u> , Haruki Kobayashi, Ryuichi Akiyama (Kyoto Institute of Technology, Japan) and Masami Nakano (Tohoku University, Japan)	360
OS5-18 14:00-14:20	Micro System of Vibration Generator of Magnetic Fluid Droplet Driven by Alternating Magnetic Field <u>Sota Inomata</u> , Seiichi Sudo (Akita Prefectural University, Japan), Hidemasa Takana and Hideya Nishiyama (Tohoku University, Japan)	362
OS5-19 14:20-14:40	Control Problems for the Stationary Navier-Stokes and MHD and Equations <u>Roman Brizitskii</u> (Institute of Applied Mathematics FEB RAS, Russia)	364
Chair: Katsufumi Tanaka (Kyoto Institute of Technology, Japan)		
OS5-20 14:50-15:20	Fabrication and Characterization of Novel PDMS based Magnetorheological Elastomers (<i>Invited</i>) <u>Weihua Li</u> (University of Wollongong, Australia)	366
OS5-21 15:20-15:40	Optical Characteristics of Magnetic Fluid Hole in Alternating Fields <u>Michihiro Shinozaki</u> , Seiichi Sudo (Akita Prefectural University, Japan), Hidemasa Takana and Hideya Nishiyama (Tohoku University, Japan)	368
OS5-22 15:40-16:00	The Bubble Deformation Shih-Wei Liu, <u>Chun-Liang Lai</u> (National Taiwan University, Taiwan)	370

OS6: Multiphase Science and Ultra Clean Technology

FUJI

September 21, 2012

Chair: Jun Ishimoto (Tohoku University, Japan)

OS6-1 13:10-13:55	Challenges in 1x Design Node Semiconductor Device Cleaning (<i>Invited</i>) <u>Jin-Goo Park</u> , Bong-Kyun Kang and Manivannan Ramachandran (Hanyang University, Korea)	374
OS6-2 13:55-14:40	Novel Quantum Dot Solar Cells Realized by Fusion of Bio-template and Defect-Free Neutral Beam Etching (<i>Invited</i>) <u>Seiji Samukawa</u> (Tohoku University, Japan)	376
14:40-14:50	BREAK	
OS6-3 14:50-15:30	Ultrapure Water-Related Problems and Waterless Cleaning Challenges in Leading-Edge Semiconductor Manufacturing (<i>Invited</i>) <u>Takeshi Hattori</u> (Hattori Consulting International, Japan)	378
OS6-4 15:30-16:00	Droplet Impact as an Elementary Process of Physical Cleaning (<i>Invited</i>) Kazumichi Kobayashi, Ryuichi Uemura, <u>Masao Watanabe</u> (Hokkaido University, Japan), Toshiyuki Sanada (Shizuoka University, Japan) and Atsushi Hayashida (Aqua Science Corporation, Japan)	380
OS6-5 16:00-16:20	The Removal of Nanoparticles from Surfaces and 3-D Structures using High-frequency Acoustic Streaming (<i>Invited</i>) <u>Ahmed Busnaina</u> (Northeastern University, USA), Jinguo Park (Hanyang University, Korea)	382
16:20-16:30	BREAK	
OS6-6 16:30-16:48	Non-spherical Bodies With Particle and Fluid Inertia: Rotating or Surfing? (<i>ISC Invited</i>) <u>Fredrik Lundell</u> , Tomas Rosén (Royal Institute of Technology, Sweden)	384
OS6-7 16:48-17:06	Experimental and Theoretical Investigation of Acoustic Cavitation Behavior in the Megasonic Cleaning <u>Bong-Kyun Kang</u> , Ji-Hyun Jeong, Yoon-Sik Cho, Min-Su Kim (Hanyang University, Korea), Hong-Seong Sohn (Akrion Systems LLC, USA), Ahmed A. Busnaina (Northeastern University, USA) and Jin-Goo Park (Hanyang University, Korea)	386
OS6-8 17:06-17:24	Evaluation of Cleaning Performance of Nano-sized CO₂ Gas Cluster for Damage Free Semiconductor Cleaning <u>Min-Su Kim</u> , Bong-Kyun Kang (Hanyang University, Korea), Hoo-Mi Choi, Tae-Sung Kim (Sungkyunkwan University, Korea) and Jin-Goo Park (Hanyang University, Korea)	388

OS6-9 17:24-17:42	Numerical Study of Influence of Initial Standoff Distance on Impulsive Pressure Induced by Single Bubble Collapse near Wall Boundary (Integration to the Next-generation Megasonic Cavitation Cleaning Technology) <u>Naoya Ochiai</u> , Yuka Iga (Tohoku University, Japan), Motohiko Nohmi (EBARA Corporation, Japan), Toshiyuki Ikohagi (Open University of Japan, Japan) and Jun Ishimoto (Tohoku University, Japan)	390
OS6-10 17:42-18:00	Effect of Turbulence on Nonlinear Sloshing in a Rectangular Pool <u>Ken Uzawa</u> (Japan Atomic Energy Agency, Japan)	392

OS7: Blood Flow for Medical Equipment

AKEBONO (EAST)

September 19, 2012

Chair: Toshio Nakayama (Tohoku University, Japan) & Aike Qiao (Beijing University of Technology, China)

- | | | |
|---|--|-----|
| OS7-1
13:00-13:30 | Numerical Simulation of Vertebral Artery Stenosis Treated with Different Stents (<i>Invited</i>)
<u>Zhanzhu Zhang</u> , <u>Aike Qiao</u> (Beijing University of Technology, China) | 396 |
| OS7-2
13:30-13:45 | Pressure-Driven Flow Characteristics in the Lymphatic Vessel for Lymphatic Drug Delivery System
<u>Yuriko Hatakeyama</u> , Nicolas Sax, Shigeki Kato, Tatsuki Okuno, Maya Sakamoto, Shiro Mori and Tetsuya Kodama (Tohoku University, Japan) | 398 |
| OS7-3
13:45-14:00 | Cancer Treatment via the Lymphatic Vessel using Nano/Micro Bubbles
<u>Shigeki Kato</u> , Sax Nicolas, Yuriko Hatakeyama, Tatsuki Okuno, Shiro Mori, Maya Sakamoto and Tetsuya Kodama (Tohoku University, Japan) | 400 |
| OS7-4
14:00-14:15 | Thermal Therapy using Plasmonic Nano Particles for Lymph Node Metastasis
<u>Tatsuki Okuno</u> , Shigeki Kato, Yuriko Hatakeyama, Takuma Sato, Maya Sakamoto, Shiro Mori and Tetsuya Kodama (Tohoku University, Japan) | 402 |
| OS7-5
14:15-14:30 | Intra-left Atrial Flow
<u>Muneichi Shibata</u> (Miyagi Cardiovascular and Respiratory Center, Japan / Tohoku University, Japan), Tomoyuki Yambe, Kenichi Funamoto and Toshiyuki Hayase (Tohoku University, Japan) | 404 |
| Chair: Makoto Ohta (Tohoku University, Japan) & Guy Courbebaisse (INSA de Lyon, France) | | |
| OS7-6
14:40-15:10 | Blood Flow Simulation within Stented Intracranial Aneurysm (<i>Invited</i>)
<u>Guy Courbebaisse</u> (INSA de Lyon, France), Jonas Latt, Orestis Malaspinas (University of Geneva, Switzerland), Maciej Orkisz (INSA de Lyon, France) and Bastien Chopard (University of Geneva, Switzerland) | 406 |
| OS7-7
15:10-15:25 | Hemodynamic Effects of Y-configuration Stent for Cerebral Aneurysms
<u>Kenichi Kono</u> , Tomoaki Terada (Wakayama Rosai Hospital, Japan) | 408 |
| OS7-8
15:25-15:40 | Simulation of Hemodynamics in Artery with Aneurysm and Stenosis
<u>Yujie Li</u> (Beijing University of Technology, China / Tohoku University, Japan), Hitomi Anzai, Toshio Nakayama, Yasutomo Shimizu, Yukihisa Miura (Tohoku University, Japan), Aike Qiao (Beijing University of Technology, China) and Makoto Ohta (Tohoku University, Japan) | 410 |
| OS7-9
15:40-15:55 | A Development of Lattice Boltzmann Model and Lumped Parameter Model Connection for Cardiovascular Multiscale Analysis
<u>Mingzi Zhang</u> (Beijing University of Technology, China / Tohoku University, Japan), Hitomi Anzai (Tohoku University, Japan), Youjun Liu (Beijing University of Technology, China) and Makoto Ohta (Tohoku University, Japan) | 412 |

OS7-10 **Optimum Design of Flow Diverter Stent Associated with Arterial Geometries** 414
 15:55-16:10 Hitomi Anzai (Tohoku University, Japan), Jean-Juc Falcone, Bastien Chopard
 (University of Geneva, Switzerland) and Makoto Ohta (Tohoku University,
 Japan)

FUJI

September 21, 2012

Chair: Makoto Ohta & Toshio Nakayama (Tohoku University, Japan)

OS7-11 **Assessment of Three Non-Newtonian Models in Steady State Blood Flow** 416
 9:00-9:15 **through an Aneurysm (*Invited*)**
 Mantulal Basumatary, Suresh Sahoo, Ganesh Natarajan and Subhash C.
Mishra (Indian Institute of Technology Guwahati, India)

OS7-12 **Heat Conduction in Soft Tissues Modelled by Hydrogels (*Invited*)** 418
 9:15-9:30 András Tél, Rita A. Bauer, Zsófia Varga and Miklós Zrinyi (Semmelweis
 University, Hungary)

OS7-13 **Effect of Parent Artery Expansion by Stent Placement for Saccular Cerebral** 420
 9:30-9:45 **Aneurysms**
Futoshi Mori (The University of Tokyo, Japan), Nhat Minh Bui and Teuro
 Matsuzawa (Japan Advanced Institute of Science and Technology, Japan)

OS7-14 **Numerical and Experimental Study of Flow in Stenosis Models with Several** 422
 9:45-10:00 **Mechanical Properties**
Yasutomo Shimizu, Shuya Shida (Tohoku University, Japan), Ashkan
 Javadzadegan (The University of Sydney, Australia), Kenichi Funamoto,
 Toshiyuki Hayase and Makoto Ohta (Tohoku University, Japan)

OS7-15 **Effect of the Aspect Ratio of Cerebral Aneurysms on Blood Flow Reduction after** 424
 10:00-10:30 **Optimized Stent Placement (*Invited*)**
Toshio Nakayama, Shinkyu Jeong (Tohoku University, Japan), Karkenahalli
 Srinivas (The University of Sydney, Australia) and Makoto Ohta (Tohoku
 University, Japan)

OS8: Membrane Micro Channel for Health Care

FUJI

September 20, 2012

Chair: Makoto Ohta (Tohoku University, Japan)

- OS8-1 **Structural Elements which Control the Signal Transduction Pathway of GPCR.** 428
8:00-8:20 ***(Invited)***
 Minoru Sugihara (Aoyamagakuin University, Japan), Makiko Suwa
 (Aoyamagakuin University, Japan / National Institute of Advanced Industrial
 Science and Technology, Japan)
- OS8-2 **Computational Detection of Organelle Sorting Signals in Membrane Localized** 430
8:20-8:40 **Proteins *(Invited)***
 Yuri Mukai, Hirotaka Tanaka, Tatsuya Konishi, Hiromu Takata, Naoyuki
 Takachio (Meiji University, Japan), Masami Ikeda (Aoyama Gakuin University,
 Japan) and Takanori Sasaki (Meiji University, Japan)
- OS8-3 **Electrophysiological Properties of Bacterial Membrane Channel Proteins** 432
8:40-9:00 **Depending on Lipid Component and Bilayer Stability *(Invited)***
 Noriko Tomita (Tohoku University, Japan), Liviu Movileanu (Syracuse
 University, USA) and Makoto Ohta (Tohoku University, Japan)

FUJI

September 21, 2012

Chair: Noriko Tomita (Tohoku University, Japan)

- OS8-4 **Engineering Membrane Protein Nanopores for Biomolecular Detection** 434
8:00-8:30 ***(Invited)***
 Mohammad M. Mohammad, Raghuvaran Iyer, Khalil R. Howard (Syracuse
 University, USA), Mark P. McPike (AptaMatrix, Inc., USA), Philip N. Borer
 (Syracuse University, USA / AptaMatrix, Inc., USA) and Liviu Movileanu
 (Syracuse University, USA)
- OS8-5 **Crosstalk between *Helicobacter pylori* and Host Cells *(Invited)*** 436
8:30-9:00 ***(Invited)***
 Hitomi Mimuro (The University of Tokyo, Japan)

September 19, 2012 in US

- OS8-1 7:00-7:20 pm in US
OS8-2 7:20-7:40 pm in US
OS8-3 7:40-8:00 pm in US

September 20, 2012 in US

- OS8-4 7:00-7:30 pm in US
OS8-5 7:30-8:00 pm in US

OS10: Thermal-Fluid Flows and Plasma Physics

FUYOH

September 19, 2012

Session I

Chair: Chien-Yuh Yang (National Central University, Taiwan)

- OS10-1 **Heat Transfer Performance of HFO - 1234yf - A Quick Overview (*Invited*)** 440
13:00-13:30 Chi-Chuan Wang (National Chiao Tung University, Taiwan)
- OS10-2 **Outflow Boundary Condition Ensuring Mass Conservation in Finite Volume Method and its Application to Incompressible Unsteady-state Reactive Thermal Fluid Flow Computation** 442
13:30-13:45 Sohey Nozawa, Yohsuke Matsushita (Kyushu University, Japan)
- OS10-3 **Numerical Simulation of Unexposed Temperature and Deformation for Fire Door** 444
13:45-14:00 San-Yih Lin, Chong-Wei Ho (National Cheng Kung University, Taiwan)
- OS10-4 **Detailed CFD Analysis of Convective Heat Transfer of Alumina Nanofluid in Subchannel Geometry** 446
14:00-14:15 Mohammad Nazififard (Shiraz University, Iran / Seoul National University, Korea / PHILOSOPHIA, Korea), M. R. Nematollahi and Khosrow Jafarpour (Shiraz University, Iran) and Kune Y. Suh (Seoul National University, Korea / PHILOSOPHIA, Korea)
- OS10-5 **Effect of Angled Grooves on Heat Transfer in an Impingement Channel with Crossflow** 448
14:15-14:30 Yuan-Hsiang Lo, Yao-Hsien Liu (National Chiao-Tung University, Taiwan)

Session II

Chair: San Yih Lin (National Cheng Kung University, Taiwan)

- OS10-6 **Direct Numerical Simulation of Particulate Flows with Heat Transfer (*Invited*)** 450
14:40-15:10 Xueming Shao, Zhaosheng Yu and Yang Shi (Zhejiang University, China)
- OS10-7 **Transient Liquid Crystal Measurement of Heat Transfer in a Rotating Rectangular Channel with the Entrance Geometry of Sudden Contraction** 452
15:10-15:25 Ching-Shii Wang, Yu-Shun Lin and Yao-Hsien Liu (National Chiao-Tung University, Taiwan)
- OS10-8 **Numerical Investigations of Unexposed Temperature Distribution for Fire Doors under Different Sizes** 454
15:25-15:40 San-Yih Lin, Tzu-Chieh Lin, George C. Yao and Tsung-Chia Wu (National Cheng Kung University, Taiwan)
- OS10-9 **A Three-dimensional Numerical Analysis of Heat Transfer and Flow in Sinusoidal Wavy Passages** 456
15:40-15:55 Kuen-Rung Huang, Wu-Shung Fu and Chi-Xiu Lo (National Chiao Tung University, Taiwan)

OS10-10 15:55-16:10	Investigation of Mixed Convection in a Three-Dimensional Vertical Channel at High Richardson Number <u>Yun Huang</u> , Wu-Shung Fu and Pei-Jung Wu (National Chiao Tung University, Taiwan)	458
Session III		
Chair: Kuo-Long Pan (National Taiwan University, Taiwan)		
OS10-11 16:20-16:50	Phenomena of Natural Convection in Multiple Open Boundaries Condition Problem (<i>Invited</i>) <u>Wu Shung Fu</u> , Wei Hsiang Wang and Chung Gang Li (National Chiao Tung University, Taiwan)	460
OS10-12 16:50-17:05	An Experimental Investigation on Air-Water Two-Flow Distribution in Plate Heat Exchangers with Inlet Distributor <u>Chien-Yuh Yang</u> , Yueh-Hung Lin and Fan-Yu Meng (National Central University, Taiwan)	462
OS10-13 17:05-17:20	Effect of Heater Size on the Critical Heat Flux of Pool Boiling on Micropillar Array-coated Surfaces Chih-Hung Huang, <u>Ming-Chang Lu</u> (National Chiao Tung University, Taiwan)	464
OS10-14 17:20-17:35	An Investigation of the Effects of a Height on Natural Convection between Two Horizontal Parallel Plates with a Heated Bottom Surface <u>Shang-Hao Huang</u> , Wu-Shung Fu and Wei-Hsiang Wang (National Chiao Tung University, Taiwan)	466
OS10-15 17:35-17:50	Numerical Simulation of Heat Transfer of Closed Loop Pulsating Heat Pipe <u>Rong-Jer Lai</u> , Jia-Wei Chiou (National Kaohsiung University of Applied Sciences, Taiwan)	468

FUYOH

September 20, 2012

Session IV

Chair: Yuichiro Nagatsu (Tokyo University of Agriculture and Technology, Japan)

OS10-16 9:00-9:30	From Miscible to Immiscible: Modeling of a Diffuse Interface and Its Implementations in Hele-Shaw Flows (<i>Invited</i>) <u>Ching-Yao Chen</u> (National Chiao Tung University, Taiwan)	470
OS10-17 9:30-9:45	Experimental Study on Viscous Fingering with a Decrease in Interfacial Tension by a Chemical Reaction <u>Masanari Fujimura</u> , Yuichiro Nagatsu (Tokyo University of Agriculture and Technology, Japan) and Yutaka Tada (Nagoya Institute of Technology, Japan)	472
OS10-18 9:45-10:00	Pattern Transition from Fingering to Fracturing in a Reacting Flow Producing Gel <u>Tomohiro Ujiie</u> (Nagoya Institute of Technology, Japan), Yuichiro Nagatsu (Tokyo University of Agriculture and Technology, Japan), Shuichi Iwata, Yoshihito Kato and Yutaka Tada (Nagoya Institute of Technology, Japan)	474
OS10-19 10:00-10:15	On The Off-center Separation in Binary Droplet Collision <u>Kuo-Long Pan</u> , Chi-Ru Lu (National Taiwan University, Taiwan)	476

OS10-20 10:15-10:30	Implicit Large Eddy Simulation using Truncated Navier-Stokes Equations for Low Mach Number Compressible Flows <u>ChungGang Li</u> (National Chiao Tung University, Taiwan), J. Andrzej Domaradzki (University of Southern California, USA), Wu Shung Fu (National Chiao Tung University, Taiwan) and T. Tantikul (University of Southern California, USA)	478
Session V		
Chair: Jong-Shinn Wu (National Chiao Tung University, Taiwan)		
OS10-21 10:40-10:55	Experimental Determination of Plasma Parameters by Laser-Induced Breakdown Spectroscopy <u>Ardian B. Gojani</u> (Tohoku University, Japan)	480
OS10-22 10:55-11:10	Comprehensive Modeling of Particle-Plasma Flow in Plasma Spray Process <u>Hongbing Xiong</u> , Xueming Shao (Zhejiang University, China)	482
OS10-23 11:10-11:25	Numerical and Experimental Investigation of Light Emission of a Planar Nitrogen Atmospheric-Pressure Dielectric Barrier Discharge Due to Addition of Ammonia Considering Oxygen Impurity <u>Fu-Li Li</u> , Yi-Wei Yang, Kun-Mo Lin and Jong-Shinn Wu (National Chiao Tung University, Taiwan)	484
OS10-24 11:25-11:40	Simulation of CH₄-H₂-air Turbulent Non-premixed Flame by Vortex Method <u>Kazui Fukumoto</u> , Yoshifumi Ogami (Ritsumeikan University, Japan)	486
OS10-25 11:40-11:55	A True-Direction Flux Reconstruction Scheme to the Quiet Direct Simulation Method for Inviscid Gas Flows <u>Ya-Ju Lin</u> (National Chiao Tung University, Taiwan), Matthew. R. Smith (National Center for High-performance Computing, Taiwan) and Jong-Shinn Wu (National Chiao Tung University, Taiwan)	488
OS10-26 11:55-12:10	Ultra-short Pulse Laser: A Potential Tool for Breast Cancer Detection Arka Bhowmik, <u>Ramjee Repaka</u> (Indian Institute of Technology Ropar, India) and Subhash C. Mishra (Indian Institute of Technology Guwahati, India)	490
Session VI		
Chair: Ramjee Repaka (Indian Institute of Technology Ropar, India)		
OS10-27 13:10-13:25	Numerical Investigation of Flow Characteristics of Fuel/Oxidizer Channels in a Solid Oxide Fuel Cell Stack Shih-Sin Wei, <u>Jong-Shinn Wu</u> (National Chiao Tung University, Taiwan)	492
OS10-28 13:25-13:40	Reversible Motion of Microchains <u>Yan-Hom Li</u> , Ching-Yao Chen (National Chiao Tung University, Taiwan)	494
OS10-29 13:40-13:55	Auxiliary Injection for Combustion Enhancement in RBCC Engine Operating in Hypersonic Flow <u>Shohei Takagi</u> (Tohoku University, Japan), Sadatake Tomioka, Tomoyuki Komuro, Katsuhiko Itoh (Japan Aerospace Exploration Agency, Japan) and Goro Masuya (Tohoku University, Japan)	496
OS10-30 13:55-14:10	Investigation on Fundamental Characteristics of Synthetic Jet Actuator with Cavity in Resonances <u>Fei-Bin Hsiao</u> , Chi-Yu Lin (National Cheng Kung University, Taiwan)	498

OS10-31 14:10-14:25	Estimation of Mode Transition in a Supersonic Combustor <u>Junji Noda</u> (Tohoku University, Japan), Sadatake Tomioka (Japan Aerospace Exploration Agency, Japan)	500
OS10-32 14:25-14:40	The Linear Stability of a Compositional Plume in the Presence of Material Diffusion <u>Khaled Suleiman Mohammed AL-Mashrafi</u> (Sultan Qaboos University, Sultanate of Oman)	502
<u>La Boaine</u>		
<u>September 20, 2012</u>		
Session VII		
Chair: Yao-Hsien Liu (National Chiao Tung University, Taiwan)		
OS10-33 14:50-15:05	Numerical Simulations of Viscous Fingerings by a Phase Field Method <u>Yu-Sheng Huang</u> , Li-Chieh Wang and Ching-Yao Chen (National Chiao Tung University, Taiwan)	504
OS10-34 15:05-15:20	Fingering Instability Induced by a Precipitation Reaction <u>Yuki Ishii</u> (Nagoya Institute of Technology, Japan), Yuichiro Nagatsu (Tokyo University of Agriculture and Technology, Japan), Yutaka Tada (Nagoya Institute of Technology, Japan) and Anne De Wit (Free University of Brussels, Belgium)	506
OS10-35 15:20-15:35	Parallel Cartesian-Grid Direct Simulation Monte Carlo Method with Cut Cells on Multiple Graphics Processor Units <u>Ming-Chung Lo</u> , Cheng-Chin Su, Fang-An Kuo, Jong-Shinn Wu (National Chiao Tung University, Taiwan) and Matthew R. Smith (National Center for High-performance Computing, Taiwan)	508
OS10-36 15:35-15:50	An Investigation of Natural Convection in Parallel Square Plates with a Heated Top Surface by a Hybrid Boundary Condition Wu Shung Fu, <u>Wei Hsiang Wang</u> and Chung Gang Li (National Chiao Tung University, Taiwan)	510
OS10-37 15:50-16:05	Effects Of Reciprocating Motions On Transfer Rate Of Hazardous Gas In A Curved Channel Wu-Shung Fu, <u>Yu-Chih Lai</u> and Yun Huang (National Chiao Tung University, Taiwan)	512

**OS11: The Eighth International Students/Young Birds
Seminar on Multi-Scale Flow**

AKEBONO (WEST)

September 19, 2012

13:00-13:05	Opening	
Session 1 13:05-(14:08)	-Award Session - Short Oral Presentation 3 min for Short Oral Presentation without PC preparation	
OS11-1	Effect of Bubble Wake on Mass Transfer from a Bubble to Liquid Phase <u>Masahiko Toriu</u> , Takayuki Saito (Shizuoka University, Japan)	516
OS11-2	Effects of Thermal and Mass Diffusions on Combustion Characteristics of Methane/Air Premixed Flame with Equivalence Ratio using Micro-flow Reactor with Controlled Temperature Profile <u>Takuro Nishida</u> , Takuhiro Matsumoto, Toshihisa Ueda, Takeshi Yokomori (Keio University, Japan) and Kaoru Maruta (Tohoku University, Japan)	518
OS11-3	Development of a Micro-tube Gas Separator Utilizing Soret Effect <u>Takahiro Wako</u> , Masae Shimizu and Naoki Ono (Shibaura Institute of Technology, Japan)	520
OS11-4	A Study on Controlling Bubble Size by Magnetically Driving Metallic Powder in Liquid Phase <u>Keiichi Igari</u> , Kazushi Kunimatsu and Naoki Ono (Shibaura Institute of Technology, Japan)	522
OS11-5	Estimation of Thermal Conductivity of Biological Tissue by Inverse Analysis <u>Takahiro Okabe</u> , Junnosuke Okajima, Atsuki Komiya (Tohoku University, Japan), Yun Luo (Shanghai Jiao Tong University, China), Ichiro Takahashi (Yamagata University, Japan) and Shigenao Maruyama (Tohoku University, Japan)	524
OS11-6	Experimental Study on Shock Wave and Bubble Evolution Induced by Underwater Electric Discharge <u>Kentarō Hayashi</u> , Taketoshi Koita and Mingyu Sun (Tohoku University, Japan)	526
OS11-7	Numerical Study on Receptivity of Flat-Plate Boundary Layer to Outer Freestream Disturbances <u>Shuta Noro</u> (Japan Aerospace Exploration Agency, Japan), Masaya Shigeta, Seiichiro Izawa and Yu Fukunishi (Tohoku University, Japan)	528
OS11-8	Conceptual Design Method for a Mars Airplane: Formulation of Aerodynamic Characteristics at Low Reynolds Numbers <u>Koji Fujita</u> , Hiroki Nagai and Keisuke Asai (Tohoku University, Japan)	530

OS11-9	Prototype Experiment and Numerical Simulation on Processing of Noncontact Thin Plate Utilizing Alloy with Low Melting Temperature <u>Yoshiyuki Mitsuhasi</u> , Kazuki Matsumura, Takashi Yamada, Mitsutaka Umeta and Naoki Ono (Shibaura Institute of Technology, Japan)	532
OS11-10	Design of Interferometer System with Phase-shifting Koester Prism <u>Eita Shoji</u> , Atsuki Komiiya, Junnosuke Okajima and Shigenao Maruyama (Tohoku University, Japan)	534
OS11-11	Dryout of Boiling with Impinging Flow in T-shaped Mini Channel with High-carbon Alcohol Aqueous Solutions <u>Minoru Ootuka</u> , Yuki Kumagai, Haruki Taguchi and Naoki Ono (Shibaura Institute of Technology, Japan)	536
OS11-12	Leading Edge Receptivity to Freestream with Velocity Profile Sinusoidal in the Spanwise Direction <u>Yu Nishio</u> , Masaya Shigeta, Seiichiro Izawa and Yu Fukunishi (Tohoku University, Japan)	538
OS11-13	Effect of Bio-Nano Fibres on Centrifugal- and Curvature-Induced Hydrodynamic Stability <u>Mathias Kwick</u> , Fredrik Lundell, Lisa PrahL Wittberg (Royal Institute of Technology, Sweden) and L. Daniel Söderberg (Royal Institute of Technology / Innventia AB, Sweden)	540
OS11-14	Water Purification by Spraying Solution into DBD Plasma Reactor <u>Tomohiro Shibata</u> , Hideya Nishiyama (Tohoku University, Japan)	542
OS11-15	Synthesis of Functional Nano-Powder through Solution Precursor Plasma Spraying in a DC-RF Hybrid Plasma Flow System <u>Juyong Jang</u> , Hidemasa Takana (Tohoku University, Japan), Yasutaka Ando (Ashikaga Institute of Technology, Japan), Oleg P. Solonenko (Khristianovich Institute of Theoretical and Applied Mechanics, Russia) and Hideya Nishiyama (Tohoku University, Japan)	544
OS11-16	Conditional Spatial Correlation of Velocity Fluctuation in Supersonic Flow with Transverse Injection <u>Shohei Uramoto</u> , Toshinori Kouchi and Goro Masuya (Tohoku University, Japan)	546
OS11-17	Effect of Supersonic Micro Nozzle Shape on the Heat Transfer in a Surface Wall <u>Yuya Takahashi</u> , Junnosuke Okajima, Atsuki Komiiya and Shigenao Maruyama (Tohoku University, Japan)	548
OS11-18	Wheel Design for Planetary Rovers Traveling over Loose Soil <u>Masataku Sutoh</u> , Keiji Nagatani and Kazuya Yoshida (Tohoku University, Japan)	550
OS11-19	The Numerical Setup of Conditions for Point Energy Release in Water <u>Daiki Ishikawa</u> , Mingyu Sun (Tohoku University, Japan)	552

OS11-20	Applications of LCS to the Study of Transport Trajectories in Space Mission <u>Kenta Oshima</u> , Shintaro Wada and Tomohiro Yanao (Waseda University, Japan)	554
OS11-21	Effects of Redox Cycling on the Mechanical Properties of Ni-YSZ Cermets for SOFC Anodes as a Function of Porosity <u>Taihei Miyasaka</u> , Shinji Sukinou, Satoshi Watanabe, Kazuhisa Sato, Tatsuya Kawada and Toshiyuki Hashida (Tohoku University, Japan)	556
(14:10-16:10)	Poster Presentation	
 <u>AKEBONO (WEST)</u> <u>September 20, 2012</u>		
Session 2 9:00-(10:00)	Short Oral Presentation 3min for Short Oral Presentation without PC preparation	
OS11-22	Estimation of Heat Conduction and Thermal Radiation in Porous Insulation Materials Using Diffuse Approximation <u>Tatsuya Kobari</u> , Junnosuke Okajima, Atsuki Komiya and Shigenao Maruyama (Tohoku University, Japan)	558
OS11-23	Low Friction Mechanism of Hydrogen and Fluorine Terminated Diamond Like Carbon Film Using Tight-Binding Quantum Chemical and First-Principles Molecular Dynamics Methods <u>Shandan Bai</u> , Seiichiro Sato, Takeshi Ishikawa, Yuji Higuchi, Nobuki Ozawa, Tomomi Shimazaki, Koshi Adachi (Tohoku University, Japan), Jean-Michel Martin (Ecole Centrale de Lyon, France) and Momoji Kubo (Tohoku University, Japan)	560
OS11-24	Molecular Dynamics Study on Recycling Mechanism of Used CeO₂ Abrasive Grain for CMP of Glass Surface <u>Kang Zhou</u> , Takeshi Ishikawa, Yuji Higuchi, Nobuki Ozawa, Tomomi Shimazaki and Momoji Kubo (Tohoku University, Japan)	562
OS11-25	Configurations of CH₄/O₂/Xe Counterflow Premixed Flames at Small Stretch Rates under Microgravity <u>Koichi Takase</u> (Tohoku University, Japan), Xing Li (Tohoku University, Japan / Beijing Jiaotong University, China), Hisashi Nakamura, Takuya Tezuka, Susumu Hasegawa (Tohoku University, Japan), Masato Katsuta, Masao Kikuchi (Japan Aerospace Exploration Agency, Japan) and Kaoru Maruta (Tohoku University, Japan)	564
OS11-26	Cetane Number and Weak Flames of Diesel Surrogates in a Micro Flow Reactor with a Controlled Temperature Profile <u>Satoshi Suzuki</u> , Mikito Hori, Hisashi Nakamura, Takuya Tezuka, Susumu Hasegawa and Kaoru Maruta (Tohoku University, Japan)	566

OS11-27	Chemical Stability of the Cubic Phase of $\text{Ba}_{0.5}\text{Sr}_{0.5}\text{Co}_{0.8}\text{Fe}_{0.2}\text{O}_{3-\delta}$ (BSCF) <u>Wang Fang</u> , Keiji Yashiro, Koji Amezawa and Junichiro Mizusaki (Tohoku University, Japan)	568
OS11-28	Transient Analysis of Loop Heat Pipes with Secondary Wick <u>Kouhei Magome</u> , Masahiko Taketani and Hiroki Nagai (Tohoku University, Japan)	570
OS11-29	Numerical Simulation for Catalytic Reaction over Pt in $\text{CH}_4/\text{O}_2/\text{CO}_2$ Mixture <u>Kenji Yamada</u> , Kazuya Iwata, Toshihisa Ueda and Takeshi Yokomori (Keio University, Japan)	572
OS11-30	Effect of Surface Reactions on Gas Phase Reactions of $\text{H}_2/\text{O}_2/\text{N}_2$ and CH_4/Air Mixtures in a Micro Flow Reactor with a Controlled Temperature Profile <u>Yuta Kizaki</u> , Kenichiro Saruwatari, Hisashi Nakamura, Takuya Tezuka, Susumu Hasegawa and Kaoru Maruta (Tohoku University, Japan)	574
OS11-31	Nongray Radiative Transfer and Convective Heat Transfer Modeling in a Trapezoidal Cavity Receiver for the CLFR Atsushi Sakurai, <u>Shumpei Yoshimura</u> (Niigata University, Japan), Masud Behnia (The University of Sydney, Australia) and Koji Matsubara (Niigata University, Japan)	576
OS11-32	In-situ Measurements of Mechanical Properties of High Temperature Ionics Materials <u>Yuta Kimura</u> , Yoshikazu Shirai, Tatsuya Kawada, Shin-ichi Hashimoto and Koji Amezawa (Tohoku University, Japan)	578
OS11-33	Optical and Thermal Characteristic of a Solar Concentrator with Compound Parabolic and Involute Reflector <u>Abid Ustaoglu</u> , Junnosuke Okajima (Tohoku University, Japan), Xin-Rong (Ron.) Zhang (Peking University, China) and Shigenao Maruyama (Tohoku University, Japan)	580
OS11-34	Non-Condensable Gas Effect in Oscillating Heat Pipe <u>Takurou Daimaru</u> , Hiroki Nagai (Tohoku University, Japan)	582
OS11-35	Friction and Thermal Properties in Drilling of Bone Biomodels <u>Kei Ozawa</u> (Tohoku University, Japan), Yuji Katakura, Yukihiro Shibata (TECNO CAST, Japan), Philippe Kapsa, Vincent Fridrici, Gaëtan Bouvard (Ecole Centrale de Lyon, France) and Makoto Ohta (Tohoku University, Japan)	584
OS11-36	A Molecular Dynamics Study on the Thermodynamic Analysis of Cryogenic Hydrogen <u>Hiroki Nagashima</u> , Takashi Tokumasu (Tohoku University, Japan), Shin-ichi Tsuda (Shinshu University, Japan), Nobuyuki Tsuboi (Kyushu Institute of Technology, Japan), Mitsuo Koshi (The University of Tokyo, Japan) and A. Koichi Hayashi (Aoyama Gakuin University, Japan)	586
OS11-37	SPH Simulation of Gas Flow Accompanying Thermal Expansion <u>Masumi Ito</u> , Seiichiro Izawa, Yu Fukunishi and Masaya Shigeta (Tohoku University, Japan)	588

OS11-38	Thermal Analysis on a Remountable High Temperature Superconducting Magnet around Jointing Region <u>Yusuke Tanno</u> , Satoshi Ito and Hidetoshi Hashizume (Tohoku University, Japan)	590
OS11-39	Effects of Incident Shock Wave and Cavity on Flameholding in Supersonic Flow <u>Yu Kitahara</u> , Yumi Ishimoto, Yoshitaka Iwamura, Taku Kudo and Hideaki Kobayashi (Tohoku University, Japan)	592
OS11-40	Combustion Characteristics of Propanol/Air Turbulent Premixed Flames at High Pressure <u>Shungo Souyoshi</u> , Takuro Suzuki, Taku Kudo and Hideaki Kobayashi (Tohoku University, Japan)	594
OS11-41	Measurement of the Ion Specific Heat Ratio in Fast-flowing Plasma using a Mach Probe <u>Yuko Hashima</u> , Kohei Okawa, Hiroshi Watanabe, Yuki Izawa, Kazuya Yashima, Kiyotaka Suzuki, Nozomi Tanaka and Akira Ando (Tohoku University, Japan)	596
OS11-42	Response Time Evaluation of Temperature-Sensitive Paint <u>Takehito Horagiri</u> , Hiroki Nagai (Tohoku University, Japan)	598
(10:00-12:00)	Poster Presentation	
Session 3 13:00-(13:30)	Short Oral Presentation 3 min for Short Oral Presentation without PC preparation	
OS11-43	Delay Time Compensation of a Hardware in the Loop Simulation Based on Contact Dynamics Model <u>Fumihito Sugai</u> , Satoko Abiko, Xin Jiang (Tohoku University, Japan), Atsushi Konno (Hokkaido University, Japan) and Masaru Uchiyama (Tohoku University, Japan)	600
OS11-44	Optical Microscope to Understand Motility <u>Takeshi Obara</u> (Tohoku University, Japan), Yasunobu Igarashi (Olympus Software Technology Corp., Japan) and Koichi Hashimoto (Tohoku University, Japan)	602
OS11-45	Characterization of Young's Modulus of MWCNT-Carbon Cantilevered Microstructures <u>Liang He</u> , Masaya Toda, Yusuke Kawai, Mamoru Omori, Toshiyuki Hashida and Takahito Ono (Tohoku University, Japan)	604
OS11-46	Thickness Evaluation of Thermal Spraying on Boiler Tubes by Eddy Current Testing <u>Yohei Takahashi</u> , Ryoichi Urayama, Tetsuya Uchimoto, Toshiyuki Takagi (Tohoku University, Japan), Hiroshi Naganuma, Kazufumi Sugawara and Yoriaki Sasaki (Tohoku Electric Power Engineering & Construction Co. Inc, Japan)	606

OS11-47	Deposition of Micro-crystalline Diamond Films on Curved Steel Surface with Ti Interlayer <u>Kyohei Naito</u> , Hiroyuki Miki, Takanori Takeno and Toshiyuki Takagi (Tohoku University, Japan)	608
OS11-48	Evaluation of Fatigue Properties of Mo-DLC Coatings under Cyclic Bending. <u>Mami Takahashi</u> , Hiroyuki Miki, Takanori Takeno and Toshiyuki Takagi (Tohoku University, Japan)	610
OS11-49	Quantitative Evaluation of Residual Strain in Austenitic Stainless Steels using Electromagnetic Nondestructive Evaluation <u>Seiya Sato</u> , Ryoichi Urayama, Takeshi Sato, Tetsuya Uchimoto, Toshiyuki Takagi (Tohoku University, Japan), Zhenmao Chen (Xi'an Jiaotong University, China) and Yasuhiko Yoshida (The Kansai Electric Power Company, Inc., Japan)	612
OS11-50	Relationship between Fluid Shear Stress and the Phenotype Change of Smooth Muscle Cells in a Co-culture Model <u>Xiaobo Han</u> (Tohoku University, Japan), Naoya Sakamoto (Kawasaki University of Medical Welfare, Japan), Noriko Tomita (Tohoku University, Japan), Meng Hui (State University of New York, USA), Masaaki Sato and Makoto Ohta (Tohoku University, Japan)	614
OS11-51	Comparison between Agarose Gel and PVA-H Biomodels for Evaluation of Ablation Catheter <u>Kaihong Yu</u> (Tohoku University, Japan), Tetsuya Yamashita (JMS Co. LTD., Japan) and Makoto Ohta (Tohoku University, Japan)	616
OS11-52	Experimental Studying of Metallic Splats Formation in the Condition of Substrate Submelting in a Contact Spot <u>Andrey V. Perfilyev</u> , Oleg P. Solonenko and Andrey V. Smirnov (Khristianovich Institute of Theoretical and Applied Mechanics SB RAS, Russia)	618
OS11-53	Size Validation of an Adrenal Vein Model for Development of an In Vitro Model with Realistic Geometrical Structure <u>Yusuke Hoshino</u> (Tohoku University, Japan), Kei Takase, Kazumasa Seiji (Tohoku University Hospital, Japan) and Makoto Ohta (Tohoku University, Japan)	620

(13:30-14:40) **Poster Presentation**

AKEBONO (WEST)
September 21, 2012

Session 4 **Short Oral Presentation**
9:00-(9:45) 3 min for Short Oral Presentation without PC preparation

OS11-54	<p>Effect of Liquid Properties on Velocity Field over a High Speed Rotary Bell Cup Atomizer</p> <p><u>Tatsuya Soma</u>, Tomoyuki Katayama, Yasuhiro Saito, Hideyuki Aoki (Tohoku University, Japan), Toshiki Haneda, Yosuke Hatayama, Minori Shirota, Takao Inamura (Hirosaki University, Japan), Daichi Nakai, Genki Kitamura, Masanari Miura, Masatoshi Daikoku (Hachinohe Institute of Technology, Japan)</p>	622
OS11-55	<p>Numerical Analysis of Cryogenic Slush Flow in a Triangular Pipe (SLUSH-3D)</p> <p><u>Takumi Hosono</u>, Daisuke Naka and Katsuhide Ohira (Tohoku University, Japan)</p>	624
OS11-56	<p>Flow and Heat Transfer Characteristics of Cryogenic Solid-Liquid Slush Nitrogen in a Square Pipe</p> <p><u>Jun Okuyama</u>, Kei Nakagomi, Koichi Takahashi and Katsuhide Ohira (Tohoku University, Japan)</p>	626
OS11-57	<p>A Numerical Study of Cavitating Flows over a Hydrofoil</p> <p><u>Daichi Matsubara</u>, Mingyu Sun (Tohoku University, Japan)</p>	628
OS11-58	<p>The Numerical Analysis of Inverse Problems for Mass Transfer Model</p> <p><u>Olga V. Soboleva</u>, Ilya S. Vakhitov (Institute of Applied Mathematics FEB RAS, Russia)</p>	630
OS11-59	<p>Development of Safety and Quick-response Actuator using MR Fluid Clutch for Walk Rehabilitation Device</p> <p><u>Hiroshi Nakano</u>, Kohki Tsuchiya and Masami Nakano (Tohoku University, Japan)</p>	632
OS11-60	<p>Implementation of Surface Chemistry Models in SMILE++ Software System</p> <p><u>Alexandra Shumakova</u>, Alexander Kashkovsky, Mikhail Ivanov and Yevgeniy Bondar (Khristianovich Institute of Theoretical and Applied Mechanics, Russia)</p>	634
OS11-61	<p>Atomistic Simulation of Proton and Water Transport in Hydrated Nafion Membrane</p> <p><u>Takuya Mabuchi</u>, Takashi Tokumasu (Tohoku University, Japan)</p>	636
OS11-62	<p>A Study of the Effect of Surface Tension on Gas-Liquid Free Interface in the Application of Micromixing</p> <p><u>Takashi Yamada</u>, Naoki Ono (Shibaura Institute of Technology, Japan)</p>	638
OS11-63	<p>Numerical Study of the Effect of Cavitation Models on the Cavitating Flow Induced by Underwater Explosion in a Rectangular Tube</p> <p><u>Taketoshi Koita</u>, Mingyu Sun (Tohoku University, Japan)</p>	640
OS11-64	<p>Scalability Study of Water Treatment System with Multiple Plasmas in Gas-Bubbles</p> <p><u>Hayato Obo</u>, Nozomi Takeuchi and Koichi Yasuoka (Tokyo Institute of Technology, Japan)</p>	642

OS11-65	Effect of Injection Interval on Flow Characteristics of High Pressure Pulse Sprays <u>Ryuichi Sagawa</u> , Satoki Yokoi, Yoshinori Kojima, Yasuhiro Saito and Hideyuki Aoki (Tohoku University, Japan)	644
OS11-66	Study of Deep-Throttleable Rocket Injector <u>Mitsuhiro Soejima</u> (Tohoku University, Japan), Sadatake Tomioka (Japan Aerospace Exploration Agency, Japan) and Goro Masuya (Tohoku University, Japan)	646
(9:45-11:45)	Poster Presentation	
Session 5 13:00-(13:45)	Short Oral Presentation 3 min for Short Oral Presentation without PC preparation	
OS11-67	Development of Back Surface TSP Measurement Technique for Shock Interaction Aerodynamic Heating in High Enthalpy Flow <u>Kazuki Nishigata</u> , Hiroki Nagai and Keisuke Asai (Tohoku University, Japan)	648
OS11-68	Molecular Dynamics Study of Oxygen Permeation in the Ionomer on Pt Catalyst of PEFC <u>Yuta Sugaya</u> , Takashi Tokumasu (Tohoku University, Japan)	650
OS11-69	Experiment Verification of Acoustic Feedback Loop around NACA0012 Airfoil at Low Reynolds Number <u>Nobuaki Sakai</u> , Hiroki Nagai, Keisuke Asai (Tohoku University, Japan), Tomoaki Ikeda and Takashi Atohe (Japan Aerospace Exploration Agency, Japan)	652
OS11-70	Compressibility Effects on Aerodynamic Characteristics of Low Reynolds Number Airfoils <u>Tetsuya Suwa</u> , Daiju Numata, Hiroki Nagai and Keisuke Asai (Tohoku University, Japan)	654
OS11-71	Flow Analysis in Cerebral Aneurysm Model with Transparent Coils Placement <u>Masanori Kuze</u> , Makoto Ohta (Tohoku University, Japan)	656
OS11-72	Measurement of Pressure Drop for Modeling Intracranial Flow Diverter Stent Using Porous Medium <u>Yukihisa Miura</u> , Hitomi Anzai, Toshio Nakayama, Toshiyuki Hayase and Makoto Ohta (Tohoku University, Japan)	658
OS11-73	Assessment of Supersonic Free-flight Experiment using a Plate Shaped Sabot Aimed at the Biplane Model <u>Yuta Saito</u> (Tohoku University, Japan), Kakuei Suzuki (Nagoya University, Japan), Takahiro Ukai (Tohoku University, Japan), Takahiro Imaizumi, Atsushi Toyoda (Nagoya University, Japan), Takaya Uchida (Tohoku University, Japan), Akihiro Sasoh (Nagoya University, Japan) and Shigeru Obayashi (Tohoku University, Japan)	660

OS11-74	<p>A Study for Transport Phenomena of Nanoscale Gas Flow in Porous Media <u>Tomoya Oshima</u>, Shigeru Yonemura and Takashi Tokumasu (Tohoku University, Japan)</p>	662
OS11-75	<p>Characterization of Fluid Flow in Fractured Geothermal Reservoirs based on Fractional Derivative Mathematical Model <u>Hiroshi Makita</u>, Anna Suzuki, Yuichi Niibori and Toshiyuki Hashida (Tohoku University, Japan)</p>	664
OS11-76	<p>Development of Micro-satellite for International Scientific Missions <u>Yoshihiro Tomioka</u>, Kazufumi Fukuda, Nobuo Sugimura, Yuji Sakamoto, Toshinori Kuwahara and Kazuya Yoshida (Tohoku University, Japan)</p>	666
OS11-77	<p>Design and Hovering Control of an Asterisk Type Quad Rotor Tail-Sitter Unmanned Aerial Vehicle <u>Atsushi Oosedo</u> (Tohoku University, Japan), Atsushi Konno (Hokkaido University, Japan), Satoko Abiko and Masaru Uchiyama (Tohoku University, Japan)</p>	668
OS11-78	<p>Development and Evaluation of Autonomous Mobile Manipulator for Sensing Device Deployment <u>Takeshi Ohki</u>, Keiji Nagatani and Kazuya Yoshida (Tohoku University, Japan)</p>	670
OS11-79	<p>Robust Mobile Robot Design for Fukushima Nuclear Plant Exploration <u>Seiga Kiribayashi</u>, Keiji Nagatani (Tohoku University, Japan)</p>	672
OS11-80	<p>Hybrid Simulation of Capturing a Massive Payload by Space Manipulators <u>Ipppei Takahashi</u>, Satoko Abiko, Xin Jiang (Tohoku University, Japan), Atsushi Konno (Hokkaido University, Japan) and Masaru Uchiyama (Tohoku University, Japan)</p>	674
(13:45-15:45)	Poster Presentation	

PS1: IFS Collaborative Research Forum (AFI/TFI-2012)

SENDAI (WEST)

September 20, 2012

Chair: Kenichi Funamoto (Tohoku University, Japan)

9:00-10:30

Short Oral Presentation

(3 min for Short Oral Presentation)

- CRF-1 **Aerodynamic Performance of an Airfoil with VGJs for Lift Augmentation**
Tetsuya Miyakoshi, Hiroaki Hasegawa, Syuko Ito (Akita University, Japan) and Shigeru Obayashi (Tohoku University, Japan)
- CRF-2 **High Aerodynamic Drag and Flow Behavior of a Badminton Shuttlecock with Spin at High Reynolds Numbers**
Kenichi Nakagawa, Hiroaki Hasegawa (Akita University, Japan), Masahide Murakami (Tsukuba University, Japan) and Shigeru Obayashi (Tohoku University, Japan)
- CRF-3 **Stepped Pressure Rise of Tail Boom with Staged Aft-Body**
Kakuei Suzuki, Takahiro Imaizumi, Atsushi Toyoda and Akihiro Sasoh (Nagoya University, Japan)
- CRF-4 **Study for Development of Flapping Wing Vehicle based on Multidisciplinary Analysis**
Shun Takahashi, Mizuki Yamate, Takeshi Sumita, Yoshihiro Tajika and Norio Arai (Tokyo University of Agriculture and Technology, Japan)
- CRF-5 **Design and Data Mining for Hull Form**
Shinkyu Jeong (Tohoku University, Japan) and Hyunyul Kim (George Mason University, USA)
- CRF-6 **Implementation of Adaptive Wavelet Method for the Efficient Design of Helicopter Rotors**
Sanghyun Chae (Pusan National University, Korea), Shinkyu Jeong (Tohoku University, Japan) and Kwanjung Yee (Pusan National University, Korea)
- CRF-7 **Flow Instabilities of Boiling Nitrogen in a Horizontal Pipe**
Ren Sakata, Katsuhide Ohira, Kazushi Miyata, Koichi Takahashi (Tohoku University, Japan), Hiroaki Kobayashi, Hideyuki Taguchi, Motoyuki Hongoh and Takayuki Kojima (Japan Aerospace Exploration Agency, Japan)
- CRF-8 **Shock Induced Temperature Measurement Using Laser-Induced Thermal Acoustics**
Toshiharu Mizukaki (Tokai University, Japan) and Shigeru Obayashi (Tohoku University, Japan)
- CRF-9 **Numerical Studies of Rarefied Chemically Reacting Flows about Space Vehicles**
Alexander Shevyrin, Mikhail Ivanov, Yevgeniy Bondar (ITAM SB RAS, Russia) and Shigeru Yonemura (Tohoku University, Japan)

- CRF-10 **Mechanism of Thermal Effects in Micro-Bubble Cavitation**
Yuka Iga (Tohoku University, Japan) and Kazuki Niiyama (Kanazawa Institute of Technology, Japan)
- CRF-11 **Development of a Compact Three-Component Force Balance and Its Application**
Hiroshi Suemura, Kouhei Takishita, Gouji Yamada, Takashi Matsuno (Tottori University, Japan), Shigeru Obayashi (Tohoku University, Japan) and Hiromitsu Kawazoe (Tottori University, Japan)
- CRF-12 **Shock Tube Study for Electron Behavior in the Shock Layer**
Shota Ago, Gouji Yamada, Yuto Kubo, Takashi Matsuno, Hiromitsu Kawazoe (Tottori University, Japan) and Shigeru Obayashi (Tohoku University, Japan)
- CRF-13 **Formation of Cellular Fronts in High-Temperature Premixed Flames**
Satoshi Kadowaki (Nagaoka University of Technology, Japan) and Hideaki Kobayashi (Tohoku University, Japan)
- CRF-14 **Numerical Investigations on the Influence of Rear Spoiler of Road Vehicle on Wake Structure**
Chenguang Lai, Yuting Zhou, Limin Fu (Chongqing University of Technology, China) and Shigeru Obayashi (Tohoku University, Japan)
- CRF-15 **Numerical Prediction of Cavitation Erosion Using a Coupled Analysis of Cavitating Flow Field and Bubbles**
Naoya Ochiai, Yuka Iga (Tohoku University, Japan), Motohiko Nohmi (EBARA Corporation, Japan), Toshiaki Ikohagi (The Open University, Japan), Jun Ishimoto (Tohoku University, Japan) and Kozo Saito (IR4TD, University of Kentucky, USA)
- CRF-16 **Super Computational Study of High-Speed Droplet-Vapor Flow and LDI Erosion**
Jun Ishimoto (Tohoku University, Japan), Guanghao Wu (SoftFlow Co., Ltd., Japan) and Kazuo Matsuura (Ehime University, Japan)
- CRF-17 **Parallel Computations on the Base of GPU for Modeling of Gas Combustion Processes**
Roman Fursenko, Evgeniy Sereshchenko, Sergey Minaev (ITAM SB RAS / FEFU, Russia), Kaoru Maruta and Hisashi Nakamura (Tohoku University, Japan)
- CRF-18 **Investigations of Sporadic Regimes of Gas Combustion**
Sergey Minaev (ITAM SB RAS, Russia), Evgeniy Sereshchenko (Far Eastern Federal University, Russia), Dmitrii Mazurok, Roman Fursenko (ITAM SB RAS, Russia), Hisashi Nakamura, Koichi Takase, Xing Li, Takuya Tezuka and Kaoru Maruta (Tohoku University, Japan)
- CRF-19 **Visualization, "Real Time" Algorithms and Parallel Computations of Reacting Flows**
Boris Mazurok (IAE SB RAS, Russia), Dmitrii Mazurok (ITAM SB RAS, Russia), Boris Dolgovesov (IAE SB RAS, Russia), Roman Fursenko, Sergey Minaev (ITAM SB RAS / FEFU, Russia), Hisashi Nakamura and Kaoru Maruta (Tohoku University, Japan)

- CRF-20 **Development of the Heat Transfer Surface with Micro-Pits to Enhance the Critical Heat Flux in Nucleate Boiling**
Kazushi Miyata, Katsuhide Ohira (Tohoku University, Japan) and Hideo Mori (Kyushu University, Japan)
- CRF-21 **Measurement of Radiative Properties of Controlled-Films**
Hiroki Gonome (Tohoku University, Japan), Mehdi Baneshi (Shiraz University, Iran), Rodolphe Vaillon (Université de Lyon, CNRS, INSA-Lyon, France), Adil Al Mahdouri, Junnosuke Okajima, Atsuki Komiya and Shigenao Maruyama (Tohoku University, Japan)
- CRF-22 **Experimentally and Numerically Investigations for Light and Heat Transport inside Biological Tissues**
Atsushi Sakurai (Niigata University, Japan), Yoshiyuki Sato, Junnosuke Okajima, Atsuki Komiya and Shigenao Maruyama (Tohoku University, Japan)
- CRF-23 **Dynamic Behavior of Flame Front Instability in Two-Dimensional Radial Microchannels**
Satoshi Onodera, Yuta Shinoda, Shinya Fujita, Hiroshi Gotoda (Ritsumeikan University, Japan), Sergey Minaev (ITAM SB RAS, Russia) and Kaoru Maruta (Tohoku University, Japan)
- CRF-24 **Investigation of Subsonic-Supersonic Hybrid-Stabilized Argon-Water Electric Arc With Inhomogeneous Mixing of Plasma Species: Role of Turbulence and Radiative Transfer Method**
Jiří Jeništa (Institute of Plasma Physics, Czech Republic), Hidemasa Takana, Hideya Nishiyama (Tohoku University, Japan), Milan Hrabovský and Tetyana Kavka (Institute of Plasma Physics, Czech Republic)
- CRF-25 **Instability of Rayleigh-Bénard Convection: Comparison between Experimental and Numerical Approaches**
Juan F. Torres (Tohoku University, Japan / École Centrale de Lyon, France), Daniel Henry (École Centrale de Lyon, France), Atsuki Komiya, Junnosuke Okajima and Shigenao Maruyama (Tohoku University, Japan)
- CRF-26 **Evaluation and Analysis of Atmospheric Radiative Energy Transfer**
Noboru Yamada (Nagaoka University of Technology, Japan), Junnosuke Okajima (Tohoku University, Japan), Atsushi Sakurai (Niigata University, Japan), Atsuki Komiya and Shigenao Maruyama (Tohoku University, Japan)
- CRF-27 **Simulation Analysis on Grain Boundaries Thought Relation between Cr Depletion Distribution and Local Magnetic Properties**
Kenji Suzuki, Katsuhiko Yamaguchi (Fukushima University, Japan), Tetsuya Uchimoto and Toshiyuki Takagi (Tohoku University, Japan)
- 10:30-10:40 BREAK

Chair: Kazushi Miyata (Tohoku University, Japan)

10:40-12:10

Short Oral Presentation

(3 min for Short Oral Presentation)

- CRF-28 **Development of Observation Method for Plasma-Generated Bubbles**
Takehiko Sato (Tohoku University, Japan), Takashi Miyahara (Shizuoka University, Japan) and Tatsuyuki Nakatani (Toyo Advanced Technologies Co., Ltd., Japan)
- CRF-29 **Studies on Non-Equilibrium Feature of Radio-Frequency Helium Plasma Flow at Atmospheric-Pressure**
Hidemasa Takana, Hideya Nishiyama (Tohoku University, Japan), Zhi-Bin Wang, Pei-Si Le, He-Ping Li and Cheng-Yu Bao (Tsinghua University, China)
- CRF-30 **Perspectives for the Next Generation Sensors for Super-High Temperature Environment and Their Industrial Applications**
Toshiyuki Takagi (Tohoku University, Japan), Kazuo Shoji (Intelligent Cosmos Research Institute, Japan), Tetsuya Uchimoto, Hiroyuki Miki (Tohoku University, Japan) and the executive board
- CRF-31 **Optimization of a Heavily Aluminized Energetic Material**
Fumiya Togashi (SAIC, USA), Shinkyu Jeong (Tohoku University, Japan) and Rainald Lohner (George Mason University, USA)
- CRF-32 **Comparison of Inversion Methods for Reconstructon of Defect from Pulsed Eddy Current Testing Signals**
Zhenmao Chen (Xi'an Jiaotong University, China), Shejuan Xie (Tohoku University, Japan), Xiaowei Wang, Yong Li (Xi'an Jiaotong University, China), Tetsuya Uchimoto and Toshiyuki Takagi (Tohoku University, Japan)
- CRF-33 **Ultrasound Radiation Force Driven B-Flow Twinkling Sign for Microcalcification Detection**
Lei Liu (GE Healthcare Japan Corporation, Japan), Kenichi Funamoto, Kei Ozawa, Makoto Ohta, Toshiyuki Hayase (Tohoku University, Japan) and Masafumi Ogasawara (GE Healthcare Japan Corporation, Japan)
- CRF-34 **Computational Simulation to Create Low Oxygen Tension in a Microfluidic Device for Cell Culture**
Kenichi Funamoto (Tohoku University, Japan), Ioannis K. Zervantonakis (Massachusetts Institute of Technology, USA), Yuchun Liu (National University of Singapore, Singapore), Christopher J. Ochs (SMART BioSystems & Micromechanics, Singapore) and Roger D. Kamm (Massachusetts Institute of Technology, USA / SMART BioSystems & Micromechanics, Singapore)
- CRF-35 **Study on the Biological Actuation with the Magnetic Stimulation**
Hitoshi Mori (IFG Co.,Ltd., Japan), Toshiyuki Takagi, Shinichi Izumi, Hiroyasu Kanetaka, Eizaburo Suzuki (Tohoku University, Japan), Kazumi Mori, Risa Sasaki and Toshihiko Abe (IFG Co.,Ltd., Japan)
- CRF-36 **Inactivation of MDCK Cell Viability by Exposure to Plasma-Treated Medium**
Yuji Kudo, Michiko Okamoto, Takehiko Sato, Daisuke Yoshino, Akira Suzuki and Hitoshi Oshitani (Tohoku University, Japan)

- CRF-37 **Anti-Bacterial Effect of a Plasma Irradiation against Biofilm-Producing Pseudomonas Aeruginosa and Acinetobacter Baumanni**
Yoshihisa Nakano, Sigeru Fujimura and Takehiko Sato (Tohoku University, Japan)
- CRF-38 **Formation of Thermal Flow Field in Shallow Water Cell by Plasma Flow**
Naoya Kishimoto (Tohoku University, Japan), Tetsuji Shimizu, Gregor E Morfill (Max Planck Institute for Extraterrestrial Physics, Germany) and Takehiko Sato (Tohoku University, Japan)
- CRF-39 **Characterization of Design of Stent Strut Positioning Using LBM Method**
Makoto Ohta (Tohoku University, Japan), Bastien Chopard (Geneva University, Switzerland) and Hitomi Anzai (Tohoku University, Japan)
- CRF-40 **Channel Properties of Membrane Proteins on Lipid Bilayers**
Makoto Ohta (Tohoku University, Japan), Liviu Movileanu (Syracuse University, USA) and Noriko Tomita (Tohoku University, Japan)
- CRF-41 **Tribology of Medical Materials on PVA-H Biomodel**
Hiroyuki Kosukegawa (École Centrale de Lyon, France), Makoto Ohta (Tohoku University, Japan), Vincent Fridrici and Philippe Kapsa (École Centrale de Lyon, France)
- CRF-42 **Possibility of Emission Energy Control of Individual Quantum Dots Using Volume Expansion of Phase Change Material**
Nurrul Syafawati Binti Humam, Motoki Takahashi, Nobuhiro Tsumori and Toshiharu Saiki (Keio University, Japan)
- CRF-43 **Management of Light by Si/SiO₂ Stack Photonic Band Gap Structure for Neutral Beam Technology based Tandem Solar Cell**
Jingnan Cai (The University of Tokyo, Japan), Seiji Samukawa (Tohoku University, Japan) and Kazumi Wada (The University of Tokyo, Japan)
- CRF-44 **Development and Micro-Channel Flow Evaluation of Electro-Rheological Nano-Suspensions**
Katsufumi Tanaka, Takanobu Hira, Ryuichi Fukui, Haruki Kobayashi, Ryuichi Akiyama (Kyoto Institute of Technology, Japan), Masami Nakano and Shouta Enami (Tohoku University, Japan)
- CRF-45 **A Study of the Next Generation CMOS by the Neutral Beam Process**
Kazuhiko Endo (AIST, Japan), Akira Wada and Seiji Samukawa (Tohoku University, Japan)
- CRF-46 **Intelligent Information Processing Circuits Using Nanodisk Array Structure**
Takashi Morie, Haichao Liang, Takashi Tohara (Kyushu Institute of Technology, Japan), Kazuhiko Endo (National Institute of Advanced Industrial Science and Technology, Japan), Makoto Igarashi and Seiji Samukawa (Tohoku University, Japan)
- CRF-47 **Thermomechanical Nano Device Resist Removal-Cleaning Technology by Using Cryogenic Spray Flow of Solid Nitrogen**
U Oh, Jun Ishimoto (Tohoku University, Japan) and Jin-Goo Park (Hanyang University, Korea)

- CRF-48 **Rheological Analysis of the Mechanism of Fetal Brain Hemorrhage**
Takuya Ito, Kenichi Funamoto, Kiyoe Funamoto, Toshiyuki Hayase and Yoshitaka Kimura (Tohoku University, Japan)
- CRF-49 **Magnetic Resonance Fluid Dynamics for Intracranial Aneurysms**
Shin-ichiro Sugiyama (Kohnan Hospital, Japan), Kenichi Funamoto, Toshiyuki Hayase and Teiji Tominaga (Tohoku University, Japan)
- CRF-50 **Oscillatory and Stagnant Flow in Intracranial Aneurysms : A Possible Association with Atherosclerosis**
Shin-ichiro Sugiyama, Hiroaki Shimizu (Kohnan Hospital, Japan), Toshio Nakayama, Makoto Ohta and Teiji Tominaga (Tohoku University, Japan)
- CRF-51 **Observation of Hypoxia Cellular Response by Using Microfluidic Devices**
Shuichiro Fukushima, Reiko Maehara (Osaka University, Japan) and Kenichi Funamoto (Tohoku University, Japan)
- CRF-52 **Propagation of Shock Wave within Complex Biomaterial Layer: Implications for the Mechanism Blast-Induced Traumatic Brain Injury**
Atsuhiko Nakagawa, Kiyonobu Ohtani (Tohoku University, Japan), Keisuke Goda (University of California, Los Angeles, USA), Tatsuhiko Arafune (Tokyo University, Japan), Toshikatsu Washio (National Institute of Advanced Industrial and Science Technology, Japan), Toshiyuki Hayase and Teiji Tominaga (Tohoku University, Japan)
- CRF-B1 **Integrated Research Collaboration for Frontier Science of Next Generation Reactive Fluid**
Jun Ishimoto, Kaoru Maruta and Takehiko Sato (Tohoku University, Japan)
- 12:10-13:10 **Lunch and Poster Session**
- Chair: Yuriko Takeshima (Tohoku University, Japan)
- 13:10-14:40 **Short Oral Presentation**
(3 min for Short Oral Presentation)
- CRF-53 **High-Frequency Characteristics of Si Single-Electron Transistor**
Hiroto Takenaka, Michito Shinohara, Takafumi Uchida, Masashi Arita (Hokkaido University, Japan), Seiji Samukawa (Tohoku University, Japan) and Yasuo Takahashi (Hokkaido University, Japan)
- CRF-54 **Development of High Performance Strained-Ge Channel Device Utilizing Neutral-Beam Oxidized Film**
Kentarou Sawano, Masato Watanabe, Arata Komatsu, Hiroshi Nohira (Tokyo City University, Japan), Akira Wada and Seiji Samukawa (Tohoku University, Japan)
- CRF-55 **Numerical Study of Shock Wave Entering and Propagation in Microchannel**
Georgy Shoen, Yevgeniy Bondar (ITAM SB RAS, Russia), Kaoru Maruta (Tohoku University, Japan) and Mikhail Ivanov (ITAM SB RAS, Russia)

- CRF-56 **Towards Development of Micromotors Based on Electrorotation of Smart Polymers**
Miklós Zrínyi (Semmelweis University, Hungary) and Masami Nakano (Tohoku University, Japan)
- CRF-57 **Thermal Resistance between Nano-Structured Surfaces and Liquids**
Masahiko Shibahara (Osaka University, Japan), Taku Ohara and Gota Kikugawa (Tohoku University, Japan)
- CRF-58 **Fabrication of Ti/Al Composite Material by Compression Shearing Method at Room Temperature**
Syou Takeda, Noboru Nakayama, Masaomi Horita, Shintaro Abe (Shinshu University, Japan), Hiroyuki Miki (Tohoku University, Japan) and Hiroyuku Takeishi (Chiba Institute of Technology, Japan)
- CRF-59 **Study of Contact Alignment for the Slider Specimen of Tribometer.**
Minoru Goto (Ube National College of Technology, Japan), Kosuke Ito (Nihon University, Japan), Hiroyuki Miki, Takanori Takeno and Toshiyuki Takagi (Tohoku University, Japan)
- CRF-60 **Effect of Cavitation Generation on Dissolved Oxygen Concentration in the Cavitation Tunnel Downstream**
Naoya Kishimoto, Takehiko Sato (Tohoku University, Japan), Marc Tinguely, Matthieu Dreyer and Mohamed Farhat (École Polytechnique Fédérale de Lausanne, Switzerland)
- CRF-61 **Development of Visualization Methods of Streamers in Water**
Hidemasa Fujita (Tohoku University, Japan), Seiji Kanazawa (Oita University, Japan), Kiyonobu Ohtani, Atsuki Komiya and Takehiko Sato (Tohoku University, Japan)
- CRF-62 **A Molecular Dynamics Study on the Density Fluctuation of Diatomic Fluid around the Critical Point**
Masato Tomi, Nobuyuki Tsuboi (Kyushu Institute of Technology, Japan), Shin-ichi Tsuda (Shinshu University, Japan), Hiroki Nagashima and Takashi Tokumasu (Tohoku University, Japan)
- CRF-63 **Construction of Interaction Models of Dissipative Particle Dynamics by Coarse-Graining Lennard-Jones Fluids**
Yuta Yoshimoto, Toshiki Mima (The University of Tokyo, Japan), Akinori Fukushima (Tohoku University, Japan), Ikuya Kinefuchi (The University of Tokyo, Japan), Takashi Tokumasu (Tohoku University, Japan), Shu Takagi and Yoichiro Matsumoto (The University of Tokyo, Japan)
- CRF-64 **Nano-Scale Modeling of Confined Liquid Films and Bridges**
Takashi Tokumasu (Tohoku University, Japan), Marie-Hélène Meurisse, Nicolas Fillot and Philippe Vergne (Université de Lyon, CNRS, INSA-Lyon, France)
- CRF-65 **Dynamics of Micro Magnetic Fluid Hole in an Alternating Field**
Michihiro Shinozaki, Seiichi Sudo (Akita Prefectural University, Japan), Hidemasa Takana and Hideya Nishiyama (Tohoku University, Japan)

- CRF-66 **Rheology of Magnetorheological Shear Thickening Fluid**
Weihua Li (University of Wollongong, Australia) and Masami Nakano (Tohoku University, Japan)
- CRF-67 **A Numerical Study of the Effect of Large Deformations of a Trailing Vortex on Its Breakdown**
Naoya Takahashi (Tokyo Denki University, Japan), Takeshi Miyazaki (University of Electro-Communications, Japan), Nozomu Hatakeyama and Yuji Hattori (Tohoku University, Japan)
- CRF-68 **Effects of External Disturbances on Spatially Developing Turbulence and Its Application to Control of Thermo-Fluid Dynamics**
Yasuhiko Sakai, Kouji Nagata (Nagoya University, Japan), Toshiyuki Hayase (Tohoku University, Japan), Osamu Terashima, Nannan Wu, Shuang Xia, Tomoaki Watanabe, Takuya Kitamura, Kosuke Hiruta, Hiroki Saito, Takeharu Sakai, Akihiro Sasoh and Yasumasa Ito (Nagoya University, Japan)
- CRF-69 **Generation Mechanism of Rising Film Flow along the Rotating Conical Outer Surface and the Subsequent Atomization Characteristics**
Keisuke Matsuda, Takahiro Adachi, Yusuke Ryu (Akita University, Japan), Junnosuke Okajima (Tohoku University, Japan) and Takeshi Akinaga (Aston University, UK)
- CRF-70 **Improvement of Reality of CG Motion Pictures by Hydrodynamic Effects: Effects of Turbulence**
Takashi Ishihara (Nagoya University, Japan) and Yuji Hattori (Tohoku University, Japan)
- CRF-71 **Quantitative Visualization of Flow Field around High-Speed Projectiles by Using Background-Oriented Schlieren**
Toshiharu Mizukaki (Tokai University, Japan), Kiyonobu Ohtani and Shigeru Obayashi (Tohoku University, Japan)
- CRF-72 **Researches on the Suppression Control of Hole-Tone Phenomena**
Kazuo Matsuura (Ehime University, Japan) and Masami Nakano (Tohoku University, Japan)
- CRF-73 **Contour Dynamics of Vortex Rings with Swirl and Magnetic Field**
Yuji Hattori (Tohoku University, Japan) and Stefan G. Llewellyn Smith (UCSD, USA)
- CRF-74 **Modal Stability Analysis of a Helical Vortex Tube with Axial Flow**
Yuji Hattori (Tohoku University, Japan) and Yasuhide Fukumoto (Kyushu University, Japan)
- CRF-75 **Magnetic Field Induced Entropy Change in Ni-Mn(Cu)-Ga Heusler Alloys**
Vladimir Khovaylo (National University of Science and Technology "MISiS", Russia), Konstantin Skokov (Tver State University, Russia), Ekaterina Avilova (National University of Science and Technology "MISiS", Russia), Vladimir Sokolovskiy, Vasiliy Buchelnikov, Sergey Taskaev (Chelyabinsk State University, Russia), Hiroyuki Miki and Toshiyuki Takagi (Tohoku University, Japan)

CRF-76 **Two-Particle and One-Particle Kinetic Equations in Landau-Fokker-Planck like Form**
Vladimir Saveliev (National Center of Space Researches and Technologies, Kazakhstan) and Shigeru Yonemura (Tohoku University, Japan)

CRF-77 **Development of Numerical Solver to Calculate Eddy Current Testing Signals for Anisotropic Laminated Epoxy-Carbon Fibre Composite**
Jun Cheng, Jinhao Qiu (Nanjing University of Aeronautics and Astronautics, China), Toshiyuki Takagi, Tetsuya Uchimoto (Tohoku University, Japan) and Ning Hu (Chiba University, Japan)

CRF-78 **Development of a Field Effect Transistor with Channel Surface Covered by Probe-Biomolecules with a Newly Developed Aptamer**
Ichiro Yamashita (NAIST, Japan) and Seiji Samukawa (Tohoku University, Japan)

CRF-79 **Metal-Containing DLC: Toward a Smart Coating**
Hiroyuki Miki, Toshiyuki Takagi, Takanori Takeno, Koshi Adachi (Tohoku University, Japan), Julien Fontaine, Michel Belin, Sandrine Bec and Thierry Le Mogne (École Centrale de Lyon, France)

14:40-14:50 BREAK

The 1st Young Researcher Overseas Visits Program Research Forum

Chair: Hidemasa Takana (Tohoku University, Japan)

14:50-15:05 **Moving on to the Small World: Microfluidic Cell Culture**
Kenichi Funamoto (Tohoku University, Japan)

15:05-15:20 **Chemical Kinetics of Biofuels and Its Experimental Validation - Collaboration between Quantum Chemistry and Combustion Engineering -**
Hisashi Nakamura (Tohoku University, Japan)

15:20-15:35 **Nondestructive Evaluation of Material Degradation and Damage in Power Plants**
Tetsuya Uchimoto (Tohoku University, Japan)

15:35-16:20 **Poster Session**

16:20-16:30 BREAK

Fluids Science Research Award Lecture

Chair: Toshiyuki Hayase (Tohoku University, Japan)

16:30-17:10 **Developing Advanced Thermal Plasma Processes of Coatings Spraying and Hollow Powders Production**
Oleg Solonenko (ITAM SB RAS, Russia)

17:10-17:50 **Aeronautical CFD: Past, Present and Future**
Kazuhiro Nakahashi (Japan Aerospace Exploration Agency, Japan)

PS2: Transdisciplinary Fluid Integration (AFI/TFI-2012)

HAGI

September 19, 2012

Chair: Shigeru Obayashi (Tohoku University, Japan)

14:40-14:50

Opening

Shigeru Obayashi (Tohoku University, Japan)

TFI-1

14:50-15:10

Activity Report of Integrated Fluid Informatics Laboratory

Shigeru Obayashi, Shinkyu Jeong, Koji Shimoyama, Kiyonobu Ohtani and Takashi Misaka (Tohoku University, Japan)

TFI-2

15:10-15:30

Collaborative Visualization for Integrated Visual Informatics

Yuriko Takeshima, Shigeru Obayashi (Tohoku University, Japan) and Issei Fujishiro (Keio University, Japan)

TFI-3

15:30-15:50

Numerical Simulation of Gas-Liquid Flows with Subgrid-Scale Interface Structures

Mingyu Sun (Tohoku University, Japan)

TFI-4

15:50-16:10

Measurement-Integrated Simulation for Biomedical Applications

Toshiyuki Hayase, Atsushi Shirai and Kenichi Funamoto (Tohoku University, Japan)

16:10-16:20

BREAK

TFI-5

16:20-16:40

Feature Profile Evolution in Plasma Processing Using Wireless On-Wafer Monitoring System

Seiji Samukawa and Tomohiro Kubota (Tohoku University, Japan)

TFI-6

16:40-17:00

Activity Report of Energy Dynamics Laboratory, IFS, Tohoku University

Kaoru Maruta (Tohoku University, Japan)

TFI-7

17:00-17:20

Innovative Development of Frontier Multiphase Flow Systems by Reality Coupled Computation

Jun Ishimoto (Tohoku University, Japan)

PS3: Functional Plasma Flow Dynamics and its Innovative Applications

HAGI

September 20, 2012

- 9:00-9:10 **Opening**
Hideya Nishiyama (Tohoku University, Japan)
- Session 1: Plasma Flow Control
Chair: Hideya Nishiyama (Tohoku University, Japan)
- PS3-1 **Nanosecond Pulse Surface Discharges for High-Speed Flow Control: Experiments and Modeling (*Invited*)** 682
9:10-9:40
Igor V. Adamovich, Jesse Little, Munetake Nishihara, Keisuke Takashima and Mo Samimy (The Ohio State University, USA)
- PS3-2 **High-Temperature Inert-Gas Plasma Magnetohydrodynamic Electrical Power Generation** 684
9:40-10:00
Tomoyuki Murakami, Yoshihiro Okuno (Tokyo Institute of Technology, Japan)
- PS3-3 **Numerical Investigation of DC Plasma Jet Effect on Thermofluid Field in a DC-RF Hybrid Plasma Torch by Three-Dimensional Simulation** 686
10:00-10:20
Masaya Shigeta (Tohoku University, Japan)
- Session 2: Thermal Plasma Flow, Material Process
Chair: Manabu Tanaka (Tokyo Institute of Technology, Japan)
- PS3-4 **Optimization of Combined Technology "Plasma Spraying - Pulsed Electron-Beam Post-Irradiation" of Cermet Wear-Resistant Coatings by Numerical Simulation (*Invited*)** 688
10:40-11:10
Oleg P. Solonenko, Vladimir I. Iordan, Vitaly A. Blednov and Alexey A. Golovin (Khristianovich Institute of Theoretical and Applied Mechanics SB RAS, Russia)
- PS3-5 **Titanium Oxide Film Deposition by TPCVD using Vortex Ar Plasma Jet** 690
11:10-11:30
Yasutaka Ando, Sheng Yuan Chen and Yoshimasa Noda (Ashikaga Institute of Technology, Japan)
- PS3-6 **Anode Jet Characteristics of Argon-Hydrogen Arc for Nanoparticle Production** 692
11:30-11:50
Takayuki Watanabe, Manabu Tanaka, Tasuku Shimizu and Feng Linag (Tokyo Institute of Technology, Japan)
- PS3-7 **Innovative Applications of Modulated Induction Thermal Plasma Flow for Materials Processings** 694
11:50-12:10
Yasunori Tanaka (Kanazawa University, Japan)
- Session 3: Arc
Chair: Yasunori Tanaka (Kanazawa University, Japan)
- PS3-8 **Mass and Energy Balances of Organic Waste Gasification in Steam Plasma (*Invited*)** 696
13:40-14:10
Milan Hrabovsky, M. Hlina, M. Konrad, V. Kopecky, O. Chumak, T. Kavka and A. Maslani (Institute of Plasma Physics ASCR, Czech Republic)

PS3-9 14:10-14:30	The Influence of Turbulence on Characteristics of a Hybrid-Stabilized Argon-Water Electric Arc <u>Jiří Jeništa</u> (Institute of Plasma Physics AS CR, Czech Republic), Hidemasa Takana, Hideya Nishiyama (Tohoku University, Japan), Milada Bartlová, Vladimír Aubrecht (Brno University of Technology, Czech Republic) and Petr Křenek (Institute of Plasma Physics AS CR, Czech Republic)	698
Session 4: Arc, Welding		
Chair: He-Ping Li (Tsinghua University, China)		
PS3-10 14:50-15:10	Numerical Modeling of Fume Formation Process in Welding <u>Shinichi Tashiro</u> , Sho Matsui and Manabu Tanaka (Osaka University, Japan)	700
PS3-11 15:10-15:30	Visualizations and Predictions of Gas Metal Arcs during Welding <u>Yoshihiro Tsujimura</u> , Manabu Tanaka (Osaka University, Japan)	702
PS3-12 15:30-15:50	Electrode Temperature Estimation of Multi-Phase AC Arc by High-Speed Video Camera <u>Manabu Tanaka</u> , Tomoki Ikeba, Yaping Liu, Sooseok Choi and Takayuki Watanabe (Tokyo Institute of Technology, Japan)	704
Session 5: Reactive Flow, Environmental Process		
Chair: Hidemasa Takana (Tohoku University, Japan)		
PS3-13 16:30-16:50	Hybrid Simulation of Gas Flow and Gas Discharge of Atmospheric-Pressure Plasma Jet with Helium Considering Impurity Effect Kun-Mou Lin, <u>Meng-Hua Hu</u> , Chieh-Tsan Hung, Jong-Shinn Wu (National Chiao Tung University, Taiwan), Feng-Nan Hwang (National Central University, Taiwan), Gary Cheng (University of Alabama, USA) and Yen-Sen Chen (National Space Organization, Taiwan)	706
PS3-14 16:50-17:10	Degradation of Organic Compounds Using a Two-Dimensional Capillary Discharge Array in Water Qiu-Yue Nie, Jian-Yu Chen, <u>He-Ping Li</u> , Zhi-Bin Wang, Wei Xing and Cheng-Yu Bao (Tsinghua University, China)	708
PS3-15 17:10-17:30	Decomposition Processes of Perfluoro Compounds Using Plasma inside Bubbles Related to Surfactant Behavior <u>Nozomi Takeuchi</u> , Akihiro Kosugi, Yuriko Matsuya and Koichi Yasuoka (Tokyo Institute of Technology, Japan)	710
PS3-16 17:30-17:50	Streamer Dynamics for Radical Generation in Air/methane Mixture under High Temperature and High Pressure <u>Hidemasa Takana</u> , Hideya Nishiyama (Tohoku University, Japan)	712
17:50-17:55	Closing Hideya Nishiyama (Tohoku University, Japan)	

PS4: Advanced Physical Stimuli and Biological Responses of Cells

FUJI

September 19, 2012

- 13:00-13:05 **Opening**
 Takehiko Sato (Tohoku University, Japan)
- Chair: Takehiko Sato (Tohoku University, Japan)
- PS4-1 **The Increment of Cell Activity by Plasma Treatment (*Plenary Talk*)** 716
13:05-13:45 Jeong-Hae Choi, Sang-Rye Park, Sung-Kil Kang, Seoul-Hee Nam, Jae-Koo Lee, Jin-Woo Hong, Jae-Koo Lee and Gyoo-Cheon Kim (Pusan National University, Korea)
- Chair: Toshiro Ohashi (Hokkaido University, Japan)
- PS4-2 **The Biomechanics and Mechanobiology of Primary Cilia (*Plenary Talk*)** 718
13:45-14:30 Mathew Downs, Kristen Lee, David Hoey, Sara Temiyasathit and Christopher Jacobs (Columbia University, USA)
- 14:30-14:40 BREAK
- Chair: Takehiko Sato (Tohoku University, Japan)
- PS4-3 **Cold Atmospheric Plasma for Skin Treatment (*Invited*)** 720
14:40-15:10 Tetsuji Shimizu (Max-Planck Institute for extraterrestrial physics, Germany), Georg Isbary (Hospital Munich Schwabing, Germany), Julia L. Zimmermann (Max-Planck Institute for extraterrestrial physics, Germany), Wilhelm Stolz (Hospital Munich Schwabing, Germany) and Gregor E. Morfill (Max-Planck Institute for extraterrestrial physics, Germany)
- PS4-4 **Response of Mammalian Cells to Intense Pulsed Electric Fields (*Invited*)** 722
15:10-15:40 Sunao Katsuki, Misako Yano, Kazunori Mitsutake, Keisuke Abe and Hidenori Akiyama (Kumamoto University, Japan)
- PS4-5 **Oxygen Tension Control in a Microfluidic Device for Cell Culture (*Invited*)** 724
15:40-16:10 Kenichi Funamoto (Tohoku University, Japan), Ioannis K. Zervantonakis (Massachusetts Institute of Technology, USA), Yuchun Liu (National University of Singapore, Singapore) and Roger D. Kamm (Massachusetts Institute of Technology, USA)
- 16:10-16:20 BREAK
- Chair: Toshiro Ohashi (Hokkaido University, Japan)
- PS4-6 **Stimuli Responsible Biointerfaces for Biological Responses of Human Cells (*Invited*)** 726
16:20-16:50 Masaru Tanaka, Kazuhiro Sato (Yamagata University, Japan)
- PS4-7 **Mechanical Stimulation Induces Movement of Protein Kinase C in Vascular Endothelial Cells (*Invited*)** 728
16:50-17:20 Susumu Kudo (Kyushu University, Japan), Tomoya Shimada, Marie Terada and Keita Hamasaki (Shibaura Institute of Technology, Japan)

PS4-8 **Vascular Cell Responses to Biomechanical Forces (*Invited*)** 730
17:20-17:50 Kimiko Yamamoto (The University of Tokyo, Japan), Joji Ando (Dokkyo
Medical University, Japan)

FUJI

September 20, 2012

Chair: Tetsuji Shimizu (Max-Planck Institute for extraterrestrial physics, Germany)
PS4-9 **Role of Fluid Mechanics in Collective Motions of Bacteria (*Invited*)** 732
9:00-9:30 Takuji Ishikawa, Naoto Yoshida, Hironori Ueno, Matthias Wiedeman, Yohsuke
Imai and Takami Yamaguchi (Tohoku University, Japan)

PS4-10 **Microscopic Analysis of Bacterial Motility at High Pressure (*Invited*)** 734
9:30-10:00 Masayoshi Nishiyama (Kyoto University, Japan)

PS4-11 **Inactivation Mechanism of Fungal Spores by Atmospheric Pressure Plasma (*Invited*)** 736
10:00-10:30 Takayuki Ohta, Hiroshi Hasizume and Masafumi Ito (Meijo University, Japan)

10:30-10:40 BREAK

Chair: Susumu Kudo (Kyushu University, Japan)
PS4-12 **In-Situ Measurement of Traction Force at Focal Adhesions during
Macroscopic Cell Stretching Using an Elastic Micropillar Substrate:
Tensional Homeostasis of Vascular Smooth Muscle Cells (*Invited*)** 738
10:40-11:10 Kazuaki Nagayama, Akifumi Adachi, Keisuke Sasashima and Takeo
Matsumoto (Nagoya Institute of Technology, Japan)

PS4-13 **Biophysical Regulation of Pro-inflammatory Signaling under Mechanical
Stimuli (*Invited*)** 740
11:10-11:40 Shinji Deguchi (Tohoku University, Japan)

PS4-14 **Cyclic Stretch Recovers Ischemic Damage in Myoblasts (*Invited*)** 742
11:40-12:10 Takeru Naiki (Okayama University of Science, Japan), Satoko Fujii (Oshu
Corporation, Japan) and Kozaburo Hayashi (Okayama University of Science,
Japan)

12:10-13:10 LUNCH

Chair: Gyoo-Cheon Kim (Pusan National University, Korea)
PS4-15 **The Enhancement of C₂C₁₂ Myoblast Cell Growth on Modified Polylactide
Surface Using a Highly Efficient Two-step Atmospheric Pressure Plasma
Treatment Procedure (*Invited*)** 744
13:10-13:40 Yi-Wei Yang, Chih-Tung Liu, Guo-Chun Liao, Ming-Hung Chiang (National
Chiao Tung University, Taiwan), Jane-Yii Wu (Da Yeh University, Taiwan) and
Jong-Shinn Wu (National Chiao Tung University, Taiwan)

PS4-16 **Traction Force Measurement of Sheared Endothelial Cells by using Micropillar
Substrate (*Invited*)** 746
13:40-14:10 Toshiro Ohashi, Yusaku Niida (Hokkaido University, Japan) and Masaaki Sato
(Tohoku University, Japan)

PS4-17 14:10-14:40	Comprehensive Gene Expression Analysis of HeLa Cells in Response to Plasma Stimuli (<i>Invited</i>) Mayo Yokoyama, <u>Takehiko Sato</u> , (Tohoku University, Japan) and Kohei Johkura (Shinshu University, Japan)	748
14:40-14:50	BREAK	
Chair: Takeru Naiki (Okayama University of Science, Japan)		
PS4-18 14:50-15:05	Effect of Spatial Gradient in Fluid Shear Stress on Distribution of Endothelial Cell Focal Adhesion in Response to Flow <u>Daisuke Yoshino</u> (Tohoku University, Japan), Naoya Sakamoto (Kawasaki University of Medical Welfare, Japan), Keita Takahashi, Eri Inoue and Masaaki Sato (Tohoku University, Japan)	750
PS4-19 15:05-15:20	Molecular Dynamics Simulations of a DPPC/Cholesterol Bilayer under Equibiaxial Stretching <u>Taiki Shigematsu</u> , Kenichiro Koshiyama and Shigeo Wada (Osaka University, Japan)	752
PS4-20 15:20-15:35	JNK and P38MAPK Mediate Low Level Shear Stress-induced Migration of Human Mesenchymal Stem Cells <u>Lin Yuan</u> (Tohoku University, Japan / Chongqing University, China), Naoya Sakamoto (Kawasaki University of Medical Welfare, Japan), Guanbin Song (Chongqing University, China) and Masaaki Sato (Tohoku University, Japan)	754
PS4-21 15:35-15:50	Numerical Analysis of Levitation Mechanism of Red Blood Cell in Inclined Centrifuge Microscope - Effect of Asymmetric Cell Shape on the Motion <u>Takashi Oshibe</u> , Toshiyuki Hayase, Kenichi Funamoto and Atsushi Shirai (Tohoku University, Japan)	756
	Closing Toshiro Ohashi (Hokkaido University, Japan)	

PS5: 6th Functionality DEsign of the COn tact Dynamics: (DECO2012)

SEIUN

September 21, 2012

Chairs: Toshiyuki Takagi (Tohoku University, Japan)

PS5-1 **An Evaluation Method for Tangential Contact Stiffness Evaluation** 760
14:50-15:10 *(Invited)*
Zahrul Fuadi (Syiah Kuala University, Indonesia / Tohoku University, Japan), Toshiyuki Takagi, Hiroyuki Miki and Koshi Adachi (Tohoku University, Japan)

PS5-2 **Tribological Behavior of Multiply-alkylated Cyclopentane Lubricated with Diamond-like Carbon Coating in the Running-in Period** 762
15:10-15:25 Masanori Iwaki (Tohoku University, Japan / Japan Aerospace Exploration Agency, Japan), Takanori Takeno, Hiroyuki Miki and Toshiyuki Takagi (Tohoku University, Japan)

PS5-3 **Effects of Substrate Bias Voltage and Target Sputtering Power on the Structural and Tribological Properties of Carbon Nitride Coatings** 764
15:25-15:40 Pengfei Wang, Takanori Takeno (Tohoku University, Japan), Fontaine Julien (Ecole Centrale de Lyon, France), Masami Aono (National Defense Academy, Japan), Koshi Adachi, Hiroyuki Miki and Toshiyuki Takagi (Tohoku University, Japan)

Chairs: Minoru Goto (Ube National College of Technology, Japan)

PS5-4 **Towards Super-low Friction with Carbon-Based Coatings** *(Invited)* 766
15:40-16:05 Michel Belin (Ecole Centrale de Lyon, France), Hiroyuki Miki (Tohoku University, Japan), Maria-Isabel De Barros-Bouchet, Julien Fontaine (Ecole Centrale de Lyon, France), Takanori Takeno and Toshiyuki Takagi (Tohoku University, Japan)

PS5-5 **Adhesion and Friction Properties of Partially Polished CVD Diamond Films on Steel Substrates** 768
16:05-16:20 Hiroyuki Miki, Yosuke Nakayama, Takanori Takeno and Toshiyuki Takagi (Tohoku University, Japan)

Chairs: Zahrul Fuadi (Syiah Kuala University, Indonesia)

PS5-6 **Tribological Properties of Ag-DLC under Various Loading Conditions** 770
16:30-16:50 *(Invited)*
Minoru Goto (Ube National College of Technology, Japan), Julien Fontaine (Ecole Centrale de Lyon, France), Takanori Takeno and Hiroyuki Miki (Tohoku University, Japan)

PS5-7 **A Method to Reduce Commutation Spark for Wear Reduction of Carbon Brush Installed in Automotive DC Motor** *(Invited)* 772
16:50-17:10 Ryoichi Hombo, Naruhiko Inayoshi and Naoki Kato (DENSO Corporation, Japan)

PS5-8
17:10-17:35

**Some Considerations on the Tribology of Solid Lubricant Coatings
(Invited)**

774

Philippe Kapsa, Vincent Fridrici, Jiao Yang, Marine Bernard (Ecole Centrale de Lyon, France) and Dabing Luo (Southwest Jiaotong University, China)

Chairs: Hiroyuki Miki (Tohoku University, Japan)

17:35-18:30

Panel Discussion

“Design paradigm for the next contact dynamics”

Special Session: Liaison Office Session

Thursday, September 20, 2012

La Boaune

16:30-17:45 Present Status and Future Plan of Liaison Office Activities

Chair: Toshiyuki Takagi

Moscow State University, Alexander Vasiliev (8 min)

UNSW and University of Sydney, Srinivas Karkenahalli (8 min)

KTH Royal Institute of Technology, Fredrik Lundell (8 min)

KAIST, Sung Jin Kim (8 min)

Syracuse University, Jeongin Ahn (8 min)

INSA-Lyon, Marie Pierre Favre (8 min)

IFS, Makoto Ohta (10 min)

Discussion (17 min)

SENDAI (WEST)

18:00-18:30 ICFD - Past and Future

Chair: Alexander Vasiliev

Shigenao Maruyama “International Activities of 21COE and GCOE”

Toshiyuki Takagi “Liaison Office Activities”

Toshiyuki Hayase “IFS International Activities and Future ICFD”

Plenary Lectures

Green Aircraft Concepts and Enabling Technology Research at NASA

Richard A. Wahls
NASA Langley Research Center
Mail Stop 267
Hampton, Virginia 23681
USA
richard.a.wahls@nasa.gov

ABSTRACT

NASA Aeronautics is addressing the challenge of enabling the sustained growth of the air transportation system through the research and development of systems and technologies for future aircraft and airspace operations. Current research programs are addressing energy and environmental issues, as well as expanded mobility/capacity options and enhanced aviation safety. This presentation highlights select subsonic transport aircraft concepts and enabling technologies that address solutions for the revolutionary energy efficiency and dramatic reductions in harmful emissions and perceived community noise that will be required in the coming decades.

1. Introduction

Commercial aviation relies almost entirely on subsonic transport aircraft to constantly move people and goods from one place to another across the globe. While air travel is an effective means of transportation providing an unmatched combination of speed and range, future subsonic aircraft must continue to improve to meet efficiency and environmental targets that are being established around the world (see, for example, Fig. 1).

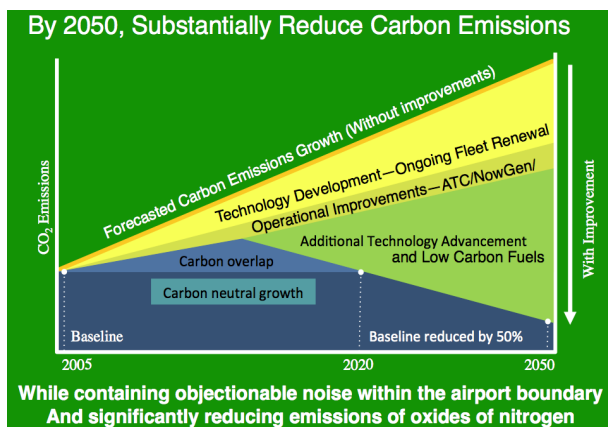


Fig. 1 Aviation Grand Challenge
(CO₂ reduction timeline adapted from IATA [1])

NASA Aeronautics is addressing the challenge of revolutionary energy efficiency improvements for subsonic transport aircraft combined with dramatic reductions in harmful emissions and perceived community noise to facilitate sustained growth of the air transportation system. This “green aviation” research includes the study of technologies and concepts for aircraft and airspace operations in the context of other goals and constraints including safety and economics. Additionally, research is conducted to characterize the properties, emissions, and performance of alternative aviation fuels.

Two projects within NASA are focused on future green aircraft: 1) Subsonic Fixed Wing Project (SFW) in the Fundamental Aeronautics Program, and 2) Environmentally Responsible Aviation Project (ERA) in the Integrated Systems Research Program. Extensive

systems analysis and technology studies have guided development of time-phased aircraft system-level metrics for NASA subsonic transport research (Fig. 2). These metrics address noise, emissions, and energy consumption for near-term (N+1), mid-term (N+2), and far-term (N+3) timeframes, and “N+x” indicates research targeted at aircraft “x” generations beyond today (N). These metrics are intentionally challenging to draw out new ideas. The SFW project focuses on the N+3 metrics, ERA on the simultaneous achievement of the N+2 metrics, and the FAA CLEEN Program has adopted the N+1 metrics [2]. N+1 research contributes to the N+2 solution space, and both contribute to N+3. At the same time, N+3 and N+2 research produce results that are leveraged forward for near-term impact.

TECHNOLOGY BENEFITS*	TECHNOLOGY GENERATIONS (Technology Readiness Level = 4-6)		
	N+1 (2015)	N+2 (2020**)	N+3 (2025)
Noise (cum margin rel. to Stage 4)	-32 dB	-42 dB	-71 dB
LTO NOx Emissions (rel. to CAEP 6)	-60%	-75%	-80%
Cruise NOx Emissions (rel. to 2005 best in class)	-55%	-70%	-80%
Aircraft Fuel/Energy Consumption† (rel. to 2005 best in class)	-33%	-50%	-60%

* Projected benefits once technologies are matured and implemented by industry. Benefits vary by vehicle size and mission. N+1 and N+3 values are referenced to a 737-800 with CFM56-7B engines. N+2 values are referenced to a 777-200 with GE90 engines

** ERA's time-phased approach includes advancing "long-pole" technologies to TRL 6 by 2015

† CO₂ emission benefits dependent on life-cycle CO₂, per MJ for fuel and/or energy source used

Fig. 2 NASA Subsonic Transport System Level Metrics

2. Goal-Driven Advanced Concept Studies

Over the last 5 years, NASA has conducted aircraft-level advanced concept studies targeted at meeting the goals set forth in Fig. 2. Generally, the idea is to put forth a set of goals for a given timeframe, and ask what is needed from a capability perspective (a future scenario), what aircraft concepts can deliver the capability, what technologies are needed to enable such aircraft, and how do we get there from here (a roadmap). With mid- and far-term research, the intent is to have researchers think “outside of the box” and deliver more

revolutionary, rather than near-term evolutionary, ideas. Research is then pursued to further understand the aircraft concepts, but more importantly to address the key enabling technologies. It is also important to baseline the studies with well-established aircraft representative of current technology, and a reference advanced technology conventional configuration if an advanced technology unconventional configuration is proposed; it is important to isolate as best as possible the effect of technology versus the effect of configuration.

Fig. 3 shows examples of N+2 aircraft concepts that resulted from studies completed in early 2012, including a flying-wing concept from Northrop Grumman, a box-wing concept from Lockheed Martin, and a blended-wing-body concept from Boeing. Fig. 4 shows examples of N+3 aircraft concepts resulting from initial studies completed in 2010, including double-bubble and hybrid-wing-body concepts from MIT, and a truss-braced-wing concept from Boeing. Although not as obvious to the eye, each of these advanced aircraft has substantial advanced technology included in the propulsion systems, and in some cases revolutionary propulsion system architecture changes – for example the hybrid gas-electric propulsion system proposed by the Boeing N+3 team. The presentation will highlight results from these and other studies. Further details can be found on the ERA studies in references [3-5], and on the SFW studies in references [6-10].



Fig. 3 N+2 Aircraft Concepts



Fig. 4 N+3 Aircraft Concepts

3. Subsystem Concepts and Enabling Technologies

Examination of the various aircraft system and subsystem concepts, whether conventional or unconventional, indicates many similarities and common needs. Most technologies are broadly applicable to many aircraft concepts, while some are uniquely enabling to specific concepts. Advances are required in aerodynamic efficiency to reduce drag (e.g. laminar flow, higher aspect ratio), structural efficiency to reduce aircraft empty weight (e.g. tailored, unitized structures) and propulsive and thermal efficiency to

reduce thrust-specific energy consumption (e.g. hot section materials, higher bypass ratios). Advances are also required to reduce perceived community noise without adversely affecting performance (e.g. shielding, liners), and to reduce harmful emissions without adversely affecting energy efficiency or noise (e.g. injection/control concepts). Finally, these advances will be tradable in an expanded design space for overall system benefit to meet specific market-driven requirements. The presentation will highlight select subsystem concepts and enabling technologies.

4. Concluding remarks

Advanced technologies and unconventional aircraft concepts offer the potential to meet the energy efficiency and environmental challenges facing aviation. There is no single solution – advances are required in all facets of aircraft technology and beyond to include operations and energy technologies. These are exciting times for aeronautics research with game-changing ideas needed to meet the challenges of the future.

This paper is a brief discussion the challenges, concepts, and technologies that are highlighted in more detail in the oral presentation.

References

- [1] J. Mamen: "IATA Perspectives on Alternative Jet Fuels," Toronto, Canada, 2010.
http://goldfinger.utias.utoronto.ca/~IWACC2/IWACC2/Program_files/Mamen.pdf
- [2] FAA CLEEN Fact Sheet, 2010.
http://www.faa.gov/news/fact_sheets/news_story.cfm?newsId=11538
- [3] J. Bonet: "Boeing ERA N+2 Advanced Vehicle Concept Study Results," Toronto, Canada, 2012.
http://goldfinger.utias.utoronto.ca/~IWACC3/IWACC3/Program_files/Bonet_IWACC_2012.pdf
- [4] C. Harris: "NASA ERA N+2 Advanced Vehicle Concepts," Toronto, Canada, 2012.
http://goldfinger.utias.utoronto.ca/~IWACC3/IWACC3/Program_files/Harris_IWACC_2012.pdf
- [5] K. Martin: "Lockheed Martin Skunk Works Green Aviation: NASA ERA and N+2 Supersonic Projects," Toronto, Canada, 2012
http://goldfinger.utias.utoronto.ca/~IWACC3/IWACC3/Program_files/Martin_IWACC_2012.pdf
- [6] E. Greitzer, et al.: "N+3 Aircraft Concept Designs and Trade Studies," NASA/CR-2010-216794, 2010.
- [7] M. D'Angelo, et al.: "N+3 Small Commercial Efficient and Quiet Transportation for Year 2030-2035," NASA/CR-2010-216691, 2010.
- [8] M. Bradley, et al.: "Subsonic Ultra Green Aircraft Research: Phase 1 Final Report," NASA/CR-2011-216847, 2011.
- [9] S. Bruner, et al.: "NASA N+3 Subsonic Fixed Wing Silent Efficient Low-Emissions Commercial Transport Vehicle Study," NASA/CR-2010-216798, 2010.
- [10] J. Felder, et al.: "Turboelectric Distributed Propulsion in a Hybrid Wing Body Aircraft," ISABE-2011-1340, Gothenburg, Sweden, 2011.

HEAT—A Weighty Compressive Fluid

Zeng-Yuan Guo

Key Laboratory for Thermal Science and Power Engineering of Ministry of Education,
Department of Engineering Mechanics, Tsinghua University, Beijing 100084, P. R. China
demgzy@tsinghua.edu.cn

ABSTRACT

Unlike the existing methodology of heat transfer study, the concept of thermomass is defined as the equivalent mass of thermal energy according to the Einstein's mass-energy relation, which differs from caloric and kinetic theories. Hence, the heat can be regarded as a compressive fluid with finite mass. Newton mechanics has been applied to establish the equation of state and motion for the phonon gas as in fluid mechanics. The latter is in fact the general heat conduction law, which may reduce to different phenomenological models, including Fourier's heat conduction model and CV model etc. under different simplified conditions.

1. Introduction

Heat transfer, as a branch of general physics, studies thermal phenomena using concepts that differ from other fields of study. As early as 1822, Fourier, a France mathematical and physical scientist, pointed out in his famous monograph "Analytical Theory of Heat": "... These (the effects of heat) make up a special order of phenomena, which cannot be explained by the principles of motion and equilibrium. ... This part of natural philosophy cannot be connected with dynamical theories, it has principles peculiar to itself ..." [1] He then proposed the famous Fourier's heat conduction law to characterize heat motion, which has been widely applied in a variety of engineering areas.

However for transient heat conduction process, Fourier's law leads to the unphysical conclusion that the heat propagation speed is infinite since the heat conduction equation based on Fourier's law is parabolic. This physical drawback has attracted many attempts to improve Fourier's model. Cattaneo [2], and subsequently Vernotte [3] developed a new heat conduction model, often called the CV equation, which adds a term of the time derivative of heat flux to Fourier's law. In recent years, the applicability of Fourier's heat conduction law has been further questioned even for steady state conditions. Lepri et al. [4] found that the thermal conductivity of molecular chains is approximately proportional to the square root of the particle number, which indicates the breakdown of Fourier's law. Different from the phenomenological analysis of heat transfer, this paper identifies the quantity, thermomass, which is the equivalent mass of thermal energy according to the Einstein's mass-energy relation. Hence, heat transfer in dielectrics can be described by mechanical principles.

2. Thermomass

According to Einstein's special theory of relativity [5], the mass of an object increases with its speed and its mass and energy of an object is related by

$$E = Mc^2 = \frac{M_0 c^2}{\sqrt{1 - u^2/c^2}}, \quad (1)$$

in which M is the moving mass or the relativistic mass of the object, M_0 is the rest mass, u is the velocity, c is

the speed of light in vacuum, E is the total energy or the relativistic energy of the object, and $M_0 c^2$ is the energy of the rest object. We now consider a rest object with mass, M_0 , and temperature, T . M_0 is the sum of all the atomic masses in the object. The thermal vibration energy is assumed to be E_{D0} , and the atomic relativistic mass will then be larger than the rest mass. For moving ideal gas molecules in stationary container, Feynman indicated [6] "when the gas is heated, the speed of the molecules is increased, and the mass is also increased and the gas is heavier". The increased mass of dielectrics due to thermal vibration is

$$M_h = \frac{E_{D0}}{c^2}. \quad (2)$$

Thus, M_h can be called the thermomass by Guo et al. [7]. The thermomass of lattice, or the equivalent mass of the phonon gas, though it is tiny compared with the rest mass of lattices, must be taken into account during heat conduction, because the equivalent mass of the phonon gas is able to move independent of the rest mass of lattices.

The state equation of phonon gas was deduced from the Debye state equation by Guo et al. [7]

$$p_h = \frac{\gamma C M_h T}{V} = \left(\frac{\gamma c^2}{\rho} \right) \rho_h^2, \quad (3)$$

where ρ is the density of dielectrics. This equation is the state equation of phonon gas.

When a temperature gradient occurs in a solid, thermal energy flows from the hot to the cold regions. The thermal energy motion (transport) is usually described by the heat flux. The thermal energy motion can be better described by its velocity defined by an advection transport term as

$$q = \rho C T u_h. \quad (4)$$

Where ρ is the mass density, C is the specific heat and T is the temperature. Thus, u_h is the velocity of the thermal energy motion, which is equivalent to the mean phonon drift velocity or the macroscopic velocity of the phonon gas.

3. Dynamics of thermomass fluid

The transport of phonons in a solid is really like fluid flows in channels. The previous phonon hydrodynamics

is based on solving Boltzmann equations of phonons. Here, based on the concept of thermomass for the phonon gas, we can establish the conservation equations to characterize the dynamics of phonon gas in a solid using Newtonian mechanics.

I. Continuity equation for a phonon gas: For heat transport in a solid without an internal heat source, the equivalent mass of the phonon gas remains constant during the motion of the phonon gas. Its continuity equation is

$$\frac{\partial \rho_h}{\partial t} + \text{div}(\rho_h U_h) = 0. \quad (5)$$

II. Equation of motion for a phonon gas: As stated above, the driving force for heat transport (phonon gas motion) is the thermomass pressure gradient in the phonon gas. The momentum variation in the phonon gas results in a inertial force. Note that the momentum here refers to the physical momentum carried by the finite mass of the phonon gas, which differs from the quasi-momentum of a phonon defined in solid physics. In addition, a resistance must exist because of the non-linearity of the lattice vibrations and defects in the solid. Thus, the equation of motion for the phonon gas can be written as in fluid mechanics

$$\rho_h \frac{dU_h}{dt} + \nabla P_h + f_h = 0. \quad (6)$$

Here, the first term represents the inertial force of the phonon gas motion, the second term is the pressure gradient and the third term is the resistance. The resistance is assumed to be linearly related to the velocity

$$f_h = \beta_h u_h \quad \left(\beta = \frac{2c^2 \gamma \rho_h^2 C}{K} \right). \quad (7)$$

III. General heat conduction law: Since the motion equation of the thermomass is based on the first principle and takes no artificial assumptions, it is just a general heat conduction equation. We can get the equation for one-dimensional heat conduction in dielectrics as follows:

$$\tau_{\text{TM}} \frac{\partial q}{\partial t} - l \rho C \frac{\partial T}{\partial t} + l \frac{\partial q}{\partial x} - bk \frac{\partial T}{\partial x} + k \frac{\partial T}{\partial x} + q = 0, \quad (8)$$

in which

$$\tau_{\text{TM}} = \frac{k}{2\gamma \rho C^2 T}, \quad (9)$$

$$l = \frac{qk}{2\gamma C(\rho CT)^2} = u_h \tau_{\text{TM}}, \quad (10)$$

$$b = \frac{q^2}{2\gamma \rho^2 C^3 T^3}. \quad (11)$$

The quantities τ_{TM} and l have dimensions of time and length, respectively, while b is a dimensionless number less than unity and its physical meaning will be given later. For silicon at room temperature, τ_{TM} is on the order of 10^{-10} s. For the heat conduction with a heat flux $q=10^4$ W/m², l is on the order of 10^{-15} m, and b is on the order of 10^{-15} . The first four terms on the left side of Eq. (8) result from the inertial effects, the fifth term represents the effect from the pressure gradient (driving force), and the sixth term results from the resistance as the phonon

gas flows through the lattices. Equation (8) inheriting from the concept of mass of heat, which describes the general relation between the temperature gradient and the heat flux vector, is referred to as the general heat conduction law.

The general heat conduction law degenerates to Fourier's law of heat conduction when the phonon gas velocity is so small that the inertial force may be neglected. Therefore, the physical essence of Fourier's law is a balance between the driving force and the resistance in the phonon gas. The general heat conduction law can also reduce to similar appearances to CV model but with different characteristic times. The characteristic time τ_{CV} in the CV model is the relaxation time, while the characteristic time τ_{TM} in the thermomass model describes a lagging response, in time, between the heat flux and the temperature gradient. When the heat flux density (drift velocity) is so large that the inertial force of the phonon gas cannot be neglected, Fourier's law breaks down, resulting in non-Fourier heat conduction even for steady state conditions. The heat flux is then no longer related linearly to the temperature gradient.

4. Concluding remarks

i) The concept of thermomass is defined as the equivalent mass of thermal energy according to the Einstein's mass-energy relation, so that the phonon gas in dielectrics can be regarded as a compressive fluid with finite mass and heat conduction in the medium resembles the gas flow through the porous medium.

ii) Newton mechanics has been applied to establish the equation of state and the equation of motion for the phonon gas as in fluid mechanics, showing that thermal and mechanical fields are mutually implied.

iii) The momentum equation of the thermomass gas, including the driving, inertial and resistant forces, is in fact the general heat conduction law, which reduces to Fourier's heat conduction law as all inertial terms are neglected and reduces to the CV model or the single phase-lag model as the heat flux related inertial terms are neglected. The general conduction law is also applicable for ultra-short pulse laser heating or heat conduction in carbon nanotubes at ultra-high heat flux.

References

- [1]. J. Fourier, *Analytical Theory of Heat* (Dover Publications, New York, 1955).
- [2]. C. Cattaneo, *Atti. Sem. Mat. Fis. Univ. Modena*, **3** (1948), 3.
- [3]. P. Vernotte, *C. R. Acad. Sci.*, **246** (1958), 3154.
- [4]. S. Lepri, R. Livi and A. Politi, *Phys. Rev. Lett.*, **78**(1997), 1896.
- [5]. A. Einstein, H. A. Lorentz, H. Minkowski and H. Weyl, *The Principle of Relativity* (Dover publications, New York, 1952).
- [6]. R.P. Feynman, *The Feynman Lectures on Physics* (Basic Books, New York, 2010).
- [7]. Z.Y. Guo, B.Y. Cao, H.Y. Zhu, *Acta Phys. Sin.*, **56** (2007), 3306.

Data Assimilation: Challenge for Big Data through Numerical Simulation

Tomoyuki Higuchi

The Institute of Statistical Mathematics, 10-3 Midori-cho, Tachikawa, Tokyo, Japan
higuchi@ism.ac.jp

ABSTRACT

Data Assimilation (DA) is a technique for a synthesis of information from a dynamical numerical model and observation data. It is an emerging area in earth sciences, particularly oceanography, stimulated by recent improvements in computational and modeling capabilities and the increase in the amount of available observations. DA can be applicable to any scientific domains involving numerical simulation models. We give a brief introduction to DA within a framework of the statistical modeling and demonstrate several examples to show how we can extract useful knowledge from big data through numerical simulation.

1. Introduction

Both theories and experiments have been widely accepted as the driving force to promote research in any fields of science. It passed about 40 years since a computer simulation is called as the third method of science. A recent explosion of data, so-called big data appearance, strengthens the research domain to study a method of tools for analyzing big data such as statistics, machine learning, data mining, and visualization technologies. This phenomenon is called the fourth paradigm after a publication [1].

The data assimilation is a synthesis technique based on the Bayesian filtering method by embedding observation/experiment data in a numerical simulation. DA is an emerging area in earth sciences, particularly oceanography. Its research motivation is easily understood simply if we notice that there are too many uncertainties in the model such as the boundary condition, initial condition, unknown parameters, and unknown dynamics. It yields an accommodation ability to make a simulation real, and the better initial and boundary conditions can be automatically obtained.

Major objects of DA can be categorized in the following five aspects: 1) To produce the best (better) initial condition for forecasting. It is actually realized in the real weather forecast. 2) To find the best (better) boundary condition in constructing a simulation model. This procedure includes a setting of appropriate boundary conditions necessary for dealing with the coupled phenomena. 3) To attain an optimal parameter vector that appears in an empirical law (scheme) employed for describing complicated phenomena which possesses the different time and spatial scales. A validation of the empirically given values is regarded as this problem. 4) To inter/extrapolate (estimate) physical quantity at times and locations without observations based on a numerical simulation model. This procedure is called “a generation of re-analysis dataset (product)”. This dataset is used to discover a new scientific finding by general geophysical researchers. 5) To conduct an experiment with a virtual observation network and perform a sensitivity analysis in an attempt to construct an effective observation network system with less budgetary cost and less consuming time.

2. Mathematical framework

In statistical methodology, DA can be formulated in

the state space model that draws much interest of the researchers in various domains such as the time series analysis, signal processing, and control theory [2-4]. A numerical simulation model is usually carried out with the discrete version of a partial differential equations (PDE) which is assumed to represent a real system. The discretization in time and space for PDE produces the finite difference equations (FDE) given by

$$x_t = f_t(x_{t-1}, v_t), \quad v_t \approx N(0, Q) \quad (1)$$

where x_t is called the state vector and defined by setting all variables at discrete time t in a numerical simulation to an element of x_t . The system noise vector v_t , which is introduced to produce the stochastic disturbances, is assumed to follow a normal distribution $N(0, Q)$ with mean 0 and variance-covariance matrix of Q . A usual setting of DA assumes that observations are obtained by a partial measurement of the state vector or a weighted linear combination of the elements with a measurement error. Thus an observation vector at time t , y_t , is represented with a prescribed matrix of H_t as follows;

$$y_t = H_t x_{t-1} + w_t, \quad w_t \approx N(0, R). \quad (2)$$

A combination of Eq. (1) and (2) yields the state space model (SSM). Major objects in DA can be reduced to be a state estimation problem and inference problem on parameters. However, to realize DA is hampered by a large dimension of the state vector, which is much larger than that of the observation vector. To deal with this difficulty, there are two approaches of DA: four-dimensional variational method (4Dvar) [5] and ensemble-based sequential DA (EnSDA) [6,7]. 4Dvar is regarded as an off-line estimation procedure because it is applied to the fixed data set. Meanwhile, EnSDA is an online estimation procedure because an estimator is improved every time we have a new observation.

3. Ensemble-based sequential data assimilation

EnSDA relies on various benefits of SSM in computations for obtaining the marginal distribution: predictive distribution $p(x_t|y_{1:t-1})$ and filter distribution $p(x_t|y_{1:t})$, where $p(A|B)$ is a conditional distribution of A given B , and $y_{1:j}$ denotes data obtained from an initial time up to time j . EnSDA has an advantage in terms of less human resources which is achieved by plugging into the existing “forward” simulation codes, and now widely used in a wide variety of scientific domains

instead of the 4Dvar. In particular, the ensemble Kalman filter (EnKF) [6] becomes very popular in the EnSDA because of having less difficulties in a numerical computation rather than other methods in EnSDA. Although the particle filter (PF) [3,7] has a drawback in terms of an ability to approximate the conditional distribution, both simple idea and less computational burden are very attractive.

4. Applications to an analysis of earthquakes

We are studying the EnSDA methods such as the EnKF and PF, and conducting the DA experiments in several specific areas: atmosphere-ocean system, tsunami, ocean tide, outer space, genome information, and social science with the multi-agent-based simulation. We here show an application to analyze an acoustic wave which is generated by earthquake followed by tsunami [8]. As you might well know, Japan is an earthquake-prone country, so our government has been promoting many researches related to earthquake prediction and earthquake disaster prevention. In spite of such efforts, a disastrous earthquake sometimes causes landslides or tsunamis that wreak human lives, cause enormous physical damage and human suffering.

Figure 1 shows the locations of recent disastrous earthquakes; one is the Iwate-Miyagi Nairiku Earthquake in 2008 having the magnitude of 7.2, and another is the Great East Japan Earthquake in 2011 having the magnitude of 9.0.

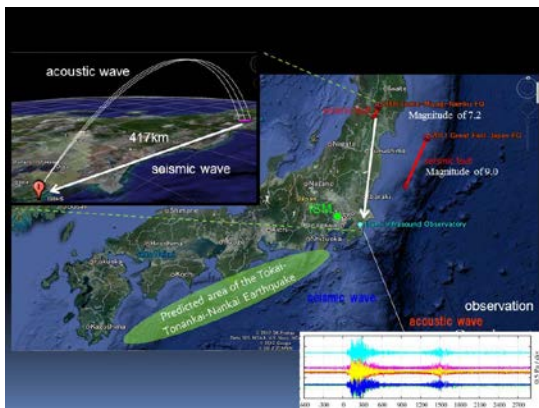


Fig. 1 Locations of earthquakes and observation point.

When each earthquake occurred, many micro-barometer sensors located at distances of hundreds or thousands of kilometers from the epicenter observed “the sound of the earthquake” in the form of atmospheric pressure perturbations. In the case of the Iwate-Miyagi Nairiku Earthquake, for example, micro-barometer sensors 417 km away from the epicenter observed acoustic waves excited by the earthquake.

We simulate the observed waveforms by assuming a physical structure model of the Earth and a seismic fault model. The structure model consists of the standard models of the solid Earth and the atmosphere, and the

seismic fault model consists of nine sub-earthquakes that continuously occur with an appropriate rupture velocity. The model parameters contained in the current model are D: depth of the hypocenter, m: magnitude of each sub-earthquake, V: rupture velocity of the seismic fault, and t_0 : time delay due to wind blowing in the atmosphere. These parameters are estimated within the framework of data assimilation.

The synthetic waveform reproduced from previous models, which determined the depth of the hypocenter to be 6km, was not consistent with the observation. On the other hand, the assimilated waveform, which found the depth to be 4km, successfully explains the observation. In the case of the Great East Japan Earthquake, the dense array of GPS receivers in Japan clearly observed the acoustic waves causing oscillations in the ionosphere at the altitude of a few hundred kilometers. We successfully reproduced this phenomenon by applying the same technique used in Iwate-Miyagi Nairiku Earthquake.

The acoustic wave generated by an earthquake propagates with much faster velocity than tsunami, therefore we could know in advance the magnitude of tsunami before it arrives. Such acoustic signals may be useful in predicting the magnitude of approaching tsunami such as in the case of the large earthquake predicted to occur in the near future. But to establish a tsunami early warning system requires to carry out a high-speed data assimilation, combining the proposed numerical simulation and barometer records.

5. Concluding remarks

We would like to emphasize that a research on the DA can be regarded as the “Creation of meta-simulation model”. We give a platform to design a measurement system in an attempt to enhance a scientific return together with reducing a total budgetary cost.

References

- [1] T. Hey, S. Tansley, and K. Tolle eds., “The Fourth Paradigm: Data-Intensive Scientific Discovery,” Microsoft Press (2009).
- [2] G. Kitagawa, W. Gersch, “Smoothness Priors Analysis of Time Series,” Springer (1996).
- [3] G. Kitagawa, “Introduction to Time Series Modeling,” Chapman & Hall Book/CRC (2010).
- [4] J. Durbin, and S.J. Koopman, “Time Series Analysis by State Space Models,” Oxford University Press (2001).
- [5] E. Kalnay, “Atmospheric Modeling, Data Assimilation and Predictability,” Cambridge University Press (2002).
- [6] G. Evensen, “Data Assimilation: The Ensemble Kalman Filter,” Springer (2007).
- [7] T. Higuchi, Proceedings of 14th International Conference Fusion (2011).
- [8] H. Nagao, N. Kobayashi, S. Nakano and T. Higuchi, Proceedings of 14th International Conference Fusion (2011).

GS1: General Session

On Numerical Modeling of Heterogeneous Combustion in Porous Media under Free Convection

Nickolay A. Lutsenko

Far Eastern Federal University. Address: 8, Sukhanova St., Vladivostok, 690950, Russia
Institute of Automation and Control Processes, FEB RAS. Address: 5, Radio St., Vladivostok, 690041, Russia
NickL@inbox.ru

ABSTRACT

A mathematical model and a numerical method have been developed for investigating the unsteady gas flows in porous objects with zones of heterogeneous combustion when gas pressure at object boundaries is known. Used approach enables to solve problems of filtration combustion for both forced filtration and free convection. One-dimensional unsteady processes of heterogeneous combustion in porous object under free convection have been investigated. Two regimes of combustion wave propagation have been revealed – wave movement up the object (cocurrent burning) and down the object (countercurrent burning).

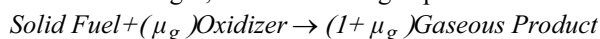
1. Introduction

Combustion in porous media is quite common in nature. Porous media in terms of mechanics are soils, peat, rocks, debris of ruined buildings and so on. Thus, the centers of combustion in porous media can arise, for example, during the explosions at atomic and industrial facilities, in underground explosions and fires in places of the extraction of natural resources. Recently, active researches on the application of the ideas of filtration combustion in various technological processes are carrying out. One application of the theory of filtration combustion is the study of spontaneous combustion of solid waste dumps (landfills). This work is devoted to the unsteady flow of gas in porous objects with zones of heterogeneous combustion at a given pressure on the borders of the object and the unknown flow of gas passing through the object.

2. Physical and mathematical models

Consider a homogeneous motionless porous object, which is bounded of impermeable non-heat-conducting side walls and opened at the top and at the bottom. The heat-evolutional process in solid phase results from the process of chemical reaction. The cold gas may flow into the inlet of the porous object (at the bottom); the gas may flows up through porous medium, is heated as a result of the heat exchange, and flows out into a free space with given pressure (at the top).

We assume that a solid porous substance consists of fuel and an inert component, and the solid fuel substance transformed by reaction with the gaseous oxidizer into a gas, so the following expression is true:



Here and below μ_g – the stoichiometric mass coefficient for the oxidizer.

The model is based on the assumption of interacting interpenetrating continua [1] using the classical approaches of the theory of filtration combustion [2, 3]. In the energy equation for the solid components not only heat release is taken into account but also the thermal conductivity and the intensity of the interphase heat exchange which is assumed to be proportional to the difference of the phase temperatures at the considered point of the medium. In the energy equation for the gas thermal conductivity is not considered because of its

smallness, and it is assumed that homogeneous reactions do not occur. To describe the dynamics of gas the conservation of momentum equation for porous media is used, which is more correct than the classical Darcy's equation. The solid phase is assumed to be fixed, so the equation of motion for it degenerates. The model takes into account changes in volume and weight of the phases at the interaction, the presence of diffusion of the oxidant as well as the validity of the of the perfect gas equation. Combustion processes are described by one-step chemical reaction of first order with respect to both arguments. As in [5, 6] it is shown that the allowance for the temperature dependence of gas in its motion through a porous heat-evolutional medium would change the solution both quantitatively and qualitatively, we will assume that the dynamical viscosity of gas is temperature dependent by Sutherland's formula.

At the inlet of the porous object (at its lower boundary) gas temperature, gas pressure and mass concentration for the oxidizer are known. At the outlet, the pressure is known because the gas flow is into the open space. The conditions of heat exchange at the inlet and outlet from the porous object and on the bounding impermeable walls are also known. A distinctive feature of the considered model is that the flow rate and gas velocity at the inlet to the porous object are unknown and have to be found from the solution of the problem.

3. Numerical method

The boundary conditions in the problems of given class differ substantially from the conditions in classical problems of the mechanics of multi-component media, and this fact impedes here the application of widely known finite-difference schemes. Therefore, an original numerical method has been developed, which is based on a combination of explicit and implicit finite-difference schemes, for the investigation of unsteady gas flow in a porous object with zones of heterogeneous combustion. This method is the development of earlier proposed numerical algorithm for the computation of the gas flows through porous objects with heat sources when gas pressure at object boundaries is known [4, 6-8]. The energy equations, momentum conservation equation and equation for oxidizer concentration are transformed into the explicit

finite difference equations. The gas temperature, solid phase temperature, gas velocity and oxidizer concentration are determined from these equations. The continuity equation is transformed into the implicit finite difference equation. From this equation taking into account the perfect gas equation of state the gas pressure is determined using Thomas algorithm [9]. The effective density of gas is determined from the perfect gas equation of state.

4. Numerical Results

One-dimensional time-dependent problems of heterogeneous combustion in a porous medium under free convection have been considered. Calculations showed that when the ignition is located at the bottom or at the central part of the object the combustion wave may arise and move up the object. As the directions of combustion wave propagation and gas movement coincide, this case is named cocurrent burning. The solid combustible substance burns completely in this case; the temperature in the combustion zone increases quite significantly; the velocity of combustion wave increases with temperature increasing. When the combustion wave passes through the porous object, the burning process is stopped and the slow cooling of a porous object is started.

When the ignition is located at the top or at the central part of the object the combustion wave may arise and move down the object. Fig. 1 shows an example of distribution of the solid medium temperature in the porous object at different times in this case of countercurrent burning. The temperature in the combustion zone and the velocity of combustion wave are significantly lower than in the case of cocurrent burning. The solid combustible material burns incompletely when the combustion wave moves down. When the combustion wave reaches the lower boundary of the object, it is reflected and starts to move up with reburning completely the remaining solid combustible substance.

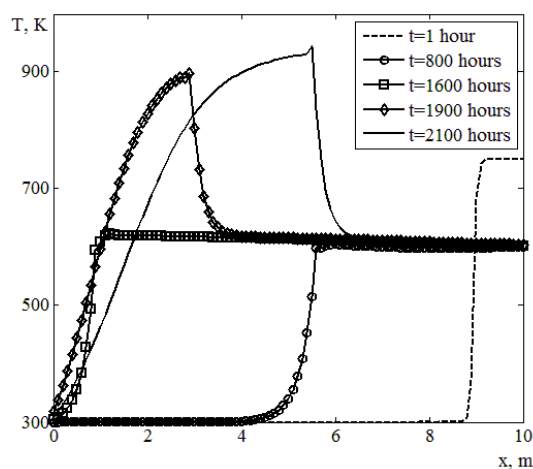


Fig. 1. Distribution of the solid medium temperature in the porous object at different times when the ignition zone is located at the top of the object.

The temperature in the combustion zone and the velocity of combustion wave increase significantly in reflected wave.

5. Conclusions

A mathematical model and original numerical method, based on a combination of explicit and implicit finite difference schemes, have been developed for investigating the time-dependent gas flows through porous objects with zones of heterogeneous combustion when gas pressure at object boundaries is known. The approach allows to solve the problem of filtration combustion for both forced filtration and free convection, so it can be efficiently applied for modeling the combustion zones in porous media, which may arise from natural or man-caused disasters. One-dimensional non-stationary processes of heterogeneous combustion in a porous object under free convection have been investigated by means of computational experiment. Two regimes of combustion wave propagation have been revealed – wave movement up the object (cocurrent burning) and down the object (countercurrent burning). It has been shown that these regimes differ significantly from each other by the degree of burnout of solid combustible material, the temperature in the combustion zone and the speed of combustion wave propagation.

6. Acknowledgements

The work was supported financially by the President of the Russian Federation (grant No. MK-2198.2011.1), the Russian Foundation for Basic Research (grant No. 11-01-98510-r_vostok_a), the Far-Eastern Branch of the Russian Academy of Sciences.

References

- [1] R.I. Nigmatulin, Principles of the Mechanics of Heterogeneous Media, Moscow: Nauka (1978). (in Russian)
- [2] A.P. Aldushin, B.J. Matkowsky, D.A. Schult, Journal of Engineering Mathematics, **31** (1997), pp. 205-234.
- [3] A.P. Aldushin, I.E. Rumanov, B.J. Matkowsky, Combustion and flame, **118** (1999), pp. 76-90.
- [4] V.A. Levin, N.A. Lutsenko, Combustion and Plasmochimistry, **3** (2005), No. 2, pp. 81-90. (in Russian)
- [5] V.A. Levin, N.A. Lutsenko, Journal of Engineering Physics and Thermophysics, **79** (2006), pp. 33-39.
- [6] V.A. Levin, N.A. Lutsenko, Computational Technology, **11** (2006), pp. 44-58. (in Russian)
- [7] V.A. Levin, N.A. Lutsenko, Mathematical Models and Computer Simulations, **2** (2010), pp. 635-647.
- [8] V.A. Levin, N.A. Lutsenko, Fluid Dynamics, **46** (2011), pp. 826-834.
- [9] J.C. Tannehill, D.A. Anderson, R.H. Pletcher, Computational Fluid Mechanics and Heat Transfer, Taylor&Francis (1997).

Investigation of Dopant Effects on Sintering Process in Solid Oxide Fuel Cell Anode Based on Molecular Dynamics Simulation

Jingxiang Xu, Ryota Sakanoi, Takeshi Ishikawa, Yuji Higuchi, Nobuki Ozawa, Tomomi Shimazaki, Kazuhisa Sato, Toshiyuki Hashida, and Momoji Kubo
Fracture and Reliability Research Institute, Graduate School of Engineering, Tohoku University,
6-6-11 Aoba, Aramaki, Aoba-ku, Sendai 980-8579, Japan
E-mail: jingxiang.xu@rift.mech.tohoku.ac.jp

ABSTRACT

The dopant effects on the sintering process of nickel nanoparticles in the nickel and doped zirconia cermet anode were investigated using molecular dynamics (MD) simulation. In this study, we observed that the extent of sintering in the Ni/YSZ is larger than that in the Ni/ScSZ due to the dopant effect. The mechanism of the dopant effect is that the strong adsorption energy between the nickel and the doped zirconia decreases the movement of the nickel nanoparticles and inhibits the sintering of the nickel nanoparticles on the doped zirconia surface.

1. Introduction

A solid oxide fuel cell (SOFC) as a power generator has been an area of active research in recent years due to their properties, such as efficient energy production, low pollutant emission, and low cost by removing the need for a precious metal catalyst like platinum, etc. Currently, the nickel and doped zirconia cermet material, which has the high conductivity ions and the stability, is widely used in the SOFC. Particularly, the nickel and the yttria-stabilized zirconia (Ni/YSZ) is the most widely used in the SOFC because of its stability and high conductivity at the high operating temperature. However, the sintering of nickel nanoparticles takes place easily at the high operating temperature and will lead to the degradation of the anode. Therefore, to improve a new anode material of low degradation is required.

The anode material consisting of the nickel and the scandia-stabilized zirconia (Ni/ScSZ) has some advantages. Ukai et al. [1] reported that the degradation of the Ni/ScSZ as an anode of SOFC is lower than that of the Ni/YSZ. However, the influence of the dopant on the sintering of nickel nanoparticles and the degradation of the anode has not been revealed. Thus, to improve the performance and inhibit the sintering in the anode during the operation, the dopant effect on the sintering is needed to be investigated. For this purpose, we employed the MD simulation method to investigate the dopant effect. However, it is difficult to determine the potential parameters between metal and metal oxide, because it is impossible to obtain the physical properties of nickel and metal oxide interface from experiments. In this study, we applied our previous developed method to determining the parameters between nickel and metal oxide [2]. Then, we investigated the dopant effect on the sintering in the representative anodes (Ni/YSZ and Ni/ScSZ) materials and discussed the mechanisms.

2. Computational Details

To investigate the dopant effect on the sintering process of nickel nanoparticles in the Ni/YSZ and the Ni/ScSZ anodes, we used the MD method for the sintering simulation by our MD program package, New-Ryudo. The MD simulations were executed with a 2.0 fs time-step, and the NVT canonical ensemble was employed in all simulations at a temperature of 1073 K.

In this study, the BMH potential was used for ionic interactions of the doped zirconia system in all calculation and the BMH potential parameters were determined in our previous work [3]. The Morse potential was used for reproducing the interactions between nickel atoms. Then, considering interactions between the nickel and the doped zirconia, we chose Morse potential to describe their interactions. The Morse parameters between the nickel and the metal oxide were determined by using the the Levenberg-Marquardt method to fit the following Morse potential function (1) against the interaction energies obtained by density functional theory (DFT) calculations [2].

$$E = \sum_{Zr} D_{Ni-Zr} \{ \exp[-2\beta_{Ni-Zr}(r_{Ni-Zr} - r_{Ni-Zr}^*)] - 2 \exp[-\beta_{Ni-Zr}(r_{Ni-Zr} - r_{Ni-Zr}^*)] \} + \sum_O D_{Ni-O} \{ \exp[-2\beta_{Ni-O}(r_{Ni-O} - r_{Ni-O}^*)] - 2 \exp[-\beta_{Ni-O}(r_{Ni-O} - r_{Ni-O}^*)] \} + \sum_Y D_{Ni-i} \{ \exp[-2\beta_{Ni-i}(r_{Ni-i} - r_{Ni-i}^*)] - 2 \exp[-\beta_{Ni-i}(r_{Ni-i} - r_{Ni-i}^*)] \} \quad (1)$$

where the parameters D_{Ni-A} , β_{Ni-A} , and r_{Ni-A}^* are related to the bond energy, stiffness, and the bond length between nickel and A , respectively. Here, A stands for any atom of Y and Sc doped zirconia surfaces (Zr, O, and i (Y or Sc)).

3. Results and Discussion

To unravel the dopant effect on the sintering process of nickel nanoparticles in the Ni/YSZ and the Ni/ScSZ systems, we adopted the simplified models consisting of two nickel nanoparticle on the YSZ(111) and the ScSZ(111) surfaces, respectively. Figure 1 shows the snapshots of the sintering of nickel nanoparticles on the YSZ(111) and the ScSZ(111) surfaces at 0 and 500 ps. As shown in Figure 1(b) and (d), we observed that the shapes of the nickel nanoparticles on the YSZ(111) and the ScSZ(111) surfaces are different after the sintering. The size of the neck between the two nickel nanoparticles on the YSZ and the ScSZ surfaces is 23.1

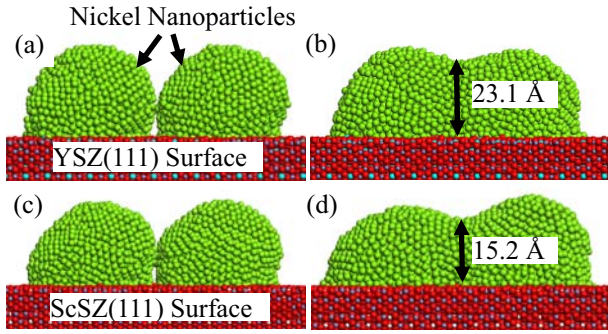


Fig 1. The snapshots of the nickel nanoparticles on the YSZ(111) surface ((a)-(b)) and the ScSZ(111) surface ((c)-(d)) during the sintering at 1073 K: (a) and (c) $t = 0$ ps, (b) and (d) 500 ps.

Å and 15.2 Å, respectively. Thus, we assume that the extent of sintering of nickel nanoparticles on the YSZ surface is larger than that on the ScSZ surface.

Here, to evaluate the differences of the sintering process in the Ni/YSZ and the Ni/ScSZ systems, the shrinkage is calculated:

$$\text{shrinkage} = \frac{R_1 + R_2 - L}{R_1 + R_2}, \quad (2)$$

where R_1 and R_2 is the radius of each nanoparticle at the initial state and L is the distance between the two centers of mass of nickel nanoparticles. The shrinkage takes a negative value before the sintering and the value becomes to zero, indicating the occurrence of the sintering. Simultaneously, the positive value of the shrinkage indicates the extent of sintering. Figure 2 shows the changes in the shrinkage for the Ni/YSZ and the Ni/ScSZ systems. When the sintering of nickel nanoparticles in the Ni/YSZ and the Ni/ScSZ systems takes place from 0 ps, a sharp increase in the shrinkage both in the Ni/YSZ and the Ni/ScSZ systems is observed as shown in Figure 2. Then, a difference of the shrinkage between the two systems increases after 2 ps. The shrinkage of nickel nanoparticles in the Ni/YSZ and the Ni/ScSZ systems are saturated to 0.19 and 0.12 after 100 ps, respectively. This indicates that the extent of sintering in the Ni/YSZ is larger than that in the Ni/ScSZ. Thus, we suggest that the sintering on the YSZ surface takes place more easily than that on the ScSZ surface.

Then, to elucidate the mechanism of the dopant effect on the sintering process on the zirconia surfaces, the adsorption energies between the nickel and the YSZ, and between the nickel and the ScSZ were calculated by using the DFT package, DMol³. We observed that the difference of the adsorption energy ($E_{\text{Ni/YSZ}} - E_{\text{Ni/ScSZ}}$) on the top of dopant site (Y and Sc) is 0.93 eV and the other adsorption energies of the nickel on the ScSZ are also lower than that of the nickel on the YSZ. This depicted that the nickel nanoparticles on the ScSZ surface is more difficult to move than that on the YSZ surface. As a result, the sintering process of nickel nanoparticles on the ScSZ(111) surface is inhibited.

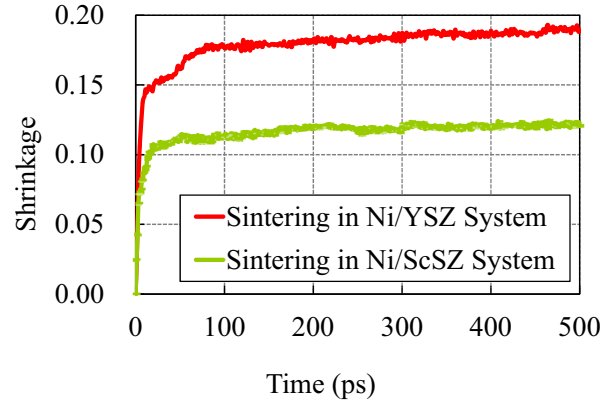


Fig 2. Changes in the shrinkage for the Ni/YSZ(111) and the Ni/ScSZ(111) systems at 1073 K.

In the Ni/YSZ and the Ni/ScSZ anodes, the electrode chemical reaction occurs at triple phase boundary (TPB) sites where the nickel nanoparticles, the hydrogen gas and the ceramic nanoparticles meet together. To unravel the effect of the sintering on the TPB length, we discussed the changes in the TPB length in the Ni/YSZ and the Ni/ScSZ systems. The TPB lengths decrease after the sintering takes place both in the Ni/YSZ and the Ni/ScSZ systems, indicating that the number of chemical reaction sites in the anode declines and the anode degrades. Meanwhile, we observed that the reduction of the TPB length of the Ni/YSZ system is larger than that of the Ni/ScSZ system, because the extent of sintering in the Ni/YSZ is larger than that in the Ni/ScSZ. The large reduction of the TPB length in the Ni/YSZ shows that the number of chemical reaction sites in the Ni/YSZ is less than that in the Ni/ScSZ after sintering. According to this result we suggest that the decrease in catalytic activity of the Ni/ScSZ is smaller than that of the Ni/YSZ with sintering time. This may explain the experimental results [1] in which the degradation of the output voltage of the Ni/ScSZ anode is smaller than that of Ni/YSZ anode in the same current density during the operation.

4. Concluding remarks

We investigated the dopant effect on the sintering process and the degradation on the YSZ(111) and the ScSZ(111) surfaces via molecular dynamics method. We found that sintering on the YSZ surface takes place more easily than that on the ScSZ surface, because the strong adsorption energies of the nickel on the ScSZ inhibits the movement of the nickel nanoparticles. Moreover, the decrease in TPB length with the sintering time reflects the smaller decrease in the output voltage of the Ni/ScSZ than that of the Ni/YSZ due to the dopant effect.

References

- [1] K. Ukai, *et al.*, Proc. Solid Oxide Fuel Cells VII, The Electrochem. Soc. (2001) 375.
- [2] A. Endou, *et al.*, *Jpn. J. Appl. Phys.* **39** (2000) 4255.
- [3] K. Suzuki, *et al.*, *Appl. Phys. Lett.* **73** (1998) 1502.

Sizing of Stirling Engine as the Prime Mover of a Coal Mine CHP System

Mehdi Aghaei Meybodi, Masud Behnia

School of Aerospace, Mechanical and Mechatronics Engineering, The University of Sydney, NSW 2006, Australia
m.meybodi@sydney.edu.au

ABSTRACT

Methane, as a major contributor to the global warming, is the greenhouse gas emitted from coal mines. Abundance of coal mines and consequently a considerable amount of methane emissions requires drastic measures to effectively mitigate harmful effects of coal mining on the environment. We have developed a thermo-economic methodology for conducting an optimisation-based feasibility study on the application of Stirling engines as the prime movers of coal mine combined heat and power (CHP) systems from an economic and an environmental point of view.

1. Introduction

Formation of coal through compression and heating of organic materials, results in generation of methane entrapped in fissures and pores of coal beds. Coal Mine Methane (CMM), which is released during active coal mining, typically has a methane content of 25% to 60%. Stirling engine is an external combustion engine and its working fluid is not involved in the combustion process. External combustion allows for better capability to deal with fuel instability as well as complete combustion and consequently minimizing the production of carbon monoxide. Therefore, Stirling engine-based system can be considered as a potential alternative to the conventional power generation systems. In this study, we aim to conduct an optimization-based feasibility analysis of a Stirling engine-based combined heat and power system installed at a coal mine and to examine the CHP system from a thermo-economic as well as an environmental point of view. Two operational modes have been considered; namely, one-way connection mode (OWC) and two-way connection mode (TWC). With OWC mode, it is only allowed to purchase electricity from the grid (i.e. grid acts as a backup source of electricity to offset the shortfall in generation) while in TWC it is also possible to sell the surplus produced electricity to the grid.

2. Present worth analysis

As a commonly applied method of analyzing engineering projects from an economic point of view, present worth approach is adopted. Net Present Worth (NPW), which is the decisive criterion in this method, is obtained by deduction of Present Worth of Cost (PWC) from Present Worth of Benefits (PWB). Positive NPW values imply that the project is economical. In addition, the maximum value indicates the optimum option. The proposed objective function is defined as:

$$NPW = \sum_{j=1}^k (SV_j \left(\frac{1}{(1+i)^{LT}} \right) - CC_j) - \left(\frac{(1+i)^{LT} - 1}{i(1+i)^{LT}} \right) [ET + \sum_{m=1}^N \left[\sum_{j=1}^k (MC_j + COF_j) + P_b \times C_{el,b} - P_{CHP,r} \times C_{el} - \dot{H}_{CHP,r} \times C_h - P_{CHP,s} \times C_{el,s} \right]_m \times \tau_m] \quad (1)$$

3. Optimization of nominal power

The following procedure is adopted to optimally determine the nominal capacity of the Stirling engine-based combined heat and power system. It is based on the assumption that the CHP system supplies the based load and the shortfall is purchased from the grid.

- For the CHP system nominal capacities from 100 kW to 1 MW (the upper limit in the first iteration) and for each time interval of demand profile (τ_m) calculating NPW (which is represented by NPW_m).
- Adding up the NPW_m values for all time intervals to calculate NPW.
- If the maximum value of NPW (NPW_{max}) corresponds to the upper limit of the CHP system nominal capacity range, the range is increased by an increment of 1 MW and steps 1&2 are repeated. This process continues until a nominal capacity within the considered range leads to the maximum NPW value.
- The nominal capacity associated with the maximum net present worth value is the optimum nominal capacity of the CHP system (which is designated by $P_{CHP,opt}$).
- For all time intervals, the operational strategy of the system is working at $P_{CHP,opt}$.

4. Results and Discussion

To demonstrate the proposed method, it has been used for a case study. Fig. 1 shows the monthly electricity and heat demand profile of a coal mine located south of Sydney. Fig. 2 shows variation of NPW versus the Stirling engine-based CHP system nominal power for TWC mode of operation under the carbon tax and ETS schemes. As shown in the figure, nominal system capacities of 6700 kW and 6300 kW have led to the maximum NPW values under the carbon tax and ETS schemes, respectively. As is evident, carbon tax curve has a steeper slope compared to that of ETS curve. This is due to the fact that the carbon tax scheme has a considerably greater impact on the economics of the system.

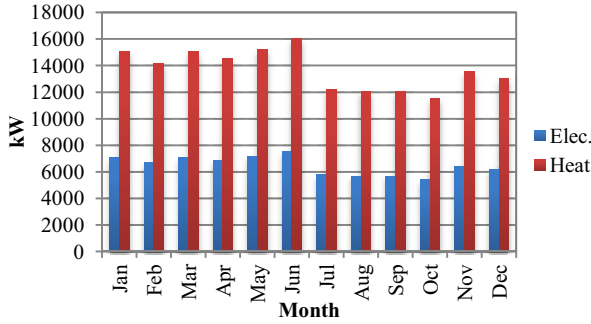


Fig. 1 Demand profile for the case study

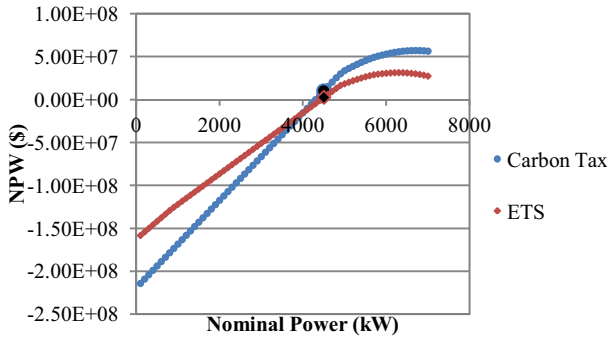


Fig. 2 NPW versus CHP system nominal power in TWC mode

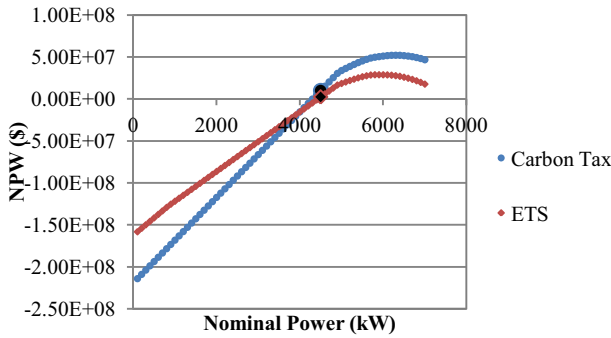


Fig. 3 NPW versus CHP system nominal power in OWC mode

Variation of NPW as a function of CHP system nominal power for OWC mode of operation is depicted in Fig. 3. Maximum NPW values are provided by nominal powers of 6300 kW for the carbon tax scheme and 5900 kW under ETS. As seen from the figure, optimum nominal power and NPW values are less than that of TWC mode due to the fact that selling the excess produced electricity in OWC mode is not allowed. It should be noted that in estimating NPW values for the considered range of nominal powers, the assumption is made that the mine produces enough methane to provide fuel for the system. However, the maximum possible nominal power of the CHP system in order to be continuously supplied by CMM for both operational modes and under both schemes is 4500 kW (the highlighted points on the graphs). Consequently, in spite of not being the optimum option, the selected nominal power of the Stirling engine-based CHP system is 4500 kW.

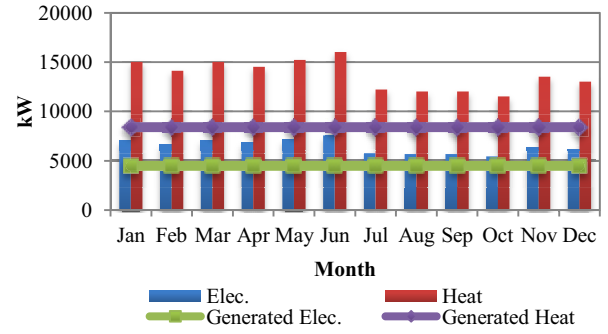


Fig. 4 Operational strategy of selected prime movers

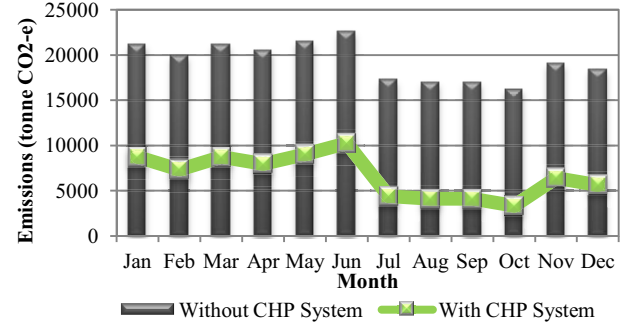


Fig. 5 Monthly greenhouse gas emissions

Fig. 4 shows the operational strategy of the selected prime movers of the Stirling engine-based CHP system. As noted before, prime movers work at their nominal capacity throughout the year. The studied CHP system is substantially effective and supplies 70.6% of the annual electricity demand as well as 62.2% of the annual thermal needs. Further, as Fig. 7 shows, a huge reduction in annual greenhouse gas emissions, a 65.4% decrease, can be achieved by incorporating the CHP system at the mine.

Nomenclature

C = cost (\$/kWh)
 CC = capital cost (\$)
 COF = cost of fuel per hour (\$/hr)
 ET = the emissions term
 \dot{H} = heat rate (kW)
 i = interest rate (%)
 K = number of equipment
 LT = lifetime (year)
 MC = maintenance cost per hour (\$/hr)
 N = number of time intervals of demand profile
 NPW = Net Present Worth (\$)
 P = electric power (kW)
 SV = salvage value (\$)
 τ_m = time interval of demand profile (hr)

Subscripts

b = buying electricity
 CHP = combined heat and power
 el = electricity
 h = heat
 r = required
 s = selling electricity

Experimental and Numerical Investigation on Ignition and Combustion Characteristics of CH₄/O₂/CO₂ Mixture Using a Micro Flow Reactor with a Controlled Temperature Profile

Xing Li^{1,2}, Li Jia², Takakazu Onishi¹, Takuya Tezuka¹, Susumu Hasegawa¹, Kaoru Maruta¹

1, Institute of Fluid Science, Tohoku University, 2-1-1 Katahira, Aoba-ku, Sendai, 980-8577 Japan

2, School of Mechanical and Electronic Control Engineering, Beijing Jiaotong University, No.3 Shang Yuan Cun, Hai Dian District, Beijing, 100044 China

lixing@edyn.ifs.tohoku.ac.jp

ABSTRACT

Stoichiometric CH₄/O₂/CO₂ ($X_{O_2}/X_{CO_2}=0.62$) premixed flame is tested in a micro flow reactor with a controlled temperature profile. Results show that the transition velocities from normal flame to FREI (flame with repetitive extinction and ignition), and FREI to weak flame are different from those of CH₄/air mixture. The flame temperature of the weak flame which corresponding to ignition temperature of the CH₄/O₂/CO₂ ($X_{O_2}/X_{CO_2}=0.62$) mixture was found to be 1235K experimentally. The computation results show that the flame structure of weak flame is quite different from that of normal flame.

1. Introduction

Oxy-fuel combustion technologies combined with carbon dioxide capture and sequestration are expected to contribute reducing global warming [1-3]. For realizing this technology, it is required to enrich our fundamental knowledge on flame characteristics of oxy-fuel combustion. However, studies on oxy-fuel combustion are generally focusing on solid fossil fuels since coal-fired power plants contribute extensively to the world energy and electric power demands [2,3].

Premixed flames are frequently employed to study combustion characteristics and of importance for comparing the property of different fuels [5-8]. Recently, CH₄/air mixture was applied to a micro flow reactor with a controlled temperature profile [5]. The experiment showed that the CH₄/air mixture exhibited three kinds of flame responses, that is, normal flame, FREI and weak flame. Among these flames, weak flame has specific characteristics which indicate the ignition temperature of the given mixture. Weak flames were successfully applied for study on the general ignition and combustion characteristics of various fuels [6-8].

In this study, stoichiometric CH₄/O₂/CO₂ mixture which has the same laminar burning velocity as stoichiometric CH₄/air mixture (36.9 cm/s) [4] was selected for examining a mixture for oxyfuel combustion. Based on PREMIX [9] with GRI-mech 3.0 [10] $X_{O_2}/X_{CO_2}=0.62$ was chosen. The aim of present work is to study combustion characteristics and ignition property of CH₄/O₂/CO₂ ($X_{O_2}/X_{CO_2}=0.62$) mixture by using micro flow reactor with a controlled temperature profile [5].

2. Experimental and Numerical Methods

Fig. 1 shows a schematic of experimental setup. A quartz tube with 2 mm inner diameter and a H₂/Air burner were employed. A smooth temperature gradient, ramping from 300K to 1300K, along the inner surface of the tube wall in x-axis direction can be obtained by adjusting the H₂/Air burner. The H₂/Air burner also benefits a better visualization of chemiluminescence from hydrocarbon flames in the micro flow reactor. Inner wall temperature was measured by a K-type thermocouple (diameter of 50 μm) inserted from the exit

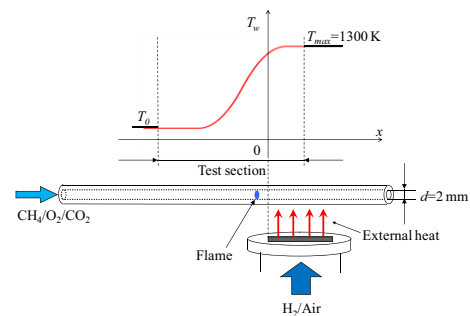


Fig. 1. Schematic of experimental system.

of the tube. The effect of air flow velocity on the wall temperature profile was confirmed to be almost negligible in the velocity range of the present interest [5]. A single-lens reflex digital camera (Nikon D-300) with a CH filter was employed for recording flame images. In the experiment, stoichiometric CH₄/O₂/CO₂ ($X_{O_2}/X_{CO_2}=0.62$) mixture was supplied into the micro flow reactor. Gas flow rates were controlled by digital mass flow controllers. Flame positions were defined by the peak of luminosities from the detected images [5-8].

To elucidate experimental results, one-dimensional computations with detailed chemistry were conducted. A steady-state code [5] based on PREMIX [9] and GRI-mech 3.0 [10] was used.

3. Results and Discussion

Fig. 2 shows CH₄/O₂/CO₂ ($X_{O_2}/X_{CO_2}=0.62$) premixed flame images with different mean flow velocity in the micro flow reactor. Flow direction is from left to right. At the mean velocity of 60 cm/s, a stable normal flame with high luminosity was observed. Non-stationary flames termed FREI formed at 10 cm/s. Stationary flame with extremely low luminosities was observed at mean velocity of 1 cm/s. Note that the color in Fig. 2c was converted to a gray scale to show weak luminescence from the flame clearly.

Flame positions of normal and weak flames, and extinction and ignition points of FREI as a function of mean flow velocity at equivalence ratio $\phi = 1$ are shown in Fig. 3. Dashed line denotes tube wall temperature profile. Similar to CH₄/Air premixed flame behaviors in previous study [5], stable flames (Fig. 2a and c) were observed in

a

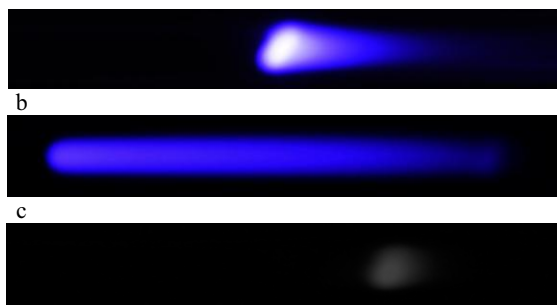


Fig. 2. Flame images ($\phi = 1.0$); (a) normal flame (60 cm/s), (b) FREI (10 cm/s), and (c) weak flame (1 cm/s).

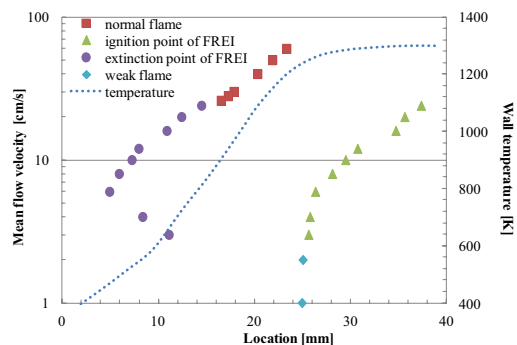


Fig. 3. Measured flame positions and extinction and ignition points of FREI for variable mean flow velocity at $\phi = 1.0$.

high and low velocity regimes, and non-stationary flame termed FREI (Fig. 2b) was observed in the moderate velocity regime. However the transition velocities from normal flame to FREI and FREI to weak flame are 25 cm/s and 2 cm/s for $\text{CH}_4/\text{O}_2/\text{CO}_2$ ($X_{\text{O}_2}/X_{\text{CO}_2}=0.62$) mixture while 40 cm/s and 5 cm/s for CH_4/Air flame [5]. The position of $\text{CH}_4/\text{O}_2/\text{CO}_2$ ($X_{\text{O}_2}/X_{\text{CO}_2}=0.62$) weak flame when the mean velocity is 1 cm/s locate at 1235K, and CH_4/Air weak flame is at 1225K from the previous study [5]. This means stoichiometric $\text{CH}_4/\text{O}_2/\text{CO}_2$ ($X_{\text{O}_2}/X_{\text{CO}_2}=0.62$) mixture which has the same laminar burning velocity as stoichiometric CH_4/Air needs higher temperature to be ignited.

Fig. 4 shows the computational profiles of THRR (total heat release rate) and major species mole fractions at mean flow velocity of 60 cm/s. It can be found that $\text{CH}_4/\text{O}_2/\text{CO}_2$ ($X_{\text{O}_2}/X_{\text{CO}_2}=0.62$) normal flame shows conventional premixed flame structure under given temperature profile. However, as shown in Fig. 5, when the mean flow velocity is 1 cm/s, the reaction zone is thicker than that of 60 cm/s with a dual peak of total heat release rate. For further investigation, the contributions of elementary reactions on total heat release rate were analyzed. Fig. 6 shows that the computational heat release rate profiles of the selected elementary reactions which have large contributions to the dual peak of total heat release rate at 1 cm/s. Seven reactions with large contributions to the total heat release rate profile were chosen. It can be seen that, R 35 plays the leading role in both peaks, R 168, R 119 and R 101 are other three main reactions for the first peak. Except R 35, three reactions of R 99, R 46 and R 33 contribute to the second peak, and it can be found that R 33 also affects the first peak.

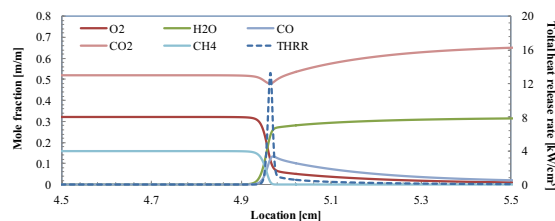


Fig. 4. Computational profiles of total heat release rate and major species mole fraction at 60 cm/s.

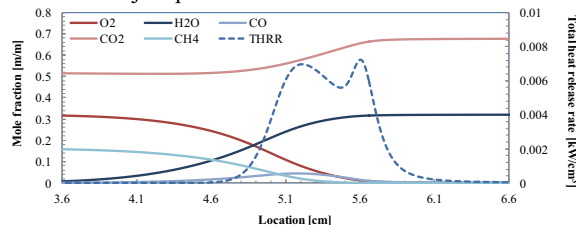


Fig. 5. Computational profiles of total heat release rate and major species mole fraction at 1 cm/s.

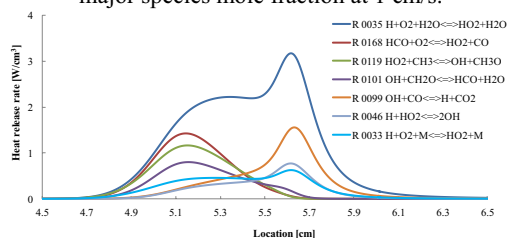


Fig. 6. Computational heat release rate profiles of the selected elementary reactions which have large contributions to the dual peak total heat release rate at 1 cm/s.

4. Concluding remarks

$\text{CH}_4/\text{O}_2/\text{CO}_2$ ($X_{\text{O}_2}/X_{\text{CO}_2}=0.62$) premixed flame shows normal flame, FREI and weak flame in different mean flow velocity regimes. The ignition temperature of weak flame was found at 1235K experimentally which is 10K higher than CH_4/Air flame. Computation results show a thin reaction zone with single peak total heat release rate of normal flame, while a thicker reaction zone with dual peak total heat release rate of weak flame.

Acknowledgements

Mr. Xing Li expresses sincere appreciation to Chinese Scholarship Council and Innovation Fund of Excellent Doctorial Candidate Program of Beijing Jiaotong University (No.141087522) for the scholarship.

References

- [1] B.J.P. Buhre, L.K. Elliott, C.D. Sheng, R.P. Gupta. *Prog. Energy Combust. Sci.*, 31 (2005), pp. 283–307.
- [2] M.B. Toftegaard, J. Brix, P.A. Jensen, P. Glarborg, A.D. Jensen, *Prog. Energy Combust. Sci.*, 36(5)(2010), pp 581–625.
- [3] F. Normann, K. Andersson, B. Leckner, F. Johnsson. *Prog. Energy Combust. Sci.*, 35 (5) (2009), pp. 385–397.
- [4] L. Selle, T. Poinsot, B. Ferret. *Combust. Flame*, 158 (1) (2011), pp 146–154.
- [5] Y. Tsuboi, T. Yokomori, K. Maruta. *Proc. Combust. Inst.*, 32 (2009), pp. 3075–3081.
- [6] H. Oshibe, K. Maruta, et al. *Combust. Flame*, 157 (8) (2010), pp. 1572–1580.
- [7] A. Yamamoto, K. Maruta, et al. *Proc. Combust. Inst.*, 33 (2) (2011), pp. 3259–3266.
- [8] M. Hori, K. Maruta, et al. *Combust. Flame*, 159 (3) (2012), pp 959–967.
- [9] R.J. Kee, J.F. Grcar, M.D. Smooke, J.A. Miller, A Fortran Program for Modeling Steady Laminar One-dimensional Premixed Flames, Report No. SAND85-8240, Sandia National Laboratories, 1985.
- [10] http://www.me.berkeley.edu/gri_mech.

Error Analysis for the Volume Penalization Method with Continuous Mask Functions

Wakana Iwakami Nakano¹, Nozomu Hatakeyama², Yuji Hattori¹

¹Institute of Fluid Science, Tohoku University, 2-1-1 Katahira, Aoba-ku, Sendai, 980-8577, Japan

²Department of applied chemistry, Tohoku University, 6-6-10 Aoba, Aramaki-aza, Aoba-ku, Sendai, 980-8579, Japan
wakana@dragon.ifs.tohoku.ac.jp

ABSTRACT

We have investigated the characteristics of the error caused by the volume penalization method. The method features the applicability to the numerical simulations of the flow passing moving and deforming solid bodies with complicated geometry. The penalization term, multiplied by the mask function $\chi(x)$, is added to the governing equation. The convergence property of the discretization error is improved if we use the continuous hyperbolic tangent function instead of the discontinuous step function for $\chi(x)$. Meanwhile, we found that the penalization error decreases as $\chi(x)$ becomes close to the discontinuous step function.

1. Introduction

The volume penalization method (VPM)^[1] is one of the useful methods to numerically investigate the flow dynamics including the interactions between a flow and a solid boundary. In VPM it is not required to generate a boundary-fitted grid and to impose a boundary condition on a solid surface. A force term, called a penalization term, is just added to the incompressible Navier-Stokes (N-S) equations. The penalization term is activated by the mask function $\chi(x)$ only on the solid region so that the penalized N-S equation turn to the Darcy equation^[2] in the solid region and the original N-S equation in the fluid region. Darcy equation is one of the equations governing the fluid in the porous medium with permeability η . Generally, the step function is chosen as $\chi(x)$, whose value is 1 on the solid region and 0 on the fluid region. However, the smoothed mask function is needed to suppress the numerical oscillation, if a solid object moves around in the computational region, at least when we use the spectral method^[3]. In this study, we pay a special attention to the continuous mask function.

In the recent years, using the discontinuous mask function, we have examined the characteristics of the error for VPM^[4], and have proposed a new approach for the error reduction^[5]. The total error is composed of the discretization error, the penalization error, and the other negligible error. As the grid/mode number N increases, the penalization error becomes dominant, and the error converges to a constant value. We found that the penalization error decreases with increasing N if the mask function is converted for the boundary between solid and fluid regions to be shifted toward fluid region with $(\nu\eta)^{1/2}$. However, it shows the second order of convergence due to the C^1 continuity of the penalized solution. In this study, using the continuous mask function, we examine the characteristics of the total error for the continuous mask function, and confirm whether the order of convergence is improved or not.

2. Numerical Method

We select the simple basic equation for this study. It is the one-dimensional Burgers equation with a penalization term

$$\frac{\partial u}{\partial t} + u \frac{\partial u}{\partial x} = \nu \frac{\partial^2 u}{\partial x^2} - \frac{\chi(x)}{\eta} u, \quad (1)$$

where t , x , u , ν , and η denote time, spatial coordinate, velocity, kinetic viscosity coefficient, and permeability, respectively. The discontinuous mask function is described as

$$\chi(x) = \begin{cases} 0 & \text{in } \Omega_f, \\ 1 & \text{in } \Omega_s \end{cases}, \quad (2)$$

where $\Omega_f = \{x \mid 0 \leq |x| < L_{VP}\}$ denotes the fluid region, $\Omega_s = \{x \mid L_{VP} \leq |x| \leq L\}$ the solid region, and $\Omega = \{x \mid 0 \leq |x| \leq L\}$ the whole region. The distance from the origin to the outer boundary is $L \approx 2\pi$, the distance from the origin to the boundary between Ω_f and Ω_s is $L_b = \pi$, and the distance from the origin to the penalization boundary is $L_{VP} = L_b - (\nu\eta)^{1/2}$, satisfying $\chi(\pm L_{VP}) = 1/2$. On the other hand, the continuous mask function is written in

$$\chi(x) = 1 + \frac{1}{2} \left(1 - \tanh \frac{x + L_{VP}}{\delta w} \right) - \frac{1}{2} \left(1 - \tanh \frac{x - L_{VP}}{\delta w} \right), \quad (3)$$

where δw is related to the smoothness of the hyperbolic tangent function. Initial value is given by

$$u(x) = \begin{cases} 0 & \text{in } \Omega_s, \\ -\sin(x) & \text{in } \Omega_f \end{cases}. \quad (4)$$

The 4th-order Runge-Kutta method is applied for the time integration, and the 4th-order compact scheme is used for the space discretization.

3. Results and Discussion

First, we verify whether our new approach for error reduction is also effective for the continuous mask function or not. The distribution of $\chi(x)$ near a solid boundary is shown in Fig.1. The smoothness of δw is variable depending on Δx . The total error is defined as

$$\delta_{tot} \equiv \sqrt{\frac{\int_{\Omega_f} |u(x) - u_{\text{exact}}(x)|^2 dx}{\int_{\Omega} dx}}, \quad (5)$$

where u_{exact} is the exact solution. In Fig.2, the dependency of the total error on N indicates that the total error decreases with increasing N so that our error reduction method is considered of value even if the mask function is continuous.

Next, we increase N while the smoothness of δw is

constant, as shown in Fig.3. Here, we define the discretization error as

$$\delta_{dis} \equiv \sqrt{\frac{\int_{\Omega_f} |u(x) - u_{N_{\max}}(x)|^2 dx}{\int_{\Omega} dx}}, \quad (6)$$

where $u_{N_{\max}}$ is the numerical solution at the maximum grid number. Most of the penalization error is removed in this error. Fig.4 demonstrates that the 4th-order convergence of the discretization error is accomplished for larger δw . Thus we can say that the continuous mask function can make the convergence property of discretization error improved. However, Fig.5 shows that the total error as function of N grows with increasing δw . So the closer to the step function, the better solution we obtain. Meanwhile, in some case, we might need to use the continuous mask function in order to perform the numerical simulation for the flow around a moving solid body without any numerical oscillation. We have to choose moderate values of δw for the use of the continuous mask function.

4. Concluding remarks

The treatment of converting mask function for the boundary between solid and fluid regions to be shifted toward fluid region with $(v\eta)^{1/2}$ for error reduction is effective even if the mask function is continuous. If the mask function is sufficiently smooth, the convergence property of the discretization error is improved, but the total error increases. Depending on the numerical method, therefore, we should find the continuous mask function as sharp as possible, enough to suppress the numerical oscillation, for the simulation of the flow around a moving solid body.

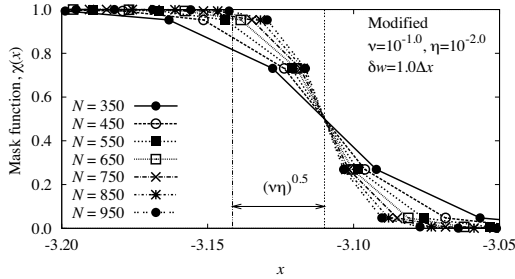


Fig. 1 The distribution of $\chi(x)$ with $\delta w \propto \Delta x$.

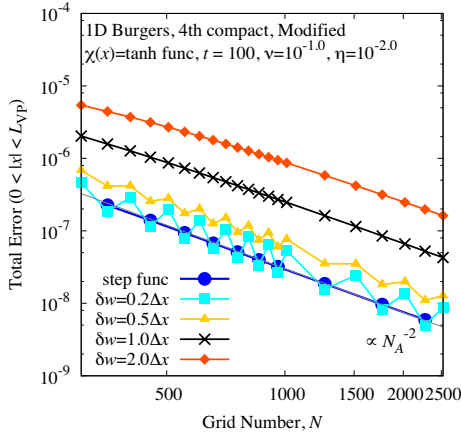


Fig. 2 The N dependency of δ_{tot} for $\delta w \propto \Delta x$.

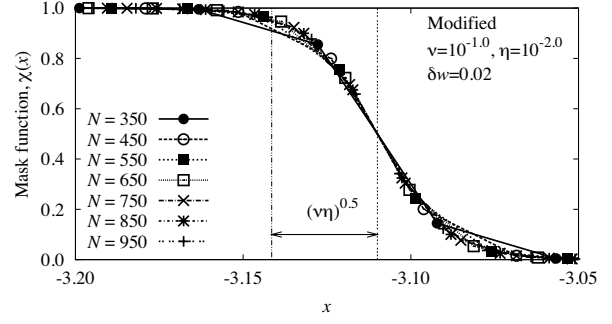


Fig.3 The distribution of $\chi(x)$ with $\delta w = \text{const}$.

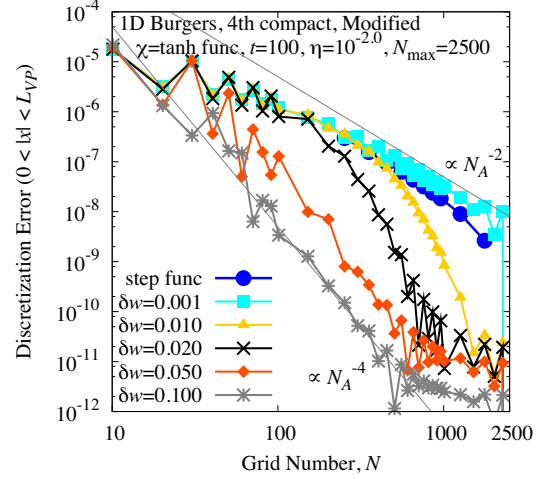


Fig. 4 The N dependency of δ_{dis} for $\delta w = \text{const}$.

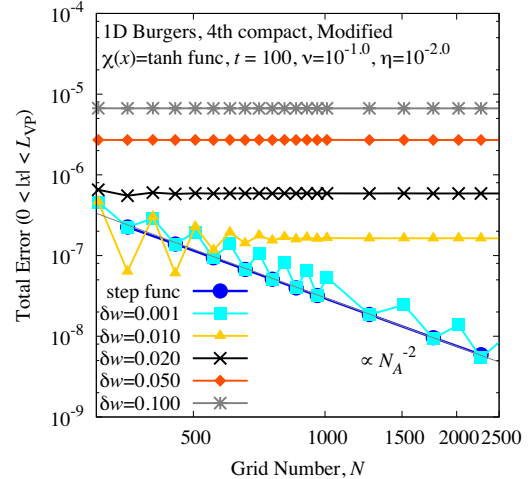


Fig. 5 The N dependency of δ_{tot} for $\delta w = \text{const}$.

References

- [1] A. Mittal and G. Iaccarino, *Annu. Rev. Fluid Mech.*, **37** (2005), pp. 239 – 261.
- [2] H. C. Brinkman, *Appl. Sci. Res.*, **1**(1949), pp.27– 34.
- [3] D. Kolomenskiy, K. Schneider, *J. Comp. Phys.*, **228** (2009), pp. 5687 – 5709.
- [4] W. I. Nakano, N. Hatakeyama, and Y. Hattori, *Proceedings of Seventh International Conference on Flow Dynamics*, (2010), pp. 138-139.
- [5] W. I. Nakano, N. Hatakeyama, and Y. Hattori, *Proceedings of Eighth International Conference on Flow Dynamics*, (2011), pp. 88-89

Numerical Study of Particle Formation in Supercritical-fluid Flows of Hydrothermal Synthesis

Takashi FURUSAWA and Satoru YAMAMOTO

Graduate School of Information Sciences, Tohoku University
Aramaki Aza Aoba 6-6-01, Aoba-ku, Sendai 980-8579, Japan
furusawa@caero.mech.tohoku.ac.jp

ABSTRACT

Mixing flows of supercritical fluid and liquid with a chemical reaction of metal salt and a particle formation of metal oxide in a supercritical hydrothermal synthesis (SCHS) reactor are numerically investigated. The flows in a T-shaped channel reactor are calculated. Then, the metal oxide particle is generated in the contact region of mixing point and the right wall of main channel. The comparison of the inlet temperature difference is performed. The distributions of number of particles are different between those at a different temperature.

1. Introduction

Supercritical fluid is in a state where the temperature and the pressure are beyond the critical point. Supercritical fluid has an intermediate property between gas and liquid. In addition, anomalous properties have been found near the critical point, such as extreme changes of density, thermal conductivity, and speed of sound. Recently supercritical fluids have been applied to nano-scale particle fabrication, coolant of light-water reactor and so on. The continuous supercritical hydrothermal synthesis (SCHS) proposed by Adschiri^{[1][2]} is one of innovative methods for fabricating nano-scale particles of metal oxide. In this method, the metal salt solution at room temperature is mixed with supercritical water in the continuous reactor. Since the solubility and the reactivity are rapidly changed near the critical point, fine and uniform particles are formed in the reactor. Understanding the mixing flow of the solution and the supercritical water; evaluating the chemical reaction and the particle formation in the continuous reactor are quite important for controlling the particle size and producing proper particles. However, the experimental observation in the supercritical state is quite difficult because of the high pressure and temperature.

We proposed a numerical method for simulating supercritical-fluid flows: Supercritical-fluids Simulator (SFS)^[3]. In this method, the preconditioning method is coupled with a program package for thermo-physical properties of fluids (PROPATH)^[4]. In PROPATH, mathematical models based on a polynomial equation approximating thermo-physical properties are defined in wide range of temperature and pressure. This program package can be adapted to the calculation of thermophysical properties near the critical point. SFS was already extended to not only high speed flows but also very slow flows of supercritical fluids^[5].

In this study, we calculate mixing flows of supercritical water and liquid solution with a chemical reaction model and a particle formation model in which four convection equations are solved.

2. Numerical method

The two-dimensional compressible Navier-Stokes (NS) equations with the preconditioning approach are

solved with a chemical reaction model and a nucleation model based on the moment method. The conservation equations of the metal salt concentration C_0 , metal oxide concentration C , zeroth-order moment μ_0 and first-order moment μ_1 are additionally solved with NS equations. The set of equations is written in vector form as

$$\Gamma \frac{\partial \hat{Q}}{\partial t} + \frac{\partial F_i}{\partial \xi_i} + \frac{\partial F_{vi}}{\partial \xi_i} + S_1 + S_2 = 0 \quad (i=1,2) \quad (1)$$

where

$$\Gamma = \begin{bmatrix} \theta & 0 & 0 & \rho_T & 0 & 0 & 0 & 0 \\ \theta u_1 & \rho & 0 & \rho_T u_1 & 0 & 0 & 0 & 0 \\ \theta u_2 & 0 & \rho & \rho_T u_2 & 0 & 0 & 0 & 0 \\ \theta h - (1 - \rho h_p) & \rho u_1 & \rho u_2 & \rho_T h + \rho h_T & 0 & 0 & 0 & 0 \\ \theta C_0 & 0 & 0 & \rho_T C_0 & \rho & 0 & 0 & 0 \\ \theta C & 0 & 0 & \rho_T C & 0 & \rho & 0 & 0 \\ \theta \mu_0 & 0 & 0 & \rho_T \mu_0 & 0 & 0 & \rho & 0 \\ \theta \mu_1 & 0 & 0 & \rho_T \mu_1 & 0 & 0 & 0 & \rho \end{bmatrix}$$

$$\hat{Q} = J \begin{bmatrix} P \\ u_1 \\ u_2 \\ T \\ C_0 \\ C \\ \mu_0 \\ \mu_1 \end{bmatrix}, \quad F_i = J \begin{bmatrix} \rho U_i \\ \rho u_1 U_i + \frac{\partial \xi_i}{\partial x_1} p \\ \rho u_2 U_i + \frac{\partial \xi_i}{\partial x_2} p \\ (e + p) U_i \\ \rho C_0 U_i \\ \rho C U_i \\ \rho \mu_0 U_i \\ \rho \mu_1 U_i \end{bmatrix}, \quad F_{vi} = J \frac{\partial \xi_i}{\partial x_j} \begin{bmatrix} 0 \\ \tau_{1i} \\ \tau_{2i} \\ \tau_{ki} u_k + \kappa \partial T / \partial x_i \\ D_0 \rho C_0 \\ D \rho C \\ 0 \\ 0 \end{bmatrix}$$

$$S_1 = - \begin{bmatrix} 0 \\ 0 \\ 0 \\ 0 \\ -k \rho C_f \\ k \rho C_f - \frac{\rho_c}{M_c} (\rho IV + \rho G \mu_0) \\ \rho I \\ \rho IV_c + \rho G \mu_0 \end{bmatrix}, \quad S_2 = - J \begin{bmatrix} 0 \\ 0 \\ (\rho_s - \rho) g \\ (\rho_s - \rho) \mu_2 g \\ 0 \\ 0 \\ 0 \\ 0 \end{bmatrix}$$

where I is the nucleation rate and G is the nuclear growth rate. k is the reaction rate. D_0 and D are the dissipation rates of metal salt and metal oxide,

respectively.

Eq. (1) is solved by the numerical method based on the preconditioned Roe's scheme and the preconditioned LU-SGS scheme [6].

Thermophysical properties are calculated from PROPATH. It contains thermo-physical properties for 48 substances such as water, carbon dioxide, oxygen, nitrogen and so on, in wide-range pressure and temperature conditions. The properties of gas, liquid and supercritical fluid are defined as numerical functions of pressure and temperature. For example, the equation of state (EOS) for water was standardized by IAPWS IF97.

3. Numerical results

Mixing flows of supercritical water and liquid solution in a T-shaped channel are calculated with the chemical reaction and the particle formation. Liquid solution from the sub channel is injected to supercritical water in the main channel. The supercritical water and the liquid solution are mixed downward and the chemical reaction is occurred and the particles are fabricated. The computational grid has 241x31 and 31x131 grid points for the main channel and the sub-channels. The channel width is 0.5mm. The inlet velocities of main and sub channels are 0.245m/s and 0.016m/s, respectively. The inlet temperature of the main channel is 750K, 700K and 650K. The inlet temperature of sub-channel is 300K. Bulk pressure is 30MPa. Liquid solutions of Al are assumed and AlO(OH) are generated in the mixing point.

Figures 1-3 show the calculated results of temperature and number of particles in each case. The solution of 750K and 700K is immediately mixed with supercritical fluid near the mixing point. The solution of 650K mainly mixed in the main channel. The particles are formed at the contact region of mixing point and the right wall of main channel. The number of particles of 650K is smaller than that of other cases because of the difference of solubility. These results show that the higher inlet temperature makes particles rapidly.

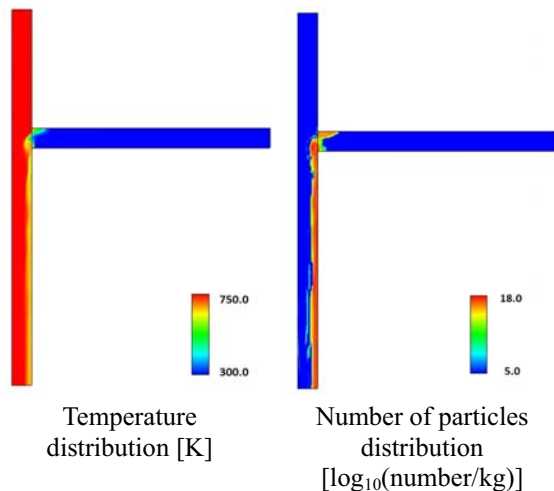


Fig.1 Numerical results of 750K.

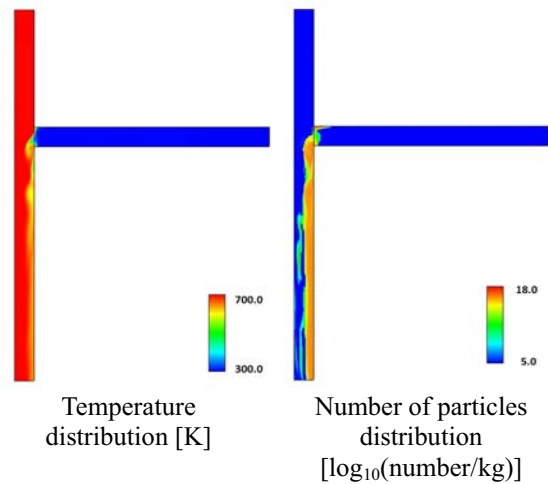


Fig.2 Numerical results of 700K.

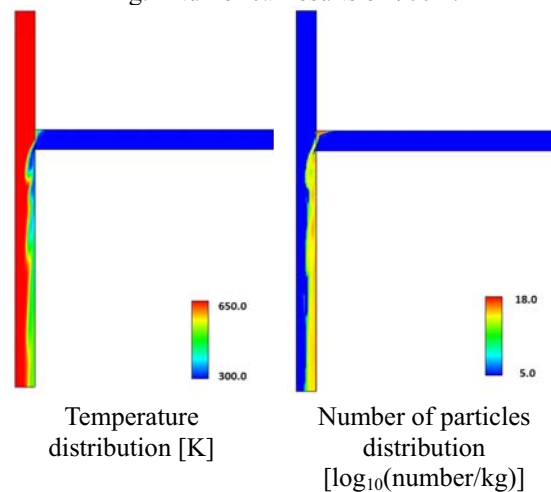


Fig.3 Numerical results of 650K.

4. Conclusions

Mixing flows of supercritical fluid and liquid solution with the chemical reaction and the particle formation in the SCHS reactor were calculated. The temperature distributions and the number of particles distributions are compared with each case of 750K, 700K and 650K as the inlet temperature. The particles are formed along the right wall of main channel and in the contact region. The number of particles distributions were different in each inlet temperature condition because of the difference of solubility.

References

- [1] T. Adschiri, K. Kanazawa and K. Arai., J. Am. Ceram. Soc., 75-4 (1992), pp. 1019-1022.
- [2] T. Adschiri, Y. Hakuta, K. Kiwamu and K. Arai, J. of Nanoparticle Research, 3 (2001), pp.227-235.
- [3] S. Yamamoto and T. Furusawa, Proc. of 6th Int. Conf. on Computational Fluid Dynamics, Computational Fluid Dynamics 2010 (2010), pp. 661-667, Springer.
- [4] A PROGRAM PACKAGE FOR THERMOPHYSICAL PROPERTIES OF FLUIDS by PROPATH group.
- [5] S. Yamamoto, T. Furusawa and R. Matsuzawa, Int. J. Heat and Mass Transfer, 54-4 (2011), pp.774-782.
- [6] S.Yamamoto, J. Comp. Phys., 207-1 (2005), pp.240-260.

Error Analysis of Volume Penalization Method for Two-Dimensional Navier-Stokes Equations

Yuzuru Yatagai¹, Wakana Iwakami Nakano², Yuji Hattori²

¹Department of Applied Information Sciences, Graduate school of Information Sciences, Tohoku University
Aramaki Aoba 6-3-09, Aoba-ku Sendai, Miyagi, 980-8579, Japan
yuzuru@dragon.ifs.tohoku.ac.jp

²Institute of Fluid Science, Tohoku University

ABSTRACT

The volume penalization method can be used for numerical simulations of flow around moving complex shaped deformable bodies. These bodies are regarded as porous media with small permeability η . In this study, we intend to reduce the error caused by the penalization term, which depends on η and on the mask function $\chi(\mathbf{x})$, for two-dimensional Navier-Stokes equations. It is found that a shift of the mask function decreases the penalization error with increasing spatial resolutions. Moreover, the penalization error mainly occurs near the boundaries between the flow and the bodies.

1. Introduction

Numerical simulations of flows around solid bodies are carried out for engineering requirement and scientific purpose. For imposing the boundary conditions, the body-fitted computational grid has been normally used. However, its numerical procedure can become complicated and it requires many computational costs when bodies move, have complicated shapes and are deformable. The volume penalization method (VPM) is one of the immersed boundary methods (IBMs). In VPM, an external force term, called a penalization term, is added instead of imposing boundary conditions of bodies. This simple procedure enables us to easily calculate flows around complex geometries which are movable and deformable. In addition, VPM can be applied to various numerical codes with high accuracy such as the spectral method and the compact scheme^{[1][2]}.

In the previous study, it was found that the modification of the mask function makes the penalization error decrease with increasing grid number in case of the one-dimensional Burgers equation^[2]. However, it has not been known that the error reduction method is effective for two-dimensional flow simulations.

In this study, we calculate the Couette flow between two cylinders to do error analysis by comparing with exact solutions. We show that the way to decrease errors in calculation by VPM is applicable to the two-dimensional Navier-Stokes equations.

2. Numerical Method

We solve the two-dimensional Navier-Stokes equations with a penalization term

$$\frac{\partial \mathbf{u}}{\partial t} + (\mathbf{u} \cdot \nabla) \mathbf{u} = -\nabla p + \nu \nabla^2 \mathbf{u} - \frac{\chi(\mathbf{x})}{\eta} (\mathbf{u} - \mathbf{u}_b), \quad (1)$$

$$\nabla \cdot \mathbf{u} = 0, \quad (2)$$

where t , p , ν , $\chi(\mathbf{x})$, η , \mathbf{u} , \mathbf{u}_b denote time, pressure, kinetic viscosity coefficient, mask function,

permeability, velocity and velocity of bodies, respectively.

We use the pseudo-spectral method for space discretization on a doubly periodic square domain $2\pi \times 2\pi$ with mode number $N^2=256^2 - 4096^2$. To remove the aliasing error, we apply the 2/3 rule. For time development, we use the 4th-order Runge-Kutta method. Since we use an explicit time integration scheme, permeability η must be larger than the time step Δt for numerical stability. In the present study, we set $\eta=1.0 \times 10^{-2}$, 10^{-3} and 10^{-4} .

We consider the Couette flow between a rotating inner cylinder with the angular velocity $\Omega=1.0$ and a stationary outer cylinder (Fig.1). The radii of the inner and the outer cylinder are $a=0.4\pi$ and $b=0.8\pi$, respectively. The Reynolds number is defined as

$$Re = \frac{\Omega a(b-a)}{\nu}. \quad (3)$$

In this calculation, we set $\nu=1.0 \times 10^{-2}$, hence $Re=158$. To avoid an initial error when the inner cylinder starts to rotate impulsively, initial values are set to the steady exact solution as follow^[3]

$$u_\theta = \frac{a\Omega}{b^2 - a^2} \left(\frac{ab^2}{r} - ar \right), \quad (4)$$

where u_θ denotes azimuthal velocity and r is the radial coordinate.

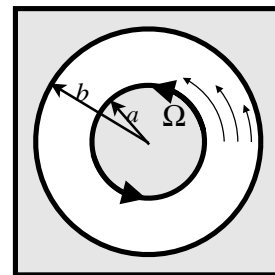


Fig.1 Couette flow between two cylinders.

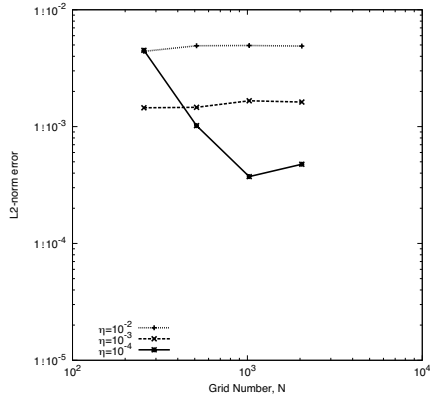
We use two types of the mask functions which define the solid and flow domains

Normal type: Step function that is equal to 1 in the solid domain and 0 in the flow domain.

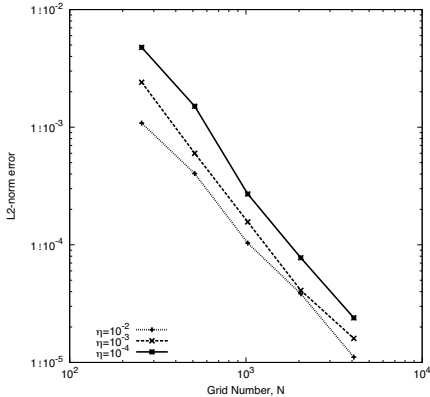
Shift type: The boundaries between $\chi(\mathbf{x})=0$ and 1 are moved $(\nu\eta)^{1/2}$ toward the flow domain.

3. Results and Discussion

We calculate the L2-norm error averaged in the flow domain where the mask function is 0 (Fig.2). This shows the dependence of the total error on the mode number N . The total error is composed of the penalization error, the discretization error, and the other numerical errors. For the normal type mask function, although N is increased, the total error converges to a certain constant value which depends on η (Fig.2 (a)). The values become smaller with small η . On the other hand, for the shift type, the total errors decrease continuously with increasing N (Fig.2 (b)). In addition, the errors for the shift type are smaller than those for the normal type. This is the effect of shifting the mask function. Furthermore, for the shift type, the errors become smaller with larger η . This is because the length scale of the shift distance $(\nu\eta)^{1/2}$ is large for the grid spacing $dx (=2\pi/N)$. This result agrees with previous one-dimensional calculation[2].



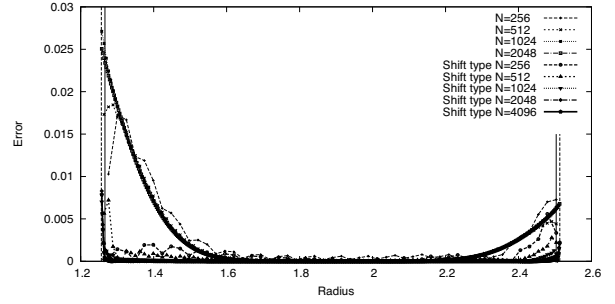
(a) Normal type



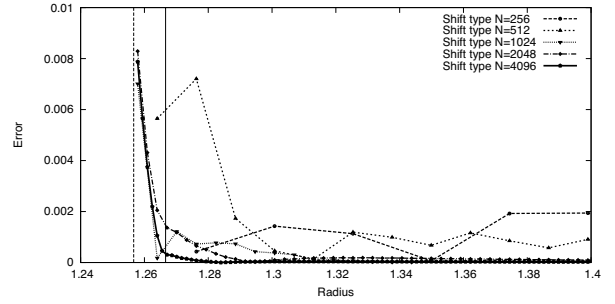
(b) Shift type

Fig.2 The total error averaged in the flow domain for (a) the normal type mask function and (b) the shift type one.

We show the error distribution at $y=0$ and $a \leq x \leq b$ in Fig.3. The errors for the shift type are smaller than those for the normal type (Fig.3 (a)). Moreover, when N increases, they collapse to a single line. This is caused by the penalization error because it does not depend on N . For the shift type, the penalization error appears in the region for $a \leq x \leq a + (\nu\eta)^{1/2}$ (Fig.3 (b)). The error around near the outer cylinder has the same tendency as that around the inner one.



(a) Whole flow domain



(b) Around the inner cylinder

Fig.3 Error distribution for $\eta=1.0 \times 10^{-2}$ (a) in the whole flow domain and (b) near the inner cylinder.

4. Concluding remarks

We carried out numerical simulation of the two-dimensional Couette flow between cylinders by volume penalization method and analyzed the errors. We found that a shift of the mask function makes the penalization error decrease continuously with increasing spatial resolutions. Furthermore, the penalization error appears only near the cylinders for the displaced region of $(\nu\eta)^{1/2}$ in the flow domain.

References

- [1] K. Schneider and M. Farge, *J. Fluids Struct.*, **20** (2005), pp. 555-566.
- [2] W. I. Nakano, N. Hatakeyama, and Y. Hattori, *Proceedings of Eighth International Conference on Flow Dynamics*, (2011), pp. 88-89.
- [3] G. I. Taylor, *Containing Papers of a Mathematical or Physical Character*, **223** (1922), pp. 289-343

A Study of Volume Penalization Method for Direct Numerical Simulation of Aeroacoustic Sound

Ryu Komatsu¹, Wakana Iwakami Nakano², Yuji Hattori²

¹Graduated School of Information Sciences, Tohoku University, 2-1-1 Aoba-ku, Sendai, 980-8577, JAPAN

²Institute of Fluid Science, Tohoku University, 2-1-1 Aoba-ku, Sendai, 980-8577, JAPAN
Komatsu@dragon.ifs.tohoku.ac.jp

ABSTRACT

We develop a method for direct numerical simulation of aeroacoustic sound generated in a flow of which geometry is complex and time-dependent. Volume penalization method, which is one of the immersed boundary methods, is applied to the compressible Navier-Stokes equations. The penalization terms proposed by Liu and Vasilyev are used. As an example the two-dimensional flow past a square cylinder is considered. Preliminary results show that both the Karman vortex street and the aeroacoustic sound are captured.

1. Introduction

The problem of aeroacoustic noise has been one of the great concerns in recent years. There is increasing need for reduction of the aeroacoustic noise. In order to reduce noise, it is necessary to predict it accurately and to understand the physical mechanisms of aeroacoustic sound generation and propagation.

A number of studies on aeroacoustic sound have been done both experimentally and computationally. However, most of the experimental approaches cannot provide detailed information about the physical phenomena generating aeroacoustic sound. Thus, there are strong needs for accurate prediction of the sound by numerical simulations. In the present study to compute the aeroacoustic sound we use direct numerical simulation (DNS), which has advantages in capturing flow and sound waves simultaneously.

Most of the previous DNS studies are based on body-fitted grid methods for the complex geometry problems. However, there are some disadvantages for this method. For example, the grid generation process can be very expensive for moving boundary problems. In an alternative approach, the immersed boundary method (IBM), simulations are carried out on fixed Cartesian grids which are not body-conforming; its main advantage is the efficient implementation for stationary and moving solid boundaries of arbitrary complexity.

The volume penalization method (VPM) is one of IBM. The main idea is to model solid obstacles as porous media with porosity and viscous permeability which are close to zero. By this approach the flow problems which contain bodies of arbitrary shapes can be calculated faster and effectively. VPM had been developed for the incompressible viscous flows around complex solid boundary. On the other hand it has seldom been developed for the compressible viscous flows. Liu and Vasilyev proposed the penalization technique for compressible Navier-Stokes equations and applied it to linear acoustic problems^[1].

In this study, we compute the aeroacoustic sound generated in the flow past a simple shape obstacle by using VPM proposed by Liu and Vasilyev. The objective of our study is to develop a direct numerical method for capturing aeroacoustic sound using VPM.

2. Numerical Method

The 2D unsteady compressible Navier-Stokes equations with penalization terms are solved. In this study, we use the governing equations proposed by Liu and Vasilyev as follows

$$\frac{\partial \rho}{\partial t} = - \left[1 + \left(\frac{1}{\phi} - 1 \right) \chi \right] \frac{\partial m_j}{\partial x_j}, \quad (1)$$

$$\frac{\partial m_i}{\partial t} = - \frac{\partial m_i u_j}{\partial x_j} - \frac{\partial p}{\partial x_i} + \frac{\partial \tau_{ij}}{\partial x_j} - \frac{\chi}{\eta} (u_i - U_{0i}), \quad (2)$$

$$\frac{\partial e}{\partial t} = - \frac{\partial}{\partial x_j} [(e + p)u_j] + \frac{\partial}{\partial x_j} (u_j \tau_{ij}) + \frac{\partial}{\partial x_j} \left(\kappa \frac{\partial T}{\partial x_j} \right) - \frac{\chi}{\eta_T} (T - T_0), \quad (3)$$

where ρ is the density of the fluid, $m_i = \rho u_i$ is the momentum, p is the pressure, τ_{ij} is the shear stress tensor, e is the total energy, κ is the thermal conductivity, U_{0i} and T_0 are the velocity and the temperature of the obstacle respectively. ϕ is the porosity, η is a viscous permeability, η_T is a thermal permeability. Note that $0 < \eta, \eta_T \ll 1$ is assumed.

Here the thermal conductivity κ is given by

$$\kappa = \frac{\gamma \mu}{Pr} \quad (4)$$

Where γ is the specific heat ratio, μ is the coefficient of dynamic viscosity of the fluid, Pr is the Prandtl number. In this study, μ and κ are assumed constant. The pressure p is obtained from the equation of state for ideal gas as follows

$$p = (\gamma - 1) \left[e - \frac{\rho}{2} (u^2 + v^2) \right] \quad (5)$$

In Eqs.(1)-(3) χ denotes the mask function

$$\chi(x_i, t) = \begin{cases} 1 & \text{if } x_i \in \text{obstacle} \\ 0 & \text{otherwise} \end{cases} \quad (6)$$

that defines the location of the solid obstacles.

In this study, a sixth-order-accurate compact Pade scheme is applied for spatial derivatives^[2]. The forth-order Runge-Kutta scheme is used for time-integration. Non-reflecting boundary condition is

used at the outer boundary of the computational domain^[3].

3. Flow model and parameters

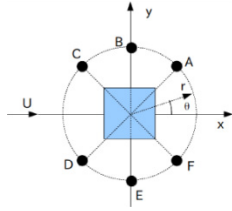


Fig. 1 Schematic diagram of the flow model.

In this study, we analyze the aeroacoustic sound generated in the flow past a square cylinder. Each physical quantity is respectively non-dimensionalized by the reference speed of sound c_0 , the side length of the cylinder L , the reference density ρ_0 . A schematic diagram of the flow model is presented in Fig.1. The computational domain is $[-1000L, 1000L]^2$.

A cylinder is fixed at the origin, and the coordinates parallel and normal to the free stream are denoted by x and y , respectively. The origin of the polar coordinates are denoted by r and θ . The Reynolds number is defined by $Re = \frac{\rho_0 U L}{\mu} = 150$, and the Mach number M of the uniform flow is defined by $M = \frac{U}{c_0} = 0.2$, where U is the velocity of the uniform flow. In this problem, $\phi = 1.0$, $\eta = 5.0 \times 10^{-3}$, $\eta_T = 5.0 \times 10^{-3}$ are used.

We adopt a rectangular grid system with non-uniform meshes. The total number of grid points is 1770×1570 .

4. Results and Discussion

It is well known that, in the case of a rectangular cylinder, vortices are shed alternately from the upper and lower sides of the cylinder and the Karman vortex street is formed behind the cylinder. The vorticity field at $t = 600$ is presented in Fig.2

In this figure, red/blue region correspond to positive/negative vorticity. It shows that alternate vortex shedding from the upper and lower sides of the cylinder produces negative and positive vorticity alternately and the Karman vortex street is well captured.

The pressure field at $t = 600$ is presented in Fig.3 in term of fluctuation pressure Δp . Here Δp denotes the fluctuation pressure defined by $\Delta p = p - p_0$, where p_0 denotes the hydrostatic pressure. Red/blue region corresponds to positive/negative fluctuation pressure..

Presented in Figs.2 and 3 are that the alternate vortex shedding generates the pressure pulses. When a vortex is shed from the upper side of the cylinder, a negative pressure pulse is generated on the upper side whereas a positive pressure pulse is generated on the lower side. Therefore, alternate vortex shedding from the upper and lower sides of the cylinder produces positive and negative pressure pulses alternately on the both sides of the cylinder, and these pressure pulses propagate as sound waves in each direction. It implies that the

aeroacoustic sound is successfully captured in the simulation.

Presented in Fig.4 is the time histories of Δp . The fluctuation Δp is measured at the location B ($r = 40, \theta = 90^\circ$) on the upper side and the location E ($r = 40, \theta = 270^\circ$) on the lower side. The result shows the pressure pulses are generated from the upper and lower side of the cylinder with a half period phase shift, and fluctuate with order 10^{-4} . These results are in good agreement with previous results^[4].

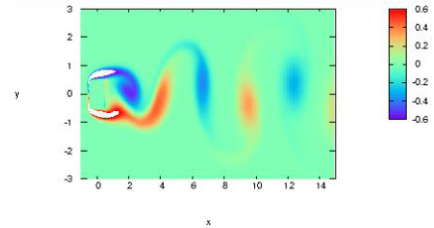


Fig. 2 Instantaneous vorticity field. $M = 0.2, Re = 150$.

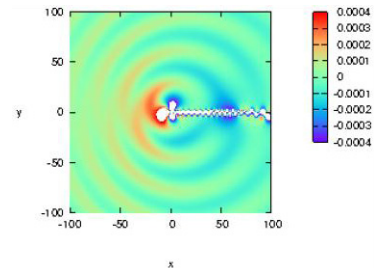


Fig. 3 Instantaneous pressure field for the square cylinder. $M = 0.2, Re = 150$.

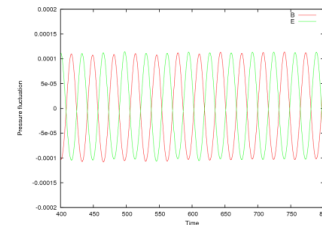


Fig. 4 Time histories of the pressure fluctuation. $M = 0.2, Re = 150$.

5. Concluding remarks

In this study, we have investigated the validity of VPM for compressible flow by direct numerical simulation of the aeroacoustic sound generated from the two-dimensional flow past a square cylinder. The results showed that both the Karman vortex street and the aeroacoustic sound are well captured.

References

- [1] Q. Liu, and O. V. Vasilyev, J. Comp. Phys. **227**, 946-966(2007).
- [2] S. K. Lele, J. Comp. Phys. **103**, 16-42(1992).
- [3] T. J. Poinsot, and S. K. Lele, J. Comp. Phys. **101**, 104-129(1992).
- [4] O. Inoue, M. Mori, and N. Hatakeyama, Phys. Fluids **18**, 046101(2006)

Effect of Orifice Shape on Liquid Jet Breakup

Sivakumar Deivandren

Department of Aerospace Engineering Indian Institute of Science, Bangalore 560012, India

E-mail of corresponding author: dskumar@aero.iisc.ernet.in

ABSTRACT

The manuscript reports an experimental study on the breakup behavior of liquid jets discharging from circular and non-circular orifices. Systematic experiments were conducted on water jets discharging from circular, elliptical, triangular, square, and rectangular orifices with same orifice exit area. Breakup curves (jet breakup length versus velocity) of liquid jets discharging from these orifices were obtained. An orifice shape-driven jet breakup was identified in the regime of low velocity liquid jets. The breakup length data for the high velocity liquid jets discharging from the non-circular orifices almost merge with that of equivalent circular liquid jets.

1. Introduction

Academic interest in the problem of liquid jet breakup started in the nineteenth century, well before the development of technologies which make use of it. A majority of these studies were confined to liquid jets discharging from circular orifices, *i.e.*, circular liquid jets. When a liquid jet emanates from an orifice, it experiences various forces, some of which are cohesive and others are disruptive in nature. When the magnitude of disruptive forces exceeds that of cohesive forces, the liquid jet breaks and produces droplets. Current developments in miniaturization techniques help to design subsystems of smaller size for several key technological applications. Recent studies involving MEMS (Micro Electro Mechanical Systems) based fuel injectors have considered non-circular orifices for liquid atomization process [1]. A systematic study on the fundamental aspects of atomization process for liquid jets discharging from non-circular orifices is still missing in current literature. The present work analyzes the breakup behavior of liquid jets discharging from non-circular orifices of different shapes.

2. Method

The experiments were carried out in a standard spray test facility. It consisted of a large stainless steel tank containing the working fluid kept under pressure by means of a compressed air supply and an air pressure regulator. A liquid flow meter was employed to monitor the flow. A group of one circular orifice and four non-circular orifices were used in the study. The non-circular orifices were of different cross sectional shapes: elliptical, equilateral triangle, square, and rectangle. The orifices were of approximately same cross sectional area. Figure 1 shows high resolution images of the circular orifice and the non-circular orifices. An equivalent diameter, D_{eq} , estimated from the exit area of orifice, was used to compare non-circular jets with that of circular jets. The hydraulic diameter, D_h of the circular and non-circular orifices was estimated as $D_h = 4A/P$ where A and P are the exit area and wetted perimeter of the orifice respectively. The length of orifice was kept at 25 mm. Table 2.1 highlights major geometrical details of the circular and non-circular orifices. Experiments were carried out with water (dynamic viscosity, $\mu = 0.802 \times 10^{-3}$ kg/ms, surface

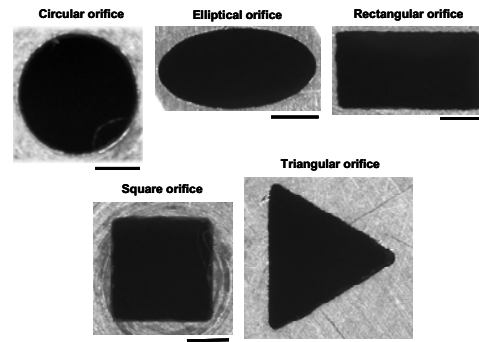


Fig. 1. High resolution images of the orifices. The horizontal lines correspond to a scale length of 1 mm.

Table 1. Geometrical details of the orifices.

Orifices	Geometric details	D_{eq} (mm)	D_h (mm)
Circular	Diameter, $D_o = 2.52$ mm	2.52	2.52
Elliptical	Major axis = 3.4 mm; Minor axis = 1.79 mm	2.49	2.24
Triangular	Side length = 3.31 mm	2.46	1.91
Square	Side length = 2.19 mm	2.47	2.19
Rectangular	Length = 3.11 mm and width = 1.66 mm	2.56	2.16

tension, $\sigma = 0.073$ N/m, and density, $\rho_l = 1000$ kg/m³) as the experimental liquid. The non-dimensionalized numbers, Re and We were estimated as

$$We = \frac{\rho U_o^2 D_o}{\sigma} \quad \text{and} \quad Re = \frac{\rho U_o D_o}{\mu} \quad (1)$$

A Nikon D1X camera was used to take photographs of the jet. In the present study, the jet breakup length is defined as the distance measured from the orifice exit to the point of the first break in the jet along the jet axis. Mean breakup length, L_b was estimated from the individual measurements of jet breakup length obtained from photographs available for each flow condition.

3. Results and discussion

Figure 2 shows the breakup curves for liquid jets discharging from the non-circular orifices with that of the circular orifice. The liquid jets discharging from non-circular orifices exhibit shorter breakup lengths compared to the circular jet in values of U_o which are much smaller the critical point velocity, $U_{o,cri}$ ($= 1.23$

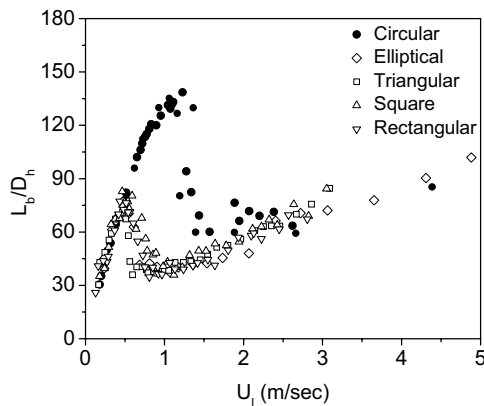


Fig. 2. The breakup curves for liquid jets discharging from the circular and non-circular orifices.

m/sec) of circular liquid jets. The images of liquid jets at these flow conditions revealed that the liquid jets discharging from the non-circular orifices exhibit a change in breakup mechanism, from axisymmetric wave breakup to transverse/sinuuous wave breakup, at flow velocities which are significantly smaller than $U_{o,cri} = 1.23$ m/sec of circular liquid jets. In other words, the possibility of aerodynamic forces in bringing the change in breakup mechanism for liquid jets discharging from the non-circular orifices at these low flow velocities is ruled out. Thus the orifice shape alters the breakup mechanism at these low flow velocities. The plot given in Fig. 2 also illustrates the influence of orifice shape within the group of non-circular orifices. For a given U_o in this range of low jet velocities, the liquid jets discharging from the triangular orifice show shorter breakup lengths compared to those from the square and rectangular orifices. This suggests that liquid jets discharging from the triangular orifice undergo rapid changes in wave growth compared to the liquid jets discharging from the square and rectangular orifices.

Figure 3 shows the comparison of breakup curves at higher values U_o where the jet breakup is dominantly

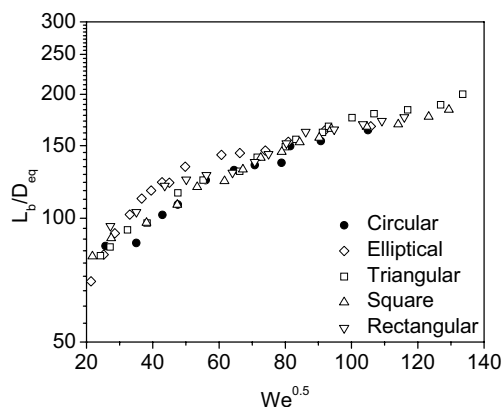


Fig. 3. The breakup curves for liquid jets with high U_o discharging from the circular and non-circular orifices.

driven by aerodynamic forces and flow turbulence. With an intention to compare the trend with those reported in the literature [2], the measurements are shown as L_b/D_{eq} versus $We^{0.5}$. It is observed that the experimental measurements of L_b obtained for the liquid jets discharging from the non-circular orifices collapse in a single line as seen in Fig. 3. The increasing trend of L_b with U_o is in agreement with the previous studies [2]. It can be concluded from Fig. 3 that the orifice shape is not influencing the jet breakup at higher values of U_o .

It can be observed from the breakup curves of liquid jets given in Fig. 2 that Rayleigh breakup regime ends with a peak, which is often referred as the critical point in the breakup curve. With the increase of U_o beyond the critical point, the breakup length decreases with U_o as seen in Fig. 2. The breakup mechanism begins to change from axisymmetric type breakup to transverse or sinuous type breakup somewhere in the zone of negative slope after the critical point. The details of critical point of the breakup curves for liquid jets discharging from the noncircular orifices were extracted from the experimental measurements. For liquid jets discharging from a given orifice, a change in critical point condition suggests the changing influence of aerodynamic forces on the liquid jet breakup. From the present experiments, the critical velocity of liquid jets discharging from the non-circular orifices was found to be much smaller compared to that of circular liquid jets. This eliminates the possible role of aerodynamic forces in changing the critical point parameters. One can definitely say that the critical point changes due to the orifice geometry. According to Ref. [3], the change of the critical point is associated with the change in the growth rate of perturbation due to the effect of the velocity profile rearrangement. .

4. Conclusions

A systematic experimental investigation on the breakup behavior of liquid jets discharging from non-circular orifices has been carried out. Non-circular orifices of various geometric shapes (elliptical, triangular, rectangular, and square) were considered. The breakup curve for liquid jets discharging from the non-circular orifices exhibits differences with that of circular liquid jets. An orifice shape-driven jet breakup, characterized by the behavior of shortened jet breakup length compared to the equivalent circular liquid jet, is seen in the regime of low velocity liquid jets.

The research work is supported by Aeronautical Research & Development Board (AR&DB), India.

References

- [1] S. Baik, J.P. Blanchard, and M.L. Corradini, *J. Gas Turbine Power* **125** (2003) 427-434.
- [2] R. P. Grant and S. Middleman, *AIChE J.* **12** (1966) 669-678.
- [3] M. Sterling and C.A. Sleicher, *J. Fluid Mech.* **68** (1975) 477-495.

Analysis Of Flow Characteristics Of Turbulent Plane Jets Based On Velocity And Scalar Fields Using DNS

Nannan Wu¹, Yasuhiko Sakai¹, Kouji Nagata¹, Hiroki Suzuki², Osamu Terashima¹, and Toshiyuki Hayase³

1) Department of Mechanical Science and Engineering, Nagoya University, Furo-cho, Chikusa-ku, Nagoya, Aichi, 464-8603, Japan 2) Department of Engineering Physics, Electronics and Mechanics, Nagoya Institute of Technology, Gokiso-cho, Showa-ku, Nagoya, Aichi, 466-8555, Japan 3) Institute of Fluid Science, Tohoku University, 1-1-2 Katahira, Aoba-ku, Sendai, Miyagi, 980-8577, Japan
wu.nannan@b.mbox.nagoya-u.ac.jp

ABSTRACT

The flow characteristics of the turbulent plane jet are studied by means of direct numerical simulation (DNS). The effects of the flow conditions at the jet exit (i.e. typical Reynolds number and velocity distribution) on the spatial development of velocity and scalar fields are mainly investigated. The results suggest that the effects of initial conditions on the plane jet evolution observed will be related to differences in the underlying turbulence structure of the jet and the initial velocity distribution will mainly affect the flow characteristics in the near field region, meanwhile the Re_d dependence will be more presented in the far field region.

1. Introduction

The investigation of the plane jet can be traced to 1930's, and later the significant research work has been carried out.^[1,2] Even though both the experimental data and numerical results will be required to study the features of the plane jet, the numerical simulation is quite promising accompanied by the improvement of capacity of scientific computer, which can easily achieve the simultaneous parameters' obtainment and avoid the effects of external disturbances on the evolution of jet flows in the experiments.

In this paper, the numerical simulations of plane jets are carried out based on direct numerical simulation (DNS) and the flow characteristics of turbulent plane jets are mainly investigated from the viewpoint of the velocity and scalar fields, meanwhile we focus on the effects of the flow conditions at the jet exit on the spatial development of flow.

2. DNS details

Three-dimensional coordinate system is set: x is the streamwise coordinate, y is the lateral coordinate and z is the spanwise coordinate. The coordinate origin is placed in the middle of the slit (jet exit). Figure 1 shows the schematic of the computational domain ($12\pi d \times 16\pi d \times 3\pi d$). The fractional step method is used to solve the governing equations which are the continuity equation, the Navier-Stokes equations and the scalar transport equations. The typical Reynolds number (Re_d) is defined by the bulk velocity (U_j) and the half of the jet height (d). The variables are located on the staggered grids ($357 \times 385 \times 65$). And the Runge-Kutta scheme and

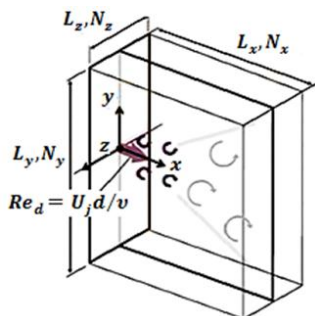


Fig. 1 Schematic of the computational domain.

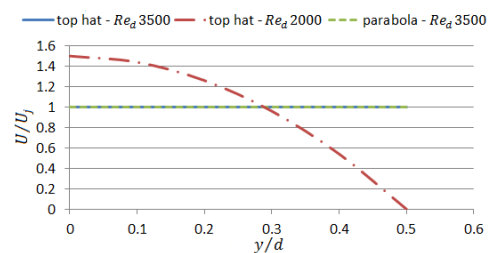


Fig. 2 Velocity profiles at jet exit.

the Crank-Nicolson scheme are used for temporal discretization and the central differences are used for spatial discretization. The accuracy of the simulation code has been confirmed^[3].

The lateral boundary condition is set as the traction-free boundary condition, the convection outflow condition is applied at the downstream exit and the periodic boundary condition is imposed at the spanwise direction.

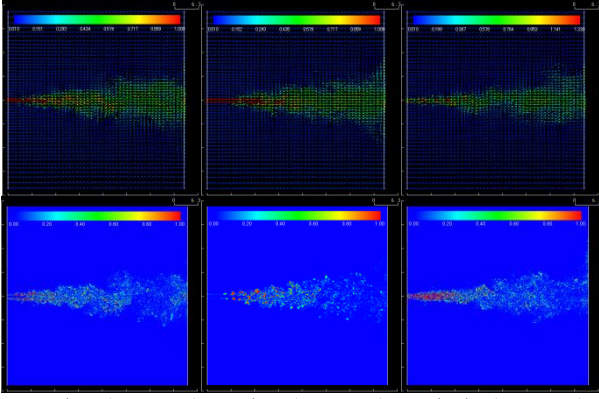
3. Flow Conditions at jet exit

The initial boundary layer characteristics are confirmed to cause significant differences in the flow evolving properties of plane jets.⁽⁴⁾ Therefore, for investigating this phenomenon here three flow conditions at the jet exit are defined by combining two different kinds of velocity distributions (i.e. top hat and parabola) and Re_d (i.e. 3500 and 2000). Figure 2 shows the velocity profiles at the jet exit.

4. Results and discussion

4.1 Instantaneous flow field

Figure 3 shows the instantaneous velocity vector (upper) and the instantaneous second invariant of velocity-gradient tensor (lower) respectively. Based on two conditions set as the same velocity profiles at jet exit, the dependency of Re_d may be studied. High Re_d obviously enhances the oscillation of flow, especially in the interacting region, and increases the velocity-gradient in the near-field zone. In the downstream region of the jet, the effects of small-scale mixing due to the strong turbulence have greatly reduced the presence of patches of the main flow and ambient flows. Moreover, the longer length of potential core can be observed for low Re_d , which is related with



Top hat ($Re_d=3500$) Top hat ($Re_d=2000$) Parabola ($Re_d=3500$)
Fig. 3 Instantaneous flow field.

the relative small velocity-gradient in the shear layer at both sides for this region, in comparison with the high Re_d conditions.

Based on two conditions at same Re_d , it makes us focus on the effects of initial velocity distribution on the flow characteristics of turbulent plane jets. It seems that the parabola shape will strengthen the velocity gradient, especially in the near-field zone.

4.2 mean flow field

The streamwise evolutions of the mean velocity and scalar along the jet centerline (i.e. U_C and Θ_c) normalized by U_j and Θ_j respectively are revealed by figure 4. It is found that after crossing the potential core, two conditions at same high Re_d present the similar evolution features. Furthermore let us focus on the near-field zone so as to reveal the effects of initial velocity profile on the mean flow field, where the parabola velocity initial profile enhances the mixing between the jet and ambient flow, and the shorter length of potential core can be seen.

Shifting to the effects of Re_d , the low Re_d condition conserves the longer length of potential core, which is well revealed by others' research. Moreover, the higher level of flow intermittency, larger entrainment of ambient fluid, and faster jet decay are shown in the interacting region as the flow structure of a low Re_d jet is dominated by large scale vortices here, as compared with high Re_d jets.

In figure 5, the streamwise evolution of r.m.s fluctuation along the jet centerline (u_{rmsc} , θ_{rmsc}) normalized by U_C and Θ_c respectively are shown, this kind of flow structure in interacting region for low Re_d jets also induce the high velocity and scalar fluctuations. But in far field region, high Re_d condition, corresponding to more various turbulent structures, shows high fluctuation for both velocity and scalar.

Comparing two kinds of velocity distributions at jet exit, parabola condition presents higher velocity fluctuation, here the K-H instability is strengthened by parabola velocity distribution, which may be incentive, based on the position of the occurrence of fluctuation peak, but this kind of feature seems not to affect the scalar fields, as for these two conditions they have the similar fluctuation evolution.

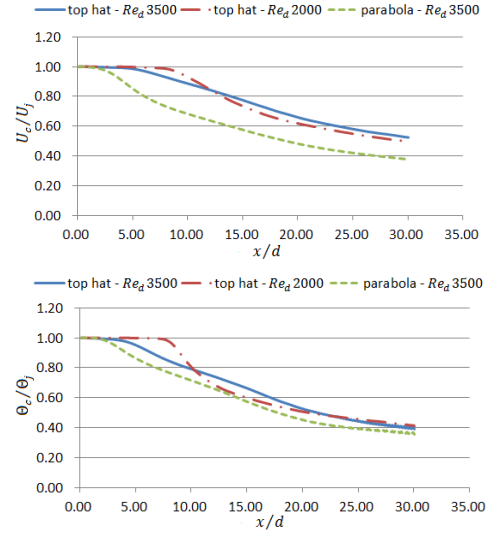


Fig. 4 Streamwise evolution of mean profiles.

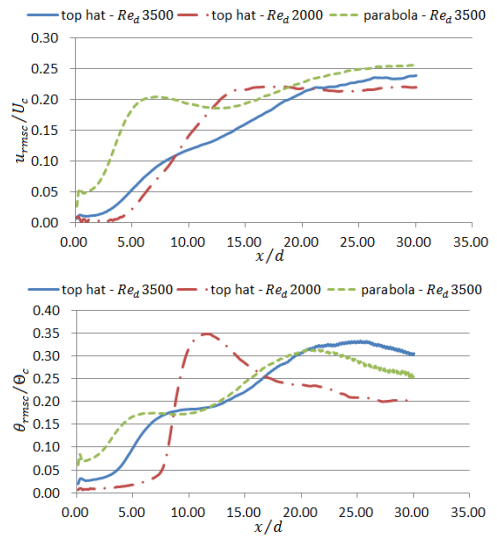


Fig. 5 Streamwise evolution of fluctuation profiles.

5. Conclusion

The simulation results reveal that the change of the flow conditions at plane jet exit will affect the flow structure and characteristics. And it is found that the initial velocity distribution will mainly take the effects in near field region and different Re_d will more affect the far field characteristics of the plane jets.

Acknowledgements

A part of this study was carried out under the Collaborative Research Project of the Institute of Fluid Science, Tohoku University and supported by Grants-in-Aid (Nos. 22360076, 2236077) from the MEXT in Japan.

References

- [1] H. Schlichting, Z. Angew. Math. Mech., **13** (1933), 260-263.
- [2] E. Gutmark, I. Wygnanski, J. Fluid Mech., **73** (1976) 465-495.
- [3] H. Suzuki, K. Nagata, Y. Sakai, et al, Trans. JSME, **75-752 B**(2009) 642-649.
- [4] A.K.M.F. Hussain, A.R., Phys. Fluids, **20**(9) (1977) 1416-1426.

Supersonic Flight of Beam Riding Vehicle Sustained by Actively Controlled Laser

Masayuki Takahashi, Naofumi Ohnishi

Department of Aerospace Engineering, Tohoku University
6-6-01 Aramaki-Aza-Aoba, Aoba-ku, Sendai 980-8579, Japan
mtakahashi@rhd.mech.tohoku.ac.jp

ABSTRACT

In order to present a feasibility of high-altitude flight of an aero-driving-type laser vehicle in a supersonic speed, we have developed a flight simulator. We newly propose an active laser control using genetic algorithm (GA) and demonstrate that the vehicle successfully flies into km-order altitude with the active control. Additionally, a concept using arrayed lasers and GA controlled sub-laser is presented in order to achieve a supersonic flight. These laser incidents can propel the vehicle into a supersonic speed with the optimized beaming strategy in which the incident positions are controlled within 50 cm around the starting point on the ground.

1. Introduction

Demands of small artificial satellites are increasing, and launch missions are usually conducted by shared-ride piggyback transportation. Since the launch timing and orbit of small satellites are restricted by a main satellite in the shared-ride system, it is necessary to establish the exclusive launch system for small satellites at lower cost. An aero-driving laser vehicle obtains thrust through interactions with a blast wave induced by repetitive laser pulse irradiated from a ground base. The blast wave can propel the vehicle to higher altitude; however, if the vehicle cannot capture the laser beam, no thrust may be obtained. Beam riding performance assessed by centering and tipping performances is crucial for the vehicle to receive continuous thrust.

One of the best beam riding vehicles at present is the "lightcraft" proposed by Myrabo, and the type-200 spinning lightcraft achieved 71-m altitude flight in 2001. In past studies of the lightcraft, some experiments were conducted to examine recentering and angular impulses for lateral offset with a single pulse. Also, flight simulations were performed with multiple laser pulses based on the impulse data for lateral offsets [1]. However, the deviation mechanism from the laser beam line was not specified from past studies because the angular offset and angular-lateral combined offset were not introduced.

In our previous work [2], we have developed a hydrodynamics-orbit coupling calculation code and a ray-tracing code. For a single pulse, data-maps of vehicle reactions against lateral, angular, and these combination offsets have been made by our numerical code. Flight calculations for multiple pulses were successfully reproduced based on the data-maps, and we found that the growth of the angular offset causes the deviation from the laser beam line. Based on the obtained flight dynamics we proposed a "laser rotation" concept to achieve higher altitude of flight as compared with the conventional flight. However, it is necessary to keep stable flight in a km-order altitude for the launch of small satellites.

The objective of the present study is improving the flight performance of a laser propulsion vehicle by introducing new concepts of laser irradiation. We propose an active laser control using genetic algorithm (GA) to obtain a stable flight, and the laser beam is controlled to keep the angular offset as small as possible. Additionally, since it is desirable that the vehicle is accelerated into a supersonic speed using pulse laser beam for a launch of small satellites, we assess arrayed lasers that can supply large energy enough to achieve the

supersonic speed even with the conventional power for each single laser.

2. Numerical Methods

2.1 Flowfield Calculation

The flowfield around a spinning lightcraft is to be obtained for forces and moments acting on the vehicle. We predict an unsteady flowfield involving the blast wave by computational fluid dynamics. The three-dimensional Navier-Stokes equation is numerically solved to reproduce the compressible gas dynamics around the vehicle.

Discretization is performed by a cell-centered finite volume manner. The AUSM-DV method is employed for numerical flux with the second-order MUSCL method. The viscous flux is estimated by the second-order central difference method, and the viscous coefficient is determined by Sutherland's formula. The Spalart-Allmaras model with an assumption of fully developed turbulence due to the axial spin of the lightcraft is employed to introduce the effect of the turbulent flow. The LU-SSOR method is utilized for the time integration of steady flow problems (e.g., measurements of aerodynamic coefficients) to save the computational time. Time integration for unsteady flows is performed by the first-order explicit Euler method. In early stage of blast wave propagation, we couple the flowfield calculation with the orbital one to introduce the effects of the unsteady vehicle motion. For initial condition, the ray-tracing method is carried out to deposit an energy source of the blast wave.

2.2 Orbital Calculation

An flight orbit of the vehicle can be determined by 6-DOF equations of motion with aerodynamic forces and moments estimated from a flowfield solution. When the blast wave has strong interaction with the vehicle, the aerodynamic forces and moments are estimated by integrating surface pressure distribution given by the flowfield solution. When the interaction between blast wave and vehicle can be ignored, 6-DOF equations of motion is integrated using aerodynamic coefficient for steady flow. The time integration is conducted using 4th-order Runge-Kutta method.

2.3 Laser Position Control Using Genetic Algorithm

The active control module for laser incident position using the real-coded GA is incorporated into flight

simulator to achieve better flight performance. BLX- α model is employed for a crossover in the GA. Minimal Generation Gap (MGG) model is used for a generation alternation while a mutation is not installed in this study. The present GA procedure is as follows. At first, fifty laser position vectors are randomly created. Parents are selected from this group, and BLX- α is operated 50 times to generate one hundred children. After that, using MGG model, two individuals are selected from the group including original parents and children, and parents are replaced by these individuals. This process is repeated until the terminal condition is satisfied. For the optimization, the evaluation function Π is primarily defined to the angular offset, but sometimes set to translational position of the vehicle.

3. Results

3.1 Flight Performance Improvement Using GA

The conventional flight trajectory deviates from the laser beam line due to the growth of the angular offset. To suppress the angular offset, we propose the active laser control using the GA. The laser is actively controlled to minimize the angular offset or the vehicle lateral position based on the evaluation function. Using the GA, the angular offset is suppressed less than 0.001 degree, and the vehicle can fly to the altitude of more than 7.0 km (Fig. 1). Suppressing the angular offset is especially important to attain km-order flight rather than translational position. However, the vehicle only obtains the velocity of several ten m/s due to low laser power.

3.2 Examination for Supersonic Flight

The possibility of the stable flight was demonstrated using the GA; however, the flight speed is not so large. It is preferable that the supersonic flight is realized at 15 s after the launch in the aero-driving mode; therefore, a novel manner to accelerate the vehicle is needed with keeping a stable flight. We propose a new concept of laser configuration in which arrayed laser beams whose axes are paralleled to the vehicle axis are irradiated to the vehicle center for obtaining larger thrust and stable moments. In addition, a sub-laser which is controlled using the GA is irradiated for posture control.

A supersonic flight is achieved by the arrayed lasers and sub-laser irradiations (Fig. 2), and the flight altitude is attained to more than 2.2 km (Fig. 3). However, the vehicle velocity has large oscillation, it is therefore necessary to divide the number of arrayed lasers during one pulse duration of the pulse laser. The arrayed laser position is controlled within 50 cm on the ground because the angular offset is minimized by the sub-laser posture control. The lateral position of the vehicle is successfully maintained in the vicinity of the starting point in the subsonic region. However, in the supersonic flight, the lateral vehicle velocity becomes larger due to the aerodynamic moments caused by the wave drag. It is still necessary to improve the scheme of the centering feedback in the supersonic speed. In addition, because it is desirable to obtain higher flight Mach number, we should increase the number of arrayed laser beams.

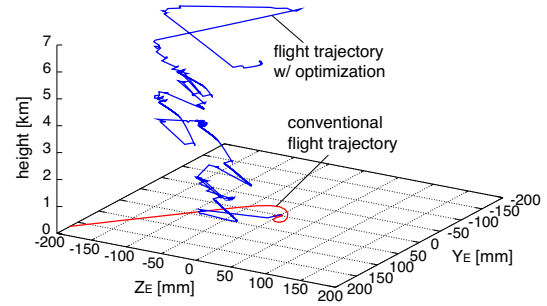


Fig.1 Flight trajectory using the GA control.

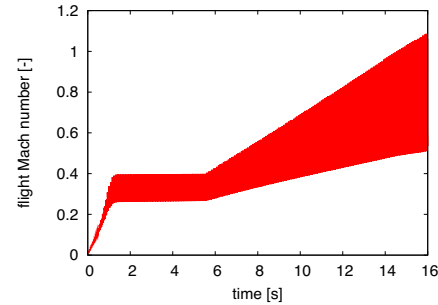


Fig. 2 Time evolution of flight Mach number using arrayed lasers and sub-laser.

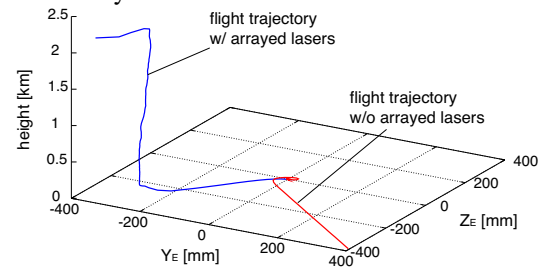


Fig. 3 Flight trajectory with arrayed lasers and sub-laser.

4. Conclusion

We have incorporated the laser control module using genetic algorithm into flight simulator to obtain km-order flight altitude. Also, the arrayed lasers and GA controlled sub-laser are irradiated for accelerating the vehicle into supersonic speed with maintaining the stable flight for the launch of small satellites.

The flight performance is improved using active laser control by the genetic algorithm whose evaluation function is defined by the translational position of the vehicle and the angular offset. Minimizing the angular offset is especially important to attain the km-order flight using actively controlled laser beam. Also, it is effective that arrayed lasers and a posture control laser are irradiated at the same time to achieve the supersonic speed with the beam riding flight.

It is necessary to improve the evaluation function in the supersonic regime for the feedback control of the vehicle lateral position with a different strategy from subsonic one. Additionally, we assess larger number of arrayed lasers in order to achieve higher Mach number toward the launch of small satellites with the laser propulsion system.

5. References

- [1] C. G. Ballard et al., Journal of Computational and Nonlinear Dynamics, 4 (2009), pp. 041005-1–041005-8.
- [2] M. Takahashi and N. Ohnishi, AIAA Journal (2012).

Numerical Simulation of a Reactive Liquid Jet by Combination of DNS and PDF Method

Tomoaki Watanabe¹, Yasuhiko Sakai¹, Kouji Nagata¹, Osamu Terashima¹, Yasumasa Ito¹ and Toshiyuki Hayase²

¹ Department of Mechanical Science and Engineering, Nagoya University, Japan

² Institute of Fluid Science, Tohoku University, Japan

watanabe.tomoaki@c.nagoya-u.jp

ABSTRACT

A planar liquid jet with a second-order chemical reaction ($A + B \rightarrow R$) is simulated by using direct numerical simulation (DNS) and probability density function (PDF) methods. The rms value of the mixture fraction fluctuation is well predicted by adjusting the parameter which appears in the mixing model. The results show that the mean mixture fraction predicted by the DNS—PDF methods is smaller than the experimental value in the upstream region of the jet, but is well predicted in the downstream region. The results also show that the mean concentration of product R predicted by the DNS—PDF methods is larger than the experimental value.

1. Introduction

Turbulent reactive flows are important in various science fields, and the numerical methods to predict the turbulent reactive flows are widely needed. The probability density function (PDF) method [1] is one of the most promising approaches to simulate turbulent reactive flows. In PDF methods, the chemical source terms appear in a closed form, whereas most simulation methods have difficulty closing the chemical source terms.

In this study, we conduct the numerical simulation of a planar liquid jet with a chemical reaction. Because of the high Schmidt number, DNS cannot be applied to the scalar fields. Hence, we apply the PDF methods by combining the PDF methods with DNS.

2. Numerical Method

A liquid planar jet with a second-order chemical reaction $A + B \rightarrow R$ is simulated by the DNS—PDF methods. Figure 1 shows a sketch of the flow. In the DNS—PDF methods, velocity fields are solved by DNS. The governing equations for the velocity fields are the incompressible Navier—Stokes equations and the continuity equation. As shown in Fig. 1, the computational domain of DNS is $L_{xDNS} = 13.5\pi d$ in the x direction, $L_{yDNS} = 13\pi d$ in the y direction, and $L_{zDNS} = 2.6\pi d$ in the z direction. The computational domain is resolved by $475 \times 425 \times 65$ grid points. At the outflow boundary, the convective outflow condition is applied. The velocity data at the plane of jet exit is generated by superimposing random fluctuations on the mean velocity profiles. The ratio of the streamwise mean velocity in the main flow, U_M , to the streamwise velocity averaged in the jet exit, U_J , is $U_M/U_J = 0.056$. The traction-free condition and the periodic boundary condition are applied at the lateral boundary and the z direction, respectively. The Reynolds number based on U_J and d is set to 2,200.

In the PDF methods, the transport equations for the velocity—scalar joint PDFs are solved by using Lagrangian particles. Each Lagrangian particle has the scalar properties denoted by $\phi = \{\Gamma_A, \Gamma_B, \Gamma_R\}$. Here, Γ_α is the concentration of species α . Lagrangian particles evolve according to the following equations;

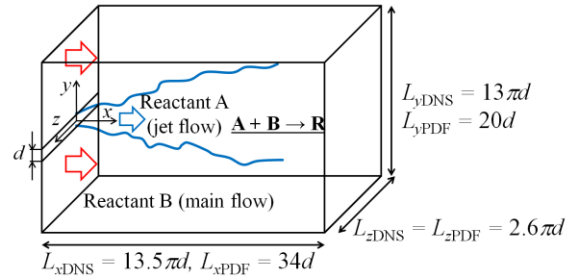


Fig. 1 Sketch of the flow.

$$d\mathbf{x}^n = \mathbf{U}^n dt, \quad (1)$$

$$d\Gamma_\alpha^n = \left[\frac{d\Gamma_\alpha^n}{dt} \right]_{\text{mix}} dt + W_\alpha(\phi^n) dt. \quad (2)$$

Here, dt is the time increment, the superscript n denotes that the quantity is related to the n th particle, and W_α is the reaction rate for Γ_α ($\alpha = A, B$, or R). For $A + B \rightarrow R$, $W_R = -W_A = -W_B = k\Gamma_A\Gamma_B$. In Eq. (1), \mathbf{U}^n is obtained from DNS results. $[d\Gamma_\alpha^n/dt]_{\text{mix}}$ is the effect of the mixing on Γ_α^n , and determined by the mixing model. We use the Curl-type mixing model, in which $[d\Gamma_\alpha^n/dt]_{\text{mix}}$ is given by

$$\left[\frac{d\Gamma_\alpha^n}{dt} \right]_{\text{mix}} dt = \beta \left[\frac{1}{2}(\Gamma_\alpha^m + \Gamma_\alpha^n) - \Gamma_\alpha^n \right]. \quad (3)$$

Particle m , which is the closest to particle n in the physical space, is selected as the mixing partner of particle n . In Eq. (3), $\beta = 1$ with probability P , and $\beta = 0$ (no mixing) with probability $1 - P$, where $P = dt/\tau_L$. τ_L is the mixing time scale, and is proportional to $(\Delta_L^2/\varepsilon)^{1/3}$ [2]. Here, Δ_L is the distance between mixing particles in the physical space, and ε is the turbulent kinetic energy dissipation rate obtained by DNS. Hence, τ_L can be given by $\tau_L = C_L^{-1}(\Delta_L^2/\varepsilon)^{1/3}$, where C_L is a model parameter. Simulation is performed for $C_L = 10$.

Equation (2) is solved for Γ_R and the mixture fraction ξ defined by $\xi \equiv (\Gamma_A - \Gamma_B + \Gamma_{B0})/(\Gamma_{A0} + \Gamma_{B0})$, where $\Gamma_{\alpha 0}$ is the initial concentration of species α .

Equation (2) for ξ can be obtained from Eq. (2) for reactant A and B. The concentrations of reactant A and B are calculated from the mass conservation law written by $\Gamma_A = \Gamma_{A0}\xi - \Gamma_R$, $\Gamma_B = \Gamma_{B0}(1-\xi) - \Gamma_R$.

The computational domain of the PDF methods is $L_{xPDF} = 34d$ in the x direction, $L_{yPDF} = 20d$ in the y direction, and $L_{zPDF} = 2.6\pi d$ in the z direction. 1,220,000 particles are introduced in the computational domain. In the z direction, the periodic boundary condition is applied to the particle moving. The particle which reaches at the inflow, the outflow, or the lateral boundary is removed, and then is introduced at the inflow or the lateral boundary according to the mean flow rate across the boundary. When the particle is introduced in the flow field, the concentrations of reactive species are imposed on particles to satisfy that $\Gamma_A = \Gamma_{A0} = 0.4 \text{ mol/m}^3$ and $\Gamma_B = \Gamma_R = 0$ in the jet exit, and $\Gamma_B = \Gamma_{B0} = 0.2 \text{ mol/m}^3$ and $\Gamma_A = \Gamma_R = 0$ in the main flow.

Statistics are calculated by taking the ensemble averages of the scalar quantity of particles in Euler cells which have $80 \times 61 \times 10$ grid points.

3. Results and Discussion

Figure 2 shows the rms value of mixture fraction fluctuation, ξ_{rms} , on the jet centerline obtained by the experiment [3] and the DNS—PDF methods. ξ_{rms} calculated by the PDF methods depends on the mixing parameter C_L , and for $C_L = 10$, ξ_{rms} is well predicted by the DNS—PDF methods.

Figure 3 shows the mean mixture fraction $\langle \xi \rangle$ on the jet centerline obtained by the experiment and the DNS—PDF methods. The DNS—PDF methods predict smaller $\langle \xi \rangle$ than the experimental value in the upstream region. However, in the region of $x/d > 20$, $\langle \xi \rangle$ predicted by the DNS—PDF methods is consistent with the experimental results.

Figure 4 shows the mean concentration of product R, $\langle \Gamma_R \rangle$, on the jet centerline obtained by the experiment and the DNS—PDF methods. $\langle \Gamma_R \rangle$ is normalized by $\Gamma_{R0} = \Gamma_{A0}\Gamma_{B0}/(\Gamma_{A0} + \Gamma_{B0})$. Figure 4 also shows the results for the equilibrium limit, which is the limiting case of the fast reaction. Figure 4 shows that the DNS—PDF methods overestimates $\langle \Gamma_R \rangle$, especially in the upstream region. This error is caused by the poor prediction of ξ in the upstream region.

4. Concluding remarks

A planar liquid jet with a chemical reaction $A + B \rightarrow R$ is simulated by the DNS—PDF methods. The rms value of the mixture fraction fluctuation is well predicted by adjusting the parameter which appears in the mixing model. The mean mixture fraction $\langle \xi \rangle$ predicted by the DNS—PDF methods is smaller than the experimental value in the upstream region of the jet whereas $\langle \xi \rangle$ is well predicted in the downstream region. The mean concentration of product R predicted by the DNS—PDF methods is larger than the experimental value.

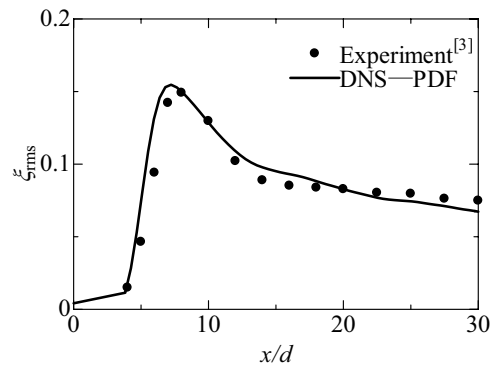


Fig. 2 The axial profile of the rms value of the mixture fraction fluctuation on the jet centerline.

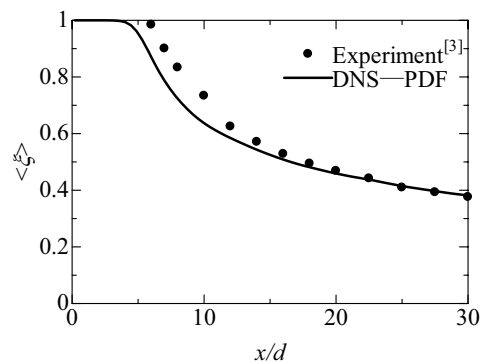


Fig. 3 The axial profile of the mean mixture fraction on the jet centerline.

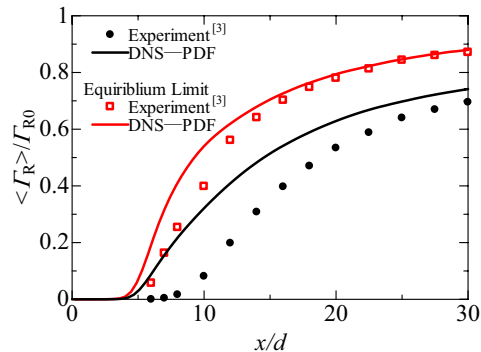


Fig. 4 The axial profile of the mean concentration of product R on the jet centerline.

Acknowledgments

Part of the work was carried out under the Collaborative Research Project of the Institute of Fluid Science, Tohoku University. Part of this work was supported by Grants-in-Aid (Nos. 22360076, 22360077, 23656133, and 23656134) from the Japanese Ministry of Education, Culture, Sports, Science and Technology.

References

- [1] Pope, S. B., Prog. Energy Combust. Sci., **11** (1985), 119–92.
- [2] Cleary, M. J. and Klimenko, A. Y., Flow, Turbulence and Combust., **82** (2009), 477–211.
- [3] Watanabe T., Sakai Y., Yasuhara H., Nagata K., Terashima O. and Kubo T., Trans. JSME, **78** (2012), 769–782.

Micromixing of Fluids within Droplets Generated on Centrifugal Microfluidics

Jerry Min Chen, Yu-Jen Chen and Lung-Sheng Tseng
Department of Mechanical Engineering
National Chung Hsing University
Taichung 40227, Taiwan
jerryrc@dragon.nchu.edu.tw

ABSTRACT

Experiments were carried out to visualize mixing and reaction of two water-based solutions inside the droplets generated in the microchannels on a rotating disk. The microchannels were composed of a Y-junction to bring the two solutions into contact, a flow-focusing junction to form water-in-oil droplets, and a U-shaped channel to further enhance the droplet mixing. In the centrifugal microfluidics, plug-type droplets of 582-820 μm in length were formed at rotational speeds in the range 400-500 rpm. The mixing efficiency can be highly enhanced to reach as much as 85% for the lower rotational speed where smaller droplets are formed.

1. Introduction

Droplet-based microfluidics has emerged as a widely used technique for its promising applications in chemical synthesis, protein crystallization and screening, and microanalysis [1,2]. In droplet-based microfluidics, micro/nanoliter-sized droplets are generated, transported, mixed, reacted, synthesized, or analyzed with the advantages of precise control of the droplet volume and reaction time, parallel operations at a high rate of throughputs, and flexible and adaptable to a variety of assays [3]. Moreover, the isolated micro-environment created in the individual droplets may provide unique culture and growth space for single cell study [4]. Mixing has been found to have excellent performance inside the droplets as chaotic advection occurs [5].

While most of microfluidic devices used for droplet generation are the one with a T-junction geometry and the other with a cross-junction or flow-focusing geometry, a few studies have demonstrated producing droplets with good uniformity on centrifugal microfluidics [6,7]. In centrifugal microfluidics, microchannels integrated with other components such as microvalves and micromixers are fabricated onto a compact disk (CD)-like substrate. Fluid mixing and other functions may be performed on the CD-like microfluidics with the advantages of safety as well as low-cost, high throughput rate and parallel detection. For the droplet generated on centrifugal microfluidics, its size and rate of generation can be controlled by variation of the rotational speed. Nevertheless, mixing inside the droplets formed on centrifugal microfluidic has never been investigated.

In this study, we present mixing and reaction of two fluids within the droplets generated in the flow-focusing microchannels on a rotating disk. The rotational speed of the microfluidic disk was varied to generate droplet of different sizes. Flow of the droplet-based mixing on the rotating microfluidic was visualized with a micro-image-synchronizing-capturing system.

2. Microfluidics Fabrication and Experimental Setup

Experiments for the droplet generation and fluid mixing and reaction were carried out on a rotating microfluidics. Figure 1 shows the schematic of the centrifugal microfluidics in which the fluids can be

driven through rotation at a speed of Ω . The dispersed phase fluids A and B were first brought in contact at the Y-junction. Then at the flow focusing junction where the continuous phase flow channel intercepts the dispersed phase channel at an angle $\alpha = 73^\circ$, droplets containing the mixed fluids were formed. At an immediate downstream, the droplets were driven through a U-shaped channel of which the right-angle turns would induce asymmetric forces to help the mixing. All of the channels had the same depth $H = 100 \mu\text{m}$ and the same width of $W = 300 \mu\text{m}$ except for the dispersed channels in which the width was $W_d = 200 \mu\text{m}$. The microfluidics was made of PDMS using the photolithography and soft lithography techniques on a PMMA substrate disk of 10 cm in diameter and 2 mm thick. The PDMS chip bonded on PMMA substrate provides excellent optical access for flow visualization.

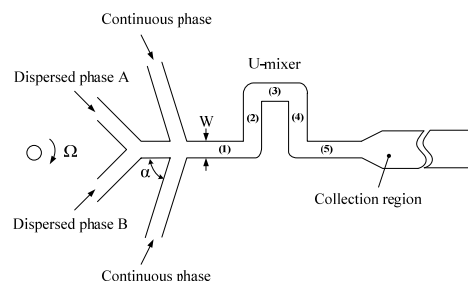


Fig. 1 Schematic of the rotating microfluidics (top view)

Visualization of the mixing and reaction on a rotating disk was performed on the apparatus including the rotation platform and the micro-image-synchronizing-capturing unit. The microfluidic disk was spun by a step motor. The micro-image-capturing unit was composed of a CCD camera (CV-M71CL, JAI, 768×576 pixels, 60 frames/s), a frame grabber (Metero-II/CL, Matrox), and a microscope ($2\times$ objective) above the disk. In order to synchronize the image capturing unit with the rotational motion, the CCD camera was triggered through a photo diode (wavelength 320-730 nm). A He-Ne laser (wavelength 633 nm) of 5 mW was used as the triggering light source. A halogen light (MHF-G150LR, Moritex) was placed beneath the disk to produce sufficient light for illuminating the flow field undergoing fast rotation. In

synchronization with the rotational motion, the CCD camera could be triggered to allow only one shot of the targeted object on the rotating disk per revolution.

3. Results and Discussion

For the present experiments, sunflower oil was used as the continuous fluid sunflower oil. The two dispersed fluids used for mixing and reaction were ferric chloride ($\text{FeCl}_3 \cdot 6\text{H}_2\text{O}$) and ammonium thiocyanate (NH_4SCN) dissolved in deionized (DI) water at the same concentration of 0.2 mol/kg. The ferric chloride solution is pale yellow while the ammonium thiocyanate solution is colorless. When these two solutions come into contact, the ferric ions bind with the thiocyanate ions instead of the chloride ions to produce blood-red color. The intensity of the red-blood color may represent the amount of fluids that mixed and reacted and was quantified as the index of mixing efficiency between the two fluids.

Figure 2 shows the formation of droplets containing the mixing solutions at $\Omega = 400$ and 500 rpm. The dispersed fluid was squeezed by the continuous fluid at the flow-focusing junction to elongate and then break up to form plug-type droplets of length between 582-820 μm . The droplets become larger at the higher rotational speed because the dispersed fluid is driven faster than that at the lower rotational speed. The mixing efficiency appears to be better in the smaller droplets at $\Omega = 400$ rpm. It should be noted that the dispersed fluids have been mixed beginning at the Y-junction prior to formation of the droplet. As the droplet flows downstream along the U-shaped channel, it can be observed that the mixing is further enhanced as the droplet makes each of the right-angle turns.

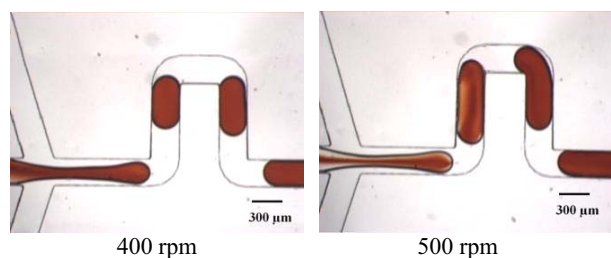


Fig. 2 Flow images of mixing between ferric chloride and ammonium thiocyanate solutions within the droplets formed on the rotating flow-focusing microfluidics at $\Omega = 400$ and 500 rpm.

In order to quantify the enhancement of mixing for the present experiments, the mixing efficiency is calculated based on the concentration measurement of the pixel intensity I of averaged RGB values in the imaged area as follows [8]:

$$\eta_{\text{mix}} = \frac{I - I_{\text{min}}}{I_{\text{max}} - I_{\text{min}}} \times 100\% \quad (1)$$

where the maximum red intensity I_{max} is observed in a fully mixed image and the minimum intensity I_{min} is observed in an image of the DI water. Figure 3 compares the mixing efficiencies measured at the positions along

the U-shaped channel as indicated in Fig. 1 for two rotational speeds $\Omega = 400$ and 500 rpm. The fluids were well mixed before entering the U-mixer at an efficiency of higher than 60%. The mixing efficiency increases progressively along the U-mixer to gain approximately 15% more at the end position (5). The comparison again shows the mixing efficiency for the lower rotational speed $\Omega = 400$ rpm exceeds that for the higher speed $\Omega = 500$ rpm to reach as much as 85% at the exit of the U-mixer.

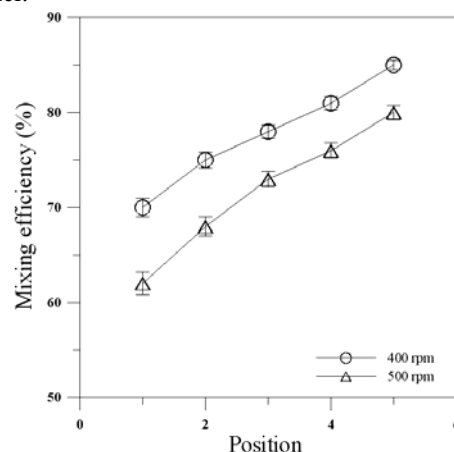


Fig. 3 Comparison of mixing efficiency measured along the U-shaped channel for $\Omega = 400$ and 500 rpm

4. Conclusions

Droplets of plug type are generated in the present centrifuge-driven microfluidics at rotational speeds in the range 400-500 rpm. It is found that the mixing efficiency can be enhanced inside the droplet and further increased along the U-shaped channel by an increment of 15%. The mixing efficiency can reach as much as 85% for the lower rotation speed smaller at which smaller droplets are generated.

Acknowledgements

The authors are grateful for the financial support from National Science Council of Taiwan under contract NSF 99-2212-E-005-028.

References

- [1] A. J. DeMello, *Nature*, **442** (2006), 394-402.
- [2] S. Y. Teh, R. Lin, L. H. Hung, A.P Lee, *Lab Chip*, **8** (2008), 198-220.
- [3] A. T.-H. Hsieh, P. J.-H Pan, A. P. Lee, *Microfluidics and Nanofluidics*, **6** (2009), 391-401.
- [4] J. F. Edd, D. D. Carlo, K. J. Humphry, S. Koster, D. Irimia, D. A. Weitz, and M. Toner, *Lab Chip*, **8** (2008), 1262-1264.
- [5] H. Song, J. D. Tice, R. F. Ismagilov, *Angewandte Chemie International Edition*, **42** (2003), 768-772.
- [6] P. Garstecki, H. A. Stone, G. M. Whitesides, *Physical Review Letters*, **94** (2005), 164501.
- [7] S. Haeberle, R. Zengerle, J. Duerée, *Microfluidics and Nanofluidics*, **3** (2006), 65-75.
- [8] J. M. Chen, T. L. Horng, W. Y. Tan, *Microfluidics and Nanofluidics*, **2** (2006), 455-469.

Flow Induced Acceleration in Vertical Axis Wind Turbine System

Chien-Chang Chen and Cheng-Hsiung Kuo

Department of Mechanical Engineering, National Chung Hsing University

Taichung 402, Taiwan

E-mail of corresponding author: chkuo@dragon.nchu.edu.tw

ABSTRACT

The performance of a small-sized VAWT system is studied by two-dimensional numerical simulation via Ansys/Fluent. The VAWT system has three blades which are separated 120 degrees in the circumferential direction and is driven passively by the incoming wind to rotate from rest. Usually, the angular rotating speed increases exponentially and reaches a steady value; whereas under certain conditions, the angular rotating speed exhibits multiple acceleration stages. This flow-induced acceleration phenomenon will be addressed in this paper.

1. Introduction

Due to excess use of the fossil fuels, the pollutants such as carbon dioxide, nitrogen oxide and sulfur dioxide form the acid rain and enhance the greenhouse effect of the world. This causes the rising of sea level and the unexpected global climate change to threaten the human life and the worldwide ecosystem. Therefore, development and use of the renewable energy is urgent to reduce the use of fossil fuel and to mitigate the unexpected global climate change. To avoid aggravating the environment, the human is looking for the new renewable energy. Among the renewable energy, the wind energy is the cleanest choices.

The VAWT system accepts the coming wind from any directions, produces insignificant aerodynamic noise, needs small operating space, and is simple to design and maintain. Based on the above advantages, the VAWT system can be set up in the densely populated city areas. However, because of the relatively low power efficiency and poor self-starting ability, the design tools of the VAWT are far from matured than those of HAWT. Thus it requires further insightful investigations on the performance of the VAWT system. The Savonius turbine is primarily driven by the drag force and is suitable at low TSR. In addition, the power coefficient is no more than 25%. On the other hand, the driving force of the Darrieus wind turbine is primarily caused by the lift force. Since the relative speed to the blade can exceed much of the coming speed, the Darrieus turbine usually operates at high TSR. Due to the low cost of manufacturing and maintenance, the straight-bladed wind turbine is more attractive to the small-scale wind turbine market.

Strickland (1977) use the multiple stream tube method to study the performance of small VAWT system. This method calculates the overall performance reasonably as the rotor is lightly loaded. Paraschivoiu and Delclaux (1983) employ the double multiple stream tube (DMS) model to predict the aerodynamic loads and the performance of Darrieus turbine. Migliore (1983) studied the effects of blade geometry on aerodynamic efficiency of Darrieus wind turbine. He concluded that the NACA 6-series airfoil not only yielded a peak power coefficient as large as the NACA 4-digit airfoil; it also had broader and flatter power coefficient in relation to the tip speed ratio (TSR). Thanks to the rapid progress of CFD technology, the numerical simulation can be

employed to research the fluid structure of the VAWT system. Ferreira et al. (2009) adopted the CFD method with various turbulence models to simulate the flow structures surrounding the blades of the VAWT system, and compared with the results obtained by the PIV method. Their results showed that the $k-\epsilon$ and the DES models can efficiently elucidate the actual flow structures, and evaluate the normal and tangential force acting on the blade as function of the azimuthal angle.

2. NUMERICAL METHODS

2.1. Physical Model and Grid Patterns

The blade profile is NACA0012 and its chord length is $C=0.1\text{m}$. The small-sized VAWT system has three blades of the same profile, located 120° apart in the azimuthal direction. The radius of rotation of these blades is $R=5C$ and the uniform inflow velocity is 10 m/s . The unsteady, 2-D and incompressible fluid with constant properties is assumed to simulate the flow structures around the VAWT system. The computational domain lies within a region $-35 \leq X/C \leq 45$ and $-30 \leq Y/C \leq 30$. The uniform inflow enters the left boundary of the flow domain. To simulate the flow characteristics and the loadings on each blade efficiently and accurately, the flow domain is divided into three regions depicted in Fig. 1. The small circular region around each blade is denoted as region A, the region B is located between the three small circular zones and large circular zone; the region outside the large circle is called region C. The digital symbols 1, 2, and 3 in Fig. 1 indicate each blade at three different azimuthal positions. The azimuthal angle (φ) starts from the vertical position shown in Fig. 1.

2.2. Process of Numerical Simulation

To determine the rotation of the VAWT system, the ANSYS/Fluent (2009) software employs the user defined function (UDF) to control the rotating motion at each instant. The Fluent solver links the UDF code through the built-in compiler. The SST- $k\omega$ turbulence model is selected for the computation because this model is suitable to calculate the flow characteristics with strong adverse pressure gradient and flow separation at large AOA. Also, the Pressure Staggering Option (PRESTO) algorithm is adapted to solve the flow field with strong pressure gradient and highly rotating flow. The SIMPLE algorithm is employed for

the coupling between the pressure and the velocity in the momentum equations. The first order upwind method is employed to solve the momentum, turbulence kinetic energy and turbulence diffusion. The iteration process stops as long as the absolute residuals in all variables are less than 10^{-4} .

4. RESULTS AND DISCUSSIONS:

The results in the left plot of Figure 2 show the temporal variations of the rotating speed, $\omega(t)$, of the VAWT system at different pitch angles (θ). Evidently, the rotating speed increases exponentially in acceleration stage and finally reaches a steady rotating speed (ω_s).

The dynamic equation $I_{zz}\ddot{\phi} + b\dot{\phi} + k\phi = M_a$ shows that the magnitude of steady rotating speed (ω_s) depends on the aerodynamic torque M_a . The larger the aerodynamic torque, the higher will be the steady rotating speed. For a VAWT system, the aerodynamic torque M_a is strong functions of the blade profile, the inflow speed (V_∞), the pitch angle (θ) and the azimuthal position (φ). The results in the left plot of Figure 2 shows that the steady rotating speed is the largest for the case $\theta = 5^\circ$. Further increase in the pitch angle ($\theta = 10^\circ$) causes a significant decrease in the value of steady rotating speed. The value of ω_s decreases monotonously but mildly as the pitch angle decreases from $\theta = 5^\circ$ to $\theta = -10^\circ$. On the contrary, in the right plot of Figure 2, the temporal variation of rotating speed experiences a secondary accelerating stage as the magnitudes of the damping coefficient and the moment of inertia reduce. On the right plot, there are two accelerating stages during the operating period. The aerodynamic moment is functions of the azimuthal position φ and rotating speed $\dot{\phi}$ depicted in eqn. (1)

$$M_a(\varphi, \dot{\phi}) = kU^2 \left[\sin^2 \varphi + (R\dot{\phi}/U + \cos \varphi)^2 \right] \quad (1)$$

This causes the dynamic equation to form a nonlinear self-excited oscillator (Neyfeh and Mook 1979). Based on the illustration in the book of Blevins (1994), the aerodynamic moment at various azimuthal positions φ and rotating speeds $\dot{\phi}$ provide the effects to decrease the damping coefficient b . Within certain time of the rotating period, the damping coefficient will become negative. Negative value of b in the dynamic equation is primarily responsible for the onset of the secondary acceleration.

5. CONCLUSIONS

In this paper, the rotation response of a small-sized VAWT system is studied by two-dimensional numerical simulation via Ansys/Fluent. The VAWT system has three blades which are separated 120 degrees in the circumferential direction and is driven passively by the incoming wind to rotate from rest. As

the VAWT is subjected to a uniform incoming flow speed, the angular rotating speed usually increases exponentially and reaches a steady value; whereas under certain conditions, the angular rotating speed exhibits a secondary acceleration stage. This flow-induced acceleration phenomenon is primarily caused by the contribution from the aerodynamic moment leading to the negative damping coefficient in the dynamic equation.

6. ACKNOWLEDGEMENTS

The authors are grateful for the financial support from the project of the National Science Foundation of Taiwan, the Republic of China, under the Grant No. NSC-99-2221-E-005-029-MY3.

7. REFERENCES

- [1] Fluent User manual (2009).
- [2] Fiedler AJ and Tullis S (2009) Wind Engineering 33 (3):237-246
- [3] Migliore P (1983) Journal of Energy 7:291
- [4] Paraschivoiu I, Delclaux F (1983) Journal of Energy 7:250-255
- [5] Strickland J (1977) International Symposium on Wind Energy 36:56.
- [6] Neyfeh AH and Mook DT (1979), Nonlinear Oscillations, Wiley Publishing Company, New York.
- [7] Blevins R (1994) Flow-Induced Vibration, Krieger Publishing Company, Malabar, Florida.

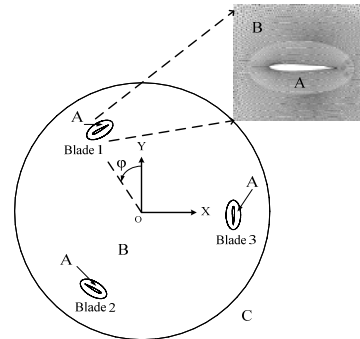


Figure 1 Coordinate of VAWT system, divisions of flow domain, grid patterns around the blades.

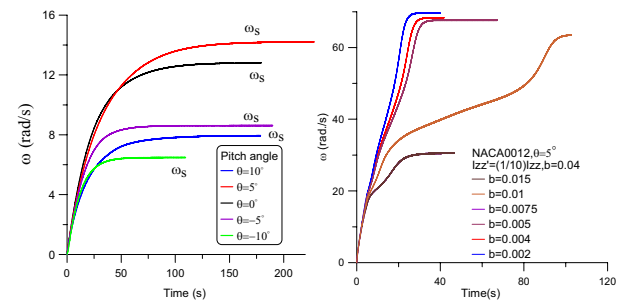


Figure 2 Temporal variations of the rotating speed of the VAWT system. The inflow speed is 10 m/s. The profile of the blades is NACA 0012. (left): without secondary acceleration, and (right): with secondary acceleration

Region of the Negative Magnus Force on Rotating Sphere

Yasufumi Konishi, Tatsuo Itami, Hiroyuki Okuizumi, Tomoyuki Ohno, Shigeru Obayashi
Institute of Fluid Science, Tohoku University, Aobaku, Katahira 2-1-1, Sendai, Miyagi, Japan.
konishi@edge.ifs.tohoku.ac.jp

ABSTRACT

It is a well-known phenomenon that the sphere rotating about an axis perpendicular to the flow is subjected to lateral force, called Magnus force. At the moderate Reynolds number and the moderate spin rate which is defined by the ratio of the circumferential velocity to the free stream velocity, the direction of the lateral force changes from usual Magnus force to negative Magnus force. We conducted force measurements at a low turbulent wind tunnel to reveal the region of the negative Magnus force. As the result, the negative Magnus force was observed at Reynolds numbers higher than 53500.

1. Introduction

It is a well-known phenomenon that the sphere rotating about an axis perpendicular to the flow is subjected to lateral force, called Magnus force. This phenomenon is often seen in a baseball, a golf ball and a table-tennis ball. Some papers showed that the direction of the lateral force changes to opposite direction at the moderate Reynolds number. This phenomenon was first reported by Maccoll[1]. Recently, Muto et al.[2] investigated to reveal the mechanism of negative Magnus force using large-eddy simulations at around the critical Reynolds number and showed that the negative Magnus force was related to the boundary layer transition of the both side of the rotating sphere. Taneda[3] also investigated the region of the negative Magnus force and explained the phenomenon by flow visualization. Moreover, Briggs[4] and Davies[5] showed that the negative Magnus force appeared in their experiment, but the occurring regions do not coincide each other. Tanaka et al.[6] also conducted a wind tunnel experiment on spheres and non-spherical bodies, including both prelate and oblate spheroids, and investigated the relationship between the spinning rate and Reynolds number. However their results of region range is higher than Taneda's result. These differences between the experiments suggest that the freestream disturbances and/or surface roughness greatly influences. Therefore, this phenomenon is closely related to the boundary layer transition. To understand this phenomenon in detail, further investigations on the accuracy of the experimental measurements should be conducted.

In this experiment, we conducted a force measurement of a spinning sphere and aimed to acquire basic data of the region of the negative Magnus force.

2. Experimental Set-up

The experiments are conducted in the low-turbulent wind tunnel at the Institute of Fluid Science, Tohoku University, Japan. The further details regarding the wind tunnel are provided by Kohama et al.[7]. The test-section is a closed octagonal shape whose diameter is 290 mm. In order to keep the static pressure of the test-section close to the atmosphere pressure of the outside, four diffuser flaps are attached to the rear part of the test section. The sphere is suspended at the center

of the test section by the thin wire whose diameter is 0.55 mm. This wire is connected to the brushless DC motor and frames. This set up is based on Naruo et al.[8] We attached a three-component balance (Nisshou Electric Works Co. Ltd, LMC-3501-50N) to the bottom of the frame, and measured the lift and drag of the sphere including the wire. Therefore, the lift and drag of the wire are measured independently and those values are subtracted to correct the lift and drag of the sphere. The overall experimental configuration is shown in Figure 1.

The sphere is a commercially available table tennis ball called Large Ball, 44 mm in diameter. It is made of celluloid and its weight is about 2.2 to 2.4 grams. We chose the three star ball specified by Japan Table Tennis Association.

Regarding the coordinate system, x is the streamwise direction, y is the normal-to-wall direction, and z is the spanwise direction. The origin is the center of the sphere.

3. Results and Discussion

To reveal the region of the negative Magnus force, the force measurements are conducted. The coefficients of the lift, C_L and drag, C_D against the spin parameter, SP for each measured Reynolds number based on the diameter of sphere, d and free stream velocity, U are plotted in Figure 2 (a) and (b) respectively. These coefficients, C_L and C_D and the spin parameter, SP is defined as follows.

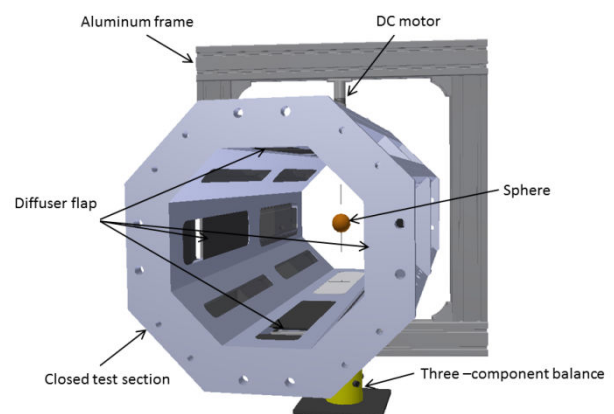


Fig. 1 Schematic of Experimental set-up

$$C_L = \frac{F_y}{1/2\rho U^2 S} \quad (1)$$

$$C_D = \frac{F_x}{1/2\rho U^2 S} \quad (2)$$

$$SP = \frac{v}{U} = \frac{r\omega}{U} \quad (3)$$

F_x and F_y are the force of the x -direction and the y -direction, respectively. S is the projected area and r is the radius of the sphere, and ω is the angular velocity. C_L increases linearly at the region of small SP and abruptly drops to negative value. After that, C_L gently increases again for higher SP . It is important to note that the gradients of C_L/SP for smaller SP are independent to Reynolds numbers and for $Re=3.0 \times 10^4$ or higher, C_L curves correlate with each other after the transition region. These gradual decreases of C_L are related to the decrease of C_D . From Fig. 2(b), we can see that C_D starts to decrease simultaneously with the decrease in C_L . In contrast with C_L which recovers immediately after drop, C_D starts to increase after continuing its decrease for a while. C_D curves also coincide with each other except the transitional region. These phenomena are observed in a rotating circular cylinder. It suggests that the mechanism of occurrence of the negative Magnus force is similar to the two-dimensional circular cylinder[9].

The region of the negative Magnus force obtained in this experiment is presented by the $Re - SP$ plane in figure 3. The line indicates the neutral line which means C_D is zero and C_L is negative within the indicated area. In this figure, previous results from Taneda and Tanaka et al. are also shown. The present result coincides with Taneda's result, and the critical Reynolds number is approximately 5.35×10^4 .

4. Concluding remarks

The force measurements were conducted to reveal the region of the negative Magnus force appearance. The results showed that the neutral line of the negative Magnus force coincides with Taneda's previous result. The results suggest that the occurrence of the negative Magnus force on the sphere can be explained by the case of the rotating two-dimensional circular cylinder.

Acknowledgement

We would like to express our gratitude to visiting Prof. Hideo Sawada, IFS, Tohoku University, for his great support and discussion.

References

- [1] Maccoll, J. H., *J. Roy. Aero. Soc.*, **32**, (1928), pp.777-798.
- [2] Muto M., Tsubokura M., and Oshima N., *Physics of Fluids*, **24**(1), (2012), 014102.
- [3] Taneda S., *Reports of Research Institute for Applied Mechanics*, **5**(20),(1957), pp. 123-128.
- [4] Briggs L., *Am. J. Phys.*, **47**(8), (1959), pp. 589-596.

- [5] Davies J. M., *Journal of Applied Physics*, **20**(9), (1949), pp. 821-828.
- [6] Tanaka T., and Yamagata K., *Proc. of the 2nd KSME-JSME Fluids Engineering*, (1990), pp. 366-369.
- [7] Kohama, Y., Kobayashi, R., Ito, H., *The Memoirs of Inst. High Speed Mech. Tohoku Univ.*, **48**, (1982), 422
- [8] Naruo, T., Mizota, T., *Nagare*, **23**, (2004), pp. 203-211.(in Japanese)
- [9] Swanson, W. M. 1961, *J. Basic Eng. Tran. ASME*, **83**, (1961), pp461-470.

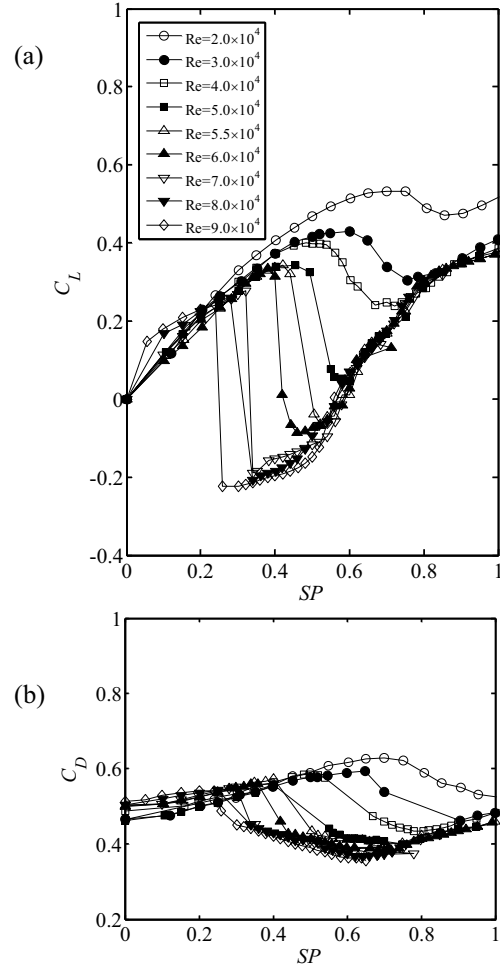


Fig. 2 Lift and Drag coefficient against spin parameter. (a) Lift, (b) Drag.

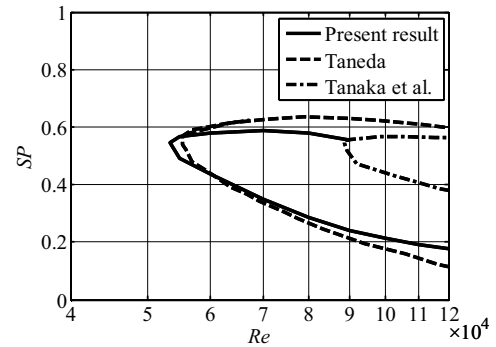


Fig. 3 Region of the negative Magnus force

Free-Flight Test Techniques Based on Ground Test Facilities

Hideyuki Tanno^{*1}, Tomoyuki Komuro, Kazuo Sato and Katsuhiro Itoh

^{*1}Japan Aerospace Exploration Agency Kakuda Space Center, Miyagi, 981-1525 JAPAN
tanno.hideyuki@jaxa.jp

ABSTRACT

Free-flight test technique with scaled models based on ground test facilities has been developing in JAXA Kakuda Space Center. The key technology for the test technique is a JAXA in-housed miniature data-recorders, which are small enough to be on-boarded in free-flight projectiles. Preliminary free-flight test was conducted in the air driven two-stage light gas gun HEK-G with the newly built 120mm-diameter gun barrel. In the present test campaign we successfully conducted to launch capsule shaped projectiles, which velocity at the gun barrel muzzle was approximately 220m/s.

1. Introduction

JAXA has studied aerodynamic characteristics of capsule shaped reentry vehicles for a candidate of JAXA's future space transporter from LEO¹. Transonic instability of capsule is one of the major technical issues for the design of capsule shaped reentry vehicles, however, this phenomenon is quite complicated because it is deeply affected from the wake of the vehicles. The exact analysis of the wake flow is heavily time consuming even with the most up-to-date CFD. In addition, accurate wind tunnel test is also difficult due to the support system such as sting which may interfere with the wake flow. Hence, numerical simulations, wind tunnel tests and free-flight tests including ballistic ranges are generally both used to observe the transonic characteristics for the capsule shaped reentry vehicles^{2,3}. In JAXA-Kakuda Space Center, we build air driven two-stage light gas gun HEK-G for free-flight test of capsule shaped projectiles⁴. The measurement results in this study are going to be used as benchmarks of transonic aerodynamic characteristics to compare with wind tunnel results and with numerical simulation results.

2. Experimental set-up

The air-driven two-stage light gas gun HEK-G was originally built as a free-piston shock tunnel⁵, and its free-piston driver was used as a pump tube for ballistic range. The facility can launch 100mm diameter projectile with 2kg mass at Mach 2. Fig.1 shows the HEK-G with its 120mm-diameter gun barrel. For direct measurement of aerodynamic force with free-flight projectiles, a miniature model-onboard data-recorder

was also developed in order to store the measured data (Fig.2). The data-recorder was originally designed to be small enough to be instrumented in wind tunnel test models⁶, with an overall size of 60 mm-diameter x 60 mm-height, including batteries. Since the recorder was configured to measure aerodynamic force or pressure, it includes eight piezoelectric amplifiers as well as high-speed analogue-digital converters, which digitize the measured data with 16-bit resolution. The recorder's sampling rate and sample size are 100 kHz and 1300 ms, respectively. For the autonomous operation, the recorder waits for a trigger signal (accelerometer output) and then starts to take measurements with arbitrary adjustable trigger threshold level and pre-trigger delay time. Measured data is stored to static memory for transfer to a PC via a USB interface after a wind tunnel test

3. Preliminary results

Projectile used in this study was 100mm diameter HRV-option II, which was manufactured with aluminum alloy. The Fig.3 shows the HRV projectile with two-pieces polyethylene Sabot. The first test campaign of the measurement as preliminary trial has already conducted in Feb.2012 at JAXA-KRC. The objective of the campaign was to secure the projectile and instruments can be survived over thousand G condition caused through acceleration and deceleration. The capsule shaped projectile was launched with flight speed of approximately 220m/s at the exit of gun muzzle. The projectile flew for 4m length and has been successfully recovered without any damages. Fig.4 shows the sequential images of the projectile and sabot flying in the open space, which images were taken with a

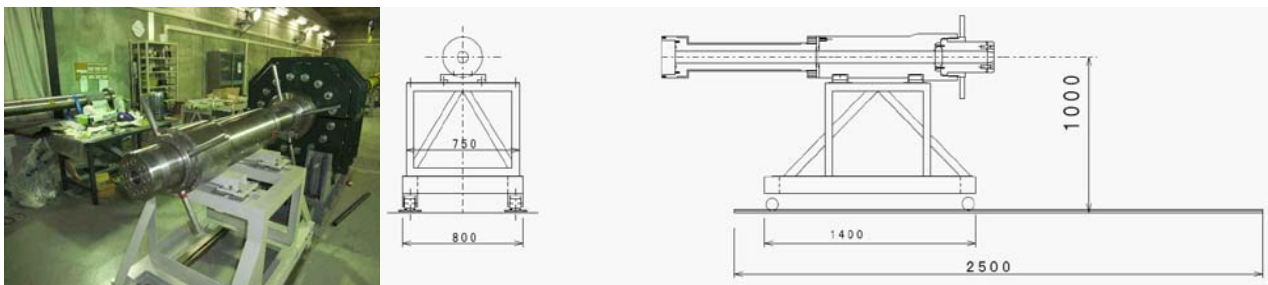


Fig.1 Gas driven two-stage gas-gun HEK-G with a newly built gun barrel which bore is 120mm.

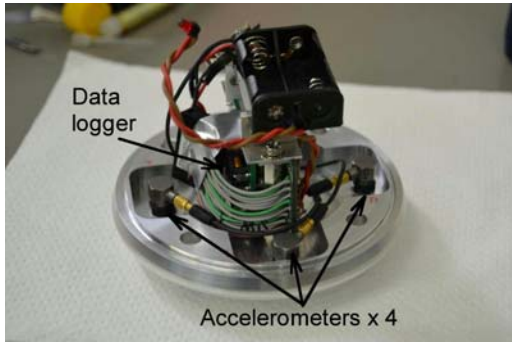


Fig.2 Miniature data-recorder and accelerometers installed on the bottom plate of the HRV projectile.

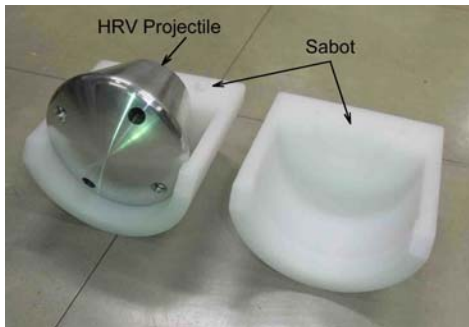


Fig.3 HRV Capsule shaped projectile and polyethylene two-pieces sabot for HEK-G.

high-speed video camera. From these images, sabot was successfully separated from the projectile even with the short flight path.

The direct force measurement of free-flight HRV projectile with the data-recorder will be conducted in the next test campaign, which will be planned in the Sep.2012. In the AIAA script the latest test results obtained in the campaign will be also reported.

References

- [1]Imada T.(2011) Concept and Technology of HTV-RAn Advanced Type of H-II Transfer Vehicle, Proceedings of the 28th ISTS
- [2]Berner C,Fleck V, Sommer E and Tran P(2008) Aerodynamic coefficients of entry vehicle demonstrator from free flight range testing, Proceedings of the 6th European Symposium on Aerothermodynamics for Space Vehicles.
- [3]Brown JD and Bogdanoff W(2008) Free-flight dynamic aero data for a lifting CEV capsule. AIAA 2008-1232
- [4]Tanno H., Komuro T., Kodera M., Sato. K., Itoh K.(2011) A two-stage light gas gun drove from free-piston shock tunnel technology, Proceedings of the 28th ISTS.
- [5]Itoh K, Ueda S, Tanno H, Komuro T, Sato K (2002) Hypersonic aerothermodynamic and scramjet research using high-enthalpy shock tunnel, Shock Waves, 12:93-98.
- [6]Tanno H, Komuro T, Sato K, Itoh K and Takahashi M (2012) Free-flight force measurement technique in shock tunnel, AIAA 2012-1241



Fig.4 Sequential high-speed video Images of free-flight test (flight length = 4m).

Heat Transfer Enhancement Using 2-Phase Flow Oscillation

Sung Jin Kim, Young Jik Youn

School of Mechanical, Aerospace & Systems Engineering
Korea Advanced Institute of Science and Technology, Daejeon, 305-701, South Korea
sungjinkim@kaist.ac.kr

ABSTRACT

A micro oscillating heat spreader was fabricated and its thermal performance was experimentally investigated. The micro channel forming a serpentine closed loop has a hydraulic diameter of 570 μm and ethanol was used as a working fluid. The heat spreader achieved maximum effective thermal conductivity of 600 $\text{W/m}\cdot\text{K}$ which is 1.5 times higher than copper. Flow visualization was performed to investigate oscillating flow characteristics. As the frequency and amplitude of the oscillating flow increase, the thermal performance increases. The frequency and amplitude are 0.67 Hz and 15 mm, respectively, at the maximum thermal performance.

1. Introduction

Heat can be effectively transported using oscillating flow. Nishio et al. [1] proposed the COSMOS (Counter-Stream-Mode Oscillating Flow) heat transport device, utilizing liquid oscillation in a small channel completely filled with liquid. However, the COSMOS device requires an additional external power to sustain liquid oscillation. Akachi [2] suggested the oscillating heat pipe (OHP) which can transport heat, using self-excited oscillation of the liquid slugs and vapor plugs without an additional external power. The OHP can be used as a thin heat transport device because the OHP uses simple mini channels. A wide range of experimental studies have been conducted for thermal performance of OHP [3, 4]. However, most studies were conducted for OHP with macro channels ($D > 2\sim 3$ mm). In order to develop the OHP with thinner profile, study on the OHP with micro channels ($D < 1$ mm) are needed.

The objectives of the present study are to experimentally evaluate the thermal performance of a silicon based micro oscillating heat spreader and investigated the effect of oscillating motion of the liquid slugs and vapor plugs on the heat transfer characteristics of the micro oscillating heat spreader.

2. Experimental setup and procedures

A total of 10 parallel interconnected rectangular channels forming a meandering closed loop were engraved on a silicon wafer using a deep reactive ion etching (DRIE) process. The width and height of the microchannel are 1 mm and 0.4 mm, and the hydraulic diameter is 570 μm . The top of the silicon wafer was covered by a transparent glass plate with a thickness of 0.5 mm to allow flow visualization. The fabricated micro oscillating heat spreader has a length of 50 mm, width of 15.5 mm, and thickness of 1.5 mm. Once fabricated, the micro oscillating heat spreader was charged with a tightly-controlled amount of working fluid (ethanol). Fig. 1 shows the fabricated micro oscillating heat spreader. The evaporator of the micro oscillating heat spreader was heated using a thin film heater. When DC electric current is applied to the heater, a nearly-uniform wall heat flux condition is established. The condenser of the micro oscillating heat spreader is cooled by a water jacket. All experiments were

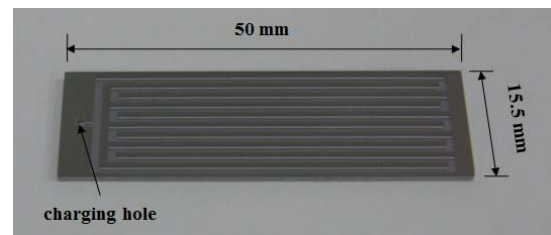


Fig. 1 Fabricated micro oscillating heat spreader

performed in a vacuum chamber ($10^{-2}\sim 10^{-3}$ torr) made of acrylic glass to minimize the heat loss from the micro oscillating heat spreader to the environment and to obtain reliable experimental data.

3. Results and Discussion

The wall temperature variations with time at the evaporator and condenser are presented in Fig. 2. When the evaporator is heated and the condenser is cooled, the evaporator wall temperature drastically increases and reaches a maximum temperature of 70 $^{\circ}\text{C}$ without temperature oscillation. At $t = 120\text{s}$, the evaporator temperature and the condenser temperature start to oscillate and the evaporator temperature sharply decreases (start-up operation). Beyond $t = 500\text{s}$, the evaporator and condenser temperature oscillates stably with nearly constant frequency and amplitude (steady operation).

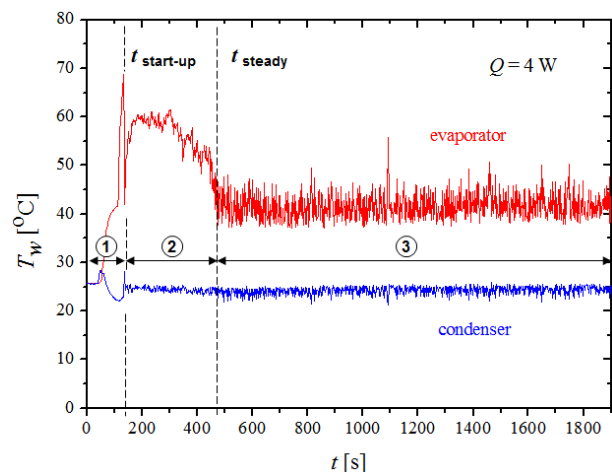


Fig. 2 Wall temperature variations with time

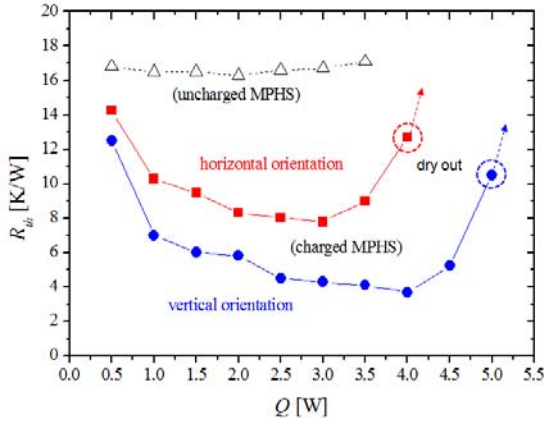


Fig. 3 Thermal resistance variations with input power

In an attempt to better quantify the thermal performance of the micro oscillating heat spreader, thermal resistance was calculated utilizing the average temperature difference between the evaporator and the condenser. The thermal resistance is obtained from

$$R_{th} = \frac{T_{avg,e} - T_{avg,c}}{Q_{in}} \quad (1)$$

where Q_{in} is the input power and $T_{avg,e} - T_{avg,c}$ is the average temperature difference between the evaporator and condenser. The variation of the thermal resistance of the micro oscillating heat spreader with input power is presented in Fig. 3. The vertically oriented micro oscillating heat spreader shows better thermal performance than the horizontally oriented micro oscillating heat spreader. The maximum effective thermal conductivity of the micro pulsating heat spreader is about 600 W/m·K corresponding to minimum thermal resistance of 3.8 K/W, which is 3.5 times higher than that of silicon and 1.5 times higher than that of copper.

Fig. 4 presents photography of the oscillating motion of liquid slugs and vapor plugs of the micro oscillating heat spreader recorded by high speed camera. The liquid slugs and vapor plugs in a micro channel oscillate with respect to time. The relative displacements (x) of meniscus between the liquid slugs and vapor plugs were measured to get the frequency and amplitude of the oscillating motion.

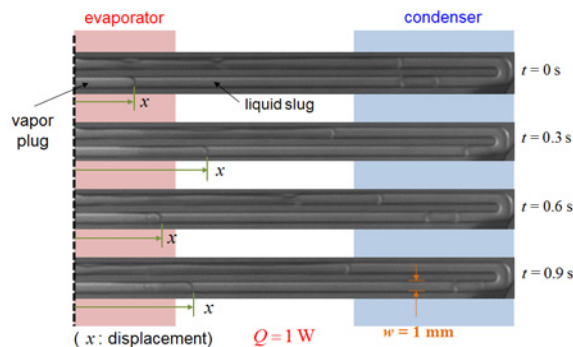


Fig. 4 Oscillating motion recorded by high speed camera

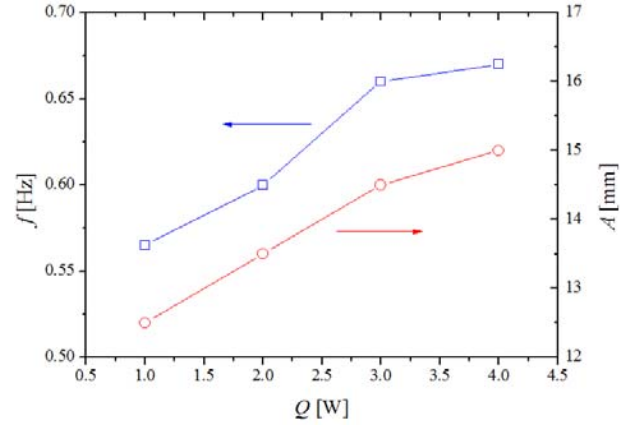


Fig. 5 Frequency and amplitude of the oscillating motion

The frequency and amplitude of the oscillating motion with respect to the input power are presented in Fig. 5. As the input power increases, the frequency increases from 0.56 Hz at input 1 W to 0.67 Hz at input power of 4 W. The amplitude also increases with increasing input power from 12.5 mm to 15 mm. As the input power increases, the rate of volume expansion of the vapor plugs increases which stimulate the oscillating motion and the thermal performance increases.

4. Concluding remarks

A silicon-based micro oscillating heat spreader was fabricated and its thermal performance was experimentally investigated. The microchannel forming a serpentine closed loop has a hydraulic diameter of 570 μm and ethanol was used as the working fluid. The micro oscillating heat spreader achieved maximum effective thermal conductivity of 600 W/m·K which is 1.5 times higher than copper. Flow visualization was performed using high speed video camera to investigate oscillating flow characteristics. As the frequency and amplitude of the oscillating flow increase, the thermal performance of the micro oscillating heat spreader increases. The frequency and the amplitude are 0.67 Hz and 15 mm, at the maximum thermal performance.

Acknowledgement

This work was supported by the Korea Science and Engineering Foundation through the National Creative Research Initiatives program, which is funded by the Ministry of Education, Science and Technology (No. 2112R1A3A2026427)

References

- [1] S. Nishio X.H. Shi, and W.M. Zhang, *Int. J. Heat Mass Transfer*, **38** (1995), 2457–2470.
- [2] H. Akachi, Japanese Patent No. Hei6–97147.
- [3] P. Charoensawan, S. Khandekar, M. Grol, and Terdtoon, *Applied Thermal Engineering*, **23** (2003), 2009–2020.
- [4] B.Y. Tong, T.N. Wong and K.T. Ooi, *Applied Thermal Engineering*, **21** (2001), 1845–1862.

Thermal Transpiration Based Pumping and Power Generation Devices

Kang Wang¹, Pingying Zeng¹, Jeongmin Ahn¹, Paul D. Ronney²
Syracuse University, USA¹; University of Southern California, USA²
jeongahn@syr.edu

ABSTRACT

Catalytic combustion-driven thermal transpiration was employed to build a miniature pump in this study. This designed pump was further used to build a miniature power generator that has self-pumping and power generation integrated into one device, has no moving parts and operates only on thermal and electrochemical energy supplied by hydrocarbon fuels. A solid oxide fuel cell tested with this power generator obtained a power density of 40 mW/cm².

1. Introduction

It is well known that hydrocarbon fuels possess far higher energy densities than the best available batteries, thus power generation devices employing hydrocarbon fuels rather than electrochemical storage as the energy feedstock have been studied extensively in recent years as potential alternatives to batteries in portable electronic systems [1 - 3]. While many devices have been proposed in order to attain high net energy density, nearly all require the use of air so that only one reactant (fuel) need be carried. Since air must be ingested and exhaust expelled at ambient pressure, some means to draw air into the device is required. This is problematic because small gas pumps are extremely inefficient and may consume most of the electrical power generated. For example, a recently reported novel electrostatic gas pump [4] consumes at least 0.87 mW of power per cm³/min of gas flow, corresponding to 3.0 % of the enthalpy of a stoichiometric propane-air mixture. Considering the low efficiency of conversion of fuel enthalpy to electrical power at small scales, it seems unlikely that such pumps could be practical for portable power devices. More traditional devices such as electric motors coupled to fans are similarly inefficient due to substantial friction losses at small scales.

In this work, we aim to develop a microscale or mesoscale self-pumping system based on a catalytic combustion-driven thermal transpiration. Thermal transpiration [5], first described by Reynolds in 1879, that occurs in narrow channels or porous media with an imposed temperature gradient. In this study, thermal transpiration (thus pressurization) is completed by using microporous materials whose pore size is comparable to the mean free path of gas molecules at relevant conditions. The pump is further used to build a miniature power generator that has self-pumping and power generation integrated into one device, has no moving parts and operates only on thermal and electrochemical energy supplied by hydrocarbon fuels, thus it has no parasitic electrical energy losses. This system has no moving parts, no supplemental working or pressurization fluids, very low mass and integrates pressurization and thrust generation. The system consists of a catalytic combustion-driven thermal transpiration-based pumping device, and integrated with single-chamber Solid Oxide Fuel Cells (SCSOFC). This SCSOFC has demonstrated an outstanding performance in previous research [6].

2. Experiment

For fabrication simplicity and ease of incorporating transpiration membranes, a cubic combustor (3 cm × 3 cm × 3 cm) design was employed (Figure 1). All six faces employed Ahlstrom™ glass microfiber filters, 1.1 mm thick with nominal pore radii of 1.6 μm as transpiration membranes. The membranes were enveloped by a high thermal conductivity cubic thermal guard fabricated using a 3D printing process using commercially available stainless steel powders having 30 μm average particle diameter. The guards were 1.2 mm thick with 250 μm holes spaced 500 μm apart.

Five faces of the cube were exposed to ambient and thus transpired air only. The sixth face (Figure 1, right side) transpired both fuel (propane) fed and air into a mixing chamber. Fuel was fed via a thermal mass flow controller and air was drawn via a T-fitting in the fuel line with one leg open to ambient. This configuration requires that both fuel and air must be transpired, otherwise fuel would escape to ambient through the open leg. In this way it is not possible for any reactant flow to occur as a result of the fuel supply pressure; only thermal transpiration can draw reactants into the device. Soap film tests confirmed that the air was drawn into (rather than fuel expelled from) the open leg. Device performance was found to be independent of orientation, thus buoyant flow is insignificant compared to transpiration flow. The side opposite the mixing chamber was fitted with a 1.5 mm diameter (large enough to avoid reverse thermal transpiration) exhaust pipe and electrical feed-throughs for a hot-wire igniter, fuel cell leads and K-type thermocouples to measure gas, catalyst and SCSOFC temperatures. A 2.5 cm × 1.25 cm Pt mesh catalyst placed at the center of the membrane chamber (Figure 1) was used for all tests.

The starting materials for the SCSOFC electrolyte, anode and cathode were, respectively, Sm_{0.2}Ce_{0.8}O_{1.9} (SDC, NexTech materials); NiO+SDC (60:40 w/w, NexTech materials); and Ba_{0.5}Sr_{0.5}Co_{0.8}Fe_{0.2}O_{3-δ} (BSCF)+SDC, the SCSOFCs were prepared [12]. The effective cell surface area of the SCSOFC was 0.95 cm². Silver wires were used for electrical connections. Current-voltage polarization curves were collected using a Keithley 2420 source meter.

3. Results and Discussion

First, thermal transpiration system performance was tested without SCSOFCs. Tests were initiated by passing a current through the hot-wire igniter until the

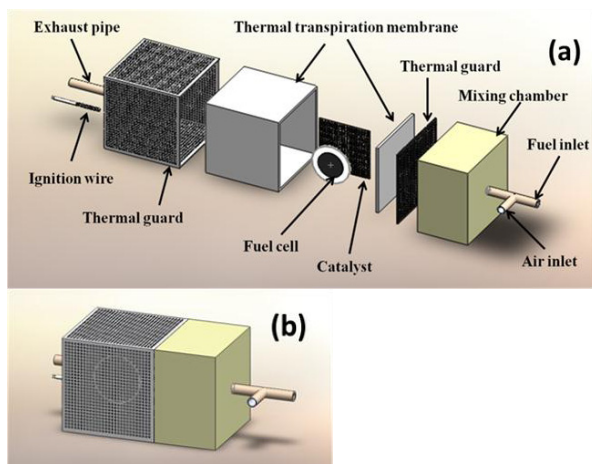


Fig. 1 Schematic of the thermal transpiration device: (a) exploded view; (b) assembled view.

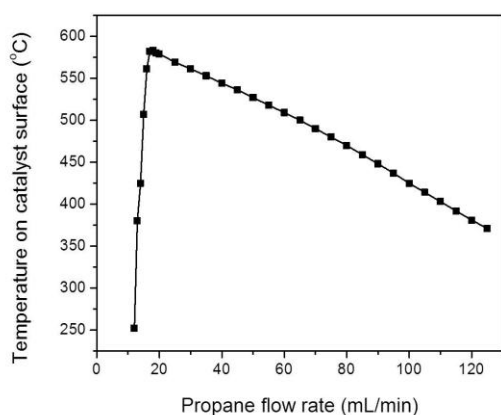


Fig. 2 Catalyst temperature curves under various propane flow rates

catalyst temperature reached about 280°C, then the fuel flow was started. When ignition occurred (as evidenced by a rapid rise in catalyst temperature) the current was switched off. After typically 2 minutes, the catalyst temperature stabilized, indicating that self-sustaining operation had been attained.

Figure 2 shows the effect of propane flow rate on catalyst temperatures. The catalyst temperature increases rapidly with increasing fuel flow up to an optimum value of about 575 °C then decreases more slowly for higher flows. This is probably due to overall near-stoichiometric mixtures being attained near the maximum temperature condition.

Since it was demonstrated that self-sustaining catalytic combustion and thermal transpiration pumping is feasible and that the maximum achievable temperatures (≈ 575 °C) are even higher than the optimal values for propane-air SCSOFCs (≈ 550 °C) [7]. Consequently, we were encouraged to test a power generator using a SCSOFC coupled to a thermal transpiration driven catalytic combustor.

Figure 3 shows the SCSOFC polarization curve obtained using the optimal (maximum power) cell location and fuel flow. The optimal SCSOFC location and orientation yielding the highest power was found to

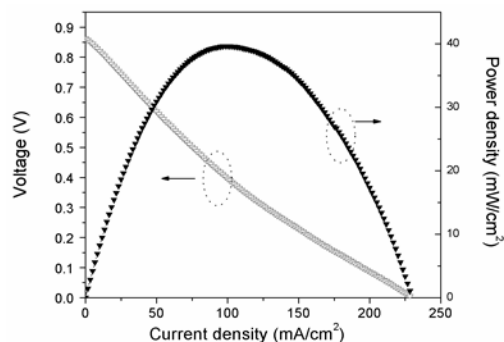


Fig. 3 Polarization curve at the location and fuel flow corresponding to maximum power

be about 0.5 cm away from the transpiration membrane with the cathode facing outward to maximize its exposure to transpired air. This is expected since if the cell is too close to the membrane, the cell temperature is low, whereas if it is too close to the catalyst, there is more fuel flow to the cathode side and thus more opportunity for undesired fuel oxidation on the cathode. The Open-Circuit Voltage (OCV) is 0.85 V, the peak current and power densities are 230 mA/cm² and 40 mW/cm², respectively, which are nearly 10 times smaller than the best reported in other propane-air SCSOFC studies [7]. Measurements of in-situ anode and cathode temperatures showed that both reached their maxima (400 and 430 °C, respectively) at the same fuel flow rate (30 mL/min) at which the maximum temperature is reached without the SCSOFC, but these SCSOFC temperatures are considerably lower than those measured in the combustor without the fuel cell.

4. Concluding remarks

It was demonstrated that self-sustaining catalytic combustion, thermal transpiration pumping and power generation were feasible in the designed combustor proposed in this paper. The highest power density obtained was 40 mW/cm² at a propane flow rate of 30 mL/min corresponding to a chemical enthalpy flux of 41.4 W, leading to an overall efficiency of 0.092 %. This is obviously far lower than necessary for a power source to be competitive with batteries. So more work has to be done in the future to improve the power.

References

- [1] A. C. Fernandez-Pello, Proc. Combust. Inst. **29** (2003), R883.
- [2] D. Dunn-Rankin D; E. M. Leal, D. C. Walther, Prog. Energy Combust. Sci. **31** (2005), R422.
- [3] D. C. Walther, J. M. Ahn, Prog. Energy Combust. Sci. **37** (2011), R583.
- [4] B. Kim, K. S. Lee, M. A. Shannon, J. Korean Phys. Soc. **57** (2010), R1494.
- [5] O. Reynolds, Phil. Trans. Royal Soc. (London) **170** (1879), R727.
- [6] K. Wang, R. Ran, W. Zhou, H.X. Gu, Z.P. Shao, J. Power Sources **179** (2008), R60.
- [7] Z. P. Shao, S. M. Haile, J. M. Ahn, P. D. Ronney, Z. L. Zhan, S. A. Barnett, Nature **435** (2005), R795.

Passive Control of the Free-Stream Turbulence Intensity of the Mars Wind Tunnel by the Turbulence Screen

Daiju Numata, Takaaki Tsuchiya and Keisuke Asai

Department of Aerospace Engineering, Graduate School of Engineering, Tohoku University
6-6-01 Aramaki Aza Aoba, Aoba-ku, Sendai, Miyagi, 980-8579 JAPAN
numata.daiju@aero.mech.tohoku.ac.jp

ABSTRACT

The objective of this study is to control flow condition, especially turbulence intensity, of the Mars Wind Tunnel (MWT) by using turbulence grids. In this study, we built three types of the turbulence grids, and evaluated the flow field behind them in the MWT at total pressure of 5, 11 and 22 kPa. The velocity fluctuation in the test section was measured by using a hot-wire anemometer (HWA). The results indicated that the free-stream turbulence intensity increased by installing the turbulence grids, and flow condition behind them indicate a transitional or fully-turbulent condition depending on the flow velocity.

1. Introduction

Recently, a great attention has been paid to explore the Mars. Many probe vehicles have been sent to the Mars to investigate the origin of life and so on. Among many kinds of vehicle, aerial vehicles have been considered as a suitable means of exploring the Mars. The advantage of the aerial vehicles is to cover greater distance than that of rovers and at lower imaging altitudes than those of satellites. However, the flight condition of "Mars airplane" becomes low Reynolds number condition because density of Martian atmosphere is one-hundredth as same as that of Earth's. For example, Fujita assumed that Reynolds number of Mars airplane was 26,000 [1]. In low Reynolds number condition, aerodynamic characteristics of airfoils are affected by the free-stream turbulence intensity [2, 3]. Mueller et al. clarified that the problems associated with obtaining accurate wind tunnel data at low chord Reynolds number are compounded by the sensitivity of the boundary layers to the free-stream disturbance environment [2]. However, the influence of turbulence intensity at low Reynolds number condition has not been clarified below Reynolds number of 50,000 because it was hard to achieve test condition.

The objective of this study is to control flow condition, especially turbulence intensity, of the Mars Wind Tunnel (MWT) at Tohoku University by using turbulence grid. We developed passive-type turbulence grids and evaluated the flow field behind them in the MWT at low pressure condition. We measured velocity fluctuation in the test section of the MWT by using a hot-wire anemometer (HWA). In addition, we conducted a frequency analysis to the flow field in the MWT, and clarified the flow condition in the MWT.

2. Experimental facilities and experimental condition

2.1. Mars Wind Tunnel (MWT)

The MWT is composed of a vacuum chamber, an induction-type wind tunnel and a buffer tank [4]. The wind tunnel is located inside the vacuum chamber so that the pressure condition of Martian atmosphere can be simulated by reducing the pressure. The test gas is dry air in usual tests and can be replaced with carbon dioxide. This wind tunnel is driven by a multiple-nozzle supersonic ejector located downstream the test section.

Ejection of high pressure gas from the ejector induces the flow in the test section. The gas inside the vacuum chamber is exhausted to the buffer tank through a connecting flexible pipe. During the test time, the pressure in the vacuum chamber is kept constant by controlling a butterfly valve placed in the flexible pipe.

2.2. Turbulence grid

In this study, to control turbulence intensity of the MWT, turbulence grid was installed between the contraction section and the test section of the MWT. The grid acts simply as an obstacle to the flow and generates turbulence [5]. For the passive grid, it is widely and experimentally known that it typically takes a downstream separation of $40m$ for the flow to become approximately homogeneous and isotropic [6], which m is a mesh size of the turbulence grid. Moreover, turbulence in the wind tunnel rises rapidly when ratio of blockage R_b is larger than 0.4 (40%) [3]. Therefore, we selected the combination of wire diameter d and mesh size m for this research as shown in table 1.

Table 1. Turbulence grid parameter

Grid No.	d [mm]	m [mm]
1	0.6	4.23
2	0.9	4.23
3	0.6	3.18

2.3. Experimental setup and experimental condition

Velocity fluctuation in the center of the test section was measured by the HWA. The HWA was connected to the CTA and output signals from CTA were recorded in PC. The number of sampling points was 200,000 and sampling frequency was 20,000 Hz. To cut off high-frequency noise, low-pass filter of cut-off frequency of 10,000 Hz was applied. Experiment was conducted by three types of turbulence grids and no grid. Total pressures of this experiment were 5, 11 and 22 kPa and flow velocity was from 10 m/s to 100 m/s.

3. Results and Discussion

Figs. 1 and 2 shows the one-dimensional power spectra of the flow field in the MWT at the center of the test section behind no grid and grid 1. As shown in Fig.

1, all case represented typical waveform of laminar flow. This indicates that flow of the test section with no grid condition was laminar, not turbulent at all total pressure.

In Fig. 2, although power spectrum of low velocity at $P_t = 5$ kPa is similar as laminar flow, other spectrum was enhanced in the low frequency range (from 10 to 8,000 Hz). At $P_t = 5$ kPa, a prominent peak was detected in frequency of about 700 Hz for the velocity from 62.9 to 78.8 m/s. At these points, energy was supposed to inject in and these level of component was dominant, hence, these flow were not turbulent but being transition. That's why it was supposed that the flow at velocity of between 41.7 and 55.2 m/s was also being transition. It was not detected prominent peak over the velocity of 84.0 m/s so the flow was turbulent flow at this range.

Fig. 3 shows the turbulence intensity behind grid 1 in comparison to no grid. By installing grid 1, turbulence intensity rises regardless of total pressure. Fig. 3 (a) shows when turbulence grid was installed, turbulence intensity increased as flow velocity increased and turbulence intensity reached its peak at flow velocity of about 60 m/s. After that turbulence intensity decreased as flow velocity increased. As shown in Fig. 2 (a), at low velocity range, power spectrum was similar as that of no grid so flow was laminar. In short, turbulence grid behaved as not turbulence generator but honeycomb. Hence, turbulence intensity was lower than or as same as that of no grid. As flow velocity increased, flow of the test section became transition. In this condition, there were several frequency peaks so turbulence intensity was supposed to be up and down. When frequency peak disappeared, turbulence intensity kept

constant. As shown in Figs. 2 (b) and (c), there were not much frequency peak so flow was turbulent at wide range of flow velocity. Therefore, turbulence intensity kept constant. Figs. 3 (b) and (c) represented when turbulence grid was installed, turbulence intensity kept constant except for the case of minimum flow velocity. In the case of installing grid 2 and 3, turbulence intensity shows the similar trend as the case of grid 1, although there was the difference of the absolute value.

4. Concluding remarks

To control flow condition, especially turbulence intensity, of the MWT, we developed passive-type turbulence grids, and evaluated the flow field behind them in the MWT at low pressure condition. Results indicated that the free-stream turbulence intensity increased by installing the turbulence grids, and flow condition behind them showed a transitional or fully-turbulent condition depending on the flow velocity.

References

- [1] K. Fujita et al., 28th International Symposium on Space Technology and Science, 2011-e-56p (2011)
- [2] T. J. Mueller et al., Experiments in Fluids 1, 3-14 (1983)
- [3] H. Abe, Report of Mechanical Engineering Laboratory No. 186 (2000) (in Japanese)
- [4] M. Anyoji, Ph.D thesis, Tohoku University (2011)
- [5] M. Gad-el-Hak and S. Corrsin, Journal of Fluid Mechanism, Vol. 62, part 1, pp. 115-143 (1974)
- [6] Hakki Ergun Cekli and Willem van de Water, Exp Fluids, 49:409-416 (2010)

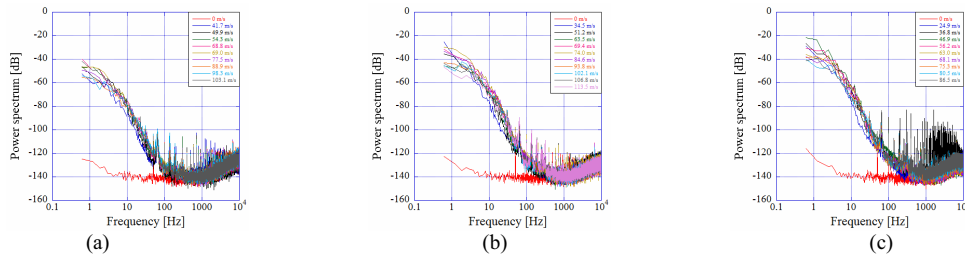


Fig. 1 Power spectra of the test section with no grid; (a) $P_t = 5$ kPa, (b) $P_t = 11$ kPa, (c) $P_t = 22$ kPa

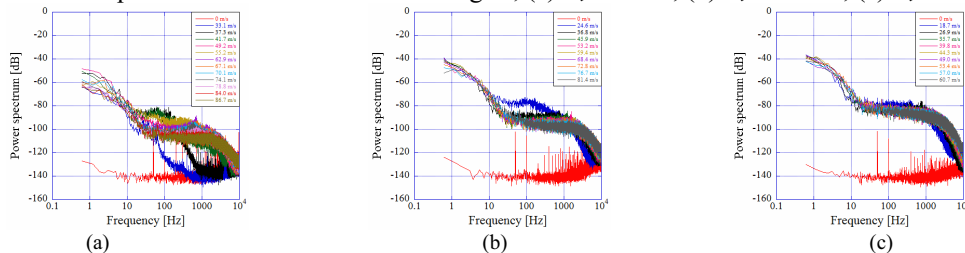


Fig. 2 Power spectra of the test section with grid 1; (a) $P_t = 5$ kPa, (b) $P_t = 11$ kPa, (c) $P_t = 22$ kPa

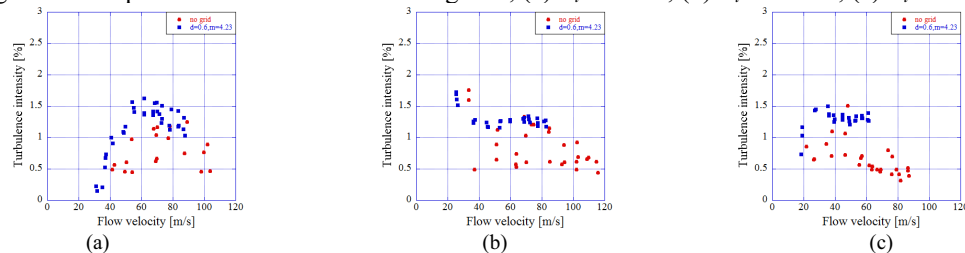


Fig. 3 Turbulence intensity for no grid versus grid 1; (a) $P_t = 5$ kPa, (b) $P_t = 11$ kPa, (c) $P_t = 22$ kPa

Numerical Temperature Analysis of Optimized TiO₂ Pigmented Coatings under Sendai Climate Conditions

Mehdi Baneshi¹, Hiroki Gonome², Shigenao Maruyama³

¹ School of Mechanical Engineering, Shiraz University, Shiraz 7193616548, Iran

² Dep. of Mech. Systems and Design, Tohoku University, 6-6 Aramaki Aza Aoba, Aoba-ku, Sendai 980-8579, Japan

³ Institute of Fluid Science, Tohoku University, 2-1-1, Katahira, Aoba-ku, Sendai 980-8577, Japan
mbaneshi@shirazu.ac.ir

ABSTRACT

Designing dark coatings that can stay cool against sunlight is of interest for painting applications to satisfy both visual appearance and thermal aspects at the same time. In this paper TiO₂ coatings on black substrates were studied. The radiative properties of TiO₂ particles in polyethylene resin as an absorbing medium were calculated in UV–IR (0.3–36 μm) region. The radiative heat transfer was simulated using radiation element method by ray emission model (REM²). The effect of particles size and surface tilt angle on temperature were analyzed.

1. Introduction

Pigmented coatings with dark visual appearance that can stay cool in sun are desired to paint buildings and cars in warm climates to satisfy simultaneously both aesthetic and thermal demands. To design such these coatings Baneshi et al. [1] proposed a design method by controlling the material, size and concentration of pigment particles in order to control the spectral behavior of paint layer. The objective of that optimization was to minimize the reflectivity at visible wavelengths specially at those with higher eye sensitivity and maximizing the reflectivity of NIR region. Based on this objective the optimum size of TiO₂ particles were found to be 0.8 μm while the typical size of TiO₂ particles used in making white paints is about 0.2 μm.

For thermal calculation the radiative properties of TiO₂ particles in resin are required in a wide range of wavelength from UV to IR. The radiative properties were calculated based on Mie theory and the effective scattering and absorption coefficients were evaluated taking into account the absorptivity of resin. The detail of this calculation can be found in authors' previous work [2].

To conduct radiative heat transfer analysis the radiation element method by ray emission model (REM²) [3] was utilized.

In this paper the effect of typical and optimum particles sizes on coating temperature is discussed. In addition the effect of surface tilt angle on temperature is studied.

2. Analysis model

A one-dimensional plane-parallel system shown in Fig. 1 is considered as the analysis model for REM². Spectral solar irradiation at the noon of June 22nd in Sendai (Latitude: 31° 50' N, Longitude: 130° 20' E) evaluated using Bird's model is considered for calculations. At the noon of June 22nd the solar zenith angle is 15° and solar heat flux on a horizontal surface is about 1024 W/m². At the coating surface the specular reflection produced by difference between the refractive indices, is calculated using Fresnel's equation.

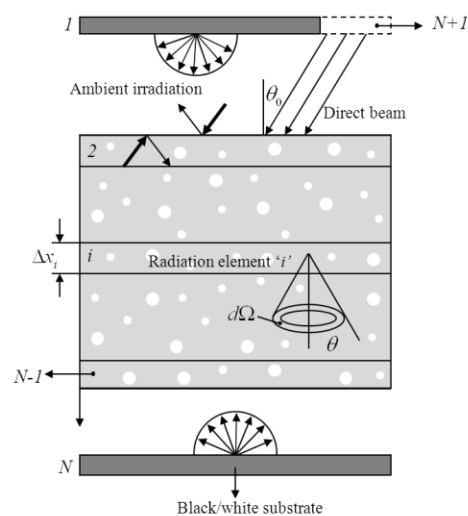


Fig. 1 Analysis model and boundary conditions

The convection heat transfer is calculated using the following empirical equation [4]:

$$h = 2.8 + 3v \quad (1)$$

where v is wind speed. The ambient temperature and wind speed are set to 29.4 °C and 2 m/s. The bottom boundary is assumed black with adiabatic thermal condition. Since the coating is thin enough, the conductive heat transfer in the coating layer is neglected and hence the coating is assumed to be isothermal.

Table 1. calculation conditions at noon of June 22nd, 2008

	Solar irradiation (W/m ²)	T_{∞} (°C)	Wind speed (m/s)	Solar zenith angle (°)
Sendai, Japan	1024	25	2.1	15

3. Results and discussions

Figure 2 shows the effective scattering and absorption coefficients for typical TiO₂ particle 0.2 μm in diameter in polyethylene resin as absorbing host medium.

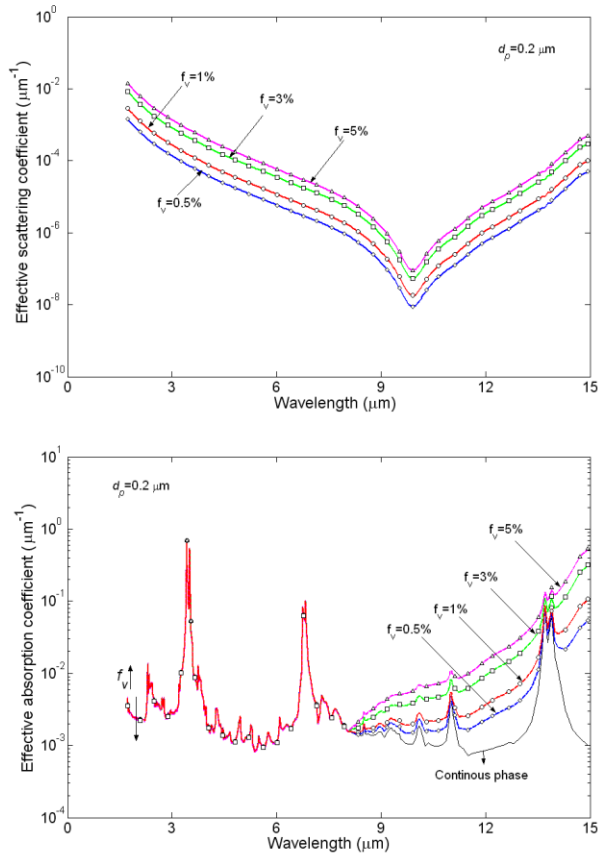


Fig. 2 Effective scattering and absorption coefficients of 0.2 μm TiO_2 particle

Table 2 compares the properties of two TiO_2 pigmented coatings made using 0.2 μm particles as the typical size of commercial TiO_2 powder and 0.8 μm particles as the proposed optimum size.

When the size of particles changes from 0.2 μm to 0.8 μm , the VIS reflectance is reduced by about 25% while the NIR reflectance increases about 14%. Also, the brightness reduced from 91.5% to 60.8%. Temperature of bare black substrate is 85 $^\circ\text{C}$. The temperature of 0.2 μm and 0.8 μm particles pigmented coating is about 54 $^\circ\text{C}$ and 60 $^\circ\text{C}$, respectively.

Table 2. Comparison between the properties of 0.2 μm and 0.8 μm TiO_2 pigment particles in polyethylene resin when $f_v=5\%$ and $t=50 \mu\text{m}$

	VIS ref. (%)	NIR ref. (%)	Total ref. (%)
$d_p=0.2 \mu\text{m}$	81.6	49.1	66.4
$d_p=0.8 \mu\text{m}$	55.5	63.1	57.5

This result shows that using the proposed optimum particles size can reduce the temperature by 25 $^\circ\text{C}$ in comparison with a bare black surface. Using the optimized coating can reduce the brightness by about 30% in comparison with the typical size of TiO_2 pigment particles. Thus, using proposed particle size we can have a coating with reasonable temperature and

Table 3. comparison between the temperature and brightness of bare and coated surfaces

	Bare Black	Coated black with $d_p=0.2 \mu\text{m}$	Coated black with $d_p=0.8 \mu\text{m}$
Temperature ($^\circ\text{C}$)	84.9	54	60
Brightness (%)	0	91.5	60.8

Table 4. The effect of surface tilt angle on temperature

Tilt angle (degree)	0		30	
Solar irradiation (W/m^2)	1056		979	
	Black	Optimum coating	Black	Optimum coating
Temperature ($^\circ\text{C}$)	90.8	66.1	86.9	63.9
Tilt angle (degree)	60		90	
Solar irradiation (W/m^2)	640		130	
	Black	Optimum coating	Black	Optimum coating
Temperature ($^\circ\text{C}$)	68.6	53.8	38	37.9

moderate brightness.

Table 4 shows the effect of substrate tilt angle on temperature. By increasing the tilt angle both the temperature of coated substrate and the difference between the temperature of bare and coated surface decrease.

4. Conclusions

Radiative properties of TiO_2 particles in an absorbing medium were calculated from UV to IR wavelengths. Then the temperature of coated substrate was calculated and the effects of particles size and surface tilt angle were discussed. Using the optimum particle size one can make a coating on black substrate with reasonable temperature and moderate brightness.

5. References

- [1] M. Baneshi, et al., JQSRT, **110** (2009), pp. 192-204.
- [2] M. Baneshi, et al., JHT, **132** (2010), pp. 023306 1-12.
- [3] S. Maruyama, Light energy engineering, (2004), Yokendo, Tokyo
- [4] M. Khoukhi, et al., Solar Energy, **75** (2003), pp. 285-292.

Numerical Analysis of Swimming Patterns and Energy-Saving Mechanism in Fish School

Szu-Yung Chen¹, Jing-Tang Yang¹

¹Department of Mechanical Engineering, National Taiwan University, Taipei 10617, Taiwan

E-mail of corresponding author: jtyang@ntu.edu.tw

ABSTRACT

In this study, the interaction between swimming patterns and energy-saving mechanism in fish school is numerically investigated. We qualitatively and quantitatively characterized the wake flow structures, forces, and power consumption with respect to various swimming patterns. The results reveal that the spatial arrangement of school and the shed vortices are highly correlated and significantly affects the performances of the thrusts and power consumption of the fish group. This mechanism reduces the power consumption of each fish in school by 23% averagely compared with that in solo.

1. Introduction

Energy-saving devices have received increasingly more attention recently, especially, the energy saving strategy of fish. For example, Yu *et al.*¹ demonstrated that the suction forces of the shed pectoral-fin vortices drifting downstream enhance lateral movements of the fish body, leading to less power consumption. The hydrodynamics in fish schooling was first proposed by Weihs and Webb³; they suggested that the diamond-shaped pattern is the optimal configuration for schooling fish to gain hydrodynamics advantages. A great deal of speculations about fish school has been proposed, such as benefits in escaping, foraging and migrations.^{2,7} The technique of Computational Fluid Dynamics was widely used in the analysis of the hydrodynamics interaction of two foils,^{4,5} and also of three foils.⁶ In this work, simulation is carried out to find the optimum schooling arrangement based on diamond patterns.

2. Method

The subject in this study is Carangiform fish; the 2D model of the fish body is based on the profile of NACA0012 foil as shown in Fig. 1. The length of the fish is L , and the free-stream velocity is U . The spacing between two rows and columns are S and D . The lateral undulation of the fish body is described as

$$y(x, t) = a(x) \sin [2\pi(\frac{x}{\lambda} - ft)] , \quad (1)$$

where t , λ , f are time, the wavelength and frequency of fish undulation. In most fish swimming with Carangiform locomotion, wavelength is observed in the range of 0.89 - $1.10 L$, so λ is given to be the body length ($=L$) in all simulations. $a(x)$ portrays the amplitude envelope of the lateral motion of the body wave and is approximated by a quadratic form,

$$a(x) = 0.002 - 0.12x + 2x^2 , \quad (2)$$

The governing equations are the two-dimensional viscous incompressible Navier-Stokes equations, which were discretized using finite-volume method. The discrete time and space are solved with Euler scheme and second-order upwind scheme. The simulations were solved with commercial software (CFD-RC, France) applying the SIMPLEC algorithm. In this work, the Strouhal number was set at 0.3 for better swimming

performance and the Reynolds number was set to be 1.2×10^4 . We adjusted the lateral distance from $S = 0$ to $1 L$ and the row distance from $D = 0.15 L$ to $0.60 L$ to reveal the hydrodynamic interaction between the members of fish as well as the energy-saving mechanism.

3. Results and Discussion

According to the results of simulation, the hydrodynamic forces and power consumption of undulating fish are defined as follows. The total drag force (F_D) consists of friction force (F_{FX}) and pressure force (F_{PX}) by integrating the whole fish body.

$$C_{DP} = \frac{F_{PX}}{\frac{1}{2}(\rho U^2 L^2)} , \quad C_{DF} = \frac{F_{FX}}{\frac{1}{2}(\rho U^2 L^2)} ,$$

$$C_D = \frac{F_D}{\frac{1}{2}(\rho U^2 L^2)} , \quad (7)$$

The power (P_S) required to perform a lateral body wave motion is defined as

$$P_S = \oint (pn) \cdot v_s \cdot dS , \quad (8)$$

in which p is the pressure of the fish surface, n the normal factor of the fish surface element, v_s the lateral velocity of the fish surface element, and dS the differential surface element. The coefficient of power consumption, C_P is defined as follow

$$C_P = \frac{P_S}{\frac{1}{2}(\rho U^3 L^2)} , \quad (9)$$

Figure 2 shows that when $D = 0.3 L$, the thrusts of fish in schooling are less than that of fish in solo, except for $S = 0$. This specific phenomenon could be attributed to the collision between the tail of the upstream fish and the high pressure region near the front of the downstream fish, as shown in Fig. 3. When the upstream fish gradually swims far away from the downstream fish, the thrust of the upstream fish decreases while the thrusts of the downstream fish increase, which stabilizes the fish school pattern.

As shown in Fig. 4, the time-dependent drag force indicates that the downstream fish gain the thrust alternately. It is noted that the reverse Kármán vortex shed by the undulating fish causes the low pressure region. In Figs. 5(a)-5(d), the head of the downstream fish takes turns of capturing the low pressure regions generated by the leader fish, thus, decreases the form

drag and increase the thrust.

The swimming power of the downstream fish is highly related to the fish school pattern. The case of $S = 0.5 L$ corresponds to a trough point for P_S in Fig. 6. At $S = 0.5 L$, the low-pressure suction force arising from the reverse Kármán vortices generated by the upstream fish assists the undulating movement of the downstream fish periodically as shown in Fig. 7. When $S > 0.5 L$, the vortices diffused by the viscous friction force, leading to the increased P_S for the downstream fish.

4. Concluding remarks

In this work, we exploit numerical methods to scrutinize the flow field and discuss the influences of fish school patterns on the thrust and power consumption. As the row spacing decreases, thrust of the upstream fish arises while that of the downstream fish reduce, which stabilize the swimming pattern. The numerical results showed that the low pressure suction force produced by the reverse Kármán vortex shed by the upstream fish decreases the pressure difference of the downstream fish, reducing the form drag and assisting the undulating movement periodically when the downstream fish at specific position, $S = 0.5 L$. This mechanism reduces the power consumption of one fish in school by 23% averagely compared with that in solo. The energy-saving revealed in this work offer a physical insight into bio-inspired arrays for the underwater vehicles.

References

- [1] C. L. Yu, S. C. Ting, M. K. Yeh, and J. T. Yang, *Phys Fluids* **23** (9) (2011).
- [2] D. H. Cushing and F. R. H. Jones, *Nature* **218** (5145), 918 (1968).
- [3] D. Weihs, *Nature* **241** (5387), 290 (1973).
- [4] G. J. Dong and X. Y. Lu, *Phys Fluids* **19** (5) (2007).
- [5] J. Deng, X. M. Shao, and Z. S. Yu, *Phys Fluids* **19** (11) (2007).
- [6] M. H. Chung, *J Mech* **27** (2), 177 (2011).
- [7] M. Larsson, *Curr Zool* **58** (1), 116 (2012).

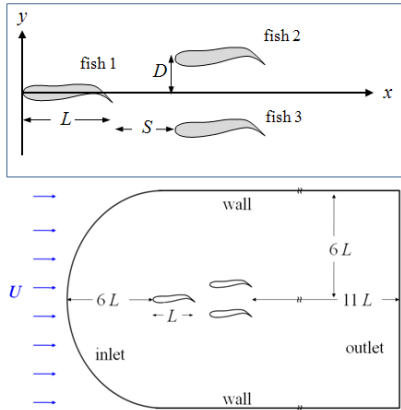


Fig. 1. Dimensions of the physical model and computational domain.

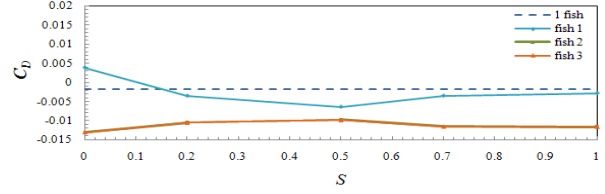


Fig. 2. Time-averaged drag force coefficient at $D = 0.3 L$.

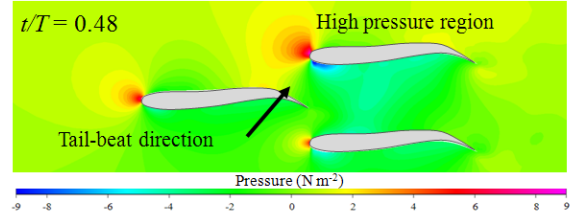


Fig. 3. The pressure contour of flow fields observed at $D = 0.3L$ and $S = 0$.

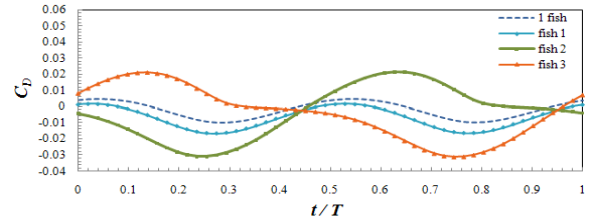


Fig. 4. Time-dependent drag force coefficient during one cycle at $D = 0.15 L$ and $S = 0.5 L$.

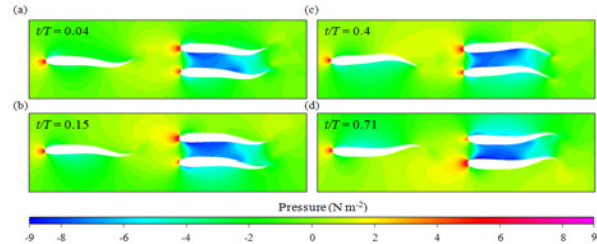


Fig. 5. The pressure contour of flow fields observed at $D = 0.15 L$ and $S = 0.5 L$.

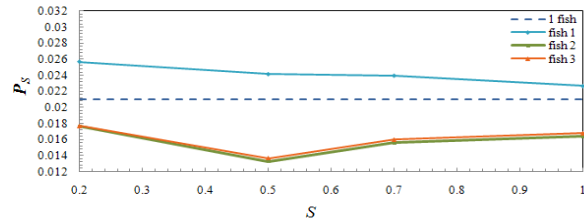


Fig. 6. Time-averaged drag force coefficient with respect to S at $D = 0.15 L$.

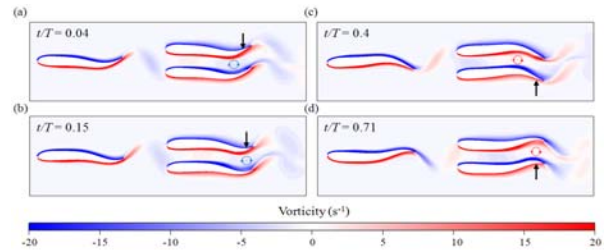


Fig. 7. The vorticity contour of flow fields observed at $D = 0.15 L$ and $S = 0.5 L$ with sequential images illustrating the periodical shedding vortices.

Experimental Study on Low Mach Number Grid Turbulence modulated by a Spherical Shock Wave

Takuya KITAMURA, Tatsuya HARASAKI, Kouji NAGATA, Yasuhiko SAKAI,
Akihiro SASOH and Osamu TERASHIAMA

Dept. of Mech. Sci. and Eng., Nagoya University, Furo-cho, Chikusa-ku, Nagoya-shi, Aichi, 464-8603, Japan

Dept. of Aerospace Eng., Nagoya University, Furo-cho, Chikusa-ku, Nagoya-shi, Aichi, 464-8603, Japan

kitamura.takuya@e.mbox.nagoya-u.ac.jp

ABSTRACT

Characteristics of low Mach number grid turbulence interacted with a shock wave are investigated by means of laboratory experiments using a wind tunnel and a diaphragm-less shock tube. Instantaneous streamwise velocity before and after passing of a shock wave is measured by hot wire anemometry. The probe is set-up in the upstream of the open end of the shock tube. The results show that streamwise turbulent intensity is increased after interaction with a shock wave.

1. Introduction

Sonic boom is known as a flight problem on supersonic transport (SST). It is known that over-pressure and rise time of sonic boom are affected by atmospheric turbulence.

In past studies^{[1]-[5]}, experimental study on a compressible grid turbulence interacted with a shock wave and numerical simulation of interaction between homogeneous turbulence and a shock wave are mainly investigated. Keller and Merzkirch^[1] measured density fluctuation and showed that Taylor's microscale increased by interaction with a shock wave. Honkan and Andreopoulos^[2] also showed that streamwise turbulent energy and streamwise integral length scale are increased by interaction with a shock wave. On the other hand, Agui et al.^[3] showed that integral length scale is decreased by interaction with a shock wave. Barre et al.^[4] also showed that streamwise integral length scale is decreased and high wavenumber energy is increased by interaction with a shock wave. However, no previous studies focused on the interaction between low Mach number turbulence and a shock wave, which appears in atmospheric turbulence.

In this study, therefore, characteristics of low Mach number turbulence interacted with a spherical shock wave are investigated using a grid turbulence and a diaphragm-less shock tube.

2. Experimental Method

A shock wave is generated by a diaphragm-less shock tube using a quick piston valve and is emitted from the open end of the shock tube, which is directed vertically downward across the turbulent flow. The low pressure room of this shock tube has a total length of 3,565 mm and has an internal diameter of 21.3 mm. Dry air of 910 kPa is used as a driver gas. This shock tube could be driven automatically and it generates shock waves in succession with good repeatability. Mach number M_s is measured by using two pressure sensors (H112A21, PCB Piezotronics Inc.), which are set-up in the shock tube. Average mach number $M_{s, Ave}$ on 100 measurements is 1.62, and its standard deviation is 0.1%.

Turbulence-generating grids (Table. 1) are installed

at the entrance to the test section of the wind tunnel to generate nearly isotropic turbulence. A schematic view of experimental apparatus is shown in Fig. 1. The experimental conditions of grid turbulence are shown in Table 2. Instantaneous streamwise velocity is measured by using hot wire anemometry (DANTEC: Streamline).

The open end of the shock tube is set-up 1,500 mm downstream of the grids, and, the hot wire probe is set-up 600 mm upstream from the open end. The experiments are performed 250 times for each condition in order to obtain reliable statistics. The sampling rate is 100 kHz. Frequency response of hot wire anemometry is about 60 kHz at $U_{mean} \sim 10$ m/s, and is about 100 kHz at $U_{mean} \sim 20$ m/s, where, U_{mean} is a mean wind speed.

Table 1. Detail of grids.

M [mm]	d [mm]
15	3
25	5
50	10
100	20

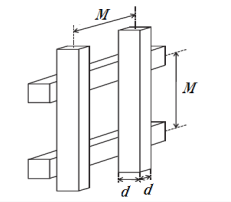
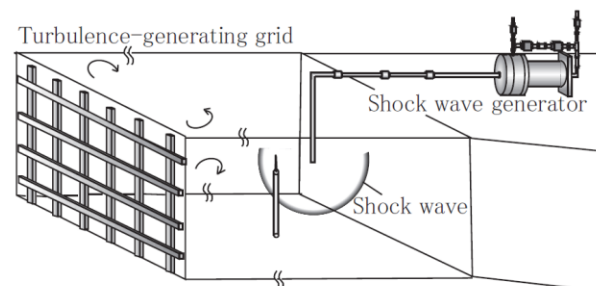



Fig. 1 Schematic diagram of experimental apparatus.

Table 2. Experimental condition.

Mesh size M [mm]	15	25	50	100
U_{mean} [m/s]	10~20	10~20	10~18	10
Re_λ	51~70	64~92	105~148	136

3. Results and Discussion

Fig. 2 shows the instantaneous velocity signal before and after passing of a shock wave (SW). In order to investigate instantaneous streamwise velocity fluctuations before and after passing of a SW on each experiments and different experimental condition, the following indicator Δ was used.

$$\Delta = \frac{1}{t_2 - t_1} \int_{t_1}^{t_2} |u(t) - U| dt \quad (1)$$

Here, U is the time average during $t_2 - t_1 = 0.01024$ s and u is the instantaneous streamwise velocity.

Fig. 3 shows the joint probability density function between amplitude of the velocity fluctuation before passing of a SW (Δ_{BS}) and that after passing of a SW (Δ_{AS}). The line in Fig. 3 indicates a borderline whether streamwise velocity fluctuations are amplified or not. There is a positive correlation between Δ_{BS} and Δ_{AS} . Fig. 3 also shows that for interaction with weak turbulence, instantaneous streamwise velocity fluctuations are amplified, whereas for interaction with strong turbulence, there are some cases, where streamwise velocity fluctuations are decreased.

In above discussion, results are based on streamwise velocity fluctuation in local short time. Thus, it is needed to discuss in perspective of statistics with data of 250 experiments. Root mean square values of streamwise velocity fluctuation $u_{r.m.s}$, are defined as follows.

$$u_{r.m.s} = \frac{1}{N} \sum_{k=1}^N \left[\frac{1}{t_2 - t_1} \int_{t_1}^{t_2} (u(t) - U_{ENS})^2 dt \right] \quad (2)$$

$$U_{ENS}(t) = \frac{1}{N} \sum_{k=1}^N u_k(t) \quad (3)$$

Here, U_{ENS} is the ensemble average of 250 ($= N$) experiments. It was confirmed that U_{ENS} are decreased after interacting with a shock wave because of the induced velocity. $u_{r.m.s BS}$, $u_{r.m.s AS}$ and its ratio are shown in Table 3. It is found that streamwise turbulent intensities are increased after interaction with a SW and the magnitude of amplification is larger for weak turbulence.

4. Concluding remarks

Characteristics of low Mach number grid turbulence interacted with a shock wave are investigated by means of laboratory experiments using a wind tunnel and a diaphragm-less shock tube. The results show that streamwise turbulent intensity is increased after interaction with a shock wave in perspective of statistics. Other statistics, relating length scale and derivative quantity will be reported in a presentation.

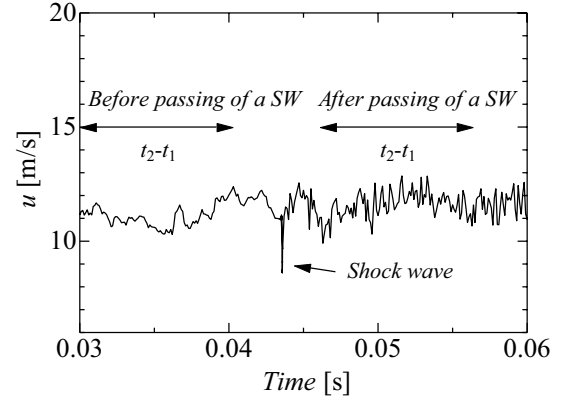


Fig. 2 Instantaneous velocity signal before passing of a shock wave and after passing of a shock wave.

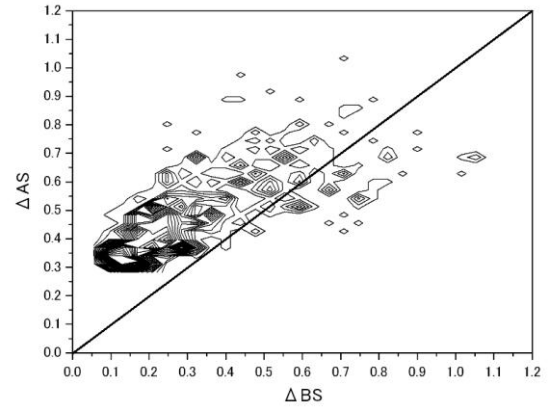


Fig. 3 Joint probability density function between Δ_{BS} and Δ_{AS} .

Table 3. r.m.s value of streamwise velocity fluctuations before and after passing of a SW.

M	U_{mean}	$u_{r.m.s BS}$	$u_{r.m.s AS}$	$u_{r.m.s AS} / u_{r.m.s BS}$
15	10	0.242	0.442	1.826
25	10	0.309	0.493	1.595
15	20	0.455	0.588	1.292
25	20	0.637	0.726	1.140
50	10	0.801	0.883	1.102
100	10	0.907	1.007	1.110
50	18	0.956	1.087	1.137

Acknowledgement

The authors would like to express their gratitude to Messrs. Kazushi Tachibana and Takao Sumi in Technical Division of Nagoya University. This research was supported by Grants-in-Aid for scientific research (22226014).

References

- [1] J. Keller and W. Merzkirch, *Exp. Fluid*, **8** (1990), 241-248.
- [2] A. Honkan and J. Andreopoulos, *Phys. Fluids*, **4** (1992), 2562-2575.
- [3] J. H. Agui et al., *J. Fluid Mech.*, **34** (1996), 968-974.
- [4] S. Barre et al., *AIAA*, **34** (1996), 968-974.
- [5] S. Lee et al., *J. Fluid Mech.*, **251**(1993), 533-562.

Solving the Nonlinear Kinetic Boltzmann Equation on GPGPU

Evgeniy Malkov, Sergey Poleshkin and Mikhail Ivanov

Khristianovich Institute of Theoretical and Applied Mechanics, Institutskaya 4/1, Novosibirsk, 630090, Russia
ivanov@itam.nsc.ru

ABSTRACT

A scheme of solving the nonlinear kinetic Boltzmann equation with the use of General Purpose Graphics Processing Units (GPGPUs) is described. A problem of the shock wave structure is solved as a test computation. Owing to parallelization of collision integral computations, two GPGPUs Tesla M2090 provide an 800-fold speedup as compared with sequential computations on a CPU with a frequency of 2.66 GHz. The computations are performed on a hybrid cluster of the Novosibirsk State University.

1. Introduction

Computations of rarefied gas flows by means of the direct numerical solution of the nonlinear kinetic Boltzmann equation offer certain advantages over Direct Simulation Monte Carlo (DSMC) methods owing to the absence of statistical noise. This advantage is particularly pronounced in computing slow flows or in the case of minor deviations from the equilibrium distribution function. However, the direct solution of the Boltzmann equation requires large computational resources. This fact appreciably retarded the development of numerical methods of solving this equation and application of these methods for modeling rarefied gas dynamics. Certain recent revival of activities in this field was initiated, on the one hand, by the development of miniaturization technologies, which involve computations of slow rarefied gas flows, and, on the other hand, by the development of computational technologies that allow solving problems that require many resources [1-2].

A bottleneck of the numerical solution of the Boltzmann equation from the viewpoint of processor time cost is the computation of the collision integral. An obvious and simple idea of parallelization of these computations on multiprocessor systems is three-dimensional decomposition in the phase space where each process implements a sequential algorithm of the collision integral computation for its node in the physical space. Deeper decomposition that involves the velocity space is more optimal for GPGPU computations. The chosen model of parallelization of data with allowance for specific features of the CUDA architecture made it possible to reach a significant (up to 800 times) speedup of computations by performing them on a GPU cluster. A problem of the shock wave structure at Mach numbers 2 and 10 was solved as a test computation.

2. Scheme of the collision integral computation

The Boltzmann equation for a one-particle distribution function in the phase space $f = f(t, \vec{r}, \vec{u})$ has the form

$$\frac{\partial f}{\partial t} + u \frac{\partial f}{\partial \vec{r}} = St(f, f) \quad (1)$$

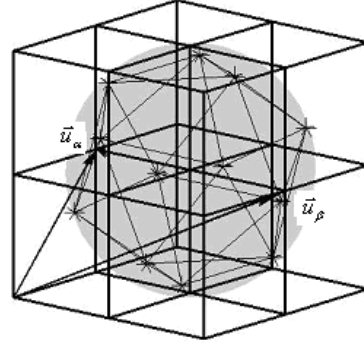


Fig. 1 Fragment of the computational grid and quadrature nodes on a sphere (marked by “stars”).

The right side of this equation contains a nonlinear integral operator, which is a collision integral:

$$St(f, f) = \int_{R^3} d^3 u_1 \int_{S^2} d^2 n (f f_1' - f f_1) |\vec{V}| \sigma(V, \cos \theta). \quad (2)$$

Here

$$\begin{aligned} f &= f(t, \vec{r}, \vec{u}), & f_1 &= f_1(t, \vec{r}, \vec{u}_1), \\ f' &= f(t, \vec{r}, \vec{u}'), & f_1' &= f_1(t, \vec{r}, \vec{u}_1'), \end{aligned} \quad (3)$$

$$\vec{u}' = \frac{\vec{u} + \vec{u}_1}{2} + \frac{|\vec{V}|}{2} \vec{n}, \quad \vec{u}_1' = \frac{\vec{u} + \vec{u}_1}{2} - \frac{|\vec{V}|}{2} \vec{n}, \quad (4)$$

where $\vec{V} = \vec{u} - \vec{u}_1$, \vec{n} is the unit vector (collision parameter) defining the direction of the relative velocity after the collision, $\sigma(V, \cos \theta)$ is the differential scattering section, and θ is the angle between the vectors of the relative velocities of the particles before and after the collision.

Figure 1 helps in understanding the procedure of computing the collision integral. For each pair of computational grid nodes $\{\alpha, \beta\}$ and a pair of quadrature nodes $\{\alpha', -\alpha'\}$ on a sphere with a diameter $|\vec{u}_\alpha - \vec{u}_\beta|$ and the center at $(\vec{u}_\alpha + \vec{u}_\beta)/2$, the value of $\Delta m = f_\alpha f_\beta \sigma_{\alpha, \beta, \alpha'} w_{\alpha'}$ is calculated ($\sigma_{\alpha, \beta, \alpha'}$ is the discrete approximation of the differential scattering section and $w_{\alpha'}$ are the weights of the quadrature nodes on the sphere. Then the value of the collision integral in the nodes $\{\alpha, \beta\}$ is reduced by

Δm , and its value in the nodes $\{\alpha', -\alpha'\}$ is increased by the same value. If the quadrature nodes $\{\alpha', -\alpha'\}$ on the sphere do not coincide with the computational grid nodes, conservative interpolation is used: the distribution of Δm between the computational grid nodes in the velocity space, which are neighbors of the quadrature node α' on the sphere, is such that the mass, momentum, and energy are conserved.

3. Parallelization of the collision integral computation over CUDA threads

The most important specific features of the CUDA architecture, which exert a crucial effect on the code execution time and read/write synchronization, and which were taken into account in our study, were the coalescing (shared access to the memory of the operating set of threads) and atomic functions [3].

Let df and st be arrays of length $I \times J \times K \times L \times M \times N$ storing the values of the distribution function and the collision integral in the computational grid nodes in the phase space (I, J, K, L, M, N are the grid dimensions in the velocity space and physical space, respectively). The index of the grid node in the physical space is $q = n + m \cdot N + l \cdot N \cdot M$, and the index of the grid node in the velocity space is $\alpha = k + j \cdot K + i \cdot K \cdot J$. Using these notations, we write the main actions to be parallelized: computation of the lost mass fraction

$$\Delta m = df[q + \alpha_1 * L * M * N] * df[q + \alpha_2 * L * M * N] * weight, \quad (5)$$

and distribution of this mass over the neighboring nodes

$$st[q + \alpha'_{1p} * L * M * N] += \Delta m * s_{1p}, \quad (6)$$

$$st[q + \alpha'_{2p} * L * M * N] += \Delta m * s_{2p},$$

or, with alternative indexation,

$$st[\alpha'_{1p} + q * I * J * K] += \Delta m * s_{1p}, \quad (7)$$

$$st[\alpha'_{2p} + q * I * J * K] += \Delta m * s_{2p},$$

where s_{1p}, s_{2p} are the distribution fractions.

The coalescing is only possible if the requested data are sequentially arranged in the GPU memory. The coalescing provides a 16-fold gain in the code execution time. In our case, this can be done by using the indexation of (6) and the following configuration of threads:

```
__global__ void gStossTerm(...) { q = threadIdx.x;
i = blockIdx.x; j = blockIdx.y; k = blockIdx.z; }
.....
gStossTerm <<< dim3(I, J, K), L * M * N >>> (...);
```

Parallel execution of actions (6) by threads can lead to a read/write conflict. Therefore, the mass distribution to the neighboring nodes is performed in the transaction mode with the use of atomic functions. Actions (6) are realized as follows:

$$atomicAdd(&st[q + \alpha'_{1p} * L * M * N], \Delta m * s_{1p}), \quad (8)$$

$$atomicAdd(&st[q + \alpha'_{2p} * L * M * N], \Delta m * s_{2p}).$$

Table 1. Parallelization efficiency.

Number of threads	Execution time (ms)	Speedup
1	676	1
2	523	2.59
4	462	5.85
8	416	13
16	349	30.99
32	523	41.36
64	1045	41.4

The results of relaxation computations with different numbers of spatial cells (threads in a block) performed on the GPGPU Tesla M2090 are summarized in Table 1. As is seen from Table 1, the maximum speedup over the computation with one thread is approximately 41. Saturation occurs at 32 threads. Parallel computations with one spatial node ensure a 12-fold speedup as compared with sequential computations on a processor with a frequency of 2.66 GHz. Thus, the total speedup reached by using Tesla M 2090 was $12 \times 41 = 492$. A further speedup was reached by using two GPGPUs. In this case, parallelization was performed via CUDA Streams with the use of the `cudaSetDevice` function for changing the context of the device and of the `cudaEventSynchronize` function for synchronization of streams. An additional speedup owing to the use of two GPGPUs was 1.6. The total speedup was $492 \times 1.6 = 787.2$.

4. Acknowledgments

This study was performed within the framework of the Integration Projects No. 39, 47 and 130 in 2012 of the Siberian Branch of the Russian Academy of Sciences.

References

- [1] O.I. Dodulad, Yu.Yu. Kloss, V.V. Ryabchenkov, and F.G. Tcheremissine, *Vych. Tekhnol.*, **12**, (2011), P40.
- [2] A.B. Morris, P.L. Varghese, D.B. Goldstein, *Journal of Computational Physics*, **230** (2011), P1265.
- [3] NVIDIA CUDA Programming Guide, <http://www.nvidia.com>

Establishment Length for a Fully Developed Solitary Wave in Viscous Fluid

Chih-Hua Chang^{1,*} Keh-Han Wang²

1. Assistant Professor, Department of Information Management, Ling-Tung University, 408, Taiwan., No. 1, Ling-Tung Rd., Taichung, 408, Taiwan.

2. Professor, Department of Civil and Environmental Engineering, University of Houston, Houston, TX 77204-4003, USA.

(*Corresponding author) E-mail: changbox@teemail.ltu.edu.tw

ABSTRACT

When a solitary wave is generated for a subsequent propagation, it is noticed the existence of an establishment length required for reaching a fully developed solitary wave and velocity profile. An understanding of the establishment length and its functional variation is important to the determination of the proper locations for the measurements of the solitary-wave velocity profiles in a short wave flume. Let us consider a solitary wave that is moving in a viscous fluid subject to laminar flow condition. The establishment length and the reattachment point on the fluid bottom in its deceleration phase are presented and discussed.

1. Introduction

In the past, studies in water wave theory have been mostly focused on the potential flow regime, where the viscous effect is neglected. However, the bottom boundary layer under wave motion plays an important role in sediment transport and morphological evolutions in coastal zone. Solitary waves are commonly assumed to represent long sea waves as they approach a shallow water region. Keulegan [1] pioneered the study of viscous effect on waves by deriving a set of analytical solutions for the laminar boundary layer under a solitary wave, which was later extended to the cnoidal waves by Tanaka et al. [2]. Recently, Liu and Orfila [3] rederived an analytical solution of the laminar boundary layer under a solitary wave. The method presented in [3] was extended by Liu et al. [4] to examine the boundary layer characteristics for fully nonlinear laminar flows. They also performed the PIV (Particle Image Velocimetry) technique to explore the flow fields and bottom shear stresses under a solitary wave. The turbulent boundary layer flow under a solitary wave was examined by Liu [5] using the Reynolds averaged equations assuming the eddy viscosity to be a power function of the distance from the bottom. Vittori and Blondeaux ([6], [7]) investigated the quantitative information on the flows generated in a region close to the bottom by direct numerical simulation (DNS). Later, Blondeaux and Vittori [8] applied the two-equation ($k-\epsilon$) formulations in RANS model to study this problem.

Similar to the concept of the entrance length for flows reaching a fully developed status when entering a pipe, a propagating solitary wave from its initial generation also requires a certain distance, defined as the establishment distance, to appear as a solitary wave with a fully developed velocity profile. In the present study, the streamfunction-vorticity equations based model that are combined with the application of the free surface conditions is employed to effectively generate the flow field in streamline patterns. For the initial developing period, we consider the wave induced fluid motion is within a laminar flow regime. We focus on the evaluation of the establishment length and the development of reattachment point for a solitary wave propagating along a constant depth channel.

2. Numerical model

In this study, we consider a solitary wave advancing along the x direction in a vertical two-dimensional domain of uniform water depth. This problem can be conveniently solved in an evolving (ξ, η) -curvilinear coordinate system. Let all flow variables be non-dimensionalized by the chosen scales of undisturbed water depth, fluid density and linear long-wave speed. With the viscous effect included in the analysis, the flow field and wave motion are modeled by solving the transformed streamfunction-vorticity ($\psi-\omega$) equations with specified initial and boundary conditions.

The initial solitary wave adopted for the simulation is the analytical solution of Grimshaw [9]. The vorticity values in the entire fluid region are set to be zero initially. The dynamic and kinematic free-surface boundary conditions are expressed with the vorticity and streamfunction in the transformed coordinate system. On the bottom, a constant streamfunction is specified whereas the vorticity can be related to the streamfunction with the no-slip condition satisfied. For the outgoing boundaries, a simple wave equation is chosen to radiate all physical variables out of the computational domain.

We employ a transient boundary-conformed grid system in the region of fluid motion. The Finite Analytic method is applied to solve the governing equations numerically. This discretization consistently improves the solution accuracy and the scheme stability [10]. For a small cell, those geometric coefficients are updated iteratively with the free-surface evolution for an instantaneous grid system.

3. Results

Fig. 1 illustrates a typical streamline pattern of the flow field under a solitary wave. A dividing line is separated from the free surface, then reattach at the bottom with a distance L_R measured from the wave peak location. Liu et al. [4] studied the laminar bottom boundary layer flow induced by a solitary wave. Their typical Reynolds numbers in experiments were about 10^5 . Since the action time is relative short for a solitary wave passing by a fixed point on the bottom, it requires a much higher value of Re for an unsteady flow to induce the fluid from its initial rest state to develop a

motion of turbulence. Here, we consider only the laminar flow analysis. Fig. 2 compares the present calculated horizontal velocity profiles with Liu's measured data and their numerical results at three different phases for a solitary wave with wave height $A_0=0.2$. Excellent agreement between the presented results can be noticed. It reveals that while the flows above the boundary layer always move in the same direction as the wave movement, the flow near the bottom inside the boundary layer may reverse the direction during the wave deceleration phase. Fig. 3 shows the horizontal velocity profiles at different phase ($t=0.5$ to 7.5) and the development of boundary layer for incident wave height $A_0=0.2$. The boundary layer thickness is determined at the position where the flow velocity has essentially reached 99% of the free-stream velocity. It is found the establishment length is about 6.5 (at the phase $t=6.0$). Fig. 4 shows the variation of reattachment length (L_R) versus the incident wave height (A_0). Fig. 4(a) shows that L_R 's for cases with various values of A_0 (0.2~0.6) decreases rapidly to an almost steady value when time increases. A trend for the steady L_R versus A_0 is plotted in Fig. 4(b). A weaker A_0 reflects a larger L_R . That is related to the effective wave length for solitary wave.

4. Conclusions

It is found in this study the location reaching the establishment length of a solitary wave is about at $x=6.5$, although it varies slightly among the cases with various incident wave heights. The reattachment length is shorter for a larger solitary wave. The present work has been supported by the National Science Council of R.O.C. under Contract No. NSC 100-2221-E-275 -001.

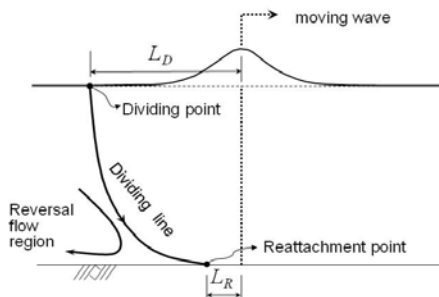


Fig. 1 Definition sketch for the flow field under a moving solitary.

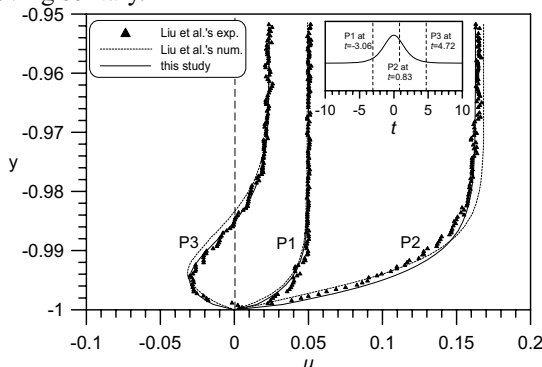


Fig. 2 Comparisons of three horizontal velocity profiles in a flat-bottom boundary layer.

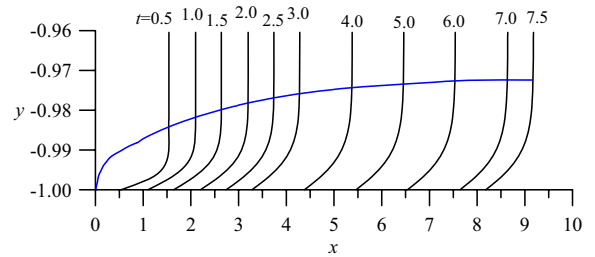


Fig. 3 Horizontal velocity plotted versus the vertical coordinate at different phases and the development of establishment length for $A_0=0.2$.

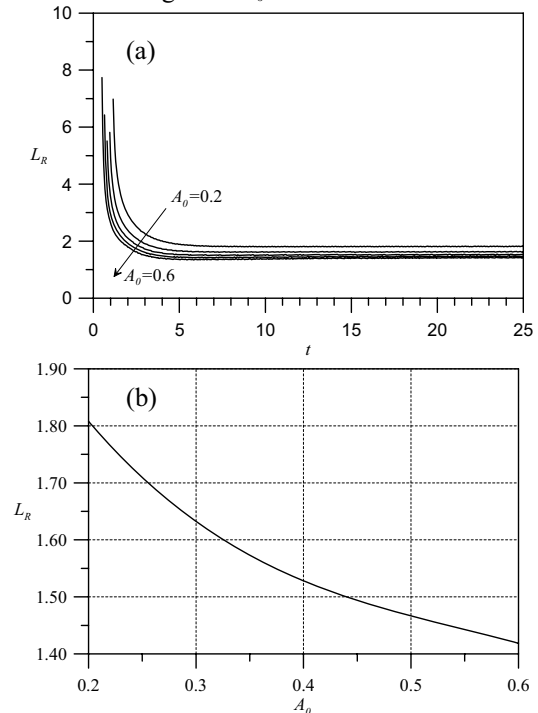


Fig. 4 Reattachment lengths (L_R) for different incident wave heights (A_0): (a) Variation of L_R versus time for various A_0 's; (b) fully developed L_R versus various A_0 's.

References

- [1]. G. H. Keulegan, J. Res. Natl Bur. Stand., **40** (1948), 607–614.
- [2]. H. Tanaka, Sumer, B.M., Lodahl, C., Coast. Eng. J. **40** (1), (1998), 81-98.
- [3]. P. L. F. Liu, Orfila, A., J. Fluid Mech., **520** (2004), 83-92.
- [4]. P. L. F. Liu, Park, Y. S. and Cowen, E. A., J. Fluid Mech., **574** (2007), 449–463.
- [5]. P. L. F. Liu, Proc. R. Soc. Lond. A, **462** (2006), 3431–3491.
- [6]. G. Vittori, and Blondeaux, P., J. Fluid Mech., **615** (2008), 433–443.
- [7]. G. Vittori, and Blondeaux, P., Coastal Eng., **58** (2011), 206–213.
- [8]. P. Blondeaux, and Vittori, G., Coastal Engineering, **60** (2012), 1–10.
- [9]. R. Grimshaw, J Fluid Mech, **46**(3) (1971), 611-622.
- [10]. C.J. Chen, and Chen, H.C., J Comp Phys, **53** (1984), 209-226.

The Shear-thinning Effect in Core-annular Flow Stability of Power-law Fluid

X.-W. Sun¹, J. Peng² and K.-Q. Zhu²

¹ Beijing Aeronautical Science & Technology Research Institute of COMAC, Future Science & Technology Park,
Xiaotangshan, Changping District, Beijing 102211, P. R. China

² School of Aerospace, Tsinghua University, Beijing 100084, P. R. China
Email: sunxuewei@comac.cc

ABSTRACT

Linear stability analysis is performed to study the core-annular flow of two power-law fluids inside an infinitely-long pipe. The influence of shear-thinning property on the flow stability is mainly concerned. It is found that shear-thinning effect equivalently amplifies the viscosity ratio or changes the capillary number. When viscosity stratification and capillary force both exist, the shear-thinning action may lead to an unstable “island” in the neutral stability curve plane.

1. Introduction

Core-annular flow appears in extensive applications, e.g. the pipeline transport of crude oil with a low viscosity fluid (usually water) used as lubricant [1, 2]. In this case a stable interface is desired to keep oil remain wrapped by the lubricant. The type of air flow inside pulmonary bronchi is core-annular flow too, where the instability of the interface between air and the liquid layer could cause respiratory distress [3, 4]. Researchers have shown much interest in studying the core-annular flow stability in the past half century and much progress has been made [2, 5].

The working fluids in core-annular flow often show non-Newtonian properties. The Upper-Convected Maxwell model has been used to study the influence of first normal stress difference on the core-annular flow stability [6, 7]. The present paper concerns the role of shear-thinning property in the core-annular flow stability by using a normal-mode linear stability analysis. Main discussion is focused on the coaction of shear-thinning property with interfacial tension and viscosity stratification effects.

2. Method

Consider the axisymmetric stratified flow of two immiscible power-law fluids driven by axial pressure gradient inside an infinitely long straight pipe with the pipe radius $r = b$. The power-law constitutive relation $\boldsymbol{\tau} = \mu \Pi^{m-1} \dot{\boldsymbol{\gamma}}$ applies, where $\boldsymbol{\tau}$ is the viscous stress tensor, $\dot{\boldsymbol{\gamma}}$ is the strain rate tensor, μ is the fluid consistency and m is the power-law index. $\Pi = \sqrt{(\dot{\boldsymbol{\gamma}} : \dot{\boldsymbol{\gamma}})/2}$ is the second invariant of $\dot{\boldsymbol{\gamma}}$.

The cylindrical coordinate system is used to establish the control equations, with r, θ, z being the radial, azimuthal and axial coordinates respectively. The z -axis coincides with the central pipeline. The interface of the two fluids is located at $r = R_I$, with its unperturbed value $\bar{R}_I = a$, where the overbar denotes unperturbed variables. Both fluids are incompressible and their densities are the same.

The flow is described by the N-S equation:

$$\partial_t \mathbf{u}^{[q]} + \mathbf{u}^{[q]} \cdot \nabla \mathbf{u}^{[q]} = -\frac{1}{Re} \nabla p^{[q]} + \frac{1}{Re} \nabla \cdot \boldsymbol{\tau}^{[q]} \quad (1)$$

where $Re = \rho \bar{u}_I^{2-m} b^m / \mu^{[2]}$ is the Reynolds number. \bar{u}_I is the unperturbed axial velocity at the interface. $q = 1, 2$ represents the core and annular fluids respectively. The boundary conditions include the immiscibility, velocity continuity and stress balance conditions at the interface, the non-slip and non-penetration conditions at the wall, the limited velocity condition at the centerline and the pseudo pressure condition at the centerline and the wall.

In order to derive the stability control equations, infinitesimal perturbation is added to the base flow, as follows:

$$\mathbf{u}^{[q]} = \bar{\mathbf{u}}^{[q]} + \mathbf{v}^{[q]}, p^{[q]} = \bar{p}^{[q]} + p^{[q]}, R_I = \varepsilon + \chi \quad (2)$$

where $\varepsilon = a/b$ is the unperturbed radial location of the interface. The perturbation is assumed to be axisymmetric and the perturbed variables are expressed in normal-mode form as:

$$\begin{aligned} & \left[(v_r, v_z, p)^{[q]}, \chi \right] \\ & = \left[(V_r(r), V_z(r), P(r))^{[q]}, X \right] \exp[i(kz + ct)] \end{aligned} \quad (3)$$

where k is the axial wave number. Substituting the expression (3) into the control equations and subtracting the basic flow leads to the perturbation equations, which can be transformed to the generalized matrix eigenvalue problem after linearization and discretization:

$$\mathbf{Ax} = \lambda \mathbf{Bx} \quad (4)$$

where $\lambda = \max[\text{Re}(ic)]$ is the perturbation growth rate.

The flow is linearly unstable when $\lambda > 0$, neutrally stable when $\lambda = 0$ and linearly stable when $\lambda < 0$. Eqn. (4) is numerically solved using a spectral collocation method based on Chebyshev polynomials.

3. Results and Discussion

The “lubricating flow” is discussed where the core layer is more viscous and the interface is close to the wall. For the present case, the consistency ratio and radial interface location is set to $\alpha = \mu^{[1]} / \mu^{[2]} = 2.0$ and $\varepsilon = 0.8$ respectively.

The influence of shear-thinning property can be deduced preliminarily through theoretical analysis. The normal stress balance equation is derived as [8]:

$$2DV_r + \frac{1}{Ca'} \frac{(1-k^2\varepsilon^2)X}{\varepsilon^2} = 0 \quad (5)$$

where $Ca' = Ca |D\bar{u}_z|^{m-1}$ can be regarded as the equivalent capillary number. For the Newtonian fluid $Ca' = Ca$. For the shear-thinning fluid, it is found that $Ca' < Ca$ when the interface is close to the wall. Consequently the shear-thinning property acts to amplify the capillary force effect.

The shear-thinning property also amplifies the viscosity stratification effect compared to the Newtonian fluid case under the same α . This is easy to understand. As the shear rate in the annular layer is higher than in the core layer, the viscosity of the annular fluid gets a larger reduce under shearing action.

In Fig. 1 the neutral stability curves in the $Re-k$ plane is shown for the Newtonian fluid. “U” and “S” in the figure denote unstable and stable regions respectively. The long wave instability region caused by interfacial tension under low Reynolds number is limited to a very small area around the zero point. Short wave Yin instability [9] appears due to the viscosity stratification effect under large Reynolds number. The area of Yih instability region is decreased when the capillary number becomes smaller, as the interfacial tension stabilizes short wave perturbations.

The results of shear-thinning fluid are shown in Fig. 2. Compared to Fig. 1, the long wave capillary instability region is larger under the same capillary number, as demonstrated in eqn. (5), the shear-thinning property amplifies the interfacial tension effect. While the short wave instability region is much smaller. This is because the shear-thinning property strengthens the stabilizing effect of the interfacial tension on short wave perturbations.

An interesting phenomena appears when $Ca = 10.0$. An unstable “island” appears in the short wave region, The “island” disappears when $Ca = 1.0$, which indicates that the instability is inhibited by interfacial tension. The unstable “island” in Fig. 2 corresponds to a region around the neutral stability curve in Fig. 1, where

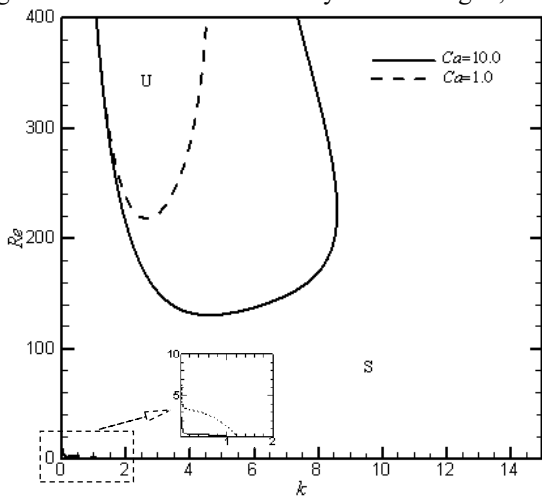


Fig. 1 Neutral stability curves in the $Re-k$ plane, $m = 1.0$

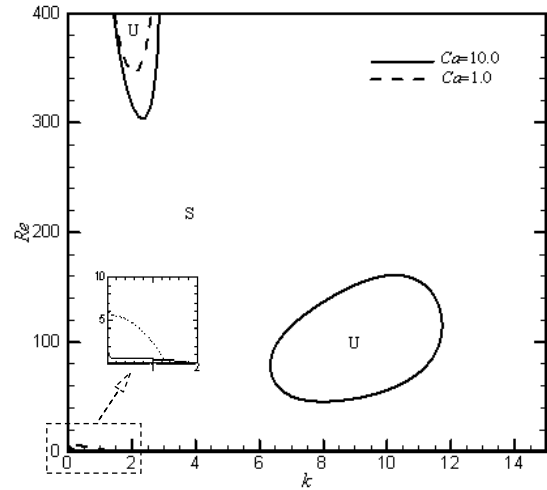


Fig. 2 Neutral stability curves in the $Re-k$ plane, $m = 0.7$

the stabilizing effect of the interfacial tension just counterbalances the Yih instability. The “island” does not appear in the Newtonian fluid case. It can be inferred that the shear-thinning property amplifies the Yih instability within the “island”. While out of the “island” the shear-thinning property strengthens the stabilizing effect of the interfacial tension.

4. Concluding remarks

The present results demonstrate that the shear-thinning property influences both the interfacial tension and viscosity stratification effects. When the interfacial tension dominates the flow stability, shear-thinning property appears to strengthen the interfacial tension effect. Otherwise, shear-thinning property enhances the viscosity stratification effect. When the effects of interfacial tension and viscosity stratification nearly counteract each other, the shear-thinning property may amplify the viscosity stratification action in the short wave region and results in the formation of the unstable “island”.

References

- [1] M. S. Arney, R. Bai, E. Guevara, D. D. Joseph & K. Liu, *Int. J. Multiphase Flow* **19**(6), 1061 (1993).
- [2] D. D. Joseph, R. Bai, K.-P. Chen, & Y. Y. Renardy, *Annu. Rev. Fluid Mech.* **29**, 65 (1997).
- [3] D. R. Otis, M. Johnson, T. J. Pedley & R. D. Kamm, *J. Appl. Physiol.* **75** 1323 (1993).
- [4] F. F. Espinosa & R. D. Kamm, *J. Appl. Physiol.* **86** 391 (1999).
- [5] S. Ghosh, T. K. Mandal, G. Das, & P. K. Das, *Renewable and Sustainable Energy Reviews* **13**, 1957 (2009).
- [6] K.-P. Chen, & Y. Zhang, *J. Fluid Mech.* **247**, 489 (1993).
- [7] A. V. Coward, & Y. Y. Renardy, *J. Non-Newtonian Fluid Mech.* **70**, 155 (1997).
- [8] X.-W. Sun, J. Peng & K.-Q. Zhu, *Sci. China Ser. G-Phys. Mech. Astron.* **53**, 933 (2010).
- [9] C. S. Yih, *J. Fluid Mech.* **27**, 337 (1967).

Time Series Analysis of Flow Instability in a Natural Convection Loop

Hiroyuki Nishikawa, Shigeki Okino, and Fujio Suda

Department of Resources and Environment Science, Tokai University, 4-1-1 Kitakaname, Hiratsuka, Kanagawa, 259-1292, Japan.

E-mail: fsuda@keyaki.cc.u-tokai.ac.jp

ABSTRACT

An experimental study has been made on various flows in a rectangular natural convection loop. Based on time series temperature data of the system, an attractor in a phase space has been reconstructed. Consequently, geometrical structures and orbital instability for this attractor were evaluated by various chaos analysis methods. The unstable flow is low-dimensional deterministic chaos. Moreover, it was suggested that the transition from the unstable to turbulent flows was caused by a dynamic noise of the system. It was confirmed by the application of the prediction for theoretical data with additive noise.

1. Introduction

A natural convection is driven by buoyancy due to a density difference of the fluid. It has attracted much attention from the viewpoint of turbulence and chaotic instability. There have been reported many studies on the flow instability in the natural convection loops since two early analyses by Welander [1] and Keller [2]. Creveling *et al.* [3] clearly observed the instabilities of water flow in a toroidal loop. The fluid flow oscillated with increasing amplitude, reversed direction and resumed oscillation. The chaotic behavior of the flow has been much investigated theoretically or experimentally, but there have been only a few studies on the comparison between experimental and theoretical results. In particular, the process of transition from an unstable flow to turbulence is not clearly understood yet.

In the present study, various chaos analyses of measurements and predictions and their comparison have been made on unstable and turbulent flows in a rectangular natural convection loop [4].

2. Experimental Apparatus and Method

The rectangular natural convection loop made of Pyrex glass tube of inner radius 1.5cm is close to a square with side length of 40cm [4, 5]. The lower and the upper branches are heated at constant heat flux and cooled at constant wall temperature, respectively, and both right and left branches are thermally insulated, its working fluid is water. Heat input Q ranges from 0 to 950W (0 to 26.5kW/m²). Sampling rate was 0.5sec, and the number of data in each measurement were 30000. Two cases of temperature data ΔT_{AB} were collected; one was the case where the heat input Q was increased in a stepwise manner from 10 to 900W (Q_{up}), and the other Q was decreased from 950 to 10W (Q_{down}).

Scalar time series data were normalized by the maximum $|\Delta T_{AB}|$. And then, an m -dimensional state space is reconstructed using the delay time method [6] by defining reconstructed vectors as $\mathbf{v}(t) = (y(t), y(t + \tau), y(t + 2\tau), \dots, y(t + (m-1)\tau))$, where τ is the delay time. The optimum delay time τ_{opt} was determined by the method of high-order autocorrelation function [6].

3. Results and Discussion

With increasing Q , the flow in the loop shows the transitions from a laminar to an unstable flow, and the unstable to a turbulent flow. In this experiment, the

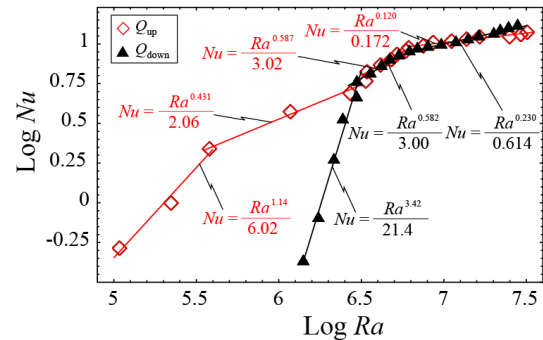


Fig. 1. Nusselt number versus Rayleigh number.

critical Reynolds number is 1202 for $Q_{up} = 200W$, and 941 for $Q_{down} = 100W$, and then, the Reynolds number of turbulence onset is 9415 for $Q_{up} = 900W$ and 8527 for $Q_{down} = 950W$. In this rectangular loop, the unstable flow with reversal occurs in a wide heating region of 150~850W.

In Fig. 1, Nusselt numbers Nu are plotted against Rayleigh numbers Ra for various Q , where the diamonds and the triangles correspond to Q_{up} and Q_{down} , respectively.

In the region of $Ra \leq 3.2 \times 10^6$, the exponents α of the $Nu \propto Ra^\alpha$ in the cases of Q_{up} and Q_{down} are quite different. These results are due to the fact that, in the case of Q_{up} , the flow changes from the local convection state to the laminar flow, while, in the case of Q_{down} , the convection did not stop even down to less than 50W. More important is the change in α in the turbulent region. Generally, between Nu and Ra is the relation: $Nu \propto Ra^{1/3}$ in the soft turbulence region. When the flow is the hard turbulence, as is well known, this exponent value becomes smaller than 1/3 [7]. In the present experimental conditions, there is a possibility of the transition from the soft to the hard turbulence in a region of $10^7 \leq Ra$. Indeed, in Fig. 1, the exponent α of Nu against Ra in the turbulent region was lower than 0.3: Q_{up} : $\alpha = 0.120$, Q_{down} : $\alpha = 0.230$

These results suggest that the unstable flow in $10^7 \leq Ra$ begins to be turbulent. The unstable flow, however, is a very chaotic behavior.

Figures 2 (a) and (b) shows a typical pattern of ΔT_{AB} variation at $Q_{up} = 700W$ and its attractor reconstructed in the phase space ($m = 3$, $\tau_{opt} = 5$), respectively. Here, the time series data were obtained from 20-point moving

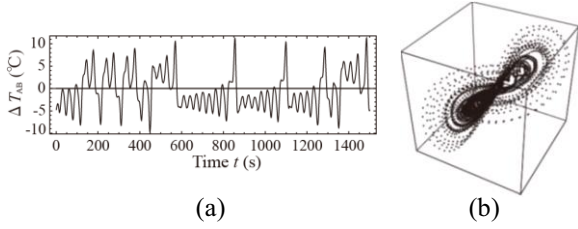


Fig. 2. An example of a ΔT_{AB} time series data and a reconstructed attractor (3-dim.) for the unstable flow.

average. In Fig. 2 (a), flow reversal occurs every 120 sec in average. The reconstructed attractor in Fig. 2 (b) is similar to the Lorenz attractor in shape, and it reflects the repeating flow reversal.

The correlation dimension D_c has been estimated by the correlation integration method [6]; we obtained $D_c = 2.16$ for this attractor. As an average value of D_c over the unstable region, we got the value of 1.8. This indicates that the unstable flow is a low-dimensional deterministic chaos. Moreover, these values are in agreement with the prediction of the one-dimensional model [5]. And then, the embedding dimension m_c was estimated by the false near neighbor method and Lyapunov spectrum [6]. As a result, $m_c = 3\sim 4$ in the unstable region, and $m_c = 5\sim 6$ in the turbulent region. Their degrees of freedom obtained from the embedding theorem are low: $2\sim 3$ in both regions. Moreover, the Lyapunov exponents in both are positive.

Next, examples of the recurrence plot [8] are shown in Fig. 3 ($Q_{up} = 500W$). We can observe flow reversals, (quasi) periodic oscillations and intermittent turbulence. Fig. 3 (a) shows the time series data. (b) and (c) are recurrence plots of a duration of the unstable flow. Then, (d) and (e) are those of a duration of the turbulent flow. One can observe regular intervals, vertical and horizontal lines, and diagonal lines from Fig. 4 (b) and (c). These structures indicate that the periodicity, a presence of deterministic dynamics and an asymptotically stable orbit on the reconstructed attractor [8].

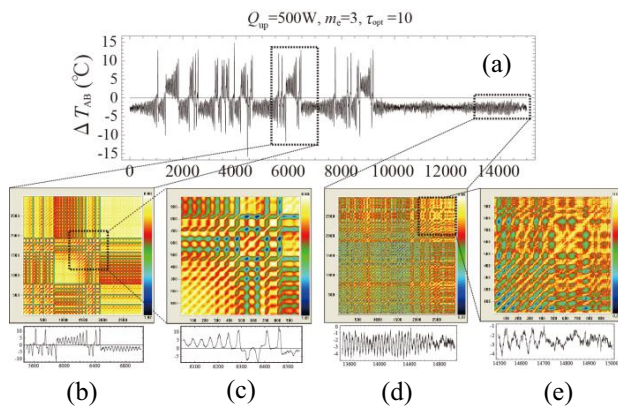


Fig. 3. Examples of the recurrence plots for the unstable flow which contain an intermittent turbulence.

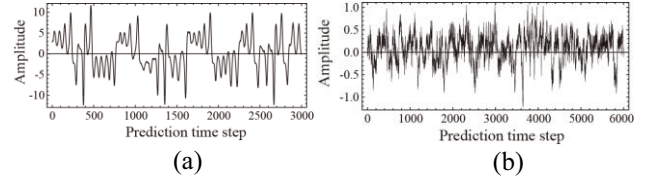


Fig. 4. Examples of predicted time series. The case of (a) is input data 700W (Q_{up}), and that of (b) is a typical unstable oscillation generated from the one-dimensional model with an additive Gaussian noise.

These features can also be observed in Figs. 4 (d) and (e). In addition, structures of the recurrence plot in Fig. 3 (e) are similar to those in (c). These points and lines are disrupted. Thus, it was found that although the unstable and the intermittent turbulence have quite different appearances, both systems have the same dynamics. A similar structure is also recognized in the developed turbulence for $10^{7.4} \leq Ra$ (Fig. 1). These results suggest that the transition from unstable to turbulent flow was caused by a dynamic noise of the system.

To confirm this conjecture, we applied the nonlinear prediction by the use of local linear approximation method [6] for the theoretical unstable flow data [5] with additive noises. Its results are shown in Fig 4; in (a) $Q_{up} = 700W$ and (b) is a typical unstable oscillation generated from one-dimensional model with an additive Gaussian noise. Its signal to noise ratio is 30%. In each case, the number of input data is 3000, and that of prediction steps is 6000. In the case of (a), the predicted time series has maintained the characteristics of its original time series [Fig. 2 (a)]. Also, D_c and m_c of (a) are estimated at 2.21 and 4, respectively. On the other hand, in the case of (b), the oscillation is similar to the turbulence. The estimated m_c is 6 ± 1 for this data, which is in agreement with the experimental results.

4. Concluding remarks

It was found that the transition from the unstable to the turbulent flow was caused by a dynamic noise of the system. The unstable flow with reversal is low-dimensional deterministic chaos.

References

- [1] P. Welander, J. Fluid Mech. **29** (1967), 17.
- [2] J.B.Keller, J.Fluid Mech. **26** (1966), 599.
- [3] H. F. Creveling, J. F. De Paz, J. Y. Baladi and R. J. Schoenhals, J. Fluid Mech., **67** (1975), 65.
- [4] H. Nishikawa, S. Okino, and F. Suda, J.Adv. Sci. **21** (2009), 20.
- [5] F. Suda, Experimental Heat Transfer, Fluid Mechanics and Thermodynamics (1997), 2191.
- [6] K. Aihara edit. “CHAOS JIKEIRETHU KAISEKI NO KISO TO OYO”, Sangyo Tosyo, 2002. Chapter 1~5, in Japanese.
- [7] M. Sano, X.Z. Wu, and A. Libchaber, Phys. Rev. A **40** (1989), 6421.
- [8] N. Marwan, M. C. Romano, M. Thiel, J. Kurths, Physics Reports **438** (2007), 237.

Sizing of Pipe Wall Thinning Using Pulsed Eddy Current Testing Method Based on Inversion Analysis

Shejuan Xie¹, Zhenmao Chen², Toshiyuki Takagi^{1,*} and Tetsuya Uchimoto¹

¹Institute of Fluid Science, Tohoku University, Katahira 2-1-1 Aoba-ku, Sendai 980-8577, Japan

²State Key Laboratory for Strength and Vibration of Mechanical Structures, Xi'an Jiaotong University, Xi'an, China

*Corresponding author: Toshiyuki Takagi, takagi@ifs.tohoku.ac.jp

ABSTRACT

In this paper, an inversion algorithm has been proposed and validated, based on a fast simulator of pulsed eddy current testing (PECT) signals and a deterministic optimization strategy, for the profile reconstruction of wall thinning in pipes of nuclear power plants. Local wall thinning is modelled as a group of planar defects with different length and depth, reconstructed from two-dimensional PECT signals. Through inverse analysis of experimental PECT signals, the efficiency and the robustness of the proposed algorithm have been demonstrated.

1. Introduction

In nuclear power plants (NPPs), local wall thinning is one type of pipe defect caused by flow accelerated corrosion (FAC) and/or liquid droplet impingement (LDI) on the inner side of the coolant pipes. Concerning the material of pipes, there are mainly two types, low-carbon steel and stainless steel where the stainless steel pipes are targeted in this study. To guarantee the integrity of NPPs, periodic non-destructive testing (NDT) is mandated to evaluate wall thinning. Another important issue is to check whether the wall thinning exceeds the safe tolerance range. This can not only guarantee safety but also save on unnecessary renewal of pipes. This requires a so-called quantitative NDT (QNDT) method. However, the defect profile characterization of pipe wall thinning in NPPs has so far not been studied.

Recently, the pulsed eddy current testing (PECT) method has been considered as a promising candidate for the detection of wall thinning. In addition, a high efficiency 3D numerical tool to simulate PECT signals has recently been developed by authors [1, 2] which give a good basis for quantitative wall thinning analysis based on inversion techniques.

Based on the backgrounds above, the objective of this paper is to propose and develop an inverse analysis scheme for the sizing of pipe wall thinning in NPPs, based on a deterministic optimization strategy and the fast PECT signal simulator developed by the authors.

2. Fast simulator for PECT signals

In PECT, the transient response signal due to the pulsed excitation can be obtained through a summation of response signals due to excitations of a series of single harmonic frequency with the corresponding Fourier transformation coefficients.

To simulate PECT signal based on the Fourier series method, the response signal due to single frequency excitation, has to be obtained in advance. In this work, the database approach for fast simulation of ECT signals has been imported for the simulation of the single frequency signals. To deal with wall thinning of 3D (3 dimension) geometry, the conventional fast simulator for 2D defect [3] has been upgraded with help of an interpolation strategy. Through comparing with the numerical results of the full FEM analysis, it was demonstrated that the proposed fast simulation scheme is of high accuracy and over 100 times

faster.

3. Principle of inversion algorithm and Results

In this study, sizing of wall thinning is conducted based on the inverse analysis strategy, which converts the sizing process to an optimization problem of minimizing the objective function,

$$\mathcal{E}(\mathbf{c}^k) = \sum_{l=1}^L \sum_{m=1}^M (P_{l,m}(\mathbf{c}^k) - P_{l,m}^{obs})^2 / \sum_{l=1}^L \sum_{m=1}^M (P_{l,m}^{obs})^2, \quad (1)$$

where k means the iteration step, l and m represent the position of 2D scanning point, \mathbf{c}^k the shape parameter vector of wall thinning after k -th iteration, $\mathcal{E}(\mathbf{c}^k)$ the objective function (residual error), $P_{l,m}(\mathbf{c}^k)$ the feature parameter (this study, peak value is employed) extracted from the PECT signal $\mathbf{B}(t)$ at (l, m) scanning point for defect shape \mathbf{c}^k , and $P_{l,m}^{obs}$ is the corresponding measured signal.

As shown in Fig. 1, the local wall thinning is modelled as a group of planar slit defects (rows) of given width but with different length (for example, in the w -th row, length of wall thinning equals $bw-aw$) and depth (in the w -th row, depth of wall thinning to total thickness of specimen is d_w (%)), which are selected as the defect shape parameters to be reconstructed. As these parameters have to be reconstructed at the same time, 2D PECT signals (Probe scans along the length and width direction in Fig. 1) scanned over the wall thinning in the far side are used for the reconstruction. In cases where the defect length and depth are close to 0 in some rows after reconstruction, then these rows will be treated as unflawed region. In this way, the width information of the wall thinning can also be properly reconstructed.

The conjugate gradient based reconstruction scheme is employed to predict the lengths and depths of each row. In this study, Eq. (2) is adopted for the direct calculation of gradient vector from the calculated electric fields for the TR type PECT probe [4].

$$\frac{\partial B(\mathbf{r}, t)}{\partial c_{w,i}} = -\sigma_0 \times \sum_{n=1}^N F_n \left(\alpha \int_S \mathbf{E}_p^u \cdot (\mathbf{E}_e^u + \mathbf{E}_e^f) \frac{\partial S_w(\mathbf{c}, \mathbf{r})}{\partial c_{w,i}} ds \right) e^{j\omega_n t}, \quad (2)$$

where, σ_0 is the conductivity of specimen in unflawed region, \mathbf{E}_p^u is the unflawed electric field generated by unit current in the pickup coil, $\mathbf{E}_e^u + \mathbf{E}_e^f$ is the flawed electric field generated by excitation coil (including unflawed and perturbed field), α is a coefficient to correspond the output of pickup coil and the PECT signal, $C_{w,i}$ is the i -th wall thinning shape parameter at the w -th planar row in width direction and $s_w(\mathbf{c}, \mathbf{r}) = 0$ is the equation of the defect boundary surface in w -th row.

According to the above theory, an inverse analysis code of PECT has been developed. The inversion algorithm preceding and the corresponding developed inverse analysis code are validated by 3D wall thinning reconstruction from the experimental PECT signals. A block of austenitic stainless steel 316L (AISI316L), with conductivity of 1.35×10^6 S/m, is employed to simulate the big diameter pipe in NPPs as the host conductor, with length 300 mm, width 300 mm, and thickness 10.5 mm as shown in Fig. 2. Wall thinning is located in the bottom side of the specimen which is shown in Fig. 2. The size of the wall thinning is length 41.0 mm, width 15.0 mm, depth 6.0 mm. The shape of length-depth cross-section is part of circle which is extended along width direction.

Figure 3 shows the reconstructed result of wall thinning from experimental PECT signals after reconstruction of 150 steps iteration. In this case, the depth, length and width of the initial wall thinning are 4.20 mm, 15.00 mm and 9.00 mm respectively. The reconstructed ones are 5.74 mm, 37.81 mm and 15.00 mm respectively which are close to the true wall thinning shape. The reconstruction errors of length and depth are -7.8% and -4.3% respectively.

Figure 4 shows the relative residual error where the relative reconstruction residual error is close to 2% up to 150th step. From these reconstructed results, we can see that the size of the wall thinning can be properly reconstructed from the experimental signals.

4. Summary

An inversion algorithm is proposed based on a fast simulator of pulsed ECT signals and a deterministic optimization strategy. Reconstruction results show that the profile of the wall thinning can be properly reconstructed using this inversion scheme.

This work was supported by the Grant-in-Aid for the Global COE Program, "World Centre of Education and Research for Trans-Disciplinary Flow Dynamics", from the Ministry of Education, Culture, Sports, Science and Technology (MEXT) of Japan.

References

- [1] S. Xie, Z. Chen, T. Takagi and T. Uchimoto, Efficient numerical solver for simulation of pulsed eddy current testing signals, IEEE Transactions on Magnetics, Vol. 47, pp. 4582-4591, 2011.
- [2] S. Xie, Z. Chen, T. Takagi and T. Uchimoto, Development of a very fast simulator for pulsed eddy current testing signals of local wall thinning, NDT&E International (In press, 2012).
- [3] T. Takagi, H. Huang, H. Fukutomi, and J. Tani, Numerical evaluation of correlation between crack size and eddy current testing signal by a very fast simulator, IEEE Transactions on Magnetics, Vol. 34, pp. 2581-2584, 1998.
- [4] S. J. Norton and J. R. Bowler, Theory of eddy current inversion, J. Appl. Phys., Vol. 73, pp. 501-512, 1993.

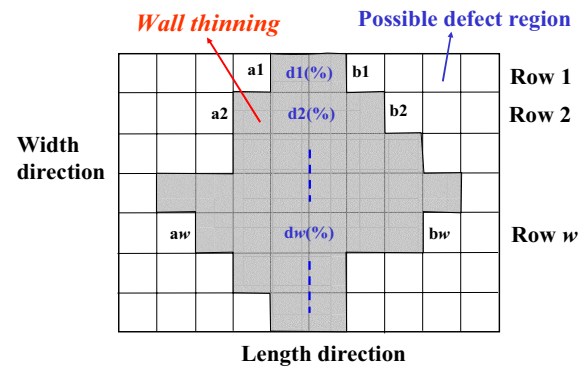


Fig. 1 Reconstruction strategy schematic for 3D wall thinning

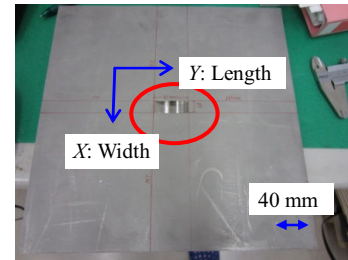
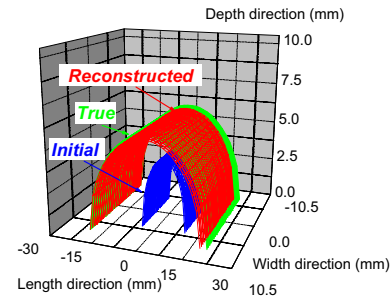
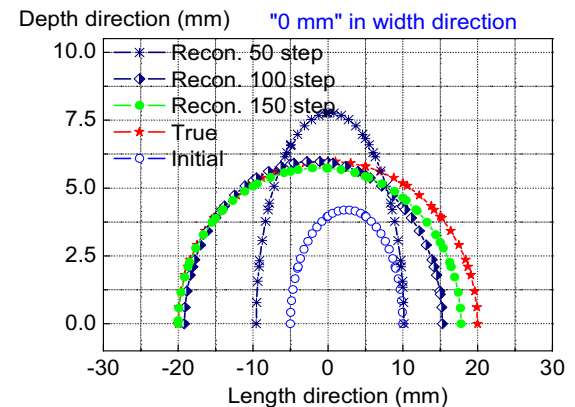


Fig. 2 AISI316L specimen and wall thinning shape



(a) 3D wall thinning: true, initial and reconstructed



(b) Cross-section of wall thinning, '0 mm' plane in width direction

Fig. 3 Wall thinning: true, initial and reconstructed

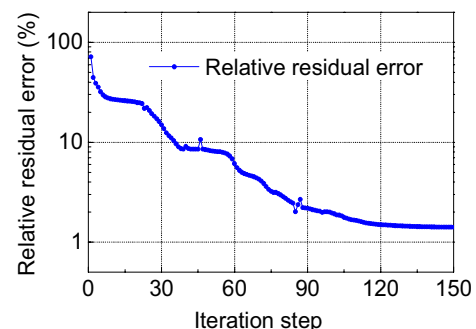


Fig. 4 Relative reconstruction residual error

A Simple Method for Three Dimensional Characteristic Boundary Conditions with Cell-centered Solver

Xinrong Su¹, Satoru Yamamoto¹, Kazuhiro Nakahashi²

1 Department of Computer and Mathematical Sciences, Tohoku University, Aoba 6-6-01, Sendai, Japan

2 Japan Aerospace Exploration Agency, Chofu Research Center, Tokyo, Japan

su@caero.mech.tohoku.ac.jp

ABSTRACT

In this paper we explore a new method for the implementation of three dimensional characteristic boundary conditions for cell-centered solver. The current method is based on the characteristic interpolation, instead of the characteristic decomposition in the existing method. Compared to current characteristic decomposition based method, it is very simple and can be used with cell-centered scheme for which the implementation of existing method is not straightforward. Also it can be extended to unstructured solver without difficulty. The accuracy and non-reflection property are verified with structured and unstructured numerical examples.

1. Introduction

Treatment of boundary conditions is an important aspect of Computational Fluid Dynamics (CFD) solver, especially for high-fidelity simulations where small scale flow features, such as vortices and pressure waves should traverse the artificial boundary with minimized reflected waves. There are many manners to implement the non-reflecting boundary and among these techniques, the characteristic wave based method is extensively exploited and widely used [1]. By identifying different waves according to the eigenvalue information, the incoming wave can be separated from outgoing waves and the identification of waves allows the precise control of boundary condition. In the literature this method is mostly used with the assumption the flow-field near the boundary can be simplified as one dimensional and this simplification is denoted as Local One Dimensional Inviscid (LODI) [2]. However, Yoo et al. [3] found that by accounting all the transverse terms, the improved boundary condition yields significantly reduced flow distortion and this approach is always named 3D-NSCBC.

In most of the papers, 3D-NSCBC is tested with Cartesian mesh based finite difference codes because in the formulation the computation of transverse term is required. On the other hand, for cell-centered scheme, as the variables are defined at the center and does not support the direct computation of transverse term, in general it is difficult to implement 3D-NSCBC with cell-centered scheme, especially with curvilinear mesh and unstructured solver. In this work a simple method to implement 3D-NSCBC is proposed for cell-centered scheme and characteristic interpolation, instead of characteristic decomposition is used and this new method can be used with both structured and unstructured solvers. Several numerical examples are given in this paper.

2. 3D-NSCBC

For clarity, denote the governing equation in the curvilinear coordinate system as

$$\frac{\partial \mathbf{U}}{\partial t} + \frac{\partial \mathbf{F}_j \xi_{i,j}}{\partial \xi_i} + \frac{\partial \mathbf{F}_{v,j} \xi_{i,j}}{\partial \xi_i} = 0 \quad (1)$$

where \mathbf{F}_j and $\mathbf{F}_{v,j}$ denote the inviscid and viscous fluxes, respectively. The 3D-NSCBC is always

implemented with primitive variable and also using the eigen-decomposition, the above equation can be written as

$$\frac{\partial \mathbf{W}}{\partial t} + \mathbf{R}_i \Lambda_i \mathbf{L}_i \frac{\partial \mathbf{W}}{\partial \xi_i} + \frac{\partial \mathbf{W}}{\partial \mathbf{U}} \frac{\partial \mathbf{F}_{v,j} \xi_{i,j}}{\partial \xi_i} = 0 \quad (2)$$

In the above equation, the second term represents the characteristic waves and the third term is the transverse term. For the second term, positive eigenvalue means the corresponding wave is transported from interior to outside and thus this term should be computed using one-sided finite difference. For wave with negative eigenvalue, the amplitude of this wave should be zero for perfect non-reflecting; however, to specify the target boundary value, some reflection is needed, especially at the outflow boundary surface.

To summarize the numerical implementation of characteristic decomposition based 3D-NSCBC, we have to setup local coordinate system to facilitate the characteristic decomposition, also the computation of transverse term. As a result finite difference method naturally supports 3D-NSCBC. However, for cell-centered scheme, as variables are defined at centers. If 3D-NSCBC is implemented at surface-center, the computation of characteristic wave is not so hard; however difficulty lies in the computation of transverse term. Also for unstructured code, it is hard to define the curvilinear coordinate system and thus the use of 3D-NSCBC is not straightforward.

3. Characteristic interpolation based method

Instead of computing the characteristic waves and the transverse term along the curvilinear coordinates, in this work another method to implement non-reflecting boundary condition is proposed and the basic idea will be introduced in the following. Similar as in the characteristic decomposition method, the eigenvalues of characteristic waves can be used to define the ingoing waves and outgoing waves. With eigen-decomposition, the amplitude of characteristic waves can be defined as

$$\mathcal{L}^+ = L^+ \mathbf{W}, \quad \mathcal{L}^- = L^- \mathbf{W} \quad (3)$$

where L is the left eigen-matrix of the flux Jacobian. As demonstrated in Fig. 1, for cell-centered solver the variables are defined at the centers and in order to complete the spatial residual computation, the physical values at the cell centers outside the computation

domain are required. Thus by specifying these values outside the computation domain with some constraints, the reflection from the boundary can be minimized.

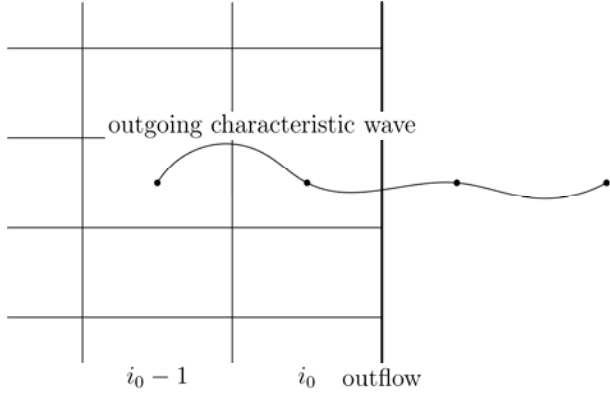


Fig. 1 Definition of outgoing characteristic wave.

For a non-reflecting boundary, the physical variables should be continuous across the boundary and the same in the characteristic space, in that the characteristic wave should be continuous. For high order accuracy, we can also require the characteristic waves are continuously differentiable. This analysis is very simple, however it can be used to constructing non-reflecting boundary. For the outgoing characteristic waves, they are available inside the domain and based on the continuous assumption, the amplitude of outgoing characteristic wave can be interpolated from the inside part and in this work they are obtained using Lagrange interpolation as

$$\mathcal{L}_{\text{outside}}^+ = \mathcal{L}_{\text{interpolation}}^+ \quad (4)$$

The ingoing characteristic wave is computed as

$$\mathcal{L}_{\text{outside}}^- = \alpha L^- W_0 \quad (5)$$

where α is a small number and W_0 is the target value. The physical value can be obtained by

$$W_{\text{outwise}} = R(\mathcal{L}_{\text{outwise}}^+ + \mathcal{L}_{\text{outwise}}^-) \quad (6)$$

4. Results and Discussion

Several test cases are used to validate the current method and of which the results of isentropic vortex case will be given in this manuscript. This a widely used test case for open boundary and it is often employed to evaluate the outflow boundary with passing vortical structures. A single vortex is positioned in the domain center and the flow is assumed to be isentropic. The flow is initialized as

$$p = p_\infty \exp \left[-\frac{\gamma}{2} \left(\frac{C_v}{a_\infty R_v} \right)^2 \exp \left(-\frac{r^2}{R_v^2} \right) \right]$$

$$\mathbf{u} = \frac{C_v}{R_v^2} \exp \left(-\frac{r^2}{2R_v^2} \right) \mathbf{e}_\theta + \mathbf{u}_\infty \quad (7)$$

$$\rho = \frac{p}{RT_\infty}$$

The computation is first conducted with a structured cell-centered finite volume solver and the computed numerical results are compared with the theoretical solution to assess the non-reflecting property and the normalized error is defined as

$$\text{Error}_p = \frac{p(\mathbf{x}, t) - p_{\text{theory}}(\mathbf{x}, t)}{p_\infty} \quad (8)$$

and the evolution of normalized error is given in Fig. 2.

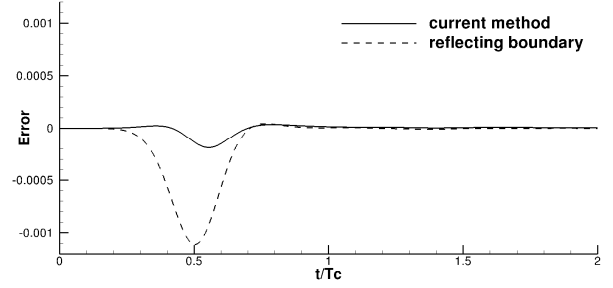


Fig. 2 Error evolution for the non-reflecting boundary.

From the comparison of current method and non-reflecting boundary, the current method works very well and the error is reduced by about one order. The current method is also implemented in an unstructured code. For test, two sets of unstructured meshes, including quadrilateral based and triangle based meshes are used. The error evolutions are given in Fig. 3.

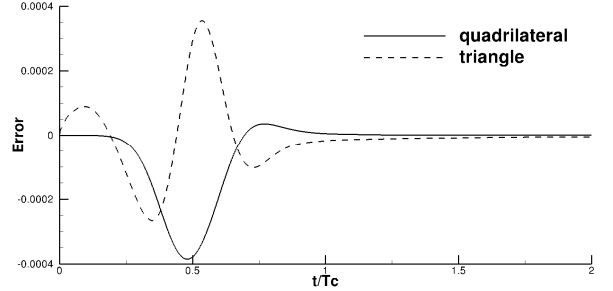


Fig. 3 Results of the method for unstructured meshes.

From the error evolutions in Fig. 3, the current method is proved to be also applicable with unstructured cell-centered solver and the numerical reflections are very small. Thus the current method is proved to be accurate and can be used with wide varieties of solvers.

5. Concluding remarks

In this paper a characteristic non-reflecting boundary condition for cell-centered solver is proposed. In this new method characteristic interpolation is used to obtain the physical values outside the domain. The resulted method is very simple and can be used with both structured and unstructured solvers. The applicability, accuracy and non-reflecting property of this method are verified with several numerical examples.

Acknowledgement

This work was supported by JSPS KAKENHI (21226018).

References

- [1] K. W. Thompson, *J. Comput. Phys.*, **68** (1987), 1-24.
- [2] T. J. Poinsot, S. K. Lele, *J. Comput. Phys.*, **101** (1992), 104-129.
- [3] C. S. Yoo, Y. Wang, A. Trounev, *Combustion Theory and Modeling*, **9** (2005), 617-646.

Numerical Simulation of Unsteady 3-D Condensate Flows through Three-Stage Stator-Rotor Blade Rows

Satoshi Miyake, Takashi Furusawa, Satoru Yamamoto
Dept. of Computer and Mathematical Sciences, Tohoku University, Sendai, 980-8579, JAPAN
s.miyake@caero.mech.tohoku.ac.jp

Yasuhiro Sasao
Dept. of Aerospace Engineering, Teikyo University, Utsunomiya, 320-0003, JAPAN

ABSTRACT

Unsteady flows through a three-stage low-pressure steam-turbine model developed by Mitsubishi Heavy Industry (MHI) is calculated by the numerical code developed by the authors. The code is based on the 3-D Reynolds averaged Navier–Stokes equations coupled with SST turbulence model and additional equations for condensation. The calculated results are compared with the experiments conducted by MHI to validate the code. Finally unsteady condensate structures obtained are discussed.

1. Introduction

Condensation of water vapor occurs occasionally in steam turbines and it certainly affects the performance of steam turbines. Yamamoto, et al. [1] calculated flows in a two-stage model turbine assuming equilibrium condensation. Miyake, et al. [2] calculated flows in a three-stage model turbine assuming equilibrium and nonequilibrium condensations. Since, few researches validating unsteady 3-D wet-steam flows through multi-stage stator-rotor blade rows in steam turbines have been reported yet. So it is crucial to get more insights of wet-steam flows through steam turbines to improve the turbine efficiency.

In this paper, calculated results in the previous research[2] are briefly introduced especially as focusing on the flow difference between dry and wet-steam conditions. In the experiments, flow measurements in dry and wet steam conditions were conducted. Then, the wet steam was produced by spraying micro-scale water droplets to the working gas. Total pressures, static pressures and yaw angles of flow velocities are measured in both conditions at the outlets of first-stage rotors, second-stage stators and second-stage rotors. In addition, unsteady condensate mass fractions are numerically visualized and the influence of three-dimensional flows to the condensation is discussed.

2. Numerical Method

The fundamental equations simulating flows of wet steam consist of conservation laws of the total density, the momentums, the total energy, the density of water liquid, and the number density of water droplets, and they are coupled with SST turbulence model[3]. Flows simulated by the equations are supposed to be a homogeneous flow without any slip between gas and water droplets. The set of equations related to condensation was derived by Ishizaka et al.[4] assuming single phase of water droplets. The equation of state and the sound speed in wet steam were also derived by Ishizaka et al.[4] assuming that the condensate mass fraction β is sufficiently small ($\beta < 0.1$) as

$$p = \rho RT(1 - \beta) \quad (1)$$

$$c^2 = \frac{C_{pm}}{C_{pm} - (1 - \beta)R} \frac{p}{\rho} \quad (2)$$

where C_{pm} is defined by the linear combination of the isobaric specific heat between gas phase and liquid phase using the mass fraction β .

The mass generation rate Γ for water droplets is formed as a sum of the mass generation rate of nucleus with critical size and the growth rate of a water droplet based on the classical condensation theory and the equation was further simplified by Ishizaka et al. [4] as

$$\Gamma = \frac{4}{3} \pi \rho_l \left(I r_*^3 + 3 \rho n r^2 \frac{dr}{dt} \right) \quad (3)$$

where the homogeneous nucleation rate I defined by Frenkel[5] and the growth rate of a water droplet dr/dt proposed by Gyarmathy[6] are employed.

The high-order high-resolution finite-difference method based on the fourth-order compact MUSCL TVD (Compact MUSCL) scheme and the Roe's approximate Riemann solver is used for space discretization of convection terms in the fundamental equations. The viscosity term is calculated by the second-order central-difference scheme. In the time integration, LU-SGS scheme is used.

3. Computational Grid and Flow conditions

Figure 1 shows the perspective view of the three-stage steam turbine. It is noted that the number of blades is approximated to 100 in each stator and rotor in the calculation, and each one passage is computed to save the computational cost, although the number is different in the experiment. Totally six blocks of the grid for stator and rotor channels, and seven blocks for the interaction areas are simultaneously calculated assuming the sliding boundary condition. Each block for the blade rows has 91x91x91 grid points and each block for interaction areas has 46x91x91 grid points.

Table 1 shows the flow conditions. CASE 1 is a dry-steam condition and CASE 2 is a wet-steam condition. In the wet-steam condition, since the working gas is wet at the inlet, condensation is supposed to be in almost equilibrium condition. So I is supposed to be 0. Because the number density of the droplets at the inlet

in the experiment is difficult to count, the value is assumed to be $1.0 \times 10^{14} [1/m^3]$ in this study.

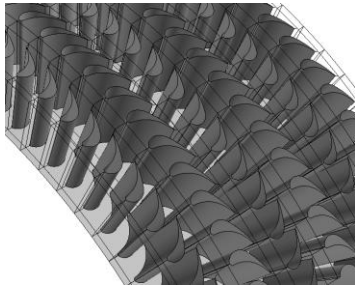


Fig. 1 Perspective view of the computational grid.

Table 1 Flow conditions.

	CASE 1	CASE 2
Inlet total pressure[MPa]	0.353	0.330
Outlet static pressure[MPa]	0.179	0.172
Inlet total temperature[K]	470.3	409.3
Inlet wetness[%]	0	4.8

4.Results and Discussion

Figures 2 and 3 show the yaw angles of flow velocity vectors of CASE 2 at the outlet of the 1st rotors and the 2nd rotors, respectively. These values are time-wise and span-wise averaged at the same diameter. The calculated results at 1st rotors are overestimated from the experiments. The reason has not been resolved yet, but it may be due to the approximated number of blades at 1st stage stators and rotors, or due to the inaccurate estimation of inlet wetness. The calculated results at 2nd rotors are in good agreement with those of experiments.

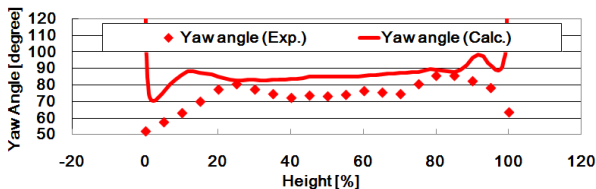


Fig. 2 Yaw angles of flow velocity vectors at the outlet of 1st stage rotors.

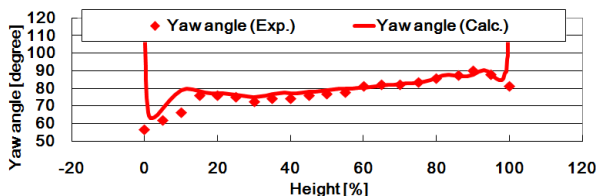


Fig. 3 Yaw angles of flow velocity vectors at the outlet of 2nd stage rotors.

Figure 4 shows the calculated instantaneous unsteady condensate mass fraction contours at the outlet cross section of the second-stage rotor blade rows. At the region A, the condensate mass fraction is relatively high, and at the wake region B, that value is relatively low because of the boundary layer. Lower condensate regions are also found at both shroud and hub corners C. These regions are corresponding to the regions with

corner vortices. The point with the lowest value coincides with the core of the vortex. These results indicate that the centrifugal force induced by the vortex flies heavier water droplets to the outer of the vortex. In addition, lower condensate regions are found near the shroud and the hub at the region D. These regions may be influenced by the corner vortices incoming from the prefaced stator blade rows.

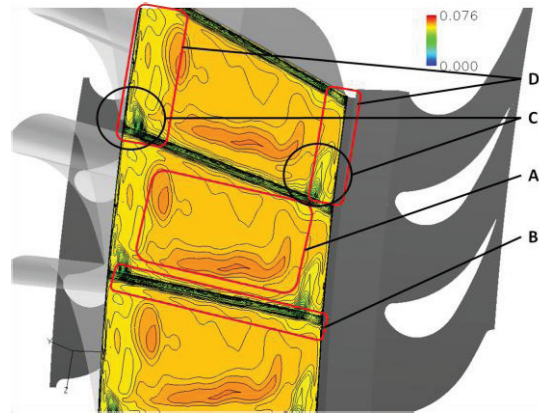


Fig. 4 Calculated instantaneous condensates mass fraction contours at a cross section of outlet of the 2nd rotor.

5.Conclusions

Flows through the three-stage stator-rotor blade rows in the low-pressure steam turbine model developed by MHI were numerically investigated. Calculated results were partially in good agreement with those of experiments. It is found that Wetness distributions were strongly affected by the corner vortex and wakes. We may need to consider the number of blade more accurately and to estimate correct inlet wetness to get more accurate results which is more in good agreement with the experiments.

References

- [1] Yamamoto, et al., Numerical and Experimental Investigation of Unsteady 3-D Wet-steam Flows through Two-stage Stator-rotor Cascade Channels, Proc. ASME Turbo Expo 2010, GT2010-22796, (2010).
- [2] Miyake, et al., Simulation of Unsteady 3-D Wet-Steam Flows through Three-Stage Stator-Rotor Cascade Channels with Equilibrium and Nonequilibrium Condensations, Proc. ASME Turbo Expo 2012, GT2012-68828, (2012).
- [3] Menter, F.R., Two-equation Eddy-viscosity Turbulence Models for Engineering Applications, AIAA Journal, 32-8(1994), 1598-1605.
- [4] Ishizaka, et al., High-Resolution Finite Difference Scheme for Supersonic Wet-Stream Flows, Proc. 6th Int. Symp. on Computational Fluid Dynamics, 1(1995), 479-484.
- [5] Frenkel. J., "Kinetic Theory of Liquids", (1955), Dover.
- [6] Gyarmathy G., Z. Angew Math. Phys., 14-3 (1963), 280-293

Statistical Properties of Two-Dimensional Decaying Weakly Compressible Turbulence

Daiki Terakado¹, Yuji Hattori²

¹Department of Applied Information Sciences, Graduate school of Information Sciences, Tohoku University
Aramaki aza Aoba 6-3-09, Aoba-ku Sendai Miyagi, 980-8579, Japan

daiki@dragon.ifs.tohoku.ac.jp

²Institute of Fluid Science, Tohoku University

ABSTRACT

Compressible turbulence appears in a wide range of flows, especially in aerospace field. However, compressible turbulence has been less understood than incompressible turbulence. In this study we carry out direct numerical simulations (DNS) of weakly compressible turbulence as a first step to clarify the whole picture of compressible turbulence. It is found that the sheet structures in the density field appear for the case with non-uniform initial entropy distributions. Moreover, the amplitudes increase with Mach number.

1. Introduction

There are various types of flows in nature, most of which are turbulent. For example, oceanic and atmospheric flows are often turbulent. Flow around vehicles such as aircrafts, cars and trains are also turbulent. Since compressibility has important effects in high speed flow in aerospace, we have to consider compressible effects on turbulence for these flows. However, the effects of compressibility on turbulence have not been fully understood yet. In this study, we investigate two-dimensional weakly compressible turbulence by DNS. Devoting our attention to the weakly compressible case enables us to study compressible effects without shock waves. Moreover, in two dimensions it is easier to simulate high Reynolds number flow than in three dimensions. Thereby we can study the effects of compressibility in detail. The results of this study would be useful in studying more complex transonic or subsonic flows in which shock waves occur.

So far, some researchers have investigated weakly compressible turbulence. Shaikh et al.^[1] carried out two-dimensional nearly incompressible hydrodynamic simulation and showed inertial ranges for direct cascade of the energy and density spectrum which are proportional to k^{-3} . Samtaney et al.^[2] investigated three-dimensional compressible turbulence using DNS and found that the effects of initial conditions on the statistics of kinetic energy are negligible. However, the spatial resolutions of those studies were low. We have carried out DNS of two-dimensional compressible turbulence with higher resolution than previous studies and found that initial non-uniform entropy distribution creates sheet structures in the density fields.^[3]

In this paper, we study the properties, especially Mach number dependency, of the sheet structures in detail.

2. Method

2-1. Equation

The compressible Navier-Stokes equations in the following form are used

$$\frac{\partial \rho}{\partial t} + \nabla \cdot \mathbf{m} = 0, \quad (1)$$

$$\frac{\partial \mathbf{m}}{\partial t} + \frac{1}{2} \frac{\partial m_i u_j}{\partial x_j} + \frac{1}{2} (\mathbf{m} \cdot \nabla) \mathbf{u} + \frac{1}{2} (\nabla \cdot \mathbf{m}) \mathbf{u} = -\nabla p + \frac{\partial \tau_{ij}}{\partial x_j}, \quad (2)$$

$$\frac{\partial p}{\partial t} + \mathbf{u} \cdot \nabla p + \gamma p \nabla \cdot \mathbf{u} = (\gamma - 1) \nabla \cdot (\kappa \nabla T) + (\gamma - 1) \phi, \quad (3)$$

where ρ is density, \mathbf{m} is momentum, \mathbf{u} is velocity, p is pressure, τ_{ij} is viscosity stress tensor, γ is ratio of specific heat, κ is thermal conductivity, T is temperature and ϕ is viscosity dissipation.

2-2. Numerical Method

Eqs. (1)-(3) are discretized by Fourier collocation spectral method on a doubly periodic square domain of side $L_x=L_y=2\pi$ with spatial resolution $N=1024^2$. We use the 4th-order Runge-Kutta method for time marching. We normalize the physical quantities by the initial speed of sound, the length 2π , and the initial density.

2-3. Initial Condition

The initial velocity field is solenoidal

$$\nabla \cdot \mathbf{u} = 0, \quad (4)$$

with three different values of mean Mach number $M=0.05, 0.1$ and 0.2 . We set the initial kinetic energy spectrum as

$$E(k) = \lambda_2 k \exp(-k^2/k_0^2), \quad (5)$$

where k is wave number, k_0 is the wave number at which the spectrum is maximum, and λ_1, λ_2 are constants chosen to obtain the specified values of initial kinetic energy.

We also consider two types of the initial density and pressure fields: A: Non-uniform entropy distribution; and B: Uniform entropy distribution.

A: Non-uniform entropy distribution

With the solenoidal velocity field, the Poisson equation for pressure is obtained by taking the divergence of the momentum equations. Density

distribution is set to 1.0 uniformly.

$$\nabla^2 p = -\rho_0 \frac{\partial u_i}{\partial x_j} \frac{\partial u_j}{\partial x_i}, \quad \rho_0 = 1. \quad (8)$$

B: Uniform entropy distribution^[3]

If the initial field is assumed homentropic, the following Poisson equation can be derived using the relation $p/\rho^\gamma = 1/\gamma$ where γ is 1.4.

$$\nabla^2 \left(\frac{p}{\rho} \right) = -\frac{\gamma-1}{\gamma} \frac{\partial u_i}{\partial x_j} \frac{\partial u_j}{\partial x_i}, \quad \frac{p}{\rho^\gamma} = \frac{1}{\gamma}. \quad (9)$$

3. Results and Discussion

The Reynolds number for the direct cascade or enstrophy cascade is given by $R_\lambda = Z^{3/2}/\eta_Z$ where Z is the enstrophy and η_Z is the enstrophy dissipative rate. In this calculation, $R_\lambda \approx 50$ at $t=70$ for $M=0.1$.

We show the density field for $M=0.1$ in Fig.1. For the non-uniform entropy case (A), sheet structures appear; on the other hand, they do not appear for uniform-entropy case (B).

The appearance of sheet structures leads to difference in the density spectrum. Two modes are observed in Fig.2. The red line is for A, and the green line is for B. The spectrum for case B with homentropic initial condition has an inertial range which is proportional to $k^{-5.6}$; by contrast, the spectrum is flatter for case A with non-uniform entropy.

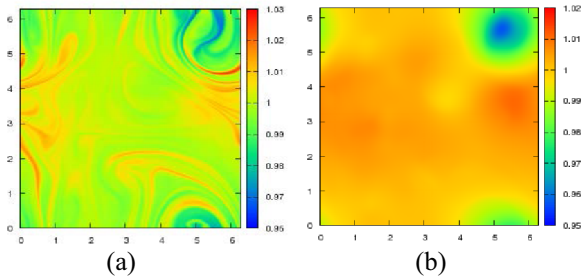


Fig.1 Density field of (a)A, (b)B for $M=0.1$ at $t=70$.

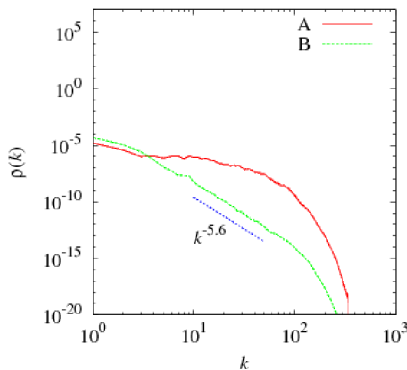


Fig.2 Density spectrum for $M=0.1$ at $t=70$.

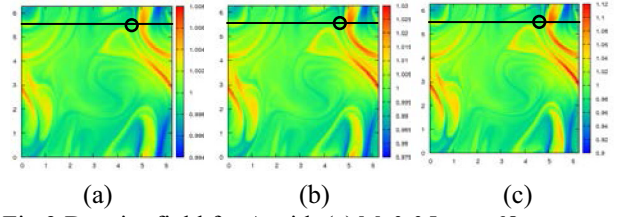


Fig.3 Density field for A with (a) $M=0.05$ at $t=68$, (b) $M=0.1$ at $t=34$, (c) $M=0.2$ at $t=17$.

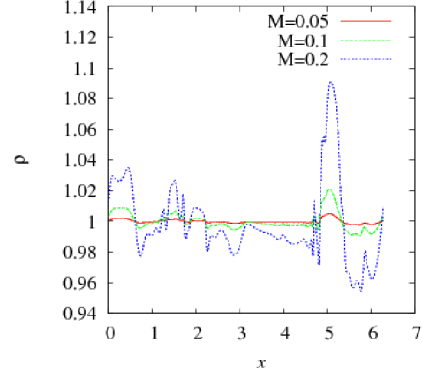


Fig.4 Cross section of Fig.3 at $y=5.5$

In order to study the effects of Mach number on the sheet structures, we choose three values of initial mean Mach number $M=0.05, 0.1$ and 0.2 . Fig.3 shows density fields for non-uniform entropy case A with different Mach number.

In Fig.3, we choose $t=68$ for a reference time of $M=0.05$, and then choose each time to be inversely proportional to Mach number. Three figures have similar distributions, so the time development of sheet structures is in proportion to Mach number.

The cross section of Fig.3 at $y=5.5$ is shown in Fig.4. Focusing on around $x=5$, we confirm the amplitudes of sheet structures increase with Mach number. On the other hand, the differences of widths are negligible. Therefore, the amplitudes of sheet structures depend on Mach number, but the widths do not.

4. Concluding remarks

We carried out DNS of two-dimensional decaying weakly compressible turbulence. We confirmed that non-uniformity of initial entropy field creates sheet structures in density field. In addition, it is found that the time development and amplitudes of the sheet structures depend on initial mean Mach number.

References

- [1] D. Shaikh and G. P. Zank. *Astrophys. J.*, **602**(2004), pp.29-32.
- [2] R. Samtaney, D. I. Pullin, and B. Kosovic, *Phys. Fluids* **13** (2001), pp.1415-1430.
- [3] D. Terakado and Y. Hattori. in the Abstract Book of the 9th European Fluid Mechanics Conference.

Study on Flame Stabilization in Curved Wall Jet Burner with Time Resolved OH-PLIF and PIV

Alaa Dawood, Morkous Shoukry Mansour, Suk Ho Chung
Clean Combustion Research Center,
King Abdullah University of Science and Technology,
Thuwal 23955-6900, Kingdom of Saudi Arabia
sukho.chung@kaust.edu.sa

ABSTRACT

The stabilization characteristics and structure of premixed flames at the exit of an axisymmetric curved-wall jet burner have been experimentally investigated. Simultaneous time resolved measurements of flame and flow structure at different mixtures and burner configurations were carried out using 10 KHz OH-PLIF and Stereoscopic Particle Image Velocimetry (SPIV). The continuous mapping of the reaction zone, traced by the existence of OH radicals, using the high speed PLIF system shows that small islands of burned gasses detach from the recirculation region and move downstream. Such pockets work as a stream of ignition sources for downstream unburned gasses.

1. Introduction

Different techniques can be implemented to stabilize the premixed flames by creating a recirculation zone to provide a sufficient residence time for active radicals [1]. These include a bluff body, sudden expansion of a combustor wall and swirl or jet-induced recirculating flows. A special jet technique was investigated in the current study using simultaneous measurements of flow velocity and flame front tracer. Using this technique, the Coanda effect [2, 3] is exploited to create a recirculation zone, enhancing the flame stabilization, air-fuel mixing and subsequently flame height control [4]. Limited applications of this effect in combustion were found in the literature [4, 5, 6 and 7].

Higher turbulence intensity in the interaction jet region was generated controlling the degree of strain rate and consequently flame intermittence. Different burner tip configurations were employed to improve flame stabilization. Higher blow-off velocity and smaller flame height were achieved as compared to a tube jet burner. Moreover, flashback could be eliminated by changing jet velocity through slit height adjustment. Thus the goal of the present work is to investigate the current burner flame stability characteristics and its structure as well as the flow field interaction using time resolved SPIV and OH-PLIF.

2. Experiment

The experimental apparatus is shown in Figure 1, a curved-wall jet burner with different tips. It is fully described in detail in [4,5]. These different semi-sphere tips associated with different concave shapes were employed. Two concave parts of 16 and 24 mm diameter with 3.37 mm depth were used. Mixture of air and propane is injected along the annular gap.

Stereo PIV could be operated at a sustained repetition rate of 10 KHz in the central flow plane. Laser double pulsed (532 nm, 5 ns pulse and 20 μ s pulses separation time) repeating at 1 KHz. The Mie scattered light from TiO₂ particles of 18 μ m nominal diameter was collected into two Imager Pro HS 4M CMOS cameras using a 105 mm focal length.

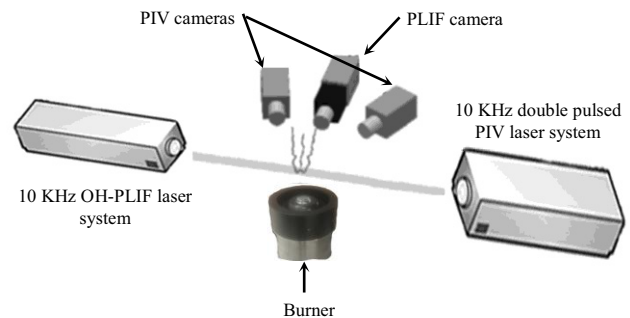


Fig. 1 Schematic diagram of simultaneous measurement system for PIV and OH-PLIF.

The SPIV cameras were placed equidistant from the laser sheet to collect a forward and backward scattered light at angles of 45 degree with the laser sheet.

Image sequences of OH-PLIF were acquired in the same plane of the SPIV. The PLIF system used a frequency-doubled dye laser pumped with the frequency-doubled, diode-pumped solid state Nd:Yag laser (Edgewave). The OH radical was excited at 283.574 nm within the laser sheet heaving a height of about 200 mm. In the present study the laser delivered 300 μ J/pulse at 10 KHz and 283.574 nm. fluorescence signal was acquired, at a right angle to the laser sheet, at 10 KHz with a HighSpeedStar 8 CMOS camera and an external two-stage lens-coupled intensifier.

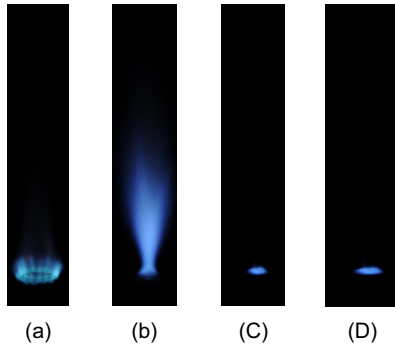
According to different considerations as the required field of view size and OH-PLIF system maximum power output, the SPIV and OH-PLIF systems have to run at the specified frequencies. The SPIV can run faster if a smaller field of view is required. The size of the quartz cuvette, used for OH-PLIF beam profile calibration, put more restriction on the size of field of view.

3. Results and Discussion

Shown in Figure 2 are direct photographs of, stoichiometric air-propane premixed flames at various jet velocities for the two modified semi-sphere tips. As seen before in the previous study [5], concave tip, over the flat tip, enrich flame stabilization through the enhancement of the role of recirculation zone. Moreover,

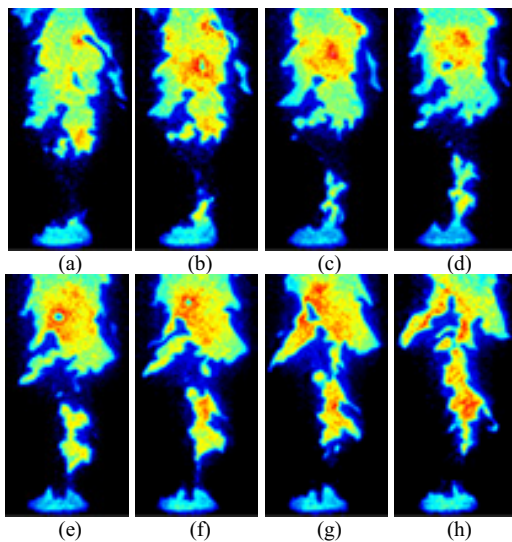
it can be shown that the larger concave tip provided larger recirculation zone and consequentially a more stabilized flame where larger jet velocity can be adopted and blow off limits increased significantly.

Fig.2 Direct photographs of stoichiometric air-propane premixed flames, for concave tip with 16 mm diameter at jet velocity of (a) 2.05, (b) 5.6 and (c) 9.86 m/s while (d) is for concave diameter of 24 mm at jet velocity of 38 m/s.



A sequence of typical OH border flame, captured at 10 KHz, is presented in Figure 3. The high speed imaging of the flame contour enables the tracing of the initiation and development of the isolated OH pockets detached from the recirculation zone and moving downstream. This provides an ignition source to the downstream unburned gasses and enhances flame stability. The recirculation zone provides a continuous stream of isolated flamelets. This phenomenon was not detected in the previous study as a low frequency OH-PLIF system was employed and considered as extinction and re-ignition phenomenon.

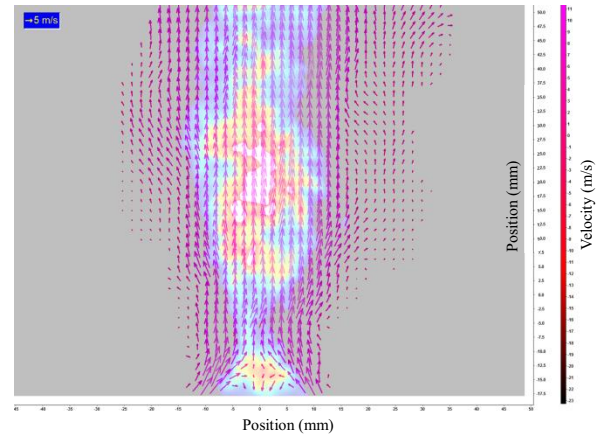
Fig. 3 (a-h) Sequence of OH-PLIF images at the rate of 10 KHz $\phi=1.6$ and $Re=18650$.



Shown in Figure 4 are the instantaneous images of simultaneously measured SPIV and OHPLIF for a representative case. The corrected PLIF image is overlaid with the three-component velocity-field measurements.

The first two components are represented by vector field; the absolute velocity magnitude is represented by the vector line lengths, while vector color represents the third velocity component (through-image-plane). This facilitates studying the local effect of flow on flame structure and vice versa. The recirculation zone and the collision of inwardly injected axisymmetric curved-wall jets can be obviously observed.

Fig.4 simultaneous SPIV and OH-PLIF images for the case of 24 mm concave diameter, $\phi=1.6$ and $Re=18650$.



4. Concluding remarks

Time resolved SPIV and OH-PLIF can provide valuable means to study flame-flow interaction phenomena. It has been shown that the detached flamelet from the recirculation zone ignites downstream unburned gasses. High speed SPIV resulted in finding out the effect of the degree of the strain rate on flame intermittence. The modified burner improved flame stabilization. Maximum blow-off velocity occurs for rich mixtures. The detailed influence of flow field intensity on flame structure will be investigated in the future work.

References

- [1] S. Chaudhuri and B.M. Cetegen, *Combustion and Flame*, 156, 706 (2009).
- [2] R.Wille and H., J. Fernholz, *Fluid Mech.* 23, 801–819 (1965).
- [3] P.W Carpenter and P.N. Green, *J. Sound Vib.*, 208, 777 (1997).
- [4] Y. S. Gil, H. S. Jung, and S. H. Chung, *Combustion and Flame*, 113, 348–357 (1998).
- [5] D. Kim a, Y. S. Gil b, T. W. Chung c & S. H. Chung, *Combust. Sci. and Tech.*, 18, 1397–1412 (2009).
- [6] M.M. Vahdati, and P. O’Nions, *J. Inst. Energy*, 7, 12 (2000).
- [7] A.G. Gaydon and H.G. Wolfhard *Flames*, 4th ed., Chapman and Hall, New York, 169 (1979).

Deflection and Orientation Measurement of Moving Delta Wing Using Photogrammetry

K. S. N. Abhinav Kumar, Tatsuya Hara, Takahiro Ito, Daiju Numata, Keisuke Asai
6-6-01, Aramaki Aza-aoba, Aoba-ku, Sendai, Miyagi, 980-8579, JAPAN
Dept. of Aerospace Engineering, Tohoku University
abhinav.kumar@aero.mech.tohoku.ac.jp

ABSTRACT

Experimental study of a delta wing with sweep angle of 80° and thickness of 3 mm is done in forced rolling motion and dutch-roll motion is carried out to determine the deflections and orientations using photogrammetry and force measurements using force balance. The photogrammetry results show that the orientation of the model changes under wind-on condition due to the aerodynamic forces acting on it. The model primarily bends along its length and the bending along the span-wise direction is negligible. Also it is observed that bending of the sting support contributes to the orientation change of the model.

1. Introduction

In dynamic wind tunnel testing determining the exact orientation of the model in wind-on testing is important as the orientation may change due to the aerodynamic forces acting on the model. This exact orientation can be determined by using sensors such as inclinometers in the model or by using photogrammetry. Placing of inclinometers in the model may not be possible in all cases and they are not sensitive to yaw. So usage of photogrammetry is more useful as it is accurate and non-intrusive.

Photogrammetry has been used to determine the deflections in static wind tunnel testing for some time[1][2]. These results show that deformation measurements and orientation measurements can be achieved with high accuracy using photogrammetry. In the present work to determine the actual orientations of a delta wing model, of leading edge sweep angle of 80° , in motion is determined using photogrammetry.

2. Experimental setup and method

Experiments were conducted in the Low Turbulence Wind Tunnel of Tohoku University. The model is mounted in the wind tunnel by using the robotic arm as shown in the Fig. 1. This robotic arm (MHI PA-10 Serial Robot Manipulator) is used to fix the model in a certain position or move the model in a pre-determined manner.



Fig. 1 Delta wing mounted using robotic arm

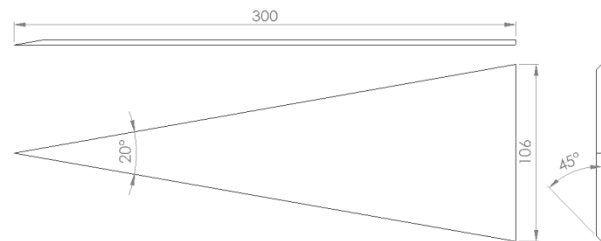


Fig. 2 Delta Wing

The model was tested at different velocities of 10 m/s, 20 m/s and 30 m/s. Forced rolling of $\pm 30^\circ$ at a frequency of 1 Hz and at angles of attack of 30° and 35° is observed at given velocities and wind-off conditions. Also dutch roll motion with rolling of $\pm 30^\circ$ and yaw of $\pm 5^\circ$ at a frequency of 1 Hz and at angles of attack of 30° and 35° is also observed.

The dynamic motion is done by moving the robotic arm to simulate the motion. The model used for this study is a delta wing (Fig. 2) of $\Lambda = 80^\circ$ sweep angle with a root chord of $c = 300$ mm and a span of $b = 106$ mm. The thickness of the model tested is 3 mm. The model has a beveled leading edge on the windward side to give it a sharp leading edge.

The deflection measurements are done by using photogrammetry. Two high-speed video cameras (Basler Ace acA2000-340km) are mounted at the top of the frame as shown in the Fig. 1. These cameras have a resolution of 2040×1088 pixels with bit depth of 8 bit at a speed of 340 fps. Though for experiments 50 fps speed is used. The lens used for these experiments are PENTAX 1218A, at a fixed focal length of 12.5 mm and the aperture of 1.8. The lighting conditions used are the room lighting, which is sufficient for detecting high contrast imaging targets and the image exposure time was set to 1 ms.

Firstly, the cameras are calibrated using Zhengyou Zhang's method[3]. In this camera calibration method a planar checker board is held at different positions and images are taken by both the cameras in a synchronized manner. Using these images the cameras are calibrated individually and after the individual calibration they are calibrated again simultaneously to determine the camera parameters with respect to each other.

After calibration of cameras the model is tested by moving the robotic arm to simulate the dynamic

pitching. A single signal generated from the robotic arm is used to trigger the cameras. This will give a synchronized image sequence capturing of the motion. Using target markers of 4 mm diameter the deflections of the corresponding target markers are found by using photogrammetric principles on the images taken by the two cameras. The procedure of coordinate determination is well known and given in literature[1][2]. The coordinate measurement is done by determining the image coordinates of the target markers using both the cameras as shown in Fig. 3. After that using the camera parameters and the collinearity equations, Eqs. 1 & 2, of the two cameras, the 3D-coordinates of the target markers can be determined.

$$x_n - x_p + dx = -c \frac{m_{11}(X_n - X_c) + m_{12}(Y_n - Y_c) + m_{13}(Z_n - Z_c)}{m_{31}(X_n - X_c) + m_{32}(Y_n - Y_c) + m_{33}(Z_n - Z_c)} \quad (1)$$

$$y_n - y_p + dy = -c \frac{m_{21}(X_n - X_c) + m_{22}(Y_n - Y_c) + m_{23}(Z_n - Z_c)}{m_{31}(X_n - X_c) + m_{32}(Y_n - Y_c) + m_{33}(Z_n - Z_c)} \quad (2)$$

where (x_n, y_n) are the image coordinates of the target markers with 3D coordinates of (X_n, Y_n, Z_n) , (X_c, Y_c, Z_c) are the position coordinates of the cameras, m_{11} to m_{33} are the rotational matrix elements of the camera orientation parameters, c is principal distance of the camera (x_p, y_p) is the principal point, and dx, dy are the distortion terms

Now using the 3D-coordinates of the target markers from wind-off and wind-on condition the deflections are determined. The flow chart for the deflection measurement is given in Fig. 4.

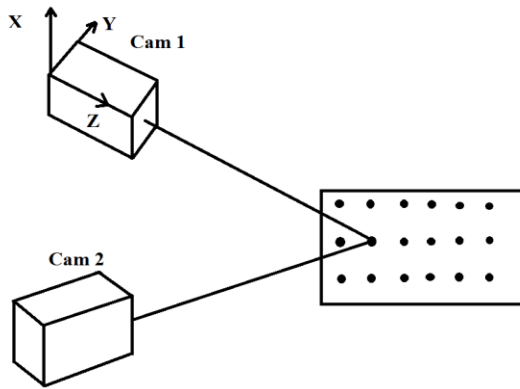


Fig. 3 3D coordinate measurement

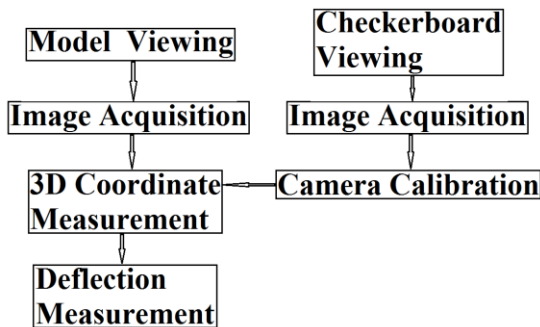


Fig. 4 Flow chart for deflection measurement

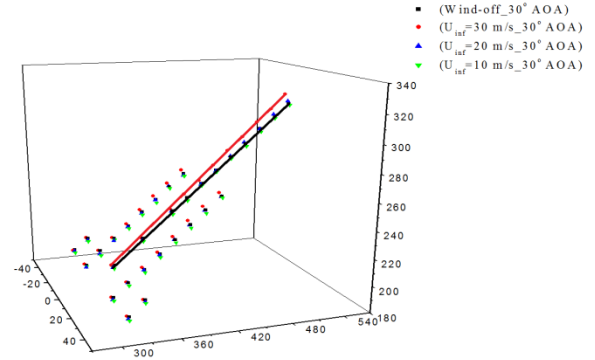


Fig. 5 Deflection measurement

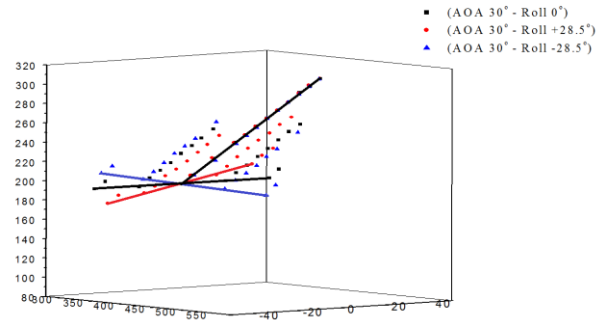


Fig. 6 Orientation measurement

3. Results and Discussion

The deflection measurements of the initial position of the delta wing are shown in Fig. 5. The positions of the markers for different velocities are given. From this result we can see that the deformation of the delta wing is minimum and the model is changing orientation due the deflection of the sting as the root chord is not deforming. The orientation of the model in forced rolling is measured using photogrammetry and is shown in the Fig. 6.

4. Concluding remarks

Deflection measurements and orientation measurements in dynamic wind tunnel have been done in dynamic wind tunnel testing. Also it is seen that there is orientation change of the model during wind-on conditions due to the bending of the sting.

References

[1] Ruyten, W., Sellers, M. E., "Demonstration of Optical Wing Deformation Measurements at the Arnold Engineering Development Center," 47th AIAA Aerospace Sciences Meeting Including The New Horizons Forum and Aerospace Exposition, 5 - 8 January 2009, Orlando, Florida.

[2] Tianshu Liu, L. N. Cattafesta III, and R. H. Radeztsky, "Photogrammetry Applied to Wind Tunnel Testing," AIAA Journal, Vol. 38, No. 6, pp. 964-971, June 2000.

[3] Z. Zhang, "Flexible Camera Calibration By Viewing a Plane From Unknown Orientations," International Conference on Computer Vision (ICCV'99), Corfu, Greece, September 1999, pp. 666-673.

A Novel Approach of Microwaves on Remote and Nondestructive Detection of both Gradual and Abrupt Wall Thinning inside a Metal Pipe

Linsheng Liu, Kota Sasaki, Noritaka Yusa, and Hidetoshi Hashizume.

Department of Quantum Science and Energy Engineering, Graduate School of Engineering,
Tohoku University, 6-6-01-2, Aramaki Aza Aoba, Aoba-ku, Sendai, Miyagi, 980-8579, Japan.

E-mail of corresponding author: linl@karma.qse.tohoku.ac.jp.

ABSTRACT

The authors have previously proposed microwave nondestructive testing (NDT) method on detecting pipe wall thinning (PWT) with an abrupt diameter-change interface. However, PWT with a gradual diameter-change interface is a more general condition at practical industrial pipelines. Here we focus on establishing a novel microwave NDT method that not only can remote NDT of PWT under these two kinds of conditions but also can distinguish them through extracting and analyzing their corresponding characteristic signals. This work is an original attempt to remote image the shapes of PWT defects inside a long distance metal pipe using microwaves.

1. Introduction

Metal pipes are widely used in industries, such as oil and gas transportation, chemical industry, and power plants. Many pipes have been in service for more than half a century, and accidents took place frequently all around the world from twenties years ago in these pipelines. Among the problems, pipe wall thinning (PWT) is one of the prime culprits. As piping systems are generally complicated and long, efficient detection and quantitative evaluation of the PWT location and degree (depth and length) are quite important issues for effective maintenance and lifetime prediction of pipelines so as to economically avoid severe accidents and ensure a safe working environment.

During recent years, X-ray, ultrasonic, electrical potential drop, and eddy current method have been used for solving the PWT problem. However, all of them attenuate fast and can only used for local examination. Ultrasonic guided wave was then adopted for long-distance inspection of piping systems [1]; however, the test results are relevant to the pipes' surrounding conditions such as outer support, weld, and the buried conditions. Since a metal pipe can be taken as a circular waveguide of microwaves, microwave NDT has been utilized to solve the PWT problems [2-7]. However, these method mainly used for PWT defects having an abrupt diameter-change interface, which happens much less than a gradual PWT interface in practical use. In our former research [7], although some experimental approach and evaluation results for PWT with a gradual wall thinning interface have been presented, the inverse problem to distinguish PWT shapes from the signals is a little far to accomplish at that stage.

In this work, we focus on analyzing the more practical PWT condition with a gradual diameter-change interface, and aim to establish a relationship between the reflection signal and the PWT interface. It is based on our former research that the reflection impulse for an abrupt PWT interface contains response resolution information, which is equal to the 50% (-6.0206 dB) points of the reflection peaks [8,9]. By comparing the response resolution evaluated using the pipe under test (PUT) with the one evaluated using a reference PWT specimen having an abrupt PWT interface, the shape of the PWT interface of the PUT can be qualitatively (and possible to be later quantitatively) evaluated. This work is a primary and original attempt to using microwaves for remote imaging of the shape of a

PWT defect located inside a long distance metal pipe.

2. Method

Figure 1 shows the overall schematic diagram of the experimental approach, during which the vector network analyzer (VNA) E8383B (Agilent Tech.) is utilized for generating and receiving microwave signals, and a T&R coaxial line adaptor is used as a bridge to introduce the signals to the pipe under test (PUT). Because it is a little difficult to machine the inner surface of a long pipe, the PWT of different degree and condition are approached by setting short pipe joints (with artificial flaws) in turn between two long pipes in a sandwich structure. The two long pipes have inner and outer diameters of 19.0 and 25.0 mm, and lengths of 1000.0 and 750.0 mm.

During the experiment, two joints with different inner diameters are used for simulating pipes with abrupt PWT interface with different PWT degrees, and another three joints having gradual PWT (using two 1/4 ellipses to approach the PWT edge [7]) of different length and degree are used together to test the effectiveness of this method. The sketch maps of joints are shown in Fig. 2. The former two specimens are numbered as A1 and A2, and the later three ones are numbered as B1 to B3. Detailed information of these five joints is shown in Table 1. The lengths of these joints ranged from 40 to 80 mm, and all of the PWT defects used here are axially symmetrical. The two long pipes together with the joints are utilized to construct long pipes under different PWT conditions.

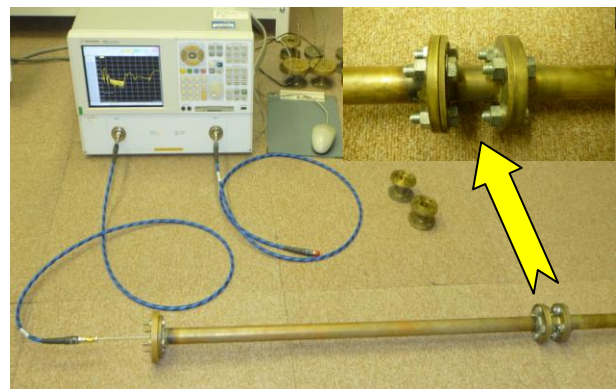


Fig. 1 Overall schematic diagram of experimental setup

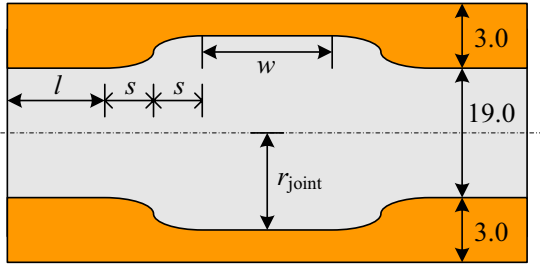
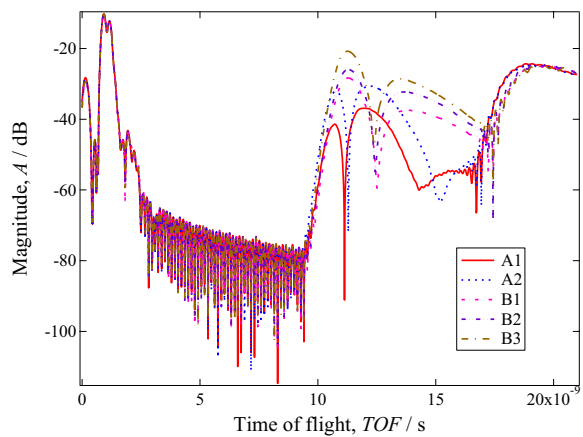


Fig. 2 Sketch map of the joints for simulating PWT

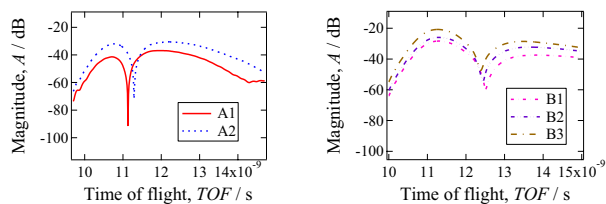
Set the “sweeping points” to be 1601, and calibration and then measure the PUT using the VNA working at S11 mode. Using the frequency range between the cutoff frequencies of dominant TM_{01} mode and the first high order TM_{11} mode, i.e., 12.1 to 19.2 GHz.

3. Results and Discussion

When the VNA works at S11 mode, time domain measurement (TDM) results have been obtained and shown in Fig. 3, in which Fig. 3(a) shows together all of the TDM results for PWT defects with both abrupt and gradual wall thinning interface. It can be easily found that the reflection peaks of abrupt PWT defects (using joints A1 and A2) are much narrower and sharper than the gradual PWT defects (using B1 ~ B3). To show the results clearer, enlarged figures for results of both of the two kinds of PWT interfaces are shown in Fig. 3(b) and (c), respectively.



(a) TDM results of all specimens



(b) TDM of abrupt PWT (c) TDM of gradual PWT

Fig. 3 TDM results of different PWT conditions

Table 1. Geometry of joints used to simulate PWT

No.	Add. length, $2l$ (mm)	Semi-major axis, s (mm)	Length, w (mm)	Inner radius, r_{joint} (mm)
A1	0	0	40	9.7
A2	0	0	40	10.0
B1	35	2.5	35	11.2
B2	30	5	30	11.4
B3	30	5	30	11.5

Moreover, when using the method mentioned in the introduction [8,9], response resolution which is relevant to the sharpness of the impulse (reflection peak) can be easily evaluated from the results shown in both Fig. 3(b) and (c). The evaluated response resolutions from A1 and A2 are similar and they are much higher than ones obtained from Fig. 3(c) of B1 ~ B3. The best response resolution is obtained from the abrupt PWT, and we can use this rule for reference. Thereafter, the degree of difference on evaluated resolution from this best one can be used for estimate the sharpness of the PWT interface.

4. Concluding remarks

Pipe wall thinning is severe defect in ageing metal pipes employed in industry. While our former models on microwave NDT of PWT are a little simple when mainly studying PWT with a sharp diameter-change interface. Because wall thinning with a gradual diameter-change interface is a much more situation, we have proposed a microwave NDT method that can not only remote test and evaluate PWT locations and degrees but also be capable of remotely obtaining information of the profile and shape of PWT defects. This work is potential for more practical application in PWT detection.

Acknowledgement

This work was supported by the Tohoku University Global COE Program - World Center of Education and Research for Transdisciplinary Flow Dynamics, and supported by Grait-in-Aid for Young Scientists (23760684).

References

- [1] H. Nishino, M. Takemoto and N. Chubachi, *Appl. Phys. Lett.*, **85** (2004), 1077.
- [2] K. Sugawara, H. Hashizume and S. Kitajima, *JSAEM Studies. Appl. Electromag. Mech.*, **10** (2001), 313.
- [3] H. Hashizume, T. Shibata and K. Yuki, *Int. J. Appl. Electromag. Mech.*, **20** (2004), 171.
- [4] L. Liu and Y. Ju, *NDT&E Int.*, **44** (2011), 106.
- [5] L. Liu, *EJAM*, **2** (2010), 101.
- [6] L. Liu, Y. Ju, M. Chen and D. Fang, *Mater. Trans.*, **52** (2011), 2091.
- [7] Y. Sakai, N. Yusa and H. Hashizume, *Nondestr. Test. Eval.*, **27** (2012), 171.
- [8] L. Liu, PhD Thesis, <http://hdl.handle.net/2237/16498> (pp. 119-120 of Chapter 5).
- [9] Agilent Tech., Time domain analysis using network analyzer, Application note 1287-12, March 2007.

Development of Ultrafast Time Response Pressure-Sensitive Paint for Visualization of Shock Wave Phenomena

Shota Fujii, Daiju Numata, Hiroki Nagai and Keisuke Asai

Department of Aerospace Engineering, Graduate School of Engineering, Tohoku University
6-6-01 Aramaki Aza Aoba, Aoba-ku, Sendai, Miyagi, 980-8579 JAPAN
fujii.shota@aero.mech.tohoku.ac.jp

ABSTRACT

It is necessary to improve the time response of Pressure-Sensitive Paint (PSP) for applying PSP to high-speed and unsteady aerodynamic phenomena, as represented by shock wave phenomena. Anodized Aluminum PSP (AA-PSP) samples with ever-larger pore diameter were fabricated by using phosphoric acid electrolyte in order to improve response time of PSP. A shock tube was used to evaluate the step time response characteristics. The results show that the obtained data included the effect of the exposure time of a detector, although the response time of the fastest PSP achieved in this study was 1.3 μ s.

1. Introduction

Pressure-Sensitive Paint (PSP) is an optical pressure measurement technique widely used in aerodynamic experiments. PSP has been applied to unsteady shock wave phenomena [1, 2]. However, one of the largest problems to apply PSP to high-speed and unsteady phenomena is the response time of PSP. The response time of PSP has to be much faster than the rate of pressure change caused by phenomena.

Kameda et al. [3] investigated the effect of the luminescence lifetime and gaseous diffusion on the time response of AA-PSP theoretically and the response time to reach 99%, $t_{0.99}$, is given in equation (1).

$$t_{0.99} = 1.8 \frac{h^2}{D_{eff}} \quad (1)$$

where h is the thickness of a binder layer and D_{eff} is the effective diffusion coefficient. The effective diffusion coefficient is proportional to the pore diameter, therefore the response time of AA-PSP is proportional to the square of the pore depth and inversely proportional to the pore diameter.

Hangai et al. [4] investigated the time response of pressure-sensitive paint using porous alumina as a binder, called Anodized Aluminum PSP (AA-PSP), by using a shock tube and concluded that the response time of AA-PSP reduces as the pore depth decreases and the pore diameter increases. The fastest response time achieved in their study was 1.8 μ s. However, further improvement of the response time is necessary in order to measure the pressure fields induced by high-speed and unsteady phenomena more accurately, and there still is much room for further development of faster PSP.

In this study, we fabricated porous anodized aluminum layer with ever-larger pore diameter by using phosphoric acid electrolyte for anodizing in order to develop ultrafast response PSP with O (~ 1 μ s) response time. In addition, the time response characteristics of three AA-PSP samples with different pore depths were evaluated from PSP images obtained by using a shock tube.

2. Experiments

2.1 Sample fabrication

Anodic porous alumina layer can be formed on aluminum surface by an electro-chemical process called

anodization. In this study, pure aluminum (A1050) was used as sample material and its size was 60 mm \times 30 mm \times 5 mm. Phosphoric acid (0.3 mol/l) was used as electrolyte in order to enlarge the pore diameter. The electrolyte temperature was controlled at 30 degrees in Celsius. We changed anodizing time, 10 min, 30 min, 60 min, and three sample plates were fabricated in order to make samples with different pore depths.

Figure 1 shows the SEM images of the sample 1 surface. The pore depths of each sample were measured by using an eddy current film thickness meter (Kett DUALSCOPE MP0R). The pore diameters and depths are listed in Table 1. We successfully fabricated AA-PSP samples with much larger pore diameters than conventional AA-PSP with 18~25 nm pore diameters. We used 1-pyrene butyric acid (PBA) as luminophore which has short lifetime (10 ns).

2.2 Experimental method

Figure 2 shows the experimental setup for the time response test. We used 60 mm \times 150 mm diaphragm-less shock tube at Institute of Fluid Science, Tohoku University. Dry air was used as working gas. The initial pressure in the high-pressure chamber was 240kPa and that in low pressure chamber was 30kPa. Mach number of a shock wave was about 1.5.

PSP sample was placed on the side wall of the shock tube. Emission light from PSP sample can be observed from outside the tube through an optical window. A Xe flash lamp (Nissin electronic co. SHORT ARC POWER FLASH SA-200F) with optical bandpass filter (transparent wavelength 340 ± 50 nm) was used to illuminate the sample. A 12bit cooled CCD camera was used to take the image of luminescence from the sample. An image intensifier (I.I.) (Hamamatsu Photonics C9547MOD) was set in front of the CCD camera as an amplifier of emission intensity and as an electrical shutter. The exposure time was set at 1 μ s. A shortcut filter (over 400nm) was set in front of I.I. to obtain appropriate wavelength of luminescence.

The measurement is started by the arrival of shock wave at an upstream pressure sensor (Kistler 603B). The activations of a Xe flash lamp, an image intensifier, a CCD camera are controlled with appropriate delay time by using a pulse generator and a delay generator. The delay time was determined in consideration of the shock

speed measured by two pressure sensor and the distance between the pressure sensor and the sample and PSP image at the moment shock passes over the sample can be acquired.

2.3 Data analysis

First, the pressure image is calculated from the emission intensity image by using Stern Volmer plot obtained from calibration test conducted with the same setup as the time response test. Second, the horizontal pressure profile is acquired by averaging vertical 600pixels of the pressure distribution image and converting horizontal distance in pixels to real distance. Finally, the pressure profile is converted into time response curve of PSP by dividing the horizontal axis with shock speed.

3. Results and Discussion

Figure 3 shows the pressure distribution in the central part of sample 1 at the moment shock wave passed over the sample plates measured by PSP. Shock wave propagates from left to right and the step change of pressure induced by shock wave can be visualized. Figure 4 shows the time response curve of PSP samples calculated from PSP images. Sample 1 with shallowest pores has the fastest response time and the rise time of sample 1, 2, 3 were respectively 1.3 μ s, 2.2 μ s, 3.5 μ s. We achieved faster response time than ever in this study. However, these results include the effect of exposure time of I.I. because shock wave transfers during this time. Therefore the real response time should be shorter than these values.

4. Concluding remarks

In this study, AA-PSP samples with ever-larger pore diameter were fabricated by using phosphoric acid electrolyte. The step time response characteristics of three samples with different pore depths were evaluated by using a shock tube. The difference of response time of these samples was detected and the fastest response time achieved in this study was 1.3 μ s under the condition that the pore diameter was 180 nm and the pore depth was about 2 μ m This response time included the effect of exposure time of a detector, therefore we plan to exclude the effect of exposure time on the time response characteristics in order to measure response time of PSP more accurately as future work.

References

- [1] Asai, K., et al., The 19th ICIASF, IEEE, Piscataway, NJ, 2000 pp. 25–36, ICIASF, (2001).
- [2] Miura, U., et al., JSSW, Yokohama, Japan, (2006).
- [3] Kameda, M., et al., Rev. Sci. Instrum., (2002).
- [4] Hangai, T., et al., The 10th ISFV, Japan, (2002).

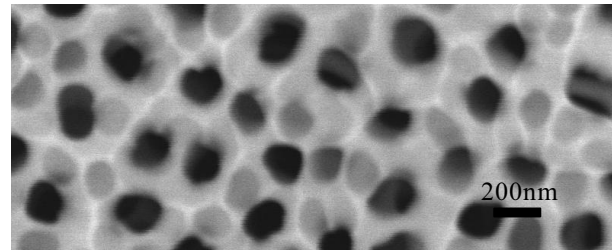


Fig. 1 SEM images of AA-PSP surfaces (Anodizing time is 10 min).

Table 1 Pore diameters and depths of samples.

Sample	Pore diameter[nm]	Pore depth [μ m]
1	180	2
2	190	5
3	220	10

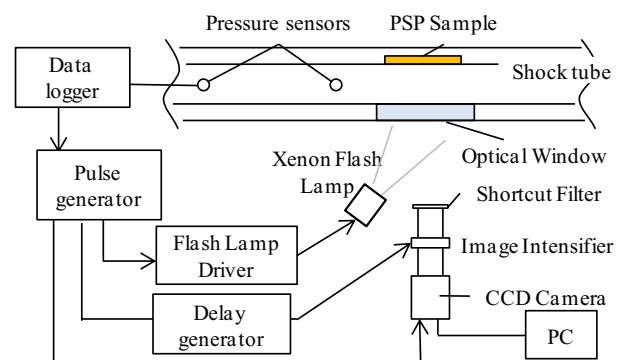


Fig. 2 Schematic of experimental setup.

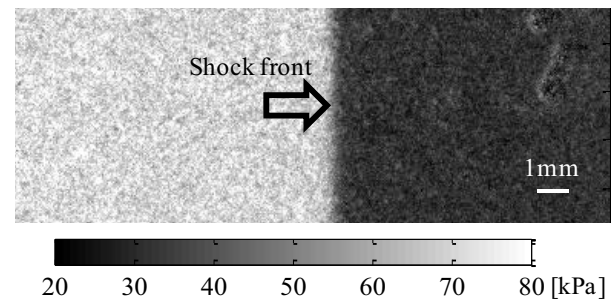


Fig. 3 Pressure distribution images obtained by PSP.

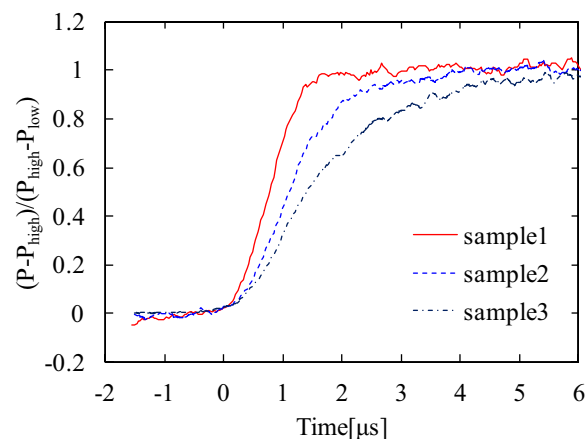


Fig. 4 Time response curves of PSP samples.

The Influence of Air Inlet of Indoor Substation on Cooling and Ventilation Effect

Chenguang Lai¹⁾, Yuting Zhou²⁾, Haibin Xing²⁾ and Limin Fu²⁾

1) Key Laboratory of Manufacture and Test Techniques for Automobile Parts (Chongqing University of Technology),
Ministry of Education, No.69, Hongguang Rd., Banan, Chongqing 400054 P.R. China

2) Chongqing University of Technology, No.69, Hongguang Rd., Banan, Chongqing 400054 P.R. China
chenguanglai@cqut.edu.cn

ABSTRACT

According to a practical example of the indoor substation in Chongqing city, four different inlet arrangements were designed to investigate the influence of air inlet of indoor substation on cooling and ventilation effect. The temperature distribution on the surfaces of the transformer and the flow field distribution in the transformer room were analyzed. Through the comparison and analysis, a recommend inlet arrangement of the indoor substation was proposed.

1. Introduction

With the rapid development of the economy in China, the electric network has penetrated into the city, and the transformer substation in the downtown becomes unprecedentedly dense. Subject to the urban construction, land saving, and especially to the noise control, most of the transformer substation is indoor substation with a narrow room. Because the service life of the power transformer in the substation is mainly determined by its temperature rise in the long-time working situation [1], a better cooling and ventilation effect of the indoor substation is much important to satisfy the temperature requirement of the power transformer.

Yangjiaping substation in Chongqing city is one of the typical indoor substations in the center of the downtown. It faces a big problem in the cooling and ventilation, and over-heat of the main power transformers in summer is the primary problem confining the normal operation of the station.

This study based on the Yangjiaping substation. Several inlet arrangements were designed to investigate the influence of air inlet of indoor substation on cooling and ventilation effect.

2. Method

The digital model was constructed based on the practical structure of the Yangjiaping substation. Necessary simplify was performed to meet the computing requirement. The practical arrangement of the transformer substation, which is defined as case 1 in this study, is shown in Fig. 1 (a), two outlets are located in the roof of the room, and the inlet is placed on one side of the room. Fixing the outlets, 3 different arrangements of the inlet are designed to observe the airflow field in the room and investigate the cooling and ventilation effect. As shown in Fig. 1, case 2 places 8 inlets in four side corners, case 3 places 4 inlets in the ground corners, case 4 places 2 inlets in the ground under the cooling plates. To better compare the cooling and ventilation effect, all these cases have the same total inlet area, as well as the input air, which is obtained by field measurement.

The heat dissipation of the transformer includes radiated heat transfer and convective heat transfer [2]. In

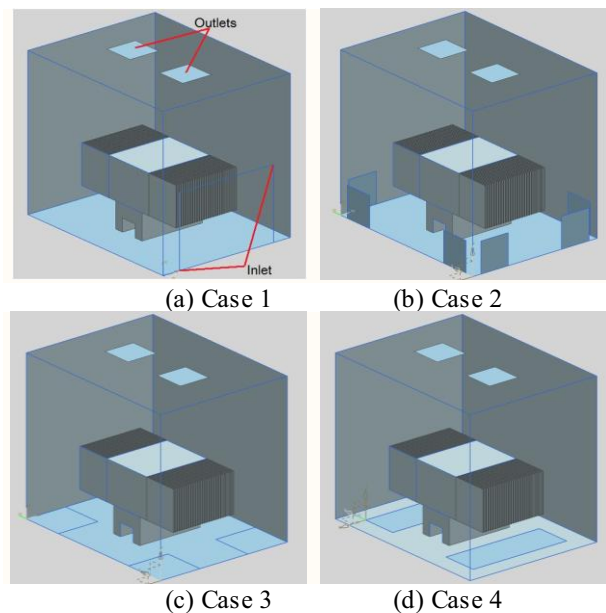


Fig. 1 Different arrangements of the inlets.

these cases, the radiated heat transfer can be calculated by equation (1):

$$Q_f = 5.67 A_r \varepsilon \left[\left(\frac{T_w}{100} \right)^4 - \left(\frac{T_f}{100} \right)^4 \right] \quad (1)$$

here, Q_f is the radiated heat transfer; T_w is the wall temperature of the transformer, T_f is the ambient temperature; A_r is the radiation surface area; ε is the slim emissivity.

In this study, T_w and T_f were obtained through field measurement, and Q_f was calculated to be 8.71 kW.

The convective heat transfer can be calculated by the equations (2) and (3):

$$Q_d = hA(T_w - T_f) \quad (2)$$

$$h = \lambda \bullet Nu / l \quad (3)$$

here, Q_d is the convective heat transfer; h is the convective heat transfer coefficient; A is the convective heat transfer area; λ is the air thermal conductivity; Nu is the Nusselt coefficient; l is the characteristic length, in this study, it is the height of the transformer.

Through the calculation, the convective heat transfer in this substation is 174.87 kW. Therefore, the total heat dissipation of the transformer is 183.58 kW.

Numerical simulations were performed through

ANSYS 13.0. The grid was meshed in Meshing module of the software, and about 8 millions structure cells were generated for each case; the calculations were carried out in Fluent. All numerical simulations were performed on a work station with six processors, equipped with 48 GB of main memory.

3. Results and Discussion

The temperature distribution on the surfaces of the transformer and the flow field distribution in the transformer room were analyzed.

In case 1, the temperature distribution is extremely uneven on the surfaces of the transformer. As shown in Fig. 2, the air in far side of the inlet flows much slower, and the cooling plates in this side cannot obtain sufficient cooling, which makes the surface temperature of the transformer in this side be much higher. The local highest temperature reaches 631 K, and it appears on the bottom outer margin of the cooling plates in far side of the inlet.

In case 2, due to the symmetry of the inlets, the flow field in the transformer room is relatively even, and the ventilation effect of the transformer room is very well. The local highest temperature on the surface of the transformer is 357 K, which is much lower than case 1. This highest temperature appears on the upper outer margin of the cooling plates, and the temperature gradually reduces from side plates to center plates in the shape of “V” (as shown in Fig. 3).

In case 3, as shown in Fig. 4, the air flows well outside of the transformer, but seldom flows through the transformer directly. As results, the cooling and ventilation effect for the cooling plates is very poor. The local highest temperature on the surface of the transformer reaches up to 627 K, and the high temperature area in the cooling plates is also very large.

In case 4, as shown in Fig. 5, the air directly flows through most of the cooling plates, and the airflow passes through the room smoothly, which reduces the energy loss caused by the turbulence and the vortex, and

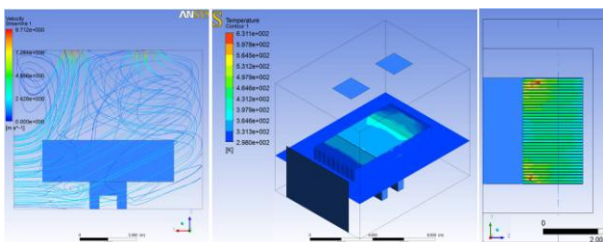


Fig. 2 Streamlines and temperature distribution (case 1).

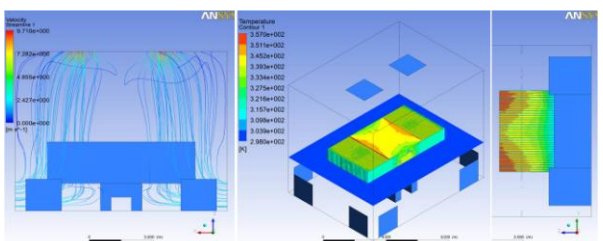


Fig. 3 Streamlines and temperature distribution (case 2).

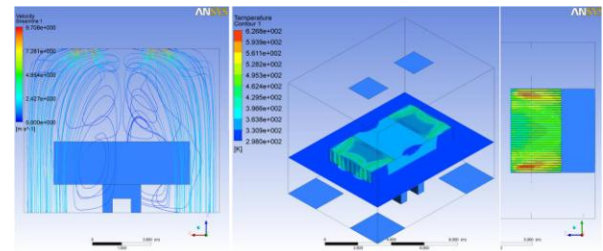


Fig. 4 Streamlines and temperature distribution (case 3).

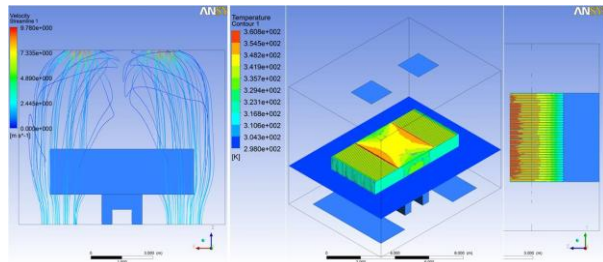


Fig. 5 Streamlines and temperature distribution (case 4).

favors to improve the work efficiency of the draughtfans in the outlets. Well convection takes most of the heat away from the plates, and the local highest temperature on the surfaces of the transformer is 360 K.

Comparing these schemes, case 2 and 4 have much better cooling and ventilation effect than other cases. But in case 2, all the inlets are located in the side corners of the walls, it takes a stricter requirement for the building structure. Moreover, case 2 may face a larger challenge in noise control. Therefore, case 4 is the preferred scheme to arrange the inlet of this substation.

4. Concluding remarks

The following conclusions were made based on the numerical simulation presented here:

- 1) Air inlet is one of the deciding factors affecting the cooling and ventilation effect of substation.
- 2) Placing the inlet in the ground under the cooling plates is a better arrangement for cooling and ventilation.

Acknowledgments

This research is supported by Natural Science Foundation Project of CQ CSTC (CSTC, 2011BB6113), supported by the Key Laboratory of Manufacture and Test Techniques for Automobile Parts (Chongqing University of Technology), Ministry of Education (2010KLMT09).

References

- [1] L. Jin: Analysis on Convection Exchange in Transformer Room, Electric Power Construction, Vol. 8 (2000), pp.19-22.
- [2] M. W. Nanstell et al.: Convection in Undivided and Partially Divided Rectangular Enclosures. Journal of Heat Transfer, Vol.103 (1981), pp: 623-629.

CFD designing on Air Flow Circulation with Branching Perforating Duct and Fan System

Ryuta Ibuki, Masud Behnia

School of Food, Agricultural and Environmental Sciences, Miyagi University, Sendai, Japan

School of Aerospace, Mechanical and Mechatronic Engineering, University of Sydney, Sydney, Australia
ibuki@myu.ac.jp

ABSTRACT

Air mixing performance of branching ducting system in greenhouse was evaluated with computational fluid dynamics (CFD). Numerical model of greenhouse, which has size of 10m×5m×2m, installing ducting system was settled as a simulation model. Simulation conditions were changed by size of holes on duct and fan locations. Large hole and double fan case shows best performance on the special uniformity of the air flow pattern.

1. Introduction

Atmospheric environmental control in greenhouse is utilizing air flow to eliminate spatial distribution about temperature, humidity and CO₂ concentration. Weather condition like air temperature and humidity in Japan have larger annual range compared with that in Western Europe. In Japan branching ducting system is generally utilized in winter to maintain warm and spatially uniform temperature condition with heater with fan but not for humidity controlling. We are aiming to model and evaluate humid season use of the systems which mixes air for humidity averaging in order to avoid fungus propagation especially for the greenhouse of tall product like cucumber. Branching ducting system is suitable to maintain uniform air condition in smaller size greenhouse with less numbers of fans.

On the other hand, Perforating branching ducting system has spatial distributions of pressure and air jet. One of the solutions of the distribution reduction is compression of the inner pressure by adjusting size of holes. However this way induces reduction of mass flow rate. Then fan will work under loading condition, it will reduce life of it and mechanical performance is not fully utilized. Size of holes for air jet has to be decided for the total performance of the system.

This work is in fundamental stage to evaluate the system through Computational Fluid Dynamics (CFD) and measurement. There are some former numerical work reported in literature about ducting system, which is one duct is connected to one ventilator, was contributed by Wells and Amos[1], and Campen et al.[2]. We worked on the branching duct system modeling under the condition of uniform mass flow rate at fans[3]. Arrangement of fan position and numbers influenced flow trend was evaluated. In this work we enhanced former work with involving the performance curve of fan. This change leads increasing the calculation loads of iteration. Then we adapted small size model of greenhouse, which is suit for reduction of the calculation load. Fundamental flow behavior was compared on this simulation under the different arrangement of fans and size of hole for air jet.

2. Method

Air in the numerical model of the greenhouse was settled as simulation domain. ANSYS CFX was utilized

to solve governing equations, continuity equation (eq.1) and the momentum equation (eq.2):

$$\rho \nabla \cdot \mathbf{U} = 0 \quad (1)$$

$$\rho \frac{\partial \mathbf{U}}{\partial t} + \nabla \cdot (\rho \mathbf{U} \times \mathbf{U}) = -\nabla p + \nabla \cdot \boldsymbol{\tau} \quad (2)$$

where ρ is density of air, \mathbf{U} is the velocity vector, t is time, p is static pressure and $\boldsymbol{\tau}$ is shear stress tensor. These equations are discretised to solve by finite element method. Isothermal condition of air at 25°C and constant density was assumed as simulation domain with k- ϵ turbulence model. All cases are compared each other after reaching steady state.

Numerical model structures simulated in this work are shown in Figure 1. Greenhouse, 5m in width, 10m in length and 2m in height, without plants but with the circulation system of fan and ducts are modeled. Two types of fan locations are considered. First structure is single fan model and this is closer to conventional fan location. The other structure is double fan model. This model was adapted to develop a symmetrical air flow in the greenhouse. In these two models, air is sucked into large duct by fan/fans from domain of greenhouse, and then air jets are made at

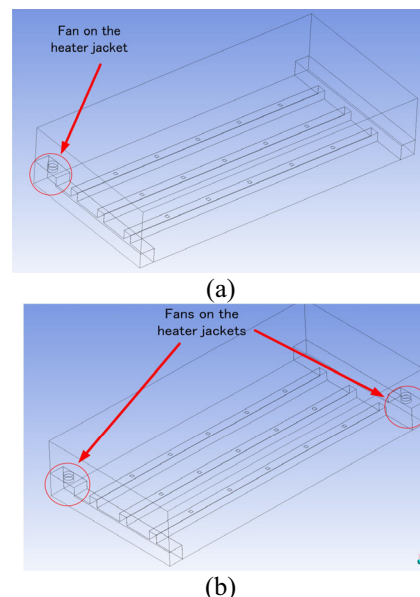


Fig.1 Numerical model of greenhouse installing branching duct and fan. (a) single fan model, (b) double fans model.

square shaped holes on branched ducts. 5holes are opened with 2m of interval on each 3ducts. 2size of the holes, 3cm x 3cm and 10cm x 10cm, are compared in the calculation. Greenhouse was assumed as closed and independent from outer environment to simulate a rainy day. Fan performance curve was considered at fan part in simulation. Normally flow rate of fan changes as function of pressure loss, which caused by resistance of flow pass. To consider this effect, fan performance curve measured by experiment was involved in simulation. Figure shows a fan curve involved in this work, which is assuming collinear approximation.

Meshing scale of this simulation had to make three length scales to simulate flow in this system. At the part of air flows with large velocity gradient have to be made layer of smaller mesh to simulate real flow pattern. Then mesh size are varied at room, ducts and fan walls and ducts part near holes. Representing mesh size are 0.1m on greenhouse, 0.05m on fan and duct walls and 0.005m on duct near holes. Then number of total elements was about 6.5million in this model. This is one of difficulty to calculate the system in full scale greenhouse.

3. Results and Discussion

Figure 2 is comparing vertical air jet velocity distribution of air jet of each case. $Z/H=0$ means surface of duct and $Z/H=1$ means ceiling. LH (large holes) model have a larger velocity along duct surface to ceiling region. LHDF(LH double fan)model has most stable and large velocity model. However, DF model used twice mass flow rate compared to SF(single fan)model. Then, LHDF and LHSF with twice mass flow rate model are compared.

Figure 3 comparing horizontal velocity distributions of the LHDF and LHSFx2 models. LHDF models have uniform distribution made by uniform strength of air jets from all holes. LHSFx2 model has large spatial bias, which is air flow at corner near fan has large velocity compared to opposite corner. These horizontal patterns are concerning dominant 3-dimensional flow pattern in models. Vertical flow like Bénard cells in LHDF and a large horizontal flow like washing machine in LHSF.

Figure 4 shows Share Strain Rate(SSR) distribution along ducts. SSR is utilized to mixing performance. Quite large SSR were observed at lower positions in LHSF model but not in higher positions. Concerning spatial uniformity of SSR, LHDF shows better trend.

Measurement was carried out to obtain fundamental value for calculation and confirmation of effectiveness of this system. Room experiment was also carried out to evaluate validity of this simulation results. Next stage of this work will be a designing of the system in greenhouse with experimental confirmation for real scale.

4. Concluding remarks

Flow pattern with air circulation system using

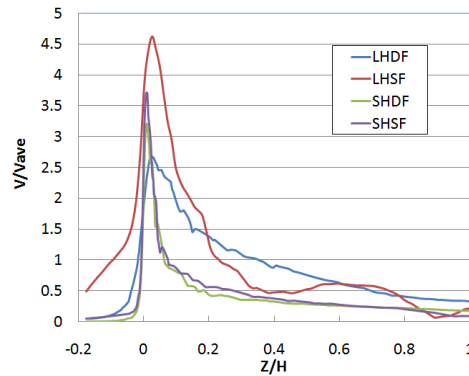


Fig. 2 Normalized vertical velocity distribution of air jet at the Centre hole on the centre duct.

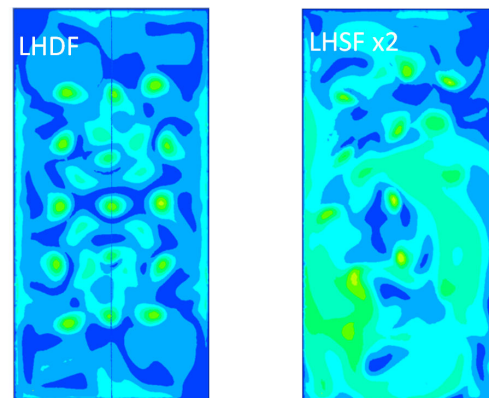


Fig.3 Velocity distribution on horizontal plane at 1m height from duct surface.

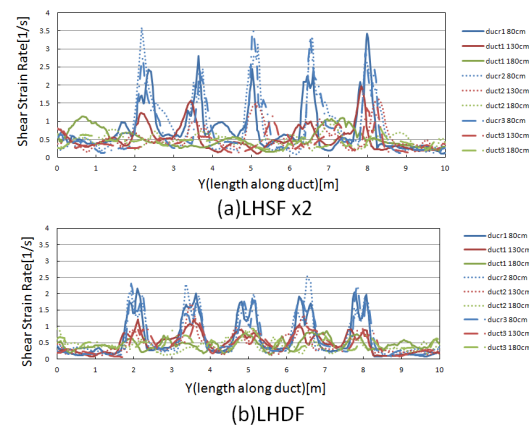


Fig.4 Share Strain Rate distribution along duct.

branching duct and fan installed in greenhouse was evaluated on size of holes and fan location with fan performance curve involving numerical simulation. Large hole with double fan system shows best performance on the spatial uniformity of air flow.

References

- [1] C.M.Wells and N.D.Amos, Acta Horticulture. 361: (1994), 93-104.
- [2] J.B.Campen, et al., BIOSYSTEM ENGINEERING IO2(2009)424-432.
- [3] R.Ibuki, and M.Behnia, 9AHMTC(2011), PIV09.

Effect of Shape of Shield on Sensitivity of Remote Field Eddy Current Testing for Inspecting Flaw of Large Diameter Tube

Jing Wang^{1,2}, Noritaka Yusa¹, Hongliang Pan², Hidetoshi Hashizume¹

¹Department of Quantum Science and Energy Engineering, Graduate School of Engineering, Tohoku University.
6-6-01-2, Aramaki Aza Aoba, Aoba-Ku, Sendai, Miyagi, Japan

²School of Mechanical and Power Engineering, East China University of Science and Technology
200237, Meilong, Xuhui, Shanghai, China

jwang@karma.qse.tohoku.ac.jp

Abstract

This paper studies the effect of shape of shield on the sensitivity of remote field eddy current testing for inspecting flaw of large diameter tube through finite element numerical simulations. The discussions are carried out on the basis of the dependency of change of phase on the depth of flaw. The results show that the higher sensitivity of remote field eddy current testing can be obtained using U-type shield compared to box-type shield.

1. Introduction

Remote field eddy current testing (RFECT) is regarded as one of the most effective non-destructive method for the inspection of tubes because of the similar sensitivity for inner and outer flaws^[1,2]. However in the case of tube with large diameter, carrying out of RFECT is facing up several hindrances, e.g. locating of coils is hardly realized because the inner region of tube is not always accessible and it is difficult to fix large coils encircling the tube from outer side.

Due to the large diameter, it is reasonable to treat big tube as plate. Several groups have successfully reported the applications of RFECT in inspection of plate by experiments and simulations^[3-5], which indicate that large diameter tube can be inspected by setting coils above outer surface of tube. The utilization of shield in their studies enables that magnetic flux propagating along the opposite of plate can be dominant at where is far from exciter. Even though it has been proved that plate can be inspected by RFECT, shield, as a key component and enables the generation of remote filed region, has not been studied in detailed.

In this study, the effect of shape of shield on the sensitivity of remote field eddy current testing for inspecting flaw of large diameter tube is investigated. Two kinds of shield, U type and box type, are studied. Signals due to inner flaw of large diameter tube are analyzed in numerical simulation from view point change of phase.

2. Materials and methods

Figure 1 and figure 2 illustrate finite element models with two kinds of shields used in this study. For these two models, the sizes of plates (simplified from larger diameter tube) are both 300 mm in length, 300 mm in width and 10 mm in thickness. Bottom flaws with the same width (2 mm) but different depth (2 mm, 4 mm, 6 mm, 8 mm) shown by character of d in these Figures are considered. Model of figure 1 employs a U-type shield with 300 mm in length, 34 mm in width, 24 mm in height and 10 mm in thickness. The axes of exciter and

detector run parallel to the surface of plate. Model of figure 2 employs a box-type shield with 34 mm in length, 34 mm in width, 24 mm in height and 10 mm in thickness. The axes of exciter and detector are perpendicular to the surface of plate. There is no air gap between the shield and the plate. Centers of coils are 7 mm far from the surface of plate in these two models. Material characteristics of model and parameters of coils are shown in Table 1. The frequency is 20 Hz which provides skin depth of 17.8 mm. The distance between exciter and detector is 60 mm which is obtained on the basis of preliminary simulations and guarantees the utilization of remote field region.

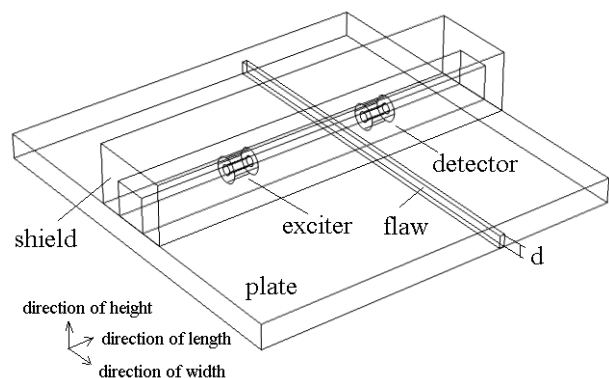


Fig. 1 Geometric model of simulation with U-type shield.

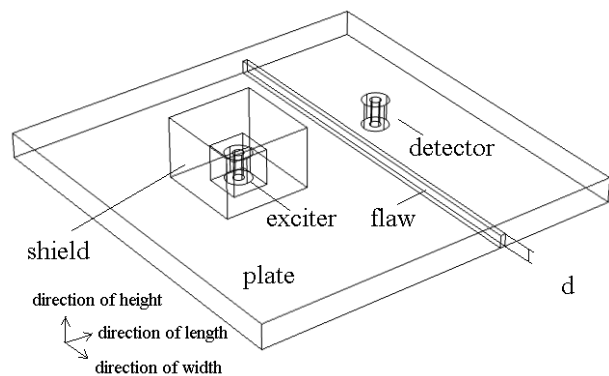


Fig. 2 Geometric model of simulation with U-type shield.

Table 1. Material characteristics of model and parameters of coils.

Item	Value
Conductivity of plate and shield	4×10^6 S/m
Relative permeability of plate and shield	10
Inner radius of exciter and detector	2 mm
Outer radius of exciter and detector	5 mm
Length of exciter and detector	10 mm
Current density of exciter	1.25×10^6 A/m ²
The number of detector coil turns	120

The simulations were carried out using the AC/DC module of commercial software Comsol multiphysics 4.2. The magnetic flux density is small ($B \approx 4 \times 10^{-3}$ T) in these simulations, therefore the governing equation is

$$(j\omega\sigma - \omega^2\epsilon)A + \mu^{-1} \nabla \times \nabla \times A = J_e \quad (1)$$

Where ω is the angular frequency, σ is the conductivity, ϵ is the permittivity, A is the magnetic vector potential, μ is the permeability, J_e is the current density of exciter. The model was discretized by edge element. The size of computational domain is 800 mm \times 800 mm \times 800 mm. Boundary condition was imposed so that the tangential component of magnetic vector potential is zero. The total number of elements is about 300,000 and it costs around 6 minutes to simulate one step during scanning of inspection.

3. Results and discussion

Figure 3 shows the effect of the distance between the exciter and the detector on induced voltage when there is no flaw. Based on the results, coil distance of 60 mm is chosen in the simulations because the indirect flux can be dominant at the region

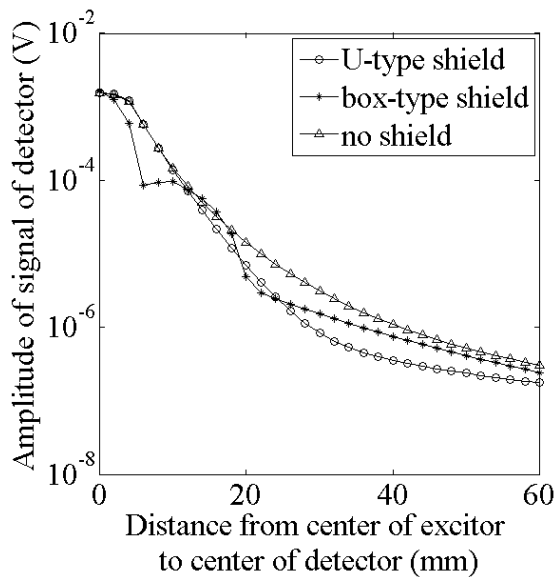


Fig. 3 The effect of coil interval on the amplitude of induced voltage.

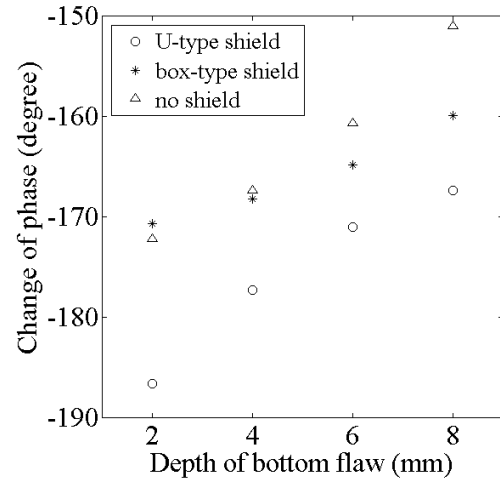


Fig. 4 Change of phase with variation of depth of bottom flaw in plate using different kinds of shield.

Figure 4 shows the changes of phase during the inspection of bottom flaws by different kinds of shields, U-type and box-type. Change of phase is also shown in the Fig. 4 when there is no shield. As the description of RFECT, change of phase basically has a linear relation with depth of flaw. It is demonstrated that sensitivity of RFECT by U-type shield is higher than sensitivity of RFECT by box-type shield from view point of change of phase, since the slope of change of signal is bigger when U-type is employed. However it should be noticed that even no shield is used, the bottom flaw of plate can still be inspected and the sensitivity of this case is similar to that obtained by U-type shield.

4. Concluding remarks

This study investigated the effect of shape of shield on the sensitivity of remote field eddy current testing for inspecting flaw of large diameter tube. The results revealed that sensitivity of RFECT using U-type shield is higher than that using box-type shield by analyzing the change in phase.

Reference

- [1] M. Isobe, R. Iwata, M. Nishikawa, High sensitive remote field eddy current testing by using dual exciting coils, *Nondestructive Testing of Materials* (1995), pp.145-152.
- [2] H. Fukutomi, T. Takagi, M. Nishikawa, Remote field eddy current technique applied to non-magnetic steam generator tubes, *NDT&E Int.*, **34** (2001), pp.17-23.
- [3] Y.S. Sun, et al., A remote field eddy current NDT probe for the inspection of metallic plates, *Materials Evaluation*, **54**(4) (1996), pp.510-512.
- [4] N. Kasai, et al., Evaluation of back-side flaws of the bottom plates of an oil-storage tank by the RFECT, *NDT&E Int.*, **41** (2008), pp.525-529.
- [5] H. Wang, et al., Simulation and experimental study of remote eddy current testing on flat conductive plate, *Int. J. Appl. Electromag. Mech.*, **33** (2010), pp.1261-1266.

Kinetomass Model for Wake Flow Simulation of Wind Turbine

Kai CHEN, Mengxuan SONG, Xing ZHANG

Key Laboratory for Thermal Science and Power Engineering of Ministry of Education,
Department of Engineering Mechanics, Tsinghua University, Beijing, P. R. China

Email: x-zhang@tsinghua.edu.cn

ABSTRACT

In this paper, a novel wind turbine wake model based on kinetomass diffusion is proposed. The kinetic energy is transformed into kinetomass and the kinetic equation is simplified into a convection-diffusion equation about kinetomass through linearization. The convection-diffusion equation is solved through the particle randomly walking method and the velocity deficit is obtained through transformation. The proposed model is compared to the experimental data and is validated by a test case. The results indicate that the kinetomass model can be used to calculate the wake flow of wind turbine.

1. Introduction

In recent years, the diminishing of the conventional fossil energies has awakened the need of developing renewable energies. As one of the most important alternative energy sources, wind energy has been taken worldwide attention due to the rich resources and widely distribution. Wind turbine micro-siting is to determine the layout of wind turbines with the target of maximizing the power output, according to site conditions, wind resources and wind turbine characteristics.

Turbine wake is one of the most important topics because it will impact the wind power distribution in the field. The most commonly used wake model in micro-siting optimization is the linear model proposed by Jensen et.al^[1]. Jensen model is good approximation to the turbine wake over flat terrain. However, for complex terrain, turbine wake will twist due to the shape of the ground and linear models are not applicable.

In this paper, a turbine wake model based on kinetomass diffusion is proposed. The kinetic energy equation is simplified into a convection-diffusion equation. The velocity deficit is obtained through the transformation. The proposed model is validated by the experimental data and a test case.

2. Kinetomass wake model

The concept of the kinetomass wake model is to add the velocity deficit to the flow field without wind turbines (background flow field).

The background flow field is calculated through the Reynolds Average Numerical Simulation (RANS). Standard $k-\varepsilon$ model are introduced to calculate the turbulence. SIMPLE algorithm is used to solve the equations. The computational domain is a rectangular domain and is large enough so that symmetric conditions can be applied in the top, left and right sides. The inlet velocity is uniform and the outflow is considered to be fully developed. Non-slip condition is applied to the ground. The calculation parameters are listed in Table 1.

A turbine rotor is placed in the domain. Assume that the kinetic energies before and after placing the rotor are K and K' , respectively. The governing equations are shown as

$$\rho u_j \frac{\partial K}{\partial x_j} = -u_j \frac{\partial p}{\partial x_j} + \mu_t \frac{\partial^2 K}{\partial x_j \partial x_j} - \mu_t \frac{\partial u_i}{\partial x_j} \frac{\partial u_i}{\partial x_j} \quad (1)$$

$$\rho u_j \frac{\partial K'}{\partial x_j} = -u_j \frac{\partial p'}{\partial x_j} + \mu_t \frac{\partial^2 K'}{\partial x_j \partial x_j} - \mu_t \frac{\partial u_i'}{\partial x_j} \frac{\partial u_i'}{\partial x_j} \quad (2)$$

where $K = u_i u_i / 2$ and $K' = u_i' u_i' / 2$.

(2) minus (1), obtaining

$$u_j \frac{\partial \rho_k}{\partial x_j} = v_t \frac{\partial^2 \rho_k}{\partial x_j \partial x_j} + \Phi \quad (3)$$

where $\rho_k = \rho (K' - K) / c^2$ and Φ is calculated by

$$\Phi = \frac{(u_j - u_j')}{c^2} \frac{\partial K'}{\partial x_j} + \frac{1}{\rho c^2} \left(u_j \frac{\partial p}{\partial x_j} - u_j' \frac{\partial p'}{\partial x_j} \right) + \frac{(v_t - v_t')}{c^2} \frac{\partial^2 K'}{\partial x_j \partial x_j} + \left(\frac{v_t}{c^2} \frac{\partial u_i}{\partial x_j} \frac{\partial u_i}{\partial x_j} - \frac{v_t'}{c^2} \frac{\partial u_i'}{\partial x_j} \frac{\partial u_i'}{\partial x_j} \right) \quad (4)$$

where c is speed of light in vacuum and Φ is the source term of equation (3). ρ_k is the kinetomass density, which is the equivalent quality of $(K' - K)$ ^[2]. It can be concluded that the convection-diffusion mechanism of kinetic energy is similar to that of the mass. ρ_k is a negative energy and describes the density of wake flow. The velocity deficit in the wake region increases with ρ_k . In equation (3), u_i is the background velocity and the kinetic energy equation is degenerated into a convection-diffusion equation with the known flow field.

For the linear wake model, the velocity after the rotor is calculated by^[1]

Table 1. Calculation parameters.

Parameter	Value
Rotor diameter	40m
Trust coefficient	0.88
Tower height	60m
Inlet velocity	8.5, 9.65, 11.52m/s
Domain size	800m * 200m * 200m
Grid number	201*51* 51
Grid size	4m *4m *4m

$$u'|_{\Gamma} = u_0 \sqrt{1 - C_T} \quad (5)$$

Where u_0 is the incoming wind speed, C_T is the trust coefficient and Γ represents the surface of the rotor. The boundary condition (5) is transformed into the condition of equation (3), shown as

$$\rho_k|_{\Gamma} = \frac{\rho C_T u_0^2}{2 c^2} \quad (6)$$

Equation (3) is solved approximately by particle randomly walking method. The steps are shown as

a) The particles are created randomly in the rotor area;

b) The diffusive displace $\Delta x = \sigma \sqrt{-2u_0 r \Delta t \log R_i}$ is added to each particle;

c) The convective displace $\Delta x = u_0 \Delta t$ is added to each particle;

d) Each particle disappears at a attenuation probability $p_y = \gamma \Delta t$;

After simulate for some time, the particle concentration C_k is obtained.

The velocity downstream the rotor is calculated by

$$u'_i = u_i \sqrt{\frac{K'}{K}} = u_i \sqrt{1 - C_T C_k} \quad (7)$$

3. Result

The experimental data from Ref. [3] is used to fit the parameters in the particle method. The results are shown as

$$\sigma = 0.18, \gamma = 0.005 \quad (8)$$

Figure 1 shows the transform results of different cross-wind sections downstream for various incoming velocities compared with the experimental data [3]. Equation (7) makes sure that the flow is not disturbed where $C=0$. That is, the region where is far from the hub is not affected by the fan blades. The near wake's results are not fit well. In this region, the disturbance of rotor is strong and the source term (4) is big. Therefore, the error of the wake model is big. In far wake region, the influence of the rotor is small, so the agreement is excellent for far wake. In fact, the far wake is the only thing that is necessary to be considered when optimizing micro-siting. Furthermore, the wake characteristics connect with the kinetomass density through the Equation (7) while the concentration changes according to the shape of the ground, suggesting that the model can be applied to complex terrain.

A case over a cube is applied to validate the model. The schematic of the domain is shown in Fig. 2(a). A turbine with the same characteristics as in Table 1 is placed before a cubic obstacle and the turbine is simulated through the volume force and the proposed wake model. The comparison of the results for the section that $X = 150\text{m}$ is presented in Fig. 2(b). The results show that the kinetomass wake model fits the volume force method and can be used to calculate the wake flow.

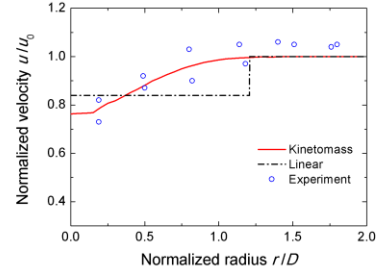
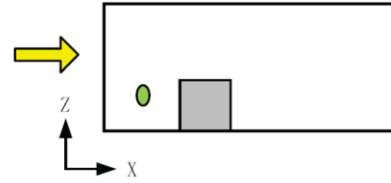
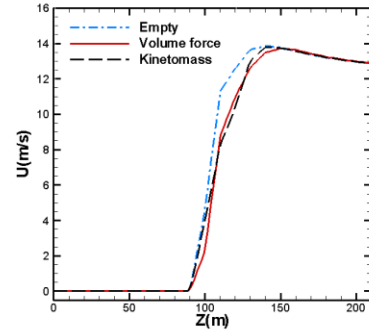


Fig. 1 The velocities obtained by the model compared with experimental data [3] ($U_{in}=9.65\text{m/s}$, $X=7.5D$).



(a) The schematic of the test case



(b) Comparison of velocity profiles at $X = 150\text{m}$

Fig. 2 The case with a turbine placed before an obstacle.

4. Conclusions

In the paper, a wake model is proposed based on kinetomass diffusion and particle randomly walking method. Comparisons with experimental data and the test case show that the model is a good approximation for turbine wake flow, especially for far wake. This model is able to bend with the ground and expected to be applied for complex terrain.

Acknowledgements

This research is supported by the National High-Tech R&D Program (863 Program) of China (No.2007AA05Z426) and the International Scientific and Technological Cooperation Program (No. 2011DFG13020).

References

- [1] N. O. Jensen, A note on wind generator interaction, Risø National Laboratory, DK-4000 Roskilde, Denmark, 1993.
- [2] Y. Dong, Journal of Engineering Thermophysics. **33** (2012)
- [3] Amina El Kasmi, J. Wind Eng. Ind. Aerodyn. **96** (2008), R103.

Flow separation control by vortex-cell

Arpiruk Hokpunna

Department of Mechanical Engineering, King Mongkut's University 126 Prachautid Rd., Bangkok, Thailand 10140
 Email: arpiruk.hok@kmutt.ac.th,

ABSTRACT

This paper presents the control of flow separation of a boundary layer above flat plate under adverse pressure gradient by mean of vortex cell with active control. Two control methods are consider, the suction method and the zero-mass-flux method. Both can suppress flow separations. The suction method is found to be more effective.

1. Introduction

Lift enhancement and drag reduction is one of the most demanding technologies in aviation industry. To ensure a high lift-to-drag ratio, wings of modern aircraft are thin and streamlined. However, from a structural-strength point of view, having thick wings would be beneficial in order to carry a larger load. As the progress in aviation leads to an increase in the size of transport aircraft, the balance between structural-strength and aerodynamic quality shifts in favour of a thick wing. The flow past a thick airfoil, however, is likely to separate, which affects the aerodynamic performance of the wing. Trapping vortices by a so-called vortex cell is considered to be able to prevent flow separation and large-scale vortex shedding which would in turn reduce the drag.

In order to achieve such desired effects, the vortex cell have to be controlled. EKIP aircraft [1] uses central body suction. In this work we consider two alternatives. The first approach is the pure suction similar to that of the EKIP aircraft. but the suction slots are placed at the surface of the vortex cell. In the second approach, we used a zero-mass-flux control where one slot draws the fluid in and the other one blows the fluid out.

2. Method

The investigation in this work is carried out using large-eddy simulation. The geometry of the cavity holding the vortex cell is shown in Fig.1. This shape is exactly the same as the one we used investigated earlier [berlin], except that two control slots are appended to the horizontal tangent of the cavity. The width of both control slot is $0.08\delta_0$ and the slots span the whole spanwise domain.

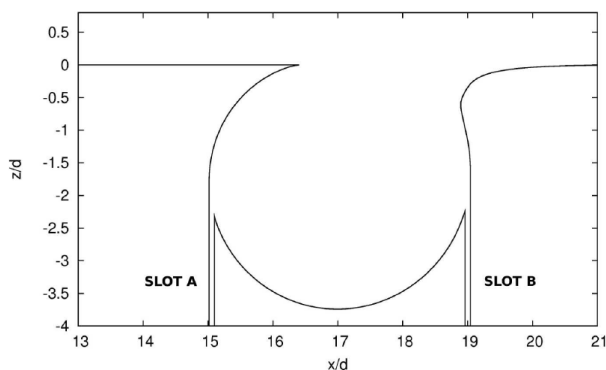


Fig 1 Geometry of the cavity with two blowing/suction channel.

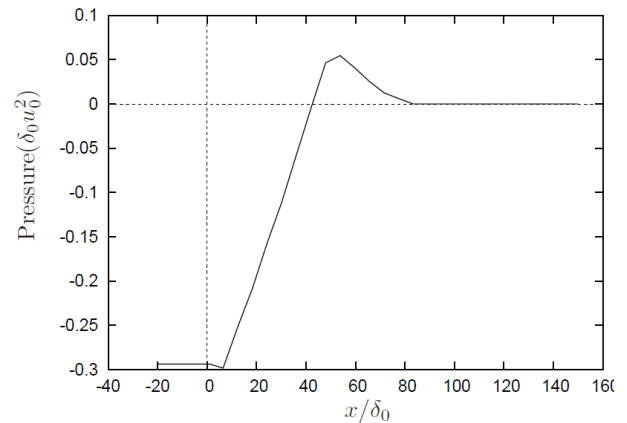


Fig. 2 :The pressure profile prescribed at the top boundary ($z = 10.2\delta_0$)

The computational box for the flat plate above the cavity is $[135\delta_0, 5\delta_0, 10.2\delta_0]$ in the streamwise, spanwise and wall-normal direction. The time-dependent turbulent inflow condition is constructed by a superposition of fluctuations onto a time-averaged velocity profile. The time-averaged inflow profile was self-similar profile of Spalart's with $Re_0 = 1410$. Since this profile is not the self-similar profile of this Reynolds number, the flat plate in front of the cavity is extended to $20\delta_0$. The fluctuations are extracted at $x = 11.5\delta_0$ downstream of the inlet by computing the difference between the instantaneous velocity and the one which was averaged in spanwise direction. The periodic boundary conditions are applied in the spanwise direction since the homogeneous conditions were assumed. On the top boundary of the domain, an adverse pressure gradient profile is prescribed as shown in Fig.2 and the Neumann conditions are applied for velocity. This adverse pressure gradient (APG) profile is obtained from DNS in [2] with a slight modification by shifting the pressure level up in order to allow a region of favourable pressure gradient which helps stabilising the large-eddy simulation. The grid resolutions in the vortex cell on xz -plane are similar to the one used in [3]. The total number of grid cells grows to 12M since we have to cover a much larger domain.

Extreme care must be taken to achieve a stable numerical simulation of a separating boundary layer using large-eddy simulation. This simulation is very sensitive to grid resolutions, initial conditions and the prescribed pressure gradient. First the initial condition

must be a fully developed zero pressure gradient(ZPG)

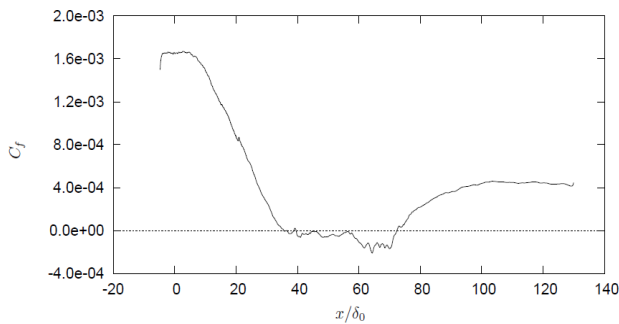


Fig. 3 C_f of the boundary layer with separation (without vortex cell).

boundary layer then the adverse pressure gradient profile must be significantly scaled down and imposed on the top boundary. Once an (approximately) statistically steady state has been reached, the scale factor can then be slowly increased. In this work we used four steps of pressure gradient with a scale factor of 0.25, 0.5, 0.75 and 1.0. It must be emphasized that the full pressure gradient cannot be imposed immediately on the ZPG solution since it leads to a very fast separation and the boundary layer will exit at the top boundary which later destabilizes the simulation.

3. Results and Discussion

Since the goal of this work is to investigate the mechanism of the vortex cell on the adverse pressure gradient, we only sample the statistics of this case for a short time and the coefficient of friction is plotted in Fig.3 showing that averaged separation bubble is located in $x \in [32, 72.5]$.

The cavity is then appended to the flat plate and the simulation is restarted with the same level of pressure gradient. Without turning on the control in the vortex cell, a massive separation starts as soon as half of the pressure level. (see Fig.4). This indicates that the vortex cell alone, under a significant adverse pressure gradient, promotes the separation.

Next, the controls are turned on while we scale up the adverse pressure gradient. Two types of control method are used: (i) suction only and (ii) blowing/suction with zero-mass-flux. They are acronymed as DS and BS, respectively. In the first method, suction is applied at both slots (A and B) in Fig.1. In the second method, blowing is applied at slot A and the suction is applied at slot B. The uniform velocities at the bottom boundary are imposed within the slot area. The control velocity (w_c) used for suction and blowing are $0.3u_0$, $0.5u_0$, and $0.7u_0$. The control velocity is kept constant in each simulation. When the control is turned on with the lowest control velocity, the massive separations can be eliminated by both methods up to the full level of the adverse pressure gradient, however the separation is not entirely suppressed.

When the controlled velocity is increased to $0.7u_0$, the BS control can eliminate the separation entirely while the DS control suppresses the separation already

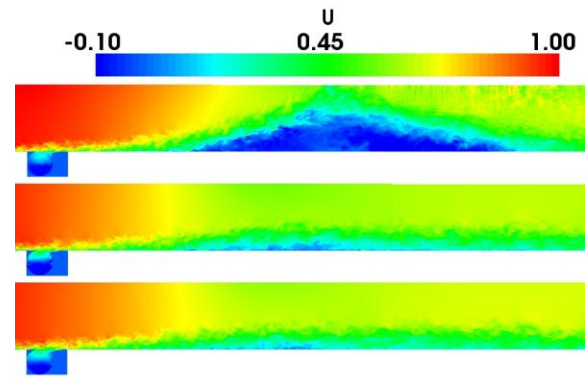


Fig.4 Instantaneous contour of the streamwise velocity of vortex cell of VC without control under 50% APG (top) and VC under full APG: with BS control using $w_c=0.7u_0$ (middle) and DS control using the same suction velocity (bottom).

when $w_c = 0.5u_0$. Instantaneous snapshots of streamwise velocity contour in Fig.4 also shows that the double suction method is more effective than the blowing/suction method. Nonetheless, it shows that the zero-mass-flux control is able to achieve the design purpose.

It should be however, noted that control algorithm which rely on the suction should not be very sensitive to the placement of the mass control slot since the effects of the control is the pressure gradient and fluid removal. The blowing/suction control, on the other hand, can be very sensitive to the positioning and the shape of the control slot because the injected mass interacts directly with the fluid. The shape of the slot and the direction of the injection are thus important. Unfortunately, we did not make an attempt to investigate the optimal positioning of the injection slot.

4. Concluding remarks

In this work, we have found that both active controls studied in this work can suppress the separation when the velocities of the control fluids reach a certain value. The suction control effectively brought down the boundary layer above the vortex cell and affected the whole boundary layer. Even though it is more effective in suppressing the separation, from the energetic point of view, it is less efficient as the blowing/suction control. The blowing/suction control offers a promising alternative to the suction control. It only interacts with the inner part of the boundary layer and does not alter the outer part of the boundary layer. This property, together with a convenient design offered by its closed circuit, make blowing/suction control a better choice for vortex cell control at cruise condition.

References

- [1] MP. A. Baranov, S. A. Isaev, Yu. S. Prigorodov and A. G. Sudakov, *Fluid Dyn.*, **47**(2003)
- [2] M. Manhart and R. Friedrich, *Int. J. Heat. Fluid Fl.*, **22**(2002)
- [3] A. Hokpunna, M. Manhart. 2nd ICWJS (2008)

Studies on Flow Transition Under Simulated Low Pressure Turbine Conditions Based on a High Order LES model

Debasish Biswas and Tomohiko Jimbo
Toshiba Research and Development Center
1, Komukai Toshiba-Cho, Saiwai-ku, Kawasaki 212-8582, Japan.
Debasish.biswas@toshiba.co.jp.

ABSTRACT

Boundary layer transition is an important phenomenon experienced by the flow through gas turbine engines. A substantial fraction of the boundary layer on both sides of a gas turbine airfoil may be transitional. The intermittent nature of transition need to be taken into account in developing improved transition model. Much has been learned from the to date, but the nature of separated flow transition is still not completely clear, and existing models are still not robust as needed for accurate prediction. Therefore, in the present work a high order LES turbulent model proposed by the author is used to predict the separated flow transition.

1. Introduction

Boundary layer transition process makes the separation on Low Pressure (LP) turbine airfoil more complicated. Turbulent boundary layers are much more resistant to separation than laminar boundary layers. In the case of flow, that were subject to only small disturbances, the transition process can be studied using linear stability analysis. They undergo what is known as Tollmien-Schlichting (TS) transition, which involves the growth of small perturbation in the boundary layer into two-dimensional disturbances known as Tollmien-Schlichting waves. The TS waves eventually become three-dimensional due to secondary instabilities as they move downstream. Such instabilities culminate as turbulent spots in the boundary layer flow.

Bypass transition occurs in flows disturbed by finite perturbations such as free-stream turbulence, surface roughness, or acoustic excitation. Under high free-stream turbulence conditions, turbulent eddies in the free-stream are expected to buffet the boundary layer, providing a non-linear transition mechanism, which acts either in place of or in combination with the linear growth of disturbances within the boundary layer. During bypass transition TS transition stages are not visible. However, bypass transition is poorly understood in part because it thus far has not been amenable to analysis. It is the mode of transition expected to be operational in gas turbine engine internal flows. In such flows, turbulence intensities of 5 to 10% are common. In the present work a high order LES turbulent model proposed by the author is used to predict the separated flow transition to test the prediction accuracy of this model regarding such complicated flow phenomena. The experimental data of Volino(1) is chosen for this comparison purpose. In his experimental work, the flow through a single-passage cascade simulator is documented under both high and low FSTI (Free Stream Turbulence Intensity) conditions at several different Reynolds numbers. The geometry of the passage (in Volino's work) corresponds to that of the "Pak-B" airfoil, which is an industry supplied research airfoil that is representative of a modern, aggressive LP turbine design. The reason behind choosing Volino's data for the present simulation study is that, Volino's data included a complete documentation of cases with Re as low as 25,000 and also the documentation of turbulent shear stress in the boundary layer under both high and low FSTI.

2. Numerical Method and Physics Based Model

The basic equations are unsteady three-dimensional continuity and momentum equations for incompressible flows. A Poisson type equation for pressure derived from the momentum equations is solved to obtain the pressure field. The dependent variables have been non-dimensionalized by

some characteristic velocity and length scale. All the equations are written in generalized coordinate to have sufficient grid resolutions in the near wall boundary layer region and to generate grids to fit the body configuration. Accurate spatial discretization is crucial in LES. In LES, numerical diffusion however small it is, can easily overwhelm physical diffusion. Also, one of the problems encountered in LES of turbulent flow is the control of aliasing error. Use of schemes, which do not have a mechanism of controlling aliasing error can result in decay of the turbulence in a given flow field or an unbounded growth of the solution. In the present work, this problem is overcome by using a spatially high order accurate, WENO (Weighted Essentially Non-Oscillatory) type upwind-biased finite difference scheme developed for incompressible N-S equations in three-dimensions. In the present method a fifth order upwind differencing technique is used for convective terms and fourth order central differencing technique is used for viscous diffusion terms. All these equations are solved using an efficient high order finite difference scheme of second order accuracy in time. In this approach, fully implicit finite difference equations are solved performing several iterations at each time step to make the differencing errors zero. In our work, in a dynamic eddy viscosity model, transfer of information between the sub-grid and large scale eddies is improved by solving an additional transport equation for turbulent kinetic energy in the grid scale level. Here, sub-grid-scale turbulent stresses are closed using a dynamic turbulent kinetic energy transport model. The sub-grid scale length scale is represented by the minimum of the universal length scale and the grid scale. A test filter was used for the dynamic procedure, which is applicable to stretched grid near the body surface. The advantages of such model include resolution of interesting scales, simultaneous modeling of high shear regions and large scale unsteadiness, and use of stretched grids. In the kinetic energy transport equation, dissipation of turbulent energy is defined on the basis of time scale.

2.1 Experimental Set Up

The experimental facility of Volino consisted of a low speed wind tunnel. Briefly, air enters through blowers and passes through a series of screens, a honeycomb, two settling chambers, and a three-dimensional contraction before entering the test section. The test sections shown in Fig.1, consisted of the passage between two airfoils. A large span to chord ratio of 4.3 was chosen to insure two-dimensional flow at the span-wise centerline of the airfoils, where he made all the measurements. Upstream of each airfoil are flaps, which control the amount of bleed air allowed to escape from the passage. These are adjusted to produce the correct leading edge flow and pressure gradient along the airfoils. A tailboard

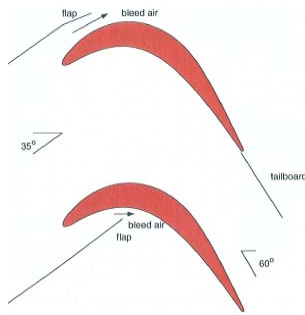


Fig.1 Schematic of test section.

on the pressure side of the flow passage also helped setting the pressure gradient in his experiment. In the case of low FSTI, it is set to a value of 0.5% and in the case of high FSTI, it is set to approximately 9%. The experiment was conducted over a wide range of Reynolds number from 25,000 to 4×10^5 .

2.2 Grid Topology

As a typical example, in Fig.2 is presented computation grids used in the numerical simulation of the experiment on separated flow transition under low-pressure turbine airfoil conditions performed by Volino. In the computations zonal grid approach is adopted. The whole computation domain is divided into three zones and patched together to form the experimental model. Zone-1 and zone-3 represent the lower portion and upper portion of the test section, respectively. Zone-2 represents the single passage cascade of “Pak-B” rotor airfoil. 469 and 201 grid points in the x and y direction respectively, are used in zone-2, 469 and 91 grid points in x and y direction are used in each of the zone 1 and 3. Experiment was carried out using a large span to chord ratio of 4.3 to insure two-dimensional flow at the span-wise centerline of the airfoils. In this work, 3-D computations are carried out and 401 grid points are used between the lower and upper wall separated by 4.3 times chord length to ensure two dimensional flows.

3. Results and Discussion

A three-dimensional representation of the flow under lower Reynolds number condition is depicted by iso-surface fluctuation pressure, axial velocity, normal velocity and vorticity based on fluctuating components of velocity along with the near wall axial and normal velocity distribution on LP turbine airfoil presented in Fig.3. These figures help to have some understanding that away from the span-wise the flow is basically 2-d in nature. Turbulent flow in the boundary layer is defined here as a flow which includes a range of large and small scales turbulence production and dissipation. Using this definition, a boundary layer may be characterized by significant fluctuations but still be non-turbulent if these fluctuations are induced by an external source which does not cause near wall turbulence production. Such is the case under high FSTI conditions, which are considered here. Free-stream

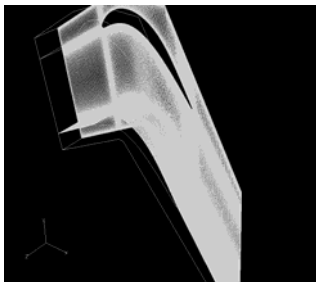


Fig.2 Computational grid.

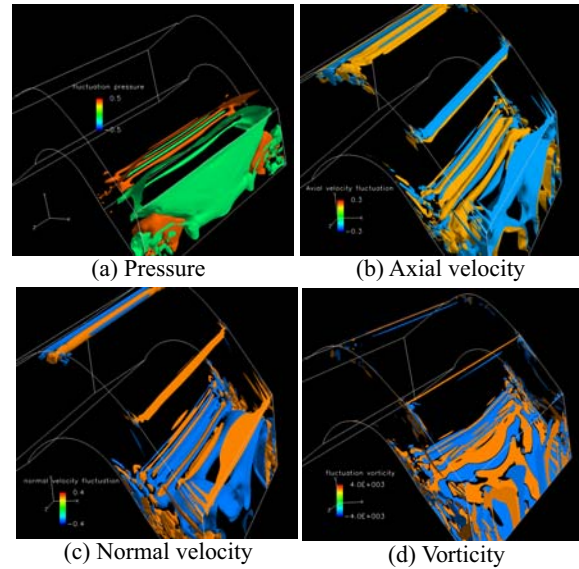


Fig.3 Iso-surface of respective fluctuating components.

eddies “buffet” the boundary layer, inducing non-turbulent boundary layer fluctuations. Buffeting occur through pressure fluctuations as was observed from other results. Boundary layer fluid is pushed in the wall normal direction across the mean gradient of the stream-wise velocity, resulting in significant (u') fluctuations. This type of motion is termed “inactive” since it does not result in momentum transport, in spite of potentially high (u') levels as can be observed here. Results also reveal that in addition to buffeting, some free-stream eddies penetrate into the boundary layer and cause some mixing. Transition to turbulence is characterized not so much by large increases in (u') levels, but by the appearance of higher frequencies superimposed on the low frequencies. Spectrum analysis of u' and v' indicated the above mentioned fact. Free-stream pressure fluctuation disturbs the near wall boundary layer region by flapping the boundary layer edge. The results also reveal that non-turbulent zone velocity fluctuations are induced by the free-stream unsteadiness through pressure fluctuations. The turbulent zone included a range of both large and small scale eddies, much like a fully turbulent boundary layer. The non-turbulent zone and the pre-transitional boundary layer under high FSTI were not laminar-like, but instead can be characterized by high amplitude, large scale fluctuations and an absence of smaller scales. Near wall turbulence production is found to be largely absent in the non-turbulent zone. The intermittent nature of transition need to be taken into account in developing improved transition model. As a whole, Fig.3 helped to have a good understanding of the flow behavior on the suction surface of LP turbine blade.

4. Concluding remarks

The present study helped to have a very good understanding of basic mechanism involved in the unsteady transition from laminar to turbulent, and the intermittency of transition from laminar to turbulent boundary layer flow.

References

- [1] Volino, R. J., ASME Paper GT-2002-30236, 2002.
- [2] Narashima, R., Progress in Aerospace Science, Vol.22, No.1, PP.29-80, 1985.
- [3] Volino, R. J. ASME Journal of Turbomachinery, 123, pp.189-197, 2001. ,
- [4] Biswas, D., AIAA Paper, 2006-2881, 2006.
- [5] Biswas, D., AIAA Paper, 2006-3684, 2006.

Turbulent Boundary Layer Influenced by Cylinder Wake in a Freestream

Kosuke Hiruta, Kouji Nagata, Yasuhiko Sakai, Osamu Terashima and Yasumasa Ito
Department of Mechanical Science and Engineering, Nagoya University, Japan
hiruta.kosuke@a.mbox.nagoya-u.ac.jp

ABSTRACT

Effects of the cylinder wake in a freestream on statistical properties of a turbulent boundary layer over a flat plate are experimentally investigated in a wind tunnel. The bursting events are detected by the variable interval time average (VITA) technique. The results show that the time-averaged mean velocity in the inner layer with the cylinder wake coincides with that without the cylinder wake. However, turbulence intensities normalized by the inner parameters are suppressed in the outer layer by the cylinder wake. It is found that the velocity fluctuation during the sweep phase in the bursting event is increased by the cylinder wake.

1. Introduction

A turbulent boundary layer with a freestream turbulence can be seen in many industrial and environmental flows. Therefore, for the prediction and control of turbulence and the better design of industrial apparatus, it is important to elucidate the interaction between turbulent boundary layer and freestream turbulence. Past researches on turbulent boundary layers have shown that the turbulence intensities are strongly affected by freestream turbulence [1]. In the previous studies, nearly isotropic grid turbulence has been used as freestream turbulence. In this study, we investigated the effects of anisotropic freestream turbulence generated by a cylinder on statistical properties of the turbulent boundary layer. Experiments were carried out in a wind tunnel and the streamwise velocity was measured by a hot wire anemometer.

2. Experimental Method

Experiments were carried out in a Eiffel-type wind tunnel. Figure 1 shows the experimental apparatus. The apparatus of the bottom wall is a flat plate which is made of a Bakelite plate to reduce the heat loss of hot wire probe. The length of the plate is 2,100 mm. The coordinate system is as follows (fig. 1): the x -axis is along the streamwise direction, the y -axis is in the vertical direction starting from the wall surface, and the z -axis is in the spanwise direction with $z=0$ being the center of the channel. To generate a fully developed turbulent boundary layer in a short distance, the transition was promoted by using the tripping wire of 1×10^{-3} m diameter placed on the bottom wall at 50 mm from the leading edge. We measured the turbulent boundary layer at $x = 1,880$ mm and the measuring region was from 0.2 mm to 150 mm (y direction).

Instantaneous streamwise velocity was measured by using a constant-temperature hot-wire anemometer. The hot wire was 5×10^{-6} m tungsten wire with a length-to-diameter ratio l/d_w of 200.

We used the variable interval time average (VITA) technique to detect the bursting event. The bursting event is detected when

$$\frac{1}{T} \int_{t-\frac{T}{2}}^{t+\frac{T}{2}} u'(t')^2 dt' - \left[\frac{1}{T} \int_{t-\frac{T}{2}}^{t+\frac{T}{2}} u'(t') dt' \right]^2 > Ku_{rms}^2 \text{ and } \frac{d}{dt} u' > 0, \quad (1)$$

where T is the averaging time, u' is the instantaneous

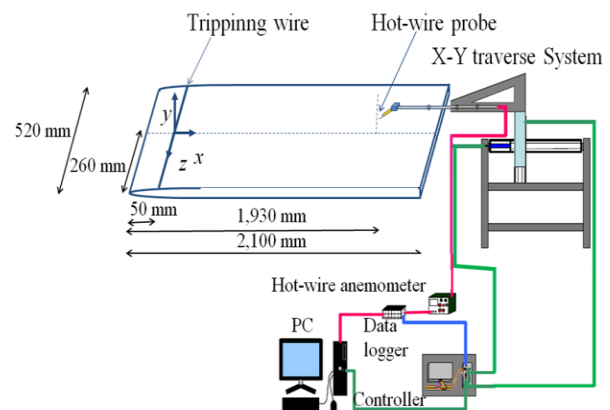


Fig. 1 Schematic view of the experimental apparatus.

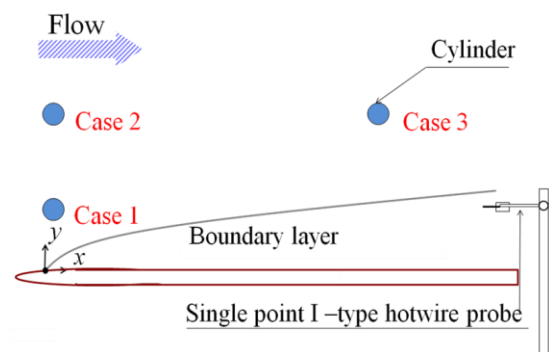


Fig. 2 Experimental setup.

Table 1. Experimental conditions for turbulent boundary layer without freestream turbulence.

Re [m ⁻¹]	Re _θ	δ [mm]	u _τ [m/s]
738,000	3,140	44	0.583

Table 2. Experimental conditions for turbulent boundary layer with freestream turbulence.

	Symbol	Location of the Cylinder (x _c [mm], y _c [mm])
Pure TBL	•	-
Case1	CWT(0, 50)	△ (0, 50)
	CWT(0, 60)	× (0, 60)
	CWT(0, 80)	◇ (0, 80)
Case2	CWT(0, 100)	▽ (0, 100)
	CWT(0, 130)	⊕ (0, 130)
	CWT(0, 150)	⊗ (0, 150)
Case3	CWT(1,680, 100)	★ (1,680, 100)
	CWT(1,680, 130)	⊕ (1,680, 130)
	CWT(0,680, 150)	□ (1,680, 150)

velocity fluctuation, and K is the threshold. In this study, $K = 1.0$ and $T^+ = Tu_\tau^2/\nu = 20$. Here, u_τ is the friction velocity and ν is the kinetic viscosity of air.

For the experiments with cylinder wake turbulence (CWT), the cylinder was horizontally set at the entrance to the test section (case 1 and case 2) and near the measuring point at $x = 1,680$ mm (case 3) (figure 2). The diameter of the cylinder is 1×10^{-2} m and the frequency of the Kármán vortex is around 200 Hz which is about 5 times of the bursting frequency of turbulent boundary layer without freestream turbulence (pure TBL).

Table 1 lists the experimental condition of turbulent boundary layer without freestream turbulence. Here, δ is the boundary layer thickness at the measuring point, u_τ is the friction velocity and Re_θ is the Reynolds number based on the momentum thickness θ and the mean freestream speed U_0 at the measuring point. Table 2 lists the location of the cylinder and the symbols of experimental results. We investigated 3 types of experimental conditions:

- Case 1: Turbulent boundary layer is directly influenced by the cylinder far-wake (non-periodical) turbulence in a freestream
- Case 2: Turbulent boundary layer is indirectly influenced by the cylinder far-wake (non-periodical) turbulence in a freestream
- Case 3: Turbulent boundary layer is indirectly influenced by the cylinder near-wake (periodical) turbulence in a freestream

3. Results and Discussion

Due to the limitation of the available pages, we show only the results of case 1. Other results will be shown in our presentation.

Figure 4 shows the vertical profiles of time-averaged mean velocity U^+ normalized by the inner parameters. It is shown that U^+ in the inner layer with cylinder wake coincided with that without cylinder wake. On the other hand, U^+ is decreased in the outer layer by the cylinder wake.

Figure 5 shows the vertical profiles of rms velocity u_{rms}^+ normalized by the inner parameters. In the inner layer, u_{rms}^+ with cylinder wake coincided with that without cylinder wake. On the other hand, u_{rms}^+ is suppressed in the outer layer by the cylinder wake.

Figure 6 shows the ensemble average of instantaneous velocity in the bursting event. Here, $\tau = 0$ is the time when the bursting event is detected. It is found that the velocity fluctuation during the sweep phase in the bursting event is increased by the cylinder wake. On the other hand, the velocity fluctuation during the ejection phase does not significantly change.

4. Concluding remarks

Effects of the cylinder wake in a freestream on statistical properties of a turbulent boundary layer over a flat plate are experimentally investigated in a wind tunnel. The results show that the rms velocity with the cylinder wake is suppressed in the outer layer. The

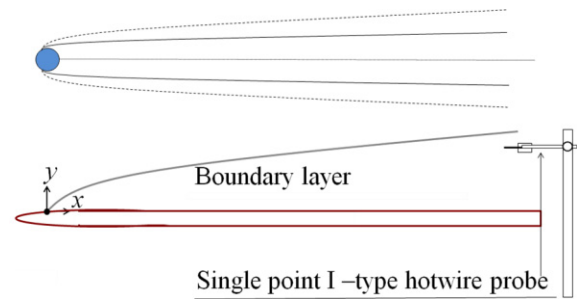


Fig. 3 Experimental setup for case 1.

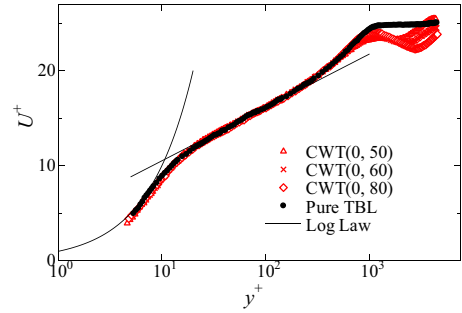


Fig. 4 Vertical profiles of time-averaged mean velocity.

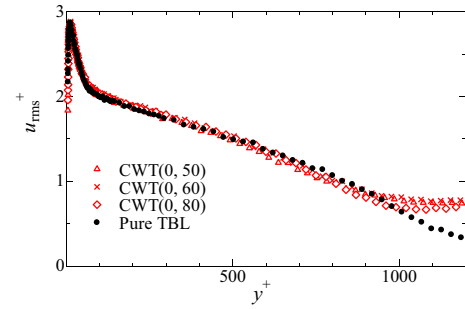


Fig. 5 Vertical profiles of rms velocity.

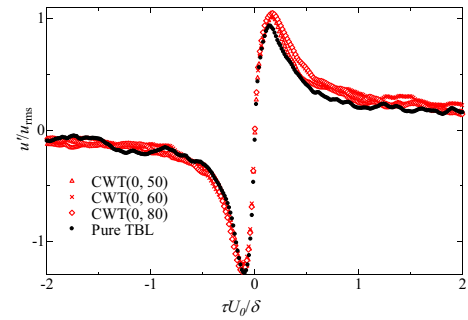


Fig. 6 Ensemble average of instantaneous velocity in the bursting event ($y^+ = 36$).

bursting event is affected by the cylinder wake.

Acknowledgments

Part of this work was supported by Grants-in-Aid (Nos. 22360076, 22360077) from the Japanese Ministry of Education, Culture, Sports, Science and Technology.

References

- [1] K. Nagata, Y. Sakai, and S. Komori, Phys. Fluids, vol.23, (2011), 065111.

Direct Numerical Simulation on the Effects of Free-stream Turbulence on the Growth of Turbulent Boundary Layer

Shuang Xia¹⁾, Kousuke Hiruta¹⁾, Kouji Nagata¹⁾, Yasuhiko Sakai¹⁾, Hiroki Suzuki²⁾, Osamu Terashima¹⁾
and Toshiyuki Hayase³⁾

1) Dept. of Mechanical Science and Engineering, Nagoya University, Nagoya, 464-8603, Japan

2) Dept. of Engineering Phys., Electronics and Mechanics, Nagoya Institute of Technology, Nagoya, 466-8555, Japan

3) Institute of Fluid Science, Tohoku University, Sendai, 980-8577, Japan

E-mail: xia.shuang@f.mbox.nagoya-u.ac.jp

ABSTRACT

Direct numerical simulation (DNS) is used to investigate the effects of free-stream turbulence on the growth of turbulent boundary layer. Free-stream turbulence is generated by a square rod. The development of turbulent boundary layer along streamwise direction under the wake of the square rod are presented and discussed.

1. Introduction

Turbulent boundary layer subjected to free-stream turbulence occurs in many natural and engineering applications, such as in turbomachinery and heat exchangers. The effects of the free-stream turbulence on turbulent boundary layer have been investigated in many researches. For instance, the effects of free-stream turbulence on bypass transition in boundary layer[1], surface friction in turbulent boundary layer[2], heat transfer in turbulent boundary layer[3,4] and so on. The free-stream turbulence may have a length scale that is smaller or larger than that of the boundary layer, which can affect not only the outer region but also the inner region of turbulent boundary layer.

The aim of this research is to investigate the effects of free-stream turbulence on the growth of turbulent boundary layer by means of direct numerical simulation (DNS). In previous researches, the free-stream turbulence is mostly generated by a grid, which is nearly isotropic turbulence. In our research, the free-stream turbulence is generated by a square rod.

2. DNS Method

2.1 Computational domain

The computational domain is a rectangular parallelepiped which is shown in figure 1. The size of the computational domain is $4.6D \times 1.5D \times 1.5D$ in the streamwise, vertical and spanwise direction, respectively. D is the characteristic length of the computational domain. The mesh number is $574 \times 320 \times 160$. The square rod with a cross section of $0.05D \times 0.05D$ is placed at $x = 0.36D$ and $y = 0.625D$. We also set a tripping wire on the bottom at the same location as the location of the square rod, which can generate a developed turbulent boundary layer in a short distance from the inlet.

The non-uniform mesh is used in the streamwise and the vertical direction. In the streamwise direction mesh points are concentrated in the region where the square rod is placed. Figure 2 shows the spatial resolution along the streamwise direction. This kind of mesh arrangement prevents the numerical instability around the square rod. In the spanwise direction the meshes are uniform. The Reynolds number based on U_{in} and D is 13333, where U_{in} is $2.5m/s$.

2.2 Boundary conditions

The velocity profile at the inlet is set to have a 1/7 power law near the lower boundary and the uniform value away from the wall. The convective outflow condition is applied at the outlet. The non-slip and the slip condition are imposed on the bottom and the top of computational domain, respectively. In the spanwise direction the periodic boundary condition is used.

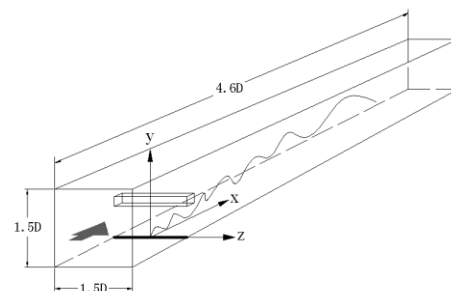


Fig. 1 Computational domain.

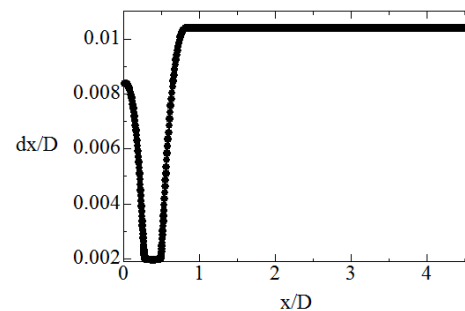


Fig. 2 Spatial resolution along the streamwise direction.

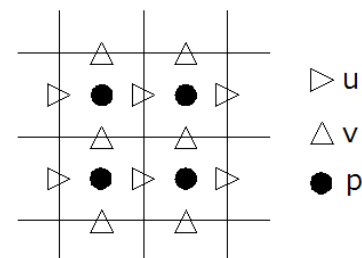


Fig. 3 Staggered meshes.

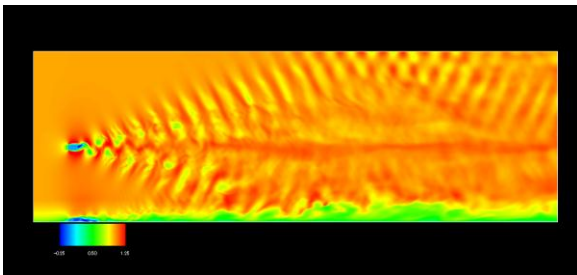
2.3 Numerical method

The governing equations are the incompressible Navier-Stokes equation and the continuity equation. The fractional step method is used to solve these governing equations. The 2nd-order Crank-Nicolson method is used for the time advancement of viscous term along the vertical direction and the 3rd-order Runge-Kutta method is used for time advancement of other terms. The 4th-order central difference method is applied in the spatial discretization. The Poisson equation is solved by the BiCGstab method. The staggered meshes are applied in the arrangement of velocity and pressure on mesh points, which is shown in figure 3.

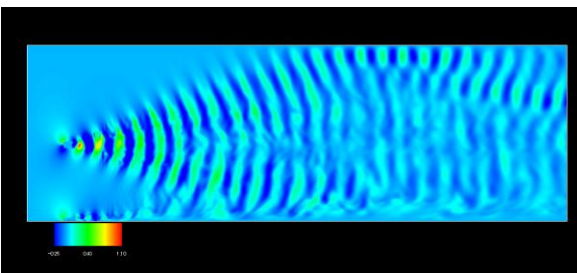
3. Results and Discussion

3.1 Instantaneous velocity field

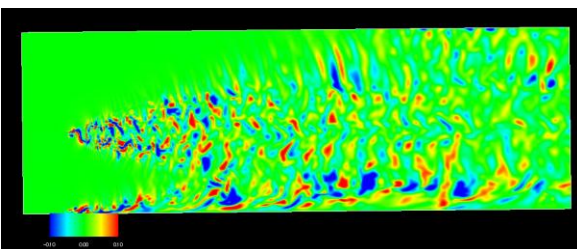
Figures 4(a), (b) and (c) show the instantaneous streamwise, vertical and spanwise velocities, respectively. From these figures we can know that at the rear of the square rod, vortices are generated successively. Near the wall turbulent boundary layer is formed and it interacts with the wake of the square rod.



(a) Instantaneous streamwise velocity
red: $U/U_0 = 1.25$, blue: $U/U_0 = -0.25$



(b) Instantaneous vertical velocity
red: $U/U_0 = 1.10$, blue: $U/U_0 = -0.25$



(c) Instantaneous spanwise velocity
red: $U/U_0 = 0.10$, blue: $U/U_0 = -0.10$
Fig. 4 Instantaneous velocity field.



Fig.5 Pressure and velocity vector.
black: high pressure, white: low pressure

3.2 Pressure and velocity vector

Figure 5 shows the pressure (background color) and the velocity vector near the square bar and the tripping wire. From this figure we can know that the pressure is low at the top, the bottom and the rear of the square rod. Vortices are generated at the rear and then they shed. At the same time, near the wall, vortices are generated behind the tripping wire. Then they flow along the downstream direction and lift gradually and are affected by the wake of the square rod.

4. Concluding remarks

By means of DNS, we showed that vortices are generated by a square rod and the wake of the square rod can affect the growth of turbulent boundary layer. In the future research, we will improve this simulation and get the turbulence statistics to clarify the mechanism of the interaction between the wake of a square rod (i.e., the free-stream turbulence) and the turbulent boundary layer.

Acknowledgements

A part of this study was carried out under the Collaborative Research Project of the Institute of Fluid Science, Tohoku University. A part of this study was also supported by Grants-in-Aid (Nos. 22360076, 2236077) from the Japanese Ministry of Education, Culture, Sports, Science and Technology.

References

- [1] V. Ovchinnikov, M. M. Choudhari and U. Piomelli, *J. Fluid Mech.* (2008), vol. 613, pp. 135-169.
- [2] V. K. Kuzenkov, V. N. Levitskii, E. U. Repik and Yu. P. Sosedko, *Fluid Dynamics* (1995), vol. 30, pp. 210-218.
- [3] M. J. Barrett and D. K. Hollingsworth, *J. Turbomachinery* (2003), vol. 125, pp. 232-251.
- [4] K. Nagata, Y. Sakai and S. Komori, *Phys. Fluids* 23 (2011), 065111.

Modal Analysis of Pressure Sensitive Paint Data

Markus Pastuhoff¹, Daisuke Yorita², Nils Tillmark¹, P. Henrik Alfredsson¹ and Keisuke Asai²

¹CCGEx, KTH Royal Institute of Technology, Dept. of Mechanics, SE-100 44 Stockholm, Sweden

²Dept. of Aerospace Engineering, Graduate School of Engineering, Tohoku University, Aoba-ku, Sendai, Japan
markuspa@mech.kth.se

ABSTRACT

In this work, proper orthogonal decomposition (POD) was used to separate coherent structures from noise in pressure sensitive paint (PSP) data acquired by high-speed photography on the side of a square cylinder in a natural periodically fluctuating flow.

1. Introduction

Pressure sensitive paint (PSP) is an optical technique for measuring surface pressure by utilizing the effect of oxygen quenching found in certain luminescent substances. In the luminescent process, photons are absorbed as energy by the electrons of a molecule, bringing them to a higher energy state. Upon relaxation back to the ground state the excess energy is released as photons of lower energy, and hence of longer wavelength. If the excited molecule is in contact with an oxygen molecule the excess energy may instead be transferred to the oxygen; the luminescence is quenched by oxygen and no photon is emitted. On a macroscopic scale the intensity of the emitted light is inversely proportional to the partial pressure of oxygen in the surrounding gas, and in case of constant oxygen concentration: pressure.

To use PSP to measure the pressure on a surface, the luminescent substance is usually bound in an oxygen permeable polymer binder that is painted on the surface. The paint is excited by LED or laser light and luminescence is captured using photo multiplier tubes or digital cameras. For further information on PSP, see reference [1].

With the introduction of high-speed high dynamic range cameras, a new realm has opened in the PSP area. However, with the large amount of raw data associated to these experiments there is a need for good data reduction methods in order to interpret the results.

In computational fluid dynamics as well as for some experimental methods that gives spatial information (e.g. particle image velocimetry) proper orthogonal decomposition (POD) is a common technique that is used to divide a flow field into spatially coherent structures evolving in time such that

$$\xi(\bar{x}, t) = \sum_{j=0}^{\infty} a_j(t) \cdot \bar{\phi}_j(\bar{x}) \quad (1)$$

where ξ represents some property (e.g. velocity or pressure) of the flow, a denotes temporal modes, ϕ spatial modes, and j is the mode number.

Features of POD are that the lower modes contain the structures with the most energy and that the structures of each mode are uncorrelated (orthogonal) to those of all other modes. In addition, POD is optimal in an energy sense; no other decomposition of equal order can capture the same amount of energy.

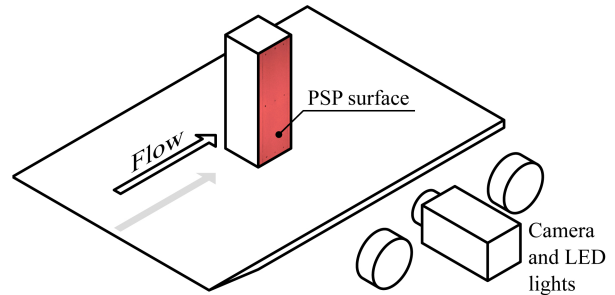


Fig. 1 Experiment setup.

For a more thorough treatment on the POD technique the reader is referred to reference [2].

Other evaluation methods, covered in reference [3], have previously been used on similar experiment data.

2. Experimental set-up and data evaluation

A square cylinder with a base of 40x40 mm² and a height of 120 mm had one of its sides painted with a PtTFPP based polymer-ceramic pressure-sensitive paint on a titanium-dioxide base layer as described in reference [4]. The model was placed on a flat plate in a wind tunnel such that the painted side was parallel to the flow, as illustrated in figure 1. The free-stream velocity of the flow was 50 m/s.

Continuous LED light was used as the source for illumination and luminescence was captured using a high-speed digital camera set to a frame rate of 2000 fps. The experiment was performed at Tohoku University in the basic aerodynamic wind tunnel (T-BART).

A subset of 2000 images was chosen for the POD-analysis carried out according to the so-called snapshot method. An n -by- m matrix \mathbf{X} was formed from the image intensities, I , such that n was the spatial, and m the temporal dimension. For each point, the temporal mean of that point was subtracted.

The \mathbf{X} matrix was subjected to singular value decomposition, solving

$$\mathbf{X} = \mathbf{U}\mathbf{\Sigma}\mathbf{V}^T \quad (2)$$

where \mathbf{U} and \mathbf{V} are orthonormal matrices and $\mathbf{\Sigma}$ diagonal. Obtaining \mathbf{U} , \mathbf{V} , and $\mathbf{\Sigma}$ the spatial and temporal modes was calculated according to

$$[\bar{\phi}_0(\bar{x}), \dots, \bar{\phi}_{m-1}(\bar{x})] = \mathbf{U} \quad (3)$$

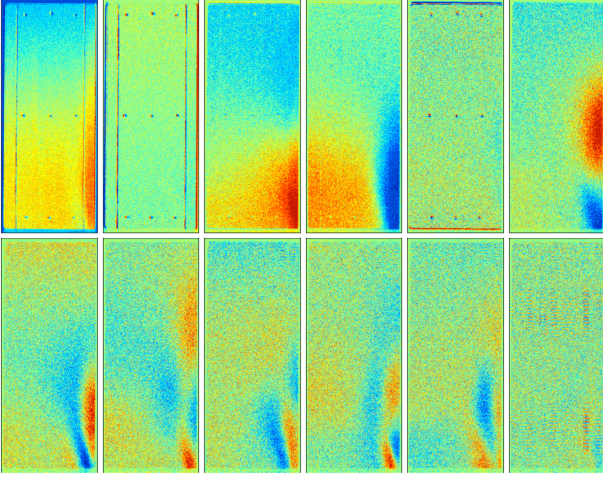


Fig. 2 First 12 spatial modes. Amplitudes are normalized by the standard deviation of respective field. Flow is from left to right.

$$\begin{bmatrix} a_0(t_0) & \cdots & a_0(t_{m-1}) \\ \vdots & \ddots & \vdots \\ a_{m-1}(t_0) & \cdots & a_{m-1}(t_{m-1}) \end{bmatrix} = \Sigma \mathbf{V}^T. \quad (4)$$

The relative modal energies λ_j were obtained from

$$[\lambda_0, \dots, \lambda_{m-1}] = [(\Sigma_{0,0})^2, \dots, (\Sigma_{m-1,m-1})^2]. \quad (5)$$

The spatial modes were inspected (figure 2) and unwanted modes were removed; in this case modes one and four, showing structural vibration in the horizontal and vertical directions respectively, and modes 11 and above, which show small scale structures and incoherent noise. For comparison, modes 11 and those above each contain less than 2.2% of the energy of mode 0.

The intensity field was then reconstructed according to (1) with $j = [0, 2, 3, 5, \dots, 10]$, the previously subtracted mean field was added and also used as the reference intensity to calculate I_{ref}/I , which relates to the pressure by the well known Stern-Vollmer relation,

$$\frac{I_{ref}}{I} = A + B \frac{p}{p_{ref}} \quad (6)$$

where A and B are calibration coefficients and I_{ref} the intensity at a reference pressure p_{ref} . The comparison was made between the intensity ratios of the raw intensity field and the reconstructed field.

3. Results and Discussion

Figure 3 shows the comparison between the raw intensity ratios and the reconstructed ratios. Note that what is shown in figure 3b is an instantaneous field and that no phase averaging or similar has been performed.

In figures 3c and 3d reconstruction is shown for two points in time compared to the spatial averages of 7 by 7 pixels from the raw intensity ratios. This comparison shows that the reconstruction follows the true behaviour well and that phase information is not lost.

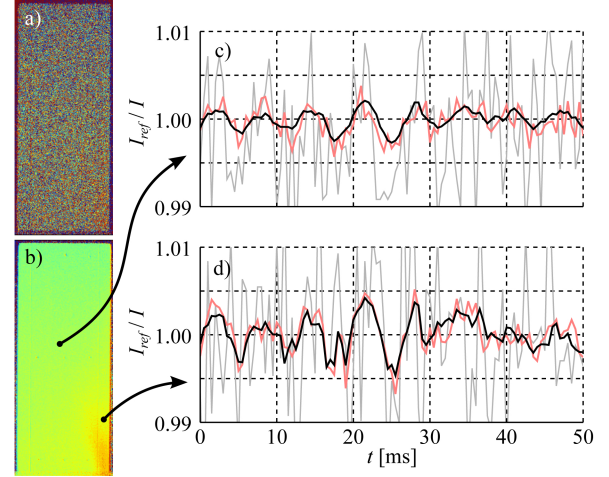


Fig. 3 I_{ref}/I for a) raw data at $t = 2$ ms, b) reconstructed data at $t = 2$ ms and c-d) time series for raw data single pixel (grey), raw data 7x7 pixel average (red) and reconstructed single pixel (black). For a) and b) the range is 0.99 (blue) to 1.01 (red).

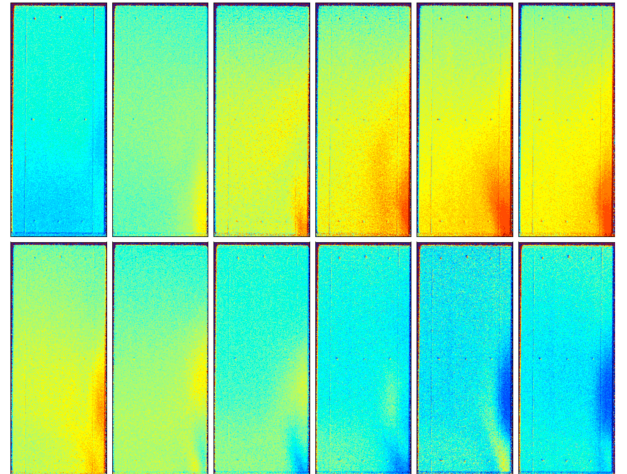


Fig. 4 First 12 reconstructed I_{ref}/I fields ranging from 0.995 (blue) to 1.005 (red). Time between snapshots is 0.5 ms.

A series of 12 instantaneous snapshots (out of the set of 2000) of the reconstructed field is shown in figure 4, clearly indicating the pressure variations over one period of the vortex shedding frequency.

4. Acknowledgements

This research was financed through the Japanese Global Centers of Excellence Program and the Swedish Energy Agency, which is greatly acknowledged.

References

- [1] T. Liu and J. P. Sullivan, *Pressure and Temperature Sensitive Paints*, Springer Verlag (2005)
- [2] H. Nobach et al, In *Springer Handbook of Experimental fluid mechanics*, ed C. Tropea et al, Springer Verlag (2007), p 1346–69
- [3] K. Asai and D. Yorita, AIAA-2011-847 (2011)
- [4] J. Gregory et al, In *Proc. IMechE G* **222** (2008)

Propagation Process of Streamer Discharge in Water

Hidemasa Fujita¹, Seiji Kanazawa², Kiyonobu Ohtani³, Atsuki Komiya³ and Takehiko Sato³

¹Graduate School of Engineering, Tohoku University, 2-1-1 Katahira, Aoba-ku, Sendai, 980-8577, Japan

²Department of Electrical and Electronic Engineering, Faculty of Engineering, Oita University, Oita, 870-1192, Japan

³Institute of Fluid Science, Tohoku University, 2-1-1 Katahira, Aoba-ku, Sendai, 980-8577, Japan

E-mail: sato@ifs.tohoku.ac.jp

ABSTRACT

A series of the processes of streamer propagations was successfully visualized using an ultra high-speed camera with a microscope lens. After 600 – 800 ns from a single-shot pulse voltage of 16.5 kV applied, a primary streamer accompanying a shock wave started to propagate with current pulses of less than 300 mA. It was clarified that secondary streamers propagated both inside and outside of the shock wave was occurred during the primary streamer propagation process. The discharge current of the secondary streamers was less than 500 mA in the case of inside of the shockwave though the current was more than 3 A in the case of outside of the shockwave.

1. Introduction

A streamer in water is known as a pre-breakdown phenomenon, which forms a strong electric field at the tip, shock waves, micro bubbles, ultraviolet rays and active species such as reactive oxygen species. These phenomena can degrade organic compounds [1] and destruct microorganisms in water [2]. Therefore water purification is considered to be one of expected applications of water discharges [3]. A streamer discharge in water has been also applied to a medical field in recent years [4].

A propagation mechanism of a streamer discharge has been studied for a long time [5-8]. The proposed mechanisms for the streamer propagation in water are (1) mechanisms are (1) ionization breakdown and (2) gas phase breakdown. However, both mechanisms have been still supported by researchers since it is difficult to observe the details of the phenomena due to the nano-micro temporal and spatial scale, and its statistical phenomenon.

In this study, a series of the streamer discharge connected with the discharge current was visualized using an ultra high-speed camera with a microscope lens, to elucidate the processes of the streamer discharge in water. To observe the fundamental phenomena, a single-shot pulse voltage was applied in the ultrapure water.

2. Experimental Methods

A needle-wire discharge system was set in a quartz glass cell, which is 45 mm in height, 10 mm in width and 10 mm in depth. For the electrodes the platinum wire of 0.5 mm in diameter was applied. Both the needle and wire electrodes were covered with insulation tubes that have 1.2 mm in outside diameter except the discharge parts. The tip of the needle electrode was sharpened to be about 40 μm in curvature. A single-shot pulse voltage of 16.5 kV with the width of 10 μs was applied to the needle electrode. The wire ground electrode was set at 6

mm below the tip of the needle electrode. The cell was filled with ultrapure water of about 0.8 $\mu\text{S}/\text{cm}$.

To generate a single-shot pulse voltage, a MOS-FET switch (BHELIKE, HTS 651-03-LC) was used. This switch was turned on by a signal from a function generator (NF, WF11976) and the voltage was applied to the pin electrode. The signal was transferred to a delay generator (Stanford Research Systems, DG645), which sent a signal with some delay and the delay adjust the shutter timing of an ultra high-speed camera (DRS Technologies, IMACON200) with a microscope lens (Keyence, VH-Z50L) to the moment of the streamer discharge. The applied voltage and the discharge current were measured by a high voltage probe (Iwatsu, HV-P30) and a current probe (Pearson, Model 2878), respectively. The waveforms are monitored by an oscilloscope (LeCroy, WaveSurfer 104MXs) in addition to the shutter gate signal from the camera. To visualize the phenomena a He-Ne laser (NEOARK, NEO-50MS) was applied as a light source. All images were taken by shadowgraph technique.

3. Results and Discussion

Figure 1 show the sequence images of the primary streamer propagation from the initiation. The interval of each photographs from (a) to (g) was 100 ns and the applied voltage was 16.5 kV as shown in (h). The displacement current was observed when the voltage rose, and then the small pulse currents started to appear with generation of the primary streamer. The shockwave shown in Fig.1 (b)-(g) was also observed at the front edge of the primary streamer and the fan-shaped primary streamer expanded shown in (b)-(d). At 400 ns shown in (e), ramosé shadows appeared and elongated with the expansion of the primary streamer. The discharge current was less than 500 mA through the propagation process.

Figure 2 shows the sequence images of the secondary streamer propagation. All images were taken continuously with the interval and exposure times of 80

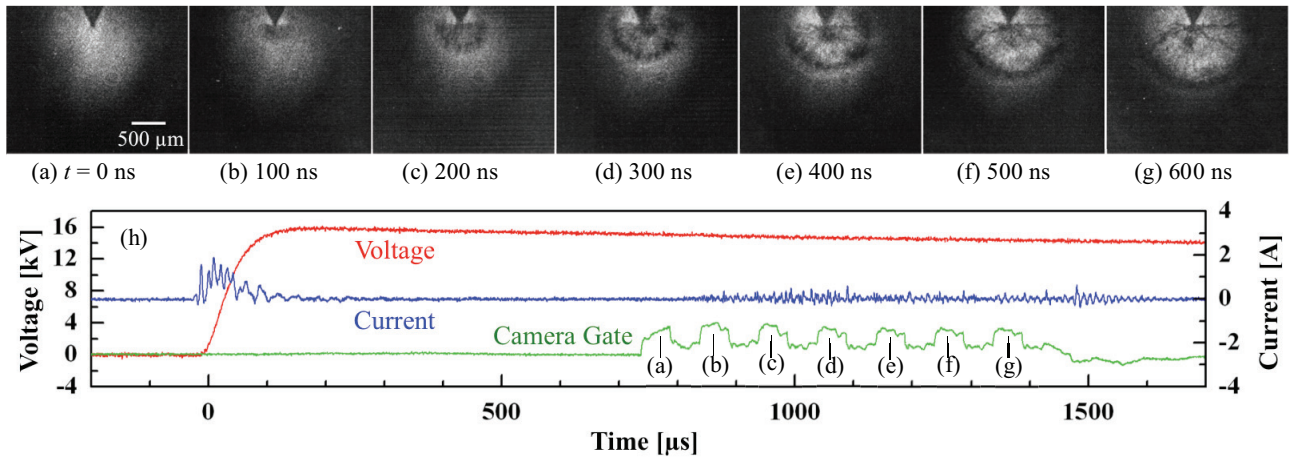


Fig. 1 (a)-(g) A series of successive shadow images of initiation and primary streamer (Voltage: 16.5 kV, Exposure time: 100 ns); (h) waveform of applied voltage and discharge current connected with the moment of (a)-(g).

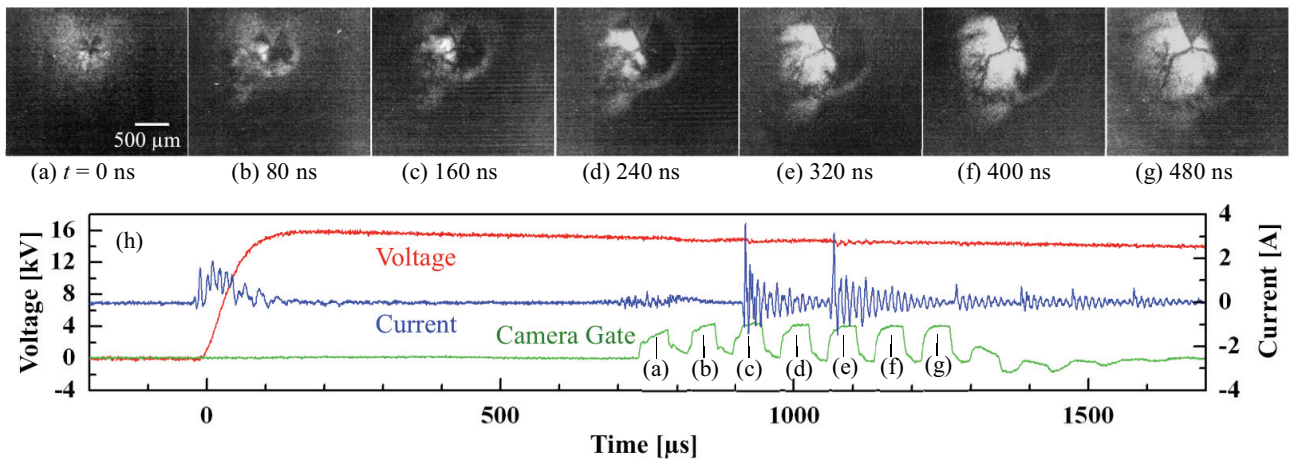


Fig. 2 (a)-(g) A series of successive shadow images of initiation and primary streamer (Voltage: 16.5 kV, Exposure time: 80 ns); (h) waveform of applied voltage and discharge current connected with the moment of (a)-(g).

ns. After primary streamers initiated with current pulses as shown in (a), a secondary streamer started to propagate with the non-pulse current of about 300 mA as shown in (b). During this current flowing, the secondary streamer cut across the front edge of the shock wave of the primary streamer and elongated to outside. The secondary streamer extended with large current pulses of more than 3 A. These current pulses are considered to flow in the gas channels formed by joule heating after the streamer propagation. Besides the minus current might imply the current flows in the gas channels reversely.

4. Conclusion

A series of the streamer propagation in water was successfully visualized using an ultra high-speed camera system with a microscope lens, connected with the discharge current. After 600 - 800 ns from the applying voltage of 16.5 kV, a primary streamer started to propagate accompanying with the shock wave from the tip of the needle electrode and with the maximum current pulses of less than 300 mA. A secondary streamer, which follows a primary streamer, has two propagation modes: the propagation outside of the shock wave, which is launched with a primary streamer, with the non-pulse

current of about 300 mA and the repeated current pulses of about 3 A, and the propagation inside of the shock wave with current pulses of about 500 mA.

Acknowledgements

This study was partly supported by the JSPS, Grant-in-Aid for Scientific Research and the Collaborative Research Project of the Institute of Fluid Science, Tohoku University and We thank Tomoki Nakajima (Tohoku University) for technical support.

References

- [1] B. Sun *et al.*, *J. Phys. D: Appl. Phys.* **32** (1999), 1908.
- [2] A. Mizuno and Y. Hori, *IEEE Trans. Ind. Appl.*, vol. **24**, No. 3 (1988), 387.
- [3] A. M. Anpilov *et al.*, *Lett. Appl. Microbiol.*, vol. **35**, No. 1 (2002), 90.
- [4] K. R. Stalder *et al.*, *J. Phys. D: Appl. Phys.*, vol. **38** (2005), 1728.
- [5] W. An *et al.*, *J. Appl. Phys.*, **101** (2007), 053302.
- [6] S. Kanazawa *et al.*, *IEEE Trans. Plasma Sci.*, **36** (2008), 922.
- [7] P. H. Ceccato *et al.*, *J. Phys. D: Appl. Phys.*, **43** (2010), 175202.
- [8] S. Kanazawa *et al.*, *I. J. PEST*, Vol. 6, No. 1 (2012), 49.

Combined Pressure- and Temperature-Sensitive Paint Using Porphyrins and Quantum Dots

Tomohiro Kameya^{*1}, Yu Matsuda^{*1}, Yasuhiro Egami^{*2}, Hiroki Yamaguchi^{*1} and Tomohide Niimi^{*1}
^{*1} Dept. of Micro-Nano Systems Engineering, Nagoya University, Nagoya, Aichi 464-8603, Japan
^{*2} Dept. of Mechanical Engineering, Aichi Institute of Technology, Toyota, Aichi 470-0392, Japan
kameya.tomohiro@c.mbox.nagoya-u.ac.jp

ABSTRACT

In the pressure-sensitive paint (PSP) measurements, temperature sensitivity of PSP is one of the crucial problems from the view point of its measurement accuracy. We fabricated a combined PSP and temperature-sensitive paint (TSP) using platinum porphyrin (PtTFPP) and a quantum dot (CdSe/ZnS) as PSP and TSP luminophores, respectively. Quantum dots have favorable features as TSP luminophore such as high quantum yield, tunable luminescence peak, narrow full width at half maximum, and broad absorption band. In this paper, we examined pressure and temperature sensitivities of the combined paint.

1. Introduction

Pressure-sensitive paint (PSP) [1] has been used for pressure measurements on a solid surface. The surface pressure is non-intrusively obtained from the luminescence intensity of PSP. In general, since the luminescence is also thermally quenched, PSP result has to be compensated by surface temperature when the temperature distribution is not uniform on a measured surface. Temperature-sensitive paint (TSP), whose pressure sensitivity is negligibly small, is promising temperature sensor for the compensation, because most of the apparatuses can be shared with the PSP measurement. In previous studies, for symmetric flow fields around a symmetric model, temperature correction was carried out by coating PSP and TSP on starboard and port side of the model, respectively, under the assumption that pressure and temperature distributions were also symmetric [2]; however, this method cannot be applied to asymmetric flow fields.

To overcome this drawback, we fabricated a combined pressure- and temperature-sensitive paint, mixture paint of PSP and TSP. The combined paint was composed of PSP luminophore: platinum porphyrin (PtTFPP), and TSP luminophore: quantum dot (CdSe/ZnS). This paper reports pressure and temperature sensitivities of the combined paint.

2. Composition of combined PSP and TSP

A combined pressure- and temperature-sensitive paint enables us to simultaneously measure the surface pressure and temperature by separately detecting luminescence from each luminophore. It is preferable that both luminophores are excited by a single illumination light source, and that their luminescence can be separated each other by only optical filters, because the measurement system is favorable to be simple.

We employed PtTFPP as a pressure sensitive luminophore due to its high pressure sensitivity near an atmospheric pressure. The absorption and emission spectra of PtTFPP have peaks at 395nm and 650nm, respectively [3, 4]. CdSe/ZnS is one of favorable candidates of the temperature sensitive luminophore due to its following notable features: high quantum yield (30-50%), tunable peak wavelength of the luminescence (from 480 to 640nm), narrow full width at half maximum (narrower than 40nm), and broad absorption

spectrum (from UV to visible light) [5]. We employed CdSe/ZnS with luminescence peak at 530nm (Lumidot 530, Sigma-Aldrich) as TSP luminophore.

3. Sample preparation and experimental apparatus

3.1 Sample preparation

PtTFPP and CdSe/ZnS mixture cocktail was prepared by dissolving 0.1mg of PtTFPP and 0.5mg of CdSe/ZnS into 1mL of toluene. A sample coupon of combined paint was made by dipping a TLC plate into the solution for 60min. For comparison, sample coupons of mono paint (PtTFPP or CdSe/ZnS) were also made in the same way as the combined paint one. Concentrations of the toluene solutions for mono paints were 0.1mg/mL (PtTFPP) and 0.5mg/mL (CdSe/ZnS), respectively.

3.2 Experimental apparatus and procedure

Figure 1 shows an experimental apparatus for pressure and temperature calibrations. The prepared sample coupons were placed on a Peltier device set in a chamber, and illuminated by the light of a xenon short arc lamp through a band-pass filter (395±5nm). The pressure in the chamber was adjusted by using a pump and dry air (O₂: 21%, N₂: 79%). The luminescence emitted from the sample was detected by a 12-bit CCD camera (Imager Compact, LaVision). An appropriate band-pass filter, 670±60nm for PtTFPP and 530±60nm for CdSe/ZnS, was set to a camera lens to detect only the luminescence emitted from each luminophore of the combined paint.

Pressure sensitivity was examined at 293K. The pressure in the chamber was varied every 10kPa from 80 to 120kPa. Temperature sensitivity was examined at 101kPa. The sample temperature was varied every 5K from 293 to 313K by the Peltier device. In the calibrations, four images were averaged at each measuring point to reduce shot noise.

4. Results and Discussion

Pressure sensitivity of the combined pressure- and temperature-sensitive paint is shown in Fig. 2. The results of PtTFPP and CdSe/ZnS mono paint are also plotted in the figure. PtTFPP of the combined paint has a pressure sensitivity of 0.77%/kPa. The sensitivity is almost the same as that of PtTFPP mono paint. On the other hand, CdSe/ZnS of the combined paint has little sensitivity against pressure variation, less than

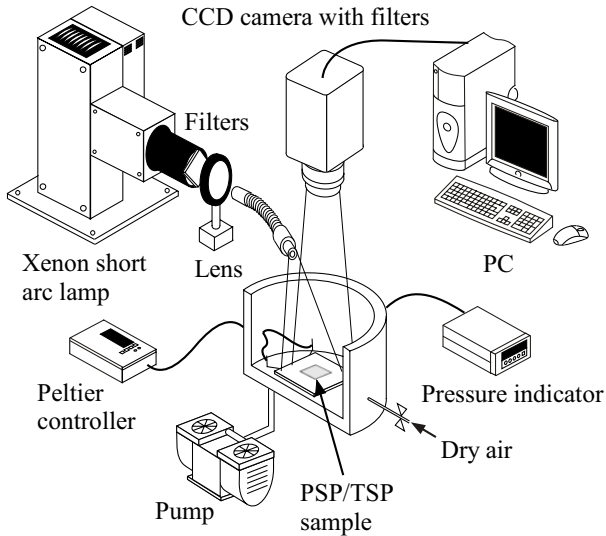


Fig. 1 Experimental apparatus.

0.04%/kPa, which is almost the same as that of CdSe/ZnS mono paint.

Figure 3 shows temperature sensitivity of the combined paint and those of mono paints. It can be seen that PtTFPP has a large temperature sensitivity of $-1.23\%/K$, and CdSe/ZnS has the sensitivity of $-0.84\%/K$, which were comparable to mono paints.

These results show that PtTFPP and CdSe/ZnS do not suffer from the degradation of pressure and temperature sensitivities, even when they are mixed in the same paint.

5. Conclusions

A combined pressure- and temperature-sensitive paint was fabricated by dipping a TLC plate into PtTFPP and CdSe/ZnS mixture cocktail. As a result of the pressure sensitivity and temperature sensitivity tests, the following conclusions were obtained;

1. PtTFPP kept its large pressure sensitivity ($0.77\%/kPa$) even when mixed with CdSe/ZnS.
2. CdSe/ZnS had little pressure sensitivity (less than $0.04\%/kPa$) and had sufficient temperature sensitivity of $-0.84\%/K$.

Acknowledgment

This research was supported in part by Grant-in-Aid for Scientific Research of the MEXT and JSPS, by research grants from the Circle for the Promotion of Science and Engineering and from the Nagoya University Global Center of Excellence (GCOE) Program. We would like to acknowledge here the generosity of these organizations.

References

[1] Liu T. and Sullivan J. P., *Pressure and temperature sensitive paints*, Springer, 2005.

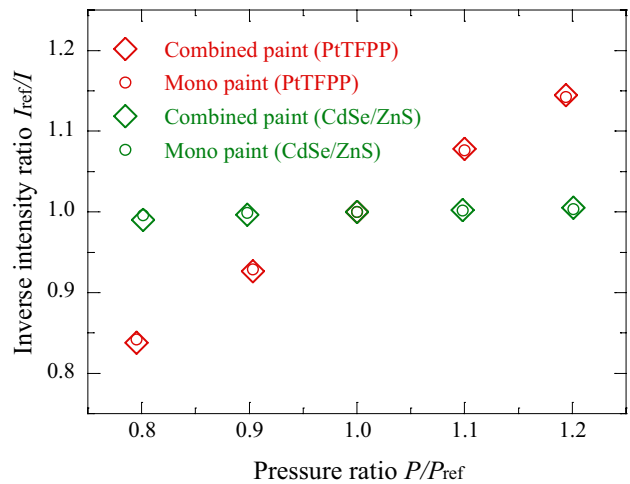


Fig. 2 Pressure sensitivity; Stern-Volmer plot.

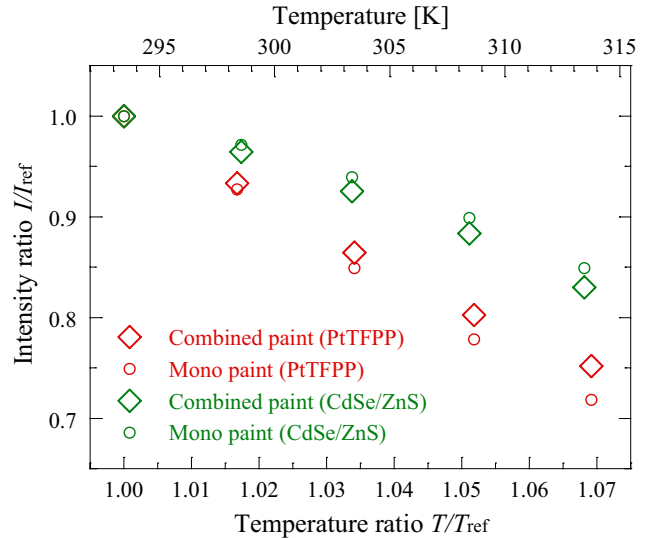


Fig. 3 Temperature sensitivity.

- [2] Kameda M. et al., Unsteady measurement of a transonic delta wing flow by a novel PSP, *26th AIAA applied Aerodynamics Conference*, AIAA Paper 2008-6418.
- [3] Amao Y. et al., Platinum tetrakis (pentafluorophenyl)porphyrin immobilized in polytrifluoroethylmethacrylate film as a photostable optical oxygen detection material, *Journal of Fluorine Chemistry*, Vol. 107, Issue 1, (2001), pp. 101-106.
- [4] Borisoc S. et al., New NIR-emitting complexes of platinum(II) and palladium(II) with fluorinated benzoporphyrins", *Journal of Photochemistry and Photobiology A: Chemistry*, Vol. 201, Issue 2-3, (2009), pp. 128-135.
- [5] <http://www.sigmaldrich.com>

Quantitative Evaluation of Flow Visualization

Ardian B. Gojani, Shigeru Obayashi
Institute of Fluid Science, Tohoku University
2-1-1 Katahira, Aoba, Sendai 980-8577, Japan
gojani@edge.ifs.tohoku.ac.jp

ABSTRACT

Development of background oriented schlieren technique for flow visualization is advanced by studying the extraction of quantitative data from images of flow. The sensitivity and uncertainties of the technique are investigated. Geometrical arrangement of the instruments can be adjusted so that sufficient sensitivity and accuracy achieved. The main factor in uncertainty of measurements comes from image evaluation, which is usually done by cross-correlation. The image blurring is investigated and found to effect the evaluation of the amount of pixel shift. As an example, quantitative visualization of cooling by natural convection is given.

1. Introduction

In the previous ICFD, preliminary results related to the development of background oriented schlieren (BOS) were given [1]. This current paper presents further developments, with a focus on the extraction of quantitative measurements of flow field from BOS visualization. The renewed interest in quantitative schlieren based visualization is primarily due to the advances in digital image analysis. This paper will treat changes in an imaged pattern due to flow field (pattern deflectometry), rather than the change in the image illuminance (photometry, as applied in standard schlieren).

2. Image Recording

A light ray that images a dot from a background to an image sensor can be deflected in its path, if it transverses a medium with a spatially changing density. Assuming a minute angle of deflection ε , the imaged dot shift will be

$$\Delta = M s_t \varepsilon \quad (1)$$

where M is the optical magnification of the BOS imaging system, and s_t is the distance between the flow field and the background. The relationship between the angle of deflection and the density gradient of the medium is given by

$$\varepsilon = \frac{L}{(1+K\rho(0))} \frac{\partial(1+K\rho(r))}{\partial r} \quad (2)$$

where L is the distance flow field -- image sensor, K is the Gladstone-Dale constant, ρ is density, and r is the distance of the medium point where the density is being measured from the optical axis [2]. $\rho(0)$ is the reference density of unperturbed medium. Elimination of ε from Eqs. (1) and (2) gives the density gradient as a function of measurable (Δ , s_t , L) and tabulated ($\rho(0)$, K) parameters.

The sensitivity of the system is

$$S = M s_t \quad (3)$$

On the other hand, since the imaging sensor is made of a rectangular grid of pixels, each integrating the light acquired from the incident cone of light, a point from the background is imaged into an area corresponding to the size of the pixel Δ_{px} . Thus, the image plane gives a

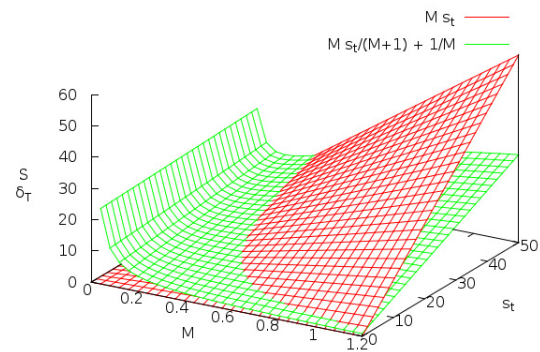


Fig. 1 Surface plot of sensitivity (red, Eq. 3) and uncertainty (green, Eq. 4) of a BOS system.

discretized picture of the field of view, a feature that provides the lower limit for the spatial resolution of the BOS system. Numerically, this value is

$$\delta_t = \frac{M}{M+1} \frac{s_t}{f_{\#}} + \frac{\Delta_{px}}{M} \quad (4)$$

where $f_{\#}$ is the f-number of the lens. Figure 1 shows the plot of the sensitivity S and uncertainty δ , as functions of magnification M and distance background-flow field s_t for unit values of $f_{\#}$ and Δ_{px} .

3. Image Evaluation

While the measurements of s_t and L are quite straightforward, evaluation of Δ is done only through image analysis, which for a BOS measurement consists of comparison of an image pair by the cross-correlation method, each image of the pair corresponding to a different state of the fluid flow. Initially, a subsection of one of the images (representing the interrogation window IW) is defined, and then its grayscale values are compared to grayscale values of all equal subsets of the other image. The result of the cross-correlation is a spatial displacement vector \mathbf{d} , which relates the correlation peaks. Applying a three point Gaussian peak detection scheme, this vector can be determined with an accuracy better than 0.1 pixel. The magnitude of \mathbf{d} is the amount of pixel shift of a background pattern due to light ray deflection, Δ .

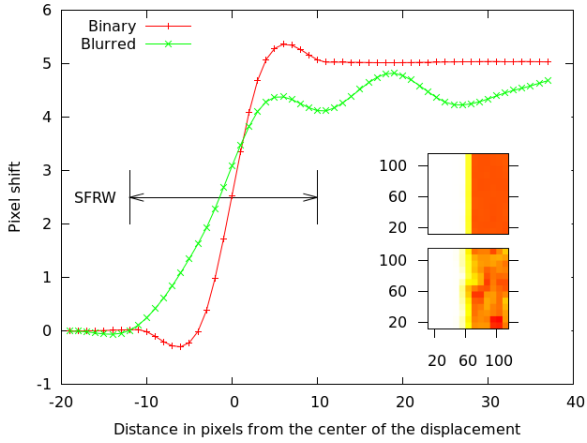


Fig. 2 Pixel shift evaluation by cross-correlation of binary (inset, up) and Gaussian blurred (inset, bottom) synthetic images. Tics in insets are image pixels.

4. Uncertainties

There are several sources of uncertainties in flow visualization measurements, which can be divided into two main categories: (i) those due to specifications of instruments, and (ii) those that arise from image analysis. In practice, the dominant type of uncertainties belong to the second type, because the arrangement of the instrumentation in a BOS system allows adjustments of sensitivity and spatial resolution.

Displacement vector obtained by image analysis is influenced by IW, pattern size, spatial frequency of pattern texture, and gradients within IW, which are responsible for error sources such as peak locking effect, pattern smoothing from non uniform image blur, etc. An example of the last effect will be given. A binary synthetic image (128×128 pixels, 50% dot coverage) is treated by a step function

$$H[N]=\begin{cases} 0, N < 0 \\ 1, N \geq 0 \end{cases} \quad (5)$$

In the simulation, half of a synthetic image (so, $N=i_{\max}/2$, where i_{\max} is the horizontal pixel count) is displaced horizontally for 5 pixels. Then, a Gaussian smoothing with 2 px radius is applied to both images, to simulate image blur. The comparison of cross-correlation based evaluations with IW=16 px is shown in Fig. 2. The effect of blurring in the step function response width (SFRW, as defined in [3]) is negligible, but this is not the case for the evaluation of the amount of pixel shift Δ . The blurring of the image has the effect of reducing the value of Δ for about 10% and introducing fluctuations in its behavior, because, as compared to a binary image, now the image is populated by all possible grayscale values and pattern spatial frequency is not conserved.

5. Quantitative Visualization of Natural Convection

BOS has been applied to visualization of natural convection. The quasi-steady flow field around an horizontally placed radiating cylinder, enclosed in a box and monitored by 8 thermocouples, was photographed by a DSLR camera (4928×3264 pixel count, 5 μm pixel

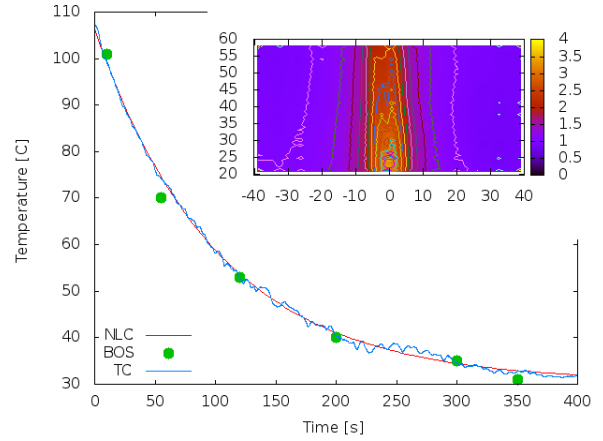


Fig. 3 Quantitative BOS results for cooling by natural convection (in the inset), and the comparison of BOS data to thermocouple readings (TC) and Newton's Law of cooling (NLC). Coordinates in the inset give the the distance in mm from the center of the heat source, and the magnitude bar shows the pixel shift.

size). A uniform random distribution of black dots printed on a white sheet of paper constituted the imaged background. A dot covered 8×8 pixels, and the background had a dot coverage of 50%. The magnification of the system was $M=0.15$, with 30 px imaging 1 mm of the field of view. The result of the measurement is shown in Fig. 3. Overall, a satisfactory agreement between BOS, thermocouple, and theory based on Newton's Law of cooling is achieved, with BOS uncertainty comparable to that of thermocouples, namely 0.1 degree.

6. Conclusion

The development of BOS is advanced by looking at the extraction of quantitative data from images. Investigation of the geometrical arrangement of the instruments used for a BOS visualization reveal that arbitrary sensitivity and accuracy can be achieved. This, though, is later influenced by image evaluation. Uncertainties related to the point of measurement are influenced by the IW, defining the spatial resolution of the measurement, while image blurring influences determination of pixel shift. BOS technique was applied to cooling by natural convection, in which case results comparable to thermocouple readings were achieved.

Acknowledgements

This work was supported by Global COE Program "World Center of Education and Research for Trans-disciplinary Flow Dynamics," Tohoku University, Japan.

References

- [1] A. B. Gojani, T. Mizukaki, T. Ogawa, K. Ohtani, T. Kikuchi, T. Yoneyama and S. Obayashi, Proc. 8th ICFD, (2011), p. 96.
- [2] G. S. Settles, *Schlieren and Shadowgraph Techniques*, Springer, (2006), p. 27.
- [3] C. J. Kahler, S. Scharnowski and C. Cierpka, Exp. Fluids **52**(2012), p. 1269.

A Realizable Microelectromechanical-System-Based Triple-Axis Fluidic Gyroscope Sensor

Thien X. Dinh, Yoshifumi Ogami

Department of Mechanical Engineering, Ritsumeikan University
1-1-1 Nojihigashi, Kusatsu, Shiga, 525-8577 Japan
thien@cf.ritsumei.ac.jp

ABSTRACT

In this paper, we present a realizable structure and simulation of a triple-axis microelectromechanical system (MEMS)-based fluidic gyroscope sensor. In the sensor, four axisymmetric jets comprising two perpendicular pairs of flows are generated in a fluidic network by a piezoelectric actuator, without requiring any check valve. The structure of the sensor is considered to diminish the cross-sensitivity between the horizontal and vertical components of angular rate. The hot wires can be fabricated by a mass standard MEMS process with only one mask.

1. Introduction

Recently, the market for microelectromechanical system (MEMS)-based inertial sensors has broadened to include newer applications, such as in airplanes, spacecraft, missiles, automobiles, video games, gesture recognition, and robotics. In this study, we develop and aim to realize a triple-axis MEMS-based fluidic gyroscope. The fluidic network structure of the gyroscope is simple and is compatible with the hot embossing technique. The sensing elements are located on a cavity surface; therefore, they can be easily fabricated by MEMS technology using only one mask. The characteristics of the gyroscope are fully analyzed with the effect of the boundary and applied angular rate.

2. Design and simulation

The schematic design of the sensor is shown in Fig. 1. The fluidic network and pump chamber are fabricated on a polymer layer by a hot embossing technique. A vibratory diaphragm on the top of the pump chamber will periodically inspire and expel gas from the pump chamber. Then, on account of the rectification effect of the network channel, a net jet flow is generated in the four measured chamber.

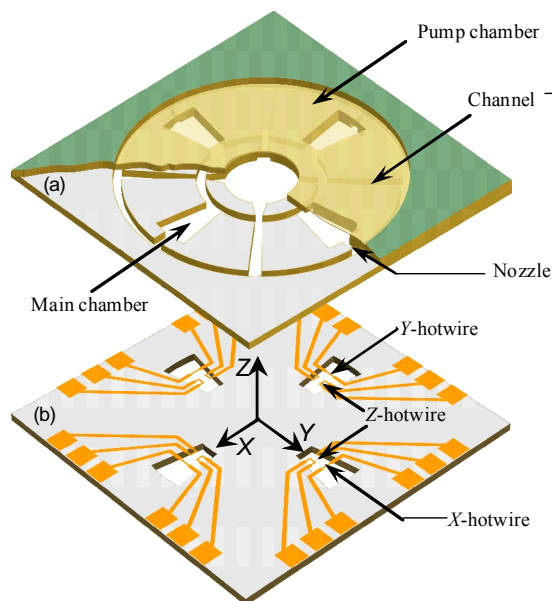


Fig. 1 Schematic design of the sensor.

The operation of the gyroscope relies on the Coriolis acceleration, which is proportional to the jet flow velocity \vec{V} and the angular rate $\vec{\Omega}$ applied to the gyroscope $\vec{a}_{\text{coriolis}} = -2\vec{\Omega} \times \vec{V}$.

The simulation is performed by using FLUENT 14, ANSYS Inc. which uses a control-volume-based technique to convert the Navier-Stokes equations to numerically solvable algebraic equations. SIMPLE algorithm is employed for pressure-velocity coupling. For spatial discretization of the momentum, density, and energy, the second-order upwind scheme is used. The calculation is advanced with time by implicit second-order scheme.

3. Results and discussion

3.1 Flow characteristics

The variation of the time-averaged velocity at a probe located in the hotwire region with the excitation frequency on the diaphragm is plotted in Fig. 2. The time-averaged velocity increases up to a certain frequency and then decreases with increasing frequency. Above this particular frequency, the gas does not have enough time to respond to the diaphragm frequency. As shown in the figure, the resonant frequency of the response is $f = 6.5$ kHz, regardless of the angular rate applied to the sensor.

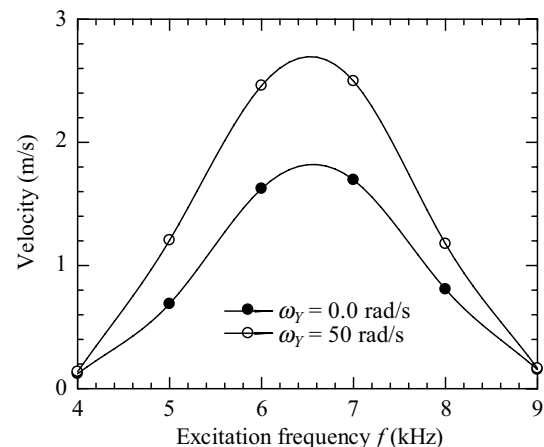


Fig. 2 Response of the velocity at a probe point in the region containing the hotwire under application of an excitation frequency to the diaphragm.

3.2 Angular rate measurement

As the flow frequency is 6.5 kHz and frequency response of the hotwire is up to 300 kHz, we can characterize the heat transfer of the hotwire in equilibrium condition with the time-averaged velocity of the jet

$$I^2 R_{HW} = hA(T_{HW} - T_a) \quad (1)$$

where the radiation and conduction to the wire supports are neglected, c_{HW} , R , and A are the heat capacity, resistance, and surface area, respectively, of the hotwire; h is the heat transfer coefficient; and T_a is the reference temperature. The left-hand side represents the Joule heating power with current I , while the right-hand side represents heat transfer to the surroundings. The resistance R_{HW} of the hotwire depends on temperature:

$$R_{HW} = R_a [1 + \alpha(T_{HW} - T_a)] \quad (2)$$

where R_a and α are the resistance at temperature T_a and the temperature coefficient of resistance of the hotwire, respectively.

Figure 3 plots the variation in the simulated output of a pair of hotwires Y and Z with changes in the applied angular rate. The measurement of the X -component of the angular rate is equivalent to the Y -component, because the X -hotwire is simply rotated 90° about the Z -axis. The measurement principle is based on hotwire anemometry, where the output voltage is approximated by King's law. In addition, the velocity difference due to the angular rate has a linear relation with the applied angular rate, since the flow deflection is small and the hotwire is placed in a narrow region. Therefore, the profiles of G/E are in a polynomial shape, as shown in Fig. 3. In this figure, the results are fitted with a second-order polynomial function by the least squares technique. It is observed that the sensor is applicable for triple-axis measurements for an angular rate of up to 50–60 rad/s, whereas the sensor can be used up to an angular rate of 80 rad/s for dual-axis measurement (for the X -axis and Y -axis).

Figure 4 shows the percentage of cross-sensitivities of the sensor, S_{ZY} and S_{YZ} . The cross-sensitivity S_{ZY} indicates the ratio of the output voltage G/E on the Y -hotwire caused by ω_z to that caused by ω_y . Similarly,

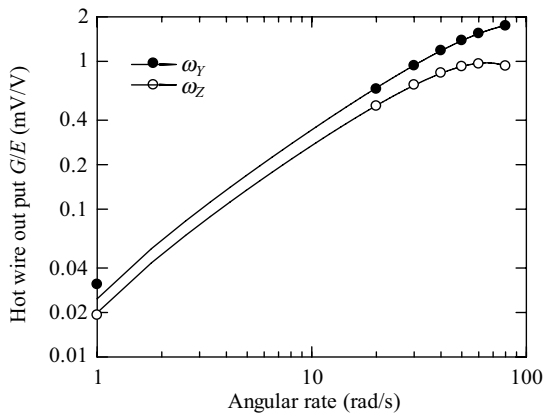


Fig. 3 Variation in sensor output voltage with angular rate.

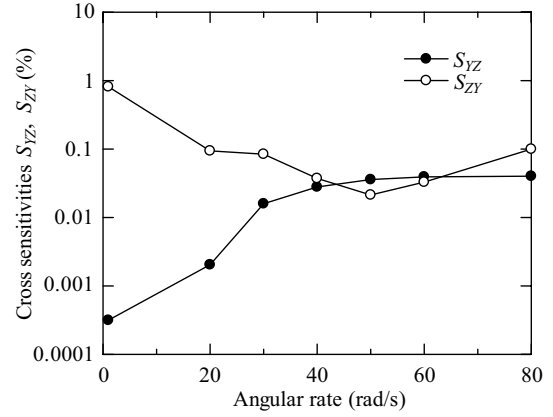


Fig. 4 Variation in cross-sensitivity with angular rate.

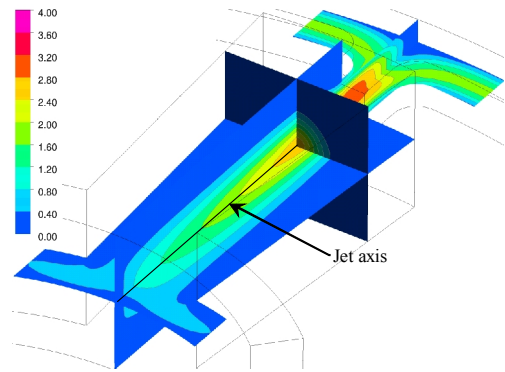


Fig. 5 Axisymmetric characteristics of the jet in the main chamber. The color bar indicates the velocity magnitude (m/s).

we have the cross-sensitivities S_{YZ} and S_{YX} . The figure shows that the cross-sensitivities are less than 1% over the entire range applied angular rates. A possible explanation is that the flow in the measurement chamber is axisymmetric respective to the jet axis, as shown in Fig. 5. The cross-sensitivity S_{YX} should be zero, because the X -hotwires are perpendicular to ω_y .

4. Conclusions

A triple-axis fluidic gyroscope sensor that is highly realizable by MEMS has been designed and examined by numerical simulation. The fabrication process requires only a one-mask MEMS process and the hot embossing technique. Four axisymmetric jets are simply generated by a vibrating piezoelectric diaphragm in a valveless network channel of the sensor. An analysis of the output of the sensor shows that the measurement resolutions of the horizontal and vertical angular rate components are equivalent. The sensor shows promise in high-sensitivity industrial applications because it has low cross-sensitivities and avoids the misalignment of number that occurs with dual- and single-axis sensors.

Acknowledgement

This work was partially funded by Grant-in-Aid for Scientific Research (C)-22510127 and the Japanese Science Promotion Society Program.

Kinematic Analysis on Unique Jump of Springtail

Toshiya Kainuma, Seiichi Sudo

Akita Prefectural University, Ebinokuchi 84-4, Yurihonjo 015-0055, Japan

Atsushi Shirai, Toshiyuki Hayase

Tohoku University, Katahira 2-1-1, Aoba-ku, Sendai 980-8577, Japan

E-mail: sudo@akita-pu.ac.jp

ABSTRACT

The jumping movements of springtails from the inside of the bubble at the air-water interface were analyzed from high-speed sequences of images captured at rate of 4500 frames per second. The results of an experiment aimed at elucidating the jumping mechanisms of water-floating springtails are described. The variation of vertical velocity during the springtail jump was analyzed. The microscopic structure of body was also clarified by a laser scanning microscope.

1. Introduction

A wide variety of living creatures live on the planet. Many adult insects have a remarkable flying capacity. The study of the flying function of insects is of fundamental interest and importance with respect to a variety of applications. In our previous papers, therefore, extensive investigations of the flapping motions and aerodynamic functions of flying insects have been conducted [1-5]. There are insects flying without wings. Springtails are minute insects without wings in the order Collembola. Various springtail species range in size from 0.2 mm to 10 mm. They are expected to find in the ancestors of modern flying insects. An analysis of the mechanism of the jumping organ was presented based on morphological examination and high-speed photography [6]. However, there is no study on the jumping behavior of springtail on the water surface. Old insects must have gone back and forth on the sea and land. The research of springtails is important from the viewpoint of the evolution study.

In this paper, the dynamic behavior of jumping springtail from the inside of the bubble at the air-water interface was analyzed. Furthermore, the microscopic observation of the body surface was conducted using the microscope.

2. Springtail

Springtails are abundant, jumping insects that inhabit a variety of moist environments. They are minute insects without wings in the order Collembola. They can rapidly move 70 to 150 mm in a single motion. They have the ability to jump by means of a taillike mechanism tucked under the abdomen. The furcula is a hinged appendage that is bent forward and is held in place by a latch mechanism called a tenaculum. When disturbed, this appendage functions as a spring, propelling them into the air away from the danger.

3. Experimental Apparatus and Procedures

A schematic diagram of the experimental apparatus to study jumping characteristics of springtail is shown in Fig.1. The experimental apparatus consists of small rectangular water container system and the optical measurement system. The container was filled with water partially. Jumping behavior of springtail from the

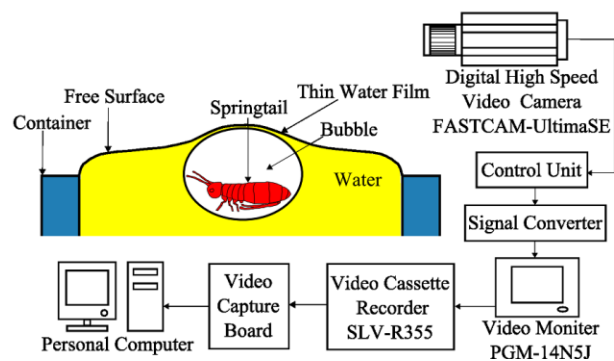


Fig.1 Block diagram of experimental apparatus

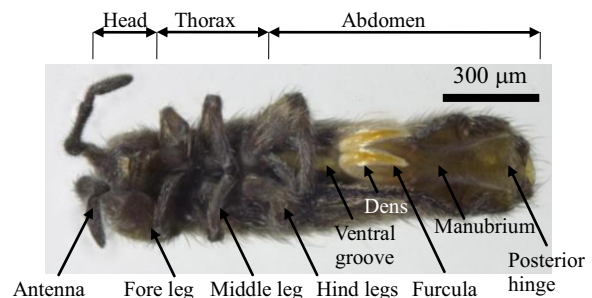


Fig.2 Microscopic photograph of test springtail

inside bubble in the container was examined. The test springtail was mixed with the water, and was injected into the container. Free jumping of the springtail was observed optically. A series of frames of jumping behavior were analyzed by the personal computer. The detailed structure of the spring body was observed with the microscope.

4. Experimental Results and Discussion

4.1 Microscopic observation of springtail

Microscopic observations of the test springtail were conducted with the laser scanning electron microscope to investigate the relationship between the body structure and the locomotive functions of the insects.

Figure 2 shows a view of the whole body of the springtail from below. The body of springtail is composed of separate sections-the head, thorax, and abdomen. The head carries the mouthparts, antennae, and eyes. The thorax has three segments with legs. The abdomen has the curved jumping organ. In Fig.2, the

structure of the springing organ as furcula can be seen. The main part of the organ articulates with the abdomen. The springing organ is normally stowed away in the ventral groove on the underside of the abdomen. It can be seen from Fig.2 that the abdomen occupies a wider area in the body. The springing organ is the immediate source of energy for jumping. The location of the springing organ is very important in the dynamics of the jump. In most insects, jumping is performed by storing energy in the flexed legs and by releasing it impulsively at the initial stage of a jump. In general, the jumping animal encounters the effect of the aerodynamic drag. In engineering situations friction is usually thought of as a source of wasted energy. Any moving body surface presented to the air will create friction. It is considered that the springtail as shown in Fig.2 has the rational profile in order to reduce frictional effects. At the microscopic level the surface of springtail body is anything but smooth. The body of springtail is clothed in minute hairs measuring less than 0.08 mm in height. It is considered that their minute hairs are related to the control of the boundary layer flow.

4.2 Jumping motion of springtail

Many test springtails were mixed with water in the container by stirring. Each springtail was covered with air in the water, that is, the bubble contained a springtail was generated in the water. Such bubble was injected into the water container by the pipette. When the bubble rose at the air water interface, the springtail jumped up out of the bubble into the air. Figure 3 shows a sequence of photographs showing the free jumping behavior from the inside of the bubble. Springtails have a jumping forked appendage called furcula. It can be seen from Fig.3 that the furcula of the test springtail functions in the bubble. Then, incompressibility of the water is kept, because impact velocity of furcula is higher. Figure 4 shows the change of vertical velocity of the springtail during the jump. The vertical velocity was obtained by measurement of the displacement change of springtail head with time. In this case, the maximum of vertical velocity is $v_{max} = dz_w/dt = 0.8$ m/s. Bubble rupture at the air-water interface has been analyzed extensively by many researchers. The maximum speed of the receding bubble film is described as follows [7]:

$$u = (2\sigma / \rho h)^{1/2} \quad (1)$$

Where σ is the surface tension of the liquid film, ρ is the density, and h is the film thickness. The receding water flow pushes the liquid to flow inward underneath the bubble cavity. When this symmetric flow meets at the bottom of the bubble cavity, a stagnation point is created, resulting in high pressure. This high pressure pushes the liquid to form upward liquid jet. The springtail may subject to the upward force. After the springing organ has lifted off from the water surface, the springtail undergoes "free fall" due to the force of gravity, although its velocity is still directed upward and it continues to climb. The jumping springtail also encounters the effect of the aerodynamic drag. The velocity change in Fig.4 shows such fact.

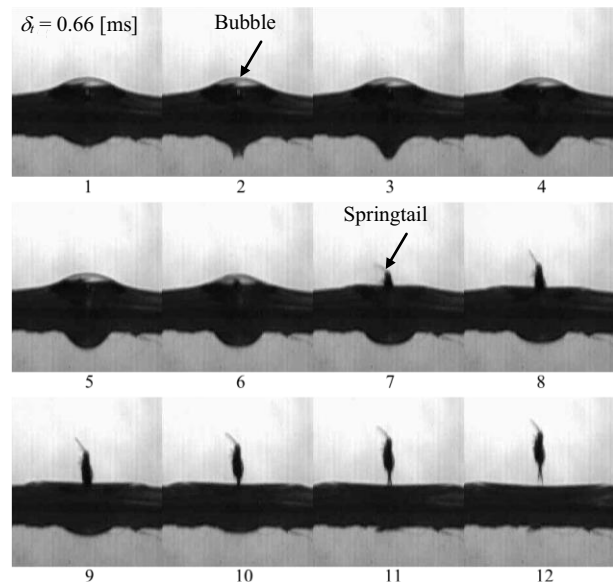


Fig.3 High-speed video sequence of the jump behavior

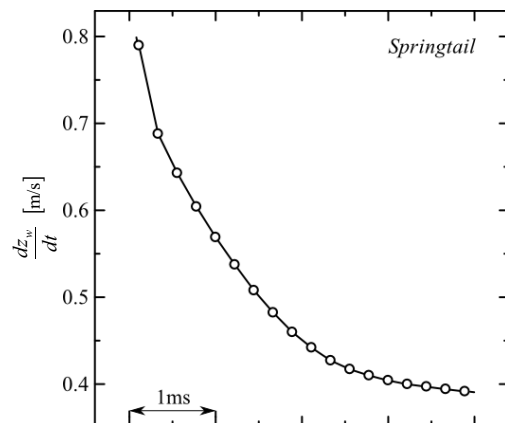


Fig.4 Velocity change in jump movement

4. Conclusions

The dynamic behavior of unique jump for small springtail from the inside of the bubble at the air-water interface was analyzed kinematically using the high-speed video camera system. The results obtained are summarized as follows;

- (1) The springtail in the bubble at the air-water interface can rupture the bubble and jump into the air.
- (2) The body of springtail is clothed in a lot of minute hairs measuring less than 80 μm in height. The springtails have well development springing organ.

References

- [1] S.Sudo et al., JSME Int. J., **42** (1999), 721.
- [2] S.Sudo et al., JSME Int. J., **43** (2000), 895.
- [3] S.Sudo et al., Exp. Mech., **45** (2005), 550.
- [4] S.Sudo et al., J. Japn. Soc. Exp. Mech., **8** (2008), 163.
- [5] S.Sudo et al., J. Aero Aqua Bio. Mech., **1** (2010), 80.
- [6] J. Brackenbury and H. Hunt, J. Zool., Lond., **229** (1993), 217.
- [7] J.Wu, J.Biotech., **43** (1995), 81.

Molecular Dynamics Study on Effect of Chain Length on Liquid-Vapor Interfacial Properties of Alkanes

Hari Krishna Chilukoti¹, Gota Kikugawa¹, Taku Ohara¹

¹Institute of Fluid Science, Tohoku University, 2-1-1 Katahira, Aoba-ku, Sendai, 980-8577, Japan
E-mail of corresponding author: chilukoti@microheat.ifs.tohoku.ac.jp.

ABSTRACT

In the present paper, effect of chain length of n-alkanes on ordering parameter and surface tension has been studied by using molecular dynamics simulations. Alkane molecules were modeled using united NERD force field. To study the effect of chain length, quantities are compared at the reduced temperature for three species of n-alkanes. Alkane molecules exhibited a triply layered structure in the vicinity of interface for a particular temperature. At the reduced temperature, all three alkanes show similar tendency to have molecular alignment in the vicinity of the interface parallel to the interface and have surface tension value about 10 mN/m.

1. Introduction

Liquids of hydrocarbon chain molecules have many industrial applications such as lubrication and coating, and are major building blocks for long polymers. Due to their essential importance for many technological and biological processes, liquid interfaces have attracted the attention of many scientists. Studies of the structure and transport properties in the vicinity of interfaces play an important role in understanding of adhesion, wetting and lubrication. Coating films with a thickness of the order of nanometers have been realized and are coming into industrial use^[1]. Understanding of equilibrium and non-equilibrium properties is also important for such nonoscale materials, since their coating flow behavior and quality of the residual films are dominated by surface effects. Thermodynamic properties and structure of the materials at the interface region are different from that of bulk liquid region. This is related to the difference in the interaction between the molecules in the bulk liquid and in the interface region.

Using molecular dynamics simulation we can study structure and thermodynamic properties of alkanes in molecular dynamics point of view. To perform the molecular dynamic simulation of alkanes we need to describe inter- and intramolecular potential energy of alkanes with proper model. Reliability of the result from the simulations using potential function depend on how accurately the inter- and intramolecular interactions were considered. The objective of the present work is to examine the interfacial properties of different alkanes at reduced temperature.

2. Simulation Details

This simulation system is a film wise liquid of n-alkane in vacuum with two liquid-vapor interfaces. We used a united atom model to describe alkanes. In united atom model, methyl (CH₃) or methylene (CH₂) groups were treated as separate atomic structures. In the NERD force field, bond bending and bond stretching are modeled in terms of harmonic potentials. Torsional potential is modeled using Ryckaert-Bellemans (RB) model. Interaction between two atoms is given by Lennard-Jones (LJ) potential. We truncated the LJ interactions at a distance of 13.8 Å.

The time integration was implemented by the r-RESPA method with multiple time scale (MTS). An integration time step of 1fs for intermolecular motion

and 0.2fs for intramolecular motion were used in all simulations. Initially the system was gradually raised to the required temperature and then simulations were performed for NVT ensemble for 6×10^6 time steps. The simulation system was maintained at constant temperature using the Nose-Hoover thermostat. In all simulations, periodic boundary conditions and minimum image convention were applied in three spatial directions. The system was enclosed in a box of length $L_x=L_y=50$ Å and $L_z=240$ Å for decane, $L_x=L_y=70$ Å and $L_z=320$ Å for tetracosane. The size of the system investigated in this work is 500 molecules for both decane (C₁₀H₂₂) and tetracosane (C₂₄H₅₀) and 1000 for hexatriacontane (C₃₆H₇₄).

3. Results and Discussion

All quantities were calculated after the system has reached equilibrium and interface has been formed. First, liquid densities obtained in our simulations have been validated by comparing them with literature. For decane, the present liquid density (624 kg/m³ at 400K) is slightly lower than the liquid density (652 kg/m³) reported by Nath et al.^[2] for the NERD potential. The cut-off radius for the LJ interactions may influence on the density. Molecular dynamics predictions of critical points of C₁₀H₂₂, C₂₄H₅₀ and C₃₆H₇₄ are 617K, 805K and 862K by

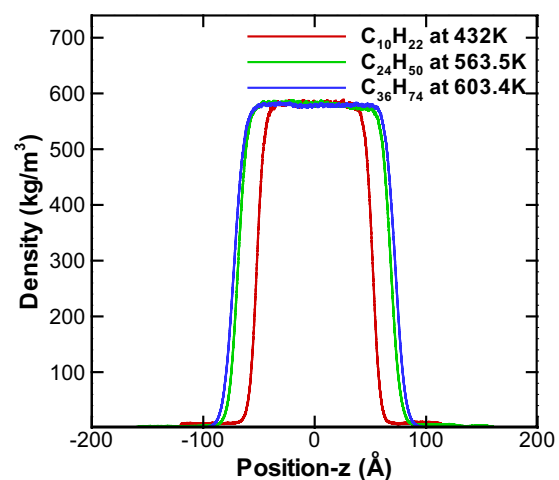


Fig.1. Density profiles for decane, tetracosane and hexatriacontane at $0.7T_{cr}$.

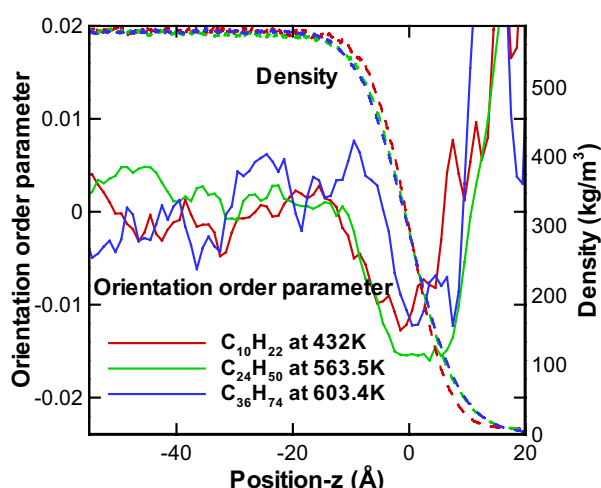


Fig.2. Orientation order parameter as a function of distance for $C_{10}H_{22}$, $C_{24}H_{50}$ and $C_{36}H_{74}$ at $0.7T_{cr}$.

Nath et al. [2]. Figure 1 shows the variation of density along z -axis for decane, tetracosane and hexatriacontane at the reduced temperature $0.7T_{cr}$. At the same reduced temperature ($0.7T_{cr}$), all alkanes have nearly equal liquid density. Vapor density decreases with increase in chain length.

The orientation order parameter can be used to quantify the effect of interface on the chain length ordering. A convenient orientation order parameter is defined as follows.

$$H(z) = \frac{1}{2} \langle 3 \cos^2 \theta - 1 \rangle \quad (1)$$

where θ is the angle between a vector connecting two carbon atoms which are two units apart in a molecule and interface normal. The average $\langle \rangle$ is taken over all vectors and time steps. The range of this parameter is $[-0.5, 1]$. A positive value indicates preferential alignment normal to the interface. Negative value indicates preferential alignment parallel to the interface. Zero indicates completely random arrangement of molecules. The ordering parameter is presented by taking Gibbs dividing surface as the origin. Figure 2 shows the ordering parameter for three alkanes at the same reduced temperature. In respect to the orientation

Table 1. Comparison of surface tension values for different alkanes at different temperatures with experimental values and reported simulation results with NERD model.

Molecule	$T(K)$	Present work (mN/m)	Experimental value ^[3] (mN/m)	NERD ^[3] (mN/m)
$C_{10}H_{22}$	300	25.5	23.1	24.8
	350	19.3	18.6	20.8
	400	13.5	14.4	16.5
	$0.7T_{cr}$	11.2	N/A	N/A
$C_{24}H_{50}$	$0.7T_{cr}$	9.5	N/A	N/A
$C_{36}H_{74}$	$0.7T_{cr}$	10.1	N/A	N/A

parameter, the vicinity of interface region consists of three layers for an alkane. In the inner most layer close to the bulk liquid, molecules are oriented preferentially perpendicular to the interface. In the middle layer next to the above layer, molecules are oriented preferentially parallel to the interface. In the outer most layer close to the vapor side, the orientation order parameter increases rapidly to a positive value again. It is considered that the parameter decreases and approaches zero towards the bulk vapor phase, although reliable data for vapor phase was not obtained in the present simulations due to the small number of samples. All three molecules show nearly the same tendency to align parallel to the interface in the middle layer at the reduced temperature.

Kirkwood-Buff formula was applied to calculate the surface tension (γ_p) during the simulation and is expressed by the following formulae [3].

$$\gamma_p = \frac{L_z}{2} \left[\langle P_{zz} \rangle - \frac{\langle P_{xx} \rangle + \langle P_{yy} \rangle}{2} \right] \quad (2)$$

where $\langle P_{zz} \rangle$ and $\frac{\langle P_{xx} \rangle + \langle P_{yy} \rangle}{2}$ are the averaged normal and tangential components of pressure. L_z is the length of the simulation box in the z direction. To take into account the effect of truncated LJ potential, the long-range corrections are implemented based on the molecular virial formula. In Table 1, surface tension of three alkanes obtained in the present simulation at several temperatures are presented and decane surface tension values at different temperatures are compared with surface tension values obtained for a system by the NERD force field and with experimental values available in the literature [3]. As we can see from the table, present simulations over-predict the surface tension of decane at lower temperature, and the error becomes smaller at higher temperatures. Overall, present results are in good agreement with the results of Mendoza et al. [3] and experimental values. Another new finding is that at the same reduced temperature of $0.7T_{cr}$ all the three alkanes have surface tension values close to 10 mN/m.

4. Concluding remarks

Effect of alkane chain length on interfacial properties has been studied using molecular dynamics simulations. It is observed that all three studied alkanes show triply layered structure in the vicinity of interface region and have surface tension value close to 10 mN/m at the reduced temperature.

References

- [1] C.B. Walsh, E.I. Franses, *Thin Solid Films*, **429** (2003), R71.
- [2] S.K. Nath, F.A. Escobedo, J.J. De Pablo, *J. Chem. Phys.*, **108** (1998), R9905.
- [3] F.N. Mendoza, R. L-Rendon, L.L-Lemus, J. Cruz, J. Alejandro, *Molec. Phys.*, **106** (2008), R1055.

Ignition Characteristics of Lower Alkane Fuels in a Micro Flow Reactor with a Controlled Temperature Profile

Taiki Kamada, Takuya Tezuka, Susumu Hasegawa, Kaoru Maruta

Institute of fluid science, Tohoku University, 2-1-1 Katahira, Aoba-ku, Sendai, Miyagi 980-8577, Japan
kamada@edyn.ifs.tohoku.ac.jp.

ABSTRACT

Ignitability of methane, ethane, propane and *n*-butane are investigated experimentally using a micro flow reactor with a controlled temperature profile. Additionally, mixtures of methane/*n*-butane blended fuel are also investigated. One-dimensional computations using detailed reaction scheme are conducted. Computational results agreed with experimental result qualitatively. The experiment using blended fuel revealed that small addition of *n*-butane to methane enhanced the ignitability of the blended fuel.

1. Introduction

Natural gas is one of the promising fuels due to its advantages such as low CO₂ and SO_x emission. It has been extensively used for various applications; gas turbine, boilers, gas engine and so on. For improving the efficiencies of such combustion devices, knowledge on ignition and combustion characteristics is essential. Therefore, we focus on methane, ethane, propane, and *n*-butane in this study which are the main components of natural gas. Although numerous studies on ignition characteristics of these pure fuels based on ignition delay times are conducted using RCM or shock tube, we are going to focus on a micro flow reactor with a controlled temperature profile [1] in this study. Using this reactor, ignition and combustion characteristics of methane [2], dimethyl ether [3] and gasoline primary reference fuel [4, 5] were studied. In these works, they paid their attentions to weak flames which are observed at low flow rate condition in the reactor. Observations of weak flames provided new knowledge on ignition and combustion characteristics.

In this study, we investigated the ignitability of pure alkane fuels which are main components of natural gas. In addition, effect of large hydrocarbon on ignitability was investigated using methane/*n*-butane blended fuels.

2. Experimental and computational methods

Figure 1 shows a schematic of experimental setup. We employed 2 mm inner diameter quartz tube as a reactor and heated it using premixed H₂/air flat flame burner to give a steady temperature profile of maximum temperature of 1300 K in axial direction. The stoichiometric premixed fuel/air mixture was introduced into the quartz tube with low flow rate. The mixture was heated by hot wall and formed a weak flame at specific point. The mean flow velocity at the entrance of the tube was set to $U = 2$ cm/s. We used a digital still camera with a band pass filter to observe weak flame in the reactor. We defined maximum brightness point as a weak flame position in the experiment. The wall temperature was measured by a K-type thermocouple.

1-D steady computations were conducted by PREMIX-based code [1]. We added the term of heat transfer between gas and wall to the gas phase energy equation. In computation, experimental wall temperature profile was given as the wall temperature profile of the channel. We used detailed reaction schemes of Natural

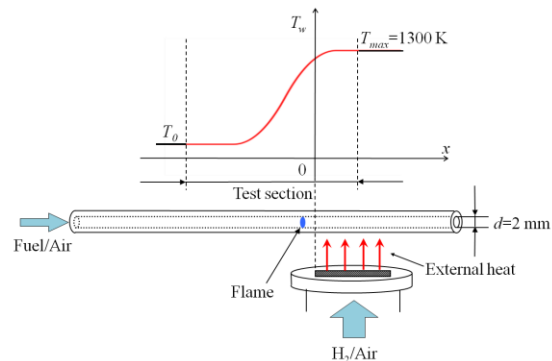


Fig. 1. Schematic of experimental setup.

gas III [6]. Computational condition was the same as experiment; $\phi = 1$, $U = 2$ cm/s, pressure $p = 1$ atm.

3. Results and discussion

3.1 Weak flame positions of pure fuels

Figure 2 shows the weak flame images of methane, ethane, propane and *n*-butane. We observed only one luminous zone in each fuel. Using these experimental images, we identified wall temperatures at the weak flame locations. The averaged values are shown in Fig. 2. From these results, methane weak flame located at the most downstream side, i.e., the highest wall temperature position in them. The weak flame of propane and *n*-butane followed methane and, weak flame of ethane located at the most upstream side. This result shows that oxidation of ethane occurs at lower temperature region than other higher hydrocarbons such as propane and *n*-butane. Computational heat release rate (HRR) profiles of each fuel are shown in Figure 3. Strong

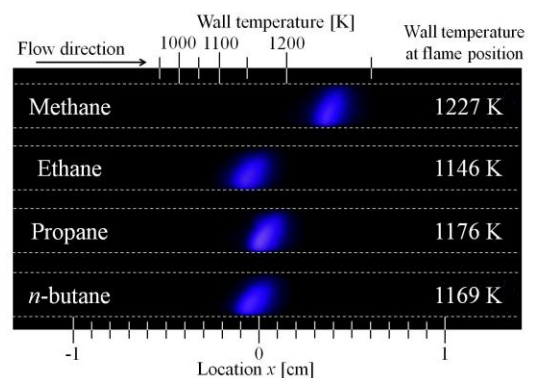


Fig. 2. Weak flame images of pure fuels.

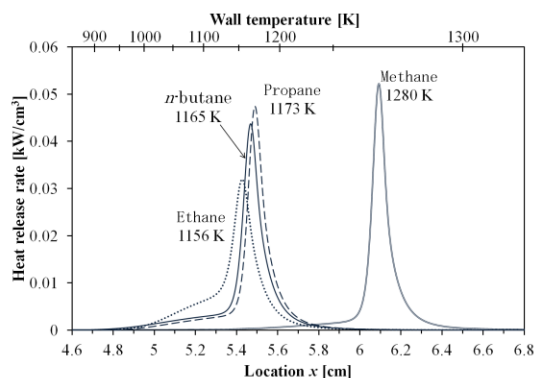
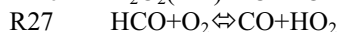
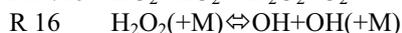
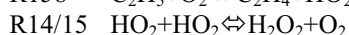
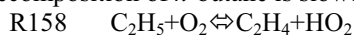


Fig. 3. Computational HRR profiles of pure fuels.

correlation between HRR and CH profiles was confirmed in our past study, and CH peak has strong correlation with chemi-luminescence observed in experiments. Therefore, we defined the HRR peak position as weak flame position in computations. Single HRR peak was obtained in each fuel case, which corresponded to the experimental luminous zone. Besides, the order of the flame position was qualitatively agreed with experimental results.

In general, higher hydrocarbons tend to be more reactive than the lower. Thus, reaction path analysis was conducted to understand the reasons why ethane is more reactive than *n*-butane and propane. We mainly focused on decomposition of ethane and *n*-butane. We found that the reaction 158 described below played a significant role to promote the ethane oxidation. Ethane mainly reacts with OH, and then C_2H_5 and H_2O are produced. The OH radical is produced mainly through the reactions of R14/15 and R16. HO_2 , which is reactant in R14/15, is produced by R158 and R27. R158 has large reaction rate due to high concentration of the reactants in ethane oxidation. On the other hand, in *n*-butane case, HO_2 is mainly provided by R27. R158 is not a key reaction because of low concentration of C_2H_5 . This causes low production rate of OH, and as a result, decomposition of *n*-butane is slower than that of ethane.



3.2 Effect of higher hydrocarbons in methane

To clarify the effect of higher hydrocarbon components in natural gas, methane/*n*-butane blended fuel with various blend ratios were tested. The experimental weak flame images and computational flame positions are shown in Figures 4 and 5, respectively. The flame position shifted to upstream with increasing the ratio of *n*-butane in blended fuels in both experiment and computation. It should be noted that small addition of *n*-butane changed the flame position dramatically. On the other hand, further addition of *n*-butane to high *n*-butane ratio fuel made only small influence on flame position. This result indicates that small percentages of higher hydrocarbons in natural gas significantly influence on the ignition and combustion characteristics of the natural gas.

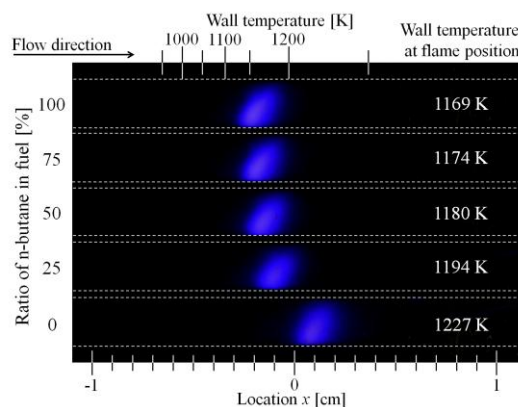


Fig. 4. Weak flame images of blended fuels.

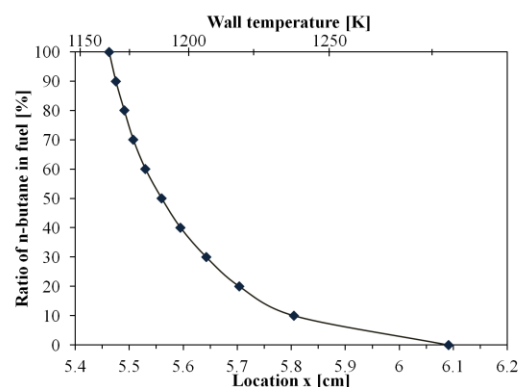


Fig. 5. Computational flame position of blended fuels.

4. Conclusions

Ignition characteristics of lower alkane fuels and its blended fuels were investigated using a micro flow reactor with a controlled temperature profile. We observed one luminous zone in each fuel case, which was reproduced by 1-D computation. The order of flame positions was qualitatively agreed between experiment and computation in both pure and blended fuel case. Reaction of $C_2H_5 + O_2 \rightleftharpoons C_2H_4 + HO_2$ played a significant role in ethane oxidation and made ethane more reactive than other fuels. As a result of blended fuel experiment and computation, it was revealed that small addition of *n*-butane improves ignitability of the blended fuel. This fact indicates that small compositions of large hydrocarbons in natural gas significantly affect on its ignition and combustion characteristics.

References

- [1] K. Maruta et al., Proc. Combust. Inst. 30 (2005) 2429-2436.
- [2] Y. Tsuboi et al., Proc. Combust. Inst. 32 (2) (2009) 3075-3081.
- [3] H. Oshibe et al., Combust. Flame 157 (8) (2010) 1572-1580.
- [4] A. Yamamoto et al., Proc. Combust. Inst. 33 (3) (2011) 3259-3266.
- [5] M. Hori et al., Combust. Flame 159 (3) (2012) 959-967.
- [6] Natural gas III, Combustion Chemistry Centre, National University of Ireland, Galway. <http://c3.nuigalway.ie/naturalgas3.html>.

OS1: Heat and Mass Transfer Issues in Materials

Interactions Between Process and Structure in Polymer Materials: Case of Non-Isothermal Crystallization Kinetics During Processing

Mhamed Boutaous, Patrick Bourgin, Matthieu Zinet
INSA de Lyon, CETHIL UMR 5008 CNRS INSA UCBL.
Mhamed.boutaous@insa-lyon.fr

ABSTRACT

Numerical simulation of thermoplastics polymer behavior during processing requires a large amount of physical phenomena. In semi-crystalline polymers, the properties of the final product are strongly dependent on the thermo-mechanical history experienced by the material during processing. Structural heterogeneities such as rigidity gradients and shrinkage anisotropy are directly related to the crystalline microstructure. Therefore, simulation requires a relevant crystallization kinetics model including both the effects of thermal and flow induced nucleation. This paper aims to highlight this strong coupling between the structure, the material and its intrinsic properties

1. Introduction

To simulate heat transfer in polymer materials during their processing, it is necessary to take into account all the thermodynamical and physical transformations. One of them, which concerns specifically semicrystalline polymers, is the crystallization phenomenon.

The thermomechanical histories of polymers affect strongly their crystallization kinetics. The experienced stresses modify both the crystallization morphology and kinetics. They align macromolecular chains, help nucleation, accelerate crystallization and generate oriented morphologies.

The study of flow-induced crystallization, usually, aims to find a set of simple and experimentally accessible parameters to describe the crystallization kinetics.

A variety of approaches have been proposed to model flow effects on crystallization kinetics. The most interesting ones explicitly take into account the nucleation and growth processes. Indeed, experimental observations have clearly shown that the number of nuclei per unit volume (nucleation density) is considerably increased under shear conditions [1, 2]. This additional nucleation rate can be linked to various parameters: free energy related quantities [3], shear rate [4], combination of shear strain and shear rate [5], recoverable strain tensor [6]

For a more detailed review on crystallization kinetics modeling, see for example ref. [7].

In this work, we have developed a numerical model able to simulate the crystallization of polymers under non isothermal flow condition [7]. We make the assumption that the polymer melt elasticity, quantified by the trace of the extra-stress tensor is the driving force of flow-induced extra nucleation. Thus, the sensitivity of the crystallization kinetics to the flow is not only a consequence of the flow kinematics, but is also determined by the rheological behavior of the melt. All the details on the mathematical model are developed in [7] or [8].

With our assumptions, the crystallization kinetics model links the flow-induced extra nucleation to the trace of the extra-stress tensor, thus Upper Convected Maxwell

(UCM) differential multimode is introduced to describe the rheological behavior of the polymer.

2. The Couette Flow Configuration

The 1D shear flow (or plane Couette flow) is one of the simplest shear flow configuration. It can model quite well a rotational rheometry experiment (cone-plate). The flow is assumed to be incompressible. The polymer is confined between two parallel plane plates separated by a gap of constant width w (Fig. 1). The lower plate (n° 1) is fixed ($U_1 = 0$), whereas the upper plate (n° 2) is moving with a velocity U_2 :

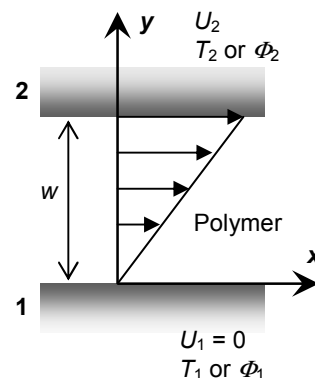


Fig.1 Flow configuration geometry

$0 < t < t_s$: $U_2 = w \cdot \dot{\gamma}_N$: Imposed shear rate

$t_s \leq t$: $U_2 = 0$: no slip condition

where $\dot{\gamma}_N$ is the nominal shear rate, i.e. the shear rate averaged over the flow width. Thermal boundary conditions can be either prescribed temperatures (T_1, T_2) or prescribed heat flux densities (Φ_1, Φ_2).

3. Results and discussion

The general model described with more details in [7] is applied to a polypropylene melt in a simple shear flow configuration, under non isothermal conditions and two types of rheological behaviors: linear and nonlinear viscoelastic behaviors. All the polymer characterization data are taken from [9]

Computations are carried out by using a transient numerical procedure based on finite elements method.

The aim is to analyze the effect of the thermo-mechanical conditions of the polymer during processing on the obtained final crystalline structure.

Connection between the process parameters and the polymer behavior will be highlighted.

Flow induced crystallinity distribution in the polymer thickness at the end of crystallization ($\alpha = 1$) is represented in Fig.2, after the application of a one-second shearing at several shear rates. Near the fixed cold plate ('wall'), the polymer is subjected to a tempering effect and the formed crystallites are quasi completely of the thermally induced type. As one come closer to the 'core' zone (boundary no.2), the flow induced crystalline fraction increases. At identical shearing time, the higher the shear rate, the closer to 100 % this fraction. It is worth noticing that in the present case, a shear rate lower than 10 s^{-1} applied only during one second does not have any significant influence on the final distribution of the flow induced crystallinity. Nevertheless, as we will see later, it influences the crystalline nucleation.

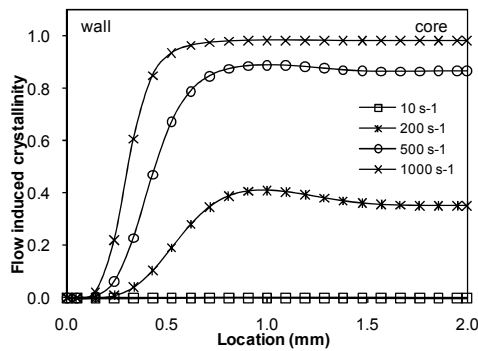


Fig.2 Flow induced crystalline fraction α^f obtained at the end of crystallization for several shear rates (shearing time: 1 s)

We consider here a configuration of homogeneous temperature decreasing according a linear law:

$$T(y, t) = T_0 - V_{cool} \cdot t$$

where $T_0 = 210 \text{ }^\circ\text{C}$ is the initial temperature and V_{cool} is the cooling rate.

As soon as the cooling starts, the polymer is subjected to a short term shearing treatment (1 s), then it is allowed to crystallize in quiescent conditions. In order to quantify the relative impact of the mechanical and the thermal conditions on crystallization, the final crystallinity distribution is examined. For that purpose, the thermally induced crystalline fraction and the flow induced crystalline fraction, respectively denoted by α^T and α^f , are calculated. These quantities are linked to the global relative crystallinity α by: $\alpha = \alpha^T + \alpha^f$

The evolutions of the global crystallinity and the crystalline fractions for two different cooling rates ($10 \text{ }^\circ\text{C}/\text{min}$ and $40 \text{ }^\circ\text{C}/\text{min}$) and several shear rates ranging from 10 s^{-1} to 200 s^{-1} are shown on Fig. 3. It is important to notice that the crystallization times are here strongly related to the cooling rate. Nevertheless, when the shearing is faster, the acceleration of the crystallization

kinetics is still noticeable. At lower temperature kinetics $10 \text{ }^\circ\text{C}/\text{min}$, the flow affects strongly the crystallization rate, and inversely, at faster thermal kinetics, temperature plays more important role.

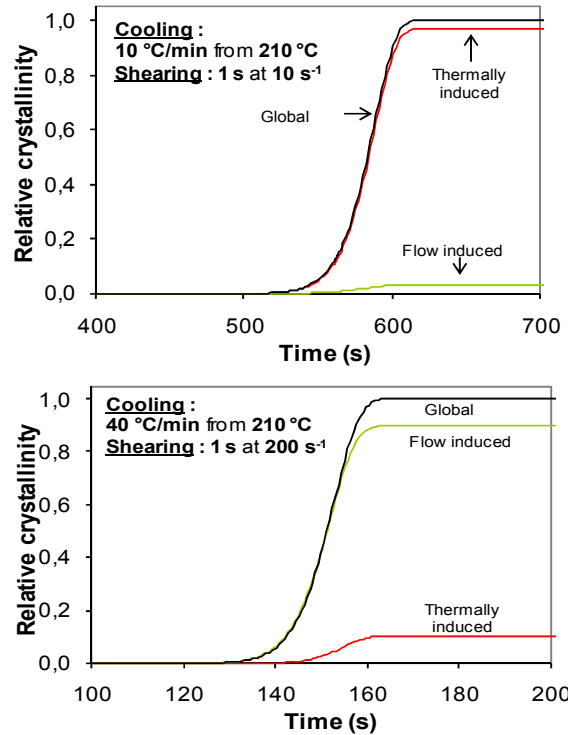


Fig. 3 Time evolution of the thermal and flow induced crystallinity

4. Concluding remarks

Flow induced crystallization model is developed taking into account the viscoelastic behavior of semi-crystalline polymers.

The quantification of the crystalline structure in terms of average density and size of the thermally and flow induced crystallites is a very interesting result within the perspective of predicting the mechanical properties of final solidified polymer parts.

References

- [1] K. Nakamura, et al., J. Appl. Polym. Sci. 17 (4), 1031, (1973)
- [2] B. Monasse, J. Mater. Sci., 30(19), 5002, (1995).
- [3] R.I. Tanner, J. Non-Newtonian Fluid Mech., 102, 397 (2002).
- [4] H. Ito et al. Int. Polym. Proc., 11, 363, (1996).
- [5] A.C. Bushman J. Polym. Sci., Part B: Polym. Phys., 34, 2393 (1996).
- [6] O. Verhoyen, PhD Thesis, Université Catholique de Louvain, Belgium, (1997).
- [7] M. Zinet, M. Boutaous, R. El Othmani,, P. Chantrenne, Polym Eng. Sci, Vol. 50, pp 2044-2059, (2010).
- [8] M. Zinet, PhD Thesis, INSA Lyon, France (2010).
- [9] Koscher, E., and Fulchiron, R., Polymer, 43, pp. 6931-6942, (2002).

Thermal Estimation of Properties and Location of Tumor in a 2-D Biological Tissue using Surface Temperature Profile

Subhash C. Mishra¹, Koushik Das¹, Mohit Ganguly² and Pranab Goswami²

¹Dept. of Mechanical Engineering, ²Dept. of Biotechnology,
Indian Institute of Technology Guwahati, India – 781039

Corresponding author: scm_iit@yahoo.com

ABSTRACT

Bioheat equation is solved for two-dimensional tissue geometry with tumor. With surface temperature known, estimations of tissue properties and the location of the tumor present inside a breast tissue are done using inverse analysis. Finite volume method is used to solve the bioheat equation. In the inverse analysis, the optimization is done using genetic algorithm.

1. Introduction

In curing any malignancy or disease, the first step is the diagnosis to know its various attributes. For a tissue the thermo-physical properties are unique. Even the properties of a healthy and a malignant tissue do not have a match. This change in property leads to change in the thermal signals of the tissue. With increased number of cancer cases, now-a-days, study of various thermal signals may prove to be a useful diagnostic tool for thermal detection of malignancy.

From heat transfer point of view, a tissue is a thermal system. Pennes' bioheat equation, proposed by Pennes in 1948, gives the mathematical expression for heat transfer in a biological system. The Pennes' bioheat equation is a modified energy equation with a simplified volumetric heat generation term. The heat generation term contains two thermo-physical properties of the tissue, viz., metabolic heat generation rate and blood perfusion rate. For a particular tissue under healthy and malignant condition, these properties are unique.

Present work is about exploring a thermal means of detection of a tumor present inside a tissue with the help of surface temperature data, and estimation of its thermo-physical properties. Simple 2-D geometry of breast tissue with tumor in it is considered for the study. The governing equations are discretized using finite volume method (FVM). The location of the tumor is estimated by optimization of the surface temperature profile using genetic algorithm.

2. Formulation

A 2-D planar rectangular geometry of tissue of size $2L \times L$ having tumor of size $L/4 \times L/4$ at the center is shown in Fig 1. The governing Pennes' bioheat equation for the shown geometry can be written as [1],

$$\rho C_p \frac{\partial T}{\partial t} = k \left(\frac{\partial^2 T}{\partial x^2} + \frac{\partial^2 T}{\partial y^2} \right) + \eta_b \rho_b C_{pb} (T_a - T) + Q_m + Q_s \quad (1)$$

where $t, T, k, \rho, c_p, \rho_b, c_{pb}, \eta_b, Q_m, Q_s$ and T_a are time, temperature, thermal conductivity, density, specific heat of the tissue, density of blood, specific heat of the blood, blood perfusion, metabolic heat generation of the tissue, distributed volumetric heat source due to spatial heating and temperature of the artery, respectively.

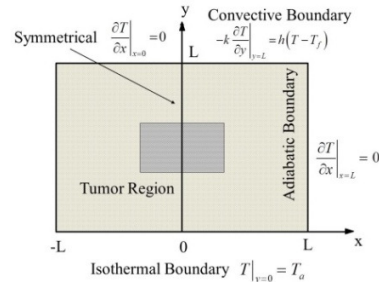


Fig.1: Schematic of the 2-D planar tissue.

With heat generation rate Q and the effective local heat source temperature T_e as defined below [1]

$$Q = \eta_b \rho_b C_{pb} (T_e - T), \quad T_e = T_a + \frac{Q_m + Q_s}{\eta_b \rho_b C_{pb}} \quad (2)$$

Eq. (1) is written as:

$$\rho C_p \frac{\partial T}{\partial t} = k \left(\frac{\partial^2 T}{\partial x^2} + \frac{\partial^2 T}{\partial y^2} \right) + Q \quad (3)$$

In the FVM formulation, the Pennes' bioheat equation takes the form:

$$T_P^{n+1} = T_P^n + \frac{\Delta t k}{\rho C_p \Delta x} (T_E^n - 2T_P^n + T_W^n) + \frac{\Delta t}{\rho C_p} \left[\eta_b \rho_b C_{pb} (T_a^n - T_P^n) + Q_m + Q_s \right] \quad (4)$$

With temperature distribution $T(x, L)$ of the surface at discrete n points known, next an inverse problem is solved to estimate the unknown attributes. In this work, we estimate blood perfusion rate, metabolic heat generation rate, and the location of the tumor, and for

this the objective function (Eq. (5)) is minimized using the genetic algorithm.

$$J = \sum_{n=1}^N (T_n - T_{n,ref})^2 \quad (5)$$

3. Results and Discussion

A healthy tissue and a tissue with a centrally located tumor are considered as shown in Fig 1. With $T_a = 37^\circ\text{C}$, tumors of type 1 and type 2 are considered, and the thermo-physical properties are $k = 0.5 \text{ W} \cdot \text{m}^{-1} \cdot \text{K}^{-1}$, $c_p = c_{p,b} = 3800 \text{ J} \cdot \text{kg}^{-1} \cdot \text{K}^{-1}$, and $\rho = \rho_b = 1052 \text{ kg} \cdot \text{m}^{-3}$. For tissue at normal condition, the value of Q_m and η_b considered are $400 \text{ W} \cdot \text{m}^{-3}$ and 0.0001 s^{-1} , respectively. Due to symmetry, only right half of the domain is solved, and steady-state temperature distribution along the surface is compared in Fig. 2, with Zhang [1].

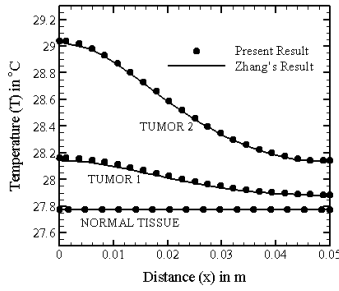


Fig. 2: Steady state surface temperature plots, and comparison of temperature distributions with Zhang [1].

For breast tissue the properties considered are $k = 0.42 \text{ W} \cdot \text{m}^{-1} \cdot \text{K}^{-1}$, $\rho = 920 \text{ kg} \cdot \text{m}^{-3}$, $c_p = 3000 \text{ J} \cdot \text{kg}^{-1} \cdot \text{K}^{-1}$ and $T_a = 37^\circ\text{C}$. For a normal breast tissue, the value of Q_m and η_b are $450 \text{ W} \cdot \text{m}^{-3}$ and 0.00018 s^{-1} , while in cancerous condition, the values become $29000 \text{ W} \cdot \text{m}^{-3}$ and 0.009 s^{-1} , respectively [2]. The steady-state surface temperature $T(x, L)$ distributions of a breast tissue for normal condition and with a tumor of size $L/4 \times L/4$ at different locations are shown in Fig. 3. Tumors are assumed to be located at constant $x (= 0 - 0.125L)$ and different y locations: top, center and bottom. For a normal tissue, surface temperature is constant, and for the tumor located at top, center, and bottom, the maximum rise of temperatures are 0.56°C , 0.05°C and 0.01°C , respectively.

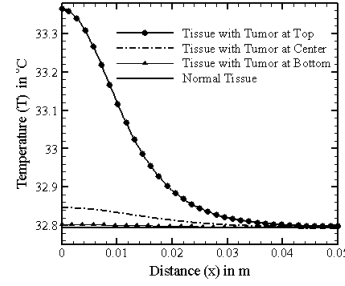


Fig. 3. Steady state surface temperature variation in breast tissue with change in location of the tumor.

Tumor Locations:

$$\begin{aligned} \text{Top} & y = 0.125L - 0.375L \\ \text{Center} & y = 0.375L - 0.625L \\ \text{Bottom} & y = 0.625L - 0.875L \end{aligned}$$

In the inverse analysis, in the GA, for a population size 100, single point crossover with constrained dependent mutation was considered. As seen from Table 1, the errors in the estimated values of η_b and Q_m are 0.0% and 0.972%, respectively.

Table 1: Estimated thermo physical parameters

Design Variable	Exact value	Estimated value	Error (%)
$\eta_b (\text{s}^{-1})$	0.01	0.01	0.0
$Q_m (\text{W} \cdot \text{m}^{-3})$	29000	28718.1	0.972

Estimated location of the tumor is also found close to the actual values, assuming that the properties of the tumor are known. The values obtained are shown in terms of x and y location of the tumor (table 2).

Table 2: Estimated location of tumor

Actual distance		Estimated distance	
x	y	x	y
0.0 - 0.125L	0.375L - 0.625L	-	0.364L - 0.621L
0.0 - 0.125L	0.125L - 0.375L	-	0.122L - 0.369L
0.0 - 0.25L	0.125L - 0.375L	0.0 - 0.248L	-

4. Conclusions

Blood perfusion rate and metabolic heat generation rate of the tumor inside a tissue was estimated for a 2-D biological tissue with errors within acceptable limit. The x and y position of the tumor inside the tissue is also estimated with good accuracy. FVM was used to solve the bioheat transfer and in the inverse method, GA was used for the optimization of the objective function. Hence, thermal means can be a useful non-invasive tool for detection of any malignancy inside a tissue.

References

- [1] Zhang H., 2008. *Lattice Boltzmann method for solving the bioheat equation*, Phys. Med. Biol.53 (2008) N15-N23.
- [2] F.J. Gonz'alez, Thermal simulation of breast tumors, Revista Mexicana De F'isica 53, pp. 323-326, 2007.

Flows of Polymer Melts through Nanopores: Experiments and Modelling

Bing-Yang Cao, Guo-Jie Hu

Key Laboratory for Thermal Science and Power Engineering of Ministry of Education,
Department of Engineering Mechanics, Tsinghua University, Beijing 100084, P. R. China
caoby@tsinghua.edu.cn

ABSTRACT

The polymer melts flow behaviors through nanopores are investigated in our study. The experimental observation obtained by using the nanoporous template wetting technique indicates that the meniscus rises according to a $(\text{time})^{1/2}$ law that agrees with the Lucas-Washburn law. Comparing the experimental results with the Lucas-Washburn equation, we also demonstrate that the viscosities of polymer melts decrease in their flow through nanopores.

1. Introduction

In recent years, polymer nanostructures, such as nanorods, nanowires, and nanotubes have drawn increasing attention for their applications in widely different areas [1]. For the fabrication of these nanoproducts, many processing approaches, such as capillary lithography [2], nanoimprint lithography [3], electrospinning [4] and micro-/nano-injection [5] have been reported. In these fabrication technologies especially in nanomoulding the nanoflow behavior of polymer melts through nanoscale channels is the key point and it becomes an active focus of current research. Lots of work has been done in this field. Steinhart et al. [6] studied the wetting behaviors of polymer melts on ordered porous templates and reported the fabrication of polymer nanotubes in 2002. Afterwards, Zhang et al. [7] reported a systematic study of the wetting of cylindrical alumina nanopores with polystyrene melts in 2006. They believed the capillary force drove the nanoflow of polymer melts in the partial wetting regime and the rate of the flow of polymer melts in the nanopore can be estimated by the Lucas-Washburn equation [8]. However, they did not analyze such capillary rise processes quantitatively, and the Lucas-Washburn equation was proposed on macroscopic scales, then its applicability on the nanoscale is still uncertain. For example, Mastic et al. [9] demonstrated a reduction in the rate of penetration due to the dependence of the contact angle on the rate of wetting based their molecular dynamics (MD) simulation of a simple Lennard-Jones (LJ) fluid, while Dimitrov et al. [10] found for both a simple LJ fluid and a polymer melt the meniscus rose according to the Lucas-Washburn law after a transient period of a few nanoseconds by MD simulation.

In our study, the flow behaviors of polymer melts in anodized aluminum oxide (AAO) nanoporous templates is investigated experimentally, and based the experimental results the theoretical model of the flow of polymer melts through nanopores is discussed.

2. Experimental method

Here we use the nanoporous template wetting technique [6] to investigate the flows of polyethylene (PE) melts through nanopores. The AAO nanoporous templates used here are purchased from Whatman, Inc..

The templates are freestanding disks and their pores are all through-hole. The diameter and pore diameter are 13 mm and 200 nm respectively. The PE films with thickness of about 300 μm , density of 0.945 g/cm^3 are obtained from Qilu Petroleum and Chemical Co. of China. The vacuum drying oven used here is purchased from Shanghai Hasuc Instrument Manufacture Co., Ltd..

In the experiment, a PE film is placed on the top of a template with a good contact, and the PE film and template sample are then put into the vacuum drying oven with the temperature of 160 $^{\circ}\text{C}$ at which the PE film will melt and infiltrate into the nanopores of the template. After a period of time the PE nanowire array with certain thickness is produced. Choosing different wetting time we get different thicknesses of nanowire arrays, i.e. different wetting displacements of PE melts. Then, the sample is taken out of the vacuum drying oven and cooled down to ambient temperature. At last, the PE nanowire arrays are released by removing the template in NaOH aqueous solution and being rinsed with deionized water and ethanol and being dry at 30 $^{\circ}\text{C}$ in vacuum in sequence. Here, the thicknesses of nanowire arrays are used to describe the nanoflow behaviors of PE melts.

3. Results and Discussion

Tian et al. [11] have reported the dependence of displacements of polystyrene (PS) melts in AAO templates with the nanopore diameter of 200 nm on the wetting time at the wetting temperature of 170 $^{\circ}\text{C}$, but they only analyzed the results qualitatively. We rearrange their results and obtain the dependence of the displacements on the square root of the wetting time, shown in Fig. 1.

From Fig. 1 we can see the displacement $H(t)$ increases with the time according to a $(\text{time})^{1/2}$ law, which agrees with the Lucas-Washburn equation, and the slope is about 2.54 $\mu\text{m}/\text{min}^{0.5}$. The Lucas-Washburn equation predicts the rise of the fluid meniscus in a small capillary and can be expressed as

$$H(t) = \left(\frac{\gamma_{LV} R \cos \theta}{2\eta} \right)^{1/2} \sqrt{t}, \quad (1)$$

where t is the wetting time, γ_{LV} is the surface tension of the liquid, η is the viscosity, R is the pore radius and θ is

the contact angle between the meniscus and the wall. The applicability of the Lucas-Washburn equation on the nanoscale and for non-Newtonian fluids is not yet conclusive. Our results provide an experimental evidence for the Lucas-Washburn equation.

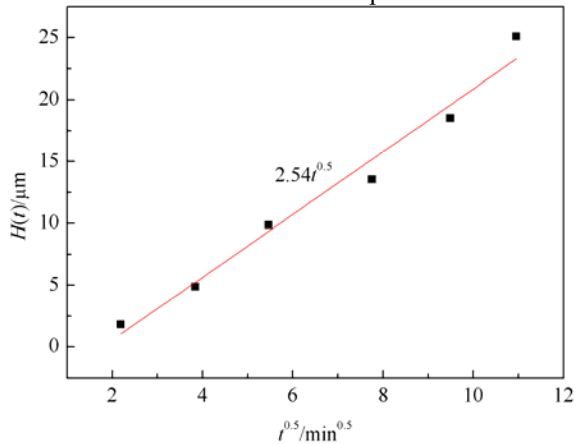


Fig. 1 Dependence of displacements of PS melts on the square root of the wetting time

To prove that the $(\text{time})^{1/2}$ increase is not just a mere coincidence and verify the applicability of Eq. (1), it is crucial to estimate the prefactor. Here, $R=100$ nm and there are other three parameter to determine. The surface tensions of polymer melts can be measured by the pendant drop method which was firstly reported by Wu [12] in 1969. He measured the surface tensions of PS melts in the temperature range of 100 to 180 °C and gave the results as a function of temperature. For PS, the function is

$$\gamma_{LV} = 40.7 - 0.072(T - 20), \quad (2)$$

where the surface tension value γ_{LV} is in dyn/cm and the temperature T is in °C. Thus, we can get the surface tension of PS melts at 170 °C is 29.9 dyn/cm ($=0.0299 \text{ N}\cdot\text{m}^{-1}$).

In our study, the capillary refers to the nanopore of AAO templates with a high-energy surface, so the polymer melts with low surface energy can completely wet it in an adequate time scale which is met in our experiment. According to the definition of the contact angle, which can be expressed as

$$\cos \theta = \frac{\gamma_{SV} - \gamma_{SL}}{\gamma_{LV}}, \quad (3)$$

where γ_{SV} , γ_{SL} and γ_{LV} represent the solid-vapor, solid-liquid and liquid-vapor interfacial tensions respectively, θ equals to 0° for the complete wetting. Thus, we can assume $\cos(\theta)=1$ here.

For the viscosities of polymer melts there are many experimental results, but under different conditions, such as at different temperatures or under different shear rates the values will be quite different. Following Ref. [13] we find the viscosity of PS melts at 170 °C under zero shear rate is about $8.2 \times 10^6 \text{ Pa}\cdot\text{s}$. then we obtain a slop $H(t)/\sqrt{t} = 0.104 \mu\text{m}/\text{min}^{0.5} < 2.54 \mu\text{m}/\text{min}^{0.5}$ which

is observed from the experimental results. Nevertheless, it was reported that the polymer melt exhibited rheological behavior in its flowing through microchannels [14]. In micro/nano-channels, the high orientation of chains of polymer nanowires may arise and the wall slip may not be ignored, which both induce the viscosities of polymer melts decrease in the micro/nano-flow. Considering the effect of the nanopores, the viscosity of PS melts in our study should be smaller than that measured on macroscopic scales. When the viscosity of PS melts $\eta = 1.4 \times 10^4 \text{ Pa}\cdot\text{s}$, the slop $H(t)/\sqrt{t}$ will be $2.53 \mu\text{m}/\text{min}^{0.5}$ which agree within error limit with the observation in Fig 1. Thus, we believe the Lucas-Washburn equation can model the nanoflow behaviors of polymer melts and their viscosities decrease during the nanoflow.

4. Concluding remarks

In this paper, we have studied the flow behaviors of PE melts through nanopores experimentally by using the nanoporous template wetting technique. Based on the experimental results we find the displacement of PS melts changes according to a $(\text{time})^{1/2}$, which verifies the applicability of the Lucas-Washburn equation in modeling the flows of polymer melts through nanopores. Comparing the experimental results and the Lucas-Washburn equation quantitatively, we observe the decrease of the viscosity of polymer melts during their flow through nanopores, which means the polymer melts exhibit rheological behavior in the nano-wetting process.

References

- [1] R. Dersch, M. Steinhart, U. Boudriot, A. Greiner, J. H. Wendorff, *Polym. Adv. Technol.*, **16** (2005), pp.276-282.
- [2] E. Kim, Y. Xia, G. M. Whitesides, *Nature*, **376** (1995), pp.581-584.
- [3] S. Y. Chou, P. R. Krauss, P. J. Renstrom, *Science*, **272** (1996), pp.85-87.
- [4] D. Li, Y. Xia, *Nano Lett.*, **4** (2004), pp. 933-938.
- [5] U. M. Attia, S. Marson, J. R. Alcock, *Microfluid. Naonofluid.*, **7** (2009), pp. 1-28.
- [6] M. Steinhart, J. H. Wendorff, A. Greiner, R. B. Wehrspohn, K. Nielsch, J. Schilling, J. Choi, U. Gösele *Science*, **296** (2002), pp. 1997.
- [7] M. Zhang, P. Dobriyal, J. T. Chen, T. P. Russell, *Nano Lett.*, **6** (2006), pp. 1075-1079.
- [8] E. W. Washburn, *Phys. Rev.*, **17** (1921), pp. 273-283.
- [9] G. Martic, F. Gentner, D. Seveno, D. Coulon, J. D. Coninck, *Langmuir*, **18** (2002), pp. 7971-7976.
- [10] D. I. Dimitrov, A. Milchev, K. Binder, *Phys. Rev. Lett.*, **99** (2007), 054501.
- [11] W. Tian, K. L. Yung, Y. Xu, L. Huang, J. Kong, Y. Xie, *Nanoscale*, **3** (2011), 4094.
- [12] S. Wu, *J. Phys. Chem.*, **74** (1970), pp. 632-638.
- [13] Q. Y. Wu, J. A. Wu, *Polymer Rheology* (Higher Education Press, Beijing, 2002).
- [14] C. S. Chen, S. C. Chen, W. L. Liaw, R. D. Chien, *Eur. Polym. J.*, **44** (2008), pp. 1891-1898.

Three Dimensional Numerical Investigation of Hydrogen-Absorption Process in Metal Hydride Container

P.Suresh, B. Satya Sekhar, P. Muthukumar, Subhash C. Mishra
Department of Mechanical Engineering
Indian Institute of Technology Guwahati, Guwahati, 781039, India
pmkumar@iitg.ernet.in

ABSTRACT

In this paper, 3-D numerical investigation of hydrogen-absorption process in a cylindrical metal hydride container is presented. Energy equation consists of three-dimensional unsteady coupled heat and mass transfer with chemical reaction is solved for cylindrical coordinates using commercial software, COMSOL multiphysics. The absorption characteristics of low temperature alloy $MmNi_{4.6}Al_{0.4}$ is studied by varying the operating parameters such as hydrogen supply pressure and absorption temperature.

1. Introduction

Many metals have the property of combining chemically with hydrogen directly to form a class of solid compounds called metal hydrides. In recent years, metal hydrides have attracted the attention of hydrogen energy advocates because of their large hydrogen storage capacity at ambient pressure. Per unit of volume, they hold more hydrogen than even liquid hydrogen. Besides large hydrogen capacity, metal hydrides offer several other practical advantages. Unlike compressed hydrogen and liquid hydrogen, metal hydrides can be kept for longer period of time in a container at atmospheric temperatures and pressures. The formation of metal hydrides does not require any special process or machinery as they form simply by coming with the hydrogen gas. Further the hydrogen absorption and delivery rates of metal hydride based hydrogen storage system can be easily controlled by adjusting the supply pressure of hydrogen and varying the absorption temperature.

Many investigators have studied the coupled heat and mass transfer characteristics of hydride bed during the absorption of hydrogen using two-dimensional mathematical model without considering the effect of heat transport by convection [1] and using two-dimensional mathematical model considering the convection effect [2-4]. The single outer cooling tube design has been widely studied in literature referred above, mainly to understand the heat and mass transfer mechanisms. For practical hydrogen storage system the absorption and desorption time should be short. A well designed multiple internal cooling tubes configuration provides high reaction rates for the short charging and discharging. In the light of the above, three dimensional numerical investigation of hydrogen-absorption process in metal hydride bed with embedded cooling tubes is presented in this paper. The variation in cooling fluid temperature along the axial direction is also considered in the present analysis.

2. Mathematical model

Fig. 1 shows the geometry of the cylindrical metal hydride container ($\phi = 79.4\text{mm}$). The container contains one filter at the centre and six embedded cooling tubes ($\phi = 11\text{ mm}$) spaced uniformly inside a

cylindrical reactor. Hydrogen storage material filled in the cylindrical container. Heat transfer fluid is passes through the cooling tubes to carry away the reaction heat generated during the absorption process. Hydrogen is supplied through the porous filter. The filter ensures the instantaneous availability of hydrogen throughout the hydride bed.

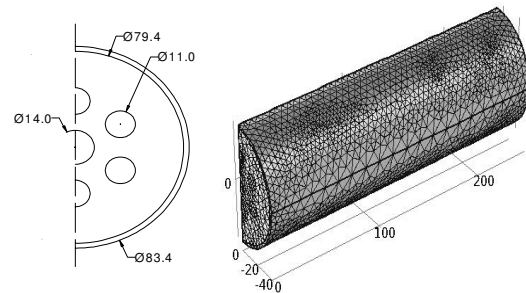


Fig. 1 Three dimensional geometry and mesh

Energy equation

Assuming thermal equilibrium between the hydride bed and hydrogen, a combined energy equation is considered instead of separate equations for both solid and gas phases [3].

$$(\rho C_p)_{eq} \frac{\partial T}{\partial t} + (\rho_g C_{pg}) (\overline{U}_g \cdot \nabla T) = \nabla \cdot (k_e \nabla T) + Q \quad (1)$$

where Q is the source term.

$$Q = m \left[\frac{\Delta H}{M_g} - T^* (C_{pg} - C_{ps}) \right] \quad (2)$$

$$(\rho C_p)_e = \varepsilon (\rho C_p)_g + (1 - \varepsilon) (\rho C_p)_m$$

$$\text{and } k_e = \varepsilon k_g - (1 - \varepsilon) k_m$$

where ρC_p is the heat capacitance, k_e is the thermal conductivity, ε is the porosity.

The hydrogen mass balance is expressed using the continuity equation [3].

$$\varepsilon \frac{\partial (\rho_g)}{\partial t} + \nabla \cdot (\rho_g \overline{U}_g) = m \quad (3)$$

The equilibrium pressure (P_{eq}) is estimated by using van't Hoff equation [2]. The rate of mass of hydrogen absorbed by the metal hydride is given in [1]. Velocity of hydrogen is calculated using the Darcy law.

Initial and Boundary conditions

Initially the pressure and temperature of the container are assumed to be uniform. Therefore,

$$p = p_0; T = T_0; \rho = \rho_s \text{ at } t = 0. \quad (4)$$

The boundary conditions for the energy balance are: Thermal insulation boundaries of the bed,

$$\hat{n} \cdot (k_e \nabla T) = 0 \quad (5)$$

and on the walls of the cooling tubes,

$$\hat{n} \cdot (k_e \nabla T) = h \cdot (T_{wall} - T) \quad (6)$$

where, h is overall heat transfer coefficient.

3. Results and discussion

Fig. 2 shows that the numerically predicted hydrogen storage capacities at different supply pressures are in good agreement with the experimental results reported by Muthukumar et al. [5]. The maximum deviation of numerical prediction from the experimental results is about 3.5 % (20 bar supply pressure) for hydrogen storage capacity, respectively. Fig. 3 shows the variation of cooling fluid temperature along the axial position at different time intervals. It is observed that at a particular time, the variation in cooling fluid temperature is linear along the axial length. Initially due to rapid absorption of hydrogen, the rise in cooling fluid temperature is high.

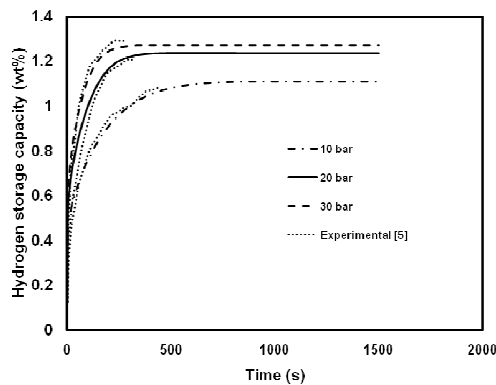


Fig. 2 Effect of supply pressure on hydrogen storage capacity

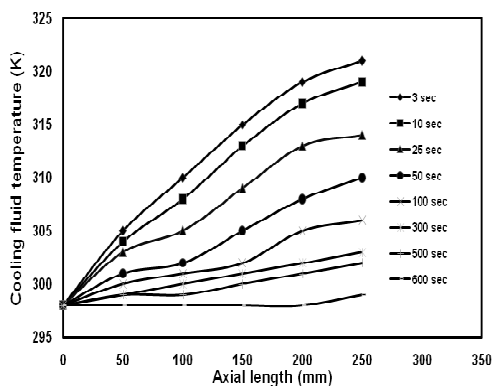


Fig. 3 Variation in cooling fluid temperature at different time intervals

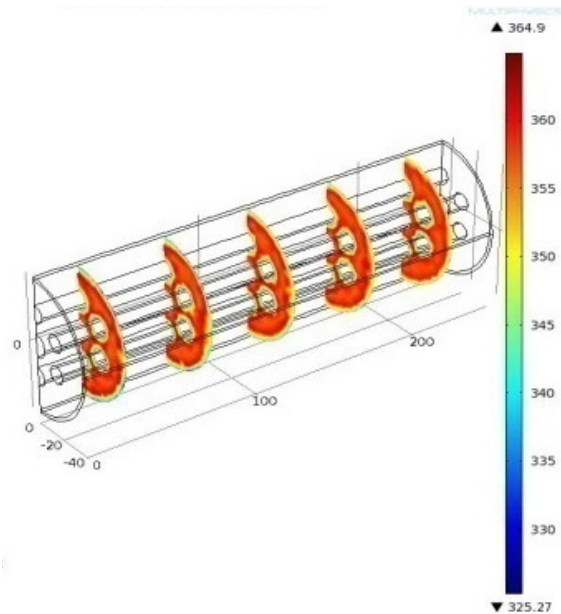


Fig. 4 Bed temperature at 3s absorption time

But as the reaction progresses, the slope of temperature profile decreases with time and finally reaches to zero slope at the end of absorption process. The variation of metal hydride bed along the axial direct is illustrated in Fig. 4. At the beginning ($t = 3$ s) of the absorption process, owing to the rapid exothermic reaction, there is an abrupt rise in the bed temperature. Later, due to effective heat removal around the cooling tubes, the temperature in these regions decrease at a faster rate than in the other regions of the bed.

4. Concluding remarks

A finite element based mathematical model for simulating 3-D $MmNi_{4.6}Al_{0.4}$ based hydrogen storage container embedded with internal cooling tubes is presented. As supply pressure increases both the hydrogen storage capacity and hydrogen absorption rates increase significantly. At the supply condition of 30 bar supply pressure and 303 K absorption temperature, $MmNi_{4.6}Al_{0.4}$ stores about 12.8 g of hydrogen per kg of alloy.

References

- [1] Mayer U, Groll M, Supper W., *J Less Common Metals* 131(1987), pp. 235–44.
- [2] Mat D, Kaplan Y., *Int. J. Hydrogen Energy* 26(2001), pp. 957–63.
- [3] Muthukumar P, Madhavakrishna U, Anupam Dewam., *Int. J. Hydrogen Energy* 32 (2007), pp. 4988-97.
- [4] Muthukumar P and Ramana V., *J. Alloys Compd.*, 472 (2009), pp. 466-472.
- [5] Muthukumar P, Prakash Maiya M, Srinivasa Murthy S., *Int. J. Hydrogen Energy* 30 (2005), pp.1569-1581.

Thermal Modelling of A Double-Stage Metal Hydride Based Heat Transformer

B. Satya Sekhar and P. Muthukumar

Department of Mechanical Engineering

Indian Institute of Technology Guwahati, Guwahati, 781039, India

pmkumar@iitg.ernet.in

ABSTRACT

In this paper, thermal modelling of a double-stage metal hydride based heat transformer (DS-MHHT) working with $\text{LaNi}_{4.88}\text{Al}_{0.23}$, $\text{MmNi}_{4.57}\text{Al}_{0.46}\text{Fe}_{0.05}$ and $\text{MmNi}_{3.98}\text{Fe}_{1.04}$ is presented using an unsteady two-dimensional mathematical model in an annular cylindrical configuration. The mathematical equations of the system are numerically solved by the fully implicit finite volume method (FVM). The variation of bed temperature within the reaction bed and heat interaction for the entire cycle is presented. For a given operating temperatures of 403/353/30 °C, the coefficient of performance (COP_{HT}) and specific heating power (SHP) of the system is estimated as 0.32, and 44 W/kg of total alloy mass, respectively.

1. Introduction

In recent years, many countries have been investing heavily on the development of the equipments that facilitate the recovery and efficient use of energy. Heat transformer is one of such devices, which has the ability to upgrade the low-grade heat to a higher level. Recovery of waste heat not only contributes to the lower energy consumption, but also to the pollution less environment. Although the conventional vapour compression heat pumps are having higher coefficient of performance than the thermally operated heat transformer, but they consume high-grade electrical energy and can be used only at low operating temperatures (less than 100 °C). Metal hydride based heat transformer (MHHT) is a type of thermally operated chemical heat transformer, which can upgrade the temperature of low grade heat such as industrial waste heat, solar energy, geothermal energy, etc. up to the temperature range of 150-220 °C. It also provides higher heat storage capacity.

Suda et al, 1991 developed a two-stage metal hydride heat pump for heat up gradation with a capacity of about 77 kW. Willers and Groll, 1999 built and tested a two-stage MHHT. The operating temperatures were 190-200 °C for the useful heat, 130-135 °C for the driving heat and 40 °C for the waste heat. Isselhorst and Groll, 1995 developed a prototype heat transformer with a capacity of about 8 kW. They showed that an upgrading of thermal energy from 130-140 °C to 200 °C with a heat sink temperature of 30- 40 °C could be possible. Gopal and Murthy, 1995 numerically investigated a single-stage metal hydride heat transformer working with $\text{ZrCrFe}_{1.4}/\text{LaNi}_5$ using a one-dimensional model. Kang and Yabe, 1995 formulated a reaction front model of heat transformer based on MHs, for upgrading the waste heat at 110 °C to more than 140 °C. It is observed from the literature that there was no study on the thermal modelling of a DS-MHHT reported. Therefore, in this paper, the authors present the thermal modelling of a double-stage metal hydride based heat transformer (DS-MHHT). The performance of the system is predicted by solving the coupled heat and hydrogen transfer processes between the paired metal hydride reactors.

2. Mathematical model

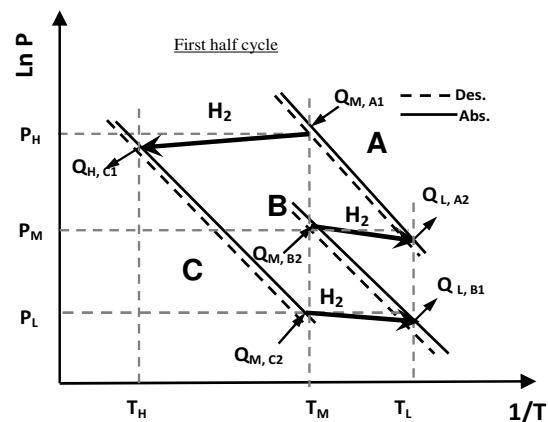


Fig.1 Operating principle DS-MHHT.

Figure 1 shows the operating principle of a DS-MHHT. This system consists of six reactors, namely, A1, A2, B1, B2, C1 and C2. Each hydride is filled in two reactors. Initially, A1 is fully hydrided at heat source temperature T_M , while C1 and B1 are dehydrided at heat output temperature T_H and heat sink temperature T_L , respectively. Reactor A1 desorbs hydrogen by taking the heat at T_M which gets absorbed by C1 at high pressure, thereby forming the hydride and releasing the heat of absorption at high temperature, T_H . This high temperature heat ($Q_{H,C1}$) is the output from the system. During the same period, C2 and B2 desorb hydrogen by taking the heat ($Q_{M,C2}$ and $Q_{M,B2}$) at temperature, T_M and the desorbed hydrogen are respectively absorbed by B1 and A2 at T_L by releasing $Q_{L,B1}$ and $Q_{L,A2}$. Thus, the system completes the first half cycle. Now, the valves between the coupled reactors are closed. Reactors A2 and B1 are heated to T_M , while C2 is heated to T_H . The other reactors, A1 and B2 are cooled down to T_L , while C1 is cooled to T_M . The hydrogen transfer processes during the second half cycle are similar to the first half cycle. The details of the thermal modeling of the coupled metal hydride reactors for a single – stage MHHT and the solution procedure were already reported by authors [6]. The same model with necessary modification is adapted here for predicting the performances of a DS-MHHT.

The performances of the DS-MHHT system are designated by the coefficient of performance (COP_{HT}) and the specific heating power (SHP). These quantities are defined as;

$$COP_{HT} = \frac{Q_{H,C1}}{Q_{M,A1} + Q_{M,B2} + Q_{M,C2}} \quad (1)$$

where, $Q_{H,C1}$ denote the heat output obtained from C1 ($Q_{H,C2}$ during second half cycle). $Q_{M,A1}$, $Q_{M,B2}$ and $Q_{M,C2}$ are the heat supplied to A1, B2 and C2, respectively. Heat output from reactor C1 is expressed as

$$Q_{H,C1} = n_{a,C1} \Delta H_{a,C1} - [C_{p,C1} (m_r + m_h)_{C1} (T_H - T_M)] \quad (2)$$

where, $n_{a,C1}$ and $\Delta H_{a,C1}$ denote the number of moles of hydrogen absorbed by C1 and the enthalpy of formation of hydride C, respectively. m_r and m_h are the mass of the reactor and the mass of the metal hydride alloy.

Heat supplied to A1 is expressed as

$$Q_{D,A1} = n_{d,A1} \Delta H_{d,A1} + [C_{p,A1} (m_r + m_h)_{A1} (T_M - T_L)] \quad (3)$$

Similarly, the heat supplied to B2 and C2 are calculated. The specific heating power (SHP) is defined as the net heat output obtained over a cycle per unit mass of alloy.

$$SHP = \frac{(Q_{H,C1} + Q_{H,C2})}{m_T t_{cy}} \quad (4)$$

where, m_T denotes the total hydride mass filled in all the reaction beds and t_{cy} denotes the total cycle time.

3. Results and discussion

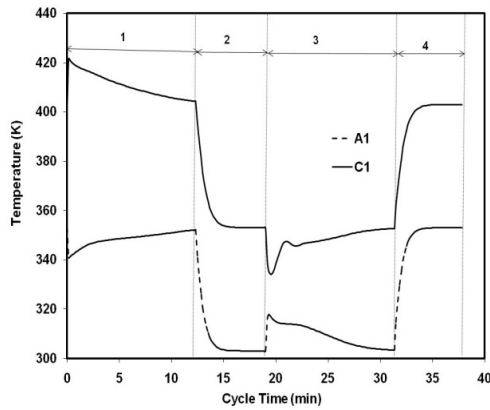


Fig. 2. Variation of bed temperature for A1 and C1

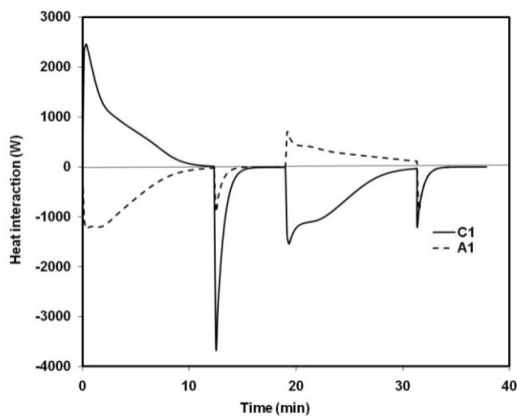


Fig. 3. Heat interactions for A1 and C1

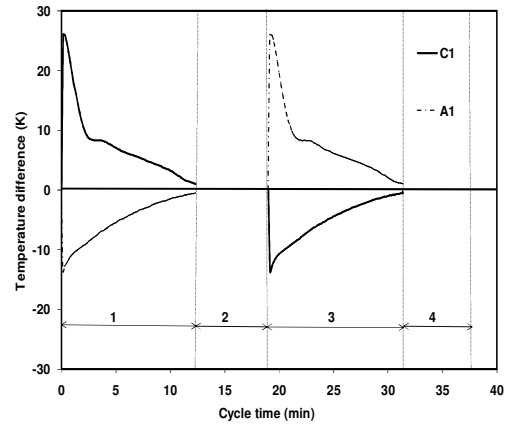


Fig. 4 Variation of HTF temperature difference

Figure 2 shows the variation of hydride bed temperatures for A1 and C1 over a complete cycle. It is observed that due to the poor thermal conductivity of the hydride bed, the required amount of heat is not being transferred from/to the heat transfer fluid (HTF) during initial rapid desorption/absorption process. Hence, the sudden fall/rise in temperature of the reaction beds of A1/C1 occurs as soon as the process started, and it reaches the HTF temperature gradually. The heat interaction between the hydride bed and the heat transfer fluid for A1 and C1 over a complete cycle time is shown in Fig. 3. Due to the exothermic/endothermic processes, heat is carried away/supplied to the reactors and their temperatures increase/decrease accordingly. The maximum rate of heat supplied to C is about 1.2 kW (total heat supplied rate is ≈ 3.4 kW) and useful heat output is 2.3 kW. Figure 4 shows the variation of heat transfer fluid (HTF) temperature difference (between inlet and outlet). The average gain in HTF temperature during the output is about 7.3 K.

4. Concluding remarks

Thermal modeling of DS-MHHT is presented. The variation of hydride bed temperature within the reaction bed and heat interactions between the coupled reaction beds over a cycle is studied. For a given operating temperatures of 403/353/303 K, the coefficient of performance (COP_{HT}) and specific heating power (SHP) of the DS-MHHT is estimated as 0.32, and 44 W/kg of total alloy mass, respectively.

References

- [1] Suda S, Komazaki Y, Narasaki H, Uchida M., *J. Less Common Metals* 172(1991), pp. 1092-110.
- [2] Willers E, Groll M., *Int. J. Hydrogen Energy* 24 (1999), pp. 269-276.
- [3] Isselhorst A, Groll M., *J. Alloys and Compounds* 231(1995), pp. 888-894.
- [4] Ram Gopal M, Murthy SS., *Ind. Eng. Chem. Res* 34 (1995), pp. 2305-13.
- [5] Kang B, Yabe A., *J. Applied Thermal Engineering* 16 (1995), pp. 677-90.
- [6] Satya Sekhar B, Muthukumar P., *21st National & 10th ISHMT-ASME Heat and Mass Transfer Conference*, (2011), pp. 27-30.

Comparative Analysis of Transient Heat Conduction in a Planar Medium Using Smoothed Particle Hydrodynamics, Finite Volume Method and Lattice Boltzmann Method

Subhash C. Mishra and Harsh Sahai
Dept. of Mechanical Engineering,
Indian Institute of Technology Guwahati, India – 781039
Corresponding author: scm_iit@yahoo.com

ABSTRACT

Smoothed particle hydrodynamics has been used to simulate transient heat conduction in one-dimensional planar medium. With bottom and top boundaries of the medium subjected to fixed temperatures, temporal and steady-state temperature distributions have been compared against the results of the finite volume method and the lattice Boltzmann method. Results from smoothed particle hydrodynamics have been found to be in excellent comparison. However, computationally, it has no advantage.

1. Introduction

Smoothed particle hydrodynamics (SPH) is notable as a mesh free method for its robustness and ease of use. SPH is particularly easy to work with, especially when complicated physics is involved for example in cases involving combined mode heat transfers and phase change, heat transfer in free surface flows, etc.

The central idea of a SPH formulation is to calculate the spatial derivatives using an approximation of the ‘Dirac Delta’ function. The ‘Dirac Delta’ function is commonly modeled by what is known as a ‘kernel’. The choice of the kernel has a significant effect on the accuracy of the solution. All other properties $A(x)$ are interpolated between particles using the following equation [1].

$$A(x) = \sum_i^N m_i \frac{A_i}{\rho_i} W(|x_i - x|; h) \quad (1)$$

where m_i and ρ_i represent the mass and density of the particle located at x_i , respectively and h represents the smoothing length. In interpolating values of a property at a point, particles located beyond this length have no contribution.

In the present work, SPH has been compared with the lattice Boltzmann method (LBM) [2] and the finite volume method (FVM). LBM is also a ‘discrete particles based’ method that has been shown to be the finite difference counterpart of the Boltzmann equation. It is amenable to extensive parallelization which makes it a suitable technique for the more involved problems that are often examined using SPH method. FVM, being a widely used and robust method to evaluate partial

differential equations in the form of algebraic equations, provides a suitable benchmark for these two methods.

2. Formulation

The SPH form used for this solution was based on the Taylor series expansion approach proposed by Brookshaw [1].

The formulation used in this work employs a cubic spline for all SPH solutions. It can be shown that the use of B-Spline kernel M_4 reduces the governing SPH equation to the familiar central finite difference form.

Heat transfer by conduction in one dimension planar medium is given by [2],

$$\rho C_p \frac{\partial T}{\partial t} = k \frac{\partial^2 T}{\partial x^2} + Q \quad (2)$$

where t , T , k , ρ , C_p and Q are time, temperature, thermal conductivity, density, specific heat and volumetric heat source, respectively.

Temperature can be expanded into a Taylor series about point x as shown below

$$T(x) - T(x') = (x - x') \frac{\partial T}{\partial x} + \frac{1}{2} (x - x')^2 \frac{\partial^2 T}{\partial x^2} + \dots \quad (3)$$

This equation can be used to derive the integral interpolant form the following equation.

$$\begin{aligned} & \int \frac{T(x) - T(x')}{x - x'} \frac{\partial W(x - x')}{\partial x} dx' \\ &= \frac{1}{2} \frac{\partial^2 T}{\partial x^2} \int (x - x') \frac{\partial W(x - x')}{\partial x} dx' + O(h^2) \end{aligned} \quad (4)$$

where h is the half width of the interpolating function $\frac{\partial W}{\partial x}$. Interpolating particles considered in this work are distributed equally throughout the solution domain.

3. Results and Discussion

With entire system initially at the temperature of the bottom boundary at 0°C and for time $t > 0$, the top raised to non-dimensional temperature unity, for a medium with constant thermal conductivity and heat capacity, comparison of non-dimensional temperature distributions in the medium at two non-dimensional time levels, viz., $\tau = 0.3$ and 0.6, and in the steady-state are shown in Fig. 1. Temperature distributions obtained from the SPH have been compared against that obtained using the LBM and the FVM. Results are found to compare exceedingly well.

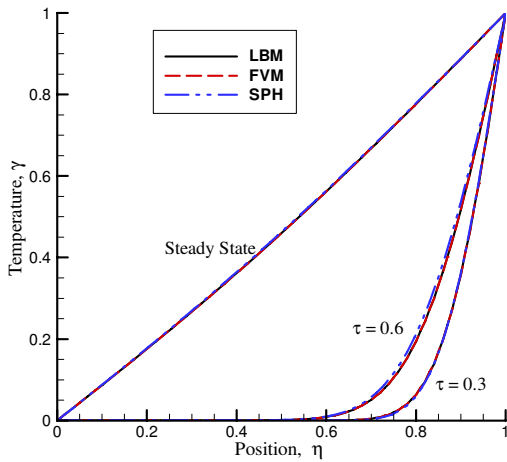


Fig. 1 Comparison of non-dimensional temperature distribution obtained from LBM, FVM and SPH in a one-dimensional planar homogeneous medium when one of its boundaries is suddenly elevated to a higher temperature.

Computational efficiency of the SPH against the LBM and the FVM has been compared in Tables 1-3. All computations were performed on an Intel Core i3 processor. Table 1 compares the number of iterations each numerical scheme took to reach the steady-state with 0.001 as the steady-state tolerance criteria. Tables 2 and 3 compare the time taken to compute the solution at the non-dimensional time $\tau = 0.6$ and the steady-state respectively.

From Table 1, it is observed that for any resolution $\Delta\tau = \Delta\eta$, the number of iterations to reach the steady-state is the minimum with the FVM and maximum with SPH except for $\Delta\tau = \Delta\eta = 0.0001$, in which case, it is the maximum for the LBM. The CPU times for computation of temperature at $\tau = 0.6$ and at the steady-state are found to be the minimum with the LBM and the maximum with the FVM.

Table 1: Comparison of the number of iterations for the steady-state solution in the FVM, the LBM and the SPH.

Resolution $\Delta\tau = \Delta\eta$	Iterations for the steady-state		
	FVM	LBM	SPH
0.001	10876	12004	12426
0.0005	22066	23096	22532
0.0001	124231	898861	126062

Table 2: Comparison of the CPU times in the FVM, the LBM and the SPH for estimation of temperature at time $\tau = 0.6$.

Resolution $\Delta\tau = \Delta\eta$	CPU time(s)		
	$\tau = 0.6$		
	FVM	LBM	SPH
0.001	8.945	0.529	9.224
0.0005	38.723	1.739	39.960
0.0001	2742.2	29.572	2801.3

Table 3: Comparison of the CPU times in the FVM, the LBM and the SPH for estimation of temperature at steady-state.

Resolution $\Delta\tau = \Delta\eta$	CPU time(s)		
	Steady-state		
	FVM	LBM	SPH
0.001	198.934	66.4564	221.8342
0.0005	876.045	127.9222	882.9144
0.0001	493500	5331.7	498860

4. Conclusions

Smoothed particle hydrodynamics was used to analyze transient heat conduction in 1-D planar medium. Temperature distributions, number of iterations to reach the steady-state and CPU times to calculate temperature at $\tau = 0.6$ and at the steady-state were compared against the FVM and the LBM. The SPH was found to provide correct results, but computationally, it was not so.

References

- [1] L. Brookshaw, A method of calculating radiative heat diffusion in particle simulations, Proc. Astron. Soc. Aust. 6 (1985) 207–210.
- [2] S.C. Mishra, B. Mondal, T. Kush and B.S.R. Krishna, Solving transient heat conduction problems on uniform and non-uniform lattices using the lattice Boltzmann method, Int. Commun. Heat Mass Transfer, 36 (2009) 322-238.

Analysis of Rayleigh-Bénard Convection with and without Volumetric Radiation

Subhash C. Mishra, Adnan Akhtar and Anshul Garg

Department of Mechanical Engineering,

Indian Institute of Technology Guwahati, India – 781039

Corresponding author: scm_iit@yahoo.com

ABSTRACT

Rayleigh-Bénard convection in a 2-D rectangular channel in the presence of volumetric radiation is analyzed. Momentum and energy equations are formulated and solved using the lattice Boltzmann method. Volumetric radiative information needed in the energy equation is computed using the finite volume method. Effects of the extinction coefficient are analyzed on streamlines and isotherms.

1. Introduction

Owing to its diverse applications from natural to man-made systems, Rayleigh-Bénard convection has been studied extensively. A good volume of work pertaining to theoretical, numerical and experimental studies is available [1]. In many situations, consideration of volumetric radiation needs to be considered. This in one way gives interesting results, on the other hand, adds to the complexity of the formulation and its solution. In the present work, Rayleigh-Bénard convection in a 2-D rectangular channel is numerically analyzed.

Lattice Boltzmann method (LBM) has found extensive application in the analysis of a wide range of fluid flow and heat transfer problems. In the recent past, it too has been used in the formulation and solution of energy equations of heat transfer problems involving volumetric radiation in which radiative information was computed using the finite volume method (FVM) [2]. With volumetric radiation, literature on Rayleigh-Bénard convection is scarce. The present work is a study in this direction.

2. Formulation

Consideration is given to a rectangular channel containing an absorbing, emitting and scattering medium. Initially, the system is at temperature T_c , and for time $t > 0.0$, the system is perturbed by raising the temperature T_h of the bottom wall, i.e., $T_h > T_c$. The thermal gradient results in a density gradient in the medium giving rise to a gravity opposing buoyancy force. This results in Rayleigh-Bénard convection.

Thermo-physical properties, except density, are assumed constant and density is considered to vary in the Boussinesq sense. Radiatively, the homogeneous medium in the channel is absorbing, emitting and scattering, and its optical properties such as the extinction coefficient β and scattering albedo ω are constant. The boundaries of the channel are considered diffuse-gray.

In the LBM formulation, for computation of density (and velocity) and thermal fields, separate particle distribution functions are used. For computation of velocity field, the governing lattice Boltzmann equation is given by

$$f_i(\vec{r} + c_i \Delta t, t + \Delta t) = f_i(\vec{r}, t) - \frac{\Delta t}{\tau_v} [f_i(\vec{r}, t) - f_i^{(eq)}(\vec{r}, t)] + J_i \quad (1)$$

where f_i is the particle distribution function, c_i is the velocity, τ_v is the relaxation time, $f_i^{(eq)}$ is the equilibrium distribution function and J_i is the buoyant body force term. With ν as the kinematic viscosity and c_s as the speed of sound, for the D2Q9 lattice used in the present work, the relaxation time τ_v is computed

$$\text{from } \tau_v = \frac{3\nu}{c_s^2 \Delta t} + \frac{1}{2}.$$

With Prandtl number Pr and Rayleigh number Ra known, the kinetic viscosity ν is computed from simultaneously solving the following:

$$\text{Pr} = \frac{\nu}{\alpha}, \quad \text{Ra} = \frac{\beta_t g_0 (T_h - T_c) \times H^3}{\nu \alpha} \quad \text{where } \alpha = \frac{k}{\rho c_p}$$

is the thermal diffusivity, $\beta_t = -\frac{1}{\bar{\rho}} \left(\frac{\partial \rho}{\partial T} \right)_p$ is the

coefficient of thermal expansion, g_0 is the acceleration due to gravity, and H is height of the channel. In the

above, with $\bar{u} = Ma \times c_s$, $\beta_t g_0 = \frac{|\bar{u}|^2}{\Delta T \times H}$ where Ma is

the Mach number and c_s is the characteristic flow velocity.

The external force term J_i in Eq. (1) is given by $J_i = 3w_i g_0 \beta_t [T(r, t) - T_\infty] \rho(r, t) c_{iy}$, where ρ and T are the local density and temperature at the lattice

site, respectively, and T_∞ is the lowest reference temperature in the domain.

For computation of thermal field, in the presence of volumetric radiation, the governing lattice Boltzmann equation is given by

$$g_i(\vec{r} + \vec{c}_i \Delta t, t + \Delta t) = g_i(\vec{r}, t) - \frac{\Delta t}{\tau_i} \left[g(\vec{r}, t) - g_i^{(eq)}(\vec{r}, t) \right] - \left(\frac{\Delta t}{\rho c_p} \right) w_i \nabla \cdot \vec{q}_R \quad (2)$$

where g_i is the particle distribution function denoting the evolution of the internal energy, τ_i is the relaxation time, $g_i^{(eq)}$ is the equilibrium distribution function and \vec{q}_R is the radiative heat flux. Formulation and calculation procedure for the calculation of volumetric radiation $\nabla \cdot \vec{q}_R$ are involved, and for page limitation, the same are skipped. These details can be found in [2].

3. Results and Discussion

The LBM formulation for the Rayleigh-Bénard convection without volumetric radiation is first validated against the results available in the literature [1]. For Prandtl number $Pr = 0.71$, in Fig. 1, this validation is shown for the variation of the average

Nusselt number $\bar{Nu} = 1 + \frac{\langle u_y \cdot T \rangle}{\alpha(T_H - T_C)/H}$ with Ra in the

range [1700, 50000]. Results of the present work compare exceedingly well with those reported in the literature.

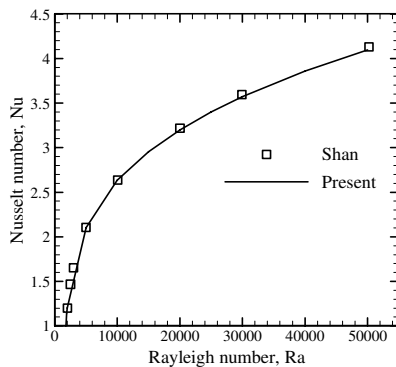
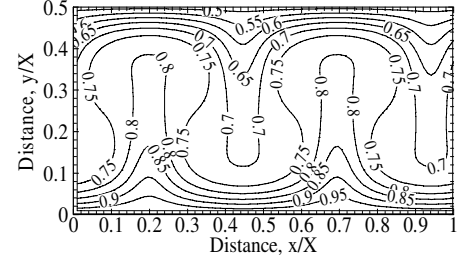


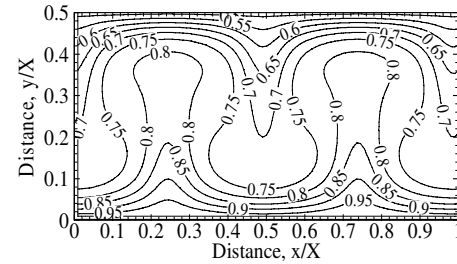
Fig. 1: Comparison of variation of steady-state average Nusselt number with Rayleigh number.

With convection to radiation parameter $CR = 250$ and scattering albedo $\omega = 0.0$, at time step 20000 for $Ra = 10000$, for extinction coefficient $\beta = 0.1$ and 3.0 , isotherms and streamlines are shown in Figs. 2a-d. As

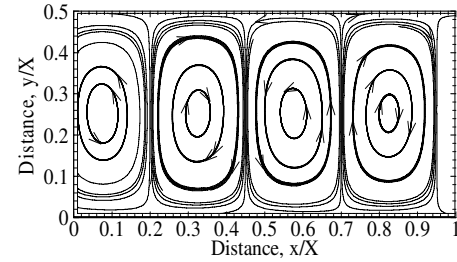
medium becomes more radiatively participating, distinct change in the isotherms is observed. However, no significant change is observed in streamline patterns.



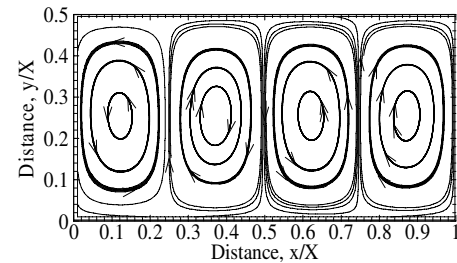
(a)



(b)



(c)



(d)

Fig. 2. Isotherms (a, b) and streamlines (c, d) at time step = 20000 for $Ra = 10000$ for (a, c) extinction coefficient $\beta = 0.1$ and (b, d) $\beta = 3.0$.

4. Conclusions

Rayleigh-Bénard convection in a 2-D rectangular channel was analyzed. Volumetric radiation was accounted. The velocity and temperature fields were computed using the LBM, and in the energy equation, radiative information was computed using the FVM.

References

- [1] X. Shan, Physical Review E, 55(1997) 2780-2788.
- [2] S.C. Mishra and H.K. Roy, J. Comput. Phys., 233 (2007) 89-107.

the bulk fluid is supercritical. Further details of the simulation method are provided elsewhere.³

We apply the external force of 0.05 pN in the x -direction to each water molecule, creating a density gradient in the bulk fluid towards the cold wall for Case 2 and the hot wall for Case 2a. The intermolecular forces in water are larger than this applied force by at least an order of magnitude. The interaction between water and the Si surface is hydrophobic, since it primarily involves van der Waals interactions. The Si surface is prepared to mimic a hydrophobic interface by manipulating q_i and q_j . The values of the charges on adjacent atoms are specified as positive and negative ($+q$, $-q$) to mimic a polar surface but yet maintain overall charge neutrality.

3. Results and Discussion

In the absence of an applied force or hydrophilic solid-fluid interactions at the interfaces, the fluid density on the colder side of the reservoir is larger than on its warmer side. N increases slightly adjacent to the cold wall when an external force is applied as compared to the case for a hydrophobic wall.³ The corresponding interfacial resistance is also comparable for Cases 1 and 2 as exhibited through their temperature profiles, which are alike. Consequently, the corresponding heat fluxes are not too dissimilar. There is a greater increase in the fluid density for Case 3 when the cold wall is rendered hydrophilic due to the adsorption and layering of fluid molecules^{7, 8, 11-13} as compared to Cases 1 and 2. This significantly decreases the interfacial resistance to heat transfer^{11, 12} and leads to a larger overall heat flux.

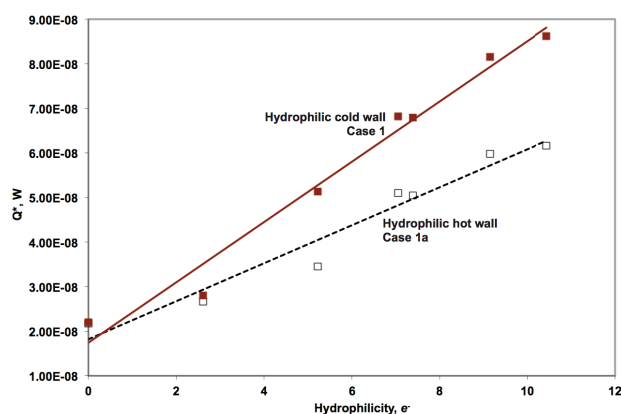


Figure 2. The variation in the heat flux in units of W with the magnitude of the hydrophilic nature of a hot (■) or cold (□) wall. The magnitude of the electron charge imparted to the (i, j) sites is taken as a surrogate for a wall's hydrophilic nature. This charge is converted into units of e^- by dividing its value by 10.45, which is the charge on a monovalent ion such as Na^+ or Cl^- . The slope of the heat flux for increasing charge on the cold wall is 75% greater than the corresponding slope for a cold wall.

The applied force is less effective in overcoming the intermolecular interactions among the water molecules in the fluid layer adjacent to the hot than are the

hydrophilic water-Si interactions. Hence, when the hot walls are rendered hydrophilic for Case 2a, the corresponding heat flux exceeds that for Cases 1a and 3.

Increasing the values of the ($+q$, $-q$) charges makes a wall more hydrophilic. Hence, in Fig. 2, the magnitude of the electron charge imparted to the (i, j) sites is taken as a surrogate for a wall's hydrophilic nature. The figure shows that the heat flux increases with e^- , i.e., making either of the hot or cold walls more hydrophilic also enhances the overall thermal transport through the reservoir. Consistent with our hypothesis, making the cold wall hydrophilic allows for greater heat transfer than is possible with a similar hydrophilic hot wall. The slopes of heat flux vs. e^- for the two conditions illustrate this response. That for Case 3 is greater than for Case 3a by 75%.

4. Concluding remarks

This observation forms the basis for thermal rectification. Clearly, in the reservoir, when the hydrophilic wall is on the cold side, there is greater heat transfer than when this wall is placed on the hot side. Thermal rectification devices that include fluid-solid interfaces should therefore focus on reducing the interfacial resistance on the cold side.

References

- [1] G. Balasubramanian, I. K. Puri, M. C. Bohm and F. Leroy, *Nanoscale* **3** (9), 3714-3720 (2011).
- [2] S. Pal, G. Balasubramanian and I. K. Puri, *The Journal of Chemical Physics* **136** (4), 044901-044907 (2012).
- [3] S. Murad and I. K. Puri, *Applied Physics Letters* **100** (12), 121901-121905 (2012).
- [4] C. W. Chang, D. Okawa, A. Majumdar and A. Zettl, *Science* **314** (5802), 1121-1124 (2006).
- [5] J. Hu, X. Ruan and Y. P. Chen, *Nano Lett* **9** (7), 2730-2735 (2009).
- [6] P. L. Kapitza, *Journal of Physics, USSR* **4**, 181 (1941).
- [7] S. Murad and I. K. Puri, *Applied Physics Letters* **92** (13), 133105 (2008).
- [8] S. Murad and I. K. Puri, *Chemical Physics Letters* **476** (4-6), 267-270 (2009).
- [9] G. L. Pollack, *Reviews of Modern Physics* **41** (1), 48-81 (1969).
- [10] P. A. E. Schoen, B. Michel, A. Curioni and D. Poulidakos, *Chemical Physics Letters* **476** (4-6), 271-276 (2009).
- [11] S. Murad and I. K. Puri, *Chemical Physics Letters* **467** (1-3), 110-113 (2008).
- [12] G. Balasubramanian, S. Banerjee and I. K. Puri, *Journal of Applied Physics* **104** (6), 064306 (2008).
- [13] S. Murad and I. K. Puri, *Physics of Fluids* **19**, 128102 (2007).

Heat and Mass Transfer in Confined Lubricated Films

Philippe Vergne¹, Nicolas Fillot¹, Wassim Habchi², Vincent Bruyere¹, Thomas Doki-Thonon¹
¹ Université de Lyon, CNRS, INSA-Lyon, LaMCoS UMR 5259, F-69621, France
² School of Engineering, Lebanese American University, Byblos, Lebanon
philippe.vergne@insa-lyon.fr

ABSTRACT

Nowadays the accurate prediction of the actual tribological parameters that characterize lubricated systems requires the development of more and more advanced tools. Concerning the numerical ones, this leads to new challenges to model and predict in a proper way the strong couplings between mass (lubricant flow) and heat (dissipation, friction) transfer that appear within and around highly confined lubricating films. This paper presents some recent advances achieved in modeling TEHL problems where shear heating and its consequences can dominate other effects.

1. Introduction

Nowadays the prediction of the actual tribological parameters that characterize lubricated systems requires the development of more and more advanced tools, experimental or numerical. This demand is mainly motivated by the increasing severity of the operating conditions that occur within lubricated contacts. More precisely, this trend comes with the significant rise of the power density experienced by lubricated contacts and simultaneously with the continuous film thickness drop towards the nanometer scale.

Concerning the numerical approach, new challenges emerge to model and predict in a proper way the strong multi-physics couplings between mass (lubricant flow) and heat (dissipation, friction) transfer that appear within and around the contact. This perspective represents a real breakthrough regarding the current knowledge and tools available for mechanical designers and engineers, mostly based on isothermal models.

2. Context and background

Thin lubricated films are formed under the thermo-elastohydrodynamic (TEHD) lubrication regime that is encountered in non-conforming mechanical lubricated contacts of many machine elements. The expression thermo-elastohydrodynamic means that a strong coupling occurs between three main effects: elastic deformations of the solid surfaces subjected to relatively high pressures, hydrodynamic effect due to the fluid entrainment through the contact inlet and finally shear and compressive heating. Thus, the lubricant undergoes extreme operating conditions:

- high pressures, typically between 0.5 to 3 GPa,
- large shear rates up to 10^5 - 10^8 s⁻¹,
- short transit times, usually much less than 1 ms,
- temperature elevation of some tens of degrees,
- very thin lubricant film thickness, from initially about 1 μm to nowadays some tens of nanometers.

Controlling such conditions and ensuring reliable operation of lubricated mechanisms has been possible thanks to numerous contributions – both experimental and numerical – on film thickness build-up mechanisms and friction in TEHD lubricated contacts published over the last 30 years. In this work, we focus on a brief description of a full-system finite element approach of TEHD lubrication and on the use of numerical models to

highlight the important couplings between heat and mass transfers that occur in these confined interfaces.

3. Numerical approach

The first solutions of the elastohydrodynamic (EHD) problem were provided by the pioneering works of Dowson and Higginson [1] and then Hamrock and Dowson [2]. Their approach called "iterative semi-system approach" consisted in solving the different equations separately and establishing an iterative scheme to reach the problem solution. This methodology has been regularly improved by numerous contributors, but the vast majority of the literature remained focused on isothermal approaches that make these works unable to address the TEHD problem.

An alternative method to the iterative semi-system approach has recently emerged based on the FEM and a full-system approach. It was driven by the need:

- to overcome the restrictive assumptions specific to the semi-system approach,
- to improve the convergence rate and thus the computing effort,
- to use more general equations,
- to take into account important issues such as the non-Newtonian behavior of the lubricant and / or heat dissipation by fluid shearing and compression.

This was successfully achieved by Habchi et al. [3-4] who solved the generalized Reynolds equation, the film thickness equation (that includes the elastic deformation of the solid bodies) and the load balance equation in a fully coupled Newton-Raphson procedure, for a given temperature distribution. Then the energy equation (applied to both the solid bodies and the lubricating film) is solved for a given pressure and film thickness profiles provided by the solution of the EHD problem. An iterative procedure is thus established between the respective solutions of the EHD and thermal problems until convergence of both the temperature and pressure fields is attained. Two steps further were accomplished in order to provide more physical insight on TEHL:

- The pressure and temperature dependence of the thermo-physical properties of the lubricant was implemented [5] in the generalized Reynolds-based model. This offered the opportunity to carry out a detailed analysis on how heat transfers can take

place at different locations within a TEHL contact.

- Navier-Stokes, full elasticity and full energy conservation equations have been used [6] to reduce the number of assumptions classically considered in TEHL. High SRR cases have been computed, showing thermal effects dominating rheological ones. The occurrence of dimples was explained with the viscosity wedge theory by analyzing the gradients of viscosity, pressure and temperature.

4. Results and Discussion

Regarding energy conservation, two heat sources are active in the contact (see fig. 1), the compression of the fluid and its shearing. Convection in the film thickness and conduction in the plane are usually neglected compared to convection in the film plane and conduction in the film thickness, due to the Reynolds thin film assumption.

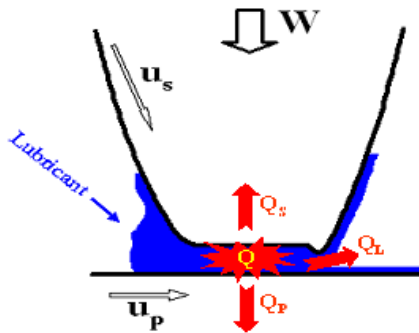


Fig. 1 Energy source terms in a TEHL case, lubricant enters the contact at the left side

A classical result in TEHL lies in the inflexion of traction curves beyond a certain amount of relative slip. This is illustrated in fig. 2: when shear heating becomes important a significant drop of friction is observed.

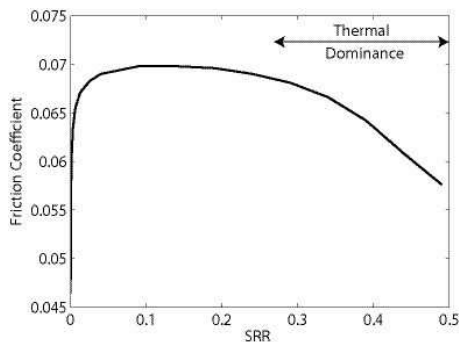


Fig. 2 Typical friction curve obtained in TEHL regime

Fig. 3 shows the heat source distribution for a pure sliding case. A strong dissymmetry is observed across the film thickness, the stationary upper surface witnesses much larger heat dissipation. In addition, the heat flux through that surface is much smaller than the one going through the lower moving surface as heat is removed from the film only by conduction. For the lower surface, heat is removed by both conduction and advection. Consequently, the temperature elevation at the moving surface will be significantly lower than the one at the upper surface. These results were obtained by solving the Navier-Stokes equations, meaning that the

consequences of viscosity or temperature gradients appearing across the film thickness are well described. Two extreme cases are presented in fig. 4 and 5, where both surfaces are moving but in opposite directions and where the upper surface is moving according a spinning motion, respectively. In both cases, the lubricant heats up at the contact inlet due to thermal conduction in the solids produced by its shearing in the central area. This sheds light another type of coupling, between the contact central zone where friction is generated and the inlet area where film thickness is built-up.

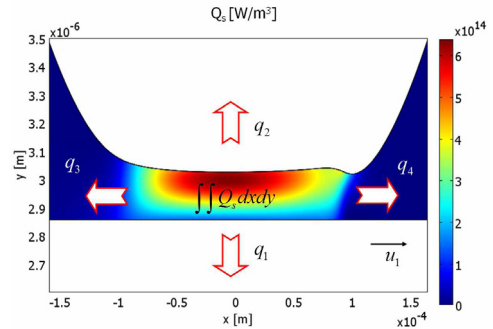


Fig. 3 Energy source term and thermal fluxes for a pure sliding case, lubricant enters the contact at the left side.

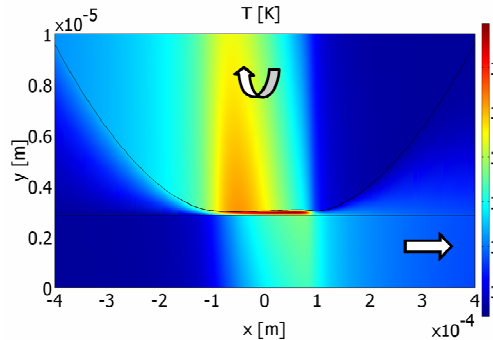


Fig. 4 Temperature distribution in the fluid and the two solids for a high sliding case, lubricant enters the contact from both sides.

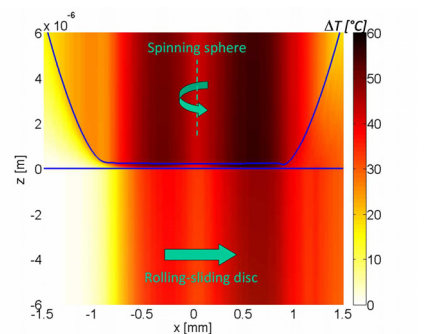


Fig. 5 Temperature rise in a longitudinal cross section of a spinning contact.

References

- [1] D. Dowson, G.R. Higginson, Pergamon Press, 1966
- [2] B.J. Hamrock, D. Dowson, JolT, 98, (1976), 223-229
- [3] W. Habchi et al., J. of Trib., 130, 2 (2008), 021501
- [4] W. Habchi et al., Trib. Letters, 30, 1 (2008), 41-52
- [5] W. Habchi et al. Trib. Int., 43, 10 (2010), 1842-1850
- [6] V. Bruyere et al., Trib. Int., 46, 1 (2012), 3-13
- [7] T. Doki-Thonon et al., JET, 226, 1 (2012), 23-35

Entransy, Entransy Dissipation and Entransy Loss for Analyses of Heat transfer and Thermodynamics

Xin-Gang Liang

School of Aerospace, Tsinghua University, Beijing 100084, China.

E-mail: liangxg@tsinghua.edu.cn

ABSTRACT

Entransy is a parameter proposed in the recent years that describes the potential of heat in an object. Its balance equation was established based on energy equation of heat transfer, which contains entransy, entransy flow, entransy dissipation, entransy production due to heat source. It has been proved that the total entransy must be reduced whenever there is heat transfer in an isolated system, leading to entransy dissipation. Entransy dissipation and entransy-based thermal resistance can be used to optimize entransy heat transfer. Entransy loss (sum of dissipation and change due to work) is defined and is related to thermodynamics processes.

1. Introduction

The method of improving heat transfer is a very important topic in heat transfer research. Entropy generation is very often applied to the optimization of heat transfer but sometimes the minimum entropy generation is not related to the best heat transfer performance^[1]. In recent years, a parameter, entransy, was proposed based on the analogy between heat and electrical conduction and was deduced from energy conservation equation of heat transfer^[2]. It is proved that entransy is reduced during heat transfer in isolated systems^[3] and the reduced entransy is called entransy dissipation which can be used to optimized heat transfer^[4-6]. The effective thermal resistance can be defined based on entransy dissipation for multi-temperature system and the minimum resistance correspond the optimum heat transfer performance^[2]. Later, the entransy balance equation was developed based energy conservation equation, the influence of work on entransy was investigated. Entransy loss that consider the entransy dissipation and entransy change due to work output is defined and is related to work output of thermodynamic cycles.

2. Entransy, its balance equation and dissipation

In the analogy between heat and electrical conduction, heat flow corresponds to electrical current, thermal resistance to electrical resistance, temperature to electric voltage, and heat capacity to capacitance. A quantity, entransy, is defined in thermal system so as to correspond to electrical potential energy of a capacitor,

$$G = UT / 2 \quad (1)$$

where U is the internal energy of object at temperature T . Entransy is the "potential energy" of heat at temperature T in an object. Higher temperature and higher internal energy imply that the object has higher ability to release heat. When two objects with different temperatures are put into contact their temperature will finally reach equilibrium. Their entransy at equilibrium state is smaller than the initial state^[2]. The entransy difference between the initial and final state is called entransy dissipation. It has been proved that the total entransy of an isolated system always decreases during spontaneous heat transfer^[3].

The entransy balance equation can be derived from the energy equation of heat transfer without considering

heat source and viscosity dissipation by multiplying temperature T ^[2,7,8],

$$\partial g / \partial t + \mathbf{v} \cdot \nabla g = -\nabla \cdot (\mathbf{q}T) + \mathbf{q} \cdot \nabla T \quad (2)$$

where \mathbf{v} is velocity, $g = 0.5uT$ is the specific entransy, u is internal energy per unit volume, \mathbf{q} is heat flux. On the left, the 1st term is time variation of entransy, the 2nd term is entransy accompanying fluid flow; on the right, the 1st term is boundary entransy flow, the 2nd term is the entransy dissipation $g_{dis} = \mathbf{q} \cdot \nabla T$. It is clear that the heat transport ability is reduced when heat is transferred from high temperature to low temperature. For steady state, the net entransy exchange due to fluid flow and heat flow at boundary equal the entransy dissipation^[4, 8].

3. Extremum principle for heat transfer optimization

For steady-state convective heat transfer of a fluid with constant boundary heat flux and ignoring the heat generated by viscous dissipation, integrating eq. (2), and transforming the volume integral to the surface integral on the domain boundary yields^[8]

$$Q_0 \delta(\overline{\Delta T}) = \delta \iiint_V [k(\nabla T)^2] dV \quad (3)$$

where Q_0 is the heat input into fluid, the temperature difference is

$$\overline{\Delta T} = T_w - 0.5(T_{in} + T_{out}) \quad (4a)$$

for open system and is

$$\overline{\Delta T} = T_{wH} - T_{wL} \quad (4b)$$

for enclosed system. Here T_w is the mean temperature of the boundary wall; subscripts H and L stand for the high and low temperature of walls, *in* and *out* for inlet and outlet. Eq. (3) indicates that minimum entransy dissipation corresponds to the minimum heat transfer temperature.

Similarly, from eq. (2) the maximum entransy dissipation is obtained for given heat exchange temperature difference,

$$\overline{\Delta T} \delta Q_0 = \delta \iiint_V [k(\nabla T)^2] dV, \quad (5)$$

where

$$\overline{\Delta T} = T_w - T_{out} \quad (6a)$$

for open system and

$$\overline{\Delta T} = T_{wH} - T_{wL} \quad (6b)$$

for enclosed system. Eq. (5) confirms that maximum

entransy dissipation results in the maximum boundary heat flux for given temperatures.

For multi-inlets and outlets, or multi boundary temperatures/heat fluxes, the averaged or equivalent temperature difference should be weighted by the heat flux fraction at corresponding boundary.

Eqs (3) and (5) are called entransy dissipation extremum (EDE) principles. Thus, the entransy dissipation can be used to optimize the flow field with given constraints [2, 4-5, 7-9].

By analogy to the definition of electrical resistance, we can define the effective thermal resistance based on entransy dissipation^[2]

$$R_G = G_{dis} / Q^2 \quad (7)$$

where G_{dis} is the entransy dissipation in the control volume, Q is the net heat exchange flow rate. This definition can be used in heat transfer with multi-temperatures and is also can applied to heat exchanger^[4, 6-7]. The extremum entransy dissipation principles become the minimum thermal resistance principle^[2, 6-8] and there is no paradox observed.

4. Entransy loss for thermodynamic analyses

For a thermodynamic process, the energy conservation gives

$$T\delta Q = TdU + T\delta W \quad (8)$$

where the left term is heat entransy flow as it is associated with heat δQ , the first term on the right is the entransy change of the working fluid, and the second term on the right is called work entransy flow as it is associated with work δW ^[10-11]. For a cycle, there is

$$G_Q = \oint T\delta Q = \oint T\delta W = G_W \quad (9)$$

where the left term is the entransy that flows into the working fluid with the heat, the right term is the entransy flow out of the working fluid with work. It could be found that the heat entransy flow that the working fluid absorbs all turns into work entransy flow.

The heat entransy flow comes from the heat sources. When Q_H is absorbed from the high temperature heat sources, entransy flows into the working fluid. Entransy will flow out of the working fluid when Q_L is released to the low temperature heat sources. Some net entransy flow from the heat sources will be dissipated if there is a temperature difference between the heat sources and the working fluid, and the rest would flow into the working fluid. Then, we get

$$G_{hs} - G_{dis} - G_Q = 0, \quad (10)$$

where G_{hs} is net entransy flow that comes from the heat sources/sink. Combination of eq. (9) and (10) leads to

$$G_{hs} - G_{dis} - G_W = 0, \quad (11)$$

Some of the entransy flow from the high temperature heat sources is dissipated in heating or cooling the working fluid, some is used to do work, and the rest flows into the low temperature heat sources. Therefore, in the view of the heat sources, the entransy is lost in the thermodynamic process and the entransy loss could be expressed as

$$G_{loss} = G_{hs} = G_H - G_L = G_{dis} + G_W. \quad (12)$$

The thermodynamic process is reversible when G_{dis} is zero. For a thermodynamic system shown in Fig.1 the entransy loss can be expressed as^[10]

$$G_{loss} = \sum_{i=1}^n \frac{1}{2} C_i (T_{in-i} - T_0)^2 + WT_0 \quad (13)$$

where C_i is the heat capacity flow rate of the i th high temperature fluid, T_{in-i} is the inlet temperature of the i th fluid, n is the number of the high temperature fluids, and T_0 is the environment temperature.

As C_i , T_{in-i} and T_0 are prescribed, the entransy

loss would increase monotonously with the increase of the output work of the thermodynamic process.

Numerical examples have shown that entransy loss always increases with the increase in output work

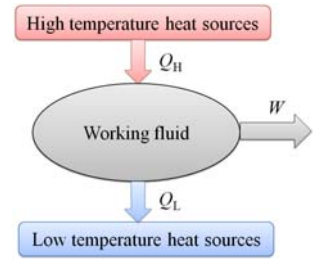


Fig.1 Thermodynamic cycle

5. Concluding remarks

The concept of entransy, together with its extension, has found applications in heat transfer and thermodynamic optimizations. The extremum entransy dissipation principles relates the minimum temperature difference to the minimum entransy dissipation for prescribed net heat exchange and relates the maximum heat exchange flow to the maximum entransy dissipation for prescribed temperature. The entransy loss is related to output work for thermodynamic processes. It always increases with increasing output work.

References

- [1] A Bejan, Entropy Generation Minimization, CRC Press, Florida, 1996, 47-112.
- [2] Z Y Guo, H Y Zhu, X G Liang, Int J Heat Mass Tran, **50**(2007), 2545-2556.
- [3] X T Cheng, X G Liang, Z Y Guo, Chin. Sci. Bull., **56**(2011), 847-854.
- [4] X T Cheng, Q Z Zhang, X G Liang, Appl. Therm. Eng. 2012; 38: 31-39.
- [5] L Chen, S Wei, F Sun, Int. J. Heat Mass Transfer; **54**(2011): 210-216.
- [6] Z Y Guo, X B Liu, W Q Tao, R K Shah, Int. J. Heat Mass Transfer, **53**(2010): 2877-2884.
- [7] X T Cheng, X G Liang, Energy Convers. Manage., **58**(2012), 163-170.
- [8] X G Liang, Q Chen, Mass Nature of Heat and Its Applications V: Entransy, Entransy Dissipation and Heat Transfer Irreversibility, 14th Int. Heat Transfer Conf., IHTC14-22422 pp. 847-856/ <http://dx.doi.org/10.1115/IHTC14-22422>.
- [9] J A Meng, X G Liang, Z X Li, Int. J. Heat Mass Transfer, **48** (2005): 3331-3337.
- [10] X T Cheng, X G Liang, Energy, 2012, doi:10.1016/j.energy.2012.04.054.
- [11] X T Cheng, W H Wang, X G Liang, Sci. China Tech. Sci., 2012, doi: 10.1007/s11431-012-4915-5.

OS2: Geometric and Probabilistic Methods in Flow Dynamics

Geodesic Detection of Transport Barriers in 2D Turbulence

George Haller and Mohammad Farazmand
Department of Mechanical and Process Engineering
ETH Zürich, Sonneggstrasse 3, 8092 Zürich, Switzerland
Email: georgehaller@ethz.ch

ABSTRACT

As shown in [1], transport barriers defined as least-stretching material lines in the flow are closely shadowed by geodesics of the Cauchy—Green strain tensor. This enables the direct computation of hyperbolic barriers (generalized stable and unstable manifolds), parabolic barriers (generalized shear jets) and elliptic barriers (Lagrangian vortex boundaries) as solutions of ordinary differential equations. Here we review the theory from [1], and use it to extract hyperbolic mixing barriers and impenetrable Lagrangian vortex cores from a direct numerical simulation of 2D turbulence.

1. Introduction

Consider a velocity field

$$\dot{x} = v(x, t), \quad x \in U \subset \mathbb{R}^2, \quad t \in [t_0, t_0 + T], \quad (1)$$

which defines a two-dimensional flow over the finite time interval $[t_0, t_0 + T]$, over the spatial domain U . Our objective is to locate all material lines that act as transport barriers to the Lagrangian particle motion generated by (1).

While transport barriers are routinely observed and intuitively described in fluid flows, an objective definition of such barriers has not emerged until recently [1]. Here we review the theory developed in [1], and show its application to objective barrier detection in a direct numerical simulation of two-dimensional turbulence.

2. Method

Material transport in (1) is governed by the flow map

$$F_{t_0}^t : x_0 \mapsto x(t; t_0, x_0), \quad (2)$$

which takes initial particle positions at time t_0 to their positions at time t along trajectories of (1). The classic Cauchy—Green strain tensor associated with the deformation field (2) is the symmetric, positive definite tensor defined as

$$C_{t_0}^t(x_0) = \left[DF_{t_0}^t(x_0) \right]^* DF_{t_0}^t(x_0), \quad (3)$$

with $DF_{t_0}^t$ referring to the gradient of the flow map (2), and with star denoting matrix transposition. The eigenvalues $\lambda_i(x_0)$ and eigenvectors $\xi_i(x_0)$ of $C_{t_0}^t(x_0)$ are fixed in a way so that they satisfy the relations

$$\begin{aligned} C_{t_0}^t \xi_i &= \lambda_i \xi_i, \quad 0 < \lambda_1 \leq \lambda_2, \quad |\xi_i| = 1, \\ \xi_2 &= \Omega \xi_1, \quad \Omega = \begin{pmatrix} 0 & -1 \\ 1 & 0 \end{pmatrix}. \end{aligned} \quad (4)$$

As shown in [1], transport barriers of the velocity field (1) are material lines whose time- t_0 positions are most closely shadowed by geodesics of the metric defined by the tensor $C_{t_0}^t(x_0)$ on the flow domain U .

Furthermore, the barriers obtained in this fashion can be classified as hyperbolic and shear-type barriers,

depending on the type of influence they exert on nearby fluid particles. Specifically, a hyperbolic barrier repels or attracts particles at the largest rate along its normals. By contrast, a shear barrier smears out nearby material elements at locally the largest rate along its tangents.

As shown in [1], hyperbolic barriers at time t_0 can be found as distinguished *strainlines*, i.e., special trajectories of the vector field defined by the minimal Lagrangian strain directions:

$$r' = \xi_1(r), \quad r \in U \subset \mathbb{R}^2. \quad (5)$$

What makes a strainline a hyperbolic barrier is that it is the most closely shadowed by least-stretching Cauchy—Green geodesics when compared to other nearby strainlines. A measure of how closely a strainline is shadowed by least-stretching geodesics is provided by the *geodesic deviation*, the pointwise C^2 -distance of a strainline from the locally least-stretching geodesic starting from the same point. As shown in [1], this geodesic deviation can be computed at any point r of a strainline as

$$d_g^{\xi_1}(r) = \frac{\left| \langle \nabla \lambda_2, \xi_2 \rangle + 2\lambda_2 \kappa_1 \right|}{2\lambda_2^3}, \quad (6)$$

with κ_1 denoting the curvature of the strainline at r .

Similarly, shear barriers at time t_0 are distinguished *shearlines*, i.e., special trajectories of the two vector fields defined by the maximal Lagrangian shear directions:

$$\begin{aligned} r' &= \eta_{\pm}(r), \quad r \in U \subset \mathbb{R}^2, \\ \eta_{\pm}(r) &= \sqrt{\frac{\sqrt{\lambda_2(r)}}{\sqrt{\lambda_1(r)} + \sqrt{\lambda_2(r)}}} \xi_1(r) \pm \sqrt{\frac{\sqrt{\lambda_1(r)}}{\sqrt{\lambda_1(r)} + \sqrt{\lambda_2(r)}}} \xi_2(r). \end{aligned} \quad (7)$$

A shearline is a hyperbolic barrier if its geodesic deviation is small. To assess this closeness, the geodesic deviation of a shearline can be computed as

$$\begin{aligned} d_s^{\eta_{\pm}} &= \frac{\sqrt{1+\lambda_2} - \sqrt{\lambda_2}}{\sqrt{1+\lambda_2}} + \left| \frac{\langle \nabla \lambda_2, \xi_1 \rangle}{2\lambda_2 \sqrt{1+\lambda_2}} \mp \frac{\langle \nabla \lambda_2, \xi_2 \rangle (\sqrt{1+\lambda_2} - \sqrt{\lambda_2})}{2\lambda_2^3 \sqrt{1+\lambda_2}} \right. \\ &\quad \left. \mp \frac{\kappa_1 \left[\sqrt{\lambda_2} + (1-\lambda_2)\sqrt{1+\lambda_2} \right]}{\lambda_2^2 \sqrt{1+\lambda_2}} + \frac{\kappa_2}{\sqrt{1+\lambda_2}} \right|, \end{aligned} \quad (8)$$

with κ_2 denoting the curvature of the ξ_2 vector field at r (cf. [1]).

Locating hyperbolic barriers in a given flow amounts to constructing the phase portrait of the strain vector field (5), then finding strainline segments that minimize the average of the geodesic deviation (6) relative to nearby strainlines.

Similarly, locating shear barriers in a given flow amounts to constructing the phase portrait of the shear vector field (7), then finding shearline segments that minimize the average of the geodesic deviation (8) relative to nearby shearlines. Numerical challenges arising in the computation of hyperbolic and shear barriers are discussed in [1].

Open shear barriers can be considered as Lagrangian shear jet filaments. We refer to such barriers as *parabolic barriers*. By contrast, closed shear barriers (limit cycles of the shear vector fields) can be considered as generalizations of the KAM curves familiar from the Lagrangian dynamics of time-periodic incompressible flows [2]. We refer to such transport barriers as *elliptic barriers*.

When advected as material lines, hyperbolic material lines extracted from forward-time calculations (i.e., for $t > t_0$) act as finite-time generalizations of classic stable manifolds [2], creating exponential material separation between particles on their opposite sides. Likewise, when hyperbolic barriers are identified from a backward-time calculation (i.e., for $t < t_0$), the material lines arising from their advection act as generalized unstable manifolds, forming the backbones of tracer filaments in forward time.

The material lines obtained from the advection of elliptic barriers act as coherent Lagrangian vortex boundaries in incompressible flows. This is because such advected elliptic barriers preserve both their enclosed area, as well as their arclength [1]. As a result, they may translate and rotate, but otherwise can only exhibit minor deformation.

3. Results and Discussion

We have applied the geodesic transport-barrier detection method reviewed above to a direct numerical simulation of forced two-dimensional turbulence on a doubly periodic domain [3]. For reference, Fig. 1 shows a snapshot of the evolution of the vorticity at $t_0 = 50$ from an initially randomized state.

Figure 2 shows geodesic transport barriers extracted for the same flow. Red curves indicate the $t_0 = 50$ positions of forward-hyperbolic barriers (generalized stable manifolds), extracted using $t = 100$. Blue curves indicate backward-hyperbolic barriers (generalized unstable manifolds) at $t_0 = 50$, extracted using $t = 50$.

The blue barriers are responsible for the formation of thin vorticity filaments, whereas the red barriers are the hidden Lagrangian mixers of the vorticity field. Green regions indicate the interior of elliptic barriers extracted for $t = 100$. These regions act as impermeable Lagrangian vortices, with their boundaries showing no filamentation up to $t = 100$. These Lagrangian vortices provide visible barriers to the diffusion of vorticity as

well, whereas other Eulerian vortex regions inferred from Fig. 1 diffuse away by $t = 100$.

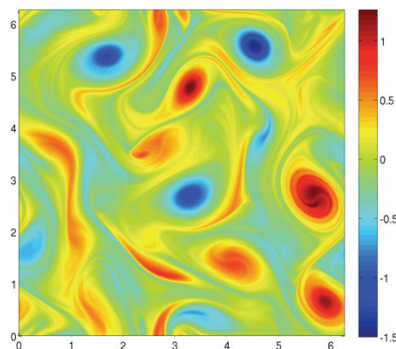


Fig. 1 Vorticity distribution at $t_0 = 100$.

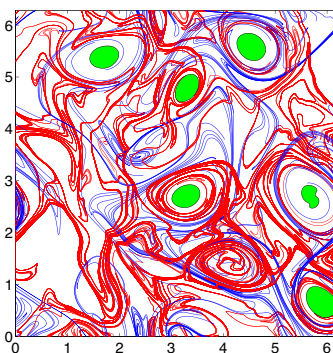


Fig. 2 Geodesic transport barriers at $t_0 = 100$.

4. Concluding remarks

We have reviewed the recent geodesic theory of transport barriers for two-dimensional flows [2], and showed results from the application of this theory to two-dimensional turbulence simulations. Our results give an objective (i.e., frame independent) way to extract all transport barriers as parametrized curves. The exact dynamical properties of these extracted barriers are guaranteed by mathematical theorems [1]. Further applications to coherent eddy detection in satellite altimetry data are given in [4]. An extension of our approach to three-dimensional flows will appear elsewhere.

5. Acknowledgements

This research was partially supported by the Canadian NSERC grant 401839-11.

References

- [1] G. Haller & F. J. Beron-Vera, *Physica D*, in press (2012).
- [2] J. M. Ottino, *The Kinematics of Mixing: Stretching, Chaos, and Transport*. Cambridge University Press, (1989).
- [3] M. Farazmand & G. Haller, submitted preprint (2012).
- [4] F. J. Beron-Vera, Y. Wang, M. J. Olascoaga, J. G. Goni & G. Haller, submitted preprint (2012).

Ridge Surface Methods for the Visualization of Lagrangian Coherent Structures

Ronald Peikert, Benjamin Schindler, Robert Carnecky
 ETH Zurich, Dept. of Computer Science
 peikert@in.ethz.ch

ABSTRACT

In the visualization of unsteady flow, Lagrangian coherent structures (LCSs) have received much attention in recent years. The standard approach is to compute the finite-time Lyapunov exponent (FTLE) on a regular grid and use a transfer function to generate a color image. In the 2D case, this is sufficient because the ridges in the image, i.e., the LCSs are easy to recognize. However, a direct volume rendering of 3D FTLE data shows high FTLE values rather than ridges. Therefore, an explicit ridge extraction method is often preferred. We describe a method for efficiently computing FTLEs and ridge surfaces, while avoiding aliasing artifacts.

1. Introduction

Lagrangian coherent structures (LCSs) can be defined [1] as the ridges of the finite-time Lyapunov exponent (FTLE). There exist methods for computing FTLEs at high accuracy. However, if FTLEs are computed for the pixels of an image, point-wise accuracy is not the goal, as it would create aliasing artifacts, but a low-pass filtered FTLE signal is needed. The appropriate method is therefore to compute trajectories on the nodes of a grid, resulting in a *flow map*, and then to estimate its gradient tensor \mathbf{F} . From \mathbf{F} , the (largest) FTLE is obtained as

$$f = \ln \sqrt{\lambda_1} / |\tau| \quad (1)$$

where λ_1 is the largest eigenvalue of the Cauchy-Green tensor $\mathbf{C} = \mathbf{F}^T \mathbf{F}$ and τ is the integration time.

Estimation of the gradient, and of first and second derivatives in the subsequent ridge extraction, is best done by convolution with derivatives of a Gaussian, to avoid that high frequencies are (re-)introduced. The spread of the Gaussian to be chosen depends on the flow data and the integration time, but we found 1-1.5 times the grid resolution to be typically sufficient.

2. Ridge Surfaces

The *height ridge* [2,3] is defined for scalar functions $f: \mathbb{R}^n \rightarrow \mathbb{R}$ and generalizes the notion of a local maximum to k -dimensional structures ($0 \leq k < n$). In the case of our interest, where f is an FTLE field, the most interesting ridges are $n-1$ -dimensional. The two conditions for a point $\mathbf{x} \in \mathbb{R}^n$ to lie on a height ridge of co-dimension 1 are

$$\nabla f(\mathbf{x}) \cdot \mathbf{e}(\mathbf{x}) = 0 \quad (2)$$

$$\mathbf{e}(\mathbf{x})^T \nabla^2 f(\mathbf{x}) \mathbf{e}(\mathbf{x}) < 0 \quad (3)$$

where $\mathbf{e}(\mathbf{x})$ is the eigenvector of the Hessian $\nabla^2 f(\mathbf{x})$ corresponding to the smallest eigenvalue (by signed, not absolute value).

By substituting a different *transverse direction* for $\mathbf{e}(\mathbf{x})$, other ridge definitions can be obtained. A simple example is the use of a constant direction, which leads to poor results at places where $\mathbf{e}(\mathbf{x})$ is far from orthogonal to the ridge. If f is an FTLE field, however, a good choice for $\mathbf{e}(\mathbf{x})$ is the eigenvector of the Cauchy-Green tensor \mathbf{C} corresponding to the largest eigenvalue λ_1 . By this choice, (2) becomes one of the requirements for a

weak LCS (see [4], Thm. 7). The resulting *C-ridges* [5] have the computational advantage over height ridges that only first derivatives have to be estimated for (2), which reflects in a smoother surface. Second derivatives are still needed for (3), which algorithmically means to trim the triangle mesh at the curve where the left hand side of (3) equals zero.

In principle, (2) amounts to an isosurface extraction by a method such as *Marching Cubes* or *Marching Tetrahedra*. However, in the cases where $\mathbf{e}(\mathbf{x})$ is not a vector but an eigenvector, the additional step of making these eigenvectors cell-wise consistently oriented is necessary. In the *Marching Ridges* method [6], principal component analysis is used for this step.

The standard *Marching Ridges* method generates a triangle mesh with vertices lying on the edges of the volume grid, obtained by linear interpolation. If the fields $f(\mathbf{x})$ and $\mathbf{e}(\mathbf{x})$ are given analytically, a *corrector step* can be added to improve the interpolation along the edge. This is the case, e.g., if convolution with kernels is used for estimating derivatives. We observed that the corrector step improves the quality of the triangle mesh and obtained corrections of up to a third of the edge length, with an average in the order of one percent of the edge length [7].

The final step in computing the ridge surface is the *trimming* of the triangle mesh. The minimum is to remove parts of the mesh where (3) does not hold. Typically, one also wants to remove “weak” and noisy ridges, which can be achieved by trimming the ridge at a lower threshold for $f(\mathbf{x})$. Finally, part of the points solving (2) and (3) do not have the characteristic of a ridge, namely if $\nabla f(\mathbf{x})$ is far from being tangent to the ridge. Therefore, it is advisable to also trim away parts of the triangle mesh where this angle exceeds a certain threshold such as 45° [8].

3. Nonorientability

The fact that ridge surfaces are in general not orientable causes some problems in their further processing. Gouraud shading, the standard method in computer graphics, requires the vertex normals to be consistently oriented. The use of two-sided lighting does not solve the problem.

A possible solution is to re-orient the normals on the fly in the vertex shader. However, it is wrong to simply orient them toward the camera (see Fig. 1). Rather, vertex normals need to be oriented consistently with the facet normal oriented to the camera. For orienting the facet normal, a geometry shader is required.

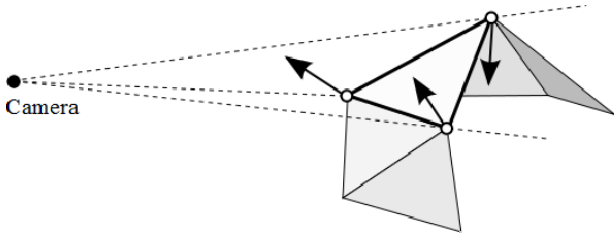


Fig. 1. Example of a triangle with inconsistent vertex normals (thick outlined). Nevertheless, all normals (i.e., their projections onto corresponding view rays) are oriented toward the camera.

An alternative solution is to traverse the triangle mesh, orient normals consistently where possible and cut the mesh where needed. Along cuts, vertices are duplicated, and the copy of the vertex is given the opposite normal. Cutting the mesh does not cause visible artifacts, provided that normals have been computed based on the full and correctly oriented neighborhood. Cuts can affect other processing, however, such as texturing, hatching, or “smart transparency” calculation. This limitation does not apply if a multilayer screen-space data structure as in [9] is used.

4. Results

We computed LCSs from simulation results of a revolving door where an air curtain has been added to prevent cold air entering the building along the floor (Fig.2). Since the flow barrier generated by the air curtain has a dynamically changing geometry, LCSs are well suited to track it over time. Using interactive viewing of the LCSs (Fig.3), we were able to find a “leak” in the flow barrier represented by the system of LCSs that opens for a fraction of the rotational period of the door. With a modified design (using an asymmetric air curtain), a more tight flow barrier was achieved.

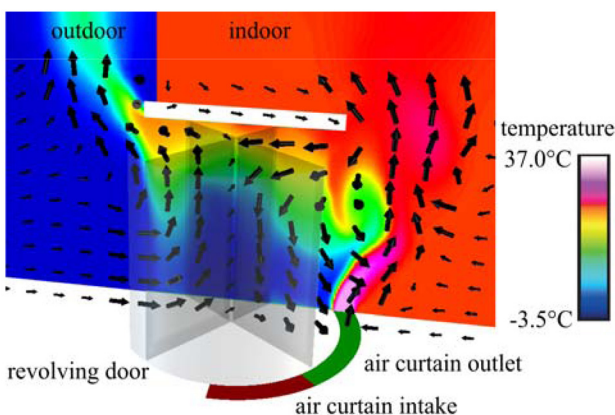


Fig. 2. Overview of the simulated setup with revolving door and air curtain.

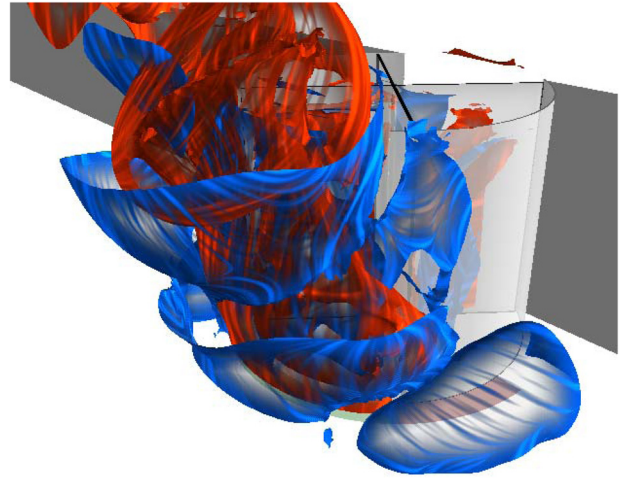


Fig. 3. Repelling (blue) and attracting (red) LCSs, visualized with context-sensitive transparency and texture along projected velocity.

Acknowledgments

This work was supported by the 7th Framework Programme for Research of the European Commission, under FET-Open grant 226042. We thank Stefan Barp and Matthias Röthlin for the CFD simulation.

References

- [1] G. Haller, “Lagrangian coherent structures from approximate velocity data”, *Phys. Fluids A*, **14** (2002) 1851–1861.
- [2] D. Eberly, *Ridges in Image and Data Analysis*, Kluwer (1996).
- [3] J. Damon, “Properties of Ridges and Cores in Two-Dimensional Images”, *J Math Imaging Vis*, **10**, 2 (1999) 163–174.
- [4] G. Haller, “A variational theory of hyperbolic Lagrangian Coherent Structures”, *Physica D*, **240** (2011) 574–598.
- [5] B. Schindler, R. Peikert, R. Fuchs, H. Theisel, “Ridge Concepts for the Visualization of Lagrangian Coherent Structures”, in: *Topological Methods in Data Analysis and Visualization II*, Springer (2012) 221–236.
- [6] J.D. Furst and S.M. Pizer, “Marching ridges”, in: *Proc. IASTED Int’l Conf. on Signal and Image Processing* (2001) 22–26.
- [7] B. Schindler, R. Fuchs, J. Waser, R. Peikert, “Marching Correctors — Fast and Precise Polygonal Isosurfaces of SPH Data”, in *Proc. 6th SPHERIC workshop* (2011) 125–132.
- [8] R. Peikert, F. Sadlo, “Height Ridge Computation and Filtering for Visualization”, in *Proc. IEEE PacificVis* (2008) 119–126.
- [9] R. Carneky, B. Schindler, R. Fuchs, R. Peikert, “Multi-layer illustrative dense flow visualization”, *Computer Graphics Forum*, **31**,3 (2012) 895–904.
- [10] B. Schindler, R. Fuchs, S. Barp, J. Waser, A. Pobitzer, K. Matković, R. Peikert, “Lagrangian coherent structures for design analysis of revolving doors”, *IEEE Trans. Vis. Comp. Graph.* (to appear).

An Analytic Framework For Finite-Time Coherent Sets In Time-Dependent Flows

Gary Froyland

School of Mathematics and Statistics
University of New South Wales
Sydney NSW 2052, Australia
G.Froyland@unsw.edu.au

ABSTRACT

Precis: The study of transport and mixing processes in dynamical systems is particularly important for the analysis of mathematical models of physical systems. In the autonomous setting, the use of transfer operators (Perron-Frobenius operators) to identify invariant and almost-invariant sets has been particularly successful. This talk introduces a new analytic transfer operator construction that enables the calculation of *finite-time coherent sets* (a time-parameterised family of sets are that minimally dispersive over a finite time interval). The construction can be applied to general Markov processes on continuous state space.

Transport and mixing processes play an important role in many natural phenomena and their mathematical analysis has received considerable interest in the last two decades. Transport is a key descriptor of the impact of the system's dynamics in the physical world, and coherent structures and metastability provide information on the multiple timescales of the system, which is crucial for efficient modelling approaches. Persistent barriers to transport play fundamental roles in geophysical systems by organising fluid flow and obstructing transport.

Probabilistic approaches to studying transport, based around the transfer operator (or Perron-Frobenius operator) have emerged over the last 15 years for autonomous systems. These approaches use the transfer operator (a linear operator providing a global description of the action of the flow on densities) to answer questions about global transport properties. Transfer operator-based methods have been very successful in resolving metastable or almost-invariant objects in a variety of settings, including molecular dynamics, astrodynamics, oil spills, and atmospheric science. The methods have been particularly effective in the analysis of global ocean models.

The paper [1] introduced the notion of finite-time coherent sets. The construction in [1] is a novel matrix-based approach for determining regions in phase space that are maximally coherent over a *finite* period of time. The main idea is to study the singular values and singular vectors of a discretised form of the transfer operator that describes the flow over the finite duration of interest. Optimality properties of the singular vectors lead to the optimal coherence properties of the sets extracted from the singular vectors. Numerical experiments using European Centre for Medium Range Weather Forecasting (ECMWF) data to delimit the stratospheric Antarctic polar vortex [1] and a global ocean model (ORCA025) to map and track Agulhas Rings between the Indian and Atlantic Oceans [2], have shown that this new approach outperforms existing methods, often significantly so.

The mathematical framework of [1] is purely finitary, which obscures the important role played by diffusion,

inherent in the numerical scheme. This talk discusses a new extension of the matrix-based numerical approach of [1] to an operator-theoretic framework in order to formalise the constructions in a transfer operator setting, and to enable an analytic understanding of the interplay between advection and diffusion.

In this talk, we formalise the framework of [1] by casting the constructions using bounded linear operators; specifically using Perron-Frobenius operators to effect the advective dynamics and diffusion operators to effect the diffusive dynamics. This operator-theoretic setting clarifies the coherent set framework and isolates the important role played by diffusion in the computations. The full paper will be published in [3].

References

- [1] Gary Froyland, Naratip Santitissadeekorn, and Adam Monahan. "Transport in time-dependent dynamical systems: Finite-time coherent sets". *Chaos*, 20:043116, 2010.
- [2] Gary Froyland, Christian Horenkamp, Vincent Rossi, Naratip Santitissadeekorn, and Alex Sen Gupta. "Three-dimensional characterization and tracking of an Agulhas Ring". *Ocean Modelling*, V52-53:69-75, 2012.
- [3] Gary Froyland. "An analytic framework for finite-time coherent sets in time-dependent flows". In preparation, 2012.

Topological Chaos and Braiding of Almost-cyclic Sets

Piyush Grover¹, Shane D. Ross², Mark A. Stremler², and Pankaj Kumar³

¹Mitsubishi Electric Research Laboratories, Cambridge, MA 02139, USA

²Engineering Science and Mechanics, Virginia Tech, Blacksburg, VA 24061, USA

³Aerospace and Ocean Engineering, Virginia Tech, Blacksburg, VA 24061, USA
 grover@merl.com

Abstract

In certain two-dimensional time-dependent flows, the braiding of periodic orbits provides a way to analyze chaos in the system through application of the Thurston-Nielsen classification theorem (TNCT). We apply the TNCT to braiding of almost-cyclic sets. In this context, almost-cyclic sets are periodic regions in the flow with high local residence time that act as stirrers or ‘ghost rods’ around which the surrounding fluid appears to be stretched and folded. We make the case that a topological analysis based on spatiotemporal braiding of almost-cyclic sets can be used for analyzing chaos in fluid flows.

1. Introduction

Given an incompressible fluid moving with a velocity field $\mathbf{V} = (u, v, w)$, one can write the advection equations of motion for a passive fluid particle at position $\mathbf{x}(t)$ as

$$\frac{d\mathbf{x}}{dt} = \mathbf{V}(\mathbf{x}, t). \quad (1)$$

Non-autonomous two-dimensional systems or autonomous three-dimensional systems are capable of generating chaotic particle trajectories even if the underlying velocity field is not chaotic or stochastic [1]. In the dynamical systems vernacular, a mixing system is one that generates chaotic trajectories. This approach to understanding and predicting mixing has played an important role in the engineering analysis of laminar flows, and it has been particularly valuable in the development of microfluidics [2, 3]. One recent approach to analyzing chaos in a fluid system is the identification of topological chaos, or chaos due to the topology of internal boundary motions such as moving rods [4]. This approach is based on application of the Thurston-Nielsen classification theorem (TNCT) to certain $(2 + 1)$ -dimensional flows: either two-dimensional, time-dependent flows or certain three-dimensional flows. The TNCT provides quantitative lower bounds on maximum stretching rates in such flows using only information from the boundary motions. Ghost rods, or periodic orbits generated by the dynamics, can also behave as physical obstructions that stir the surrounding fluid, providing a basis for the topological analysis in place of physical boundaries.

We consider the problem of examining topological chaos in flows without physical rods and with no low-order periodic orbits on which to base a topological analysis [5, 6]. In this view, the domain is divided into distinct subsets such that there is a very small probability that typical trajectories beginning in each subset will leave this subset in a short time. These *Almost-Invariant Sets* (AISs) [7] can be determined from the eigenspectrum of the discretized Perron-Frobenius transfer operator via a set-oriented approach. In some cases, disconnected components of an AIS correspond to almost-periodic regions, or what has been referred to as *Almost-Cyclic Sets* (ACSS) [7]. Since the ACSSs consist of trajectories that move together for a relatively long time, the region of the domain corresponding to an ACS can be identified as a (leaky) ghost rod, and a representative trajectory from each ACS can be

used to reveal the underlying braid structure. Furthermore, since these ACSSs contain almost-periodic orbits, the aperiodic braid they generate can be approximated by periodic continuation to a time-periodic braid. This time-periodic braid can be characterized using the TNCT, and an estimate of the topological entropy can hence be determined. We demonstrate that this estimate can give a good representation of the flow.

2. Method and Results

The fluid system model that we analyze in this work is as follows [8]. We consider a two-dimensional lid-driven cavity flow in an infinitely-wide cavity with height $2b$. Under the assumption of Stokes’ flow, the stream function $\psi(x, y)$ satisfies the two-dimensional biharmonic equation,

$$\nabla^2 \nabla^2 \psi(x, y) = 0. \quad (2)$$

We assume that the flow is driven by prescribed tangential velocities on the top and bottom boundaries at $y = \pm b$. By the time periodicity of the boundary conditions, the flow pattern is reflected about the line $x = a/2$ every $\tau_f/2$ units of time. We consider the one-parameter family of stroboscopic global Poincaré maps,

$$\phi_t^{t+\tau_f} : D \rightarrow D, \quad (3)$$

where $\phi_t^{t+\tau_f}$ is the solution map (i.e., flow map) from time t to $t + \tau_f$; that is, $\phi_t^{t+\tau_f}$ represents the motion of all fluid particles over one period of the velocity field starting at time $t \in [0, \tau_f]$.

We choose parameters in the reference case so that there exist three period-3 points in the domain with trajectories that form the $(2+1)$ -dimensional space-time braid structure shown in figure 1(c). According to the TNCT, for reference case the lower bound on the stretching of material lines is $\lambda_{\text{TN}} = (3 + \sqrt{5})/2$ and $h_{\text{TN}} = \log(\lambda_{\text{TN}}) \approx 0.962$. In general, the train-tracks algorithm [9] is used to compute h_{TN} for a given braid. The actual topological entropy, h_f , can be determined by computing the asymptotic stretching rate of topologically non-trivial lines [10], such as lines that join a periodic point with the outer boundary. For this reference case, these computations give $h_f \approx 0.97$, which is reasonably well represented by the lower bound, h_{TN} . For the analysis discussed here, we keep all other parameters fixed while changing the value of τ_f away from unity. This perturbation increases (for $\tau_f > 1$) or decreases (for $\tau_f < 1$) the amount of rotation in the domain before switching,

which has a direct effect on the stretching of material lines.

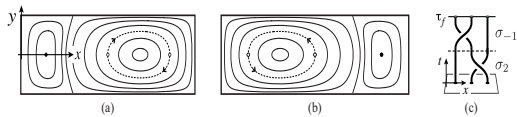


Figure 1: (a–b) Representative streamlines for the reference case for (a) $0 \leq t < \tau_f/2$ and (b) $\tau_f/2 \leq t < \tau_f$. Points marked by solid circles are stagnation points in the flow. For chosen parameters, the fluid particles starting at the open circles have exchanged positions after $\Delta t = \tau_f/2 = 1/2$. (c) The braid diagram generated by the periodic orbit trajectories in the reference case.

In the reference case with $\tau_f = 1$, the three period-3 points are parabolic points, which are structurally unstable. When the value of τ_f is decreased below 1, the parabolic points disappear and no low-order periodic points are found in the flow. Thus, there are no apparent periodic ‘ghost rods’ available to form a braid and predict a lower bound on the topological entropy of the flow. However, $h_{TN,3}$ is a lower bound for h_f for approximately a 7% perturbation in τ_f . Hence we consider the validity of the topological entropy predicted by TNCT even if we cannot identify exactly periodic orbits that produce the expected braiding motion. We accomplish this by using a transfer operator approach to reveal phase space structures that braid non-trivially and persist under perturbations in the τ_f values. We use a set-oriented method to compute AISs for the lid-driven cavity flow system. Our aim is to partition the phase space into a given number (say k) of sets $\{A_1, A_2, \dots, A_k\}$ such that the phase space transport between these sets is very unlikely. We also want these sets to be important statistically with respect to the long term dynamics of the system. Using the Ulam-Galerkin method [7], we define the *transition matrix* P_{t,τ_f} with entries

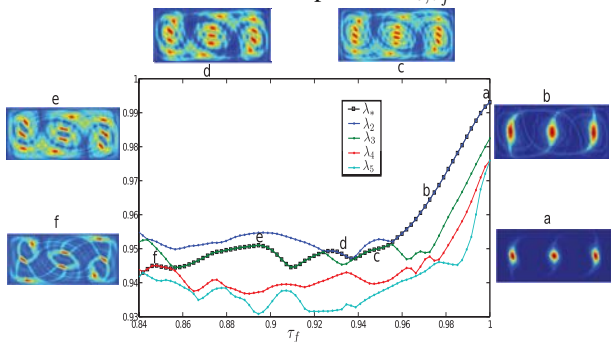
$$p_{ij} = \frac{m(f^{-1}(B_i) \cap B_j)}{m(B_j)} \text{ where } f = \phi_t^{t+\tau_f} \text{ and } B_1, \dots, B_n \text{ are the boxes covering the phase space and } m \text{ is the area measure, i.e., the phase space volume measure. We use the sign structure of right eigenvectors } v_k, \text{ corresponding to eigenvalues } \lambda_k \text{ of the related reversibilized operator } R_{t,\tau_f}, \text{ to detect AISs [7].}$$


Figure 2: Almost-invariant set structure via continuation of the 3-strand eigenvector found at (a) for various values of τ_f . One of these is singled out as the λ_* branch (shown with large squares), which is the eigenvalue corresponding to $v_*^{\tau_f}$, the continuous eigenvector family of interest.

If an AIS (over one period- τ_f map, $\phi_t^{t+\tau_f}$) can be further decomposed into period- N subsets, then those subsets are ACSs of the flow of period $N\tau_f$ (see figure 2).

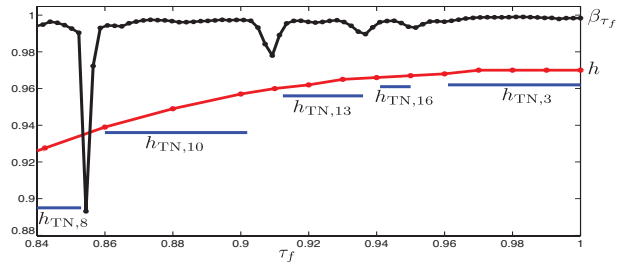


Figure 3: β_{τ_f} is an inner product used for continuation of the 3-strand eigenvector found at reference point. The topological entropy of the flow, h_f , computed by line stretching is shown in red. The lower bounds computed by TNCT are shown in blue.

The ACS found using the above method can each be identified with a braid, with the number of strands in the braid corresponding to the number of ACS in the domain. We see that the lower bounds provided by the TNCT for these braids, $h_{TN,N}$, are indeed sharp lower bounds on the actual topological entropy for the flow, h_f (see figure 3). Furthermore, $h_{TN,N}$ is a good estimate of h_f in these cases.

3. Conclusions

We have used almost-invariant sets as central objects in the application of the TNCT by looking at non-trivial braids corresponding to the space-time trajectories of these sets. We demonstrate that the lower bound given by this procedure holds even in the case where the braid word is not the one originally formed by periodic points; that is, in case of braid bifurcation under perturbation, the new braid dictates the complexity of the flow.

References

- [1] H. Aref, *J. Fluid Mech.* **143**, 1 (1984).
- [2] J. Ottino and S. Wiggins, *Philosophical Transactions of the Royal Society of London Series A* **362**, 923 (2004).
- [3] M. Stremler, F. Haselton, and H. Aref, *Philosophical Transactions: Mathematical, Physical and Engineering Sciences* **362**, 1019 (2004).
- [4] P. L. Boyland, H. Aref, and M. A. Stremler, *J. Fluid Mech.* **403**, 227 (2000).
- [5] M. A. Stremler, S. D. Ross, P. Grover, and P. Kumar, *Physical Review Letters* **106**, 114101 (2011).
- [6] P. Grover, S. D. Ross, M. A. Stremler, and P. Kumar, arXiv:1206.2321 (2012).
- [7] G. Froyland and M. Dellnitz, *SIAM Journal of Scientific Computing* **24**, 1839 (2003).
- [8] V. V. Meleshko and A. M. Gomilko, *Proc. R. Soc. Lond. A* **460**, 807 (2004), Our choice of boundary conditions allows for an exact solution with a finite number of terms.
- [9] M. Bestvina and M. Handel, *Topology* **34**, 109 (1995).
- [10] S. Newhouse and T. Pignataro, *J. Stat. Phys.* **72**, 1331 (1993).

Identifying Coherence In Flows Using Lagrangian Averages

Marko Budišić¹, Igor Mezić¹

¹*Department of Mechanical Engineering, University of California, Santa Barbara, USA,*
{mbudisic, mezić}@engr.ucsb.edu

ABSTRACT

We describe an analysis of coherent structures in state spaces of dynamical systems, particularly appropriate for the use in analysis of tracer paths in incompressible fluid flows. By averaging observables along tracer paths, we construct and evaluate a basis for the set of functions invariant to dynamics; collectively they are referred to as *ergodic quotient*. Their level sets are then aggregated to larger coherent structures based on a particular metric structure. The method is demonstrated on several numerical fluid flows.

1. Introduction

Complicated fluid flows, e.g., oceans and atmosphere, are commonly understood by extracting smaller features in them, e.g., eddies and currents, within which the behavior of the flow is more-or-less homogeneous. Moreover, analytical results about theoretical concepts, e.g., vortices, ballistic transport, or mixing, can be used to draw conclusions within the coherent regions. Unfortunately, detection of such coherent regions is difficult in realistic flows, especially when they can be accessed only through simulation or experiments.

Instead of trying to start from local features, e.g., eyes of vortices, and test the boundaries to which they organize the global flows, we present an approach that addresses the problem of decomposition in a global fashion. We construct a set of invariant functions of the flow whose level sets partition the state space into invariant sets. Using a large number of independent invariant functions it is possible to obtain very fine invariant features by intersecting associated partitions. We then aggregate them into larger coherent structures based on similarity of their dynamics. This approach, termed *ergodic quotient analysis*, can be seen as a part of a group of algorithms that analyze dynamics using operators associated to the flow map: the Koopman operator [1, 2] and the Perron-Frobenius operator [3].

2. Analysis of ergodic quotients

Let $T^t : M \rightarrow M$ be a continuous flow map on a bounded state space M . Curves $t \mapsto T^t(x)$ are Lagrangian trajectories: solutions to a set of ODEs $\dot{x} = F(x, t)$, tangential to the vector field $F : M \rightarrow \mathcal{T}M$. In fluid flows, F is usually the velocity field of the fluid where the incompressibility condition is $\nabla \cdot F \equiv 0$. Instead of studying properties of trajectories $t \mapsto T^t(x)$ directly, we capture the behavior of the flow as it acts on observables: scalar functions $f : M \rightarrow \mathbb{R}$ chosen from a function space \mathcal{F} , typically volume-integrable functions $\mathcal{F} = L^1(M, dx)$ for incompressible fluid flows. The action of the flow on any $f \in \mathcal{F}$ is given by the Koopman operator $U^t : \mathcal{F} \rightarrow \mathcal{F}$, as $[U^t f](x) = f[T^t(x)]$.

In practical terms, observables f could be, e.g., salinity or temperature of an ocean, while evolutions $t \mapsto U^t f(x)$ would represent time evolutions of those quantities as seen by a tracer released at point x and advected

by the ocean flow. The reason for adapting the formalism of the Koopman operator is that it makes it easy to study quantities that remain invariant over Lagrangian trajectories, through eigenfunctions $\varphi \in \mathcal{F}$ of linear Koopman operators, $U^t \varphi(x) = \lambda^t \varphi(x)$. When flow is in a steady state, the operators U^t are unitary and, consequently, all of their eigenvalues are on the unit circle in the complex plane.

Given a countable set of uniformly bounded eigenfunctions $(\varphi_k)_{k \in \mathbb{N}}$ that span the eigenspace at an isolated eigenvalue λ , we form a map $\pi_\lambda : M \rightarrow l^\infty(\mathbb{N})$,

$$\pi_\lambda(x) := (\varphi_1(x), \varphi_2(x), \varphi_3(x), \dots). \quad (1)$$

When $\lambda = 1$, if for two different points $x, y \in M$ it holds $\pi_1(x) = \pi_1(y)$, it means that tracers released at x and y will see the same values of *any* observable invariant under the flow. Level sets of π_1 are equivalent to a partition of the state space into minimal invariant sets, i.e., into an ergodic partition [4, 5]. As a generalization of this concept, we call partitions into level sets of π_λ *Fourier partitions*. The image set $\xi_\lambda = \pi_\lambda(M)$ is the *Fourier quotient* (ergodic quotient for $\lambda = 1$). While ergodic partitions and quotients describe time-invariant features, their Fourier analogues at $\lambda = e^{i2\pi\omega}$ describe periodic features when $\omega \in \mathbb{Q}$ and aperiodic features when $\omega \notin \mathbb{Q}$.

Numerically, eigenfunctions φ_k are obtained by averaging a function basis f_k for the space of observables \mathcal{F} along trajectories of the flow. For almost any (in volume) initial condition $x \in M$ we can form *Fourier averages*

$$\tilde{f}_k^{(\omega)}(x) := \lim_{t \rightarrow \infty} \int_0^t f_k[T^\tau(x)] e^{-i2\pi\omega\tau} d\tau, \quad (2)$$

to obtain a projection of f_k onto the eigenspace at $\lambda = e^{i2\pi\omega}$. The map $x \mapsto (\tilde{f}_1^{(\omega)}(x), \tilde{f}_2^{(\omega)}(x), \dots)$ is a representation of the Fourier quotient map associated to $e^{i2\pi\omega}$. The details of this process are studied in [1, 5–7].

In practical applications, data that describes locations of minimal invariant sets can be overwhelming. Instead, we would like to group those invariant sets that contains dynamics that is similar on a macro scale. For example, in an incompressible vortex, tracers at different distances from the center rotate within different invariant sets. However, we perceive the entire vortex as one region of coherent dynamics. In [1] we described how studying geometry of quotients $\xi \subset l^\infty$ allows us to aggregate

minimal invariant sets using a numerically-practical algorithm. A negative-index Sobolev distance on the ambient set l^∞ can be used to correctly capture the differences in behavior of each invariant set [8].

We start from a uniform distribution of initial conditions $x_n \in M$ and sample the quotient ξ through computing averages of Fourier harmonics via (2). Between any two points we compute the negative-index Sobolev distance, which in this particular set of eigenfunctions amounts to a weighed euclidean distance between points $\pi_1(x_n) \in \xi$. The pair-wise distances are inputs into the Diffusion Maps manifold learning algorithm [9] which constructs a low-dimensional representation of ξ where euclidean distance is equivalent to an intrinsic (coordinate-free) distance along ξ . This makes it easy to identify components of ξ using stock algorithms, e.g., k -means or proximity graphs. These components correspond to one-parameter families of dynamical orbits, e.g., vortices parametrized by radius from the core of the vortex.

As presented so far, the analysis applies to autonomous flows, where the flow map T^t forms a group preserving a measure. The extension to periodically forced flows, where the vector field $F(x, t)$ is periodic in time, is simple and proceeds through introduction of an extended time variable, casting it into autonomous framework on the extended state space $M_e = M \times \mathbb{T}$. Nevertheless, using observables that have only factor M for the domain instead of M_e provides full detail about the system (Fig. 1), based on the same arguments used to justify Poincaré section analysis of periodic dynamical systems [1].

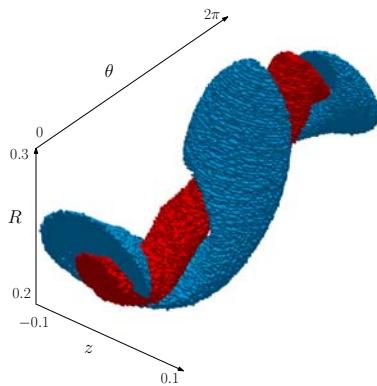


Figure 1: Primary and secondary vortices in the state space of a numerical periodically driven flow (periodic 3D Hill's vortex), extracted using ergodic quotient analysis. (Reprinted from [1].)

3. Conclusions

Averaging of observables along Lagrangian trajectories casts the problem of detection of coherent structure into analysis of topology of the quotients ξ . A practical numerical algorithm was implemented, based on sampling of the quotient, construction of a negative-index Sobolev metric, and its low-dimensional parametrization via Diffusion maps. Its results have a clear interpretation for autonomous and periodically forced flows: the algorithm

detects asymptotically invariant sets and aggregates them into larger coherent structures.

Even if the averaging process (2) is not taken to $t \rightarrow \infty$ limit, but rather only a fixed time T averages are analyzed for all trajectories, the same construction and geometric analysis can be performed. In that case, there are no claims of invariance or ergodicity of sets in the asymptotics. Nevertheless, the computational geometric analysis of such finite-time quotients can be interpreted as a scale-ordered analysis of the material transport in flows over finite times. Conclusions drawn based on such analysis are still not fully investigated and will be the topic of our future efforts.

References

- [1] M. Budišić and I. Mezić. *Physica D. Nonlinear Phenomena* 241.15 (Aug. 2012), pp. 1255–1269. DOI: [10.1016/j.physd.2012.04.006](https://doi.org/10.1016/j.physd.2012.04.006).
- [2] C. W. Rowley et al. *Journal of Fluid Mechanics* 641 (2009), pp. 115–127. DOI: [10.1017/S0022112009992059](https://doi.org/10.1017/S0022112009992059).
- [3] G. Froyland et al. *Chaos: An Interdisciplinary Journal of Nonlinear Science* 20.4 (Jan. 2010), p. 043116. DOI: [10.1063/1.3502450](https://doi.org/10.1063/1.3502450).
- [4] I. Mezić and S. Wiggins. *Chaos: An Interdisciplinary Journal of Nonlinear Science* 9.1 (Jan. 1999), pp. 213–218. DOI: [10.1063/1.166399](https://doi.org/10.1063/1.166399).
- [5] I. Mezić and A. Banaszuk. *Physica D. Nonlinear Phenomena* 197.1-2 (Jan. 2004), pp. 101–133. DOI: [10.1016/j.physd.2004.06.015](https://doi.org/10.1016/j.physd.2004.06.015).
- [6] Y. Susuki and I. Mezić. *Decision and Control, 2009 held jointly with the 2009 28th Chinese Control Conference. CDC/CCC 2009. Proceedings of the 48th IEEE Conference on*. 2009, pp. 7497–7502. DOI: [10.1109/CDC.2009.5400911](https://doi.org/10.1109/CDC.2009.5400911).
- [7] Z. Levnajić and I. Mezić. *Chaos: An Interdisciplinary Journal of Nonlinear Science* 20.3 (2010), DOI: [10.1063/1.3458896](https://doi.org/10.1063/1.3458896).
- [8] G. Mathew and I. Mezić. *Physica D. Nonlinear Phenomena* 240.4-5 (Feb. 2011), pp. 432–442. DOI: [10.1016/j.physd.2010.10.010](https://doi.org/10.1016/j.physd.2010.10.010).
- [9] R. Coifman and S. Lafon. *Applied and Computational Harmonic Analysis* 21 (Jan. 2006), pp. 5–30. DOI: [10.1016/j.acha.2006.04.006](https://doi.org/10.1016/j.acha.2006.04.006).

Lagrangian data assimilation in geophysical flows

Kayo Ide
University of Maryland
ide@umd.edu

ABSTRACT

The Lagrangian data assimilation (LaDA) is a method for the assimilation of Lagrangian observations directly into the model. By augmenting the model state vector with the coordinates of the Lagrangian instruments and computing their trajectories based on the model velocity, the LaDA removes the need for any commonly used approximations to transform the Lagrangian observations into the Eulerian velocity observations. Using the theory of observability and applications, we demonstrate the information content of Lagrangian data and LaDA's effectiveness to extract it.

1. Introduction

The problem of assimilating data into a geophysical system is both fundamental, in that it aims at applying all available information to the task of estimation and prediction of an unknown true state, and challenging in that it does not naturally afford a clean mathematical solution. Geophysical data assimilation draws information from two equally important sources: observations and computational models. Observations acquired by instruments provide direct information about the true state. In contrast, computational models use knowledge of underlying physics and dynamics to provide a complete description of state evolution in time, but models alone cannot provide detailed descriptions of the geophysical fluid system.

A natural question arises as to how much data is needed, in a given situation, to get certain key features of the correct in the model forecast. Geophysical fluid motion ultimately involves the movement of material elements of fluid, and this movement is essential for the transport of heat, momentum, matter, dissolved and suspended materials in geophysical fluid systems. Thus capturing Lagrangian structures of the geophysical fluid system in the model is essential in enhancing the predictive skill. Lagrangian observations of the geophysical systems represented by sequences of position data along the trajectories of instruments that move according to the local velocity, such as balloons in the atmosphere or drifters and floats in the oceans, naturally contain Lagrangian information of the underlying flow. Most numerical simulations are conducted in an Eulerian framework, in which the velocity field is represented on a fixed grid, and the pathways of Lagrangian particle are usually not explicitly computed. A challenge of capturing Lagrangian coherent structures in the data assimilation framework is thus how to incorporate the Lagrangian information in to the model that makes the forecast.

In this work, we present a method for incorporating Lagrangian observations directly into the model, Eulerian or Lagrangian, by augmenting the Lagrangian variables into the forecast model. We call this method the Lagrangian Data Assimilation (LaDA). We show theoretically how LaDA can offer more information than Eulerian observations of the geophysical systems. The LaDA is then applied to the monitoring and forecasting of the nonlinear process of ocean eddy shedding.

2. Method

We follow the Lagrangian data assimilation (LaDA) method developed by Ide et al. [1] for the assimilation of the drifter trajectories. The method was originally developed based on the extended Kalman filter [1,2] and has been applied to ocean data assimilation using the ensemble Kalman filter [3,4,5]. To address the nonlinearity in model dynamics and non-Gaussianity of the error distribution in the model forecast, the method can also be formulated as the particle filter [6,7].

To formulate the model, the LaDA, we write the augmented state vector \mathbf{x} as

$$\mathbf{x}^T = (\mathbf{x}_F^T, \mathbf{x}_D^T), \quad (1)$$

where \mathbf{x}_F^T is the geophysical fluid system model and \mathbf{x}_D^T is the coordinate of the Lagrangian data that freely advect in the flow. Corresponding forecast model for the augmented system is

$$\begin{aligned} d\mathbf{x}^T &= m(\mathbf{x})^T dt \\ &= (m_F(\mathbf{x}_F)^T, m_D(\mathbf{x}_F, \mathbf{x}_D)^T) dt. \end{aligned} \quad (2)$$

To assimilate observation \mathbf{y} into the model for the forecast \mathbf{x} of requires that \mathbf{y} is a function of \mathbf{x} . Thus, the use of the augmented state vector, any conventional or Lagrangian observations can be directly assimilated in the LaDA.

3. Application to Ocean Eddy Tracking

The Observing System Simulation Experiment (OSSE) is a commonly used approach in data assimilation. It examines the effectiveness of the observations using a "control" run generated by the model forecast and making observations from that control. We use the OSSEs and study the efficiency of Lagrangian data using 4 drifters deployed in the Gulf of Mexico (Figure 1). By assimilating four drifter positions once a daily in sequence, the LaDA quickly produces an ocean eddy in a matter of a few days, whereas the assimilation of Eulerian-type observations sampled at the fixed stations fails with such a small number of observations as four.

4. Measure of observability

The remarkable efficiency of the LaDA arises from its ability to extract the hidden information regarding the underlying Lagrangian coherent structures, i.e., the eddy in this case. Advantage of the LaDA in extracting the

hidden flow information associated with the Lagrangian structures can be highlighted formally in the framework of control theory applied to an idealized flow field with Lagrangian coherent structures represented by the point vortices.

The local unobservability index [8,9] measures how hard it is to distinguish an initial state from its neighbors. Any data assimilation scheme that is exact when no observation is present will have a local singular value at least as large the local unobservability index. These are very useful for measuring the relative observability or unobservability of the model dynamics and hence capacity for the data assimilation system. By applying to a pair of point vortex system, the unobservability indicates that the best Lagrangian observation is superior to the best Eulerian observation. This implies not only the usefulness of Lagrangian data but also the importance of the observing system design.

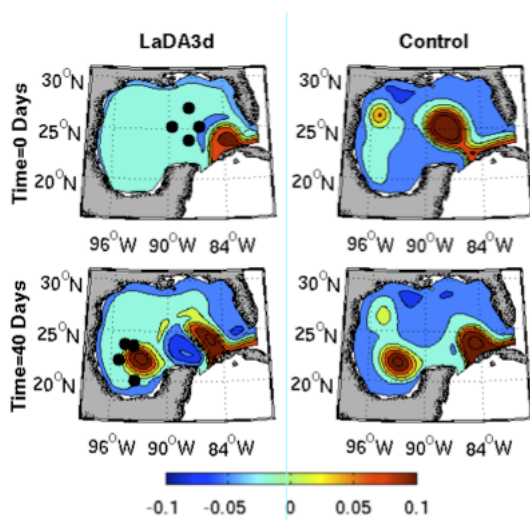


Fig. 1 SSH (color) of OSSEs and positions of 4 drifters: LaDA (left) and Control (right). Top is the initial condition, bottom is after 40days of assimilation.

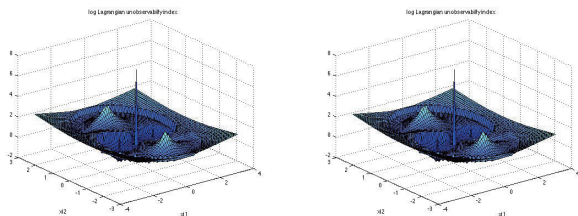


Figure 2. Log of Lagrangian (left) and Eulerian (right) unobservability index for a pair of two point vortices.

5. Results and Discussion

Lagrangian observations of geophysical fluid systems contain different nature of information from Eulerian observations. We demonstrate the efficiency of

the LaDA to extract the information hidden in Lagrangian data. The effectiveness of the LaDA is presented in terms of the unobservability index. Our study suggests the importance of observing system design for monitoring and prediction of the geophysical fluid systems.

References

- [1] K. Ide, L. Kuznetsov, C.K.R.T., Jones. *Turbul.* 3 (2002).
- [2] L. Kuznetsov, C.K.R.T., Jones. K. Ide. *Mon. Wea. Rev.*, 131, (2003), 2247-2260
- [3] H. Salman, L. Kuznetsov, C.K.R.T., Jones, K. Ide, *Mon. Wea. Rev.* 134, (2006), 1081-1101
- [4] H. Salman, K. Ide, C.K.R.T. Jones. *Tellus* 60, (2008), 321-355
- [5] G. Vernieres, C.K.R.T. Jones, K. Ide. *Physica D*, 240, (2011), 166-179
- [6] E. Spiller, C.K.R.T., Jones. K. Ide. *Physica D*, 237, (2008), 1498-1506
- [7] H. Salman. *Q. J. Royal Meteor. Soc.* (2008), 134, 1551-1565
- [8] A. J. Krener. *Tellus* (2008), 60A, 1089-1102
- [9] A. J. Krener, K. Ide. *Proc.*, 48th IEEE.

On the Performance of Lagrangian Descriptors in 2D and 3D Flows

Ana M Mancho¹, J. Curbelo^{1,2}, S. Wiggins³, C. Mendoza⁴

¹ICMAT (CSIC-UAM-UC3M-UCM). C/ Nicolás Cabrera 15, Campus Cantoblanco UAM, 28049 Madrid, Spain

²Departamento de Matemáticas, Campus Cantoblanco, Universidad Autónoma de Madrid, 28049 Madrid, Spain

³School of Mathematics, University of Bristol, University Walk, Bristol, BS8 1TW, UK

⁴ETSI Navales, U. Politécnica de Madrid, Av. Arco de la Victoria 4, 28040 Madrid, Spain.
a.m.mancho@icmat.es.

ABSTRACT

We explore the performance of Lagrangian descriptors. These are functions based on the integration along trajectories of bounded positive scalars, which express an intrinsic geometrical or physical property of the trajectory. We analyze the convenience of different descriptors from several points of view, study them in 2D and 3D flows and compare outputs with other methods proposed in the literature.

1. Introduction

Lagrangian Descriptors have been recently proposed by [1, 2] as a useful tool for identifying invariant manifolds in arbitrary time dependent flows and have been successfully applied to several geophysical contexts [2, 3]. These techniques are based on integrations along trajectories and have a spirit similar to the recent methods developed in [4]. This article further explores the results provided in [1, 2] providing a general the expression for Lagrangian descriptors and analyzing their efficiency in 2D and 3D flows with a general time dependence. The motivation of this research is to find out the aspects in which alternatives are more advantageous than others and in what aspects in some aspects.

We compare their performance with other Lagrangian methods for visualizing flow structures, in particular FTLE and time averages along trajectories.

2. Lagrangian Descriptors

We consider a general vector field:

$$\frac{d\mathbf{x}}{dt} = \mathbf{v}(\mathbf{x}, t) \quad \mathbf{x} \in \mathbb{R}^n \quad (1)$$

The Lagrangian descriptor described in [6] is a function M which measures the Euclidean arc-length on the phase space of the curve defined by a trajectory passing through \mathbf{x}^* at time t^* . The trajectory is integrated from $t^* - \tau$ to $t^* + \tau$. An explicit expression for M is:

$$M = \int_{t^* - \tau}^{t^* + \tau} \|\mathbf{v}(\mathbf{x}, t)\| dt. \quad (2)$$

The function M successfully allows us the realice time-dependent phase portraits of systems like (1). In particular for the periodically forced Duffing equation the computation of M provides a picture such as that in figure 1 where stable and instable manifolds are highlighted as abrupt changes in M . In order to reveal such features a sufficiently long integration time is required, which in Figure 1 is $\tau=10$. A heuristic argument as to why M succeeds in revealing the geometry of objects such as the stable and unstable manifolds of hyperbolic trajectories is as follows. M measures the arc-length of trajectories on a time interval

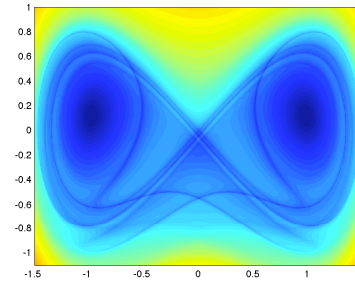


Fig. 1. Evaluation of M for $|F(\mathbf{x}, t)| = \|\mathbf{v}(\mathbf{x}, t)\|$ on the periodically forced Duffing Equation.

$(t^* - \tau, t^* + \tau)$. Trajectories evolving close to each other during this time interval are expected to have similar arc-lengths, since their geometrical evolution on the phase space will be similar. However at the boundaries of regions comprising trajectories with qualitatively different evolutions arc-lengths, on a fixed time interval, will change abruptly, and these regions are exactly what the stable and unstable manifolds separate. This argument motivates the exploration of studying the accumulation of other positive intrinsic geometrical or physical property along trajectories. Thus, in general it suggests an expresión for M of the following form

$$M = \int_{t^* - \tau}^{t^* + \tau} |F(\mathbf{x}, t)| dt. \quad (3)$$

where $|F(\mathbf{x}, t)|$ is a positive bounded scalar evaluated along a trajectory $\mathbf{x}(t)$. A particular choice that we discuss in this abstract is the magnitude of the acceleration, $|F(\mathbf{x}, t)| = \|\mathbf{a}(\mathbf{x}, t)\|$.

3. Lagrangian Descriptors in 3D flows

Lagrangian descriptors succeed in resrepresentating manifolds in time dependent 3D flows. We analyze the stationary Hill's vortex flow, \mathbf{H} , when it is perturbed by a time dependent strain, \mathbf{S} , in the following way:

$$\mathbf{v}(\mathbf{x}, t) = \mathbf{H}(x, y, z) + \mathbf{S}(x, y, z, t) \quad (4)$$

The explicit expression for (4) and the output of the directly computed manifolds is found in section 6.1.2 in [5]. Figure 2 shows the evaluation of the function M for the case in which $|F(\mathbf{x}, t)| = \|\mathbf{a}(\mathbf{x}, t)\|$ in two perpendicular

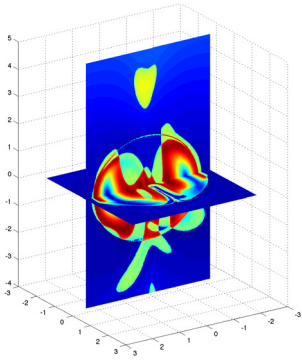


Fig. 2. Evaluation of M for $F(\mathbf{x},t)=\|\mathbf{a}(\mathbf{x},t)\|$ on the perturbed Hill's vortex flow.

planes. A zoom of a region in the horizontal plane is given in Figure 3. There one can see the high quality of detail provided by M .

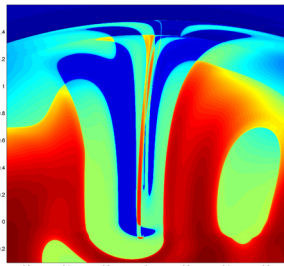


Fig. 3. A zoom of Fig. 2 on the horizontal plane.

4. FTLE and time averages

Another tool commonly used in the study of time dependent flows are finite time Lyapunov exponents (FTLE). These have been very successful in the study of this type of flows, however as noted in [6], ridges of FTLE may give rise to spurious structures.

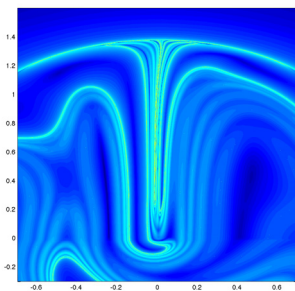


Fig. 4. Backwards FTLE on a zoom on the horizontal plane of Fig. 2. This is the analogue of Fig. 3.

Figure 4 displays the backwards FTLE field, where similar structures to those in Fig. 3 are detected although not so clean and sharp. Artifact ridges are also perceived.

There are differences between the approach embodied in Eq. (3) and the results obtained by applying the Ergodic Partition Theorem [7]. The most important difference is that the theorem is not proven in the context in which (3) is applied: continuous time dynamical systems with an arbitrary time dependence

and for finite time intervals. Results on the ability of finite time averages for highlighting manifolds in aperiodic flows are discussed in [8]. This work does not impose the integration of *positive* scalars along trajectories, thus producing oscillations that distort the manifold output. This is confirmed in the output shown in Fig. 5 for the forwards time average of the horizontal component of the velocity, as considered in [8].

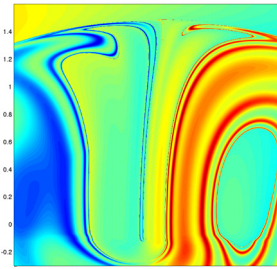


Fig. 5. Analogue of Fig. 3 computed with forwards time averages of the horizontal component of the velocity.

This quantity oscillates along trajectories producing oscillations in the output.

5. Conclusions

Lagrangian descriptors are shown to be a useful tool for highlighting stable and unstable manifold in general time dependent flows in 2D and 3D. We have shown that they may provide sharper and cleaner outputs than those obtained with alternative tools such as finite time averages and FTLE.

Acknowledgements

The computational part of this work was done using the CESGA computer FINIS TERRAE and computers at Centro de Computación Científica (UAM). The authors have been supported by CSIC grant ILINK06-09 and MINECO Grants: ICMAT Severo Ochoa project SEV-2011-0087 and MTM2011-26696. SW acknowledges the support of the Office of Naval Research (Grant No.~N00014-01-1-0769).

References

- [1] C. Mendoza, A. M. Mancho, Phys. Rev. Lett. **105** (2010) (3) 038501.
- [2] C. Mendoza, A. M. Mancho, arXiv:1006.3496
- [3] A. de la Cámara, A. M. Mancho, K. Ide, E. Serrano, C.R. Mechoso. J. Atmos. Sci. **69** (2) (2012) 753-767.
- [4] I. I. Rypina, S. E. Scott, L. J. Pratt, M. G. Brown. Nonlin. Processes Geophys., **18**, (2011) 977-987.
- [5] M. Branicki, S. Wiggins. Physica D 238 (2009) 1625-1657.
- [6] M. Branicki, S. Wiggins. Nonlinear Processes in Geophysics, **17** (2010) 1-36
- [7] I. Mezic and S. Wiggins. Chaos **9** (1999) 213
- [8] A.C. Poje, G. Haller, and I. Mezic. Physics of Fluids, **11** (1999) 2963.

Short-Term Dispersal of Fukushima-Derived Radionuclides off Japan: Modeling Efforts and Model-Data Intercomparison

Irina I. Rypina¹, Steven R. Jayne¹, Ken O. Buesseler¹, Sashiko Yoshida¹, Elizabeth M. Douglass², Alison M. Macdonald¹

Affiliation and address: 1. Woods Hole Oceanographic Institution, Woods Hole, MA, 02543, USA.

2. Naval Research Laboratory, Stennis Space Center, Stennis Space Center, MS 39529, USA.

E-mail of corresponding author: irypina@whoi.edu.

ABSTRACT

As a result of the Tohoku earthquake and tsunami on March 11, 2011, the Fukushima nuclear power plants were damaged and radioactive material was released to the atmosphere and into the ocean. In order to assess the levels of contamination in the water off Japan, a field study was carried out on June 4-18, during which the water samples were collected. To interpret these field measurements, we carried out numerical simulations of the spreading of the contaminated waters. The simulations provide the physical oceanographic insight into which oceanic features and processes influenced the short-term dispersal of the radionuclides.

1. Introduction

As a result of the Tohoku earthquake and tsunami that occurred on March 11, 2011, the Fukushima Dai-ichi nuclear power plants were damaged and radioactive material was released both to the atmosphere and into the waters of the Northwest Pacific Ocean. The peak of the airborne fallout of radioactive contaminants occurred in mid-March whereas the direct discharge of contaminated waters to the near-shore ocean off the coast of Japan peaked in early April.

In order to assess the levels of contamination in the water, fish and plankton off Japan, a comprehensive field study was carried out on June 4-18 using the R/V Ka'imikai-o-Kanaloa (Buesseler et al. (2012)). We will refer to this field study as the KOK cruise. During the KOK cruise, water and biological samples were collected at 50 stations spanning the ocean from 30 to 600 km off the Fukushima coast. The samples were later analyzed to produce a map of ¹³⁷Cs concentrations throughout the 150000 km² area of the KOK cruise. The highest activities were detected at stations located in the near-shore area but not at stations closest to the coast. The smallest activities were detected at southernmost stations.

2. Methods

To interpret these findings, we carried out numerical simulations of the spreading of the contaminated waters using both data-based and numerically-generated velocity fields. More specifically, the numerical velocities were produced by the data-assimilative NCOM model, whereas the data-based velocities were obtained by combining the near-surface geostrophic velocity estimates from AVISO with Ekman velocities due to winds inferred from the NCEP/NCAR reanalysis wind stresses. Both the data-based and numerical-model-based velocity fields were validated against, and showed good agreement with, the measured trajectories of 24 near-surface drifters that were deployed as part of the KOK cruise.

To estimate the spreading of contaminated waters, we used the Lagrangian advection scheme with variable-step Runge-Kutta 4(5) integration and a bilinear interpolation in time and space between grid points. The source function for the deposition of ¹³⁷Cs

from the air was based on the study by Stohl et al. (2011) and assumes the total source strength of about 27PBq with the peak fallout on March 16 over a broad area of the Pacific Ocean. The source function for the direct ocean discharge of ¹³⁷Cs uses a measured time-series of input from Buesseler et al. (2011) and assumes the total discharge of 3.5 PBq of ¹³⁷Cs into a small area centered at the Fukushima power plant; the direct discharge peaked on April 7.

3. Results and Discussion

Our numerical studies suggest that by the time of the KOK cruise, a large volume of the contaminated water had already moved out of the KOK domain heading eastward and into the Pacific. The distribution of the remaining contaminated water in the region was streaky and patchy, with the largest concentrations associated with the outer edge of the robust semi-permanent near-shore mesoscale eddy. Our simulations also suggest that the core of the Kuroshio Current was acting as a (leaky) boundary for the southward spreading of the contaminated waters, which explains the very low concentrations detected at southernmost stations. Finally, the relatively low ¹³⁷Cs concentrations at stations closest to shore were likely due to the fact that this water leaked from the damaged power plant long after the accident and thus contained lower levels of radioactivity than the water that was discharged at the peak of the radioactive release in early April.

Our simulations also suggest that most of the detected ¹³⁷Cs was from the direct discharge rather than from the airborne fallout. This is supported by the fact that the distribution of the measured concentrations of ⁹⁰Strontium, which, unlike ¹³⁷Cs, was only discharged directly to the ocean, is similar to that for the ¹³⁷Cs.

References

- [1] Buesseler K. O., Aoyama M., Fukasawa M. (2011). Impacts of the Fukushima nuclear power plants on marine radioactivity. *Environ Sci Technol*, 45:9931-9935.
- [2] Stohl A., Seibert P., Wotawa G., Arnold D., Burkhart J. F., Eckhardt S., Tapia C., Vargas A., and Yasunari T. J. (2011). Xenon-133 and Caesium-137 releases into the atmosphere from the Fukushima Dai-ichi nuclear power

plant: Determination of the source term, atmospheric dispersion, and deposition. *Atmos Chem Phys Discuss*, 11:28319–28394.

[3] Buesseler K. O., Jayne, S. R., Fisher N. S., Rypina I. I., Baumann H., Baumann Z., Breier C. F., Douglass E. M., George J., Macdonald A. M., Miyamoto H., Nishikawa J., Pike S. M., and Yoshida S. (2012). Fukushima-derived radionuclides in the ocean and biota off Japan. *PNAS*, 109(16), 5984-5988

Bifurcation Structures In Flapping Flight Problems

Makoto Iima

Graduate School of Science, Hiroshima University,
1-7-1, Kagamiyama, Higashi-Hiroshima, 739-8251, Japan
makoto@mis.hiroshima-u.ac.jp.

ABSTRACT

In insect's flight, vortices separated from flapping wings and its dynamics are important to account for the lift which is larger than that expected by steady-state aerodynamics. If the body motion is coupled, we can discuss the stability of the center-of-mass motion, which is related to the maneuverability, although the behavior of the whole system becomes much more complex. In this paper we focus on the mathematical structure of the insect's flight. In particular, we show that the bifurcation diagram, the parameter dependence of the steady flapping flight state, is useful for analysis.

1. Introduction

Insect's flight can be understood as a coupled system between the airflow driven by the flapping wing and the center-of-mass motion according to the hydrodynamic force and the gravity. Because the hydrodynamic force is determined by the unsteady flow, which is in general complicated due to the separation vortices, the behavior of the system is not simple. However, real-life insects actually control such complex flow not only to achieve steady flights but also to move to the place they want to go. To understand the mismatch between the complicated flow and the high maneuverability, we need a new viewpoint. Here, we focus on the mathematical structure embedded in the flapping flight using vortices. In this paper, we focus on the bifurcation structure in parameter space in which fruitful information is included.

2. Flapping Models

We consider several flapping models in two-dimensional fluid. The detailed configurations depend on the model, but in all models, we consider the equation of motion for the center-of-mass:

$$M \frac{d^2 \mathbf{G}}{dt^2} = \mathbf{F}_{\text{hydro}} - M g \mathbf{e}_y \quad (1)$$

where $\mathbf{G}=(x,y)$ is the position of the center of mass, $\mathbf{F}_{\text{hydro}}$ is the hydrodynamic force acting on the wing(s), M is the mass, and g is the gravitational acceleration. The following flight models have been considered so far.

(a) Symmetric flapping model [1-6].

Two line segments are considered as two wings. They flap around a hinge, and their motion is symmetric with respect to the vertical line. Also, wing motion is symmetric with respect to the horizontal line, i.e., a symmetric flapping. Due to the mirror symmetry with respect to the vertical line, the center of mass can move along the vertical line: $\mathbf{G}=(0,y)$ where $x=0$ represents the vertical line. In this model, we observe a symmetry breaking. When $g=0$, the situation is symmetric with respect to the horizontal line. Thus the mean velocity of the center of mass looks to be zero at a first glance. However,

Due to the interaction among the separation vortices and wing, the center of mass moves in one direction [1]. This is a symmetry-breaking which can be clarified by bifurcation analysis [2]. In this model, the fluid flow is solved by the discrete vortex method and the effect of the separation vortices are controlled by an artificial viscosity, by which the bifurcation structure is obtained clearly. Similar model has been analyzed by solving the Navier-Stokes equations, and similar results are obtained [4]. The effect of the gravity has been also investigated by using the bifurcation diagram [5]. Surprisingly, the bifurcation branch suddenly disappears if the gravity acceleration is gradually increased. The flight state at the critical point is close to hovering, i.e., the mean velocity of the center of mass is almost zero.

(b) Horizontal flapping model [6].

In this model, single wing moves horizontally with changing its angle of attack. Such motion is often observed in hovering flight. The center-of-mass motion is restricted to the vertical one: $\mathbf{G}=(0,y)$. Bifurcation branch representing upward flight also ends at a critical gravity where the mean vertical velocity is almost zero, which is similar to the result of the symmetric flapping model [5]; the result is universal. An analytical study shows that the hovering flight in two-dimensional space is a singular flight [7].

(c) Forward-flight flapping model [7].

Maneuverability of the flapping flight is considered using a forward-flight flapping model. In this model, single wing flaps along a line corresponding to the stroke plane with changing the angle of attack. The center of mass can move in both horizontal and vertical direction, but the pitching angle is assumed constant: $\mathbf{G}=(x,y)$. Due to two degrees of freedom for the center-of-mass motion, the possible flight modes have a variety. We found an unstable flight that separates the final flapping states, which coexist as stable steady flight. Such unstable flight can be achieved by a simple flapping motion.

3. Concluding remarks

The flapping-flight models have been analyzed in terms of bifurcation analysis. Possible flight states at given parameter sets determine the possible flight behavior, thus, the bifurcation analysis is important. In other configuration other than flapping flight, similar analysis has been applied. In the thermal convection of binary fluid mixture, a spatially localized convection cells are observed, and their interaction is related to the bifurcation structure [9]. Such analysis is useful to understand the formation process of a hierarchical multi-scale structure [10]. Even in experimental system, such mathematical structure is observed. In a rotating flow with free surface in a cylinder [11,12], an unstable state is observed as a transient state [13]. When the parameter is near the critical point between the laminar-turbulent transition, the bifurcation diagram shows a bistability for laminar and turbulent states [14]. A discussion is given for the relationship between such bifurcation structure and “Surface switching phenomena”, a non-periodic surface shape transition between these states.

Flow in nature is complicated because the boundary shape and its motion are complex, the flow transition occurs, and hierarchical structures are generated in general: a global flow structure [15]. Although it is tough to analyze such systems, there are several approaches we can tackle with. Bifurcation analysis is one of the mathematical tools useful for investigation.

Acknowledgments

This study is partially supported by Grant-in-Aid for Scientific Research (KAKENHI) No.21340019, No. 2236105, No. 23540433, and Core Research for Evolutional Science and Technology (CREST) No. PJ74100011.

References

- [1] M. Iima and T. Yanagita, J. Phys. Soc. Japan, **70** (2001), 5.
- [2] M. Iima and T. Yanagita, Theor. Appl. Mech., **50** (2001), 237.
- [3] M. Iima and T. Yanagita, Fluid Dyn. Res. , **36** (2005), 407.
- [4] K. Ota, K. Suzuki and T. Inamuro, Fluid Dyn. Res. **44** (2012), 045504.
- [5] M. Iima and T. Yanagita, Europhys. Lett., **74** (2006) 55.
- [6] M. Iima, J. Theor. Biol., **247** (2007), 657.
- [7] M. Iima, J. Fluid Mech. **617** (2008), 207.
- [8] M. Iima, N. Yokoyama, N. Hirai, and K. Senda, Adv. Sci. Tech., *in press*.
- [9] T. Watanabe, K. Toyabe, M. Iima and Y. Nishiura, Theor. Appl. Mech. Jpn., **59** (2011), 211.
- [10] T. Watanabe, M. Iima and Y. Nishiura, *submitted*.
- [11] T. Suzuki, M. Iima and Y. Hayase, Phys. Fluids, **18** (2006), 101701.
- [12] T. R. N. Jansson, M. P. Haspang, K. H. Jensen, P. Hersen, and T. Bohr, Phys. Rev. Lett., **96** (2006), 174502,.
- [13] R. Bergmanna, L. Tophøj, T. A. M. Homan, P. Hersen, A. Andersen and T. Bohr, J. Fluid Mech. **679** (2011), 415.
- [14] Y. Tasaka and M. Iima, J. Fluid. Mech., **636** (2009),475.
- [15] M. Iima, Y. Tasaka and T. Watanabe, GAKUTO International Series **34** (2012), 25.

Symmetries and Constraints in Aquatic Propulsion via Vortex Shedding

Scott David Kelly Phanindra Tallapragada
Department of Mechanical Engineering and Engineering Science
University of North Carolina at Charlotte
9201 University City Boulevard
Charlotte, NC 28223-0001 USA
scott@kellyfish.net

ABSTRACT

This paper presents a qualitative summary of the role played by symmetry-breaking velocity constraints in certain models for aquatic locomotion via propulsive vortex shedding, and introduces a pair of simple examples to illustrate the analogy between such models and traditional models for wheeled mobile robots subject to nonholonomic rolling constraints.

1. Introduction

The goal of this paper is to draw attention to a fundamental analogy that exists between certain idealized models for locomotion in viscous fluids and certain models for the locomotion of wheeled mobile robots. A substantial literature addresses motion planning and control for systems of the latter kind. The authors have recently applied an algorithm developed for the planar navigation of a wheeled robot to the planar navigation of an idealized fishlike swimmer [1], and hope to clarify the general class of systems to which similar methods are applicable.

Central to the analogy in question is the phenomenon of symmetry breaking by nonholonomic constraints. In the context of terrestrial robotics, such constraints arise when wheels are assumed to roll longitudinally without slipping laterally. In the context of fluid-body interactions, such constraints may be introduced in the form of Kutta-like conditions to compel flow separation without explicitly accounting for viscous boundary-layer dynamics. In either context, symmetry breaking can lead to the supersession of a set of independent conservation laws by a set of differential equations governing the coupled evolution of multiple momentum-like quantities. The self-propulsion of an aquatic vehicle hinges on the coupled evolution of the fluid impulse associated with the vehicle's motion and the vorticity in the vehicle's wake, both of which exemplify such quantities.

For the present (short) paper, we forgo a general treatment of these ideas and instead describe a pair of simple systems that illustrate the analogy we have in mind.

2. Chaplygin and Joukowski Beanies

The system we call the *Chaplygin beanie*, depicted in Fig. 1, was introduced in [1] as an amalgam of two canonical mechanical systems. The *Chaplygin sleigh* [2] comprises a cart supported in the front by a pair of casters and in the rear by a massless passive wheel constrained not to slip sideways. Atop the center of mass of such a cart, displaced longitudinally from the center of the wheel, we mount a rotor. If the cart is placed on solid ground and the rotor is induced to rotate relative to the cart, the cart will acquire forward momentum. In the absence of the no-slip constraint on the wheel, this system corresponds

to *Elroy's beanie* [3].

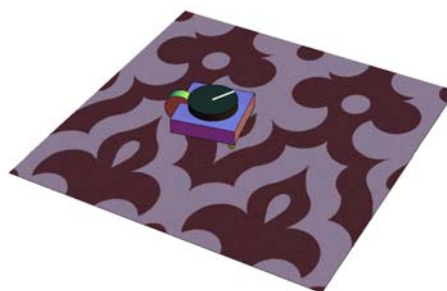


Fig. 1 The Chaplygin beanie on a plate with finite mass

In Fig. 1, the Chaplygin beanie is shown not on solid ground but atop a platform with finite mass that's free to translate as a result of the time-varying lateral force applied to it by the wheel. The dynamics of the resulting system may be understood as follows.

In the absence of the no-slip constraint, the kinetic energy due to translation and rotation of the cart alone exhibits an $SE(2)$ symmetry that results, via Noether's theorem, in the conservation of the cart's linear and angular momentum in the plane parallel to the plate. If the rotor is induced to rotate relative to the cart, the cart will counter-rotate to conserve angular momentum, but will not translate. Concurrently, the kinetic energy of the plate alone exhibits a symmetry with respect to translation, resulting in the conservation of the plate's linear momentum. Because the kinetic energy of the cart and plate together is invariant under planar translation as well, the total linear momentum in the system is also conserved.

The introduction of the no-slip constraint couples the momentum of the cart to that of the plate. The total linear momentum in the system is still conserved, but inducing the rotor to rotate relative to the cart will result in the translation of the cart and the counter-translation of the plate.

Like the conservation laws described above, the conservation of vorticity in a planar inviscid fluid corresponds to a symmetry via Noether's theorem. When such a fluid is bounded internally, the value of the momentum map corresponding to this symmetry incorporates both the vorticity field and the set of scalar circulations around

internal boundaries [4].

Fig. 2 depicts a single frame from a simulation of a planar aquatic vehicle analogous to the Chaplygin beanie. A Joukowski foil with zero camber is surrounded by an infinite ideal fluid; coupled to the foil internally is a rotor like that in Fig. 1. The angular position of the rotor has been induced to vary sinusoidally relative to that of the foil, causing vorticity to be shed from the foil's trailing point and causing the foil to accelerate from rest. Vorticity is shed discretely in accordance with the (frequent) periodic application of a Kutta condition at the foil's trailing point; vortices with positive strength are shown in blue and vortices of negative strength in red. Between vortex-shedding events, the positions of the foil and the vortices evolve according to a non-canonical Hamiltonian system of equations [5].

If vorticity is initially absent from the fluid in Fig. 2, then the dynamics of the system — for the sake of analogy, the *Joukowski beanie* — may be understood as follows. The reader should compare the following two paragraphs to the second and third paragraphs that follow Fig. 1.

In the absence of the Kutta condition, the kinetic energy due to translation and rotation of the foil — including that associated with the foil's added mass and added rotational inertia — exhibits an $SE(2)$ symmetry that results in the conservation of linear and angular impulse in the system. If the rotor is induced to rotate relative to the foil, the foil will counter-rotate to conserve angular impulse, but will not translate. Concurrently, the kinetic energy of the fluid alone exhibits a symmetry that results (as described above) in the conservation of the (initially null) vorticity in the fluid and the (initially null) circulation around the foil.

The introduction of the Kutta condition couples the impulse due to translation and rotation of the foil to the fluid vorticity and the circulation around the foil. The total impulse in the system is still conserved, but inducing the rotor to rotate relative to the foil will result in the translation of the foil and the counterbalancing introduction of vorticity and circulation to the fluid.

The parallelism between the Chaplygin and Joukowski beanies is not superficial, but follows from the formal equivalence of the rolling constraint affecting the former to the Kutta condition — imagined to be applied continuously — affecting the latter. Each is a constraint on the direction of the relative velocity between vehicle and medium at a single vehicle-fixed point, representable in terms of an $SE(2)$ -invariant constraint distribution on the appropriate configuration manifold.

The study of symmetries in mechanics underpins the technique of dynamic *reduction*, whereby the essential dimension of a system's phase space may be determined to be less than that suggested by canonical Lagrangian or Hamiltonian formalism. In the absence of the no-slip constraint, the Chaplygin beanie conserves linear and angular momentum as it moves over a planar medium, and its dynamics are reduced in dimension by these conservation laws. With the no-slip constraint in place, these conservation laws fail, but a partial reduction is still pos-

sible.

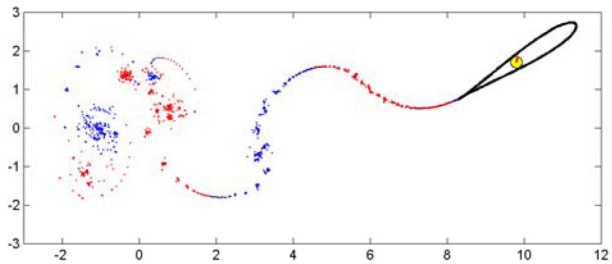


Fig. 2 The Joukowski beanie accelerating from rest as a result of sinusoidal variations in relative rotor velocity

The dynamics of the Chaplygin beanie atop a fixed plate are discussed in detail in [1]. Instantaneously, the motion of the cart is the superposition of longitudinal translation and rotation about the point of contact between the wheel and the plate. Each of these primitive motions corresponds to a vector field on the system's configuration manifold; associated with the span of these vector fields is a two-dimensional quantity called the system's *nonholonomic momentum* [6]. This quantity is not conserved, but its evolution encodes the complete dynamics of the cart's translation and rotation, reduced in dimension by one — corresponding to the single nonholonomic constraint — from the number of independent scalar momenta defined in the unconstrained case. In a forthcoming paper, the authors detail the reduced dynamics of the Joukowski beanie in terms of the evolution of an analogous nonholonomic momentum.

3. Acknowledgements

Support for this work was provided in part by the NSF grants CMMI-1000652 and CMMI-1000656.

References

- [1] S. D. Kelly, M. J. Fairchild, P. M. Hasing, and P. Tallapragada. Proportional Heading Control for Planar Navigation: The Chaplygin Beanie and Fishlike Robotic Swimming. In *Proceedings of the American Control Conference*, 2012.
- [2] A. M. Bloch. *Nonholonomic Mechanics and Control*. Springer Verlag, 2003.
- [3] J. E. Marsden, R. Montgomery, and T. S. Ratiu. Reduction, Symmetry, and Phases in Mechanics. *Memoirs of the American Mathematical Society*, 436, 1990.
- [4] J. E. Marsden and A. Weinstein. Coadjoint Orbits, Vortices, and Clebsch Variables for Incompressible Fluids. *Physica 7D*, 7:305–323, 1983.
- [5] B. N. Shashikanth. Poisson Brackets for the Dynamically Interacting System of A 2D Rigid Cylinder and N Point Vortices: the Case of Arbitrary Smooth Cylinder Shapes. *Regular and Chaotic Dynamics*, 10(1):1–14, 2005.
- [6] A. M. Bloch, P. S. Krishnaprasad, J. E. Marsden, and R. M. Murray. Nonholonomic Mechanical Systems with Symmetry. *Archive for Rational Mechanics and Analysis*, 136:21–99, 1996.

Atmospheric Coherent Structures and Biological Invasions

Shane D. Ross, David G. Schmale III, Binbin Lin, Amir E. BozorgMagham, Aaron J. Prussin II, Shibabrat Naik
(Virginia Tech, USA), Phanindra Tallapragada (University of North Carolina at Charlotte, USA)
E-mail of corresponding author: sdross@vt.edu

Abstract

The language of coherent structures provides a new means for discussion of certain aspects of aeroecology, particularly transport and mixing of atmospheric pathogens, paving the way for new modeling and management strategies for the spread of infectious diseases affecting plants, domestic animals, and humans. We report on a recent integration of experimental biology and applied mathematics uncovering how Lagrangian coherent structures and their boundaries, provide a framework for understanding how airborne microbe populations are dispersed and mixed.

Introduction

Many spores, seeds, dust particles and chemical pollutants can be transported across very large distances in the troposphere, sometimes on a continental scale. The atmosphere serves as a medium of transport as well as a reservoir for many of these particles. Several studies show the existence of such long range transport of dust, trace chemicals and biota in the atmosphere [1, 2]. Focusing on airborne fungal spores, our group has demonstrated that there are chaotic fluctuations in the spore concentration, particularly of the genus *Fusarium* [3–5], collected with autonomous unmanned aerial vehicles (UAVs) at a single geographic location. A phenomenon of particular interest are the abrupt changes in the spore concentration. In this study, we explore the possibility that these ‘punctuated changes’ in concentrations of *Fusarium* are related to the passage of large-scale, moving, transport barriers over the sampling location.

Many *Fusarium* species use the atmosphere to travel from one habitat to another, yet their atmospheric transport is poorly understood. Some members of the genus are important plant and animal pathogens, others are producers of dangerous toxins. Atmospheric transport of *Fusarium* can be broadly categorized into distinct stages [2] - (1) release and ascent of *Fusarium* into the planetary boundary layer (PBL), (2) long range transport of *Fusarium* in the PBL or above and (3) deposition of *Fusarium* into a new habitat.

In the release and ascent stage, spores of *Fusarium* (or any passively moving particles) have to cross a relatively thin boundary layer that can extend in height up to 50 m. Thus surface boundary layer (SBL) is the lowest layer of the atmosphere and being in contact with the ground, it has very strong vertical gradients in wind speed, temperature and humidity. The flow in the SBL is highly turbulent because of surface effects [6, 7]. Above the SBL is the PBL, a well-mixed layer in which the turbulence due to the surface forcing decreases. The height of the PBL extends from ~ 50 m to ~ 3 km above the ground, with the upper limit decreasing to as little as 300 m during the night. Once spores manage to cross the SBL and enter the PBL they have the potential to be transported over long distances. Indeed, in the PBL and above, on the meso- to synoptic (~ 10 - 100 km) scale, motion over time-scales of a day is quasi-2D along constant pressure surfaces, following the homogeneous geostrophic equa-

tions appropriate to this scale [6].

The first and third stages have received considerable attention in terms of developing computational models, for example in the works of Aylor, Schmale, and co-workers [8, 9]. The long range transport stage has usually been studied using a few sample trajectories [10]. However, the study of individual trajectories cannot fully resolve the complex motion of the atmosphere, nor the resulting changes in the observed concentrations of *Fusarium* in the lower atmosphere. Rather than individual trajectories, the qualitative properties of sets of trajectories are more reliable.

Here we discuss a more systematic, geometric framework for discussing the changes in atmospherically advected microorganism concentrations, based on computations of atmospheric transport barriers (ATBs). The ATBs are approximated as Lagrangian coherent structures boundaries (LCSBs) extracted as ridges from the finite-time Lyapunov exponent (FTLE) field [11]. The LCSBs serve as the most important material surfaces within the flow which effectively separate air masses of qualitatively different dynamics, e.g., different spore composition, different origin, different destination.

We have found [5] that (i) the autocorrelation of *Fusarium* spore concentration decreases with time, Fig. 1, and gives a correlation time of about 6-9 hours and (ii) in the absence of punctuated changes, spore concentration is distributed according to a slowly-varying inhomogeneous Poisson process. Large changes in spore concentration over short times would be highly improbable based on a Poisson process. We have suggested that punctuated changes are correlated with the passage of atmospheric LCSBs.

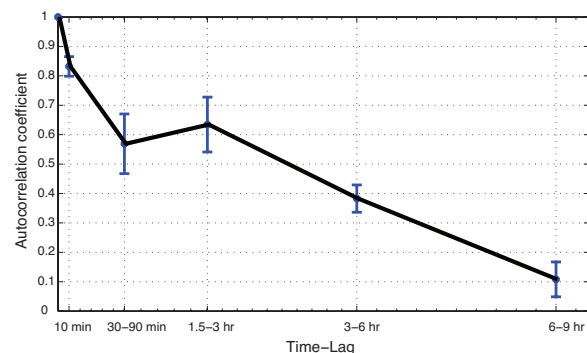


Figure 1. Fluctuations in fungal spore concentration: auto-correlation vs. time-lag.

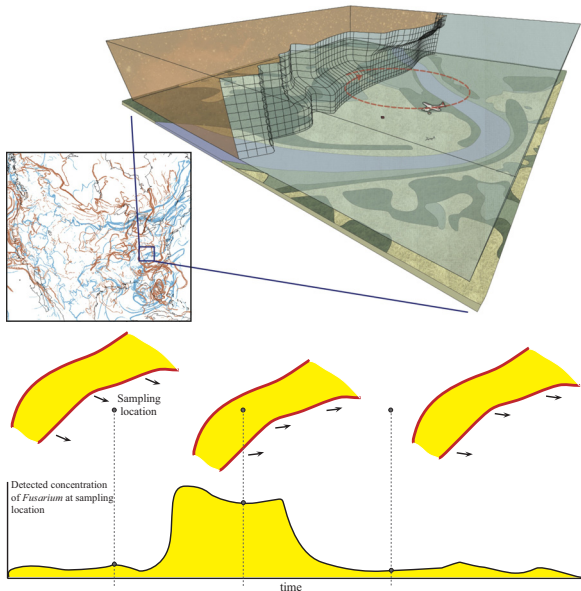


Figure 2. (a) Atmospheric LCSBs are large-scale features with local effects. An LCSB (shown as undulating mesh) separates two volumes of air as it moves over topography, shown schematically on a scale of several kilometers near our sampling site at Virginia Tech’s Kentland Farm in Blacksburg, Virginia, USA. We use autonomous UAVs to collect *Fusarium* in the lower atmosphere. We hypothesize that mixed populations of *Fusarium* in the lower atmosphere are mediated by LCSB, as an LCSB is a highly repelling material surface separating two relatively well-mixed air masses. This LCSB is just one of a large-scale network of repelling and attracting LCSB on the continental scale (left). (b) Movement of a ‘cloud’ of relatively high concentration of *Fusarium* bracketed by repelling LCSBs (upper panel, three time snapshots going from left to right) and the corresponding abrupt changes in detected concentrations of *Fusarium* at a geographically fixed sampling location (below). The continuous signal with time is hypothetical. Sampling yields only a discrete number of observations, as sampling takes a finite duration and the time between samples can be significant. In this example, two punctuated changes are shown (an abrupt increase followed by an abrupt decrease), which are a consequence of the particular LCSB movement with respect to the sampling location.

Hypotheses on role of LCSBs in abrupt changes

The role of transport barriers as separatrices that influence both mixing and separation processes has been investigated in many problems of geophysical flows [12]. However, the relationship between the movement of atmospheric LCSBs over the landscape and abrupt changes in concentration of microorganisms has not yet been investigated. Microbes belonging to the genus *Fusarium* were selected for this study because of the relative abundance of *Fusarium* in the atmosphere and the existence of reliable methods for selectively collecting *Fusarium* in the lower atmosphere [13]. Moreover, many members of this genus cause important diseases in animals and crops with serious economic consequences, as discussed in the introduction.

Observed changes in the atmospheric concentrations of *Fusarium* suggest that we are sampling masses of air that differ not only in the relative amount of *Fusarium*, but also in their composition of different species and/or strains of *Fusarium*. We hypothesize that moving three-

dimensional atmospheric LCSBs are partitioning large-scale air masses, a small portion of which we are sampling with UAVs, as illustrated in Fig. 2.

Results, Conclusions, and Future Work

Based on over 200 samples, we found that most consecutive samples do not show much variation, consistent with the auto-correlation relationship described above. On the other hand, punctuated changes, defined by a probabilistic criterion, are associated with the movement of LCSBs, and particularly repelling LCSBs, in a one-way correlation [3]. That is, when a punctuated change occurs between two sampling times, there is a high probability that a repelling LCSB passed over the sampling location between the two sampling times. It is possible that the magnitude of punctuated changes can depend on ‘repelling strength’ of the repelling LCSB. Furthermore, the results of our hypotheses testing are influenced by several parameters, including the time-scale used to determine punctuated changes, (12 or 24 hours). Future studies are expected to systematically investigate the influence of these factors. The role of coherent fluid structures in biological invasion in other contexts should be considered, as well as the role of dynamic barriers in shaping the large-scale migration of organisms more generally.

Acknowledgments. This material is based upon work supported by the National Science Foundation under Grant Numbers DEB-0919088 and CMMI-1100263.

References

- [1] Aylor, D. E. [2002] *Agricultural and Forest Meteorology* **38**:263–288.
- [2] Isard, S. and Gage, S. H. [2001] *Flow of Life in the Atmosphere: An Airscape Approach to Understanding Invasive Organisms*. Michigan State University Press, East Lansing, MI.
- [3] Tallapragada, P., Ross, S. D. and Schmale, D. [2011]. *Chaos*, 21:033122.
- [4] Schmale, D. G., Ross, S. D., Fetters, T. L., Tallapragada, P., Wood-Jones, A. K. and Dings, B. [2012] *Aerobiologia* **28**:1–11.
- [5] Lin, B., BozorgMagham, A. E., Ross, S. D. and Schmale, D. G. [2012] *Aerobiologia* :doi: 10.1007/s10453-012-9261-3.
- [6] Zdunkowski, W. and Bott, A. [2003]. *Dynamics of the atmosphere, A course in theoretical meteorology*. Cambridge University Press, 2003.
- [7] Boehm, M. T. and Aylor, D. E. [2005] *Atmospheric Environment* **39**:4841–4850.
- [8] Aylor, D. E. and Flesch, T. K. [2001] *Journal of Applied Meteorology* **40**:1196–1208.
- [9] Schmale, D. G. and Bergstrom, G. C. [2004] *Canadian Journal of Plant Pathology* **26**:591–595.
- [10] Davis, J. M. [1987] *Annual review of phytopathology* **25**:169–188.
- [11] Lekien, F. and Ross, S. D. [2010] *Chaos* **20**:017505.
- [12] Coulliette, C., Lekien, F., Paduan, J. D., Haller, G. and Marsden, J. [2007] *Environmental Science and Technology* **41**:6562–6572.
- [13] Schmale, D. G., Dings, B. R. and Reinholtz, C. [2008] *Journal of Field Robotics* **25**:133–147.

Invariant Manifolds and the Geometry of Front Propagation in Fluid Flows

Kevin A. Mitchell and John R. Mahoney
School of Natural Sciences, University of California, Merced
5200 North Lake Road, Merced, CA, 95343, USA
kmitchell@ucmerced.edu

ABSTRACT

Recent theoretical and experimental work has demonstrated the existence of one-sided, invariant barriers to the propagation of reaction-diffusion fronts in quasi-two-dimensional, periodically-driven fluid flows. These barriers are called burning invariant manifolds (BIMs). We develop a detailed theoretical analysis of BIMs, providing criteria for their existence, a classification of their stability, a formalization of their barrier property, and mechanisms by which the barriers can be circumvented. This analysis assumes the sharp front limit and negligible feedback of the front on the fluid velocity field.

1. Introduction

The passive advection of particles in a two-dimensional fluid flow is a well-studied problem important both for its direct relevance to fluid mixing and for its broader connection to Hamiltonian dynamics. The latter finds applications ranging from chaotic ionization in atomic physics [1,2] to the motion of asteroids in the solar system [3]. A key observation in passive chaotic advection is that invariant manifolds form barriers to particle transport [4-7]. The question addressed here is to what extent an *active* material within a fluid flow is subject to such barriers. We are particularly concerned with active systems that generate fronts, e.g., chemical reactions [8,9] or sound waves in moving fluids, plankton blooms [9,10] in ocean flows, optical pulses in an evolving optical medium, phase transitions in liquid crystals, or even the spreading of disease within a mixing population.

2. Burning invariant manifolds

The existence of robust barriers to the propagation of reaction fronts in advection-reaction-diffusion systems has recently been experimentally demonstrated in both time-independent and time-periodic, vortex-dominated flows [11]. These flows are magneto-hydrodynamically-generated and quasi-two-dimensional. The reaction is a ferroin-catalyzed, Belousov-Zhabotinsky reaction. The barriers are experimentally shown to be both (i) one-sided, preventing front propagation in one direction, but not the reverse and (ii) invariant, staying either fixed in the lab frame or periodically varying (for periodically driven flows). These barriers therefore play an important role in pattern formation in such systems; they also limit, and could potentially be used to control, the average front propagation speed through the fluid.

The theoretical explanation for the front barriers is based on a low-dimensional dynamical systems approach, which interprets the experimental barriers as invariant manifolds attached to unstable periodic orbits. Hence, these barriers are named *burning invariant manifolds* (BIMs), where “burning”¹ emphasizes their

relevance to reaction-front propagation and distinguishes them from the well-established invariant manifolds controlling advection of *passive* tracers [4-7].

A complete model of a general advection-reaction-diffusion system is typically built, at least initially, around a partial differential equation that couples the local chemical dynamics to the local fluid flow and vice versa. In general, the reaction dynamics can profoundly impact the fluid velocity (e.g. in combustion). However, such feedback is relatively small in some cases, such as the experiments in Refs. [11-13] considered here. Thus, we take the fluid velocity field $\mathbf{u}(\mathbf{r})$ to be prescribed at the outset and to be unaffected by the subsequent chemical dynamics. Furthermore, we take the “geometric optics” limit in which the reaction is sufficiently fast that a sharp front develops between those regions that are fully reacted and those that are completely unreacted.

The above assumptions lead to a three-dimensional ODE for the propagation of a point along the front. This allows us to treat front propagation dynamics as a modification of passive advection. A point along the front is viewed as an active “particle” (or “swimmer”) that evolves according to both fluid advection and its own internal locomotion, fixed at a constant speed v_0 (the “burning” speed) in the moving frame of the fluid. The corresponding dynamical system is thus three-dimensional, with two dimensions for the xy -position within the fluid and a third dimension for the orientation angle of the local front element. Initially, it may seem that the invariant manifolds defined for passive advection are irrelevant for reactive front propagation, since the reaction can burn right through an advective separatrix. However--and this is the central point of this presentation--the invariant manifolds of the advection dynamics can be suitably and naturally modified to the reaction front scenario; these are the burning invariant manifolds (BIMs). The BIMs reduce to traditional advective invariant manifolds when $v_0 = 0$, but otherwise may differ dramatically from them.

We give a brief overview of the physical role played by BIMs. Figure 1 illustrates the BIMs (bold, red) for a

¹Throughout, we use the term “burned” or “burning”

generically for front propagation.

time-independent flow, confined to a horizontal channel with counter-rotating vortices. In Fig. 1a, the reaction is catalyzed at the channel bottom between the BIMs, and then generates the sequence of reaction fronts, forming an upward propagating plume, ultimately rolled up by the vortices. The fronts are bounded by the BIMs on either side, with the arrows normal to the BIMs denoting the “burning” direction of each BIM. A BIM forms a barrier to fronts propagating in its burning direction (as in Fig. 1a), but not to fronts impinging in the opposite direction, as illustrated in Figs. 1b–d. In Figs. 1b–d the fronts are catalyzed at different stimulation points (small open circles) and approach the BIMs from different directions. In each case, the fronts pass through a BIM when approaching opposite the BIM’s burning direction but are stopped when approaching in the burning direction.

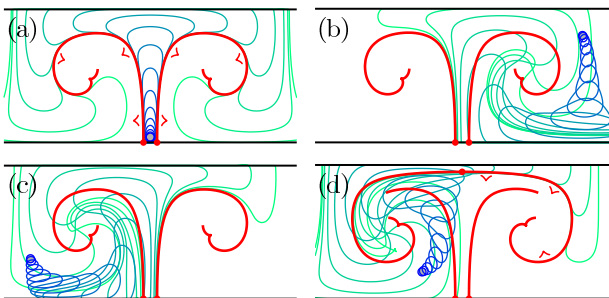


Fig. 1. (a) Fronts converging (blue to green) upon BIMs (bold, red) in a time-independent vortex flow. Panels b–d show fronts initialized at different stimulation points (small open circles) burning through BIMs opposite their burning direction but bounded by BIMs in their burning direction. Panel d includes a BIM attached to a burning fixed point near the top of the channel, which restricts the front in the upper right.

In Fig. 2, the vortices oscillate periodically in the horizontal direction. The BIMs are shown at a single phase of the driving. An initial stimulation between the BIMs in Fig. 2a grows outward in a series of reaction fronts. During the first period, the front migrates outside the BIM channel in Fig. 2a, but returns to it exactly one driving period T after initialization (shown by the gray “burned” region in Fig. 2b.) Figures 2c and 2d show two additional stimulation points, and their subsequent evolution after two driving periods (in gray). In both cases, BIMs bound the front evolution in their burning direction, but not in the opposite direction.

3. Further Developments and Applications

In addition to the properties of BIMs discussed above, we have succeeded in developing a number of further results and applications, including: (i) existence and stability criteria for burning fixed points, including a topological index theory, (ii) mechanisms for fronts to circumvent BIMs, (iii) methods for experimentally measuring BIMs in the laboratory, (iv) connections to finite-time Lyapunov exponents (FTLEs) [14,15], (v) mode-locking and pinning of fronts, and (vi) lobe dynamics for front propagation. The latter two are

discussed in a separate presentation.

4. Acknowledgements

This work was supported by the US National Science Foundation under grant PHY-0748828. The authors gratefully acknowledge extensive discussions with, and experimental results from, our collaborators Tom Solomon, Dylan Bargteil, and Mark Kingsbury.

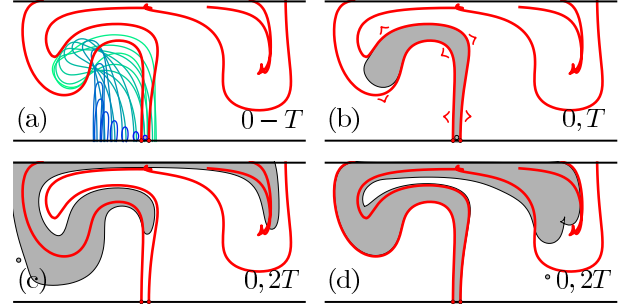


Fig. 2. BIMs in a time-periodic flow. An initial stimulation between the BIMs moves outside the BIMs during the forcing cycle (panel a) but returns by time T (panel b). A stimulation to the left of the BIM pair evolves through one BIM but not the other (panel c), and similarly for a stimulation on the right (panel d).

References

- [1] P. M. Koch and K. A. H. van Leeuwen, *Phys. Rep.* **255**, 289 (1995).
- [2] K. Burke, K. A. Mitchell, B. Wyker, S. Ye, and F. B. Dunning, *Phys. Rev. Lett.* **107**, 113002 (2011).
- [3] C. Jaffe, S. D. Ross, M. W. Lo, J. Marsden, D. Farrelly, and T. Uzer, *Phys. Rev. Lett.* **89**, 011101 (2002).
- [4] R. S. MacKay, J. D. Meiss, and I. C. Percival, *Physica D* **13**, 55 (1984).
- [5] J. M. Ottino, *The kinematics of mixing: stretching, chaos, and transport* (Cambridge University Press, United Kingdom, 1989).
- [6] V. Rom-Kedar and S. Wiggins, *Archive for Rational Mechanics and Analysis* **109**, 239 (1990).
- [7] S. Wiggins, *Chaotic Transport in Dynamical Systems* (Springer-Verlag, New York, 1992).
- [8] T. Tel, A. de Moura, C. Grebogi, and G. Karolyi, *Phys. Rep.* **413**, 91 (2005).
- [9] Z. Neufeld and E. Hernandez-Garcia, *Chemical and Biological Processes in Fluid Flows: A Dynamical Systems Approach* (Imperial College Press, 2009).
- [10] M. Sandulescu, C. Lopez, E. Hernandez-Garcia, and U. Feudel, *Ecological Complexity* **5**, 228 (2008).
- [11] J. Mahoney, D. Bargteil, M. Kingsbury, K. Mitchell, and T. Solomon, *Euro. Phys. Lett.* **98**, 44005 (2012).
- [12] M. S. Paoletti and T. H. Solomon, *Phys. Rev. E* **72**, 046204 (2005).
- [13] A. Pocheau and F. Harambat, *Phys. Rev. E* **77**, 036304 (2008).
- [14] G. Haller, *Phys. Fluids* **14**, 1851 (2002).
- [15] S. C. Shadden, F. Lekien, and J. E. Marsden, *Physica D* **212**, 271 (2005).

Classification of Streamline Topologies for Structurally Stable Vortex Flows in Multiply Connected Domains

Takashi Sakajo and Tomoo Yokoyama

Department of Mathematics, Hokkaido University, Sapporo Hokkaido 060-0810, Japan & JST CREST
E-mail: sakajo@math.sci.hokudai.ac.jp

ABSTRACT

We consider the inviscid and incompressible flows in two-dimensional multiply connected exterior domains. The instantaneous flow field is described by a Hamiltonian vector field whose Hamiltonian is the stream function and it is characterized topologically by the streamline pattern, which is described as the contour plot of the stream function. The present paper is concerned with topological classification of the structurally stable streamline patterns generated by many vortex points in the presence of the uniform flow. We propose an inductive procedure to determine all possible streamline patterns.

1. Introduction

Let us consider fluid flows generated by many vortex structures in the presence of the uniform flow in two-dimensional multiply connected exterior domains. The flows are regarded as mathematical models for biofluids such as insect flights[1] and vertical descend of rotating plant seeds[2] and for environmental flows in rivers and coastal flows[3,4]. For the sake of theoretical simplicity, we suppose that the fluid is incompressible and inviscid (or slightly viscid), and that the vortex structures are approximated by point vortices. Then the instantaneous flow field in the two-dimensional domain is constructed from the stream function, which is defined as the imaginary part of the complex potential, and it defines a Hamiltonian, i.e. divergence-free, vector field whose Hamiltonian is the stream function. Complex potentials for a given exterior domain are obtained from those for a canonical multiply connected domain with the same multiplicity by constructing the conformal mapping from the canonical one to the target one, since the complex potentials are conformally invariant. Crowdy and Marshall[5] considered multiply connected domains in the unit circle with circular holes, called *circular domains*, for which they gave an explicit formula of the complex potential representing a point vortex. Moreover, Crowdy[6] also has constructed the complex potential representing the uniform flow in multiply connected exterior domains.

In the present talk, we are concerned with global topological structure of the streamline patterns generated by point vortices in the uniform flow. Classification of the streamline patterns has been investigated in the unbounded plane without boundary by Aref and Brøns[7] and on the sphere without boundary by Kidambi and Newton[8]. The present study is not only an extension of the preceding studies to the case of multiply connected domains, but it also adds the following new aspects that have not been considered so far. First, the uniform flow is taken into considerations. This is an essential element in the study of biofluids and environmental flows, and it adds a new streamline structure to the flow profile topologically. Second we focus on the structurally stable streamline structure, which is of significance since the stable flow patterns are more probable to be observed in real flow

phenomena. Let us note that even if we restrict our attention to the structurally stable velocity field, we still obtain many non-trivial streamline patterns, since Ma and Wang have shown that homoclinic orbits generated by the divergence-free vector fields on 2D manifold are structurally stable[9]. Third, owing to the existence of boundaries, we need to consider the streamlines separated from the boundaries, which append another structurally stable streamline structure. Thus, the topological classification of the streamline patterns in multiply connected domains provides us with non-trivial new results mathematically that are applicable to many fluid phenomena.

2. Mathematical Method

A mathematical difficulty arises when we need to take the uniform flow into considerations, since the complex potential for the uniform flow has a pole at infinity of the complex plane. The set of streamlines converges to the pole in its vicinity and thus it has a non empty interior point, at which we are unable to define a Hamiltonian vector field. Thus the standard definition of the structural stability for Hamiltonian vector fields cannot be used as it is. In order to eliminate this drawback, we modify the definition of Hamiltonian vector fields on which we introduce an extended notion of the structural stability. Thanks to the modification, we can show that the structurally stable Hamiltonian vector fields in the presence of the uniform flow are identified topologically with homoclinic saddle connections and saddle connections between two points at one boundary.

Our topological classification is based on a constructive procedure. That is to say, starting from some structurally stable initial streamline patterns in genus zero and one, we construct new structurally stable streamline patterns in multiply connected domains with higher genus by inductively adding one genus. Thanks to the procedure, we not only classify the structurally stable streamline patterns systematically, but we also determine all possible streamline patterns for a given genus of multiply connected domain in a combinatorial manner.

3. Results and Discussion

In the present talk, I will explain the procedure to construct the structurally stable streamline patterns generated by point vortices in the presence of the uniform flow in multiply connected domains. In addition, applying the procedure, I will obtain all structurally stable streamline patterns in the multiply connected domain of genus one and two.

In what follows, as the simplest example, I show in Figure 1(a) and (b) the schematic pictures of the streamline pattern, called *the saddle connection diagram*, generated by the structurally stable Hamiltonian vector field in the presence of the uniform flow in the unit disk, which has zero genus. The saddle connection diagrams are obtained by mapping the pole of the complex potential for the uniform flow at infinity to the origin of the unit disk, and the hole to the region exterior to the unit disk with a conformal mapping whose existence is assured by Riemann's mapping theorem. Owing to the existence of the pole singularity corresponding to the uniform flow at the origin, there exist infinite closed streamlines starting from and return to the origin.

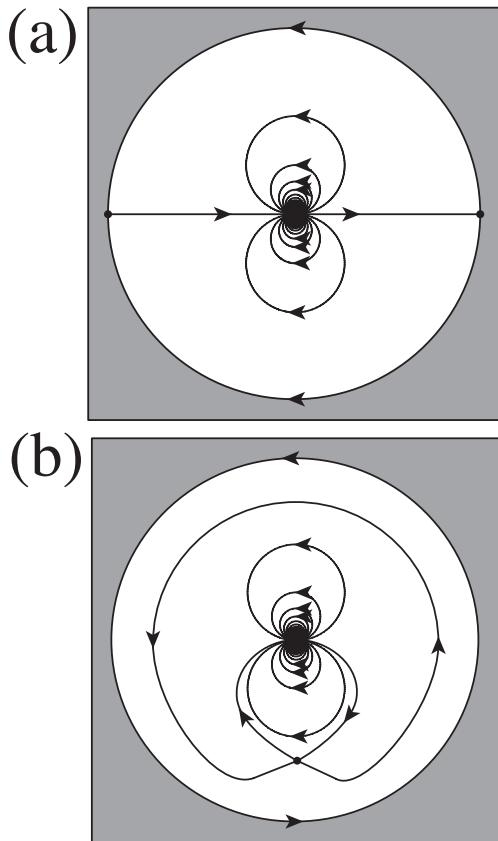


Fig. 1 Two structurally stable streamline patterns in the presence of the uniform flow in the unit disk, i.e. the domain with genus zero.

The difference between these two saddle connection diagrams is explained with using the topological index of the pole, a saddle in the unit disk and a saddle at the boundary, which are 2, -1 and -1/2 respectively. By Poincaré-Hopf theorem, the Euler number of the unit

disk is one and it equals to the sum of the indices of saddles. Hence, the streamline patterns in Figure 1(a) and (b) correspond to $1=2+(-1)$ and $1=2+2 \cdot (-1/2)$ in terms of the equality between the indices. Since the structurally stable Hamiltonian vector field with the uniform flow consists of homoclinic saddle connections and saddle connections between point at the boundary, no other stable patterns exists in the unit disk except for the streamline patterns shown in Figure 1(a) and (b).

References

- [1] M. Iima and T. Yanagita 2001 *Is a two-dimensional butterfly able to fly by symmetric flapping?* J. Phys. Soc. Japan **70**, 939-954.
- [2] D. Lentink, W. B. Dickson, J. L. van Leeuwen and M. H. Dickinson 2009 *Leading edge vortices elevate lift of autorotating plant seeds*, Science **324**, 1348-1440.
- [3] E. R. Johnson and N. R. McDonald 2004 *The motion of a vortex near two circular cylinders*, Proc. Roy. Soc. A **460**, 939-954.
- [4] E. R. Johnson and N. R. McDonald 2005 *Vortices near barriers with multiple gaps*, J. Fluid Mech **531**, 335-358.
- [5] D. G. Crowdy and J. S. Marshall 2005 *Analytical formulae for the Kirchhoff-Routh path function in multiply connected domains*, Proc. Roy. Soc. A **461**, 2477-2501.
- [6] D. G. Crowdy 2006 *Calculating the lift on a finite stack of cylindrical aerofoils*, Proc. Roy. Soc. A **462**, 1387-1407.
- [7] H. Aref and M. Brøns 1998 *On stagnation points and streamline topology in vortex flows*, J. Fluid Mech. **370**, 1-27.
- [8] R. Kidambi and P. K. Newton 2000 *Streamline topologies for integrable vortex motion on a sphere*, Physica D **140**, 95-125.
- [9] T. Ma and S. Wang 2005 *Geometric theory of incompressible flows with applications to fluid dynamics*, Mathematical Surveys and Monographs **119**, American Mathematical Society, Providence RI.

Bubbles and Flux: Scalar Transport Around Coherent Structures in Laminar Flow

Guy Metcalfe¹, Marc Horner², J.M. Ottino³

¹CSIRO Materials Science & Engineering, Box 56, Highett Vic 3190 AUSTRALIA

²ANSYS Inc., Evanston IL 60201 USA

³McCormick School of Engineering & Applied Science, Northwestern University, Evanston IL 60201 USA

guy.metcalfe@csiro.au

Abstract

Coherent flow structures, arising from natural vortical features or through interaction of the fluid with boundaries, are ubiquitous, and their presence greatly impacts local fluxes of heat and mass (scalar fields). Here we give an example of mass flux mediated by coherent structures in a chaotic flow. In cavities arising in aneurysms or stents, measured mass flux into flow bubbles shows a surprising minimum at a bifurcation from one bubble to two bubbles in the cavity as the cavity aspect ratio increases. We use a novel form of symmetric bifurcation analysis to predict the flux up to an overall constant.

1 Introduction

Vortical features (tubes or bubbles) in steady, laminar flows are material lines of the dynamical system describing fluid particle orbits. Material lines are transport barriers in the flow [1, 2]. Figure 1a–c shows several examples of wall-attached material lines, labeled Ψ_s , that in steady flow prevent transport between a free stream and flow cells in a cavity.

When the free stream flow is periodically perturbed, the material lines stretch and fold to periodically form lobes that transport parcels of material in to and out of the cavities. In an earlier paper we measured this cavity material flux as a function of the amplitude, frequency and type of perturbation [3]. Here we address the effect of cavity geometry at a fixed perturbation. In particular we examine the flux ϕ as a function of the cavity aspect ratio $A = W/H$, W and H respectively the cavity width and height.

For $A \approx 1$ there is one cell in the cavity (figure 1a), while for A large there are two cells (figure 1c) at the forward- and backward-facing steps of the cavity. At some intermediate A there is a flow bifurcation. It is fairly clear what happens to ϕ in the limits of both very small and very large A . As A goes to zero, ϕ also goes to zero: as the cavity disappears, there is less and less flux. On the other hand, as A becomes large, the cells on the forward- and backward-facing steps go further apart and have independent, constant fluxes: ϕ goes to some constant value as A becomes large. For A in the mesoscale range what happens to ϕ ?

2 Bubbles and Flux

It is somewhat simpler to understand the transport behavior by imagining that the cavity wall has been pulled flat. This conformal transformation turns cells in the cavity into “bubbles” attached to a flat wall. Figure 1d shows $A \approx 1$ where there is a single cell/bubble. Fig-

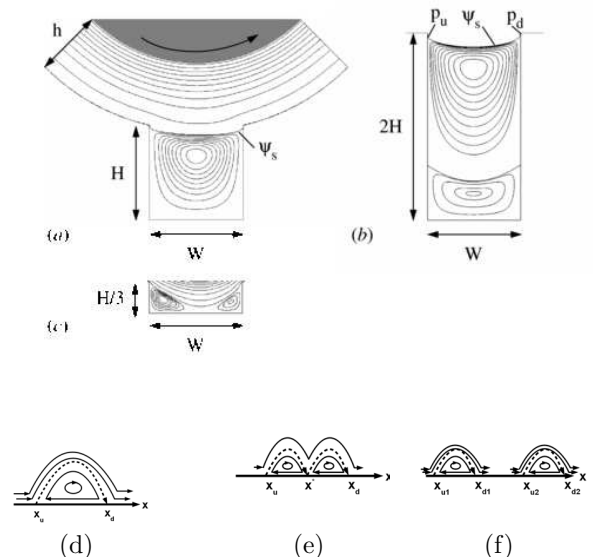


Figure 1: (top) Cavity flows of various aspect ratios. (c) As the cavity width increases, a single roll becomes two. (d–f) The cavity “pulled” flat and the rolls as bubbles. Dashed lines show the streamline separating the cavity from the channel.

ure 1f shows A large where there are two bubbles. Figure 1e shows intermediate A where the bifurcation has just occurred and two bubbles touch at the point labeled x^* .

Exchange of material between the cavity and channel occurs via the lobe mechanism only at the down-stream attachment critical points of the separatrices (dashed lines in figure 1d–f), the material lines that in steady flow divide the cavity’s primary cell flows from the channel flow. At every critical point where the velocity goes from positive to negative as x increases, that critical point is stable. Conversely every critical point where the velocity goes from negative to positive as x increases is unstable. All upstream attachment points in cavity

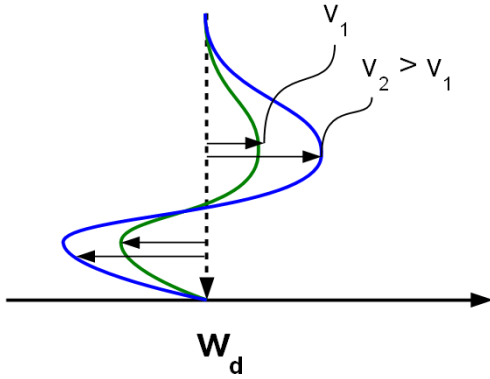


Figure 2: Separating manifold forming lobes at the unstable downstream attachment point w_d . Lobe area per cycle is proportional to the local velocity. A local minimum occurs at the bifurcation point.

flows are stable, and all downstream attachment points are unstable. Lobes form at unstable points. The point x^* is special in that precisely at the bifurcation, x^* is neutrally stable. Past the bifurcation two new critical points are born that complete the splitting into two cells.

The above physical description of cavity flow stability and transition can be made explicit through an equation describing the velocity around the the critical points. Since we are interested in describing events around the bifurcation from one bubble to two, we define a new space coordinate $w = x - x^*$ to shift the origin of the coordinate axis. Further we define the bifurcation parameter $\mu = A - A_c$, where A_c is the critical aspect ratio of the bifurcation. A_c will come from our measurements. With these preliminaries we can write the symmetric normal form equation [4] for the cavity bubble bifurcation as

$$\dot{w} = \mu - \left(\frac{1}{2}A_c\right)^2 w^2 + (1 - \mu)^2 w^4, \quad (1)$$

which is valid only near the bifurcation. For a given value of μ the critical attachment points are located at the roots of equation 1.

Consider figure 2a which shows as a dotted line the separating manifold at the unstable downstream attachment point w_d . In unsteady flow for $A < A_c$ this point is the location of all the cavity transport and is the location for the bulk of the transport even for A above A_c . As a lobe forms near w_d , the local velocity determines how much the manifold is pulled in the direction of the arrows during one cycle of the unsteady flow. If the local velocity is larger (c.f. the curve labeled v_2 compared to the curve labeled v_1), then the lobe area per cycle will be larger. As the flux is given by the lobe area times the frequency of lobe formation, for a constant frequency of lobe formation ϕ is proportional to the velocity gradient at w_d , which is given by the derivative of equation 1 evaluated at w_d . This slope $f(w_d)$ is a function of μ .

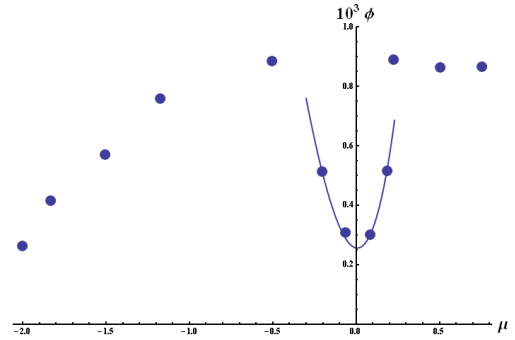


Figure 3: Experimental flux measurements as a function of reduced aspect ratio $\mu = A - A_c$, where $A_c = 2.5$. The predicted flux minimum occurs at $\mu = 0$, and the solid line is from theory as described in the text.

Figure 3 shows experimental data for ϕ as a function of μ ; $A_c = 2.5$ [5]. As expected, as cavity width goes to zero ($\mu \ll 0$), the flux tends to zero, and, as cavity width becomes very large ($\mu \gg 0$), the flux goes to a constant value. However, there is a flux dip at the bifurcation. The solid line is a fit of $\phi = C_0 + f(w_d)$ to the data points in the interval $\mu = \pm 0.2$, with $C_0 = -3.65$. Equation 1 predicts the flux dip at the bifurcation.

3 Conclusions and Discussion

Measurements of material flux into wall-attached cavity bubbles show a surprising dip at the bifurcation from one bubble to two as the cavity aspect ratio increases; away from the bifurcation flux behaves as expected. A novel use of normal form symmetric bifurcation analysis is able to predict the measured flux up to an overall constant. Moreover, the analysis has physical meaning in terms of changes to the local velocity gradient at the downstream attachment point.

References

- [1] Guy Metcalfe. *Complex Physical, Biophysical, and Econophysical Systems*, volume 9 of *Lecture Notes in Complex Systems*, chapter Applied Fluid Chaos: Designing Advection with Periodically Reoriented Flows for Micro to Geophysical Mixing and Transport Enhancement, pages 189–242. World Scientific, 2010.
- [2] Guy Metcalfe, M.F.M. Speetjens, D.R. Lester, and H.J.H. Clercx. *Advances in Applied Mechanics*, chapter Beyond Passive: Chaotic Transport in Stirred Fluids, pages 109–188. Academic Press, 2012. doi:10.1016/B978-0-12-380876-9.00004-5.
- [3] M. Horner, Guy Metcalfe, S. Wiggins, and J.M. Ottino. Transport mechanisms in open cavities: Effects of transient and periodic boundary flows. *Journal of Fluid Mechanics*, 452:199–229, 2002.
- [4] M. Golubitsky and D.G. Schaeffer. *Singularities and Groups in Bifurcation Theory.*, volume 1. Springer, 1985.
- [5] M. Horner, Guy Metcalfe, and J.M. Ottino. Convection-enhanced transport into open cavities. In preparation for *Annals of Biomedical Engineering*, 2012.

Global Bifurcations and the Onset of Turbulence in Shear Flows

Authors names: Lennaert van Veen¹, Genta Kawahara²

¹University of Ontario Institute of Technology, 2000 Simcoe Street North, L1H7K4 Oshawa, Ontario, Canada

²Graduate School of Engineering Science, Osaka University, 1-3 Machikaneyama, Toyonaka, Osaka 560-8531, Japan
E-mail of corresponding author: lennaert.vanveen@uoit.ca

ABSTRACT

Plane Couette flow is laminar at low Reynolds numbers and turbulent at high Reynolds numbers, but the laminar state is always asymptotically stable. The *edge state hypothesis* asserts that this transition is regulated by the invariant manifolds of simple invariant solutions. One possible edge state is a periodic solution with small energy dissipation, and its stable and unstable manifolds intersect in a homoclinic tangle. The presence of this tangle may explain irregular bursting. We search for the lowest Reynolds number for which the tangle exists and investigate its relation to transition Reynolds numbers observed in experiments and simulations.

1. Introduction

Recent studies have shown that in transitional wall-bounded shear flows without linear instability of the laminar state the boundary between laminar and turbulent flows can be identified in phase space as the edge of chaos [1]. A particularly interesting situation arises when the laminar-turbulent boundary is formed by the stable manifold of a traveling wave or periodic solution, which is then called an “edge state.” Edge states have now been computed for flow in channels as well as pipes, with various numerical schemes and resolutions, and there is some consensus that they are a robust feature of subcritical shear flow.

Here we study the two-dimensional unstable manifold of an edge-state periodic solution [2, 3] to the incompressible Navier–Stokes equation in plane Couette flow, and find that it contains two orbits which return to the edge state along its stable manifold. We conjecture, that these homoclinic orbits collide and disappear in a tangency bifurcation at lower Reynolds number. Away from this bifurcation, these orbits are transversal intersections of the stable and unstable manifolds. Thus, their presence generically implies the existence of an intricate tangle of these manifolds through the classical Smale–Birkhoff theorem. This, in turn, may explain the observed irregular turbulent bursting.

2. Computational method

We consider plane Couette flow at a Reynolds number of $Re=400$ in the minimal flow unit of dimensions $L_x \times 2h \times L_z = (1.755\pi, 1.2\pi)$ [3], where Re is based on half the velocity difference between the two walls, U , and half the wall separation, h . We used resolutions of $16 \times 33 \times 16$ up to $32 \times 65 \times 32$ grid points in the streamwise, wall-normal and spanwise directions, respectively, and checked that the behaviour is qualitatively the same.

The edge state in this computational domain is a time-periodic variation, which shows weak, meandering streamwise streaks [2]. This gentle periodic orbit has a single unstable Floquet multiplier and thus its unstable manifold has dimension two and its stable manifold has codimension one in phase space. The stable manifold can thus separate the phase space into two parts, one of

which is thought to be the domain of attraction of the laminar flow.

A piece of the two-dimensional unstable manifold can be computed by Newton–Krylov continuation of orbit segments. A boundary value problem is set up which specifies that the initial point of the segment must lie in the linear approximation of the manifold, whereas the final point satisfies a scalar condition. This boundary value problem is under-determined by a single degree of freedom and thus we can compute a family of orbit segments by arclength continuation [4].

Since a connecting orbit separates the manifold into two components, consecutive orbit segments converge to a connecting orbit during continuations with an appropriate right boundary condition. Each such connecting orbit is generically a transversal intersection of the stable and unstable manifolds of the edge state.

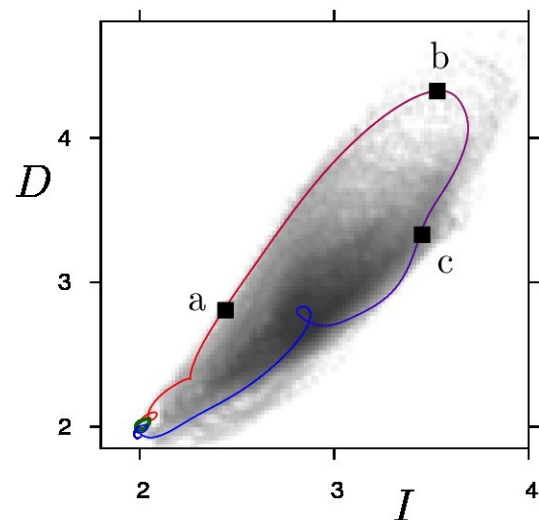


Fig. 1 Projection of the homoclinic orbit in plane Couette flow at $Re=400$ onto the energy input rate, I , and the dissipation rate, D , normalised by their value in laminar flow [1]. The piece of orbit leaving the gentle periodic solution is shown in red and the one approaching it in blue. In the background, the probability density function of transient turbulence is shown in gray scale. The labels a–c correspond to the snapshots in Fig. 2.

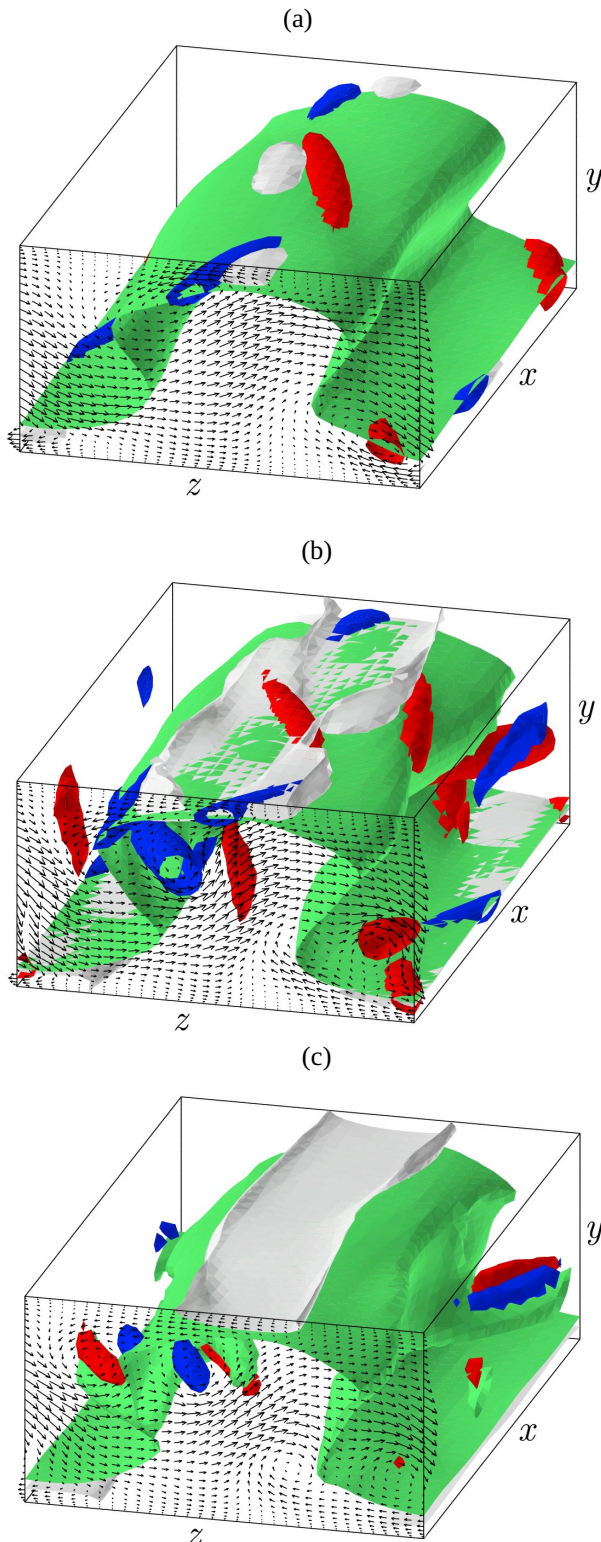


Fig 2. Visualizations of flow structures in one periodic box at three phases on the homoclinic orbit at $Re=400$, labeled as in Fig. 1. Green corrugated isosurfaces of the null streamwise velocity represent a streamwise streak. Shown in red and blue are isosurfaces of the Laplacian of the pressure, which denote the vortex tubes of the positive and negative streamwise vorticity. Gray isosurfaces show the isosurface of local energy dissipation rate at 20 times the value in laminar flow.

In Fig. 1 such a homoclinic orbit is shown. It makes a large excursion during which the energy dissipation rate reaches more than twice the mean value in periodic motion and four times that at the laminar equilibrium. In the dissipative phase of this bursting cycle, at the valley and the crest of the streaks small quasi-streamwise vortices are formed and move rapidly in the spanwise direction, and the larger part of the energy dissipation takes place there. In fact, about 40% of the energy dissipation takes place in the region denoted by gray isosurfaces in Fig. 2, which occupies only 5% of the spatial domain. Similar flow structures are also observed during bursting in a turbulent state, and they are very different from the near-wall regeneration cycle [2, 3].

3. Discussion

The existence of orbits homoclinic to the edge state implies that the geometry of the laminar-turbulent boundary is rather complex. At the same time, it generically implies the existence of infinitely many unstable periodic orbits which correspond to flows with arbitrarily many, arbitrarily long, near laminarization events. It is natural then to think of turbulent shear flow as governed by a large chaotic attractor which comprises both unstable periodic orbits in the turbulent regime, which reproduce the regeneration cycle, and ones which reproduce near-laminarization and bursting events.

In ongoing work, we search for the lowest Re for which this attractor exists, hypothesizing that the onset Re is set by a tangency bifurcation of two homoclinic orbits. Preliminary results indicate that the homoclinic connections persist at least down to $Re=260$. Interestingly, chaotic sets were recently uncovered in plane Couette flow through the bifurcation analysis of periodic orbits around $Re=200$ [6]. The appearance of homoclinic chaos and these chaotic sets may be related.

Another possibility is that the homoclinic orbits persist to the point where the periodic orbit undergoes a fold bifurcation. Several global bifurcations might then take place that could explain the subcritical transition.

The continuation of the homoclinic orbits in Re is not straightforward, since we cannot compute all stable and unstable perturbations to the periodic orbit. A possible alternative would be to solve the adjoint equations as proposed by Pringle and Kerswell [7].

References

- [1] B. Eckhardt, *et al.*, *Philos. T. R. Soc. A* **366**, pp. 1297–1315, 2008.
- [2] G. Kawahara and S. Kida, *J. Fluid Mech.* **449**, pp. 291–300, 2001.
- [3] J. M. Hamilton *et al.*, *J. Fluid Mech.* **287**, pp. 317–348, 1995.
- [4] L. van Veen, G. Kawahara and A. Matsumura, *SIAM J. Sci. Comp.* **33**, pp. 25–44, 2011.
- [5] L. van Veen and G. Kawahara, *Phys. Rev. Lett.* **107**, pp. 114501, 2011.
- [6] T. Kreilos and B. Eckhardt, *arXiv:1205.0347*.
- [7] C. C. T. Pringle and R. R. Kerswell, *Phys. Rev. Lett.* **105**, pp. 154502, 2012.

Intramolecular Energy Flow and the Mechanisms for Collective Motions of Complex Molecular Systems

Tomohiro Yanao¹, Yurie Oka¹, and Wang Sang Koon²

¹Department of Applied Mechanics and Aerospace Engineering, Waseda University, Tokyo 169-8555, Japan

²Control and Dynamical Systems, California Institute of Technology, MC107-81, Pasadena, CA 91125, USA

E-mail: yanao@waseda.jp

ABSTRACT

This study explores the mechanisms for structural transitions of atomic clusters from the viewpoint of intramolecular energy flow. We apply the hyperspherical coordinates and associated mode analysis to study the directionality of energy flow among internal vibrational modes of atomic clusters. Equations of motion for the hyperspherical coordinates reveal a hierarchical nature of the coupling among slow modes and fast modes. It is shown that slow-scale variables called gyration radii accumulate energy upon the onset of structural transitions of the clusters. Mechanisms for the accumulation of energy in the gyration radii are highlighted.

1. Introduction

Mechanisms for large-amplitude collective motions of complex molecular systems, such as chemical reactions and structural phase transitions, have been the central issues in current chemical physics and biophysics. Information on energy flow over molecular vibrational modes is crucial for the understanding and control of collective motions of molecules.

While the conventional normal-mode analysis is useful for the study of small-amplitude vibrations of molecules, its applicability to large-amplitude motions may be limited. This is because the coupling among vibrational as well as rotational modes can be intensive at the energy (or temperature) levels where collective motions set in, and the dynamics of molecules can be highly nonlinear.

In the present study, we examine a novel method of mode analysis for the study of the mechanisms for structural transitions of atomic clusters. This method is based on the hyperspherical coordinates [1,2] and the framework of gauge theory for the separation of rotations and vibrations of n -body systems [3]. This method takes into account the coupling between molecular vibrations and rotations in an appropriate manner and reveals a hierarchical nature of the coupling between slow modes and fast modes of molecules.

2. Method: Hyperspherical-Mode Analysis

The hyperspherical coordinates for internal (shape) dynamics of an n -atom system consist of three gyration radii, a_1, a_2, a_3 ($a_1 \geq a_2 \geq a_3 \geq 0$), and $3n-9$ hyperangles, $\varphi_1, \dots, \varphi_{3n-9}$. The three gyration radii characterize inflation and contraction of the overall mass distribution of the system along the three instantaneous principal axes. The $3n-9$ hyperangular degrees of freedom are further classified into three twisting modes and $3n-12$ shearing modes [4]. Angular velocities of the twisting modes and those of the shearing modes are denoted as ω_{ij} and γ_{ik} respectively.

Internal kinetic energy of an n -atom system is given compactly as

$$K = \sum_{i=1}^3 \frac{\dot{a}_i^2}{2} + \sum_{ij=12,23,31} \frac{(a_i^2 - a_j^2)^2}{2(a_i^2 + a_j^2)} \omega_{ij}^2 + \sum_{i=1}^3 \sum_{k=4}^{n-1} \frac{a_i^2 \gamma_{ik}^2}{2}, \quad (1)$$

where the terms containing \dot{a}_i^2 represent kinetic energies of gyration radii, and those containing ω_{ij}^2 or γ_{ij}^2 represent kinetic energies of the twisting modes or the shearing modes respectively. Lagrangian of the n -atom system with zero total angular momentum is given by $L = K - V$, where V is the potential energy of the system. The resulting equations of motion for the three gyration radii are

$$\frac{d^2 a_i}{dt^2} = \Gamma_{ij} \omega_{ij}^2 + \Gamma_{ik} \omega_{ik}^2 + a_i \sum_{m=4}^{n-1} \gamma_{im}^2 - \frac{\partial V}{\partial a_i}, \quad (2)$$

where $(i, j, k) = (1, 2, 3), (2, 3, 1), (3, 1, 2)$, $\omega_{ij} = -\omega_{ji}$, and

$$\Gamma_{ij} = \frac{a_i(a_i^2 + 3a_j^2)(a_i^2 - a_j^2)}{(a_i^2 + a_j^2)^2} \quad (i, j = 1, 2, 3, i \neq j). \quad (3)$$

In Eq. (2), the terms containing the factor ω_{ij}^2 or ω_{ik}^2 represent the coupling between gyration radii and twisting modes. These terms have the physical meaning of “twist centrifugal force” that originates from twisting of the system. The terms containing the factor γ_{im}^2 represent the coupling between gyration radii and the shearing modes, having the physical meaning of “shear centrifugal force”. These centrifugal forces are internal ones, arising even in the systems with zero total angular momentum. Equations of motion for the twisting modes and the shearing modes are written in the form,

$$\frac{dl_\alpha}{dt} + c_{\alpha\beta}^\gamma \omega^\beta l_\gamma = -X_\alpha^\mu \frac{\partial V}{\partial \varphi^\mu}, \quad (4)$$

where l_α represents momentum conjugate to ω^α , which is a simplified notation of ω_{ij} or γ_{ik} . In Eq. (4), Einstein convention for summation is adopted for the Greek indices from 1 to $3n-9$. Both $c_{\alpha\beta}^\gamma$ and X_α^μ are dependent on the hyperangles φ^μ . Eqs. (1)-(4) constitute the basis for the study of intramolecular energy flow and mode coupling.

3. Intramolecular Energy Flow and Mode Coupling

We apply the hyperspherical-mode analysis to the structural transition dynamics of Lennard-Jones (LJ) clusters as a prototypical model of collective motions of

complex molecular systems. It has been revealed [4] for a six-atom cluster that the gyration radii change slowly and serve as good reaction coordinates, characterizing large-amplitude structural transitions of the cluster. The twisting modes and shearing modes change rapidly and may be regarded as “bath modes”. Thus, activation of the gyration radii is crucial for the onset of structural transitions of a system.

Fig. 1 shows an example of time evolution of the hyperspherical variables introduced above for a dissociation process of a six-atom Lennard-Jones cluster, where the total energy is conserved and the total angular momentum is zero. In this time evolution, the system initially assumes the CTBP structure, as is schematically depicted in (a), and finally dissociates. At the beginning, kinetic energy was selectively assigned in one of the shearing modes, γ_{24} -mode. Since this is a dissociation process, the largest gyration radius a_1 monotonically increases and goes to infinity in the end (see (a)). As expected, a_1 acquires the large amount of energy when a_1 starts to increase (see (c)). These results are indicative of the fact that a_1 is an essential reaction coordinate for dissociation.

Equations of motion, Eqs. (2)-(4), can qualitatively explain the course of energy flow leading to the dissociation of the cluster. The following is a digest: Eq. (2) indicates that when γ_{24} -mode is active, this mode can activate a_2 via the shear centrifugal force. This is indeed the case (see (c) at around $t=0.1$). Once a_2 becomes active, the value of a_2 can approach a_1 (see (a)). One can validate that when two gyration radii, a_i and a_j , are close to each other, the twisting mode ω_{ij} becomes active and a strong twist centrifugal force $f_{ij} \equiv \Gamma_{ij}\omega_{ij}^2$ arises. This is indeed the case as shown in (b) and (c) at around $t=0.2$. The strong twist centrifugal force in turn can activate a_1 as is indicated by Eq. (2), and the system finally dissociates.

Fig. 2 confirms the course of energy flow observed above in a statistical manner, where the time evolutions of the partitioning of kinetic energy are averaged over many dissociating trajectories having initial kinetic energy only in the γ_{24} - or γ_{25} -mode. Since the respective trajectories have different time spans, they were scaled so that they have the same initial and dissociation time, which are denoted as “I” and “D” respectively. It is noteworthy that, at the very instant of the dissociation time, ω_{12} -mode tends to be active, as is consistent with the result of Fig. 1. This indicates that the twist centrifugal force is the major driving force for dissociation of the cluster. This can also be regarded as an extension of Ref. [4], where it was shown that the twist centrifugal force mediates symmetry-breaking and symmetry-restoring transitions of the cluster.

4. Concluding Remarks

We have investigated the directionality of energy flow among the internal modes of atomic clusters. The hyperspherical mode analysis has made it possible to

explain the course of energy flow in terms of the mode coupling and has revealed a driving force for large-amplitude collective motions of atomic clusters. It is an ongoing issue to clarify the directionality of energy flow in a much longer time scale, information on which will be useful for the control of molecular reactions.

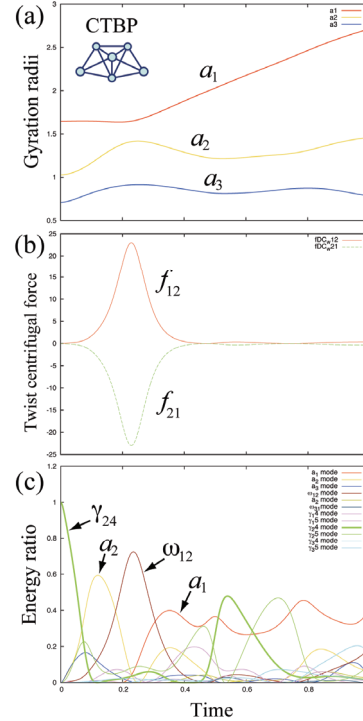


Fig. 1: Time evolution of three gyration radii, (a), that of the components of twist centrifugal force, (b), and that of the partitioning of kinetic energy, (c), in a dissociation process of the six-atom LJ cluster.

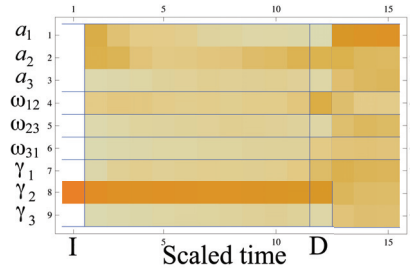


Fig. 2: Averaged and scaled time evolution of the partitioning of kinetic energy among the hyperspherical modes in the dissociation process of the LJ clusters. Darker color represents larger amount of energy.

Acknowledgements

This work has been partially supported by NSF grant (NSF-CMMI-092600) and JSPS grant (23740300).

References

- [1] C. Eckart, Phys. Rev. **46** (1934), 383.
- [2] X. Chapuisat and A. Nauts, Phys. Rev. A **44** (1991), 1328.
- [3] R. G. Littlejohn and M. Reinsch, Rev. Mod. Phys. **69** (1997), 213.
- [4] T. Yanao, W. S. Koon, and J. E. Marsden, J. Chem. Phys. **130** (2009), 144111.

Coherent Structures in Homogeneous Turbulence Sustained by Steady Force

Susumu Goto, Tatsuya Yasuda, and Genta Kawahara
Graduate School of Engineering Science, Osaka University,
1-3 Machikaneyama, Toyonaka, Osaka, 560-8531 Japan
goto@me.es.osaka-u.ac.jp

ABSTRACT

Direct numerical simulation of turbulence sustained by steady external force in a periodic cube is conducted to investigate energy cascade in turbulence. Temporal evolution of the turbulent velocity field in a statistically stationary state is quasi-periodic, and consists of roughly two stages. One is the energy cascading period in which smaller-scale structures are created due to vortex stretching in larger-scale strain fields around the quadruplet of vortex tubes, which are generated directly by the external force in the other period.

1. Introduction

Turbulence is *not* a random velocity field, but it consists of coherent structures. Such coherent structures in turbulence are likely to serve as a foundation for us to understand its sustaining or transition mechanism, its statistics, and its functions such as mixing and diffusion. For example, Fig. 1 shows that there coexists a hierarchy of multiple-scale coherent vortex tubes in turbulence at a high Reynolds number. As shown in [1, 2], these multiple-scale coherent vortical structures are indeed the key ingredient to understand the sustaining mechanism (i.e. the energy cascade process) of such high-Reynolds-number turbulence.

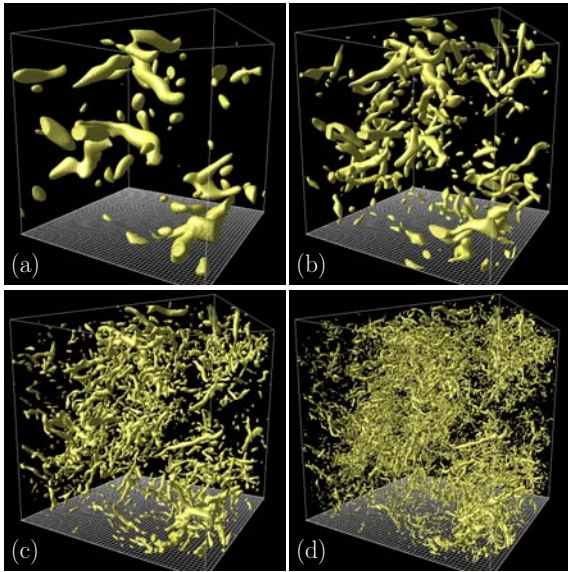


Fig. 1 Multiple-scale vortex tubes in turbulence at Taylor-length Reynolds number $R_\lambda = 550$. (a) Vortices coarse-grained at 680η , (b) 340η , (c) 170η and (d) 84η , where η is the smallest length scale (the Kolmogorov length). See [2] for details.

Here, the term “energy cascade” denotes the process in which large-scale structures (sustained by external force or shearing motions) create smaller ones. Understanding this energy cascade has been a central issue, since the process is the cause of the small-scale universality of turbulence. (More concretely, through the scale-by-scale energy cascade, the large-scale dependence on the boundary condition might well be lost.) The small-scale

universality was originally predicted by Kolmogorov [3], and it states that statistics of any turbulence at small scales are independent of the boundary condition if the Reynolds number is high enough. This similarity has been supported by many experiments; but, despite of its very long history of the notion, the physics of the energy cascade (and the small-scale universality) is not fully understood. So, the main objective of the present paper is to investigate the energy cascade by the help of systematic and precise numerical simulations.

It is very recently that we could numerically simulate developed turbulence in which energy cascade takes place. In such a simulation, we have to simulate turbulence at a sufficiently high Reynolds number with limited numerical resources. It is therefore conventional to simulate turbulence in a periodic cube, since then we do not need to resolve fine structures near solid walls. However, in such a simulation under the periodic boundary condition, we must employ artificial force to sustain turbulence, which is expected to be statistically homogeneous and isotropic. The simplest way might be to use Gaussian random (i.e. statistically homogeneous and isotropic) force. As another strategy [4], for example, the viscous term with a negative viscosity acting only at large scales is also sometimes used. In our previous studies [1, 2], on the other hand, the magnitudes of Fourier modes of velocity field at low wave numbers are kept constants (only their phases evolve) to avoid the turbulence to decay.

As far as we are interested in small-scale statistics and structures, which should be independent of the forcing scheme, detailed nature of artificial large-scale force does not matter. However, the above-mentioned large-scale artificial force is not necessarily appropriate to investigate the energy cascade process, which, or at least the first few stages of which, seem to depend on large-scale structures sustained directly by the external force. So, here, we conduct numerical simulation of turbulence sustained by more *natural* force. It is then revealed that the cascade process becomes clearer than in the turbulence in the previous studies where the largest-scale structures are somewhat random because of the randomness of the external force.

2. Direct numerical simulation

We numerically solve the Navier-Stokes equation,

$$\frac{\partial \mathbf{u}}{\partial t} + \mathbf{u} \cdot \nabla \mathbf{u} = -\frac{1}{\rho} \nabla p + \nu \nabla^2 \mathbf{u} + \mathbf{f}, \quad (1)$$

supplemented with the continuity equation, $\nabla \cdot \mathbf{u} = 0$, for an incompressible fluid under periodic boundary conditions in all the three orthogonal directions. In these governing equations, $\mathbf{u}(\mathbf{x}, t)$ denotes the velocity field, $p(\mathbf{x}, t)$ the pressure field, ρ the constant density, and ν the kinematic viscosity of the simulated fluid. The last term on the right-hand side of (1) stands for the steady external force; which is set, in our numerical simulations, to be such that

$$\nabla \times \mathbf{f}(\mathbf{x}) = C \sin\left(\frac{x}{\mathcal{L}}\right) \sin\left(\frac{y}{\mathcal{L}}\right) \mathbf{e}_z \quad (2)$$

where $\mathbf{x} = (x, y, z)$ is the position vector, C is a constant, \mathbf{e}_z is the unit vector in the z -direction, and \mathcal{L} is the period of the boundary condition. Note that this force leads to a steady velocity field accompanied by a quadruplet of vortex tubes (Fig. 2) when the Reynolds number is sufficiently low.

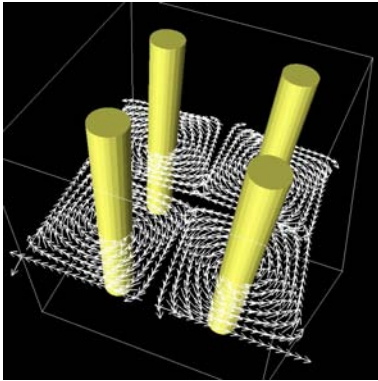


Fig. 2 Steady flow sustained by the steady large-scale force. Iso-surfaces of vorticity magnitude are shown together with the velocity vectors on a cross-section.

The fourth-order Runge-Kutta-Gill method is employed for the temporal integration of (1), and the spatial derivatives in the governing equations are estimated by the Fourier spectral method. Alias errors are removed by the phase-shift technique.

3. Results

We conduct numerical simulations of turbulence at higher Reynolds numbers (with smaller kinematic viscosity ν) starting from the steady state shown in Fig. 2 as the initial condition. After a sufficiently longer duration (typically about $100T_e$) than the turnover time T_e of the largest eddies, turbulence reaches a statistically stationary state. It is interesting that this state is far from a steady state, but it is quasi-periodic and consists of roughly two typical stages. One is the period in which smaller-scale eddies are created from the largest-scale vortices. In other words, this is the energy-cascading stage where the energy possessed by the large-scale vortex tubes transfers to smaller scales to be dissipated. The other stage is the one in which the largest-scale quadruplet eddies are re-generated by the action of the external force.

It is further interesting to observe that, in the former period, smaller-scale eddies are created by the vortex stretching in strongly straining regions around the quadruplet vortex tubes. This is verified that the created smaller-vortex tubes are aligned in the perpendicular direction to the quadruplet (Fig. 3). Note that the quadruplet is regarded as a pair of anti-parallel pairs of vortex

tubes, and that strong strain fields are located around the hyperbolic stagnation points (i.e. stagnation lines in the three-dimensional space) between an pair of tubes. In other words, smaller-scale eddies are created in larger-scale strain fields around the hyperbolic stagnation lines. These observations rather clarify the argument on the energy cascade [1, 2] developed on the basis of numerical simulations of turbulence with unsteady, and random, external force.

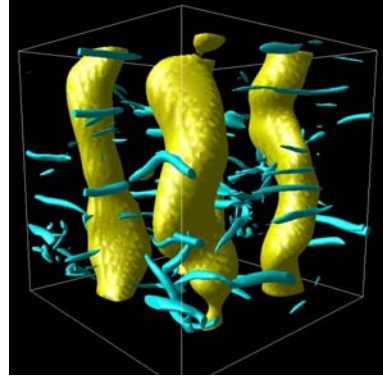


Fig. 3 Creation of smaller-scale vortex tubes (blue objects) around the larger-scale vortex tubes (yellow ones), which are visualized by the iso-surfaces of vorticity magnitude coarse-grained at two different scales. Turbulence at $R_\lambda \approx 100$.

4. Conclusion

Turbulence sustained by the steady external force (2) in a periodic cube is simulated numerically. Focus is on coherent structures in the sustained turbulence. The largest coherent structures are quadruplet vortex tubes shown in Fig. 2, which are directly created by the external force; while the second generation of coherent structures are thinner vortex tubes (Fig. 3), which are aligned in the perpendicular direction to the largest-scale vortex tubes. This is because they are created by vortex stretching rather than vortex breakups due to an instability. This observation of smaller-scale vortex creation caused by vortex stretching in larger-scale strain fields around parent vortex tubes clearly supports the scenario of the energy cascade proposed and discussed in [1, 2]. Further investigation on the third generation, for example, is a near-future target, and will be presented in the conference.

Acknowledgments

This work was partly supported by a Grant-in-Aid for Scientific Research B (No. 24360071) from the Japan Society for the Promotion of Science. The numerical simulations were performed under the auspices of the NIFS Collaboration Research Program (11KNSS023).

References

- [1] S. Goto, *J. Fluid Mech.* **605** (2008) 355.
- [2] S. Goto, *Prog. Theor. Phys. Suppl.* **195** (2012) in press.
- [3] A. N. Kolmogorov, *Dokl. Akad. Nauk SSSR* **30** (1941) 301; English translation in *Proc. R. Soc. London, Ser. A* **434** (1991) 9.
- [4] T. Ishihara, Y. Kaneda, M. Yokokawa, K. Itakura and A. Uno, *J. Fluid Mech.* **592** (2007) 335.

Front Propagation In Fluid Flows: Structure, Transport And Invariant Barriers

John Mahoney and Kevin Mitchell
 University of California, Merced
 School of Natural Sciences
 5200 North Lake Road
 Merced, CA 95343, USA
 jmahoney3@ucmerced.edu

ABSTRACT

Recent experimental and theoretical studies have demonstrated the existence of invariant barriers (BIMs) to fronts propagating in fluid flows. These barriers are similar in many respects to the invariant manifolds important in the theory of passive advection. While some features of these advective manifolds remain, the addition of front propagation dynamics introduces several new properties. We discover the central role played by BIMs in such diverse phenomena as mode-locking, lobe dynamics, and front pinning.

1. Introduction

The notion of fronts propagating in flows is important for a broad range of physical systems. A small sample includes acoustic fronts in a rapidly flowing atmosphere, growth fronts of algae in the ocean, and chemical reaction fronts propagating in a stirred fluid. Our contribution emerges by viewing this front propagation system from a dynamical systems perspective and, most importantly, making use of tools developed for passive advective systems (without fronts). In this particular work, we illustrate the utility of these adapted tools in explaining a variety of phenomena observed in experiments involving chemical fronts.

2. Background theory

The study of advecting fluids, and particularly of Lagrangian chaos in such flows, has firmly established the importance of invariant manifolds in theories of transport and mixing [Wiggins]. It has recently been shown, in theory and experiment, that invariant barriers also exist for fronts propagating in fluids, and that these barriers correspond to invariant manifolds of the dynamics of front elements [Mahoney, Mitchell]; A front element is an infinitesimal oriented line element along a front.

These new invariant manifolds, what we call burning invariant manifolds (BIMs) because of the interpretation of front propagation as a flame spreading, are co-dimension 2 manifolds in a 3D phase space. That these manifolds serve as barriers to front propagation follows after understanding that fronts may only dynamically cross other fronts in particular ways, and that BIMs are a special class of front.

Just as fluid advection can be analyzed in terms of stagnation points and their attached invariant manifolds, our hybrid system of flow and fronts admits a similar analysis in terms of burning fixed points and their attached BIMs.

3. Experimental system

A series of experiments [Solomon] has verified the presence and function of BIMs. These experiments involve the progress of an autocatalytic chemical

reaction ongoing in one of several two-dimensional fluid flows. These include a periodically forced linear array of alternating vortices (Fig. 1) and a two-dimensional disordered array of vortices in the presence of a “wind”. These two flows were used to produce the phenomena of mode-locking, lobe-dynamics, and front pinning.

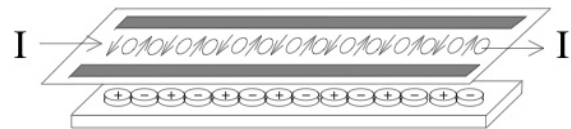


Fig. 1. Alternating vortex flow is induced in a thin fluid layer.

4. Mode-locking

We observe mode-locking using the periodically forced vortex array [Abel, Paoletti]. The chemical front proceeds down the 1D channel while twisting under the influence of the vortices. We observe that the front pattern may reappear an integer N forcing periods later and M vortex units down the channel. This behavior is defined as (N, M) mode-locking. By varying parameters, a variety of these types may be obtained.

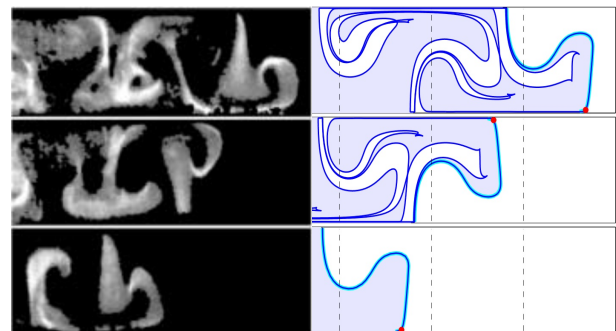


Fig. 2. Type (1,2) mode-locking. (left) experiment. (right) simulation. Burning fixed point on front generates BIM which is the front.

The key result here is that the mode-locking behavior implies that a burning fixed point exists on this front, and that the attached BIM is itself the mode-locking front. The mode-locking front is not fixed in the

laboratory; the burning fixed point and BIM we seek emerge when the front element dynamics is viewed in a comoving frame.

One advantage of the BIM perspective of mode-locking is that we can study the passage between different mode-locking types in terms of bifurcations in the BIM geometry.

5. Lobe dynamics

Lobe dynamics is a theory important for understanding transport in systems with Lagrangian chaos [Wiggins]. As the lobes used in describing advective systems are regions delimited by advective invariant manifolds, it is natural to ask whether BIMs also bound regions which effectively describe the transport of fronts.

We focus on the central process in lobe dynamics--the turnstile mechanism [MacKay]. Here we define the lobes involved in the turnstile and show how a set-based definition leads, as desired, to regions bounded by BIMs (Fig. 3). Thus, the BIMs underlie the primary mechanism of front transport.

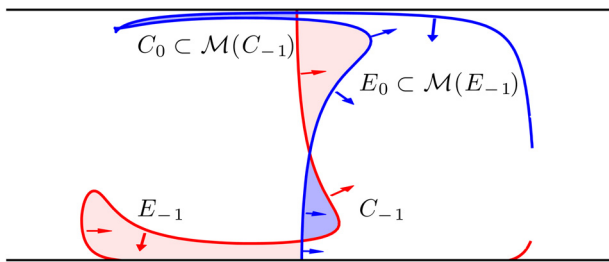


Fig. 3. Front propagation turnstile mechanism. Lobes E_{-1} and C_{-1} map forward into E_0 and C_0 . Front propagation is not area preserving and neither is the turnstile.

This modified turnstile is relevant to questions of front control. Here is a model control problem where the objective is to prevent an impinging front from entering a protected region (Fig. 4). While several control protocols suggest themselves, it is shown that the lobe-based protocol is optimal in requiring the minimal amount of front suppression agent.

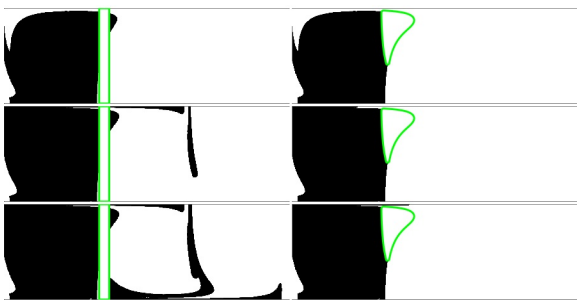


Fig. 4. A reaction front impinges from the left in periodically forced vortex array. Two control protocols are compared. The naïve rectangle approach is outperformed by the lobe-based protocol of equal area.

6. Front pinning

We now turn to the other flow of interest – the disordered 2D array of vortices with an added fluid wind. As the wind speed is increased, the upwind propagation of the front is slowed. Beyond a critical value of the wind, the front no longer proceeds upwind, and notably is not necessarily blown downstream either. The front may remain pinned to structures in the fluid flow [Schwartz].

Previously, the fluid vortices were understood as being responsible for this pinning. Now we see that the relevant structures are the burning fixed points which lie near advective stagnation points located between the vortices. These burning fixed points generate BIMs which again are the pinning fronts.

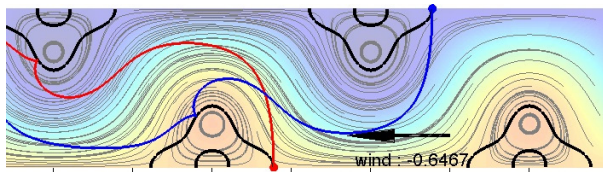


Fig. 5. In a vortex array with wind (to the left), fronts pin to the two BIMs (red, blue).

7. Concluding remarks

These cases illustrate the extent to which the BIM concept permeates the study of fronts in fluid flows, thus unifying a set of diverse phenomena.

Preliminary evidence suggests that this formalism may be generalized to describe front propagation structures in time aperiodic flows. Much attention has been given to propagation through random flows and porous media. The success of this method in mesoscale flows bodes well for its application in more statistical settings.

8. Acknowledgements

This work was supported by the US National Science Foundation under grant PHY-0748828. The authors gratefully acknowledge both extensive discussions with and experimental results from Tom Solomon, Mark Kingsbury and Dylan Bargteil.

References

- [Wiggins] S. Wiggins, Chaotic Transport in Dynamical Systems.
- [Mahoney] J. Mahoney, et al., EPL, **98** (2012), 44005.
- [Mitchell] K. Mitchell, et al., submitted (2012).
- [Solomon] J. P. Gollub, et al., Physica Scripta, **40**, (1989).
- [Abel] M. Abel, PRE, **64**, (2001), 046347.
- [Paoletti] M. S. Paoletti, et al., PRE, **72**, (2005), 046204.
- [MacKay] R. S. MacKay, et al., Physica D, **13**, (1984).
- [Schwartz] M. E. Schwartz, et al., PRL, **100** (2008), 028302.

OS3: Hybrid Rockets: A Quest for
Next-Generation
Environmentally-Compatible
Space Transportation

Scalable Regression Rate Expressions for Hybrid Rockets

Arif Karabeyoglu

Space Propulsion Group Inc.
Sunnyvale, CA
arif@spg-corp.com

Abstract

The fuel regression rate expressions reported in the hybrid literature often depend explicitly on the physical dimensions of the system such as the fuel port diameter. Typically, when these dimensional formulas are applied to systems with significantly different scales, they produce grossly inaccurate results. This paper addresses the development of scalable space-time averaged regression rate formulas for hybrid rockets. The derivation process hinges on the assumption that the local instantaneous regression rate is a function of the local mass flux and the axial port distance in the power law format as predicted by the classical theory developed by Marxman.

1. Introduction

As discussed extensively in the literature, hybrid rockets offer many advantages over conventional liquid and solid systems. One of the most important advantages is the hybrid's inherent safety, which is a direct consequence of the storage of the fuel and oxidizer remotely from each other in different phases (one in liquid, the other in solid, making it virtually impossible for them to mix and react spontaneously). The two-phase propellant system also forces hybrids to operate in a heterogeneous, boundary layer, combustion configuration. Typically, the hybrid combustion process is diffusion limited, making the fuel regression rate primarily mass flux dependent. In practice, the accurate ballistic design of a hybrid system requires the full understanding of the dependence of the regression rate on the mass flux and other key operational parameters such as pressure and grain length. This functional relation is commonly referred to as the "regression rate law" and each propellant combination has its unique regression rate formula due to the differences in the thermophysical and thermochemical properties of the components of the propellant. Because of the lack of fidelity in the combustion models presently available for hybrid rockets, an accurate theoretical determination of the regression rate law based on the fundamental properties of the propellants is still not possible. Even though there are theories that can predict the form of the regression rate dependency on system properties, none of these prediction tools can accurately estimate the regression rate behavior of a system in a manner that is required in the internal ballistic design process.

Consequently, in practice, the regression rate law for each hybrid propellant system of interest must be constructed from extensive motor testing. The interpretation of the motor data and the reduction to a scalable regression rate law is a difficult

process. The methods of data reduction are not unique due to the nonlinear nature of the problem and, for certain test conditions, each method may yield significantly different results. In many reports and papers, the technique used in the data reduction process is not adequately discussed, decreasing the value of the information. In certain cases, the regression rate is written in terms of dimensional parameters other than the oxidizer or total mass flux, resulting in formulas that are accurate for interpolation purposes but potentially highly problematic when they are used to extrapolate to other scales. One example to such a scaling formula is given in [1], which assumes a regression rate law that shows an explicit and strong dependency on the average port diameter.

$$\bar{r} = 0.065 G_{ox}^{0.77} \left[\frac{\bar{D}}{3} \right]^{0.71}$$

Here G_{ox} is the average oxidizer mass flux, \bar{D} is the average port diameter and \bar{r} is the space-time averaged regression rate. When this formula is used to predict the regression rate of a system 10 times larger in scale, one estimates a regression rate approximately five times higher. Clearly, such an increase in regression rate with motor scale is highly unrealistic.

Our goal in this study is to develop space-time averaged regression rate expressions from the classical local instantaneous regression rate equation in the power law format. The mass flux and axial distance exponents will be kept as free parameters to preserve the generality in the derived formulas. Details of the derivations are discussed in reference 2.

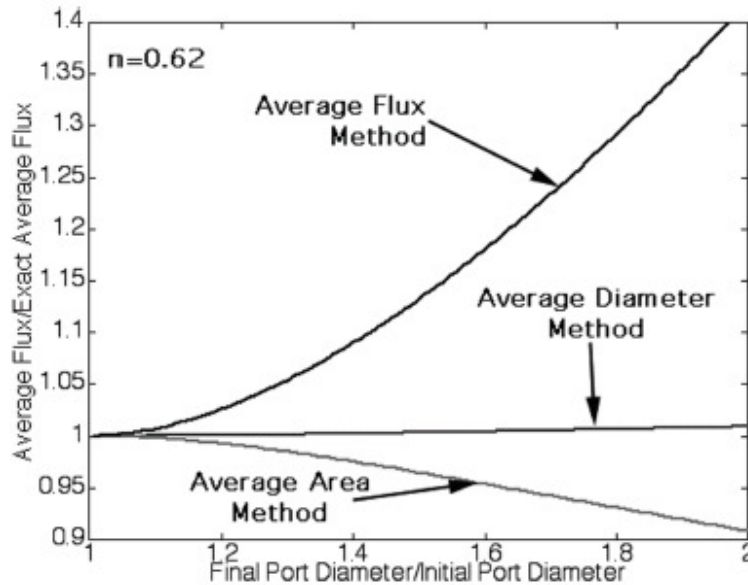


Fig. 1 Error induced by various averaging methods as a function of port diameter ratio (Data from Ref. 2)

2. Conclusions

The following conclusions can be drawn from this study.

1) Nondimensional formulas for space-averaging have been derived for the separate cases of oxidizer and total mass flux dependent regression rate laws. The correction term which only depends on the motor O/F is determined to be more pronounced for systems operating under fuel rich conditions. The case of oxidizer mass flux requires a slightly higher correction compared to the total mass flux formula. The O/F correction reduced the scatter in data for the paraffin/GOX motors tested at Stanford and NASA Ames facilities. The effect of correction on the JIRAD data (HTPB/GOX propellant system) was not conclusive, possibly due to the narrow range of operational parameters for this particular data set. At this point, we would like to emphasize that none of the assumptions introduced in the derivations are related to the type or properties of the selected fuel. Thus, we fully expect that the results are universal for any inert hybrid fuel system.

2) Various time-averaging techniques for the mass flux have been evaluated based on their relative accuracies compared to the exact expression. It has been determined that the diameter-based averaging method is by far the most accurate technique (see Figure 1). It is important that each separate method selected to reduce the oxidizer mass flux data results in a significantly different regression rate law even for the same set of motor data. Therefore, the method used in the analysis must be explicitly stated in reporting the regression rate/mass flux data.

3) The systematic and random measurement errors for the regression rate and the oxidizer mass flux have been investigated. Several equations to predict both kinds of error

have been derived. It has been determined that the most important variable that affects the combined error is the final to initial port diameter of the test articles. There exists an optimal value for the diameter ratio that minimizes the combined error in the regression rate and the oxidizer mass flux. For the example considered in this paper, the optimal ratio is determined to be around 2.0.

4) Finally, the partial differential equations that govern the space-time coupled dynamics of the port geometry in the simple case of a circular port have been derived. An exact solution for the special case of $n=0.5$ has been developed. For all other mass flux exponents, an efficient and accurate numerical solution method has been suggested. The method has been applied to the case of paraffin-based fuels burned with GOX. The results indicated a very weak length dependency in the regression rate law. This observation is consistent with the experimental results which showed no measurable change in the regression rate as the motor scale has been increased by a factor of 3.0.

References

- [1] Boardman, T. A., Carpenter, R. L., Goldberg, B. E., and Shaeffer, C. W., AIAA/SAE/ASME/ ASEE 29th Joint Propulsion Conference and Exhibit, Monterey, CA, AIAA Paper No. 93-2552, June 1993.
- [2] Karabeyoglu M.A., Cantwell B. J. and Zilliac, G., *Jour. Prop. Power*, **Vol. 23**, **No. 4**, [2007].p 737.

Scaling In Hybrid Rocket Motors

C. Palani Kumar, Amit Kumar
Dept. of Aerospace Engineering, IIT Madras, Chennai, India - 600036
amitk@ae.iitm.ac.in

ABSTRACT

Hybrid rocket motors have distinct advantages over both the solid rockets (being safer) and liquid rockets (being simpler). The regression rate of hybrid rockets vary spatially as well as temporally. It also exhibits strong dependence on the size of the combustion chamber. In the present study, an effort has been made to study the effect of scaling up on the regression rate and the performance parameters of hybrid rockets. It is seen that while the regression rate increases with length of the motor, it decreases with the motor diameter due to corresponding variation in mass flux. It is also seen that the specific impulse attains a maximum at an optimal L/D.

1. Introduction

Rockets with propellant in more than one phase are called hybrid rockets. The most important design parameter in hybrid rockets is the regression rate (r_b). It is the rate at which the solid fuel is consumed and it is commonly expressed in terms of the fuel thickness consumed per unit time.

Extensive research conducted over the past few decades on hybrid rocket motors has contributed greatly towards the fundamental understanding of its working. Previous researches on the effect of scaling indicate that the regression rate decreases with increasing diameter [1]-[3]. However, scaling studies had been done with motors of fixed L/D ratio as they maintain the geometric similarity. In the present study, an effort is made towards studying the effect of scaling at various lengths and diameters of the combustion chamber.

2. Numerical method

The processes occurring inside the hybrid rocket combustion chamber can adequately be described by basic flow equations of continuity, momentum, energy and species. These unsteady governing equations in axi-symmetric coordinates were solved in 2D single port cylindrical computational domain. The computational domain consisted of the combustion chamber alone and the solid-gas interface was defined as the fuel inlet where mass and energy balance was applied. They were given by the following equations respectively.

$$\dot{m} = \rho_s r_b = -\rho v \quad (1)$$

$$\lambda_{eff} (\partial T / \partial y)_g - \lambda_s (\partial T / \partial y)_s + \rho_s r_b (H_p) = 0 \quad (2)$$

The first term in equation (2) is the heat conduction into solid fuel from gas phase, the second term is heat lost into solid fuel by conduction and the third term is the heat of solid fuel pyrolysis. Since the solid fuel is not included in the computational domain, the heat lost inside was determined by an analytical solution of 1D heat conduction inside the solid with moving hot boundary. The analytical temperature profile inside the solid fuel is given by

$$T(y) = (T_s - T_\infty) * \exp(-r_b y / \alpha) + T_\infty \quad (3)$$

Combustion processes inside the rocket motor were modeled using a single step global reaction, whose reaction rate was modeled as second order Arrhenius

equation [4]. The pyrolysis of solid fuel was modeled as zeroth order Arrhenius equation following [5]. The governing equations were discretized to second order accuracy in both space and time. They were solved with the above mentioned models using a pressure based, double precision solver [6].

3. Results and Discussion

Simulations were performed with motors of various diameters viz., 20mm, 30mm, 40mm and 90mm for L/D ranging from 3.75 to 25. The results are discussed here.

For all the cases, the inlet oxidizer mass flux was maintained at constant value of 132kg/m²s. Since the regression rate is known to strongly depend on the mass flux, one can expect similar regression rates for all these motors. However, with large diameter, the increase in local mass flux at any axial location is not as large as that for the small motor. Hence, the heat transferred to the fuel surface is higher for smaller diameter motor and consecutively the regression rate is also higher.

Figure 1 illustrates the temperature contours in the combustion chamber for motors with diameters 30mm and 90mm and L/D ratio of 25. It is observed for the large motor that the flame reaches the core at an axial location which is larger than that of the small motor.

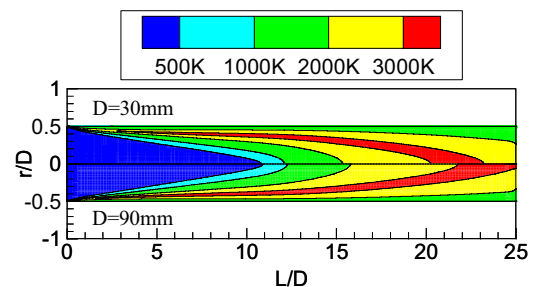


Figure 1 Temperature contours in combustion chambers with two different diameters

Figure 2 represents the average regression rate for all the motor configurations considered in the present study. The average regression rate increases with length due to increased local mass flux downstream as the fuel is progressively added. As discussed earlier, it decreased with increasing in diameter.

The inset in the Figure 2 shows the axial variation of local regression rate for motors with fixed diameter (30mm) and various lengths. The local regression rate increases up to an axial location of about 500mm and then decreases. The increase is due to increased heat transfer caused by higher mass flux. When the flame reaches the core, the downstream flow becomes non-reacting hot flow. With fuel being added progressively, the bulk temperature of the gas mixture decreases and hence the heat transfer decreases. This results in decreasing local regression rate.

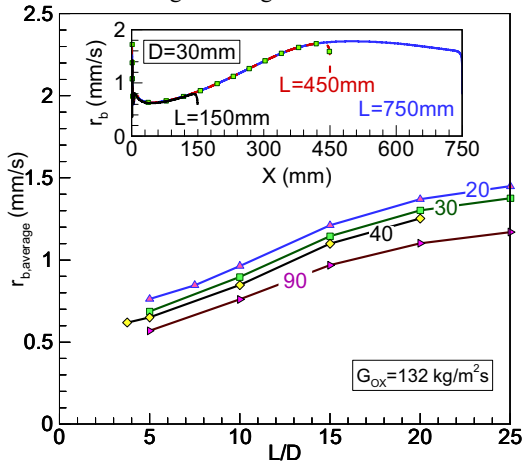


Figure 2 Effect of combustion chamber dimensions on the average regression rate of the hybrid rocket; the inset figure shows the effect of length (with fixed diameter) on the local regression rate

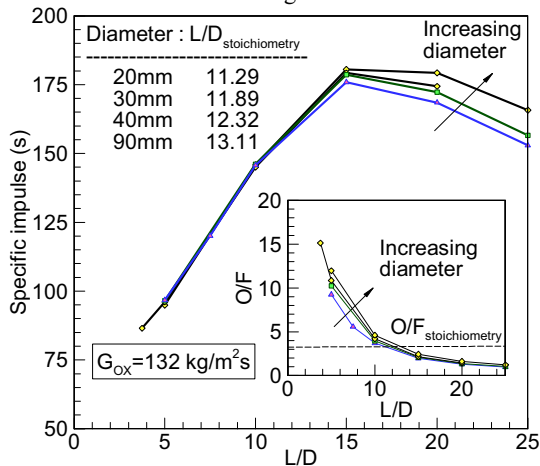


Figure 3 Effect of combustion chamber diameter on the specific impulse of hybrid rocket motors; the inset figure shows the O/F ratio for corresponding cases

Figure 3 illustrates the specific impulse (I_{sp}) for the corresponding simulations. The O/F ratios are plotted in the inset figure. I_{sp} is a strong function of bulk temperature of the mixture at the nozzle inlet. The presence of diffusion flame inside the hybrid rocket combustion chamber results in strong temperature variation both in axial and radial directions (Figure 1). Thus, I_{sp} becomes a strong function of L/D.

The bulk temperature of the mixture reaches maximum when the flame is somewhere in between the axis and the fuel surface (an optimal L/D~15). At shorter L/D ratios, the cold oxidizer at the core decreases the I_{sp} of the motor, whereas at longer L/D ratios, the fresh fuel addition from interface decreases the I_{sp} .

The stoichiometric O/F ratio for the considered propellant combination is 3.25, where theoretically the I_{sp} is expected to be maximum (L/D when stoichiometric O/F occur is represented in the figure). However, in the present simulations, maximum I_{sp} occurs at a fuel rich O/F=2. At optimal L/D, some un-burnt fuel passes out between the flame and the fuel surface resulting in a fuel rich condition. This also results in poor combustion efficiency (~70% at optimal L/D). This may be avoided by providing a post combustion chamber where un-burnt fuel and oxidizer are allowed to mix and react.

4. Conclusions

Simulations were carried out for hybrid rocket combustion chambers for various diameters and lengths, for a fixed inlet oxidizer mass flux. Based on these studies, the following conclusions may be drawn.

1. The local regression rate in a hybrid rocket motor increases up to a length where the flame exists. After the flame meets the core, further fuel addition cools the gas mixture and hence the local regression rate decreases. However, the average regression rate increases monotonically with length. It may decrease with further longer motors (L/D>25) as the local regression rate has a decreasing trend.
2. The average regression rate drops with increase in diameter. In large diameter motor, the increase in local mass flux with fuel addition is lower compared to small diameter motor. This results in lower heat transfer to the fuel surface and lower regression rate.
3. There exists an optimal L/D (~15) where the I_{sp} attains peak value. It is attained for a fuel rich mixture (O/F~2). This is caused by poor combustion efficiency which may be improved by providing a post combustion chamber.

References

- [1] S. Venkateswaran, and C.L. Merkle, AIAA paper 1996-0647, (1996).
- [2] R. D. Swami, A. Gany, Acta Astronautica, **52** (2003), pp.619–628.
- [3] G. Cai, P. Zeng, X. Li, H. Tian, and N. Yu, Aerosp. Sci. Technol, (2011); doi: 10.1016/j.ast.2011.11.001
- [4] G. C. Cheng, R. C. Farmer, H. S. Jones and J. S. McFarlane, AIAA paper 1994-0554, (1994).
- [5] P. A. Ramakrishna, P. J. Paul and H. S. Mukunda, Proceedings of the Combustion Institute, **29**, (2002) 2963-2973
- [6] ANSYS-Fluent Software Release Version No. 6.3.26, (2006).

Enhancement of Regression Rate Using a Bluff Body in Hybrid Fuels

Rajiv Kumar and P. A. Ramakrishna

Department of Aerospace Engineering, Indian Institute of Technology Madras,
Chennai-600036, India
rajiv1203@gmail.com

ABSTRACT

In this paper, an attempt is made to increase the regression rate of hybrid fuel (wax) using a bluff body placed near the head end of the motor. The oxidizer used for the present study is gaseous oxygen. The results show that the use of a bluff body increases the regression rate by around two times at the higher G_{ox} and by around 3 – 4 times at the lower G_{ox} . In addition, the port diameter was nearly uniform from the head end to the nozzle end minimizing the sliver losses.

1. Introduction

Hybrid rocket contains fuel and oxidizer in different phase, generally fuel is in solid phase and oxidizer is in gaseous or liquid phase. Hybrid rocket is known to be safest system as compared to the solid and liquid rocket engines. The advantages of hybrids are well documented in Sutton and Biblarz [1].

On the disadvantage side, hybrid rocket have a low regression rate. Although various techniques have been adopted by researchers to increase the regression rate of the hybrid fuel, yet it has not been enough to be used in any practical application.

Karabeyoglu et al. [2] used paraffin wax as hybrid fuel and gaseous oxygen as oxidizer. It was observed that the regression rate was around 3-4 times higher than any other conventional hybrid fuel. Goose [3] used diaphragm in the combustion chamber to improve the regression rate as well as the combustion efficiency. He observed a maximum increment in the regression rate of about 80 % depending on the type of diaphragm used.

In this paper an effort is made to increase the regression rate by using a bluff body. The study of bluff body in hybrid rocket has important implications, as the bluff body alters the flow behaviour within the combustion chamber and hence will be independent of the type of fuel or oxidizer used. In the present study, regression rate was obtained using a weight loss method as in Ref. [4]. The fuel used in the present study is a combination of 30% of micro-crystalline wax and 70% of paraffin wax. It was manufactured by Mahatha Petroleum Private Limited, Chennai, specifically for this purpose. It has a density of 890 kg/m^3 and a melting point of 337 K. Gaseous oxygen is used as the oxidizer.

2. Experimental set up and test procedure

The schematic of the experimental set-up used and the experimental procedure used in the current study are given in Ref. [4]. Here, experiments were carried out with a burn time of 0.5 s and it has been verified in Ref. [4] that 0.5 s burn time is possible. In the present study, an interrupted test was carried out for obtaining the burn rate. In an interrupted test, the same fuel grain was used for obtaining the burn rate by stopping the combustion after each 0.5 s and restarting. The mass of fuel burnt after each 0.5 s was used to calculate the regression rate, using weight loss method (Ref. [4]). The final port diameter calculated in the first time

period of 0.5 s was considered as the initial port diameter for next time step. The mass flow rate of oxidizer used in the present study is 30 g/s.

In the present study a bluff body was used for the enhancement of the regression rate. A schematic diagram of hybrid rocket motor along with bluff body arrangement is shown in Fig. 1. The bluff body, which is made up of high density graphite is fixed to the injector plate with the help of two 2 mm stainless steel screws at a distance of 2 mm from injector plate. It is a semi-hemispherical body of diameter 12 mm. Initially, experiments were carried out without the hole at the

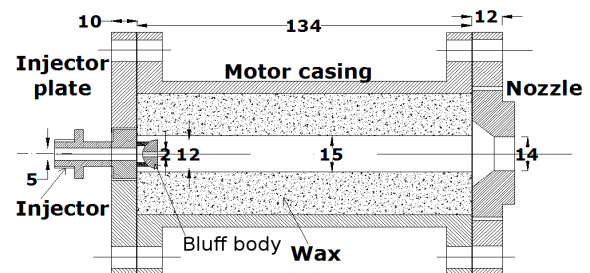


Fig. 1 Schematic diagram of hybrid rocket motor along with bluff body

centre of bluff body, but due to very high G_{ox} (oxidizer mass flux) near the head end, the motor got burnt off. Hence, a hole was drilled at the centre of the bluff body, which is seen in Fig. 1. Experiments were carried out with hole size of 2 mm. The initial port diameter of the fuel was 15 mm. The length of the fuel grain was 134 mm. The motor used for the experiments has an injector diameter of 5 mm and convergent nozzle of throat diameter of 14 mm, which was made of high density graphite. The mild steel rod of 15 mm was used as a mandrel for casting the wax.

3. Results and Discussion

Experiments were carried out with a hole size of 2 mm in bluff body and a burnt time of 0.5 s. The mass of fuel consumed during combustion is determined by weighing the motor before and after combustion using a weighing balance, which has a least count of 100 mg. During experiments care was taken to ensure that the shape of the bluff body does not change. The results obtained with bluff body were compared with the regression rate results obtained without the bluff body, which are shown in Fig. 2. It is seen from Fig. 2 that the regression rate for the case with the bluff body

improves by around two times at higher G_{ox} and around 3-4 times at lower G_{ox} when compared with the burn

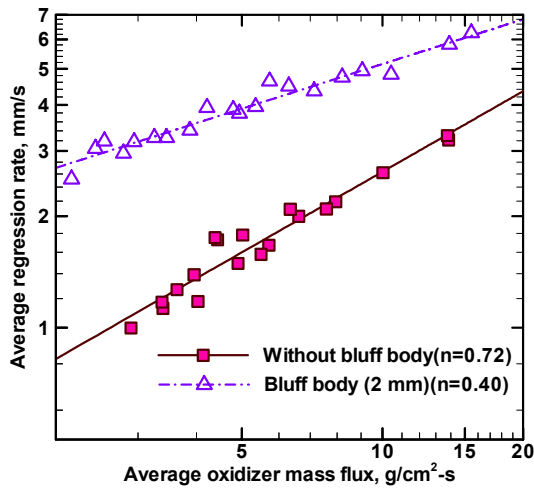


Fig. 2 Comparison of regression rate vs. G_{ox} with and without bluff body

rates obtained without the bluff body. The increase in regression rate is due to the reduction in boundary layer thickness as the velocity of oxidizer is higher near the fuel surface, which increases the convective heat transfer to the fuel.

Apart from this, it has been observed in Ref. [5] that the presence of large recirculation zone near the head end influences the regression rate. Hence, here an attempt was made to compare the recirculation zone formed with the bluff body being present and without it. The recirculation zone was obtained with a cold flow CFD study using Fluent [6]. The details of the domain and the boundary conditions are explained in ref. [5]. The streamline profiles obtained from the CFD study are shown in Fig. 3 (a) and (b). It can be seen from the Fig. 3 (a) that the length of the recirculation zone without the bluff body is around 25 % of the total length of the fuel. While, with the presence of the bluff body, the length of recirculation zone is very small around 3 % of the total length of the fuel (ref. Fig. 3 (b)). Hence, one can conclude that the presence of bluff body reduces the recirculation zone length and hence, increases the burn rate.

It is also observed from Fig. 2 that the mass flux exponent n reduces from 0.72 to 0.40 with the use of a bluff body, which is close to 0.5. This is desirable for the hybrid rocket, as it eliminates the change in O/F ratio with the burn time. The reason for the reduction in n is that as the port diameter increases with the burn time during combustion, the growth rate of recirculation length is higher for the case without the bluff body as compared to that with the bluff body being present.

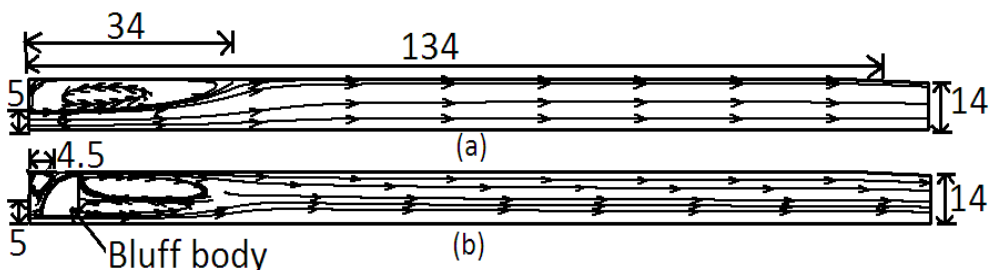


Fig. 3 Comparison of streamline profile (a) without bluff body, (b) with bluff body

An attempt was also made to compare the burnt profile with the bluff body and without it. The burnt profiles obtained after a burn time of 5 s are shown in Fig. 4. It is seen that with the use of bluff body, burnt surface is more uniform, except very close to the head end. The thickness of unburnt fuel at the head end is 21 and 8 mm, for without and with bluff body respectively. The thickness of unburnt fuel at the

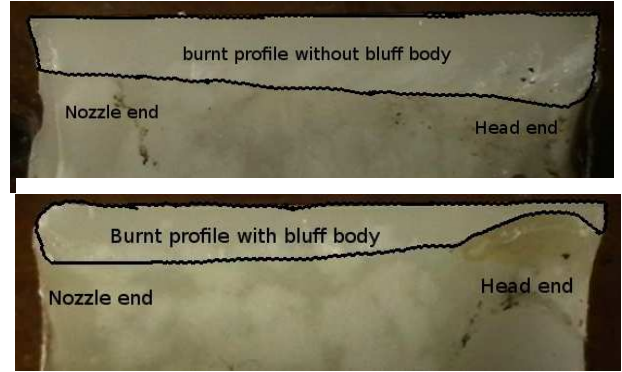


Fig. 4 Comparison of burnt profile with and without bluff body after burn time of 5 s

nozzle end is 12 and 13 mm for without and with bluff body respectively. The higher regression rate near the head end with the bluff body is due to high radial component of velocity impinging on the fuel surface. The effect of bluff body on the regression rate diminishes as one move from the head end to the nozzle end. This is compensated by the increased fuel regression rate near the head due to which there is an increase in the mass flux in the port.

4. Conclusions

It can be concluded from the present study that:

1. The bluff body increases the regression rate by around two times at higher G_{ox} and around 3-4 times at lower G_{ox} .
2. The mass flux exponent n reduces from 0.72 to 0.40.
3. The burnt surface becomes more uniform from head end to the nozzle end, with the use of bluff body.

References

- [1] G. P. Sutton, O. BibLarz, Rocket Propulsion Elements, John Wiley & Sons
- [2] A. Karabeyoglu, G. Zilliac, B. J. Cantwell, S. Dezilwa, P. Castellucci, Journal of Propulsion and Power 20 (2004) 1037-1045.
- [3] M. Grosse, AIAA-2009-5113.
- [4] R. Kumar, P. A. Ramakrishna, AIAA-2011-5913
- [5] R. Kumar and P. A. Ramakrishna, 8th Asia Pacific Conference on Combustion, Hyderabad, India, 2012, pp. 652-659.
- [6] Ansys-Fluent Version 6.3, 2007.

Scale Effect Between 2500 and 5000 N Thrust Class CAMUI-type Hybrid Rocket Motors

Harunori Nagata¹, Tsuyoshi Totani¹, Masashi Wakita¹, Tsutomu Uematsu²

¹ Division of Mechanical and Space Engineering, Hokkaido Univ., Sapporo 060-8628, Japan.

² Camuispaceworks Co. Ltd., Kyowa 230-50, Akabira 079-1101, Japan.
nagata@eng.hokudai.ac.jp

ABSTRACT

The authors have developed CAMUI type hybrid rockets as an explosive-free small-scale sounding rocket. In this paper, the authors propose a scaling rule for weight loss of a fuel block in a CAMUI type hybrid rocket. This scaling rule comes from our previous findings that similarity conditions based on convective heat transfer are valid for most burning surfaces. To confirm the validity of the scaling rule, we made static firing tests with two motors having geometrically-similar fuel grain. Results show that weight loss of a fuel block obey the scaling rule, showing the scaling rule is valid.

1. Introduction

The authors have developed CAMUI type hybrid rockets as a nontoxic propellant sounding rocket system[1]. Figure 1 shows the key idea, a distinctive fuel grain design to accelerate gasification rates of solid fuels. Because regressions of these surfaces progress simultaneously with different regression rates among them, temporal variation of grain geometry is complicated. Previous experimental researches show that the amount of fuel consumption calculated from a simple model, assuming uniform fuel regression for each burning surface, includes error up to 10%. Static firing tests are necessary to correct for variations of the predicted fuel regression progress. Because many static firing tests are necessary to fine-tune the grain geometry, employing a subscale motor is preferable to save time and expense. We have been working to obtain a rule to define a similarity condition under which subscale tests should be conducted. Previous research revealed that similarity conditions based on convective heat transfer mechanisms are valid for most burning surfaces[2]. To explore comprehensive effects of scaling on rocket motor performance, we conducted static firing tests with two motors having geometrically-similar fuel grain with the scale ratio of 1.5.

2. Test motor and fuel grain

Figure 2 shows a schematic of test motors. Both motors use polyethylene (PE) and liquid oxygen (LOX) as propellants. There is a pair of outer and inner tubes in the LOX tank. A three-way valve connects a high-pressure helium tank to the LOX tank during the burning. Before supplying the LOX, the valve prevents pressure rising in the LOX tank by releasing gasified oxygen into the combustion chamber through the inner tube. After the ignition, the valve closes the gas release line and opens the pressurizing line simultaneously. The orifice between the LOX tank and the combustion

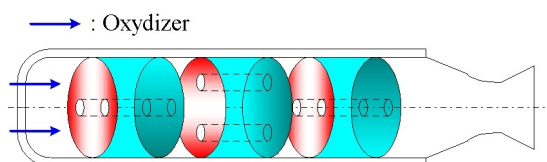


Fig. 1 Basic concept of CAMUI fuel grain.

chamber is to measure the LOX flow rate. A fuel grain consists of nine stages of fuel blocks and one tubular fuel as a mixing chamber, as Fig. 3 shows. For each stage, fuel blocks for two motors are geometrically-similar with each other.

3. Results and Discussion

Figures 4 and 5 show histories of chamber pressure and propellant (fuel and LOX) flow rates. The fuel flow rates are calculated by a reconstruction technique. The reconstruction technique calculates fuel flow rate from histories of LOX flow rate and chamber pressure, assuming a constant c^* efficiency. The large fluctuation around five seconds in the fuel flow rate of the large motor case (Fig. 5) is due to calculation instability of this method. After each firing test, we collected residual fuel to measure the weight loss of each fuel block.

Our previous research revealed that similarity conditions based on convective heat transfer mechanisms are valid for most of burning surfaces[2]. Accordingly, fuel flow rate is proportional to:

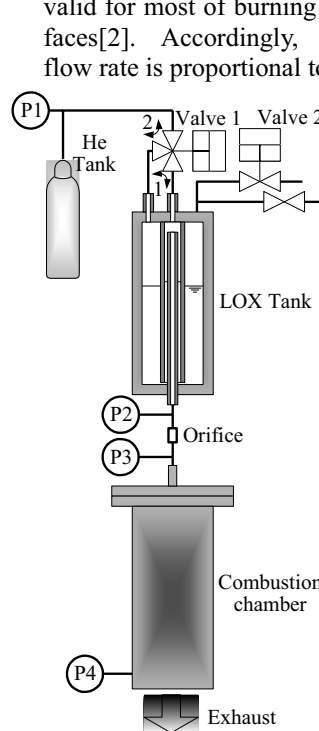


Fig. 2. Schematic of the test motors.

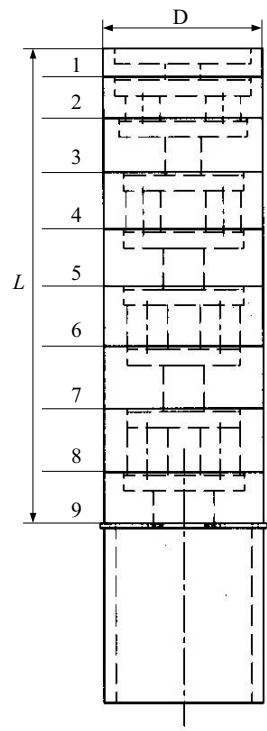


Fig. 3. A CAMUI-type fuel grain.

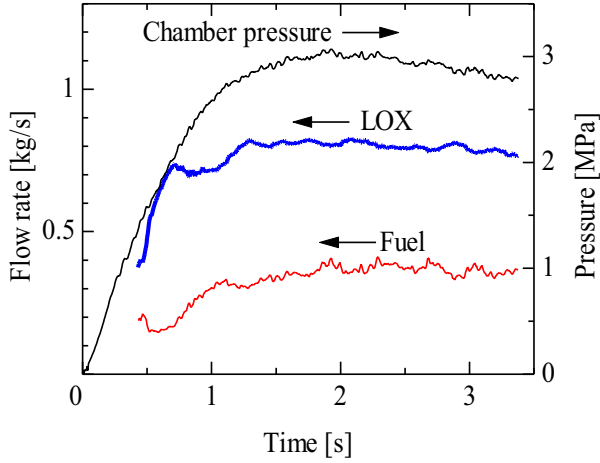


Fig. 4 Histories of chamber pressure and propellant flow rates (Small motor).

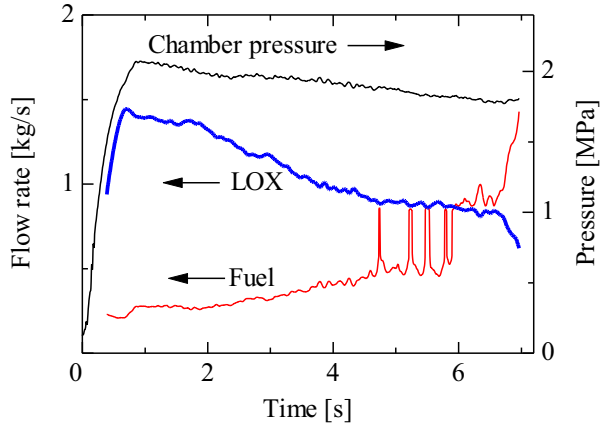


Fig. 5 Histories of chamber pressure and propellant flow rates (Large motor).

$$\dot{m}_f \propto D^2 Nu \left(\frac{\Delta T}{D} \right) \lambda \propto D^2 Re^n \frac{1}{D} \propto D \left(\frac{\rho U D}{\mu} \right) \propto D^{(1+n)} G_o^n$$

where ΔT , λ , ρ , U , μ , and G are temperature difference between fuel surface and combustion gas, heat conductivity, gas density, gas velocity, viscosity coefficient, and mass flow density, respectively. Although the numerical value of the exponent n varies among burning surfaces, our previous experiments show that they from 0.75 to 0.80[2], being reasonably close to 0.8. Therefore,

$$\dot{m}_f \propto D^{(1+n)} G_o^n \propto D^{1.8} \left(\frac{\dot{m}_o}{D^2} \right)^{0.8} = \dot{m}_o^{0.8} D^{0.2} \propto \dot{m}_o^{0.8} S^{0.2}$$

where S is scale ratio. By integrating the both sides of the equation,

$$\Delta m_f \propto S^{0.2} \int_0^{t_b} \dot{m}_o^{0.8} dt$$

where Δm and t_b are amount of weight loss of a fuel block and burning duration, respectively. This equation is a scaling rule for weight loss of a fuel block in a CAMUI type hybrid rocket. Figure 6 shows validity of the scaling rule, showing close agreement between the results of two scales.

Table 1 Specifications of small and large motors.

	Small	Large
Scale ratio	1	1.5
D [mm]	100	150
L [mm]	302	453
Burning duration [s]	3.4	7.0
Initial fuel weight [kg]	1.65	5.60
Final fuel weight [kg]	0.76	2.92
Fraction of fuel consumption	0.54	0.48
Total LOX weight [kg]	2.3	5.3
Nozzle diameter [mm]	27	40.5

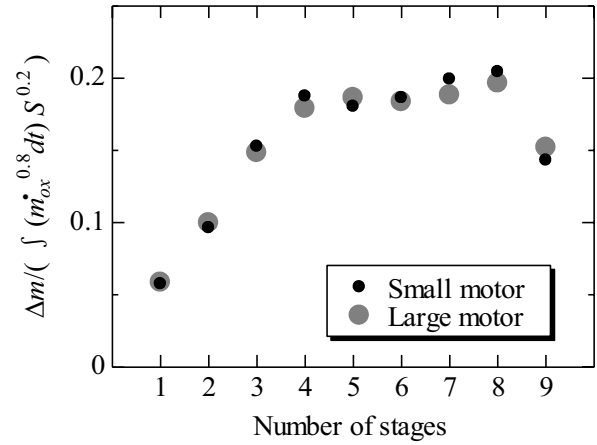


Fig. 6 Validity of the scaling rule.

4. Concluding remarks

We proposed a scaling rule for weight loss of a fuel block in a CAMUI type hybrid rocket. This scaling rule comes from our previous findings that similarity conditions based on convective heat transfer mechanisms are valid for most burning surfaces. To confirm the validity of the scaling rule, we made static firing tests with two motors having geometrically-similar fuel grain. Results show that weight loss of a fuel block obey the scaling rule, showing that the scaling rule is valid.

Acknowledgements

This research is supported by the Ministry of Education, Science, Sports and Culture, Grant-in-Aid for Scientific Research (A), 40281787, 2012.

This research is supported by the Hybrid Rocket Research Working Group (HRrWG) of Institute of Space and Astronautical Science, Japan Aerospace Exploration Agency. The authors thank members of HRrWG for their helpful discussion.

References

- [1] H. Nagata, et al., 49th International Astronautical Congress, IAF-98-S.3.09, 1998.
- [2] H. Nagata, 46th AIAA/ASME/SAE/ASEE Joint Propulsion Conference & Exhibit, AIAA 2010-7117, 2010.

Reactive and Additive Routes to Novel Polymer-based Fuels for Hybrid Propulsion

Paul Joseph¹, Koki Kitagawa², Vasily Novozhilov¹ and Toru Shimada²

¹School of the Built Environment and the Built Environment Research Institute, University of Ulster, Newtownabbey, BT37 0QB, County Antrim, UK

²Japan Aerospace Exploration Agency, Sagami-hara, Kanagawa, 252-5210, Japan

p.joseph@ulster.ac.uk

ABSTRACT

Polymer combustion is a complex phenomenon, involving the gaseous phase, an inter-phase and the solid phase. Through physically mixing other additive(s) with, or by chemically modifying, an appropriate polymer matrix, its degradation profiles and rates can be substantially modified. In the present paper both strategies, i.e. a *reactive* or an *additive* approach, with a view to enhancing the degradation and combustion propensities of some commercially important chain-growth polymers are discussed in the wake of their potential use in hybrid rocket propulsion technologies.

1. Introduction

When subjected to a sufficient length of time to an external heat source, organic polymeric materials undergo thermal degradation, generating various products in varying concentrations over different ranges. The chemical steps leading to the formation of volatiles may be homolytic or heterolytic, that is, be radical or ionic. In addition, the presence of oxygen has an influence on the degradation profiles of polymers—however, this strongly depends on the chemical nature of the polymer in question as well [1].

One of the most serious problems of a hybrid rocket engine currently is its low fuel regression rate. To address this problem, physical techniques like swirling flow or impinging flow, and chemical technique like energetic additives or advanced fuel have been tried. However, in recent years, we have been attracted to the *reactive* and *additive* routes of increasing the fuel regression rates of some of the common fuels used for hybrid rocket propulsion, such as polymethyl methacrylate (PMMA) and polypropylene (PP). For instance, this could involve chemically-modifying the base polymers with silicone (Si)- or Boron (B)-containing groups or mixing the polymers with nano-metric scale Carbon (C) or B [2].

The following sessions, mainly, cover the synthetic strategies for achieving chemical modifications for producing some promising polymeric fuels and the laboratory-scale analytical techniques to screen their degradation and combustion behaviours.

2. Synthetic strategies

2.1 Material selection and chemical modifications

The main purpose here is to select a variety of polymeric substrates, some homopolymers and closely associated chemically modified systems, with a view to extensively investigating their microstructures, thermal- and thermo-oxidative degradation behaviours and combustion characteristics. The homopolymers of styrene (St), α -methyl styrene (α -MSt), methyl methacrylate (MMA), and polyolefins (PE, PP, PiB and PE/PP) and functionalized telechelic polybutadienes will be the primary focus of study (Fig. 1). As the second step, copolymers of styrene (St) and methyl

methacrylate (MMA), among themselves as well as with α -methyl styrene (α -MSt), and with a wide variety of compositions, will be prepared through copolymerization reactions, under radical initiation, in solutions. This will be followed by copolymerization reactions of MMA and St with Silicon (Si) or Boron (B) containing monomers. Finally, modified polymers based on PP will be obtained through grafting reactions utilizing Si- or B-containing reagents. Post-modification reactions for incorporating B into polyhydroxylic substrates such as polyvinyl alcohol, or transition metal chelates (for example, VO(AcAc)₂) with appropriately modified base polymers (PST or PMMA), will be prepared following literature precedents (Fig. 2) [3].

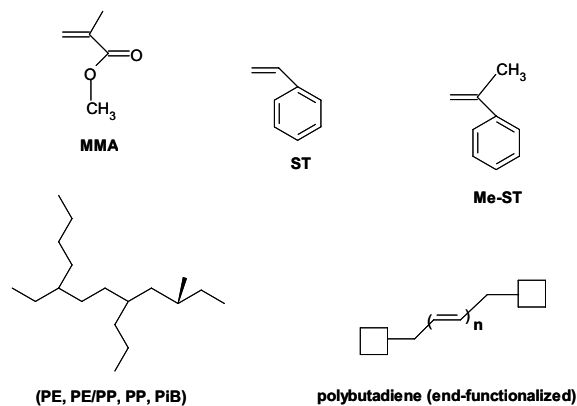


Fig. 1 Chemical structures of the common monomers and the base polymers

For homo- and copolymerization reactions, standard methods described in literature precedents will be followed [4]. The procedures for grafting reactions and other chemical modifications, which were developed in our laboratories, will be followed as means of appropriate post-modification strategies and in accordance with the task in hand. As for obtaining the physical mixtures either melt blending (for low melting PE or for PP), or solution casting (for PMMA and similar systems), technique will be used as appropriate. The recovered polymeric materials, after purification (primarily through re-precipitation method) will be dried in a vacuum oven at elevated temperatures (*ca.* 60 °C), to constant weights, before further characterization.

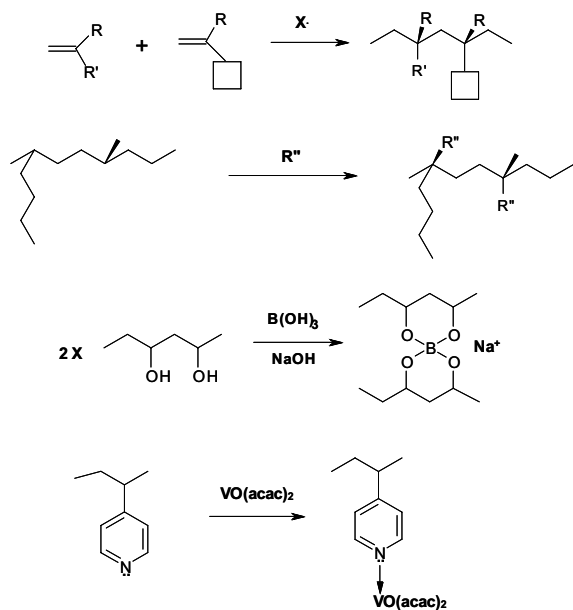


Fig. 2 Synthetic Strategies

3. Characterization of polymers

Spectroscopic (NMR and FT-IR) and elemental analyses: High field (500 MHz) solution state ^1H and ^{13}C NMR will be carried out with a view to deciphering the microstructures of the polymers (this includes tacticity, composition, monomer sequencing, minor structures including structural defects etc.). Limited, but complementary, information regarding the structural features of the polymer will be obtained from the FT-IR spectra and hetero-atom elemental analyses.

Chromatographic and related techniques: These are primarily aimed at obtaining the molecular weights and their distributions. For polyolefin based-polymers, optionally the melt-flow index measurements will be also carried out.

Thermo-gravimetric analyses (TGA): TGA runs will be carried out on *ca.* 10-15 mg of the resin in nitrogen, air and in oxygen atmospheres, say, at $10\text{ }^\circ\text{C min}^{-1}$, and from 30 to $1000\text{ }^\circ\text{C}$. The idea behind these runs is to get the general thermal- and thermo-oxidative degradation profiles of the material (i.e. under different oxidative atmospheres). This could be followed by repeating the runs, in a chosen atmosphere(s), with a view to estimating the Arrhenius parameters.

Differential Scanning Calorimetry (DSC): Here, milligrams of samples are heated, under a nitrogen atmospheres and usually at a heating rate of $10\text{ }^\circ\text{C min}^{-1}$, in sealed aluminum pans, up to a point where substantial thermal degradation starts- a very useful technique that often yields information regarding melting behaviours, glass transition temperatures etc. that the material might undergo under the heating conditions imposed.

Parallel Plate Rheometry: Here again the sample, ideally in the shape of thin films, will be heated whilst sandwiched between two heated parallel plates, at the same time a sinusoidal mechanical stress is applied- a good methods for determining the moduli of elasticity

(store and loss), the glass transition temperatures, and more importantly the *melt flow behaviour* of the resin

Bomb Calorimeter: This instrumentation will be used to determine the heats of combustion (ΔH_{comb}) of the resin- a good indicator of the maximum heat out put on complete oxidation.

Pyrolysis Combustion Flow Calorimetry (PCFC): This piece of instrumentation, often dubbed as the *micro cone calorimeter*, produces plots of Heat Release Rates against time, as well as generates parameters like the heat release capacity on milligrams of a material (i.e. the maximum amount of heat released per unit mass per degree of temperature ($\text{Jg}^{-1}\text{K}^{-1}$), is a material property that appears to be a good predictor of flammability)

Hyphenated techniques: Attempts to identify the volatiles formed from thermal degradation of the materials will be made by hyphenating the TGA to an FT-IR. Such a hyphenated technique is also available in a larger scale that, primarily, involves two consecutive tube furnaces in connected in series. Optionally, some of the gaseous-products formed upon degradation, in ambient atmosphere, collected through by using proprietary containers, will be subjected to GC/MS.

4. Correlation of results

The overriding principle here is to obtain, as fully as possible, the structure property relationships of the materials tested. The main areas of interest are: a) try to find the influence of the molecular weights (i.e. the chain lengths, or the degree of polymerization), structural defects and other microstructure on the thermal/thermo-oxidation behaviours; b) gauge the 'ease' of thermal/thermo-oxidative degradation, and thus hopefully leading to correlations with the regression rates; c) estimate the influences of combustion energetics (such as the heats of combustion, the heat release and its rate, residue left), the effects of the heteroatom bearing groups/transition metal (Si and B, or V), the morphology, melt-drip behaviours etc. on the overall performance of the material as a rocket fuel d) carryout further chemical modifications, in the wake of the results obtained through c, with a view to improving the overall performance of the polymeric substrates as components of hybrid rocket engine systems.

References

- [1]. P. Joseph and J. R. Ebdon, In Fire Retardant Materials, A. R. Horrocks and D. Price (Eds.), (2000), Woodhead Publishing Limited, Cambridge, UK
- [2]. K. Kitagawa, P. Joseph, V. Novozhilov and T. Shimada, 9th ISICP, (2012), Quebec, Canada (accepted)
- [3]. J. R. Ebdon, B. J. Hunt, P. Joseph and C. S. Konkel, In Speciality Polymer Additives: Principles and Applications, S. Al-Malaika, A. Golvoy and C. A. Wilkie (Eds.), (2001), Blackwell Science, Oxford, UK
- [4]. J. R. Ebdon, D. Price, B. J. Hunt, P. Joseph, F. Gao, G. J. Milnes and L. K. Cunliffe, Polym. Deg. and Stab., **69**, (2000), pp.267-277

Enhancement of Regression Rate in HTPB Based Hybrid Rocket using Recrystallized AP and Pyral

Gaurav Marothia, P.A. Ramakrishna

Indian Institute of Technology Madras, Chennai-36, India

gaurav.marothiya29@gmail.com

ABSTRACT

Recrystallization of ammonium per-chlorate along with iron oxide enhances the regression rate significantly in hybrid rockets. Pyral is used to enhance the regression rate of Hydroxyl Terminated Poly-butadiene (HTPB) based hybrid fuel. A combination of 28 % pyral and 7 % micron size aluminium give the best performance and give enhancement in regression rate of more the 100 % over micron sized aluminium.

1. Introduction

A combination of solid and liquid rockets is known as a hybrid rocket. It possesses the collective advantages of both liquid and solid rockets. A hybrid rocket, similar to a liquid rocket, is safe since the fuel and oxidizer are stored separately, has the start-stop-restart capability and like solid rockets they does not have transverse mode of instability. But, disadvantages like low regression rate, low combustion efficiency etc. prevent its practical application.

A number of researchers have tried, over the years to eliminate the low regression rate. Karabeyoglu et al. [1] suggested the use of wax as fuel. Although wax has significant regression rate value in hybrid rockets, it has very poor mechanical properties. Because it is an extensively used fuel in solid rockets, HTPB was recommended. However, since it is a polymeric fuel, it also has low regression rates in hybrid rockets.

To overcome this disadvantage of HTPB, the use of a solid oxidizer like ammonium perchlorate (AP) within the fuel grain of a hybrid rocket was proposed. Risha et al. [2] report about the use of nano sized aluminium within the fuel grain to increase regression rate of HTPB based hybrid rockets. George et al. [3] also reported that using 6% AP (98 μm) with 18% Al (28 μm) enhances the regression rate by more than 100% over pure HTPB.

In the current study, we propose the use of pyral and recrystallized AP within the fuel grain to enhance the regression rate of HTPB based fuel. Following Verma and Ramakrishna [4], it was thought that use of pyral would yield higher burn rates. Pyral used here has mean diameter of 8.23 μm . Pyral is flake like particles of very large specific surface area ($\sim 22599.3 \text{ m}^2/\text{kg}$) as compared to 5 μm aluminum which is spherical in shape. Since the burn rate of non aluminized solid propellants can be enhanced by recrystallization of AP (Ishitha and Ramakrishna [5]), here AP is recrystallized with iron oxide (IO) using water as a solvent and after recrystallization R(AP+IO) is

passed through a fluid energy mill and reduced to particle size of less than 15 μm .

2. Preparation of propellants

All the ingredients (HTPB, DOA, IPDI, AP, Al, and IO) in appropriate proportions were mixed in a 250g sigma type solid propellant mixer. The slurry was then transferred in parts into two PVC pipes of $\sim 160 \text{ mm}$ length and filled upto half of the length. To remove gases trapped inside the propellant slurry, the filled PVC pipes were kept overnight in vacuum. After which the samples were kept under ambient conditions for 14-15 days' to cure the propellant. The two pipes were then joined together and machined to make a fuel grain of 134 mm length with an internal port diameter of 9 mm. The hybrid rocket motor used for carrying out the experiments had an injector diameter of 5 mm and a nozzle throat diameter of 8 mm. Brief schematic of motor design is given in Fig. 1.

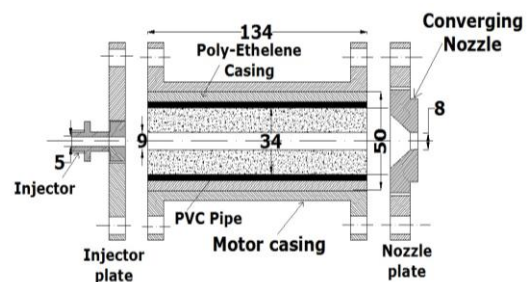


Fig. 1: Schematic of Hybrid motor design

Mass flow rate of the oxidizer was maintained at $\sim 30 \text{ g/s}$. Elaborate explanation of experimental setup and motor design are given in Ref. [6].

3. Result and Discussion

Various mixes as indicated in Table 1 were prepared. Average particle size of AP used in all the mixes were less than 15 μm . Mix 1 is used only for a comparison with different mixes and taken from Ref. [6]. Mix-2 was prepared with AP recrystallized with IO. Results of experiments with mix-2 were compared with Mix-1 (Fig 2) and it was observed that recrystallization of AP with IO

Table.1: Composition of Propellants

Mix	Composition
1	35% Al(5 μ m)+15% AP + 50% Binder (From Ref. [6])
2	35% Al(5 μ m)+ R(3% IO+15% AP) + 47% Binder
3	35% Al(50% Pyral+50% 5 μ m Al) + 15% AP + 50% Binder
4	35% Al(80% Pyral+20% 5 μ m Al) + 15% AP +50% Binder

gives enhancement in the regression rates of around 33% when compared with Mix-1 and around 50% when compared with pure HTPB.

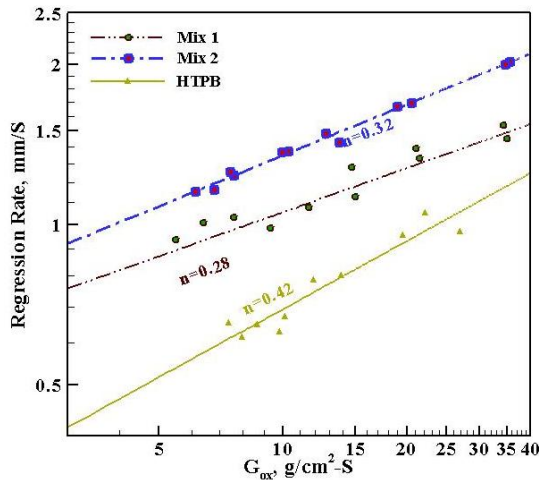


Fig. 2: Comparison of Regression rate vs. G_{ox} for Recrystallization of AP along with IO

De Luca et al. [7] reported that the burn rate in solid propellants can be enhanced by increasing the surface area of aluminium particles. Verma and Ramakrishna [4] had reported that pyral significantly enhances the burn rate in solid propellants. Because pyral is a thin flake its combustion possibly occurs more to the burning surface as compared to the spherical particles of micron sized aluminum. Due to this the heat transferred to the propellant surface is higher with pyral which causes the increase in the burn rates of solid propellants. Therefore propellants were prepared with the same composition as of Mix-1, but instead of micron sized aluminum, Pyral was used. In experiments conducted with the propellants which were prepared with the entire aluminum content (35 %) being pyral, it was observed that propellants did not quench and burn like solid propellants. So Mix-3 was prepared as given in Table 1. Mix-3 quenched after the oxidizer supply was stopped, but did not enhance the regression rate significantly. So Mix-4 (refer Table 1) was prepared. Pyral As shown in Fig 3, Mix-4 gives an enhancement of more than 100 %

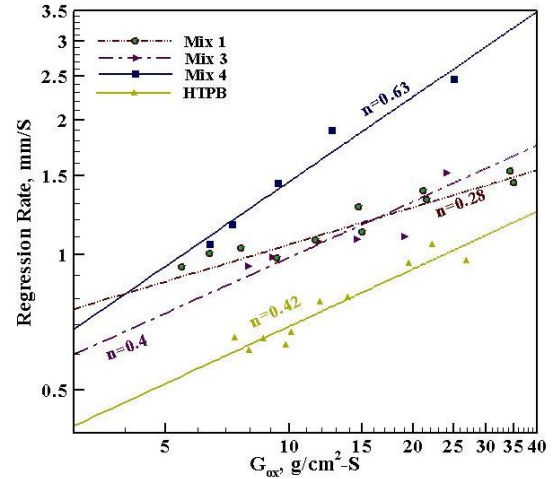


Fig. 3: Comparison of Regression rate vs. G_{ox} for Pyral

of regression rate when compared to Mix-1. It also quenched upon stoppage of the oxidizer supply.

4. Conclusion

1. Recrystallization of AP with IO enhances the regression rate in hybrid rockets.
2. Propellants made with the entire aluminium content being Pyro Al, the propellants do not quench and burn like solid propellants.
3. Propellants with a combination of 28 % pyral and 7 % micron sized aluminium produce the highest enhancement in regression rate and yet do not burn like solid propellants.

5. References

- [1] M. A. Karabeyoglu, B. J. Cantwell, and D. Altman, *37th AIAA/ASME/SAE/ASEE Joint Propulsion Conference and Exhibit*, 2001.
- [2] G. A. Risha, A. Ulas, E. Boyer, S. Kumar, and K. K. Kuo, *37th AIAA/ASME/SAE/ASEE Joint Propulsion Conference and Exhibit*, 2001.
- [3] P. George and S. Krishnan, *Journal of Propulsion and Power*, vol. **17**(2001), no. 1, pp. 35-42.
- [4] S. Verma and P. A. Ramakrishna, *Combustion and Flame* (under review).
- [5] K. Ishitha and P. A. Ramakrishna, *47th AIAA/ASME/SAE/ASEE Joint Propulsion Conference and Exhibit (JPC)*, 2011.
- [6] G. Marothiya, R. Kumar, and P. A. Ramakrishna, *47th AIAA/ASME/SAE/ASEE Joint Propulsion Conference and Exhibit (JPC)*, 2011.
- [7] L. T. De Luca et al., *Combustion Explosion and Shock Waves*, vol. **41**(2005), no. 6, pp. 680-692.

Improving the Mechanical Properties of Paraffin Based Hybrid Fuels

Hiteshwar Brahma, [Rajiv Kumar](#) and P. A. Ramakrishna
Department of Aerospace Engineering, Indian Institute of Technology Madras,
Chennai-600036, India
rajiv1203@gmail.com

ABSTRACT

Although the regression rates recorded with paraffin wax is around 3-4 times higher than any polymeric fuel, it has poor mechanical properties. In this paper, an attempt is made to improve the mechanical properties of paraffin wax using EVA (Ethylene Vinyl Acetate). The results showed that use of 20% EVA improved the mechanical properties significantly. The percentage elongation increased from 4% for wax to around 14% for 80% wax with 20% EVA. The tensile strength recorded with 20% EVA was 45 kgf/cm².

1. Introduction

In a hybrid rocket engine, the fuel is generally in solid phase and the oxidizer is in gaseous or liquid phase. Hybrid rocket is known to be the safest system as compared to the solid and liquid rocket engine. The advantages of hybrid rockets are well documented in Sutton and Biblarz [1].

On the disadvantage side, hybrid rocket has a low fuel regression rate. There were various techniques which have been adopted by researchers to increase its regression rate. The work carried out by Karabeyoglu et al. [2] using paraffin wax as fuel has shown that the regression rate is around 3 – 4 times higher than any other polymer fuel. The advantages of using wax as fuel over other polymer fuels is that it is easily available, and it is eco-friendly. The combusted products do not contain any hazardous gases. Hence, use of wax as hybrid fuel reduces the overall costs.

Although, wax has advantages over other hybrid fuels, it has very poor mechanical properties like lower percentage elongation. Work has been carried out by various authors to improve its mechanical properties. DeSain et al. [3] have used the LDPE (low density polyethylene) in wax to improve the mechanical properties. They observed that tensile strength and percentage elongation increases with the increase in the percentage of LDPE. The 4% addition of LDPE in wax was observed to increase tensile strength by 100 % and percentage elongation by around 50 %. Maruyama et al. [4] have added EVA (ethylene vinyl acetate), which had 28 % vinyl acetate to paraffin wax. They observed that with an increase in the percentage of EVA of 20 %, the tensile stress as well as percentage strain increases to 60 % and 100 %. The results reported by them shows highly scattered data.

In this paper, an effort is made to improve the mechanical properties of wax. An attempt is also made to compare the regression rate. The wax used in the present study is a combination of 30% of micro-crystalline wax and 70% of paraffin wax. It was manufactured by Mahatha Petroleum Private Limited, Chennai, specifically for this purpose. It has a density of 890 kg/m³ and melting point of 337 K. Here, following Maruyama et al. [4] EVA was used as additive to improve mechanical properties of wax. An attempt is also made to determine the mechanical properties of wax when HTPB (Hydroxyl-terminated polybutadiene)

is added.

2. Studies on the mechanical properties

In order to find the mechanical properties, experiments were carried out on an Instron uniaxial testing machine (IUTM-3365), which has a capacity of 5 KN and least count of 0.001 N. The wax is cast into a bone shaped specimen using a stainless steel die. The fuel specimen obtained from this die is similar to one shown in Fig. 1. The specimen obtained had a thickness of 10 mm.

Wax was heated and once it started melting it was mixed with appropriate percentage of either HTPB or EVA. The molten mixture was properly mixed for around 20 min at high temperature and the mixture was cast into the die. This is allowed to cure in closed room at around 298 K. It was observed that the cured specimen obtained with HTPB had no problem, while the cured specimen obtained with EVA had cracks similar to that seen in Fig. 2. The reason for this could have been the rapid rate of cooling. To avoid this EVA mixed with wax was allowed to cure under the hot sun (for around 5 hours) when the temperatures were in excess of 313 K. This slow cooling ensured that specimen had no cracks as seen in Fig. 3.

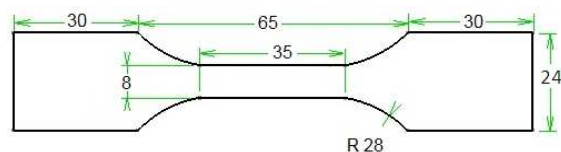


Fig. 1 Bone shape fuel specimen obtained from stainless steel die (dimensions are in mm)



Fig. 2 Fuel specimen obtained by cooling at 300 K



Fig. 3 Fuel specimen obtained by cooling at 313 K

Initial studies on the mechanical properties were carried out by mixing 20 % of HTPB with wax with the hope that it might improve its mechanical properties. The mechanical properties obtained with HTPB are shown in Table 1.

Table 1. Comparison of mechanical properties of wax with other additives

Properties	Pure wax	Wax+ 20% HTPB	Wax+ 20% HTPB +DOA	Wax + 10% EVA	Wax+ 20 % EVA
Tensile Strength (kgf/cm ²)	14.2	14.1	14.0	30.8	45.5
Young's Modulus (kgf/cm ²)	14.7	12.7	13.6	31.3	44.5
	15.7	13.4	13.9	31.1	40.4
% elongation	663	778	1086	402	530
	651	812	950	398	570
	630	862	1017	410	537
	4.3	4.0	4.1	7.37	13.5
	4.6	4.1	3.85	6.98	14.3
	4.5	3.95	3.8	8.3	13.3

In Table 1 the mechanical properties obtained with pure wax are also presented for comparison. It is seen from the Table 1, the addition of 20% HTPB does not show any improvement in the mechanical properties over those obtained with pure wax. Further, an attempt was made by adding around 6 % of DOA (Di-octyle adipate) along with HTPB. This addition of DOA led to a slight increase in tensile strength. Further, wax was mixed with EVA, which was observed by Maruyama et al. [4] to yield better mechanical properties. Here, the mechanical properties studies were carried out by adding 10 % and 20 % of EVA. The results of this study are shown in Table 1. It is observed that addition of 10 % EVA increases the tensile strength by around 100 %. The improvement in percentage elongation is around 50 %. The addition of 20 % EVA in wax led to an increase in the tensile strength as well as the percentage elongation. The improvement in percentage elongation is around 4.5 times the value obtained with wax. Thus, the mechanical properties of 80 % wax with 20 % EVA in it are attractive enough to envisage its use in a hybrid rocket, with a simple cylindrical grain.

3. Regression rate studies

It is observed from the above study, with the addition of 10 % and 20 % EVA in wax, the mechanical properties is improved sufficiently to be used in a practical application. Hence, an attempt is made here to find the regression rate with this combination. In order to determine the regression rate, the experimental set-up used is explained in ref. [5]. The burn time used was 0.5 s. The regression rate was obtained using a weight loss method with interrupted burn test. The mass flow rate of oxidizer was 30 g/s.

The regression rate results obtained with 10 % and 20 % EVA in wax are shown in Fig. 4. The results are also compared with the pure wax. It is observed that the addition of EVA reduces the regression rate by around 50 to 60 % depending on the fraction of EVA added to wax. The reason for the reduction of the regression rate is that the melting point of 20 % EVA mixed wax is

around 350 K which is higher than the melting temperature of pure wax (around 337). Due to the

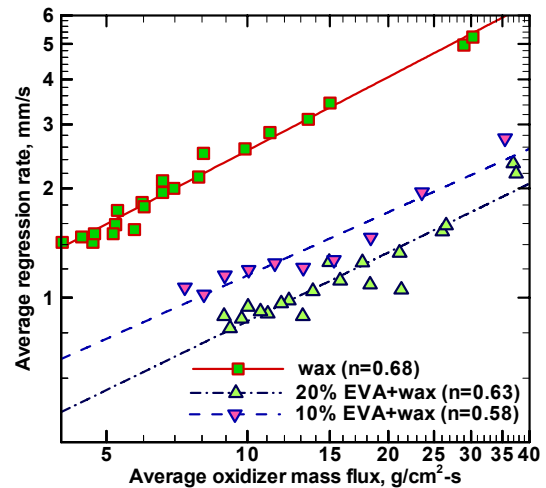


Fig. 4 Comparison of regression rate vs. G_{ox} with 10 and 20 % EVA along with pure wax

higher melting temperature, the melt layer formation is probably lower in 20 % EVA and wax. As the melt layer formation is lower here, the droplet entrainment from the melt layer into the gas stream will be lower compared to that of pure wax. As observed by Karabeyoglu et al. [6] the higher the entrainment of the droplet into the gas phase from the melt layer, higher will be the regression rate. This could be the reason for the low regression rate obtained with 20 % EVA and wax.

4. Conclusions

The following conclusion can be drawn from the present study.

1. The addition of 20% EVA in wax increases the strain at breakage or percentage elongation from 4% for pure wax to 14% with 20% EVA and 80% wax.
2. The tensile strength was observed to improve by about 3 times as compared to pure wax.
3. The addition of HTPB to the wax does not show any improvement in the mechanical properties.
4. Regression rate reduces by around 60 % with the addition of 20 % EVA.

References

- [1] G. P. Sutton, O. BibLarz, Rocket Propulsion Elements, John Wiley & Sons.
- [2] A. Karabeyoglu, G. Zilliac, B. J. Cantwell, S. Dezilwa, P. Castellucci, Journal of Propulsion and Power 20 (2004) 1037-1045.
- [3] J. D. DeSain, B. B. Brady, K. M. Metzler, T. J. Curtiss and T. V. Albright, AIAA-2009-5115.
- [4] S. Maruyama, T. Ishiguro, K. Shinohara and I. Nakagawa, Eighth International Conference on Flow Dynamics, 2011, pp. 306-307.
- [5] R. Kumar, P. A. Ramakrishna, AIAA-2011-5913
- [6] M. A. Karabeyoglu, B. J. Cantwell, D. Altman, AIAA-2001-4503

Development of lab scale hybrid rocket motor using low melting point thermoplastics

Yutaka Wada¹, Yo Kawabata¹, Ryuichi Kato¹, Nobuji Kato², Keiichi Hori³

¹Akita University, Akita, Japan ²Katazen corporation, Aichi, Japan, ³ISAS/JAXA, Kanagawa, Japan
E-mail: wada@mono.akita-u.ac.jp

ABSTRACT

The low melting point thermo plastics was chosen as a hybrid rocket fuel because of its better mechanical property and high regression rate. In this study, the lab scale hybrid rocket motor is developed for measurement fuel regression rate using liquid nitrous oxide (N₂O) as a oxidizer, and the result is compared and discussed to examinations results of the gas oxygen case. From the results, regression rate of the liquid N₂O oxidizer was same order to the gas oxygen result. Therefore, we suggested that the fuel regression rate is no oxidizer dependency, and the detail is discussed in this paper.

1. Introduction

The hybrid rocket is focused / expected as a next sounding rocket motor and a manned space vehicle engine because of having low cost system and high safety design due to the non-explosive propellant. However, the hybrid rocket system has not established of commercial base as a mainstream the space system. The reason is difficult to generate the large thrust due to the low combustion efficiency, the low fuel regression rate and poor fuel mechanical property of the hybrid rocket.

Therefore, the thermoplastic polymer of the low melting point excellent in the mechanical property is focused in this study. Low melting point thermoplastics (LT) fuel has a prospect of high regression rate because it has a similar physical property with low melting point of paraffin fuel. Katazen Corporation developed LT fuel which lowered the melting point down to hot water temperature range. The uniaxial tensile test of the LT fuel was carried out and evaluated[1]. The maximum strain is over 300% at the test sample, and they have enough elongation better than the conventional solid motor propellant. Therefore, in this study, two types of the lab scale hybrid rocket motor is developed for measurement of the fuel regression rate using gas oxygen and liquid nitrous oxide (N₂O) as a oxidizer. And both of results are compared and discussed.

2. Measurement of regression rate test

The two types of the combustion chambers using gas oxygen and N₂O were made and used for the measurement of the surface regression rate. The schematic view of the small combustion chamber is shown in Fig. 1.

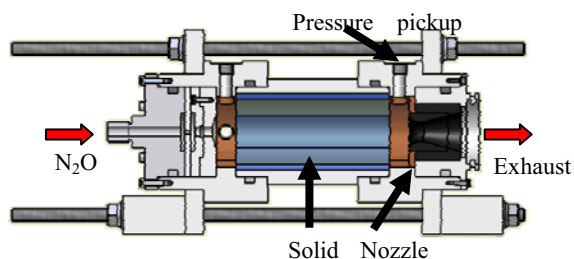


Fig. 1 Schematic view of the combustion chamber

The experimental setup of gas oxygen type uses gas oxygen of small flux at the time of ignition, and when thin ignition fuel made from acrylics ignites, the oxygen gas flow flux is raised to the predetermined level, and nitrogen is supplied into a chamber promptly at the time of terminated of combustion. The ignition energy is given by electronic spark energy. The mainstream oxygen line is controlled by the pneumatic driven ball valve, and the oxygen flow measurement uses the sonic orifice whose coefficient of resistance is known. The strain gauge pressure sensors (KYOWA PGS-100kA) were used for the measurement of the upstream pressure of gas oxygen and chamber pressure. In this study, oxidizer mass flux and chamber pressure are changed between 5 to 80 kg/m²s and 0.5 to 2.2MPa because of investigation of influence of the regression rate.

The experimental setup of N₂O type is using liquid N₂O as oxidizer. Assembly of the liquid N₂O feed system and ignition system is based upon HyperTEK system[2]. The N₂O is a self-pressurizing condensed gas, which is stored within the aluminum oxidizer tank that the tank volume is 300cc. As liquid N₂O are supplied to combustion chamber during motor burn by the self pressure, the tank pressure drop due to the drop temperature for heat of vaporization. Thus, the time history of thrust profile is also a declining trend. After the end of combustion, the combustion flame automatically extinguishes. The measurement of pressure, which is N₂O tank pressure and combustion chamber pressure, is using same equipment of the gas oxygen type setup, and the thrust was measured by load cell sensors (KYOWA LMA-1kN).

3. Results and Discussion

Results from an exemplary test with liquid N₂O as oxidizer are shown in Fig.2. At Fig.2, the motor have also good ignition performance used by electronically spark wire, however; the large ignition peak was observed as compared with gas oxygen motor. This reason is that many amount of gaseous fuels, which gasification of fuel is driven by ignition energy, encountered liquid N₂O suddenly. And also initial thrust is up concurrently to ignition peak however; it is helpful to a small rocket launching, because the small rocket is able to obtain enough flight velocity for aeromechanical stability. The ignition peak of chamber pressure is up to

4.5MPa, and after, the pressure is decreasing to 3MPa, and finally the pressure is gradually decreasing to 2MPa. The average combustion pressure was 2.3MPa, the largest thrust was 600N, and average thrust was 300N.

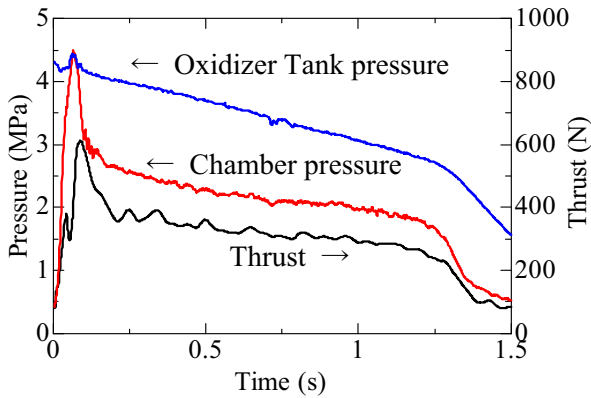


Fig. 2 An example of time histories of pressure and thrust

The result of LT fuel regression rate using gas oxygen and liquid N_2O as oxidizer is shown in Fig. 3. The regression rate was calculated as an averaged value from the mass difference of the firing test before and after an experiment. After the firing test, the LT fuel melted slightly and accumulated into the bottom of the chamber, therefore direct inside diameter measurement is omitted. And the inside diameter after combustion was calculated from the mass difference, and the oxidizer mass flux also calculated as an average oxidizer mass flux from average inside diameter before and after an experiment.

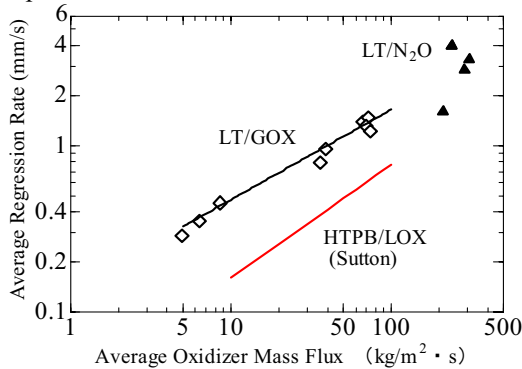


Fig. 3 Comparison of regression rate of LT fuel and classical hybrid fuel

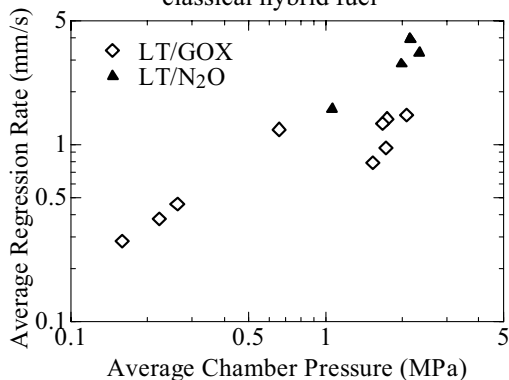


Fig. 4 Effect of chamber pressure to regression rate

The LT/GOX average regression rate is shown as following equation.

$$\bar{r} = 0.137\bar{G}^{0.54} \quad (1)$$

The average regression rate is in millimeter per second and average mass flux is kilogram per square meter per second. The mass flux exponent is 0.54, which is smaller than mass flux exponent of paraffin based fuel[3] and classical fuel HTPB. The value of LT/GOX fuel average regression rate is also 2 to 3 times high compared to the classical fuel HTPB, and is slightly small or same as compared to paraffin based fuel. The LT/ N_2O average regression rate seems to the same order as LT/GOX average regression rate. These results mean that as regression rate characteristics of hybrid rocket fuels, the value of regression rate does not depend to type of oxidizer. It is confirmed that it is dominant in regression rate that droplets are carried away by the oxidizer mass flux from the fuel surface by the entrainment effect[1] the result of the fuel regression rate independent of the type of oxidizer.

Figure 4 show the effect of chamber pressure to regression rate. The regression rate seems to be proportional to chamber pressure. Especially as for the tendency, N_2O appears strongly rather than oxygen. From Fig.3, no large distribution of the average oxidizer mass flux is observed at LT/ N_2O data. This means that the internal flow condition of chamber by oxidizer is not changed, however average regression rate is increasing with average chamber pressure rising. This phenomenon suggested that the average chamber pressure rising is increasing flame temperature, that is decreasing surface tension of melt fuel. The reduction in surface tension may contribute of the increasing of fuel regression rate due to the entrainment effect.

4. Summary

Two types of hybrid rocket motors which use the gas oxygen and N_2O as oxidizer are used for investigation of regression rate of the LT fuel. The regression rate was compared between gas oxygen and N_2O , and the value of LT/GOX regression rate is described by regression curve of oxidizer mass flux, and the exponent is 0.54. The regression rate is 2 to 3 times high compared to classical fuel of the hybrid rocket. The results suggested that the LT fuel have a same combustion mechanism of paraffin based fuel because of its own low melting temperature. Therefore, the LT fuel is good candidate for hybrid rocket fuel in order to have excellent mechanical property and high regression rate performance.

References

- [1]Wada Y. et al., Transactions of JSASS, **10**, (2012), pp1-5.
- [2]HyperTEK, <http://www.hypertekhybrids.com/>
- [3]Karabeyoglu M. A. et al., AIAA Paper, **2001-4503**, (2001).

Sounding Rocket Development with Hybrid Combustion Technology

Yen-Sen Chen¹, T. H. Chou², J. S. Wu², G. Cheng³

¹National Space Organization, Hsinchu Science Park, Hsinchu, Taiwan

²Department of Mechanical Engineering, National Chiao Tung University, Hsinchu, Taiwan

³Department of Mechanical Engineering, University of Alabama in Birmingham, Alabama, U. S. A.

e-mail: yench@nspo.narl.org.tw

ABSTRACT

Hybrid rocket technology was recently introduced in the sounding rocket developments to support the science experiments of academic application and the establishment of a viable flight test platform for space components development. Due to its safety nature in material handling and combustion processes, hybrid rockets are suitable for university and research institute environments for advanced technology developments and to enable the hands-on experience in rocket science education. Hybrid combustion sounding rocket development approach and strategy are described and its future plan is outlined in this paper.

1. Introduction

Over the past 60 years, sounding rockets have been demonstrated to be particularly useful for flight experiments above 50 km altitude, under which airplanes and balloons are also readily available. Although it has almost always been motivated by military applications, for many space faring countries, sounding rockets also served as rocket technology research and development platforms for the establishment of their space launch capabilities. Today, sounding rockets are often used for science experiments in atmospheric studies, microgravity environment, advanced aerospace technologies and space components developments and qualifications. And, solid rockets are commonly employed for these applications, which are mostly fabricated by military or well-established aerospace organizations in technically qualified facilities with skilled personnel.

In the recent development of sounding rockets and space launch systems, hybrid rocket propulsion has drawn a lot of attention, especially in the civilian space tourism community, and has been demonstrated to become a viable alternative to the liquid and solid rockets. The hybrid rocket is a combination of both the solid and liquid systems with half of the plumbing of the liquid rockets but retaining the flexibility of operation and avoiding the explosive nature of the solid rockets [1]. It is therefore suitable for advanced hybrid technology developments in university and research institute environments for academic research and educational purpose.

In combining both theoretical and experimental approaches, the hybrid rocket development programs have been demonstrated to be very effective and efficient. For the theoretical approach, since the early 1980s, computational modeling approaches have been gradually adopted in the aerospace community in the development of combustion devices and space launch systems. Numerical models using computational fluid dynamics (CFD) methods have been applied to liquid and solid rocket combustion systems with successful results in supporting the technical programs [2-7]. These computational tools allow design studies in hybrid rocket propulsion, rocket aerodynamics, rocket structural dynamics and flight mechanics, etc. Among these

disciplines, rocket propulsion and combustion is the key and the most complicated technology.

There are many types of hybrid combustion systems, in which fuel is classically a solid and the oxidizer is a liquid or gas. Typical examples of combination of fuel and oxidizer with optimum O/F ratio, specific impulse Isp (184 to 326 sec) and characteristic velocity (1224 to 2118 m/sec) are summarized and discussed in [1]. For material local availability, N₂O-HTPB propulsion system is selected in the present hybrid rocket development. The maximum vacuum Isp demonstrated in practice so far for the N₂O-HTPB propulsion system is only fair around 250 seconds while its theoretical limit can be as high as 320 seconds. This indicates that it is worthwhile to invest in this research to push the thrust performance close to the theoretical limit.

Very few [8,9] have attempted to model the complicated reactive flow phenomena of a realistic hybrid propulsion system that an energy-balanced surface decomposition model is employed. The modeling efforts have reached successes to some extent based on fitting of experiments and numerical simulations with real-fluid effects considered in the models. The real-fluid properties affect the overall flow structure in the combustion chamber, especially near the injectors, and affect the combustion processes and heat transfer characteristics, which is the key to the regression rates of the solid grain.

Thrust performance, propellant mass fraction, reliability and cost are the major factors that determine the overall performance of a rocket system. Theoretically, hybrid rocket systems are advantageous among many of these factors as compared to solid and liquid rocket systems. However, the thrust performance aspect of hybrid rockets still need further investigations to improve their combustion efficiency, Isp and stable O/F ratio control, etc. And, these are good research topics for universities and research institutes.

2. Hybrid Rocket Technology Demonstration

The sounding rocket program of National Space Organization of Taiwan was initiated in 1998 with the aim to establish a flight test platform for ionosphere studies and space technology developments. The long-

term goal of this program is for building up the technical capabilities for designing space launch systems.

In 2009, a hybrid rocket development program was launched with two university research teams selected to bring lab-scale hybrid combustion devices to their maturity that can be integrated into flight-worthy small-scale sounding rocket systems. This technology demonstration program gave the university team research opportunities in extending the results of their fundamental studies to multi-disciplinary systems engineering practices in order to realize the system integration, testing and flight operations. This program is unprecedented in Taiwan's research community and has broadened the views and hands-on experience of the researchers and students involved in the program. As part of the results of the program, successful hybrid rocket flight tests were demonstrated in 2010 and 2011 to altitudes around 10 km.

In this program, two combustion design concepts were employed. They are a N_2O -HTPB system with mixing enhancer of NCTU (National Chiao Tung University) [9] and a N_2O -50%HTPB+50%Paraffin system of NCKU (National Cheng Kung University) [10]. The thrust level (around 300 kgf) and Isp (around 220 seconds) of these two approaches are comparable. The rocket system is completed with composite N_2O pressure tank, flight computer and telemetry data link. During the propulsion system development, hybrid rocket motors with flight specifications and configurations were hot-fire tested in the laboratory to measure the thrust performance, solid regression rates, thermal protection environment and nozzle erosion characteristics. In the meantime, a comprehensive numerical model with finite-rate chemistry and real-fluid properties [9,11] was developed and employed by the NCTU team to study the internal ballistics of the hybrid rocket motor and compared with the hot-fire test data.

3. Hybrid Sounding Rocket Development

Based on the successful program of the hybrid technology demonstration, the National Science Council has approved proposals of the two university teams in 2011 for continuing developments of the sounding rocket technology in the next phase. The main goal of the new program is to develop viable sounding rockets in three years, capable of performing science experiments in altitude above 100 km.

With the mission descriptions of the next-phase sounding rocket using hybrid propulsion one design concept has required that the thrust level for a 600 kg rocket is to be greater than 3,000 kgf. For the new rocket motor development, the comprehensive numerical model is employed in the extensive design analysis work while a hot-fire ground test facility is being built. A final design of the hybrid motor will be selected based on theoretical and experimental studies.

A two-stage hybrid rocket system is resulted based on the system design. The first-stage motor will be similar in design as that used in the previous study with direct scaled up and fine-tuned. For the second-stage

motor, a low slenderness form factor design using dual vortical flow concept is proposed. This new design also ends up with higher combustion efficiency based on numerical optimization process. The new design gives 292 seconds vacuum Isp, which is one big step closer to the theoretical optimum value for the N_2O -HTPB hybrid system. This finding will be confirmed by hot-fire experimental data later during the preliminary design phase of the program.

The 8 meter long sounding rocket will carry three nano-size satellite engineering models to be deployed at around 100 km altitude after nose fairing separation. The scientific instruments onboard will conduct ionosphere measurements and send the data to the ground stations through the downlink telemetry system. The second-stage of the rocket is designed to deploy parachute after reentry and splash down the Pacific Ocean about 50 km off the southeast coast of Taiwan. The second-stage, which contains the flight computer and some position and attitude sensors, will be recovered from the sea. To accomplish the mission, reliable flight computer avionics and telemetry subsystems is also important for the hybrid rocket system.

4. Conclusions

The sounding rocket development program of Taiwan using hybrid rocket propulsion has been described in the paper. A comprehensive computational model with hot-fire test data validations has played an important role in the development of N_2O -HTPB hybrid rocket motors.

In the 2nd-phase of the sounding rocket R&D program using hybrid propulsion technology, a two-stage rocket has been designed and analyzed using the numerical model and will be verified using experimental data. A new motor has been designed numerically for the second-stage of the rocket that has shown good combustion efficiency and Isp. The overall thrust performance of the new design will be further validated using hot-fire test data.

Acknowledgements

This work is supported by the Sounding Rocket Program of the National Space Organization of the National Applied Research Laboratory of Taiwan. The computational resources and services are provided by the National Center for High-performance Computing of the National Applied Research Laboratory.

References

- [1] M. Chiaverini, K. Kuo, *Prog. Astro. & Aero.* (2007) **218**.
- [2] Y.S. Chen, et al., *J.Prop. & Power* (1998), **11**:4.
- [3] P. Liaw, et al., *AIAA-94-2780* (1994).
- [4] Y.S. Chen, *JENNAF 28th Exhaust Plume* (2004).
- [5] T.S. Wang, et al., *J.Prop. & Power* (2002) **18**:6.
- [6] T.S. Wang, *J.Prop. & Power*, (2005) **22**:1.
- [7] T.S. Wang, *AIAA-2005-3942* (2005).
- [8] R.C. Farmer, et al., *JANNAF 35th* (1998).
- [9] Y.S. Chen, et al., *Computers & Fluids*, (2011) **45**.
- [10] T.S. Lee, et al., *5th Taiwan-Indonesia Wkshp.* (2006).
- [11] T.S. Wang, Y.S. Chen, *J. of Prop. & Power*, (1993) **9**:5.

Computation of Swirling Flowfield Coupled with Fuel Surface Regression in Combustion Chamber for Hybrid Rocket Engine

Takaya Koda, Yousuke Ogino, and Keisuke Sawada
Department of Aerospace Engineering, Tohoku University, Sendai 980-0579, Japan
koda@cfm.mech.tohoku.ac.jp

Abstract

The purpose of this study is to reproduce the three-dimensional regression pattern in combustion chamber for hybrid rocket engine. The chemical equilibrium gas model is employed to compute the chemically reactive flow. Surface regression rate is determined by solving the heat balance equation at the fuel surface. As the test case, the calculation of diffusion flame over a flat plate is examined. The computed results shows higher regression rate is obtained at the leading edge of the fuel.

1. Introduction

Hybrid rocket uses solid fuel and liquid oxidizer as propellant. Compared with the conventional solid rocket motor, hybrid rocket is superior in terms of safety and cost because propellants are separated physically. Additionally, it can be applicable to various missions because of throttling, shutdown and reignite ability. Compared with the liquid rocket engine, its propellant feed systems are dramatically reducible.

In spite of a number of advantages, hybrid rocket is not so popular. This is because the inherent drawback of lower regression rate of solid fuel. Swirling injection of oxidizer enhances the regression rate of solid fuel in the combustion chamber of hybrid rocket [1, 2]. In the experimental studies of Yuasa et al. [2], a higher regression rate was indeed demonstrated when oxidizer was injected tangentially at the upstream side of the combustion chamber.

As the feature of the flowfield in combustion chamber of hybrid rocket, the interaction of the flowfield and surface regression is known. This is because the regression is caused by the heat transfer from fluid to the fuel surface, and the regression of surface effects the inner flowfield. The surface regression of solid fuel is larger near the leading edge of the grain, but the regression is almost constant at downstream. Additionally, helical pattern are observed due to swirling injection of oxidizer. It is thought that these three-dimensional patterns are appeared by interaction of flowfield and surface regression. When we attempts to reproduce these regression patterns by calculation, the coupled computation of flowfield with surface regression is needed. Some preceding numerical studies of the two-dimensional flowfield with surface regression was conducted [3, 4]. However, the three-dimensional flowfield computation coupled with the surface regression has not been examined yet.

In our previous works, three-dimensional computation of the swirling oxidizer flowfield was carried out [5, 6], but the surface regression was not considered. In this study, we attempt to compute the swirling flowfield coupled with surface regression of solid fuel in the combustion chamber using chemical equilibrium NS gas solver. As a preliminary study, computation of diffusion flame over a flat plate is examined.

2. Numerical Methods

2.1. CFD Code

The governing equations are the Navier-Stokes equations that have two mass conservation equations without mass generation term. Mass conservation for fuel and oxidizer gas, and momentum and energy conservation for gas mixture are considered.

We assume 1,3-butadiene (C_4H_6) as fuel and gaseous oxygen as oxidizer, and then obtain an equilibrium state for a gas mixture consisting of 9 chemical species such as CO, CO_2 , H, H_2 , H_2O , O, O_2 , OH and C_4H_6 . Equilibrium composition and thermodynamic properties of gas mixture are determined by utilizing NASA CEA [7]. As input variables of CEA, we choose density and temperature for easier curve fitting. Hence, total density and temperature of gas mixture and weight fraction of fuel gas are required in order to obtain the properties of gas mixture. We consider the total density range of 0.1 to 100kg/m³ divided into 25 data points equally spaced in logarithmic space. On the other hand, the weight fraction of fuel is considered from 0 to 100% divided into 21 data points equally spaced. We fit thermochemical properties of gas mixture in terms of temperature with assigned total density and weight fraction of fuel gas. The fitted curve is described as

$$q(T) = c_1 T^{-1} + c_2 + c_3 \ln T + c_4 T + c_5 T^2, \quad (1)$$

where coefficients are determined by least square fitting.

The governing equations are discretized by the discontinuous Galerkin finite element method [8]. The current version is second order accurate in space with the BR2 formulation for the viscous and diffusion terms. The time integration is made by the cellwise relaxation implicit scheme developed by Yasue et al. [9].

2.2. Surface regression model

The regression rate is given by solving following equations iteratively.

$$\kappa_g \frac{\partial T}{\partial y} \Big|_{+0} - \rho_f \dot{r} \sum_i Y_i h_i - \kappa_f \frac{\partial T}{\partial y} \Big|_{-0} + \rho_f \dot{r} H_v = 0, \quad (2)$$

$$\dot{r} = A \exp\left(-\frac{E_a}{RT_s}\right), \quad (3)$$

where κ is the thermal conductivity, y is the vertical direction coordinate from the fuel surface, ρ_f is the density of the fuel, \dot{r} is the regression rate, Y_i is the mass fraction of i species, h_i is the enthalpy of pyrolyzed gas, H_v is the energy of vaporization, A is the frequency factor, E_a is the activation energy, R is the universal gas constant and T_s is surface temperature.

Eq. (2) denotes the heat balance on the fuel surface and Eq. (3) denotes the relation between the pyrolysis rate of the solid fuel and the temperature of fuel surface. The first term of L.H.S. in the Eq. (2) is the convective heat flux and evaluated by fluid variables. The third term is heat conduction in the solid fuel and evaluated by solving the one-dimensional heat conduction equation.

3. Results and Discussion

Calculation of diffusion flame over a flat plate is conducted. Figure 1 shows a schematic of the computational domain. A non-slip flat plate is located at the bottom of the domain. The downstream region of the flat plate is fuel injection wall whose length L_f is 1 m. The length of the domain L is 2 m, the height H is 1 m, and the depth is 0.05 m. The free stream of oxidizer is assumed whose velocity is 65 m/s. The pressure and the temperature of the free stream are 1 MPa and 300 K, respectively. The mass flux and temperature of the fuel gas inflow correspond to $\rho_f \dot{r}$ and surface temperature T_s , respectively.

The computed temperature contours and velocity vectors are plotted in Fig. 2. The diffusion flame is formed over the fuel injection wall and the maximum temperature is about 3,800 K. At the leading edge of the fuel ($x = 0$), the high temperature region is close to the fuel surface. The distance between the flame and the fuel is almost constant at the far downstream. Figure 3 shows the surface temperature and regression rate distribution along the x direction. The surface temperature has peak value of 2,200 K near the upstream end of the fuel, and the constant value of 700 K at the far downstream. Because the flame is close to the fuel surface at the L.E., the higher convective heat flux results in higher regression rate. It is seemed that the surface regression at the L.E. of the fuel effects the downstream flowfield.

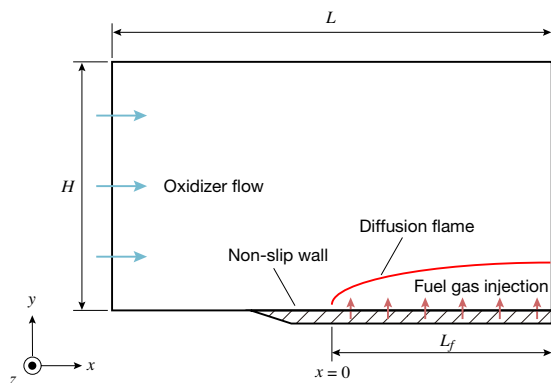


Fig. 1 Schematic of computational domain.

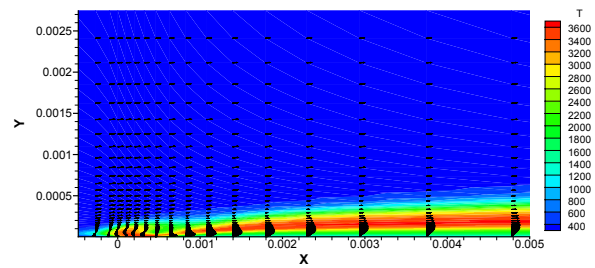


Fig. 2 Obtained temperature contours and velocity vectors in xy -plane.

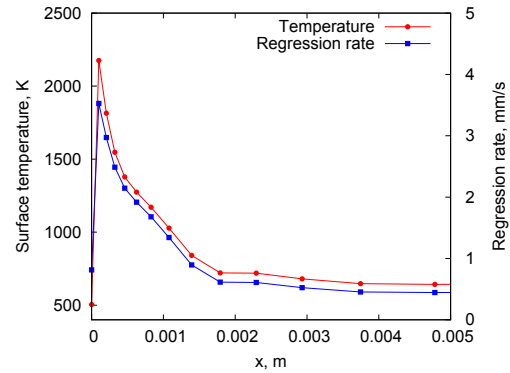


Fig. 3 Surface temperature and regression rate distribution along the x direction.

4. Conclusoin

In order to compute the swirling oxidizer flowfield coupled with surface regression, we employed chemical equilibrium NS gas solver and surface regression model based on the heat balance at the fuel surface. The computation of the diffusion flame over flat plate is carried out. The obtained regression rate is higher at the upstream end of the fuel and constant at the downstream. The results of flowfield calculation coupled with the surface regression will be shown in the conference presentation.

References

- [1] Knuth, W. H., et al., AIAA paper 98-3348, 1998.
- [2] Yuasa, S., et al., AIAA paper 99-2322, 1999.
- [3] Antoniou, A. and Akyuzlu, K. M., AIAA paper 2005-3541, 2005.
- [4] Funami, Y., at al., AIAA paper 2010-6873, 2010.
- [5] Yoshimura, K. and Sawada, K., AIAA paper 2010-905, 2010.
- [6] Koda, K., et al., Proc. of 8th ICFD, 2011, 310-311.
- [7] Gordon, S. and McBride, B. J., NASA RP-1311, 1996.
- [8] Cockburn, B. and Shu, C.-W., *J. Comput. Phys.*, **141**(1989), 199-244.
- [9] Yasue, K., et al., *CiCP*, **7**(2010), 510-533.

Improvement of Two-Equation Turbulence Model with Anisotropic Eddy-Viscosity for Swirl-Injected Hybrid Rocket Research

Mikiro Motoe*, Toru Shimada**

* Department of Aeronautics and Astronautics, School of Engineering, the University of Tokyo, Japan.

** Institute of Space and Astronautical Science, Japan Aerospace Exploration Agency.

8367791179@mail.ecc.u-tokyo.ac.jp

ABSTRACT

For a hybrid rocket engine, it has been proven by ground and flight experiments that the fuel regression rate can be accelerated by swirling injection of the oxidizer. It is known a swirling turbulent flow has anisotropic nature in its turbulent viscosity. In this study, the objective is to improve the applicability of existing treatment of isotropic turbulent model such as two-equation, eddy viscosity, model by introducing anisotropic eddy-viscosity coefficients, in order to simulate swirling turbulent flows in hybrid rocket engines. Simulation results for some swirling turbulent flows with the existing model and with an improved model will be compared.

1. Background and Objectives

Hybrid rocket propulsion is one of space propulsion techniques for the next generation now researched actively. As shown in Figure 1, this type of rocket consists of solid fuel and liquid oxidizer. Typically, acrylic or wax is used as the solid fuel, and liquid oxygen is used as the oxidizer. Therefore, it has high safety because the fuel does not contain explosives as ingredients and low environmental load by exhaust than that of a solid rocket motor. In addition, the rocket shows good characteristics of capability that thrust modulation like a liquid rocket engine, and higher specific impulse than a solid rocket motor.

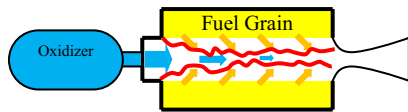


Fig. 1 Outline of a hybrid rocket engine

Though, in case a conventional fuel, such as, HTPB or PE, etc., a hybrid rocket engine has limitation that only low fuel regression rate can be obtained. As one of methods for enhancing fuel regression rate, a swirling-oxidizer-typed hybrid rocket engine that induces swirling flow in the chamber was invented. It has been clarified by experimental investigations that the regression rate can be improved by this method. Also, some numerical studies are reported.

In general, for the case that CFD is employed as a design tool of the combustion chamber, the Reynolds Averaged Navier-Stokes (RANS) equations have been used because of their reasonable computational costs compared to those of LES and DNS. On this occasion, a two-equation turbulence model, such as $k - \varepsilon$ model, has been often selected in order to obtain turbulence stresses. However, as is well known, ordinary linear turbulence models based on the eddy-viscosity assumption cannot simulate flow field like swirling turbulence in pipe precisely. Because the turbulence transport in swirling flows is usually anisotropic which is small in selective directions, a turbulent model assuming isotropic turbulence transport cannot describe swirling flow in principle.

Recently, Yoshizawa, et al. have developed the improved two-equation turbulence model, which is usable for simulating swirling turbulence flow [1]. This

model is based on the standard $k - \varepsilon$ model. An eddy-viscosity of this model is reduced by a coefficient constructed with substantial derivative of vorticity indicating swirling of mean flow. So, the turbulence stresses of all directions are reduced uniformly.

Authors simulated the experiment of low velocity swirling flow in a pipe by Murakami, et al. [2] as a prior case for evaluating applicability of the improved model to the swirling-oxidizer-typed hybrid rocket engine [3]. And it was confirmed that the predictive accuracy for weak swirling flow is clearly improved than the result of standard $k - \varepsilon$ model. Though, the result that applying improved model to strong swirling flow for instance vortex-tube was not favorable. It is considered that these flow fields have strong anisotropic turbulence. Hence, authors attempt to that improvement simulation result of Yoshizawa model by adding nonlinear term of turbulent stress formulation of helicity model[4] in order to append property of anisotropy to eddy viscosity. Objective of this study is to comprehend characteristic of this model by means of simulate existing experimental results and to validate availability.

2. Turbulence Model

The turbulence model using in this study is composed by that adding nonlinear term of turbulent stress of helicity model to that of Yoshizawa model. The formulas of this model are showed as follows.

Turbulent energy transport:

$$\frac{\partial(\rho k)}{\partial t} + \frac{\partial(\rho u_j k)}{\partial x_j} = R_{ij} \frac{\partial u_i}{\partial x_j} - \rho \varepsilon + \frac{\partial}{\partial x_j} \left[\left(\mu + \frac{\mu_t}{\sigma_k} \right) \frac{\partial k}{\partial x_j} \right] \quad (1)$$

Turbulent energy dissipation rate transport:

$$\begin{aligned} \frac{\partial(\rho \varepsilon)}{\partial t} + \frac{\partial(\rho u_j \varepsilon)}{\partial x_j} = & C_{\varepsilon 1} \frac{\varepsilon}{k} R_{ij} \frac{\partial u_i}{\partial x_j} - C_{\varepsilon 2} f_2 \rho \frac{\varepsilon^2}{k} \\ & - C_{\varepsilon 3} \frac{k^2}{\varepsilon} \boldsymbol{\Omega} \cdot \nabla H + \frac{\partial}{\partial x_j} \left[\left(\mu + \frac{\mu_t}{\sigma_\varepsilon} \right) \frac{\partial \varepsilon}{\partial x_j} \right] \end{aligned} \quad (2)$$

And where

$$R_{ij} = 2\mu_i \left[\mathbf{S}_{ij} - \frac{1}{3} \frac{\partial u_j}{\partial x_i} \delta_{ij} \right] - \frac{2}{3} \delta_{ij} \rho k - \eta \left[\Omega_i \frac{\partial H}{\partial x_j} + \Omega_j \frac{\partial H}{\partial x_i} - \frac{2}{3} (\boldsymbol{\Omega} \cdot \nabla H) \delta_{ij} \right]$$

$$\eta = C_\eta \frac{k^4}{\varepsilon^3}, \quad H = \frac{1}{C_H} \frac{k}{\rho \varepsilon} \left(R_{ij} \frac{\partial \Omega_i}{\partial x_j} - \Omega_i \frac{\partial R_{ij}}{\partial x_j} \right)$$

$$C_V = 0.12, \quad C_S = 0.015, \quad C_{\Omega L} = 0.3, \quad \sigma_k = 1.4, \quad \sigma_\varepsilon = 1.4, \quad C_{\varepsilon 1} = 1.5, \\ C_{\varepsilon 2} = 1.9, \quad C_\eta = 1 \times 10^{-6}, \quad C_{\varepsilon 3} = 1 \times 10^{-4}, \quad 1/C_H = 1 \times 10^{-2}$$

Yoshizawa model is the turbulence model that has isotropic eddy viscosity, but by adding nonlinear term to turbulent stress, it can be considered that the isotropic eddy viscosity is converted into anisotropic eddy viscosity as follows.

$$R_{ij} = 2 \left\{ \mu_t - \eta \left[\Omega_i \frac{\partial H}{\partial x_j} + \Omega_j \frac{\partial H}{\partial x_i} - \frac{2}{3} (\boldsymbol{\Omega} \cdot \nabla H) \delta_{ij} \right] \right\} / 2 \left[\mathbf{S}_{ij} - \frac{1}{3} \frac{\partial u_j}{\partial x_i} \delta_{ij} \right] \\ \times \left[\mathbf{S}_{ij} - \frac{1}{3} \frac{\partial u_j}{\partial x_i} \delta_{ij} \right] - \frac{2}{3} \delta_{ij} \rho k \\ R_{ij} = 2 \bar{\mu}_{t ij} \left[\mathbf{S}_{ij} - \frac{1}{3} \frac{\partial u_j}{\partial x_i} \delta_{ij} \right] - \frac{2}{3} \delta_{ij} \rho k$$

3. Numerical Method

The governing equations are specially discretized by finite volume method. Numerical flux of convection term is calculated due to SLAU scheme constructed by Shima et al. [5] The 3rd order MUSCL scheme regulated by Van-Albada slope limiter with primitive variable interpolation is used to obtain higher order accuracy at cell boundary. Numerical flux of viscous term is evaluated by 2nd order central difference scheme. 2nd order 2 stages Runge-Kutta scheme is used to integrate time derivative term.

4. Numerical Setup

A case of swirling flow is selected as analysis objects which is an experiment conducted by Murakami et. al. which has retard flow in center of the pipe and use water as working fluid. The numerical grid point number for the case is about 0.3 million, and the number of each directions of axial, radius and circumferential are 71, 51 and 81 points respectively. The minimum grid length is about 10 μm at wall. The velocity boundary conditions of axial and circumferential direction at inlet are adopted velocity profiles which were measured by experiment, and radius direction velocity set to "0". In case of experiment of Murakami et. al., the position measuring velocity is at distance of 50 times of pipe radius R_0 from the swirler. Because the data of velocity profile have been nondimensionalized by bulk velocity, in this study, the bulk velocity is set to 5 m/s. In this case, the Reynolds number is about order of 10^5 .

5. Results and Discussion

The simulation results for the experiment by Murakami et. al. are shown. Figure 2 and Figure 3 indicate radial distribution of axial velocity and circumferential velocity, respectively, both of them are averaged circumferentially and are nondimensionalized. In Figure 2, about axial velocity distribution, it can be seen that the current model simulate better results than that of the Yoshizawa model in central and near wall regions. In central region, the current model estimates smaller absolutes of axial velocity than the results of Yoshizawa model, and in near wall region, it estimates bigger absolutes of velocity. In figure 3, about circumferential velocity distribution, differences between the current model and the Yoshizawa model are

seen only in near wall region at both sections. In this situation, current model estimates bigger absolutes of velocity than the results of Yoshizawa model.

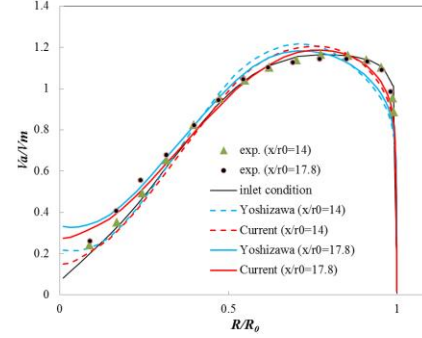


Fig. 2 Axial velocity distributions

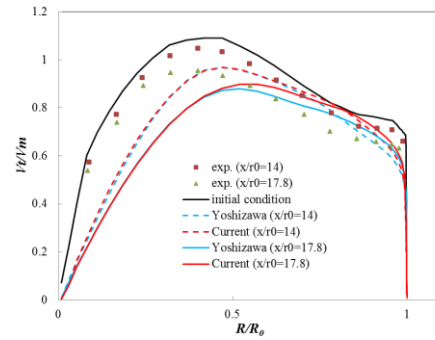


Fig. 3 Circumferential velocity distributions

6. Summary

In this study, Yoshizawa model is improved by adding nonlinear term of turbulent stress formulation of helicity model in order to append property of anisotropy to eddy viscosity. In the case of simulation for experiment of Murakami et al., axial velocity distributions are slightly improved at central and near wall region, and absolute value of circumferential velocity become bigger than that of Yoshizawa model.

References

- [1] Yoshizawa, A., et al., Journal of Turbulence, vol. 12, 2011.
- [2] Murakami, M., et al., Transactions of the Japan Society of Mechanical Engineers. B, vol.41, No.346, pp.1793-1801, 1975.
- [3] Motoe, M, et al., , AIAA 2011-560
- [4] Yokoi, N., et al., Transactions of the Japan Society of Mechanical Engineers. B, vol.58, No.553, pp.2714-2721, 1992.
- [5] Shima, E., et al., AIAA Paper 2009-0136

Numerical Investigation of Flow Characteristics Past a Mixing Enhancer in a Single-Port Hybrid Combustion Chamber

T.-H. Chou¹, J.-S. Wu^{1*}, Y.-S. Chen² and G. Cheng³

¹Department of Mechanical Engineer, National Chiao Tung University, Hsinchu, Taiwan

²National Space Organization, Hsinchu Science Park, Hsinchu, Taiwan

³Department of Mechanical Engineer, University of Alabama, Birmingham, Alabama, USA

*e-mail: chongsin@faculty.nctu.edu.tw

ABSTRACT

In this paper, gas flow field past a mixing enhancer with eight blades in a single-port hybrid combustion chamber is thoroughly investigated using a parallel Navier-Stokes equation solver. Results show that the velocity gradients (or shear stress) on port surface decrease with increasing downstream distance from the mixing enhancer and the strongly non-uniform circumferential distribution is found to correlate very well with experimental regression at the solid surface from a static-burn test.

1. Introduction

Recently, hybrid rocket propulsion has attracted much attention because of many advantages, including good ISP (as compared to solid rocket propulsion), simplicity of system (as compared to liquid rocket propulsion), high safety of operation and throttling capability [1]. Because of these rationales, hybrid rocket propulsion is one of excellent research topics, especially, for universities and academic institutions.

Hybrid propulsion system generally employs solid fuel and liquid oxidizer, in which combustion takes place in a form of diffusion flame. The combustion efficiency of diffusion flame is generally low because of poor mixing between fuel and oxidizer. Thus, mixing enhancer [2] had been developed to efficiently improve the mixing between fuel and oxidizer while keeping the simplicity of the system.

In [2], 4-8 planar blades are inserted in a single-port hybrid combustor with different angles of attack with respect to the axial flow, as shown in Fig. 1. Several experimental results have demonstrated that ISP can be boosted by this mixing enhancer. However, detailed flow structure past this kind of mixing enhancer is still required to further understand the complex flow field, which may lead to better performance in practical applications.

In this paper, we would like to numerically investigate and present the flow structure due to the mixing enhancer, especially the wall velocity gradient at the port surface.

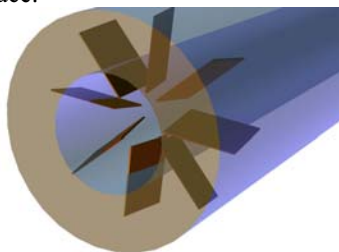


Fig. 1 A mixing enhancer in a single-port hybrid combustor with eight blades.

2. Numerical Method

In this paper, we solve the governing equations including the continuity equation, the momentum equations, the energy equation, the species continuity

equations and the extended k- ϵ turbulence modeling equations [3].

By taking the advantage of symmetry, we only take 1/8 of original port for production run (Fig. 2). Note that we have also performed a full-scale simulation to make sure this simplification is appropriate.

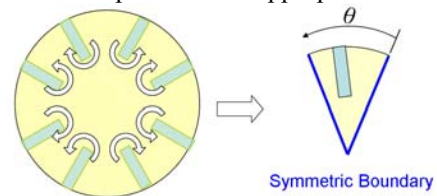


Fig. 2 Symmetric boundary condition in 1/8 cylinder.

To further save simulation time, we have used two different types of mesh for some cases, which include a multi-zone unstructured mesh (Fig. 3 left) and an I-blanking mesh (Fig. 3 right). Results from both types of mesh are found to be slightly different but the trends of the flow properties we are interested in, such as vorticity and wall shear stresses at the port surface, are similar.

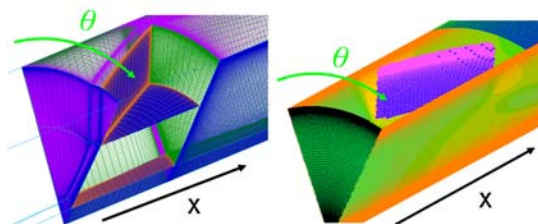


Fig. 3 Multi-zone unstructured mesh (left) and I-blanking mesh (right).

In hybrid combustion, the typical value of Prandtl number is close to 1 ($Pr \approx 1$) [4], which means that thermal boundary layer thickness almost equal to velocity one. Based on the wall shear stresses, we can easily infer the heat flux approximately, and thus the distribution of surface regression rate [4]. Therefore, we will focus on the velocity gradients at port surface and compare them to the measured distribution of surface regression at solid fuel due to hybrid combustion.

3. Results and Discussion

Note all the results presented hereafter are for a

single port having 30 mm in diameter port, a cold flow (air) inlet axial velocity with 20 m/s and an initial pressure of 30 bars that is appropriate to a real combustion chamber pressure.

Fig. 4 and Fig. 5 show the averaged axial vorticity magnitude at different locations after the blade tip following the presentation in [5]. In this case we fix chord length as 15 mm with different combinations of span and angles of attack. These two results are different, but the trends are almost the same. Results show that the combination of span with 6 mm in length and angle of attack with 23.5° has the best performance (highest vorticity).

Fig. 6 shows the axial velocity gradient with respect to radial direction (dU_x/dR) at the port surface using the combination of best performance. Results show that there exist very large positive values at the blade tips and very large negative values right behind the blade that is caused by a reverse flow. Fig. 7 is the azimuthal velocity gradient (dU_θ/dR) with respect to radial direction. We can see the peak value that is smaller than those presented in Fig. 6 appears in the tip at the downside. We expect those downstream regions at the solid fuel surface behind the large axial velocity gradients would be burned faster with a larger regression rate. Fig. 8 shows that burned HTPB fuel surface behind a mixing enhancer with eight blades. It clearly shows the pattern as we have found from the numerical simulation.

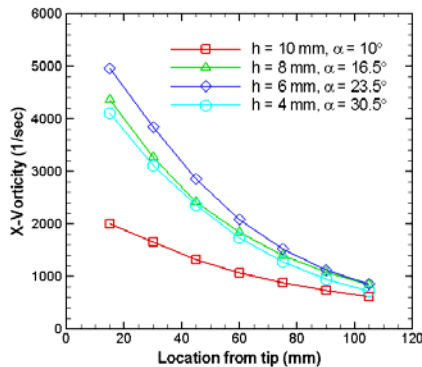


Fig. 4 Normal multi-zone structure grid results: Axial vorticity magnitude with fixed chord length (15 mm) and different combination of span & angle of attack.

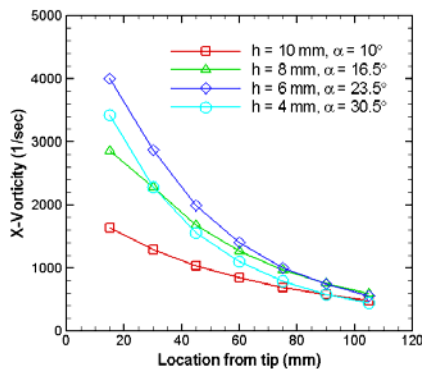


Fig. 5 I-blanking grid results: Axial vorticity magnitude with fixed chord length (15 mm) and different combination of span & angle of attack.

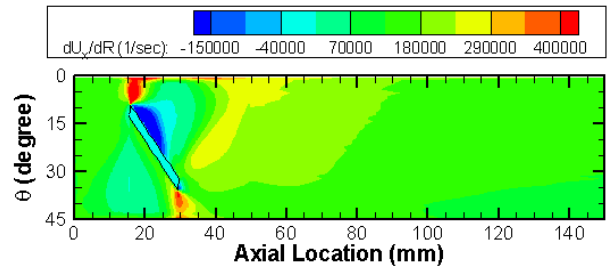


Fig. 6 Axial velocity gradient on port surface.

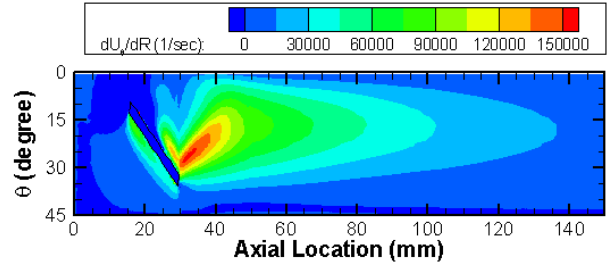


Fig. 7 Rotational velocity gradient on port surface.



Fig. 8 The burned fuel surface just after mixing enhancer.

4. Concluding remarks

In this paper, we have presented a numerical simulation of gas flow past a mixing enhancer in a single-port hybrid combustion chamber [2]. Results of axial and azimuthal velocity gradients with respect to radial direction show that very large localized shear stresses can be found near the blade tips. This finding also correlates well with experimental observations from a static-burn test.

To further understand the improvement of the hybrid combustion efficiency due to the addition of the mixing enhancer, 3-D simulation of reacting flows considering real fluid model and finite-rate chemistry of HTPB-N2O is currently in progress.

References

- [1] M. J. Chiaverini, K. K. Kuo, *Fundamentals of Hybrid Rocket Combustion and Propulsion*, AIAA (2007).
- [2] U.S Patent, 2011/0203256 (2011)
- [3] Wang & Chen, *J. of Prop. & Power*, 9:5 (1993)
- [4] Marxman, G. and Gilbert, M., Ninth Symposium (International) on Combustion, Academic Press, pp 371-372 (1963).
- [5] B. J. Wendt, AIAA-95-1797 (1995).

Injection Effects on Hybrid Rocket Combustion Instability

Mario Kobald^{1,2}, Tobias Willerding², Alexander Schindler², Helmut Ciezki¹ and Stefan Schlechtriem^{1,3}.

1 - DLR - Institute of Space Propulsion, 74239 Hardthausen, Germany.

2 - HyEnD – Hybrid Engine Development, DGLR student group, 70569 Stuttgart, Germany.

3 – Institute of Space Systems, University of Stuttgart, 70569 Stuttgart, Germany.

E-mail of corresponding author: Mario.Kobald@dlr.de.

ABSTRACT

There exists a growing interest in Hybrid rocket engines over the last years. But only minor work has been done on the design and performance of the injector type. This is especially important since combustion stability can be closely linked to the type of injector and configuration of the pre-combustion chamber. In the present paper hot flow experiments have been carried out to evaluate the performance of different injector types. Characteristic velocity and combustion stability during hot fire tests are evaluated and compared. Impingement injectors with high impingement angles produced unstable combustion.

1. Introduction

Hybrid rocket engines combine the advantages of solid and liquid propulsion systems: Simple and safe storability due to separately stored oxidizers and fuels, straightforward control of mixture ratio by variation of the oxidizer mass flow and the possibility for immediate shut-down. The most well-known application of a hybrid rocket engine is the one flown on June 21, 2004: SpaceShipOne achieved the first privately funded human spaceflight.

The work in this paper has been done from HyEnD (Hybrid Engine Development) Stuttgart; a student group of DGLR (German Aerospace Association) Stuttgart was founded in 2006 with the goal of building and developing hybrid rocket engines [1].

2. Injectors

Injectors are said to be the component with the greatest impact on rocket engine performance and stability [2]. A rapid and efficient atomization of the oxidizer is the main task of the injector head. Three different types of injectors are under investigation in this research:

Showerhead injectors produce straight parallel jets of oxidizer penetrating through the fuel. In a showerhead the individual streams do not interact with each other and atomization properties are controlled by Rayleigh jet break-up length [3]. Therefore mixing with the fuel is restricted and combustion efficiencies can be rather low.

Impingement injectors generally offer a higher performance due to their improved atomization behavior. For our research we use four different quintuplet impingement injectors. Their difference is in the impingement angle which was built as 45°, 60° and 90°.

Swirl injectors set the fluid in rotational motion. The swirling ruptures the fluid by the centrifugal forces in droplets of varying sizes, about 2.5 times smaller droplets than jet injectors for the same pressure drop and mass flow rate [4]. Additionally this swirling motion also improves the turbulent mixing for higher combustion efficiency. Our swirl injector has a characteristic geometric parameter of 10 [5].

3. Combustion instability

Combustion is defined to be instable when the

fluctuations in chamber pressure exceed more than 5%-10% of the mean pressure value. Oscillations in chamber pressure p' can grow if they are in phase with the heat release oscillations q' of the combustion. This is known as the criterion of Rayleigh [6]

$$\iiint_0^t p' q' dt dV > 0 \quad (1)$$

During these oscillations energy from the combustion can be transferred in the acoustic modes of the chamber. These oscillations can lead to different failure mechanisms, for example increased chamber pressure. Non-acoustic instabilities can generally be caused by poor atomization from the injector, chuffing of the solid fuel, pressure sensitivity of the combustion, flow oscillations caused by vortex shedding or hydrodynamic coupling between the oxidizer in the feed system and the combustion process. Acoustic oscillations are higher in amplitude and often coexist or can be triggered by the low frequency instabilities. They mostly appear together with intrinsic low frequency instabilities [7]. A transient model by Karabeyoglu has shown that these instabilities can be based on a complex coupling between thermal transients in the solid fuel, wall heat transfer blocking and the transients in the boundary layer [8]. Instabilities can also be related to inadequate flame holding [7] or vortex shedding [9].

4. Test data

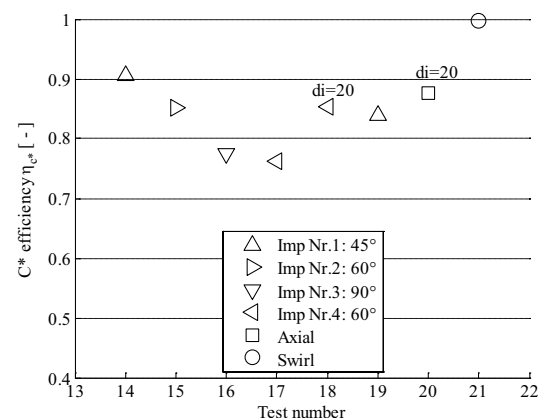


Fig. 1 C* efficiencies

All tests were performed in fuel rich conditions. Solid paraffin as fuel and liquid nitrous oxide (N₂O) as oxidizer was used in a 250 N hybrid engine. The initial tank pressure during all tests was approximately 60 bar to have similar conditions at injector inlet. Detailed test data is referenced in [10]. If we have a look at the combustion efficiencies in Figure 1 we can see that the impingement injectors produce high efficiencies between 75%-91%. The showerhead injector in test 20 also had a high efficiency. The swirl injector delivers the best performance with an efficiency of almost 100%. Test 15 and Test 16 have been done under comparable operating conditions concerning oxidizer mass flow, chamber pressure, fuel geometry, regression rate and burn time. The main difference was the injector configuration. Test 15 used an impingement injector with 60° angle while test 16 used a 90° angle. Test 16 showed a sudden increase in mean chamber pressure at 1 sec after test begins which lasted for about 1 sec as can be seen in Figure 2. The amplitude of the oscillation is

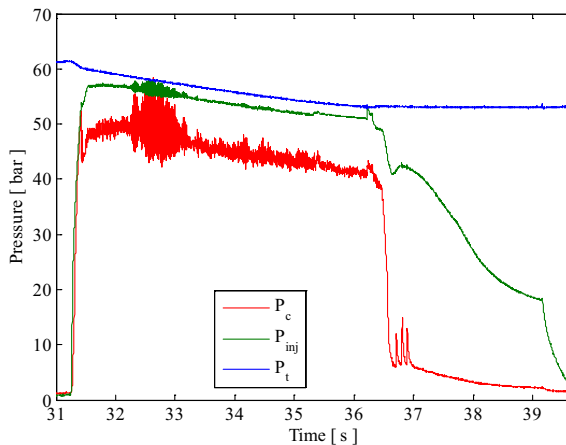


Fig. 2 Pressure time trace test 16

approximately 20% of the mean pressure. This indicates that due to the strong radial flow field of the injector no continuous recirculation zone before the paraffin grain could be established. In contrary test 15 in Figure 3 shows a stable combustion without oscillation. The unsteady flow field in the precombustion chamber in test 16 is

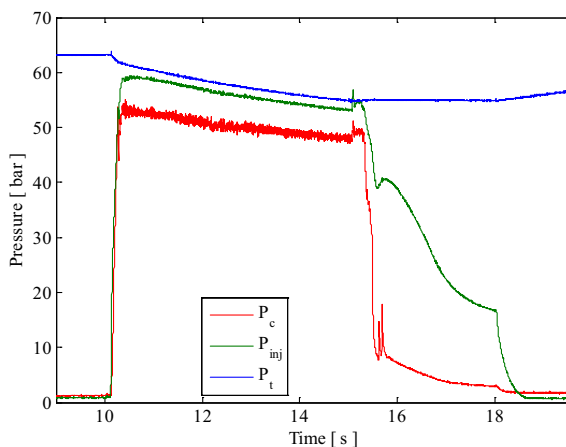


Fig. 3 Pressure time trace test 15

also likely to induce vortex shedding which then excites the vortex shedding in the postcombustion chamber. A spectral analysis of test 15 and 16 shows that oscillations at 90-100 Hz exist but only in test 16 strong oscillations evolved. A lower frequency around 90 Hz is associated with vortex shedding while the frequency at about 180 Hz can be either related to a higher mode vortex shedding or the Helmholtz frequency.

5. Conclusions

Vortex shedding related instabilities are also appearing with liquefying hybrid rocket fuels. Impingement injectors with high angles produce unstable combustion similar to radial injectors. Their unsteady flow field in the precombustion chamber can promote instabilities. The oscillations were limited in their amplitude and did not exceed 20% of mean chamber pressure. The intrinsic low frequency instability of hybrid rocket engines has been not been observed during most of the tests.

6. Acknowledgements

The authors would like to thank all the persons, institutes and companies who supported the presented work in several manners, especially the Klaus Tschira Stiftung GmbH for their fundamental sponsorship. The experimental tests have been performed in cooperation with the Institute for Space Propulsion at DLR Lampoldshausen at test complex M11 in Support of the department of propellants which is greatly acknowledged. We also would like to thank Sasol Wax for generously providing us the different paraffin wax blends to be tested and Endress + Hauser for the Coriolis mass flow sensor. A complete list of our supporters is presented under: www.hybrid-engine-development.de.

References

- [1] M. Kobald, H. Moser, A. Bohr, and S. Mielke, in DLRK, (2009).
- [2] D. Huzel and D. H. Huang, *Modern Engineering for Design of Liquid-Propellant Rocket Engines*, vol. 147 (1992).
- [3] K. Lin, C. Rajniecek, J. McCall, B. Fischer, C. Carter, and K. Fezzaa, no. AIAA 2011-232, (2011).
- [4] V. Yang, M. Habiballah, J. Hulka, and M. Popp, *Liquid Rocket Thrust Chambers: Aspects of Modeling, Analysis, and Design*, vol. 200 (2004).
- [5] S. Yuasa, O. Shimada, T. Imamura, T. Tamura, and K. Yamamoto, no. AIAA 99-2322, (1999).
- [6] J. W. S. Rayleigh, *Nature*, vol. 18, no. 4551, (1878), pp. 319–32.
- [7] T. A. Boardman, D. H. Brinton, R. L. Carpenter, and T. F. Zoladz, no. AIAA 95-268, (1995).
- [8] M. A. Karabeyoglu, S. De Zilwa, B. Cantwell, and G. Zilliac, *JPP*, vol. 21, no. 6, (2005), pp. 1107–1116.
- [9] C. Carmicino, *JPP*, vol. 25, no. 6, (2009), pp. 1322–1335.
- [10] M. Kobald, T. Willerding, A. Schindler, M. Kott, M. Hahn, H. Ciezki, and S. Schleichtriem, SPC, (2012).

Low-Frequency Oscillatory Combustion in Hybrid Rocket Motors

Takakazu Morita¹, Saburo Yuasa², Koki Kitagawa³, Toru Shimada³ and Shigeru Yamaguchi⁴

¹Department of Aeronautics and Astronautics, Tokai University, Hiratsuka, Japan

²Department of Aerospace Engineering, Tokyo Metropolitan University, Hino, Japan

³Institute of Space and Astronautical Science, Sagami-hara, Japan

⁴Department of Physics, Tokai University, Hiratsuka, Japan

E-mail: morita@tokai-u.jp

ABSTRACT

The low-frequency unstable combustion of hybrid rocket motors was investigated using the transfer function of the full thermal-combustion-gasdynamic coupled system that was coupled with a liquid propellant feed system. The transfer function was obtained based on the method developed by Karabeyoglu et al. This transfer function is applicable to the motors that have a long fuel port length. The linear stability limits and the frequencies of pressure oscillations in hybrid rocket motors were obtained theoretically using the transfer function.

1. Introduction

Many previous studies on the theoretical treatment of feed system coupled combustion instabilities in hybrid rocket motors were done using the assumption that various physical quantities in a combustion chamber change in bulk mode⁽¹⁻³⁾. However, the axial variation of various physical quantities in large L/D motors cannot be ignored. Here L and D are chamber port length and port diameter, respectively. Therefore, it is necessary to incorporate the spatial non-uniformities into the chamber transfer function of the motors. Moreover, considering the effect of heat loss on a combustion chamber wall, we assume that the gas temperature in the combustion chamber changes in a polytropic process⁽³⁾. In order to examine the low-frequency combustion instabilities of large L/D motors, the transfer function of a liquid-fed system was coupled with that of the full thermal-combustion-gasdynamic (TCG) coupled system, which was obtained based on the method developed by Karabeyoglu et al^(2,4,5). The linear stability limits and the frequencies of the neutral oscillation in a combustion chamber were obtained theoretically using this analysis. In addition, the results obtained by the above analysis were compared with the results obtained under the assumption that various physical quantities change in bulk mode.

2. Analytical Method

Coupled the full TCG coupled transfer function with the transfer function of a liquid propellant feed system, we can obtain the transfer function that describe the low-frequency unstable combustion caused by non-steadiness of a liquid-fed system. The result shows in the following equation.

$$\frac{\hat{p}_a^*}{\hat{p}_T^*} = \frac{1}{1 + S_1 + \{\sigma(1 + S_1) + S_2\} \exp(\tau_{ox}s) / H_a} \quad (1)$$

H_a is the transfer function of the full TCG coupled system. S_1 and S_2 are the parameters that represent the non-steady characteristics of a liquid propellant feed system. The condition that unstable combustion occurs can be obtained by setting the denominator of Eq.(1) to zero. Moreover, setting α to zero yields the condition of

the combustion stability limit. The result is written as shown below.

$$1 + S_1 + \{\sigma(1 + S_1) + S_2\} \exp(i\omega^*) / H_a = 0 \quad (2)$$

The above equation is separated into the real and imaginary parts as follows.

$$\frac{\Delta p}{\bar{p}_a} = \frac{|H|}{2}, \quad (3)$$

$$\tan \omega^* = \frac{H_i}{H_r}, \quad (4)$$

$$\text{where } H = H_a + \exp(\tau_{ox}s) S_2 / (1 + S_1). \quad (5)$$

In order to calculate the combustion stability limit, Equation (4) must be solved numerically. The solution is the non-dimensional angular frequency of the neutral oscillation in a combustion chamber. Substituting it into Eq.(3), we can obtain the combustion stability limit.

3. Results and Discussion

The theoretical combustion stability limits were calculated using the above-mentioned transfer function. We also calculated the stability limits using the assumption that various physical quantities change in bulk mode. The former is almost the same as the latter. However, it gives the correct results only to the low-frequency oscillatory combustion in small-scale hybrid motors. These results are shown in Fig.1. This figure also indicates that the area of stable combustion becomes large as the gas residence time of a combustion chamber increases. When the polytropic exponent is equal to one, it corresponds to an isothermal model. The ratio of specific heats of combustion product gas was equal to 1.24 in this study. When the polytropic exponent has the same value, it corresponds to the assumption that gas temperature changes adiabatically in a combustion chamber. Compared with the adiabatic case, the isothermal case yields more stable results.

Figure 2 shows the non-dimensional frequencies of the neutral oscillation in a combustion chamber. In this figure, the above-mentioned transfer function gives almost the same as the result in the case of the bulk mode. Moreover, although the polytropic exponent is assumed to be 1 or 1.24, few differences were seen among them in the range of the horizontal axis on this

figure. Therefore, the frequency characteristics of the oscillatory combustion are almost independent of the polytropic exponent.

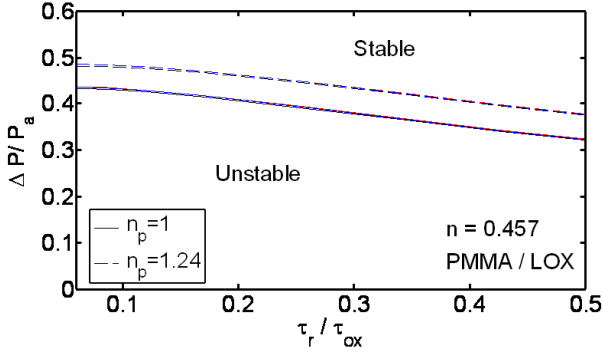


Fig. 1 Stability limits of the low-frequency unstable combustion.

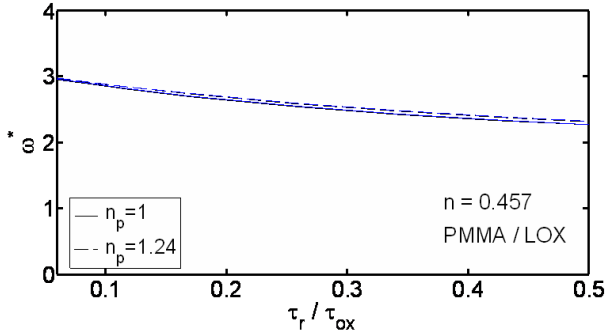


Fig. 2 Non-dimensional frequencies of the pressure oscillation in a combustion chamber

4. Concluding remarks

A transfer function of the low-frequency unstable combustion caused by the combustion time lag of liquid oxidizer was obtained. The combustion stability limits and the frequencies of the neutral oscillation in a combustion chamber were calculated using this transfer function. For small scale hybrids, the combustion stability limit can be described approximately by the following parameters: the ratio of the gas residence time to the combustion delay time of liquid oxidizer, the polytropic exponent of the gas in a combustion chamber. The frequencies of the neutral oscillation can be described approximately by the above-mentioned ratio. Therefore, the frequency of the neutral oscillation is almost independent of the polytropic exponent.

Nomenclature

$$H_a : H_a = \hat{p}_a^* / \hat{M}_a^*$$

i : imaginary unit

$$\dot{M}_a^* : \dot{M}_a^* = \dot{M}_a / \bar{M}_a$$

n_p : polytropic exponent

p : pressure

$$p_a^* : p_a^* = p_a / \bar{p}_a$$

$$p_T^* : p_T^* = p_T / \bar{p}_a$$

s : Laplace transform variable, $s = \alpha + i\omega$

α : growth rate constant

$$\Delta p : \Delta p = \bar{p}_j - \bar{p}_a$$

$$\sigma : \sigma = 2\Delta p / \bar{p}_a$$

τ_{ox} : combustion time lag of liquid oxidizer

τ_r : gas residence time of a combustion chamber

ω : angular frequency

$$\omega^* : \omega^* = \tau_{ox}\omega$$

Subscripts

a : precombustion chamber

i : imaginary part

j : injector

r : real part

T : oxidizer tank

Superscripts

$*$: nondimensional value

\wedge : Laplace transform of the perturbation quantity

$-$: steady-state

Acknowledgments

This research is supported by the Hybrid Rocket Research Working Group (HRrWG) of Institute of Space and Astronautical Science, Japan Aerospace Exploration Agency. The authors thank members of HRrWG for helpful discussions.

References

- [1] A. Karabeyoglu, J. Stevens, and B. Cantwell, AIAA Paper 2007-5366 (2007).
- [2] M. A. Karabeyoglu, Ph.D. Thesis, Stanford University (1998).
- [3] T. Morita, K. Kitagawa, S. Yuasa, S. Yamaguchi, and T. Shimada, Transactions of the Japan Society for Aeronautical and Space Sciences, Aerospace Technology Japan, **10** (2012), pp.37-41.
- [4] T. Morita, K. Fujiwara, A. Matsuki, S. Yamaguchi, and T. Shimada, Proc. of the 55th Space Sciences and Technology Conference, JSASS-2011-4459, (2011), (in Japanese).
- [5] T. Morita, K. Kitagawa, T. Shimada and S. Yamaguchi, Proc. of 9th International Symposium on Special Topics in Chemical Propulsion, pp.145-146.

Validation of Integral Method for Numerical Prediction of Hybrid Rocket Internal Ballistics

Yuki Funami[†] and Toru Shimada^{††}

[†]The University of Tokyo, 7-3-1 Hongo, Bunkyo-ku, Tokyo, Japan

^{††}Japan Aerospace Exploration Agency, 3-1-1 Yoshinodai, Chuo-ku, Sagami-hara, Kanagawa, Japan
funami.yuki@ac.jaxa.jp

ABSTRACT

In order to design hybrid rocket engines, we have developed a numerical prediction approach to the internal ballistics. The key point is its cost performance. Therefore simple but efficient models are required. Fluid phenomenon and thermal conduction phenomenon in a solid fuel should be treated time-dependently, because characteristic times of these phenomena are longer than those of other phenomena. Besides, they are solved with the energy-flux balance equation at the solid fuel surface to determine the regression rate. It is confirmed that numerical evaluation of time-space averaged regression rate is the same order of magnitude as that in experiments.

1. Introduction

The purpose of this study is to develop a design tool for prediction of hybrid rocket performance, such as regression rate characteristics through the whole burning period. A very physically rigorous mathematical model, such as direct numerical simulation of turbulence flame, is not appropriate for this purpose. On the other hand, physico-chemical phenomena in a combustion chamber of hybrid rocket consist of various processes that are mutually interacting. Therefore moderately complex models that are appropriate for this present purpose are required. In this study, fluid phenomenon of main stream and thermal conduction phenomenon in a solid fuel are considered, because characteristic times of these phenomena are longer than those of other phenomena. On the other hand, characteristic times of combustion reactions are short enough, and quasi-steady flame is assumed. The energy-flux balance equation at the solid fuel surface is solved to estimate regression rate. In order to validate the method, numerical results are compared with experimental results.

2. Method

The developed method is outlined in the following sections. The details of it are described in Ref. [1].

2.1 Configuration

Calculation domain is in a chamber and a nozzle. A fuel grain has a circular single port. Oxidizer injection type is axial-flow injection. Configuration of the port and the nozzle is shown in Fig 1.

Fuel is high density polyethylene. Oxidizer is oxygen. It is assumed that any polyethylene becomes ethylene when the solid fuel gasifies and that liquid oxygen has already evaporated when it is injected into the chamber.

Calculation conditions are in Table 1.

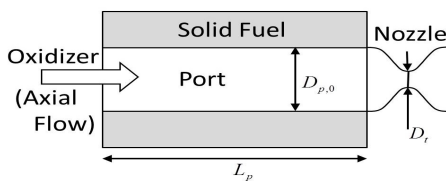


Fig. 1 Configuration of a hybrid rocket engine.

2.2 Governing equations

Basic equations for flowfield are the quasi-one-dimensional compressible Euler equations with a conservation equation for the mixture fraction ξ . Mass addition from the solid fuel surface is considered as a source term.

$$\begin{aligned} \frac{\partial A\mathbf{Q}}{\partial t} + \frac{\partial A\mathbf{F}}{\partial x} &= \mathbf{S}_{Q1D} + \mathbf{S}_{Mass}, \quad (1) \\ \mathbf{Q} &= (\rho, \rho u, \rho e_t, \rho \xi)^t, \\ \mathbf{F} &= (\rho u, \rho u^2 + p, (\rho e_t + p)u, \rho \xi u)^t, \\ \mathbf{S}_{Q1D} &= \left(0, p \frac{dA}{dx}, 0, 0\right)^t, \\ \mathbf{S}_{Mass} &= (l_p \dot{m}_F, 0, l_p \dot{m}_F h_w, l_p \dot{m}_F)^t \end{aligned}$$

In addition, definition equations of specific total energy and specific enthalpy, and the equation of state of ideal gas are used.

Mass addition \dot{m}_F is estimated by solving the energy-flux balance equation at the solid fuel surface. When radiation heat transfer is not considered for the moment, energy-flux balance is expressed as follows;

$$\lambda_g \left(\frac{\partial T}{\partial y} \right)_{y=+0} = \lambda_s \left(\frac{\partial T}{\partial y} \right)_{y=-0} + \rho_s \dot{r} h_v \quad (2)$$

The term in the left-hand side of Eq. (2) is evaluated by Karabeyoglu's model [2]. Regression rate behavior depends on mass flux in this model. In the first term of the right-hand side, temperature profile in the solid fuel is obtained by solving one-dimensional thermal conduction equation. In steady state, there is the analytical solution of it. In Eq. (2), \dot{r} is eliminated by using Arrhenius type function. Hence, Eq. (2) is expressed as the equation of surface temperature T_S . When this equation is solved for T_S , $\dot{m}_F (= \rho_s \dot{r})$ are obtained.

2.3 Combustion model

It is assumed that fuel gas and oxidizer are mixed and reacted instantly in the control volume. Nine chemical species C_2H_4 , O_2 , CO_2 , H_2O , CO , H_2 , OH , O , H are considered. Temperature and chemical composition are obtained with chemical equilibrium calculation. In this calculation, Helmholtz free energy is minimized by Lagrange's method of undetermined multipliers under the

Table 1. Calculation conditions.

Case No.	Port length, L_p [cm]	Diameter of initial port, $D_{p,0}$ [mm]	Diameter of nozzle throat, D_t [mm]	Injection oxygen mass flow rate, \dot{m}_{ox} [kg/s]	Burning period, t_b [s]
Calc.1	30.48	12.8 - 22.0	9.53 - 9.91	0.0328 - 0.0454	3.00
Calc.2	57.00	25.0 - 50.0	16.0	0.0800 - 0.210	21.2 - 54.9

constraint condition that mole numbers of elements are conserved [3].

2.4 Numerical scheme

Eq. (1) are discretized with finite volume method. Numerical flux is evaluated with AUSMDV scheme. Second order MUSCL method is used. Time integration is two-stage Runge-Kutta time integration.

It is assumed that surface regression is a quasi-static change. At a certain time t , the convergence result of Eq. (1) is calculated. Port configuration at $t + \Delta t$ is evaluated with the obtained regression rate, and the convergence result is calculated again. This procedure is iterated. Time-histories of the state in the chamber can be obtained by compiling the convergence results.

3. Results

Pressure time-history for a typical case of Calc.1 is shown in Fig. 2. Regression rate profile for a typical case of Calc.1 is shown in Fig. 3. In Fig. 4, numerical evaluation of time- and space-averaged regression rate \bar{r} is compared with that in experiments. The averaging method of numerical results is described as follow.

$$\Delta m_F = \rho_s \int_0^{L_p} \pi(r_{final}^2 - r_{initial}^2) dx \quad (3)$$

$$\bar{r}_{final} = \sqrt{r_{initial}^2 + \Delta m_F / (\pi \rho_s L_p)} \quad (4)$$

$$\bar{r} = (\bar{r}_{final} - r_{initial}) / t_b \quad (5)$$

$$\bar{G}_{ox} = 4\dot{m}_{ox} / \pi(r_{initial} + \bar{r}_{final})^2 \quad (6)$$

The order of averaged regression rate in Calc.1, whose conditions are conformed to Karabeyoglu's experimental conditions [4], is the same order as that of the experiments. The values of \bar{r} in Calc.1 are within $\pm 30\%$ of that in Expt. [4]. The data in the near range of oxygen mass flux, Lee's experiments [5], is close to the result in Calc.2. The values of \bar{r} in Calc.2 also are within $\pm 30\%$ of that in Expt. [5]. However, the slopes n ($\bar{r} = a\bar{G}_{ox}^n$) for calculation results differ from that for experiments. The factors n are listed in Table 2. The values of n in calculations are larger than that in experiments.

Table 2. The factor n in $\bar{r} = a\bar{G}_{ox}^n$.

	Expt. [4]	Expt. [5]	Calc.1	Calc.2
n	0.50	0.61	0.84	0.82

4. Summary

In order to validate the developed method, numerical results were compared with experimental results. While numerical evaluation of time- and space-averaged regression rate was the same order of magnitude as that in experiments, the factors n for calculations differed from

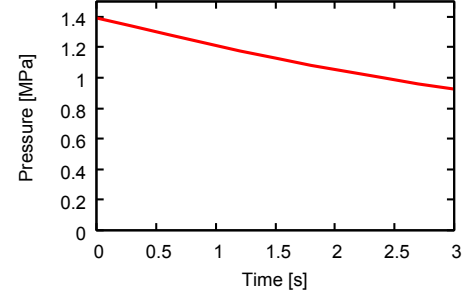


Fig. 2 Pressure time-history for a typical case of Calc.1.

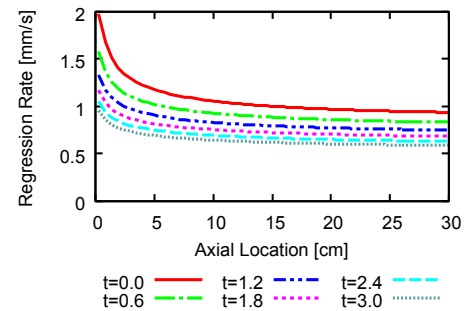


Fig. 3 Regression rate profile for a typical case of Calc.1.

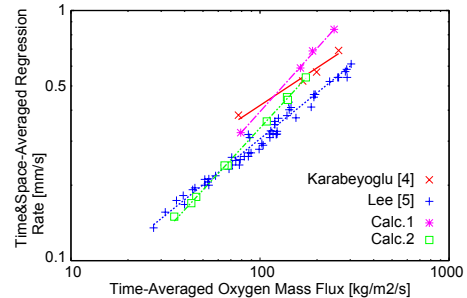


Fig. 4 Time-averaged oxygen mass flux vs. Time- and space-averaged regression rate.

that for experiments. Future works are to examine the reason of the difference of n and to modify the model.

Acknowledgements

This research is supported by the Hybrid Rocket Research Working Group (HRrWG) of ISAS/JAXA. The authors thank members of HRrWG for their helpful discussion.

References

- [1] Y. Funami, 27th ISTS, 2011-a-33s, 2011.
- [2] A. Karabeyoglu, *Fundamentals of Hybrid Rocket Combustion and Propulsion*, AIAA, 2007, pp.351-411.
- [3] S. Gordon, et al., NASA-RP-1311, 1994.
- [4] M. A. Karabeyoglu, et al., AIAA 2005-3908, 2005.
- [5] J. Lee, et al., AIAA 2011-5754, 2011.

Local and Spontaneous Regression Rate Measurement of Hybrid Rocket Using Ultrasonic's

Po-Jul Chang¹, Yutaka Wada², Toshiyuki Katsumi³, Keiichi Hori³, Hideo Nakayama⁴, Motoyasu Kimura⁵
¹Tokyo University, Tokyo, Japan ²Akita University, Akita, Japan ³ISAS/JAXA, Kanagawa, Japan
⁴Ihi Aerospace Co., Ltd. ⁵Nof Corporation
E-mail: chang.po-jul@ac.jaxa.jp

ABSTRACT

An experimental measurement of instantaneous regression-rate by using ultrasonic sensor has been studied. Glycidyl Azide Polymer (GAP) was diluted by Polyethylene Glycol (PEG) and this mixture was chosen as a hybrid rocket fuel. Three sensors were set up at upstream, middle stream and downstream of 1300mm long motor which gave the information of how the burning proceeds. Regression rate measurements indicated that propellant burns as a function of positions along the inner port of grain.

1. Introduction

Hybrid rocket systems have been studied for many years for the purpose of detailed knowledge of regression rate [1]. The complex relationship among pressure, overall size, mass fluxes, and geometric configuration is required for the design of hybrid rocket. Generally, regression rate is a mean value, however, experimental parameter changes gradually as the burning proceeds, hence instantaneous surface regression rate of solid fuel (rb) is needed for further research. So far, instantaneous rate (rb) has been mainly approached by x-ray radiography system [1]. X-ray can analyze regression rate easily, but it is costly and of less accuracy when the regression rate has a displacement of several millimeters per second. Hence the method of using ultrasonic wave with the help of sensors is rather cheap, more accurate and easy to design the combustion chamber used for experiment. But it is difficult to calibrate, because the sonic speed changes with temperature and pressure. Herein a mixture containing 25% GAP with 75% PEG is prepared for the test of regression rate. GAP is known for its higher burning rate, so PEG is added for suppressing regression rate [2].

2. Method

Propulsion test was conducted using 1300 mm long, and inside diameter 90mm motor. The motor was made using stainless steel, and has three special designed ports for ultrasonic sensors and the other three ports for thermocouples as shown in Fig. 1. The grains were loaded into the chamber having a single inner port for delivering oxidizer. The port size is 30 mm in diameter. Oxygen flow rate was controlled using two different supply lines which had different sizes of orifice.

Ultrasonic sensors were manufactured by Honda Electronics Co., LTD. Each sensor was composed of two sets, pulsar and receiver which are shown in Fig. 2. The sonic wave frequency was set at 1MHz to have a good penetration in rubber material, and the surfaces of sensors were attached to the holder with the help of grease to have a better contact. From previous study, 10V of excitement voltage for the sensor was not sensitive enough to deduce the regression rate, so voltage was enhanced to 100V. By measuring the time of flight of ultrasonic wave, we have a series of signals.

These signals were obtained from within the stainless steel holder, along the peripheral part of the combustor, and directly from the grain surface. Using the measured time of flight of pulse, the regression distance was calculated by the calibrated ultrasonic speed. Regression rate was obtained by differentiating the surface trace of grain as shown in Fig. 3.

OmniScan MX (OLYMPUS) was used to calibrate sonic speed. Another chamber was prepared and was pressurized with nitrogen. Inside the chamber was a specific size of fuel which was covered by the heater. The sonic speed was measured as functions of temperature and pressure.

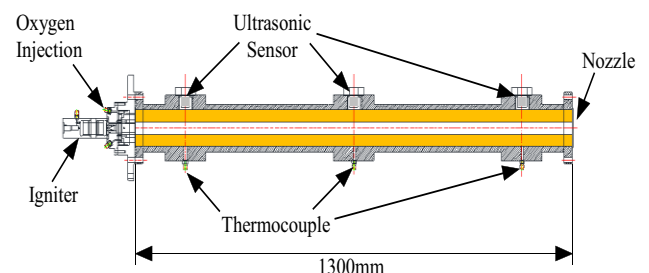


Fig. 1 Schematic diagram of hybrid motor with ultrasonic sensors and thermocouples.



Fig. 2 Ultrasonic sensor with two cables, one is for pulsar and the other one is for receiver.

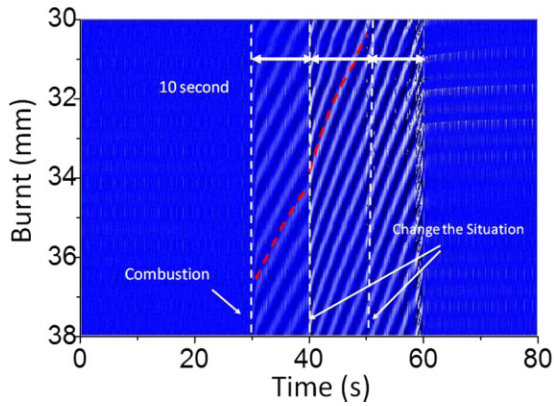


Fig. 3 Trace of fuel burnt using ultrasonic sensors

3. Results and Discussion

Fuel was made with a mixture of 25%GAP and 75%PEG. The burning test was conducted for 30 seconds and oxygen flow rate was changed at every 10 seconds. Figure 4 (a) shows the pressure at each second. Middle and downstream part of the motor have higher regression distance than upstream; due to the gas from the decomposed fuel increases the total mass flow rate. At downstream, the lower concentration of oxygen resulted in the lower regression distance than middle stream as shown in Fig. 4. (b).

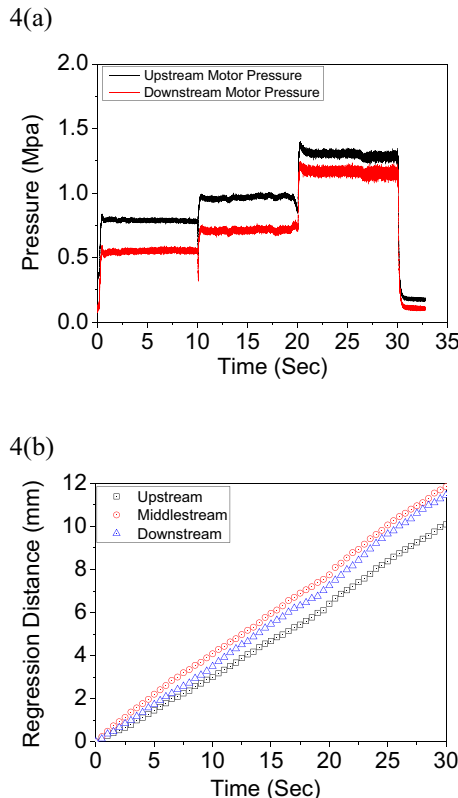


Fig. 4 (a) Pressure pattern (b) The instantaneously regression distance of grain at up, middle, and down part of motor.

Table 1 shows the results of regression rates. When the combustor pressure increased, the regression rate at up and downstream increased distinctly. In the middle position, regression rate kept at relative high value, due to the balance of increase in fuel flow and decrease in oxygen concentration.

Table 1. Summary of experimental regression rate

Regression rate (mm/s)			
Time (sec)	Up	middle	down
0-10	0.31	0.41	0.35
11-20	0.32	0.37	0.37
21-30	0.37	0.40	0.42

4. Concluding remarks

Ultrasonic technique successfully measured the instantaneous regression rate. The results suggest that the fuel regression rate depend on mass flow rate, and also on the positions along the length of motor. The application of ultrasonic method is a strong help to establish the comprehensive combustion model of hybrid rocket motor.

References

- [1] Robert A. Frederick Jr., Joshua Whitehead, L. Richard Knox, and Marlow D. Moser, *Journal of Propulsion and Power*, **Vol.23**, No. 1, Jan.-Feb. (2007), pp. 175-180.
- [2] Hori K., *AIAA Paper*, (2009), 2009-5348.

Internal Flow Characteristics in Combustor of Hybrid Rocket Engine

Khin Oo Mon*, Heeseok Koo**, Changjin Lee*

*Konkuk University, Gwangjin-gu, Seoul 143-701, Korea

**Seoul National University, Seoul, Korea

purenov@konkuk.ac.kr, heeseokkoo@gmail.com, cjlee@konkuk.ac.kr

The stability and combustion behavior in hybrid rockets are significantly dependent on the generation of unsteady vorticity and the coupling of acoustical motion with vortex shedding on the burning surfaces. Experimental results also show the change in flow conditions prior to entering the fuel grain may alter the regression rate and pressure fluctuations. This study focuses on the numerical calculation with LES to simulate the evolution of flow interactions including vortex dynamics and pressure oscillations without chemical reaction.

I. Introduction

The stability and combustion behavior of unsteady motion in solid propellant rockets are significantly affected by two mechanisms. These are the generation of unsteady vorticity at the burning surfaces and the coupling between acoustical motion and vortex shedding at obstacles or near the region adjacent to the burning surfaces. Despite of fundamental differences flow conditions at entrance of combustor; fully turbulent incoming flow in hybrid rockets and accumulated mass driven flow in solid motors, it is expected to observe a similar behavior of hydrodynamic instability in hybrid rocket associated with the interaction of vortex shedding. From the hydrodynamic point of view, flow dynamics in solid propellant rocket is very analogous to those in hybrid rocket in that flow instabilities are found as a consequence of coupling between mean flow and evaporative fuel flow from the surface. French research groups concentrated on the flow instability in solid propellant motor extensively.

The numerical studies with LES methodology by Na & Lee showed very interesting features of flow behavior near the wall surface. Their calculation results showed that the interaction of oxidizer turbulent flow with the wall injected flow can completely alter the structure of turbulent boundary layer and produce isolated cell-like contours of streamwise velocity near the surface.

Camicino et al. recently performed a series of combustion test with two different injector configurations; axial and radial types. They found that combustion behaviors were strongly dependent upon the interaction of vortex shedding and acoustic oscillations determined by injector configurations. However, more research is still required to understand the physics of the interaction of vortex shedding and acoustic oscillations. Thus, it is also quite interesting to ask what would happen if vortex shedding induced in the pre-chamber could interact with vortices formed as the result of instabilities with evaporative normal flow in the vicinity of burning surfaces.

Motivated by the question related to the flow conditions in hybrid rocket combustion, LES calculation has conducted to find the behavior of hydrodynamic instability in the flow if vortex shedding from the pre-chamber interacts with vortices in the vicinity of burning surfaces as observed in solid motors. In the present study, the objective is to investigate the interaction of vortex shedding in the pre-chamber and small-scale vortices adjacent to burning surfaces by using combustion tests and numerical simulation for non-reactive flow. Special attentions are put on responses of the streamwise velocity to vortex interaction and the evolution of vorticity in the flow.

II. Numerical Simulations

As depicted in Figure 1, the pipe consists of two regions: recycled part ($-5 < x/D < 0$) and wall injecting part ($0 < x/D < 10$) where D is the diameter of the pipe. The recycled pipe is added to provide realistic turbulence without any discontinuity to the main region of interest. The wall injecting region is applied to simulate effect of a regression process of a hybrid rocket. The numbers of grid points used to discretize the computational domain in axial, radial, and azimuthal directions are 192, 64, and 128, respectively. In radial direction, meshes are gathered using hyperbolic tangent function to capture near-wall flow accurately.

Secondly, a pipe with a ring-type block attached in front of wall blowing region is simulated. A schematic of this configuration is available in Figure 2. Lengths of the recycling and mass injecting parts are identical to the previous case. Length and height of the block is one-tenth of the diameter, from which vortex flow with substantial strength is generated. Then, interactions between the generated vortex and vortex shedding due to wall injection would occur.

Averaged axial velocity at inlet is 23.3m/s in this study, thus Mach number for substantial portion of the domain is very low. Therefore, a preconditioned compressible flow solver is used. A modified Roe-type flux difference scheme is used which is suitable

for LES and viscous terms are calculated by central differencing. Time integration is done using a dual-time stepping method to allow larger time-step size. A dynamic Smagorinsky sub-filter model is used to closure LES terms.

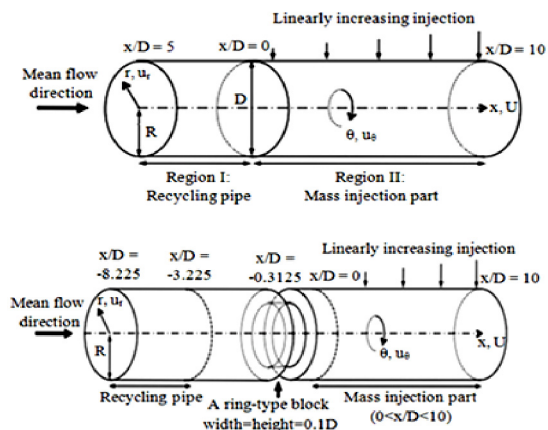


Figure 1. Computational domain for the case without and with a block

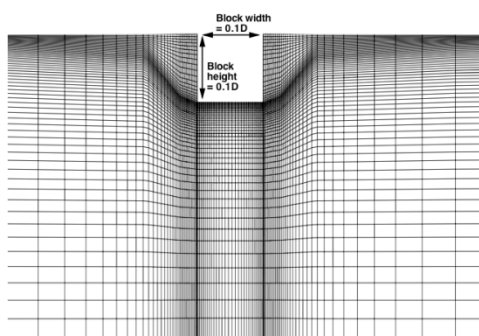


Figure 2. Mesh system around the block

No-slip, isothermal wall boundary condition is applied for all wall boundaries except for mass injecting walls. Wall temperature is set to be identical to free stream temperature, 288K. For $0 < x/D < 10$, mass fluxes is continuously injected into the domain. Radial velocity is specified along the wall in this region and it linearly varies from 0% (at $x/D=0$) to 3% (at $x/D=10$) of the mainstream bulk velocity. At the interface between recycling and injecting parts, all flow information is passed through except pressure since pressure-related wave is assumed to ravel backward. Note that the similar philosophy is used for the exit boundary condition where back pressure value is used and all other properties are extrapolated. Reynolds number for the calculations is set to 30,600. The simulations were performed until statistically converged profiles are obtained. The solver is parallelized using an MPI-based domain decomposed strategy. Each calculation took 2 (without block) or 4 (with block) weeks using 40 processors.

In this study, recycling (or recirculation) technique follows a method suggested by Lenormand et al. While maintaining velocity and thermal fields at the same time is hard to achieve in a compressible flow, it was not a huge bottleneck for such low-speed flow.

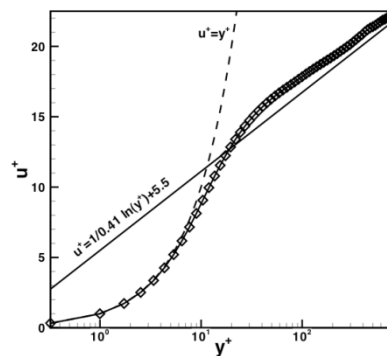


Figure 3. Mean axial velocity profile for the recycling pipe

Figure 3 shows velocity profiles after statistically converged, and log-law layer is slightly over-predicted than a theoretical profile with $k=0.41$ and $B=5.5$. $U\tau$ is calculated as 1.235m/s and mesh size of the first cell from the wall is $126.9+ \times 0.65+ \times 39.0+$ in axial, radial, and azimuthal directions using the wall unit. A snapshot of axial velocity at $y+=10$ location is plotted at Figure 4. The figure is from an expanded view at the given radial location. Therefore, vertical axis of the figure is in azimuthal direction. The velocity streaks are well developed in this plot and some streaks are as long as two thirds of the recycling part. These results justify the use of present LES solver for the analysis of the turbulent flow structures and their modifications by the interaction with mass injection from the wall.

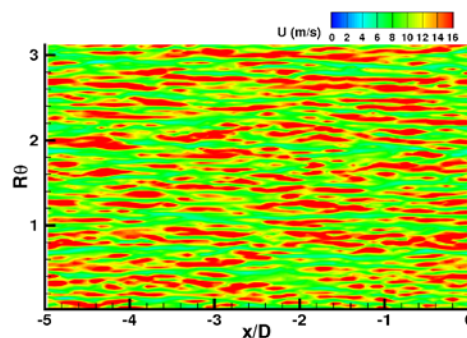


Figure 4. Expanded view of a snapshot of axial velocity at $y+=10$ for the recycling pipe

Numerical Analysis of the Inside Flow of Ramjet Engine

Yorimoto Tokiwa, Ichiro Nakagawa
Tokai University, Hiratsuka, Kanagawa, 259-1292, Japan
1bmjm023@mail.tokai-u.jp

ABSTRACT

We proposed hybrid rocket & ram jet combined engine as an engine for next generation space transfer vehicles. Ignition at the time of shifting to ram jet mode is considered to be the most important technical problem. In order to improve ignition reliability, the phenomenon in a ram jet combustion chamber should be grasped and searching for the conditions which can make the ignition easier is important. In this study, build of the calculation code is done for the design of the ram jet combustion chamber combined with a hybrid rocket.

1. Introduction

Many researchers studied space transfer vehicle using air breathing engines, such as a ram jet engine, NASA predicted in 1994 that space activity expands and develops by entry of a different user from former, when space transportation cost became about 1/10 or less. [1] In order to realize it, expendable rocket system is difficult and a completeness re-use type space transportation system is required. [1]

We proposed Hybrid rocket & Ram jet combined engine. It is used for TSTO booster engine. In low-speed region, the ejector jet with a hybrid rocket, and in high-speed region, a ram jet engine is operated. (Fig.1) Ignition of a ramjet is performed using the exhaust gas of the hybrid rocket final stage combustion.

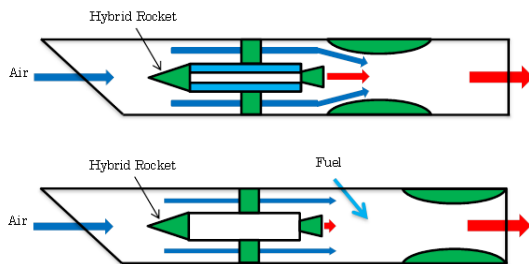


Fig.1 Hybrid rocket & ramjet combined engine
(Above: Ejector mode, below: Ram jet mode)

The combustion experiments were conducted with the combustion wind tunnel in Tokyo University Kashiwa campus. Fig.2 shows the ram jet combustion device used in the experiments. Mach 2, altitude sea level condition simulated air was supplied from the wind tunnel, methane was injected in the engine as ram jet fuel, and ignition was conducted by the exhaust gas of the hybrid rocket. In some cases, ignition was succeeded but in another cases, no ignition as shown in Fig.3.

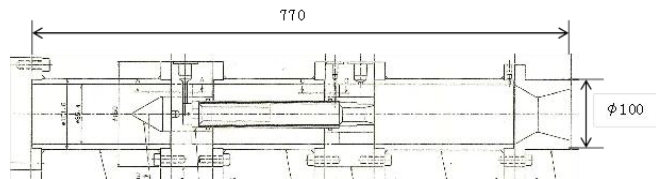


Fig.2 Ram jet combustion device

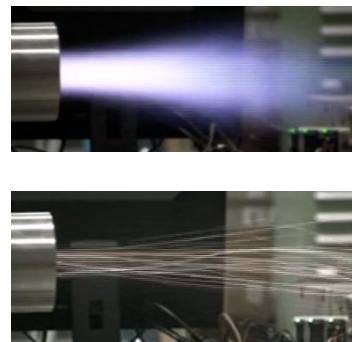


Fig.3 Combustion experiment images
(Above: ignition was succeeded,
below: no ignition)

In order to make the ignition reliable, it's important to grasp the phenomenon in a combustion chamber. This research purpose is to build the calculation code used for the design of a ram combustion chamber combined with a hybrid rocket, moreover, to grasp the phenomenon in the combustion chamber in ram jet mode, and search for the conditions which can make ignition reliable.

2. CFD Method

The calculation grid was created based on the experiments devices shown as Fig.4.

Governing equations are a two dimensional compressibility Navier-Stokes equation and a transport equation of a mass fraction.

$$\frac{\partial \mathbf{q}}{\partial t} + \frac{\partial \mathbf{E}}{\partial x} + \frac{\partial \mathbf{F}}{\partial y} = \frac{\partial (\mathbf{E}_v + \mathbf{E}_{mass})}{\partial x} + \frac{\partial (\mathbf{F}_v + \mathbf{F}_{mass})}{\partial y} \quad (1)$$

$$\mathbf{q} = \begin{bmatrix} \rho \\ \rho u \\ \rho v \\ E \\ \rho Y_{fuel} \\ \rho Y_{air} \end{bmatrix}, \mathbf{E} = \begin{bmatrix} \rho u \\ \rho u^2 + p \\ \rho uv \\ \rho uH \\ \rho u Y_{fuel} \\ \rho u Y_{air} \end{bmatrix}, \mathbf{F} = \begin{bmatrix} \rho v \\ \rho uv \\ \rho v^2 + p \\ \rho vH \\ \rho v Y_{fuel} \\ \rho v Y_{air} \end{bmatrix}$$

$$E_v = \begin{bmatrix} 0 \\ \tau_{xx} \\ \tau_{xy} \\ \tau_{xx}u + \tau_{yx}v + \kappa \frac{\partial T}{\partial x} \\ 0 \\ 0 \end{bmatrix}, F_v = \begin{bmatrix} 0 \\ \tau_{yx} \\ \tau_{yy} \\ \tau_{xy}u + \tau_{yy}v + \kappa \frac{\partial T}{\partial y} \\ 0 \\ 0 \end{bmatrix}$$

$$E_{mass} = \begin{bmatrix} 0 \\ 0 \\ 0 \\ 0 \\ \frac{\mu_{mix}}{Sc} \frac{\partial Y_{fuel}}{\partial x} \\ \frac{\mu_{mix}}{Sc} \frac{\partial Y_{air}}{\partial x} \end{bmatrix}, F_{mass} = \begin{bmatrix} 0 \\ 0 \\ 0 \\ 0 \\ \frac{\mu_{mix}}{Sc} \frac{\partial Y_{fuel}}{\partial y} \\ \frac{\mu_{mix}}{Sc} \frac{\partial Y_{air}}{\partial y} \end{bmatrix}$$

$$p = \rho R_0 T \sum_i \frac{Y_i}{M_i} \quad (2)$$

$$E = \rho c_v T + \frac{1}{2} \rho (u^2 + v^2) \quad (3)$$

Where ρ denote the density, u and v the Cartesian velocity, p the pressure, H the total enthalpy, E the total energy, T the temperature, Y_{fuel} the mass fraction of methane, Y_{air} the mass fraction of air, Y_i the mass fraction for i th chemical species, M_i the molecular weight for i th chemical species, c_v the specific heat at constant volume, R_0 the universal gas constant, κ the thermal conductivity, μ_{mix} the viscous coefficient, and Sc the Schmidt number.

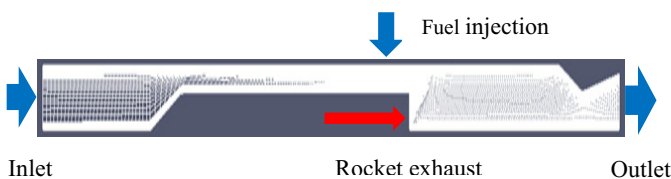


Fig.4 Calculation grid

The governing equation was dispersed with the finite volume method. The numerical flux is evaluated by AUSM-DV scheme and MUSCL approach is used. Two-stage Runge-Kutta method was used for time integration. The viscous flux is evaluated by second order central difference scheme. The diffusion member of a mass fraction is evaluated by second order central difference scheme.

In order to evaluate mass fraction, five chemical species CH_4, O_2, CO_2, H_2O and N_2 , are considered. CO_2 and H_2O are given as the mass fraction of rocket exhaust, assuming that a hybrid rocket carries out in

perfect combustion condition. The purpose is to search for the conditions which can make ignition reliable from total pressure, temperature, and mass fraction.

3. Results and Discussion

A result is shown orally.

References

- [1] N. Tanatsugu, Introduction, ISAS Report, 1 .No.46, 2003.

Three-dimensional Numerical Simulation on Unsteady Compressible Flow Using Preconditioning Method in Hybrid Rocket Engine: Effects of Preconditioning Schemes

Nobuyuki Tsuboi¹, Katsuyoshi Fukiba², Toru Shimada³

¹Kyushu Institute of Technology, 1-1 Sensui-chou, Tobata-ku, Kitakyushu, Fukuoka, Japan

²Shizuoka University, 3-5-1 Johoku, Naka-ku, Hamamatsu, Shizuoka, Japan

³Japan Aerospace Exploration Agency, 3-1-1 Yoshinodai, Chuo-ku, Sagami-hara, Japan

tsuboi@mech.kyutech.ac.jp.

Abstract

The swirling flow in the hybrid rocket motor with high Re number and low speed is simulated by using the time-dependent preconditioned compressible Navier-Stokes solver. The preconditioning numerical fluxes are the preconditioning AUSMDV, AUSM+-up, and SLAU. The time integration adopts the preconditioning LU-SGS method. The stable swirling flow in the chamber is observed except the region near the injection ports and converging section of the nozzle. The effects of the numerical schemes are small on the swirl intensity and the time-averaged axial velocity.

1. Introduction

The hybrid rocket engine uses a solid fuel and gas oxidizer to become more safety and less expensive than the solid rocket engine because the fuel and oxidizer are separated and solid fuel is typically made of polymer materials. Therefore the hybrid rocket is a candidate for the transportation of the manned space mission. An oxidizer is injected axially through the core of the solid fuel in the conventional hybrid rockets. After the ignition, the combustion of the oxidizer and fuel provides the heat release required to vaporize the solid fuel. The combustion process is strongly coupled with the flowfield in the hybrid rocket engine. The engine requires high combustion efficiency and large regression rate to obtain enough thrust performance. Its thrust performance can be increased by the tangential or impingement injection of oxidizer than the axial injection[1, 2]. The tangential injection generates complex flowfield in the combustion chamber and exhaust nozzle. Therefore the flow structure should be understood by using the numerical simulations as well as the experiments.

Although the numerical simulations are necessary for the design of the hybrid rocket motor, common compressible flow solvers are "density-based" schemes, which are impossible to solve incompressible flow lower than free-stream Mach number of 0.1 due to small time step and slow converging rate. This causes a stiffness problem in which the ratio of maximum eigen value to minimum one in inviscid flux is of the order of 100. This stiffness problem also arises in the simulations with chemical reaction. The preconditioned Euler or Navier-Stokes equations [3], which is control the eigenvalues without stiffness, can be solved for such the low speed as well as high Mach number. Recently some preconditioning schemes are developed, however, their advantages and disadvantages for the simulations of the hybrid rocket motor are not discussed in detail.

We have recently developed the time-dependent preconditioning Navier-Stokes code to solve such the high Re number and low speed flow in order to understand flow mechanism in the hybrid rocket combustion chamber. In this paper, we discuss the effects of the preconditioning schemes in the hybrid rocket motor.

2. Numerical Method

The three-dimensional compressible Navier-Stokes equations are used. The governing equations are transformed by using the preconditioning method proposed by Weiss and Smith[3]. The reference Mach number sets 3.0 in the preconditioned scheme.

The inviscid flux adopts three preconditioned schemes: preconditioning AUSMDV(pAUSMDV)[4], AUSM+-up[5], and SLAU[6]. The second-order MUSCL with van Albada limiter is used and time integration uses preconditioned LU-SGS scheme[7]. The turbulent model adopts Baldwin-Lomax model. In this simulation, the number of sub-iterations in the pseudo-time-derivative is thirty to preserve time-accuracy. The viscous terms are second-order central difference without preconditioned scheme. The results for the preconditioning schemes are compared with those for AUSMDV scheme with LU-ADI time integration. The detail of the current procedures is presented in Ref. 8.

3. Computational Grids and Simulation Conditions

The computational grid in the cylindrical chamber is shown in Fig.1. The tangential inflow conditions employed the experiments conducted by Yuasa et al[9, 10]. The number of grid points is $146 \times 93 \times 51$. The number of injection ports is eight near the closed end wall in the chamber. The injection pressure, temperature, and specific heat ratio are 1.37 MPa, 300 K, and 1.21, respectively. Therefore Re number is $3.9 \times 10^8/m$. The injection mass flux equals 136 g/s. The wall boundary conditions are non-slip and adiabatic wall. The non-dimensional computational time step uses 1×10^{-4} and the corresponding CFL number becomes approximately 100.

4. Results and Discussion

Figure 2(a) shows the instantaneous Mach number contours in the chamber and the close-up view near the nozzle section is shown in Fig. 2(a). The swirl flow becomes unsteady therefore the downstream of the throat section is affected. The time-averaged axial and rotational velocity profiles along the axis are plotted in Fig.

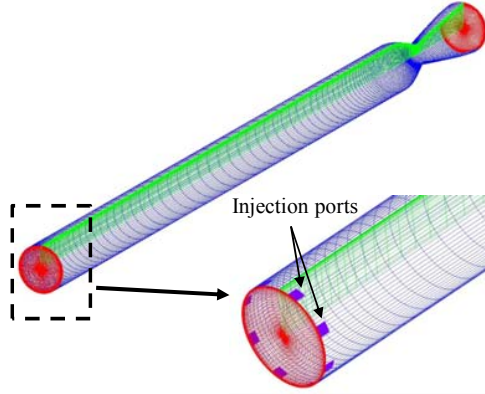


Fig. 1 Computational grid in the hybrid rocket engine.

3(a) and (b). The averaged rotating velocity profiles without precondition scheme near the nozzle inlet section do not agree with those for the preconditioning schemes. Figure 3(c) show the comparison of the time-averaged swirl intensity along the axis. The effects of these schemes are small on the swirl intensity.

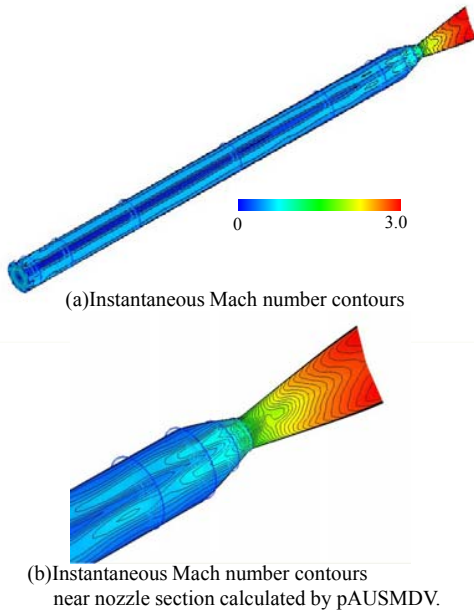


Fig. 2 Computational results in the hybrid rocket engine.

5. Conclusions

The swirling flow in the hybrid rocket motor with high Re number and low speed is simulated by using the time-dependent preconditioned compressible Navier-Stokes solver. The stable swirling flow in the chamber is observed except the region near the injection ports and converging section of the nozzle. The effects of the numerical schemes are small on the swirl intensity and the time-averaged axial velocity.

Acknowledgements

This research is conducted as a contribution to the

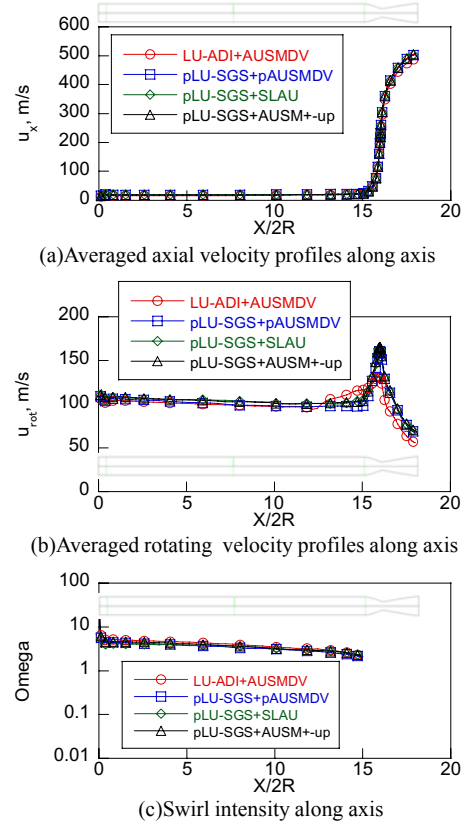


Fig. 3 Effects of preconditioning numerical fluxes.

Hybrid Rocket Research Working Group (HRrWG) with the approval of the Space Engineering Steering Committee of Institute of Space and Astronautical Science, Japan Aerospace Exploration Agency.

This research has also been supported by the Ministry of Education, Science, Sports and Culture, Grant-in-Aid for Scientific Research (B) (No.23360380). The present numerical simulations are collaborated with Cybermedia Center in Osaka University and V system in JAXA supercomputer system.

References

- [1] T. Tamura, S. Yuasa, and K. Yamamoto, AIAA paper 99-2323 (1999).
- [2] H. Nagata, M. Ito, V. Maeda, M. Watanabe, T. Uematsu, T. Totani, and I. Kudo, *Acta Astro.*, **59**, (2006), 253.
- [3] J.M. Weiss and W.A. Smith, *AIAA J.*, **33**, **11**, (1995), 2050.
- [4] J.R. Edwards and M.-S. Liou, *AIAA J.*, **36**, **9**, (1998), 1610.
- [5] M.-S. Liou, *Journal of Computational Physics* 214, pp.137-170 (2006).
- [6] E. Shima, K. Kitamura, *AIAA J.*, **49**, **8**, pp.1693-(2011).
- [7] S. Yamamoto, *J. Comp. Phys.*, **207**, (2005), 240.
- [8] N.Tsuboi, K. Fukiba and T. Shimada, *AJCPP2010-088*, *AJCPP* (2010).
- [9] K. Kitagawa, T. Sakurazawa, and S. Yuasa, *JSASS*, **6**, (2007), 47.
- [10] R. Itakura, K. Okamoto, S.Teramoto, T.Nagashima, *AJCPP2010-079*, *AJCPP* (2010).

Numerical and Experimental Study of Venturi Flow Meters for Nitrous Oxide

K.-M. Chuang¹, Jhe-Wei Lin¹, Jong-Shinn Wu^{1*}, Gary Cheng² and Yensen Chen³

¹Department of Mechanical Engineering, National Chiao Tung University, Taiwan

²University of Alabama, Birmingham, Alabama, USA

³National Space Organization, Hsinchu Science Park, Hsinchu, Taiwan

*e-mail: chongsin@faculty.nctu.edu.tw

ABSTRACT

In this paper, numerical simulations and experiments of several Venturi flow meters for nitrous oxide are performed and compared. In the numerical part, a parallel all-speed finite-volume flow solver considering real fluid model is employed to simulate the multi-phase flow inside flow meters. In the experimental part, carbon dioxide is used for cost reduction since its vapor pressure varying with temperature is very similar to those of nitrous oxide. Design of several Venturi flow meters in the range of 1-12 kg/s of nitrous oxide is completed which can be used for a hybrid rocket motor with thrust levels in the range of 300-3,000 kgf.

1. Introduction

Recently, hybrid propulsion has attracted much attention for its good specific impulse performance, nontoxicity, low cost, high safety and throttling capability for advanced rocket technology. One of the simplest hybrid propulsion systems employs HTPB and nitrous oxide, e.g., SpaceShipOne developed by Paul Allen and Scaled Composites [1]. In addition to the hybrid motor development, thrust control through throttling is one of the major components that require careful design and investigation. For a precise thrust control, an accurate flow meter which can accurately measure the flow rates of flowing nitrous oxide under high pressure and high flow rates is required. In this study, we intend to apply Venturi tube as the potential flow meter for nitrous oxide flow rate measurements.

Venturi tube is one of the forms of flow meter, which pressure loss is very low with a proper design. For the design purpose, we need the pressure difference between the inlet and throat is large enough for measurement, while the pressure drop at the inlet and outlet are small enough not to lose too much total pressure. Pressurized water had been used to confirm the mass flow rate of a designed cavitating venturi flow meter [2]. Unfortunately, the physical properties of water are very different from liquid nitrous oxide, and this study was performed experimentally based on the Bernoulli equation, which is only accurate for incompressible flow. On the other hand, vapor pressure variation with temperature of carbon dioxide is found to be very close to nitrous oxide. This motivates us to use carbon dioxide for experiments, instead of nitrous oxide since it is much cheaper as compared to nitrous oxide. For a design purpose, numerical simulation can be very helpful, especially for a real fluid such as nitrous oxide or carbon monoxide.

In this study, we intend to investigate the flow behaviors of several Venturi flow meters numerically and experimentally.

2. Method

Experimental Part

Fig. 1 shows the experimental setup for measuring the flow rates of CO₂ through a Venturi flow meter. A CO₂ tank, as pressurized by a helium tank, provides a stable source of pressurized CO₂ liquid flow flowing through the Venturi flow meter. A load cell placed under the CO₂ tank is used to measure instantaneous weight during the test, from which the instantaneous flow rates can be deduced. In addition, a pressure transducer with a fast response is used to measure the pressure difference between the upstream and throat, and also the pressure drop before and after the Venturi flow meter. These data are collected with a preset sampling frequency by a data acquisition system (NI 9205, NI9213 and NI cDAQ-9172) and a personal computer.

Numerical Part

We have applied a parallel Navier-Stokes equation solver [3] with the HBMS real-fluid model [4] for modeling the flow past the Venturi flow meters with different geometries. This code solves the continuity equation, the momentum equations and the energy equation with extended k-ε turbulence model using collocated cell-centered finite-volume method with unstructured grid. Because of axisymmetry, a 2D axisymmetric coordinate system is used for saving computational time. In the simulations, we consider a fixed mass flow rate and inlet pressure. Pressures at the throat and downstream locations are obtained as part of the simulations. With these, we are able to obtain the flow rates as a function of pressure difference between the inlet and throat locations.

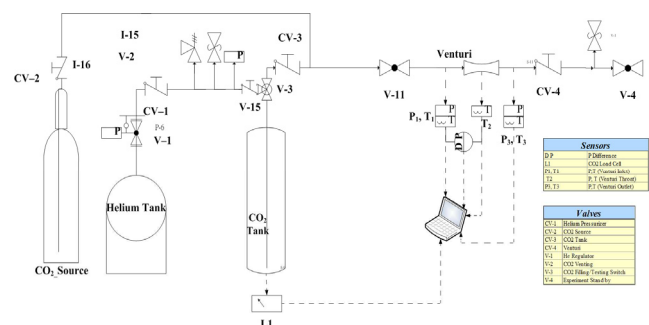


Fig. 1 Experiment setup for measuring flow rates of CO₂ or N₂O through a Venturi flow meter.

3. Results and Discussion

Fig. 2 shows the geometry and dimensions of a typical Venturi flow meter designed in this study. These Venturi flow meters are kept as 200 mm in length, while the diameters of inlet (and outlet) and throat are varied. Throat is kept as 10 mm in length. Convergent and divergent parts of the flow meter are kept as 20 mm and 60 mm respectively. Table 1 summarizes various combinations of D and d we have performed in the experiments and simulations.

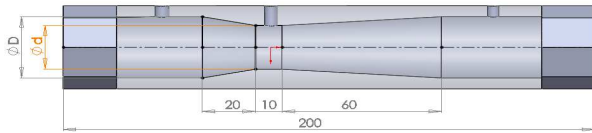


Fig. 2 Dimensions of Venturi flow meters under tests.

Table 1. Dimension design of venturi flow meters.

D (mm)	d (mm)
10	8
10	9
28	16
28	20
28	24

Fig. 3 shows the simulated flow properties in the Venturi flow is nearly constant everywhere, while both the density and pressure changes appreciably (smaller) at the throat at the same time, which is unlike an incompressible flow that density is a constant. This justifies the use of a CFD code with real-fluid model without using the simple Bernoulli equation for modeling the flow inside the Venturi flow meter.

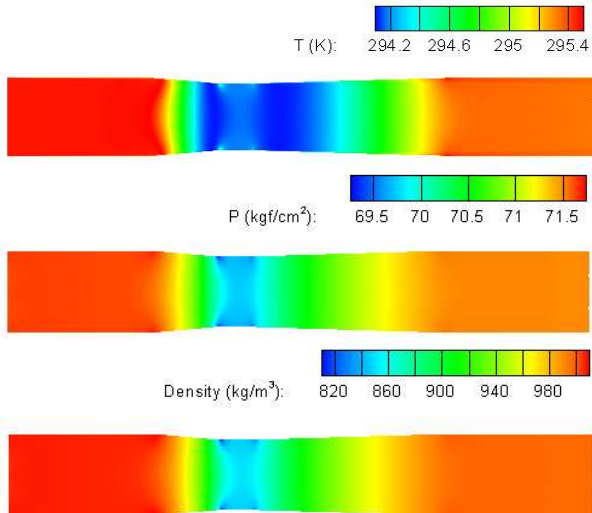


Fig. 3 Simulated flow properties of nitrous oxide in the Venturi flow meter (D=28 mm and d=24 mm).

Fig. 4 and Fig. 5 show the simulation results of the pressure difference and pressure drop of venturi flow meter at D=10 and 28 mm respectively. Results show that, for smaller flow rates less than 1.5 kg/s, one can choose the combination of d=9 mm and D=10 mm for a pressure drop less than 1 kgf/cm². For larger flow rates,

d= 20-24 mm and D=28 mm is a better combination for a pressure drop less than 2-3 kgf/cm². These simulated data will be compared by the experiments, which are currently in progress. A simplified formula similar to the Bernoulli equation will be derived based on the experiments. The range of flow rates for the above Venturi flow meter is 1-12 kg/s, which can potentially produce 300-3,000 kgf for a two-stage hybrid rocket that is currently under development. All the above will be reported in detail in the meeting.

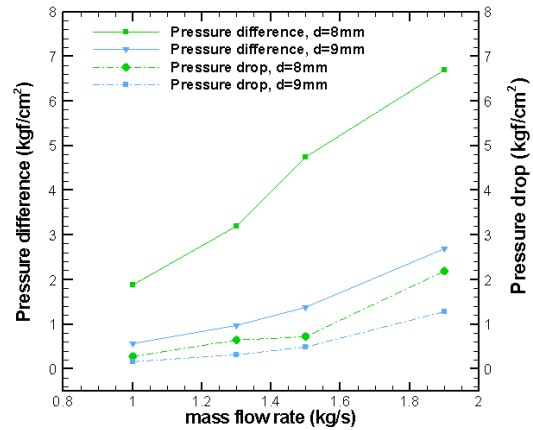


Fig. 4 Simulated pressure difference and pressure drop as a function of mass flow rates (D=10 mm).

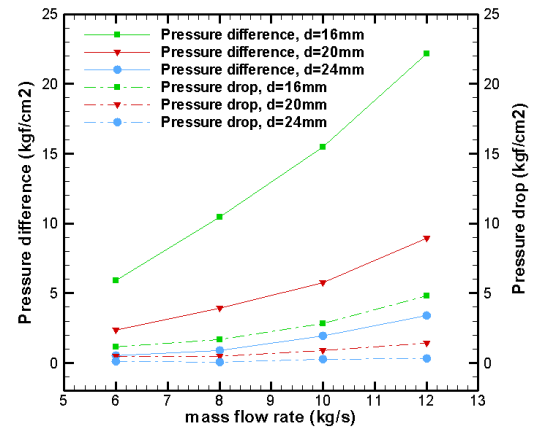


Fig. 5 Simulated pressure difference and pressure drop as a function of mass flow rates (D=28 mm).

4. Concluding remarks

In the current study, we have investigated the flow behavior in various Venturi flow meters experimentally and numerically. Preliminary design has been completed based on simulation results, which will be verified by experiments that are currently in progress.

References

- [1] Zachary Thicksten, et al., Handling Considerations of Nitrous Oxide in Hybrid Rocket Motor Testing, SpaceDev Inc., AIAA 2008-4830
- [2] A. Ulas, Passive flow control in liquid-propellant rocket engines with cavitating venturi, Flow Measurement and Instrumentation 17 (2006) 93–97.
- [3] B. J. Wendt, AIAA-95-1797 (1995).
- [4] Richard C. Farmer, et al., Computational Transport Phenomena for Engineering Analyses, (2009)

Hybrid Rocket Propulsion: State of the Art and Perspectives for Space Activities Applications

Luigi T. DeLuca¹, Pietro Tadini¹, Carmen Pardini², and Luciano Anselmo²

¹ Politecnico di Milano, Dipartimento di Ingegneria Aerospaziale
SPLab, Campus Bovisa, I-20156 Milan, MI, Italy

² Space Flight Dynamics Laboratory, Consiglio Nazionale delle Ricerche, ISTI-CNR
1 Via G. Moruzzi, I-56124 Pisa, PI, Italy.

luigi.deluca@polimi.it

ABSTRACT

Ballistic characterization of solid fuels for hybrid rocket propulsion was performed in several lab-scale burners. An optical time-resolved technique was used to evaluate the quasi-steady regression history of single perforation, cylindrical fuel samples. The effects of oxidizer injection, metallized additives and radiant heat transfer on regression rates were assessed. Under the investigated operating conditions, comparative analyses of the collected experimental data show an appreciable influence of metal hydrides and properly coated selected metals on ballistic properties. A specific application for active space debris removal is shortly discussed.

1. Introduction

Hybrid Rocket Engines (HREs) are propulsive systems combining chemical reactants in both a solid and a fluid (liquid or gaseous) state. The main points of interest for this architecture include relatively large specific impulse, high thrust throttleability, operational flexibility, overall system simplicity in manufacture and operations, intrinsic safety in handling and operations, possible reduced environment impact, and cost effectiveness. On the other hand, a serious drawback of HREs is the low regression rate of the gasifying solid fuel surface for applications requiring large thrust levels. The main reason of such behavior is the well-known essentially diffusive nature of the resulting flame.

The development of novel energetic additives brought about a new generation of hybrid solid fuels, with improved performance in terms of specific impulse, density, and throat erosion. In addition, a swirling injection providing a vortex combustion can promote a better heat exchange, higher combustion efficiency, and larger as well as more uniform fuel regression rates [1]. By combining a swirling injection with energetic additives in the solid fuel superior regression rates can be obtained. Thus, HREs are today an attractive “new” option for a range of applications including minilaunchers, boosters, upper stage propulsion, lander systems, private human space access, active space debris removal (ADR) [2], and so on.

SPLab of Politecnico di Milano has developed a variety of experimental techniques and diagnostics in order to investigate ballistics of hybrid fuels. The present study is focused on a time-resolved technique for regression rate measurements of a variety of solid fuels burning in gaseous Oxygen (GOX).

2. Method and Representative Results

The SPLab 2-D radial burner used in this work enables a relative ballistic grading of different fuel formulations in terms of regression rate under controlled operating conditions. The tested strands have a cylindrical shape and a single central port perforation. Each solid fuel grain is accommodated in a stainless steel case with 30 mm length. The strand outer diameter is 18 mm while its nominal initial port diameter is 4 mm.

Different cases enable testing of samples with different outer diameters (thus increasing or reducing the solid grain web thickness for a given D_0). Likewise, use of different mandrels enables testing of fuel strands with different D_0 .

The implemented experimental rig provides a continuous visualization of the tested strand head-end, thus it is possible to track the central port diameter during combustion. Video recording of the combustion processes enables regression rates measurement by an optical, non-intrusive technique. Independent regulations of the oxidizer mass flux and burning pressure are possible. Sample burning is initiated by a pyrotechnic primer charge, in turn ignited by a CO₂ laser. Video acquisition is obtained with dedicated analog or digital cameras capable of speed up to 500 fps and resolution up to 1024 x 1024 pixels (see Fig. 1).



Figure 1 – Swirling injection of GOX in HTPB fuel grain.

It should be stressed that the above experimental facility is a strand burner, rather than a motor, used for relative grading of solid fuels. At the same way that the well-known strand-burners used in solid propulsion are a tremendous help in preliminary processing of solid propellant formulations, the proposed hybrid burner is meant to help in discriminating among different solid fuel formulations before moving to the more expensive and time-consuming hybrid motor testing. The implemented injection head avoids significant entrance effects while the short length of the solid fuel sample favors a rather uniform regression rate in the axial direction. Both effects are confirmed by pictures of the fuel surface after a forced burning interruption.

Moreover, on PMMA cylindrical samples, this kind of tests provided a well-defined trace of the swirl decay during the combustion.

A software package able to detect automatically the regressing surface is also available. In the case of pure HTPB, automatic processing was verified to yield essentially the same results as the manual processing. Yet, the manual procedure is believed to be of broader validity since it can be applied also to solid fuels whose regression surface is obscured by a variety of noise sources affecting its capture (such as those typically observed when testing high-energy additives). In addition, the manual procedure allows the operator to directly observe all details of the regressing surface possibly underlining strong irregularities and anisotropies of the combustion surface (such as those typically seen for wax-based samples). Furthermore, peculiar phenomena that may occur during burning (such as solid fuel fragmentation) are not easily captured by an automatic software. In summary, an automatic procedure is certainly more convenient and expedite, but in general the manual procedure allows more careful and pregnant data analyses.

All experiments were conducted for a variety of solid fuels under GOX up to 20 bar of pressure. The results collected clearly point out that regression rates exhibit a peculiar monotonic growth with oxidizer mass flux, whose power law approximation however features an exponent close to the 0.8 value predicted by Marxman [3]. Differently than for solid propellants, μAl does not contribute to specific impulse. But hydrides (AlH_3 , LiAlH_4 , MgH_2) and properly coated metals ($n\text{Al}$ or MgB) are effective promoters of the solid fuel regression rate. In addition, AlH_3 and LiAlH_4 offer outstanding ideal specific impulse increases, while $n\text{Al}$ helps to increase the actually delivered specific impulse by reducing 2P losses. However, limited chemical compatibility of hydrides with HTPB requires a suitable solid fuel matrix, above a certain level of additive.

3. A Space Activity Application

During the last 40 years, the mass of the artificial objects in orbit increased quite steadily at the rate of about 145 metric tons annually, leading to a total of approximately 7000 metric tons. But in just a couple of years, from Jan 2007 to Feb 2009, two collisions in space involving the catastrophic destruction of three intact satellites (Fengyun 1C, Cosmos 2251 and Iridium 33) in high inclination orbits took place. This increased the population of cataloged orbital debris in low Earth orbit by approximately 50%. Both events occurred in the altitude range already most affected by previous launch activity and breakup events, leading to the progressive formation of new shells of long lasting debris.

Most of the cross sectional area and mass (97% in LEO) is concentrated in about 4500 intact objects, i.e. abandoned spacecraft and rocket bodies, plus a further 1000 operational spacecraft. The most efficient and effective way to prevent the long-term exponential growth of the cataloged debris population ("Kessler

syndrome"), would be to remove enough cross-sectional area and mass from densely populated orbits. In practice, the active yearly removal of approximately 0.1% of the abandoned intact objects would be sufficient to stabilize the cataloged debris in low Earth orbit, together with the worldwide adoption of the mitigation measures recommended by the Inter-Agency Space Debris Coordination Committee (IADC) and the United Nations. The candidate targets for removal would have typical masses between 500 and 1000 kg, in the case of spacecraft, and of more than 1000 kg, in the case of rocket upper stages. Current data suggest that optimal active debris removal missions should be carried out in a range between 750 and 1400 km of altitude (critical altitude-inclination bands). In these bands, if the technical solution(s) devised during this research activity will make it possible, multiple rendez-vous with different targets might be carried out. In this way, one single chaser mother-ship could be able to reach several abandoned objects per mission in the selected altitude-inclination band, by modifying the relative orbital node through a variation of the semi-major axis. This kind of mission requires an advanced propulsion system, able to perform rendez-vous maneuvers, attitude control and deorbiting of the selected debris.

Hybrid rocket technology for deorbiting applications is considered one valuable option because, in addition to its standard features, it allows commandable cut-off and low regression rates to limit vehicle acceleration. Suitable propellant features include clean combustion, storability, insensitivity to space environment, and easy re-ignition capability. Using a tangentially oxidizer injection, very compact and highly combustion efficient units would result. These characteristics can be the right solution for space debris mitigation, by supplementing with this engine all new satellites that will reach space in the future. It would be possible to deorbit large space debris (several tons) by placing on their surface one hybrid motor, for the reentry maneuver, and few small hybrid thrusters for the attitude control. Thus a family of these engines, of different size, could be able to support micro satellite deorbiting, attitude control, and large debris deorbiting maneuvers.

4. Concluding remarks

In this framework, the objective of the proposed ADR project is to design and demonstrate a hybrid engine module including scalability of design, integration and validation at lab-scale (cold and hot-fire testing), and demonstration at medium-scale.

References

- [1] M. J. Chiaverini, K. K. Kuo, *Fundamentals of Hybrid Rocket Combustion and Propulsion*, Progress in Astronautics and Aeronautics, Vol. 218, 2007.
- [2] L. T. DeLuca et al., *2nd European Workshop on Active Debris Removal*, CNES HQ, Paris, France, 18-19 Jun 2012.
- [3] G. A. Marxman, *9th International Symposium on Combustion*, Vol. 9, pp. 371–383, 1963.

Development of Hybrid Rocket Engines with Multi-Section Swirl Injection Method for Higher Regression Rate and Combustion Efficiency

Shigeru Aso¹, Yasuhiro Tani¹, Yoshihide Hirata¹, Sho Ohyama¹, Kentaro Araki¹, Kengo Ohe¹ and Toru Shimada²

¹ Department of Aeronautics and Astronautics, Kyushu University, Fukuoka 819-0395, Japan

² ISAS, JAXA, Sagamihara 252-5210, Japan

aso@aero.kyushu-u.ac.jp

ABSTRACT

In order to improve fuel regression rate of hybrid rockets, a new method with multi-section swirl injection has been proposed. The new method is to introduce swirling flow within fuel port through multi-section swirl injection holes, which are placed at several locations along the fuel grain. The method is applied for high density polyethylene fuel and paraffin fuel (FT-0070) with pressurized gaseous oxygen. In the previous study combustion duration was rather short. In the present study longer combustion duration has been established for 8 seconds. The increase of combustion efficiency has been realized.

1. Introduction

Recently, hybrid rocket engine becomes one of the promising space propulsion systems. The advantages of hybrid rocket engines are 1) safety, 2) low cost, 3) throttling of thrust, 4) re-ignition, 5) nontoxic and nonhazardous propellant. However, hybrid rocket engines have low fuel regression rate and low combustion efficiency. In order to overcome those disadvantages, there are several research activities[1-3].

In the present study the new method that can improve the fuel regression rate more than that of conventional methods is proposed. The method is multi-section swirl injection method[4]. In the previous, though the proposed method showed excellent increase of fuel regression rate, the combustion duration was rather short. In the present study longer combustion duration has been established for 8 seconds. The increase of combustion efficiency has been realized.

2. Method

Figure 1 shows the schematic diagram of multi-section swirl injection method. The injection of the oxidizer through a number of injector holes that are set in the fuel grain causes swirling flow.

High density polyethylene fuel and paraffin fuel (FT-0070) are used for the present study. Three different grain length of fuel grain with inside diameter of 35 mm are tested in high density polyethylene fuel and paraffin fuel. Diameter of the injector holes, which inject the oxidizer, are 1 or 2 mm. In the present study four injector holes are located at four cross-sections along the axis of the fuel grain.

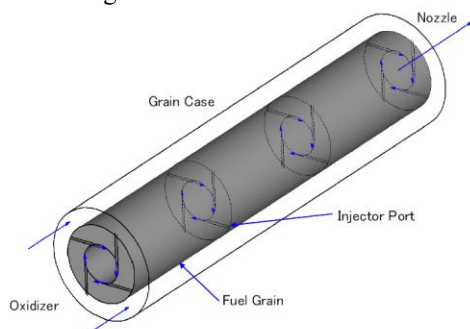


Fig. 1 Schematic diagram of multi-section swirl injection method.

3. Results and Discussion

3.1 High Density Polyethylene Fuel Cases

In the tests of shorter grain the average regression rate is improved. In addition to that, average O/F is improved in the tests of shorter grain. The picture during combustion and the time histories of combustion pressure and thrust for 8 seconds combustion duration are shown in Figs. 2 and 3.

The comparison of the average regression rate obtained from the present study with the conventional method is shown in Fig. 4. The regression rate law of HTPB fuel[5] and paraffin fuel[6] are also plotted. In the tests of high density polyethylene fuel the average regression rate is about 2 or 3 times that of the conventional method with HTPB fuel.



Fig. 2 Picture during combustion in high density polyethylene fuel.(upper: from downstream, lower: from side, $\bar{r} = 0.64$ mm/s, O/F=2.56, c^* efficiency = 0.84, combustion duration = 8sec.)

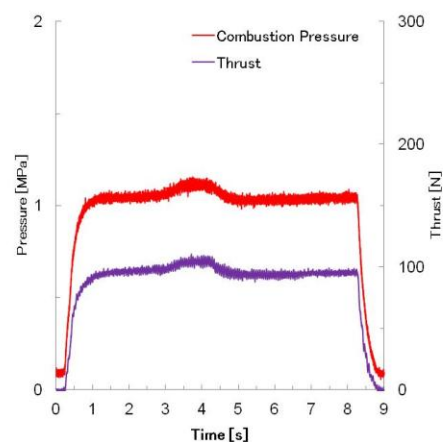


Fig. 3 Time histories of combustion pressure and thrust in high density polyethylene fuel of case of Fig.3.

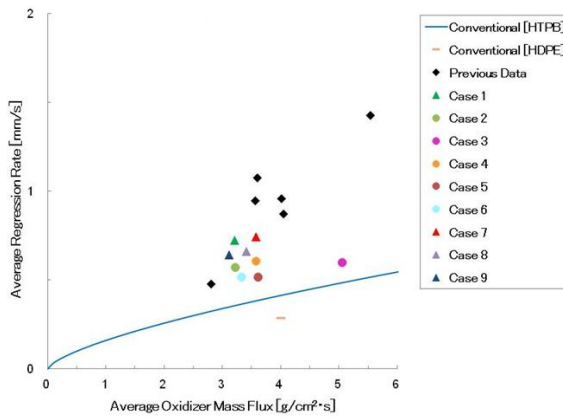


Fig. 4 Relationship between regression rate and oxidizer mass flux with high density polyethylene fuel.

3.2 Paraffin Fuel Cases

Same as the tests of high density polyethylene fuel, in the tests of shorter grain (grain length of 80 mm or 40 mm) significant increase of the average regression rate is realized in the tests of paraffin fuel. Combustion experiments have been conducted in order to increase combustion efficiency by increasing oxidizer mass flux for paraffin fuel. The results show higher combustion efficiency. The picture during combustion and the time histories of combustion pressure and thrust are shown in Figs. 5 and 6.

The comparison of the average regression rate obtained from the present study with the conventional method is shown in Fig. 7. In the case of grain length of 40 mm the average regression rate is about 10 times that of the conventional method with paraffin fuel.

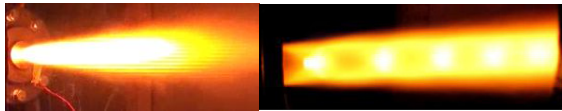


Fig. 5 Picture during combustion with paraffin fuel. (upper: from downstream, lower: from side, $\bar{r} = 3.9$ mm/s, O/F=1.5, c^* efficiency=0.93, combustion duration=3 sec.)

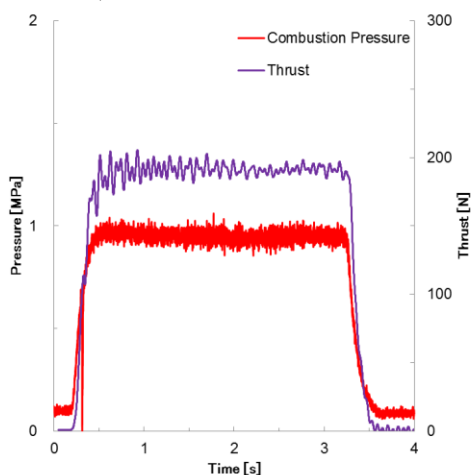


Fig. 6 Time histories of combustion pressure and thrust in paraffin fuel of case of Fig.6.

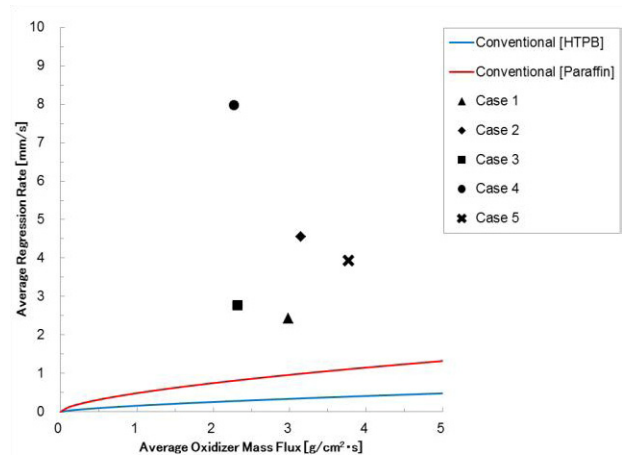


Fig. 7 Comparison of the average regression rate in paraffin fuel.

4. Conclusions

- 1) The new method with multi-section swirl injection is proposed in order to improve fuel regression rate of hybrid rockets.
- 2) By using multi-section swirl injection method with longer combustion duration, precise average regression rate is obtained for high density polyethylene fuel. Combustion experiments with larger oxidizer mass flux with paraffin fuel show higher combustion efficiency. Also regression rate is 10 times compared with that of the conventional no-swirl injection method.
- 3) A lot of data are required to obtain new correlation in multi-section swirl injection method.

References

- [1] H. Nagata et al., Acta Astronautica, **59** (1-5) (2006), 253-258.
- [2] T. Tamura et. al., AIAA paper 99-2323 (1999).
- [3] H. William et. al., AIAA paper 99-2318 (1999).
- [4] S. Aso et. al., AIAA paper 2011-5907 (2011).
- [5] G. P. Sutton, Rocket Propulsion Elements, John Willey & Sons, New York, 6th Edition (1992).
- [6] A. Karabeyoglu et. al., Journal of Propulsion and Power, **20**, No. 6 (2004), 1037-1045.

Numerical Investigation of a Dual Vortical Flow Hybrid Rocket Motor

Yen-Sen Chen¹, B. Wu¹, T. H. Chou², J. S. Wu², Gary Cheng³

¹National Space Organization, Hsinchu Science Park, Hsinchu, Taiwan

²Department of Mechanical Engineering, National Chiao Tung University, Hsinchu, Taiwan

³Department of Mechanical Engineering, University of Alabama in Birmingham, Alabama, U. S. A.

e-mail: yench@nspo.narl.org.tw

ABSTRACT

A dual vortical flow hybrid rocket motor design is proposed in the present study to improve the overall combustion efficiency of the motor and its form factor effect in the design of the rocket system. Diffusion flame is a basic combustion feature in the conventional hybrid rocket motor designs. A comprehensive three-dimensional computational model is employed to investigate the effects of the dual vortical flow N₂O-HTPB hybrid rocket motor design on the diffusion flame development and mixing enhancement in the combustion chamber. Promising results are obtained for the present design.

1. Introduction

In searching for payload mass fraction performance enhancement of human's access to space technical capabilities, ramjet and scramjet (supersonic combustion ramjet) studies have been a long-term research effort in the aerospace community since the 1960's. Since the 1980s, computational modeling approaches have been gradually adopted in the aerospace community in the development of combustion devices and space launch systems. Numerical models using computational fluid dynamics (CFD) methods have been applied to liquid and solid rocket combustion systems with successful supports to the technical programs [1-6].

In the recent development of space launch systems, hybrid rocket propulsion has drawn a lot of attention, especially in the civilian space tourism community, and has been demonstrated to become a viable alternative to the liquid and solid rockets. The hybrid rocket is a combination of both the solid and liquid systems with half of the plumbing of the liquid rockets but retaining the flexibility of operation and avoiding the explosive nature of the solid rockets [7].

There are many types of hybrid combustion systems, in which fuel is classically a solid and the oxidizer is a liquid or gas. Typical examples of combination of fuel and oxidizer with optimum O/F, Isp (184 to 326 sec) and characteristic velocity (1224 to 2118 m/sec) are discussed in [7]. The maximum vacuum Isp of the N₂O-HTPB propulsion system demonstrated so far is only fair around 250 seconds, while its theoretical value for using an 80 expansion ratio nozzle is around 320 seconds. Therefore, there is room for improvement to increase the thrust performance of N₂O-HTPB hybrid rocket motors. Comprehensive computational models allow effective numerical studies for improving the motor designs. Very few [8,9] have attempted to model complicated reactive flow phenomena of a realistic hybrid propulsion system, they employ an energy-balanced surface decomposition model.

The modeling efforts have reached success to some extent based on fitting of experiments and numerical simulations. With the real-fluid effects considered in the model, the overall flow structure in the combustion chamber, especially near the injectors, which affects the

combustion processes and heat transfer characteristics, is better represented by the numerical method.

In the present study, a dual vortical flow N₂O-HTPB hybrid rocket motor is designed and analyzed with much improved overall combustion efficiency and thrust performance. The improved form factor of the present motor design also gives improved versatility in the design of a rocket system.

2. Numerical Method

The present numerical method solves a set of governing equations describe the conservation of mass, momentum (Navier-Stokes equations), energy, species concentration and turbulence quantities [10].

For complete description of the thermal environment in the combustion chamber, a radiative heat transfer model with discrete-ordinate solution method [11,12] is employed in the present model. The turbulence fields are calculated using an extended two-equation model [13,14]. An efficient method for comprehensive real-fluid equations of state and fluid properties is also employed for liquid propellant combustion flows.

In order to analyze the phase change phenomena of liquid sprays and/or cryogenic fluid flows, real-fluid thermal and caloric equations of state (EOS) were developed and used in the present computational model. The HBMS equations of state [15-17] were chosen for this purpose. Thermal and caloric equations of state, vapor pressure, heat of vaporization, and transport properties are modeled with the equations of state proposed by Hirshfelder, et al. [18,19] (we term these the HBMS equations of state) and with conventional correlations [18], for the other properties. This model has been validated with subcritical and supercritical spray combustion experiments of DLR [20].

3. Hybrid Combustion with Mixing Enhancer

The present hybrid rocket combustion model include a 580 mm combustion chamber with the design of forward-end and aft-end mixing chambers. A simple convergent-divergent conical nozzle is attached to the end of the combustion chamber. A single-port simple solid grain of HTPB is cast in two sections and assembled into a single segment through bonding. To boost the mixing efficiency, a mixing enhancer (patent

pending) is also installed near the forward corner of the solid grain. A pintle-type injector made of stainless steel is employed for steady injection of the N_2O oxidizer. Due to the properties of the oxidizer and the absence of thermal control for the oxidizer tank and without using a pressurant tank upstream, the injection flow rates of this pressure-fed injection system depend directly on the temperature of the environment. A small pyro grain is attached to the forward face of the solid grain, which is ignited at engine start-up to melt the HTPB solid and start the combustion process after the N_2O control valve is commanded to open.

Overall, the experimental data show that the solid regression rate is around 1 mm/sec for the current design. The measured specific impulse, sea-level I_{sp} , of the motor with the mixing enhancer is around 213 sec (or vacuum I_{sp} of 222.18 sec). For cases without mixing enhancer, the measured sea-level I_{sp} was around 178 sec (or vacuum I_{sp} of 187.18). The numerically predicted averaged sea-level I_{sp} of an axisymmetric model is 181.2 sec, which is close to the measured data for the case without mixing enhancer. The numerical solutions of 3D models show an averaged vacuum I_{sp} of 223.77 sec and 190.82 sec for the cases with and without the mixing enhancer, respectively. Figure 1 shows predicted flowfield for the hybrid motor.

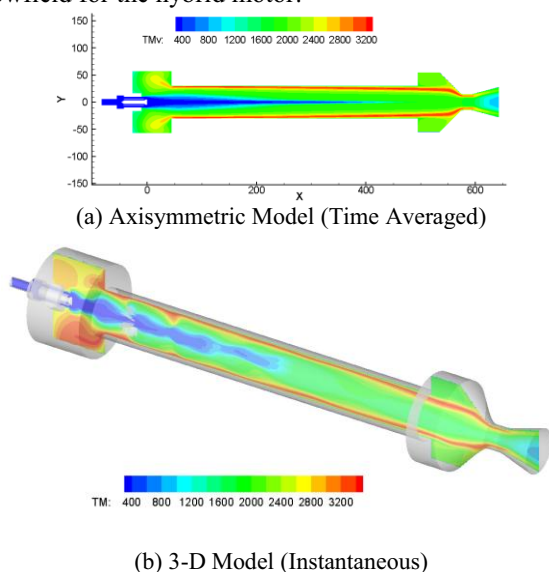


Fig. 1 Predicted temperature distributions in a N_2O -HTPB hybrid rocket motor.

4. Dual Vortical Flow Hybrid Motor Study

Conventional hybrid rocket motors are excessively long in order to obtain good combustion efficiency due to the nature of its diffusion flame structure. This makes hybrid rockets usually very slender with reduced overall rigidity and hamper its flight performance. To overcome this shortcoming and still achieve the purpose of improved combustion efficiency, a dual vortical flow design is proposed in the present study. The effects of the dual vortical flow design are in increasing the combustion length through spiral flow pattern and enhancing the overall mixing by the increased stresses as the flow goes through sharp turns and counter rotation.

The predicted vacuum I_{sp} of this design is 292 seconds, which represents a major improvement for a N_2O -HTPB system. Figure 2 shows the predicted flowfield of the present dual vortical flow hybrid rocket motor.

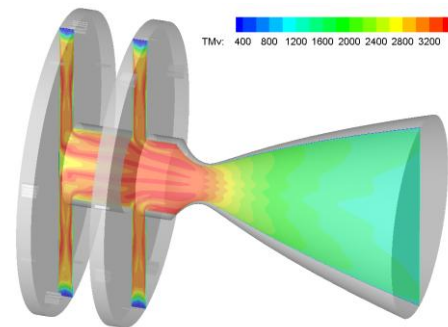


Fig. 2 Predicted temperature distributions in a N_2O -HTPB dual vortical flow hybrid rocket motor.

5. Conclusions

In the present study, a comprehensive numerical model for predicting the combustion flowfield of hybrid rocket motors is employed to evaluate the motor performance. A real-fluid model has been employed for accurate description of the fluid dynamics of the N_2O -HTPB hybrid rocket combustion system.

The experimental investigation of the N_2O -HTPB hybrid rocket combustion system has demonstrated the effective, reliable and low-cost setup of the present designs. The present numerical solutions and test data have shown enhanced combustion efficiency for the hybrid motor with mixing enhancer and a dual vortical flow design.

Acknowledgements

This work is supported by the Sounding Rocket Program of the National Space Organization of the National Applied Research Laboratory of Taiwan. The computational resources and services are provided by the National Center for High-performance Computing of the National Applied Research Laboratory.

References

- [1] Y.S. Chen, et al., *J.Prop. & Power* (1998), **11**:4.
- [2] P. Liaw, et al., AIAA-94-2780 (1994).
- [3] Y.S. Chen, JENNAF 28th Exhaust Plume (2004).
- [4] T.S. Wang, et al., *J.Prop. & Power* (2002) **18**:6.
- [5] T.S. Wang, *J.Prop. & Power*, (2005) **22**:1.
- [6] T.S. Wang, AIAA-2005-3942 (2005).
- [7] M. Chiaverini, K. Kuo, *Prog. Astro. & Aero.* (2007) **218**.
- [8] R.C. Farmer, et al., JANNAF 35th (1998).
- [9] Y.S. Chen, et al., *Computers & Fluids*, (2011) **45**.
- [10] T.S. Wang, Y.S. Chen, *J. of Prop. & Power*, (1993) **9**:5.
- [11] J. Liu, Y.S. Chen, *Num. Heat Trans.*, (1999) **B, 36**,
- [12] J. Liu, Y.S. Chen, *J.Quant.Spec.Radi.Transfer.* (2000) **22**.
- [13] Y.M. Kim, et al., AIAA-92-3763 (1992).
- [14] Y.S. Chen, et al., AIAA-92-3602 (1992).
- [15] O.A. Uyehara, et al., *National Petro. News* (1944).
- [16] J.B. Maxwell, *Data Book on Hydrocarbons*, (1950).
- [17] R.C. Farmer, et al., SECA-FR-02-02 (2002).
- [18] R.B. Dooley, Sept. (1997) Release, IAPWS web.
- [19] L.E. Dean, L.A. Shurley, TCR-70, (1957).
- [20] G. Cheng, et al., RCM-2 Workshop (2001).

Status Summary of FY 2011 Hybrid Rocket Research Working Group

Toru Shimada

Japan Aerospace Exploration Agency, Sagami-hara, Kanagawa, 252-5210, Japan
shimada.toru@jaxa.jp

ABSTRACT

In this report, the status of Hybrid Rocket research Working Group (HRrWG) activities of the fiscal year of 2011. HRrWG is working for R&D of next-generation hybrid rockets (HR), with the approval of the Space Engineering Steering Committee of ISAS/JAXA, as an inter-university research activity in Japan. The activities covers preliminary design of Hybrid Test Engine (HTE-5-1), review of space transportation evolution utilizing the features of hybrid rockets, review of growing community of hybrid rocket, and technologies research and development.

1. Introduction

In this report, we describe the status of Hybrid Rocket research Working Group (HRrWG) activities in the fiscal year of 2011. With the approval of the Space Engineering Steering Committee of ISAS/JAXA, HRrWG is working for R&D of next-generation hybrid rockets (HR) as an inter-university research activity in Japan.

2. Preliminary design of Hybrid Test Engine (HTE-5-1)

As the first step to demonstrate technologies for next-generation hybrid rockets, we have been working on the preliminary design of HTE-5-1 that operates at 5kN thrust for more than 30 s with LOX at above 95% C* efficiency in the Akiruno testing facility of ISAS/JAXA. We have added the goal one constraint that the averaged regression rate is more than 3mm/s.

HTE-5-1 is consisting of a static firing test facility (SFTF) and various test engines and combustors (TEC). As for SFTF, we have finished preliminary design of feed system for GOX, LOX, N₂, etc., have defined a system diagram, and have selected high-pressure gas feeding equipment, such as valves, filters, and orifices, so that they are appropriate for design pressure, temperature, and flow rates. We have conducted case studies on the capability of GOX and LOX to define the system requirement. We have defined requirements and conducted preliminary design about a test bench that supports the test engines for the thrust measurement. In addition to these, we defined the outline of measurement system and control system.

As for TEC, we have defined two sub-goals before reaching the above-mentioned final goal. The sub-goal No.1 is to achieve 5kN thrust for more than 10s with GOX at above 95% C* efficiency with average regression rate of 3mm/s. The sub-goal No.2 is to achieve the gasification of LOX, that is, to heat LOX to more than 160K and vaporize it for more than 30s at the flow rate of 1.5kg/s. Preliminary design peer reviews (PDPR) have been conducted on proposed 9 TEC's to evaluate their progress situation and to determine the order of priority. We have confirmed the completion of the PDPR for the two TEC's for the sub-goal No.1 and another two TEC's for the sub-goal No.2. They are approved to proceed to detailed design.

3. Review of space transportation evolution utilizing the features of hybrid rockets

We have made questionnaire investigation, as well as quantitative evaluations, in order to clarify the features of HR and to figure out the method of utilizing them. Three sizes of engines with thrust levels of 100tonf, 10tonf, and 1tonf are considered. We have evaluated about solid rockets, liquid rockets, and hybrid rockets of each of the engine size from the viewpoint of safety, cost, environmental friendliness, reliability, quality assurance, propulsion capability, response capability, environment resistance, structural efficiency, storability, launch operation period, reusability, requirement for new launch site, payload burden, and propellant characteristics. The investigation shows that HR overtops the others in the viewpoint of safety, environmental friendliness, reliability, requirement for new launch site, and propellant characteristics (exhaust of CO₂ and depletion risk of law material). The overall rating of HR is the best of the three.

As applications utilizing these features of HR, the investigation gives higher rating in comparison with the others to 100tonf-class boosters, 10tonf-class manned ballistic sub-orbital spaceship, and 1tonf-class sounding rockets. In other words, because of its safety and environmental friendliness, HR is compatible with the contemporary society where environmental issues are emphasized. Because of the good operability, HR is easy for future evolution. From the viewpoint of safety, reliability, and operability, HR is expected to be applicable for extraterrestrial activities and HR is hard to generate space debris. We have summed up that HR has significance in its high applicability to the coming society, in comparison with the other engine systems.

4. Review of growing community of hybrid rocket R&D

It is very important for HRrWG to contribute the realization of hybrid rockets by returning our research achievement, expanding our community, and leading people to better understanding of HR. In HRrWG, as of March 2012, there are 20 researchers (JAXA 6, Hokkaido Univ. 3, Tohoku Univ. 2, Akita Univ. 1, Tokyo Metropolitan Univ. 3, Tokai Univ. 2, Kyushu Univ. 2, and Kyushu Inst. Tech. 1) and 6 research

partners. In addition, there have been 17 graduate-student participants (49 in gross) to monthly meetings and research activities based on inter-university research cooperation. Apart from the monthly meetings, organized sessions on HR were held at the 28th ISTS (Okinawa, June), at the 8th ICFD (Sendai, Nov.) and at the 55th Space Sciences and Technology Conference (Matsuyama, Dec.). In 2011, seven refereed articles have been published and 78 conference presentations have been made including 40 international and 2 invited lectures. The frequency of conference presentations by members of HRrWG is increasing year by year. At the same time, the number of articles on HR in major academic societies is increasing as seen in Fig.1. We have confirmed that the number of collaborations on HR among research organizations is growing by investigating the authors and their affiliations of papers published from 2008 to 2011(Fig.2).

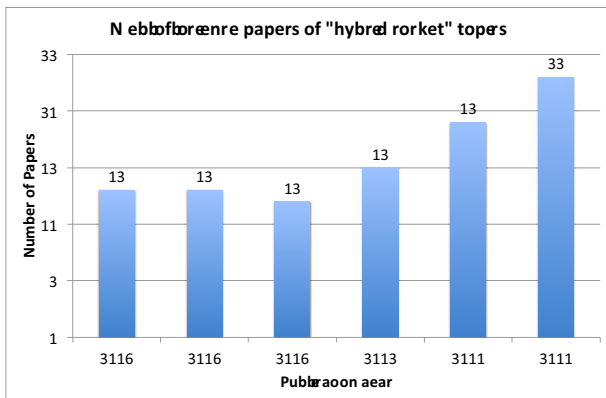


Fig. 1 Number of papers on hybrid rockets searched in Thomson-Reuter's Web of Science®.

University activities on HR have been active recently. In FY2011, more than 200 static firing tests and more than 35 launch experiments have been conducted by about 20 organizations. Due to its safety, HR is used as means of learn-by-doing teaching in schools and is effective for the education of young engineers.

5. Technology R&D

In next-generation hybrid rockets, it is expected that innovative technologies will be used to achieve higher fuel regression rate. We conducted studies on fuel characteristics of low-melting point thermoplastics and the regression rate of paraffin-based fuels. We also have been working on fundamental study on chemically-modified polymers with Si for hybrid rocket fuel. We investigated the fuel regression characteristics in swirling-oxidizer-flow-type hybrid engines, as well as the effect of oblique injection angle. It is found that significant enhancement of regression rate is possible by paraffin-based fuels with multi-section swirl injection method. We are also working on the development of local and real-time regression rate measurement technique using ultrasonic sensors.

We have studied the evaluation method of C* efficiency of swirling-oxidizer-flow-type hybrid engines,

where significant pressure distribution in radial direction exists due to the centrifugal force. Also, we have studied on combustion efficiency of paraffin-based hybrid rockets to evaluate effects of baffle plates and post combustion chambers.

We are working on the development of theoretical and numerical technologies for hybrid engines, such as design optimization using genetic algorithm, computational fluid dynamic simulation for turbulent diffusion flame, turbulence model improvement for swirling flow, numerical tools for internal ballistics prediction, and the linear stability analysis.

6. Summary

The activities of Hybrid Rocket research Working Group of FY 2011 are described. The activities covers preliminary design of Hybrid Test Engine (HTE-5-1), review of space transportation evolution utilizing the features of hybrid rockets, review of growing community of hybrid rocket, and technologies research and development. We would like to continue these activities toward the establishment of next-generation rocket technologies that meet the future social demands.

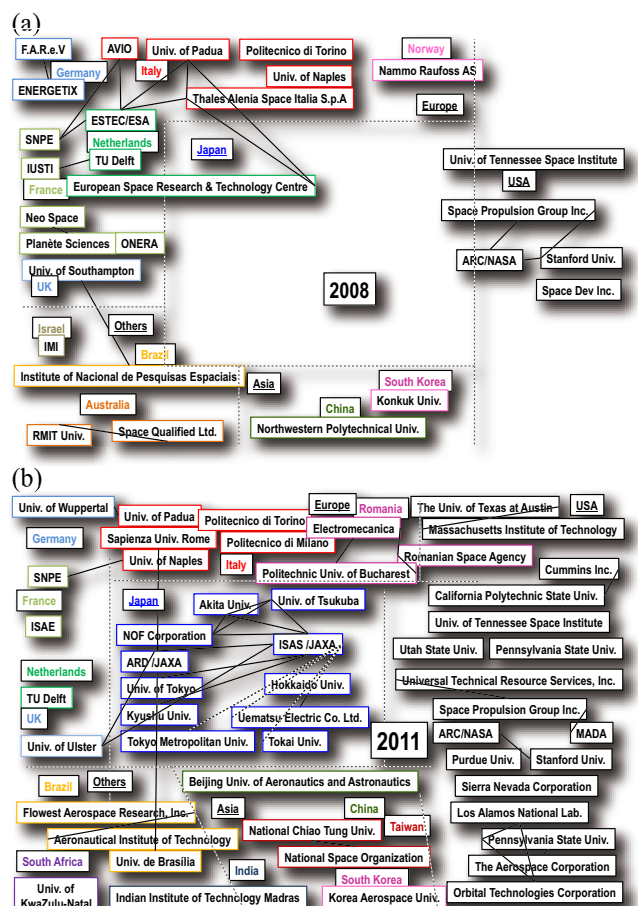


Fig. 2 Collaborations among organizations viewed from author lists of papers in (a)2008 and (b)2011.

Acknowledgments

The author would like to thank for the support of the members of Hybrid Rocket research Working Group.

Nammo Hybrid and Monopropellant Rocket Propulsion Work, an Overview

Jan-Erik Rønningen

Technical Manager Hybrid Rocket Propulsion Technology
Nammo Raufoss, Missile Products Division, Enggata 10, 2830 Raufoss, NORWAY

www.nammo.com

jan-erik.ronningen@nammo.com

ABSTRACT

This paper gives an overview over hybrid and monopropellant rocket propulsion work that Nammo Raufoss (Nammo) has been involved with since 2003. Nammo is a leading company producing rocket motors for tactical missiles and space applications.

1. Introduction

Nammo Raufoss (Nammo) is a world-leading company producing solid propellant based rocket motors for small to medium sized tactical missiles and for space launchers. In 2003 Nammo started to invest and work on hybrid rocket propulsion. Over the years Nammo developed the technology mainly for sounding rocket use. Later, European Space Agency (ESA) became interested, with the focus on developing the technology for Ariane 5 ME use and for up-scaling the technology. As a spin-off from the hybrid rocket propulsion technology work, the monopropellant thruster technology emerged. The success of using high-concentration hydrogen peroxide in hybrids paved the way for reassessing the “green” potential of developing a monopropellant hot-gas reaction system for the Ariane 5 ME launcher. Currently, Nammo is also developing a hybrid rocket propulsion system for a lander demonstrator; the goal of the program is to develop a robust and highly throttleable hybrid rocket engine. The focus of this technology is to be used for landing spacecraft’s on other planets, e.g. Mars.

2. Nammo’s past hybrid rocket programs

In 2003 Nammo started to work on hybrid rocket propulsion within a technology program [1]. The focus was to develop a modular lab-scale rocket engine using gaseous oxygen as the oxidizer. It was early decided to develop the solid fuel based on in-house competence and ingredients as used in solid propellants formulations. In September 2004, Nammo’s first hybrid rocket engine (HRE) was static fired. The engine contained a solid fuel based on HTPB (Hydroxy-Terminated PolyButadiene) with enhanced mechanical properties over the baseline polymer. The engine ran for 7.5 s before intentionality being terminated. No pyrotechnical device was used to ignite the engine, only a special prepared heating device. The engine burned very stable and produced an average regression rate above 1 mm/s. This encouraging test initiated further work.

In 2003 a second program was initiated. This program ran in cooperation with Lockheed Martin Michoud Operations (LMMO) in the United States (US). The goal of the program was to let LMMO educate Nammo in hybrid rocket propulsion technology and to develop a demonstration rocket to be flight tested from Norway. LMMO was design lead and Nammo

responsible for building, test, and fly the rocket. The rocket flight was supposed to occur from Andøya Rocket Range (ARR). The design work and cooperation went smoothly, and in the period of 2005 to 2006, several sub-scale and full-scale engine tests were successfully performed at Nammo’s own test center [2].

The rocket engine used liquid oxygen (LOX) as the oxidizer and “HTPB/C” as the solid fuel, the same fuel formulation as developed under Nammo’s own technology program. The propulsion system used a staged-combustion cycle in order to efficiently evaporate and heat-up the injected liquid oxygen before taking part in the combustion. On 3th May 2007 Nammo’s first hybrid rocket was successfully flown from ARR. The rocket flew a 12 kg technological payload for monitoring and recording a multitude of rocket parameters [3].



Fig. 2 Static firing and flight of a LOX fed staged-combustion HRE

In 2009, Nammo received its first contract with ESA with the goal of investigating Nammo’s hybrid propulsion technology in relation to the preliminary functional requirements of an upper-stage attitude control and propellants settling system (SCATE) for ESA’s next generation Ariane 5 launcher, the Ariane 5 Mid-life Evolution (A5ME). The A5ME will be a versatile heavy-lift launcher, which can place satellites with a mass of up to 12 tons into a geostationary transfer orbit (GTO). For the launcher, the keywords are high precision, safety, and flexibility on a system level as well as mastered recurring costs. These are features that are natural for a well-established hybrid propulsion technology.

In 2010, Nammo initiated an ESA-funded hybrid propulsion Technology Readiness Level (TRL) improvement program based on the proposed HRE technology from a previously performed study. In less

than one year, Nammo executed 29 hybrid rocket firing tests using hydrogen peroxide as the oxidizer. Critical to the success was the close support and cooperation with the Swedish company SAAB Dynamics (SAAB). The highly successful program demonstrated HRE engines with high combustion efficiency, stable combustion, thrust modulation (1:5), rapid pulsing, termination and re-ignition on demand, precise thrust reproducibility and ignition under ambient and low temperature conditions. Regression rates as high as 8 mm/s was recorded [4].



Fig. 3 H₂O₂ fed HRE during burn

3. Nammo's current hybrid rocket programs

Currently, Nammo is up-scaling its hydrogen peroxide based HRE technology to large-scale through a three year ESA FLPP (Future Launcher Preparatory Programme) program. The plan is to scale-up to a size suitable for sounding rocket use, ultimately leading to a small multi-stage launcher for placing nano-satellites into low Earth orbits from Norway. So far small-scale HRE tests have been carried out testing new fuel formulations [5].

Nammo is also engaged in a European Union (EU) funded technology program led by ThalesAlenia Space in Italy. The program is named "SPARTAN" and the goal is to develop a highly throttleable HRE [6]. The system shall demonstrate 1:10 throttling. Four engines will be placed inside a lander demonstrator and drop tested from a helicopter hovering at 100 m altitude. The vehicle has to soft land automatically.

4. Monopropellant thruster technology

As a direct result of A5ME systems studies and the highly successful results obtained from the ESA-funded HRE maturation program, ESA saw an interest in improving the maturation level on monopropellant thruster technology utilizing hydrogen peroxide as well. The main reason for this is that hydrogen peroxide is a "green" propellant, being environmental friendly and non-toxic.

In 2011 Nammo and SAAB was awarded a TRL maturation program on the development of monopropellant thruster technology. 38 separate tests were performed at ambient and low temperature (-15°C) accumulation to about 1100 seconds of operation and 380 pulses with varying frequency. The program did show that Nammo & SAAB could efficiently produce a robust and reliable hot-gas reaction system suitable for launchers like Ariane 5.

5. Summary

Nammo has since 2003 actively through several

challenging technology programs successfully developed and worked on several aspects of hybrid rocket propulsion technology. Today Nammo is continuing this development with a new generation of hybrid engines that hopefully will see a market use within near future. In parallel Nammo has initiated the process of perfecting "green" monopropellant thruster technology for attitude, distancing, de-orbit, and propellant settlement for large launchers and/or spacecraft's.

References

- [1] Jan-Erik Rønningen & Nils Kubberud, Hybrid Rocket Testing at Raufoss, 17th ESA Symposium on European Rocket and Balloon Programmes and Related Research, 2005
- [2] Jan-Erik Rønningen, The HTR Program – An Overview of the Rocket System and Program Achievements, 18th ESA Symposium on European Rocket and Balloon Programmes and Related Research, 2007
- [3] Jan-Erik Rønningen, Post-Flight Analysis of a Hybrid Test Rocket Flight, 59th International Aeronautical Conference in Glasgow, 2008
- [4] Jan-Erik Rønningen, Nammo hybrid rocket propulsion TRL improvement program, AIAA Joint Propulsion Conference, Atlanta USA, 2012
- [5] Jan-Erik Rønningen, ESA FLPP: Test results from small-scale hybrid rocket testing, Space Propulsion 2012. 07-10 May in Bordeaux, France, 2012
- [6] www.spartanproject.eu

Development Plan of Hybrid Rocket Test Engine Facility in Hybrid Rocket Research Working Group

Koki Kitagawa¹, Toru Shimada¹, Keiichi Hori¹, Toshiaki Takemae¹, Noriko Shiraishi¹, Toshio Tomizawa¹,
Naohiro Suzuki¹, Tsuyoshi Yagishita¹, Nobuyuki Oshima², Harunori Nagata², Masashi Wakita², Keisuke Sawada³,
Hiroyuki Nagai³, Yutaka Wada⁴, Saburo Yuasa⁵, Takashi Sakurai⁵, Masahiro Kanazaki⁵, Ichiro Nakagawa⁶,
Takakazu Morita⁶, Masaki Nakamiya⁷, Shigeru Aso⁸, Yasuhiro Tani⁸ and Nobuyuki Tsuboi⁹

¹Japan Aerospace Exploration Agency, Sagamihara, Kanagawa, 252-5210, Japan

²Hokkaido University, Japan, ³Tohoku University, Japan, ⁴Akita University, ⁵Tokyo Metropolitan University, Japan,

⁶Tokai University, Japan, ⁷Kyoto University, Japan, ⁸Kyushu University, Japan, ⁹ Kyushu Institute of Technology, Japan
kitagawa.koki@jaxa.jp

ABSTRACT

To demonstrate the technologies of the hybrid rocket engine, the goals were decided. 9 demonstrators were designed preliminary and the preliminary design review was carried out. 4 demonstrators passed the review. Preliminary design of HTE-5-1 test facility which can be used for combustion tests of 5 kN in thrust was carried out. In this paper, the outlines of the preliminary design of the demonstrators and the test facility are introduced.

1. Introduction

Hybrid Rocket research Working Group (HRrWG) with the approval of the Space Engineering Steering Committee of ISAS/JAXA consists of scientists on hybrid rockets from many Japanese universities and from JAXA in order to research hybrid rockets scientifically. From 2008, basic researches, such as development of new fuel, clarifying hybrid combustion mechanism, development of element technology, development of numerical analysis code and clarifying future concept, are carried out. To some extent, technology for the hybrid rocket engine is matured in HRrWG. It becomes the step of performing demonstration of the technologies at present.

For the first step of the demonstration of the technologies, we set the target to the thrust of 5 kN. The demonstrator of Hybrid rocket Test Engine (HTE-5-1) and the test facility in Akiruno facility, which belongs to JAXA, were designed preliminary. In this paper, the outlines of the preliminary design of the demonstrators and the test facility are introduced.

2. Demonstrator

3 goals are set in HTE-5-1 as shown in Table 1.

Table 1 Goals of HTE-5-1

Goal I	Oxidizer is GOX, average thrust is more than 5 kN, burning duration is more than 10 s, average regression rate is more than 3 mm/s, average C* efficiency is more than 95 %.
Goal II	Oxidizer is LOX, LOX flow rate is 1.5 kg/s, LOX is heated to more than 160 K and vaporized for more than 30 s.
Goal III	Oxidizer is LOX, average thrust is more than 5 kN, burning duration is more than 30 s, average regression rate is more than 3 mm/s, average C* efficiency is more than 95 %.

In the case of the swirling oxidizer flow type engine[1] which is one of the techniques developed in HRrWG, LOX should be vaporized before the injector, because the effect of the swirling flow with LOX is smaller than that with GOX[2]. However, LOX vaporizing technique[3] like a regenerative cooling nozzle has not matured yet. So, the target is divided into two as the goal I and the goal II. If the goal I and the goal II are achieved, the goal III can be achieved.

Nine demonstrators were proposed in HRrWG. The preliminary designs of these proposals and the preliminary design review were carried out. A process to achieve the goal, an experimental method and an example design of the demonstrator were evaluated in this review. Four proposals have passed the review. A swirling oxidizer flow type demonstrator and a high combustion pressure demonstrator with GAP are for the goal I. A regenerative cooling nozzle to vaporize LOX and GAP gas generator to vaporize LOX are for the goal II.

At the next step, these proposals will go to the detailed design phase and the critical design review will be carried out. The other proposals are continuing the preliminary design.

3. Test facility

Preliminary design of HTE-5-1 test facility which can be used for combustion tests of 5 kN in thrust was carried out. The main components of the test facility are a feed system, a test stand, a measurement system and a control system.

3.1 Feed system

The feed system is schematically represented in Fig.1. This system mainly consists of a GOX feed line, a LOX feed line, a GOX line for ignition and a N₂ purge line. About the GOX feed line, it can supply GOX more than 2 kg/s for 15 s or more at the condition of 5 MPa in the injector upper-stream pressure. About the LOX feed line, it can supply GOX more than 2 kg/s for 35 s or more at the condition of 5 MPa in the injector upper-stream pressure. LOX in the tank is pressurized

by GOX. The envelopes of both of oxygen mass flow rates are shown in Fig. 2 and 3. It is capable to arrange the feed condition within these limits.

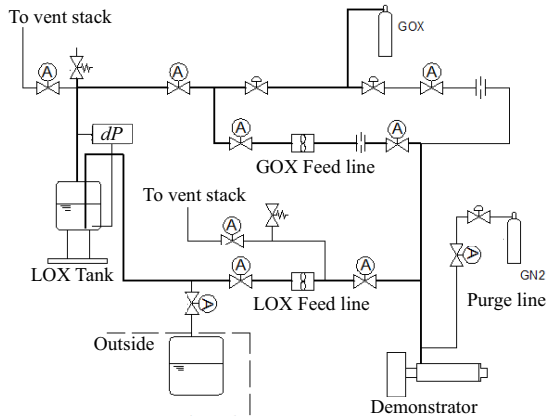


Fig. 1 Schematic of feed system

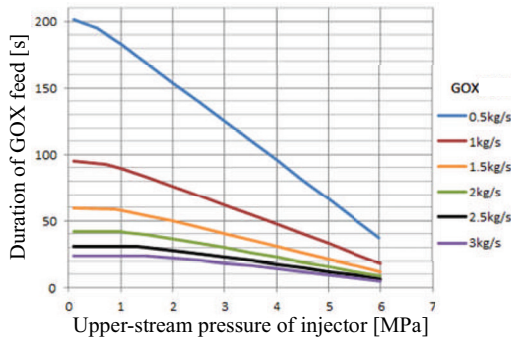


Fig. 2 Envelope of GOX flow line

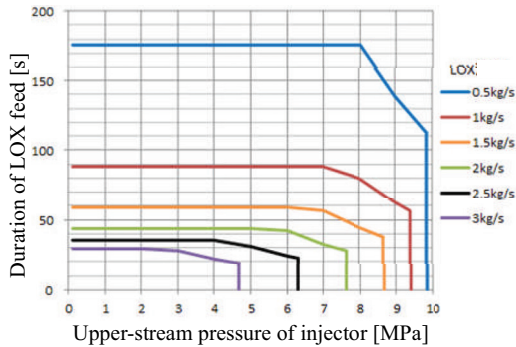


Fig. 3 Envelope of LOX flow line

3.2 Test stand

The test stand contains the thrust measurement system. This test stand is hanging or lifting type using flexures or plate springs to measure the thrust. The u-shaped frame with all corners in straight angles is hanged from the portal frame and the test engine is set inside the u-shaped frame. The permissible size of the test engine is up to 1 m in diameter, up to 1.5 m in length and up to 1.5 t in weight. The thrust can be measured up to 10 kN.

3.3 Measurement system

The main parameters for the measurement are shown in Table 2. Both oxidizer flow rates are measured with turbine flow meters. The combustion pressure is measured with not only a low frequency pressure gage but also a high frequency pressure gage to confirm the combustion instability. LabVIEW (National Instruments) is used for the data logger. The sampling rate is normally up to 10 ms excluding the high frequency pressure gage.

Table 2 Main measurement parameters

Component	Parameter
Feed system	Primary pressure of reducing valve
	Secondary pressure of reducing valve
	Upper-stream pressure of GOX flow meter
	Upper-stream pressure of LOX flow meter
	Differential pressure in LOX tank
	LOX tank pressure
	Upper-stream temp. of GOX flow meter
	Upper-stream temp. of LOX flow meter
	LOX temperature in LOX tank
	GOX flow rate
	LOX flow rate
Demonstrator	Upper-stream pressure of injector
	Combustion pressure (upper)
	Combustion pressure (down)
	Upper-stream temperature of injector
	Nozzle throat wall temperature
	Nozzle throat case temperature
	Thrust

3.4 Control system

LabVIEW is used for the sequencer to control the valves and the ignition. If the start condition of the combustion test is not proper, a system is interlocked. Two feed valves are shut off, when the combustion pressure, the nozzle throat wall temperature or the nozzle case temperature exceeds a limit during the combustion test. Also, an emergency stop button is equipped. When the combustion test finishes, the purge gas is fed automatically to extinguish the combustion.

4. Summary

To demonstrate the technologies of the hybrid rocket engine, the goals were decided. Nine demonstrators were designed preliminary and the design review was carried out. Four demonstrators passed the review.

Preliminary design of HTE-5-1 test facility which can be used for combustion tests of 5 kN in thrust was carried out.

At the next step, the demonstrators passed the preliminary design review and HTE-5-1 test facility will go to the detailed design phase. Manufacture of some demonstrators and mainly GOX feed line will be completed by the end of this fiscal year. LOX feed line will be constructed after that.

References

- [1] S. Yuasa, et al., AIAA Paper 99-2322, 1999.
- [2] K. Kitagawa, et al., AIAA-2004-3479.
- [3] T. Mitsutani, et al., AJCPP 2005-22001.

OS4: Green Aviation: Prospects for
Environmentally
– Compatible Air Transportation

Green Aviation Activities in Korea with UAV Platform Case Studies

Jinsoo Cho

School of Mechanical Engineering, Hanyang University, Seoul Korea
 jscho@hanyang.ac.kr

ABSTRACT

Some activities for green aviation in Korea will be introduced. Korean research teams are studying UAV systems and electric power systems more than manned aircraft or large gas turbine engines for aircraft. Many research teams are developing the high efficiency UAV platforms, renewable electric power system such as fuel cell battery and high efficiency embedded distributed propulsion system. A small battery company is developing high-end secondary battery. Major airliners are adopting green technologies to reduce emissions and fuel consumption. As developing these technology, Korea researcher are ready to green electric manned aircraft.

1. Introduction

Because of the Global warming problem, many researchers are developing new technologies for green aviation in worldwide. Aircraft configurations for low drag and technologies for high efficiency and low emission engine are most big issues for green aviation.

But the Korean aerospace industry is not large enough to develop the high tech airliner and gas turbine engine. Because of this, the Korean researchers are focusing on the high efficiency UAV platform and eco-friendly electric powered propulsion system are researching. Especially, technologies for rechargeable battery and fuel cell battery for electric aircraft are developed very well.

Other activities for green aviation are performed by major airliners. They are trying to reduce the emission and wastes through adapting green technologies for ground service, flight planning and new aircraft and engine.

In this paper, those activities for green aviation and case study of the green BWB UAV platform will describe.

2. Green Aviation Activities in Korea

2.1 Electric powered UAVs

Research team of KAIST(Korea Advanced Institute of Science and Technology) developed small fuel cell system as a power source for UAV and perform a flight test using BWB type UAV test bed in 2007[1]. The fuel cell was PEM(Polymer Electrolyte Membrane) type and produce 20W. The fuel cell system and the BWB UAV are shown in fig.1.

The research group consist of Chosun University, Chungnam National and KAIST a fuel cell unmanned aircraft and verified the performance by long endurance flight test in 2009[2]. The fuel power cell system and the unmanned aircraft are shown in fig.2.

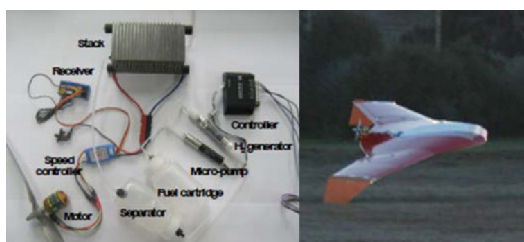


Fig. 1 20W Fuel cell system and BWB UAV test bed

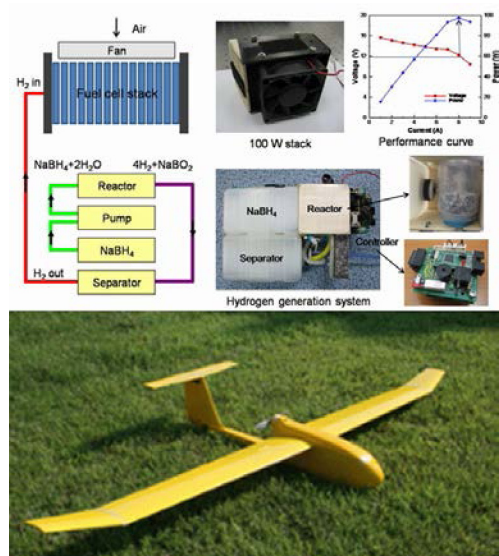


Fig. 2 Fuel cell power system and unmanned aircraft

KAIST and Samsung developed weight reduction technology of fuel cell using aluminum bipolar plate and verified performance under various operation condition by using a small reconnaissance UAV in 2010 [3].

From 2010, the green BWB UAV platform has been developed in Hanyang University, funded by the KAI (Korea Aerospace Industries, LTD.). Concepts of The green BWB UAV are long endurance, low noise and emission [4, 5].

The BWB configuration is selected for long endurance, and distributed electric jet propulsion system is selected for maximize the efficiency and minimize emission. The aerodynamic analysis result and prototype of the green BWB UAV platform are shown in fig. 3 and fig. 4.

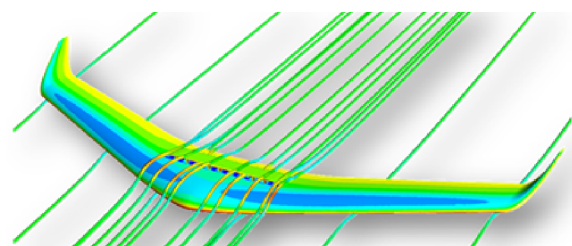


Fig. 3 Aerodynamic analysis result of the Green BWB UAV Platform



Fig. 4 Prototype of the Green BWB UAV Platform

Another research group consisting of Korea Aerospace University and KIST (Korea Institute of Science and Technology) developed the solar-powered UAV and demonstrated over 11 hours of flight in 2011 [6]. The solar-powered UAV is shown in Fig. 5.



Fig. 5 Solar-powered UAV

Korean green aviation will start with green UAVs and light airplanes.

References

- [1] T.G Kim, H.C Sim, S.J Kwon, Proceeding of the 2007 KASAS Fall Conference, 2007, pp.733-734
- [2] T.G Kim, G.S Lee, S.J Kwon, Proceeding of the 2009 KASAS Spring Conference, 2009, pp.508-511
- [3] K.I Kim, J.K Lee, B.S Jang, S.J Kwon, J. of The KSAS, Vol.38, No10, 2010, pp. 1031-1037
- [4] H. Choi, J. Kim, Y. Kim, J. Cho, 2010, 2010 KSAS Fall Conference.
- [5] T. Kim, H. Choi, J. Cho, 2012, 2012 KSAS Spring Conference
- [6] J.S Bae, S.H Park, H.B Kim, S.Y Lee, Y.S Hong, I.Y Ahn, M.J Jung, S.M Choi, S.J Kim, Proceeding of the 2011 KASAS Fall Conference, 2011, pp. 1052-1056

2.2 Rechargeable battery

A small company named Kokam has world class technologies for high energy density and safety. And they supply their battery to defense applications, F-15 and Apache helicopter, solar cell aircraft named "solar impulse". The solar impulse

2.3 Eco-friendly Airliners

The Korean Air and Asiana Airlines, two major airlines in Korea, are doing good activities for green aviation. They publish the sustainability report annually. According to the report, they try to reduce carbon emissions by introducing new aircraft and engines of high fuel efficiency and weight management, flight planning, optimal flight procedures.

2.4 Green Aviation plans of the government

Gyeongangnam-do holds a briefing session of "validity report for commercialization of the green aircraft using hybrid electric power system". According to the report, 11,321 new light airplanes, over 5,000 modified light airplanes and over 27,500 general airplanes are operated with electric power systems until 2025.

3. Results and Discussion

Korean aviation industry is not enough to develop the large green aircraft. But many research teams are developing green technologies for green aviation. And the green technologies are ready to be commercialized.

JAXA's Environment Conscious Aircraft Technology Program Initiative

Takeshi Ohnuki

Japan Aerospace Exploration Agency, JAXA
6-13-1, Osawa, Mitaka-City, Tokyo, 181-0015, JAPAN
E-mail: ohnuki.takeshi@jaxa.jp

ABSTRACT

JAXA is preparing Environmental Conscious Aircraft Technology Program Initiative commencing in 2013 which is the first year of the 3rd JAXA's Mid-Term R&D Period. This paper introduces the provisional plan of "Environment Conscious Aircraft Technology (ECAT) R&D Program". In the program, Technology Reference Aircrafts (TRA), TRA2022 is defined to identify technological goal in 2022. Based on TRA's technological goals, the ECAT R&D program consists of three R&D projects and aircraft system concept research & technology evaluation.

1. Introduction

Both Airbus and Boeing predict that passenger traffic alone will grow more than 2 times (based on revenue passenger kilometer) in the next 20 years[1,2]. Reducing greenhouse gas is one of aviation's biggest challenges today along with safety and security. This paper introduces JAXA's research and development challenge of environmental conscious aircraft technologies.

2. E-CAT Program Initiative

JAXA's Environment Conscious Aircraft Technology (E-CAT) Program Initiative is composed of three research and development (R&D) projects and concept research/ technology evaluation as shown in Figure 1. Element researches on environmental technologies JAXA has been conducted so far are strategically integrated into this program.

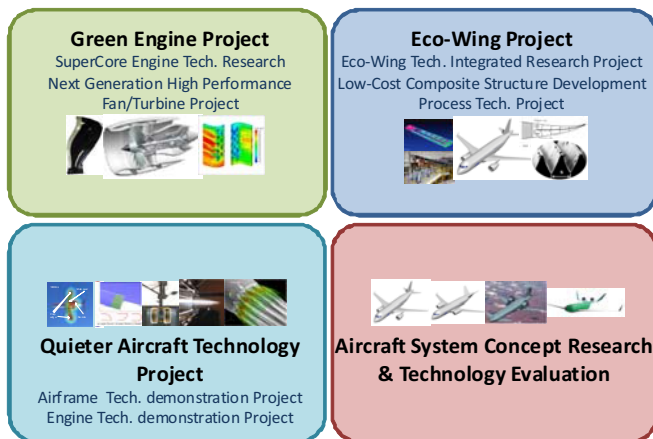


Fig. 1 Framework of E-CAT Program Initiative

Green Engine Project

Technologies for the next generation high performance fan/turbine engines with drastic reduction of fuel burn CO2 emission will be verified in this project. This includes application of composite materials to the fan blades and low pressure turbine blades and/or the case(Fig.2). Also, R&D of elemental technologies such as cooling technology for super-high pressure turbine,

high load compressor technology, and low NOx combustor technology will be conducted.

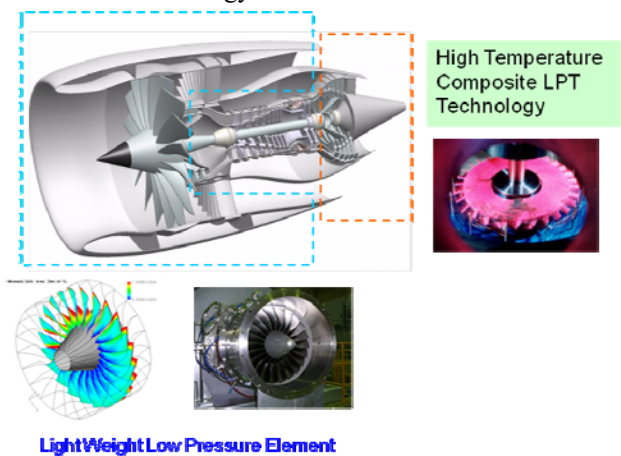


Fig.2 Next Generation High Performance Fan/Turbine Technology

Eco-Wing Project

The purpose of this project is to improve airframe fuel efficiency by increasing aerodynamic efficiency and reducing airframe weight. To increase airframe efficiency, the boundary layer control technologies and morphing technologies will be demonstrated(Fig.3). Also, research on improving type certificate process with development of highly reliable structure design technology and database of composite materials will be conducted in order to decrease airframe weigh without cost penalty.

Quieter Aircraft Technology Project

Noise reducing technologies for both airframe noise and engine noise will be demonstrated in this project. Noise reduction technology using devices for flaps and landing gears will be applied to JAXA's Flying Test Bed(Fig.4).

Aircraft System Concept Research & Technology Evaluation

This is to clarify the position of above projects/initiative in an airplane system and to pursue creation of innovative airplane concepts. Also, fundamental

technology R&D such as MDO will be conducted.

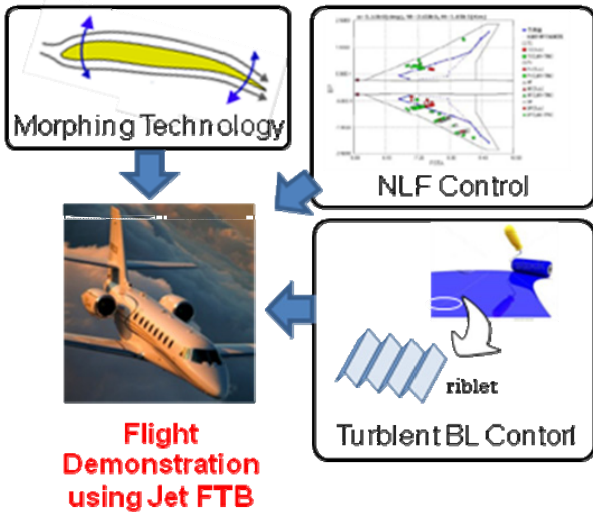


Fig.3 Flight Demonstration of Drag Reduction Technologies

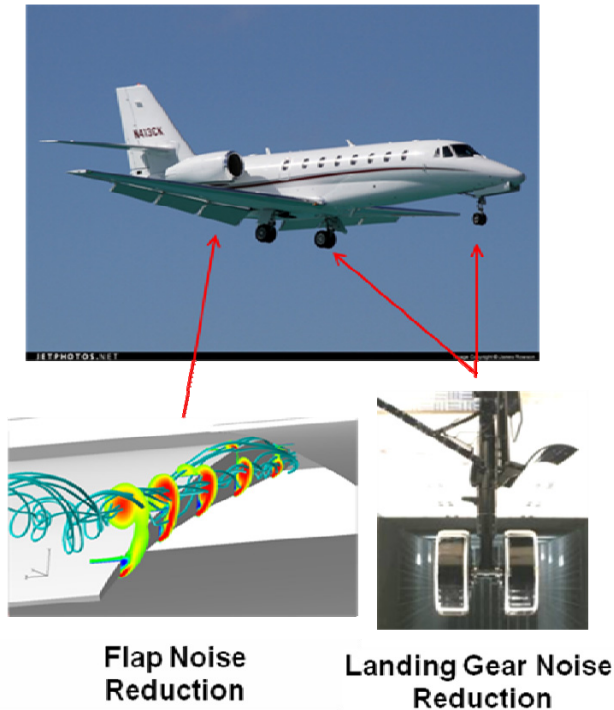


Fig.4 Flight Demonstration of Airframe Noise Reduction Technologies

3. Technology Reference Aircraft

Technology Reference Aircraft (TRA) 2022 and TRA 2035 are defined as aircrafts to be entry in service in 2022 and 2035, respectively. They are defined with technological goals expected in 2022 and 2035. Figure 5 shows the image of TRA 2022 with technical goals of 30% reduction of CO₂ emission relative to the same sized in-production aircrafts, 20dB reduction in airport noise relative to ICAO Chapter 4 regulation, and 70%

reduction of NO_x emission relative to CAEP/6 regulation.

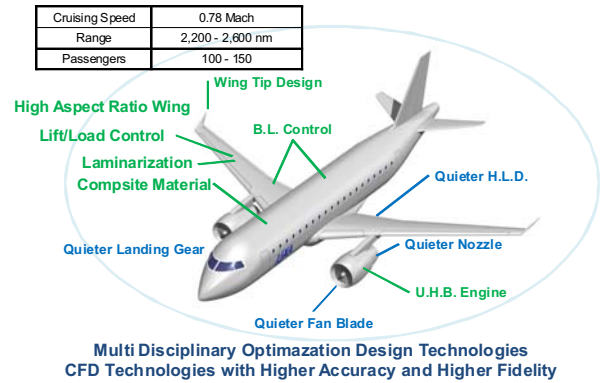


Fig. 5 Technology Reference Aircraft 2022

4. Concluding remarks

This program is supposed to be launched in 2013 coincidentally with commencement of the 3rd JAXA's Mid-Term R&D Period 2013-2017, though all of above mentioned projects could not be launched at the same time. Detailed planning is required for all of the projects.

References

- [1] Airbus, "Global Market Forecast 2010-2029", <http://www.airbus.com/company/market/gmf2010/>
- [2] Boeing, "Current Market Outlook 2011-2030", <http://www.boeing.com/commercial/cmo/>

A Meshless and Matrix-free Approach to Aerodynamic Modeling

Matthew Wilkinson and Andrew J. Meade
William Marsh Rice University, Houston, TX 77251-1892
meade@ruf.rice.edu.

ABSTRACT

We introduce a meshless and matrix-free fluid dynamics solver called SOMA that avoids the need for user generated and/or analyzed grids, volumes, and meshes. Incremental building of the approximation avoids the creation and inversion of possibly dense block diagonal matrices and significantly reduces user interaction. Results will be presented of efforts to apply SOMA to both two- and three-dimensional forms of the unsteady and compressible RANS equations.

1. Introduction

Numerical methods have been an active area of research for decades. The inherent difficulty and frequent impossibility in finding closed form solutions to many of the most important governing differential equations has given rise to the field of Computational Fluid Dynamics (CFD). The cost associated with any CFD analysis has helped fuel the drive for programming methods that aim to maximize numerical data gathering capacity for a given level of computational effort and memory allocation. We believe that the Sequentially Optimized Meshfree Approximation (SOMA) method is another step in this direction [1].

SOMA is a meshless, volume-free, and matrix-free flow solver that can handle elliptical, parabolic, hyperbolic, and mixed governing differential equations in one, two, or three dimensions. Flow simulations solvable by SOMA can be compressible or incompressible, viscous or inviscid, rotational or irrotational. The temporal nature of these flows can be steady, time marching to steady state, or unsteady/periodic. When flows are not solved purely steady state, SOMA has both explicit and implicit time stepping methods, as well as the ability to switch dynamically between the two methods depending upon either computational efficiency or convergence criteria.

As a meshless method, SOMA does not require mesh connectivity data, geometry Jacobians, or conformal maps to transform between physical and computational domains. Further, the element and volume edge crossing restrictions on the distribution of discrete evaluation points associated with meshed methods is eliminated, simplifying the application of standard Adaptive Domain Refinement (ADR) techniques [2].

Other benefits and advancements associated with SOMA improve on both meshed and other meshless methods. Foremost among these, SOMA eliminates the need to invert large, possibly dense, block diagonal matrices in the solution of the governing equations. Solutions to the flow variables are determined through incrementally built approximations, and the governing equations can remain in vector form. By this, SOMA eliminates the computational costs both of calculating and of inverting the system mass matrix.

Additionally, the decades of analysis and work associated with the finite difference method (FDM) and

finite volume method (FVM) with respect to numerical stability, upwinding, CFL number, characteristic lines, system eigenvalues, and many others can be directly applied to SOMA. Fortunately, this application can occur with little to no modification to account for the meshfree nature of SOMA. Additionally, boundary condition enforcement at farfield and surface locations can follow the methods used in FDM and FVM, including extrapolation and ghost points.

Finally, SOMA greatly reduces the required human-in-the-loop cost for domain discretization and adaptation, since there is no mesh to inspect, and eliminates the need for user involvement during solution, since the solution is determined through optimization methods.

2. Method

SOMA employs a sequential greedy optimization procedure. A greedy function approximation approach is often referred as highly non-linear because the target function is used to pick the best approximant or basis from a given set of basis and is then used to form the best k -term representation [3]. We start our approximation of an unknown function u by noting that a continuous d -dimensional function evaluated at N collocation points can be approximated arbitrarily well with a linear combination of one-dimensional basis functions, ϕ .

$$u \approx u_k(x) = \sum_{i=1}^k c_i \phi(x, x_{c,i}, \beta_i) = c_k \phi(x, x_{c,k}, \beta_k) + u_{k-1}(x) \quad (1)$$

where $x \in \mathbb{R}^d$, $\beta_i \in \mathbb{R}^m$, and $c_i \in \mathbb{R}$ represent the function argument, independent variables, function parameters, and linear coefficients, respectively. The variable $x_{c,k}$ represents the spatial location of the center of the k -th basis function in the problem domain. There are no restrictions on the distribution of these bases and a broad class of functions can be used in combination (e.g. low-order polynomials, B-splines, and radial basis functions).

We can write the residual to a differential equation at the k -th stage, and its objective function ε_k , as

$$R_k(x) = H[u_k(x)] - f \quad \text{and} \quad \varepsilon_k = \sum_{j=1}^N (R_k(x_j))^2 / \varepsilon_1 \quad (2)$$

with boundary condition $B[u_k]=0$. Here $H[\cdot]$ and f represent the differential operator and forcing function, respectively.

In this work, a Gaussian radial basis is used along with a multiquadratic quadrature to calculate spatial derivatives. The objective function ε_k is minimized with a tailored genetic algorithm. In combination with the collocation points, the multiquadratic quadrature works with general problem domains and boundary irregularity without the need for Jacobian grid transformations.

3. Results and Discussion

The SOMA method has been applied to both two- and three-dimensional forms of the unsteady and compressible RANS with a minimum of user interaction. Figure 1 compares the accuracy of the computed nondimensional turbulent eddy frequency from Menter's SST-V two equation model along a flat plate in compressible flow. Figure 2 compares the accuracy of the computed C_p surface distribution about the ONERA M-6 wing in transonic conditions.

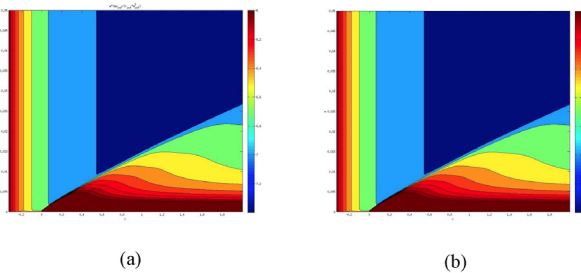


Figure 1: Comparison of computed nondimensional turbulent eddy frequency about a flat plate at $M = 0.2$ and $Re = 5e6$
(a) Reference [4], (b) SOMA

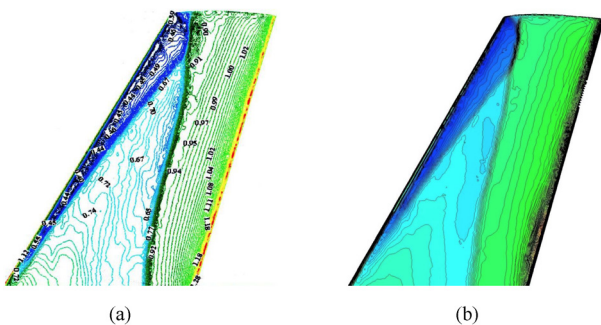


Figure 2: Comparison of the inviscid C_p distribution along the upper surface of the ONERA M6 wing at $M = 0.8358$
(a) Reference [5], (b) SOMA

4. Concluding remarks

The cost and time consumption associated with experimental methods, coupled with the lack of closed form solutions to fluid dynamic governing equations, has fueled the drive for ever better numerical methods. However, the standard modeling techniques still have significant human-in-the-loop overhead, along with the

need to generate and invert large, possibly dense, block diagonal matrices. As an alternate approach, the SOMA method significantly reduces user interaction time while maintaining or decreasing computation cost by eliminating the need for the aforementioned matrices.

Unlike traditional solvers, which require grids, volumes, or meshes, along with the corresponding connectivity data, SOMA requires only a list of spatial coordinates to solve the flow problem. SOMA has two major benefits from this freedom from connectivity. First, there is no need for a human user to inspect a mesh, something which can be difficult and time consuming in three dimensions, especially for users without extensive experience. Second, modification of the domain discretization can occur without the face and element crossing restrictions associated with mesh and volume methods, and without the need to re-mesh the entire domain while performing the domain adaptation.

References

- [1] M. Wilkinson, "Sequentially Optimized Meshfree Approximation as a New Computational Fluid Dynamics Solver," Doctor of Philosophy Thesis, Department of Engineering and Materials Science, Rice University, Houston, TX, April, 2012.
- [2] T. Plewa, *Adaptive Mesh Refinement – Theory and Applications: Proceedings of the Chicago Workshop on Adaptive Mesh Refinement Methods, Sept. 3-5, 2003*, Springer, Berlin, 2005.
- [3] R.A. DeVore, "Nonlinear Approximation," *Acta Numerica*, 1998, pp.51-150.
- [4] M.T. Manzari, "Inviscid Compressible Flow Computations on 3D Unstructured Grids," *Scientia Iranica*, **12**, 2, 2005, pp.207-216.
- [5] C. Rumsey, Langley Research Center Turbulence Modeling Resource, 2011, <http://turbmodels.larc.nasa.gov/index.html/>

Wall Shear Stress Measurement

Ebenezer Gnanamanickam and John Sullivan
Purdue University, West Lafayette, IN
sullivan@purdue.edu

ABSTRACT

Wall-bounded flows are among the most common flows encountered in fluid mechanics. Wall shear stress on the walls of these flow fields is an important engineering quantity as it is responsible for skin friction drag, which is a significant portion of the drag on bodies ranging from airplanes to flow in biological systems. Measuring, understanding and eventually controlling the wall shear stress has implicit financial significance. A wall shear stress sensor, referred to as the micro-pillar wall shear stress sensor is presented from concept to actual measurements in a wall jet flow field.

1. Introduction

The measurement of wall shear stress or skin friction is important for many everyday engineering problems. The time averaged values of the wall shear stress are used to determine global quantities such as skin friction drag on a body moving in a fluid. The time resolved measurement of wall shear stress gives an estimate of the turbulent activity in the flow and describes the individual momentum transfer events between the body and the fluid. The instantaneous wall shear stress is a foot print of the individual unsteady flow structures that transfer momentum to the wall

Wall shear stress is significant especially in improving the performance and efficiency of transportation vehicles by reducing drag. In the airline industry skin friction drag accounts for about 45 % of the drag on an aircraft at cruise conditions. Measurement of the wall shear stress, thus assumes significance as a reduction in drag directly results in a reduction in fuel consumption.

For a commercial aircraft such as the Boeing 787 the Reynolds number based on chord is a $Re \sim 40$ million at cruise with a viscous length scales ~ 5 microns

Wall shear stress sensor requirements are:

1. high spatial resolution
length scales $O(10^{-5}$ mm)
2. high temporal resolution
time scales O (kHz's)
3. high sensitivity
resolve very small forces O (mPa's)

All these requirements are very challenging.

The review papers by Naughton and Sheplak [1] and Plesniak and Peterson[2], presents in detail the recent developments in wall shear stress sensors. In general, there is a need for sensors with high spatial and temporal resolution to measure the wall shear stress.

These papers review the many types of direct and indirect shear stress sensors but this paper will concentrate on one type- the micro-pillar array.

2. Method

The Micro pillar shear stress sensor is an array of micron scale pillars manufactured out of a flexible material and placed on the wall of a wall bounded flow, such that the pillars protrude into the viscous sub layer.

In the presence of a shear field these pillars deflect an amount proportional to the drag force on it which is in turn proportional to the wall shear stress.

A schematic of the concept is shown in Fig. 1.

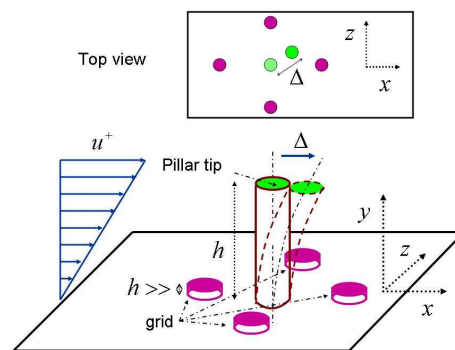


Fig. 1 Wall shear stress sensor concept schematic.

A mechanical model of the micro-pillar sensor based on first principles will predict the response of the micro-pillar shear stress sensor to a static load. Using the Euler-Bernoulli beam theory and Oseen's approximation Venier et al.[3] have calculated the tip deflection Δ_{tip} for a micro-tubule under the loading of a velocity field. If the velocity field that a micro-pillar is subjected to is substituted into the expression developed by Venier et al.[3] the following is obtained,

$$\Delta_{tip} \approx \frac{32h\tau_w}{E \ln(h/2d)} \left(\frac{h}{d}\right)^4 \quad (1)$$

The micro pillar arrays are manufactured out of a PDMS elastomer using a lost wax [4][5]

Characteristics of a typical micro pillar array are:

- $25 \times 25 = 625$ micropillars
- Overall sensor size
 - 10 mm x 10 mm
- Micropillar dimensions
 - height ~ 200 microns
 - tip diameters ~ 10 microns
 - base diameter ~ 35 microns
 - Spacing ~ 400 microns

Pictures of this array are shown in Figure 3.

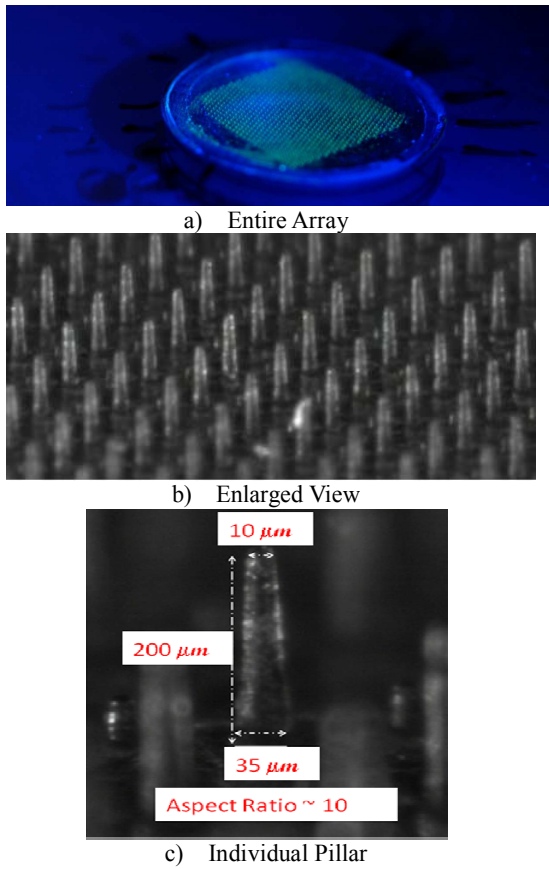


Fig. 2 Photographs of the micro pillar array

Considering the micro-pillar to behave as a micro-tubule, Eq. 1 states that as a first approximation the pillar tip deflection is proportional to the wall shear stress, flexibility of the pillar and the fourth power of the aspect ratio.

Static calibration of the micro-pillar shear stress sensor was carried out in a fully developed channel flow. By measuring the pressure drop across the micro-pillar sensor an estimate of the wall shear stress can be obtained. A typical calibration curve is shown in Fig. 3.

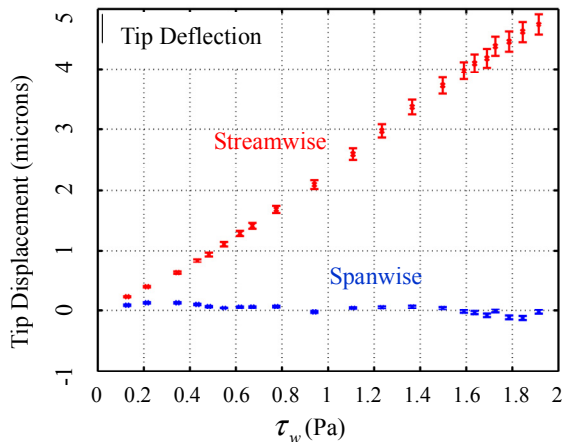


Fig. 3. Mean wall shear stress calibration

Wall jets are formed when a jet exits such that the fluid stream exiting the jet is along or parallel to a solid boundary. The wall shear stress is measured on the wall of the wall jet demonstrating the ability of the micro pillars to measure the distributed unsteady wall shear stress. The three-dimensional wall jet schematic is shown in Fig. 4 and an instantaneous image of the wall shear stress distribution showing turbulent wall stress structure in Fig. 5.

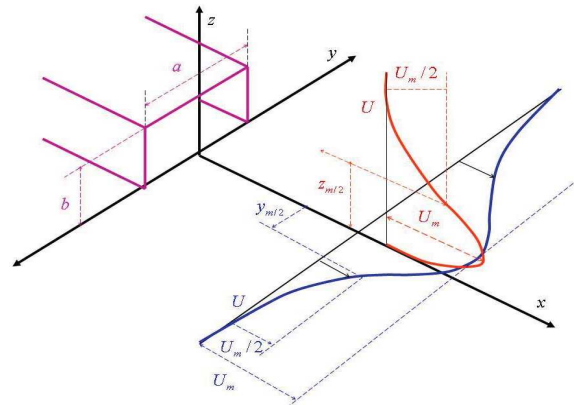


Fig. 4. 3D Wall jet set-up

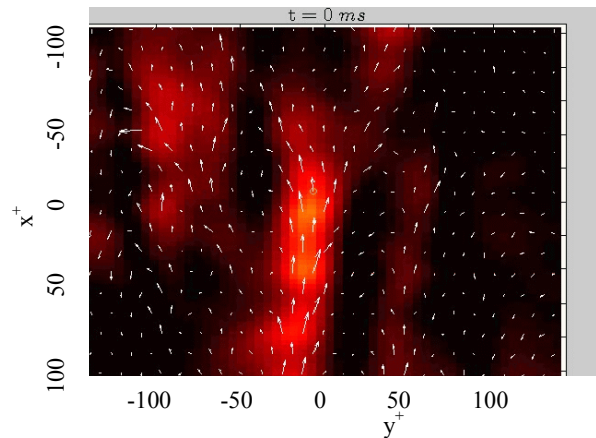


Fig. 5. Turbulent shear stress structure

Several large data sets have been acquired and are currently being reduced.

References

- [1] W. Naughton and M. Sheplak *Progress in Aerospace Sciences*, 38:515–570, 2002.
- [2] Plesniak and S. S. Peterson. AIAA-2004-2301, June 28-1, 2004.
- [3] P. Venier, A. C. Maggs, M. F. Carlier, and D. Pantaloni. *Journal of Biological Chemistry*, 269:13353–13360, 1994.
- [4] E. Gnanamanickam, PhD thesis, Purdue University, August 2010.
- [5] E. Gnanamanickam and J. Sullivan, AIAA 2011-1097, 2011, Orlando, Florida

Evaluation of Four-Engines Configuration for Near-Future Fuel Efficient Transonic Transports with Geared Turbo Fan Engines

Masaya Oshimizu^[1], Shinkyu Jeong^[1], Shigeru Obayashi^[1], Daisuke Sasaki^[2], Kazuhiro Nakahashi^[3].

^[1]Tohoku University, Sendai, 980-8577, Japan.

^[2]Kanazawa Institute of Technology, Nonoichi, 921-8501, Japan.

^[3]Japan Aerospace Exploration Agency, Chofu, 182-8522, Japan.

oshimizu@edge.ifs.tohoku.ac.jp.

ABSTRACT

This study evaluated four-engines configuration for near-future aircraft. Future geared turbo fan engines were designed preliminary to estimate the efficiency and diameter. Engine drag and weights are calculated by empirical method. Three different technology levels were applied to recognize the influence of technology development. The disadvantage the conventional two-engines low wing configuration due to its engine diameter limitation was estimated from its fuel burn reduction. Approximately 1 % of advantage in fuel burn was estimated for four-engines configuration compared to the conventional configuration.

1. Introduction

The problem of ground clearance is getting much more serious for future aircrafts. For near future Tube-and-Wing (TAW) aircrafts, one of the keys to reduce fuel burn is the development in engines, which has been achieving much higher efficiency values. We can expect large fuel burn reduction by installing advanced engines. Engine dependent concepts, like Airbus320neo[1] or Boeing737MAX[2], might be one of the big trends for near future aircrafts until advanced new configurations, such as blended-wing-body, become feasible enough both technologically and industrially. However, the idea of installation of advanced engines for conventional aircrafts has a serious problem, ground clearance. The conventional configuration, which has two engines potted under the low wing, allows installation of only limited diameters of engines, though it excels other varieties of TAW concepts in aerodynamics, structure and versatility. The diameter of engines has been increasing with increase in bypass ratio (BPR) which causes reduction in fuel burn, emission and noise. Especially for new types of engine, geared turbo fan (GTF), a great increase in diameter is expected. The conventional TAW aircraft might not incorporate with the best BPR of GTF engines due to its diameter limitation. To deal with this problem, four-engines configuration, which can use smaller engines, has been proposed.

This study estimates the difference in fuel consumption between four-engines configuration and the conventional configuration related to their diameter limitation and the increase in the best BPR caused by development in technologies.

2. Estimation Method

In this study, 4500 km of range with 150 of passengers in Mach 0.785 was set as a requirement. Boeing737-600, one of the best seller aircraft in this class, was chosen as a reference aircraft. Fuel consumption in this study was calculated comparing specific fuel consumption (SFC), engine drag, and engine weight with Boeing737-600.

2.1 Geared Turbo Fan Engine Design

GTF engines were designed to estimate their SFC

with a preliminary gas turbine design application, GasTurb[3]. In GasTurb, engines were designed mainly by basic thermodynamics and some empirical methods introduced in literatures. The base engine is CFM56-7B, which is the power plant of Boeing737-600. Present technology level GTF engine was designed by referring PW1100G[4], which is the power plant of Airbus320neo. Near future GTF engines were designed for three technology development cases summarized in Table 1. Smaller engines for four-engines configuration were also designed by halving required thrust. Engine diameters were calculated from their inlet mass flows.

2.2 Engine Drag Estimation

Parasite drag from engines were calculated by the modified Raymer's empirical method (1)[5].

$$CD_{0,component} = \frac{Cf * FF * Q * S_{wet,component}}{S_{ref}} \quad (1)$$

The method cannot be applied to very high BPR of engines. To improve the accuracy of the estimation for very high BPR of engines, drag calculations were done for the axially split nacelles. Drag for nacelles were estimated by integrating the calculated drag of the split small parts.

2.3 Engine Weight Estimation

Engine weights were calculated empirically by the original equation (2).

$$W_e = \frac{0.11T}{1 + 0.6BPR} + \frac{0.7T}{1 - \sqrt{1 + 0.088BPR}} + 0.033T + 800 \quad (2)$$

The equation is constructed empirically from about 250 of existing aero engine data referring Torenbeek[6]. The average error for this equation to the data is less than 10 %. For future engines, fan and fan case will be lighter with composite. To apply this effect, the second term of the right hand side of the equation (2), which expresses the parts whose weights are increased with increase in BPR, is decreased 5 %, 10 %, and 15 % for the slow, the normal, and the high development cases. Engine weights are adjusted proportionally to engine diameter referring the base engine.

Table 1 Summary of Technology Development Cases

	Overall Pressure Ratio	Turbine Inlet Temperature	Weight of Fan & Fan Case
Slow Development	+ 20 %	+ 70 K	- 5 %
Normal Development	+ 40 %	+ 140 K	- 10 %
High Development	+ 60 %	+ 210 K	- 15 %

3. Results and Discussions

The resultant difference in fuel burn for the each case and the engine diameters are shown in Figs. 1 and 2. As BPR increases, SFC decreases while drag and weight increase (Fig. 3). Decreasing rate of SFC at high BPR becomes bigger with higher technology. As a result, indicated in Fig. 1, the more technology is developed, the larger the best BPR becomes (purple arrow). On Fig. 2, three diameter limitations are drawn: 1.54 m for Boeing737-600, 1.77 m for Boeing737MAX, and 2.06 m for Airbus320neo. With the 1.77 m of diameter limitation, conventional configuration aircrafts cannot use the best BPR of GTF engines (brown arrow in Fig. 2). Its disadvantage is approximately 1.4 % in fuel burn for the highly developed case, while it is less than 0.9 % for the present technology case. Thus, the disadvantage of the conventional configuration will be increased as technology developed.

For the four-engines configuration, diameter limitation never affects to fuel burn with GTF engines. Its fuel burn is approximately same as two-engines configuration for the same BPR although the SFC of the smaller engines are worse than SFC of the bigger engines because total weight gets lighter as engines become smaller. As a result, approximately 1.3 % of fuel burn benefit is expected for the four-engines compared to the conventional configuration for the highly developed case.

The diameter limitation of the conventional configurations causes disadvantage which can be solved by the four-engines configuration as expected. However, the difference is too small which is about 1% even for the highly developed case with GFT engines. This small benefit in fuel burn can be easily cancelled out by other disadvantages such as increase in maintenance cost due to the increase in the number of engines. Thus, four-engines configuration seems not worth to invest in development with GTF engines for near future.

4. Concluding Remarks

Geared turbo fan engines were designed to evaluate four-engines configuration. The advantage of the four-engines configuration is too small to ignore, although it can solve the problem of ground clearance for the conventional configuration. Thus, the four-engines configuration is not adequate for near future aircrafts with GTF engines. To bring out the advantage of four-engines configuration, much larger diameter of engines with high efficiency are required. For future work, open rotor engines will be applied to this study to maximize the superiority of four-engines configuration.

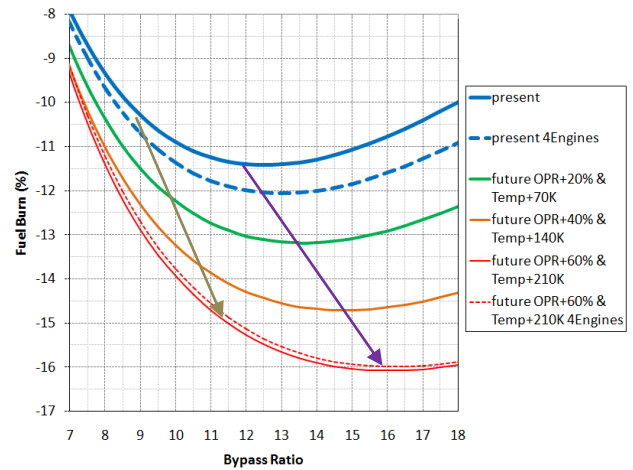


Figure 1 Fuel Burn Reductions Related to Bypass Ratio

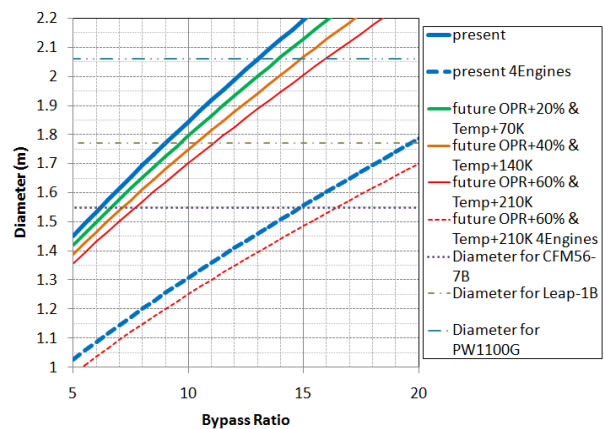


Figure 2 Engine Diameters Related to Bypass Ratio

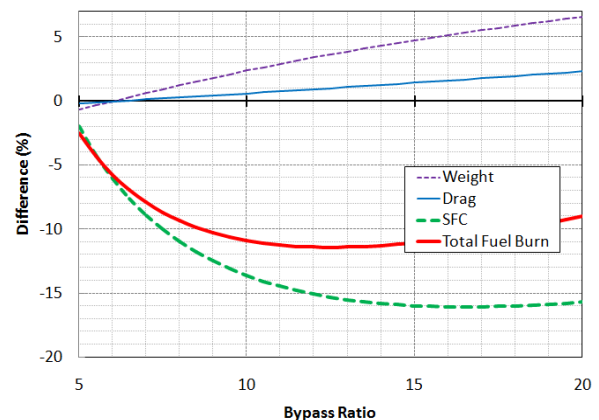


Figure 3 Effect of Bypass Ratio for the Present Case

References

- [1] Airbus, <<http://www.airbus.com/aircraftfamilies/passengeraircraft/a320family/spotlight-on-a320neo/>>, (accessed May 23, 2012).
- [2] Boeing, <<http://boeing.mediaroom.com/index.php?s=43&item=2212>>, (accessed May 23, 2012).
- [3] Joachim Kurzke, <<http://www.gasturb.de/>>, (accessed May 23, 2012).
- [4] Pratt & Whitney, PW1000G broucher.
- [5] Daniel P. Raymer, AIAA education series, 2006.
- [6] Egbert Torenbeek, Kluwer Academic Publisher, 1982.

Wind Tunnel Tests on Aerodynamic Performance of Clustered Linear Aerospike Nozzles

Kohei Kuwamori¹, Goro Masuya¹

¹Tohoku University, Dept. of Aerospace Engineering, Sendai, Miyagi, Japan

Hidemi Takahashi², Sadatake Tomioka², Noboru Sakuranaka² and Takeo Tomita²

²Japan Aerospace Exploration Agency, Kakuda Space Center, Kakuda, Miyagi, Japan

tomioka.sadatake@jaxa.jp

ABSTRACT

The aerodynamic performance of clustered linear aerospike nozzles was investigated by conducting cold flow tests with simplified models of clustered linear aerospike nozzles. The effect of external flow on the aerodynamic performance of the aerospike nozzle was investigated using two kinds of models which defer on ratio of width of cell-nozzle exit and distance among adjoined cell-nozzles. In cases of with-external flow condition the pressure distribution on the ramp surface were raised by the external flow, compared to those for the without-external flow one.

1. Introduction

Future fully reusable TSTOs(Two State to Orbit) to reduce launch costs are under development. Propulsion systems for TSTO vehicles are required to have good performance for a wide range of flight altitude and light weight. Aerospike nozzles are thought to meet these requirements because of its altitude compensating ability. However, the flow structure around the aerospike nozzles is very complex because of the interference between the external flow surrounding the vehicle and flows evacuated from the combustion chambers, each flows evacuated from adjoined combustion chambers of clustered aerospike nozzles resulting in the performance of aerospike nozzles changes. Therefore, it is needed to investigate the effect of these interferences on the performance of aerospike nozzles.

Until now experimental studies have been investigated clustering effects on the performance of clustered linear aerospike nozzles without external flow surrounding the vehicle [1], [2]. However there are not enough experimental studies investigating about effects of external flow surrounding the vehicle on performance of aerospike nozzles. Therefore this study aims to investigate effects of external flow on the performance of clustered linear aerospike nozzles by setting simplified models into the M2.0 wind tunnel.

2. Method

In this study, two kinds of the models which were different in the ratio of cell nozzle exit width (L_{cxe}) to distance among adjoined cell nozzles (L_{cg}) was compared about effect on the aerodynamic performance. It is because flows advocated from adjoined cell-nozzles interfere each other and the interference is largely effected on L_{cg} / L_{cxe} . Figure 1 shows one schematic of the simplified models of the clustered linear aerospike nozzle. The model is composed of four cell-nozzles connecting to the 77-mm-length straight section and the 210-mm-length straight ramp section. The ramp angle is 12 degrees inclined against the straight section. The nozzle contour is made in the horizontal direction where the exit width is 22 mm and the throat width is 2.95 mm resulting in the nozzle Mach number of 3.47 and $L_{cg} / L_{cxe} = 0.18$. The reason why the ramp section is

flat plate is to focus on the effect of interferences between the external flow and flows evacuated from combustion chambers. The another model is composed of three cell-nozzles and $L_{cg} / L_{cxe} = 0.77$. Figure 2 shows the experimental apparatus. The experimental apparatus is set into the low pressure room where pressure is kept low(approximately 10 kPa) by operating ejector set into the downstream of the room. The wall static pressure on ramp surface is measured by the PSI (Pressure measurement system, PSI ESP-64). In this experiment, NPR which is the pressure ratio expressed by the following equation is changed as the main experimental parameter.

$$NPR = P_{0r} / P_b \quad (1)$$

where P_{0r} is total pressure of cell nozzle flow and P_b is pressure in low pressure room. The NPR corresponds to flight condition: higher flight altitude condition corresponds to NPR bigger. The designed NPR of the cell-nozzle which is the condition of optimal expansion is 73.6. The experimental conditions are summarized in Table 1.

3. Results and Discussion

Figure 3 shows relation between cell-base pressure P_{cb} divided by P_b and NPR . It is important to investigate the cell-base pressure behavior because total area of the cell-base is so large that it effects on the performance of the aerospike nozzle as an additional thrust. In case of without-external flow condition P_{cb} / P_b is value despite NPR change. And in case of 3 cell-nozzle model P_{cb} / P_b is nearly unity, namely P_{cb} always balances with P_b . On the other hand, in case of with-external flow P_{cb} / P_b increase as NPR increase.

Figures 4 and 5 show pressure distributions as NDP distribution on the straight section and the ramp section for case of 3 cell-nozzle and 4 cell-nozzle models. The NDP is a non-dimensional parameter introduced to eliminate the effects of P_b and P_{0r} for different experimental conditions, and therefore NDP enables each condition comparable expressed by the following equation.

$$NDP = (P_w - P_b) / P_{0r} \quad (2)$$

where P_w is wall pressure on the straight and ramp sections. The upper sides of figures 4 and 5 are the result for the case of without-external flow and the lower sides are that for the case of with-external flow in under-expansion conditions. In case of 3 cell-nozzles model high pressure spots were seen at about 90 mm and 120 mm from cell-nozzle exit.(Fig.4) On the other hand, in case of 4 cell-nozzle model the pressure distribution does not almost change along y direction. It means the flow is nearly two dimensional form. Figure 6 compares NDP along the flow direction at the center line of the second cell-nozzle from right wall of 4 cell-nozzles model for the cases of without- and with-external flows. Figure 6 shows that in cases of with-external flow the pressure distribution along x direction on the ramp section were raised by external flow. Especially in case of over-expression condition($NPR = 26.1$) repetition of pressure increase and decrease along x direction for case of without-external flow condition was vanished by external flow.

4. Concluding remarks

- 1) In case of without-external flow conditions P_{cb} / P_b of 3 cell-nozzles model ($L_{cg} / L_{cze} = 0.18$) and 4 cell-nozzles model ($L_{cg} / L_{cze} = 0.77$) is almost constant value despite NPR increase.
- 2) In each case of with-external flow, pressure distribution were raised to constant value on the ramp surface.
- 3) High pressure spots were observed on the ramp surface of 3 cell-nozzle model because of interference in flows from adjoined cell-nozzles.

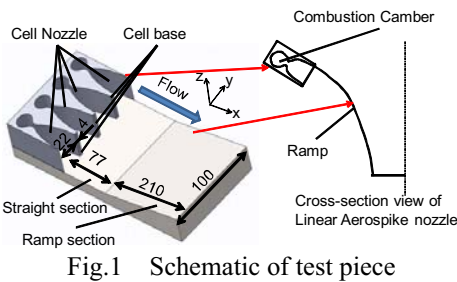


Fig.1 Schematic of test piece

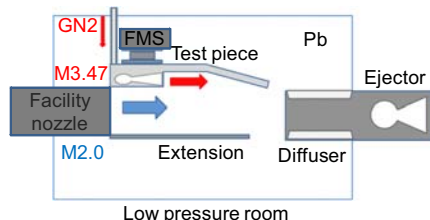


Fig.2 Schematic of experiment apparatus

Table1 Experimental conditions

	w/o external flow	w/ external flow
4 cell-nozzle model	16 conditions NPR = 8.7 - 142.1	7 conditions NPR = 16.5 - 104.5
3 cell-nozzle model	10 conditions NPR = 24.4 - 156.5	6 conditions NPR = 22.7 - 102.1

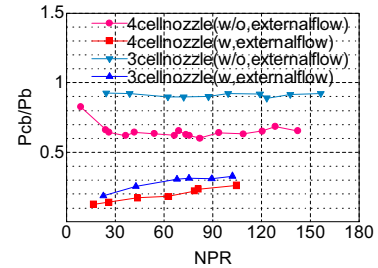


Fig.3 Relation between P_{cb} / P_b and NPR

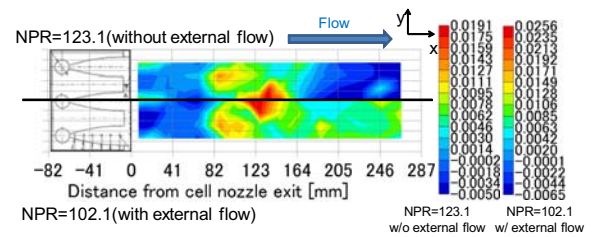


Fig.4 NDP distribution (3 cell-nozzle model)

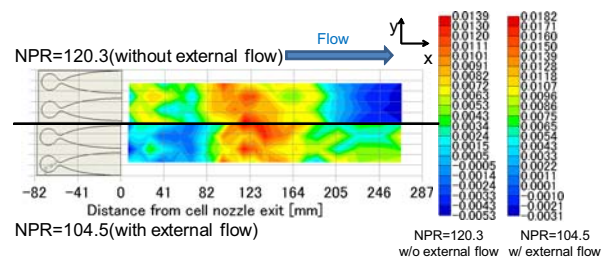


Fig.5 NDP distribution (4 cell-nozzle model)

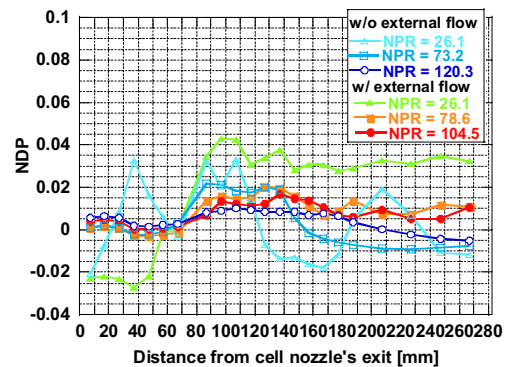


Fig.6 NDP distribution along flow direction (4 cell-nozzle model)

References

- [1] Tomita.T. and Takahashi,M., 37th AIAA/ASME/SAE/ASEE Joint Propulsion Conf. and Exhibit, 2001
- [2] Tomita,T. and Takahashi,M., 36th AIAA ASME/SAE/ASEE Joint Propulsion Conf. and Exhibit, 2000

Effects of Leading-Edge Truncation and Stunting on Drag and Efficiency of Busemann Intakes for Axisymmetric Scramjet Engines

Hideaki Ogawa^{*}, Russell R. Boyce^{*}, and Sannu Mölder[†]

^{*} Centre for Hypersonics, School of Mechanical and Mining Engineering
The University of Queensland, St. Lucia, Brisbane, QLD 4072, Australia

[†] Ryerson University, Toronto, Ontario, M5B 2K3, Canada
h.ogawa@uq.edu.au

ABSTRACT

Designing high-performance air intakes is of crucial importance for the successful operation of hypersonic scramjet propulsion. This paper investigates the flowfields and performance of axisymmetric intakes obtained by applying two shortening methods, namely, leading-edge truncation and stunting (longitudinal contraction), to the full Busemann intake. The aim is to balance viscous and shock losses so as to optimize performance and intake weight. The effects of intake shortening on performance are similar for the two methods for moderate (25%) decreases in intake length, conducting to considerable reduction in intake weight.

1. Introduction

Scramjet propulsion is a promising technology for reliable and economical access to space and high-speed atmospheric transport. An axisymmetric configuration is currently being explored in the SCRAMSPACE project [1] led by The University of Queensland (UQ), due to the advantages offered in numerous aspects including aerodynamic and combustion efficiency, aerothermal and structural management as well as manufacture.

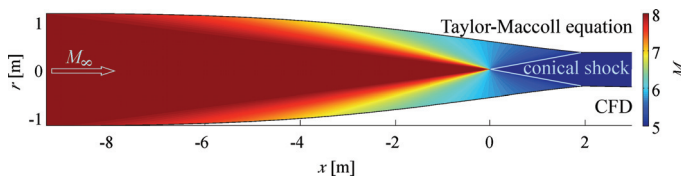


Fig. 1 Full Busemann intake for $M_\infty = 8$ and inviscid flowfields from theory (top) and CFD (bottom)

The air intake plays a crucial role in scramjet operation, being responsible for the compression of inflow to high pressure and temperature required for combustion, while maintaining high total pressure. The full Busemann intake (Fig. 1) can achieve high compression on a fully concave inlet surface in the inviscid flowfield, attaining a total pressure recovery of 97% with a minimum entropy rise across a single conical shock wave [2]. However, it inherently features an extremely long geometry hence heavy structure as well as high viscous losses, which subsequently reduce the total pressure recovery to 43% for the full Busemann intake. An examination of Fig. 1 shows that the leading edge surface of the full Busemann intake contributes little to compression. These findings encourage the present study involving two representative methods for shortening the full Busemann intake in order to find an optimum intake length that can minimize the sum of boundary layer and shock losses, striking the balance.

This paper presents the results and insight obtained from parametric studies performed numerically for leading-edge truncation of the Busemann intake as well as an alternative shortening method, namely, stunting (contraction in the axial direction). The performance is assessed with respect to various criteria required for scramjet intake design aiming at high compression and total pressure recovery with minimum structural weight.

2. Methods

1. Flow conditions and configurations

The present study focuses on the internal flowfield in the axisymmetric scramjet intake. The captured airflow is a uniform freestream at Mach 8 with a static pressure and temperature of 1197 Pa and 226.5 K, respectively, assuming scramjet operation at an altitude of 30 km. The Reynolds number based on the nominal inlet exit radius of 0.1m is 1.79×10^6 . The contour for the full Busemann intake is obtained analytically from the Taylor-Maccoll equation. The intake-shortening factor indicates the degree of shortening, defined as $\Delta L / L_{full}$, that is, the length reduction normalised by the full Busemann length. The contraction ratio decreases steadily from 11.2 (for the full Busemann intake) with leading-edge truncation, whereas it remains constant at 11.2 with stunting. The leading-edge truncated intake geometry is sized for the constant entrance radius of 0.335 m to ensure constant mass flow capture for fair comparison¹.

2. Computational fluid dynamics

The inlet flowfields are computed by utilising a commercial high-fidelity code CFD++. An advanced wall-function technique is used for near-wall treatment and turbulence is modelled by the two-equation SST $k-\omega$ RANS model. The airflow is treated as calorically perfect gas and the inlet surface is assumed to be adiabatic. A commercial grid generator Pointwise is utilised to generate two-dimensional structured computational meshes comprising 55,000 cells, with the minimum cell thickness on the wall of 10^{-5} m.

3. Results

Steady flowfields have been computed in parametric studies where the shortening factor is varied from 0 (full Busemann intake) to 0.99 in leading-edge truncation and to 0.52 in stunting² with an increment of 0.01.

1. Flowfields

The Mach number distributions in the truncated and stunted intakes are compared in Fig. 2 and Fig. 3 for the shortening factor of 0.2 and 0.4, respectively. It is

¹ This leads to the difference in the length of the intakes shortened by the two methods for the same shortening factor.

² Stunted intakes unstart when $\Delta L / L_{full}$ is greater than 0.52.

notable that the truncated intake flowfields are relatively insensitive to shortening in this range, maintaining the features of the full Busemann intake including isentropic compression through a series of Mach waves and a terminating conical shock wave. On the other hand, influence on the flow structure can be evidently seen in the intake flowfield shortened by $\Delta L / L_{full} = 0.4$ (Fig. 3), where Mach waves emanating from concave curvature coalesce into a curved shock wave, leading to the emergence of a Mach disk at the centreline. The reflected conical shock enters the combustor section, resulting in high non-uniformity flow at the exit (throat).

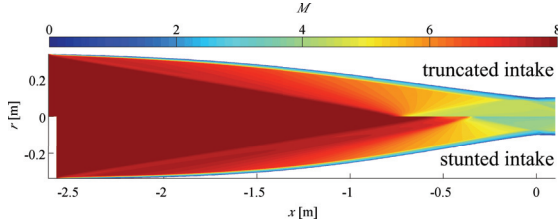


Fig. 2 Flowfield comparison for $\Delta L / L_{full} = 0.2$

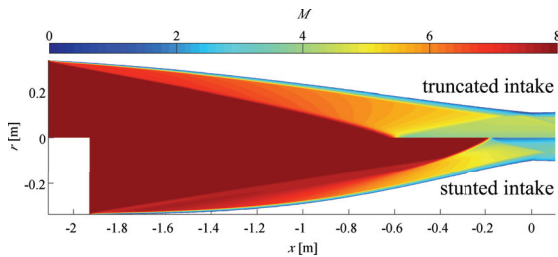


Fig. 3 Flowfield comparison for $\Delta L / L_{full} = 0.4$

2. Compression efficiency

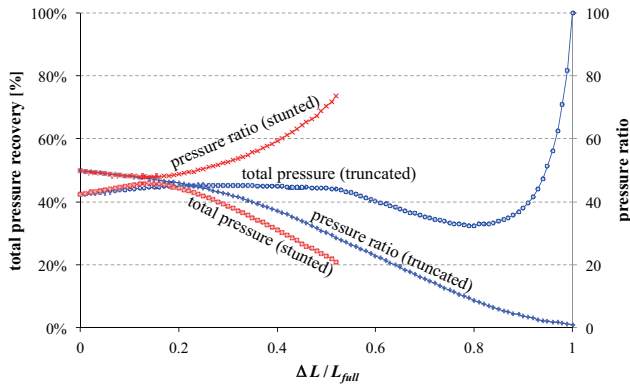


Fig. 4 Variations of total pressure recovery and pressure ratio

The variations of the total pressure recovery and pressure ratio³ are compared between the two methods in Fig. 4 in order to evaluate the compression efficiency. Similar variations can be seen for both quantities for shortening up to about $\Delta L / L_{full} = 0.2$, above which the total pressure recovery decreases and pressure ratio increases rather rapidly in the stunting case due to the formation of curved hence stronger shock waves. The truncated intakes, on the other hand, are characterised by a rather mild variation of the total pressure over a large

³ The total pressure recovery and pressure ratio are calculated from the stream-thrust averaged total pressure and static pressure, respectively, at the entrance and exit stations.

extent up to $\Delta L / L_{full} \leq 0.5$ (further truncation beyond this is impractical due to inadequate flow compression).

3. Drag and wetted area

The variations of the overall drag and its inviscid and viscous components are plotted in Fig. 5, along with the variations of the wetted area. It is observed that the inviscid drag from both shortening methods initially follows similar trends ($\Delta L / L_{full} \leq 0.2$), beyond which the stunted intake undergoes rapid rise as a result of curved shock waves, while the viscous drag decays steadily in both methods. The wetted area can be regarded as a measure of weight reduction in the assumption that the intake surface is made of constant thickness material. It can be seen that the wetted area decreases at similar rates with both methods of shortening, indicating similar degree of weight reduction achieved by both methods.

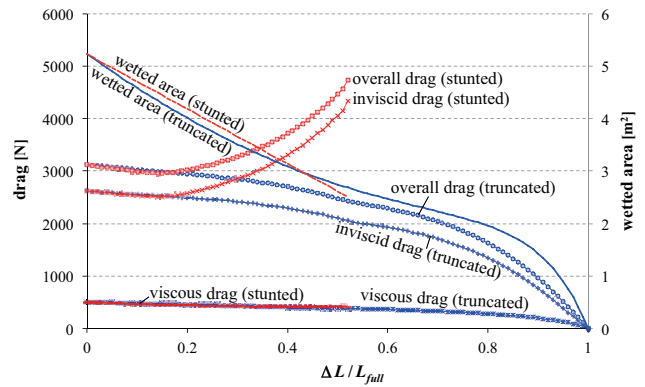


Fig. 5 Variations of drag components and wetted area

4. Concluding remarks

Numerical simulations have been performed to investigate the performance and flowfields of Busemann intakes shortened by two methods, namely, leading-edge truncation and stunting, aiming at the application to an axisymmetric scramjet engine operating at Mach 8. The performance of shortened intakes has been assessed with respect to various criteria including the total pressure recovery, pressure ratio, drag, and wetted area. Both shortening methods have result in similar variations for all criteria within a mild degree of shortening up to about 20%. However, further stunting has resulted in somewhat rapid decrease in the total pressure recovery and increase in the pressure ratio and intake drag due to shock formation, which may render this method useful if high exit pressure and temperature are needed at the cost of the total pressure loss and drag. On the other hand, truncated intakes are characterized by relatively constant total pressure recovery and gradual variations of the other quantities over a larger extent. Shortening the intake can achieve weight reduction of the order of 50%.

References

- [1] Boyce, R. R., Tirtey, S. C., Brown, L., Creagh, M., and Ogawa, H., AIAA Paper 2011-2297, 17th AIAA International Space Planes and Hypersonic Systems and Technologies Conference, San Francisco, CA, (2011).
- [2] Mölder, S., and Szpiro, E. J., *Journal of Spacecraft*, Vol. 3, 8 (1966), pp. 1303-1304.

Sabot Separation Schemes in the Rectangular Aeroballistic Range

Akihiro Sasoh, Kakuei Suzuki, Takahiro Imaizumi, Atsushi Toyoda,
Department of Aerospace Engineering, Nagoya University, Furocho Chikusa-ku Nagoya 464-8603, JAPAN
sasoh@nuae.nagoya-u.ac.jp

ABSTRACT

This paper reports the method of launching a model without rolling, pitching and yawing to an acceptable extent. The hybrid sabot separation scheme of in-tube aerodynamic with mechanical impingement is developed. The practical performance was examined.

1. Introduction

Ballistic range is a free-flight test facility, being characterized as an aerodynamics tool in which test flow condition can be well controlled without serious fluctuation and non-uniformity because quiescent air or any kind of gas in a test chamber is utilized as the test flow. However, in practice launching a flight model (or ‘projectile’) in ‘straight’ manner, with acceptable uncertainty in its flight trajectory, rolling, pitching and yawing motion, is not at all an easy task. Usually, in order to launch a flight model that has a different cross-section from that of the bore, the model is held by a so-called ‘sabot’ which plugs the aftbody of the model during acceleration. In a large facility, the sabot separation is done in a test chamber by aerodynamically exerting a pitching moment only to sabot segments so that they are blocked out by mechanical impingement, see for example Ref. [1]. However, in a facility of modest dimensions it is difficult to separate the sabot segments within a limited length.

In this paper, we have further improved the in-tube aerodynamics sabot separation method[2,3] by combining the assistance of mechanical impingement.

2. Sabot separation scheme

The ballistic range in Nagoya University[3] comprises of a high-pressure helium driver, acceleration section, ventilation section, sabot separation section and test chamber. The acceleration, ventilation and sabot separation sections have a 25 mm × 25 mm square bore. The tubes are made using aluminum extrusion technique. Figure 1 illustrates the sabot separation method in the sabot separation section. The sabot and the model are accelerated together in the acceleration section, then the frontal and rear pressures are decreased in the ventilation section. When they enter the sabot separation section, the sabot acts as a piston, drives a shock wave in front. The negative or decelerating pressure balance is produced. However, the model does not experience the deceleration because it is surrounded by the post-shock air with an equal speed to itself. Therefore, the sabot is separated from the model.

Here, let the coordinate along the motion and the separation distance be designated by x and d , respectively. d is given by solving the following differential equation.

$$m_{\text{sabot}} \frac{dX}{dt} = P_{\text{front}} - P_{\text{rear}} \quad (1)$$

where m_{sabot} , P_{front} , P_{rear} and t denote the mass of the sabot, pressure on the frontal surface of sabot, pressure on the rear surface and time, respectively.

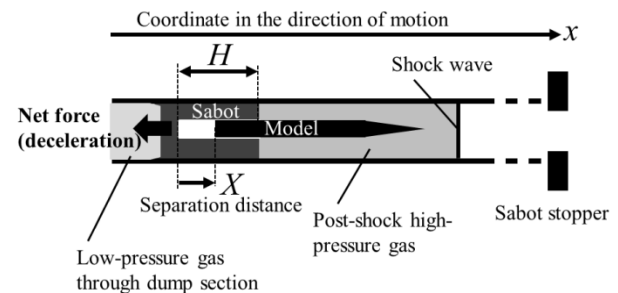


Fig. 1 Schematic illustration of in-tube aerodynamics and mechanical impingement hybrid sabot separation method.

The time integration is done during the period, τ , in which the sabot passed through the sabot separation section.

$$X = \int_0^{\tau} \frac{P_{\text{front}} - P_{\text{rear}}}{m_{\text{sabot}}} dt \quad (2)$$

$$L_{\text{SS}} = \int_0^{\tau} U_{\text{sabot}}(t) dt \approx U_{\text{sabot}}(0) \tau \quad (3)$$

where the time is originated by the moment of entry to the sabot separation section; L_{SS} and U_{sabot} denote the length of the sabot separation section and the sabot velocity, respectively. The important parameter in the sabot separation is $X(\tau)$, which should be compared to H , the model holding depth in the sabot.

3. Criterion for best sabot separation

Figures 2 to 4 shows examples of model flight with different values of $X(\tau)/H$. In the case of $X(\tau)/H \ll 1$, see Fig. 2, the sabot experiences the mechanical impact against the sabot stopper. It is crashed before releasing the model so that the model attitude is disturbed by the crash. When $X(\tau)/H \gg 1$, see Fig. 3, the model free flies even in the sabot separation section. Since it is not supported by the sabot, the probability that the model attitude failed to be kept straight is decreased. From many operation tests, we have concluded that the criterion for the best keeping the model attitude is $X(\tau)/H = 1$, see Fig. 4. In this case, the sabot releases the model at the muzzle. Before the release, the model is supported by the sabot even not through the full depth.

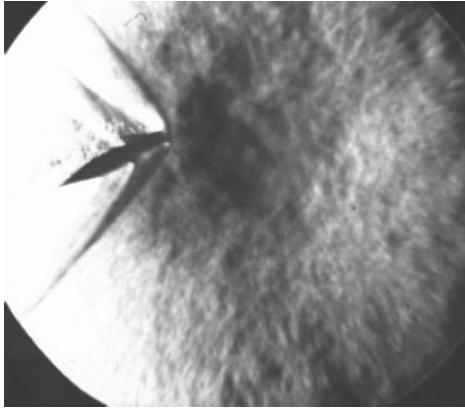


Fig. 2 Example of Schlieren image around a flight model launched with only with mechanical impingement sabot separation Mach number at the muzzle 1.4.

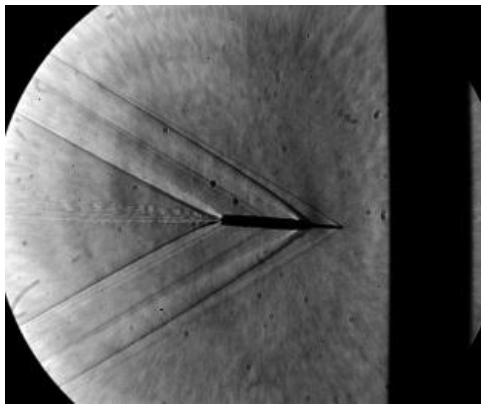


Fig. 3 Example of Schlieren image around a flight model launched with only with in-tube aerodynamics sabot separation, Mach number at the muzzle 1.7.

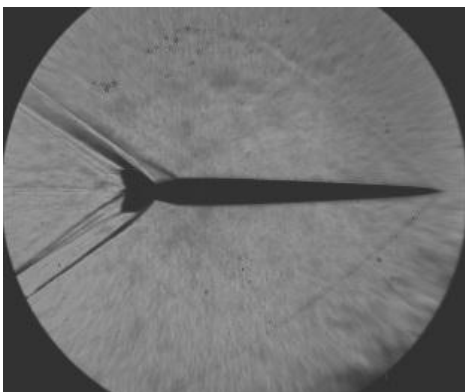


Fig. 4 Example of Schlieren image around a flight model launched with the hybrid sabot separation, Mach number at the muzzle 1.7, $X(\tau)/H$ equals about unity.

parameters in this ballistic range:

P_{driver}	= initial pressure of driver
m_{sabot}	= mass of sabot
m_{model}	= mass of model
P_{chamber}	= initial pressure in test chamber

The parameters which characterize the operation performance are

$U_{\text{model}}(\tau)$ = muzzle speed of the model
 $X(\tau)$ = sabot separation distance

$U_{\text{model}}(\tau)$ is approximately equals the speed of the sabot with the model at the interface between the acceleration section and the ventilation section, U_{AV} . Under the present operation conditions, the following relations were obtained.

$$U_{AV} \approx f_1(P_{\text{driver}}, m_{\text{sabot}}, m_{\text{m}}) \quad (4)$$

$$X(\tau) \approx f_2(U_{AV}, P_{\text{chamber}}, m_{\text{sabot}}) \quad (5)$$

The functions, f_1 and f_2 , can be obtained from fitting to experimental data.

4. Summary

The in-tube aerodynamics sabot separation method is improved by combining the mechanical impact against the sabot stopper at the muzzle. The criterion that the model is released from the sabot at the muzzle yield best probability to keep the model attitude straight.

The authors would like to thank Messrs. K. Yamamoto, N. Shiraki, Y. Masanaka and A. Saito, Technical Division, Nagoya University for their valuable technical assistance. We acknowledge valuable technical discussions with Dr. S. Yokota. This research was supported by Japan Society for Promotion of Science as Grant-in-Aid for Scientific Research (S), No. 22226014.

References

- [1] Canning, T. N., Seiff, A., and James, C. S., AGARDograph 138, Aug. 1970.
- [2] A. Sasoh and S. Oshiba, Review of Scientific Instruments, 2006, **77**(10), article 105106.
- [3] Sasoh, A., Kikuchi, K., Shimizu, K., Matsuda, A., International Journal of Aerospace Innovations, **2**, No.3, pp. 147-156. (2010).

4. Operation characterization

There are four independent operation control

One experimental technique of detecting the trajectory of a free-flight projectile launched by a ballistic range

Takamasa Kikuchi, Takahiro Ukai, Kiyonobu Ohtani and Shigeru Obayashi
Institute of Fluids Science, Tohoku University: 2-1-1, Katahira, Aoba-ku, Sendai, Miyagi, Japan 980-8755
takamasa.kikuchi@gmail.com

ABSTRACT

In experiment of Fluid Science using a ballistic range which can launch a object at high-speed, the trajectory of a free-flight projectile is important information for evaluation of validity of measurement results. This paper introduces a novel experimental technique of detecting the trajectory and reports evaluation result of accuracy of the technique. Verification using impact to target plate as reference revealed that this technique was able to detect the trajectory qualitatively.

1. Introduction

Experiment using a ballistic range which can launch a object at high speed has a merit which is possible to produce the whole flow field around the object, since the object flies freely in stationary gas. It has a demerit which is impossible to control the flight attitude and the trajectory of a projectile which means a flying object, since the projectile is not supported by a sting. The trajectory is not constant and has some scatters on every shoot. Therefore, to detect the flight attitude and the trajectory is necessary for accurate measurement of the flow field in ballistic experiments. This paper introduces a novel method for detecting the trajectory and reports evaluation results about its validity.

2. Experimental facilities

2.1 Ballistic range

A horizontal ballistic range in Institute of Fluids Science, Tohoku University is shown in Figure 1. The ballistic range consists of a high-pressure chamber (30 liters in volume and 5.0 MPa in maximum charge pressure), a launch tube (51 mm in inner diameter and 6.7 m in length) and a recovery tank which serves a test tank (1.66 m in inner diameter and 12 m in length). This ballistic range is able to accelerate a projectile, of 100 g in weight, on atmospheric condition to Mach number 2.0 by using only helium gas pressure[1].

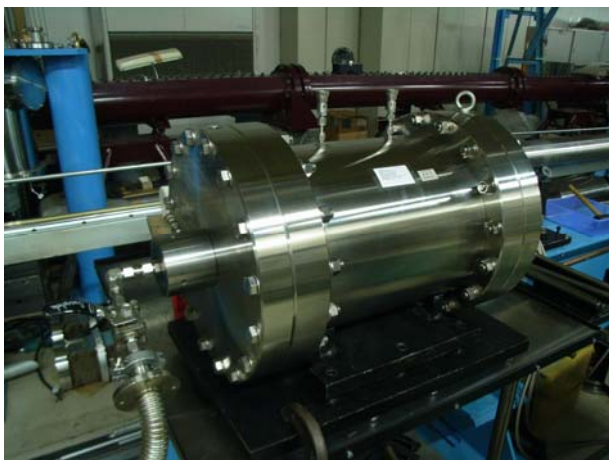


Fig.1 The ballistic range in IFS, TU

2.2 Projectile and sabot

A projectile and a sabot are shown in Figure 2. The

projectile is a 30 mm diameter sphere made of polyamide resin and the sabot shapes cylinder of 51 mm in outer diameter and 55 mm in length made of polycarbonate. The sabot is 4-parts type sabot. After the sabot separates from the projectile by receiving aerodynamic resistance of air in the recovery tank, the sabot is stopped by impact to a steel plate with a hole at the center where the projectile passes through. Only the projectile flies in observation region.

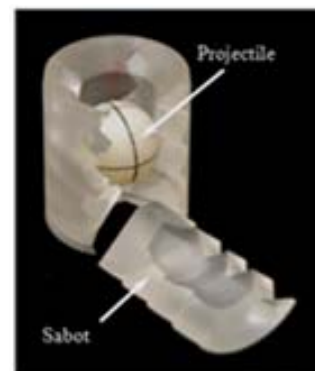


Fig. 2 Projectile and sabot

2.3 Pressure measurement equipment

A pressure measurement equipment is shown in Figure 3. 6 channels piezo-type pressure transducers are plugged in its top plate at regular intervals. This equipment is able to measure pressure distribution around the projectile.

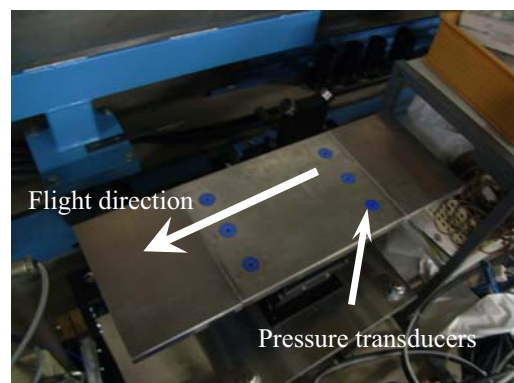


Fig. 3 Pressure measurement equipment

3. Detecting method

The trajectory was determined by two methods which were both analyzing pressure measurement results and calculating from impact scar of a target plate. The trajectory detecting method from pressure measurement results is illustrated in Figure 4. Since a detached shock wave around a spherical projectile shapes axisymmetric blunt cone, left and right pressure transducer detects the detached shock wave at completely same timing if the projectile flies above a center pressure transducer. If the projectile flies with prejudiced trajectory to left or right, the timing of detecting the detached shock wave is different. The trajectory is calculated analytically by using this different timing. This novel method[2] has a merit that the trajectory is able to be calculated by only data analysis without some additional experimental equipments. Another method which calculates the trajectory from impact scar of a target plate is often used since the method is able to measure spatial trajectory. A projectile which is launched from a muzzle flies following a ballistic course which is affected by the earth rotation[3]. The trajectory can be considered as straight if the flight distance is short. A polyethylene terephthalate sheet was set at downrange of the observation region as a target plate. A line between the center of the muzzle and the center of the impact scar was considered as the trajectory.

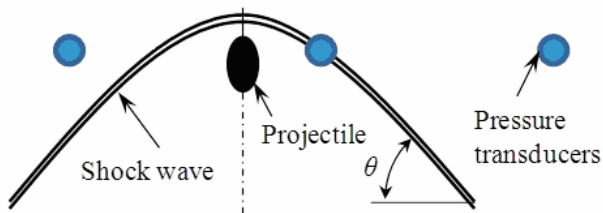


Fig. 4 Schematic diagram of the trajectory calculation

4. Results and Discussion

The result is shown in Figure 5. The ordinate designates difference from the center probe which is cross direction against the trajectory, the abscissa designates distance from the leading edge of the pressure measurement equipment, which is the same direction against the trajectory. The solid line is the trajectory calculated from the target plate scar and the white circle is the trajectory calculated from the pressure measurement results respectively. The flight height was removed from consideration in this experiment since the height is not able to be calculated from the pressure measurement result. In comparison with the trajectory by using the target plate, trajectories did not coincide sufficiently. But, both trajectory located on same side of the center probe. The difference from the center probe increased on both method. It means that the missing directions were same. Therefore, the tendency of the trajectory coincided.

The reason why two results did not coincide may be

the influence of the flight height. Present analysis way, a detached shock wave around a projectile is treated as two-dimensional view. Since actual shapes of a detached shock wave is three-dimension, the timing that both pressure transducers detects the detached shock wave changes depending on the flight height. This carelessness of consideration could cause disagreement between two detecting method. This is point that can be improved in future work.

In case that the flow field and the pressure distribution around the projectile are measured, the flow field and the pressure distribution are usually measured by the combination of the optical visualization and a pressure measurement equipment. In this measurement way, the horizontal trajectory can not be calculated though the flight height can be calculated from the visualization images. By this novel method, the horizontal trajectory may be able to be measured without some additional equipments. Moreover, the trajectory of past experimental data could be calculated from additional analysis and the accuracy of experimental result will be improved.

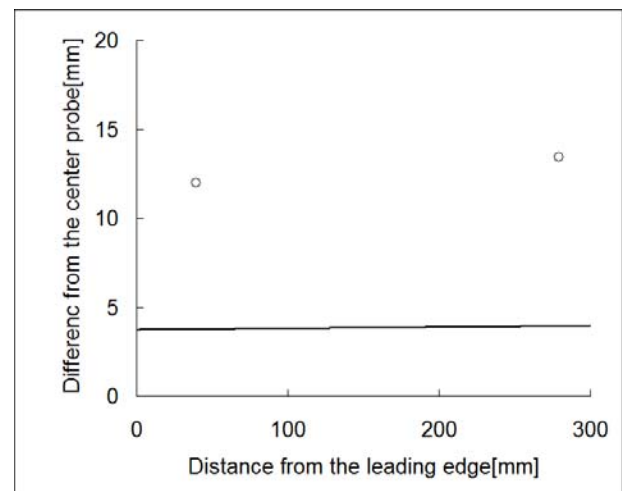


Fig. 5 The trajectory

4. Concluding remarks

The measurement accuracy of a novel trajectory detecting method by analyzing pressure measurement results was verified by comparison with usual method by using impact scar of a target plate. This method can detect the trajectory qualitatively. A possibility of improving accuracy of past experiment data is suggested.

References

- [1] S. Obayashi, H. Yamashita, K. Ohtani, T. Kikuchi, T. Ogawa and T. Ukai, Aeronautical and space science Japan (in Japanese, acceptance)
- [2] T. Ukai, Master thesis of Tohoku University (2012)
- [3] Ballistics Research Association (ed.), Handbook of Weapon and Bomb Technology, Defence Technology Foundation (2003) (in Japanese)

Near-Field Pressure Measurement of a Projectile Flying up to Mach Number 2.0

Takahiro Ukai, Takamasa Kikuchi, Kiyonobu Ohtani, Takaya Uchida, Yuta Saito and Shigeru Obayashi
Institute of Fluid Science, Tohoku University, Sendai, Miyagi, 980-8577, Japan
ukai@edge.ifs.tohoku.ac.jp

ABSTRACT

This paper reports an investigation about the effect of the flight conditions to the near-field pressure waveform. A spherical projectile was launched at Mach number ranging from 1.2 to 1.4 by a ballistic range in the Institute of Fluid Science, Tohoku University. Then the influence of the angular velocity, the flight height and Mach number to the near-field peak pressure was evaluated by correlation analysis. As a result, Mach number most affected the near-field peak pressure.

1. Introduction

The near-field pressure waveform of an airplane model is measured for a study of the sonic boom reduction of a supersonic transport [1-3]. The near-field pressure of a model is generally measured in a wind tunnel, in which the model is supported by a sting. Since disturbances generated from the sting affects pressure waves generated from the tail of the model, it is difficult to accurately measure a near-field pressure along entire length of the model. Although a ballistic range which launches a model into free flight can be used to avoid this problem [4-9], the experiment in a ballistic range has a demerit that the flight attitude and the flight path of the model may be irregular. Since, the flight attitude interferes with the near-field pressure waveform in a ballistic range [10], the control of the flight conditions is an important topic in the ballistic range experiment. However, the control of the flight conditions is very difficult. If the most important factor which influences the near-field pressure waveform is found and it is improved, the influence of the near-field pressure waveform can be readily reduced. Hence, the most dominant factor to the near-field pressure waveform has to be investigated.

This paper reports an investigation about the effect on the flight conditions to the near-field pressure waveform in a ballistic range.

2. Experimental setup

The experiment was performed in a ballistic range at the Institute of Fluid Science, Tohoku University. The schematic diagram of the ballistic range is illustrated in Fig. 1. The ballistic range at a single-stage light gas gun consists of a high-pressure driver gas chamber, a recovery tank and a launch tube of 51 [mm] in inner diameter and 6.7 [m] in length. The recovery tank of 1.66 [m] in inner diameter and 12 [m] in length has three pairs of observation windows of 600 [mm] in diameter for optical visualization.

A spherical projectile and a sabot are shown in Fig. 2. The projectile with three line markings on surface is made of polyamide resin, with 16 [g] in mass and 30 [mm] in diameter. The four-piece cylindrical sabot is made of polycarbonate with 51 [mm] in diameter, 60 [mm] in length and 110 [g] in mass. The sabot in which the projectile is stored is launched by the high-pressure driver gas into the recovery tank.

The sabot parts are separated from the projectile by aerodynamic force in the recovery tank whose pressure was 101 [kPa] (atmospheric pressure). The flight velocity was measured from the transit time when the projectile passed between two laser beams cross the flight path.

A pressure instrumentation for measuring the near-field pressure was located at approximately 8 [m] long from the end of the launch tube and 270 [mm] high under the flight path. Three pressure transducers (model 113B28, PCB Corp.) were embedded in the front and rear positions on a plate of the pressure instrumentation, respectively. To avoid an influence of shock diffraction from the edges, those pressure transducers were arranged at 189.5 [mm] long from the rear and front edges.

To measure the flight attitude, the optical arrangement of the simultaneous visualization method [8] with a pair of 480 [mm] diameter schlieren mirror, a continuous light source (metal halide lamp LS-M210, Sumita Optical Glass, Inc. 290 [W]) and a zoom lens (AF ASPHERICAL LD MACRO 285D, TAMRON Corp., AF28-300 [mm], F/3.5-6.3) were used. This method can visualize the flow field around a projectile and a projectile surface simultaneously. The images were recorded by a high-speed video camera (HPV-1, Shimadzu Corp., 102 frames at 312×260 pixel spatial resolution, maximal framing rate 1,000,000 [frames/sec]).

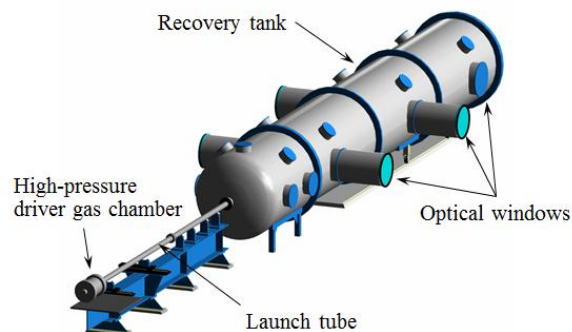


Fig. 1 Schematic diagram of a ballistic range at single-stage light gas gun mode in the Institute of Fluid Science, Tohoku University

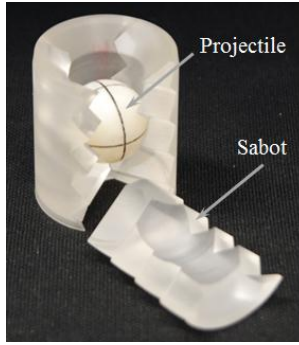


Fig. 2 A spherical projectile and a sabot

3. Results and Discussion

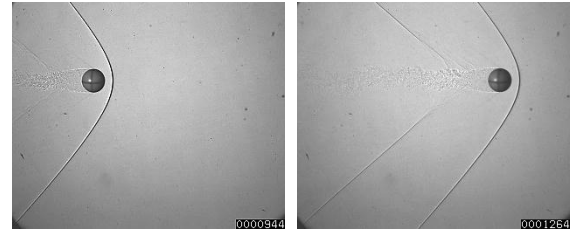
The Sequential images by the simultaneous visualization method are shown in Fig. 3. The lines marked on the surface of the projectile were able to be visualized clearly. Where, the time when the projectile arrived at the left side of the visualization region was defined as 0 [μs]. The flight attitudes (the angles of the pitch, the yaw and the roll) were calculated from the amount of displacement of the marking lines. The time evolution of the flight attitudes is shown in Fig. 4. The green dot, the red dot and the blue dot is corresponding to the angle of the pitch, the roll and the yaw respectively. The solid lines are linear approximation curves by the least-squares method. Each angular velocity of the pitch, the roll and the yaw obtained from these approximation curves. The flight height was obtained from the visualization image.

A near-field pressure of the spherical projectile was measured at Mach number ranging from 1.2 to 1.4. Since the projectile flies into free-flight, the conditions of the angular velocity and the flight height cannot be set up arbitrarily. The effect of each angular velocity, the flight height and Mach number to $\Delta P/P_\infty$ was evaluated by the Spearman rank correlation coefficient [11]. $\Delta P/P_\infty$ is a dimensionless coefficient of the near-field peak pressure divided by the recovery tank pressure. The Spearman Rank correlation coefficient r_s was calculated by using following equation

$$r_s = 1 - 6 \frac{\sum_{i=1}^n d_i^2}{(n^3 - n)} \quad (1)$$

n is the sample numbers and d_i is the difference of a ranking between variables.

The correlation coefficients at each flight conditions to $\Delta P/P_\infty$ are shown in Table 1. M_s is the Mach number of the projectile, ω_p is the pitch angular velocity, ω_y is the yaw angular velocity, ω_r is the roll angular velocity and H is the flight height. Mach number is the strongest to the correlation of the near-field peak pressure. However, it is unknown whether the near-field pressure waveform by a flying complex shaped projectile is affected by the angular velocity or flight height.



(a) $t = 0.176$ [ms] (b) $t = 0.496$ [ms]
Fig. 3 Sequential images ($M_s = 1.43$)

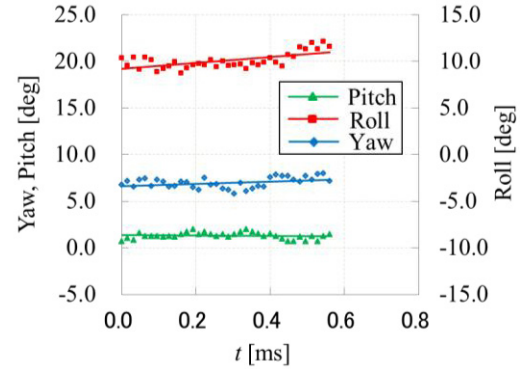


Fig. 4 Time evolution of the flight attitudes ($M_s = 1.43$)

Table 1. The correlation coefficients for pressure rate $\Delta P/P_\infty$

	M_s	ω_p	ω_y	ω_r	H
$\Delta P/P_\infty$	0.83	0.14	0.46	0.36	0.46

4. Conclusions

The effect of the flight conditions to the near-field pressure waveform around a flying spherical projectile launched by a ballistic range was investigated. As a result, the near-field peak pressure was most affected by Mach number as compared with other flight conditions. The investigation about the effect of the flight conditions to the near-field pressure waveform by a flying complex shaped projectile is required as a future work.

References

- [1] D. S. Miller et al, NASA TN-6201 (1971).
- [2] H. W. Carlson, NASA TN D-881 (1961).
- [3] H. W. Carlson et al, NASA TN D-3106 (1965).
- [4] J. G. Callagban, NASA CR-603 (1966).
- [5] T. Tam et al, AIAA Paper 2000-1011 (2000).
- [6] A. Sasoh et al, Review of Scientific Instrumentations **77**, 105106 (2006).
- [7] A. Matsuda et al, Transactions of JSASS Space Technology of Japan, Vol.9, pp.37-41 (2011).
- [8] T. Ukai et al, 8th International Conference on Flow Dynamics, pp.280-281 (2011).
- [9] T. Ukai et al, 6th SUN-Tohoku University Joint Workshop on Next Generation Aero Vehicle, pp. 65-68 (2011).
- [10] A. Toyoda et al, 7th International Conference on Flow Dynamics, pp.48-49 (2010).
- [11] J. H. Zar, Journal of the American Statistical Association, Vol. 67, No. 339, pp.578-580 (1972).

Attitude Measurement of a Projectile by Flash X-ray Stereography

Takaya Uchida, Takahiro Ukai, Kiyonobu Ohtani, Shigeru Obayashi
Institute of Fluid Science, Tohoku University, Sendai, Miyagi, 980-8577, Japan
uchida@edge.ifs.tohoku.ac.jp

ABSTRACT

This study performed the preliminary flash X-ray stereography experiment for measuring an attitude of a supersonic projectile in a ballistic range at the Institute of Fluid Science, Tohoku University. The position coordinates of a stationary spherical model was estimated by using simple geometric relationship between a model, X-ray source points and sensitive plates. The position coordinates were obtained with a less than ± 0.2 [mm] of errors.

1. Introduction

A sonic boom is a big noise associated with the shock wave created by a supersonic traveling aircraft. This noise is one of the most important problems in realizing the Super-Sonic Transport (SST). Hence, it is necessary to mitigate the sonic boom.

To develop a low-boom SST, it is important to estimate the sonic boom accurately. The waveform parameter method is one of the most famous methods to estimate the sonic boom. In this method, a near-field pressure waveform from an aircraft model is used as an input value, and then calculations of the propagation of the waveform are performed. In general, a supersonic wind tunnel is used to measure the near-field waveform. However, a sting which supports a model affects a flow field. Hence, it is difficult to measure a near-field pressure generated from the rearward of the model accurately.

On the other hand, a ballistic range which launches a projectile into calm environment can realize the accurate measurement of the near-field pressure. Nevertheless there is a demerit that it is difficult to keep the attitudes of the projectiles stable. Hence, it is important to establish the method to launch projectiles in stable attitudes. To realize this, it is necessary to establish the method of estimating the attitudes of the projectiles before establishing the method to control the flight attitude.

The flight attitude can be measured by visualizing a supersonic projectile surface directly using a high-speed camera [1]. However, the method has some disadvantages such as an effect of the distortion by the lenses. Moreover, the images have only two-dimensional information. On the other hand, the X-ray images have no effect of the distortion. Furthermore, by taking an X-ray stereograph, three-dimensional information of the attitude of a projectile can be read from the stereo images.

In this study, the flash X-ray stereography on behalf of the high speed camera is used to measure the attitude of a model. In this paper, the preliminary experiment was performed to do accuracy validation of this stereographic method using a simple metallic spherical model. First, the stereo images of the stationary model, which is supported by a sting, were taken. Then, the position of the model was estimated from the stereo images.

2. Method

2.1 Experiment system

The preliminary flash X-ray stereography experiment was performed in a ballistic range at the Institute of Fluid Science (IFS), Tohoku University [2]. A schematic of the ballistic range is illustrated in Fig. 1. The ballistic range test section is 1.66 [m] in inner diameter and 12 [m] in length. A schematic of the X-ray stereography system is illustrated in Fig. 2. This figure is a cross-section view of the test section with a dot lined plane in Fig.1. Two flash X-ray sources were installed to the upper parts of the test section of the ballistic range and two sensitive plates were placed in the test section.

A flash x-ray electron beam system (MODEL 43731A, TITAN Systems Corp.) and X-ray tubes (130-529000) of 70 [ns] pulse duration were used. A model is a metallic spherical model (Aluminum) with 7.94 [mm] in diameter.

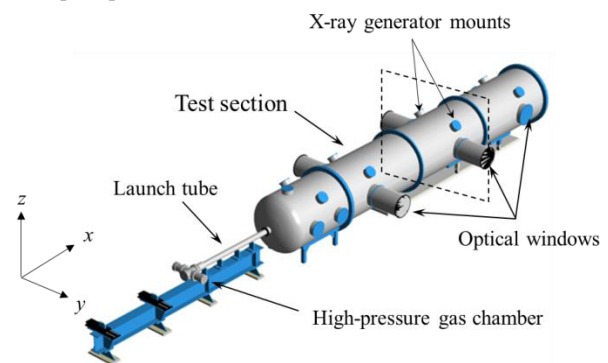


Fig. 1 Overall view of a ballistic range at the Institute of Fluid Science, Tohoku University

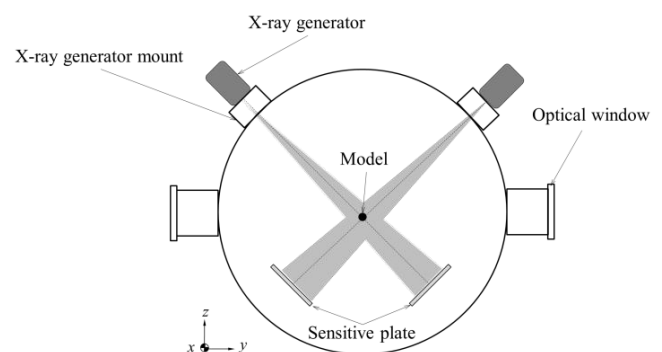


Fig. 2 Schematic of the X-ray stereography system

2.2 Measurement technique of a model position

In this study, the position of the spherical model is estimated by the geometric relationship of flash X-ray source point, the position of the model and the sensitive plates. A schematic of the geometric relationship in the case of photographing from the top-left part of the test section is illustrated in Fig. 3. The geometric relationship of them is represented as follows:

$$\theta = \tan^{-1}\left(\frac{u}{f \cdot \sin \alpha}\right) \quad (1)$$

$$\varphi = \tan^{-1}\left(\frac{v}{f}\right) \quad (2)$$

where u and v are coordinate values of the projected image, f is the focusing length, θ and φ are angles of depression and α is the tilt of the sensitive plate respectively. Since f and α are known, θ and φ can be determined by measuring u and v in the image. Then the straight lines can be drawn from the X-ray source point on an x - y plane and y - z plane respectively. The coordinate points of the model are on these lines. On the other hand, in case of photographing from the top-right part in the test section, the straight lines can be drawn by the same technique. Then, the position of the model is obtained as the intersections of these lines.

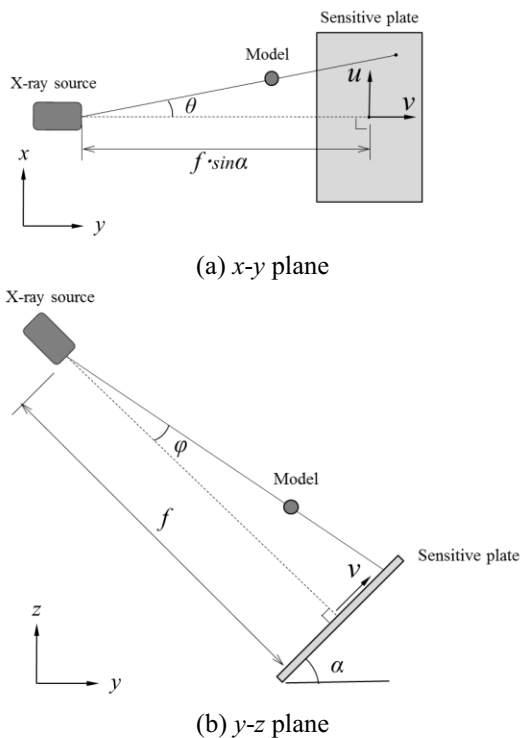


Fig. 3 Schematics of the geometric relationship of the X-ray optical system

The experimental conditions are as below; the focal length is $f = 1300$ [mm], the angle of sensitive plates are $\alpha = 45$ [degree], and the distances between the flight path axis and sensitive plates are $x = 200$ [mm]. The settings of flash X-ray are the output voltage is 20 [kV], the pressure of dry nitrogen is 15 [psi]. The size of the images is 2860 [pixel] \times 2280 [pixel]. The coordinates

of the model is set $x = -5.0 \sim 5.0$ [mm], $y = -7.0 \sim 7.0$ [mm], $z = -7.0 \sim 7.0$ [mm].

3. Results and Discussion

The X-ray image is illustrated in Fig.4. The coordinates of the model in this image are $(x, y, z) = (0, 0, 0)$. The coordinates (u and v) of this image are used as an origin.

Table.1 shows the set coordinates and the result values of the calculations by using the stereo images. The resolution of the X-ray image is so high that 1 [pixel] equals 0.087 [mm]. The coordinates of the model are measured with a high degree of accuracy. Errors are within ± 0.2 [mm]. In this method, the accuracy of the result value depends on the accuracy of measuring u and v . Hence, it is very important to measure u and v of congruent points of stereo images accurately.

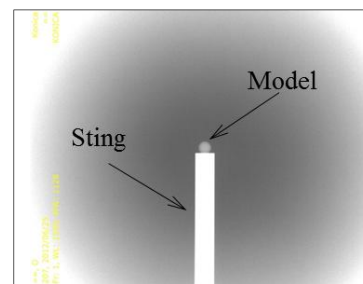


Fig. 4 X-ray image $(x, y, z) = (0, 0, 0)$

Table.1 Set values and result values of the coordinates of the model

	x		y		z	
	set value	result (error)	set value	result (error)	set value	result (error)
1	5.0	5.0 (0.0)	0.0	0.0 (0.0)	0.0	0.0 (0.0)
2	-5.0	-5.0 (0.0)	0.0	0.0 (0.0)	0.0	0.0 (0.0)
3	0.0	0.0 (0.0)	7.0	7.0 (0.0)	0.0	-0.1 (-0.1)
4	0.0	0.0 (0.0)	-7.0	-7.0 (0.0)	0.0	-0.1 (-0.1)
5	0.0	0.0 (0.0)	0.0	0.0 (0.0)	7.0	6.8 (-0.2)
6	0.0	0.0 (0.0)	0.0	0.0 (0.0)	-7.0	-7.1 (-0.1)
7	5.0	5.0 (0.0)	7.0	7.0 (0.0)	0.0	-0.1 (-0.1)
8	-5.0	-5.0 (0.0)	7.0	7.1 (+0.1)	0.0	-0.2 (-0.2)
9	5.0	5.2 (+0.2)	3.5	3.5 (0.0)	3.5	3.3 (-0.2)

4. Concluding remarks

In this study, flash X-ray stereography was used to estimate the position coordinates of a stationary spherical model. The position coordinates are obtained within a tolerance of ± 0.2 [mm] by using simple geometric relationship of the X-ray optical system. These results show that this method is effective.

Based on the result, this method will be applied to a projectile at supersonic flight. The attitude (pitch, yaw and roll) and the trajectory of the projectile will be obtained by multipoint measurements of the coordinates of the points on the projectile.

References

- [1] Ukai, T. et al., The 8th International Conference on Flow Dynamics, pp.280-281 (2011).
- [2] Saito, T. et al., Shock Waves **21**, 483 – 489 (2011).

Near-field Pressure Signature Measurement of D-SEND#1 Models

Yoshikazu Makino, Masayoshi Noguchi
 Japan Aerospace Exploration Agency
 6-13-1 Osawa, Mitaka, Tokyo 181-0015, JAPAN
 makino.yoshikazu@jaxa.jp

ABSTRACT

The near-field pressure signatures of two models named NWM and LBM used in the D-SEND#1 drop tests are measured in supersonic wind-tunnel tests for the purpose of validating some sonic-boom prediction tools. A static pressure rail which has 111 static pressure taps with 4mm interval is used on the wind-tunnel wall. The height of the rail from the wind-tunnel wall can be changed in order to investigate the effects of the rail geometry and the shock/boundary layer interaction effects on the measured signatures. Several types of model support system are used to correct the support interference effects on the measured signatures.

1. Introduction

Japan Aerospace Exploration Agency(JAXA) has been promoting the Silent Super-Sonic(S-cube) research program for future supersonic airliners with economically viable and environmentally friendly characteristics since 2006. In this program, the flight test project named D-SEND(Drop test for Simplified Evaluation of Non-symmetrically Distributed sonic boom) is planned in order to demonstrate the advanced low-boom design concepts. The project comprises two experimental phases. In the first phase of the project (D-SEND#1), two axisymmetrical models named NWM (N-Wave Model) and LBM (Low-Boom Model) shown in Fig.1 are dropped back to back from a stratospheric balloon and the sonic-booms generated from both models are measured both on the ground and at about 1km above the ground. The purpose of the D-SEND#1 tests is to make sure the possibility of demonstrating low-boom concepts with the 8m-long scaled airplane model in the second phase of the project(D-SEND#2).

In this paper, supersonic wind-tunnel tests for measuring the near-field pressure signatures of the NWM and LBM configuration are summarized. The data obtained in these tests will be utilized to validate some sonic-boom prediction tools together with the sonic-boom pressure signature data measured in the D-SEND#1 drop tests.[1]

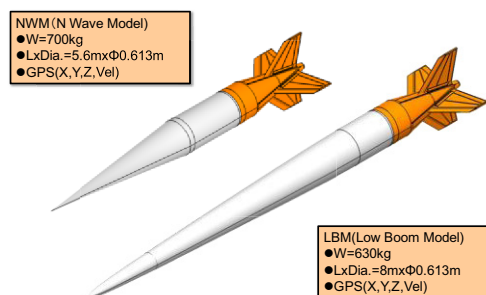


Fig.1 D-SEND#1 models (NWM, LBM)

2. Wind-tunnel Test

The wind-tunnel test is conducted in JAXA's 1m x 1m blow-down type supersonic wind-tunnel (JSWT). The wind-tunnel models are the 5% of the NWM and LBM models used in the D-SEND#1 drop tests (NWM: 280mm, LBM: 400mm in length). A static pressure rail

which has 111 static pressure taps on its surface with 4mm interval is used on the wind-tunnel wall. The freestream Mach number is 1.7 and the model is held at the angle-of-attack of 0 degree and at the vertical position of H/L=1.18 (H: model nose height from the rail surface, L: LBM model length of 400mm). The experimental apparatus for the LBM model is shown in Fig.2. Two 15psi-range 64-port modules of the ZOC system are used for the pressure taps and the pressure waves generated from the models are obtained by subtracting the pressure without the models from the data with the models. The height of the rail from the wind-tunnel wall can be changed from 0mm (wind-tunnel wall) to 12mm in order to investigate the effects of the rail geometry and the shock/boundary layer interaction effects on the measured signatures. Several types of model support system shown in Fig.3 are used to correct the support interference effects on the measured signatures.

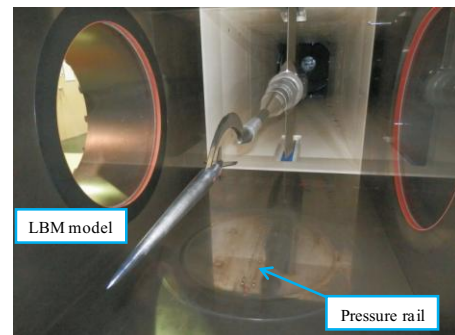


Fig.2 LBM model setup in JSWT

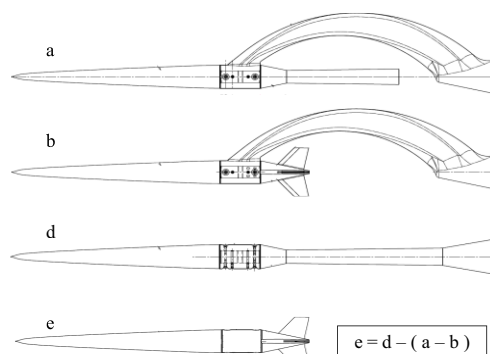


Fig.3 Support systems

3. Results and Discussion

Figure 4 shows the measured pressure signatures with/without the LBM model with the rail height of 0mm. Some pressure changes are shown on the wind-tunnel wall even without the model. The result that C_p difference before $X=-1060\text{mm}$ are almost zero shows the model on/off correction works well in the tests. Figure 5 shows the C_p variation during the blow without the model for 8 seconds. It shows that the measurement accuracy is within 0.0005 in C_p . (The standard deviation is about 0.00015 in C_p .) Figure 6 shows the effects of the rail height. Although the pressure signature becomes slightly sharper with the rail height of 12mm, it qualitatively agrees well with the signature with the rail height of 0mm. Figure 7 shows the effects of the support interference. It shows that the signature gets closer to the CFD results in the aft part of the signature with the support interference correction.

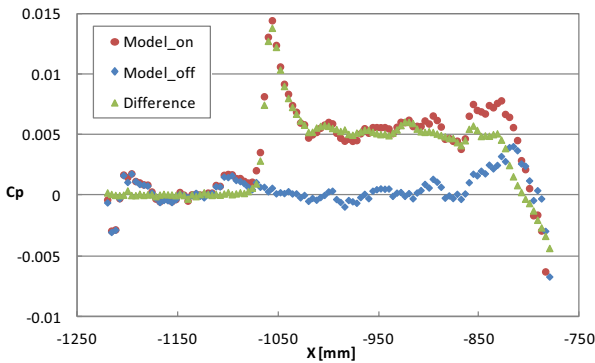


Fig.4 Model on/off difference

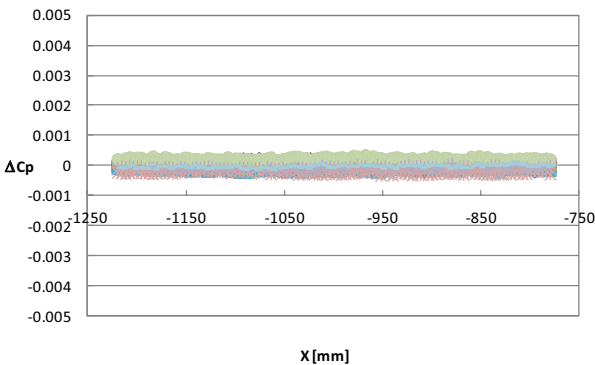


Fig.5 Pressure variation (Model off case)

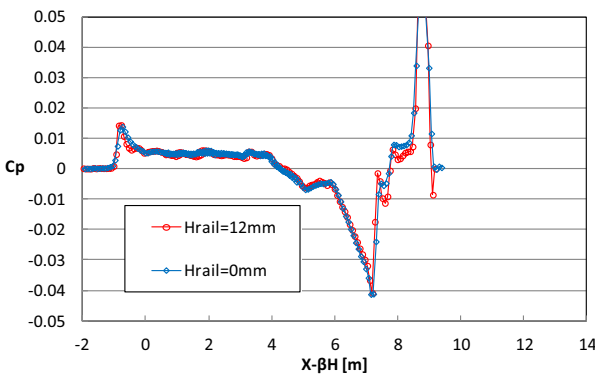


Fig.6 Rail height effects

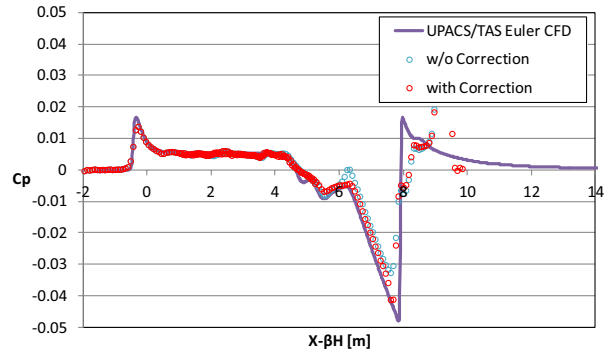


Fig.7 Support interference correction

Figure 8 and 9 show the measured pressure signature with all of the above corrections of the NWM and LBM models, respectively. The measured data are compared to some prediction data.

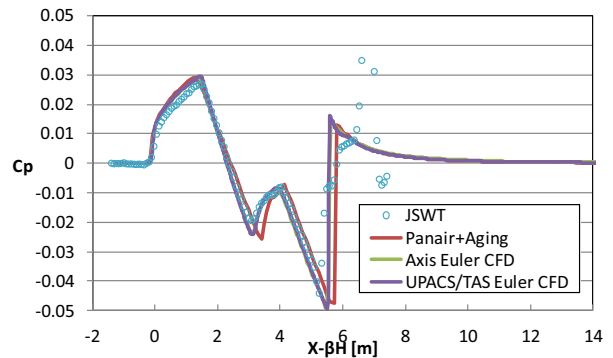


Fig.8 Near-field pressure signatures of the NWM

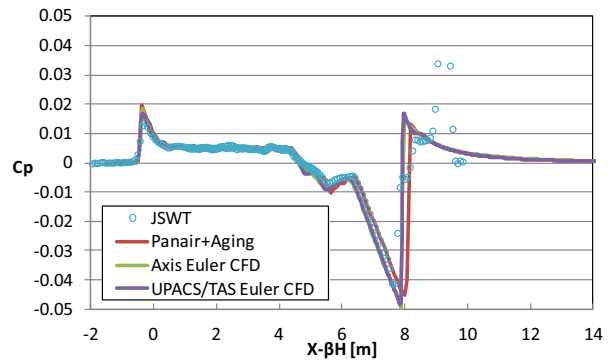


Fig.9 Near-field pressure signatures of the LBM

4. Concluding remarks

Supersonic wind-tunnel tests for measuring the near-field pressure signatures of the D-SEND#1 models are summarized. Some data correction methods are applied and the measurement accuracy is shown. The data will be utilized for the prediction tool validation.

Acknowledgements

The authors express their sincere gratitude to the JSWT staff for their support in the wind-tunnel test and to Mr.Hiroaki Ishikawa for his cooperation on CFD analysis of the models.

References

[1] http://d-send.jaxa.jp/d_send_e/index.html

Investigation of Micro-scale Phenomenon of Clear Air Turbulence by High Accuracy Meteorological Analysis

Keita Morimoto¹, Hamaki Inokuchi², Soshi Kawai³, Koji Shimoyama¹, Shinkyu Jeong¹ and Shigeru Obayashi¹

¹Institute of Fluid Science, Tohoku University, Sendai, Miyagi, 980-8577, Japan

²Aviation Program Group, Japan Aerospace Exploration Agency, Mitaka, Tokyo, 181-0015, Japan

³Institute of Space and Astronautical Science, Sagami-hara, Kanagawa, 252-5277, Japan

morimoto@edge.ifs.tohoku.ac.jp

ABSTRACT

In this research, the sixth-order compact difference scheme was introduced for the large eddy simulation. First, the vortex advection problem was investigated to validate the numerical accuracy. Roe's upwind scheme was used for the comparison. From the results, the compact difference scheme can maintain the vortex while minimizing numerical viscosity compared to the Roe's upwind scheme. Additionally, both schemes were applied to meteorological analysis for the horizontal roll convection currents. The results confirmed that the compact difference scheme tends to constrict diffusion in the downstream in particular.

1. Introduction

Over the last two decades, the number of air passengers has been increasing continuously at a rate of 4.1% per year. Over the next 20 years, global air passenger numbers are expected to increase by an average of 5% every year. On the other hand, airplane accidents caused by turbulence, such as United Airlines Flight 826 (1997) and FedEx Express Flight 80 (2009), occur frequently, and the failure rate associated with turbulence shows an upward trend. There is a concern regarding the increase in turbulence accidents due to the growth of air traffic. Turbulence can be classified as that associated with thunderclouds and clear air turbulence (CAT), which occurs in clear skies. The former can be avoided by detecting the position of thundercloud by both visual observation and radar. In this way, countermeasures for turbulence associated with thunderclouds can be implemented. On the other hand, CAT can be detected by neither visual observation nor radar because it occurs in clear skies. Thus, it is difficult to develop countermeasures for CAT. A number of studies have been conducted to predict CAT using meteorological simulation and Doppler Lidar as airborne turbulence sensors. If it is possible to detect CAT in advance, a pilot would be able to change the flight route and avoid the CAT.

In the USA, a prediction method called Graphical Turbulence Guidance2 (GTG2) was developed by the FAA Aviation Weather Research Program Turbulence Product Team. In Japan, Forecast Bad weather Japan (FBJP) was developed by the Tokyo Aviation Weather Service Center. However, in both methods, the forecasting range is too large to allow flight plans to be changed in advance to avoid the predicted CAT area. This is because these methods are based on macro- or synoptic-scale meteorological features, while CAT is a micro-scale phenomenon.

The main purpose of this study was to gain insight into the mechanisms of CAT, such as the causes and process of development of CAT, using methods that can show the micro-scale features of CAT. In this study, we employed Japan Meteorological Agency Non-Hydrostatic Model (JMANHM) and large eddy simulation (LES) to capture 50-m scale vortex structures that have the greatest effect on airplanes [1]. The initial

and boundary conditions for LES are determined from JMANHM. As the first step of this study, a compact difference scheme was introduced into LES to improve its spatial accuracy. This scheme is easily extended to higher-order accuracy with a small number of stencils. In this paper, as the most standard scheme today, Roe's upwind scheme is also used. The calculation results using these schemes are compared. First, vortex advection problem is investigated for the both schemes respectively. Second, meteorological analysis for horizontal roll convection currents is calculated by using both schemes, and the results were compared.

2. Numerical Method

The basic equations are the three-dimensional compressible Navier-Stokes equations. For calculation of the sub-grid-scale variations, Shen's Smagorinsky model with the modification of minimizing overmuch eddy viscosity at the center of the vortex was used. As the calculation method of spatial derivatives, the sixth-order compact difference scheme [2] is introduced. For any scalar quantity f , the spatial derivatives are obtained as

$$\alpha \left(\frac{\partial f}{\partial \xi} \right)_{i-1} + \left(\frac{\partial f}{\partial \xi} \right)_i + \alpha \left(\frac{\partial f}{\partial \xi} \right)_{i+1} = a \frac{f_{i+1} - f_{i-1}}{2} + b \frac{f_{i+2} - f_{i-2}}{4} \quad (1)$$

with $\alpha = 1/3$, $a = 14/9$, and $b = 1/9$ for a sixth-order scheme. This method was applied to all of the spatial derivatives in convective terms, viscous terms, metrics, and Jacobians. At the points on the boundaries, a fourth-order explicit one-sided finite difference scheme was used for evaluation of the derivatives. Similarly, a one-sided biased finite difference method scheme was used at the first interior point.

The filtering procedure is an important component of the compact difference scheme to suppress numerical instabilities arising from unresolved scales, mesh non-uniformities, and boundary conditions. The following filtering scheme is used at interior points:

$$\alpha_f \hat{q}_{i-1} + \hat{q}_i + \alpha_f \hat{q}_{i+1} = \sum_{n=0}^N \frac{a_n}{2} (q_{i+n} + q_{i-n}) \quad (2)$$

where α_f is a free parameter satisfying the inequality $-0.5 < \alpha_f \leq 0.5$. In this range, a higher value of α_f corresponds to a less dissipative filter. A fourth-order filter is adopted at the first interior point. For

multidimensional problems, the described procedure is sequentially applied for each direction.

Roe's upwind scheme extended to the fourth-order accuracy by compact MUSCL interpolation was also used for the comparison. The viscous terms are evaluated by the second-order central difference for the scheme. In addition, a time integration algorithm was applied by the fourth-order Runge-Kutta method for both schemes.

3. Results and Discussion

3.1 Vortex Advection Problem

The effect of compact difference scheme is investigated by vortex advection problem. The initial vortex conditions are given as

$$v_\theta = \frac{\Gamma}{2\pi r} \frac{r^2}{r^2 + r_c^2}, \quad \frac{dp}{dr} = \frac{\rho v_\theta^2}{r}, \quad (3)$$

$$\frac{\gamma p / \rho}{\gamma - 1} + \frac{v_\theta^2}{2} = \frac{\gamma p_\infty / \rho_\infty}{\gamma - 1}$$

where v_θ is the velocity magnitude in the circumferential direction, $\Gamma = 480$ and $r_c = 16$. The vortex is set in crosswind 2m/s. Figure 1 shows the time histories of the pressure at the vortex core and a comparison of Roe's fourth-order scheme and the sixth-order compact difference schemes. Figure 1 shows low pressure was maintained much better by the compact difference scheme than the Roe's upwind scheme. Therefore, the calculation accuracy was improved by introduction of the compact difference scheme.

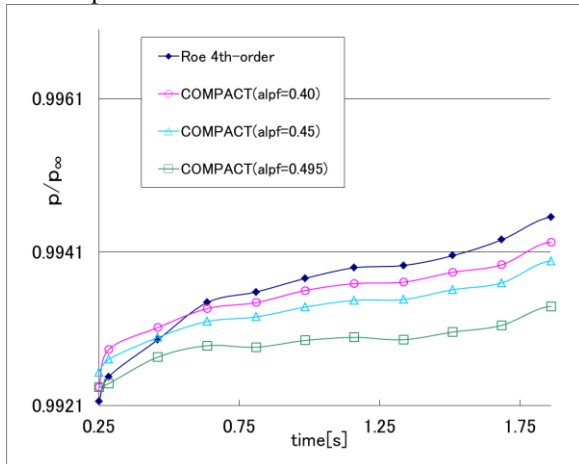
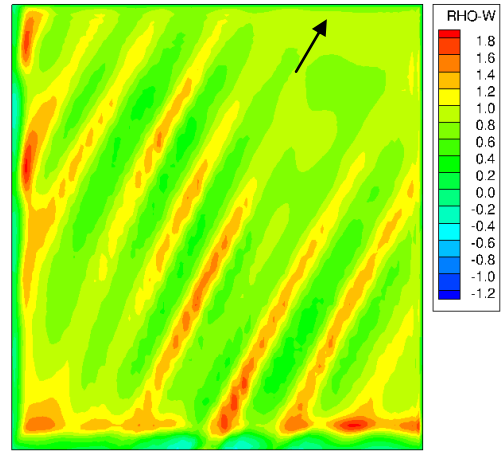


Fig. 1 Time histories of the pressure at the vortex core

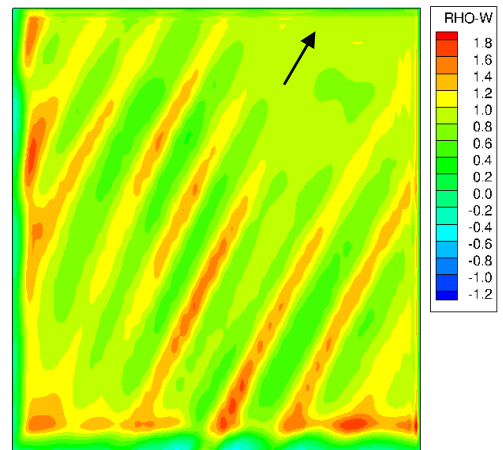
3.2 Application to the Meteorological Analysis

The horizontal roll convection currents [3], which occurred at Sendai Airport in June 19 2007, were employed as the analysis target of actual phenomena. Horizontal roll convection currents have multiple, horizontal, counter-rotating vortices in the atmospheric boundary layer, and the axes of the vortices are parallel or nearly parallel. Initial and boundary conditions for LES were calculated by JMANHM. The computational area for LES has $307 \times 208 \times 172$ grid points, with a grid size of 18m. Also, $\alpha_f = 0.495$ and 10th-order compact filter were employed in the compact difference scheme. Figure 2 shows the calculation results of LES : contour plots the vertical momentum on the XY-section

calculated by compact difference scheme and Roe's upwind scheme respectively. From Figure 2, the compact difference scheme constricts diffusion much better than the Roe's upwind scheme, and this tendency becomes remarkable especially in the downstream.



(a) Calculation result by compact difference scheme



(b) Calculation result by Roe's upwind scheme

Fig. 2 Horizontal roll convection currents

4. Concluding Remarks

The sixth-order compact difference scheme was introduced for the LES to improve its calculation accuracy. Roe's upwind scheme was used for the comparison. From the result of vortex advection problem for each scheme, low pressure was maintained much better by the compact difference scheme than the Roe's upwind scheme. Additionally both schemes were applied to meteorological analysis for the horizontal roll convection currents. Analysis results indicated that the compact difference scheme can constrict diffusion much better than the Roe's upwind scheme, and this tendency becomes remarkable in the downstream region in particular. Further studies are required to realize the analysis of meteorological events that airplanes encountered such as clear air turbulence.

References

- [1] R. Sharman et al, *Weather and Forecasting*, **21**, (2001).
- [2] S. K. Lele, *J. Computational Physics*, **103**, (1993).
- [3] S. Ogawa et al, *J. Meteorological Society of Japan*, **81**, (2003).

Study on Aerodynamic Optimization Using Compressible Euler Solver on Block-Structured Cartesian Mesh

Yoshinori Andoh, Shinkyu Jeong, and Shigeru Obayashi
Institute of Fluid Science, Tohoku University, Sendai, Miyagi, 980-8577, Japan
andoh@edge.ifs.tohoku.ac.jp

ABSTRACT

In this study, the computational accuracy of BCM compressible Euler solver was firstly validated with NACA0012 airfoil. The result showed that BCM was in good agreement with the TAS Code. Next, the BCM solver was applied to the aerodynamic design optimization problem of shock free airfoil. The airfoil without shock wave was successfully designed.

1. Introduction

Aerodynamic analysis using Computational Fluid Dynamics (CFD) is an inevitable tool for development of airplane in recent years. For the complex aircraft configuration, unstructured mesh methods have been widely used during the past two decades. However, the unstructured grid method has drawbacks such as the grid generation time, the complicated data structure, the difficulty of extending to high-order accuracy and so on. In order to solve the drawbacks, Building-Cube Method (BCM), which is based on Block-Structured Cartesian Mesh, was developed.

BCM has many advantages over the unstructured mesh method as follows:

- 1) Simplicity of data structure
- 2) Ease to parallelize
- 3) Ease to construct high-order accuracy
- 4) Rapid grid generation
- 5) Ease for post-processing for large scale data

The objective of this study is to confirm the validity of the BCM solver for aerodynamic optimization. The present method was applied to the design problem of shock free airfoil.

2. CFD Analysis Method

In this study, BCM compressible Euler solver developed by Nishimura is used [1]. This solver adopts an immersed boundary method to improve the accuracy of wall boundaries and reduce the number of cells. Numerical schemes used in the present solver are shown in Table 1.

Table 1. Numerical Scheme.

Governing Equations	Compressible Euler equation
Discretization Method	Cell centered finite volume method
Inviscid flux	HLLEW
High order solution algorithm	3 rd order MUSCL
Time integral method	LU-SGS implicit method

3. Optimization Method

In this study, Multi-purpose Engineering Design Optimization Code (MEDOC) developed by Jeong [2] is used as the optimization tool. The method consists of Generic Algorithm (GA) and Kriging model to reduce the computation time needed to evaluate objective

functions in optimization. The Kriging model is able to approximate a strongly non-linear objective function. The Kriging model constructs a response surface by interpolating the values of real objective function sampled in search region. The values of objective function at unknown design point and those of uncertainty are estimated at the same time. Based on these estimated values, the response surface is renewed by adding new sample points which have maximum Expected Improvement (EI) value. By repeating the renewing of response surface, not only improvement of accuracy of the response surface, but also discovering of global optimal solutions can be achieved as shown in Fig. 1.

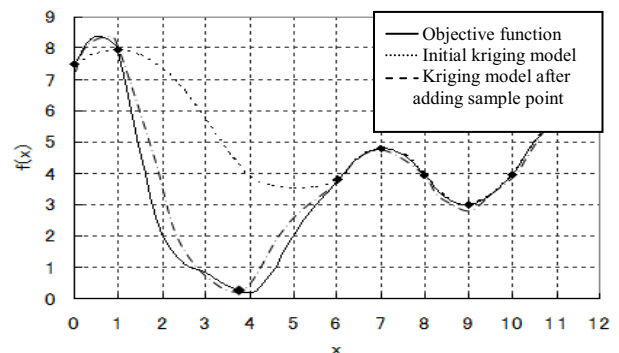


Fig. 1 Improvement of the accuracy for Kriging model.

4. Design Problem Definition of Airfoil

PARSEC airfoil is used for the definition of airfoil geometry. As parameters of PARSEC airfoil have close relations with aerodynamic features around airfoil, it's easy to discuss the influence of parameter on aerodynamic performance. The parameters of PARSEC airfoil is shown in Fig. 2. In this study, the thickness ΔZ_{TE} and Z coordinates of trailing edge are set to zero, thus the total number of design variables is nine.

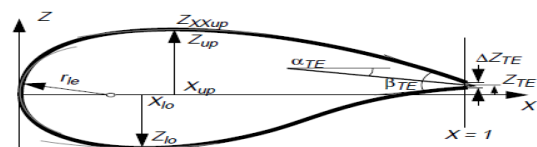


Fig. 2 PARSEC airfoil.

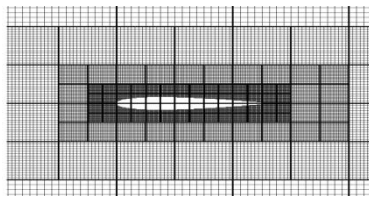
5. Results and Discussion

5.1 Verification of Computational Accuracy

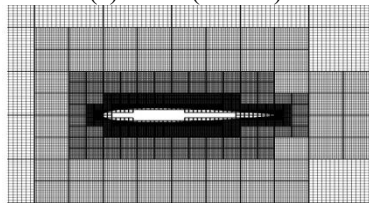
In order to confirm the computational validity of the present BCM, the flow field around NACA0012 airfoil was computed with two different resolutions of BCM mesh and unstructured mesh (TAS-Code). Table 2 shows the computational condition. Each computational mesh is shown in Fig. 3.

Table 2. Computational condition.

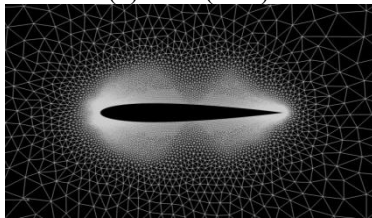
Mach number		0.8
Angle of attack [degree]		2.0
Minimum grid size	BCM (Coarse)	0.01
	BCM (Fine)	0.001
	TAS-Code	0.001



(a) BCM (Coarse)



(b) BCM (Fine)



(c) TAS-Code

Fig. 3 Computational mesh

Fig. 4 shows the comparisons of C_p distribution between BCMs and TAS-Code. As shown in Fig. 4, C_p distribution of BCM fine mesh was in good agreement with that of TAS-Code. Compared with BCM coarse mesh, BCM fine mesh obtains smoother C_p distribution and captures the location of shock wave accurately. Therefore, BCM fine mesh will be applied to the following aerodynamic design optimization.

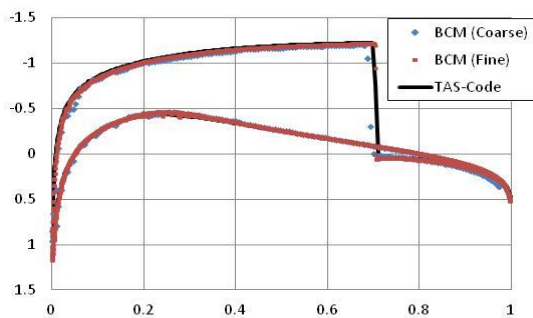


Fig. 4 C_p distribution around NACA0012.

5.2 Design of shock free airfoil

The shock free airfoil was designed using optimization technique. The objectives of the problem are

$$\begin{aligned} & \text{Maximize } C_l \\ & \text{Minimize } |C_p^* - C_{pmin}| \\ & \text{subject to } t/c \geq 0.12 \end{aligned}$$

at the flow condition of Mach 0.74 and an angle of attack is 0.0 degree. C_p^* and C_{pmin} are critical pressure and minimum pressure coefficients, respectively. t is maximum thickness of airfoil and c is the chord length of the designed airfoil.

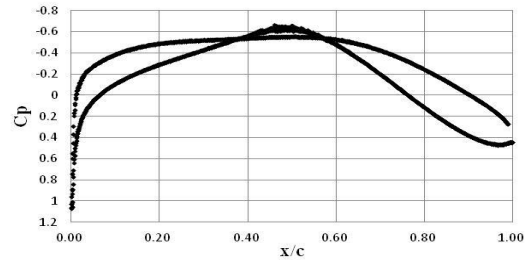


Fig. 5 Obtained C_p distribution.

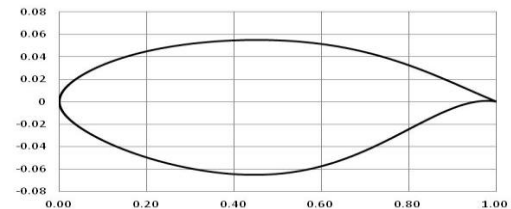


Fig. 6 Obtained shock free airfoil.

Figs. 5 and 6 show the result of C_p distribution and the shock free airfoil obtained by optimization, respectively. The result in Fig. 5 indicates that the negative peak value of C_p is minimized and the optimized airfoil does not generate shock on the surface of the airfoil.

6. Concluding remarks

In this study, the computational accuracy of BCM compressible Euler solver was firstly validated with NACA0012 airfoil. The result showed that BCM was in good agreement with the TAS Code. Next, the BCM solver was applied to the aerodynamic design optimization problem of shock free airfoil. The flow condition was Mach 0.74 and the airfoil thickness was constrained at 12%. The airfoil without shock wave was successfully designed. In the future, in order to understand the characteristics of configuration for the obtained shock free airfoil, data mining will be performed using Proper Orthogonal Decomposition (POD) [3], which is able to analyze the data of configuration and flow field.

References

- [1] Yasutaka Nishimura, Daisuke Sasaki, and Kazuhiro Nakahashi, 43rd Fluid Dynamics Conference/Aerospace Numerical Simulation Symposium 325-334 (2011).
- [2] S. Jeong, K. Yamamoto, and S. Obayashi, AIAA paper, 2004-6437, 2004.
- [3] A. Oyama, Transactions of JSCES, Vol.14, 2009.

GUI tool for Creation of Aircraft Configuration

Tomoki Taira^[1], Shinkyu Jeong^[1], Shigeru Obayashi^[1], Daisuke Sasaki^[2], Kazuhiro Nakahashi^[3].

^[1]Tohoku University, Sendai, 980-8577, Japan.

^[2]Kanazawa Institute of Technology, Nonoichi, 921-8501, Japan.

^[3]Japanese Aerospace Exploration Agency, Chofu, 182-8522, Japan.

E-mail of corresponding author: taira@edge.ifs.tohoku.ac.jp

ABSTRACT

A GUI-based form deformation tool is developed to improve the efficiency of conceptual design. This tool allows the designer to deform the configuration interactively by mouse operation. In addition, the user can also estimate the flow around the configuration quickly with CFD solver. This tool has the advantage that the user can deform the configuration and calculate the aerodynamic performance interactively in the same tool. Therefore, it enables deformation of the configuration according to the computation results and allows the creation of a high performance configuration with a short development time.

1. Introduction

For next-generation aircraft design, it is necessary to take into consideration stringent economic and environmental requirements, such as fuel efficiency, noise, emissions, etc. However, it is difficult to satisfy these requirements with the conventional aircraft design concept[1]. There has been a great deal of recent research and development in new aircraft concepts to fulfill these requirements[2]

In the conceptual design phase, many different configurations are considered and numerous geometry changes are made. Due to this feature of conceptual design, a design tool that allows interactive geometry modification is essential for comparison of many configurations[3]. Another requirement for the conceptual design tool is the ability to conduct rapid performance evaluation. Such tools will be helpful for the designer to determine the configuration that meets the design goal. Optimization methods are widely employed in the conceptual design phase. By coupling the configuration deformation tool and optimization engine, the configuration satisfying the design goal can be found efficiently.

In this study, a GUI (Graphical User Interface)-based form deformation tool is developed to improve the efficiency of conceptual design. This tool allows both global and local configuration changes, using a modified free form deformation method implementing physics-based direct manipulation[4] and coordinate transformation. This tool also supplies two aerodynamic analysis solvers. One is based on the panel method[5] and the other uses the Cartesian meshed-based Euler solver[6] The designer can select the analysis solver depending on the required accuracy level.

2. Form Deformation

In this study, a modified Free Form Deformation (FFD) implementing physics-based direct manipulation and coordinate transformation was introduced. FFD is a versatile deformation method, because it is able to express the object deformation with only the displacement of a parallelepiped volume domain surrounding the object (this domain is called control box or control lattice), instead of the displacement of the object surface itself. That is, parameterization based on

FFD is represented by the coordinates of the node points of the control box. Therefore, it can be easily applied to any kind of complex object. This standard FFD method has the following specific merits:

- It can be used for any kind of complex object;
- The deformed objects can be fairly general and continuous;
- The differentiability and degree-elevation properties of Bézier curves are preserved;
- B-spline/NURBS-based FFD can be formulated easily using the B-spline/NURBS basis function instead of the Bernstein polynomials.

However, one of the limitations of this control point-based method is that there is no direct (intuitive) relationship between the displaced control points and the deformed object. For shape optimization, it is better to use the control points on the object. To meet this requirement, the original FFD was modified by implementing the physics-based direction manipulation and coordinate transformation method.

In the physics-based method, the solution is determined by minimization of deformation energy with user-specified constraints. In this study, the deformation energy is defined with the assumption of isotropic elastic material:

For coordinate transformation, the displacement of control points are computed from mouse movement. Then, the coordinates of the airfoil are transformed. Deformation takes place in a different coordinate system. After computing the displacement of node points in space, the displacement of node points in the coordinate system is computed by inverse coordinate transformation. This modified FFD method allows the user to deform the configuration both globally and locally. This method also allows the configuration to be represented with a small number of control points.

3. Aerodynamic Analysis Methods

A. PANAIR

PANAIR is a program developed to predict inviscid subsonic and supersonic flows about arbitrary configurations. Generally, a panel method solves a linear partial differential equation numerically by approximating the configuration surface by a set of

panels on which unknown "singularity strengths" are defined, imposing boundary conditions at a discrete set of points, thereby generating a system of linear equations relating the unknown singularity strength. These equations are solved for the singularity strength that provides information on the properties of the flow. PANAIR differs from earlier panel methods by employing a "higher order" panel method; that is, the singularity strengths are not constant in each panel. This is necessitated by more stringent requirements of supersonic problems. The potential for numerical error is greatly reduced in the PANAIR program by requiring the singularity strength to be continuous. It is also this "higher order" attribute that allows PANAIR to be used to analyze flows about arbitrary configurations.

B. Building-Cube Method

The BCM is based on a multi-block structure of equally spaced Cartesian meshes to achieve simplicity in mesh generation and in postprocessing. The computational mesh consists of many cuboids called 'cubes,' which include equally spaced small Cartesian mesh 'cell'. As the number of mesh points is identical in all of the cubes regardless of the cube size, and the computation is parallelized based on each cube, high parallel efficiency is achieved. Because the mesh resolution is controlled by the size of each cube, the geometrical cube size becomes large as the distance from the object increases. In the present approach, the body surface is approximated as a staircase pattern.

The governing equation in the present BCM is the compressible Euler equation, which is discretized using the cell-centered finite volume method. The HLLW (Harten-Lax-van Leer-Einfeldt-Wada) scheme, a type of approximate Riemann solver, is implemented to solve the inviscid flux, and 3rd order MUSCL is used to construct the high-order scheme satisfying the TVD condition. For time integration, the LU-SGS (Lower-Upper Symmetric Gauss-Seidel) implicit method is employed. In this study, three points backward difference scheme is adopted to achieve 2nd order time accuracy for unsteady calculations. For the wall boundary treatment, an immersed boundary method using the ghost cell and the image point is used.

4. Results and Discussion

The procedure of deformation, mesh generation, and CFD is shown here. Deformation is performed by clicking and holding the control point and dragging and dropping it using the mouse. Then, clicking the "Mesh" button generates the mesh around the model. Finally, clicking the "CFD" button shows the flow around the model. As soon as the calculation finishes, the Cp distribution graph updates automatically (Fig. 1).

For 3D case, DLR F6 was selected for the analysis. The pressure distribution around the model is shown in Fig. 2.

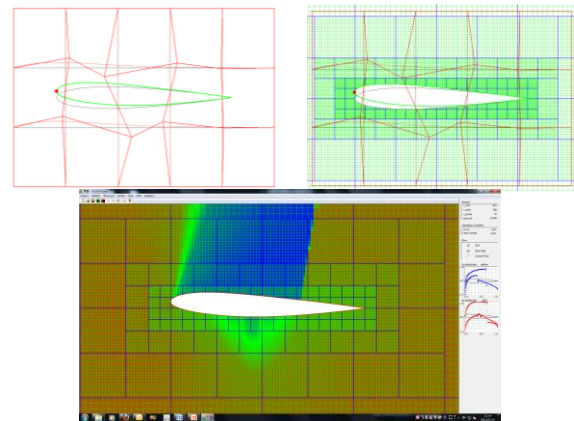


Fig. 1 GUI tool for 2D

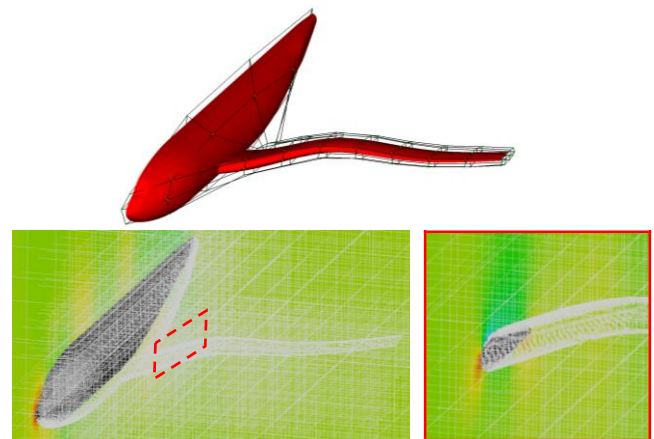


Fig. 2 GUI tool for 3D

3. Conclusion and future work

A GUI-based form deformation tool was developed to improve the efficiency of conceptual design. This tool allows the designer to deform the configuration interactively by mouse operation. A modified Free Form Deformation implementing physics-based direct manipulation and coordinate transformation was introduced, and it was shown to enable the user to deform the configuration both locally and generally.

In addition, the user can also estimate the flow around the configuration quickly with the panel method and Cartesian mesh-based solver. The designer can select the analysis solver depending on the required accuracy level.

References

- [1] John T. Bonet , 50th AIAA Aerospace Sciences Meeting, January 11, 2012.
- [2] Mark Mangelsdorf, Turbo Expo, June 6 - 10, 2011.
- [3] Byounsoo Kim , Japan-Korea CFD workshop 2008.
- [4] W. Yamazaki, S. Mouton, G. Carrier 12th AIAA/ISSMO Multidisciplinary Analysis and Optimization Conference, 2008.
- [5] Magnus, A. and Epton, M., Tech. Rep. CR-3251, NASA, 1980.
- [6] K. Nakahashi, Computational Fluid Dynamics 2002, Eds. S. Armfield, R. Morgan, K. Srinivas, Springer, pp.77-81. 2003.

OS5: Advanced Control of Smart Fluids and Fluid Flows

Wandering Correction of a Wing-Tip Vortex Velocity Field via Deconvolution

Adam Edstrand, Eric Deem, Louis Cattafesta
 Department of Mechanical Engineering, Florida State University, Tallahassee, FL 32310
 Florida Center for Advanced Aero-Propulsion (FCAAP)
cattafes@ufl.edu

ABSTRACT

Wind tunnel experiments of wing-tip vortices have been shown to have an inherent problem with wandering of the vortex core within the test section. This wandering corrupts fixed probe measurements, which results in an under-prediction of the vortex core velocity levels, and an over-prediction in vortex core size. An experimental study has been performed with stereo particle image velocimetry, and a post-processing wandering correction via a deconvolution method has been used in an attempt to reconstruct the original vortex velocity field without wandering contamination.

1. Introduction

Wing-tip vortices are a negative byproduct of a three-dimensional lifting surface, created by the flow generated by the pressure difference on the upper and lower surfaces of the airfoil at the tip. These vortices dictate the timing in between aircraft landing at airports and also cause induced drag on the airfoil and aerodynamic noise. Because of these effects, tip vortices and their attenuation are a prominent area of research.

Tip vortices in wind tunnels exhibit random motion referred to as wandering. The wandering corrupts measurement data when using fixed probes [1-2]. The corrupted measurements under-predict the core velocities, over-predict the core radius, and increase the apparent Reynolds stresses within the core [1-3]. Therefore, the wandering causes a problem in obtaining accurate measurements of the tip vortex. Researchers have proposed a deconvolution method for removing the effects of wandering [4]. A deconvolution method using a Wiener filter for this correction is explored and the results are compared with uncorrupted vortex measurements.

2. Experimental Setup and Methodology

The tip vortex is generated with a NACA0012 airfoil at a chord Reynolds number of 530k, rotated about its quarter-chord to an angle of attack of 5 degrees. Stereo particle image velocimetry (SPIV) data are obtained 5 chords downstream of the leading edge. With SPIV, 500 image pairs are acquired, resulting in 500 velocity fields for statistical analysis. All measurements are taken in the University of Florida Anechoic Flow Facility [5].

The time between the two images taken for SPIV is small relative to the time scale of the wandering. Because of this, the velocity field provided by each image pair can be assumed to be an instantaneous measurement of the vortex velocity field. This allows an observation of the vortex core location for each image pair. A bivariate probability density function (PDF) is constructed from the vortex core locations and is determined to represent the wandering.

The mean vortex velocity field is determined simply by averaging the SPIV data. This is equivalent to having fixed probe measurements at each SPIV measurement location. Since it is possible to find the vortex location for each image pair using SPIV, shifting each image pair to the mean vortex center location, then averaging the

shifted velocities can determine the true vortex mean velocity field. This can be used as a comparison between the deconvolution and the true vortex.

Since the PDF is not directly measurable in fixed probe measurements, an estimate of the PDF must be found. Devenport [1] postulated that the PDF can be assumed to be a bivariate Gaussian PDF. The standard deviation in the y -direction is determined via the relation [1]

$$\sigma_y = \frac{\sqrt{u_{rms}^2 + v_{rms}^2}}{\nabla(w)}$$

where σ_y is the standard deviation of y , and the standard deviation of z can be found similarly. With the mean velocity field known, and the wandering PDF estimated, an estimation of the true velocity field could now be determined by inverse filtering theory.

The mean vortex velocity caused by the wandering is defined as the convolution of the true mean vortex velocity and the PDF of the wandering location

$$v_m(y, z) = \int \int p(y, z) v(y - y_v, z - z_v) dy_v dz_v,$$

where v_m is the mean velocity, p is the PDF, and v is the true velocity field. The variables y and z are the probe locations, and y_v and z_v are the location of the vortex center.

Since convolution in the time domain is equivalent to multiplication in the Fourier domain, the true vortex velocity can be reconstructed if the wandering PDF is known. Therefore, by taking the inverse Fourier transform of the measured mean velocity field, then point-by-point division by the Fourier transform of the wandering PDF gives the estimated velocity field sans wandering.

However, this process is highly dependent on noise within the data. In order to minimize the effect of the noise, a Wiener deconvolution is used [6]. The Wiener deconvolution takes into account the noise and minimizes its impact given a signal-to-noise ratio. The inverse Wiener filter is defined as

$$G(\lambda_y, \lambda_z) = \frac{1}{P(\lambda_y, \lambda_z)} \left[\frac{|P(\lambda_y, \lambda_z)|^2}{|P(\lambda_y, \lambda_z)|^2 + \frac{1}{SNR(\lambda_y, \lambda_z)}} \right]$$

where P is the PDF in the Fourier domain, and SNR is the signal-to-noise ratio. The error is defined as the

difference between the deconvolved vortex and the true mean vortex. This error is used to determine the optimal signal-to-noise ratio at each measurement location by minimizing the impact of the measurement noise.

Once the inverse Wiener filter is found, the true velocity field is then estimated as

$$v(y, z) = \mathcal{F}^{-1}\{G(\lambda_y, \lambda_z)V_m(\lambda_y, \lambda_z)\}, \dots$$

where $\mathcal{F}^{-1}()$ denotes the inverse Fourier transform.

3. Results and Discussion

In the following section, the results from the theory laid out above are discussed. First, a comparison between the PDF determined from the measurements of 500 vortex center locations, seen in Fig. 1a, and the estimated PDF from the mean flow “fixed probe” data, seen in Fig. 1b. As shown, the estimation proposed by Devenport seems to over-predict the standard deviations and under-predict the anisotropy coefficient, seen by the smaller amount of rotation of the PDF. However, since the PDF cannot be directly measured in a fixed probe measurement, the PDF in Fig. 1b will be used in order to simulate the fixed probe measurement situation.

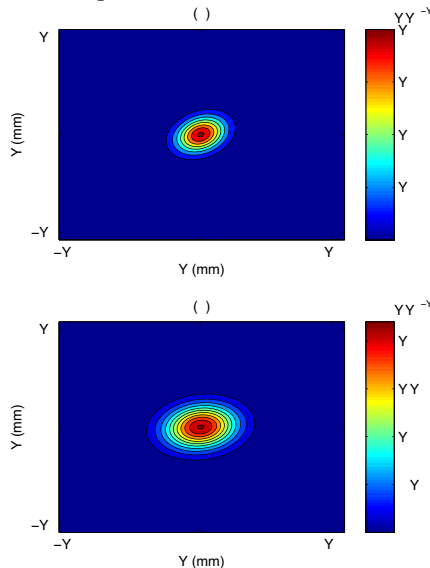


Fig. 1 Comparison of PDF found from (a) the SPIV core locations and (b) the mean velocity field data.

Fig. 2 shows the results of the streamwise velocity of the vortex for the mean flow case, the true flow case, and the deconvolved case. Observing the comparison between the mean flow case and the true vortex case, seen in Fig. 2a and 2b, the mean flow under-predicts the velocity deficit seen within the core, and over-predicts the core size as seen in [1]. The velocity deficit has an error of approximately 2.5%. There also appears to be a U-shaped structure within the core center that is removed completely by the effects of the wandering.

In comparing the deconvolved flow field, it can be seen that it does a better job at the velocity deficit levels within the core. The error of the velocity deficit is less than 1% in the core. The deconvolution method seems to partially reconstruct the U-shaped core flow field that is removed by the effects of the wandering in the mean

flow case.

However, with the advantages of the better-predicted velocity deficits, the deconvolved flow field is noisy due to the estimation procedure. In particular, this noise characteristic is exacerbated outside of the core.

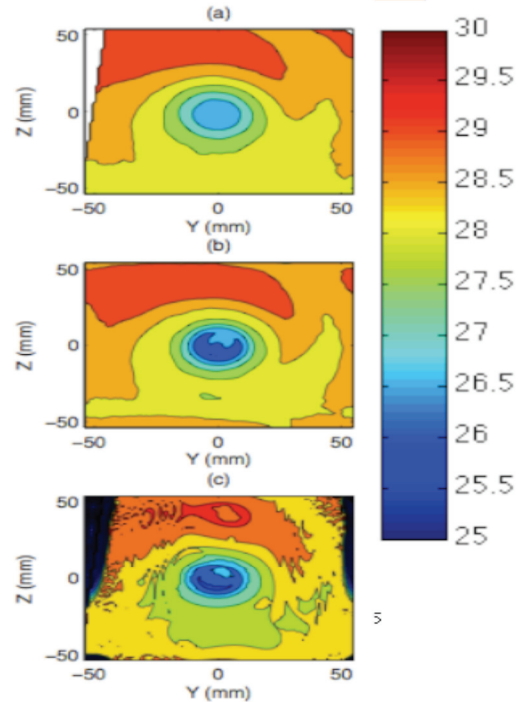


Fig. 2 Streamwise velocity comparison of the vortex fields of the (a) mean flow field, (b) true flow field and (c) deconvolved flow field.

4. Conclusions and Future Work

A deconvolution technique for correcting the effects of wandering using a Wiener deconvolution method is explored. The wandering causes an under-prediction of velocity levels and an over-prediction of core radius. Additionally, there are flow field characteristics that are completely removed due to the effects of wandering.

The deconvolution method helps reconstruct the streamwise velocity in the core with errors less than 1% and reconstructs the flow field characteristics seen in the true vortex. However, these improvements do not come without a penalty. Spatial “high frequency” noise is created as a result of the deconvolution process.

Future work includes efforts to minimize the effects of noise in the deconvolved flow field. This can be done by applying a low pass filter to the data and/or changing the size of the interrogation window of the deconvolution process.

References

- [1] W. Devenport et al., *J. Fluid Mech.*, **312** (1996), pp. 67-106.
- [2] V. Corsiglia et al., *J. Aircraft*, **10** (1973), No. 12.
- [3] S. Green and A. Acosta, *J. Fluid Mech.*, **227**, (1991), pp. 107-134.
- [4] G. Iungo et al., *Exp Fluids*, **46** (2009), pp. 435-452.
- [5] J. Mathew, Ph.D Dissertation, (2006).
- [6] R. Gonzalez et al., (2004), *Digital Image Processing using MATLAB*, Pearson Prentice Hall.

Multiparametric Control Problems for Boussinesq Equations

Gennady Alekseev, Dmitry Tereshko

Institute of Applied Mathematics FEB RAS, 7, Radio St., Vladivostok, 690041, Russia
alekseev@iam.dvo.ru

ABSTRACT

This work is concerned with a numerical solution of optimal control problems for the heat convection model. In these problems the velocity of fluid and the heat flux on some parts of the boundary are used to minimize a quadratic functional depending on the velocity. Optimality systems describing the first-order necessary optimality conditions are deduced and analyzed. Based on results of this theoretical analysis we propose numerical algorithm for solution of boundary control problems under consideration and discuss some results of numerical experiments.

1. Introduction

In the last decade much effort was focused on optimal control problems for models of heat transfer in viscous incompressible fluid. This interest to control problems is connected with a variety of technical applications in science and engineering such as the crystal growth process, the aerodynamic drag reduction, the suppression of a turbulence and flow separation. In these problems the unknown densities of boundary or distributed sources, the coefficients of model differential equations or boundary conditions are recovered from additional information on the solution to the original boundary value problem. Importantly, inverse problems for models of heat transfer can be reduced to corresponding extremum problems by choosing a suitable minimized cost functional that adequately describes the inverse problem in question. As a result, both control and inverse problems can be analyzed by applying a unified approach based on the constrained optimization theory in Hilbert or Banach spaces [1-4]. These theoretical results, the increasing power of computers and the development of numerical methods for the flow simulation itself motivate the numerical study of the optimal flow control problems under consideration.

Let Ω be a bounded domain in the space \mathbf{R}^m , $m=2, 3$ with Lipschitz boundary Γ . We consider the boundary value problem for the stationary Boussinesq equations

$$-\nu\Delta\mathbf{u} + (\mathbf{u} \cdot \nabla)\mathbf{u} + \nabla p = -\beta T\mathbf{G}, \quad \text{div } \mathbf{u} = 0 \quad \text{in } \Omega, \quad (1)$$

$$-\lambda\Delta T + \mathbf{u} \cdot \nabla T = f \quad \text{in } \Omega, \quad (2)$$

$$\mathbf{u} = \mathbf{g} \text{ on } \Gamma, \quad T = \psi \text{ on } \Gamma_D, \quad \lambda \partial T / \partial n = \chi \text{ on } \Gamma_N \quad (3)$$

which describes the steady flow of viscous incompressible heat-conducting fluid in the domain Ω . Here \mathbf{u} , p and T denote the velocity, pressure and temperature fields respectively, ν is the kinematic viscosity coefficient, \mathbf{G} is the gravitational acceleration vector, β is the volumetric thermal expansion coefficient, λ is the thermal conductivity coefficient, \mathbf{g} is a given vector-function on Γ , ψ is a given function on a part Γ_D of Γ , χ is a function given on another part Γ_N of Γ , \mathbf{n} is the unit outer normal. We shall refer to problem (1)-(3) as Problem 1.

Together with (1)-(3) we consider nonstationary boundary value problem

$$\mathbf{u}_t - \nu\Delta\mathbf{u} + (\mathbf{u} \cdot \nabla)\mathbf{u} + \nabla p = -\beta T\mathbf{G} \quad \text{in } \Omega \times (0, t_1), \quad (4)$$

$$\text{div } \mathbf{u} = 0 \quad \text{in } \Omega \times (0, t_1), \quad \mathbf{u} = \mathbf{g} \quad \text{on } \Gamma \times (0, t_1), \quad (5)$$

$$T_t - \lambda\Delta T + \mathbf{u} \cdot \nabla T = f \quad \text{in } \Omega \times (0, t_1), \quad (6)$$

$$T = \psi \text{ on } \Gamma_D \times (0, t_1), \quad \lambda \partial T / \partial n = \chi \text{ on } \Gamma_N \times (0, t_1), \quad (7)$$

$$\mathbf{u}|_{t=0} = \mathbf{u}_0 \text{ in } \Omega, \quad T|_{t=0} = T_0 \text{ in } \Omega \quad (8)$$

as a model of unsteady flow of viscous heat-conducting fluid on time interval $(0, t_1)$.

2. Optimal Control Problems

Our goal is the theoretical and numerical study of the boundary control problems for the models under consideration. The problems consist in minimization of certain cost functional depending on the state and controls. In order to formulate control problem for the model (1)-(3) we split the set of all data of Problem 1 into two groups: the group of controls containing the functions $\mathbf{g} \in \mathbf{H}^{1/2}(\Gamma)$ and $\chi \in L^2(\Gamma_N)$ and the group of fixed functions f and ψ . We assume that the controls \mathbf{g} and χ vary in some closed convex sets $K_1 \subset \mathbf{H}^{1/2}(\Gamma)$ and $K_2 \subset L^2(\Gamma_N)$. The mathematical statement of the optimal control problem is as follows: find a pair (\mathbf{x}, u) , where $\mathbf{x} = (\mathbf{u}, p, T) \in X$, and $u = (\mathbf{g}, \chi) \in K_1 \times K_2 = K$ such that $F(\mathbf{x}, u) = 0$ and

$$J(\mathbf{x}, u) = J_i(\mathbf{u}) + \frac{\mu_1}{2} \|\mathbf{g}\|_{\mathbf{H}^{1/2}(\Gamma)}^2 + \frac{\mu_2}{2} \|\chi\|_{L^2(\Gamma_N)}^2 \rightarrow \inf.$$

Here $F(\mathbf{x}, u) = 0$ is the operator constraint in the form of the weak formulation of Problem 1; μ_1, μ_2 are nonnegative constants, $J_i(\mathbf{u})$ is a cost functional. The possible cost functionals are usually defined as

$$J_1(\mathbf{u}) = \frac{1}{2} \int_Q |\text{curl } \mathbf{u}|^2 d\Omega, \quad J_2(T) = \frac{1}{2} \int_\gamma |\mathbf{u} \cdot \mathbf{n}|^2 d\Gamma$$

in the cases where the vorticity in some subdomain Q and fluid flow through the curve γ are minimized.

The existence of an optimal solution is based on the a priori estimates and standard techniques (see [2]). Optimality systems describing first-order necessary optimality conditions were obtained, and, by analysis of their properties, conditions ensuring the uniqueness and stability of solutions were established. Similarly the optimal control problems for the unsteady model (4)-(8) are formulated.

3. Numerical Experiments

A numerical algorithm, based on the solution of the optimality system applying Newton's method, was proposed. The open source software freeFEM++ (www.freefem.org) is used for the discretization of boundary-value problems by the finite element method.

Following example is connected with the separation of 2D viscous fluid flow in a cavity. The original uncontrolled flow is the solution of the Boussinesq equations with no-slip boundary conditions for velocity and Dirichlet boundary condition $T=\psi$ for temperature when $\psi=0$ on the left, top and bottom boundaries and $\psi=1$ on the right boundary. The velocity field for uncontrolled flow is shown in Figure 1.

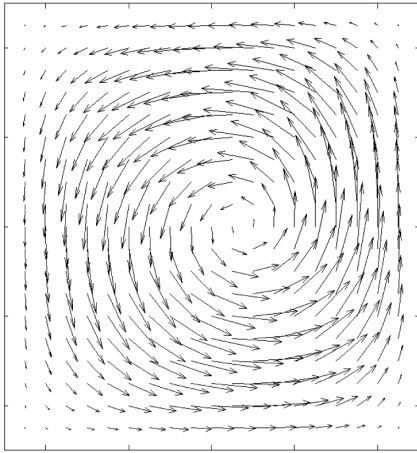


Fig. 1 Velocity field for the uncontrolled flow

In order to eliminate the heat and mass transfer from one to another part of the domain the functional $J_2(\mathbf{u})$ is minimized using an optimal control approach for the models (1)-(3) and (4)-(8).

In the first case we use the heat flux χ on the left boundary as the control. The vertical line γ divides the domain Ω into two equal parts. The velocity field for controlled flow is shown in Figure 2.

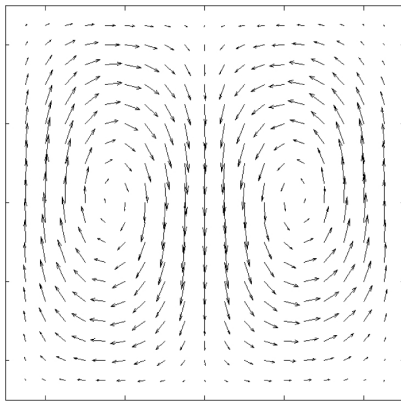


Fig. 2 Velocity field for the controlled flow with a boundary heat flux control

Let us note that in this case a functional depending on velocity is minimized by means of temperature control. Analysis of the temperature field in the computational domain allows us to understand the physical mechanisms of the velocity field correction due to the thermal convection. Additional heat flux generates heating on the left boundary. This thermal action separates the fluid flow on the given line γ .

In the next example we use two types of control. The heat flux on the left and bottom boundary sections is used to separate the flow on the diagonal line γ . Additionally we use the tangent velocity control on in the vicinity of the left upper corner. The velocity vector field for controlled flow is shown in Figure 3.

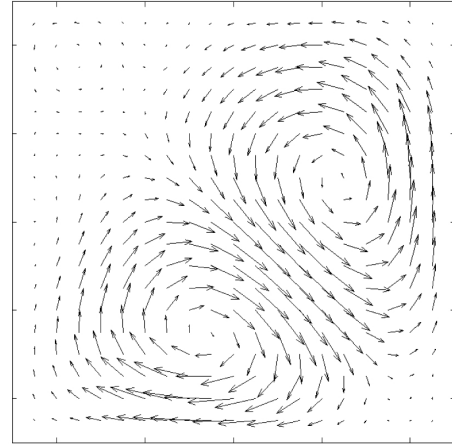


Fig. 3 Velocity field for the controlled flow with velocity and heat flux controls

Unsteady controlled flows for the model (4)-(8) are stable and converge to the corresponding stationary flows shown in Figures 2 and 3.

Separation of the flow can significantly limit the transfer of harmful impurities from one to another part of the domain, and thus prevent the pollution of significant subdomain. Some results of other numerical experiments can be found in [2-4].

Acknowledgments

This work was supported by the Russian Foundation for Basic Research (project no. 10-01-00219-a) and the Far Eastern Branch of the Russian Academy of Sciences (project no. 12-I-P17-03).

References

- [1] M.D. Gunzburger, Perspectives in flow control and optimization. SIAM, (2003).
- [2] G.V. Alekseev and D.A. Tereshko, Analysis and optimization in hydrodynamics of viscous fluid. Dalnauka, (2008).
- [3] G.V. Alekseev and D.A. Tereshko, J. Appl. Mech. Tech. Phys., **51** (2010), 510-520.
- [4] G.V. Alekseev and D.A. Tereshko, Comp. Math. Math Phys., **51** (2011), 1539-1557.

Verification of CFD Analysis for Vortex Generators on a Super Critical Infinite-Wing

Nobuo Namura, Shinkyu Jeong, and Shigeru Obayashi

Institute of Fluid Science, Tohoku University, 2-1-1 Katahira, Aoba-ku, Sendai 980-8577, Japan
namura@edge.ifs.tohoku.ac.jp

ABSTRACT

A transonic wing with vortex generator (VG) is analyzed by using computational fluid dynamics (CFD) with two types of turbulence models: modified Spalart Allmaras (MSA) model with the nonlinear Reynolds-stress tensor and $k-\omega$ shear stress transport (SST) model. By using VG, the shock wave location moves downstream with MSA while the pressure coefficients behind the shock wave decrease with SST. It becomes obvious that the pressure coefficient distributions of the wing with VG depend on the turbulence models significantly, which also affect lift coefficient characteristics against angles of attack.

1. Introduction

Shock-induced separation can be caused by small increment of angle of attack and Mach number in transonic flight. This phenomenon decreases lift and increases drag and pitching moment drastically as in the case with the stall at high angle of attack in subsonic flight. In order to reduce shock-induced separation, an array of vortex generators (VGs) is frequently employed. A small vane, whose height is almost the same as the thickness of a boundary layer, is often used as VG, and generates vortex which supplies the fresh flow into the boundary layer. VGs can be applied without any change of the primary design of the aircraft. However, the design of VGs array strongly depends on the engineer's experience because the scale difference between VG and the wing makes it difficult to perform the experiment and the numerical analysis. In the experiment, the size of VG becomes too small to properly measure the effect because the wing model is scaled down. On the other hand, the numerical analysis requires the high-resolution mesh which can capture the shape of VG and its vortex. For these reasons, there are few papers reporting the effect of VGs on the wing.

Wik & Shaw [1] compared the results of computational fluid dynamics (CFD) with different turbulence models to experimental data by the vortexes from one VG on a flat plate. They reported that the Spalart Allmaras (SA) model with rotation correction [2], [3] and the $k-\omega$ shear stress transport (SST) model [4] could predict the vortex well and further improvements were obtained using the Reynolds stress model. Bur et al [5]. created a shock wave by a ramp in a transonic wind tunnel. They tested six types of VGs arrays and investigated the VG's effect to the shock wave. However, it was not mentioned how VG affects the aerodynamic characteristics of the transonic aircraft because these studies were performed on the flat and ramp plane. Huang et al. [6] performed the CFD analysis of a 3-dimensional transonic wing and confirmed that VGs array could improve the aerodynamic characteristics. However, it was not clear how VG's parameters (height, spacing, location, deflection angle) affect the aerodynamic characteristics because the 3-dimensional analysis was performed in only one case of angle of attack and VGs arrangements were three limited cases.

In order to confirm the effects of each VG's parameter properly, the high-resolution mesh and the suitable turbulence model must be applied to CFD analysis. In this paper, two types of turbulence models are compared. We use the wing model in which one VG is equipped on a super critical rectangular wing and the periodic boundary condition is adopted to employ the mesh as fine as possible.

2. Computational Method

In this paper, a three-dimensional unstructured mesh flow solver named Tohoku University aerodynamic simulation (TAS) code is used to simulate the flow field. Navier-Stokes equations are computed by the cell-vertex finite-volume scheme. Numerical flux is computed using the approximate Riemann solver of Harten-Lax-van Leer-Einfeldt-Wada (HLLIW). Second-order spatial accuracy is realized by a linear reconstruction of the primitive variables with Vankatakrisnan's limiter. The lower/upper symmetric Gauss-Seidel (LU-SGS) implicit method is used for time integration. Turbulence models used in this study are the modified SA (MSA) model with the nonlinear Reynolds-stress tensor [2], [7] and SST. Hybrid volume mesh consisting of tetrahedron, prism and pyramid is used to resolve the boundary layer accuracy in unstructured mesh computation.

3. Flow Conditions and Model Geometries

Flow conditions and model geometry were chosen based on the experiments planed by Japan aerospace exploration agency (JAXA): the free stream temperature 266 [K], Mach number 0.7, Reynolds number based on the chord length 5×10^6 , and angle of attack from 0 to 5 [deg]. In the CFD analysis, one VG is equipped on a rectangular wing with a super critical airfoil SC(2)-0518 because the periodic boundary condition is adopted, while some VGs are equipped on a finite-wing in the experiment. The shape of VG vane is rectangle whose height is 0.6 [%], length is 2.4 [%], and thickness is 0.072 [%] of the chord length respectively. In this paper, VG is located at 20 [%] of the chord length with 20 [deg] of incidence angle to the flow direction and spaced at intervals of 10 times of the VG height. The unstructured mesh with 3,428,323 nodes, in which the upper surface of the wing has 13 times more nodes than

the lower surface to capture the vortex from VG, was generated for VG model. To confirm the effects of VG, a reference model without VG, whose mesh has 2,939,303 nodes, was employed.

4. Results and Discussion

The wings with and without VG are analyzed to explore the effect of VG with the different turbulence models. Figure 1 shows the lift coefficients, C_L , of each model against angle of attack, α . Comparing the reference models with MSA and SST, the qualitative $C_L - \alpha$ characteristics between $\alpha = 0$ and 4 [deg] are the same although the C_L values with SST are lower than those with MSA. This is because the shock wave of the reference model with SST is located more upstream than that with MSA as shown in Fig. 2. These differences between the shock wave locations with MSA and SST increase with α , and change the qualitative characteristics between $\alpha = 4$ and 5 [deg] in Fig. 1.

The qualitative $C_L - \alpha$ characteristics of the VG models with MSA and SST in Fig. 1 also have some differences. The VG model with SST has higher C_L by about 0.03 than the reference model between $\alpha = 1$ and 5 [deg], while the VG model with MSA shows their advantage when α is more than 3 [deg]. Characteristic pressure coefficient, C_p , distributions generated by VG with each turbulence model cause this difference. Figure 3 shows C_p distributions at $\alpha = 4$. Using MSA, the shock wave location of the VG model moves downstream compared to that of the reference model, which increases C_L of the VG model. In contrast, C_p of the VG model with SST is lower than that of the reference model behind the shock wave (between $x/c = 0.35$ and 0.5). This characteristic is also shown in Fig. 2 though the shock wave locations of the VG model and the reference model with MSA are the same. It should be noted that the C_p distributions of the VG models change drastically depending on the choice of the turbulence models. Additionally, angles of attack for maximum C_L are different depending on the difference in C_p distribution characteristics as well.

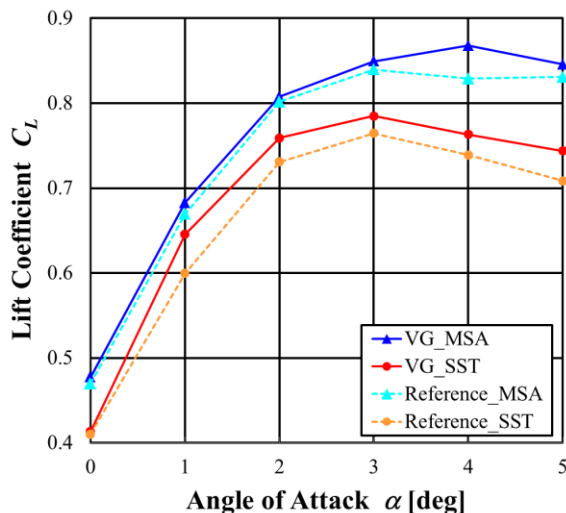


Fig. 1 Lift coefficients against angle of attack

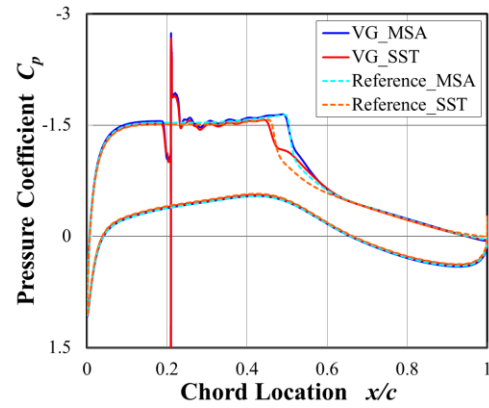


Fig. 2 Pressure coefficient distributions at $\alpha = 2$ [deg]

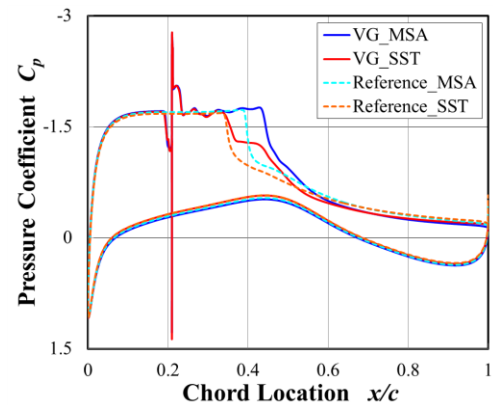


Fig. 3 Pressure coefficient distributions at $\alpha = 4$ [deg]

5. Concluding Remarks

In this paper, a transonic wing with vortex generator (VG) was analyzed by using two types of turbulence models. It became obvious that the pressure coefficient distributions of the wing with VG depend on the turbulence models significantly, which also affected lift coefficient characteristics against angles of attack.

It cannot be mentioned based on only these results which turbulence model is suitable for VG analysis. Experiment of VG on a wing is required to verify the results of this numerical analysis.

Acknowledgements

The authors would like to thank Dr. Mitsuhiro Murayama of JAXA, Dr. Keizo Takenaka of Mitsubishi Heavy Industries, Ltd., and Mr. Keita Hatanaka of Mitsubishi Aircraft Corporation for their kind supports.

References

- [1] E. Wik and S. T. Shaw, AIAA 2004-2697 (2004).
- [2] P. R. Spalart and S. R. Allmaras, Recherche Aerospatiale, No. 1 (1994).
- [3] J. Dacles-Mariani et al, AIAA J., Vol. 33, No. 9 (1995).
- [4] F. R. Menter, AIAA J., Vol. 32, No. 8 (1994).
- [5] R. Bur et al, Shock Waves, Vol. 19, No. 6 (2009).
- [6] J. Huang et al, J. of Fluid Science and Technology, Vol. 6, No. 1 (2011).
- [7] P. R. Spalart, Intl. J. of Heat and Fluid Flow, Vol.21 (2000).

Study on Drag Reduction of a Ship due to a Drainage Slit

Liu Aiming

Wuhan University of Technology, Wuhan City, Hubei Province, China
E-mail of corresponding author: lamfluid@126.com

ABSTRACT

In this paper, research on drag reduction of a two-tailed ship with bulbous bow due to a drainage slit is carried out using numerical simulation, and the computational result is verified by measuring the total drag force and velocity distribution for the ship models in the wind tunnel. The numerical total force and pressure accords with the experimental result. Furthermore the influence of flow field and drag reduction that effected by the drainage are analyzed. The research results show: The reasons for the drag reduction are the pressure drop on the bow and the variation at the flow field of the stern by opening the drainage slit.

1. Introduction

There are many kinds of drag reduction technologies, such as drag reduction by compliant wall[1], groove surface[2,3], riblet surface[4] and micro bubble[5,6]. Nowadays people try to seek new way to reduce drag force. Yajima and Sano[7] investigated the drag reduction of a circular cylinder due to double rows of hole. The research indicated that the reduction effect is good. Moreover Tan Guang-kun[8] studied the flow around a hollow circular cylinder with several splits and the drag reduction mechanism. The experimental result indicates that the drag force is decreased obviously.

In this paper, drag reduction mechanism of a ship due to leading edge hole is explored using the simulation and experimental method. Firstly the flow field around different ship model including original ship model, ship model with leading edge hole are calculated. Secondly the drag force, wall surface pressure and velocity distribution for the ship models were respectively measured in wind tunnel. Furthermore the influence of flow field and drag reduction that effected by leading edge hole are analyzed.

2. Ship model

One two-tailed ship with bulbous bow and no rudder was selected as the test ship. The scale ratio of model ship to original ship was 1/97.5. Table 1 provided the principal particulars of the original ship.

Table 1. Principal particulars of the test ship

Particular	Prototype	Model
Lpp(m)	78	0.8
B(m)	31.2	0.32
Draft(m)	4	0.041
Wetted surface area(m ²)	1592	0.1675

The flow field of three cases(shown in fig. 1~3), such as original ship model, ship model with leading edge hole from the bow to stern and ship model with leading edge hole from the bow to step are carried out by numerical simulation method.

The drag force, wall surface pressure and velocity distribution for case 1 and 2 were carried out by the experiment in wind tunnel. The test ship and the incoming velocity is the same during the calculation and experiment. The speed is 32m/s.

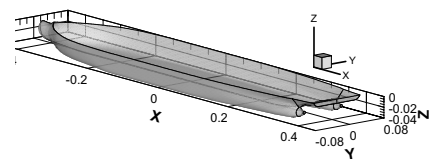


Fig.1 case1: Original ship model

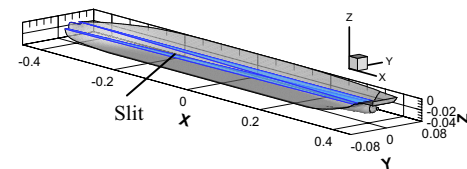


Fig. 2 case 2: Ship model with a slit from bow to stern

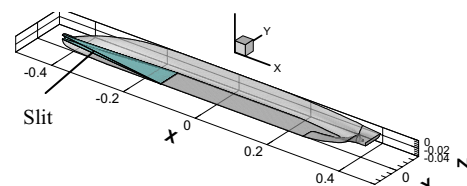


Fig. 3 case 3: Ship model with a slit from bow to step

3. Results and Discussion

3.1 Drag coefficient

The Strain gauge was employed to measure total drag force. Calculated drag coefficient of three ship models is listed in table 2, where C_D , C_f , C_R represent the form drag coefficient, total friction drag coefficient and total viscosity drag coefficient respectively. M_D , M_f , M_R are defined as follows:

$$M_D = (C_{Di} - C_{D0}) / C_{D0}$$

$$M_f = (C_{fi} - C_{f0}) / C_{f0}$$

$$M_R = (C_{Ri} - C_{R0}) / C_{R0}$$

Subscript 0 and i represent the data of case 1 and case 2 (or case 3) respectively.

For experimental total viscosity drag coefficient C_f of case1 is 0.0076, and or case 2 is 0.0072, so the reduction rate is 5.26%

Table 2. Drag coefficient ($\times 10^{-3}$)

	C_D	C_f	C_R	M_D	M_f	M_R
Case1	1.693	4.064	5.757	—	—	—
Case2	1.302	4.246	5.548	-23.1	4.92	-3.63
Case3	1.364	4.135	5.499	-19.4	1.75	-4.48

The calculated viscosity drag accords with the experimental result. Although the friction drag coefficient increases owing to the increase of the wet area of the ship hull in considering the slit surface area. The form coefficient drag of the ship reduces dramatically due to leading edge hole, so the total viscosity drag coefficient of the ship reduces to about 5% as well.

3.2 Pressure results

The ship surface pressure were obtained through the silicon-based micro mezo-resistive pressure sensors. 10 pressure holes are set up at bow and stern of the ship body surface, which are located under the waterline $z=-0.27$. The pressure holes can not be set up at the inlet or outlet of the slit, so it's impossible to measure the pressure at these place. The location of the experimental and computational measuring point is listed table 3. Here point -1,-2,0 is located near the inlet of the slit and point 11 is situated at the outlet.

Table 3 The location of the measuring point ($z=-0.27$)

Points	1	2	3	4	5
x/L_{pp}	-0.485	-0.47	-0.455	-0.44	-0.425
Points	6	7	8	9	10
x/L_{pp}	0.4	0.4125	0.425	0.4375	0.45
Points	-2	-1	0	11	
x/L_{pp}	-0.54	-0.525	-0.51	0.4625	

Fig. 4 show that the simulation results of the 10 measuring point are in accordance with that of the experimental data. From the numerical results we can see that the C_p on the bow of original ship model is close to 1. However C_p at bow of case 2 decreases to 0.1, which that pressure coefficient at bow reduces clearly due to the slit. But the change of C_p at stern before and after opening the slit is less than that on bow. So the pressure difference between bow and stern reduces due to the slit. Consequently the pressure drag decreases.

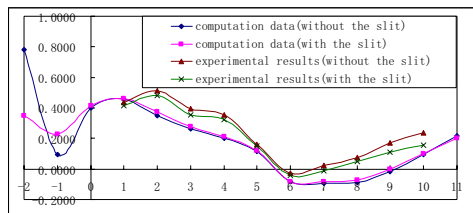


Fig. 4 C_p of the measuring point

3.3 Local mean velocity

A five-hole Pitot tube was utilized to measure the velocity. Two dimensional velocity vector at cross section ($x/L_{pp}=-0.56, 0.46$) is given in fig.5~fig.6. These figures indicate that the velocity of the cross section change very slightly at bow and stern after opening the slit except near the inlet and outlet of the slit. Furthermore, due to the propeller shaft, a circumfluence exists in the wake of case

1 as well as case 2. In general the flow velocity is not changed obviously after opening the slit.

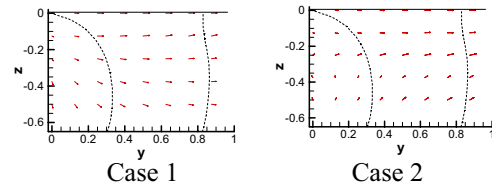


Fig. 5 Velocity vector at section $x/L_{pp}=-0.56$

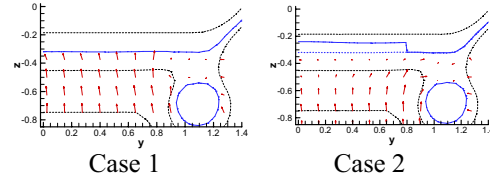


Fig. 6 Velocity vector at section $x/L_{pp}=0.46$

4 Conclusions

The following conclusions can be made:

- (1) The change of the wake velocity is slight after opening the slit.
- (2) The change of C_p at stern before and after opening the slit is less than that on bow. So the pressure difference between bow and stern reduces due to the slit. Consequently the pressure drag decrease.
- (3) The drag force of the ship model with drainage slit decreases. The drag reduction ratio is greater than 5%.
- (4) The free surface is not considered during carrying out the experiment, which is not consistent with the actual conditions. Therefore further research work should be done.

Acknowledgements

The present research was supported by the National Natural Science Foundation of China (NSFC-10972167).

References

- [1] Dixon A. E, Lucey A. D, Carpenter P. W.(1994).. *AIAA Journal*, 32(2), 256-267
- [2] Bacher E V, Smith C R. A(1985), *AIAA Journal*, 85-0548.
- [3] Luchini P.(1991). *J Fluid Mech* , 228 :87 - 109.
- [4] Merkle C L, Detusch S.(1985).. AIAA Paper 85-0348, *AIAA Shear Flow Control Conference*, Boulder, Co. 12~14
- [5] Kato H.(1983).. *Journal of Marine Science and Technology*, 3(3), 122-129.
- [6] Walsh M J, Sellers W L, McGinley G B(1989). *Journal of Aircraft*, 26(6), 570-575.
- [7] Yajima Y,Sano O.(1996). *Fluid Dynamics Research*, Vol. 18, 237-243.
- [8] Tan Guang-kun, Wang Jin-jun, LI Qiu-sheng.(2001). *Journal of Beijing University of Aeronautics and Astronautics*, Vol. 27, No.16,658-661.

Statistical Properties of Disturbances in a Transitional Channel Flow

Kenta Watanabe, Syunsuke Akaoka, Masaharu Matsubara and Kvik Mathias
Department of Mechanical Systems Engineering, Shinshu University,
4-17-1 Wakasato, Nagano, 380-8553, Japan
11ta144k@shinshu-u.ac.jp

ABSTRACT

A planar channel flow undergoing Reynolds number reduction was visualized by flake particles and image processing for the visualization was conducted. In the flow, turbulent patches and large-scale streaks intermittently appear above the minimum transitional Reynolds number. The intermittency factor quantified from the visualization is in good agreement with that by the hot wire measurement. The streamwise length scale of the streaks in non-turbulent regions is twice as large as that of the turbulent disturbance, suggesting its characteristic production process.

1. Introduction

In the two dimensional channel flow, the flow becomes turbulence even under the critical Reynolds number if initial disturbance is sufficiently strong. However, decreasing Reynolds number, the flow inversely transit from this turbulent state to a laminar flow at a certain Reynolds number. This Reynolds number is defined as the minimal Reynolds number in this study.

In the experiment [1], when Reynolds number is higher than the minimal Reynolds number, turbulent patches and streaks appeared, then transitional flow becomes an intermittent flow consist of turbulence structure, streak, and laminar. In this study we focused on statistical quantification for length scales of streak structure and turbulent disturbance utilizing flow visualization, and comparison between them was attempted.

2. Experimental apparatus and method

Experiments were made in a closed water facility. Water pressurized by a pump ran through a settling chamber followed by a 24:1 contraction and entered into an entrance channel. The flow was disturbed by a tripping wire of 0.9 mm diameter mounted 220 mm downstream of the channel entry, then flow at the end of the entrance channel became fully development turbulent. A expansion channel following the entrance channel widened from 360mm to 580 mm in the spanwise direction so that Reynolds number of the flow decreases 0.62%. The water gushed from the test channel returned to the pump via a pipe. The entrance, expansion and test channel are 2000mm, 400mm, and 4550mm long, respectively. The flow rate are measured a orifice flowmeter inserted between the pump and the settling chamber. Coordinate origin is at the inlet of test section on one of the walls. Coordinate systems are x , y , z for streamwise, wall-normal and spanwise directions, respectively.

The flow visualization was made using a 6.0 megapixel video camera. The frame rate was 20fps and the shutter speed was 1/1600 for the recording pictures for the image processing and the camera set at 300fps and 1/1000 shutter speed for the video observation. Pearl flakes that had specific gravity of 3.1 and $7 \sim 8\mu\text{m}$ size were used as flow tracer. Three 500 W halogen lamps were used for flow illumination. Visualization experiment was made at a position of $x = 4200\text{mm}$. The bulk

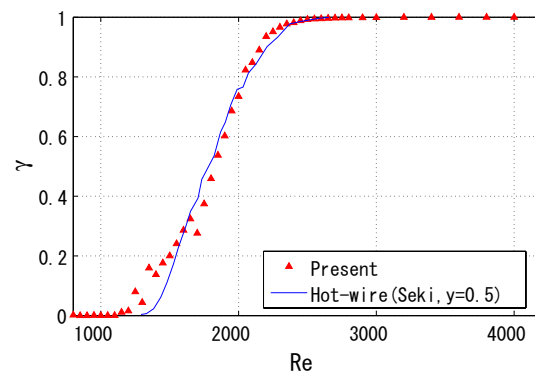


Figure 1: Intermittency factor

Reynolds number is defined as $Re = U_m d / \nu$, where U_m is mean velocity and ν is the kinematic viscosity. Since the glass deflection by the water pressure broke uniformity of the channel width, we controlled compressive stress to beams mounting the test glass plates by inserting the shim thickness, then the channel width was adjusted at $7.1 \pm 0.1\text{mm}$ in the center region of the test channel. The orifice meter was calibrated by Laser Doppler Velocimeter and the bulk velocity was determined from its differential pressure.

3. Results

The intermittency factor was estimated by image processing. At first, average pictures brightness values of 1200 original pictures subtracted from the values each original picture in order to remove blots of the glass and unevenness of illumination. To prevent difference of the brightness values by changing the amount of tracer particles, every image is normalized by the standard deviation of the brightness values. After the band-pass filtering using two dimensional the Fourier transform, the local standard deviation was obtained in the size of 199 pixel square that corresponds to 21 mm square in the real scale. The threshold value for judging laminar or turbulence was determined by human-eye checking and the intermittency factor γ was obtained the ration of turbulent area to the total picture area.

In Fig. 1, the intermittency factor γ is compared to the hot wire measurement[2]. The visualization result, at

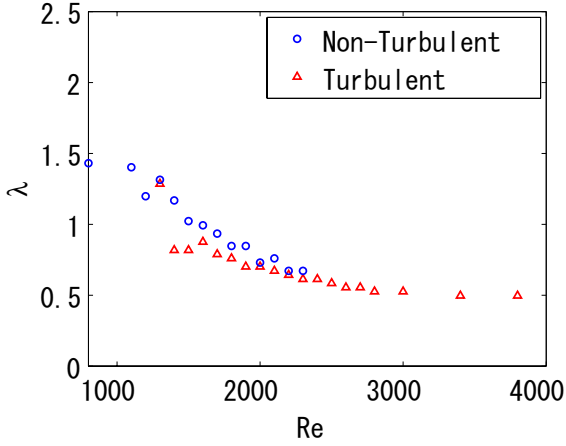


Figure 2: The spanwise scales of the flow disturbance.

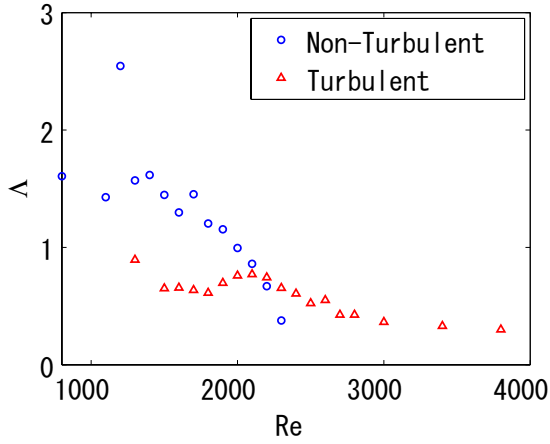


Figure 3: The streamwise scales of the flow disturbance.

under the $Re = 1200$, γ have an almost constant value 0, and gradually increases up to $Re = 2500$, and over $Re = 2500$, γ approaches one. Though there is a little difference with the hot wire measurement at a low Reynolds number part, they are in good agreement. The two facilities are different in terms of the expansion ratio and inclination of the end wall in the expansion section so that it is confirmed that their influence is insignificant. From the intermittency factor variation the transition region is approximately between $Re = 1200 \sim 2500$.

Fig. 2 shows the spanwise scales of the disturbance. The spanwise scale is estimated from auto-correlation of the images with shifting overlap regions of the image in the spanwise direction. The length scale λ is defined as

$$\lambda = \frac{2\Delta z_{min}}{d}, \quad (1)$$

where Δz_{min} is the spanwise sift at minimum value of the correlation coefficient. This estimation was performed separately for the laminar and turbulent regions. The spanwise length scale λ of the non-turbulent region is 0.7 at $Re = 2300$. The scales becomes larger with de-

creasing the Reynolds number and it is about 1.4 around $Re = 1200$. The turbulent disturbance scales is almost constant at 0.5 over $Re = 2500$. This scale is getting larger with decreasing the Reynolds numbers, though the enlargement is less than that of the non-turbulent disturbance.

Fig.3 shows the streamwise scale of the flow disturbance. Streamwise scale is defined as

$$\Lambda = \frac{1}{d} \int_0^{\infty} R_x dx, \quad (2)$$

where R_x is the correlation coefficient with the streamwise shift. The streamwise scale of the non-turbulent disturbance rapidly gets larger with decreasing the Reynolds number, while the turbulent streamwise scale is roughly constant in the range of the transitional Reynolds number. The non-turbulent scale is about twice as large as the turbulent scale. From the visualization, streak structures are confirmed in the non-turbulent region. The streamwise scale suggests characteristic production mechanism for this disturbance dissimilar from the turbulent one.

4. Summary

The quantified intermittency factor from the flow visualization is in good agreement with the hot wire measurement. The streamwise length scale of the streaks in non-turbulent regions is twice as large as that of the turbulent disturbance, suggesting its characteristic production process.

References

- [1] Numano, T., Matsubara, M, Proceedings of 2008 Annual Meeting, Japan Society of Fluid Mechanics, (2008), pp.29.
- [2] Seki, D., Matsubara, M, Proceedings of 2010 Annual Meeting, Japan Society of Fluid Mechanics, (2010), pp.24.

Experimental Study of Linear Disturbance in a Turbulent Boundary Layer

Konosuke Matsumoto, Taiki Mishiba, Yasuyuki Sendai, Masaharu Matsubara
Department of Mechanical Systems Engineering, Shinshu University,
4-17-1 Wakasato, Nagano, 380-8553, Japan
11ta137g@shinshu-u.ac.jp

ABSTRACT

As the first step of the investigation of the linear disturbance in a turbulent boundary layer, we developed a pressure sensor array for capture of the linear disturbance, and then as a test for the sensor, measurements of the spatiotemporal correlation between the streamwise velocity and the wall pressure fluctuation were performed in turbulent boundary layers with several tripping conditions. The result demonstrates that the sensor gives rich information relating to both outer layer and near-wall disturbance structures, suggesting that it would be very useful tool for the linear disturbance investigation.

1. Introduction

Recently, it was confirmed that there exists a linear large scale disturbance in a planar turbulent jet. This strongly suggests that the linear disturbances are ubiquitous in turbulent shear flows. On the other hand, an extensive comparison of numerical results for a turbulent boundary layer indicated considerable discrepancies in both peak fluctuation values and the outer layer profiles [1]. One possible explanation for this inconsistency is dependence of upstream disturbance condition that strictly governs boundary layer transition. The final goal of the series of the present experiment is to discover the linear disturbance in the turbulent boundary layer. As the first step, we developed a pressure sensor array for capture of the linear disturbance. And then as a test for the sensor we measured the tempo-spatial correlation between the streamwise velocity and the wall pressure fluctuation in turbulent boundary layers that were tripped by several kinds of roughness.

2. Experimental apparatus and method

The experiments were performed in a closed wind tunnel, which had a vertically mounted test plate of a 2.1 m length and a 580 mm width. The sidewall faced to the test surface and a trailing-edge flap were carefully adjusted to prevent separation around the leading edge and to obtain constant streamwise distribution of pressure in the free stream. The coordinate system is denoted by the streamwise, wall-normal and spanwise distances x , y and z from the origin at the center of the leading edge, respectively. The pressure sensor array as shown in Fig. 1 had 32 holes of a 0.5 mm diameter with the spanwise space of 0.8 mm. Each hole was connected to a MEMS (Micro Electro Mechanical Systems) microphone. Five tripping sets were tested. One set labeled 'Case 1' consists five plastic tapes embossed with letter 'V's located between $315 \text{ mm} \leq x \leq 415 \text{ mm}$. Another set of 'Case 2' had seven plastic tapes but they placed between $150 \text{ mm} \leq x \leq 400 \text{ mm}$. In case 2, a strip of 100 grit sandpaper was fixed downstream of the plastic tapes and this tripping is very similar to that used by Österlund [2]. In both cases the tapes were placed at regular intervals. Cases 3, 4 and 5 were for the classical tripping with a round cylinder of 1, 2, 6 mm diameter, respectively. The cylinders were placed on the test plate surface at $x = 150$



Figure 1: Pressure sensor array and hot wire probe.

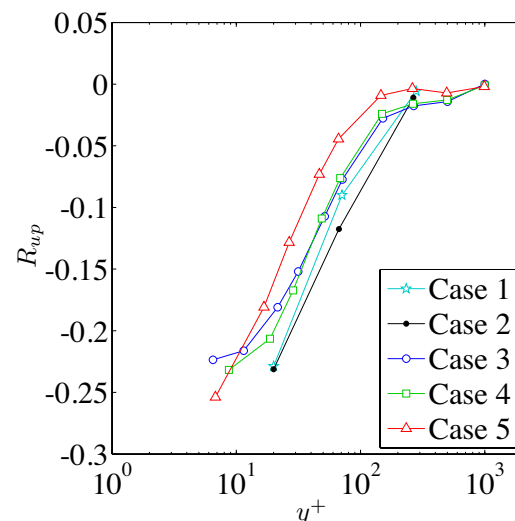


Figure 2: The wall-normal distributions of R_{up} .

mm. Roughly speaking, tempestuousness of the tripping is in order of the case number. The larger for the number, the more tempestuous. In all cases, the free stream velocities U_f were adjusted so that $2860 < Re_\theta < 3020$.

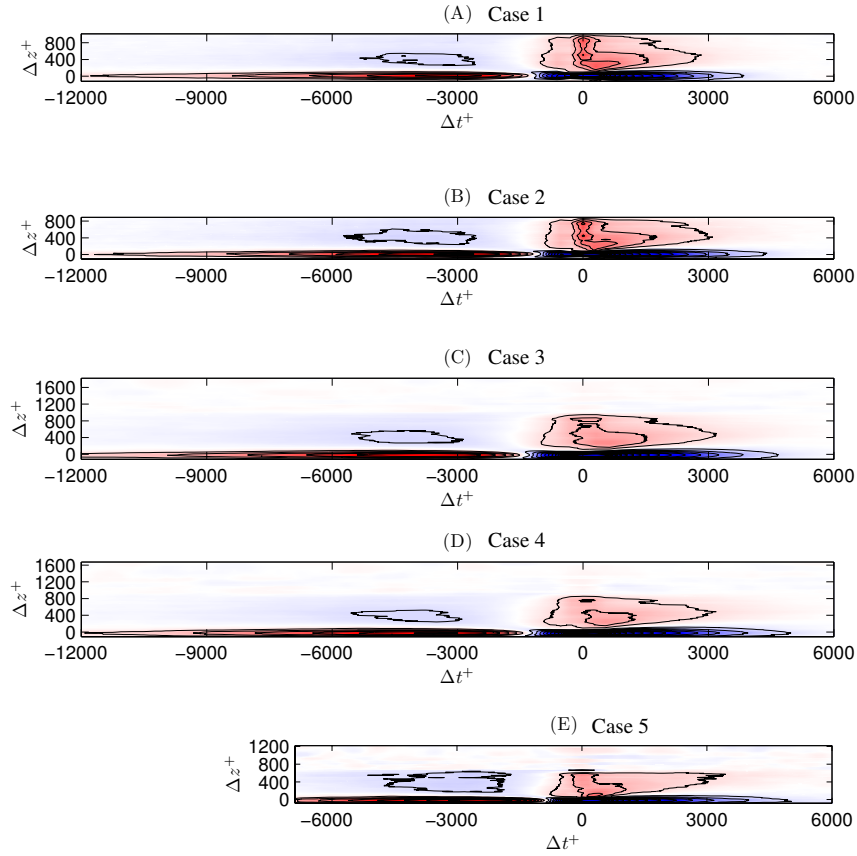


Figure 3: Counter maps of the spatiotemporal correlation R_{up} at $y^+ = 20$. Contour spacing is 0.01. The plus and minus zones are shaded by red and blue, respectively. The zero contours are removed.

3. Results

The wall-normal distributions of the spatial correlation between the streamwise velocity and the wall pressure fluctuations, R_{up} , shown in Fig. 2 have exponential decay with the height around $y^+ = 40$ regardless of the tripping set. The level of R_{up} is increasing with tempestuousness of the tripping.

Figure 3 shows the spatiotemporal correlation between the streamwise velocity and the wall pressure fluctuations at $y^+ = 20$. Both temporal and spatial scales are normalized in the wall unit as $\Delta z^+ = \Delta z u_\tau / \nu$ and $\Delta t^+ = \Delta t u_\tau U_f / \nu$. The time difference is defined as $\Delta t = t_u - t_p$, where t_u and t_p is the time of the streamwise velocity and the pressure, respectively. The fine spanwise traversing step of the hot wire of 0.1 mm enables high spanwise resolution of these correlation maps. These maps of the spatiotemporal correlation clearly indicate a longitudinal distribution of high correlated region that elongates in the streamwise direction longer than 10000 in the wall unit. The Correlation maps are drastically affected by the tripping configuration in terms of the peak value. It seems that the cross-correlation is very sensitive to transition process and/or transition position.

Correlations between velocities and velocity-pressure are indispensable statistics for the turbulent analysis so that great care of the tripping and the transition process should be taken for both experiments and numerical simulations. The pressure fluctuation on the wall includes rich information that relates to the near-wall disturbance structures, so that the pressure array would be a very useful tool for surveying of the linear disturbance in a turbulent boundary layer.

References

- [1] Schlatter P. and Örlü R., *J. Fluid Mech.*, **659**, (2010), pp. 116–126.
- [2] Österlund J. M., Experimental studies of zero pressure-gradient turbulent boundary layer flow, *Ph.D. thesis*, Royal Institute of Technology, Stockholm, Sweden. (1999).

The Effect of Actuator Length-Scale on Excited Waves

Hajime Okawa, Masaya Shigeta, Seiichiro Izawa, Yu Fukunishi
Department of Mechanical Systems and Design,
Graduate School of Engineering, Tohoku University
6-6-01 Aramaki-Aoba, Aoba-ku, Sendai, Miyagi, Japan
okawa@fluid.mech.tohoku.ac.jp

ABSTRACT

Wind tunnel experiment is carried out to investigate the effect of the streamwise length-scale of an actuator on the T-S wave generation. Although the results of previous works indicated that the optimum size of the actuator was related to the wavelength of the T-S waves, the current result of the experiment indicates that the optimum size of the actuator relative to the T-S wavelength changes depending on the operating frequency.

1. Introduction

In the early stage of a boundary layer transition, the linear growth of a periodical velocity fluctuation namely the Tollmien-Schlichting (T-S) waves and the oblique T-S waves are observed. These instability waves inside the laminar boundary layer can be excited by a combination of an acoustic wave in the freestream and a roughness element attached on the flat-plate[1]. Sound waves are taken into the boundary layer at the upstream and downstream corners of the roughness element. The amplitude of resulting instability waves depends on the interaction between the waves from the both corners.

From an engineering point of view, it is important to suppress the growth of such instability waves and thus delaying the transition. Several types of the actuators were proposed to control T-S waves and consequently to delay the turbulence transition[2][3]. We reported that the feedforward system could successfully suppress the growth of T-S waves by counter waves induced by piezo-electric actuators[4]. In this study, the actuators of four different streamwise lengths were tested to find out the method to effectively generate the T-S waves.

2. Experiment setup

Figure 1 shows the experiment setup. The experiment was carried out in the low-turbulence wind tunnel at the Institute of Fluid Science, Tohoku University. The device including a flush-mounted actuator was attached on a flat-plate which was vertically installed inside the tunnel. The thickness of the device was 2mm and a slope was added to the upstream end to eliminate undesirable receptivity at the edge. The x axis is in the streamwise direction at the center of the actuator, whose origin is at the leading edge of the flat-plate. The y axis is in the wall normal direction starting from the surface of the device. The dimensionless wall normal distance η is defined as $\eta = y\sqrt{U_\infty/\nu}$, where U_∞ is the freestream velocity set at 14 m/s and ν is the kinematic viscosity.

The detailed design of the actuator is shown in Fig. 2. The actuator consisted of a piezo-electric element which expanded and shrank by a AC electric signal and a steel plate glued at the tip of the element by candle wax. They were embedded inside an acrylic base with small gaps so that they could freely move back and forth. The gaps

were covered with thin Scotch tapes at the surface. Four types of actuators with steel plates of different streamwise lengths L were used, as shown in Table 1. The length of each type was set close to either the T-S wavelength λ_{T-S} or its half, and the frequency was either 78Hz or 100Hz. The downstream side of each actuator was located at $x = 870\text{mm}$.

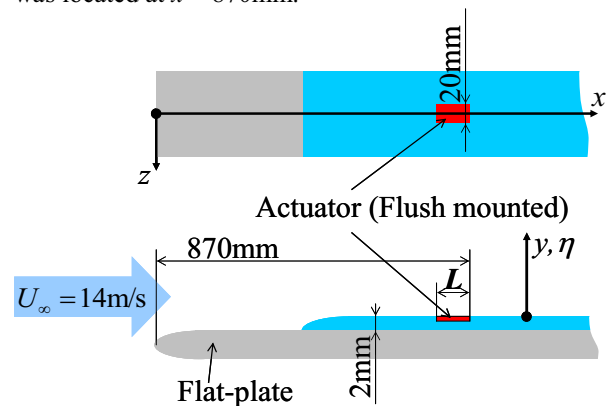


Fig. 1 Schematic view of the experiment setup

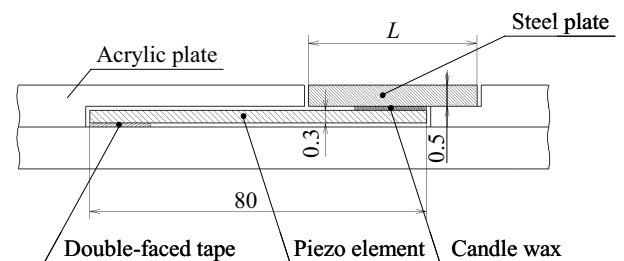


Fig.2 Assembly drawing of the actuator

Table 1. The length-scale of actuators

Type	L [mm]	$L / \lambda_{T-S,78\text{Hz}}$ [%]	$L / \lambda_{T-S,100\text{Hz}}$ [%]
1	24	40	51
2	28	47	60
3	47	79	101
4	60	100	129

The driving sinusoidal signal whose frequency was 78Hz or 100Hz with a voltage of 100V was applied to the actuators. These frequencies were selected to be inside the neutral stability curves predicted by the linear stability theory. The measurements were conducted

using a single hot-wire probe sweeping above the spanwise center of the actuator.

3. Results and Discussion

The ensemble-averaged vorticity fluctuation is given by

$$\omega'_{z,ens} = \frac{\partial v'_{ens}}{\partial x} - \frac{\partial u'_{ens}}{\partial y}, \quad (1)$$

where ω'_z is the spanwise vorticity fluctuation. And u' and v' are the streamwise and wall-normal velocity fluctuations, respectively. The suffix "ens" indicate that the values are obtained by ensemble-averaging. In this study, the vorticity fluctuation is evaluated only by the second term in Eq. (1). It is based on assumption that the first term is much smaller than the second term near the wall. Figures 3 and 4 show the distributions of the "vorticity fluctuation" excited by the Type 1 and Type 3 actuators, respectively. The driving signal is 100Hz. The blank areas in these figures are the region where the measurement could not be conducted to avoid the hot-wire touching the surface. A stronger T-S wave pattern can be observed for the Type 1 actuator whose streamwise length is half of the T-S wavelength, compared to the Type 3 actuator with a T-S wavelength.

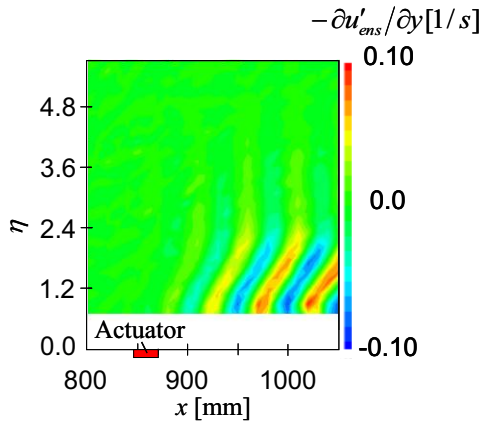


Fig. 3 Contour map of $-\partial u'_{ens}/\partial y$ (Type 1 with 100Hz signal)

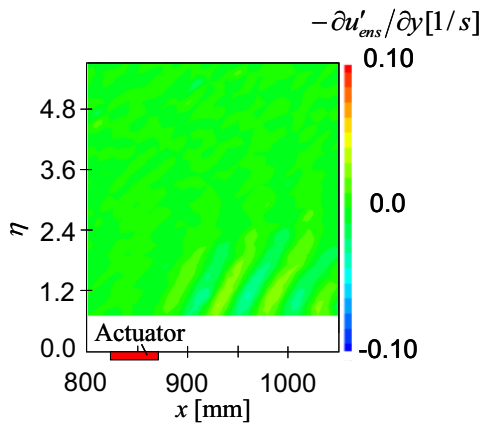


Fig. 4 Contour map of $-\partial u'_{ens}/\partial y$ (Type 3 with 100Hz signal)

However, the opposite tendency is observed when the actuator is operated at 78Hz. Figures 5 and 6 show

the distributions of the vorticity fluctuation by the Type 2 and Type 4 actuators, respectively. The observed waves were weaker when the half-wavelength size actuator, Type 2, was used.

From Fig. 6, using the longest Type 4 actuator, it can be clearly confirmed that the T-S waves starts above the surface of the flush-mounted actuator. However, the relation between the actuator length-scale and the generated T-S waves, hence how the waves are generated is still unclear and needs further investigations.

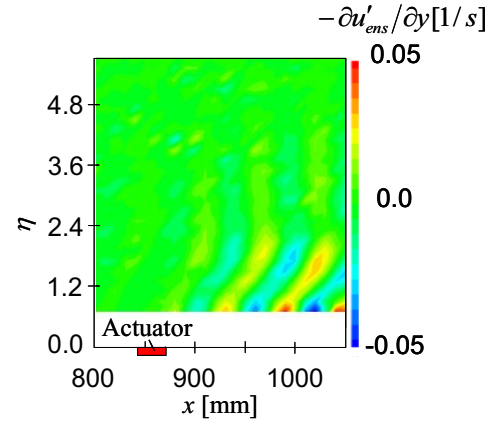


Fig. 5 Contour map of $-\partial u'_{ens}/\partial y$ (Type 2 with 78Hz signal)

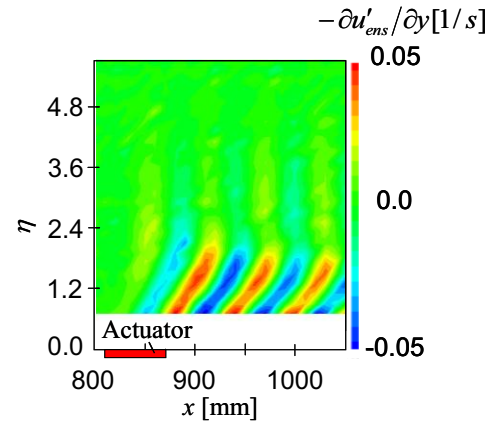


Fig. 6 Contour map of $-\partial u'_{ens}/\partial y$ (Type 4 with 78Hz signal)

4. Concluding remarks

Experiments generating T-S waves were conducted using actuators of different streamwise lengths operated at different frequencies. The optimum size of the actuator differed by the operating frequency.

References

- [1] R. Kobayashi, *et. al.*, *Laminar-Turbulent Transition: IUTAM Symposium*, Springer-Verlag, pp.507-514, 1995.
- [2] M. Baumann, D. Sturzebecher and W. Nitsche, *Proc. the IUTAM Symposium*, 2000, pp. 155-160.
- [3] S. Grundmann and C. Tropea, *Experiments in Fluids*, **44**(5), pp. 795-806.
- [4] H. Okawa, *et. al.*, *Proc. 13th Asian Congress of Fluid Mechanics, Dhaka, Bangladesh*, (17-21 December, 2010), pp.256-258 CD-ROM.

Jet flow-sound interaction in a modified hole tone system with a tail pipe

Mikael A. Langthjem¹, Masami Nakano²

¹Graduate School of Science and Engineering, Yamagata University

²Institute of Fluid Science, Tohoku University

E-mail of corresponding author: mikael@yz.yamagata-u.ac.jp

Abstract

We consider the interaction between the self-sustained flow oscillations in a hole tone feedback system and the standing acoustic waves in a connected tail pipe. Of special interest is the possibility of lock-in of the former type of oscillations to the latter. The unstable shear layer is modeled via the discrete vortex method, based on axisymmetric vortex rings. The aeroacoustic model is based on the Powell-Howe theory of vortex sound. Boundary integrals that represent scattering by the end plate and the tailpipe are discretized via the boundary element method.

1. Introduction

Interaction between self-sustained flow oscillations and standing waves in pipes can take place in a variety of systems, such as automotive silencers and wind instruments [1, 2]. Self-sustained flow oscillations may occur when an unstable shear layer is coupled with acoustic waves via a feedback loop. A feedback loop is typically established when the shear layer hits an edge. The (two-dimensional) edge tone and the (three-dimensional) hole tone are prototypical examples.

The present work is concerned with the hole tone problem, where a circular jet goes through a hole in a plate placed downstream from the jet nozzle. When a pipe is connected to the plate - as illustrated in Fig. 1 - there will be interaction between the hole tone oscillations and standing acoustic waves in the pipe. In particular, when the dominating hole tone frequency (which is a function of the flow speed) passes through one of the pipe resonances (by continuous increase of the flow speed) it may ‘lock-on’ to that frequency, that is, remain constant at that frequency even when the flow speed is increased further.

The lock-in mechanism is not understood in detail and a main motivation of the present work is to contribute to a better understanding.

2. Mathematical model

The flow model is based on the discrete vortex method [3]. The acoustic model is based on Howe’s equation for vortex sound at low Mach numbers [1]. Let \mathbf{u} denote the flow velocity, $\boldsymbol{\omega} = \nabla \times \mathbf{u}$ the vorticity, c_0 the speed of sound, and ρ the fluid density. Then the sound pressure $p(\mathbf{x}, t)$ at the position $\mathbf{x} = (z, r)$ and time t is related to the vortex force (Lamb vector) $\mathcal{L}(\mathbf{x}, t) = \boldsymbol{\omega}(\mathbf{x}, t) \times \mathbf{u}(\mathbf{x}, t)$ via the non-homogeneous wave equation

$$\left(\frac{1}{c_0^2} \frac{\partial^2}{\partial t^2} - \nabla^2 \right) p = \rho \nabla \cdot \mathcal{L}.$$

This equation is solved by using the Green’s function method. The boundary integrals are evaluated by applying the boundary element method.

Finally, the flow field and the acoustic field are coupled by evaluating the acoustic particle velocities via the Euler equations, and imposing them on the flow field.

3. Numerical examples

Figure 1 illustrates the discrete vortex ring simulations during one period of oscillation.

Figure 2 shows the sound pressure level at the position $(z, r) = (3, 3)d_0$, measured from the symmetry axis at the downstream tailpipe exit. Here d_0 is the pipe diameter, which is 50 mm. In parts (a) and (b) the tailpipe length $L = 13.6d_0$, which gives a resonance frequency of 250 Hz for a half-wave (‘mode 1’) and 500 Hz for a full wave (‘mode 2’). Mode 1 is not represented clearly in the spectra, but mode 2 can be recognized clearly.

The fundamental hole tone frequency $f_0 = 158$ Hz. The higher modes are apparently the higher harmonics of this frequency. In part (a) the flow speed $U = 10$ m/s; in part (b) $U = 20$ m/s.

Parts (c) and (d) are similar to (a) and (b), but here the pipe length is $L = 21.5d_0$. This gives a resonance frequency of 158 Hz for a half-wave, that is, the same as the fundamental hole tone frequency f_0 .

References

- [1] M. S. Howe, *Acoustics of Fluid-Structure Interactions*, Cambridge University Press, Cambridge, 1998.
- [2] B. Fabre, J. Gilbert, A. Hirschberg, X. Pelorson, *Aeroacoustics of musical instruments*. *Annu. Rev. Fluid Mech.* 2012, 44:1-25.
- [3] M.A. Langthjem, M. Nakano. A numerical simulation of the hole-tone feedback cycle based on an axisymmetric discrete vortex method and Curle’s equation. *J. Sound Vibr.* 2005, 288:133-176.

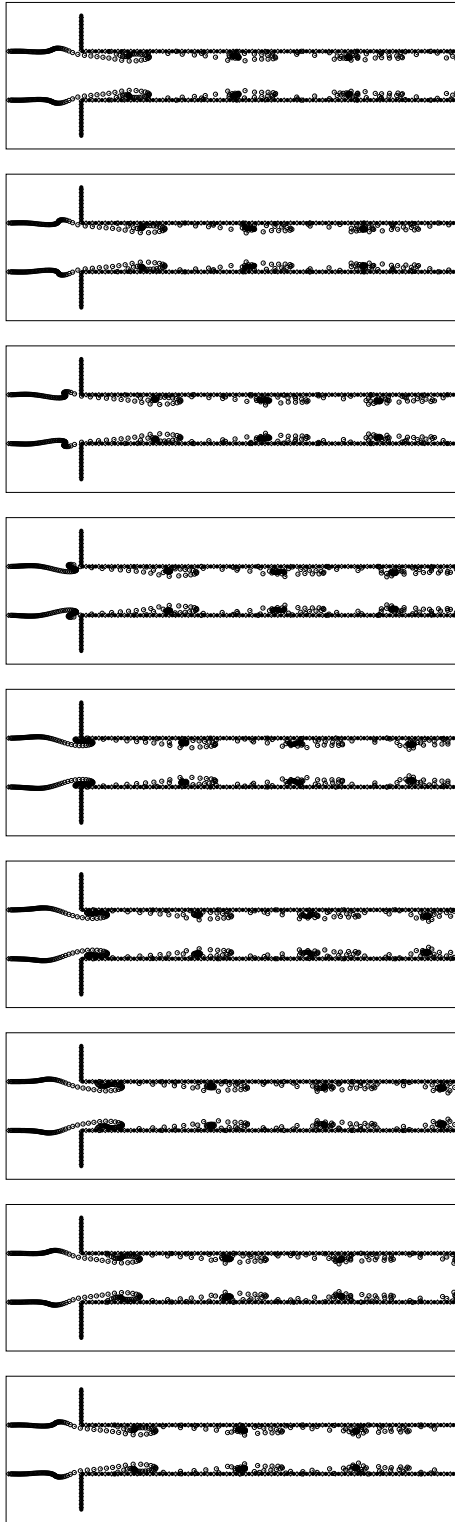


Fig. 1. Discrete vortex ring simulations of the hole tone system with a tailpipe. The sequence (from top to bottom) shows the flow during one period of oscillation. The flow is from left to right.

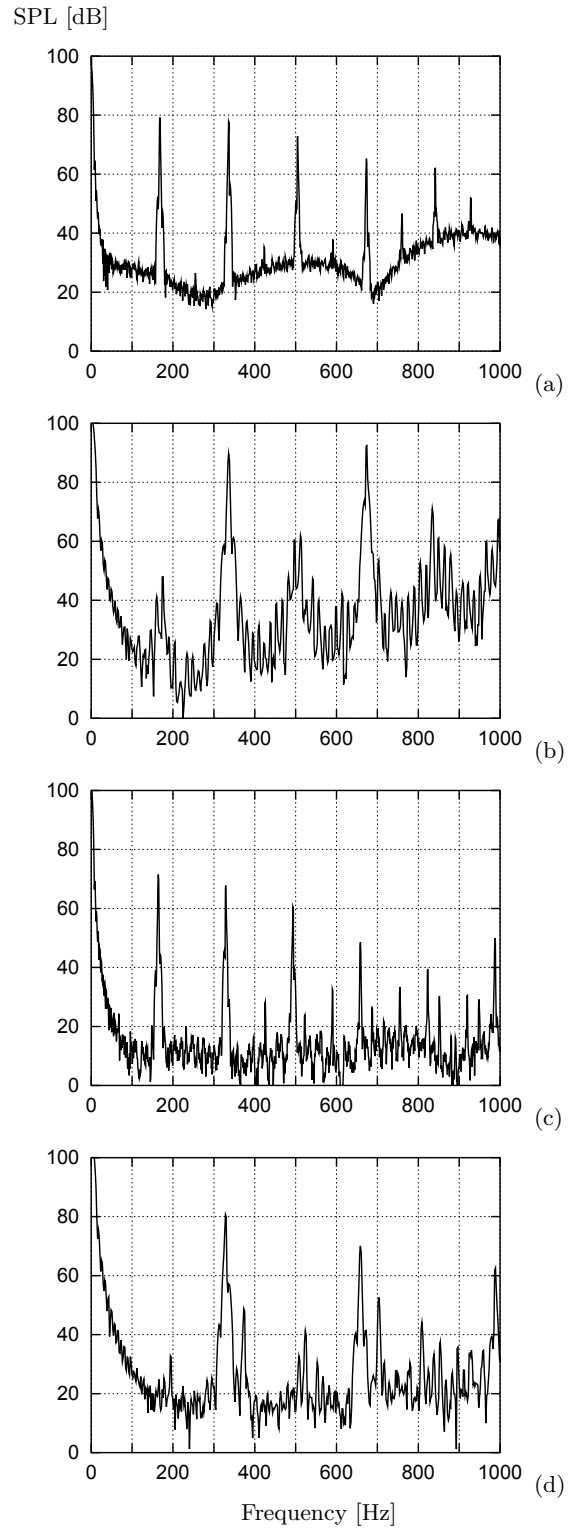


Fig. 2. Sound pressure levels at the position $(z, r) = (3, 3)d_0$, measured from the downstream tailpipe exit. (a) Flow speed $U = 10$ m/s, tailpipe length $L = 13.6d_0$. (b) $U = 20$ m/s, $L = 13.6d_0$. (c) $U = 10$ m/s, $L = 21.5d_0$. (d) $U = 20$ m/s, $L = 21.5d_0$.

An Experimental Investigation of Wing-Tip Vortex Attenuation via Circulation Control

Adam Edstrand, Eric Deem, Louis Cattafesta
Department of Mechanical Engineering, Florida State University, Tallahassee, FL 32310
Florida Center for Advanced Aero-Propulsion (FCAAP)
lcattafesta@fsu.edu

ABSTRACT

Circulation control is a well-known technique using tangential blowing over a curved surface for modifying the pressure forces about an airfoil, usually to augment its lift characteristics. The effect of using tangential blowing about the side of a rounded wing-tip, rather than from the trailing edge of an airfoil, opposing the natural flow of the wing-tip vortex, is being experimentally studied. A baseline configuration of a rectangular wing-tip is presented and preliminary circulation control experiments are also described.

1. Introduction

Wing-tip vortices are caused by the pressure difference between the upper and lower surface of a lifting surface equalizing at the tip. This swirling flow causes an increase in drag, dictates timing between subsequent aircraft landings, and is a source of aerodynamic noise. These negative effects make the study of wing-tip vortex attenuation a prominent area of research.

Since passive devices are optimized for a specific flight condition, off-design implementation may result with poor or even adverse performance. This motivates the implementation of active control. One such implementation employs the use of plasma actuators. Studies have shown a reduction in the strength of the wing-tip vortex [1]. However, plasma actuators provide modest control authority and thus limited effects on the wing-tip vortex.

Circulation control is a technique that is normally used to increase the lift on an airfoil through the ejection of air from a pressurized plenum. The air is issued, generally from a slot, over a curved surface of the trailing edge of an airfoil, increasing circulation about the airfoil.

This idea is extended to the wing-tip, where a slot along the upper-edge of a lifting surface issues a jet over a rounded wing-tip, intending to counteract the naturally occurring tip vortex. First, the experimental setup and the measurement techniques are presented. Then, the experimental results of the measured baseline, rectangular tip vortex are shown and interpreted. Finally, the measurements involving the characterization of the control are explained, and the experimental plan for control is given.

2. Experimental Setup

Within the University of Florida Anechoic Flow Facility [2], a NACA0012 airfoil generates a wing-tip vortex. The vortex is generated at a chord Reynolds number of 530k, or 27.1 m/s, for 5 degrees angle of attack rotated about its quarter-chord. The chord of the airfoil is 0.305 m with a span of 0.381 m.

Stereo particle image velocimetry (SPIV) data are obtained 2 chords and 6 chords downstream of the leading edge of the airfoil for the investigation of the near-field and far-field vortex development. For each

case, 500 image pairs are acquired, resulting in 500 velocity fields used for statistical analysis. To remove the problem of wing-tip vortex wandering [3, 4], the SPIV vector fields are shifted to the point of maximum vorticity, assumed to be the vortex center, and averaged at these points.

For the baseline case, a rectangular wing-tip, manufactured via selective laser sintering, is mounted to the tip of the airfoil. For the control case, a rounded wing-tip is used, with the NACA0012 half profile on the edge. The slot is 75% of the chord, beginning at the leading edge. Figure 1 shows the image of the circulation control wing-tip.

A compressor supplies pressurized air to the plenum. Prior to entering the plenum, the air is dried through desiccant dryers to remove moisture. The pressure is then stepped down with a pressure regulator. Downstream of the regulator, a Venturi meter is placed in line to measure the average mass flow rate through the pipe. An air filter removes potential debris, and then the air flows into the airfoil plenum. A steady pressure transducer placed within the plenum measures the plenum pressure.



Fig. 1 CAD rendering of the circulation control wing tip, highlighting the Coanda surface and slot.

To characterize the flow leaving the slot, a hot-wire anemometer is placed in the middle of the slot. A thermocouple is used to allow for the implementation of King's law [5], providing more accurate results in the presence of temperature variation. Hot-wire data are acquired at a sampling rate of 40,960 Hz for 10 seconds.

With the hotwire measurements, it is possible to calculate the amount of momentum being injected into the flow-field. The non-dimensional momentum coefficient is defined as

$$C_{\mu} = \frac{\dot{m}_{jet} U_{jet}}{\frac{1}{2} \rho_{\infty} U_{\infty}^2 S} \quad (1)$$

where \dot{m}_{jet} is the mass flow rate leaving the slot, U_{jet} is the jet velocity, ρ_{∞} is the ambient density of air, U_{∞} is the freestream velocity and S is the planform area of the airfoil.

3. Results and Discussion

In this section, the results of the baseline case and the characterization of the flow leaving the slot are presented. Figure 2a shows a contour plot of the streamwise velocity of the vortex at two-chords downstream of the leading edge. As can be seen, the core exhibits a velocity deficit, which has been observed in prior literature [3]. The presence of the wake of the airfoil is also apparent in Figure 2a. The shear layer from the wake of the airfoil feeds into the vortex, wrapping around the core of the vortex.

As the vortex convects downstream to six-chords downstream of the leading edge, the velocity deficit seen by the wake of the airfoil separates from the vortex. The deficit within the core also decreases. The transverse velocities begin to become fairly axisymmetric within the core. The application of control will determine the effect of the circulation control blowing on the near field and far field behavior of the vortex.

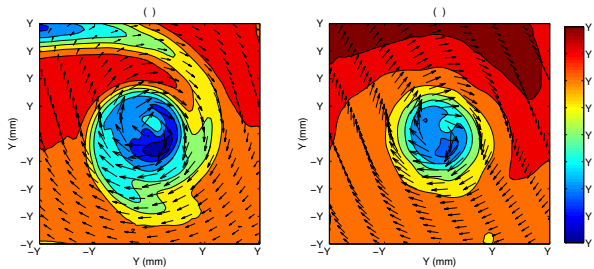


Fig. 2 A streamwise velocity component contour plot with a quiver plot of spanwise (Y) and transverse (Z) velocities superimposed. This is for (a) $x/c = 2$ and (b) $x/c = 6$.

Before control is applied to the wing-tip vortex, the flow leaving the slot must be characterized. A relation is derived for the speed of the flow out of the slot as a function of plenum pressure and ambient pressure. The relation is derived and seen in the equation

$$U_{jet} = \sqrt{\frac{2RT}{\gamma-1} \left(\left(\frac{p_{plen}}{p_{\infty}} \right)^{\frac{\gamma-1}{\gamma}} - 1 \right)}, \quad (2)$$

where R is the universal gas constant for air, T is the temperature, γ is the ratio of specific heats, p_{∞} is the ambient pressure, and p_{plen} is the plenum pressure, assumed to be the stagnation pressure. From this relation, the plenum pressure is set for jet velocities from 20 to 100 m/s in 10 m/s increments.

The results of the jet velocity at different chordwise locations are seen in Figure 3. The slight variation in slot velocity along its length is attributed primarily to experimental error in the placement of the hot-wire probe within the 1 mm slot height. The black line in

Figure 3 shows the relation in equation 2. The velocities are slightly lower than the theoretically calculated value. This is attributed to major and minor losses of the flow within the flow path. The slot lip deformation is also measured (not shown), and shows the lip deforms approximately 40% of the slot height for higher plenum pressures. This deformation in the slot slip does not significantly change the speed of the flow leaving the slot.

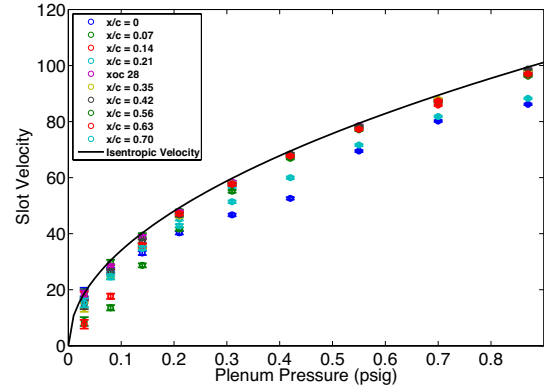


Fig. 3 The slot velocity as a function of plenum pressure for different chordwise locations along the slot. Shows comparison to theoretical relation, Eq. (2), in black.

4. Current and Future Work

The baseline case shows that a wing-tip vortex similar to that observed in the literature is generated in the University of Florida Anechoic Flow Facility. Both a near-field and far-field measurement of the vortex is acquired via SPIV. Through shifting the SPIV vector fields to the vortex center, average velocity fields are obtained. The baseline case measurements presented in this paper allow for a good comparison for analysis of the effects of control on the wing-tip vortex.

Currently underway, SPIV data are being acquired in the University of Florida Anechoic Flow Facility. The test matrix includes near-field and far-field measurements at 5 degrees angle of attack for different momentum coefficients. These preliminary results will help show the effects of momentum added in the direction opposing the naturally occurring flow of the wing-tip vortex.

When the effects of the control are determined, further studies can be performed on the effects of blowing in specific areas of the chord. Since circulation control is known for adding acoustic noise, the noise contributed (and potentially attenuated) by the control can also be studied.

References

- [1] A. Leroy et al., AIAA Flow Control Conference, 2012-2951.
- [2] J. Mathew, Ph.D Dissertation, (2006).
- [3] V. Corsiglia et al., J. Aircraft, **10** (1973), No. 12.
- [4] W. Devenport et al., J. Fluid Mech., **312** (1996), pp. 67-106.
- [5] H. Bruun, (1995), *Hot-wire Anemometry*, Oxford Science Publications.

Flow Structures under Passive Control in a Hole-Tone System

Kazuo Matsuura¹, Masami Nakano²

¹Graduate School of Science and Engineering, Ehime University
3 Bunkyo-cho, Matsuyama, Ehime, 790-8577, Japan

²Institute of Fluid Science, Tohoku University
2-1-1 Katahira, Aoba-ku, Sendai, Miyagi, 980-8577, Japan
E-mail: matsuura.kazuo.mm@ehime-u.ac.jp

ABSTRACT

The passive control of a hole-tone phenomenon is investigated by direct computations and experiments. The mean velocities of air-jets are 10 m/s in both the computations and experiments. The diameters of a nozzle and an end plate hole are both 51 mm, and an impingement length between the nozzle and the end plate is 50 mm. Computed pressure distribution around the hole indicates that the axisymmetric throttling mechanism we proposed previously still holds even when the obstacle is attached.

1. Introduction

The sound produced when a jet, issued from a circular nozzle or hole in a plate, goes through a second plate with a hole of the same diameter as the jet is referred to as a hole-tone. We encounter the tone in many practical situations such as solid propellant rocket motors, automobile intake- & exhaust-systems, ventilation systems, gas distribution systems, whistling kettle, etc. The mechanism of the tone is considered that the sound is maintained by a feedback mechanism in which pressure fluctuations generated at the second hole cause pulsations in the jet flow rate that excite axisymmetric instabilities of the jet [1]. Despite the long history of the hole-tone problem, a comprehensive analytical/numerical solution including methods to minimize the tone has not yet been given [2]. The authors have conducted both direct computations and experiments to investigate the details of the hole-tone [3, 4].

In this paper, the passive control of the hole-tone phenomenon is investigated.

2. Numerical Method

The governing equations are the unsteady three-dimensional compressible Favre-filtered Navier-Stokes equations. To close the system the perfect gas law is assumed. The equations are solved by the finite-difference method. Spatial derivatives that appear in metrics, convective and viscous terms are basically evaluated by the 6th-order tridiagonal compact scheme [5]. Time-accurate solutions to the governing equations are obtained by the 3rd-order Runge-Kutta scheme. In addition to the above-mentioned spatial discretization and time integration, a 10th-order implicit filtering [6] is introduced to suppress instabilities of the computations. The parameter that appears in the left-hand side of the filtering formulation is set to be 0.492 in interior grid points. The details of the present numerical method are shown in [7].

3. Computational and Experimental Systems

Figs. 1 and 2 show the computational overview of the present problem, and an experimental system with an obstacle for the passive control of the hole-tone

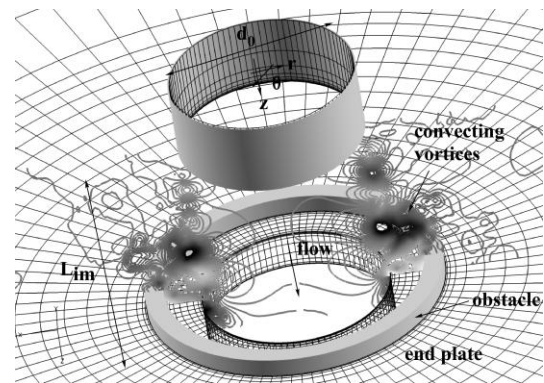


Fig. 1 Hole-tone system
(Contours: instantaneous pressure by CFD)

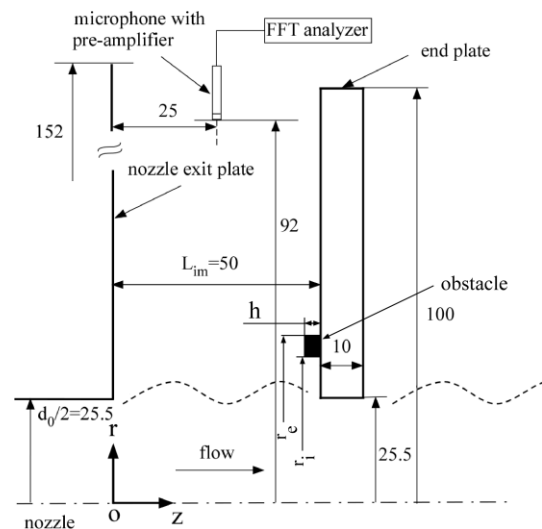


Fig. 2 Experimental system with an obstacle

Table 1. Obstacle geometries used in the computations and experiments

	r_i	r_e	h
exp	35.5	40.5	0, 2, 3, 5
cfD	35.5	40.5	0, 5

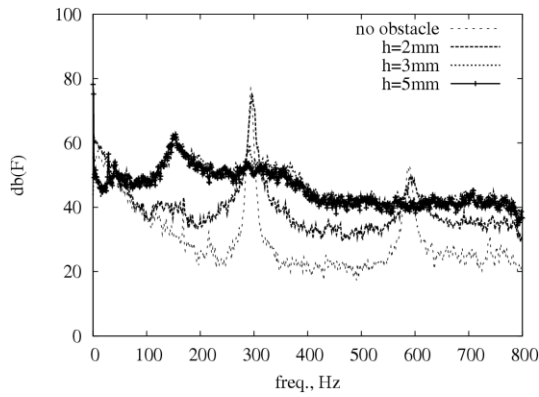


Fig. 3 Measured sound pressure levels for $h=0, 2, 3, 5$ mm

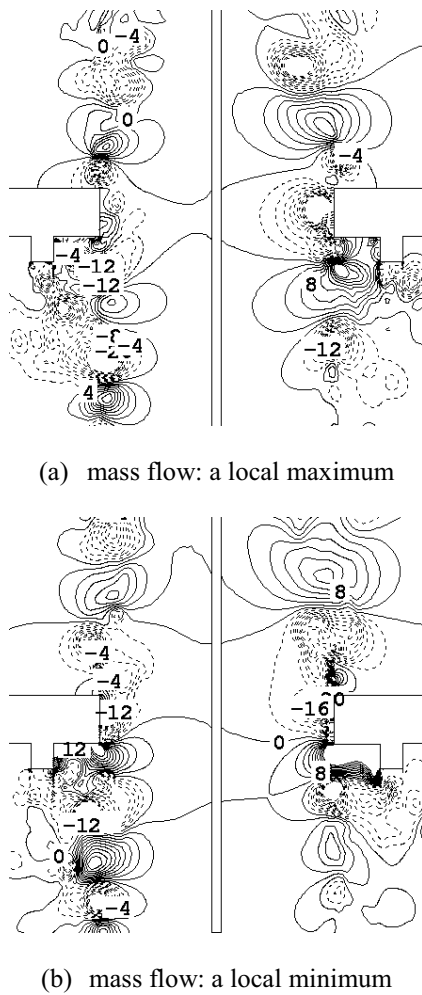


Fig. 4 Distribution of $\Delta p = p - p_\infty$ when mass flows become local maxima/minima

phenomenon, respectively. The diameters of the nozzle and the end plate hole are $d_0=51$ mm. In the numerical model, the outer diameter of the end plate is taken to be 250 mm. The impingement length between the nozzle and the end plate L_{im} is 50 mm. The thickness of the end plate is 10 mm. The mean velocities u_0 of the air-jets are At 15°C, this corresponds to a Reynolds number

$Re=u_0d_0/\nu\approx 3.42\times 10^4$. The overall computational domain consists of 7 zones, and cylindrical-coordinate grids of the O-type topology are generated in each zone. The total numbers of grid points are 9.21×10^6 points when the obstacle height $h=0$ mm, and 24.6×10^6 points when $h=5$ mm. Table 1 shows the geometries of the obstacles used in the computations and experiments.

4. Results and Discussion

Fig. 3 shows measured sound pressure levels for $h=0$ (no obstacle), 2, 3, 5 mm. Peaks observed around 300 Hz for $h=0$ and 2 mm disappear when $h=3$ and 5 mm, which means that the present obstacle is effective in suppressing the hole-tone. Fig. 4 shows the distribution of $\Delta p = p - p_\infty$, $p_\infty = 101,325$ Pa when mass flows become local maxima/minima. When the mass flow becomes a local maximum, low pressure regions are observed upstream of the end plate hole. While, when the mass flow becomes a local minimum, high pressure regions are observed there. From these results, it is thought that the axisymmetric throttling mechanism [4] we proposed previously still holds even when the obstacle is attached.

5. Concluding Remarks

The passive control of a hole-tone phenomenon is investigated by the direct computations and the experiments. When the mass flows become local maxima/minima, low/high pressure regions are observed upstream of the end plate hole, which indicates the axisymmetric throttling mechanism we proposed previously still holds even when the obstacle is attached.

Acknowledgements

This research was supported by the Global COE Program “World Center for Education and Research for Transdisciplinary Flow Dynamics,” of Tohoku University. Part of the work was carried out under the Collaborative Research Project of the Institute of Fluid Science, Tohoku University. Computational resources are provided by Advanced Fluid Information Research Center of Institute of Fluid Science, Tohoku University.

References

- [1] M. S. Howe, Acoustics of Fluid-Structure Interactions, (1998), Cambridge Univ. Press.
- [2] M. A. Langthjem, M. Nakano, J. Sound and Vibration, **28** (2005), p. 133.
- [3] K. Matsuura, M. Nakano, J. Fluid Sci. Tech., **6**(4) (2011), p. 548.
- [4] K. Matsuura, M. Nakano, J. Fluid Mech., (2011) (submitted).
- [5] S. K. Lele, J. Compt Phys., **103**(1) (1992), p. 16.
- [6] D. V. Gaitonde, M. R. Visbal, AIAA J., **38**(11) (2000), p. 2103.
- [7] K. Matsuura, C. Kato, AIAA J., **45**(2) (2007), p. 442.

Increased Lift Airfoil of Vibration Flow Control Technology

Dawei Li, Jinhao Qiu, Rui Nie, Hongli Ji

State Key Laboratory of Mechanics and Control for Mechanical Structures, Nanjing University of Aeronautics & Astronautics, #29 Yudao Street, Nanjing 210016, China
qiu@nuaa.edu.cn

ABSTRACT

This article aims at study the technology of active flow control to increase the lift of wing and weaken the shock wave by method of fluid mechanics. A three-dimensional wing model is used to verify the validity of this new control method. Research shows that partial active deformation can improve the aerodynamic characteristics of airfoil. In the condition of low mach number, the lift coefficient can be increased by 17%. In the condition of high mach number, the lift coefficient of symmetrical airfoil can be increased by 12%.

1. Introduction

Active control is an active field in fluid dynamics. Development of lift-rising techniques is very important. In order to complete requirements of environmental protection of N+2 generation civil aircraft, researchers had put forward a lot of control methods to improve the aerodynamic characteristics of wing, such as contour bump^[1] and synthetic jets^[2]. These technologies, however, would increase the weight or destroy the structure of wing. Because piezoelectric active control technology has several advantages, for example small structure, light, convenient control and doing no damage to the wing structure. Therefore, the piezoelectric material with high performance has a broad development trend. Based on this idea, the paper conducts several numerical simulations about active control.

2. Model and Simulation

NASA0012 airfoil has been used to verify the validity of this method, the span is one meter ($c=1$). A two-dimensional model of airfoil was used in parallelogram grid, on the other hand three-dimensional model of wing was used in hexahedral grid. The wingspan of model is one meter. Figure 1 is the picture of three-dimensional mesh model. The three-dimensional wing model can demonstrate better the pressure distribution and aerodynamic characteristics.

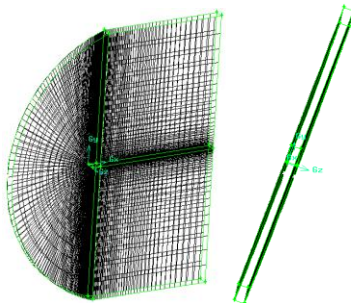


Figure 1 Three-dimensional mesh model

The INVISCID, SIMPLE solution of control and the two order upwind scheme have been used in the simulation. When Mach number (Ma) is 0.3783, the results of simulation and the results of experiment were shown in figure 2. The result of the experiment is get

from the research of G. Solbrekken^[3]. A conclusion is made that the results of calculate and experiment are consistent in the range of small angle of attack. Therefore, the angle of attack is 4° , unless otherwise noted. The UDF has been use to drive a sinusoidal vibration on the upper surface of the airfoil. The disturbance of boundary layer have been shown in the figure 3, when the amplitude (A) is 0.005m, wavelength (λ) is 0.2m and position of vibration is from $x_1=0.2c$ to $x_2=0.4c$. The amplitude value is relatively large when A is 0.005m. The amplitude has been from 0.0005m to 0.002m in the simulation. The function of displacement of every position is presently defined by $y = A \times \sin(2 \times \frac{x-x_1}{x_2-x_1} \pi) \times \sin(ft)$, where f denoted the frequency.

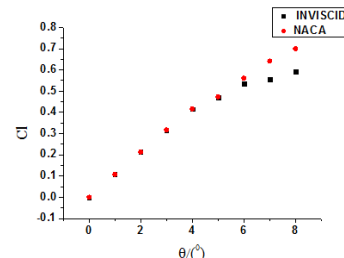


Figure 2 Comparison of both results

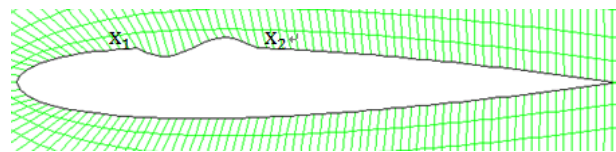


Figure 3 Sinusoidal vibration

3. Results and Discussion

The two-dimensional symmetric NASA0012 airfoil is used in calculation, and wingspan is one meter. When the cycle of calculated result coincides with cycle of physical vibrations, the calculations end. Parameters of sinusoidal vibration are comprehensive. The result would be influenced by several parameters. In low mach number, Ma is 0.3783, sinusoidal vibration is introduced to the position of 0.2c-0.4c. The amplitude of vibration is 0.001m and wavelength is 0.2m. Convergent curves of lift coefficient have been shown in the Figure 4, 0Hz is a steady flow. If frequency is 2000Hz, average value of lift coefficient is 0.438, increased by 6%.

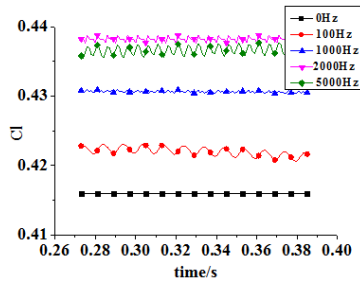


Figure 4 Convergent curves

Three-quarters of power would be consumed by shock wave drag, in the high mach number ($Ma=0.8$). The drag will rise several times, that is because a shock resistance came from the aircraft. $A=0.001m$, $\lambda=0.2m$ and vibratory width is $0.2m$. DCL is an added value of lift coefficient. The vibration can obtain a better effect of lift-enhancement, when vibratory position is close to the original shock, so vibratory position can be fixed on $0.6m-0.8m$. The effects of amplitude and frequency have been shown in Figure 5, through this research we can see that lift coefficient increases first, and decreases later. When the frequency reached about $2000Hz$ the DCL went up to the maximum. The lift coefficient would rise from 0.737 to 0.832 , increased by 12% . Based on the results a conclusion can be found that the vibration which was put into the upper surface of the wing can improve the characteristics of airfoil.

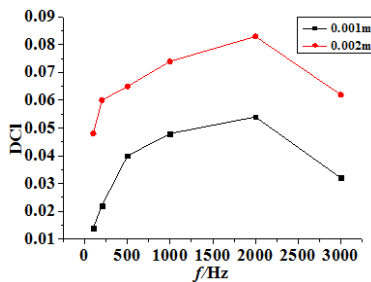


Figure 5 Added value of lift coefficient

The wing is a three-dimensional structure, so it is necessary to use the 3D model to verify the validity of the control method. $Ma=0.8$, model of wing has chosen NASA0012. The simulations have been conducted when the A is $0.001m$ or $0.002m$ and the λ is $0.1m$ or $0.2m$. As the DCL, lift-to-drag ratio of wing increases first, and decreases later. Figure 6 shows the effect of vibratory parameters. The lift-to-drag ratio can be increased by 5% , when $A = 0.002m$, $\lambda = 0.2m$, $f = 1000Hz$.

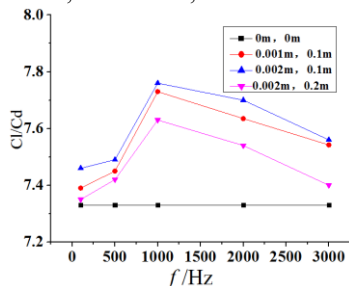


Figure6 Change of lift-to-drag ratio

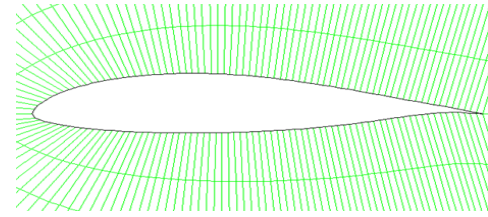


Figure 7 Asymmetric airfoil

This section $Ma=0.1$. Asymmetric model of wing has been researched in this section. The wingspan is 1.5 meter, as shown in the figure 7. The vibratory position is from $0.9m$ to $1.1m$. Figure 8 shows the effect of vibratory parameters. The effect of lift enhancement becomes the best, when $A=0.002m$, $\lambda = 0.2m$, $f=2000Hz$, and the lift coefficient increases by 17% . The total pressure loss is smaller when airflow pass-through a series of oblique shock waves than a straight shock wave. Sinusoidal vibration has been introduced to upper surface of the wing, because strong interference can weak shock. The vibration can inject energy to boundary layer, the position of shock will move backwards and supersonic region in the upper surface will expand. The backward of shock wave position is show in figure 9.

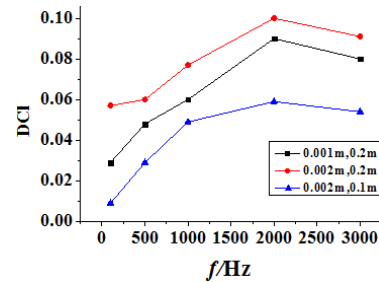


Figure 8 Effect of vibratory parameters

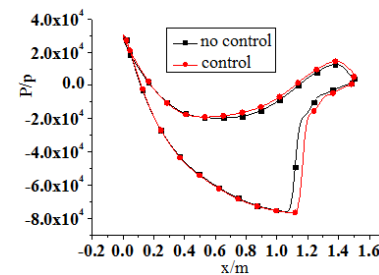


Figure 9 Change of position of shock wave

4. Acknowledgement

This research is supported by NSFC (No.50830201), PCSIRT (IRT0968), Funding of Jiangsu Innovation Program for Graduate Education (CXLX12_0165), The Fundamental Research Funds for the Central Universities.

References:

- [1] B. Smith, AIAA. **0213** (1997).
- [2] J. Reneaux, European Congress on Computation Methods in Applied Science and Engineering. (2004).
- [3]G. Solbrekken, University of Missouri. Columbia. (2006).

Parallel Hypersonic Flow Field Simulation around a Spiked Body using Hydraulic Analogy

Shashank Khurana¹, Kojiro Suzuki¹ and Ethirajan Rathakrishnan²

¹Department of Advanced Energy, University of Tokyo, 5-1-5 Kashiwanoha, Chiba 277-8561

²Department of Aerospace Engineering, IIT-Kanpur, India 208016
shashank@daedalus.k.u-tokyo.ac.jp

ABSTRACT

Flow field around a cylindrical body with hemispherical nose, with and without a spike was simulated in a water flow channel using water color dyes at Froude number 6 utilizing Hydraulic analogy. The prime focus was visualizing the formation of vortices near the stagnation area of the forebody, and the effect of spike, otherwise difficult in hypersonic wind tunnel experiments. The effect of spike-nose configuration on the base region and flow field was also studied. Two vortices of opposite family were observed on either side of the spike, with the largest for hemispherical-nose spike, corroborating with wind tunnel results.

1. Introduction

A forward-facing spike attached to the nose of the body, as a passive control device, has been the focus of attention for a long time subjected to numerous experiments and numerical analysis, for simultaneous reduction of drag and aerodynamic heating at high-speed applications [1]. The flow physics around a spiked body accompanying recirculation region (comprising of vortices), as shown in Fig. 1, have been discussed, but literature review of the past research fails to report any information about the mechanism of formation of the vortices and its quantitative measurement. Hence, an attempt has been made to understand the flow physics of vortex formation near the stagnation zone and the shedding of vortices at the spike-root, using a low-cost device. The present work aims to assess the applicability of hydraulic analogy (similarity of Froude Number in Water Channel with that of Mach Number of Gas Flow) in running a parallel flow field simulation in a two-dimensional water channel, and comparing that with flow field from experiments [2] around a spiked body at Mach 6, by analyzing the accuracy and effectiveness of the former in prediction of the flow field around the spike and the effect of spike-nose configuration on the same.

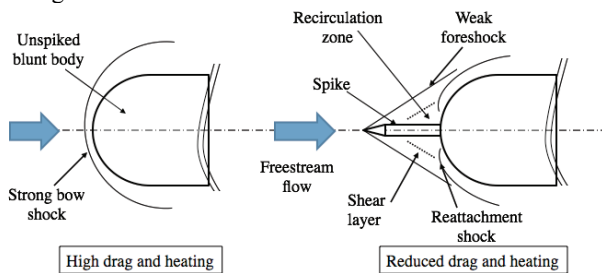


Fig. 1 Spiked-body concept

2. Experimental facility and method

In the present study, the flow around a spiked body, comprising of vortices near the stagnation area, was visualized using a rectangular water flow channel [3-4], manufactured in-house in the Suzuki K. Laboratory, University of Tokyo. Khurana et al. [4] made a first-of-its-kind attempt to visualize the flow field around a spiked body at Reynolds number 3070 and quantified the flow field parameters, concluding the dependence of body-nose vortices on the spike-nose configuration. Schematic diagram and a pictorial view of the channel are shown in Fig. 2(a) and Fig. 2(b), respectively. Water from the chamber, spills over the inclined plate and is

conditioned using an array of wire-meshes, before reaching the downstream of the test-section. The flow quality is ensured to be fairly uniform in the test-section before the start of the experiments. The velocity of the flow is measured using the floating-particle method technique, over the length of the test-section. The average of a set of measured velocities is taken as the representative velocity of the flow.

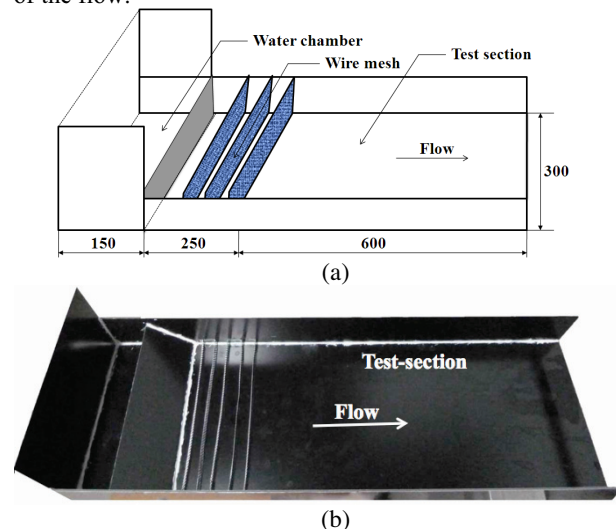


Fig. 2 (a) Schematic diagram of experimental set-up (all dimensions in mm), (b) pictorial view of the set-up

The schematic diagrams of the test models and spike geometries, manufactured from ABS and Bakelite material, respectively, using PC-controlled Modela MDX-504A (Roland DG Corporation) Rapid-prototyping machine available onsite in the laboratory, are shown in Fig. 3. The axis of the model was aligned parallel to the flow direction at the middle of test-section for every test. The model consists of a hemisphere-cylindrical forebody with various spike-nose configurations (hemispherical, conical and flat nose). All the tests of the present study were carried out at equivalent Froude number (given by $v/(gh)^{1/2}$) of 6 (similar to Mach 6 experiments [2] using Hydraulic Analogy). After ensuring the flow field in the test-section to be parallel and uniform, by observing parallel streak lines of dye (acting as visualizing elements) injected upstream of the empty test-section, the model was placed in the test-section and the flow field was recorded on a video camera (PANASONIC, Model DMC-ZX3) at 30 frames per second. The videos recorded were processed to obtain the visualization images from the experiments.

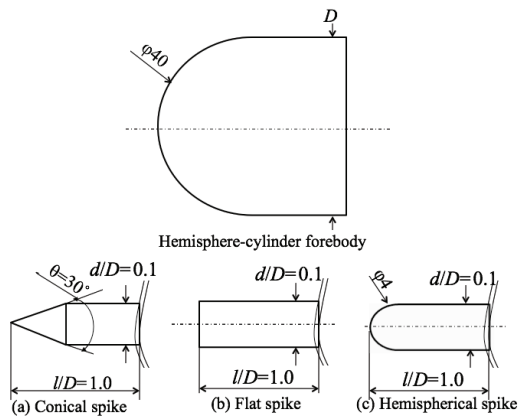
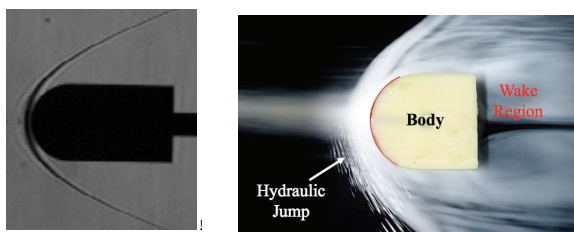


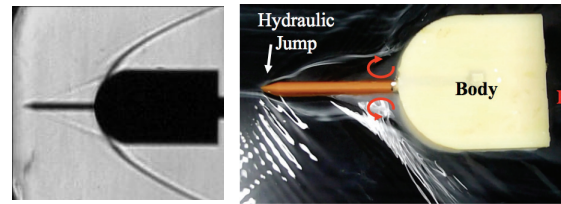
Fig. 3 Test geometry with spike configurations

3. Results and Discussion

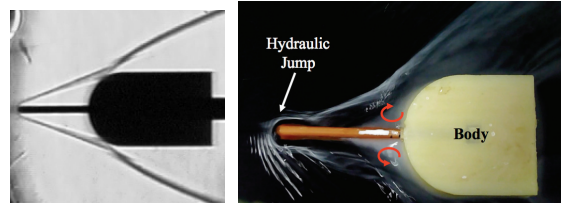
The drag-reduction with the introduction of the spike has long been considered as a result of the generation of vortices at the base of the spike (around the stagnation area) but the large inertia in high-speed flow renders the capturing of vortices in visualization. The use of axisymmetric configurations will be suited for a two-dimensional correlation in the water channel with gas flow. Figures 4-7 illustrate some representative visualization pictures of the flow field comparison using hypersonic wind tunnel [2] and water channel experiments, for with and without spike cases. On a closer look and analysis, it can be established from the water channel visualization pictures that the equivalent hydraulic jump (analogous to shock in gas-flow) from the spike-nose and the other flow properties, corroborates to that from hypersonic wind tunnel results, to a significantly fair accuracy, together with the presence of vortices. Figure 8 shows visualization pictures of vortices, around the base body without and with spikes of different nose-configurations at Froude number 6 captured from the video clippings. It can be seen that for all spike cases visualized, two vortices, one clockwise and other anticlockwise, were positioned at the root of the model on either side. The magnitude of these vortices dominates the strength of the recirculation region around the body nose responsible for affecting the pressure distribution. It can be seen that the relative magnitude of vortex size is the largest for the hemispherical-nose case, which is in coordination with, and responsible for the minimum-drag condition [2] amongst all the four cases shown in Fig. 8. With this inference it may be summarized that the water channel technique has an edge in providing an insight into flow physics, with the latter being capable of serving as a low cost, quick and fairly accurate visualization technique with appropriate analogies, with a finite amount of uncertainty on its applicability in real gas flow.



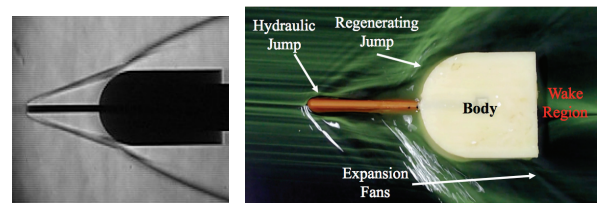
(a) Wind tunnel [2] (b) Water Channel
Fig. 4 Flow field for no-spiked body



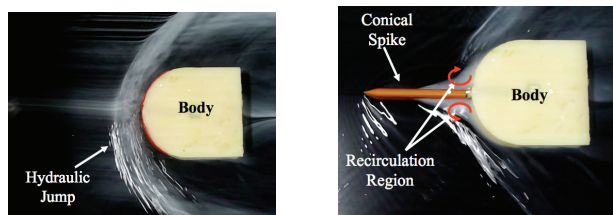
(a) Wind tunnel [2] (b) Water channel
Fig. 5 Flow field for conical-nose spiked body



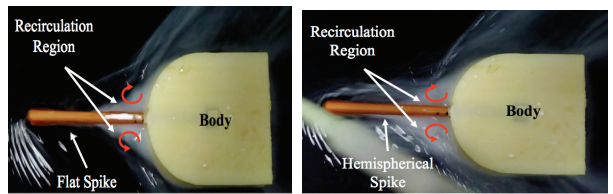
(a) Wind tunnel [2] (b) Water channel
Fig. 6 Flow field for flat-nose spiked body



(a) Wind tunnel [2] (b) Water channel
Fig. 7 Flow field for hemispherical-nose spiked body



(a) (b)



(c) (d)

Fig. 8 Visualization of vortices

References

- [1] M.Y.M. Ahmed and N. Qin, Prog. in Aerosp. Sciences, **47**, 6 (2011), pp. 425-449.
- [2] R. Kalimuthu, PhD Thesis, Indian Institute of Technology (I.I.T.)-Kanpur (2009).
- [3] H. Sharma, A. Vashishtha and E. Rathakrishnan, Proc. IMechE, Part J. Aerosp. Engg. **222**, 6 (2008) pp. 783-788.
- [4] S. Khurana, K. Suzuki and E. Rathakrishnan, Int. J. Turb. Jet. Eng., **29** (2012).

Design and Simulation of Low Voltage Cascade Electroosmotic Pump

Ujjal Barman, Subhash C. Mishra, Ashis K. Sen*
Indian Institute of Technology Guwahati, Guwahati – 781039, India
*Indian Institute of Technology Madras, Chennai – 600036, India
Corresponding author: scm_iitg@yahoo.com

ABSTRACT

A low voltage electroosmotic micropump is proposed here with improvements over current literature. To minimize drag losses, the pump has two arrays of interdigitated planar electrodes at the top and the bottom surfaces of a rectangular microchannel. For channel width $10\ \mu\text{m}$ and depth $1\ \mu\text{m}$, a flow rate of more than $0.2 \times 10^{-4}\ \mu\text{l/s}$ is achieved with the maximum back pressure of 54 Pa for 3 pumping stages at 2V applied voltage.

1. Introduction

The use of Electroosmotic (EO) pump has become very suitable for pumping and controlling fluids of miniscule quantities for miniaturized lab on chip systems. The absence of mechanical elements reduces inertia of the system and improves its sensitivity. Simplicity in design allows ease of microfabrication and applied voltage dependence of flow rate provides better control.

2. Method

The use of interdigitated electrodes in microfluidics is preferred for its ability to create strong electric fields within a very limited space. In this work, arrays of interdigitated electrodes at the top and the bottom surfaces along the length of a microchannel are used to create sufficient pressure head while driving the fluid in the microchannel. The direction of electric field gets reversed at adjacent spaces between electrodes. So, naturally, the EO flows at these adjacent spaces are in opposite directions. The smaller of the two adjacent spaces would have stronger electric field and hence stronger EO flow. Guo et al. [1] designed such a pump where a part of the stronger EO flow neutralized the effect of opposing EO flow at the adjacent space and the balance determined the net flow rate. Barman et al. [2] used non-planar electrodes to contain the interaction of these opposing flows and showed that net flow rate is determined by the weaker EO flow due to physical hindrance provided by the electrode walls to the stronger EO flow.

In this work, further improvement in the design proposed by Barman et al. [2] is reported. Here, the electrode pairs are planar but are separated by slots into the top and the bottom surfaces of the microchannel. This allows forward EO flow smoothly but traps the reverse EO flow within the slots. This not only reduces the momentum dissipation attributed to direct contact of opposing EO flows but also minimizes drag losses because of the planarity of electrode pairs. Simulations were carried out with Comsol Multiphysics 4.0

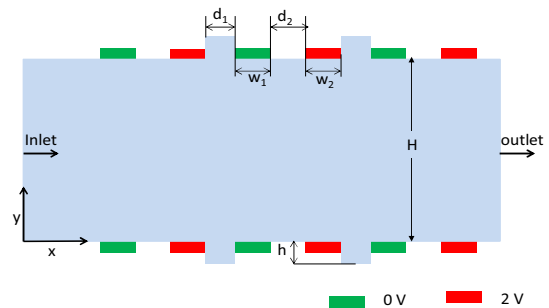


Fig. 1 A two dimensional schematic of the EO pump.

2.1 Formulation

The governing equations for EO flow are

$$\text{Conservation of mass: } \frac{\partial(\rho\mathbf{v})}{\partial t} + \nabla \cdot (\rho\mathbf{v}) = 0 \quad (1)$$

where ρ and \mathbf{v} are the fluid density and velocity respectively. Conservation of momentum:

$$\frac{\partial(\rho\mathbf{v})}{\partial t} + \mathbf{v} \cdot \nabla(\rho\mathbf{v}) = -\nabla p + \eta \nabla^2 \mathbf{v} + \rho \mathbf{g} + \rho_{e1} \mathbf{E} \quad (2)$$

where, p is the pressure, η is the dynamic viscosity, \mathbf{g} is the acceleration due to all body forces except the Coulombic forces $\rho_{e1} \mathbf{E}$ for electric field $\mathbf{E} = -\nabla \phi$, ϕ being the applied potential and ρ_{e1} the electric charge density.

$$\text{Conservation of charge: } \frac{\partial \rho_{e1}}{\partial t} + \nabla \cdot \mathbf{J} = 0 \quad (3)$$

where \mathbf{J} is current density which is studied in electrohydrodynamics using Nernst-Planck equation [3].

$$\mathbf{J} = n_{\pm} \mathbf{v} - D_{\pm} \nabla n_{\pm} - \left(Z_{\pm} n_{\pm} \frac{e D_{\pm}}{k_b T} \nabla \phi \right) \quad (4)$$

where, n_{\pm} , D_{\pm} and Z_{\pm} are ionic densities, diffusion coefficients and valences of positive and negative ions and k_b is the Boltzmann constant, respectively. Using Eq. (3) and (4), for invariant ionic concentration at

inlet

$$\begin{aligned} \nabla \cdot (n_{\pm} \mathbf{v}) + \nabla \cdot (D_{\pm} \nabla n_{\pm}) \\ - \nabla \cdot \left(Z_{\pm} n_{\pm} \frac{eD_{\pm}}{k_b T} \nabla \phi \right) = 0 \end{aligned} \quad (5)$$

2.2 Boundary conditions

The Dirichlet B.C.s for applied voltage at the electrodes are

$$\begin{pmatrix} \text{At anode: } \phi_p = V_0 \\ \text{At cathode: } \phi_n = 0.0 \end{pmatrix} \quad (6)$$

The pressure and gradient of electric potentials at the two ends of the microchannel are invariant

$$\begin{pmatrix} p|_{x=0,L} = p_0 \\ \frac{\partial \phi}{\partial x}|_{x=0,L} = 0 \end{pmatrix} \quad (7)$$

The ionic concentration at the inlet is kept constant

$$n_{\pm}|_{x=0} = n_0 \quad (8)$$

At the walls, zeta potential and ionic concentration (using Boltzmann distribution) are

$$\begin{pmatrix} \zeta = 0.1 \text{ V} \\ n_{\pm} = n_0 \exp\left(-Z_{\pm} \frac{e\zeta}{k_b T}\right) \end{pmatrix} \quad (9)$$

Also, no-slip Navier-Stokes flow at the walls is assumed

$$u_i|_{y=0,H} = 0 \quad (10)$$

3. Results and Discussion

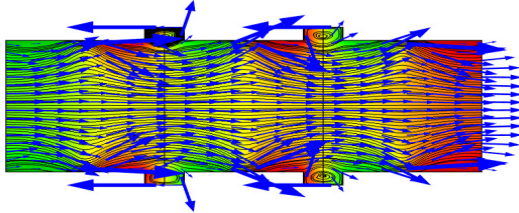


Fig. 2 Simulation plot of 2-D model.

In Fig. 2 surface plot of electric potential with red for positive and green for ground potentials, respectively are shown. Velocity streamlines are represented by black lines and velocity vectors are depicted by blue arrows at steady-state condition at 2 V. It is quite clear from Fig. 2 that the EO flow between a pair of electrodes is smooth and the reverse EO flow is trapped within the slots between two such pairs.

In Fig. 3 variation of flow rate with the depression h is plotted. Rapid rise in flow rate is observed initially with increasing h . This is attributed to high resistance to reverse EO flow at d_1 because the thickness of electrical

double layer is $O(10.0 \times 10^{-9} \text{ m})$. The flow rate reaches a maximum value just above $0.2 \times 10^{-4} \mu\text{l/s}$ and then starts decreasing due to increasing drag losses. In Fig. 4, the flow rate plotted against back pressure indicates a maximum back pressure of 54 Pa for all values of $r = w_1/w_2$. Also, the best performance is found with $w_1 = w_2 = 2 \mu\text{m}$ with $h = 1 \mu\text{m}$.

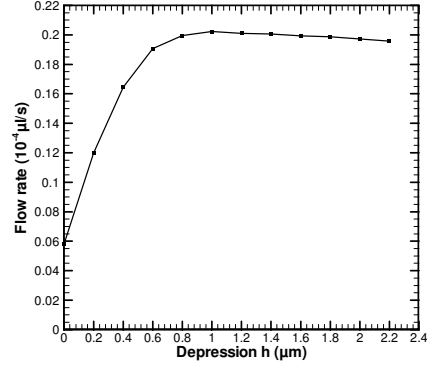


Fig. 3 Variation of flow rate with h for $d_1 = 2 \mu\text{m}$, $d_2 = 2 \mu\text{m}$, $w_1 = 2 \mu\text{m}$ and $w_2 = 2 \mu\text{m}$.

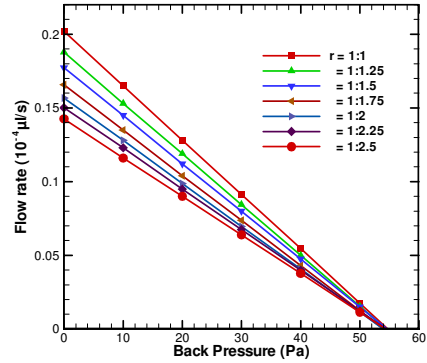


Fig. 4 Variation of flow rate with back pressure with $h = 1 \mu\text{m}$, $d_1 = 2 \mu\text{m}$, $d_2 = 2 \mu\text{m}$, $w_1 = 2 \mu\text{m}$ and for different $r = w_1/w_2$.

4. Conclusions

An electroosmotic micropump was proposed with minimum drag losses and high flow rate. It was realized that any non-uniformity in the microchannel surface has telling effects on the flow rate due to the narrowness of the electrical double layer.

References

- [1] Q. Guo, Y. Liu, X. Wu and J. Yang, *Microsyst Technol* 15(2009) 1009–1015.
- [2] U. Barman, A.K. Sen, S.C. Mishra, P. Baruah, R. Pator, *Microsyst Technol* (2012) communicated.
- [3] R. Probstein (1994) *Physicochemical Hydrodynamics - An Introduction* 2nd. Edition. John Wiley and Sons, Massachusetts Institute of Technology.

Various quantum ground states of low – dimensional nickel - based nitrates

Olga Volkova, Igor Morozov, Viktor Shutov, Alexander Vasiliev
Moscow State University, Leninskie Gory 119991, Russia
vasil@mig.phys.msu.ru

In present work we studied two new members of nickel nitrates family of compounds $\text{Rb}_3\text{Ni}_2(\text{NO}_3)_7$ and $\text{Ni}(\text{NO}_3)_2$. The spin – liquid behaviour was found in $\text{Rb}_3\text{Ni}_2(\text{NO}_3)_7$ and explained in the frames of $S = 1$ spin liquid dimer model. The $\text{Ni}(\text{NO}_3)_2$ is shown to be the rare case of insulating ferromagnet with $T_C = 5.5 \pm 0.25\text{K}$ possessing unusually low effective magnetic moment.

1. Introduction

Special feature of nitrates family is connection of metal – oxygen polyhedra via nitrate groups and/or water molecules, if presented in the structure. Till recently among nickel nitrates the structure was defined for $\text{Ni}(\text{NO}_3)_2$, $\text{Ni}(\text{NO}_3)_2 \cdot 2\text{H}_2\text{O}$, $\text{Ni}(\text{NO}_3)_2 \cdot 4\text{H}_2\text{O}$ and $\text{Ni}(\text{NO}_3)_2 \cdot 6\text{H}_2\text{O}$ [1-4]. Magnetic ground state was estimated only for hydrated compounds. Namely, dehydrate compound $\text{Ni}(\text{NO}_3)_2 \cdot 2\text{H}_2\text{O}$ was identified as two – dimensional antiferromagnet with $T_N = 4.2\text{K}$. The magnetic exchange integrals were estimated as ferromagnetic one in plane $J \sim -1\text{K}$, and antiferromagnetic one between the planes $J' = 0.25\text{K}$ [5-7]. Other hydrates $\text{Ni}(\text{NO}_3)_2 \cdot 4\text{H}_2\text{O}$ and $\text{Ni}(\text{NO}_3)_2 \cdot 6\text{H}_2\text{O}$ were found to be paramagnets [5].

In present work we studied two new members of nickel nitrates family of compounds $\text{Rb}_3\text{Ni}_2(\text{NO}_3)_7$ and $\text{Ni}(\text{NO}_3)_2$.

2. Method

The powder samples were prepared by crystallization from nitric acid solution in presence of adsorbent – dessicant [8]. Magnetic properties were measured by MPMS XL 5 “Quantum Design” SQUID magnetometer. The specific heat was measured by PPMS “Quantum Design”.

3. Results and Discussion

The $\text{Rb}_3\text{Ni}_2(\text{NO}_3)_7$ contains the ladders of Ni^{2+} ($S = 1$) ions as shown in Fig. 1. The model of ladders can transform into the dimers or separate chains in the cases of strong intradimer or intrachain exchange interactions. The temperature dependence of magnetic susceptibility χ of $\text{Rb}_3\text{Ni}_2(\text{NO}_3)_7$ measured in 0.1 T magnetic field, see Fig. 2, demonstrates broad maximum at about $T_{\text{max}} \sim 11\text{K}$. The reverse magnetic susceptibility obeys Curie – Weiss law at high temperatures with negative Weiss temperature $\Theta = -27\text{K}$, indicating the predominance of antiferromagnetic exchange interaction. For $S = 1$ dimer case the exchange integral J is connected with the T_{max} by the equation: $kT_{\text{max}}/|J| = 2,05$ [6] which allows estimating $J \sim 5.4\text{K}$. The fit of $\chi(T)$ dependence with $S = 1$ dimer model is shown by solid line in Fig. 1.

Other thermodynamic properties, i.e. specific heat and high – field magnetization confirm the $S = 1$ dimer model in this compound.

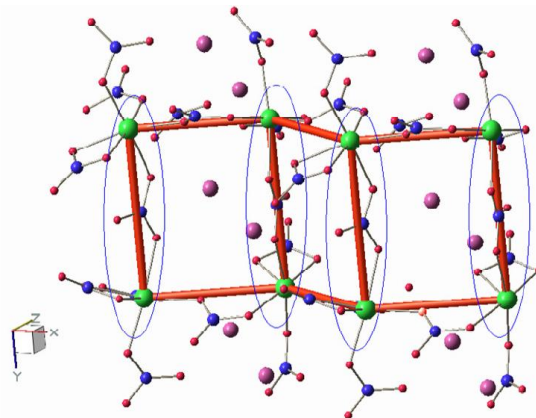


Fig. 1. The fragment of the crystal structure of $\text{Rb}_3\text{Ni}_2(\text{NO}_3)_7$. The Ni^{2+} ions are shown with large spheres in octahedral oxygen coordination. The NO_3^- ligands are shown with triangular clusters. The Rb^+ ions are the middle size spheres.

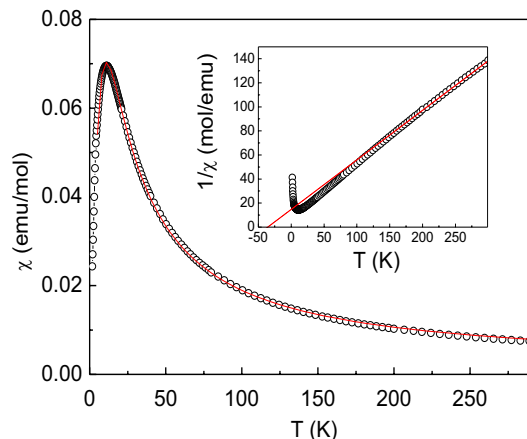


Fig. 2. The temperature dependence of magnetic susceptibility of $\text{Rb}_3\text{Ni}_2(\text{NO}_3)_7$. The inset represents the temperature dependence of the inverse magnetic susceptibility of $\text{Rb}_3\text{Ni}_2(\text{NO}_3)_7$. The solid line indicates the fit in the frames of $S = 1$ dimer model.

Available information about nickel nitrate $\text{Ni}(\text{NO}_3)_2$ was limited only by its crystal structure. Initially it was described as cubic $\text{Pa}\bar{3}$ ($a = 7.31\text{Å}$, $\alpha = 90^\circ$) with one position for nickel ion [1]. Later it was defined more exactly as $\text{R}\bar{3}$ ($a = 10.332\text{Å}$, $c = 12.658\text{Å}$) with two positions for nickel ions in the ratio $\text{Ni}_1:\text{Ni}_2 = 3:1$ [9]. Both positions possess octahedral oxygen environment. Every NiO_6 octahedron is connected via six nitrate

groups with twelve neighbouring octahedra. Therefore, the number of neighbours for every magnetically active cation is twice larger than six which is typical for three – dimensional structures. Certain simplification of $\text{Ni}(\text{NO}_3)_2$ structure can be made, if to take into account the distortion of NiO_6 octahedra. In both Ni_1 and Ni_2 positions the apical oxygen anions are shifted aside from the symmetric vertical location to 11° and 12° , respectively. We believe that this distortion may decrease the overlap of metal d_{z^2} and oxygen p orbitals. This in turn, may result in d_{z^2} energy level decrease and weakening of magnetic exchange interaction along d_{z^2} orbital. Then we may exclude these oxygen ions from the nickel environment. As shown in Fig. 3, the Ni_1 ions form two – dimensional kagome lattice in the ab – plane, and Ni_2 ions occupy its hexagonal cavities. Besides, the Ni_2 ions are not connected with other cations within the layer, they are linked via nitrate groups with Ni_1 ions in upper and lower planes.

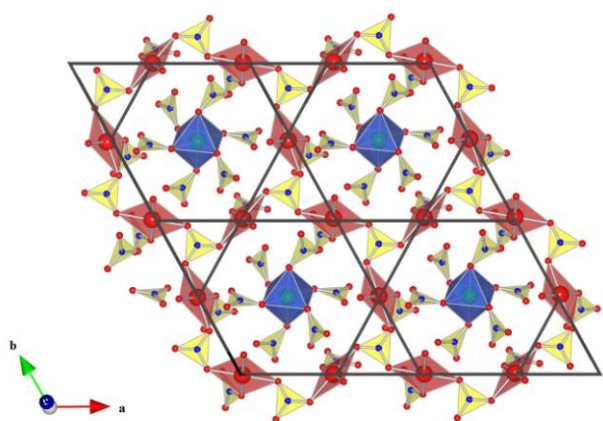


Fig. 3. The fragment of the crystal structure of $\text{Ni}(\text{NO}_3)_2$ in the ab – plane. The Ni_1 ions are shown in square oxygen coordination, the Ni_2 ions are shown in octahedral oxygen environment, the nitrate groups are shown by triangulars. Solid lines are the guides for an eye to accentuate kagome layers in the structure of $\text{Ni}(\text{NO}_3)_2$.

The temperature dependence of dc - magnetic susceptibility $\chi = M/B$ in $\text{Ni}(\text{NO}_3)_2$ is shown in Fig. 4. Rapid increase of magnetic susceptibility replaced by saturation at low temperatures indicates the formation of ferromagnetic order. At high temperatures, the magnetic susceptibility follows the Curie – Weiss law $\chi_{\text{CW}} = \chi_0 + C/(T - \Theta)$ with temperature independent term equal to $\chi_0 = 2.7 \cdot 10^{-4}$ emu/mol, Curie constant $C = 0.8$ K-emu/mol and Weiss temperature $\Theta = 6.0$ K.

The magnetization curves of $\text{Ni}(\text{NO}_3)_2$ measured at various temperatures allow estimating in Below – Arrott's scale the Curie temperature as $T_C = 5.5 \pm 0.25$ K, see Fig. 5. Unusually low value of Curie constant in this compound deserves additional investigations.

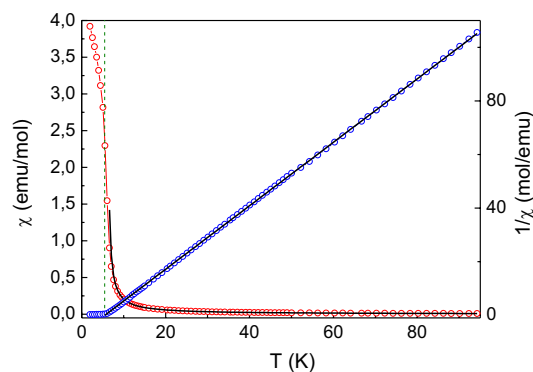


Fig. 4. The temperature dependences of magnetic susceptibility and reverse magnetic susceptibility of $\text{Ni}(\text{NO}_3)_2$. Solid lines are the fits by the Curie – Weiss law, dotted line indicates the Curie temperature T_C , obtained from Arrott's plots.

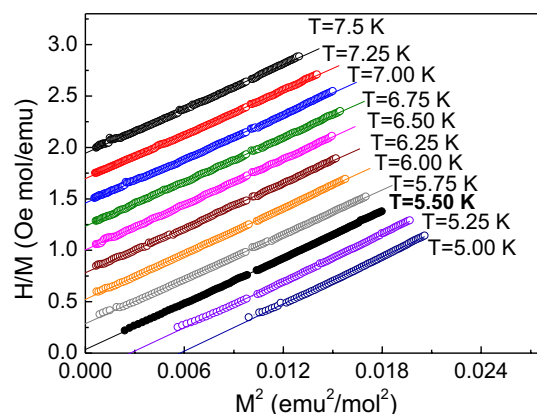


Fig.5. Magnetization curves of $\text{Ni}(\text{NO}_3)_2$ in Below – Arrott's coordinates.

4. Concluding remarks

Two novel low-dimensional nickel based nitrates $\text{Rb}_3\text{Ni}_2(\text{NO}_3)_7$ and $\text{Ni}(\text{NO}_3)_2$ were studied. The first one presents spin – liquid behavior typical for $S=1$ dimers while the second is the insulating ferromagnet.

References

- [1] D. Weigel, B. Imelik, M. Prettre, Bull. Soc. Chim. Fr., 2600 (1964).
- [2] B. Ribar, N. Milinski, Zeitschrift fuer Kristallographie **144**, 126 (1976).
- [3] P. Gallezot, D. Weigel, M. Prettre, Acta Crystallographica **22**, 699 (1967).
- [4] F. Bigoli, A. Braibanti, A. Tiripicchio, M. Tiripicchio Camellini, Acta Crystallographica B **27**, 1427 (1971).
- [5] L. Berger, S.A. Friedberg, Phys. Rev. B, 136, A158 (1964).
- [6] V.A. Schmidt, S.A. Friedberg, Phys. Rev. B **1**, 2250 (1970).
- [7] S. Salem-Sugui Jr., A.-D. Alvarenga, J. Magn. Magn. Mater. **74**, 281 (1988).
- [8] K. O. Znamenkov, I. V. Morozov, S. I. Troyanov, Russian Journal of Inorganic Chemistry **49**, 172 (2004).
- [9] G. Giester, C. L. Lengauer, M. Wildner, J. Zemann, Z. Kristallogr. **223**, 408 (2008).

A Microfluidic Device Demonstrated by Two-color Fluorescence MPIV

Ming-Wen Wang

Department of Mechanical Engineering, Oriental Institute of Technology, New Taipei City 220, Taiwan
avian@mail.oit.edu.tw

ABSTRACT

An extension of two-color micro particle image velocimetry (MPIV) has been described where the color images recorded onto a single high-resolution (3060×2036 pixel) color camera. The fluidic dynamics in a microfluidic device was obtained by measuring the motion of two different sizes fluorescence particles that contain different fluorescent dyes, 0.8 and 5.0 μm , and allowing them to be distinguished using single epi-fluorescent filter cubes. By comparing the images of fluorescence particles, the underlying Stokes drag effects of micro particles in a microfluidic device can be uniquely determined, without expensive experimental setup or technique.

1. Introduction

Micro Particle Image Velocimetry (MPIV) is a popular technique that allows detailed measurements of particle and fluid velocity in the microfluidic devices [1, 2]. Typically, MPIV measures the fluid velocity by tracking the motion of fluorescent particles with an assumption that the tiny particles faithfully follow the fluid flow. However, the alternate action and influence of unusual dimensional particles was a popular application in a microfluidic device. Under steady state conditions, the particles with different size experience unequal forces induced by the Stokes' drag forces due to viscous interactions with the fluid. The particle velocity with unusual size was therefore different from the fluid velocity because of the effect of drag force. This had a great effect upon the Stokes drag force of the larger particle comparatively in the microfluidic device. For measure two different physical components of flow phenomena, the multicolor confocal micro PIV system has been developed [3-5]. It uses two color lasers for illumination and records two different fluorescent lights. The one camera catches short pass filtered image of fluorescent of larger particle, and long pass filtered the image of surrounding flow tiny particles also be captured by another camera. The two color cameras recording technique has two sets of laser and camera been adopted, and that is expensive and complex. For the reasons of economy and simplified image recording system, a simplified two-color MPIV has been applied which the color images were recorded onto a single high-resolution (3060×2036 pixel) color camera and the algorithm has been archived by image processing behind the procedure. This technique has been successfully implemented for the measuring the fluidic dynamics of two different sizes fluorescence particles, 0.8 and 5.0 μm in a microfluidic device. The different sizes of particles contain different fluorescent dyes, allowing them to be distinguished using single epi-fluorescent filter cubes. By comparing the images of fluorescence particles, the underlying Stokes drag effects of micro particles in a microfluidic device can be uniquely determined.

2. Experimental Setup

In this work the experimental investigation of the fluidic dynamics of two different sizes fluorescence

particles in a microfluidic device is performed using the experimental setup in Fig. 1.

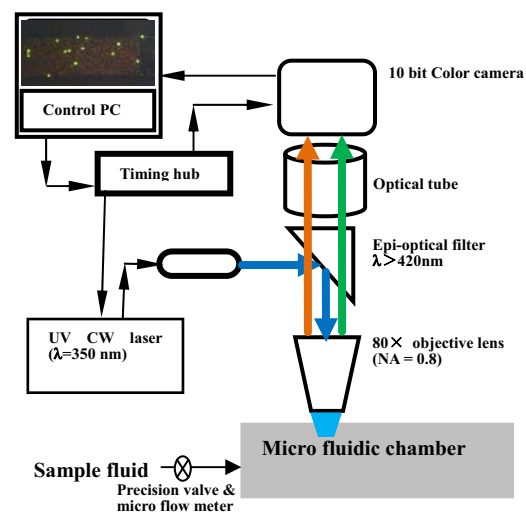


Fig. 1 The experimental setup

The micro-fluidic device has an inlet port connected to fluid supply system through a firm silicone tube. The sample fluid are driven by pressurized air and regulated by valves. A micro flow meter is used in measuring the flow rate. Two kinds of fluorescence particles ($d_p = 0.8$ and $5.0 \mu\text{m}$) with high emitting (550nm and 460nm) respecting UV laser were used as tracer particles in the experiments. The particles are usually stored as suspensions in deionized water. However, the agglutinate substance occurred because of chemical activity under long time deposit, the experimental fluids needed to be carefully filtered. An UV CW diode laser (350 nm) beam was direct through a set of optical lens to illuminate the micro-fluidic chamber. The two different sizes fluorescence particles images were captured using a single high-resolution (3060×2036 pixel) color camera capable of recording 2500 pairs images via a optical tube equipped with an epi-optical filter ($\lambda > 420\text{nm}$) and objective lens ($M=80$, $NA=0.8$). Following Inoue and Spring [6], the depths of focus was expressed as $\delta z = n_0 \lambda_0 / NA^2 + n_0 e / (M \times NA)$, where n_0 is the refractive index of the immersion medium, λ_0 is the wavelength of light imaged,

e is the space between neighboring pixels of the camera, and NA and M are the numerical aperture and magnification of the objective lens, respectively. Meinhart et al. [7, 8] derived the following expression for the depth-of-correlation: $\delta z_c = 3[n_0 \lambda_0 / NA^2] + 2.16 [d_p / (\tan \theta_0)_{\max}] + d_p$, where d_p is the particle size and θ_0 is the small light collection angle. In the study, n_0 was 1.3, λ_0 were 460 and 550nm, NA was 0.8, d_p were 0.8 and 5 μm , and $\tan \theta_0$ was 0.782. Therefore, the depth of correlation was calculated to be 5 – 7 μm .

The micro fluidic chamber was fabricated by bonding a polydimethylsiloxane (PDMS) replica onto a pyrex glass slide. The cross sectional size and streamwise length of the channel were $200 \times 50 \mu\text{m}^2$ and 10mm, respectively.

3. Results and Discussion

Under conditions of constant outlet pressure, the two colors fluorescence image can be observed by a single high-resolution color CCD camera, where the larger particles emitted green spots and the smaller particles emitted orange spots, respectively (Figure 2). We maintained stable flow rate $Re = 9.0$. For the reasons of economy and simplified image recording system, the fluorescence color image was separate into a pair of individual color images by post image processing (Figure 2a, 2b).

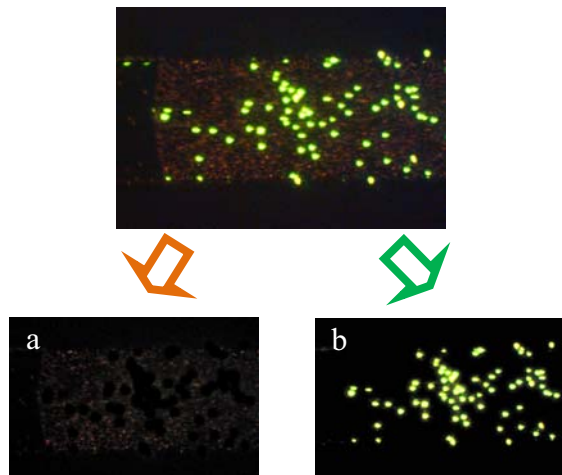


Fig. 2 The two colors fluorescence image can be observed by a single high-resolution color CCD camera, and the fluorescence color image was separate into a pair of individual color images by post image processing (a, b)

The different sizes of particles with a different fluorescent color image can be distinguished and separated into two groups easily. The algorithm of MPIV has been archived by above imaging groups analyze (Figure 3), alternately. Furthermore, the underlying Stoke drag effects of micro particles in a microfluidic device can be uniquely determined by comparing the analyzing results of MPIV algorithm. The moving velocity of smaller particles is faster than larger particles due to the Stoke drag force exits in a microfluidic

device.

4. Concluding remarks

Single camera recording two-color fluorescence imaging micro particle image velocimetry (MPIV) technique has been developed and used to uniquely determine the velocity of different size micro particles in a microfluidic device. By comparing the images of fluorescence particles, the underlying Stoke drag effects of micro particles in a microfluidic device can be uniquely determined, without expensive experimental setup or technique. According the results of MPIV analyze, the underlying Stoke drag effects of unusual size particles has been demonstrated and cannot be neglected in a microfluidic device.

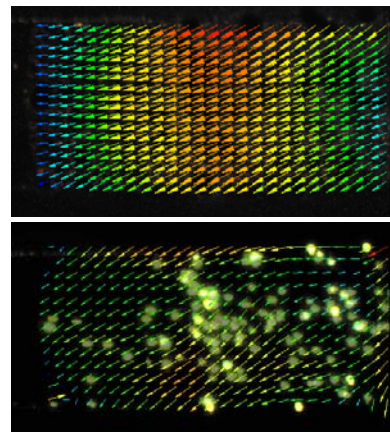


Fig. 3 The algorithm of MPIV has been archived by the fluorescence color image was separate into a pair of individual color imaging groups.

Acknowledge

The financial support from National Science Council NSC100-2221-E-161-008-MY2 of R.O.C. (Taiwan) is greatly appreciated.

References

- [1] C.D. Meinhart, S.T. Wereley, and M.H.B. Gray, *Meas. Sci. Technol.*, **11** (2000), 809.
- [2] E.B. Cummings, *Exp Fluids Suppl* (2000) S42–S50.
- [3] M. Oishi, H. Kinoshita, T. Fujii and M. Oshima, *Measurement Science and Technology*, **22** (2011), 105401.
- [4] M. Oishi, H. Kinoshita, T. Fujii and M. Oshima, *14th International Conference on Miniaturized Systems for Chemistry and Life Sciences*, Groningen, Netherlands (2010), 569.
- [5] M. Oishi, H. Kinoshita, T. Fujii and M. Oshima, *Proc. Micro Total Analysis Systems* (2009), T14A.
- [6] S. Inoue and Spring K, *Video Microscopic: The Fundamentals*, N.Y.: Plenum, 1997.
- [7] C.D. Meinhart, S.T. Wereley ST, *Meas Sci Technol*, **14** (2003), 1047.
- [8] S.T. Wereley and C.D. Meinhart: *Micro and nano scale diagnostic techniques*, N.Y.: Springer, 2004.

Suppressing Turbulence in Flows of Liquid Suspensions with Electromagnetic Fields

R. Tao

Department of Physics, Temple University, Philadelphia, PA 19122, USA
rtao@temple.edu

ABSTRACT

When a strong electric field is applied along the flow direction in pipeline, the suspended particles inside liquid suspensions aggregate into short chains along the flow direction. This aggregation breaks the symmetry and makes the viscosity anisotropic. Along the flow direction, the viscosity is reduced, but along the directions perpendicular to the flow, the viscosity is actually increased. All these suppress the turbulence and improve the flow of liquid suspension in pipeline. The above theoretical prediction has been verified by experiment.

1. Introduction

Suppressing turbulence in flows of liquid suspensions is important [1, 2]. This is especially true for crude oil flow in pipeline. Typically, when the Reynolds number N_R is less than 2300, the flow in pipeline is laminar (Fig.1). The friction factor for laminar flow is

$$f = 64 / N_R \quad (1)$$

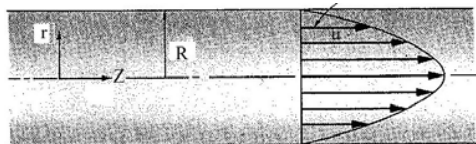


Fig.1 Laminar flow inside the pipeline.

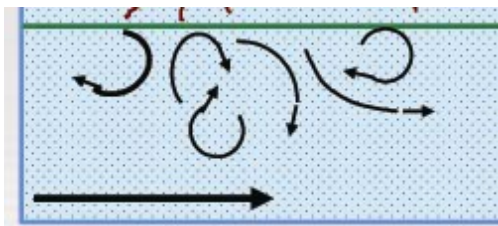


Fig.2 Turbulence occurs when the Reynolds number exceeds 2300.

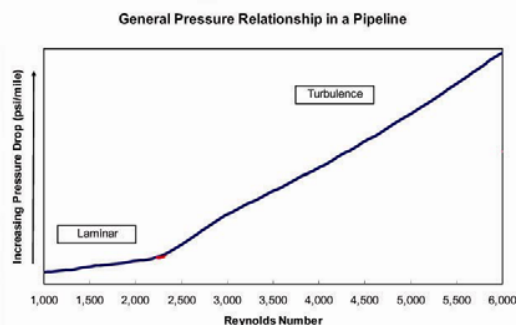


Fig.3 The pressure drop increases much faster in the turbulence region than that in the laminar flow region.

When the Reynolds number exceeds 2300, the flow becomes turbulent (Fig.2) and the pressure drop goes up much faster than that for the laminar flow (Fig.3). For $2300 < N_R < 100000$, the friction factor is given by

$$f = 0.3164 / (N_R)^{0.25} \quad (2)$$

It is clear that in presence of turbulence, we need much more energy to transport crude oil and other liquid suspensions.

Presently the dominate method to suppress turbulence is to add drag reducing agent (DRA) into the flow. DRA is long chain polymer. After DRA is injected into crude oil or refinery products, the turbulence in the radial direction is minimized and the flow in the axial direction is thus improved. On the other hand, DRA is not only expensive, but also raises concerns at refineries.

Here we show that when a strong electric field is applied along the flow direction in pipeline, the suspended particles inside liquid suspensions aggregate into short chains along the flow direction. This aggregation breaks the symmetry and makes the viscosity anisotropic. Along the flow direction, the viscosity is reduced, but along the directions perpendicular to the flow, the viscosity is actually increased [3-5]. All these suppress the turbulence in flow of liquid suspension in pipeline and improve the flow. The above theoretical prediction has been verified by our experiment.

2. Method

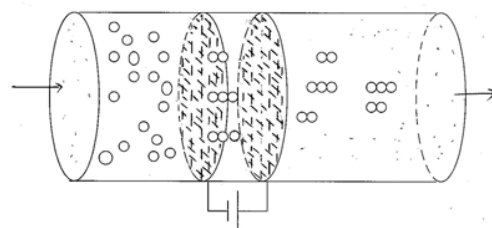


Fig.4 As the flow passes a strong local electric field, the suspended particles aggregate along the field direction, and the viscosity is reduced.

We use the electric field and crude oil as an example. As shown in Fig.4, a strong electric field is applied along the flow direction in a small section of the pipeline. Because the suspended particles and the base liquid have different dielectric constants, the suspended particles are polarized with a dipolar moment

$$\vec{p} = \vec{E} a^3 (\epsilon_p - \epsilon_f) / (\epsilon_p + 2\epsilon_f), \quad (3)$$

where a is the radius of the suspended particle, ϵ_p and

ϵ_f are the dielectric constants for the particle and base liquid respectively. The interaction between two dipoles,

$$U = \epsilon_f p^2 (1 - 3 \cos^2 \theta) / r^3 \quad (4)$$

where r is their distance and θ is the angle between the field and the line joining the two dipoles. If this interaction is strong enough to overcome the Brownian motion, $U > k_B T$, the particles aggregate and align in the field direction to form short chains.

Once the particles form short chains along the field direction, the symmetry is breaking. Under such a condition, similar to flow of nematic liquid crystal with its molecule alignment in one direction, the viscosity is no longer isotropic. Along the axial direction, viscosity η_z is the minimum. The viscosity along the radial direction η_r and the viscosity along the circular direction, η_θ are much higher than η_z . We can approximate the short chain by a prolate spheroid with its rotational axis along the flow direction,

$$(x^2 + y^2) / a^2 + z^2 / c^2 = 1 \quad (5)$$

For such spheroid, the intrinsic viscosity along the z-axis ν_z is much smaller than that of the intrinsic viscosity along the other direction, such as ν_x [6]. For example, if $(c-a)/c=0.9$, we have $\nu_z=2.01$, while $\nu_x=4.48$. From the Krieger-Dougherty equation [7],

$$\eta_i / \eta_0 = (1 - \phi / \phi_m)^{-[\eta] \phi_m} \quad (6)$$

Hence it is clear that η_z is much lower than the viscosity along the other directions. For example, if we assume $\phi=0.40$ and $\phi_m=0.64$, then we have the original viscosity $\eta/\eta_0=4.80$, while $\eta_z/\eta_0=3.535$, reduced by 26.4% and $\eta_x/\eta_0=16.64$, increased by 246.7%. As the viscosities in the directions other than the flow direction are increased substantially, the turbulence is suppressed. Only the axial direction is the favourable direction for the flow as its viscosity is reduced significantly.

3. Results and Discussion



Fig. 5. The viscosity reduction device is connected in the pipeline.

Recently we conducted field test on crude oil pipeline. As shown in figure 5, our viscosity reduction device is connected in the testing pipeline route at DOE facility, Rocky Mountain Oilfield Testing Center (RMOTC), near Casper, Wyoming, USA. The testing

route is about 8 km. Our viscosity reduction device has a strong local electric field applied along the flow direction when the field is turned on. As shown in Fig.5, the device is located immediately after the pump. The crude oil flows through our device, then to the south route, east route, west route, and return to the original place to circulate around. There are sensors to monitor pressure and temperature along the test route.

The inner diameter of the pipeline is $D=5.576in$. The pump used for our test is a PD pump. During our test, we set the pump at flow rate of 420 gallons per minute, which has flow velocity $v=168.2$ cm/s.

Before we turned on our device, the crude oil has viscosity 93.6 cp. The crude oil density is $\rho=0.85$ g/cm³. This corresponds to a Reynolds number 2163.127 and the flow is in laminar region, which gives the friction factor 0.028449 from Eq.(1). The pressure drops along the pipeline confirm that the flow is laminar. For example, the south loop has 1291 m and on the same level and the pressure loss is 47 Psi. If we ignore any secondary loss and use

$$\Delta P = 0.5 \rho v^2 f L / D, \quad (7)$$

the calculation confirms the flow is laminar.

After we turn on the electric field, the viscosity along the flow direction is reduced to 85.5 cp. Thus the Reynolds number is increased to 2368.1, which should be in the turbulence region under the normal situation. If the flow were in the turbulence region, the friction factor would be 0.045356 from Eq.(2) and the pressure loss along the south route should be increased to 72 psi or more. In fact, the pressure loss along the pipeline is actually reduced to 43 Psi from 47 Psi. This confirms that the flow remains laminar. Using Eq.(7), we further verify that the flow is in the laminar region. The tests were repeated many times and the results remain the same: in spite of the fact that the Reynolds number along the flow direction exceeds 2300, the flow remains laminar.

4. Conclusion Remarks

The above finding fully confirms that application of a strong electric field can reduce the viscosity and suppress turbulence for flow of liquid suspensions in pipeline. If the suspended particles are sensitive to magnetic field, we can employ magnetic field [5].

This work is supported in part by STWA.

References

- [1] K. Avila, et al Science, **V333**, Issue 6039 (2011) 192..
- [2]. B. Hof, et al, Science, **V327**, Issue 5972 (2010), 1491.
- [3] R. Tao R. and X. Xu, Energy & Fuels, **20** (2006), 2046.
- [4]R. Tao, J. of Intelligent Material Systems and Structure, **V22** (2011) 1667-1671.
- [5] R. Tao & K. Huang, Physical Review E, **84** (2011), 011905.
- [6] G. B. Jeffery, Proceedings of the Royal Society of London Series A, **V.102**, Issue 715 (1922), 161.
- [7] I. M. Krieger & T. J. Dougherty, *Tans. Soc. Rheol.* **3** (1959), 137.

Electro-Rheological Properties of Nano-Suspensions based on Titanium Dioxide Nano-Particles

Katsufumi Tanaka^{*1}, Haruki Kobayashi^{*1}, Ryuichi Akiyama^{*1}, and Masami Nakano^{*2}

^{*1}Department of Macromolecular Science and Engineering, Kyoto Institute of Technology,
Matsugasaki, Kyoto 606-8585, Japan

^{*2}Institute of Fluid Science, Tohoku University, Katahira, Sendai 980-8577, Japan

E-mail of corresponding author: ktanaka@kit.ac.jp

ABSTRACT

Flow behavior and microstructure were discussed for electro-rheological (ER) nano-suspensions based on titanium dioxide nano-particles with particle diameter on the order of 100 nm. The ER effect was also discussed in relation to the microstructure developed between parallel plates of the rheometer.

1. Introduction

A suspension composed of micro-particles and insulating oil is known to show the electro-rheological (ER) effect [1]. The flow of the ER micro-suspension under no electric fields is generally assumed to be the Newtonian flow. Under an electric field, the flow is well assumed to be the Bingham flow. In such a micro-suspension, a chain-like microstructure along the electric field is induced, the ground state of which was found to be a body-centered tetragonal (bct) lattice [2]. Because a characteristic response time of the ER micro-suspension is on the order of milliseconds [3, 4], there are expectations for applications [5], such as dampers, clutches, valves, robotics, force display devices, and so on.

For practical applications, however, there are still demands for the ER fluid to be improved. Although a much higher yield stress has been a major demand, stability in the ER effect would also be a demand. Recently, a suspension based on rutile titanium dioxide (TiO₂) nano-particles with diameter of primary particles around 15 nm has been reported [6, 7]. The suspended secondary particles were remarkably stable against sedimentation and electrical breakdown. The nano-suspension showed a good fluidity within a narrow gap, while it showed a plateau stress at the lower shear rates under no electric fields.

At a given particle volume fraction of ϕ , it is expected that secondary particles based on the larger particles are smaller than those based on the smaller particles (of the same chemical nature, crystal structure, and so on), because the surface to volume ratio (as well as the number density) of the larger particles is much smaller than that of the smaller particles. In such a nano-suspension, a lower apparent yield stress under no electric fields can be observed, the lower apparent yield stress of which will be favorable for the flow within a narrow gap [8].

In the present paper, flow behavior and microstructure will be discussed for electro-rheological nano-suspensions based on TiO₂ nano-particles with particle diameter on the order of 100 nm.

2. Experimental

Nano-particles of anatase TiO₂ with diameter of the primary particles around 300 nm were suspended in a

silicone oil with a viscosity η_c of 5×10^{-2} Pa·s. The nano-particles were also suspended in a hydrocarbon oil with η_c of 1.5×10^{-2} Pa·s, and a chemically-modified silicone oil with η_c of 1.0×10^{-1} Pa·s. The volume fraction of the particles was 8.8 vol%. The rheological measurements were performed at room temperature using rotational rheometers with fixtures of parallel plates. Particle behavior was observed using an optical microscope equipped with a CCD camera. Furthermore, the effect of shearing time on the ER responses was also investigated.

3. Results and Discussion

Under no electric fields, the silicone oil based sample of 300 nm and 8.8 vol% showed a plateau stress around 5 Pa at the lower shear rates. At the higher shear rates, the stress of the sample of 300 nm gradually approached that previously reported for the sample of 15 nm and 8.8 vol% [6]. The ER responses to the dc electric field measured at a shear rate of 1.88 s^{-1} were studied for the silicone oil based sample of 300 nm. The stress around 2 kPa was induced by the dc electric field with a strength of 16 kV/mm. The stress around 2 kPa was comparable to (but slightly lower than) that observed for the sample of 15 nm and 8.8 vol% [6].

The stability of the micro-gap flow under the dc electric field of 2 kV/mm was further evaluated for the sample of 300 nm and 8.8 vol%. Figures 1 and 2 show, respectively, the shear stress and flow behavior under the electric field plotted against shearing time. The shear rate was 100 s^{-1} . The gap h was set to be 50 μm .

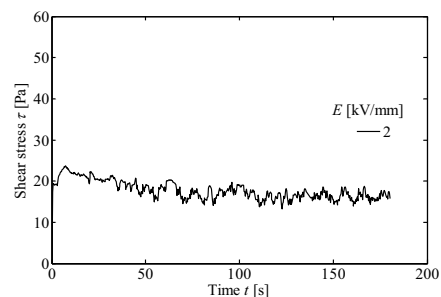


Fig. 1 Changes of shear stress with shearing time in the silicone oil based nano-suspension. The shear rate was 100 s^{-1} . The strength of the electric field was 2 kV/mm, and the gap between parallel plates was 50 μm .

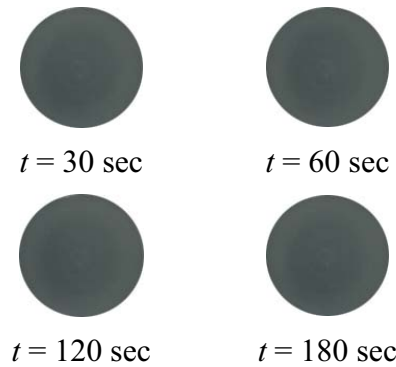


Fig. 2 Changes of flow behavior with shearing time simultaneously observed with shear stress under the electric field of 2 kV/mm shown in Fig. 1.

As shown in Fig. 1, the stress under shear and electric fields was stable during the period on the order of 10^2 s at the electric field of 2 kV/mm for $h = 50$ μm . In Fig. 2, the flow behavior observed simultaneously with the ER behavior is also stable, and ring-like microstructure [9-11] cannot be seen in the figure.

However, a gradual increase, or a very slow mode of the ER response at 5 kV/mm was observed for $h = 50$ (or 70) μm . For the flow of $h = 100$ μm , a more stable flow than that of $h = 50$ μm was found. Especially, the stability of the flow of $h = 100$ μm was fairly well even at 5 kV/mm [8]. The development and gradual changes in a ring-like microstructure were also observed simultaneously for the flow of the sample of 15 nm and 8.8 vol% with the very slow mode [9, 10], suggesting the close relation between the very slow mode and the development of the ring-like microstructure.

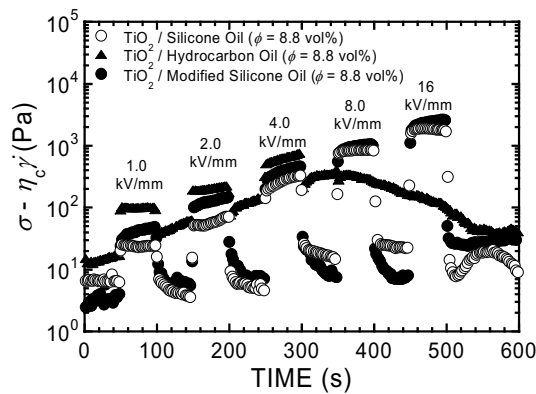


Fig. 3 Responses of $\sigma - \eta_c \dot{\gamma}$ to the dc electric field for the sample based on the modified silicone oil. The data for silicone oil and hydrocarbon oil based samples are also plotted. The shear rate was 1.88 s^{-1} .

For the nano-suspension based on the hydrocarbon oil, a plateau stress at the lower shear rates was observed, the plateau stress of which was slightly higher than that of the silicone oil based sample. On the other hand, a plateau stress was also observed for the sample based on the modified silicone oil, the plateau stress was lower

than that of the silicone oil based sample. These results of the plateau stress were closely related to microstructures of the nano-particles developed in the nano-suspensions.

Figure 3 shows responses of the subtracted shear stress to the dc electric field measured at a shear rate of 1.88 s^{-1} for the sample based on the modified silicone oil. For comparison, the data for silicone oil and hydrocarbon oil based nano-suspensions are also plotted. In Fig. 3, the induced stress for the sample based on the modified silicone oil is larger than that of the silicone oil based sample, whereas it is slightly smaller than that of the hydrocarbon oil based sample. It should be pointed out that the recovery after removal of the electric field in Fig. 3 is fairly well for the sample based on the modified silicone oil.

4. Conclusions

Nano-suspensions based on titanium dioxide nano-particles with particle diameter on the order of 100 nm were prepared. The plateau stress under no electric fields was closely related to the microstructure developed in the nano-suspension. The ER effect for the nano-suspension based on a chemically modified silicone oil was effectively induced by the electric field, and the reversibility of the ER responses was fairly well.

Acknowledgement

This work was partially supported by the Cooperative Research Program of the Institute of Fluid Science, Tohoku University.

References

- [1] W. M. Winslow, *J. Appl. Phys.*, **20** (1949), 1137.
- [2] R. Tao, and J. M. Sun, *Phys. Rev. Lett.*, **67** (1991), 398.
- [3] A. Hosseini-Sianaki, W. A. Bullough, R. Firoozian, J. Makin, and R. C. Tozer, *Int. J. Mod. Phys. B*, **6** (1992), 2667.
- [4] K. Tanaka, A. Sahashi, R. Akiyama, and K. Koyama, *Phys. Rev. E*, **52** (1995), R3325.
- [5] M. Nakano, and K. Koyama (eds.), *Proc. of 6th Int. Conf. on ER Fluids, MR Suspensions and Their Applications* (World Scientific, Singapore, 1998).
- [6] K. Tanaka, T. Wakayasu, A. Kubono, and R. Akiyama, *Sensors and Actuators A*, **112** (2004), 376.
- [7] K. Tanaka, H. Nakahori, K. Katayama, and R. Akiyama, *Colloid Polym. Sci.*, **285** (2007), 1201.
- [8] K. Tanaka, T. Hira, R. Fukui, N. Nakagawa, R. Akiyama, M. Nakano, K. Yoshida, and T. Tsujita, *Colloid Polym. Sci.*, **289** (2011), 855.
- [9] M. Nakano, S. Yamamura, R. Keta, K. Tanaka, *Proc. of Mechanical Engineering Congress, Japan*, vol. 2, (2006), 25.
- [10] M. Nakano, *Jpn. J. Multiphase Flow*, **23** (2009), 135.
- [11] S. Henley, and F. E. Filisko, *J. Rheol.*, **43** (1999), 1323.

Micro System of Vibration Generator of Magnetic Fluid Droplet Driven by Alternating Magnetic Field

Sota Inomata¹, Seiichi Sudo¹, Hidemasa Takana² and Hideya Nishiyama²
¹Akita Prefectural University, Ebinokuchi 84-4, Yurihonjyo 015-0055, Japan
²Tohoku University, Katahira 2-1-1, Aoba-ku, Sendai 980-8577, Japan
 E-mail: M13A002@akita-pu.ac.jp

ABSTRACT

This paper is concerned with the development of the micro system of vibration generator of magnetic fluid droplet driven by alternating magnetic field. The micro system is composed of a needle, NdFeB magnets, magnetic fluid, and the micro coil. The elongation and contraction oscillations of magnetic fluid droplet were produced by the micro system. The validity of a miniaturization using the micro coil was shown experimentally even in the reduction of the voltage and current.

1. Introduction

Since high-quality magnetic fluids composed of solid magnetic particles of subdomain size dispersed colloidally in a liquid carrier were developed, the fundamental responses of magnetic fluids by applied magnetic fields have been studied by a number of researchers [1]. Especially, the responses of magnetic fluid droplet to applied magnetic fields are of fundamental interest and great importance in many technological applications. Therefore, extensive investigations on the magnetic fluid droplet under various applied magnetic fields have been conducted. For example, an experimental investigation of the elongation of a magnetic fluid droplet in homogeneous magnetic field was conducted [2]. In our previous papers, authors reported the shape responses of droplets of some magnetic functional fluids in alternating magnetic fields [3], and the study on surface oscillations of magnetic fluid droplet system using an iron needle, NdFeB magnets, magnetic fluid, and the Helmholtz coil [4]. In spite of many investigations, there is no study on the micro system of vibration generator of magnetic fluid droplet driven by alternating magnetic field. The study on the micro system of vibration generator of magnetic fluid droplet driven by alternating magnetic field is useful for the development of various types of micro magnetic fluid devices.

In this paper, the system for vibration generator of magnetic fluid droplet driven by alternating magnetic field was miniaturized. The surface oscillation of magnetic fluid droplet in the micro system compared with our previous Helmholtz coil system was examined. The validity of a miniaturization using the micro coil was revealed experimentally.

2. Experimental apparatus and procedures

Figure 1 shows the test micro system for vibration generator and its dimensions. The micro system of vibration generator is composed of an iron needle, NdFeB magnets, magnetic fluid, and a micro coil with smaller diameter instead of the Helmholtz coil with larger diameter [4]. The diameter of the iron needle was 0.5 mm. The needle was bonded to the column permanent magnet with the magnetic flux density $B=440$ mT. The volume of magnetic fluid droplet was $V_m=4 \times 10^{-9} \text{ m}^3$ (4 μl). Sample magnetic fluid was

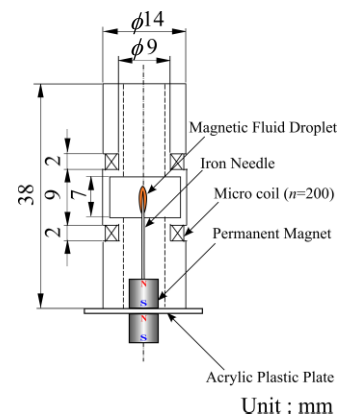


Fig. 1 Test micro system for vibration generator

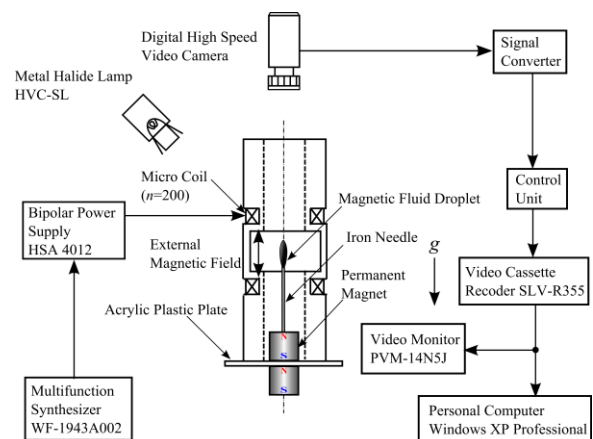


Fig. 2 A schematic diagram of experimental apparatus

kerosene-based ferricolloid HC-50. The surface tension of the magnetic fluid was 0.0277 N/m (magnetic fluid/air at a temperature of 19°C). The Inner diameter of the micro coil was 9 mm. The micro coil was consisted of a pair of coil, which were wound in same direction and connected in series. The turn number of each coil was 200 turns. The diameter of coil wire was 0.1 mm. A block diagram of the experimental apparatus is shown in Fig. 2. The alternating magnetic field was generated by applying alternating voltage to the coil. The alternating current signal was supplied by the frequency synthesizer. The direction of the magnetic field was parallel and anti-parallel in the gravity

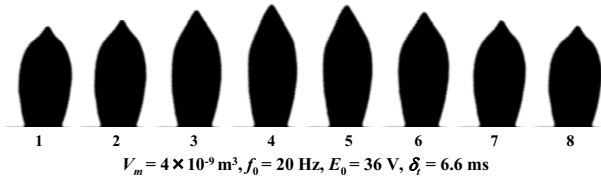


Fig. 3 Photographs showing dynamic response of magnetic fluid droplet by alternating field

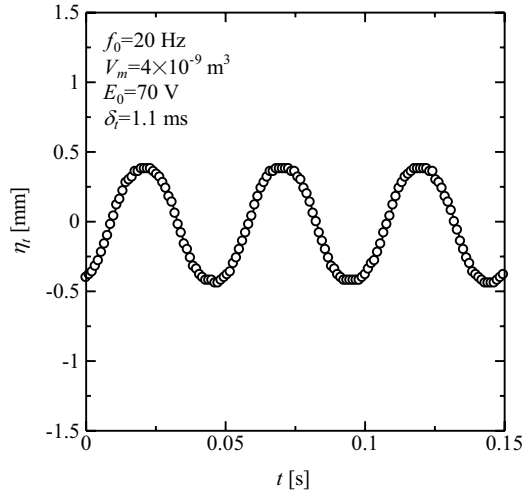


Fig. 4 Surface oscillation of magnetic fluid droplet in alternating magnetic field generated by the Helmholtz coil

direction. In this experiment, the applied voltage E was given in the sinusoidal form as follows:

$$E = \frac{E_0}{2} \sin(2\pi f_0 t) \quad (1)$$

where $E_0/2$ is the amplitude of alternating voltage, f_0 is the frequency, and t is the time. The surface oscillation of magnetic fluid droplet in the micro coil system was compared with our previous Helmholtz coil system at the same level condition of magnetic field intensity [4]. The behavior of magnetic fluid droplet was observed with the high-speed video camera system. A series of frames of the magnetic fluid droplet motions were analyzed by the personal computer. The experiment was performed under the condition of the room temperature.

3. Results and Discussion

The dynamic behavior of the magnetic fluid droplet in the micro system as shown in Fig. 2 was observed under the condition of external alternating magnetic field with the high speed video camera system. Figure 3 shows a sequence of photographs of the shape oscillation of magnetic fluid droplet subject to alternating magnetic field. The time interval between frames in Fig. 3 is $\delta_t=6.6$ ms. The pictures reveal the process of surface elongation and contraction of magnetic fluid droplet adsorbed to magnetized needlepoint. The magnetic fluid droplet is elongated when the external field is parallel to the magnetic field produced by the needle. The droplet is contracted when the external field is anti-parallel to the magnetic field of

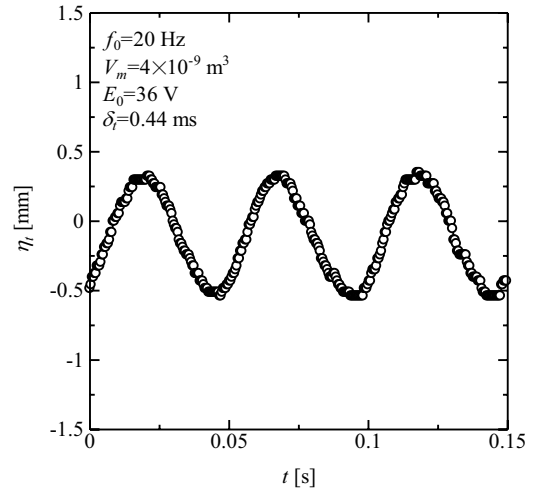


Fig. 5 Surface oscillation of magnetic fluid droplet in alternating magnetic field generated by the micro coil

needle [4].

Figure 4 shows the response of the top of droplet η_r in the alternating magnetic field generated by the Helmholtz coil [4]. In Fig. 4, the applied voltage to the coil is $E_0=70$ V and the frequency of alternating magnetic field is $f_0=20$ Hz. Figure 5 shows the response of magnetic fluid droplet in alternating magnetic field generated by the micro coil. In Fig. 5, the applied voltage to the coil is $E_0=36$ V and the frequency of alternating magnetic field is $f_0=20$ Hz. Even though the applied voltage to the micro coil is lower than that of the Helmholtz coil, the amplitude of η_r -oscillation in Fig. 5 is almost equal to that of η_r -oscillation in Fig. 4. Due to the miniaturization of the coil, the current through the micro coil can be reduced in comparison with that of the Helmholtz coil.

4. Concluding remarks

The surface oscillation of magnetic fluid droplet driven by alternating magnetic field in the micro system was examined. The surface oscillation of magnetic fluid droplet in the micro system was shown the same response with that of the system using the Helmholtz coil with larger diameter. The response of the top of droplet η_r was accomplished with lower voltage and current.

References

- [1] R.E. Rosensweig, Ferrohydrodynamic (Cambridge Univ. Press, Cambridge, 1985).
- [2] V. I. Arkhipenko, Yu. D. Barkov, V. G. Bashtovoi, Magnetshydrodynamics, **14** (1978), 373.
- [3] S. Sudo, A. Nakagawa, K. Shimada, H. Nishiyama, J. Magn. Mater., **289** (2005), 321.
- [4] S. Inomata, S. Sudo, H. Takana, H. Nishiyama, J. Jpn. Soc. Appl. Electromagn. Mech., **20-1** (2012), 174.

Control Problems for the Stationary Navier–Stokes and MHD Equations

Roman Brizitskii

Institute of Applied Mathematics FEB RAS, 7, Radio St., Vladivostok, 690041, Russia
mlnwizard@mail.ru

ABSTRACT

The optimal control problems for the stationary Navier–Stokes and magnetohydrodynamic equations are considered. For MHD equations the role of controls in control problems is played by density of electric current. Quadratic tracking-type functionals for the velocity or pressure play the role of cost functionals. A local stability of optimal solutions with respect to some perturbations of both cost functional and state equation is proved.

1. Introduction. Statement of Problem

The development of new technologies in engineering fluid mechanics leads to new statements of problems in theoretical hydrodynamics and magnetohydrodynamics. Optimal control problems for the Navier–Stokes and magnetohydrodynamics equations can serve as examples of such problems. There are a number of papers (e.g., see [1–8]) dealing with such problems. In these papers, the solvability of extremal problems was studied, optimality systems were derived, and numerical algorithms for solving control problems were developed. In addition, the uniqueness and stability of solutions of extremal problems for the stationary Navier–Stokes and MHD equations were analyzed.

In the present work, we state and study control problems for the stationary magnetohydrodynamic equations of a viscous incompressible fluid

$$-\nu \Delta \mathbf{u} + (\mathbf{u} \cdot \nabla) \mathbf{u} + \nabla p - \kappa \operatorname{rot} \mathbf{H} \times \mathbf{H} = \mathbf{f}, \quad \operatorname{div} \mathbf{u} = 0, \quad (1)$$

$$\nu_1 \operatorname{rot} \mathbf{H} - \rho_0^{-1} \mathbf{E} + \kappa \mathbf{H} \times \mathbf{u} = \nu_1 \mathbf{j}, \quad \operatorname{div} \mathbf{H} = 0, \quad \operatorname{rot} \mathbf{H} = 0, \quad (2)$$

considering in domain Ω under following inhomogeneous boundary conditions:

$$\mathbf{u} = \mathbf{g} \text{ on } \Gamma, \quad \mathbf{H} \cdot \mathbf{n} = 0 \text{ on } \Gamma_N, \quad \mathbf{H} \times \mathbf{n} = 0 \text{ on } \Gamma_T, \\ \text{and } \mathbf{E} \times \mathbf{n} = \mathbf{k} \text{ on } \Gamma_N \quad (3)$$

Here $\Omega \in \mathbf{R}^3$ is a bounded domain with boundary Γ , consisting of two parts: Γ_N and Γ_T , \mathbf{u} is the velocity vector; \mathbf{H} and \mathbf{E} are the magnetic and electric field intensity vectors, respectively; $p = P/\rho_0$ where P is the pressure, $\rho_0 = \text{const}$ is a density, \mathbf{j} is the external current density vector, \mathbf{g} and \mathbf{k} are given functions on Γ and Γ_N . We shall refer to problem (1)–(3) as Problem 1.

The mixed formulation of the boundary conditions for the magnetic field corresponds to a situation where different parts of the boundary Γ have different physical properties (see [9]).

The papers [8], [10–12] deal with the theoretical study of extremal problems for the model (1), (2). The solvability of these extremal problems was proved in these papers, and optimality systems describing necessary extremum conditions were derived and analyzed. The uniqueness and stability issues for solutions of extremal problems are much less studied. We note only the papers [13–16], in which uniqueness issues for solutions of extremal problems were considered for a model of magnetohydrodynamics of a viscous heat-conducting fluid. Below we mainly pay attention to the analysis of the uniqueness and stability

of solutions of extremal problems for the model (1), (2) on the basis of new a priori estimates of solutions of the boundary value problem (1)–(3) and an auxiliary theorem on properties of the difference of solutions of the original control problem and a perturbed control problem obtained by a perturbation of the original performance functional. The resulting stability estimates are cumbersome. However, by using specially introduced dimensionless parameters, which are analogs of the Reynolds, Hartmann, and Prandtl numbers used in hydrodynamics, we represent these estimates in a fairly concise and clear form.

2. Optimal Control Problems

A typical extremal problem for the considered model of magnetohydrodynamics is to find one or several unctional parameters (controls) occurring in weak formulation of Problem 1 and its solution $(\mathbf{u}, p, \mathbf{H})$ from the minimum condition for a certain performance functional. In what follows, we consider an extremal problem in which the performance functional depends either only on the velocity or only on the pressure and the function \mathbf{j} occurring in the right-hand side of equation (2) is used as a control. We assume that the control \mathbf{j} can vary over a set K , where $K \subset \mathbf{L}^2(\Omega)$ is a nonempty convex closed set.

The mathematical statement of the optimal control problem is as follows: find a pair (\mathbf{x}, \mathbf{j}) , where $\mathbf{x} = (\mathbf{u}, H, p) \in X$, and $\mathbf{j} \in K$ such that

$$J(\mathbf{x}, \mathbf{j}) = I_i(\mathbf{u}, p) + \frac{\mu_1}{2} \|\mathbf{j}\|^2 \rightarrow \inf.$$

$$F(\mathbf{x}, \mathbf{j}) = 0, \quad \mathbf{x} \in X, \quad \mathbf{j} \in K \quad (4)$$

Here $F(\mathbf{x}, \mathbf{j}) = 0$ is the operators form of the weak formulation of Problem 1 (see [8, 17]); μ_1 is nonnegative parameter, $I_i(\mathbf{u}, p)$ is a cost functional. The possible cost functionals are usually defined as

$$I_1(\mathbf{v}) = \|\mathbf{v} - \mathbf{v}_d\|_Q^2, \quad I_2(\mathbf{v}) = \|\mathbf{v} - \mathbf{v}_d\|_{1,Q}^2 \\ I_3(\mathbf{v}) = \|\operatorname{rot} \mathbf{v} - \eta_d\|_Q^2, \quad I_4(p) = \|p - p_d\|_Q^2 \quad (5)$$

Here Q is a some subset of domain Ω , $\mathbf{v}_d \in \mathbf{L}^2(Q)$ (or $\mathbf{v}_d \in \mathbf{H}^1(Q)$) is function, which simulates a given distribution of the velocity field in Q . Functions $\eta_d \in \mathbf{L}^2(Q)$ and $p_d \in \mathbf{L}^2(Q)$ have a similar sense.

The existence of an optimal solution is based on the a priori estimates and standard techniques (see [3]). Optimality systems describing first-order necessary optimality conditions were obtained, and, by analysis of

their properties, conditions ensuring the uniqueness and stability of the solution were established.

3. Uniqueness and Stability of Solutions to Control Problems

To study the stability of solutions of control problems we have developed an approach that is based on the analysis of fundamental properties of the optimality system for the general control problem and using special estimates for the difference of solutions to the original and perturbed control problems. The latter is obtained by perturbing both the cost functional and the boundary function entering into the Dirichlet boundary condition for the velocity. Using this approach allows us to obtain the local stability estimates of optimal solutions with respect to small perturbations of both the cost functional and one of the given functions entering into the state equation in an explicit and sufficiently easy-to-interpret form.

We consider the extremum problem for MHD system

$$J(\mathbf{v}, \mathbf{j}) \equiv \frac{\mu_0}{2} \|\mathbf{v} - \mathbf{v}_d\|_Q^2 + \frac{\mu_1}{2} \|\mathbf{j}\|^2 \rightarrow \inf,$$

$$F(\mathbf{x}, \mathbf{j}, \mathbf{g}) = 0, \quad \mathbf{x} \in X, \mathbf{j} \in K, \quad (6)$$

corresponding to the cost functional $I_1(\mathbf{v})$. Let us assume below, that the boundary function \mathbf{g} in (6) can change in some bounded set $G \subset \mathbf{H}_T^{1/2}(\Gamma)$. Denote by $(\mathbf{x}_1, \mathbf{j}_1) \equiv (\mathbf{u}_1, \mathbf{H}_1, \mathbf{p}_1, \mathbf{j}_1)$ a solution to problem (6) that corresponds to given functions $\mathbf{v}_d \equiv \mathbf{u}_d^{(1)} \in L^2(Q)$ and $\mathbf{g} = \mathbf{g}_1 \in G$. By $(\mathbf{x}_2, \mathbf{j}_2) \equiv (\mathbf{u}_2, \mathbf{H}_2, \mathbf{p}_2, \mathbf{j}_2)$ we denote a solution to problem (6) that corresponds to perturbed functions $\mathbf{v}_d \equiv \mathbf{u}_d^{(2)} \in L^2(Q)$ and $\mathbf{g} = \mathbf{g}_2 \in G$.

Denote by

$$\Delta \equiv \|\mathbf{u}_d^{(1)} - \mathbf{u}_d^{(2)}\|_Q + (a\|\mathbf{g}_1 - \mathbf{g}_2\|_{1/2,\Gamma} + b\|\mathbf{g}_1 - \mathbf{g}_2\|_{1/2,\Gamma}^2)^{1/2}.$$

We obtained local stability estimates for the solutions of problem (6):

$$\|\mathbf{u}_1 - \mathbf{u}_2\|_{\mathbf{H}^1(\Omega)} \leq M_u \Delta, \quad \|\mathbf{H}_1 - \mathbf{H}_2\|_{\mathbf{H}^1(\Omega)} \leq M_H \Delta,$$

$$\|p_1 - p_2\| \leq M_p \Delta, \quad \|\mathbf{j}_1 - \mathbf{j}_2\| \leq M_j \Delta,$$

where a , b , M_u , M_H , M_p and M_j are not decreasing functions of norms of the initial data of Problem 1.

For Navier-Stokes equations we consider the following control problem:

$$J(\mathbf{v}, \mathbf{g}) \equiv \frac{\mu_0}{2} \|\mathbf{v} - \mathbf{v}_d\|_Q^2 + \frac{\mu_1}{2} \|\mathbf{g}\|_{1/2,\Gamma}^2 \rightarrow \inf,$$

$$F(\mathbf{x}, \mathbf{g}, \mathbf{f}) = 0, \quad \mathbf{x} \in X, \mathbf{g} \in K. \quad (7)$$

We assume that the control \mathbf{g} can vary over in a nonempty convex closed set $K \subset \mathbf{H}^{1/2}(\Gamma)$. Similarly we assume that the function \mathbf{f} in (7) can change in some bounded set $F \subset L^2(\Omega)$. Denote by $(\mathbf{x}_1, \mathbf{g}_1) \equiv (\mathbf{u}_1, \mathbf{p}_1, \mathbf{g}_1)$ a solution to problem (7) corresponding to given functions $\mathbf{v}_d \equiv \mathbf{u}_d^{(1)} \in L^2(Q)$ and $\mathbf{f} = \mathbf{f}_1 \in F$. By $(\mathbf{x}_2, \mathbf{g}_2) \equiv (\mathbf{u}_2, \mathbf{p}_2, \mathbf{g}_2)$ we denote a solution to problem (7) that corresponds to perturbed functions $\mathbf{v}_d \equiv \mathbf{u}_d^{(2)} \in L^2(Q)$ and $\mathbf{f} = \mathbf{f}_2 \in F$.

Denote by

$$\Delta \equiv \|\mathbf{u}_d^{(1)} - \mathbf{u}_d^{(2)}\|_Q + \|\mathbf{f}_1 - \mathbf{f}_2\|$$

We obtained linear local stability estimates for the

solutions of problem (7):

$$\|\mathbf{u}_1 - \mathbf{u}_2\|_{\mathbf{H}^1(\Omega)} \leq M_u \Delta, \quad \|p_1 - p_2\| \leq M_p \Delta,$$

$$\|\mathbf{g}_1 - \mathbf{g}_2\|_{1/2,\Gamma} \leq M_g \Delta,$$

where M_u , M_p and M_g are not decreasing functions of norms of the initial data for Navier-Stokes system.

Acknowledgments

The work was supported by the Council for Grants of the President of the Russian Federation for Young scientists support (project no. MK-3311.2011.1), Federal Program "Scientific and scientific-pedagogical personnel of innovative Russia" in 2009 – 2013 years (project no. 14.740.12.0835), Russian Foundation for Basic Research (project no. 10-01-00219-a) and the Far Eastern Branch of the Russian Academy of Sciences (project no. 12-I-P17-03).

References

- [1] A.V. Fursikov, *Mat. Sb.*, **118** (1982), 323–349.
- [2] M. Gunzburger, L. Hou and T. Svobodny, *Math. Model. Numer. Anal.*, **25** (1991), 711–748.
- [3] G.V. Alekseev and V.V. Malikin, *Comp. Fluid Dynamics J.*, **3** (1994), 1–26.
- [4] A.V. Fursikov, *Discrete Contin. Dyn. Syst.*, **46** (2004), 289–314.
- [5] A.V. Fursikov, M.D. Gunzburger and L.S. Hou, *SIAM J. Control Optim.*, **46** (2005), 2191–2232.
- [6] G.V. Alekseev and D.A. Tereshko, *Analysis and optimization in hydrodynamics of viscous fluid*. Dalnauka, (2008).
- [7] G.V. Alekseev and R.V. Brizitskii, *Differential Equations*, **46** (2010), 70–82.
- [8] G.V. Alekseev and R.V. Brizitskii, *Differential Equations*, **48** (2012), 397–409.
- [9] P. Fernandes and G. Gilardi, *Math. Mod. Meth. Appl. Sci.*, **7** (1997), 957–991.
- [10] L.S. Hou and A.J. Meir, *Appl. Math. Optim.*, **32** (1995), 143–162.
- [11] G.V. Alekseev, *Prikl. Mekh. Tekhn. Fiz.*, **44** (2003), 170–179.
- [12] G.V. Alekseev, *Sibirsk. Mat. Zh.*, **45** (2004), 243–262.
- [13] M. Gunzburger and C. Trenchea, *J. Math. Anal. Appl.*, **333** (2007), 295–310.
- [14] M. Gunzburger, J. Peterson and C. Trenchea, *Int. J. Pure Appl. Math.*, **42** (2008), 289–296.
- [15] G.V. Alekseev, R.V. Brizitskii, *J. Comp. Math. Math. Physics*, **45** (2005), 2049–2065.
- [16] G.V. Alekseev, *Uspekhi Mekh.*, **2** (2006), 66–116.
- [17] R.V. Brizitskii and D.A. Tereshko, *Differential Equations*, **43** (2007), 1–13.

Fabrication and Characterization of Novel PDMS based Magnetorheological Elastomers

Weihua Li

School of Mechanical, Materials and Mechatronic Engineering, University of Wollongong,
Wollongong, NSW 2522, Australia
E-mail: weihuali@uow.edu.au

ABSTRACT

This paper presents the fabrication and characterization of Polydimethylsiloxane (PDMS) based new magnetorheological elastomers (MREs). A total of four PDMS based MRE samples, with different weight fractions of 64.5%, 78.4%, 84.5%, and 87.9%, were fabricated. Their mechanical and rheological properties under both steady-state and dynamic loading conditions were tested. The effects of particle composition, magnetic field, strain amplitude and frequency on the MRE effects were summarized. The comparison of the new PDMS based new MRE samples with conventional MREs was reported.

1. Introduction

Magnetorheological elastomers (MREs) are smart materials where polarized particles are suspended in a solid or gel-like matrix. These materials have found a variety of applications because they exhibit characteristics that their moduli can be reversely controlled by an external magnetic field [1]. Both natural rubber and silicone are commonly used as matrix for fabricating MREs. Polydimethylsiloxanes (PDMS) is one example of silicon rubber. The PDMS have a low surface tension and are capable of wetting most surfaces. The stability and chemical neutrality of the system also enables the adhesive to bond to the metals [2]. PDMS is the most widely used silicon-based organic polymer, and is particularly known for its unique properties such as curing at low temperatures, rapid curing at high temperature, deformation reversibility and surface chemistry controllable by reasonably well-developed techniques. PDMS is optically clear, and, in general, is considered to be inert, non-toxic and non-flammable. In this project we used PDMS as the matrix of MREs and studied the mechanical properties of the new MREs. Carbonyl iron particles can easily blend into PDMS because of its liquid initial state, meanwhile, the rapid curing of PMDS under certain temperature provides a quick method to fabricate MREs.

2. Method

The base and curing agent of PDMS, type Sylgard 184 (Dow Corning Pty. LTD) at weight ratio 10:1 were firstly mixed evenly to be used as the carrying matrix, and then added to the carbonyl iron particles, type C3518 (Sigma-Aldrich Pty. LTD) and stirred sufficiently. The iron particles' diameter is between $3\mu\text{m}$ and $5\mu\text{m}$ at normal distribution. The density of iron particles and PMDS are 7.86 g/cm^3 and 1.1 g/cm^3 , respectively. The final mixtures were placed in a vacuum chamber to eliminate bubbles in 30 minutes and were placed between two pieces of plastic paper and pressed to be membranes. Some small cylinders with 1mm thickness were used to ensure the thickness of MREs is 1mm. Then the mixture was curing in an oven at 100°C for 35 minutes and then cut by a punch to disks with 20mm diameter. The total time to fabricate PDMS was no more than 100 minutes, which saves lot of time than the conventional MREs made of natural rubber or silicone

rubber that need more than 24 hours to curing. In this study, four PDMS MRE samples were fabricated whose iron particles' weight fraction (iron wt. %) were 60%, 70%, 80% and 90%. All MRE samples were isotropic. Microstructures of these MRE samples were observed using SEM (JSM 6490LV SEM). Their mechanical and rheological performances were measured with a MR rheometer (MCR301, Anton Paar).

3. Results and Discussion

Figure 1 shows that the carbonyl iron particles disperse randomly in the PDMS matrix due to the isotropy of all samples. The sample having higher iron weight fraction of 90% shows more iron particles in the same area.

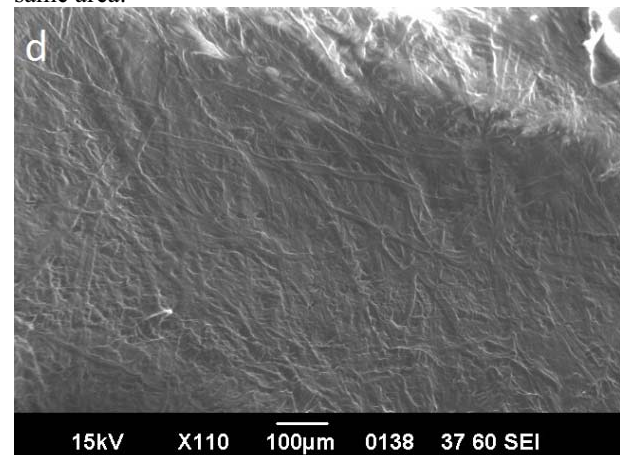


Fig. 1 Microstructure of PDMS MREs with iron 90%.

Figures 2 show the strain–stress curve of the MRE sample at five different magnetic field intensities ranging from 0 to 440 mT. The slope of the strain–stress curve is the shear modulus of the material.

As can be seen in the figures, the sample' shear modulus show an increasing trend with magnetic field before they reach magnetic saturation at high field strength, which proves that all the MRE samples exhibit obvious MR effects. We can see that the curve at 0 mT, which is the zero-field modulus of the 90 wt.% sample, shows a bigger slope of stress-strain curve compared with the lower graphite concentration samples, which means 90wt.% sample has a higher zero-field modulus. When the strain is above the limitation, the shear stress

reaches a saturation (maximum value) and decreases steadily. This might be due to the sliding effect. Additionally, other factors, such as the sample surface roughness and the normal force, could contribute to the resultant stress. In particular, they influence the static friction between the MRE sample and the upper plate, which consequently result in overshoots, as shown in Fig. 2.

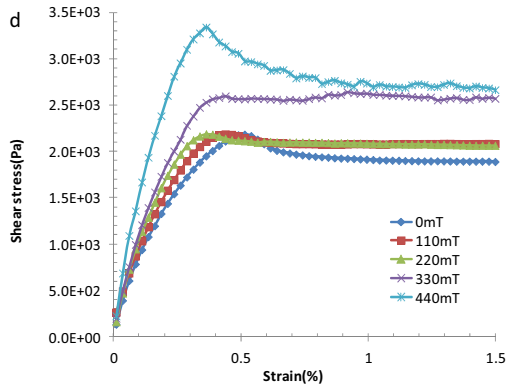


Fig. 2 Strain-stress curve versus magnetic field.

Also from this figure, the shear stress shows a linear relationship with the shear strain when the strain is within a range. This means the MRE acts with linear viscoelastic properties when the strain is below a limitation. Table 1 summarized the linear ranges of all samples at various magnetic field intensities.

Table 1. Linear range of the four MRE samples.

Samples	Linear range (%)				
	0 (mT)	110 mT	220 (mT)	330 (mT)	440 (mT)
60% iron	150	127	127	123	120
70% iron	80	37	33	31	30
80% iron	40	10	9	9	8
90% iron	0.5	0.4	0.35	0.35	0.35

Both strain amplitude sweep and frequency sweep modes were employed to study dynamic properties of the samples. In the strain sweep test, the storage and loss moduli were tested by varying strain from 0.1% to 100% at different magnetic fields and room temperature. Figures 3 show the changing of storage modulus and loss moduli at the strain amplitude sweep. As can be seen from this figure, the overall trend of storage modulus is decreasing with the strain amplitude. It goes down smoothly within a critical shear strain and begins to drop significantly over the critical value and to go crossing with loss modulus, with which we can say that within the critical shear strain, the storage modulus shows approximately a linear relationship with the shear strain. Take sample containing 80% iron as an example, within 10% strain, its storage modulus versus strain as linear. In the frequency sweep mode, the strain

amplitude is set as a constant of 1% while the frequency was varied from 1 to 100 rad/s at different magnetic field of 0, 110, 220, 330, and 440 mT. The storage modulus and loss modulus were tested and shown in Figure 4. As can be seen from these figures, the storage and loss moduli of the sample are both increasing linearly with the growth of angular frequency. This means that at a higher angular frequency, the samples have bigger storage and loss moduli. This logarithmically linear relationship of the storage and loss moduli to the angular frequency can be used to predict the storage and loss moduli at a certain frequency.

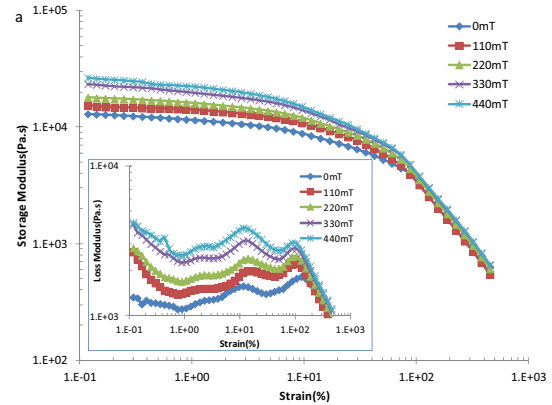


Fig. 3 Storage and Loss Modulus versus sweep strain.

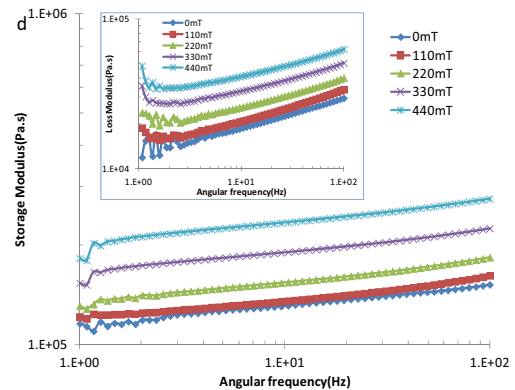


Fig. 4 Storage and Loss Modulus versus sweep frequency for four sample.

4. Conclusions

The fabrication time for PDMS MREs is less than 100 minutes which is much shorter than the time needed for conventional MREs based on natural rubber or silicone rubber. LV SEM was used to observe their microstructures. This observation shows that iron particles disperse randomly in the isotropic samples. Both steady and dynamic testing of the samples demonstrated that they perform similar behaviors as conventional MREs. The higher the iron weight fraction, the higher initial storage and loss modulus and also the higher MR effects.

References

- [1] G. Y. Zhou, Smart Mater. Struct., **12** (2003), 139.
- [2] F. De Buyl, Int. J. Adhes., **21** (2001), 411.

Optical Characteristics of Magnetic Fluid Hole in Alternating Fields

Michihiro Shinozaki¹, Seiichi Sudo¹, Hidemasa Takana², Hideya Nishiyama²

¹Akita Prefectural University, Ebinokuchi 84-4, Yurihonjo 015-0055, Japan

²Tohoku University, Katahira 2-1-1, Aoba-ku, Sendai 980-8577, Japan

E-mail : sudo@akita-pu.ac.jp

ABSTRACT

Experimental study on the optical characteristics of a hole formed with magnetic fluid and thin annular permanent magnet in the alternating magnetic fields were performed by using the Helmholtz coil. The light intensity through the magnetic fluid hole is measured by the photodiode sensor system. It was found that the hole oscillation of magnetic fluid was generated by external alternating magnetic field. The optical characteristics of magnetic fluid hole in alternating fields were revealed.

1. Introduction

With the development of space technology, stable colloidal suspensions (magnetic fluids) of solid magnetic particles of subdomain size dispersed in a nonmagnetic carrier liquid were developed [1]. The fluids respond to magnetic fields and have a magnetization. Magnetic field based micro mechanical system devices using the magnetic fluids were proposed [2]. In our previous papers, authors proposed novel micro electromechanical actuators using a permanent magnet and magnetic fluid [3-5], and novel type of micro wind energy converter using insect wings, NdFeB permanent magnet, magnetic fluid, and the coil [6]. The driving characteristics of these micro magnetic fluid devices were revealed. However, there is no study on the dynamic behavior of the hole formed with magnetic fluid and thin annular permanent magnet in the alternating fields using a photodiode sensor system.

In this paper, the optical characteristics of hole formed with annular magnet and magnetic fluid system in the alternating magnetic field were studied with the photodiode sensor system.

2. Experimental apparatus and procedures

A block diagram of the experimental apparatus used in the study is shown in Fig.1. The test magnet-magnetic fluid system is composed of small thin annular permanent magnet and magnetic fluid. The photodiode system may measure the intensity of LED light. The photodiode sensor system is composed of a LED light source system and a photodiode detector system. The hole oscillation is observed by the light, using the photodiode sensor system. When the size of hole expands, the intensity of light increases. Also the size of hole contracts, the intensity of light decreases. Sample magnetic fluid used in the experiment was kerosene-based ferricolloid HC-50. The saturation magnetization was $M_S = 33.42$ kA/m. The surface tension of magnetic fluid was 0.0277 N/m (magnetic fluid/air at a temperature of 19 °C). The magnetic fluid of a prescribed volume ($V_m = 200$ μ l) was adsorbed by annular magnet as shown in Fig.2. The alternating magnetic field was generated by applying alternating voltage E to the Helmholtz coil.

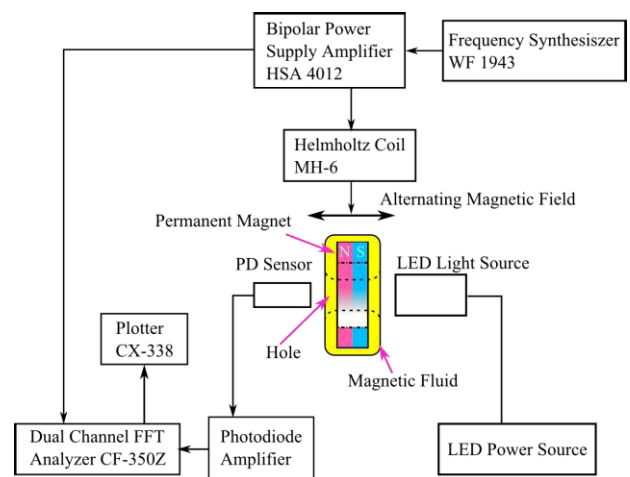


Fig.1 A schematic diagram of experimental apparatus

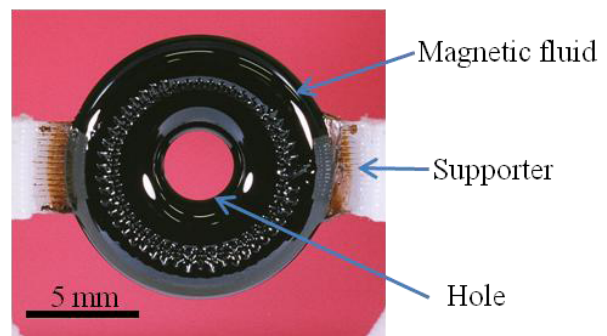


Fig.2 Photograph of magnetic fluid hole system

$$E = \frac{E_0}{2} \sin(2\pi f_0 t) \quad (1)$$

where $E_0/2$ is the amplitude of alternating voltage, f_0 is the frequency, and t is the time. When the alternating voltage E was applied to the coil, current I was described as follows:

$$I = \frac{E}{j(2\pi f_0)L} \quad (2)$$

where L is the inductance of the coil, j is the imaginary unit. In this experiment, the magnetic flux density of permanent magnet was $B_m = 190$ mT at the surface of magnet, and the magnetic flux densities of the external

magnetic field were less than 5 mT. The size of annular magnet is 10 mm in outer diameter, 6 mm in inner diameter, and 1 mm in thickness. The alternating current signal was supplied from the frequency synthesizer. The direction of the magnetic field was parallel and anti-parallel in the magnetic moment direction as shown by the arrow in Fig.1. When the direction of external field corresponds to the magnetic moment direction of the permanent magnet, the magnetic fluid hole expands. While the direction of magnetic field opposes the magnetic moment direction, the hole contracts. The output signal from the photodiode system was analyzed by the dual channel FFT analyzer.

3. Experimental results and discussion

The dynamic response of hole formed with permanent magnet and magnetic fluid element subject to alternating magnetic field was investigated using photodiode sensor system. Figure 3 (a) shows input signal to the coil. Figure 3 (b) shows output optical signal from the photodiode sensor system. The output optical signal, E_{photo} is the voltage signal from the photodiode sensor system. In Fig.3, the frequency of alternating magnetic field is $f_0=20\text{Hz}$ and the total amplitude of voltage is $E_0=40\text{V}$. Figure 3 (c) shows the hole diameter oscillation. It can be seen from Fig.3 (c) that the frequency of hole of magnetic fluid for alternating magnetic field corresponds precisely to the forcing frequency.

The hole response was obtained from the output optical signal. Both the optical signal frequency and the hole diameter frequency correspond precisely to the input signal frequency. The optical signal and the hole oscillation delineate precisely to the same curve. Therefore, the optical signal response corresponds the hole oscillation.

By comparing Fig.3(a) with Fig.3 (c), The phase difference between input signal and optical signal is recognized. The phase difference is 14.7° between applied alternating voltage E and the diameter of hole D_h at $f_0=20\text{Hz}$ and $V_m=2\times 10^{-7}\text{m}^3$. The resonance frequency may obtain by using of the photodiode sensor system.

Figure 4 (b) shows the response of magnetic fluid hole in alternating magnetic field generated by the Helmholtz coil. In Fig.4, the frequency of alternating magnetic field is $f_0=1\text{kHz}$ and the total amplitude of voltage is $E_0=40\text{V}$. It can be seen from Fig.4 that magnetic fluid hole responds even at applied frequency, $f_0=1\text{kHz}$. The diameter oscillations of magnetic fluid hole were observed even at higher frequencies ($>1\text{kHz}$).

4. Conclusions

The dynamic responses of magnetic fluid hole in alternating magnetic field were studied with the photodiode sensor system. The signal from the photodiode system revealed the detail of the magnetic fluid hole response to the alternating magnetic field. The phase difference between applied alternating voltage E and the diameter of hole D_h was recognized.

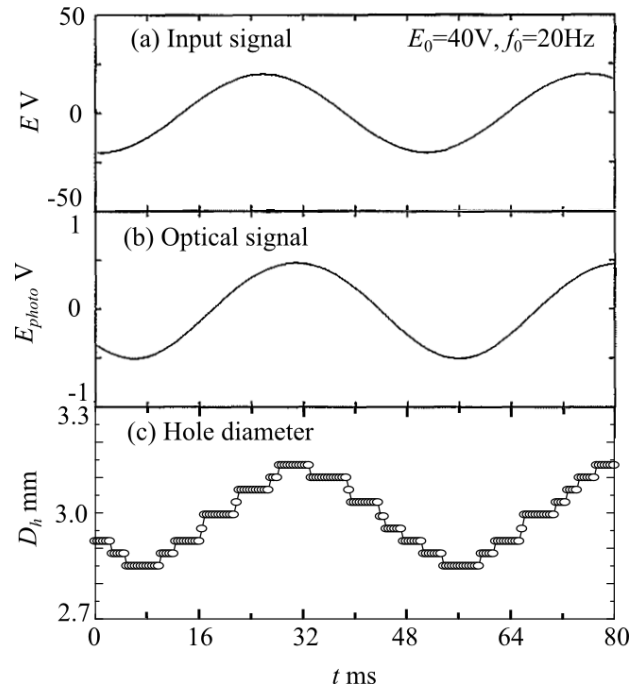


Fig.3 Variations of (a) the input signal, (b) the optical signal and (c) the hole diameter ($E_0=40\text{V}$, $f_0=20\text{Hz}$, $V_m=2\times 10^{-7}\text{m}^3$)

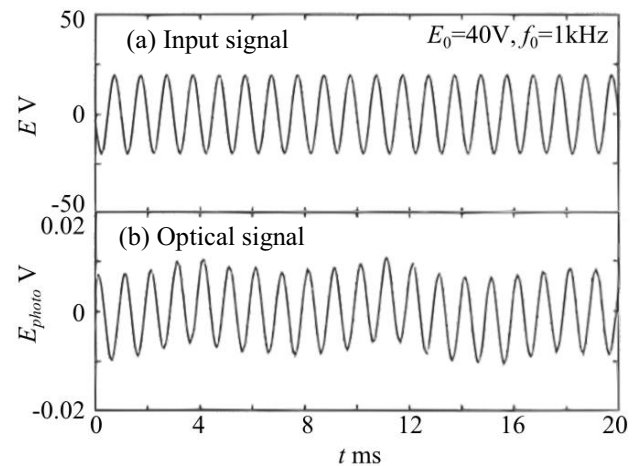


Fig.4 Variations of (a) the input signal and (b) the optical signal ($E_0=40\text{V}$, $f_0=1\text{kHz}$, $V_m=2\times 10^{-7}\text{m}^3$)

References

- [1] R.E. Rosensweig, Ferrohydrodynamic (Cambridge Univ. Press, Cambridge, 1985).
- [2] M. Zahn, J. Nanoparticle Res., **3** (2001), 73.
- [3] S. Sudo, Y. Takaki, Y. Hashiguchi, H. Nishiyama, JSME Int. J., **48-3** (2005), 464.
- [4] S. Sudo, T. Yano, M. Okabe, T. Komatsu, Int. J. Appl. Electromagn. Mech., **25** (2007), 95.
- [5] S. Sudo, A. Nakagawa, Int. J. Modn. Phys., **19**(2005), 1520.
- [6] S. Sudo, K. Tsuyuki, T. Yano, K. Takagi, J. Phys. : Cond. Matter., **20** (2008), 204142.

The Bubble Deformation

Shih-Wei Liu and Chun-Liang Lai

Department of Mechanical Engineering

National Taiwan University

Taipei, Taiwan 106 R.O.C.

E-mail: cllai@ntu.edu.tw

ABSTRACT

A zero-net-force, self-driven, deformation-induced bubble motion, named bubble deformation, is defined and clearly demonstrated in this study through a theoretical analysis of a long bubble migration in a conical tube.

1. Introduction and Physical Model

The present study is aimed at investigating and analyzing theoretically and systematically the unsteady migration and shape variation of a long bubble moving in a conical tube.

The schematic of the physical model and coordinate system are shown in Fig. 1. The coordinate system employed is the *conical coordinates* with r denoting the radial coordinate pointing outward from the vertex and along the tube wall, and z , the inward coordinate normal to the wall. The half angle of the conical tube is α . A long bubble of length ℓ with a rear spherical cap of radius \bar{R}_1 and a front spherical cap of radius \bar{R}_2 will migrate with a speed $U(t)$ through the conical tube from the narrower end toward the wider end due to capillary pressure gradient. In the mean time, the surrounding liquid with viscosity μ will flow from the wider end toward the narrower end through the thin film region between the tube wall and the long gas bubble. The surface tension between the liquid and the gas

bubble is denoted by σ . Three flow regimes were usually defined in the previous studies: the creeping liquid flow along the thin film region between the tube wall and the side surface of the long bubble, the nearly stagnant regions around the two end caps of the bubble, and the transition regions in between.

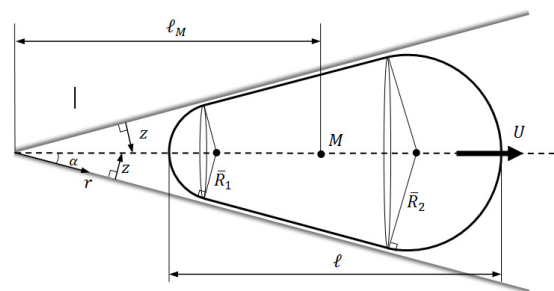


Fig. 1 The schematic of a long bubble in a conical tube

2. Method and Results

The logic and procedure for solving the problem are shown in Fig. 2, where Q and h denote, respectively, the volume flow rate through and the thickness of the thin liquid film, V is the volume of the

enclosure region bounded by the rear cap and the tube wall, and $U(t)$ represents the migration speed of the bubble.

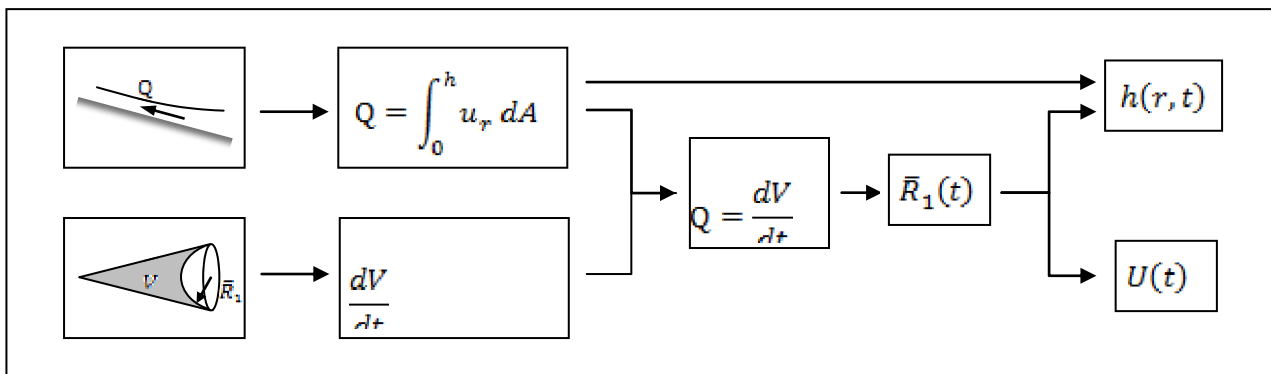


Fig. 2 The solution logic and procedure.

The following two conditions are employed to accomplish the analysis: (1) the conservation of the surrounding liquid flow, and (2) the constant-volume constraint of the gas bubble. The results indicate that the bubble always migrate from the narrower end toward the wider end with a reduced migration speed. Consequently, the bubble becomes wider and shorter, approaching spherical shape finally as required by the second law of thermodynamics, Fig. 3.

The most important conclusion from all the findings is that the net force acting on the bubble during migration vanishes always. The migration is due to the unequal deformation of the front and rear caps of the bubble; it is different from the rigid body motion determined by the Newton's second law. The present study thus defines and names such a "deformation induced motion" as "deformation"!

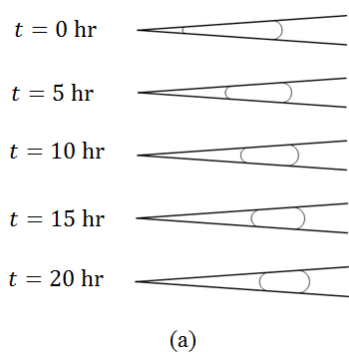


Fig. 3 (a) The bubble migration in a conical tube

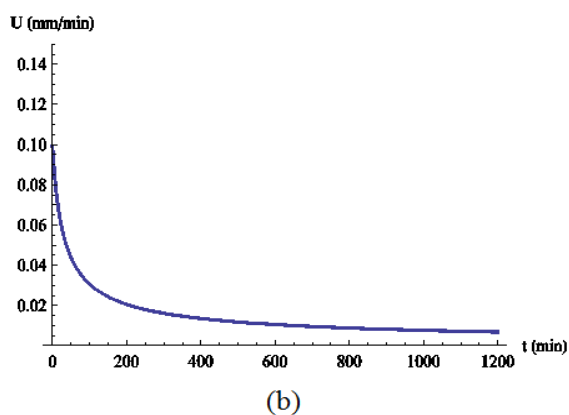


Fig.3 (b) the time variation of the bubble migration speed U with $\sigma/\mu = 80 \text{ m/s}$, $\alpha = 4^\circ$, $R_0 = 5 \text{ mm}$, $\ell_1(0) = 1.5 \text{ cm}$, and $h_1 = 0.01 \text{ mm}$.

OS6: Multiphase Science and Ultra Clean Technology

Challenges in 1x Design Node Semiconductor Device Cleaning

Jin-Goo Park^{1,a}, Bong-Kyun Kang¹ and Manivannan Ramachandran¹

¹Department of Bionano Technology and Materials Engineering, Hanyang University, Ansan 426-791, Korea
^ajgpark@hanyang.ac.kr

ABSTRACT

Physical force induced wet and dry cleaning methods have been investigated to remove the killing contaminants from the surface without collapsing any pattern. To address the critical issues of cleaning process for 1x design node semiconductor, cleaning process window between the fragile pattern and nano sized particle were quantitatively measured and analyzed by using the nano manipulation mode of atomic force microscope (AFM). Subsequently, we could find out critical margin of cleaning process between the pattern collapse force and particle removal force by our proposed physical force induced cleaning method.

1. Introduction

As the design rule for the semiconductor device becomes tighter, the formation of nanopatterns as well as the cleaning process becomes important in device of 1x design rules [1]. Also, the concentration of chemicals becomes diluted to minimize the materials loss, but it is difficult to remove the contaminants such as particles due to lower reactivity [2]. In order to enhance the particle removal efficiency (PRE) with a minimum material loss, physical forces have been applied in both wet cleaning methods such as a megasonic (MS) irradiation and a high speed jet spray with very dilute chemicals and dry cleaning methods such as cryogenic aerosol and laser induced plasma (LIP) shock wave.

Particle diameter of a few tens of nanometers should be considered as killer defects for the features sizes below 50 nm. As the particle size decreases, higher cleaning forces are required due to the higher particle adhesion forces. However, an increase in cleaning force can have negative impacts on pattern damage. In order to secure an effective cleaning process without pattern damages, the mechanism for the pattern collapse and particle removal should be understood and measured quantitatively with various physical force induced cleaning method as mentioned earlier and its possibility as a cleaning method below 1x pattern devices.

2. Method

Collapse force measurement of nano pattern: An AFM was employed to measure the lateral deflection signal. When an AFM tip touches a nano pattern and the signal was quantified by the lateral force calibration method [3] to define the strength of nano patterns and the particle removal force. Those forces were measured by an AFM (XE-100, Park Systems) with nano manipulation software to control the motion of the AFM probe and a signal access module with a data acquisition system (PCI-6123, National Instrument) to simultaneously collect the signals of cantilever bending and twisting as shown in Fig. 1.

Evaluation of cleaning ability: In order to evaluate the cleaning efficiency of various cleaning methods, the surface was intentionally contaminated either by slurry dipping or by spin drying method regardless of their type and size. Coupon sized pattern wafers were used for pattern damage test and the number and density of damage in line pattern were observed by optical

microscope.

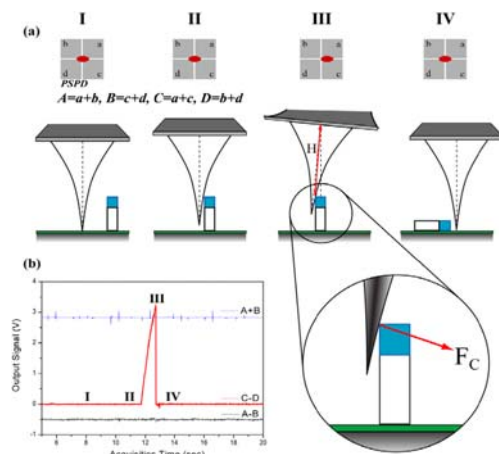


Fig. 1. (a) Illustration of AFM probe motions and (b) their signal gains to measure the collapse force of nano pattern.

3. Results and Discussion

Fig. 2 shows the measured collapse force of two different patterns as a function of line width. The collapse force of photoresist (PR) pattern was about 10 times lower value than that of poly Si pattern at the same line width, which is due to the weak mechanical strength of the PR pattern material. The collapse force of poly Si line pattern below 50 nm line widths could also be predicted based on the fitted line. The collapse force of PR pattern at 300 nm line width showed about 1.4 μN . This collapse force corresponds to 50 nm line width in the case of poly Si pattern.

Fig. 3 shows the PRE of various gas dissolved deionized water (DIW) types as a function of their pressurized level. PRE of various gas dissolved DIW increases gradually with the pressurized level. But there exist a large difference in cleaning ability of various dissolved gases, which may be due to difference in the cavitation effect affected by a change in physical properties associated with acoustic bubble growth rate. Fig. 4 shows the line density of damage sites on PR pattern as a function of the dissolved gas types with their concentration level. The density of damaged sites on the PR patterns is reduced when DIW and Ar-DIW is used for cleaning. On the other hand, the PR pattern had a lot of damage sites when H_2 gas was used irrespective of its concentration level, owing to its much stronger

cavitation effect than other gases.

Also, to define the relationship between pattern collapse and particle removal force in practical LIP shock wave cleaning process, the resisting moment for patterns M_p was calculated by

$$M_p = F_p \times h_p$$

where F_p is a minimum resisting force of pattern against the collapse force and h_p is the height of poly Si pattern. The removal moment ratio of the pattern resisting moment and moment of the LIP shock wave could be calculated as shown Fig. 5. To verify this theoretical relationship between the particle removal moment ratio (RMR) and the pattern collapse moment ratio, 1 μm silica contaminated poly Si pattern wafer was cleaned by using the laser shock wave. Particles were removed effectively without any pattern damages after exposing to the shock wave radiation as shown in Fig. 6. The relation between measured RMR for 1 μm and the pattern collapse moment ratio agreed well with the actual cleaning experiment.

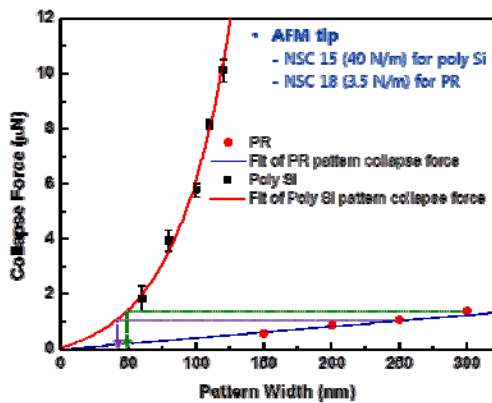


Fig. 2. The collapse forces of SiO₂/poly Si/SiO₂ gate stack and PR line patterns as a function of the line width.

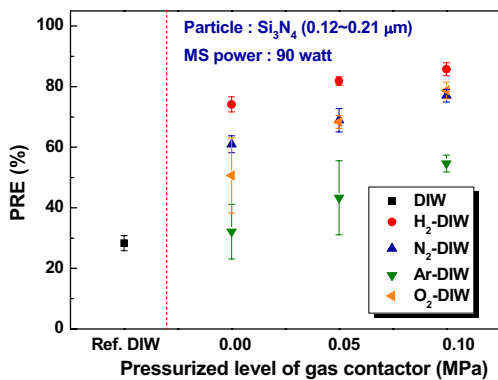


Fig. 3. Comparison of particle removal efficiency as a function of pressure at the contactor for various gas dissolved DIW.

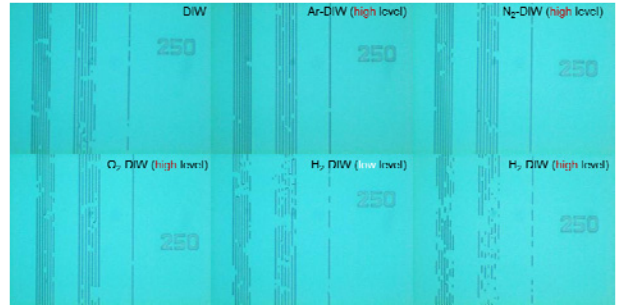


Fig. 4. Optical microscope images of PR line width of 250nm showing damage sites after MS cleaning for 1 min using various gas dissolved DIW.

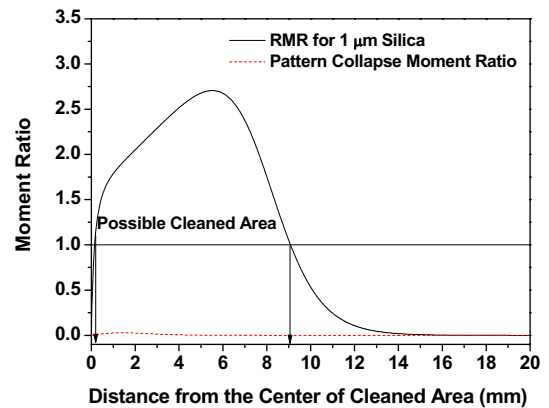


Fig. 5. The calculated moment ratio for the silica particle removal with a diameter of 1 μm and for the pattern collapse of the poly Si at line width of 80 nm.

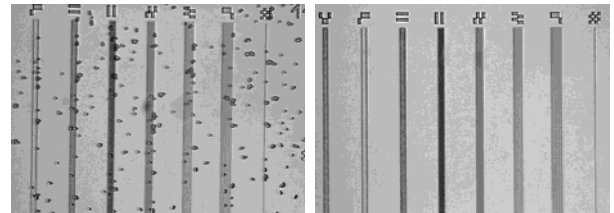


Fig. 6. Optical microscope images of (a) 1 μm silica particles deposited on poly Si patterns of 80 nm line width and (b) after particle removal by cleaning with laser energy of 1.8 J at a gap distance of 3 mm.

4. Concluding remarks

In this study, pattern collapse force and particle removal force were measured by using AFM manipulation mode. We could also propose an alternative method to predict the physical cleaning process window regardless of wet and drying cleaning method to achieve damage free cleaning.

References

- [1] K. A. Reinhardt et al., Handbook of Silicon Wafer Cleaning Technology, William Andrew, Norwich (2008).
- [2] T. Hattori et al., IEEE Transactions on Semiconductor Manufacturing, **20**, 252 (2007).
- [3] J. E. Sader et al., Rev. Sci. Instrum., **70**, 3967 (1999).

Novel Quantum Dot Solar Cells realized by Fusion of Bio-template and Defect-Free Neutral Beam Etching

Seiji Samukawa^{1,2,3}

¹Institute of Fluid Science, Tohoku University, Sendai, 980-8577, Japan, samukawa@ifs.tohoku.ac.jp

²WPI Advanced Institute for Materials Research, Tohoku University, Sendai, 980-8577, Japan

³Japan Science and Technology Agency, CREST, Tokyo, 102-0076, Japan

ABSTRACT

A 2-dimensional Si nanodisk (ND) array with a high-density and well-ordered arrangement could be fabricated by using bio-template and an etching process combined with nitrogen trifluoride (NF₃) gas/hydrogen radical treatment (NF₃ treatment) and Cl NB etching. In this structure, the controllable band gap energy (from 2.2eV to 1.4eV) and high photon absorption coefficient ($>10^5 \text{ cm}^{-1}$) could be obtained at RT by controlling the Si-ND structure. Our proposed processes for 2D Si-ND array and stacked ND are very feasible for the all-Si tandem solar cells comprising quantum dot superlattice (QDSL).

1. Introduction

Recently, an all-silicon tandem solar cell comprising a quantum dot superlattice (QDSL) has attracted much attention due to its potential to breakthrough the Shockley-Queisser limit.^{1,2)} One of the advantages of the QDSL is that the required energy band gap for each cell can be engineered by changing the quantum dot size.³⁾ Reportedly, the maximum conversion efficiency can be improved up to 47.5% for three-cell tandem stacks.⁴⁾ However, not only the uniformity and control of QD size but also of the spacing between QDs are equivalently essential to generate the miniband in the QDSL for carrier transport.⁵⁾ The ideal spacing between QDs is approximately 2 nm or less in the SiO₂ matrix.⁶⁾ The technique widely used to fabricate the Si quantum dot superlattice is depositing alternately multiple layers of amorphous silicon-rich oxide (SiO_x, $x < 2$) and stoichiometric silicon dioxide (SiO₂) by sputtering or plasma-enhanced chemical vapor deposition followed by annealing at a high temperature.^{6,7)} However, the results showed nonuniform dot size and dot spacing.

To address these problems, we have developed a sub-10nm-silicon-nano-disk (Si-ND) structure using the bio-template (ϕ 7-nm-etching-mask) and damage-free chlorine (Cl) neutral beam (NB) etching.⁸⁾ The fabricated ND had a quantum effect, i.e. Coulomb staircase, at room temperature (RT). Two geometrical parameters of thickness and diameter in Si-ND can be independently controlled. Interestingly, the quantum effect of a single Si-ND is strongly dependent on its thickness, while almost independent of its diameter.⁸⁾ In this study, a 2D Si ND array with a high-density and well-ordered arrangement could be fabricated by using bio-template and an etching process combined with nitrogen trifluoride (NF₃) gas/hydrogen radical treatment (NF₃ treatment) and Cl NB etching. In this structure, the controllable band gap energy (from 2.2eV to 1.4eV) and high photon absorption coefficient ($>10^5 \text{ cm}^{-1}$) could be obtained at RT by controlling the Si-ND structure.

2. Fabrication of high-density 2D array of Si-ND

The fabrication of a 2D Si-ND array using the bio-template and damage-free NB etching⁸⁾ is schematically shown in Fig. 1(a). The steps are as follows: multilayer films of 1.4-nm SiO₂, several nm-thick poly-Si and 3-nm SiO₂ (the 3-nm SiO₂ was fabricated by our developed neutral beam oxidation at a low temperature of 300 °C and is called NBO SiO₂ hereafter) were sequentially prepared on a Si wafer as shown in Fig.1(1), Fig.1(2), and Fig.1(3), re-

spectively; (4) a 2D array of ferritin molecules (protein including iron oxide core (Fe-core) in the cavity) was placed through directed selforganization on the surface of NBO SiO₂; (5) ferritin protein shells were removed by heat treatment in oxygen atmosphere to obtain 2D Fe-core as a template; (6) etching was carried out using a NF₃ treatment and Cl NB etching to remove NBO SiO₂ and poly-Si, respectively; (7) and finally 2D Fe core was removed by using hydrochloric solution. The sample underwent NF₃ treatment for 30 min to remove NBO SiO₂ and NB etching for 90 seconds to remove 4-nm poly-Si. Figure 2 shows a SEM image of the top view of the sample after etching. We can see that the 2D Si-ND array has a high-density ($>7 \times 10^{11} \text{ cm}^{-2}$) and well-ordered arrangement. The 2D array is what remained after etching, proving that a good-quality 2D Si-ND array was successfully fabricated using the bio-template and Cl NB etching with NF₃ treatment. We performed NF₃ treatment to investigate the controllability of the ND diameter, i.e. the spacing between NDs. When the NF₃ treatment times were 15 and 30 min, the average gaps were about 1 and 3 nm (G_{ii} and G_{iii}), and the diameters were about 10 and 8 nm (D_{ii} and D_{iii}), respectively. These results suggest that the spacing between adjacent NDs can be controlled by changing the NF₃ treatment time, which also indicates that the formation of miniband in a 2D Si-ND array can be controlled. Although the spacing control by NF₃ treatment is accompanied by inevitable changes in diameter, as shown in Fig. 4, the diameter changes do not affect the quantum effect, which was proven in a previous work.⁸⁾

3. Optical Properties of 2D Si-ND array

The absorption properties of the structure were studied by measuring the transmission for samples by UV-vis-NIR. The absorption coefficient has been calculated in accordance with the equation below⁹⁾

$$T = e^{-ad}$$

a being the absorption coefficient, d the total thickness of the ND thickness and surface oxide thickness (3-nm thick), and T the transmittance of light passing through the structure. Figure 3(a) shows the results of an absorption coefficient of the structure as a function of ND thickness. We found that the absorption spectra strongly depend on the ND thickness and the absorption edge is blue-shifted when the ND thickness decreases due to the quantum size effect. Additionally, the absorption coefficient ($>10^5 \text{ cm}^{-1}$) of 2D Si-ND array is extremely high, and therefore it is possible

to obtain sufficient absorption if the NDs can be integrated into the 3rd dimension. To determine the optical band gap energy of the structure, the Tauc formula was used:

$$(ah\nu)^{1/2} = A(h\nu - E_g),$$

where A is a constant, h is Planck's constant, ν is frequency, E_g is the band gap energy, and n is 1/2 in the case of indirect allowed and forbidden electronic transitions. The Tauc formulation as a function of ND thickness is plotted in Fig. 3(b). As the ND thickness changes from 2 to 12 nm, the E_g could be controlled from 2.2 to 1.4eV as shown in Fig. 4. From these results, we found that E_g could be certainly controlled by simply changing ND thickness by thin-film deposition in our proposed fabrication. Based on the processes, all-Si tandem solar cells assembled with 3D ND array fabricated by stacking 2D Si-ND array as schematically shown in Fig. 5 could be constructed.

4. Conclusions

We created a 2D Si-ND array with a high-density and well-ordered arrangement using bio-template and an advanced etching process that included NF_3 treatment and damage-free Cl NB etching. The spacing between Si NDs can be controlled in the structure by changing NF_3 treatment time. The E_g can be easily controlled by changing the ND thickness during thin film deposition. The absorption coefficient of single layer 2D Si-ND is comparable to that of 3D QDSL. Our proposed processes for 2D Si-ND array and stacked ND are very feasible for the all-Si tandem solar cells comprising QDSL.

References

- [1] W. Shockley and H. J. Queisser, J. Appl. Phys. **32** (1961) 510.
- [2] M. A. Green et al., 20th EU-PVSEC (2005), 1AP.1.1.
- [3] A. Kongkanand et al., J. Am. Chem. Soc. **130** (2008) 4007.
- [4] G. Conibeer et al., Thin Solid Films **516** (2008) 6748.
- [5] A. J. Nozik: Physica E **14** (2002) 115.
- [6] E. C. Cho et al., Nanotechnology. **19** (2008) 245201.
- [7] Y. Kurokawa et al., Jpn. J. Appl. Phys. **45** (2007) L1064.
- [8] S. Samukawa et al., Appl. Phys. Express **1** (2008) 074002.
- [9] B. Pejova and I. Grozdanov, Mater. Chem. Phys. **90** (2005) 35.

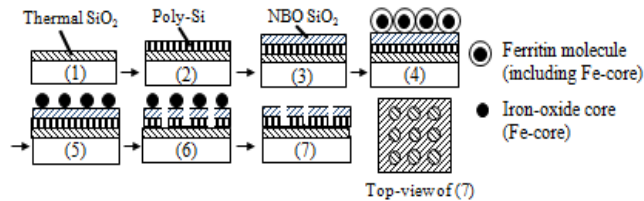


Fig. 1. Fabrication flow of 2 dimensional Si nano-disk array by bio-template and chlorine neutral beam etching.

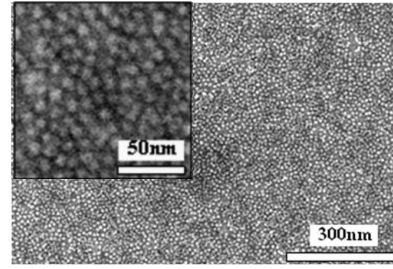


Fig. 2. SEM images of 2 dimensional Si nano-disk array fabricated by Cl neutral beam etching with bio-template.

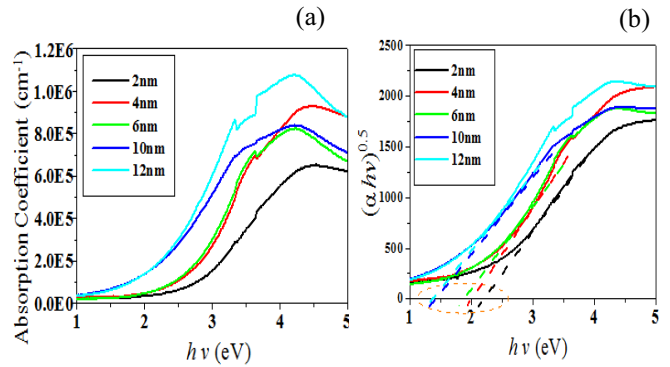


Fig. 3. (a) Absorption coefficient (b) Tauc plot of 2 dimensional Si nano-disk array with different nano-disk thicknesses from 2 nm to 12 nm.

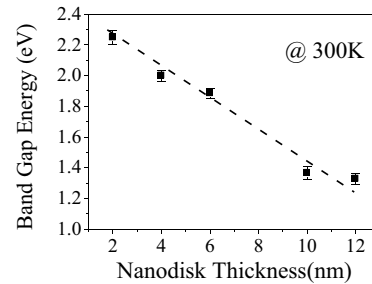


Fig. 4. Band gap energy (E_g) of nano-disk with different Si nano-disk thicknesses by using UV-vis-NIR.

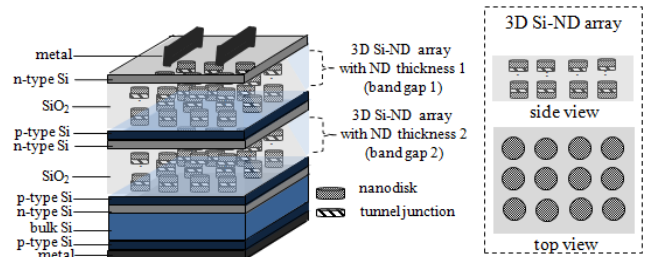


Fig. 5. Scheme of all-silicon tandem solar cell assembled with 3 dimensional Si nano-disk array.

Ultrapure Water-Related Problems and Waterless Cleaning Challenges in Leading-Edge Semiconductor Manufacturing

Takeshi Hattori

Hattori Consulting International, 5-17-82, Nango, Chigasaki 253-0061, Japan
hattori@stanfordalumni.org

ABSTRACT

Ultrapure water can cause several serious problems in leading-edge semiconductor device manufacturing, such as nano-structure collapse, watermark formation, material dissolution, and flow electrification, among others. The solutions to these problems are presented. As the ultimate solutions, waterless cleaning techniques are also described and discussed, which include HF vapor cleaning, cryogenic nitrogen aerosol cleaning, supercritical carbon-dioxide cleaning, and pinpoint cleaning, such as MEMS-tweezer pickup.

1. Introduction

Ultrapure water (UPW) plays an essential and important role in the semiconductor industry for cleaning and rinsing silicon wafer surfaces as well as diluting aqueous chemicals¹⁾. As semiconductor device geometry shrinks to the nanometer range, it becomes clear that UPW causes several serious problems in the most advanced semiconductor manufacturing²⁾.

In this paper, these UPW-related problems are described and practical solutions to these problems are presented. This paper then demonstrates and discusses several waterless cleaning techniques as the ultimate solutions to the problems.

2. UPW-Related Problems and their Solutions

High Resistivity of Water: During water rinsing of silicon wafers, water jet impacted against the surface of a silicon wafer can generate streaming electrification on the silicon surface with highly resistive water, resulting in the degradation of gate oxide integrity as well as accelerated electrostatic adhesion of particles onto the wafer surface. The use of carbon-dioxide dissolved water can prevent the electrostatic-charge generation even at the highest speed. Connecting the wafer to ground is another solution but it will be sometimes difficult to modify the tool-component materials.

High Reactivity of Water with Silicon: In the aqueous processing of silicon wafers, drying after water rinsing is a critical step in terms of the prevention of both particle adhesion and watermark formation. The easy reaction of water with oxygen in air and substrate silicon at room temperature forms silicic acid ($\text{SiO}_2 \cdot x\text{H}_2\text{O}$), resulting in, after wafer drying, the formation of its residues or so-called watermarks on the silicon surface. The watermarks cause prevention of both etching and epitaxial growth. It has become increasingly more difficult to reduce the watermarks to the extent desirable as the device geometry has shrunk. Conventional drying methods such as centrifugal spin drying, IPA vapor drying, and even Marangoni (or Rotagoni) drying can not meet the stringent requirement for watermark prevention in the most advanced wafer processing lines for nano-device fabrication. In order to prevent watermark formation, various novel methods have been employed, which include drying in an inert-gas ambient with a seal plate and more preferably in a sealed chamber in the single-wafer spin cleaning

system and blowing ultra-dry air with a dew point of -96°C or below along the wafer surface in the batch immersion cleaning equipment. Very recently, the replacement of water with liquid IPA during rinsing and subsequent wafer drying with IPA evaporation is employed in some of the most advanced lines, but the excess consumption of IPA is unfavorable from the environmental viewpoint. Introduction of non aqueous cleaning will be the ultimate solution^{2,3)}.

High Permittivity of Water: In the BEOL, the k value of interlayer insulating films has been being decreased from 4 (SiO_2) through 3 (SiOC) and 2 (ULK) toward 1 (airgap) in order to reduce RC time delay of LSI circuits and increase the system performance. If water remains in porous low- k interlayer films after wet cleaning and drying, the effective k -value of the film increases due to the high k value of water ($k=78$), causing delayed signal propagation in the circuits. The use of thermal curing or non-aqueous processing will be able to solve the problem.

Dissolution/Corrosion of Metals in Water: In the FEOL, some high- k gate capping materials such as La_2O_3 dissolve in water while, in the BEOL, Cu is corroded in water during wafer rinsing. These metal losses result in the degradation of electrical characteristics of semiconductor devices. The solution to the former issue is to employ organic-solvent cleaning and that for the latter case is to lower the oxidation-reduction potential of UPW by eliminating dissolved oxygen in UPW or more preferably by using electrolyzed reducing water or Hydrogen water. It should be noted that UV treatments of water to eliminate total organic carbons in on-site UPW plants generate unexpected hydrogen peroxide in the ppb range in UPW, which can cause metal corrosion as well as chemical oxidation of the silicon surface.

High Surface Tension of Water: The last but not least problem of aqueous cleaning is the high surface tension of rinsing water, which was able to be completely ignored when the device geometry was big enough, so that the surface tension of water had virtually no influence on the mechanical strength of the circuit structures. However, with semiconductor-device geometry shrinking and becoming more complex, conventional aqueous cleaning/drying tends to collapse high-aspect-ratio fragile photoresist and

ULSI/MEMS device patterns due to the comparatively high surface tension of water during wafer drying³⁾, as shown in Fig. 1. Pattern collapse occurs not only in thin gate-stack and STI structures in the FEOL but also in porous ultra- low-k interlayer structures in the BEOL for most advanced devices. In many cases, conventional aqueous cleaning/drying will be inadequate and impractical for free-standing MEMS structures and high aspect-ratio LSI structures. Aqueous cleaning/ drying should be further modified or avoided in the near future.

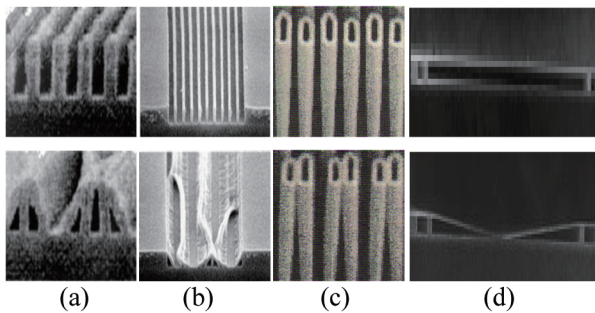


Fig. 1. SEM images of typical collapse/stiction of nano-structures: normal patterns (upper) and collapsed patterns (lower) of photoresists (a,b), DRAM cylindrical capacitors (c) and a MEMS beam structure. (Not to scale)

3. Wafer Cleaning without Using Water

Finally, as the ultimate solutions, several techniques of wafer cleaning without using water are demonstrated and discussed³⁾.

HF Vapor Cleaning: Vapor-phase etching/cleaning to use a controlled mixture of anhydrous HF/MeOH has been employed for etching thin silicon dioxide films without causing pattern collapse or stiction. The chemical reactions produce not only residues but also water as a product of etching which can sometimes cause stiction of fragile MEMS structures such as RF switches having air-filled cavity structures. In such a case, an elevated-temperature, low-pressure HF vapor treatment is preferable in order to prevent water condensation on the silicon surface. Temperature and pressure should be carefully selected to prevent the condensation of water on the etched surface as well as to prevent non-volatile residues left behind.

Cryogenic Aerosol Cleaning: Cryogenic aerosol-based cleaning is one of the most promising dry cleaning techniques that can remove particles and process residues. Conventionally used carbon-dioxide and argon aerosols, however, can cause the destruction of fragile fine structures. High aspect-ratio structures can be cleaned without causing damage by employing nitrogen as a source of aerosols, whose force of impact against the structures is smaller than argon and CO₂ due to its smaller molecular weight. Our simulation based on molecular dynamics showed that the pressure and temperature of impacting nitrogen aerosols against the surface reach the critical point of nitrogen. Hence resulted supercritical nitrogen fluid will be considered to

generate relatively large shear force to remove particles out of silicon wafers even when the force of the impacting nitrogen is smaller than argon and CO₂ due to the smaller size of the aerosols.

Supercritical Fluid Cleaning: Supercritical carbon dioxide (SCCO₂)-based technology has been proposed for various steps in device fabrication, such as wafer drying, cleaning and metal deposition. SCCO₂ has no surface tension like gas, and thus, can penetrate easily into deep trenches and vias, and also enables cleaning and drying without pattern collapse or stiction. We have successfully stripped high-dose ion-implanted photoresists by using SCCO₂ without damage and silicon recess^{4,6)}. SCCO₂ can also be applied for stripping the post-etch photoresists on ultra low-k films by adding chemical formulations without causing damage and k-value change^{4,6)}. In MEMS fabrication, etching of nanometer-thick sacrificial SiO₂ layers and *in-situ* drying in SCCO₂ can form nano-gap beam structures without stiction. The potential of particle removal using SCCO₂ has also been shown^{4,6)}. The unique properties and capabilities of SCCO₂ will continue to draw interest for various applications in the future semiconductor and nano-electronics industries

Pinpoint Cleaning: While all the methods described above clean the whole surface of a wafer in a single operation, novel local-area or pinpoint cleaning, in which particulate contaminants are targeted one by one without affecting the surrounding non-contaminated areas of the wafer surface, will become necessary as the required level of cleanliness gets even higher. Several pinpoint cleaning methods have been proposed³⁾, which include femto-second laser illumination to create abrupt surface expansion, laser shockwave irradiation, AFM nano-probe sweeping, and MEMS-based nano-tweezer pickup.

4. Concluding Remarks

Practical solutions to UPW-related problems were given and several waterless cleaning techniques as the ultimate solutions to the problems were described and discussed. As we work to develop non-aqueous/dry cleaning methods, we are encouraged by knowing that these methods are environmentally-friendly. There will be more research challenges and opportunities in the damage-free waterless cleaning technologies for more fragile, finer nano-structures in the near future.

References

- 1) T.Hattori: Ultra Clean Surface Processing of Silicon Wafers, Springer, Berlin and New York (1998).
- 2) T. Hattori: ECS Transactions, **34** (1) (2011), 371.
- 3) T. Hattori: ECS Transactions, **25** (5) (2009), 3.
- 4) K. Saga and T. Hattori, Solid State Phenomena, **134**, (2008), 97, and references therein.
- 5) K. Saga, H. Hirano, and T. Hattori: 8th Int'l Symp. on Supercritical Fluids, Kyoto, BO-2-16 (2006).
- 6) T. Hattori: in Supercritical Fluids for Semiconductor and MEMS Devices, Corona Publishing, Tokyo (2012) <in Japanese>.

Droplet Impact as an Elementary Process of Physical Cleaning

Kazumichi Kobayashi^a, Ryuichi Uemura^a, Masao Watanabe^a, Toshiyuki Sanada^b, Atsushi Hayashida^c

^aDivision of Mechanical and Space Engineering, Hokkaido University, Sapporo, Japan

^bDepartment of Mechanical Engineering, Shizuoka University, Hamamatsu, Japan

^cAqua Science Corporation, Yokohama, Japan

masao.watanabe@eng.hokudai.ac.jp

ABSTRACT

In the steam-water mixed spray-cleaning technique, droplet impact on the solid surface is the one of the primarily important physical processes. We experimentally studied a freely falling droplet impact on a solid plate that moves with a speed ranging from 5 to 50 m/s using high-speed video camera. We observed that high-speed liquid film flows radially outward along the surface just after the impact. In addition, we also observed that liquid turns into splash in the cases of higher impact velocities.

1. Introduction

We have been proposing that steam-water mixed spray on silicon surface is quite effective in both cleaning and photo-resist stripping [1, 2]. We assume that the pressure field generated by the droplet impact on a surface causes the primary physical force in this method [3]. The impacting high pressure may contribute to detaching particles from the wafer surface; however, particles should be advected by either gas or liquid for a cleaning process to be completed. These flow fields are mainly generated due to the high-speed droplet impact.

We experimentally study a millimeter sized droplet impacting on a solid plate that moves with a speed ranging from about 5 to about 50 m/s toward a freely falling single droplet. We discuss the deformation process of the single droplet due to the impact and the consequently generated liquid flow field. In the cases of lower impact velocities, we observe liquid film flow radially outward along the surface just after the impact. We also observe fingers in the cases of higher impact velocities. These outwardly generated flow field due to the droplet impact may play an important role in cleaning.

2. Method

We observed that an accelerated solid plate, which we refer to as impact plate hereafter, impacts on a freely falling single droplet which was generated with the use of the needle whose inner diameter was 0.1mm. The diameters of the droplet were approximately 2 mm. The impact plate was made of a square piece of silicon wafer, which was adhered to the surface of the circular transparent acrylic resin plate, whose outer diameter and height were 8.0 mm and 1.0 mm, respectively. The impact plate was accelerated by a compressed air whose pressure ranged from 0.05 to 0.60 MPa in gauge. The distance that a droplet falls from the generation to the impact was 400 mm. The droplet fall velocity was approximately 2.5 m/s just before the impact. Schematic of experimental setup is shown in Fig. 1.

The rates of changes of both the shape of droplet and the flow field upon the impact of the impact plate on the droplet were measured from the pictures taken by a high-speed video camera (Shimadzu, HPV-1) with a

strobe light (Nisshin Electronic, SA-200F) as the backlight light source. The frame rates of this camera ranged from 500,000 to 1,000,000 fps.

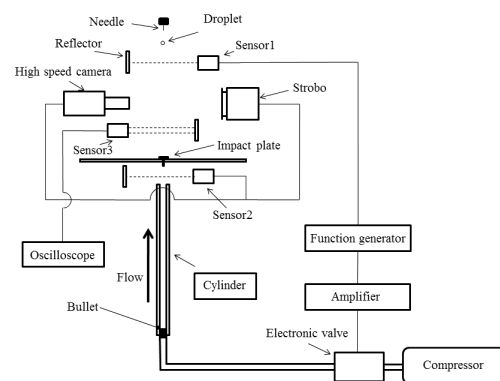


Fig.1 Schematic of experimental setup.

3. Results and Discussion

The deformation of a single droplet impacting on a solid surface was observed. Figures 2 and 3 show the case of impact plate velocity $U_{ip} = 10$ m/s. We observed an axisymmetric liquid film that flows radially outward (Fig. 3). We refer to this liquid film spread flow along the impact plate surface as lamella hereafter. Although lamella smoothly flows on the plate, at the rim of the lamella, small surface disturbance was observed.

Figures 4 and 5 show the deformation of the droplet on impact plate when impact plate impacts on the droplet with higher velocities: $U_{ip} = 15$ m/s. In the cases of higher impact velocities, in addition to the lamella, we observed the liquid spread from the rim of lamella in the obliquely upward direction. The development of thin-thread type liquid flow, which is generally referred to as finger, was observed.

Figure 6 shows the deformation of single droplets with various impact velocities observed with a camera angle of 60 degrees from horizontal. In the case of $U_{ip} = 10.1$ m/s, clean lamella is well developed and flows outwardly. In the case of $U_{ip} = 16.3$ m/s, the development of fingers from the rim of the lamella. Further increment of the impact velocities ($U_{ip} = 22.5$ m/s, 50.3 m/s) results in the increase of the number of fingers. In the case of 16.3 m/s, fingers stem from the rim of lamella. It should

be noted that most of the surface of lamella is not disturbed but disturbed surface is only be found near the rim of lamella. On the other hand, in the case of higher impact velocities, the multifold finger layer flow developed. It should be noted that the rim of lamella cannot be clearly identified and that disturbed surface area on lamella significantly increases. These characteristic outwardly generated flow fields due to the droplet impact may play an important role in cleaning since particles should be advected away for a cleaning process to be completed.

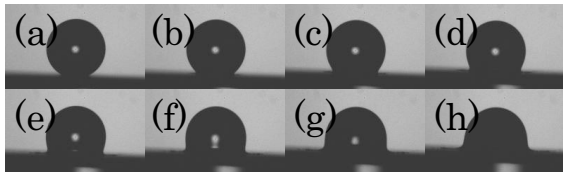


Fig.2 Snapshots of droplet impact observed with a horizontal camera angle; $U_{ip}=10\text{m/s}$, $\Delta t=8\mu\text{s}$.

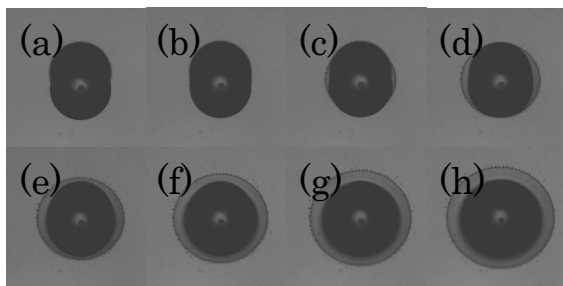


Fig.3 Snapshots of droplet impact observed with a camera angle of 70 degrees; $U_{ip}=10\text{m/s}$, $\Delta t=8\mu\text{s}$.

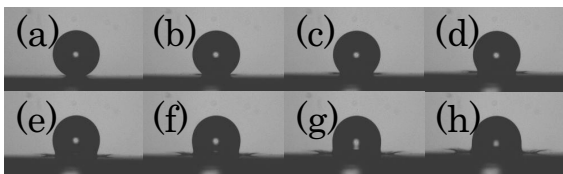


Fig.4 Snapshots of droplet impact observed with a horizontal camera angle; $U_{ip}=15\text{m/s}$, $\Delta t=4\mu\text{s}$.

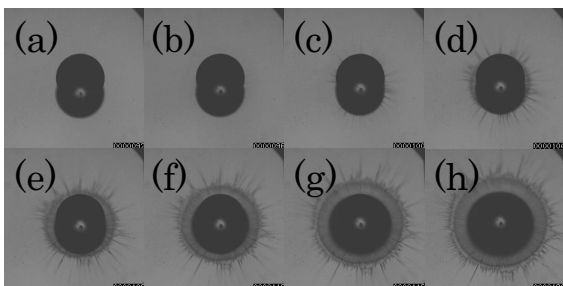


Fig.5 Snapshots of droplet impact observed with a camera angle of 70 degrees; $U_{ip}=15\text{m/s}$, $\Delta t=4\mu\text{s}$.

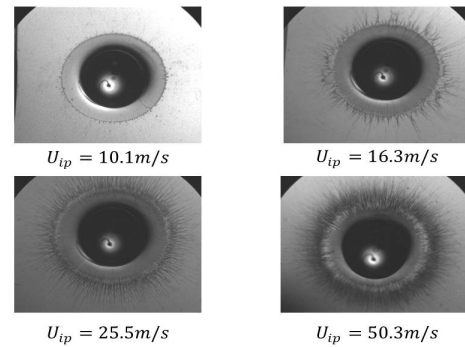


Fig.6 Snapshots of droplet impact observed with a camera angle of 60 degrees.

4. Concluding remarks

We observed a single droplet impact on a solid surface experimentally by impacting a solid plate on a freely falling droplet by using high-speed camera with the frame rate up to 1,000,000 fps. We observed the deformation process of the single droplet due to the impact and the consequently generated liquid flow field.

When an impact plate impacts on a droplet, we observed a liquid film spread flow along the impact surface i.e. lamella, and also in the cases of higher impact velocities, we observed the instabilities of liquid flow that turns into the generation of fingers that spreads obliquely upward and radially. These outwardly generated flow field due to the droplet impact may contribute to particle removal or photo-resist stripping.

Acknowledgements

The authors would like to show their gratitude to Professor Emeritus Shigeo Fujikawa of Hokkaido University for the most important advice, and to Mr. Yasutaka Sakurai for his devoted efforts in carrying out experiments. This work is supported in part by Grant-in-Aid for Scientific Research (B) 22360073 of JSPS and by Grant-in-Aid for Challenging Exploratory Research 21656048 of JSPS.

References

- [1] T. Sanada, A. Hayashida, M. Shirota, M. Yamase, M. Watanabe, *Fluid Dyn. Res.*, **54** (2008), 627.
- [2] T. Sanada, M. Watanabe, A. Hayashida, Y. Isago, *Solid State Phenom.*, **146** (2009), 273.
- [3] M. Watanabe, T. Sanada, A. Hayashida, Y. Isago, *Solid State Phenom.*, **145** (2009), 43.

The Removal of Nanoparticles from Surfaces and 3-D Structures Using High-frequency Acoustic Streaming

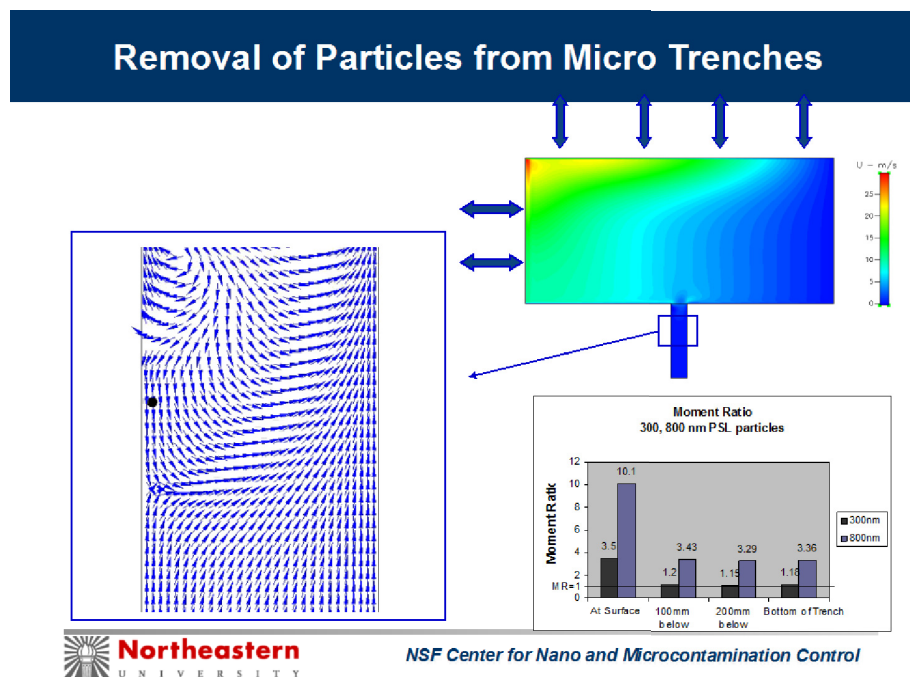
Ahmed Busnaina¹ and Jingoo Park²

¹NSF Center for Nano and Microcontamination Control,
Northeastern University, Boston, MA 02115

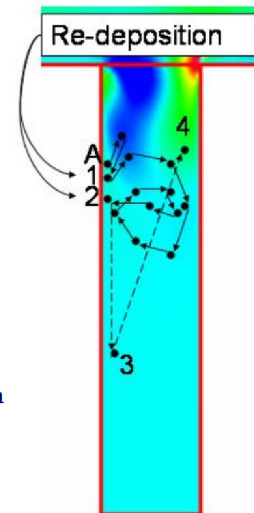
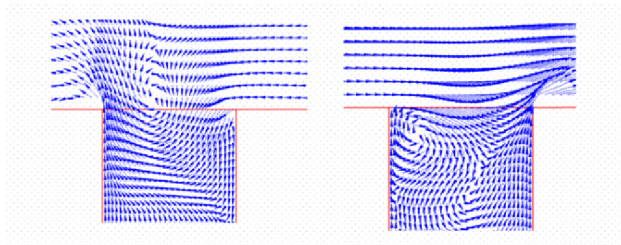
²Nano-bio Electronic Materials Processing Laboratory
Hanyang University, Ansan, Korea

Email: a.busnaina@neu.edu, URL: www.nano.neu.edu

The removal of nanoparticles from patterned wafers is one of the main challenges facing the semiconductor industry. As the size of structures shrinks with each new generation of devices, it becomes more difficult to remove nanoscale particles. The removal of nanoparticles from patterned wafers is one of the main challenges in semiconductor industry. Megasonics utilizes high frequency acoustic streaming to reduce the acoustic boundary layer and utilize the generated pulsating flow to remove nanoscale particle from trenches and other structures on the wafer. The removal of different size particles from silicon trenches is investigated. Complete removal of 200nm particles from 2 micron trenches was achieved. Smaller trenches took longer to clean than larger trenches. In addition, complete removal was possible at lower power but took longer time. This was explained by understanding the removal mechanism and the large impact of the acoustic boundary layer on the particle removal force using CFD.



Particle Redeposition in Micro Trenches



The simulation shows:

- **The vortex in the trench is transient**
 - The particle is trapped inside the vortex
 - The vortex moves the particle inside the trench
- **The flow is parallel to the trench wall**
 - Favorable for particle detachment
- **The re-deposition slows down the removal process**



NSF Center for Nano and Microcontamination Control

Nanostructures (specially, poly silicon lines) were found to be vulnerable to damage when megasonic cleaning is utilized. Although Megasonics is believed to be a solution for many of these cleaning challenges, it has been shown to cause severe damage to nanoscale device structures such as poly-silicon lines. The cause of damage in megasonics cleaning was investigated and the results showed that cavitation damage does not occur at megasonic frequencies as shown by many over the last 3-4 decades but rather, secondary frequencies as low as 40 KHz exist in megasonic tanks with sufficiently high power to generate ultrasonic cavitation responsible for damage. Elimination all of the low frequencies (using a narrow band transducer) demonstrated that damage does not occur even at high power once the low ultrasonic frequencies (with high amplitude) are eliminated. Effective damage free removal of nanoscale particles was also demonstrated at high amplitude (power).

Non-spherical Bodies With Particle and Fluid Inertia: Rotating or Surfing?

Fredrik Lundell & Tomas Rosén

Linné FLOW Centre, KTH Mechanics, Royal Institute of Technology, SE-100 44 Stockholm, Sweden
Fredrik@mech.kth.se

ABSTRACT

The motion of non-spherical particles in shear flow and extensional flow is studied numerically and theoretically. The purpose of the study is to provide fundamental knowledge that is necessary in order to model flows with non-spherical particles. Here, two flow cases will be studied and presented. The first is an ellipsoid in extensional flow under the Stokes flow assumption. It is shown that particle inertia controls whether the particle align monotonously or oscillate with a decreasing amplitude. The second is an ellipsoid in shear flow. It is shown that there might be both steady and tumbling solutions at elevated Reynolds numbers.

1. Introduction

The motion of particles in elementary flows is the fundamenta of all modeling of particle suspensions. Non-spherical particles occur in many geophysical and engineering applications, volcanic ash and papermaking are two examples.

Here, two fundamental flow cases are studied: extensional flow (see Fig. 1a) and linear shear flow (see Fig. 2a). Particles in shear flow have been studied extensively and they can exhibit a number of different behaviours depending on the Reynolds number[1],

$$Re = \frac{\dot{\gamma} l^2}{\nu}$$

where $\dot{\gamma}$ is the rate of shear, l is the length of the particle and ν is the kinematic viscosity of the fluid. These motions include tumbling, log-rolling, inclined rolling and a steady particle. These effects all appear due to effects of fluid inertia. However, there are also effects due to particles inertia[2,3], which is quantified by the Stokes number;

$$St = \kappa Re$$

where κ is the density ratio between the particle and the fluid.

The same parameters (Re , St) control the particle behaviour in extensional flow, although the shear is replaced by the rate of extension.

Here, a few aspects of these flow cases will be studied, primarily the effect of particle inertia (St) in extensional flow and combined effects of (Re , St) in shear flow.

2. Method

This study is based on integrating the equations of rotation of the particle based on the torques exerted on the particle by the flow. Two methods are used to determine the torques on the particles. The first is direct use of Jeffery's solution[4] for the torques on ellipsoids in linearly varying Stokes flow. The second method, which is used for non-zero Re , is the Lattice Boltzmann Method together with Element Boundary Forcing[5].

3. Results and Discussion

In Fig. 1, extensional flow is shown. A sketch of the particle in the flow is shown in (a). In (b), the orientation angle φ as a function of time is shown for in

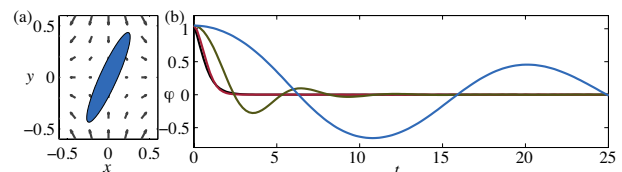


Fig. 1 (a): An ellipsoid in extensional flow. (b): Orientation angle to the horizontal φ as a function of time for increasing Stokes number from red via black and green to blue. $Re=0$.

Increasing Stokes numbers from red via black and green to blue. At low St , the particle aligns rapidly whereas at high St , the particle oscillates considerably before it reaches the aligned state. The mechanism behind this behaviour is that at high St , the particle carries particle inertia, which gives the overshoot of the orientation.

In Fig. 2a, a particle in linear shear flow is shown and in (b), the effects of St on rotation period at $Re=0$ are shown in order to highlight effects of particle inertia[2]. At low St , the particle performs a tumbling motion around the vorticity axis (z' in Fig. 2a). As St is increased, the particle motion undergoes a transition and the particle starts to rotate with a constant angular velocity, which is equal to the vorticity, i.e. $\dot{\gamma}/2$.

The different curves in Fig. 2b show different aspect ratio combinations. The longer the particle is, the longer the rotation period at low St . The results also show that as particle gets wider, the St at which the rotation rate changes from high to low becomes lower.

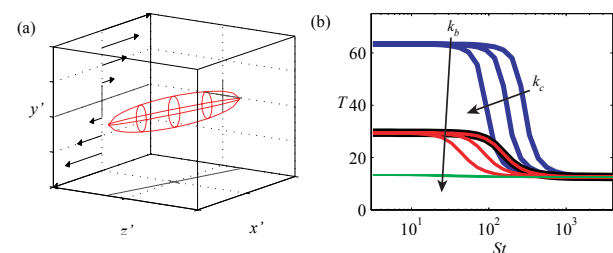


Fig. 2 (a) An ellipsoid in linear shear flow. (b): Rotation period as a function of Stokes number for different aspect ratio combinations, $Re=0$.

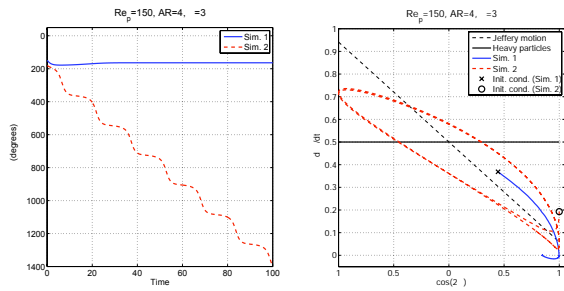


Fig. 3 Time evolution of orientation in shear flow at $Re=150$. (a): Angle as a function of time for two different initial conditions. (b): State space diagram of the two motions.

At higher Re , however, the situation is quite different, as is illustrated in figure 3. In this figure, a single combination of $Re=150$ and $St=450$ is studied and the particle is forced to rotate with its longest axis in the flow-gradient plane. The left plate shows the orientation angle as a function of time for two different initial conditions. The red curve shows a tumbling motion, which is only a slight modification of the motion at $Re=0$.

The blue curve, on the other hand, shows a completely different behaviour. After some slow initial variations, the orientation angle becomes constant, i.e. the particle is steady.

The difference between these two behaviours is detailed in the state-space diagrams shown to the right in Fig. 3. Here, the angular velocity $-\dot{\phi}$ (where the dot denotes differentiation with respect to time) is plotted vs. $\cos 2\phi$. In this plane, the two motions at $Re=0$ discussed in relation to Fig. 2 becomes straight lines: the tumbling at low St is the straight dashed line and the rotation with constant angular velocity at high St is the horizontal full line. The red and blue lines are the same cases as in the left plate.

The red curve is seen to enter a periodic orbit (going clockwise in the figure). Although there exists regions with zero, or even counteracting torque due to flow separation, during this rotation, the particle still performs complete rotations due to its particle inertia. In order to do so, however, the initial condition must be such that the particle has enough rotary inertia when being exposed to the braking torque.

The blue curve is an example of when this is not the case. The starting point of the blue curve (marked with a cross) is seen to be considerably below the red orbit. From this combination of orientation and angular velocity, the particle does not possess sufficient particle inertia when being exposed to the counteracting torque. As a result, the particle stops and rotates backwards to a steady position, where the torque on the particle is zero (this process can be seen in some detail in blue curve of the left plate of Fig. 3).

4. Concluding remarks

It has been shown that particle in linear shear flow

and extensional flow presents a wide variety of behaviour at increased Re and St . In extensional flow, the system becomes underdamped and the particle starts to rotate when St is increased. In linear shear flow, it was shown that the combination of fluid and particle inertia can give rise to multiple solutions. Thus, the answer to the question in the title becomes: it depends (on the initial condition).

References

- [1] Huang, H., Yang, X., Krafczyk, M. and Lu, X.-Y. 2012 Rotation of spheroidal particles in Couette flows. *J. Fluid Mech.* **692**, pp. 369-394.
- [2] Lundell, F. & Carlsson, A. 2010 Heavy ellipsoids in creeping shear flow: Transitions of the particle rotation rate and orbit shape. *Phys. Rev. E* **81**, 016323.
- [3] Lundell, F. 2011 The effect of particle inertia on triaxial ellipsoids in creeping shear: From drift toward chaos to a single periodic solution. *Phys. Fluids* **23**, 011704.
- [4] Jeffery, G. B. 1922 The motion of ellipsoidal particles immersed in a viscous fluid. *Proc. Roy. Soc. London* **102** (715), 161–179.
- [5] Wu, J. & Aidun, C. K. 2010 A method for direct simulation of flexible fiber suspensions using lattice Boltzmann equation with external boundary force. *Int. J. Multiphase Flows* **36**, 202–209.

Experimental and Theoretical Investigation of Acoustic Cavitation Behavior in the Megasonic Cleaning

Bong-Kyun Kang^{1,2}, Ji-Hyun Jeong^{1,2}, Yoon-Sik Cho^{1,2}, Min-Su Kim^{1,2}, Hong-Seong Sohn³
Ahmed A. Busnaina⁴ and Jin-Goo Park^{1,2,a}

¹Department of Bionano Technology and ²Materials Engineering, Hanyang University, Ansan 426-791, Korea

³Akron Systems LLC, 6330 Hedgewood Drive, Suite 150 Allentown, PA 18106 USA

⁴Center for Microcontamination Control, Northeastern University, Boston, MA 02115

^a jgpark@hanyang.ac.kr.

ABSTRACT

High power ultrasound has brought a technology innovation in electronic device cleaning process. However it still faces a difficult problem in controlling the random behavior of acoustic bubbles, which should be controlled to prevent the undesired defect on the surface. In order to render the unstable motion of acoustic bubble to stabilize, acoustic bubble growth mechanisms relating to cavitation effect were comprehensively investigated by both theoretical calculations and experimental results. It was found that cavitation phenomena could remarkably reduce with small amounts of isopropyl alcohol (IPA) addition in water.

1. Introduction

As the semiconductor manufacturing technology for ultra-large scale integration devices continues to shrink beyond 32 nm, stringent measures have to be taken to obtain damage free patterns during cleaning process. The patterns are no longer cleaned with the megasonic (MS) irradiation in advanced device node due to severe pattern damages during cleaning. Several research activities are currently carried out to control the cavitation effect of MS to reduce the pattern damages. The pattern damages were due to unstable acoustic bubble motion, which was mainly attributed to the high sound pressure associated with violent bubble collapse [1]. In particular, cavitation effect induced during MS cleaning can be controlled by adjusting the acoustic bubble growth rate. Also the bubble growth rate change can be well explained by both rectified diffusion for single bubble and bubble coalescence for multi-bubble, respectively. Similarly, it is a well-known fact that surface active solute (SAS) in ultrasound field can play a critical role in controlling the cavitation effect. The explanation about the acoustic bubble growth rate, cavitation threshold and their relationship with type of SAS and its concentration from biomedical and chemical reactions perspective have been reported elsewhere [2,3]. Their studies were demonstrated that the change of cavitation effect depends not only on the chain length of the alcohol in solution but also on the physical properties such as surface tension and viscosity of SAS solutions.

In this study, MS cleaning was performed using IPA based cleaning solution. Its physical property relating to acoustic bubble growth rate was studied extensively. Also the change of cavitation effect as a function of IPA concentration was indirectly confirmed through the particle removal efficiency (PRE) and pattern damage test in a single wafer cleaning system.

2. Method

IPA was mixed with de-ionized water (DIW) for 10 min in a closed system to achieve complete mixing and supplied to single tool (Velocity, Akron systems) set up with MS (0.83 MHz, Akron systems) to perform the

PRE tests. Silicon wafers (200 mm, P type, <100>) were intentionally contaminated with Si₃N₄ particles (0.1~10 μm, Sigma-Aldrich) dispersed in DIW by a spin drying method. PRE was precisely analyzed by a surface particle scanner (Surfscan 6200, KLA-Tencor) within the particle range from 120 to 210 nm.

Photoresist (PR, PAR817, Sumitomo) patterns with line width of 250 and 300 nm were used for the pattern damage evaluation in MS cleaning to quantify an unstable cavitation power using various concentration of IPA solution. The pattern collapse forces were measured and also compared with the previous study [2]. After MS cleaning with IPA mixture, damage features on PR line patterns were observed by using bright mode in the optical microscope (LV100D, Nikon).

3. Results and Discussion

Initially bubble nuclei in solution are acoustically grown by rectified diffusion of gas in solution into the bubbles or bubble coalescence or the combination of both processes, until it reaches a critical size which induces the cavitation effect [4]. Collapsed bubbles generate new nuclei and those nuclei subsequently grow to their critical resonance size. Therefore the power of cavitation can be determined by the bubble growth rate and its population under ultrasound. In particular, it is well known that cavitation power can be regulated with SAS adsorption at the air/water or bubble/water [5]. Those changes were affected not only by the type of SAS and difference of chain length but also by the variation of concentration in solution due to the repulsive force that include steric and electrostatic forces. The total bubble volume can be experimentally measured by using a simple capillary technique with ultrasonic energy as shown in Figure 1 [6]. Though these theories do not inform us the change of cavitation effect with SAS concentration in MS cleaning, but provide the relation between acoustic bubble growth rate and SAS concentration. In practice, the effect of SAS on bubble growth might significantly affect the PRE and pattern damage which rely on its concentration, due to change in cavitation effect.

Figure 2 shows the PRE results as a function of IPA

concentration. Experiments were performed by fixing the MS power level at 10, 50 and 90 W to evaluate the effect of an unstable cavitation against pattern damage events in solutions. PRE vary significantly with the IPA concentration. It is evident that PRE decreased with the IPA concentration increasing from 0.1vol% to 5.0 vol% when compared with pure DIW (0% IPA). This may be attributed to the decrease in the number of cavitation event by inhibiting the bubble coalescence related to the repulsive force, mentioned earlier. The pattern damage test for IPA contained DIW with MS was performed on PR patterns of 250 and 300 nm line width under the same experimental condition like PRE test. Figure 3 shows the pattern damage density (%) on PR pattern as a function of IPA concentration in DIW. The damage density on the PR patterns was significantly reduced when the IPA concentration is 1.0 vol% similar to PRE results. Figure 4 shows the image of the PR after cleaning with various concentration of IPA. It is clear from the image that the PR treated with 1.0 vol% has very less damages when compared with the other IPA concentrations. On the other hand, the PR pattern had a lot of damage sites when IPA concentration is more than 10 vol%. This may be due to the stronger cavitation power in IPA solutions than in pure DIW as shown in Figure 3 and 4. Thus, we could confirm through the experimental results of PRE and pattern damage that the cavitation effect can be controlled by changing the acoustic bubble growth rate as a function of SAS concentration.

4. Concluding remarks

In this study, we have demonstrated the possibility to control the cavitation by using mixtures of IPA and DIW. The cavitation effect can be varied with the IPA concentration. When small amounts of IPA was mixed in DIW (0.2~5.0 vol%), bubble coalescence was reduced by the inhibition of absorbed IPA on bubbles. At higher concentration ranges from 10~20 vol%, it was shown that cavitation effect was fairly improved by the dominant rectified diffusion with the increase of bubble growth rate.

References

- [1] W. Kim, K. Park, J. Oh, J. Choi and H. Y. Kim, *Ultrasonics* **50** (8), 798-802 (2010).
- [2] B. Kang, M. Kim, S. Lee, H. Sohn and J. Park, *ECS Transactions*, **41** (5) 101-107, (2011).
- [3] J. Lee, S. E. Kentish and M. Ashokkumar, *The Journal of Physical Chemistry B* **109** (11), 5095-5099 (2005).
- [4] M. Ashokkumar, J. Lee, S. Kentish and F. Grieser, *Ultrasonics Sonochemistry* **14** (4), 470-475 (2007).
- [5] M. Ashokkumar, R. Hall, P. Mulvaney and F. Grieser, *Journal of Physical Chemistry B* **101** (50), 10845-10850 (1997).
- [6] J. Lee, M. Ashokkumar, S. Kentish and F. Grieser, *The Journal of Physical Chemistry B* **110** (34), 17282-17285 (2006).

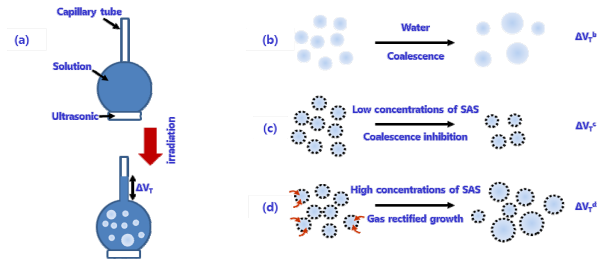


Fig. 1. The effect of SAS concentration on the total bubble volume (ΔV_T). (a) capillary tube showing the change in liquid level that occurs during ultrasonic irradiation. (b) For pure water: ΔV_T^b (c) At low concentrations of SAS: ΔV_T^c . (d) At high concentrations of SAS: ΔV_T^d , $\Delta V_T^b > \Delta V_T^c > \Delta V_T^d$.

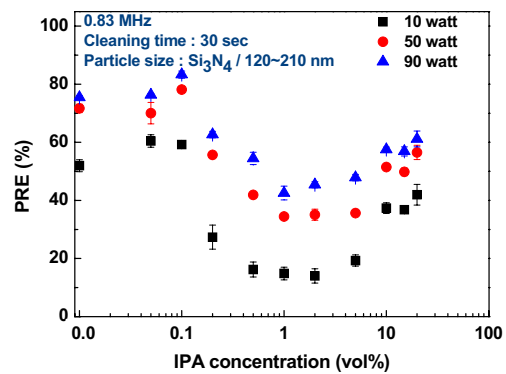


Fig. 2. PRE on Si wafer as a function of IPA concentration

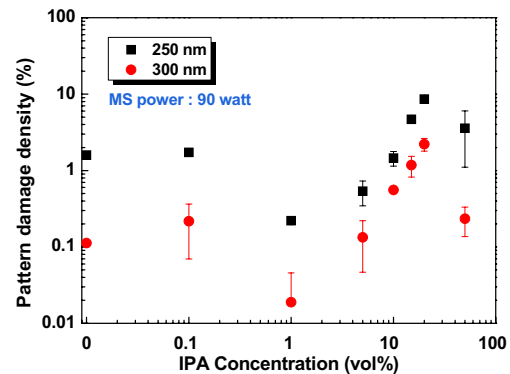


Fig. 3. Pattern damage density on PR line pattern as a function of IPA concentration

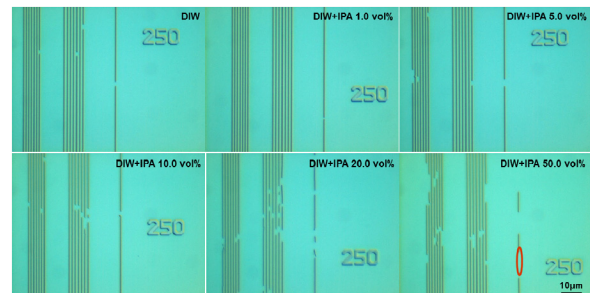


Fig 4. Optical microscope images of PR line pattern (250 nm) after megasonic cleaning process for 1 min.

Evaluation of Cleaning Performance of Nano-sized CO₂ gas cluster for Damage Free Semiconductor Cleaning

Min-Su Kim^a, Bong-Kyun Kang^a, Hoo-Mi Choi^b, Tae-Sung Kim^b, and Jin-Goo Park^{a,*}

^a Department of Bio-Nano Technology, Hanyang University, Ansan 426-791, Korea

^b SKKU Advanced Institute of Nanotechnology (SAINT), Sungkyunkwan University, Suwon 300, Korea

* jgpark@hanyang.ac.kr

ABSTRACT

CO₂ gas cluster cleaning process for nano particles removal without pattern damage was investigated. When pressurized CO₂ gas was passed through the convergence-divergence (C-D) nozzle, the high speed and high energy gas clusters were generated in vacuum chamber. The cleaning force of CO₂ gas cluster is related to flow rate of the gas and gap distance between the nozzle and substrate. In this study, the optimum gas flow rate and gap distance for nano-sized particles removal was found, respectively. Pattern damage test of the poly-Si and a-Si pattern were also evaluated by SEM images. No pattern damages were observed at these optimum conditions.

1. Introduction

In Semiconductor cleaning process, the critical nano size of particles should be dislodged without material loss and damage of nano pattern. However, this could not be achieved with physical force induced wet cleaning processes such as megasonic and jet spray nozzle cleaning due to their uncertainty of cleaning force. Among other feasible cleaning methods, cryogenic aerosol cleaning was one of the leading candidate technologies for damage free cleaning as it has been successfully used to remove contaminant particles from the surface of semiconductor wafers [1]. However, damage issue was not resolved fully because it is difficult to generate the size of cryogenic aerosol below sub-micrometer level. On the other hand, gas cluster cleaning technology has potential to be a replacement because the size of gas cluster is below 100 nm [2]. A gas cluster is an aggregate of a few to several thousands of gaseous atoms or molecules, and it can be made by supersonic expansion when the gas expands from a high-pressure stagnation region into a vacuum through a small orifice [3]. The random velocity of gas atoms is reduced by the adiabatic expansion, causing all the atoms to move at nearly the same speed [4]. The gas cluster has a kinetic energy to dislodge the contaminants from the surface to be cleaned through collisions. Since the typical size of gas cluster is less than 50 nm, it is expected to cause no damage on the surface.

2. Method

In this study, a newly developed dry cleaning process using CO₂ gas cluster was performed. CO₂ gas cluster cleaning system consists of pre-chamber and cleaning chamber. Cleaning chamber is kept at vacuum atmosphere of about 5.0×10^{-1} Torr. CO₂ gas pressure in converging-diverging nozzle changed from 0 to 105 psi when gas flow rate changed from 0 to 15 LPM. Also, gas temperature could be critically controlled by a chilling system. For particle removal efficiency (PRE) test, coupon wafers were dipped into contaminant solution which contains silica and PSL particles. In pattern damage test, two kinds of patterned wafer were used which consist of gate pattern structures: Si/SiON/a-Si/SiO₂ and Si/SiO₂/poly-Si/SiO₂ (below 120 nm). PRE was evaluated as functions of gas flow rate, gas temperature and gap distance between nozzle and

substrate. PRE and pattern damage were analyzed by OM (Optical Microscope) dark field mode and SEM (Scanning Electron Microscopy).

3. Results and Discussion

PRE was evaluated as functions of gas flow rate and gap distance for 300 nm Silica and PSL particles (Fig. 1). The PRE is proportional to gas flow rate and saturated at 10 LPM of gas flow rate as over 97 % for silica and over 80 % for PSL particles. There was a drastic increase in the PRE when the flow rate changes from 5 LPM to 10 LPM. Moreover, PRE is inversely proportional to gap distance between the nozzle and the substrate at 5 LPM of gas flow rate for both silica and PSL. This is mainly attributed to the fact that gas cluster has high speed and high energy at low gap distance and high gas flow rate.

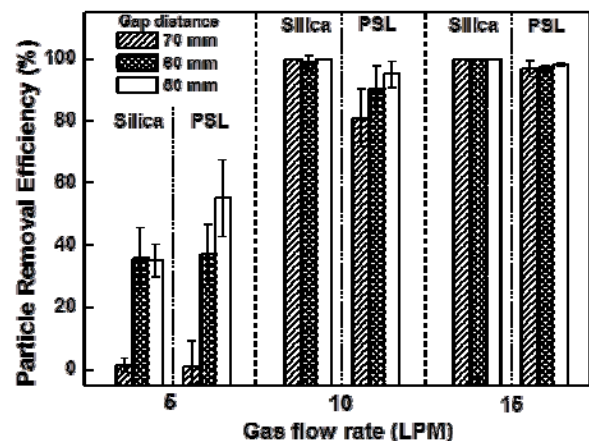


Fig. 1 300 nm silica and PSL particles removal efficiency as functions of gas flow rate and gap distance between nozzles and substrate.

In order to find out the critical gas flow rate in detail, particle removal efficiency was tested between 5 and 10 LPM of gas flow rate which can remove the particles and the gap distance is fixed at 50 mm for achieving high PRE. Fig. 2 shows the 300 nm silica particle removal efficiency and nozzle pressure as a function of gas flow rate. The PRE is rapidly increased at 6 LPM gas flow rate which might be a critical flow rate for gas cluster generation for the effective particle removal. To

confirm the difference of cleaning force of gas cluster with change gas flow rate, we also measured the pressure in nozzle. The nozzle pressure is steadily increased as increasing gas flow rate.

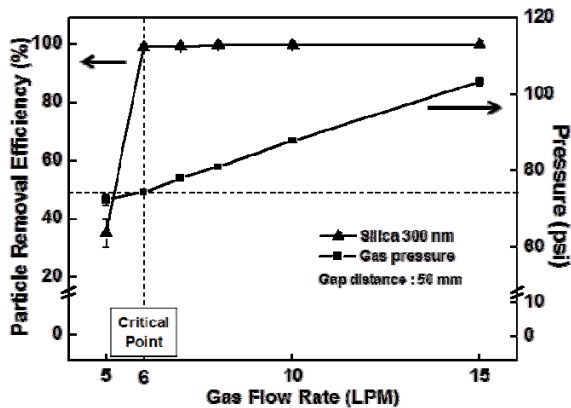


Fig. 2 300 nm silica particle removal efficiency and nozzle pressure as a function of gas flow rate.

We evaluated the nano-sized particle removal using below 50 nm silica particles to confirm the possibility of nano-sized particle removal in CO₂ gas cluster cleaning process. In Fig. 3(a), 25 nm silica particles were contaminated uniformly on the wafer. After cleaning, in common with result of 300 nm particle removal test, more number of particles is removed at 6 LPM which is critical point in CO₂ gas cluster cleaning (Fig. 3(c)). Since the size of CO₂ gas cluster is less than submicron, gas cluster is able to remove the nano-sized silica particles.

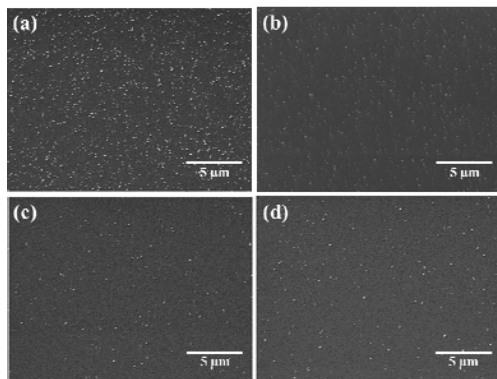


Fig. 3 SEM images of 25 nm silica particles: (a) silica particles contaminated on wafer, (b) after cleaning at 5 LPM, (c) 6 LPM, and (d) 7 LPM of gas flow rate.

To evaluate the pattern damage, we used Si/SiON/a-Si/SiO₂ and Si/SiO₂/poly-Si/SiO₂ (60 nm) patterned wafer which has gate stack pattern structure. These patterned wafers consist of gate dielectric material/gate material/ hard mask material structure and very similar to actual gate stack pattern structure. Pattern damage test was performed at 5 LPM to 7 LPM and the results are shown in Fig. 4.

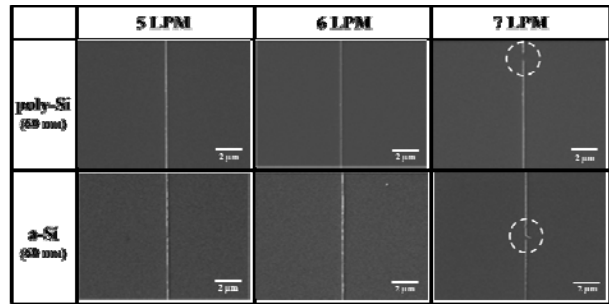


Fig. 4 Pattern damage test with poly-Si and a-Si gate structure patterned wafer as a function of gas flow rate.

As shown in Fig. 4, there is no pattern damage at 5 LPM and 6 LPM. However, pattern damage is occurred on both poly-Si and a-Si patterned wafer at 7 LPM. In figure 5, CO₂ gas cluster has large size and high energy because the phase of CO₂ is liquid before passed through the nozzle and CO₂ molecules are easily agglomerated. As a result, pattern damage is occurred due to large size of gas cluster and high cleaning force at 7 LPM.

Hence, it can be concluded from the above studies that it is possible to remove the nano-sized particles without pattern damage at 6 LPM in CO₂ gas cluster cleaning process.

4. Concluding remarks

In this study, we evaluated CO₂ gas cluster cleaning process for nano-sized particle removal without pattern damage. We confirmed the CO₂ gas cluster was affected by gas flow rate and gap distance between nozzle and substrate. From the experiments, it was found that not only nano-sized particles removal but also damage free cleaning could be achieved at 6 LPM gas flow rate. Thus, CO₂ gas cluster cleaning could be applied to damage free cleaning only at a specific gas flow rate.

Acknowledgements

The gas cluster cleaning system was supported by Zeus Co. LTD., Korea.

References

- [1]. S. Banerjee and A. Campbell, *J. Adhesion Science and Technology*, **19**, 739 (2005).
- [2]. K. S. Hwang, M. J. Lee, M. Y. Yi and J. W. Lee, *Thin Solid Films*, **517**, 3866 (2009).
- [3]. H. Choi, Y. Kim, D. Yoon and T. Kim, 'Development of CO₂ Cluster Beam Based Wafer Cleaning Process', UCPSS Conference 2010
- [4]. N. Toyoda and I. Yamada, *IEEE Trans. on Plasma Science*, **36**, 1471 (2008).

Numerical Study of Influence of Initial Standoff Distance on Impulsive Pressure Induced by Single Bubble Collapse near Wall Boundary (Integration to the next-generation megasonic cavitation cleaning technology)

Naoya Ochiai¹, Yuka Iga¹, Motohiko Nohmi², Toshiaki Ikohagi³ and Jun Ishimoto¹.

¹Institute of Fluid Science, Tohoku University, 2-1-1 Katahira, Aoba-ku, Sendai, 980-8577, Japan

²EBARA Corporation, 78-1 Shintomi, Futtsu, 293-0011, Japan

³Open University of Japan, 2-1-1 Katahira, Aoba-ku, Sendai, 980-8577, Japan
ochiai@alba.ifs.tohoku.ac.jp

ABSTRACT

The non-spherical bubble fluctuating in acoustic field is necessary to be analyzed for the clarification of the cavitation cleaning and the improvement of the cleaning efficiency. In the present study, a bubble collapse near the wall boundary is numerically analyzed by the two-dimensional axisymmetric calculation using a locally homogeneous model of a gas-liquid two-phase medium. The numerical results of the cases of three initial conditions indicate that all three cases have the similar tendencies of the maximum wall pressure during the first and second collapses against the initial standoff distance.

1. Introduction

A cavitation bubble collapse locally induces high impulsive pressure. The physical effect have been utilised for the cleaning and the sterilization. The efficient particle removal without device damage is required in the wafer cleaning in semiconductor manufacturing. Acoustic cavitation cleaning has the potential to meet the requirement. The complex interactions between the non-spherical bubble collapse, the rectified diffusion, the Bjerknes force and so on largely influence the cleaning efficiency and damage. Therefore, the non-spherical bubble fluctuating in acoustic field is necessary to be analyzed for the clarification of the cavitation cleaning and the improvement of the cleaning efficiency. At the beginning of the study, a bubble collapse near the wall boundary is numerically analyzed, and the influence of the initial standoff distance on the impulsive pressure investigated in the present study.

2. Numerical Method

A locally homogeneous model of a gas-liquid two-phase medium [1, 2] is used. The governing equations which are the continuity, the momentum, the total energy equations of a compressible two-phase medium, and the continuity equations of the mixture gas and noncondensable gas, are expressed as follows:

$$\frac{\partial \mathbf{Q}}{\partial t} + \frac{\partial (\mathbf{E}_j - \mathbf{E}_{vj})}{\partial x_j} = \mathbf{S} \quad (1)$$

$$\mathbf{Q} = \begin{bmatrix} \rho \\ \rho u_i \\ e \\ \rho Y \\ \rho Y D_a \end{bmatrix}, \mathbf{E}_j = \begin{bmatrix} \rho u_j \\ \rho u_i u_j + \delta_{ij} p \\ \rho u_j H \\ \rho u_j Y \\ \rho u_j Y D_a \end{bmatrix}, \mathbf{E}_{vj} = \begin{bmatrix} 0 \\ \tau_{ij} \\ -q_j + \tau_{jk} u_k \\ 0 \\ 0 \end{bmatrix}, \quad (2)$$

where Y and D_a are the mass fraction of a gas and the density ratio of noncondensable gas, respectively. The source terms $\mathbf{S} = [0 \ 0 \ 0 \ \dot{m} \ 0]^t$ where \dot{m} is the evaporation and condensation rate [2]. The void fraction inside and outside a bubble are 1 and 8.5×10^{-7} , respectively, and the bubble interface is described as the region with large void fraction jump. The phase change occurs at the bubble interface. The surface tension is not considered.

3. Calculation Condition

The two-dimensional axisymmetric calculation, in which the symmetric axis is perpendicular to the wall, of the bubble collapse due to the pressure difference between the internal and external pressures of a bubble is performed with working fluids of water, vapor and air. The initial external pressure of a bubble p_{out} is 100 kPa, and the initial internal and external temperatures T_{in} and T_{out} are 293.15 K. And the three different initial conditions (R_0 [mm], p_{in} [kPa]) = case 1 (1.5, 3), case 2 (1.5, 10) and case 3 (0.5, 3) are picked up, in which R_0 and p_{in} are the initial bubble radius and the initial internal pressure of a bubble, respectively.

4. Results and Discussion

Figure 1 shows the time evolution of the non-spherical bubble collapse (the distribution of the void fraction and the isolines of the pressure) at $R_0 = 1.5$ mm, $p_{in} = 10$ kPa, $\gamma = l_0/R_0 = 1.4$ (l_0 : initial standoff distance from wall boundary to the bubble center). Ochiai et al. [2] showed the calculation results at $R_0 = 1.5$ mm, $p_{in} = 3$ kPa, $\gamma = 1.4$. The bubble behaviors of the two cases are similar. A micro jet occurs (Fig. 1(ii)) and penetrates (Fig. 1(iii)) during the first collapse. The bubble move to the wall boundary and attaches to the wall boundary during the rebound (Fig. 1(iv)). A toroidal bubble forms during the second collapse (Fig. 1(v)) and the toroidal bubble collapse induces a pressure wave (Fig. 1(vi)).

Figure 2 shows the maximum wall pressure against initial standoff distance γ at three calculation conditions, (R_0 [mm], p_{in} [kPa]) = (1.5, 3), (1.5, 10) and (0.5, 3). We performed the bubble calculations until the bubble second collapse, and Fig. 2 shows the maximum wall pressure during the first (Fig. 2(i)) and second collapses (Fig. 2(ii)). The first collapses induce the maximum pressures in the central area at all γ . During the second collapse, a toroidal bubble attached the wall boundary forms at a certain γ . The toroidal bubble collapse induces the peak wall pressure near the collapse position. Therefore, the maximum wall pressures during the second collapse in Fig. 2 correspond to the peak wall pressure due to the

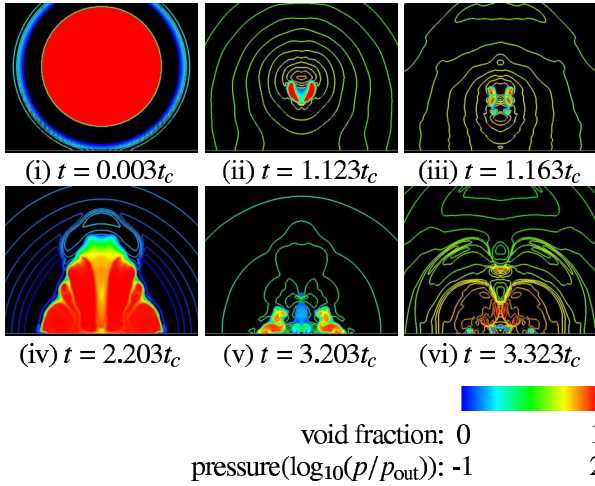


Fig. 1 Time evolution of bubble behavior and isoline of pressure ($R_0 = 1.5$ mm, $p_{in} = 10$ kPa, $\gamma = 1.4$, $t_c = R_0/\sqrt{p_c/\rho_c}$).

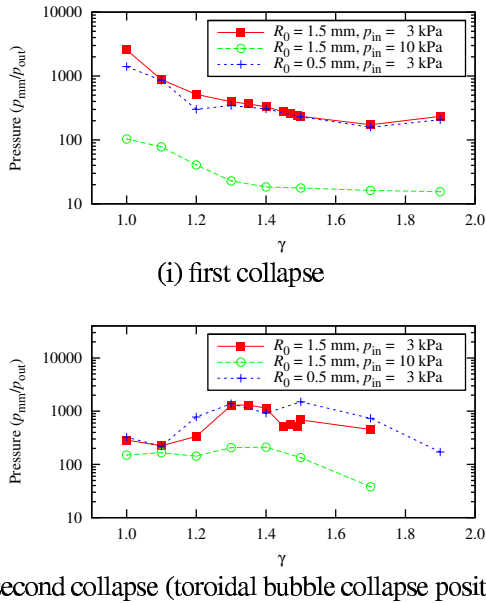


Fig. 2 Maximum wall pressure against initial standoff distance.

toroidal bubble collapse. First, the maximum wall pressures during the first collapse are discussed. Figure 2(i) indicates that the maximum wall pressure during the first collapse becomes large with the decrease in γ . The bubble translational motion to the wall boundary during the first collapse largely influences the maximum wall pressure. Figure 3 shows the bubble position at the first collapse against γ , in which l_{min} is the distance from a bubble to the wall boundary at the first collapse. Figure 3 also shows the experimental results by Shima et al. [3]. At small γ the bubble is found to largely move to the wall boundary. The characteristic corresponds well to the experimental result. Figure 4 shows the minimum bubble radius during the first collapse. At small γ the minimum bubble radius is found to be large, and the bubble collapse is thought to be suppressed. Although the bubble collapse is suppressed at small γ , the maximum wall pres-

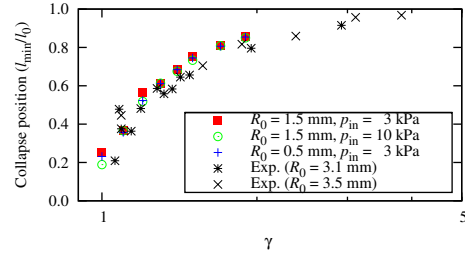


Fig. 3 Bubble position at bubble first collapse against initial standoff distance.

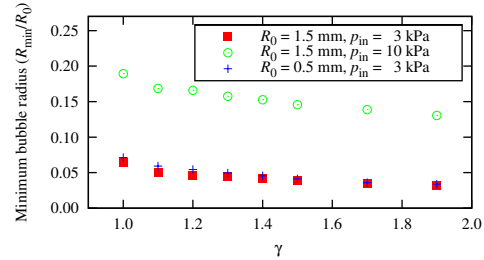


Fig. 4 Minimum bubble radius during first collapse against initial standoff distance.

sure is large at small γ as shown in Fig. 2. Therefore, the translational motion is found to largely influence the wall pressure during the first collapse. All three cases have the similar tendencies of the maximum wall pressure, the translational motion and the minimum bubble radius against the initial standoff distance during the first collapse. However, case 2 which is the larger initial internal pressure, shows the larger minimum bubble radius and the lower maximum pressure.

Next, the second collapse is discussed. The maximum wall pressure during the second collapse is maximum at medium γ in all three cases (Fig. 2(ii)), and all three cases are found to have the similar characteristics of the wall pressure during the second collapse. And the maximum wall pressure during the second collapses are found to be higher than these during the first collapse in the range of $1.3 \leq \gamma \leq 1.7$ comparing the maximum wall pressures (Figs. 2(i) and 2(ii)).

5. Conclusions

Numerical analysis of the non-spherical bubble collapse near the wall boundary is performed at three cases (initial conditions). The influence of the initial standoff distance on the impulsive pressure is investigated, and it is found that all three cases have the similar tendencies of the maximum wall pressure during the first and the second collapses against the initial standoff distance.

References

- [1] K. Okuda and T. Ikohagi, Trans. JSME Ser. B, **62-603** (1996), 3792-3797 (in Japanese).
- [2] N. Ochiai et al., J. Fluid Science and Tech., **6-6** (2011), 860-874.
- [3] A. Shima et al., Rep. Inst. High Speed Mech., **48-367**, (1984), 77-97.

Effect of Turbulence on Nonlinear Sloshing in a Rectangular Pool

Ken Uzawa

The Center for Computational Sciences and E-systems, Japan Atomic Energy Agency
Kashiwanoha 5-1-5, Kashiwa, Chiba 277-8587, JAPAN
uzawa.ken@jaea.go.jp

ABSTRACT

The effect of turbulence on nonlinear sloshing in a rectangular pool is numerically investigated. The fluid pressure on the wall in a large eddy simulation (LES) model is found to be in good agreement with experimental results. The water overflow in the LES model is also found to improve numerical predictions compared to the laminar model, suggesting that nonlinear sloshing phenomena can be predicted without an empirical damping factor by precisely solving the turbulent dissipation.

1. Introduction

During an earthquake, the water surface in the spent fuel pool of a nuclear reactor will undergo sloshing. This sloshing may lead to overflow of the radioactive water, as well as damage to the pool and structure attached to it owing to increase in the fluid pressure. To preclude such an event, knowing the wave height and fluid pressure resulting from sloshing is crucial.

Conventionally, velocity potential analysis has been adopted as a theoretical method to estimate the maximum sloshing height [1]. When the sloshing height and initial water height are of the same order of magnitude, turbulent behavior is non-negligible [2]. In such a situation, the conventional analysis is invalid. Until now, numerical simulations based on Reynolds-averaged Navier-Stokes (RANS) turbulence models have been performed and revealed that the sloshing height and pressure are in good agreement with experimental results in the strong nonlinear regime [3].

The sloshing energy dissipates owing to the turbulence near the wall, and the sloshing height decays. The damping factor must be determined with respect to each pool because the sloshing behavior depends on the shape of the pool and initial water height. However, as shaking a real spent fuel pool is impossible, empirical values from 0.1% to 1% have been used for the damping factor thus far. In this work, to substitute the empirical value with turbulence dissipation, the effect of turbulence on nonlinear sloshing is numerically investigated and examined applicability of turbulence models.

2. Numerical model

Based on the range of modeled spatio-temporal scales, turbulence models can be classified into RANS and large eddy simulation (LES) models. RANS models can be divided into two categories: eddy viscosity (EV) models and second-order-moment closure (SMC) models. Here, the realizable k - ϵ model [4] is employed as an EV model, the Launder-Gibson model (LG) model [5] is employed as the SMC model, and the Smagorinsky model [6] is employed as a standard model for the LES model.

The sloshing in a pool can be interpreted as a phenomenon in which water with large deformation of the free surface moves periodically between closed walls. In this work, the dam-break phenomenon is

chosen as the subject matter of an introductory investigation into sloshing, and the fluid pressure on the wall is numerically investigated. Subsequently, the turbulence effect on water overflow in a rectangular pool is examined.

3. Fluid pressure on the wall

Figure 1 shows the computational domain and initial setting for the water column. The numerical conditions are the same as those used in Hu [7], $(W, H, D, w_0, h_0) = (1.18, 0.24, 0.12, 0.68, 0.12)$ [m]. The total cell numbers are $(N_x, N_y, N_z) = (472, 96, 48)$.

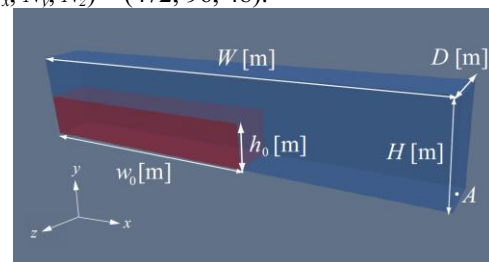


Figure 1 Computational domain and initial water column.

Figure 2 shows the temporal evolution of the fluid pressure at point $A = (1.18, 0.01, 0.06)$ [m]. The circles indicate experimental results repeated eight times by Hu, and their averages are shown by the solid lines. The blue, green, red, and aqua lines show the results calculated with the laminar, RKE, LG, and Smagorinsky models, respectively. The pressure predictions are improved by considering anisotropic turbulence near the wall. The pressure curve including two peaks in the Smagorinsky model is in good agreement with experimental results.

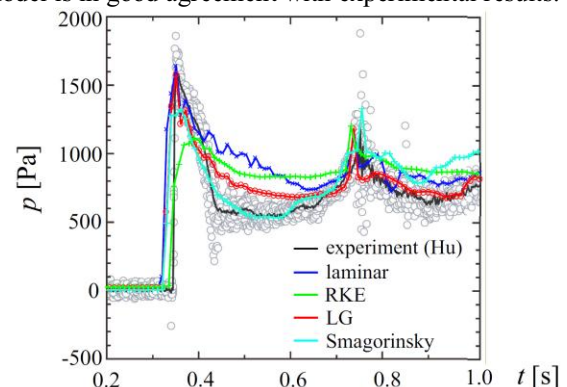


Figure 2 Temporal evolution of the fluid pressure in various models with experimental results.

4. Sloshing height and water overflow in the pool

The computational domain and shape of the rectangular pool are shown in Fig. 3. The computational domain is $(W, H, D, h, w_0, h_0) = (3.2, 2.0, 0.5, 2.0, 1.5, 1.45)$ [m]. The N-S component of the K-Net [8] Tomakomai wave is added to the water in the pool to excite sloshing. Here, the peak spectral frequency of the seismic wave is shifted to the eigen frequency of the pool by changing the temporal axis to excite the sloshing efficiently. The cell numbers are $(N_x, N_y, N_z) = (160, 100, 25)$. These conditions are same as those used in a previous study by Sakai [3].

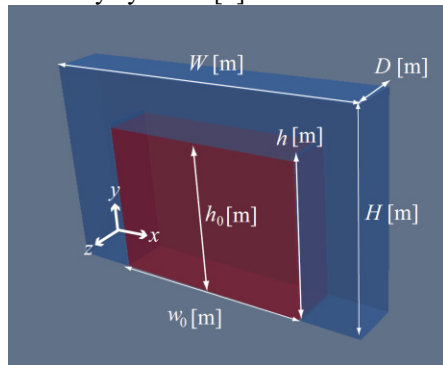


Figure 3 Computational domain and initial setting of the rectangular pool.

Figure 4(a) shows the temporal evolution of sloshing height at the left wall of the pool in each turbulence model. The black, green, red, and aqua lines show the laminar, RKE, LG, and Smagorinsky models, respectively. Experimental (square) and simulated (dotted line) results by Sakai are also shown as a reference. Figure 4(b) is a close-up of Fig. 4(a) at around $t = 50$ [s]. The wave height in the Smagorinsky model is closest to the experimental result. The difference between the wave height in the LG model and that in the Smagorinsky model is small, whereas the wave height is underestimated in the laminar and RKE models.

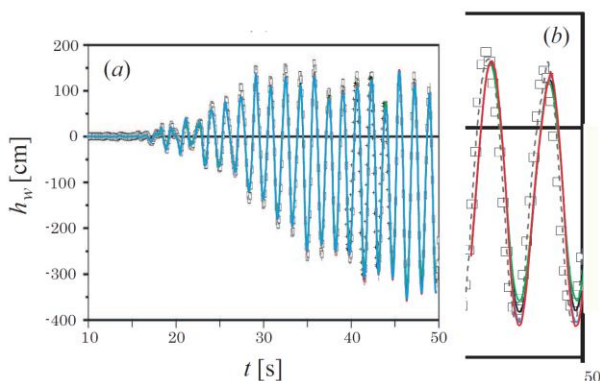


Figure 4 Temporal evolution of sloshing height at the left wall in the pool.

Figure 5 shows the temporal evolution of water height at the left wall. The dotted black line represents the final experimental water height by Sakai. The blue line shows numerical results by Sakai, and the red line indicates the numerical results of the Smagorinsky model. The

difference between the experimental and Smagorinsky results is approximately 8%. This value is of the same order as that of the numerical result by Sakai, suggesting that sloshing in the strong nonlinear regime can be simulated by precisely solving the turbulent dissipation.

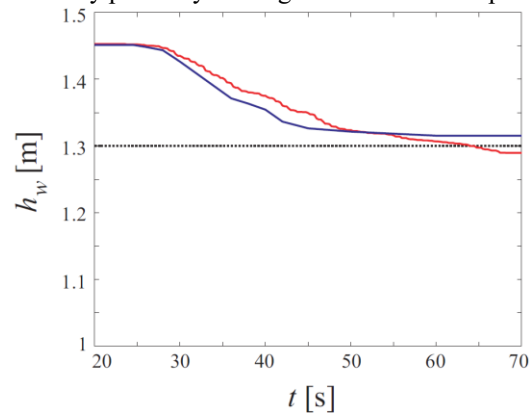


Figure 5 Temporal evolution of water height with final experimental value.

5. Concluding remarks

The effect of turbulence on nonlinear sloshing in a rectangular pool is numerically investigated. The fluid pressure on the wall in the Smagorinsky model is found to be in good agreement with experimental results. Pressure predictions are improved by considering anisotropic turbulence near the wall. The water overflow in the Smagorinsky model without the damping factor improves numerical predictions compared to the laminar model, suggesting that nonlinear sloshing phenomena can be predicted without any empirical values by precisely solving the turbulent dissipation.

Acknowledgements

I would like to thank Prof. S. Koshizuka, Prof. H. Okuda, and Dr. M. Sakai for their fruitful comments. I would also like to express my gratitude to Drs. M. Tani, N. Nakajima, H. Takemiya, A. Nishida, and Y. Suzuki for their support. I also thank the National Research Institute for Earth Science and Disaster Prevention (NIED) for providing the K-Net data.

References

- [1] Fire Service Act, Firefighting Hazards No. 14.
- [2] K. Muto *et al.*, Proc. Pressure Vessels and Piping Conference, p. 209 (1985).
- [3] M. Sakai *et al.*, J. Structural Engineering, **53A** p. 597 (2007).
- [4] T. H. Shih *et al.*, Computers Fluids, **24** p. 227 (1995).
- [5] G. G. Gibson *et al.*, J. Fluid Mechanics, **85** p. 491 (1978).
- [6] J. Smagorinsky, Monthly Weather Review, **91** p. 99 (1965).
- [7] C. Hu, J. Mar. Sci. Technol, **9** p.143 (2004).
- [8] <http://www.kyoshin.bosai.go.jp/kyoshin/>

OS7: Blood Flow for Medical Equipment

Numerical Simulation of Vertebral Artery Stenosis Treated with Different Stents

Zhanzhu Zhang, Aike Qiao

College of Life Science and Bio-engineering, Beijing University of Technology, Beijing, 100124, China
E-mail of corresponding author: qak@bjut.edu.cn

ABSTRACT

To investigate the effect of stents with different links on treating stenotic vertebral artery and the relation between the shape of link and in-stent restenosis (ISR), numerical simulations of solid mechanics and hemodynamics were performed. From the view point of combination of solid mechanics and hemodynamics, S-stent has better therapeutic effect because of its lower potential possibility of inducing ISR, and better prospects in clinical application more than L-stent and V-stent.

1. Introduction

Stenting technology has emerged as an alternative for treating the stenotic artery, which recovers blood fluency through mechanical scaffold using struts. Different kinds of stent cause different injury on the artery wall, inducing different ratios of postoperative in-stent restenosis (ISR) [1]. Therefore, the design of stent structure has a significant influence on therapeutic effect of stent intervention. To investigate the effect of stents with different links on treating stenotic vertebral artery and the relation between the shape of link and ISR, as well as provide scientific guidelines for designing stent structure and selecting stent in clinical procedure, numerical simulations of solid mechanics and hemodynamics were performed in this paper, which coupled the stent with three kinds of link, the plaque and the blood in the vertebral artery.

2. Method

Three kinds of stent with different links and idealized stenotic vertebral artery were established using Pro/Engineering. The three kinds of stent are L-stent, V-stent and S-stent respectively according to the different shape of link (Fig.1). The idealized vertebral artery was constructed based on physiological anatomy parameters. Solid mechanics simulations of the deployment of stent were performed using ABAQUS. Stents were deployed in the vertebral artery under the same boundary condition. Then, the deformed meshes of stent and artery after deployment were extracted and used to construct their surfaces. Boolean operation of these deformed surfaces was carried out so that the hemodynamic boundary surface was obtained and imported into ICEM. The finite element model was established by meshing the flow domain. Finally, numerical simulations of hemodynamics under physiologically pulsatile flow condition were performed using ANSYS-CFX.

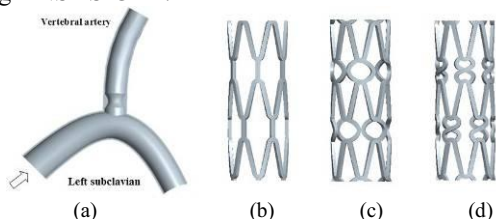


Fig. 1 Geometry Models of artery and stent. (a)Artery; (b)L-stent; (c)V-stent; (d)S-stent

3. Results and Discussion

3.1 Stress distribution in vertebral artery

Figure 2 shows the stress contour of the vertebral artery after stenting. The peak stresses caused by the three kinds of stent are located on the plaque at the outer bend of artery (left side). The peak stress caused by S-stent is the minimum, and the peak stress caused by L-stent is the maximum. The extent of stent embed in artery increases as stress increases in the artery, so the potential possibility of injury of endothelial cells caused by stenting may increase. It is apt to the rupture of plaque because of higher stress, causing vascular occlusion, even inducing stroke. Therefore, compared with L-stent and V-stent, S-stent has a better therapeutic effect because of its decreasing the potential possibility of inducing ISR.

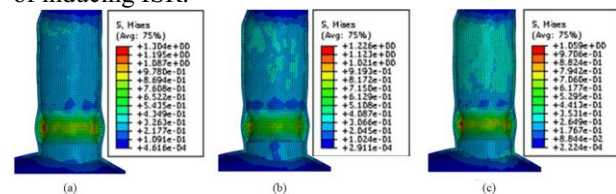


Fig.2 Contours of the Von Mises stress in arterial wall: (a)L-stent; (b)V-stent; (c)S-stent

3.2 Straightening of curved artery

Artery is more flexible than stent, so curved artery is straightened because of stent implantation in the artery, which agrees with the result of Wu [2]. The displacement of the middle point of the distal section of the vertebral artery could indirectly indicate the straightening of artery, so it is obtained and depict in Table 1. The degree to which artery is straightened because of implantation of L-stent is significant, S-stent is the least significant, and their relative difference is just 3.7%. This coincides with the flexibility of stents in sequence. The flexibility of L-stent is the worst, and the flexibility of S-stent is the best. The shape of link has little effect on the straightening of curved artery, but the straightening of artery is related with flexibility of stent to some extent.

Table 1 The displacement of the middle point of the distal section of the vertebral artery

Stent type	Displacement
L-stent	1.41mm
V-stent	1.38mm
S-stent	1.36mm

3.3 Foreshortening of stent

The axial length of stent will foreshorten with its radial expansion. This behavior is described as foreshortening, which can be illustrated as equation (1).

$$C = \frac{L_0 - L}{L_0} \times 100\% \quad (1)$$

where L_0 is the initial length, and L is the deployed length. Table 2 shows the foreshortening of stents. The foreshortening of S-stent is the minimum, and the foreshortening of L-stent is the maximum. It is favorable to clinical application of stent that smaller foreshortening could ensure the precise position of stent in the artery. Therefore, compared with L-stent and V-stent, S-stent ensures the precise position of stent in the artery, and it has better prospect of clinical application.

3.4 Wall shear stress distribution on artery wall

Figure 3 shows the contour of wall shear stress (WSS) at the peak velocity, using scale of 0-10Pa. Lower WSS is located mainly in the region around struts and links of stent, while higher WSS is located in the middle region of mesh of stent, specifically the highest WSS is located in the stenotic region.

Table 3 shows the area ratio of time-averaged WSS distribution on artery wall. The area ratio caused by S-stent is the maximum, the area ratio caused by L-stent is the minimum, and the difference between these two area ratios is only 2.56%. The distinction between S-stent and L-stent is not significant from the viewpoint of area ratio difference. However, low WSS distributes mainly in the region where stent was implanted, which covers around 1/8 of the whole area of artery. The area ratio difference will be above 10% if the area ratio is derived from the ratio of the area of low time-averaged WSS and the arterial region where stent was implanted. In such a manner, the distinction between S-stent and L-stent will be significant.

Table 2 Foreshortening of stents

Stent	Initial length	Deployed length	Foreshortening
L-stent	11.5mm	9.37mm	18.5%
V-stent	11.5mm	9.82mm	14.6%
S-stent	11.5mm	10.04mm	12.7%

Table 3 The area ratio of time-averaged WSS distribution on artery wall

WSS	L-stent	V-stent	S-stent
0~0.4Pa	9.05%	10.22%	11.61%

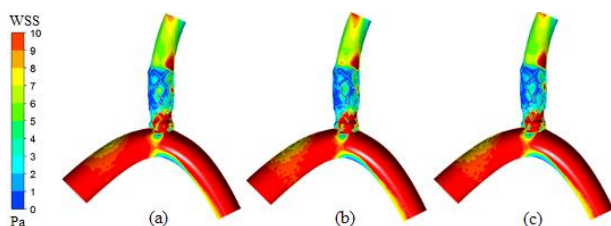


Fig.3 Contour of the instantaneous WSS. Using a scale of 0-10Pa: (a)L-stent; (b)V-stent; (c)S-stent

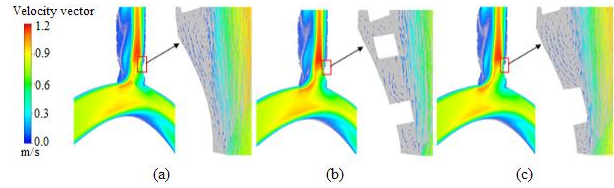


Fig.4 Contour of velocity vector in the longitudinal plane: (a)L-stent; (b)V-stent; (c)S-stent

3.5 Blood flow

Figure 4 shows the contour of velocity vector of blood flow at peak velocity. The region of contour displayed is magnified just in the proximity of stent. The range of velocity is 0-1.2m/s. Compared with L-stent, the links of V-stent and S-stent has transverse structure in the longitudinal profile, which has blocking effect on blood flow. Blood flow hardly exists in the region close to the artery wall between strut and link as well as between links. So blood stagnation zone, as well as low WSS, occurs in that region, increasing the stagnation time of toxic substances in blood. Moreover, a vortex appears in L-stent between two struts, while two vortexes appear in V-stent and S-stent. Vortex could cause flow separation, low WSS and blood stagnation zone, which induce stagnation of toxic substances such as hemocyte, lipid etc^[3]. Compared with V-stent and S-stent, L-stent has better blood flow patterns close to the artery wall, so it could decrease the potential possibility of inducing ISR from the viewpoint of hemodynamics.

4. Concluding remarks

1) Better shape of link could decrease foreshortening of stent and the potential possibility of denudating plaques and inducing ISR; 2) Better flexibility of stent could lessen potential possibility of ISR; 3) Less blood stagnation area and better blood flow pattern close to the artery wall could decrease the potential possibility of inducing ISR.

S-stent has better therapeutic effect from the viewpoint of solid mechanics, and L-stent has better therapeutic effect from the viewpoint of hemodynamics. Considering the short-term step effect of stent and the long-term mechanical effect of stent scaffold, S-stent has better therapeutic effect and better prospects in clinical application because of its decreasing the potential possibility of inducing ISR.

5. Acknowledgement

This work was supported by National Natural Science Foundation of China (10972016, 81171107) and Natural Science Foundation of Beijing (3092004). Cooperative Laboratory Study Program in Tohoku University also supported this study.

References

- [1] Gu LX, J. Med. Devices, 4(2010).
- [2] Wu W, J. Biomech, 40(2007).
- [3] Pakala R, Cardio. Rad. Med, 3(2002).

Pressure-Driven Flow Characteristics in the Lymphatic Vessel for Lymphatic Drug Delivery System

Yuriko Hatakeyama, Nicolas Sax, Shigeki Kato, Tatsuki Okuno, Maya Sakamoto, Shiro Mori, Tetsuya Kodama
Graduate School of Biomedical Engineering, Tohoku University, 4-1 Seiryomachi, Aoba-ku, Sendai, Miyagi, Japan
yuriko.hatakeyama@bme.tohoku.ac.jp

ABSTRACT

The lymphatic system plays an important, but its mechanism has not been understood. Due to the absence of useful experimental animal models, a lymphatic administration method has not been developed. We have developed a mouse model of the pressure-driven lymph node metastasis (LNM) via the efferent lymphatic vessel (LV). Using this model, we succeeded in measuring the pressures in the LNs and visualizing the lymphatic flow with a real-time pressure measurement system. We also elucidated the characterization of lymphatic flow for lymphatic administration. These results allow a new drug delivery system through the LV.

1. Introduction

The major pathways of tumor cells dissemination are the lymphatic and circulatory system. However, the role of the lymphatic system in metastasis is less well understood compared with the circulatory system [1]. The lymphatic system is a complex network of nodes, vessels and thin-walled capillaries that drain the protein-rich lymph, excess fluids, and waste products from the extracellular space within most organs to the vascular system. Current lymphatic imaging modalities with newer tools using nanocarriers, quantum dots, and magnetic resonance imaging promise to vastly improve the staging of lymphatic spread without needless biopsies [2, 3]. Normal mice have small lymph nodes (of 2mm diameter), these small lymphatic organs are often difficult to identify in mice using standard dissection techniques, so that a lymphatic administration method has not been reported. The lymphatic flow dynamics relating to mechanisms of lymph node metastasis also has not been elucidated because of the absence of useful experimental animal models [4].

Recently, we have developed a LNM mouse model. The mice used in this model have enlarged lymph nodes, whose size is similar to human lymph node [5]. We established a real-time measurement system which can measure pressures in the LNs and visualize the lymphatic flow, simultaneously. Here we report the pressure-driven flow characteristics through the efferent lymphatic vessel (ELV) with a real-time pressure measurement system using these mice.

2. Method

In vivo experiments were done in accordance with the ethical guidelines of Tohoku University.

2.1 Mouse model

We have developed a mouse model of LNM via the efferent LV by which the time and location of the occurring metastasis are determined. MXH-10 /Mo/lpr/lpr (MXH-10) mice have enlarged LNs, which size is similar to human LNs (10mm diameter) [5]. In this model, metastasis is induced by injection of tumor cells into the inguinal lymph node (ILN), followed by induction in the axillary lymph node (ALN). We made a skin incision in the mice under anesthesia to expose two LNs (ILN, ALN) and LV between these LNs.

2.2 Visualization of lymphatic flow

Visualization of the flow in the LNs and LV was carried out *in vivo* by a fluorescence stereo-microscopy Leica M165-FC (fluorescent filter:GFP2, λ_{ex} :460-500nm, λ_{em} :>510nm), Leica camera AG, Bensheim, Germany) with a high-speed camera (Cool SNAP HQ2, Photometrics, Tokyo, Japan), using fluorescein isothiocyanate (FITC) (5(6)-Carboxyfluorescein, 376.32MW, λ_{ex} :492nm, λ_{em} :517nm, SIGMA-Aldrich Japan, Tokyo, Japan) solutions. We injected FITC into the ILN at a constant volume and flow rate.

2.3 Real-time pressure measurement system

We established the real-time multichannel pressure measurement system (Fig.1). We simultaneously measured the pressure changes in the LNs with two pressure transducers (Operating pressure range : -50 to +300 mmHg, sensitivity : $5\mu V/V/mmHg$, $\pm 2\%$ (typically $< \pm 1\%$), World Precision Instruments, Sarasota FL, USA) using syringe pump (Legato100, KD scientific, Massachusetts, USA) and visualize lymphatic flow in the LNs and LVs with a stereoscopic fluorescent microscope. The trigger signal was switched on by the syringe pump. Pressures were measured by 50 readings/sec about 10 min after FITC injection.

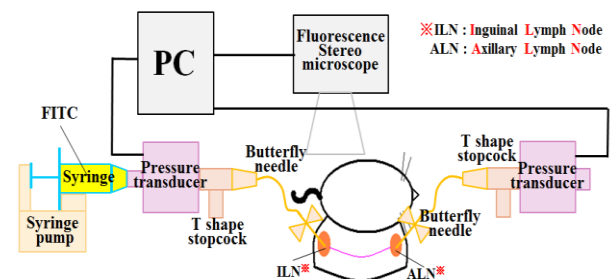


Fig. 1 Real-time pressure measurement system
Synchronized measurement among three equipment (syringe pump, pressure transducer and stereoscopic fluorescent microscopy) was carried out by the trigger signal from the syringe pump. Set the syringe filled up with FITC on the syringe pump, and connected through the pressure transducer and the T-shape stopcock to a butterfly needle. We injected FITC into the ILN at a constant rate to visualize the flow in LNs and LVs.

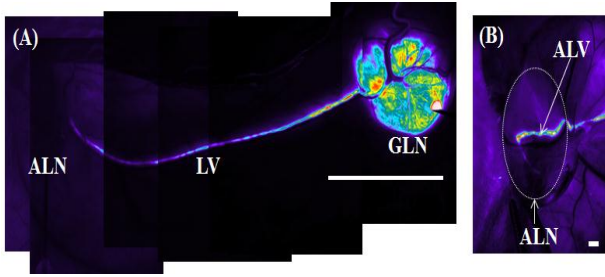


Fig. 2 FITC flow visualization

(A) Distribution of FITC solutions in the ILN. FITC flow from the ILN toward the ALN via the LV was observed. (B) FITC flow to the ALN via the afferent lymphatic vessel (ALV). Scale bars of Fig.2 (A), (B) = 10mm, 1mm, respectively.

3. Results and Discussion

3.1 Visualization of lymphatic flow

The flow of FITC solutions from the ILN to the ALN via the LV was visualized by injecting FITC into the ILN with a fluorescence stereo-microscopy (volume: 60 μ L, flow rate : 50 μ L/min). Figure 2(A) shows the FITC concentration distribution in the ILN and FITC flow from the ILN toward the ALN via the LV. We also visualized the flow of FITC solutions to the ALN via the afferent lymphatic vessel (ALV) in Fig.2(B).

3.2 Real-time pressure measurement system

Figure 3 shows the pressure changes in the ILN and ALN by injecting FITC solution into the ILN. We can see a sharp increase rise of pressure followed by a plateau in the ILN. The pressure in the ILN increases up to about 7 [kPa] and remains at the same value during the injection of FITC solution. We can see the gradual pressure decrease in the ILN after FITC injection. Pressure increase/decrease in the ALN is delayed by about 50 seconds following FITC injection in the ILN and injection end, respectively.

3.3 Development of theoretical modeling

Theoretical model focused on the pressure change in the ILN and flow into the ELV was established based on Hagen-Poiseuille flow with the real-time pressure measurement. Volume flow Q can be expressed as

$$Q = \frac{\pi d^4 (\Delta P)}{128 \mu l} \quad (1)$$

and mean flow rate v in the LV can be expressed as

$$v = \frac{d^2 (\Delta P)}{32 \mu l} \quad (2)$$

where d is the diameter of the LV, ΔP is the pressure change in the LN, μ is the viscosity coefficient, and l is the length of the LV. These formula are expressed in a plateau in the ILN. The volume elasticity K at the ILN was $K = 1.45 \times 10^5$ [Pa].

At $t > t_d$ (t_d : time of FITC injection end) time domain, rate of pressure change can be expressed

$$\Delta p(t) = (\Delta P) \cdot \exp \left[-\frac{\pi d^4 K}{128 \mu l V_0} (t - t_d) \right] \quad (3)$$

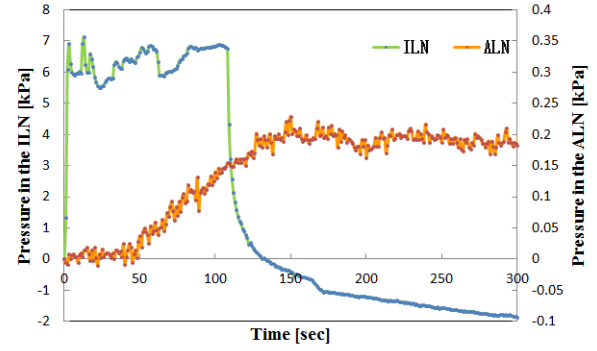


Fig. 3 Pressure changes in the ILN and ALN
Pressure changes in the ILN and ALN by injecting FITC into the ILN were measured with real-time pressure measurement system.

and mean flow rate in the LV also expressed as

$$v(t) = \frac{d^2 (\Delta P)}{32 \mu l} \exp \left[-\frac{\pi d^4 K}{128 \mu l V_0} (\tau - t_d) \right] \quad (4)$$

where V_0 is the initial LN volume.

4. Concluding remarks

We developed a system allowing simultaneous imaging of the FITC flow in LNs, and the pressure measurement inside the LNs of MXH-10 mice. We also obtained the FITC flow characteristics from ILN to ALN through the LV, and investigated the administration induced pressure increase, drug dosage, administration speed and volume of liquid delivered from ILN to ALN.

Acknowledgements

T. Kodama received grant-in-aid for scientific research (B) (23300183) and challenging exploratory research (24650286). S. Mori received grant-in-aid for scientific research (B) (22390378) and challenging exploratory research (24659884). M. Sakamoto received grant-in-aid for scientific research (B) (21390500) and challenging exploratory research (24659834).

References

- [1] Nathanson SD, Insights into the mechanisms of lymph node metastasis, *Cancer*, (2003), 98.
- [2] Satish K.Nune, Padmaja Gunda, Bharat K. Majeti, et al. Advances in lymphatic imaging and drug delivery, *Adv Drug Deliv Rev*, (2011), 63.
- [3] Kosaka, N., Ogawa, M., Sato, N. et al. In vivo real-time, multicolor, quantum dot lymphatic imaging, *J Invest Dermatol*, (2009), 129.
- [4] Harrell, M. I., Iritani, B. M., Ruddell, A., Lymph node mapping in the mouse, *J Immunol Methods*, (2008), 332.
- [5] Tanaka Y, Komori H, Mori S, et al. Evaluating the role of rheumatoid factors for the development of rheumatoid arthritis in a mouse model with a newly established ELISA system, *Tohoku J Exp Med*, 220.

Cancer Treatment Via The Lymphatic Vessel Using Nano/Micro Bubbles

Shigeki Kato, Sax Nicolas, Yuriko Hatakeyama, Tatsuki Okuno, Shiro Mori, Maya Sakamoto, Tetsuya Kodama
Graduate School of Biomedical Engineering, 4-1, Seiryu-machi, Aoba-ku, Sendai, Miyagi, 980-8575, Japan
Shigeki.kato@bme.tohoku.ac.jp

ABSTRACT

Cancer invasion that is spread to the lymphatic system is a common occurrence and is often the first step of the metastatic pathway. The most common administration route of drugs to metastatic lymph nodes (LNs) is blood circulation. However, this delivery system causes severe side effects. The lymphatic vessels are directly connected to the lymph node (LN), thus have potential of delivering drugs to the targeted metastatic LN with metastasis. Here we show a drug delivery system to the LN via a single lymphatic vessel using acoustic liposomes (ALs) and ultrasound (US).

1. Introduction

Cancer invasion that is spread to the lymphatic system is a common occurrence and is often the first step of the metastatic pathway[1]. Therefore, lymphatic spread is an important factor of staging and prognosis. Chemotherapy plays a central role in treatment for clinically-evident lymph metastasis, and systemic administration of anti-tumor agents is mainstream in clinical practice[2, 3]. Systemic administration causes severe side effects to normal cells, and only a small fraction of the drug is delivered to the lymphatic system[4]. If anti-tumor agents are delivered to tumors growing in the LNs through the lymphatic system, anti-tumor agents can be delivered into the tumors efficiently, resulting in decreased side effects. US mediated drug delivery with nano/microbubbles (NMBs) allows control of the drug concentration at the target sites non-invasively. NMBs are small gas-filled microspheres with a radius of less than 5 μ m, and have specific acoustic properties that make them useful as contrast agents in the field of US. Therefore, image guided treatment of US triggered drug delivery system can be achieved by characterizing the localization and behavior of ALs with US imaging system. The aim of the present study is to develop a novel administration route via the lymphatic vessels by US and NMBs. We used MXH-10/Mo/lpr/lpr (MXH-10) mice which have enlarged lymph node, and visualized ALs flowing in the lymphatic vessel and the ALN by high-frequency US system. We found that exogenous molecules were delivered into the ALN via the lymphatic vessel using US and NMBs.

2. Method

All *in vivo* studies were done in accordance with the ethical guidelines of Tohoku University.

Preparation of NMBs

The NMBs used in this study were acoustic liposomes (ALs) [5]. The acoustic liposomes (lipid concentration, 1 mg/mL) were composed of DSPC (NOF Co., Tokyo, Japan) and 1,2 - distearoyl -sn - glycerol - 3 - phosphatidyl - ethanolamine - methoxy - polyethylenglycol (DSPE-PEG2000-OMe) (NOF Co.) (94:6 [mol/mol]) containing C₃F₈ gas. Liposomes were prepared by the reverse phase evaporation method. ALs were created from the liposomes by sonication in the presence of C₃F₈ gas for 1 min with a 20 kHz stick

sonicator (130 W, Vibra Cell, Sonics & Materials Inc., Daubury, CT, USA). The mean diameter of ALs was 199 \pm 84.4 nm; < 0.01% are ALs with diameters exceeding a few micrometers.

Animal model

MXH-10 mice were used in this study. This animal model develops systemic lymphadenopathy enlarged to a size similar to human LN. The lymphatic vessel from the inguinal lymph node (ILN) to the axillary lymph node (ALN) is the metastatic route depicted in Fig.1.

Fluorescent molecules

TOTO-3 fluorophore (T-3604; Molecular Probes, Eugene, OR, USA; MW: 1355, absorption: 642 nm, emission: 660 nm) was used as molecular markers at a concentration of 10 μ M[6]. TOTO-3 fluorophore was injected into the ILN by a butterfly needle at a speed of 50 μ L/min and delivered to the ALN.

Delivery of fluorescent molecules into the ALN

Four mice (age 15 - 18 weeks) were used for molecular delivery. The mice were divided into four groups (A, B, C, D). In group A, 200 μ L of PBS was injected into the ILN. In group B and D, 200 μ L of solution (100 μ L of ALs and 100 μ L of TOTO-3) was injected into ILN. In group C, 200 μ L of solution (100 μ L of PBS and 100 μ L of TOTO-3) was injected into the ILN. And in group C and D, solutions were exposed to US when they were reached the LN. US was generated by a 1.0 MHz submersible US transducer with a diameter of 12 mm (Honda Electronics, Toyohashi, Japan). Signals were generated using a multifunction synthesizer (WF1946A; NF Co., Yokohama, Japan) and amplified with a high-speed bipolar amplifier (HSA4101; NF Co.). The ALN was exposed to US with a pressure of 0.67 MPa at a duty ratio of 20% for 60 s, as verified with a calibrated PVDF needle hydrophone (ONDA, Sunnyvale, CA, USA). The number of cycles in the pulse was 200. Each ALN was extracted immediately after the treatment. These samples were mounted in OCT compound (Sakura Finetek Japan, Tokyo, Japan), taking not to slant the sample and frozen with liquid nitrogen and stored at -80°C before sectioning at 10 μ m.

Immunofluorescent staining

The LNs that were used for the fluorescent

delivery as described above were then excised to make frozen sections. The frozen samples were sectioned into 10 μm . LYVE-1 positive lymphatic endothelial cells were stained using the primary antibody LYVE-1 (RELIATech GmbH, Germany). Secondary antibody Alexa Fluor 488 (Invitrogen, America) was applied next day. The nuclei were stained with DAPI. Images showing DAPI, LYVE-1 and TOTO-3 fluorescence were captured on a confocal laser scanning microscope (FV1000, Olympus).

3. Results and Discussion

Figure 2 shows images of immunofluorescent staining in the ALNs. The nuclei of the lymphocytes were stained with DAPI (blue). The lymphatic vessels were stained by LYVE-1 (green) and the area in which TOTO-3 was delivered was stained in red. PBS injection alone did not show any signals (Fig.2A). TOTO-3 alone was weakly detected in the nuclei of the lymphocytes (Fig.2B, white arrow). US with TOTO-3 delivered TOTO-3 in the nuclei of lymphocytes (Fig.2C). US and in the presence of TOTO-3 and ALs delivered TOTO-3 in the nuclei of lymphocytes (Fig.2D). Surprisingly, the amount of TOTO-3 delivered by US with TOTO-3 was larger than that of US in the presence of TOTO-3 and ALs

We demonstrated that US exposure induced cell permeability, resulting in successful delivery of exogenous fluorescent molecules into the lymphocytes of the ALN. In the previous studies, the combination of ALs and US exposure could enhance the delivery efficiency compared to without ALs [7]. However, in the present study, TOTO-3 and US enhanced delivery of TOTO-3, compared to TOTO-3, US and ALs.

We have to optimize the delivery conditions in the presence of US and ALs.

4. Concluding remarks

We demonstrated that a molecular delivery system via the lymphatic vessel with US and NMBs can deliver exogenous molecules into the ALN.

References

1. McElroy, M., et al., *Fluorescent LYVE-1 antibody to image dynamically lymphatic trafficking of cancer cells in vivo*. J Surg Res, 2009. **151**(1): p. 68-73.
2. Celikoglu, F., S.I. Celikoglu, and E.P. Goldberg, *Intratumoural chemotherapy of lung cancer for diagnosis and treatment of draining lymph node metastasis*. J Pharm Pharmacol, 2010. **62**(3): p. 287-95.
3. Spiro, S.G. and J.C. Porter, *Lung cancer--where are we today? Current advances in staging and nonsurgical treatment*. Am J Respir Crit Care Med, 2002. **166**(9): p. 1166-96.
4. Lentacker, I., et al., *Design and evaluation of doxorubicin-containing microbubbles for ultrasound-triggered doxorubicin delivery: cytotoxicity and mechanisms involved*. Mol Ther, 2010. **18**(1): p. 101-8.

5. Kodama, T., et al., *Morphological study of acoustic liposomes using transmission electron microscopy*. J Electron Microsc (Tokyo), 2010. **59**(3): p. 187-96.
6. Horie, S., et al., *Development of localized gene delivery using a dual-intensity ultrasound system in the bladder*. Ultrasound Med Biol, 2010. **36**(11): p. 1867-75.
7. Kodama, T., et al., *Evaluation of transfection efficiency in skeletal muscle using nano/microbubbles and ultrasound*. Ultrasound Med Biol, 2010. **36**(7): p. 1196-205.

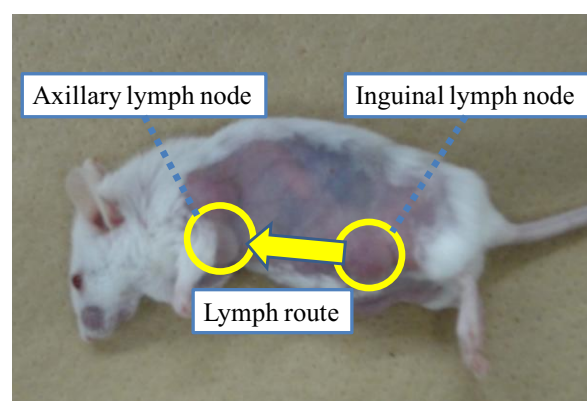


Fig 1. MXH-10 mouse. LNs are enlarged and the size is as large as human. The ILN is connected by a single lymphatic vessel to the ALN. Injected solution into the ILN reaches the ALN via the lymphatic vessel.

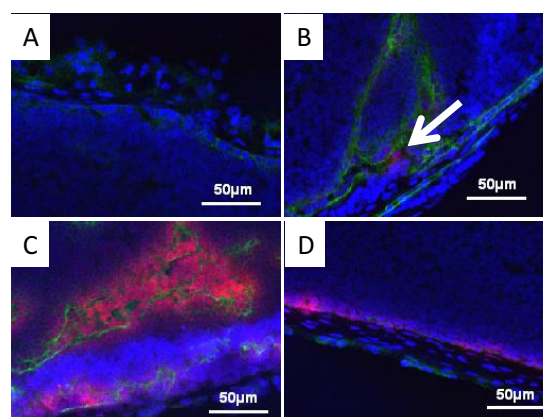


Fig. 2 Immunofluorescent staining images of the ALN. (A) PBS injection, (B) TOTO-3 + ALs, (C) TOTO-3 + US, (D) TOTO-3 +US+ALs.

Thermal Therapy Using Plasmonic Nano Particles for Lymph Node Metastasis

Tatsuki Okuno, Shigeki Kato, Yuriko Hatakeyama, Takuma Sato, Maya Sakamoto, Shiro Mori, Tetsuya Kodama;
Graduate School of Biomedical Engineering, Tohoku University, 4-1 Seiryō, Aoba Sendai, Miyagi, Japan,
tatsuki.okuno@bme.tohoku.ac.jp

ABSTRACT

The present study examines the plasmonic nanoparticle assisted photo-thermal therapy (PPTT). This technique takes advantage of the surface plasmonic resonance by near infrared laser (NIR –laser) and gold nanorods(AuNRs). Tumor cells were injected in human size lymph node of MXH10/Mo/*lpr/lpr* mice. After 3days, tumor bearing lymph node was injected AuNRs and irradiated with NIR laser beam (1064 nm, 1.5 W/cm², 3 min). Mice in PPTT group appeared temporary anti-tumor effect. This is the first result of PPTT effect to tumor in the human size lymph node.

1. Introduction

Lymphatic metastasis is serious problem for patient, and its progression leads to poor prognosis [1, 2]. Treatment of lymphatic metastasis is a combination of lymph node removal and systemic chemotherapy. These methods have serious side effects due to tissue invasiveness, thus low-invasive methods are required [3, 4]. Here we show that a novel low-invasive thermal therapy using gold nanorods (AuNRs) and near infrared laser (NIR-laser) beam for treatment of lymphatic metastasis. AuNRs generate surface plasmonic resonance (SPR) by NIR-laser beam irradiation. Under the SPR, AuNRs convert laser beam energy to thermal energy, and this thermal energy is able to treat tumor. In this study, we evaluated anticancer effect of this thermal therapy using tumor-bearing mice. Mice were injected AuNRs and irradiated laser beam. Our results demonstrate that our thermal therapy is effective to tumor in human size lymph node. This is the first result of PPTT effect to tumor in the human size lymph node.

2. Method

In vivo experiments were done in accordance with the ethical guidelines of Tohoku University.

2-1. Mouse model

MXH10/Mo/*lpr/lpr*(MXH10) mice were used in this experiment. This mouse is hybrid of MRL/Mp/*lpr/lpr* (MRL/*lpr*)mouse and C3H/HeJ/*lpr/lpr*(C3H) mouse, and this mouse has large lymph node as the same as human's. It is possible that close to clinical experiment by this mouse model(Fig.1).

2-2. Gold nanorods

Avidin polymer coated gold nanorods(AuNRs) were used in this experiment(ZZZ Ntherapy Nanorods, axial diameter 10 nm, long diameter 67 nm, surface plasmon resonance peak 1064 nm, aspect ratio 6.7, Nanopartz, America, Colorado). Solution of AuNRs was dissolved in PBS and the concentration was 3.3×10^5 cells/mL. Au nanorods were observed by transmission electron microscope (HT7700,HITACHI, Japan, Ibaraki).(Fig.2)

2-3. Cell culture

KM-luc/GFP cells were MRL/MpTn-*gld/gld* fibroblast cells, and were transfected with a luciferase

pEGFP-Luc plasmid. Cells were seeded onto a 10 cm dish and incubated in DMEM (Sigma-Aldrich, St. Louis, MO) containing 10% heat-inactivated fetal bovine serum (hyclone, Utah, USA), 1% Penicillin – Streptomycin – L - Glutamine Solution (Sigma-Aldrich, St. Louis, MO) and 1% Genetin(G418 sulfate, 1 mg/mL ; Sigma-Aldrich, St. Louis, MO).

2-4. Photothermal ablation of cancer in vivo

All MXH10 mice(age : 17 weeks, n = 12) were inoculated with 30 μ L (3.3×10^5 cells/mL) KM-Luc/GFP cells in the one-sided axillary lymph node(Day 0). On 3 days, mice were randomly allocated into four groups (n=3). Mice in group A were injected PBS in the tumor - bearing proper axillary lymph node (Control). Mice in group B were injected AuNRs. Mice in group C were injected PBS and irradiated with 1064 nm laser beam. Mice in group D were injected AuNRs and irradiated laser beam. All mice were injected 30 μ L PBS or AuNRs and mice in group C and D were irradiated with the NIR laser at 1.5 W/cm² for 3 min. Temperature of tumor bearing lymph node was measured with thermography(TVS-500, NEC/Avio, Tokyo, Japan). On 3 , 7 , 10 , 14days, luciferase activity of tumor were measured by small animal bio luminescent system (IVIS Lumina , Caliper, Alameda, CA ,USA). Before 10 min of taking luminescent image, mice were injected 200 μ L(15 mg/mL) luciferin to interperitoneal.

3. Results and Discussion

Effectiveness of *in vivo* SPR was evaluated by thermo image (Fig .3). Temperature of group D(Fig.3 A) is approximately 2 °C higher than group C(Fig.3 B). According to the result, SPR phenomenon is generated in the lymph node under the skin layer (approximately 2 mm in thickness) .

Anti-cancer effect of PPTT was evaluated by luciferase activity of tumor in the lymph nodes (Fig. 4, Fig5). Fig.4 shows luminescent image of tumor bearing lymph nodes. The upper side is control, the lower side is AuNRs+laser (PPTT). Fig.5 shows time dependence of luciferase activity of tumor in the lymph lymph nodes. Group A(Control) , Group B(AuNRs), and Group C(laser) is not observed anti-tumor effect. In contrast of Group D(AuNRs+laser : PPTT), on day 7, anti-tumor

effect is observed. However, on day 10, anti-tumor effect of PPTT is not observed.

4. Concluding remarks

In this study, the temporary effectiveness of PPTT to tumor in human size lymph node is observed. This is the first result of PPTT effect to tumor in the human size lymph node. Utilizing the laser situation and number of irradiation times, anti-tumor effect would be enhanced. This study opens new perspectives for laser beam and nano particle therapy.

Acknowledgements

T. Kodama received grant-in-aid for scientific research (B) (23300183) and challenging exploratory research (24650286). S. Mori received grant-in-aid for scientific research (B) (22390378) and challenging exploratory research (24659884). M. Sakamoto received grant-in-aid for scientific research (B) (21390500) and challenging exploratory research (24659834).

References

- [1] S.F. Schoppmann, R. Horvat, P. Birner, *Oncol. Rep.* **9** (2002) 455–460
- [2] P.A. Kyzas, S. Geleff, A. Batistatou, N.J. Agnantis, D. Stefanou, *J. Pathol.* **206** (2005)170–177
- [3] E.C .Behm, J.M. Buckingham, *ANZ. J. Surg.* **78** (2008)151–157.
- [4] L.Ine, G .Bart, D. Joseph, C. Stefaan, S. De , N.S. Niek , *Molecular Therapy*, **18(1)**(2010)101–108



Fig.1 MXH10/Mo/lpr/lpr
The mouse has large lymph node as the same as human's.

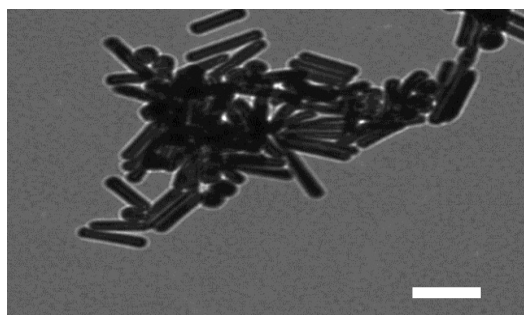


Fig.2 TEM image of gold nanorods.
Axial diameter 10 nm, long diameter 67 nm, surface plasmon resonance peak 1065 nm, aspect ratio 6.7 , scale bar : 100 μm

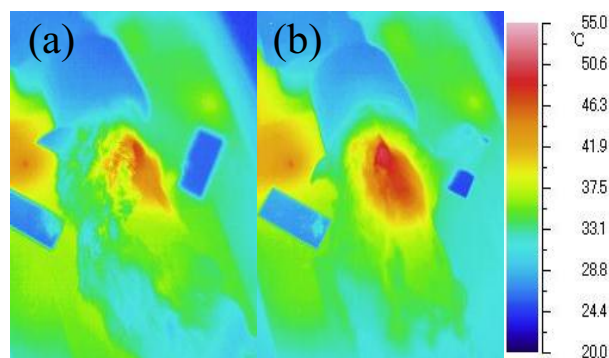


Fig.3 Thermo image. (a) Group C , (b) Group D
Blue(the lowest temperature) : 20 °C , red(the highest temperature) : 55 °C. Temperature of group D(Fig.3 A) is approximately 2 °C higher than group C.

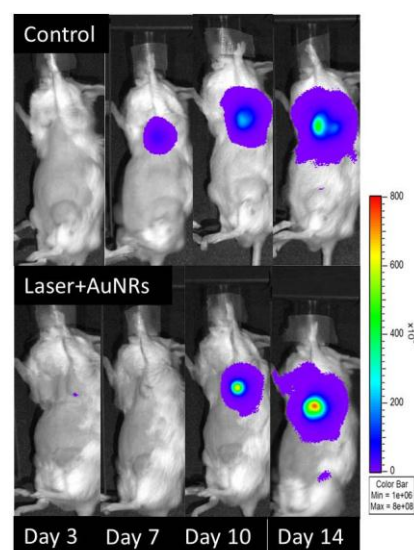


Fig.4 Luminescent image of tumor in the lymph.
Upper side : Control, lower side : AuNRs+laser (PPTT)
Temporary anti-tumor effect is observed.in group D(PPTT cause) on Day7

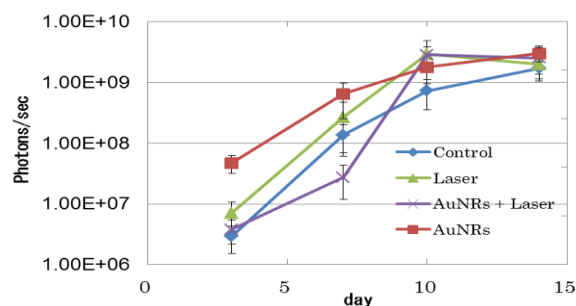


Fig.5 Luciferase activity of tumor in the lymph node.
blue : Control, red : AuNRs, green : laser, purple :
AuNRs+laser (PPTT) Temporary anti-tumor effect is
observed.in group D(PPTT cause)

Intra-left Atrial Flow

Muneichi Shibata*,**, T. Yambe**, K. Funamoto*** and T. Hayase***

* Miyagi Cardiovascular and Respiratory Center, 55-2 Semine-Negishi, Kurihara, Miyagi 989-4513, Japan

** Institute of Development, Aging and Cancer, Tohoku University, 4-1 Seiryō, Aoba, Sendai, Miyagi 980-8575, Japan

*** Institute of Fluid Science, Tohoku University, Tohoku University, 2-1-1 Katahira, Aoba, Sendai, Miyagi 980-8577, Japan

E-mail: muneichi@idac.tohoku.ac.jp

ABSTRACT

The left atrial appendage (LAA), a pouch of the left atrium (LA), is the origin of at least 90% of all left atrial thrombi. Flow dynamics simulations of the LA and clinical data from computational tomography measurements have shown that the mechanism of LAA tends to be the origin of thrombi. Intra-LAA flow runs off from the main flow of the LA. Wall shear stress of the LAA is lower than the other areas of the LA. When atrial fibrillation occurs, the intra-left atrial flow pattern becomes stationary and the LAA contraction decreases.

1. Introduction

From 2009 to 2012, a collaborative research project between the Miyagi Cardiovascular and Respiratory Center and the Institute of Fluid Science of Tohoku University demonstrated physiological findings regarding intra-left atrial flow. We performed a wide variety of experiments, computational fluid dynamics, animal experiments, and collecting clinical data using magnetic resonance imaging (MRI) and computational tomography (CT).

The left atrial appendage (LAA) is a muscular pouch connected to the left atrium (LA) of the heart. It is derived from the left wall of the primary atrium, which forms during the 4th week of embryonic development. It has different characteristics from the body of the LA. The LAA has been found to be the origin of at least 90% of all left atrial thrombi [1], and systematic emboli cause approximately 25% of all strokes [2].

This paper summarizes the reasons why patients with atrial fibrillation have a high risk of left atrial thrombosis based on our findings.

2. Method

2.1 Intra-left atrial flow simulation

A geometrical model of the LA was constructed based on MR images of a healthy male volunteer acquired using a 1.5 T MRI scanner system. This study was approved by the regional ethics committee of Miyagi Cardiovascular and Respiratory Center. Images were reconstructed using the commercial software Mimics 7.3, and a computational model was created using tetrahedral mesh. To include consecutive temporal changes in the model, we presumed that deformation of the LA was related to annular movement of the mitral valve. Then we traced its temporal changes and approximated.

The flow simulation was performed using FLUENT. Pressure boundary conditions were set based on data in the literature [3]. A fully opened exit or free flow was simulated when flow was permitted through the mitral orifice, while no-flow boundary conditions were applied at the exit while the mitral valve was in the closed position.

To imitate atrial fibrillation, we added low

amplitude and high frequency contractions to the sinus rhythm mode, and subtracted an active contraction while the mitral valve was opening.

2.2 Virtual left atrial appendage elimination

The orifice of the LAA was virtually closed with a patch on STL data. Deformation rules were also applied to this model. Flow simulation was then performed with FLUENT. Pressure boundary conditions were set the same as in an intact model.

2.3 CT measurement of left atrial appendage dimension

The LAA changes shape by its active contraction and relaxation, and passive drainage and filling. We selected 10 subjects who had intact coronary arteries and normal left ventricle contraction among 1500 cardiac CT cases. These subjects were divided into two groups (age adjusted): the sinus rhythm (SR) group, with 5 subjects; and the atrial fibrillation (AF) group, with 5 subjects. Image acquisition was performed using a dual-source CT scanner (SOMATOM Definition; Siemens Healthcare, Forchheim, Germany). The examination protocol was as follows: kV = 100-120 kV, Effective mAs = 400 mAs/rot, Rotation time = 0.33 sec, Slice width = 0.75mm, Position increment = 0.40mm, Pitch = 0.2-0.5mm. Iodinated contrast was administered at a rate of 3.5-5 ml/sec and to a total amount of 40-80 ml with a bolus tracking technique. Image reconstruction was performed using commercial software (AquariusNet, TeraRecon, Foster City, CA, USA). Measurements of LAA length, width, and orifice thickness were recorded at systole and diastole (Fig. 1).

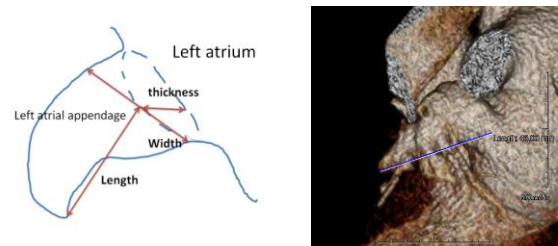


Fig. 1. Measurement of left atrial appendage dimension.

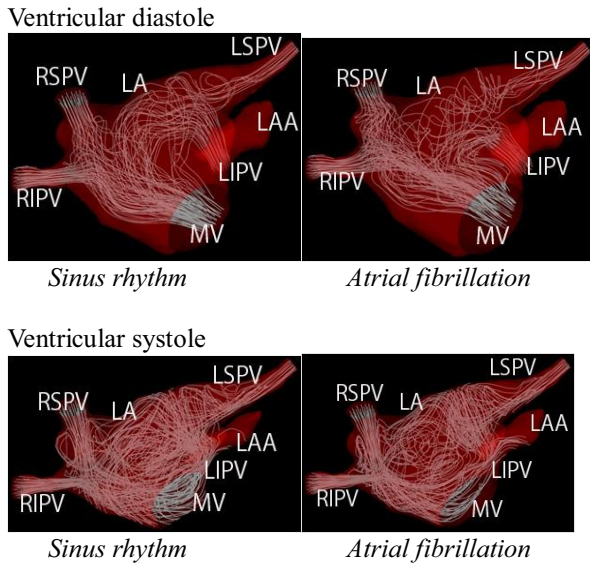


Fig. 2 Comparison of atrial blood flow associated with sinus rhythm and atrial fibrillation in the simulation model. LA: left atrium; MV: mitral valve; LAA: left atrial appendage; LSPV: left superior pulmonary vein; LIPV: left inferior pulmonary vein; RSPV: right superior pulmonary vein; RIPV: right inferior pulmonary vein.

Length was defined as the length from the tip to the orifice. Width was defined as the maximal width orthogonal to the length-line. Thickness was defined as the maximum thickness of the orifice. The shortening ratio was calculated by the following equation:

$$\text{Shortening ratio} = \text{diastolic dimension} / \text{systolic dimension}$$

3. Results and Discussion

3.1 Intra-left atrial flow

In sinus rhythm, during ventricular diastole, a small rotational flow was observed. Flow from the inferior left pulmonary vein was changed in the direction toward the mitral valve. A small number of eddies occurred along the superior left pulmonary vein. During ventricular systole, as blood moved towards the closed mitral valve, a vortex developed and gained strength (Fig. 2).

In atrial fibrillation, during ventricular diastole, a small rotational flow was not observed. A large number of eddies were evident along the superior left pulmonary vein. During ventricular systole, although a vortex formed, the density of streamlines was lower than the sinus rhythm (Fig. 2).

Intra-LAA flow runs off from the main flow of the LA in both heart rhythms. When atrial fibrillation occurs, the intra-left atrial flow pattern becomes stationary.

3.2 Virtual left atrial appendage elimination

There was no remarkable change through elimination of the LAA on a velocity vector field pattern and wall shear stress distribution (Fig 3). Wall shear stress of the LAA was lower than the other areas of the LA.

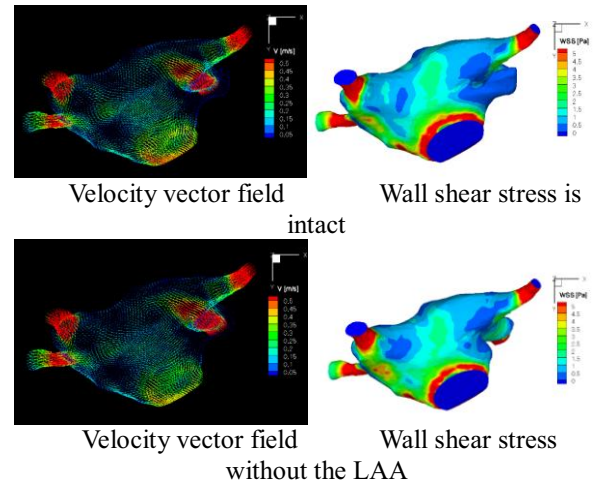


Fig. 3 flow patterns and wall shear stress distribution.

Table 1. Comparison of the dimension and shortening ratio between sinus rhythm and atrial fibrillation patients.

	SR (n = 5)	AF (n = 5)	p-value
Age (y)	66.4±6.6	66.4±7.4	1.000
Diastolic dimension (mm)			
Length	38.14±5.2	43.16±6.2	0.205
Width	31.92±8.8	32±8.9	0.989
Thickness	18.2±5.4	21.34±3.7	0.320
Systolic dimension (mm)			
Length	25.3±2.7	38.2±2.3	<0.001††
Width	17.7±2.9	27.2±12.3	0.131
Thickness	10.8±1.5	18.1±4.3	0.016†
Shortening ratio (%)			
Length	33.4±3.9	10.2±12.6	0.012†
Width	42.4±13.6	16.8±23.1	0.074
Thickness	36.7±18.9	14.2±19.2	0.099
Volume	85.8±6.7	54.6±23.8	0.041†

the data are mean ± SD, † † P < 0.01, † P < 0.05

3.3 Left atrial appendage contraction

Originally, it was difficult to distinguish the contribution to LAA deformation between active contraction and passive drainage, as well as active relaxation and passive filling. Simulation data showed that the contribution of passive drainage and filling to LAA deformation was small. The difference in the shortening ratio between SR and AF was considered the decrease of LAA contraction (Table1).

4. Concluding remarks

Intra-LAA flow runs off from the main flow of the LA in both heart rhythms. Wall shear stress of the LAA is lower than the other areas of the LA. When atrial fibrillation occurs, the pattern of intra-left atrial flow becomes stationary. Moreover, contraction of the LAA decreases when atrial fibrillation occurs. This is the mechanism whereby the LAA tends to be the origin of thrombi.

References

- [1] A.L. Saady, Heart, **82** (1999), 547-554.
- [2] Vemmos KN, et al., Stroke 30 (1999), 363–370.

Blood flow simulation within Stented Intracranial Aneurysm

Guy Courbebaisse¹, Jonas Latt², Orestis Malaspinas², Maciej Orkisz¹, Bastien Chopard²

(1) CREATIS; Université de Lyon; CNRS UMR 5220; INSERM U1024; UCB Lyon 1; INSA Lyon
7Av. Jean Capelle – Bat. Blaise Pascal, 69621 VILLEURBANNE – France

(2) University of Geneva, Computer Science Department, 1211 Geneva 4, Switzerland
guy.courbebaisse@insa-lyon.fr

ABSTRACT

This paper highlights the first results delivered when modelling the blood flow within a stented intracranial aneurysm. This research takes place in the framework of the THROMBUS project (European FP7 project), whose the main objective is the theoretical understanding of the complex thrombosis process within intracranial aneurysms, its cause in terms of the local flow properties and the biology of the wall and of the blood. As a first step of the project, the blood flow simulation is performed within a patient specific aneurysm in which a virtual flow diverter has been deployed.

1. Introduction

Cerebral aneurysms are undesired local deformations of the wall of a brain vessel whose rupture can be lethal (Fig. 1). The natural repair of an aneurysm is through a thrombosis process that fills in the cavity, eventually leading to the remodelling of the wall vessel. Such a clot can be induced by deploying a flow diverter stent in the parent vessel, across the aneurysm neck. The effect of the flow diverter is to modify the blood flow pattern in the aneurysmal cavity, thus creating favourable conditions for the aggregation of platelets allowing the thrombosis to start.

In this way, a validated multiscale numerical simulation of blood flow is implemented when a specific stent ‘a flow diverter’ is introduced in the blood vessel. Then a comparison is provided with the case without stent. One of the objectives is to find the best positioning of the stent associated with the validation of the neuroradiologist.

2. Image Processing

The image processing offers advanced image segmentation methods developed in the active contours framework (Fig. 2), known for its robustness and adequacy to complex multidimensional image segmentation problems [1].

Also segmentation of the lumen and of the thrombus is optimized by using Lattice Boltzmann Method associated to a collision function based on a diffusion equation [2]. In addition, image processing operators and mathematical models (Simplex, RGC model) allow the modelling of the flow diverter stent (42 wires) and of the virtual stent deployment (Fig. 3) [3].

3. Numerical simulation

The herein used models are implemented within the lattice Boltzmann (LB) framework [4]. More precisely, 3D and 4D BGK Lattice Boltzmann codes to solve the Navier-Stokes equations and a

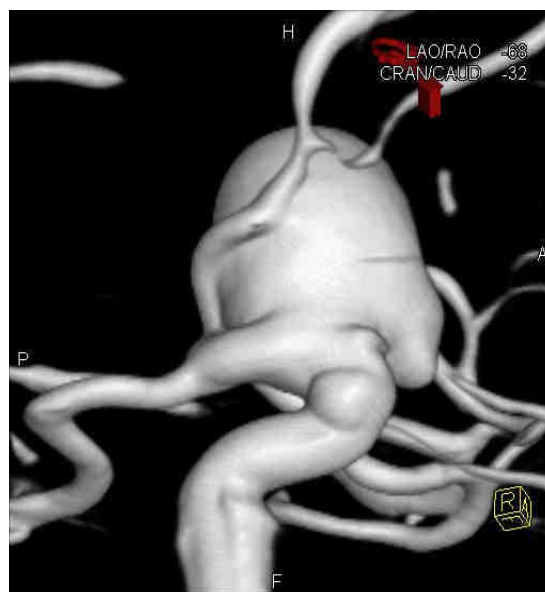


Fig. 1 Intracranial Aneurysm ‘IA’

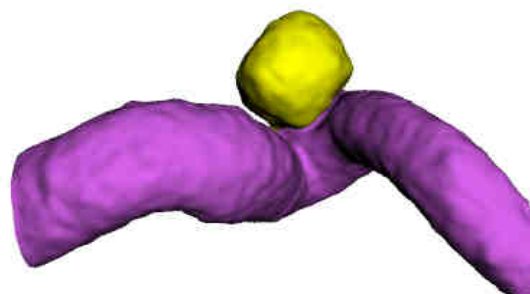


Fig. 2 Segmentation of an IA

Carreau-Yasuda constitutive law [5] have been taken in consideration. The Fig. 4 is an image issued from a BGK D3Q19 simulation. The mean velocity is 0.05 m/s. The Reynolds number is 200. The Inlet has a 4mm diameter. The numbers of grid nodes of the lattice is upper than 40 millions.

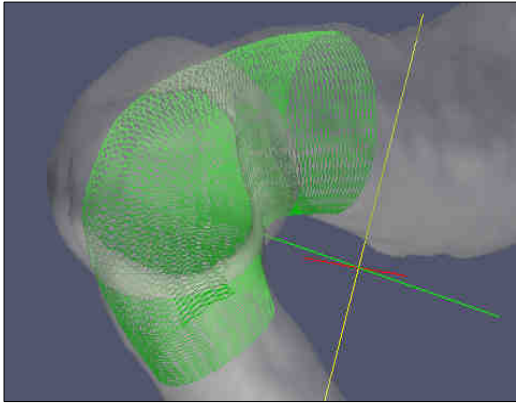


Fig. 3 Virtual flow diverter deployment within IA



Fig. 4 3D Blood Flow simulation

A parallel computation has been realized with a 120 cores cluster to optimize the time consuming (200 hours). The result of such a study is a crucial step for the understanding of aneurysm mechanisms (genesis, growth or not, healing ...), the numerical simulation providing a realistic numerical simulation where blood flows are quantified in the cavity of the aneurysm and in the parent vessel, with or without a stent (Fig. 4).

The objective of these simulations with stent is the test of several configurations in order to find the relevant blood flow and adapted near wall shear stresses which will contribute to the best thrombosis phenomena [6][7][8]. The next crucial step is to strengthen focus our research in the understanding and on the analysis of the secretions of the endothelium when submitted to wall shear stresses, and its ability to catalyse the aggregation of platelets process to form the thrombus.

4. Conclusion

This paper focuses on recent results provided by 3D and 4D (3D + time) CFD simulation for parent vessels and aneurysms stented or not. The next objective of this research is to adapt a biological model of thrombosis within a Lattice Boltzmann model and to merge into a multiscale model of thrombosis in cerebral aneurysms. The success of

the research will be conditioned in major part, by the level of our expertise reached leading to implement in our codes of numerical simulation the complex biological processes and biophysical data in order to provide a realistic modelling of the thrombosis.

Acknowledgment

This study is partially funded by the European Commission under the FP7 THROMBUS project (<http://www.thrombus-vph.eu>).

References

- [1]D.C.Barbosa, T.Dietenbeck, J.Schaerer, J.D'hooge, D.Friboulet, and O.Bernard, "B-Spline Explicit Active Surfaces: An efficient framework for real-time 3D region-based segmentation", *IEEE Trans. on Image Processing*, vol. 21, no. 1 (2012), pp. 241-251.
- [2]Y.Wang, G.Courbebaisse, and Y.M.Zhu, "Segmentation of Giant Cerebral Aneurysm Using a Multilevel Object Detection Scheme Based on Lattice Boltzmann Method", *IEEE International Conference on Signal Processing, Communications and Computing*, vol. 3799 (2011), XI'AN, IEEE.
- [3]L.Flórez Valencia, J.Montagnat, and M.Orkisz, "3D graphical models for vascular-stent pose simulation", *Mach Graph Vision*, vol. 13, no. 3 (2004), pp. 235-248.
- [4]R.Ouared and B.Chopard, Lattice Boltzmann simulations of blood flow: non-Newtonian rheology and clotting processes, *J. Stat. Phys*, Vol 121 (1-2) (2005), pp. 209--221.
- [5]O.Malaspinas, G.Courbebaisse, and M.O.Deville, "Simulation of a generalized Newtonian fluid by the Lattice Boltzmann Method", *International Journal of Modern Physics C (IJMPC)*, vol. 18, no. 12 (2007), pp. 1939-1949.
- [6]B.Chopard, R.Ouared and D.A.Rufenacht, A lattice Boltzmann simulation of clotting in stented aneurysms and comparison with velocity or shear stress reductions}, *Mathematics and Computers in Simulation*, Vol 72 (2006), pp. 108-112.
- [7]R. Ouared, B. Chopard, B. Stahl, D. A. Rufenacht, H. Yilmaz, and G. Courbebaisse, "Thrombosis Modeling in Intracranial Aneurysms : a Lattice Boltzmann Numerical Algorithm", *Computer Physics Communications Elsevier Journal*, vol. 179, no. 1-3 (2008), pp. 128-131.
- [8]R.Ouared, B.Chopard, D.Rufenacht, K.O. Lovblad and V.M. Pereira, Thrombosis Engineering in Intracranial Aneurysms using a Lattice Boltzmann Numerical Method, *Medical Physics and Biomedical Engineering World Congress WC2009, IFMBE Proceedings, ISSN1680-0737, Vol 25/4 (2010), pp. 1538--1541, Springer Berlin Heidelberg.*

Hemodynamic Effects of Y-configuration Stent for Cerebral Aneurysms

Kenichi Kono, Tomoaki Terada

Department of Neurosurgery, Wakayama Rosai Hospital, Wakayama, Japan
Corresponding author: Kenichi Kono (vyr01450@gmail.com)

ABSTRACT

Y-configuration stenting with closed- or open-cell stents is used for endovascular treatment of cerebral aneurysms. Using double closed-cell stents causes narrowing of the second stent. Computational fluid dynamics simulations were performed using Y-stent placed in a silicone model to clarify the unique hemodynamic effects of this narrowed structure in Y-configuration stenting. The narrowed structure of Y-configuration stenting redirects flow and increases flow diversion. This may be a desirable reconstruction of flow hemodynamics and may decrease the recanalization rate compared with Y-stents using open-cell stents.

1. Introduction

Y-configuration stenting with closed- or open-cell stents is used for endovascular treatment of cerebral aneurysms. Using double closed-cell stents causes narrowing of the second stent. It is uncertain whether this narrowing is beneficial or harmful.

Using micro-computed tomography (micro-CT), we obtained precise three-dimensional (3D) images of a Y-stent with a narrowed structure deployed in a silicone block model of an aneurysm. Pulsatile computational fluid dynamics (CFD) simulations were performed using this image to clarify the unique hemodynamic effects of this narrowed structure in Y-configuration stenting.

2. Method

A Silicone Model of An Aneurysm

A 3D image of an aneurysm at the basilar tip of a patient was obtained by 3D rotational angiography (Philips Healthcare) (Figure 1). Using an engineering design software, 3-matic (Version 6.1, Materialise NV, Leuven, Belgium), the 3D image was reconstructed by trimming small vessels, such as the superior cerebellar arteries. The image consisted of the aneurysm, the bilateral posterior cerebral arteries (PCAs), and the basilar artery. Based on the reconstructed image, a rigid silicone block model of the aneurysm was created.

Stent Placement

The first Enterprise stent with the length of 28 mm (Figure 2) was deployed into the left PCA in the silicone model. The stent was scanned by micro-CT. The image of the single stent in the silicone model was obtained as the standard triangulated language (STL) format. The second Enterprise stent with the same length was deployed into the right PCA through the interstices of the initial stent, which caused narrowing of the second stent. The Y-stent was scanned by micro-CT. The image of the Y-stent was obtained as STL format.



Fig. 1 An aneurysm at the basilar tip.

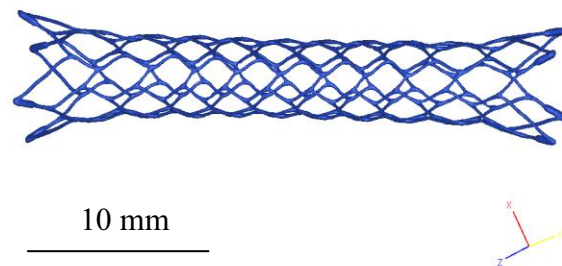


Fig. 2 Enterprise stent with the length of 28 mm.

CFD simulations

Using 3-matic, we constructed the aneurysm models with five different types of stent placements as follows: no-stent; a single stent into the left or right PCA; and a Y-stent with or without narrowing. We merged the image of the aneurysm with that of the stent by 3-matic.

We extruded the inlet of each model by approximately 30 cm. The images were meshed using ANSYS ICEM CFD software (Version 14.0, ANSYS Inc., Canonsburg, PA, USA) to create finite volume tetrahedral elements. The number of elements in each model ranged from approximately 1,100,000 to 1,800,000. Blood was modeled as a Newtonian fluid with a density of 1056 kg/m³ and a viscosity of 0.0035 kg/ms. A rigid-wall no-slip boundary condition was implemented at the vessel walls. We performed a pulsatile flow simulation with ANSYS CFX (Version 14.0, ANSYS Inc.). We examined the following hemodynamic parameters: area-averaged velocity on the neck orifice, volume-averaged velocity in the dome, and area-averaged wall shear stress (WSS) on the dome. The results were evaluated by CFD-POST (Version 14.0, ANSYS Inc.). To perform the CFD simulations, we used a lap top computer DELL precision M4500 (Dell Computer Corporation, Austin, Texas, USA).

3. Results and Discussion

A single stent placement into the right or left PCA decreased flow velocity in the aneurysm and WSS on the dome compared with the no-stent model. A Y-stent with or without narrowing decreased these hemodynamic values more than single stent placement. A Y-stent with narrowing decreased these hemodynamic values more than a Y-stent without narrowing because of narrowing of the second stent. This narrowed structure decreased porosity of the second stent, which redirected the flow into the right PCA and decreased impingement flow into the aneurysm. These flow diversion effects indicate reconstruction of hemodynamic flow. On the other hand, a Y-stent without narrowing maintained the original porosity of the stent and did not redirect or decrease flow into the aneurysm compared with a Y-stent with narrowing. These results showed unique differences between a Y-stent with narrowing and that without narrowing.

Time-averaged, peak systolic, and end-diastolic hemodynamic parameters were quantitatively measured. Anytime in the cardiac cycle, hemodynamic values showed the same trend with regard to effect on flow diversion as follows: a Y-stent with narrowing > Y-stent without narrowing > a single stent > no stent. A single stent, a Y-stent without narrowing, or a Y-stent with narrowing reduced flow velocity and WSS by

approximately 20%, 30%, or 50%, respectively. This suggests that the narrowed structure in the Y-stent significantly increases flow diversion.

4. Concluding remarks

Y-stenting with a narrowed structure using closed-cell stents for treatment of cerebral aneurysms has reconstructive flow diversion effects because of a decreased porosity of the second stent around the narrowed area. These strong flow diversion effects appear to be better for reducing the recanalization rate. From the viewpoint of hemodynamic effects, a Y-stent with narrowing using double closed-cell stents may be beneficial compared with a Y-stent using open-cell stents.

Simulation of Hemodynamics in Artery with Aneurysm and Stenosis

Yujie LI^{1,4}, Hitomi ANZAI², Toshio NAKAYAMA³, Yasutomo SHIMIZU³, Yukihiisa MIURA², Aike QIAO¹, Makoto OHTA⁴

1: College of Life Science and Bioengineering, Beijing University of Technology, Beijing 100124, China

2: Graduate School of Engineering, Tohoku University, 6-6, Aramaki Aza Aoba, Aoba-ku, Sendai 980-8579, Japan

3: Graduate School of Biomedical Engineering, Tohoku University, 6-6, Aramaki Aza Aoba, Aoba-ku, Sendai 980-8579, Japan

4: Institute of Fluid Science, Tohoku University, 2-1-1 Katahira, Aoba-ku, Sendai 980-8577, Japan

E-mail: yujie.li@biofluid.ifs.tohoku.ac.jp

Abstract

Few CFD studies have focused on stenosis and aneurysm occurred in the same artery. The purpose of this study is to establish an idealized model of this complicated case. Numerical simulations were performed to analyze the hemodynamics of this model influenced by different geometric parameters as altering the percent stenosis and the distance between the stenosis and the aneurysm. As the percent stenosis increases, the reattachment length increases. Varied reattachment point changes the inflow zone and the flow pattern in the aneurysm. The study provides the possibility of further study for the treatment of complex arterial diseases.

1. Introduction

Blood flow characteristics in arteries can be altered significantly by arterial disease, such as stenosis and aneurysm^[1], which may lead to stroke and cerebral hemorrhage threatening people's health and life severely. During the last two decades, many studies about stenosis and aneurysm have been performed by using computational fluid dynamics (CFD) method, while few focused on the case with both stenosis and aneurysm occurred simultaneously in the same artery which may cause higher possibility of either arterial occlusion or hemorrhage.

This research focuses on the case of artery with stenosis and aneurysm occurred simultaneously. It is necessary to investigate the hemodynamic behavior of flow through the vascular based on numerical approaches. Idealized models of blood vessel with both aneurysm and pre-aneurysm stenosis will be studied to understand the complicated flow condition.

2. Material and Method

2.1 Geometry Model Construction

Geometries were established by using 3D CAD software (Pro/ENGINEER Wildfire 4.0, PTC, USA). Geometry parameters are as follows: length of the blood vessel is 140mm, which gives the flow enough space to fully develop from the inlet, diameter of normal artery is 4mm, diameter of stenotic artery depends on the level of stenosis, diameter of aneurysm is 8mm, aneurysm is located at 70mm from the inlet, which is connected to the blood vessel by a 1mm high aneurysm neck, as shown in Fig. 1.

Considering the reattachment of blood flow, the distance between the stenosis and the aneurysm should range widely to show the relationship between the recirculation and the different distances. Models with the distance of 1mm, 10mm and 30mm between stenosis and aneurysm were established respectively.

Stenosis was described with a spline curve. In North American Symptomatic Carotid Endarterectomy Trail, the percent stenosis was determined by calculating the ratio of the luminal diameter at the point of the greatest stenosis and the normal part of the artery beyond the

carotid bulb^[2]. Therefore, in this research, percent stenosis = $(d_1 - d_2) / d_1 * 100\%$, where d_1 is the normal artery diameter and d_2 is the minimal luminal diameter.

As the disease develops, the percent stenosis also increases. Two separate studies were performed in this research, stenotic arteries with a mild stenosis of 30% or a moderate stenosis of 50%, to obtain and analyze detailed flow patterns.

2.2 Numerical Simulation Method

Considering the complexity of the model feature, the tetrahedral mesh was generated (GAMBIT 2.4.6, Ansys Inc., USA) in the entire flow domain, using a size function to refine the mesh around the wall. The 3D flow domains were discretized to 2,067,472 to 2,077,388 meshes in all cases.

Assumptions of Newtonian fluid, incompressible and laminar flow were adopted^[3], with the density of 1050kg/m³ and the kinetic viscosity of 0.0035Pa·s.

A steady flow condition was applied for the simulation. Velocity of 0.2m/s was set at the model inlet with a relatively low Reynolds Number of 240, which is in the range from 110 to 850 of Reynolds Number in large artery^[4]. Free pressure condition was set at the model outlet. Stationary and no-slip condition was set on the model wall.

The flow simulation was performed by using a commercial solver (Fluent 6.3.26, Ansys Inc., USA) based on finite volume method. APRESTO! scheme was used for pressure discretization and a QUICK scheme was used to discretize momentum.

3. Result and Discussion

The maximum velocity in the middle plane along the axial direction and the maximum wall shear stress (WSS) with different degrees of stenosis are shown in Fig. 2. With the increase of percent stenosis, the maximum velocity of the flow as well as the maximum WSS increase and they are distributed in the stenosis area. These maximum values keep in approximate consistent numbers with the same percent stenosis. As to the low velocities, they appear in the aneurysm and the recirculation area locates at the distal zone of stenosis. In several areas close to the wall after the stenosis, the velocity is so small that made the flow little short of static. The distribution of low WSS is influenced by that

of velocity, while the low WSS affected by the recirculation appears at the radial plane of the reattachment point.

Figure 3 shows the relationship between the percent stenosis and the reattachment length. The reattachment length is obtained from the velocity vector plot of the middle plane along the axial direction. As the percent stenosis increases, the reattachment length increases.

Different distance between stenosis and aneurysm will result in different condition of the flow pattern in the aneurysm according to the varied reattachment points to aneurysm.

For the case of blood vessel with only aneurysm without stenosis, a part of flow from parent artery enters into aneurysm as inflow at the distal neck and goes out from the aneurysm as outflow at the proximal neck. Parts of the outflow join the laminar flow in the parent artery trending to the outlet, while the other parts join the inflow zone at the distal neck. Simultaneously, a rotation flow is generated in the center of the aneurysm. This flow pattern is called the normal flow pattern.

For the 30% stenosis cases, the reattachment length is about 1.6mm on the aneurysm side, which means under the case of 1mm distance, the reattachment point appears at the aneurysm neck, causing the direction of the velocity at inflow zone different from the normal flow pattern. Instead of flowing along the aneurysm wall, this inflow runs directly to the center of the aneurysm in a straight line from the distal neck. It starts to circulate until reaches close to the top of the aneurysm, which separates the flow zone inside the aneurysm into two rotations on the two sides of this inflow, as shown in Fig. 4. As to the cases of 10mm distance and 30mm distance with 30% stenosis, recirculation occurred at the upstream of the aneurysm. In this situation, the laminar flow going through the aneurysm neck won't change the flow pattern inside the aneurysm.

For the 50% stenosis cases, the reattachment length is around 13mm on the aneurysm side, which means under cases of 1mm distance and 10mm distance, the reattachment point locates after or near the aneurysm. The recirculation flows through the aneurysm neck on the aneurysm side along the negative axial direction. The flow patterns in aneurysm will be changed to different patterns similar to that of the 1mm distance model in 30% stenosis.

4. Conclusion

Simulation results show that as the degree of stenosis increases, the reattachment point moves to the downstream of the parent artery. Differences of reattachment length and position of aneurysm have greatly affected the flow pattern inside the aneurysm. This study gives the basic hemodynamic condition of flow in artery suffered with both stenosis and aneurysm, and provides elementary understanding for further research and treatment of this complicated arterial disease.

5. Acknowledge

This work was supported by National Natural Science Foundation of China (10972016, 81171107) and Natural Science Foundation of Beijing (3092004). Cooperative Laboratory Study Program in Tohoku University also supported this study.

References

- [1]Q. Long et al., J Biomech, 34(2001).
- [2]NASCET Collaborators, N Engl J Med, 325(1991).
- [3]H. Meng et al., ANJR Am J Neuroradiol, 27(2006).
- [4]Ku et al., Ann Biomed Eng, 33(2005).

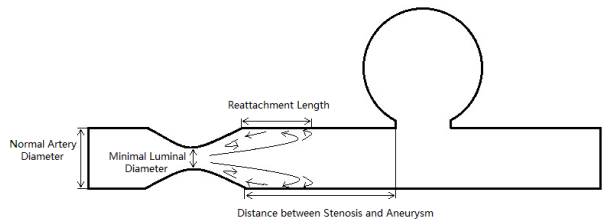


Fig.1 Sketch of the geometry

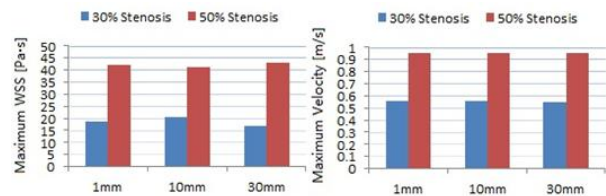


Fig.2 Maximum WSS and velocity with different degrees of stenosis in all cases

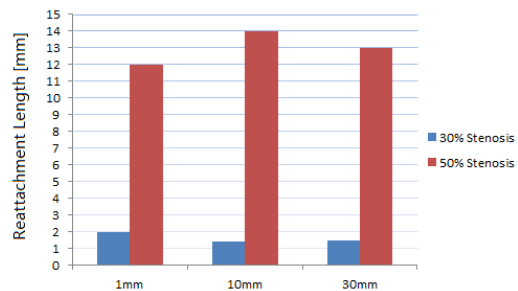


Fig. 3 Reattachment length with different degree of stenosis in all cases

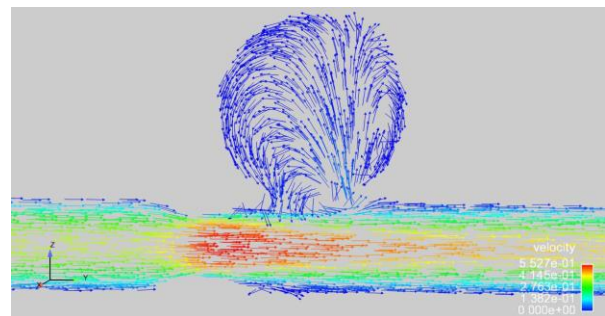


Fig. 4 The unusual flow pattern in aneurysm

A Development of Lattice Boltzmann Model and Lumped Parameter Model Connection for Cardiovascular Multiscale Analysis

Mingzi Zhang^{1,3}, Hitomi Anzai², Youjun Liu¹, Makoto Ohta³

¹Department of Life-science and Bio-engineering, Beijing University of Technology, No.100 Pingleyuan, Chaoyang District, Beijing, P.R.China

²Graduate School of Engineering, Tohoku University, Japan

³Institute of Fluid Science, Tohoku University, Japan

E-mail: mingzi.zhang@biofluid.ifs.tohoku.ac.jp

ABSTRACT

Multiscale computing for biomedical fluid dynamics is a challenging and promising method to do numerical study on cardiovascular diseases. In this report, a geometrical multiscale model consists of a Lumped Parameter network (LPN) and a Lattice Boltzmann (LB) model based on the modified Norwood procedure was simulated using the open source software Palabos. The comparison between LPN and multiscale simulation suggests the necessity of multiscale model providing the 3-dimensional (3D) simulation a relatively real physical boundary condition and Palabos shows its good features of flexible and publicly available environment for LB method.

1. Introduction

Hypoplastic left heart syndrome (HLHS) is a congenital heart condition which is usually made up of a complex combination of cardiac malformations including hypoplasia or atresia of the aortic and mitral valves and hypoplasia of the left ventricle and ascending aorta. [1] Modified Norwood procedure is the first stage palliative surgery HLHS patients. During this procedure, the aortic root, aortic arch and pulmonary artery are anastomosed to create a neo-aorta and a shunt between the innominate and pulmonary arteries regulates flow to the pulmonary circulation.

It has been a few years since numerical method was applied to study the hemodynamic behavior of Norwood Procedure. The outstanding feature of using multiscale simulation [2] is the interaction between LB model and LPN which can reflect the influence of local surgical change to global circulation and vice versa.

In this paper, we introduce the possibility of using LB [4] blood flow simulation for 3D ideal geometry in combination with LPN (zero dimensional) simulation under Palabos environment to predict hemodynamic behaviors in arteries of modified Norwood procedure. The purpose of this research is to study the volume flow rate and pressure changing under the interaction of LB model and 0D model connection.

2. Method

2.1 Lumped Parameter Model

A lumped parameter model is constructed following the methodology illustrated in Cardiovascular Mathematics [2]. By relating current and voltage with flow and pressure, components like resistors, capacitors and inductors can therefore be related with blood viscosity, inertia and wall compliance respectively. The model is made of three main parts: The single hypoplastic heart, the systemic circulation and pulmonary circulation. Systemic circulation is detailed around the procedure region which could later be used in coupling with patient-specific 3D geometry.

In the model, the single ventricle is described as a time-varying capacitor and elastance function is used to represent the relationship of pressure and volume

change:

$$En(t) = (Emax - Emin) \cdot En(tn) + Emin \quad (1)$$

where $En(tn)$ is the double hill function [3]. $Emax$ and $Emin$ are associated with the end-systolic and end-diastolic pressure volume relationship and the whole network is represented by a non-linear algebraic-differential equations system in the form:

$$F(\dot{\mathbf{y}}(t), \mathbf{y}(t), t, \mathbf{b}) = 0 \quad (2)$$

where $\mathbf{y}(t)$ stands for the unknown time-dependent vector (flow rate or pressure) at the inlet and the outlet of each block. t is time and \mathbf{b} is forcing terms. After several substitutions, this form (2) can be transformed into a list of ordinary differential equations (ODEs).

2.2 LB Model for 3D Simulation

The LB method for hydrodynamics is a mesoscopic approach in which the fluid is described in terms of density distribution $f_i(\mathbf{r}, t)$ of idealized fluid particles moving and colliding on a regular lattice. These collision-propagation dynamics could be written as

$$f_i(\mathbf{r} + \Delta t \mathbf{v}_i, t + \Delta t) = f_i(\mathbf{r}, t) + \frac{1}{\tau} (f_i^{eq} - f_i) \quad (3)$$

where f^{eq} is called the local equilibrium distribution and τ is called the relaxation time [4,6].

The computational fluid dynamics (CFD) simulation was performed based on the D3Q19 lattice topologies. The 3D ideal geometry was set up as a tube to describe the shunt. The diameter of the tube was 4mm with the spatial discretization $\Delta r = 0.2$ mm. Incompressible fluid was set up with the density of 1080 kg/m³ and the kinematic viscosity of 4.0e-6 m²/s. At the inlet and outlet of the tube, time-dependent parabolic velocity boundary condition and uniform pressure boundary condition were added respectively from the results of 0D simulation. Bounce-back boundary algorithm was implemented and lattice viscosity was chosen as $\mu = 0.01$, giving a relaxation time $\tau = (6\mu + 1)/2 = 0.53$. In this study, the open source software Palabos v1.0 [5] was used and ODEs solver was built into it in order to obtain a coupled solution.

2.3 Multiscale Simulation

In multiscale simulation, according to the algorithm illustrated in Multiscale Model of the Vascular System [2], we set up the initialization using the velocity by

transforming the flow rate from the result of 0D simulation at the corresponding upstream block (Innominate Artery, IA) as the LB model inlet boundary condition $Q_{in}^{(k)}$ and the pressure at the corresponding downstream block (Pulmonary Artery, PA) as the outlet boundary condition $P_{out}^{(k)}$.

The coupling loop is designed as the following: 1. Solving the LB model by using the boundary condition to get the average normal stress $P_{in}^{(k)}$ at the inlet cross-section and flow rate $Q_{out}^{(k)}$ at the outlet cross-section. 2. Solving the 0D model by using the forcing term $P_{in}^{(k)}$, $Q_{out}^{(k)}$ to compute the variables $Q_{in}^{(k+1)}$ and $P_{out}^{(k+1)}$. After each iteration a convergence test is designed: $|Q_{in}^{(k+1)} - Q_{in}^{(k)}| \leq \epsilon, |P_{out}^{(k+1)} - P_{out}^{(k)}| \leq \epsilon$. In our case, the multiscale model converged after 4 iterations as we set the convergence precision $\epsilon = 0.1$. Time required for the simulation was nearly 3 hours and all the simulations were performed with the heart rate at 75 beats/min. Mean aortic pressure (MAP) was around 93 mmHg and cardiac output (CO) was around 2.5 L/min.

3. Results and discussion

Comparison between LPN simulation and 0D-3D simulation is demonstrated by depicting the flow rate and pressure before and after coupling respectively in the particular nodes and inter-sections.

Figure 1 shows the curve of pressure and flow rate tracing at the inlet and outlet interface under conditions of LPN simulation and multiscale simulation.

The values tracing of multiscale simulation slightly decreases in comparison with LPN simulation, which reflects that after 0D-3D connection, LPN system read the feedback of LB simulation. And the decreasing flow rate is also resulted from increasing flow resistance, since a tube is added to the system. Average pressure and flow at both initial and final state is given in table 1.

Figure 2 shows the curve of average energy of fluid cells changing with respect to time. With setting up the time dependent boundary condition, pulsatile flow inside the tube reaches at a periodically stable condition after three periods' simulation.

During the simulation, Palabos shows its benefits of flexibility, highly parallelized which makes the coupling code easy to be organized. Based on the good features, patient-specific geometry with more interfaces will be proposed to carry out evaluation of the local hemodynamic behaviors in the operation area.

4. Concluding remarks

A geometrical multiscale model based on a 0D-3D connection was evaluated. Simulation results suggest that the connection delivers the influence from one model to the other. Relatively real boundary conditions will be reproduced during the interaction between the two models.

Acknowledgement

This work was supported by National Natural Science Foundation of China (11172016). Part of the work was carried out under the Cooperative Laboratory

Study Program (COLABS) of Tohoku University.

Reference

- [1] D. Frankel, Education Exhibit, 6 pp.701-706, 2001
- [2] L. Formaggia, Cardiovascular Mathematics, ISBN 9788847011519, Milano 2009
- [3] N. Stergiopoulos, Am J Physiol., vol.270, pp.H2050-2059, 1996
- [4] S. Succi, The Lattice Boltzmann Equation, For Fluid Dynamics and Beyond, Oxford Univ. Press 2001
- [5] <http://www.palabos.org/>
- [6] H. Anzai, Journal of Computational Science, 3 pp.1-7, 2012

Table 1 Average pressure, flow rate and rate of change (CR) values at initial and final states

	Pressure (mmHg)		Flow rate (ml/s)	
	Inlet	Outlet	Inlet	Outlet
Initial	89.13	16.22	26.24	23.35
Final	87.82	15.43	24.38	22.56
CR (%)	1.47	4.87	7.08	3.38

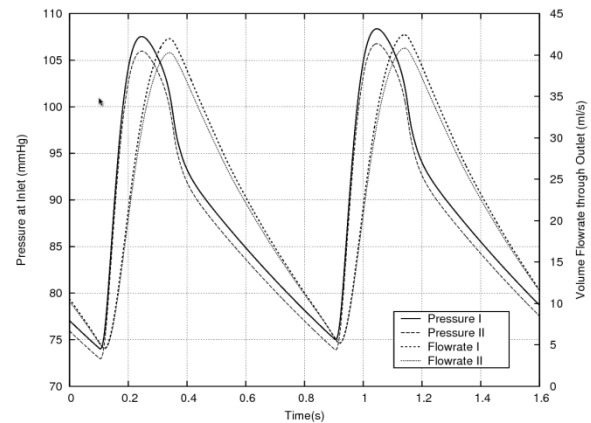


Fig. 1 Outlet flow rate and inlet pressure comparisons between LPN and multiscale simulation. (State I and II stand for LPN and multiscale results, respectively)

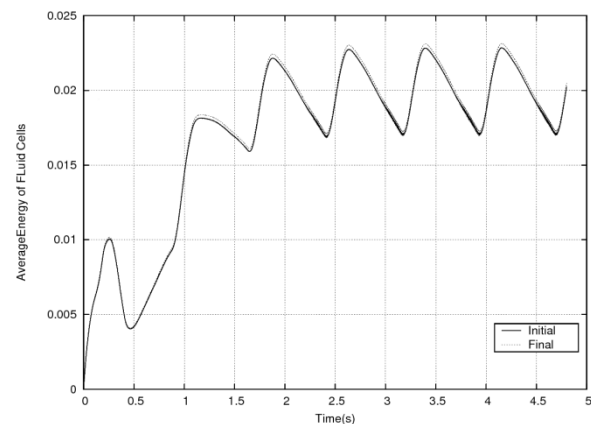


Fig. 2 Initial and Final curve of average energy.

Optimum Design of Flow Diverter Stent Associated with Arterial Geometries

Hitomi Anzai¹, Jean-Juc Falcone², Bastien Chopard², Makoto Ohta³

¹Graduate School of Engineering, Tohoku University, 6-6 Aramaki Aza Aoba, Aoba-ku, Sendai, Miyagi, Japan

²University of Geneva, 7 route de Drize CH-1227 Carouge, Switzerland

³Institute of Fluid Science, Tohoku University, Tohoku University, 2-1-1 Katahira Aoba-ku, Sendai, Miyagi, Japan

anzai@biofluid.ifs.tohoku.ac.jp

ABSTRACT

To design optimal stents that efficiently reduce the flow of blood inside cerebral aneurysms, we utilized a methodology in which simulated annealing optimization was combined with lattice Boltzmann simulations. As a result, optimized stents were characterized by denser struts in the inflow area observed with initially uniform stents. The variety of stent geometry indicates the requirement of tailor-made implants for the efficient treatment of aneurysms.

1. Introduction

Cerebral aneurysm is a vascular disorder characterized by distension of the vessel wall. In recent years, a medical device called a flow diverter (FD) stent which reduces intra-aneurysmal flow and promotes a clotting has attracted much attention [1]. Our previous research has suggested that the strut in the inflow zone of an aneurysm is an important factor of stent design for flow reduction based on the concept of the bundle of inflow (BOI) [2]. One way to find an optimal stent design has been proposed by Srinivas [3] and Nakayama [4], i.e., through the application of an optimization procedure to construct a detailed structure of the stent. However, conventional methods for stent optimization require manual handling to generate stent structure and numerical meshes. Therefore, we have introduced the possibility of using lattice Boltzmann (LB) blood flow simulations in combination with simulated annealing (SA) optimization to explore the design of stents for 2-D aneurysms in a fully automated way [5]. The 3-D extension of the computer program and examination of optimal stent design for several types of aneurysms were conducted.

2. Methods

2.1 Fluid simulation

The LB method for hydrodynamics is a mesoscopic approach in which a fluid is described in terms of density distributions $f_i(\vec{r}, t)$ of idealized fluid particles moving and colliding on a regular lattice. These collision-propagation dynamics are written as

$$f_i(\mathbf{r} + \Delta t \mathbf{v}_i, t + \Delta t) = f_i(\mathbf{r}, t) + \frac{1}{\tau} (f_i^{eq} - f_i), \quad (1)$$

where f_i^{eq} is the local equilibrium distribution and τ is the relaxation time.

Computed fluid dynamics (CFD) simulations were performed based on D3Q19 lattice topologies. Arterial geometries assuming an arterial diameter of 3.5 mm and an aneurysmal diameter of 4.8 mm with a spatial discretization $\Delta r = 5.0 \times 10^{-2}$ mm are illustrated in Fig. 1. All models have a neck diameter of 2.8 mm and an aneurysmal height of 4.5 mm. U-shaped models have a curvature of 1.7×10^2 m⁻¹. The non-slip boundary condition was imposed using the so-called bounce-back rule on the walls of the vessel and the aneurysm, as well

as on the stent struts. The inlet boundary was defined as a velocity boundary condition, a steady parabolic profile with an average velocity 0.11 m/s. At the outlet, a pressure boundary was imposed. In order to achieve a Reynolds number of 100, the kinetic viscosity for LB simulation was chosen as $\nu = UL / \text{Re} = 0.027$, giving a relaxation time $\tau = (6\nu + 1) / 2 = 0.58$. The open source software Palabos, ver. 1.1 (www.palabos.org) was applied in this study.

2.2 Optimization method

The average velocity inside the aneurysm V_{ave} was taken as the objective function of the problem. The SA process was performed with application of random modifications of the current stent geometry with a fictitious temperature varying from 5.0×10^{-5} to 5.0×10^{-6} . The stent had about 80% porosity and consisted of thin struts with a volume of $0.07 \times 0.07 \times 0.71$ mm along the cross section of the neck. The various stent geometries were generated by placing 36 small strut segments on 72 possible locations, with two possible orientation $\theta = \pi/4$ or $\theta = -\pi/4$, as illustrated in Fig. 2.. All stent models had a uniform distribution of struts as the initial state. Stent modification was obtained by randomly moving a strut segment to an empty position. Stent improvement was computed as the variation ΔD of the fitness function

$$\Delta D = V_{new} - V_{current}. \quad (2)$$

Even if $\Delta D < 0$, the modification was accepted if

$$\exp\left(\frac{-\Delta D}{T}\right) > R[0,1], \quad (3)$$

where $R[0,1]$ was a random number between 0 and 1 and T was the current temperature of the SA process. This temperature was gradually decreased based on a cooling schedule described as

$$T_{n+1} = \beta T_n, \quad (4)$$

where $\beta = 0.9$.

3. Results and Discussion

Table 1 shows the velocity reduction due to the stent placement in each artery. The left side of Fig. 3 shows streamlines through the neck and top views of the inflow/outflow zone in the neck with the optimum stent shown on the right side.

In the case of a straight parent artery, the inflow area into the aneurysm is observed at the distal end of neck before stenting. After placement of the initial uniform stent, the inflow enters the aneurysm from the center of the neck through gaps in the stent struts. The optimum stent has denser struts at the center of the neck.

The inflow zone of a U-shaped artery with an aneurysm at the side of a curvature ($\gamma = \pi/2$) is on the outer distal curvature of the neck. Due to the deployment of the initial stent, the inflow area slightly moves to the proximal region of the neck. The optimum stent has denser struts at the outer side of a curvature and a large space at the center of the neck.

A U-shaped artery with an aneurysm at the top of a curvature ($\gamma = \pi$) has the inflow zone at the distal end of neck. The initial stent changes the inflow zone to the proximal half of neck. The optimum stent has denser struts in the proximal half of the neck.

The results show the change of flow direction in an aneurysm as well as the change of inflow/outflow position due to the deployment of the initial stent. The initial stent decreases the momentum of the inflow, and then the rotation direction of flow inside an aneurysm reverses directions in the no stent case. The optimum stent has denser struts in the inflow zone observed with the initial stent. The relationship between the inflow zone and denser area of struts is consistent with our previous report dealing with a 2-D aneurysm. The struts located in the inflow zone disperse the BOI and slows down the flow inside the aneurysm. Thus, strut placement in the BOI may assume a critical role for velocity reduction in an aneurysm, and this relationship can be an important concept for strut design that especially focuses on the BOI. In addition, the variety of strut patterns for each aneurysm may indicate the requirement for tailor-made implants for the treatment of aneurysms.

4. Concluding remarks

Development of stent design based on a combination of LB flow simulation and SA optimization was performed for several 3-D aneurysms. The optimum stents have a common characteristic, namely, denser struts in the inflow area observed with the initial stent. The variety of optimum stents indicates the importance of stent design for inflow and the requirement of tailor-made implants for aneurysms.

Acknowledgement

This study was supported by a Research Fellowship of the Japan Society for the Promotion of Science for Young Scientists and was done in collaboration with the THROMBUS VPH European project. Part of the work was carried out under the Collaborative Research Project of the Institute of Fluid Science, Tohoku University.

References

- [1] L. Augusburger, Clin. Neurorad., **19**(2009), 204
- [2] H. Anzai, ASME FEDSM-ICBNN2010, 30591.
- [3] K. Srinivas, J. Med. Devices, **4** (2010), 021003.

- [4] T. Nakayama, ASME FEDSM-ICBNN2010, 30592.
- [5] H. Anzai, J. Comput. Sci., **3**(2012), 1

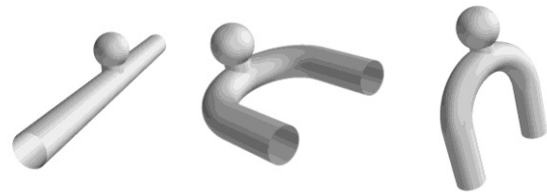


Fig. 1 Images of computational models (left: straight artery, center: U-shape artery ($\gamma = \pi/2$), right: U-shape artery ($\gamma = \pi$), where γ is the angle of an aneurysm to a parent artery)

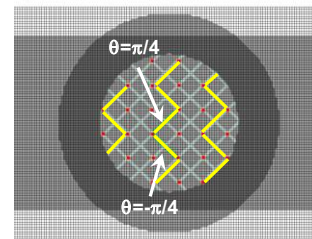


Fig. 2 Schematic image of stent model, where yellow line represents struts

Geometry	Initial stent	Optimum stent
Straight	85.0	92.8
U-shape ($\gamma = \pi/2$)	83.8	88.6
U-shape ($\gamma = \pi$)	86.1	94.8

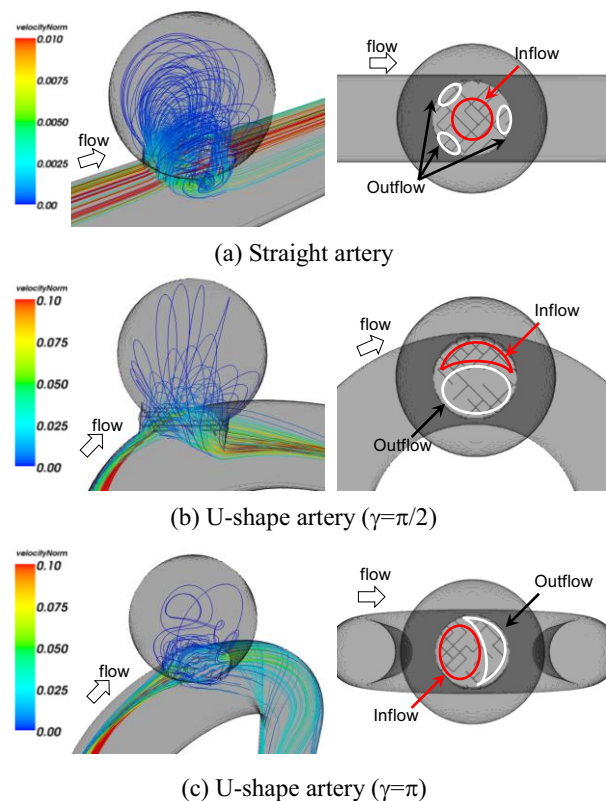


Fig. 3 Images of flow pattern entering an aneurysm with optimum stent (left: Streamlines, right: Inflow/Outflow zone on a neck)

Assessment of Three Non-Newtonian Models in Steady State Blood Flow through an Aneurysm

Mantulal Basumatary, Suresh Sahoo, Ganesh Natarajan, Subhash C. Mishra
Department of Mechanical Engineering,
Indian Institute of Technology Guwahati, India – 781039
Corresponding author: scm_iitg@yahoo.com

ABSTRACT

The effect of non-Newtonian behavior of blood on the flow dynamics in an intracranial aneurysm is investigated. Three different non-Newtonian models, viz., Power Law (PL), Carreau-Yasuda (CY) and Casson model are employed for this study. Computations are performed using a second order accurate fractional step method in conjunction with novel hybrid staggered/non staggered finite volume framework. Preliminary results for a two-dimensional aneurysm with unit ratio of height to neck indicate that non-Newtonian effects are not significant in steady flows.

1. Introduction

Blood is a complex mixture of red blood cells (RBC), white blood cells (WBC), platelets and plasma, and is a non-Newtonian fluid. Nevertheless, many researchers have modelled blood as a Newtonian fluid for many biomedical studies. This assumption may hold well in some situations, but could be erroneous especially at low shear rates. A better understanding of dynamics of flow in blood vessel can play a key role in the diagnosis and cure of many diseases. In the present study, we assess the importance of non-Newtonian modeling of blood flow in aneurysm, which is a bulge in blood vessel and poses a huge health risk, especially rupture.

2. Formulation

Blood is considered as a non-Newtonian fluid and its flow is considered to be incompressible. The governing continuity and momentum equations are the following:

Continuity equation:

$$\nabla \cdot U = 0 \quad (1)$$

Momentum equation:

$$\rho \left(\frac{\partial U}{\partial t} + U \cdot \nabla U \right) = -\nabla p + \nabla \cdot \tau \quad (2)$$

where $U=(u,v)$, τ , p , ρ are velocity vector, stress tensor, pressure and density of blood, respectively. The shear stress, τ is related to the strain rate, $\dot{\gamma}$ through a shear rate dependent viscosity, $\mu(\dot{\gamma})$ as

$$\tau = \mu(\dot{\gamma})\dot{\gamma} \quad (3)$$

The non-dimensional forms of viscosity relations used for the three models are given in Table1.

The governing equations in non-dimensional form are solved using the finite volume method in a hybrid staggered/non-staggered framework [1].

Table 1 Effective viscosity relation for the three models

Constitutive model	Effective viscosity relation
PL	$\mu = \dot{\gamma} ^{n-1}$
CY	$\mu = 1 + \left(\frac{\mu_0}{\mu_\infty} - 1 \right) [1 + (W_i \lambda)^a]^{(\frac{n-1}{a})}$
Casson	$\mu = [1 + \sqrt{\frac{Bi}{ \dot{\gamma} }} (1 - e^{-\sqrt{W_i \dot{\gamma} }})]^{\frac{1}{2}}$

The momentum and pressure correction equations, arising from a segregated approach of solution are solved in an implicit manner. The convective fluxes are computed using a second order upwind scheme, and viscous gradients at the faces are computed using a least-square based reconstruction [2]. The equations are marched in time using a second order accurate time integrator.

3. Results and Discussion

The geometry of the idealized two-dimensional intracranial aneurysm is shown in Fig. 1. An unstructured mesh with 7059 volumes is used for the computations. A unit height to neck ratio ($\frac{H}{n} = 1$) is considered and all computations are performed at $Re = 291$ using the three constitutive models. Other parameters pertaining to the models are given in Table 2. The Weissenberg number and Bingham number are calculated based on an average blood vessel diameter of 2.5 mm.

Figure 2 shows the wall shear stress (WSS) distribution of the three models on the aneurysm dome. The maximum WSS for all three models are at the distal end of the aneurysm, which agrees well with the results in [3]. The WSS distributions predicted by different models do not show significant differences and are qualitatively similar.

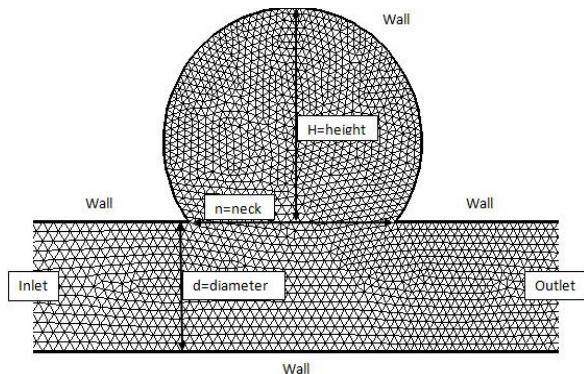


Fig. 1: Unstructured grid used in aneurysm geometry with boundary conditions.

Streamline pattern (for PL model) in Fig. 3 clearly indicates a “driven-cavity” like flow as obtained in [4].

Table 2 Parameters used for the three models

Parameters	PL	CY	Casson
Non-Newtonian exponent (n)	0.8	0.392	-
Zero shear rate viscosity (μ_0)	-	.0022	-
High shear rate viscosity (μ_∞)	-	0.022	-
Model constant (a)	-	0.64	-
Weissenberg number (Wi)	-	15.2	15.2
Bingham number (Bi)	-	-	0.02

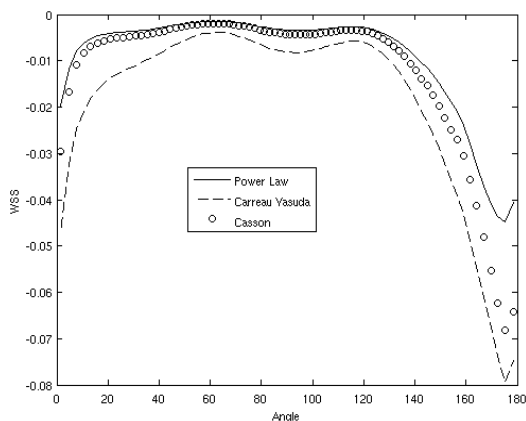


Fig. 2: WSS distribution on aneurysm dome

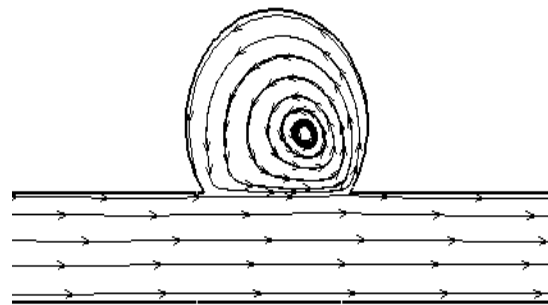


Fig. 3: Streamline plot for PL models

In this flow pattern the flow in the parent blood vessel is demarcated from the circulation inside the aneurysm dome.

4. Conclusions

Computations of steady flow in a two-dimensional aneurysm with three different non-Newtonian models are carried out. WSS distribution and streamline patterns are indicative of the fact that non-Newtonian effects are less significance for steady flows in such geometries. The modeling of pulsatile flow which are realistic in such configuration is currently underway.

References

- [1] G. Liang, S. Fotis, A numerical method for solving the 3D unsteady incompressible Navier-Stokes equations in curvilinear domains with complex immersed boundaries, *J. Comput. Phys.*, **225** (2007), 1782-1809.
- [2] N. Ganesh and F. Sotiropoulos, IDEC(k): A new velocity reconstruction algorithm on arbitrary polygonal staggered meshes, *J. Comput. Phys.*, **230** (2011), 6583-6604.
- [3] J. Arter, A. Ramme, and B. Walsh, CFD analysis of intracranial aneurysms, The University of IOWA, 2009.
- [4] B.L. Trung, I. Borazjani and S. Fotis, Pulsatile flow effects on the hemodynamics of intracranial aneurysms, *J. Biomech. Eng.*, **132** (2010), 111009-11.

Heat Conduction In Soft Tissues Modelled By Hydrogels

András Tél, Rita A. Bauer, Zsófia Varga and Miklós Zrinyi
Semmelweis University, Department of Biophysics and Radiation Biology
H-1089 Budapest, Nagyvarad ter 4, HUNGARY,
E-mail of corresponding author: mikloszrinyi@gmail.com

ABSTRACT

Biological tissues are a combination of liquids and fibrous solids, therefore polymer hydrogels can be used as model heat transfer system for soft tissues. Cylindrical poly(N-iso-propyl acrylamide) gel which shows LCST phase transition at $T_{ph}=35\text{ }^{\circ}\text{C}$ was used as heat conducting medium. The phase transition temperature defines a visible front that moves forward in the opposite direction to temperature gradient. The kinetics of moving turbid front was analysed on the basis of Fourier's- and Stefan's theories. Our novel technique can be successfully applied to determine heat conductivity and heat diffusibility of loosely crosslinked hydrogel.

1. Introduction

If the heat transfer experiment is achieved in a cross-linked polymer gel, then the convective motion of fluid is hindered by the presence of network chains and the only mechanism is heat conduction. By using poly(N-iso-propyl acrylamide) (PNIPA) gels we are able to visualize the phase transition temperature front, that moves forward in the opposite direction to temperature gradient. When the temperature exceeds a critical value of $T_{ph} = 35\text{ }^{\circ}\text{C}$, the originally transparent gel becomes opaque. This opacity which is separated from the clear gel phase with a sharp interface boundary, makes us possible to follow the evolution of $35\text{ }^{\circ}\text{C}$ temperature front during the heat transfer experiment.

The experimental data are interpreted on the basis of two different approaches. One dimensional case of Fourier's laws relate the heat flux to the temperature gradient as well as the evolution of temperature distribution in space, but the latent heat, due to the phase transition of PNIPA gel as well as the possible difference in the heat capacity of the two gel phases are completely neglected [1-5]. The Stefan's approach takes into consideration all of these effects.

For a one dimension case (x), if the thermal conductivity can be assumed to be independent from the temperature, one can write the governing equation of heat transport as

$$\frac{\partial T}{\partial t} = \alpha \frac{\partial^2 T}{\partial x^2} \quad (1)$$

where $\alpha = \frac{k}{\rho \cdot c_p}$, ρ stands for the density of the material and c_p denotes the heat capacity per unit mass at constant pressure.

2. Method

The experimental set up is shown in Fig. 1.

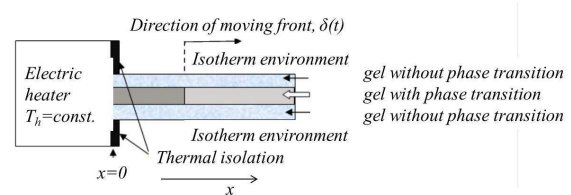


Fig.1 Schematic representation of experimental set up to study the heat convection in PNIPA gel.

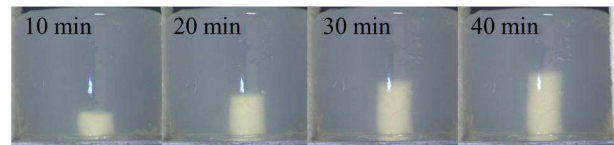


Fig.2 Visualization of moving temperature front of $T_{ph} = 35^{\circ}\text{C}$ by PNIPA gels

The electric heater maintains constant steady temperature T_h at $x \leq 0$ positions. Semi-infinite PNIPA cylindrical gel occupying the region $x \geq 0$ and has the initial temperature, T_o . This gel is placed in the center of cylindrical polyvinylalcohol (PVA) gel, which has no phase transition. The role of PVA gel is to minimize the heat transfer, perpendicular to the direction of x axis. We have measured the position of turbid interface (penetration length) as a function of time as shown in Fig. 2.

3. Results and Discussion

Fig. 3 shows the time evolution of penetration length, $\delta(t)$ as a function of square root of time, measured at different initial conditions in which the temperature of the heater, T_h was varied from 44.5 to 78 $^{\circ}\text{C}$.

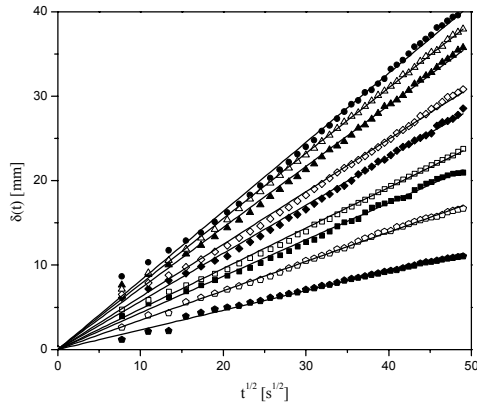


Fig.3 Dependence of penetration length on the square root of temperature.

The slope of the straight lines, K_{exp} were determined and analysed on the basis Fourier's and Stefan's theories.

In order to determine the basic parameters that characterize the phenomenon and evaluate thermal material properties, the problem of moving boundary has to be solved for this special case. According to Fourier's theory ($K_F = K_{exp}$) the thermal diffusibility, α_F can be expressed as:

$$\alpha_F = \frac{K_{exp}^2}{4\left(\text{erfc}^{-1}(T^*)\right)^2} \quad (2)$$

where $T^* = (T_{ph} - T_0) / (T_h - T_0)$

From seven series of measurements, the thermal diffusivity was found to be $1.78 \cdot 10^{-7} \text{ m}^2/\text{s}$ with a standard deviation of $1.09 \cdot 10^{-8} \text{ m}^2/\text{s}$.

According to Stefan's theory ($K_{St} = K_{exp}$) the thermal diffusibility, α_{St} can be obtained by numerical solution of nonlinear equation :

$$\frac{-(1-)e^{-\frac{m^2}{4}}}{\sqrt{\pi}\text{erf}\left(\frac{m}{2}\right)} + \frac{\frac{k_c}{k_t}e^{-\frac{m^2}{4}}}{\sqrt{\pi}\text{erfc}\left(\frac{m}{2}\right)} = \frac{Q}{2}m \quad (3)$$

Taking into account that $m = \frac{K_{St}}{\sqrt{\alpha_{St}}}$ and

$$Q = \frac{q_{ph}\alpha_{St}\rho_{PNIPA}}{2k_{St}(T_h - T_0)} = \frac{q_{ph}}{2c_{p,t}(T_h - T_0)} \quad (4)$$

where $q_{ph} = -2.08 \text{ J/g}$ represents the latent heat of PNIPA phase transition, $c_{p,t} = 3.97 \text{ J/gK}$ means the

Table 1. Thermal diffusibility of PNIPA gels determined by Fourier's and Stefan's law.

T_h	$\alpha_{St} (\text{m}^2/\text{s})$	$\alpha_F (\text{m}^2/\text{s})$
40.3	$1.815 \cdot 10^{-7}$	$1.658 \cdot 10^{-7}$
43.6	$2.169 \cdot 10^{-7}$	$1.981 \cdot 10^{-7}$
46.9	$2.095 \cdot 10^{-7}$	$1.904 \cdot 10^{-7}$
50.3	$2.256 \cdot 10^{-7}$	$2.064 \cdot 10^{-7}$
53.6	$2.229 \cdot 10^{-7}$	$2.037 \cdot 10^{-7}$
56.9	$2.042 \cdot 10^{-7}$	$1.870 \cdot 10^{-7}$
60.3	$1.919 \cdot 10^{-7}$	$1.748 \cdot 10^{-7}$
63.6	$1.821 \cdot 10^{-7}$	$1.663 \cdot 10^{-7}$

heat capacity of the PNIPA gel. It was assumed that the thermal conductivity, the heat capacity and the density of both PNIPA phases are identical. The results of calculation are summarized in Table I.

Comparing the values of α_F and α_{St} one can see that Stefan analysis has provided a little higher numerical data. The average values are $\alpha_F = 1.866 \times 10^{-7} \text{ m}^2/\text{s}$ and $\alpha_{St} = 2.043 \times 10^{-7} \text{ m}^2/\text{s}$.

4. Concluding remarks

The heat diffusibility coefficient of loosely crosslinked poly(N-iso-propyl acrylamide) gels have been determined. It was found the Fourier and Stefan theories provide a slightly different heat diffusibility coefficient. No significant effect of crosslinking density on heat conductivity has been observed.

Acknowledgements

This research was supported by OTKA Foundation (Grant number: NK 101704), as well as by the Hungarian National Development Agency Grant TAMOP-4.2.1.B-09/1/KMR-2010-0001.

References

- [1]G.A.Truskey, F. Yuan and D.F.Katz: Transport Phenomena in Biological Systems, Spearson Education Inc., Publishing as Prentice Hall, Upper Saddle River, New Jersey, (2010)
- [2]R.B.Bird, W.E. Stewart, E.N. Lightfoot: Transport Phenomena, John Wiley and Sons , Inc. (2012)
- [3]F.Hafner, D. Sames, H-D Voight: Wärme- und Stofftransport, Springer Verlag, Berlin, Heidelberg New York (1992)
- [4]F.P. Incropera, D.P. Dewitt, T.L. Bergman and A.S. Lavine: Principles of Heat and mass Transfer, John Wiley and Sons , Inc. (2012)
- [5]James M. Hill: One-dimensional Stefan Problems: an Introduction, volume of Pitman Monographs and Surveys in Pure and Applied Mathematics. Longman Scientific & Technical, Essex, (1987).

Effect of Parent Artery Expansion by Stent Placement for Saccular Cerebral Aneurysms

Futoshi MORI^{1,2}, Nhat Minh BUI³, Teuro MATSUZAWA⁴

¹Interfaculty Initiative in Information Studies, The University of Tokyo, 1-1-1 Yayoi, Bunkyo-ku, Tokyo 113-0032, JAPAN, f-mori@eri.u-tokyo.ac.jp

²Earthquake Research Institute, The University of Tokyo, JAPAN

³School of Information Science, Japan Advanced Institute of Science and Technology, 1-1 Asahidai, Nomi, Ishikawa 923-1292, JAPAN

⁴Research Center for Simulation Science, Japan Advanced Institute of Science and Technology, 1-1 Asahidai, Nomi, Ishikawa 923-1292, JAPAN
E-mail: matuzawa@jaist.ac.jp

ABSTRACT

The parent artery shape is related to the influence on the aneurysm. We paid attention to the transformation of the parent artery by the stent implantation. The purpose of this study is to clarify the effect of deformation between the mechanical property of stent and blood vessel. The parent artery in stent placement region has been expanded virtually by changing the diameter. As results, the parent artery expansion could be reduced for inflow rate and WSS distribution on the aneurysm wall than no considered parent artery expansion. The effect of parent artery expansion was effective.

1. Introduction

Saccular cerebral aneurysms develop at arterial bifurcations and bends in the Circle of Willis. Aneurysm rupture leads to a subarachnoid hemorrhage, which has high mortality and morbidity rates [1] [2]. Stent treatment is minimally invasive for cerebral aneurysm [3]. Recently, the effect of stent treatment was examined using CFD analysis.

The parent artery shape is related to the influence on the aneurysm. The inflow to the aneurysm and the stress on the aneurysm wall were influenced by the parent artery configuration and angle between parent artery and aneurysm [4]. Moreover, Castro et al [5] showed that the wall shear stress distribution on the aneurysm wall decreased by transforming parent artery forward from the aneurysm. In addition, the result after the stent treatment was influenced by the parent artery configuration [6]. Consequently, the parent artery configuration is important. We paid attention to the transformation of the parent artery by the stent implantation. The effect of the stent expansion is reported. In the animal experiment of the rabbit, the expansion of parent artery is observed [7]. Moreover, the implanted stent diameter is larger than the diameter of the blood vessel in order to prevent release from the blood vessel as the procedure of stent treatment. However, the flow considered the deformation between the mechanical property of stent and blood vessel is not clarified.

The purpose is to clarify the inflow to aneurysm and the wall shear stress on the aneurysm at parent artery expansion by the stent placement. In this research, we examined the possibility of inflow to aneurysm as the stent expansion effect.

2. Method

2.1 Computational geometry

A patient-specific geometry of a human internal carotid artery with an aneurysm was used in this study. Moreover, the stent geometry for the aneurysm was

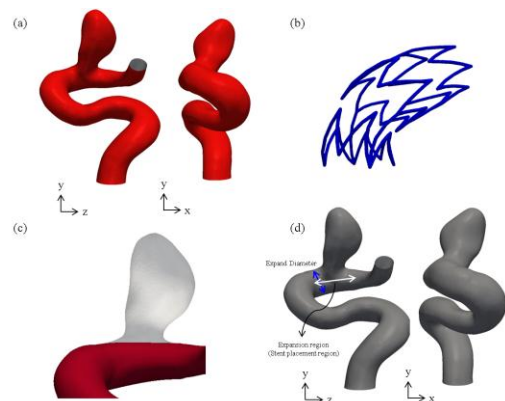


Fig.1 Computational models: (a) Patient-specific geometry of a human internal carotid artery with an aneurysm (b) Self-expandable Stent geometry(c) Reconstructed parent artery (red color) without an aneurysm (d) Reconstructed expansion geometry with an aneurysm

Z-link stent (self-expandable). Fig.1 (a) and (b) showed the geometries provided by the Virtual Intracranial Stenting Challenge [8]. The numerical data for the geometry were provided in the form of STL data.

The parent artery in stent placement region was expanded to consider the deformation between the mechanical property of stent and blood vessel. We reconstructed the excluded aneurysm part shape using a Voronoi diagram and centerlines [9] [10]. Fig.1 (c) shows the reconstructed geometry without the aneurysm part as shown in red color. The parent artery of the stent placement region has been expanded based on Fig.1 (c) geometry. The expansion rate in the stent placement region was set to 6% from the observation of literature [7]. The aneurysm part united with the reconstructed parent artery shape to change the diameter of the stent placement region. Fig.1 (d) shows the reconstructed expansion geometry with the aneurysm. These procedures build upon methods implemented in the Vascular Modeling ToolKit (VMTK).

2.2 Calculation method in CFD

We calculated the steady-state solution. The governing equations were the Navier-Stokes equation and the continuity equation. The boundary conditions for the inlet, outlet, blood vessel, aneurysm wall, and stent were time-independent [8]. The inlet boundary condition had a uniform velocity profile of 0.189 m/s. The outlet boundary condition was set to 0 Pa and the Reynolds number was 477. A no-slip condition was employed on the blood vessel, aneurysm wall, and stent. The wall boundary was set to rigid. Calculations using the finite volume method were performed using a commercial solver (Fluent 6.3.26, ANSYS, Inc.).

3. Results

Fig.2 shows the flow without stent using streamline in no-expansion and 6% expansion. The flow changed in upstream side of aneurysm by the expansion of parent artery. Moreover, the inflow to aneurysm and flow within the aneurysm were also decreasing. Fig.3 shows the inflow rate comparison without- and with stent. In case of the without stent, the 6% expansion was decreased 17.9% than no-expansion. The inflow to aneurysm at the stent placement was almost no change in case of no-expansion. On the other hand, the inflow to aneurysm has decreased 13.5% in case of 6% expansion with stent. However, the inflow rate of 6% expansion with stent was increased 5.5% than that of 6% expansion without stent in this stent position. As this reason, it is thought that the effects of induced flow were larger than those of obstructed flow.

Fig.4 shows the wall shear stress (WSS) using contour in case without stent of no-expansion and 6% expansion. In the center on the aneurysm part, the high WSS of 6% expansion was more decrease than that of no-expansion. Moreover, the mean WSS distribution on aneurysm wall of 6% expansion without stent was decreased 14.6% than no-expansion without stent. Further, the mean WSS distribution on aneurysm wall in no-expansion with stent was decreased 13.9% than that in no-expansion without stent. By stent placement, the mean WSS distribution can be reduced. In addition, the mean WSS distribution was reduced further by considering the parent artery expansion.

4. Conclusion

This study examined the inflow to aneurysm about the possibility of the decrease by the stent expansion effect. The parent artery expansion could be reduced for inflow rate and WSS distribution on the aneurysm wall than not consider blood expansion. These data suggested that the effect of parent artery expansion was effective.

Acknowledgement

We thank the Virtual Intracranial Stenting Challenge (VISC) committee for providing the arterial geometry data through the VISC 2006 project.

References

[1] F Tomasello et al. Journal of Neurosurgical Science,

42 (1998), 47-51.

[2] JM Wardlaw et al. Brain, **123** (2000), 205-221.

[3] DA Rufenacht et al. Swiss Archives of Neurology and Psychiatry, **155** (2004), 348-352.

[4] Y Imai et al. Annals of Biomedical Engineering **36** (2008), 1489-1495.

[5] MA Castro et al. American Journal of Neuroradiology **27** (2006), 1703-1709.

[6] H Meng et al. American Journal of Neuroradiology **27** (2006), 1861-1865.

[7] CN Iontia et al. American Journal of Neuroradiology **32** (2011), 1399-1407.

[8] AG Radaelli et al. Journal of Biomechanics, **41** (2008), 2069-2081.

[9] L Antiga et al. Medical and biological engineering and computing, **46** (2008), 1097-1112.

[10] MD Ford et al. The British Journal of Radiology, **82** (2009), S55-S61.

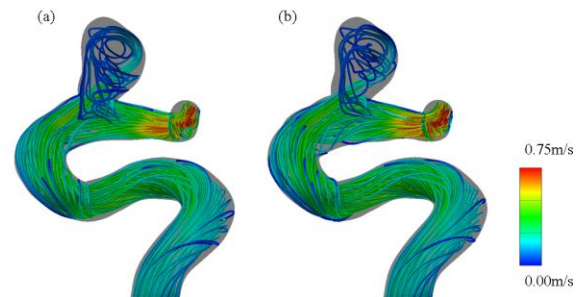


Fig.2 Flow without stent placement using streamline: no-expansion (left) and 6% expansion (right). Blue is low speed and Red is high speed.

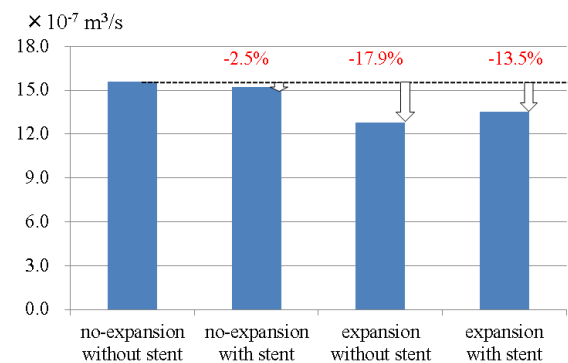


Fig.3 Inflow rate comparison without- and with stent

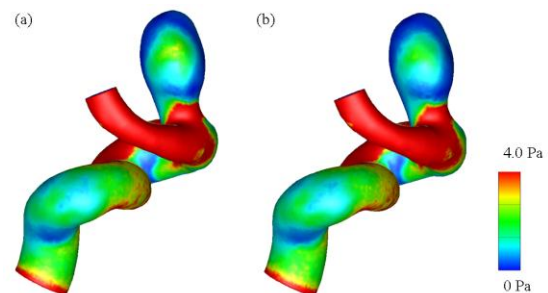


Fig.4 Wall shear stress without stent placement using contour: no-expansion (left) and 6% expansion (right). Blue is low WSS and Red is high WSS.

Numerical and Experimental Study of Flow in Stenosis Models with Several Mechanical Properties

Yasutomo Shimizu¹, Shuya Shida¹, Ashkan Javadzadegan², Kenichi Funamoto³, Toshiyuki Hayase³, Makoto Ohta³

1: Graduate School of Biomedical Engineering, Tohoku University, 6-6-01, Aobayama, Sendai, 980-8579, Japan

2: School of Mechanical Engineering, The University of Sydney, NSW 2006, Sydney, Australia

3: Institute of Fluid Science, Tohoku University, 2-1-1, Katahira, Aoba-ku, Sendai, 980-8577, Japan

E-mail: shimizu@biofluid.ifs.tohoku.ac.jp

ABSTRACT

Stenosis is one of the most serious diseases because it can cause circulatory diseases with high mortality. We performed PIV experiments using 2 kinds of stenosis biomodels and numerical simulations for finding the difference of flow conditions in the models. Depending on mechanical properties of the models, the parent arteries can expand and the plaque geometries also change in accordance with increasing the internal pressure. These geometrical changes will affect blood flow patterns. These findings may suggest the importance of focus on the mechanical properties of models for analysis of disease using PIV experiments.

1. Introduction

Endovascular disease is one of the most common causes of death, and even in non-fatal cases, serious sequelae may persist. Vascular stenosis in particular is a serious symptom because it can reduce the volume of blood flow, or result in embolization or rupture of blood vessels. A plaque component consisting stenosis has a wide range of stiffness depending on disease conditions [1], with stiffness being an important factor in plaque behavior [2].

For proper diagnoses, it is important to determine not only blood flow distribution but also behavior of blood vessels and change in the geometry of plaques. In order to elucidate the effect of changes in plaque geometry or stenosis severity, flow observation is required using biomodels with varying plaque stiffness. However, it is insufficient to evaluate the influence of the plaque stiffness on blood flow condition because only rigid tubes have been used in previous studies. Instead, a model mimicking the mechanical properties in the body is also required.

Recently, a biomodel made of poly (vinyl alcohol) hydrogel (PVA-H) has been developed [3]. PVA-H is useful for observations of flow such as particle image velocimetry (PIV) method [4] and of deformation. It is important to clarify the relationship between plaque geometry and blood flow because these factors influence each other. The purpose of this study is to find out the influence of mechanical properties of models on flow patterns. PIV experiments using PVA-H and silicone models with stenoses were performed, and then, a numerical simulation was performed for validation and parameter studies.

2. Method

To clarify the relationship, both PIV experiments and a numerical simulation were performed.

2-1. Stenosis models for PIV

A PVA-H stenosis model was prepared using the previous developed method [5]. The PVA-H stenosis model had 4mm diameter and 70% blockage by the NASCET method as calculated by equation (1).

$$SS = \left(1 - \frac{D_s}{D}\right) \times 100 \quad (1)$$

In eq. (1), D_s is the diameter of stenosis and D is the

diameter of the parent artery, as shown in Fig. 1. Concentration of the PVA solution was 12 wt %. Additionally, a silicone model of the same geometry of the PVA-H model was prepared as a rigid model.

2-2. Circuit for PIV

A Nd:YAG laser (532NM-X-300MW, B&W TEK) was used to provide a 1 mm-thick laser sheet through the center plane of the channel with a power of 100 mW and a wavelength of 532 nm. One hundred photographic images of 1024×512 pixels were captured using a high speed camera (Fastcam SA3, Photron Limited) with a telescopic micro-lens with a focal length of 105 mm and an F ratio of 2.8 (Micro-Nikkor, Nikon). The images were analyzed using a PIV software (DaVis 8.1, LaVision), and reattachment lengths and widths of D_s and D were measured by ImageJ (1.43u, NIH). Re is calculated by equation (2).

$$Re = \frac{U_{max} D}{\nu} \quad (2)$$

In eq. (2), ν is the kinematic viscosity and U_{max} is the velocity at the center of the parent artery. The flow rate was fixed at 150 mL/min of steady flow using a screw pump (NBL30PU, R'Tech) and was measured using a Coriolis flow meter (FD-SS2, Keyence). The pressures upstream and downstream of stenosis were measured using pressure meters (PW-100KPA, Tokyo Sokki Kenkyujo). The height of the fluid column in the reservoir loaded hydrostatic pressures to the circuit.

2-3. Working fluid

The working fluid consisted of a mixed solvent of glycerol/ distilled water solution and sodium iodide/ water solution, and included particles based on a previous report [4]. The final working fluid for the PVA-H model had a refractive index of 1.455, density of 1.476 g/mL, and kinematic viscosity of 4.03 mm²s⁻¹ at 21.0 °C, and that for the silicone model had a refractive index of 1.411, density of 1.194 g/mL, and kinematic viscosity of 4.58 mm²s⁻¹ at 21.6 °C.

2-4. Numerical Simulation process

All processes of finite element analysis were performed using a commercial software package (Comsol 4.2a, Comsol). The same geometry of the models for PIV, and a hypothetical geometry with a larger parent artery of 4.8mm diameter and with deformed plaque section of 3.36 mm width under high

pressure were adopted as model geometries. The number of tetrahedron mesh was about 700,000 in all cases. A laminar flow rate of 150 mL/min was introduced at the inlet, and several constant pressures with no viscous stress were set on the outlet. The basic equations of continuity and the Navier-Stokes equation were solved to determine the flow field.

3. Results and Discussion

Figure 2 shows the stenosis severity in each model with relation to internal pressure. This figure indicates that stenosis severity in the PVA-H model decreases linearly in accordance with upstream pressure, and that in the silicone model is almost constant. Change of pressure drop in each pressure depends on the mechanical properties of models, as shown in Fig. 3. It suggests the mechanical properties of models can influence on the deformation ratio of the models themselves, and change flow conditions despite the same initial geometry. *In vivo* arteries show the compliance decreases nonlinearly according to increase of inner pressure in diameter-pressure curve [6]. From this report, the mechanical properties of a biomodel should be reproduced corresponding condition of blood vessels to reproduce the deformation and the flow.

Figure 4 shows the relationship between Re and upstream pressure. PVA-H model with the decrease of Re with increasing pressure can be described based on the reduced speed, even though the diameter increases. On the other hand, Re increases in accordance with the increase in the upstream pressure in the silicone model. Reattachment lengths tend to decrease in accordance with the increase in Re, as shown in Fig. 5. This reduction can be exhibited with dependence on expansions of the parent arteries and deformations of the plaques due to inlet pressure. In other words, the reattachment lengths could depend on the mechanical properties of models. On the contrary, the reattachment lengths in the model of the numerical simulation are always constant in spite of increasing inlet pressure. These results indicate the expansion of the parent arteries and geometrical change of the plaques in accordance with increasing the internal pressure depends on the mechanical properties of the models. Therefore, it is suggested that the mechanical properties of biomodels can be one of the important parameters in PIV experiment for analysis of diseases.

4. Concluding remarks

PIV experiments in two kinds biomodels with stenoses and the numerical simulations were performed. The mechanical properties of models determined the final geometries of models, and the final geometries affected flow patterns. This results suggested that the mechanical properties of biomodels can be one of the important parameters in PIV experiment with disease model.

Acknowledgments

This study was mainly supported by Tohoku University Global COE program on World Center of Education and Research for Trans-disciplinary Flow dynamics, and

partly by the Sasakawa Scientific Research Grant from the Japan Science Society.

References

- [1] T. Yamagishi, J. Athe. Throm., **16** (2009), 662
- [2] H.R. Shi, Phys. Med. Bio., **53** (2008), 6377
- [3] M. Ohta, Tech. Health Care, **12** (2004), 225
- [4] S. Shida, ASME IMECE2011-64388, (2011)
- [5] Y. Shimizu, ICFD proceedings, (2010)
- [6] Y. Tardy, Clin. Phys. Physiol. Meas., **12** (1991), 39

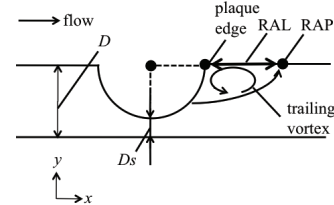


Fig. 1 Flow and geometry of the channel with the stenotic part.

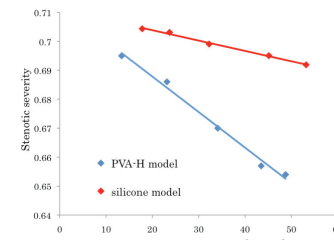


Fig. 2 Relationship between stenosis severity and pressure upstream of PIV.

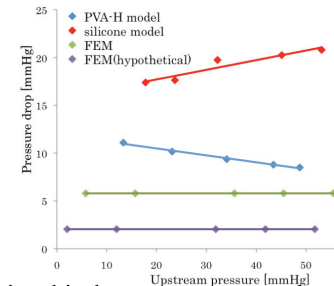


Fig. 3 Relationship between pressure drop and pressure upstream.

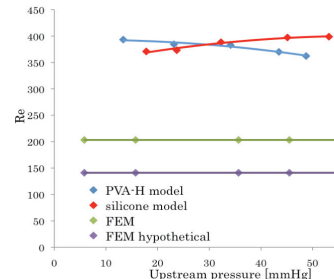


Fig. 4 Relationship between Re and pressure upstream.

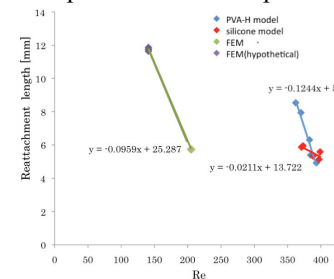


Fig. 5 Relationship between reattachment length and Re.

Effect of the Aspect Ratio of Cerebral Aneurysms on Blood Flow Reduction after Optimized Stent Placement

Toshio Nakayama¹, Shinkyu Jeong², Karkenahalli Srinivas³, Makoto Ohta²

¹Graduate School of Biomedical Engineering, Tohoku University, 2-1 Seiryō-Machi Aoba-ku Sendai Miyagi, 980-8575, JAPAN

²Institute of Fluid Science, Tohoku University 2-1-1 Katahira Aoba-ku Sendai Miyagi, 980-8577, JAPAN

³School of Aerospace, Mechanical and Mechatronic Engineering, University of Sydney, NSW 2006, AUSTRALIA

nakayama@biofluid.ifs.tohoku.ac.jp.

ABSTRACT

The effect of stent strut in aneurysm neck was analyzed by computational fluid dynamics (CFD), and the design method of stent strut pattern using optimization has been reported. In this report, the classified cerebral aneurysm by Aspect ratio (AR) is introduced. The CFD analysis was performed to aneurysm of each AR, and the optimization was performed to CFD result. The blood flow speed and the wall shear stress (WSS) were reduced in almost case after optimization of stent strut pattern. The problem of the development of stent strut pattern was able to be clarified at the same time.

1. Introduction

The rupture of a cerebral aneurysm causes massive bleeding in the brain, which is life threatening and carries a high probability of brain sequelae. As the method of treatment, there is endovascular treatment that is called stent implantation in intracranial artery. Stents have become increasingly popular because the surgical damage that results from this treatment seems to be less severe than that from other treatments. The role of stenting for cerebral aneurysm is thought as reducing the blood flow in cerebral aneurysm. We developed the computational fluid dynamics (CFD) using a realistic stent and aneurysm for the evaluation of stenting [1]. From these results, the stent strut pattern is very effect on the blood flow reduction in cerebral aneurysm. Then we have thought that development of a methodology for stent strut pattern may be necessary. We performed an optimization way to design stent strut pattern with three-dimensional techniques [2]. And the results say that several optimized designs can be proposed.

Ujje et al. introduced aspect ratio (AR) of aneurysm and rupture of aneurysm is related to AR [ref]. AR is a geometrical function and also induces the flow aspect. Therefore, the relation of stent pattern to AR will be important.

In this study, the relationship between cerebral aneurysms classified by using Aspect Ratio (AR) and stent strut pattern is focused. We performed optimization of stent strut and observed the flow patterns.

2. Method

2.1. Cerebral aneurysm

The target was a side wall type aneurysm. An ideal shape shown in Figure 1 was used in this calculation for simplification. The shape of the parent artery was a straight pipe with 4 mm diameter and 50 mm length. The aneurysm was a combination of a straight pipe and a half sphere. The range of AR was between 0.5–2.0; therefore, the height of the aneurysm was variable between 2–8 mm with constant neck size. The construction of these shapes was performed using CAD software (MagicsRP 13.1; Materialise, Belgium).

2.2. Intracranial stent

Z-type strut was applied because of the effective flow reduction in previous researches [2]. The variation

of stent strut width was from 60 to 160[μm]. The length of stent strut was changed under the condition of porosity keeping 80%. The stent strut height was constant at 150 [μm]. The stent was implanted at 1.9 [mm] position from the center of parent artery. Then 10 cases of stent strut pattern were constructed by using CAD software (Pro/Engineer, Parametric Technology Corp., U.S.).

2.3. Numerical simulation

The constructed shape data were transferred to a personal computer and a tetrahedral numerical mesh was generated (ICEM CFD 11.0; Ansys Inc., PA, USA). The mesh number was around 1,300,000–1,700,000 in all cases. To improve analytical accuracy, mesh refinement was performed near the stent strut. The size of the mesh near the stent strut was made finer than that at other parts. The constructed mesh data were transferred to a supercomputer at the Institute of Fluid Science (UV, Silicon Graphics Inc., CA, USA). Figure 4 shows fine mesh near the stent strut.

In previous research [3], the Reynolds number in cerebral blood vessels was assumed to be about 200; on this basis, it was assumed to be 240 in this study. The blood flow speed at the inlet was calculated on the basis of Reynolds number and the characteristic length, which was calculated as 0.200 m/s. The blood flow in the blood vessel was considered to be laminar. The blood flow had a density of 1050 kg/m³ and a viscosity of 0.0035 Pa·s. Therefore, the governing equations for describing this fluid were the continuity and Navier – Stokes equations.

Numerical simulation of blood flow was performed by using the commercial software package ANSYS Fluent 6.3 (Ansys Inc., PA, USA) on the IFS super computer (UV, Silicon Graphics Inc., CA, USA). Time-independent boundary conditions were applied to the inlet, outlet, vessel, aneurysm wall, and stent.

2.4. Optimization

In the spirit of the method used, namely, exploration of design space, one examines a large number of candidate designs and evolves an optimum. The results of CFD analysis were evaluated using several objective functions. The objective functions in this study were the maximum velocity and WSS. This evaluation method

was followed by using the process of Multi-Objective Genetic Algorithm and Kriging [5], to produce a response surface [6], which represents the relationship between the objective functions and the design variables. The process essentially predicts unknown values from the data collected by computations. The procedure also yields with nondominated solutions.

3. Results and Discussion

Figure 2 shows a result of optimization in AR=0.5 case. The x-axis means the maximum blood flow speed in cerebral aneurysm and the y-axis means the maximum wall shear stress. The blue point means the results of CFD analysis and the red point means the non-dominated fronts for stent strut pattern.

From the optimized result, the optimized size of strut of AR=0.5 is similar to that of AR=2.0. The highest reduction rate of the maximum WSS is stent with the diameter of 65 [μm], whereas that of the flow speed is stent with 145 [μm] shown in table 1(a) and (b). The reduction rate is defined as follows.

$$\text{reduction rate} = \frac{\text{with stent}}{\text{no stent}} \quad (1)$$

In previous research, we reported that the maximum WSS increased after stent placement when AR is 0.5 or 0.7 (4). However, this study reveals that stents with over 115 [μm] after optimization could reduce the maximum WSS in comparison with no-stent case(0.58[Pa], AR=0.5).

The high blood flow speed is observed in an area encircled by the distal aneurysm wall and stent struts. The flow in the area goes from aneurysm to the parent artery. The high blood flow also produces the maximum at the distal aneurysm wall. The area size between the distal aneurysm wall and stent strut will affect the speed. And the blood flow speed will affect the maximum WSS at the distal wall. The area size is very important and is considered in parameter in future work.

The flow patterns of all AR on the necks are almost same. However, as table 1 and 2 show, the reduction rate of AR=0.5 are relatively bigger than that of AR=2.0. The relationship between the flow pattern on neck and reduction rate will be a future task.

The two rotational flows in cerebral aneurysm are observed before stent implantation when AR was over 1.5. After the stent implantation, the two rotational flows disappeared and a rotational flow is observed.

It is difficult to implant of stent at a strict position in the aneurysm neck by present medical equipment performance and medical Technology. Then, the development of high performance stent with independent on the implantation position will be necessary.

4. Concluding remarks

The optimizations of stent strut pattern using cerebral aneurysms classified by using AR were performed. AR has relation to the reduction rate small effect on the blood flow pattern on neck.

5. Acknowledgments

CFD analysis was performed by the super-computer of Institute Fluid Science, Tohoku University.

References

- [1]T. Nakayama et al, Proceedings of the 6th International Symposium on Advanced Fluid Information., (2006), 47-48.
- [2]T. Nakayama et al, Proceedings ASME. (2010) FEDSM / ICNMM 2010, 30592
- [3] M. Ohta et al, Interventional Neuroradiology., 10(2) (2004), 85-94
- [4]T. Nakayama et al, Proceedings of the 8th International Symposium on Advanced Fluid Information., (2011), 458-459.
- [5]R. J. Donald et al, J. Global Optim., (1998), 13, 455-492.
- [6] R. H. Myers et al, Process and Product Optimization Using Designed Experiments, Wiley, New York, pp. 1-8

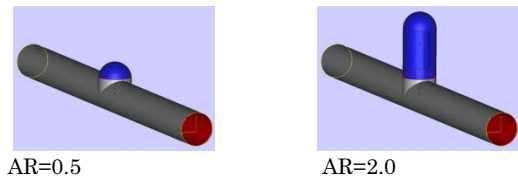


Fig. 1 The cerebral aneurysm shape. Blue region is the cerebral aneurysm and Gray region is the parent artery.

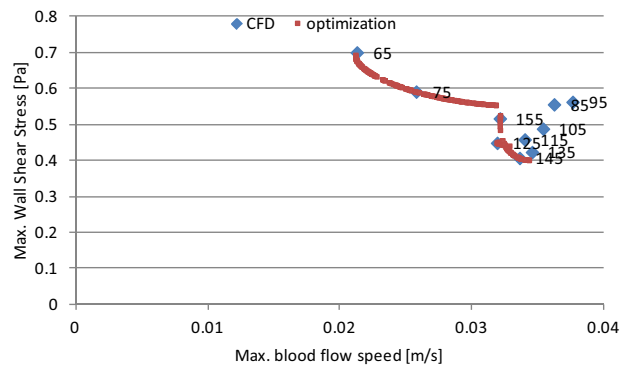


Fig. 2 Results of optimization. Non - dominated front for stent strut pattern (Red) and CFD results (Blue)

Table 1 The maximum WSS value and blood flow speed in the cerebral aneurysm

(a)The maximum WSS

AR	0.5	2.0
with stent [Pa]	0.55	0.37
no stent [Pa]	0.59	0.83
reduction rate	0.93	0.45

(b)The maximum blood flow speed

AR	0.5	2.0
with stent [m/s]	0.022	0.022
no stent [m/s]	0.024	0.037
reduction rate	0.92	0.59

OS8: Membrane Micro Channel for Health Care

Structural Elements which Control the Signal Transduction Pathway of GPCR.

Minoru Sugihara¹, Makiko Suwa^{1,2}

¹ Aoyamagakuin University, College of Science and Technology, Department of Chemistry and Bioscience, 5-10-1, Fuchinobe, Chuo-ku Sagamihara-shi, Kanagawa, 252-5258, Japan.

² Computational Biology Research Center (CBRC), National Institute of Advanced Industrial Science and Technology, AIST Tokyo Water Front BIO-IT Research Building, 10F, 2-4-7 Aomi, Kotou-ku, Tokyo, 135-0064, Japan
suwa@chem.aoyama.ac.jp

ABSTRACT

Recent optogenetic technology intends to control the intracellular signal of G-protein coupled receptor (GPCR) by using light instead of chemical substances. This technology made a chimera in which cytoplasmic loops of a rhodopsin are exchanged to those of other GPCR. We address a question of how specific partial structural elements of GPCRs contribute to control the G-protein coupling selectivity by performing combined QM/MM, MD studies of rhodopsin structure and sequence analysis of GPCRs. The different structural stability was observed in the retinal binding pocket, inter-helical region and loops at cytoplasmic side.

1. Introduction

G-protein coupled receptors (GPCRs) are the target of ~30% of the total marketed drugs, and it is strongly required to reveal the functional mechanisms of these receptors. Recent optogenetic technology intends to control the intracellular signal of G-protein coupled receptor (GPCR) by using light instead of chemical substances. This technology made a chimera in which cytoplasmic loops of a rhodopsin are exchanged to those of other GPCR [1]. We address a question of how specific partial structural elements of GPCRs contribute to control the signaling pathway (G-protein coupling selectivity) by performing combined quantum/molecular mechanical (QM/MM), molecular dynamics (MD) studies of rhodopsin structure and sequence analysis of GPCRs.

2. Method and Results [2]

The analysis of amino acid occurrence at each site of protein family indicates whether the site is common or specific in all family members. We retrieved 1272 class A GPCR sequences of 48 subfamilies (24 vertebrates) from the SEVENS database ([3], <http://sevens.cbrc.jp>) and five invertebrate rhodopsins from UNIPROT (<http://www.ebi.ac.uk/uniprot/>). Transmembrane helical regions were determined based on available crystal structures of rhodopsin, adrenergic receptor, and adenosine receptor to which the multiple sequence alignments performed by MAFFT [4].

The simulation was performed for evaluating structure of squid and bovine rhodopsin [5, 6, 7] with CHARMM package [8]. The retinal structure was calculated quantum mechanically by employing SCC-DFTB [9]. Water molecules are described with the TIP3P model. Our model protein contained no lipids and a harmonic constraint was applied to the peptide backbone atoms to maintain the shape of the protein. Time step was 1 fs. and the simulation was prolonged to 10 ns at 300 K.

We firstly compared the structures of Bovine and Squid rhodopsin which bind to G proteins of different kinds, as a model case. (Fig. 1)

The retinal binding pocket of squid rhodopsin contains many highly conserved aromatic residues, most of

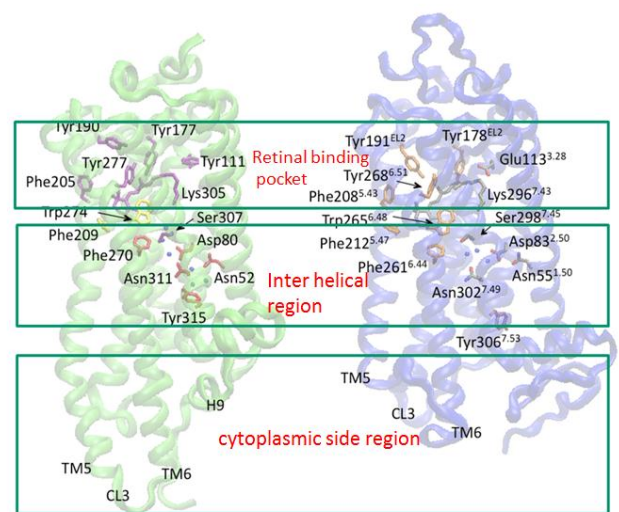


Fig. 1. Three structural regions, where we analyzed; the retinal binding pocket, the inter-helical region, and the cytoplasmic side region.

which were also found in bovine rhodopsin. Some of these residues were specific in rhodopsin.

In contrast, most of the conserved residues in GPCRs were localized in the helical domains, including the D(E)RY motif in the third transmembrane helix(TM3), the CWxPY motif in TM6, and the NPxxY motif in TM7. Significant differences between both rhodopsin are found in the regions of the third cytoplasmic loop (CL 3) and N-terminal where squid rhodopsin has more numbers of charged residues than bovine rhodopsin.

Accurate description of the retinal geometry is essential for understanding the signal transduction, because the retinal geometry is a key structural determinant of the isomerization that initiates the downstream signal propagation. The calculated geometry (bond length alternation, bond angles and dihedral angles) of retinal showed good agreement in squid and bovine rhodopsin, although experimentally determined geometry was slightly different from each other. The minimized retinal binding pocket near the

β -ionone ring of retinal is occupied with highly conserved aromatic residues both between squid and bovine rhodopsin. The coordinates of the aromatic residues showed only small changes in squid and bovine rhodopsin, except for a tyrosine residue (tyr190 in squid and Tyr 191 in bovine rhodopsin) in extracellular loops.

Water molecules present in the inter-helical cavity of GPCRs are likely to be important for the proper function of activation. Starting from the Trp274 of squid rhodopsin (Trp265 of bovine rhodopsin), a “ladder” of the hydrogen-bond network mediated by the water molecules was observed in the inter-helical cavity of both squid and bovine rhodopsin. In squid rhodopsin, a hydrogen bond network, which extends approximately 13 Å to Tyr315 on the cytoplasm side, is maintained regardless of the protonation state of Asp80. In contrast, the extended hydrogen-bonded network is interrupted at Tyr306 in bovine rhodopsin after QM/MM computation.

It has been suggested that CL3 between transmembrane helices 5 (TMH5) and 6 has significant roles in the interaction with G-proteins. A remarkable difference between the crystal structures of squid and bovine rhodopsin is that TMH5 and TMH6 of squid rhodopsin protrude into the cytoplasmic medium and are longer than in bovine rhodopsin (Fig. 1). Furthermore, squid rhodopsin possesses an additional helix (H9) located after H8. To clarify the influence of H9 on the stability of TMH5 and TMH6, we performed a set of MD runs with and without H9. Two rhodopsins show the significant difference about the number of salt bridges formed on cytoplasmic side loops. The MD work demonstrated that the elongated conformation of TMH6 in squid rhodopsin is stabilized by salt bridges with H 9.

Based on our observation, we considered the following signal transduction pathway. The similar environment of retinal binding pocket, containing highly conserved aromatic residues, stabilizes the inactive retinal to the same geometry in the two rhodopsins. The signal induced by a photon propagates from the retinal binding pocket and the highly conserved Trp274 (Trp265) in squid (bovine) rhodopsin is the first residue to interact with the isomerized retinal. This tryptophan residue interacts with water and causes the first perturbation of the signal propagation. In squid rhodopsin, the stable hydrogen bond network extends to Tyr315 at the cytoplasmic side. On the contrary, in bovine rhodopsin, the hydrogen bond network is interrupted at the coincident Tyr306, and the inter-helical hydrogen bond network is rather loose compared with that of squid rhodopsin. Moreover, in squid rhodopsin, the salt bridges on the cytoplasmic surface stabilize the protein conformation, and consequently, rather small changes are likely to occur on the cytoplasmic side in the later intermediates.

We also indicate difference of simulated structure of cytoplasmic side of rhodopsin according to the interaction with different type (Gq, Gt, Gs) of G-protein. Paying attention to these regions (retinal binding pocket, inter-helical environment, cytoplasmic loop regions)

distributions of hydrogen bonding residues and charged residues were summarized as profiles. And the correlation of it and G protein coupling selectivity was investigated.

Although we still not know the actual functional mechanism of GPCRs, these observations may lead to understand general concept of structural elements which control the G-protein binding selectivity.

References

- [1] Raag, D. A., *et al.*, *Nature*, **458**(2009), 1025-1029.
- [2] Sugihara, M., Fujibuchi, W., Suwa, M., *J. Phys. Chem. B*, **115** (2011), 6172–6179.
- [3] Suwa, M., Ono, Y., In *Methods in Molecular Biology*. Koga, H., Ed. Springer-Verlag: Berlin, Heidelberg, Tokyo, **577** (2009), 41-54.
- [4] Katoh, K., Toh, H., *Briefings in Bioinformatics*. **9** (2008), 286–298.
- [5] Park, J. H., Scheerer, P., Hofmann, K. P., Choe, H.-W., Ernst, O. P., *Nature*, **454** (2008), 185-187.
- [6] Murakami, M., Kouyama, T., *Nature*, **453** (2008), 363-368.
- [7] Shimamura, T., *et al.*, *J. Biol. Chem.*, **283**(2008), 17753-17756.
- [8] MacKerell, A. D., *et al.*, *J. Phys. Chem. B*, **102** (1988), 3586-3616.
- [9] Cui, Q., Elstner, M., Kaxiras, E., Frauenheim, T., Karplus, M., *J. Phys. Chem. B*, **105** (2001), 569–585.

Computational Detection of Organelle Sorting Signals in Membrane Localized Proteins

Yuri Mukai^{1,2}, Hirotaka Tanaka¹, Tatsuya Konishi¹, Hiromu Takata¹, Naoyuki Takachio²,
Masami Ikeda³ and Takanori Sasaki^{1,2}

¹Faculty of Electrical Engineering, Graduate School of Science and Technology, Meiji University, Kawasaki, Kanagawa 214-8571, Japan, ²Department of Electronics and Bioinformatics, School of Science and Technology, Meiji University, Kawasaki, Kanagawa 214-8571, Japan, ³Department of Chemistry and Biological Science, School of Science and Technology, Aoyama Gakuin University, Sagamihara, Kanagawa 252-5258, Japan
yuri@isc.meiji.ac.jp

ABSTRACT

Methods for the detection of golgi localized membrane proteins and GPI-anchored proteins, which are secreted on the surface of the plasma membrane, were developed by alignment position specific amino acid scoring matrix for the purpose of computational detecting of weak consensus motifs for golgi membrane targeting and plasma membrane sorting. Subcellular distribution of artificial signal-peptide-GFP fusion proteins also could be observed by the GFP fluorescence detection using a confocal laser scanning microscope.

1. Introduction

Protein subcellular localization is an important key problem in the post-genome era. The computational approaches including NNPSL, PSORT II, TargetP, SubLoc, iPSORT, LOC3D, PLOC, WoLF PSORT among many others for predicting protein subcellular localization have been developed. Although these systems predict soluble proteins well, they cannot predict membrane localized proteins with high accuracy. The reasons are following: (i) there are no clear consensus signals or motifs for organelle membrane transport and (ii) few membrane localized proteins are available for the construction of training datasets for developing these prediction systems. Therefore, the development of an original computational detection system for membrane localized proteins is required. In this study, methods for the detection of golgi localized membrane proteins and GPI-anchored proteins, which are secreted on the surface of the plasma membrane, were developed for the purpose of computational detecting of weak consensus motifs for golgi membrane targeting and plasma membrane sorting. Experimental validation for the protein localization using artificial signal-peptide (SP) sequence which helps importing proteins to the Endoplasmic Reticulum (ER) is also reported.

2. Detection of Golgi membrane proteins focusing on their transmembrane regions

The Golgi apparatus is an important organelle which is involved mainly in the modification of protein oligosaccharides and vesicular transport. There are various proteins in the Golgi apparatus with important roles in their function, notably Golgi-localized type II membrane proteins (GLs), including epimerases, nucleotidases, decarboxylases, oligosaccharide synthases, polysaccharide-degrading enzymes, and glycosyltransferases. Glycosyltransferases are major members of the GL and are one of the most important types of proteins involved in the modification of protein oligosaccharides. Oligosaccharides play important roles in many vital reactions, including cell adhesion, signal transfer, and subcellular localization. Variations in

oligosaccharide modification depend on the localization of the protein and families of oligosaccharide-related proteins in the Golgi apparatus, including the glycosyltransferases. Hence identification and classification of GLs is essential in clarifying the mechanisms underlying oligosaccharide modification. To this end, the development of a computational method to distinguish the genes encoding GLs in mammalian genomes is desired. In this study, a method for the detection of golgi localized membrane proteins was developed [1].

The non-redundant datasets of GLs and post-Golgi type II membrane proteins (PGs) were obtained from Swiss-Prot database. GLs were detected by combining hydrophathy alignment and position-specific scoring matrix (PSSM) around the transmembrane region. Each sequences was aligned by superpositioning the highest average hydrophobicity position. The PSSM was estimated based on position-specific amino acid propensities of the alignment position in the region of -14 to +18. This method can discriminate GLs from PGs with 89.8% sensitivity and 87.0% specificity was achieved in 5-fold cross-validation test. This study is expected to pave the way for comprehensive identification of GL genes not only in mammalian genomes, but also in other genomes by generating the PSSM for each phylum/class.

3. Detection of GPI-anchored proteins and their GPI modification sites

Glycosylphosphatidylinositol (GPI) is a post-translational modification molecule which plays important roles in the vital activities of Eukaryotic cells. Each GPI binds to a singular amino acid at a site called the omega-site in soluble proteins (GPI-anchored proteins, GPI-APs) in the Endoplasmic Reticulum and is secreted on the surface of the plasma membrane (Fig. 1). There are various GPI-APs related to human incurable disorders including bovine spongiform encephalopathy and paroxysmal nocturnal hemoglobinuria among many others. Thus, identification and functional analysis of GPI-APs are believed to be crucial for the understanding of vital activities of Eukaryote cells and the resolution of

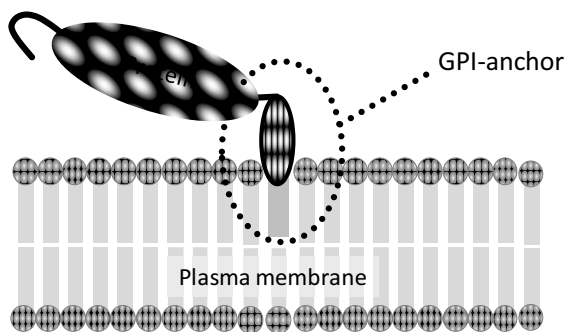


Fig. 1 Schematic diagram of GPI-anchored protein.

molecular mechanisms of human incurable disorders. Therefore, development of computational methods to predict GPI-APs and their omega-sites with high accuracy from genome/protein sequences is of utmost importance.

In this study, new methods for the detection of GPI-APs and for the prediction of the location of omega-sites by physicochemical properties, PSSM and back-propagation artificial neural networks (BP-ANNs) were developed [2]. GPI-AP and omega-site datasets were obtained from the Swiss-Prot database. The non-GPI-AP dataset was collected based on the hydrophathy of N- and C-terminal sequences, and sequences around A, C, D, G, N and S residues in GPI-AP sequences without omega-sites were extracted as a non-omega-site dataset. PSSs were calculated based on amino acid propensities around the omega-sites. PSSs were applied to BP-ANNs which consist of a three-layered structure. This method could distinguish GPI-APs from non-GPI-APs (92.9% sensitivity and 94.8% specificity) and also could discriminate omega-sites from non-omega-sites with higher accuracy (95.6% sensitivity and 97.0% specificity) than other GPI-APs detection tools reported previously.

4. Subcellular localization and transport efficiency of protein sorting signal sequence using green fluorescent protein

Signal-peptide (SP) is a sequence which consists of about twenty-five amino acids which are responsible for protein transport to the ER. After being localized in the ER, the main part of the protein is detached from the SP and becomes a mature-form protein attached by modification molecules including oligosaccharides, lipids and glycolipids. However, why various sequence patterns exist in SP is still unclear.

In this study, the relation between subcellular localization, organelle transport efficiency and physicochemical properties of amino acids which consist of SPs were evaluated using microscopic study and immunoassay by examining the fusion of green fluorescence proteins (GFPs) to SP. SPs derived from native GPI-anchored proteins and several artificial sequences like SPs were introduced into GFP. GFP fluorescence in HeLa cells transfected by the expression

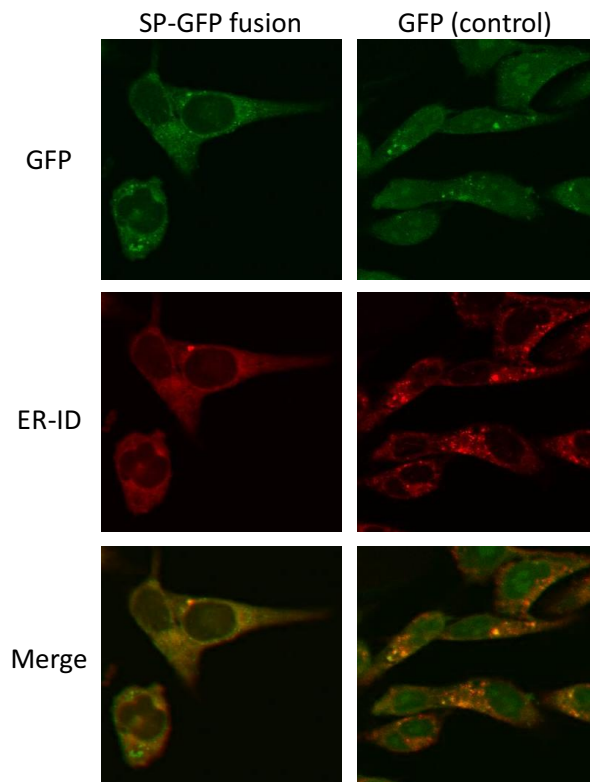


Fig. 2 Confocal laser microscope images of HeLa cells expressed SP-GFP fusion proteins

vector for SP-GFP fusion protein was observed by a confocal laser scanning microscope (Fig. 2). Subcellular localizations of SP-GFP fusion proteins were examined by comparison with the fluorescence image using organelle markers.

4. Concluding remarks

Methods in this study using PSSMs could detect membrane-localized proteins, including golgi transmembrane proteins and GPI-anchored proteins with high accuracies. Subcellular localization of artificial SP-GFP fusion proteins could be observed by GFP fluorescence detection using a confocal laser scanning microscope.

Acknowledgement

This work was financially supported by the Research for Promoting Technological Seeds from the Japan Science and Technology Agency (JST) and KAKENHI Grant-in-Aid for Young Scientists (B) from Japan Society for the Promotion of Science (JSPS).

References

- [1] Y. Mukai, M. Yoshizawa, T. Sasaki, M. Ikeda, K. Tomii, T. Hirokawa, M. Suwa, *Biosci. Biotech. Biochem.*, **75** (2011), 82-88.
- [2] Y. Mukai, H. Tanaka, M. Yoshizawa, O. Oura, T. Sasaki, M. Ikeda, *Current Bioinform.*, **7** (2012), 125-131.

Electrophysiological Properties of Bacterial Membrane Channel Proteins Depending on Lipid Component and Bilayer Stability

Noriko Tomita¹, Liviu Movileanu^{2,3,4}, and Makoto Ohta¹

1. Institute of Fluid Science, Tohoku University, 2-1-1 Katahira, Aoba-ku, Sendai, Japan

2. Department of Physics, Syracuse University, Syracuse, New York, USA

3. Structural Biology, Biochemistry, and Biophysics Program, Syracuse University, Syracuse, New York, USA

4. Syracuse Biomaterials Institute, Syracuse University, Syracuse, New York 13244, USA
tomita@biofluid.ifs.tohoku.ac.jp

ABSTRACT

Activities and structures of membrane proteins are affected by the lipid bilayer environment. We herein show diversity in channel properties of engineered ferric hydroxamate protein uptake component A (FhuA $\Delta C/\Delta 4L$), an outer membrane receptor of *Escherichia coli*, on planar lipid bilayers consisting of various types of phospholipids. Single-channel electrical analysis revealed that the shape of phospholipids affects the sensitivity of the FhuA $\Delta C/\Delta 4L$ channel to closure under high-voltages. This study expands the versatility of the engineered FhuA $\Delta C/\Delta 4L$ channel, making the channel suitable for biosensors and nanodevices.

1. Introduction

FhuA (Ferric hydroxamate protein uptake component A) is a ligand-gated channel in the outer membrane of *Escherichia coli*, which forms a monomeric 22-stranded β -barrel protein [1]. Based on the versatile properties of the FhuA channel, including dynamics, robustness, and thermal stability, focus has been placed on its application as a stochastic biosensing element [2]. Mohammad et al. have created new engineered FhuA $\Delta C/\Delta 4L$ by a removal of almost one-third of the total number of amino acids of the wild-type FhuA (Fig. 1) [3], and revealed that FhuA $\Delta C/\Delta 4L$ forms a functional, open pore in planar lipid bilayers with a more stable and greater conductance than the other engineered FhuA proteins recorded previously [3], which implied FhuA $\Delta C/\Delta 4L$ has promising potential to be applied as a more useful stochastic sensor for protein and DNA

While protein engineering techniques have been applied to improve its utility and advantages as stochastic sensor, electrophysiological properties of the FhuA $\Delta C/\Delta 4L$ affecting the lipid bilayer environment, such as gating with conformational change and voltage-dependency, had yet to be elucidated. In this study, we investigate the effect of the phospholipid component on the voltage-dependent gating of the FhuA $\Delta C/\Delta 4L$ channel by using single-channel electrical analysis in planar lipid bilayer. We selected either neutral or negative-charge, cylindrical or cone-shape, and different lipid mixtures to explore a wide variety of lipid types that might effect gating. This work should contribute not only to providing new insights into the FhuA $\Delta C/\Delta 4L$ channel properties and their dependence on the membrane environment, but also the expansion of the availability of the FhuA $\Delta C/\Delta 4L$ channel as a nanodevice that can be regulated by phospholipid component.

2. Method

2.1. Preparation on planar lipid bilayers

For preparation of the planar lipid bilayer, we used five types of phospholipid, 1,2-diphytanoyl-sn-glycerophosphatidylcholine (DPhPC), 1,2-diphytanoyl-sn-glycero-3-phosphoethanolamine, (DPhPE), 1,2-diphytanoyl-sn-glycero-3-phospho-L-serine, (DPhPS),

N-palmitoyl-D-erythro-sphingosylphosphorylcholine (SM) and *E. coli* Polar Lipid Extract (ECTPL) containing of PE (phosphatidylethanolamine):PG (phosphatidylglycerol):CL (cardiolipin) in a volume ratio of 6.7:2.3:1.0. These phospholipids were purchased from Avanti Polar Lipids (Alabaster, AL). Powders of DPhPC, DPhPE, DPhPS and ECTPL were solubilized with pentane at a concentration of 10 mg/mL. SM powder was solubilized with a mixture of chloroform and methanol (2:1, v/v). Phospholipid solutions for bilayer formation were prepared by mixing DPhPE and DPhPC in a volume ratio of 3:7 and 1:1, and SM:DPh in a volume ratio of 1:1. To investigate an effect of charge, DPhPS was used without being mixed with DPhPC..

2.2 Preparation of the FhuA $\Delta C/\Delta 4L$ protein

The construction of the plasmid for the expression of the engineered FhuA $\Delta C/\Delta 4L$ protein nanopores and modifications of the protocol for obtaining the FhuA $\Delta C/\Delta 4L$ protein nanopore through rapid-dilution refolding have been performed as described previously [3]. Briefly, 40 μ L of His⁺-tag purified, denatured FhuA $\Delta C/\Delta 4L$ was diluted 50-fold into a 1.5 % n-Dodecyl- β -D-maltopyranoside (DDM), in 50 mM Tris-HCl, containing 200 mM NaCl, 1 mM EDTA, pH 8.0. The diluted protein samples were left overnight at 23°C to complete the refolding of FhuA $\Delta C/\Delta 4L$ protein.

2.3. Electrical recordings on planar lipid bilayers

The *cis* and *trans* chambers (1.5 ml each) of the apparatus were separated by a 25- μ m-thick Teflon septum (Goodfellow Corp., Malvern, PA). An aperture in the septum, ~ 80–120 μ m in diameter, was pretreated with hexadecane (Sigma-Aldrich Co. LLC. St. Louis, MO) dissolved in highly purified pentane (Fisher HPLC grade, Fair Lawn, NJ) at a concentration of 10% (v/v). DPhPE: DPhPC = 3:7, DPhPE: DPhPC = 1:1, SM: DPhPC = 1:1, ECTPL and DPhPS bilayers were formed across the aperture. Single channels of the engineered FhuA $\Delta C/\Delta 4L$ protein were obtained by adding purified and refolded protein into the *cis* chamber at a final amount of 150-300 ng. Electrical recordings were carried out an Axon 200B patch clamp amplifier (Axon

Instruments, Foster City, CA) in the voltage-clamp mode. Data was collected by an Intel Core Duo PC (Dell, Austin, TX) connected to a Digidata 1440A (Axon Instruments). Output was filtered using a Frequency Devices Model 900B 8-pole Bessel filter (Frequency Devices, Ottawa, IL) at 10 kHz. The acquisition rate was 50 kHz.

2.4. Analysis of voltage-dependent channel properties

A first closure time (FCT) of the channel is defined as the number of seconds taken for the channel to enter its first closure state, normalized to the total duration of the experiment, 60 seconds. If the channel did not close within 60 seconds, the normalized FCT (NFCT) was calculated as 1. The three distinct single-channel experiments were performed for analyzing the NSS, the number of states, and NFCT on each kind of lipid bilayer.

4. Results

We investigated the sensitivity of FhuA $\Delta C/\Delta 4L$ channel for closure under high-voltage when reconstituted in lipid bilayers that include cylindrical phospholipids (Bcyl) and cone-shaped phospholipid (Bcon). Figure 5A show representative traces of FhuA $\Delta C/\Delta 4L$ single channel at +180 mV on Bcyl (upper panel) and Bcon (lower panel). As shown in Fig. 5B, the NFCTs of the channels on the SM: DPhPC = 1:1 and DPhPS bilayers, which are Bcyl bilayer, are significantly greater than those on the DPhPE: DPhPC = 3:7, DPhPE: DPhPC = 1:1 and ECTPL bilayer, which are Bcon bilayer. On the contrary, there are no significant differences between the Bcon bilayers and between the Bcyl bilayers (Tukey-Kramer method). While, channel closing did not take place on any of the bilayer at +40 mV.

Taken together, the FhuA $\Delta C/\Delta 4L$ channels are susceptible to high voltage for closing and the degree of sensitivity will be influenced by the shape of phospholipid rather than by lipid charge.

4. Discussion

By adding cone-shaped phospholipids into a Bcyl, spontaneous curvature stress is produced within the bilayer and lateral pressure is imparted on the embedded membrane protein [4]. Actually, previous study reported that thermodynamic stability and folding efficacy of the *Escherichia coli* β -barrel outer membrane proteins (OMPs) increased by insertion of PE into PC bilayer [5], and the frequency of gating of the *E. coli* OmpG channel was changed by lipid charge [6]. Our results in the present study, in which the conductance, the NSS and the number of state of FhuA $\Delta C/\Delta 4L$ channel were similar but the sensitivities to high-voltage for closure were significantly different between Bcon and Bcyl, indicate the shape of the phospholipid can alter the sensitivity of the FhuA $\Delta C/\Delta 4L$ channel without any substantial change in the structure. Because there are no significant differences in the NFCTs between DPhPE: DPhPC = 3:7 and 1:1 bilayers, the ratio of cone-shaped

phospholipid to cylindrical-shaped phospholipid does not appear to affect high-voltage sensitivity of the channel. Our result indicates a little difference in the number of states for closure between SM: DPhPC and DPhPS bilayers. However, further analysis is needed to evince whether the significant difference could be induced by lipid charge.

To our knowledge, this is the first experimental study suggesting that the electrophysiological properties of β -barrel membrane protein could be affected by lipid shape. The phospholipid shape-dependent nature of FhuA $\Delta C/\Delta 4L$ channel can expand the versatility of the FhuA $\Delta C/\Delta 4L$ channel for nanopore engineering. The feature of FhuA $\Delta C/\Delta 4L$ channel formed on Bcon, which can keep opening for a longer time than that on Bcyl at the high-voltage, should be useful for future stochastic sensing applications, allowing for the measurements to be taken at high voltage, thus improving the signal to noise ratio, for long periods of time.

Acknowledgements

The authors thank Jiaming Liu, Belete R. Cheneke and Aaron J. Wolfe from Syracuse University for their technical assistance. This work was partially supported by a Grant-in-Aid for JSPS Fellows (RPD), Young Researcher Overseas Visits Program for Vitalizing Brain Circulation (IFS, JSPS) and a Global COE Program Grant of the World Center of Education and Research for Trans-disciplinary Flow Dynamics from Tohoku University.

N. Tomita is the recipient of a postdoctoral fellowship from JSPS.

References

- [1] Locher, K.P., Rees, B., Koebnik, R., Mitschler, A., Moulinier, L. Rosenbusch, J.P., and Moras, D. (1998). Transmembrane signaling across the ligand-gated FhuA receptor: crystal structures of free and ferrichrome-bound states reveal allosteric changes. *Cell*. 95, 771–778.
- [2] Mohammad M.M., Howard, K.R., and Movileanu, L. (2011). Redesign of a plugged β -barrel membrane protein. *J. Biol. Chem.* 286, 8000–8013.
- [3] Braun, M., Killman, H., Maier, E., Benz, R., and Braun, V. (2002). Diffusion through channel derivatives of the *Escherichia coli* FhuA transport protein. *Eur. J. Biochem.*, 269, 4948–4959.
- [4] Gruner S. M. (1985). Intrinsic curvature hypothesis for biomembrane lipid composition: A role for nonbilayer lipids. *Proc. Natl. Acad. Sci. USA*. 82, 3665–3669
- [5] Tamm, L.K., Hong, H., and Liang, B. (2004). Folding and assembly of beta-barrel membrane proteins. *Biochim. Biophys. Acta*. 1666, 250–263.
- [6] Hwang, W.L., Chen, M., Cronin, B., Holden, M.A., and Bayley, H. (2008). Asymmetric droplet interface bilayers, *J. Am. Chem. Soc.* 130, 5878–5879.

Engineering Membrane Protein Nanopores for Biomolecular Detection

Mohamamd M. Mohammad¹, Raghuvaram Iyer², Khalil R. Howard³, Mark P. McPike⁴, Philip N. Borer^{2,3,4} and Liviu Movileanu^{1,3,5}

¹Department of Physics, Syracuse University, 201 Physics Building, ²Department of Chemistry, Syracuse University, ³Structural Biology, Biochemistry, and Biophysics Program, Syracuse University, Syracuse, NY 13244, United States. ⁴AptaMatrix, Inc., 100 Intrepid Lane Suite 1, Syracuse, NY 13205, United States. ⁵The Syracuse Biomaterials Institute, Syracuse University, 121 Link Hall, Syracuse, NY 13244, United States.
mohammad@physics.syr.edu

ABSTRACT

Membrane proteins are desired for developing sensing technologies. Yet, many challenges persist in designing protein nanopores that can sustain various detection conditions. Using a bacterial β -barrel membrane protein as a template for protein engineering, we produced an exceptionally functional nanopore for sampling biomolecular events. Pore-forming activity of the engineered protein is maintained at low salt and high acidic conditions. We also show that the protein can act as a sensor for enzymatic activity at low pH. This work demonstrates that nanopores are indispensable tool for building analytical devices and nanosensors.

1. Introduction

Protein nanopores have become an indispensable tool for creating novel devices for biomolecular detection and molecular manipulation at the single-molecule level, and they present an alternative to current analytical devices in biomedical molecular diagnosis (1-4). The principle behind the detection of biomolecules by nanopore is simple. The biomolecules (or analytes) alter the current created by the nanopore through their specific interaction with the nanopore (3). Pore-forming toxins and bacterial outer membrane proteins, are highly attractive for building sensing and analytical devices because of their robust β -barrel structure (5), their resolved atomic structure, their customizability for specific functions, and their prospect in integration into nanodevices. Yet, one challenge is to produce rigid proteins that maintain their assigned tasks under a wide spectrum of environmental conditions. To address the above challenge, we extensively engineered the bacterial ferric hydroxamate uptake component A (FhuA) (6-9) (**Fig. 1a**). We reduced 4 extracellular loops and removed the N-terminal cork domain (**Fig. 1b**). Using electrical recordings, we show that the engineered FhuA protein (FhuA $\Delta C/\Delta 4L$) forms a robust pore in synthetic bilayer and we demonstrate that this protein is capable of sensing analyte in various harsh experimental and physiological conditions (10).

2. Method

Genetic engineering- We used the plasmid containing *wt fhuA* to derive the new gene that lacks the extracellular loops (L3, L4, L5, L11) and the cork (plug), called *fhuA $\Delta c/\Delta 4l$* (**Fig. 1b**) (9). **Protein purification and refolding-** The FhuA $\Delta C/\Delta 4L$ was expressed in *E. coli* and was purified from inclusion bodies using metal affinity chromatography under denaturing condition. The refolded proteins were obtained by diluting denatured protein into solution that contained 1.5% n-Dodecyl- β -D-maltopyranoside (DDM) (11). **Electrical Recordings-** Recordings were carried out utilizing planar bilayer lipid membranes separating two chambers. Current was created when FhuA $\Delta C/\Delta 4L$ protein forms

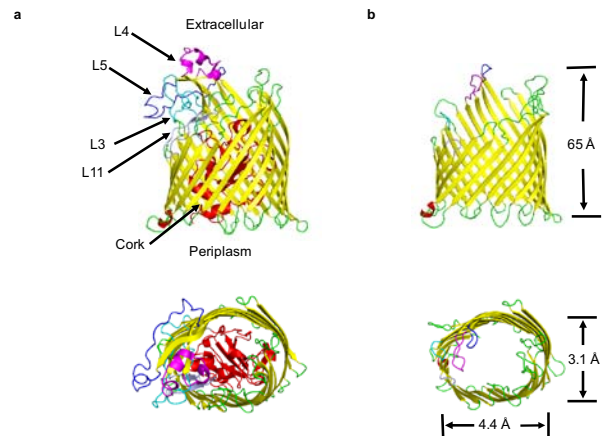


Fig. 1. Structure of FhuA protein. a, the wild-type FhuA. b, the engineered FhuA $\Delta C/\Delta 4L$. Top and bottom panels show side and extracellular views, respectively.

pores in bilayer lipids allowing electrolytes to pass through between two chambers (12).

3. Results and Discussion

We used high-resolution, single-channel electrical recordings to inspect the properties of the engineered FhuA $\Delta C/\Delta 4L$ protein nanopore. **Fig. 2** shows that the newly engineered protein forms pores in the synthetic bilayer and it is very stable in low salt and very acidic pH environments, giving the FhuA $\Delta C/\Delta 4L$ protein nanopore a great advantage to detect biomolecules in harsh conditions. Here, we present one application for using the engineered FhuA $\Delta C/\Delta 4L$ protein nanopore.

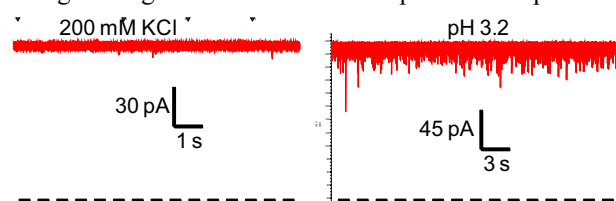


Fig. 2. FhuA $\Delta C/\Delta 4L$ is stable at low salt (left panel) and high acidic (right panel) conditions. Applied voltage was +100 mV. Dashed lines represent 0 current.

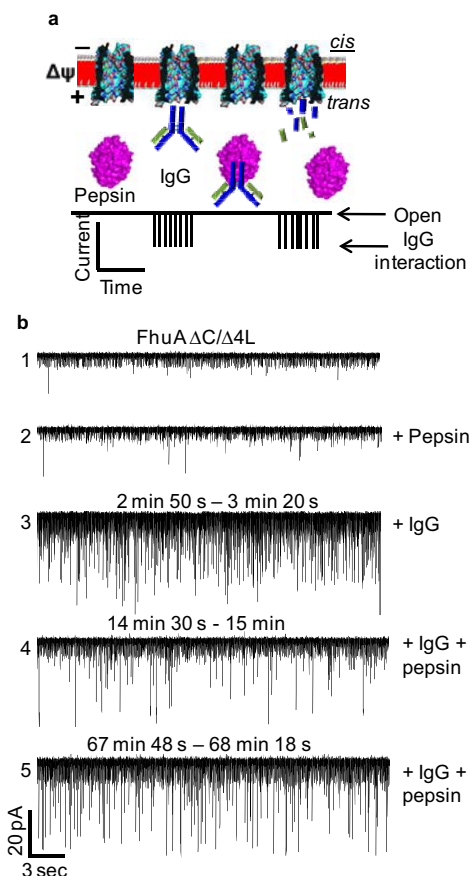


Fig. 3. FhuA $\Delta C/\Delta 4L$ nanopore detects enzymatic activity of proteins in high acidic condition. a, Cartoon presenting the sensing mechanism for the digestion of IgG by pepsin. b, Nanopore-based assay for the digestion of IgG by pepsin. 2.6 μM IgG and 1.5 units of pepsin were used in 1 M NaCl, phosphate-citrate buffer, pH 3.9. The applied voltage was +40 mV. Represented traces were taken at the indicated times during the assay.

In **Fig. 3** we show that the engineered FhuA $\Delta C/\Delta 4L$ nanopore is capable of sensing the digestion of the serum immunoglobulin (IgG) protein at very acidic pH. The pepsin protease is routinely used to produce antigen-binding fragments (Fab) by digesting the Fc part of IgG at very low pH condition (13). The principle of nanopore-based detection is that the IgG fragments are detected by the nanopore upon pepsin digestion (**Fig. 3a**).

The nanopore-based detection of the pepsin digestion activity is shown in **Fig. 3b**. As expected, the FhuA $\Delta C/\Delta 4L$ nanopore is stable in the digestion buffer (**Fig. 3b, trace 1**). The addition of pepsin to the chamber did not significantly alter the current recordings (**Fig. 3b, trace 2**), most probably due to a large size of the enzyme as compared to openings of the nanopore. Unlike pepsin, addition of IgG to the chamber resulted in transient current blockades with an event frequency $f = 30 \pm 8 \text{ s}^{-1}$ ($n=3$, **Fig. 4b, trace 3**). Remarkably, adding pepsin to IgG decreases the event frequency dramatically ($f = 5 \pm 2 \text{ s}^{-1}$ at $t=10 \text{ min}$) (**Fig. 3b, trace 4**). As expected, further digestion of IgG produced

frequent transient current blockades ($f = 10 \pm 2 \text{ s}^{-1}$ at $t \approx 70 \text{ min}$) (**Fig. 3b, trace 5**). Again, this experiment indicates that the reconstitution of the engineered FhuA $\Delta C/\Delta 4L$ in bilayer provides a system that is stable under this very acidic condition for long periods.

4. Concluding remarks

The stability of the engineered FhuA $\Delta C/\Delta 4L$ protein at low salt concentration will open previously-unavailable avenues for investigating biomolecular events under physiological conditions. For example, it is possible to detect very weak binding events between an analyte and FhuA $\Delta C/\Delta 4L$ nanopore or among a complex of analytes. A pH-resistant FhuA $\Delta C/\Delta 4L$ protein nanopore shows prospects for customizing nanopores; for example, drug delivery in harsh conditions. Recently, protein nanopores have been incorporated into artificial solid-state membranes to overcome the softness of the membranes (14), increasing the prospect that the engineered FhuA $\Delta C/\Delta 4L$ nanopores can be integrated into nanodevices. Finally, the convenient method of producing the engineered FhuA $\Delta C/\Delta 4L$ protein nanopore makes it an excellent platform for medical applications bionanotechnology.

Acknowledgments

This work was funded by the U.S. National Science Foundation Grants DMR-1006332 (L.M.) and DGE-1068780 (IGERT Program), and the National Institutes of Health grants R01 GM088403 (L.M.), R01 GM032691 (P.N.B.), and R44 GM076811 (M.P.M.).

References

1. T. Braun *et al.*, *Nature Nanotechnology* **4**, 179(2009).
2. L. Movileanu, *Journal of Biomolecular Structure & Dynamics* **26**, 804 (2009).
3. H. Bayley, P. S. Cremer, *Nature* **413**, 226 (2001).
4. M. Wanunu, *Physics of Life Reviews*, e-pub. May 2012
5. S. Majd *et al.*, *Current Opinion in Biotechnology* **21**, 439 (2010).
6. A. D. Ferguson, E. Hofmann, J. W. Coulton, K. Diederichs, W. Welte, *Science* **282**, 2215(1998).
7. H. Killmann, R. Benz, V. Braun, *J. Bacteriol.* **178**, 6913 (1996).
8. M. Braun, H. Killmann, E. Maier, R. Benz, V. Braun, *Eur. J. Biochem.* **269**, 4948 (2002).
9. M. M. Mohammad, K. R. Howard, L. Movileanu, *Journal of Biological Chemistry*.
10. M. M. Mohammad *et al.*, *Journal of the American Chemical Society* **134**, 9521 (2012).
11. J. H. Kleinschmidt, L. K. Tamm, *Biochemistry* **38**, 4996 (1999).
12. Mohammad M. Mohammad, Liviu Movileanu, *Methods in Molecular Biology* **870**, 21 (2012).
13. R. G. A. Jones, J. Landon, *Journal of Immunological Methods* **263**, 57 (2002).
14. A. R. Hall *et al.*, *Nature Nanotechnology* **5**, 874 (2010).

Crosstalk between *Helicobacter pylori* and Host Cells

Hitomi Mimuro

Division of Bacteriology, Department of Infectious Diseases Control, International Research Center for Infectious Diseases, Institute of Medical Science, The University of Tokyo
4-6-1, Shirokanedai, Minato-ku, Tokyo 108-8639, Japan
mim@ims.u-tokyo.ac.jp

ABSTRACT

Persistent colonization of the gastric mucosa by *Helicobacter pylori* elicits chronic inflammation and aberrant epithelial cell proliferation, which increase the risk of gastric diseases such as gastritis, ulcers, and gastric cancer. In this session, I would like to summarize recent our findings of how *H. pylori* functionally interact with gastric epithelial cells as well as Peyer's patches within the intestine, and how *H. pylori* establish long-term colonization in host stomach and contribute to the pathogenesis.

1. Outline

Persistent colonization of the gastric mucosa by *Helicobacter pylori* elicits chronic inflammation and aberrant epithelial cell proliferation, which increase the risk of gastric diseases such as gastritis, ulcers, and gastric cancer.

More virulent *H. pylori* isolates harbors numerous bacterial outer membrane proteins adhesins and *cag* (cytotoxin-associated genes) pathogenicity island encoding a type IV secretion system (TFSS) (Fig. 1 and Fig. 2). The adhesins establish bacterial contact with the surface of host epithelial cells, and the TFSS represents a needle-like pilus apparatus for the delivery of bacterial effector protein CagA into host epithelial cells. The intracellular CagA proteins alter several intracellular regulatory cascades that, in turn impact on cell structure and cell fate in ways that ultimately contribute to overt disease.

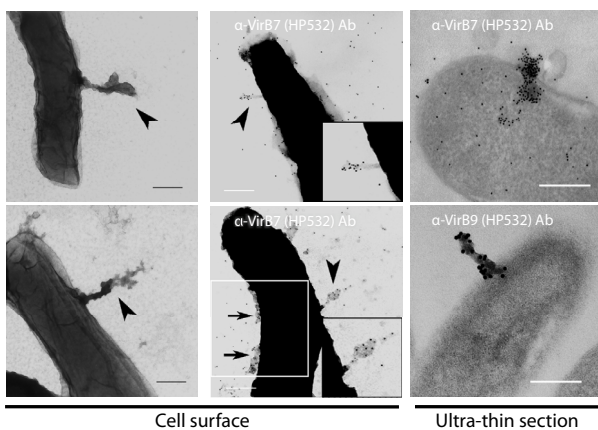


Fig. 1 Immunoelectron micrographs of *H. pylori* Type IV secretion system. (T. Tanaka, et. al., Cell Microbiol, 2003)

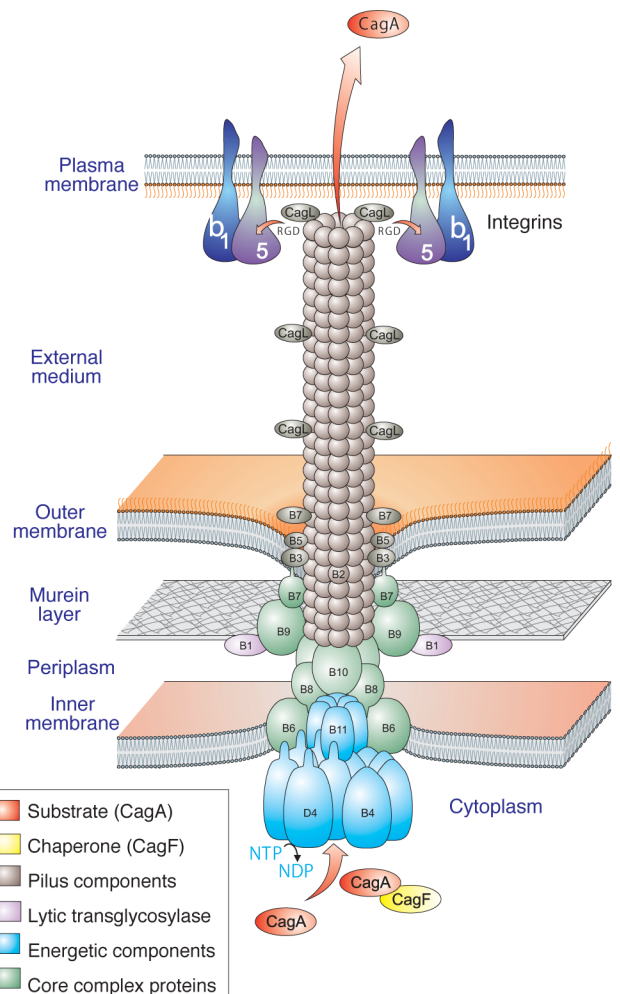


Fig. 2 Schematic model structure of *H. pylori* Type IV secretion system. (Modified from S. Backert, H. Mimuro, et al., in "Helicobacter pylori in the 21st Century, Advances in Molecular and Cellular Microbiology 17", 2011)

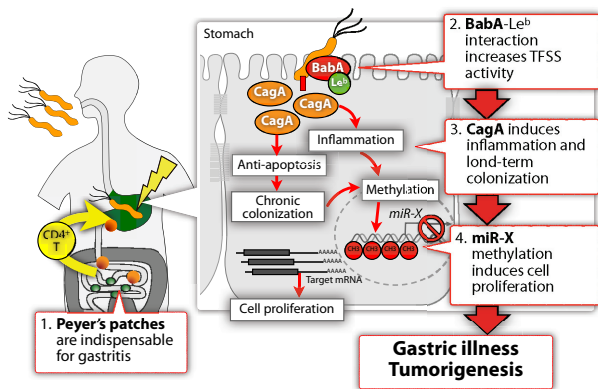


Fig. 3 The overall control of host cell responses by *H. pylori* infection.

2. Conclusions

In this session, I would like to summarize recent our findings of how *H. pylori* functionally interact with gastric epithelial cells as well as Peyer's patches within the intestine, and how *H. pylori* establish long-term colonization in host stomach and contribute to the pathogenesis (Fig. 3).

3. Acknowledgements

The author would like to thank Kotaro Kiga, Masato Suzuki, Nozomi Ishijima, Toshihiko Suzuki, Shigenori Nagai, Aya Shinozaki, Rainer Haas, Thomas Borén, Douglas E. Berg, Shigeo Koyasu, Takeshi Nagai, Yukihiko Fujita, Yusuke Ichikawa, Kanna Nagamatsu, Jiro Tanaka, Momoyo Asahi, Taira Kobayashi, Takahito Sanada, Hiroshi Ashida, Yumi Kanegae, Izumu Saito, Minsoo Kim, Michinaga Ogawa, Yuka Watanabe, Hiroyuki Kayo, Yoko Fukuda, Hiroki Iwai, Teruo Kirikae, Masashi Fukayama, Taro Fukao, Dangeruta Kersulyte, Jaime Cok, Catherine C. Hooper, Shiho Suzuki, Masaaki Oyama, Hiroko Kozuka-Hata, Shigeru Kamiya, Quan-Ming Zou, Robert H. Gilman, Gabriele Rieder, and all members of the Sasakawa and the Mimuro laboratories. The author also would like to express special thanks to Chihiro Sasakawa.

References

- [1] H. Mimuro, et al., *Mol Cell*, **10** (2002), 745.
- [2] J. Tanaka, et al., *Cell Microbiol.*, **5** (2003), 395.
- [3] S. Nagai, et al., *Proc. Natl. Acad. Sci. USA*, **104** (2007), 897.
- [4] H. Mimuro, et al., *Cell Host Microbe.*, **2** (2007), 250.
- [5] H. Mimuro, et al., *Bioessays*, **30** (2008), 515.
- [6] N. Ishijima, et al., *J. Biol. Chem.*, **286** (2011), 25256.

OS10: Thermal-Fluid Flows and Plasma Physics

Heat Transfer Performance Of HFO-1234yf - A Quick Overview

Chi-Chuan Wang

Department of Mechanical Engineering, National Chiao Tung University

E-mail: ccwang@mail.nctu.edu.tw

ABSTRACT

This study provides an overview about the two-phase heat transfer performance for HFO-1234yf which is made to substitute R-134a. Based on the limited information, it is found that the nucleate boiling heat transfer coefficient (HTC) and convective boiling HTC for HFO-1234yf are comparable to R-134a provided $q < 200 \text{ kW m}^{-2}$. For external condensation, the only database shows that the HTC between HFO-1234yf and R-134a is also negligible. For in-tube condensation, it is found that the condensation HTCs for HFO-1234yf are inferior to those of R-134a, and the difference increases with the rise of vapor quality.

1. Introduction

Vehicle air conditioning is a significant and growing source of greenhouse gas (GHG) pollution. At present stage, most mobile air conditioning (MAC) systems use R-134a as the working fluid whose 100-yr global warming potential (GWP) is as high as 1,430 and MAC is the largest and most emissive sales market for R-134a (Papasavva et al. [1]). As a result, efforts were made to search for new refrigerants that is environmentally benign and can be used to globally replace refrigerants used in future mobile (cars and light trucks) air conditioning systems. Among the candidates, HFO-1234yf is regarded as the promising candidate for its GWP is as low as 4. The thermophysical properties, cycle performance, and two-phase heat transfer performance of HFO-1234yf are the key parameters to estimate the feasibility of using this new refrigerant in mobile air conditioners. The thermophysical properties of refrigerant mixture were reported to be similar to those of R-134a (Arakawa et al., [2]), thereby offering an opportunity as a drop-in solution for current mobile air conditioners. Normally a drop-in solution yields a lower system performance for lacking optimization. For instance, Lee and Jung [3] had shown that the coefficient of performance and capacity of HFO-1234yf are up to 2.7% and 4.0% lower than those of R-134a, respectively during a typical drop-in experiment. The compressor discharge temperature and amount of charge of HFO-1234yf are 6.5°C and 10% lower than those of R-134a.

Until now, only very limited information associated with the two-phase heat transfer characteristics as far as HFO-1234yf are concerned. The only published literatures regarding to the two-phase flow characteristics are from Moreno et al. [4] and Park and Jung [5] concerning nucleate boiling, Park et al. [6] for external condensation, Saitoh et al. [7] regarding to in-tube evaporation, Padilla et al. [8] in association with two-phase flow pattern, and Col et al. [9] for in-tube condensation. The following is a brief summary and discussion from the aforementioned results associated with R-134a counterpart.

2. Heat Transfer Performance for HFO-1234yf

2.1 Results for nucleate boiling

Moreno et al. [4] conducted pool boiling experiments for HFO-1234yf and R-134a at system

pressures ranging from 0.7 to 1.7 MPa using horizontally oriented 1 cm^2 heat sources. The test surfaces include a plain and microporous surfaces. And it shows that the boiling heat transfer coefficients of HFO-1234yf and R-134a are nearly identical at lower heat fluxes ($q < 200 \text{ kW m}^{-2}$) while HFO-1234yf yielded lower heat transfer coefficients at higher heat fluxes and lower critical heat flux (CHF) as compared with R-134a.

It is often recognized that three mechanisms, namely bubble agitation, vapor-liquid change phenomenon, and evaporation are associated with basic mechanisms of the nucleate boiling heat transfer (Thome, [10]). As shown by Akasaka et al. [2] and Tanaka et al. [11], the HFO-1234yf has a higher reduced pressure at the same saturation temperature. This is because its critical pressure is about 17% lower than of R-134a. In fact, at a saturation temperature of 40 °C the reduced pressure p^* is approximately 20% higher than that of R-134a, thereby leading to a larger activation sites that would boost the heat transfer coefficient.

2.2 Results of external condensation

Park et al. [6] conducted experiments concerning external condensation experiments for plain, low fin, and Turbo-C tubes at a saturated vapor temperature of 39 °C with the wall subcooling ranging from 3 to 8 °C. Test results show that the condensation HTCs of HFO-1234yf are very similar to those of R-134a for all three surfaces tested. At first glance, it seems that the condensation HTCs for HFO-1234yf is also identical to that of R-134 as nucleate boiling. However, the authors also made comparisons (smooth tube) with their condensation HTCs against the well accepted Nusselt's equation.

Their comparison revealed that the measured data for R-134a and HFO-1234yf were 9.0% and 27.1% larger than the predicted values. They argued that the relatively large deviation associated with HFO-1234yf were from the large uncertainties of various properties of HFO-1234yf. A similar calculation was made by the present author for plain tube with $d_o = 19.05 \text{ mm}$ and $T_w = 20 \text{ °C}$. The calculated results show that the condensation HTCs for R-134a are much higher than that of HFO-1234yf (around 30~60%). It is not totally clear why the tested condensation HTC for R-134a and HFO-1234yf (Park et al. [6]) are comparable for all the

test tubes at the same condensation temperature. One of the possible reasons may be associated the large uncertainty of their measurements. This is because their test tube is quite short and the acquired heat transfer rate (temperature difference subtracted from the inlet and outlet of cooling water) and temperature difference between the surface and saturation temperature ($T_s - T_w$) are comparatively small. This is especially pronounced when enhanced tubes (low fin and turbo C) were used. In addition to the uncertainty, another possible explanation may be attributed to their relative short test length ($L = 290$ mm) which may cause some end effect (lateral conduction from the test tube to the flange) that inevitably promotes condensation. Note that most of properties influencing the condensation HTC suggest a lower condensation HTC of HFO-1234yf.

2.3 Results of in-tube evaporation

Saitoh et al. [7] conducted study for boiling heat transfer of the refrigerant HFO-1234yf flowing in a smooth small-diameter horizontal tube. The test tube was heated by direct electrification using a DC power supply connected to two electrodes soldered at the flanges of the two ends of the test tube. Their experimental conditions are $T_s = 15$ °C, $q = 6\sim 24$ kW/m², and $G = 100 \sim 400$ kg/m²s. At the lowest heat flux of 6 kW/m², the measured heat transfer coefficient increased with the vapor quality, showing that the convective heat transfer intensifies with increasing quality. The dryout quality was about 0.8 and did not change with heat flux. Increasing the heat flux from 6 kW/m² to 12 and 24 kW/m² showed that the heat transfer coefficient increases with heat flux at low vapor quality; thus, nucleate boiling is the dominant heat transfer coefficient mechanism at low vapor quality. On the other hand, the detectable rise of HTC (heat transfer coefficient) vs. vapor quality for a low heat flux of 6 kW/m² is associated with the change of flow pattern since annular flow may prevail at high quality region. However, as claimed by the authors who argues that nucleate boiling is dominant heat transfer process when $q = 12$ and 24 kW/m², thereby showing a moderate change of HTC as vapor quality is increased. This seems feasible but the relative effect of heat flux, based on the test results of Saitoh et al. [7], is in fact much lower. A rough estimation of the heat flux dependency is about $q^{0.42}$ which is generally much lower than the pure nucleate boiling where $h \sim q^{0.6-0.7}$. In this sense, it is expected that convective evaporation still plays certain role rather than pure nucleate boiling.

2.4 In-tube condensation

Col et al. [9] conducted experiments for measurement of local heat transfer coefficients during condensation of HFO-1234yf within a single circular 0.96 mm diameter microchannel at 40 °C saturation temperature and compares them to the ones of R-134a. Condensation tests are carried out at mass fluxes ranging between 200 and 1000 kg/m²s. They reported sufficient heat transfer deterioration for the HFO-1234yf

as compared to the ones of R-134a. Except for the lowest values of vapor quality, R-134a displays a heat transfer coefficient higher than HFO-1234yf for all three values of mass velocities. At a mass flux of 200 kg/m²s, the heat transfer coefficient of HFO-1234yf is lower than that of R-134a by 15% at 0.4 vapor quality and by 30% at 0.8 vapor quality. One of the explanations about the pronounced difference in HTC between HFO-1234yf and R-134a at a higher vapor quality region is due to film thickness on the periphery. Notice that at higher vapor quality regime the annular flow prevails. On the other hand, the liquid density for R-134a is about 11% higher than that of HFO-1234yf. This implies a thinner film thickness of R-134a provided the vapor quality is the same, thereby leading to a higher HTC for R-134a.

3. Concluding remarks

This short overview gives the heat transfer performance for refrigerant HFO-1234yf which is made to substitute R-134a. At present, the associated studies concerning the heat transfer performance is still limited. However, based on the limited information, the associated comparison of heat transfer performance, including nucleate boiling, in-tube convective evaporation, external condensation, in-tube condensation, and flow pattern, between HFO-1234yf and R-134a is made in the brief overview, it is found the HTC deviates mainly in the condensation regime.

4. Acknowledgements

The author would like to express gratitude for supporting funding from the National Science Council of Taiwan (100-2221-E-009-087-MY3).

References

- [1] S. Papasavva, D.J. Luceken, R.L. Waterland RL, K.N. Taddonio, S.O. Andersen. *Env. Sci. & Tech.* **43** (2009) 9252.
- [2] R. Akasaka, K. Tanaka, Y. Higashi, *Int. J. Refrig.* **33** (2010), 52.
- [3] Y. Lee, D. Jung, *App. Ther. Engng.* **35** (2012); 240.
- [4] G. Moreno, S. Narumanchi, C. King. *Proceedings of the ASME 2011 International Mechanical Engineering Congress & Exposition IMECE2011 November 11-17, 2011, Denver, Colorado, USA, paper no. IMECE2011-64002.*
- [5] K.J. Park, D. Jung, *Int. J. Refrig.* **33** (2010) 553.
- [6] K.J. Park, D.G. Kang, D. Jung. *Int. J. Refrig.* **34** (2011) 317.
- [7] S. Saitoh, C. Dang, Y. Nakamura, E. Hihara, *Int. J. Refrig.* **34** (2011) 1846.
- [8] M. Padilla, R. Revellin, P. Haberschill, A. Bensafi, J. Bonjour. *Exp. Ther. Fluid Sci.* **35** (2011) 1113.
- [9] D.D. Col, D. Torresin, A. Cavallini. *Int. J. Refrig.* **33** (2010) 1307.
- [10] J. Thome, *Wolverine Engineering Data book III, chapter 9.*
- [11] K. Tanaka, Y. Higashi, *Int. J. Refrig.* **33** (2010); 474.

Outflow Boundary Condition Ensuring Mass Conservation in Finite Volume Method and its Application to Incompressible Unsteady-state Reactive Thermal Fluid Flow Computation

Sohey Nozawa, Yohsuke Matsushita
Research and Education Center of Carbon Resources, Kyushu University
6-1 Kasuga-koen, Kasuga, Fukuoka 816-8580, Japan
matsushita@cm.kyushu-u.ac.jp

ABSTRACT

This paper presents the application of the outflow boundary condition ensuring mass conservation in Finite Volume Method (FVM) to the incompressible unsteady-state reactive thermal fluid flow computation using unstructured grid. The concept is to satisfy the mass flow rate between the inflow and the outflow boundary conditions exactly and the summation of the transient terms in the whole of the computational domain. When the outflow boundary condition is applied to the reactive thermal fluid flow calculation, the stable, robust and high accuracy in the mass conservation are obtained.

1. Introduction

The boundary conditions such as the wall, inflow, and outflow boundary conditions are important in the fluid flow computations since they usually determine the numerical results. When we consider the mass conservation, the inflow and outflow boundary conditions should be prescribed carefully. Therefore, Matsushita *et al.* propose the outflow boundary condition in Finite Volume Method (FVM) for steady-state, variable density, incompressible fluid flow, which ensures the mass conservation exactly between inflow and outflow boundaries [1]. In previous studies of author's group, it is extended to the unsteady-state, variable density, incompressible fluid flow computations and applied to the structured (Staggered grid [2], Co-located grid [3]) grid and unstructured grid [4]. Aforementioned outflow boundary condition is expected to be applicable in incompressible reactive thermal fluid flow computation, since it is a typical example of variable density, incompressible thermal fluid flow.

In this study, the outflow boundary conditions are applied to incompressible unsteady-state reactive thermal fluid flow computation using unstructured grid and the accuracy of the mass conservation and the stability of the calculation are discussed.

2. Outflow boundary condition

The unsteady-state continuity equation with variable density, Eq. (1) can be discretized as Eq. (2).

$$\partial\rho/\partial t + \nabla \cdot (\rho\mathbf{U}) = 0 \quad (1)$$

$$\frac{\rho_p^{n+1} - \rho_p^n}{\Delta t} \Delta V_p + \sum (\mathbf{A} \cdot \rho\mathbf{U})_f = 0 \quad (2)$$

The summation of the discretized continuity equation with inflow and outflow boundaries for all cells in the computational domain yields the following equation,

$$u_o \cong \dot{u}_o + \frac{F_1 - F_o - \sum \frac{\rho_p^{n+1} - \rho_p^n}{\Delta t} \Delta V_p}{\sum \rho A|_o} \quad (3)$$

where \dot{u}_o is the velocity on the outflow boundary obtained by applying Neumann condition for the solution of discretized momentum equation. The second term corrects the mass imbalance between the mass flow rate through the inflow and the outflow boundary, and becomes sufficient small when the convergence is

obtained. If the second term is removed, Eq. (3) becomes the outflow boundary condition for the steady-state calculation. This outflow boundary condition ensures the mass balance of the mass flow rate through the inflow and the outflow boundary condition and all of the transient terms in the computational domain corresponding to the continuity equation used in SIMPLE algorithm. By applying the outflow boundary condition as a part of SIMPLE calculation procedure, the stable, robust, and high accuracy in the mass conservation in unreactive thermal fluid flow has already presented in previous studies.

3. Mathematical models, numerical schemes and solutions

To demonstrate the validity of the outflow boundary condition, coaxial jet combustor is considered [5]. The computational grid is shown in Fig. 1.

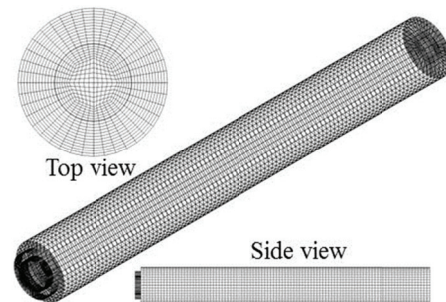
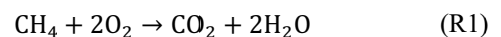


Fig. 1 Computational grid

The fuel used in the experiment was natural gas but for the present study is assumed to be pure methane. The following one step, overall reaction (R1) is considered as the combustion reaction.



Standard $k-\varepsilon$ two-equation model is employed to describe the turbulence flow. Wall function and Pee function are used with the turbulence model to estimate the share stress and the convective heat transfer coefficient on the wall boundary. Eddy Dissipation Concept (EDC) is used to estimate the chemical reaction rate. P-1 method and Weighted Sum of Gray Gasses (WSGG) model are used to estimate the radiative heat transfer and its absorption coefficient. The governing equations for mass, momentum, enthalpy, kinetic energy

of turbulence and its dissipation rate, and chemical species are discretized by FVM, with the unstructured grid. Fluid density is evaluated by the ideal gas equation with respect to temperature. The hybrid method and Euler's implicit method are used as the discretization schemes for the space, convection and, diffusion terms and for the time and transient term, respectively. The SIMPLE is chosen to execute the pressure and velocity field calculations. The discretized equations are iteratively solved by the Bi-Conjugate Gradient Stabilized (BiCGStab) method, with the polynomial preconditioning until the convergence is obtained for every time steps. Note that the under-relaxation method is used for the iterative calculation.

4. Results and Discussion

The residual histories for the iterations of the continuity equation with the outflow boundary conditions for the steady-state and unsteady-state calculations are shown in Fig. 2. In case of the boundary condition for the steady-state, result for first step ($t = \Delta t$) is shown, and for the unsteady-state, results for first and second step ($t = \Delta t, 2\Delta t$) are shown. The converged solution is obtained with the boundary condition for the unsteady-state calculation in both of first and second step. This fact indicates to satisfy the continuity equation with high accuracy. On the other hand, the converged solution cannot be obtained with the outflow boundary condition for the steady-state calculations even if under-relaxation factors are changed, because of the unsuitable outflow boundary condition.

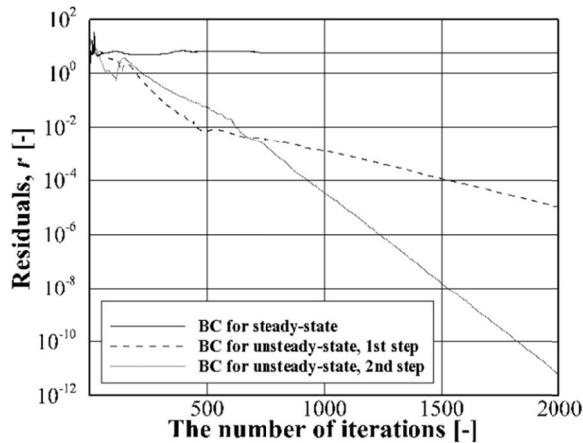


Fig. 2 Residual history for the iterations

In the initial conditions of present calculation, the fluid flow is stationary state. The evolution of the unsteady-state flow field and ignition of the temperature field from a stationary state cannot be reproduced with the outflow boundary condition for the steady-state calculations even if under-relaxation factors are changed. On the other hand, the evolution of the unsteady-state flow field and the ignition of the temperature field from a stationary state are reproduced with the outflow boundary condition for the unsteady-state calculation as shown in Fig. 3, due to the residuals decreases rapidly and the convergence solution with high accuracy is obtained.

4. Concluding remarks

In this study, the outflow boundary conditions are applied incompressible unsteady-state reactive thermal fluid flow computation using unstructured grid.

When the outflow boundary condition ensuring mass conservation is applied to the reactive thermal fluid flow calculation, the stable, robust and high accuracy in the continuity equation is obtained. Therefore, the effectiveness of the boundary condition ensuring mass conservation to the reactive thermal fluid flow computation is indicated.

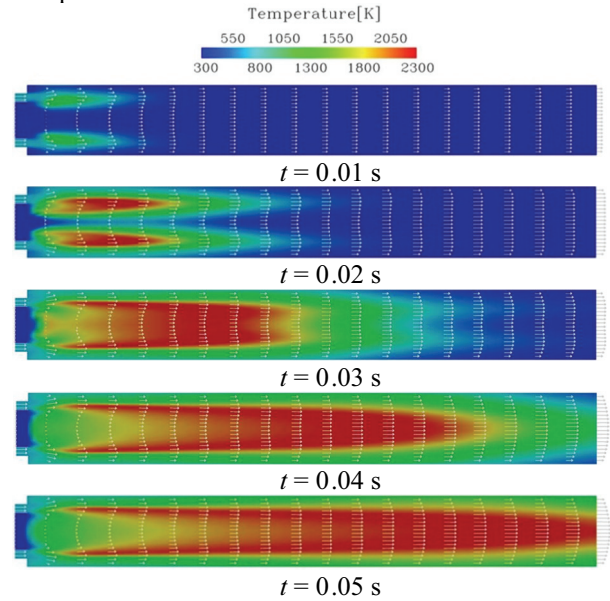


Fig. 3 Fluid flow and temperature field in the computational domain

Nomenclature

A	cell face area	[m ²]
F	mass flow rate	[kg/s]
u	velocity component	[m/s]
x	coordinate	[m]
	Greek symbols	
ρ	fluid density	[kg/m ³]
Δt	time step	[s]
ΔV	cell volume	[m ³]
	Subscripts	
I	inflow boundary	
O	outflow boundary	
P	present cell	
	Superscript	
n	time level	

References

- [1] Y. Matsushita *et al.*, The 42th National Heat Transfer Symposium, (2005), H224.
- [2] Y. Matsushita, Computational Thermal Science, **3**, (2011), pp. 531-537.
- [3] S. Nozawa *et al.*, SCEJ 43rd Autumn meeting, (2011), G115.
- [4] S. Nozawa *et al.*, The 7th International Conference on Flow Dynamics, (2011), OS7-13.
- [5] F. K. Owen *et al.*, Symp. (Int.) on Combust., **16**, (1976), pp. 105-117.

Numerical Simulation of Unexposed Temperature and Deformation for Fire Door

San-Yih Lin^{* **} and Chong-Wei Ho^{*}

^{*} Department of Aeronautics and Astronautics, National Cheng Kung University, Tainan, Taiwan

^{**} Fire Protection and Safety Research Center, National Cheng Kung University, Tainan, Taiwan

E-mail: sylin@mail.ncku.edu.tw

ABSTRACT

This paper is to investigate the unexposed temperature distribution and deformation of a standard fire safety door in a furnace under a given elevated temperature curve by numerical simulations. The finite element method by the software ANSYS is used for the numerical simulation tool. The unexposed temperature distribution and deformation of a steel fire door heated in the furnace is simulated. The numerical results are compared with the experimental data performed by the Fire Protection and Safety Research Center, National Cheng Kung University.

1. Introduction

The thermal resistance and deformation of a fire door are two important issues for a fire door. Liew et al.[1] proposed a finite element method for studying the large-displacement inelastic behavior of building frames subjected to the standard time-temperature curve ISO 834-1 [2]. Zhao and Shen [3] investigated the deformation behavior of unprotected steel framed structures exposed to the real fire condition. Zhao [4] used a finite element method to predict the nonlinear behavior of steel frames at a given elevated temperature curve. In this study, results from a standard fire endurance test and from a numerical model by the commercial finite element software ANSYS are compared.

2. Method

The governing equation for the thermal analysis of fire doors exposed to high temperatures is presented by the three-dimensional heat diffusion equation:

$$\rho c \frac{\partial T}{\partial t} = \frac{\partial}{\partial x} \left(k \frac{\partial T}{\partial x} \right) + \frac{\partial}{\partial y} \left(k \frac{\partial T}{\partial y} \right) + \frac{\partial}{\partial z} \left(k \frac{\partial T}{\partial z} \right) \quad (1)$$

where ρ, T, k , and c are density, temperature, thermal conductivity, and specific heat, respectively.

The boundary condition on the exposed side can be given as:

$$\dot{Q} = \dot{Q}_{conv} + \dot{Q}_{rad} = (h + h_r) A_s (T_\infty - T_s) \quad (2)$$

where $\dot{Q}, h, h_r, A_s, T_s$ and T_∞ are heat transform rate, heat convection coefficient, radiation heat convection coefficient, surface area, surface temperature, and CNS11227 elevated temperature, respectively.

$$h_r = \varepsilon \sigma (T_\infty + T_s)(T_\infty^2 + T_s^2), \sigma = 5.67 \times 10^{-8} \quad (3)$$

where ε and σ are radiation emissivity and Stefan-Boltzmann number, respectively. Similar to the boundary condition on the unexposed side, except $T_\infty = 30^\circ C$. This is the ambient temperature at the test. The boundary conditions on the other four sides of the steel fire door are simplified as the adiabatic boundary condition.

The deformation is very important about fire doors. because every materials has different expansion or contraction rate. In the finite element method,

Elements of the relationship between displacement and thermal load can be expressed as:

$$[k_e] \{u\} = \{F_e^{th}\} \quad (4)$$

where $[k_e]$ is stiffness matrix, $\{u\}$ is displacement vector and $\{F_e^{th}\}$ is thermal load vector. The thermal load vector can be written as an integral vector form, as:

$$\{F_e^{th}\} = \int_{vol} [B]^T [D] [\varepsilon^{th}] d(vol) \quad (5)$$

where $[B]$ is strain-displacement matrix, $[D]$ is material matrix and $[\varepsilon^{th}]$ is thermal strain vector.

$$[\varepsilon^{th}] = \Delta T [\alpha_x \quad \alpha_y \quad \alpha_z \quad 0 \quad 0 \quad 0]^T \quad (6)$$

Therefore, If we has the coefficient of thermal expansion (α), the Young's modulus (E), Poisson ratio (ν), we can obtain static deformation of each element node by Eqs. (4)-(6).

On the part of thermal analysis, the thermal elements such as Solid 87 and Solid 90 are used. Since the effects of convection and radiation on the door surface are considered, the element Surf152 is also used on the panels facing the furnace. In the structural analysis, the structural elements such as Solid 186 and Solid 187 are used.

3. Results and Discussions

A steel fire safety door has the dimensions of 1.080m width, 2.00m height, and 64mm depth. It is consisted of Galvanized steel board, Magnesium oxide board, Perlite board, Ceramic fiber, and Iron. The hardware fittings of the door include of lock, tamper latch, and hinge. We investigate the unexposed temperature distribution and deformation under two-hour heating with the UL10C time-dependent elevated temperature curve.

Fig.1 shows the temperature and deflection measurement locations on the unexposed side, T11~T15 are for temperature measurement, and D1~D8 are for deflection measurement. Fig.2 shows the comparisons of the unexposed temperature histories at the measurement positions. The position of the highest

temperature situates at the door edge where means the location of steel skeleton. The steel skeleton is composed of galvanized steel board and steel and the heat can transfer effectively from the exposed side to the unexposed side by mechanism due to the galvanized steel board and steel are thermal conductivity well. The temperature around the lock is slightly lower than the steel skeleton. This is due to the surface of the steel coated by MgO board and ceramic fiber which will decrease the heat transfer rate. According to the result of simulation, the temperature at the region of gauging point is approximately 99°C , and the experimental value is approximately 96°C , both the results are well matched. Also, one can see that the temperature from the experiment data is raised rapidly from 2000 seconds to 2500 seconds. We guess this is due to chemical reaction since the sandwich board and laminated plank in the door are belonged to the chemical composite insulation material. In this study, the chemical reaction is not considered in this simulation. After 2500 seconds, the good comparisons between experiment data and numerical results are presented.

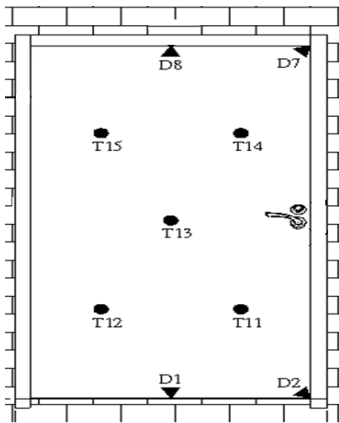


Fig 1: Unexposed side temperature and deflection measure locations.

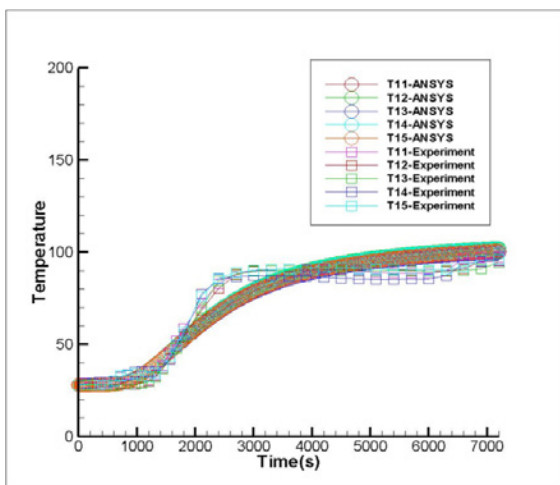


Fig 2: The comparisons of the unexposed temperature histories on the measurement positions.

About the deformation simulation, Table 1 shows the comparison of the numerical and experimental data. One can see that deformations at D7 and D8 are greater than those at D1 and D2 since the constraint area at the upper location of the door is greater than that at the lower location. The numerical results at D1, D7 and D8 are compared well with the experimental data. Also, the experimental data at D2 is unusual, which might be due to the construction mistake.

Table 1: Comparison of the deformation between experimental and numerical data.

	Experiment(mm)	ANSYS (mm)
D1	0.3	0.2135
D2	9.2	0.5871
D7	1.5	1.1315
D8	1.9	1.1521

4. Concluding remarks

The numerical results indicate that the finite element software has a good performance in the temperature distribution and deformation prediction. Using the finite element method to predict the unexposed temperature and deformation of the fire safety door can provide the suggestion to the door designer to prevent the waste of the test resources and costs.

Acknowledgements

The authors wish to extend their appreciation for the supports awarded by the National Science Council of the Republic of China under the contact NSC 100-2221-E-006-106 and by the Fire Protection and Safety Research Center, National Cheng Kung University.

References

- [1] Liew J.Y.R., Tang L.K., Holmaas Tore, Choo Y.S., Advanced Analysis for the Assessment of Steel Frames in Fire, Journal of Constructional Steel Research, Vol. 47, pp. 19-45, 1998.
- [2] International Standard ISO 834-1, Fire resistance tests-Elements of building construction-Part 1: General requirements, 1999.
- [3] Zhao, J.C., Shen Z.Y., Experimental Studies of the Behavior of Unprotected Steel Frames in Fire, Journal of Constructional Steel Research, Vol. 50, pp. 137-150, 1999.
- [4] Zhao, J. C., Application of the Direct Iteration Method for Non-linear Analysis of Steel Frames in Fire, Fire Safety Journal, Vol. 35, pp. 241-255, 2000.

Detailed CFD Analysis of Convective Heat Transfer of Alumina Nanofluid in Subchannel Geometry

Mohammad Nazifard^{1,2,3}, M.R. Nematollahi¹, K. Jafarpour¹, K.Y. Suh^{*2,3}

¹School of Mechanical Engineering, Shiraz University, Shiraz, Iran

²Department of Energy Systems Engineering, Seoul National University

³PHILOSOPHIA, 1 Gwanak Ro, Gwanak Gu, Seoul 151-744, Korea

kysuh@snu.ac.kr

ABSTRACT

This paper is aimed at understanding convective heat transfer of water based alumina (Al_2O_3) nanofluid in a subchannel geometry. The Al_2O_3 /water nanofluid of 1% and 4% by volume has been used for the numerical simulation resorting to the homogenous fluid assumptions with modified thermophysical properties. Results revealed that the heat transfer increases with nanoparticle volume concentrations in the subchannel. The maximum heat transfer enhancement at the center of a subchannel formed by heated rods is 14.97% for the particle volume concentration of 4% corresponding to the Reynolds number of 80,000.

1. Introduction

A novel way to improve the thermal conductivity of a fluid is to suspend nano-sized particles on the order of 1~100 nm with high thermal conductivity in the base fluid with a low thermal conductivity. This paper aims to make a further contribution to nanofluids turbulent convection in a subchannel by numerically studying the developing turbulent forced convection flow of the alumina (Al_2O_3)/water nanofluid in a subchannel of the fusion-fission thorium hybrid reactor.

2. Method

A single subchannel (Fig. 1) of of the fusion-fission thorium hybrid reactor was modeled using the flow symmetry. The computational model geometry and grid were generated using GAMBIT, the preprocessing module for the FLUENT solver [1].

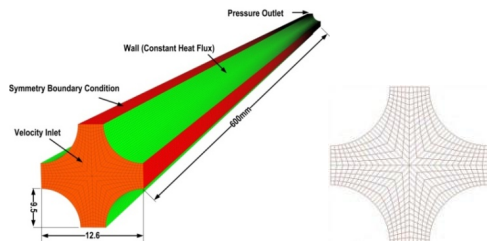


Fig. 1
Computational domain and mesh distribution on channel inlet.

The modeled cases were solved using the ANSYS FLUENT software version 12.1 (ANSYS FLUENT 12.0/12.1 Documentation). The fluid enters with uniform temperature of $T_0 = 293$ K and velocity V_0 profiles at the inlet. At the outlet of the computational model a relative average pressure equaling zero was defined.

The surface of the walls was assumed hydraulically smooth. A constant heat flux $q = 50$ kW/m² was given at the wall. A segregated, implicit solver option was used to solve the governing equations. The first order upwind discrimination scheme was employed for the terms in the energy, momentum, and turbulence parameters.

A standard pressure interpolation scheme and the SIMPLE pressure velocity coupling were implemented.

A residual root-mean-square (RMS) target value of 10^{-5} was defined for the FLUENT simulations. The number of iterations for convergence was 4000 to 5000. The single phase approach was chosen to calculate the thermophysical properties of nanofluids as is widely used in the literature [2-5]. The homogenous mixture was assumed prior to solving the governing equations of continuity, momentum and energy for the single phase fluid flow that the presence of nanoparticles is realized by modifying thermophysical properties of the mixture fluid [2, 3].

Table 1. Equations used to compute Al_2O_3 /water nanofluid thermophysical properties [2]

Property	Equation
Density	$\rho_{nf} = (1 - \varphi)\rho_{bf} + \varphi\rho_p$
Specific heat	$(\rho c_p)_{nf} = (1 - \varphi)(\rho c_p)_{bf} + \varphi(\rho c_p)_p$
Dynamic viscosity	$\mu_{nf} = (123\varphi^2 + 7.3\varphi + 1)\mu_{bf}$
Thermal conductivity	$k_{nf} = (4.97\varphi^2 + 2.72\varphi + 1)k_{bf}$

3. Results and Discussion

Results are reported in terms of the average Nusselt number Nu , convective heat transfer coefficient, as a function of the Reynolds number Re ranging from 20×10^3 to 80×10^3 , and particle volume concentrations of 0%, 1% and 4%.

The local and average heat transfer coefficients are defined as

$$h(z) = \frac{q}{T(z)_w - T(z)_b} \quad (1)$$

$$h_{av} = \frac{1}{L} \int_0^L h(z) dz \quad (2)$$

The average heat transfer coefficient for all the concentrations and considered Re is reported in Fig. 2. Notice the useful contribution to the heat transfer provided by the inclusion of nanoparticles in comparison to the case with the base fluid only. Also note that heat transfer increases with the particles volume concentration and Re . The highest heat transfer rates are identified, for each concentration, at the highest Re .

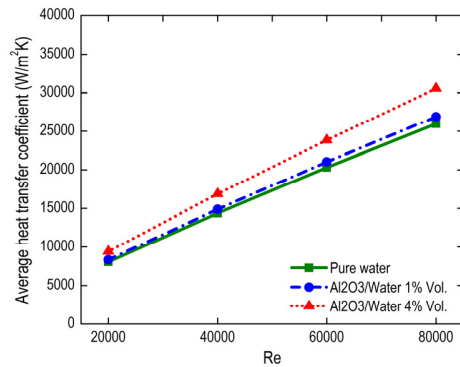


Fig. 2 Average heat transfer coefficient for all concentrations and Re .

The observed increase in heat transfer coefficient could be attributed to improved thermophysical properties of the mixture with respect to the base fluid [2-5]. Thus, a nanofluid with higher thermal conductivity increases the heat transfer along the channel [3]. Moreover, the term $\rho \cdot c_p$ increases, therefore more energy is required to increase the bulk temperature with respect to the case of the base water [2]. However, the difference between the wall and bulk temperatures decreases with respect to the case of the base fluid provoking the increase of the heat transfer coefficient. Earlier studies [2-5] have yet shown that the increase in heat transfer is generally higher than that in the thermophysical properties. The explanations are not convincing enough to enlighten the increase in the heat transfer due to a nanofluid

Fig. 3 demonstrates the average Nu for all the concentrations and Re against the experimental and numerical correlations available in the literature. The ANSYS FLUENT results are compared against the experimental correlations proposed by Pak and Cho [5] and the numerical correlation proposed by Maiga et al. [2]. Bianco et al. [2] reported that the [4] correlation overestimates the values provided by Pak and Cho [5] by about 20% which is clearly shown in Fig. 3. However, this overestimation can be considered acceptable, as reported also by Buongiorno [3]. The Pak and Cho [5] correlation concurs with the FLUENT result at $Re = 20 \times 10^3$, while at higher $Re = 80 \times 10^3$ the Maiga et al. [4] correlation agrees with the FLUENT result.

4. Conclusion

Results showed enhancement of the heat transfer using nanofluid in comparison to the base fluid only. The convective heat transfer as well as the thermal performance factor tends to increase with the increasing Al_2O_3 nanoparticle concentration. The study indicates that the Pak and Cho [5] correlation concurs with the FLUENT result at $Re = 20 \times 10^3$, while at higher $Re = 80 \times 10^3$, the Maiga et al. [4] correlation estimates the result precisely. Albeit the nanofluids may have great potential for enhancing heat transfer, research is in its infancy on the concept, enhancement mechanism, and application of the nanofluids in different industries.

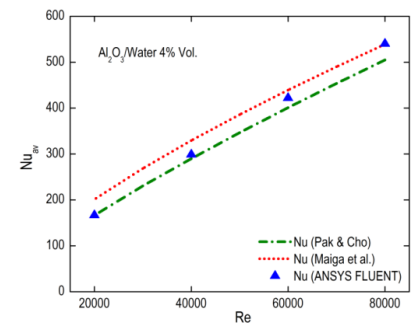
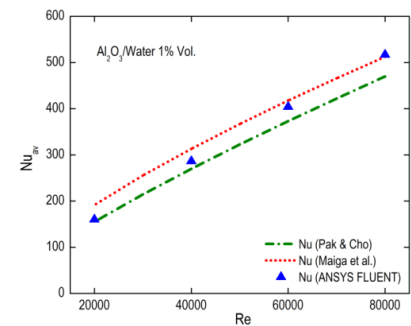
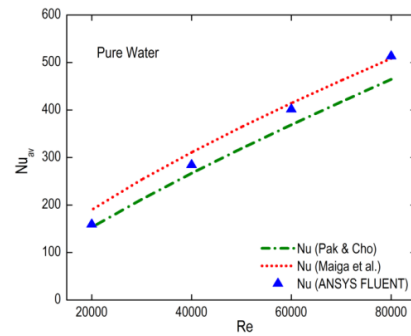


Fig. 3 Comparison of average Nu with the correlations proposed by Maiga et al. [4], and Pak and Cho [5] for (a) pure water, (b) $\phi = 1\%$, (c) $\phi = 4\%$.

Acknowledgements

This work was performed as part of the Basic Science Research Program through National Research Foundation of Korea (NRF) funded by the Ministry of Education, Science and Technology (MEST) (NRF-2011-0000906).

References

- [1] M.R. Nematollahi, M. Nazifi, Energy Convers. Manage., **49** (2008), 1981-1988.
- [2] V. Bianco, O. Manca, S. Nardini, Int. J. Therm. Sci. **50** (2011), 341-349.
- [3] J. Buongiorno, J. Heat Transfer, **128** (2006), 240-250.
- [4] S.E.B. Maiga et al., Int. J. Numer. Methods Heat Fluid Flow, **16** (2006), 275-292.
- [5] B.C. Pak, Y.I. Cho, Exp. Heat Transfer, **11** (1998), 151-170.

Effect of Angled Grooves on Heat Transfer in an Impingement Channel with Crossflow

Yuan-Hsiang Lo, and Yao-Hsien Liu

Department of Mechanical Engineering, National Chiao-Tung University, Hsinchu, Taiwan, 30010

E-mail: yhliu@mail.nctu.edu.tw

ABSTRACT

Transient liquid crystal technology is used for measuring the heat transfer coefficient in the impingement cooling channel. Reynolds numbers are from 2500-7700 and the target surface is roughened with rectangular grooves. These rectangular grooves inclined at an angle of 45° with the exit flow direction, and the jets impinge on the grooves (inline) or between the grooves (staggered). The jet-to-jet spacing is 4 and the jet-to-target plate spacing is 3. Effect of crossflow pushes impinging jets away from the target surface and the heat transfer reduces downstream. When Reynolds number increases, the Nusselt number also increases.

1. Introduction

Lowering the surface temperature with the impingement jet is imperative for cooling of the electronic products, combustion chambers, and turbine blades. Jet impingement cooling technology provides high convective heat transfer by directing the coolant jets on the hot target surfaces. The development of the cross-flow from spent air may reduce the effectiveness of the impinging jets in the multiple jet impingement system [1-3]. Extended studies can be found in the literatures such as the impingement with the elliptic jet arrays [4] and the effect of the film cooling extraction [5]. Heat transfer measurement with liquid crystal can provide detailed distribution on the target surface [6-7]. Lim et al. [8] measured local heat transfer coefficients on a hemi-spherically convex surface and the surface inclined at an angle with a round oblique impinging jet. Jet impingement heat transfer is also influenced by the surface roughness on the target plate. This study investigates the effect of the angled grooves aligned with the jet holes (inline) or between the jet holes (staggered) and the heat transfer variation on the target surface is presented.

2. Method

The schematic of experimental setup is shown in Fig. 1. The flow is provided by a blower and the temperature of the flow is heated and controlled by a pipe heater. A three-way ball valve controls the direction of the inlet flow. This heated air flows into the test section and goes through an orifice plate. This hot impinging jet is directed to the target surface which affects the color of the liquid crystal layer coated on the test plate. A CCD camera takes the image of the reflected color of the liquid crystal. The liquid crystal (R30C5W) is manufactured by Hallcrest Inc. The orifice plate setting between the pressure chamber and impingement channel has an array of 4 by 12 rows of circular holes. The diameter of the jet hole (d) is 0.5 cm and the jet-to-jet spacing (S) is 2 cm. The impingement test section is shown in Fig. 2. The cross sectional areas of the inlet pressure chamber and the impingement chamber are $2\text{ cm} \times 8\text{ cm}$ and $1.5\text{ cm} \times 8\text{ cm}$, respectively. The heights of the pressure chamber and impingement channel are 2 cm and 1.5 cm, respectively. The mainstream temperature during the transient test is measured by the thermocouples installed at the inlet of the pressure

chamber. The target plate has the surface area of $24\text{ cm} \times 8\text{ cm}$. The rectangular grooves on the surface have the width of 0.5 cm and the depth of 0.25 cm. The inline and staggered patterns of the current test are shown in Fig. 3.

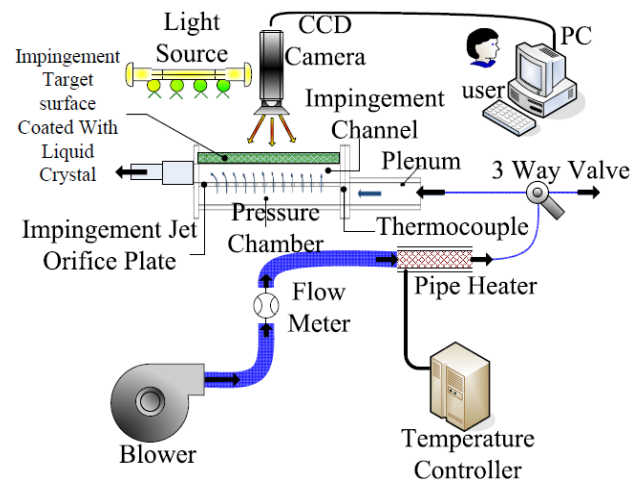


Fig. 1 Schematics of the experimental setup

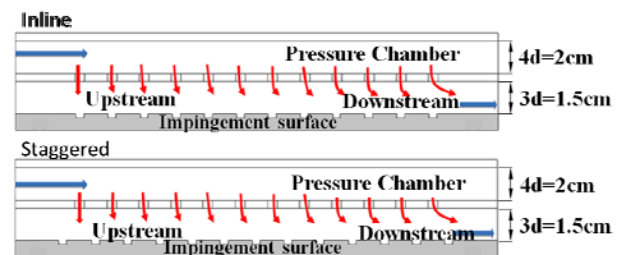


Fig. 2 Impingement test section

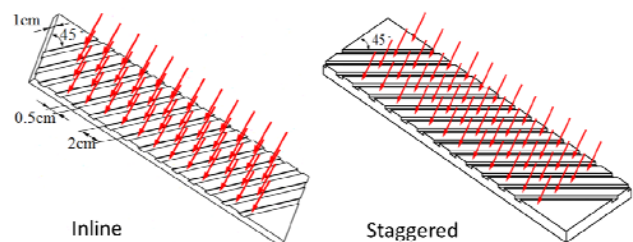


Fig. 3 Inline and stagger of pattern of the current test

A calibration process is performed to obtain the relationship between the color of the liquid crystal and

the corresponding temperature. One-dimensional transient heat conduction equation of the semi-infinite solid is used to obtain the heat transfer coefficient on the test surface. Since the mainstream temperature changes with time, the equation is modified by Duhamel's superposition theorem:

$$T_w - T_i = \sum_{i=1}^N \left\{ 1 - \exp\left(-\frac{h^2 \alpha (t - \tau_j)}{k^2}\right) \operatorname{erfc}\left(\frac{h \sqrt{\alpha (t - \tau_j)}}{k}\right) \right\} [\Delta T_m] \quad (1)$$

where T_w and T_i are the test surface temperature and the initial temperature. τ_j and ΔT_m are the time-step and the change of the mainstream temperature. With the heat transfer coefficient obtained from the above equation, Nusselt number can be calculated:

$$Nu = \frac{hd}{k_a} \quad (2)$$

where k_a is the thermal conductivity of air and d is the diameter of jet hole.

3. Results and Discussion

The experiments test three different Reynolds numbers of 2575, 5150, and 7730. Fig. 4 shows the temperature distribution and the Nusselt number distribution when the impinging jets striking on the angled grooves (inline). The grooves break the impingement jet core the heat transfer reduces inside grooves. The Nusselt number reduces due to the development of the crossflow as the flow moves downstream. The effectiveness of the impingement heat transfer is also reduced. Grooves induce flow recirculation and additional mixing around the grooves. This may hinder the impinging jet and the associated heat transfer decreases. Results also show that the Nusselt number inside grooves is smaller than the areas between the grooves.

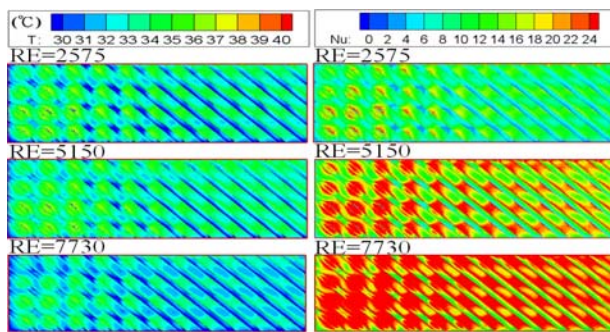


Fig. 4 Nusselt number distribution for the inline case

When the impinging jets striking between the grooves, the Nusselt number distribution is shown in Fig. 5. It produces higher Nusselt number distribution upstream due to impinging jet. It can also be observed that the Nusselt number is smaller inside the grooves. Both cases show that the effect of crossflow is strong downstream and heat transfer reduces.

Span-wise averaged Nusselt numbers along the streamwise direction are plotted in Fig. 6. The local high

heat transfer due to impinging jets can be clearly observed upstream. But the effectiveness of the impinging jet heat transfer also reduces downstream due to crossflow.

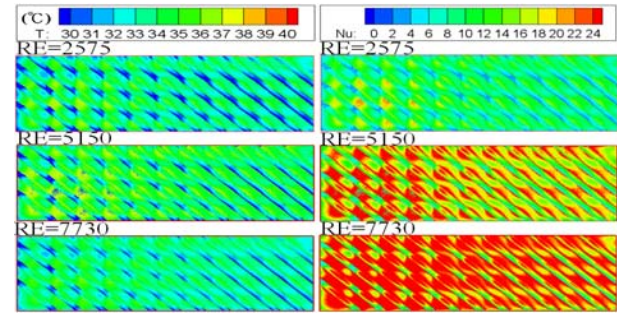


Fig. 5 Nusselt number distribution for the staggered case

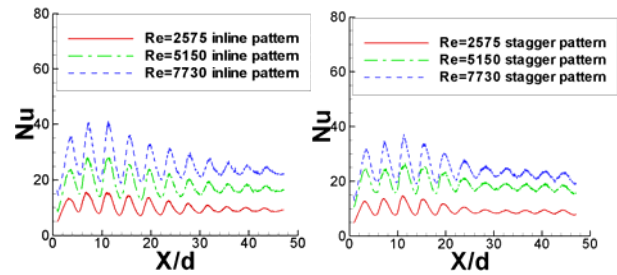


Fig. 6 Span-wise averaged Nusselt numbers

4. Concluding remarks

Impingement heat transfer distributions on a target surface with angled grooves are experimentally measured by the transient liquid crystal technique. The Nusselt number decreases downstream due to crossflow. The inline case shows slightly higher heat transfer than the stagger case near upstream of the channel at higher Reynolds numbers.

5. Acknowledgements

This research has been funded by National Science Council in Taiwan (NSC 100-2221-E-009-100).

References

- [1] R. J. Goldstein, and A. I. Behbahani, *Int. J. of Heat and Mass Trans.*, **25** (1982), pp. 1377-1382.
- [2] L. W. Florschuetz, D. E. Metzger, and C. C. Su, *ASME J. of Heat Trans.*, **106** (1984), pp. 34-41.
- [3] U. Uysal, P. W. Li, and M. K. Chyu, and F. J. Cunha, *ASME J. of Turbomach.*, **128** (2006), pp.158-165.
- [4] W. M. Yan, S. C. Mei, *Int. J. of Heat and Mass Trans.*, **49** (2006), pp. 159-170.
- [5] S. V. Ekkad, Y. Huang, and J. C. Han, *AIAA J. of Thermo. and Heat Trans.*, **13** (1999), pp. 522-528.
- [6] M. Amro, B. Weigand, R. Poser, M. Schnieder, *Int. J. of Thermo. Sci.*, **46** (2007), pp. 491-500.
- [7] B. Facchini, L. Innocenti, M. Surace, *Int. J. of Heat and Mass Trans.*, **49** (2006), pp. 3130-3141.
- [8] K. B. Lim, N. W. Sung, S. H. Lee, *Experimental Thermal and Fluid Science*, **31** (2007), pp. 711-719.

Direct Numerical Simulation of Particulate Flows with Heat Transfer

Xueming Shao, Zhaosheng Yu, Yang Shi

State Key laboratory of Fluid Power Transmission and Control, Department of Mechanics,
Zhejiang University, 310027, Hangzhou, China
E-mail of corresponding author: mecsxm@zju.edu.cn

ABSTRACT

A new method is proposed by combing the fictitious domain (FD) method and the sharp interface (SI) method for the direct numerical simulation of particulate flows with heat transfer in three dimensions. The flow field and particle motion are solved with the FD method. The temperature field is solved in both fluid and solid media with the SI method. The proposed FD/SI method is validated via test problems, and then applied to several typical particulate flows including the rising of spherical catalyst particles in an enclosure. The effects of the thermal conductivity ratio on the particle motion are examined.

1. Introduction

Particulate flows with heat transfer exist widely in both nature and industrial applications. In recent years, the direct numerical simulation(DNS) has become a practical and important tool to probe the mechanism of these complex flows. So far, there have been a variety of the DNS works on general particulate flows. However, there are only limited works on the DNS of the heat transfer between the fluid and freely moving particles.

The aim of the present study is to propose a new DNS method for the particulate flows with heat transfer by combining the direct-forcing fictitious domain (FD) method and the sharp interface (SI) method. The FD method is a non-boundary-fitted method, and has been demonstrated to be a stable and efficient method for the solution of the fluid-solid motion^[1]. The sharp interface (SI) method^[2] was developed to handle the Poisson equation with jump coefficients across the interface. Its main feature is that the jump condition on the interface is used to modify the discretization of the differential operators on the Cartesian grids in the vicinity of the interface, and then the jump condition on the interface is accurately captured^[3].

2. Method

The basic idea of the fictitious domain method is that the interior of particles is filled with the fluid and the inner fictitious fluid is enforced to satisfy the rigid body motion constraint via a pseudo-body force. In this study, the Boussinesq approximation is used to deal with the effect of temperature variation on the flow field. Then, the dimensionless governing equations for the flow field and the particle motion can be written as follows:

$$\frac{\partial \mathbf{u}}{\partial t} + \mathbf{u} \cdot \nabla \mathbf{u} = \frac{\nabla^2 \mathbf{u}}{Re} - \nabla p - \frac{Gr}{Re^2} \bar{T}_f \frac{\mathbf{g}}{g} + \boldsymbol{\lambda} \quad \text{in } \Omega \quad (1)$$

$$\mathbf{u} = \mathbf{U} + \boldsymbol{\omega}_s \times \mathbf{r} \quad \text{in } P \quad (2)$$

$$\nabla \cdot \mathbf{u} = 0 \quad \text{in } \Omega \quad (3)$$

$$(\rho_r - 1) \rho_p^* \left(\frac{d\mathbf{U}}{dt} - Fr \frac{\mathbf{g}}{g} \right) = - \int_p \boldsymbol{\lambda} d\mathbf{x} - \int_p (\rho_r \beta_r - 1) \frac{Gr}{Re^2} \bar{T}_f \frac{\mathbf{g}}{g} d\mathbf{x} \quad (4)$$

$$(\rho_r - 1) \frac{d(\mathbf{J}^* \cdot \boldsymbol{\omega}_s)}{dt} = - \int_p \mathbf{r} \times \boldsymbol{\lambda} d\mathbf{x} - \int_p \mathbf{r} \times \left[(\rho_r \beta_r - 1) \frac{Gr}{Re^2} \bar{T}_f \frac{\mathbf{g}}{g} \right] d\mathbf{x} \quad (5)$$

The dimensionless governing equation for the temperature field is

$$\rho^* c_p^* \left(\frac{\partial \bar{T}}{\partial t} + \mathbf{u} \cdot \nabla \bar{T} \right) = \nabla \cdot \left(\frac{k^*}{Pe} \nabla \bar{T} \right) + \bar{Q} \quad (6)$$

with the following jump conditions on the solid-fluid interface:

$$[\bar{T}]_I = 0 \quad \text{on } \partial P \quad (7)$$

$$\left[k^* \frac{\partial \bar{T}}{\partial \mathbf{n}} \right]_I = 0 \quad \text{on } \partial P \quad (8)$$

We employ the FD method and the SI method to solve the Eqs.(1)~(6), and thus the new proposed method is referred to as FD/SI method.

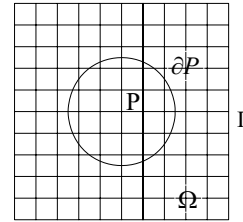


Fig.1 Schematic diagram of the fictitious domain method

3. Results and Discussion

3.1 Natural convection in cavity with fixed particles

The first validation problem is the natural convection in a two dimensional cavity with four fixed particles. The adiabatic boundary condition is imposed on the bottom and top walls of the cavity. On the left and right boundaries, the dimensionless temperatures are fixed to be $T_1 = 1$ and $T_2 = 0$, respectively. We set $k_r = 1$, $Pr = 1$ and $Gr = 1221300$. The steady temperature field obtained with the grid number of 128×128 is shown in Fig. 2. Our values of the Nusselt number Nu are 9.28, 9.35 and 9.36 for the grid number of 128×128 , 256×256 and 512×512 , respectively, and compare favorably with that of Braga and de Lemos^[4] who obtained $Nu = 9.4945$.

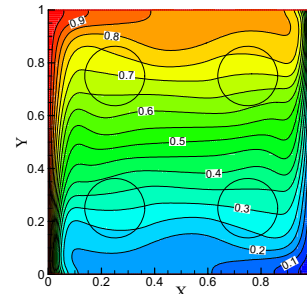


Fig.2 The temperature field at steady-state

3.2 Flow over a cold sphere

The thermal evolution of a fixed cold sphere in a uniform flow was simulated as another test problem. It is shown that the sphere's temperature rises faster for a larger k_r . The rates are roughly the same for $k_r = 100$ and $k_r = 1000$, indicating that the sphere can be considered isothermal for $k_r \geq 100$. We compare our results at $k_r = 1000$ to those of Balachandar and Ha^[5] in Fig. 3. The agreement is favorably good.

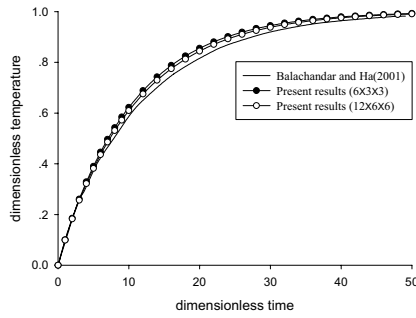


Fig.3 Comparison of the results on the temperature variation of the sphere in a uniform flow.

3.3 Rising of spherical catalyst particles in an enclosure

The proposed FD/SI method was applied to simulate the rising of a single spherical catalyst particle from the center of an enclosure and 500 particles from the bottom. The temperature on the boundaries of the enclosure is fixed, and the heat source is assumed to homogeneous over the particle domain and time.

For the single particle case, the dimensionless size of the enclosure is $8 \times 8 \times 16$, and the parameters are set to be $(Re, \rho_r, Gr, \beta_r, c_{pr}, Pr, Q_s) = (40, 1.1, 1000, 0, 1, 0.7, 1)$, with k_r ranging from 0.1 to 50. The time evolution of the vertical velocity of the spherical catalyst particle at different k_r is shown in fig.4. We see that the particle with a larger thermal conductivity rises faster. The reason is that the enhancement in k_r causes more rapid heat transfer from the solid bulk region to the boundary and then to the fluids, resulting stronger natural convection which is responsible for the rising of the particle. From Fig.4, the effect of the thermal conductivity becomes insignificant for $k_r > 10$, and our result for $k_r = 50$ is in remarkably good agreement with that of Wachs^[6] who employed a finite-element-based fictitious domain method and assumed a homogeneous temperature over the particle domain (a nice approximation for large k_r).

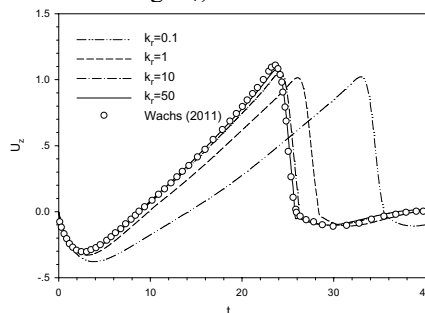


Fig.4 the vertical velocity of the catalyst particle.

For the case of 500 particles, the enclosure dimension is $8 \times 8 \times 32$, and the parameters are set to be $(Re, \rho_r, Gr, \beta_r, c_{pr}, Pr, Q_s) = (40, 1.1, 1000, 0, 1, 0.7, 4.64)$. The rising of catalyst particles was simulated for $k_r = 1$ and $k_r = 50$. The results show that the effects of thermal conductivity on the rising of 500 particles from the bottom are different from the case of a single particle released at the center: at the early stage of the rising ($t < 12$) the effect of k_r on the average particle vertical position is small and at the late stage ($t > 25$), the particles even rise faster for smaller k_r . Fig.5 shows the iso-therms in the center plane and particle distributions at different times during the rising of 500 particles for $k_r = 1$.

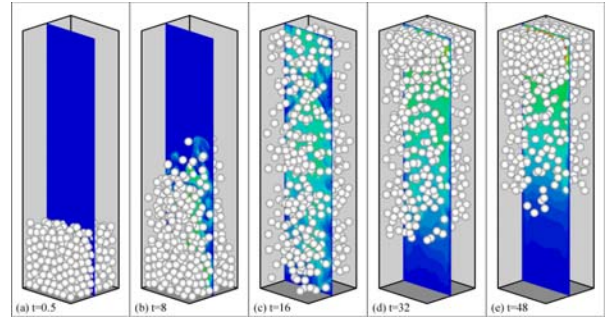


Fig.5 The rising of 500 spherical catalyst particles

4. Concluding remarks

We have presented a new method for the direct numerical simulations of particulate flows with heat transfer in three dimensions. The new method is a combination of the fictitious domain method and the sharp interface method. The accuracy of the proposed method is validated via two test problems: the natural convection in a two dimensional cavity with fixed particles, and the flow around a sphere. The method is then applied to the simulation of the rising of spherical catalyst particles in an enclosure.

Acknowledgements

The work was supported by the National Natural Science Foundation of China (Nos. 11072217, 10872181 and 11132008), and the Program for New Century Excellent Talents in University.

References

- [1] Z. Yu, X. Shao, J. Comput. Phys., **227** (2007), P292-314.
- [2] X.D. Liu, R. P. Fedkiw, M. Kang, J. Comput. Phys., **160** (2000), P151-178.
- [3] H. Liu, S. Krishnan, S. Marella, H. S. Udaykumar, J. Comput. Phys., **210** (2005), P32-54.
- [4] E. J. Braga, M. J.S. de Lemos, Int. Commun. Heat Mass Trans., **32** (2005), P1289-1297.
- [5] S. Balachandar, M. Y. Ha, Phys. Fluids, **13**(2001) , P3714-3728.
- [6] A. Wachs, Comput. Chem. Eng., **35** (2011), P2169-2185.

Transient Liquid Crystal Measurement of Heat Transfer in a Rotating Rectangular Channel with the Entrance Geometry of Sudden Contraction

Ching-Shii Wang, Yu-Shun Lin, Yao-Hsien Liu

Department of Mechanical Engineering, National Chiao-Tung University, Hsinchu, Taiwan, 30010

Email: yhliu@mail.nctu.edu.tw

ABSTRACT

The effect of entrance geometry and rotation number on heat transfer in a rectangular cooling channel (Aspect ratio =2:3) with 45° angled ribs is investigated in this study. Two entrance conditions are considered in this rectangular channel: fully developed and sudden contraction. The rib spacing-to-height ratio (P/e) is 10 and rib height-to-hydraulic diameter ratio (e/D_h) is 0.125. Two Reynolds numbers of 15000 and 25000 are tested, and the rotation number is from 0 to 0.023. Detailed Nusselt number distributions on roughened walls are obtained by transient liquid crystal technique using a stroboscopic light and a digital camera. Results show that the sudden contraction geometry produces higher heat transfer under stationary and rotation conditions.

1. Introduction

The gas turbine inlet temperature keeps increasing to reach the higher efficiency for aircraft engines and power generation. This extremely high temperature may destroy the gas turbine blades and cooling of the engine components is necessary. Heat transfer measurement under rotating condition is very useful for actual applications. Lock et al. [1] uses liquid crystal technique with the stroboscope to obtain the heat transfer on a rotating disk, which models the pre-swirl nozzle system in gas turbines. For internal cooling channel inside turbine blade, effect of entrance geometry on heat transfer under rotating condition is an interesting topic. Wright et al. [2] investigated entrance effects on a 4:1 aspect ratio channel with three entrance geometries: fully-developed, sudden contraction, and sudden partial contraction. Results showed that the entrance effect on heat transfer is more apparent in the smooth channel than the ribbed channel. Liu et al. [3] investigated heat transfer in a 1:4 aspect ratio rectangular channel with the rotation number up to 0.67. They also presented a comparison of the entrance effect on heat transfer with the literature data [4-5]. Entrance geometry of sudden contraction or re-direction has the tendency to enhance heat transfer.

2. Method

The facility and the detailed components for rotating heat transfer research are shown in Fig. 1. A motor is used to drive the rotating shaft and a frequency controller is used to control the rotational speed from 0 to 360 rpm. This rotating shaft connects to a rotating arm with the test section. Heated air entering into the test section is supplied by a compressor. The flow rate is measured by a Tokyo KEISO thermal mass flow meter. A slip-ring, serving as an interface between stationary and rotating components, is used to transfer thermocouple signals. A stroboscope synchronized with the rotating speed of the rotating arm can be used for the CCD camera to record the color change of the liquid crystal under rotating condition.

Fig. 2 shows the rib configuration in the rectangular channel. This test section is manufactured from transparent acrylic material. The channel width and height are 15mm and 10mm, respectively. The heated air

enters a smooth region before it enters the roughened region of the test section. Effect of sudden contraction entrance can be achieved by enlarging the channel height from 10mm to 30mm in the flow entry region, which gives a contraction ratio of 3:1. The square ribs have a cross-section of 1.5mm x 1.5mm. They are put on the leading and trailing surfaces with the angle of attack of 45°. The rib spacing-to-height ratio (P/e) is 10 and rib height-to-hydraulic diameter ratio (e/D_h) is 0.125.

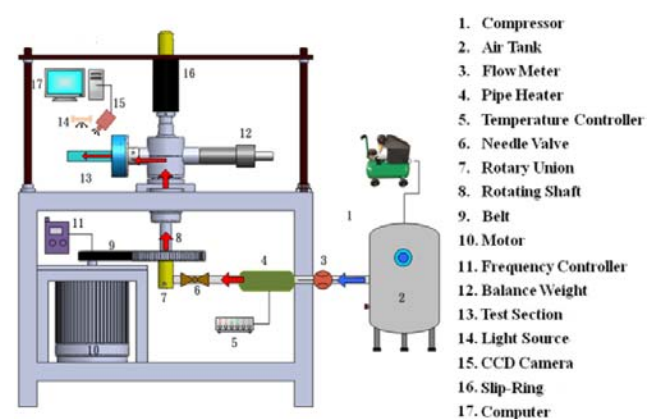


Fig. 1 Rotating facility

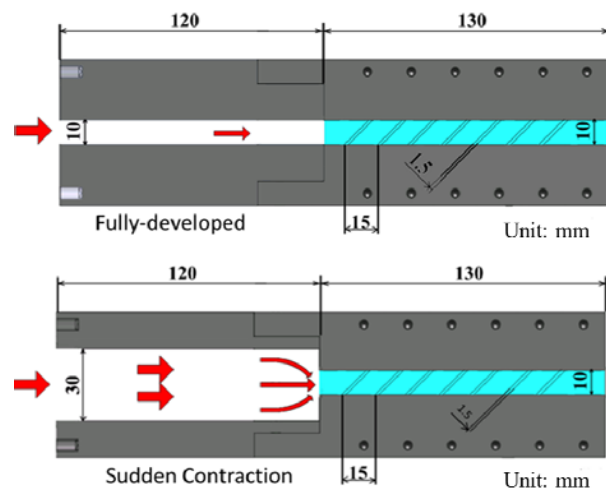


Fig. 2 Test section and with 45° angled ribs

A calibration process is performed to obtain the relationship between the temperature and the reflected color of the liquid crystal. Also, the effect of the stroboscope flashing has been tested as shown in Fig. 3. Results indicated that the difference due to flashing is less than 2.1%.

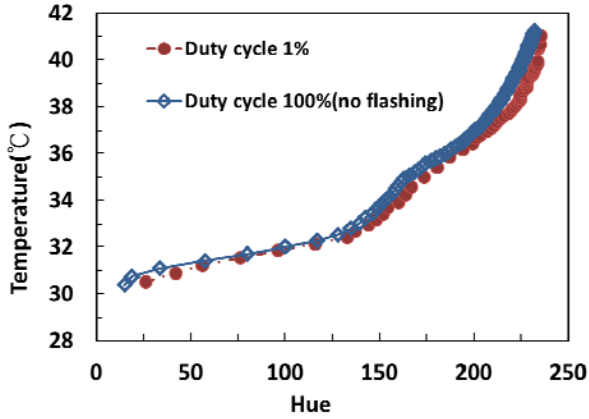


Fig. 3 Effect of stroboscope flashing on the liquid crystal calibration curve

The 1-D unsteady heat conduction through the semi-infinite solid with the convective boundary condition can be used to model the current test plate. With the mainstream temperature changing with time, the equation is modified by Duhamel's superposition theorem:

$$T_w - T_{w,i} = \sum_{j=1}^N \left[1 - \exp\left(-\frac{h^2 \alpha (t - \tau_j)}{k^2}\right) \times \operatorname{erfc}\left(\frac{h \sqrt{\alpha (t - \tau_j)}}{k}\right) \right] [\Delta T_m] \quad (1)$$

where ΔT_m and τ_j are the change of the mainstream temperature and the time-step. The surface temperature is obtained from the liquid crystal and the initial temperature is measured by the thermocouples.

The Nusselt number (Nu) is presented based on the heat transfer coefficient obtained from the measurement. The Dittus–Boelter/McAdams correlation for turbulent flow in the smooth tube (Nu_0) is chosen as the reference:

$$\frac{Nu}{Nu_0} = \frac{hD_h / k}{0.023 \operatorname{Re}^{0.8} \operatorname{Pr}^{0.4}} \quad (2)$$

where k is the thermal conductivity of the air and Pr is the Prandtl number of the air. In order to determine the effect of rotation on heat transfer inside cooling channels, Rotation number (Ro) is considered based on the bulk flow velocity (V) and the rotational speed (Ω) as shown below:

$$Ro = \Omega D_h / V \quad (3)$$

3. Results and Discussion

Fig. 4 shows the Nusselt number distribution with the fully-developed flow entrance condition. The results presented here are the regions between the ribs only. It clearly shows that there is a higher heat transfer region between ribs due to secondary flow along the angled rib orientation. Flow reattachment to the surface enhances

heat transfer over that region. As the channel starts to rotate, Nusselt number decreases on the leading surface while increases on the trailing surface. However, this heat transfer enhancement/degradation is not significant due to the relatively small rotation number tested in this study.

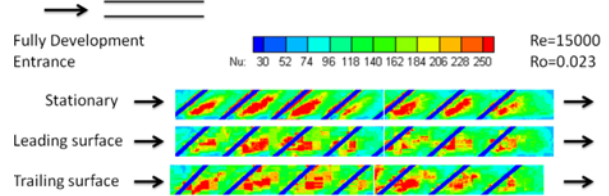


Fig. 4 Nusselt number distribution in the channel with fully-developed entrance

Fig. 5 shows heat transfer distribution in this channel with sudden contraction entrance geometry. It has higher Nusselt number than the fully-developed flow case as shown in Fig. 4. Under rotation condition, Nusselt number is higher on both the leading and trailing surfaces than the fully-developed flow condition.

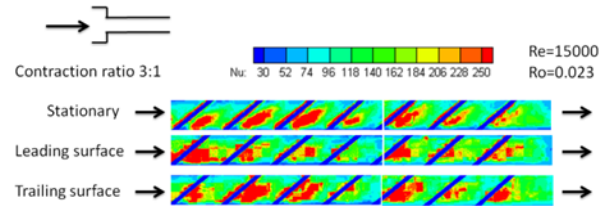


Fig. 5 Nusselt number distribution in the channel with sudden contraction entrance geometry

4. Concluding remarks

Transient liquid crystal technique, combined with a stroboscope, is used to experimentally obtain the heat transfer in a rotating internal cooling channel. This technique has the potential to reach very high rotational speed close to the real engine condition. Effect of entrance geometry is tested and it shows that the sudden contraction geometry produces higher heat transfer.

5. Acknowledgements

This research has been funded by National Science Council in Taiwan (NSC 100-2221-E-009-100).

References

- [1] G.D. Lock, Y. Yan, P.J. Newton, M. Wilson, and J. M. Owen, *J. of Eng. for Gas Turbines and Power*, **127**(2005), 375-382.
- [2] L.M. Wright, W.L. Fu, and J.C. Han, *J. of Heat Transfer*, **127**(2005), 378-387.
- [3] Y.H. Liu, M. Huh, and J.C. Han, *J. of Heat Transfer*, **130**(2008), 081701.
- [4] W.L. Fu, L.M. Wright, and J.C. Han, ASME Paper No. GT 2005-68493.
- [5] W. Kays, M. Crawford, and B. Weigand, 2005, *Convective Heat and Mass Transfer*, McGraw Hill, New York.

Numerical Investigations of Unexposed Temperature Distribution for Fire Doors under Different Sizes

San-Yih Lin^{*,**}, Tzu-Chieh Lin^{***}, George C. Yao^{***}, and Tsung-Chia Wu^{*}

^{*} Department of Aeronautics and Astronautics, National Cheng Kung University, Tainan, Taiwan

^{**} Fire Protection and Safety Research Center, National Cheng Kung University, Tainan, Taiwan

^{***} Department of Architecture, National Cheng Kung University, Tainan, Taiwan

E-mail: sylin@mail.ncku.edu.tw

ABSTRACT

The unexposed temperature distributions of steel fire doors under different areas are investigated by a finite element method. The finite element software ANSYS is used for the numerical simulation tool. The CNS elevated temperature curve is exposed on one side of a fire door. A series of simulations of the unexposed temperature distributions under different fire door areas with the same door structure are investigated. According to this study, one can establish a fire safety rule to judge a standard fire safety door to be a fire safety door or not when it is reduced its dimensions.

1. Introduction

Fire doors are one of the key elements in the fire safety designs of buildings. For this propose, a complex structure made of different materials are used either in the movable part (leaf) or in the fixed part (frame). In different country areas, there are different fire safety regulations to examine the thermal and mechanical stability for a fire door under certain fire condition, such as UL10B for USA, EN1363 for Europe, and CNS11227 for Taiwan [1,2,3]. There are also a large variety of door frames that can be combined with a large variety of door leaves. This leads different dimension combinations for length, width, and height. This variety of products leads a large number of costly fire tests for a fire door factory. Although this number can be reduced partly by means of the similar rules given in the standard [2,3], there is a need for further reduction that can be done by means of numerical and experimental analysis. The present study the unexposed temperature distributions of steel fire doors under different areas are investigated by a finite element method. The finite element software ANSYS is used for the numerical simulation tool. A series of simulations of the unexposed temperature distributions under different fire door areas with the same door structure are investigated. According to this study, one can establish a fire safety rule to judge a standard fire safety door to be a fire safety door or not when it is reduced its dimensions.

2. Method

The governing equation for the thermal analysis of fire doors exposed to high temperatures is presented by the three-dimensional heat diffusion equation:

$$\rho c \frac{\partial T}{\partial t} = \frac{\partial}{\partial x} \left(k \frac{\partial T}{\partial x} \right) + \frac{\partial}{\partial y} \left(k \frac{\partial T}{\partial y} \right) + \frac{\partial}{\partial z} \left(k \frac{\partial T}{\partial z} \right) \quad (1)$$

where ρ , T , k , and c are density, temperature, thermal conductivity, and specific heat, respectively.

The boundary condition on the exposed side can be given as:

$$\dot{Q} = \dot{Q}_{conv} + \dot{Q}_{rad} = (h + h_r) A_s (T_\infty - T_s) \quad (2)$$

where \dot{Q} , h , h_r , A_s , T_s and T_∞ are heat transform rate, heat convection coefficient, radiation heat convection coefficient, surface area, surface temperature, and

CNS11227 elevated temperature, respectively.

$$h_r = \varepsilon \sigma (T_\infty + T_s)(T_\infty^2 + T_s^2), \sigma = 5.67 \times 10^{-8} \quad (3)$$

where ε and σ are radiation emissivity and Stefan-Boltzmann number, respectively. Similar to the boundary condition on the unexposed side, except $T_\infty = 30^\circ\text{C}$. This is the ambient temperature at the test. The boundary conditions on the other four sides of the steel fire door are simplified as the adiabatic boundary condition.

The finite element software ANSYS is used for the numerical simulation tool. The thermal element Solid 70 is used. Since the effects of convection and radiation on the door surface are considered, the element Surf152 on the surface is also used.

3. Results and Discussions

In this section, a series of simulations of the unexposed temperature distributions under different fire door areas with the same door structure are investigated. The steel fire door with the dimension of 1.157m width, 2.16m height, and 64mm depth is served as the original door. This fire door and frame assembly in this study were tested at the Fire Protection and Safety Research Center, NCKU in Tainan, Taiwan. During this test, thermocouple measurements on the unexposed side of the fire door at the seven locations shown in Fig. 1 were gathered.

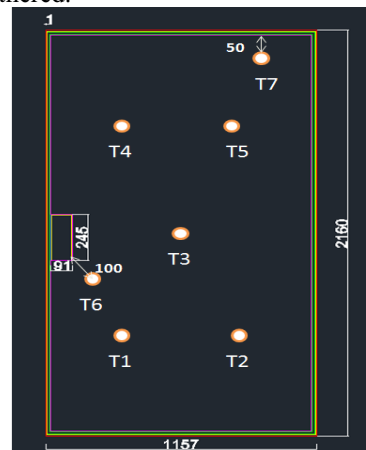


Fig 1 The seven measured positions in this test.

3.1 The Effect of Reduced Door Area

First, under fixed door depth, the door area is reduced by reducing the dimension of width or height to see the effect on the unexposed temperature distribution. Five cases are performed:

- (1) 9095: width reduced to 90% and height reduced to 95%.
- (2) 8095: width reduced to 80% and height reduced to 90%.
- (3) 7085: width reduced to 70% and height reduced to 85%.
- (4) 6085: width reduced to 60% and height reduced to 80%.
- (5) 5075: width reduced to 50% and height reduced to 75%.

Table 1 shows the increase of the averaged temperature on the unexposed side due to the decrease of the door area. One can see that the averaged temperature is very sensitive to the change of the door area. The numerical results indicate that the averaged temperature is increased if the door area is reduced. The increase ratio (increased temperature/reduced area(%)) is about 0.75.

Table 1. The increase of the averaged temperature on the unexposed side.

Reduced Area(%)	12.5	28	41.5	52	62.5
Increase Temperature	9.06	16.4	29.6	40.6	49

3.2 The Effect of Ratio of Width and Height

Then, by a fixed door area, we investigate the effect on the unexposed temperature distributions by changing the ratio of width and height of the fire safety door. Three cases are performed:

(A) door area is reduced to 85.5% width (1) height is reduced to 85.5%, (2) width is reduced to 95% and height is reduced to 90%, (3) width is reduced to 92.466% and height is reduced to 92.466%, (4) width is reduced to 90% and height is reduced to 95%, and (5) width is reduced to 85.5%.

(B) door area is reduced to 72% width (1) height is reduced to 72%, (2) width is reduced to 90% and height is reduced to 80%, (3) width is reduced to 84.853% and height is reduced to 84.853%, (4) width is reduced to 80% and height is reduced to 90%, and (5) width is reduced to 72%.

Figs. 2 and 3 show the temperatures at the seven positions on the unexposed side for Cases A and B, respectively. One can see temperatures are almost equal to each other for each width-height reduced ratio. This indicates that the temperature distribution on the unexposed side just depend on the door area and are not sensitive to the width-height reduced ratio.

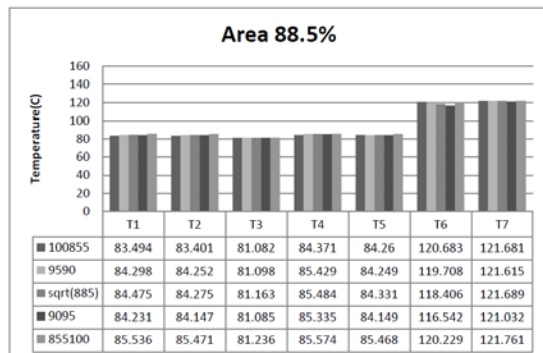


Fig 2 The temperatures at the seven positions on the unexposed side for Case A.

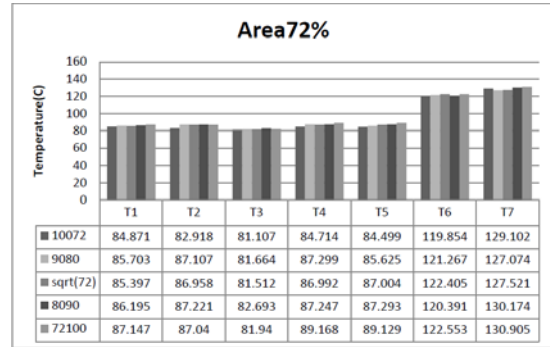


Fig 3 The temperatures at the seven positions on the unexposed side for Case B.

4. Concluding remarks

The unexposed temperature distributions of steel fire doors under different areas are investigated by a finite element method. A series of simulations of the unexposed temperature distributions under different fire door areas with the same door structure are investigated. From the above numerical results, one can conclude that:

- (1) For a standard fire safety door, the averaged temperature on the unexposed side is increased if the door area is reduced. The increase ratio (increased temperature/reduced area (%)) is about 0.75.
- (2) By a fixed door area, the temperature distributions on the unexposed side just depend on the door area and are not sensitive to the width-height reduced ratio.

According to this study, one can establish a fire safety rule to judge a standard fire safety door to be a fire safety door or not when it is reduced its dimensions.

Acknowledgements

The authors wish to extend their appreciation for the supports awarded by the National Science Council of the Republic of China under the contact NSC 100-2221-E-006-106 and by the Fire Protection and Safety Research Center, National Cheng Kung University.

References

- [1] UL 10 B, Standard for Safety for Fire Tests of Door Assemblies, Ninth Edition, Underwriters Laboratories Inc., Northbrook, IL USA, 1997.
- [2] European Standard EN 1363-1, Fire Resistance Tests – Part 1: General requirements, European Committee for Standardization CEN, Brussels, 2000.
- [3] CNS11227, Standard for Test Method of Fire Door, Taiwan, ROC, 2002.

A Three-dimensional Numerical Analysis of Heat Transfer and Flow in Sinusoidal Wavy Passages

Kuen-Rung Huang, Hsinchu (National Chiao Tung University, Taiwan), Wu-Shung Fu, Hsinchu (National Chiao Tung University, Taiwan), Chi-Xiu Lo, Hsinchu (National Chiao Tung University, Taiwan)
gibu.me95@nctu.edu.tw; wsfu@mail.nctu.edu.tw; beel305@msn.com

ABSTRACT

The research is talk about the difference between wavy and flat vertical wall in three dimensional channel flow field. To compare the heat transfer in different channels, this research compared the velocity, temperature and local Nusselt number by simulating various amplitude and width cases.

1. Introduction

Now days, in order to remove the waste heat of electric devices; heat convection technology is one of useful way to remove it. Heat convection can divide to three types: force, natural and mixed, and free convection can cool the element by itself; so it is the most economical way to cooling. There are many researches of natural convection about the flat plate flow, and some special geometry has the remarkable effect. The phenomenon at opened-ended finite length channel is a very important issue in both academic and industrial fields.

In this research, Boussinesq assumption is not appropriate to simulate the flow with high temperature and deformed channel. The compressible flow is taken into consideration instead of renunciation of the Boussinesq assumption.

In the past, Bhavnani [1] investigated the heat transfer rate of two-dimensional wavy heating wall which is better than that of flat plate. The heat transfer rate of 2-dimensional wavy heating wall is better than flat plate, and there is no research talking about three-dimensional wavy heating channel. So this research will extend to three-dimensional model for advance research.

2. Physical model

2.1 Physical model

The three-dimensional wavy channel is investigated and the model is shown on Fig. 1.

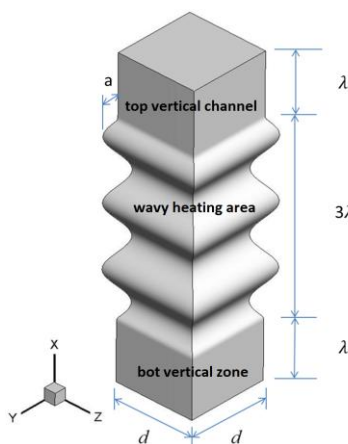


Fig. 1 Physical model of wavy channel

The structure can be divided to three parts: top vertical channel, wavy heating area and bot vertical zone. The side lengths of two square vertical channels are “ d ” and the height is “ λ ”. The height of wavy channel, the amplitude of the wave and the wavelength are 3λ , a and λ , respectively.

The boundary conditions of constant temperature are set on waved walls; the other walls are no slip condition. Initial temperature is 298K and pressure is 101.3kPa. In this case with high Richardson number, non-reflection boundary conditions are adopted on both the inlet and the outlet instead of fully-developed flow condition for saving computing grids.

The constant temperature “ T_h ” boundary condition is set on wavy wall, and the inlet and outlet are non-reflection boundaries.

2.2 Governing equations

The continuity, momentum and energy equations are writing in general partial form in which the parameters of viscosity and compressibility of the fluid and gravity are considered simultaneously are shown in the following equations.

$$\frac{\partial U}{\partial t} + \frac{\partial F}{\partial x} + \frac{\partial G}{\partial y} + \frac{\partial H}{\partial z} = S \quad (1)$$

$$P = \rho RT \quad (2)$$

In which

$$U = (\rho \quad \rho u \quad \rho v \quad \rho w \quad \rho e)^T \quad (3)$$

$$F = \left(\begin{array}{c} \rho u \\ \rho u^2 + P - \tau_{xx} \\ \rho uv - \tau_{xy} \\ \rho uw - \tau_{xz} \\ \rho \left(e + \frac{V^2}{2} \right) u + Pu - k \frac{\partial T}{\partial x} - u\tau_{xx} - v\tau_{xy} - w\tau_{xz} \end{array} \right) \quad (4)$$

ρ : density

p : pressure

u, v, w : velocity of $x, y,$ and z direction

k : thermal diffusivity

$e = C_v T + 0.5(u^2 + v^2 + w^2)$

3. Numerical method

Using the Roe scheme [2] to match preconditioning

method [3] and applying the coordinate transformation technology [4] solves the equations which with Jacobian transformation.

$$\Gamma \frac{\partial U_p}{\partial \tau} + \frac{\partial \tilde{U}}{dt} + \frac{\partial \tilde{F}}{dx} + \frac{\partial \tilde{G}}{dy} + \frac{\partial \tilde{H}}{dz} = S' \quad (5)$$

Then use 3th order MUSCL proposed by Abalakin et al. [5] to compute the inviscid terms. Viscid terms are solved by second order central difference. Finally, sue the LUSGS [6] to solve temporal advancements.

4. Result and discussion

In order to confirm the flow and temperature field of the program, we compare with previous researches [7, 1] who considered the cases of low Reynolds number on the wavy wall. Bhavnani [1] proposed the experiment with wavy heating vertical wall of natural convection. The boundary condition of three flat sides are opened space i.e. p=100kPa T=298K and the waved wall is 328K, the periodic boundary was set in z-direction; the physical model and comparisons are shown in Fig. 2.

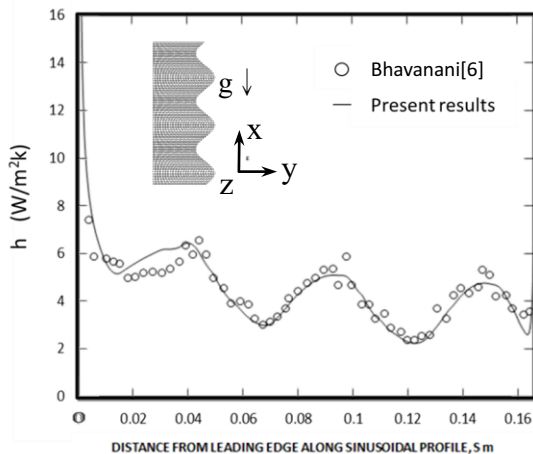


Fig. 2 Heat transfer coefficient distribution along the streamwise, $\lambda = 50.8\text{mm}$, $a = 5.08$, $Ra = 3 \times 10^5$

Although the higher amplitude of wavy heating walls is the lower h_{average} are. The wavy surface provides extra heat transfer area than flat heating wall, that makes it has higher total heat transfer rate. Both in Bhavnani and present researches have similar results and the error is smaller than 3% that can confirm the program is adaptive.

In this three-dimensional simulation, we change the Rayleigh number to compare the heat transfer rate of different models. However Rayleigh number is function of temperature, scale, etc..., so we divided the research to two parts, different temperature and scale.

Part A : Base on Temperature

In part A, we simulate the Rayleigh number in 2.5×10^4 , 5.5×10^4 and 1.0×10^5 , and non-dimension amplitude α equals 0, 0.1 and 0.2, in which $\alpha = a/\lambda$; and the results of simulation are shown in Fig. 3

Part B : Base on Scale

Part B is the simulation of three different

characteristic lengths in $Ra = 10^4$, 10^5 and 10^6 ; the non-dimension amplitude α equals 0.1 and 0.2. The comparisons are shown in Fig. 4.

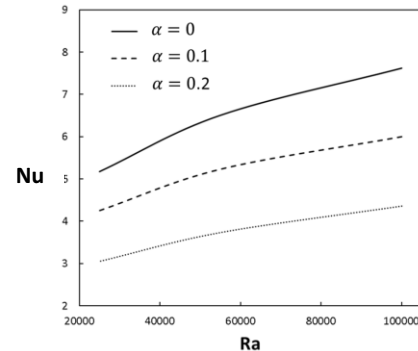


Fig. 3 Average Nu versus Ra of different non-dimension amplitude base on different temperature

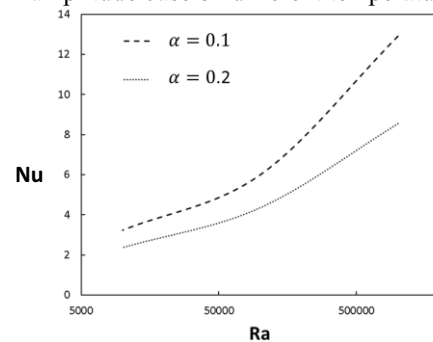


Fig. 4 Average Nu versus Ra of different non-dimension amplitude base on different characteristic length

In Fig.3 and 4, both results are similar; the higher “ α ” the lower heat transfer rate, although the model of high “ α ” has large heat transfer area, eddies will be restrained and spin in expansion corner zone that the energy can’t be bring to exit. Finally it causes the average Nu lower than flat heating wall.

5. Concluding remarks

1. As the main flow passes through the taper section, the better heat transfer rate occurred.
2. Eddies occurred in the expansion zones, which reduce the heat transfer rate.
3. Although the larger amplitude model has more heat transfer area, but which fills with eddy and makes small heat transfer rate, i.e. high amplitude is inefficient.

References

- [1]Bhavanani S.H. and Bergles A.E, Int. J. heat and mass transfer (33) No. 5 pp-no.965, 1990
- [2]P. L. Roe, J. Comput. Phys. 43(1981)357-372
- [3]J. M. Weiss and W. A. Simth, AIAA. 33 (1995)2050-2056.
- [4]Upender K. Kaul *NASA Ames Research Center,M/S 258-5, Moffett Field, CA 94035, United States
- [5]I. Abalakin, A. Dervieux, T. Kozubskaya, INRIA (2002) No4459.
- [6]S. Yoon, A. Jameson, AIAA. 26 (1988) 1025-1026
- [7]A.M. Guzzman and C. H. Amon, Phys. Fluids 6 (6) June 1994

$$M_{in} = \frac{m_{in}}{m_f} \quad (3)$$

Where m_{in} is the mass flow rate at the inlet and the mass flow rate provided by the forced convection m_f at the inlet expressed as follows, respectively.

$$m_{in} = \iint_A \rho u dy dz \quad (4)$$

$$m_f = \rho u_0 l_2^2 \quad (5)$$

To investigate the heat transfer and the influence in the situations of different ratios of free region under a high Richardson number represented by buoyancy force to inertia force as follows.

$$Ri = Gr / Re^2 \quad (6)$$

From Table 1, there is an optimization of the efficiency of heat transfer in the situation of the ratio of free region of 0.175. The streamlines, velocity field and thermal field in the situation of the ratio of free region of 0.175 are indicated in Fig. 2. The results show that in a large Richardson number situation the amount of fluid induced by natural convection is huge which causes part of the amount of fluid from the outside via the free region at the inlet to be sucked into the channel. Since those fluids sucked into the channel are larger than those flowing into the channel via the inlet provided by forced convection, and then the interacting impingement between both amounts of fluid mentioned above occurs which leads the flow field to be unsteady. In addition, the flow and thermal field in the situation of the ratio of free region of 0.25 is relatively steady shown in Fig. 3.

5. Concluding remarks

Several conclusions may be summarized as follows.

1. It can be concluded that the efficiency of heat transfer in the situation of $\alpha = 0.175$ is superior to the other situations of this study.
2. The mass flow rates and velocities of the fluids induced by buoyancy force are affected by the ratio of free region that lead different heat transfer mechanisms under the same Richardson number.

Table 1 the ratios of free region, mass flow rates and Nusselt numbers of this study.

α	M_{in}	U_{max}	Nu
0.3	5.27	1.14	8.41
0.25	5.47	1.45	8.94
0.225	5.73	1.67	9.23
0.2	5.8	1.59	9.87
0.175	5.6	1.76	9.95
0.15	4.8	1.82	9.08
0.125	4.07	1.78	9.5
0.1	3.67	1.76	9.5
0.075	2.93	1.61	9.75
0.05	2.07	1.2	7.3

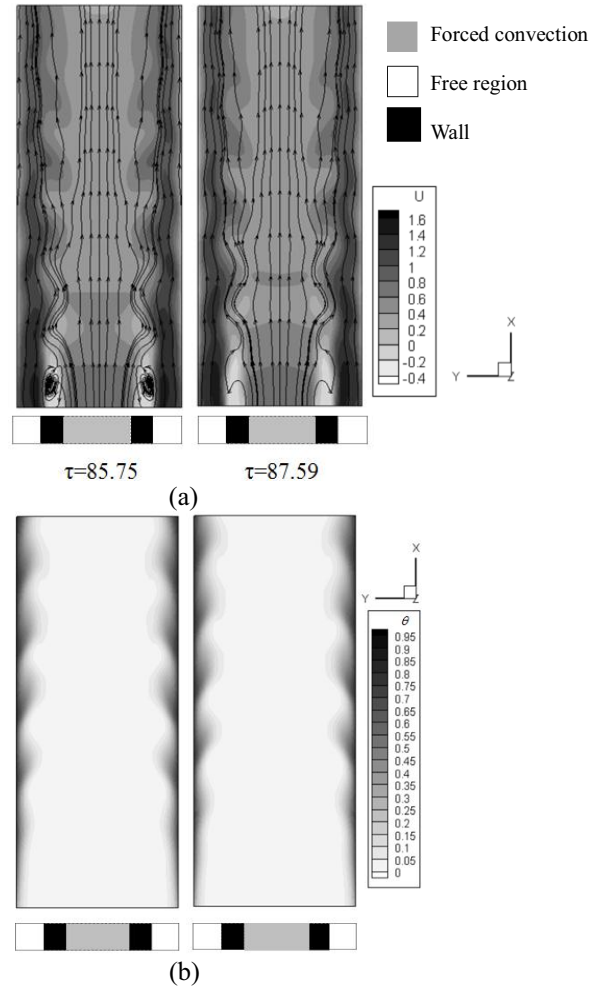


Fig. 2 the variations of streamlines, velocity field and thermal field. ($\alpha = 0.175, Ri = 3.77$)

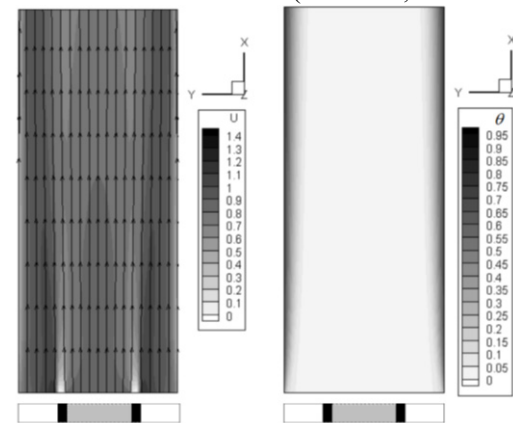


Fig. 3 the variations of streamlines, velocity field and thermal field. ($\alpha = 0.25, Ri = 3.77$)

References

- [1] T.J. Poinsot, and S.K. Lele, J. Compu. Phys. **101** (1992) 104-129.
- [2] W.S. Fu, C.G. Li, C.C. Tseng, Int. J. Heat Mass Transfer **53** (2010) 1575-1585.
- [3] P.L. Roe, J. Compu. Phys. **43**(1981) 357-372.
- [4] J. M. Weiss and W. A. Smith, AIAA. **33** (1995) 2050-2056
- [5] S. Yoon, A. Jameson, AIAA. **26** (1988) 1025-1026.

Phenomena of Natural Convection in Multiple Open Boundaries Condition Problem

Wu Shung Fu, Wei Hsiang Wang, Chung Gang Li

EE306, Department of Mechanical Engineering, No.1001, Daxue Rd., East Dist., Hsinchu City 300, Taiwan (R.O.C.)
wsfu@mail.nctu.edu.tw

ABSTRACT

A study of natural convection in three dimensional square plates is investigated numerically. Multiple open boundaries co-exist in the physical domain, and a non-reflecting boundary condition applied at the aperture is no longer suitable for solving the problem of this study. An absorbing boundary condition is then adopted and modified in solution processes. The geometry of the physical model is the parallel square plates, and then phenomena observed are almost symmetrical.

1. Introduction

A subject of natural convection is an important and attractive topic in both research of fundament and application. The subject, except a physical geometry of an enclosure, indispensably involves a problem of an open boundary. Therefore, characteristics of the open boundary deeply affect the phenomena of the inside of the domain. From a view point of theoretical analysis, a correct and appropriate treatment of the open boundary becomes a complex and serious topic.

In order to facilitate the problem induced by the open boundary in an incompressible flow problem Poinot and Lele [1] developed an ingenious method of Navier-Stokes characteristics boundary condition (NSCBC) to treat compressible fluids flowing through open boundaries of the domain. Fu and Li [2] modified the method of the NSCBC being adopted in all speeds of compressible flows. However, sequential methods of the NSCBC are limited in the treatment of the problem of the non-reflecting boundary on the cross section of the open boundary having one normal direction such as the physical model shown in [2]. And these methods have difficulties to solve the domain having neighboring open boundaries.

In order to match the demand of the neighboring open boundaries for viscous fluid flow problems, Freund [3] proposed an absorbing layer to substitute the PML method to solve one dimensional compressible problems in viscous fluid flow situations. However, when the method was used to apply to a three dimensional open boundary problem, it is rather difficult to determine correct directions of the artificial convection and damping terms in the intersection zone. Therefore, the study aims to develop a new available method to solve natural convection in multiple open boundaries condition problem.

2. Physical model and Numerical method

A physical model of three dimensional parallel square plates is indicated in Fig. 1, and since the absorbing boundary is used, an additional zone called an artificial buffer zone is necessarily added to the original domain. The heated bottom surface is cdhg.

The governing equations described in the original domain in which the parameters of viscosity and compressibility of the fluid and gravity are considered

simultaneously are shown in the following equation.

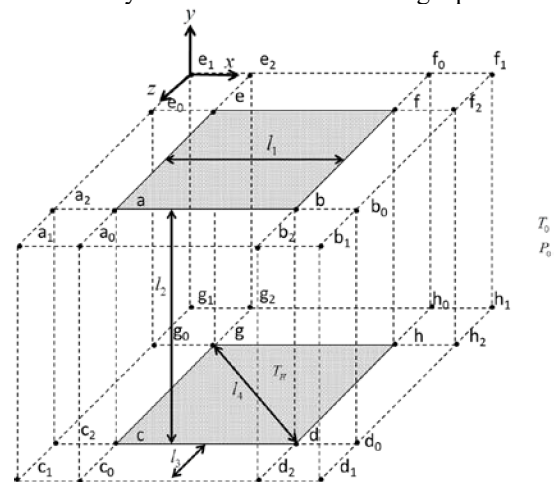


Fig. 1 Physical model of three dimensional parallel square plates

$$\frac{\partial U}{\partial t} + \frac{\partial F}{\partial x} + \frac{\partial G}{\partial y} + \frac{\partial H}{\partial z} = S \quad (1)$$

As for the governing equations described in the artificial buffer zone [15], the artificial convection and damping terms are newly adopted. Then general forms of the governing equations in the artificial buffer zone can be described as Eq. (2).

$$\frac{\partial U}{\partial t} + \frac{\partial \tilde{F}}{\partial x} + \frac{\partial \tilde{G}}{\partial y} + \frac{\partial \tilde{H}}{\partial z} + \tilde{\sigma} = 0 \quad (2)$$

\tilde{F} , \tilde{G} and \tilde{H} are modified physical quantities by adopting artificial convection terms to F , G and H shown as follows.

$$\tilde{\phi} = \phi + \tilde{\eta}_{\phi} \quad (3)$$

Where $\phi = F, G, H$ and $\tilde{\eta}_{\phi}$ is the artificial convection term and $\tilde{\sigma}$ is the three dimensional artificial damping term. Methods of the Roe scheme, preconditioning and dual time stepping matching LSUGS scheme are used to solve the situation of a low speed compressible flow.

3. Results and Discussion

In Fig. 2(a) and 2(b), velocity vectors distributed on the edge of the cross section of $ijnm$ and the diagonal plane of $gdbe$ are indicated. The bottom surface is heated, then cool fluids are sucked from surroundings and flow into the parallel square plates along the bottom surface. Due to the effect of the buoyance force, the cool fluids heated by the bottom surface ascend and impinge on the top surface. Finally, the cooling fluids turn moving directions and flow out of the parallel square plates.

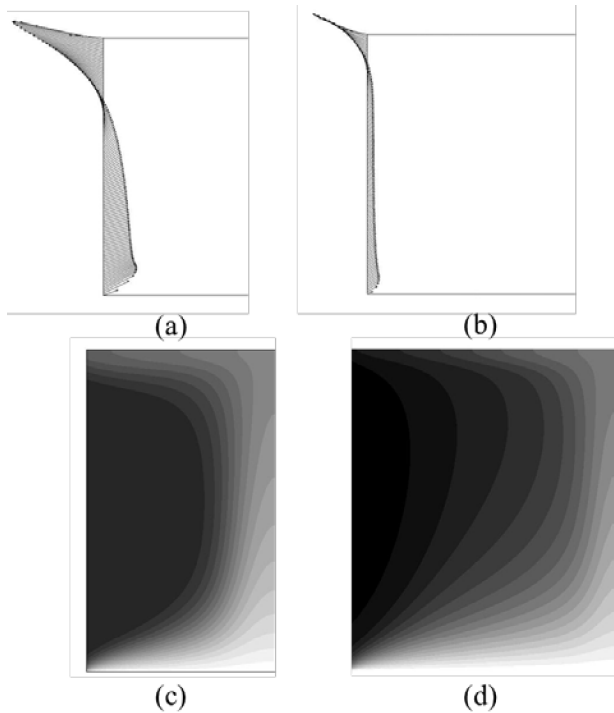


Figure 2 Distributions of velocity vectors and thermal fields of different cross-sections under $Ra^* = 1.55 \times 10^6$

In Fig. 2(c) and 2(d), a thermal field which is the left half side is indicated. The cooling fluids are gradually heated by the bottom surface from the edge to the center. Then a higher temperature region is concentrated in a central region of the plates. The phenomenon means that some cool fluids in the dark region flowing into and out of the plates are just induced by the ascending cool fluids in the central region and not directly heated by the bottom surface.

In Fig. 3(a), the temperatures of the fluids in the central region are higher than those in the other regions which cause the local Nusselt numbers in the central region to be lower than those in the other regions. Shown in Fig. 3(b), local Nusselt numbers distributed on the heated bottom surface are indicated. Heated distances from the center to the locations of i and j are shorter than those from the center to the location of g and d . Consequently, the shape formed by the

same local Nusselt numbers is similar to a concave quadrangle.

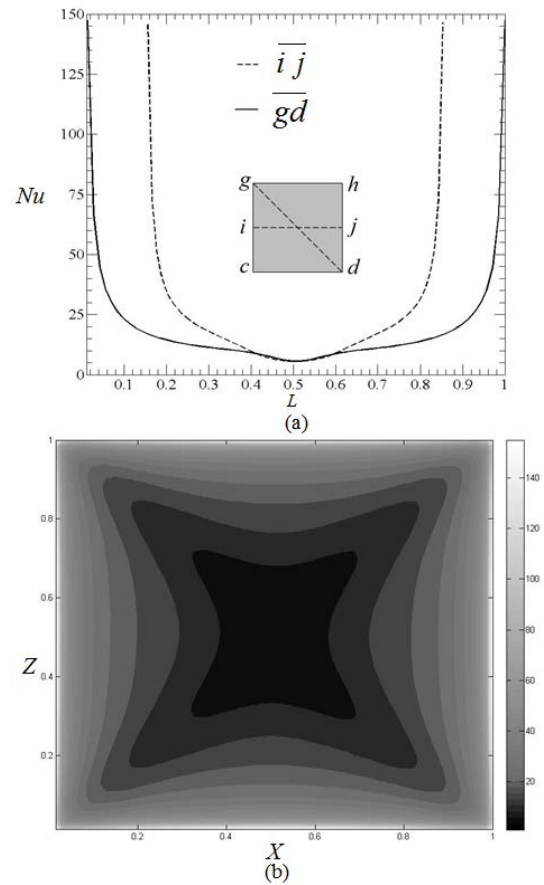


Fig.3 Distributions of (a) local Nusselt numbers along \overline{ij} and \overline{gd} (b) contour of local Nusselt numbers on the heated bottom surface

4. Concluding remarks

A study of natural convection in multiple open boundaries is investigated numerically and some conclusions are drawn as follows.

- (1) The model is parallel square plates, and phenomena occurring in the domain are mainly symmetrical.
- (2) The cooling fluids are gradually heated by the bottom surface from the edge to the center and flow out at the top surface.
- (3) The absorbing boundary condition is effective for the multiple open boundaries problem.

References

- [1] T. J. Poinot and S. K. Lele, J. Comput. Phys., 101 (1992), 104-129.
- [2] Wu-Shung Fu, Chung-Gang Li, Tseng Ching-Chi, Int. J. Heat Mass Transfer 53(2010), 1575-1585.
- [3] J. B. Freund, AIAA 35(4)(1997), 740-742.

An Experimental Investigation on Air-Water Two-Flow Distribution in Plate Heat Exchangers with Inlet Distributor

Chien-Yuh Yang, Yueh-Hung Lin and Fan-Yu Meng
Graduate Institute of Energy Engineering, National Central University
No. 300, Zhong-Da Road, 320 Zhong-Li, Taiwan
cyyang@ncu.edu.tw

ABSTRACT

This study provides an experimental observation of air-water two-phase flow distribution in plate heat exchanger with various inlet distributors. Air injected in the direction 12 (upward), 3, 4, 5, 6 (downward) and 9 with inlet void fraction of 0.7 and Reynolds number 500 and 1,500 were investigated. The experimental results show that the air inlet distributor is able to significantly improve the air flow uniformity for air-water two-phase in a plate heat exchanger. For lower Re (= 500), air injected from direction 6 provides the most uniform distribution of the air flow. However, for higher Re (= 1,500), air injected from direction 3 is the best.

1. Introduction

A plate heat exchanger is made by combing several corrugated stainless plates. Working fluids pass through the channels between adjacent plates and exchange heat through the plate. It is commonly used as evaporators in air-condition and refrigeration systems because of their compactness and high heat transfer performance. Figure 1 shows the schematic diagram of fluid flowing through a plate. Since the flow distance through the left portion of the plate is shorter than it through the right portion of the plate if the inlet and exit port are at the side of the plate, most of the fluid will flow through the left portion and caused the flow mal-distribution. This effect will be more significant for two-phase flow in an evaporator.

Recently, a so-called inlet distributor as shown in Figure 2 has been designed for reducing the flow mal-distribution. The inlet fluid passes through a small hole to restrict it flow in a specified direction and increase the air flow through the longer portion of the flow passage. Numerous analyses have been done for flow in corrugate plates [1-8]. But very few research results were published regarding to the flow distribution in a plate heat exchanger with inlet distributor. Chu [9] provided a numerical analysis of the flow distribution in plate heat exchangers through various inlet distributors. The present study provides an experimental observation for further understanding of the flow distribution through various inlet distributors.

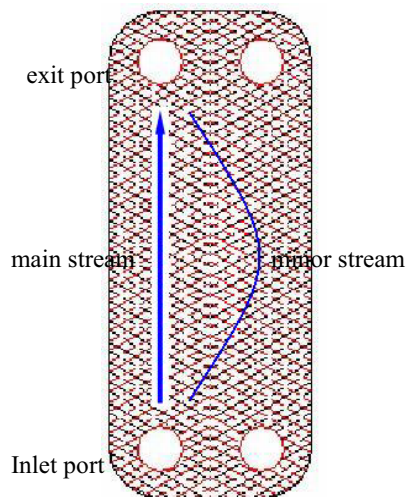


Fig. 1. Schematic diagram of the fluid flowing through a

corrugated plate

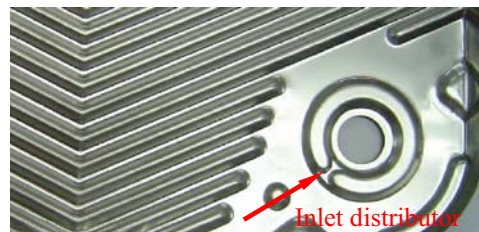


Fig. 2. Inlet distributor in a plate heat exchanger

2. Experimental Setup

A chevron corrugated stainless plate and a Pyrex plate with reverse chevron corrugates is combined together to form the test section for flow visualization as shown in Figure 3. Water flows uniformly outward from the inlet port of the plate. Air flows inward and injected from various inlet positions with angles from 0° to 360° with direction numbered from 0 to 12 respectively. Figure 4 shows details of the inlet distributor. A high speed camera is installed in front of the plate to record the flow images.

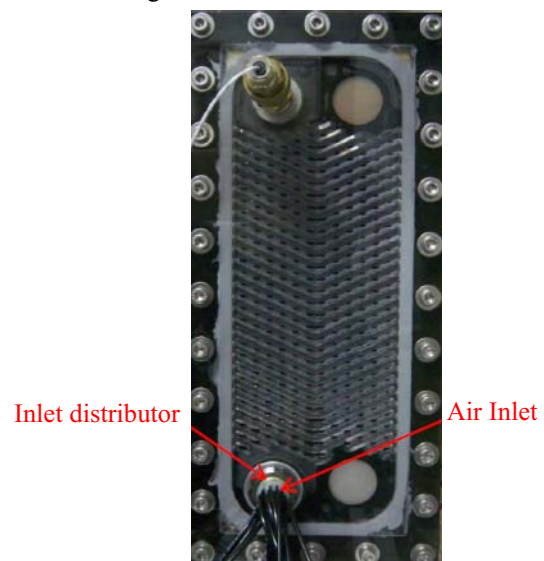


Fig. 3. Test section for flow visualization

3. Results and Discussion

Air-water two-phase flow with inlet void fraction 0.7 and Reynolds number 500 and 1,500 was studied in this

research. The volume fraction distribution and flow rate of air injected in the direction 12 (upward), 3, 4, 5, 6 (downward) and 9 were investigated. Figure 5 shows the observation result for air injected directly upward (direction 12) at Reynolds number = 500. The volume fraction distribution analyzed by Chu [9] was also plotted for comparison. A significant flow mal-distribution can be observed from the figure. Most of the air flows through the left portion of the plate. The air volume fraction is in the range of 0.8 to 1.0 in this portion in comparing to that only 0 to 0.2 in the right portion of the plate.

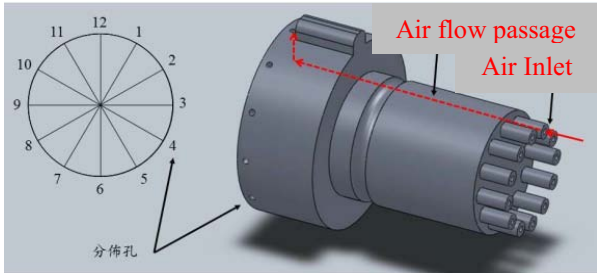


Fig. 4. Details of the inlet distributor

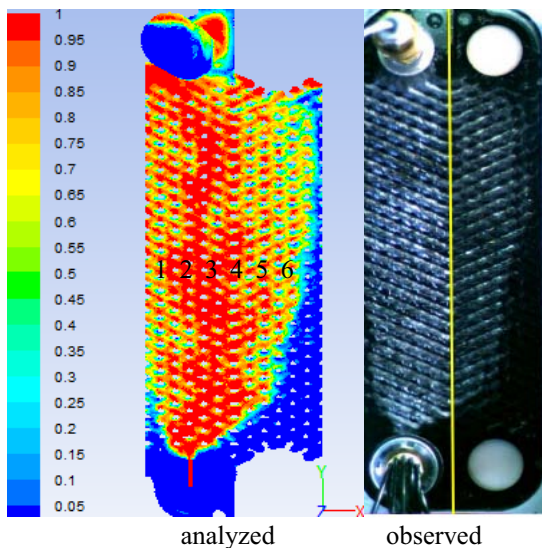


Fig. 5. Volume fraction distribution, air direction 12, Re = 500

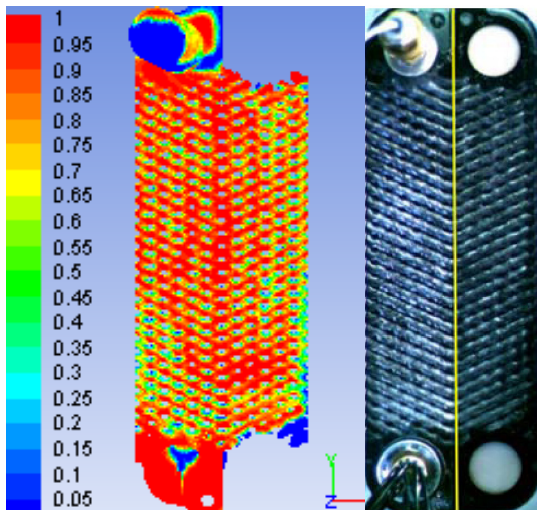


Fig. 6. Volume fraction distribution, air direction 6, Re = 500

Figure 6 shows the volume fraction distribution for air injected from direction 6 at Reynolds number = 500. Flow mal-distribution is almost not able to be observed in this situation. Air flows evenly through the entire plate.

4. Concluding remarks

From the previous experimental observation, we may clearly investigate that the air inlet distributor is able to significantly improve the air flow uniformity for air-water two-phase in a plate heat exchanger. For lower air flow velocity, $Re = 500$, air injected from direction 6 provides the most uniform distribution of the air flow. However, for higher air flow velocity, air injected from direction 3 provides the most uniform distribution of the air flow.

Acknowledgments

This study was financially supported by the Taiwan National Science Council under grant number NSC 99-2622-E-008 -005 -CC2.

References

- [1] Paras S.V., Kanaris A.G, Mouza A.A., Karabelas A.J., 15th International Congress of Chemical and Process Engineering. Prague, August, 2002.
- [2] Kanaris A.G, Mouza A.A., Paras S.V., Chem. Eng. Res. Des., 83 (A5), 2005, 460-468.
- [3] Pelletier O., Stromer F., Carlson A., ASHRAE Trans., 111, 2005, 846-854.
- [4] Kanaris A.G, Mouza A.A., Paras S.V., Chem. Eng. & Technology 2006, 29, 8, 923-930.
- [5] Tsai Y.C., Liu F.B., Shen P.T., Intern. Comm. in Heat and Mass Transfer 2009, 36, 574-578.
- [6] Jain S., Joshi A., Bansal P.K., J. Heat Transfer 2007, 129, 291-297.
- [7] Han X.H., Cui L.Q., Chen S.J., Chen G.M., Wang Q., Intern. Comm. in Heat and Mass Transfer 2010, 37, 1008-1014.
- [8] Gherasim, N. Galanis, C. T. Nguyen., Applied Thermal Eng. 2011, 31, 4113-4124.
- [9] Y.-C. Chu, 2012, Master Thesis, National Central University, Jhong-Li, Taiwan.

Effect of Heater Size on the Critical Heat Flux of Pool Boiling on Micropillar Array-coated Surfaces

Authors names: Chih-Hung Huang and Ming-Chang Lu

Affiliation and address: Department of Mechanical Engineering, National Chiao Tung University

E-mail of corresponding author: mclu@mail.nctu.edu.tw

ABSTRACT

In this work, pool boiling on micropillar array-coated surfaces for three different heater sizes (0.5×0.5 , 1×1 , and 1.5×1.5 cm²) was studied. The obtained Critical Heat Fluxes (CHF) after subtracting conduction heat losses for the corresponded heater sizes are 168.1 ± 4.8 , 173 ± 3.6 , and 164.4 ± 3.6 W/cm², respectively, and the percentages of the heat losses for the three heater sizes are 16.4 ± 0.9 , 7.6 ± 0.3 , and 5 ± 0.1 %, respectively. The highest CHF on the micropillar array-coated surface is 173 ± 3.6 W/cm² for the 1×1 cm² heater. After subtracting the conduction heat losses from the CHFs, there is no apparently heater size dependence of the CHF observed. It is found that the percentage of the conduction heat loss increases as the heater size reduces. The increased conduction heat loss is due to the fact that an augmentation of the edge effect as the heater size reduces.

1. Introduction

About 40% of world's electricity is generated by the heat engines based on Rankine cycle. The efficiency and output power of such heat engines are determined by the Critical Heat Flux (CHF) of boiling. Thus, an increased CHF will have a large impact on the world's total energy. The mechanisms causing the CHF of pool boiling have been extensively discussed [1]. Besides, it is generally agreed that the CHF increases as heater size reduces [2]. But the proposed mechanisms causing the heater size effect and the size of the heater at which heater size effect appears among previous studies are not consistent [2].

For example, Bar-Cohen and Mcneil [2] found that the effect of heater size takes place once the non-dimensional heater size L' is smaller than 20, where L' is defined as L/L_c , whereas L is the size of the heater and L_c is the capillary length:

$$L_c = \sqrt{\sigma/[g(\rho_l - \rho_v)]} \quad (1)$$

In the above equation, σ , ρ_l and ρ_v are surface tension of liquid, liquid density and vapor density, respectively.

Lienhard and Dhir [3] showed that the CHF is a function of heater size when $L' < 32$. They attributed the effect of heater size to the fact that the number of vapor columns is reduced by decreasing the size of the heater.

Further, Gogonin and Kutateadze [4] found that the size of the heater will affect the CHF when $L' < 2$.

Rainey and You [5] also found that CHF increases as heater size decreases. They argued that the heater size effect is due to the fact that the rewetting of liquid for a small-sized heater is easier.

Kwark *et al.* [6] also found that CHF increases as heater size decreases. The increased CHF is attributed to a smaller flow resistance for the small-sized heater.

In addition, our previous study [7] found that the heater size effect appears when $L' < 8$. We conjectured that it is the limited Helmholtz wavelength on a small-sized heater causing the heater size effect.

In this work, the mechanism causing the heater size effect was examined by conducting pool boiling on silicon micropillar array-coated surfaces for three

different heater sizes.

2. Experimental Method

The silicon micropillar array was fabricated using deep reactive-ion etching (DRIE). The scanning electron microscope (SEM) and the optical microscope (OM) images of the silicon micropillar array-coated surface are shown in Fig. 1(a) and Fig. 1(b), respectively. Fig. 1(a) shows the cross-sectional view of the silicon micropillar and Fig. 1(b) shows the top view of the silicon micropillar array. The height, diameter and pitch between the pillars are about 52, 8 and 8 μ m, respectively, whereas the size of each patch in the array is about 344 μ m and the channel width is about 64 μ m.

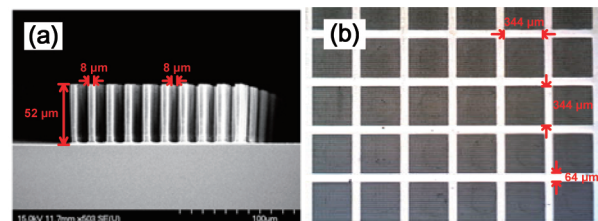


Fig. 1 (a) SEM image of the cross-sectional view of the silicon micropillar array; (b) OM image of the top view of the silicon micropillar array.

Three different heater sizes (0.5×0.5 , 1×1 , and 1.5×1.5 cm²) were studied to examine the effect of heater size on the CHF. The fabrication procedure of the heaters and the test section assembly are the same as that in our previous study [7].

The experimental setup is shown in Fig. 2(a) and the layout of the thermocouples on the backside of the silicon wafer is shown in Fig. 2(b). The temperature of the heater was measured by the two thermocouples at the center of the heater (dark solid circles in Fig. 2(b)). In addition, three more thermocouples were bounded at the edge of the heater separated in equal distance (2mm) from the edge to measure the conduction heat loss (see Fig. 2(b)). The temperature data was collected by a data acquisition (DAQ) unit. Furthermore, a high speed camera was used to take the boiling images at each applied power. The conduction heat loss was obtained from the Fourier's law using the measured temperature

gradient at the edge of the heater [7].

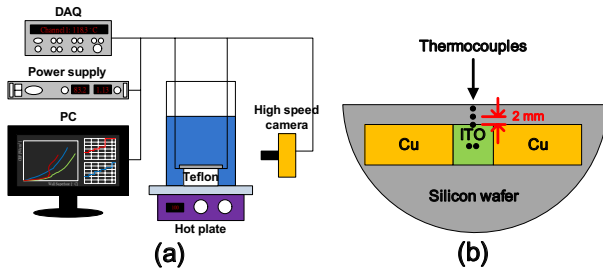


Fig. 2 (a) Experimental setup; (b) backside of the silicon wafer, in which the area of Indium Tin Oxide (ITO) defines the heater size and two Cu electrodes are used for passing electrical current to heat the ITO heater.

3. Results and Discussion

The effect of heater size on the CHF was examined by conducting pool boiling experiments on the silicon micropillary array-coated surfaces for three different heater sizes (0.5×0.5 , 1×1 , and 1.5×1.5 cm²). The obtained CHF_s and the CHF_s after subtracting conduction heat losses are shown in Fig. 3. The red open triangle and blue solid circles shown in the figure are the obtained CHF_s and the CHF_s after subtracting conduction heat losses, respectively, for the three different sizes of the heaters. In the figure, the points of the CHF_s are the average of the obtained CHF_s on at least three samples having the same morphology, while the error bars represent the standard error of the means.

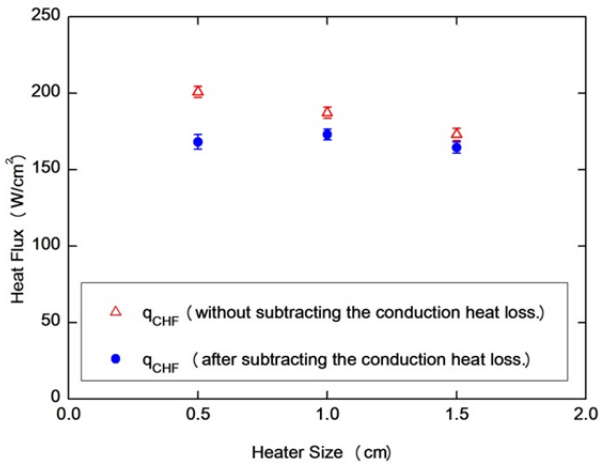


Fig. 3 CHF versus heater size. The red open triangles are the CHF_s without subtracting the conduction heat losses, while the blue filled circles are the CHF_s after subtracting the conduction heat losses.

It is observed that the CHF increases as heater size reduces, which is similar to previous findings [2]. However, there was no apparently heater size dependent found for the values of the CHF_s after subtracting conduction heat losses on the corresponded sizes of the heaters (see blue solid circles in Fig. 4). The highest obtained CHF (after subtracting the conduction heat loss) is 173 ± 3.6 W/cm² on the 1 cm² sized heater. Further, it

is found that the conduction heat loss is dependent on the heater size, i.e., the conduction heat loss increases as the heater size reduces. We conjectured that the increased conduction heat loss is a result of the augmentation of the edge effect as the size of the heater reduces.

4. Concluding remarks

The effect of heater size on the CHF has been examined by studying pool boiling on the micropillar array-coated surfaces with three different sizes of the heaters (0.5×0.5 , 1×1 , and 1.5×1.5 cm²). The highest obtained CHF (after subtracting the conduction heat loss) is 173 ± 3.6 W/cm² on the 1 cm² sized heater. It is observed that the CHF increases as heater size reduces. However, there is no apparently size-dependence observed for the values of the CHF_s after subtracting conduction heat losses. In addition, the percentage of the conduction heat loss also increases as heater size reduces. Thus, the increase of CHF with reducing heater size is a result of the increased conduction heat loss for a small-sized heater.

References

- [1] V.P. Carey, Liquid–Vapor Phase-Change Phenomena: An Introduction to the Thermophysics of Vaporization and Condensation Processes in Heat Transfer Equipment, second ed., Taylor and Francis, New York, (2008).
- [2] A. Bar-Cohen and A. McNeil, Parametric effects of pool boiling critical heat flux in dielectric liquids, in: Proceedings of the Engineering Foundation Conference on Pool and External Flow Boiling, ASME, Santa Barbara, CA, (1992) 171–175.
- [3] J.H. Lienhard and V.K. Dhir, Hydrodynamic Theory of the Peak and Minimum Pool Boiling Heat Fluxes, CR-2270 (1973).
- [4] I.I. Gogonin and S. S. Kutateadze, Critical heat flux as a function of heater size for a liquid boiling in a large enclosure, J. Eng. Phys., 33 (1977) 1286-1289.
- [5] K.N. Rainey and S.M. You, Effects of heater size and orientation on pool boiling heat transfer from microporous coated surfaces, Int. J. Heat Mass Transfer, 44 (14) (2001) 2589-2599.
- [6] S.M. Kwark *et al.*, Effects of pressure, orientation, and heater size on pool boiling of water with nanocoated heaters, Int. J. Heat Mass Transfer, 53 (23-24) (2010) 5199-5208.
- [7] M.C. Lu, R. Chen, V. Srinivasan, V.P. Carey, A. Majumdar, Critical heat flux of pool boiling on Si nanowire array-coated surfaces, Int. J. Heat Mass Transfer, 54 (25-26) (2011) 5359-5367.

An Investigation of the Effects of a Height on Natural Convection between Two Horizontal Parallel Plates with a Heated Bottom Surface

Shang-Hao Huang, Wu-Shung Fu, Wei-Hsiang Wang (National Chiao Tung University, Taiwan)
1001 Ta Hsueh Road, Hsinchu, Taiwan
shhuang.me98g@g2.nctu.edu.tw; wsfu@mail.nctu.edu.tw; flyman.me98g@g2.nctu.edu.tw

The effect of a height on natural convection between two horizontal parallel plates with a heated bottom surface is investigated numerically. Numerical methods of the Roe scheme, preconditioning and dual time stepping are adopted for solving governing equations of a low speed compressible flow. By increasing the height of horizontal parallel plates, the thermal and flow fields changing from a steady to an unsteady situation are observed and the Nusselt number also increases.

1. Introduction

Natural convection in opened-ended horizontal parallel plates is a very important subject in both academic and industrial researches. A low-speed compressible fluid flow is taken into consideration instead of Boussinesq assumption in high temperature difference [1]. Kitamura and Asakawa [2] showed that the unsteady situation that appeared over the heated plate gradually disappear with decreasing distance between parallel plates. The process of variation of flow field from a steady to an unsteady situation was difficult to express because of the limitation of time-averaged experimental results. Turgut and Onur [3] revealed that the increment of the average Nusselt number by the increment of the separation distance. It is observed that plate separation distance has influence on the natural convection heat transfer between parallel plates. Both results of numerical and experimental works had good agreements. Due to the presentation of time-averaged results, the phenomenon of unsteady natural convection was not discussed. Yang et al. [4] investigated the thermal fluid instability between two horizontal parallel plates with three different thermal condition cases numerically. The phenomenon of instability was mainly induced by a thermal perturbation of temperature obtained from a Gaussian random number generator. Because of the initial assumption of the perturbed temperature, the process of stability changing to instability could not be indicated. In those past study, the effect of distance between horizontal parallel plates that is very important and the phenomena of natural convection varying from a steady to an unsteady situation in a heating process are hardly studied. Therefore, the aim of this study investigates of the effects of a height on natural convection between two horizontal parallel plates with a heated bottom surface numerically.

2. Physical Model

A physical model of three dimensional horizontal parallel plates is indicated in Fig.1. The length, height and width are l , h and d , respectively. The temperature of the heated bottom surface is $T_h(700K)$, and the top plate is adiabatic. The gravity is downward and the temperature and pressure of the surroundings are $T_0(298K)$ and $P_0(101300Pa)$, respectively.

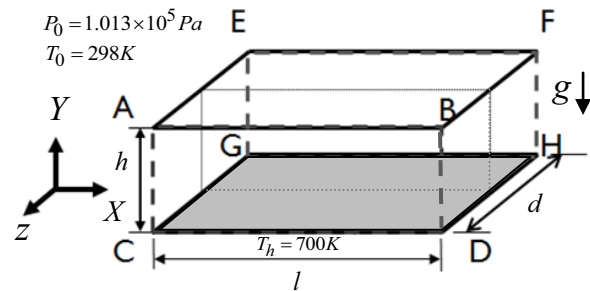


Fig. 1 Physical model

3. Numerical Method

For the investigation of the heat transfer with high temperature difference, the numerical method of compressible flow without Boussinesq assumption is considered. The governing equations of a compressible flow can be divided into two parts. One is the inviscid term and the other is the viscous term. The Roe scheme with 3rd order MUSCL proposed by Abalakin et al. [5] are used to compute the inviscid terms. The method of dual time stepping is added to calculate the transient state. And a second order central difference method is adopted to calculate the magnitudes of the viscous terms. Finally, the LUSGS was modified by [6] to suitable for preconditioning in solving temporal term. The non-reflecting boundary conditions are used at the apertures of the channel in order to avoid a low speed compressible flow to be polluted by the reflections of acoustic waves. And both sides of the width are periodic conditions.

And governing equations can be obtained.

$$\Gamma \frac{\partial U_p}{\partial \tau} + \frac{\partial U}{\partial t} + \frac{\partial F}{\partial x} + \frac{\partial G}{\partial y} + \frac{\partial H}{\partial z} = S \quad (1)$$

where τ is the artificial time, t is the physical time. Γ is a preconditioning matrix proposed by Weiss and Smith [7]

4. Results and Discussion

In Fig.2, histories of development of thermal fields and streamlines are indicated under the $Ra^* = 2.18 \times 10^6$ situation. In Fig.2 (a), Fluids close to the heat wall are heated and expanded, and then part of the fluids is discharged through the apertures. In Fig. 2(b) ~2(e), heated fluids with light density exerted by the buoyancy force ascend to the top wall. Ascending fluids along the

longer heated bottom wall continuously accumulate and start to form several circulations. And as time passes, the circulations is gradually disappear. In Fig. 2(f), ascending fluids impinge the top wall and separately flow to both apertures. Thermal and flow fields incline to a steady situation.

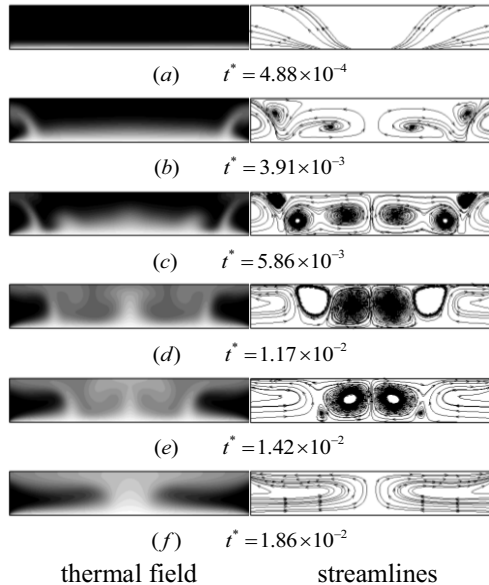


Figure 2 Histories of development of thermal field and streamlines under $Ra^* = 2.18 \times 10^6$

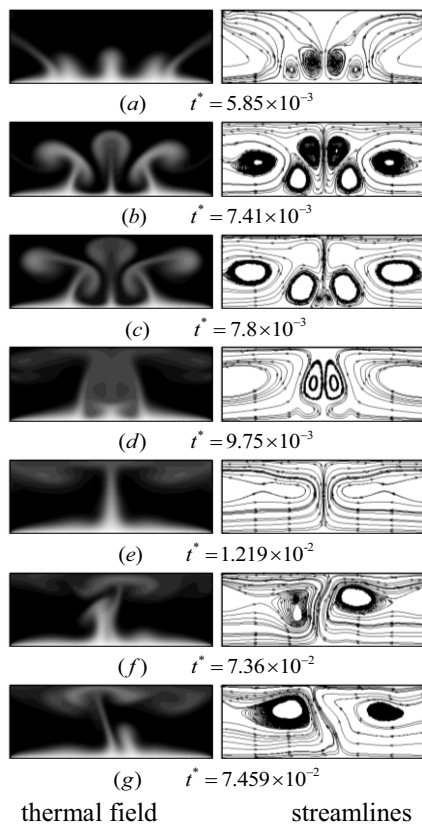


Figure 3 Histories of development of thermal field and streamlines under $Ra^* = 8.66 \times 10^6$

In Fig.3, Since the heated bottom surface is long, two couples of circulations appear simultaneously in Fig. 3(a). In Fig. 3(b) ~3(d), two couples of circulations are sequentially enlarged and raised by the strong strength of the buoyancy force. Meanwhile, two new circulations are also produced as fluids are sucked from the apertures periodically. In Fig. 3(e), the variations of thermal and flow fields are symmetric based on the centerline. As a result, shown in Fig.3 (f) ~3(g), the thermal and flow fields separately distributed in both half regions begin to swing unsteadily.

In Fig. 4, the distributions of variations of area average Nusselt numbers with time under different Rayleigh numbers are shown. For $Ra^* = 2.18 \times 10^6$, the average Nusselt numbers fluctuates in $t^* = 0.02$, and then stabilizes after 3s. But for $Ra^* = 8.66 \times 10^6$, the average Nusselt numbers with time oscillates and never becomes a steady state.

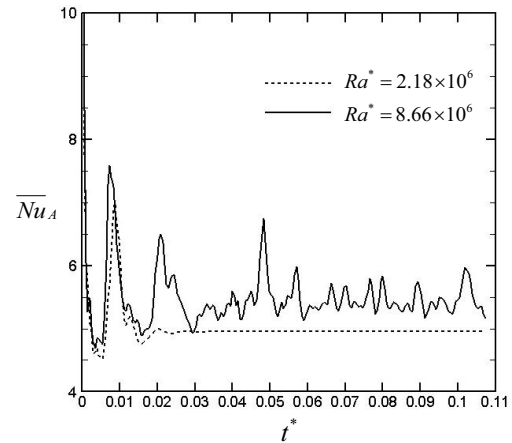


Figure 4 Distributions of variations of area average Nusselt numbers with time under different Rayleigh numbers.

5. Concluding remarks

Several conclusions are summarized as follows.

1. By increasing the height, behaviors of both thermal and flow fields changing from a steady to an unsteady situation are observed.
2. The Nusselt number increase under high natural convection condition.

References

- [1] D.D. Gray, A. Giorigini, Int. J. Heat Mass Transfer, **19** (1976) 545-551.
- [2] K. Kitamura, T. Asakawa, Heat Transfer Asian Research **29** (2000) 333-346.
- [3] Oğuz Turgut, Nevzat Onur, Int. J. Heat Mass Transfer **34** (2007) 644-652.
- [4] H. Yang, Z. Zhu, J. Gilleard, Int. J. Heat Mass Transfer **44** (2001) 1485-1493
- [5] I. Abalakin, A. Dervieux, T. Kozubskaya, INRIA (2002) No4459.
- [6] W. S. Fu, C. G. Li, W. F. Lin and Y. H. Chen, Int. J. Nume. Meth. Fluids (2008).
- [7] J. M. Weiss and W. A. Smith, AIAA. **33** (1995) 2050-2056

Numerical Simulation of Heat Transfer of Closed Loop Pulsating Heat Pipe

Rong-Jer Lai Jia-Wei Chiou
Department of Mechanical Engineering
National Kaohsiung University of Applied Sciences
Kaohsiung, Taiwan
rjlai@cc.kuas.edu.tw 1098303135@cc.kuas.edu.tw

ABSTRACT

In this study numerical simulations based on the κ -epsilon model are carried out to analyze the heat transfer of closed loop pulsating heat pipe. Existing experimental research is chosen as the object of simulation. The predicted average evaporator temperatures show in good agreement with the experimental data.

1. Introduction

Due to the relatively simple structure and cost effectiveness the pulsating heat pipe (PHP) becomes an attractive heat transfer device, but the fluid dynamics governing the two-phase oscillating flow and the heat transfer are complicated, so that despite the efforts made in modeling and experiments on PHP in the last decades the results up to now remain diversified [1]. In this study existing experimental research is chosen as the object of simulation. The volume of fluid (VOF) model is selected for the multiphase system [2], and numerical simulations based on the κ -epsilon turbulence model are undertaken through the use of CFD software FLUENT.

2. Method

In general, there are three variants of κ -epsilon model, namely standard, renormalization group (RNG) and realizable. All three models have similar forms, with transport equations for turbulent kinetic energy (κ) and its dissipation rate (ϵ). The features that are essentially common to all models include the turbulent production, generation due to buoyancy, accounting for the effects of compressibility, and modeling heat and mass transfer. The major differences in the models are the method of calculating turbulent viscosity, the turbulent Prandtl numbers governing the turbulent diffusion of κ and ϵ , and the generation and destruction terms in the ϵ equation [3].

The standard κ - ϵ model consists of the turbulent kinetic energy equation:

$$\frac{\partial}{\partial t}(\rho\kappa) + \frac{\partial}{\partial x_i}(\rho\kappa u_i) = \frac{\partial}{\partial x_j} \left[\left(\mu + \frac{\mu_t}{\sigma_\kappa} \right) \frac{\partial \kappa}{\partial x_j} \right] + G_\kappa + G_b - \rho\epsilon - Y_M + S_\kappa \quad (1)$$

, and the dissipation rate equation:

$$\frac{\partial}{\partial t}(\rho\epsilon) + \frac{\partial}{\partial x_i}(\rho\epsilon u_i) = \frac{\partial}{\partial x_j} \left[\left(\mu + \frac{\mu_t}{\sigma_\epsilon} \right) \frac{\partial \epsilon}{\partial x_j} \right] + C_{1\epsilon} \frac{\epsilon}{\kappa} (G_\kappa + C_{3\epsilon} G_b) - C_{2\epsilon} \rho \frac{\epsilon^2}{\kappa} + S_\epsilon \quad (2)$$

The turbulent heat transport is modeled by the following:

$$\frac{\partial}{\partial t}(\rho E) + \frac{\partial}{\partial x_i} [u_i(\rho E + p)] = \frac{\partial}{\partial x_j} \left(k_{eff} \frac{\partial T}{\partial x_j} + u_i(\tau_{ij})_{eff} \right) + S_h \quad (3)$$

Implicit option of the coupled solver is chosen for all variables in the fields of pressure, velocity and temperature.

3. Results and Discussion

The object of numerical simulation is an existing experimental research on closed loop pulsating heat pipe (CLPHP) with copper tubes of ID 2.0 mm and OD 3.0 mm, in vertical mode with ethanol as working medium in various fill ratios (Fig.1) [4]. Following the model mentioned above, the periodic oscillations of liquid slugs and vapor plugs in the CLPHP were observed through the predicted average evaporator temperature curves, as illustrated in Fig. 2 - Fig. 4. The numerical simulations show in good agreement with the experimental data. In addition, for the case with ethanol in filling ratio 55%, heating power up to 15 W there are almost no differences for the average evaporator oscillation temperature to be observed between the predictions using standard, RNG and realizable κ -epsilon model (about 72,75,70°C respectively).

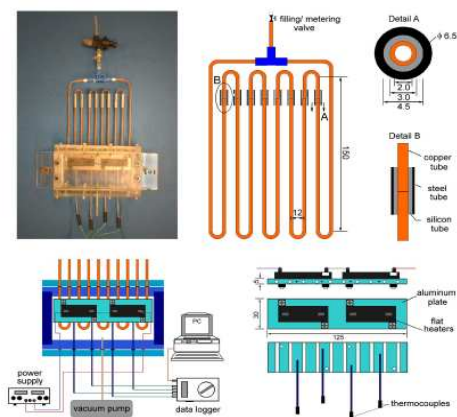
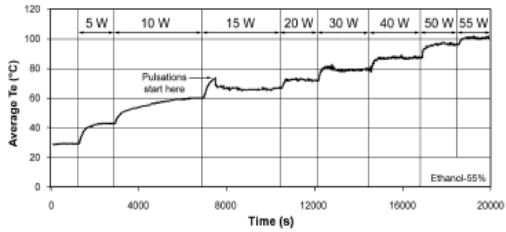
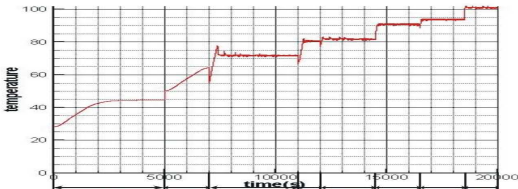


Fig. 1 Closed loop pulsating heat pipes (CLPHP) [4]

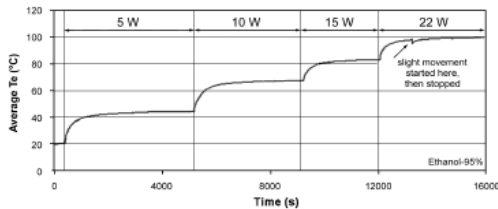


(a) experimental data

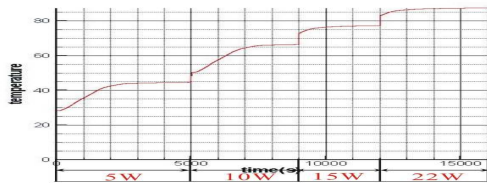


(b) numerical prediction

Fig. 2 Average evaporator temperatures with ethanol in filling ratio 55%

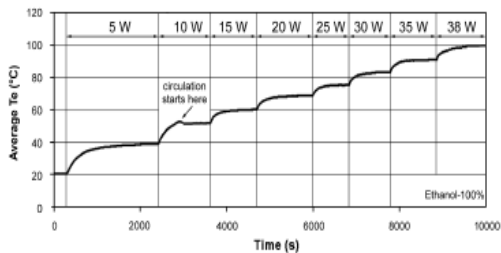


(a) experimental data



(b) numerical prediction

Fig. 3 Average evaporator temperatures with ethanol in filling ratio 95%

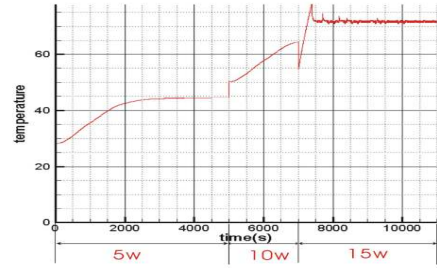


(a) experimental data

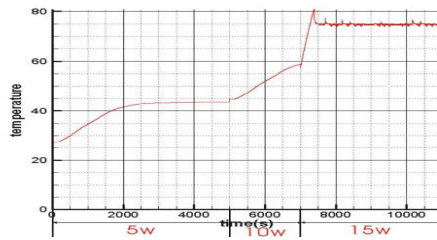


(b) numerical prediction

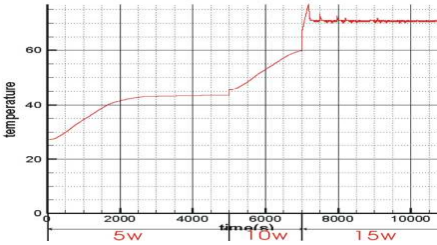
Fig. 4 Average evaporator temperatures with ethanol in filling ratio 100%



(a) standard κ -epsilon



(b) RNG κ -epsilon



(c) realizable κ -epsilon

Fig. 5 Predictions of evaporator oscillation temperature with ethanol in filling ratio 55% using (a) standard, (b) RNG and (c) realizable κ -epsilon model for heating power up to 15 W

4. Concluding remarks

In this study numerical simulations based on the κ -epsilon model are carried out to analyze the heat transfer of closed loop pulsating heat pipe. The published experiment is chosen as object of simulation. The numerical predictions of average evaporator temperatures show in good agreement with the experimental data, and should be applicable for the engineering purpose. In addition, for the CLPHP under study with heating power 15 W there are almost no differences between the predictions of evaporator oscillation temperature using different κ -epsilon models.

References

- [1] Y. Zhang and A. Faghri, Heat Transfer Engineering, **29**:1(2008), pp.20-44.
- [2] FLUENT 6.3 User's Guide, Fluent Inc., (2006), Chap. 24.
- [3] FLUENT 6.3 User's Guide, Fluent Inc., (2006), Chap. 11.
- [4] S. Khandekar, Dr.-Ing. Diss., Universität Stuttgart, Germany,(2004), http://elib.uni-stuttgart.de/opus/volltexte/2004/1939/pdf/Diss_Khandekar.pdf

From Miscible to Immiscible:

Modeling of a Diffuse Interface and Its Implementations in Hele-Shaw Flows

Ching-Yao Chen

Department of Mechanical Engineering, National Chiao Tung University
E-mail of corresponding author: chingyao@mail.nctu.edu.tw

ABSTRACT

In this presentation, the diffuse-interface model by the classical Cahn-Hilliard approach is applied to flows in a Hele-Shaw cell. By considering different types of the free surface energy within the diffuse interface, the approach is capable, if properly applied, to catch the interfacial phenomena for both a miscible system in which the interface diffuses continuously, and an immiscible system whose surface is confined within an extremely thin region.

1. Introduction

The mixing phenomena of fluids are generally classified as being miscible or immiscible. An immiscible system is characterized by a strict interface, whose boundary cannot be crossed by the molecules of adjoining liquids. This high potential barrier can be explained by different intermolecular interactions within the mixture components on molecular scale. A surface tension is commonly introduced to define the macroscopic effects of the interfacial potential barrier. On the other hand, the intermolecular forces between miscible fluids are much smaller. The molecules of initially separated components are assumed to freely codiffuse, so that there is no surface tension on the fluids' boundary. Based on the above arguments, the two systems of miscible/immiscible are usually modeled differently into the governing equations. For instance, an additional term of surface tension acting at a moving boundary is included into the momentum equations for an immiscible system, while the miscible system is solved associated with a conventional advection-diffusion equation of concentration followed by the Fick's Law. Nevertheless, there are cases of the miscible liquids, for which the intermolecular forces cannot be neglected, and apparent interfaces are visible for a long period time. As a result, it is also necessary to describe the concept of interfacial tension of a slowly miscible system.

In this presentation, the diffuse-interface model [1,2] by the classical Cahn-Hilliard approach is discussed. By considering the free surface energy within the diffuse interface, the approach is capable, if properly applied, to catch the interfacial phenomena for both a miscible system in which the interface diffuses continuously, and an immiscible system whose surface is confined within an extremely thin region.

2. Method

We investigate the interfacial instability between two miscible/immiscible fluids in a rotating Hele-Shaw cell (Fig. 1). The cell has gap spacing h and turns around an axis perpendicular to the plane of the flow with constant angular velocity Ω . Inside the cell an initially circular drop (radius R_0) of fluid 2 is surrounded by an outer fluid 1. The densities and viscosities of the fluids are

denoted by ρ_j and η_j , respectively ($j = 1, 2$). We focus on the centrifugally-induced motion where $\rho_2 > \rho_1$, but allow the inner fluid to be either more or less viscous than the outer fluid.

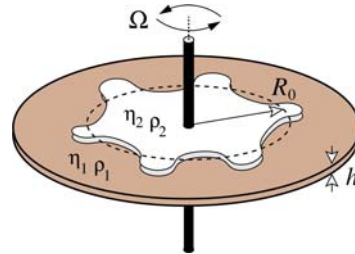


Fig. 1 Sketch of a rotating Hele-Shaw cell

The governing equations of such a diffuse interface problem are based on a model proposed by Cahn and Hilliard [1]. In the context of a rotating Hele-Shaw cell system the dimensionless equations can be written as

$$\nabla \cdot \mathbf{u} = 0, \quad (1)$$

$$\nabla p = -\eta \mathbf{u} - \left(c + \frac{\rho_2}{\Delta \rho}\right) [\mathbf{r} + 2 \text{Re}(\mathbf{e}_z \times \mathbf{u})] - \frac{C}{Ga} \nabla \cdot [(\nabla c)(\nabla c)^T] \quad (2)$$

$$\frac{\partial c}{\partial t} + \mathbf{u} \cdot \nabla c = \frac{1}{Pe} \nabla^2 \mu, \quad \mu = \frac{\partial f_0}{\partial c} - C \nabla^2 c \quad (3)$$

$$f_0 = c^2(1-c)^2 \quad \text{for an immiscible interface;} \quad (4)$$

$$f_0 = 0.5(c-0.5)^2 \quad \text{for a miscible interface.}$$

Here, \mathbf{u} denotes the fluid velocity vector, p the pressure, η the viscosity, and ρ the density of the binary fluid system. The phase-field variable is represented by c , so that $c = 1$ in the bulk of fluid 1 (phase 1), and $c = 0$ in the bulk of fluid 2 (phase 2). The chemical potential is denoted by μ , and f_0 is a free energy. \mathbf{r} is the radial position vector, and \mathbf{e}_z represents the unit vector along the rotation axis (z -axis). Equations (1)-(4) define the so-called Hele-Shaw-Cahn-Hilliard model [3-4]. It is worth noticing that the choice of free energy in equation (4) leads to different interpretations of the model [3-4]. The choice of a quartic free energy indicates the phases are separated, so that is suitable for an immiscible

interface. If a convex free energy is applied, fluid diffusion is allowed. By further assuming an extremely small, the model is identical to the miscible simulations including Korteweg stresses.

3. Results and Discussion

If an immiscible interface is at equilibrium, a rotating Bond number, which represent the ratio between surface tension and centrifugal force, can be obtained as $Bo=(C/2)^{0.5}/3Ga$. In the linear regime, it has been found that the number of fingers (N) follows a correlation of $N \sim \{1/3 Bo\}^{0.5}$, which is used to quantitatively validate the numerical codes. Excellent agreements are obtained as shown in Fig. 2 for a wide range of Bond number. In addition, the fingering patterns obtained resemble the existing experimental results remarkably, including different fingering competition behaviors for Atwood number varying from a negative value to positive [5]. Various flow conditions, including radial injections or cell lifting conditions for immiscible/miscible interfaces, are simulated to further demonstrate the capability of the present numerical scheme. Shown in Fig. 3 are cases which demonstrate the effects of Coriolis to an immiscible interface. The fingers show interesting pinch-off. The emissive droplets and fingers appear an apparent rotating orientation. Correspondent cases in a fully miscible condition with effects of the effective Korteweg stresses [6] are shown in Figs. 4 and 5, respectively.

4. Concluding remarks

Numerical simulations for miscible and immiscible systems are demonstrated to illustrate their interfacial morphologies and dynamics. In a miscible system, the effects of interfacial tension are investigated in various situations and models, such as conditions of zero surface tension in the conventional Fick's law, inclusion of effective interfacial tension by a simplified model of the Korteweg stresses and results from the completed Cahn-Hilliard equations. The Cahn-Hilliard equations are also implemented to simulate an immiscible system with a sharp interface whose interfacial free energy is prominent.

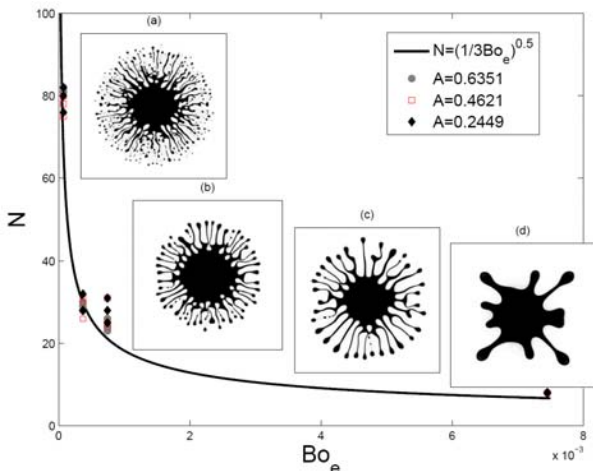


Fig. 2: Immiscible simulations without effects of Coriolis

force: Numbers of fingers (N) versus the rotating Bond number (Bo). The curve represents an analytical relationship, which agrees well with the numerical results.

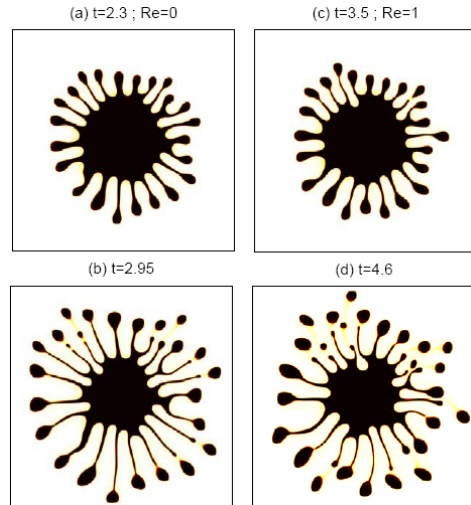


Fig. 3: Immiscible simulations with effects of Coriolis force for a case of $A=0$, $Bo=1.9 \times 10^{-3}$, and $C=10^{-5}$. Apparent finger distortion can be observed at (c,d).

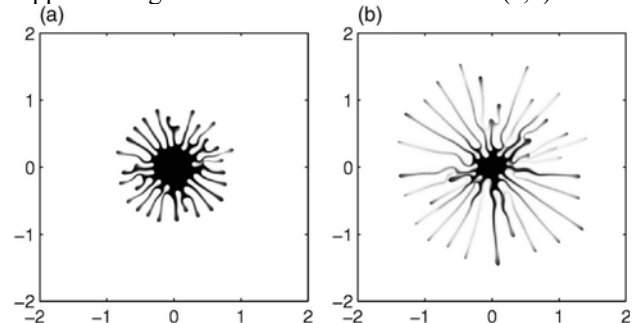


Fig. 4: Miscible simulations with effective interfacial Korteweg stresses and the Coriolis force.

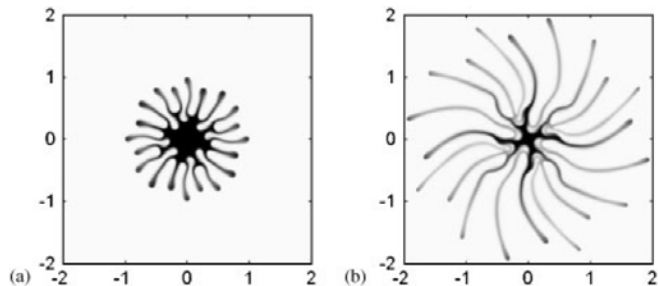


Fig. 5: Miscible simulations with effective interfacial Korteweg stresses but no Coriolis force.

References

- [1] J. W. Cahn and J. E. Hilliard, *J. Chem. Phys.* **28**, 258 (1958).
- [2] D. Jacqmin, *J. Comput. Phys.* **155**, 96 (1999).
- [3] H.-G. Lee, J. Lowengrub, and J. Goodman, *Phys. Fluids* **14**, 492 (2002).
- [4] H.-G. Lee, J. Lowengrub, and J. Goodman, *Phys. Fluids* **14**, 514 (2002).
- [5] C.-Y. Chen, Y.-S. Huang and J. Miranda, *Phys. Rev. E*, **84**, 046302 (2011).
- [6] C.-Y. Chen, C.-H. Chen and J. Miranda, *Phys. Rev. E*, **73**, 046306 (2006).

Experimental Study on Viscous Fingering with a Decrease in Interfacial Tension by a Chemical Reaction

Masanari Fujimura, Yuichiro Nagastu (Tokyo University of Agriculture and Technology),
Yutaka Tada (Nagoya Institute of Technology)
E-mail: 50012648034@st.tuat.ac.jp

ABSTRACT

To reveal recovery efficiency of alkaline flooding for wide ranges of flow rate and concentration of alkali, we perform flow experiments by using a radial Hele-Shaw cell. The reaction is a neutralization of a linoleic acid by sodium hydroxide (NaOH) to form a surfactant, which decreases the interfacial tension. We observe the non-reactive system had more recovery efficiency for the low flow rate, but for the high flow rate, reactive fingering leads to the increment of oil recovery. In addition, the VF pattern transmuted with the concentrations of NaOH. We speculate this mechanism is associated with Marangoni stresses.

1. Introduction

Viscous fingering (VF) is a hydrodynamic instability that typically occurs when a more viscous fluid is displaced by a less viscous one in a porous medium or a Hele-Shaw cell [1] Homsy 1987. The interface between the two fluids becomes unstable undergoing finger-like patterns. This situation is commonly encountered in oil recovery. When heavy oil in oil reservoir is swept by water, the displaced interface become finger pattern which cause a decrease in oil recovery. In general, alkaline flooding indeed improves oil recovery compared to waterflooding. Alkaline flooding is a well-known technique of enhanced oil recovery (EOR) [2]. When an alkaline solution is injected into the reservoir, an interfacial reaction takes place between the oil-based acid and the water-based alkali. This results in time-dependent (dynamic) interfacial tension at the oil-water interface [3].

In past times, some studies of alkaline flooding in the Hele-Shaw cell have been conducted with different conditions [2-4]. Despite these previous works, it has not been revealed which is more efficiency, alkaline flooding or waterflooding. In order to reveal alkaline flooding efficiency, we performed the experiments in the Hele-Shaw cell with wider experimental condition.

2. Experiment

Our Hele-Shaw cell is formed by two transparent glass plates of 140 mm × 140 mm × 10 mm thickness with a constant gap width b . The gap width b is set as $b = 0.1$ mm by placing four metal triangular plates at four corners between the two glass plates. For liquid injection, the upper glass plate has a small hole of 4 mm in diameter in the centre. A syringe pump was used to inject the liquids. The viscous fingering formed in the Hele-Shaw cell was videotaped by a CCD camera mounted below the cell.

In the alkaline flooding, 0.01 M linoleic acid in paraffin oil (viscosity = 126 mPa·s) was displaced by 0.2, 0.02, 0.002 M aqueous sodium hydroxide solutions (NaOH) with a given concentration, C_{NaOH} . In the waterflooding, the same oil (0.01 M linoleic) was displaced by deionized water. The injected solutions were colored by adding 0.1 wt% trypan blue.

The cell was first filled with the oil to be displaced. The syringe pump was adjusted to the required flow rate

($q = 0.526 \times 10^{-9} - 71.4 \times 10^{-9} \text{ m}^3/\text{s}$). Then, the displacing fluid entered into the cell. In the present experiments, the oil recovery efficiency of each system was evaluated by a time (t_b) until which the longest finger reaches at a certain radius. Based on the evaluation, larger t_b means the high efficiency.

3. Results and Discussion

The images of waterflooding and alkaline flooding with different NaOH concentrations at $q = 8.21 \times 10^{-9} \text{ m}^3/\text{s}$ (low flow rate) are shown in Figure 1. It is observed that the fingers become thinner as C_{NaOH} increases. Furthermore, then when $C_{\text{NaOH}}=0.02$ and 0.2 M, water drops are formed. As a result, t_b is smaller as C_{NaOH} increases. In other words, the efficiency is smaller in alkaline flooding.

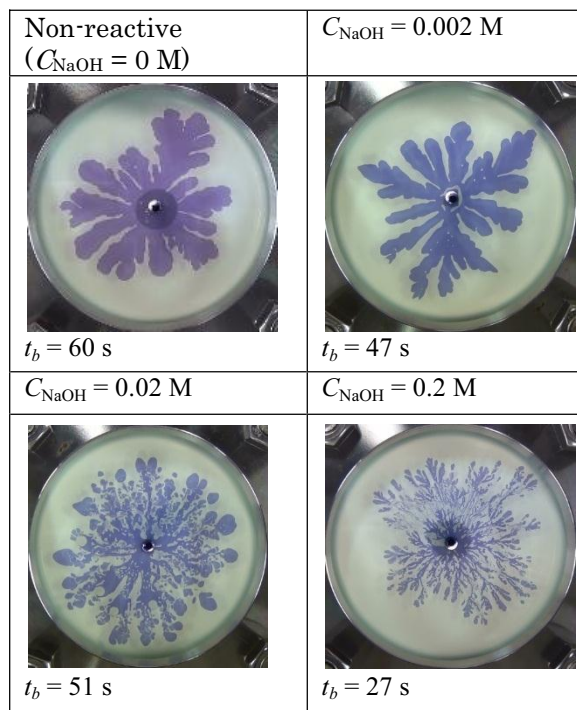


Figure 1, Images of waterflooding and alkaline flooding ($q = 8.21 \times 10^{-9} \text{ m}^3/\text{s}$)

Figure 2 shows the images at $q = 36.2 \times 10^{-9} \text{ m}^3/\text{s}$ (high flow rate). We find the fingers in alkaline flooding become wider than those in waterflooding. As a result, t_b

is larger in alkaline flooding. This indicates the efficiency is larger in alkaline flooding. It should be emphasized that the result for low flow rate is opposite to those for high flow rate.

Non-reactive ($C_{\text{NaOH}} = 0$)	$C_{\text{NaOH}} = 0.002 \text{ M}$
	
$t_b = 6.2 \text{ s}$	$t_b = 14.0 \text{ s}$
$C_{\text{NaOH}} = 0.02 \text{ M}$	$C_{\text{NaOH}} = 0.2 \text{ M}$
	
$t_b = 9.2 \text{ s}$	$t_b = 13.2 \text{ s}$

Figure 2, Images of waterflooding and alkaline flooding ($q = 36.2 \times 10^{-9} \text{ m}^3/\text{s}$)

We speculate that the opposite effects of the chemical reaction on the fingering pattern depending on the flow rate would be caused by difference in how Marangoni stresses act on the finger. Interfacial tension would not be constant along the finger as result of the chemical reaction taking place at the interface. The Marangoni stresses cause flow from regions of low tension to high.

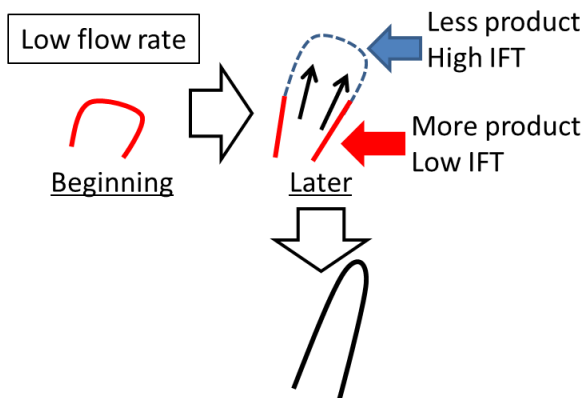


Figure 3, Marangoni stress acting on the finger at low flow rate

At low flow rate, at the tips of finger the interface are freshly created. Farther down along the finger the interface has had time to react and form interfacially-active species. As a result of this, surfactant concentration gradients will be produced at the

interface; the tips are higher interfacial tension (Figure 3). Such conditions induce Marangoni flow toward the tips and make finger thinner.

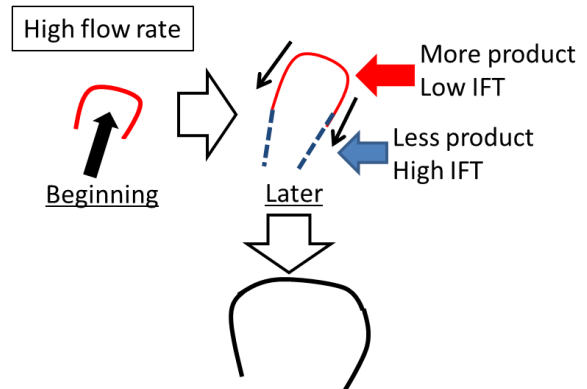


Figure 4, Marangoni stress acting on the finger at high flow rate

At high flow rate, in the troughs, the reaction is diffusional limitations. Otherwise, the reaction goes to higher completion near the tips than the troughs. As a result, the interface of the tips is relatively lower interfacial tension than that of the troughs (Figure 4). Such interfacial tension gradient cause Marangoni flow toward the troughs, which makes finger wider.

4. Conclusion

We conducted flow experiments of alkaline flooding in the Hele-Shaw cell with wide range of experiment conditions. The effect of chemical reaction on the finger pattern and recovery efficiency depend on flow rate. At low flow rate, the waterflooding is more efficiency. But at high flow rate, alkaline flooding improves oil recovery. We speculate that this mechanism is due to Marangoni flow caused by the interfacial tension gradient.

Reference

- [1] Homsy, G. M. 1987 *Annu. Rev. Fluid Mech.* **19**, 271-311.
- [2] Hornof, V., Neale, G. M., Hosseini, G. M. 2000 *J Colloid Interf Sci.* **231**, 196-198
- [3] Hornof, V., Baig, F. U., 1995 *Exp Fluids.* **18**, 448-453
- [4] Fernandez, J., Homsy, G. M. 2003 *J. Fluid Mech.* **480**, 267-281

Pattern Transition from Fingering to Fracturing in a Reacting Flow Producing Gel

Tomohiro Ujiie¹, Yuichiro Nagatsu², Shuichi Iwata¹, Yoshihito Kato¹, Yutaka Tada¹

¹Nagoya Institute of Technology, Gokisocho, Showa-ku, Nagoya, Aichi, 466-8555, Japan

²Tokyo University of Agriculture and Technology, Naka-cho, Koganei, Tokyo 184-8588, Japan
nagatsu@cc.tuat.ac.jp

ABSTRACT

We have experimentally investigated pattern formation obtained when a more viscous aqueous polymer solution is displaced by a less viscous solution including a metal ion in a Hele-Shaw cell. When the two liquids contact, a chemical reaction takes place and a gel is formed. For some concentrations of the polymer and the metal ion, a transition from fingering pattern to fracturing pattern is demonstrated as the injection rate exceeds threshold value. We have measured the rheological property of the gel and investigated the relationship between the observed fingering-fracturing transition and the measured rheological property.

1. Introduction

Zhao and Maher, in 1993 [1], reported a displacement experiment in the Hele-Shaw cell in which associating polymer and homopolymer solutions were displaced by water. They observed abrupt pattern transition from viscous fingering (VF) to fracturing when the injection rate of water exceeds threshold value. In fact, both the fingering and fracture patterns were observed under the same condition beyond the threshold injection rate. They never observed fracturing for the homopolymer solution. In addition, they showed the fracturing pattern occurred at the same Deborah number for the associating polymer cases, but, this rule could not be applicable for the homopolymer cases. Here, Deborah number (De) is sometimes used to characterize the flow of a viscoelastic material and defined as the ratio of the gel relaxation time τ_r to the characteristic time of the fluid flow τ_f .

In the present study, we observed similar phenomena in a displacement experiment using a homopolymer solution but with a chemical reaction producing a gel. Here, xanthan gum (XG) solution and ferric ion (Fe^{3+}) solution were used as the more and less viscous liquids, respectively. When we mix the two solutions being initially non-premixed, gel is produced. This paper shows the results of the displacement experiment and characterizes the results based on rheological measurements of the gel.

2. Experimental apparatus

2.1 VF experiment

Fig.1 shows experimental apparatus for VF. We used a radial Hele-Shaw cell. The more viscous liquid was dyed by indigo carmine for visualization of the fingering. In the present study, the injection rate (q), and the concentration of ferric ion ($C_{Fe^{3+}}$) were varied, while the gap of the cell (b) and the concentration of (C_{XG}) were fixed. Table 1 shows the detail experimental conditions.

Table 1. Experimental conditions

C_{XG}	0.3 wt%
$C_{Fe^{3+}}$	0.1 M, 1.0 M
q	$5.3 \times 10^{-10} \text{ m}^3/\text{s} \sim 82 \times 10^{-10} \text{ m}^3/\text{s}$
b	0.2 mm

2.2 Rheological measurement of the gel

We used a rheometer with a double wall ring (DWR) type sensor named AR-G2 from TA instrument [2]. Fig.2 shows the schematics of cross section of the sensor. For the measurement, XG solution was first poured into the trough with the circular channel, and then the ring set at the surface. A time sweep experiment was started at fixed frequency and strain. At $t=0$, Fe^{3+} solution was sprayed on the top of the XG solution phase and the gel began to be produced by the reaction in the interface region. After the spray the time sweep was continued. Finally, frequency sweep experiment of the gel was performed.

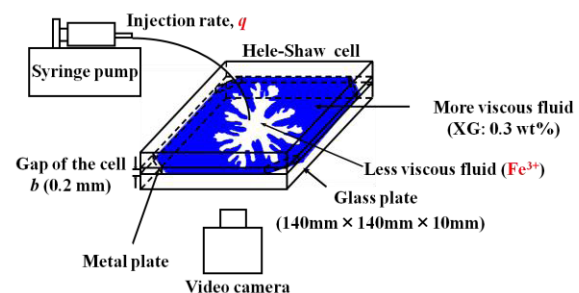


Fig. 1 Apparatus for VF experiment

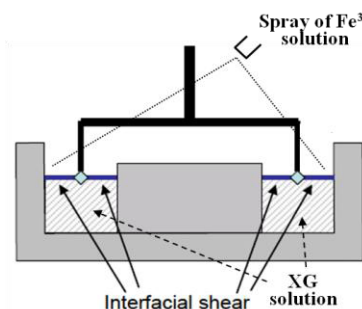


Fig. 2 Schematics of cross section of DWR type sensor

3. Results and Discussion

Fig.3 shows the typical displacement patterns for the various q and $C_{Fe^{3+}}$. When $C_{Fe^{3+}}=0$ M, that is, the nonreactive case, the fingering pattern was observed regardless of q . In addition, there is little influence of q

on the fingering pattern. When $C_{\text{Fe}^{3+}}=0.1$ M, the fingering pattern was observed for the smaller q . We found that there existed a threshold injection rate beyond which the fracture patterns appeared. The transition between the fingering and fracture patterns was very drastic. Actually, in some condition of q , we observed the fingering patterns in some cases whereas the fracture patterns in other cases. For sufficiently larger q , the fracture pattern was always obtained. When $C_{\text{Fe}^{3+}}=1$ M, similar phenomena were observed. It should be noted that the threshold injection rate becomes smaller.

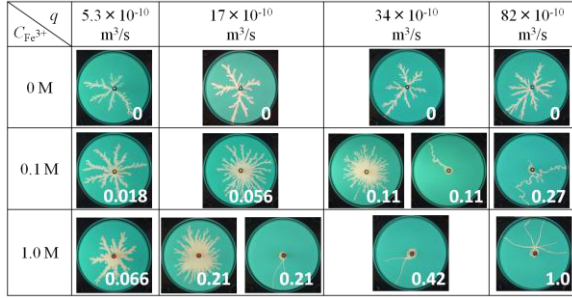


Fig. 3 Typical VF patterns for the various q and $C_{\text{Fe}^{3+}}$

In the present study, we tried characterizing rheological property of the gel produced by the reaction in the interface region between the two liquids in order to explain the obtained displacement results.

Fig.4 shows the results of the time sweep. At $t=0$, both storage modulus (G') and loss modulus (G'') rapidly increased for both $C_{\text{Fe}^{3+}}$. Gradual increase in G' and G'' after the rapid increase is supposed to be caused by an increase in the gel thickness induced by the penetration of the Fe^{3+} into XG. These results indicate that the gel is instantaneously produced. In other words, the chemical reaction employed here can be treated as instantaneous one regardless of $C_{\text{Fe}^{3+}}$.

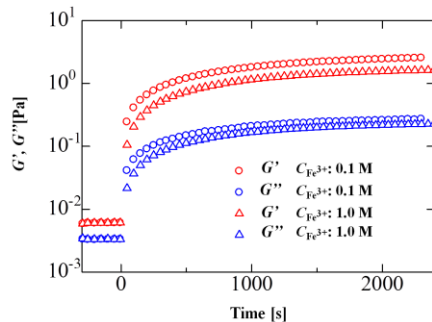


Fig. 4 G' and G'' of the time sweep experiment

Fig.5 shows the shear stress imposed on the gel in the interface region measured after the time sweep. For both the gel, the shear stress increased until a critical shear rate. Beyond the critical value, the shear stress remains almost constant regardless the shear rate. However, the critical shear rate was larger for the ferric ion 0.1 M than that for 1.0 M.

As well as Zhao and Maher, here, we introduce De (Eq. 1~4). We define the characteristic time for the Hele-Shaw flow (τ_f) as Eq. (2). Here, R is the radius which is 58 mm. We used the inverse of the onset shear rate of the shear thinning regime in Fig. 5 as the gel relaxation time (τ_r). Therefore, in the present displacement experiments, we change the De by changing q and $C_{\text{Fe}^{3+}}$.

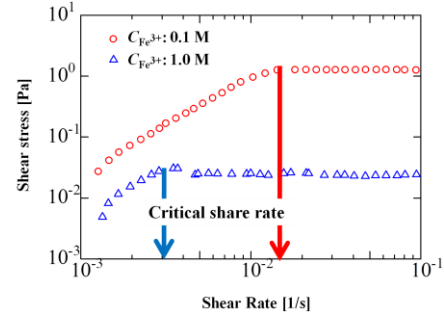


Fig. 5 Shear stress measurement of gel

$$De = \frac{\tau_r}{\tau_f} \quad (1)$$

$$\tau_f = \frac{\pi R^2 b}{q} \quad (2)$$

$$\tau_r = \frac{1}{\dot{\gamma}_0} \quad (3)$$

$$De = \frac{q}{\pi R^2 b \dot{\gamma}_0} \quad (4)$$

We show the results of displacement experiment with the calculated De (Fig. 1). In the nonreactive case, $De=0$. For each $C_{\text{Fe}^{3+}}$, De becomes larger as q is larger. For each q , De becomes larger as $C_{\text{Fe}^{3+}}$ is larger. As shown here, the fracturing pattern is formed when De exceeds around 0.11.

4. Conclusion

We performed experiment on VF with a chemical reaction producing a gel. The transition from the fingering to the fracturing was observed. In addition, we succeeded in characterizing the rheological property of the gel produced by the reaction in the interface region. Finally, we showed that the transition occurred when De exceeds threshold value.

References

- [1] H. Zhao and J. V. Maher
PHYSICAL REVIEW E, 47 (1993), 4278-4283
- [2] Steven Vandebriel, Aly Franck, Gerald G. Fuller
Paula Moldenaers, Jan Vermant
Rheologica Acta, 49 (2010), 131-144

On The Off-center Separation in Binary Droplet Collision

Kuo-Long Pan and Chi-Ru Lu

Department of Mechanical Engineering, National Taiwan University, Taipei 106, Taiwan, R. O. C.

E-mail of corresponding author: panpeter@ntu.edu.tw.

ABSTRACT

We have studied experimentally the collision regimes between two droplets made of hydrocarbon fuels or water. In contrast to five basic regimes generally known, i.e., (I) coalescence after minor deformation, (II) bouncing, (III) coalescence after substantial deformation, (IV) reflective separation, and (V) stretching separation, we have found additional regime named as (VI) second reflexive separation. This regime is characterized by separation of a merged droplet with a scenario different from that proposed in previous studies. In comparison with the existing models, we provide likely interpretation for the unique phenomenon that has been overlooked in the literature.

1. Introduction

The collision dynamics between two droplets plays a crucial role in various disciplines of nature and practical interests. For example, meteorological phenomena such as formation of raindrops, operation of nuclear reactors, spray combustion in liquid-fueled combustors, fire fighting via liquid injection, and relevant applications of spraying processes such as painting, coating, and cooling. The scenarios have been widely investigated [1-5], as demonstrated in Fig. 1, showing characteristic transitions from (I) coalescence after minor droplet deformation to (II) bouncing, to (III) coalescence after substantial droplet deformation, and to (IV) temporary coalescence followed by separation of primary binary droplets and further formation of satellite droplets when a governing dimensionless parameter of Weber number is increased. It is defined as $We = \rho_l U^2 D / \sigma$, where U is the relative velocity, D the diameter of the droplet, and ρ_l and σ respectively the density and surface tension of the liquid.

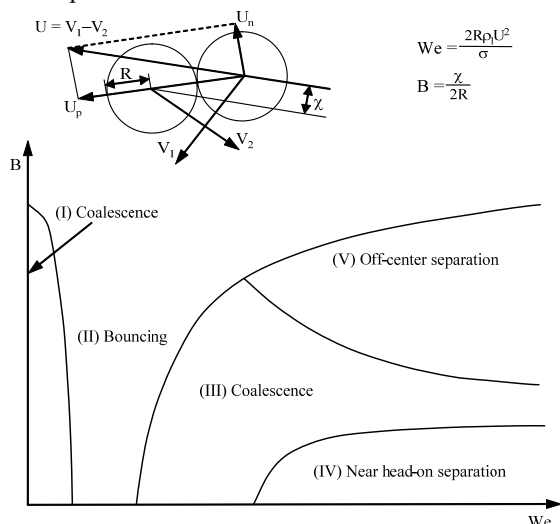


Fig. 1 The regime diagram of hydrocarbon at 1 atm [4].

Another key factor dominating the collision is the impact parameter, $B = \chi / D$, where χ is the projection of the separation distance between the droplet centers in the direction normal to the vector U . Thus $B = 0$ indicates head-on collision and $B = 1$ means grazing

condition. If We is sufficiently large, with increase of B , two distinct scenarios of separation after merging of droplets have been reported. That is, reflexive separation in near head-on impact due to reflection of colliding masses and stretching (or off-center) separation at large B caused by stretching of temporarily coalesced masses that are however not aligned in a collinear path. Various models and mechanisms have been proposed for comprehensive interpretation of these phenomena. The results nonetheless are somehow not consistent with each other and the accuracy may degenerate in different studies. In this work we propose a new regime diagram according to the experimental finding. As shown in Fig. 2, a different type of separation structure is caught in the middle range of B . The elucidation would eliminate the inconsistency raised in previous studies.

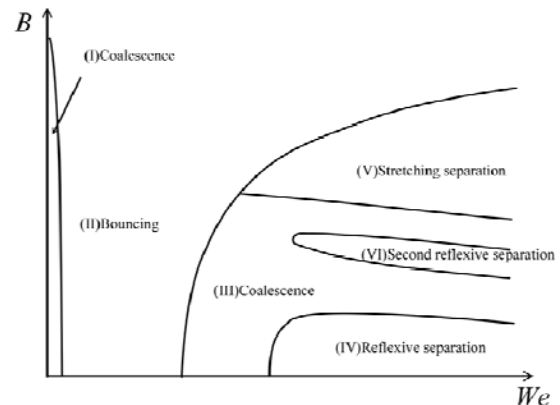


Fig. 2 The new regime diagram of hydrocarbon at 1 atm.

2. Method

The experimental setup was similar to that described in Refs. [5] and [6]. Two identical droplets were generated by nozzles that were triggered by the vibration of piezoelectric plates. They were made to impinge onto each other with adjusted angles of the colliding path. Time-resolved images were either taken through stroboscopy synchronized with the droplet generation circuit or recorded by a high-speed CMOS digital camera (X-StreamTM Vision, XS-4), which supported a maximum resolution of 512×512 pixels with 5100 frames per second (fps). In the test condition requiring high resolution in time, the frame rate was raised to

20,000 fps while the resolution was shrunk to 128×512. The shutter of the high-speed camera was synchronized with a LED lamp that can support the shortest duration of 1 μ s, so as to capture images with sufficiently small exposure and adequate light intensity while avoiding slurring due to background scattering. In contrast, for high spatial resolution, a standard CCD was used to take droplet pictures as the motion was synchronized with the stroboscopic light. With precise control of the delays of electronic signals, a digital imaging system then accurately time-resolved the collision event, recorded the droplet image, and processed the data. This yielded the fine temporal resolution of the transitional behavior between different regimes. Due to stringent requirement of droplet steadiness, however, this technique might not readily render desired points on the regime diagram; thus a complimentary approach using the high-speed camera was implemented. More details are referred to [7].

3. Results and Discussion

Different hydrocarbons and water have been tested. They all demonstrated the existence of a new regime of separation following temporary merging of two identical droplets. Figures 2 and 3 are the integrative results of decane, dodecane, and tetradecane. Specifically in Fig. 3, as B is increased, the collision outcome can be compared for the selected points. The sequences of images are shown in Figs. 4a and 4b, demonstrating that the coalesced droplet is stretched out and eventually separated after a rotation of about π phase difference (Fig. 4b). This is distinct from the known scenarios of near head-on and off-center separation regimes.

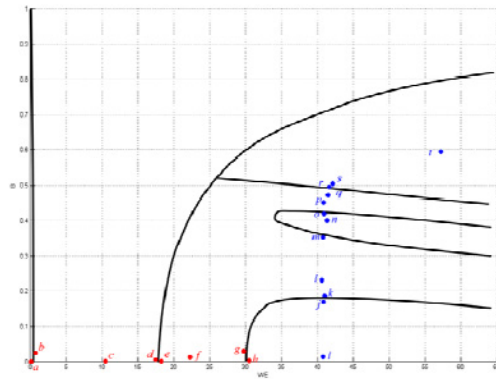


Fig. 3 The new regime diagram of hydrocarbon at 1 atm.

4. Concluding remarks

The transformations of characteristic regimes in drop impact have long been investigated due to the significance of delineating the parametric conditions that can be readily applied to various topics. In this work, a new regime of droplet separation following temporary coalescence has been found. The mechanism could link the difference of previous studies and resolve certain discrepancy on the similar topic. We have been working on the modeling and planning numerical simulation for further interpretation of these phenomena.

References

- [1] P. R. Brazier-Smith, S. G. Jennings, J. Latham, Proc. R. Soc. Lond. A, **326** (1972), 393.
- [2] N. Ashgriz, J. Y. Poo, J. Fluid Mech., **221** (1990), 183.
- [3] Y. J. Jiang, A. Umemura, C. K. Law, J. Fluid Mech., **234** (1992), 171.
- [4] J. Qian, C. K. Law, J. Fluid Mech., **331** (1997), 59.
- [5] K. L. Pan, C. K. Law, B. Zhou, J. Appl. Phys., **103** (2008), 064901.
- [6] C. H. Wang, K. L. Pan, S. Y. Fu, W. C. Huang, J. Y. Yang, J. Mech., **23** (2007), 415.
- [7] K. L. Pan, M. W. Liao, J. Chinese Inst. Engr., accepted.

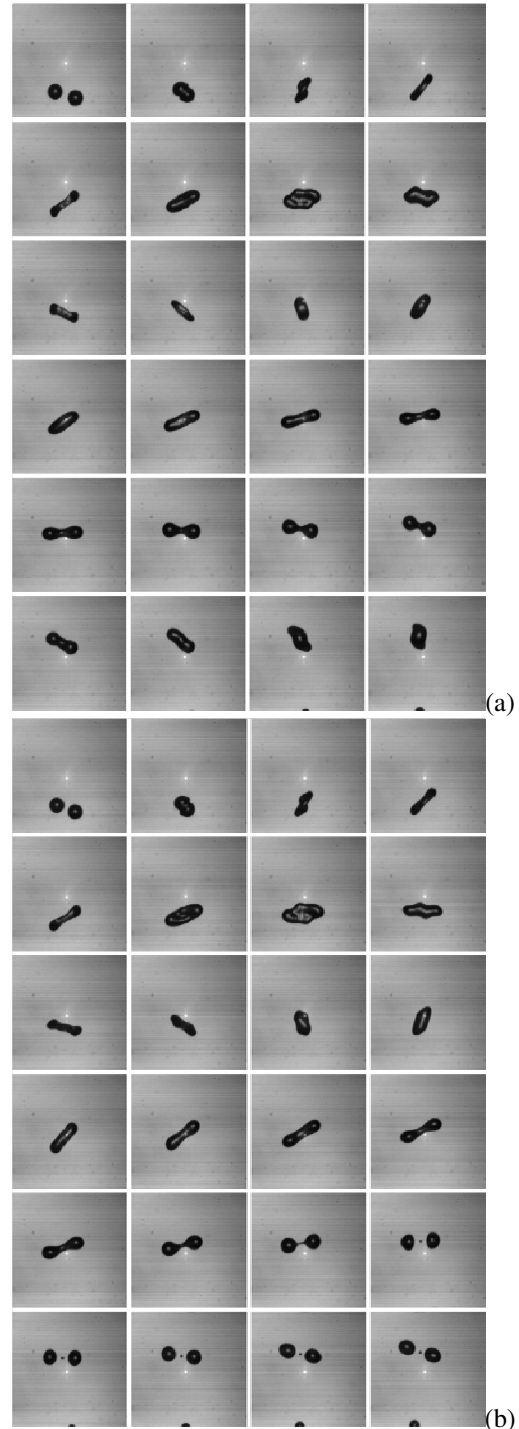


Fig. 4 Sequences of droplet impact for point (a) m and (b) n in Fig. 3.

Implicit Large Eddy Simulation using Truncated Navier-Stokes Equations for Low Mach Number Compressible Flows

ChungGang Li^a, J.Andrzej Domaradzki^b, WuShung Fu^a and T. Tantikul^b

^a Department of Mechanical Engineering, National Chiao Tung University,

^b Department of Aerospace and Mechanical Engineering, University of Southern California,
ricklee.rick@msa.hinet.net

ABSTRACT

A new turbulence model named a dissipative model for compressible turbulent flows at low Mach numbers is proposed. The model is implemented in a numerical code which uses the Roe scheme, preconditioning method, and dual time stepping. It is validated in simulations of the turbulent channel flow for a range of Reynolds numbers from $Re_\tau = 180$ to 950. We show that by changing the value of the Roe upwinding dissipation term it can act as an implicit large eddy simulation (ILES) for turbulent flows.

1. Introduction

Recently, compressible turbulent flows at extremely low Mach numbers, such as encountered in aeroacoustics, combustion, and natural convection induced by high temperature difference, etc., have attracted much attention. The direct use of compressible flow solvers developed for high Mach numbers is not appropriate for low Mach number flows because of slow convergence and low efficiency.

Besides numerical complexities of simulating compressible flows at low Mach numbers, another aspect is how to simulate accurately and efficiently turbulent flows in such situations. Large eddy simulations (LES) is preferred due to its applicability for time-evolving turbulent flows.

To address a broad range of practical, compressible flow problems we need urgently turbulence models that are easily implementable for high Reynolds number flows. Implicit LES is one such a method because in this approach the Navier-Stokes equations are solved numerically on a coarse LES with the truncation error of a numerical scheme serving as a turbulence model.

Therefore, the aim of this study is to propose a new turbulence model in the ILES framework for low Mach number compressible flows. In this turbulence model named dissipative model, the Roe upwinding dissipation term acts to provide model dissipation. With the advantages of an easy implementation because no explicit modeling terms are needed in the governing equations, the availability of the curvilinear coordinates formulation, and the validation for a wide range of Reynolds numbers, the dissipative model can be expected to become an useful and a reliable tool for practical flow simulations for turbulent, low Mach number flows.

2. Numerical Method

The Roe upwind difference scheme [1] is employed

$$F_{inviscid,i+\frac{1}{2}} = \frac{1}{2}(F_R + F_L) - \frac{1}{2}\varepsilon \left\{ \left[\Gamma^{-1} A_p \right] \Delta U_p \right\}. \quad (1)$$

In the original Roe scheme for DNS, ε in Eq. (1) is always set to 1 to stabilize the numerical scheme. However, in this study, ε is a variable coefficient which is used to adjust the Roe upwinding dissipation

term $1/2 \times \varepsilon \left\{ \left[\Gamma^{-1} A_p \right] \Delta U_p \right\}$ as an implicit turbulence model.

In order to adjust ε automatically, the energy ratio ER obtained by [2] should be calculated at every grid point

$$ER = I(\Delta) / I(2\Delta) = \sum_{i=1}^3 (u_i - \bar{u}_i)^2 / \sum_{i=1}^3 (u_i - \hat{u}_i)^2 \quad (2)$$

In Eq. (2) u_i is the original velocity field in the TNS equations, \bar{u}_i is the velocity field filtered with the filter width equal to the mesh size Δ and \hat{u}_i is the filtered velocity field obtained using the filter width equal to twice the mesh size 2Δ . Here, the secondary filter constructed from the box filter as a primary filter is adopted.

According to [2], this ratio ER should be in a range between 0.007 and 0.01. If ER is larger than 0.01, it is an indication that the energy in small scales is excessive and should be dissipated by increasing ε . On the other hand, if ER is smaller than 0.007, it means that the flow field is already too dissipative and ε should be made as small as possible while keeping the simulations stable. The selected values of ε in different ER ranges are based on the following reasoning. If $0.007 \leq ER \leq 0.01$, ε should be the optimal value to keep ER in this range. According to our tests at lower Reynolds number, $\varepsilon = 0.1$ gives the best results. If ER is larger than 0.01, ε should be large enough to dissipate the excess energy, but not as dissipative as underresolved DNS. The value of 0.5 is selected for this range as a compromise between the DNS value ($\varepsilon = 1$) and the constant turbulent value ($\varepsilon = 0.1$). If ER is smaller than 0.01, ε should be made as small as possible but not as small as to cause numerical instability. The recommended value is 0.05

Roe scheme with 5th order MUSCL proposed by are used to compute the inviscid terms. Other derivative terms are solved by the fourth order central difference. Besides, usage of preconditioning method with dual time stepping and curved linear coordinate transformation skills to stabilize transient situation and increase grids near the channel walls are performed. Finally, the original LUSGS was modified by [3] to match preconditioning skill in solving temporal

advancements.

The original N-S equation is then transformed into the following equation.

$$\Gamma \frac{\partial U_p}{\partial \tau} + \frac{\partial U}{\partial t} + \frac{\partial F_1}{\partial \xi} + \frac{\partial F_2}{\partial \eta} + \frac{\partial F_3}{\partial \zeta} = 0 \quad (3)$$

3. Results and Discussion

In order to validate the dissipative model, first simulations for cases at $Re_\tau = 180$ and $Re_\tau = 550$ are performed. The results for mean velocity and turbulent intensities are shown in Fig. 1 through Fig. 2 and are in good agreement with the DNS data of Kim et al [5] and of del Alamo and Jimenez [4]. We can conclude that for these two lower Reynolds numbers the Roe upwinding dissipation term with $\varepsilon = 0.1$ acts as a viable ILES model.

The same model is used for ILES at higher Reynolds number, $Re_\tau = 950$, the case Re950. The mean velocity for this case shown in Fig. 3 is still in a good agreement with the DNS data obtained by del Alamo et al. [6]. However, turbulent intensities in x_2 and x_3 directions shown in Fig. 3 are over predicted, indicating insufficient dissipation to remove the energy in small scales. To correct this problem, simulations for the case Re950ER are performed where the numerical dissipation is controlled by adjusting ε using the procedure described in the previous section. In Fig 4, we show the mean velocity and turbulent intensities, respectively, for this case. The distribution of the mean velocity is basically unaffected by the change in the model from the constant to variable ε . However, as seen in Fig. 4, because of the automatic adjustment procedure for ε , the turbulent intensity distributions in x_2 and x_3 directions improve significantly and are in a very good agreement with DNS data. The results for the turbulent intensity in x_1 direction do not change much though the overall increase in the model dissipation causes a slight drop in the central parts of the channel. Based on the results for case Re950ER we can conclude that the automatic adjustment procedure for the parameter ε improves simulation results compared with the case of setting ε to a constant 0.1.

Therefore, the dissipative model with variable ε provides overall good quality results, indicating that it is a promising simulation tool for practical applications.

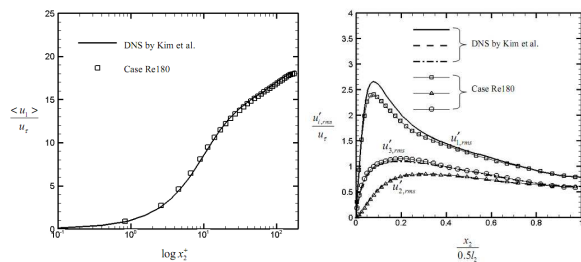


Fig. 1 The mean velocity profiles and turbulent intensities for $Re_\tau = 180$

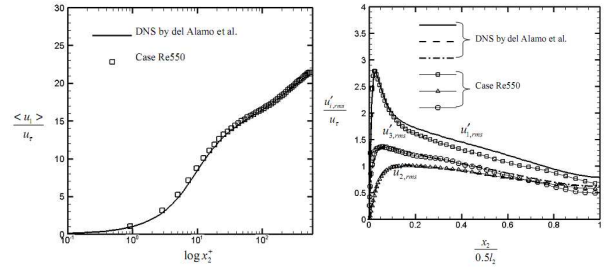


Fig. 2 The mean velocity profiles and turbulent intensities for $Re_\tau = 550$

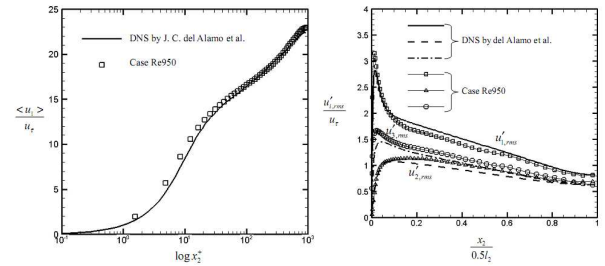


Fig. 3 The mean velocity profiles and turbulent intensities for $Re_\tau = 950$

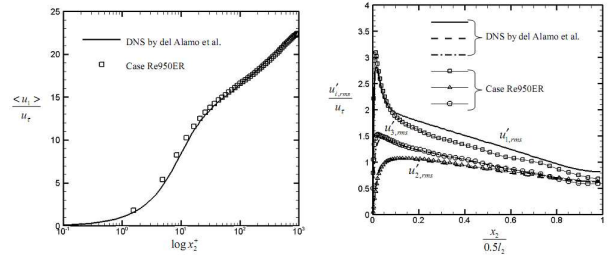


Fig. 4 The mean velocity profiles and turbulent intensities for $Re_\tau = 950ER$

4. Concluding remarks

In this study, a new turbulence model named the dissipative model for ILES has been proposed. Because of that and the validation of the model in this work we believe that it can become a useful tool for numerical simulations of turbulent low Mach number flows encountered in practical applications.

References

- [1] P. L. Roe, J. Comput. Phys. **43** (1981) 357-372.
- [2] T. Tankitil and J. A. Domaradzki, Journal of Turbulence **11** (2010) 1468-5248.
- [3] W. S. Fu, C. G. Li, W. F. Lin and Y. H. Chen, Int. J. Nume. Meth. Fluids **61** (2009) 888-910.
- [4] J. Kim, P. Moin, R. Moser, J. Fluid Mech. **177** (1987) 133-166.
- [5] J. C. del Alamo and J. Jimenez, Phys. Fluids **15** (2003) 41-44.
- [6] J. C. del Alamo, J. Jimenez, P. Zandonade and R. D. Moser, J. Fluid Mech. **500** (2004) 135-144.

Experimental Determination of Plasma Parameters by Laser-Induced Breakdown Spectroscopy

Ardian B. Gojani

Institute of Fluid Science, Tohoku University
2-1-1 Katahira, Aoba, Sendai 980-8577, Japan
gojani@edge.ifs.tohoku.ac.jp

ABSTRACT

Time resolved and space integrated copper and brass plasma is analyzed by laser-induced breakdown spectroscopy. Conditions for plasma diagnostics, in particular the state of local thermodynamic equilibrium, are discussed.

1. Introduction

Laser-induced breakdown spectroscopy (LIBS) is recognized as a fairly reliable technique for chemical analysis. But, with regards to plasma diagnostics, many important questions still remain open. A recent review outlining the technique and its applications can be found in the set of papers by Hahn and Omenetto [1-2]. As it is discussed there, two issues that require attention are:

- (i) characterization and quantification of the ablation process, with focus on the extraction of useful data for spectroscopic analysis, and
- (ii) investigation of the thermodynamic state of the plasma and the applicability of local thermodynamic equilibrium (LTE) relations.

The topic of the present paper is (ii).

The importance of plasma being in LTE lays in the fact that LTE relations allow for the complete plasma characterization only through the knowledge of three parameters: temperature, electron number density, and total number density of species in plasma. However, demonstration that plasma is in LTE is quite demanding, because this requires the confirmation that the energy loss by radiation is negligible in comparison to energy exchange within plasma through other processes, i. e. collisions.

The aim of this paper is to show that plasmas used for LIBS may be approximated as being in LTE, after which the electron number density and temperature can be determined.

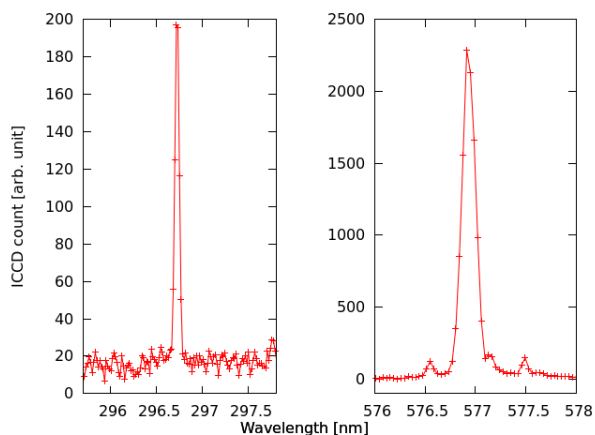


Figure 1: Instrument function obtained from mercury lamp. FWHM values are 0.07 and 0.11 nm.

2. Method

For this study, plasma was generated by ablation of copper (99% pure) and brass (60% Cu, 40%Zn) samples by focusing a laser beam ($\lambda_{\text{laser}}=532$ nm, $\tau_{\text{pulse}}=3$ ns, $E_{\text{laser}}=25$ mJ) onto a 100 μm diameter spot. Plasma radiation is collected by a fiber (50 μm core diameter), cross-dispersed by an echelle grating (resolving power $\lambda/\Delta\lambda=5000$), and recorded by a gated ICCD camera, operated with 100 ns gate time at four distinct moments: 0.32 μs , 0.64 μs , 1.28 μs , and 2.28 μs . Fig. 1 shows the instrument function of the spectrometer, with full width half maximum values.

One method to determine electron density of the plasma is by using the Stark broadening, while plasma temperature can be determined by means of the Boltzmann plot. Both these methods make use of lines collected from optically thin plasma. Fig. 2 shows the emission from Zn I (472.2 nm) collected at two different distances from the ablation spot: in one instance, the fiber was placed 0.5 mm perpendicularly from the surface of the ablation spot, and on the other, at 10 mm distance (in both cases, the fiber was 20 mm away from the centerline of the expansion of the plasma). Since plasma itself was about 5-6 mm long, its density at these different distances obviously is different. But, the line width of the shown emission is the same, thus, the condition that the plasma is optically thin can be considered fulfilled. Similar behavior was also found for other emission lines.

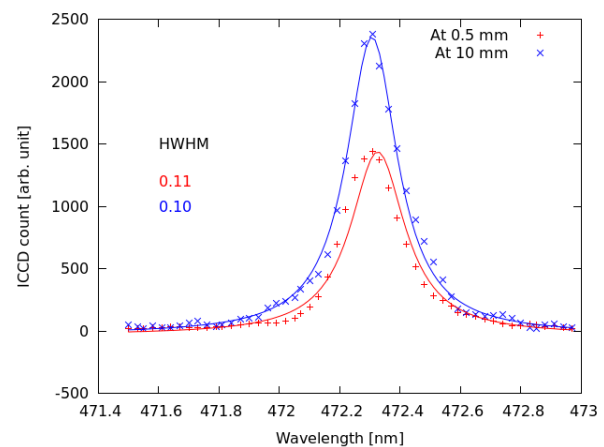


Figure 2: Line emission with fiber at two different distances perpendicular to the ablation spot.

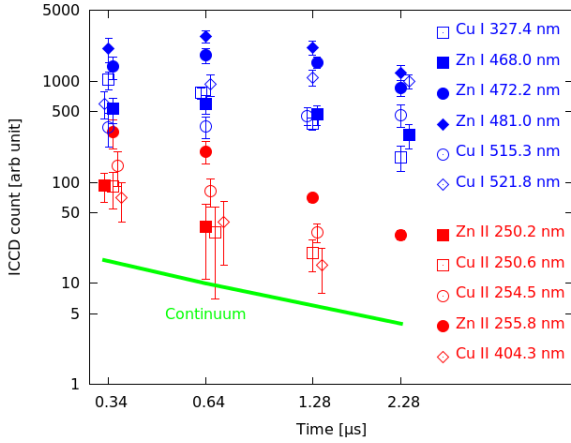


Figure 3: Time evolution of line intensities.

3. Results and Discussion

Temporal evolution of the plasma can be deduced from the variation of emission line intensities with time, as shown in Fig. 3 for emission from neutral and singly ionized copper and zinc atoms, as well as from the continuum (bremsstrahlung) radiation. A general observation is that the emissions from ions decrease in intensity most rapidly, followed by the continuum. The only ionic emission observed after 2.28 μs in the life of plasma was that of Zn II 255.8 nm.

Laser induced plasmas are transient and with great spatial gradients. Therefore, not in equilibrium. For LIBS plasmas, Cristoforetti et al. in [3] state that the right approach is to investigate how far the plasma is from the equilibrium.

This can be tested by determining Boltzmann plot of several elements in plasma. In this study, the temperature of the plasma is calculated from the Boltzmann plot using integrated intensities of several nonresonant and well-resolved copper (578.2 nm, 515.3 nm, 521.8 nm, 458.7 nm, and 427.5 nm) and zinc lines (330.3 nm, 334.5 nm, 468.1 nm, 472.2 nm, and 481.0 nm), and the temperature evolution with time is shown in Fig. 4. Since the temperature difference between zinc and copper atoms is not so large, the within certain limits LTE is assumed.

For the calculation of electron number density, a Lorentzian curve is fitted to the zinc line at 472.2 nm and it is assumed that only the Stark effect causes line broadening. In this case, the line width at FWHM is given by

$$\Delta\lambda_{Stark} = 2\omega \frac{n_e}{10^{16}}, \quad (1)$$

where $\omega=0.1$ nm is the electron impact width parameter and n_e is the electron number density. The change of the electron number density with time is shown in Fig. 5. A power curve fit to the data shows that the electron number density decreases as

$$n_e \propto t^{-1.33}. \quad (2)$$

Comparison of the temperature and electron number density shows that the necessary condition for the application of LTE (McWhirters criterion) is satisfied.

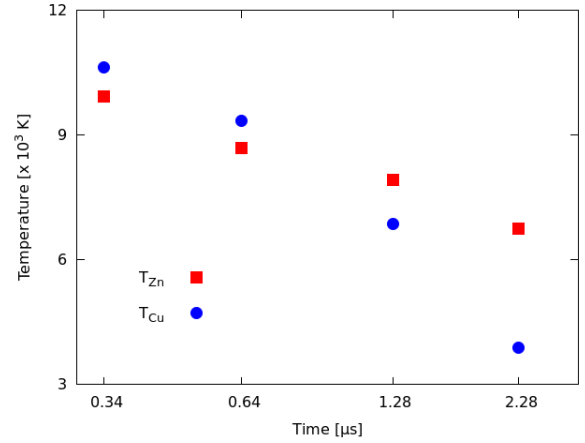


Figure 4: Temperature of plasma.

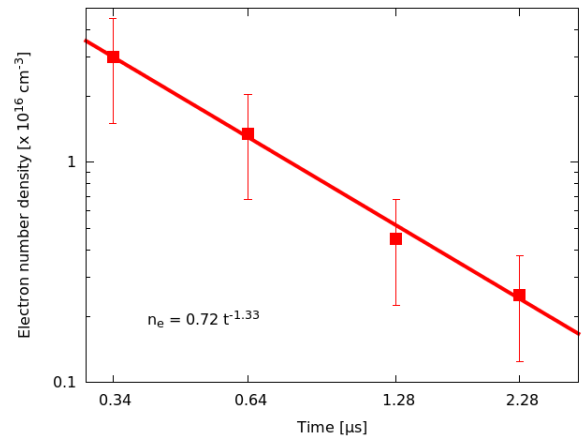


Figure 5: Electron number density.

4. Conclusion

Electron number density and temperature of a laser-induced plasma has been determined using LIBS method, demonstrating the viability of the technique for plasma diagnostics.

References

- [1] D. W. Hahn and N. Omenetto, *Appl. Spectro.* **64**(2010), 335A-366A.
- [2] D. W. Hahn and N. Omenetto, *Appl. Spectro.* **66**(2012), 347-419.
- [3] G. Cristoforetti, A. De Giacomo, M. Dell'Aglio, S. Legnaioli, E. Tognoni, V. Palleschi, and N. Omenetto, *Spectrochim. Acta B* **65**(2010) 86-95.

Comprehensive Modeling of Particle-Plasma Flow in Plasma Spray Process

Hongbing Xiong*, Xueming Shao
Department of Mechanics, Zhejiang University, Hangzhou, 310027, China
Email: *hbxiong@zju.edu.cn

ABSTRACT

Plasma spray is one kind of thermal spray methods, in which micro or nano size articles are injected into the plasma jet with the help of suspension droplet to achieve thin and finely structured coatings. Good melting and enough momentum energy of in-flight particles achieving from the plasma flow are of vital importance to the coating quality. This paper develops a fundamental understanding of the transport phenomena in the particle-laden plasma flow for investigating the complex process including the nanoparticle injection, discharge, acceleration, heating, melting and evaporation.

1. Introduction

Plasma spray is widely utilized to deposit micro or nano size particles in a prepared substrate [1]. The combination of coating and base-material can provide resistance to heat, wear, erosion and/or corrosion, as well as unique sets of surface characteristics. The increased demand for thin film coatings of high quality at low cost has motivated extensive research efforts on thermal spraying science and technologies. However, the scientific research has lagged far behind the technological applications due to the complexity of the phenomena involved, e.g., plasma flame generation, heat and momentum transfer to particles, powder injection and reaction with the environment. This dissertation is aimed at developing a fundamental understanding of the transport phenomena during the particles in flight, and investigating the process conditions and optimization. For this purpose, we have developed a comprehensive model for the particle injection, discharge, acceleration, heating, melting and evaporation. Initial values of suspension droplet size and agglomerate size are selected according to typical experimental data. Non-continuum effects on particle acceleration and heating, known as Knudsen effects, is considered, as well as the influence of evaporation on the heat transfer. After compared with the experimental data, this nanoparticle model is applied for the zirconia and alumina axially injected into the suspension plasma spray. Trajectory, velocity and temperature of the in-flight nanoparticles are predicted for different initial sizes ranged from 30 nm to 1.5 μm ; the distributions of the particle characteristics for multiple particles in the spray are also presented. The effects of powder size and material, power input, plasma gas flow rate and standoff distance on the nanoparticle characteristics have been investigated and discussed.

2. Method

The plasma jet is treated as a compressible, continuous multi-component, chemically reacting ideal gas with temperature-dependent thermodynamic and transport properties. With the assumption of a local thermodynamic equilibrium, the governing equations for plasma are described as follows,

$$\frac{\partial \rho_i}{\partial t} + \nabla \cdot (\rho_i \vec{u}) = -\nabla \cdot \vec{J}_i + \dot{\rho}_i^c \quad (1)$$

$$\frac{\partial \rho}{\partial t} + \nabla \cdot (\rho \vec{u}) = 0 \quad (2)$$

$$\frac{\partial (\rho \vec{u})}{\partial t} + \nabla \cdot (\rho \vec{u} \vec{u}) = -\nabla \left(p + \frac{2}{3} \rho k \right) + \nabla \cdot [\sigma] + \vec{F}_p \quad (3)$$

$$\frac{\partial (\rho e)}{\partial t} + \nabla \cdot (\rho e \vec{u}) = -p \nabla \cdot \vec{u} - \nabla \cdot \vec{q} + \rho \varepsilon + \dot{Q}_c - \dot{Q}_R + \dot{Q}_p \quad (4)$$

In Eq. (1), ρ_i , ρ_i^c , and J_i are the density, the rate of density change due to chemical reaction, and the diffusive mass flux for the species i , respectively. \vec{F}_p in Eq. (3) represents the momentum source or sink due to particles injection, k is the turbulent kinetic energy per unit mass, σ is the viscous shear stress tensor. In Eq. (4), the six terms on the right-hand side accounts for pressure work, heat flux vector, turbulence dissipation, chemical reactions, radiation, and heat source or sink due to injected particles. The ionization, dissociation, recombination, and other chemical reactions are treated using a general kinetic and equilibrium reaction algorithm [2].

The suspension droplet or nanoparticle is treated as a discrete Lagrangian entity that exchanges mass, momentum, and energy with the plasma gas. The mathematical models for nanoparticles in suspension plasma spray system includes three sub-models, i.e., (1) heating of suspension droplet and discharge of the nanoparticles and agglomerates, (2) acceleration and tracking of individual particles, and (3) nanoparticles heating, melting and evaporation.

For particle momentum transfer, we considered the viscous drag, Saffman lift force and Brownian force as:

$$\vec{F}_p = \pi r_p^2 C_D f_{Kn}^{0.45} f_{prop}^{-0.45} \frac{\rho |\vec{V}_g - \vec{V}_p| (\vec{V}_g - \vec{V}_p)}{2} + \frac{2K_c (\eta / \rho_g)^{0.5} d_{ij} \rho_g (\vec{V}_g - \vec{V}_p)}{\rho_p d_p (d_p d_{kl})^{0.25}} + G_0 \sqrt{\frac{\pi S_0}{\Delta t}} \quad (5)$$

where C_D is drag force coefficient, f_{Kn} represents the non-continuum effects, K_c is the constant coefficient of Saffman force, and d_{ij} is the deformation tensor, G_0 is zero-mean, unit-variance independent Gaussian random number, and S_0 is the spectral intensity. The nanoparticle energy conservation equation can be expressed as:

$$m C_p \frac{dT_p}{dt} = 4\pi r_p^2 \dot{q} \quad (\text{for } T_p \neq T_m) \quad (6)$$

$$m L_m \frac{dY_m}{dt} = 4\pi r_p^2 \dot{q} \quad (\text{for } T_p = T_m) \quad (7)$$

where Y_m is the mass fraction of melt in the particle, L_m is the latent heat of fusion, and \dot{q} is the heat flux at the

particle surface which considers the heat transfer by convection, evaporation and radiation.

3. Results and Discussion

The simulated particle temperature and velocity are plotted against the experimental data in Fig. 1. A good agreement between the simulation results and experimental data [3] has been obtained; the difference between the experiment and simulation is within 10%.

The gas temperature contour of the baseline case is shown in Fig. 2. The core of the plasma jet, at the distance of 1 cm from the torch exit, has very high temperature and velocity, more than 10,000 K and 2000 m/s. The droplet suspension resides in the plasma core, and rapidly heated up to evaporation. After the discharge of agglomerate and nanoparticles, particles flying through the plasma jet are driven to a high speed up to 2,500 m/s, and heated up to 4,500 K.

Figure 3 show nanoparticle or agglomerate trajectory. Each particle is injected in the torch axis. Results show that the radial displacement is quite small, about 0.01 cm. Nanoparticles have different trajectories compared to the microsize agglomerates. The microsize suspension droplet is accelerated steadily by the gas stream and its trajectory goes straight. When the suspension solvent vaporized at the standoff distance of about 0.5 to 0.7 cm, the nanoparticle or the agglomerates are discharged to the plasma jet. For the nanoparticles, the trajectories are highly fluctuating since the inertia is small and thus more sensitive to the gas turbulence. It should be pointed out that the turbulence model is important for the calculation of the nanoparticles tracking. Though $k-\varepsilon$ model could provide quantitative results of the gas turbulent energy, better turbulence model such as large eddy simulation would be helpful for more accurate prediction of the nanoparticles trajectories.

Nanoparticles have similar temperature and velocity if they experience the same gas environment. Large nanoparticles have lower temperature and may have a higher velocity depending on the local gas velocity. During the suspension droplet continually evaporation, the nanoparticle agglomerates originally embedded in the evaporated solvent will be discharged to the plasma jet. In current case, the agglomerates are discharged to the plasma jet at the standoff distance of 0.5 to 0.7 cm, depending on the particle material properties. After being discharged to the plasma jet, the nanoparticles might stay within the agglomerate, or explode to free nanoparticle. For the free nanoparticle, the speeding rate is increased immediately after the discharge. If the nanoparticles are further discharged to the plasma jet after agglomerate explosion, its velocity and temperature are steeply increased, followed by a slow deceleration and cooling rate at the downstream of the spray. The main reason for this phenomenon is that the mass of the nanoparticle is much smaller than that of their parent agglomerate and suspension droplet. For the nanoparticle agglomerates, the speeding and heating rate are smaller compared to the nanoparticles. However, the

agglomerates have higher impact velocity than the nanoparticles due to its less deceleration at the downstream of the spray, whereas its impact temperature is lower. For ZrO_2 agglomerate, the surface temperature is at the melting point when impact, but the interior of the agglomerate is not totally melted due to its large latent heat of melting and high melting temperature.

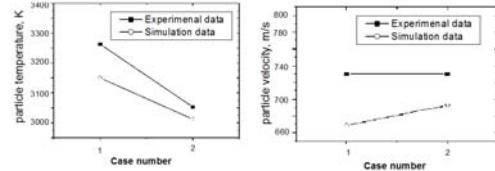


Figure 1: Comparison of averaged particle temperature and velocity with the published experimental data.

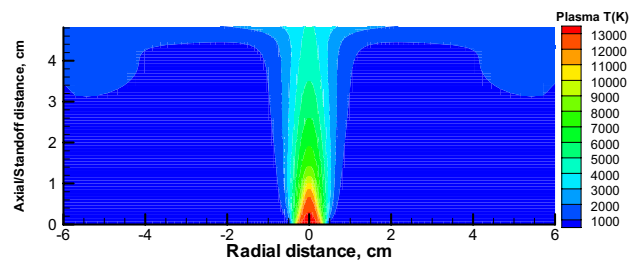


Figure 2: Plasma temperature.

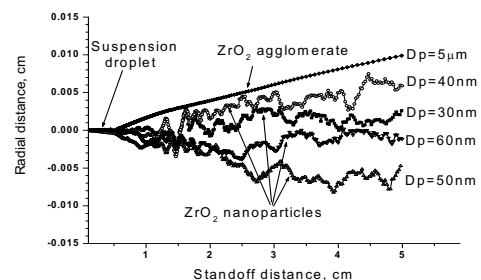


Figure 3: Trajectories of micro-size agglomerate and nanoparticles.

4. Concluding remarks

A numerical particle model is proposed to study nanoparticles tracking, acceleration, heating, melting and evaporation in suspension plasma spray. Results show that the trajectory of the suspension droplet and agglomerates follows steadily in the injection direction with certain expansion angle, while the nanoparticles have fluctuating trajectories.

Acknowledgement: This work is supported by the National Natural Science Foundation of China (11072216) and the Fundamental Research Funds For the Central Universities (2012FZA4027)

References

- [1] P. Fauchais, G. Montavon, J. Therm. Spray Technol., 19 (2010) 226-239.
- [2] Hong-Bing Xiong, Li-Juan Qian et al., J. Therm. Spray Technol., 2012 (21) 2, 226-239
- [3] F. Tarasi, M. Medraj, et al., J. Therm. Spray Technol., 2008, 17(5-6), p 685-691.

Numerical and Experimental Investigation of Light Emission of a Planar Nitrogen Atmospheric-Pressure Dielectric Barrier Discharge Due to Addition of Ammonia Considering Oxygen Impurity

Fu-Li Li, Yi-Wei Yang, Kun-Mo Lin, and Jong-Shinn Wu*

Department of Mechanical Engineering, National Chiao Tung University, Hsinchu, Taiwan

*E-mail: chongsin@faculty.nctu.edu.tw

ABSTRACT

In this work, mechanism of light emissions, including NO- γ , NO- β and N₂-SPS, of N₂/NH₃ atmospheric-pressure dielectric barrier discharge considering oxygen impurity is investigated numerically and experimentally. Results show that, NO- γ decreases with increasing NH₃ addition due to the loss of N₂(A) by the reaction of NH₃ with N₂(A). NO- β decreases with increasing NH₃ due to the depletion of NO(B) because of NH₃. N₂-SPS decreases with increasing NH₃ because metastable-metastable associative ionization NH₃ becomes weaker.

1. Introduction

Recently, nitrogen/ammonia atmospheric pressure dielectric barrier discharges have attracted attention because of its use in enhancing biocompatibility of PLA surface. Few experiments [1-3] and simulation [4] have been performed to understand the detailed discharge physics and chemistry. However, in these studies, mechanisms of light emission and oxygen impurity were not explored, which is important in further understanding the complex plasma chemistry.

Li *et al.* [4] have performed a detailed 1-D fluid modeling of N₂/NH₃ discharge without considering the detailed mechanism of light emission (NO- γ , NO- β and N₂-SPS) because they combined all excited/metastable nitrogen to be excited nitrogen and the impurity of oxygen was not considered, either. We specially single out these three emission bands mainly because they are often detected clearly in a nitrogen-based discharge. In the commercial nitrogen bottle (99.99%) we have found oxygen could be up to 30 ppm using gas chromatography [1-2]. Therefore, for a realistic modeling of N₂/O₂/NH₃ AP-DBD, mechanism of these light emissions need to be considered as well as the oxygen impurity.

In the present study, the emission results of a planar N₂/NH₃ AP-DBD with O₂ impurity driven by a realistic distorted sinusoidal voltage waveform is simulated using a 1-D fluid modeling code. The results are compared with the measurements obtained by optical emission spectroscopy. A set of plasma chemistry of N₂/NH₃/O₂ AP-DBD is developed to elucidate mechanism of light emission of discharge. Trends of simulated light intensities are shown to agree reasonably well with the experiments. Then, effect of ammonia addition into N₂/O₂ on the light intensity is presented and discussed in detail in this paper.

2. Methods

For simulating such complicated AP discharge physics and chemistry, 1-D fluid modeling is employed. We solved a set of model equations self-consistently, including the continuity equations of charged species with drift-diffusion approximation for the momentum equations, the excited state and neutral species continuity equations, the electron energy density

equations, and the Poisson equations [5]. The cell-centered finite-volume method is used to discretize these equations. Discretized equations are solved by semi-implicit method. Corresponding numerical schemes and algorithms are described in detail and are not repeated here for brevity [5].

In the current study, a set of plasma chemistry of N₂/O₂/NH₃ is proposed, including 48 species (e^- , H⁺, H₂⁺, H₃⁺, N⁺, N₂⁺, N₄⁺, NH⁺, NH₂⁺, NH₃⁺, NH₄⁺, O₂⁺, H⁻, O⁻, O₂⁻, N(²D), N(²P), N₂(^A $^3\Sigma_u^+$), N₂(^B $^3\Pi_g$), N₂(^a $^1\Sigma_u^-$), N₂(^C $^3\Pi_u$), O(¹S), O(¹D), O₂(a), O(¹S)N₂, NO(A), NO(B), H, H₂, H₂O, H₂O₂, HNO, N, N₂, NH, NH₂, NH₃, N₂H, N₂H₂, N₂H₃, N₂H₄, NO, N₂O, NO₂, O, O₂, O₃, and OH) and 244 reaction channels, providing an extensive view of the chemical processes. The corresponding reaction channels and the rate constant are given elsewhere [4]. The light emission of excited species of nitrogen and nitrogen oxide, and electronegative ions are all taken into account in the model. For NO- γ emission bands, direct electronic excitation ($e^- + \text{NO} \rightarrow \text{NO}(A) + e^-$) is negligible as compared to the N₂(A) quenching channel (N₂(A) + NO \rightarrow N₂ + NO(A)) [6]. Thus, we do not consider the reaction of $e^- + \text{NO} \rightarrow \text{NO}(A) + e^-$ in this model.

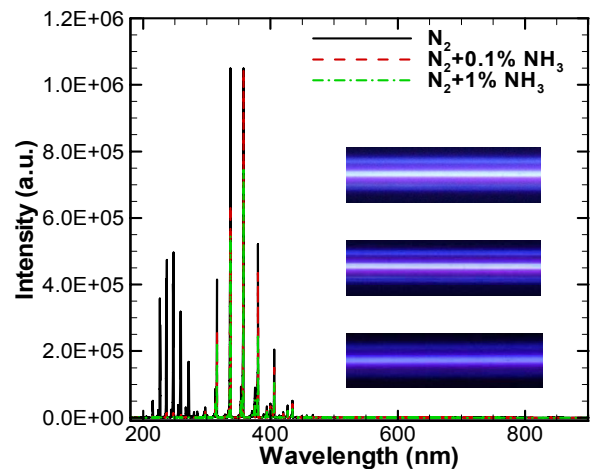


Fig. 1 Optical emission spectra of N₂/(0-1%)NH₃ AP-DBD from 180 to 900 nm. (30 kHz, 8 kV, 50 SLM, 400W)

3. Results and Discussion

All of the experiments and simulated results presented in the paper are performed under the conditions of 30 kHz (power supply), 8 kV (voltage), 1 mm (gap distance), 25 cm² (electrode area), 4.76 (quartz plate having measured relative permittivity), 1 mm (quartz thickness), 400 K (temperature of background gas) and 30 ppm (oxygen).

Fig. 1 shows the optical emission spectra of OES measurement in the range of 180-900 nm in the discharge region under different concentration of ammonia addition from 0 to 1% and the emission bands of N₂ second positive system, NO- γ and NO- β have been detected. The experimental setup as described in Chiang *et al.* [7] was used. The wavelength range of N₂-SPS and NO- γ emission are 313.6-466.7 nm and 220-280 nm, respectively. Note that it is unlikely to detect the emission containing O such as NO- γ and NO- β under condition of pure gas with N₂ and NH₃. The reason for obtaining NO- γ and NO- β emission in our experiment is owing to an inevitable existence of impurities in commercial bottles such as O₂ which has been carefully verified through gas chromatography in our laboratory [1-2]. Results show NO- γ , NO- β and N₂-SPS decrease with increasing NH₃ addition. Furthermore, the emission of NO- γ diminishes much rapidly and totally vanishes after 0.5% addition. In contrast, the other two emission lines decrease slightly with increasing addition of NH₃.

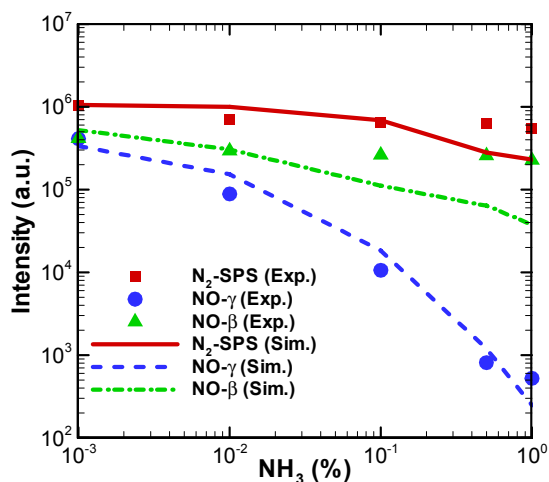


Fig. 2 Optical emission spectra comparison of simulation with experiment

Fig. 2 shows the comparison of predicted and measured light intensities of the discharge. The wavelengths of light emission have been selected at 337.1 nm (N₂-SPS), 236 nm (NO- γ) and 316 nm (NO- β). All light intensities of the discharges decrease with increasing concentration of ammonia, especially NO- γ , which decreases dramatically. The spectra in the discharges are dominated by the nitrogen second positive system which is directly excited by electron impact and N₂(C), whose effective lifetime is in order of nanosecond. Based on the simulations, electron density decreases with increasing NH₃ because NH₃ is an electronegative gas which has high electron affinity [8]. Therefore, negative atomic hydrogen, increasing with

increasing NH₃, is produced by electron attachment ($e+\text{NH}_3\rightarrow\text{NH}_2+\text{H}^-$). In addition, N₂(C) is also generated by electron-ion recombination ($e+\text{N}_4^+\rightarrow\text{N}_2(\text{C})+\text{N}_2$). N₄⁺ is produced by metastable-metastable associative ionization ($\text{N}_2(\text{a}^1)+\text{N}_2(\text{A})\rightarrow\text{N}_4^++e$) and charge exchange ($\text{N}_2^++\text{N}_2+\text{N}_2\rightarrow\text{N}_4^++\text{N}_2$) which become less efficient because N₂(A) and N₂⁺ decrease with NH₃. In addition, the emission of NO- γ diminishes much rapidly and totally vanishes after addition of 0.5% NH₃ because N₂(A) is consumed mainly through $\text{N}_2(\text{A})+\text{NH}_3\rightarrow\text{N}_2+\text{NH}_2+\text{H}$ and $\text{NO}(\text{A})+\text{NH}_3\rightarrow\text{NO}+\text{NH}_3$. NO- γ is created by the two-body reaction ($\text{N}_2(\text{A})+\text{NO}\rightarrow\text{N}_2+\text{NO}(\text{A})$) which involves N₂(A) and NO. From the simulations (not shown), N₂(A) and NO(A) decrease with increasing NH₃. Thus, NO- γ depends on densities of N₂(A) and NH₃. Moreover, NO- β is created by the three-body reaction ($\text{N}+\text{O}+\text{N}_2\rightarrow\text{NO}(\text{B})+\text{N}_2$) which involves atomic nitrogen and atomic oxygen also decreases with increasing NH₃ because decreasing N and O with increasing NH₃. More details will be presented in the meeting.

4. Conclusion

In present study, we investigate the mechanism of the light emissions (NO- γ , NO- β and N₂-SPS) in a planar N₂/NH₃ AP-DBD considering oxygen impurity. Results of 1D fluid modeling is validated by reasonable agreement with OES measurements. Results show that all emission bands decrease with increasing N₂-SPS decrease is caused by electron attached by NH₃ and weaker metastable-metastable associative ionization. NO- γ decrease is caused by decreasing N₂(A) and NO(A), and NO- β decrease is caused by decreasing N and O.

References

- [1] Y.W. Yang, *et al.*, 7th International Conference on Flow Dynamics, Sendai, Japan, 2010, 164.
- [2] Y.W. Yang, *et al.*, 8th International Conference on Flow Dynamics, Sendai, Japan, 2011.
- [3] C.-P. Klages, A. Grishin, *Plasma Process Polymer*, **5** (2008), 368.
- [4] F. L. Li, K. M. Lin, Y. W. Yang, C. T. Hung, J. S. Wu, and J. P. Yu, *Plasma Chem. Plasma Process*, **32** (2012), 547.
- [5] K. M. Lin, C. T. Hung, F. N. Hwang, M. R. Smith, Y. W. Yang, and J. S. Wu, *Comput. Phys. Commun.*, **183** (2012), 1225.
- [6] N. Gherardi, E. Gat, F. Massines, S. Lemoing, P. Ségur, *Proc. 15th Int. Symp. on Plasma Chemistry* (Orleans, France), **1** (2001), 97.
- [7] M.H. Chiang, K.C. Liao, I.M. Lin, C.C. Lu, H.Y. Huang, C.L. Kuo, J.S. Wu, C.C. Hsu, S.H. Chen, *Plasma Chem Plasma Process*, **30** (2010), 553.
- [8] A. Fateev, F. Leipold, Y. Kusano, B. Stenum, E. Tsakadze, H. Bindslev, *Plasma Process. Polym.* **2** (2005), 193.

Simulation of CH₄-H₂-air Turbulent Non-premixed Flame by Vortex Method

Kazui Fukumoto and Yoshifumi Ogami

Department of Mechanical Engineering and Science, Ritsumeikan University
1-1-1 Nojihigashi, Kusatsu, Shiga 525-8577, Japan
fukumoto@cf.d.ritsumei.ac.jp

ABSTRACT

In this paper, we present a turbulent non-premixed combustion model for the vortex method. In this model, it is assumed that combustion occurs in the vortex particle, and detailed chemical mechanisms can be taken into account by solving ordinary differential equations. Our model is validated through a simulation of a CH₄-H₂-air non-premixed flame. The tendency of the production and consumption of the chemical species is similar to the experimental data.

1. Introduction

Vortex methods, grid-free Lagrangian computational methods, have been used as modeling tools to study various flows because they are simpler and have lower computational overhead than other methods.

In this paper, we present a turbulent non-premixed combustion model for the vortex method. The proposed model is validated through a simulation of a CH₄-H₂-air non-premixed flame called DLR flame [1].

2. Method

The vortex method was performed for flow simulation in this study.

$$\frac{\partial \rho \boldsymbol{\omega}}{\partial t} = -\{(\rho \mathbf{u} + \rho \mathbf{u}_d) \cdot \text{grad}\} \boldsymbol{\omega} \quad (1)$$

where ρ denotes the density; $\boldsymbol{\omega}$, the vorticity vector; t , the time; \mathbf{u} , the convection velocity; and \mathbf{u}_d , the diffusion velocity. \mathbf{u} is calculated as

$$\rho \mathbf{u} = \sum_j \frac{\Gamma_j (\mathbf{k} \times \mathbf{R})}{2\pi R_j^2} \left(1 - \exp\left(-\frac{R_j^2}{\sigma_j^2}\right) \right) \quad (2)$$

where $\mathbf{R} = \mathbf{x} - \mathbf{x}_j$ and $R_j = |\mathbf{R}|$. Γ_j denotes the strength of particles j ; \mathbf{x} , the position vector of the particle; \mathbf{x}_j , the position vector of particle j ; \mathbf{k} , the unit vector; and σ_j , the radius of particles j . \mathbf{u}_d is computed as

$$\rho \mathbf{u}_d = -\frac{\mu}{\boldsymbol{\omega}} \text{grad} \boldsymbol{\omega} \quad (3)$$

where μ denotes the viscosity. The additional particle is defined to compute the mixture fraction f .

$$\frac{\partial \rho f}{\partial t} = -\{(\rho \mathbf{u} + \rho \mathbf{u}_d) \cdot \text{grad}\} f - \rho \chi \quad (4)$$

$$\chi = 2D(\text{grad} f)^2 \quad (5)$$

$$\rho \mathbf{u}_d = -\frac{\rho D}{\boldsymbol{\omega}} \text{grad} \boldsymbol{\omega} \quad (6)$$

where χ denotes the scalar dissipation rate; D , the diffusion coefficient; and \mathbf{u}_d , the diffusion velocity of the mixture fraction. In this study, a detailed chemical mechanism was considered, and it is assumed that combustion occurs in the vortex particle. The vortex particle is considered a perfectly stirred reactor and the steady state of the following equations are solved under the initial conditions obtained from the current mixture fraction, density, and initial temperature T_0 in each particle:

$$\frac{\partial Y_J}{\partial t} = \frac{w_J}{\rho} + \chi(Y_{in,J} - Y_J) \quad (7)$$

$$Y_{in,J} = fY_{fu,J} + (1-f)Y_{ox,J} \quad (8)$$

where Y_J denotes the mass fraction of chemical species J ; w_J , the reaction rate of chemical species J ; $Y_{in,J}$, the mass fraction of chemical species J that enters the particle; $Y_{fu,J}$, the mass fraction of chemical species J of the fuel; and $Y_{ox,J}$, the mass fraction of chemical species J of the oxidant. T_0 is computed as

$$\alpha = \frac{f-1.0}{f_{st}-1.0} \quad f \geq f_{st} \quad (9)$$

$$T_0 = (1-\alpha)T_{st} + \alpha T_{fu} \quad (10)$$

$$\alpha = \frac{f-0}{f_{st}-0} \quad f < f_{st} \quad (11)$$

$$T_0 = (1-\alpha)T_{st} + \alpha T_{ox} \quad (12)$$

where f_{st} denotes the mixture fraction at the stoichiometric ratio; T_{st} , the temperature at the stoichiometric ratio; T_{fu} , the temperature of the fuel; and T_{ox} , the temperature of the oxidant. Once the mass fraction Y_J is obtained, the temperature T is modified by

$$T = T_{ref} + \frac{h - \sum_J Y_J \Delta_f h_J^0}{\sum_J Y_J C_{p,mj}} \quad (13)$$

where $T_{ref}=298.15$. $\Delta_f h_J^0$ denotes the standard enthalpy of formation of chemical species J . h is the

enthalpy computed as

$$h = fh_{fu} + (1-f)h_{ox} \quad (14)$$

where h_{fu} is the enthalpy of the fuel, and h_{ox} is the enthalpy of the oxidant. Cp_{mJ} is the mean specific heat at constant pressure of chemical species J .

$$Cp_{mJ} = \frac{\int_{T_{ref}}^T Cp_J dT}{T - T_{ref}} \quad (15)$$

where Cp_J denotes the specific heat at constant pressure of chemical species J .

3. Numerical conditions

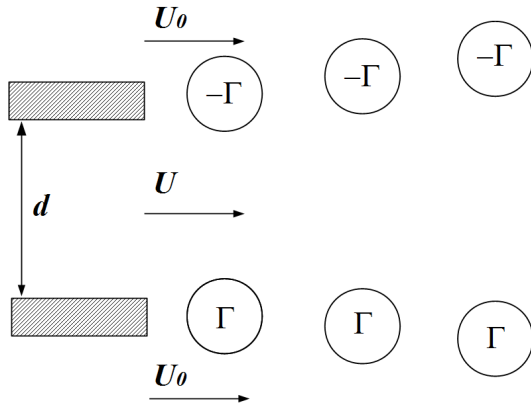


Fig. 1 Vortices released from the edges of the upper and the lower walls of the nozzle

A $\text{CH}_4\text{-H}_2\text{-air}$ turbulent non-premixed flame was simulated to verify the accuracy of the proposed model. The numerical conditions were based on DLR flame A [1]. Fig. 1 shows the sketch of the vortices released from the edges of the upper and the lower walls of the nozzle. The mass fractions of CH_4 , H_2 , and N_2 in the fuel Y_{fu} were 0.212, 0.0397, and 0.7483, respectively. The mass fractions of the oxidant Y_{ox} of O_2 and N_2 were 0.233 and 0.767, respectively. The fuel was injected from a nozzle with a radius of $d=8$ mm. The velocities of the fuel and ambient air were $U=51.35$ and $U_0=0.3$ m/s, respectively. T_{fu} , T_{ox} , T_{st} were set to 298.15 K, 298.15 K, and 1900 K, respectively. Γ is computed as

$$\Gamma = \frac{\Delta t(U - U_0)^2}{2} \quad (16)$$

μ and D were calculated by the simplified transport model suggested by Smooke [2], and ρ was set to 1 in this study. Also, the detailed chemical mechanism suggested by Kee [3] was used to compute the reaction rates.

4. Results and Discussion

Fig. 2 shows the axial mass fractions and temperature predicted by the proposed model. The mass fraction of CO_2 is slightly lower than the experimental data because the consumption of CH_4 is underestimated when $30 < x/d$. The predicted mass fraction of H_2O and

temperature are similar to the experimental data. However, the tendency of the production and consumption of the chemical species is similar to the experimental data.

Fig. 3 shows the distribution of the instantaneous temperature distribution. The local extinction can be seen in the flame. The fluctuation is taken into account because the vortex method can consider the interaction of momentum between each vortex particle.

The temperature and mass fractions were relied on the mixture fraction. Thus, we found that the prediction accuracy in this simulation is relied on the accuracy of the particle distribution of the mixture fraction. A method to improve the accuracy of the mixture fraction should be investigated.

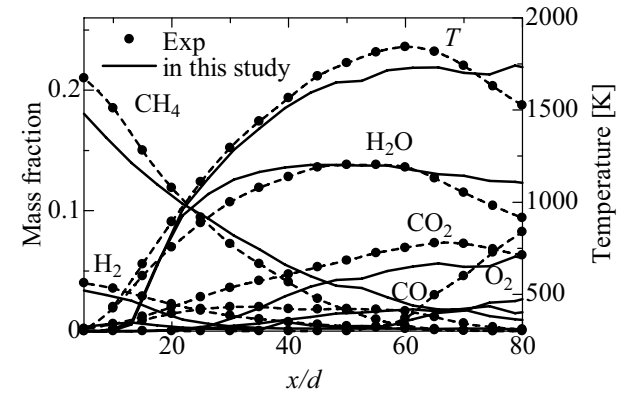


Fig. 2 Axial mass fractions and temperature

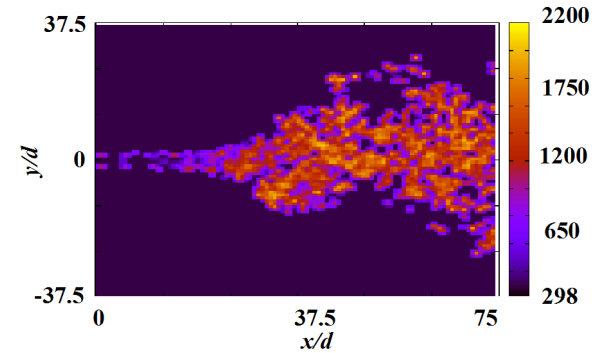


Fig. 3 Instantaneous temperature distribution

5. Concluding remarks

We have proposed the turbulent non-premixed combustion model for the vortex method. The tendency of the production and consumption of the chemical species was similar to the experimental data. The prediction accuracy for the mass fractions and temperature is relied on the accuracy of the particle distribution of the mixture fraction.

References

- [1] V. Bergmann, et al., Appl. Phys. B, **66** (1998) 489.
- [2] M. D. Smooke, Reduced kinetic mechanisms and asymptotic approximations for methane-air flame, Lecture note in physics Springer-Verlag (1991)
- [3] R. J. Kee, et al. SANDIA REPORT, SAND85-8240 UC-4 (1987), 47

A True-Direction Flux Reconstruction Scheme to the Quiet Direct Simulation Method for Inviscid Gas Flows

Ya-Ju Lin¹, Matthew. R. Smith² and Jong-Shinn Wu^{1*}

¹Department of Mechanical Engineering, National Chiao Tung University, Hsinchu, Taiwan

²National Center for High-performance Computing, Hsinchu

*E-mail of corresponding author: chongsin@faculty.nctu.edu.tw

ABSTRACT

In this paper, a new true-direction flux reconstruction of the 2nd order quiet direct simulation (QDS) as an equivalent Euler equation solver, named N²-QDS, is proposed. This method is demonstrated in several verification studies to compare 2N-QDS method (Smith J. Comp. Phys., 2009) and analysis of the flux difference between two methods in analytical equation is performed. Results show that our proposed multi-dimensional reconstruction provides a significant increase in the accuracy of the solution for inviscid flow simulation.

1. Introduction

Computational fluid dynamics (CFD) typically uses the finite volume method to solve a set of discretized governing equations, usually the Euler or Navier-Stokes equations. The particle-based Direct Simulation Monte Carlo (DSMC) method has been arguably the most successful method for simulating rarefied gas flows since its development by Bird in the 1960s [1]. Albright et al. [2] developed a numerical scheme for the solution of the Euler equations, known as the Quiet Direct Simulation Monte Carlo (QDSMC) method. The method was later renamed the Quiet Direct Simulation (QDS) method by Smith (named 2N-QDS) [3], due to the lack of stochastic processes, and extended to second order spatial accuracy. For the application, the 2nd order 2N-QDS method is applied to simulate highly unsteady low pressure flows encountered in a Pulsed Pressure Chemical Vapor Deposition (PP-CVD) reactor by Cave [4,5].

In this paper, we extend the 2nd order QDS algorithm to high-order reconstruction through the polynomial multidimensional reconstruction of conserved properties across each cell width. Validation simulations of four two-dimensional cases are carried out to show the improved accuracy of the proposed N²-QDS scheme for inviscid gas flow simulations.

2. Method

The normal random variable $N(0,1)$ is defined by the probability density:

$$p(x) = \frac{e^{-x^2/2}}{\sqrt{2\pi}} \quad (1)$$

By using a Gaussian quadrature approximation, the integral of equation (1) over its limits can be approximated by:

$$\int_{-\infty}^{\infty} \frac{e^{-x^2/2}}{\sqrt{2\pi}} f(x) dx \approx \sum_{j=1}^N w_j f(q_j) \quad (2)$$

where w_j and q_j are the weights and abscissas of the Gaussian quadrature (also known as the Gauss-Hermite parameters) shown in Figure 1 and Table 1, and N is the number of terms. The abscissas are the roots of the Hermite polynomials, which can be defined by the recurrence equation:

$$H_{n+1}(q) = 2qH_n - 2nH_{n-1} \quad (3)$$

where $H_{-1}=0$, and $H_0=1$. The weights can be determined from:

$$w_j = \frac{2^{n-1} n! \sqrt{\pi}}{n^2 [H_{n-1}(q_j)]^2} \quad (4)$$

where the particle mass m_j , particle velocity v_j , and particle internal energy ε_j are:

$$m_j = \frac{\rho \Delta x w_j}{\sqrt{\pi}} \quad v_j = u + \sqrt{2} \sigma q_j \quad \varepsilon_j = \frac{(\xi - \Omega) \sigma^2}{2} \quad (5)$$

where ρ is the density, u is the bulk (or mean) flow velocity, and $\sigma = (RT)^{1/2}$ in a given source cell. The total number of degrees of freedom ξ is defined as $\xi = 2(\gamma - 1)^{-1}$ and Ω is the number of simulated degrees of freedom (e.g., $\Omega = 1$ for one dimensional flow).

In the current study, Fig. 1 described briefly the N²-QDS method how to deal with the volume-to-volume flux reconstruction. The value of a conserved property (mass, momentum, or energy) $Q(x)$ obtained from Taylor series is computed for the flux out value of average conserved quantity successfully moving from the source cell into the destination cell (denoted by \bar{Q}_r).

$$\begin{aligned} \bar{Q}_r &= \frac{1}{(x_r - x_l)} \int_{x_l}^{x_r} Q(x) dx = \frac{1}{(x_r - x_l)} \left[Q_c + \frac{1}{2} \left(\frac{dQ}{dx} \right) (x - 0.5\Delta x)^2 + \dots \right]_{x=0.5\Delta x}^{x=\Delta x} \quad (6) \\ &= Q_c + \frac{1}{(x_r - x_l)} \left[\frac{1}{2} \left(\frac{dQ}{dx} \right) (x - 0.5\Delta x)^2 + \dots \right]_{x=\Delta x - \Delta x}^{x=\Delta x} \end{aligned}$$

Where Q_c is the value of Q at the central cell during a time step Δt presented below:

$$Q_c = \bar{Q}_c - \frac{\Delta x^2}{24} \left(\frac{d^2 Q}{dx^2} \right) - \frac{\Delta x^4}{1920} \left(\frac{d^4 Q}{dx^4} \right) - \dots - \frac{2\Delta x^{n-1}}{n!} \left(\frac{1}{2} \right)^n \left(\frac{d^{n-1} Q}{dx^{n-1}} \right) \quad (7)$$

3. Results and Discussion

3.1 Error Analysis

The purpose of this simulation is to observe the difference fluxes that between 2N and N²-QDS method in mass flux, momentum flux and energy flux using variation of density, velocity and energy when the source cell travelled to the diagonal destination cell. We compare the case which the difference of density ($\Delta \rho$), velocity (Δu) and temperature (ΔT) are $1.0e^{-2}$.

Fig. 3 shows the mass result of the difference between 2N and N² method at the range of the density, velocity and temperature in 0.1 to 5.0.

3.2 Shock-bubble

The strength of correct multi-dimension reconstruction is demonstrated in two dimensions with the shock/bubble interaction problem [23]. The initial conditions for this problem are shown in Fig. 4.

Fig. 5 displays two QDS schemes with same numbers of cells. Obviously, the multi-dimensional computation (N2 scheme) achieves higher accuracy than the 2N scheme.

References

[1] Bird GA. Molecular Gas Dynamics and the Direct Simulation of Gas Flows. Oxford: Clarendon Press; 1994.
 [2] B.J. Albright, D.S. Lemons, M.E. Jones and D. Winske, Phys. Rev. E 65 (2002) 1.
 [3] M.R. Smith, H.M. Cave, J.-S. Wu, M.C. Jermy, Y.-S. Chen, J. Comp. Phys. 2009; 228: 2213–2224
 [4] Chin Wai Lima,b, Hadley M. Cavea,c, Mark C. Jermya, Susan P. Krumdiecka and Jong-Shinn Wuc, The 27th International Symposium on Rarefied Gas Dynamics, California, July 10-16, 2010.
 [5] H.M. Cavea,b, C.-W. Lima,c, M.C. Jermya, S.P. Krumdiecka, M.R. Smithd Y.-J. Linb, and J.-S. Wub, The 27th International Symposium on Rarefied Gas Dynamics, California, July 10-16, 2010.

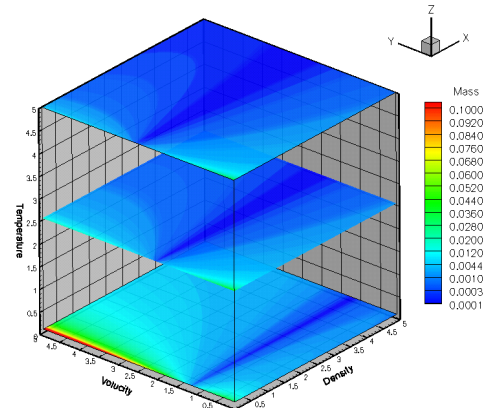


Fig. 3 The value of mass flux for the difference of 2N and N² method.

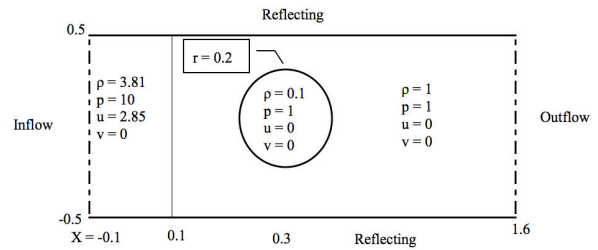


Fig. 4 The structure of shock bubble interaction.

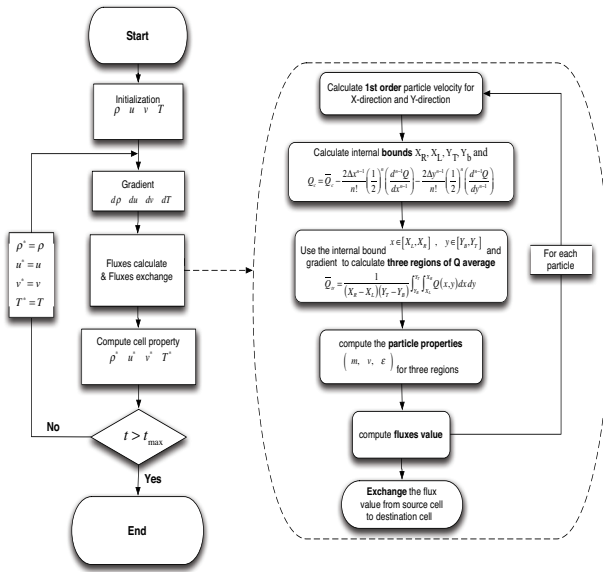


Fig. 1 Flowchart describing N2-QDS particle computation with gradient inclusion.

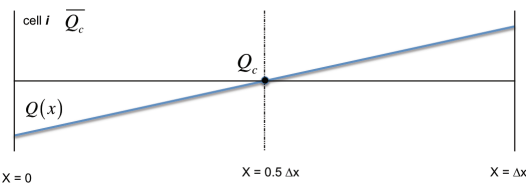


Fig. 2 The special reconstruction convention for current amount of conserved quantity Q. The list of references must be

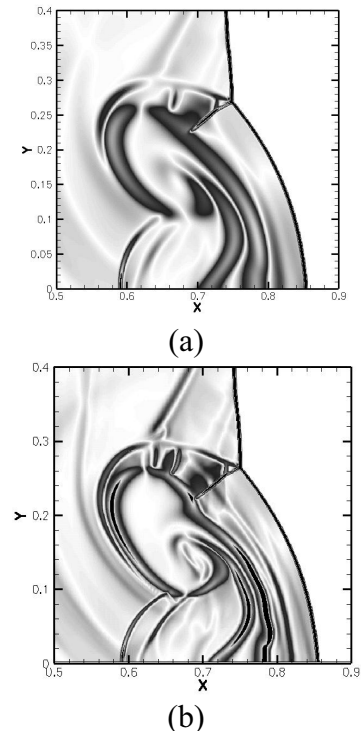


Fig. 5 Zoom of shock-bubble Schlieren image with 1000x500 cells at time of 0.2. QDS 2nd order (a) 2N scheme with van Leer's limiter, (b) N2 scheme.

Ultra-short Pulse Laser: A Potential Tool for Breast Cancer Detection

Arka Bhowmik¹, Ramjee Repaka^{1*}, Subhash C. Mishra²

¹ School of Mechanical Materials and Energy Engineering, Indian Institute of Technology Ropar, Punjab, India

² Department of Mechanical Engineering, Indian Institute of Technology Guwahati, Guwahati, India

* Corresponding author: ramjee.repaka@iitrpr.ac.in

ABSTRACT

A preliminary study on ultra-short pulse laser transport within normal and abnormal human breast tissues is performed. The characteristic signals of laser irradiated human breast with and without malignant lesion analyzed are within the therapeutic optical window of 600-1200 nm. These signals are found to be medium specific as well as specific to source configurations. The associated changes in the characteristic signals due to the change in properties and conditions can be a means to detect traces of cancer.

1. Introduction

Mostly cancer cells are capable to replicate faster in an uncontrollable manner and exhibit different growth stages. As a result, it should be detected as early as possible, for better treatment. Now, from the standpoint of early detection of cancer, the present non-invasive imaging techniques (X-ray, CT scan and MRI etc) are incapable to image small number cancer cells at an early stage [1]. However, using a low power short-pulse laser source and the time resolved detection technique, there is a possibility to detect the cancer at an early stage as well as to avoid significant cases of false negative cases. Thus, in order to determine the distinguishing features of the characteristic signals, the article performs a parametric study on the breast with and without cancerous lesion subjected to short-pulse laser. The aim of this study is to essentially boost the future use of laser as a potential clinical tool for breast cancer detection.

2. Mathematical Formulation

The general relation that governs the radiative heat transfer within a participating medium is given by [2].

$$\frac{1}{c} \frac{\partial I_d}{\partial t} + \hat{s} \cdot \nabla I_d = -\beta I_d + \kappa_a I_b + \frac{\sigma_s}{4\pi} \int (I_d + I_c) \Phi(\hat{s}, \hat{s}_i) d\Omega_i \quad (1)$$

where I is the intensity, $\Delta\Omega$ is the solid angle, t is the time, \hat{s} is the direction vector, c is the speed of light in the medium ($= c_{vac}/n$), n is the refractive index, κ_a is the absorption coefficient, σ_s is the scattering coefficient, β is the extinction coefficient ($=\kappa_a+\sigma_s$), $\Phi(\hat{s}, \hat{s}_i)$ is the scattering phase function, subscript i indicates incident direction, I_d is the diffuse intensity, I_b is the black body intensity and I_c is the collimated intensity. For simplification, the breast is approximated as 1-d planar medium (Fig. 1) and a longitudinal section of tissue has been considered along the dorsoventral axis of the breast with the assumption that, there are negligible changes in the condition at other lateral directions.

The scattering phase functions in Eq. (1) has been approximated using the Henyey-Greenstein scattering phase function in terms of Legendre polynomial P_m for azimuthally symmetrical case and can be given by

$$\Phi(\theta, \theta_i) = 1 + \sum_{m=1}^M (2m+1) g^m P_m(\cos\theta) P_m(\cos\theta_i) \quad (2)$$

where θ is the polar angle, g is the asymmetry factor and M is the order of approximation, is equal to 10 for present case. In Eq. (1), the collimated intensity I_c is due to pulsating laser of step temporal profile.

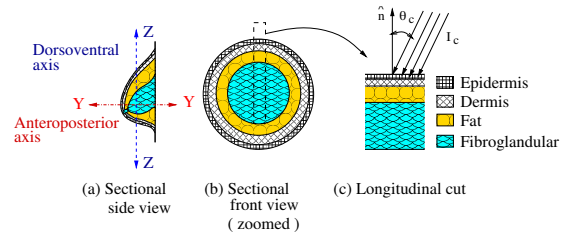


Fig. 1 Schematic of Breast: a) side view, b) sectional front view (zoomed) and c) longitudinal cut.

Relations for the collimated remnant of pulsating laser source as well as boundary conditions can be obtained from Mishra et al. [2]. The Finite volume method (FVM) has been used to solve the Eq. (1) and has been elaborated in [2].

3. Results and Discussions

The optical properties and the thickness of normal as well as abnormal breast tissues are given in Table 1. Breast is an inhomogeneous anatomic structure composed of layers of fat, fibroglandular and connective tissues. Among those the majority of tissues in the breast are fatty and fibroglandular tissues. Present study has been carried out by considering commonly found breasts (BI-RADS-IV), i.e., the breast contains 75 % of fibroglandular tissues and 25% other tissues. More details on the classification of breast can be obtained from American college of radiology. The abnormal breast has been modeled by considering two cases: (a) benign breast lesion, fibroadenoma found throughout the fibrous tissues and (b) ductal carcinoma found in the inside lining of ducts that carry milk from the glands. The thickness, d , of various layers of tissue varies for breast along the anteroposterior axis of the breast as can be seen from Fig. 1. It can be seen that, the thickness of

layers at anterior end reduces compared to that of posterior end. Further, the ductal carcinomas are normally found at the anterior end where ducts are located due to which the thickness in Table 1 has been reduced approximately from that of the original thickness [3]. Similarly, the thickness of outer skin has been approximated as 0.11 cm. The epidermis is of 0.01 cm and the dermis is of 0.1 cm. For numerical simulations the refractive index, $n = 1.4$ has been considered. The ductal carcinoma and fibroadenoma have been modeled at the upper 5 mm of fibro-glandular tissue.

Table 1. Optical properties of normal and cancerous breast tissues [4] at wavelength 1100 nm.

Tissues	d (mm)	β (mm^{-1})	σ_s (mm^{-1})	g
Epidermis	0.1	29.217	29.2	0.9
Dermis	1.0	17.646	17.6	0.9
Fat	1.5	31.6433	31.513	0.977
Fibroglandular ^[5]	10	12.247	12.175	0.9384
Ductal cancer	5	12.998	12.939	0.946
Fibroadenoma	5	20.817	20.753	0.979

The transmittance and the reflectance from the normal and the abnormal breasts subjected to single step laser pulse having pulse width of 1ps have been compared in Figs. 2 and 3 respectively. It can be seen from Fig. 2 that, there is a significant demarcation in the peak magnitude of the transmitted signals for normal breast compared to that of abnormal breast (i.e., benign fibroadenoma and ductal carcinoma). On the other hand, the peak magnitude of the transmitted signals from the breast with benign fibroadenoma exhibit small demarcation compared to that of ductal carcinoma. Further, it has been noticed from Fig. 2 that, there are significant variations in the temporal broadening of the transmitted signals.

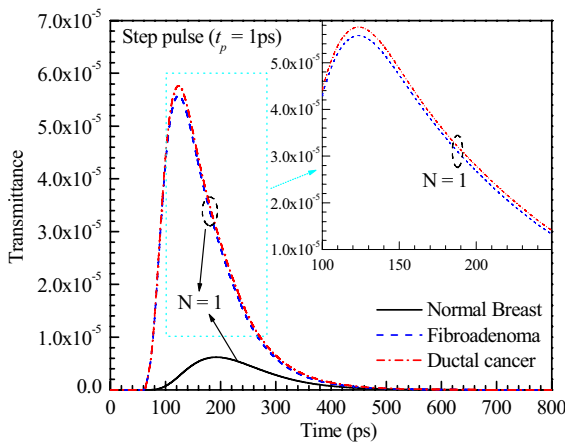


Fig. 2 Transmittance from normal and abnormal breasts subjected to single ($N=1$) step pulse of 1ps pulse width.

On the contrary, the peak magnitude and the temporal broadening of the reflected signals from the normal and abnormal breasts (Fig. 3) exhibit small variations. The observed distinguishing feature is the variation of the temporal spread of the signals within the temporal range of 0.9–1.7 ps. Further, it should be noted that, the small-scale deviation of reflected signals can be easily differentiated using a sensitive time gating detection technique.

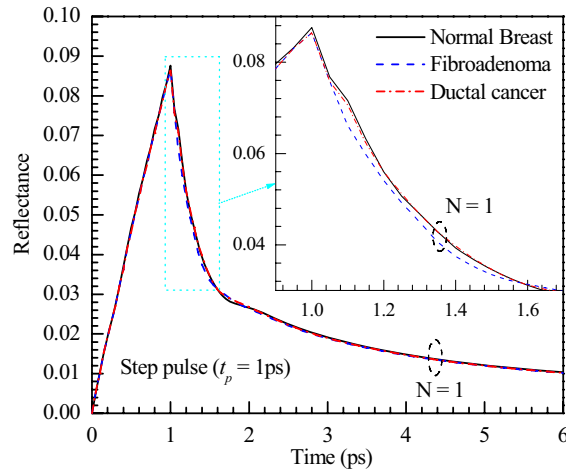


Fig. 3 Reflectance from normal and abnormal breasts subjected to single ($N=1$) step pulse of 1ps pulse width.

4. Conclusions

The numerical analysis of normal and abnormal breasts subjected to low power pulsating laser source has been done to determine the distinguishing features. The study affirmed that abnormal lesion within the breast exhibit distinctive features in the temporal spectra of characteristic signals when compared to that of the normal breast. The observed distinctive features are mainly due to the change in the medium configurations (i.e., optical properties, growth of lesion and depth of lesion, etc.) as well as due to change in the input laser configurations (i.e., wavelength, pulse width, pulse temporal profile, etc.). The changes in the characteristic signals due to the associated changes in the optical properties of breast with and without anomalies will serve as a means to determine the cancer in the breast at an early stage.

References

- [1] J.V. Frangioni, *J. Clin. Oncol.*, **26** (2008), 4012.
- [2] S.C. Mishra, P. Chugh, P. Kumar, K. Mitra, *Int. J. Heat and Mass Transfer*, **49** (2006), 1820.
- [3] M.B. Tayel, A.T. Ibrahim, M.I. Badwai, *CJBET*, **2** (2011), 43
- [4] V.G. Peters, D.R. Wyman, M.S. Patterson, G.L. Frank, *Phys. Med. Biol.*, **35** (1990), 1317.
- [5] H. Key, E.R. Davis, P.C. Jackson, P.N.T. Wells, *Phys. Med. Biol.*, **36** (1991), 579.

Numerical Investigation of Flow Characteristics of Fuel/Oxidizer Channels in a Solid Oxide Fuel Cell Stack

S.-S. Wei and J.-S. Wu*

Department of Mechanical Engineering, National Chiao Tung University, Hsinchu, Taiwan

*E-mail of corresponding author: chongsin@faculty.nctu.edu.tw

ABSTRACT

In this paper, we study numerically the effect of flow channel design of a planar solid oxide fuel cell stack on the efficiency and fuel utilization. Results show that a new design of flow channel, termed as type B, by directing the gas flow diagonally through the conducting interconnects performs with a 12% increase of power density and a 14.6% increase of fuel utilization as compared with a conventional design using counter-flow concept, termed as type A.

1. Introduction

Fuel cells have demonstrated very high efficiency as compared to combustion engines and are also much less harmful to the environment. Among these, solid oxide fuel cell (SOFC) has been considered as one of the promising energy technologies due to much higher efficiency (up to 90%) can be achieved by hybridizing with combined heat and power (CHP) system because of its operation at high temperature (700-900 °C). By applying the concept of cell stacks, one can build 1kW-10MW power generators. It is thus highly suitable for applications in distributed power stations.

To better design the cell stacks, it is necessary to consider mass and heat transports, and electrochemical reactions simultaneously to obtain the distributions of power density, current density, fuel and oxidizer concentrations. This makes computational fluid dynamics (CFD) an inevitable tool in the design process. Recknagle et al. [1] showed that counter-flow channel design results in higher power density than co-flow and cross-flow designs. However, for a cell stack design using counter-flow channels [2], it was shown that there exist many disadvantages. These include non-uniform flow distribution and often very complex structures needed. Thus, we would like to propose a simple but effective design of flow channels in a cell stack based on CFD simulations.

For this aim, we use the commercial CFD code FLUENT to create the stack model and simulate. The research focus on 50×50 mm² anode support planar SOFC, because of to decrease the time of design.

2. Method

In this study, we employed a commercial CFD package, named FLUENT, to simulate the thermal-fluid field within a cell stack. It is used to solve the conservations of mass, momentum, energy, species and electrochemical reactions. The details of the numerical method were described by Qu *et al.* [3] and are not repeated here for brevity.

Following the idea of Sembler *et al.* [4], we can estimate the performance of a cell stack by simulating a single cell. Thus, we simulate the single-cell to improve the stack flow channel design. After the flow channel design is completed, we will simulate the thermal-fluid field within a multi-cell stack.

Fig.1 shows the design of multi-cell stack. In type A,

it is a hexagonal cell stack consisting of planar SOFC with 50×50 mm² anode support with a single-inlet/double-outlet design having many parallel rectangular channels in the middle. The air and fuel flows in opposite directions. Each flow pipe is shared by three stacks. If we include more stacks, it looks like a honeycomb (Fig.2). This design has the potential in reducing the amount of material used. For the same concept, type B is a square stack with a single-inlet/single-outlet design and having tessellated channel. It is a cross flow type along different cell diagonal directions. This design can save more material than type A and having perfect symmetry.

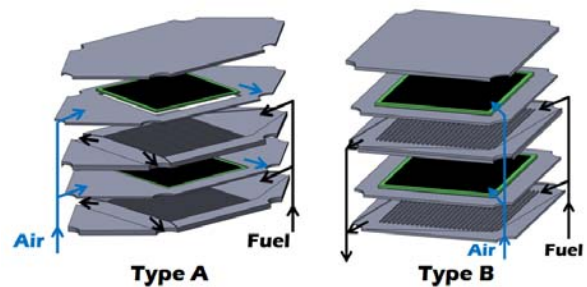


Fig. 1 Multi-cell stack designs.

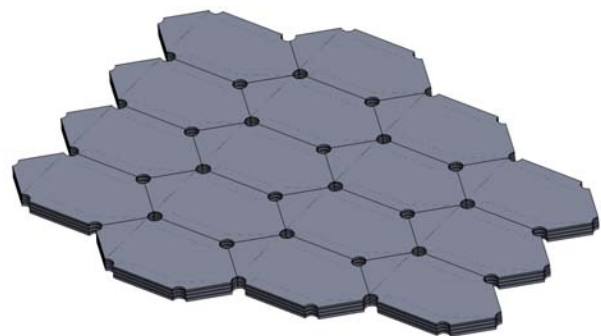


Fig. 2 A diagram of multi-cell multi-stack organization.

In the simulation of air and fuel flow channels, we use porous material for interconnect. Because of the anode-supported structure, the cathode is comparatively thin and the geometric configuration of the air supply has remarkable effect on oxygen distribution and thus overall cell performance. [3]

The material properties we employed in the current study are summarized in Table 1. The boundary

conditions are adiabatic at the top of stack and radiation wall in side of stack at 973K. To make sure our simulation setup is correct, we have benchmarked our simulation with Sembler *et al.* [4] as follows;

- anode (fuel) inlet composition: 97% H₂, 3% H₂O
- anode inlet mass flow rate: 4.48×10^{-7} kg/s
- cathode (oxidizer) inlet composition: 100% dry air
- cathode inlet mass flow rate: 2.17×10^{-5} kg/s
- operating pressure: 1 atm
- air and fuel supply temperature: 973 K

Table 1. Single-cell SOFC properties

Part	Anode	Cathode	Electrolyte
Thickness	1 mm	100 μ m	20 μ m
Material	Ni-YSZ ^a	LSM ^b	YSZ ^c
Density (kg/m ³)	6500	5620	5480
Specific heat	450	450	450
Thermal conductivity	10	11	2
Porosity	0.24	0.375	N/A
Tortuosity	3	3	N/A

^aNickel oxide+yttria-stabilized zirconia.

^bStrontium-doped lanthanum manganite.

^cYttria-stabilized zirconia.

3. Results and Discussion

Fig. 3 shows I-V curves of type A and type B for single-cell simulations. Results show that Type B has a maximum power density of 744.48 mW/cm² at 0.6V, which is ~12% as compared to type A. The most important reason is that type B consumes more hydrogen than Type A. Fig. 4 shows the distributions of H₂ concentration of type A and type B. There are some regions at the end of fuel channel having no hydrogen at all, which means it is all consumed, especially in the case of Type B. Fuel utilization in Type B increases ~14.6% as compared to type A. We can also see similar trend of oxygen consumption in Fig.5, in which the oxygen of type B is consumed more than type A.

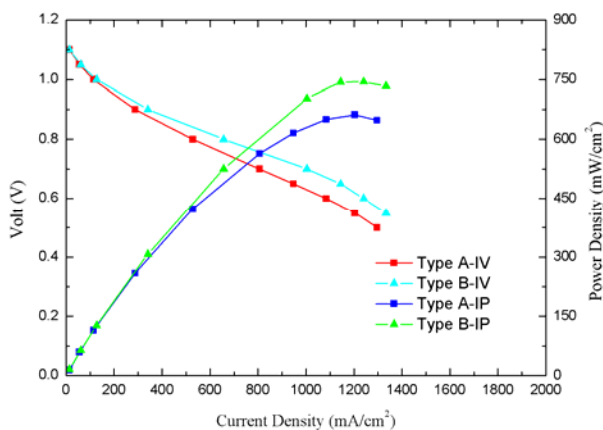


Fig. 3 I-V curves of Type A and type B SOFC.

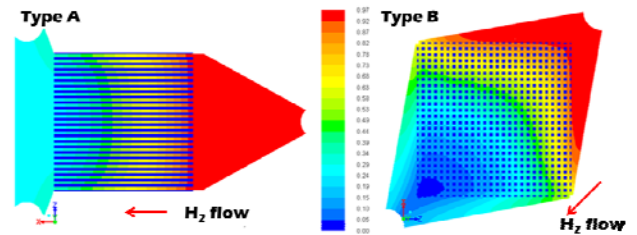


Fig. 4 Type A and type B H₂ mole fraction at 0.65V

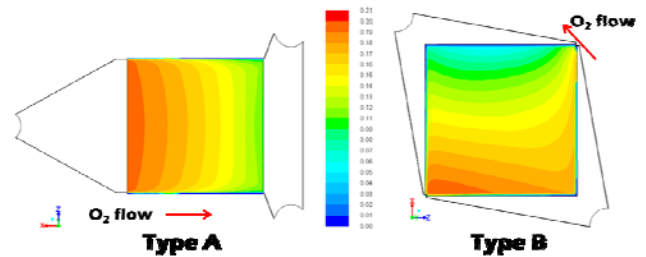


Fig. 5 Type A and type B O₂ mole fraction at 0.65V

4. Concluding remarks

In the current study, a new type of fuel and air flow channels is proposed to increase the power density and fuel consumption. Results show that 12% increase of power density and a 14.6% increase of fuel utilization of Type B as compared with a conventional design using counter-flow concept, termed as type A can be achieved. A large-scale simulation by including more than 10 fuel stack is currently in progress and the results will be reported in the meeting.

References

- [1] K. P. Recknagle, R. E. Williford, L. A. Chick, D. R. Rector and M. A. Khaleel, *J. Power Sources* **113** (2003) 109.
- [2] C.M. Huang, S.S. Shy, C.H. Lee, *J. Power Sources* **183** (2008) 205
- [3] Zuopeng Qu, P.V. Aravind, S.Z. Boksteen, N.J.J. Dekker, A.H.H. Janssen, N. Woudstra, A.H.M. Verkkooijen, *International journal of hydrogen energy* **36** (2011) 10209.
- [4] William J. Sembler, Sunil Kumar, *Journal of Fuel Cell Science and Technology* **vol.8** (2011).

Reversible Motion of Microchains

Yan-Hom Li, Ching-Yao Chen

Department of Mechanical Engineering, National Chiao Tung University
Hsinchu, Taiwan, Republic of China

E-mail of corresponding author: chingyao@mail.nctu.edu.tw

ABSTRACT

This article outlines and illustrates the reverse motion of microchains subjected to an oscillating field by experimental analysis. A chain consisting of superparamagnetic particles whose radius are about $2.25 \mu\text{m}$ is first formed by a static directional field and then manipulated by an additional dynamical perpendicular field. The chain oscillates reversely to the orientation of the external field under either a certain higher perpendicular field or a lower static unidirectional field, which leads the maximum instantaneous phase lag to reach the critical value.

1. Introduction

Magnetorheological (MR) suspension is an artificial and smart fluid consisting of paramagnetic solid particles suspended in a nonmagnetic solvent. The dynamics and aggregation processes of magnetorheological fluids subjected to rotating magnetic fields have been investigated experimentally [1][2]. The rotating chain reverses align along the external field while the phase lag angle of the chain relative to the external field reaches $\pi/2$ [3]. As for the behaviors of microchains in an oscillating field, Li et al. have detailed discussion [4][5].

In this work, we study the reverse motion of the magnetic chains under an oscillating field. This study may lead to a better understanding of the dynamics and behaviors of an oscillating chain, which can be effectively employed as a micro-swimmer or to other MEMS applications.

2. Experimental Procedure

Fig. 1 shows the schematic of our experimental setup. Micro-size magnetic particles are initially dispersed in distilled water. The magnetic particles used in our experiments are aqueous superparamagnetic polystyrene microspheres coated with iron oxide grains produced by Invitrogen Life Tech.. The mean radius of the microspheres (denoted as a) are $a=2.25\mu\text{m}$, with a susceptibility of $\chi=1.6$ and no magnetic hysteresis or remanence. A static unidirectional magnetic field, denoted as H_d , is generated first by a pair of coils powered by DC power sources. Magnetic particles magnetized by the unidirectional field tend to aggregate and form chains because of dipolar attractive forces. To create an oscillating field, another pair of coils are placed perpendicularly to the former pair and connected to AC power supplies to generate a sinusoidal dynamical perpendicular field (H_p) with a maximum field strength H_p and frequency f , i.e. $H_p = H_p \sin(2\pi ft)$. This additional perpendicular field and the original static directional field result in an overall oscillating field (\mathbf{H}) of $\mathbf{H} = H_d \mathbf{i} + H_p \mathbf{j}$, in which \mathbf{i} and \mathbf{j} are unit vectors in the directional and perpendicular axis, respectively. Under such a field configuration, the phase angle trajectory (θ) of the external field is prescribed as $\theta(t) = \tan^{-1}[(H_p/H_d)\sin(2\pi ft)]$ associated with an amplitude

(denoted as θ_{Amax}) of $\theta_{Amax} = \tan^{-1}(H_p/H_d)$. The magnetic particle chains, which tend to align along the orientation of the external field, would oscillate under the presence of such an oscillating field. The motion of the particle chains is recorded by an optical microscope connected to a digital camera (Silicon Video 643C) whose shooting rate is 200 frames/sec.

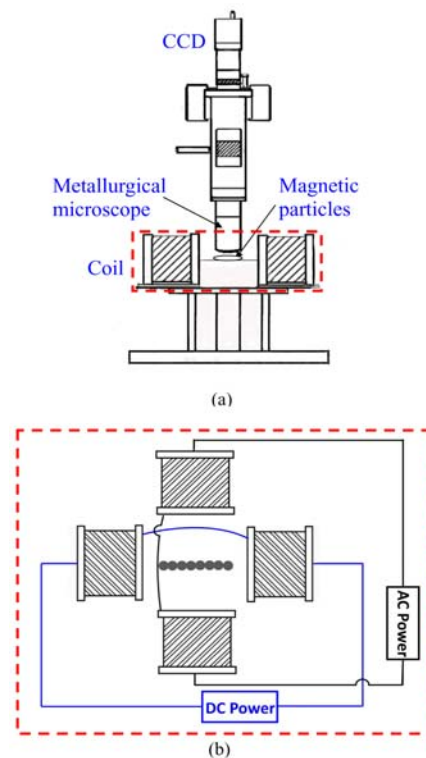


Fig 1. (a) Schematic of experimental setup, and (b) top view configuration of coil pairs for generation of oscillating magnetic field. The size of the particle chain in (b) is exaggerated and not in actual scale.

3. Results and Discussion

Fig. 2 shows the sequential images taken from a chain consisting of 8 particles (denoted as a P8 chain) subjected to an oscillating field configuration of $H_d = 24.15 \text{ Oe}$, $H_p = 176.13 \text{ Oe}$ and $f = 1 \text{ Hz}$ (or period $P = 1 \text{ s}$) within one and half periods, i.e. $0 \leq t \leq 3P/2$. Under such a field condition, the chain behaves as a rigid beam and oscillates asynchronously with the orientation of the

external field. Actually, an interesting phenomenon of reverse oscillation is observed. Instead of concurrent oscillation with the external field, the chain moves reversely (counter-clockwise) at $17P/30 < t < 20P/30$. Afterward, the chain oscillates along the perpendicular axis (or $\theta = 90^\circ$), rather than the horizontal axis (or $\theta = 0^\circ$) of external field. The reverse motion can be observed more clearly by the phase angle trajectory also shown in Fig. 3. At $t=17P/30$, an apparently reverse motion of the chain from the external field can be identified. Consequently, the chain's trajectory completely deviates from the external field during the time at $17P/30 < t < 32P/30$. The chain changes its oscillating orientation dramatically at about $t=33P/30$ and resumes to follow the trajectory of the external field. Excluding the initial start at $t < 4P/30$, a distinct pattern of oscillation along the perpendicular axis of $\theta = 90^\circ$ is resulted.

The actual maximum instantaneous phase lags ($\Delta \theta_{Lmax}$) of chains composed of different numbers of particles subjected to various perpendicular field strengths are shown in fig 4. Note, for longest P21 chain, stable chaining structure can only be sustained up to a perpendicular field of $H_p = 42.03$ Oe. Ruptures occur when the field strength exceeds $H_p = 56.7$ Oe. The sustainable field for a P15 chain is higher at $H_p = 70.88$ Oe, while P8 chain remains stable up to a stronger $H_p = 176.13$ Oe causing to oscillates reversely along the perpendicular axis because of the instantaneous excessive phase lag of $|\Delta \theta_{Lmax}| > 90^\circ$.

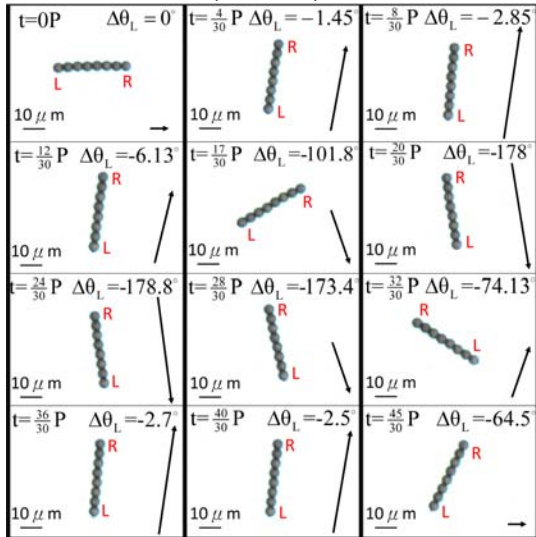


Fig.2 Images of 8-particle (P8) chain oscillating under a field of $H_d = 24.15$ Oe, $H_p = 176.13$ Oe and $f = 1$ Hz. Due to the instantaneous excessive phase lag of $|\Delta \theta_{Lmax}| > 90^\circ$, the chain oscillates reversely along the perpendicular axis within $17P/30 < t < 32P/30$.

4. Concluding remarks

In the present work, the motion of a magnetic chain oscillating reversely to the external field is experimented and analyzed. By increasing the strength of perpendicular field, the maximum instantaneous phase lag of $|\Delta \theta_{Lmax}| > 90^\circ$ lead the chain to oscillate along

the perpendicular axis, rather than the horizontal axis of external field. Those findings support the applicability to manipulation of micro swimmers.

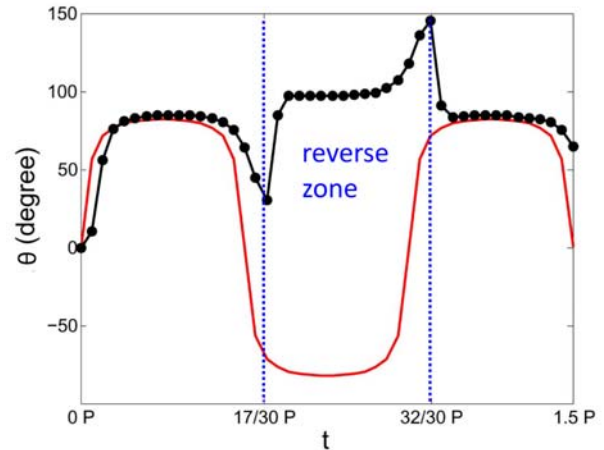


Fig.3 The trajectories of phase angle (θ) of a P8 chain and its corresponding external field of $H_d = 24.15$ Oe, $H_p = 176.13$ Oe and $f = 1$ Hz. Reverse motion of the oscillating chain is observed due to the excessive phase lag of $|\Delta \theta_L| > 90^\circ$ at $17P/30 < t < 32P/30$.

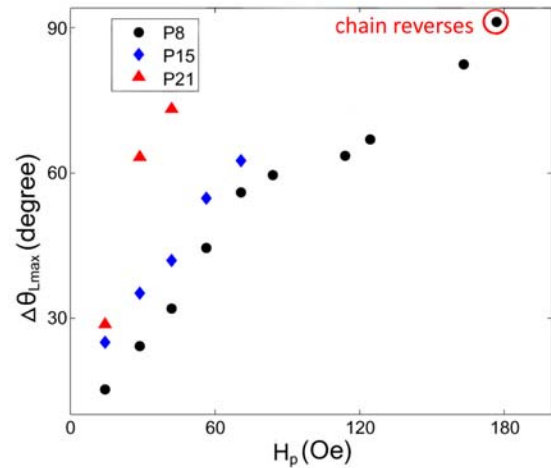


Fig 4. Maximum instantaneous phase lag ($\Delta \theta_{Lmax}$) of chains composed of different numbers of particles subjected to various perpendicular field strengths in a fixed directional field of $H_d = 24.15$ Oe and $f = 1$ Hz.

Acknowledgements

The financial support from the National Science Council of Republic of China (Taiwan) through Grant NSC 99-2221-E-009-057-MY3 is acknowledged.

References

- [1] S. Melle, G. G. Fuller and M. A. Rubio, Phys. Rev. E 61, 4111(2000).
- [2] S. Melle, J. E. Martin, J Chem Phys: Vol. 118, no. 21 June(2003).
- [3] S. Biswal, A. Gast. Phys. Rev. E 69: 041406(2004.)
- [4] YH Li, ST Sheu, JM Pai, CY Chen, J. Appl. Phys., 111: 07A924. (2012).
- [5] YH Li, ST Sheu, JM Pai, CY Chen, accepted for publication in Microfluid Nanofluid. (2012).

Auxiliary Injection for Combustion Enhancement in RBCC Engine Operating in Hypersonic Flow

Shohei Takagi¹⁾, Sadatake Tomioka²⁾, Tomoyuki Komuro²⁾, Katsuhiro Itoh²⁾, Goro Masuya¹⁾

¹⁾Department of Aerospace Engineering, Tohoku University, Sendai, Japan : takagi@scrj.mech.tohoku.ac.jp
1 Koganezawa, Kimigaya, Kakuda City, Miyagi Prefecture, Japan

²⁾JAXA-Kakuda Space Center, Kakuda, Japan

ABSTRACT

The purpose of this study is to accomplish combustion in RBCC engine operating in hypersonic flow at Mach 11 flight condition. Auxiliary injection for combustion enhancement in RBCC engine was tested experimental at JAXA-Kakuda Space Center using high enthalpy shock tunnel (HIEST). By injecting a portion of fuel besides in residual fuel in the rocket exhaust, incoming air and residual hydrogen in the rocket exhaust were started reaction.

Nomenclature

φ_i : Equivalence ratio of the auxiliary injection against airflow
 φ_r : Equivalence ratio of the rocket
 Φ_r : Equivalence ratio of residual fuel in the rocket exhaust
 p_0 : Stagnation pressure
 p_w : Wall pressure
 X : Stream wise location from the rocket base

1. Introduction

Rocket Based Combined Cycle (RBCC) engine is expected to be the most effective propulsion system for booster stage of launch vehicles. Our RBCC engine is scramjet flow-pass with embedded rocket engines. It has four operation modes, ejector mode (flight Mach number 0~3), ramjet mode (flight Mach number 3~7), scramjet mode (flight Mach number 7~11) and rocket mode (flight Mach number 11~). The object of this research is to accomplish combustion in scramjet mode operation of RBCC engine. In the scramjet mode operation, the incoming airflow and the residual fuel in the rocket exhaust run downstream at high speed. Therefore, accomplishment of combustion is very difficult due to insufficient combustion velocity. This is the major problem of the scramjet mode operation. Thus, auxiliary injection in upstream of the rocket base was thought. Temperature and pressure raise due to combustion of this fuel enforce combustion enhancement between incoming air and the residual fuel in the rocket exhaust. The effect of this expedient was confirmed in the Mach 7 flight condition (lowest condition of scramjet mode operation) by Tomioka and Kobayashi. [1][2] This experiment confirms the effect of this expedient in more high condition of Mach 11.

2. Test apparatus and engine model

2.1 HIEST (high enthalpy shock tunnel)

This experiment was run at JAXA-Kakuda Space Center, using high enthalpy shock tunnel (HIEST). HIEST is free piston type shock tunnel. It is the largest and the most high-performance shock tunnel that can make airflow condition of maximum stagnation enthalpy 25MJ/kg and maximum stagnation pressure 150MPa. Either air or nitrogen was used as the test gas to conduct both reacting and non-reacting tests. Table 1

shows airflow condition of Mach11 flight condition that was used in this experiment.

Table.1 Free stream condition at M11 flight condition

Stagnation Condition	Total temp.	4550K
	Total pres.	17MPa
	Enthalpy	7.0MJ/kg
Condition at nozzle exit	Mach number	6.7
	Static temp.	640K
	Static pres.	1.9kPa
	Dynamic pres.	62kPa

2.2 Engine model

Engine model is shown in Fig.1. It had a single ramp with angle of 10 degrees, the airflow pass after compression was 100mm in width and 25mm in height. Two rockets were located at a backward-facing base (40mm in height) at the exit of isolator section. The wall surface where rockets are installed was termed as rocket side and the other side wall surface as cowl side. The auxiliary injector (1.5mm in pore diameter×8, vertical injection) was installed in 50mm upstream of the rocket base on both cowl side and rocket side. Fuel of the auxiliary injection was hydrogen. A combustor which had ramp side wall of 3 degrees was installed in downstream of the rocket base, and it was 800mm in length. The combustor had pressure taps at 50mm interval on the centerline of both rocket and cowl side walls. Two rocket chambers were connected to a detonation tube to generate rocket exhaust gas. The detonation tube was filled with hydrogen and oxygen. Table 2 shows the typical operation conditions of the detonation tube. The equivalence ratio of residual fuel in the rocket exhaust (Φ_r) was defined against air flow.

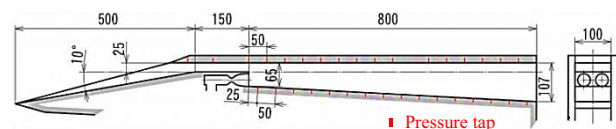


Fig.1 Test model of RBCC Engine

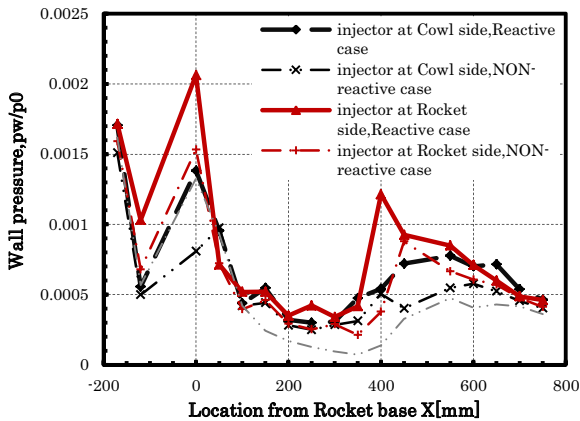
Table.2 Rocket chamber operation condition

Detonation tube premixed gas condition	Equivalence ratio	1.0	1.5
	Initial Pressure	0.5MPa	0.5MPa
	Φ_r against airflow	0	0.5

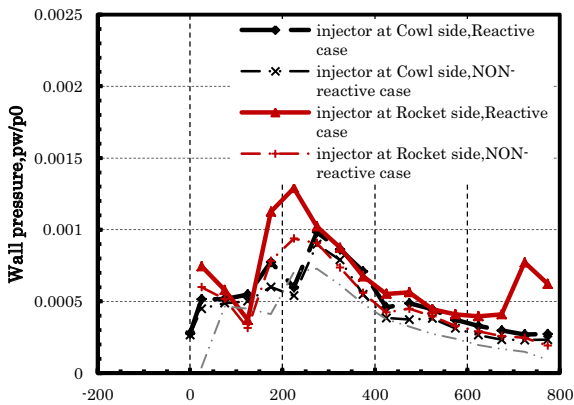
3. Results and discussion

3.1 Wall pressure distribution

Figure 2 shows wall pressure distributions on cowl side and rocket side at Mach 11 flight condition. The condition of the auxiliary injection was equivalence ratio of $(\phi_i)=0.5$, and the condition of the rocket was equivalence ratio of $(\phi_r)=1.5$. The abscissa axis is stream wise location from the rocket base, and the vertical axis is non-dimensional wall pressure (p_w/p_0).



(a)Cowl side wall pressure distribution



(b)Rocket side wall pressure distribution

Fig.2 Wall pressure distribution at Mach11 flight condition

The wall pressure distribution in both reactive case and non-reactive case has some peaks. Thus, the result means that these peaks were occurred by shock waves. The peaks of rocket side injection are higher than these of cowl side injection. Therefore, the bow shock associated with injection on the rocket side is stronger than that of cowl side injection. Both cowl side and rocket side, however, the wall pressure distributions in reactive case are higher than that in non-reactive case. The combustion reaction started in the engine. Additionally, it is known that the position of shock wave move upstream when combustion occurs. [3] This phenomenon can be confirmed from the difference of positions around $X=400mm$ between the reacting case and non-reacting case in the cowl side wall distribution. The peak around $X=650mm$ in the rocket side distribution moved upstream due to this phenomenon. This result also could interpret that the combustion

reaction started.

3.2 Schlieren photographs

Figure 3 shows three schlieren photographs around the rocket base, and the flow direction is from left to right. Figure 3 a) is with rocket side injection, b) is with cowl side injection and c) is freestream alone.

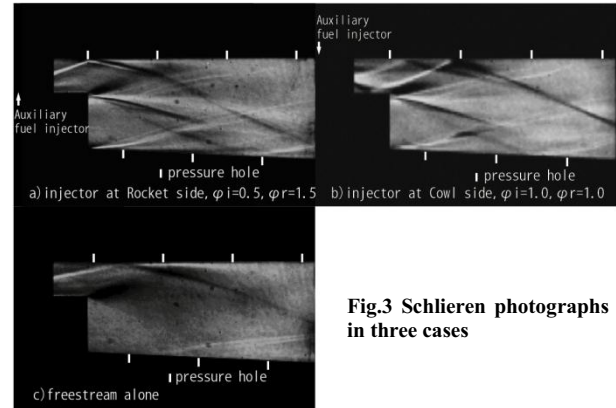


Fig.3 Schlieren photographs in three cases

In cowl side injection case, the bow shock that was occurred by the auxiliary injection reflects at rocket side wall in upstream of the rocket base. It rode another shock wave that was from inlet after it reflects again. Meanwhile, in rocket side injection, the bow shock reflected at cowl side wall. And this shock wave rode another shock wave from the inlet. Due to this merged shock wave, in rocket side injection case, the high peak was appeared $X=0mm$ on cowl side wall. Additionally, this merged shock wave got temperature and pressure raise. These increase the rate of reacting. Moreover, Mach number was decreased by this shock, the distance that the incoming airflow and the auxiliary fuel were mixed was decreased. Therefore, the pressure distribution of rocket side injection was higher than that of cowl side injection.

4. Conclusions

- 1) The auxiliary injection got auxiliary fuel and residual hydrogen in the rocket exhaust to start reaction.
- 2) The pressure distribution of rocket side injection was higher than that of cowl side injection.
- 3) The rocket side injection got strong shock waves due to the merged shock wave.

References

- [1]Sadatake Tomioka,Kenji Kudo,Kanenori Kato,Atsuo Murakami,and Takeshi Kanda"Auxiliary Injection for Combustion Augmentation of G/G Plume in RBCC combustor",AIAA 2005-4284
- [2]Sadatake Tomioka, Ryohei Kobayashi, Atsuo Murakami, Shuichi Ueda, Tomoyuki Komuro, and Katsuhiko Itoh " Combustion Enhancement in Scramjet-Operation of a RBCC Engine",2011
- [3] Masahiro Takahashi,Tetsuji Sunami,Hideyuki Tanno, Tomoyuki Komuro,Masatoshi Kodera and Katsuhiko Itoh."Performance Characteristics of a Scramjet Engine at Mach 10 to 15 Flight Condition", AIAA 2005-3350

Investigation on Fundamental Characteristics of Synthetic Jet Actuator with Cavity in Resonances

Fei-Bin Hsiao* and Chi-Yu Lin

Institute of Aeronautics and Astronautics, National Cheng Kung University, Tainan 70101, Taiwan, RO.C.

* fbhsiao@mail.ncku.edu.tw

ABSTRACT

This paper uses the loudspeaker as driving mechanism for conducting the synthetic jet actuator (SJA) to study the resonance frequencies of the SJA in variations with some relevant parameters. The SJA system has the opening orifice in two-dimensional shape with a large cavity. The diaphragm of the loudspeaker is driven by an amplifier with a sine waveform as input to produce the ejected velocities at the orifice exit from the SJA. Results indicate that two resonance frequencies were measured and confirmed to be respectively corresponding to the membrane resonance and the cavity as Helmholtz resonator.

Keywords: Synthetic jet, Resonance, Helmholtz Resonator

1. Introduction

The piezoelectric-driven synthetic jet actuators (SJAs) have been extensively applied in many areas for flow control. Such as through the piezoelectric-driven SJAs applied in a NACA 633018 wing for boundary flow control, its aerodynamic performance could effectively be improved in our previous study [1]. Interestingly, two peak frequencies in exit velocity fluctuations for the piezoelectric-driven actuator were found by a few papers [2, 3], which can be referred to resonance frequencies associated with the resonance frequency of the diaphragm and the Helmholtz frequency of the cavity. As it is difficult to investigate experimentally the flow characteristics of the small synthetic jet flow, this paper is hence aimed to explore the detailed flow characteristics using the synthetic jet actuator model tailor-designed to be two-dimensional and in a bigger scale as well for better measurements and analyses. This paper will also report the difference of the resonance frequencies regarding the diaphragm resonance and the Helmholtz cavity frequency of this synthetic jet actuator.

2. Experimental Measurement

In stead of using the piezoelectric material as the driving scheme in our previous study [1], this paper now adopts a loud speaker, 203 mm in diameter, as the driving mechanism for the synthetic jet actuators. Both the cavity and rectangular orifice are made of acrylic material. The dimension of the cavity is 175 mm in depth and 140 mm in diameter with the opening rectangular orifice 280 mm in length and 8 mm in width. The loud speaker was seamlessly bounded to the outside surface of the diaphragm without any leakage. In operating the experiments, the synthetic jet actuator is driven by a sine wave from a standard electrical signal generator with a sinewave form. The schematic flowchart of the experiment is shown in Fig. 1. The instantaneous streamwise velocities at exit slot of the jet are measured using a single hot-wire probe of HW-110 anemometric system. The sampling rate and sample number of the Analog/Digital Converter are respectively adjustable according to the forcing frequency used from the signal generator between 10 and 280 Hz. For instance, the sample rate and sample data were respectively set at 1000 Hz and at 2048

points when the forcing frequency is within 100 Hz measured for 2 seconds.

3. Results and Discussion

The experimental arrangement was mainly made to investigate the resonance characteristics of the natural resonance and cavity resonance of the SJA system. Figure 2 shows the results of the maximum amplitude of the diaphragm with respect to the forcing frequency at various driving voltage, which indicates that the frequency of 40 Hz is the resonance frequency and to be the maximum for all input voltages at the same sine wave. The higher the voltage of amplifier provided, the better the amplitude is obtained. Interestingly, two peak values in maximum amplitude of the exit velocity fluctuations take place at 40 Hz and 160 Hz shown in Fig. 3. This result also indicates that with the new model tested, the same trend of the resonance frequencies is obtained as those in our previous study using the piezoelectric-driven SJA [1]. It is evident that the voltage of amplifier as a driving input is the function of amplitude as well. According to the maximum amplitude observed at 40 Hz in Fig. 2, it is very obviously to make difference between the resonance frequency of the diaphragm and the cavity resonance. In theory, the resonance frequency of the diaphragm is independent of such parameters as the amplifier voltage, input waveform, the changed area of exit slot (width is fixed) and the like, but those parameters may somehow influence the intensity of the ejected velocity at the exit. On the contrast, the resonance frequency in the cavity strongly depends on the area of exit slot in this study. Shown in Equation (1), the resonance frequency of the cavity or so-called Helmholtz resonator is reduced with the decreasing area of the exit slot. In addition, the intensity of the ejected velocity for every cavity resonance is increased with the decreasing area of exit slot. The Equation of Helmholtz resonator [4] was represented as follows

$$w_r = c \left(\frac{A}{l'V} \right)^{1/2} \quad (1)$$

where w_r is the resonance frequency, A is a cross-section area in the opening, c is speed of sound, l' is effect neck length and V is volume in cavity. The

area of exit slot (width is fixed) is decreased with the decreasing resonance frequency of cavity as indicated in Fig. 4 (a), while the maximum ejected velocity reduces with the increasing resonance frequency of cavity at the changed area of exit slot in Fig. 4 (b). The trend of the resonance frequency in cavity is in good agreement with the Helmholtz frequency of the cavity.

4. Conclusion

This paper has clearly identified the difference between the resonance frequency of diaphragm and the resonance frequency in cavity. In spite of the changed area of exit slot and voltage of the amplifier, the resonance frequency of the diaphragm is independent of these parameters, but they may somehow influence the intensity of ejected velocity at exit slot for the resonance frequency of diaphragm. On the contrast, the resonance frequency in the cavity depends on the changed area of exit slot in this experiment. The resonance frequency in cavity is reduced with decreasing area of exit slot. The intensity of the ejected velocity for every cavity resonance is increased with the decreasing area of exit slot. In summary, the trend of the resonance frequency in cavity is in good agreement with the Helmholtz frequency of the cavity. These results have explicitly indicated the difference in resonance frequency of diaphragm and Helmholtz frequency of the cavity for a synthetic jet actuator, and this result may be useful for designing the synthetic jet actuator for flow control.

Acknowledgement

This work is supported by National Science Council of Taiwan under Contract NSC 98-2221-E-006-134-MY3.

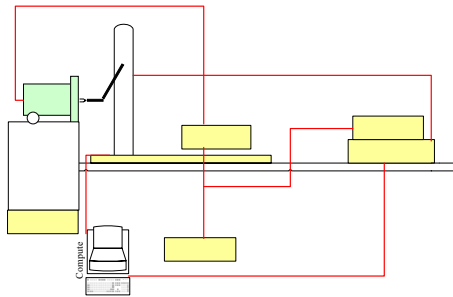


Fig. 1 Schematic flowchart of experiment

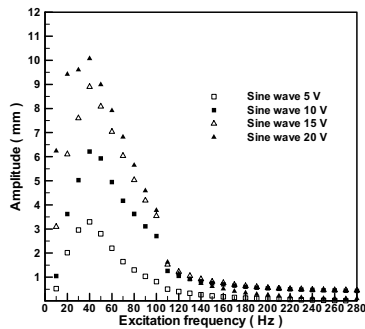


Fig. 2 Variation of velocity amplitude with excitation frequency at various forcing voltage

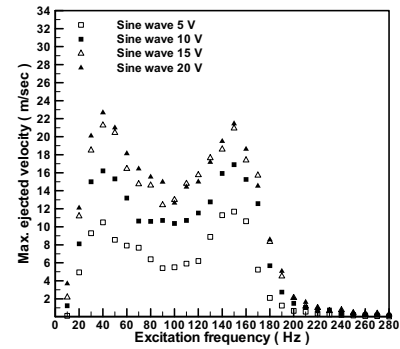


Fig. 3 Variation of maximum ejected velocity with excitation frequency at various forcing voltage

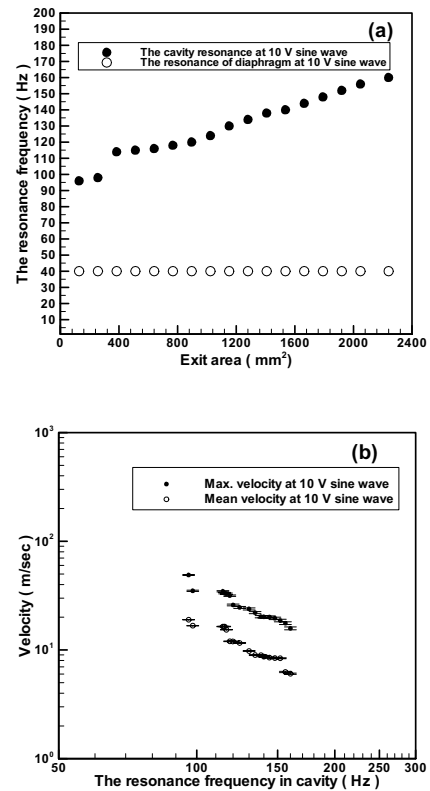


Fig. 4 (a) The resonance frequency in cavity is reduced with the decreasing area of exit slot while (b) the maximum ejected velocity is increasing

References

- [1] C.Y. Lin and F.B. Hsiao, accepted for publication in *Journal of Mechanics* (2012).
- [2] C. Lee, G. Hong, Q.P. Ha and S.G. Mallinson, *Sensors and Actuators A*. Vol. 108, No. 15, pp. 168-174 (Nov. 2003).
- [3] M. Chaudhari, G. Verma, B. Puranik and A. Agrawal, *Experimental Thermal and Fluid Science*, Vol. 33, pp. 439-448 (2009).
- [4] A.D. Pierce, McGraw-Hill, New York, pp. 330-333 (1981).

Estimation of Mode Transition in a Supersonic Combustor

Junji Noda¹ and Sadatake Tomioka²

¹Tohoku University, 6-6-01, Aramaki-Aza-Aoba, Aoba-ku, Sendai, Miyagi 980-8579, Japan

²Japan Aerospace Exploration Agency, 1 Koganesawa, Kimigaya, Kakuda, Miyagi 981-1525, Japan
noda@scrj.mech.tohoku.ac.jp

ABSTRACT

Quasi-one dimensional calculation was carried out to figure out the supersonic combustor performances. Three flow tubes were considered in the combustor region. Those were a main air flow tube, a combustion flow tube and a fuel flow tube. Mach 1 condition was assumed in the combustion flow tube. The estimation of mode transition was considered as a result of compound choking. The calculated results were compared with the previously tested experimental result. It showed that both mode transition equivalence ratios of calculated value and that of previously tested experimental value were well matched.

1. Introduction

Supersonic combustion ramjet (scramjet) engine is one of the options for the future transportation systems. The specific impulse of this engine is higher than that of rocket engines in wide flight Mach number range. However, because the scramjet engine needs ram pressure to compress air for combustion, it is not able to make any significant thrust at a static condition. In other words, about Mach 5 flight speed is demanded for scramjet engine starting.

In the scramjet operation, there is one critical problem in the combustor. At relatively low flight Mach number conditions for scramjet engine, the flow separation in the combustor sometimes goes upstream and it touches the engine inlet. This is so-called the engine un-start. Some previously experimental tests showed that considerable thrust reduction occurred with engine un-start [1]. They also showed that the flow speed in the combustor reduced from supersonic to subsonic due to pseudo shock wave (PSW) as to increasing fuel equivalence ratio [1]. This flow mode transition is known as a dual-mode. Because of this PSW, the combustor pressure level become very higher than without it. Thus, to understand such mode transition is very important for scramjet engines.

There are some previous works about PSW. Waltrup et al. showed the relation between the PSW length and its pressure rise ratio, experimentally [2]. Crocco investigated the quasi-one-dimensional modeling to explain the pressure increase in PSW [3]. Though these study explain the PSW phenomena, they did not mention about the conditions that the PSW can exist or not. Hence, to estimate the mode-transition condition is not enough with only previous study.

In this study, quasi-one dimensional calculation was carried out to estimate mode-transition condition. Quasi-one dimensional approach is very attractive from the standpoint of the calculation costs. This point is important to perform a parametric study. Thus in this paper, the flame holding modeling was considered on a quasi-one-dimensional sense. First of all, quasi one dimensional method is explained. Then the calculated results and previously experimentally tested results for mode transition were compared each other.

2. Method

2.1 General method for calculation

The method for quasi-one dimensional calculation was based on three fundamental conservations, i.e., mass, impulse function (momentum) and enthalpy. In addition, both wall friction[4] and heat transfer[5] were considered. Thirteen species were taken into account. The calculation starts at the point of nozzle throat using target total pressure (823kPaA), total temperature (1170K) and mass flow rates (525g/s). Because the candidate flow state is supersonic, the calculation was only carried out from upstream to downstream. The detail of this calculation is noted in [6]. The target combustor configuration is shown in Fig. 1. The gaseous H₂ fuel was injected through a ramp injector at Mach 1.7. The origin was set at the ramp injector. All distance was normalized by the ramp injector height, H=6.35mm.

2.2 Estimation of Fuel Mixing Schedule

Gas sampling and pitot pressure measurement was previously carried out to calculate mixing efficiency at mid and exit point of the combustor those are X/H = 26 and 58, respectively [6]. Finally, we obtained a modified mixing equation for supersonic flow, written in Eq. (1),

$$\eta_{\text{mod}} = \xi + \psi \frac{x}{x_{\phi}} + \zeta \ln \frac{x}{x_{\phi}} \quad (1)$$

where

$$x_{\ell} = 60G \quad \text{and} \quad x_{\phi} = 0.179e^{1.72\phi} x_{\ell} \quad (2)$$

Here, G and ϕ are Gap (=8H) and equivalence ratio, respectively. Additionally, coefficients ξ , ψ and ζ were estimated as 0.925, 0.529 and 0.124, respectively for supersonic mode.

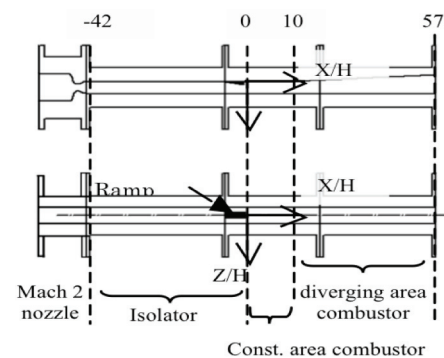


Fig. 1 Combustor configuration

2.3 Modeling for Frame Holding

One stream tube assumption seems enough for the isolator region of supersonic flow. After the fuel injector region, however, the flow state becomes more complex. For instance, mixing and combustion occurs. Especially in supersonic combustible flow, the Mach number is easily changed by the fuel heat release. Tomioka et al. carried out quasi-one-dimensional-one-stream-tube-flow calculation for supersonic combustible flow [7]. Their flame holding modeling contained an experimental coefficient. It completely depends on experimental results. Thus, it is difficult to obtain the coefficient before the experimental tests.

To avoid such special situation, at flame holding region, three flow tubes model was introduced in this study. An air flow tube, a mixing-combustion flow tube and an unburned fuel flow tube were considered. Figure 2 shows the schematic diagram of the flow tubes and flame holding. As we can see in Fig. 2, three stream tubes begin from at a fuel injection hole, which locates at $X/H = 0$. Before this position, only one stream tube was considered. Mass transfers and impulse functions that interact with each flow tube were considered. In addition, constant cross-sectional-pressure was assumed.

At three stream-tubes region in the constant cross-sectional area combustor, chemical equilibrium calculation was carried out. The mass flow from fuel-tube to mixing-tube was calculated by mixing schedule. On the other hand, the mass transfer from the air flow to the mixing & combustion flow was applied to satisfy Mach 1 in the mixing & combustion flow region. This is a model of thermal choke at flame holding region.

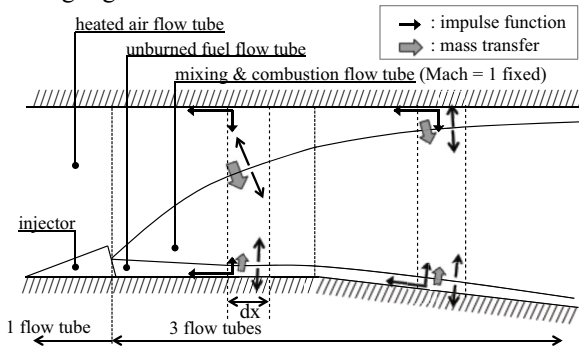


Fig. 2 Schematic diagram of flame holding model

3. Results and Discussion

Figure 3 (a) shows the wall pressure distributions based on some inflow and fuel equivalence ratio conditions. EAH and VAH mean clean and vitiated air inflow, respectively. ER means fuel equivalence ratio. The calculated pressure was normalized by the static pressure at the nozzle exit position, $X/H = -42$. Because this calculation considered wall frictions, the normalized pressures at $X/H = -10$ show a little higher value than 1. In combustor region, the pressure magnitudes with VAH were smaller than that with EAH at same ER. This trend qualitatively matches to the experimental results [7].

Figure 3(b) shows the Mach number distributions for an air flow tube. As noted on this figure, Mach = 1 insists a choke condition. At low equivalence ratio cases, Mach numbers were enough higher compared to the choke condition. However, in cases of EAH-ER-0.15 and VAH-ER-0.17, the air flow Mach number reached 1 before $X/H = 10$. This insists a compound choking. A previous experimental test showed that mode transition occurred at around VAH-ER-0.18 condition. Thus, this calculation model well estimated the mode transition.

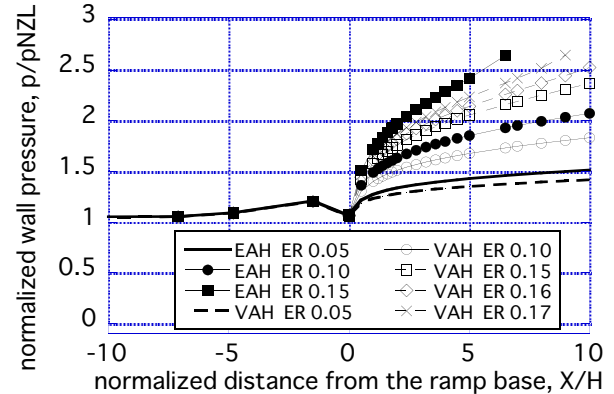


Fig. 3(a) Wall pressure distributions

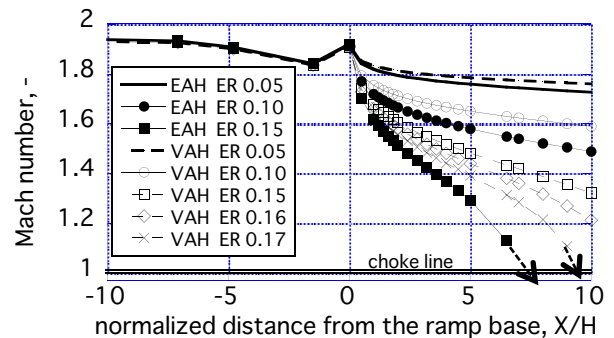


Fig. 3(b) Mach number distributions in air flow

4. Concluding remarks

Quasi-one dimensional calculation was developed to estimate supersonic-subsonic mode transition. Three flow tubes were considered to divide an air flow tube, a mixing & combustion flow tube and a fuel flow tubes. In the combustion flow tube, Mach 1 condition was adopted for frame holding. Calculation results showed wall pressure magnitudes with VAH were smaller than that of with EAH. Additionally, mode transition equivalence ratio was quantitatively well matched with the experimental results.

References

- [1] T. Mitani, et al., J. Prop. Pow., 13, (5), 1997, pp635
- [2] P.J. Waltrup, et al., J. Spacecraft & Rockets, 10, (9), 1973, pp. 620
- [3] Crocco, L., Highspeed Aerodynamics & Jet Prop., III-B (1985), 110, Princeton.
- [4] E.R. Van Driest, J. Aero. Science, 18, (3), pp145
- [5] F.M. White, Viscous Fluid Flow, Chap. 7, 1974
- [6] J. Noda et al., AIAA-2011-6087
- [7] S. Tomioka et al., J. Prop. Pow., 23, (4), 2007, pp789

The Linear Stability of a Compositional Plume in the Presence of Material Diffusion

Khaled Suleiman Mohammed AL-Mashrafi

Department of Mathematics and Statistics, College of Science, Sultan Qaboos University,
P.O. Box 36, Muscat, Sultanate of Oman
E-mail: p001175@squ.edu.om

ABSTRACT

The mathematical modeling of the dynamics of compositional plumes is important for the understanding of the properties of fluid alloys in the presence of heat and pressure. Such understanding is useful for industrial [1], and geophysics [2], [3], [4], [5]. A number of authors have recently studied the directional solidification of fluid alloys giving rise to one or more compositional plumes. These studies showed that the plumes are unstable for all values of the Grashoff (Reynolds) number [6]. These studies have neglected the diffusion of material. In this study, we extend the previous work on the stability of a plume by including material diffusion.

1. Introduction

If a fluid of two components of different densities is cooled from below, the component with the higher melting temperature solidifies first and settles at the bottom of the container to form a layer of mixed solid crystals and fluid. The layer so produces at the bottom is known as a mushy layer. If solid crystals so formed belong to the heavier component, they will settle at the bottom to produce a solid layer. As the solidification process continues, the mushy layer becomes thicker and eventually becomes unstable [7]. Due to its instability, compositional plumes of the light component rise from the mushy layer through the melt layer to the top. These types of plumes can be defined as a directional fluid flow rising in another fluid of different properties and composition. Such a channel flow is defined as a compositional plume.

The theoretical works on stability of the compositional plumes showed that the plumes are unstable. All these studies neglected material diffusion. Experimental studies indicated that the plume flow seems stable [8]. Since diffusion is generally stabilizing, it is of interest to examine the influence of material diffusion, k_m , on the stability of the plume in order to see whether the plume can be stabilized.

The recent study focused on extending the previous work on the stability of compositional plumes by including compositional diffusion.

2. Formulation of the model

The studies of the dynamics of compositional plumes used the equations of conservation of mass, conservation of momentum in the presence of the Boussinesq approximation together with equations of heat, concentration of light material, and state. These equations in dimensionless form are

$$\left[\frac{\partial \mathbf{u}}{\partial t} + (\mathbf{u} \cdot \nabla) \mathbf{u} \right] = -\nabla \left(p + \frac{z}{\beta \tilde{C}} \right) + \nabla^2 \mathbf{u} + (T - T_0 + C - C_0) \hat{z}, \quad (1)$$

$$\nabla \cdot \mathbf{u} = 0, \quad (2)$$

$$R \sigma \left[\frac{\partial T}{\partial t} + \mathbf{u} \cdot \nabla T \right] = \nabla^2 T, \quad (3)$$

$$R S_C \left[\frac{\partial C}{\partial t} + \mathbf{u} \cdot \nabla C \right] = \nabla^2 C, \quad (4)$$

$$\rho / \rho_0 = 1 - \beta \tilde{C} (T - T_0 + C - C_0), \quad (5)$$

where, \mathbf{u} is the velocity vector, ρ the density, p the pressure, \hat{z} an upward unit vector in the direction opposite to that of the gravity, t the time, β the coefficient of compositional expansion, (T_0, C_0, ρ_0) the constant reference values, \tilde{C} the amplitude of the concentration, C the concentration of the solvent component (light material) in the fluid and T is the temperature of the fluid. The three dimensionless numbers, R the Grashoff (Reynolds) number, σ the Prandtl number and S_C the Schmidt number are defined by

$$R = \frac{UL}{\nu}, \quad \sigma = \frac{\nu}{k}, \quad S_C = \frac{\nu}{k_m}, \quad (6)$$

where ν , κ are kinematic viscosity and thermal diffusivity, respectively, U is a typical velocity and L a characteristic length, defined by

$$U = \beta \tilde{C} \left(\frac{g \kappa}{\alpha \nu \gamma} \right)^{\frac{1}{2}}, \quad L = \left(\frac{\nu \kappa}{\alpha g \gamma} \right)^{\frac{1}{4}}, \quad (7)$$

, where α is the coefficient of thermal expansion, g is the uniform acceleration of gravity, and γ is the uniform vertical temperature gradient of the hydrostatic state.

3. Stability analysis and Conclusions

Two geometric shapes of the plume are assumed in the analysis: (i) a single plane interface in an infinite fluid where this case represents a plume of infinite thickness, and (ii) two parallel interfaces which represents a plume of finite thickness, and there is a sharp jump in the composition across the interfaces. The stability problem is governed by the dimensionless parameters R, σ, S_c and the dimensionless thickness of the plume x_0 in the case of two parallel interfaces. The analysis is restricted to small values of R . The growth rate, Ω , is maximized over the horizontal and vertical wave numbers m and n , respectively, for different values of σ, S_c , and x_0 . The preferred mode of instability is identified in the space of parameters of the problem. The preferred mode for any values of σ, S_c , and x_0 is the maximum possible value over the plane (m, n) . In conclusion, the addition of the material diffusion doesn't affect the stability of the single plane interface. The stability of the two parallel interfaces can take the form of a varicose mode, in which the two interfaces are out-of-phase, or a sinuous mode, in which the interfaces are in-phase. In general, the presence of material diffusion tends to stabilise the plume with the consequences that the growth rate is reduced but the plume is always unstable. Moreover, it was found that the influence of material diffusion is independent of the type of the mode considered. Also it is shown that material has a stronger stability influence on two dimensional ($m = 0$) than it has on three dimensional ($m \neq 0$) disturbances. We present graphically the preferred mode a function of S_c, σ, x_0 . Figures 1 presents the preferred mode of instability as a function of Schmidt number S_c for different values of x_0 ($x_0 = 0.5, 3.0, 10.0$).

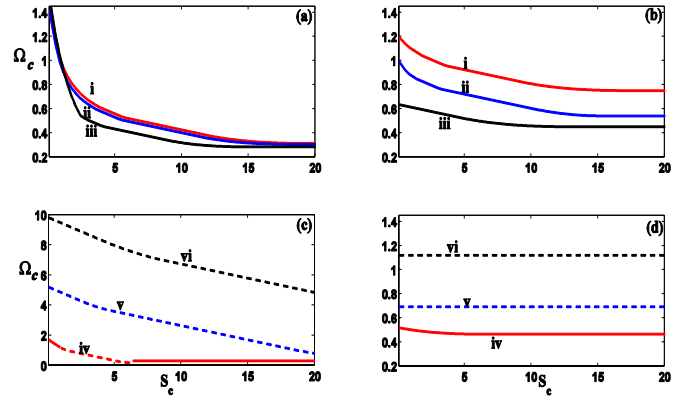


Figure 1. Illustration of the growth rate, Ω_c , of the preferred mode as a function of the Schmidt number, S_c , for different values of x_0 and σ . The solid (broken) curves refer to sinuous (varicose) modes. (a) and (c) refer to $x_0 = 1.0$ while (b) and (d) refer to $x_0 = 3.0$. The roman numbers (i) – (vi) correspond to $\sigma = 0.0, 1.0, 5.0, 10.0, 50.0, 100.0$, respectively. Note that the value of the growth rate increases with x_0 for moderate values of x_0 and σ is not too large, and the preferred mode is sinuous for small values of σ and varicose for large values of σ .

References

- [1] Copley, S.M., Giamel, A. F., Johnson, S.M. and Hornbecker, M.F. 1970. The origin of freckles in unidirectionally solidified castings. *Metall. Trans.* **1**: 2193-2204.
- [2] Loper, D.E. and Roberts, P.H. 1983. Compositional convection and the gravitationally powered dynamo. In *Stellar and Planetary Magnetism* (ed. A.M. Soward), pp. 297-327. Gordon and Breach, New York.
- [3] Morgan, W. J., 1972. Plate motions and deep mantle convection. *Studies in Earth and Space Sciences, Geol. Soc. Am. Mem.*, **132**, 7-22
- [4] Howard, L.N. and Veronis, G., 1992 Stability of salt fingers with negligible diffusivity. *Journal of Fluid Mechanics.* **239**, 511 – 522
- [5] Wettlauffer, H. K., Worster, M. G. and Huppert, H. E. 1997 Natural convection during solidification of an alloy from above with application to the evolution of sea ice. *J. Fluid Mech.* **344**, 291 – 316.
- [6] Eltayeb, I.A. and Loper, D.E. 1994. On the stability of vertical double-diffusive interfaces. Part 2. Two parallel interfaces. *J. Fluid Mech.* **267**: 251-271.
- [7] Worster, M.G. 1992 Instabilities of the liquid and mushy regions during solidification of alloys. *J. Fluid Mech.* **237**, 649-669.
- [8] Classen, S., Heimpel, M. and Christensen, U., Blob instability in rotating compositional convection. *Geophys. Res. Lett.* 1999, **26**(1), 135-138.

Numerical Simulations of Viscous Fingerings by a Phase Field Method

Yu-Sheng Huang, Li-Chieh Wang, Ching-Yao Chen

Department of Mechanical Engineering National Chiao Tung University, Hsinchu Taiwan, 30010 Republic of China
chingyao@mail.nctu.edu.tw

ABSTRACT

We present numerical simulations based on a diffuse interface model for this particular two-phase displacement that capture a variety of pattern forming behaviors. This is implemented by employing a Boussinesq Hele-Shaw-Cahn-Hilliard approach, considering different effect of possible value for the viscosity contrast and surface tension. The role played by these two physical contributions on the development of interface singularities is illustrated and discussed.

1. Introduction

The interfacial evolution of multiphase flows plays a crucial role in a variety of instabilities vital to industrial. Especially the phenomenon of viscous fingering in porous media, which reduce the efficiency of the displacement process, is of special interesting in the field of enhanced oil recovery.

It arises at the interface separating two viscous fluids constrained to flow in the narrow gap between closely-spaced parallel plates of a Hele-Shaw cell. Under constant injection radial flow rate [1] the most typical signature of such an instability is the occurrence of fingerlike structures which split at their tips, leading to the emergence of a convoluted dense-branching morphology. Over the years this constant injection rate radial viscous fingering problem has been extensively studied both experimentally [2-3] and theoretically [4-5].

In this work, we consider a diffuse interface approach which is based on a simplified version of the Navier-Stokes-Cahn-Hilliard model [6-7], and compared to miscible injection research. We extend the results obtained to the injecting Hele-Shaw setup, and used intensive numerical simulations to analyze the fully nonlinear behavior of the evolving inter- facial patterns.

2. Physical Problem and Governing Equation

Consider a Hele-Shaw cell of constant gap thickness h_0 containing two miscible, incompressible, viscous fluids (Fig. 1). Denote the viscosities of the fluids as η_1 and η_2 , and assume that $\eta_2 > \eta_1$. Fluid 1 is injected into fluid 2 at a given injection rate Q (equal to the area covered per unit time) which may depend on time.

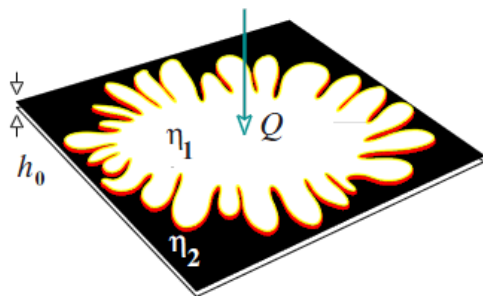


Fig. 1 Schematic setup for the injection-driven radial

Hele-Shaw flow with miscible fluids. The constant cell gap width is denoted by h_0 , and the less viscous fluid 1 is injected into the more viscous fluid 2.

The governing equations of such a diffuse interface problem are based on a model proposed by Cahn and Hilliard. In the context of a rotating Hele-Shaw cell system, the equations can be written as

$$\frac{\partial \rho}{\partial t} + \nabla \cdot (\rho \mathbf{u}) = 0 \quad (1)$$

$$\nabla p = -\eta \mathbf{u} - \varepsilon \nabla \cdot [\rho (\nabla c) (\nabla c)^T] \quad (2)$$

$$\rho \left(\frac{\partial c}{\partial t} + \mathbf{u} \cdot \nabla c \right) = \alpha \nabla^2 \mu \quad (3)$$

$$\mu = \frac{\partial f_0}{\partial c} - \frac{\varepsilon}{\rho} \nabla \cdot (\rho \nabla c) - \frac{p}{\rho^2} \frac{d\rho}{dc} \quad (4)$$

$$f_0 = f^* c^2 (1-c)^2 \quad (5)$$

Here, \mathbf{u} denotes the fluid velocity vector, p the pressure, η the viscosity, and ρ the density of the binary fluid system. The phase-field variable is represented by c , so that $c = 1$ in the bulk of fluid 1 (phase 1), and $c = 0$ in the bulk of fluid 2 (phase 2). The chemical potential is denoted by μ , and f_0 is a free energy. Equations (1)-(5) define the so-called Hele -Shaw- Cahn -Hilliard model [6-7]

Correlations of viscosity (η) and density (ρ) with the phase-field variable c are required by the present approach and are taken as

$$\eta(c) = \eta_1 e^{[R(1-c)]}, R = \ln(\eta_2/\eta_1) \quad (6)$$

$$\rho(c) = \rho_1 c + \rho_2 (1-c) \quad (7)$$

Dimensionless parameters, such as the Peclet number Pe , the viscosity contrast A , the Cahn number C , and the modified Galileo number Ga are defined as

$$Pe = \frac{\rho_b Q_c}{2\pi \alpha f^*}, \quad A = \frac{e^R - 1}{e^R + 1},$$

$$C = \frac{\varepsilon}{f^* l^2}, \quad Ga = \frac{\eta_1 Q_c}{2\pi\rho_b f^*} \quad (8)$$

To reproduce the fine fingering structures, a highly accurate pseudospectral method is employed to solve the streamfunction equation. Time integration is fully explicit by a third order Runge-Kutta procedure. The numerical code has been successfully used for immiscible rotating Hele-Shaw cell, and is quantitatively validated by comparing the experiment. [8]

3. Results and Discussion

First, we introduce numerical results for injecting Hele-Shaw flows with different viscosity contrast. Numerical simulations illustrating the effect of viscosity contrast for three different value of $A=0.941$ [(a) and (d)], $A=0.848$ [(b) and (e)], and $A=0.635$ [(e) and (f)] are depicted in Fig. 2 for three different values. It point out that the number of fingers is growth and more unstable when increase the Atwood number. Before fingers touched the boundary, more larger viscosity contrast made the top of fingers become more thinner.

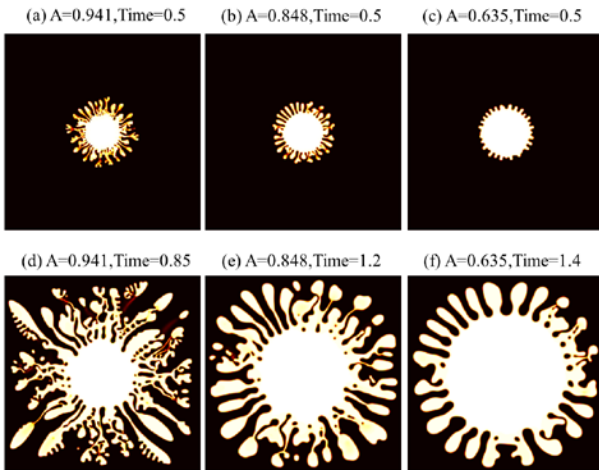


Fig. 2 Typical fingering patterns for $A=0.941$ [(a) and (d)], $A=0.848$ [(b) and (e)], and $A=0.635$ [(e) and (f)]. The remaining parameters are: $Pe=12 \cdot 10^3$, $Ga=10$ and $C=10^{-5}$. The top panel shows fingers start growth and the bottom panel shows fingers touched the boundary.

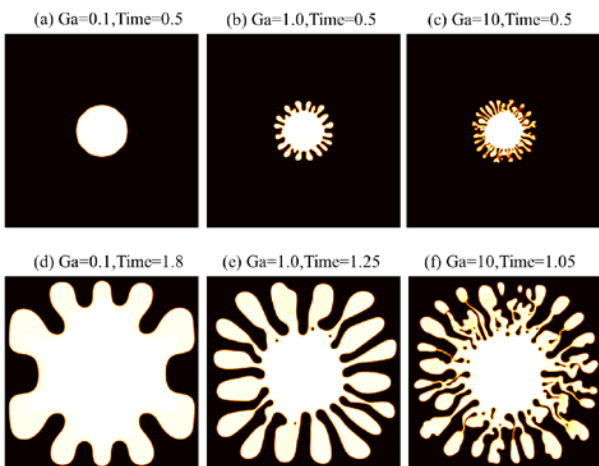


Fig. 3 Typical fingering patterns for $Ga=0.1$ [(a) and (d)], $Ga=1.0$ [(b) and (e)], and $Ga=10$ [(e) and (f)]. The remaining parameters are: $Pe=12 \cdot 10^3$, $A=0.905$ and $C=10^{-5}$. The top panel shows fingers start growth and the bottom panel shows fingers touched the boundary.

The effect of three different Galileo number of $Ga=0.1$ [(a) and (d)], $Ga=1.0$ [(b) and (e)], and $Ga=10$ [(e) and (f)] is depicted in Fig. 3. Dimensionless Galileo number is the ratio between inertia and surface energy. When Galileo number is decrease, the number of fingers is decrease and become thicker. In the other hand, when increase the Galileo number also increase the probability of pinch-off and emission.

4. Concluding remarks

We have presented a diffuse interface numerical study for the injecting Hele-Shaw problem, which has been implemented by utilizing a Boussinesq Hele-Shaw-Cahn-Hilliard (BHSC) approach. We point out the usefulness of our diffuse interface approach in addressing two very important behaviors which arise at nonlinear stages of the dynamics in injecting Hele-Shaw flows: the phenomena of (a) finger competition, and (b) droplet pinch-off, and their sensitivity to changes in the value of the viscosity contrast and surface tension. All these features are in line with what has been obtained by previous simulating investigations of the problem, which employed distinct numerical techniques.

References

- [1] L. Paterson, *J. Fluid Mech.* 113, 513 □1981.
- [2] J.-D. Chen, *J. Fluid Mech.* 201, 223 1989; *Exp. Fluids* 5,363 1987.
- [3] O. Praud and H. L. Swinney, *Phys. Rev. E* 72, 011406 2005.
- [4] J. A. Miranda and M. Widom, *Physica D* 120, 315 1998.
- [5] C.-Y. Chen, C.-W. Huang, H. Gadêlha, and J. A. Miranda, *Phys. Rev. E* 78, 016306 2008.
- [6] J. W. Cahn and J. E. Hilliard, *J. Chem. Phys.* 28 (1958), 258.
- [7] D. Jacqmin, *J. Comput. Phys.* 155 (1999), 96.
- [8] Ching-Yao Chen, Y.-S. Huang, and *Miranda, J., *Phys. Rev. E*, 84, 046302, 2011.

Fingering Instability Induced by a Precipitation Reaction

Yuki Ishii¹, Yuichiro Nagatsu², Yutaka Tada¹, Anne De Wit³

¹Nagoya Institute of Technology, Gokiso-cho, Showa-ku, Nagoya, Aichi, 466-8555, Japan

²Tokyo University of Agriculture and Technology, 3-8-1 Harumi-cho, Fuchu-shi, Tokyo 183-8538, Japan

³Free University of Brussels, Boulevard du Triomphe, B-1050 Bruxelles

nagatsu@cc.tuat.ac.jp

ABSTRACT

We experimentally demonstrated hydrodynamic instability fully driven by an $A+B \rightarrow C$ type chemical reaction producing precipitation C in a Hele-Shaw cell. In the present system, the fingering patterns were different depending on whether A displaced B or B displaced A . Mathematical modelling for the system was set up. The origin of the instability was clarified based on the underlying mobility profile reconstructed by concentration profiles obtained by the one-dimensional diffusion-reaction equations. The nonlinear simulation for the governing equations reproduced the instability experimentally observed.

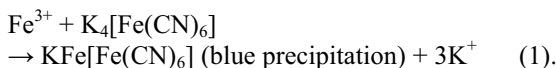
1. Introduction

It is well known that the hydrodynamic instabilities develop when a less viscous fluid displaces a more viscous one in porous media or in Hele-Shaw cells. In such a situation, the interface of boundary between two fluids forms finger like pattern. In the reverse situation or the case where the two fluids have the same viscosity, the fingering patterns are not obtained. In 2007 Podgorski et al.[1] experimentally showed the fingering pattern takes place if high viscous product is produced by chemical reaction between the two fluids even when the two fluids have the same viscosity. We can say this type of fingering is induced by the chemical reaction because the fingering does not occur in the case without reaction.

Here, we show different type of hydrodynamic instability driven by chemical reaction in a Hele-Shaw cell. In the present system, the reaction does not change fluid property. However, the reaction produces solid precipitation reducing permeability which is able to trigger the instability otherwise the system is stable.

2. Method

In the present study, we have performed an experiment in which a solution including reactant A (ion) displaces another solution including reactant B (ion) in a horizontal Hele-Shaw cell. The displacing and the displaced solution have the same viscosity as that of water. Here, an $A+B \rightarrow C$ type chemical reaction takes place and the product C is precipitation. We used a following precipitation reaction.



In the present study, a case involving a non-precipitation reaction was also examined as a reference. The non-precipitation reaction used was as follows.



Both the reactions are very fast ones and can be treated as instantaneous ones. In both cases, the selected liquids

and chemical reactions mentioned above allow us to recognize the fingering pattern by color difference. These reactions were the same as those employed in our previous study, Nagatsu et al. [2] which investigated the effects of precipitation reaction on viscous fingering. We performed 4 kinds of reactive experiments depending on the combinations of the displacing and displaced solutions. (a) Fe^{3+} solution displaces SCN^- solution (non-precipitation) (b) Fe^{3+} solution displaces $\text{K}_4[\text{Fe}(\text{CN})_6]$ solution (precipitation) (c) SCN^- solution displaces Fe^{3+} solution (non-precipitation) (d) $\text{K}_4[\text{Fe}(\text{CN})_6]$ solution displaces Fe^{3+} solution (precipitation).

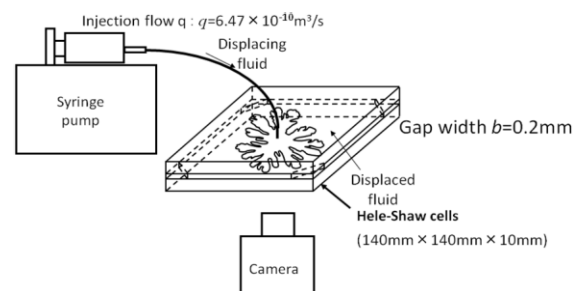


Fig.1 Experimental apparatus

Displacement experiments were conducted using a radial Hele-Shaw cell. This apparatus is the same as that used in our previous studies. In the present study, the gap width b was set to be 0.2 mm. In the radial Hele-Shaw geometry, it is common to define the Péclet number, Pe as $Pe=q/2\pi bD$, where q is the volumetric flow rate of the injection of the less-viscous liquid D is the diffusion coefficient between the displacing and displaced liquids. Here, D was estimated to be $1 \times 10^{-9} \text{ m}^2/\text{s}$.

We will set up mathematical model for the present system as follows.

$$\nabla \cdot \underline{u} = 0 \quad (3)$$

$$\nabla p = -\frac{\underline{u}}{\kappa(c)} \quad (4)$$

$$\frac{\partial a}{\partial t} + \underline{u} \cdot \nabla a = \delta_A \nabla^2 a - D_a ab \quad (5)$$

$$\frac{\partial b}{\partial t} + \underline{u} \cdot \nabla b = \delta_B \nabla^2 b - D_a ab \quad (6)$$

$$\frac{\partial c}{\partial t} + \underline{u} \cdot \nabla c = \nabla^2 c + D_a ab \quad (7)$$

We consider two-dimensional rectilinear flow in porous media. A solution including reactant A displaces another solution including reactant B. An $A+B \rightarrow C$ type chemical reaction takes place. We denote concentrations of species A,B and C as a,b and c , respectively. The governing equations in non-dimension for the present reacting flow consist of continuity equation and Darcy's law coupled with three reaction-diffusion-convection equations for chemical species A,B and C. We assume the permeability of porous media κ is impacted by the concentration c . Here, $\delta_{A,B} = D_{A,B}/D_c$, where $D_{A,B,C}$ is diffusion coefficient of species A,B,C. And D_a is Damköhler number, defined as here.

3. Results and Discussion

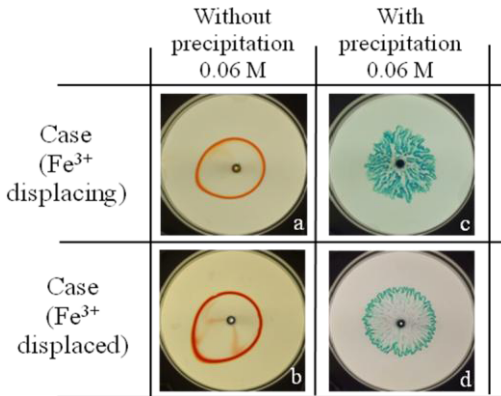


Fig.2 Reactive displacement patterns with and without the precipitation.

Fig. 2 shows the results of the reactive displacement experiment with and without the precipitation. In both the cases without the precipitation, circular like patterns were obtained. In both the cases with the precipitation, finger like patterns were obtained. Comparison between the precipitation and non-precipitation cases clearly shows the hydrodynamic instability is induced by precipitation. In this instability, asymmetric characteristic was observed. In other words, the product is more concentrated at the boundary in Case (d), while it spreads in broad area in Case (c). Molecular weight of Fe³⁺ and that of K₄[Fe(CN)₆] are 56 and 368, respectively. Thus, we can consider the former ion has a

larger diffusivity, and this is the origin of asymmetric characteristics. This point will be discussed later in detail. Note that the asymmetry does not exist in the case without the precipitation as expected.

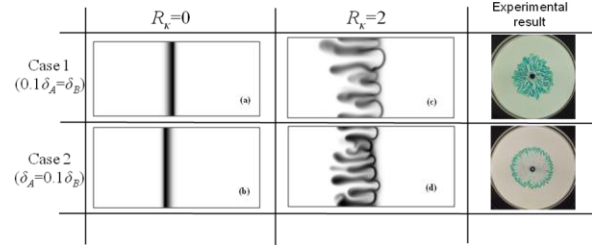


Fig.3 Results of numerical simulation, $t=1500$, $D_a=1$. In Case A, $0.1\delta_A=\delta_B$, in Case B, $\delta_A=0.1\delta_B$.

The governing equations are numerically integrated by the spectral method. This Fig.3 shows the results of the numerical simulation. In these figures, the distribution of the product is drawn in gray scale. In this column, the result at $R_k=0$ without the precipitation are described, while in this column, the result at $R_k=2$ with the precipitation are shown. In the upper column, $\delta_A > \delta_B$, which corresponds to Case (1) in the experiment. In the lower column, $\delta_A < \delta_B$, which corresponds to Case (2) in the experiment. First, we can find that the fingering instability is certainly reproduced only when $R_k=2$. Composition between the results in the upper and lower columns at $R_k=2$ shows that the product is more concentrated at the boundary in the lower column. These result have good agreement with experimental result. We propose the asymmetry can be caused by difference in diffusivity between reactant A and B.

4. Concluding remarks

In conclusion, we have experimentally demonstrated hydrodynamic instability driven by chemical reaction producing precipitation for the first time. In the present system, an asymmetric property is present, i.e. the fingering patterns are different depending on the cases where A displaces B or B displaces A. We propose the asymmetry can be caused by difference in diffusivity between reactant A and B. We set up mathematical model for the present system involving precipitation. Non-linear simulation for our model equations reproduces the instability and its asymmetric property.

References

- [1]Podgorski et al. PHYSICAL REVIEW E 76, (2007) 016202
- [2]Nagatsu et al. PHYSICAL REVIEW E 77 (2008) 067302

Parallel Cartesian-Grid Direct Simulation Monte Carlo Method with Cut Cells on Multiple Graphics Processor Units

Ming-Chung Lo¹, Cheng-Chin Su¹, Fang-An Kuo¹, Jong-Shinn Wu^{1*}, Matthew R. Smith²

¹Department of Mechanical Engineering, National Chiao Tung University, Hsinchu, Taiwan

²National Center for High-performance Computing, National Applied Research Laboratories, Hsinchu, Taiwan

*E-mail: chongsin@faculty.nctu.edu.tw

ABSTRACT

A cut-cell approach is implemented in a recently proposed parallel two-dimensional DSMC (Direct Simulation Monte Carlo) method using hybrid MPI-CUDA paradigm [1] for improving the capability of treating complex geometry under rarefied condition. In the current study, we have verified the accuracy of our implementation and demonstrated that a high parallel speedup up to 100-200 times using 16 GPUs (Graphics Processing Units) can be reached for a near continuum flow problem.

1. Introduction

The Boltzmann equation, which is appropriate for modeling the rarefied flows, is extremely difficult to solve numerically due to its high dimensionality and the complexity of the collision term. The DSMC method introduced by Bird [2] provides a particle-based method that reproduces the realistic flow behavior by no more than collision kinetics. It had been the dominant numerical technique for modeling rarefied gas flows for several decades since its invention in 1960s.

It is well-known that DSMC is very time-consuming as compared to computational fluid dynamics. General wisdom in speeding up the computation is to parallelize the code using message passing interface (MPI) on distributed memory machines. Recently, the Cartesian-grid DSMC was parallelized using hybrid CUDA-MPI paradigm [1]. Note CUDA [3] (Compute Unified Device Architecture) is a parallel protocol developed by NVIDIA Inc. for GPU computing. However, its capability in treating complex geometry is limited. Thus, we would like to further extend its capability for treating complex geometry using cut-cell approach.

2. Method

2.1 Cut-cell scheme

In the cut-cell approach, solid bodies in the flow domain are cut out of a background Cartesian grid with their boundaries represented by different types of cut cells. A special treatment procedure is proposed to properly handle particle interactions with these solid boundaries.

Ray casting algorithm [4] is used to find the intersection points between the Cartesian mesh and the solid surfaces. Once all the intersection points have been located, a simple collating procedure is used to determine the cut-cell information. In the current study, we only consider three basic types of cut cells (A, B and C) that are shown in Fig. 1.

2.2 Parallel DSMC on GPUs

Fig. 2 shows a hybrid MPI-CUDA paradigm for DSMC computing on multiple GPUs. In this method, the MPI protocol is used to distributed/gather data into/from memory of different processors and

communicate among all processors (CPU). CUDA is used to accelerate the DSMC-related simulation components. Each GPU is controlled using a unique thread (core) on a CPU.

Fig. 3 shows the flowchart of DSMC computation using CUDA in each CPU processor. During the initialization stage, input data are loaded into the memory of the primary cluster node and distributed to all processors using the MPI protocol. The initial states are computed on each host CPU. This information (including particle and computational cell information) is then transferred to global memory of each GPU device. Following this, an unsteady phase of the DSMC simulation is performed - particle moving, indexing between particles and cells, particle collision and sampling in each cell are executed on each GPU - until a steady state is reached.

3. Results and Discussion

To validate the cut-cell approach, a simulation is performed for the hypersonic flow over a compression ramp. The distance between the leading edge of the flat plate and the ramp corner is equal to 71.4 mm. The ramp angle is 35-deg and also its length is equal to 71.4 mm. Further details of the ramp geometry are provided in Fig. 4 [5].

The flow of nitrogen gas is considered with the following free-stream conditions: density $\rho=1.401 \times 10^{-4}$ kg/m³, velocity $V=1521$ m/s, temperature $T=9.06$ K. The corresponding free-stream Mach number and Reynolds number are 24.8 and 12,020, respectively. The wall is perfectly diffusive with wall temperature set to be 403.2 K [5]. Simulation time step is chosen as 1/3 of the mean collision time in the free stream and near-wall region. Typical number of particles and number of cells are about 240,000 and 24,000 respectively.

The ramp geometry is employed to study the effects of flap deflection on the flow past a space vehicle. Figs. 5 and 6 report the streamlines obtained by the cut-cell approach and Moss *et al.* [5], respectively. Both streamlines contours show the typical features of shock wave-boundary layer interaction with flow separation and re-attachment. Figs. 7 and 8 provide the density contours, obtained by the cut-cell approach and Moss *et al.* [5] respectively. The agreement is reasonably well

both qualitatively and quantitatively.

In the meeting, we will demonstrate a maximum speed up of 100-200 times using 16 GPUs (M2070) when compared to the use of a single core of an Intel X5670 CPU depending upon the level of rarefaction encountered in the simulation.

4. Concluding remarks

In this study, we have proposed and validated a cut-cell approach for treating complex geometry in a recently developed Cartesian-grid DSMC using multiple GPUs. Results show that parallel performance is not affected by this cut-cell approach in general. It could be a very powerful tool in simulating rarefied gas dynamics.

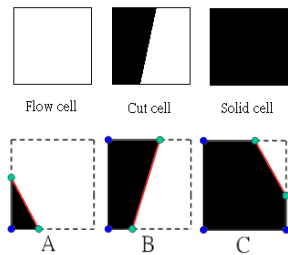


Fig. 1 Different types of cut cells.

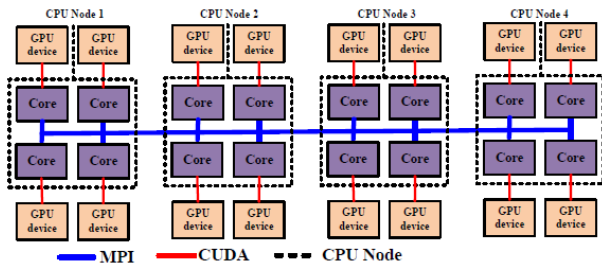


Fig. 2 Hybrid MPI-CUDA paradigm.

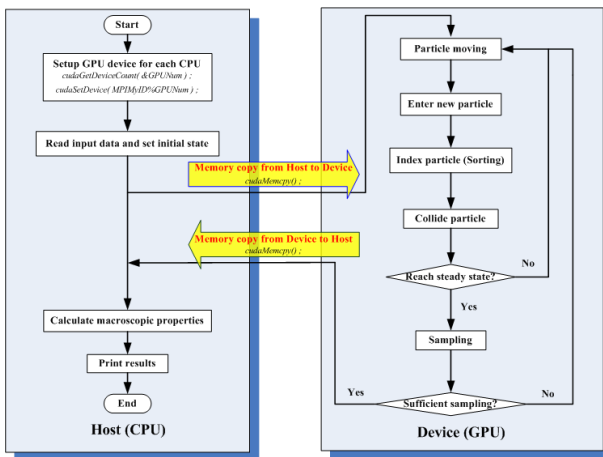


Fig. 3 Flowchart of DSMC on a single GPU.

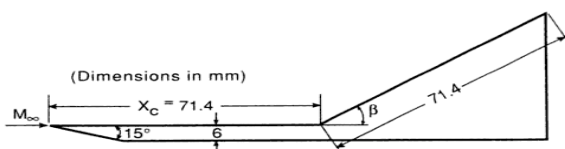


Fig. 4 Sketch of the 2-D hypersonic ramp flow.

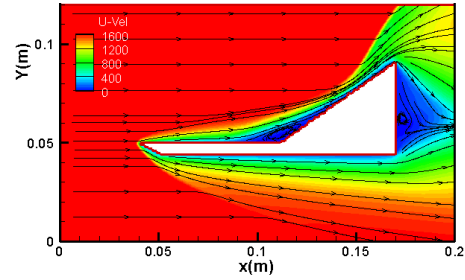


Fig. 5 Streamlines contours (cut-cell approach).

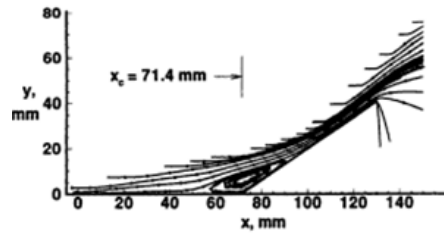


Fig. 6 Streamlines contours (Moss *et al.* [5]).

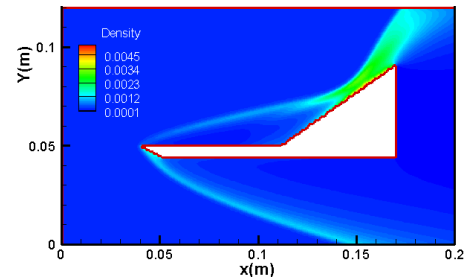


Fig. 7 Density contours (cut-cell approach).

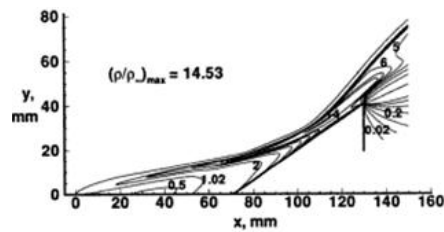


Fig. 8 Density contours (Moss *et al.* [5]).

References

- [1] C.-C. Su, M.R. Smith, J.-S. Wu*, C.-W. Hsieh, K.-C. Tseng and F.-A. Kuo, Large-Scale Simulations on Multiple Graphics Processing Units (GPUs) for the Direct Simulation Monte Carlo Method, *Journal of Computational Physics*, 2012 (under 2nd review).
- [2] G.A. Bird, *Molecular Gas Dynamics and the Direct Simulation of Gas Flows*, Clarendon Press, Oxford, 1994.
- [3] NVIDIA Inc., *NVIDIA CUDA C Programming Guide Version 3.2*, 2010.
- [4] Haines, Eric, "Point in Polygon Strategies," *Graphics Gems IV*, ed. Paul Heckbert, Academic Press, p. 24-46, 1994.
- [5] Moss, J.N., Rault, D.F., and Price, J.M., "Direct Monte Carlo Simulations of Hypersonic Viscous Interactions Including Separation," *Rarefied Gas Dynamics: Space Science and Engineering*, edited by B.D. Shzgal and D.P. Weave., 1994.

An Investigation of Natural Convection in Parallel Square Plates with a Heated Top Surface by a Hybrid Boundary Condition

Wu Shung Fu, Wei Hsiang Wang, Chung Gang Li

EE306, Department of Mechanical Engineering, No.1001, Daxue Rd., East Dist., Hsinchu City 300, Taiwan (R.O.C.)
wsfu@mail.nctu.edu.tw

ABSTRACT

A study of natural convection in three dimensional square plates is investigated numerically. The geometry of the physical model is the parallel square plates, and hybrid boundary condition which combined non-reflecting boundary condition and absorbing boundary condition is adopted. This kind of boundary condition is effective for solving the problem of this study, and the results of the work have good agreements with the experimental results of a previous paper.

1. Introduction

A natural convection with open boundary which has always attracted much attention is a very important subject in both academic and industrial researches. The subject, except a physical geometry of an enclosure, indispensably involves a problem of an open boundary. Therefore, characteristics of the open boundary deeply affect the phenomena of the inside of the domain.

The Navier-Stokes characteristics boundary condition (NSCBC), also called non-reflecting boundary condition, developed by Poinso and Lele [1] is an ingenious method to treat compressible fluids flowing through open boundaries. Fu and Li [2] modified the method of the NSCBC for all speeds of compressible flows. However, the method has pointed out by Yoo [3] et al. that it has difficulties to solve the domain having neighboring open boundaries. Therefore, a method of absorbing boundary was proposed to solve the domain of the problem including several neighboring open boundaries

Freund [4] proposed an absorbing boundary zone to solve one dimensional compressible problems in viscous fluid flow situations. Fu and Li [5] modified the absorbing layer for treating a two dimensional open boundary problem and applied it to solve a two dimensional compressible flow problem with the open boundaries. However, when the method was used to apply to a complex three dimensional open boundary problem, the physical quantities could not be eliminated in the artificial domain and affect the results of physical domain. Therefore, the study aims to develop a new available method combined non-reflecting boundary condition and absorbing boundary condition to solve natural convection in three dimensional open boundaries condition problem.

2. Physical model and Numerical method

A physical model of three dimensional parallel square plates is indicated in Fig. 1. The absorbing boundary is used and the artificial buffer zone is added to the original domain. The non-reflecting boundary condition is adopted at the outside boundary of artificial buffer zone. The heated top square is abfe, and the bottom square cdhg is adiabatic. Three different magnitudes of $Ra^* = Ra \times (l_1/l_2)$ equal to 1.72×10^5 ,

1.55×10^6 and 4.31×10^6 are considered.

The governing equations of the original domain in which the parameters of viscosity and compressibility of the fluid are considered are shown in the following equation.

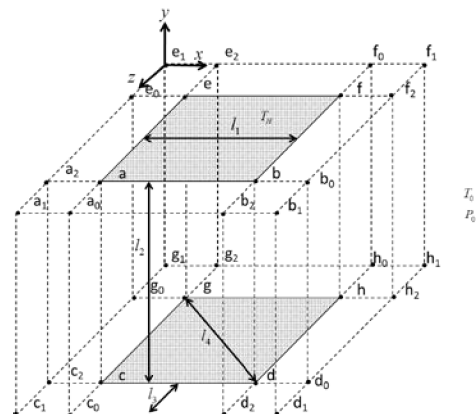


Fig. 1 Physical model of three dimensional parallel square plates

$$\frac{\partial U}{\partial t} + \frac{\partial F}{\partial x} + \frac{\partial G}{\partial y} + \frac{\partial H}{\partial z} = S \quad (1)$$

The artificial convection and damping terms are newly adopted to Eq. and the general form of the governing equations in the artificial buffer zone can be described as Eq. (2).

$$\frac{\partial U}{\partial t} + \frac{\partial \tilde{F}}{\partial x} + \frac{\partial \tilde{G}}{\partial y} + \frac{\partial \tilde{H}}{\partial z} + \tilde{\sigma} = 0 \quad (2)$$

\tilde{F} , \tilde{G} and \tilde{H} are modified physical quantities by adopting artificial convection terms to F , G and H and $\tilde{\sigma}$ is the three dimensional artificial damping term.

Methods of the Roe scheme, preconditioning and dual time stepping matching LSUGS scheme are used to solve the situation of a low speed compressible flow.

The non-reflecting boundary condition is adopted at the outer surfaces of artificial boundary zone. The

equations of NSCBC are shown as follow.

$$L = \begin{pmatrix} L_1 \\ L_2 \\ L_3 \\ L_4 \\ L_5 \end{pmatrix} = \begin{pmatrix} u \frac{\partial T}{\partial x} + \frac{1}{\rho \gamma} \left(\frac{\partial P}{\partial x} - \gamma \frac{\partial P}{\partial x} \right) \\ u \frac{\partial w}{\partial x} \\ u \left(-\frac{\partial v}{\partial x} \right) \\ (u' + c') \left[\frac{\partial P}{\partial x} - \rho(u' - c' - u) \frac{\partial u}{\partial x} \right] \\ (u' - c') \left[\frac{\partial P}{\partial x} - \rho(u' + c' - u) \frac{\partial u}{\partial x} \right] \end{pmatrix} \quad (3)$$

3. Results and Discussion

In Fig. 2, velocity vectors distributed on central cross section are indicated. The top surface is heated, and fluids near the top surface expand and flow out of the domain, then cool fluids are sucked from surroundings to top surface.

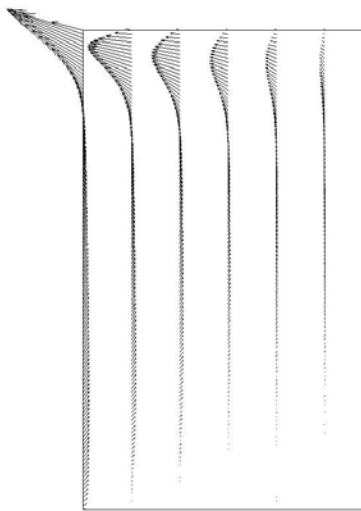


Fig.2 Distributions of velocity vectors on central cross-section

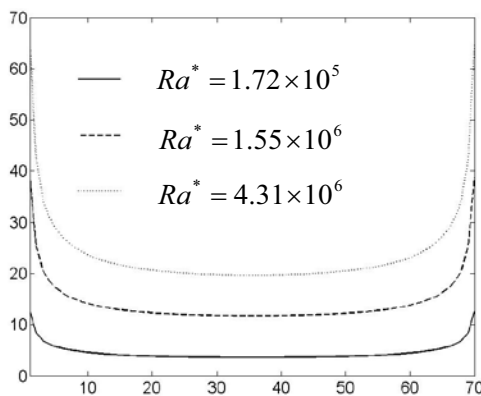


Fig.3 Distributions of local Nusselt numbers under

different modified Rayleigh numbers

In Fig. 3, distributions of local Nusselt numbers along under different modified Rayleigh numbers are shown. Naturally, the larger the Rayleigh number is, the more remarkable heat transfer rate can be achieved. The cool fluids from the outside flow into the plates that lead the magnitudes of local Nusselt numbers to be decreased from the edge to center of the bottom surface.

In Fig. 4, variations of area averaged Nusselt numbers obtained by three different Rayleigh numbers with a time are shown, respectively. Naturally, the larger the Rayleigh number is, the larger area averaged Nusselt number can be obtained. Except an early stage of development, the variations of the local Nusselt numbers reveal a steady phenomenon.

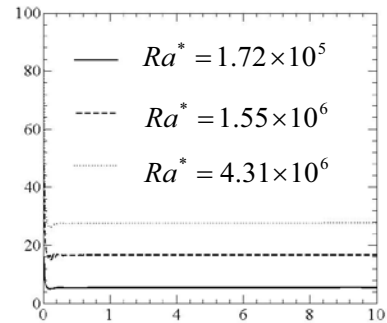


Fig.4 Distributions of area averaged Nusselt numbers with time under different modified Rayleigh numbers

4. Concluding remarks

A study of natural convection in multiple open boundaries is investigated numerically and some conclusions are drawn as follows.

- (1) Hybrid boundary condition which combined non-reflecting boundary condition and absorbing boundary condition is successful used to calculate complex three dimensional open boundary problem
- (2) The model is parallel square plates, and phenomena occurring in the domain are mainly symmetrical.
- (3) The cooling fluids are sucked from surroundings to top surface and heated by the heated top square and expanded out of the domain .

References

- [1] T. J. Poinso and S. K. Lele, J. Comput. Phys., 101 (1992), 104-129.
- [2] W. S. Fu, C. G. Li, C. C. Tseng, Int. J. Heat Mass Transfer 53(2010), 1575-1585.
- [3] C. Yoo, Y. Wang, A. Trouvé and H. Im, Combustion Theory and Modeling 9 (4) (2005) 617-646.
- [4] J. B. Freund, AIAA 35(4)(1997), 740-742.
- [5] W. S. Fu, C. G. Li, Y. Huang, The 7th International Conference on Flow Dynamics (2010).

Effects Of Reciprocating Motions On Transfer Rate Of Hazardous Gas In A Curved Channel

Wu-Shung Fu, Yu-Chih Lai, Yun Huang
Department of Mechanical Engineering
National Chiao Tung University
1001 Ta Hsueh Road, Hsinchu, 30056,
Taiwan
E-mail: wsfu@mail.nctu.edu.tw

ABSTRACT

This study focus on numerical investigation of hazardous gas and gaseous waste transfer enhancement in exhaust channels by exerting reciprocating motion to the channel. The Arbitrary Lagrangian-Eulerian method (ALE) with finite element method (FEM) is applied in this study. The mass transfer mechanisms affected by the main parameters such as frequency, amplitude and Reynolds number are discussed in detail.

1. Introduction

This study utilize a curved exhaust channel to lower the pollutants in industrial applications. Several studies focusing on enhancement of mass flow rate in channels are reviewed. Watson [1] showed that the mass transfer rate of a diffusing substance along a pipe was augmented by an oscillatory motion of the ambient fluid in the pipe. Nishimura et al. [2-5] utilized a sinusoidal wavy-walled channel to investigate mass transfer enhancement by pulsating and oscillatory flows numerically and experimentally. The results indicated that the higher mass transfer rates appeared as Reynolds numbers rose, and the flow patterns which affected mass transfer rates were directly influenced by the frequency of oscillating remarkably. Due to the limitation of curve shaped channels, the above methods of literatures mentioned do not always assure enhancement of fine mass transfer rate, and the aim of this study is to exert reciprocating motion on a curved channel to enhance mass transfer rate.

2. Physical Model

A two-dimensional curved channel which is composed of two vertical and a horizontal channels used in this study is shown in Fig. 1 with dimensions indicated. The region between \overline{OP} and \overline{MN} is flexible and the reciprocating amplitude is l_c . The meshes above \overline{OP} are movable, meshes below \overline{MN} are fixed. The value of moving velocity of the horizontal channel subject to the reciprocating motion is v_c , and can be expressed in terms of $v_c = v_m \sin(2\pi f_c t)$, where v_m is the maximum reciprocating velocity of the channel and equals to $2\pi l_c f_c$. For facilitating the analysis, the assumptions of this study are described as follows:

- (1) Fluid is laminar and incompressible.
- (2) Fluid properties are constant and the effect of the gravity is neglected.
- (3) No-slip condition is held on all surfaces. The fluid velocities on moving boundaries equal to the boundary moving velocities.
- (4) No chemical reaction between mass species and

working fluid.

- (5) The concentration gradient at wall surfaces except the top surface is zero.
- (6) The body force of hazardous gas particle is neglected.

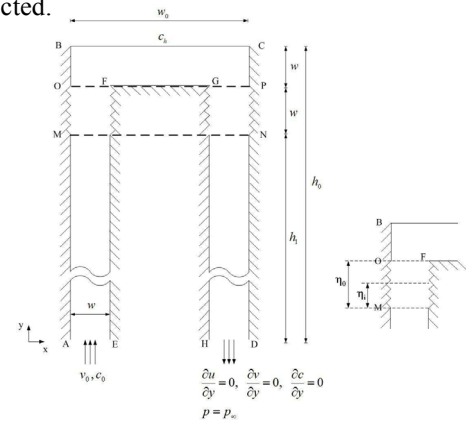


Fig. 1 Physical model

The dimensionless ALE governing equations are expressed as the following equations:

Continuity equation

$$\frac{\partial U}{\partial X} + \frac{\partial V}{\partial Y} = 0 \quad (2)$$

Momentum equation

$$\frac{\partial U}{\partial \tau} + U \frac{\partial U}{\partial X} + (V - \hat{V}) \frac{\partial U}{\partial Y} = -\frac{\partial P}{\partial X} + \frac{1}{\text{Re}} \left(\frac{\partial^2 U}{\partial X^2} + \frac{\partial^2 U}{\partial Y^2} \right) \quad (3)$$

$$\frac{\partial V}{\partial \tau} + U \frac{\partial V}{\partial X} + (V - \hat{V}) \frac{\partial V}{\partial Y} = -\frac{\partial P}{\partial Y} + \frac{1}{\text{Re}} \left(\frac{\partial^2 V}{\partial X^2} + \frac{\partial^2 V}{\partial Y^2} \right) \quad (4)$$

Mass transportation equation

$$\frac{\partial C}{\partial \tau} + U \frac{\partial C}{\partial X} + (V - \hat{V}) \frac{\partial C}{\partial Y} = \frac{1}{\text{ReSc}} \left(\frac{\partial^2 C}{\partial X^2} + \frac{\partial^2 C}{\partial Y^2} \right) \quad (5)$$

3. Numerical Method

The governing equations and boundary conditions are solved by the Galerkin finite element formulation and a backward scheme is adopted to deal with the time terms of the governing equations. The continuity equation (2), momentum equation (3) and (4) can be expressed as the following matrix form:

$$\sum_1^{ne} [A]^{(e)} \{\varphi\}_{t+\Delta t} = \sum_1^{ne} \{b\}^{(e)} \quad (6)$$

The mass transportation equation (5) can be expressed as the following matrix form:

$$\sum_1^{ne} [Z]^{(e)} \{0\}_{t+\Delta t} = \sum_1^{ne} \{f\}^{(e)} \quad (7)$$

The GMRES method [6] with pressure convection-diffusion [7] preconditioned method is applied to solve Eq. (6) and (7), and the operations of preconditioning operator matrixes in compressed CRS sparse form are solved by LU direct solving method, furthermore, suggested Robin boundary condition [7] is applied to preconditioning matrix to enhance the convergence rate.

4. Results and Discussion

The Schmidt number is 0.71. Combinations of main parameters are tabulated in Table 1.

CASE	Re	L_c	F_c	V_m	\overline{Sh}	En
Stationary	100	-	-	-	2.692	1
Stationary	400	-	-	-	4.717	1
1	400	0.2	0.5	0.628	5.470	1.159
2	100	0.2	0.5	0.628	2.805	1.041
3	400	0.2	0.1	0.126	4.921	1.043
4	400	0.4	0.5	1.256	6.011	1.274

Table 1. Combination of computational parameters and enhancement factor En

The local mass flux m_x generated on surface \overline{BC} is defined as:

$$m_x = D \frac{\partial c}{\partial y} \Big|_x = K_x (c_h - c_0) \quad (8)$$

The Sherwood number for indicating dimensionless local mass flux can be expressed as:

$$Sh_x = \frac{\partial C}{\partial Y} \Big|_x = \frac{K_x w}{D} \quad (9)$$

The time and area average Sherwood number \overline{Sh} is defined as:

$$\overline{Sh} = \frac{1}{\tau_p} \int_0^{\tau_p} \left(\frac{1}{w} \int_{\overline{BC}} Sh_x dX \right) d\tau \quad (10)$$

Fig. 2 shows distributions of local Sherwood numbers on the \overline{BC} surface for $Re = 400$, $L_c = 0.2$, $F_c = 0.5$ and $F_c = 0.1$ situations in a cycle time, and the ‘ \uparrow ’ and ‘ \downarrow ’ signs indicate the moving directions of curved channel. The durations of same and opposite directions relative to the direction of inlet fluid individually occupy a half cycle time, the volume of curved channel is then enlarged in a half cycle time when both directions of the moving channel and inlet fluids are same and vice versa. Except the impingement of inlet fluid at the inlet of horizontal channel, those behaviors mentioned above mainly cause several summits of distributions of local Sherwood numbers to be produced, where the flow structure causing accumulating of hazardous gas was destroyed, and the magnitudes of local Sherwood numbers obtained by the reciprocating motion of curved channel to be much larger than those at the stationary situation.

The smaller magnitude of F_c causes the behaviors

of interaction between the horizontal channel and inlet fluids being not drastically as shown in Fig. 5. Naturally, the magnitudes of the difference of local Sherwood numbers between both distributions of reciprocating and stationary situations are contracted in whole surface of \overline{BC} .

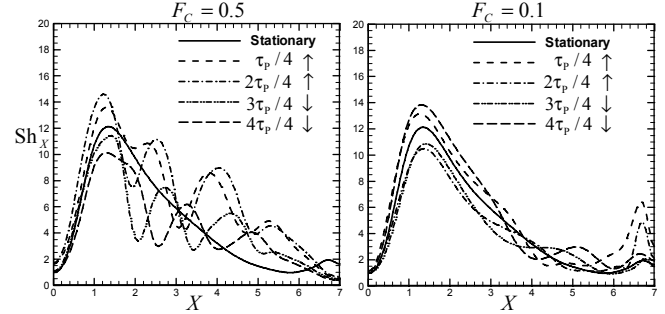


Fig. 2 Distributions of local Sherwood numbers on \overline{BC} surface for $Re=400$, $L_c = 0.2$.

The definition of enhancement factor En of hazardous gas transfer rate in a curved channel under the same Reynolds number is expressed as follows:

$$En = \frac{\overline{Sh} \text{ subject to reciprocating motion}}{\overline{Sh} \text{ stationary situation}} \quad (11)$$

The interaction effect between the horizontal channel and inlet fluids is seriously affected by Reynolds number. Then the smaller the Reynolds number is, the smaller magnitude of En is obtained and tabulated in Table 1.

5. Conclusion

Several conclusions are drawn.

- (1) Usage of reciprocating motion to enhance the hazardous gas transfer rate in a curved channel is achievable.
- (2) The larger magnitudes of Reynolds number, amplitude and frequency can gain more remarkable results.
- (3) The numerical method adopted in this study is accurate and available adopted for solving moving boundary problems.

References

- [1] E.J. Watson, J. Fluid Mech. 133 (1983) 233–244.
- [2] T. Nishimura, N. Kojima, Int. J. Heat Mass Transfer 38 (9) (1995) 1719–1731.
- [3] T. Nishimura, A. Taurmoto, Y. Kawamura, Int. J. Heat Mass Transfer 38 (1987) 1007–1015.
- [4] T. Nishimura, S. Arakawa, D. Murakami, Y. Kawamura, Chem. Eng. Sci. 46 (1991) 757–771.
- [5] T. Nishimura, S. Arakawa, D. Murakami, Y. Kawamura, Chem. Eng. Sci. 44 (1989) 2137–2148.
- [6] Y. Saad and M. Schultz, SIAM J. Sci. Stat. Comput. 7 (1986), pp. 856–869.
- [7] H.C. Elman, D.J. Silvester, And A.J. Wathen, Oxford University Press, Oxford, 2005.

OS11: The Eighth International
Students/Young Birds
Seminar on Multi-Scale Flow

Effect of Bubble Wake on Mass Transfer from a Bubble to Liquid Phase

Masahiko Toriu¹, Takayuki Saito²

¹Graduate School of Engineering, Shizuoka University

²Graduate School of Science and Technology, Shizuoka University
3-5-1, Johoku, Naka-ku, Hamamatsu, Shizuoka, 432-8561, Japan
ttsaito@ipc.shizuoka.ac.jp

ABSTRACT

Knowledge of the effects of flow structure on the mass transfer from a bubble is still insufficient. 1-pentanol, a surfactant substance, was used as a contamination to control hydrodynamic conditions. The flow structure around the bubble rising in stagnant water changed remarkably due to the surface contamination. The mass transfer rate from the bubble to the surrounding liquid must be affected by the difference in the flow structures. The bubble wake and the bubble volume were respectively visualized and measured experimentally. We discussed the effect of the flow structures on the instantaneous mass transfer, based on the experimental results.

1. Introduction

A bubbly flow having high mass/heat transfer rates is a common flow in industrial plants and useful for reducing their operation cost. A clear understanding of the flow structure related to mass transfer is important for achieving more efficient and safer operations. To understand in detail what actually happens in a reactor, stepwise approaches considering the number of the bubbles (i.e. a single bubble, a bubble cluster and a bubbly flow) are required. Moreover, industrial operations are usually contaminated system. In the bubbly flow with contamination, its flow structure and mass transfer rate must be different from those without contamination. Many studies of a single bubble associated with mass transfer have been investigated experimentally and numerically, but those results are insufficient for understanding cause and effect between the bubble wake and instantaneous mass transfer.

In the present study, we discussed the effects of the flow around a single bubble on the instantaneous mass transfer. The flow around the single bubble changed with an added surfactant in the liquid phase. The bubble wake was visualized through the LIF (Laser Induced Fluorescent) method with a pH-sensitive fluorescent substance. Additionally, bubble projection images were captured through two high-speed cameras. The bubble shape was reconstructed from the bubble images, and its volume and surface area were calculated precisely. We discussed the relation between the flow structure around the bubble and the instantaneous mass transfer, combining both results of the visualization of mass transportation process and the bubble volume measurement.

2. Experimental setup

Figs. 1 and 2 show the schematic diagrams of the experimental setup used in two types experiment: water containing a very small amount of a surfactant (1-pentanol mass concentration of 500ppm, molecular formula of $C_5H_{12}O$, and molecular mass of 88.15), and pure water. Table 1 shows the liquid properties with or without the surfactant.

2.1 Visualization of convective mass transportation

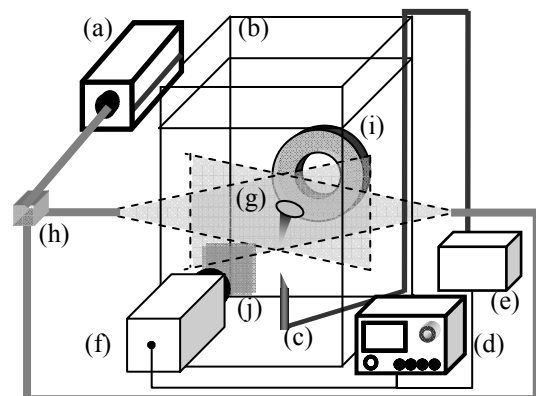
Fig. 1 shows a schematic diagram of the experimental setup used in the LIF/HPTS experiments.

HPTS (8-hydroxypyrene-1, 3, 6-trisulfonic acid) is a pH-sensitive fluorescent substance for LIF. Temperature dependency of HPTS emission intensity is negligible [1]. Since HPTS changes the emission intensity remarkably in a pH range of 6–9, HPTS easily visualizes convective transportation of CO_2 -rich regions in the surrounding liquid phase of the bubble.

An acrylic water vessel (b) was filled with ion-exchanged and degassed water. A very small amount of HPTS was added in the water (HPTS concentration 0.0001 mol/L). An Ar⁺ ion laser (wavelength: 488nm) system (a) was used for exciting HPTS. The laser beams were sheeted by a cylindrical lens and illuminated on a visualization area. A high-speed camera (f) equipped with a zoom lens was used to obtain high spatial resolution (number of pixels 1024×1024 pixels, spatial resolution 17.5 μ m/pixel, and shutter speed 1000fps).

Table 1 Liquid property

1-pentanol concentration[ppm]	Surface tension [mN/m]	Viscosity [mPa·s]
0	72.7±0.2	0.83
500	70.1±0.4	0.84



(a) Ar ion laser system, (b) Vessel & water, (c) Hypodermic needle, (d) Function generator, (e) Bubble generator, (f) High-speed camera, (g) Bubble, (h) Half mirror, (i) LED light, (j) Optical filter

Fig. 1 Experimental setup for LIF/HPTS method.

A red LED light (i) was used for visualization of the sharp bubble image. A highly-reproducible bubble was launched from a bubble generator (e); the device consists of a hypodermic needle (c), an audio speaker and two precise pressure controllers, and precisely controls the zigzag motion, size, surface oscillations, position and orientation. While the bubble rises in the HPTS solution, the emission intensity decreased in association with amount of dissolved CO₂. Thus the region containing the dissolved CO₂ was clearly distinguished from the region without CO₂.

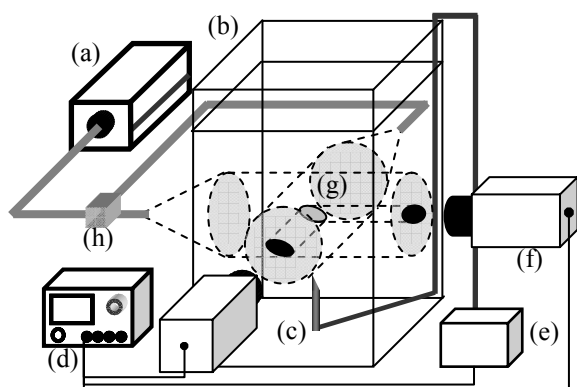
2.2 Measurement of bubble volume

Fig. 2 shows a schematic diagram of experimental setup used in the bubble volume measurement. An acrylic water vessel (b) was filled with ion-exchanged and degassed water. An Ar⁺ ion laser system (a) was used as back lighting. The laser beams were split by a half mirror, and the beams were expanded/collimated by a beam expander and then illuminated an interrogation area. The bubble was formed by the same bubble generator (e) described above. The bubble generator formed and launched a single uniform bubble repeatedly; hence measurement was achieved in high accuracy and consistency in both experiments. The bubble generator and high-speed cameras (f) (exposure time 10μs, spatial resolution 6.01μm/pixel, and temporal resolution 1700fps) were synchronized with a function generator (d), i.e. launching the single bubble and filming the shape and motion of the bubble in the same timing were realized repeatedly. As a result, the zigzag motion and surface oscillation of every examined bubble were visualized from two directions simultaneously.

The captured bubble images were analyzed, and the volume and surface area of every examined bubble were precisely calculated.

3. Results and Discussion

Fig. 3 shows two snapshots of a typical bubble wake (i.e. a part of CO₂ transportation). A bright ring shows the contour of the bubble. A dark region at the right side of the bubble is the shadow area created by the bubble.



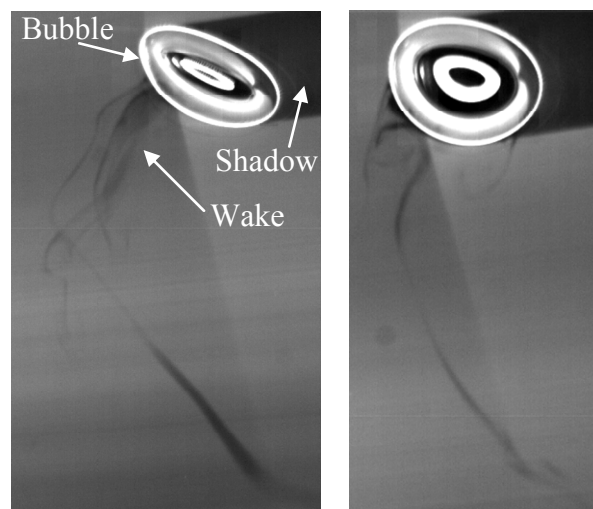
(a) Ar ion laser system, (b) Vessel & water,
(c) Hypodermic needle, (d) Function generator,
(e) Bubble generator, (f) High-speed camera,
(g) Bubble, (h) Half mirror

Fig. 2 Experimental setup for bubble projection images.

Fig. 3-(a), (b) are snapshots obtained in the purified water and in the 500-ppm solution, respectively. The bubble shape and the bubble wake structure in the purified water was different from those in the 500-ppm solution. The changes of the flow structure and the bubble shape arose from adhesion of the surfactant on the gas-liquid interface. The surfactant contaminating the interface decreased the surface tension. It led the bubble in contaminated water to the different shape from that in the purified water. In the contaminated water the flow structure around the bubble must differ from that in the purified water. In association with the bubble ascent, the attached surfactant was accumulated to the rear of the bubble; i.e. the distribution of the attached on the bubble surface was non-uniform. The non-uniform distribution of the attached surfactant caused the gradient of surface tension on the bubble surface, and the gradient of surface tension induced the Marangoni effect [2]. As a result, the significant effects of the attached surfactant brought the bubble wake to be unlike hairpin vortex shown in Fig. 3(b). These effects of contaminant on the flow around the bubble must be supposed to affect not only the bubble motion but also the mass transfer. A. Koynov et al. studied mass transfer of a two-dimensional elliptical bubble with different hydrodynamic conditions numerically [3]. Their results indicated that vortex shedding promote convective diffusion of CO₂ and prevent the dissolved CO₂ from accumulating on the bubble-rear interface. Our results can also be considered in the same way as their results. We are going to discuss the effects of the flow structure around the bubble on its mass transfer based on both results of bubble volume measurement and visualization of the convective diffusion of dissolved CO₂.

References

- [1] J. Coppeta, *Exp. Fluids*, **25** (1998) 1-15.
- [2] T. Saito, *Chem. Eng. J.*, **158** (2010) 39-50.
- [3] A. Koynov, *Chem. Eng. Sci.*, **59** (2005) 2786-2800.



(a) Without surfactant (Pure water)
(b) With surfactant (500 ppm)

Fig. 3 Convective diffusion and bubble wake structure.

Effects of Thermal and Mass Diffusions on Combustion Characteristics of Methane/Air Premixed Flame with Equivalence Ratio Using Micro-flow Reactor with Controlled Temperature Profile

Takuro Nishida¹, Takuhiro Matsumoto², Toshihisa Ueda², Takeshi Yokomori², Kaoru Maruta³

¹ School of Science for Open and Environmental Systems, Keio University,
3-14-1 Hiyoshi Kohoku-ku, Yokohama 223-8522, Japan

² Department of Mechanical Engineering, Keio University, 3-14-1 Hiyoshi Kohoku-ku, Yokohama 223-8522, Japan

³ Institute of Fluid Science, Tohoku University, 2-1-1 Katahira, Aoba-ku, Sendai 980-8577, Japan
takuronishida@a5.keio.jp

ABSTRACT

The effects of thermal and mass diffusions on combustion characteristics for methane/air premixed flames with various equivalence ratios were investigated numerically. To evaluate those diffusion effects, a micro-flow reactor model with controlled temperature profile was adopted. The results showed that the thermal diffusion effect was limited but the mass diffusion effect was crucial to the reaction. The reaction was accelerated by mass diffusion effect by supplying radicals to the upstream side, and it strongly depended on the equivalence ratio.

1. Introduction

To clarify the detailed mechanism of self-ignition process which depends on chemical reaction, such as HCCI combustion, tough challenges were conducted experimentally and numerically. However, there were few researches focused on the non-uniformity of the temperature and the species concentrations, which cause the thermal and mass diffusions, before and after the ignition [1].

In this study, the micro flow reactor with controlled temperature profile was adopted [2]. This reactor has the axially one-dimensional temperature distribution from 300 to 1300 K by the external heat source. The premixed gas is flowed inside of the tube and it is reacted under the influence of heated wall. At the low temperature rise rate, the unique flame, which is called “weak flame,” is observed. Since the weak flame has so little heat release that the gas temperature is anchored to that of wall surface, the characteristics of this flame are coincident with that of ignition, for example the temperature of the flame location corresponded to the ignition temperature [2]. Therefore, it becomes possible from this feature to also discuss about the effects of thermal and mass diffusions on ignition by using this model.

The purpose of this study was to investigate the effects of thermal and mass diffusion on CH₄/Air combustion for various equivalence ratios numerically by using the micro flow reactor model with the controlled temperature profile.

2. Numerical model

The simulations were conducted by solving 1D conservation equations of mass, energy, species and equation of state with detailed chemical reactions. The energy and species conservation equations are as follows:

$$\dot{M} \frac{dT}{dx} - \frac{A}{c_p} \frac{d}{dx} \left(\lambda \frac{dT}{dx} \right) + \frac{A}{c_p} \sum_{k=1}^K \rho Y_k V_k C_{p,k} \frac{dT}{dx} + \frac{A}{c_p} \sum_{k=1}^K \dot{\omega}_k h_k W_k - \frac{A}{c_p} \frac{4\lambda Nu}{d^2} (T_w - T) = 0 \quad (1)$$

$$\dot{M} \frac{dY_k}{dx} + \frac{d}{dx} (\rho A Y_k V_k) - A \dot{\omega}_k W_k = 0 \quad (2)$$

where \dot{M} , T , x , c_p , λ , A and ρ are mass flow rate, gas phase temperature, spatial coordinate, specific heat, thermal conductivity, cross-sectional area and density, respectively. Y_k , V_k , $\dot{\omega}_k$, h_k , W_k are mass fraction, diffusion velocity, production rate, specific enthalpy and mass weight of species k . d and Nu are channel diameter and Nusselt number. T_w is a fixed wall-temperature profile given by the external heat source. The simulation was conducted by PREMIX code [3] with a modification of the energy equation by including convective heat transfer between gas-phase and wall, and GRI-mech 3.0 [4] without reactions related to N₂ (36 species and 218 reactions). The equivalence ratio was parametrically varied from 0.5 to 1.5 and the pressure was fixed at 1.0 atm.

To evaluate the effects of thermal and mass diffusions, the terms related to those diffusions in governing equations were turned-off artificially as follows; Case 1 (normal model): thermal and mass diffusions are taken into consideration, Case 2 (no thermal diffusion model): turned-off the terms related to heat transport by temperature gradient, that is, heat conduction and enthalpy transport by mass diffusion in the energy equation, Case 3 (no mass diffusion model): turned-off the terms related to mass transport by species concentration gradient, that is, enthalpy transport by mass diffusion term in the energy equation and diffusion term in the species equation, Case 4 (no thermal and mass diffusion model): turned-off the terms related to both thermal and mass diffusions.

3. Result and Discussion

Figure 1 shows a variation of the flame position to an inlet flow velocity for all cases at $\phi = 1.0$. The flame locations were defined by the peak of the heat release rate (hrr) of the steady-state solutions. In case 4, the flame position shifted toward the upstream side with the decrease of the flow velocity. This case does not include thermal and mass diffusions. Therefore, case4 is equivalent to a zero-dimensional computation and the spatial coordinate corresponds to the time. In other cases, flame locations are different from that of case 4. Those differences prove an important role of thermal and mass

diffusion effects. In low velocity regime (< 3.0 cm/s), where weak flames are observed, flame locations show a good agreement between cases 1 and 2, or cases 3 and 4. This means that the thermal diffusion effect has no influence on the flame characteristics in this regime.

In order to examine the effect of an equivalence ratio, a variation of the flame location for each equivalence ratio at a mixture velocity of 1.0 cm/s is shown in Fig. 2. With the increase of the equivalence ratio, the flame location changes toward downstream side monotonously in case 3. In case 1, on the other hand, the flame locates at the upstream side compared with that of case 3 for lean and rich mixtures. This feature was caused by the change of the flame structure due to the mass diffusion effect.

Figure 3 shows the heat release rate (hrr) distribution with equivalence ratio at the inlet velocity of 1.0 cm/s in case 1. In this figure, it can be seen that the flame has the broad hrr distribution for each equivalence ratio. This is because the species were extensively spread by the mass diffusion. In addition, the double peak can be observed on hrr distribution for $\phi = 0.6$ to 1.0 and, in particular, the peak value at the downstream side is higher than that at the upstream side for $\phi = 0.8$ and 1.0 . These distributions imply that the reaction mechanism was changed with equivalence ratio.

Figure 4 shows the location of the peak value of CH_3 and CHO in cases 1 and 3 at the inlet velocity of 1.0 cm/s. CH_3 and CHO are major species which appear in the reaction pathway of CH_4/air premixed flame. Since CH_3 and CHO peak locations agree well each other and with the flame location shown in Fig. 2. In this case, therefore, the reactions related to CH_3 and CHO species were occurred at almost same location so that the flame has thin reaction zone. CH_3 and CHO peaks in case 1 locate at more upstream side than that in case 3. This means that the reaction was accelerated by supplying radicals to the upstream side by the mass diffusion effect. Note here that CH_3 peak location monotonously shifts toward the downstream side as increasing equivalence ratio, while CHO peak location reaches to most downstream side at $\phi = 1.0$ and it moves back to the upstream side for rich mixture. Furthermore, the flame location shown in Fig. 2 does not agree with CH_3 peak location but agrees with CHO peak one. These features imply that a certain species such as CHO was predominant on the flame reaction, and it was strongly influenced by the mass diffusion.

4. Concluding remarks

For the weak flame which was formed in the micro flow reactor, the thermal diffusion effect was small, but the mass diffusion effect was predominant on the reaction.

References

[1] R. Sankaran, H.G. Im, E.R. Hawkes, J.H. Chen, Proc. Combust. Inst. **30** (2005) 875.
 [2] K. Maruta, T. Kataoka, N.I. Kim, S. Minaev, R. fursenko, Proc. Combust. Inst. **30** (2005) 2429.

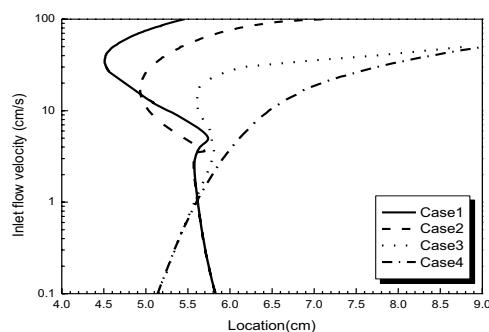


Fig. 1 Flame locations as a function of inlet flow velocity ($\phi = 1.0$).

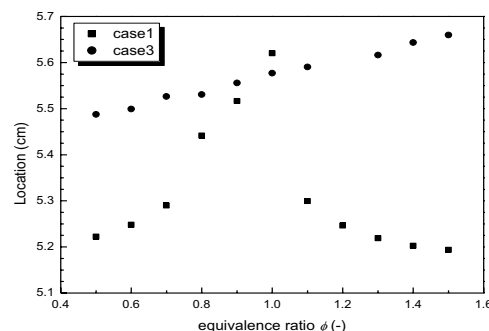


Fig. 2 Flame locations as a function of equivalence ratio ($v = 1.0$ cm/s).

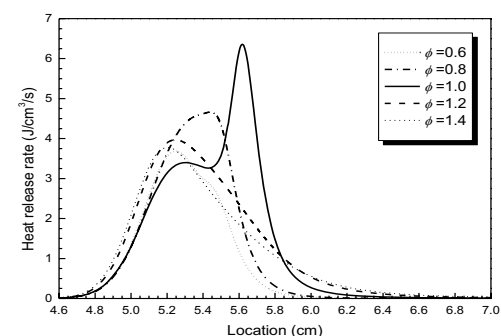


Fig. 3 Distributions of heat release rate for various equivalence ratios ($v = 1.0$ cm/s, case 1).

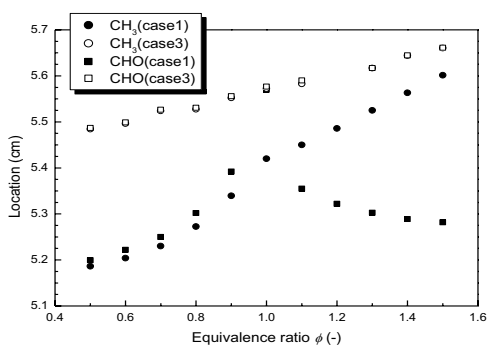


Fig. 4 Locations of peak of species concentration as a function of equivalence ratio ($v = 1.0$ cm/s).

[3] R. J. Kee, J. F. Grcar, M. D. Smooke, J. A. Miller, Sandia National Lab. Report SAND85-8240 (1985).
 [4] Information available at: http://www.me.berkeley.edu/gri_mech.

Development of a Micro-tube Gas Separator Utilizing Soret Effect

Takahiro Wako, Masae Shimizu and Naoki Ono
Shibaura Institute of Technology
3-7-5, Toyosu, Koto-ku, Tokyo, 135-8548, Japan
naokiono@shibaura-it.ac.jp

ABSTRACT

We developed a gas separator of hydrogen-carbon dioxide binary mixture utilizing Soret effect. More precisely, the Soret effect is: "Mass flux due to a temperature gradient". In nonsteady conditions, there might be a mass flux without any concentration gradient.

In this study, we performed an experiment with fluid separating device using a stainless tube. We located heating section just before the branch in order to give the sudden temperature gradient, and to increase concentration difference. From the experiment, we obtained the concentration difference of 4.6%. In the future, in order to downsize the an experimental apparatus, we introduce MEMS to our system.

1.Introduction

These days, technology has developed toward the sustainable society where environmental conservation and de-fossil, de-atomic energy are regarded as key issues. Above all, the energy system using hydrogen is expected as a new energy source because it has little environmental load and high energy conversion rate.

In the field of hydrogen technology, the steam reforming has been adopted as a main hydrogen manufacturing method. It uses the fossil fuel. The reformed gas is composed of H₂ and CO₂. Therefore, we attempt to use Soret effect which is driven by a temperature gradient in order to separate the mixed gases of H₂ and CO₂. We assume using exhausted heat, for example, absorbed heat when LNG is vaporized. Furthermore, the Soret effect enables gas separation to be completed in very short distance and time in miniature size. To establish the effective in hydrogen refinement technology using this characteristic, we performed the experiment with gas flow in a mini/micro tube.

2.Theory

We illustrate the principle of the Soret effect in Fig.1. The mass flux is occurred by the temperature gradient when heating temperature T₁ and cooling temperature T₂ are given in domain one or two, respectively. This phenomenon is called Soret effect. A property of this phenomenon is that the concentration gradient increases with the increase of the temperature gradient. On the other hand, the mass flux based on the concentration gradient, i.e. Fick's law influences to relieve concentration gradient when the system with the concentration gradient. In the system of two ingredients (chemical species A and B), Soret effect and Fick's law is expressed to (1) and (2), respectively.

$$j_i^{(T)} = -\frac{c^2}{\rho} M_A M_B D_{AB} \frac{k_T \Delta T}{T L}. \quad (1)$$

$$j_i^{(x)} = -\frac{c^2}{\rho} M_A M_B D_{AB} \frac{\Delta x_i}{L}. \quad (2)$$

In those equations, c and ρ are the molar density and mass density, respectively, M is the molecular weight, D_{AB} is the diffusion coefficient, x is the molar fraction. k_T is the thermal diffusion ratio, T is the temperature, and L is the separation distance. The subscripts i indicates chemical species A and B. When these two

mass fluxes are balanced, it is in a condition that species was completed. The separation density difference is expressed as: (3).

$$\Delta x_i = x_{i2} - x_{i1} = k_T \ln \frac{T_2}{T_1}. \quad (3)$$

Between two ingredients, the value of k_T takes a positive value with light molecules and takes a negative value with the heavy molecules. In the system of H₂-CO₂, the value of k_T is 0.0899. This value is detected by Bastick.

Therefore, the light molecules move to the high temperature domain, and the heavy molecules move to the low temperature domain, respectively.

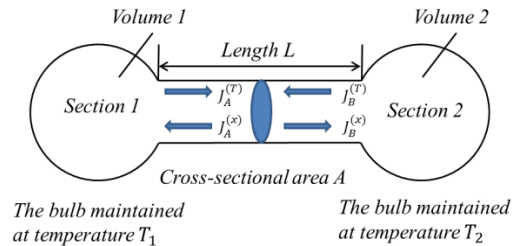


Fig.1 Steady-state binary thermodiffusion

3.Numerical analysis

We simulated separating situation in the tube by using software Phoenics. In order to simplify the calculation, we used a rectangular tube, which one side of the length was the same as the tube in the experiment, namely, 2.4 millimeters. We set the cooling part at the upper part entirely and the heating part at the under part locally. And we adopted thermal conductivity of stainless steel.

4.The outline of the experiment

We illustrate experimental apparatus in Fig.2. From the gas cylinder, we supply the gas into the tube. The gas is composed of 48% H₂ and 52% CO₂. After feeding the gas into the tube, the species separation process is started. In this apparatus, we set the cooling part at the upper part and the heating part at the under part, we created temperature gradient which cross at right angles to the flow direction. In addition, the temperature of cooling section is 263 K, and heating section is 723 K. The separated gas is divided into two branches, they are analyzed by gas chromatography. We measured the difference between the concentration of separated gas

and that density of gas cylinder.

This apparatus could collect high concentration gas effectively by making sudden temperature gradient. Furthermore, we modified the heating block to ensure temperature difference between heating and cooling section, as illustrated in Fig.3.

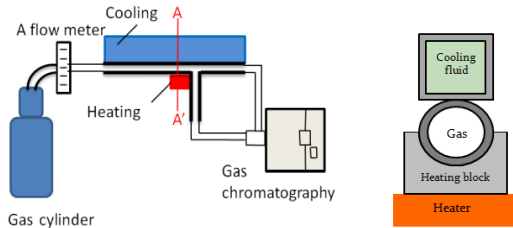


Fig.2 Experimental apparatus Fig.3A-A' cross section

5.Results and Discussion

We illustrate the result of experiment and numerical analysis. Fig.4 shows the average concentration difference and the error. From this result, the concentration difference increases drastically in low flow rate, especially below 50ml/min.

We think this is because of the thick concentration boundary layer nearby surface, re-mixing of high concentration gas and low concentration gas was restrained.

We illustrate the result of the numerical simulations in Figs.5 and 6 which show the separation state in the tube when flow velocity was changed. In Fig.5, the case of inflow velocity 0.13m/s, in Fig.6, the case of inflow 1.0m/s. These results show the difference in heating and cooling section around the branch part.

First, near the heating section, there was the high concentration gas layer as shown in Figs.5 and 6. The case of inflow velocity Fig.5, the layer was thick just before the branch part and the layer flowed into the branch tube. On the other hand, the case of inflow velocity Fig.6, the layer was not thick just before the branch part. Then, near the cooling section, there was the low concentration gas layer as shown in Figs.5 and 6. However, in Fig.5, the layer was floated back of the tube, concentration difference declined in just before the separation branch. Namely, we think that the separation rate was higher in the low flow velocity than in high flow velocity.

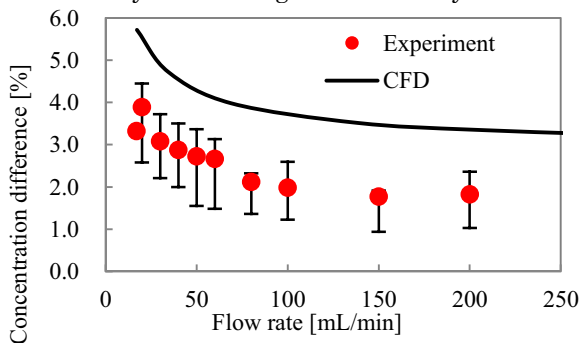


Fig.4 Experimental result

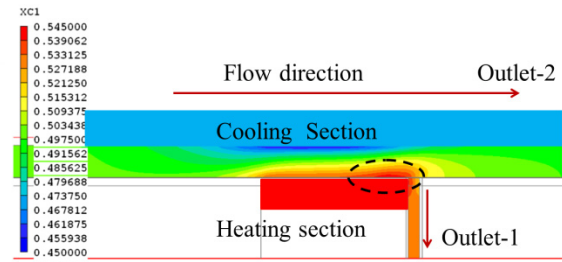


Fig.5 Hydrogen concentration distribution at inflow velocity 0.13m/s

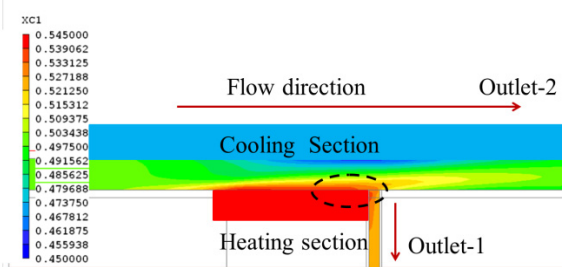


Fig.6 Hydrogen concentration distribution at inflow velocity 1.0m/s

6.Concluding remarks

- 1.From the experiment, we confirmed that the maximum gas separation difference was 4.6%.
2. From the result of the experiment and numerical analysis, it was found that the low inflow velocity was more effective than the high velocity because the thick concentration boundary layer was thought to be formed just before the branch part.

7.Future plans

We plan to optimize the shape and the size of the channel and branch tube in order to increase separation difference.

To combine the tubes for multi processes in order to obtain higher separation at the final outlet, the apparatus would become larger and larger. Therefore, by introducing MEMS technology, we plan to downsize our experimental apparatus in near future.

References

- [1] K.Yamaji, Hydrogen Energy Society, JSER, (2008), pp.136-143
- [2] T.Wako, graduation thesis, Shibaura Institute of Technology, (2011)
- [3] R.Byron Bird, Watten E. Stewart, Edwin N. Lightfoot Transport phenomena, John Wiley & Sons, (1976), pp.554-575.
- [4] R.E.Bastick, H. R. Heath, T. L. Ibbs, The molecular fields of carbon dioxide and nitrous oxide, Proc.Roy.Soc, A173(1939), pp.543-546.

A Study on Controlling Bubble Size by Magnetically Driving Metallic Powder in Liquid Phase

Keiichi Igari, Kazushi Kunimatsu and Naoki Ono

Shibaura Institute of Technology, 3-7-5 Toyosu, Koto-ku, Tokyo 135-8548, Japan

naokiono@sic.shibaura-it.ac.jp

ABSTRACT

This study is a basic research about boiling heat transfer aiming to promote miniaturization and detachment of boiling bubbles, and suppression of dryout. The pure water containing metallic powder was placed inside a Hele-Shaw cell. The metallic powder was expected to drive the flow by using rotation of magnetic field and bubbles were supplied from the bottom. Force caused by the metallic powder affected the gas-liquid interface and decreased the size of bubbles. We think that this method could have possibility of enhancing the wetting of the heated surface.

1. Introduction

In recent years, it is necessary to study the property of working fluid itself for apparatus of cooling the heat-emitting devices.

In the application of electromagnetic effect to the boiling heat transfer, there are already precedent studies about the usage of electric field, but there have been very few studies using magnetic field. In relation to boiling heat transfer, the decrease of the size of boiling bubbles as well as the frequent detachment of bubbles from the heated surface is thought to be important.

This study is a basic experiment attempting to make the size of bubbles smaller in boiling. Metallic powder was driven in the fluid by using rotation of magnetic field. Metallic powder gave force to gas-liquid interface and promoted miniaturization of bubbles. Also, after confirming the effect in air-bubble experiments, this method was applied for real boiling bubbles and investigated the frequency of bubble detachment from the heated surface.

2. Metallic powder and Experimental system

2-1. Triiron tetraoxide

Triiron tetraoxide (oxide of iron) is ferromagnetic material. The metallic powder used by this experiment was originally main components of ferrofluid. Mean diameter of this metallic powder was about 270nm.

2-2. Hele-Shaw Cell

Test fluid was contained in vertical Hele-Shaw cell, as sketched in Fig.1. Hele-Shaw cell is apparatus which holds two plates of glass in parallel with small gap between them. The observation of bubbles can be made easy by this experimental apparatus.

In the experiment about boiling bubbles, the right and left sides were made of white Teflon plate having low thermal conductivity and the top surface was open to atmosphere, as sketched in Fig.1. Heating unit was a copper plate. The tip of protruding portion was the heated surface. Face of Teflon plate did not offer boiling sites.

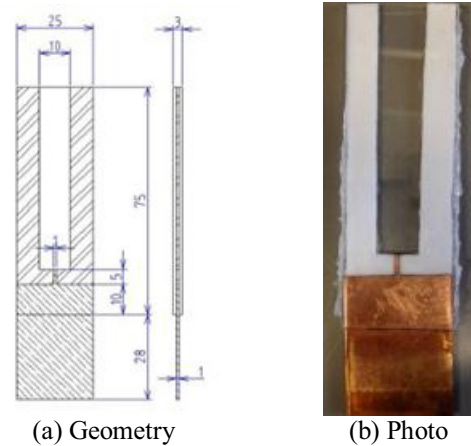
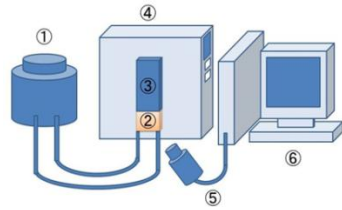


Fig.1 Hele-Shaw cell

3. Experimental apparatus and Method

Schematic drawing of experimental apparatus is shown in Fig.2. Magnetic flux density distribution (component in the direction of the thickness of Hele-Shaw cell) of magnet in the experiment is shown in Fig.3. 1 wt% of surfactant was added in the pure water. This solution of 0.45ml and triiron tetraoxide of 0.04g, was contained in the Hele-Shaw cell.

Ceramic heater was attached to the copper plate. AC 40 volts was applied to the heater and the fluid was heated from the bottom of Hele-Shaw cell. The heated area of tip of protruding portion of copper plate was 1×1 mm. Temperature of heated surface was about 110°C . Magnetic stirrer was used for magnetically driving the metallic powder (Condition: Clockwise rotation, Number of revolution 50~ 500rpm, Four neodymium solid magnets were used, the center of rotation was the second magnet from the end). Boiling bubbles when metallic powder was driven magnetically, was observed by video camera. Bubbles diameter and frequency of bubble detachment were measured.



- ① Variable transformer
- ② Ceramic heater
- ③ Hele-Shaw cell
- ④ Stirrer
- ⑤ High speed camera
- ⑥ PC

Fig.2 Experimental apparatus

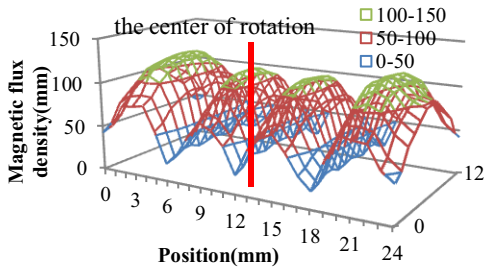


Fig.3 Magnetic flux density distribution

4. Results and Discussion

A boiling bubble without magnetic field is shown in Fig.4. The diameter and the averaged frequency of bubble detachment in Fig.4 were defined as the reference diameter and the reference frequency. They were 3.26mm and 22.3Hz, respectively.

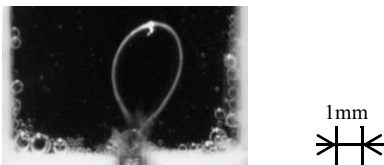


Fig.4 Bubble with no magnetic field

Boiling bubbles in powder rotating at 50rpm and 450rpm are shown in Fig.5 and Fig.6, respectively. The relation between number of rotation and bubble diameter is shown in Fig.7. The relation between number of rotation and frequency of bubble detachment is shown in Fig.8.



Fig.5 Bubble in 50rpm



Fig.6 Bubble in 450rpm

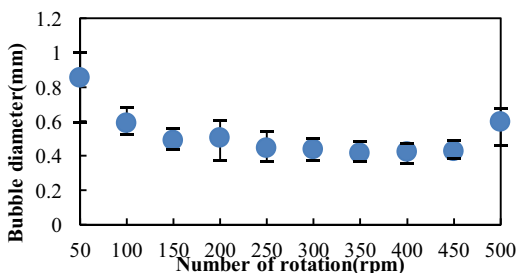


Fig.7 Number of rotation vs Bubble diameter

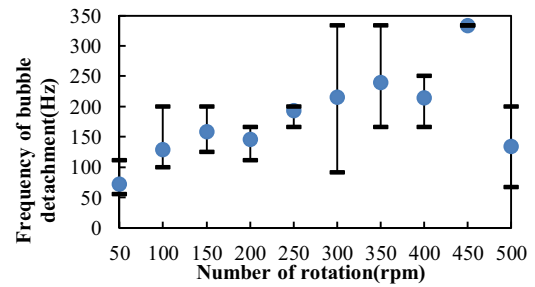


Fig.8 Number of rotation vs Frequency of bubble detachment

From the results of the relation between number of rotation and bubble diameter, in the case of 50~150rpm, bubble diameter was decreasing, as the rotation increased. In the case 150~450rpm, bubble diameter was nearly constant. In the case of number of rotation 350rpm, bubble diameter was the smallest. It was 0.42mm and one-eighth of the reference boiling bubble diameter. Compared to the experiment of the reference bubble diameter, this experiment with magnetically-driven metallic powder had the effects of miniaturization of bubbles. We suppose that the metallic powder could supply the heated surface with liquid and could have an ability of suppressing dryout of the heated surface.

The relation between number of rotation and frequency of bubble detachment was thought to be strongly reflected by the relation between number of rotation and bubble diameter. In the case of 450rpm, the frequency of bubble detachment was the largest, which was 3.33×10^2 Hz and one-fifteenth of the reference frequency of bubble detachment.

5. Concluding remarks

In the case of number of rotation 350rpm, the bubble diameter was the smallest. It was 0.42mm and one-eighth of the reference boiling bubble diameter without magnetic field.

In the case of number of rotation 450rpm, the average frequency of bubble detachment was the largest. It was 3.33×10^2 Hz and one-fifteenth of the reference frequency of bubble detachment without magnetic field.

As a conclusion, we think that this new method could have a potential ability of enhancing the wetting of the heated surface and suppressing the dryout, which we plan to investigate in future experiments.

References

- [1] Tadashi CHIKA, Yuta HIGUCHI and Ichiro KANO, JSME, (2011), J054073.
- [2] Yoshimichi OKI, Yasuhiro TANAKA, Shinji WAKAO, (2011), pp.140-157
- [3] Kei ISHIKAWA, Masahiro SHOJI, Makoto WATANABE and Shigeo MARUYAMA, Therm. Sci. Eng. (2005), pp.10-11.

Estimation of Thermal Conductivity of Biological Tissue by Inverse Analysis

Takahiro Okabe¹, Junnosuke Okajima², Atsuki Komiya², Yun Luo³, Ichiro Takahashi⁴, Shigenao Maruyama²

¹ Graduate School of Engineering, Tohoku University, 6-6 Aoba, Aramaki-aza, Aoba-ku, Sendai, Miyagi 980-8579, Japan

² Institute of Fluid Science, Tohoku University, 2-1-1 Katahira, Aoba-ku, Sendai, Miyagi 980-8577, Japan

³ Institute of Biomedical Manufacturing and Life Quality Engineering, School of Mechanical Engineering, Shanghai Jiao Tong University, A825 Mech. Bldg., 800 Dong Chuan Rd Shanghai 200240, China

⁴ Graduate School of Science and Engineering, Yamagata University, 4-3-6 Jonan, Yonezawa, Yamagata 992-8510, Japan

E-mail of corresponding author: okabe@pixy.ifs.tohoku.ac.jp

ABSTRACT

This paper describes a method to measure the thermal conductivity of the biological tissue by a point contact method. The thermal conductivities of the biological tissue such as the fat and muscle of the pig were estimated by the inverse analysis using a multilayered numerical model. In this study, a real-coded Genetic Algorithm which is a global search method for solving optimization problems was selected as optimization method. Measurements of the thermal conductivity of the biological tissue were carried out, and reasonable values of thermal conductivity could be obtained by a proposed method.

1. Introduction

In order to understand heat transfer mechanism in living tissues, the accurate knowledge of the thermophysical properties of the biological tissues such as thermal conductivity, thermal diffusivity and blood perfusion are required. These parameters play an important role in both the theoretical research of bioheat transfer and clinical applications including thermal therapy^[1] and laser therapy^[2]. Therefore, it is necessary to measure the thermophysical properties of the living tissue *in vivo* to ensure accuracy. In addition, it is preferable to undertake *in situ* measurements rather than establishing a constant value, because the thermophysical properties of the biological tissue differ among individuals, different regions and different states. Thus, a reliable, a short time, *in situ* and noninvasive measuring method is required.

We focused on the thermophysical handy tester^[3] utilizing a point contact method^[4] which is a short time, noninvasive, *in-situ* measurement of the thermophysical properties of metals and resins. However, the thermophysical handy tester cannot obtain the thermal conductivity of soft and liquid materials precisely.

The purpose of this study is to establish a measurement method of the thermal conductivity of the biological tissue *in vivo* by the inverse analysis which can optimize multivariable using the thermophysical handy tester, and to estimate the thermal conductivities of the biological tissue. Moreover, the measurable range of method is estimated experimentally. The final goal is the *in-vivo* measurement of living tissue, but measurement in this study was conducted using a piece of meat as evaluation experiment.

2. Thermophysical Handy Tester

Figure 1 shows the schematic of the experimental apparatus. First, the thermal probe with a sheathed thermocouple is heated at a constant temperature which is higher than that of the sample. The thermal probe is placed on the sample so that only an exposed junction of

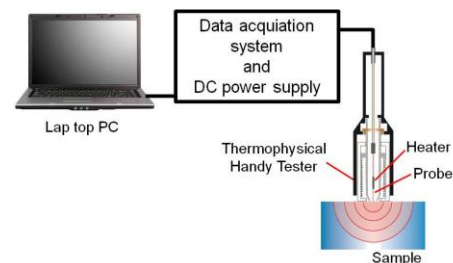


Fig.1 Experimental apparatus

the probe is in point contact. Then, thermal propagation in the sample spreads spherically around the contact point. Temperature response of the probe is observed for several seconds just after contact. The thermophysical properties are determined from comparison between the theoretical and the measured response. For the case of the measurement of soft and liquid materials, a tensioned polyimide film of thickness 50 μ m which is bonded to circular aluminum ring is used to stabilize the contact radius of the probe^[5]. However, the estimated results were affected according to the polyimide film.

3. Inverse analysis

Figure 2 shows 1D and 1D spherically-symmetric analytical model proposed in this study, and means that the tip of the probe in the thermophysical handy tester is contacting with the sample through the polyimide film.

This model assumes that heat conduction in the probe is one dimensional, that in the sample is one dimensional spherically symmetry. Thus, CPU time can be reduced by using this analytical model. There is a heater from $x = 15$ mm to 25 mm.

The governing equation is expressed as follows:

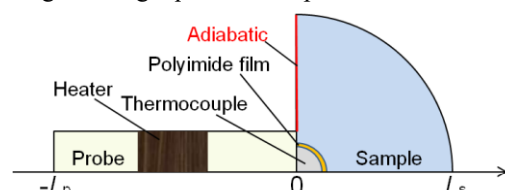


Fig.2 1D and 1D spherically-symmetric analytical model

$$A_i \rho c \frac{\partial T}{\partial t} = \frac{\partial}{\partial x} \left(A_i k \frac{\partial T}{\partial x} \right), \quad (1)$$

where ρ , c , k , T and t are density, specific heat, thermal conductivity, temperature and time, respectively.

In order to consider the three-dimensional heat transfer in the sample, the area at each position x are as changed as follows:

$$A = \pi R_p^2 \quad (-L_p \leq x \leq 0), \quad (2)$$

$$A = 2\pi x^2 \quad (R_c \leq x), \quad (3)$$

where L_p and R_c are length of the probe and radius of the probe, respectively.

The objective function of the inverse problem is defined as integration value of the difference between experimental and calculated temperature response, which is expressed as,

$$OF(\mathbf{r}) = \int_0^{t_{end}} |T_{exp} - T_{cal}| d\tau, \quad (4)$$

where \mathbf{r} is optimization vector expressed as,

$$\mathbf{r} = (k_{sam}, R_c, k_{TC}, S_{c_h}), \quad (5)$$

where k_{sam} , R_c , k_{TC} and S_{c_h} are thermal conductivity of the sample, contact radius, thermal conductivity of the thermocouple and heat generation rate per unit volume, respectively. By using these vectors, the errors in the measurement can be optimized. Thermal conductivity of the sample can be estimated by minimizing the objective function. In this study, Real-coded Genetic Algorithm utilizing Unimodal Normal Distribution Crossover proposed by Ono et al.^[6] which is a global search method for solving optimization problems was selected as optimization method of the objective function.

4. Results and Discussion

First of all, it was verified whether the thermal conductivity of water could be successfully measured by the method developed in this study. Figure 3 shows the result of the estimated and measured temperature response. The estimated result shows the good agreement with the measured result, and is 0.59 W/(m·K) which is a reasonable value. The difference between the estimated and reference value was about -3%, and it was thus concluded that the values obtained using a method proposed in this study was reliable.

Figure 4 shows the comparison between estimated and reference value of thermal conductivity of other samples. The measurement objects were fat of pig, muscle of pig, silicone oil and agar. In addition, brass, aluminum and Styrofoam which is extremely bigger or smaller than thermal conductivity of the polyimide film were selected as sample in order to estimate the measureable range of new measurement method.

The results shown in Fig.4 show that the estimated results of fat of pig, muscle of pig, silicone oil and agar agree well with reference results. However, There are upper and lower limit in the measureable range which is 0.19 - 1.2 W/(m·K). Thus, a method proposed in this study is effective for the measurement for thermal conductivity of the biological tissue, because the range

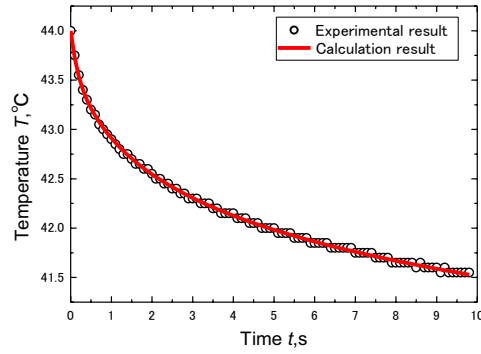


Fig.3 Comparison between estimated and measured temperature response of water

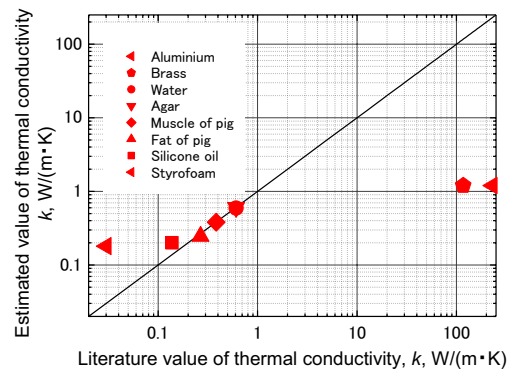


Fig.4 Comparison between estimated and reference value of thermal conductivity

of the thermal conductivity of biological tissue is generally 0.2 - 0.5 W/(m·K).

5. Concluding remarks

In this study, the inverse analytical technique which can optimize multivariable using a multilayered numerical model was established to estimate the thermal conductivities of the biological materials and other samples.

- (1) Estimated results indicated that more accurate values of thermal conductivity could be estimated.
- (2) It was estimated that there were upper and lower limit in the measureable range of new method which is 0.19 - 1.2 W/(m·K).
- (3) The inverse method proposed in this study has a possibility to consider the effect of blood flow and metabolism in the future.

References

- [1] S. Maruyama et al., Heat Transfer Asian Research, **40**(2) (2011), 114-124.
- [2] S. Maruyama et al., Proc. 8th ICFD, (2011) 534-535.
- [3] Takahashi et al., J. J. Thermophys., **13** (1999), 246-251.
- [4] Takahashi et al., J. J. Thermophys., **17** (2003), 18-23.
- [5] Komiya et al., Proc.31st Jpn. Symp. Thermophys. Prop., (2010), A204.
- [6] Ono et al., J. J. Soc. Artif. Intell., **14** (1999), 1146-1155.

Experimental Study on Shock Wave and Bubble Evolution Induced by Underwater Electric Discharge

Kentaro Hayashi¹, Taketoshi Koita¹, Mingyu Sun²

¹Graduate School of Engineering, Tohoku University, 6-3 Aoba, Aramaki aza, Aoba-ku, Sendai 980-8578, Japan

²Institute of Fluid Science, Tohoku University, 2-1-1, Katahira, Aoba-ku, Sendai 980-8577, Japan
hayashi@iswi.cir.tohoku.ac.jp

ABSTRACT

The shock wave and bubble phenomenon associated with the underwater explosion by electric discharge in a narrow channel were studied. In previous studies, the appearance and disappearance of cavitation bubbles are observed behind the shock wave by direct visualization. In order to clarify their mechanism, in this study, we try to measure the pressure in the cavitation zone, and simultaneously visualize the flow features by shadowgraph method photograph. The head-on or reflected pressure is measured experimentally using a Müller-Platte needle probe.

1. Introduction

When underwater explosion occurs near a free surface, the water above the bubble can be accelerated, forming a water jet. The mechanism of this water jet is similar to explosive volcano eruptions that are caused by expanding high pressure gases [1] in volcanic channels. It also shares the similar mechanism as the laser-induced liquid jet that has been studied in biology and medicine [2]. In this application, the water jet and the bubble are induced in a narrow pipe. In the rectangular tube, the second cavitation occurs between the bubble and the bottom of the tube [3, 4], mainly due to the shock waves reflected from the bottom wall. Interestingly enough, the formation of cavitation bubbles was also observed immediately behind the cylindrical shock wave without any reflection [5] over walls. This phenomenon is different from what have been seen in extracorporeal shock wave lithotripsy (ESWL) that produces a reflected focusing shock wave followed by a negative pressure [8].

In this study, we try to measure the pressure and simultaneously conduct flow visualization of shock wave and associated cavitation phenomenon.

2. Experimental Method

Fig.1 shows the test section in this study. The thickness (L) of the container is 5mm, and the width(W) is 240mm. The purified water is filled up to 300mm in the 320mm high container. The bottom wall and two side walls are made of stainless steel, and other two sides are optical windows made of acrylic glass. Underwater explosion is created with a high voltage electric discharge system using a cooper wire. The shock wave and cavitation are visualized by shadow photograph using a high speed camera. The exposure time is 2 μ sec. The metal halide lamp with power of 350w is used as the light source. The experimental equipment and the optical system in this study are shown in Fig.2. The driver circuit in high voltage discharge consists of a high voltage power, a capacitor, a spark trigger and two electrodes (P and N). These electrodes are installed at $Y = 150$ mm and connected with a copper wire of 50 micrometers in diameter in water. Capacitor is connected in parallel with voltage power and its capacity C is 0.2 μ F. The circuit is triggered manually. When the circuit is triggered, electric discharge is instantly generated and then explosion bubble appears. Previous research shows that the cavitation occurs around electrodes in the container [5]. The distance between the needle hydrophones and electrodes D is changed with 8 patterns, $D = 45, 40, 35, 30, 25, 20, 15, 10$ mm, are tested. The oscilloscope is used for the purpose of

recording the pressure waveform. The voltage power V is changed with 3 patterns, $V = 5.0, 4.5, 4.0$ kv. The location and the velocity of the shock wave are also obtained by analyzing recorded photos. This paper reports at $V = 4.5$ kv, $D = 30$ mm.

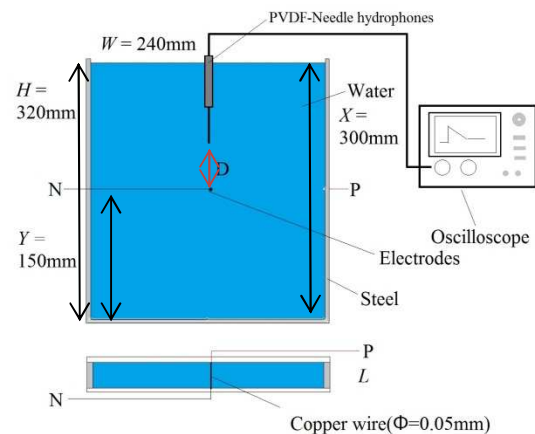


Fig.1 Test section

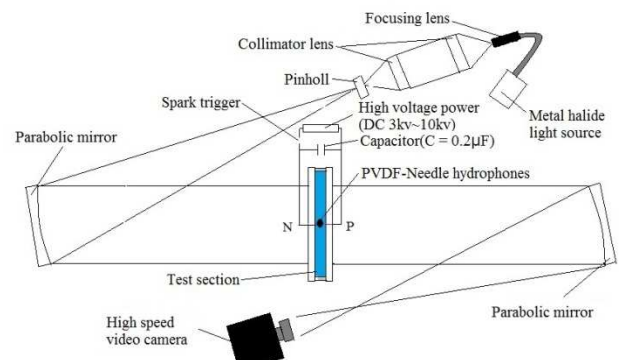


Fig.2 Schematic diagram of experimental equipment and optical system of shadow photograph

3. Results and Discussion

Fig.3 shows the sequential shadow photograph images of shock wave and cavitation for $V = 4.5$ kv, $D = 30$ mm. The PVDF-Needle hydrophone is seen over the electrodes. At the two electrodes, electric energy is released and a shock wave is caused. In Fig.3, it is seen that the shock wave propagates in the water. This blast wave propagates in water and it creates the low pressure region. In Fig.3 at the time of 31.6 μ s, the cavitation is observed near the electrodes. With the passing on the shock wave, the cavitation zone transits more far from the electrodes. The sequential shadow photograph images of the collapsing stage of the primary bubble is

shown in Fig.4. It is seen that the secondary cavitation occurs over the needle probe after the collapse of the primary bubble. This secondary cavitation may be induced by the shock wave created by the collapse of the primary bubble. The trajectory of the shock wave is measured from the photos and is shown in Fig.5. The velocity of the shock wave is evaluated from displacement and the time interval between two frames. Fig.6 shows the pressure history measured at $D = 30\text{mm}$. This result is the simultaneous measurement with the optical visualization. Two high pressure pulses are observed in experiment.

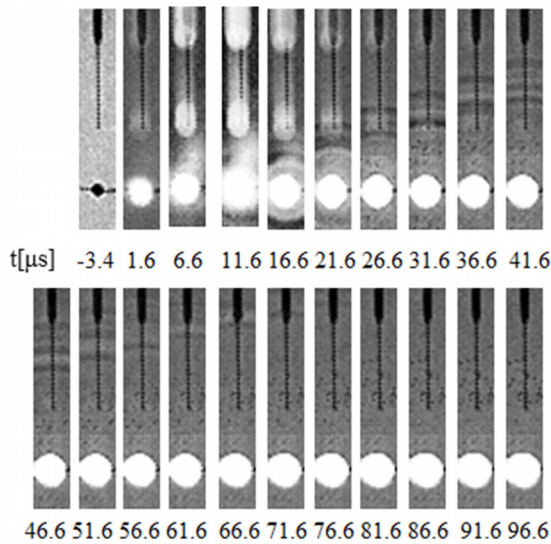


Fig.3 Sequential shadow photograph images of underwater electric discharge ($V = 4.5\text{kv}$) with a pressure gauge, 30mm above the wire.

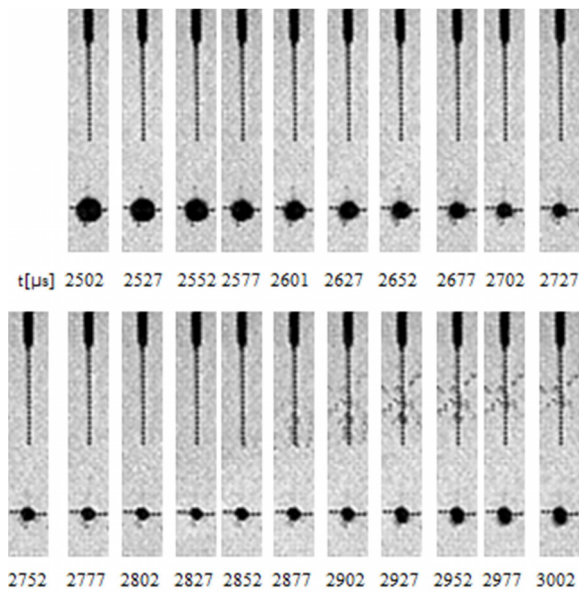


Fig.4 Sequential shadow photograph images during the collapse of the primary bubble for $V = 4.5\text{kv}$ at $D = 30\text{mm}$

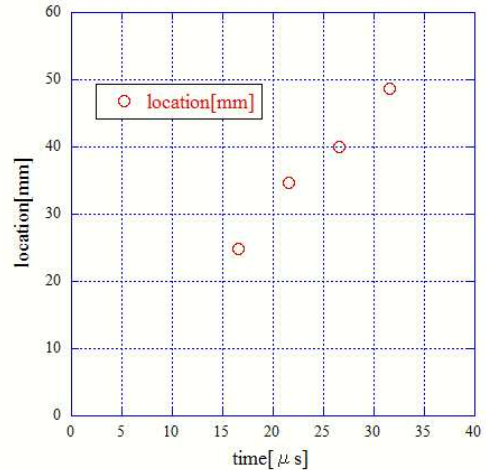


Fig.5 Trajectory of the primary shock wave front

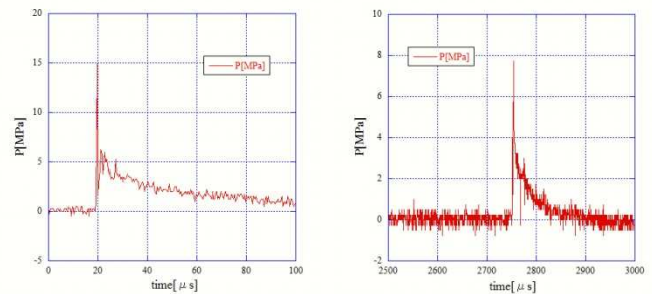


Fig.6 Pressure history of two pulses ($D = 30\text{mm}$)

4. Concluding Remarks

The shock wave and the cavitation induced by underwater electric discharge are visualized by shadow photograph. The velocity of the shock wave is evaluated from displacement and the time interval between two frames. The pressure in cavitation zone is measured simultaneous with the optical visualization.

References

- [1]H.Yamamoto, K.Takayama and K.Ishokawa, Journal of Mineralogical and Petrological Sciences, **103**(2008), No.3:192-203.
- [2]T.Tominaga, A.Nakagawa, Shock Waves, **15**(2006), R55-67.
- [3]A.Nakagawa, T.Kumabe, Y.Ogawa, T.Hirano, M.Kanamori, R.Saito, M.Watanabe, T.Hashimoto, T.Nakano, T.Kamei, H.Uenohara, K.Takayama, T.Tominaga, JJSLSM, **30**(2009), No.2:119-125
- [4]Kedriniskiy.V, Shock Waves, **18** (2009)
- [5]T.Koita, M.Sun, Symposium of Shock Waves in Japan (2010) pp.191-194
- [6]K.Hayashi, T.Koita, M.Sun, Symposium of Shock Waves (2012) pp.157-158
- [7]T.Koita, Y.Zhu and M.Sun, The 28th International Symposium on Shock Waves, Manchester, UK, (2011).
- [8]Church CC, J. Acoust. Soc. Am. **86**, (1989), pp. 215-227

Numerical Study on Receptivity of Flat-Plate Boundary Layer to Outer Freestream Disturbances

Shuta Noro^{*1}, Masaya Shigeta^{*2}, Seiichiro Izawa^{*2}, Yu Fukunishi^{*2}

^{*1} Japan Aerospace Exploration Agency, Tokyo, Japan

^{*2} Department of Mechanical Systems and Design, Tohoku University, Sendai, Japan

E-mail: noro.shuta@jaxa.jp

ABSTRACT

Numerical studies were carried out to investigate the boundary layer receptivity to localized freestream disturbances. The disturbances were indirectly taken account into through the vorticity patterns on a wall generated by the vortical disturbances in the freestream. As a result, it was shown that only the low wavenumber fluctuations could generate the vorticity pattern on the wall, and the interaction between the longitudinal vortices and the boundary layer promoted the rapid growth of the flow field.

1. Introduction

Laminar-turbulent transition in a low freestream turbulence environment generally starts from a receptivity process at the leading edge, in which the infinitesimal disturbances in freestream are taken into a boundary layer [1]. Almost all the studies on the receptivity have been performed, premised on the leading-edge receptivity [2]. On the other hand, the present study focuses on the receptivity of developed Blasius boundary layer far from the leading edge to the localized disturbances in freestream. The receptivity of such a smooth flat surface is generally negligible since there is no singular point on it and the curvature is constantly zero everywhere. However, if the freestream acquires local intense fluctuations downstream from the leading edge, they might influence the boundary layer directly. These direct effects of external disturbances on the boundary layer are still unclear.

Shigeta et al. [3] used a turbulence-generating bar located outside a boundary layer, in order to generate a disturbance free of the leading edge receptivity. The bar was a hollow circular pipe with several holes for ejecting jets into its wake. The device generated a peak-valley structure near the wall. Besides, velocity fluctuations consisted of low-frequency components below 50 Hz were observed near the wall before the outer disturbance directly reached the boundary layer. However, the physical mechanism was still not clear due to the limitation of the experimental measurement.

The objective of this study is to investigate the boundary layer receptivity to localized outer disturbances in detail using the three-dimensional numerical simulation. In particular, the receptivity is discussed from a point of view of the vorticity patterns on the wall generated by the outer disturbances.

2. Computational Method

The computational domain is the cuboid shown in Fig. 1. The inflow Reynolds number based on the displacement thickness $\delta^* = 2.11$ mm is 704. The origin of coordinate system is set at the center of leading edge. The axes x , y and z are in the streamwise, wall-normal and spanwise directions, respectively. The inlet flow has a Blasius profile. The governing equations are the non-dimensionalized differential equations for three perturbation velocity components relative to the steady

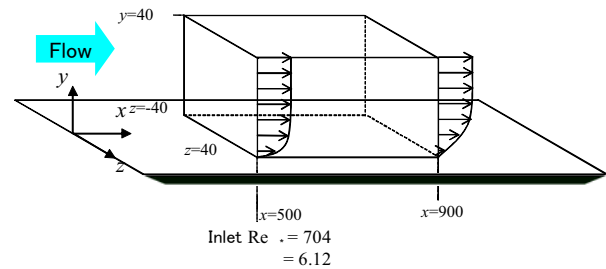


Fig. 1 Computational region.

Blasius base flow, not the incompressible Navier-Stokes equations,

$$\frac{\partial u_i'}{\partial t} + \bar{u}_j \frac{\partial u_i'}{\partial x_j} + u_j' \frac{\partial u_i'}{\partial x_j} = -\frac{\partial p'}{\partial x_i} + \frac{1}{\text{Re}} \frac{\partial^2 u_i'}{\partial x_j \partial x_j}, \quad (1)$$

Uniform grid systems are used in the streamwise and spanwise directions, while the grid points are concentrated near the wall. The grid points are $N_x \times N_y \times N_z = 256 \times 65 \times 129$. As for the velocity boundary conditions, a non-slip condition is applied at the wall, and Neumann condition is applied at the boundaries in the streamwise and wall-normal directions. As for the pressure boundary conditions, Neumann condition is applied. The computational region covers $500 \leq x \leq 900$, $0 \leq y \leq 40$, $-40 \leq z \leq 40$ mm at freestream velocity $U = 5$ m/s. The periodical condition is used in the spanwise direction. Sommerfeld radiation condition is used at the outlet boundary. The multi-directional difference method is applied. The third-order upwind method is used in the convection term. For the others, the second-order central difference method is used. The Crank-Nicolson implicit scheme is used for the time advancement.

The effect of outer disturbances in freestream is incorporated into the computation as follows. First, the counter-rotating vortex pairs of circulation Γ_0 are aligned at a certain interval in the streamwise or spanwise direction outside a boundary layer, $y = h$, and the slip velocities on the wall position are calculated. Then, the velocities that cancel these slip velocities are given as a boundary condition on a wall. It should be noted that the outer disturbances is only taken into account through the wall boundary condition to get rid of the effect of their convection.

3. Results and Discussion

Figure 2 shows the variation of circulation for various streamwise vortex spacings. The circulation is calculated by integrating the vorticity generated at the wall. As the vortex spacing ratio $\Delta x/h$ (vortex interval divided by its height) increases, the circulation Γ divided by the circulation of each vortex line Γ_0 gradually asymptotically approaches 1.0 because the influence of neighboring vortices becomes negligible. This means that only the low wavenumber fluctuations can generate vorticity fluctuations on the wall surface. In other words, the smooth flat wall surface is sensitive only for the low wavenumber fluctuations.

The absolute value of circulation of each vortex line is $\Gamma_0=0.264 \text{ m}^2/\text{s}$. The interval spacing s ($\Delta x, \Delta z$)=10.6 mm and height is $h=2.11 \text{ mm}$. The condition corresponds to the spacing ratio $s/h=5$ in Fig. 2. Figures 3 and 4 show the contour maps of spanwise and streamwise vorticity fluctuations on the wall, when the vortex pairs are aligned in the spanwise and streamwise directions, respectively. In Fig.3, only a clear pattern of the stripes appear on the wall vorticity pattern. In Fig. 4, the vorticity pattern is patchy. Figure 5 shows the isosurface of the second invariant of velocity gradient tensor, $Q=0.01$, for the latter case. A number of longitudinal vortices appearing can be found and they become entangled with each other in the downstream region. Consequently, the horseshoe-type vortices randomly appear inside the boundary layer. It is also found that owing to these vortical motions, the boundary layer becomes turbulent as shown in Fig. 6.

4. Conclusions

The receptivity of Blasius boundary layer to local vorticity fluctuations was investigated by a numerical simulation. It was shown that only the low wavenumber fluctuations could effectively generate vorticity patterns on the wall. In addition, it was found that the arrangement of longitudinal vortices promoted the boundary layer transition.

References

- [1] Saric, W. S., Reed, H. L. and Kerschen, E. J., *Annu. Rev. Fluid Mech.*, **34** (2002), pp.291-319.
- [2] Fransson, J. H. M., Matsubara, M., Alfredsson, P. H., *J. Fluid Mech.*, **527** (2005), pp.1-25.
- [3] Shigeta, M., Ohno, T., Izawa, S. and Fukunishi, Y., *Proc. 12th ACFM*, (2008), pp.1-4.

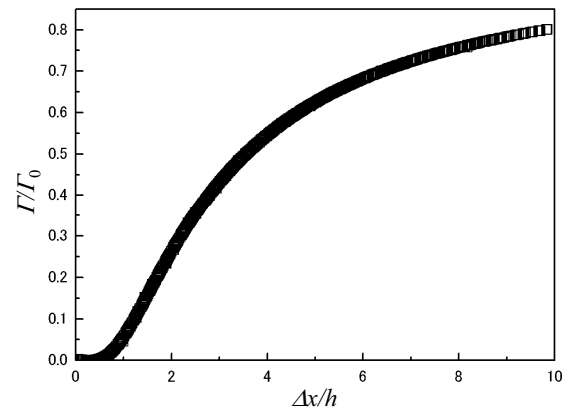


Fig. 2 Relation between spacing ratio $\Delta x/h$ and nondimensionalized circulation Γ/Γ_0 .

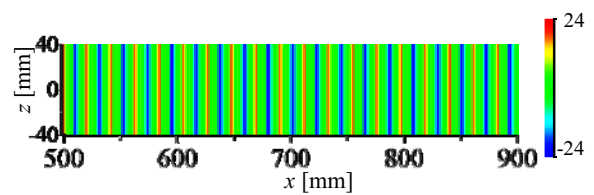


Fig. 3 Vorticity fluctuation ω_z' generated spanwise vortex lines on wall in x - z plane at $t=199$.

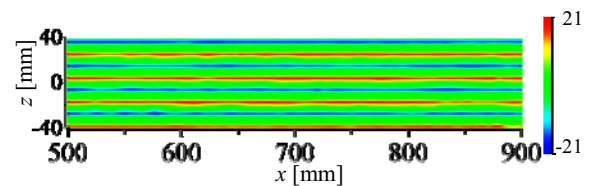


Fig. 4 Vorticity fluctuation ω_x' generated streamwise vortex lines on wall in x - z plane at $t=199$.

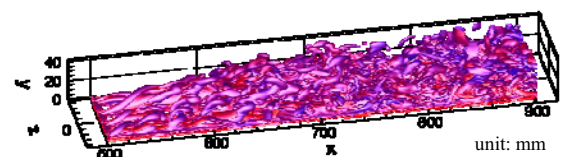


Fig. 5 Iso-surface of $Q=0.01$ criterion at $t=199$.

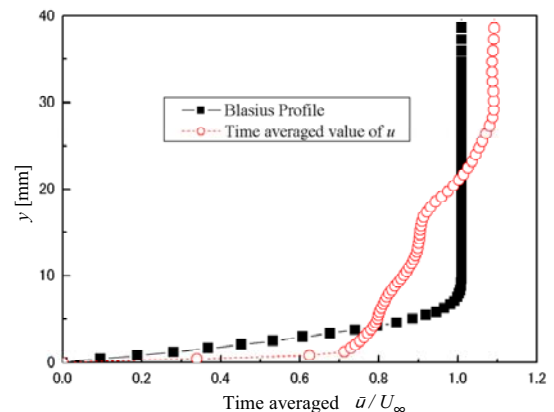


Fig. 6 Time averaged velocity \bar{u}/U at $x=844 \text{ mm}$ in Fig. 5.

Conceptual Design Method for a Mars Airplane: Formulation of Aerodynamic Characteristics at Low Reynolds Numbers

Koji Fujita^{*1}, Hiroki Nagai^{*1} and Keisuke Asai^{*1}

^{*1} Dept. of Aerospace Engineering, Tohoku University,
6-6-01, Aramaki-Aza-Aoba, Aoba-ku, Sendai 980-8579, JAPAN
fujita.koji@aero.mech.tohoku.ac.jp

ABSTRACT

A reconnaissance airplane for Mars exploration offers the possibility to obtain high-resolution data on a regional scale of several hundreds of kilometers. In this design process, an accurate estimation of aerodynamic characteristics at low Reynolds number is one of the important problems. This paper presents formulas of aerodynamic characteristics as a function of Reynolds number, Mach number, and Aspect ratio. A lightweight, fixed-wing, propeller-driven, deployable airplane for the Mars exploration was designed using the formulas. And sensitivities for the total mass to each input parameter are shown in this paper.

1. Introduction

Airplanes have been seriously considered as a new effective method of exploring Mars at NASA¹. It offers the possibility to obtain high-resolution data on a regional scale of several hundreds of kilometers, which cannot be achieved with rovers or satellites.

An atmospheric density on Mars is only one thousandth of that on Earth. Therefore Reynolds number of flow field is usually on the order of 10^4 . Generally aerodynamic characteristics change depending on the Reynolds number. Estimation techniques for aerodynamic characteristics used in existing conceptual design methods are inaccurate at low Reynolds number region because the estimation is based on aerodynamic characteristics at high Reynolds number.

Recently some aerodynamic test results of high performance wing at low Reynolds number region were reported^{2,3}. This paper presents accurate formulas of aerodynamic characteristics at low Reynolds number as a function of Reynolds number, Mach number, and aspect ratio using those data. A conceptual design of a fixed-wing, miniature, and propeller-driven airplane for Mars was performed using the formulas. Based on the design method, parametric studies were performed and effects of input parameters on a total mass were evaluated quantitatively.

2. Conceptual design process

A conceptual design process followed “*Aircraft Design: A Conceptual Approach*”⁴ by Raymer. First, the design requirements and constraints were defined. Next, a first guess on sizing was made from a sketch. Then, the values about aerodynamics, weight, propulsion system, etc. were estimated. Finally, the design was revised based on that result and sizing was made again. Through iterating this cycle, the design was optimized and detailed. In consideration of the low Reynolds number flow, this study uses results of aerodynamic characteristics experiments at low Reynolds number^{2,3}.

3. Current Mission Scenario

The Mars airplane will be transported to Mars packed in an aeroshell. At Mars, the aeroshell will enter and descend into Martian atmosphere. When the aeroshell arrives at a predefined position, the Mars

airplane will be released. Then it will deploy, control its attitude, and start horizontal flight. It will observe a Martian magnetic field and take pictures of a Martian surface closely in vast area.

4. Requirements and Constraints

Table 1 shows requirements and constraints assumed on the basis of the mission scenario. These were used in following estimation method as inputs.

Table 1. Requirements and constraints

Item	Value / Comment
Allowable total mass	3.5 kg
Equipment mass	1.4 kg
Allowable propeller Mach #	0.8 -
Range	300 km
Configuration	Fixed wing
Propulsion	Propeller / DC motor
Payloads	Magnetometer
	High-resolution camera

5. Specifications estimation method

The specifications of the Mars airplane were estimated through iterations. This method was made up of three sections: aerodynamic performance estimation, propulsion performance estimation, and mass build-up.

In order to reduce energy consumption for the propulsion system, the Mars airplane was designed to maximize a lift-drag ratio during non-accelerated level flight while satisfying requirements and constraints. A main wing area S_{ref} was given using Eq. (1).

$$S_{ref} = \frac{2M_{total}g}{\rho V^2 C_L} \quad (1)$$

At first, a total mass M_{total} was assumed to be 2.1 kg as an initial value. The acceleration due to gravity g was set to 3.7 m/s². A density ρ and a cruise velocity V were input parameters. A lift coefficient of a main wing C_L was given by the experiment². Equation (2) and (3) show lift coefficient formulated as a function of Reynolds number Re and aspect ratio AR .

$$\begin{aligned} (Re < 2.1 \times 10^4) \\ C_L = 1.7 \times 10^{-5} \times Re + 0.012AR + 0.084 \end{aligned} \quad (2)$$

$$(Re \geq 2.1 \times 10^4) \quad (3)$$

$$C_L = -0.036 \ln(Re - 1.5 \times 10^4) + 0.0095AR + 0.75$$

Then a drag was estimated. A drag coefficient of the main wing was also given by the experiment². Equation (4) shows the drag coefficient formulated as a function of Reynolds number Re and aspect ratio AR .

$$C_D = 3.4Re^{-0.51} - 0.0021AR + 0.018 \quad (4)$$

A drag coefficient of a tail wing was assumed as a zero lift drag coefficient and converted to another form using the main wing area. A drag coefficient of a fuselage C_{Df} was represented as Eq. (5)⁴, where Re_l is Reynolds number by fuselage length, f is a fuselage taper ratio, and $S_{f_{wet}}$ is a wetted area of the fuselage.

$$C_{Df} = \frac{1.328}{\sqrt{Re_l}} \left(1 + \frac{60}{f^3} + \frac{f}{400} \right) \frac{S_{f_{wet}}}{S_{ref}} \quad (5)$$

A total drag coefficient was obtained as a sum of those drag coefficients.

A propulsion performance was estimated in accordance with a method developed by Adkins and Liebeck⁵. Aerodynamic characteristics of an airfoil for the propeller, C_{lp} and C_{dp} , were given by the experiment³ and formulated as shown in Eq. (6) and (7).

$$C_{lp} = 0.065 \ln(Re_p) - 0.42M_p + 0.17 \quad (6)$$

$$C_{dp} = \frac{4.2}{(Re_p - 2.3 \times 10^3)(M_p - 0.087)} + 0.060 \quad (7)$$

where Re_p and M_p are Reynolds number and Mach number of propeller element, respectively. However, the minimum lift coefficient of propeller was restricted to 0.02 to prevent the value becoming negative.

A total mass was estimated as a sum of mass of each section. A wing mass was obtained by assuming that the mass is proportional to the wing area and 0.34 kg per 1 m². As a battery, the lightest Li-ion battery was selected⁶. Its energy density is 118 Wh/kg. A mass of the battery M_{bat} was estimated using Eq. (8).

$$M_{bat} = \frac{P_{total}E}{\rho_{energy}} \quad (8)$$

Here, P_{total} is the total input power, E is endurance, and ρ_{energy} is energy density of the battery. An input power for the motor was obtained from the propulsion performance calculation described above.

By reentering the obtained total mass to Eq. (1), these calculations were iterated until a difference of the total mass became less than 0.001 kg.

6. Results

Table 2 shows obtained baseline specification result. Specifications satisfied requirements and constraints. Remarks of this result are a high lift coefficient and a

high aspect ratio. Therefore this result shows a small wing area and a high lift-drag ratio.

Parametric studies for the total mass to each input parameter were performed. Major results are shown in Table 3. These results can be used for a quick estimation at design modification in a conceptual design process.

Table 2. Baseline specification result

Parameter	Value
Total mass M_{total}	2.8 kg
Reynolds # of wing Re	2.1×10^4 -
Max. Mach # of propeller $M_p _{max}$	0.72 -
Aspect ratio of wing AR	9.5 -
Wing area S_{ref}	0.82 m ²
Lift coefficient of wing C_L	0.55 -
Drag coefficient C_D	2.2×10^{-2} -
Drag D	0.42 N
Lift-Drag ratio L/D	25 -
Propeller torque Q	3.8×10^{-2} N·m
Propeller power P_{axi}	34 W

Table 3. Sensitivity

Parameter	Sensitivity
Area density of wing structure	1.5 kg/(kg/m ²)
Cruise velocity	-0.043 kg/(m/s)
Range	3.3×10^{-6} kg/m
Wing span	-0.42 kg/m
Altitude	0.00016 kg/m

7. Conclusion

The estimation formulas of aerodynamic characteristics at low Reynolds number and the conceptual design of the Mars airplane were presented. The proposed design satisfied requirements and constraints. A parametric study result for the total mass to inputs was shown as a quick modification tool.

References

- [1] M. D. Gynn, et al., AIAA paper 2003-6578, San Diego, CA, 2003.
- [2] S. Shigeoka, et al., Proc. of the 64th Kyushu Branch Regular Meeting of the JSME, C42, Kyushu University, Fukuoka, 2011.
- [3] T. Suwa, et al., Proc. of the 43rd Fluid Dynamics Conf. / Aerospace Numerical Simulation Symposium 2011, 1D09, Tokyo, 2011.
- [4] D. P. Raymer, AIAA Education Series.
- [5] C. N. Adkins, R. H. Liebeck, Proc. of the AIAA 21st Aerospace Science Meeting, AIAA-83-0190, Reno, 1983.
- [6] H. Toyota, et al., Proc. of the Space Sciences and Technology Conf., JSASS-2010-4479.

Prototype Experiment and Numerical Simulation on Processing of Noncontact Thin Plate Utilizing Alloy with Low Melting Temperature

Yoshiyuki Mitsuhashi, Kazuki Matsumura, Takashi Yamada, Mitsutaka Umeta, Naoki Ono
Department of Engineering Science and Mechanics, Shibaura Institute of Technology
3-7-5 Toyosu Koto-ku, Tokyo 135-8548, Japan
naokiono@sic.shibaura-it.ac.jp

ABSTRACT

Two types of ribbon growth methods, edge-defined film-fed growth method (EFG) and ribbon growth method on substrate (RGS) are already utilized to produce a silicon plate in photovoltaic industry. By combining the advantages of the two methods we attempted to make a thin metal plate, which was horizontally pulled and solidified in the air by means of forming meniscus shape. We report the experimental results by using low-melting-temperature alloy and the simulation analysis. Consequently, we found that the thickness of solidified metal depended on the liquid level in the container, and ~ 0.2 mm thickness was achieved experimentally.

1. Introduction

Ribbon growth methods have some advantages which are cost reduction and high production speed in the photovoltaic industry, compared with the silicon wafer produced from ingots[1].

The two classical methods are edge-defined film-fed growth (EFG) and ribbon growth on substrate (RGS). The liquid metal in these two methods is exposed to a die or substrate while solidifying. We are concerned that the solidified metal contains some impurities mixed from the substrate. Therefore, we here propose a new method to produce a thin plate which can contain less impurity.

Figure 1 illustrates the concept of our method. The seed was dipped into liquid metal in the container, and pulled horizontally. The liquid metal attaching to the seed was cooled down and was solidified in the air while it was being pulled.

In this study, we conducted experiments and computational fluid dynamics (CFD) simulations by using the low melting temperature metal alloy instead of silicon, whose melting temperature is 1410°C , for the sake of building the experimental device.

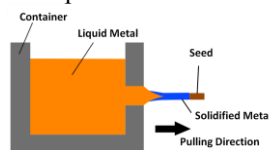


Fig.1 Concept of noncontact thin plate growth method

2. Method

Figure 2(a) schematically shows the experimental apparatus around the container. The seed metal made of copper, whose thickness and width were 0.1mm and 2.5cm correspondingly, was inserted into the 0.3mm high and 3cm wide slit in the container which was made of poly-ester-pate. Bismuth- Indium alloy of 60°C melting temperature in the container was heated from the top and cooled with the Peltier device at the bottom, since the liquid metal was drained at near melting temperature in the air.

As shown in figure 2 (b), once the power supplier connecting to the motor was on, the screw started rotating. Then, the seed metal that was held on the stage

gradually moved away from the container with the speed of about $3\text{mm}/\text{min}$. At that time, the temperature of liquid metal inside of the container was measured with a thermocouple and adjusted to about 61°C . A CCD camera was also used to record the liquid metal in front of the slit while it was solidifying.

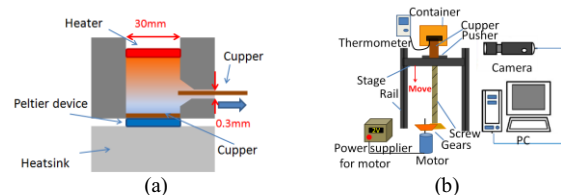


Fig. 2 Sketches of container (a) and experimental apparatuses (b)

The CFD analysis was conducted by using femLego[2], which was developed by Gustav Amberg and extended by Minh Do-Quang. This software can be used for the computation based on the finite element method.

The two-dimensional analysis was performed under the similar condition to that experiment. The cooling temperature was set as 23°C of room temperature at the free surface. The temperature at the inlet was 61°C and the inlet velocity was set to be $3\text{mm}/\text{min}$. The computation system and boundary condition are illustrated in Figure 3.

The governing equations of motion, deformation, energy, and volume fraction of liquid-solid were computed with the dimensionless numbers in Table 1[3],[4]. Thus, the velocity, pressure, deformation of liquid at free surface, temperature, and volume fraction of liquid- solid fields were obtained.

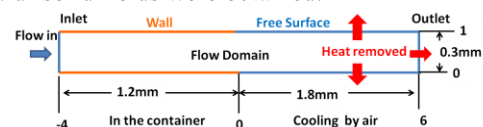


Fig. 3 Sketch of computational system

Table 1 Non-dimensional numbers

Reynolds number	0.12
Prandtl number	$6.1\text{E-}03$
Stephen number	0.12
Biot number	$3.2\text{E-}04$
Weber number	$1.41\text{E-}08$

3 Results and Discussion

The results of the experiment are illustrated in Figure 4. The solidified metal attached to the seed was leaving out of the container after about 6 minutes, and the liquid part was drained after about 8 minutes. The metal was thick at first, but it gradually became thinner due to the decrease of the amount of liquid in the container. The liquid in the container flooded out due to the gravity effect at first. As a result, the metal could become thick. 30 minutes later, thickness turned to be less than 0.2 mm.

As illustrated in Figure 5, we could produce about 10 cm long, and the average width and thickness were about 15 mm and 0.4 mm correspondingly.

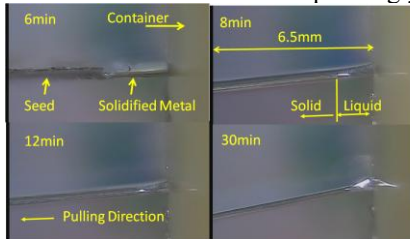


Fig. 4 Liquid metal pulled from the container



Fig. 5 Produced solid plate

3.2 Results of the simulation

The results of simulation are shown in Figure 6. The red color shows the volume fraction of liquid and the blue color indicates the solid. In addition, yellow-green color implies the liquid-solid interface. After 3 minutes, the solidified metal was thicker than the slit. After that, the interface came closer to the slit, and the metal gradually became thinner as can be seen in the experimental results.

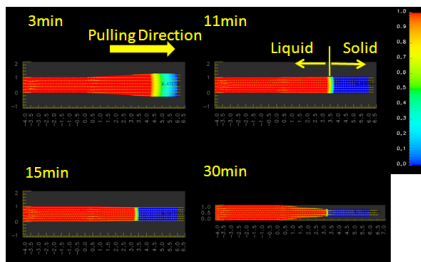


Fig. 6 Liquid metal pulled from the container

3.3 Discussion

As seen in Figure 7, the experiment was compared with the simulation with respect to the thickness. In the simulation, the thickness was 300 μm at initial and the metal had not started solidification yet, so the thickness could be compared from about 470 μm . The trend of the simulation and the experimental results shows that the metal became thick at first, and the thickness was gradually reduced.

Figure 8 indicates the position of interface of liquid and solid depends on time. The results of the simulation shifted to the experimental data at 1.6 mm from the slit, which means the initial condition of the simulation was fitted with the one of the experiment. The slope of the

position of interface altered near 11 minutes, supposing that the metal was thinner than the slit. Moreover, the position of interface in the simulation was a little farther from the slit than the one in the experiment around 12 minute. This was because the thermal conductivity near the melting point of the simulation was a little small.

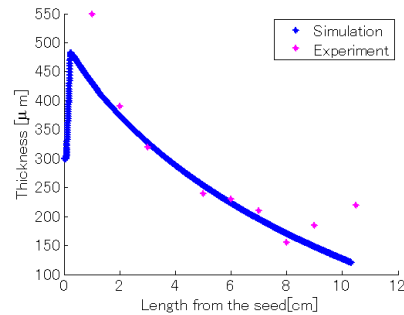


Fig.7 Comparison of simulation with experiment with respect to the thickness of produced metal depending on the length of the core metal

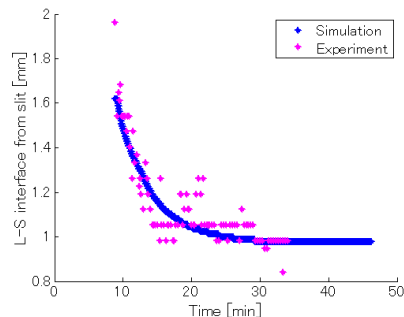


Fig.8 Comparison of simulation with experiment in terms of the position of interface of liquid and solid with time

4 CONCLUSION

We conducted the prototype experiment and simulation based on the new process to produce the thin silicon plate of solar cell.

Less than 0.1mm thick plate was aimed to be produced. However, the minimum thickness approached to about 160 μm . We found the level of liquid metal in the container strongly affected on the thickness.

We will control the level of liquid metal in the container in order to produce less than 0.1mm thick plate at constant, and utilize the simulation to realize the optimum process to produce the silicon plate near future.

References

- [1] K. Nakajima , N. Usami, Crystal growth of Si for solar cells, Springer Verlag (2009), 96-117
- [2] G. Amberg , R. Tönhardt , C. Winkler , Finite element simulations using symbolic computing, Math. Comput. Simul. 49,4(1999),257-274.
- [3] M. Do-Quang, G. Amberg, Modelling of Time-Dependent 3D Weld Pool Flow Due to a Moving Arc, Simulation and Optimization of Complex Processes (2003),127-138
- [4] R.V. Birikh, V.A. Briskman, M.G. Velarde, Liquid Interfacial Systems Oscillations and Instability, Marcel Dekker(2003),1-28

Design of Interferometer System with Phase-shifting Koester Prism

Eita Shoji¹, Atsuki Komiya², Junnosuke Okajima², and Shigenao Maruyama²

¹School of Engineering, Tohoku University

6-6-04, Aramaki Aza Aoba Aoba-ku, Sendai, Miyagi, 980-8579, Japan

²Institute of Fluid Science, Tohoku University

2-1-1 Katahira, Aoba-ku, Sendai, Miyagi, 980-8577, Japan

eita@pixy.ifs.tohoku.ac.jp

ABSTRACT

An interferometer system with a phase-shifting Koester prism to study density fields was proposed in this study. Accurate measurement with high resolutions and visualization with a large visualization area can be performed by a phase-shifting technique and the optical configuration, respectively. In addition, a phase-shifting Koester prism was designed to expand the versatility of the system. In order to validate the system, temperature in natural convection were measured and compared with analytical solution. It was confirmed that the interferometer system with the prism is effective for temperature measurement in natural convection.

1. Introduction

There are many experimental methods for the investigation of flow fields[1]. In those methods, optical methods have been established because non-intrusive method is desirable for flow fields. Typical methods include shadowgraphy, Schlieren method and interferometry. Both the shadowgraphy and Schlieren method provide qualitative information. On the other hand, interferometry is quantitative.

Mach-Zehnder interferometry has long been applied to study flow fields, such as natural convection. Nevertheless, a conventional Mach-Zehnder interferometry has some drawbacks, e.g. phase and spatial resolutions, air disturbance effects and visualization area size.

In order to improve phase and spatial resolutions, phase-shifting technique[2][3] was installed to Mach-Zehnder interferometer in this study. Special optical elements are necessary to implement the technique. Nevertheless, previously developed optical elements have problems.

Therefore, the objective of this study is a design of a quasi common path phase-shifting interferometer with phase-shifting Koester prism in order to overcome the drawbacks. In addition, natural convection were visualized and measured to validate the interferometer system.

2. Experimental Apparatus

In this study, a quasi common path phase-shifting interferometer was constructed. Figure 1 shows the schematic of the interferometer. This interferometer was designed to accomplish three objectives: to reduce the

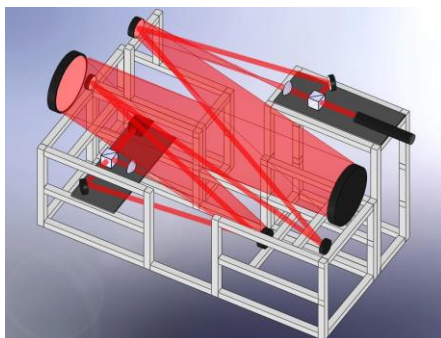


Fig. 1. Schematic of quasi common path phase-shifting interferometer.

air disturbance effect, to achieve a large visualization area, and to improve phase, spatial and time resolutions. This interferometer features a quasi common path, a non-conventional optical configuration, and a phase-shifting technique.

A phase-shifting technique was installed to conduct measurement accurately. The phase-shifting technique is an image processing technique, which produces phase-shifted data. The phase-shifted data were obtained from three interferogram in different polarization state.

Here, a method to acquire the three interferograms is important in the technique. Though some optical elements were developed[2][3] to acquire the interferograms, the optical elements have problems, such as time resolution and availability to CCD camera.

Thus, a phase-shifting Koester prism was designed. Figure 2 shows a schematic of the phase-shifting Koester prism. The prism has features: to split a beam into 4 beams and filter each beam, to output 4 beams in the same direction.

Figure 3 shows the processing screen of obtained 4 images by the prism. The prism outputs the three interferogram in different polarization state and a shadowgraph. Accordingly, phase-shifted data can be obtained with one CCD camera. In addition, quantitative measurements as well as qualitative measurements are conducted since a shadowgraph can be also obtained.

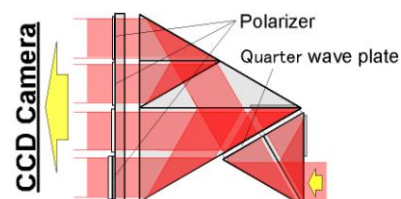


Fig. 2. Phase-shifting Koester Prism.

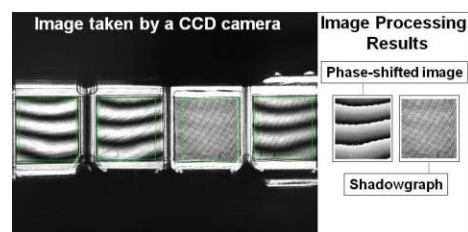


Fig. 3. The processing screen of obtained images by phase-shifting Koester prism.

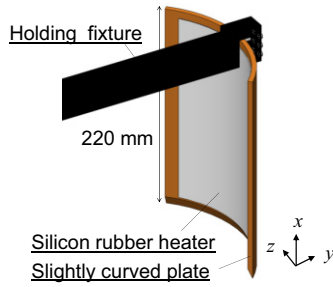


Fig. 4. The slightly curved vertical plate.

3. Data processing

The effect of a three-dimensional structure of measurement object is not negligible in measurement by interferometry[4]. Hence, inverse Abel transform and a slightly curved plate were used in this study.

A line integral value distribution σ can be converted to a radial distribution γ by inverse Abel transform in cases where a physical quantity distributes axisymmetrically. Inverse Abel transform[5] is expressed as Eq. (1).

$$\gamma(r) = -\frac{1}{\pi} \left\{ \begin{aligned} & [\sigma(a) - \sigma(r)](a^2 - r^2)^{-1/2} \\ & + \int_r^a [\sigma(y) - \sigma(r)] y(y^2 - r^2)^{-3/2} dy \end{aligned} \right\}, \quad (1)$$

where r is a axis along a radial direction, y is an axis perpendicular to an optical axis, a is an integral interval.

The natural convection which has an axisymmetric temperature field was generated by the slightly curved plate. Given the natural convection is approximately the same as natural convection around a vertical heated flat plate, temperature distributions are measured removing the effect of three-dimensional structure by Eq. (2).

4. Experimental condition

The slightly curved vertical plate was heated by a silicon rubber heater, and a thermocouple was attached to measure the surface temperature. The schematic of experimental apparatuses is shown in Fig. 4.

The material of the plate is copper by virtue of its high thermal conductivity. The length, the thickness and the radius value are 220 mm, 5 mm and 95 mm respectively. The radius was selected to form approximately the same phenomena as the natural convection around a vertical heated flat plate. In addition, the uniformity was validated by the plate's Biot number and fin efficiency[6].

The experiments are conducted in a room maintained at 20°C and the plate was heated to 40°C. Rayleigh number is 5.3×10^6 in the experimental condition.

5. Results and Discussion

Figure 5 shows phase-shifting images of the natural convection for visualization. The whole image was obtained from Fig. 5 (a). In addition, magnified image was obtained as shown by Fig. 5 (b) because interference fringes are unclear in the thermal boundary layer due to insufficient CCD camera resolution.

The temperature distribution was obtained by Fig. 5 (b) and Eq. (2). Though only one interference fringe was

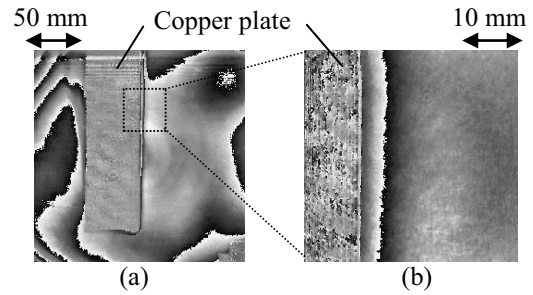


Fig. 5. Phase-shifted data (a) whole image 200×200 mm, (b) magnified image 35×35 mm.

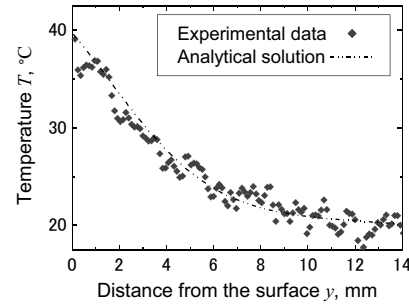


Fig. 6. Comparison with analytical solution.

observed in Fig. 5 (b), a large number of the measurement points were obtained. The experimental data was compared with analytical solution in laminar natural convection from isothermal vertical flat plate[6].

The comparison result is shown in Fig. 6. A temperature fluctuation by noise is observed. Nevertheless, the result denotes the same tendency as an analytical solution. The fluctuation is caused by an alignment problem in image processing of three interferogram. Phase-shifting processing using phase-shifting Koester prism requires a correct alignment since three images are obtained in different position of one CCD sensor.

6. Concluding remarks

An interferometer system with phase-shifting Koester prism has been proposed in this study. The following conclusions were reached.

- (1) The system was validated by measurements of temperature field in natural convection.
- (2) An accurate alignment of three images is indicated to be significant in the image processing using the phase-shifting Koester prism.

Acknowledgement

This work was supported by a special research student of international leading researcher hatchery program in Tohoku university Global COE program.

References

- [1] W. Merzkirch, Flow Visualization, (1987).
- [2] S. Maruyama et al., Exp. Therm. Fluid. Sci., Vol.19, (1999), pp.34–48.
- [3] A. Komiya et al., Proc. 13th IHTC, (2006), MST-10.
- [4] E. Shoji, Proc. ISTP-23, (2011), tracking number 62.
- [5] Deutsch et al., Appl. Phys. Lett. Vol.41, (1982), p.27.
- [6] F.P. Incropera et al., Fundamentals of heat and mass transfer, Wiley, (2001).

Dryout of Boiling with Impinging Flow in T-shaped Mini Channel with High-carbon Alcohol Aqueous Solutions

Minoru Ootuka, Yuki Kumagai, Taguchi Haruki and Naoki Ono
Shibaura Institute of Technology, 3-7-5 Toyosu, Koto-ku, Tokyo 135-8548, Japan
naokiono@sic.shibaura-it.ac.jp

ABSTRACT

We investigated combination of impinging flow and high-carbon alcohol aqueous solutions in mini channel. We used two types of the glass tubes. One of them was a square cross section whose side length was 5.4mm, and the other one was circular cross section of 5.4mm in diameter. We compared heat transfer characteristics including dryout point with butanol aqueous solution and pure water. It was found from the experiments that the liquid film of the butanol aqueous solution extended in the direction toward high-temperature region and the butanol aqueous solution of 3.00wt% gave high dryout heat flux.

1. Introduction

In recent years, a variety of electronic control equipment has been widely used for computers, automotive and industrial machineries. CPU used for the control equipment emits larger amount of heat than before due to the needs of rapid performance gain and drastic miniaturization. Therefore, to prevent from heat damage or performance degradation, it is necessary to remove heat and to cool the CPU. However, it is to be concerned that cooling technologies may not keep up well enough with the increase of heat in future.

In this experiment, we used high-carbon alcohol aqueous solutions as working fluid. In our method, the fluid was impinging against the heated surface to promote heat transfer and to suppress the onset of the dryout. We combined high-carbon alcohol aqueous solutions and impinging flow to realize compact cooling device with high efficiency.

2. Method

Figure 1 shows the flow loop used in the experiment. This was mainly for the observation of boiling bubble and fluid motion. Figure 2 shows the test section (each glass tube A and B). After filling the tank with the test fluid, the fluid was fed into the test section by using a pump. Fluid passing through the test section will be then pumped to a disposal tank without circulation. Quartz glass was used for each glass tube of a test section. Glass tube A was a square cross section whose side length was 5.4mm, and Glass tube B was a circular cross section of 5.4mm in diameter. The flow rate to the test section was 35.0ml/min. Pulsation of a pump was suppressed by Pressure tank. At the top center portion of the test section, the copper block was plugged into the holes of the glass tube. After inserting the cartridge heater inside the copper block, we applied direct current to the heater for joule heating. The values of the three K-type thermocouples which were inserted into the copper block at three locations (3mm, 7mm and 11mm from the heat transfer surface) were measured. Then the temperature data were used to calculate the temperature gradient and the heat flux at the heated surface by using Fourier's law. We also observed the boiling bubble and the motion of liquid film with a High speed camera. Table 1 shows the experimental conditions.

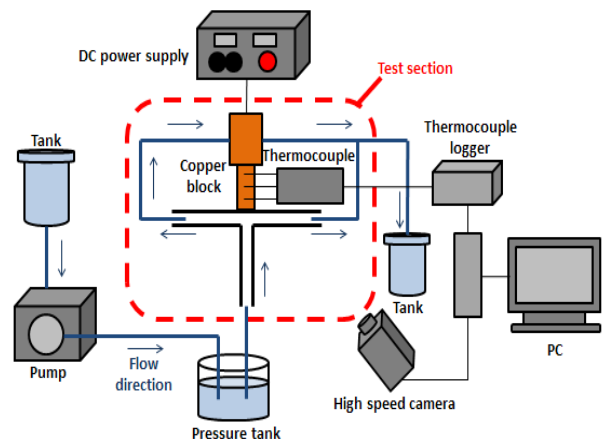


Fig. 1 Experimental apparatus

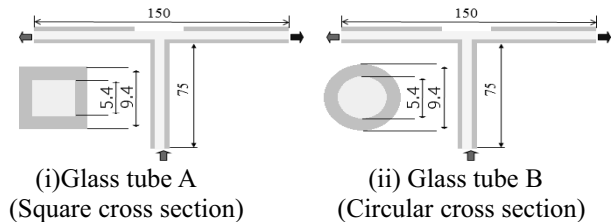


Fig. 2 Test section

Table 1. Experimental conditions

Flow rate [ml/min]	Flow velocity[m/s]	Reynolds number	Subcooling [°C]
35.0	2.0×10^{-2}	120.94	75

3. Results and Discussion

In this experiment, we used butanol aqueous solution (3.00wt%) and pure water which was degassed sufficiently, as working fluids. Butanol aqueous solution is a kind of high-carbon alcohol aqueous solutions.

(i) Heat transfer characteristics

Figure 3 shows boiling curves which compare the butanol aqueous solutions and the pure water when using glass tubes A and B, respectively. Note that CHF in the figures for each of the working fluid indicates the dryout point.

From these results, in the case of butanol aqueous solution, the heat transfer characteristics were better than in the case of pure water in square cross section and

circular cross section. Moreover, the boiling curve indicated a sudden increase in heat flux near CHF point when the butanol aqueous solution was applied. This could be because the peculiarity of high-carbon alcohol aqueous solutions is related. The experiment of R.Vochten and G.Petre, J.Colloidal^[1] shows that the surface tension of high-carbon alcohol aqueous solutions increases by the rise of temperature. The increases of the surface tension by the rise of temperature, arises unique thermal Marangoni convection as shown in a Fig.4. Detachment of bubbles was promoted by unique thermal Marangoni convection and gave high dryout heat flux. However, in the case of pure water, Surface tension decreases by the rise of temperature. It becomes as shown in a Fig.5. Therefore, detachment of bubble was not promoted and gave low dryout heat flux.

From the Fig.3, we found that the heat flux of circular cross section higher than in the case of square cross section. Therefore, the cross-sectional shape influenced heat flux. The reasons and its mechanism are currently under investigation.

(ii) Observation of boiling bubble

The photos of the observed behavior of the boiling bubbles are shown in Fig.6 and Fig.7. In the case of pure water, the boiling bubbles tended to stay around the cross position, as shown in Fig. 6 (ii) and Fig.7(ii). The staying bubble made the heated surface perfectly dry and worsened the heat transfer. In the case of butanol aqueous solution, the liquid film seemingly extended to the heated surface and cooled that, as shown in Fig. 6(i) and Fig. 7(i). In addition, bubbles tended to vibrate more than in the case of pure water. We think that the unique Marangoni convection of high-carbon alcohol aqueous solutions influenced that motion.

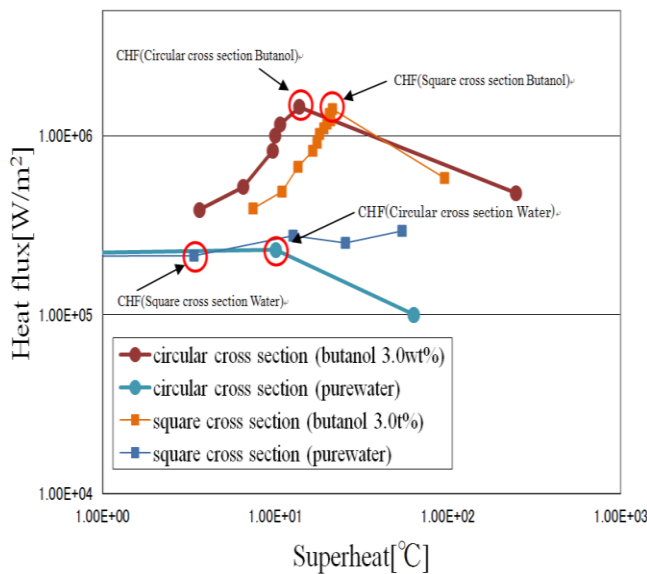


Fig. 3 Boiling curve

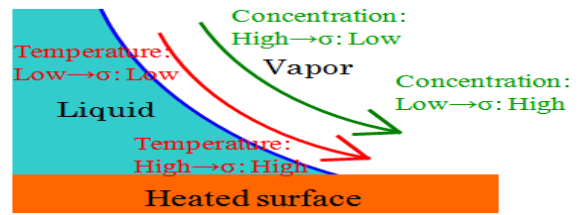


Fig.4 Marangoni convection (High-carbon alcohol aqueous solutions)

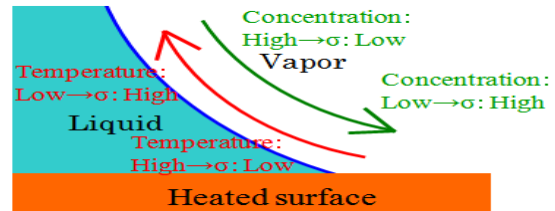
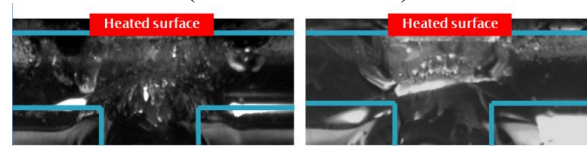
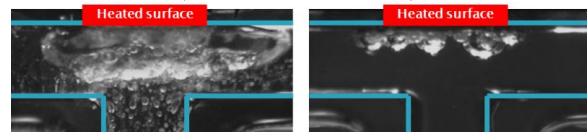


Fig.5 Marangoni convection (The other solutions)



(i) Butanol aq.sol of 3.00wt% (ii) Pure water
Fig.6 Behavior of the boiling bubbles in glass tube (circular cross section)



(i) Butanol aq.sol of 3.00wt% (ii) Pure water
Fig.7 Behavior of the boiling bubbles in glass tube (square cross section)

4. Concluding remarks

It was found from this experiment that using the butanol aqueous solutions, the boiling curve indicated a sudden increase in heat flux near CHF point. Moreover, the liquid film seemingly extended to the heated surface.

We think that the unique Marangoni convection of high-carbon alcohol aqueous solutions influenced these results. In addition the combination of high-carbon alcohol aqueous solutions and impinging flow made influence of unique Marangoni convection more remarkable and gave the better heat transfer characteristics.

References

[1] R.Vochten and G.Petre, J.Colloidal Science, 42-2(1973), pp. 320-327.
 [2] Naoki Ono, Takahiro Yoshida, Takahiro Kaneko, Syotaro Nishiguchi and Masahiro Shoji, Proc 46th Japan Heat Transfer Symposium(2009), pp. 367-368.
 [3] Naoki Ono, Takahiro Yoshida, Takahiro Kaneko, Syotaro Nishiguchi and Masahiro Shoji, Proc 46th Japan Heat Transfer Symposium(2009), pp. 367-368.
 [4] Minoru Otsuka, Atsushi Hamaoka, Yuki Kumagai, Kazushi Kunimatsu and Naoki Ono, Proc 48th Japan Heat Transfer Symposium(2011), pp. 277-278.

Leading Edge Receptivity to Freestream with Velocity Profile Sinusoidal in the Spanwise Direction

Yu Nishio, Masaya Shigeta, Seiichiro Izawa and Yu Fukunishi

Department of Mechanical Systems and Design, Graduate School of Engineering, Tohoku University
nishio@fluid.mech.tohoku.ac.jp

ABSTRACT

Numerical simulation of the flow around a flat plate with an elliptic leading edge is performed to understand the receptivity of the leading edge to a disturbance with a velocity profile sinusoidal in the spanwise direction. As a result, the strong vorticity deformation that leads to a difference in the disturbance growth rate depending on the spanwise location is observed.

1. Introduction

Boundary-layer receptivity has been studied analytically and experimentally for last several decades. In recent years, the numerical approaches became more practical thanks to the rapid advance in computer technology. For example, Nagarajan et al.^[1] performed a numerical simulation to observe the effect of the bluntness of a leading edge on a bypass transition. They reported that the stretching of vortices at the leading edge is the important factor in the receptivity process and the leading edge amplifies the vortices. Lars-Uve Schrader et al.^[2] discussed the receptivity of a flat plate with an elliptic leading edge using a numerical simulation. They showed that the vertical and streamwise vortices with low frequency trigger the bypass transition and the spanwise vortices affect the T-S waves. Besides, they also found that the receptivity to vertical vortices depends on the leading edge bluntness, whereas the receptivity to streamwise vortices is independent of it.

In this study, a three dimensional simulation is performed, focusing on a leading edge receptivity to freestream with a velocity profile sinusoidal in the spanwise direction. Then, the growth of the disturbance inside a boundary layer is observed.

2. Numerical Method

The three-dimensional incompressible unsteady Navier-Stokes equations are solved by a finite difference method using a body-fitted coordinate on a regular grid system. A third-order upwind difference scheme is used for the convection term written in a gradient form. For the other terms, the second-order central difference scheme is employed. In addition, the multi-directional finite different scheme is also implemented for the discretization of the all terms of the N-S equations. The third-order Adams-Bashforth explicit scheme is applied for the convection term and the Crank-Nicolson implicit scheme is used for the viscous term.

Figure 1 shows the computational domain around a flat plate with a leading edge of an aspect ratio 1:5. The origin of the Cartesian coordinate system is set at the center of the leading edge of the plate, where x , y and z axes denote the streamwise, vertical and spanwise directions, respectively. The numbers of grids are 449 points in ξ direction, 193 points in η direction, and 16 points in ζ direction. The flat plate

length is four times larger than the length of the leading edge. Reynolds number based on the leading edge length is 4.0×10^4 . The spanwise scale of the computation grid is $1.5a$.

As for the velocity boundary conditions, the non-slip condition is applied to the wall, the Neumann condition is prescribed at the outlet boundary and the Dirichlet condition is used for the outer elliptic boundary. As for the pressure boundary conditions, the Neumann condition is enforced to the inlet and the wall and the Dirichlet condition is employed at the outlets. The outlet pressure is fixed at 1. The periodic boundary condition is used in the spanwise direction.

Freestream disturbances are given by changing only the streamwise velocity component at the inlet according to the following equation,

$$\frac{u'}{U_\infty} = \begin{cases} A \times \sin(2\pi ft) \times \sin(\beta z) & -\frac{l_y}{2} \leq \frac{y}{a} \leq \frac{l_y}{2} \\ 0 & \text{otherwise} \end{cases}$$

where the non-dimensional frequency $f (= 1/T) = 1$, and the amplitude A is 1% of the freestream velocity. It should be noted that $f = 1$ corresponds to a frequency higher than those in the Schrader et al.'s simulation^[2]. $t = 0$ indicates the moment the disturbance was added. $\beta (= 2\pi/1.6a)$ is the spanwise wavenumber and in this study the β is 1.

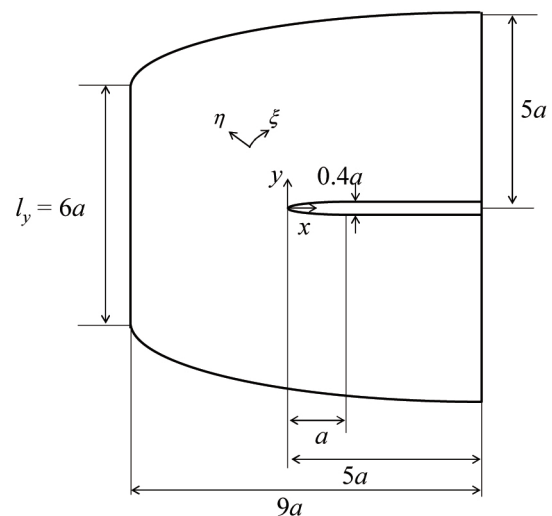


Fig. 1 Computational domain

3. Results and Discussion

Figure 2 shows the distribution of the wall-normal vorticity in the x - y plane at $z/a = 0.8$ where the velocity shear at the upstream boundary becomes the highest, and the x - z plane at $y/a = 0$. The introduced vorticity becomes high at $z/a = 0$ and 0.8 .

Figure 3 shows the contour maps of $\sqrt{\omega_x^2 + \omega_y^2}$ near the leading edge at $t/T = 11.0, 11.125, 11.25$ and 11.375 . The color map shows the magnitude of the vorticity fluctuation ω' . The oncoming vorticity fluctuation pattern is distorted passing the leading edge. The vorticity fluctuation becomes stronger in front of the leading edge at $t/T = 11.25$.

Figure 4 shows the profile of u' in the spanwise direction at $t/T = 11.0, 11.25, 11.5$ and 11.75 . The velocity periodically changes in time and space. The frequency of velocity fluctuation is equal to the forcing frequency f . In addition, the streamwise velocity fluctuation becomes high in between the oncoming vortices at $z/a = 0.4$ and 1.2 . The streamwise variation of u'_{rms} at one grid point away from the wall is shown in Fig. 5. It is found that the vorticity fluctuation becomes stronger where the initial velocity fluctuation near the leading edge is higher.

4. Concluding remarks

A numerical study is performed to investigate the leading edge receptivity to a freestream disturbance with a velocity profile sinusoidal in the spanwise direction. As a result, it is found that the growth of disturbance inside a boundary layer depends on the spanwisely local interaction between the oncoming vortices and the leading edge.

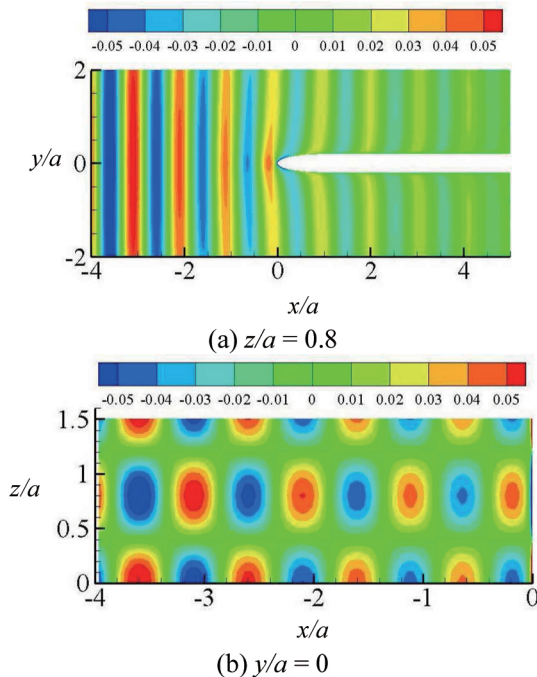


Fig. 2 Contour maps of ω_y at $t/T = 12.0$

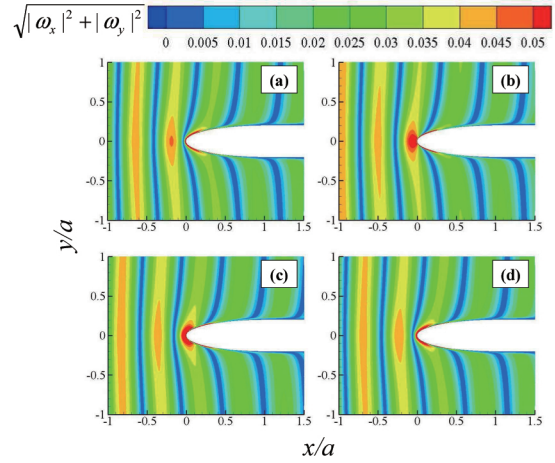


Fig. 3 Contour maps of $\sqrt{\omega_x^2 + \omega_y^2}$ near the leading edge at $z/a = 0.8$ and $t/T =$ (a)11.0, (b)11.125, (c)11.25 and (d)11.375.

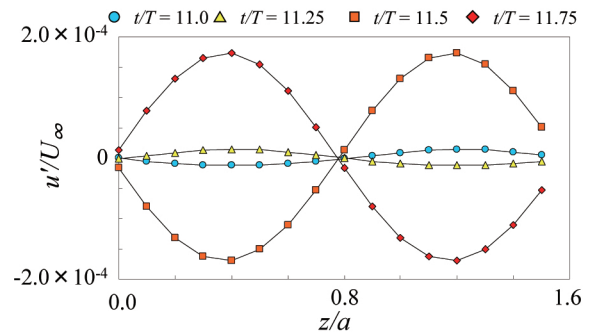


Fig. 4 Spanwise distribution of u' near the wall at $x/a = 0.06$

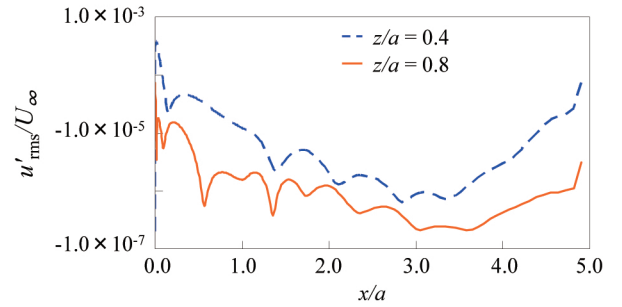


Fig. 5 Streamwise distribution of u'_{rms} near the wall

References

- [1] S. Nagarajan, S.K. Lele and J.H. Ferziger, *J. Fluid Mech.*, **572**(2007), 471-504.
- [2] L.-U. Schrader, L. Brandt, C. Mavriplis and D.S. Henningson, *J. Fluid Mech.*, **653**(2010), 245-271.

Effect of Bio-Nano Fibres on Centrifugal- and Curvature-Induced Hydrodynamic Stability

Mathias Kvik^{†*}, Fredrik Lundell^{†*}, Lisa Prahll Wittberg^{†*}, L. Daniel Söderberg^{†‡}

[†]Wallenberg Wood Science Center, Royal Institute of Technology, KTH Mechanics, SE-100 44 Stockholm, Sweden

^{*}Linné FLOW Centre, Royal Institute of Technology, KTH Mechanics, SE-100 44 Stockholm, Sweden

[‡]Inventia AB, Box 5604, SE-114 86 Stockholm, Sweden

E-mail of corresponding author: kvick@mech.kth.se

ABSTRACT

In order to investigate the effects of nano-fibrillated cellulose on hydrodynamic stability, experiments are performed in a curved rotating channel. Images of the structures in the flow are acquired and evaluated by visual examination. The experiments are analysed together with a linear stability analysis. In both theory and experiments, the effect of the addition of fibres is found to be greater on the bulk viscosity compared to the stability.

1. Introduction

In this work, the effect of nano-fibrillated cellulose (NFC) on curvature- and rotation-induced instabilities is investigated. NFC is produced from pulp, resulting in cellulose fibrils with diameters of the order of 100 nm and lengths up to 2 μm .

Not many experimental studies exist concerning the effects of fibres on hydrodynamic stability, and the studies are contradicting, indicating that fibres may act either stabilising [1] or destabilising [2].

2. Method

The experimental setup used is a curved rotating channel, shown in figure 1. The channel has a radius of curvature of 400 mm and covers 180°.

The curvature of the channel gives rise to a centrifugal force, this force will destabilise the flow. The rotation of the channel induces an additional centrifugal forces as well as a Coriolis force. Depending on the direction of the rotation, the Coriolis force either counteracts or enhances the centrifugal instability.

The two non-dimensional numbers governing the flow are the Reynolds number and the Rotational number, defined as;

$$\text{Re} = \frac{U_b d}{\nu}, \quad (1)$$

$$\text{Ro} = \frac{\Omega d}{U_b}, \quad (2)$$

where U_b is the bulk velocity, d the channel width, ν the fluid viscosity and Ω the angular velocity defined positive in the direction of the flow.

The flow is visualised by the addition of a small amount of Iridin (plate like particles), and images of the flow-structures are acquired. Experiments are performed with pure water as well as an NFC suspension with a volume fraction of 0.0308%. The images are inspected visually, and each case is assigned to be either in the *laminar*, *primary instability*, *secondary instability* or *turbulent* regime.

In the theoretical work carried out, the fibres are

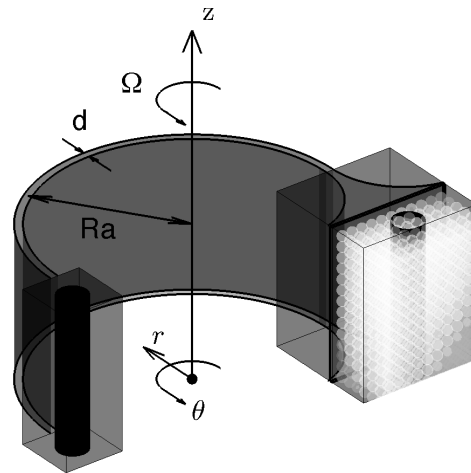


Fig. 1 Experimental setup

modelled as an additional stress, appearing in the Navier-Stokes equations as;

$$\sigma_f = A\Phi(\dot{\gamma} : a_4), \quad (3)$$

where A is a rheological parameter depending on the fibre aspect ratio and the volume fraction of fibres Φ , $\dot{\gamma}$ is the shear rate and a_4 the fourth order orientation tensor. The closure problem of the orientation tensor is solved by assuming that the fibres are performing Jeffery orbits in the flow-gradient plane and thereby obtaining the angular velocities of the fibres. The orientation distribution is thereafter calculated with the Smoluchowski equation. The orientation distribution is in this work assumed to be stationary.

The linear stability equations are derived assuming perturbations of the general form;

$$f' = F(r)e^{i\beta z + st}, \quad (4)$$

where β is the spanwise wavenumber and s the temporal growth rate. The eigenvalue problem found by inserting the perturbations in the Navier-Stokes equation is solved for different values of β , Re and Ro . The lowest Re/Ro at which the imaginary part of the temporal growth rate is positive is the critical Re/Ro .

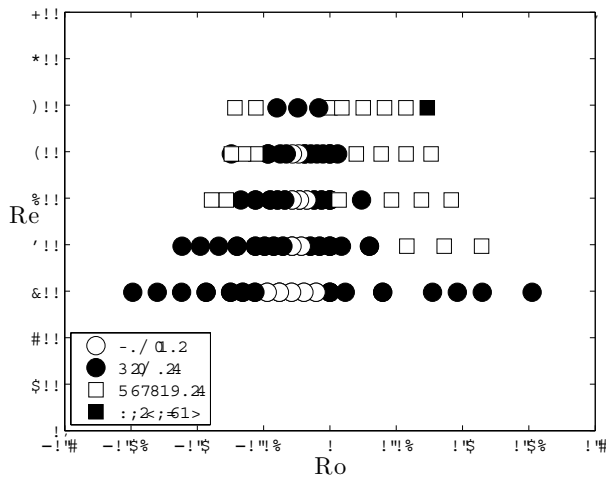


Fig. 2 State diagram for experiments with pure water.

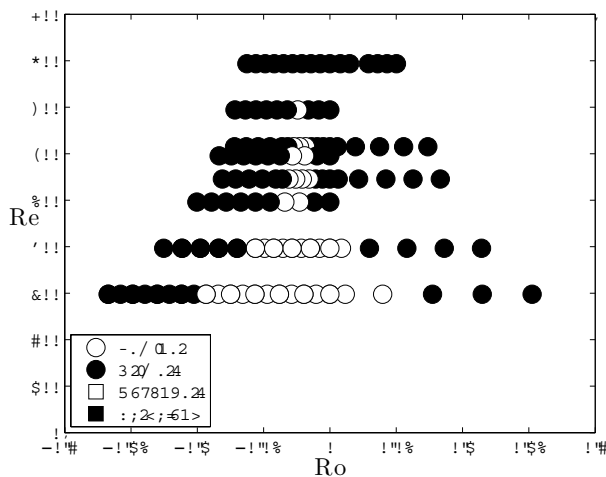


Fig. 3 State diagram for experiments with the NFC suspension, the Reynolds number is based on the viscosity of water.

3. Results and Discussion

In figure 2 and 3, the state diagrams obtained from the experiments for pure water and the NFC suspension are shown in the $ReRo$ -plane. The Reynolds number is in both cases based on the viscosity of water. In both figures, the largest laminar Re is reached at $Ro = -0.03$. At this rotational number, the centrifugal (due to curvature) and the Coriolis force (due to rotation) balances each other. When comparing the two figures it is clearly seen that the addition of NFC stabilises the flow (the laminar region is greater).

In figure 4 the neutral stability curves (solid lines) obtained from the linear stability analysis are shown for different volume fractions of fibres. Here the contours (dashed lines) of the transition from laminar flow to the primary instability in the experiments is also depicted.

From the neutral stability curves it is clearly seen that the addition of fibres stabilises the flow according to theory. However, the calculated shear viscosity of 1.4

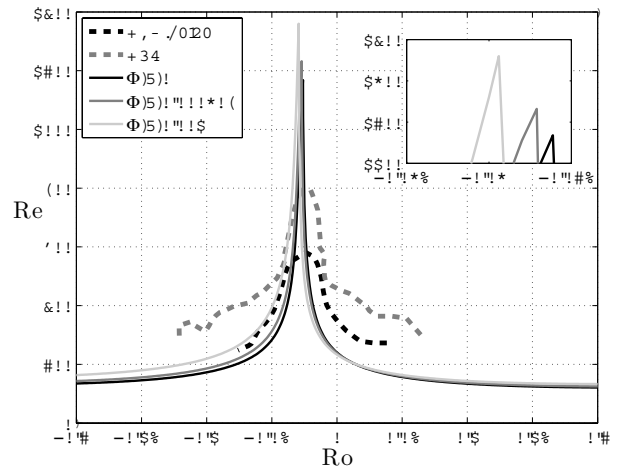


Fig. 4. Neutral stability curves from linear stability analysis and contours of the transition from laminar flow to the primary instability in the experiments.

times the viscosity of the solvent is not sufficient to explain the increase in critical Reynolds numbers, which is of the order of 1.1.

Furthermore, the contour of the transition from laminar flow to the primary instability in the NFC experiment is found to fit the experiment with pure water when scaled by a factor of 1.4. This is lower than the mean measured shear viscosity of 1.8, obtained with a rotational viscometer.

4. Concluding remarks

The addition of NFC clearly stabilises the flow. However, the addition of fibres has greater effect on the bulk viscosity compared to the effects on the primary instability, both for the experiments and the theoretical considerations. Due to the spanning of the parameter space, no conclusions can be made regarding the secondary instability.

Furthermore, the linear stability under predicts the addition of fibres.

References

- [1] Vaseleski RC, Metzner AB, (1974), *AIChE J.* 20(2):301-306
- [2] Pilipenko VN, Kalinichenko NM, Lemak AS, (1981), *Soviet Phys. Doklady* 26:646

Water Purification by Spraying Solution into DBD Plasma Reactor

Tomohiro Shibata¹, Hideya Nishiyama².

¹Graduate School of Engineering, Tohoku University, 2-1-1 Katahira Aoba-ku, Sendai 980-8577, Japan

²Institute of Fluid Science, Tohoku University, 2-1-1 Katahira Aoba-ku, Sendai 980-8577, Japan
shibata@paris.ifs.tohoku.ac.jp

ABSTRACT

The world has been faced with serious problems of water pollution. Recently, conventional chemical treatment has been replaced by a water treatment system using plasma. In this study, using a newly developed mist-flow plasma reactor, a method for decomposing organic compound by directly spraying solution as mist into reactive plasma was investigated. An atomized solution containing micro-sized droplets was introduced into the reactor. The decomposition characteristics were clarified through decolorization experiments of methylene blue solution. In addition, the acetic acid decomposition is observed by ion chromatography.

1. Introduction

Water pollution is serious problem not only for humans but also for the entire ecological system. Recently, conventional waste water treatment, e.g., biological and chemical methods, has been replaced by a water treatment system using plasma because functional plasma treatment is environmentally adaptive. In plasma treatment, organic compounds are generally decomposed by the ozone. Although a variety of radicals are also generated by reactive plasma, the radicals and some of the ozone cannot be used for water purification due to their short lifetime. If the reactive plasma is generated near the solution interface, the radicals can be utilized efficiently for water purification. A water treatment system utilizing the discharge of bubbles, above water and in gas-liquid two phase flow has been developed. It has been reported that the method of spraying waste water into reactive plasma shows the highest relative energy efficiency[1]. Furthermore, there are some Persistent Organic Pollutants (POPs) requiring higher oxidation potential to decompose. Since the oxidation potential of ozone is insufficient, these POPs cannot be decomposed only by ozone. Therefore, attention has been focused on advanced oxidation processes utilizing OH radicals.

In this study, a method for decomposing organic compounds by spraying solution as mist into reactive plasma directly was investigated, using a newly developed mist-flow plasma reactor. Reactive plasma is generated by dielectric barrier discharge (DBD) on the inner wall of a tube. An atomized solution containing micro-sized droplets was introduced into the plasma reactor. Liquid properties of dissolved chemical species such as H₂O₂, reactive oxidation species (ROS) and O₃ are measured. The decomposition characteristics of this method were experimentally clarified through decolorization experiments using methylene blue solution. The methylene blue solution is about 100 % decomposed by one treatment under certain operating conditions. In addition, the feasibility of decomposing acetic acid using the plasma reactor is demonstrated.

2. Experimental apparatus and measurement procedure

Figure 1 shows a schematic of the experimental

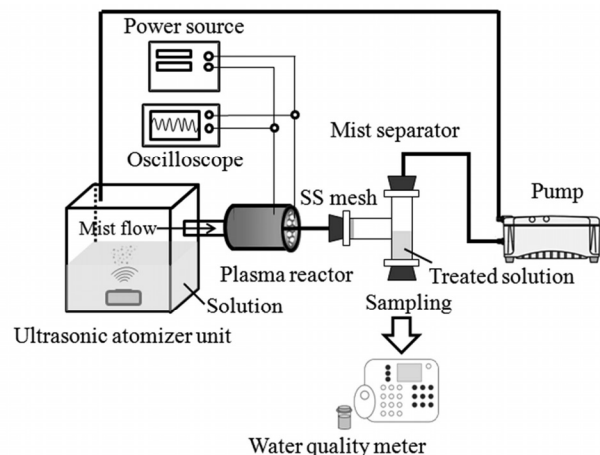


Fig. 1 Schematic illustration of experimental setup.

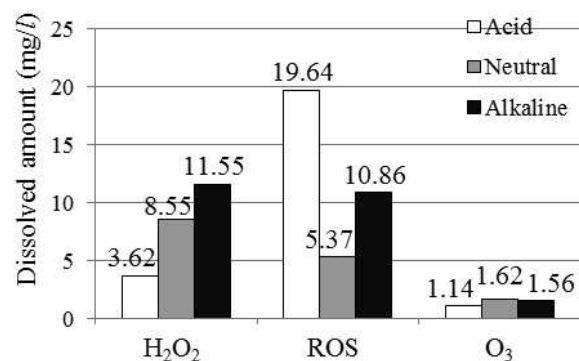


Fig. 2 Increase in concentration of dissolved species for various solution pH.

setup, which mainly consists of electric power supply, ultrasonic atomizer units, a mist-flow plasma reactor, a mist separator and an air pump. Two ultrasonic atomizer units are used to generate sufficient amount of mist. Air and Ar are used as carrier gases. The mist flow plasma reactor made of Teflon with a thickness of 0.5 mm has an inner mesh electrode made of stainless and an outer grounded electrode made of copper. Sinusoidal voltage is applied to the inner mesh electrode.

The amount of generated ozone is measured by an ultraviolet absorption ozone monitor. The decomposition efficiency of organic compounds is evaluated by

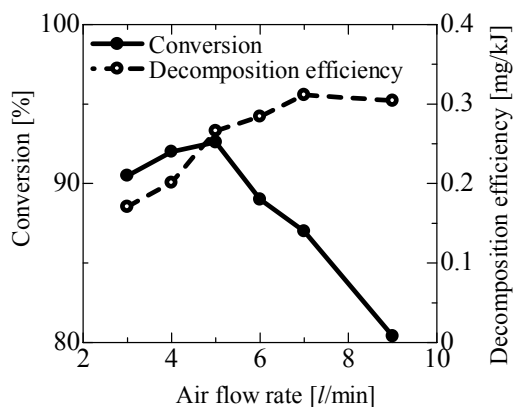


Fig. 3 Methyleneblue conversion and decomposition efficiency with air flow rate.

absorptiometry using methylene blue solution. In addition, the decomposing acetic acid is observed by ion chromatography.

3. Results and Discussion

Figure 2 shows the amount of dissolved chemical species such as hydrogen peroxide (H_2O_2), reactive oxidation species (ROS) and ozone (O_3) with applied voltage of 10 kV and applied frequency of 1000 Hz. The solution is purified water and the solution pH is adjusted by HCl and NaOH. The amount of dissolved H_2O_2 increases as pH increases. The ROS is effectively dissolved especially in acid solution. The dissolved ozone concentration is almost the same at any pH. This is because ozone, free radicals and UV generated by air plasma react with water droplet. Ozone decomposes by itself in water. Ozone self-decomposition reaction starts with (1) and (2).



O_2^- generated in (2) reacts with O_3 and the radical chain reaction starts. Reactive oxidation species such as OH are generated in this reaction. Finally, H_2O_2 is generated as the final product of this reaction. As shown in (1), the ozone self-decomposition reaction depends on pH and is enhanced in alkaline solution. Therefore, the H_2O_2 concentration increases especially in alkaline solution. On the other hand, the ROS increases especially in acid solution because HO_2 radicals are generated by (2) in H^+ rich solution.

Figure 3 shows an influence of the air flow rate on the methylene blue conversion and the decomposition efficiency. The maximum conversion is shown with air flow rate of 5 l/min. This is because the mist cannot be transported and water film generated on inner wall weakens the plasma in low air flow rate. On the other hand, the residence time of mist is insufficient in high air flow rate. So the methylene blue conversion decreases with air flow rate. The methylene blue decomposition efficiency increase as air flow rate increases. This is because the amount of transported mist increases.

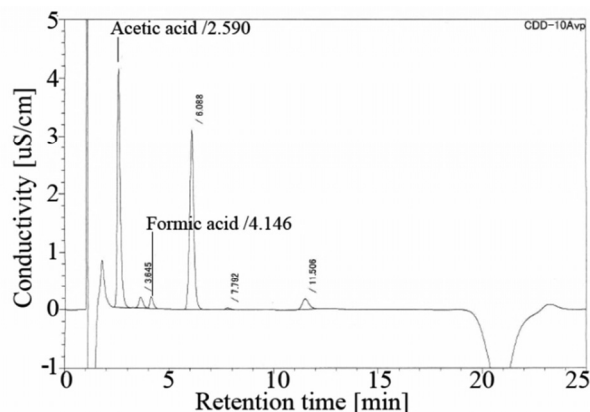


Fig. 4 Ion species generated in the acetic acid solution after plasma treatment.

Table 1 Concentration of acetic acid and formic acid before and after treatment (N.D. = Not detected).

	Concentrations [mg/l]	
	Acetic acid	Formic acid
Before treatment	68.3	N.D.
After treatment	65.8	0.565

Figure 4 shows the ion species in the acetic acid solution with plasma treatment. Ar is used as a carrier gas because the OH radical can be generated in Ar. The applied sinusoidal voltage is 12 kV and the frequency is 1000 Hz. The formic acid is generated from the acetic acid decomposition by OH radical.

Table 1 shows the concentrations of solution before and after treatment by the area of peaks in fig. 4. The initial concentration of acetic acid is equal to 68.3 mg/l and decreases to 65.8 mg/l after one treatment.

4. Concluding remarks

The results obtained in the present study are summarized as follows.

- (1) Reactive species including H_2O_2 , ROS and O_3 are dissolved in the droplets effectively. The amount of dissolved H_2O_2 increases as pH increases. ROS is dissolved especially in acid solution. The dissolved ozone concentration was almost the same at any pH.
- (2) The methylene blue solution is decomposed more than 90 % using newly developed air plasma reactor. The influence of the air flow rate on the methylene blue conversion and efficiency are experimentally clarified.
- (3) Acetic acid is also decomposed successfully using newly developed argon plasma reactor.

5. Acknowledgment

This work was partly supported by Grant-in-Aid for Challenging Exploratory Research (24656117) in JSPS and a Grant-in-Aid for JSPS Fellows (24·9008).

References

- [1] M. A. Malik, Plasma Chem. Plasma Process, no. 30, 21–31 (2010).

Synthesis of Functional Nano-Powder through Solution Precursor Plasma Spraying in a DC-RF Hybrid Plasma Flow System

Juyong Jang¹, Hidemasa Takana², Yasutaka Ando³, Oleg P. Solonenko⁴ and Hideya Nishiyama²

¹ Graduate School of Engineering, Tohoku University, 2-1-1 Katahira, Aoba-ku, Sendai, Japan

² Institute of Fluid Science, Tohoku University, 2-1-1 Katahira, Aoba-ku, Sendai, Japan

³ Faculty of Engineering, Ashikaga Institute of Technology, Ashikaga, Japan

⁴ Khristianovich Institute of Theoretical and Applied Mechanics, SB RAS, Novosibirsk, Russia
jang@paris.ifs.tohoku.ac.jp

ABSTRACT

In the present study, a functional nano-sized TiO₂ coated by carbon black is synthesized through solution precursor plasma spraying in a DC-RF hybrid plasma flow system. Carbon black helps TiO₂ to increase absorption of visible light irradiation, a functional nanohybrid powder at a mixture ratio of 0.1 was shown in higher photocatalytic activity though photodegradation of methylene blue solution than pure TiO₂ under visible light irradiation.

1. Introduction

Titanium dioxide (TiO₂) is an attractive material for environmental applications commercially used as a photocatalytic material because of its outstanding physicochemical properties. However, TiO₂ is active only under ultraviolet light irradiation because of its wide band gap. Many works were focused on the preparation to obtain functional TiO₂ by coupling processes with metal and non-metal atoms. One of the remarkable authors prepared carbon coated TiO₂. The carbon coated TiO₂ showed that a photocatalytic activity in the decomposition of methyl orange under UV irradiation depended on the ratio of TiO₂ to carbon [1].

In this study, TiO₂ combined with carbon black was synthesized by solution precursor spraying into plasma flow in a DC-RF hybrid plasma flow system in order to carry out a highly photocatalytic activity under visible light irradiation. Physicochemical characteristics of functional TiO₂ coated by carbon black were investigated and kinetics of methylene blue degradation for photocatalytic activity of functional TiO₂ coated by carbon black was analyzed under visible light irradiation.

2. Experimental setup

Figure 1 shows a schematic of a DC-RF hybrid plasma flow system for solution precursor plasma spraying. The operating pressure of 250 torr is kept. A DC power of 1.1 kW and an RF power of 6.6 kW (4 MHz) are supplied to this system. The working gas is argon. The flow rates of DC plasma forming gas and swirling sheath gas are 5 and 20 Sl/min, respectively. A two-phase atomizer (YS-03, Yaezaki, Japan) is installed at $r = 95$ mm and $z = 195$ mm in order to spray a solution precursor into downstream plasma flow. Atomizing gas of the atomizer is kept at 6 Sl/min during spraying. Further details of this system can be obtained from Refs. [2] to [5].

A solution precursor of titanium tetrabutoxide (TTB, TiO₄C₁₆H₃₆, Wako Pure Chemicals Industries, Ltd.) is used to synthesize functional nano-sized TiO₂ coated by carbon black (TiO₂-CB). Mixture solution precursor (MSP) that TTB is diluted in ethanol is prepared to form smaller its droplets. Mixture ratios of TTB to ethanol for

MSP preparation are 0.25, 0.125, and 0.1. The MSP with mass flow rate of 1.6 g/min on average is sprayed by the two-phase atomizer at $z = 195$ mm.

A functional TiO₂-CB powder is synthesized from MSP in plasma flow and collected at the chamber wall. All of such powders are annealed for two hours at 573 K. Physicochemical characteristics of functional TiO₂-CB powder are evaluated by UV-visible spectroscopy (V-7200, JASCO Inc., Japan) and morphological analysis of that is carried out by scanning electron microscopy (SEM, SU6600, Hitachi Inc., Japan). Additionally, its photocatalytic activity is assessed by photodegradation rate of methylene blue solution under visible light irradiation.

3. Experimental results and discussion

Figure 2 shows optical spectra measured at $z = 70$ mm with and without MSP spraying. After droplets of the MSP are successfully vaporized in the downstream plasma flow, vapor is rise to upstream plasma flow below the RF coils by characteristic backflows and successfully dissociated into titanium and carbon in the plasma flow and detected though a optical spectrum with MSP spraying [5].

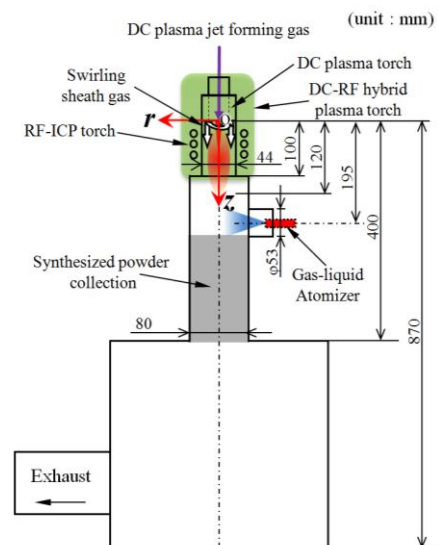


Fig. 1 Schematic of a DC-RF hybrid plasma flow system for solution precursor plasma spraying

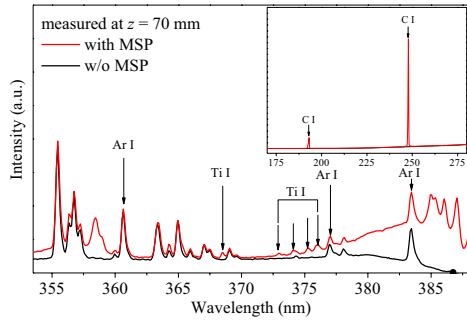


Fig. 2 Optical spectra measured at $z = 70$ mm with and without MSP spraying

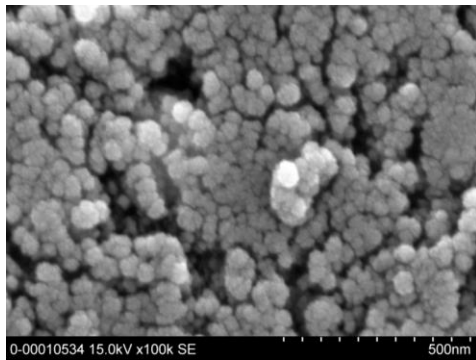


Fig. 3 SEM micrograph of functional TiO_2 -CB powder at a mixture ratio of 0.25

Figure 3 shows a SEM micrograph of a functional TiO_2 -CB powder at a mixture ratio of 0.25. SEM micrographs of synthesized all functional TiO_2 -CB powders are shown similarly. Functional TiO_2 -CB particles with a particle size of several ten nanometers are easily formed to agglomerated large particles due to strong Van der Waals force of attraction between carbons.

Figure 4 shows optical absorption spectra of TiO_2 -CB powders depending on mixture ratios of TTB to ethanol. In the case of a mixture ratio of 0.1, absorption spectrum is similar to typical anatase-phase TiO_2 . In the cases of higher mixture ratios of 0.25 and 0.125, increase of absorption range toward visible light may be explained by overlapping absorption spectra of CB and TiO_2 [1]. Optical absorption spectra are sensitively changed by depending on mixture ratios.

Figure 5 shows photodegradation of methylene blue solution under only visible light irradiation. While photocatalytic activity of pure TiO_2 with anatase-phase is lower efficient for photodegradation of methylene blue solution, functional TiO_2 -CB powders are more efficient. This means CB coated helps TiO_2 to be more photocatalytically active under visible light irradiation. Photodegradation of methylene blue solution by only visible light irradiation follows the pseudo-first-order kinetics, as following equation;

$$\ln\left(\frac{C_0}{C}\right) = k_{app}t, \quad (1)$$

where C_0 is the initial concentration of methylene blue solution at $t = 0$, C is the evolutionary concentration of that, k_{app} is the apparent pseudo-first-order rate constant, and t is time [1]. A rate constant of functional TiO_2 -CB

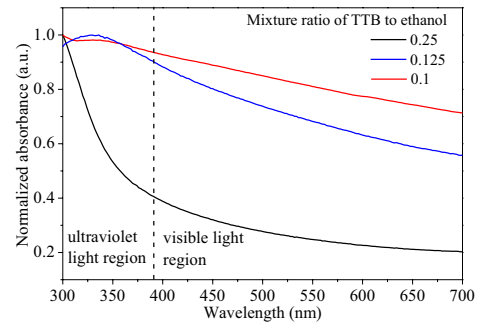


Fig. 4 Optical absorption spectra of functional TiO_2 -CB powders depending on mixture ratios

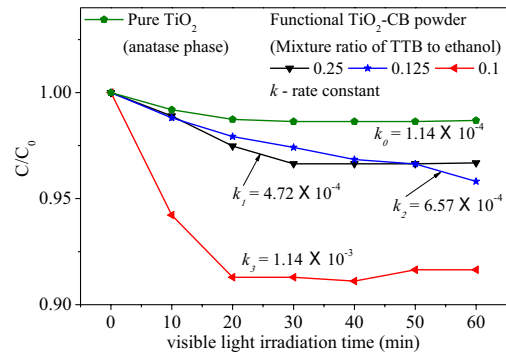


Fig. 5 Photodegradation of methylene blue solution under only visible light irradiation

powder at a mixture ratio of 0.1 is ten times higher than that of pure TiO_2 under visible light irradiation.

4. Conclusions

In the present paper, functional TiO_2 -CB powders are synthesized by solution precursor plasma spraying in the DC-RF hybrid plasma flow system and investigated. The results are summarized as follows;

- Droplets of MSP spraying are vaporized and successfully dissociated in plasma flow. This is verified by the presence of titanium and carbon in the optical spectra.
- Optical absorption spectra of functional TiO_2 -CB powders are sensitively changed by mixture ratios of TTB to ethanol.
- Functional TiO_2 -CB powders are more effective for photodegradation of methylene blue solution than pure TiO_2 under visible light irradiation.

References

- [1] Y. Li, X. Li, J. Li and J. Yin, Water research, **40** (2006), pp.1119-1126.
- [2] H. Nishiyama, M. Onodera, J. Igawa and T. Nakajima, et al, J. Therm. Spray Tech., **18-4** (2009), pp. 593-599.
- [3] H. Takana, J. Jang, J. Igawa, T. Nakajima, O. P. Solonenko and H. Nishiyama, et al, J. Therm. Spray Tech., **20-3** (2011), pp. 432-439.
- [4] J. Jang, H. Takana, O. P. Solonenko, and H. Nishiyama, et al, J. Fluid Sci. & Tech., **6-5** (2011), pp.729-739.
- [5] J. Jang, H. Takana, S. Park and H. Nishiyama, J. Therm. Spray Tech., (2012), on-line

Conditional Spatial Correlation of Velocity Fluctuation in Supersonic Flow with Transverse Injection

Shohei Uramoto, Toshinori Kouchi, Goro Masuya
Department of Aerospace Engineering, Tohoku University
6-6-01, Aramaki-aza-Aoba, Aoba-ku, Sendai, Miyagi, 980-8579, Japan
uramoto@scrj.mech.tohoku.ac.jp

ABSTRACT

We measured the velocity field induced by the transverse injection into a supersonic flow to investigate relation between the upstream boundary layer and downstream other flowfield. We calculated single-time two-point spatial correlations taking the reference point in the upstream boundary layer. The streamwise velocity fluctuation of the upstream boundary layer had strong correlation with ones near the bow shock wave and the jet flow. Furthermore, we conditioned the instantaneous velocity by the bow shock position and calculated spatial correlations, but we could not find clear difference between two conditional correlations.

1. Introduction

As a propulsion system of hypersonic flight vehicles, a supersonic combustion ramjet (scramjet) engine has been studied. The Flow in the combustor of this engine is supersonic and the time for mixing fuel and air is very short. Therefore, a fuel injection and mixing are required to be highly efficient.

Transverse injection into a supersonic flow from the wall is one of the typical injection methods. This injection method causes large pressure losses by the bow shock wave in the airflow, Mach disc in the fuel jet and so on. However, it had high penetration of fuel into the mainstream and induces a three dimensional disturbance to enhance the mixing.

For efficient fuel mixing, Shida [1] changed configuration of the injector-side wall from flat one to a riblet shape (Height: 2.8 mm). He measured density of this flowfield by planer laser induced fluorescence (PLIF) technique. He found that the jet penetration became higher when the riblet wall was used and suggested that the surface flow induced by the riblet caused this improvement. This result showed that disturbance in the upstream boundary layer could change the penetration and mixing characteristics of jet.

In the present study, we measured the velocity field around the injection port by a stereoscopic particle image velocimetry (SPIV) and investigated relation between the upstream boundary layer and downstream other flowfield induced by injection by taking single-time two-point spatial correlation of fluctuation velocity. In addition, we conditioned the instantaneous velocity by the bow shock position and calculated spatial correlation to obtain further information about turbulent structure of this flowfield.

2. Experimental equipment and Calculate method

We used a suction-type supersonic wind tunnel with a two-dimensional Laval nozzle. The nominal Mach number of the mainstream was 2.0. A seeding chamber was placed at the entrance of the nozzle to supply tracer particles into the mainstream for SPIV.

The test section had a 30-mm square cross section and was 290 mm long. The walls of the test section were made of transparent acrylic resin. The wall with the injection hole was made of red acrylic resin to reduce

the reflection of laser sheet light. The diameter of injection hole was 2.5 mm. It was located on the center line of the lower wall at 75 mm downstream from the entrance of test section. The jet-to-mainstream momentum flux ratio is 1.96 ± 0.02 . The SPIV system used a double-pulse Nd-YAG laser (wave length: 532 nm, power: 15 mJ/pulse, frequency: 15Hz) as a light source. The tracer particles were droplets of dioctyl sebacate (density: 913.5 kg/m^3 of about $1 \mu\text{m}$ diameter [2]) produced with a Laskin nozzle in the mist generator. Other measurement conditions of SPIV are shown in Table 1.

Table 1. Measurement conditions of SPIV

Camera Configuration	Scheimpflug	
Camera Angle	27	[deg]
Lens Tilt angle	8	[deg]
Aperture	6.7	
Number of Picture pairs	1700	[pairs]
Laser Delay Time	300	[ns]
Thickness of Laser Sheet	1	[mm]

The original point is located on the center of the injection hole. x , y and z indicated streamwise, transverse and spanwise. The single-time two-point spatial correlation $C_{u_i u_j}$ is calculated by Eq. (1). Point (x, y) is a location of reference point of spatial correlation. Δx and Δy are distances from the reference point, respectively. We took reference point that is half height of the upstream boundary layer to investigate the relation of the velocity fluctuations in the upstream boundary layer and the injection flow. In this equation, u , v and w are streamwise, transverse and spanwise component velocities, respectively.

$$C_{u_i u_j}(x, y; \Delta x, \Delta y) = \frac{\frac{1}{N} \sum_{n=1}^N [u'_{i,n}(x, y) \cdot u'_{j,n}(x + \Delta x, y + \Delta y)]}{u_{i_rms}(x, y) \cdot u_{j_rms}(x + \Delta x, y + \Delta y)} \quad (1)$$

$(u_i, u_j; u, v, w)$

u'_i : velocity fluctuation of u_i
 u_{i_rms} : root-mean-square of u'_i

3. Results and Discussion

Figure 1 showed the non-conditional single-time two-point spatial correlation of velocity fluctuation: C_{uu} . Symbol + shown in Fig. 1 is the reference point of the

correlation. Figure 1 indicates that streamwise velocity fluctuation in the upstream boundary layer had strong correlation with the regions near the bow shock wave and along the jet flow. There was no strong correlated region with the upstream boundary layer for fluctuations of other velocity components, C_{vv} and C_{ww} . So, we selected only the streamwise velocity to calculate the conditional spatial correlation. At the point shown by symbol \circ in Figs. 1 and 2, we conditioned the instantaneous streamwise velocity whether the bow shock wave passed through the point or not, because the non conditional correlation in Fig. 1 shown strong correlation among the upstream boundary layer and the bow shock wave and the jet flow.

Figure 2 show the conditional spatial correlations C_{uu} . Condition (a) and (b) correspond to the upstream and downstream bow shock wave position comparing with its mean value at the circle point in Fig. 2, respectively. An instantaneous velocity was classified into condition (a) when the streamwise component was less than 480 m/s, and into condition (b) when u was more than 510 m/s at the conditioning point. The data number was 246 for condition (a) and that was 229 for condition (b). The regions enclosed by the black solid lines in Fig. 2 had a strong correlation with the reference point.

In condition (a), the region above the injection hole had a strong positive correlation. Because the penetration height increased comparing with its mean value, the streamwise velocity fluctuation at this region became negative, and the velocity fluctuation had negative value in condition (a) at the circle point. It suggested that the penetration height increased when the bow shock wave moved to upstream. In condition (b), the region above the injection hole also had strong correlation region with the reference point because the penetration height changed from its mean value. Thus, the velocity fluctuation in the upstream boundary layer had the relation with the penetration height of jet.

When we qualitatively compared correlations for conditions (a) and (b), we could not find clear difference between them. Such low sensitivity of the flow field to the position of the bow shock wave may be the result of its continuous movement about its mean position. Therefore, the bow shock wave position is not suitable as a conditioning parameter.

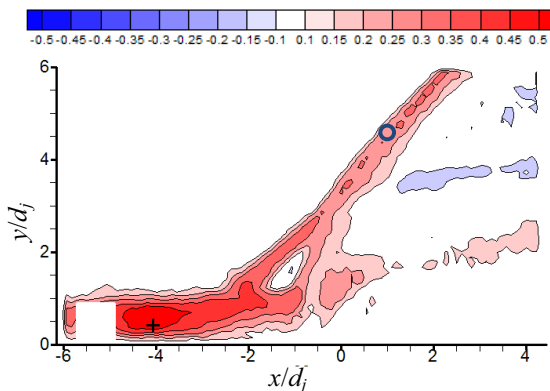


Fig. 1 Non-conditional spatial correlation C_{uu}

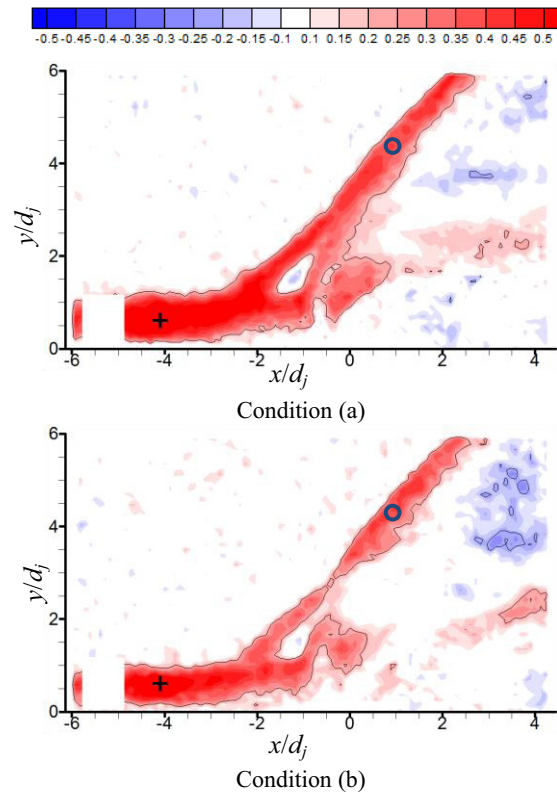


Fig. 2 Conditional spatial correlation C_{uu}

4. Concluding remarks

We measured the velocity field with transverse injection by SPIV and calculated the conditional single-time two-point spatial correlations of velocity fluctuations. The following results were obtained.

- The streamwise velocity fluctuation of the upstream boundary layer had strong correlation with one near the separation shock wave, the bow shock wave and the jet flow.
- The velocity fluctuation in the upstream boundary layer had the relation with the penetration height of jet.
- In this condition, we could not find clear difference between two conditions because such low sensitivity of the flow field to the position of the bow shock wave may be the result of its continuous movement about its mean position.

Acknowledgments

This work was supported by the MEXT in Japan, Grant-in-Aid (B), 20360081.

References

- [1] S. Shida, Bachelor thesis, Department of Aerospace Engineering, Tohoku University, 2007. (in Japanese)
- [2] E. Kitamura, M. Matsumoto, S. Koike, G. Masuya, 30th Visualization Symposium, Visualization Society of Japan, 2002, pp. 189-192 (in Japanese)

Effect of Supersonic Micro Nozzle Shape on the Heat Transfer in a Surface Wall

Yuya Takahashi¹, Junnosuke Okajima², Atsuki Komiya², Shigenao Maruyama²

¹Graduate School of Eng., Tohoku Univ., Sendai, 980-8579

²Institute of Fluid Science, Tohoku Univ., Sendai, 980-8577

yuya@pixy.ifs.tohoku.ac.jp

ABSTRACT

In this study, micro scale cooling device using supersonic flow was studied. Numerical simulations were conducted to reveal the effect of nozzle shape for supersonic air flow in micro nozzle under the heated walls by using ANSYS FLUENT 12.1 with Roe-FDS method. The channel size is about 100 μm in width, 1600 μm in length, and its wall condition is isothermal ($T_{\text{wall}}=400\text{ K}$). The Nusselt number Nu is estimated from the calculated values to evaluate the cooling ability of the supersonic micro nozzle flow. From the results, the Laval nozzle has great ability for cooling device.

1. Introduction

In recent years, the power density of integrated circuit such as CPU comes up 1000 W/cm^2 with the increase of components per chip. It causes rise of energy consumption to cool the datacenters and its cost becoming big issue^[1]. Thus several researches about coolant, such as liquid, gas^[2] and two-phase^[1,3] flow have been conducted to improve cooling ability. However, these on-chip cooling systems are not enough to cool CPU, so in the present state, these are used with air conditioner and the integration degree is suppressed.

When this kind of small heat sources are treated as a target, downsized cooling devices are required. It can be achieved with the development of Micro Electro Mechanical System (MEMS) technology. In a micro channel, velocity and thermal boundary layers considerably affect inner flow because of its viscosity. The liquid cooling system requires higher energy to drive and two-phase cooling system has an issue about its instability^[3].

To decrease the driving energy, air flow which has low viscosity should be used as working fluid. Furthermore, to decrease the energy loss, closed cycle that performs heat transfer on the surface of the channel should be used in place of impingement type cooling system. In addition, air cooling can use the temperature drop due to an isentropic expansion and the supersonic flow can be generated under relatively low pressure. However the supersonic micro nozzle flow is affected by the boundary condition and the nozzle shape, the nozzle shape depend on the required flow condition. Hence, in order to design and optimize the cooling channel using supersonic flow, the both of heat transfer from the heated wall to supersonic flow and supersonic flow generated by the nozzle have to be considered simultaneously.

To develop an effective on-chip air cooling device, the effect of nozzle shape on heat transfer in a supersonic flow is discussed by the comparison between arc shape nozzle and traditional supersonic nozzle shape (Laval nozzle).

2. Calculation Method

2.1. Governing equations

The numerical simulations were conducted by

ANSYS FLUENT 12.1. The governing equations are equations of state, continuity, momentum and energy, which are expressed as,

$$\frac{dp}{p} = \frac{d\rho}{\rho} + \frac{dT}{T}, \quad (1)$$

$$\frac{\partial \rho}{\partial t} + \nabla \cdot (\rho \mathbf{v}) = 0, \quad (2)$$

$$\frac{\partial}{\partial t} (\rho \mathbf{v}) + \nabla \cdot (\rho \mathbf{v} \mathbf{v}) = -\nabla p + \nabla \cdot \mu \left\{ (\nabla \mathbf{v} + \nabla \mathbf{v}^T) - \frac{2}{3} \nabla \cdot \mathbf{v} \mathbf{I} \right\}, \quad (3)$$

$$\frac{\partial}{\partial t} (\rho E) + \nabla \cdot (\mathbf{v} (\rho E + p)) = \nabla \cdot \left(k_{\text{eff}} \nabla T + \left(\bar{\tau}_{\text{eff}} \cdot \mathbf{v} \right) \right), \quad (4)$$

$$E = h - \frac{p}{\rho} + \frac{v^2}{2},$$

where p , μ , I , $\bar{\tau}_{\text{eff}}$, k_{eff} and T_{ref} are static pressure, viscosity, unit tensor, share stress, effective thermal conductivity and reference temperature (298.15 K) respectively. The Roe's Flux Difference Splitting (Roe-FDS) method was used for discretization.

2.2. Calculation conditions

Two-dimensional calculation domains are shown in Fig.1(a) and (b). These meshes are created by ANSYS GAMBIT. Figure 1(a) shows simple arc geometry at throat and its size. The grid number is 100 in width, 320 in length. The cross section ratio of throat A^* to nozzle end A_e (A^*/A_e) is 0.8502 (85.02 μm) that is the value for $Ma=1.5$ on the isentropic flow.

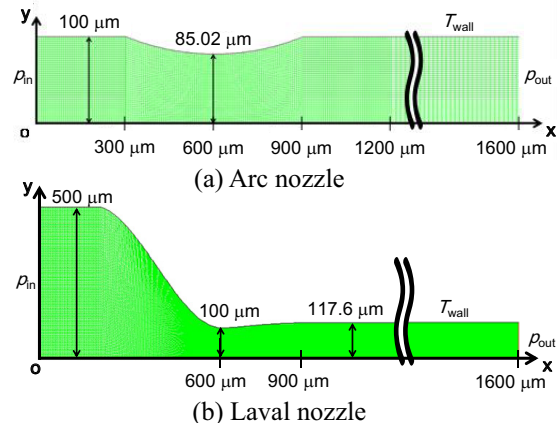


Fig. 1 Two dimensional calculation domains

Figure 1 (b) shows supersonic nozzle geometry and its size. The grid number is 100 in width, 456 in length. The shape of Laval nozzle is designed by Foelsch's method^[4] and the length of convergent section is 343.1 μm , width of nozzle end is 117.6 μm , namely A^*/A_c is same as the arc nozzle. The shape of divergent section is expressed by cubic function with 15 degree at inlet. The inlet and outlet pressures are 360 kPaA and 100 kPaA, and stagnation temperature and pressure are 300 K and 500 kPaA. The working fluid is air and the walls are assumed as isothermal ($T_{\text{wall}}=400$ K). The Reynolds number Re is about 5000 and the flow is assumed to be laminar. The temperature dependency of thermophysical properties of air is considered.

3. Results and Discussion

The calculated Mach number Ma and pressure p distributions are shown in Fig.2. Between two different nozzles, both of them show same tendency. Ma achieved to 1.0 at the throat ($X=600$ μm) and then still increased in the expansion section to 1.5 that is desired Mach number. Pressure distributions in a downstream show same tendency between two nozzles but there are about 100 kPaA different in the inlet region. This is caused by the difference of nozzle shape. The pressure loss on the Laval nozzle is lower than arc nozzle because it was designed from spread of expansion wave. This contributes to decrease of energy consumption and make the flow fast. In fact, Fig.2 shows Ma in Laval nozzle is larger than that of arc nozzle. In addition, temperature ratio to stagnation on the state in Ma under the quasi-one-dimensional steady isentropic flow is expressed as

$$\frac{T_0}{T} = 1 + \frac{\gamma-1}{2} Ma^2, \quad (5)$$

where γ is specific-heat ratio. This equation describes that temperature becomes lower as Ma increases. The lower temperature makes heat transfer on the surface walls increase. This is described by following eqs. (6)–(7). The above suggests that supersonic flow in a Laval nozzle has a great potentiality of cooling. However the flow detail such as an interaction between the heated walls and flow is unknown.

The Nusselt number Nu was estimated from following equations.

$$T_b = \frac{\int \rho \cdot C_p \cdot u \cdot T}{\int \rho \cdot C_p \cdot u}, \quad (6)$$

$$Nu = -\theta'(1), \quad \theta\left(\frac{y}{H}\right) = \frac{T - T_w}{T_b - T_w}, \quad (7)$$

where T_b , C_p , u and H are bulk mean temperature, specific heat, velocity, channel width, respectively. The Nu and the T_b distributions in downstream of the nozzle are shown in Fig. 3. Both of nozzles have a same tendency. However the Nu distributions of Laval nozzle are higher than that of arc nozzle because of its low temperature and the values are twice as large as theoretical ones ($=7.54$) for the forced convection in a parallel plated under the isothermal wall condition.

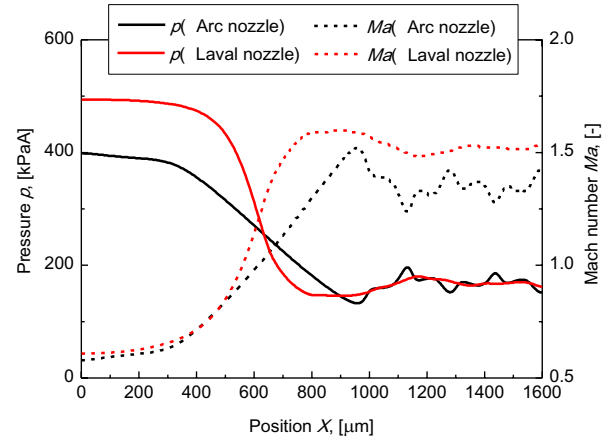


Fig. 2 Mach number Ma and pressure p distributions

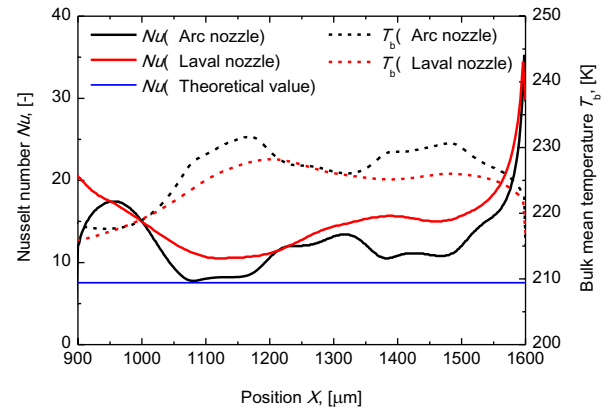


Fig. 3 Nusselt number Nu and bulk mean temperature T_b distributions in downstream of the nozzle

The rapid increase of Nu from 600 μm to 700 μm is caused by the expansion in the outlet region.

4. Concluding remarks

In this study, supersonic micro nozzle flows were analyzed under different nozzle shape to propose the micro sized on-chip cooling device using supersonic air flow. Then the values of Nu were compared on different nozzles and knowledge was obtained as follows.

- (1) The lower bulk mean temperature T_b distributions of supersonic flow by Laval nozzle makes great potentiality for the heat transfer on the surface wall.
- (2) The Nu in downstream of the Laval nozzle is double of theoretical value on laminar convective heat transfer. However, the optimum shape of the nozzle for cooling device is still unknown.

References

- [1] J.B. Marcinichen, J. A. Olivier, J. R. Thome, Applied Thermal Engineering (2012), pp.1–16.
- [2] C. Hong, Y. Asako, J. Lee, Int. J. Thermal Sciences 46 (2007), pp.1153–1162.
- [3] J. Xu, G. Liu, W. Zhang, Q. Li, B. Wan, Int. J. Multiphase Flow 35 (2009), pp.773–790.
- [4] J. Conrad Crown, NACA Technical note No.1651 (1948), pp.8–15.

Wheel Design for Planetary Rovers Traveling over Loose Soil

Masataku Sutoh, Keiji Nagatani, and Kazuya Yoshida

Graduate School of Engineering, Tohoku University, 6-6-01 Aoba Aramaki Aoba-ku, Sendai, Miyagi, 980-8579, Japan
sutoh@astro.mech.tohoku.ac.jp

ABSTRACT

The surfaces of the Moon and Mars are covered with loose soil. In such conditions, planetary rovers can get stuck and even cause failure of an exploration mission. To avoid such problems, the wheels of planetary rovers typically have lugs (i.e., protrusions) on their surface, which substantially improve their traveling performance. However, there exists no theoretical method to determine a suitable lug interval. In this study, we model the linear traveling speed of wheel equipped with lugs and provide fundamental guidelines for determining the lug interval on a wheel.

1. Introduction

Mobile robots, also called rovers, have played a significant role in NASA's Martian geological investigations. However, the Martian surfaces are covered with loose soil, and numerous steep slopes are found along their crater rims. In such conditions, rovers can get stuck and even cause mission failure. To avoid such problems, many research groups have studied the traveling performances of rovers on the basis of terramechanics [1, 2].

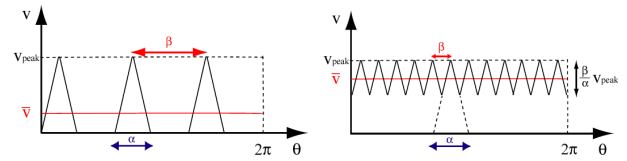
Terramechanics has mainly studied large vehicles, such as dump trucks. Lugs (i.e., protrusions) on the wheels of large vehicles have little influence on their traveling performances. On the other hand, it has been reported that lugs substantially influence the traveling performances of lightweight vehicles such as planetary rovers. However, from the point of view of designing wheels, there exists no theoretical method to determine a suitable lug interval.

The objective of this study is to provide guidelines for determining the lug interval on a wheel. To this end, we first model the linear traveling speed of a wheel, along with introducing the wheel models in terramechanics. Finally, we report traveling tests using a two-wheeled rover and verify the proposed model.

2. Linear traveling speed model of wheel with lugs

For a rover to travel over a slope, its wheel is required a force to pull its weight, called a drawbar pull. A wheel with lugs obtains its drawbar pull from shear stress developed by the surface of the wheel and lugs. However, over a steep slope, where significant drawbar pull is required, the wheel surface could not generate enough drawbar pull to move the rover forward. Thus, only when the lugs contact with the ground, the rover moves; the rover's linear traveling speed periodically changes in cycle corresponding to lug interval.

Assuming that the peak values of the linear speed would be the same for wheels with different lug intervals, the relationship between the rotation angle of the wheel, θ , and the linear speed, v , of the wheel over a steep slope is obtained, as shown in Fig.1. In the figure, α denotes an angle where lugs develop thrust and β denotes an angle between lugs (see Fig.2). According to Fig.1, when β is greater than α , using the peak speed, v_{peak} , the mean linear speed \bar{v} of the wheel is calculated



(a) In case $\beta > \alpha$. (b) In case $\beta \leq \alpha$.
Fig. 1 Linear traveling speed of wheel with lugs.

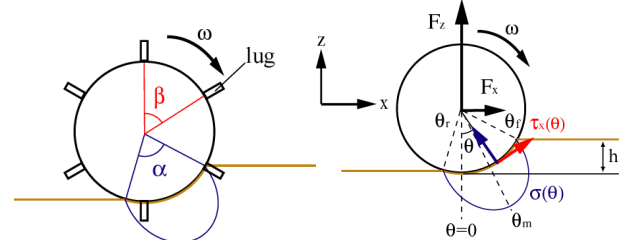


Fig. 2 Overview of α and β .

Fig. 3 Wheel model.

as

$$\bar{v} = \frac{1}{2} \frac{\alpha v_{peak} \times \frac{2\pi}{\beta}}{2\pi} = \frac{1}{2} \frac{\alpha}{\beta} v_{peak} \quad (1)$$

On the other hand, when β is smaller than α , \bar{v} is calculated as

$$\bar{v} = \frac{2\pi v_{peak} - \frac{1}{2} \frac{\beta}{\alpha} v_{peak} \beta \times \frac{2\pi}{\beta}}{2\pi} = v_{peak} \left(1 - \frac{1}{2} \frac{\beta}{\alpha} \right) \quad (2)$$

Using Eqs. (1) and (2), the relationship between α/β and \bar{v}/v_{peak} is obtained as a curve shown in Fig.5. According to the curve, when α/β is smaller than 2, shorting the lug interval substantially contributes to improving the mean speed. On the other hand, when α/β is greater than 2, it only slightly improves the mean speed. From this finding, we believe that if the lugs are at least equipped with an interval of $\alpha/2$ on a wheel, the wheel will have a high traveling performance.

3. Estimation of stress distribution beneath wheel

As mentioned above, α , the angle where lugs develop thrust (see Fig.2), is a key parameter to determine a suitable lug interval. We considered α as the range where normal stress is generated beneath the wheel. Therefore, α can be estimated on the basis of the terramechanical normal stress distribution models. In this section, we discuss α of a wheel, along with introducing the terramechanical wheel models.

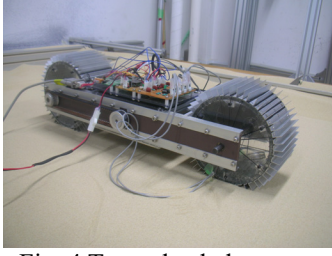


Fig. 4 Two-wheeled rover.

3.1 Stress distribution models

When a wheel without lugs travels over loose soil, a normal σ and a shear stresses τ_x , are generated beneath it (see Fig. 3). In terramechanics, the normal stress σ is determined from the following equation [1]:

$$\sigma(\theta) = \sigma_{\max} [\cos \theta - \cos \theta_f]^n \quad (\theta_m \leq \theta \leq \theta_f)$$

$$\sigma(\theta) = \sigma_{\max} \left[\cos \left\{ \theta_f - \frac{\theta - \theta_r}{\theta_m - \theta_r} (\theta_f - \theta_m) \right\} - \cos \theta_f \right]^n \quad (\theta_r \leq \theta \leq \theta_m) \quad (3)$$

where σ_{\max} denotes the maximum stress, which is derived using soil parameters; θ_f and θ_r denote the entry angle and departure angle of the wheel, respectively (see Fig. 3).

The shear stress τ_x beneath a wheel was formulated as follows [1]:

$$\tau_x = (c + \sigma(\theta) \tan \phi) \left[1 - e^{-j_x(\theta)/k_x} \right] \quad (4)$$

where c denotes the cohesion stress of the soil, ϕ is the internal friction angle of the soil; k_x and j_x are the shear deformation modulus and the soil deformation, respectively.

3.2 Vertical force model

The vertical force F_z of wheel is obtained by integrating the vertical components of σ and τ_x from the entry angle θ_f to the departure angle θ_r , as follows [1]:

$$F_z = rb \int_{\theta_f}^{\theta_r} \{ \tau_x(\theta) \sin \theta + \sigma(\theta) \cos \theta \} d\theta \quad (5)$$

where b and r denote the wheel width and wheel radius, respectively.

Considering a case that F_z equals to normal load of wheel, using Eqs. (3), (4), and (5), we can estimate the normal and shear stress distributions beneath a wheel without lugs. Assuming that the normal stress distribution is roughly the same for a wheel with or without lugs, by estimating σ , we can obtain α and determine the suitable lug interval for the wheel from a curve in Fig. 5.

4. Verification experiments

To verify the linear traveling speed model, we performed traveling tests using a two-wheeled rover with various wheels. In this section, the experiments and experimental results are reported in detail.

4.1 Two-wheeled rover

We developed a two-wheeled rover with interchangeable wheels (see Fig.4). The distance between the front and rear wheels of the rover was 400 mm, and the rover weight was set to 4.0 kg for different wheel types. Furthermore, eight wheel types were developed. They have a diameter of 150 mm and a width of 100 mm, and two different lug heights (5 and

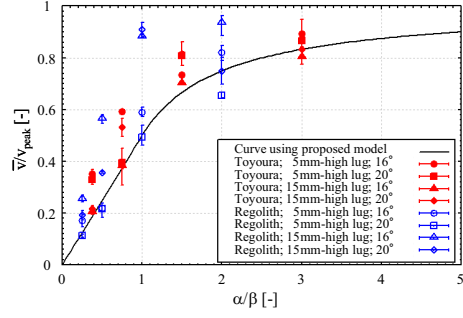


Fig. 5 α/β vs. v/v_{peak} ; model and experimental data.

15 mm) and four different lug intervals ($\beta = 120, 60, 30$ and 15°).

4.2 Experimental overview and conditions

The two-wheeled rover, with the eight types of wheels, was used to perform traveling tests in sandboxes. Each sandbox has a length, width, and depth of 1.5 m, 0.3 m, and 0.2 m, respectively, and was filled with Toyoura sand/lunar regolith simulant. In the tests, the sandbox was inclined at 16 and 20° . The angular speed of the wheel was fixed at 2.50 rpm, and we measured the linear traveling speed of the rover. Each trial was conducted under identical soil conditions, and three trials were conducted for each condition.

4.3 Experimental results and discussion

To verify the proposed linear traveling speed model, we plotted the experimental data superimposing a curve derived from the proposed model in Fig.5. Here, α of the wheel on Toyoura sand/lunar regolith simulant was calculated using Eqs. (3), (4), and (5).

According to the figure, it was found that experimental data corresponds with the curve derived from the proposed model. Thus, the model was validated and we concluded that if the lugs are at least equipped with an interval of $\alpha/2$, i.e., $\alpha/\beta \geq 2$, on a wheel, the wheel will have a high traveling performance.

5. Concluding remarks

In this study, the linear traveling speed of a wheel with lugs was modeled, along with introducing the wheel models in terramechanics. To verify the proposed model, we performed traveling tests using a two-wheeled rover with various wheels. From the validated model, it was found that when a wheel has at least two lugs in a range where normal stress is generated beneath it, it has a high traveling performance.

6. Acknowledgements

This work was partially supported by Tohoku University Global COE Program on World Center of Education and Research for Trans-disciplinary Flow Dynamics.

References

- [1] J. Y. Wong, Theory of Ground Vehicles Third edition, Wiley-Interscience, New York (2001).
- [2] K. Iagnemma, and S. Dubowsky, Mobile Robots in Rough Terrain, Springer, New York, (2004).

The Numerical Setup of Conditions for Point Energy Release in Water

Daiki Ishikawa¹, Mingyu Sun²

¹Department of Aerospace Engineering, Graduate School of Engineering, Tohoku University,
6-3, Aramaki aza aoba, Aoba-ku, Sendai 980-8578, Japan

²Institute of Fluid Science, Tohoku University, 2-1-1, Katahira, Aoba-ku, Sendai 980-8578, Japan
ishikawa@iswi.cir.tohoku.ac.jp, sun@fmail.ifs.tohoku.ac.jp

ABSTRACT

Point energy release in water is a model of the early stage of laser breakdown in water. The model is indispensable in the simulation of the laser induced underwater phenomenon. In this study, we first constructed a series of equations of states for real water and steam, covering a wide range for temperature and pressure. We further developed a physical model for the setup of initial conditions for the point energy release. Using these models, the mechanism of point energy explosion in water was investigated. The equations of states under consideration can be used to the simulation of both cavitation and boiling phenomenon.

1. Introduction

It is essential to clarify the mechanism of bubble formation in water after a rapid energy release, which is the early stage of the Laser-Induced Liquid Jet [1]. Previous studies have used equations of state of Tait, ideal gas, linearized equation of internal energy or database for the simulation of water and steam [2-5]. However, these equations are not adequate for the efficient and accurate analysis of the phenomenon in the problem of laser irradiation. For instance, the Tait EOS is valid for very high pressures under the constant temperature. The database [5] covers a large range of temperature under 1 GPa.

In this study, we try to construct an equation of state for real water based a modified Tait EOS that covers a much high temperature range. Furthermore, a model of the initial states of a point energy release in water has been proposed based on the conservation laws. The initial states are necessary for the startup of numerical simulation for laser-induced compressible fluids.

2. Construction of the equations of states for real water and steam

In this study, Eq. (1) is used as a fitting function for all analytical expressions:

$$f(T) = \sum_{i=0}^6 a_i T^i. \quad (1)$$

Eq. (2), (5)-(7) are proposed EOS and analytical expressions of specific internal energy for water and steam considering dependence of both of temperature and density. These temperature-dependent terms are fitted using the polynomial (1), based on the saturated states and initial room densities of water and steam. The fitted polynomials together with the database data are plotted in Fig. 1 and Fig. 2. Eq. (2) is a Tait equation extended from triple point to critical point ($n = 7.15$). Eq. (3), (4) are Virial equations introduced by Tanishita in 1944 [6].

Fitting coefficients a_i shown in Table. 1 are verified by high correlation from triple point to critical point. It is clear that these fitted formulas reproduce the physical data in the temperature range between 273.16K and 633.15K, from Fig 1, 2.

These equations are constructed as follows:

· Equation of states for water:

$$p(\rho, T) = K_p(T) \left\{ \left(\frac{\rho}{\rho_{lsat}(T)} \right)^n - 1 \right\} + p_{sat}(T), \quad (2)$$

· Equation of states for steam:

$$\begin{cases} p(\rho, T) = \rho RT (1 + \rho B(T)), & (3) \\ B(T) = -0.668 \left(\frac{T}{100} \right)^{-2.7} - 437 \left(\frac{T}{100} \right)^{-8.4}, & (4) \end{cases}$$

· Specific internal energy for water:

$$e(\rho, T) = e_{lsat}(T) + (\rho^{n-2} - \rho_{lsat}(T)^{n-2}) f_{la}(T) + (\rho^{-2} - \rho_{lsat}(T)^{-2}) f_{lb}(T), \quad (5)$$

$$= e_{lsat}(T) + f_{l1,2}(T), \quad (6)$$

· Specific internal energy for steam:

$$e(\rho, T) = e_{gsat}(T) + (\rho - \rho_{gsat}(T)) f_g(T). \quad (7)$$

3. Point Energy Release Model

We consider the following processes. First some amount of water of a small area Ω_0 that absorbs energy E_a is assumed to be saturated. The saturated state is compressed by an isothermal process, to initial density ρ_0 , because the mass of water remain constant if chemical process is neglected. If we consider that the water of the area is being compressed from an initial state with temperature T_0 , pressure p_0 , density ρ_0 , specific internal energy e_0 and volume Ω_0 , to a final state with T_1 , p_1 , $\rho_1 = \rho_0$, e_1 and Ω_1 , the mass and energy conservation laws are

$$\rho_0 \Omega_0 = \rho_1 \Omega_1, \quad (8)$$

$$\rho_0 \Omega_0 e_0(\rho_0, T_0) + E_a = \rho_1 \Omega_1 e_1(\rho_1, T_1). \quad (9)$$

All thermodynamic functions for water can be solved by combining Eq. (2), (5), (6), (8) and (9). Fig. 3 shows T_1 and p_1 . These are used as the initial conditions for numerical methods in fluids.

4. Numerical analysis for point energy release

The phenomenon of the underwater explosion after the energy release is simulated by the two models following,

- 1) Point Energy Release Model,
- 2) Cavitation and Boiling Model.

Table. 1: Fitting coefficients a_i and correlation coefficient R (273.16K-647.096K) of functions of temperature in analytical expressions for water and steam

$f(T)$	a_0	a_1	a_2	a_3	a_4	a_5	a_6	R
$\ln(p_{sat})$	-7.045364×10	7.037878×10^{-1}	-2.716884×10^{-3}	6.064245×10^{-6}	-7.928070×10^{-9}	5.647571×10^{-12}	$-1.692521 \times 10^{-15}$	1.000
ρ_{tsat}	-3.726770×10^3	6.675586×10	-3.900921×10^{-1}	1.217122×10^{-3}	-2.146343×10^{-6}	2.018627×10^{-9}	$-7.918682 \times 10^{-13}$	0.993
$\ln(\rho_{gsat})$	-1.989760×10	-2.089313×10^{-1}	2.821146×10^{-3}	-1.168679×10^{-5}	2.365039×10^{-8}	$-2.390330 \times 10^{-11}$	9.685766×10^{-15}	0.987
e_{tsat}	1.232021×10^6	-3.329504×10^4	2.429734×10^2	-8.280355×10^{-1}	1.565437×10^{-3}	-1.560331×10^{-6}	6.444526×10^{-10}	0.999
e_{gsat}	-5.006823×10^7	7.730674×10^5	-4.691108×10^3	1.497363×10	-2.647511×10^{-2}	2.459928×10^{-5}	-9.396962×10^{-9}	0.988
K_p	-1.318904×10^{10}	1.648058×10^8	-8.279949×10^5	2.210894×10^3	-3.328391	2.670858×10^{-3}	-8.888164×10^{-7}	0.988
f_{11}	-7.246856×10^6	1.083304×10^5	-6.713922×10^2	2.208302	-4.055142×10^{-3}	3.925001×10^{-6}	-1.566144×10^{-9}	0.992
f_{12}	-6.017620×10^7	7.259707×10^5	-3.651604×10^3	9.818312	-1.488568×10^{-2}	1.206004×10^{-5}	-4.082380×10^{-9}	0.984
f_g	-2.213051×10^6	2.195612×10^4	-9.091751×10	1.987885×10^{-1}	-2.399263×10^{-4}	1.499730×10^{-7}	$-3.731245 \times 10^{-11}$	1.000

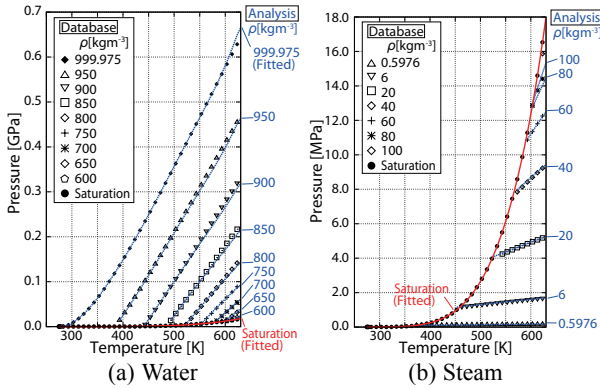


Fig. 1: Comparison between analytical equations of states (lines) and database [4, 5] (dots) of p - T diagrams for water and steam

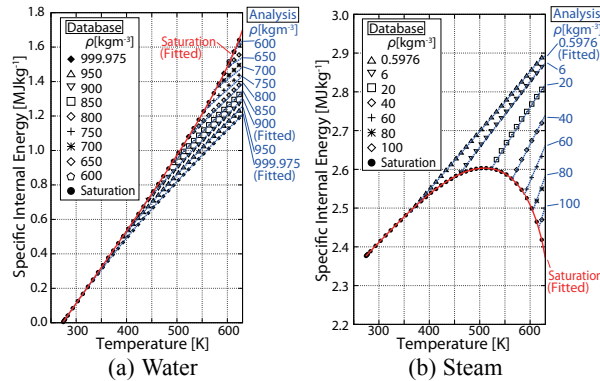


Fig. 2: Comparison between analytical expressions (lines) and database [4, 5] (dots) of e - T diagrams for water and steam

In cavitation and boiling model, Merkle cavitation model adapted to the two-fluid model [7] is improved for realistic fluids. The numerical method in fluids is based on a two-velocity two-pressure two-fluid model and Lagrange-Remap method [8, 9].

Fig. 4 shows an initial bubble formed by low pressure of the center of the explosion caused by the initial energy release in water. The water $T_0 = 293.15$ K, $p_0 = 0.101325$ MPa absorbed energy $E_a = 20$ mJ at a small area Ω_0 of a circle with a diameter of $400 \mu\text{m}$ in free space.

5. Conclusion

The equations of states of real water and steam for a wide range of temperature and pressure are constructed.

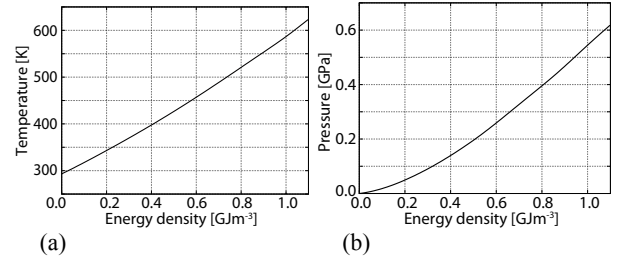


Fig. 3: Analytical results of initial conditions after point energy release in water are shown. Energy density E_a/Ω_0 is needed to be given. (a) Temperature T_1 calculated from Eq. (8) and (9); (b) Pressure p_1 at T_1 , ρ_1 calculated from Eq. (2). These values can be initial conditions for numerical methods in fluids.

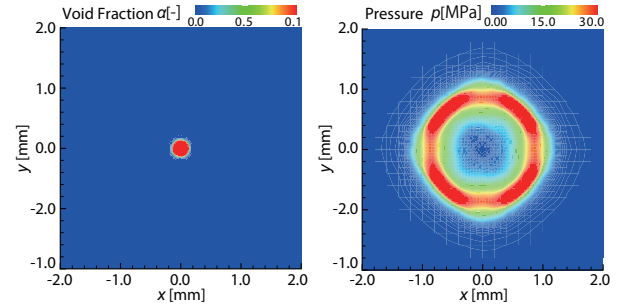


Fig. 4: An initial 2-D bubble (steam) is formed by low pressure caused by the initial energy release in water. Figures are shown at $t = 0.50 \mu\text{s}$.

We found that the model can predict the formation of steam bubble after energy release.

References

- [1] A. Nakagawa, T. Kumabe, Y. Ogawa, T. Hirano, M. Kanamori, R. Saito, M. Watanabe, T. Hashimoto, T. Nakano, T. Kamei, H. Uenohara, K. Takayama, T. Tominaga, *JJSLSM*, **30**, (2009), pp.119-125.
- [2] A.H.Koop, PhDthesis, Twente Univ. (2008), pp.39-51.
- [3] SCE ed., *Chem. Eng. Handbook* (1988), pp.6-106.
- [4] JSME ed., *JSME Steam Tables* (1999), pp.29-119.
- [5] W. Wagner, IAPWS-95 (2004).
- [6] H. Nakashima, H. Kondo, *Rep.Fac. Eng. Nagasaki Univ.*, **7** (1976), pp.21-25.
- [7] Y. Zhu, M. Sun, *Proc. AFI/TFI-2010* (2010), PS1-7.
- [8] M. Sun, *Proc. 24th CFD Symp.* (2010), A8-2.
- [9] K. Yada, M. Sun, *Proc. 24th CFD Symp.* (2010), C3-3.

Applications of LCS to the Study of Transport Trajectories in Space Mission

Kenta Oshima, Shintaro Wada, Tomohiro Yanao

Department of Applied Mechanics and Aerospace Engineering, Waseda University, Tokyo 169-8555, Japan

E-mail: kenta-oshima@akane.waseda.jp

ABSTRACT

This study is concerned with the construction of transport trajectories in the planar elliptic restricted three-body problem (ER3BP), a generalization of the planar circular restricted three-body problem (CR3BP). The main difficulty in designing trajectories in the ER3BP originates from the explicit time dependence of the system. We show that the method of Lagrangian coherent structures (LCS) and the symmetries of the system facilitate the construction of low-energy transport trajectories in the ER3BP. As an extension of this approach, we construct the horseshoe orbits in the ER3BP and discuss their practical issues.

1. Introduction

The circular restricted three-body problem (CR3BP) has been widely studied, and recently the systematic method of constructing low-energy transport trajectories has been established based on the tube dynamics and Poincaré sections method [1]. Extension of this method to the elliptic restricted three-body problem (ER3BP) is of practical and scientific interest. Major difficulty in the ER3BP is in the fact that the energy as well as tubes are time dependent [2].

Recently, the method of Lagrangian coherent structures (LCS) has been applied to reveal cross sections of tubes in the restricted three-body problem [2]. This indicates that one can infer the locations of the boundaries of tubes in the ER3BP for fixed values of true anomaly f and energy E on Poincaré sections, even though tubes pulsate periodically.

In this study, we construct low-energy transport trajectories in the planar ER3BP by using the method of LCS and symmetries of the dynamics. This approach turns out to be suitable to the construction of horseshoe orbits. Indeed, the horseshoe orbits are interesting from the viewpoints of natural science and space mission applications [3].

2. Method

The ER3BP assumes two heavy bodies m_1 and m_2 orbiting elliptically around their center of mass and asks for the motion of a light particle m_3 . In this study, m_1 , m_2 , and m_3 correspond to the Sun, Jupiter, and a spacecraft, respectively. Fig.1 shows the configuration of the system in a rotating frame, which fixes the positions of m_1 and m_2 .

We introduced Poincaré sections as shown in Fig.1 and computed LCS on the U3 section for fixed values of $f = -6.248$ and $E = -1.42$. The results are shown in Fig.2. We then made grid points of initial conditions in the rectangle, $0.03 \leq y \leq 0.07$, $-0.1 \leq x' \leq 0.1$, which is expected to have an overlap with the intersection of tubes on U3. These initial conditions are given with the energy in the range, $-1.45 \leq E \leq -1.4$, and integrated until they get to the U1 section. Out of the trajectories arrived at U1, we extracted those having small absolute values of x -velocity, x' , and f . We regarded these trajectories as “good initial guesses”, and differentially corrected them [1] until their values of x' and f converge to zero. By

virtue of the symmetry of the ER3BP, the trajectories obtained in this manner give rise to the transport trajectories as shown in Fig. 3(a), which start from the exterior region, passing through the m_2 realm, revolving around m_1 in the m_1 realm, passing through the m_2 realm again, and finally exits to the exterior region.

The transport trajectories obtained above are not periodic. One can take one of these trajectories as “good initial guess” and differentially correct it [1] to make the values of x' become zero at U4, and f become integer multiple of π at U4. By virtue of the symmetry of the ER3BP and the 2π -periodicity of the equations of motion with respect to f , the trajectory obtained in this manner gives rise to a periodic orbit called the horseshoe orbit (see Fig. 3(b)).

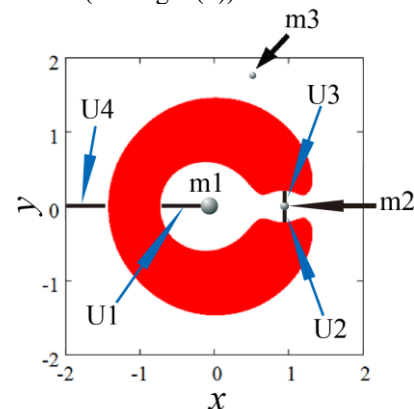


Fig. 1: The three bodies m_1 , m_2 , and m_3 in the ER3BP and the locations of Poincaré sections, U1, U2, U3, and U4. Energetically forbidden region is filled with red points.

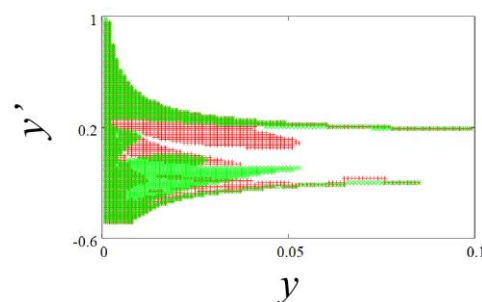


Fig. 2: LCS on U3 indicating the locations of the cross sections of the stable (red) and unstable (green) tubes on U3. (Their boundaries are not very clear. in this figure.)

3. Results and Discussion

We obtained the two transport trajectories as shown in Fig.3 based on the above procedures.

Practically, it is interesting to know the distribution of horseshoe-like orbits (quasi-horseshoe orbits) on U1. It should be noted that the quasi-horseshoe orbits (the blue points in Fig.4) having the same values of f and E as those of the horseshoe orbit, $f_h=0.0$ and $E_h=-1.4462$, distribute around the horseshoe orbit (the pink point in Fig.4) in an anisotropic manner on U1.

This is because such quasi-horseshoe orbits at U1 must be in the stable tube having f_h and E_h at U1, but not required to be in the unstable tube having f_h and E_h at U1. Indeed, the returned points of the quasi-horseshoe orbits on U1 are to be in the respective unstable tubes having the values of f and E of the returned points on U1. This situation can be verified in Fig. 5, where the values of f and E of the returned point and those of the corresponding unstable tube are $f=37.0737$ and $E=-1.4641$. It should be noted that the shape of the unstable tube has changed from Fig.5(a) to Fig.5(b) due to the time dependence.

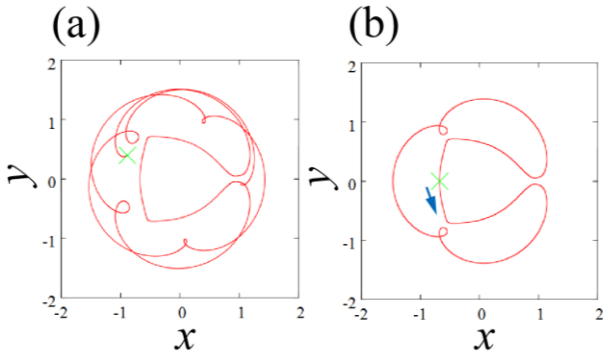


Fig. 3: (a) Transport trajectory (red) symmetrized with respect to U1 only. (b) Transport trajectory (red) symmetrized with respect to both U1 and U4 (horseshoe orbit). The green crosses represent the initial points.

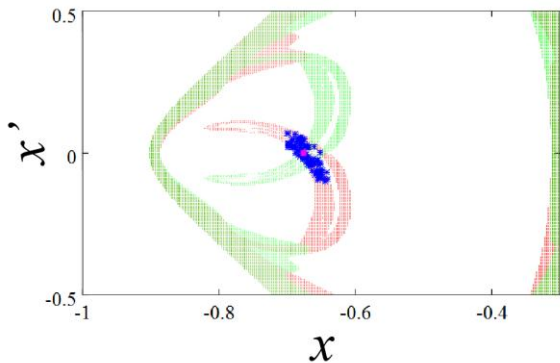


Fig. 4: The horseshoe orbit (pink) and quasi-horseshoe orbits (blue) on U1 superposed on the cross sections of stable (red) and unstable (green) tubes obtained by computing LCS for the values of f_h and E_h on U1.

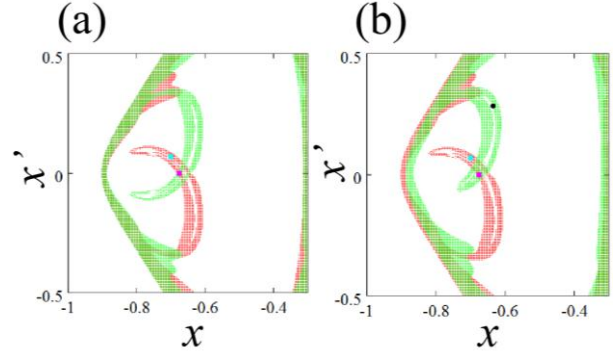


Fig. 5: (a) The horseshoe orbit (pink) lying in the intersection of stable (red) and unstable (green) tubes on U1. One quasi-horseshoe orbit (sky blue) lying inside the stable tube and outside the unstable tube. (b) The horseshoe orbit (pink), the stable tube (red), and the quasi-horseshoe orbit (sky blue) are the same as in (a). The returned point (black) lying in its corresponding unstable (green) tube after one revolution.

Thus, one should be careful enough to take into consideration the geometry of tubes in selecting initial conditions of quasi-horseshoe orbits. The distribution of quasi-horseshoe orbits in phase space around the horseshoe orbit can generally be anisotropic due to the explicit time dependence and nonlinearity of the ER3BP.

4. Concluding Remarks

This study has suggested a method of constructing low-energy transport trajectories in the planar ER3BP by using the method of LCS and symmetries of the system. The horseshoe orbits in the ER3BP have also been constructed as a natural extension.

For practical interest, we have explored the distribution of quasi-horseshoe orbits. It is important to note that the distribution of the quasi-horseshoe orbits is anisotropic on Poincaré sections because of the time dependence and nonlinearity of the system.

Finally, when a spacecraft is far from the heavy bodies, m_1 and m_2 , the planar model is a good approximation. However, when the spacecraft approaches the heavy bodies, the third dimension becomes important [1]. Thus, the extension of the present approach to the spatial model should be the next task to be solved.

References

- [1] W. S. Koon, M. W. Lo, J. E. Marsden, and S. D. Ross, *Dynamical Systems, the Three-Body Problem and Space Mission Design* (2005).
- [2] E. S. Gawlik, J. E. Marsden, P. C. Du Toit, and S. Campagnola, *Celest. Mech. Dyn. Astr.*, **103** (2009), 227-249.
- [3] J. M. Howsman, *Investigation of transfer trajectories to periodic horseshoe orbits*, Master thesis, Purdue University (2011).

Effects of Redox Cycling on the Mechanical Properties of Ni-YSZ Cermets for SOFC Anodes as a Function of Porosity

Taihei Miyasaka^a, Shinji Sukinou^a, Satoshi Watanabe^a, Kazuhisa Sato^b,
Tatsuya Kawada^a, Toshiyuki Hashida^b

^a Graduate School of Environmental Studies, Tohoku University.

6-6-11-709, Aza-Aoba, Aramaki, Aobaku, Sendai 980-8579, Japan

^b Fracture and Reliability Research Institute, Graduate School of Engineering
Tohoku University, 6-6-11-707 Aoba, Aramaki, Aoba-ku, Sendai, 980-8579, Japan

taihei.miyasaka@rift.mech.tohoku.ac.jp

ABSTRACT

Effects of redox cycling on the mechanical properties of the Ni-YSZ cermets were investigated by using a small punch (SP) testing method. The porosity range in the Ni-YSZ cermets tested in this study was 25-46%. Experimental results obtained from the in-situ SP tests demonstrated that ductile-like fracture under the reduction environment at 800°C and damage cause by redox cycling degraded the elastic modulus and fracture stress of the NiO-YSZ composites at low porosity. This study revealed that porosity makes a key contribution to the durability of Ni-YSZ cermets by the redox cycling.

1. Introduction

Solid Oxide Fuel Cell (SOFC) can realize very high power generation efficiency to convert the chemical energy of H₂ directly into electrical energy[1]. Thus, SOFCs are expected to become a major electric power sources in the future. Typical SOFC anodes are fabricated from a nickel oxide (NiO) / yttria-stabilized zirconia (YSZ) composites. When hydrogen fuel is supplied to the cell first time, NiO-YSZ composites is converted into Ni-YSZ cermets. Under normal operating conditions, fuel is supplied at the anode and Ni is kept in its reduced state. However, the Ni may reoxidize due to factors such as seal leakage, system shutdown or high fuel utilization. Thus, cyclic reduction and oxidation (redox) of the anode may occur commercial during SOFC operations. Many researchers have reported that Ni re-oxidation may cause a degradation or destruction of the cells[2,3]. However, the effect of redox cycling on the mechanical properties has not investigated yet, which is one of most important information for the reliability and durability of SOFCs. Therefore, it is important to be able to understand the change of mechanical properties of Ni-YSZ cermets during redox cycling.

The object of this work was to investigate on the relationship between mechanical properties of Ni-YSZ cermets and redox cycling, porosity, we evaluated the mechanical properties of the as-sintered NiO-YSZ composites, the reduced Ni-YSZ cermets and the re-oxidized NiO-YSZ by the in-situ small punch (SP) tests.

2. Method

2.1 Sample preparation

In this study, NiO (Sumitomo Metal Mining, Japan) and 8 mol% yttria-stabilized zirconia (YSZ) (Tosoh Co, Japan) and polymethylmethacrylate (PMMA) (Sekisui Plastics Co, Japan) were used as starting materials. The particle diameters of NiO, YSZ and PMMA are 0.48 μm, 90 nm and 2.5 μm. The volume fractions of Ni, YSZ and PMMA are shown Table 1. The powders were

Table 1 List of samples used in this study with details on volume fraction and porosity.

Ni/YSZ/PMMA fraction (vol. %)	Porosity (%)		
	As-sintered	Reduced	Re-oxidized
50 / 50 / 0	2.5	25.4	18.0
45 / 45 / 10	6.7	29.2	16.6
40 / 40 / 20	10.7	32.1	16.2
35 / 35 / 30	14.8	34.3	18.4
30 / 30 / 40	19.0	37.2	20.7
25 / 25 / 50	22.3	41.2	24.1
20 / 20 / 60	27.4	46.0	30.7

uniaxially pressed at 30 MPa into green compacts. The green bodies were then isostatically cold pressed at 100 MPa. After pressing, the samples were sintered in atmosphere condition at 1400°C for 3h. The heating rates for the sintering process were 200°C/h. The as-sintered samples were polished with 3 μm diamond paste and finally size were φ7.5 mm × 0.5 mm. The as-sintered NiO-YSZ composites were reduced at 800°C in Ar-1%H₂ environment for 12h. The reduced Ni-YSZ cermets were then re-oxidized at 800°C in 100%O₂ for 12h. After each treatment, we confirmed that all the samples were fully reduced or re-oxidized from weight measurements. The porosity of sample was estimated from the sample dimensions and weight. Table 1 shows the available porosities of the samples.

2.2 Measurement of mechanical properties

The elastic modulus and fracture stress of the as-sintered NiO-YSZ composites, the reduced Ni-YSZ cermets, and the re-oxidized NiO-YSZ composites were measured by a small punch (SP) testing method[4]. The test atmosphere of NiO-YSZ composites was in 100%O₂ (P_{O₂} = 1 atm) at 800°C and Ni-YSZ cermets was in 100%H₂ (P_{O₂} = 10⁻²⁵ atm) at 800°C. The SP tests were performed on a universal testing machine (Instron Type 5565, USA) and crosshead speed was 0.5 mm/min.

3. Results and Discussion

Under the oxidizing environment, the as-sintered NiO-YSZ composites and the re-oxidized NiO-YSZ composites show a linear elastic brittle fracture in $PO_2 = 1$ atm at $800^\circ C$. In contrast, under the reducing environment, the Ni-YSZ cermet shows a ductile-like fracture in $PO_2 = 10^{-25}$ atm at $800^\circ C$.

Figure 2 shows the elastic modulus E_{SP} and Fig.3 shows the fracture stress σ_{fsp} obtained from the in-situ SP tests as a function of the porosity. The elastic modulus of the as-sintered NiO-YSZ composites decreased with increasing porosity. About the fracture stress, the same tendency as the elastic modulus was shown. The results of the elastic modulus of the reduced Ni-YSZ cermet show only a slight decrease with increasing porosity. The fracture stress of the reduced Ni-YSZ cermet decreased with increasing porosity. After the single re-oxidation treatment, the numerous numbers of micro-cracks were observed on the surface of the NiO-YSZ composites at low porosity. Due to the micro-cracks, the elastic modulus and fracture stress was drastically decreased compared with the as-sintered NiO-YSZ. On the other hand the elastic modulus remained practically unchanged compared with the as-sintered NiO-YSZ at high porosity. Figure 4 shows the relative strength as a function of the as-sintered porosity. The relative strength is given by (1).

$$\text{Relative Strength} = \frac{E_{SP(\text{re-oxidized})}}{E_{SP(\text{as-sintered})}}, \frac{\sigma_{SP(\text{re-oxidized})}}{\sigma_{SP(\text{as-sintered})}} \quad (1)$$

A drastically decrease in relative strength was observed in the porosity range 3-8%. On the other hand, the range of porosity over 10%, observed on cyclic re-oxidations degradation of the relative strength by was reduced. Its reversibility implies that no significant damage occurred within the NiO-YSZ composites structure.

4. Conclusions

In this study, the mechanical properties of the as-sintered NiO-YSZ composites, the reduced Ni-YSZ cermet and the re-oxidized NiO-YSZ were measured at $800^\circ C$ under different partial pressures ($PO_2 = 1$ atm and $PO_2 = 10^{-25}$ atm) by the SP tests. The porosity range in the Ni-YSZ cermet tested in this study was 25-46%. The SP results revealed that the Ni-YSZ cermet shows a ductile-like fracture under the reduction environment at $800^\circ C$. Mechanical properties were gradually decreased with increasing porosity. However, degradation of the mechanical properties by redox cycling was reduced at higher porosity. It is suggested that porosity makes a key contribution to the durability of Ni-YSZ cermet by the redox cycling.

Acknowledgment

This study was partly supported by "Development of Systems and Elemental Technology on SOFCs," funded by New Energy and Industrial Technology Development Organization (NEDO).

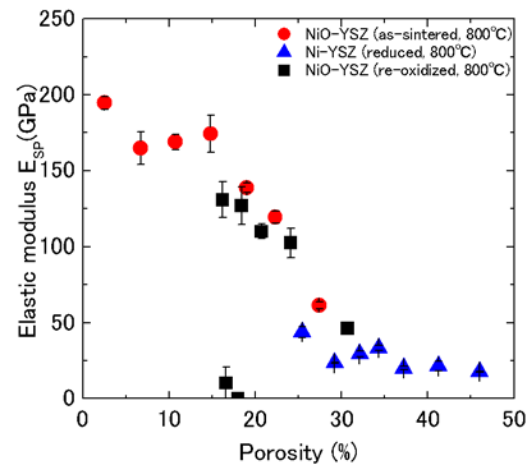


Fig. 2 Elastic modulus E_{SP} of NiO-YSZ and Ni-YSZ as a function of porosity.

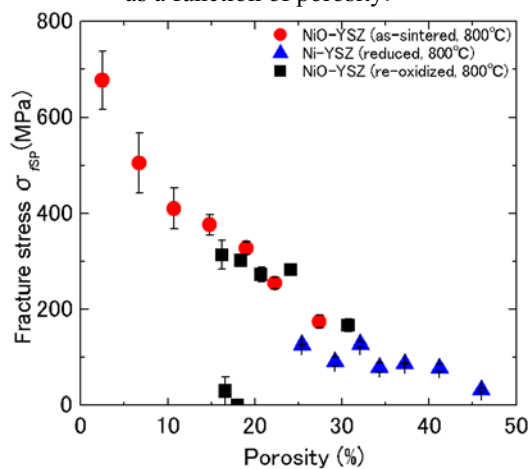


Fig. 3 Fracture stress σ_{fsp} of NiO-YSZ and Ni-YSZ as a function of porosity.

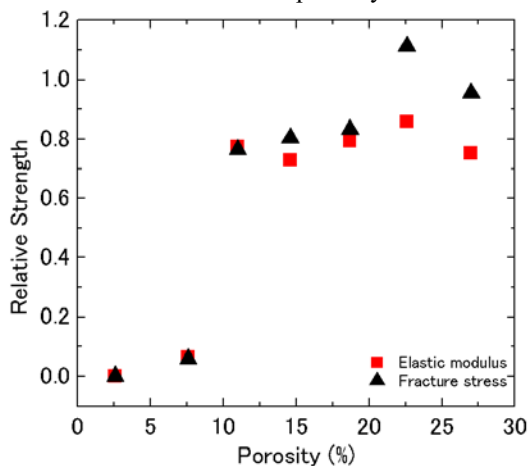


Fig.4 Relative strength of the re-oxidized NiO-YSZ as a function of porosity.

References

- [1] A. Atkinson *et al.*, *Nature. Mater.*, **3** (2004) 17-27.
- [2] D. Sarantaridis *et al.*, *J. Power Sources.*, **180** (2008), 704-710.
- [3] T. Hatae *et al.*, *J. Electrochem. Soc.*, **157** (5) (2010), B650 – B654.
- [4] S. Okuda *et al.*, *The Japan Society of Mechanical Engineers*, **53** (1991), 940-945.

Estimation of Heat Conduction and Thermal Radiation in Porous Insulation Materials Using Diffuse Approximation

Tatsuya Kobari¹, Junnosuke Okajima², Atsuki Komiya², Shigenao Maruyama²
¹ Graduate School of Engineering, Tohoku University, Sendai, 980–8579, Japan
² Institute of Fluid Science, Tohoku University, Sendai, 980–8577, Japan
 E-mail of corresponding author: kobari@pixy.ifs.tohoku.ac.jp

ABSTRACT

From the literature data of effective thermal conductivity of insulation materials, the contributions of heat conduction and thermal radiation are estimated separately. Also, the temperature dependences of each contribution are evaluated using diffuse approximation on thermal radiation. The estimation results indicate the tendencies of the contributions of each heat transfer phenomenon in rock wool, glass wool, silica aerogel and perlite. The importance of the control of radiative heat transfer to improve the insulation performance is indicated even in cryogenic condition.

1. Introduction

Porous insulation materials have widely used in many industrial areas, for instance, building, electronics, plant and aerospace. Reducing energy consumption strongly requires the development of porous insulation material with low thermal conductivity. Regarding the insulation performance, three important heat transfer modes are combined, which are the conduction and convection of residual gas, the conduction of solid material and the thermal radiation. Each heat transfer mechanism have been investigated in detail^[1]. Moreover, to improve the insulation performance of various insulation material, the design of insulation material requires the information which phenomena has most dominant influence and should be most controlled with consideration for the temperature dependence.

In this study, the contribution of solid and gaseous heat conductions and thermal radiation are separately estimated from the effective thermal conductivity in literature. It enables to indicate the influence of each heat transfer phenomena in a certain temperature condition. The contribution of thermal radiation is determined by diffuse approximation. The contribution of heat transfer is determined by porosity of insulation material and thermal conductivities of free gas and bulk solid. Then, the temperature dependences of each contribution are evaluated.

2. Effective thermal conductivity

In porous medium, heat is transferred by mainly solid conduction, gaseous conduction and radiation. The contributions of heat transfer of residual gas, solid material and radiation are represented by gas thermal conductivity k_{gas} [W/(m·K)], solid thermal conductivity k_{solid} [W/(m·K)] and radiative thermal conductivity k_{rad} [W/(m·K)], respectively. The effective thermal conductivity is expressed as,

$$k_{eff} = k_{gas} + k_{solid} + k_{rad}. \quad (1)$$

2.1 Gas thermal conductivity k_{gas}

In porous medium, the residual gas causes the convective and conductive heat transfer. Since the pore size and temperature gradient are large, the convection becomes considerable. However in this study, the

temperature difference of insulation material in the literature is assumed as small enough that the convection can be negligible. In this study, k_{gas} is estimated from the porosity ϕ [-] and thermal conductivity of free gas $k_{gas,0}$ [W/(m·K)], which does not change by pressure.

$$k_{gas} = \phi k_{gas,0}, \quad (2)$$

where the porosity ϕ is estimated by using ratio between the densities of insulation material and bulk solid material. While in vacuum condition where the Knudsen number is large, the flow condition becomes discontinuous and the heat conduction by gas becomes negligible. Therefore, k_{gas} is ignored for the reference data where k_{eff} was measured in vacuum condition.

2.2 Solid thermal conductivity k_{solid}

Many models to estimate k_{solid} of porous medium from microscopic parameters have been proposed^[2]. However, due to the lack of the microscopic information in most literatures, the following equation with the thermal conductivity of bulk solid $k_{solid,0}$ [W/(m·K)], which is applicable to many cases is adopted.

$$k_{solid} = (1 - \phi) k_{solid,0}. \quad (3)$$

Note that Eq. (3) cannot take account into the extension of heat path and the contact thermal resistance due to the internal structure. $k_{solid,0}$ has temperature dependency. The thermal conductivities of Calcium oxide, silica dioxide and aluminum oxide, which are main component of rock wool, glass wool, silica aerogel and perlite, are approximately constant in higher temperature condition. In lower temperature condition, the thermal conductivity of silica dioxide decreases, while ones of calcium oxide and aluminum oxide increase.

2.3 Radiative thermal conductivity k_{rad}

On the assumption that the insulation material has large optical thickness and optical isotropy, the diffuse approximation can be applied to estimate radiative heat transfer. It enables to consider that radiation emitted from a point can transport the energy to an immediate vicinity. Accordingly, the radiative heat flux q_{rad} [W/m²] can be expressed using the temperature gradient in the form similar to the Fourier's law^[3].

$$q_{rad} = -\frac{16n^2\sigma T^3}{3\sigma_{e,R}} \frac{\partial T}{\partial x}, \quad (4)$$

where $\sigma_{e,R}$ [1/m] means Rosseland mean extinction coefficient. The coefficient in the right side represents k_{rad} , which is proportional to the cube of temperature.

$$k_{rad} = \frac{16n^2\sigma T^3}{3\sigma_{e,R}}. \quad (5)$$

3. Estimation of contribution by conduction and radiation

The separated estimation of k_{gas} , k_{solid} and k_{rad} is performed from the literature data of k_{eff} of insulation materials^[4]. First, k_{gas} is estimated from the porosity and $k_{gas,0}$ as Eq. (2). However, for the data measured in vacuum condition, k_{gas} is estimated as zero.

Second, k_{rad} is estimated. In higher temperature region, the variation of k_{rad} with temperature is more dominant in the variation of k_{eff} than one of k_{solid} . Therefore, the Rosseland mean extinction coefficient can be obtained from the gradient of $k_{eff}-k_{solid}$ against the cube of temperature. k_{rad} in higher temperature is estimated from Eq. (5). Also, k_{solid} in higher temperature is estimated as $k_{eff}-(k_{gas}+k_{rad})$.

Next, to consider the temperature dependence of $k_{solid,0}$, the ratio of $k_{solid}/k_{solid,0}$ at higher temperature is obtained. Then, the product of $k_{solid}/k_{solid,0}$ at higher temperature and $k_{solid,0}$ in whole temperature region is estimated as k_{solid} . Finally, k_{rad} is estimated as $k_{eff}-(k_{gas}+k_{solid})$ in whole temperature region.

4. Results and discussion

Figures 1a to 1d show the separated estimation results of k_{eff} for rock wool, glass wool, silica aerogel and perlite, respectively. The black, red, green and blue lines show k_{eff} , k_{gas} , k_{solid} and k_{rad} against the cube of temperature, respectively. Figures 1b, 1c indicate that k_{rad} of glass wool and silica aerogel are proportional to the cube of temperature even in lower temperature, especially at temperature below 100 K for silica aerogel. It is because the thermal conductivity of bulk silica dioxide is approximately constant.

Figure 1a indicates that k_{solid} of rock wool increases at temperature below 600 K with increment of the thermal conductivity of bulk solid material. While, k_{rad} decreases to negative value at temperature below 500 K. This contradiction of the present estimation may be because the influences of contact thermal resistance and extension of heat path are ignored. In a microscopic view point, the internal stress and the thermal expansion by the change of temperature cause the decrease of contact area and the extension of heat path of the inner fibers and powders. It indicates that the actual solid thermal conductivity is smaller than $(1-\phi)k_{solid,0}$.

Figure 1d indicates that the perlite has slight solid thermal conductivity at whole temperature region. It means that the control of radiative heat transfer is most important for the purpose to reduce k_{eff} of perlite.

From the results, the radiative thermal conductivities

of rock wool and perlite are not proportional to the cube of temperature in cryogenic region. Because the thermal radiation emitted from lower temperature surface has longer wavelength, the relation between wavelength and size of internal structure changes significantly in cryogenic region. Therefore, the detailed analysis of radiative heat transfer in porous insulation material requires to take account for the absorption and scattering phenomena of radiation with wavelength dependence.

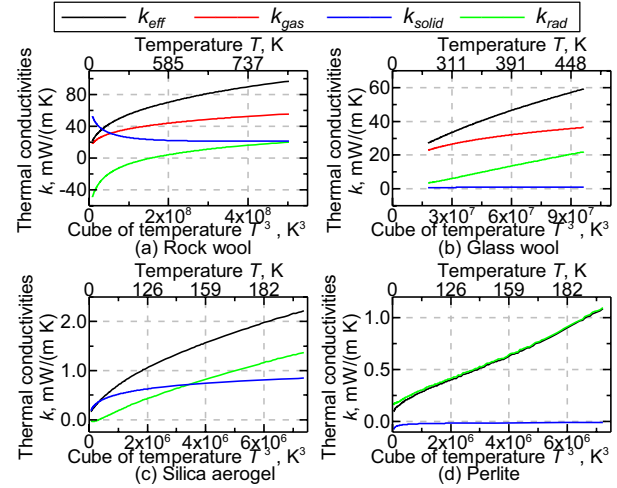


Fig. 1 The separate estimations of effective thermal conductivity of insulation materials.

5. Conclusion

In this study, the literature data of effective thermal conductivities of rock wool, glass wool, silica aerogel and perlite are separately estimated into the gas, solid and radiative thermal conductivity. The temperature dependence of thermal conductivities of free gas and bulk solid is considered. While, the diffuse approximation is applied to consider radiative heat transfer. From the estimation results of contributions by each heat transfer phenomenon, following conclusions can be obtained.

- (1) The perlite has slight solid thermal conductivity. Thus, the control of radiative heat transfer is most important to improve the insulation performance.
- (2) Because the contact thermal resistance and the extension of heat path at internal structure are not considered, the solid thermal conductivity of rock wool is overestimated in lower temperature region.
- (3) The detailed analysis of radiative heat transfer in low temperature region requires the consideration of absorption and scattering phenomena of radiation with wavelength dependence.

References

- [1] A. Milandri, F. Asllanaj, G. Jeandel and J. R. Roche, *J. Quant. Spectrosc. Radiat. Trans.*, **74**, 585–603.
- [2] J. S. Kwon, C. H. Jang, H. Y. Jung and T. H. Song, *Int. J. Heat Mass Tran.*, **52**, 5525–5532.
- [3] H. Reiss, “Radiative Transfer in Nanotransparent Dispersed Media”, Springer-Verlag, (1988).
- [4] Nihon netsu bussei kenkyukai, “Netsu bussei shiryoshu dannetsuzai-hen”, Yokendo, Japan, (1983).

Low Friction Mechanism of Hydrogen and Fluorine Terminated Diamond Like Carbon Film Using Tight-Binding Quantum Chemical and First-Principles Molecular Dynamics Methods

Shandan Bai¹, Seiichiro Sato¹, Takeshi Ishikawa¹, Yuji Higuchi¹, Nobuki Ozawa¹, Tomomi Shimazaki¹, Koshi Adachi², Jean-Michel Martin³, and Momoji Kubo¹

¹ Fracture and Reliability Research Institute, Graduate School of Engineering, Tohoku University, Aoba, Aramaki, Aoba-ku, Sendai, Japan

² Department of Nanomechanics, Graduate School of Engineering, Tohoku University, Aoba-ku, Sendai, Japan

³ Laboratoire de Tribologie et Dynamique des Systemes, Ecole Centrale de Lyon, 69134 Ecully Cedex, France

E-mail: shandan.bai@rift.mech.tohoku.ac.jp

ABSTRACT

The low friction mechanism of hydrogen terminated diamond like carbon (H-DLC) and hydrogen and fluorine terminated diamond like carbon (H-, F-DLC) films was studied by the tight-binding quantum chemical and first-principles molecular dynamics methods under pressures of 1 and 7 GPa. The results showed that both of them achieved low friction under 1 GPa. The friction coefficient of H-, F-DLC film was less than that of H-DLC film under pressure of 7 GPa, because the strong repulsive force between terminated fluorine atoms worked at the interface, leading to low friction property.

1. Introduction

Diamond like carbon (DLC) film is one of the widely used tribo-coating for industrial applications due to its superior properties, such as low friction, anti-wear, and low abrasion [1]. To improve its properties, some elements were terminated at interface of the DLC surface. In particular, fluorine termination modified the surface properties, in addition to feature of extremely low friction. The low friction and excellent chemical resistance features were reported in reference [2]. Fontaine et al. reported that the superlow friction coefficient about 0.005 was achieved by the fluorinated DLC film against an iron surface under high vacuum condition [3]. However, the details of the low friction mechanism have not been revealed.

To investigate the low friction mechanism, the computational methods are very useful. We have investigated the superlow friction mechanism using tight-binding quantum chemical molecular dynamics (TB-QCMD) method. We reported that the tribo-chemical reaction occurred at the interface of hydrogen free DLC and hydrogen terminated DLC (H-DLC) films during the friction simulation [4]. On the other hand, the tribo-chemical reaction at the interface of hydrogen and fluorine terminated DLC (H-, F-DLC) film has not been revealed. In this study, the tribo-chemical reaction mechanism of the H-, F-DLC film was investigated by computational methods on the electronic and atomic scale.

2. Methods

The low friction mechanism was investigated by our TB-QCMD code "Colors" [4, 5] and first-principles molecular dynamics (FPMD) code "Violet". The friction simulation model of H-, F-DLC film is shown in Fig. 1. The simulation using "Colors" code was performed for 100,000 steps with the interval time of 0.1 fs. To consider the boundary friction condition, external pressure of 1 and 7 GPa were applied to the top layer of upper substrate of H-, F-DLC film, while it was forcibly slid with horizontal velocity of 100 m/s. The top layer of upper substrate of H-, F-DLC and the bottom layer of

lower substrate of H-, F-DLC films were completely frozen. The friction coefficient μ is given by

$$\mu = \frac{F_x}{F_z}, \quad (1)$$

where F_x and F_z represent the sums of horizontal and perpendicular forces with respect to the fixed layer of upper substrate, respectively.

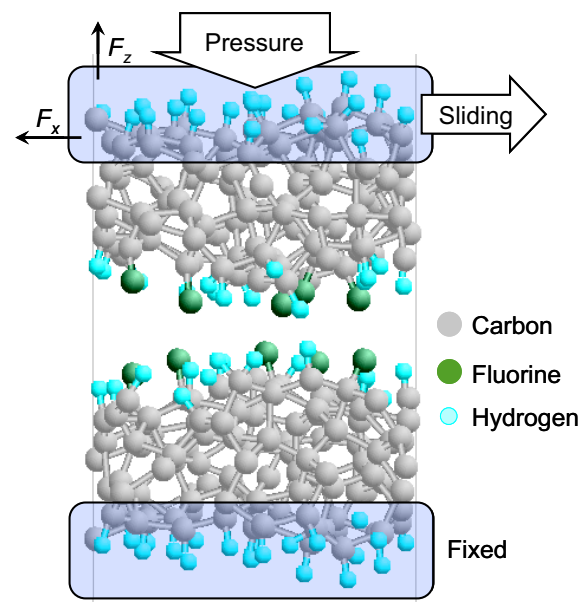


Fig. 1 Friction simulation model of H-, F-DLC film.

3. Results and Discussion

To study the friction mechanism of H-DLC and H-, F-DLC films, TB-QCMD and FPMD methods were carried out for the investigation of tribo-chemistry. In the present study, we compared the friction properties of H-DLC and H-, F-DLC films using TB-QCMD method. Fig. 2 shows that a friction coefficient of H-DLC film under pressure of 7 GPa is higher than that under pressure of 1 GPa. The values of friction coefficient are

0.38 and 0.04, respectively. The snapshots of H-DLC film are shown in Fig. 3. Under pressure of 1 GPa, no C-C bonds is generated at the interface of the H-DLC film (Fig. 3a). On the other hand, the generation of C-C bonds is observed under pressure of 7 GPa. These results indicate that the extreme pressure generates C-C bonds at the interface of H-DLC films. This generation of C-C bonds leads to the high friction coefficient. Fig. 4 shows that the friction coefficients are 0.07 and 0.10 for H-, F-DLC film under pressures of 1 and 7 GPa, respectively. From this result, we observed that low friction coefficients were achieved by the H-, F-DLC films under both pressures of 1 and 7 GPa. No bond is generated at the interface of H-, F-DLC film as shown in Fig. 5. These results indicate that terminated F atoms prevent generation of the C-C bonds, leading to low friction property even under extreme pressure.

Under pressure of 1 GPa, the friction coefficient of both H-DLC film and H-, F-DLC film is low. These are caused by the repulsive force between terminated atoms, which keep the distance between films and prevent the generation of C-C bonds. The simulation result is in good agreement with the experimental result [3]. On the other hand, the friction coefficient of H-DLC film was higher than that of H-, F-DLC film under pressure of 7 GPa. The stronger repulsive force worked at the interface of H-, F-DLC film, due to negative charge of F atoms. No generation of C-C bonds at the interface of H-, F-DLC film was observed and kept on low friction, even though it was sliding under extreme pressure. More details and the result of first-principles molecular dynamics simulation will be reported in our presentation.

4. Concluding remarks

In this study, we investigated the tribo-chemical mechanism of H-DLC and H-, F-DLC films under pressures of 1 and 7 GPa. H-, F-DLC film shows low friction properties even under extreme pressure, while the friction coefficient of H-DLC films increases under high pressure. We consider that the strong repulsive force between terminated F atoms worked at the interface of H-, F-DLC films, leading to low friction property on the H-, F-DLC films.

References

- [1] J. Brand, G. Bechmann, G. Konrath, and T. Hollstein, *Ind. Lubr. Tribol.*, **54** (2002), 291.
- [2] R. Prioli, L.G. Hacobsohn, M.E.H Maia da Costa, and F.L. Freire, Jr., *Tribology Letter*, **15** (2003), 177.
- [3] J. Fontaine, T. Le Mogne, J.L. Loubet, and M. Belin, *Thin Solid Films*, **482** (2005), 99.
- [4] K. Hayashi, K. Tezuka, N. Ozawa, T. Shimazaki, K. Adachi, and M. Kubo, *J. Phys. Chem. C*, **115** (2011), 22981.
- [5] K. Hayashi, S. Sato, S. Bai, Y. Higuchi, N. Ozawa, T. Shimazaki, K. Adachi, J.M. Martin, and M. Kubo, *Faraday Discuss.*, in press.

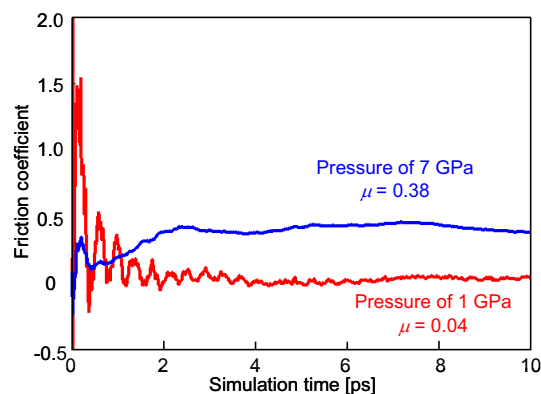


Fig. 2 Friction coefficient of H-DLC film under pressures of 1 and 7 GPa.

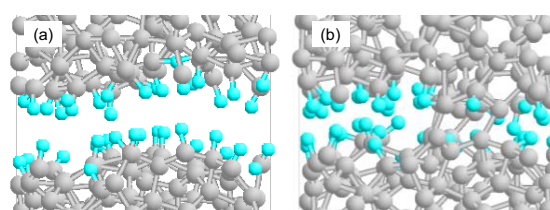


Fig. 3 Snapshots of H-DLC film under pressures of (a) 1 GPa and (b) 7 GPa at simulation time of 2.3 ps.

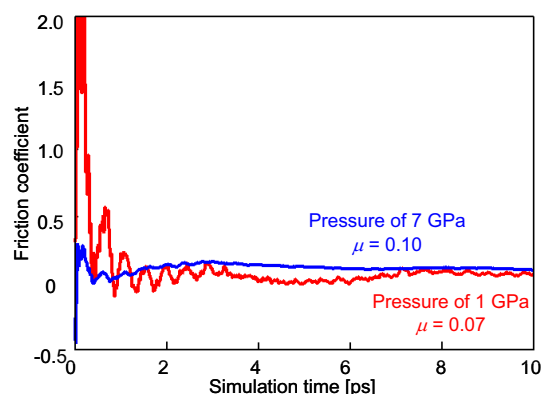


Fig. 4 Friction coefficient of H-, F-DLC film under pressures of 1 and 7 GPa.

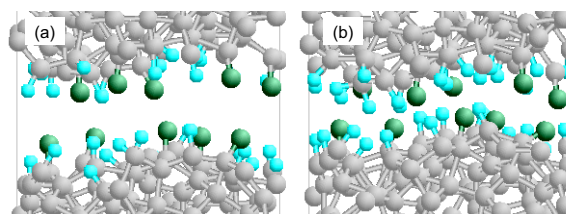


Fig. 5 Snapshots of H-, F-DLC film under pressures of (a) 1 GPa and (b) 7 GPa at simulation time of 8 ps.

Molecular Dynamics Study on Recycling Mechanism of Used CeO₂ Abrasive Grain for CMP of Glass Surface

Kang Zhou, Takeshi Ishikawa, Yuji Higuchi, Nobuki Ozawa, Tomomi Shimazaki, and Momoji Kubo
Fracture and Reliability Research Institute, Graduate School of Engineering, Tohoku University
6-6-11-703 Aoba, Aramaki, Aoba-ku, Sendai 980-8579, Japan
E-mail: kang.zhou@rift.mech.tohoku.ac.jp

ABSTRACT

To realize the recycle of the CeO₂ abrasive grain used at glass polishing, we studied the polishing process of a glass surface by a CeO₂ abrasive grain and the collision process of the CeO₂ abrasive grains via molecular dynamics simulation. We confirmed that the grain surface was partially covered with polished SiO₂ clusters after polishing. Moreover, the collision simulation of the CeO₂ particles presented the removal of the SiO₂ clusters from the CeO₂ particle surface under water environment. This result indicated that the polishing property of the CeO₂ abrasive grains recovers by the sideways collision under water environment.

1. Introduction

CeO₂ is very efficient for planarization of glass surfaces because it shows the chemical mechanical polishing (CMP) process in which chemical reactions at the interface between the CeO₂ particle and glass surface promote mechanical polishing process [1]. Therefore, CeO₂ abrasive grains are used for planarization of glass materials for many applicants such as IC photo masks, liquid crystal display (LCD), and glass disks of HDD etc. However, its stable supply is difficult since CeO₂ resources are closely located in few countries. Then, the development of recycling technology for used CeO₂ abrasive grains is quite expected. Here, during the polishing process, the abrasive grains were partially covered with the polished SiO₂ clusters, which disturbed the reaction of CeO₂ particle with glass surface and reduced the polishing rate [2]. Therefore, the used CeO₂ particles were impacted by manual stirring under water environment for the recovery of the polishing ability.

However, the polishing rate of those recycled particles was still low. Hence, to improve the polishing property of recycled CeO₂ abrasive grains, the understanding of the removal mechanism of the SiO₂ clusters from the grains is necessary. Since some bonds between the CeO₂ particle and the polished SiO₂ clusters are dissociated at the removal process of the clusters, an analysis at atomic and molecular scale is required. Then, in this study, we investigated the removal mechanism of the polished SiO₂ cluster from the used CeO₂ abrasive grain by the molecular dynamics method.

2. Method

In this study, we simulated the polishing process of SiO₂ glass surface by CeO₂ abrasive grains first. Then, we simulated the collision process of the CeO₂ abrasive grains covered with the polished SiO₂ clusters obtained by the polishing simulation. The simulation program NEW-RYUDO was used for these molecular dynamics calculations. Since commercial CeO₂ particles contain La, the La was added to the models of the CeO₂ grains.

3. Results and Discussion

3.1 Polishing simulation of the glass surface by a CeO₂ abrasive grain

For studying the structure of the SiO₂ clusters adhered on the surface of the CeO₂ abrasive grain, we simulated the polishing process as shown in Fig. 1. In this simulation, the CeO₂ abrasive grain was pushed down to the SiO₂ surface. Then, it was added a friction field in the horizontal direction. At last, it was pulled out from the surface. Fig. 2 shows the structure of the abrasive grains after the polishing simulation. With pulling out the CeO₂ abrasive grain, the polished SiO₂ clusters adhere to the surface of the grain. At the interface between the abrasive grain and polished SiO₂ clusters, O atoms of the polished SiO₂ clusters are bonded with Ce atoms of the CeO₂ abrasive grain. It implies that the removal of these SiO₂ clusters is important for recovery of the polishing property of the abrasive grain, because the Ce atoms of the surface chemically react with the glass surface in the CMP process.

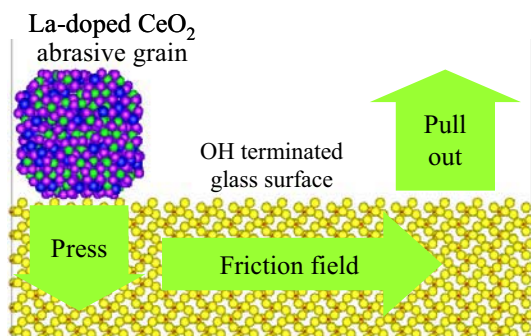


Fig. 1. The simulation model of polishing the SiO₂ surface by the La-doped CeO₂ abrasive grain.

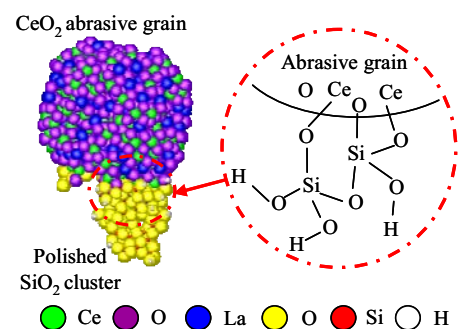


Fig. 2. The CeO₂ abrasive grain after polishing (left) and the schematic of the interface between the grain and polished the SiO₂ cluster (right).

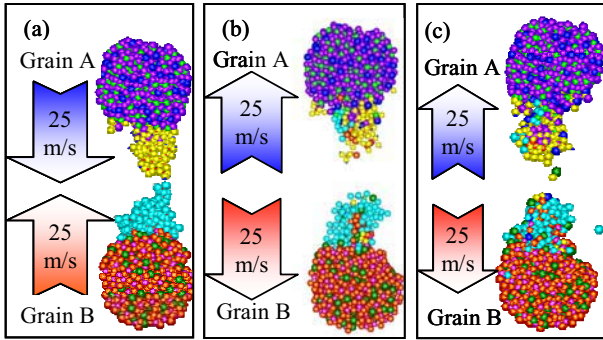


Fig. 3. The deformation of the SiO₂ clusters on the CeO₂ abrasive grains at the frontways collision process. (a) Before the 1st collision. (b) Separated after the 1st collision. (c) Separated after the 3rd collision.

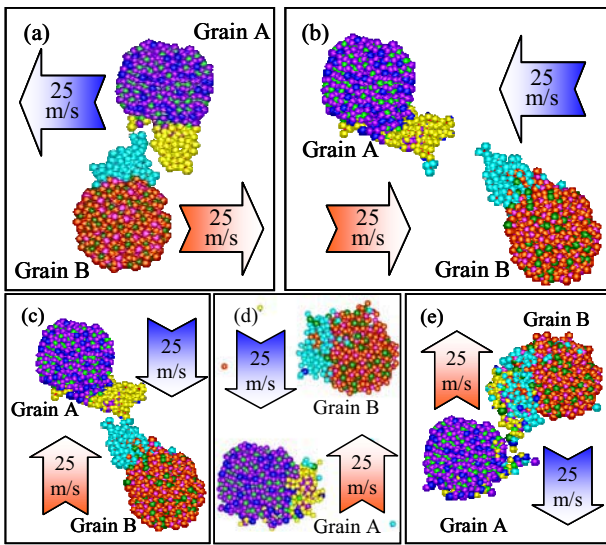


Fig. 4. The deformation of the SiO₂ clusters on the CeO₂ abrasive grains at the sideways collision process. (a) Before the 1st collision. (b) After the 1st collision. (c) Before the 2nd collision. (d) After the 2nd collision. (e) After the 3rd collision.

3.2 Result of the collision simulation

In order to clarify the removal mechanism of the SiO₂ clusters from the CeO₂ grain by stirring, we carried out the collision simulations using the abrasive grains partially covered with the SiO₂ clusters obtained by the above simulation. Here, we terminated the dangling bonds on the SiO₂ clusters adhered to the CeO₂ grain by OH groups, and then crashed the grains three times in each case of the collisions. As shown in Fig. 3(a), the grains moved to each other in front at a velocity of 25 m/s. The deformation of the SiO₂ clusters after the 1st collision is shown in Fig. 3(b). Some SiO₂ clusters attach from the grain to the other but haven't removed from the grains even after the 3rd collision (Fig. 3 (c)). Fig. 4(a) shows the sideways collision simulation at the same velocity of 25 m/s. The SiO₂ clusters on the surface of the grain A are moved after the 1st collision (Fig. 4(b)). Moreover, we performed the sideways collision simulation twice. Here, we turned the direction

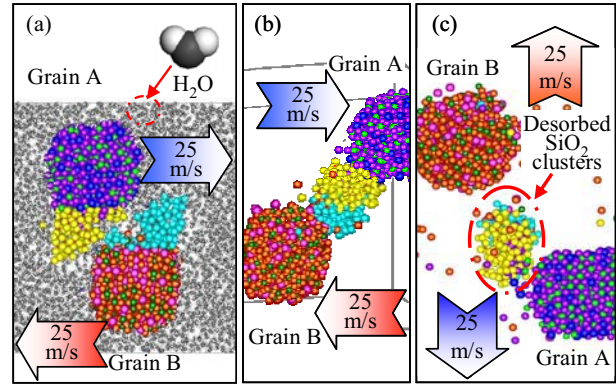


Fig. 5. The deformation of the SiO₂ clusters on the CeO₂ abrasive grains at collision process under water environment. The display of water molecules is turned off in (b) and (c). (a) Before the 1st collision. (b) After the 1st collision. (c) After the 3rd collision.

at the 2nd collision (Fig. 4(c)). According to the results, the most SiO₂ clusters moved and adsorbed on the grain surface again after the 2nd and 3rd collision (Fig. 4(d) and (e)). This implies that the sideways collision are possible to take away the clusters if the reattachment is prevented. Next, we performed the sideways collision simulation under water environment as shown in Fig. 5(a). The deformation of the SiO₂ clusters after the first collision is shown in Fig. 5(b). In this simulation, the Si-O bonds between the SiO₂ clusters and the CeO₂ grains are broken, and OH groups generated from water molecules terminate on the dangling bonds of the Si atoms. These OH terminations prevent reattachment of the SiO₂ clusters from the grains. Fig. 5(c) shows the abrasive grains after the 3rd collision. The SiO₂ clusters are removed from both of the grains. Since Ce atoms of the abrasive grain are exposed on the surface again by the collision under water environment, the chemical reaction between the CeO₂ abrasive grains and the glass surface becomes possible. In other words, for recover of the polishing ability of the CeO₂ abrasive grains, the sideways collision and water environment are effective.

4. Concluding remarks

In this study, we simulated the glass polishing process and removal process of SiO₂ clusters by CeO₂ abrasive grains via the molecular dynamics method. After polishing of the SiO₂ surface by the grain, the Ce atoms of the grain surface are covered by the polished SiO₂ clusters, which disturb the polishing process of the glass surface and reduce the polishing rate of the abrasive grain. In order to recover the polishing rate, we revealed that the sideways collision of the grains under water environment is efficient for the removal of the SiO₂ cluster from the CeO₂ abrasive grain.

References

- [1] L. M. Cook, *J. Non-Crystalline Solid*, 120 (1990), 152.
- [2] K. Kato, T. Yoshioka, A. Okuwaki, *Ind. Eng. Chem. Res.*, 39 (2000), 943.

Configurations of CH₄/O₂/Xe Counterflow Premixed Flames at Small Stretch Rates under Microgravity

Koichi Takase¹, Xing Li^{1,2}, Hisashi Nakamura¹, Takuya Tezuka¹, Susumu Hasegawa¹,
Masato Katsuta³, Masao Kikuchi³, Kaoru Maruta¹

1. Institute of Fluid Science, Tohoku University, Japan

2. School of Mechanical and Electronic Control Engineering, Beijing Jiaotong University, China

3. Tsukuba Space Center, Japan Aerospace Exploration Agency, Japan

takase@edyn.ifs.tohoku.ac.jp

ABSTRACT

The formation of ball-like flame in a low-stretched counterflow field of premixed CH₄/O₂/Xe mixture was examined by microgravity experiment and two-dimensional computations. Transition from planar flame to ball-like flame was experimentally observed near the extinction limit. Two-dimensional duplicated the transition and computations revealed that the ball-like flame had similar characteristics with flame ball.

1. Introduction

The knowledge on near-limit flame behavior is important for the development of advanced combustion devices and their control technology. In 1941, Zeldovich [1] firstly suggested theoretical description of the flammability limit in which the flammability limit was the result of the competition between heat generation by combustion and heat loss mechanism. Spalding [2] described that the flammability limit should be determined based on the ratio of heat loss to total heat production. In 1996, radiation-induced extinction of counterflow premixed flame at extremely small stretch rate under microgravity was experimentally confirmed [3]. At extremely small stretch rate, heat and species transports are significantly governed by molecular diffusion. On the other hand, steady-state spherical premixed flame in a quiescent mixture which was later termed 'Flame ball [4]' was observed under microgravity when Lewis number is small. Flame ball is intensified when mass diffusion exceeds thermal diffusion and stabilized by the balance between energy transportation by diffusion and emission by the radiative heat loss. However, the interaction and transition between these two kinds of flames have not been studied yet. Therefore, the verification of the possibility of the transition of flame configuration could improve our knowledge on the near-limit flames.

The objective of the study is qualitative clarification of the behavior of low-Lewis-number counterflow premixed flame at small stretch rate under microgravity. Ground-based microgravity experiments by the airplane and two-dimensional computations were conducted for examinations on the behavior of the target phenomena. These examinations contribute future space experiment which was selected as the candidate theme for International Space Station.

2. Experimental and Computational Methods

Microgravity experiments were conducted by the parabolic flight of airplane. One pair of 3.0 cm inner diameter counterflow burner was set in a combustion chamber. The distance between burner lips, d , was kept at 3.0 cm. Nominal stretch rate, a , defined by $a = 2u_0/d$ was used as stretch rate, where u_0 is flow velocity at the

burner exit and d is twice of the distance from inlet ($x = -1.5$) to stagnation plane ($x = 0$). After establishing counterflow twin flames, equivalence ratio, ϕ , was gradually decreased linearly from 0.58 to 0.30 in 20 seconds.

To identify the limits of counterflow premixed flame at small stretch rate, axisymmetric two-dimensional computation with one-step overall chemistry [5] was conducted. Xenon (Xe) was selected as an inert gas in the present study to obtain the mixture with Lewis number smaller than unity. Two-dimensional computations using FLUENT 6.3.26 were conducted for the investigation of the possibility of transition from planar flame to flame ball in a counterflow field. The counterflow burner used in the experiment was modeled and the coordinate of burner lip was $r = 1.5$ cm and $x = -1.5$ cm. Due to the symmetries of counterflow field, a quarter of counterflow field was computed for saving computational cost. Therefore the boundary condition at $r = 0$ and $x = 0$ were axisymmetrical and symmetrical boundary conditions, respectively. Mixture with uniform flow velocity was issued from the burner exit. Discrete ordinate method was adopted to solve radiative transfer equation and Weighted-Sum of Gray-Gas Model [6, 7] was used for the computation of radiative absorption coefficient. In transient computations, equivalence ratio was decreased with the rate around 0.016/sec.

3. Results and Discussion

First, experimental results under microgravity were shown in Fig. 1. Planar twin flame was observed at first and then the twin flame merged to single planar flame. Flame shape changed from planar to ball-like shape near the extinction limit ($\phi = 0.35$).

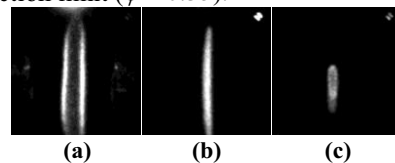


Fig. 1 The images of experimental counterflow premixed flame at $a = 3.2 \text{ s}^{-1}$.
(a) Planar twin flames, $\phi = 0.47$.
(b) Planar single flame, $\phi = 0.38$.
(c) Ball-like flame, $\phi = 0.35$.

Next, observed transition of flame configuration was investigated by both the transient and steady-state two-dimensional computations. From the results of transient computations, the transition from planar single flame to ring-like flame at extinction limit was obtained at $a = 3.2 \text{ s}^{-1}$, as shown in Fig. 2.

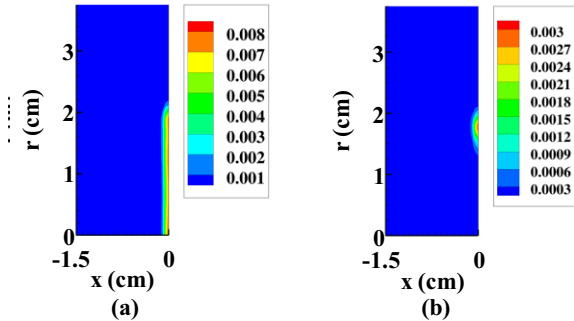


Fig. 2 Flames obtained by transient computation of counterflow premixed flame at $a = 3.2 \text{ s}^{-1}$ ($\text{kmol/m}^3/\text{s}$).
(a) Planar single flame.
(b) Ring-like flame at extinction limit ($\phi = 0.37$).

However, by steady-state computation, only planar flame was obtained. The flame configuration at extinction limit was shown in Fig. 3. Therefore, ring-like flame would be an intermediate status from counterflow planar flame to complete extinction.

Flame ball was the spherical flame formed in the steady-state mixture, namely, the field with no flame stretch. Therefore, computations of the conditions with smaller stretch rate were conducted. The results of transient computation shows that a ball-like flame was obtained at extinction limit at $a = 0.50 \text{ s}^{-1}$. With steady-state computation, ball-like flame was also obtained at near-limit region. The ball-like flame obtained by steady-state computation was shown in Fig. 4. At near-limit region, flame temperature decreased at $a = 3.2 \text{ s}^{-1}$ and increased at $a = 0.50 \text{ s}^{-1}$ with decrease of equivalence ratio, as shown in Fig. 5. The characteristics of flame temperature at $a = 0.50 \text{ s}^{-1}$ was similar to that of flame ball. Therefore, obtained ball-like flame at extinction limit of counterflow flame at $a = 0.50 \text{ s}^{-1}$ should have steadiness, similar to that of flame ball. These results indicated that the characteristics of ball-like flames obtained at small stretch rate qualitatively resemble that of flame ball.

4. Concluding remarks

Ball-like flame in the counterflow field at small stretch rates were observed experimentally and simulated numerically. The findings are as follows.

1. The transition from planar flame to ball-like flame was observed near the extinction limit at small stretch rates under microgravity.
2. The ball-like flame was obtained from transient and steady computational results at $a = 0.50 \text{ s}^{-1}$.
3. From the computational results, the increase of flame temperature was exhibited with decrease of equivalence ratio near extinction limit.
4. Obtained ball-like flame at small stretch rate has a qualitative resemblance to the flame ball.

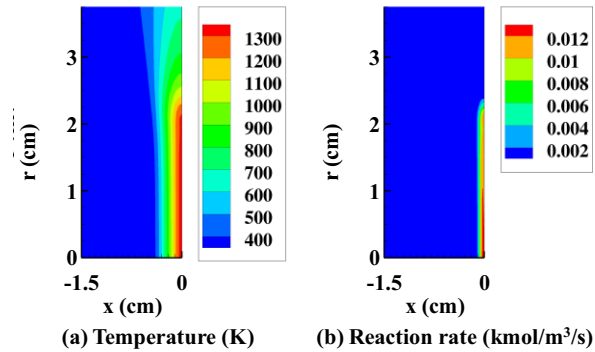


Fig. 3 Temperature and reaction rate of counterflow premixed flame at extinction limit ($\phi = 0.40$, $a = 3.2 \text{ s}^{-1}$).

(a) Temperature.
(b) Reaction rate.

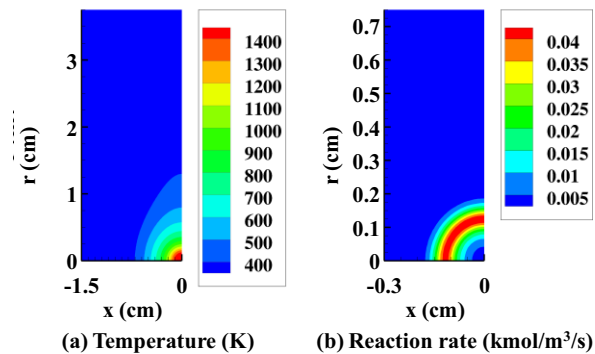


Fig. 4 Temperature and reaction rate of counterflow premixed flame at extinction limit.

($\phi = 0.30$, $a = 0.50 \text{ s}^{-1}$).

(a) Temperature.
(b) Reaction rate.

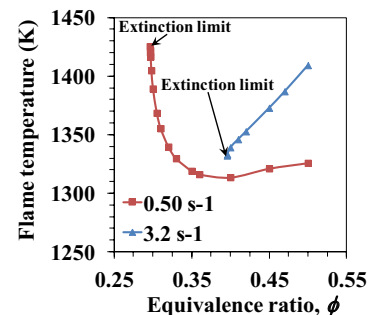


Fig. 5 Computational temperature of steady-state counterflow premixed flames.

References

- [1] Ya. B. Zeldovich, Zhurn. Exsp. Teoret. Fiz., **11** (1941), 159-168.
- [2] D. B. Spalding, Proc. Roy. Soc. London, Ser. A **240** (1957), 83-100.
- [3] K. Maruta, M. Yoshida, Y. Ju and T. Niioka, Proc. Combust. Inst., **26** (1996), 1283-1289.
- [4] P. D. Ronney, Combust. Flame, **82** (1990), 1-14.
- [5] C. K. Westbrook and F. L. Dryer, Combust. Sci. Technol., **27** (1981), 31-43.
- [6] A. Coppalle and P. Vervisch, Combust. Flame, **49** (1983), 101-108.
- [7] T. F. Smith, Z. F. Shen and J. N. Friedman, J. Heat Trans., **104** (1982), 602-608.

Cetane Number and Weak Flames of Diesel Surrogates in a Micro Flow Reactor with a Controlled Temperature Profile

Satoshi Suzuki*, Mikito Hori, Hisashi Nakamura, Takuya Tezuka, Susumu Hasegawa, and Kaoru Maruta
Institute of Fluid Science, Tohoku University
2-1-1 Katahira, Aoba-ku, Sendai, Miyagi 980-8577, Japan
suzuki@edyn.ifs.tohoku.ac.jp

ABSTRACT

Ignition and combustion characteristics of a stoichiometric gaseous diesel surrogates (*n*-cetane, *n*-decane, *n*-heptane, iso-cetane and 1-methylnaphthalene)/air mixtures were investigated using a micro flow reactor with a controlled temperature profile. At the low velocity region, multi-stage oxidation process of the fuels (weak flames) can be observed as separated multiple stationary flames, and also gas sampling and analysis were conducted. The predictions of 1-D steady simulations with detailed reaction kinetics agreed with the trends of the multi-stage oxidation processes.

1. Introduction

Reaction modeling of diesel fuel is an effective tool to accelerate further improvement of diesel engines. Major contributions to obtain experimental data for development of the modeling capability were made by the experiments with a shock tube. However conventional shock tube is suitable for the gaseous fuels or liquid fuels with sufficiently high vapor pressures [1], and special technique is required for liquid fuels with low vapor pressure such as diesel fuels. As a new approach, we employed a micro flow reactor with a controlled temperature profile [2-6]. In our previous studies, combustion characteristics of methane/air [3], DME/air [4], *n*-heptane/air [5], and gasoline PRF/air [6] mixtures were examined by using the micro flow reactor. These studies clearly indicated the possibility of the micro flow reactor as a method to investigate the ignition and combustion process of given fuels.

The present study is focusing on the combustion characteristics of five fuels (*n*-cetane, *n*-decane, *n*-heptane, iso-cetane and 1-methylnaphthalene: AMN) known as diesel surrogates. Each fuel has cetane number (CN), 100 for *n*-cetane, 76 for *n*-decane, 53 for *n*-heptane, 15 for iso-cetane, and 0 for AMN. Diesel fuel ignition is rated by its CN, where fuels with higher values of CN ignite more readily than fuels with lower CN values. *n*-Cetane (CN 100) is the most reactive fuel among the applied fuels. The objective of this study is to investigate ignition and combustion characteristics of five diesel surrogate fuels by using a micro flow reactor with a controlled temperature profile. Flame responses with the various CN were examined.

2. Experimental and computational method

Figure 1 shows a schematic of the experimental setup. A quartz tube with an inner diameter of 2 mm was employed as a micro flow reactor, and heated by H₂/air premixed burner so as to have a stationary temperature profile (400-1300 K) in a flow direction. Due to the small inner diameter of the tube, temperature of the gas phase in the tube strongly depends on the temperature of the inside surface of the tube.

A gaseous diesel surrogates/air mixture was produced by injecting the each liquid fuel with a micro syringe into air which was controlled by mass flow controller. Injection volume of the each fuel was

controlled by a stepping motor. The mixture coming into the quartz tube ignites in the heated tube and the flame remains at a certain location. This flame was captured with a digital single lens reflex camera with a CH filter. All of the experiments were conducted under the atmospheric pressure.

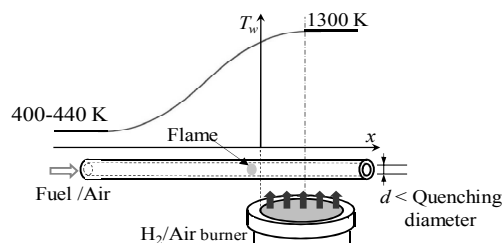


Figure 1 Schematic of the experimental setup.

Computations were carried out by employing one-dimensional steady code based on PREMIX, and heat convection term between gas phase and wall was added to its energy equation [2], so as to examine the experimental results. The temperature gradient with maximum wall temperature 1300 K is the same with that of the experiment. Detailed reaction mechanism developed by LLNL for *n*-cetane [7], *n*-heptane [8], iso-cetane [9], and by Pitsch for AMN [10] were selected. Flame location was defined as the peak of the heat release rate.

3. Results and discussion

Three kinds of flame responses were observed by changing inlet flow velocity. This tendency agrees with the previous experimental results for methane [2-6]. In this study, we focus on the weak flames (shown in figure 2), which were observed in the lower flow velocity region. The multiple luminous zones were observed in a long exposure image. Reaction zone at the highest temperature region has strong luminosity accompanied with another weak luminous zone, and that at the lowest temperature region has weak luminosity. Luminous zones at high temperature region are separated hot flame, and weak luminescence at the lowest temperature region is cool flame. Fig. 2 shows the weak flame images of the five fuels. A cool flame was recognized in CN from 100 to 53 at around 800 K, while AMN (CN 0) only showed hot flame which located at over 1200 K. Figure 3 shows

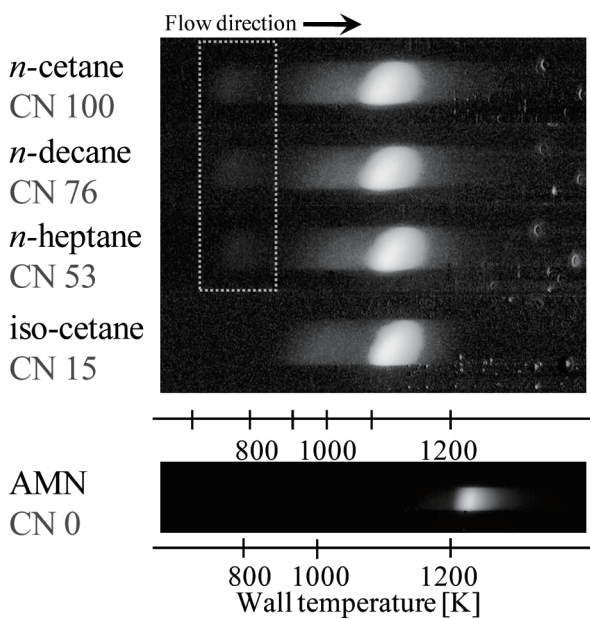


Figure 2 Weak flame images with various CN.

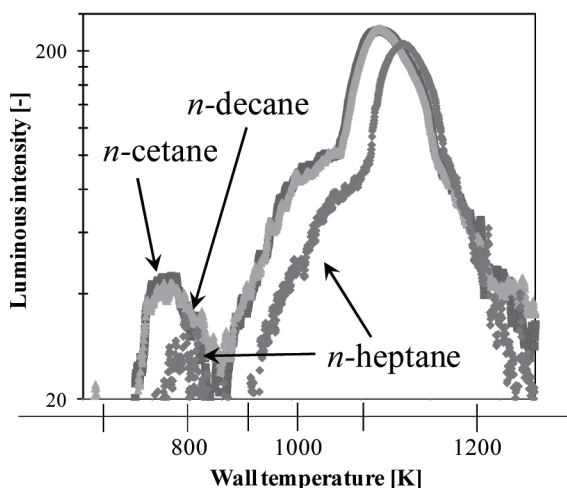


Figure 3 Luminous intensity profiles of weak flames in various CN. Average values of the digital intensity data.

luminous intensity profiles of the weak flames in Fig. 2 except the iso-cetane and AMN cases. Focusing on cool flame peaks around 800 K, *n*-cetane (CN 100) has the largest peak among the three fuels, and *n*-heptane (CN 53) peak is the smallest. Difference between CN 100 and CN 76 is small, but decreasing trends of luminous intensity can be seen with decreasing CN. In addition, as the CN decreased, locations of the cool and hot flames slightly shift to downstream.

Figure 4 presents the computational heat release rate (HRR) profiles of the five fuels at the flow velocity of 3.0 cm/sec, that is the same as experiments. For CN 100, 76 and 53, three peaks of the heat release rate were confirmed. It is confirmed that these peaks correspond to the three luminous zones observed in Fig. 2, according to the study on *n*-heptane [5] and a CH_2O profile of *n*-cetane by a gas analysis, although it is not shown. Computational results show that HRR peak of cool and hot flames shift to the higher temperature region in lower CN, this tendency qualitatively agrees with the

experimental data shown in Figs. 2 and 3. These results in the present micro flow reactor and the cetane number showed analogous trends; higher CN fuels showed that brighter cool flame than that of lower CN fuel, and also the cool and hot flames of higher CN located at lower temperature range than those of lower CN fuels.

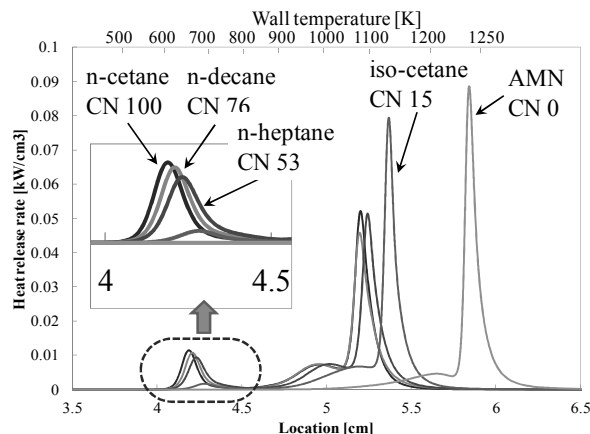


Figure 4 Heat release rate profiles for various CN.

4. Conclusions

Ignition and combustion characteristics of diesel surrogates/air mixtures were investigated using a micro flow reactor with a controlled temperature profile.

- Responses of weak flames with various cetane numbers were examined by using five diesel surrogates whose cetane number varies 0 to 100. The 1-D computational results with detailed chemical kinetics agreed with the experimental ones.
- Low temperature oxidation of a fuel (cool flame) was observed in higher cetane number fuels.
- It was indicated that the present reactor has a capability to measure characteristics of high boiling point fuels such as diesel fuel.

References

- [1] D.R. Haylett, et al., *Combust. Flame.* 159 (2) (2012) 552-561.
- [2] K. Maruta, et al., *Proc. Combust. Inst.* 30 (2005) 2429.
- [3] Y. Tsuboi, T. et al., *Proc. Combust. Inst.* 32 (2009) 3075.
- [4] H. Oshibe, et al., *Combust. Flame.* 157 (8) (2010) 1572.
- [5] A. Yamamoto, et al., *Combust. Inst.* 33 (2) (2011) 3259.
- [6] M. Hori, et al., *Combust. Flame.* (2011) 159 (3) (2012) 959.
- [7] Matthew A. O. et al., *Combust. Flame.* 156 (2009) 2165.
- [8] H.J. Curran et al., *Combust. Flame* 114 (1-2) (1998) 149.
- [9] Charles K. et al., *Combust. Flame.* 156 (2009) 181-199.
- [10] K. Narayanaswamy et al., *Combust. Flame.* 157 (2010) 1879.

Chemical Stability of the Cubic Phase of $\text{Ba}_{0.5}\text{Sr}_{0.5}\text{Co}_{0.8}\text{Fe}_{0.2}\text{O}_{3-\delta}$ (BSCF)

Wang Fang, Keiji Yashiro, Koji Amezawa, Junichiro Mizusaki
Institute of Multidisciplinary Research for Advanced Materials, Tohoku University
2-1-1 Katahira, Aoba-ku, Sendai 980-8577, Japan
f-wang@mail.tagen.tohoku.ac.jp.

ABSTRACT

The objective of this research is to investigate the chemical stability of perovskite BSCF phase. To this end the BSCF was studied by using an *in situ* HT-XRD analysis, while annealing it in the HT-XRD chamber under controlled oxygen partial pressure ($p(\text{O}_2)$, $1\text{-}10^{-4}$ bar) and temperature (RT-1100 °C). The results showed that the cubic phase of BSCF is decomposed at lower temperature in relatively high $p(\text{O}_2)$ and the boundary of the stability $p(\text{O}_2)$ region shifts to lower $p(\text{O}_2)$ with increasing temperature. It implied the phase stability of the cubic BSCF depends on $p(\text{O}_2)$ as well as temperature.

1. Introduction

$\text{Ba}_{0.5}\text{Sr}_{0.5}\text{Co}_{0.8}\text{Fe}_{0.2}\text{O}_{3-\delta}$ (henceforth denoted as BSCF) in the cubic perovskite phase has excellent oxygen ionic and electronic conducting property. Due to such a mixed ionic-electronic conduction, BSCF was found to exhibit excellent performance as a cathode for intermediate temperature solid oxide fuel cells (IT-SOFCs) [1]. Recently, however, the performance degradation of BSCF cathodes was reported after the long-term operation [2-4]. This might be caused by the instability of BSCF at intermediate temperature range in air. More recently, attentions have been paid on the phase transition of BSCF depending on temperature and time [5-14]. Svarcova *et al.* found the coexistence of hexagonal and cubic polymorphs after long time annealing at 800°C [5]. D. N. Müller *et al.* detected phase equilibrium between hexagonal and cubic perovskite phase at 800°C by a combined study with XRD and electron microscopy [8]. P. Müller observed a trigonal phase besides the hexagonal and the cubic phases by TEM analysis on a bulk BSCF sample [11]. All of these results indicated the instability of the cubic BSCF in air around 800°C. But the chemical stability of BSCF, particularly the influence of oxygen partial pressure, $p(\text{O}_2)$, is not fully understood. In this work, the chemical stability of BSCF were investigated by using *in situ* HT-XRD measurements in $p(\text{O}_2)$ range of $\log(p\text{O}_2/\text{bar}) = -4$ to 0 by a stepwise heating process from 400°C to 1100°C.

2. Method

Single-phase perovskite $\text{Ba}_{0.5}\text{Sr}_{0.5}\text{Co}_{0.8}\text{Fe}_{0.2}\text{O}_{3-\delta}$ (BSCF) powders were synthesized by the Pechini method. Firstly, nitrate solutions of Ba^{2+} , Sr^{2+} , Co^{2+} and Fe^{3+} were prepared. The concentration of each solution was determined by a chelate titration for Ba^{2+} , Sr^{2+} , Co^{2+} and by ICP-AES for Fe^{3+} . The nitrate solutions were then mixed in the appropriate stoichiometric ratio. Ethylene glycol and citric acid were added to the solution and heated up to 473 K to obtain a polymeric precursor. The pulverized precursor was calcined at 1073 K for 5 hours, and then sintered at 1373 K for 10 h. The phase state of the sample was analyzed by powder X-ray diffraction (M21X, MAC Science Co., Yokohama, Japan) with a $\text{CuK}\alpha$ anode at room

temperature in air, and was confirmed as the single-phase perovskite.

X-ray diffractometer (D8 Advance with LYNXEYE™ Super Speed Detector, Bruker AXS, and $\text{CuK}\alpha$ radiation) was used for the *in situ* high-temperature powder X-ray diffraction (HT-XRD) measurement as a function of oxygen partial pressure $p(\text{O}_2)$, temperature and annealing time. The BSCF powder was set on a platinum heater inside the XRD chamber (Fig. 1).

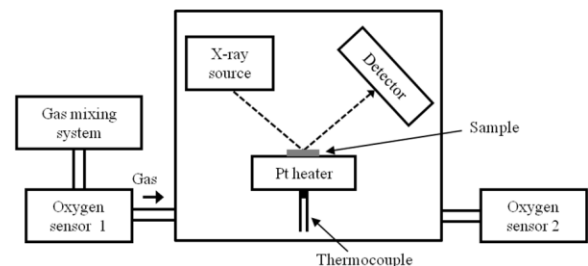


Fig.1 Schematic illustrations of experimental setup for high-temperature X-ray diffraction measurements.

In order to investigate the chemical stability depending on $p(\text{O}_2)$, the XRD patterns were measured in the $p(\text{O}_2)$ range of $\log(p\text{O}_2/\text{bar}) = -4$ to 0 using $\text{O}_2\text{-N}_2$ mixture gases. The $p(\text{O}_2)$ was monitored at the inlet and the outlet of the XRD chamber by two zirconia sensors.

3. Results and Discussion

The XRD patterns were obtained at every 100°C between 400°C and 1100°C in each $p(\text{O}_2)$. For ensuring equilibrium we programmed the heating process with the holding time of 20, 20, 15, 10, 5, 5, 5, and 5 hours at 400, 500, 600, 700, 800, 900, 1000, and 1100°C, respectively. Figures 2 (a)-(d) show HT-XRD patterns of BSCF after annealing at 400°C to 800°C in $p(\text{O}_2)$ range of $\log(p\text{O}_2/\text{bar}) = -4$ to 0. Figure 2 (a) shows no impurity phase was observed when $\log(p\text{O}_2/\text{bar}) \leq -2$ at 400°C after 20 hours annealing. When $\log(p\text{O}_2/\text{bar}) \geq -1$, however, peaks of an impurity phase (phase A) appeared. This means that the cubic perovskite phase of BSCF is not thermodynamically stable under these $p\text{O}_2$ conditions at 400°C. Figure 2 (b) shows the decomposition of the cubic phase BSCF occurred when $\log(p\text{O}_2/\text{bar}) > -1$ at 500°C. This means that the

boundary of the stable pO_2 condition for the cubic BSCF shifted to lower with increasing temperature.

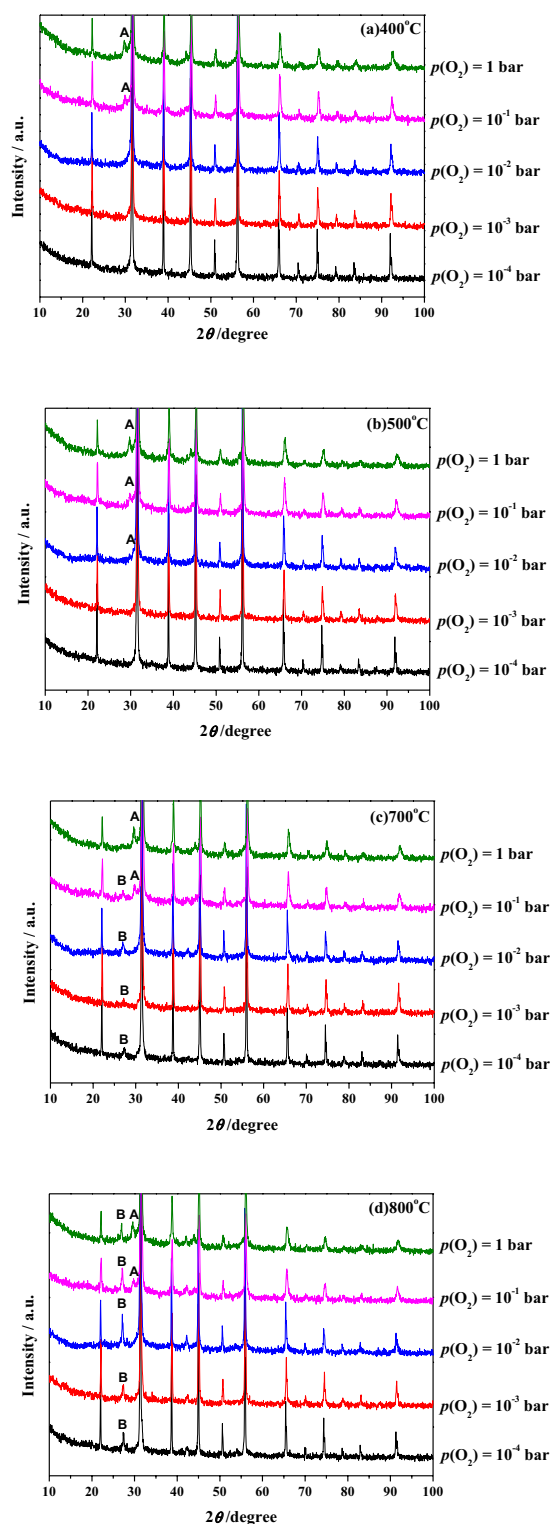


Fig. 2 HT-XRD patterns of BSCF powder after long time annealing at (a) 400 °C, (b) 500 °C, (c) 700 °C and (d) 800 °C.

Figure 2(c) shows the HT-XRD results of BSCF powder after annealing with 10 hours at 700 °C. At this temperature, another impurity phase (phase B) was

observed in addition to the impurity phase A and the cubic BSCF in $\log(pO_2/\text{bar}) = -4$ to 1. As seen in Fig. 2(d), at 800 °C, BSCF powders were all decomposed to multiphase, showing complicated decomposition behaviors of cubic BSCF. The impurity phase B seems more stable at higher temperature.

4. Concluding remarks

The *in situ* HT-XRD measurements were employed for the chemical stability analysis of BSCF in $\log(pO_2/\text{bar}) = -4$ to 0 from 400 °C to 1100 °C. The results indicated the instability of BSCF at intermediate temperatures. Additionally, the results implied the stability of the cubic phase of BSCF is influenced by not only temperature but also $p(O_2)$.

Acknowledgements

The Japan Society for the Promotion of Science and the Tohoku University Global COE program were acknowledged.

References

- [1] Z.P. Shao, S.M. Haile, *Nature* **431**, 170 (2004)
- [2] W. Zhou, R. Ran, Z.P. Shao, *J. Power Sources* **192**, 231 (2009)
- [3] A. Yan, M. Cheng, Y. L. Dong, W. S. Yang, V. Maragou, S. Q. Song and P. Tsiakaras, *App. Catalysis B-Environmental* **66**, 64 (2006)..
- [4] Z.P. Shao, W.S. Yang, Y. Cong, H. Dong, J.H. Tong, G.X. Xiong, *J. Membrane Science* **172**, 177 (2000) .
- [5] S. Svarcova, K. Wiik , J. Tolchard , H. J.M. Bouwmeester, T. Grande, *Solid State Ionics* **178**, 1787 (2008).
- [6] S. McIntosh, J.F. Vente, W. G. Haije, D. H.A. Blank, H. J.M. Bouwmeester, *Solid State Ionics* **177**, 1737 (2006).
- [7] J. Ovenstone, J.Jung, J. S. White, D.D. Edwards, S. T. Misture, *J. Solid State Chem.* **181**, 576 (2008).
- [8] D. N. Mueller, R. A. D. Souza, T.E. Weirich, D. Roehrens, J. Mayer, M. Martin, *Phys. Chem. Chem. Phys.*, **12**, 10320 (2010).
- [9] S. Yakovlev, C.Y. Yoo, S. Fang, H. J. M. Bouwmeester, *Appl. Phys. Letter*, **96**, 254101 (2010).
- [10] Z. Yang, J. Martynczuk, K. Efimov, A.S. Harvey, A. Infortuna, P. Kocher, L. J. Gauckler, *Chem. Mater.*, **23**, 3169 (2011).
- [11] P. Müller, H. Störmer, L. Dieterle, C. Niedrig, E. Ivers-Tiffée b, D. Gerthsen, *Solid State Ionics* **206**, 57 (2012).
- [12] C. Niedrig, S. Taufall, M. Burriel, W. Menesklou , S. F. Wagner, S. Baumann , E. I.Tiffée, *Solid State Ionics* **197**, 25(2011).
- [13] K. Efimov, Q. Xu, Armin Feldhoff, *Chem. Mater.*, **22**, 5866 (2010).
- [14] D.N. Mueller, R.A. De Souza, H. Yoo, M. Martin, *Chem. Mater.*, **24**, 269 (2012).

Transient Analysis of Loop Heat Pipes with Secondary Wick

Kouhei Magome, Masahiko Taketani, and Hiroki Nagai
 Department of Aerospace Engineering, Tohoku University
 6-6-01, Aramaki-Aza-Aoba, Aoba-ku, Sendai 980-8579, JAPAN
 magome.kohei@aero.mech.tohoku.ac.jp

ABSTRACT

Loop Heat Pipe (LHP) is a heat transfer device utilizing a phase change of fluid, it has highly thermal performance and robustness for fluctuating the ambient temperature. However, a strict prediction of LHP inside behavior is very difficult because of a complex inner mechanism. Especially, under specific condition, an LHP startup becomes unstable temporarily. A solution for this problem is to attach a secondary wick. In this study, the effect of the secondary wick on the LHP startup was investigated numerically. As a result, it showed that the secondary wick improved unstable behavior in the LHP startup.

1. Introduction

Thermal control on the spacecraft is very important to operate its equipment surely under strict thermal environment, which changes ambient temperatures heavily. In addition, recent spacecraft is needed for more heat transferring from inside to outside of its structure due to miniaturization. Loop Heat Pipes (LHPs) are devices that meet these requirements, have highly thermal transfer performance and robustness for severe ambient temperature changes.

But while an accurate prediction of LHP inside behavior is difficult because a mechanism of the LHP inside, dominated by thermal fluid dynamics, is very complex and LHP operation depends on various ambient condition. Moreover, with vapor in the central core, an evaporator temperature becomes high in the startup.

A solution for this problem, there is a method of using a secondary wick. Attaching the secondary wick, it can supply liquid enough for the central core, LHP startup characteristics are stabilized. Therefore, in this research, LHP models with the secondary wick were simulated numerically to conduct the secondary wick effect on the LHP startup.

2. Principle

2-1. Operating of Loop Heat Pipes

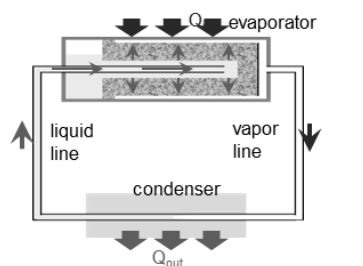
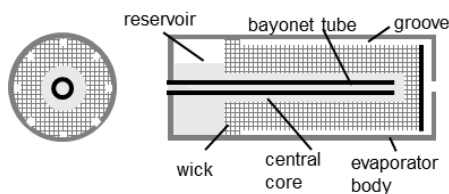


Fig. 1 Schematic of overall LHP



(a) radius (b) along with z axis

Fig. 2 Section of LHP evaporator

Fig. 1 is a schematic of overall LHP. LHP consists of evaporator, condenser, vapor line, liquid line and the

working fluid is enclosed. Fig. 2 is a detailed figure of the evaporator, which composes of a reservoir and a heating zone. In the heating area, a porous material called wick is inserted, the capillary force generated in this material is a driving force of the LHP circulation. The reservoir accumulates extra liquid and always makes possible to supply liquid for the wick.

LHP transfers heat as follows. At first, the working fluid is vaporized in grooves by heat input and vapor flows to the condenser. At the condenser, heat is removed from vapor to environment, fluid returns into liquid and flows to the evaporator. Returning liquid is pumped to the wick outside by its capillary force, and vaporized again.

2-2. Startup Behavior

For a feature of LHP, it is known that vapor – liquid distribution in the evaporator the operating before influences on startup behavior. Maydanik et al. classified LHP's startup into four patterns (Fig. 3) [1]. According to Fig. 3, situation 2 and 4 existing vapor in the central core appear a high temperature peak. This peak should avoid generating, more moderate startups are desired. To operate safely in these situation, it is required that transfer liquid from the reservoir to the wick. For the one of the solution of this problem, there is the way to install the secondary wick.

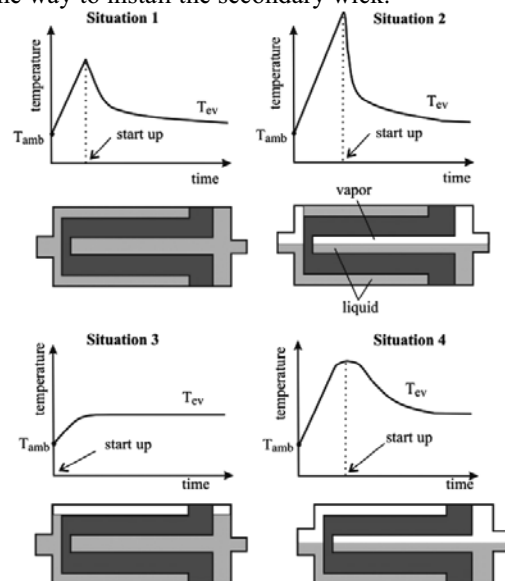


Fig. 3 Classification of LHP Startup

2-3. Secondary wick

Fig. 4 shows the shape of the secondary wick arrangement. The main function of the secondary wick, which is made of the rougher porous material, is a supplying liquid to the primary wick certainly. With the secondary wick, it can transport more smoothly the working fluid from the reservoir to the primary wick. As a result, it is expected that unstable startups such as situation 2 and 4 become moderate.

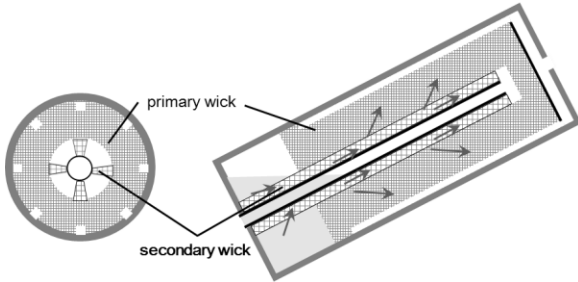


Fig. 4 Secondary Wick Arrangement

3. Analysis Model

The numerical simulation was conducted for the LHP model with the secondary wick programmed by SINDA/FLUINT. This model includes the overall LHP, and has a detailed cylindrical evaporator area. Fig. 5 is a nodal network of the evaporator, composed of main two groups, the thermal network and the fluid flow network. The wick area is divided into 3 parts along with the axial direction, the secondary wick is placed just under the primary wick in parallel with central core's flow paths. In this network, it is assumed that the fluid flow inner evaporator is an axial symmetry, the flow passing through the primary and secondary wicks are one dimensional, a flow direction in the primary is radius, while in the secondary is axial. The size of the reservoir is 38 mm in diameter and 76 mm in length, while the size of the heating zone is 25 mm in diameter and 152 mm in length. The working fluid is ammonia, the initial temperature T_{init} is 293 K, and the sink temperature T_{sink} is 273 K. The initial vapor – liquid distribution is close to situation 4 as depicted Fig. 3.

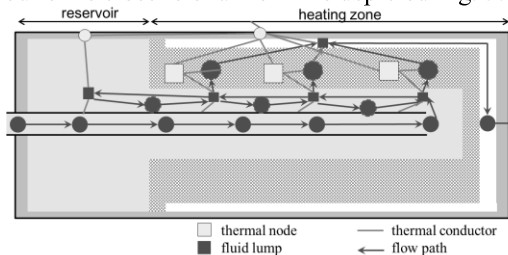


Fig. 5 Network Model of Evaporator Section

4. Results and Discussion

Fig. 6 gives the simulation result of the evaporator temperature without the secondary wick and existing vapor in the central core. A sharp peak was observed in LHP startup. A cause of this peak is vapor in the central core, which prevents liquid from permeating the primary wick and leads reduction of the whole LHP circulation. In other words, heat added the heating zone tends to stay

in the evaporator inside.

On the other hand, Fig. 7 presents the same vapor – liquid distribution condition model attached the secondary wick. There is no peak and the startup is more moderate. This is because the secondary wick supplies liquid from the reservoir to the primary wick and the LHP transfer heat favorably.

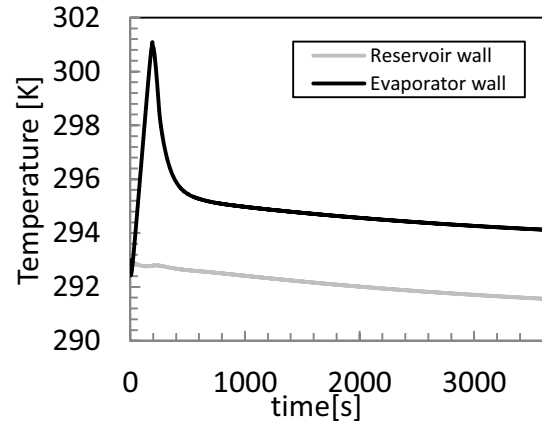


Fig. 6 Evaporator Temperature (without secondary wick)

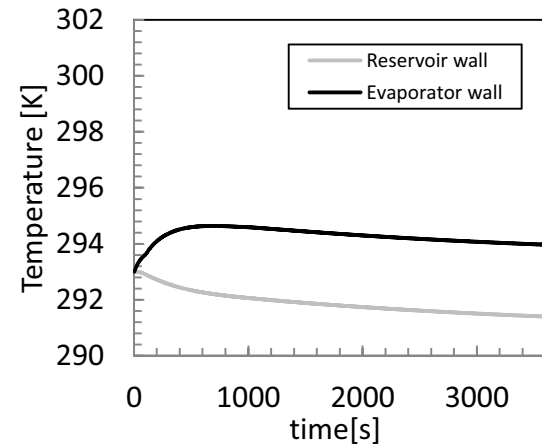


Fig. 7 Evaporator Temperature (with secondary wick)

5. Concluding remarks

To investigate the secondary wick effect on the LHP startup, the numerical simulation was calculated for the LHP models. For the same condition, with and without the secondary wick cases were simulated. As a result, it is showed that the behavior of the LHP startup was improved by using the secondary wick. In the future works, the influence of the secondary wick for overall LHP performance will research.

References

- [1] M. A. Chernysheva, Y. F. Maydanik, J. M. Ochterbeck, 'Heat Transfer Investigation in Evaporator of Loop Heat Pipe During Startup', JOURNAL OF THERMOPHYSICS AND HEAT TRANSFER, Vol. 22, No. 4, October–December 2008
- [2] Trim T. Hoang, 'Mathematical Modeling of Loop Heat Pipes Part II: Secondary Wick Analysis', 5th IECEC 25-27 June 2007, St. Louis, Missouri

Numerical Simulation for Catalytic Reaction over Pt in CH₄/O₂/CO₂ Mixture

Kenji Yamada¹, Kazuya Iwata², Toshihisa Ueda², Takeshi Yokomori²

¹School of Science for Open and Environmental Systems, Keio University,
3-14-1 Hiyoshi, Kohoku-ku, Yokohama 223-8522, Japan

²Department of Mechanical Engineering, Keio University, 3-14-1 Hiyoshi, Kohoku-ku, Yokohama 223-8522, Japan.
Email:fr062381@a6.keio.jp

ABSTRACT

In order to investigate the characteristics of the catalytic reaction under high dilution of CO₂, two-dimensional numerical simulation under steady-state with detailed elementary surface and gas-phase reactions was conducted by using ANSYS FLUENT 13.0 in this study. As a result, the stability reduction of catalytic reaction was confirmed under CH₄/CO₂/O₂ mixture compared to CH₄/N₂/O₂ mixture in wide range of conditions (equivalence ratio ϕ , inlet velocity V). At the same time, the temperature, Pt(s) coverage and heat of reaction on catalyst surface was decreased.

1. Introduction

In recent years, CO₂ capture and storage (CCS) technology is an effective approach to reduce emissions of CO₂. This technology can achieve (Zero emission) virtually zero CO₂ emissions into the atmosphere. There are three methods of CO₂ separation on the combustion technology, oxy-fuel combustion has attracted a great attention from the point of view of simplicity of the device among them.

Oxy-fuel combustion is a combustion system using only oxygen as an oxidizer, so that the increase of CO₂ fraction in the exhaust gas is attained. The separation of water vapor from the exhaust gas by the condenser is an advantage that can separate easily the high concentration of CO₂ of more than 90%. In oxy-fuel combustion, the exhaust gas recirculation has frequently adopted for the purification of CO₂. However, since high CO₂ concentration causes the low flame stability,^[1] the amount of CO₂ recirculation is limited and the supply of oxygen is relatively increased. This feature also leads to increase the operating cost due to the necessity of large production of oxygen.

In order to improve the flame stability in oxy-fuel combustion, the use of the catalytic pre-combustion was proposed in this study. However, the details of catalytic combustion under high concentration of CO₂ have not been reported yet. The purpose of this study is to clarify the characteristics of catalytic combustion under high concentration CO₂.

2. Computational method

Figure 1 shows a schematic diagram of the computational domain. It was assumed that the catalyst was a tube with 5.0 mm in radius and 30.0 mm in length, and the reaction was occurred inside of it. Hence, the computational area had an axial symmetry so that only two-dimensional analysis was examined. The catalyst consisted of pure platinum and the convective heat transfer from the catalyst tube to circumstance was taken into account. The convective heat transfer coefficient was calculated from the Nusselt number for forced convection in laminar flow parallel to the cylinder; $h = 12.11 \text{ W}/(\text{m}^2 \cdot \text{K})$. In order to ignore the effect of inlet and outlet boundaries, the extended sections with adiabatic

non-catalyst walls were set at the upstream and the downstream side of the catalyst as shown in Fig. 1. From the inlet boundary, the pre-mixture of CH₄/CO₂/O₂ (or CH₄/N₂/O₂) was injected with equivalence ratio ϕ and the inlet Velocity V . The volumetric ratio of O₂ : CO₂ (or N₂) was fixed at 20.95 : 79.05.

The numerical calculation was performed under the steady-state condition by using ANSYS FLUENT 13.0. The elementary gas-phase reactions with 18 species and 58 steps [2], and the elementary surface reactions with 11 species and 24 steps [3] were respectively adopted in this calculation.

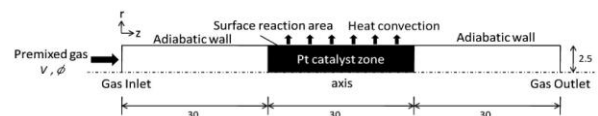


Fig. 1 Schematic diagram of computational domain.

3. Results and Discussion

3.1. Reaction stability limit on catalyst.

Figure 2 shows the reaction stability limit on Pt catalyst under N₂ or CO₂ dilution. From this figure, the upper and lower velocity limits exist for lean mixture, while only the lower limit exists for rich mixture, in both of CO₂ and N₂.

For the upper limit, reactants were supplied to the catalyst surface by the diffusion in the concentration boundary layer, which became thinner with the increase of the flow velocity. On the other hand, a heat generated by the surface reaction is carried more to the mainstream as decreasing the thermal boundary layer thickness. At the same time, the characteristic time of flow was shortened as increasing the flow velocity, so that the reactants were washed away to downstream before initiating the reaction. Hence, the heat to maintain the surface reaction was no longer obtained, and it led to extinction. For the lower limit, the rate of diffusion of the reactants to the catalyst surface was reduced by thickening the concentration boundary layer as decreasing the flow velocity. In addition, there was a heat loss by the convective heat transfer from the outer wall surface of the catalyst in this model. Therefore, the catalyst temperature became so low that the reaction was no longer sustained, and it led to extinction.

Note here that the stability limit for CO₂ was narrowed in comparison with that for N₂.

3.2. Temperature distribution of reactant gas

Figure 3 shows the temperature distributions of reactant gas at $\phi = 2.0$ and $V = 0.5$ m/s for N₂ and CO₂ dilutions. From this figure, there is clearly a temperature difference between N₂ and CO₂ dilution conditions. This is due to a difference in the gas phase component, in particular, the difference of specific heat between N₂ and CO₂ has a significant impact for the temperature. Specific heats of N₂ and CO₂ are 32.7 J/(kg·K) and 54.3 J/(kg·K) at 1273 K, respectively, so that the temperature rise was prevented for CO₂.

3.3. Catalyst wall temperature

Figure 4 shows the temperature averaged over the catalyst wall surface at $\phi = 2.0$. This shows that the catalyst wall temperature for CO₂ is lower than that for N₂. This reason is mainly because the gas phase temperature for CO₂ dilution was lower than that for N₂ as shown in Fig. 3. As described later, in addition, the heat of reaction on the catalyst surface for CO₂ was also lower than that for N₂, so that it caused the decrease of the temperature. This temperature difference strongly influenced to the stability limit as shown in Fig. 2.

3.4. Catalyst surface coverage of Pt(s)

Figure 5 shows the averaged surface coverage of Pt(s) for N₂ and CO₂. For CO₂ dilution, the coverage of Pt(s) shows lower compared to that for N₂ dilution. This feature causes that the activation of catalyst surface reduced for CO₂ compared to N₂. A possible reason for this is the reduction of the desorption rate of chemical species due to the decrease of catalyst wall temperature.

3.5. Heat of reaction

Figure 6 shows the total heat of reaction on the catalyst wall at $\phi = 2.0$. This result shows that there is a difference of the heat of reaction on the catalyst surface between N₂ and CO₂, as well as the surface temperature and Pt(s) coverage as shown in Figs. 4 and 5. As shown in Fig. 5, the coverage of Pt(s) on the catalyst surface was greatly affected by CO₂ dilution and it was deactivated. In addition, the feed of CH₄ on the catalyst surface for CO₂ dilution should be smaller than that for N₂ dilution, because the binary diffusion coefficient between CH₄ and CO₂ (1.39 cm²/s) is smaller than that between CH₄ and N₂ (1.72 cm²/s). Therefore, the reductions of Pt(s) coverage and of CH₄ feed led to decreasing the heat of reaction.

4. Concluding remarks

The stability of the catalytic reaction under CH₄/O₂/CO₂ mixture was worse than that under CH₄/O₂/N₂ mixture, because of low catalyst wall temperature, low Pt(s) coverage, and accordingly low heat of reaction on the surface.

References

- [1] Y. Tan et al., Fuel **81**, 1007-1016 (2002).
- [2] O. Deutschmann et al., Combust. Inst. Vol. **26**, pp1747-1754(1996).
- [3] R. J. Kee et al, National Lab. Report SAND **85-8240** (1991).

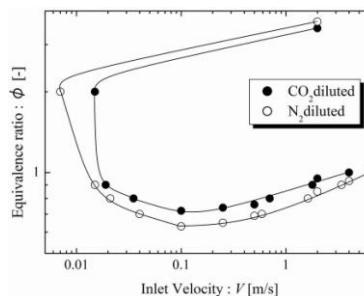


Fig. 2 Reaction stability limit on Pt catalyst.

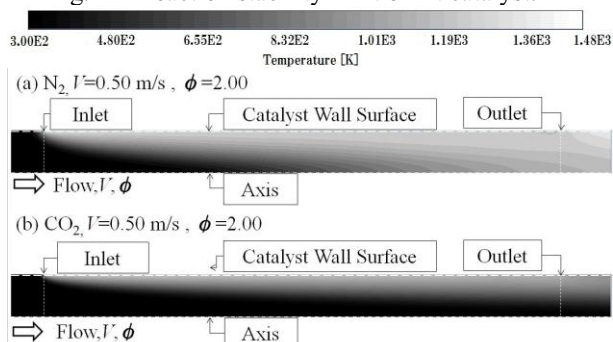


Fig. 3 Temperature distribution at $\phi=2.0$ and $V=0.5$ m/s for (a) N₂ dilution and (b) CO₂ dilution.

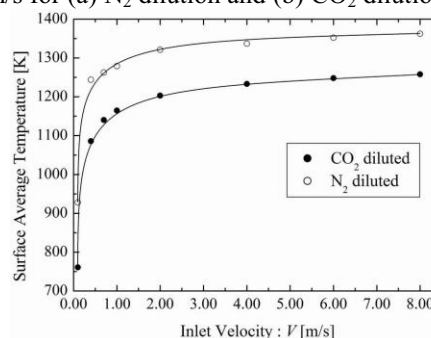


Fig. 4 Averaged catalyst Wall Temperature.

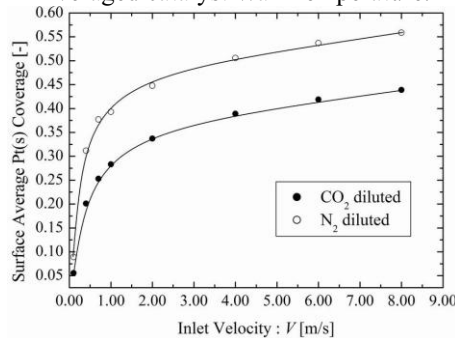


Fig. 5 Averaged catalyst surface coverage of Pt(s).

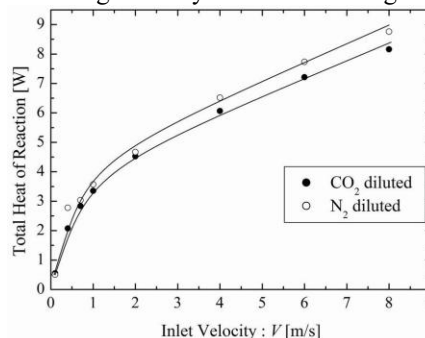


Fig. 6 Total Heat of Reaction on catalyst surface.

Effect of Surface Reactions on Gas Phase Reactions of $H_2/O_2/N_2$ and CH_4 /Air Mixture in a Micro Flow Reactor with a Controlled Temperature Profile

Yuta Kizaki, Kenichiro Saruwatari, Hisashi Nakamura, Takuya Tezuka, Susumu Hasegawa and Kaoru Maruta
Institute of Fluid Science, Tohoku University, 2-1-1 Katahira Aoba-ku Sendai Miyagi 980-8577, Japan
kizaki@edyn.ifs.tohoku.ac.jp

ABSTRACT

Combustion characteristics of $H_2/O_2/N_2$ and CH_4 /air mixtures were investigated by using a micro flow reactor with a controlled temperature profile. 2-D computations with detailed chemical mechanisms of gas phase and surface reactions were conducted to examine the effect of radical quenching on the wall surface. By comparing the computation with gas sampling analysis, it was found that the surface reaction mechanism for radical quenching may overestimate the effect of radical quenching on the gas phase reaction.

1. Introduction

With the downsizing and technology advance of mobile devices, the demands on micro power source are increasing. Micro combustion systems are expected to be one of the possible power sources having high energy density. Due to large surface-to-volume ratio, heat loss to the wall is increased in micro combustion and it is difficult to maintain a stable combustion. In addition, the effect of radical quenching on the wall surface is not negligible in micro system and it is important to clarify it. However, there are a few experimental and numerical studies on radical quenching [1, 2].

This study focused on a micro flow reactor with a controlled temperature profile [3]. A narrow channel, which diameter is smaller than ordinary quenching diameter, was heated by an external heat source and a stationary wall temperature gradient was established. This technique can simulate heat recirculation and enable a stable combustion. In previous studies, combustion characteristics of methane/air [4], DME/air [5] and *n*-heptane/air [6] mixtures were investigated in the micro flow reactor. These studies established the availability of the micro flow reactor with a controlled temperature profile as the method to examine the combustion characteristics of various hydrocarbons.

In this study, we applied H_2 to the micro flow reactor as a fuel which is sensitive to surface radical quenching. As second target, CH_4 was used as a general fuel. The objective of this study is to examine the effect of radical quenching on the gas phase reaction of H_2 and CH_4 .

2. Experimental and computational method

Figure 1 shows the schematic of the experimental setup. A quartz glass tube with an inner diameter of 1 mm was used as a micro flow reactor and heated by a H_2 /air flat flame burner to obtain a stationary temperature profile from 300 K to 1300 K. A stoichiometric $H_2/O_2/N_2$ mixture which was controlled by mass flow controllers was supplied into the tube in atmospheric pressure. In order to decrease the ordinary quenching diameter less than 1 mm, the mole fractions of H_2 and O_2 were diluted with N_2 ($X_{H_2}:X_{O_2}:X_{N_2}=2:1:9$). The exhaust gas was analyzed by a gas chromatograph with a thermal conductivity detector. Argon was used as a carrier gas. Molecular Sieve 5A 60/80 was used.

To investigate the experimental result and the effect of radical quenching, 2-D computation was conducted by FLUENT 6.3 with detailed reaction mechanisms. CH_4

case was studied only by computation at present. The conservation equations of mass, momentum, energy and species were solved. Because of the symmetry of the cylindrical tube, the computational domain was a half of the tube from central axis ($r=0$ mm) to the wall ($r=0.5$ mm). As a boundary condition, the wall surface was assumed as nonslip wall and given a stationary wall temperature profile which is the same as the experimental wall temperature profile. H_2 oxidation mechanism [7] and GRI3.0[8] without reactions for N were used to represent the gas phase reaction. In order to evaluate the effect of radical quenching on the wall, two surface conditions were assumed; (a) inert wall without any surface reaction, (b) quench wall with surface reaction mechanism for radical quenching [1].

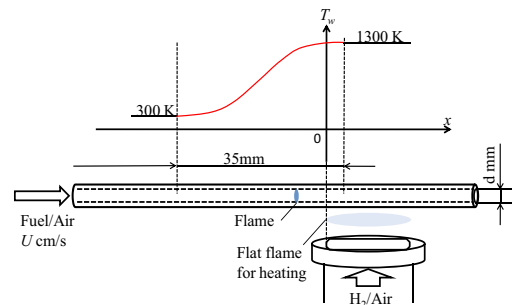


Fig. 1 Schematic of experimental setup and provided wall temperature profile.

3. Results and discussion

Figure 2 shows the computational distributions of H_2 , O_2 and H_2O mole fractions, gas phase temperature and wall temperature at inlet mixture flow velocity of 200 cm/s on (a) inert wall and (b) quench wall. Except for wall temperature profiles, the other distributions are the results on the tube center at $r=0$ mm. The wall temperature is illustrated the result on the wall surface where $r = 0.5$ mm. In inert wall condition (Fig. 2a), H_2 and O_2 were rapidly consumed and H_2O was produced in a reaction zone. In the quench wall condition (Fig. 2b), a reaction zone was also formed. However, even though the gas phase temperature is high enough for hydrogen combustion, 8 % of reactants remained in the downstream of the reaction zone. Figure 3 shows distributions of OH mass fraction and wall temperature. The OH mass fraction peak in the quench wall condition was smaller than that in the inert wall condition and shifted to downstream in the quench wall.

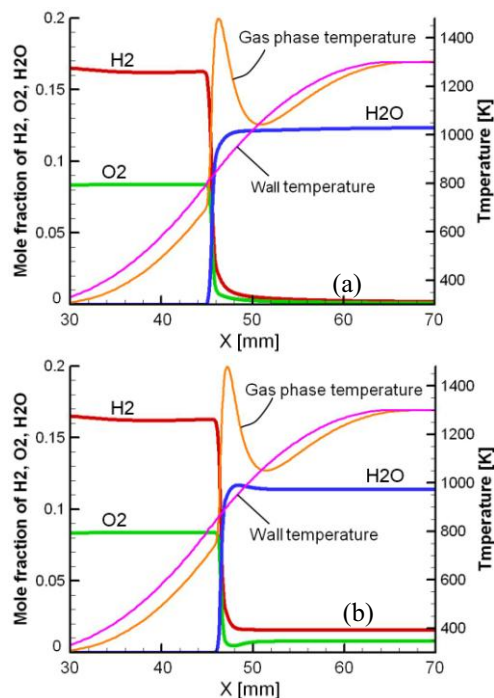


Fig. 2 Distributions of mole fractions (H_2 , O_2 and H_2O), gas phase temperature and wall temperature at $U=200$ cm/s in (a) inert wall and (b) quench wall.

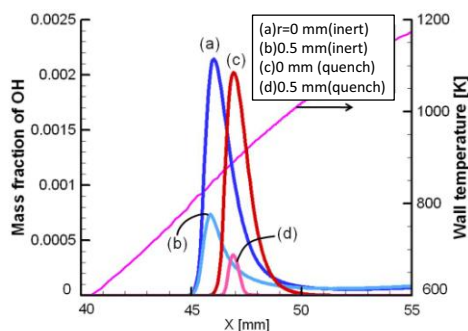


Fig. 3 Distributions of OH mole fraction in gas phase and wall temperature at $U=200$ cm/s.

These differences between inert and quench walls would be attributed to the suppression of oxidation reaction because of reduction of radicals by the effect of radical quenching on the wall surface. However, since H_2 was completely consumed in experiment, computations couldn't reproduce the experiment. Thus it was concluded that the radical quenching mechanism may overestimate the effect of radical quenching on the wall surface.

Subsequently, the effect of surface reactions for CH_4 case is examined. Figure 4 shows the computational distributions of CH_4 , O_2 , CO_2 and H_2O mole fractions, gas phase temperature and wall temperature at inlet mixture flow velocity of 80 cm/s on (a) inert wall and (b) quench wall. As is the case in H_2 , the gas phase temperature is high enough for methane combustion, 3 % of O_2 remained in the downstream of the reaction zone. And, flame location move to downstream on quench wall. This difference of wall temperature is about 100 K. This result indicates that significant effect of surface reactions

for CH_4 case. Therefore, gas analysis is needed to clarify the effect of surface reactions for CH_4 case.

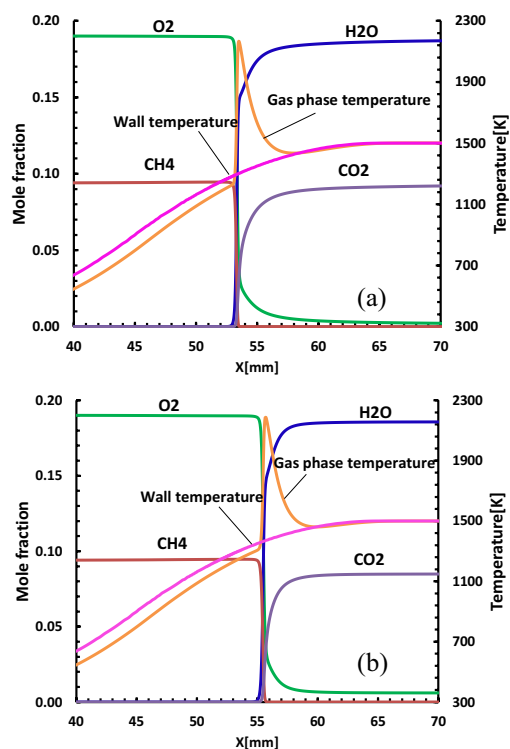


Fig. 4 Distributions of mole fractions (CH_4 , O_2 , CO_2 and H_2O), gas phase temperature and wall temperature at $U=80$ cm/s in (a) inert wall and (b) quench wall.

4. Conclusions

The effects of radical quenching were examined by 2-D computations for H_2 and CH_4 cases. For H_2 case, by comparing the computational results of two types of the wall condition with the result of gas sampling analysis, it was found that radical quenching mechanism may overestimate the effect of radical quenching on the wall surface. For CH_4 case, it was found the same tendency as H_2 case. Therefore, the comparison of the current computational result with gas analysis will be needed.

References

- [1] S. Raimondeau, D. Norton, D. G. Vlachos and R. I. Masel, Proc. Combust. Inst. **29** (2002) 901-907.
- [2] P. Aghalayam, P-A. Bui and D. G. Vlachos, Combust. Theory Modeling **2** (1998) 515-530.
- [3] K. Maruta, T. Kataoka, N. I. Kim, S. Minaev and R. Fursenko, Proc. Combust. Inst. **30** (2005) 2429-2436.
- [4] Y. Tsuboi, T. Yokomori and K. Maruta, Proc. Combust. Inst. **32** (2009) 3075-3081.
- [5] H. Oshibe, et al., Combust. Flame **157** (2010) 1572-1580.
- [6] A. Yamamoto et al., Proc. Combust. Inst. **33** (2011) 3259-3266.
- [7] J. Mantzaras, R. Bombach and R. Schaeren, Proc. Combust. Inst. **32** (2009) 1937-1945.
- [8] G.P. Smith et al., http://www.me.berkeley.edu/gri_mech/.

Nongray Radiative Transfer and Convective Heat Transfer Modeling in a Trapezoidal Cavity Receiver for the CLFR

Atsushi Sakurai*, Shumpei Yoshimura**, Masud Behnia*** and Koji Matsubara*

*Faculty of Engineering, Niigata University, Niigata 950-2181, Japan

**Graduate School of Science and Technology, Niigata University, Niigata 950-2181, Japan

*** Aerospace, Mechanical and Mechatronic Engineering, University of Sydney, Sydney, NSW 2006, Australia

E-mail: sakurai@eng.niigata-u.ac.jp

ABSTRACT

The Compact Linear Fresnel Reflector (CLFR) is a promising technology of solar thermal power plant. The objective of this study is to develop a coupled simulation model of nongray radiation and convective heat transfer. Effects of optical properties of glass on nongray radiation are investigated in order to enhance efficiency of energy trapping. The present study shows the results of nongray radiation model for glass of solar receiver. Since visible light transmission and infrared light absorption of the glass are considered, the obtained results clarify the role of nongray radiative heat transfer in the solar receiver.

1. Introduction

Solar thermal power plant is an attracting technology for renewable energy source. The Compact Linear Fresnel Reflector (CLFR) is a solar concentrator designed for use in solar power plant [1]. The collector consists of mirror arrays that concentrate solar energy and a trapezoidal cavity receiver that absorb the energy.

In order to collect solar energy, glass plate plays an important role. Due to the nongray behavior of optical properties of glass, the glass plate can trap the infrared radiation in the receiver, and transmit the solar irradiation. However, the previous studies have not paid attention to the nongray radiation.

The objective of this study is to validate a coupled simulation of nongray radiation and convective heat transfer by comparing with the experiment. Then, effects of optical properties of glass on nongray radiation are investigated in order to enhance efficiency of energy trapping.

2. Numerical Method

A numerical model of the solar receiver has been developed using the FLUENT ver.12 commercial CFD software package. Fig. 1 shows the 2D trapezoidal solar receiver model. The solar receiver surface is modeled as an isothermal with a specified temperature of 573K and an internal emissivity of 0.1. The side wall is modeled as convective heat transfer boundary exchanging heat with ambient temperature. An internal emissivity of 0.9 is used for the side wall. The computational condition is summarized in Table. 1.

The bottom surface is modeled as a glass. A semi-transparent medium is assumed for radiative heat transfer analysis. Figure 2 shows the absorption coefficient of the glass. The 10 band model is employed for the nongray radiative heat transfer analysis[2]. As shown in this figure, visible light can be transmitted but infrared light cannot be transmitted. The optical characteristics are very useful for decreasing radiative heat loss from solar receiver. External convection heat transfer coefficients were modeled by following Reynolds et al.'s experiment[3].

The flow in the solar receiver is modeled as laminar. The discrete transfer method and discrete ordinate method is employed for radiative heat transfer[4,5].

Table 1. Computational condition

Temperature, T_{wd} [K]	573
Temperature, T_w [K]	293
External temperature, T_{ww} [K]	404
Heat transfer coef., h_{wd} [W/m ² K]	0
Heat transfer coef., h_w [W/m ² K]	0.65
Heat transfer coef., h_{ww} [W/m ² K]	0.33
Emissivity, ε_{wd} [-]	0.1
Emissivity, ε_w [-]	0.92
Length, D , L , and W [m]	0.26, 0.41, 0.465

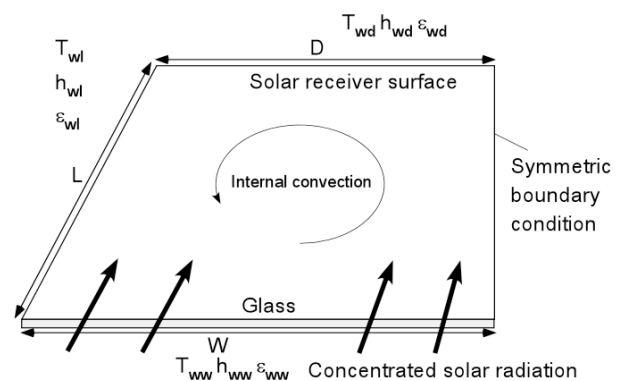


Fig. 1 2D solar receiver model

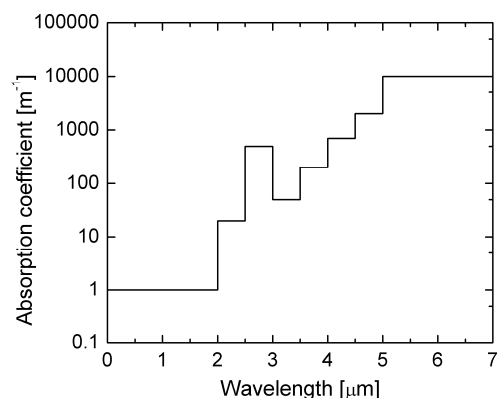


Fig. 2 Absorption coefficient of glass and modeling band approximation[2]

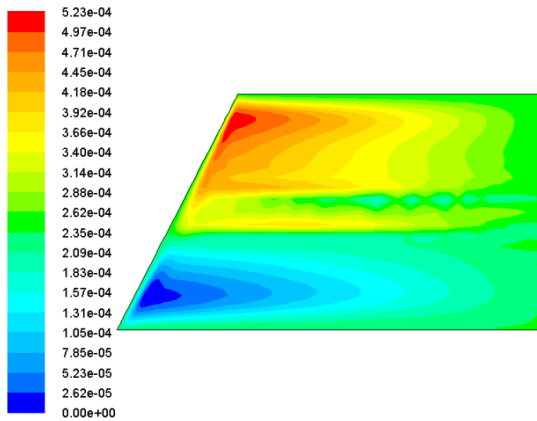


Fig. 3 2D contour of the stream function with the discrete transfer method

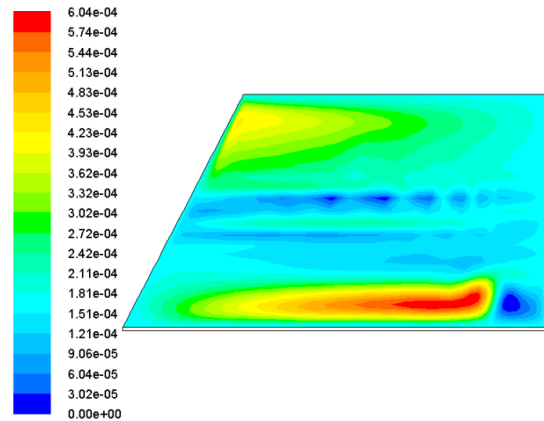


Fig. 5 2D contour of the stream function using nongray radiation model

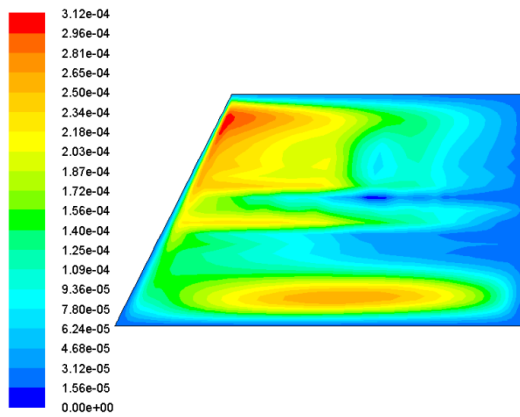


Fig. 4 2D contour of the stream function with the discrete ordinate method

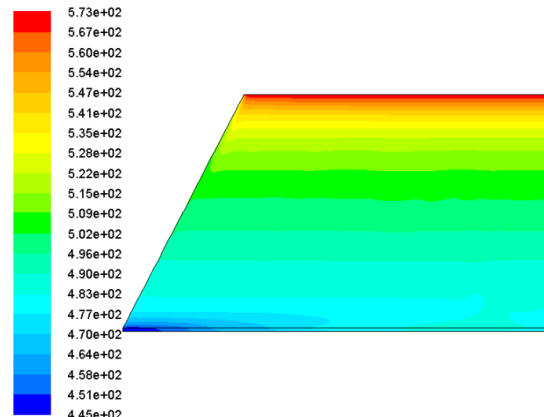


Fig. 6 2D contour of the temperature distribution using nongray radiation model

3. Results and Discussion

Figures 3 and 4 show the streamline by the CFD with gray and opaque assumption using the discrete transfer method and the discrete ordinate method for comparing with the Reynolds et al's experiment[3]. We have confirmed our numerical data shows similar tendency with the experimental results. Since the result with the discrete ordinate method shows better performance, the method is employed for the next analyzes.

Figure 5 shows the streamline by the CFD with nongray and semitransparent assumption for modeling of real glass. These flow patterns were appeared to have a basically stratified upper layer, with a large convective eddies in the lower half of the cavity. Rising hot fluid from the bottom causes local instability in the flow, and eddy entrainment occurs near side wall. Since the glass transmits visible light and traps infrared light, the clear eddy structure can be found near the glass. On the other hand, the temperature distribution shows clearly stratified at steady-state solution as shown in Fig. 6.

4. Conclusion

The present study has investigated the fundamental heat transfer of solar receiver using compact linear

fresnel reflector. Conclusions are summarized as;

1. We have confirmed our simulation model using FLUENT ver.12 shows similar tendency with the experimental results, and the discrete ordinate method is suitable for radiative heat transfer modeling for the analysis.
2. Nongray radiative heat transfer analysis of glass showed the different flow pattern with the gray and the opaque assumption because we have considered the visible light transmission and the infrared light trapping.

Nongray gas model and nongray concentrated solar radiation model will be incorporated in our future work, and the work will more clarify the role of radiative heat transfer for solar receiver.

References

- [1] Milles et al., *Solar Energy*, **68**(3) (2000) 263-283.
- [2] Bauer et al., *Solar Energy Mat. & Solar Cells*, **88** (2005) 257-268.
- [3] Reynolds et al., *Solar Energy*, **76** (2004) 229-234.
- [4] Modest M.F., *Radiative Heat Transfer*, Academic press (2003).
- [5] Maruyama S., *Light Energy Engineering*, Yokendo, (2004). (In Japanese)

In-situ Measurements of Mechanical Properties of High Temperature Ionics Materials

Yuta Kimura^a, Yoshikazu Shirai^a, Tatsuya Kawada^a, Shin-ichi Hashimoto^b, Koji Amezawa^c

^a Graduate School of Environmental Studies, Tohoku University, Sendai, Miyagi
980-8579, Japan

^b Graduate School of Engineering, Tohoku University, Sendai, Miyagi 980-8579, Japan

^c IMRAM, Tohoku University, Sendai, Miyagi 980-8577, Japan
kimura@ee.mech.tohoku.ac.jp

ABSTRACT

Elastic moduli and stress-strain relationships of $\text{La}_{0.6}\text{Sr}_{0.4}\text{Co}_{1-y}\text{Fe}_y\text{O}_{3-\delta}$ (LSCF) were evaluated at high temperatures under controlled atmospheres by using a resonance method and uniaxial compression tests. The elastic moduli of LSCF drastically changed with the change in oxygen nonstoichiometry, crystal structure. The stress-strain relationships of LSCF showed nonlinear behaviors, which is considered due to ferroelasticity.

1. Introduction

Solid oxide fuel cells (SOFCs) are expected as energy conversion devices having advantages such as high power-generation efficiency, fuel flexibility, a possible use of high-temperature waste heat and so on. Mechanical failures of the components are one of the serious issues to be solved for their full scale commercialization. In order to design the cell/stack suppressing mechanical failures, mechanical properties of the component materials should be precisely understood under operating conditions^[1]. SOFC are mainly composed of high temperature ionics materials. So far, their electrochemical properties have been widely studied by many researchers^[2]. However, there are few studies which focused on their mechanical properties especially at high temperatures under controlled atmospheres. From above background, we evaluated mechanical properties of $\text{La}_{0.6}\text{Sr}_{0.4}\text{Co}_{1-y}\text{Fe}_y\text{O}_{3-\delta}$ (LSCF, LSC for $y = 0$, LSCF6428 for $y = 0.8$, LSF for $y = 1$), which is one of high temperature ionics materials, by using resonance method and uniaxial compression tests.

2. Experimental

LSCF powders synthesized by Pechini method were sintered at 1473-1573 K for 6 hours. Relative densities of the samples were over 95 %. Young's modulus, E , shear modulus, G , were measured by a resonance method. The measurements were performed in the temperature range from 298 to 1173 K and in $P(\text{O}_2)$ range from 1×10^{-1} to 1×10^{-4} bar by using an elastic modulus meter (EGII-HT, Nihon Technoplus Co., Ltd.). Detailed procedures for the measurements were described elsewhere^[3]. The uniaxial compression tests were performed in the temperature range between room temperature to 1073 K in air. A 20 kN uniaxial actuator (Cormet digital control) was used to apply a load. The load was measured with 20 kN load cells (Cormet), while the deformation of a sample by an extensometer (MTS 634.31F-25 S/N 1144123). The samples were held one hour to attain equilibrium before each measurement. Once a measurement was performed, temperature was elevated to 1173 K and held 1 hour to anneal a sample. And then temperature was cooled and

the next measurement was successively performed with the same sample.

3. Results and Discussion

3.1. Temperature dependence of E , G

Fig. 1 shows temperature dependence of the Young's and shear moduli of LSC, LSCF6428 and LSF under $P(\text{O}_2)$ of 1.0×10^{-1} bar. The elastic moduli first decreased with increasing temperature, then they drastically increased at high temperatures. For all the compositions of LSCF, the temperatures at which the drastic increase started corresponded with respective phase transition temperatures from rhombohedral to cubic^[4-6]. It is reported that the elastic modulus of perovskite oxides are highly influenced by the phase transition^[7]. Thus, the drastic increase above at high temperatures is considered to be associated with the phase transition.

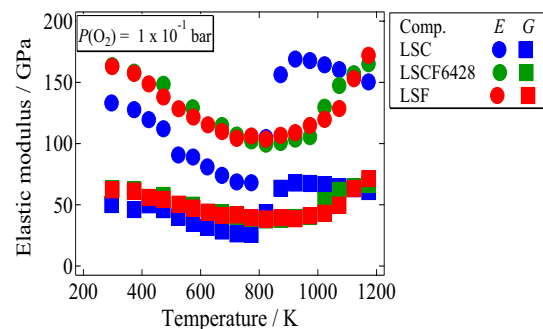


Fig. 1. Temperature dependence of the Young's and shear moduli of LSC, LSCF6428 and LSF under $P(\text{O}_2)$ of 1.0×10^{-1} bar.

3.2. $P(\text{O}_2)$ dependence of E , G

Fig. 2. shows $P(\text{O}_2)$ dependence of the Young's and the shear modulus of LSCF6428 at various temperatures. The $P(\text{O}_2)$ dependence was different depending on temperature. At 873K, the elastic moduli was almost independent of $P(\text{O}_2)$, while they increased with decreasing $P(\text{O}_2)$ at 973 K. At 1073 K, they first increased with decreasing $P(\text{O}_2)$ under higher $P(\text{O}_2)$ and then gradually decreased under lower $P(\text{O}_2)$. At 1173K, they monotonically decreased with decreasing $P(\text{O}_2)$. The complicated $P(\text{O}_2)$ dependence of the elastic moduli

may be interpreted by complex influences of the second-order phase transition and the variation of the oxygen nonstoichiometry. The structure change of LSCF gradually proceeds with decreasing $P(O_2)$. As demonstrated in Fig. 1, the phase transition of LSCF is considered to increase the elastic moduli. On the other hand, the decrease in $P(O_2)$ causes the increase in the oxygen vacancy concentration, which leads to the chemical expansion. The expansion weakens the bond strength and thus decreases the elastic moduli. It was considered these conflicting changes competed during changing $P(O_2)$ and each contribution to the elastic moduli differs depending on temperature.

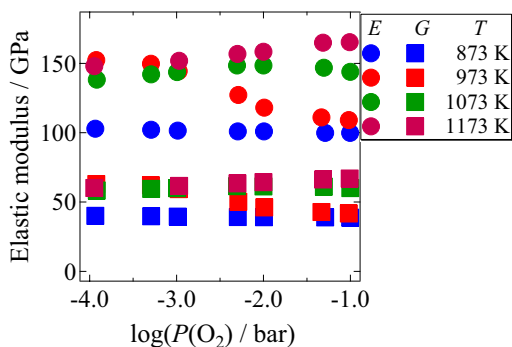


Fig. 2. $P(O_2)$ dependence of the Young's and the shear modulus of LSCF6428 at various temperatures.

3. 3. The stress-strain relationships of $La_{0.6}Sr_{0.4}Co_{1-y}Fe_yO_{3-\delta}$

Figs. 3 (a), (b) show the stress-strain relationship of LSC at room temperature and 873 K. At room temperature, the stress-strain curve nonlinearly changed during loading. While it changed almost linearly during unloading. A residual strain was observed after unloading. Such a stress-strain relationship corresponds with the ones of other $LaCoO_3$ -based oxides reported in the literatures^[8]. In rhombohedral $LaCoO_3$ -based oxides, there can exist 4 domain states which have a different rhombohedral principal axis. When a certain level of stress is applied to the $LaCoO_3$ -based oxide, a domain state can switch to the other and twins are formed. Such domain switching and twin formations can relieve the stress and result in a nonlinear stress-strain relationship and a residual strain. Such a peculiar stress-strain relationship is called ferroelasticity. Considering the above discussion, the nonlinear stress-strain curve of LSC is considered due to the ferroelasticity. In addition, the stress relaxation due to the ferroelasticity is expected to vary the effective Young's modulus, which is the inverse of the slope of the stress-strain curve. The comparatively large decrease in the Young's modulus of LSC under low temperatures (see Fig. 1) might be related with the ferroelasticity.

At 873 K, the stress-strain curve during both loading and unloading was almost linear and almost no hysteresis was observed. This agrees with the fact that LSC has the cubic structure at 873 K and thus no ferroelastic behavior can be observed in the stress-strain curve.

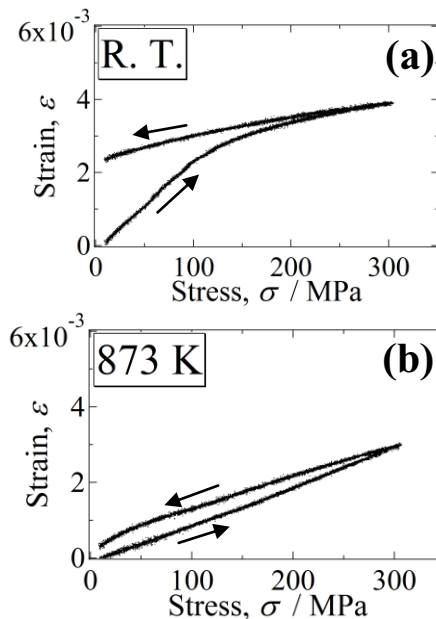


Fig. 3. Stress-strain behavior of LSC at (a) room temperature, (b) 873 K.

4. Conclusions

The Young's and shear moduli of LSCF were evaluated as functions of temperature and $P(O_2)$ by using the resonance method. It was revealed that the elastic moduli of LSCF drastically changed with temperature and $P(O_2)$ due to the phase transition and the variation of the oxygen nonstoichiometry. The stress-strain relationships of LSCF were evaluated by the uniaxial compression tests. It was suggested that the stress-strain relationship of rhombohedral LSCF is influenced by the ferroelasticity.

Such a variation of the elastic modulus with temperature and $P(O_2)$ and the complicated stress-strain relationship can greatly influence the stress distribution in SOFCs under operations. Thus, those should be taken in consideration for determining the operational margin and the design of SOFCs.

Acknowledgement

This investigation was supported by the New Energy and Industrial Technology development Organization (NEDO), Japan. The authors gratefully acknowledge Dr. M.-A. Einarsrud, Dr. J. Tolchard, Dr. T. Grande for their help in performing the uniaxial compression tests.

References

- [1] K. Hosoi *et al.*, *ECS Trans.*, **35** (2011) 11.
- [2] M. Katsuki *et al.*, *Solid State Ionics*, **156** (2003) 453.
- [3] Y. Kimura *et al.*, (2012) to be published.
- [4] J. Mastin *et al.*, *Chem. Mater.*, **18** (2006) 6047-6053.
- [5] B. X. Huang *et al.*, *Solid State Ionics*, **180** (2009) 241.
- [6] A. Fossdal *et al.*, *J. Am. Ceram. Soc.*, **87** (2004) 1952-1958.
- [7] M. A. Carpenter *et al.*, *J. Phys. Condens. Matter*, **22** (2010) 035404.
- [8] P. E. Vullum *et al.*, *Adv. Mater.*, **19** (2007) 4399-4403.

Optical and Thermal Characteristic of a Solar Concentrator with Compound Parabolic and Involute Reflector

Abid Ustaoglu¹, Junnosuke Okajima², Xin-Rong (Ron.) Zhang³, Shigenao Maruyama²

¹Graduate School of Engineering, Tohoku University, Sendai, 980-8577, Japan

²Institute of Fluid Science, Tohoku University, Sendai, 980-8577, Japan

³Department of Energy and Resources Engineering, Peking University, Beijing 100871, China

E-mail: abid@pixy.ifs.tohoku.ac.jp

ABSTRACT

A solar concentrator has been designed and investigated with an emphasis on its optical and thermal performance. The primary objective of this concentrator is the manufacturing of lower cost solar concentrator with enhanced thermal performance and no the convective heat loss by using an evacuated glass tube. A ray-tracing model was developed to evaluate the optical and thermal properties of the concentrator. The concentrator, even at a high absorber temperature of 373 K, with a concentrator rate of 2.51 would operate with a reasonably high average efficiency of 47.8%, although the absorber is assumed a gray surface.

1. Introduction

Compound parabolic concentrators (CPC) are relevant for solar energy collection because they achieve the highest possible concentration for any acceptance angle [1]. A CPC can gather solar irradiation on the absorber with a reflector or a refractor and utilize direct and diffuse solar irradiation. The heat losses of a CPC are far less than those of a flat plate solar collector [2,3]. Thus, CPC are always more effective than a normal flat plate solar collector. Rabl [1] evaluated the CPC the optical and thermal properties of the CPC and compared it with those of a truncated CPC. Maruyama [4] proposed an involute reflector to generate uniform and homogeneous emission and carried out ray-tracing calculation to evaluate optical characteristics of that reflector. An integrated Collector storage (ICS) solar water heater was designed, constructed and studied with an emphasis on its optical and thermal performances [5]. The efficiency in the solar concentrators decreases with aging, because the reflector surface is affected by environmental factors, such as dust and climate variation. Furthermore, thermal efficiency abates due to heat losses. Heat losses mainly arise from convective heat loss, which can reach 3-6 times radiative and conductive heat losses [1].

The objective of this study is to investigate the development of a solar concentrator with an emphasis on its optical and thermal performance. An evacuated glass tube used to protect the reflector surface from degradation caused by external conditions and to eliminate convective heat losses. The all side of absorber can be illuminated; In other words, the collector has no back losses because it has no back. A ray-tracing model was developed to evaluate the optical and thermal properties of the concentrator.

2. Concept

The concentrator is composed of a conventional CPC and an involute reflector. The involute reflector is added to the focus points of the conventional compound parabolic reflector and a tubular absorber exists in the cusp region of the involute reflector. The tubular absorber is illuminated on all sides. This achieves better performances owing to the fact that back-side heat transfer loss is eliminated. The concentrator is covered

by an evacuated glass tube, which not only averts the performance decline of the reflector caused by external conditions such as dust, rain and wind, but also reduces natural and forced convective heat loss.

The CPC reflector profile has been designed for a half-acceptance angle of 23.44°, which is for the Sendai location. The involute reflector has a half-acceptance angle of 90° and all radiation which crosses the aperture of involute reflector concentrate on the absorber. The diameter, thickness and length of the absorber are assumed to be 0.02 m, 0.002 m and 1 m, respectively. Figure 1 gives the basic details of the concentrator. The CPC part is comprised of two identical parabolic curves, AB and CD and the identical curves AE and DE constitute the involute reflector of the concentrator.

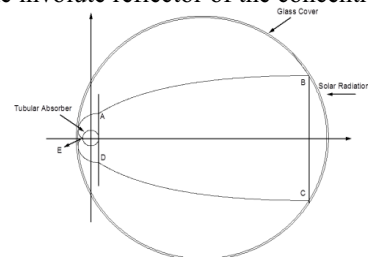


Fig. 1 Geometry of the solar concentrator

3. Optical Performance

The ray-tracing method has been used to evaluate the optical and thermal efficiency as a function of the incidence angle of solar irradiance for the 2-D model. Optical efficiency can be determined by

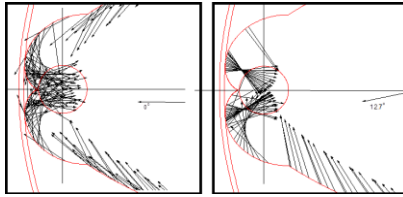
$$\eta_{opt} = \alpha_{ab} \tau_c \rho_r^n \quad (1)$$

where α_{ab} is the absorptivity of the absorber, τ_c is the transmissivity of the glass tube, ρ_r is the reflectivity, and n is the number of the reflection. Every ray has a different reflection number for a different angle. Therefore, ρ_r^n was defined by using the ray-tracing method for more accurate result. For any direction of rays entering the aperture within the maximum acceptance angle (θ_{max}), they will reach the absorber either directly or after s number of reflections. As can be seen in Fig. 2, in the case of the normal ray angle, the main part of rays reflected from CPC can reach the back side of the absorber after the second reflection, as most

of rays reflected from CPC can reach to the absorber directly at 12.7° ray angle. Therefore the optical efficiency of 76.8% at 12.7° ray angle is higher than the optical efficiency of 72.9% for the normal ray angle regarding the number of reflections, and the average optical efficiency is 72.7%.

Table 1. The Specifications of the concentrator material

Parameters of the concentrator	Value
Transmissivity of the glass tube (τ_c)	0.95
Absorptivity of the absorber (α_{ab})	0.90
Emissivity of the absorber (ε)	0.90
Reflectivity of the reflector material (ρ_r)	0.90



(a) 0° Normal ray angle (b) 12.7° ray angle
Fig. 2 Ray reflection around absorber

4. Thermal Performance

The thermal efficiency can be calculated considering the radiation heat loss as a first approximation by [6]

$$\eta = \eta_{opt} - \frac{\varepsilon \sigma A_a (T_a^4 - T_{amb}^4)}{q_{in} A_c}, \quad (2)$$

where q_{in} [W/m²] is the heat flux from solar, A_c is the aperture area of the CPC part, A_a is the aperture area of the involute reflector or the perimeter of the tubular absorber, σ is the Stephan-Boltzmann constant, T_{amb} is the ambient temperature, which is assumed to be 293.15 K, and T_a is the temperature of the absorber. The solar radiative heat flux is assumed to be 1000 (W/m²) and the amounts of absorbed heat flux are investigated with the incidence angle and the beam intensity.

Figure 3 shows the thermal efficiency change taking into account the radiation heat loss which depends on the ray angle. The efficiency increases, as the ray angle becomes closer to 12.7° because the reflection number decreases, and the maximum efficiency is obtained when the ray angle is about 12.7°. Subsequently, the efficiency decreases due to the fact that the reflection number increases, as the ray angle becomes closer to the maximum acceptance angle. In case of the maximum acceptance, the efficiency is minimal due to the maximum number of reflection. The maximum temperature of the absorber can be calculated by Eq. (3), when it is assumed that there is no heat transfer from absorber to the heat transfer fluid. C is the concentrator rate of the solar concentrator. The concentrator rate can be obtained in the same way as CPC in Eq. (4).

$$T_{a,max} = \left(T_{amb}^4 + \frac{q_{in} \eta_{opt} C}{\varepsilon \sigma} \right)^{\frac{1}{4}}, \quad (3)$$

$$C = \frac{A_c}{A_a} = \frac{1}{\sin \theta_{max}}, \quad (4)$$

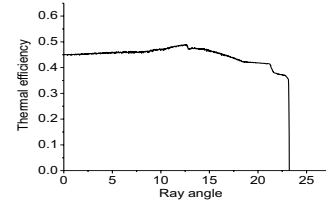


Fig. 3 The concentrator efficiency with ray angle

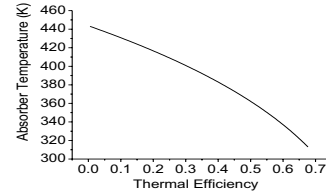


Fig. 4 The change of solar concentrator efficiency by the absorber temperature

The maximum absorber temperature is approximately 455 K for normal ray angle. Figure 4 shows the change of solar concentrator efficiency by the absorber temperature. The thermal efficiency decreases, as the absorber temperature becomes closer to the maximum absorber temperature. The concentrator, even at a high absorber temperature of 373 K, with a concentrator rate of 2.51 would operate with reasonably high average efficiency of 47.8%, although absorber is assumed a gray surface. The highest thermal efficiency of 51.9% was obtained at the ray angle of 12.7°.

5. Concluding remarks

In this study, a solar concentrator consisting of a CPC and an involute reflector, which is covered by an evacuated glass tube, was investigated as to its optical and thermal performance. Obtained results were as follows:

1. The average optical efficiency of the concentrator is 72.7% for maximum acceptance angle of 23.44°. Even at high absorber temperature, the concentrator is characterized by high thermal efficiency.
2. Convective heat loss can be eliminated by using evacuated glass tube. In the case of water boiling temperature at 373 K; the concentrator would operate with a reasonably high average thermal efficiency of 47.8%, although the absorber is assumed a gray surface. The highest thermal efficiency of 51.9% was obtained at the ray angle of 12.7°.

References

- [1] A. Rabl, Sol Energy, **18** (1976), 497-511.
- [2] Y. Kim et al, IntCommun Heat Mass, **35** (2008), 446-457.
- [3] M. Ronnelid et al., Sol Energy, **57** (1996) 177-184.
- [4] S. Maruyama, Proceedings Fourth ASME/JSME Joint Thermal Engineering Conference, Nevada, (1991)
- [5] M. Souliotis, Y. Tripanagnostopoulos, Renew Energ, **33** (2008), 846-858.
- [6] J. R. Howell, R. B. Bannerot, G.C. Vliet, Sol.-Thermal En. Sys. Analysis and Design, (1982) 22.

Non-Condensable Gas effect in Oscillating Heat Pipe

Takurou Daimaru, Hiroki Nagai

Department of Aerospace Engineering, Graduate School of Engineering, Tohoku University
6-6-01 Aoba-Aza-Aramaki, Aoba-ku, Sendai, Miyagi 980-8579 Japan
E-mail: daimaru.takurou@aero.mech.tohoku.ac.jp

ABSTRACT

In this study, the effects of Non-Condensable Gas in Oscillating Heat Pipes were evaluated. The working fluid is ethanol, and the Non-Condensable Gas is argon. The thermal performance of Oscillating Heat Pipe was investigated by the case of with and without Non-Condensable Gas. The temperature and pressure of the heat pipe were measured over the heat input range 100W to 180W, and the thermal resistances were calculated. From the result, the non-condensable gas affects the thermal performance of Oscillating Heat Pipe.

1. Introduction

Oscillating Heat Pipe (OHP) is a relatively new type of heat transfer device. OHP has higher heat transfer capability than a conventional heat pipe. The structure of OHP is very simple and consists of only a meandering tube. There is no wick structure inside the tube as in a conventional heat pipe.¹ In recent years, great attention has been paid to OHP as a thermal control device for spacecraft. However, for a long-term operation in space, Non-Condensable Gas (NCG) may be produced inside OHP, and the heat transport capability of OHP may be affected. When OHP will be applied to a spacecraft, it is necessary to investigate the influence of NCG. In this paper, the thermal performance of OHP was investigated by the case of with and without NCG.

2. Experimental setup

Figure 1 shows the OHP which consist of an evaporator, an adiabatic and a condenser section. It is made of copper tube with 3mm of outer diameter and 2 mm of inner diameter. The length of the evaporator and the condenser section are 100 mm, and the adiabatic section is 160 mm. The number of turn is 16.

An aluminum plate was attached to the evaporator and heat was applied to the evaporator through an aluminum plate on which a silicon rubber heater, capable of providing heat loads up to 180W. The other aluminum plate cooled by forced flow of water supplied by water chiller was attached on the condenser and was used for heat sinks in the experiments. In this test, the sink temperature was set to 20°C. These plates were placed with thermal grease to reduce the contact thermal resistance. The whole OHP was well insulated with grass wool.

In this study, the experiment was conducted by the case of NCG 0% and NCG 1% which were to the total inner volume of OHP. Ethanol was used as working fluid filled with 50%. The heat load Q was increased by every 10W from 100W to 180W. Temperature was measured the 18 points by using T-type thermocouples. Pressure sensor was installed in the bottom of adiabatic section.

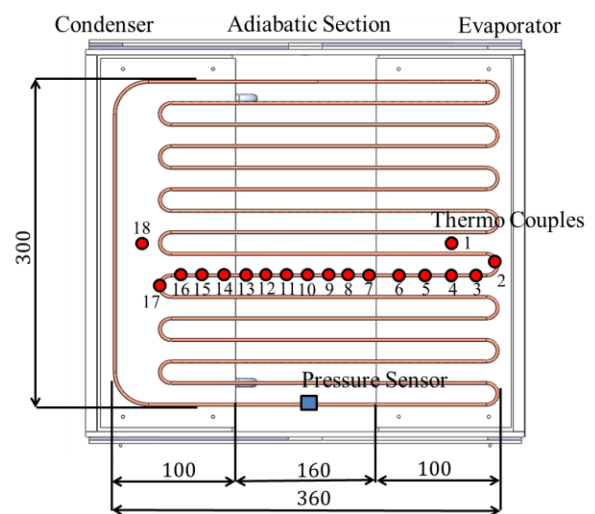


Fig.1. Configuration of OHP

3. Results and Discussion

Figure 2 shows temperature histories of thermocouples at some key points for the case of OHP working with NCG 0% and NCG 1%, applied heat load of 100W, respectively. Comparing NCG 1% to NCG 0% , each temperature histories basically show good agreement. The equilibrium temperature, the frequency of the temperature oscillation, and the amplitude at adiabatic section (No.7) were almost the same. There is no influence of NCG at heat load of 100W.

Figure 3 shows temperature histories at some key points for the case of OHP working with NCG 0% and NCG 1%, applied heat load of 160W, respectively. Comparing to NCG 1% and NCG 0%, the temperature of evaporator (No.2) and adiabatic section (No.7) of NCG 1% case are higher than NCG 0% case, and the amplitude of temperature oscillation in the adiabatic section (No.7) is smaller than NCG 0%. In addition, the amplitude of temperature oscillation in condenser (No.15, 17) is very small for the case of OHP working with NCG 1%.

This difference indicates that NCG affect thermal performance of OHP at heat load of 160W.

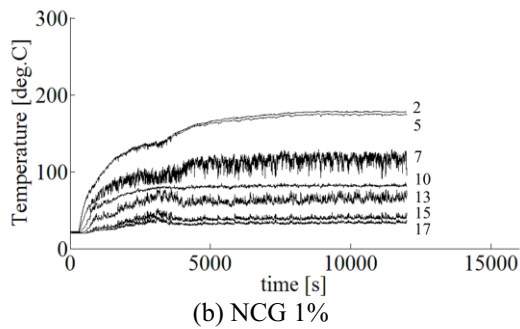
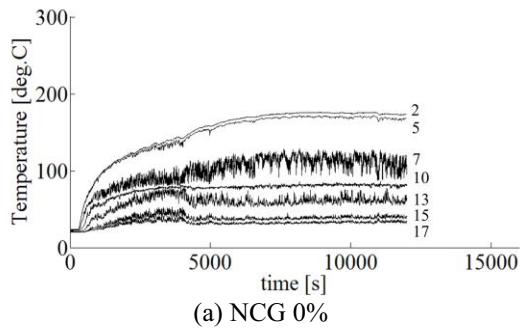


Fig.2. Temperature histories applied heat load of 100W

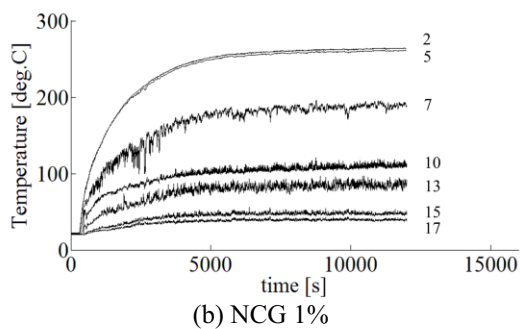
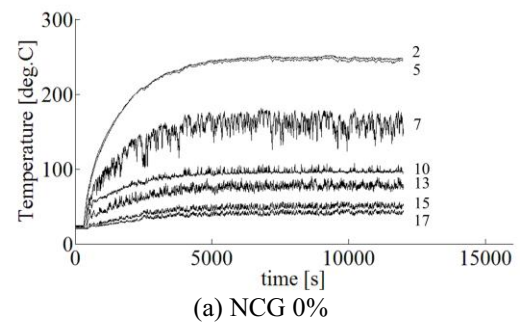


Fig.3. Temperature histories applied heat load of 160W

Figure 4 shows the relation between heat load and thermal resistance.

In this test, the thermal resistance is defined by following equation. Subscript 2 and 17 represent points of thermocouples in Fig.1.

$$R_{th} = \frac{T_2 - T_{17}}{Q} \quad (1)$$

The thermal resistance is decreasing as the heat load increases in the case of NCG 0%. However, it increases once at the heat load of 155W. This phenomenon would be caused by changing of flow pattern from slug flow to annular flow.²

In the case of NCG 1%, thermal resistance shows same trend with the case of NCG 0% from 100W to 140W. But it is higher than NCG 0% slightly overall heat load. And it also increases once at the heat load of 150W. This heat load is slightly smaller than the case of NCG 0%.

In this study, it is found that Non-Condensable Gas affected the thermal performance of OHP.

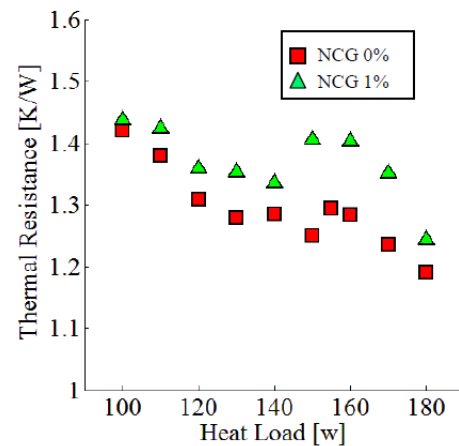


Fig.4. Thermal resistance

4. Concluding remarks

In this study, the effects of Non-Condensable Gas in Oscillating Heat Pipes were investigated for the case with NCG 0% and NCG 1%. From the results, NCG makes temperature higher in evaporator and adiabatic section, and the thermal resistance of NCG 1% is slightly higher than that of NCG 0%. So, NCG affects thermal performance of OHP.

References

- [1] Y. Miyazaki, H. Akach, "Oscillating Heat Pipe with check valves", in: Proc. 6th Int. Heat Pipe Symposium, Chiang Mai, Thailand, (1996)
- [2] S. Khandekar, M. Groll, "An insight into thermo-hydrodynamic coupling in closed loop pulsating heat pipes", International Journal of Thermal Sciences 43 (2004) 13-20
- [3] Sun, K.H. and Tien, "Thermal Performance Characteristics of Heat Pipes", Journal of Heat Mass Transfer, 18, 363 (1975).

Friction and Thermal Properties in Drilling of Bone Biomodels

Kei Ozawa¹, Yuji Katakura², Yukihiro Shibata²,

Philippe KAPSA³, Vincent FRIDRICI³, Gaëtan BOUVARD³, Makoto Ohta⁴

1. Graduate School of Biomedical Engineering, Tohoku University, 2-1-1 Katahira, Aoba-ku, Sendai, Japan

2. TECNO CAST

3. Laboratoire de Tribologie et Dynamique des Systèmes, Ecole Centrale de Lyon

4. Institute of Fluid Science, Tohoku University

E-mail : k-ozawa@biofluid.ifs.tohoku.ac.jp

ABSTRACT

It is required for doctors to acquire high-level surgical skills according to the progressing medical technology. Then, bone biomodel is required to improve the skills and evaluate the performance of medical devices. The authors have developed bone biomodel consist of composite acrylic and wood to realize the feeling of drill or screw. Thrust force and temperature rise during drilling performance under constant normal load were measured using bone models and porcine bone. The thrust force of all cases decreases after a peak. Thermal property of the material may affect the thrust force during drilling.

1. Introduction

It has progressed the medical technology and quality of medical devices. With following the progressing, doctors are necessary to acquire high level skills to treat disease safely and precisely. Then, the development of biomodel mimicking tissue shape and realistic mechanical properties will be helpful for the acquisition [1]. The model could also be applied to improve the doctors' skills, performance tests of medical devices, and *in-vitro* physical experiments[2]. To develop the model from the improvement, the reproducibility of biomodel should be evaluated based on clinical operative procedure and physical responses from medical devices.

So far, the drilling tests using animal bone, such as mainly porcine or bovine bone were carried out in order to measure the force or temperature in drilling [3-8]. These results can be applied to develop the model with the evaluation.

Composite material included polymers would be effective for casting the model and adjust mechanical properties. The mixture of polymer and wood has been applied to recycled plastics or building materials [9-12]. We have developed a method of composite bone mimicking model using acrylic and wood sawdust under the evaluation of medical doctor [13]. Then the authors measured thrust force and friction heat in surgical drilling situation based on previous studies.

2. Material and Methods

2-1. Processing procedure for specimens

The powder of acrylic resin and wood sawdust less than length of 0.55 mm were employed as the basement composite material for model mimicking bone tissue. The powder of acrylic, wood sawdust and polymerization agent were mixed. The ratio of weight of mixture defined as (Acrylic weight) / (Acrylic weight and wood sawdust). Four types specimens, Acrylic100 wt%(A100), A95, A75, A59 were prepared. The mixtures were injected to a gypsum mold with loading 1500 kg/cm². The injected materials were heated at 105 °C for 20 min for solidification. After the heating, the solid mixture was cooled in water with room temperature for 20 min. The size of specimens was set 20 mm×20 mm×20 mm. A mandible of porcine bone (male, 6 months old) was also prepared and was cut to a cubic shape for setting in the drilling machine.

2-2. Drilling test

Drilling test was designed to simulate the clinical conditions in implant osteotomy. The experimental set-up includes a driller, a force measurement system with strain gauge, strain gauge conditioner, displacement measure and thermocouple. The samples were clamped on the plate. The thermocouple was set in the sample at a depth of 3 mm. And the center of thermocouple was located at 2 mm distance for the center of the drill [3]. Thrust force and friction heat in

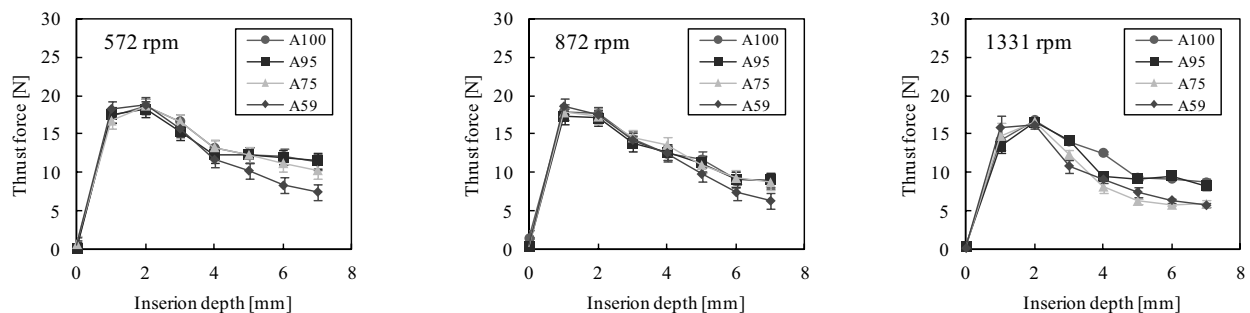


Fig.1 Comparison of profile of thrust force of composite models

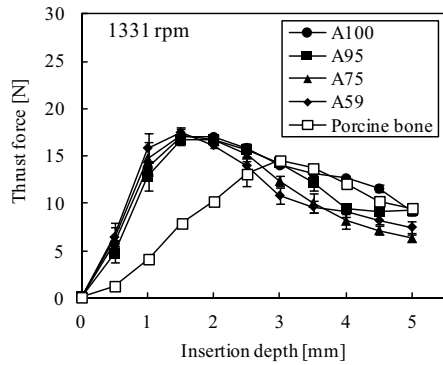


Fig.2 Comparison of thrust force profile composite models and porcine bone

specimens were measured during drilling 7 mm depth. Implant drill with diameter of 2 mm was employed (Implant drill, Nobel Biocare Japan Co., Ltd). The normal load of 20 N was forced to samples continuously. The drill speed was set 572, 872 and 1331 rpm, respectively.

3. Results and Discussion

Fig.1 shows thrust force profile during drilling. At first, the thrust force reach 20 N. Thrust forces of all types of specimen decrease with increasing insertion depth. After reaching 20 N, the thrust force of A100 and A95 cases decrease around 10 N at 7 mm depth. The thrust forces of A75 and A59 decrease around 7 N. The cutting speed also increases in accordance with increase of wood amount in composite. The results are similar to the result using porcine bone (Fig.2).

The friction heat increases with increase of insertion depth. The maximum temperature rises up to 60 °C at the 7 mm depth of the drill. According to Fig. 3, there may have strong correlation between the change of thrust force and temperature rise. This correlation indicates the viscoelasticity of acrylic may be changed during drilling and the change leads the decrease of thrust force. H. Hocheng et al. also describe that polymer chain of acrylic may be easier to slide by temperature rise during drilling. Then the model is softened and easy to be drilled [8].

This correlation will lead that the acrylic composite materials may reproduce a realistic response for drilling based on the thermal properties such as a thermal conductivity.

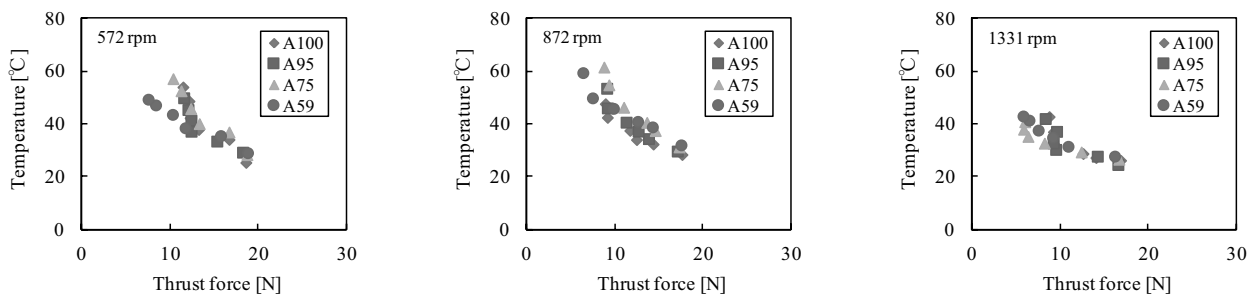


Fig.3 Relation between thrust force and temperature change during drilling

4. Concluding remarks

In the present report, bone tissue-mimicking models based on composite material were tested in surgical drilling condition. We obtained as following conclusions.

1. At first, thrust force increases around 20 N and then decrease with increase insertion depth of the drill in both composite model and porcine bone cases.
2. Wood amount of composite affects cutting speed by difference of thrust force
3. Correlation the change of thrust force and temperature rise during drilling indicates the drilling response can be reproduced by using acrylic composite materials.

References

[1] K. Alm et al., *Medical Engineering & Physics*, **33**, (2011), 234-239
 [2] Sun-Jung KIM et al., *J Appl Oral Sci.*, **18**, (2010), 522-527
 [3] Bedrettin Cem Sener et al., *Clin.Oral Impl. Res.*, **20**, (2009), 294-298
 [4] M.T. Hilley et al., *Journal of Materials Processing Technology*, 92-93, (1999), 302-308
 [5] Goran Augustin et al., *Arch Orthop. Trauma Surg.*, **128**, (2008), 71-77
 [6] Benedict Wilimes et al., *Journal of Orofacial Orthopedics*, **69**, (2008), 51-58
 [7] K. Alam et al., *Medical Engineering & Physics*, **33**, (2011), 234-239
 [8] H. Hocheng et al., *Journal of Engineering Materials and Technology*, **15**, (1993), 146-149
 [9] S.K Najafi et al., *Journal of Applied polymer Science*, **100**, (2006), 3641-3645
 [10] R. Bouza et al., *Journal of Applied polymer Science*, **102**, (2006), 6028-6036
 [11] N. Sombatsompop et al., *Journal of Applied polymer Science*, **102**, (2006), 1896-1905
 [12] P. Turgut, *Building and Environment*, **42**, (2006), 3801-3807
Materials and Technology, **15**, (1993), 146-149
 [13] K. Ozawa et al., proceedings of 6th WCB, (2010), 525

A Molecular Dynamics Study on the Thermodynamic Analysis of Cryogenic Hydrogen

Hiroki Nagashima, Takashi Tokumasu, Tohoku University, 2-1-1, Katahira, Aoba-ku, Sendai, Miyagi, Japan
Shin-ichi Tsuda, Shinshu University, 4-17-1, Wakasato, Nagano, Nagano, Japan
Nobuyuki Tsuboi, Kyushu Institute of Technology, 1-1, Sensui-chou, Tobata-ku, Kitakyushu, Fukuoka, Japan
Mitsuo Koshi, University of Tokyo, 2-11-16, Yayoi, Bunkyo-ku, Tokyo, Japan
A. Koichi Hayashi, Aoyama Gakuin University, 5-10-1, Chuo-ku, Fuchinobe, Sagami-hara Kanagawa, Japan
E-mail of corresponding author: nagashima@nanoint.ifs.tohoku.ac.jp

ABSTRACT

In this paper, we conducted analysis of thermodynamic properties of cryogenic hydrogen using classical Molecular Dynamics (MD) and path integral Centroid MD (CMD) method to understand an effect of quantum nature of hydrogen molecules. We performed NVE constant MD simulation across a wide density-temperature condition to obtain an Equation Of State (EOS). Simulation results were compared with experimental data. As a result, it was confirmed that classical MD cannot reproduce the experimental data at the high density region. On the other hand, CMD well reproduce the thermodynamic properties of liquid hydrogen.

1. Introduction

Currently environmental problems and energy problems are serious issues. Therefore, there are many studies to achieve the hydrogen energy society. Among them, we focus on nanoscale thermal flow phenomena of hydrogen. Understanding of nanoscale thermal flow phenomena is very important for safety and efficient use of hydrogen. However the nuclear quantum effect cannot be ignored because the mass of hydrogen molecules is very small. Because of this quantum nature, it is expected that conventional molecular simulation method cannot be applied for the analysis of nanoscale thermal flow phenomena of hydrogen [1]. Moreover, since the quantum nature is difficult to reproduce numerically, there is little analysis of nanoscale phenomena of hydrogen using MD method. Therefore, it is not clarified how the quantum nature affects the nanoscale phenomena of hydrogen. Besides, it affects not only its microscopic thermodynamic properties but also its macroscopic ones. From this aspect, perceiving the effect of the quantum nature on the thermodynamic properties is important for both microscopic and macroscopic analysis of hydrogen.

In this paper, therefore, we investigated the effect of the quantum nature on the thermodynamic properties of hydrogen using classical MD method and path integral Centroid Molecular Dynamics (CMD) method [2].

2. Simulation Method

In this paper, an EOS was derived to clarify the effect of quantum nature of hydrogen molecules. The EOS was determined by Kataoka's method [3]. In this method, the EOS is expressed by the excess Helmholtz free energy from an ideal gas A^e as the sum of the product of density ρ and temperature T ,

$$\frac{\beta A^e}{N} = \sum_{n=1}^5 \sum_{m=-1}^5 A_{nm} \left(\frac{\rho}{\rho_0} \right)^n \left(\frac{\beta}{\beta_0} \right)^m, \quad (1)$$

where $\beta (= 1/k_B T)$ is the inverse temperature, and N is the number of molecules. The thirty five A_{nm} coefficients were determined by a least square fitting of the simulated potential energies and pressures which were derived by MD simulation. We have performed

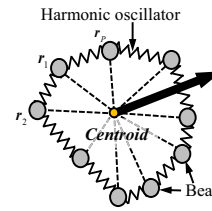


Fig. 1 Diagram of the path integral CMD.

microcanonical 300 cases of ensemble MD and CMD simulations by changing density and temperature.

The CMD method is based on a formalism in which the quantum partition function becomes the same form as the classical partition function which consists of L particles ring polymer as shown in Fig. 1. In short, the quantum partition function is described as discretized expression,

$$Z(\beta, N) = \lim_{L \rightarrow \infty} \frac{1}{N!} \left(\frac{mL}{2\pi\beta\hbar^2} \right)^{\frac{2NL}{2}} \int \cdots \int \prod_{i=1}^N \prod_{j=1}^L dr_i^{(j)} \exp[-\beta\Phi(r_i^{(j)})] \quad (2)$$

where Φ is an effective potential and it is defined by

$$\Phi(r_i^{(j)}) = \sum_{i=1}^N \sum_{j=1}^L \frac{mL}{2\beta^2\hbar^2} (r_i^{(j)} - r_i^{(j+1)})^2 + \frac{1}{L} \phi(r_i^{(j)}), \quad (3)$$

where m is the mass of molecule, L is the number of discretized points that is the number of beads composed a ring polymer, $r_i^{(j)}$ is a bead position and $r_i^{(1)} = r_i^{(L+1)}$, each bead is connected with neighbor one by a harmonic potential, ϕ is the interaction function between beads. Silvera-Goldman potential [4] is used for this interaction. The centroid is defined as the center of the paths, i.e.,

$$r_0 = \frac{1}{L} \sum_{i=1}^L r_i. \quad (5)$$

Using this centroid information, the equation of motion of hydrogen molecule becomes classical like, i.e.,

$$m \frac{d^2 r_0}{dt^2} = -\frac{1}{P} \sum_j^P \frac{\partial \Phi(r_i^{(j)})}{\partial r_i^{(j)}}. \quad (6)$$

The right side is an average force which acts on each bead. In our simulation, each bead position is transformed to normal mode coordinate [5]. This transformation leads to separate centroid motion from beads motion and the second term of Eq. (3) becomes individual harmonic oscillator. More detailed

explanation is described in Ref. 6. In this paper, the EOSs were reduced by critical points and compared using the principle of corresponding state.

3. Results and Discussion

A comparison of temperature-density saturation lines which are reduced by critical temperature T_{cr} and critical density ρ_{cr} is shown in Fig. 2. In this figure, there is a large disagreement between classical MD result and experimental data [7] at the high density region. On the other hand, CMD result agrees well with experimental data. From these results, it was clarified that the effect of quantum nature on the reduced EOS of liquid hydrogen is large.

To clarify the reason of the difference between the classical result and the CMD result, we compared the pressure formulation of each method. The pressure formulation of classical MD is described by,

$$P_{cl} = \frac{Nk_B T}{V} + \frac{1}{3V} \left\langle \sum_{i=1}^N \mathbf{F}_i \cdot \mathbf{r}_i \right\rangle, \quad (7)$$

where \mathbf{F}_i is a force acting on molecule i . The pressure formulation in path integral method is described by,

$$P_{PI} = \frac{LNk_B T}{V} + \frac{1}{3V} \left\langle \sum_{i=1}^N \sum_{j=1}^L \left[-\frac{mL}{\beta^2 \hbar^2} (\mathbf{r}_i^{(j)} - \mathbf{r}_i^{(j+1)})^2 + \frac{1}{L} \mathbf{F}_i^{(j)} \cdot \mathbf{r}_i^{(j)} \right] \right\rangle. \quad (8)$$

The first and second term of Eq. (8) is the kinetic pressure term. The differences between P_{PI} and P_{cl} in each term at $\rho = 80 \text{ kg/m}^3$ are shown in Fig. 3. As shown in this figure, the differences decrease with increase of temperature and the difference of the virial term (red line) is larger than the kinetic one (green line). These mean the quantum nature affects the virial term more than the kinetic one and makes larger the virial pressure than in classical mechanics. Therefore, the CMD result is consistent with experimental data.

To more clarify the quantum nature on the virial term, intermolecular potentials were derived using force matching method [8]. In this method, the force which acts on the centroid is achieved in a least squares senses by minimizing the objective function,

$$\chi^2 = \left| \frac{1}{3N_c N_p} \sum_{i=1}^{N_c} \sum_{j=1}^{N_p} \mathbf{F}_{ij}^c - \mathbf{F}_{ij}^p(A_1, \dots, A_M) \right|^2, \quad (9)$$

where N_c and N_p are the number of configurations and the number of particles in each configuration, \mathbf{F}_{ij}^c is a force acting on a centroid, \mathbf{F}_{ij}^p is a classical like force which is a function of intermolecular distance and depend on M adjustable parameters A_1, \dots, A_M . The fitted results are shown in Fig. 4. As shown in this figure, the potential which acts on the centroid depends on the temperature. Additionally, the potential well is shallow and the well positions are far away from the classical well position. These results suggest that taking into account the quantum nature makes smaller intermolecular interaction energy and repulsive force than classical representation.

4. Concluding remarks

In this paper, we have investigated the effect of quantum nature of hydrogen molecule on its thermodynamic properties using classical MD and CMD

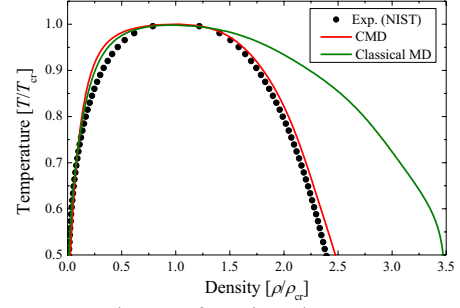


Fig. 2 Comparison of reduced temperature-density saturation line results.

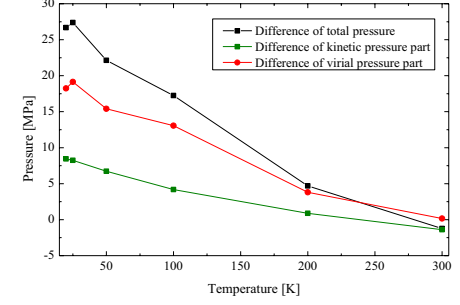


Fig. 3 Difference of total pressure and each term of pressure formulation between path integral and classical method at $\rho = 80 \text{ kg/m}^3$.

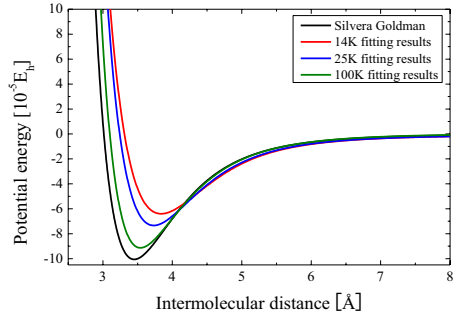


Fig. 4 Comparison of temperature dependence of effective potential as fitted results.

method. From the results, it was clarified that the effect of quantum nature on the reduced EOS is large and taking into account the quantum nature makes larger virial pressure, intermolecular interaction energy, and repulsive force than classical representation.

Acknowledgements

This study has been supported by the Ministry of Education, Science, Sports and Culture, Grant-in-Aid for Scientific Research (B) (No. 23360380), (No. 24360065) and the Collaborative Research Project of the Institute of Fluid Science, Tohoku University.

References

- [1] H. Nagashima, *et al.*, *Mol. Sim.*, (2012),
- [2] J. Cao, *et al.*, *J. Chem. Phys.*, **101**(1994), 6168.
- [3] Y. Kataoka, *J. Chem. Phys.*, **87**(1987), 589.
- [4] I. F. Silvera, *et al.*, *J. Chem. Phys.*, **69**(1978), 4209.
- [5] J. Cao, *et al.*, *J. Chem. Phys.*, **99**(1993), 2902.
- [6] T. D. Hone, *et al.*, *J. Chem. Phys.*, **121**(2004), 6412.
- [7] <http://webbook.nist.gov/chemistry/> (2012.6.26)
- [8] S. Izvekov, *et al.*, *J. Chem. Phys.*, **120**(2004), 10896.

SPH Simulation of Gas Flow Accompanying Thermal Expansion

Masumi Ito, Seiichiro Izawa, Yu Fukunishi, and Masaya Shigeta

Department of Mechanical Systems and Design, Graduate School of Engineering, Tohoku University
6-6-01 Aramaki-Aoba, Aoba-ku, Sendai, Miyagi, Japan
masumi@fluid.mech.tohoku.ac.jp.

ABSTRACT

A gas flow accompanying changes in temperature and density was simulated by an incompressible SPH (Smoothed Particle Hydrodynamics) method. The thermal expansion was modeled by changing the diameters of particles depending on their temperatures. The density evaluated in the SPH way decreased as the distance between the particles enlarged in a high temperature region. The convectonal flow where density and temperature change could be simulated.

1. Introduction

SPH is a Lagrangian-based method to simulate a fluid motion without a grid system. The fluid motion is represented by the behavior of particles that move according to their respective motion equations containing mutual interactions. In our previous study, the behavior of anode metal on the TIG (Tungsten Inert Gas) welding process was successfully simulated by the SPH method that was extended to incompressible fluid flows [1]. There, the thermal and mechanical effects of shielding gas were indirectly taken into account as the steady boundary conditions at the anode surface.

The aim of this study is to develop a method to simulate shielding gas flows using the SPH method. Since it is quite difficult to simulate them under the practical conditions, this study focuses only to the effect of thermal expansion on the gas flow and the gas flow in a container with isothermal wall is simulated.

2. Numerical Method

2.1 Model description

The mass distribution of each particle is given as a continuous function of Kernel W . The M4 spline kernel given by

$$W = W(r, h) \frac{\sigma}{h^D} \begin{cases} 1 & 0 \leq q \leq 1 \\ \frac{1}{4}(2-q)^3 & 1 \leq q \leq 2, \\ 0 & 2 \leq q \end{cases} \quad (1)$$

is used, where D is the dimension number, σ is a non-dimensional coefficient with a value of $10/7\pi$ when $D=2$, h is a parameter to define the broadening of the kernel, r is a distance between particles, and $q=r/h$ is a non dimensional distance.

The density distribution at the particle position is written as follows:

$$\rho_a = \rho(\mathbf{r}_a) = \sum_b m_b W_{ab} = \sum_b m_b W(|\mathbf{r}_a - \mathbf{r}_b|), \quad (2)$$

where a and b denote the particle indices, \mathbf{r} is the position of a particle, and m is the mass of a particle.

Thermal conduction is given as follows:

$$\frac{dT_a}{dt} = \frac{2D}{\rho_a C_a} \frac{\sum_b \kappa (T_b - T_a) W_{ab}}{\sum_b (\mathbf{r}_a - \mathbf{r}_b)^2 W_{ab}}, \quad (3)$$

where, T is the temperature, κ is the thermal conductivity, and C is the specific heat at constant pressure. This is the

same as the Laplacian model which is normally used in another particle method, namely the MPS method [2].

The detailed model description of the SPH method is found in Ref. [3].

2.2 Thermal expansion model

To adjust the particle volume accompanying the temperature change, the parameter h is redefined as a function of a particle temperature as follows:

$$h_a = h_0 \sqrt{\frac{T_a}{T_0}}, \quad (4)$$

where T_0 and h_0 are reference values.

To achieve an incompressible flow computation, particle locations are adjusted every time step to keep the density field uniform for the case of computations without the expansion. Instead of this density adjustment method, thermodynamic pressure is used and it is kept constant during the computation. The thermodynamic pressure is defined as follows:

$$p(\mathbf{r}_a) = \sum_b \frac{RT_b}{M} m_b W_{ab}, \quad (5)$$

where R is the gas constant and M is the molecular mass. This pressure is used only for the adjustment. Hence, it is different from the actual pressure related to the flow field.

3 Computational conditions

Figure 1 shows the computational domain representing gas in a container with the width of 100 mm and the height of 60 mm. The blue part indicates gas and the gray part indicates an isothermal wall. The wall and the gas in the isothermal region are forced to be 300 K. The top surface of the gas is assumed to be depressed by the floating wall which moves and deforms according to the gas movement. Hence, the gas does not diffuse above, and the geometry of this surface varies depending on the flow and the density field of the gas.

A downward gas flow, generated at the acceleration region in the figure, simulates the jet flow ejected from a welding torch, blowing towards the anode surface. In addition, the variation of gas temperature is modeled by placing a heat source in its downstream. The temperature of a particle is increased with the constant rate of 100 K/s inside the heating region.

The domain is discretized by 6,000 particles with an initial diameter of 1 mm. The material properties of argon are given to all particles. The time step length is set as 1 ms. The initial temperature is set to be uniform at 300 K. Particles are accelerated 0.05 m/s^2 up to the speed of 1.0 m/s passing through the acceleration region.

When the computation was conducted without the heating region, a circulating flow was generated. Eventually, a steady flow was obtained, which was used as the initial condition. Figure 2 shows this velocity field which is employed as the initial condition of the present simulation. A symmetric flow pattern can be observed.

4. Results and Discussion

Figure 3 shows the velocity field at the end of the simulation when the heating is turned on. Figures 4 and 5 show the temperature and the density distributions at the same moment. The temperature of a part of the gas, which passed through the heating area, increased. Corresponding to that, the density of the gas decreased. The particles are plotted with a constant radius in these figures. It can be clearly observed that the distance between the particles are larger, because the particles' diameters are extended by the thermal expansion algorithm. Hence, the density estimated in the SPH way is became lower.

When the computation of the convective flow is continued further, the flow field becomes asymmetric at $t=1 \text{ s}$. This result suggests that the momentum might not be conserved in the thermal expansion algorithm.

5. Concluding remarks

SPH method was applied to the simulation of a heated gas flow accompanying thermal expansion. The thermal expansion model, which changes the particle diameter depending on its temperature, was suggested and employed. The convective flow where the density change by the temperature could be simulated.

References

- [1] M. Shigeta *et al.*: Proceedings of Visual JW 2010, Osaka, Japan, **1** (2010), pp. 9-10.
- [2] S. Koshizuka and Y. Oka: Nucl. Sci. Eng., **123** (1996), pp. 421-434.
- [3] M. Shigeta *et al.*: Int. J. Emerging Multidisciplinary Fluid Sci., **1** (2009), pp. 1-18.

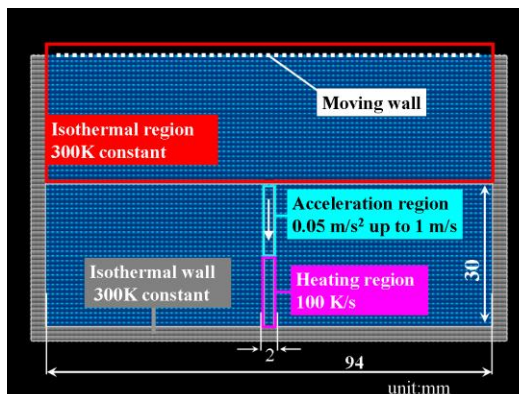


Fig. 1 2D computational domain.

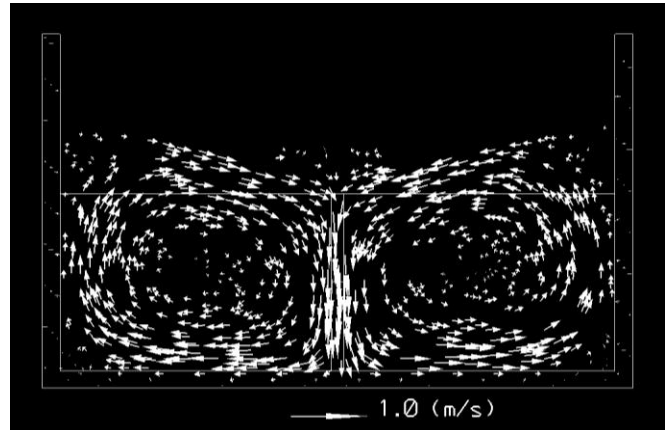


Fig. 2 Initial velocity distribution.

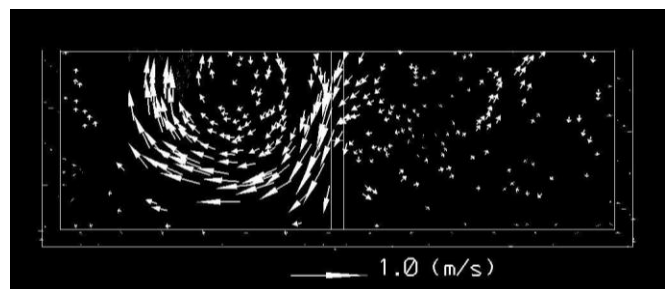


Fig. 3 Instantaneous velocity distribution at end of simulation ($t=1 \text{ s}$).

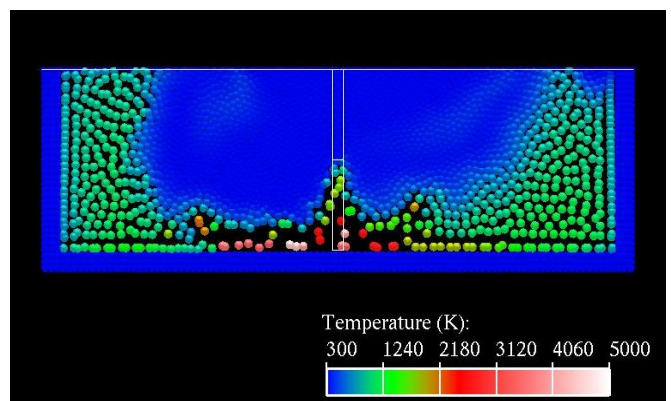


Fig. 4 Instantaneous temperature distribution at $t=1 \text{ s}$.

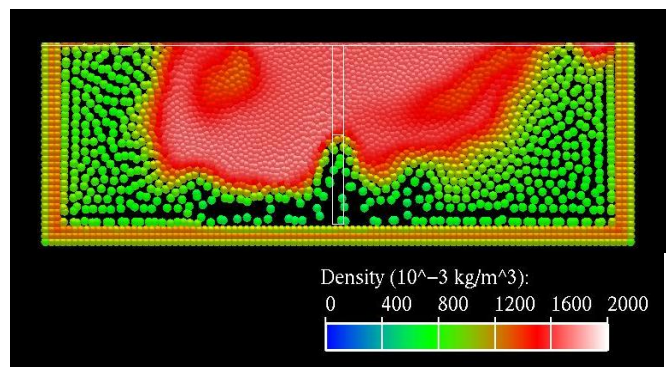


Fig. 5 Instantaneous density distribution at $t=1 \text{ s}$.

Thermal Analysis on a Remountable High Temperature Superconducting Magnet around Jointing Region

Yusuke Tanno, Satoshi Ito, Hidetoshi Hashizume
Tohoku University, Japan
ytan@karma.qse.tohoku.ac.jp

ABSTRACT

A reduction of temperature rise caused by joule heating around jointing region is one of the important issues for thermal design of a remountable high-temperature superconducting magnet proposed for future fusion reactors. We evaluated temperature distribution around the jointing region with finite element method, and then obtained performance charts indicating a relationship between temperature rise and each operating conditions such as joint resistance, cooling performance and so on. Based on the results, we discuss the thermal design of the remountable magnet.

1. Introduction

A remountable high-temperature superconducting (HTS) magnet is a segmented type superconducting magnet whose segments can be mounted and demounted repeatedly with mechanical joints [1]. The remountable magnet has some advantages; relatively easier fabrication of complicated magnets, repairability of damaged parts, and accessibility to inner reactor components. High-temperature superconductors could allow to use mechanical joints inducing joule heating because of their high critical temperatures and heat capacities. However, the excess temperature rise will decrease critical current of HTS conductors constituting the magnet and eventually lead to a quench. Therefore, reducing the temperature rise in the conductors is one of the most important issues to design the remountable HTS magnet.

As one of the design options of superconducting magnet for heliotron-type DEMO reactor, FFHR, remountable HTS magnet was proposed to be employed with indirect cooling method [2]. In a preceding study, the allowable heat load of a remountable HTS magnet applied to FFHR's helical magnets was estimated to be 990 W/m^3 for a temperature rise of 5 K [3], with assumptions that heat generates uniformly within the magnet and the temperature of cooling panel is constant. Although temperature rise around the jointing region in actual case is larger than in the above calculation, the details of temperature distribution have not yet been evaluated. In this study, therefore, temperature distribution is evaluated by thermal analysis with finite element method in a jointing region of the remountable magnet applied to FFHR, changing operating conditions such as operating temperature, joint resistance, and cooling performance. Then performance chart is obtained, which indicates relationship between maximum temperature rise and each operating condition. Based on the performance chart, we discuss the thermal design of the remountable magnet, in terms of joint resistance and heat transfer coefficient, flow rate and pressure drop of a coolant.

2. Method

Two-dimensional numerical analyses are performed on a model shown in Fig. 1 using

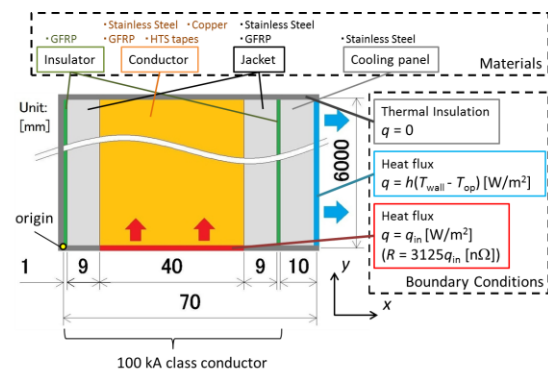


Figure 1 Schematic view of numerical model

commercial FEM software COMSOL multiphysics 4.2a. The triangular mesh is used and the number of elements is about 1,400,000. The governing heat conduction equation is

$$\nabla \cdot (k \nabla T) + Q = 0 \quad (1)$$

where k , T and Q are thermal conductivity, temperature and heat load, respectively. Here, Q is 100 W/m^3 which expresses the nuclear heat load [4].

The calculation model consists of the 100 kA class conductor and the cooling panel. The conductor consists of HTS tapes (YBCO tape consisting of silver, YBCO, Hastelloy layers), copper, stainless steel jacket, and electrical insulator. The cooling panel, which is made of stainless steel, is cooled by forced flow of a liquid coolant, such as liquid nitrogen and liquid neon, flowing through the rectangular channel located inside the cooling panel. The conductor is then conductively cooled by the cooling panel. In this calculation, the temperature of the coolant is assumed to be constant. The thermal conductivity of each material is temperature dependent, which is interpolated with sextic function over the domain. Those in certain temperatures are summarized in Table 1. In the

Table 1 Thermal conductivities of materials [5,6,7]

Materials	k [W/(m·K)]		
	20 K	64 K	77 K
Copper	1300	720	600
Hastelloy	4.4	7.5	7.7
GFRP (insulator)	0.18	0.34	0.39
Silver	3700	620	590
Stainless Steel	2.0	6.2	7.0
YBCO	0.26	0.47	0.46

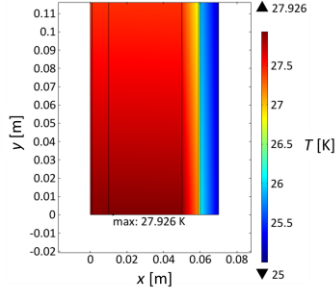


Figure 2 Temperature distribution
($T_{op} = 25$ K, $R = 1.1$ n Ω , $h = 1000$ W/(m 2 ·K))

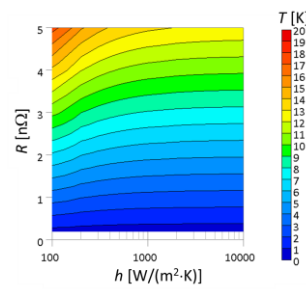


Figure 3 Performance chart
($T_{op} = 25$ K)

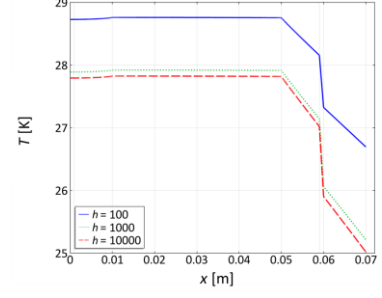


Figure 4 Temperature distribution
at $y = 0$ ($T_{op} = 25$ K, $R = 1.1$ n Ω)

two-dimensional analysis, the thermal conductivity for each region is given as effective value based on the size of the constituting structures. Parameters are joint resistance R (0.2 ~ 5 n Ω) which affects the heat generation, heat transfer coefficient h (100 ~ 10,000 W/(m 2 ·K)) on the surface of cooling channel which affects the cooling performance, and operating temperature T_{op} (25, 27 K for liquid neon, 64, 77 K for liquid nitrogen) of the remountable magnet.

The temperature rise of coolant, which is not considered in numerical analyses, is also calculated assuming single-phase flow. Flow rate of coolant G per one cooling channel system is

$$G = Q_t / (\rho \cdot C_p \cdot \Delta T \cdot N) \quad (2)$$

where ρ , C_p , ΔT , Q_t , N are density, heat capacity, temperature difference from saturated temperature, total heat load, and the number of cooling channel systems, respectively. Pressure drop per unit length is

$$\Delta P/l = \lambda \cdot \rho \cdot U^2 / 2D_h \quad (3)$$

where λ , l , U , D_h are pipe friction coefficient, length of channel, flow velocity which is obtained by dividing G by cross-section area of cooling channel A , and hydraulic diameter of channel, respectively. h is derived by following equations,

$$Nu = 0.023Re^{0.8} Pr^{0.4} \quad (4)$$

$$Nu = hD_h/k \quad (5)$$

where Nu , Re , Pr are Nusselt number, Reynolds number, and Prandtl number, respectively. The least number of cooling channel system, which satisfies that maximum stress on channel is less than yield strength of the channel, is evaluated.

3. Results and Discussion

We obtained temperature distribution for each operating condition. One example is shown in Fig 2. In addition, we made performance charts, whose example shown in Fig. 3, indicating relationship between maximum temperature rise and operating conditions. According to the performance charts, an increase in the heat transfer coefficient does not have significant effect to reduce the temperature rise especially in high h region because large temperature gradient exists in the insulator and the stainless steel having low thermal conductivities as shown in Fig. 4. Therefore, the maximum temperature rise strongly

depends on joint resistance. In recent studies, joint resistances for soldered bridge joint and mechanical butt joint were predicted to be 1.1 n Ω [8] and 5 n Ω [9], respectively. Performance charts show that the temperature rise of 3 K for soldered bridge joint and 10 K for mechanical butt joint should be accepted.

The least number of cooling channel system and corresponding heat transfer coefficient are shown in Table 2. In all cases, it can be inferred from performance chart that h is high enough to have nearly the maximum cooling performance.

4. Conclusion

In this study, we discussed thermal design of the remountable HTS magnet applied to FFHR based on numerical analyses and calculations. The maximum temperature is less influenced by heat transfer coefficient of a coolant due to existence of low thermal conductivity materials and it strongly depends on the joint resistance. The values of h can be acceptable in operating conditions based on the evaluation of the number of cooling channel systems.

References

- [1] H. Hashizume *et al.*, J. Plasma Fus. Res. SERIES, **5**, 532 (2002).
- [2] N. Yanagi *et al.*, Plasma Fusion Res. **5**, S1026 (2010).
- [3] G. Bansal *et al.*, Plasma Fusion Res. **3**, S1049 (2008).
- [4] A. Sagara *et al.*, Fus. Eng. Design **81**, 1299 (2006).
- [5] J. Heremans *et al.*, Phys. Rev. **B 37**, 1604 (1988).
- [6] S. Jang *et al.*, IEEE Trans. Appl. Supercon. **13**, 2956 (2003).
- [7] J. Lu *et al.*, J. Appl. Phys. **103**, 064908(2008).
- [8] Y. Terazaki *et al.*, Plasma Fusion Res. **7**, 2405027 (2012).
- [9] T. Ohinata *et al.*, Plasma Fusion Res. **7**, 2405045 (2012).

Table 2 The number of cooling channel system and corresponding heat transfer coefficient

Joint Type	T_{op} [K]	N	h [W/(m 2 ·K)]
Soldered Bridge Joint ($R = 1.1$ n Ω)	25	5	1.40×10^4
	27	36	3.57×10^4
	64	3	5.11×10^3
	77	20	2.06×10^4
Mechanical Butt Joint ($R = 5$ n Ω)	25	8	1.73×10^4
	27	58	4.39×10^4
	64	3	9.19×10^3
	77	26	3.01×10^4

4. Results and discussion

4-1. Experimental result

Figure 3 shows schlieren images and flame emission taken simultaneously; (1) without ISW, (2) $x_i = 47.3$ mm, (3) $x_i = 57.3$ mm and (4) $x_i = 67.3$ mm. It is confirmed that flameholding region extends to downstream without ISW. However, flame extinction is observed at the point of interaction between ISW and flame when ISW is introduced. Therefore, we investigated emission intensity of the flame region. Figure 4 shows relationship between flame length (L_f) and location of ISW. Flame length, L_f , is defined as the length from the rear edge of the cavity to the rear edge of the flame, as shown in Fig.5. When emission intensity of flame decreases to brightness of background, the location was defined as a flame extinction point. The flame extinction point means rear edge of the flame. From Fig.4, it is observed that L_f is increased linearly when ISW is introduced more downstream. From Fig.3, flow turbulence downstream of ISW is generated, which may lead to cooling of flame region and flame extinction. Also from the previous study[5], it is presumed that, when ISW is introduced, flow structure changes three-dimensionally and entrainment of main stream from the side increases, leading to flame extinction.

4-2. Numerical result

Figure 6 and 7 show the profiles of mass fraction and pressure; (1) without ISW and (2) $x_i = 47.3$ mm. Figure 7 also show streamlines of main stream. From Fig.6(1), jet flow has certain thickness downstream. However, from Fig.6(2), thickness of jet flow is decreased from the point of ISW to downstream. Also from Fig.7(2), static pressure downstream of ISW increased and streamline of main stream curved downward. The phenomenon means that jet layer downstream of ISW is pressed against the wall. Therefore, it is expected that main stream curved to downward direction promotes cooling of flame near the wall.

5. Conclusions

1. Combustion experiments in supersonic flow and visualization of flow field and flameholding were performed. Flame extinction was confirmed downstream of ISW when ISW was introduced. It is expected that entrainment of the main flow leads to the flame extinction downstream of ISW.
2. From the numerical results, the vectors of main stream were curved and the thickness of boundary layer was decreased. It is expected that the phenomenon promotes cooling of flame near the wall.

Reference

[1]Chadwick C. Rasmussen, James F. Driscoll et al., Proc.

Combust. Inst. 30 (2005), pp. 2825- 2833.

[2]Hisashi Nakamura, Hideaki Kobayashi, Susumu Hasegawa, Goro Masuya, Takashi Niioka, 19th International Colloquium on the Dynamics of Explosions and Reactive Systems, 2003, CD-ROM.

[3]Naoki Sato, Master Thesis, Tohoku University, 2007.

[4]D. C. Wilcox, Turbulence Modeling for CFD, 2nd ed., DCW Industries, 1998.

[5]Toru Mai, Yoshimune Sakimitsu, Hisashi Nakamura et al., Proc. Combust. Inst. 33 (2011), pp. 2335- 2342.

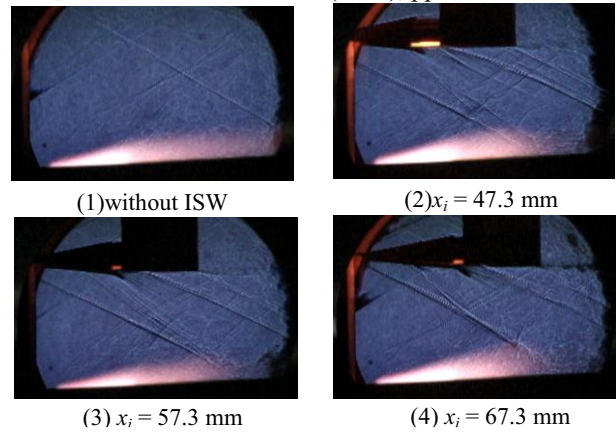


Fig.3. Flame emission and shock wave images.

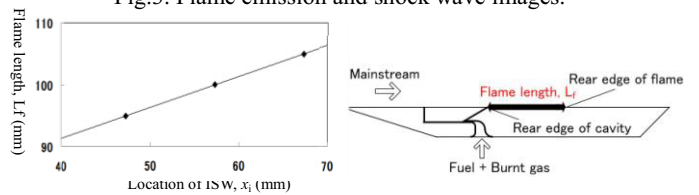
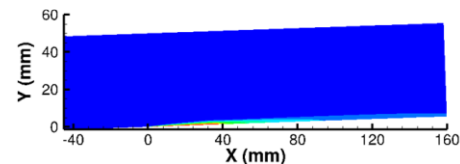
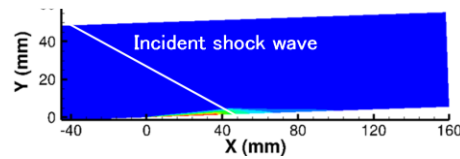


Fig.4. Relationship between x_i and L_f .

Fig.5. Definition of L_f .

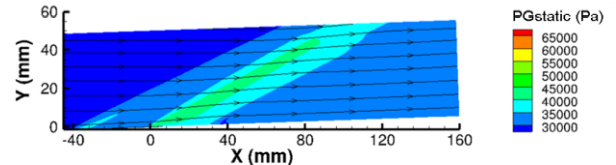


(1) without ISW

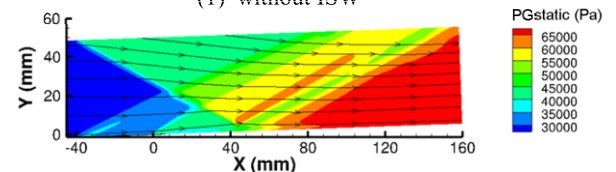


(2) $x_i = 47.3$ mm

Fig.6. Profile of mass fraction of injection gas in the flow field.



(1) without ISW



(2) $x_i = 47.3$ mm

Fig.7. Profile of static pressure in the flow field.

Combustion Characteristics of Propanol/Air Turbulent Premixed Flames at High Pressure

Shungo Souyoshi, Takuro Suzuki, Taku Kudo, Hideaki Kobayashi

Institute of Fluid Science, Tohoku University, 2-1-1 Katahira, Aoba-ku, Sendai, Miyagi 980-8577, Japan
souyoshi@flame.ifs.tohoku.ac.jp

ABSTRACT

Characteristics of turbulent premixed flames of alcohol-isomer biofuels, i.e., 1-propanol and 2-propanol, were experimentally investigated at high pressure up to 0.5 MPa. OH-PLIF measurement was performed for stabilized Bunsen-type flames using the slot-type burner installed into a high-pressure chamber. Result showed that there were differences in the flame properties between two isomers of which thermal and physical properties are almost equal. It was proved that they cannot be explained based on the previous theory of fluid dynamic and diffusive-thermal instability on turbulent premixed combustion.

1. Introduction

Biofuels have great advantages as potential alternative fuels, their renewability and carbon neutrality. In particular, high alcohols are considered to be next-generation biofuels. For implementation of these alcohols, it is essential to acquire knowledge of their turbulent premixed combustion at high pressure. As shown in Table 1, higher alcohols have several isomers with approximately same thermal and diffusive properties. Besides, the process of pyrolysis is different with ambient temperature [1]. So these isomers are thought to have different chemical reaction characteristics. By DNS result of turbulent premixed flames, it is suggested that the distribution of chemical species is different from laminar premixed flames and turbulence affects flame chemistry in the turbulent premixed flame [2]. Therefore, we need to examine the interaction between turbulence and flame chemistry independent of the mixture properties as well.

In this study, characteristics of turbulent premixed flames of alcohol-isomer biofuels, i.e., 1-propanol and 2-propanol, were experimentally investigated in a high-pressure environment to clarify the important properties of propanol/air turbulent premixed flames as well as to gain insight into the mechanism of interaction between turbulence and flames. For comparison, CH₄/air, as a typical hydrocarbon flame, was also examined.

Table 1. Properties of mixture (Pressure, P = 0.1 MPa, Equivalence ratio, $\phi = 0.9$).

	Kinematic viscosity ν [cm ² /s]	Thermal diffusivity α [cm ² /s]	Lewis number Le_{fuel}
methane/air(T = 300 K)	0.161	0.224	0.95
1-propanol/air(T = 343 K)	0.181	0.251	2.12
2-propanol/air(T = 343 K)	0.181	0.251	2.13

2. Experimental Method

Experiments were conducted using the high pressure combustion test facility at the Institute of Fluid Science, Tohoku University [3]. The mixtures provide the burner maintaining high temperature by mixing vaporized fuels with hot air. In this experiment, we used the slot-type burner to compare with recently obtained DNS results in future. Planar Laser-Induced Fluorescence (OH-PLIF) measurement was performed for 1- and 2-propanol flames at high pressure up to 0.5 MPa in a high pressure

chamber. Equivalence ratio, ϕ , of the mixture was from 0.8 to 1.0.

Laminar burning velocity, S_L , was estimated by CHEMKIN-PRO. Propanol detailed reaction mechanism by Johnson and Curran [4] was used for propanol/air flame, and GRI-Mech. 3.0 [5] was used for CH₄/air flame.

3. Results and Discussion

3.1 OH-PLIF images

Figure 1 showed OH-PLIF images of 1-propanol/air, 2-propanol/air and CH₄/air flames. Turbulent premixed flames of propanol/air had smaller cusps than those of CH₄/air. In those, 2-propanol/air flame had the smallest cusps.

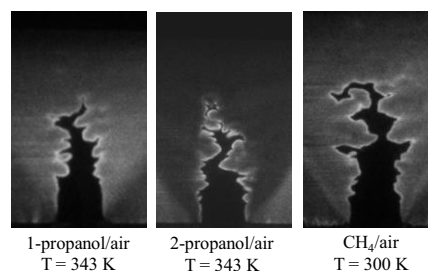


Fig. 1 OH-PLIF images of the flames ($u'/S_L = 1.35$).

Using OH-PLIF images, distribution of local flame surface density, Σ_{local} , mean progress variable, $\langle c \rangle$, fractal inner cut off, ϵ_i , turbulent burning velocity, S_T were analyzed and compared among those of 1-propanol/air, 2-propanol/air and CH₄/air flames.

3.2 Local flame surface density

Figure 2 shows the distribution of Σ_{local} . Propanol/air flames had globally larger Σ_{local} than CH₄/air flame. This means that propanol/air flame structures complicated than CH₄/air flame. Figure 3 shows the relationship between $\langle c \rangle$ and Σ_{local} of 1-propanol/air, 2-propanol/air and CH₄/air flames. The maximum Σ_{local} of 2-propanol/air flame is larger than that of 1-propanol/air flame. Markshtein length and Markshtein number of propanol/air flames, which represent the effect of flame stretch to laminar burning velocity as an element of turbulent flames, are smaller than those of CH₄/air flames. So this result corresponds to our

expectation that the flame surface density of propanol/air flames is larger than that of CH₄/air flames.

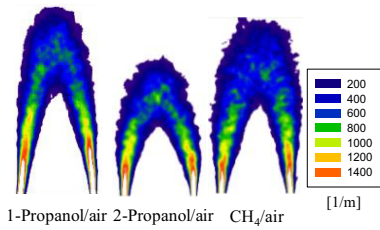


Fig. 2 Distribution of flame surface density, Σ_{local} .

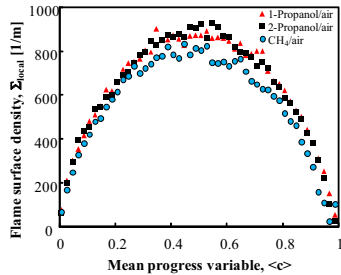


Fig. 3 Relationship between $\langle c \rangle$ and Σ_{local} .

3.3 Turbulent burning velocity

Figure 4 shows the relationship between normalized turbulent intensity, u'/S_L , and fractal inner cut off scale, ϵ_i , ten times of kolmogorov scale, $10\eta_k$, which corresponds to the mean diameter of vortex tubes. Fractal inner cut off, ϵ_i , is regarded as the smallest scale of flame wrinkles. ϵ_i of propanol/air flames is smaller than that of CH₄/air. This corresponds to the OH-PLIF images that propanol/air flames had smaller cusps than CH₄/air flames. Figure 5 shows the relationship between normalized turbulent intensity, u'/S_L , and normalized turbulent burning velocity, S_T/S_L . S_T/S_L of 2-propanol was larger than that of 1-propanol/air flame and CH₄/air flame. This means that gross flame area increased because the smallest scale of flame wrinkles get smaller. According to the previous theory of diffusive-thermal instability, S_T/S_L of propanol/air was also expected to be nearly equal between two isomers. However, S_T/S_L of the two isomers was obviously different, thus experimental results are different from the expectation. Figure 6 shows the relationship between normalized wave number, $k\delta$, and normalized disturbance growth rate, $\sigma\delta/S_L$. Disturbance growth rate, σ , means the effect of flame instability for flame complication. σ of CH₄/air flame is larger than that of propanol/air flame. As a result, CH₄/air flames were expected to become complicated. On the other hand, flame front of two propanol/air flames was expected to be nearly equal between two propanol isomers, however, 2-propanol/air flame had the smallest cusps. Therefore, they cannot be explained according to the previous theory of diffusive-thermal instability and more examinations regarding another flame instability mechanism and interaction between turbulence and flame chemistry are needed.

4. Concluding remarks

Characteristics of propanol isomers turbulent

premixed flames in a high pressure environment were examined experimentally. From OH-PLIF measurement, turbulent flame properties for propanol isomers are different each other. Further examinations regarding turbulence and flame instability are needed to clarify the effect of isomers fuels.

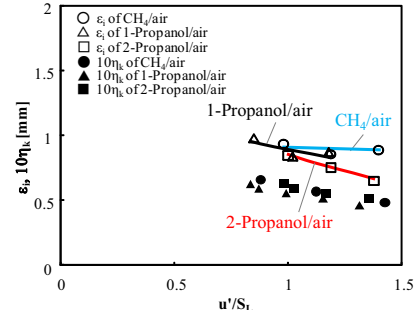


Fig. 4 Relationship between u'/S_L and ϵ_i ($P = 0.5$ MPa, $\phi = 0.9$).

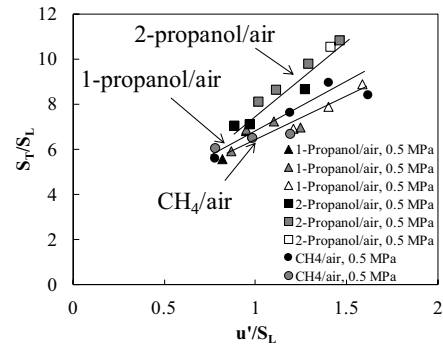


Fig. 5 Relationship between u'/S_L and S_T/S_L ($P = 0.5$ MPa).

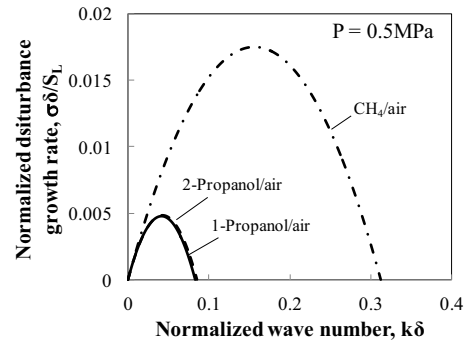


Fig. 6 Relationship between $k\delta$ and $\sigma\delta/S_L$ ($P = 0.5$ MPa, $\phi = 0.9$).

References

- [1] X. Gu, Z. Huang, S. Wu, Q. Li, Combust.Flame 157(2010) 2318-2325.
- [2] J.B. Bell, M.S. Day, J.F. Grcar, Proc. Combust. Inst. 29(2002) 1987-1993.
- [3] H. Kobayashi, T. Nakashima, T. Tamura, K. Maruta, T. Niioka, Combust. Flame 108(1997) 104-117.
- [4] M.V. Johnson, S.S. Goldsborough, Z. Serinyel, P. O'Toole, E. Larkin, G. O'Malley, H.J. Curran, Energy Fuels 23(2009),5886.
- [5] G.P. Smith, et.al, GRI-Mech homepage, <<http://www.me.berkeley.edu/gri-mech/>>.

Measurement of the Ion Specific Heat Ratio in Fast-flowing Plasma using a Mach Probe

Yuko Hashima, Kohei Okawa, Hiroshi Watanabe, Yuki Izawa, Kazuya Yashima,
Kiyotaka Suzuki, Nozomi Tanaka, Akira Ando

Department of Electrical Engineering, Graduate School of Engineering, Tohoku University
6-6-05, Aoba-yama, Aoba, Sendai, 980-8579, Japan
hashima@ecei.tohoku.ac.jp

ABSTRACT

The specific heat ratio of ions γ_i has evaluated in a fast-flowing plasma using a Mach probe. An ion Mach number M_i was measured in a plasma flow passing through a Laval type magnetic nozzle. The ratio γ_i was derived from comparing the measured M_i with isentropic relations. The ratio γ_i of 1.2 was evaluated in helium plasma with an electron density of $3.8 \times 10^{19} \text{ m}^{-3}$. The γ_i estimation was performed in various plasmas with He, Ne, Ar and Kr as working gases. The ratio γ_i decreased as electron density increased.

1. Introduction

The specific heat ratio γ is one of the important parameters specifying thermodynamic behavior in gas dynamics. An ideal gas behaves in accordance with the polytropic relation, $pV^\gamma = \text{const.}$ in an adiabatic process. The ratio γ is expressed as $\gamma = (f + 2)/f$, where f is the degree of freedom. In a process of constant pressure or constant temperature, $\gamma = 0$ or $\gamma = 1$ is used in the same polytropic relation, respectively.

In plasmas the specific heat ratio of ions γ_i is also important parameter. However, many processes of ionization and electron excitation make the derivation of γ_i difficult. The determination of γ_i has attracted much attention in observation of various space phenomena. Recently γ_i in solar corona has been estimated by observation of corona behavior from a spacecraft [1].

We have experimentally determined the ratio γ_i using an isentropic plasma flow passing through a Laval type magnetic nozzle. When the nozzle cross-section gradually changes, thermodynamic parameters of passing gas fluid, such as temperature and density, vary according to the following isentropic relations.

$$\frac{dM}{M} = \frac{2 + (\gamma - 1)M^2}{2(M^2 - 1)} \frac{dA}{A} \quad (1)$$

$$\frac{dU}{U} = \frac{1}{M^2 - 1} \frac{dA}{A} \quad (2)$$

$$\frac{dn}{n} = -\frac{M^2}{M^2 - 1} \frac{dA}{A} \quad (3)$$

$$\frac{dT}{T} = -\frac{(\gamma - 1)M^2}{M^2 - 1} \frac{dA}{A} \quad (4)$$

Here, M is Mach number, U is flow velocity, n is density, T is temperature and A is nozzle cross section.

An ion Mach number M_i in a plasma is expressed as follows,

$$M_i = \frac{U}{\sqrt{(\gamma_i T_i + \gamma_e T_e)/m_i}} \quad (5)$$

where, m_i is ion mass, γ_i and γ_e are ion and electron specific heat ratios and T_i and T_e are ion and electron temperatures, respectively.

When only electrons are magnetized, ions behave as collisional neutral particles in gas fluid surrounded with

magnetic flux tube. M_i increased from subsonic ($M_i < 1$) to supersonic ($M_i > 1$) value according to Eq. (1) when a plasma flow passes through a Laval type magnetic nozzle. It becomes unity at the nozzle throat. In this research we have measured M_i and derived γ_i in various plasma flows passing through a Laval type magnetic nozzle.

2. Experimental setup

Experiments were carried out in the HITOP (High density Tohoku Plasma) device, as is shown in Fig.1. A fast-flowing plasma was exhausted from an MPD arcjet attached on the device [2]. A quasi-steady discharge can be operated up to 1 ms in duration. Various types of axial magnetic field can be applied and a bump type magnetic configuration shown in Fig. 2 was used in the

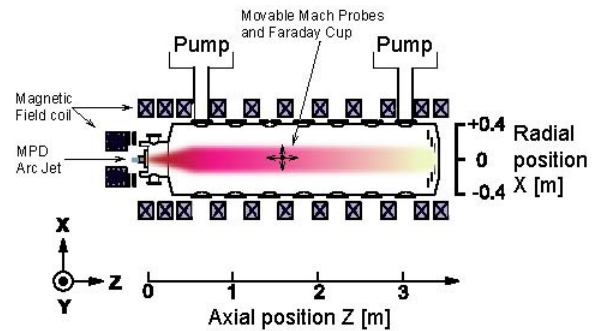


Fig. 1 Schematic of the HITOP device. The position at $Z = 0$ corresponds to the cathode tip of the MPDA.

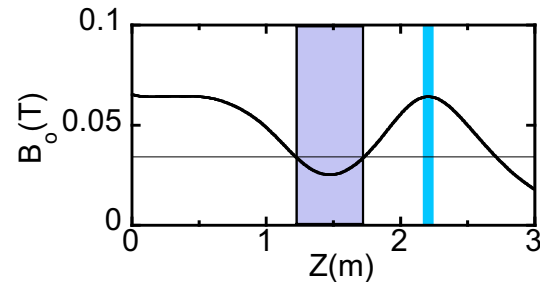


Fig. 2 An axial profile of the bump type magnetic configuration. The maximum magnetic field is 0.065 T at magnetic nozzle throat ($Z = 2.2$ m). Shock wave occurred at the hatched area and Mach number decreased below unity.

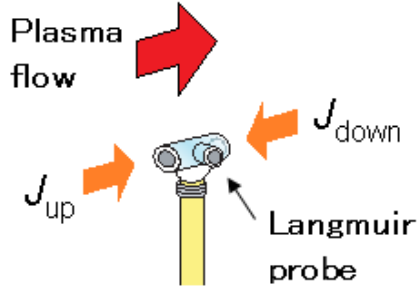


Fig. 3 Schematic of a Mach probe with perpendicular tip.

experiments. M_i decreased below unity at the hatched area ($Z=1.2-1.7\text{m}$) in Fig.2, where shock wave phenomena occurred, and increased above unity at the following Laval type magnetic nozzle. A Mach probe shown in Fig. 3 was used to measure an ion Mach number of the plasma flow. Electron density and temperature were measured by using a perpendicular tip of the probe. An energy analyzer (Faraday cup) with three grids was used for measurements of ion energy distribution. These diagnostics were set on a two-dimensionally movable table set in the vacuum chamber. He, Ne, Ar and Kr were used as working gases in the experiments.

3. Experimental results and discussion

Figure 4 shows an axial profile of ion Mach numbers measured by a Mach probe in He plasma. Discharge current was 3.6 kA and electron density was $3.8 \times 10^{19} \text{ m}^{-3}$ at the nozzle throat ($Z=2.2\text{m}$). The experimental results were compared with theoretical curves obtained by Eq. (1) assuming $\gamma_i = 1.2$. These data are in good agreement with the theoretical value.

When a plasma flow passes through a Laval type magnetic nozzle, a Mach number becomes unity at the nozzle throat. At the throat the ion specific heat ratio γ_i can be expressed as follows using Eq. (5) and $M_i = 1$.

$$\gamma_i = \frac{T_e}{T_i} (v_f^2 - \gamma_e) \quad (6)$$

Here, the normalized velocity v_f is expressed as $v_f = U / \sqrt{\gamma_e T_e / m_i}$ and can be derived by using a Mach probe as well as M_i [3]. We also evaluated γ_i at the nozzle throat using Eq.(6) and measured plasma

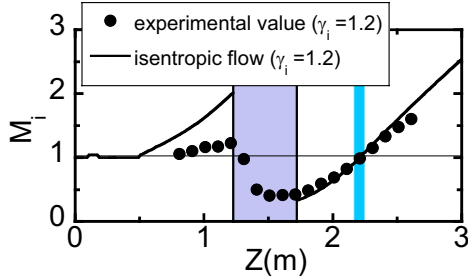


Fig. 4 Axial profile of M_i in the bump type magnetic configuration. M_i was measured by using a Mach probe and compared with the isentropic flow model.

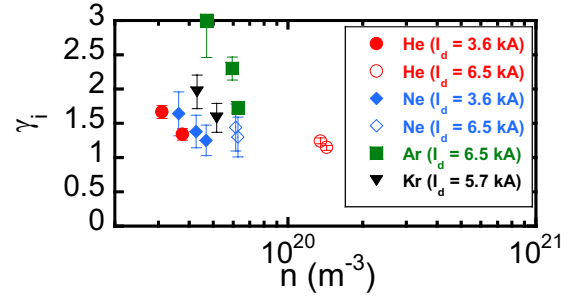


Fig. 5 Dependence of the ion specific heat ratio on a plasma density in plasmas with various gases.

parameters and obtained $\gamma_i = 1.2$.

We evaluated γ_i in the same procedure by changing a discharge current in various gases and measured time in a discharge. Figure 5 shows the evaluated γ_i as a function of electron density in various gas plasmas. The ratio γ_i varied from 1 to 3 and decreased as plasma density increased. It indicates that collisions between ion-ion and ion-neutral particles made γ_i smaller.

4. Summary

We have experimentally measured ion Mach numbers in plasma flow passing through a Laval type magnetic nozzle. The ion specific heat ratio γ_i in plasma with various gases were derived by comparing the measured M_i with isentropic relations. The obtained γ_i varied from 1 to 3 and decreased as plasma density increased. The experimental results indicated that collisions between ion-ion and ion-neutral particles made γ_i smaller. More experimental estimations of γ_i in various plasma conditions are necessary to formulate γ_i in plasmas.

References

- [1] T. V. Doorsselaere *et al.*, The Astrophysical Journal Letters **727**, L32 (2011).
- [2] M. Inutake *et al.*, J. Plasma Fusion Res. **83**, 483 (2007).
- [3] A. Ando *et al.*, Contrib. Plasma Phys. **46**, 335 (2006).

Response Time Evaluation of Temperature-Sensitive Paint

Takehito Horagiri and Hiroki Nagai

Department of Aerospace Engineering, Tohoku University
6-6-01, Aramaki-Aza-Aoba, Aoba-ku, Sendai 980-8579, JAPAN
horagiri.takehito@aero.mech.tohoku.ac.jp

ABSTRACT

Currently Temperature-Sensitive Paint (TSP) attracts attention as a temperature measurement technique. TSP is a temperature sensor based on photochemical reaction. In this conventional method, we can only obtain a discrete data and a measurement point depends on the model shape and the number of sensors. In contrast, TSP measurement provides a full-field image of the temperature distribution on a model surface with high spatial resolution. But, we need to know the response time of TSP to use a short duration wind tunnel. By comparing TSP with thermocouple data, we evaluate the response time of TSP.

1. Introduction

Heat flux measurement in hypersonic wind tunnel is one of indispensable requirements for designing a next generation reentry vehicle.

Typically, the method of measurement with a thermocouple is dependent on the model shape and the number of sensors. Thus, we can get only discrete data. In contrast, we can get a full-field image of the temperature distribution on the model surface by using Temperature-Sensitive paint (TSP) [1].

Currently, the reappearance of a spacecraft reentry is conducted with a shock tube and a wind tunnel. Test times of some of the equipment are extremely short [2] so we cannot use the TSP which does not have enough response time. Thus, we need to evaluate the response time of TSP.

In this study, we change the TSP film thicknesses and the exposed times of a pulse laser and evaluate the response time of TSP.

2. Principle

2.1 Temperature-Sensitive Paint

TSP is a coating that consists of sensor molecules dispersed in polymer binder. When illuminated with light at an appropriate wavelength, the sensor molecules become excited electronically to an elevated energy state. The molecules undergo transition back to the ground state by one of several mechanisms, each occurring at a different rate. The predominant mechanisms are radiative decay (luminescence) and non radiative decay through release of heat. A part of non radiative decay depends on temperature. Therefore, the luminescence of TSP coating decreases with increasing temperature. Thus, we can get the surface temperature of the model by using the relationship between the luminescence of TSP and the temperature. Generally, the relationship is expressed by Eq. (1).

$$\frac{I}{I_{ref}} = \sum_{n=0}^N A_n \left(\frac{T}{T_{ref}} \right)^n \quad (1)$$

where the subscript *ref* represents the reference conditions, and A_n is a calibration coefficient.

In this study, Ru(phen)₃²⁺ is used as TSP. The absorption peaks of this TSP are at wavelength of approximately 260 nm and 430 to 450 nm and the

emission peak is 610 nm.

2.2 Theoretical formula

In the method of temperature calculation with TSP, we generally use a transient 1-D semi-infinite model. The temperature change ratio when we give heat flux q on the model surface is expressed by Eq.(2).

$$\frac{T_s(t) - T_i}{T_{max} - T_i} = A_{et} \frac{2q\sqrt{t}}{\sqrt{\pi\rho ck}} \quad (2)$$

where the temperature at t , the initial temperature and the maximum temperature of the model surface are $T_s(t)$, T_i and T_{max} , respectively. The density, specific heat and heat conductivity of the model are ρ , c and k , respectively. A_{et} are calculated coefficients.

3. Experimental Setup

The measurement system is shown in Fig.1. In this test, a size of the ceramic model is 50×50 mm and the thickness is 10 mm which was half coated with TSP.

A thin-film thermocouple was set on the model surface to compare with TSP. The model was pulse heated with 30 W CO₂ laser. The UV-LED (wavelength 405nm) was used as an excitation light, and a photomultiplier tube (PMT) was used as a photo-detector. Additionally, an optical filter which was cutoff wavelength at 580 nm was placed in front of a camera lens to prevent the reflected laser light from entering the PMT. A beam-expander was set up between the model and the laser to expand the irradiation spot.

The test parameters are listed in table 1.

Table 1 Test parameter

Exposed time[ms]	20	10	5	1
Film thickness[μm]	0.05	0.1	0.6	1.2

4. Results and Discussion

Fig.2 shows the comparisons with theory which are calculated from the results of the surface temperature change of TSP. In this test, we defined an mathematical expression of the time delay, which is expressed by Eq.(3).

$$Time \ Delay = \left| \frac{t_{T_{max}} - t_{et}}{t_{max}} \right| \times 100 \quad (3)$$

where t_{Tmax} is the time that reaches the maximum temperature from start time and t_{et} is the time of the laser irradiation. Fig.2 shows the results which are normalized with difference of the maximum and initial surface temperature of the model. The theoretical value is shown in Fig.2 (black, heavy line). According to the results, there are temperature errors between experimental results and theoretical value. These errors are caused by inconsideration of the film thickness of TSP layer and hypothesis of semi-infinite model. There is time delay without relation to film thickness of TSP layer. In addition, the time delay becomes larger as the exposed time is shorter.

Fig.3 shows the quantitative evaluation of time delay of Fig.2. In cases where the exposed time are 5 ms and over, film thickness of TSP does not effect on the response time of TSP so much. In equivalent exposed time, time delay of the model which is coated with thick TSP is slightly smaller than that of thin TSP. Commonly, it is said that the rise time of thin TSP layer model is faster than thick TSP because the heat capacity of the thin TSP layer is smaller than that of thick TSP layer. In contrast, at this experiment, the result is that the rise time of thick TSP layer model is faster than thin TSP layer model.

5. Concluding remarks

In this study, used CO₂ laser and heat the models which are coated with TSP. We change the TSP thickness and the exposed time and evaluated the time delay of TSP. By coating TSP thickly, the time delay is smaller and S/N ratio is improved, so we can apply the TSP for short test time experiments.

References

- [1] T.Liu and J.P.Sullivan, "Pressure and Temperature Sensitive Paints", Springer, Berlin, 2005.
- [2] K.Itoh, S.Ueda, H.Tanno, T.Komuro and K. Sato, Hypersonic aerothermodynamic and scramjet research using high enthalpy shock tunnel, Shock Waves (2002) 12: 93–98

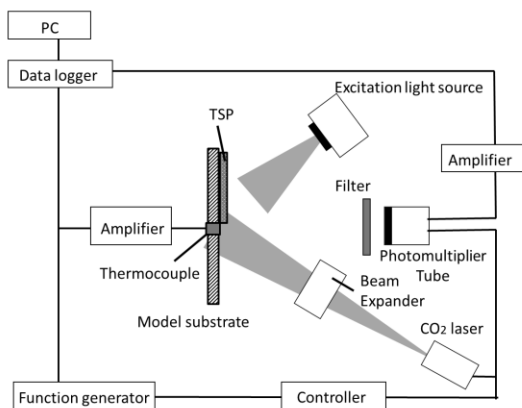


Fig.1 Experiment setup

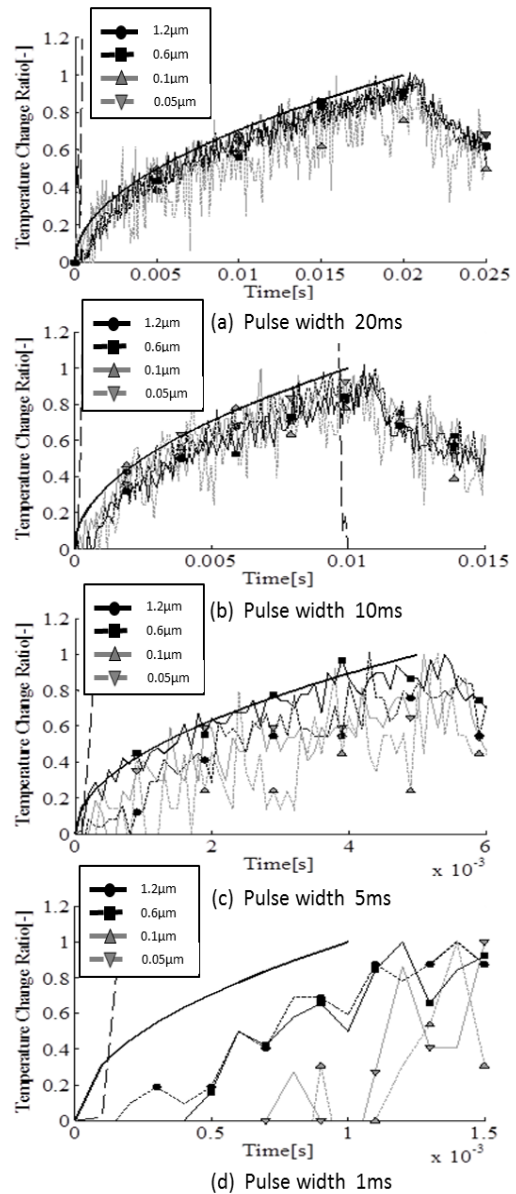


Fig.2 Comparison with theory

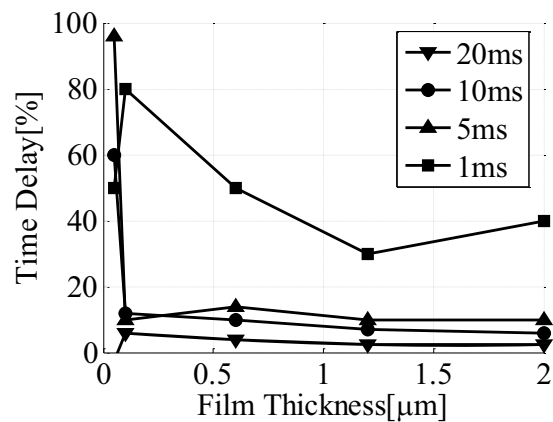


Fig.3 Quantitative evaluation of time delay

Delay Time Compensation of a Hardware in the Loop Simulation Based on Contact Dynamics Model

Fumihito Sugai⁽¹⁾, Satoko Abiko⁽¹⁾, Xin Jiang⁽¹⁾, Atsushi Konno⁽²⁾ and Masaru Uchiyama⁽¹⁾

⁽¹⁾ Department of Mechanical Systems and Design, Graduate School of Engineering, Tohoku University, 6-6-01, Aramaki-aza-Aoba, Aoba-ku, Sendai, Miyagi, 980-8579 Japan.

⁽²⁾ Division of System Science and Informatics, Graduate School of Information Science and Technology, Hokkaido University, Kita 14, Nishi 9, Kita-ku, Sapporo, Hokkaido, 060-0814, Japan.
{sugai, abiko, jiangxin, uchiyama} @space.mech.tohoku.ca.jp, konno@ssi.ist.hokudai.ac.jp

ABSTRACT

In order to develop space robotic technologies, the feasibility and reliability of the systems have to be verified by repetitive tests. Hardware in the loop (HIL) simulation is one of the effective ways to simulate micro-gravity condition on the earth. However the HIL has a problem of energy increase due to dead time of the system. In this paper, we extend a delay time compensation method to deal with contacting spring-damper environment.

1. Introduction

Hardware in the loop (HIL) simulation is one of the effective methods to test space robotic operations on the ground. The HIL can emulate three dimensional relative motion of a space robot with respect to a certain target in micro gravity environment using numerical dynamic calculation and hardware to which physical interaction occurs (Fig. 1). However, the HIL simulator generally suffers from a problem of energy increase. This problem leads to unrealistic phenomena such that, the coefficient of restitution exceeds one in the collision emulated by the HIL simulator. This problem mainly occurs due to delay time in the loop (i.e. servo delay and force/torque measuring). A number of researches tackled the energy increase problem due to the delay time [1–3]. The delay time compensation method proposed by Osaki et al. is one of the effective ways to deal with delay time. They derived the compensation method on the assumption that the contact dynamics as a spring-mass model. However, actual contact phenomena generally include damping effect. Hence, we model the contact dynamics as spring-mass-damper system in the HIL simulator and derive delay time compensation method with the spring-mass-damper model.

2. The HIL simulator

As shown in Fig. 1, the HIL simulator consists of a robotic motion table, a numerical simulator and a physical model that is designed as same as a part of the corresponding real target. The physical model is affected by physical interaction or contact. The physical contact is measured by an F/T sensor installed between the motion table and the physical model. The numerical simulator calculates dynamic motion of the entire robotic system due to the contact. Then, the relative motion is demonstrated by the motion table based on calculation result in the numerical simulation. Fig. 2 is an overview of the HIL simulator developed in our laboratory. The robotic motion table contains a 6 DOF parallel robot called HEXA, 2 DOF mobile platform termed X-Y table, and 1 DOF infinite spinning motion system.

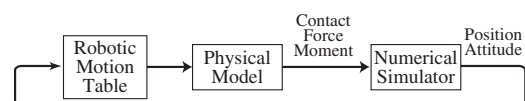


Fig. 1 Concept of HIL.

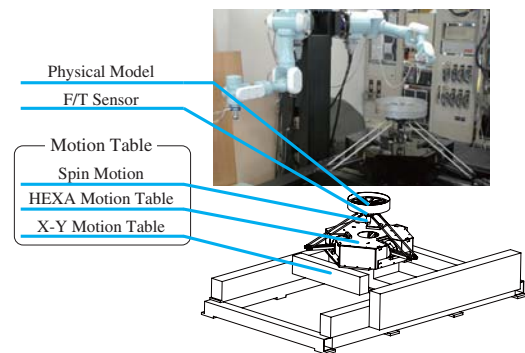


Fig. 2 Overview of the HIL simulator.

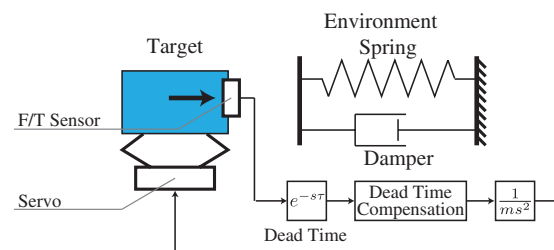


Fig. 3 Model of HIL simulation.

3. Delay time compensation

Osaki et al. proposed compensator which achieves phase lead in the loop based on the desired coefficient of restitution (C.o.R.) for the delay of servo system and force/torque measurement system in the HIL simulator. We improve the compensation method by applying the spring-mass-damper system (Fig. 3) as the contact dynamics model in order to realize the contact with various environmental characteristics.

The design of delay time compensation amounts to a problem to obtain a relation between compensated force $\hat{F}(t)$ and measured force with dead time $F'(t)$, with which the target motion can be achieved as the case that without dead time. The equation of motion of floating target with

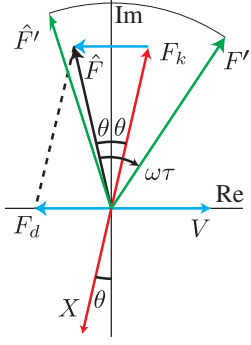


Fig. 4 Velocity and force vectors.

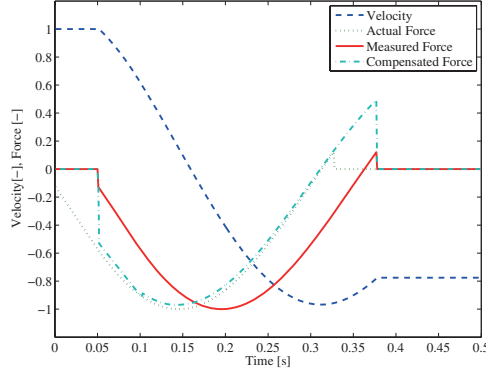


Fig. 5 Simulation result (conventional method).

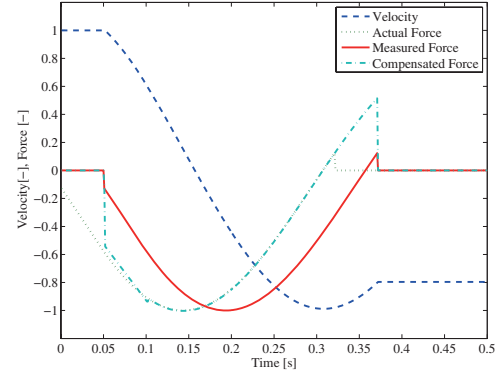


Fig. 6 Simulation result (proposed method).

compensated force in the simulator is as follows.

$$m\dot{V}(t) = \hat{F}(t), \quad (1)$$

$$F'(t) = F(t - \tau), \quad (2)$$

$$\begin{aligned} F(t) &= F_k + F_d \\ &= -kX(t) - 2\zeta\omega_n mV(t), \end{aligned} \quad (3)$$

where, F is the contact force, V is a velocity of the target, m is a mass of the target, k is a stiffness of the contact model, ζ is an attenuation coefficient of the contact model, and τ is a dead time.

The motion without dead time is expressed as following equation that can be derived from the equation of motion.

$$\begin{aligned} V &= V_0 e^{(-\zeta + j\sqrt{1-\zeta^2})\omega_n t}, \\ &= V_0 e^{Z\omega_n t} (Z = e^{j(\frac{\pi}{2} + \theta)}), \end{aligned} \quad (4)$$

$$\theta = \tan^{-1} \frac{\zeta}{\sqrt{1-\zeta^2}}. \quad (5)$$

Hence \hat{F} is expressed as follows:

$$\begin{aligned} \hat{F} &= m\dot{V}(t), \\ &= m\omega_n ZV(t), \\ &= m\omega_n e^{j(\frac{\pi}{2} + \theta)} V(t). \end{aligned} \quad (6)$$

The measured force in the case with dead time is derived with Eq. (2).

$$\begin{aligned} F' &= m\omega_n e^{j(\frac{\pi}{2} + \theta)} V(t - \tau), \\ &= m\omega_n e^{j(\frac{\pi}{2} + \theta)} e^{(\zeta - j\sqrt{1-\zeta^2})\omega_n \tau} V(t), \\ &= m\omega_n e^{\zeta\omega_n \tau} e^{j(\frac{\pi}{2} + \theta - \omega_n \tau)} V(t), \end{aligned} \quad (7)$$

where $\omega = \sqrt{1-\zeta^2}\omega_n$.

From the above equations, consequently, the relationship between $F'(t)$ and $\hat{F}(t)$ is derived as follows.

$$\frac{\hat{F}}{F'} = e^{-\zeta\omega_n \tau} e^{j\omega\tau} \quad (8)$$

The difference between the conventional compensated force $\hat{F}'(t)$ and the proposed compensated force in this paper $F'(t)$ is described as follows.

$$\hat{F}' = e^{j\omega_n \tau} F' \quad (9)$$

Table 1. Simulation result.

	Conventional	Proposed
C.o.R.[-]	0.7757	0.7963
Error [%]	3.0	0.5

The velocity and force vectors are shown in complex plane in Fig. 4. This figure shows that \hat{F}' is not equal to \hat{F} . If we compensate motion contacting spring-damper environment with spring mass model, the motion simulated with HIL will not be equivalent with the real motion.

4. Verification with numerical simulation

We verified the proposed compensation method with numerical simulation. In the simulation, we setup $m = 300$ [kg], $k = 30000$ [N/m]. The attenuation coefficient is set to realize coefficient of restitution(C.o.R.) 0.8. The result of numerical simulation is shown in Figs. 5 and 6. The data shown in the figures are normalized by peak value. The realized C.o.R. and error of C.o.R. with conventional method and with proposed method are shown in Table 1. It shows that the proposed method has better performance even though the target contacts with spring-damper environment.

5. Conclusions

In this paper, we proposed extended delay time compensation method of the HIL simulator for contacting to spring-damper environment. The numerical simulation verified the validity of the proposed compensation methods.

References

- [1] S. Ananthkrishnan et al. "Role of estimation in real-time contact dynamics enhancement of space station engineering facility," *Robotics & Automation Magazine*, IEEE, **3**, pp. 20–28 (2002)
- [2] M. Inoue et al. "Development of the Docking Dynamics Simulator," *Tran. Society of Instrument and Control Engineers*, **28**, No. 11, pp. 1306–1313 (1992)
- [3] K. Osaki et al. "Delay Time Compensation for a Hybrid Simulator," *Advanced Robotics*, **9**, No. 9, pp. 1081–1098 (2010)

Optical Microscope to Understand Motility

Takeshi Obara¹, Yasunobu Igarashi² and Koichi Hashimoto¹

¹Graduate School of Information Sciences, Tohoku University

6-6-01 Aramaki aza aoba, Aoba-ku, Sendai City, Miyagi, 980-8579, Japan

²Olympus Software Technology Corp. 2951 Ishikawa-cho, Hachioji, Tokyo, 192-8507, Japan

obara@ic.is.tohoku.ac.jp

ABSTRACT

In biological and medical sciences, optical microscopes are widely used. However, moving specimens easily escape from a field of view of it. Therefore, we propose to track a moving specimen. It is put back inside of the field of view by visual feedback controlled microscope stage. A *C.elegans* had been tracked during 40 seconds and its fluorescent images reflecting nerves' condition had been captured all that time. We are planning to combine optogenetic method to stimulate a nerve artificially. We believe that the proposed microscope is helpful to understand motility.

1. Introduction

Many microorganisms sense stimuli from the environment[1-2]. Then they move in order to approach better environment or avoid worse one[3]. This function, motility, is essential for them. However, there is a dilemma to research it. When we observe them in microscopic magnification, they easily escape from a field of view. When in macroscopic magnification, we cannot get detailed and bright images. To solve this dilemma, we propose to track a moving specimen in order to observe microorganisms in both microscopic magnification and macroscopic area at the same time.

2. Method

2.1 Outline

The proposed microscope system (Fig. 1) was mainly composed of an optical microscope (Bx 51, Olympus), a high speed camera (GRAS-03K2M/C, 640 x 480 pixel, 200 FPS, Point Grey Research), a high sensitivity camera (C9100-02, 1000 x 1000 pixel, 30 FPS, x200 EM gain, -50 °C cooling, Hamamatsu Photonics K. K.), a projector (MiLSS (ASKA COMPANY) with MS513P(800 x 600 pixel, 2700 lumen, BenQ)), a PC (OS: Linux Ubuntu 9.04(kernel 2.6.32.7) + Xenomai-2.5.1, CPU: Intel Xeon X5460 3.16 GHz, RAM: 4 GB) and an XYZ stage (special order product, Accuracy: XY 2.5 μm, Z 1 μm HEPHAIST). 20-times objective lens (UApo 20X3/340, Olympus) was used. A scheme of the proposed microscope system is shown in Fig. 2 and its details are described in following chapters.

2.2 Tracking

In order not to miss a moving specimen, it was tracked. It locomoted on a petri dish. The specimen's shape and position were monitored by bright field illumination and a high speed camera. An interest region of the specimen was tracked by ESM algorithm, a kind of texture tracking[4]. Position of the petri dish, which loads the specimen, was controlled by an electric stage in order to put the interest region back inside of the field of view. This routine above was continued in 200 Hz cycle.

2.3 Fluorescent observation

Microorganisms' nerves sense environmental stimuli

and send control signals to muscles. It is important for understanding motility to monitor nerves' condition.

In order to monitor it, a fluorescent Ca²⁺ indicator (Yellow Cameleon[5]), a fluorescent excitation light (Laser) and a high sensitivity camera were used. Intensity of emission light of the fluorescent Ca²⁺ indicator reflects nerves' condition.

2.4 Optogenetic stimulation

Using optogenetics method, we can stimulate a specific nerve artificially[6-7]. It must be helpful to understand motility. We are planning to control optogenetic stimuli at specified time, place and intensity by a projector.

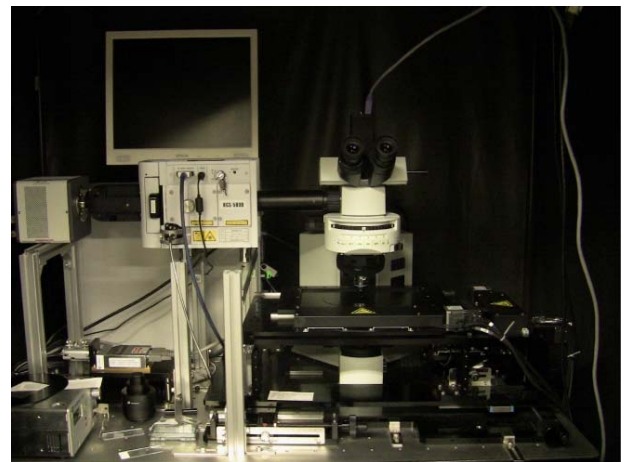


Fig. 1 An image of a proposed microscope system.

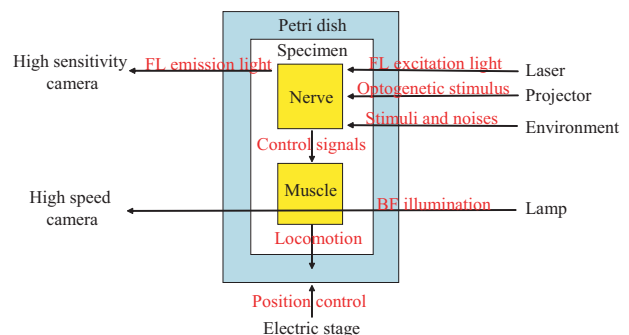


Fig. 2 A scheme of the proposed microscope system.

3. Results and Discussion

The proposed tracking and fluorescent observation were performed to a freely moving *C. elegans* mutant (a fluorescent Ca^{2+} indicator Yellow Cameleon is introduced to a sensory neuron AFD). Its time lapse images (neck region) are shown in Fig. 3. Its entire body is shown in Fig. 4.

When $t = 0$ ms, a texture of the specimen's neck region was registered as a template to track manually and then tracking was started. When $t = 0$ to 40 s, the neck region was kept inside of the field of view although the specimen had been locomoting. Fluorescent images had been captured all that time. When $t = 40$ s, observation was stopped because the tracked texture was missed by deformation.

C. elegans locomotes fast (1,000 $\mu\text{m/s}$) and its neck region is small (100 μm). It must go out of the field of view in a short time. However, it had been observed for 40 s. Without tracking, it must be unable to observe a neck region of a freely moving *C. elegans* in microscopic magnification (20-times).

4. Conclusion

Proposed microscope can track a moving microorganism and observe fluorescent images. We are planning to control optogenetic stimuli. We believe it is helpful to understand motility.

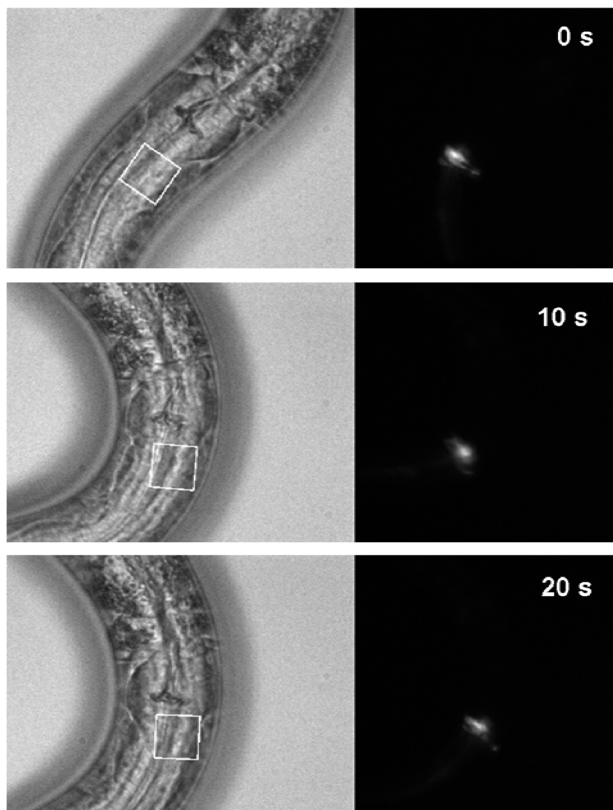


Fig. 3 Time lapse images of a freely moving *c.elegans*. Left: bright field images, Right: fluorescent images. The white squares show tracked textures. Time stamps are on upsides of each image.



Fig. 4 A bright field image of a *c.elegans*. The red square shows a neck region in which the central nerve is located.

References

- [1] Y. Nakaoka, F. Oosawa, J.PROTOZOOL, Vol24, pp. 575-580, 1977
- [2] E. M. Hedgecock, R. L. Russell, Proceedings of the National Academy of Sciences of the United States of America, Vol. 72, pp. 4061-4065, 1975.
- [3] H. S. Jennings, Behavior of the Lower Organisms, Columbia University Press, 1923.
- [4] S. Benhimane and E. Malis, International Journal of Robotic Research, vol. 26, no. 7, pp. 661–676, 2007.
- [5] A. Miyawaki, J. Llopis, R. Heim, J. M. McCaffery, J. A. Adams, M. Ikura, and R. Y. Tsien, Nature, vol. 388, no. 6645, pp. 882-887, 1997.
- [6] F. Zhang, A. M. Aravanis, A. Adamantidis, L. de Lecea, K. Deisseroth, Nature Reviews Neuroscience, No. 8, pp. 577--581, 2007
- [7] A. M. Leifer, C. Fang-Yan, Nature Methods, No. 8, pp. 147--152, 2011.

Characterization of Young's Modulus of MWCNT-Carbon Cantilevered Microstructures

Liang He¹, Masaya Toda², Yusuke Kawai¹, Mamoru Omori³, Toshiyuki Hashida³, and Takahito Ono¹

¹Graduate School of Engineering, Tohoku University, 6-6-01 Aza Aoba, Aoba-ku, Sendai 980-8579, Japan

²Micro System Integration Center (μ SIC), Tohoku University, 519-1176 Aza Aoba, Aoba-ku, Sendai 980-0845, Japan

³Fracture and Reliability Research Institute, Tohoku University, 6-6-11 Aza Aoba, Aoba-ku, Sendai 980-8579, Japan

E-mail: hl@nme.mech.tohoku.ac.jp

ABSTRACT

MWCNT-carbon cantilevered microstructures were fabricated from SU-8 50 mixed with 1 wt% MWCNTs in our process including Si micromolding and pyrolysis. The Young's modulus of the composite cantilevers was estimated from the natural resonant frequencies of the cantilevered microstructures that were measured by a laser Doppler vibrometer. The results shown the Young's modulus of MWCNT-carbon cantilevered microstructures pyrolyzed at 400 °C range from 3.50 to 8.84 GPa.

1. Introduction

Now resonant sensors such as cantilevers and microbridges are based on silicon and polysilicon have been widely investigated [1], and other materials were investigated and used since the quality of the various microsensors is so closely related to the mechanical properties of the material. In recent years, carbon nanotubes (CNTs) have been utilized as nano-fillers to enhance the mechanical strength of various matrices including polymers, ceramics and metals [2-4]. An important increase of the tensile modulus and toughness of matrices has been reported after the random dispersion of SWCNTs (Single-Walled CNTs) or MWCNTs (Multi-Walled CNTs). In this research, the cantilevered structures of CNT composite are fabricated, and their mechanical characteristics are evaluated from the mechanical resonance.

Photoresist-derived pyrolysis carbon and other amorphous carbon have been widely investigated for applications in MEMSs (Micro Electro Mechanical Systems) since its unique mechanical, electrical, chemical properties and its fabrication processes can be compatible to IC microfabrication [5]. In our research, MWCNT-carbon cantilevered microstructures with high aspect ratio was fabricated and investigated for its resonant frequencies.

2. Fabrication process and characterization method

The MWCNT-carbon cantilevered microstructures

were fabricated from SU-8 50 mixed with 1wt.% MWCNTs in our process including Si micromolding and deep ICP-RIE (Inductive Coupled Plasma Reactive Ion Etching) [6], as shown in Fig. 1.

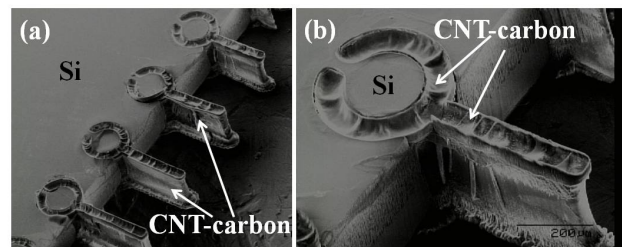


Fig. 1 SEM images of the fabricated composite cantilevers, (a) Tilt view of cantilever arrays (b) Magnified view of a cantilever.

The Young's modulus of the composite cantilevers was estimated from the natural resonant frequencies of the cantilevered microstructures that were measured by a laser Doppler vibrometer. As shown in Fig.2, the laser beam is focused at the vertical wall, and the flexural modes of lateral vibration are measured. The density of composite cantilevers was estimated from the weight and thickness of the MWCNT-carbon composite film fabricated by the same pyrolysis process, according to our measurement, the mass shrinkage and volume shrinkage were 38.9% and 53.0%, respectively. Therefore, 1 wt% MWCNT/resist became 1.65% in the pyrolysis process since the mass of the MWCNTs didn't change. The density of the composite microstructures

was $1.656 \pm 0.075 \text{ g/cm}^3$, from the resonant frequency f , the Young's modulus E of MWCNT-carbon composite can be estimated according to the rectangular shape.

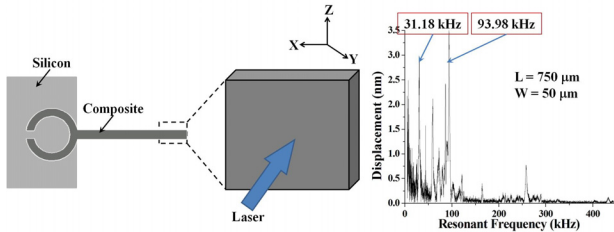


Fig. 2 Resonant frequency measurement of composite cantilever.

3. Results and discussion

The resonant frequencies are listed in Tab.1 together with the physical dimensions of the cantilevers. For the MWCNTs in this composite, Young's modulus ranged from ~ 30 to ~ 1090 GPa (average: 800 GPa) as reported in [7]. For the pyrolyzed resist film, Young's modulus ranged from 8.5-15 GPa. The linear rule of mixtures [8] is generally applied to estimate the physical properties of a composite material, such as Young's modulus and hardness, etc. According to this rule, the effective property of the composite has the upper and lower bound values that are approximated as:

$$E_{eff} = E_c f_c + E_m f_m \text{ (upper-bound)} \quad (1)$$

and
$$E_{eff} = \frac{E_m E_c}{E_m f_c + E_c f_m} \text{ (lower-bound)} \quad (2)$$

$E_c, f_c, E_m,$ and f_m are the physical parameter and volume fraction of the dopant (MWCNTs) and matrix (carbon), respectively. The calculated Young's modulus of CNT-carbon in Tab.1 was below the lower-bound model of the composite. These low Young's modulus should results from the voids in the composite microstructures.

Length (μm)	In-plane resonance (kHz)	Young's modulus (GPa)	Z direction (kHz)
650	36.35	5.92	95.08
700	38.30	8.84	94.61
750	31.18	7.72	93.98
800	18.46	3.50	93.79
850	24.18	7.66	85.94

Tab. 1 Resonant frequencies and calculated Young's modulus of the composite cantilevers with different length (width = $50 \mu\text{m}$).

4. Conclusions

Cantilevered microstructures of the MWCNT-carbon composite can be fabricated by this micromolding and pyrolysis process. The lower Young's modulus of the composite cantilevers should results from the voids in the composite microstructures.

Acknowledgements

This study was partially supported by the Global COE Program, "World Center of Education and Reaearch for Trans-disciplinary Flow Dynamics", Tohoku University, Japan Society for the promotion of Science.

References

- [1] Göran Stemme, *J. Micromech. Microeng.*, **1**, pp. 113-125 (1991)
- [2] F. T. Fisher, R. D. Bradshaw, and L. C. Brinson, *Appl. Phys. Letts.*, **80** (24), pp. 4647-4649 (2002)
- [3] Guang-Ren Shen, Yu-Ting Cheng, and Li-Nuan Tsai, *IEEE Trans. Nanotechnol.*, **4** (5), pp. 539-547 (2005)
- [4] Csaba Balázsi, Balázs Fényi, Norbert Hegman, et al., *Composites: Part B*, **37**, pp. 418-424 (2006)
- [5] Daniel H. C. Chua, B. K. Tay, W. I. Milne, et al., *Diam. Relat. Mater.*, **13**, pp. 1980-1983 (2004)
- [6] L. He, M. Toda, M. Omori, T. Hashida, T. Ono, et al., *Transducers 2011*, **16**, pp. 2331-2334 (2011)
- [7] G. Yamamoto, J. Suk, R. D. Piner, T. Hashida, et al., *Diam. Relat. Mater.*, **19**, pp. 748-751 (2010)
- [8] W. D. Callister, Jr., *Materials Science and Engineering*, 3rd ed. New York: Wiley, 1994, ch. 17, pp. 516-521

Thickness Evaluation of Thermal Spraying on Boiler Tubes by Eddy Current Testing

Y. Takahashi¹, R. Urayama², T. Uchimoto², T. Takagi², H. Naganuma³, K. Sugawara³, Y. Sasaki³

¹Graduate school of Engineering, Tohoku University, 6-6 Aramaki aza, Aoba, Sendai Miyagi 980-8579, Japan

²Institute of Fluid Science, Tohoku University, 2-1-1 Katahira, Aoba, Sendai Miyagi 980-8577, Japan

³Technical Research & Development Center, Tohoku Electric Power Engineering & Construction Co. Inc, Shin-nakabori, Iidoi, Rifu, Miyagi-gun, Miyagi 981-0113, Japan

E-mail : takahashi@wert.ifs.tohoku.ac.jp

ABSTRACT

This paper discusses the feasibility of thickness evaluation of thermal spraying on type 304 austenitic stainless steels by swept frequency eddy current testing. In the previous study, the authors discussed the electromagnetic model of coating and substrate for as-received test piece, and carried out inverse analysis. In this study, the inverse analysis is conducted for test piece which are heated in SO₂ environment and ambient air. The results of inverse analysis show good agreements with the thickness values which is measured by a micrometer.

1. Introduction

Boiler tubes in thermal power plants are used in hot corrosive environment, and thermal spraying is applied on the surface of tubes for mitigation of abrasion[1]. Cracking, delamination, and thinning of thermal spraying can occur due to aging degradation, and coating thickness should be non-destructively evaluated for the management of boiler tubes.

Ni-based alloy Hastelloy C-22 is used for the boiler tubes as thermal spraying. Because it is conductive material, the eddy current testing has capability to evaluate the thickness of coating.

In this study, the feasibility of evaluation for thickness of coating by swept frequency eddy current method is discussed. Thermal spraying specimens heated in SO₂ and ambient air are prepared and the impedance spectra are measured by an impedance analyzer. Numerical analysis is conducted to discuss the electromagnetic model of thermal spraying and sandblast layer with heat treatment. Finally, thickness of thermal spraying is evaluated through the inverse analysis based on the measured impedance spectra.

2. Experiment and numerical analysis

2.1 Test piece

Type 304 austenitic stainless steel was used as substrate. To increase the adhesion of coating, the surface of substrate was treated by sandblast. The hastelloy C-22 was sprayed on the substrate of the type 304 austenitic stainless steel. The thickness of coating was systematically changed from 100μm to 400μm. These test pieces were heated in sulfur dioxide environment and ambient air environment at the temperature of 650 degrees C. Heating time were 200h, 350h and 500h, and SO₂ concentrations were 0.01% and 0.1%.

2.2 Experimental setup

The probe used for this study is a pancake coil. The inner diameter, the outer diameter height and number of turns are 1.2mm, 3.2mm, 0.8mm, and 140 respectively. Using this coil, impedance spectra were

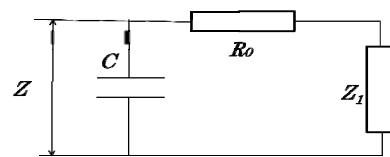


Fig. 1 Equivalent circuit of the probe with wire resistance and stray capacitance

measured by an impedance analyzer (Agilent 4294A). The test frequency was swept from 2MHz to 3MHz. The number of sampling points is 801.

2.3 Numerical Analysis

2.3.1 Forward analysis for coil impedance

The Cheng-Dodd-Deeds multilayer model[2] was used for numerical analysis of coil impedance. It makes possible to analyze the coil impedance of pancake coil on layered conductor. In order to take consideration of wire resistance R_0 and stray capacitance of coil C , the equivalent circuit as shown in Fig.1 was considered[3]. The impedance of the equivalent circuit is

$$Z = \frac{\frac{R_0 + \text{Re}(Z_1)}{\omega C} - j \left\{ (R_0 + \text{Re}(Z_1))^2 + \text{Im}(Z_1) \left(\text{Im}(Z_1) - \frac{1}{\omega C} \right) \right\}}{\omega C \left\{ (R_0 + \text{Re}(Z_1))^2 + \left(\text{Im}(Z_1) - \frac{1}{\omega C} \right)^2 \right\}}, \quad (1)$$

where Z_1 is the coil impedance calculated by the Cheng-Dodd-Deeds model, and ω is the angular frequency.

2.3.2 Inverse analysis

In the previous study, it turned out that lift-off noise is sensitive to the coil impedance, and lift-off as well as thickness should be estimated.[4] The objective function is

$$G(t, L) = \sqrt{\frac{\sum_i^L (Z_{\text{exp}}(f_i) - Z_{\text{cal}}(f_i))^2}{n}}, \quad (2)$$

where $Z_{\text{exp}}(f_i)$ and $Z_{\text{cal}}(f_i)$ are the measured and calculated complex impedance as function of frequency f_i , t , L and n are the coating thickness, lift-off, and the number of sampling points, respectively. The thickness of coating

and the lift-off are swept to find out the local minimum of object function.

3. Results

3.1 Numerical model

Heat treated test piece was modeled as three layers with uniform electromagnetic properties which represent coating, sandblast layer and substrate, respectively. Conductivity and relative permeability of each layer were determined to get good agreement with measured impedance spectra. The thickness of sandblast layer and substrate were set to $23\mu\text{m}$ and 8.0mm , respectively. The conductivity of coating layer and sand blast layer and substrate layer are 0.10×10^6 , 0.8×10^6 , and $1.35 \times 10^6 \text{S/m}$. Their relative permeability are 1.0, 1.5, and 1.1, respectively.

3.2 Inverse analysis method and calibration

The response surface of the objective function for ambient air specimen with the thickness of $287\mu\text{m}$ is shown in Fig.2. The local minimum locates at the points of thickness $312\mu\text{m}$ and lift-off $0.446\mu\text{m}$. The response surface is smooth and simple. Here, the calibration of evaluated thickness was conducted taking the consideration of lift-off. Micrometer measures the coating thickness based on the highest peak of surface. Thickness evaluated by inverse analysis is mean thickness of coating, and evaluated lift-off includes fluctuation of thickness. Here, calibration thickness is the summation of evaluated thickness and change of lift-off from the proper lift-off value of $0.455\mu\text{m}$.

3.3 Inverse analysis for SO_2 test piece

The inverse analysis was conducted for SO_2 test piece. The results after the calibration are shown in Fig.3. In the area around the micrometer thickness of $400\mu\text{m}$, the variation is large. After the calibration, the average error was $17.3\mu\text{m}$.

3.4 Inverse analysis for ambient air test piece

The inverse analysis was conducted in the same way as test pieces heated in SO_2 environment. The inverse analysis results after the calibration are shown in Fig.4. In this figure, the areas near the $100\mu\text{m}$ and $400\mu\text{m}$ had good agreements with estimated values from inverse analysis. However, the other area had large deviation from the micrometer thickness. The reason of this variation may be the measurement error of coil impedance spectra. The average error of calibrated thickness of coating was $28.4\mu\text{m}$.

4. Summary

In this study, the thickness of thermal spraying heated in SO_2 and ambient air environment was evaluated using swept frequency eddy current testing. Inverse analysis of test pieces heated in 0.01% SO_2 environment had good agreement with micrometer thickness, and for test pieces heated in 0.1% SO_2 environment, errors were larger than

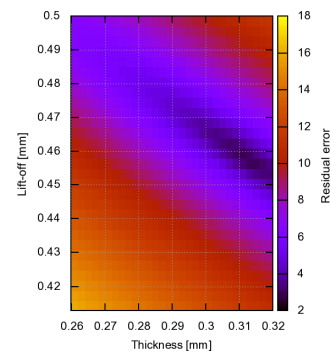


Fig. 2 Response surface of the object function

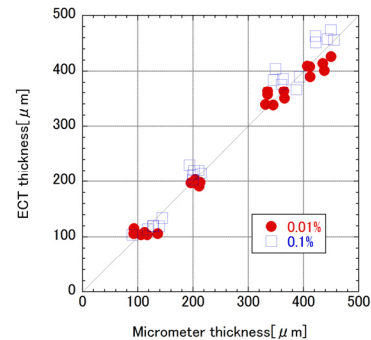


Fig. 3 Evaluated thickness of test piece heated in SO_2 environment

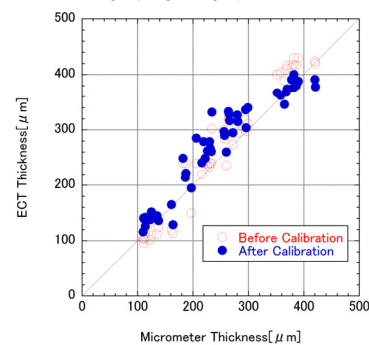


Fig. 4 Evaluated thickness of test piece heated in ambient air

that of 0.01% SO_2 test piece.

Inverse analysis for test piece heated in ambient air had good agreement around $100\mu\text{m}$ and $400\mu\text{m}$ micrometer thickness. Around the $200\mu\text{m}$ and $300\mu\text{m}$ micrometer thickness, errors were large.

References

- [1] J. Kawakita et al., Materials Transactions, **44** (2003), 253-258.
- [2] C. C. Cheng et al., International Journal of Nondestructive Testing, **3**(1971), 109-130.
- [3] T. Kojima et al., Kanagawa Industrial Technology Center Research Report, **12**(2006), 6-10.
- [4] Y. Takahashi et al., JSAEM Studies in Applied Electromagnetics and Mechanics. **14**(2011), 443-445.

Deposition of Micro-crystalline Diamond Films on Curved Steel Surface with Ti Interlayer

Kyohei Naito¹, Hiroyuki Miki², Takanori Takeno¹ and Toshiyuki Takagi³

- 1) Graduate School of Engineering, Tohoku University, Aramaki asa Aoba 6-6, Aoba-ku, Sendai, Japan
2) Center for Interdisciplinary Reserch, Tohoku University, Aramaki asa Aoba 6-3, Aoba-ku, Sendai, Japan
3) Institute of Fluid Science, Tohoku University, 2-1-1 Katahira, Aoba-ku, Sendai, Japan

E-mail: takagi@wert.ifs.tohoku.ac.jp

ABSTRACT

This study reports the deposition of diamond on curved steel substrate. It has a problem of peel resistance between substrate and diamond in previous studies. We successfully deposit diamond films on curved steel surfaces which have low detachability for substrate using a Ti interlayer. X-ray diffraction analysis and scanning electron microscope observation show that the structure of diamond film is micro-crystalline diamond, and Ti interlayer is carbonized during CVD process which makes good adhesion strength between film and substrate.

1. Introduction

Diamond has not only as the value of jewelry but also many good mechanical properties which is high hardness, low friction coefficient, wear resistance, etc. Past study even shows low friction of diamond [1,3]. According to these properties, diamond is expected to apply for solid lubrication.

Artificial diamond has been used for industrial application instead of natural diamond. It is inexpensive and has similar properties which natural one has. Chemical Vapor Deposition (CVD) is one of the method of depositing diamond films by activating raw material gas (CH₄, H₂).

Diamond films show good adhesion when it deposited on silicon or some ceramics materials. However, if we want to deposit diamond films to steel surface which is main materials of mechanical components, we have to solve some problems. For example, the large difference of thermal expansion between steel and diamond, diffusion of carbon in steel and formation of graphite induced by Fe catalysis. These phenomena cause a delamination of diamond films.

One of the approaches to solve these problems is using an interlayer between diamond films and steel substrate [4]. In previous study, we succeeded to deposit diamond films on flat stainless steel substrate with sufficiency adhesion to mechanical polishing by using Ti interlayer.

If we want to apply diamond films as a solid lubrication, deposition technique applied for more complicated geometry is required. In this study, we deposit diamond films on curved steel surface with an interlayer. We discuss its crystallographic and adhesion properties from the view point of interlayer.

2. Experiment

The substrate is AISI440C with rod shape (ϕ 18 mm×35 length). Prior to diamond deposition, we took some preparation for the substrate. First, in order to improve adhesion between diamond films and substrate, we have polished substrate surface until arithmetic average roughness $Ra \sim 0.4 \mu\text{m}$. Interlayer was

deposited by magnetron sputtering method. Material of interlayer is titanium and thickness is 2.0 μm . After the deposition of interlayer, substrate was seeded with diamond suspension in an ultrasonic chamber for 15 min. By seeding, nucleation density become higher and deposition rate of diamond films is improved.

Diamond films were deposited by Hot Filament CVD (HFCVD) method. HFCVD is the method which raw material gas was activated by electrical heating of filament. Tungsten filaments are used and their diameters are 0.3 mm. Deposition parameter of HFCVD process is shown in table 1. During the diamond deposition, substrates were set on a SiC plate at 5 mm from tungsten filament.

After the CVD process, Raman spectroscopy and X-Ray Diffraction (XRD) measurement were used for crystallographic consideration of deposited diamond films. Scanning Electron Microscopy (SEM) and Energy Dispersive X-ray Spectroscopy (EDS) were also used to perform surface and chemical analysis of diamond films.

3. Results and Discussion

Fig.1 shows SEM image of the surface of the diamond films where deposited on the nearest position from tungsten filament. This image shows each diamond grains formed facet-like structure. Besides, the result of Raman spectroscopy shows that these films contain amorphous carbon matrix. Therefore, deposited diamond films are categorized as a cauliflower like diamond films which is including both crystalline diamond and amorphous carbon [5]. Cauliflower diamond films show good friction properties when it

Table 1. Deposition parameter of HFCVD

H ₂ flow	100 ml/min
CH ₄ flow	2.3 ml/min
Total gas pressure	11.0 kPa
Deposition time	5 hours
Filament temperature	2000 K

was adequately-processed after deposition on flat substrate [1-3]. Thus cauliflower diamond films are proper structure for solid lubricant film.

The spectrum profiles of XRD measurements shown in Fig. 2. By changing an incident angle of X-ray, we have got two results: θ - 2θ scan gives the surface information of deposited diamond films and 2θ scan gives the one from interlayer and steel substrate. A sharp peak from diamond structure is seen at about 45 degree. In addition, Fe peaks which are originate from the element in steel substrate can be seen at θ - 2θ scan. However, we could not find any Ti related peaks but TiC peak at about 35 degree. Ti interlayer was supposed to be carbonized during CVD process.

Fig.3 is the cross-section area of diamond films deposited on flat substrate made by AISI440C which is deposited in order to observe the interlayer. EDS analysis point is as shown in the figure. Diamond film was deposited on the flat substrate with Ti interlayer and processed by the same parameter that deposit on curved surface. EDS analysis at this point shows that carbon present in the Ti interlayer. Its ratio of C:Ti is about 1:3. It is conceivable that chain reaction of Ti carbonizing is caused by exposing interlayer to high-temperature activated carbon gas circumstance during CVD process.

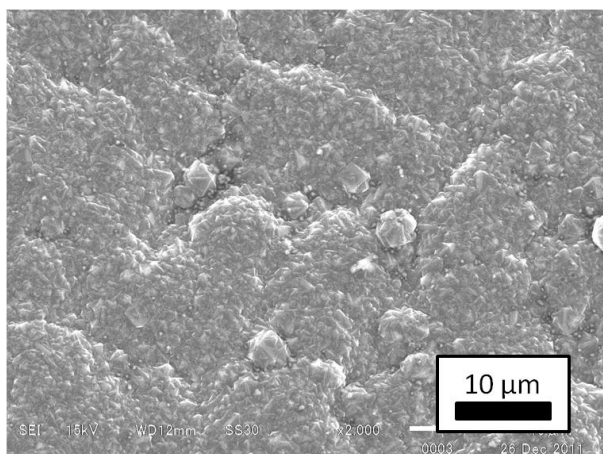


Fig.1 SEM images of diamond films

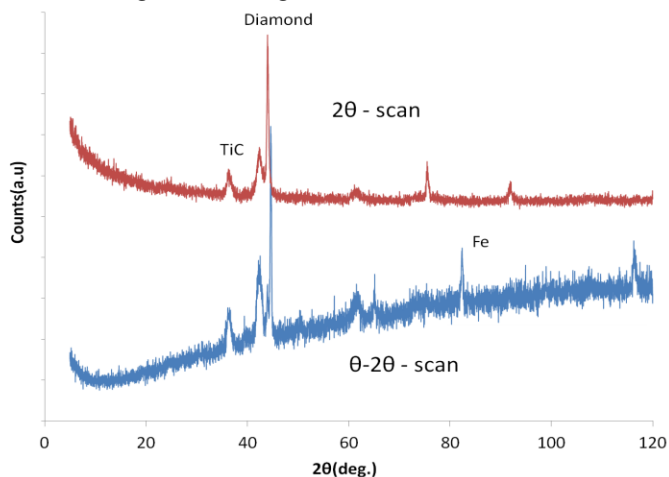


Fig.2 XRD analysis of diamond films

Therefore it suggested that amount of carbon diffusion in the Ti interlayer is largest in the outermost surface and becomes smaller toward the inside. This gradient of carbon distribution make more effective to suppress for the thermal stress due to the deference of thermal expansion between diamond films and steel substrate. As a result, it makes good adhesion.

4. Summary

- 1) It was indicated that possibility of diamond deposition on curved steel surface by HFCVD.
- 2) XRD measurement shows that Ti interlayer is carbonized. The diffusion of carbon in the interlayer becomes during CVD process.
- 3) It was suggested that the gradient of carbon density in the interlayer may have good effect to remove the difference of thermal expansion.

Acknowledgments

This work was partially supported by the Asahi Glass Foundation in Japan, Grant-in-Aid for Challenging Exploratory Research (23656113) of Japan Society for the Promotion of Science (JSPS). This study was supported by Global COE Program “World Center of Education and Research for Trans-disciplinary Flow Dynamics”. Authors are thankful to Mr. Takeshi Sato from the Institute of Fluid Science, Tohoku University, Japan, for his technical assistance.

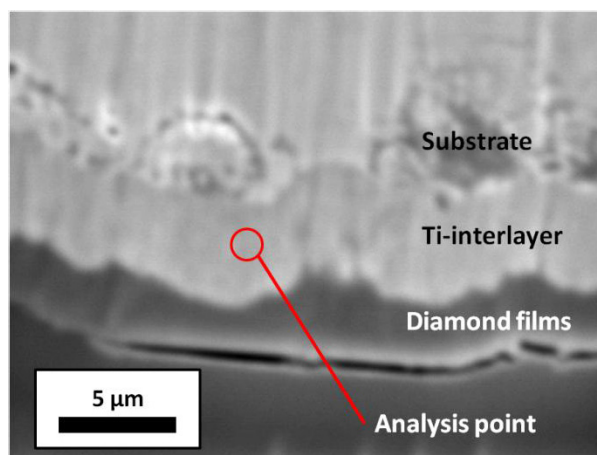


Fig.3 EDS analysis point of flat-substrate with interlayer

References

- [1] T. Takeno, T. Komiyama, H. Miki et al. *Diamond and Related Materials* **14** (2005), 2118-2121.
- [2] H. Miki, A. Tsutsui, T. Takeno, T. Takagi, *Diamond and Related Materials* **17** (2009), 868-872.
- [3] H.Miki, A.Tsusui, T.Takeno, T.Takagi, *Diamond and Related Materials* **24** (2012) 167-170.
- [4] Qi Hua Fan, A. Fernandes, J.Gracio, *Diamond and Related Materials* **7** (1998), 603-606.
- [5] Lindlbauner A, haubner R, Lux B. *Diamond films Technol* **2** (1992), 81-98.

Evaluation of Fatigue Properties of Mo-DLC Coatings under Cyclic Bending.

M. Takahashi¹, H. Miki², T. Takeno¹, T. Takagi³

¹Graduate School of Engineering, Tohoku University, Aoba 6-6-1, Aramaki, Aoba-ku, Sendai 980-8579, Japan

²Center for Interdisciplinary Research, Aoba 6-6-3, Aramaki, Aoba-ku, Sendai 980-8579, Japan

³Institute of Fluid Science, Tohoku University, Katahira 2-1-1, Aoba-ku, Sendai 980-8577, Japan
takagi@ifs.tohoku.ac.jp

ABSTRACT

A fatigue sensor using metal containing diamond like carbon (Me-DLC) film was proposed in this paper. Under the vibration test, we found that resistance change was found clearly with the number of fatigue cycles. The mechanism of these change was discussed from the view points of Raman spectra and nano indentation test.

1. Introduction

Vibrations and deformations of the pipes at plants are one of the factors that may cause structural fatigue and cracks. In order to avoid serious failure and cut back on the replacement cost of the pipes, precise and real-time monitoring technology is now strongly required. In the real plants, many pipes are placed complexly and exposed to corrosive environment. Therefore, the requirements for monitoring sensors expected to be thin, able to prepare it on the material directly and with chemical stability.

Diamond-like carbon (DLC) coatings are widely used in industrial field because of their excellent mechanical properties such as high hardness, low friction and anti-wear performance. Moreover, amorphous carbon coatings can be used in extreme environmental conditions such as a corrosive environment and the inside of a human body because of their chemical stability and high bio-compatibility. Recently, many attempts have been done to fabricate a smart sensor having good mechanical functionality by using amorphous carbon coatings [1].

We proposed Mo-DLC as a fatigue sensor, which its gauge factor decreases with number of cycles, especially high cyclic region[2]. Although it indicated the possibility to use metal-containing DLC as a fatigue sensor, it is not clear whether gauge factor is the appropriate parameter. Using Mo-DLC as a fatigue sensor, we should find other possible electrical parameters for degradation index.

2. Method

2.1 Deposition

Ceraflex(ZrO₂) was used for substrate. Ceraflex is high elastic deformation property. The size of a substrate is 7 × 4 × 0.1 mm³. Test samples were prepared by combined techniques of chemical vapor deposition and DC sputtering of molybdenum target[3]. The parameters used for the deposition in this study are listed in Table 1.

2.2 Vibration test

Dynamic strain property was measured by a vibration testing device. Fig. 1 shows a schematic illustration of the experimental setup in this study. Test samples were bonded on the cantilever beam with glue.

Dynamic strain was applied using electromagnet with an AC input. The strain applied to Mo-DLC is measured using strain gauge attached on the backside of the

Table 1. Parameters of the deposition

Substrate	ZrO ₂	Substrate bias voltage	-400 V
Target metal	Molybdenum	Ar flow	7.5 ccm
DC generator	200 W	CH ₄ flow	6.0 ccm
Thickness	1 μm	Deposition pressure	1.3 Pa

sample. The displacement of beam is measured by laser displacement sensor. In this study, the resonance frequency of cantilever was set from 60 to 80 Hz.

The electrical resistance of the Mo-DLC coatings was measured by a four-point probe method, and electrical parameters were measured with each step of number of bending cycles in the order of 10ⁱ (i = 0, 1, ... 7). The data of strain applied to the beam, displacement of the beam and the electrical resistance of Mo-DLC were monitored at a same time.

3. Results and Discussion

3.1 Variation of resistance

Fig. 2 shows result of the resistance and temperature changes with the number of cycles. As shown in this figure, measured value named "Law Z" did not change up to 10³ cycles, then increased slightly, up to 10⁴ cycles. The appearance of such drop of resistance at 10⁶ cycles may be due to the temperature fluctuation during the measurements in environmental temperature change during measurement because resistances of DLC has large temperature dependence [1].

We have measured temperature dependence on resistance and compensated "Raw R". Assuming the linear relationship between temperature and resistance in the

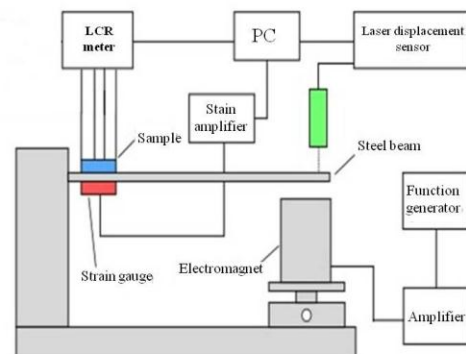


Fig. 1 Experimental setup of vibration test.

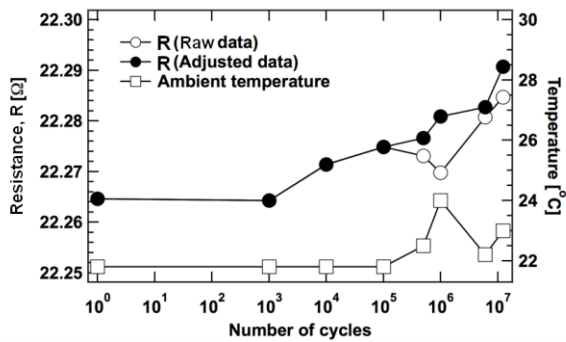


Fig. 2 Variation of resistance and number of cycle.

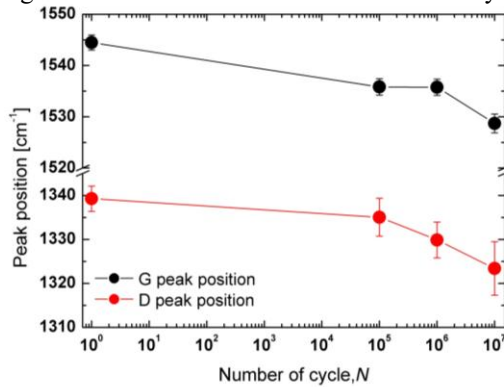


Fig. 3 Variation of peak position in Raman spectra and number of cycles.

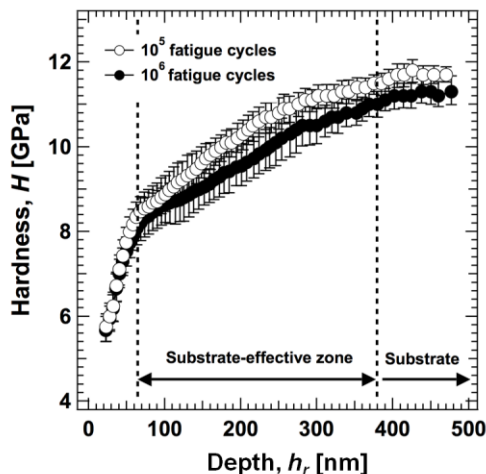


Fig. 4 Variation of hardness with depth.

temperature range in this study, gradient can be calculated as $-0.005 \Omega/^{\circ}\text{C}$. We have corrected the data according to the assumption mentioned above, and the corrected data was shown in figure 2 with the legend of "Adjusted R". It was found that the resistance value increased with the number of cycles.

3.2 Raman spectra with various cycles

The specimen with each number of cycles (1×10^0 , 10^5 , 10^6 , 10^7) were analyzed by Raman spectroscopy. Each Raman spectrum was profile-fitted using Lorentz function and Breit-Wigner-Fano function for D and G peaks, respectively. Fig. 3 shows variation of each peak position plotted against number of cycles. It was found that both D peak and G peak position moved to lower frequency with the number of cycles, which

indicates that carbon bonding state changes due to the cyclic strain.

3.3 Change of the hardness by fatigue

The hardness of Mo-DLC was investigated by nano indentation testing after the vibration test. Fig. 4 shows the result of hardness tests. No difference could not be seen on hardness in the region from the surface to the depth of 70 nm. However, slight change could be found below the depth of 70 nm. Taking into account the Raman results shown in fig. 3, the change of the hardness may be due to the structural change of carbon matrix since the decrease of D and G peak qualitatively indicates the change of bonding condition between the carbon atoms in the matrix[4]. Therefore, possible explanation is that carbon network may change due to the fatigue loading. In order to understand the mechanisms, more experiments must be required.

4. Summary

In this study, we tried to clarify the mechanisms on change in the gauge factor with the fatigue cyclic loading. What we could find were summarized as follows:

- Resistance change was found clearly with the number of fatigue cycles.
- D and G peak positions decrease with the number of cycles.
- Hardness of the specimen after the 10^6 cycles is lower than that after 10^5 cycles.

These findings suggest that carbon structural change may occur due to the cyclic fatigue tests. But more experiments are still required for understanding the mechanisms.

Acknowledgements

This work was partly supported by a Grant-in-Aid for Scientific Research (A) (23240638) and (B) (22360043). This study was supported by Global COE Program "World Center of Education and Research for Trans-disciplinary Flow Dynamics". The authors are greatly thankful to Dr. Julien Fontaine from the Laboratory of Tribology and System Dynamics, Ecole Centrale de Lyon, France for their technical assistance for nano indentation testing and useful discussions about experiments. The authors express their appreciation to Mr. Takeshi Sato from the Institute of Fluid Science at Tohoku University for his technical assistance.

References

- [1] E. Peiner et al., *Sensors and Actuators A – Physical*, **130** (2006), pp. 75-82
- [2] T. Ohno, "Investigation of electrical conductive properties of metal-containing amorphous carbon coatings for strain sensor application" Tohoku University, Master thesis, (2011).
- [3] T. Takeno et al., *Diamond and Related Materials*, **17** (2008), pp. 713-716.
- [4] J. Robertson, Diamond-like amorphous carbon, *Material Science and Engineering R*, **37** (2002), pp.129-281.

Quantitative Evaluation of Residual Strain in Austenitic Stainless Steels using Electromagnetic Nondestructive Evaluation

Seiya Sato¹, Ryoichi Urayama², Takeshi Sato², Tetsuya Uchimoto², Toshiyuki Takagi², Zhenmao Chen³, Yasuhiko Yoshida⁴

¹ Graduate School of Engineering, Tohoku University, Japan

² Institute of Fluid Science, Tohoku University, 2-1-1 Katahira Aoba-ku, Sendai, Miyagi 980-8577, Japan

³ State Key Laboratory for Strength and Vibration of Mechanical Structures, Xi'an Jiaotong University, Xi'an, China

⁴ The Kansai Electric Power Company, Inc., Japan

Email: uchimoto@ifs.tohoku.ac.jp

ABSTRACT

In this study, to evaluate residual strain in austenitic stainless steel quantitatively, eddy current testing (ECT) and non-linear eddy current testing (NLECT) are applied. Signal sensitivity to residual strain is large at the region more than 5% of strain, signal sensitivity is decreased at low strain region in ECT. In contrast, there is a linear correlation between signal and residual strain in NLECT. These changes reflect magnetic phase due to the deformation induced martensitic transformation, which is confirmed by magnetic force microscopy.

1. Introduction

When large amount of seismic load is exerted to components in nuclear power plants like the Great East Japan Earthquake, structural integrity evaluation is required. Currently, the technique based on hardness measurement which is quasi-nondestructive testing is being applied in the field tests, and it is expected to establish nondestructive evaluation techniques that are more reliable and convenient. It is well known that magnetic properties of metallic materials are sensitive to their microstructure, and several studies have reported that the magnetic properties change due to the change of dislocation and phase transition [1, 2]. In order to put this technique into practical, it is necessary to figure out the quantitative relationship between residual strain and electromagnetic properties.

In this study, nondestructive methods to evaluate residual strain due to seismic loading of nuclear structural materials, focusing on the change of electromagnetic properties. Type 304 austenitic stainless steels are discussed as a target material. Uniaxial tensile tests are carried out, and electromagnetic nondestructive evaluation method, specifically eddy current testing (ECT) and non-linear eddy current testing (NLECT) are applied to evaluate residual strain quantitatively.

2. Specimen

Table 1 shows the chemical composition of type 304 austenitic stainless steel used in this study. Specimens were cut out by machining from plates with thickness of 4.8mm. Figure 1 shows the shape and dimensions of the specimen. Tensile test was carried out using INSTRON5582 and prepared 11 specimens with residual strains from 1% to 15%. The residual strain was measured by 2 strain gauges (A and B) put on the center of both sides of specimen. Table 2 shows residual strain values together with resulting width and thickness of the specimens after tensile tests. Figure 2 shows stress - strain curves of 3, 7 and 15% specimens.

Table 1. Chemical composition of type 304 austenitic stainless steel (wt %).

C	Si	Mn	P	S	Ni	Cr	Fe
0.05	0.4	1.11	0.028	0.002	8.04	18.09	bal.

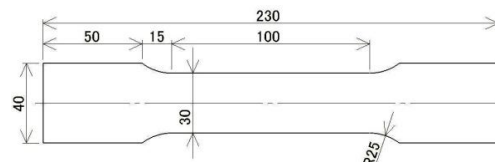


Fig. 1 Schematic drawing of tensile specimen.

Table 2. Results of tensile test.

Target strain (%)	Strain A (%)	Strain B (%)	Width (mm)	Thickness (mm)
0%	0.00	0.00	30.01	4.78
1%	1.05	1.01	29.95	4.75
2%	2.02	2.03	29.70	4.72
3%	3.15	3.15	29.70	4.69
	3.02	3.00	29.60	4.69
	3.07	3.08	29.60	4.69
5%	5.24	5.21	29.40	4.64
	5.20	5.18	29.50	4.65
7%	8.35	8.44	29.00	4.59
10%	11.22	11.18	28.50	4.52
	16.69	-	28.10	4.42
15%	16.11	15.98	28.00	4.44

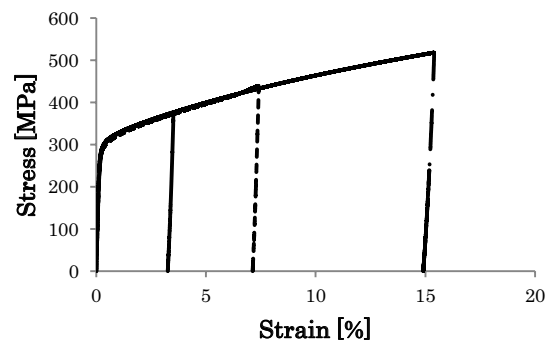


Fig. 2 Stress - strain curves of 3, 7 and 15% specimens.

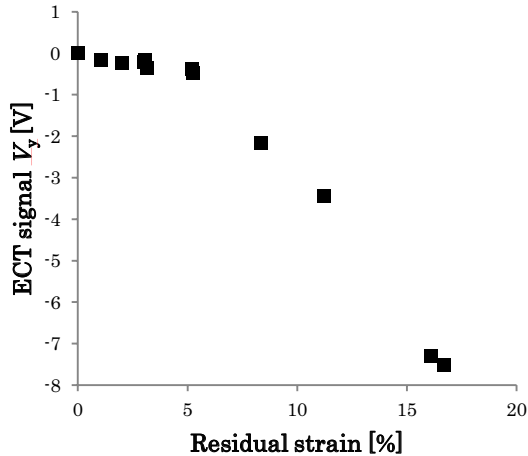


Fig. 3 Relationship between eddy current signal V_y and residual strain (100kHz).

3. Experimental Method

3.1. ECT

ECT was carried out using eddy current instrument (ASSORT PC II Aswan Ect Co., Ltd.), and eddy current signals V_x and V_y are measured. The probe has two coils with outer diameter of 5mm, inner diameter of 2mm, height of 3mm and 750 turns. These coils are arranged in tandem. This probe is self-induced differential type one. Test frequencies are 50, 100 and 200kHz, and the gain set to 50dB. ECT has a drawback that the signals are sensitive to lift-off noises. In order to decrease the lift-off noise, the signals V_y are read after shifting the signal phases so that lift-off signals coincide with the x direction.

3.2. NLECT

In NLECT, by applying AC current to exciting coil to invoke AC magnetic field into a sample, magnetization process of the sample is detected by the voltage of a pickup coil. Equivalent changes of AC hysteresis curve are easily acquired by plotting Lissajous figure composed of signals of an exciter and a detector, and the amplitude of the third harmonic wave acquired by the signal of a pickup coil. The probe has a ferrite core and two coils. The excitation coil has outer diameter of 2mm, inner diameter of 1mm, height of 2mm and 200 turns, and the detection coil has outer diameter of 2mm, inner diameter of 1mm, height of 4mm and 400 turns. Test frequency is 5kHz, applied voltage is 4.5V and sampling rate is 200 points per cycle.

In this study, third and fifth harmonic components S are used as a parameter,

$$S=20 \times \log \left(\frac{\sqrt{(A_3)^2 + (A_5)^2}}{(A_1)} \right) \text{ [dB]} \quad (1)$$

where A_1 , A_3 and A_5 are basic, third and fifth harmonic component intensity, respectively.

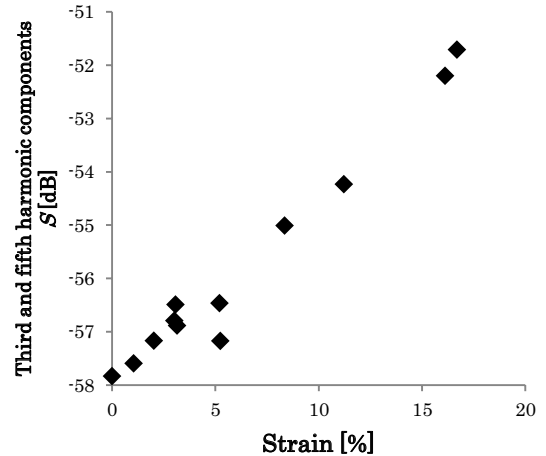


Fig. 4 Relationship between third and fifth harmonic components S and residual strain.

4. Results and Discussion

Figure 3 shows relationship between eddy current signal V_y and residual strain at the frequency of 100kHz. It shows that the eddy current signal increase with residual strain. Though signal sensitivity to residual strain is large at the region more than 5% of strain, signal sensitivity is decreased at low strain region, which leads large SN ratio. It is hard to evaluate small residual strain by ECT in this region.

Figure 4 shows third and fifth harmonic components S as function of residual strain in NLECT. There is a linear correlation between third and fifth harmonics components and residual strain. Therefore, NLECT has a capability to evaluate quantitatively residual strain less than 3%, which is hard to evaluate by eddy current testing.

These signal changes in ECT and NLECT reflect magnetic phase due to strain induced martensitic transformation, and martensite phase was observed by magnetic force microscopy.

5. Summary

In this study, ECT and NLECT were applied to evaluate quantitatively residual strain of austenitic stainless steel. As a result, correlation was observed between the signal and residual strain in both ECT and NLECT. There is a clear linear correlation between third and fifth harmonic components and residual strain in NLECT. These changes in the signal reflect magnetic phase due to the strain induced martensitic transformation.

Acknowledgment

The authors express our appreciation for making specimens and equipment and their technical assistance to Mr. K. Kuroki and Mr. S. Onuma of Institute of Fluid Science, Tohoku University.

References

- [1] M. Kamaya, INSS Journal, **16** (2009), pp.179-188.
- [2] M. Kawakubo *et al.*, Transactions of the Atomic Energy Society of Japan, **9** (2010), pp.166-173.

Relationship between Fluid Shear Stress and the Phenotype Change of Smooth Muscle Cells in a Co-culture Model

Xiaobo Han¹, Naoya Sakamoto², Noriko Tomita³, Meng Hui⁴, Masaaki Sato¹, Makoto Ohta³

1) Graduate School of Biomedical Engineering, Tohoku University, 2-1-1, Katahira, Aoba-ku, Sendai, Japan.

2) Department of Medical Engineering, Kawasaki University of Medical Welfare.

3) Institute of Fluid Science, Tohoku University.

4) Toshiba Stroke Research Center, University at Buffalo, State University of New York.

E-mail: hanxb@biofluid.ifs.tohoku.ac.jp

ABSTRACT

We developed a vascular endothelial cell (EC)–smooth muscle cell (SMC) co-culture model consisting of contractile phenotype SMCs, which mimics *in vivo* cellular interactions to explore SMC response to mechanical stimulations. We applied fluid shear stress (SS) to ECs in co-culture models and then determined SMC phenotypes. The results showed that the expression of contractile proteins in SMCs in co-culture model decreased under static conditions, while application of SS of 2 Pa to ECs in the model maintained the expression level of contractile proteins in the SMCs.

1. Introduction

Vascular smooth muscle cells (SMCs) are lying in the tunica media layer outside the intimal endothelial cell (EC) monolayer, and can regulate vessel diameter to control blood pressure and flow. SMCs generally exhibit a contractile phenotype in normal blood vessels. SMC phenotype change from contractile to synthetic involving SMC migration and excessive proliferation in atherosclerotic lesions, is normally thought contributing to the growth of atherosclerotic plaques. Since the formation of atherosclerotic plaques usually occurs at such place as blood vessel bifurcations and curves, where local fluid shear stress (SS) is lower than that at normal straight vessels, it is suggested that specific hemodynamics could affect SMC behaviors. Several groups practiced EC-SMC co-culture experiments, and revealed that ECs exposed to shear stress affect unshared SMC functions associated with the development of atherosclerosis through cellular interactions [1, 2]. Recently, Meng's group [3] surgically created new branch points in the carotid vasculature of adult dogs to explore how specific hemodynamic factors near the apex of an arterial bifurcation, including flow impingement, high SS, with high spatial gradient of SS (Shear Stress Gradient: SSG), affect vascular remodeling. A destructive remodeling was observed in the adjacent region of flow acceleration (high SS with high SSG) that resembled the initiation of an intracranial aneurysm, characterized by disruption of the internal elastic lamina, loss of medial SMCs, and reduced proliferation of SMCs. All these researches suggest that SMCs could response to the SS through cellular interactions with EC, and play a role in blood vessel pathology.

Thus, it is important to explore SMC behaviors under SS conditions. In the present study, we established an EC-SMC co-culture model with phenotype-controlled SMCs, which is similar to normal healthy arterial walls. Then, we used the co-culture model in flow-exposure experiments to explore relationship between SS and SMC phenotype change.

2. Methods

2.1 Construction of co-culture model

Human carotid artery ECs from passage 4-9 and human carotid artery SMCs from passage 4-9 (Cell Applications) were used in the present study.

The co-culture model was composed of SMCs, which were 3-D cultured in a collagen layer, a membrane filter, a spacer ring, and ECs, as shown in Fig. 1. ECs were 2-D cultured with Medium 199 (Invitrogen) containing 20% fetal bovine serum (JRH Bioscience) and 1% penicillin/streptomycin (Invitrogen) (Proliferation Medium: PM) on the membrane filter until confluent. SMCs were seeded into a solution of 0.5% type I collagen (Koken) in addition to DMEM/F12 medium (Invitrogen) at 10-fold concentration, and reconstruction buffer. Then the SMC-collagen layer was allowed to polymerize at 37 °C for 30 min. After polymerized, SMCs were cultured with the same PM as ECs in collagen layer for about 6 days, and then the medium was changed into a serum-free medium containing DMEM/F12 with 1% penicillin/streptomycin (Quiescent Medium: QM) to control SMCs into a contractile phenotype as described previously [4].

2.2 Western blotting

We firstly examined the SMC phenotype to test the effect of QM on SMC phenotypes. After SMCs were cultured in collagen gel with QM for different days,

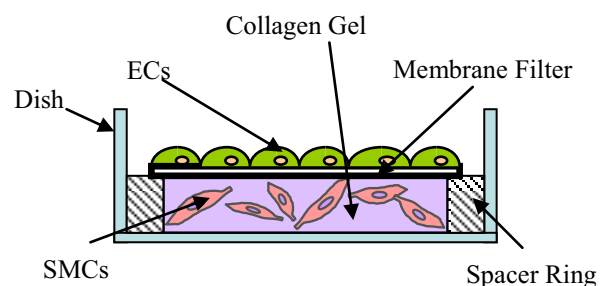


Fig. 1 A diagram of co-culture model of EC-SMC.

type I collagenase was added into dishes to melt gel, and then SMCs were recollected and added into lysis buffer to compose cell lysates for western blot analysis. After electrophoresis and transfer to membrane, three typical contractile proteins (α -smooth muscle actin (α -SMA), calponin, myosin heavy chain (MHC)) and a label protein, β -actin, were stained by their antibodies (Sigma Aldrich), and were subsequently developed by an AP-conjugated substrate kit (Bio-Rad Laboratories). The band intensities of α -SMA, calponin or MHC were quantified with the ImageJ (National Institute of Health) and normalized by that of β -actin. The phenotype of SMC in the co-culture model after flow-exposure experiment was also determined.

2.3 Flow-exposure experiment

By connecting a pulse damper, flow chambers, a reservoir, and a roller pump with silicone tubes, we constructed a flow loop used for the flow-exposure experiment. Parallel plate flow chambers were used to apply a SS of 2 Pa to the co-culture model. The flow-exposure last for 72 hours using a mixture medium of 25% PM with 75% QM (Coculture Medium: CM) at 37°C in 95% air/5% CO₂ atmosphere.

3. Results and Discussion

Figure 2 shows the related expression levels of three contractile proteins (α -SMA, calponin and MHC) in SMCs cultured in collagen gel with QM. The expression of α -SMA and calponin increased and reached to a peak after culture in QM for 6 days (QM6), and then kept at that level till QM15. Meanwhile, the expression of MHC reached to a peak later at about QM12, and there was no significant difference between QM12 and QM15. This increase of contractile proteins indicates a phenotypic differentiation of cultured SMCs from synthetic to contractile states. This suggests that we succeeded in control SMC into a contractile phenotype using a serum-free QM. Co-culture models consisting of phenotype controlled SMCs using in the present study could provide information of SMC responses to mechanical stimulations and cellular interactions relevant to *in vivo* conditions.

The co-culture model consisting of SMCs cultured with QM for 15 days was exposed to a SS of 2 Pa. Figure 3 shows a typical western blot bond of α -SMA, calponin, MHC and β -actin in SMCs after flow-exposure and after static cultured in CM for 72 h. Compared with QM 15, the expression of α -SMA and calponin of SMCs in the statically cultured models decreased, while there was no obviously difference of that between SMCs at QM 15 and SMCs in the model after flow-exposure. The expression of MHC showed quite same in all three conditions. This suggests that the serum-containing CM could change the contractile SMC phenotype to the synthetic phenotype, while a SS of 2 Pa could keep SMCs in a contractile phenotype.

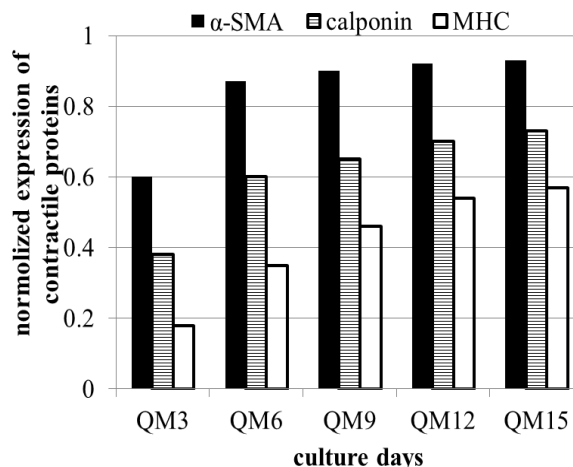


Fig.2 The expression of α -SMA, calponin and MHC of SMCs 3-D cultured in collagen gel with QM. Data were normalized to the expression of β -actin, n=1.

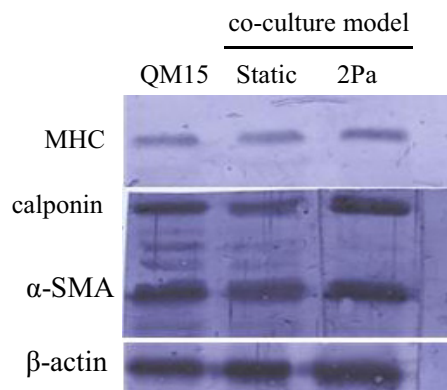


Fig.3 A typical western-blotting result of expression of calponin, MHC, α -SMA and β -actin of SMC after 15 days culturing in collagen gel with QM; under static conditions in co-culture model with CM for 72 h; after 72 h flow-exposure in co-culture model.

4. Conclusion

In the present study, we constructed an EC-SMC co-culture model that was composed of phenotype controlled SMCs. Contractile SMCs in co-culture model changed to synthetic phenotype under static conditions, while application of SS of 2 Pa to ECs in the model maintains the expression of contractile proteins of SMCs.

References

- [1] H. Wang, L. Huang, M. Qu, Z. Yan, B. Liu, B. Shen, Z. Jiang. *Endothelium* **13**(2006), 171-180.
- [2] N. Sakamoto, T. Ohashi, M. Sato. *Ann Biomed Eng* **34** (2006), 408-415
- [3] H. Meng, Z. Wang, Y. Hoi, L. Gao, E. Metaxa, D.Swartz, J. Kolega. *Stroke* **38** (2008), 1924-1931
- [4] N. Sakamoto, T. Kiuchi, M. Sato. *Ann Biomed Eng* **39** (2011), 2750-2758.

Comparison between Agarose Gel and PVA-H Biomodels for Evaluation of Ablation Catheter

Kaihong Yu *, Tetsuya Yamashita**, Makoto Ohta***

*Graduate School of Biomedical Engineering, Tohoku University, 6-6-01, Aobayama, Sendai, 980-8579, Japan

**JMS CO., LTD., 1-13-5 Minamiohi, Shinagawa, Tokyo, 140-0013, Japan

***Institute of Fluid Science, Tohoku University, 2-1-1, Katahira, Aoba, Sendai, 980-8577, Japan
kaihongmr_yu@biofluid.ifs.tohoku.ac.jp

ABSTRACT

Parameters for controlling scope and depth of ablation are still set by experiences of medical doctors. To determine the parameters under various conditions, in-vitro system called as biomodel with mimicking heart muscles and blood to measure the temperature distribution may be necessary. In this study, comparisons between agarose gel and PVA-H were performed based on Young's moduli and temperature distribution. PVA-H is suitable to observe the contact state of catheter on the surface of model as a heart muscle with a load on tissue. And agarose gel is suitable to measure temperature distribution with a power similar to the clinical conditions.

1. Introduction

Catheter ablation is a treatment technique using currents with frequency about 500 kHz applied to tissues through electrodes. Recently, the treatment is becoming more frequently used for tachyarrhythmia. Catheter with electrode on the tips is inserted into a blood vessel in groin and placed in the heart. Then high-frequency energy is introduced through the catheters to destroy abnormal heart tissue causing the heart rhythm disorder.

This treatment is attractive as minimally invasive and curative. However, in case that the temperature of electrode rises excessively, patient will have complications like thrombus. To protect the complications, recent catheter has a temperature sensor inside the tip to measure the temperature in the tissue. However, complications still occur, and so the relationship between the temperature of the catheter and the temperature distribution of heart muscle tissue is unclear.

To find that relationship, parameters such as contact state of catheter on tissue surface, power of high-frequency generator are necessary to be determined. An in-vitro evaluation system with mimicking the elastic and the thermal properties will measure the temperature distributions with changing the parameters [1, 2]. We considered two kinds of materials: one is PVA-H which has high transparency, mechanical characteristic approximated to biological soft tissue [3], and the other one is agarose gel which has thermo physical property close to the biological tissue. In this study, we compared these two materials by tensile test and temperature distribution.

2. Method

2.1 PVA-H Construction

Dimethyl sulfoxide (DMSO Toray Fine Chemicals Co., Ltd., Japan) and distilled water were mixed by 80wt% and 20wt%. PVA (JF17, JAPAN VAM & POVAL CO., LTD) (99mol% degree of saponification, 1700 degree of polymerization) of 15 wt% and NaCl of 2 wt% were dissolved into the solvent at 120°C for two hours. Then the melted PVA liquid was poured into a mold to make a heart model and cooled at -20°C for 24 hours.

2.2 Agarose Gel construction

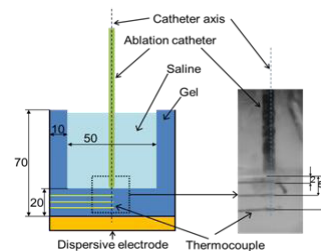


Fig. 1 Schematic side view (left) and a photo image on the catheter axis (right) of the experimental setup with mimicking interaction between heart muscle and blood (unit: mm)

Agarose gel was constructed by using agarose of 5 wt% (Agarose ST, KANTO CHEMICAL CO., INC), sucrose of 3 wt% (Sucrose, KANTO CHEMICAL CO., INC), and NaCl of 0.075 wt% in distilled water at 100°C for 2 hours. The melted agarose liquid was poured into the mold and cooled at 4°C for at least 4 hours.

2.3 Tensile Testing

Young's moduli of PVA-H and agarose gel were measured by using tensile testing machine EZ-S (SHIMADZU, Co.). The size of samples was 10×30×3 mm. The speed of tension of PVA-H was 10mm/min, and 2 mm/min for the agarose gel, because the agarose gel sample is easy to break. The measurement was performed until the break of sample, or until the strain reaching 1.0. All materials were isotropic samples and Poisson's ratio was assumed as 0.5. Then, Young's modulus was determined by the value of the stress and strain obtained.

2.4 Temperature Distribution Measurement

A high-frequency current of approximately 500 kHz was introduced into the model at the room temperature and internal temperature distributions were measured by using several thermocouples. The output energy was set at 5W or 20W, and the introduction was performed for 60s. The measurement was carried out three times for each sample and the average temperature with time was calculated. After each measurement, an interval time was set to drop the temperature to the room temperature.

2.5 Evaluation System of Ablation Catheter

Figure 1 shows the diagram of the biomodel and

experimental setup. The biomodel consists of a container for mimicking blood in heart chamber and heart muscle assumed with the gels. The mold for container was built by using acrylic boards. The inside of the container was filled with saline. The ablations were conducted using a 7Fr/4 mm ablation catheter (maker) on the bottom of container. The electrode of the catheter was set for contact with the surface of the gel with the load of 2 gf. To measure the temperature bottom side gel, K type thermocouples (maker) with the diameter of 0.5mm were located at the depth of 2mm, 5mm, and 8mm, respectively, from the surface of gel. The thermocouple tips were always placed on the catheter axis.

3. Results and Discussion

3.1 Tensile testing

Table 1 shows a list of Young's modulus of PVA-H and agarose gel from the tensile tests and Young's modulus of heart muscle from reference [4]. Young's moduli of both gels were higher than that of heart muscle. However, Young's modulus of PVA-H is closer to heart muscle with comparison to agarose gel. In addition, PVA-H is transparent and so, the inside of the container can be seen clearly. Therefore, PVA-H will be more suitable to evaluate the contact state of catheter on tissue surface in case of load on tissue using catheter.

3.2 Temperature distribution measurement

Figure 2-(a) shows an example from the results of temperature distribution measurement using PVA-H model at 5W with power control. Compared to the temperature of tip of catheter, temperature of the depth of 2mm is higher at 60 seconds. This result is similar to the agarose gel (fig.2-b) and to previous studies [1]. Therefore, the evaluation system built in the chapter of 2.5 is possible to evaluate the temperature distribution using high-frequency current electricity.

In clinical case, high-frequency generator is generally set at 10-50W with temperature control and the temperature of the electrode is set to be 50-60°C. From the viewpoint of setting to the clinical case, the setting of 20W output with temperature control at 50°C is suitable to evaluate temperature distribution. With power which is similar to the clinical conditions, as shown in figure 3, PVA-H gel in contact with the electrode is melted. The melting can be happened because the temperature of the depth of 2mm is over 70°C at 5 second and the melting point of PVA-H is 65°C.

Figure 4 shows an example from results of temperature distribution used agarose gel model at 20W output energy with temperature control at 50°C. The temperature of tip of electrode is hold at 50°C. Temperature of the depth of 2mm rises at 70°C and melting is not observed. The results show agarose gel can withstand more heat than PVA-H. Therefore, compared to PVA-H model, using agarose gel is more suitable to evaluate temperature distribution by using power similar to the clinical conditions.

4. Concluding remarks

We compared agarose gel and PVA-H biomodels for evaluation ablation catheter based on Young's moduli and temperature distribution. PVA-H is suitable to evaluate the contact state of catheter on the model as a tissue surface in case of load on tissue. On the other hand, agarose gel is suitable to evaluate temperature distribution with power similar to the clinical conditions.

References

- [1] H. Cao, Trans. Biomed. Eng., **47**(2000), 1518.
- [2] R. Blasco-Gimenez, Physiol. Meas., **31**(2010), 581.
- [3] H. Kosukegawa, J. Fluid Sci. Tech., **3**(2008), 533.
- [4] I. P. Herman, Physics of the Human Body: Biological and Medical Physics, Biomedical Engineering, (2007).

Table 1. Young's modulus of agarose, PVA-H and heart muscle

Specimen	Young's modulus (kPa)
Agarose gel (agarose 5wt%, NaCl 0.075wt%, sucrose 3wt%)	516
PVA-H (PVA 15wt%, NaCl 2wt%)	190
Heart muscle	About 100

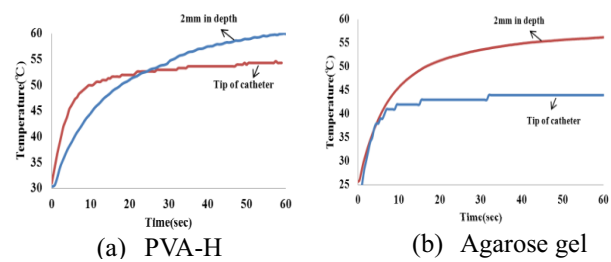


Fig. 2 An example of temperature distribution at 5W output energy with power control



Fig. 3 Condition of PVA-H after ablation of 20W output with temperature control at 50°C

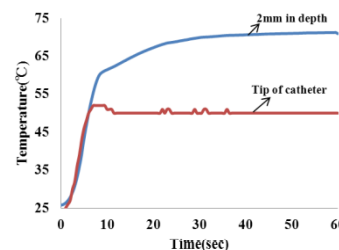


Fig. 4 An example of temperature distribution used agarose gel model at 20W output energy with temperature control at 50°C

Experimental Studying of Metallic Splats Formation in the Condition of Substrate Submelting in a Contact Spot

Andrey V. Perfilyev, Oleg P. Solonenko and Andrey V. Smirnov

Khristianovich Institute of Theoretical and Applied Mechanics, Siberian Branch of RAS, Novosibirsk, Russia
solo@itam.nsc.ru

ABSTRACT

There are presented preliminary experimental data characterizing morphology of splats (flattened and solidified droplets at collision with substrates), as well as their thickness and diameter, at metal droplets impact onto polished metallic substrates in the conditions of their submelting in contact area with particle. To provide the experiments under full control of key physical parameters (KPPs) prior to droplet-substrate interaction (temperature, velocity and size of particle, and substrate temperature) it was created a model setup to studying the above-mentioned phenomenon.

1. Introduction

During last two decades, increasingly growing interest was expressed to the problem of ultra-rapid quenching of melt micro-droplets of various materials upon their impingement on a surface. This phenomenon is the basis for various advanced technologies such as plasma, arc, detonation and flame spraying, powder micro-atomization, solder-drop-printing, production of microcrystalline materials, etc. Also, it is of great interest for materials science when it is necessary to study non-equilibrium state diagram of different alloys and composite materials under extreme exposures. It was recognized that further progress in improving both quality and structure of plasma-sprayed materials largely depends on our understanding of processes that occur during interaction of liquid particles, carried by a high – temperature jet, with substrates.

Generally speaking, we are dealing with independent scientific and technological line of investigation – micrometallurgy of a small volume of melt at its collision with substrate or, in other words, micrometallurgy of splats [1].

As it was noted in [2], in the plasma spray process, depending on the values of KPPs, along with thermophysical properties of the particle-substrate materials pair, the splat formation process at the stage of inertial spreading of the melt droplet should follows one of four basic thermophysical scenarios: (1) - spreading and simultaneous solidification of the droplet on the solid base; (2) - spreading and simultaneous solidification of the droplet, and submelting of the base in a contact spot with the droplet; (3) - spreading the droplet over the solid base surface, and subsequent cooling and solidification of a spread layer; (4) - spreading the droplet accompanied by simultaneous submelting of the base in a contact spot with the droplet, followed by subsequent cooling and solidification of both.

In paper [3] it was presented and theoretically generalized the representative set of experimental metallic splats formed on polished substrates according to scenario 1 under full control of KPPs.

At the same time, theoretical and experimental

investigation of splats formation according to scenarios 2 and 4, i.e. accompanied by simultaneous submelting of substrate in a contact spot with the droplet, are of great interest in context of plasma spraying the coatings with high bond strength with a base.

Analysis of known publications shows that by now there are no reliable representative data characterizing splats formation according to scenarios 2 and 4.

The main goal of present study is to overcome the mentioned shortcoming.

2. Model physical setup and experimental conditions

The model physical setup (see Fig. 1) was created for experimental study of interaction of melted single particle with substrate in conditions of its submelting in contact spot with substrate at full control of key physical parameters: velocity, temperature and size of particle, as well as substrate temperature and its surface state prior to impact.

Quartz tube (1), with external and inner diameters $d_1=6$ mm and $d_2=4$ mm, respectively, one end of which was profiled with the help of heating and drawing out in order to provide an inner diameter of 0.05-0.15 mm, was placed inside the ohmic heater (2).

Model material was fed in glass tube placed in a heater. First gas line (Ar), containing manometer (3), rubber bulb (4) and tap (5), was attached to upper part of tube, emerged through heaters window. Feeding an argon through second gas line was performed tangentially in order to remove remaining air, situated in annular gap between glass tube and heater. Heater was a hollow copper tube with external and inner diameters $d_3=12$ mm and $d_4=8$ mm, respectively, and two heating sections rounded from nichrome wire of 0.5 mm diameter. Between them there were placed a positioner (6), to center the tube with material in heater, and two chromel-kopel thermocouples (7 and 8) with lead-out on controllers (9 and 10). In order to prevent the heat loss, front area of heater was heat-insulated with asbestos-cement disk (11) with inner diameter of 4.5 mm and created a step. In this area behind the step took place formation of droplet. While conducting the experiment the temperatures of heaters wall, measured

by upper and lower thermocouples were identical.

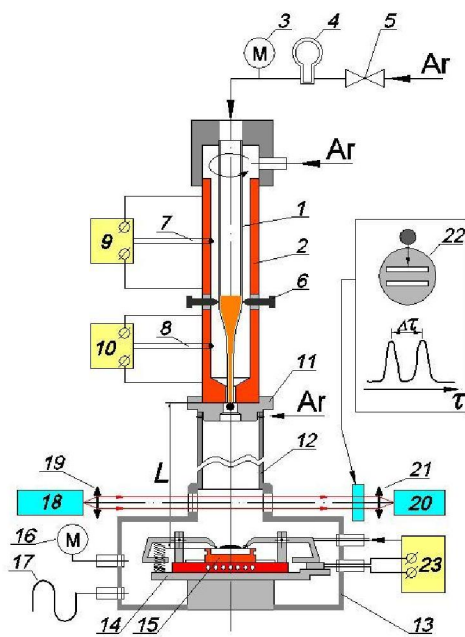


Fig. 1. Schematic diagram of model experimental setup.

The usage of distributed feeding of inert gas was performed as follows. First gas line was used for forced blowing of material with inert gas during its heating. After heating and melting of material sample placed inside the glass tube, melt filled the outlet part of capillary. It was followed by the rise of pressure, registered with manometer (3). With the help of tap (5) gas line was shutted off and after some time lag at given temperature, additional rising the pressure was provided for drops generation with the help of bulb (4). At the same time, second gas line was providing the blowing of external side of quartz tube with inert gas with flow rate $G_{Ar}=0.005$ g/sec to prevent drop from oxidation while its formation on capillary end. During implementation of free fall regime, drop, reaching some equilibrium size, which is defined by density and surface tension of melt, as well as by diameter of tube-capillary and thickness of its walls, tore off due to its own weight.

To control the temperature of substrate a corresponding temperature-controlled table (hot place) was made, including junction for substrates fixation, ohmic heater and chromel-alumel thermocouple, flattened and polished thermal junction of which pressed itself to upper surface of substrate with spring loaded ceramic pressing.

To preset given temperatures maintenance of melt and substrate and to increase the accuracy of their determining, setup was equipped with controllers of TPM151-01 type (9, 10 and 23). Readings of thermocouples are transmitted to controller inputs, which are compared with preliminary pre-installed temperatures and realize the control over heaters for the purpose of reducing their deviations of current

temperature values from given.

Furnace for melting of material sample was hermetically connected with the help of replaceable vertically oriented tubes (12) of different length with hermetical chamber (13), in which temperature-controlled table was placed (14) with substrate, fixed on it (15). At that, the length of tube (12) defines the velocity of drops during their free fall and impact with surface of substrate.

To control the velocity of drops prior their impact with substrate and for straightforward observation of process, chamber was equipped with glass windows. Pressure in chamber, measured with manometer (16), was regulated with the help of hydraulic valve (17).

To measure the velocity of drop a time-of-flight method was implemented. With the help of laser diode (18) and collecting lens (19) a parallel light beam was generated, coming through side windows of chamber in immediate vicinity of substrates surface. Receiving part consists of photodiode (20), placed in a focus of collecting lens (21) and two-slit diaphragm (22), which cuts two narrow horizontal stripes from beam on known distance. During particles crossing the parallel beam, photodiode registers sequentially two impulses from transiting particle, which are transmitted to storage of oscilloscope. Drops velocity u_{p0} was defined by signal received.

Temperature T_{p0} of a free falling droplet prior to impact with substrate was calculated with enough accuracy. Size D_p of molten falling particle is calculated in accordance with the formula $D_p = \sqrt[3]{6m_s / \pi\rho_p^{(l)}(T_{p0})}$, where m_s is mass of splat, $\rho_p^{(l)}(T_{p0})$ is density of particle material in liquid state at temperature of droplet T_{p0} . Splats mass was defined by direct weighting with the help of analytical balance Ohaus Pioneer PA214C with accuracy within 0.1 mg.

Superpure fusible metals (zinc, lead, tin, bismuth and indium) were used as model materials for drops generation and substrates preparation.

Acknowledgment

The results reported were obtained in part within Interdisciplinary Integration Project No.2 of the Siberian Branch of Russian Academy of Sciences for the year 2012-2014.

References

- [1] O.P. Solonenko, V.V. Kudinov, A.V. Smirnov et al., JSME International Journal, Series B, **48** (2005), P. 366-380.
- [2] O.P. Solonenko, Thermal Plasma and New Materials Technology, Eds. O.P. Solonenko and M.F. Zhukov, Cambridge, England: Cambridge International Science Publishing, **2** (1995), P. 7-96.
- [3] O.P. Solonenko and A.V. Smirnov, Reports of Russian Academy of Sciences, in Russian, **63** (1998), P. 46-49.

Size Validation of an Adrenal Vein Model for Development of an In Vitro Model with Realistic Geometrical Structure

Yusuke Hoshino[†], Kei Takase^{††}, Kazumasa Seiji^{††}, Makoto Ohta^{†††}

[†]Graduate School of Biomedical Engineering, Tohoku University, 6-6-01 Aramaki aza aoba, Aoba-ku, Sendai, Miyagi, Japan

^{††}Department of Diagnostic Radiology, Tohoku University Hospital, 1-1 Seiryomachi, Aoba-ku, Sendai, Miyagi, Japan

^{†††}Institute of Fluid Science, Tohoku University, 2-1-1 Katahira, Aoba-ku, Sendai, Miyagi, Japan
hoshino@biofluid.ifs.tohoku.ac.jp

ABSTRACT

Adrenal venous sampling (AVS) is an important procedure, however, the difficulties require the development of an adrenal vein model with realistic geometrical structure for training of the AVS. In this study, 3-D reconstructions of the inferior vena cava and the left renal vein, and the adrenal vein were performed from conventional CT images and specific CT images, respectively. These structures were combined, and the adrenal vein model was fabricated from the combined structure and validated in size. As a result, the finding PVA concentration for a vein will realize the softness of vein, however, the size of vein should be improved.

1. Introduction

The blood pressure has strong relation to onset of stroke or cardiovascular disease. It is reported that incidence and mortality of stroke or cardiovascular disease increase as blood pressure become higher^[1, 2]. Then, the treatment of hypertension will be essential for prevention of stroke or cardiovascular disease.

The hypertension is classified into two categories: essential hypertension and secondary hypertension. In case of the essential hypertension, firstly, the patient's lifestyle is improved for decreasing of the blood pressure. And then, in case the blood pressure isn't decreased, antihypertensive drugs are administered to the patient. In case of the secondary hypertension, most of the patients are cured by the treatment of causative disorders.

Primary aldosteronism (PA) is one of the causative disorders of secondary hypertension. The excessive secretion of aldosterone from the adrenal gland as shown in Fig. 1 leads the hypertension. Historically, the PA was thought to represent less than 1% of hypertensive patients, however more recent studies suggest that the true incidence is closer to 5-10% of cases^[3, 4]. Therefore, many hypertensive patients are cured by using the treatment of the PA. Additionally, the treatment of the PA will lead to a decrease in incidence and mortality of stroke or cardiovascular disease.

It is necessary to determine whether the excessive secretion of aldosterone is unilateral or bilateral for the decision of treatment method for the PA. The unilateral excessive secretion can be treated with surgery. Adrenal venous sampling (AVS) is performed to determine whether the excessive secretion is unilateral or bilateral. In the AVS, venous blood is sampled from right and left adrenal veins by using catheters and tested for the aldosterone. The AVS has a reputation as a difficult procedure, because insertion of the catheter is difficult due to small internal diameter and individual difference in direction and location of the adrenal vein.

A simulation of the AVS is necessary for training of the AVS or development of a catheter with curative function, and the development of an adrenal vein model with realistic geometrical structure for the AVS simulation is required.

The 3-D structure of the adrenal vein is necessary to develop the adrenal vein model with realistic geometrical structure. 3-D structures of blood vessels can be reconstructed by using angiographic CT images, however the 3-D structure of the adrenal vein is hard to be reconstructed due to low contrast between the adrenal vein and the surrounding tissue in general angiographic CT images.

In this study, at first, the 3-D reconstructions of the inferior vena cava (IVC) and the left renal vein were performed from general CT images. Next, the 3-D reconstruction of the adrenal vein was performed from specific CT images. And then, these structures were combined, and the adrenal vein model was fabricated from the combined structure and validated in size for development of an AVS simulation model.

2. Method

2.1. Angiography

Two angiography methods were performed for CT images of the veins. One is a usual method as a routine work, and the other is a specific method for more precise image. In the former, CT images were taken after injection of a contrast material via antecubital vein using power injector. The usual method was applied for CT image of the IVC and the left renal vein, and the 3-D structure was constructed by using 182 sliced images with resolution of 0.645 mm/pix and 1.0 mm intervals. In the latter, CT images were taken while the contrast material was simultaneously injected into right and left adrenal veins through catheters.

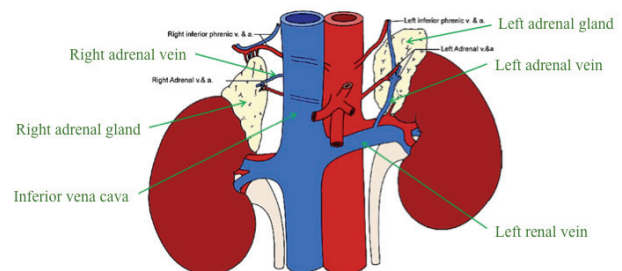


Fig. 1 Adrenal gland anatomy^[3]

Firstly, the usual method was also applied to the adrenal vein, however the segmentation of the adrenal vein was impossible. Therefore the specific method was applied for the vein on another day, and the 3-D structure was constructed by using 157 sliced images with resolution of 0.625 mm/pix and 0.8 mm intervals.

2. 2. 3-D Reconstruction and Combination of Veins

The 3-D reconstruction of veins was performed by using an image processing software package (Osirix, ver. 3.9.3, Osirix foundation). Firstly the automatic segmentation of the vein was carried out. In case that the segmentation couldn't be performed automatically, another software package (Mimics, ver. 7.30, Materialise) was applied for 3-D reconstruction. The reconstructed 3-D structures were edited such as combination, smoothing or wrapping by using an editing software package (Magics, ver. 14.0, Materialise).

2. 3. Fabrication and 3-D Reconstruction of an Adrenal Vein Model

A cast molding of the adrenal vein was fabricated from the combined structure with gypsum. Then CT scan of the mold was performed, and the 3-D structure was reconstructed by using 221 sliced images with resolution of 0.22 mm/pix and 1.0 mm intervals for comparison with the combined structure.

Firstly, Poly (vinyl alcohol) (PVA) was dissolved in a mixed solvent of dimethyl sulfoxide (DMSO) and distilled water (80/20, w/w). Concentration, degree of polymerization and saponification value of the PVA were 8 wt%, 1700 and 99 mol%, respectively. The PVA powder in the mixture solution was stirred for 2 hours at 100 °C until dissolution. Then the PVA solution was cast into an acrylic box with the cast molding. And then the acrylic box was maintained at -30°C for 24 hours to promote PVA gelation. After the gelation, the mold material was removed as the lost-wax technique. Then CT scan of the PVA hydrogel (PVA-H) model was performed, and the 3-D structure was reconstructed by using 341 sliced images with resolution of 0.37 mm/pix and 1.0 mm intervals for comparison with the combined structure.

3. Results and Discussion

3-D structures of combined structure, the cast molding, and PVA-H model using CT scan are shown in Fig. 2, respectively. The reconstruction of left adrenal vein of PVA-H model seem to be low accurate, however, as shown in Fig. 3, the reconstruction can be observed. Because the CT value of PVA-H is similar to that of water, the segmentation of the adrenal vein is failed. Contrast media will improve the segmentation.

Fig. 4 shows the images of cross section at the distal position of IVC and Table 1 shows the values of the maximum length (ML) of cross section, and area (A) of combined structure, cast molding and PVA-H model, respectively. The size of PVA-H model is 13.5% times larger than that of combined structure. The size accuracy will be improved by using the evaluation of swelling of

PVA-H.

4. Concluding remarks

Adrenal veins of a patient were reconstructed by using a specific method of injection of contrast material for accurate reconstruction and PVA-H model was developed using the similar mechanical properties for a vein. The finding PVA concentration for a vein will realize the softness of vein, however, the size of vein is larger than that of reconstruction.

References

- [1] Nippon Data 80 Research Group, Journal of Human Hypertension, **17** (2003), 851-857.
- [2] Asia Pacific Cohort Studies Collaboration, Journal of Hypertension, **21** (2003), 707-716.
- [3] S. L. Kahn and J. F. Angle, Techniques in Vascular and Interventional Radiology, **13** (2010), 110-125.
- [4] N. Daunt, Radiographics, **25** (2005), S143-S158.

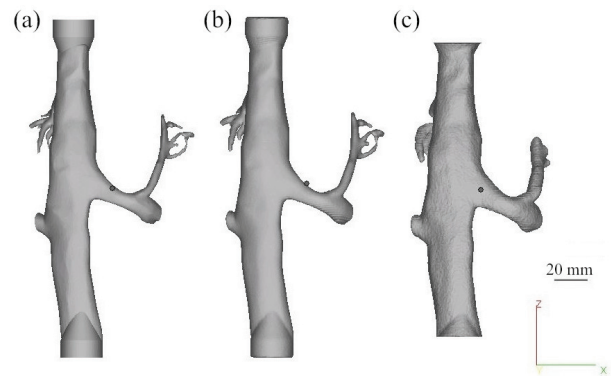


Fig. 2 3-D structures of (a) combined structure, (b) cast molding and (c) PVA-H model

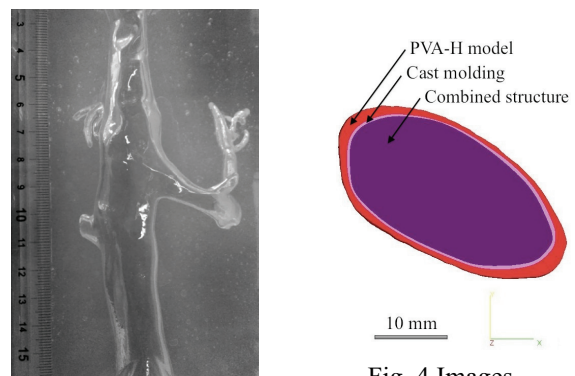


Fig. 3 PVA-H model

Fig. 4 Images of cross section

Table 1. Comparison of 3-D structures

3-D structure	ML [mm]	A [mm ²]
Combined structure	31.1	784
Cast molding	31.9	836
PVA-H model	35.3	998

Effect of Liquid Properties on Velocity Field over a High Speed Rotary Bell Cup Atomizer

Tatsuya Soma¹, Tomoyuki Katayama¹, Yasuhiro Saito¹, Hideyuki Aoki¹, Toshiki Haneda², Yosuke Hatayama²,
Minori Shirota², Takao Inamura², Daichi Nakai³, Genki Kitamura³, Masanari Miura³, Masatohi Daikoku³

¹Department of Chemical Engineering, Faculty of Engineering, Tohoku University, 6-6-07 Aoba, Aramaki, Aoba-ku, Sendai, Miyagi 980-8579, Japan, ²Department of Intelligent Machines and System Engineering, Faculty of Science and Technology, Hirosaki University, 1 Bunkyo-cho, Hirosaki, Aomori 036-8560, Japan, ³Department of Mechanical Engineering, Faculty of Engineering, Hachinohe Institute of Technology, 88-1, Ohbiraki, Myo, Hachinohe, Aomori 031-8501, Japan

E-mail: saito@tranpo.che.tohoku.ac.jp

ABSTRACT

Using the volume of fluid (VOF) method, we analyze two-dimensional fluid flow over high-speed rotary bell-cup atomizers. The fluid behavior is analyzed, and the liquid film thickness is quantitatively evaluated. The bell rotational speed is 35,000 rpm; and the liquid flow rate is 300 mL/min. The liquid viscosity is 1, 20, 40, 70, and 100 mPa·s. Surface tension coefficient of the liquid is 30, 40, 50 and 60 mN/m. The results show that the increase of viscosity diminishes the radial velocity of the liquid, and the film thickness increases. The film thickness hardly relies on surface tension coefficient.

1. Introduction

High-speed rotary bell-cup atomizers are widely used in industrial painting such as auto painting because of its high productivity and high quality. The bell-cup revolves at a high speed, and the paint is supplied through the paint supply holes. The centrifugal force pushes the paint to flow over the bell-cup surface toward the bell-cup edge and a liquid film is formed. Then, the paint flows out of the bell-cup edge and droplets are formed in the air. The droplets are sprayed to the automobile body, and the droplets help in determining the coating quality. The droplets have been already reported to be affected by the liquid film on the bell-cup surface [1], and obtaining knowledge of the liquid film is so important.

In the present study, we analytically compute the flow on a high-speed rotary bell-cup atomizer. It allows us to quantitatively analyze the fluid velocity and the liquid film thickness.

2. Method

Fig. 1 shows an analytical object, which is a two-dimensional flow over a high-speed rotary bell-cup atomizer. Here, we focus on the flow around the paint supply holes, and assume that the bell-cup surface is flat in shape. The liquid is supplied from the paint supply hole, and then flows over the surface due to the centrifugal force. The air flows around the bell-cup due to the rotation of the bell-cup. The no-slip condition is applied to the boundary of the bell-cup surface.

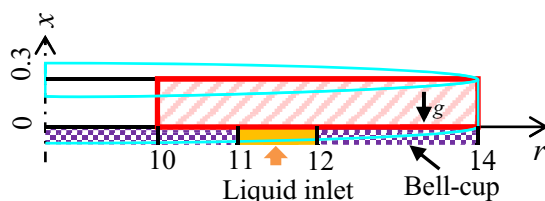


Fig. 1 Analytical object

We consider a gas–liquid two-phase flow and use the volume of fluid (VOF) method. The fluids are assumed to be viscous and incompressible. The fluid flow is governed by the continuity equation, momentum equations and the VOF equation. These governing equations are discretized via the finite volume method. A staggered grid is used as the computational grid, a Simplified marker and cell (SMAC) is used as the coupling scheme, and algebraic multigrid solvers (AMGS) are used as the matrix solver.

Table 1 shows the numerical conditions. The operating conditions correspond to real automotive painting conditions.

Table 1. Numerical conditions

Mesh size ($r \times x$) [μm]	3.3×3.3
Operating condition	
Liquid flow rate [mL/min]	300
Rotational speed [krpm]	35
Liquid property	
Density [kg/m^3]	1000
Viscosity [mPa·s]	1, 20, 40, 70, 100
Surface tension coefficient [mN/m]	30, 40, 50, 60
Gas property	
Density [kg/m^3]	1
Viscosity [mPa·s]	0.01

3. Results and Discussion

Fig. 2 shows details of the flow field. At $x = 0.3$ mm, the bell-cup rotation scarcely affects the fluid, and thus radial velocity of the liquid obtained is low. Far from the bell-cup, with decreasing x , the fluid velocity increases. That is because the fluid near the bell-cup is easily influenced by the bell-cup rotation. Near the bell-cup, with decreasing x , the velocity decreases. That is because the radial velocity is zero on the bell-cup surface due to the friction between the fluid and the bell-cup. The gas near the liquid level attains the maximum velocity because of the balance between the

effect of bell-cup rotation and friction.

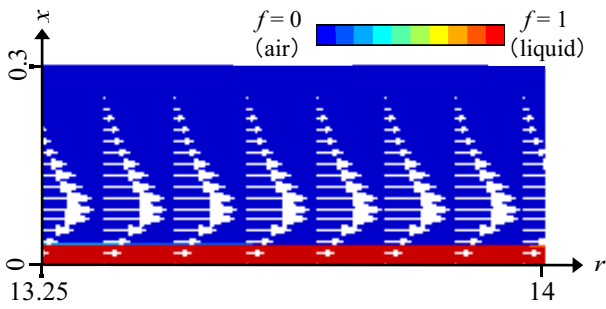
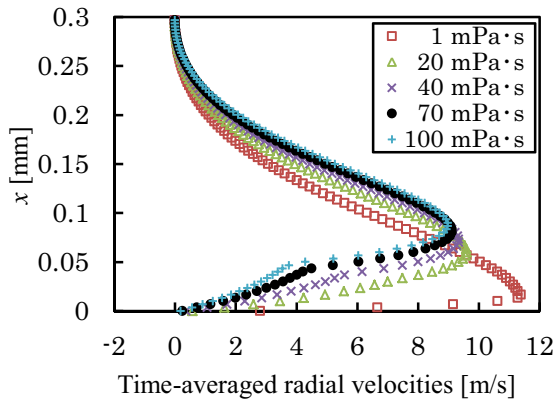
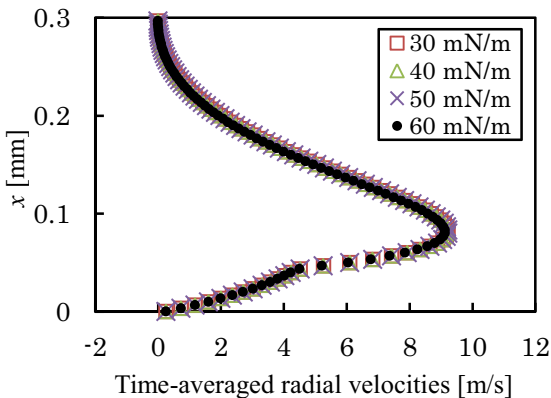


Fig. 2 Resultant of radial and axial velocity (70 mpa·s, 60 mN/m)

Fig. 3 shows the change of velocity field with paint properties. Fig. 3(a) indicates that the paint viscosity strongly affects the fluid behavior. With an increase in the liquid viscosity, a decline in the liquid mobility diminishes the radial velocity of the liquid. Fig. 3(b) indicates that surface tension coefficient of the paint hardly affects the fluid behavior. This means that surface tension has little effect on the fluid velocity field at least after the bell-cup surface get a wetting.



(a) Comparison of viscosity (60 mN/m)

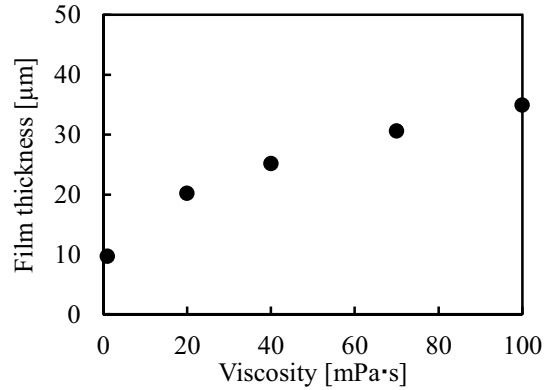


(b) Comparison of surface tension (70 mPa·s)

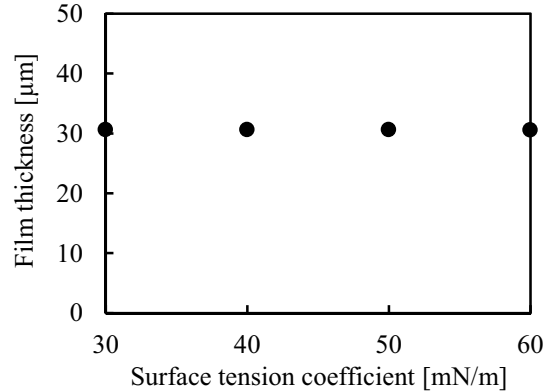
Fig. 3 Time-averaged radial velocities

Fig. 4 shows relationships between paint properties and film thickness. Fig. 4(a) shows that the increase in the viscosity causes the film thickness to increase. With

an increase in the liquid viscosity, slowing of the liquid film bring about increase in film thickness. Fig. 4(b) shows that the film thickness never depends on surface tension coefficient. That is because that surface tension has no effect on the paint velocity. That is to say the liquid viscosity is dominant factor affecting fluid behavior of the liquid film.



(a) Comparison of viscosity



(b) Comparison of surface tension coefficient

Fig. 4 Relationship between paint properties and film thickness

4. Concluding remarks

We study the liquid flow over a bell-cup atomizer. We analyze the gas–liquid two-phase flow using the VOF method, and then obtain the following results:

- The increase in viscosity affects the fluid behavior and causes the film thickness to increase.
- The increase in surface tension coefficient hardly causes the fluid behavior or film thickness.

References

- [1] S. Kazama, JSAE Review, **24** (2003), 489

Numerical Analysis of Cryogenic Slush Flow in a Triangular Pipe (SLUSH-3D)

Takumi HOSONO, Daisuke NAKA, Katsuhide OHIRA

Institute of Fluid Science, Tohoku University, 2-1-1 Katahira, Aoba, Sendai 980-8577, Japan
hosono@luna.ifs.tohoku.ac.jp

ABSTRACT

Cryogenic slush fluids such as slush hydrogen are two-phase single component fluids containing solid particles in a liquid, which have higher density and refrigerant capacity than a single-phase liquid. In this study, the slush flow in a horizontal triangular pipe which is used for heat exchanger because of its large heat-transfer area and space-saving was numerically calculated to clarify the flow characteristics of slush fluids. The results showed that the effect of solid particles on the pressure drop in a triangular pipe was smaller than those of circular and square pipes because a large turbulence occurs at the corners of a triangular pipe.

1. Introduction

Cryogenic slush fluids are two-phase single component fluids containing solid particles in a liquid. The density and refrigerant heat capacity of the slush fluids are higher than those of the liquids. And also the pressure drop reduction [1] of slush fluids is confirmed at high Reynolds number. Because of these advantages, the energy system where slush hydrogen is transported as energy and used in superconducting power transmission refrigerant is suggested [2]. In this system, the synergic effect between the transportation of fuel and electrical power at the same time and the storage of those are expected. However, flow characteristics of slush fluids in a pipe are not fully clarified.

The aim of this research is to clarify flow characteristics of slush fluids in a horizontal triangular pipe which is used for heat exchanger because of its large heat-transfer area and space-saving. The flows of slush nitrogen and hydrogen are numerically analyzed with the computational model. And the result is compared with those of circular and square pipes [3] [4].

2. Method

2.1. Governing equations

In this research, the liquid and solid phases are supposed to be the incompressible continuous phase and Newtonian fluid. And solid particles are treated as sphere. The physical properties of each phase used are the values at the triple point. The standard $k-\epsilon$ is adopted to simulate the turbulence. And the PISO algorithm is utilized for the pressure calculation.

Following equations are the modeling equations employed in the Euler-Euler coupling two-fluid model. The continuity equation for the phase φ ($\varphi = l$ for the liquid phase, s for the solid phase) is written as (1).

$$\frac{\partial \alpha_\varphi \rho_\varphi}{\partial t} + \nabla \cdot (\alpha_\varphi \rho_\varphi \mathbf{U}_\varphi) = \dot{m}_\varphi \quad (1)$$

\dot{m}_φ is the mass exchange term between liquid and solid phases. The momentum equation is written as (2).

$$\frac{\partial \alpha_\varphi \rho_\varphi \mathbf{U}_\varphi}{\partial t} + \nabla \cdot (\alpha_\varphi \rho_\varphi \mathbf{U}_\varphi \mathbf{U}_\varphi) + \nabla \cdot (\alpha_\varphi \boldsymbol{\tau}_\varphi) + \nabla \cdot (\alpha_\varphi \rho_\varphi \mathbf{R}_\varphi) = -\alpha_\varphi \nabla P + \alpha_\varphi \rho_\varphi \mathbf{g} - \dot{m}_\varphi \mathbf{U}_\varphi + \mathbf{M}_\varphi \quad (2)$$

The momentum exchange term between solid and liquid phases \mathbf{M}_φ is composed of drag and virtual mass terms. The Energy equation is written as (3).

$$C_{p,\varphi} \rho_\varphi \left(\frac{\partial \alpha_\varphi T_\varphi}{\partial t} + \nabla \cdot (\alpha_\varphi \mathbf{U}_\varphi T_\varphi) \right) = \nabla \cdot (\alpha_\varphi \kappa_\varphi^{\text{eff}} \nabla T_\varphi) + \dot{m}_\varphi h_L + Q_\varphi \quad (3)$$

The heat exchange term between solid and liquid phases Q_φ is given by the Ranz-Marshall model.

2.2. Simulation Condition

Fig. 1 shows the equilateral triangular pipe model with a side of 20 mm used in this numerical analysis. The flow path length of this model is 1500 mm. And also, another triangular pipe model with a side of 26 mm is analyzed for comparison with circular and square pipes.

The solid diameter is assumed $d_s = 1.3$ mm. And the solid fractions are $\alpha_s = 5 - 25$ vol.%, the inlet velocities are $U_{in} = 1.5 - 5.0$ m/s as the initial conditions.

3. Results and Discussions

3.1. Flow characteristics

Fig.2 shows the pressure drop of slush nitrogen in a triangular pipe with a side of 20 mm. The numerical results of subcooled liquid nitrogen agree well with the Blasius equation. Thus the validity of the numerical code is confirmed. And, the pressure drop of slush nitrogen increases with the increase of the solid fraction. It is due to the increase of turbulence with the increase of the interference between solid and liquid phases.

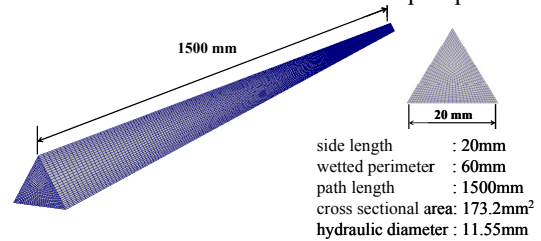


Fig.1 Triangular pipe model

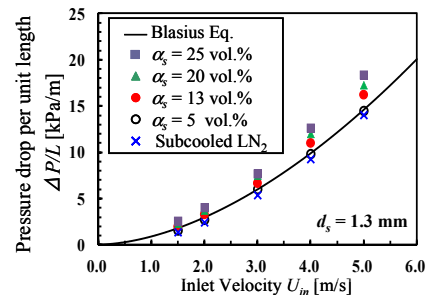


Fig.2 Pressure drop of slush nitrogen

Fig.3 shows the solid phase velocity profile of slush nitrogen for a solid fraction $\alpha_s = 13$ vol.%. In this figure, the dotted line indicates the position of gravity center. The position of velocity peak at the low inlet velocity is upper than that at the high inlet velocity. And Fig.4 shows the local solid fraction profile in the same conditions. The solid particles are concentrated in the bottom of the pipe at the low velocity, and are distributed uniformly at the high velocity. These results show that the position of velocity peak is upper than the position of gravity center at the low inlet velocity due to the interference between solid and liquid phases in the bottom of the pipe, and is consistent with the position of gravity center at the high velocity because of the uniform distribution of solid particles.

3.2 Comparison with different shaped pipes

The results of the triangular pipe are compared with those of the circular and square pipes. Hydraulic diameter of each pipe is 15 mm. Fig.5 shows the pressure drop of each pipe for a solid fraction $\alpha_s = 13$ vol.%. The pressure drops of square and triangular pipes are lower than that of circular pipe. And the pressure drop of triangular pipe is slightly lower than that of square pipe. It is because the effects of the solid particles relatively decrease due to the large turbulence of liquid phase in the corners of a triangular pipe.

3.3 Comparison of slush nitrogen and slush hydrogen

Fig.6 shows the local solid fraction profiles of slush nitrogen and slush hydrogen. There is almost no difference between them at the high velocity. But at the low velocity, the solid particles of slush hydrogen are distributed more uniformly than those of slush nitrogen because the viscosity and solid-liquid density ratio of hydrogen are smaller than those of nitrogen. Fig. 7 shows the pressure drop increase rates of slush nitrogen and slush hydrogen compared with the liquid nitrogen and liquid hydrogen, respectively. In the case of the circular pipe, the increase rate of slush hydrogen is lower than that of slush nitrogen [3]. However, in the case of the triangular pipe, the results are almost the same values except for the low velocity conditions at the high solid fraction. It is because of the large turbulence in the corners, as described above.

4. Concluding remarks

In this research, slush flow in a horizontal triangular pipe was numerically analyzed. As a result, flow characteristics of slush fluids in a triangular pipe were clarified. And it was found that the effects of solid particles of a triangular pipe were smaller than those of circular and square pipes.

References

- [1] K. Ohira, K. Nakagomi and N. Takahashi, *Cryogenics*, **51** (2011), 563-574
- [2] K. Ohira, *TEION KOGAKU*, **41** (2006), 61-72
- [3] K. Ohira, A. Ota, Y. Mukai and T. Hosono, *Cryogenics*, **52** (2012), 428-440
- [4] K. Ohira and A. Ota, *Abstracts of CSJ Conference*, **84** (2011), 172

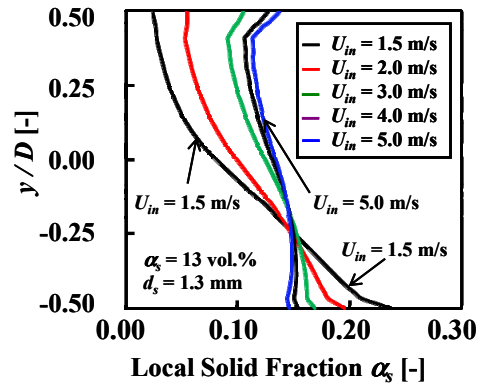


Fig.3 Solid phase velocity profile

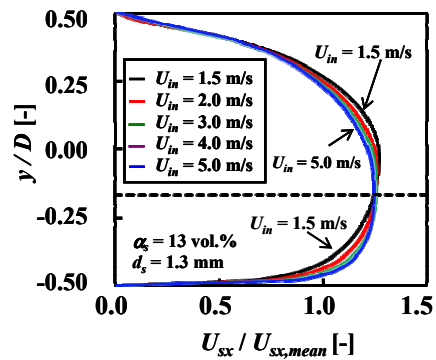


Fig.4 Solid fraction profile

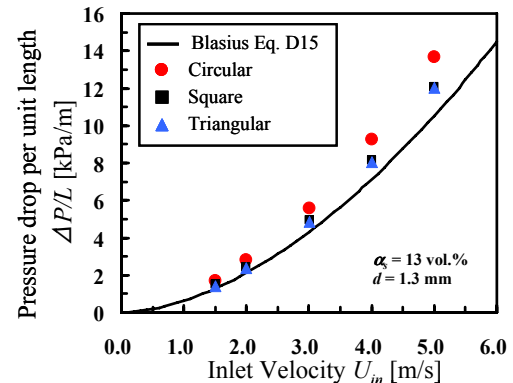


Fig.5 Comparison of pressure drop for different pipes

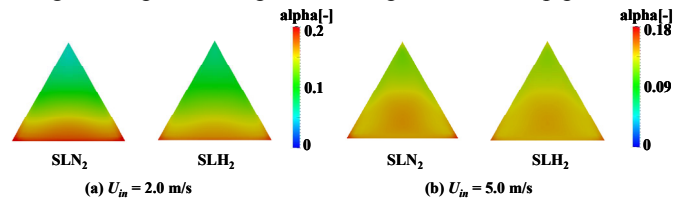


Fig.6 Comparison of solid fraction profiles
($\alpha_s = 13$ vol.%)

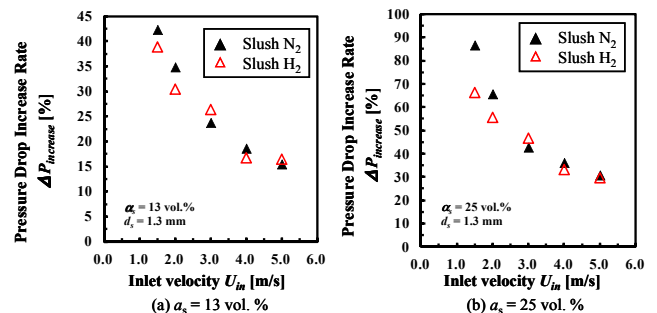


Fig.7 Comparison of pressure drop increase rates

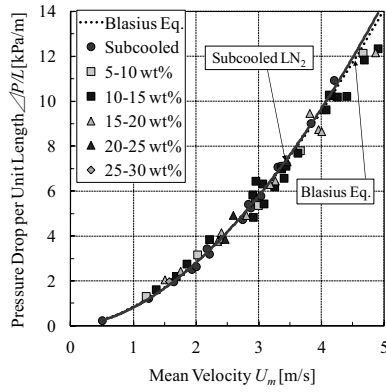


Fig. 3 Pressure drop and mean velocity of slush N₂.

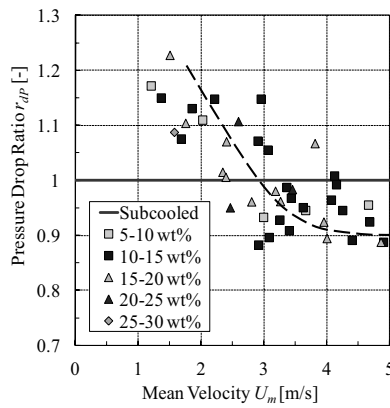


Fig. 4 Pressure drop ratio and mean velocity of slush N₂.

3.2. Heated condition ($q = 10, 20 \text{ kW/m}^2$)

Figs. 5, 6 show the result of pressure drop, local heat transfer coefficient and flow velocity in heated conditions. Local heat transfer coefficient h_5 of temperature sensor T₅ is shown. Heat flux in Figs. 5, 6 are 10 kW/m^2 and 20 kW/m^2 , respectively. Equation (2) shows the definition of the local heat transfer coefficient.

$$h = q / (T_{\text{wall}} - T_{\text{bulk}}). \quad (2)$$

Regardless of the magnitude of heat flux, in the range of over 2.5 m/s, pressure drop reduction appears in almost all the solid fraction. These tendencies are the same as a non-heated condition. Thus, the heat transfer to slush nitrogen doesn't have an influence on the flow velocity that pressure drop reduction begin to occur.

Heat transfer coefficient of slush nitrogen is less than that of liquid nitrogen in all the flow velocity and solid fraction. This feature is the same not only at the point of temperature sensor T₅ but also at the points of temperature sensors T₃ and T₄. So, in the range of over 2.5 m/s, both pressure drop reduction and heat transfer deterioration occur. However, in the range of below 2.5 m/s, heat transfer deterioration occurs only. This phenomenon are considered to occur by following reasons. In the range of high flow velocity, by the migration of the solid particles to the center of the pipe, interference between solid particles and the pipe wall is reduced. The group of solid particles in the pipe center also suppresses the diffusion of turbulence near the pipe

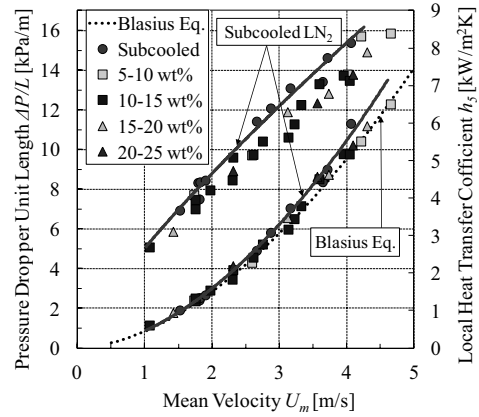


Fig. 5 Pressure drop and local heat transfer coefficient of slush N₂. ($q = 10 \text{ kW/m}^2$)

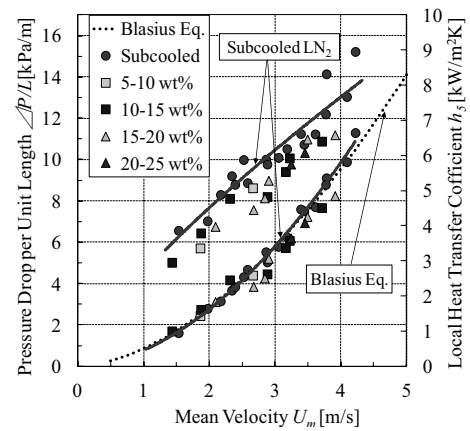


Fig. 6 Pressure drop and local heat transfer coefficient of slush N₂. ($q = 20 \text{ kW/m}^2$)

wall to the pipe center. As a result, pressure drop reduction occur. In addition, heat transfer coefficient deteriorates because heat diffusion by turbulent mixing is suppressed. On the other hand, in the range of low flow velocity, by turbulence of the liquid phase that occur at the pipe corners [3], solid particles are diffused to the pipe center. Thus, in comparison with circular pipe, the flow in a square pipe is easy to become pseudo-homogeneous flow. Therefore, owing to solid particles in the pipe center, heat diffusion by turbulent mixing is suppressed. As a result, heat-transfer deterioration occurs.

4. Conclusions

When slush nitrogen flowed in a square pipe, pressure drop reduction appeared at the flow velocity 2.5 m/s or greater. The heat transfer to slush nitrogen didn't have an influence on the flow velocity that this phenomenon began to occur. Heat transfer coefficient of slush nitrogen is less than that of liquid nitrogen in all the flow velocity and solid fraction.

References

- [1] K. Ohira, TEION KOGAKU, **41** (2006), 61-72.
- [2] K. Ohira, cryogenics, **51** (2011), 389-396.
- [3] K. Ohira, A. Ohta, Proceedings of Multiphase Flow (2011), 322-323.

A Numerical Study of Cavitating Flows over a Hydrofoil

Daichi Matsubara¹, Mingyu Sun²

¹ Graduate School of Engineering, Tohoku University, 6-3 Aoba, Aramaki aza, Aoba-ku, Sendai 980-8577, Japan

² Institute of Fluid science, Tohoku University, Katahira2-1-1, Aoba-ku, Sendai 980-8578, Japan
matsubara@iswi.cir.tohoku.ac.jp, sun@fmail.ifs.tohoku.ac.jp

ABSTRACT

This is a preliminary result of our attempt to simulate the cavitating flow over a hydrofoil by novel numerical method unifies an interface tracking method and a two-fluid model. Both methods are based on the same mathematical model for two-phase flows, and they only differentiate themselves at the definition of numerical fluxes. The former calculates the numerical fluxes for each phase, following the PLIC-VOF method reconstructs a linear interface in each cell. The latter evaluates the fluxes by using the volume fractions. Numerical results indicate it's possible to reconstruct discrete bubbles from the initial continuous volume fractions.

1. Introduction

When a flow moves around a body, the cavitation occurs if the liquid is accelerated and the pressure of liquid falls below the vapor pressure. It is a serious problem in practical applications because it may cause erosion on the wall surface, and deteriorate the performance of devices. It is still a challenge for numerical prediction of such a phenomenon.

The numerical methods for cavitating flows can be divided to two large categories. One is the diffused interface method (DIM), such as one-fluid and two-fluid models. Available commercial codes are built on the one-fluid model. The other approach is the sharp interface method (SIM), such as level set method, geometric VOF method. Both methods have advantages and disadvantages. The DIM calculates phase fluxes from volume fractions, so it can resolve two-phase phenomenon without explicitly calculating geometric interfaces, but results in a diffused interfaces between two phases. On the other hand, the SIM can resolve an interface within one cell, but necessities complex geometric calculations.

The mathematical model or the governing equations for these two methods are usually different. The DIM is based on an averaging procedure over sufficient number of bubbles. The governing equations vary with the assumptions adopted in the averaging procedure. The governing equations for the SIM are usually the same as these for two pure fluids with compatible relations between them.

We have proposed a mathematical model for two-phase flows that can handle both DIM and SIM under the same framework [2]. In this study, we introduce a switching mechanism between them, and try to investigate the behavior and the impact of such a unification on the numerical solution of the cavitation phenomena over a hydrofoil.

2. Method

In this study, the simulation is conducted with a semi-implicit Lagrange-Remap method. In the Lagrange step, it solves primitive quantities of pressure and velocity in the Lagrangian frame. The equation of continuity and the equation of motion,

$$\frac{Dp}{Dt} = -\rho c^2 \nabla \cdot \vec{u} \quad (1)$$

$$m \frac{D\vec{u}}{Dt} = -\nabla p \quad , \quad (2)$$

are discretized as follows,

$$\frac{(p_i^*)^{n+1} - (p_i^*)^n}{\Delta t} = -\frac{I_i^2}{m_i} \sum \left((u_i^*)^{n+1} S_{xij} + (v_i^*)^{n+1} S_{yij} \right) \quad (3)$$

$$m_i \frac{(u_i^*)^{n+1} - (u_i^*)^n}{\Delta t} = -\sum \left((p_i^*)^{n+1} S_{xij} \right) \quad (4)$$

$$m_i \frac{(v_i^*)^{n+1} - (v_i^*)^n}{\Delta t} = -\sum \left((p_i^*)^{n+1} S_{yij} \right) \quad , \quad (5)$$

where m is mass at cell number i , S_{xij} and S_{yij} are outward normal vectors. Superscript * indicates values in the Lagrangian coordinate. Acoustic impedance is given by

$$I_i = \rho_i c_i \quad . \quad (6)$$

The conservative quantities are then calculated from the pressure and velocity at the boundary of the particle. They are remapped to the Eulerian coordinate, as a finite volume method. For the cavitation model, Merkle's cavitation model is adapted to two-fluid model [3], and we use this cavitation model for the SIM as well. In two-fluid model, volume fluxes are given by

$$F_s = aF \quad , \quad (7)$$

where a is volume fraction. We adopt this formula for the volume fraction below 0.05.

On the other hand, the SIM is based on the PLIC/SN method [4], which belongs to the PLIC-VOF method that uses one linear segment to represent the interface in a cell. For the volume fraction over 0.05, we adopt the SIM. Since the newborn bubble is much smaller than the grid size, the surface normal method that can track the subgrid particle is used. For small bubbles, their surface normal vectors are evolved by the following surface normal equation,

$$n_i + \nabla(u \cdot n) = 0 \quad . \quad (9)$$

The reader is referred to [4] for more details of this method.

In our unified approach the interfacial phenomenon in a cell is either modeled or tracked, depending on how

their volume numerical fluxes are calculated. For the sake of clarity, we call them either interface-tracking (IT) cell or two-fluid (TF) cell.

All cells are marked either IT or TF cells. The rules for their definitions are summarized as follows.

- ① An IT cell changes to be TF if the total volume fraction in its neighborhood is below a threshold value, otherwise it remains unchanged.
- ② For a TF cell, if there is one or more IT cells in its neighborhood, and if the discrete phase in at least one of these IT cells enters the cell, it changes to be IT.
- ③ For a TF cell, if its volume fraction becomes larger than a threshold value, and if there is no IT cells in its neighborhood, it becomes a newborn IT cell.
- ④ Vectors of this newborn IT cell and the TF cells in its neighborhood set to be the gradient of volume fraction, $\vec{n} = \nabla \alpha$.

3. Results and Discussion

We calculate the water flow over the Clark-Y hydrofoil at an angle-of-attack of 8° . Fig.1 shows a computational grid structured O-type (160×56). The length of chord is 1m. Viscosity is not considered. Computations have been done for cavitation number σ of 0.7. The flow Mach number is 0.0065. All cases are done with the CFL number 0.04. The mesh adaptation grid level is 2. The steam obeys the equation of state for idea gases. All cells are marked as TF initially.

The result of the cavitating flow over a hydrofoil using the two-fluid model and using the present unified method that coupled two-fluid model and interface tracking method are recorded and compared in Fig.2. There is no difference between two methods at $t=0.0044$ sec because the volume fraction is still below the threshold value, and the IT cell has not been triggered on yet. At $t=0.0052$ sec, the former shows the existence of cavitation bubbles as a dark band, while the latter is able to resolve them as discrete bubbles.

The cavitation bubbles grow with time, and they separate from each other on the surface of a hydrofoil at $t=0.0061$ sec. It requires much fine grid for other interface tracking methods to track there small cavitation bubbles. With this unified method that incorporates the surface normal technique, we can track bubbles even with a coarse mesh. A bubble can be resolved in roughly three cells.

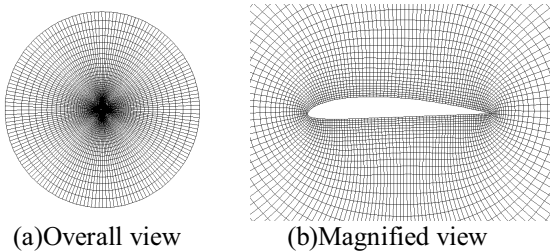


Fig.1 Computational grid

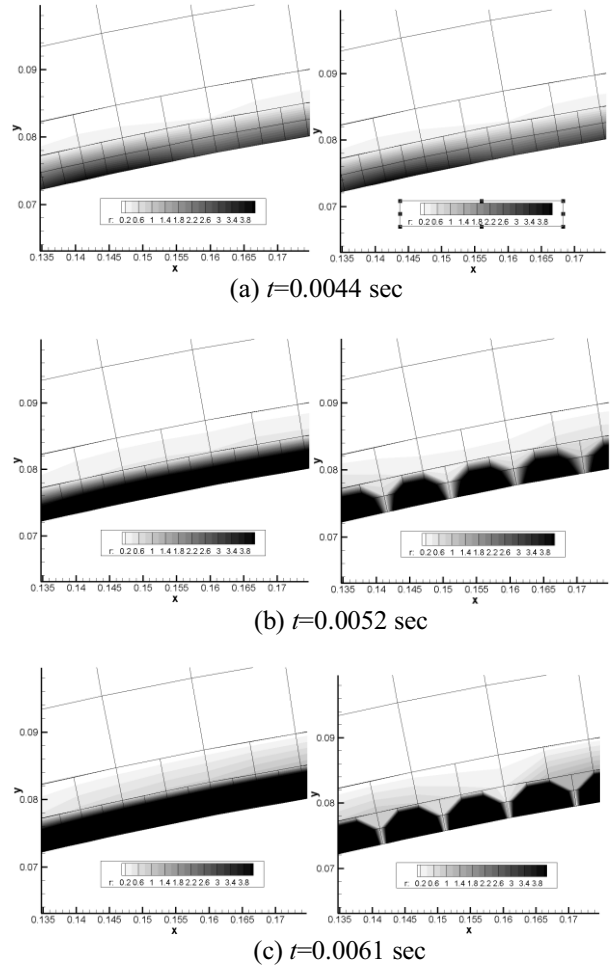


Fig.2 Comparison of the initial development of cavitation zone:
two-fluid model (left column);
the present unified method (right column)

4. Concluding remarks

The bubble in cavitating flows over a hydrofoil Clark-Y is analyzed. Using the unified calculation methods, it is possible to reconstruct discrete bubbles from the initial continuous volume fractions.

References

- [1] T. Kunugi, Mars for multiphase calculation, Computational Fluid Dynamics J, Vol.9, pp563-571(2003)
- [2] M. Sun, Direct simulation of gas-liquid two-phase flows with subgrid particles, Symposium on Computational Fluid Dynamics (2010), A8-2
- [3] Y. Zhu, M. Sun, Numerical simulation of cavitation with two-fluid method, International Conference on Fluid Dynamics (2010), Sendai, Japan
- [4] M. Sun, Volume-tracking of subgrid particles, International Journal for Numerical Methods in Fluids, 66; 1530-1554(2011)

The Numerical Analysis of Inverse Problems For Mass Transfer Model

O. V. Soboleva, I.S. Vakhitov

Institute of Applied Mathematics FEB RAS, 7, Radio St., Vladivostok, 690041, Russia
soboleva22@mail.ru

ABSTRACT

The identification problems for the stationary equation of convection-diffusion-reaction considered in on the boundary is investigated. By means of an optimization method these problems are reduced to a extremum problem in which the role of control is played by a variable diffusion coefficient and factor of chemical reaction. Dependence of solutions of the specific extremum problems on a number of parameters entering into model under study is investigated.

1. Introduction

In recent years the great attention is given to statement and research of new classes of problems for mass transfer models. They consist finding in unknown densities of boundary or distributed sources or the coefficients entering into differential equations or boundary conditions for considered model using additional information on the solution of an initial boundary value problem. It is important to note that studying these inverse problems can be reduced to corresponding extremum problems but choosing a suitable minimized functional cost [1,2,3,4,5,6,7].

The purpose of this work is the numerical analysis of inverse extremum problems for the mass transfer model looking like the stationary which has the form of the equation of convection-diffusion-reaction with variable diffusion coefficient, and factor of chemical reaction considered in bounded domain under Dirichlet condition on boundary Γ . In the work dependence of solutions of the specific extremum problem on a number of parameters entering into the model under study is investigated.

2. Direct problem

Let Ω is a bounded domain in \mathbb{R}^d , $d=2,3$ with a Lipschitz boundary Γ . We consider model of transfer of (polluting) substance, described by the following equations

$$-\operatorname{div}(\lambda \nabla \varphi) + \mathbf{u} \cdot \nabla \varphi + k\varphi = f \quad \text{in } \Omega, \quad \varphi|_{\Gamma} = \psi. \quad (1)$$

Here $\lambda \equiv \lambda(\mathbf{x}) > 0$ is a diffusivity coefficient, depending on a point $\mathbf{x} \in \Omega$, $\mathbf{u} = \mathbf{u}(\mathbf{x})$ is the velocity, $k = k(\mathbf{x}) \geq 0$ is the factor characterizing disintegration of a contaminant at the expense of chemical reactions, $f = f(\mathbf{x})$ is the density of volume sources, $\psi = \psi(\mathbf{x})$ is given on Γ function.

3. Statement of inverse problem

The boundary value problem (1) contains some parameters which should be given for ensuring uniqueness of the solution of problem (1). But in practice there are situations when some of them are unknown, and it is required to determine them together with the solution φ using additional information on the solution. As specified information it is possible to choose, for

example, values $\varphi_d(\mathbf{x})$ of concentration φ measured in points of some set $Q \subset \Omega$.

We consider a case when functions λ and k are unknown, and it is required to determine them along with the solution φ . We will apply an optimization method according to which this problem is reduced to the solution of the corresponding extremum problem [9]. We define a functional $I: H^1(\Omega) \rightarrow \mathbb{R}$ by the formula

$$I(\varphi) = \|\varphi - \varphi_d\|_{L^2(Q)}^2 = \int_Q |\varphi - \varphi_d|^2 dx = \int_{\Omega} r(\varphi - \varphi_d)^2 dx.$$

Here r is characteristic function of a set Q .

The considered extremum problem consists in finding of the triple of functions (φ, λ, k) satisfying to the weak formulation of problem (1) and minimizing a functional J , i.e.:

$$(\lambda \nabla \varphi, \nabla h) + (\mathbf{u} \cdot \nabla \varphi, h) + (k\varphi, h) = (f, h) \quad \forall h \in T, \quad \varphi|_{\Gamma} = \psi. \quad (2)$$

$$J(\varphi, \lambda, k) = \frac{\mu_0}{2} \|\varphi - \varphi_d\|_{L^2(Q)}^2 + \frac{\mu_1}{2} \|\lambda\|_{H^s(\Omega)}^2 + \frac{\mu_2}{2} \|k\|_{L^2(\Omega)}^2 \rightarrow \inf,$$

$$(\varphi, \lambda, k) \in H^1(\Omega) \times H_{\lambda_0}^s(\Omega) \times L_+^2(\Omega). \quad (3)$$

Here (2) is a weak formulation of the direct problem (1), $J: H^1(\Omega) \times H_{\lambda_0}^s(\Omega) \times L_+^2(\Omega) \rightarrow \mathbb{R}$ is a minimized functional, $\mu_0 \geq 0$, $\mu_1 \geq 0$, $l=1,2$ are some constants. The description of other used designations can be found in [4, chapter.3].

By book [4], necessary conditions of an optimality for problem (2)-(3) have the form of the following relations:

$$(\lambda \nabla \varphi, \nabla h) + (\mathbf{u} \cdot \nabla \varphi, h) + (k\varphi, h) = (f, h) \quad \forall h \in T, \quad \varphi|_{\Gamma} = \psi, \quad (4)$$

$$(\lambda \nabla \tau, \nabla \eta) + (\mathbf{u} \cdot \nabla \tau, \eta) + (k\tau, \eta) = (\varphi - \varphi_d, h)_Q \quad (5)$$

$$\forall \eta \in H^1(\Omega), \quad \eta|_{\Gamma} = 0,$$

$$(\mu_1 \lambda + \nabla \varphi \nabla \eta, \tilde{\lambda}) + (\mu_2 k + \varphi \eta, \tilde{k}) = 0, \quad \forall \lambda \in H^s(\Omega), \quad (6)$$

$$k \in L_+^2(\Omega).$$

4. Numerical experiments

The numerical solution of problem (2)–(3) in domain Ω was made by means of computer model operation in the program Scilab [10] and in a package FreeFem++ [11]. The domain Ω got out in the form of a simple square on which the even grid was entered.

In this paper we present results of the numerical experiments when only one of the control functions is

unknown and the other are given.

Let us consider a case when λ is unknown. On fig. 1 one can see schedules of the given diffusion coefficient $\lambda_d=10 + \cos(\pi*x)$ and the restored solution of the inverse problem λ . On fig. 1 the surface of the restored solution, and on fig. 2 vertical section of a surface at $x = 0.5$ are presented.

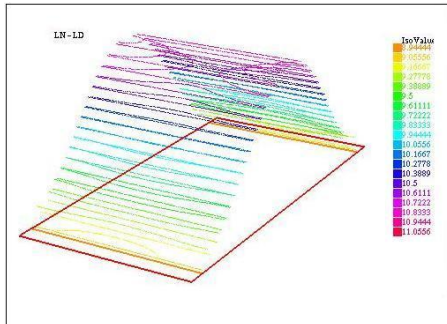


Fig. 1. The restored diffusion coefficient λ

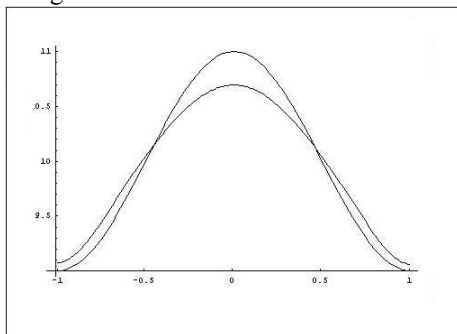


Fig. 2. The restored diffusion coefficient λ

Let us consider now a case when the factor of chemical reaction k is unknown. On fig. 3 and fig. 4 schedules similar given on fig. 1 and fig. 2 are presented.

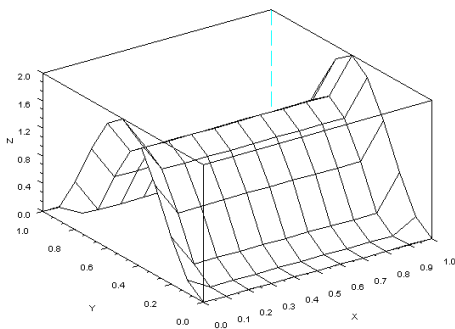


Fig. 3. The restored factor of chemical reaction k

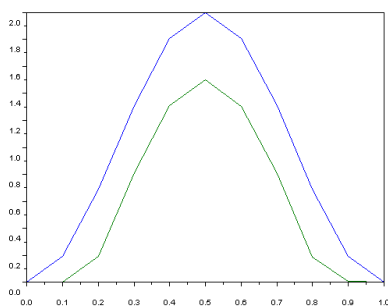


Fig. 4. The restored factor of chemical reaction k .

5. Conclusions

In this work inverse extremum problems for the convection-diffusion-reaction equation were formulated. On the basis of the analysis of the constructed system of an optimality the algorithm of the numerical solution of the inverse extremum problem is developed. The received algorithm laid down in the base of programs for the solution of inverse problems for model describing process of transfer of substance. As a result of the performed numerical experiments dependences of the solution of the inverse extremum problem on a number of parameters entering into studied model under study were revealed.

This work was supported by the Russian Foundation for Basic Research (project nos. 10-01-00219-a and 11-01-98508-r_vostok_a), and by the Far East Branch of the Russian Academy of Sciences (project nos. 12-III-A-01M-002) and by the Far East Branch of the Russian Academy of Sciences under the Programs for Basic Research of the Presidium of the Russian Academy of Sciences (project nos. 12-I-III7-03).

References

- [1] G.I. Marchook Mathematical modeling in the problem of environment protection. M.: Science. 1982. 319 p.
- [2] O.M. Alifanov, E.A. Artuhin, Roomayntcev C.V. Extremum solutions of ill-posed problems and their applications to inverse problems of heat transfer. M.: Science, 1988. 286 p.
- [3] A.A. Samarskii, P.N. Vabishevich Numerical methods of solving inverse problems of mathematical physics. 2004. 480 p.
- [4] G.V. Alekseev, D.A. Tereshko Analysis and optimization in viscous fluid hydrodynamics, Vladivostok: Dalnauka. 2008. 365 p.
- [5] G.V. Alekseev, Reports of Academy of Sciences, **416:6** (2007).
- [6] G.V. Alekseev, O.V. Soboleva, D.A. Tereshko, Applied. Mech. and Tech. Physics. **49:4** (2008).
- [7] I.S. Vakhitov, Far. Eastern Mathem Journal. **10:2** (2010). P. 93-105.
- [8] O.V. Soboleva, Far. Eastern Mathem Journal. **10:2** (2010). P. 170-184.
- [9] A.N. Tichonov, V.Ya. Arsenin, Methods of solving ill-posed problems. M.: Science. 1986. 288 p.
- [10] <http://www.scilab.org>
- [11] <http://www.freefem.org/ff++/index.htm>

Development of Safety and Quick-response Actuator using MR Fluid Clutch for Walk Rehabilitation Device

Hiroshi Nakano¹, Kohki Tsuchiya¹, and Masami Nakano²

¹Graduate School of Engineering, Tohoku University, 2-1-1 Katahira, Aoba-ku, Sendai, Japan

²Institute of Fluid Science, Tohoku University, 2-1-1 Katahira, Aoba-ku, Sendai, Japan
nakano@irs.mech.tohoku.ac.jp

ABSTRACT

The actuator of leg power assist device, which is used for walk rehabilitation, has been developed. This actuator mainly consists of the developed magneto-rheological (MR) fluid clutch and a reversible DC motor. Because MR fluid clutch produces passively the magnetic field-dependent transmitting torque almost independent of the rotational speed, it will be suitable for the power assist device of rehabilitation from a viewpoint of safety and relief. From the investigation of steady and transient performances of developed MR fluid clutch, we found that it is suitable for leg power assist device.

1. Introduction

For the power assist device of walk rehabilitation, it is necessary to have high torque, high controllability and high safety. The clutch using a magneto-rheological (MR) fluid generates the magnetic field-dependent transmitting torque almost independent of the rotational speed, because the MR fluid behaves like a Bingham fluid having variable yield stress with magnetic field. Because of this inherent feature, the use of MR fluid clutch will be suitable for an actuator of the power assist device of walk rehabilitation.

In this study, the MR fluid actuator, which consists of the MR fluid clutch and a motor, has been proposed and developed for the use of the leg power assist device, which assists the strength of knee extension and flexion during a walk rehabilitation. In this paper, the total design of the MR fluid actuator and the detailed design of the MR fluid clutch are described, and steady and transient performances of the clutch are investigated. The applicability of this actuator to the power assist device is discussed.

2. Design of MR fluid actuator

Figure 1 shows the structure of developed MR fluid actuator. The actively produced motor torque is transmitted to the MR fluid clutch through the gears (gear ratio of 5.4:1 and 15:1). The clutch torque, which is controlled by the applied coil current, is transmitted to the knee braces through the planetary gear (gear ratio of 5:1). The design goal of the clutch torque T is set to be

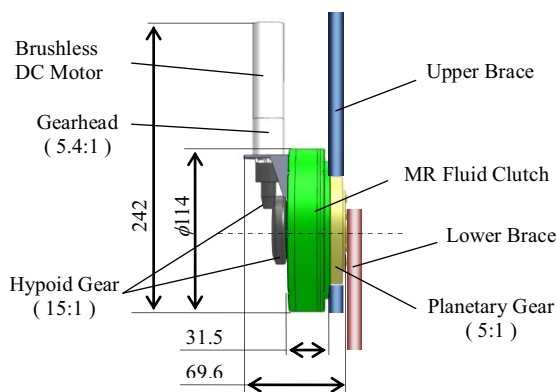


Fig. 1 Developed MR fluid actuator

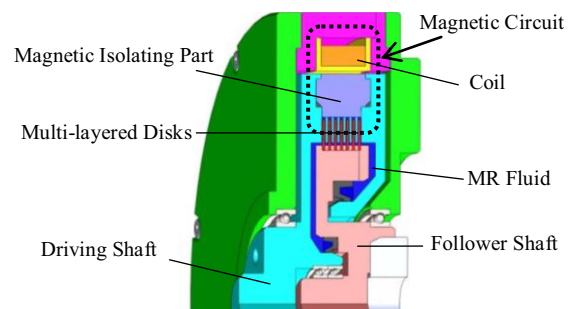


Fig. 2 Cross-sectional view of MR fluid clutch

4.5 Nm based on the requirements in the normal walking of healthy people, which is the knee torque of 20 Nm [1] and the knee rotational speed of 66 rpm [2].

In wearable power assist device, the actuator needs to be designed compactly. Therefore, the multi-layered disk type MR fluid clutch is designed as shown in Fig. 2. This clutch has 6 driving side disks (thickness of 0.5 mm), 7 follower side disks (thickness of 0.5 mm), and an MR fluid (MRF-132DG, Lord Co.) in the 14 gaps of 0.1 mm between the disks, and a magnetic coil (wire diameter; 0.3 mm, turns; 400, electric resistance; 29.9Ω) outside of the disks. The dashed line in Fig. 2 indicates the magnetic circuit, which is generated by a coil.

A steady magnetic field analysis using the JMAG (JSOL Co.) was done to optimize the design of the MR fluid clutch. Figure 3 shows the contour map of analytical steady magnetic flux density for an input coil current I of 1.0 A. It can be seen that the magnetic flux is mainly applied to the disk parts. As a result, the MR fluid particle clusters form in the gap between the drive and follower disks, and the torque T is transmitted. As shown in

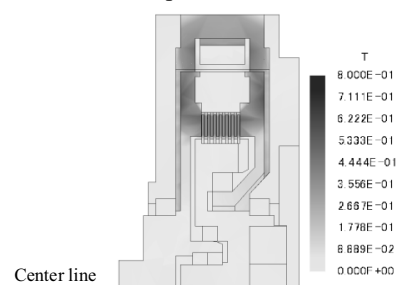


Fig. 3 Magnetic flux density distribution

Fig. 4(b), the predicted T increases in almost proportion to I . The predicted T is 7.4 Nm at $I=1.0$ A.

3. Experimental study

3.1. Steady responses of torque

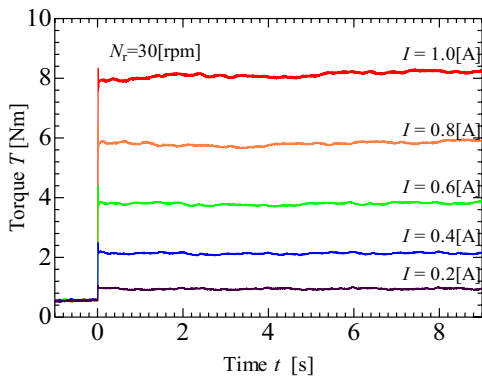
The measurements of steady T as a function of I from 0 to 1.0 A are conducted at constant rotational speed N_r of 10, 30, 50 and 100 rpm. As seen in Fig. 4(a), the MR fluid clutch generates almost constant T with time t at each I . Figure 4(b) shows that T increases with increasing I in a good agreement with the analytical one, a little depending on the rotational speed. It can be ensured that the MR fluid clutch generates T of at least 7.9 Nm at $I = 1.0$ A, and the MR fluid actuator generates the output torque of at least 39.5 Nm at $I = 1.0$ A.

3.2. Step responses of current and torque

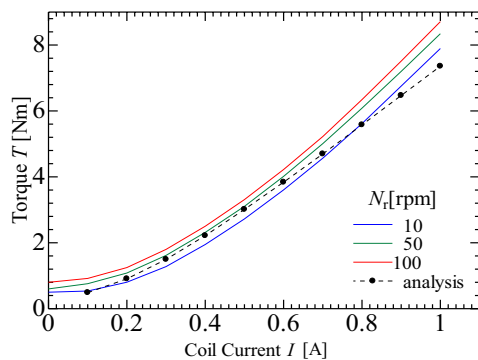
The transient responses of T and I are measured when step inputs of desired $I = 0.1\sim 1.0$ A are applied to a coil power supply (servo amplifier). Figure 5 shows the result of the desired I of 0.5 A. It can be ensured that this clutch is the second order lag element of torque, which has the rise time $T_r = 2.5\sim 5$ ms, the time to peak $T_p = 10\sim 14$ ms, the settling time $T_s = 20\sim 25$ ms and the pure time delay $L = 3$ ms.

3.3. Hysteresis of torque vs. current

The T is measured with I continuously changed from 0 through to 1.0 to 0 A at a constant N_r of 30 rpm. It



(a) Time variations of experimental torque for coil current



(b) Analytical and experimental steady torques vs. coil current.

Fig. 4 Steady torque responses

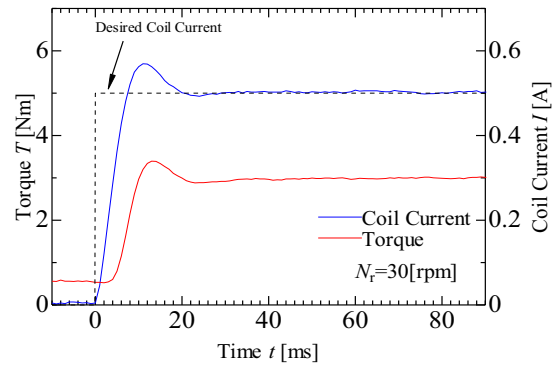


Fig. 5 Step responses of torque and coil current

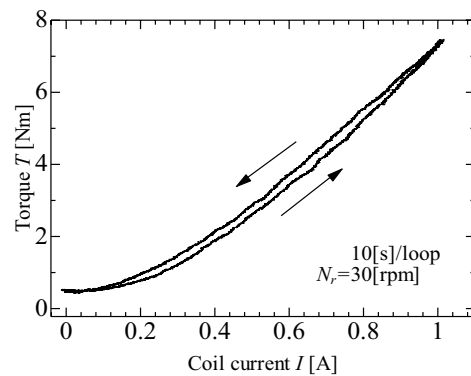


Fig. 6 Hysteresis loop of torque vs. coil current

takes 10 seconds to complete one cycle. The experimental result in Fig. 6 shows a little hysteresis of the T - I loop. At the end of loop, the difference of T becomes almost 0 Nm, meaning no residual magnetization.

3. Concluding remarks

The MR fluid actuator consisting of a servo motor and an MR fluid clutch for the use of the leg power assist device for rehabilitation is designed and manufactured, and the performances are investigated both analytically and experimentally. It is found from experiments for steady and transient torque responses of the developed MR fluid clutch that the MR fluid actuator is capable of generating the magnetic-field dependent torque up to 39.5 Nm for a coil current of 1.0 A and the MR fluid clutch has a high response speed of torque. The clutch has the features of high controllability and safety because of the above mentioned characteristics such as the low dependence on rotational speed, the simply controlled torque and the torque limiting function, showing that the developed MR fluid actuator is suitable for leg power assist device.

References

- [1] H. Kawamoto, Y. Sankai, Proc. IEEE ICSMC, 4 (2002), pp. 447-452.
- [2] Y. Hiiragi, M. Kato, H. Sato, H. Maruyama, Rigakuryoho Kagaku, 20(2) (2005), pp. 93-98.

Implementation of Surface Chemistry Models in SMILE++ Software System

Alexandra Shumakova, Alexander Kashkovsky, Mikhail Ivanov, Yevgeniy Bondar,
Khristianovich Institute of Theoretical and Applied Mechanics, 4/1 Institutskaya str., Novosibirsk, 630090, Russia.
shumakova@itam.nsc.ru

ABSTRACT

The phenomenological model of catalytic surface reaction suitable for particle DSMC computations was proposed and implemented in the SMILE++ software system. The effect of surface chemistry on the flow structure and distributed heat flux was examined using DSMC method for Mach 30 rarefied CO₂/N₂ flow comparing two limiting cases of non-catalytic and fully catalytic surface. The computational results demonstrate that even for rarefied flow the surface catalysis can contribute more than 10 % to the total heat flux to the body surface.

1. Introduction

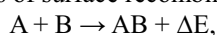
An accurate prediction of heat fluxes on space vehicles during atmospheric entry phase requires improvement of physical models and CFD codes, which are to be validated with experimental data in ground-based facilities. One of the greatest uncertainties concerning the numerical predictions of the spacecraft aerothermodynamics is related to the modeling of surface chemical reactions. Surface chemical processes have not been investigated as well as gas phase chemical reactions despite the fact that they can significantly contribute to a total heat flux to a spacecraft.

The numerical methods of continuum gas dynamics based on Navier-Stokes equations are inapplicable for high-altitudes aerothermodynamic predictions due to rarefaction and thermal non-equilibrium effects; therefore, the methods of rarefied gas dynamics as the Direct Simulation Monte Carlo (DSMC) method [1] should be employed in the computations. The SMILE++ software system [2] for numerical studies of spacecraft high-altitude aerothermodynamics by the DSMC method has been created at Khristianovich Institute of Theoretical and Applied Mechanics (ITAM). The system allows performing a complete cycle of numerical study from creation of three-dimensional geometrical model of spacecraft to visualization of numerical simulation results.

The main purpose of the present work is development of DSMC surface chemistry model to account for chemical processes on spacecraft surface and its implementation in SMILE++ software system. The study is mainly focused on the problem of Martian entry. The influence of surface catalysis on the flow structure and distributed surface heat flux in high-enthalpy CO₂/N₂ flow was studied using proposed surface chemistry model.

2. DSMC Surface Chemistry Model

The phenomenological catalytic surface model was proposed and implemented in SMILE++ software system. The parameters of the model are catalytic coefficients defined in the following manner. Lets consider the process of surface recombination reaction



where ΔE is an energy releasing in the reaction, which is fully accommodated by the surface. A and B can be both atomic and molecular species.

The procedure presented below is applied to every surface element (so called "panel") at every time step. The catalytic coefficients γ_A and γ_B are given both for the particle A and particle B for each recombination reaction in which they are involved. The catalytic coefficients assumed to be constant parameters depending only on the surface material and temperature. When particle A impinges on the surface it reflects from the surface without reaction with probability $1-\gamma_A$ according to usual reflection law (e.g. diffuse) or is selected for surface recombination reaction $A + B \rightarrow AB$ with probability γ_A .

There are two possible scenarios what can happen with the particle A selected for recombination: it can recombine with particle B or it can "stick" to the panel (it means that the particle doesn't move on, it stays at the panel for a while). First scenario occurs when there are particles B already stuck to the panel, in this case the particle A recombines with one of them. The second scenario occurs in the absence of particles B stuck to the panel. Note, that an integer parameter is chosen which limits the maximum number of particles of any species stuck to the panel. In the present study this parameter was chosen to be equal to 4. This means that if particle is chosen for recombination and there are 4 particles of the same species already stuck to the panel then this particle is reflected without recombination according to usual reflection law.

Note, that coefficients γ_A and γ_B do not equal to the probabilities of recombination. For example if there are no particles A presented in the flow the probability of recombination of the particle B can not be other than zero no matter what is the value of γ_B .

The two limiting cases of non-catalytic and fully catalytic surface are considered in the paper. In non-catalytic case no surface recombination occurs (γ_A and γ_B are equal to 0). In fully catalytic case both γ_A and γ_B are equal to 1. In fact this means that all the particles are selected for recombination and hence all particles, which can "find" a partner for recombination, recombine. Note, that this case is not similar to cases of fully catalytic wall considered in the continuum CFD when the values of mass fractions of species at the surface are set as a boundary condition. In the case of DSMC or Boltzmann equation the values of mass fractions at the surface cannot be explicitly set because they depend on the distribution function of impinging molecules and hence

can be determined only in the course of the flow simulation.

3. Results of Numerical Modeling

The implemented surface chemistry model was employed in numerical studies of the Mach 30 CO₂/N₂ flow about flat-faced 50 mm diameter cylinder with rounded edges by the SMILE++ software system. The geometry of the cylinder is shown in Fig. 1.

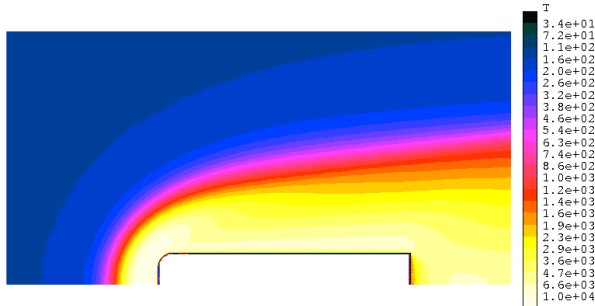


Fig. 1 Temperature flow field

The free stream conditions are presented in Table 1. The flow composition was 97 % of CO₂ and 3 % of N₂ by mass. The eight species were considered: C, O, N, CO, NO, O₂, N₂, CO₂. The reduced chemical mechanism of [3] containing 40 dissociation and 8 exchange reactions was used for gas phase reactions.

The surface was assumed to be non-catalytic in the first case and fully catalytic in the second case with temperature of 300 K. Considered surface reactions are:

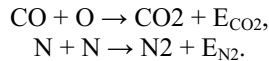


Table 1. Free stream conditions.

Velocity, m/s	5941.2
Temperature, K	155.2
Density, kg/m ³	3.21E-005
Knudsen number	2.68E-002

The translational temperature field is given in Fig. 1. The flow behind the bow shock wave heats up to temperatures higher than 10,000 K. The non-equilibrium dissociation of CO₂ occurs at such conditions. Figure 2 shows the profiles of the dissociation products' mass fraction (CO and O) along the stagnation streamline. In non-catalytic case the mass fraction of CO and O rises from zero values in the free stream up to 11 and 4 %, respectively, in the stagnation point. The catalytic reactions lead to significant decrease of the dissociation products' mass fractions. They drastically decrease in the vicinity of the stagnation point in the fully catalytic case; their stagnation point values are about four times lower than in non-catalytic case both for CO and O.

The effect of the surface chemistry on the heat transfer can be seen in Fig. 3, where the heat flux per unit area as a function of distance from the stagnation point along the body surface is presented. The

stagnation point heat flux in a case of fully-catalytic surface is 12 % greater than in a case of non-catalytic surface and it is generally greater along all of the front area of the cylinder. This effect is expected to become more pronounced for lower Knudsen number where the degree of dissociation in the shock layer is higher and hence more heat can be released in the course of the surface recombination.

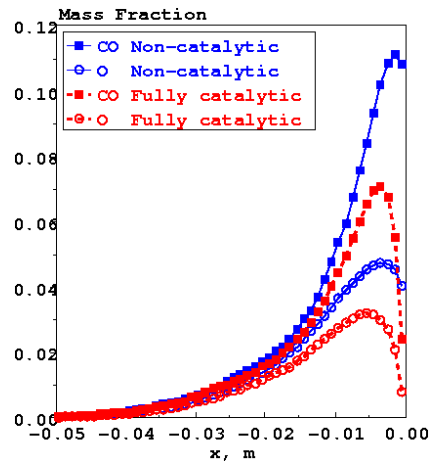


Fig. 2 Mass fractions of CO and O along the stagnation streamline

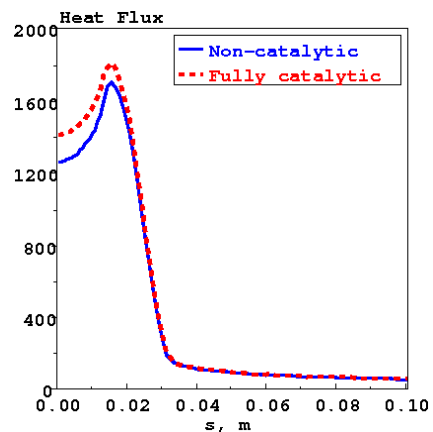


Fig. 3 Heat flux along the surface, kW/m²

Acknowledgments

The study was supported by the IFS Collaborative Research Project “Numerical studies of rarefied chemically reacting flows about space vehicles” and the SACOMAR project funded by the European Commission under Grant agreement No. 263210.

References

- [1] G. Bird, *Molecular gas dynamics and the direct simulation of gas flows*, Oxford Press, 1994
- [2] M. S. Ivanov, A. V. Kashkovsky, P. V. Vashchenkov, Ye. A. Bondar, Parallel Object-Oriented Software System for DSMC Modeling of High-Altitude Aerothermodynamic Problems, AIP Conf. Proc. 1333, 211 (2011), DOI:10.1063/1.3562650
- [3] C. Park, J. T. Howe, R. L. Jaffe, and G. V. Candler, *J. of Thermophysics and Heat Transfer*, vol. 8, no. 1, pp. 9–23, 1994

Atomistic Simulation of Proton and Water Transport in Hydrated Nafion Membrane

Takuya Mabuchi¹, and Takashi Tokumasu²

¹Graduate School of Engineering, Tohoku University, Sendai, Miyagi 980-8577 Japan

²Institute of Fluid Science, Tohoku University, Sendai, Miyagi 980-8577 Japan
mabuchi@nanoint.ifs.tohoku.ac.jp.

ABSTRACT

We have proposed a model of Nafion membrane based on DREIDING force field validated by comparing the density, water diffusivity, and Nafion morphology with experimental data. The simulated final density agrees with experiment within 1.3 % for various water contents. In addition to determination of diffusion coefficients of liquid molecules as a function of hydration level for dynamical validation, we have also calculated static structure factors among liquid molecules for mesoscopic structural validation. The diffusion coefficient of water molecules is found to be in good agreement with experimental data.

1. Introduction

Polymer electrolyte fuel cells (PEFCs) are one of the most promising systems for next-generation power supplies. They can be a reliable method to produce efficient and environmentally friendly energy for many uses. PEFCs use Perfluorosulfonic acid (PFSA) based membranes where protons transfer from anode to cathode, such as Nafion developed by DuPont. It is critical to increase the efficiency of proton transport in the membrane to make it in practical use since proton transport is one of the dominant factors controlling power generating efficiency. In the previous research, many macroscopic simulations treated as a continuous fluid have found difficult to discuss the structural and dynamics properties of proton because proton transport is largely attributed to the structure and dynamics in nanoscale [1].

To understand the quantitative transport of protons and water molecules in the nanoscopic and mesoscopic structure, we have used a molecular dynamics (MD) simulation which has been extensively applied to study the properties of PFSA membranes [2-4]. However, their molecular models of PFSA membranes have not been precisely reproduced in terms of membrane density and mesoscopic morphology at various water contents. In this study, we have performed an atomistic analysis of the vehicular transport of hydronium ions and water molecules in the nanostructure of hydrated Nafion membrane using classical molecular dynamics simulations with a model of Nafion membrane which is newly modified and validated by comparing the density, water diffusivity, and PFSA morphology with experimental data. It is critical to understand a connection between the nanoscopic and mesoscopic structure of ion clusters and the dynamics of hydronium ions and water molecules in the hydrated Nafion.

2. Method

The Nafion membrane was used as PFSA membrane. It was assumed that all sulfonate groups SO_3H were ionized to H^+ and SO_3^- in water. Nafion consists of hydrophilic SO_3^- -terminated pendants spaced evenly by seven nonpolar $-\text{CF}_2-\text{CF}_2-$ monomers (N) that form a hydrophobic backbone. We generated Nafion by linking

the polar monomeric unit (P) to the end of the nonpolar monomeric unit N_5 , repeating the procedure thirteen times to obtain $(\text{N}_7\text{P})_{13}$, in the notation of Jang et al. [6]. The potential model for Nafion was based on the DREIDING force field as referred to previous studies by other authors [5, 6] and we modified it to fit the experimental property of Nafion by adjusting the parameters of torsion potential. The flexible three-center (F3C) model [7] for water molecules and classical hydronium model [5] for hydronium ions are employed.

The initial configurations were generated by randomly placing 25 Nafion chains in a box, $x \times y \times z = 200 \times 200 \times 200 \text{ \AA}^3$, with periodic boundary condition in all directions. To ensure charge neutrality, we added a total of 325 hydronium ions and considered water contents of $\lambda = 3, 6, 12, \text{ and } 18$, where the parameter λ indicates the ratio of the number of water molecules to that of SO_3^- ($N_{\text{H}_2\text{O}, \text{H}_3\text{O}^+}/N_{\text{SO}_3^-}$). After all molecules were added, the annealing procedure was carried out to eliminate initial configuration and orientation of molecules and to establish equilibrium state. Firstly, the simulation cell was compressed gradually for 50 ps to fit with experimental density [8], and *NPT* MD simulation for 100 ps at 800 K and 100 MPa using the reduced to 1/100 magnitude of L-J potential parameters, ϵ , among Nafion atoms [4]. After that, *NPT* MD ensemble for 50 ps with the temperature and pressure gradually decreased from 800 to 300 K and 100MPa to 0 MPa, respectively. In addition, we annealed it in four steps as follows: 1. *NPT* MD simulation for 100ps at 300 K; 2. *NVT* MD simulation for 50 ps with the temperature increased gradually from 300 to 800 K; 3. *NVT* MD simulation for 50 ps at 800 K; 4. *NVT* MD simulation for 50 ps with the temperature decreased gradually from 800 to 300 K. We repeated these four steps four times and confirmed that the density variation rate by annealing procedure is less than 0.1 %. The final density was then obtained after *NPT* MD run for 200 ps at 300 K. The final density is shown in Fig. 1 with experimental density for various water contents. The agreement with experiment is within 1.3 % for all λ . Under similar conditions, the density of Nafion tends to be lower in other studies [2-4]. We used this final structure for the production *NVE* ensemble for 2.4 ns and the trajectory of molecules was collected every 0.2

ps. The temperature was held by the Nosé-Hoover thermostat [9], and the pressure was controlled by the Andersen method [10]. The multiple time method, r-RESPA [11], was employed for the time integration technique, such as intra-molecules for 1 fs, inter-molecules for 2 fs, and the long distance term in the PME method for 4 fs.

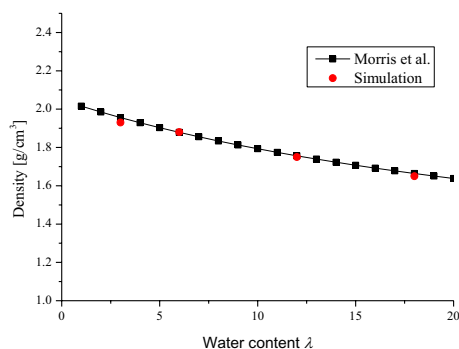


Fig. 1 Simulated density and experimental density of Nafion as a function of λ .

3. Results and discussion

The self-scattering of liquid molecules including hydronium ions and water molecules at various water contents is determined and displayed for $\lambda = 3$ and 18 in Fig. 2. The first peak on the low wave length can be found as 0.259, 0.256, 0.247, and 0.200 \AA^{-1} , respectively, at $\lambda = 3, 6, 12,$ and 18. From these values, the periodic structure distance, d , which is obtained from the expression $q = 2\pi/d$, can be found as 24.3, 24.5, 25.4, and 31.4 \AA at $\lambda = 3, 6, 12,$ and 18, respectively. Gebel [12] reported that an inter-cluster distance increases from 27 to 30 \AA comparing the dry membrane and the swelling membrane based on small-angle X-ray scattering (SAXS) and small-angle neutron scattering (SANS). The periodic structure distance at the low wave length from our simulation, which implies an inter-cluster distance, increases as hydration level increases and is consistent with the experimental data [12].

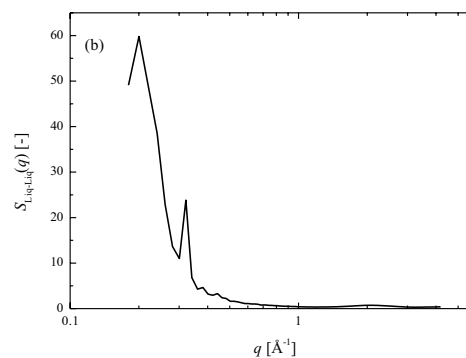
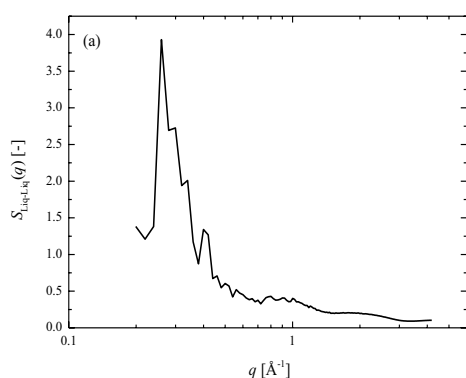


Fig. 2 Self-scattering function of liquid molecules (a) $\lambda = 3$ and (b) $\lambda = 18$.

4. Concluding remarks

We have performed an atomistic analysis of the vehicular transport of hydronium ions and water molecules in the nanostructure of hydrated Nafion membrane by systematically changing the hydration level using classical molecular dynamics simulations. The models of Nafion membrane based on DREIDING force field with modification of torsion potential are proposed and validated by comparing the density, water diffusivity, and Nafion morphology with experimental data. After annealing procedure, the final density agreement with experiment is within 1.3 % for various water contents and the trends that density decreases with increasing hydration level are reproduced. The static structure factors of H_2O molecules and H_3O^+ ions provide insights into the periodic structure of the inter-clusters which are consistent with the Gebel's model based on small-angle X-ray and neutron scattering that considers the inter-clusters of distance change from 27 to 30 \AA with increasing hydration.

References

- [1] Y. Wang, K.S. Chen, J. Mishler, S.C. Cho, X.C. Adroher, *Appl Energ*, 88 (2011) 981-1007.
- [2] A. Venkatnathan, R. Devanathan, M. Dupuis, *Journal of Physical Chemistry B*, 111 (2007) 7234-7244.
- [3] R. Devanathan, A. Venkatnathan, M. Dupuis, *Journal of Physical Chemistry B*, 111 (2007) 13006-13013.
- [4] S. Ban, C. Huang, X.Z. Yuan, H.J. Wang, *Journal of Physical Chemistry B*, 115 (2011) 11352-11358.
- [5] S.S. Jang, V. Molinero, T. Cagin, W.A. Goddard, *Journal of Physical Chemistry B*, 108 (2004) 3149-3157.
- [6] T. Li, A. Wlaschin, P.B. Balbuena, *Ind Eng Chem Res*, 40 (2001) 4789-4800.
- [7] M. Levitt, M. Hirshberg, R. Sharon, K.E. Laidig, V. Daggett, *Journal of Physical Chemistry B*, 101 (1997) 5051-5061.
- [8] D.R. Morris, X.D. Sun, *J Appl Polym Sci*, 50 (1993) 1445-1452.
- [9] W.G. Hoover, *Phys Rev A*, 34 (1986) 2499-2500.
- [10] H.C. Andersen, *J Chem Phys*, 72 (1980) 2384-2393.
- [11] M. Tuckerman, B.J. Berne, G.J. Martyna, *J Chem Phys*, 97 (1992) 1990-2001.
- [12] G. Gebel, *Polymer*, 41 (2000) 5829-5838.

A Study on the Effect of Surface Tension on Gas-Liquid Free Interface in the Application of Micromixing

Takashi Yamada and Naoki Ono

Department of Engineering Science and Mechanics, Shibaura Institute of Technology
3-7-5 Toyosu Koto-ku, Tokyo 135-8548, Japan
na12104@shibaura-it.ac.jp

ABSTRACT

For development of instant mixing in capillary channel on micro scale, we attempted to build micromixing device utilizing a gas-liquid free interface. In this study, some types of test channels which were straight-flow micro channel with a bending point of 90 degrees were designed. The device was constructed by a gas-liquid free interface in the bending point. The test channels were experimented to investigate mixing quality with the two liquids having different surface tension. As a result, remarkable effect of the advancement of 40% of mixing rate just near the gas-liquid free interface was achieved.

1. Introduction

In micro scale, mixing acceleration has depended on molecular diffusion by taking small diffusive distance as the primary mixing improvement of micromixer because of very small Reynolds number of the flow condition in that area[1]. Otherwise, the micromixing process has been developed by using electrokinetic effect or acoustic wave at liquid-liquid or gas-liquid free interface in biochemistry area. These studies have suggested that some definite effect was found by using instability on the interface about the mixing acceleration [2].

In this study, the mixing device utilizing Marangoni effect as a physical phenomenon caused by the imbalance of surface or interfacial tension on the interface was made and evaluated on mixing performance which contains to raise the mixing speed and quality.

2. The mechanism of the mixing device

In this study, the mixing device was built in the elbow point of L-type micro channel as straight-flow micro channel with bending point of 90 degrees. The outline of the mixing process is shown in Fig.1.

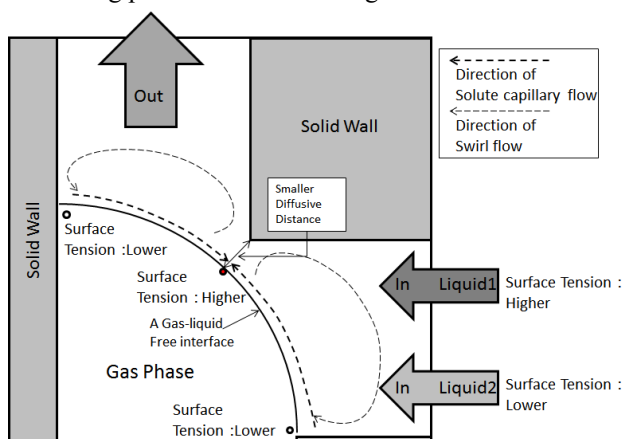


Fig.1 The mechanism of the mixing device by using the effect of Marangoni convection depending on concentration difference

When a gas-liquid free interface was put and expanded in the elbow area and the two fluids having different value of surface tension flowed into the area, it

made narrow space between the interface and inner wall at that place and the mixing of the two fluids at the local area would be developed. Therefore, it would make imbalance of the surface tension which was caused by concentration difference between the two fluids, and Marangoni convection as the flow was caused by the different surface tension just on the interface. Then it led to swirl flow to accelerate mixing in the area.

3. Method

The basic design and dimensions of the device is shown in Fig.2. The device to keep a gas-liquid free interface was built in the elbow point of the L-shaped channel.

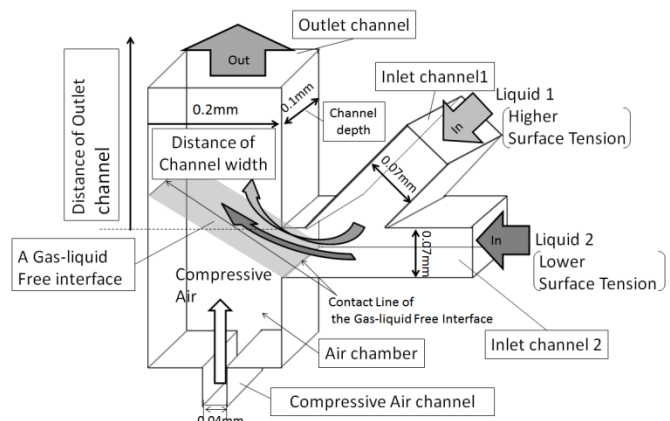


Fig. 2 Basic design at the elbow point of test channel

Three types of test channels for mixing experiments were made by photo lithography [3] as shown in Fig.3. Both Type-1 and 2 channels had no device to make the gas-liquid free interface as mixing device, but Type-2 channel had a solid structure which has quite same form of the interface built in Type-3 channel. Test fluids for the experiments were adopted the two solutions as pure water with 1.4wt% of blue dye containing the mixture of Brilliant Blue FCF (8%) and Dextrin (92%) at inlet 1 and 40wt% of acetic acid aqueous solution at inlet 2 in Fig. 2 respectively. As the evaluation of the mixing rate, maximum value of relative concentration difference was calculated by the information of brightness in the photo images of the flow experiments. Physical properties of

the two solutions are shown in Table 1. Experimental setup was same as previous studies in our laboratory [4]. Volume flow rate of both test fluids were same value of $0.8\mu\text{l}/\text{min}$ in the mixing experiments.

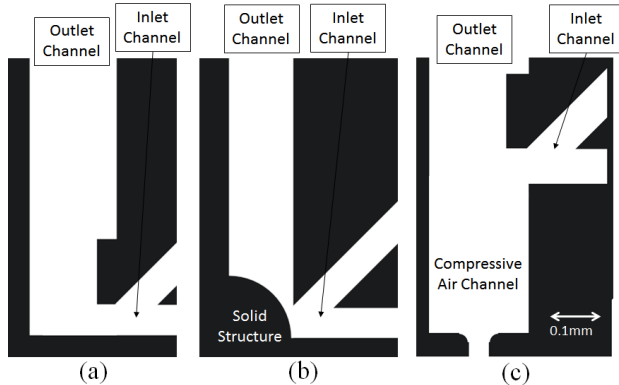


Fig.3 Designs of junction point including bubble holding section into each test channel, (a) Type-1, (b) Type-2 and (c) Type-3

Table 1 Physical property of the two fluids in the experiments

Test fluids	Surface tension	Viscosity
Pure water with blue dye 1.4wt%	69.0 (mN/m)	0.96 (mPa·s)
Acetic acid solution 30wt%	42.7 (mN/m)	1.75 (mPa·s)

4. Results and Discussion

Photos of the mixing experiments using Type-1, 2 and 3 channel and results of maximum concentration difference throughout the cross section in the each point at every 1mm of the outlet channel are illustrated in Fig. 4 and 5, respectively.

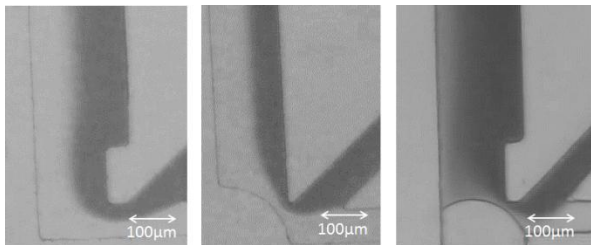


Fig.4 Photos of the mixing experiment of the test channels, (a) Type-1, (b) Type-2 and (c) Type-3 channel, volume flow rate; $0.8\mu\text{l}/\text{min}$ in each inlet

It is note that Fig.4 (a), (b) are quite obscure than Fig.4 (c), but these images were recorded under same environment and condition to the experiments, and made to confirm the different mixing character by gas-liquid free interface. In Fig.4, the mixing acceleration was not observed near the elbow point in both Type-1 and 2 channels, but in Type-3 channel, it could be seen near the gas-liquid free interface at the elbow point widely. Similarly, in Fig. 5, it was confirmed that the mixing development between the two test-fluids was completed about 40%. But it was noted that the value of diffusive coefficient of the blue dye solution ($1.67 \times 10^{-10} [\text{m}^2/\text{s}]$ at 20 degrees [4]) was smaller than that of acetic acid ($1.24 \times 10^{-9} [\text{m}^2/\text{s}]$ at 25degrees [5]), and then the concentration distribution of the blue

dye in Fig. 5 did not reflect that of acetic acid solution directly.

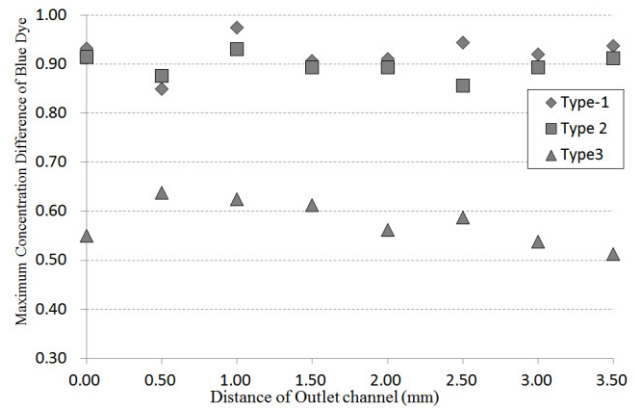


Fig.5 Results of maximum concentration difference of blue dye at some distances of outlet channel of Type-2 and 3 channels in the mixing experiments

However, it could be thought that the result of Fig.5 suggests the mixture between the two liquids having different surface tension was enhanced by the driving force depending on the different surface tension just on the gas-liquid free interface. Then the mixing ability was improved by considering the design in the mixing device, especially the bubble location.

4. Concluding Remarks

In this study, three test channels for mixing device which contained a gas-liquid free interface at the elbow point of L-type channel with a bending point of 90 degrees, were made and experimented to investigate mixing performance with the two fluids having different surface tension. As a result, at $0.8\mu\text{l}/\text{min}$ of volume flow rate in both test fluids, it was confirmed that the mixing rate near the gas-liquid free interface was enhanced widely in Type-3 channel. In the future, the visualization of the flow near the gas-liquid free interface in the mixing device and replacing the gas-liquid free interface with some liquid-liquid interface will be investigated.

References

- [1] V. Hessel, H. Löwe and W. Ehrfeld, Micromixers - a review on passive and active mixing principles, *Chemical Engineering Science* 60 (2005), 2494-2501.
- [2] N. T. Nguyen, and Z. Wu, Micromixers - a review, *Journal of Micromechanics and Microengineering*, 15, (2005)
- [3] E. Kazawa, T. Ueno, and T. Shinoda, High-aspect-ratio lithography for micro module fabrication, *Bulletin of Tokyo metropolitan industrial technology research institute* No. 5 (2002).
- [4] T. Yamada, N. Kato, K. Takeda and N. Ono, A Basic Study of a Straight-Flow Micromixing Device Utilizing a Very Thin Liquid Film, *Journal of Fluid Science and Technology*, vol.7, 64-77, (2012)
- [5] National Research Council, *International critical tables of numerical data, physics, chemistry and technology*, McGraw-Hill, 1926-30, vol.5 p.63

Numerical Study of the Effect of Cavitation Models on the Cavitating Flow Induced by Underwater Explosion in a Rectangular Tube

Taketoshi Koita¹, Mingyu Sun²

¹ Graduate School of Engineering, Tohoku University, 6-3 Aoba, Aramaki aza, Aoba-ku, Sendai 980-8578, Japan

² Institute of Fluid Science, Tohoku University, 2-1-1 Katahira, Aoba-ku, Sendai 980-8577, Japan
koita@iswi.cir.tohoku.ac.jp

ABSTRACT

Numerical analysis of cavitation generated by underwater explosion in a rectangular tube was carried out with equilibrium and non-equilibrium models of a modified Merkle's cavitation model. Two numerical models based on different definitions of sound speed for the cavitation region are also tested. One is the classic homogeneous sound speed, and the other introduces a modification in the equilibrium model, in which the liquid sound speed is adopted if the vapor volume fraction is below certain threshold value. The front velocities of cavitation zone obtained from these models were quantitatively compared with the experimental result.

1. Introduction

In experimental study of the bubble generation and water jet formation induced by the underwater explosion in the rectangular tube, cavitation bubbles are observed between the bubble and the bottom wall [1]. These cavitation bubbles are formed because of the low pressure generated by the blast wave reflected from the bottom wall [2]. In experiments, the formation and features of the cavitation have been observed with a high repeatability. These results can be therefore served as a test case to evaluate the cavitation model for highly unsteady and possibly non-equilibrium flows.

In our previous study, the equilibrium cavitation model has been compared with the model coupled with a mechanically non-equilibrium model has been tested. It is found that the front velocity of cavitation zone is affected significantly by the definition of the sound speed of the two-phase cell [2]. In this study, the non-equilibrium cavitation model is tested, and the time histories of cavitation front velocity are compared with the above-mentioned models.

2. Numerical method

The cavitating flow is calculated with the inviscid 2-pressure 2-velocity two-fluid model. The discretization is employed with the finite volume method. A semi-implicit Lagrange-Remap method [3] is used to deal with all-speed two-phase flows. In this method, basic equations are calculated implicitly in the Lagrange frame, and the resulting linear sparse matrix is solved by the ILU+GMRES method. The updated conservative quantity in the Lagrange frame is remapped back to the Euler frame, using the formulas which are formally the same as the finite volume method. In each mix cell that contains either one large interface or small bubbles, a subgrid model [4] is used to approximate the interactions between two phases at the level of subgrid scale. The EOS of gas and liquid phase are the equation of ideal gas and the Tait EOS respectively.

In this study, the original Merkle's cavitation model developed for the one-fluid model is modified to the two-fluid model [5]. The averaged pressure of two phases in a cell, \tilde{p} , is adopted as that used in the one-fluid model. Since the total mass M is not changed,

the modified cavitation model is described, for the liquid phase mass, m_l

$$\text{evaporation: } \frac{\partial m_l}{\partial t} = k_E \cdot m_l \cdot (\tilde{p} - p_{st}) \quad (1)$$

$$\text{condensation: } \frac{\partial m_l}{\partial t} = k_C \cdot (M - m_l) \cdot (\tilde{p} - p_{st}) \quad (2)$$

where k_E and k_C represent the rate of evaporation and condensation, are calculated with $C_E = 1.0 \times 10^3$, $C_C = 1.0 \times 10^3$ and a typical length scale of the flow field L_∞ .

$$k_E = \frac{C_E}{0.5 \rho_\infty U_\infty^2 t_\infty} \quad k_C = \frac{C_C}{0.5 \rho_\infty U_\infty^2 t_\infty} \quad (3)$$

$$t_\infty = \frac{L_\infty}{U_\infty} \quad (4)$$

The averaged pressure of two-fluid in a cell, \tilde{p} , is

$$\tilde{p} = \frac{\beta_v \cdot p_l + \beta_l \cdot p_v}{\beta_l + \beta_v} \quad (5)$$

$$\beta_l = \frac{c_l^2 m_l}{\Omega_l^2} \quad \beta_v = \frac{c_v^2 m_v}{\Omega_v^2}, \quad (6)$$

where subscript l and v denote liquid and vapor phase respectively, p is pressure, Ω is volume, and c is sound speed. p_{st} is the saturated vapor pressure at the temperature of a cell, and is calculated from the Tetens equation. In order to get a stable and non-iterative solution, equations (1) and (2) are further linearized in the neighborhood of equilibrium, denoting the liquid mass in equilibrium, m_{le} ,

$$\text{evaporation: } \tilde{p} < p_{st}, \quad \frac{\partial m_l}{\partial t} = \lambda_E (m_l - m_{le}) \quad (7)$$

$$\text{condensation: } \tilde{p} > p_{st}, \quad \frac{\partial m_l}{\partial t} = \lambda_C (m_l - m_{le}) \quad (8)$$

$$\text{where, } \lambda_E = k_E [(m_{le} f'(m_{le}) + f(m_{le}))] \quad (9)$$

$$\lambda_C = k_C [(m_{ve} f'(m_{ve}) + f(m_{ve}))] \quad (10)$$

$$f(m_{le}) = p_e - p_{st} \quad (11)$$

The liquid phase mass m_l , after time Δt , can be immediately solved, by the exact solution to the ODEs,

$$m_l = m_{le} + (m_{l0} - m_{le}) \cdot e^{(\lambda \Delta t)} \quad (12)$$

m_{le} is calculated as follows. At the equilibrium point,

$$\left(\frac{\partial m_l}{\partial t} \right)_{m_{le}} = 0 = \begin{cases} k_E m_{le} f(m_{le}) \\ k_C (M - m_{le}) f(m_{le}) \end{cases} \quad (13)$$

In the equation (13), when $0 < m_{le} < M$,

$$f(m_{le})=0 \Rightarrow p_{le} = p_{ve} = p_e = p_{st} \quad (14)$$

with $m_{le} + m_{ve} = M \Rightarrow \rho_{le}\Omega_{le} + \rho_{ve}\Omega_{ve} = \rho\Omega$ (15)

$$\Omega_{le} + \Omega_{ve} = \Omega \quad (16)$$

From equations (15) and (16),

$$\Omega_{le} = \frac{\rho - \rho_{ve}}{\rho_{le} - \rho_{ve}} \Omega \quad (17)$$

where, $\rho_{le} = \rho_l(p_e)$ and $\rho_{ve} = \rho_v(p_e)$ can be derived from their EOS. Therefore,

$$m_{le} = \begin{cases} 0 & (m_{le} < 0, \rho < \rho_{le}, p_e < p_{st}) \\ \rho_{le}\Omega_{le} = \frac{\rho - \rho_{ve}}{\rho_{le} - \rho_{ve}} \rho_{le}\Omega & (0 < m_{le} < M, p_e = p_{st}) \\ \frac{\rho_{le} - \rho_{ve}}{M} \rho_{le}\Omega & (m_{le} > M, \rho > \rho_{le}, p_e > p_{st}) \end{cases} \quad (18)$$

In the numerical model with a different definition for the two-phase sound speed (c^*),

$$c^* = \begin{cases} c_{\text{homogeneous}} & (\sigma > \varepsilon) \\ c_{\text{water}} & (\sigma \leq \varepsilon) \end{cases} \quad (19)$$

where σ is the vapor volume fraction, and ε is the threshold value under which the water sound speed is compared with the homogeneous sound speed. When ε is zero, the formulae become the homogeneous two-phase sound speed. The threshold value ε is varied from 0.0% to 0.2%. The effect of the two-phase sound speed on numerical solution is investigated in the equilibrium model.

Fig.1 shows the initial grid after analysis is started. The bubble is employed as the vapor and is set at $(x, y) = (0, 0)$. The region of $-140\text{mm} < y < 15\text{mm}$ is water and that of $15\text{mm} < y < 140\text{mm}$ is vapor. Initial bubble conditions are calculated with the energy conversion coefficient $\alpha = 0.3$ at the voltage $V = 4.5\text{kV}$ [2]. The traditional solution-adaptive grid technique is employed and the refinement level 4 is used.

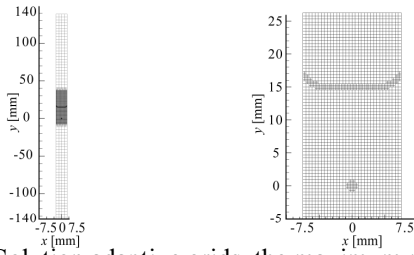


Fig.1 Solution adaptive grids, the maximum refinement level = 4: (a) Overall initial grid, (b) Zoomed view of the bubble and water surface

3. Results and Discussion

Fig.2 shows the numerical result of time variation of volume fraction analyzed by non-equilibrium cavitation model. In Fig.2, the cavitation region appears between the bubble and the bottom wall. This model can also analyze the cavitating flow in a tube. Fig.3(a) shows time histories of the front velocity of the cavitation zone obtained by equilibrium and non-equilibrium cavitation model. Both models reproduce the formation and the disappearance of the cavitation zone. The predicted velocity are slightly lower than the experimental result. The results obtained by the model with sound speed definition (ε) are plotted in Fig.3(b). It is clearly seen

that the front velocity of it varies with ε and it increases as ε becomes large. It seems that the numerical model defined by the present sound speed with a properly defined ε can be more accurate than that by the non-equilibrium model.

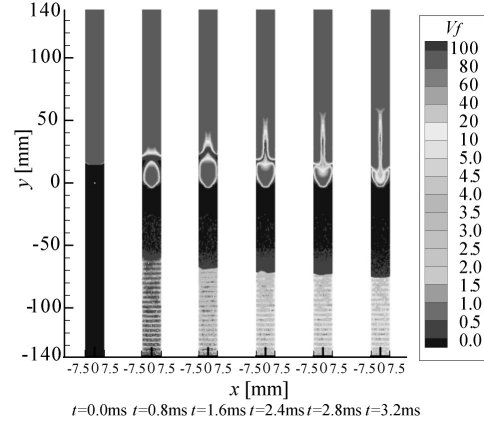


Fig.2 Gas volume fraction in a tube using the non-equilibrium cavitation model

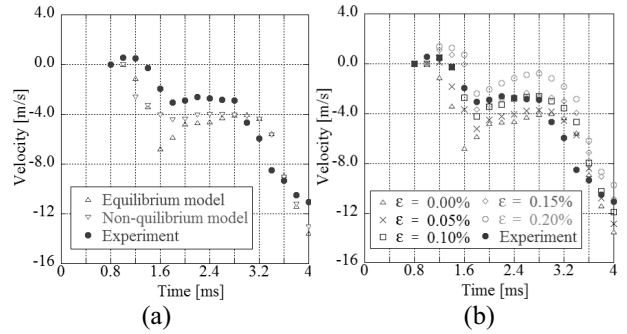


Fig.3 The front velocity of the cavitation zone: (a) results of equilibrium and non-equilibrium cavitation models; (b) results of different sound speed definition (ε) in the equilibrium cavitation model. Numerically, the vertical location where volume fraction is equals to 1.0 in the tube center is set to be the front of the cavitation zone.

4. Concluding remarks

Numerical analysis is carried out with equilibrium and non-equilibrium model of modified Merkle's cavitation model. The front velocity of cavitation zone predicted by the non-equilibrium model is similar to that of equilibrium model at the initial stage. The numerical model with a different definition for the two-phase sound speed has a similar effect on the front velocity, as the non-equilibrium model.

References

- [1] T. Koita, Y. Zhu, M. Sun, 28th International Symposium on Shock Waves, (2011).
- [2] Taketoshi Koita, Mingyu Sun, 25th Symposium on CFD, Japan, (2011),C7-3.
- [3] Kazuyuki Yada, Motoaki Shito, Mingyu Sun, 24th Symposium on CFD, Japan, (2010), C3-3.
- [4] M. Sun, 24th Computational Fluid Dynamics, (2010), A8-2.
- [5] Y. Zhu, M. Sun, AFI/TFI-2010,(2010), PS1-7

Scalability Study of Water Treatment System with Multiple Plasmas in Gas-bubbles

Hayato Obo, Nozomi Takeuchi and Koichi Yasuoka

Department of Electric and Electronic Engineering, Tokyo Institute of Technology, Tokyo 152-8552, Japan
obo@plasma.ee.titech.ac.jp

ABSTRACT

Plasma generation in bubbles has been widely studied due to their energy-efficient decomposing abilities, particularly for persistent substances. Plasma-water interactions are crucial for efficient decomposition, and thus, a new technique for synchronization of plasma generation in gas bubbles has been developed by combining pressure control of the gas chamber and pulsed plasma generation. Using this method, the plasma can be generated within bubbles via 10 holes to decompose about 10 times as much perfluorooctanoic acid (PFOA) solution as traditional methods.

1. Introduction

In recent years, studies using plasma decomposition of harmful chemical substances in water such as persistent dioxins have been conducted. Organofluoric compounds that are not decomposed by conventional methods such as the advanced oxidation process, which involves the use of hydroxyl radicals, can be decomposed using plasma generation within bubbles in water [1]. Fig. 1 shows perfluorooctanoic acid (PFOA), a chemical widely used for manufacturing industrial and commercial products due to its chemical stability and desirable physical characteristics. Biopersistence and unexpected toxicity, however, have raised environmental concerns regarding its use. PFOA can be decomposed by DC plasma generated within bubbles in the treatment water. Fig. 2 shows a schematic of the DC plasma reactor. The plasma reactor consists of a hole with a diameter of 0.3 mm for the generation of plasma and bubbles, a cooling tube, and a grounded electrode placed in 20 mL of solution. DC voltage is applied through a ballast resistor to generate stable plasma within the bubbles. Organofluoric compounds are considered to decompose at the interface of the plasma and the treatment water. However, this method is unable to decompose large amounts of treatment water using a reactor with one hole because of the limited ability of a single hole to generate plasma. Here, we present a new plasma reactor with 10 holes to generate plasma for PFOA decomposition.

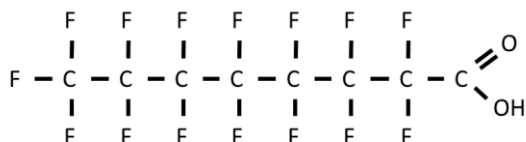


Fig. 1 Chemical structural formula of PFOA.

2. Experimental setup

Fig. 3 shows the schematic diagram of the experimental setup, which consists of a 10-hole reactor, a bubble controller, a high-voltage circuit to generate plasma, and a signal generator (National Instruments, cDAQ-9174, NI 9402, NI 9263). The bubble controller can generate bubbles from all 10 holes by creating pressure waves in the gas flow from the vibration of a speaker cone driving a sawtooth control signal. The system can then generate plasma from all 10 holes in

synchrony with bubble generation. Fig. 4 shows a timing chart of the control signals for bubble generation and plasma generation. The rising edge of the sawtooth signal can generate bubbles, and the slowly dropping edge can prevent treatment water from flooding the bottom of the reactor. The initial PFOA concentration and volume were 45 mg/L and 200 mL, respectively. Injecting argon gas into the solution at a flow rate of 500 sccm formed argon bubbles in the solution. The of bubble generation period (T_{saw}), delay time for plasma generation after bubble generation (T_{delay}), and discharge time of the plasma (T_{d}) were 20 Hz, 5 ms, and 5 ms, respectively. The high-voltage power supply was set to 5 kV.

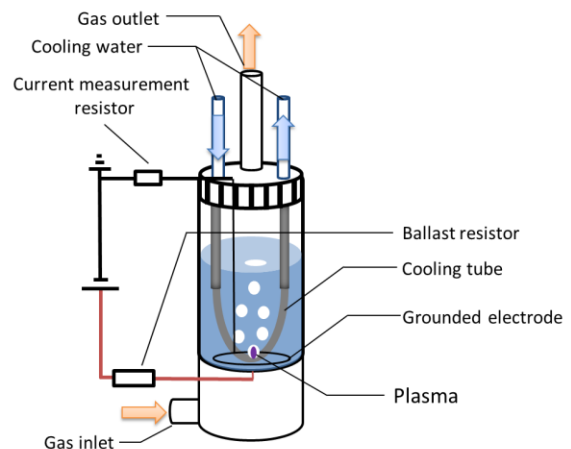


Fig. 2 Schematic of the DC plasma reactor.

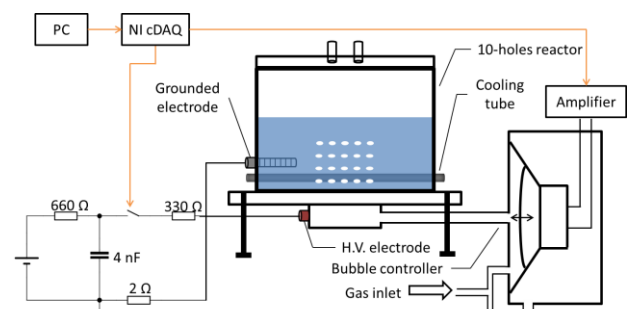


Fig. 3 Schematic diagram of the experimental setup.

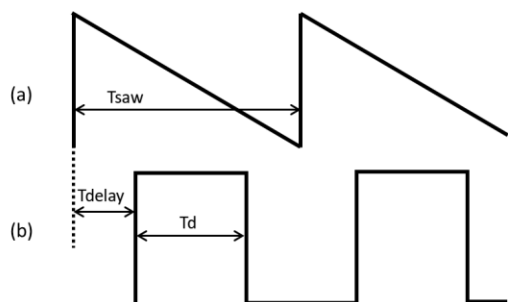


Fig. 4 Timing chart of control signals. (a: bubble generation, b: plasma generation)

3. Results and Discussion

Fig. 5 shows images of plasma within bubbles with different discharge times (T_d). White broken lines indicate the ceramic plate with 10 holes. Plasma is generated in all holes, and the emission of plasma increases with the discharge time. Fig. 6 shows typical voltage and current waveforms of the reactor. The voltage and current rose in response to the signal for plasma generation and failed. The power of the plasma generation was calculated to be 60 W when the frequency of the bubble generation (T_{saw}) was 20 Hz. Fig. 7 shows PFOA concentration as a function of the input energy per unit volume. The PFOA concentration decreased exponentially with input energy in the same manner as a conventional reactor with single plasma source. We have successfully developed this new reactor with up to 10 times the volume capacity of conventional reactors.

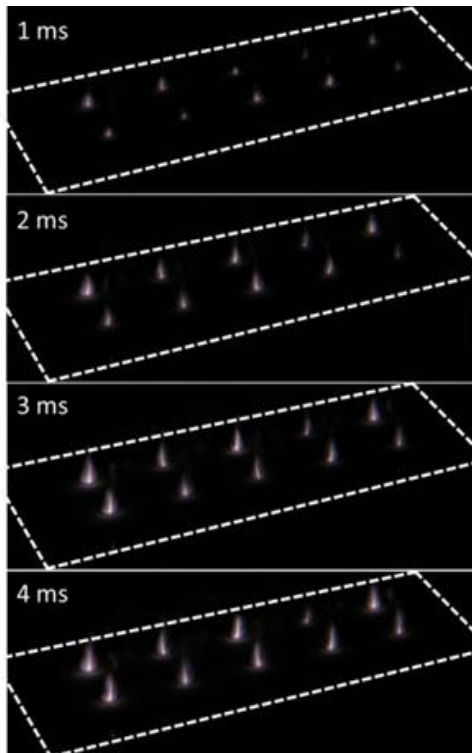


Fig. 5 Images of plasma within bubbles for different discharge times after the initiation of bubble generation.

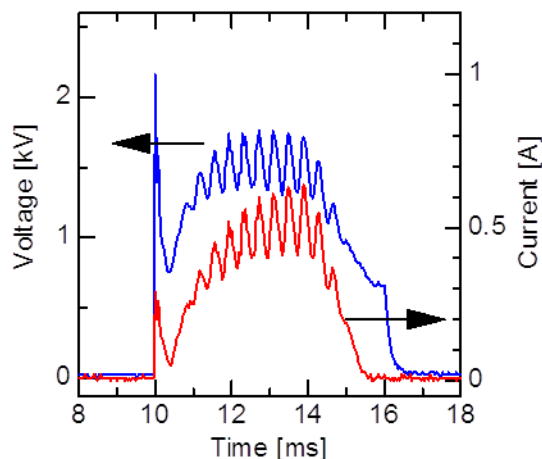


Fig. 6 Typical voltage and current waveforms with argon in a 50 mg/L PFOA solution.

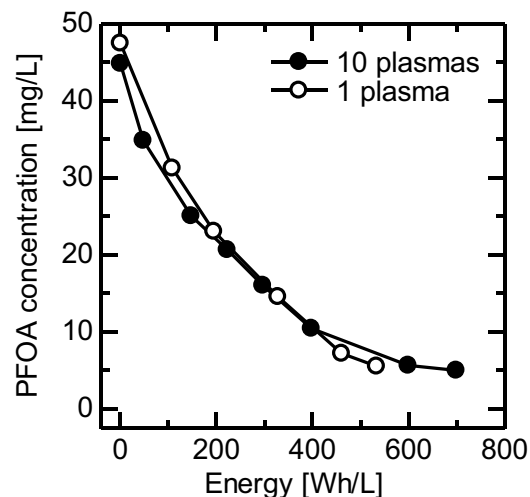


Fig. 7 PFOA concentration as a function of the input energy per unit volume.

4. Conclusion

A reactor with 10 times the volume capacity of conventional reactors was successfully developed using synchronized signals for bubble and plasma generation. The decomposition efficiency of the new reactor with 10 plasma sources is similar to a conventional reactor with a single plasma source. A simple scale-up was achieved in the new method for the generation of plasma within bubbles in water.

Acknowledgements

This work was supported by the Environment Research and Technology Development Fund of the Ministry of the Environment, Japan K2324.

References

- [1] K. Yasuoka, K. Sasaki and R. Hayashi, Plasma Sources Sci. Technol., Vol. 20, (2011)

Effect of Injection Interval on Flow Characteristics of High Pressure Pulse Sprays

Ryuichi Sagawa, Yokoi Satoki, Yoshinori Kojima, Yasuhiro Saito and Hideyuki Aoki
Department of Chemical Engineering, Graduate School of Engineering, Tohoku University,
6-6-07 Aoba, Aramaki, Aoba-ku, Sendai 980-8579, Japan
saito@tranpo.che.tohoku.ac.jp

ABSTRACT

Various injection intervals are numerical investigated. At the near the nozzle, turbulence energy is equal to the value irrespective of difference in oscillation frequency. The spray of 200 Hz has large momentum. Thus, turbulent flow field formed by pulse sprays is promoted. In the small oscillation frequency, the axial velocity of peak is larger than other oscillation far from the nozzle tip. The turbulent flow field formed by pulse sprays is promoted in the case of large injection quantity per one spray is indicated.

1. Introduction

A stationary combustor such as a gas turbine and a boiler is widely used in industry. Spray combustion is generally used for the combustor. The optimization and development of the combustor is required because the strict environmental regulation is imposed.

In an internal-combustion engine, a common rail injection system is developed. The injection system is able to control the injection of high pressure fuel and the injection timing.

We consider applying the system to the stationary combustor. If the common rail injection is applied the combustor, the injection form pulse sprays. Thus, it will be environmentally-friendly combustion because the environmental pollutants can be decreased.

In the previous study, the injection system has been aimed at internal-combustor, especially only one spray in the small space [1-3]. Since the space of stationary combustor is large scale and pulse sprays affect each other, it is necessary to evaluate the spray characteristics in the free space.

Pulse sprays using a common rail injection system generate turbulent flow field shown in Figure 1. It is known that the flow effects on combustion [4, 5]. Thus, it is important of spatiotemporal changes of sprays, because pulse sprays form complex and unsteady flow field.

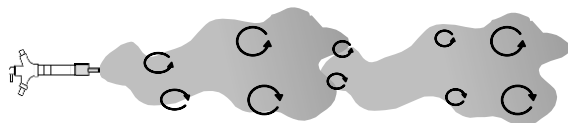


Fig. 1 Pulse sprays

In this study, we investigate flow characteristics of high pressure pulse sprays. Numerical study on pulse sprays is conducted, and we compare various injection intervals on the turbulence energy and air velocity.

2. Numerical simulation of spray flow

2.1 Analytical object

Figure 2 shows the analytical object. The analytical object is a two-dimensional spray flow. The computational domain is divided into uniform 80×62 grids. We use non-uniform grids to reduce computational loads. Turbulence energy and air velocity

data is obtained from center of spray at 50, 150 and 200 mm downstream the nozzle tip.

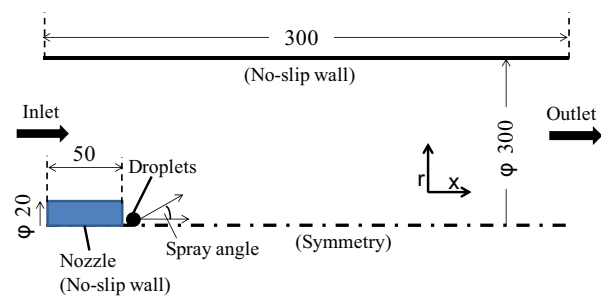


Figure 2 Analytical object

2.1 Governing equation and numerical schemes

The gas-phase flow field is described using the Navier–Stokes equations with the RNG $k-\epsilon$ turbulence model. Governing equations for the fluid flow system are expressed as:

$$\begin{aligned} \frac{\partial \rho \phi}{\partial t} + \frac{\partial}{\partial x}(\rho U \phi) + \frac{1}{r} \frac{\partial}{\partial r}(r \rho V \phi) = \\ \frac{\partial}{\partial x} \left(\Gamma_{\phi} \frac{\partial \phi}{\partial x} \right) + \frac{1}{r} \frac{\partial}{\partial r} \left(r \Gamma_{\phi} \frac{\partial \phi}{\partial r} \right) + S_{\phi} + S_{p\phi}, \quad (1) \\ \phi = 1(\text{mass}), u, v, k, \epsilon, \end{aligned}$$

where $S_{p\phi}$ is an additional source term from particle phase, and is evaluated by PSI-CELL model. Table 1 shows numerical schemes used.

In spray phase, the motion of droplets in the turbulent flow field is calculated using Lagrangian method.

Table 1 Numerical schemes

Discretization method	Finite volume method
Discretization scheme for momentum equation	
Convection term	SUPERBEE
Diffusion term	2nd-order central difference
Discretization scheme for $k-\epsilon$ equation	
Convection & diffusion	Hybrid difference
Unsteady term	1st-order Euler explicit
Coupling scheme	SMAC
Matrix solver	AMGS (for p) SOR(for $k-\epsilon$)

2.3 Numerical conditions

Table 2 shows numerical conditions. Injection time and spray cone angle are obtained from the experimental results. The fuel flow rate is constant. The gas and droplets properties are assumed to be air and diesel fuel as shown in Table 3.

Table 2 Numerical conditions

Injection pressure	[MPa]	40		
Fuel flow rate	[L/min]	0.1		
Oscillation frequency	[Hz]	200	300	400
Injection interval	[ms]	5.0	3.3	2.5
Injection time	[ms]	1.34	0.90	0.68
Initial droplets diameter	[mm]	0.21		
Spray angle	[deg]	7		
Initial air velocity	[m·s ⁻¹]	0.1		
Initial droplets velocity	[m·s ⁻¹]	198		

Table 3 Air and droplet properties

Density (Air)	[kg·m ⁻³]	1.184
Viscosity (Air)	[Pa·s]	1.84×10 ⁻⁵
Density (droplet)	[kg·m ⁻³]	850
Viscosity (droplet)	[Pa·s]	2.62×10 ⁻³
Surface tension	[mN·m ⁻¹]	26.3

3. Results and Discussion

Figure 3 shows the change of the turbulence energy on each of measuring points. The turbulence energy increase with time at the every measuring points. In the case of (a), the turbulence energy is equal to the value irrespective of difference in oscillation frequency. In the case of (b) and (c), the turbulence energy of 200 Hz is larger than other oscillation frequencies. The difference of turbulence energy is large far from the nozzle tip. This means that the injection quantity per one spray of 200 Hz is bigger than that of other oscillation frequencies. The spray of 200 Hz have large momentum. Thus, turbulent flow field formed by pulse sprays is promoted.

Figure 4 shows the change of the axial air velocity at 50 and 200 mm downstream the nozzle tip. In the case of (a'), the maximum value of the axial velocity of peak is equal to the value irrespective of difference in oscillation frequencies. On the other hand, in the case of (b'), the peak of 200 Hz is larger than other oscillation frequencies. Thus, the turbulence energy of 200 Hz is larger than others.

4. Conclusions

In this study, we carried out numerical investigation. The effect of injection interval on flow characteristics of high pressure pulse sprays is investigated. The following results are obtained.

- At the near the nozzle, turbulence energy is equal to the value irrespective of difference in oscillation frequency.
- The spray of 200 Hz has large momentum. Thus, turbulent flow field which is formed by pulse sprays is promoted.
- In the small oscillation frequency, the axial velocity of peak is larger than other oscillation far from the nozzle tip.

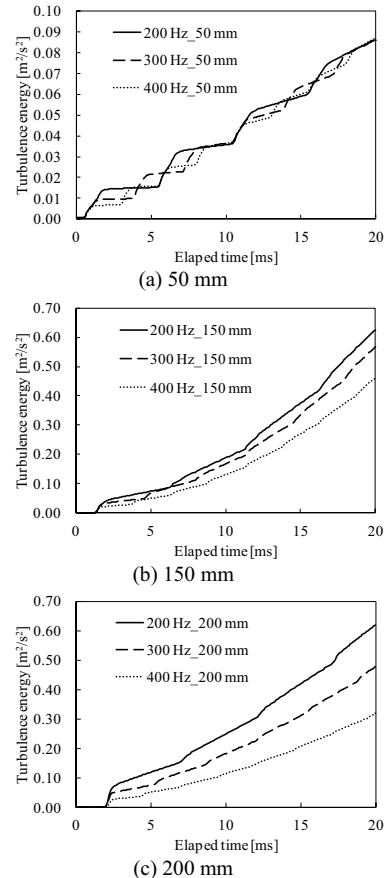


Figure 3 Change of the turbulence energy at downstream the nozzle tip

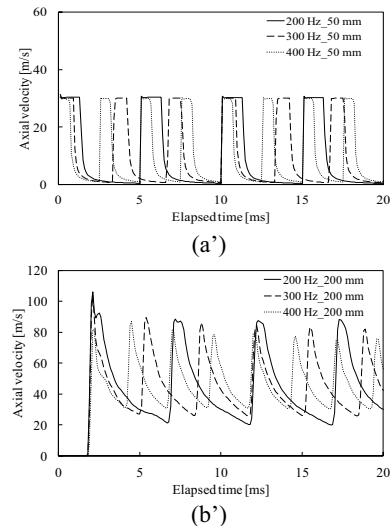


Figure 4 Change of the axial velocity at downstream the nozzle tip

References

- [1] C. S. Lee, S. W. Park, *Fuel*, **81** (2002), 2417.
- [2] H. K. Suh, S. W. Park, C. S. Lee, *Fuel*, **86** (2007), 2833.
- [3] Z. Wu, Z. Zhu, Z. Huang, *Fuel*, **85** (2006), 1458.
- [4] J. Hayashi, F. Akamatsu, *Transactions of the Japan Society of Mechanical Engineers, Series B*, **74**, (2008), 175.
- [5] K. Sison, N. Ladommatos, H. Song, H. Zhao, *Fuel*, **86** (2007), 345.

Study of Deep-Throttleable Rocket Injector

Mitsuhiro Soejima¹, Sadatake Tomioka², Goro Masuya³
1, 3: Tohoku University, 6-6, Aramaki Aza Aoba, Aoba-ku, Sendai
2: Japan Aerospace Exploration Agency, 1, Koganezawa, Kimigaya, Kakuda
1:soejima@scrj.mech.tohoku.ac.jp

ABSTRACT

A deep-throttleable rocket engine has some issue. The principal of them are related to the pressure balance of the injection system and the capacity of chamber cooling system. Then the gas/gas injector is proposed to apply to deep-throttleable rocket engine. It relieves change of the pressure balance automatically. Also, it raises the chamber cooling capacity, because it needs to gasify both fuel and oxidizer. They are stored as a liquid in the tank. This paper focuses on analysis of the chamber heat transfer, and regenerative cooling capacity.

1. Introduction

The Rocket Based Combined Cycle (RBCC) Engine is expected for the propulsion system of the next generation space transportation vehicle, and the deep-throttling capability of the embedded rocket engine is one of the key technical challenges of the system.

A rocket engine should be designed to consider some terms of reference. One of them is the balance of each engine components, such as mass flow rate, power, pressure, heat transfer.

Especially, the pressure ratio of injector and chamber heat transfer is important factor for deep-throttleable rocket engine, because the rate of change of them is not same as that of propellant mass flow rate.

The gas/gas injector can automatically control the pressure ratio by change of the density of gaseous propellant.

Then, the injector demand gaseous fuel and oxidizer, but most of rocket propellant are stored as liquid in the tank. So, these propellants have to be gasified by heat transfer from combustor, which is called regenerative cooling. That is the reason why gas/gas injector raises chamber cooling capacity and latitude compared with conventional gas/liquid injector.

This feature is useful for RBCC because the system has large duct which pass high temperature gas and needs active cooling.

For the system analysis of deep-throttleable rocket engine, this study estimate dual cooled (fuel and oxidizer cooling) chamber cooling capacity. To simplify the matter, this paper describes the LH₂/LOX rocket engine chamber heat transfer analysis as the first step of the study.

2. Method

The Basis of this analysis is heat transfer analysis^{[1],[2]}. Combustion gas (hot gas) and propellant properties are mainly calculated by NASA Chemical Equilibrium with Applications (CEA) code. The viscosity of hot gas in the boundary layer μ_{bi} was calculated by the following expression^[3].

$$\mu_{bi} = \mu_i \mathcal{M}_i^{0.5} \left(\frac{\bar{T}_{bi}}{T_i} \right)^{0.6} \quad (1)$$

Where, μ_i , \mathcal{M}_i , and T_i is viscosity, molar mass, and temperature at the main stream of same section, \bar{T}_{bi}

is the arithmetic mean temperature of the boundary layer.

The process of chamber heat transfer calculation is following Ref.2. For the heat transfer coefficient calculation, Bartz correlation and Dittus-Boelter correlation is used. But, the range of coolant temperature under 160 K, NASA CEA code cannot calculate coolant heat transfer properties. When, heat transfer calculation in this range, the coefficient of heat transfer between coolant side wall and coolant is assumed to infinity. That is to say, the temperature of coolant side wall is assumed identical with coolant.

Hot gas side wall temperature is numerically calculated by the balance of heat flux and thermal resistance, using the following relation.

$$\dot{q} = h_g (T_r - T_{wg}), \quad (2)$$

$$T_{wl} = T_{wg} - \dot{q} \frac{\delta}{\lambda}, \quad (3)$$

$$T_l = T_{wl} - \dot{q} \frac{1}{h_l}. \quad (4)$$

Where, \dot{q} , h , T , and λ is heat flux, coefficient of heat transfer, temperature, and thermal conductivity. The subscripts g , r , w , and l are gas side, recovery temperature, wall, and coolant side.

The outline of combustion chamber model is shown in Fig.1. The heat transfer of cylinder part was calculated with 50 mm interval. That of contraction part was calculated with 25 mm interval, and expansion part was calculated with 25 - 125 mm interval.

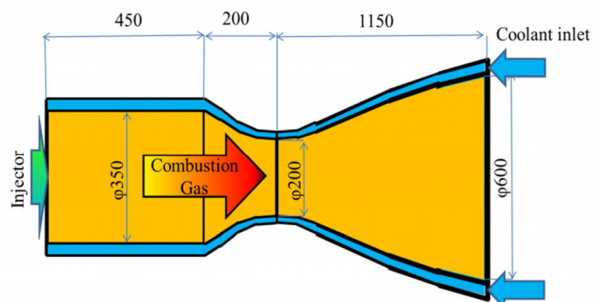


Fig. 1 Outline of combustion chamber model

The fuel comes into the cooling channel from nozzle exit side and flow opposingly to hot gas.

On this calculation, it is assumed that LOX is gasify using a heat exchanger. That cool down the H₂ as a intercooler between rocket chamber cooling channel and RBCC duct cooling channel. As a result of this, total regenerative cooling capacity will increase. The exchanged heat amount is calculated as the change of enthalpy, because this calculation need the thermal transport properties at under 160 K range.

3. Results and Discussion

The result of this analysis is shown in Fig.2 - 5. Figure 2 shows chamber wall heat flux. The maximum heat flux was 90 MW/m² at 100% P_c on nozzle throat. This tendency is same as that at the other P_c condition.

Heat flux at 60% P_c was reduced to 67~70%, and 10% P_c was 15~18% of that of at 100% P_c, shown in Fig.3. This means the cooling load per unit mass of coolant increased by decreasing P_c. As a result of this, coolant temperature at cooling channel exit increased by throttling, shown in Fig.4. The fluctuation range of coolant temperature at cooling channel exit is almost 200 K between 100 % P_c and 10 % P_c.

For RBCC engine, it means to decrease duct cooling capacity. Then, the cooling capacity of LOX is calculated as the product of mass flow rate by gap of enthalpy between 100 K and 300 K. It is 2.6MW at 10% P_c condition, which corresponds to 25% of chamber heat transfer.

Hot gas side wall temperature, especially at 10% P_c shown difference trend. As the chamber pressure reduce, the peak of chamber throat temperature become gently, shown in Fig.5. As a result of this, the maximum wall temperature at 10% P_c is place on injector faceplate side. But the temperature of that point is almost same as at 100 % P_c.

4. Concluding remarks

- The cooling load per unit mass of coolant increase to 110-170% by decreasing P_c.
- Dual cooled RBCC can have 25% larger regenerative cooling capacity than that of fuel cooled one.
- When the engine working low thrust level, the peak point of hot gas side wall temperature is not place to chamber throat.

Reference

[1] Y. Nakamura, K. Suzuki, Rocket Engine (2004), 67-69, in Japanese
 [2] K. Suzuki, Rocket Engine supplement of Section7.3 "Cooling" (2011), in Japanese
 [3] D. K. Huzel, D. H. Huang, DESIGN OF LIQUID PROPELLANT ROCKET ENGINE (1967)
 [4] D. R. Bartz, "A Simple Equation for Rapid Estimation of RocketNozzle Convective Heat Transfer Coefficients", Jet Propulsion, 27, (1) (1957)

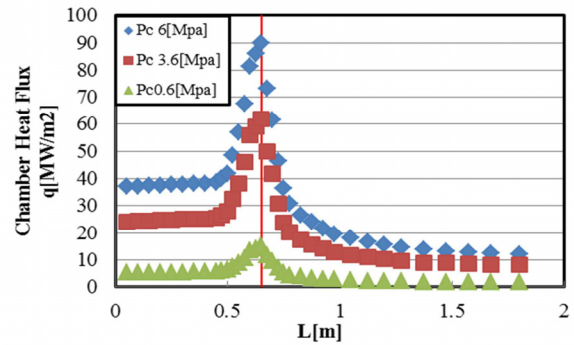


Fig. 2 Heat flux of combustion chamber wall

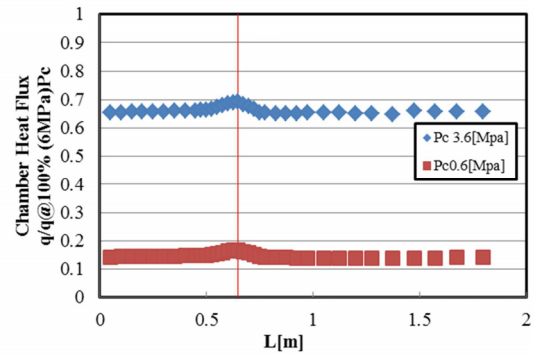


Fig. 3 Heat flux of combustion chamber wall Compared with 100% P_c

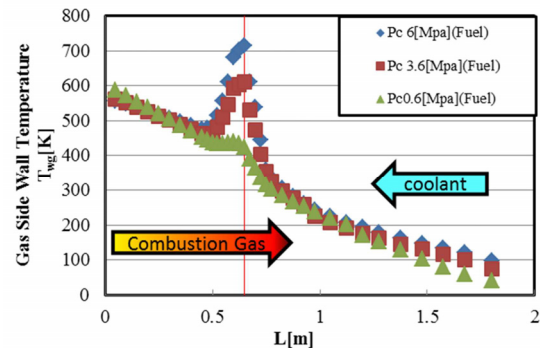


Fig. 4 Coolant temperature increase

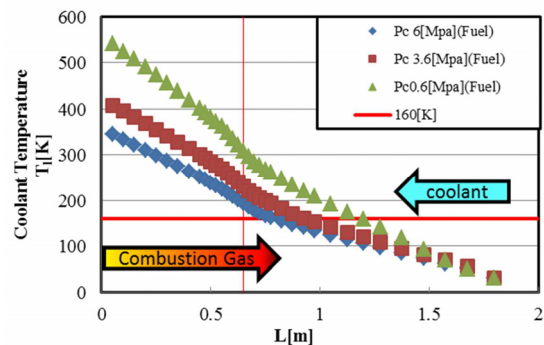


Fig. 5 Gas side chamber wall temperature

Development of Back Surface TSP Measurement Technique for Shock Interaction Aerodynamic Heating in High Enthalpy Flow

Kazuki Nishigata, Hiroki Nagai and Keisuke Asai
Department of Aerospace Engineering, Tohoku University,
6-6-01 Aramaki-Aza-Aoba, Aoba-ku, Sendai, Miyagi, 980-8579, JAPAN
nishigata.kazuki@aero.mech.tohoku.ac.jp

ABSTRACT

For the aerodynamic heating calculation, Temperature-Sensitive Paint (TSP) measurement has been applied to hypersonic wind tunnel testing. But in hypersonic flow, the air creates plasma with its high temperature and produces self-illuminating, which affects an excitation and a detection of TSP measurement and reduces an accuracy of measuring. In this study, a back surface TSP measurement technique has been proposed in order for an elimination of self-illumination of plasma, and basic experiment has been conducted. As a result, effects of model thickness have been confirmed.

1. Introduction

Aerodynamic heating is one of the most important problems in space plane development. Especially, shock or shock interaction produces high heat transfer rates locally in a heat shield. In wind tunnel experiments, various types of heatflux measurement technique have been used, and one of these is temperature-sensitive paint (TSP) measurement. TSP measurement is an optical temperature measurement technique based on photochemical reaction of luminescent molecules, and it can obtain global quantitative heatflux maps of testing models as opposed to local heatflux data obtained from sensors like thermocouple.

In existing TSP measurements, TSP is coated on the front surface of the testing model, and a heatflux calculation uses a surface temperature time history of the model. Liu et al. developed heatflux calculation method considering TSP layer and lateral heat conduction on the surface [1, 2] and applied it to wind tunnel experiment [2]. But in hi-enthalpy hypersonic flow, the air creates plasma with its high temperature and produces self-illuminating, which affects an excitation and a detection of TSP measurement and reduces an accuracy of measuring. Therefore, existing TSP measurements cannot be applied to hi-enthalpy hypersonic wind tunnel testing. So, a back surface TSP measurement has been proposed in order for an elimination of self-illumination of plasma. There, a front surface heatflux is calculated from the back surface temperature history of the model. In this study, we investigated effects of model thickness and TSP layer in the back surface TSP measurement.

2. Back Surface TSP Measurement

Fig. 1 shows an illustration of one-dimensional heat conduction model. The parameter q is a heatflux at the front surface of the model base or TSP layer. In one of an existing model called two-step method [1, 2], q is given by the discrete form of the solution of one-dimensional time-dependent heat conduction equation,

$$q(t_n) = \frac{k_p(1-\bar{\varepsilon}^2)}{\sqrt{\pi a_p}} \left[\sum_{i=1}^n \frac{T(t_i) - T(t_{i-1})}{\sqrt{t_n - t_i} + \sqrt{t_n - t_{i-1}}} \{ \bar{W}(t_n - t_i) + \bar{W}(t_n - t_{i-1}) \} \right] \quad (1)$$

where

$$a_p = k_p / \rho_p c_p, \varepsilon = \sqrt{\rho_p c_p k_p / \rho_b c_b k_b}, \bar{\varepsilon} = (1 - \varepsilon) / (1 + \varepsilon),$$

$$\bar{W}(t, \bar{\varepsilon}, L) = \frac{2}{\sqrt{\pi}} \int_0^{\infty} \frac{\exp(-\xi^2) d\xi}{1 + \bar{\varepsilon}^2 - 2\bar{\varepsilon} \cos(2L_p \xi / \sqrt{a_p t})}$$

The parameter $T(t)$ is the surface temperature given by TSP data, ρ_b, c_b, k_b is the density, specific heat and thermal conductivity of the base, respectively, the parameter ρ_p, c_p, k_p is the density, specific heat and thermal conductivity of TSP, respectively, and L_p is the TSP layer thickness.

In the back surface TSP measurement, TSP provides the back surface temperature of finite model, so the model thickness L_b could be considered in heatflux calculation as an inverse problem.

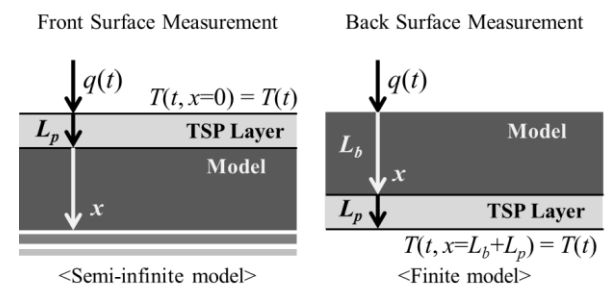


Fig. 1 One-dimensional heat conduction model in front/back surface TSP measurement

3. Basic Experiment

3.1. Experimental Setup

For the investigation of model thickness effects, TSP measurements were conducted the front and the back surface of the model simultaneously. In this experiment, a flat plate coated with TSP was heated by high temperature airflow of a non-flame torch for 16 seconds. Fig. 2 shows a schematic illustration of this experiment. The TSP was Ru-phen TSP, which was coated on each surface of stainless flat plate. Also, thermocouples were attached in the area of heating spot on each surface. The frame-rate of each high-speed camera was 500fps, with 560nm high pass filter. Plate thicknesses of 0.2mm, 0.5mm, 0.8mm, 1.0mm were tested as experiment cases.

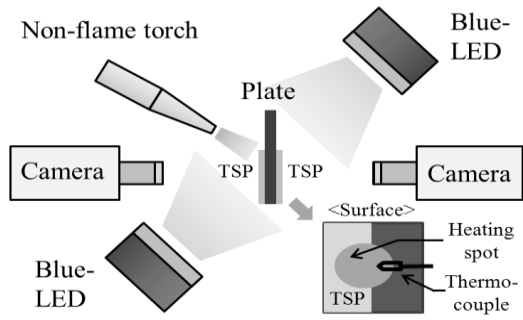


Fig. 2 Schematic illustration of TSP measurement

3.2. Result and Discussion

Fig. 3 is global temperature images at $t=15$ seconds in each case, Fig. 4 is temperature profiles at $t=15$ seconds in each case and Fig. 5 (a) ~ (d) are temperature histories obtained from TSP images of the front/back surface and thermocouple data. The time step of calculation is 0.2 seconds, and $t=0$ is the start time of heating. In the TSP measurement, as the plate thickness become thinner, temperature become higher and the heat is laterally conducted more readily. This would appear that the saturation of thickness-dependent thermal heat capacity brought higher temperature rising and induced the rising of surrounding temperature. It should be considered that lateral heat conduction causes an error in global heatflux calculation quantitatively and qualitatively. Meanwhile, temperature differences between the front surface and the back surface of plate thickness of 0.2mm, 0.5mm, 0.8mm and 1.0mm are 0.97K, 2.8K, 1.5K and 2.7K, respectively.

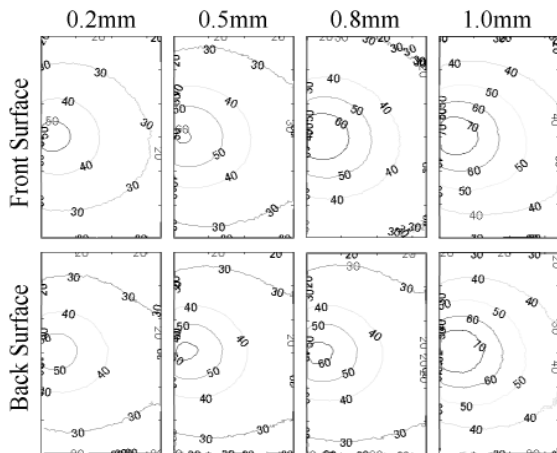


Fig. 3 Global temperature images at $t=15$ in each case

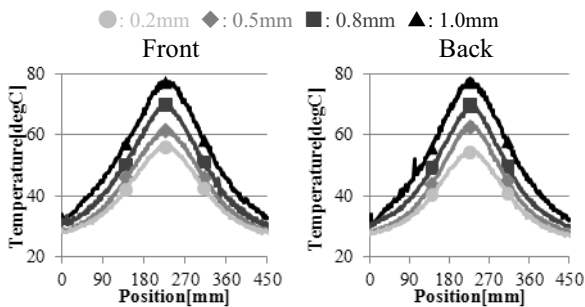


Fig. 4 Temperature profile at $t=15$ in each case

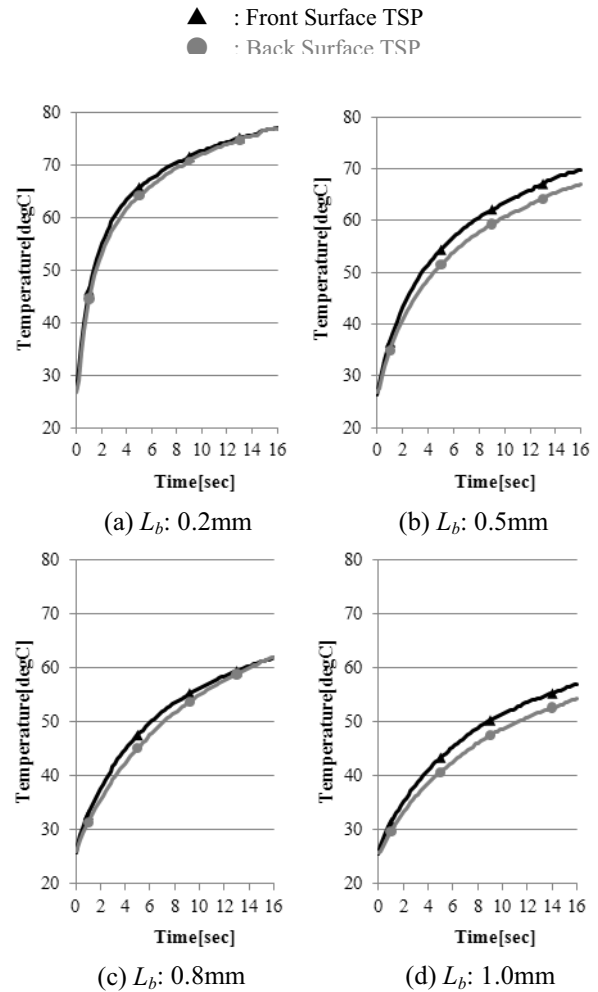


Fig. 5 Temperature histories in each case

4. Conclusion

For the investigation of effects of model thickness, front and back surface simultaneous TSP measurements were conducted. As a result, temperature differences between the front surface and the back surface are within 2.8K in all cases. Therefore, heatflux calculation methods that ignore model thickness could be applied such as thin-skin calorimeter models [3].

References

- [1] T. Liu, Z. Cai, J. Lai, J. Rubal and J. P. Sullivan: Analytical Methods for Determination of Heat Transfer Fields from Temperature Sensitive Paint Measurements in Hypersonic Tunnels, AIAA 2009-736, 2009.
- [2] T. Liu, B. Wang, J. Rubal and J. P. Sullivan: Correcting lateral heat conduction effect in image-based heat flux measurements as an inverse problem, International Journal of Heat and Mass Transfer 54 1244-1258, 2011.
- [3] D. L. Schultz, and T. V. Jones: Heat-transfer Measurements in Short-duration Hypersonic Facilities, AGARDograph No. 165, 47-52, 1973.

Molecular Dynamics Study of Oxygen Permeation in the Ionomer on Pt Catalyst of PEFC

Yuta Sugaya, and Takashi Tokumasu,
Tohoku University, Katahira 2-1-1, Sendai, Miyagi
sugaya@nanoint.ifs.tohoku.ac.jp

ABSTRACT

In Polymer electrolyte fuel cell (PEFC) cathode catalyst layer, an ionomer with which the catalyst is covered is very important on the point of transferring protons to the catalytic surface on the cathode side. On the other hand, it is said that ionomer interferes with oxygen permeation to the catalytic surface. The mechanism of oxygen permeation through the ionomer was not analyzed in detail. In this research, we constructed the system of ionomer on the Pt surface by using molecular dynamics study, and researched about the effect of the water content of the ionomer on the structure of the ionomer and oxygen permeability.

1. Introduction

Polymer electrolyte fuel cell (PEFC) is focused worldwide as the energy conversion device for next generation. However, PEFC is not widespread in general because an actual power generation efficiency is lower than a theoretical power generation efficiency.

PEFC is composed of membrane electrode assemblies (MEAs) that consist of a polymer electrolyte membrane (PEM), catalyst layers (CLs), microporous layers (MPLs), and gas diffusion layers (GDLs). In CLs, Pt catalyst is the particle which diameter is 3 ~ 4 nm and it is on a supported carbon. In addition, it is covered with an ionomer because of proton transfer to catalyst surface. The ionomer improves ability of proton transfer but it reduces oxygen permeability to Pt surface and therefore dissociative adsorption reaction becomes slow. It is necessary to research the oxygen permeation and proton transfer in such a situation to raise its efficiency. However, it is difficult to analyze by macroscopic experiment because these phenomena occur in the microscopic structure. For this reason, it is necessary to analyze the oxygen permeation and the proton transfer at the microscopic point of view.

In this research, we constructed the system of ionomer on the Pt surface by using molecular dynamics study, and researched about the effect of the water content of the ionomer on the structure of the ionomer and oxygen permeability.

2. Method

In this research, we simulated the system of CLs of the cathode side by molecular dynamics simulation. This system includes Pt wall, PFSA, water, oxonium ion and oxygen molecule.

Pt-Pt interactions were represented by spring mass model considering nearest neighbor atom. PFSA was represented by the flexible model which interaction was expressed by the DREIDING force field [1]. The F3C model [2] was adopted for water, and for oxonium ion, we selected similar model with four point charges. The Morse potential was used for intramolecular potential of oxygen molecule. The intermolecular potentials between nafion and water, nafion and oxonium ion were represented by Lennard Jones (LJ) potential and coulomb interaction. The interaction between Pt and water was represented by Spohr and Heinzinger

potential [4] and that between Pt and oxonium ion was represented by the potential that the number of hydrogen atoms changes from two to three. The intermolecular potentials between oxygen and water, oxygen and oxonium ion were represented by LJ potential and Morse potential. The others were connected by LJ potential but the interaction between Pt-O₂ was not considered because we assumed all permeated oxygen dissociated at Pt surface and this reaction speed was faster than oxygen dissolution or diffusion. We allowed oxygen molecules to pass through Pt surface and permeated oxygen were returned to gas space.

Fig. 1 shows the system of this research. In this calculation, we considered the periodic boundary condition. The temperature was set at 350K and the simulation domain was set at 66.5×57.6×150Å. The platinum surface was placed at the bottom of simulation box and ionomer which was composed of hydrated PFSA molecules were placed on the surface. A chain of PFSA molecule constructed 5 pair of 1 polar chain and 6 non-polar chains. In this system, 15 PFSA molecules were placed. Moreover, the number of water molecules was determined according to water content. We used velocity verlet and rRESPA. The calculation procedure is described as follows.

Firstly, we made the ionomer without Pt during 800ps. The temperature was controlled 350K by velocity scaling during first 720ps. After 800ps, we attached the ionomer to Pt surface. Then oxygen molecules were introduced. The number of oxygen molecule was set at the number that is in the gas space corresponds to 1MPa. The number of oxygen in the gas space was constant to keep the pressure in the gas space constant and permeated molecules were returned to gas space. By this procedure, we made the constant oxygen mass flux in the ionomer.

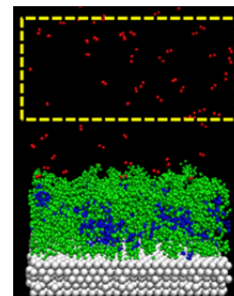


Fig. 1 The schematic diagram of this system

3. Result and Discussion

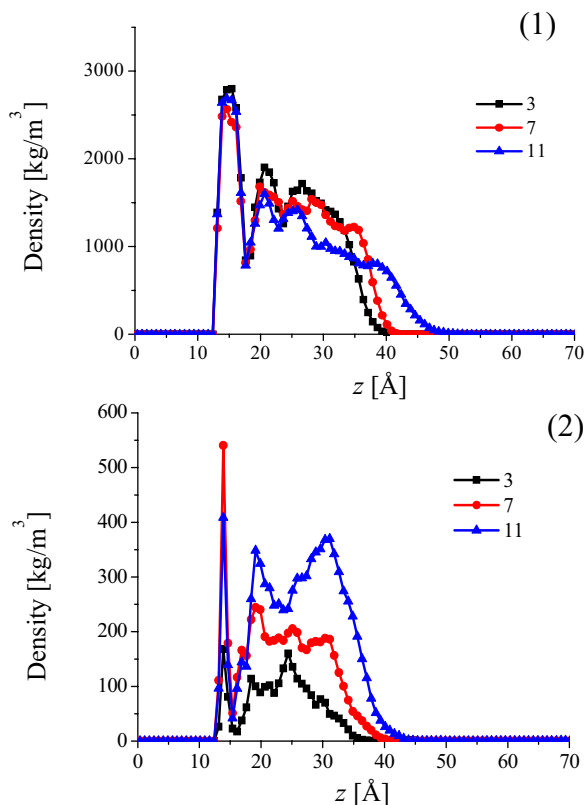


Fig. 2 Density distribution of (1)PFSA molecule, (2)water and oxonium ion along z direction

Density distribution of PFSA and liquid along z direction are shown in Fig. 2 From upper side, the density distribution of (1) PFSA molecule and (2) water and oxonium ion distribution in the case of water content $\lambda = 3, 7, 11$, respectively. From Fig. 2 (1), it is said that the PFSA gathers toward the catalyst surface. This phenomenon occurs because Pt strongly attracts the other molecules. The density of PFSA molecule on Pt surface increase in order $\lambda = 3, 11, 7$. From Fig. 2 (2), many water molecules distribute on Pt surface and inside of the ionomer. The density of water molecules on Pt surface increase in order $\lambda = 7, 11, 3$. The density of water molecules inside of the ionomer increases as water content increases. From Fig. 2 (1) and (2), Water molecule absorbs Pt surface stronger than PFSA molecules.

Table 1. The number of oxygen molecule which permeated to catalyst surface

water content λ	3	7	11
No. of permeated O ₂	36	4	3

Table 1. shows the number of oxygen molecule which permeated to catalyst surface. From TABLE1, the number of permeated oxygen molecule decreases with the increase of water content. This tendency is different from the experiment of oxygen permeation in bulk PFSA membrane [5].

Oxygen solubility along z direction on the catalyst surface is shown in Fig. 3 From this figure, oxygen permeation is interrupted by the ionomer which adsorbs on platinum surface in all cases. Minimum value of oxygen solubility are 0.0148 at $\lambda=3$, 0.0032 at $\lambda=7$, 0.0039 at $\lambda=11$. This tendency that minimum value of oxygen solubility decrease as water content increases agree with the tendency of the number of permeated oxygen. In conclusion, we think that oxygen permeability correlates highly with oxygen solubility in the ionomer.

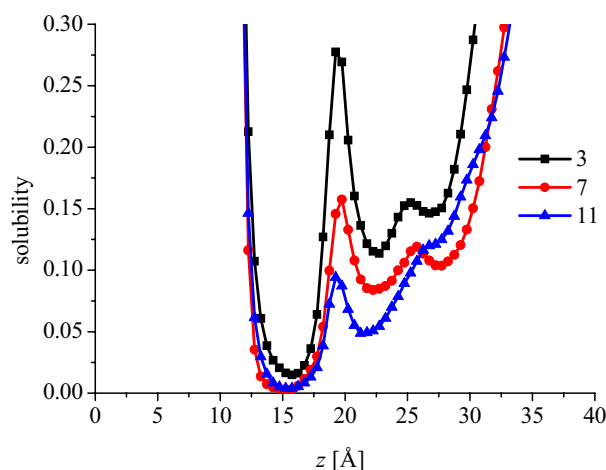


Fig. 3 Oxygen solubility along z direction on the catalyst surface.

4. Conclusion

The oxygen permeability in the ionomer of catalyst surface was examined by using molecular dynamics simulation. In this simulation, we constructed the model of ionomer on the Pt catalyst surface in the PEFC catalyst layer. PFSA ionomer adsorbed on Pt surface and forms a thin film structure and water adsorbed stronger on the Pt surface. Moreover, in this simulation, we examined the oxygen permeability in the ionomer on the catalyst surface. It is said that the oxygen permeability decreased as water content increased. Also, we think that oxygen permeation correlate highly with oxygen solubility in the ionomer.

5. Acknowledgment

This research is supported by the super computer system of Institute of Fluid Science, Tohoku University.

References

- [1] S. L. Mayo, B. D. Olafson, and W. A. Goddard III, *J. Phys. Chem.*, **94**, 8897-8909, (1990)
- [2] M. Levitt, M. Hirshberg, R. Sharon, K. E. Laidig, and V. Daggett, *J. Phys. Chem.*, **101**, 5051-5061, (1997)
- [3] Ewald, P.; *Ann. Phys.*, **1921**, *64*, 253-287
- [4] Spohr, E.; *J. Phys. Chem.*, **1989**, *93*, 8254-8282.
- [5] K. Broka, P. Ekdunge, *J. Appl. Chem.* *27*, 2 (1996), 117-123

Experiment Verification of Acoustic Feedback Loop around NACA0012 Airfoil at Low Reynolds Number

Nobuaki Sakai^{*1}, Hiroki Nagai^{*1}, Keisuke Asai^{*1}, Tomoaki Ikeda^{*2}, Takashi Atobe^{*2}

^{*1} Dept. of Aerospace Engineering, Tohoku University,
6-6-01, Aramaki-Aza-Aoba, Aoba-ku, Sendai, Miyagi 980-8579, JAPAN

^{*2} Fluid Dynamics Group, Japan Aerospace Exploration Agency,
7-44-1, Jindaiji Higashi-machi, Chofu, Tokyo 182-8522, JAPAN
sakai.nobuaki@aero.mech.tohoku.ac.jp

ABSTRACT

In this study, we measured pressure fluctuations near the trailing edge of a NACA0012 airfoil at low Reynolds number. Experiments were conducted in low-pressure environment of the Mars Wind Tunnel at Tohoku University. Reynolds number was kept constant at 1.1×10^4 and Mach number was 0.20, 0.25, 0.30, 0.35 and 0.40. It's considered that an acoustic feedback loop is formed around the model at certain angle of attack and Mach number in this experiment.

1. Introduction

Unsteady phenomena caused by the flow around airfoil affect aerodynamic characteristics of an airfoil at low Reynolds number. According to the computational study conducted by Atobe, et al. [1], pressure fluctuation on the airfoil can be increased drastically due to an acoustic feedback loop in certain conditions of the angle of attack, Reynolds number, Mach number. However, the experimental data on this unsteady phenomenon at low Reynolds number are very limited.

In this study, we investigated experimentally the unsteady phenomenon that appears around the airfoil at low Reynolds number. We measured pressure fluctuations near the trailing edge of a NACA0012 airfoil and investigated the conditions of an acoustic feedback loop.

2. Experimental method

2.1 Mars Wind Tunnel

The MWT is composed of a vacuum chamber, an induction-type wind tunnel and a buffer tank. The induction-type wind tunnel is located inside the vacuum chamber where the pressure condition of Martian atmosphere can be simulated. This wind tunnel is driven by multiple-nozzle supersonic ejector located downstream of the test section. Ejection of high-pressure gas from the ejector induces the flow in the test section. The total pressure in the wind tunnel is kept constant by exhausting the gas inside the vacuum chamber to the buffer tank.

2.2 Test Model

The test model is a NACA0012 airfoil. The chord length of the model is 50 mm and the span length is 100 mm. A high-frequency pressure transducer (kulite LQ-062-5A) was installed at $x/c = 0.9$ on both upper and lower sides of the model.

2.3 Experimental condition

Reynolds number (Re) was fixed at 1.1×10^4 . Mach number (M) was set at 0.20 ~ 0.40 to investigate the effect of Mach number to the pressure fluctuations. The angle of attack (α) was changed from 0 to 15 deg.

3. Results and Discussion

Figure 1 shows power spectrum of pressure fluctuation on upper side of the model at $M = 0.20$.

The highest peak frequency appeared approximately at 3.0kHz for all Mach number cases. For high angles of attack, the peak appeared at 0.9-1.0 kHz.

In addition, the relatively small peak appeared at low angles of attack. These frequencies are 3.6, 4.3, 5.3, 5.8, 6.6kHz, at $M = 0.20, 0.25, 0.30, 0.35, 0.40$, respectively. These frequencies were converted to non-dimensional frequencies using the following equation (1).

$$f^* = \frac{fc}{u} \quad .(1)$$

Here, f is frequency, c is chord length of the model, and u is the main flow velocity. From the equation (1), a non-dimensional frequency f^* is set to be 2.61, 2.59, 2.58, 2.54, 2.52. These frequencies are consistent with the frequency of Karman vortex that is obtained by CFD.

Therefore, it is considered that these pressure fluctuations are caused by Karman vortex emission attributed to the wake instability.

On the other hand, for middle angles of attack, the peak at the frequency of a Karman vortex disappear and the other peaks appear at a number of discrete frequencies. At a certain angle of attack and Mach number, the difference of these discrete frequencies is close to that calculated by the following equation of a phase loop condition suggested by ARBEY, et al. [2].

$$f_n = \left(n + \frac{1}{2} \right) \frac{c_r}{L} \left/ \left(1 + \frac{c_r}{a-u} \right) \right. \quad .(2)$$

Here, c_r is phase velocity of instability waves in the boundary layer on the airfoil, L is distance between the point of maximum speed on the airfoil and the point of origin of sound wave. From this equation (2), discrete frequency interval (Δf) is represented by the following equation (3).

$$\Delta f = \frac{c_r}{L} \left/ \left(1 + \frac{c_r}{a-u} \right) \right. \quad .(3)$$

The point of maximum speed on the airfoil is $x/c = 0.05$ and the point of origin of sound wave is trailing edge ($x/c = 1.0$). Therefore, $L = 0.95$. In addition, $c_r = 0.4u$ with reference to Nash, et al. [3]. Figure 2 shows comparison of experimental and theoretical (solid line) values of the interval of discrete frequency in all Mach number cases. The experimental and theoretical values show a trend similar. Therefore, in these conditions, the experimental results indicate that acoustic feedback loop has been formed.

However, the peak frequency is approximately 1.0kHz or 3.0kHz. Because this is a resonance frequency of the wind tunnel walls and model, there is a possibility that this resonance prompted the boundary layer instability, causing the acoustic feedback loop. This suggests the possibility that the sound-absorbing wall provided on the wall of wind tunnel could not absorb enough sound. For this reason, it is necessary to improve the sound-absorbing wall.

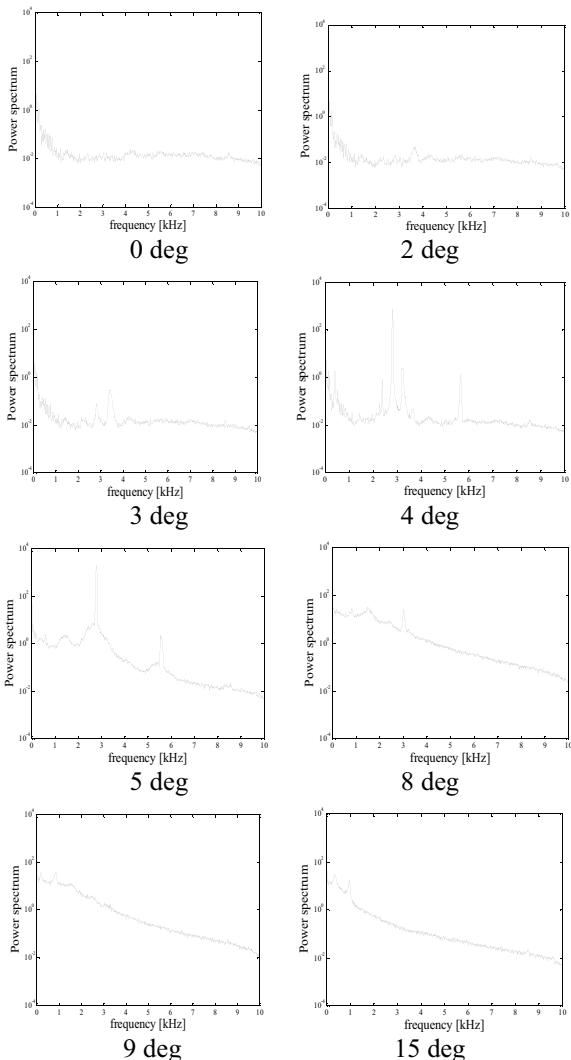


Fig. 1 The power spectrum of pressure fluctuation ($M=0.20$)

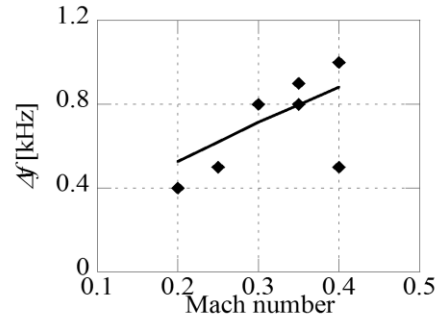


Fig. 2 Interval of discrete frequency

4. Conclusion

This study aims to clarify the conditions that can cause the acoustic feedback loop, measure the pressure fluctuation near the trailing edge by using Mars Wind Tunnel. We investigated the dependence of the angle of attack and Mach number. The summary is follows.

- Karman vortex occurs around $f^* = 2.5\sim 2.7$ non-dimensional frequency in the low angle of attack.
- Discrete frequency fluctuations which appear with the frequency of Karman vortex disappear in middle angles of attack. The peak frequency interval near the maximum peak frequency is almost consistent with the frequency interval of acoustic feedback loop forming.

References

- [1] T. Atobe, T. Ikeda, ICAS 2010-3.9.4, 27th Congress of International Council of the Aeronautical Sciences, Nice, France, 19 - 24 September, 2010.
- [2] H. ARBEY, J. BATAILLE, " Noise generated by airfoil profiles placed in a uniform flow ", Journal of Fluid Mechanics, vol. 134, pp. 33-47, 1983.
- [3] E. C. Nash, M. V. Lowson, A. McAlpine, "Boundary-layer instability noise on aerofoils", Journal of Fluid Mechanics 382, pp.27-61, 1999.

Compressibility Effects on Aerodynamic Characteristics of Low Reynolds Number Airfoils

Tetsuya Suwa, Daiju Numata, Hiroki Nagai and Keisuke Asai
Tohoku University, 6-6-01, Aramaki-Aza-Aoba, Aoba-ku, Sendai 980-8579, JAPAN
suwa.tetsuya@aero.mech.tohoku.ac.jp

ABSTRACT

The objective of this study is to clarify Mach number effect on the aerodynamic characteristics of airfoils at low Reynolds number regime. We measured aerodynamic force and pressure distributions on a flat plate and a thin triangular airfoil at low Reynolds number using a force balance and Pressure-Sensitive Paint. The results show that Mach number has an effect to delay a reattachment of shear layer, resulting in a decrease in lift near stall angle of attack. Moreover, the compressibility has an effect to move the separation point on the airfoil to downstream, that results in a decrease in maximum lift-drag ratio.

1. Introduction

Mars aerial vehicles have been considered as a feasible means of exploring Mars [1-3]. A propeller or a rotor for Mars aerial vehicles operates at low Reynolds number and high-subsonic number, meaning that these factors should be taken account in designing the blade of a propeller or a rotor. The tip speed of the blade is restricted because of the compressibility effect. Presently, there is few experimental data in this test region because it is difficult to simulate the flow condition on Mars in a conventional wind tunnel. To design the optimum propeller or rotor of Martian aerial vehicle, evaluation of the compressibility effect in the low Reynolds number regime is indispensable.

The objective of this study is to clarify Mach number effect on the aerodynamic characteristics of airfoils by conducting airfoil tests in the Mars Wind Tunnel (MWT) at Tohoku University. In this test, a flat plate and a thin triangular airfoil were used as test models. We measured aerodynamic force and pressure distributions on the model using a force balance and Pressure Sensitive Paint (PSP).

2. Experimental Devices and Condition

2-1. Mars Wind Tunnel

The MWT is composed of a vacuum chamber, an induction-type wind tunnel and a buffer tank. The induction-type wind tunnel is located inside the vacuum chamber where the pressure condition of Martian atmosphere can be simulated. The test gas is dry air in usual tests, but can be replaced with carbon dioxide. Currently, the MWT is being operated at ambient temperature only.

2-2. Two-component Balance System

A two-component balance system was used to measure aerodynamic force. This balance system is composed of two load cells and has a sufficient sensibility and accuracy to measure lift and drag at reduced pressure.

2-3. Pressure-Sensitive Paint (PSP)

PSP is a coating type pressure sensor consisting of luminescent molecules and binder. The principle of PSP is based on oxygen quenching. The rate of quenching depends on local oxygen concentration which is proportional to ambient pressure. Therefore, surface pressure can be calculated from measured luminescent

intensity of PSP. PSP is known to be affected by the temperature distribution. In this test, PSP and Temperature-Sensitive Paint (TSP) were applied on a right side and right half of the model and pressure and temperature distributions on an airfoil were measured simultaneously with PSP measurement. Temperature dependence of PSP was corrected by TSP data.

2-4. Airfoils

A flat plate and a triangular airfoil were used as test models. The thickness of the flat plate is 5 % of the chord. The maximum thickness of the triangular airfoil, located at 30 % from the leading edge, is 5 % of the chord.

2-5. Experimental Condition

For evaluating Mach number effect, Reynolds number was fixed at 3,000 or 10,000. Mach number was changed from 0.15 to 0.70. The test gas was dry air at room temperature.

3. Results and Discussion

3-1. Flat Plate

Figure 1 shows the lift curve and the drag polar of the flat plate for $Re = 3,000$. As shown in Fig. 1, below $\alpha = 2$ deg, the lift and drag are almost the same for all Mach numbers. From $\alpha = 3$ deg to 10 deg, the lift slope decreases with increasing Mach number. On the other hands above $\alpha = 10$ deg, the lift increases with increasing Mach number. The drag polar shows a trend corresponding to the observed lift change.

Figure 2 shows the effect of Mach number on the pressure profiles at $\alpha = 6$ and 8 deg for $Re = 3,000$. As shown in Fig. 2, for $M = 0.7$, the pressure coefficient at the trailing edge decreases with increasing angle of attack. It is considered that a separation bubble is not formed for all angles of attack. This could be the reason why the lift slope becomes lower than that for lower Mach numbers.

3-2. Triangular Airfoil

Figure 3 shows the lift curve and the drag polar of the triangular airfoil for $Re = 3,000$. As shown in Fig. 3, below $\alpha = 8$ deg, the lift changes linearity and there is almost no difference on the drag for all Mach numbers. For $M = 0.15$, the lift slope sharply increases at $\alpha = 8$ deg. On the other hand, for higher Mach numbers, the

lift curve keeps linearity even above $\alpha = 6$ deg and the drag increases more than for $M = 0.15$. For $M = 0.7$, the lift keeps increasing while the lift is kept constant for the other conditions above $\alpha = 14$ deg.

Figure 4 shows the effect of Mach number on the pressure profiles at $\alpha = 8$ and 10 deg for $Re = 3,000$. As shown in Fig. 4, the separation point moves to downstream with increasing Mach number. For $M = 0.5$ and 0.7, a pressure-recovering region does not appear. Hence, a low pressure region moves to downstream as Mach number increases. It is suggested this change in pressure distribution causes an increase of the drag with an increase of Mach number.

3-3. M Effect on Maximum Lift-drag ratio

Figure 5 shows the effect of Mach number on the maximum lift-drag ratio for a flat plate and a triangular airfoil. As shown in Fig. 5, for $Re = 3,000$, the maximum lift-drag ratio of the flat plate decreases with increasing Mach number. On the other hand, the maximum lift-drag ratio of the triangular airfoil decreases when Mach number increases for $Re = 10,000$.

4. Conclusions

To evaluate the compressibility effect on the characteristics of airfoils at low Reynolds number, we measured the aerodynamic force and pressure distribution of a flat plate and a triangular airfoil.

The results show that Mach number has an effect to delay a reattachment of shear layer, resulting in a decrease in lift near stall angle of attack. Moreover, the compressibility has an effect to move the separation point on the airfoil to downstream, that results a decrease in maximum lift-drag ratio. Finally, The compressibility effect on the aerodynamic performance is dependent on the shape of airfoils and Reynolds number.

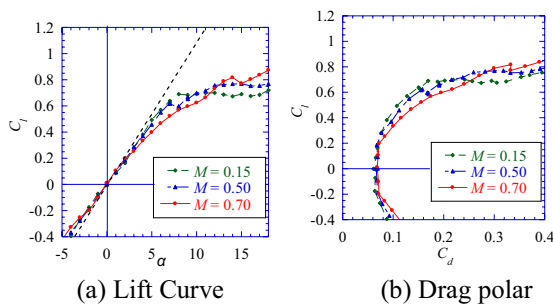


Fig. 1 Aerodynamic force of a flat plate for $Re = 3,000$

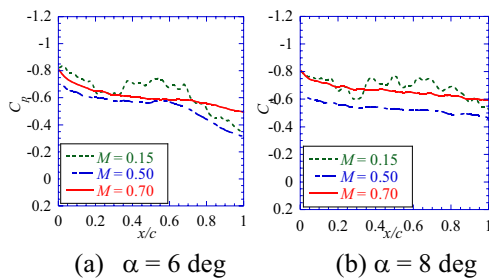


Fig. 2 Pressure profiles of a flat plate for $Re = 3,000$

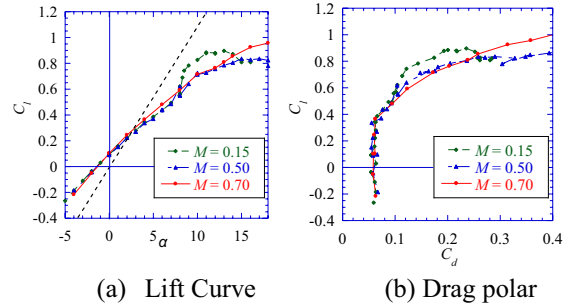


Fig. 3 Aerodynamic force of a triangular airfoil for $Re = 3,000$

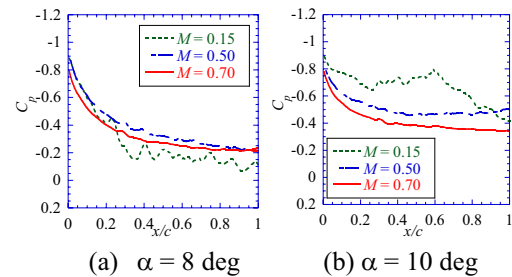


Fig. 4 Pressure profiles of a triangular airfoil for $Re = 3,000$

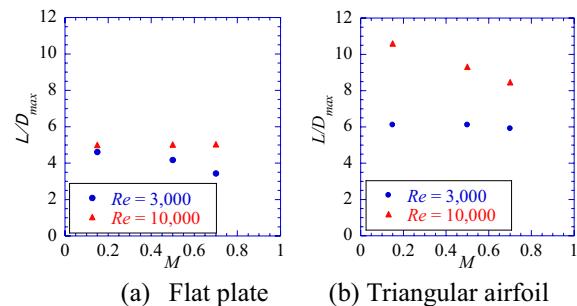


Fig. 5 M effect on maximum lift-drag ratio

References

- [1] Fujita, K., Nagai, H., Asai, K., "Conceptual Design of a Miniature, Propeller-Driven Airplane for Mars," 50th AIAA Aerospace Sciences Meeting, AIAA 2012-0847, Gaylord Opryland Resort & Convention Center Nashville Tennessee, 9-12 Jan. 2012.
- [2] Datta, A., Roget, B., Gri_ths, D., Pugliese, G., Sitaraman, J., Bao, J., Liu, L., Gamard, O., and Chopra, I., "Design of a Martian Autonomous Rotary-Wing Vehicle," Design Report, submitted to the American Helicopter Society, Winner of 17th AHS Student Design Competition, June 2000.
- [3] Tsuzuki, N. "A Study on a Miniature Rotary-Wing Vehicle for Mars Exploration: Its Feasibility and Aerodynamic Characteristics of the Rotor" Ph.D. Thesis, Tokyo University 2005.
- [4] SUWA, T., NOSE, K., Numata, D., Nagai, H., Asai, K., "Compressibility Effect on Airfoil Aerodynamics at Low Reynolds Number," AIAA Summer Conference, AIAA 2012-3029, New Orleans, 25-28 Jun. 2012.

Flow Analysis in Cerebral Aneurysm Model with Transparent Coils Placement

Masanori KUZE¹, Makoto OHTA²

1. Graduate School of Biomedical Engineering, Tohoku University, 6-6, Aramaki Aza Aoba, Aoba-ku, Sendai
2. Institute of Fluid Science, Tohoku University, 2-1-1, Katahira, Aoba-ku, Sendai
kuze@biofluid.ifs.tohoku.ac.jp

ABSTRACT

Coil embolization is one of the treatments of cerebral aneurysm. However, recanalization after the treatment will be observed frequently. The recanalization can be related to blood flow, and so flow analysis with coil is important. PIV method is one of the major ways to observe the flow in in-vitro model, however the accuracy of velocity decreases under the shade of the coils. The purpose of this study is to decrease the effect of shade of coils on the calculation and to increase the accuracy of the flow analysis in cerebral aneurysmal model inserted coils by using a transparent coil model.

1. Introduction

Cerebral aneurysm is one of the vessel diseases and the part of a cerebral artery is swelled. Rupture of a cerebral aneurysm causes fatal symptoms such as subarachnoid hemorrhage (SAH). Thus a treatment of unruptured cerebral aneurysms or an immediate treatment of ruptured cerebral aneurysms will be important.

Coil embolization is a method of embolization using metallic string called as "coil". This treatment can decrease blood flow and form the thrombus in the cerebral aneurysm. However, recanalizations of aneurysms after the treatment have been reported [1]. Preventive methods against recanalization haven't been established yet.

The blood flow in the aneurysms with coils may be related with the recanalization and regrowth. However, it is difficult to measure the flow in the aneurysm with coils, because masking will not be performed. A coil will be in the way and the shade of complicated geometries of the coils should be there, however, the shade is not observed. Then, the recognition of analysis area is not performed accurately, and as a result, the accuracy of calculation of velocity will decrease. Matsumoto [2] developed a method of masking using superimpose of images. And the accuracy of velocity around the coil will increase based on the improvement of masking method leading velocity calculation with 11% higher speed as shown in Fig.1. However, it is still not enough to measure the velocity around the coil and the shade because the more shades will increase masking area decrease the analysis area. Then, we introduced a transparent coil to reduce masking area in the analysis area.

The purpose of this study is to measure the accuracy of PIV analysis in aneurysm with coils. Analysis condition is examined when the transparent coil is inserted in a cerebral aneurysmal model.

2. Method

2-1. Making cerebral aneurysmal model

A cerebral aneurysmal model was fabricated using PVA-H (Poly Vinyl Alcohol-Hydrogel) as shown in Fig.2. The solvent was mixture of dimethylsulfoxide (DMSO, Toray Fine Chemicals Co., Ltd.) and distilled water (80/20, w/w). PVA powder (JF-17, JAPAN VAM

& POVAL Co., Ltd.) was dissolved in the solvent at 100 °C for 2 hours. The concentration of PVA solution was 15 wt%. A Metallic cylinder (ϕ 4 mm) was set in the center of the mold used as an artery, and a gypsum sphere (ϕ 10 mm) was attached on the bar used as an aneurysm. The solution was poured into an acrylic mold (98×50×50 mm). After the gelation in a freezer at -30 °C, the metallic cylinder and the gypsum sphere was removed and water displacement was performed for removing DMSO.

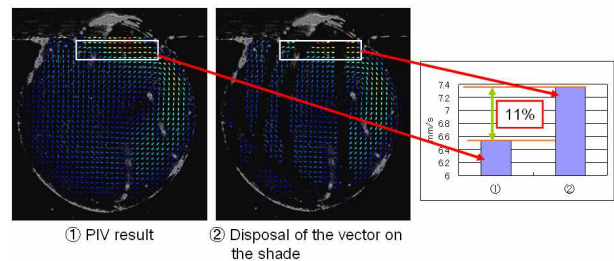


Fig. 1 Error by shade in PIV

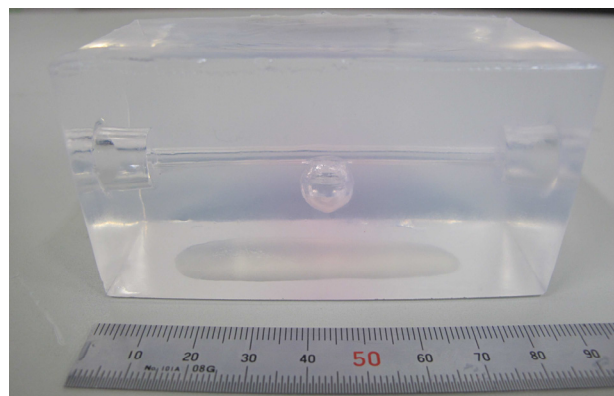


Fig. 2 PVA-H cerebral aneurysmal model

2-2. Coil model

A transparent fluorocarbon line of ϕ 0.260 mm (RIVERGE R18, KUREHA CORPORATION) was used as a transparent coil model as shown in Fig.3. The diameter of the line is similar to that of a clinical coil. The coil model was cut into 200 mm length and was inserted in the cerebral aneurysm part of the cerebral aneurysmal model.

2-3. PIV (particle image velocimetry)

Mixed solvent of 65 wt% glycerol/distilled water

solution and 35 wt% sodium iodide/distilled water solution was used as the working fluid. Glycerol/distilled water solution consisted of 61.6 wt% glycerin and 38.4 wt% distilled water, and sodium iodide/distilled water solution consisted 40.9 wt% sodium iodide and 59.1 wt% distilled water, respectively. The refractive index of the working fluid was 1.414. This refractive index was adjusted to that of the transparent coil model to vanish the shade of the transparent coil model. The kinematic viscosity of the working fluid was $4.35 \text{ mm}^2/\text{s}$ to be close to that of blood [3]. The working fluid was including particles (TECHPOLYMER MBX-20, Sekisui plastic Co., Ltd.), and the flow rate was 160 ml/min.

Nd:YAG solid-state laser (532NM-X-300MW, B&W TEK INC.) was used to provide a nominal 1mm-thick continuous laser sheet with beam splitter. The power was 100 mW and the wavelength was 532 nm. Mid-plane of the cerebral aneurismal part was illuminated with the laser sheet. Scattering particle images were acquired with high-speed camera (FASTCAM SA3, PHOTRON LIMITED) with a telescopic micro lens which had 105 mm of focal length and 2.8 of F ratio (Micro-Nikkor, Nikon Co Ltd.). The frame rate is 1000 fps and the shutter speed is 1/1000 s.

PIV analysis of cross-correlation method was performed by commercial software (DaVis version 7.2, LaVision, Inc.). The size of interrogation region (IR) ($N \times N$ pixels) was changed from 8×8 to 128×128 pixels and Overlap was 75 % as the analysis condition. After the analysis, two areas of 90×90 pixels with and without coil were defined as region of interest (ROI) and mean velocities in the area were calculated, respectively, as shown in Fig.4.

3. Results and Discussion

Figure 5 shows the mean velocities in the IRs. First, when the IR is 128×128 pixels with coil area, the mean velocity is lower than that of the other IR. To reduce the effect of the change of the brightness value pattern as much as possible, N should be set smaller [4]. Thus this size is not suitable.

In the area without coil, mean velocities in each IR is almost constant. This result indicates from 8×8 to 64×64 pixels of IR have high accuracy. On the other hand, in the area with coil, the mean velocities increase in accordance with increase of IR. This result indicates that the shade of transparent coil still remains and will decrease the velocity [2]. And the larger N makes the smaller effect of velocities reduction by coil shades. These results will lead that the IR of 64×64 pixels is the most suitable size in this ROI.

4. Concluding remarks

PIV analysis condition is examined using a cerebral aneurismal model with the transparent coil model. As the result, velocity analysis can be performed on the transparent coil, although a shade of transparent coil still remains

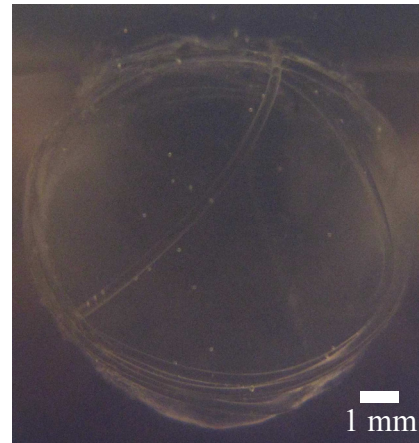


Fig. 3 Transparent coil model

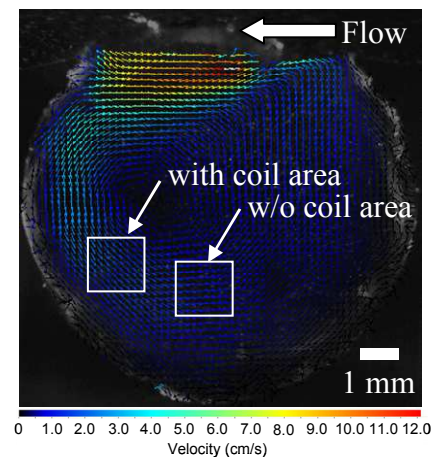


Fig. 4 PIV result and ROI

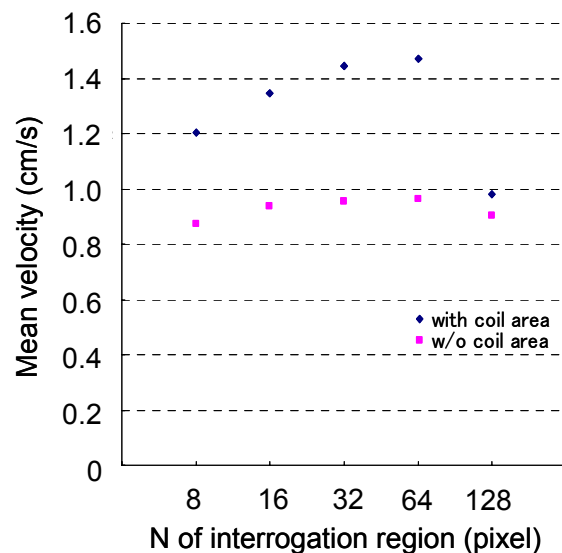


Fig.5 Mean velocity in analysis area

References

- [1] M. Hayakawa, J Neurosurg, **93** (2000), 561-568
- [2] K. Matsumoto, Master Thesis, Tohoku University (2009), In Japanese
- [3] Galduroz J.C.F., Phytomedicine, **14** (2007), 447-451
- [4] The Visualization Society of Japan, Handbook of particle image velocimetry, Morikita Publishing Co., Ltd., (2002), In Japanese

Measurement of Pressure Drop for Modeling Intracranial Flow Diverter Stent Using Porous Medium

Yukihiisa Miura¹, Hitomi Anzai¹, Toshio Nakayama², Toshiyuki Hayase³, Makoto Ohta³

¹Graduate school of engineering, Tohoku University, 6-6, Aramaki Aza Aoba, Aoba-ku, Sendai, Miyagi, Japan

²Graduate school of biomedical engineering, Tohoku University, 6-6-12, Aramaki Aza Aoba, Aoba-ku, Sendai, Miyagi, Japan

³Institute of Fluid Science, Tohoku University, 2-1-1 Katahira Aoba-ku Sendai Miyagi, Japan

miura@biofluid.ifs.tohoku.ac.jp

ABSTRACT

Method of measuring the pressure drop is proposed for characterizing flow diverter stent using porous medium based on the permeability and the friction loss to decrease the high load of computational simulation. Test section was defined and a stent was placed with several angles to flow direction to measure the permeability. The pressure drop increases in accordance with increase of the inclined angle. Pressure drops decline inversely to the diameter of the test sections, which is similar to the equation of pipe friction loss. The method may describe the values of pressure drop of each direction simultaneously.

1. Introduction

Rupture of cerebral aneurysm is a fatal disease that causes subarachnoid hemorrhage (SAH) and so the unruptured aneurysm requires early treatments. Endovascular treatment has been an attractive method because of the less-invasion. Stent is one of the main endovascular devices. It was reported that the placement of stent could reduce inflow to the aneurysm [1]. Recently, in order to emphasize the effect of flow reduction using stent, a flow diverter stent (FD) with fine and dense strut-network has been developed. On the other hand, numerical simulations allow the assessment of blood flow in the aneurysm and of effect of endovascular devices such as stent. However, in numerical simulation analysis, the reconstruction of the shape of stent requires fine numerical mesh, and huge number of mesh. Then high techniques of operators and high loads of computers are required for numerical simulations of FD. Augsburg, L. reported that modeling FD by using porous medium may solve the problem [2]. However, method for definition of parameters of pressure drop of FD has not been fixed yet. In this research, in order to establish the method of measuring pressure drop of FD, We tried several ways to measure the pressure drop and compared them.

2. Method

2.1 Construction of FD stent shape

Stent used in this research was made plane by 3D CAD software, Pro/ENGINEER Wildfire 4.0 (PTC, Needham, USA). Silk stent (Balt International, Montmorency, France) was used as a reference (Fig.1). The width of strut was 25 μm , and every strut exists at about 250 μm intervals.

2.2 Measuring pressure drop of FD

In order to measure pressure drop of FD, a test section with long pipe (1.128 mm of diameter and 100 mm length) was assumed. Firstly, FD was placed vertically to flow direction at the center of pipe to measure the pressure drop in the vertical direction. Secondary, the pressure drops with inclined stent were measured for reaching the value of pressure drop in the horizontal direction. The pressure drop was plotted in

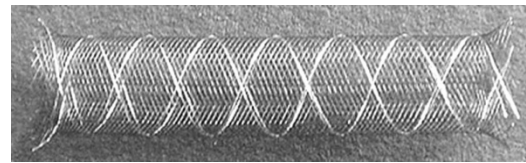


Fig.1 Image of Silk stent [3]

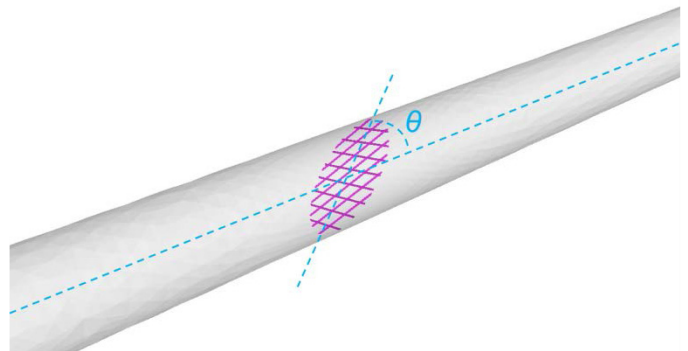


Fig.2 View of stent inclined in test section

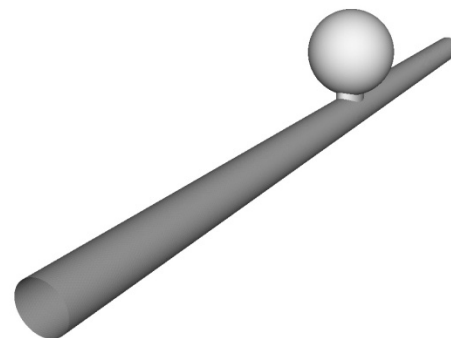


Fig.3 Ideal aneurysm model

accordance with decreasing the inclined angle. And then the pressure drop at 0 degree was obtained as the intercept of approximation formula. Next, the inlet velocity was changed and the pressure drop was measured to plot the relationships between the pressure drop and inlet velocity. This graph was used to characterize the porous medium for the stent.

2.3 Modeling the flow of FD with Porous Medium

The flow in the porous medium was modeled based

on the addition of a momentum source term to the standard fluid flow equations. This term was composed of a viscous resistance term and inertial resistance term as follows.

$$\Delta p = \left(\frac{\mu}{\alpha} v_i + C_2 \frac{1}{2} \rho v_i^2 \right) \Delta e \quad (1)$$

$$\Delta p = av^2 + bv \quad (2)$$

where, i is the i th (x , y , or z) coordinate, v is the velocity, α is the permeability, C_2 is the inertial resistance factor, μ is the viscosity, and ρ is the density. Δe is the porous medium thickness. If the pressure drop is approximated as eq. (2), we can obtain two pressure coefficient, $1/\alpha$ and C_2 .

2.4 Simulation condition

In all simulations of this study, the inlet condition was defined as velocity condition. And the outlet condition was applied by using the constant pressure. Density of working fluid was 1050 kg/m^3 , and viscosity of working fluid was 0.0035 Pas , assuming blood. The walls of artery and aneurysm were adopted as non-slip condition, and the flow was steady.

Construction of geometries and generation of mesh were performed by using GAMBIT2.4 (Ansys Inc., Canonsburg, USA) and Tgrid5.0.6 (Ansys Inc., Canonsburg, USA). FLUENT6.3 (Ansys Inc., Canonsburg, USA) was used as solver.

The aneurysm models with FD and porous medium were a 3D-ideal shape shown in Fig.3. The diameter of parent artery was 4 mm and the diameter of aneurysm was 10 mm . FD and porous medium were placed at the neck of aneurysm.

3. Results and Discussion

The relationships between pressure drop and inclined angle is shown in Fig.4. The values of pressure drop are normalized using the length of stent. The pressure drop decreases in accordance with decreasing inclined angle.

The graph of pressure drops with change of diameter of test sections is shown in Fig.5. The pressure drop of pipe without stent follows eq.(3) and eq.(4),

$$\Delta P = \lambda \frac{l}{d} \frac{\rho u_m^2}{2} \quad (3)$$

$$\lambda = \frac{64}{Re} \quad (4)$$

where, l is distance and d is diameter of pipe. u_m is mean velocity, and λ is frictional loss coefficient. This is called equation of *Darcy-Weiswach*. As the theoretical formula of pipe friction loss, the pressure drops of FD also decline inversely to diameter of the test sections.

Comparing with the vertical pressure drop, the horizontal pressure drop is strongly affected from the volume of test section. Therefore, the methodology of diameter of test section for calculation of horizontal pressure drop will be important.

Combining these methods will develop an universal method for determination of pressure drop.

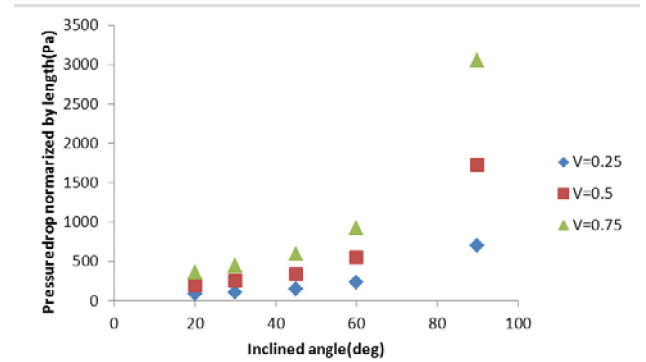


Fig.4 Relationships between pressure drop and inclined angle

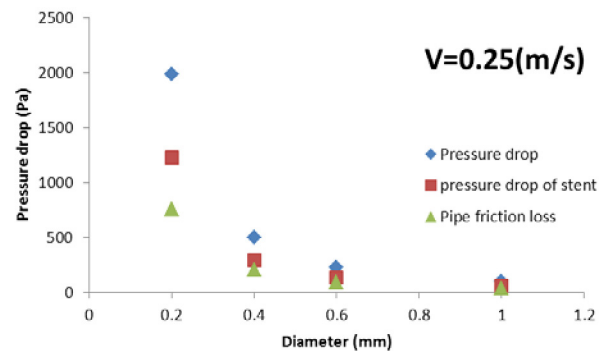


Fig.5 Relationships between pressure drop and diameter of test section

4. Concluding remarks

Pressure drop of stent was examined by using inclining to flow direction and change of diameter for horizontal direction. The pressure drop decreases in accordance with decreasing inclined angle. Whereas, the pressure drop of stent declines inversely to diameter of test section. Combining these results shows a necessity for development of an universal method for determination of pressure drop.

References

- [1] M. Aenis, J. Biomech. Eng. **199**(1997), 206 .
- [2] L. Augsburg, J. Ann. Biomed. Eng. **39**(2010), 850.
- [3] <http://jnls.bmj.com/content/early/2010/06/25/jnls.2010.002725.full>

Assessment of Supersonic Free-flight Experiment using a Plate Shaped Sabot Aimed at the Biplane Model

Yuta Saito¹, Kakuei Suzuki², Takahiro Ukai¹, Takahiro Imaizumi², Atsushi Toyoda²,
Takaya Uchida¹, Akihiro Sasoh², Shigeru Obayashi¹

¹Institute of Fluid Science, Tohoku University

²Department of Aerospace Engineering, Nagoya University

E-mail of corresponding author: saito@edge.ifs.tohoku.ac.jp

ABSTRACT

A ballistic range experiment using a plate shaped sabot aimed at biplane model is conducted. Sabot separation is one factor that causes unstable flight of projectile. This experiment was performed in order to conduct a precise free-flight experiment. In this experiment, plate shaped sabot is employed. The experiment result indicates that plate shaped sabot helps stable flight for the projectile.

1. Introduction

Aircrafts made outstanding progress since the Wright brothers' first flight. In the civil aircraft, Concorde succeeded in the supersonic flight at Mach 2. However, its actual service was ended because of the noise (Sonic boom) and fuel consumption caused by the shock wave which is created during the supersonic flight. For overcoming this problem, biplane airfoil is proposed by Adolph Busemann^[1]. The airfoil cancels the compression wave and the expansion wave between the wings, and it could be one of many solutions for these problems. However, reduction of the sonic boom using biplane airfoil has not been proofed by supersonic wind tunnel, because shock wave generated from sting which holds the model affects the measurement profoundly. In order to avoid effect of the sting, free-flight experiment using ballistic range^[2] is known as an experimental method for the evaluation of the sonic boom.

A projectile is accelerated with a sabot which envelopes the projectile. These parts are separated by difference of the air drag, and projectile flies in the test chamber. However, a problem became clear that the flight attitude is not stable in each experiment due to the effect of the sabot. During the sabot separation, the sabot exerts a force on the projectile, and projectile tilts to one side. Some studies about configuration of the sabot have been conducted, and a projectile flies stable when the sabot has a plate part behind the projectile^[3].

In this experiment, plate shaped sabot was employed to confirm its characteristic for the experiment using biplane model.

2. Experimental setup

The ballistic range placed at Nagoya University is used in this study^[2,4]. The ballistic range has a distinct and unique feature that aerodynamic sabot separation in-tube^[2]. After experiencing an acceleration driven by the driver gas (He) with 3.75 [MPa], the sabot experiences a large pressure unbalance, and thereby being decelerated, while a projectile keeps its entry speed. The projectile ejected from the muzzle to the test chamber depressurized at 30 [kPa] (air), and pressure distribution was measured by pressure transducers (PCB112A21) at 150 [mm] under from the flight pass. The flow field around the projectile was visualized by

Schlieren method.

The total weight of the model is heavy for this apparatus. Therefore, drive gas pressure must be high for getting Mach 1.7. Also, ambient gas pressure is set low, because the test chamber's pressure gets high and it could cause breaking of the equipment after the shoot of the model.

Figure 1 shows a projectile and a sabot. The projectile is shaped like a combined circular cylinder and circular cone. The sabot is shaped like a plate and it has a Bridgman seal. This structure is able to accelerate adequately thanks to the efficient high pressure behind the sabot. The total weight is 30[g] in order to simulate the mass of the biplane model.

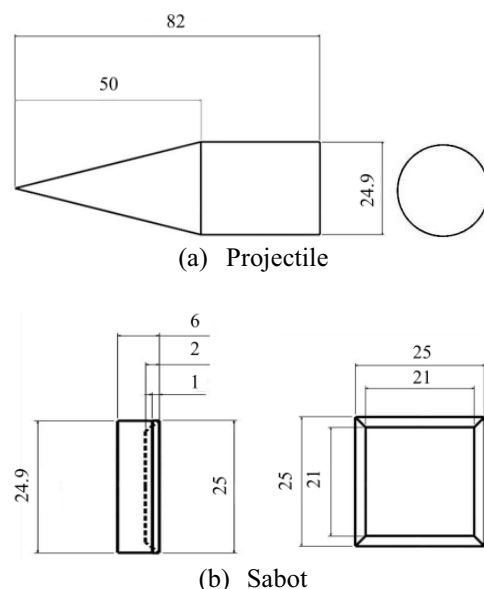


Fig. 1 Configuration of the model

3. Results and Discussion

Schlieren image of the experiment is shown in Fig. 2. The projectile flies stable around Mach = 1.7 and A.o.A = 0 [deg]. In this experiment, the used sabot shaped like a plate. For this reason, the projectile is not forced by sabot to radial and tangential direction.

However, separation distance between the projectile and sabot is not far enough for getting pressure distribution from only the projectile. Only the projectile

was calculated using Computational Fluid Dynamics (CFD) for acquiring pressure distribution of the projectile. For the CFD analysis, Euler calculation was conducted employing unstructured mesh CFD solver called TAS-code (Tohoku University Aerodynamic Simulation code)^[5-7]. The CFD result at symmetry section is shown in Fig. 3, and experiment and CFD pressure distribution at the pressure measurement position is shown in Fig. 4. C_p represents the value of the pressure fluctuation normalized by the free-stream dynamic pressure. c represents the cord length of the projectile (82 [mm]) and x is distance from position where first compression wave is observed at the pressure measurement position.

Experimental and CFD results indicate a similar profile until $x/c = 0.9$, while these results show different characteristic after that. CFD result indicates pressure declines until $x/c = 1.7$, nevertheless pressure value rises little around $x/c = 1.1$ due to recompression. On the contrary, experimental result indicates an instantaneous rise in the pressure at $x/c = 1.0$. Compression wave from sabot affects the pressure distribution profoundly, thus N wave is observed after the area. For getting enough sabot separation distance, ambient gas pressure should be higher.



Fig. 2 Schlieren image

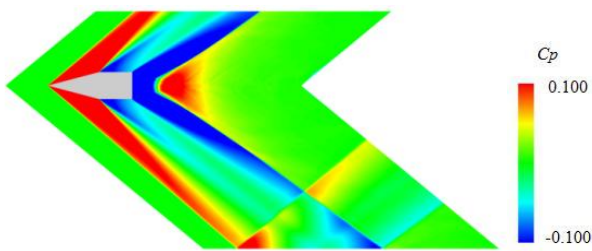


Fig. 3 CFD result at symmetry section

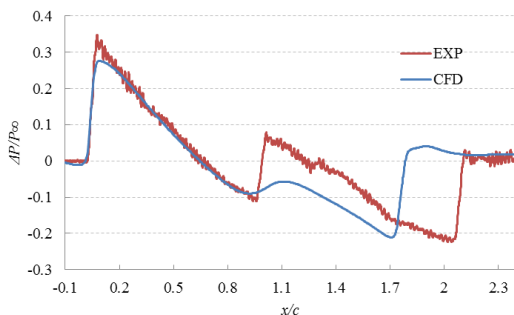


Fig. 4 Pressure distribution

4. Conclusion

For making sure to conduct the free-flight experiment precisely using the biplane model, the same gross weight mode is experimented. The unstable flight attitude is estimated to be caused by the sabot separation. As a sabot for this experiment, a plate shape type was employed. Followings were obtained.

- (1) The plate shaped sabot helps stable flight for the projectile
- (2) Ambient gas pressure must be high enough to provide sufficient

The problem about the sabot separation distance can be overcome by releasing the ambient gas to atmosphere.

5. Future works

This experiment reveals that plate shaped sabot is effective for the stable flight. In this experiment, configuration of the projectile is simple that the sabot has to have a function just for accelerating. However, biplane model is not simple. The configuration of the sabot must be complex to have a function for fixing in the acceleration section. For future works, a sabot must be designed for a non-axisymmetric model. Then, the pressure measurement using biplane models can be experimented.

References

- [1] Busemann, A., "The relation between minimized drag and noise at supersonic speed," Proc. Conference on High-Speed Aeronautics, Poly. Inst. Brooklyn, pp. 133-144, 1955.
- [2] Sasoh, A. and Oshiba, S., "Impactless, in-tube sabot separation technique useful for modest-sized supersonic ballistic ranges," Rev. Sci. Instrum., 77, 105106, 2006.
- [3] Callagban, J., "A feasibility investigation concerning the simulation of sonic boom by ballistic models," NASA contractor report, NASA CR-603, 1966.
- [4] Sasoh, A., et al., "Aluminum-extrusion, square-bore, aero-ballistic range for launching three-dimensional projectiles," International Journal of Aerospace Innovations, 1757-2258, pp. 147-156, 2010.
- [5] Ito, Y., and Nakahashi, K., "Direct Surface Triangulation Using Stereolithography (STL) Data," AIAA Paper 2000-0924, 2000.
- [6] Sharov, D., and Nakahashi, K., "Hybrid Prismatic / Tetrahedral Grid Generation for Viscous Flow Applications," AIAA Paper 96-2000, 1996.
- [7] Ito, Y., and Nakahashi, K., "Unstructured Mesh Generation for Viscous Flow Computations," Proceedings of the 11th International Meshing Roundtable, Ithaca, NY, pp. 367-377, 2002.

A Study for Transport Phenomena of Nanoscale Gas Flow in Porous Media

Tomoya Oshima, Shigeru Yonemura, and Takashi Tokumasu
Tohoku Univ., Katahira 2-1-1, Aoba-ku, Sendai, Japan, 981-8577
oshima@chapman.ifs.tohoku.ac.jp

ABSTRACT

The direct simulation Monte Carlo (DSMC) method is suitable to solve the transport phenomena in porous media with pores as small as molecular mean free paths of gases because we need to consider molecular motions directly instead of treating gas flow as continuum. In this work, we considered gas flows driven by pressure gradient in porous media imitated by locating nanoscale spheres randomly, and performed numerical simulations of gas flow without any surface reaction to clarify transport phenomena in porous media. We investigated effects of pressure gradient, diameter of spheres, and porosity on gas flow rate.

1. Introduction

Gas flow with surface reaction in porous media appears in various fields of engineering, e.g. catalytic converters and fuel cells. In order to improve the performance of such devices, it is important to understand transport phenomena in porous media. In porous media with pores as small as a molecular mean free path, i. e. Knudsen number Kn of gas flow in the narrow channel is in the order of unity. Therefore, the general solution based on the Navier-Stokes equation cannot be applied for this kind of flow, but the direct simulation Monte Carlo (DSMC) method [1-3] is suitable to solve the transport phenomena in porous media. We investigate characteristics of nanoscale gas flows in porous media by performing DSMC simulations.

2. Calculation Method

In this study, we make porous media by locating spherical particles randomly. Calculating gas flow without surface reaction, we treat simulation molecules as hard sphere particles, and treat molecular reflection at solid surface as diffusive reflection. Molecules treated here are H_2 . The temperature at inlet and outlet is 293 K, and the temperature at solid surface is also 293 K. We set gas pressure 101325 Pa at inlet, and also set negative pressure gradient by setting lower gas pressure at outlet. Here, we treat steady flows.

3. Results and Discussion

Figure 1 shows the relation between gaseous mass flux and porosity. We treated 3 sets of sphere locations for each porosity value. The gaseous mass flux, F is given by

$$F = mnU, \quad (1)$$

m is the mass of molecules, n is the number density, and U is the mean gas velocity. This figure indicates that mass fluxes for any sphere locations agree one another. In the cases treated here, the effect of sphere locations, i.e. the effect of internal structures of porous media could not be recognized. Figure 2 shows the relation between the gaseous mass flux and the pressure gradient, dp/dx . It is found that the gaseous mass flux is proportional to the pressure gradient. This trend agrees

with the Fick's law for molecular diffusion and the Poiseuille flow of a continuum. Figure 3 shows the relation between the gaseous mass flux and diameter of solid spheres for 4 different porosities in the liner scale (upper) and in the double logarithmic scale (lower). The mass flux increases with increasing diameter d of solid spheres. When we change the diameter of solid spheres under the condition of constant porosity, we put spheres at similar positions. The characteristic length of porous channel is proportional to the diameter of solid spheres. In the double logarithmic graph, the slope of the gaseous mass flux for the case of porosity = 0.6 is 1.03, whereas the slope for the case of porosity = 0.9 is 1.28. The relation between the gaseous mass flux F and the slope α is as follow.

$$F = C_0 d^\alpha \quad (2)$$

Here, C_0 is a constant. Those results indicate that the gaseous mass flux shows a curve with higher order of diameter d for high porosity. Figure 4 shows the relation between the gaseous mass flux and porosity for 5 different diameters d , in the liner graph (upper) and in the double logarithmic graph (lower). The gaseous mass flux increases with increasing porosity. And the slope in the double logarithmic scale increases when diameter of spheres increases.

4. Conclusion

We performed the Direct Simulation Monte Carlo (DSMC) simulations to analyze transport phenomena in porous media, by imitating porous media by spherical particles located randomly. Results are summarized as follows.

1. The gaseous mass fluxes for different locations of solid spheres agree well one another under the condition of the same diameter of spheres and the same porosity.
2. The gaseous mass flux is proportional to the pressure gradient, and this trend agrees with the Poiseuille flow of a continuum and the Fick's law for molecular diffusion.
3. Under the condition of the constant porosity, the gaseous mass flux increases with increasing diameter of solid spheres. It shows curves with higher order for higher porosities.

4. Under the condition of the constant diameter, the gaseous mass flux increases with increasing porosity. It shows curves with higher order for larger diameters.

References

[1] G. A. Bird, "Molecular Gas Dynamics and the Direct Simulation of Gas Flows", Clarendon, Oxford, 1994.
 [2] S. Yonemura, "Particle Modeling of High Knudsen Number Flows and Plasmas", *Nano-Mega Scale Flow Dynamics in Highly Coupled Systems*, (2008), Tohoku University Press. pp.57-99.
 [3] K. Nanbu, "Stochastic Solution Method of the Boltzmann Equation I" Institute of Fluid Science, Tohoku University Press, (1992), pp. 47-93.

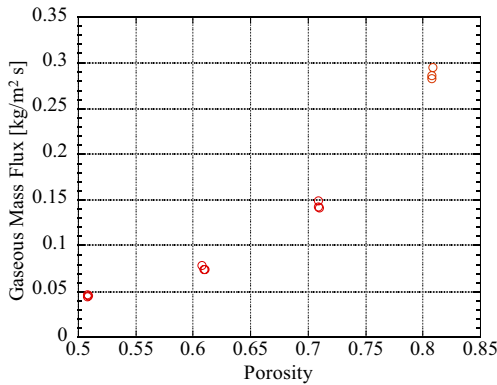


Fig. 1 Effects of sphere locations. ($d = 60$ nm, $dp/dx = -7.51$ Pa/nm)

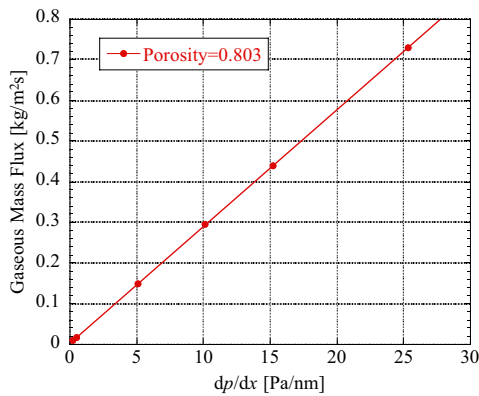


Fig. 2 Relation between the gaseous mass flux and pressure gradient. ($d = 60$ nm, Porosity=0.803)

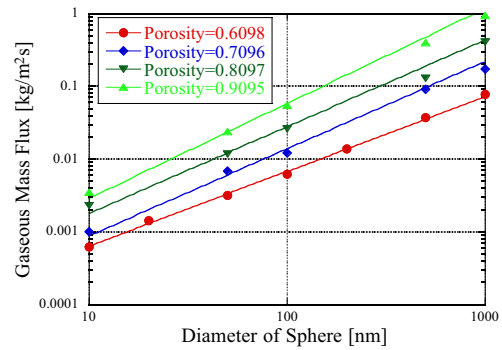
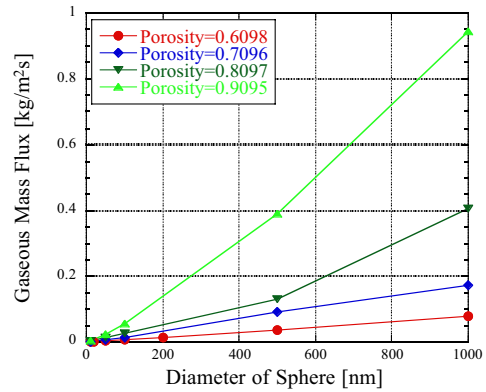


Fig. 3 Relation between the gaseous mass flux and diameter of spheres. ($dp/dx = -0.3378$ Pa/nm)

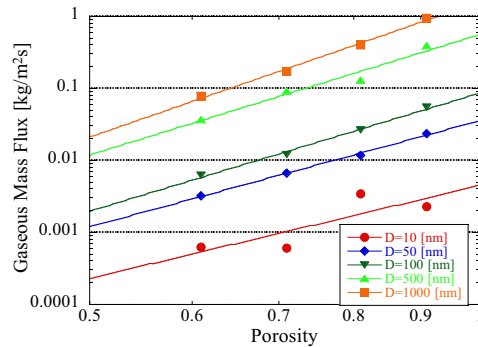
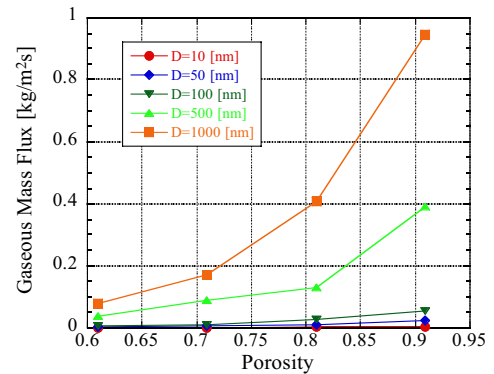


Fig. 4 Relation between the gaseous mass flux and porosity. ($dp/dx = -0.3378$ Pa/nm)

Characterization of Fluid Flow in Fractured Geothermal Reservoirs based on Fractional Derivative Mathematical Model

Hiroshi Makita¹, Anna Suzuki¹, Yuichi Niibori², Toshiyuki Hashida²

Graduate School of Environmental Studies, Tohoku University,
6-6-01 Aza-Aoba, Aramaki, Aoba-ku, Sendai 980-8579, Japan

Graduate School of Engineering, Tohoku University, 6-6-01 Aza-Aoba, Aramaki, Aoba-ku, Sendai 980-8579, Japan

E-mail: hiroshi.makita@rift.mech.tohoku.ac.jp

ABSTRACT

Modeling fractured reservoirs is a crucial step for the design of geothermal energy extraction and requires the knowledge of underground fluid flow. The objective of our study is to characterize flow through fractured rocks using a transport model that includes fractional-order derivatives. We simulate tracer transport employing fracture network models where the fractal dimensions are in the range of 2.0-3.0 and the fracture densities are 0.7 and 1.5[m²/m³]. Comparison of the flow parameters with the properties of the fracture networks has demonstrated the potential of predicting the structures of fractured reservoirs from tracer responses.

1. Introduction

It is needed to understand structures of geothermal systems in order to predict the amount of thermal energy extraction^[1]. Tracer tests are often performed to obtain hydraulic parameters and to model geothermal systems^[2]. The Advection-Dispersion Equation (ADE) based on Fick's law has generally been used to describe mass transport in the underground. In this study, we use the fractional Advection-Dispersion Equation (fADE)^{[3][4]} instead of the classical ADE to calibrate tracer curves, as follows:

$$\frac{\partial C}{\partial t} + b \frac{\partial^\gamma C}{\partial t^\gamma} = \frac{1}{Pe} \frac{\partial}{\partial X} \left(\frac{\partial^\alpha C}{\partial X^\alpha} \right) - \frac{\partial C}{\partial X}, \quad (1)$$

where C is the concentration of the fluid, X the transverse spatial coordinate, t the time, b the capacity coefficient for the fractional derivative, Pe the Peclet number, α, γ , ($0 < \alpha \leq 1$, $0 < \gamma \leq 1$) fractional space and time derivatives, respectively. The second term on the left-hand side models the retardation process associated with secondary branched fractures and matrix permeability. The first and second terms on the right-hand side express the dispersion and advection in the direction of fluid flow, respectively.

There are two main reasons why we use the fADE model for tracer analyses. First, the fADE model is more applicable than the classical ADE model^{[3][5]}. It is known that the classical ADE provides no appropriate expression for non-Fickian transport which is often observed in heterogeneous media including geothermal fields^{[3][6]}. Second, Fomin et al. have demonstrated that non-Fickian transport can be described considering fractal geometry in fractured rocks^[4]. If we can predict the fractal dimension of the underground using tracer tests with the fADE model, it will be able to contribute significantly to reservoir modeling. We examine the relationship between underground flow and fractal dimension to explore the feasibility of predicting fractal dimensions of fractured rocks based on the fADE.

2. Numerical Method

We produce tracer curves numerically using FRACSIM-3D^[7] that can calculate underground fluid flow. We assume a discrete fracture network model which is a three-dimensional discretized grid where fra-

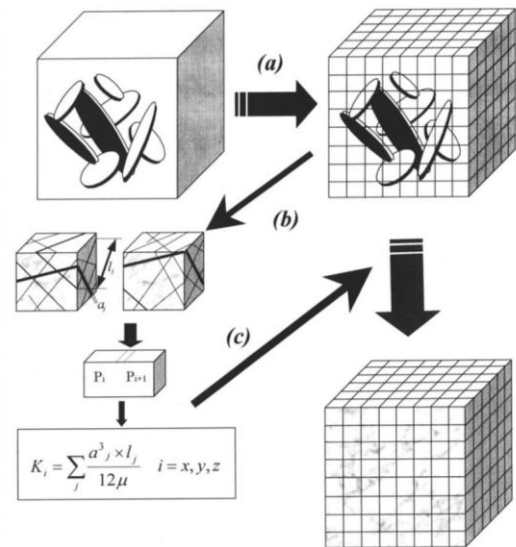


Fig. 1 Concept of converting the discrete fractures in stochastic fracture network to the equivalent permeability at the element interfaces.

ctures are embedded (Fig.1a). The fractures are generated based on fractal geometry and the governing equation given by:

$$N = C_f r^{-D_R}, \quad (2)$$

where N is the number of fractures, C_f the fracture density parameter, r the radius of fractures, D_R the fractal dimension, respectively. The procedure of mapping the flow properties to the grid is illustrated in Fig.1b, in which the quantity of fluid flow from block to block is controlled by Darcy's law with the "permeability" that is calculated as follows:

$$K_i = \sum_j \frac{a_j^3 \cdot l_j}{12 \mu}, \quad i = x, y, z \quad (3)$$

where K_i is the "equivalent permeability" connecting the grids, μ the viscosity of fluid, a_j and l_j the aperture and the length of fractures intersected to the block face, respectively. Steady state flow solutions in the 3D grid are solved numerically using an iterative multigrid algorithm (Fig.1c). Movements and traveling time of tracers are calculated by probabilities determined by flow rate. Thus, the flow pattern and tracer curve for the fracture network is solved by converting it to an equivalent

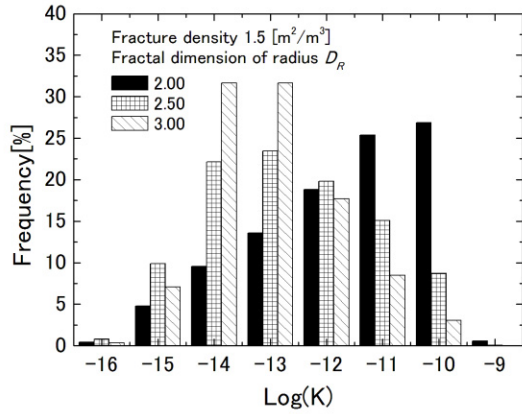


Fig.2 Log permeability histogram for fracture networks.

-ent stochastic continuum. After obtaining tracer curves, we apply the fADE model and explore the validity of the model. The fADE parameters are defined by fitting calculated tracer curves for various fractal dimensions.

3. Results and Discussion

Permeability distribution for different fractal dimensions are shown in Fig.2. The most frequently observed equivalent permeability of the elements is 10^{-10} [m²] for low fractal dimension $D_R=2.0$ and 10^{-14} [m²] for high fractal dimension $D_R=3.0$. High permeability is coupled to a low fractal dimension and vice versa. The higher the fractal dimension becomes, the more small fractures are observed. This means that the permeability histogram is related to the size of fractures and large fractures facilitate the movement of fluid. Moreover, the variance of permeability decreases when the fractal dimension increases. The higher the fractal dimension is, the more homogeneous the fracture network is. These phenomena are observed at both fracture densities 0.7 and 1.5[m²/m³]. Simulated tracer curves by FRACSIM-3D are shown in Fig.3. The fracture density is set to be 1.5[m²/m³] for all the fracture networks. Tracer curves for low fractal dimension have sharp peaks at earlier time. On the other hand, tracers are retarded for high fractal dimensions relative to low fractal dimension. Those phenomena are considered due to the permeability distribution and the size of fractures.

The fitting result for tracer curves with various fractal dimensions is shown in Fig.4. It shows that γ increases with the increase of fractal dimension. The same trend holds true for b . The space index α and Pe , however, may not always increase or decrease. The increase of index γ means the decrease of heterogeneity. This describes the phenomenon well that the fracture network becomes homogeneous when the fractal dimension becomes high. In addition, the increase of b shows the increase of small fractures in the media. This corresponds closely to the property that the small fractures increase in the fracture network when the fractal dimension becomes high. These results indicate the fADE model based on fractal geometry is capable of capturing key aspects of flow and transport in fractured rocks and it may be possible to predict fractal dimensions of fractured rocks by tracer tests.

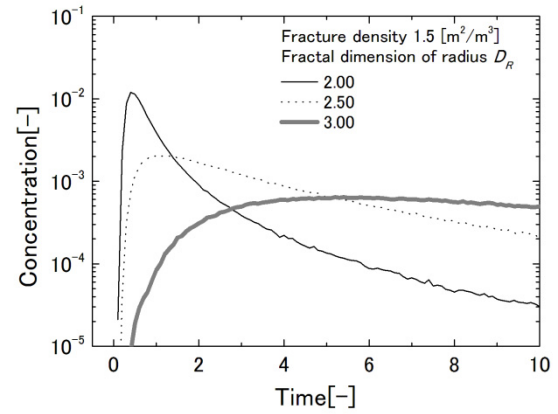


Fig.3 Simulated tracer curves for $D_R = 2.0, 2.5, 3.0$.

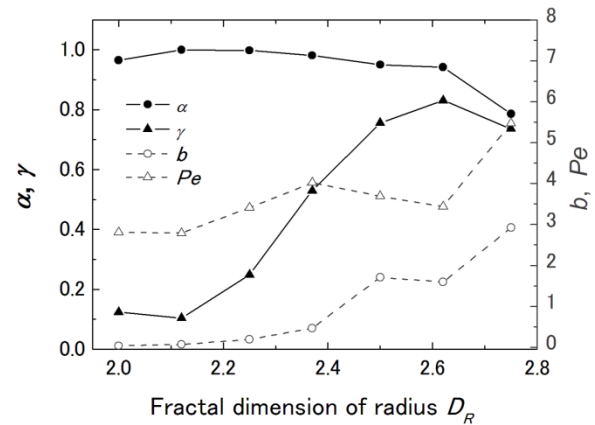


Fig.4 Relationship between the fADE parameters and fractal dimension of radius D_R at 1.5[m²/m³].

4. Concluding remarks

One of the main motivations of this study is to reveal and to quantify parameters by the fADE model in fractured networks for various fractal dimensions. Numerical experiments have been used to explore the predictability of fractal dimensions using the fADE model parameters that give the knowledge of subsurface heterogeneity. The fADE parameters deduced from the tracer analyses correspond closely to the characteristic properties of the fracture network models. Further investigation, including theoretical, numerical experiments are needed to establish the predictive model of fractal dimensions from tracer curves using the link between the parameters and the fractal dimensions.

References

- [1] S. Finsterle, *Vadose Zone J*, **3** (2004), 747-762.
- [2] P. Neuman, *Hydrogeol J*, **13** (2005), 124-147.
- [3] D. Benson, S. Wheatcraft, and M. Meerschaert, *Water Resour Res*, **36** (2000), 1403-12.
- [4] S. Fomin, V. Chugunov and T. Hashida, *Proc. R. Soc. A* **461** (2005), 2923-2939.
- [5] Y. Zhang, D. Benson and D. Reeves, *Water Resour Res*, **32** (2009), 561-568.
- [6] B. Berkowitz and H. Scher, *Water Resour Res*, **36** (2000), 149-158.
- [7] Z. Jing, *J Geophys Res*, **105** (2000), 663-679.

Development of Micro-satellite for International Scientific Missions

Yoshihiro Tomioka, Kazufumi Fukuda, Nobuo Sugimura, Yuji Sakamoto, Toshinori Kuwahara, Kazuya Yoshida
Department of Aerospace Engineering, Tohoku University
6-6-01 Aoba, Aramaki-Aza, Aobaku, Sendai, Miyagi, Japan
tomioka@astro.mech.tohoku.ac.jp

ABSTRACT

The Space Robotics Laboratory (SRL) of Tohoku University is developing 50kg-class micro-satellite "RISESAT" now. RISESAT will install some scientific observation components offered by international scientific institution because its main mission is international scientific observation. RISESAT project is aiming to develop general-purpose bus system that can be installed various mission components. In this paper, we show that overview of RISESAT bus system, mission, and system verification test.

1. Introduction

Recently, the development of micro-satellites weighing 100kg or less has been paid great attention. In the future, the needs of micro-satellites will be greater in the fields of Earth science observation and engineering demonstration with the latest technique because its risk and cost is smaller and development period can be expected shorter than bigger satellites.

The Space Robotics Laboratory (SRL) has successfully developed a class of 50kg satellite "RISING (SPRITE-SAT)" and has launched in January 2009 as a piggyback satellite of the H-IIA rocket. In Jun 2011, we have succeeded in development of "RISING-2" that is based in development of RISING. It is finalizing about software now. July 2012, we are developing the third micro-satellite "RISESAT". It is based in experience of RISING and RISING-2 development. RISESAT project is aiming to develop general-purpose bus system that can be installed various mission components.

In this paper, we show that overview of RISESAT bus system, mission, and system verification test.

2. Bus system

Fig.1 shows outer and interior view of RISESAT. Table.1 shows the specification of RISESAT. The size of RISESAT is 500x500x500[mm], and its mass is approx 55[kg]. RISESAT has two deployment solar array panel that can be improved its generating power condition. Its main structure system is "Central pillar configuration". So, many of component are installed on the central pillar is located on center of satellite. Because of it, RISESAT has superior specification about structure strength and on-orbit thermal condition for components. The central pillar configuration has been adopted in RISING and RISING-2. In RISESAT project, we have added improvement into its traditional configuration. We can install more components than previous satellites by new configuration. Furthermore, in the new configuration, we can change its mission components easily without change its bus components, because the area for installing of bus and mission components are separated. So, RISESAT bus system is general purpose bus system that can be installed various mission components.

Fig.2 shows the configuration of electrical system of RISESAT. There are four main control equipments in it,

SCU: Satellite Central Unit, PCU: Power Control Unit, ACU: Attitude Control Unit and SHU: Science Handling Unit. PCU controls charge and discharge of battery and power of each component. ACU controls sensors and actuators, for example, GYRO sensor and Reaction Wheels. It also calculates state of satellites attitude. SHU controls science observation components and processes observation data. SCU is located in center of those units and controls the telemeter and command with ground station. It is one of the most important equipment of satellite, so it is essential that it operates correctly at any time. To provide against contingencies, it has redundant system with CPU and FPGA.

Table 1. Specification of RISESAT

Size and Weight	
size	Smaller than W500 x D500 x H500 mm
weight	less than 55 kg
Orbit	
type	Sun synchronous Orbit
local time	9:00 – 15:00 (Default LTDN 10:30)
altitude	between 500 – 900 km
inclination	approx. 98 deg
Attitude determination and control	
method	3-axis stabilization
pointing accuracy	< 0.1 deg (3 σ) (Reqs.) < 0.04deg (3 σ) (Objectives)
pointing stability	6"/s
sensors	star sensor (2), Fiber Optical Gyro (3-axis) magnetometer (3-axis), GPS receiver (1)
actuators	course and accurate sun sensors (4 π) reaction wheels (4) magnetic torquers (3-axes)
Power supply	
solar cells	GaAs multijunction cell 10 series x 5 parallel x 3 panels (Deployable panels and one body panel) 10 series x 1 parallel + 10 series x 2 parallel
battery unit	9 series x 2 parallel MiMH (3.7Ah, 18V)
max. power generation	> 100 W
max. power consumption	> 50 W
Communication	
command uplink	UHF, 2400 bps at Sendai station, Japan
HK downlink	S-Band, 0.1 W, 38400 bps – max. 500 Kbps main: Sendai station, Japan sub: Fukui Univ. of Tech. station, Japan sub: Kiruna station, Sweden
Mission data downlink	X-band, max. 2.45 Mbps main: Fukui Univ. of Tech. station, Japan sub: Sendai station, Japan

3. Mission

The main mission of RISESAT is scientific observation with using scientific observation equipments. The missions are follow: (1)High precision earth imaging by "High Precision Telescope (HPT)", (2)Observation of TLE (Transient Luminous Events) in upper atmosphere by "Dual-band Optical Transient Camera (DOTCam)", (3)Observation of Ocean by "Ocean Observation Camera (OOC)", (4)Measurement of radiation quantity by "Three Dimensional Silicon Detector Telescope (TriTel)", (6)Observation of radiation particle by "TIMEPIX Space Radiation micro-Tracker (TIMEPIX)", (7)Observation of Geomagnetic by "Micro Magnetic Field Sensor (μ MAG)", (8)High speed light communication downlink by "Very Small Optical Transmitter for component validation (VSOTA)". Most of the mission equipments are offer from foreign institutes. Fig.3 shows some mission equipments of RISESAT.

4. System verification Test

Satellites will be launched to on-orbit by rocket. They will be exposed to severe vibration and acceleration environment at launch. Moreover, they will be exposed to severe thermal and radiation environment on orbit. We need to do various tests to confirm satellites endure those environments. At the same time, of course, we need to check that satellite will be not destruction at launch and operate correctly on orbit. RISESAT project is in EM (Engineering Model) development phase. EM is a test model for verification. Before EM development phase, we did a vibration test with dummy mass model (MTM: Mechanical Test Model) of RISESAT as a test of structural verification, and have confirm there is no flaw about structure. Moreover, we selected appropriate device for equipment of RISESAT by serious radiation testing. In the future, we will complete development of RISESAT EM, do vibration test, separation shock test and thermal vacuum test with checking that there is no flaw in its system. At the same time, we will do electrical test by simulating real satellite's operational environment, and make some plans of satellite's operation process.

5. Conclusion

In this paper, we showed that overview of system, mission and verification test of RISESAT. RISESAT project is in EM development phase. We will develop FM (Flight Model) after developing EM of RISESAT. It will be launched by a rocket in 2013 or 2014.

SRL is aimed to establish bus system and simulation environment for development of general-purpose mission satellite. We will realize those environments through RISESAT project.

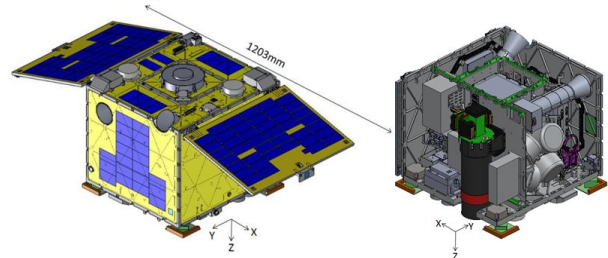


Fig.1 Outer and interior view of RISESAT

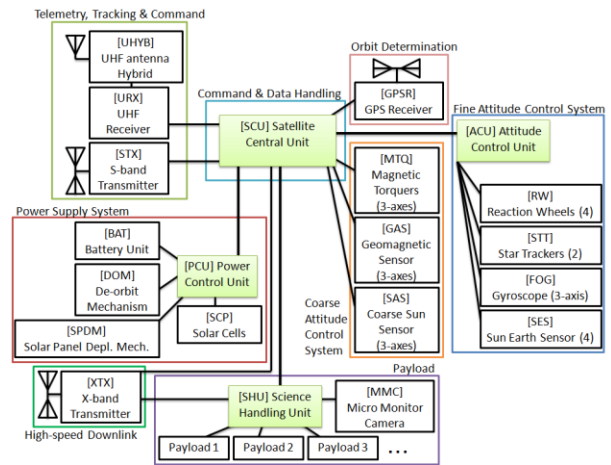


Fig.2 System Electrical Architecture of RISESAT



Fig.3 Mission Payloads

References

- [1] T. Kuwahara, K. Yoshida, Y. Sakamoto, Y. Takahashi, J. Kurihara, H. Yamakawa, A. Takada, "A Japanese Microsatellite Bus System for International Scientific Missions", 62nd International Astronautical Congress, Cape Town, South Africa, 2011, IAC-11.B4.2.10
- [2] Y. Tomioka, T. Kuwahara, Y. Sakamoto, H. Fukuchi, Y. Tanabe, K. Yoshida, "Micro-satellite structure system for cost-effective and rapid development", 3rd Nano-satellite symposium, Kitakyushu, Japan, 2011, NSS-03-0411

Design and Hovering Control of an Asterisk Type Quad Rotor Tail-Sitter Unmanned Aerial Vehicle

Atsushi Oosedo⁽¹⁾, Atsushi Konno⁽²⁾, Satoko Abiko⁽¹⁾ and Masaru Uchiyama⁽¹⁾.

⁽¹⁾Dept. of Aerospace Engineering in Tohoku University. 6-6-01 Aobayama, Sendai 980-8579, Japan
{oosedo, abiko, uchiyama} @space.mech.tohoku.ca.jp

⁽²⁾Divi. of System Science and Informatics in Hokkaido University. 14-9, Kita-ku, Sapporo, 060-0814, Japan, {konno}
@ssi.ist.hokudai.ac.jp

ABSTRACT

Quad rotor helicopters have simple mechanism and high stability. However, it is not easy for a quad rotor helicopter to fly long time and long distance. Therefore, we developed quad rotor tail-sitter Unmanned Aerial Vehicle (UAV) which can hover like a quad rotor helicopter, and can fly long distance like a fixed wing airplane. This paper presents the development of a quad rotor tail-sitter UAV termed asterisk type which composed of four rotors and a fixed wing and hovering experiment with the developed UAV.

1. Introduction

Vertical Takeoff and Landing Unmanned Aerial Vehicles (VTOL UAVs) are expected to perform dangerous mission such as rescue and exploring disaster site alone.

Quad rotor helicopters are one of the VTOL UAVs and have been commonly used in research for the reason of simple mechanism and high stability. However, it is not easy for the quad rotor helicopter to fly for long time and long distance, because most of the thrust is consumed to lift the body.

One of the solutions for this problem is to provide capability to fly like a fixed wing airplane. This strategy was proposed by Young et al. at NASA Ames Research Center in 2002 [1]. They developed an R/C airplane and succeeded in manual flight. This type of UAV is classified into the category of tail-sitter aircraft. The tail-sitter VTOL aircraft switches between level flight and hover modes by changing its pitch angle of the fuselage by 90° as shown in Fig. 1. A simple mechanism is preferable for UAVs, because weight saving is crucial for the VTOL maneuver. Up to now, several different types of tail-sitter VTOL UAVs have been developed. Kita developed a simple tail-sitter VTOL UAV whose airframe is single propeller R/C airplane [2]. Stone has developed the T-Wing tail-sitter, which has a canard wing and tandem rotors [3]. However, they achieved high stability in level flight, but stationary hovering was relatively difficult compared with a rotary wing aircraft.

On the other hand, we developed a quad rotor tail-sitter UAVs which are composed of a quad rotors and fixed wing. This type of UAVs can hover like a quad rotor helicopter, and can fly for long distance like a fixed wing airplane. First quad rotor tail-sitter UAV we developed suffered harmful effect of propeller slipstream on attitude control due to the configuration of rotors and wing [4]. This paper presents the development of new type of a quad rotor tail-sitter UAV which is not affected by slipstream. This type of UAV is termed as asterisk-type quad rotor tail-sitter UAV here. By using the developed UAV, we carried out the hovering flight experiment.

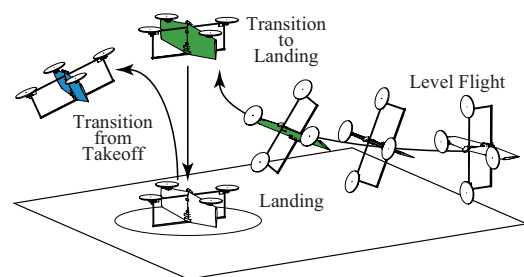


Fig. 1 Take off and landing of tail sitter VTOL

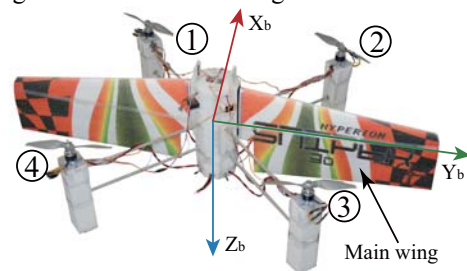


Fig. 2 An overview of quad rotor tail-sitter UAV

2. System configuration

An overview of the quad rotor tail-sitter UAV is shown in Fig. 2. The total weight is 1.36 kg, and the main wingspan is 0.99 m. The main wing is parts of commercially available R/C airplane (Hyperion Co., Sniper 3D), and other parts such as the body frames are newly developed. The motor and propeller are selected to satisfy the static thrust amounting to 130% of the fuselage weight at a continuous maximum motor load. A microcomputer board (Alpha Project Co., STK-7125) has an SH2 microcomputer made by Renesas Technology Co.

Several sensors, such as attitude sensor, GPS and ultrasonic sensor and a microcomputer board (Alpha Project Co., STK-7125) were installed in the UAV. Attitude and position information are processed by the on-board computer and the control commands are sent to each motors. The propeller revolution speed is feedback to the controller through the motor amp. Additionally an R/C receiver is equipped to be controlled by a human in emergency

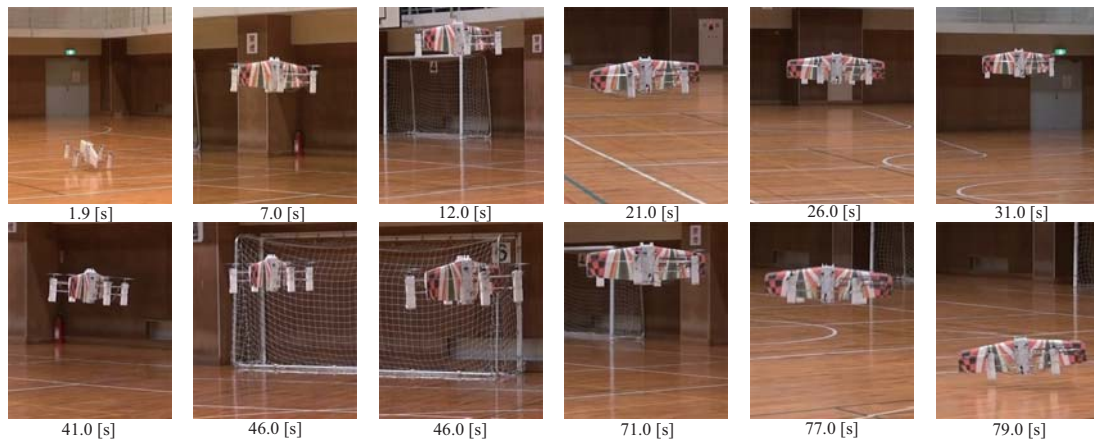


Fig. 3 Sequential photographs of the hovering control

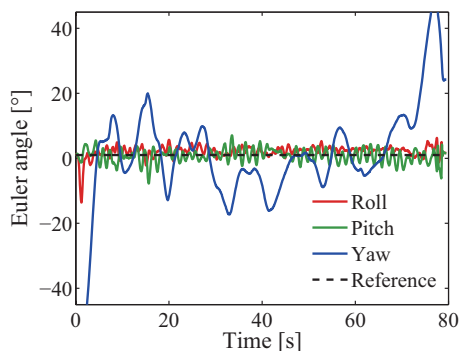


Fig. 4 Attitude change during the hovering flight

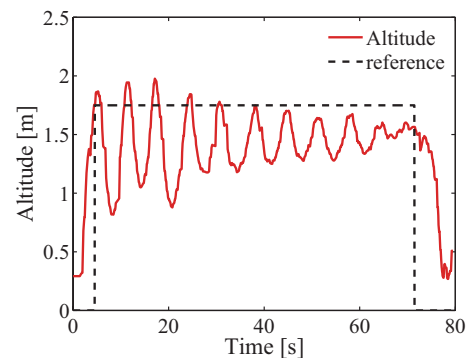


Fig. 5 Altitude change during the hovering flight

3. Hovering flight experiment

We performed hovering control experiment using the developed UAV. The reference roll, pitch and yaw angles are 0° , and reference altitude was 1.75 m. This flight experiment was performed indoors. Snapshots of the attitude control experiment are shown in Fig. 3. As can be seen in Fig. 3, the UAV maintains almost constant attitude and altitude. The UAV started flying at experimental time $t = 1.9$ s. After flying for eighty seconds, the experiment was terminated and the UAV landed on the ground.

Fig. 4 shows the attitude during the experiment. As can be seen from Fig. 4, the roll and pitch angles are oscillating at about $\pm 3^\circ$. On the other hand, the maximum yaw angle error is 20.0° in clockwise direction at 15 s. Additionally, it was found from Fig. 4 that the yaw control capability is very low. This problem was caused by air drag of fixed wing and torque limiter on software. Currently, maximum total torque for yaw control is limited to ± 0.07 Nm. It seems that yaw angle is poorly responsive since this limit is too severe for yaw control. We will relax the limit of torque and test this hypothesis.

Fig. 5 shows the altitude change. Since minimum range of ultrasonic sensor is 0.3 m, the initial altitude is 0.3 m. It was found from Fig. 5 that the altitude follows the reference. However, there is a steady-state error at about -0.2 m. This error was caused by a drop in voltage of battery. The drop in voltage of battery causes a huge change of propeller revolution speed. In this research, this influence was compensated by the propeller revolu-

tion speed feedback. However, the PI controller could not compensate propeller revolution speed because the drop in voltage of battery was larger than that was expected. This problem is resolved by means of integration gain scheduling of propeller feedback.

These flight experiment shows that the attitude and altitude of UAV are well controlled simultaneously during the hovering flight. However, we need to considerably improve the performance of yaw control.

4. Conclusion

This paper discussed the hovering flight test of an asterisk-type quad rotor tail-sitter VTOL UAV. For the future, we will conduct a level flight experiment.

References

- [1] L. A. Young et al. "New Concepts and Perspectives on Micro-Rotorcraft and Small Autonomous Rotary-Wing Vehicles", (2002), Ames Research Center, Moffett Field.
- [2] K. Kita et al. "Hovering Control of a Tail-Sitter VTOL Aerial Robot", *Journal of Robotics and Mechatronics*, Vol. **21**, (2009), pp. 277-283.
- [3] H. Stone et al. "Optimization of Transition Maneuvers for a Tail-Sitter Unmanned Air Vehicle (UAV)", in *Proc. 5th Australian International Aerospace Congress*, (2001), Canberra, pp. 105.
- [4] A. Oosedo et al. "Design and Attitude Control of a Quad Rotor Tail-Sitter Vertical Takeoff and Landing Unmanned Aerial Vehicle", *Advanced Robotics*, Vol. **26**, (2012), pp. 307-326.

Development and Evaluation of Autonomous Mobile Manipulator for Sensing Device Deployment

Takeshi Ohki, Keiji Nagatani, and Kazuya Yoshida
Department of Aerospace Engineering, Tohoku University
6-6-01 Aramaki Aza Aoba, Aoba-ku, Sendai-shi, Miyagi-ken, Japan
takeshi@astro.mech.tohoku.ac.jp

ABSTRACT

Nondestructive sensing method for underground structures using artificial earthquake and seismometer array technology requires the deployment of many sensing devices over a wide area on a target outdoor field; such work is currently conducted in manually. To automate such work, our research group has been developing an autonomous mobile manipulator system. The key technology to realize such system is "3-D localization." In this paper, we report our strategy and implementation of the localization that works well in large scale outdoor field, and the results of the field experiments to confirm the validity of our system.

1. Introduction

Even though there is a strong movement to break away the fossil fuel society, there will still be a strong demand for oil exploration activities throughout the world. Therefore, a nondestructive method of sensing underground structures to find oilfields is required. One of the methods, which involves the use of artificial earthquake and seismometer array technology to detect underground structure, has become very popular. However, detecting the earthquake waves in different locations requires deployment of many sensing devices over the wide area in the target field, which is currently done manually. To automate this work, our research group initiated a project to realize a robotics sensor deployment system for outdoor field and developed an autonomous mobile manipulator that consists of mobile base and onboard manipulator. (Fig. 1)

There are reports of autonomous mobile manipulator system. However, almost all were for indoor use [1]. By contrast, our research group has been developed many types of mobile robots for exploration in outdoor environments [2]. The aim of this research is to realize an autonomous mobile manipulator that performs well in outdoor environments by applying our experiences of developing mobile robots for outdoor field exploration. We predefined a specific scenario for the mobile robot system as follows.

1. An operator defines target positions of deployment.
2. The mobile base moves to nearest target position and places the end-effector of the onboard manipulator at a location above the target position.
3. It performs the sensing device installation motion at the target position.
4. It brings the manipulator back to the initial configuration.
5. It repeats 2-4 until all target positions have been installed.

To realize above scenario, many types of the technologies must be developed and integrated appropriately, such as "mobility on rough terrain," "localization," and "manipulation." The key to realize the accurate deployments is how to realize the accurate localization in large scale unknown outdoor fields. Therefore, in this paper, we report the overview of our localization strategy and implementation.



Fig. 1 Autonomous mobile manipulator

2. Localization strategy

Localization refers to technology for accurately determining the current position of a mobile robot. The most basic method of localization is called "dead reckoning" based on the internal sensors such as wheel encoders and gyroscopes. Dead reckoning can obtain the position and attitude online and continuously. However, the dead reckoning cannot avoid the accumulated errors.

Another popular localization method is absolute localization such as Global Positioning System (GPS). It is possible to obtain the position of the robot in a world coordinate by using the GPS. However, there is measurable error in GPS based localization and also the errors of GPS signal lost and reflection.

There is a solution to cancel the problems of each localization method by combining them. One of the most major approaches is the Monte Carlo Localization (MCL). MCL fuses the dead reckoning and absolute localization by using the particle filter algorithm [3]. Particle filter uses numerous particles that each particle expresses the hypotheses of the localization. The average of the whole particles is the results of the fused localization.

The particles are (a) initially distributed around the robot position based on GPS. When the robot moves, (b) the particles are translated based on dead reckoning. Then, (c) the particles are evaluated based on the distance from the measured GPS position if possible. And (d) if the evaluation was done successfully, resampled. By repeating the process (b) to (d), MCL

obtains the fused localization results online and avoid the problem of dead reckoning and absolute localization.

The Fig.2 shows an example image of the particle filter algorithm. By resampling the particles (orange dot with bar) based on the measured GPS position (yellow dot), the particles are converged and the average position of the particles (green robot) are derived.

3. Field experiments

We implemented above MCL method on our mobile robot (Fig.1) and conducted several field experiments. In the experiments, the robot performs the scenario we mentioned before. To evaluate our system, we used a laser measurement tool called “total station” as the ground truth.

The target environment for the experiments was along the Hirose River in Sendai, as shown in Fig.3. In the figure, there is a set of target positions (red dots) we pre-defined, and trajectories of the robot (black line segments). The robot traversed and performed the deployment motions. Fig.4 shows the errors between the set target positions and the deployed positions. The origin of the coordinates donates the center positions of the errors. In the experiments, the standard deviation (*sd*) of the X-axis is 283 mm, and that of Y-axis is 123 mm.

If we assume the errors distributes based on the normal distribution, 99.7 % samples are within the three times the values of *sd*. Therefore, it is possible to say that 99.7 % of the deployments are performed within 849 mm by using our system.

The positioning accuracy of the GPS we used is larger than 1 m. Even when the GPS is set in differential GPS mode, the accuracy is still almost 1 m. The experimental results confirmed the validity of our system.

4. Conclusion

To realize the autonomous sensing device deployment, we designed an autonomous mobile manipulator system. The key to achieve the accurate deployment is the accurate localization of the base robot of the mobile manipulator. We implemented the fused localization method that combines the localization by dead reckoning and GPS with particle filter algorithm. The field experiment was conducted and validated our approach.

References

- [1] E. Van Henten, “Field Test of an Autonomous Cucumber Picking Robot,” *Biosystems Engineering*, **86**, no. 3, pp.305-313, (2003)
- [2] T. Ohki, K. Nagatani, and K. Yoshida, “Local Path Planner for Mobile Robot in Dynamic Environment based on Distance Time Transform Method,” *Advanced Robotics*, DOI:10.1080/01691864.2012.694648, (2012)
- [3] F. Dellaert, D. Fox, W. Burgard, and S. Thrun, “Monte carlo localization for mobile robots,” *InProc. of 1999 IEEE International Conference on Robotics and Automation*, **2**, pp. 1322–1328, (1999)

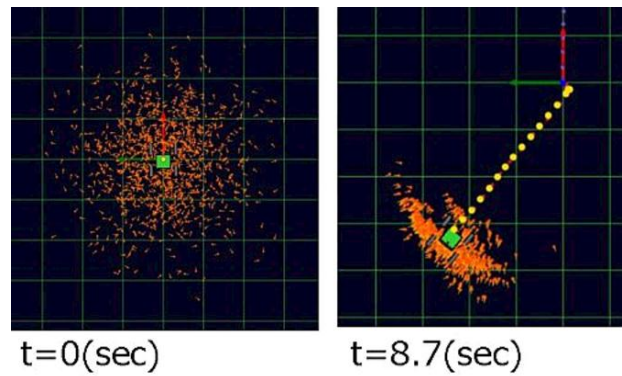


Fig. 2 Convergence of particles



Fig. 3 Target points in outdoor field

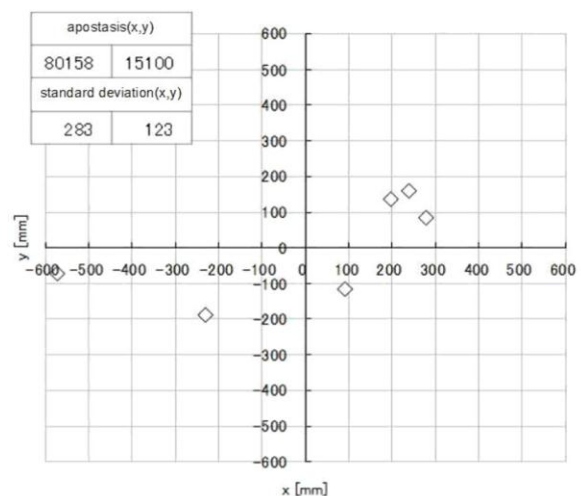


Fig. 4 Errors of deployed positions

Robust Mobile Robot Design for Fukushima Nuclear Plant Exploration

Seiga Kiribashi, Keiji Nagatani(Tohoku Univ.)
 6-6-01 Aoba, Aramaki-Aza, Aobaku, Sendai, Miyagi, Japan
 seiga@astro.mech.tohoku.ac.jp, keiji@astro.mech.tohoku.ac.jp

ABSTRACT

Nuclear plant exploration robot "Quince" has a serious problem of its power supply. The problem was that shut down a power when drivetrain got a huge load. Once we lose a power, there is a need for humans to operate power switch to recovery but, in the real field, such operation is a dangerous to human because of radiation. Therefore, in order to increase a robustness of "Quince", we employ an automatic reset feature with power down detection. This feature improves the robustness of "Quince", as a result, "Quince" has been adopted as a robot exploration nuclear power plant.

1. Introduction

We have studied the robot to explore a variety of environments. In order to explore the actual disaster area, the robot is required to operate safely and reliably. Therefore, robustness is important.

However, we were faced with the problem of inoperative about our Nuclear Power Plant Exploration robot "Quince"(Fig.1)[1][2][3], during development. It was when given a heavy load on the robot, battery protection circuit worked and all power of robot was shut down. Once the protection circuit is activated, must do the OFF-ON action a main switch of robot to restart a system. The protection circuit is effective to protect a battery from damage. Therefore, we have developed a Power Reset System that can automatically restart a system even if the protection circuit is activated.

In this paper, we introduce the Power Reset System and result of exploration.

2. Robust Control System

2.1. Problem of Power Supply

Quince is using a total of four batteries of the same standard used by video camera for broadcasts. The four batteries are connected in series parallel, its total capacity is 352Wh. In this battery, as a protection circuit, poly switch has been installed, it automatically disconnects a circuit when pass a current of about 15A per battery. This protection circuit is very effective to protect from destruction the battery, but it does not return while circuit current is larger than 20 μ A. It means necessary of all loads were removed. Therefore, protection circuit is activated, it is necessary to do an OFF-ON action in main switch to operate again the robot. Such operation in the experiment in the laboratory is not a problem, by contrast, in the exploration of nuclear power plants inside is impossible.

2.2. Solution for the problem

Fig.2 shows the system configuration of Quince. Reset circuit in the figure is the PowerResetSystem, it has been developed. this reset circuit insert between the battery and full load of the robot to reset the protection circuit of the battery. Fig.3 shows the circuit diagram of the reset circuit. This circuit can be divided into power supply part, voltage comparison part, and switch part. As indicated above, Poly-Switch will reset by remove all load. So this circuit has an electric double layer



Fig.1 Appearance of Quince

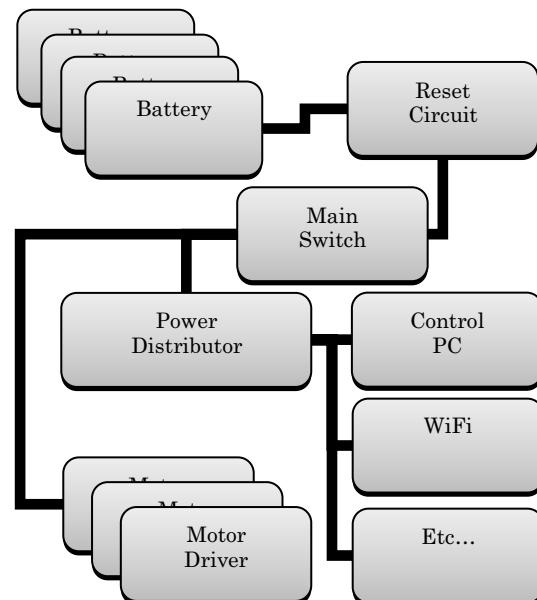


Fig.2 System configuration of Quince

capacitor and operate by it when power is disconnected. It will charge in normal operation.

Voltage comparison part is always comparing a battery voltage to reference voltage. If the battery

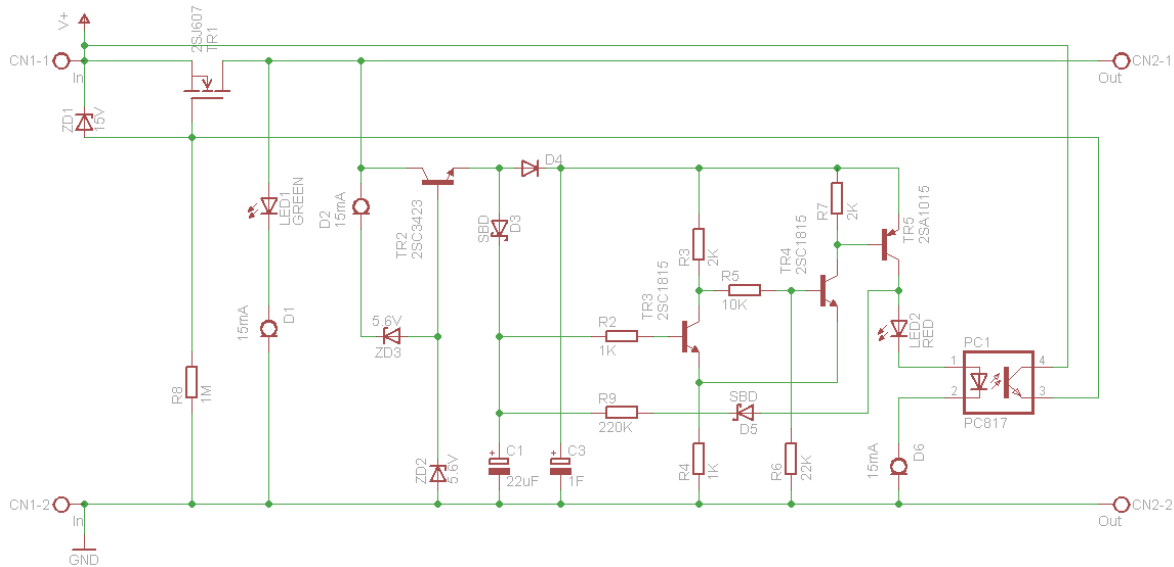


Fig.3 Circuit Diagram about Reset Circuit

voltage is lower than the reference voltage, it deem protection circuit to be activated. If determined to so, turn OFF the internal electrical switch, and operates to ON again after a few seconds.

In addition, the poly-switch recovery time varies depending on temperature. Therefore, while battery voltage is lower than reference, OFF-ON action will repeat, and reset a protection for sure.

3. Exploration Result

Quince was able to confirm that incorporating a reset circuit to operate robustly. As a result, Quince has been adopted as a exploration robot of the Fukushima Daiichi nuclear power plant, and go into the site. Shown in Fig.4 is an image taken by Quince inside of a nuclear power plant, the situation of internal damage has been taken scrupulously. Including the practice, power failure has never been reported. This means solution in this paper is to be of benefit.

4. Conclusion

There was a problem on the power supply of Nuclear Power Plant Exploration robot "Quince". So, we developed a reset circuit to solve the problem.

As a result, the problem was resolved, Quince is now able to have a robust operation. And, it has been demonstrated that withstand the operation of the actual field.

References

- [1] Keiji Nagatani, Yoshito Okada, Naoki Tokunaga, Seiga Kiribayashi, Kazuya Yoshida, Kazunori Ohno, Eijiro Takeuchi, Satoshi Tadokoro, Hidehisa Akiyama, Itsuki Noda, Tomoaki Yoshida, Eiji Koyanag, J. Field Robotics, 28(2011), 373-387
- [2] Keiji Nagatani, Seiga Kiribayashi, Yoshito Okada, Satoshi Tadokoro, Takeshi Nishimura, Tomoaki Yoshida, Eiji Koyanagi, Yasushi Hada, Security and Rescue Robotics, 11(2011), 13-18

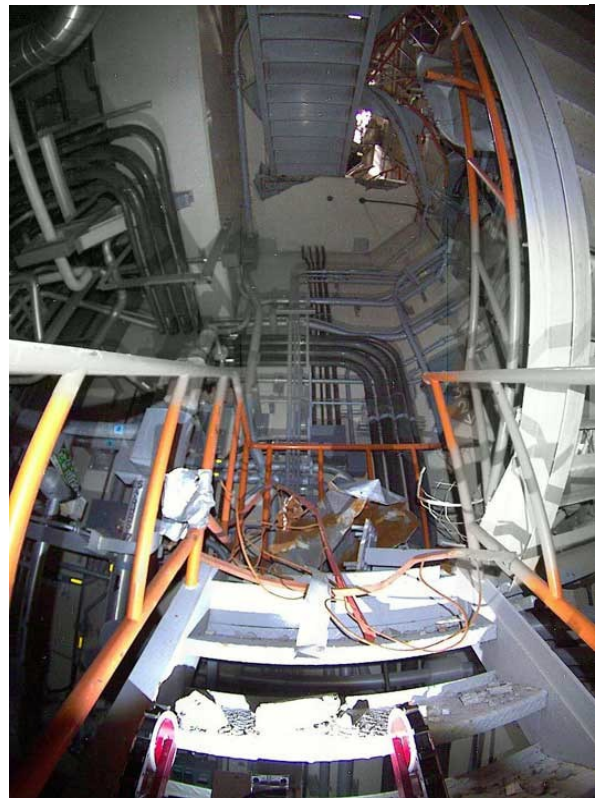


Fig.4 Inside of Fukushima Daiichi

- [3] Keiji Nagatani, Seiga Kiribayashi, Yoshito Okada, Kazuki Otake, Kazuya Yoshida, Satoshi Tadokoro, Takeshi Nishimura, Tomoaki Yoshida, Eiji Koyanagi, Mineo Fukushima, Shinji Kawatsuma, Security and Rescue Robotics, 11(2011), 56-60

Hybrid Simulation of Capturing a Massive Payload by Space Manipulators

Ippei Takahashi⁽¹⁾, Satoko Abiko⁽¹⁾, Xin Jiang⁽¹⁾, Atsushi Konno⁽²⁾ and Masaru Uchiyama⁽¹⁾

⁽¹⁾ Department of Mechanical Systems and Design, Graduate School of Engineering, Tohoku University, 6-6-01, Aramaki-aza-Aoba, Aoba-ku, Sendai, Miyagi, 980-8579 Japan.

⁽²⁾ Division of System Science and Informatics, Graduate School of Information Science and Technology, Hokkaido University, Kita 14, Nishi 9, Kita-ku, Sapporo, Hokkaido, 060-0814, Japan.

{ippei, abiko, jiangxin, uchiyama} @space.mech.tohoku.ca.jp, konno@ssi.ist.hokudai.ac.jp

ABSTRACT

In orbital operation of capturing a target by space manipulator systems, safety must be guaranteed at all times. To achieve the operation safety, relative velocity between a target and a space manipulator is determined as a criterion. However the behavior of them should be analyzed if contingent contact beyond the criterion occurs. This paper describes the development of hybrid motion simulator for the mission of capturing a target. In the simulator, the mission of capturing H-II Transfer Vehicle (HTV) by Space Station Remote Manipulator System (SSRMS) is considered as an application.

1 Introduction

This paper presents hybrid motion (hardware -in -the -loop) simulator (HMS) for capturing a massive floating target by a space manipulator. Recently many orbital operations, for example Engineering Test Satellite VII (ETS-VII) and International Space Station (ISS), have been executed. In the future, it is expected that space exploration will continue to be developed more and more. In space missions, safety is the most important beyond anything else. In order to ensure the safety of the orbital operations such as the above examples, it is necessary to precisely evaluate and verify the strategy of task before launch. Hence, it is required to develop reliable methods for verification before launch on the ground. The hybrid simulator is one of the effective methods to evaluate the feasibility and reliability of the orbital operation. Our laboratory has developed a hybrid motion simulator (HMS)[1]. The goal of this paper is to construct the hybrid simulator for capturing the HTV by the SSRMS as an application of the orbital operation.

2 Hybrid Motion Simulator

The HMS is a numerical simulator which embeds hardware experiment in the loop. It can simulate three dimensional relative motion between two objects, such as a space robot and a grasped target, under artificial micro-gravity environment on the ground. The concept of the HMS is shown in Fig. 1.

By including the hardware experiment in the loop, the HMS can use advantages of both the hardware experiment and the numerical simulation. It is generally difficult to develop a precise model of complex phenomena such as multi contacts or impacts in the numerical simulation. In the HMS, certain parts are replaced to hardware to which physical contact occurs. The hardware is called physical model in this paper. The forces and torques received at the hardware are measured by force/torque sensor and sent to numerical simulation. In the numerical simulation, dynamics of the space robot and the target are calculated. Then the motion of the objects is demonstrated by servo mechanism of the HMS in real time.

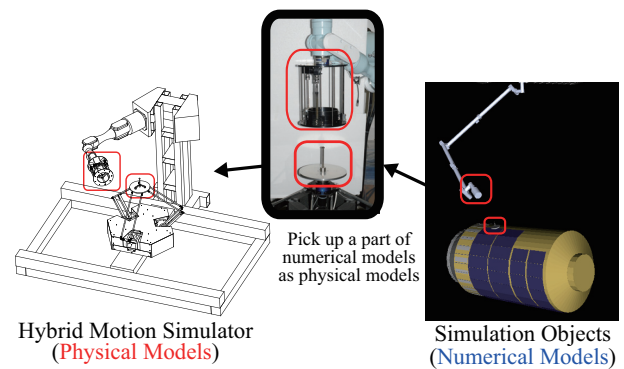


Fig. 1 Concept of HMS.

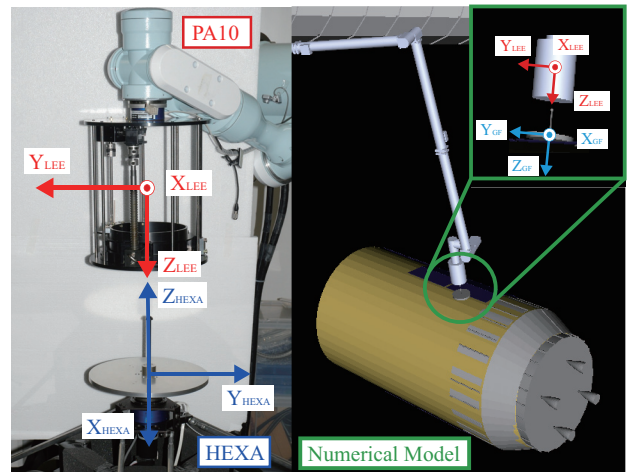


Fig. 2 Coordinate frames in physical model and numerical model

2.1 Numerical Model

In this paper, the entire dynamics of the HTV and the SSRMS are calculated in the numerical simulation. Therefore, the HTV is modeled as one rigid body and, the SSRMS is modeled as a flexible joint manipulator. It is known that the long-reach space manipulators generally have flexibility due to the stiffness of the joints and the backlash[2]. Then, the motion equation of the SSRMS can be expressed as the following equation.

$$H\ddot{q} + c(q, \dot{q}) + K\Delta q = \tau \quad (1)$$

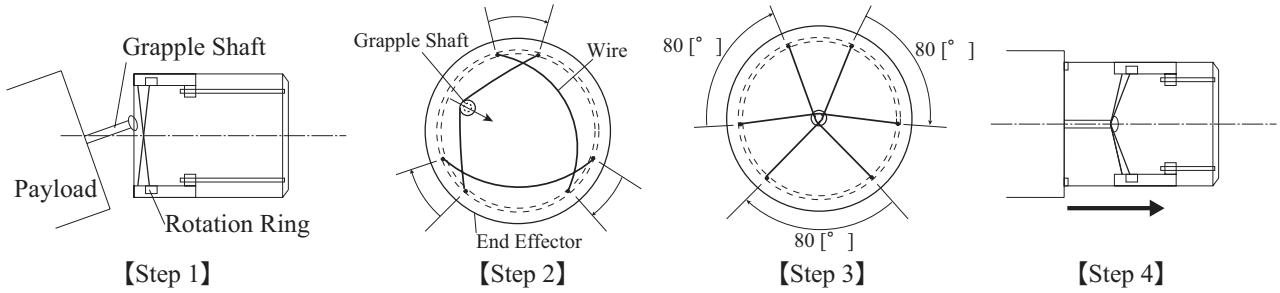


Fig. 3 Sequence of capturing the HTV © JAXA.

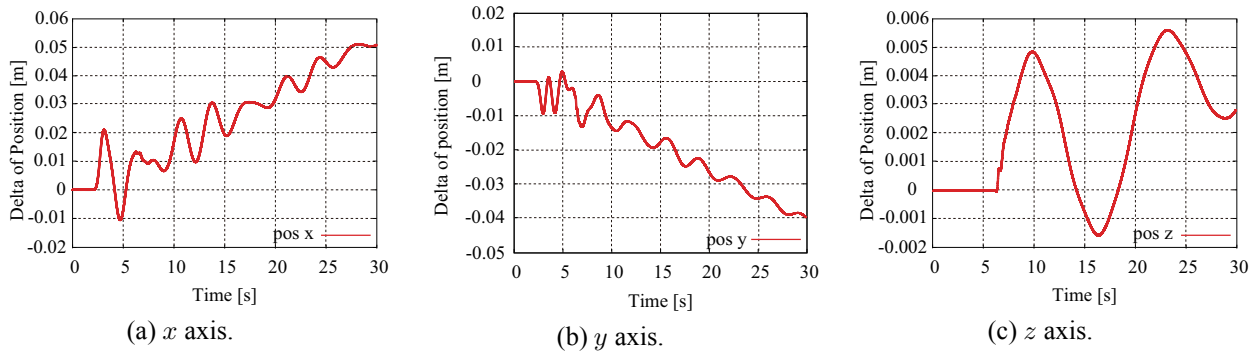


Fig. 4 Relative position of LEE and HTV.

where q and q_m represent angles of link side and of motor side. The matrix Δq and τ are joint angle difference between link side and motor side and the driving torque. The inertia matrix, H , and the stiffness matrix, K , are provided JAXA in the collaborative researchs.

2.1.1 Physical Model

In this study, scaled physical models of Latching End Effector (LEE) and Grapple Fixture (GF) are used. Both of them are used in the HTV mission. The LEE is mounted at the end-effector of the SSRMS, and GF is mounted at the payload and ISS. The LEE is used to grasp the GF in the capturing mission. The physical models of them are shown in Fig. 2. Their specifications are shown in Table 1.. Their size were designed a half size of real ones.

The LEE mockup has the following capabilities:

- part of rotation for putting the screws to the wires and fixing the grapple shaft
- part of translation for pulling in the LEE after fixing the shaft

By using the LEE, the HTV can be captured through the sequence as shown in Fig. 3.

3 Experiment

3.1 Condition of Experiment

To check the correctness of the numerical simulator, external force is applied on the z axis of the GF in the hardware. The observed external force is provided into the numerical simulator.

3.2 Results of Experiment

The results of the experiment are shown in Fig. 4 (a)–(c). The figure shows the relative position between the

Table 1. Size of physical models

	LEE	GF
Height [mm]	293	141
Diameter [mm]	250	250
Mass [kg]	3.9	1.6

HTV and the GF. It clearly shows that the simulator can represent the behavior of characteristic of the flexible joint manipulator. In the Fig. 4 (a)–(c), the static positions shift through the experiment. This is because the HTV is floating by a way from the SSRMS due to the contact force.

4 Conclusions

This paper describes the constructing the HMS of capturing the HTV by the SSRMS. In the future, the behavior of the SSRMS in this simulator is compared with the behavior data of the SSRMS when the HTV was captured by the SSRMS. We are planning to evaluate the behavior of the HTV and the SSRMS by using this simulator when the HTV is failed to be grasped by the SSRMS due to the relative velocity beyond the criterion.

5 Acknowledgement

This research is a part of a collaboration work between Tohoku University and JAXA.

References

- [1] R. Takahashi et al.:“Hybrid Simulator of a Dual-Arm Space Robot Colliding with a Floating Object”, 2008 IEEE International Conference on Robotics and Automation, Pasadena, California, 2008.
- [2] H. Hashimoto et al.:“Performance of Japanese Robotic Arms of the International Space Station,” 15th, IFAC World Congress, 2002.

PS1: IFS Collaborative Research Forum (AFI/TFI-2012)

For details, please refer to separate proceedings

PS2: Transdisciplinary Fluid Integration (AFI/TFI-2012)

For details, please refer to separate proceedings

PS3: Functional Plasma Flow Dynamics and its Innovative Applications

Nanosecond Pulse Surface Discharges For High-Speed Flow Control: Experiments And Modeling

Igor V. Adamovich, Jesse Little, Munetake Nishihara, Keisuke Takashima, and Mo Samimy
The Ohio State University, Columbus, OH 43210, USA
adamovich.1@osu.edu

ABSTRACT

The paper provides an overview of recent progress in the use of surface dielectric barrier discharges sustained by repetitive, high-voltage, nanosecond duration pulses for high-speed flow control, demonstrating their significant potential. A kinetic model of energy coupling to the plasma in a surface ionization wave discharge produced by a nanosecond voltage pulse has been developed. The model allows an analytic solution and lends itself to incorporating into compressible flow codes, for analysis of nanosecond discharge plasma flow control mechanism.

1. Introduction

One of the most critical issues of surface Dielectric Barrier Discharge (DBD) plasma flow control technology is maintaining the actuator performance and achieving flow control authority at high flow velocities. Recent experiments using surface plasma actuators powered by high-voltage nanosecond pulses (NS-DBD actuators) have demonstrated flow control authority over a much wider range of Reynolds and Mach numbers, compared to conventional AC DBD actuators. The main effect of NS-DBD actuators on the flow is due to compression waves formed during rapid localized heating in the surface nanosecond pulse discharge. Quantitative insight into the mechanism of flow forcing by NS-DBD plasma actuators requires predictive modeling of surface nanosecond pulse discharge development, thermalization of energy stored in charged and excited species, and coupling of localized thermal perturbations to the flow field. The present paper provides an overview of recent flow control experiments using NS-DBD plasma flow actuators in quiescent air, in subsonic flows, and in supersonic flows, followed by a discussion of a physics-based, self-similar surface NS-DBD plasma model.

2. NS-DBD flow control experiments

Experimental studies of diffuse and filamentary surface nanosecond pulse discharges in quiescent air demonstrate that they generate compression waves, due to rapid localized heating produced in the plasma [1-3] (see Fig. 1). Compression waves produced by individual discharge filaments have somewhat higher amplitude and higher speed compared with waves produced in a

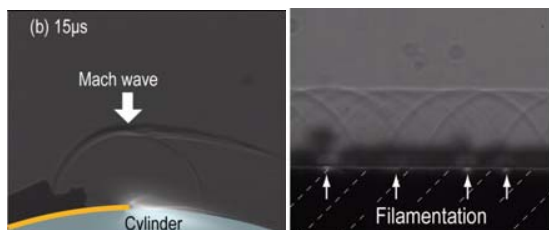


Fig. 1. Compression waves generated by an NS-DBD actuator in quiescent air on a cylinder model surface, 15 μ s after discharge pulse (end view and side view) [2].

diffuse discharge. Psec CARS, time-resolved rotational temperature measurements in a nsec pulse discharge filament in a point-to-point geometry [4] have shown that the compression waves are indeed formed by rapid heating in the filament, on a sub-acoustic time scale. Unlike surface dielectric barrier discharges sustained by AC voltage waveforms, nanosecond pulse discharges transfer little momentum to quiescent air [5], showing

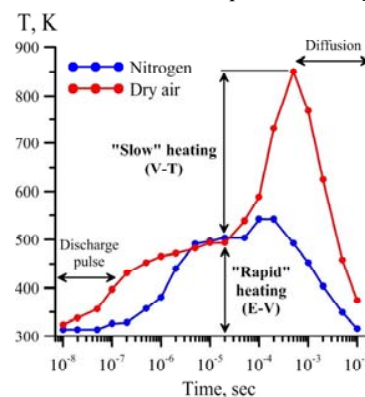


Fig. 2. Time-resolved temperature after a nsec pulse discharge in air and nitrogen at $P=100$ torr vs. time delay after the pulse [4].

that localized heating and subsequent compression wave formation is the dominant flow control mechanism.

Flow separation control using a nanosecond pulse surface discharge plasma actuator on an airfoil leading edge has been studied up to $M=0.26$, $Re=1.5 \cdot 10^6$ (free stream flow velocity 93 m/s), over a wide range of angles of attack [5,6]. The results are consistent with earlier experiments [1] and show that at pre-stall angles of attack, the actuator acts as an active boundary layer trip. At post-stall angles of attack, strong flow perturbations generated by the actuator excite shear layer instabilities and generate robust, coherent spanwise vortices (see Fig. 3). These coherent structures entrain freestream momentum, thereby reattaching the separated flow to the suction surface of the airfoil. This effect has been detected over a range of discharge pulse repetition rates (flow forcing frequencies), resulting in significant increase of lift coefficient.

Feasibility of supersonic flow control by low-temperature nanosecond pulse plasma actuators has been demonstrated in a supersonic (Mach 5) air flow

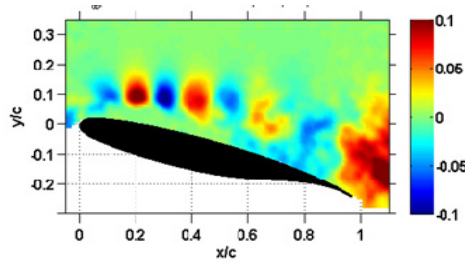


Fig. 3. Spanwise vortices generated by an NS-DBD actuator near the leading edge of the airfoil. Free stream flow velocity 45 m/s [5].

over a cylinder model [7]. Again, strong perturbations of a bow shock standing in front of the model are produced by compression waves generated by rapid localized heating in the plasma. Interaction of the compression waves and the bow shock causes its displacement in the upstream direction, increasing shock stand-off distance by up to 25% (see Fig. 4). The effect of compression waves generated by nanosecond discharge pulses on shock stand-off distance has been demonstrated both for single-pulse and quasi-continuous (pulse repetition rate 100 kHz) actuator operation.

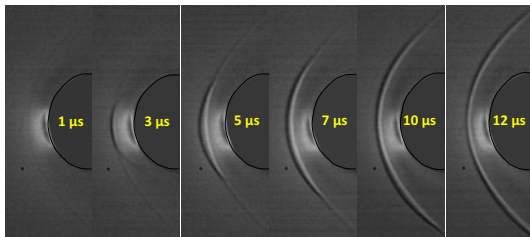


Fig. 4. A compression wave and a bow shock perturbation produced by NS-DBD actuator on a surface of a cylinder model in a Mach 5 air flow, shown vs. time delay after the pulse [7].

3. Kinetic modeling of surface NS-DBD discharge

Using an approach outlined in Ref. [8], a self-similar kinetic model has been developed to analyze energy coupling to the plasma in a surface ionization wave discharge produced by a nanosecond voltage pulse [9]. The model predicts key discharge parameters such as ionization wave speed and propagation distance, electric field, electron density, plasma layer thickness, and pulse energy coupled to the plasma, demonstrating good agreement with available experimental data [2,3] and two-dimensional kinetic modeling calculations [10]. Figure 5 shows a schematic of a surface ionization wave discharge in a NS-DBD plasma actuator and the predicted temperature distribution 1 μ s after the pulse, demonstrating that rapid (sub-acoustic) heating occurs primarily near the high-voltage electrode. The model allows an analytic solution and lends itself to incorporating into existing compressible flow codes, for in-depth analysis of the nanosecond discharge plasma flow control mechanism. This approach has a significant advantage compared to full coupling of the discharge

modeling code and a flow code, which is extremely challenging due to a wide range of time scales involved, from $\sim 10^{-11} - 10^{-7}$ s typical for propagation of surface streamer / ionization wave discharge, to $\sim 10^{-7} - 10^{-6}$ s for discharge energy thermalization and compression wave formation, to $\sim 10^{-6} - 10^{-3}$ s for flow structure formation and development.

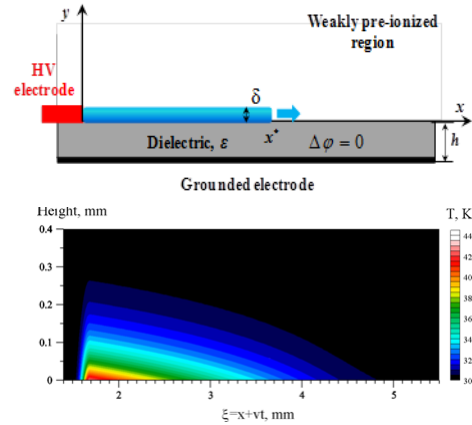


Fig. 5. Schematic of a surface ionization wave discharge in a NS-DBD plasma actuator (top); predicted temperature distribution 1 μ s after the pulse. $U_{peak}=14$ kV, $dU/dt=2$ kV/nsec (bottom).

4. Concluding remarks

The experimental results demonstrate significant potential of NS-DBD actuators for flow control, over a wide range of Reynolds and Mach numbers. Development of analytic models of nsec pulse surface discharge and their incorporation into compressible flow codes makes possible in-depth, quantitative analysis of NS-DBD flow control mechanisms.

References

- [1] D.V. Roupasov, A.A. Nikipelov, M.M. Nudnova, and A. Yu. Starikovskii, *AIAA J.*, 47 (2009) 168
- [2] K. Takashima, Y. Zuzeeck, W.R. Lempert, and I.V. Adamovich, *Plasma Sources Sci. Technol.*, 20 (2011) 055009
- [3] N. Benard, N. Zouzou, A. Claverie, J. Sotton, and E. Moreau, *J. Appl. Phys.*, 111 (2012) 033303
- [4] A. Montello, Z. Yin, D. Burnette, I.V. Adamovich, and W.R Lempert, *AIAA Paper 2012-3180*
- [5] J. Little, K. Takashima, M. Nishihara, I. Adamovich, and M Samimy, *AIAA J.*, 50 (2012) 350
- [6] C. Rethmel, J. Little, K. Takashima, A. Sinha, I. Adamovich, and M. Samimy, *AIAA Paper 2011-0487*
- [7] M. Nishihara, K. Takashima, J.W. Rich, and I.V. Adamovich, *Phys. Fluids*, 23 (2011) 066101
- [8] A.N. Lagarkov and I.M. Rutkevich, "Ionization Waves in Electric Breakdown of Gases" (Springer, New York, 1994)
- [9] K. Takashima, Z. Yin, I. Adamovich, *AIAA Paper 2012-3093*
- [10] T. Unfer and J.-P. Boeuf, *J. Phys. D: Appl. Phys.* 42 (2009) 194017

High-Temperature Inert-Gas Plasma Magnetohydrodynamic Electrical Power Generation

Tomoyuki Murakami and Yoshihiro Okuno

Department of Energy Sciences, Tokyo Institute of Technology
4259 Nagatsuta, Midori, Yokohama 226-8502 Japan
murakami@es.titech.ac.jp

ABSTRACT

The present paper describes magnetohydrodynamic (MHD) electrical power generation in a high-temperature seed-free argon plasma, for which single-pulse shock-tunnel-based experiments are conducted. The MHD power-generating experiments using a linear-shaped Faraday-type generator and a disk-shaped Hall-type generator clarify the energy conversion efficiency as functions of the total inflow temperature (7600-9600 K) and the applied magnetic-flux density (up to 4.0 T).

1. Introduction

High-efficiency MHD energy conversion is feasible in the case that the degree of ionization of a working medium is sufficiently high to attain necessary electrical conductivity. A conventional method of enhancing the electrical conductivity of a low-temperature gas (typically with a total temperature of approximately 2000 K) is to seed a low ionization potential material in a mother gas^[1,2]. One of the alternative methods, a combined scheme involving the seeding and an external energy supply, *i.e.* an RF-power assist, is also effective for creating a nonequilibrium MHD power-generating plasma^[3]. Furthermore, a feasibility demonstration of the RF-power assist nonequilibrium MHD power-generation with a “seed-free” plasma has been conducted^[4].

On the other hand, if the total gas temperature increases sufficiently to cause thermal equilibrium ionization rather than the nonequilibrium ionization, MHD energy conversion using a seed-free gas is feasible without the additional RF-power supply. In the present paper, high-density MHD energy conversion in a high-temperature seed-free argon plasma is described, for which single-pulse shock-tunnel-driven power-generating demonstrations are conducted. The results obtained using a linear-shaped Faraday-type MHD generator (in progress) and a disk-shaped Hall-type MHD generator are shown.

2. Experimental setup

[Shock-tunnel] The MHD electrical power generators are driven by a single-pulsed shock tunnel. The shock-tunnel facility consists of a shock tunnel, a MHD generator, a cryocooled superconducting magnet, a gas supply, and an exhaust system. The shock tunnel supplies a high-enthalpy argon flow to the MHD generator through the introducing duct. The total temperature are 7600 – 9600 K and the total pressure are 0.12 – 0.17 MPa. The MHD generator is completely immersed in the cylindrical bore of a continuously operating superconducting magnet. The maximum magnetic flux density on the bore axis is 4.0 T. The shock-tunnel facility provides a power generation period of approximately 1.0 ms. The thermal input to the generator is approximately 0.15 MW.

[Faraday generator] The linear-shaped Faraday-type MHD generator has a “Laval-nozzle type”

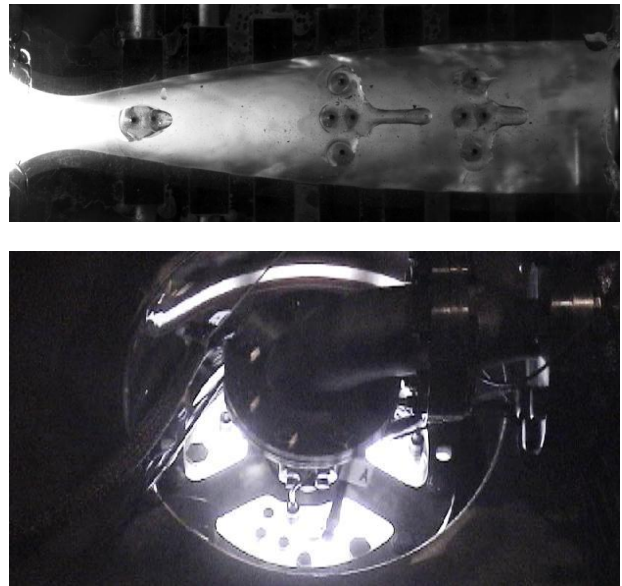


Fig. 1 Images of MHD electrical power generation plasma. Upper: linear-shaped Faraday-type generator. Lower: disk-shaped Hall-type generator.

supersonic channel. The cross sections of the rectangular channel are 10.0 mm x 50.0 mm at the throat and of 30.0 mm x 50.0 mm at the exit. The electrode walls have a convex curvature and the insulator walls have plain surfaces. Seven electrode pairs are equipped. the width of the copper electrode is 8.0 mm. The electrode pitch is 13mm. The MHD channel length is 86.0 mm and the power-generating volume is $11 \times 10^{-5} \text{ m}^3$.

[Hall generator] In the disk-shaped Hall-type generator, a working gas expands in the radial direction in a narrow gap between parallel disks corresponding to the supersonic MHD channel, where an external magnet applies magnetic flux. An electromotive force of $u \times B$ induces a Faraday current in the azimuthal direction, and a radial Hall electric field is induced by the Hall effect (u : flow velocity vector and B : magnetic flux density vector). The channel height increases linearly from 3.5 mm at the throat ($r=55.0$ mm) to 10.0 mm at the upstream edge of the cathode ($r=115.0$ mm). The MHD channel length is 50.0 mm and the power-generating volume is $21 \times 10^{-5} \text{ m}^3$.

3. Results and Discussion

Figure 1 shows the high-speed camera imaging of the MHD electrical power generation plasmas in the linear-shaped Faraday-type generator and the disk-shaped Hall-type generator. The inflow of argon with a total temperature of over 8000 K provides an electrical conductivity of several hundred S/m. The characteristic time of argon ion recombination (e-folding time for argon ion recombination) is estimated to be comparable to the plasma residence time in the generator(s). The plasma in a thermal equilibrium state provided to the channel is slowly cooled without applying magnetic flux, and the electron temperature and ionization degree gradually decreased in the channel. The application of magnetic flux enhances the electron temperature and gradually increases the ionization degree, whereby the plasma is maintained in a nonequilibrium state.

Figure 2 shows the enthalpy extraction ratio as functions of the total inflow temperature and the applied magnetic flux density; (a) Faraday-type generator (the load resistance is controlled in the range of 0.5-2.0 Ω) and (b) Hall-type generator (the load resistances are 0.02-0.5 Ω). The power generation performance varies with total inflow temperature and magnetic flux density.

For both the generator, the total inflow temperature of less than about 8000 K is not suitable for MHD energy conversion because the electrical conductivity of the inflow gas is too low to trigger the MHD interaction.

When the magnetic flux density of 4.0 T is applied to the Faraday generator, the enthalpy extraction ratio is improved with increasing total inflow temperature from 8100 to 9000 K; the maximum enthalpy extraction ratio is 13%. The increase in magnetic flux density from 2.0 T to 4.0 T improves the generator performance at the inflow temperature of 9000 K.

For the Hall generator, the enthalpy extraction ratio is improved with increasing total inflow temperature from 7600 to over 9000 K; the maximum enthalpy extraction ratios are 13.2% (9230 K and 0.5 T), 13.7% (9230 K and 1.0 T), and 15.8% (9080 K and 1.2 T). However, with increasing magnetic flux density to 2.0, 3.0, and 4.0 T, the peak enthalpy extraction ratio shifts to a lower temperature and decreases; the enthalpy extraction ratios are 8.4% (8580 K and 2.0 T), 4.4% (8500 K and 3.0 T), and 1.4% (8140 K and 4.0 T). At an excessive total inflow temperature of more than 9400 K, the generator performance deteriorates. Because the excessive total inflow temperature and magnetic flux density result in an excessive Lorentz force deteriorating the fluid-dynamical property.

4. Concluding remarks

High-temperature inert-gas (seed-free argon) MHD electrical power generation was conducted. The shock-tunnel-based experiments using the linear-shaped Faraday-type generator and the disk-shaped Hall-type generator clarify the energy conversion efficiency as functions of the total inflow temperature and the applied magnetic-flux density.

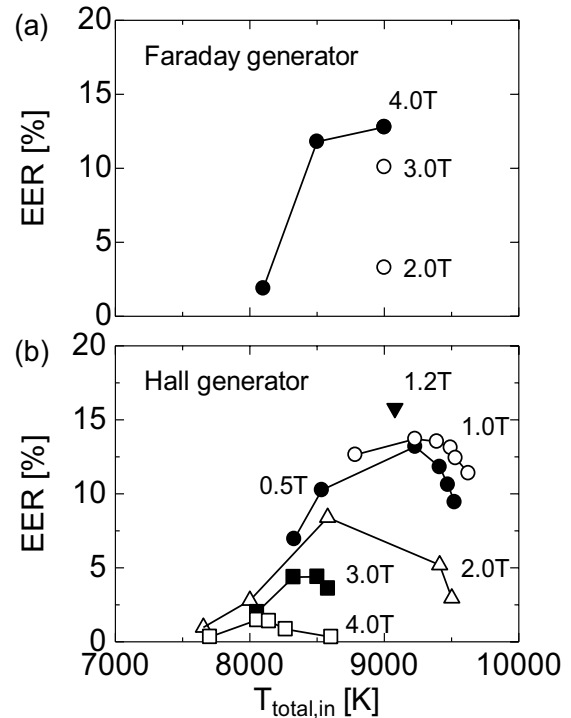


Fig. 2 Enthalpy extraction ratio (EER, power output / thermal input) as functions of total inflow temperature ($T_{total,in}$) and applied magnetic flux density.

Acknowledgements

This work was partly supported by the Grant-in-Aid for Scientific Research (A) 22246130 and (C) 24561054 of the Japan Society for the Promotion of Science (JSPS).

References

- [1] T. Murakami and Y. Okuno, *J. Phys. D: Appl. Phys.* **44** (2011), 185201.
- [2] T. Murakami and Y. Okuno, *J. Phys. D: Appl. Phys.* **44** (2011), 185202.
- [3] T. Murakami and Y. Okuno, *J. Appl. Phys.* **105** (2009), 023301.
- [4] T. Murakami, Y. Okuno and H. Yamasaki, *Appl. Phys. Lett.* **86** (2005), 171502.

Numerical Investigation of DC Plasma Jet Effect on Thermofluid Field in a DC–RF Hybrid Plasma Torch by Three-Dimensional Simulation

Masaya Shigeta

Department of Mechanical Systems and Design, Graduate School of Engineering, Tohoku University
6-6-01 Aramaki-Aoba, Aoba-ku, Sendai 980-8579, Japan
E-mail: shigeta@fluid.mech.tohoku.ac.jp

ABSTRACT

Time-dependent 3-D simulations based on a large eddy simulation (LES) are successfully performed to clarify the effect of a direct current (DC) plasma jet on the thermofluid field in a direct current – radio frequency (DC–RF) hybrid thermal plasma torch. The present simulation also shows the complex flow structure composed of multi-scale vortices in and around the plasma; in addition, it reveals that turbulent and non-turbulent regions co-exist in the flow field.

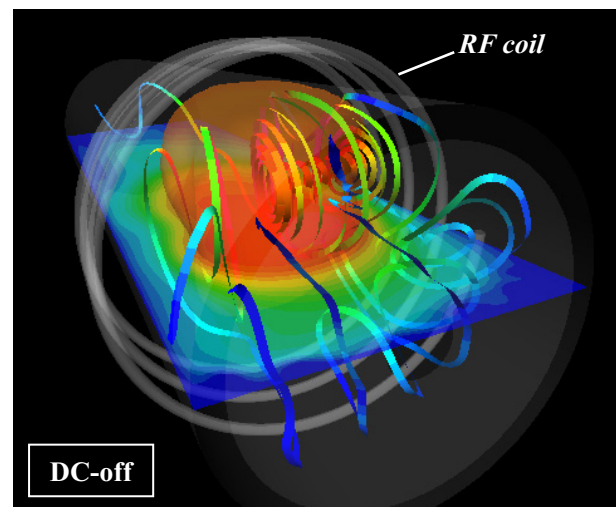
1. Introduction

A direct current – radio frequency (DC–RF) hybrid thermal plasma was originally developed by Yoshida *et al.* [1]; and it offers a unique thermofluid field with high temperature and chemical activity. Hence, it has been expected as a promising tool for effective material processes [2]. Although the control of the thermofluid field is indispensable for the effective processes, the flow structure and dynamic behaviour of the plasma is still unknown. Kawajiri *et al.* [3] only showed instantaneous snapshots of the complicated flow field by the particle tracking velocimetry, whereas the numerical works [1, 4, 5] simulated only a simple flow structure because all of them assumed steady 2-D conditions. Therefore, it is significant to simulate the plasma flow by a time-dependent 3-D approach to investigate its complex flow structure and dynamic motions. In addition, there has been no report that has revealed the “coherent structure” of multi-scale vortices in/around a thermal plasma.

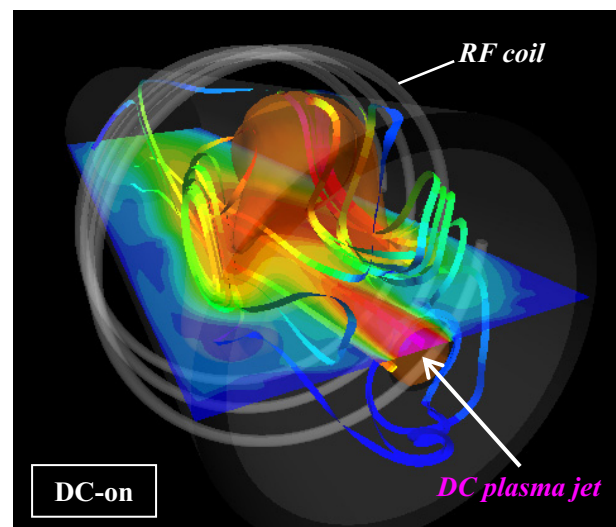
In this study, time-dependent 3-D simulations based on a large eddy simulation (LES) are performed to clarify the effect of a DC plasma jet on the thermofluid field in a DC–RF hybrid thermal plasma torch. Because the knowledge of the vortex structure will be helpful for the process design via flow control, the present simulation attempts to capture multi-scale vortices although that often destabilizes the computation.

2. Model description

The thermofluid field in a DC–RF hybrid plasma torch is determined by the simultaneous conservation equations of mass, momentum and energy, coupled with the Maxwell’s equation. The entire flow field, where the plasma at a high temperature and a cold gas at room temperature co-exist, must be treated at the same time. This is why thermal plasma simulations are very difficult. The widely ranging temperature from 300 to 12,000 K causes large spatial variations of the transport properties with several orders of magnitude. Furthermore, the density at a room-temperature region is approximately 45 times that at a high-temperature plasma. Meanwhile, the Mach number is estimated to range from 0.003 to 0.045. Hence, the partially ionized flow in a torch is treated as an incompressible flow with the density as a temperature-dependent variable to



(a) DC-off (RF discharge alone)



(b) DC-on (Hybrid discharge)

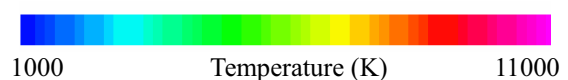


Fig. 1 Instantaneous snapshots of the thermofluid fields for (a) DC-off and (b) DC-on. (View from the torch top)

obtain the solution in a practical time-scale. Moreover, it can be conjectured that turbulent and non-turbulent regions co-exist in the flow field because a cold gas has

a low kinematic viscosity, whereas a plasma has a high kinematic viscosity. To express this feature, the coherent structure Smagorinsky model [6] is implemented to the sub-grid scale.

The governing equations are discretized by the finite volume method. Because the often-used first-order upwind-differencing scheme cannot capture eddies due to its large numerical viscosity, a central-differencing scheme should be used for the convection terms to capture vortices. However, that scheme easily causes an unstable computation. Therefore, in this study, the second-order central-differencing scheme is basically used for the convection terms; however, 10% of the first-order upwind-differencing is blended to stabilize the computation. In addition, the second-order Adams-Bashforth method is applied to time marching.

3. Computational conditions

The computational conditions are similar to Ref. [1]. The inner radii of the DC jet nozzle and the torch wall are 4 mm and 25 mm, respectively. The slit width for sheath gas is 3 mm. The input flow rates of the DC jet and the sheath gas are set at 3 Sl/min and 23 Sl/min. The RF induction coil has a spiral shape with a radius of 30 mm, a length of 30 mm and a pitch of 10 mm; and its front end is located at 25 mm from the top of the torch. The input powers to the DC and RF portions are 0.6 kW and 6 kW; and the induction frequency is 4 MHz. The axisymmetric profile is given as the initial condition. The computation is performed with a solver coded in FORTRAN using the supercomputer (SX-9, NEC, Japan) at the Cyberscience Center of Tohoku University.

4. Results and Discussion

Figures 1(a) and 1(b) show the representative results of the instantaneous thermofluid fields for an RF discharge alone and a DC–RF hybrid discharge, respectively. The high temperature plasma generated by RF discharge tends to have a large scale recirculating flow which is caused by the Lorentz forces. In Fig. 1(a), the recirculation prevents the injected cold gas from flowing downstream. On the other hand, in Fig. 1(b), the strong DC plasma jet conveys the surrounding cold gas and overcomes the recirculation occasionally. Because of this effect, the thermofluid field in a DC–RF hybrid plasma discharge tends to be more complicated and dynamical than that in a normal RF discharge.

Figure 2 depicts the coherent vortex structure visualized by the second invariant of the velocity gradient tensor whose value is 2.0 that is normalized by an arbitrary representative speed of 10 m/s and the torch diameter of 50 mm. The high temperature region has a large scale vortex structure, whereas the low temperature flow forms small eddies.

Figure 3 portrays the distribution of the viscosity ratio which is defined as the ratio of the turbulent eddy viscosity to the molecular viscosity. The flow in a torch is a very complicated field where turbulent and

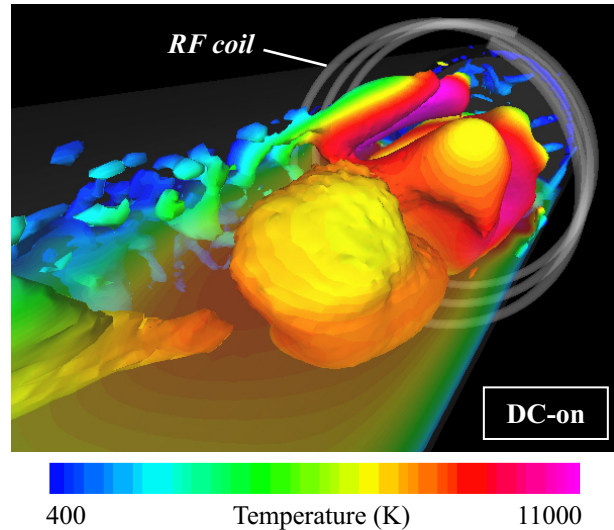


Fig. 2 Instantaneous snapshot of the coherent vortex structure. (View from the torch outlet)

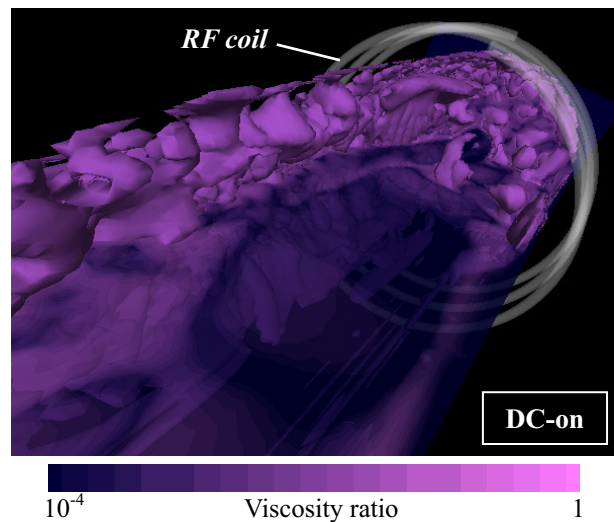


Fig. 3 Instantaneous snapshot of the viscosity ratio. (View from the torch outlet)

non-turbulent regions co-exist.

5. Summary

Time-dependent 3-D simulations based on an LES were successfully performed to clarify the effect of a DC plasma jet on the thermofluid field in a DC–RF hybrid thermal plasma torch. The complex flow structures comprising multi-scale vortices were also revealed.

References

- [1] T. Yoshida *et al.*, *J. Appl. Phys.*, **54** (1983), 640.
- [2] M. Shigeta, A.B. Murphy, *J. Phys. D: Appl. Phys.* **44** (2011), 174025.
- [3] K. Kawajiri *et al.*, *Surface Coatings Tech.*, **171** (2003), 134.
- [4] M. Shigeta, H. Nishiyama, *Trans. ASME, J. Heat Trans.* **127** (2005), 1222.
- [5] J.H. Seo *et al.*, *Plasma Sources Sci. Tech.* **17** (2008), 025011.
- [6] H. Kobayashi, *Phys. Fluid* **17** (2005), 045104.

Optimization of Combined Technology "Plasma Spraying - Pulsed Electron-Beam Post-Irradiation" of Cermet Wear-Resistant Coatings by Numerical Simulation

Oleg P. Solonenko, Vladimir I. Iordan, Vitaly A. Blednov, and Alexey A. Golovin
Khristianovich Institute of Theoretical and Applied Mechanics, Siberian Branch of RAS, Novosibirsk, Russia
Altai State University, Barnaul, Russia
solo@itam.nsc.ru

ABSTRACT

Thermal and, in particular, plasma spraying of nano- or submicron-structured cermet coatings from composite powders with particles containing a high volume concentration of ultra-fine inclusions of a very hard chemical compound dispersed in a metal alloy matrix opens up vast possibilities in the synthesis of wear-resistant coatings intended for use under severe environmental conditions. In this connection, an approach is proposed to designing and optimizing the processes of the formation of a lamellar structure and porosity of plasma-sprayed (TiC-(Ni-Cr)-alloy) ceramic-metal coatings and their post-irradiation by pulsed electron beam in vacuum.

1. Introduction

Thermal and, in particular, plasma spraying of nano- or submicron-structured ceramic-metal (cermet) coatings from composite powders with particles containing inclusions of a very hard chemical compound dispersed in a metal alloy matrix (binder) opens up vast possibilities in the synthesis of wear-resistant surface layers intended for use under severe environmental conditions.

Composite powders obtained from mechanically crushed "titanium carbide – metal binder" cermet compacts synthesized by thermal explosion of starting powder elements under high-pressure conditions, deserves special mention [1]. In cermet powders, particles have a finely dispersed inner structure formed by 1–3 μm sized equiaxed carbide inclusions uniformly distributed, throughout the whole particle volume, in a metal binder.

The high carbide phase content of ceramic-metal powder particles (50-70 vol.%) makes the melted metal binder, containing hard, finely dispersed suspended inclusions, highly viscous. Among other things, the high viscosity of sprayed particles provides for a low degree of their deformation during impingement onto substrate or previously sprayed coating layer. That is why ceramic-metal coatings plasma sprayed from above powder materials normally have a comparatively high porosity formed at the junctions between individual splats and at the coating-substrate interface [1].

Porosity in a plasma-sprayed cermet coating can be reduced, with simultaneous strengthening of the coating-to-substrate bonding, by giving the coating a post thermal treatment. The problem here consists in the necessity to heat the coating to a desired temperature without seriously affecting the ultra-fine refractory solid inclusion distributed in melted metal binder as well as the metal substrate. In practice, such a high-temperature treatment of plasma-sprayed powder coatings can be organized using pulsed laser, ion-beam, or electron-beam irradiation. Of special interest here is high-energy treatment of cermet coating with pulsed electron beams, capable of heating and remelting a

surface layer at depths of 0.1 mm [2].

There are presented the results concerning computer design and optimization of above combined technology.

2. Modeling cermet coatings formation

First, an approach is proposed to the modeling the process of the formation of a lamellar structure of thermal coatings, including plasma coatings, at the spraying of above-mentioned cermet powders. The results are presented, which concern the further development of the computational algorithm and the program code [3] for modeling the process of laying the splats in the coating with regard for its surface relief, which varies dynamically at the spraying, as well as the formation of a lamellar structure and porosity of the coating (see Fig. 1).

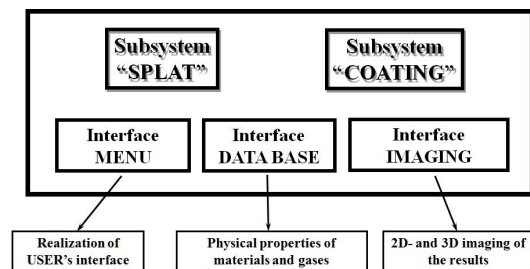


Fig. 1. Structural block diagram of program code.

The theoretical solution [4] is used to rapid prediction of splats thicknesses and diameter depends on the key physical parameters (KPPs) prior to "cermet particle with melted binder and solid carbide inclusions – substrate/base" interaction: the velocity, temperature, and particle size, the temperature of the base, and the concentration of ultra-fine solid inclusions.

Using the obtained solution included in the subsystem SPLAT, we performed the calculations which have demonstrated the possibility of formulating adequate requirements on KPPs of the spray process in designing a technology for spraying cermet coatings with predictable splat thickness and degree of particle flattening on the substrate, and also with desired contact

temperature at the coating-substrate/base interface during the formation of the first/next coating monolayer.

The results of computational experiments illustrating the performance of the developed computational technology are presented. This gives rise to a possibility of formulating the requirements for the facility and investigating its potential technological capabilities from the viewpoint of ensuring the given characteristics of the coating.

3. Modeling coatings pulsed electron post-treatment

Second, numerical experiments were carried out using the software package described in [5]. The software package was developed for modeling, by the finite-element method (FEM), of non-stationary boundary-value heat-transfer and phase-transition problems usually met in the field of treating surfaces and coatings with high-concentrated energy fluxes.

For pulsed electron-beam irradiation of the coatings, we used an electron beam experimental facility characterized by diameter of 1–3 cm and the beam current of up to 300 A, the pulse duration of electron-beam could be varied in the range 10–200 μs at an accelerating voltage of up to 25 kV, and the energy flux density in the beam of up to 100 J/cm^2 [6]. This equipment provides the operation window as far as the density of heat flux q presented in Fig. 2.

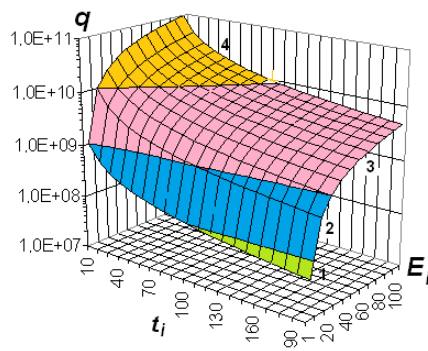


Fig. 2. The surface that defines the range of q (W/m^2) in the electron beam within the operating space of regime parameters of the experimental setup: pulse duration t_i , μs ; pulse energy E_i , J/cm^2 ; different intervals of q are indicated with different colors: 1 – $[10^7; 10^8]$; 2 – $[10^8; 10^9]$; 3 – $[10^9; 10^{10}]$; 4 – $[10^{10}; 10^{11}]$.

Numerical estimates of optimal values of process parameters corresponding to different values of porosity and volume content of ultra-fine TiC solid inclusions in plasma sprayed cermet coatings allow use of pulsed electron-beam irradiation for modification of structure of cermet coatings under conditions of solid-liquid phase interaction of cermet components with each other and with the steel substrate.

4. Concluding remarks

The computer experiments fulfilled showed that the energy flux density in the electron beam and the duration

of electron-beam pulses are parameters that have a predominant influence on the formation of the temperature profile in plasma-sprayed coatings subjected to electron-beam irradiation. Through variation of the total number of electron-beam pulses and the time intervals between the pulses, one can regulate the duration of the interphase interaction of components in the cermet composition under restrictions imposed on the temperature profile in the surface layer of the coating. Optimal values of process parameters were evaluated, suitable for implementing a controlled thermal treatment of cermet coatings under conditions of solid-liquid interaction of components in the cermet composition with each other and with the steel substrate.

Pulsed electron-beam irradiation of plasma-sprayed cermet coatings presents an efficient tool for rapid heating of powder coatings with their rapid quenching without affecting the metal base up to complete melting of metal binder in the coating. With increasing the particles' size of plasma-sprayed cermet powder and at irradiation conditions kept unchanged, the heating temperature of the coating increases.

Pulsed electron-beam irradiation of cermet coatings plasma-sprayed onto steel substrates resulting in complete remelting of the metal binder leads to the formation, in the surface layer of the coating, of a high-dispersion structure formed by submicron titanium carbide particles dispersed in the metal binder based on the solid solution of nickel and chrome in iron. In the middle part of the coating, the above structure comes into a nanostructure state defined by the formation of a cermet structure from titanium carbide nanoparticles. In the immediate vicinity of the steel substrate the coating structure is defined by the formation of an iron-based solid solution with titanium carbide nanoinclusions.

Acknowledgment

The results reported were obtained in part within Interdisciplinary Integration Project No. 2 of the SB RAS for the year 2012-2014.

References

- [1] O.P. Solonenko, V.E. Ovcharenko, Yu.I. Ivanov and A.A. Golovin, *J. of Thermal Spray Technology*, **20** (2011), P. 927-938.
- [2] V. Rotshtein, Yu. Ivanov and A. Markov, *Materials surface processing by directed energy techniques*, Ed. by Y. Pauleau, Elsevier, 2006, P. 205-240.
- [3] O.P. Solonenko, V.A. Blednov and V.I. Jordan, *Thermophysics and Aeromechanics*, **18** (2011), P. 253-271.
- [4] O.P. Solonenko, *J. of Thermal Spray Technology*, **21** (2012), to be published.
- [5] A.A. Golovin and O.P. Solonenko, *Thermophysics and Aeromechanics*, **14** (2007), P. 395-409.
- [6] V.N. Devyatkov, N.N. Koval, P.M. Schanin, V.P. Grigoryev, and T.B. Koval, *Laser and Particle Beams*, **21** (2003), P. 243-248.

Titanium Oxide Film Deposition by TPCVD using Vortex Ar Plasma Jet

Yasutaka Ando, Sheng Yuan Chen, Yoshimasa Noda
Ashikaga Institute of Technology
268-1 Omae, Ashikaga Tochigi 326-8558 Japan
E-mail: Yasutaka Ando

ABSTRACT

In order to develop an atmospheric thermal plasma CVD process without fluctuation of plasma jet, atmospheric TPCVD equipment with vortex plasma jet generator nozzle was fabricated and titanium oxide film deposition by this equipment was carried out on the condition of Ar working gas and 304 stainless steel substrate. Consequently, vortex Ar plasma jet could be generated by using the vortex generator nozzle. Besides, in the case of 40mm in deposition distance, anatase dominant film, which had enough photo catalytic property to decolor methylene blue solution by 96 hour UV irradiation, could be deposited.

1. Introduction

Thermal plasma CVD (TPCVD) is a rapid film deposition process. Various functional material films, such as SiC[1], Diamond[2], Ti-B-N-C[3], TiO₂[4] and so on, have been successfully deposited so far. Especially, in the case of oxide film deposition, film deposition can be carried out in open air. Therefore, TPCVD is hoped to be a low cost deposition process for functional material films. Besides, in cases of oxide film deposition like TiO₂, ZnO and so on, atmospheric TPCVD (ATPCVD) is thought to be available since film pollution due to the ambient oxygen during film deposition does not take into account. However, since the feedstock is injected perpendicular to the plasma jet in the case of the conventional ATPCVD using DC arc jet, it is difficult to deposit the uniform film due to the difficulty of uniform vaporization of the liquid feedstock.

In this study, in order to develop an atmospheric TPCVD process which can vaporize the feedstock uniformly, as a basic study, atmospheric TPCVD equipment using vortex Ar plasma jet was fabricated and titanium oxide film deposition by this equipment was carried out.

2. Experiments

Fig.1 shows TPCVD equipment with vortex plasma jet generator. The equipment consisted of plasma torch, DC power supplying system, micro tube pump (feedstock supplying system) and working gas supplying system. The nozzle for vortex plasma jet generation (vortex nozzle) was equipped at the head of the plasma torch. As feedstock feeding system, a commercial airbrush was used. Table 1 shows deposition conditions. The plasma torch had water cooled electrodes. The anode, which was made from copper, had the constrictor which is 6 mm in diameter. A cylindrical cathode made from tungsten had a diameter of 3 mm. Ar was used as working gas. Mass flow rate of the gas was fixed at 20 l/min. As the feedstock for titanium oxide film deposition, ethanol diluted titanium tetra iso butoxide (Ti(OC₄H₉)₄) was used. Substrates were 15mm x 15mm x 1mm 304 stainless steel plates with #400 sand paper polished surface. Film depositions were conducted on the conditions of 20mm, 40mm and 70mm in spray distance (the distance between the nozzle

outlet of the plasma torch and the surface of the substrate). The deposition time was 7 min. The discharge power was 125A/ 30V. After titanium oxide films deposition, investigations of the microstructure of the film by X-ray diffraction (CuK α , 40 kV, 100 mA). Besides, in order to confirm photo-catalytic property of the film, water droplet wettability test and methylene-blue droplet test and its decoloration test using UV irradiation equipment (Fig. 2) were carried out.

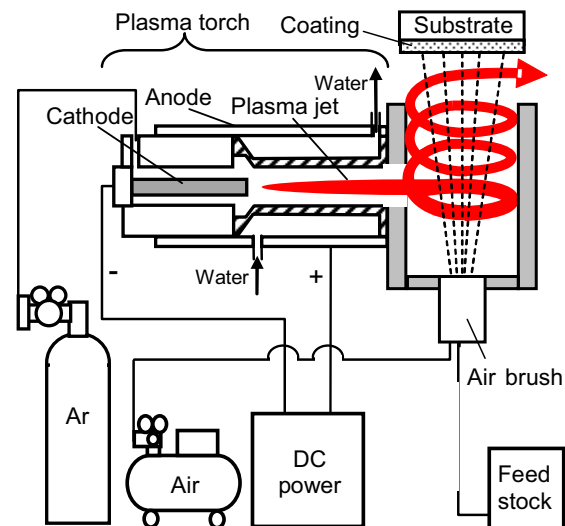


Fig. 1 Schematic diagrams of the ATPCVD equipment.

Table 1. Film deposition conditions .

Ar working gas flow	20 l/min.
Discharge Power	125A/ 30V
Deposition distance	20,40,70 mm
Feedstock	C ₂ H ₅ OH diluted TTIB* solution
Feedstock quantity	20 ml
Substrate	304 stainless steel

*TTIB: Titanium tetra iso butoxide

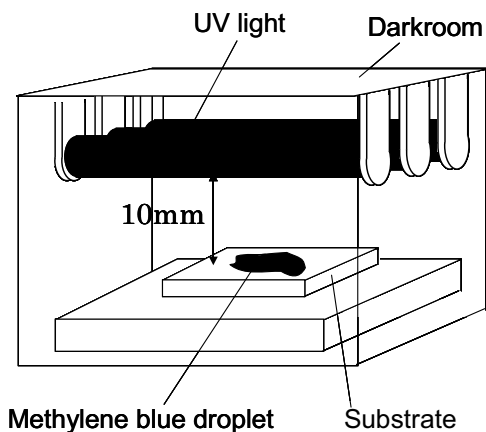


Fig. 2 Equipment for methylene-blue decoloration test.

3. Results and Discussion

3.1 Vortex Ar plasma jet

Since Ar plasma jet released from the plasma torch proceeded along the inner wall of the vortex nozzle, the Ar plasma jet became vortex flow at the nozzle outlet. The feedstock could be vaporized uniformly and provided continuously because the feedstock was transported from air brush outlet to substrate surface on the axial center of vortex plasma tunnel and continuously in this study.

3.2 Titanium oxide deposition

Fig. 3 shows XRD patterns of the titanium oxide films deposited by TPCVD with vortex plasma jets. In the case of 20mm in deposition distance ($d=20\text{mm}$), rutile/ anatase mixture film could be deposited. On the other hand, in the case of $d=40\text{mm}$, anatase dominant film could be deposited. However, in the case of $d=70\text{mm}$, amorphous film was deposited. In the case of vortex plasma jet assisted TPCVD, since the substrate could not be heated by plasma jet directly, the substrate temperature during deposition was under 623 K on the condition of $d=70\text{mm}$. Therefore, amorphous titanium oxide film was deposited. However, by post heat (723 K, 30 min.), the amorphous film could be changed into anatase dominant film.

Fig.4 shows the results of water droplet wettability test. In the cases of the film deposited on the conditions of $d=20\text{mm}$ and 40mm , the contact angles are below 10 degree, which indicated hydrophilic, in both cases. On the other hand, in the case of that on the condition of $d=70\text{mm}$, the angle was 70 degree, which indicated relatively hydrophobic. As for the methylene blue decoloration test, though the methylene blue was perfectly decolorated by 96 hour UV irradiation in the case of the titanium oxide film deposited on the condition of $d=40\text{mm}$, methylene blue decoloring ability of the films was low in the cases of $d=20\text{mm}$ and 70mm compared to the film in the case of $d=40\text{mm}$. This tendency is thought to occur due to transformation from anatase to rutile and deterioration of the degree of crystallinity of the film. In addition, it was proved that

rutile had photo-catalytic properties to indicate hydrophilic, but not enough to decolor methylene blue solution.

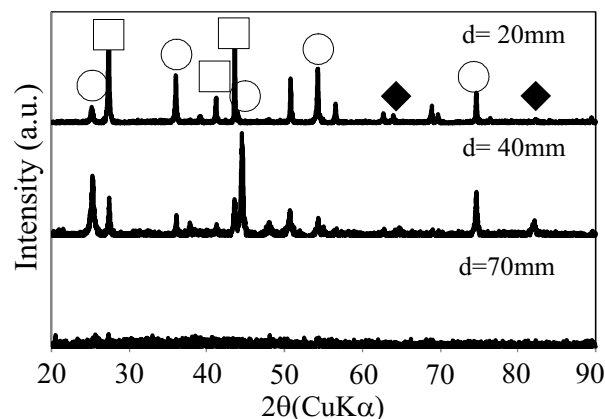


Fig. 3 XRD pattern of the titanium oxide films.

d: Deposition distance,
 [□: Rutile, ○: Anatase, ◆: Fe (Substrate)]

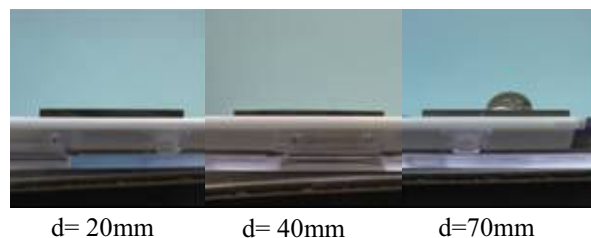


Fig. 4 Results of water droplet wettability test.

4. Concluding remarks

- 1) By equipment of the vortex nozzle at the nozzle outlet of the plasma torch, vortex Ar plasma jet could be created.
- 2) Since feedstock was injected by air brush and transported to the substrate surface on the axial center of the vortex plasma tunnel, feedstock could be vaporized uniformly and fed continuously.
- 3) By controlling the deposition temperature, hydrophobic amorphous film as well as hydrophilic rutile and anatase dominant films could be deposited.
- 4) The anatase dominant film had high photo-catalytic property to decolor methylene blue solution.

References

- [1] H. Murakami, T. Yoshida, K. Akashi, *Advanced Ceramic Materials*, 3, 4 (1988), 423.
- [2] N. Ohtake and M. Yoshikawa, *Japanese Journal of Applied Physics*, 32 (1993), 2067.
- [3] S. Shimada, M. Takahashia, J. Tsujinob, I. Yamazakic, K. Tsudac, *Surface Coatings and Technology*, 201 (2007), 7194.
- [4] H. Okayama, A. Nagata, H. Isa, *Trans. IEE Japan*, Vol. 117-A, 9 (1997), 936. (in Japanese)

Anode Jet Characteristics of Argon-Hydrogen Arc for Nanoparticle Production

Takayuki Watanabe, Manabu Tanaka, Tasuku Shimizu, and Feng Linag
Tokyo Institute of Technology, Dept. Environmental Chemistry and Engineering,
G1-22-4259 Nagatsuta, Midori-ku, Yokohama, Kanagawa 226-8502, Japan
watanabe@chemenv.titech.ac.jp

ABSTRACT

High-speed camera observations were conducted to investigate the influence of the hydrogen addition on the anode jet characteristics. The high-speed camera system with appropriate band-pass filters successfully provides the observation of anode jet image without cathode jet image. The areas of the anode jet and the cathode jet were separately evaluated from the high-speed images. The periodical fluctuation of the anode jet was confirmed. Higher hydrogen concentration leads to larger anode jet area, resulting from the enhanced evaporation of the anode material.

1. Introduction

Thermal plasmas have been widely applied to many fields because of their unique advantages such as high chemical reactivity, easy and rapid generation of high temperature, high enthalpy to enhance reaction kinetics, rapid quenching capability, and oxidation and reduction atmosphere in accordance with required chemical reaction. These advantages increase the advances and the demands in plasma chemistry and the plasma processing [1,2].

Among various thermal plasmas, DC arc plasma as an energy source with high energy efficiency has been applied to the welding and the cutting metals, the plasma spraying, synthesis of the nanoparticles. Especially, the DC arc with hydrogen addition has been applied to the production of metal, alloys, and intermetallic nanoparticles due to the evaporation enhancement of the metals by the hydrogen addition in the arc [3].

The anode region of the high-intensity arc has been studied [4,5]. As the cold ambient gas enters into the arc, the arc-anode attachment appears in mainly three different modes. Besides the well-known diffuse and constricted anode attachment modes, the transition mode, which is called multiple-attachment mode, has been observed [6-9]. The anode attachment modes are the results of the competition between the cathode jet and the anode jet. When the cathode jet is strong, the anode attachment mode is in a diffuse mode. The arc transitions to the multiple-attachment mode with reducing the cathode jet. Further decreasing the cathode jet increases the current density, which leads to the strong anode jet flow and to the entrainment of cold gas along the anode towards the arc attachment. The increase of the radial heat loss due to the anode jet makes a single constricted attachment take over the most of the current and stabilizes it.

The anode region of the argon-hydrogen arc has not been studied enough, although many efforts have been made. This lack of understandings is primarily due to the strong interaction of electrical, magnetic, thermal, and fluid-dynamic effects. In addition, the observation of only the anode jet is difficult due to the strong emissions from the cathode jet.

The purpose of the present work is to observe the anode jet without the cathode jet to characterize the

anode jet quantitatively. From the observation, the influence of the hydrogen addition on the arc-anode attachment was investigated.

2. Experimental Procedure

2.1 Experimental setup

Fig. 1 shows a schematic illustration of experimental setup. This setup consists of a power supply, an arc chamber, a particle collector, and a gas circulation pump. Nickel ingot of 50 g as an anode was placed on the water-cooled copper. Ar and Ar-H₂ arc was used for the evaporation of the raw material. Typical operating conditions are as follows: current: 50-200 A, voltage: 20-50 V, total pressure: 101 kPa, shield gas flow rate: 0-20 NL/min, H₂ concentration: 0, 10, 30, 50vol%.

2.2 Diagnostics

Fig. 2 shows the schematic illustration of the high-speed video camera (Photron, FASTCAM-SA WTI) with band-pass filters, which was used to observe the anode jet. Emissions from the arc were introduced to the optical system, which includes the band-pass filters and the beam splitter. Filtered images were then captured by the CCD plane of the high-speed camera. Therefore, high-speed images of each species in the arc were obtained with frame rate of 10,000. Typical shutter speed was 100 μ s. The vaporized species from the molten metal were identified by spectroscopic diagnostics (Horiba Jobin Yvon, iHR-550).

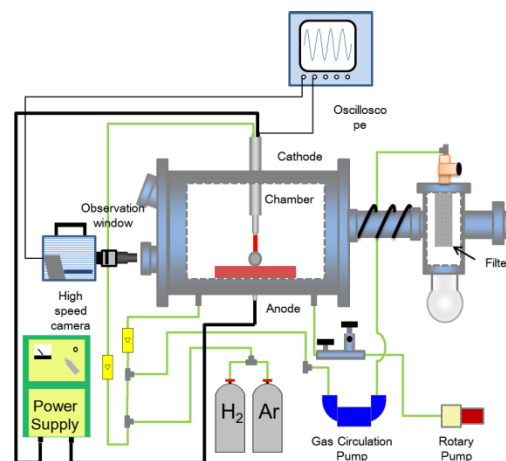


Fig. 1 Schematic of the experimental setup.

3. Results and Discussion

Fig. 3 (a)-(c) shows the high-speed images for different hydrogen concentration. Anode jet became larger with increasing the hydrogen concentration. This can be explained by two effects as follows; (i) momentum of the plasma gases from the cathode to anode became smaller with increasing the hydrogen concentration, (ii) the metal evaporation leads to higher electrical conductivity, resulting in the constriction of the arc in anode region.

Fig. 3 (d)-(f) shows the snapshots of the high-speed video images with band-pass filter at 500 nm. Since nickel vapor only exists in anode jet region, the high-speed images of anode jet were successfully obtained without the cathode jet flow images. The anode jet area was evaluated from these images.

Fig. 4 (a) shows the time variation of the anode jet area in 50%-H₂ arc. The waveforms of the arc current and the voltage synchronized with the high-speed observation were shown in Fig. 4 (b). The Ni anode jet area was strongly influenced by the ripple of the arc current. The Ni anode jet area became larger at the peak top of the arc current, while the Ni anode jet became smaller at the peak bottom of the arc current. This is because the higher arc current leads to the anode material evaporation, resulting in the enhancement of the anode jet.

4. Conclusion

High-speed camera observations with appropriate band-pass filters were conducted to investigate the influence of the hydrogen concentration on the anode jet characteristics. Only the anode jet was successfully observed without strong emissions from the cathode jet by using this high-speed camera system. Hydrogen addition in the arc leads to the formation of the anode jet. The control of the anode jet and the arc-anode attachment enable to prepare metal, alloy, and intermetallic nanoparticles with high productivity by the DC arc under atmospheric pressure.

References

- [1] T. Watanabe, et al., *Pure Appl. Chem.*, **82** (2010), 1337.
- [2] T. Watanabe, et al., *Plasma Chem. Plasma Process.*, **32** (2012), 123.
- [3] M. Tanaka, et al., *Thin Solid Films*, **526** (2008), 6645.
- [4] N. A. Sanders, et al., *J. Appl. Phys.*, **53** (1982), 4136.
- [5] N. A. Sanders, et al., *J. Appl. Phys.*, **55** (1984), 714.
- [6] G. Yang, et al., *J. Phys. D: Appl. Phys.*, **39** (2006), 2764.
- [7] G. Yang, et al., *Plasma Sources Sci. Technol.*, **16** (2007), 529.
- [8] G. Yang, et al., *Plasma Sources Sci. Technol.*, **16** (2007), 765.
- [9] G. Yang, et al., *J. Phys. D: Appl. Phys.*, **18** (2007), 5649.

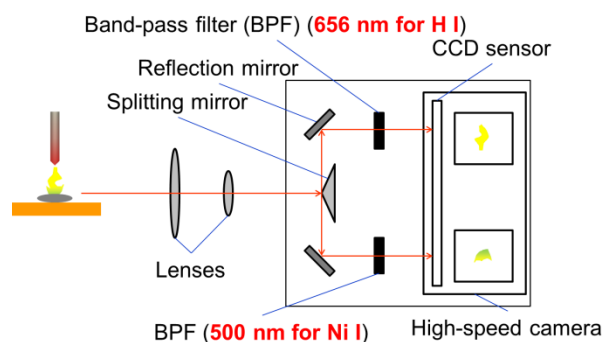


Fig. 2 Schematic illustration of the high-speed video camera with the band-pass filters.

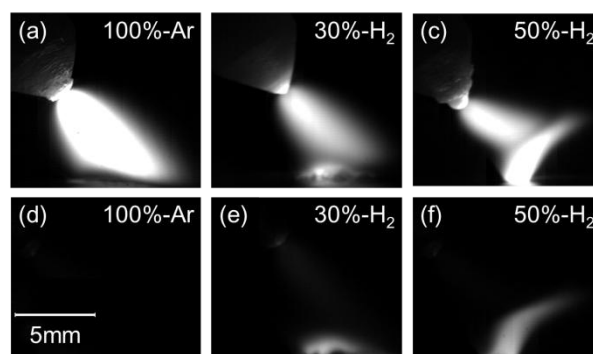


Fig. 3 Representative snapshots of the high-speed images without band-pass filter (a-c), with band-pass filter (d-f).

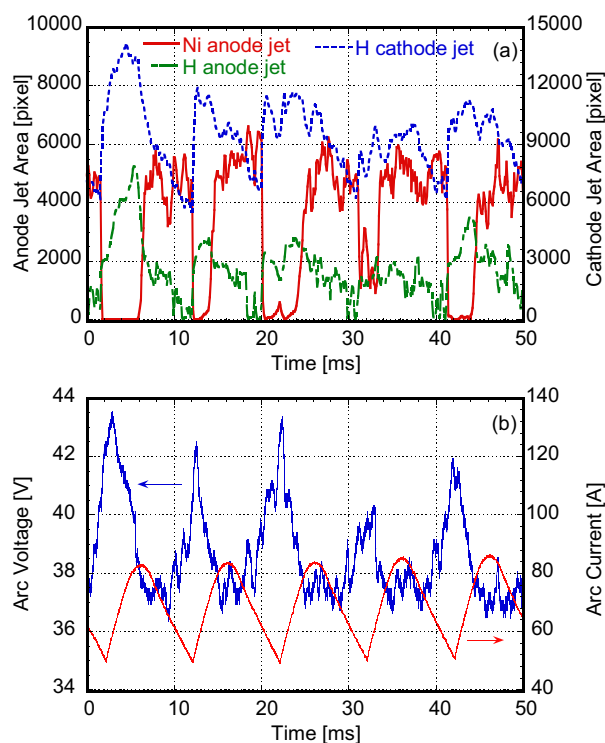


Fig. 4 Time variation of the anode jet area and the cathode jet area for 50%-H₂ arc (a), and the waveforms of the arc voltage and current (b).

Innovative Applications of Modulated Induction Thermal Plasma Flow for Materials Processings

Yasunori Tanaka

Kanazawa University, Kakuma, Kanazawa 920-1192, Japan
tanaka@ec.t.kanazawa-u.ac.jp

ABSTRACT

This paper reviews recent innovative applications of modulated induction thermal plasmas. We have so far developed various types of high-power modulated induction thermal plasma system. Some examples will be introduced on application of the modulated induction thermal plasmas to surface modification and carbon film deposition in which thermally and chemically non-equilibrium effects are essential in temperature and radical density fields.

1. Introduction

We have developed several types of systems for several-tens kW-class modulated induction thermal plasma (MITP). The MITP is sustained by the coil current modulated in milliseconds. Such the millisecond modulation in the coil current remarkably perturbs the thermal plasma, and then it can markedly change temperature, densities of atoms/molecules in thermal plasmas. This periodical perturbation on the thermal plasmas can thus control the time-averaged value of them in time domain [1]. This modulation also provides non-equilibrium effects even in high-pressure thermal plasmas. We have also studied to apply the MITP to materials processings. The simplest MITP is the pulse modulated induction thermal plasma (PMITP). The PMITP is sustained by the coil current modulated into a rectangular waveform. This rectangular waveform is characterized by the modulation parameters: the on-time, the off-time, and the higher current level (HCL) and the lower current level (LCL) [1]. The shimmer current level (SCL) is also defined as a ratio of LCL/HCL. Lower SCL corresponds to higher modulation degree.

This paper reviews recent innovative applications of modulated induction thermal plasmas such as surface modification and film deposition.

2. Experimental setup

The most possible application of the PMITP is the surface treatment. Here, results will be introduced for applications of PMITP to high-speed nitridation and diamond film deposition. In these processings, the PMITP is irradiated to the specimen surface. Fig. 1 shows a schematic diagram of the plasma torch, the reaction chamber and a specimen for processings. The 'on-time' and 'off-time' were set respectively to 10 ms and 5 ms in this experiment. The time-averaged input power was fixed to the MOSFET inverter power supply at the same value of 15 kW for any SCL condition. This power condition can be realized using a higher HCL and a lower LCL to the current amplitude in the non-modulation condition.

3. Surface nitridation using the PMITP

One application of the PMITP is the surface nitridation [2], which is widely used to enhance surface hardness for cutting tools, gears, etc. The conventional surface nitridation methods like gas nitriding, salt bath nitriding require a long time more than several tens of hours. Thermal plasma surface nitridation is one candidate for high-speed nitridation processings. The thermal plasma can provide high nitrogen atomic flux, which is an important factor. However, the steady-state thermal plasma offers high heat flux onto the specimen, which causes thermal damage of the surface. On the other hand, the PMITP can control heat flux as well as nitrogen atomic flux.

In the present nitridation processings, a 15-mm-diameter titanium specimen was used. The Ar gas was supplied as a sheath gas for a plasma, while N₂/H₂ gas mixture was supplied from the side of the downstream torch. The total gas flow rate was fixed at 100.0 slpm (= l/min). The N₂/H₂ gas flow rate was set to a value of 2.0/1.0 and 4.0/1.0 slpm. Pressure inside the chamber was fixed to 30 kPa (230 torr). The irradiation time was 180 s. The specimen surface irradiated by the PMITP was analyzed by X-ray diffraction (XRD). The XRD spectral peak $I_{42.6}$ at a diffraction angle $2\theta=42.6^\circ$ from TiN (2 0 0) and the peak $I_{39.7}$ at $2\theta=39.7^\circ$ from α -TiN_{0.3} were observed. The ratio of the above peak $I_{42.6}/I_{39.7}$ is shown in Fig. 2. As seen, the condition 60–70%SCL pro-

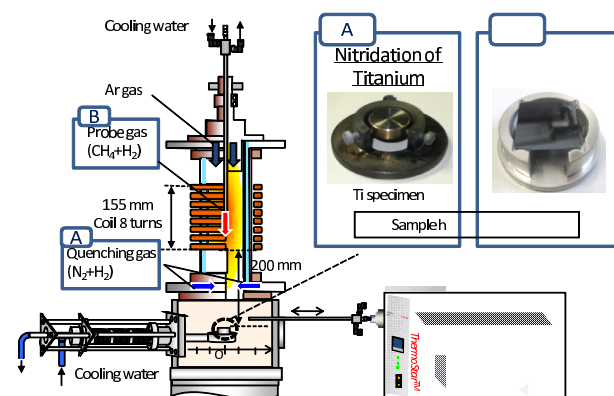


Fig. 1. Plasma torch and specimen for materials processings using PMITP.

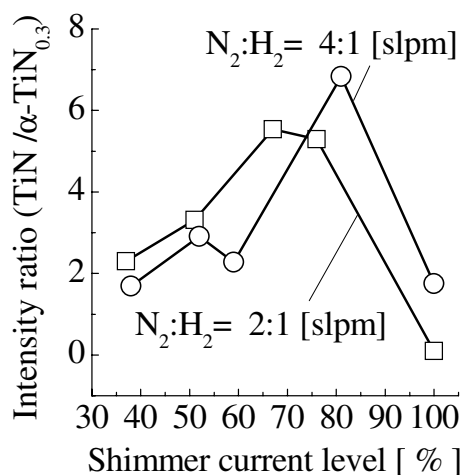


Fig.2. XRD spectral intensity ratio (TiN/ α -TiN_{0.3}) versus SCL.

vides a local maximum of the ratio $I_{42.6}/I_{39.7}$. This means that the nitriding degree is promoted at 60–70%SCL only for 180 s compared to 100%SCL, i.e. non-modulation condition. On the other hand, the specimen surface temperature was measured to decrease with decreasing SCL from 100% to 40%. Fig. 2 implies that higher nitrogen flux could be produced at 60–70%SCL.

4. Diamond film deposition by the PMITP

Another application of the PMITP is the diamond film deposition [3]. Diamond is expected to be the next generation semiconductor material operating at high voltage. High voltage semiconductors are demanded recently for electric vehicle circuits, high-voltage dc electric power distribution system.

Fig. 3 shows the photograph of the Si wafer with an area of $25 \times 25 \text{ mm}^2$ irradiated by the non-modulated induction thermal plasma (a) and the PMITP at 40%SCL (b). The Ar gas was fed as a sheath gas with a flow rate of 67 slpm, whilst CH_4/H_2 gas was supplied with a flow rate of 3.03 slpm, through the water-cooled tube inserted from the torch top to the plasma as indicated in Fig. 1. The gas mixture ratio of CH_4/H_2 was 1.0%. Pressure inside the chamber was fixed at 24 kPa (180 torr).

The non-modulated thermal plasma irradiation clearly makes non-uniform film on the Si wafer. On the other hand, the PMITP irradiation produces almost uniform film as indicated in Fig. 3(b). Fig. 4 indicates the Raman shift measured at two positions on the films deposited by the non-modulated plasma and by the PMITP. One position is the center of the substrate, the other is near the edge of the substrate. For the non-modulated plasma irradiation, we see clearly a Si spectral peak at 520 cm^{-1} and G-band spectra around 1500 cm^{-1} at the center of the substrate. The Si spectral peak originates from the Si substrate, whose appearance means that deposited film is quite thin. Observation of the G-band spectra indicates that the film mainly includes graphite. At the edge of



(a) Non modulated plasma (b) Pulse modulated plasma

Fig.3. Photographs of Si irradiated by the PMITP.

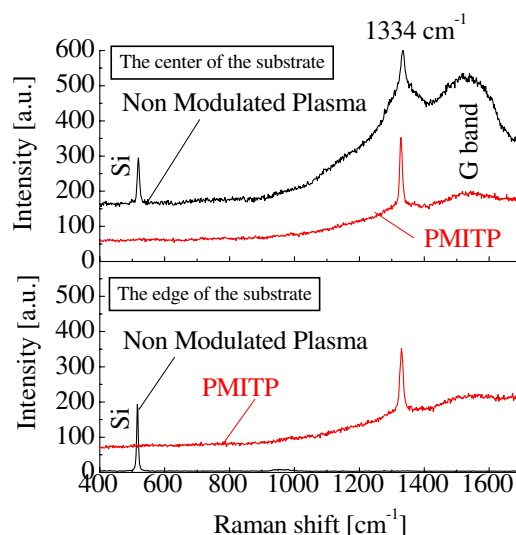


Fig.4. Raman shift measured at two positions on films deposited by the non-modulated plasma and by the PMITP.

the substrate, only the Si peak is seen; No carbon film is present. On the other hand, the film deposited by the PMITP irradiation shows the peak at 1334 cm^{-1} both for the two positions. This peak is attributed to the diamond structure. The above fact means that the PMITP can provide diamond film almost uniformly for a Si wafer of $25 \times 25 \text{ mm}^2$.

5. Conclusion

This paper introduces recent trial applications of modulated induction thermal plasmas to surface modulation and film deposition. The modulated induction thermal plasma is a promising tool being adopted for future material processing demands.

References

- [1] Y.Tanaka, The Open Plasma Phys. J., **2** (2009), 120.
- [2] Y.Haruta, et al., Plasma conference 2011 (PLASMA2011), 22P063-P (2011.11).
- [3] K.Fujimoto, et al., Plasma conference 2011 (PLASMA2011), 22P062-P (2011.11).

Mass and Energy Balances of Organic Waste Gasification in Steam Plasma

Milan Hrabovsky, M. Hlina, M. Konrad, V. Kopecky, O. Chumak, T. Kavka, A. Maslani
Institute of Plasma Physics ASCR, Prague, Czech Republic
hrabovsky@ipp.cas.cz

ABSTRACT

Production of syngas by reaction of wood with oxygen, carbon dioxide and water was studied in plasma reactor with dc arc plasma torch stabilized by combination of water vortex and argon flow. Wood saw dust and wooden pellets were supplied into plasma flow inside the reactor. Oxygen and carbon dioxide were added to the reactor, water was from wood humidity, additional oxygen was supplied by steam plasma. Syngas with high concentrations of hydrogen and carbon monoxide was produced. In the experiments we tested effect of material mass flow rate, particle size and flow rates of added oxidizing media on properties of produced syngas.

1. Introduction

Plasma gasification for production of syngas is an alternative to conventional methods of biomass treatment [1, 2]. Plasma is a medium with the highest energy content and thus substantial lower plasma flow rates are needed to supply sufficient energy needed for gasification compared with other media used for this purpose. This results in minimum contamination and dilution of produced syngas by plasma gas and easy control of syngas composition. The other advantages are higher calorific value of the gas and reduction of unwanted contaminants like tar, CO₂, CH₄ and higher hydrocarbons, as well as wide choice of treated materials. The process acts also as energy storage – electrical energy is transferred into plasma energy and then stored in produced syngas.

In this paper gasification of wood by plasma assisted reaction with oxygen, carbon dioxide and water was studied. Effect of material feed rate, material particle size, flow rate of added gases and energy available for material treatment on syngas properties was studied in experiments with wood saw dust and wooden pellets.

2. Experimental System

The principal scheme of experimental reactor is shown in Fig. 1. High enthalpy steam plasma was

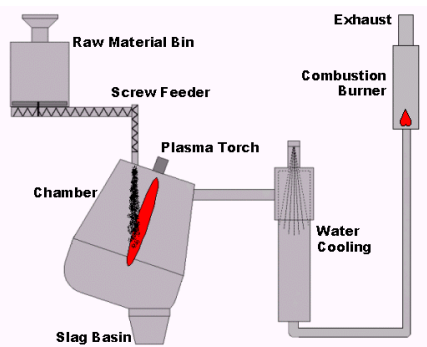


Fig. 1 Schematic of plasma reactor PlasGas

generated in dc arc torch with hybrid water/gas plasma torch [3-5]. Basic parameters of plasma torch are in Table 1. Wood saw dust and wooden pellets were supplied into plasma flow inside the reactor. As molar content of carbon is higher than oxygen content in

biomass, an oxidizing medium has to be supplied to ensure complete gasification of material and reduction of solid carbon formation. In the present experiments oxygen, carbon dioxide and water were used as an oxidizing media. Gases were supplied to the reactor, water came from wood humidity, and additional oxygen was supplied by steam plasma. Gas produced in the reactor was fed into quenching tower where the temperature was rapidly reduced to 300 °C by water spray. After filtering and cleaning the produced gas was burned in the gas burner. Measurements of temperatures and power losses in the reactor were made, composition of produced syngas in the reactor and at the output of quenching chamber were performed by mass spectrometer and analyzer of CO and H₂.

Table 1. Operation parameters of plasma torch

Arc current [A]	400 - 500
Arc power [kW]	110 - 140
Plasma flow rate [g/s]	0.3 - 0.4
Plasma enthalpy [MJ/kg]	150 - 200
Exit centerline temperature [K]	19 000 – 21 000
Exit centerline velocity [m/s]	5 000 – 6 000

3. Results and Discussion

Figures 2 to 4 show basic characteristics of material and gas inputs for ten runs of experiments with various feed rates of material, flow rates of gas and arc power.

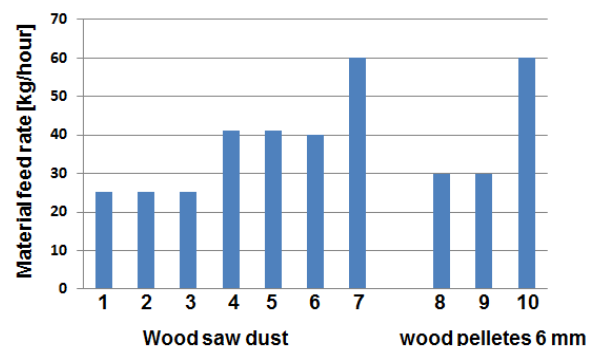


Fig. 2 Feed rates of treated material

Runs 1 to 7 were made with fine saw dust, runs 8 to 10 with wooden pellets of 6 mm diameter and 15 mm length. Fig. 3 shows ratio of arc power to material feed

rate and process enthalpy defined as ratio of energy available for material treatment to amount of material. Energy available for material treatment was determined from the difference of arc power and power loss to the plasma torch and reactor walls. Fig 4 shows amount of added oxygen as a ratio of added oxygen from water,

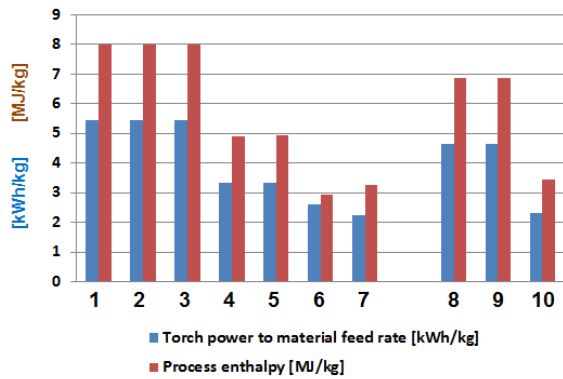


Fig. 3 Ratio of arc power to material feed rate and ratio of energy available for process to material mass (process enthalpy)

oxygen and carbon dioxide to stoichiometric oxygen needed for complete gasification of all carbon in

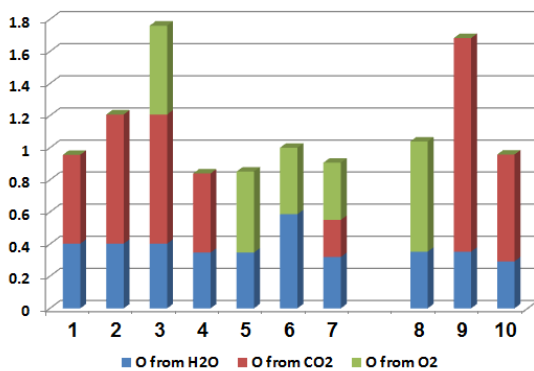


Fig. 4 Ratio of molar fraction of added oxygen to fraction needed for full gasification

material to CO. Conditions with a surplus as well as of a shortage of oxygen were tested in this series of experiments.

In Fig. 5 measured syngas composition is shown compared with the composition corresponding to complete gasification of material to syngas. Fig. 6 presents ratio of heating value of produced syngas to plasma torch power.

It can be seen that in all cases composition of produced syngas was close to the composition calculated for complete gasification of material. In cases with the highest feed rates of material (runs 7 and 10) with maximum energy yield the syngas composition as well as the gas yields were similar to runs with smaller feed rates. Maximum achieved energy gain was 3.5 in run 7. It seems that even higher feed rates and thus

lower process enthalpies can be realized which result in higher energy gain.

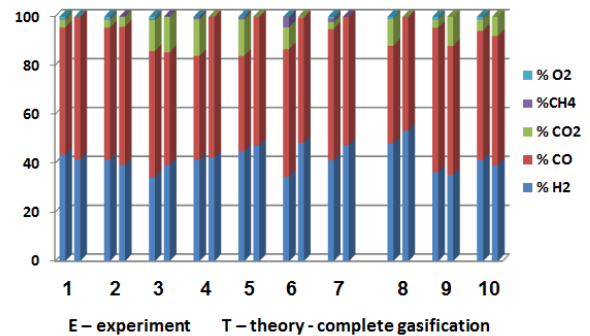


Fig. 5 Measured syngas composition and composition corresponding to complete gasification

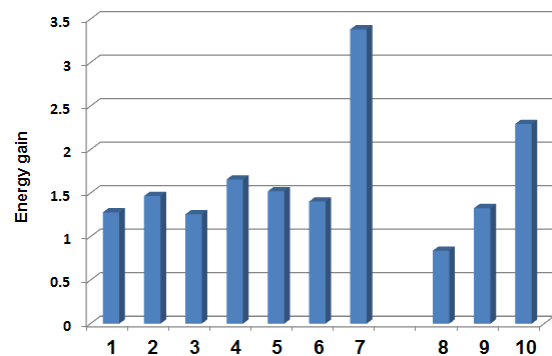


Fig. 6 Ratio of calorific value of syngas to torch power

Acknowledgement

The work was supported by the Grant Agency of the Czech Republic under the project P 205/11/2070.

References

- [1] L. Tang, H. Huang, *Energy&Fuels* **19** (2005), 1174-1178.
- [2] M. Hrabovsky, M. Konrad, V. Kopecky, M. Hlina, *High Temperature Material Processes* **10** (2006), 557-570.
- [3] M. Hrabovsky, V. Kopecky, V. Sember, T. Kavka, O. Chumak, M. Konrad, *IEEE Trans. on Plasma Science* **34** (2006), 1566- 1575
- [4] M. Hrabovsky, M. Konrad, V. Kopecky, M. Hlina, T. Kavka, O. Chumak, A. Maslani, *Proc. of 20th Int. Symp. on Plasma Chem.*, Philadelphia, 2011.
- [5] M. Hrabovsky, P. Krenek, *Proc. of 11th Int. Symp. on Plasma Chemistry*, Loughborough, 1993, Vol. 1, 315-320.

The Influence of Turbulence on Characteristics of a Hybrid-Stabilized Argon-Water Electric Arc

Jiří Jeništa¹, Hidemasa Takana², Hideya Nishiyama², Milada Bartlová³, Vladimír Aubrecht³, Petr Křenek¹

¹Institute of Plasma Physics AS CR, v.v.i., Za Slovankou 3, 182 00 Praha 8, Czech Republic

²Institute of Fluid Science, Tohoku University, 2-1-1 Katahira, Aoba-ku, Sendai, Miyagi, 980-8577, Japan

³Brno University of Technology, Technická 8, 616 00 Brno, Czech Republic

e-mail: jenista@ipp.cas.cz

ABSTRACT

The paper presents numerical simulations of the discharge and near outlet regions of the hybrid-stabilized argon-water electric arc. Calculations have been carried out for the assumption of laminar and turbulent plasma flow regimes respectively. Results of calculations for currents 300-600 A show that the influence of turbulence is weak and the maximum difference for all the monitored physical quantities is less than 10 %. Comparison with available experiments exhibits good agreement.

1. Introduction

The so-called hybrid stabilized electric arc, developed a decade ago at IPP AS CR in Prague, utilizes a combination of gas and vortex stabilization. In the hybrid argon–water plasma torch, the arc chamber is divided into the short cathode part, where the arc is stabilized by tangential argon flow, and the longer part, which is stabilized by water vortex. This arrangement provides not only the additional stabilization of the cathode region and the protection of the cathode tip but also offers the possibility of controlling plasma jet characteristics in wider range than that of pure gas- or liquid-stabilized arcs. The arc is attached to the external water-cooled rotating disk anode at a few millimeters downstream of the torch orifice. The experiments made on this type of torch showed that the plasma mass flow rate, velocity, and momentum flux in the jet can be controlled by changing the mass flow rate in the gas-stabilized section, whereas thermal characteristics are determined by the processes in the water-stabilized section. At present, this arc has been used for plasma spraying using metallic or ceramic powders injected into the plasma jet, as well as for the pyrolysis of waste (biomass) and production of syngas [1], which seems to be a promising environmentally friendly application of thermal plasma jets.

In this paper we present the influence of turbulence on parameters in the discharge and near-outlet regions of the hybrid-stabilized arc. The results between laminar and turbulent flows are discussed and compared with available experiments.

2. Physical Model and Numerical Approach

The following assumptions for the model are applied: 1) argon-water plasma itself is in local thermodynamic equilibrium, 2) the model is two-dimensional, 3) the plasma flow is laminar/turbulent and compressible, 4) argon and water create a uniform mixture in the arc chamber, 5) gravity effects are negligible, 6) the magnetic field is generated only by the arc itself, 7) the partial characteristics method for radiation losses is employed, 8) transport and thermodynamic properties for Ar + H₂O plasma mixture, calculated rigorously from the kinetic theory, depend on temperature and pressure [2].

Radiation losses from the argon-water arc are calculated by the partial characteristics method for different molar fractions of argon and water plasma species as a function of temperature and pressure. Continuous radiation, discrete radiation consisting of thousands of spectral lines, molecular bands of O₂, H₂, OH and H₂O have been included in the calculation of partial characteristics [3]. Broadening mechanisms of atomic and ionic spectral lines due to Doppler, resonance and Stark effects have been considered.

Turbulence is modelled by Large eddy simulation with the Smagorinsky subgrid-scale model and the Van Driest damping function near the walls [4].

The resulting set of conservative governing equations for density, velocity and energy (continuity, momentum and energy equations) is solved numerically by the LU-SGS method [5], which is coupled with Newtonian iterative method. To resolve compressible phenomena, convective term is calculated by using a third-order MUSCL-type TVD scheme [6]. For the electric potential, the TDMA algorithm enforced with the block correction method is applied. The task has been solved on an oblique structured grid with nonequidistant spacing finer near the walls and boundaries for the total number of 38 553 grid points.

3. Results

Calculations for turbulent and laminar models have been carried out for currents 300, 400, 500 and 600 A. Mass flow rate for water-stabilized section of the discharge was taken for each current between 300 and 600 A from our previously published work [7]. Argon mass flow rate was varied in agreement with experiments in the interval from 22.5 slm (standard liters per minute) to 40 slm, namely, 22.5, 27.5, 32.5 and 40 slm.

Fig. 1 presents the average relative difference between turbulent and laminar models within the volume of the discharge and of the near-outlet regions for temperature, velocity and the Reynolds number. The average relative difference for a given physical quantity X is calculated as

$$\Delta_{av}^X = \frac{100}{N} \cdot \sum_{i=1}^N \text{abs}(X_{\text{turb}}^i - X_{\text{lam}}^i) / X_{\text{turb}}^i \quad (1)$$

where N is the total number of grid points in the domain, representing the discharge volume and the region 2 mm downstream of the nozzle exit; “turb” and “lam” stand for the turbulent and laminar values of X respectively.

One can see that the lowest difference occurs for temperature ($\sim 2.5\%$), the highest difference for the Reynolds number ($\sim 10\%$). The difference increases with currents for all displayed quantities.

4. Conclusions

Much more results have been obtained for currents 300-600 A and for argon mass flow rates 22.5-40 slm. They can be summarized as follows:

(a) Turbulence is not significant phenomenon in the discharge and near-outlet regions of the hybrid-stabilized argon-water electric arc:

- Maximum relative difference of each of the monitored physical quantities calculated at the arc axis, along the radius near the outlet nozzle and within the volume of the discharge and near-outlet region reaches less than 10 %.

- Difference generally increases with current; the maximum value of the difference occurs for the Reynolds number. The maximum value of the Reynolds number is 13 000.

(b) Turbulent effects are stronger in small regions near sharp edges of the outlet nozzle and in the transition region between hot plasma and surrounding atmosphere in the near-outlet region with high radial temperature and velocity gradients.

(c) Comparison with available experimental data demonstrates very good agreement for temperature. Agreement between the calculated radial velocity profiles and the profiles derived from experiments is worse.

Acknowledgments

J. Jeništa is grateful for financial support under the Fluid Science International COE Program from the Institute of Fluid Science, Tohoku University, Sendai, Japan, and their computer facilities. Financial support from the project GA CR 205/11/2070 is gratefully acknowledged. The access to the METACentrum super-computing facilities provided under the research intent MSM6383917201 is highly appreciated.

References

[1] G. Van Oost, M. Hrabovsky, V. Kopecky, M. Konrad, M. Hlina, T. Kavka, O. Chumak, E. Beckman, J. Verstraeten, *Vacuum*, **80** (2006), pp. 1132-1137.
 [2] P. Křenek, *Plasma Chem. Plasma Process.*, **28** (2008), pp. 107-122.
 [3] M. Bartlova, V. Aubrecht, *Czech. J. Phys.* **56** (2006) pp. B632-B637.

[4] S. B. Pope, *Turbulent Flows*, Cambridge University Press 2000.

[5] A. Jameson, S. Yoon, *AIAA Journal*, **25** (1987), pp. 929-935.

[6] B. van Leer, *J. Comp. Phys.*, **32** (1979), pp. 101-136.

[7] J. Jeništa, *J. High Temp. Mat. Processes*, **7** (2003), pp. 11-16.

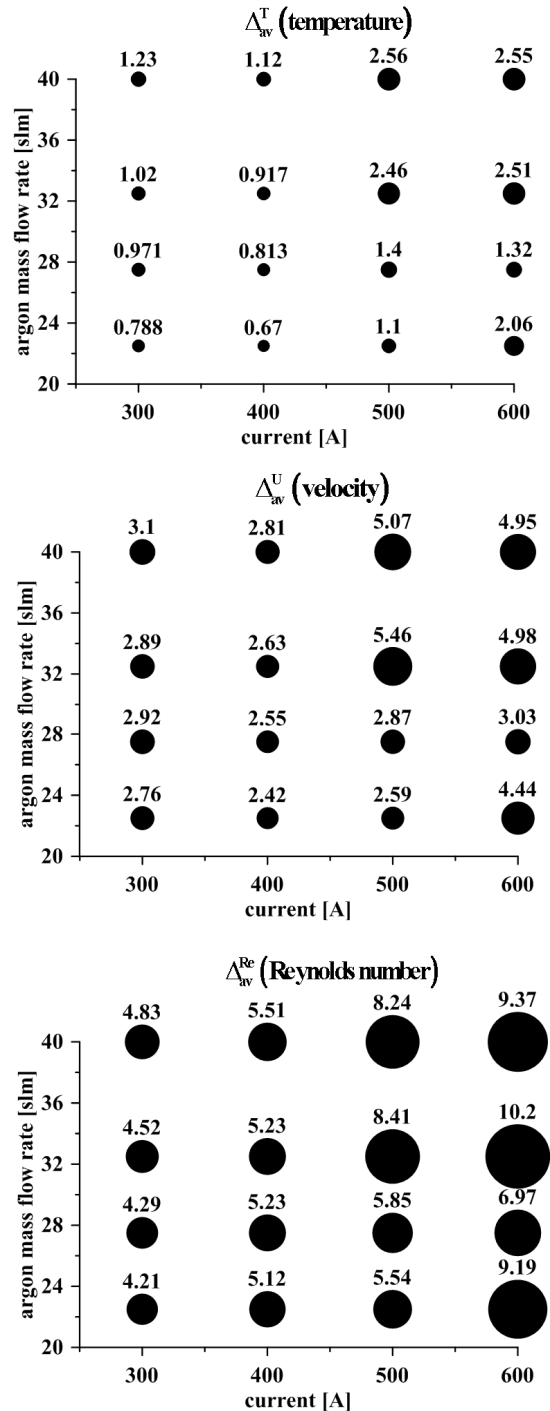


Fig. 1. Average relative difference in per cent between turbulent and laminar models within the volume of the discharge and of the near-outlet regions for temperature (top), velocity (middle) and the Reynolds number (bottom).

Numerical Modeling of Fume Formation Process in Welding

Shinichi Tashiro, Sho Matsui, Manabu Tanaka

Joining and Welding Research Institute, Osaka university, Osaka 567-0047, Japan
tashiro@jwri.osaka-u.ac.jp

ABSTRACT

This study aims to visualize the fume formation process and clarify the fume formation mechanism in arc welding theoretically through numerical analysis. Furthermore, the reliability of the simulation model was also evaluated through comparison of the simulation result with experimental result. As a result, it was found that the size of the secondary particle consisting of small particles with size of several nm which range like a chain reaches 150nm at maximum in helium GTA welding.

1. Introduction

In order to clarify the fume formation mechanism in arc welding, a quantitative investigation based on the knowledge of interaction among the electrode, arc and weld pool is indispensable. A fume formation model consisting of a heterogeneous condensation model, a homogeneous nucleation model and a coagulation model has been developed and coupled with the GTA welding model [1]. A series of processes from evaporation of metal vapor to fume formation from the metal vapor was totally investigated by employing this simulation model. The aim of this study is to visualize the fume formation process and clarify the fume formation mechanism theoretically through a numerical analysis.

2. Method

In this study, helium GTA welding model and the fume formation model considering the assumptions (1)~(7) listed below are used.

- (1) The formation of supersaturation of the metal vapor by cooling.
- (2) The formation of the primary particle by the homogeneous nucleation.
- (3) The growth of the primary particle by the heterogeneous condensation.
- (4) The formation of the secondary particle by the coagulation.
- (5) The growth of the secondary particle by the heterogeneous condensation and the coagulation.
- (6) Coulomb force and Brownian force are considered for driving force of particles in coagulation.
- (7) Particle temperature is calculated by considering heat transfer between particle and plasma.

It is required to provide the metal vapor pressure and the cooling rate obtained from the GTA welding model to the fume formation model as the initial conditions. The metal vapor pressure is referred from the value in the region at 3,000K. The cooling rate is calculated as product of temperature gradient and plasma flow velocity at 2,000K.

3. Results and Discussion

Fig. 1 shows distributions of temperature and stream lines of the plasma flow. The maximum temperature of the arc plasma reached 22,000K near the cathode tip. Since the electrical conductivity of helium plasma is extremely low especially in low temperature, the current path is constricted within the central region where the plasma is high temperature. Therefore, Joule heating is prompted in this region. The heat input from the arc into the base metal increases in the central region due to the same reason. The weld pool in the base metal is heated intensively. Consequently, the maximum temperature of the weld pool rose up to 3,056K.

Fig. 2 shows distribution of partial pressure of the metal vapor evaporated from the weld pool. It was found that the metal vapor was compressed into the region near the weld pool surface due to strong plasma flow from the cathode which was called the cathode jet and was swept away in radial direction. The maximum metal vapor pressure became 7,500Pa near the center of the weld pool surface. In this study, a cooling rate and a metal vapor pressure near the weld pool surface are selected as calculation conditions for the fume formation model, because dense metal vapor near the weld pool surface is considered to affect fume characteristics strongly. As a result, cooling rate at 2,000K and metal vapor pressure at 3,000K were 7.99×10^5 K/s and 246Pa.

Fig. 3 shows dependences of particle diameter distribution on temperature above 1,400K. Fig. 4 shows an example of history of change in particle shapes with decreasing temperature at (a) 1700K, (b) 1650K, (c) 1600K and (d) 1500K denoted at points in Fig. 3. At around 1,700K, the nucleation began and very small primary particles below diameter of 1nm were appeared in the region. The particles moved at an average velocity of 234m/s at 1,700K. Subsequently, primary particles grew up by the heterogeneous condensation and a part of them formed secondary particles due to the coagulation. Especially, diameters of secondary particles rapidly increased below 1,650K due to coagulation among secondary particles. An average velocity decreased to 21m/s at 1,600K because of increase in particle weight. All the primary particles have been coagulated and an averaged velocity became 0.8m/s at 1,550K. Around this temperature, diameters of

secondary particles approached 100nm at maximum. Finally, the size of the secondary particle consisting of small particles with size of several nm which range like a chain reaches 150nm at maximum at 300K.

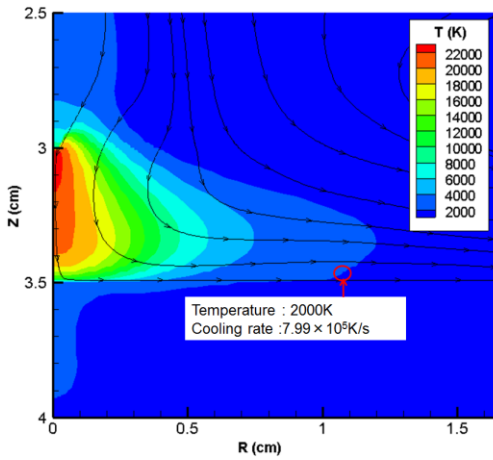


Fig. 1 Distribution of temperature and fluid flow.

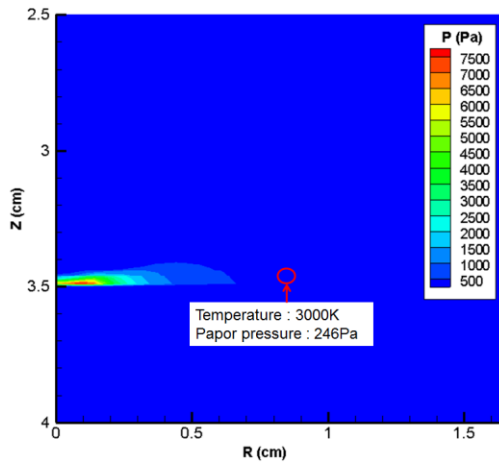


Fig. 2 Distribution of metal vapor pressure.

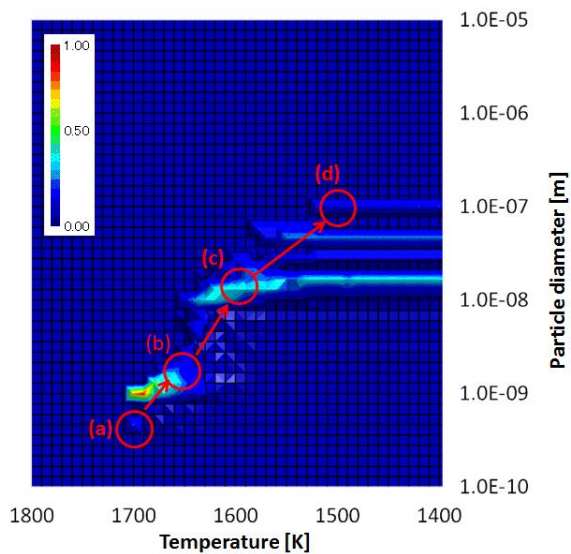


Fig. 3 Dependences of particle diameter distribution on temperature.

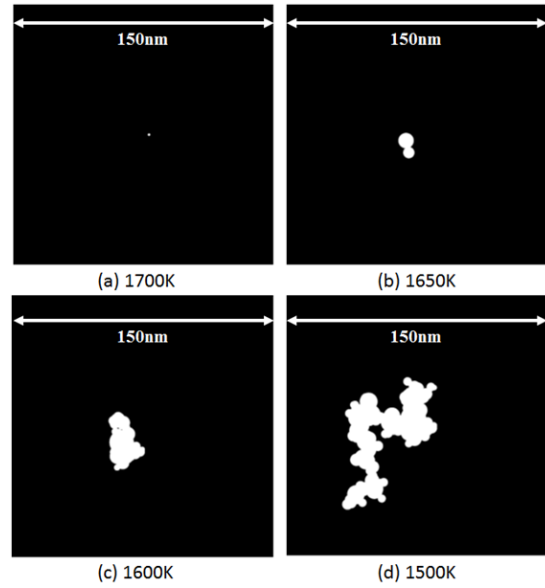


Fig. 4 An example of history of change in particle shapes with decreasing temperature at (a) 1700K, (b) 1650K, (c) 1600K and (d) 1500K denoted at points in Fig. 3

4. Concluding remarks

A fume formation model consisting of a heterogeneous condensation model, a homogeneous nucleation model and a coagulation model has been developed and coupled with the GTA welding model. Through the simulation using the coupled model, it was found that the size of the secondary particle consisting of small particles with size of several nm which range like a chain reaches 150nm at maximum in helium GTA welding.

References

- [1] S. Tashiro et al: J. Phys. D: Appl. Phys., Vol. 43, (2010), pp. 434012 (11p).

Visualizations and Predictions of Gas Metal Arcs during Welding

Yoshihiro Tsujimura, Manabu Tanaka
Joining and Welding Research Institute, Osaka University
11-1 Mihogaoka, Ibaraki, Osaka 567-0047, Japan
tsujimura@jwri.osaka-u.ac.jp

ABSTRACT

This paper gives an instance of recent progress which has led to the capability of the visualization and prediction of welding arcs, though the dynamic observations of spectral image by a high speed digital video camera with a monochromator and also the calculations by numerical models. The dynamic observations lead to visualizations of metal vapor behavior in arc plasma. Finally, we discuss plasma physics in welding arcs through numerical calculations. There is close interaction between the electrode, the arc plasma, the weld pool, and also the metal vapor, which constitute the welding process, and must be considered as a unified system.

1. Introduction

Rouffet¹⁾ suggested the possibility that the temperature of the arc near the arc axis decreased comparing with that apart from the arc axis due to influence of the metal vapor in Gas Metal Arc (GMA) welding. However, information about the metal vapor concentration obtained from the experiments was only radial distribution at a height of the arc column. The overall phenomenon of GMA welding is not yet understood accurately.

This study aims to develop method for measuring dynamical variation of two-dimensional distribution of temperature and metal vapor concentration in the arc through optical measurement and to analyze behavior of the metal vapor in GMA welding.

2. Experiment

Experimental setup consists of a GMA welding torch, an inverter power source, a wire feeder, spectroscopes, high speed video cameras and a PC.

The spectroscopes is Czerny-Turner type and has diffraction grating with wavelength resolution of 0.6nm. The recorded intensity distribution is converted to temperature distribution with Fowler-Milne method after Abel conversion. After measurement of plasma temperature, iron vapor concentration distribution is obtained from intensity distribution of FeI line spectrum (538nm).

A frame rate is set to be 2000fps. The distance between the wire tip and the base metal surface is 25mm. The pure iron wire with diameter of 1.2mm and SS400 plate are employed as the anode and cathode, respectively. Pulsed welding current is used. The peak current, the base current, the averaged welding current and the arc voltage are 450A, 50A, 250A and 35V suitable for 1pulse-1drop. The shielding gas is pure argon and the gas flow rate is 20L/min.

3. Results and Discussion

3.1 Plasma temperature distribution

Fig. 1 shows dynamic variations of distributions of (left) ArI line spectrum at 696nm, (center) FeI line spectrum at 538nm and (right) temperature measured with Fowler-Milne method.

During the base current the temperature near the arc axis was about 4,000K and that apart from the arc axis was about 7,000K. During the peak current, the temperature near the arc axis was about 6,000K and that

apart from the arc axis was about 11,000K.

From these results, decrease in temperature near the arc axis was confirmed and dynamic variation of the entire temperature distribution of the arc was presented. It was found that although the plasma temperature in GMA welding varied with the metal transfer and the welding current, the arc was basically classified into two regions (low temperature region near the arc axis and high temperature region apart from the arc axis).

3.2 Behavior of metal vapor in plasma

Fig. 2 shows dynamic variations of distributions of (left) ArI line spectrum at 696nm, (center) FeI line spectrum at 538nm and (right) iron vapor concentration in case of pulsed welding current.

During the base current, metal vapor molar fraction near the arc axis reached 100% and became metal vapor

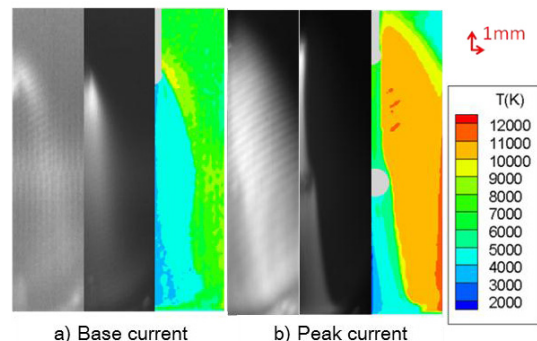


Fig.1 Time variation of (left) intensity distribution of ArI at 696nm and (center) that of FeI at 538nm and (right) distribution of plasma temperature

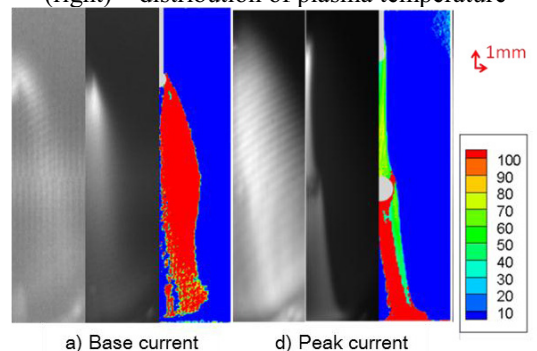


Fig.2 Time variation of (left) intensity distribution of ArI (696nm) and (center) that of FeI (538nm) and (right) distribution of iron vapor concentration

plasma in this region because dilution of the metal vapor caused by plasma jet was weakened due to decrease in plasma jet velocity. On the other hand, during the peak current, although evaporation of the metal vapor from the droplet surface was enhanced, dilution of metal vapor caused by the plasma jet was prompted because of increase in plasma jet velocity. However, concentration of the metal vapor reaching approximately 100% molar fraction was maintained between the droplet and the base metal because of the existence of the droplet in metal transfer. The plasma jet velocity was decreased in the downstream region of the droplet since the stream of the plasma jet was prevented by the droplet. Consequently, it is considered that concentration of the metal vapor became high because of weakness of dilution due to the plasma jet in addition to evaporation of the metal vapor from the droplet surface.

Consequently, the plasma temperature decreases with increase in the concentration of the metal vapor. Therefore, in GMA welding, the arc is double structure which consists of low temperature region near the arc axis occupied mainly with the metal vapor and high temperature region apart from the arc axis occupied with the shielding gas.

3.3 Physics of decrease in plasma temperature

In order to discuss physics of decrease in plasma temperature, numerical analysis was also conducted.

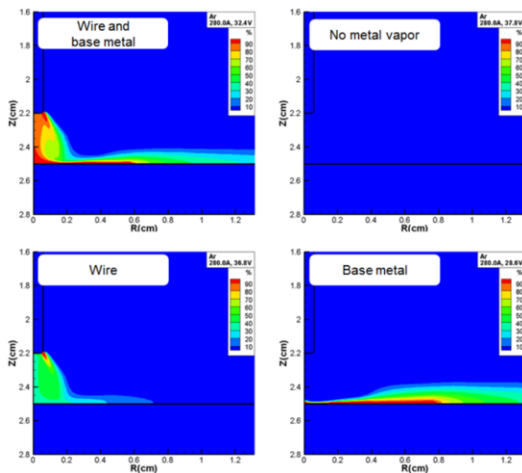


Fig.3 Distributions of iron vapor concentration

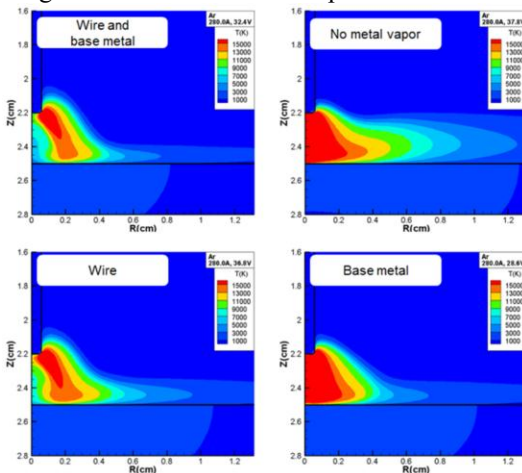


Fig.4 Distributions of plasma temperature

The simulation model was described in detail in previous paper²⁾. The numerical simulation is carried out assuming two sources of the iron vapor: the weld wire and the weld pool. The results from this are shown in Fig. 3 and Fig. 4.

In case of no metal vapor, naturally the metal vapor doesn't exist in the arc. In case of the metal vapor evaporated from the weld pool, although the metal vapor is mixed to the arc, large part of the metal vapor was swept away along the weld pool surface to outside of the arc because the metal vapor source is in downstream of the high speed plasma jet. As a result, the metal vapor hardly flows into the arc. On the other hand, in case of the metal vapor evaporated from the wire tip, the metal vapor flows into the arc through the plasma jet because the metal vapor source is in upstream of the plasma jet. In case of the metal vapor evaporated from the wire tip and weld pool corresponding to the practical situation, it was seen that mainly the metal vapor from the wire tip was transported into the arc through the plasma jet.

It was found that if the metal vapor was evaporated from the wire tip, the arc has double structure consisting of high temperature region apart from the arc axis and low temperature region near the arc axis as confirmed in the experiment. It is because the arc was cooled especially near the arc axis through the intensive radiation loss caused by high concentration of the metal vapor^{3,4)}.

4. Concluding remarks

Conclusions are summarized as follows:

- 1) In GMA welding, the arc has double structure consisting of high temperature region apart from the arc axis and low temperature region near the arc axis due to influence of the metal vapor.
- 2) The metal vapor became dense under the droplet because the droplet in metal transfer affects the stream of the plasma jet.
- 3) The low temperature region near the arc axis occurred because the arc was cooled especially through the intensive radiation loss caused by high concentration of the metal vapor.

Acknowledgement

This work was supported by KAKENHI 22246095, Grant-in-Aid for Scientific Research (A).

References

- [1] M.E. Rouffet, M. Wendt, G. Goett, R. Kozakov, H. Schoepp, K.D. Weltmann and D. Uhrlandt, *J. Phys. D: Appl. Phys.*, 43 (2010) 434003.
- [2] Y. Tsujimura and M. Tanaka, *Quarterly J. Japan Welding Soc.*,30 (2012),68.
- [3] S. Tashiro, M. Tanaka, K. Nakata, T. Iwao, F. Koshiisi, K. Suzuki and K. Yamazaki, *Sci. & Tech. Weld. Joining*, 12 (2007) 202.
- [4] M. Schnick, U. Fussel, M. Hertel, A. Spille-Kohoff and A.B. Murphy, *J. Phys. D: Appl. Phys.*, 43 (2010) 022001.

Electrode Temperature Estimation of Multi-Phase AC Arc by High-Speed Video Camera

Manabu Tanaka, Tomoki Ikeba, Yaping Liu, Sooseok Choi, and Takayuki Watanabe
Department of Environmental Chemistry and Engineering, Tokyo Institute of Technology
G1-22-4259 Nagatsuta, Midori-ku, Yokohama, 226-8502, Japan
mtanaka@chemenv.titech.ac.jp

ABSTRACT

Discharge characteristics of multi-phase AC arc were investigated based on the electrode temperature measurement in order to apply the multi-phase AC arc to an innovative glass melting. Thermal radiation from the electrode was measured by a high-speed video camera with band-pass filters. The electrode temperature was estimated from the radiations at 785 nm and 880 nm. The high-speed visualization of the electrode temperature by the high-speed video camera is a useful tool to investigate the electrode phenomena during the arc discharge.

1. Introduction

The glass industry is a large global industry that annually produces more than 100 million tons of glass products such as sheet glass, container glass, fiber glass, and optical glass. Most glass has been produced by typical Siemens-type melter fired in air with heavy oil or natural gas as the fuel. This type of melter has been used for more than 140 years because of its good large-scale performance and continuous melting system. In the air-fuel fired furnace, the heat transfer from above burner flame to glass melt is so low that the conventional melting technology is energy intensive and time consuming, especially in the melting and the refining process. With the rapid growth of glass usage and the increased energy and environment issues, it is crucial to develop a new glass melting technology to solve these problems.

Under the support of New Energy and Industrial Technology Development Organization (NEDO) in Japan, an innovative in-flight glass melting technology was developed [1]. The granulated raw material with small diameter is dispersed in thermal plasmas and the powders contact fully with the plasma and burner flame. The high heat-transfer and temperatures of the plasma lead to the quick melt of the raw material. In addition, the decomposed gas of carbonates is removed during the in-flight treatment to reduce the fining time considerably. Compared with the traditional glass production, the total vitrification time is evaluated only 2-3 h at the same productivity as the fuel-fired melter.

Arc plasmas as an energy source with high energy efficiency have been applied in in-flight glass production because the multi-phase AC arc possesses many advantages such as high energy efficiency, large plasma volume (about 100 mm in diameter), low velocity (5-20 m/s) [2,3]. However, the multi-phase arc remains to be explored because the multi-phase arc is a new type of the arc generating system.

Electrode temperature is important to understand erosion phenomena of the electrode material and the interaction between the arc and the electrodes. The purpose of the present study is to measure the electrode temperature by high-speed camera and to investigate the electrode phenomena of the multi-phase arc.

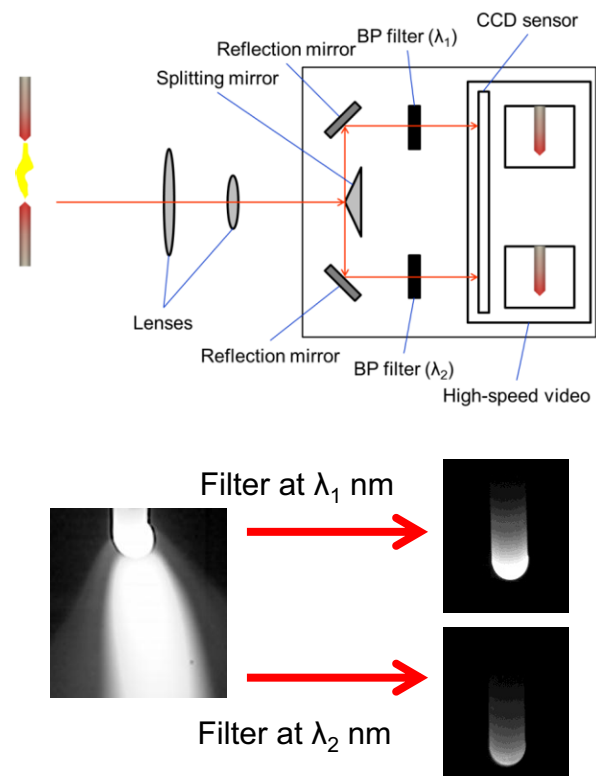


Fig. 1 Conceptual diagram of two-colour pyrometry using high-speed video camera with band-pass filters.

2. Method

The multi-phase arc generator consisted of an arc chamber, AC power supply (50 Hz), and 12 electrodes. The electrodes for the 12-phase arc were symmetrically arranged by the angle of 30 degree. The electrodes were made of 2wt%-thoriated tungsten with diameter of 6 mm. The details on the multi-phase ac arc discharge were explained in our previous report [4].

According to the Wien's approximation of Planck's law, the spectrum of thermal radiation from a blackbody is used to determine the electrode temperature at the applied wavelengths.

$$TR_{\lambda_i} = \frac{K\varepsilon(\lambda_i)d^2\lambda_i^{-5}}{e^{k_2/\lambda_i T} - 1} \quad (1)$$

A real body that emits less thermal radiation than the blackbody has surface emissivity ε less than 1. Since the emissivities are unknown for many applications, the gray body assumption $\varepsilon(\lambda_1) = \varepsilon(\lambda_2)$ is used where it is hypothesized that the surface emissivity is independent of wavelength.

Based on these approximations, the electrode temperature T is obtained from the ratio of the radiation intensity,

$$T = \frac{K_2(\lambda_1 - \lambda_2)}{\lambda_1\lambda_2} \frac{1}{\left(\ln\left(\frac{TR_{\lambda_1}}{TR_{\lambda_2}}\right) + 5 \ln\left(\frac{\lambda_1}{\lambda_2}\right) \right)} \quad (2)$$

where K_2 is the second radiation constant in Planck's law which value is $1.439 \times 10^{-2} \text{ m} \cdot \text{K}$, TR_{λ_1} and TR_{λ_2} are the thermal radiations emitted by the electrode at λ_1 and λ_2 , respectively.

Spectroscopic measurements (iHR550, Horiba Jobin Yvon) were conducted to determine appropriate wavelengths for two-colour radiations. Electrode temperature of the multi-phase arc was then measured from radiations from electrodes at 785 nm and 880 nm. High-speed video camera (FASTCAM SA-WTI, Photron) with band-pass filter system was used to measure the radiation intensities, as shown in Fig. 1. Frame rate and exposure time of the measurements were 10,000 fps and 20 μs , respectively. The voltage of each electrode was recorded at 1 MHz by an oscilloscope (Scope Corder DL 850, Yokogawa).

3. Results and Discussion

Fig. 2 shows the snapshot and the temperature distribution of the electrode for 12-phase ac arc. The tip temperature was higher than the melting point of tungsten (3695 K).

Fig. 3 shows the time dependence of the electrode tip temperature of 2-phase and 12-phase AC arc. The tip temperature at cathodic period was higher than that at anodic period, although the total heat transfer at anodic period is larger than that at cathodic period due to electron condensation. From the comparison between the 12-phase and 2-phase arc, the temperature variation of the 12-phase arc is narrower than that of the 2-phase arc. This is due to the multi-arc existence from the electrode in the case of the 12-phase arc as shown in Fig. 4 taken by the high-speed video camera.

4. Conclusions

High-speed visualization of the electrode temperature by using the high-speed video camera is a useful tool and enables to understand the electrode phenomena. The electrode tip temperature at cathodic period was higher than that at anodic period, although the total heat transfer at anodic period is larger.

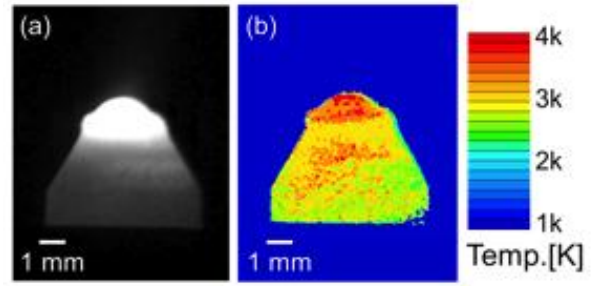


Fig. 2 (a) Snapshot of electrode, (b) 2-dimensional temperature distribution of the electrode for 12-phase AC arc.

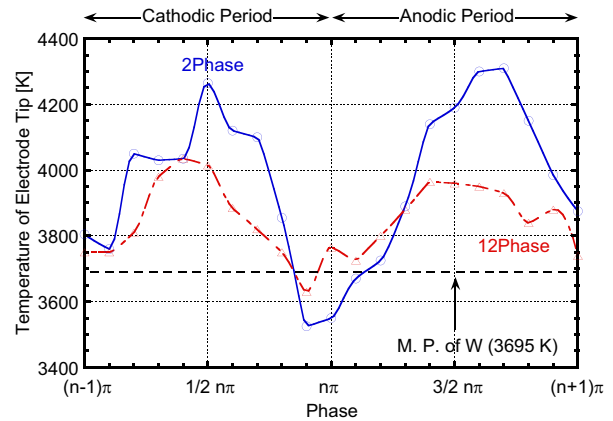


Fig. 3 Electrode tip temperature of 12-phase AC arc and 2-phase AC arc.

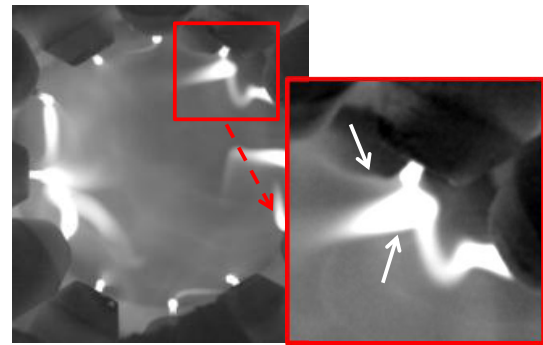


Fig. 4 High-speed video image of 12-phase AC arc.

Acknowledgments

The financial support by the Strategic Development of Energy Conservation Technology Project of NEDO (New Energy and Industry Technology Development Organization, Japan) is gratefully acknowledged.

References

- [1] Y. Yao, et al., *Sci. Technol. Adv. Mater.*, **9** (2008), 025013.
- [2] T. Watanabe, et al., *Pure Appl. Chem.*, **82** (2010), 1337.
- [3] M. Tanaka, et al., *IEEE Trans. Plasma Sci.*, **39** (2011), 2904.
- [4] Y. Liu, et al., *Thin Solid Films*, **519** (2011), 7005.

Hybrid Simulation of Gas Flow and Gas Discharge of Atmospheric-Pressure Plasma Jet with Helium Considering Impurity Effect

K.-M. Lin¹, M.-H. Hu¹, C.-T. Hung¹, J.-S. Wu^{1*}, F.-N. Hwang², G. Cheng³ and Y.-S. Chen⁴

¹Department of Mechanical Engineering, National Chiao Tung University, Hsinchu, Taiwan

²Department of Mathematics, National Central University, Jhongli, Taiwan

³Department of Mechanical Engineering, University of Alabama, Birmingham, AL, USA

⁴National Space Organization, Hsinchu, Taiwan.

*E-mail: chongsin@faculty.nctu.edu.tw

ABSTRACT

In this paper, an efficient parallel weakly coupled algorithm hybridizing 2-D gas flow model (GFM) and plasma fluid modeling (PFM) is presented. Both the GFM and PFM are discretized by the cell-centered finite-volume method. Both solvers are parallelized using domain decomposition method. A realistic APPJ with helium considering effect of measured impurities that include oxygen, nitrogen and water vapor is simulated for demonstration of the powerful capability of the proposed method.

1. Introduction

Atmospheric-pressure plasma jets (APPJ) have found wide applications in several important disciplines in recent years because they are potentially inexpensive. Optimal design of these plasma devices relies heavily on costly trial-and-error approach. Understanding of these complex plasma physics and chemistry through experimental method could be limited and difficult, if not impossible. Thus, numerical simulation becomes an inevitable tool in fully appreciating the complex physics in a gas discharge.

Helium is a commonly selected and studied as the working gas for the APPJ because it can be operated in a wide stable operating window at one atmosphere [1]. It was shown that discharge current calculated from pure helium data does not quantitatively agree with experimental results [2]. Although the impurity level is typically less than 0.01 %, it was reported that the impurity plays an important role in "pure" helium discharges [2]-[3]. However, there is no report addressing on the composition of impurities found in the literature.

Plasma fluid model (PFM) is often employed to model gas discharges when continuum assumption is valid. For low-pressure gas discharges, the PFM without considering the fluid dynamics is often considered to be valid. Nevertheless, as the pressure rises, fluid dynamics becomes important in affecting the gas discharges. Thus, understanding of the gas discharges requires proper modeling of gas flow and gas discharge simultaneously. However, there have been very few studies in the literature which have focused on this regard [4-6]. Moreover, it often takes from weeks up to months of runtime in coupling the gas flow model (GFM) and the PFM because of large disparity of characteristic time scales between fluid dynamics and plasma. Therefore, an efficient hybrid numerical algorithm to couple the GFM and the PFM for simulating APPJ is required.

In this paper, we report our recent progress in developing a parallel hybrid gas flow and fluid modeling algorithm and its application in APPJ with helium considering effect of measured impurity.

2. Numerical Methods

The GFM and the PFM are introduced in turn. It

follows the proposed TMSM applied to the PFM to reduce large amount of runtime. The procedure of a complete APPJ simulation is introduced at the end of this section.

Gas Flow Model

For the neutral gas flow simulation, a complete set of 2D compressible Cartesian-grid conservation equations, including continuity equation, momentum equations (Navier-Stokes), energy equation, species continuity equations and equation of state for ideal gas, are solved using a cell-centered finite-volume method, named extended SIMPLE (Semi-Implicit Method for Pressure Linked Equations) scheme [7]. The solver is parallelized using domain decomposition approach. In general, this solver can deal with gas flows at all speeds and can consider conjugate heat transfer involving convection in the gas and conduction in the solid.

Plasma Fluid Modeling

For modeling the gas discharge, the fluid modeling is used. The modeling equations include the continuity equations with drift-diffusion approximation for all charged species, the continuity equations for neutral species, the electron energy density equation, and the electrostatic Poisson's equation. The transport coefficients (drift and diffusion) and the rate constants related to electrons are functions of the electron temperature, which are obtained by integrating either the experimental collision cross section, or the EEDF from the solution of the simplified Boltzmann equation solver [8]. All model equations are discretized by using the backward Euler's method on the temporal domain and cell-centered finite volume with the Scharfetter-Gummel scheme for the mass fluxes on the spatial domain. To ensure stability when larger time steps are used, linearization in time and electron energy density is applied for the source term of Poisson's equation and electron energy density equation, respectively. All discretized fluid modeling equations are solved by using the libraries in PETSc package [9], in which MPI (message passing interface) is employed for parallel communication. Details of implementation are presented elsewhere [10].

Hybrid Flow-Plasma Simulation

Degradation of Organic Compounds Using a Two-dimensional Capillary Discharge Array in Water

Qiu-Yue Nie, Jian-Yu Chen, He-Ping Li, Zhi-Bin Wang, Wei Xing and Cheng-Yu Bao
Department of Engineering Physics, Tsinghua University, Beijing 100084, P. R. China
E-mail of corresponding author: liheping@tsinghua.edu.cn

ABSTRACT

The decolorization of the aqueous solution of methylene blue by means of a non-thermal plasma technique is investigated in this paper. A dual electrode structure consisting of a powered capillary electrode and a downstream floating electrode is employed as the elemental structure to construct a two-dimensional capillary discharge array. It is shown that the array features a simple set-up, good unit-unit uniformity and favorable decolorization efficiency. A significant degradation rate up to 99.16% can be obtained after 11 minutes plasma treatment with air as the plasma working gas.

1. Introduction

Wastewater generated from the textile industry represents a large portion of civil sewage. The features, such as large volume, high organic content, dark color and complex components, have made it a significant threat to the surrounding ecosystem. Because of the features of high chemical stability, non-biodegradability and high toxicity, some organic compounds in dyeing wastewater are difficult to de degrade by traditional techniques. Recently, the non-thermal discharge plasmas produced under water have been proposed as an attractive method to decompose the harmful organics in water [1]. With the combination of various effects, such as the intense electric field, high concentrations of chemically reactive species, ultra violet radiation and shock wave generation, the plasma water treatment has been demonstrated as an effective technology for wastewater treatment. Up to now, different types of discharges, including liquid phase discharge, gas phase discharge and gas-liquid discharge, have been studied as possible approaches for the treatment of the wastewater [2-6]. In this paper, a new simple scheme of plasma generation, which utilizes an upstream capillary electrode recessed within a quartz tube and a downstream perforated floating electrode placed on the quartz tube nozzle, is presented. Basing on the elementary structure, a two-dimensional capillary discharge array is constructed, and the capability of the organic compounds degradation with air as the plasma working gas is investigated.

2. Experimental Method

A scheme of the experimental setup is shown in Fig. 1(a), and the single plasma generator, which is used as the elementary structure to form the two-dimensional capillary discharge array, is given in Fig. 1(b). As shown in this figure, the lower part of the reactor is immersed in the aqueous solution, and the solution is grounded. A central capillary electrode with the inner diameter (I.D.) and outer diameter (O.D.) of 0.83 mm and 1.27 mm doubled as the powered electrode and the working gas inlet channel is enclosed tightly within a concentric dielectric quartz tube (O.D.=1.99 mm, I.D.=1.35 mm), and its tip is 7.12 mm away from the end of the quartz tube nozzle in the axial direction. A perforated metallic cover is attached on the nozzle of the quartz tube as the

floating electrode. With the metallic floating electrode assembled downstream, the electric field could be enhanced effectively. Besides, the hole ($\Phi=0.20$ mm) on the floating electrode is favorable to stabilize the discharge by reducing the interference between the gas discharge and the aqueous solution. The working gas of air with a flow rate of 0.8 slpm (standard liters per minute) is fed axially into the capillary electrode, and the discharge plasma obtained is finally spurted from the hole on the floating electrode into the aqueous solution. The single discharge generator is powered by a sinusoidal excitation voltage at $f=8.5$ kHz. The applied voltage and discharge current are measured using a high-voltage probe (Tektronix P6015A) and a current probe (Tektronix TCP202) via a digital oscilloscope (Tektronix DPO4034).

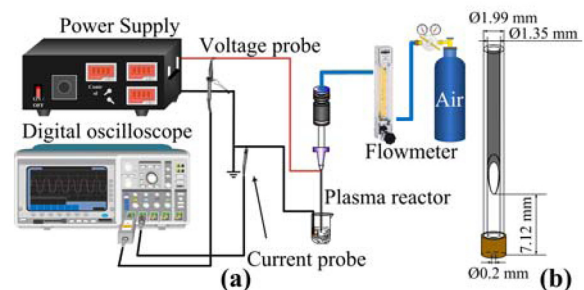


Fig. 1 Schematic of the experimental setup (a) and the plasma generation unit (b)

3. Results and Discussions

Figure 2 shows the voltage-current ($V-I$) and voltage-power ($V-P$) curves, as well as the corresponding discharge images during the discharge process. In general, the continuous increase of the applied voltage would result in the generation and evolution of the discharge from initiation to the mild discharge stage, and finally transition to the relatively acute discharge stage. When the applied voltage is raised over the breakdown threshold of $V_{pp}=3.2$ kV (point A), a localized plasma is first initiated near the capillary tip. Then, an increase of the applied voltage makes the discharge extend to the floating electrode gradually. At $V_{pp}=5.1$ kV (point B), a mild and stable air discharge plasma occupies the whole tube. As the voltage

increases further to $V_{pp}=13.3$ kV (point C), the discharge becomes acute with numerous bright discharge channels generated abruptly. Correspondingly, the discharge power increases from 0.46 W to 8.7 W with the applied voltage ranging from $V_{pp}=3.2$ kV to 10.7 kV

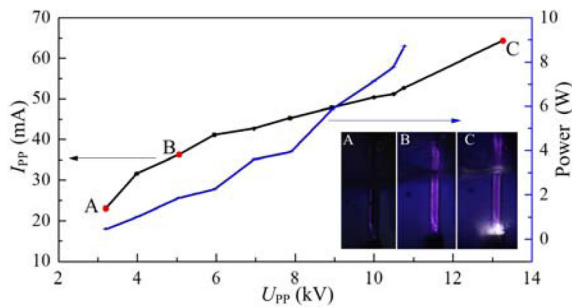


Fig. 2 The peak to peak discharge current and discharge power as a function of the peak to peak applied voltage

In actual applications of the wastewater treatment, a large volume plasma is usually required. Therefore, we parallelize nine single generators to form a two-dimensional capillary discharge array, as shown in Fig. 3(a). The two-dimensional capillary discharge array is fixed in a dielectric block with 3×3 arranged through-holes, and the working gas ($Q_{air}=7.0$ slpm) is divided into nine identical branches to feed the nine capillaries. Figures 3 (b) and (c) show the discharge images taken from both the side view and the end view. It is observed that the simultaneous discharges with good uniformity among all 9 units of the two-dimensional capillary discharge array can be achieved.

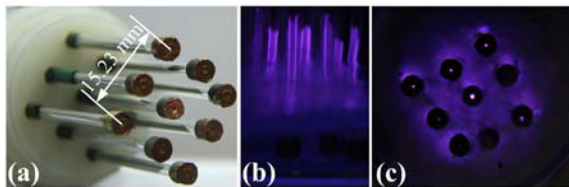


Fig. 3 Picture of the two-dimensional capillary discharge array (a) and the typical discharge images taken from the side view (b) and the end view (c)

In this work, the aqueous solution of methylene blue is selected as the model organic compounds in dyeing wastewater because of its stable molecular structure. In the experiment, 20 ml tap water containing 40 mg/l methylene blue, is used for the plasma treatment. During the treatment process, various chemical radicals are generated by the two-dimensional capillary discharge array, and subsequently dissolve in the methylene blue. Besides, the intense electric field and ultra violet radiation produced also play important roles in the degradation reaction process. Fig. 4(a) shows the color variation of the methylene blue solution with different treatment times. It is obvious that the color of the methylene blue solution faded gradually. The variations of the concentration and the degradation rate of the

methylene blue solution with different treatment times are illustrated in Fig. 4(b). It is shown that a significant degradation rate up to 99.16% can be attained after 11 minutes plasma treatment with the experimental conditions of $f=7.8$ kHz and $V_{pp}=7.9$ kV.

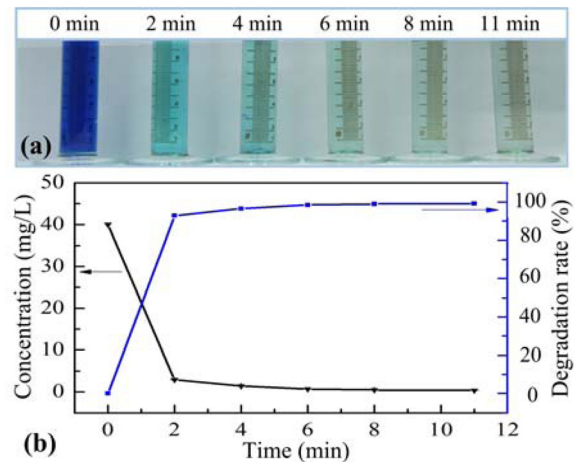


Fig. 4 Variations of the color (a), the concentration and the degradation rate (b) of the methylene blue solution with the plasma treatment time

4. Concluding Remarks

This paper presents a new atmospheric plasma source, which is shown to be a potential simple approach used for the wastewater treatment. Based on the elementary structure, a two-dimensional capillary discharge array with simultaneous discharges and good unit-unit uniformity is formed. The experimental result shows that the degradation efficiency of the methylene blue using the two-dimensional capillary discharge array can reach 99.16% after 11 minutes plasma treatment

Acknowledgement

This work has been supported by the China Postdoctoral Science Foundation (20110490418) and the National Natural Science Foundation of China (No.10972119).

References

- [1] M. A. Malik, A. Ghaffar and S. A. Malik, Plasma Sources Sci. Technol., **10** (2001), 82-91.
- [2] J. S. Clements, M. Sato and R. H. Davis, IEEE Trans. Plasma Sci., **IA-23** (1987), 224.
- [3] Q. Tang, W.-J. Jiang, Y. Zhang, W.-Y. Wei and T. M. Lim, Plasma Chem. Plasma Process, **29** (2009), 291-305.
- [4] H. Katayama, H. Honma, N. Nakagawara and K. Yasuoka, IEEE Trans. Plasma Sci., **37** (2009), 897-904.
- [5] D. H. Shin, Y. C. Hong and H. S. Uhm, IEEE Trans. Plasma Sci., **34** (2006), 2464-2465.
- [6] K. Sato and K. Yasuoka, IEEE Trans. Plasma Sci., **36** (2008), 1144-1145.

Decomposition Processes of Perfluoro Compounds Using Plasma inside Bubbles Related to Surfactant Behavior

Nozomi Takeuchi, Akihiro Kosugi, Yuriko Matsuya, and Koichi Yasuoka
Tokyo Institute of Technology, 2-12-1 Ookayama, Meguro-ku, Tokyo 152-8552, Japan
takeuchi@ee.titech.ac.jp

ABSTRACT

Perfluorooctane acid (PFOA: $C_7F_{15}COOH$) can be decomposed effectively by plasmas generated on a gas–liquid interface. During the decomposition of PFOA, perfluorocarboxylic acids (PFCAs: $C_nF_{2n+1}COOH$) with shorter carbon chains ($n = 1-6$) are generated as by-products. A PFCA with shorter carbon chain had less surfactant activity, and was hard to be decomposed by the plasma due to lower surface concentration on the gas–liquid interface. Additionally, the decomposition processes of PFOA were found to be that more than one carbon atoms in the carbon chain of PFCAs decrease by one reaction step.

1. Introduction

Recently, the biopersistence and unexpected toxicity of long-chain PFCs such as perfluorooctane acid (PFOA: $C_7F_{15}COOH$) and perfluorooctane sulfonic acid (PFOS: $C_8F_{17}SO_3H$) have raised environmental concerns, and effluent controls have been applied. Therefore, efficient decomposition methods for PFOA and PFOS in water are required and several methods such as sonochemical reactions have been reported [1].

We recently found that plasma generated on a gas–liquid interface can easily decompose PFOA and PFOS and exhibits much higher decomposition energy efficiency than other methods [2]. Since PFOA and PFOS cannot be decomposed by OH radicals [1], a surface reaction decomposing them on the plasma–liquid interface with positive ions generated in the plasma has been suggested [2]. Previous research reveals that the surface concentration of PFOS on the plasma–liquid interface is much higher than the bulk concentration, and therefore, the plasma can decompose PFOS effectively by a surface reaction [3].

During the PFOA decomposition, other perfluorocarboxylic acids (PFCAs: $C_nF_{2n+1}COOH$) with shorter carbon chains ($n = 1-6$) are generated [2]. These PFCAs also can be decomposed by the plasma; however, the decomposition rates are probably different, depending on the surfactant behavior of the PFCAs. In this study, the relationship between the adsorbed amounts of PFCAs (TFA: $n = 1$, PFPrA: $n = 2$, PFBA: $n = 3$, PFPeA: $n = 4$, PFHxA: $n = 5$, PFHpA: $n = 6$, and PFOA: $n = 7$) on the gas–liquid interface and their rate of decomposition by plasma, and the decomposition processes were investigated.

2. Surfactant Behavior and Decomposition Rate

When water contains a surfactant, the surface tension on the gas–liquid interface becomes lower than that of pure water due to the surfactant adsorption. The surface tension of the PFCA solutions was measured with a DuNouy surface tensiometer. Figure 1 shows the surface tension of the PFCA solutions as a function of the bulk concentration. The surface tension decreased with increasing bulk concentration. A solution containing a PFCA with a longer carbon chain had a lower surface tension at the same bulk concentration. In other words, a PFCA with a shorter carbon chain showed less

surfactant activity. The surface concentration of surfactant on the gas–liquid interface is related to the surface tension by the Gibbs adsorption isotherm equation [3]. It was found that a PFCA with a longer carbon chain has a higher surface concentration.

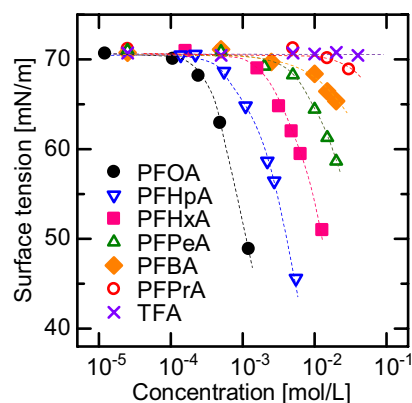


Fig. 1 Surface tension of PFCA solutions.

Decomposition experiments of the PFCAs were conducted using the reactor shown in Fig. 2(a) at an initial bulk concentration of 10^{-4} mol/L. The PFCA solutions (50 mL) were treated using dc plasma in oxygen gas over the solution. After the plasma treatment, the bulk concentrations of the PFCAs were measured with a liquid chromatography mass spectrometry (Shimadzu, LCMS-2020).

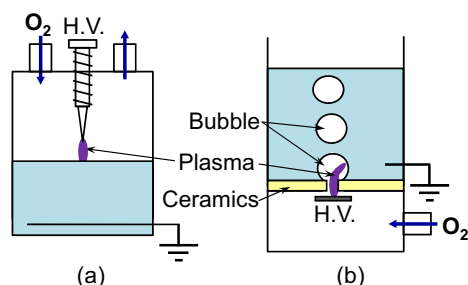


Fig. 2 Schematics of plasma reactors, (a) plasma over the solution, (b) plasma inside bubbles.

The decomposition reactions of the PFCAs were first-order reactions, of which the reaction rate constant, k , is expressed as follows:

$$k = \frac{1}{t} \ln \left(\frac{C_0}{C} \right), \quad (2)$$

where C_0 is the initial bulk concentration and C is the bulk concentration after the treatment. The decomposition reaction rate constants are plotted in Fig. 3 as a function of the number of carbon atoms in the carbon chain of the PFCAs. The rate constant was higher with larger current for the same PFCA. For PFCAs with relatively short carbon chains ($n < 3, 4,$ or 5 at currents of $5, 10,$ and 15 mA, respectively), the rate constants were smaller than those of long PFCAs. A shorter PFCA has a lower surface concentration due to the less surfactant activity. Thus, the rate-limiting factor for the decomposition of short PFCAs seems to be the amount adsorbed to the gas-liquid interface. On the other hand, the rate constants for the relatively long PFCAs have an almost constant value depending on the current. Thus, the rate-limiting factor for the decomposition of long PFCAs seems to be the decomposition capability of the plasma.

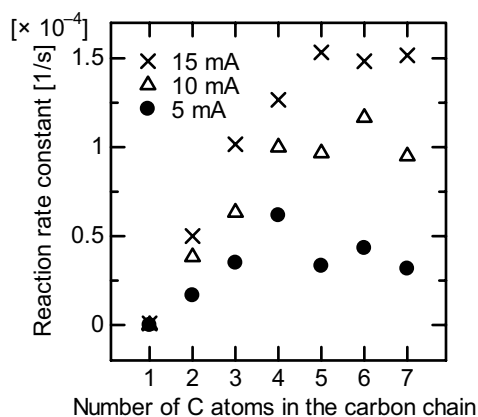


Fig. 3 Reaction rate constants of PFCAs as a function of number of carbon atoms in the carbon chain.

3. Decomposition Processes

Using the reactor shown in Fig. 2(b), decomposition of PFOA and other PFCAs ($n = 1-6$) was conducted to reveal the decomposition processes of PFOA. PFCA solutions (20 mL) were treated by dc plasma generated inside oxygen bubbles at a current of 10 mA, and the reaction rate constants were obtained. Figure 4 shows the time variation of the concentrations of PFOA and the by-products. PFOA was fully decomposed within 2.5 h. During the decomposition of PFOA, PFCAs with shorter carbon chain were generated. In previous reports [2], the decomposition processes shown in Fig. 5(a) that the number of carbon atoms in the carbon chain of PFCAs decreases one by one was suggested. However, the numerical simulation using the reaction rate constants of the PFCAs with the suggested decomposition processes showed much higher concentrations of the by-products than the experimental results. Thus, the new decomposition processes shown in Fig. 5(b) that more than one carbon atoms in the carbon chain decreases in one reaction step was

suggested, and the numerical result was in good agreement with the experimental result.

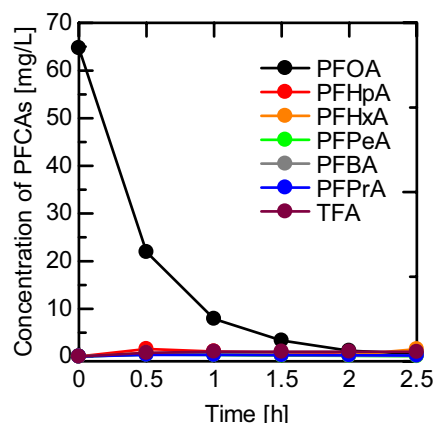


Fig. 4 Time variation of concentrations of PFOA and the by-products.

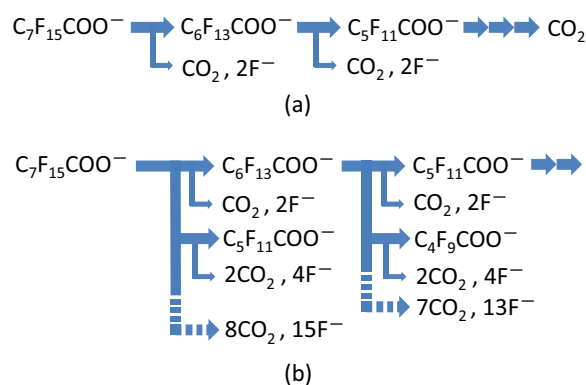


Fig. 5 Decomposition processes of PFOA, (a) previously suggested, (b) suggested in this study.

4. Concluding remarks

The following concluding remarks were obtained:

- 1) The decomposition reaction rate constant of PFCAs with less surfactant activity was smaller than that of PFCAs with strong surfactant activity.
- 2) The rate-limiting factor for the decomposition of PFCAs with strong surfactant activity was the capability of the plasma depending on the current.
- 3) The decomposition processes of PFOA by plasma were found to be that more than one carbon atoms in the carbon chain of PFCAs decrease by one reaction step.

Acknowledgements

This work was supported by the Environment Research and Technology Development Fund of the Ministry of the Environment, Japan K2324.

References

- [1] H. Moriwaki et al., *Environ. Sci. Technol.*, **39** (2005), 3388.
- [2] K. Yasuoka et al., *Plasma Sources Sci. Technol.*, **20** (2011), 034009.
- [3] N. Takeuchi et al., *IEEE Trans. Plasma Sci.*, **39** (2011), 3358.

Streamer Dynamics for Radical Generation in Air/methane Mixture under High Temperature and High Pressure

H. Takana and H. Nishiyama

Institute of Fluid Science, Tohoku University, 2-1-1 Katahira, Aoba-ku, Sendai 980-8577, JAPAN
takana@paris.ifs.tohoku.ac.jp

ABSTRACT

Computational simulation of a single streamer in DBD in lean methane-air mixture at pressure of 3 atm and temperature of 500 K was conducted for plasma enhanced chemical reactions in a closed system. The time evolution of reactive species concentration and temperature fields during streamer propagation in nano second pulse were successfully simulated.

1. Introduction

The plasma assisted combustion has been especially paid attention in aerospace and automobile engineering. Most of the experimental studies and analyses are typically carried out at pressures close to 1 atm. For the practical application of the plasma assisted combustion, it is essential to understand the radical generating process with streamer propagation and also to clarify the chemical kinetics under high pressure, especially for the application to internal engines.

In this study, the effects of surrounding pressure and temperature on the streamer dynamics and radical production characteristics by methane-air dielectric discharge are clarified by computational simulations. Furthermore, time evolutions of reactive species concentration and temperature fields with development of a single streamer in DBD are shown.

2. Governing Equations and Computational Conditions

Following continuity equations for electrons and ions with drift-diffusion approximation are solved coupled with Poisson's equation:

$$\frac{\partial n_k}{\partial t} + \nabla \cdot \mathbf{\Gamma}_k = S_k, \quad (1)$$

$$\mathbf{\Gamma}_k = \text{sgn}(q_k) \mu_k \mathbf{E} n_k - D_k \nabla n_k, \quad (2)$$

$$\nabla \cdot (\varepsilon \nabla \phi) = - \sum_k q_k n_k, \quad (3)$$

where n_k , $\mathbf{\Gamma}_k$, S_k , q_k , μ_k , D_k , are the number density, flux, source term, charge, mobility and diffusion coefficient for species k , respectively. \mathbf{E} , ε and ϕ are electric field, permittivity and electric potential, respectively. Charged particle fluxes are given by the Scharfetter-Gummel formulation. The electron transport properties and rate coefficients are given as a function of reduced electric field and they are obtained by solving Boltzmann's equation for the electron energy distribution.

The rate of photoionization in a gas volume is included in the source term in equation (1). In this study, two-exponential Helmholtz model was employed for

photoionization of oxygen. The photoionization processes in O_2 are caused by the radiation in the wave range 98 – 102.5 nm. The radiation in this range is produced by the radiative transitions from three singlets of N_2 ($b^1\Pi_u$, $b'^1\Sigma_u^+$ and $c'^1\Sigma_u^+$) to the ground state ($X^1\Sigma_g^+$).

The self-biased potential on the dielectric surface is calculated by Gauss's law, assuming a constant electric field in the dielectric. The secondary electron emission probability by ion impact on a surface is given as 0.01.

The composition ratio of methane-air mixture is $N_2:O_2:CH_4 = 15:4:1$. The chemical kinetics of methane-air mixture studied in this work includes processes with participation of species of N_2 , $N_2(A^3\Sigma_u^-)$, $N_2(B^3\Pi_g)$, $N_2(C^3\Pi_u)$, $N_2(a'^1\Sigma_u^-)$, $N_2(b^1\Pi_u, b'^1\Sigma_u^+ \text{ and } c'^1\Sigma_u^+)$, N_2^+ , O_2 , $O_2(a^1\Delta_g)$, $O_2(b^1\Sigma_g^+)$, O , O_2^+ , $O_2(c^1\Sigma_u^-, C^3\Delta_u, \text{ and } A^3\Sigma_u^+)$, O_3 , CH_4 , CH_3 , CH_2 , CH_4^+ , CH_3^+ , CH_2^+ , H_2 , H , H_2O , OH , HO_2 , CH_2O , CH_3O , NO and electron.

The chemical kinetics of methane-air mixture studied in this work is based on that developed in the model described in except for the reactions associated with argon. Moreover, the O atom decay processes through recombination with oxygen resulting in ozone formation, $O + O_2 + M \rightarrow O_3 + M$ and also through recombination with ozone, $O + O_3 \rightarrow O_2 + O_2$ are incorporated. It was shown from the sensitivity analysis that the increased atomic oxygen loss rate in methane-air occurs primarily due to reactions of H atoms and CH_3 radicals, in particular $H + O_2 + M \rightarrow HO_2 + M$, $O + HO_2 \rightarrow OH + O_2$, $OH + CH_4 \rightarrow CH_3 + H_2O$, and $O + CH_3 \rightarrow H + CH_2O$. These reactions are also taken into account. In addition to that, the following reactions of OH production and decay are also considered; $OH + HO_2 \rightarrow O_2 + H_2O$, $HO_2 + CH_3 \rightarrow OH + CH_3O$, $CH_3O + O_2 \rightarrow HO_2 + CH_2O$, and $H + O_2 \rightarrow O + OH$.

The distributions of gas temperature T_g and the mean vibrational energy of nitrogen molecules ε_{vN_2} are obtained by solving the set of following energy conservation equations;

Conservation of internal energy

$$\frac{\partial}{\partial t} \left(\rho \frac{1}{\gamma - 1} RT_g \right) = \eta_T \mathbf{j}_e \cdot \mathbf{E} + (\eta_e \mathbf{j}_e \cdot \mathbf{E} - \dot{w}) + j_i \cdot \mathbf{E} + Q_{VT} \quad (4)$$

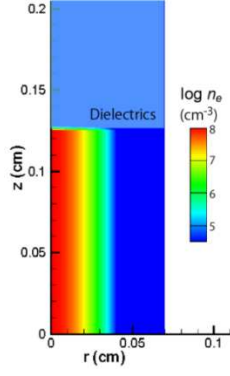


Fig. 1 Computational domain and initial condition.

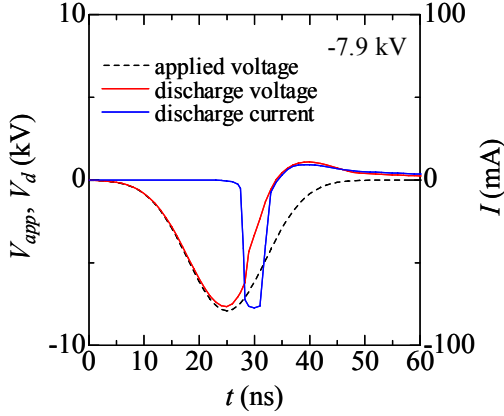


Fig. 2 Time evolutions of applied voltage, discharge voltage and discharge current. at 3 atm and 500 K.

Conservation of vibrational energy of nitrogen molecule

$$\frac{\partial}{\partial t} \varepsilon_{vN_2} = \eta_v \mathbf{j}_e \cdot \mathbf{E} - Q_{VT}. \quad (5)$$

Figure 1 shows the computational domain and initial electron distribution. Only the grounded electrode is covered with quartz glass ($\varepsilon/\varepsilon_0 = 3$) with the thickness of 0.8 mm. The flat powered electrode (cathode) and grounded electrode (anode) are separated by 2.05 mm. In order to understand the gas heating process during streamer propagation in nano second pulse, the streamer simulations are conducted at the applied voltage given by Gaussian function. The gas pressure and temperature are 3 atm and 500 K. The initial electron number density is given uniformly along the axis to consider the residual electrons from the previous pulse. The initial radial distribution of electron number density with the peak value of $1 \times 10^8 \text{ 1/cm}^3$ is given by the Gaussian function. The initial gas temperature and vibrational temperature are 500 K.

3. Results and Discussion

Figure 2 shows the time evolutions of applied voltage, discharge voltage and current. -7.9 kV of voltage is applied in 25 ns. Electric current flows sharply at $t = 30$ ns due to the streamer propagation to cathode. The voltage between discharge gap decreases to zero at 34 ns when the electric field in discharge

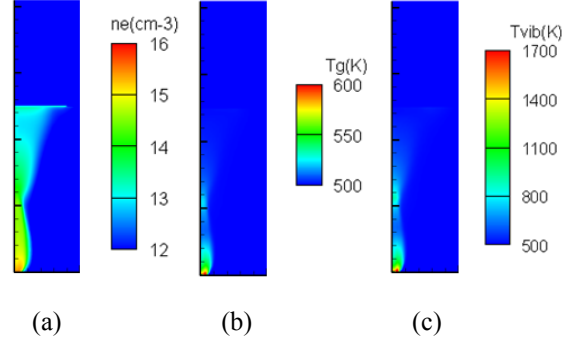


Fig. 3 Distribution of (a) electron number density, (b) gas temperature and (c) vibrational temperature of nitrogen molecules at 40 ns.

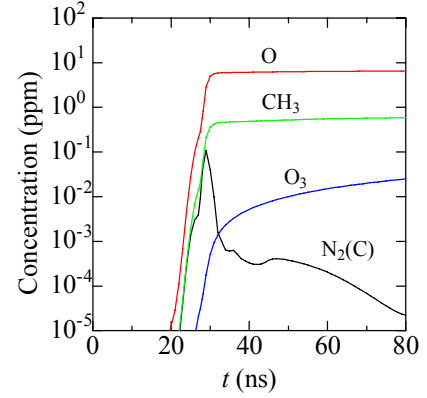


Fig. 4 Temporal distributions of volume averaged concentrations of O, CH₃, O₃ and N₂(C³Π_u).

space is shielded by the accumulation of electrons on the dielectric surface. The increase in negative surface charge on the dielectric layer decreases the electric potential on the dielectric, which results in the increase of discharge voltage. Positive current increases with increase in positive discharge voltage.

Figure 3 (a) shows the distribution of electron number density and (b) and (c) show the distributions of gas temperature and vibrational temperature of nitrogen molecules at 40 ns, respectively. Both gas temperature and vibrational temperature of nitrogen molecules become highest near the bare cathode, where gas temperature elevates by 100 K in 40 ns.

Figure 4 shows temporal distributions of volume averaged concentrations of O, CH₃, O₃ and N₂(C³Π_u). Reactive species are instantly generated with the energy deposition around $t = 30$ ns. Under this condition, approximately 60 % of input power is deposited to the streamer. N₂(C³Π_u) starts to decay just after the energy deposition, however, other reactive species gradually increase after the energy deposition.

4. Concluding remarks

The radical generation processes with rapid gas heating during streamer propagation has been clarified under high pressure and high temperature in nano pulse methane/air DBD.

PS4: Advanced Physical Stimuli and Biological Responses of Cells

The Increment of Cell Activity by Plasma Treatment

Jeong-Hae Choi^{1,3}, Sang-Rye Park¹, Sung-Kil Kang³, Seoul-Hee Nam¹, Jae-Koo Lee³, Jin-Woo Hong³, Jae-Koo Lee³,
Gyoo-Cheon Kim¹

¹Department of oral anatomy and cell biology, school of dentistry, Pusan National University, Republic of Korea

²Department of Electrical Engineering, POSTECH, Republic of Korea

³Department of Internal Medicine, School of Korean Medicine, Pusan National University, Republic of Korea
ki9100m@pusan.ac.kr

ABSTRACT

Light-based skin care devices including laser and LED device achieve their goal by using thermal energy. However, because of this, they easily create several side effects and it is very hard to elucidate their precise working mechanisms. Recently, low-thermal plasma has received big attention on the field of dermatology for their multifunction including wound healing, disinfection of skin. Nonetheless, basic studies of low-thermal plasma were just started throughout the world. Here, we elucidated the effect of low-thermal plasma on skin cells and their possible role for skin care.

1. Introduction

The purpose of anti-skin aging items, including cosmetic products, is to transform the old states of biochemical reactions within the skin to younger states. Therefore, skin-care devices are expected to enhance the enzyme activity and gene expression related to the extracellular matrix (ECM) in skin. Up to date, light-based skin care devices are most widely used, and they employ thermal energy from a specific spectrum of light to achieve their goal. However, it is very difficult to clarify how thermal energy can regulate various biological reactions and control the thermal effect for skin improvement.

Plasma describes the fourth state of matter and consists of many active components, such as radicals (reactive species), ions, electrons and photons.[1] This gives plasma devices unique properties compared to light-based devices. Although the type of plasma device and experimental conditions were different, many reports have demonstrated that low-temperature plasma can help improve the wound healing process. Nevertheless, the precise biological effects during plasma treatment remain elusive, safety concerns were not mentioned in cellular level. In previous study, we developed a microwave plasma generator for multiple biomedical purposes.[2] This new-type low-temperature plasma is generated from a small-sized handy module, and sterilizes a range of bacteria. Considering the low-temperature characteristics and sterilizing effect of microwave plasma, it might be useful for skin care. As of now, there are no reports of the efficacy of microwave plasma on skin at the cellular level.

This study examined the effect of microwave plasma on skin cells. The expression pattern of the genes related to anti-skin aging after the treatment and whether this device can induce stress responses in skin cells are reported.

2. Method

Microwave Plasma Generator A microwave type plasma generator was used for the plasma treatment of skin cells. For the plasma generator, a 900-MHz coaxial transmission line resonator was used with argon gas flow of approximately 2.5 slm. Detailed information

about this device can be found elsewhere.[2] [3]

Skin Cell culture and Plasma treatment NIH3T3 mouse fibroblasts and HaCaT human keratinocytes were cultured in Dulbecco's modified Eagle's medium containing 10% (v/v) heat-inactivated fetal bovine serum and 1% penicillin/streptomycin at 37°C in a humidified atmosphere containing 5% CO₂ and were re-fed every 2 days. For the treatment of microwave plasma, the cells were seeded in a 35 mm culture dish and incubated for 24 hours. Immediately before the treatment, the cell medium was exchanged with 2 ml of fresh growth medium. The dishes were located at distance of 1 cm under microwave plasma generator. The microwave plasma generator was turned on for the indicated times, and the dishes were placed in a CO₂ incubator.

RT-PCR (reverse transcription-PCR) analysis The total RNA from the cells was isolated using TRIzol® reagent according to the manufacturer's instructions. First strand cDNA was synthesized using an RNA template and the specific primers, as described in the One-step PreMix kit (iNtRON Biotechnology Inc., Korea). Equal amounts of cDNA were then amplified by PCR in a 20 µl reaction volume containing 2× PCR master mix, 10 µM specific primers for genes of interest. The amplification products were separated by 1.5% agarose gel electrophoresis and visualized by ethidium bromide staining under UV transillumination.

Cell growth assay Cells were seeded at 35 mm dish and incubated for 24 hours in CO₂ incubator. After plasma treatment, cells were fixed and stained with sulforhodamine B (SRB) dye, and non-specific staining was washed with 1% acetic acid for 5 times. Then, the cells were treated with 10 mM Tris solution to elute stained SRB dye, and 150 µl of each solution were transferred into 96 well plates. The absorbance was detected using microplate reader at wavelength of 515 nm.

FACS analysis The sub-G1 population was quantified by flow cytometry, as described previously [4]. The stained cells were analyzed on a FACScan flow cytometer (Becton Dickson Co., CA, USA) and DNA histograms were analyzed using WinMidi software.

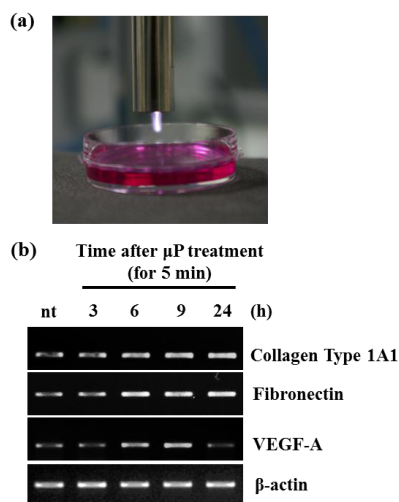


Fig. 1 The effect of microwave plasma (μP) on cellular gene expression. (a) The picture showing the methods for microwave plasma treatment. (b) The results of RT-PCR analysis.

3. Results and Discussion

The youth of skin generally can be maintained by two major biological reactions- proliferation of keratinocytes and gene expression of dermal fibroblast. In the first step of our study, the effect of microwave plasma on skin cell gene expression was elucidated. As Figure 1 shows, microwave plasma treatment on NIH3T3 mouse fibroblast increases several anti-aging genes significantly. First of all, microwave plasma enhanced expression of collagen which is a major building block of dermal tissue, and also increased fibronectin expression which is very important for formation of collagen matrix. Therefore, this data represents that microwave plasma treatment can enhance dermal collagen layer leading to increase of skin tightness. Furthermore, microwave plasma induced vesicular endothelial growth factor (VEGF) expression, so that this device also stimulates wound healing of the skin by increased angiogenesis.

In the next step, the effect of microwave plasma on the proliferation of HaCaT human keratinocytes was tested. As figure 2a shows, microwave plasma treatment inhibited cell growth in treatment dose-dependent manner (up to 40 % growth inhibition). This data was unexpected because for the application of this device on the field of skin care or wound healing, the enhancement of epithelial cell proliferation was needed. However, because of the other ability of microwave plasma (stimulation of anti-aging gene expression) was good enough for those aim, slight growth inhibition without cell damage can be neglected.

In order to figure out whether this growth inhibition was caused by microwave plasma induced cellular death or not, we adopted FACS analysis using propidium iodide. As figure 2b shows, microwave plasma treatment

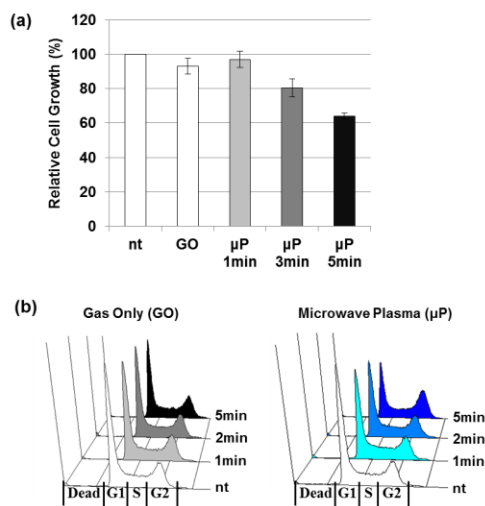


Fig. 2 The effect of microwave plasma on cell growth and cell cycle. (a) The result of cell growth assay of after the treatment. (b) The result of FACS analysis.

does not on the dead cell population as we expected. Interestingly, microwave plasma induced the population cells at G2 phase whereas reduced the population of G1 phase and S phase. Furthermore, the cells treated with argon gas flow does not affected on cell cycle representing that this phenomenon is plasma gas specific. Altogether, these data shows that cell growth inhibition after microwave plasma treatment was caused by cell cycle arrest at G2 phase, not caused by cellular damages.

4. Concluding remarks

Here, the effect of microwave plasma on skin cells was elucidated. Low-thermal atmospheric plasma from microwave plasma device enhances several gene expressions without severe cellular damages. Therefore, this study suggests that the possible role of microwave plasma device for the skin care and dermal wound healing.

5. Acknowledgements

This study was supported by Basic Science Research Program through the National Research Foundation of Korea (NRF) funded by the Ministry of Education, Science and Technology (20110013205) and a grant of the Traditional Korean Medicine R&D Project, Ministry for Health & Welfare, Republic of Korea (B11003911110000200).

References

- [1] G. Isbary, G. Morfill, J. Zimmermann, T. Shimizu, W. Stolz, *Arch Dermatol*, **147** (2011) 388-390.
- [2] S.J. Park, J. Choi, G.Y. Park, S.K. Lee, Y. Cho, J.I. Yun, S. Jeon, K.T. Kim, J.K. Lee, J.Y. Sim, *IEEE T Plasma Sci*, **38** (2010) 1956-1962.
- [3] J. Choi, F. Iza, H.J. Do, J.K. Lee, M.H. Cho, *Plasma Sources Sci T*, **18** (2009).
- [4] C.H. Kim, M. Won, C.H. Choi, J. Ahn, B.K. Kim, K.B. Song, C.M. Kang, K.S. Chung, *Biochem Biophys Res Commun*, **391** (2010) 1182-1186.

The Biomechanics and Mechanobiology of Primary Cilia

Mathew Downs, Kristen Lee, David Hoey, Sara Temiyasathit, Christopher Jacobs
Columbia University
Department of Biomedical Engineering
1210 Amsterdam Ave
New York, NY USA
crj2111@columbia.edu

ABSTRACT

Primary cilia have been implicated as a sensor of both chemical and mechanical signals in a number of cells and tissues including kidney, liver, cartilage, and embryos. In our laboratory we have demonstrated that this organelle acts as a mechanosensor in bone and have identified aspects of the intracellular signaling pathway activated by them. We have also shown that mutant mice with primary cilia missing in bone are less able to sense mechanical loading. Recently we have collected biophysical measurements of primary cilia deflections in real time and have created mathematical models of this deflection.

1. Introduction

The ability of non-specialized non-excitable cells to sense and respond to mechanical stimulation is central to proper physiologic function in a surprisingly wide range of cell types including endothelial cells, liver, lung and kidney epithelial cells, chondrocytes, neurons, and osteocytes. Cellular mechanosensation is critical in diseases responsible for enormous human suffering including atherosclerosis, osteoarthritis, cancer, and osteoporosis. Primary cilia are solitary linear cellular extensions that extend from the surface of virtually all cells. As a result, large local strains occur as they are deflected suggesting that they may act as cellular strain concentrators. For decades, the biologic function of this enigmatic structure was elusive, however, recent data suggest that it functions as a complex nexus where both physical and chemical extracellular signals are sensed and coordinated responses initiated. For example, it is important in sensing the biochemical signals such as hedgehog (Hh), wingless, and platelet derived growth factor, as well as mechanosensing in the kidney and embryonic node.

2. Method

In terms of mechanobiology in our laboratory we have collected data that primary cilia act as mechanical sensors in bone cells. In vitro methods that we utilize include biochemical removal of primary cilia and siRNA knockdown of motor proteins required in ciliogenesis [1]. We have also created a

mutant mouse with a cre-lox strategy that have primary cilia deleted in bone tissue specifically [2].

We have recently begun to examine the biomechanical behavior of primary cilia [3]. We developed a novel combined experimental/modeling approach to determine the mechanical properties of primary cilia. Specifically, we developed a large rotation formulation of cilia bending with fluid flow that accounts for rotation at the base of the cilium, the initial shape of the cilium and fluid drag at high deflection angles. We also have obtained three dimensional configurations of primary cilia in their deformed configuration at 3Hz acquired with high-speed confocal microscopy.

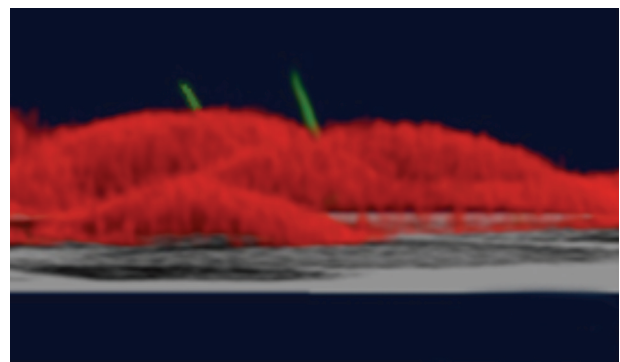


Fig. 1 Primary cilia (green) protruding from the apical surface of kidney cells (red)

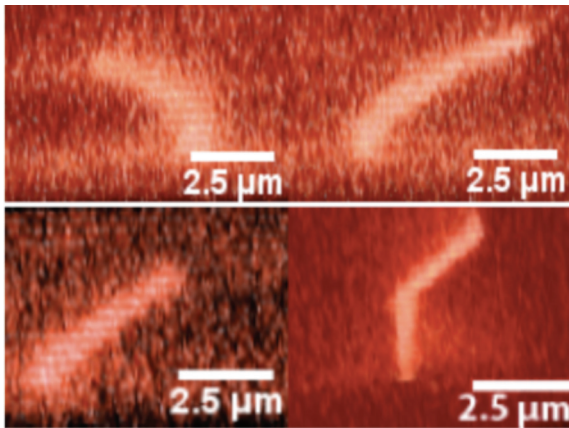


Fig. 2 Typical primary cilia deflection patterns

3. Results and Discussion

In terms of mechanobiology we have shown that osteocytes that have had their primary cilia deleted are unable to respond to dynamic fluid flow. We have also shown that mice that have had primary cilia conditionally deleted from bone cells are deficient in their ability to form bone in response to physical loading. Furthermore, we have found that the intracellular signaling pathway activated by primary cilia in bone is distinct from those observed in other tissues such as kidney. We have implicated the second messenger cAMP and the enzyme responsible for its regulation, adenylyl cyclase 6, in the primary-cilium-dependent pathway activated by dynamic flow in osteocytes. We also demonstrated a loss of mechanosensitivity in our mouse model.

In terms of biomechanics we found a wide variety of previously unreported bending shapes and behaviors. Cilia appear to deflect in smooth bending shapes, rigid-body rotation, and in a hinged or kinked pattern. This suggests that both the axoneme and basal body anchorage are important to understanding deflection patterns. We also analyzed post-flow relaxation patterns. These results indicate that with removal of force, cilia slowly return to their initial configuration. However, they also can return to a different configuration with “overcorrection” observed that suggests adaptation of mechanical properties. Results from our combined experimental and theoretical approach suggest that the average flexural rigidity of primary

cilia might be higher than previously reported. In addition our findings indicate the mechanics of primary cilia are potentially non-linear, richly varied, and mechanisms may exist to alter their mechanical behavior.

4. Concluding remarks

In conclusion, the primary cilium has a rich potential to transduce a variety of signals through multiple mechanisms and may undergo functional specialization as a function of tissue or cell type.

References

- [1] Malone, A.M., Anderson, C., Tumalla, P., Kwon, R., Johnston, T., Stearns, T., Jacobs, C.R., Primary Cilia Mediate Mechanosensing in Bone Cells by a Calcium-Independent Mechanism. *Proceedings of the National Academy of Sciences*, August 14, 104:13325-13330, 2007.
- [2] Temiyasathit, S. Tang W.J., Leucht, P., Anderson, C.T., Monica, S.D., Castillo, A.B., Helms, J.A., Sterns, T., Jacobs, C.R., Mechanosensing by the Primary cilium: Deletion of Kif3 Reduces Bone Formation in Vivo. *Plos One*, 7:e33368, 2012.
- [3] Downs, M., Herzog, F.A., Hoey, D.A., Jacobs C.R., The Mechanical Behavior of Primary Cilia Exposed to Fluid Shear, *Computer Methods in Biomechanics and Biomedical Engineering*, In Press.

Cold Atmospheric Plasma for Skin Treatment

Tetsuji Shimizu¹, Georg Isbary², Julia L. Zimmermann¹, Wilhelm Stolz², and Gregor E. Morfill¹
¹Max-Planck Institute for extraterrestrial physics, 85748 Garching, Germany

²Department of Dermatology, allergology and Environmental Medicine, Hospital Munich Schwabing, Germany
tshimizu@mpe.mpg.de

ABSTRACT

Cold atmospheric plasmas produce a large variety of species (reactive species, charged particles, UV photons, etc.) relevant to biomedical effects. The plasmas have a broad application potential in medicine and hygiene. In our group, a clinical study has been conducted for chronic wound disinfection with an argon microwave plasma torch. The results showed that the plasma treatment could reduce bacterial load with no side effects. In parallel, the Surface Micro-Discharge plasma has been prepared for another clinical trial for skin treatments including wounds. For this device, efficacy and safety of the device is discussed.

1. Introduction

Cold atmospheric plasmas have a large variety of applications in medicine and hygiene because the plasmas produce many reactive species relevant for biomedical reactions [1-6]. The plasma treatments can be applied to heat-sensitive materials including living tissues because the gas temperature is close to room temperature. The plasma components can be delivered to rough surfaces because of gaseous state. They can be transported even into small cavities like pores in the skin. In addition, the plasma enables us contact-free and waste-free treatments. By using these characteristics, a lot of studies have been conducted for medical and hygiene purposes, e.g. sterilization/ disinfection, stop bleeding, cell proliferation, wound closure. This is a highly interdisciplinary topic with plasma physics, chemistry, fluid dynamics and life sciences.

The cold atmospheric plasma can be a promising tool for disinfection on skin in public health as well as hospital care. In the health care systems, one of the major concerns is the substantial decline of the antimicrobial susceptibility of pathogens, e.g. methicillin-resistant *Staphylococcus aureus* (MRSA). In the US, Hospital acquired infections (HAI) with *Staphylococcus aureus*, especially MRSA infections, are one of the major cause of illness and death [7]. By these infections considerable costs are imposed on patients and hospitals. There are already reports that the cold atmospheric plasma can inactivate many kinds of bacteria including MRSA [8], so that the plasma can play an important role for the prevention of HAIs and infection control.

In our group, several cold atmospheric plasma devices have been developed and tested for the disinfection purpose. In this paper, two devices are briefly presented, one is for wound disinfection and the other is for more versatile skin treatments especially from the viewpoint of hygiene.

2. Plasma for disinfection

A clinical study has been carried out in collaboration with Department of Dermatology, Allergology and Environmental Medicine, Hospital Munich Schwabing [9,10]. The objective is to examine the safety and to

reduce bacterial load in chronic infected wounds in vivo as a new medical treatment because bacterial colonization of chronic wounds can impair healing.

The used device is MicroPlaSter as shown in fig. 1. The plasma system has an argon plasma torch at the end of the flexible arm. Inside the torch there are six plasmas produced by microwave at 2.45 GHz (insert in fig. 1). From the plasma torch, the plasma components are delivered to objects following the applied argon flow. Before conducting a clinical phase II study on patients, a phase I study was carried out in order to show safe operation parameters and optimized dosage in inactivation of bacteria relevant in wounds. The argon plasma was characterized especially from the viewpoint of safety. Bactericidal effects on relevant bacteria were also shown. With this information, the clinical study was approved by the Bavarian State Association for Medical Issues.

Here, one example in our clinical study is shown. In the clinical study, patients received a five-min plasma treatment on randomized wounds as an add-on therapy. Bacterial load was detected using standard bacterial swabs and nitrocellulose filters from both control and treated wounds. The usage of bacterial swabs shows the types of bacteria and the bacterial load is evaluated by the nitrocellulose filter. Chronic infected wounds were treated from about 150 patients.

It was demonstrated that there was a highly



Fig. 1 Clinical device, MicroPlaSter. At the end of the flexible arm the plasma torch is placed. Six plasmas are shown in the insert.

significant ($\sim 34\%$, $P < 10^{-6}$) reduction in bacterial load in comparison with non-treated control area. The treatments were well tolerated and no side-effects were reported. From our plasma torch, mainly reactive species and UV light play a role in bactericidal property. The argon plasma is produced inside the plasma torch and many reactive species (NO , O_3 , NO_2 , OH , etc.) are produced through mixing with the ambient air. The main source of UV light is the plasma production region in the plasma torch. Still the inactivation mechanism is not clear, however, a synergetic effect from both reactive species and UV light could play an important role.

The second is a plasma dispenser equipped with the Surface Micro-Discharge (SMD) electrode [11]. The SMD electrode consists of an insulator plate (~ 1 mm) sandwiched by a metal planar electrode and a metal mesh electrode. By applying a high voltage, ~ 10 kV_{pp}, a plasma discharge is produced on the side of the mesh electrode using the ambient air. The design of this electrode is scalable and flexible, so that many kinds of applications are expected. Moreover, the SMD plasma device can be portable since this plasma discharges require only the air and electricity.

From this plasma discharge, many reactive species are produced, e.g. O_3 , NO_2 , HNO_3 , N_2O , N_2O_5 , etc. The plasma chemistry is highly complex and we are now characterizing the plasma in detail. In our experimental setups, these reactive species play a major role because UV emission is low. Due to the distance of ~ 1 cm between the plasma discharge and objects, short lifetime species, e.g. charged particles, have a minor role. The produced reactive species can have a biomedical activity and we have shown that this plasma has a relatively strong bactericidal and sporicidal property [12]. It was shown that this plasma could inactivate adenovirus [13]. From these characteristics, another clinical study is planned.

The required electrical safety tests were carried out according to IEC60601-1. The measured UV radiation and the toxic gas emission were below the limits given by the International Commission on Non-Ionizing Radiation Protection (ICNIRP) and the US National Institute for Occupational Safety and Health (NIOSH). Furthermore, In vitro cell culture experiments showed that a parameter window exists where a high bactericidal property is achieved by the plasma treatment whereas no damage was observed in cell culture experiment. Using this information, we are currently preparing for clinical studies on human.

3. Summary

Since cold atmospheric plasmas produce a large variety of reactive species, many biomedical applications become possible, for example sterilization and disinfection. Furthermore, the plasma produces charged particles and UV light, and a synergetic effect among all the produced species should also be considered. The discharge chemistry is highly complex and more information is still needed.

Until now, we have conducted a clinical study on chronic wounds in patients using the argon plasma torch system and demonstrated that the bacterial load was reduced without possessing any side effects. Using the SMD electrode, another clinical study is currently prepared. The SMD plasma technique has a scalable and flexible design. The required resource is only air and electricity, so that a portable plasma device can be designed.

Cold atmospheric plasmas have a broad application spectrum in medical and hygiene. To improve the plasma systems, detailed research in physics, chemistry, biology, medicine, etc. is still necessary.

Acknowledgment

This study was supported by Max-Planck Society under grand 02.M.TT.A.

References

- [1] E. Stoffels, *Contrib. Plasma Phys.*, **47** (2007), 40.
- [2] G. Fridman, A. B. Shekhter, V. N. Vasilets, G. Friedman, A. Gutsol and A. Fridman, *Plasma Process. Polym.* **5** (2008), 503.
- [3] M. Laroussi, *IEEE Trans. Plasma Sci.*, **30** (2002), 1409.
- [4] E. Stoffels, Y. Sakiyama, D. B. Graves, *IEEE Trans. Plasma Sci.* **36** (2008), 1441.
- [5] M. G. Kong, G. Kroesen, G. E. Morfill, T. Nosenko, T. Shimizu, J. van Dijk and J. L. Zimmermann, *New J. Phys.* **11** (2009), 115012.
- [6] K. D. Weltmann, E. Kindel, T. von Woedtke, M. Haehnel, M. Stieber and R. Brandenburg, *Pure Appl. Chem.* **82** (2010), 1223.
- [7] E. Klein, D. L. Smith and R. Laxminarayan, *Emerg. Infect. Dis.*, **13** (2007), 1840.
- [8] T. Maisch, T. Shimizu, Y-F. Li, J. Heinlin, S. Karrer, G. Morfill and J. L. Zimmermann, *PLoS ONE*, **7** (2012), e34610.
- [9] G. Isbary, G. Morfill, H-U. Schmidt, M. Georgi, K. Ramrath, J. Heinlin, S. Karrer, M. Landthaler, T. Shimizu, B. Steffes, W. Bunk, R. Monetti, J. Zimmermann, R. Pompl, and W. Stolz, *Br. J. Dermatol.*, **163** (2010), 78.
- [10] G. Isbary, J. Heinlin, T. Shimizu, J. L. Zimmermann, G. Morfill, H-U. Schmidt, R. Monetti, B. Steffes, W. Bunk, Y. Li, T. Klaempfl, S. Karrer, M. Landthaler, and W. Stolz, *Br. J. Dermatol.*, accepted.
- [11] G. Morfill, T. Shimizu, B. Steffes, and H-U. Schmidt, *New J. Phys.*, **11** (2009), 115019.
- [12] T. G. Klaempfl, G. Isbary, T. Shimizu, Y-F. Li, J. L. Zimmermann, W. Stolz, J. Schlegel, G. E. Morfill, and H-U. Schmidt, *Appl. Environ. Microbiol.*, accepted.
- [13] J. L. Zimmermann, K. Dumler, T. Shimizu, G. E. Morfill, A. Wolf, V. Boxhammer, J. Schlegel, B. Gansbacher, and M. Anton, *J. Phys. D: Appl. Phys.*, **44** (2011), 505201.

Response of Mammalian Cells to Intense Pulsed Electric Fields

Sunao Katsuki, Misako Yano, Kazunori Mitsutake*, Keisuke Abe*, Hidenori Akiyama*
Bioelectrics Research Center, Kumamoto University
*Graduate School of Science and Technology, Kumamoto University,
39-1, Kurokami 2-chome, Kumamoto City, Kumamoto 860-8555, Japan
katsuki@cs.kumamoto-u.ac.jp

ABSTRACT

Apoptosis-related signaling pathway in HeLa S3 cells subjected to nanosecond pulsed electric fields (nsPEFs) is discussed. 120 ns-long 12.5 kV/cm electrical pulses were repetitively applied to the cells, to give sub-lethal effect to the cells. We analyzed messenger RNA (mRNA) and proteins associated with ER stress (IRE, JNK, c-Jun etc.), DNA repair and mitochondria, by means of a real-time PCR (Q-PCR) and a FACS (flow-cytometer). Also, we tried 2D-PAGE and protein sequence. All analysis we have done support the fact that the ion influx, ceramide and ER stress play important roles in the field-induced apoptosis.

1. Introduction

Apoptosis, or programmed cell death, plays a role in normal development and homeostasis. Many materials and phenomena act as apoptosis-causative agents such as anti-cancer drugs, UV, radiation, ROS and more. Also, some stimuli of an electric field can cause apoptosis signals of micro and millisecond duration, and this high voltage electric field pulse can damage the plasma membrane; this electroporation phenomenon is used with drug delivery to kill specific cells and tissue, a complex technique called electrochemotherapy. Recently, a new field called bioelectrics has arisen, which use nanosecond electric field (nsPEF) on biomaterial. In this field, some researchers have experimented with cancer therapy, using nsPEF to induce apoptosis to cancer cells. Mouse melanoma was found to decrease and finally disappear within two weeks to one month after nsPEF stimulation. Moreover, recent report has indicated that nsPEF inhibited VEGF in mouse melanoma. Because nsPEF-induced cell death was indicated by Annexin V positive, active-caspase3 positive and DNA fragmentation, many researchers think nsPEF-induced cell death is indeed apoptosis.

In this study, we anticipated that extracellular ion influx is very important for nsPEF-induced apoptosis. We thus investigated the effect of ion influx to elucidate nsPEF-induced apoptosis pathway in detail. Ca^{2+} influx is known to activate calpain and calmodulin kinase (CaMK). Also we examined which organelle, mitochondria or endoplasmic reticulum (ER) was damaged by nsPEF. Finally, we checked the expression of ceramide, which has lately become well-known famous as a second messenger. It is known that ceramide is up-regulated by physical and chemical stress, and that ceramide promotes SAPK/JNK signals to cause apoptosis. Thus, we investigated mRNA and protein related to ceramide and stress pathways.

2. Materials and Method

2.1 Cell Line and Culture Medium

We have used HeLa S3 cells (cervical cancer: ATCC CCL-2.2) for the target because their handling is relatively easy and the character is well-understood. The cells were cultured in alpha minimum essential medium (α MEM, WAKO) supplemented with 10% fetal bovine

serum (FBS, NICHIREI BIOSCIENCES) and penicillin/streptomycin at 37°C with 5% CO₂ in a humid atmosphere. The cells were moderately passaged every two or three days when the dishes reached 80% confluence. Three kinds of samples, sham control, EDTA-free and EDTA-added, were prepared to see the influence of presence of metal ions on apoptosis. EDTA (Ethylenediamine-tetraacetic acid, Nacalai) is chelate agent of metal ions.

2.2 Nanosecond PEF Application

A pulse power generator (MPC2000S, Suematsu Electronics), consisting of a control unit, a high voltage charger, and a magnetic pulse compression generator (MPC), was used to deliver 120 ns-long pulsed electric field to HeLa S3 cells in a 4 mm gap electroporation cuvette. The cells were suspended in a medium containing 10% FBS at $1-2 \times 10^6$ cells/ml. (800 μ L volume). The cuvettes were exposed to nsPEF at a room temperature (22-25°C). The pulse repetition rate was 0.5 pps, which is sufficiently slow for the temperature not to exceed 3°C during the pulse exposure. Fig. 1 shows the voltage waveform of the pulse, of which the main frequency band is 5 MHz.

Biological effects of a pulsed electric field are significantly dependent upon both the electric field strength and the number of pulses, even with no significant temperature rise. Too large field strength or too much pulse number easily kills the cells and a

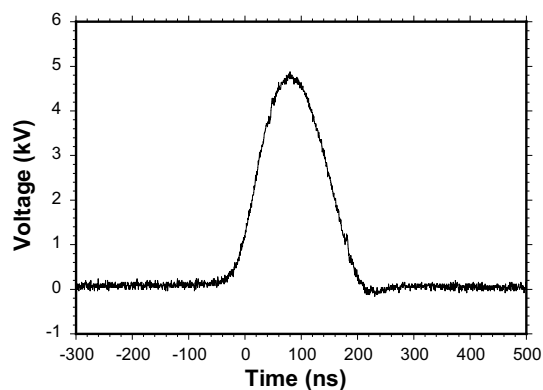


Fig. 1 Waveform of 120 ns-long pulsed voltage applied to a 4 mm-gap cuvette.

number of death mechanisms might be activated simultaneously. In order to clarify the most dominant mechanisms of the field-induced apoptosis, the electrical stress or pulse energy must not be too large. In this study, the field strength was fixed to be 12.5 kV/cm and the numbers of the pulses was chosen to be 100 to kill 50% of the cells.

2.3 Apoptosis and gene expression analysis

Apoptotic cells were detected using terminal deoxynucleotidyl transferase dUTP nick end labeling (TUNEL) assay and the ratio was evaluated using a flowcytometer. TUNEL-positive cells were marked by FITC-conjugated antibody. Total RNA was isolated using an illustra RNAspin Mini (GE Healthcare) cDNA for Quantitative PCR (Q-PCR) was reverse-transcribed by SuperScript VILO. Quantitative mRNA analysis was performed by quantitative real-time PCR using a SsoFast EvaGreen Supermix on an MJ Mini Thermal Cycler equipped with an MiniOpticon Real Time PCR system under the conditions of 35 to 45 cycles at 95°C for 5 s, and 55 to 65°C for 1-5 s using cDNA as a template. Real-time PCR data were calculated by measuring the average cycle threshold for the mRNA of interest, which was normalized to the values of the mRNA for beta-actin. In this study,

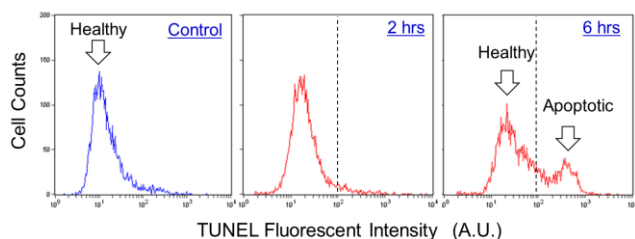


Fig. 2 Apoptotic DNA fragmentation in HeLa S3 cells induced by 120 ns-long electrical pulses detected by means of TUNEL assay and flowcytometer. From the left, control, samples 2 and 6 h after pulse exposure, respectively.

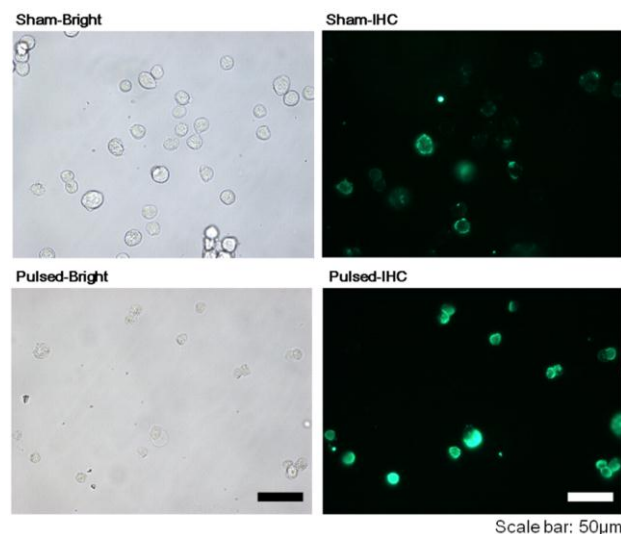


Fig. 3 Expression of ceramide in HeLa S3 cells immediately after the exposure to 120 ns-long electrical pulses.

sense and an antisense primer were designed on the basis of the nucleotide sequences from human in NCBI database.

3. Experimental Results

Histograms in Fig. 2 show degrees of the field-induced apoptotic DNA fragmentation in HeLa S3 cells. Almost all cells were healthy in the control, whereas DNA fragmentation is advanced slowly in the pulsed cells. Also active-caspase3 was upregulated. Ion influx induced by nsPEF caused cell death. Ca^{2+} and Mg^{2+} -free PBS inhibited cell death indicates that extracellular Ca^{2+} and/or Mg^{2+} are important to cause nsPEF-induced cell death. Moreover, nsPEF damaged mitochondria and ER. nsPEF-induced ion influx promoted generation of ceramide from cytomembrane into the cytoplasm, and the ceramide accumulated in blebbing area (Fig. 3). nsPEF-induced ceramide promoted ASK1/JNK/c-Jun signal and increased Bax expression, JNK inhibited mitochondria survival factors.

4. Summary

Fig. 4 shows the summary of the analysis. Our data raise the possibility that nsPEF induces ceramide activated MAPK/JNK pathway to cause apoptosis. We formulated a hypothesis that, first of all, lipid raft platforms are gathered at the anode site and damaged by nsPEF stimuli. Nano-pores are made and Ca^{2+} enters the cytoplasm along with Ca^{2+} dependent enzymes such as SMase family from the lipid raft platform and cytoplasm. These enzymes were activated with Ca^{2+} to make ceramide, and ceramide activated SAPK/JNK signal. Mitochondria were destroyed by JNK signal pathway, however, mitochondrial survival factors were activated 2 h after nsPEF exposure and were down-regulated at 6 h by nsPEF. Therefore, our result indicates survival factors inhibited DNA fragmentation within 2 h, but apoptosis factor was released about 6 h after nsPEF and initiate DNA fragmentation.

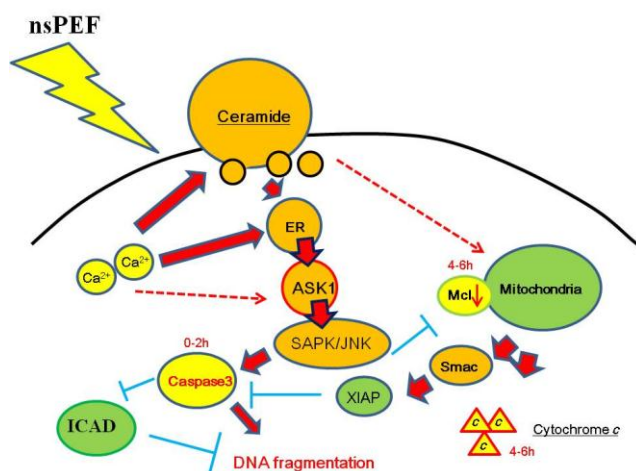


Fig. 4 Apoptosis pathway induced by the exposure to 120 ns-long electrical pulses.

Oxygen Tension Control in a Microfluidic Device for Cell Culture

Kenichi Funamoto¹, Ioannis K. Zervantonakis², Yuchun Liu³, Roger D. Kamm²

¹Institute of Fluid Science, Tohoku University, Sendai 980-8577, Japan

²Department of Mechanical Engineering, Massachusetts Institute of Technology, Cambridge, MA 02139, USA

³Faculty of Engineering, National University of Singapore, Singapore 117576, Singapore

E-mail: funamoto@reynolds.ifs.tohoku.ac.jp

ABSTRACT

Oxygen tension affects cell fate, such as viability, migration, proliferation and differentiation. A microfluidic device is designed to reveal cell responses to hypoxia or oxygen gradient. The oxygen tension in the microfluidic device was validated by using a ruthenium-coated (Ru-coated) oxygen-sensing glass cover slip, assuming the Stern-Volmer equation between the fluorescence intensity and oxygen tension. The oxygen tension decreased by supplying 0% gas, and the establishment of low uniform oxygen tensions (<3%) was confirmed. The experimental result agreed well with the corresponding computational result.

1. Introduction

Oxygen tension is one of the most important factors influencing cell viability, migration, proliferation and differentiation [1]. Conventional gas variable incubators, which create the desired oxygen environment by mixing oxygen, nitrogen and carbon dioxide in a predefined ratio, are most commonly used to study the effects of oxygen tensions on cell behaviors. However, these systems do not allow the generation of oxygen gradients and are limited by the long times required for equilibrating the gas concentration [2].

In this study, we introduce a simple microfluidic device that allows the generation of low oxygen environments or an oxygen gradient for the study of cells in a 3D environment, using the supply of predefined gas mixtures. The steady and transient oxygen tension in the microfluidic was measured based on the fluorescent intensity change of a Ru-coated oxygen-sensing glass cover slip bonded to the microfluidic channels, and compared with the corresponding numerical simulation result.

2. Methods

Figure 1 shows a schematic of microfluidic device to control oxygen tension for a cellular experiment. The device has a central gel region, sandwiched by media channels, and peripheral gas channels on both sides. Oxygen tension in the device was measured with a sample of commercially available oxygen-sensing glass cover slip coated with Ru complex dye (FOXY-SGS, Ocean Optics, FL, USA) bonded to the bottom surface of the PDMS microfluidic device mold. For microscopic imaging, a digital CCD camera (C4742-95-12ER, Hamamatsu Photonics, Japan) connected to an inverted microscope (ECLIPSE TE300, Nikon, Japan) was employed. The oxygen-sensing glass cover slip was excited with green laser ($\lambda_{ex} = 540-580$ nm) and the fluorescence ($\lambda_{em} = 595$ nm) was recorded with a 4x magnification objective. Exposure time for brightness field and fluorescence imaging was set at 2 ms and 800 ms, respectively.

Since collagen type I gel was difficult to stabilize on the oxygen-sensing cover slip, leaking to the media channels easily, it was replaced by water in this

experiment. Water purged with air overnight was added into the media channels and the gel region of the microfluidic device. The two inlets and one outlet of the media channels were connected to a water reservoir, and a syringe pump (EW-74901-00, Cole-Parmer, IL, USA), respectively. Water was withdrawn at a flow rate corresponding to $Pe_m = 10$ (10.8 $\mu\text{l/h}$ for each media channel), while blocking the gel ports so as not to cause water flow in the gel region and to prevent evaporation during the experiment. Humidified gas mixture containing 21% oxygen, 5% carbon dioxide and 74% nitrogen (Airgas East Inc., MA, USA) was first supplied to both gas channels at the flow rate of $Pe_g = 100$ (18 ml/min) to calibrate the device at 21% oxygen. Then, the gas mixture was switched to the one containing 0% oxygen, 5% carbon dioxide and 95% nitrogen (Airgas East Inc., MA, USA) at the same flow rate to decrease oxygen tension in the device. Note that the 0% oxygen gas mixture was humidified using a solution containing 10 wt% sodium sulfite (Na_2SO_3) to remove any dissolved oxygen. Fluorescence images were recorded every five min for the first 30 min, followed by every 30 min for three hrs, and six and 12 hrs after changing the gas supply. Finally, the water in the media channels and the gel region was substituted with 10 wt% Na_2SO_3 solution, and gas flow with the same 0% oxygen gas was supplied through both gas channels without any media flow ($Pe_m = 0$) for the calibration of 0% oxygen

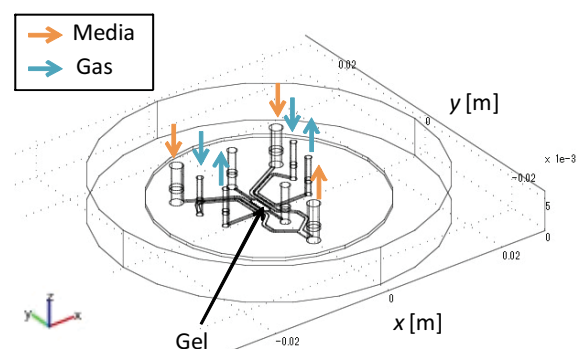


Fig. 1 Microfluidic device for a cellular experiment under hypoxia.

tension.

The fluorescence intensity in each image was quantified using image processing software (ImageJ, NIH, MD, USA). Three fluorescence intensity profiles across the media channels and gel region were obtained by setting three rectangular regions of interest (ROI) of $1,276 \times 80$ pixels ($2 \text{ mm} \times 0.13 \text{ mm}$). Each ROI was divided into small sections of $0.1 \text{ mm} \times 0.13 \text{ mm}$, and the space-averaged fluorescence intensity in each section was obtained. Then, the fluorescence intensity in each condition was converted to an oxygen tension based on the Stern-Volmer equation:

$$\frac{I_0}{I} = 1 + K_q[\text{O}_2], \quad K_q = \frac{I_0}{I_{100}} - 1 \quad (1)$$

where I and I_0 are the fluorescence intensities in oxic and anoxic atmospheres, respectively, and K_q is the quenching constant.

Three microfluidic devices, which had a 7.2 mm thickness on average, were used in the validation experiment, and the PDMS thickness below the PC film was $\sim 2.75 \text{ mm}$. The corresponding computational model of the microfluidic device was constructed (Fig. 1), and the media and gas flows through the individual channels were simulated by solving the Navier-Stokes equations and the equation of continuity. Both steady and transient oxygen tensions inside the device were calculated by solving the convection-diffusion equation. Simulations were performed by employing commercial finite element software (COMSOL Multiphysics 3.5a, COMSOL, MA, USA).

3. Results and Discussion

Figure 2 shows a representative set of microscope images. In the bright field image, the central gel region sandwiched by media channels and PDMS pillars to sustain channels are displayed. In normoxia at 21% oxygen tension, the fluorescence image was very dark though several white dots were observed due to nonuniformity of the Ru-coating (Fig. 2(b)). The fluorescence image intensity increased after supplying 0% oxygen gas through both gas channels, indicating oxygen tension decreased. The intensity was saturated after 3 hrs, and the oxygen tension reached a steady state.

The oxygen tension at each time step in each condition was correlated based on the Stern-Volmer equation (Eq. (1)). The oxygen-sensing glass cover slip was first calibrated using two known oxygen tensions of 21% and 0%, and the quenching constant, K_q , was obtained. The average value of the oxygen tension with the standard deviation is compared with the simulation result in Fig. 3. A uniform hypoxia condition with $< 3\%$ oxygen tension was created in the device, showing a good agreement with the simulation result. The reduction of oxygen tension took slightly longer than simulated. The disagreements between the measurement and the numerical simulation could possibly be attributed to non-ideal device fabrication and setup errors, resulting in diffusion of atmospheric oxygen.

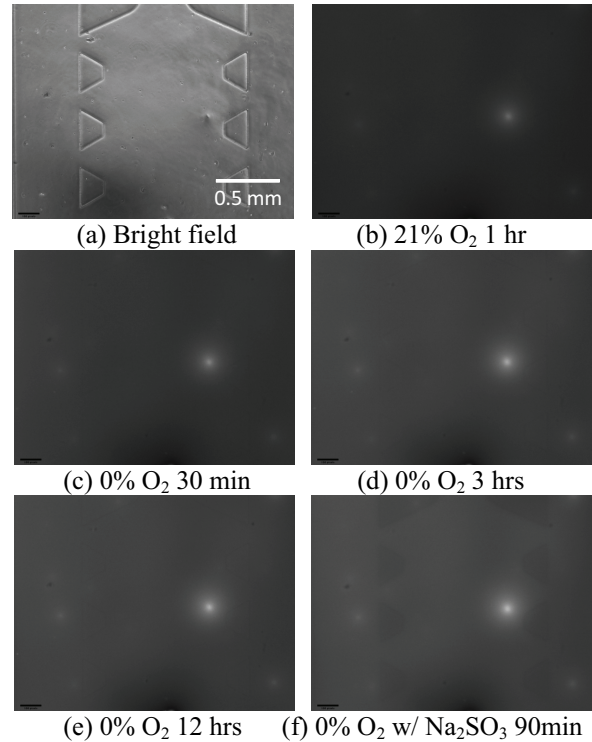


Fig. 2 Microscope images of the gel channel sandwiched by media channels in the microfluidic device: (a) a bright field image and (b) – (f) fluorescence images with 21% or 0% O_2 gas supply through both gas channels. Both gel and media channels were filled with water or Na_2SO_3 solution.

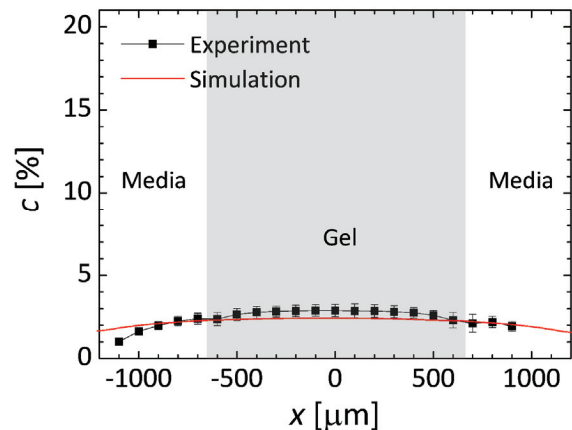


Fig. 3 Oxygen tension profile across the gel region and media channels.

4. Conclusion

A microfluidic device to control oxygen tension for a cell culture was successfully developed.

Acknowledgement

KF was supported by Young Researcher Overseas Visits Program for Vitalizing Brain Circulation, JSPS.

References

- [1] A. Mohyeldin et al., Cell Stem Cell, **7** (2010), 150-161.
- [2] C.B. Allen et al., Am J Physiol-Lung C, **281** (2001), L1021-L1027.

Stimuli Responsible Biointerfaces for Biological Responses of Human Cells

Masaru Tanaka, Kazuhiro Sato

Biomaterials Science and Tissue engineering Group,
Department of Biochemical Engineering,
Graduate School of Science and Engineering,
Yamagata University, Yonezawa, Japan
tanaka@yz.yamagata-u.ac.jp
http://www.bio-material.jp/

ABSTRACT

It has been pointed out that biocompatibility depends on the various physicochemical properties of the material surface. Water is thought to be a fundamental factor in the biological response induced by artificial materials. Detailed studies on the dynamics and structure of hydrated polymers at the biointerface are required to clarify the mechanism underlying the biocompatibility of polymers. We hypothesized that *intermediate water*, which prevents the biocomponents from directly contacting the polymer surface or *non-freezing water* on the polymer surface, plays an important role in the excellent biocompatibility.

1. Introduction

Many polymers have been studied in order to obtain biocompatible surfaces, and several mechanisms have been proposed for the biocompatibility of polymers [1]. Biocompatible surfaces can be classied into 3 main categories: hydrophilic surfaces; micro-phase-separated domain surfaces; and bioinspired biomembrane-like surfaces, including zwitterionic groups. It has been pointed out that biocompatibility depends on the various physicochemical properties of the material surface, e.g., surface charge, wettability, surface free energy, topography or roughness, stiffness, and the presence of specific chemical groups on the surface. Although considerable theoretical and experimental efforts have been devoted to clarifying this issue in the past few decades, the factors responsible for biocompatibility of polymers have not been elucidated. Water is thought to be a fundamental factor in the biological response induced by artificial materials. Many researchers have insisted that water structure on a polymer surface is one of the key factors for its biocompatibility. However, the proposed structures and/or the functions of water are different in many cases, and there is little consistency among structures. Detailed studies on the dynamics and structure of hydrated polymers at the biointerface is required to clarify the mechanism underlying the biocompatibility of polymers.

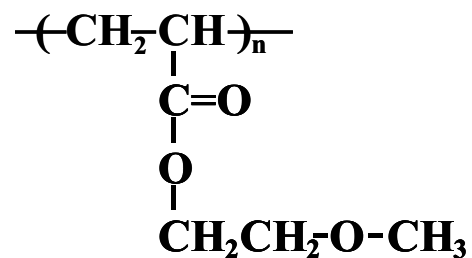
2. Method

The phase transitions of water in the polymer (poly(2-methoxyethyl acrylate) (PMEA) (Fig. 1) and poly(meth) acrylate analogs with thermo-sensitivity) were measured with a differential scanning calorimetry (DSC) equipped with a low-temperature cooling apparatus. The sample was placed in an aluminum pan and hermetically sealed. The weight of the sample used was 4-5 mg. The sample was first cooled to -100 °C at the rate of 5.0 °C/min, held at -100 °C for 10 min, and then heated to 50 °C at the same rate under a nitrogen atmosphere. The heating process was monitored. It was confirmed that there was no weight loss during the measurement. The hydrated water in polymer can be classified into 3 types: non-freezing water, intermediate

water, and free water on the basis of the equilibrium water content (EWC) and the enthalpy changes due to the phase transition observed by DSC.

3. Results and Discussion

We found that hydrated PMEA and poly(meth) acrylate analogs possessed a unique water structure, observed as cold crystallization of water in differential scanning calorimetry (DSC) [2,3]. Cold crystallization is interpreted as ice formation at low temperature, an attribute of freezing-bound water in PMEA. The presence of 3 types of water (Figs. 2 and 3) in PMEA is supported by the results of attenuated total reflection infrared (ATR-IR) spectroscopy and NMR. Intermediate water molecules interact weakly with the methoxy group of PMEA. While investigating the main factor responsible for the excellent biocompatibility of PMEA, it is important to reveal the water structure on the polymer surface.



- **excellent blood compatibility**
- **water insoluble, adhesive**
- **low protein adhesion and denaturation**
- **low blood cells adhesion and activation**
- **low toxicity, approved by FDA**

Fig. 1. Chemical structure of novel biocompatible polymer: poly(2-methoxyethyl acrylate) (PMEA)

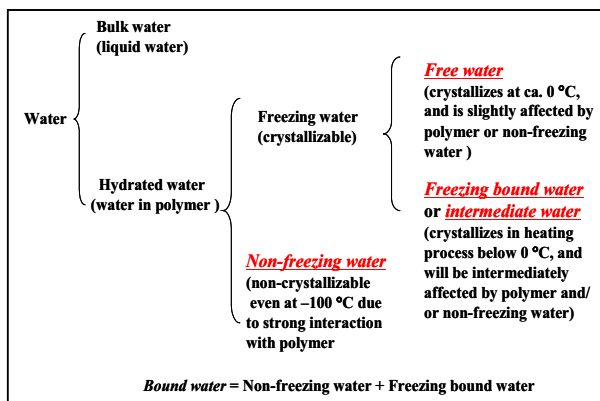


Fig. 2 Classification of water in hydrated polymer. The hydrated water in polymer can be classified into three types, non-freezing water, freezing-bound water, and free water on the basis of the equilibrium water content and the enthalpy changes due to the phase transition observed by thermal analysis.

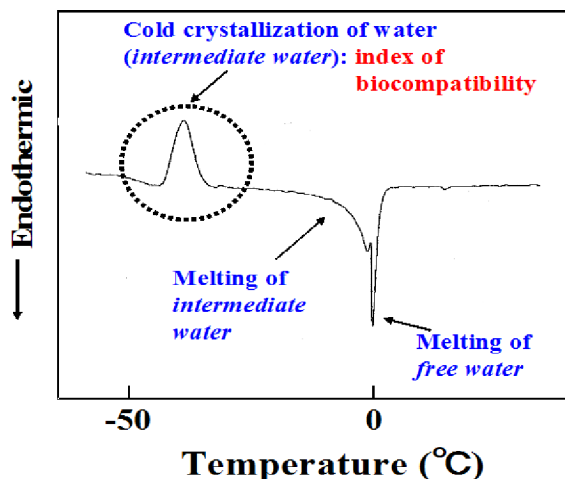


Fig. 3 Differential scanning calorimetry (DSC) heating curve of biocompatible polymer: PMEA-water system.

When the polymer surface comes in contact with blood, it first absorbs water, and a specific water structure is formed on the surface. If the resulting structure formed is the first layer, then the layers will be in the following order; polymer surface→non-freezing water→(freezing-bound water)→free water→bulk water. Free water is unlikely to activate the system, and is unable to shield the polymer surface or nonfreezing water on the polymer surface; this is because free water exchanges with bulk water very freely, resulting in a structure similar to bulk water. Since freezing-bound water is weakly (loosely) bound to the polymer molecule or non-freezing water (tightly bound water), this layer forms a rather stable structure compared to that of free water. Thus, when the freezing-bound water layer becomes adequately thick, it prevents the cell or the protein from directly contacting

the polymer surface or non-freezing water.

Our hypothesis is supported by several reports that demonstrate the formation of cold crystallizable water (in freezing-bound water) in well-known biocompatible polymers like poly(ethylene glycol), poly(methyl vinyl ether) (PMVE), polyvinylpyrrolidone (PVP), poly(2-methacryloyloxyethyl phosphorylcholine) (PMPC), poly(tetrahydrofurfuryl acrylate) (PTHFA), poly(2-(2-ethoxyethoxy)ethyl acrylate) and the analog polymers, gelatin, albumin, cytochrome C, and various polysaccharides, including hyaluronan, alginate, and gum.

Also, we have found that regular structures are formed during the casting of biocompatible polymer solutions on solid surfaces; for example, self-organized honeycomb-patterned films with highly regular porous structures can be prepared under humid casting conditions. Here, we report the growth of human normal and cancer cells cultured on the 3D films and their applications for medical devices, such as a bile-duct stent which is covered by the patterned-films. The new products are commercially available on the world clinical market. We highlight that 1) the reasons for this compatibility by comparing the structure of water in hydrated PMEA to the water structure of other polymers and 2) the reasons that honeycomb films exerted a strong influence on normal, cancer and stem cells morphology, proliferation, differentiation.

Conclusions

We hypothesized that intermediate water, which prevents the biocomponents from directly contacting the polymer surface or non-freezing water on the polymer surface, plays an important role in the excellent biocompatibility.

Acknowledgements

This work is supported by Grants-in-Aid and Special Coordination Funds for Promoting Science and Technology of Ministry of Education, Culture, Sports, Science and Technology, Japan. We greatly acknowledge the financial support from Funding Program for Next Generation World-Leading Researchers (NEXT Program, Japan)

References

- [1] T. Tsuruta, *Adv. Polym. Sci.*, **126**, (1996), 1.
- [2] M. Tanaka, *Biochim. Biophys. Acta*, **1810** (2011), 251.
- [3] M. Tanaka, A. Mochizuki, *J. Biomat. Sci. Polym. Ed.*, **21** (2010), 1849.
- [4] T. Hirata, H. Matsuno, M. Tanaka, K. Tanaka, *Physical Chemistry Chemical Physics*, **13** (2011), 4928.
- [5] M. Tanaka, *JP Patent 4746984* (2011).
- [6] T. Hatakeyama, M. Tanaka, A. Kishi, H. Hatakeyama, *Thermochim Acta*, **532** (2012), 159.
- [7] I. Javakhishvili, M. Tanaka, K. Jankova, S. Hvilsted, *Macromol. Rapid Commun.*, **33** (2012), 319.
- [8] T. Hayashi, Y. Tanaka, Y. Koide, M. Tanaka, M. Hara, *Physical Chemistry Chemical Physics*, in press.

Mechanical Stimulation Induces Movement of Protein Kinase C in Vascular Endothelial Cells

Susumu Kudo, Tomoya Shimada*, Marie Terada*, and Keita Hamasaki**

Department of Mechanical Engineering, Kyushu University, 744 Motooka, Nishi-ku, Fukuoka 819-0395, JAPAN

*Department of Mechanical Engineering, Shibaura Institute of Technology, 3-7-5 Toyosu, Koto-ku, Tokyo 135-8548, JAPAN

** Department of Applied Chemistry, Shibaura Institute of Technology, 3-7-5 Toyosu, Koto-ku, Tokyo 135-8548, JAPAN

kudos@mech.kyushu-u.ac.jp.

ABSTRACT

We investigated the translocation of protein kinase C alpha (PKC α) used by fusion protein PKC α -AcGFP in endothelial cells by point mechanical and chemical stimulation. In the cells closest to the mechanical and chemical stimulated cell, there was a time-dependent increase in PKC α -AcGFP fluorescence on the cell periphery adjacent to the target.

1. Introduction

When an endothelial cell is injured by mechanical stimulation using a microprobe, a Ca²⁺ wave is propagated. Ca²⁺ wave propagation refers to the spread of an influx of intracellular Ca²⁺ concentration in the form of a wave from the stimulated cell to the non-stimulated adjacent cells [1]. Previous research suggests the involvement of Ca²⁺ wave propagation in the lining process of damaged vasculature, and consequently, intercellular Ca²⁺ wave propagation is considered a distinct form of cell-to-cell communication [2].

Protein kinase C α (PKC α) is involved in the regulation of endothelial cell migration at the time of vascular injury [3]. PKC α is typically distributed uniformly throughout the cytoplasm. However, in response to an increase of intracellular Ca²⁺ induced by chemical stimulation, PKC α is recruited to the cell membrane, where it becomes activated thus triggering downstream intracellular signaling pathways [4, 5]. The translocation of PKC α by chemical stimulation has been investigated but not by mechanical stimulation. Therefore, an investigation of the movement of PKC α in response to Ca²⁺ wave propagation in endothelial cells by mechanical stimulation will shed light on the mechanism of endothelial cell migration.

In this study, we developed a experimental system to simultaneously visualize PKC α translocation and Ca²⁺ signaling. Using this system, we stimulated a single cell to propagate Ca²⁺ waves and then examined PKC α movement. Mechanical and biological modes of cell stimulation were compared. For mechanical stimulation, a micromanipulator-controlled glass pipette was used to deform a single cell. Alternatively, caged ATP was used to biologically stimulate a cell. This biologically inactive ATP analogue probe is converted to the active form of ATP when it is photolyzed with UV light.

2. Method

PKC α was labeled with the green fluorescent protein AcGFP (Clontech) in order to visualize its cellular localization. The PKC α -AcGFP fusion protein was

generated by attaching the gene encoding AcGFP to the C-terminus of the PKC α gene (pPKC α -AcGFP) according to Wagner et al. [3]. AcGFP releases fluorescence emissions at 510 nm when excited at 488 nm.

Cultured bovine aorta endothelial cells (Toyobo) were plated onto 27-mm diameter glass-bottom dishes (Iwaki), and transfected with pPKC α -AcGFP using the lipofection reagent HilyMax (Dojindo). Cells were examined 1 to 2 days after transfection.

Intracellular changes in Ca²⁺ concentration were visualized using the Ca²⁺ sensitive fluorescent indicator Fura-2/AM (Invitrogen). Fura-2/AM releases fluorescence at 510 nm following activation at 440 nm. The intensity of Fura-2/AM fluorescence decreases with increasing levels of calcium ions.

For mechanical stimulation due to physical cell deformation, borosilicate capillary tubing (B100-75-10, Sutter Instrument) attached to a motor-driven micromanipulator (#06004, Narishige, Tokyo, Japan) was utilized. In order to avoid breakage of the capillary glass, a planetary gear box set (#72001, Tamiya) was attached to the motor for precise control of mechanical stimulation.

In order to biologically stimulate a single cell (non-physically), caged ATP (Molecular Probes) was introduced into the target cell. Caged ATP, when irradiated with UV laser pulse at 355 nm, releases ATP that activates the cell. In this study, the cells were loaded with caged ATP, and one specific cell was subjected to irradiation using a UV light pulse.

Microscopic fluorescence studies were conducted using an inverted microscope (Eclipse TE2000-S, Nikon,) fitted with a 40x oil immersion lens (S Fluor, NA = 1.30, Nikon). In order to monitor the stimulation-induced shifts in both the PKC α location and Ca²⁺ concentration, the excitation wavelength was switched back and forth between 440 and 488 nm at 148 millisecond intervals. The excitation beam was emitted by a xenon lamp (C7773, Hamamatsu Photonics) and the wavelength was filtered using the Aquacosmos system (C7501, Hamamatsu Photonics). The

fluorescence emission from the sample was amplified with an image intensifier (C8600-03, Hamamatsu Photonics), detected by a high-speed cooled digital CCD camera (C6790, Hamamatsu Photonics), and recorded on a PC.

A pulsed Nd-YAG laser transmitter (20Hz, New Wave Research) was employed to generate 355-nm UV light for the photolysis of caged ATP. Application of the laser flash photolysis system (C7501, Hamamatsu Photonics) enabled synchronous irradiation of the target cell with the excitation light and the photolysis light, thereby allowing the measurement of the effects of ATP stimulation. The diameter of the UV spot irradiation was in the range of 2.0 to 2.5 μm .

3. Results and Discussion

Figures 1A and 1B are representative fluorescence images of the changes in intracellular Ca^{2+} levels and localization of PKC α -AcGFP in response to mechanical stimulation. As shown in Figure 1A, the fluorescence intensities were decreased in the cells surrounding the stimulated target cell (marked by 'x'), indicating the propagation of the Ca^{2+} wave. On the other hand, in the cells closest to the stimulated target cell there was a time-dependent increase in PKC α -AcGFP fluorescence on the cell periphery adjacent to the target (indicated by arrows in the lower panel of Figure 1B).

Figure 1C illustrates the changes in the ratios of post- to pre-stimulation mean fluorescence intensities after stimulation for the cells in the vicinity of the target cell. Specifically, the graph shows the fluorescence intensity ratios for the three segments of the cells—near, far, and cytoplasm—as defined by the distance relative to the target cell and based on the assumption that the cell membrane extended to a maximum length of 5 μm from the edge of the cell. Comparison between the near, far, and cytoplasm segments indicated that the near segment had significantly greater fluorescence intensity ratios than the far and cytoplasm segments between 5 to 70 seconds post-stimulation. In addition, the results showed that the fluorescence intensity ratio of the near segment did not return to the baseline level for more than 90 seconds.

The changes in the intracellular Ca^{2+} level and localization of PKC α -AcGFP in response to ATP stimulation were investigated. The fluorescence intensities were decreased in the cells surrounding the UV-irradiated target cell, which was representative of the propagation of the Ca^{2+} wave. Moreover, tracking of PKC α -AcGFP in the cells adjacent to the irradiated cell revealed a transient increase in the fluorescence intensity on the periphery adjacent to the target.

The near segment had significantly greater fluorescence intensity ratios than the far and cytoplasm segments, which were comparable to the outcomes obtained for mechanical stimulation.

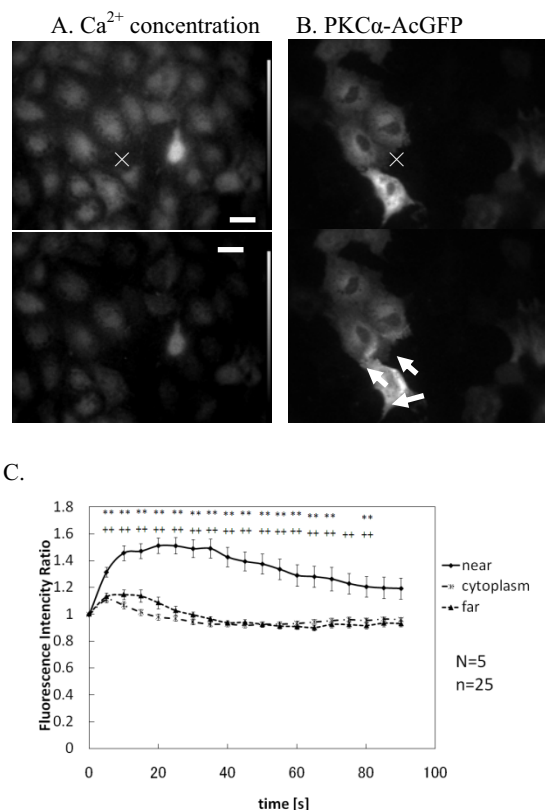


Fig. 1. Changes in intracellular calcium ion concentration and protein kinase α movement in aortic endothelial cells following mechanical stimulation of a single cell (scale bar: 10 μm . **: $P < 0.01$ near vs cytoplasm segments. ++: $P < 0.01$ near vs far segments). A: Fluorescence images reflecting the Ca^{2+} concentration before stimulation (upper panel) and after stimulation (lower panel). B: PKC α -AcGFP fluorescence images taken before stimulation (upper panel) and after stimulation (lower panel). C: Time-course changes in fluorescence intensity ratio.

4. Concluding remarks

Calcium waves were initiated and propagated among aortic endothelial cells by stimulating a single cell by mechanical stress or UV-mediated release of ATP. Both types of stimulation induced translocation of PKC α to the cell membrane of adjacent cells, on the same side as the stimulation.

References

- [1] L.L Demer et al., *Am. J. Physiol.*, **264**(1993), 2094-2102.
- [2] Z. Zhao et al., *J. Cell. Physiol.*, **214** (2008), 595-603
- [3] S.Wagner et al., *Exp. Cell Res.*, **258** (2000), 204-214.
- [4] C. Massch et al., *FASEB J.*, **14** (2000), 1653-1663.
- [5] P. J. Robinson et al., *J. Biol. Chem.*, **267**(1992), 21637-21644.

Vascular cell responses to biomechanical forces

Kimiko Yamamoto¹, Joji Ando²

¹Department of Biomedical Engineering, Graduate School of Medicine, University of Tokyo, Tokyo113-0033, Japan

²Laboratory of Biomedical Engineering, School of Medicine, Dokkyo Medical University, Tochigi 321-0293, Japan
k-yamamoto@umin.ac.jp

ABSTRACT

Endothelial cells (ECs) alter their functions in response to shear stress. Although their responses play important roles in vascular tone control, angiogenesis, and atherogenesis, how ECs recognize shear stress is poorly understood. Our previous studies demonstrated that Ca^{2+} signaling is crucial to shear-stress mechanotransduction via ATP-operated P2X4 ion channels by ECs. P2X4 KO mice have higher blood pressure values than wild-type mice and do not exhibit normal EC responses to shear stress, such as blood-flow-mediated vasodilation and remodeling. Thus, P2X4-mediated shear-transduction plays an important role in the vascular homeostasis.

1. Introduction

The endothelial cells (ECs) lining blood vessels have a variety of functions and play a central role in the homeostasis of the circulatory system. Biochemical mediators, including hormones, cytokines and neurotransmitters, have long been thought to control EC functions. Recently, however, it has become clear that biomechanical forces generated by blood flow and blood pressure regulates EC functions. ECs are constantly exposed to shear stress, a frictional force generated by flowing blood, and to cyclic strain, which is caused by pulsatile changes in blood pressure. A number of recent studies have demonstrated that ECs have the ability to sense shear stress and cyclic strain as signals and transmit them into the cell interior, where they cause the ECs to change their morphology, functions and gene expression¹⁻². The EC responses to biomechanical forces are critical to maintaining normal vascular functions, and impairment of EC responses leads to the development of vascular diseases, including hypertension, thrombosis, aneurysms, and atherosclerosis. This paper will focus on fluid shear stress and summarize the data from recent studies in the molecular mechanisms underlying shear stress mechanotransduction in ECs.

2. Endothelial cell responses to shear stress

Blood flow generates a frictional force, shear stress, in ECs, and the following formula can be used to calculate its intensity (τ): $\tau = \mu \, du/dt$, where μ is blood viscosity, u is blood flow velocity, r is the radius of the blood vessel, and du/dr is the flow velocity gradient. Under physiological conditions, arterial ECs are exposed to a shear stress of around 20 dynes/cm², and venous ECs to shear stress ranging from 1.5 to 6 dynes/cm²³.

It has well been established that ECs are sensitive to shear stress. When cultured ECs are exposed to shear stress in fluid-dynamically designed flow-loading devices, the ECs change their morphology and functions. ECs are polygonal under static culture conditions, but become elongated with their long axis oriented in the direction of flow in response to shear stress⁴. EC functions also change in response to flow⁵. For example, ECs increase production of various vasodilating substances, including nitric oxide (NO)⁶⁻⁷, prostacyclin, C-type natriuretic peptide, and adrenomedullin in response to shear stress, and decrease the production of vasoconstricting factors, including endothelin and angiotensin converting enzyme. Shear stress also results in an increase in the antithrombotic activity and fibrinolytic activity of ECs by stimulating production of thrombomodulin and plasminogen activators. Shear stress also affects EC synthesis of growth factors, cytokines, and reactive oxygen species (ROS), which are involved in EC apoptosis and adhesive interactions with leukocytes.

When shear stress modulates EC functions, it usually affects the expression of related genes. Our DNA microarray analysis showed that approximately 3% of all EC genes examined showed some kind of response to shear stress⁸. Assuming that ECs express around 20,000 genes, this finding suggests that more than 600 genes are shear-stress-responsive.

3. Shear stress mechanotransduction

The fact that ECs respond to shear stress by undergoing changes in morphology, function, and gene expression indicates the existence of a mechanotransduction mechanism by which ECs sense shear stress as a signal and transmit it into the cell interior. Numerous studies have shown that multiple pathways are involved in shear stress signal transduction (Fig. 1)⁹. However, which pathways are primary and which are secondary remains unclear, because the initial sensing mechanism or sensors that recognize shear stress have not been identified. Various membrane molecules and cellular microdomains, including ion channels, growth factor receptors, G protein-coupling receptor, caveolae, adhesion proteins, the cytoskeleton, the glycocalyx, and primary cilia, have been shown to play important roles in the shear stress sensing mechanism.

Ca^{2+} signaling is one of the pathways involved in shear stress mechanotransduction¹⁰⁻¹¹. When ECs cultured from human pulmonary arteries were subjected to laminar shear stress, the intracellular Ca^{2+} concentration increased in a dose-dependent manner¹². The Ca^{2+} response was due to an influx of extracellular Ca^{2+} via P2X4, a subtype of ATP-operated cation channel P2X purinoceptor. Treatment of ECs with an antisense oligonucleotide targeted to their P2X4 channels blocked the shear-stress-induced Ca^{2+} influx, and activation of P2X4 required ATP, which was supplied in the form of endogenous ATP released by the ECs¹³. The ECs released ATP dose-dependently in response to laminar shear stress, and suppression of ATP release with the ATP synthase inhibitor angiotatin abolished the shear-stress-induced Ca^{2+}

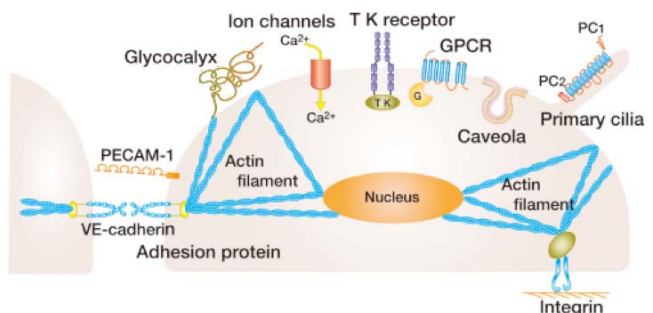


Fig. 1 Candidates for shear stress sensors: ion channels, tyrosine kinase receptor, GPCRs, caveolae, adhesion proteins, tensigrity, glycocalyx, primary cilia.

responses. These findings suggest that ECs are capable of accurately converting information regarding shear stress intensity into changes in intracellular Ca^{2+} concentrations through ATP release and P2X4 activation. We recently discovered that ATP synthase is localized in caveolae and involved in the ATP release induced by shear stress¹⁴. This finding means that ATP synthase not only produces ATP as an energy source in the mitochondria but also generates ATP as a signal transduction factor on the cell surface.

To analyze the dynamics of ATP release, we recently developed a novel chemiluminescence imaging method by using cell-surface attached firefly luciferase and a CCD camera¹⁵. Upon shear stress stimulation, cultured human pulmonary artery ECs simultaneously released ATP in two different manners, a highly concentrated, localized manner and a weakly concentrated, diffuse manner. The localized ATP release occurred at caveolin-1-rich regions of the cell membrane and was blocked by caveolin-1 knockdown with siRNA and depletion of plasma membrane cholesterol with methyl- β -cyclodextrin, indicating involvement of caveolae in localized ATP release. Ca^{2+} imaging with Fluo-4 combined with ATP imaging revealed that shear stress evoked an increase in intracellular Ca^{2+} concentration and subsequent Ca^{2+} wave that originated from the same sites as the localized ATP release (Fig. 2). These findings suggested that localized ATP release at caveolae triggers shear stress Ca^{2+} signaling in ECs.

4. Roles of shear-stress-mediated Ca^{2+} signaling via P2X4 in control of the circulatory system

In order to identify the physiological roles of P2X4-mediated shear stress signal transduction in the circulatory system, we generated P2X4 gene knockout mice (KO mice)¹⁶. The KO mice did not exhibit normal EC responses to shear stress, such as a Ca^{2+} influx and subsequent production of NO. When the ECs of wild-type mice (WT mice) were exposed to laminar shear stress, the intracellular Ca^{2+} concentration increased in a dose-dependent manner, whereas no flow-induced Ca^{2+} responses occurred in the ECs of the KO mice. Since increases in cytoplasmic Ca^{2+} concentration directly lead to the production of NO, we examined the ECs for changes in NO production with a fluorescence indicator, diamino fluorescein (DAF-2). NO

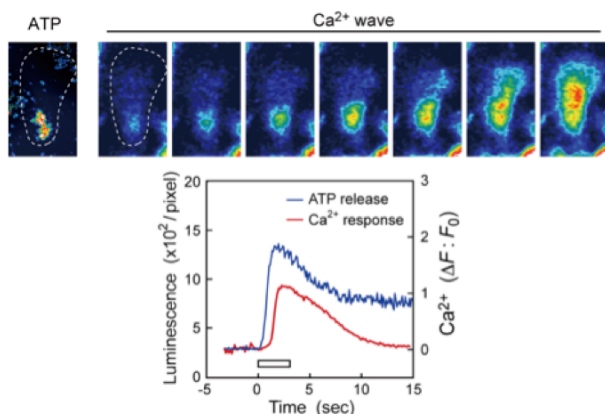


Fig. 2 Co-localization of the sites of localized ATP release and subsequent Ca^{2+} wave initiation. Pseudo-color images of shear-stress-induced ATP release and Ca^{2+} responses. Ca^{2+} imaging showed that shear stress evoked an increase in intracellular Ca^{2+} concentrations ($[\text{Ca}^{2+}]_i$) that started at a single site and propagated throughout the entire cell in the form of a Ca^{2+} wave. ATP imaging of the same cells was performed. Quantitative analysis of the rising phase of ATP release and $[\text{Ca}^{2+}]_i$ increase showed that ATP release always preceded the $[\text{Ca}^{2+}]_i$ increase.

production by the ECs of WT mice increased in response to laminar flow, and the response was shear-stress-dependent. The ECs of KO mice, however, did not show any evidence of flow-induced production of NO. Because of this impairment of NO production, the vasodilation induced by acute increases in blood flow in situ was much weaker in the KO mice, and the KO mice had higher blood pressure than the WT mice.

Chronic changes in blood flow through large arteries induce structural remodeling of the vascular wall: increases in blood flow cause vessel diameter to enlarge, while decreases in blood flow have the opposite effect. When the left external carotid artery was ligated for two weeks, thereby decreasing blood flow through the left common carotid artery (LC), the diameter of the LC had significantly decreased at the end of the two weeks in the WT mice, but not in the KO mice. The impaired vascular remodeling in the KO mice was similar to that observed in eNOS KO mice. These findings suggest that Ca^{2+} signaling of shear stress via P2X4 plays a crucial role in the control of vascular tone and in blood flow-dependent vasodilation and vascular remodeling through endothelial NO production.

5. Concluding remarks

Biomechanical studies in the past 30 years have revealed the cellular and molecular mechanisms by which ECs sense and respond to fluid mechanical forces, and they have confirmed that fluid mechanical forces actually play important roles in the control of vascular structure and function. However, many subjects remain to be investigated in future research, including fluid mechanical force sensors, the roles of fluid mechanical forces in the pathogenesis of vascular disease, such as atherosclerosis, hypertension, and aneurysm, and the relationships between fluid mechanical forces and the effects of physical exercise on human health.

References

- [1] J. Ando, K. Yamamoto, *Cir. J.*, **73** (2009), 1983-92.
- [2] S. Chien, *Am. J. Physiol.*, **292** (2007), H1209-24.
- [3] A. Kamiya, R. Bukhari, T. Togawa, *Bull. Math. Biol.*, **46** (1984), 127-37.
- [4] C. F. Dewey, Jr., S. R. Bussolari, M. A. Gimbrone, Jr., P. F. Davies, *J. Biomech. Eng.*, **103** (1981), 177-85.
- [5] J. Ando, K. Yamamoto, *Circ. J.*, **73** (2009), 1983-92
- [6] G. M. Buga, M. E. Gold, J. M. Fukuto, L. J. Ignarro, *Hypertension*, **17** (1991), 187-93.
- [7] R. Korenaga, J. Ando, H. Tsuboi, W. Yang, I. Sakuma, T. Toyo-oka, A. Kamiya, *Biochem. Biophys. Res. Commun.*, **198** (1994), 213-9.
- [8] N. Ohura, K. Yamamoto, S. Ichioka, T. Sokabe, H. Nakatsuka, A. Baba, M. Shibata, T. Nakatsuka, K. Harii, Y. Wada, T. Kohro, T. Kodama, J. Ando, *Atheroscler. Thromb.*, **10** (2003), 304-13.
- [9] K. Yamamoto, J. Ando, *Pharmacol. Sci.*, **116** (2011), 323-31.
- [10] J. Ando, T. Komatsuda, A. Kamiya, *In Vitro Cell Dev. Biol.*, **24** (1988), 871-7.
- [11] J. Ando, A. Ohtsuka, R. Korenaga, T. Kawamura, A. Kamiya, *Biochem. Biophys. Res. Commun.*, **190** (1993), 716-23.
- [12] K. Yamamoto, R. Korenaga, A. Kamiya, J. Ando, *Circ. Res.*, **87** (2000), 385-91.
- [13] K. Yamamoto, T. Sokabe, N. Ohura, H. Nakatsuka, A. Kamiya, J. Ando, *Am. J. Physiol.*, **285** (2003), H793-803.
- [14] K. Yamamoto, N. Shimizu, S. Obi, S. Kumagaya, Y. Taketani, A. Kamiya, J. Ando, *Am. J. Physiol.*, **293** (2007), H1646-53.
- [15] K. Yamamoto, K. Furuya, M. Nakamura, E. Kobatake, M. Sokabe, J. Ando, *Cell. Sci.*, **124** (2011), 3477-83.
- [16] K. Yamamoto, T. Sokabe, T. Matsumoto, K. Yoshimura, M. Shibata, N. Ohura, T. Fukuda, T. Sato, K. Sekine, S. Kato, M. Isshiki, T. Fujita, M. Kobayashi, K. Kawamura, H. Masuda, A. Kamiya, J. Ando, *Nat. Med.*, **12** (2006), 133-7.

Role of Fluid Mechanics in Collective Motions of Bacteria

Takuji Ishikawa, Naoto Yoshida, Hironori Ueno, Matthias Wiedeman, Yohsuke Imai, Takami Yamaguchi
School of Engineering, Tohoku University
6-6-01, Aoba, Aramaki, Aoba-ku, Sendai 980-8579, Japan
E-mail: ishikawa@pfs1.mech.tohoku.ac.jp

ABSTRACT

Coherent structures appear in a concentrated suspension of swimming bacteria. In this study, we carry out the first successful measurement of the three-dimensional velocity field in a dense suspension of bacteria. The results show that most of the energy generated by individual bacteria dissipates on the cellular scale. Only a small amount of energy is transported to the meso-scale, but the gain in swimming velocity and mass transport due to meso-scale coherent structures is enormous. These results indicate that collective swimming of bacteria is efficient in terms of energy.

1. Introduction

Collective behaviours of living creatures appear on various length scales, from bacteria to whales. Collective behaviours of swimming fish and flying birds are advantageous in terms of energy saved, because the undulatory movements of leading animals generate thrust-type vortices that are shed into the wake. Bacteria also exhibit collective swimming, and coherent structures appear in a concentrated suspension^[1]. However, the collective swimming of bacteria is not in analogous to collective behaviours at high Reynolds number because of the dominant viscous effect. It would be interesting to clarify whether collective swimming of bacteria is advantageous in terms of energy saved. In this study, we investigate energy transport in a concentrated suspension of bacteria by measuring the 3D velocity field experimentally.

2. Material and Method

As a model bacterium, *Escherichia coli* (*E. coli*), wild-type strain MG1655, was used. *E. coli* has a cell body about 1 μm in diameter and 2 μm in length, and swims at a velocity of about 20 $\mu\text{m}/\text{s}$. The cells were grown for 12h in tryptone broth (TB) maintained at 37°C, using a rotary shaker (160rpm)^[2]. Saturated cell culture (50 μL) was diluted in 5 mL of TB, and kept at 25°C without shaking for 10h. The cells were then separated from the media by centrifugation (2000g, 10min, 25°C), washed with motility buffer MB+, and finally suspended in MB+ with a cell density of 3×10^{10} cell/mL. To perform PIV analysis, tracer particles of diameter 1 μm were also suspended, with a number density of 5×10^9 bead/mL.

The confocal micro-PIV system^[3] enabled us to measure the velocity field even inside the dense suspension, up to 50 μm from the glass wall, with high spatial and time resolution. These advantages enabled us to calculate the 3D flow field in the dense suspension, and discuss the wall effect on the coherent structures. The system consisted of an inverted microscope, a confocal scanning system, a high-speed camera, a diode-pumped solid-state laser, a thermo plate, an objective lens, and a low-voltage piezoelectric translator controller.

A small drop of suspension, with a volume of 1 μL

and a diameter of about 1mm, was placed in a glass-bottomed Petri dish kept at 25°C for the study. To avoid evaporative flows, a high humidity was maintained in the closed chamber by enclosing additional drops. Strong coherent structures were observed for many minutes. Tracer movement was observed at the centre of the drop in planes with $z = 10, 20, 30, 40$ and 50 μm . Here, the z -axis was taken perpendicular to the wall. The x - and y -axes were parallel to the wall. We performed two kinds of measurements: (i) in-plane measurements, in which time-series images for PIV analysis were recorded in a fixed plane for 5s (100frames/s), and (ii) semi-3D measurements, in which measurements were carried out in five focal planes successively, using the piezoelectric translator, and images were recorded in each plane for 50ms (5 frames) with a 250ms interval. The PIV analysis was processed using interrogation windows of 16×16 pixels with 50% overlap (1pixel = 1.15 μm). An iterative cross-correlation method was used to calculate the velocity field. A sample image of tracer motions in a bacterial suspension is shown in Fig.1.

3. Results and Discussion

In the suspension, coherent structures similar to previous studies^[4] were observed. Fig.2(a) shows a sample sequence of velocity vectors at $z = 30 \mu\text{m}$, where the colour indicates the in-plane vorticity. The velocity field was measured by the motion of the tracer particles, and thus the figure indicates the velocity of the solvent fluid. We can see from the figure that vortices were generated on a scale much larger than that of the individual cells. Similar coherent structures were found

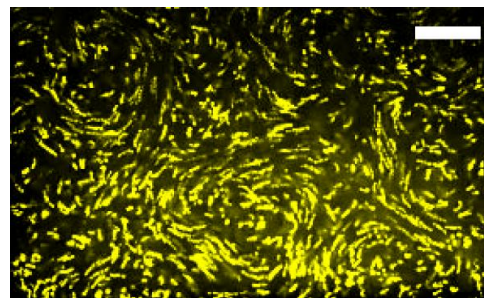


Fig.1 Flow in a bacterial suspension (scale bar=50 μm).

in all focal planes ($z = 10\text{-}50\mu\text{m}$). The average magnitude of the velocity vectors was calculated in each plane, and the results are shown in Figure 2(b). The average velocity was saturated around $z = 30\mu\text{m}$.

To clarify the scale of the collective motions, we calculated the spatial and time correlations of the velocities. Fig.2(c) and (d) show the respective spatial and time correlations for $z = 10, 30$ and $50\mu\text{m}$. These results indicate that the length scale of the vortices increased with z , whereas the time scale was not much affected by z . Fig.2(d) also shows that the time scale of the velocity fluctuations was about 1s. In our semi-3D measurements, two successive PIV measurements could be performed with an interval of 250ms. Thus, by linearly interpolating two successive velocity fields, we were able to calculate the 3D distribution of the in-plane velocity at any time. Fig.3 shows the 3D distribution of the in-plane vorticity, where the red and blue colours, respectively, indicate clockwise and counter-clockwise rotation of a vortex, viewed from the bottom. We can see that the vortices grew in the z -direction, and actually had 3D structure.

Next, we calculate the energy dissipation of the coherent structures using the velocity vectors obtained from the PIV analysis. The results are shown in Fig.4. In the range $z = 10\text{-}40\mu\text{m}$, the energy dissipation is about $3\text{-}7 \times 10^{-9} \text{J}/(\text{s.mL})$. By dividing the energy dissipation by the number density of the bacteria, we can deduce that individual bacteria dissipate energy at an average of about $1\text{-}2 \times 10^{-19} \text{J}/(\text{s.cell})$ on the meso-scale. We compared this value to the energy input from a solitary bacterium swimming in a free space, using a boundary element analysis^[2], and found that the model bacterium dissipates energy at about $3.9 \times 10^{-16} \text{J}/\text{s}$. The portion of its energy consumption that directly contributes to swimming can be approximated at $6.8 \times 10^{-18} \text{J}/\text{s}$. Thus, the swimming efficiency of a solitary cell is about 2%. The value of $1\text{-}2 \times 10^{-19} \text{J}/(\text{s.cell})$ is less than 0.1% of the total energy input from the individual bacteria.

4. Conclusions

We carry out the first successful measurement of the three-dimensional velocity field in a dense suspension of bacteria. The results show that only a small amount of energy is transported to the meso-scale, but the gain in swimming velocity and mass transport due to meso-scale coherent structures is enormous. These results indicate that collective swimming of bacteria is efficient in terms of energy. This paper demonstrates the advantages of collective swimming of bacteria, and sheds light on how energy can be transported toward smaller wave numbers in the Stokes flow regime.

References

- [1] Ishikawa T., *J. R. Soc. Interface*, **6**, 815-834, (2009)
- [2] Giacche D., *et al.*, *Phys. Rev. E*, **82**, 056309, (2010)
- [3] Saadatmand M., *et al.*, *J. Biomech.*, **44**, 170-175 (2011)
- [4] Dombrowski C. *et al.*, *Phys. Rev. Lett.*, **93**, 098103, (2004)
- [5] Ishikawa T., *et al.*, *Phys. Rev. Lett.*, **107**, 028102, (2011)

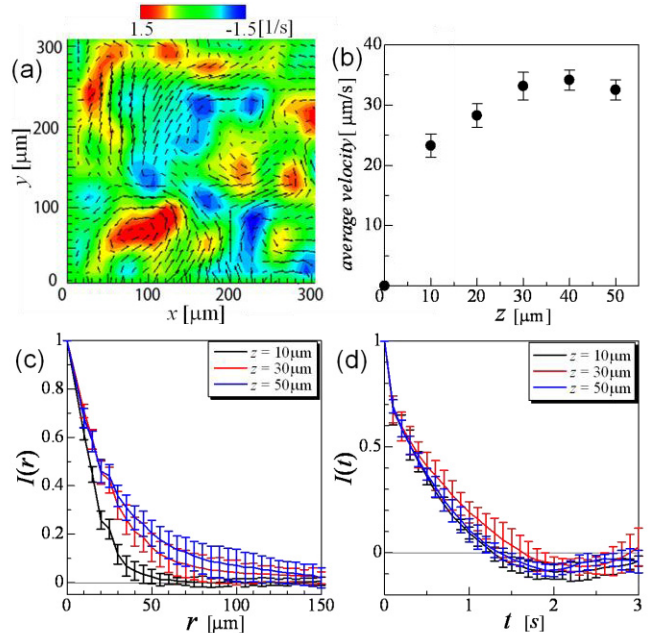


Fig.2 Velocity field in the suspension^[5]: (a) a sample sequence of velocity vectors at $z = 30\mu\text{m}$, where the colour indicates the in-plane vorticity; (b) change in the average in-plane velocity with respect to depth; (c) and (d) spatial and time correlations of the in-plane velocity vectors.

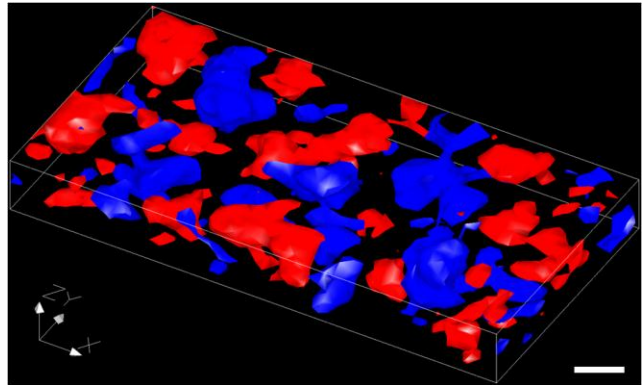


Fig.3 Distribution of in-plane vorticity in three dimensions^[5]. Iso-surfaces of 1.3 and -1.3 s^{-1} are coloured red and blue, respectively. The white scale bar is $50\mu\text{m}$.

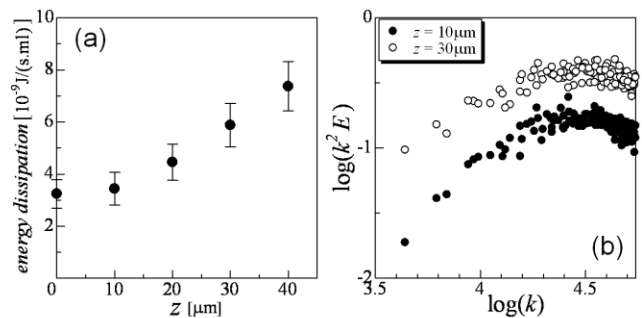


Fig.4 Energy dissipation of the meso-scale velocity field^[5]: (a) change in the energy dissipation with respect to depth; (b) spectrum of energy dissipation, $k^2 E$, at $z = 10$ and $30\mu\text{m}$.

Microscopic Analysis of Bacterial Motility at High Pressure

Masayoshi Nishiyama

The HAKUBI Center, Kyoto University, Yoshida-Ushinomiya-cho, Sakyo-ku, Kyoto 606-8302, Japan
mnishiyama@icems.kyoto-u.ac.jp

ABSTRACT

We characterized the pressure dependence of the motility of swimming *Escherichia coli* cells and the rotation of single flagellar motors. Our results showed that the fraction and speed of swimming cells decreased with increased pressure. At 80 MPa, all *E. coli* cells stopped swimming, although their flagellar motors still generate torque that should be sufficient to join rotating filaments in a bundle. The discrepancy in the behavior of free swimming cells and individual motors could be due to the applied pressure inhibiting the formation of rotating filament bundles that can propel the cell body in an aqueous environment.

1. Introduction

An *Escherichia coli* cell has 5–6 flagella, each of which consists of a long (~10 μm), thin (~20 nm) helical filament [1]. The cell turns its filament like a screw in either the counterclockwise (CCW, viewed from filament to motor) or clockwise (CW) direction. CCW rotation allows the left-handed helical filaments to form a bundle that propels the cell smoothly in a run. In contrast, CW rotation of a filament forces it out of the bundle and leads to a change in swimming direction called a tumble. The switching between CCW and CW rotation enables bacteria to migrate to more favorable environments. The bacterial flagellar motor converts an ion flux into the rotation of the flagellum. The motor consists of a rotor surrounded by multiple stator units. A maximum of 11 stator units can interact simultaneously with a single rotor, depending on the number of total stator units pooled in the inner membrane. Torque is generated by intermolecular interactions between the rotor and stator units. The chemo-mechanical energy conversion process is affected by physical and chemical conditions, such as temperature, pH, and solvation. The application of pressure is also expected to modulate the torque generation processes to the extent that *E. coli* cells stop swimming. To study in detail the effects of high pressure, it is critical to monitor the motility of *E. coli* cells under these conditions.

Here, we describe a high-pressure microscope that enables us to acquire high-resolution microscopic images under various pressure conditions [2]. The system developed allowed us to apply pressure of up to 150 MPa to any biological sample in solution, which is ~1.5-fold higher than the hydrostatic pressure in the deepest part of the Mariana Trench. Using this system, we characterized the pressure dependence of the motility of swimming *E. coli* cells and single flagellar motors [3].

2. Method

Briefly, the equipment design has been described previously [3]. We used *E. coli* strains RP4979 and YS1326. Cells were cultured from frozen stocks to late logarithmic phase at 30 °C in Tryptone broth (1% Bacto tryptone, 0.5% NaCl). The medium culture contained 50 mg ml⁻¹ ampicillin for strain YS1326. All assays were performed within 2 h after the cells were suspended in motility medium (10 mM Tris, pH 7, 0.1 mM EDTA).

3. Results and Discussion

To focus on the pressure dependence of the motor function in swimming *E. coli* cells, strain RP4979 (ΔcheY), rather than wild-type strain, was used for the following experiments. RP4979 cells lack the switch-inducing CheY protein; therefore, their flagellar motors rotate exclusively in the CCW direction, and cells swim smoothly without tumbling. The pressure of the high-pressure chamber was increased to 80 MPa, and then decreased to 0.1 MPa. Fig. 1A displays typical time courses for RP4979 cells under various pressure conditions. Under ambient conditions (0.1 MPa and 23 °C), RP4979 cells swam smoothly with a speed of 20 \pm

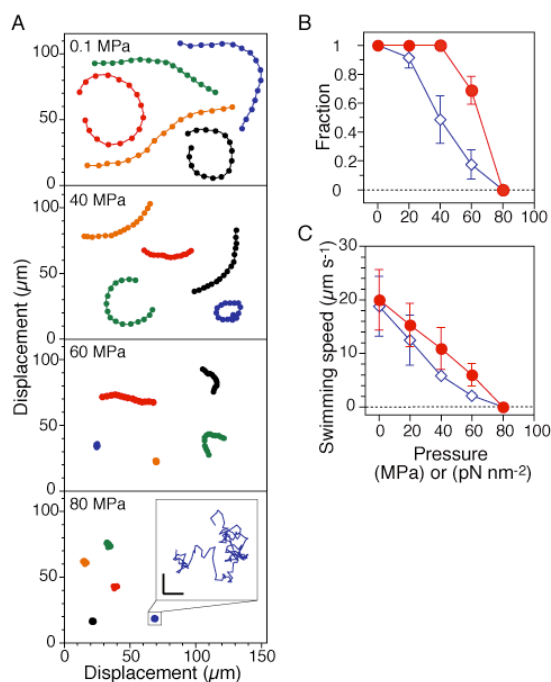


Fig. 1 Motility of smooth-swimming cells. (A) Trajectories of RP4979 cells. The positions of the cell were plotted every 10th frame for 5 s. (Inset) Trajectory of a cell at 80 MPa for 5 s on an expanded scale. Scale bar, 2 μm . (B and C) Swimming fraction and speed during the pressurization (circles) and depressurization processes (diamonds). Swimming fractions were based on the number of cells that swam with a speed of $>2 \mu\text{m s}^{-1}$ at each pressure. The speed was the average value of the swimming cells in B. Error bars represent the SD.

$6 \mu\text{m s}^{-1}$ (mean \pm SD, $n = 63$). At 40 MPa, most cells still swam smoothly, but the average speed decreased to $\sim 50\%$ of its initial value at 0.1 MPa. At 60 MPa, many cells still swam, though swimming speed had drastically decreased, and the others just jiggled without showing any translational motion. At 80 MPa, most cells stopped directional swimming and diffused freely in the translational and rotational directions. A limited number of cells seemed to show a rolling motion of their cell bodies.

Fig. 1B and C, summarizes the swimming fraction and speed of the cells during the pressurization and depressurization processes. We selected cells that swam with a speed of $>2 \mu\text{m s}^{-1}$ and calculated both their fraction of all cells in the focal plane and their average speed. Both the fraction and speed decreased with increases in pressure and reached zero at 80 MPa. Both the swimming fraction and speed showed significant hysteresis between the pressurization and depressurization processes, although the cells eventually recovered their initial motility sometime after the pressure was released.

Next, We performed a tethered-cell assay using strain YS1326, which lacks switch-inducing protein CheY and expresses FliC-sticky filaments. A single flagellar filament protruding from each cell was attached to the observation window in the chamber, and the rotation of the cells was tracked under various pressure conditions. Under ambient conditions (0.1 MPa and 23 °C), cells rotated smoothly at an average speed of $5.8 \pm$

3.0 s^{-1} (mean \pm SD, $n = 130$). Fig. 4A and B, shows sequential phase-contrast images of the same single cell at 0.1 and 80 MPa, respectively. The time courses of the rotation speeds of a single cell at 0.1, 40, and 80 MPa are displayed in Fig. 2. The cell still rotated smoothly in the CCW direction, even at 80 MPa.

A systematic analysis was performed to characterize the pressure dependence of the rotational speed of tethered cells. All cells that rotated smoothly before application of pressure were analyzed at each pressure. Fig. 2 displays a pressure-velocity relationship. The rotational speed decreased with increased pressure, but even at 80 MPa, $\sim 80\%$ of motors still rotated at $3.4 \pm 2.6 \text{ Hz}$ (mean \pm SD, $n = 102$), which is $\sim 60\%$ of the initial speed at ambient pressure. Thus, the rotation of each motor was robust under conditions of high pressure. After release of the pressure, some cells ($\sim 10\%$) did not recover to rotate, quite possibly because they had become stuck to the observation window.

Why do *E. coli* cells stop swimming at 80 MPa (Figs. 1 and 2), although their flagellar motors still function? We showed that a single motor, under conditions of lower viscous drag, rotated at $\sim 60 \text{ Hz}$ [3]. In swimming cells, this rotation speed should generate enough torque to propel the cell body. We hypothesize that the application of pressure may prevent filaments (five to six, on average, per *E. coli* cell) from rotating together in a bundle. The long filaments are exposed to water, and in general, hydrostatic pressure enhances the clustering of water molecules around hydrophilic and hydrophobic residues on protein surfaces. In fact, the helical structure of flagellar filaments is known to be sensitive to environmental factors such as temperature, pH, ionic strength, and torsional load. In previous studies, several factors involved in constructing a bundle of rotating filaments have been reported, including the flexibility of the hook and the helical form and surface conditions of the filament. Thus, interference with the ability of flagellar filaments to form coherent bundles provides a plausible explanation for the pressure-induced inhibition of the motility of swimming *E. coli* cells.

4. Conclusions

We present a novel assay that modulates the performance of a molecular machine in situ using high-pressure techniques. Application of pressure is a powerful method for modulating intermolecular interactions between protein and water molecules. This technique could be extended to study the mechanisms by which isolated molecular machines are affected by the application of high pressure.

References

- [1] Y. Sowa and R. M. Berry, *Q Rev Biophys.*, **41** (2008), 103-132.
- [2] M. Nishiyama *et al.*, *Biophys. J.*, **96** (2009), 1142-1150.
- [3] M. Nishiyama and Y. Sowa, *Biophys. J.*, **102** (2012), 1872-1880.

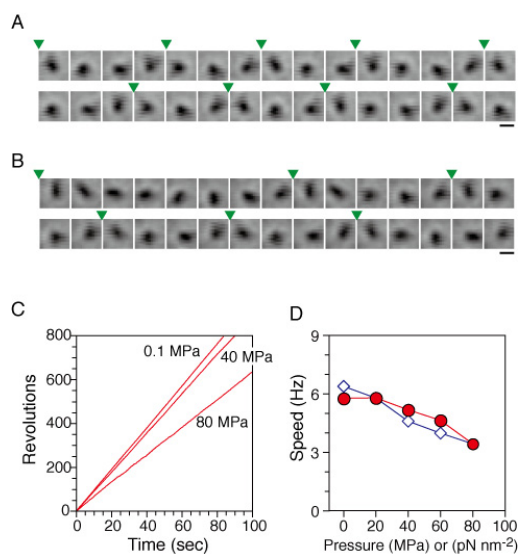


Fig. 2 Torque generation of single flagellar motors in strain YS1326. (A and B) Sequential phase-contrast images of the same rotating tethered cell were taken at every frame. The pressure was 0.1 MPa (A) or 80 MPa (B). Arrowheads indicate completion of a turn. Scale bars, $2 \mu\text{m}$. (C) Time courses of revolutions of the same cell in A and B (CCW positive). (D) Pressure and speed relation in the pressurization (circles) and depressurization processes (diamonds). Data for cells whose motors were stopped were excluded from calculations of speed.

Inactivation Mechanism of Fungal Spores by Atmospheric Pressure Plasma

Takayuki Ohta, Hiroshi Hasizume, Masafumi Ito
Faculty of Science and Technology, Meijo University
1-501 Shiogamaguchi, Tempaku, Nagoya, 468-8502, Japan
tohta@meijo-u.ac.jp

ABSTRACT

A high-density non-equilibrium atmospheric pressure plasma (NEAPP) applied for inactivating fungal spores of *P. digitatum* is introduced as an environmentally safe and rapid-inactivation method. The absolute densities of ozone and ground-state atomic oxygen were measured by using ultraviolet and vacuum ultra violet absorption spectroscopies, respectively. The contributions of ozone, ultra violet radiation and ground-state atomic oxygen in the NEAPP on the inactivation of the spores were investigated by colony count method and plasma diagnostics.

1. Introduction

In agricultural fields and plant protection stations, pesticides are sprayed to protect crops from various insects and viruses. Fungi, such as *Aspergillus* or *Penicillium*, contaminate foods, such as cereals, fruits, vegetables, meats. However, methyl bromide and residual agricultural chemicals (*e.g.*, thiabendazole, imazalil, and ortho-phenylphenol) are harmful to the human body and the environment.

Low-temperature, non-equilibrium atmospheric pressure plasmas (NEAPP), as well as low-pressure plasmas, were applied to inactivation, and showed promise as a very effective system that causes minimal damage to crops, foods, seeds, humans, and the environment. Inactivation factors, such as ultra violet (UV)-C emission, charged species, neutral species, and synergic effects, for various plasma processes from low pressure to atmospheric pressure have been intensively studied. Disinfections of crops, foods and so on by using non-equilibrium atmospheric-pressure plasma as well as low-pressure plasma were also reported. Moreover, they report only performances of disinfection but not the mechanism supported by the quantitative diagnostics of plasmas. Therefore, we investigated the individual effects of the inactivation factors to elucidate the mechanism of the rapid inactivation.

In this talk, a high-density NEAPP applied for inactivating fungal spores of *Penicillium digitatum* is introduced as an environmentally safe and rapid inactivation method. The contributions of ozone and UV radiation in the NEAPP on the inactivation of spores are evaluated using colony count method.[1]-[3] We investigate the inactivation of *P. digitatum* spores using an oxygen radical source that employs a high-density atmospheric-pressure O_2/Ar plasma. The radical source supplies neutral radicals only (*i.e.*, it does not supply charged species or optical radiation). The ground-state atomic oxygen (O) density was measured using vacuum ultra violet (VUV) absorption spectroscopy (AS). The inactivation efficiency of O radical is discussed in terms of the atomic oxygen densities estimated by quantitative analysis of the gas phase.

2. Experimental

Figure 1(a) shows a schematic diagram of the experimental setup containing an oxygen-radical source

based on the NEAPP and a VUVAS optical system. When an alternative current (AC) voltage on the order of kilovolts is applied to the two electrodes, the NEAPP generates high-density electrons of about 10^{16} cm^{-3} . A head with holes installed under the plasma exit aperture of the discharge head blocks charged species and optical radiation so that samples are exposed to only neutral species. The absolute density of ground-state atomic oxygen was measured by VUVAS using a microdischarge hollow cathode lamp (MHCL). To eliminate the influence of atmospheric gases, the chamber containing the radical source was purged with Ar gas. Two ceramic tubes with MgF_2 windows at both ends were employed in the measurements. The exit holes were arranged in a cross; the length of this cross was 6.5 mm, which corresponds to the absorption length [see Fig. 1(b)]. Measurements were performed 10 mm downstream from the filtering head. VUV light from the oxygen-MHCL passed through the MgF_2 window and was introduced into the chamber. The transition lines used for O atoms were $3s^3S^0-2p^4^3P_2$ at 130.217 nm, $3s^3S^0-2p^4^3P_1$ at 130.487 nm, and $3s^3S^0-2p^4^3P_0$ at 130.604 nm.

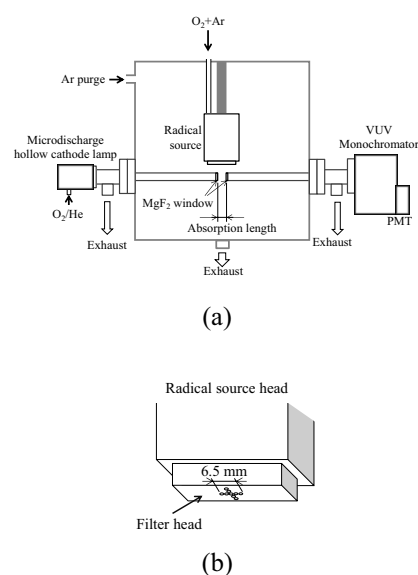


Fig. 1 Schematic diagrams of (a) experimental setup containing oxygen-radical source based on the NEAPP with VUVAS optical system and (b) radical source head.

3. Results and Discussion

The absolute density of ozone in the NEAPP was measured by using UVAS. A deuterium lamp was used as a light source. Ozone has its maximum absorption cross-section of $1.2 \times 10^{-17} \text{ cm}^2$ at a wavelength of 254 nm. The ozone density increased from 2 to 8 parts per million (ppm) with increasing the distance L from electrodes, while the inactivation rate decreased. To evaluate the effect of ozone, we compared the inactivation rate of the NEAPP to that of an ozone generator, which produced ozone with a density of 600 ppm at a flow rate of 5 slm. The number of *P. digitatum* spore survivors after inactivation as a function of the integrated number density of ozone ($N_{\text{O}_3} \times T$), the product of the ozone density (N_{O_3}) multiplied by exposure time (T), is shown in Fig. 2. The D value at a distance L of 10 mm was 1.7 min while that of the ozone generator was 6.1 min. Thus, the D value of this plasma was three times smaller than that of the ozone generator. Moreover, the $N_{\text{O}_3} \times T$ of the ozone generator was approximately two orders of magnitude larger than that of this system. Therefore, the contribution of ozone to inactivation of *P. digitatum* was small. The contribution of neutral radical oxygen species such as O or OH radicals except O_3 , produced through the dissociation of O_2 or H_2O molecules in air, would be large for the rapid inactivation of *P. digitatum*.

Figure 3 shows ground-state atomic oxygen O ($^3P_{j=0,1,2}$) densities and D values as a function of the $\text{O}_2/(\text{Ar}+\text{O}_2)$ flow rate ratio. The O densities were estimated to be between 1.4×10^{14} and $1.5 \times 10^{15} \text{ cm}^{-3}$. The O density increased with increasing $\text{O}_2/(\text{Ar}+\text{O}_2)$ mixture flow rate ratio up to 0.6% and it then decreased with increasing flow rate ratio. Atomic oxygen is generated through the collision of electrons with O_2 gas molecules and its density increases with the addition of O_2 to Ar. However, the further increase in the amount of O_2 leads to the decrease in electron density and the recombination reaction with atomic oxygen and oxygen molecule occurred frequently in the remote plasma region. Therefore, the O density decreased at $\text{O}_2/(\text{Ar}+\text{O}_2)$ mixing ratios of greater than 0.6%. The D value decreased with increasing $\text{O}_2/(\text{Ar}+\text{O}_2)$ mixture flow rate ratio up to 0.6% and increased with increasing flow rate ratio. Since the D value is the inverse of the inactivation rate, these results indicate that the behaviors of the O density correspond to that of the spore inactivation rate.

4. Concluding remarks

We developed a high-density NEAPP and inactivated spores of *P. digitatum*. We investigated the inactivation effects of ozone and the inactivation rate of this plasma was higher than that of an ozone generator using the integrated number density of ozone.

We inactivated *P. digitatum* spores using neutral ground-state atomic oxygen generated by an oxygen radical source employing a nonequilibrium atmospheric-pressure remote O_2/Ar plasma. The ground-state oxygen radical density was measured using

VUV absorption spectroscopy. The density was estimated to be on the order of $10^{14}\text{--}10^{15} \text{ cm}^{-3}$. The behavior of the inactivation rates of *P. digitatum* spores corresponded to that of the O density. Based on these results obtained by quantitative analysis of the gas phase, we conclude that O density is one of the dominant species responsible for inactivating microorganisms.

References

- [1] S. Iseki, T. Ohta, A. Aomatsu, M. Ito, H. Kano, Y. Higashijima, and M. Hori, Appl. Phys. Lett. 96, 153704 (2010).
- [2] S. Iseki, H. Hashizume, F. Jia, K. Takeda, K. Ishikawa, T. Ohta, M. Ito, and M. Hori, Appl. Phys. Express 4, 116201 (2011).
- [3] M. Ito and T. Ohta, and M. Hori, J. Korean Phys. Soc. 60, 937 (2012).

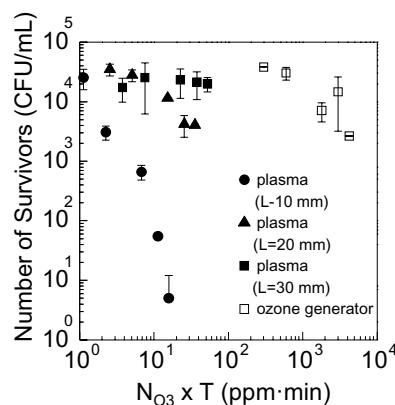


Fig. 2 Number of survivors as a function of integrated number density of ozone.

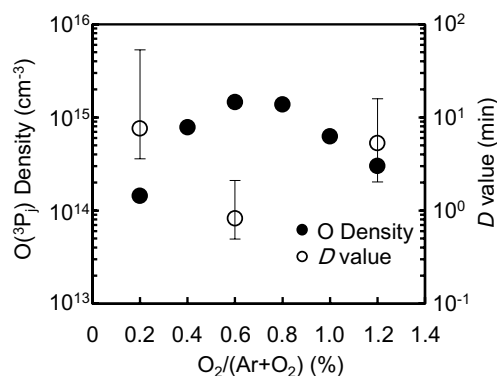


Fig. 3 O density and D value as a function of $\text{O}_2/(\text{O}_2+\text{Ar})$ flow rate ratio.

In-Situ Measurement of Traction Force at Focal Adhesions during Macroscopic Cell Stretching Using an Elastic Micropillar Substrate: Tensional Homeostasis of Vascular Smooth Muscle Cells

Kazuaki Nagayama, Akifumi Adachi, Keisuke Sasashima, and Takeo Matsumoto
Biomechanics Laboratory, Department of Mechanical Engineering, Nagoya Institute of Technology,
Gokiso-cho, Showa-ku, Nagoya 466-8555, Japan.
k-nagaym@nitech.ac.jp.

ABSTRACT

We have investigated the changes in traction force at focal adhesions (FAs) during stretching of aortic smooth muscle cells (SMCs) cultured on elastic micropillar substrates. SMCs were plated on a PDMS-based micropillar array substrate. After cell spreading, the SMCs were stretched and released in their major axis direction, and the deflection of the micropillars were measured simultaneously to obtain the traction force at each FA of SMCs. In some cases, traction forces at both ends of the cells decreased with increase of their strain and *vice versa*. This result may indicate that the SMCs showed active responses to keep their internal tension constant during the macroscopic stretch/release, namely, mechanical homeostatic responses.

1. Introduction

Adherent cells generate traction forces through contraction of the actin-myosin cytoskeleton, and transmit these forces via focal adhesions (FAs) to the underlying extracellular matrix. Cellular traction forces contribute to the mechanical properties [1] and shape stability [2] of cells, and they are believed to play pivotal roles in regulating various cellular functions.

Several studies have been performed to estimate cellular traction forces using flexible substrates. Wang et al. [3] cultured airway smooth muscle cells on a flexible polyacrylamide gel substrate and measured deformation of the substrate to estimate the distribution of cellular traction forces. Tan et al. [4] measured cellular traction forces using polydimethylsiloxane (PDMS)-based elastic substrates with a micropillar array. They showed that the cellular traction force generated at each FA was mainly towards the center of the cells, and that its magnitude was in the order of several 10 nN. However, these studies focused only on the cellular traction forces in a static culture condition. Adherent cells such as vascular smooth muscle cells (SMCs) are dynamically exposed to macroscopic cyclic stretching in the vascular wall *in vivo*. For a detailed quantification of mechanotransduction mechanisms, it is crucial to know dynamic changes in traction force at each FA during macroscopic deformation of cells.

For this purpose, we have developed a technique to measure the dynamic changes in traction forces at each FA during macroscopic stretch of the cells by stretching the micropillar array substrate under a microscope stage. We have further established a micropatterning technique to align the direction of the cell on the pillars parallel to the stretch direction, and adapted it to our cell stretching protocol. We then cultured porcine aortic SMCs on the micropillar array substrate, performed a loading/unloading test repeatedly for SMCs aligned in the stretch direction, and investigated the mechanical response of SMCs.

2. Method

Porcine aortic SMCs were used as the test model. PDMS micropillar substrates were fabricated by replica-molding [4] as previously described [5]. We used a hexagonal arrangement micropillar array whose pillar diameter, length, and center-to-center spacing were 3, 9, and 9 μm , respectively (Fig. 1A). The PDMS micropillar array substrate ($t = 1\text{ mm}$) was glued to the bottom of a rectangular silicone rubber frame (Fig. 1B). In order to align SMCs to the stretch direction, we

adjusted the adhesion region of the micropillar substrate using the following method: we attached a metal specimen grid for transmission electron microscopy with rectangular openings (Ni 100/400, VECO, Fig. 1C) firmly to the surface of a PDMS sheet ($t = \sim 2\text{ mm}$). We poured a fibronectin solution onto the PDMS sheet through the holes of the grid, air-dried them, and then peeled off the grid from the PDMS sheet. We then adjusted the long axis direction of the fibronectin-coated area of the PDMS sheet to the stretch direction, and attached the coated surface onto the top of the pillars to make the rectangular adhesion regions (Fig. 1D). We plated SMCs sparsely onto the pillars for $\sim 6\text{ h}$. SMCs elongated within the rectangular area and aligned in the stretch direction.

A cell stretching apparatus (STB-150, Strex, Japan) set on the stage of an inverted microscope was used. We modified the apparatus so as to stretch cells symmetrically using a mechanism with wires and pulleys (Fig. 2). By using this mechanism, we could observe the same cell continuously in the chamber during stretching under a 40x objective [6].

SMCs on the pillars in the culture chambers were set on the stretching apparatus. Cells were then stretched by stretching the substrate incrementally by 0.3% every 15 s and then unloaded in a similar manner. The cells and their neighboring pillars were observed with a CCD camera connected to the microscope. Deflection of pillars was measured on the recorded images with multiparticle tracking software (G-track, G-angstrom, Japan). The two-dimensional Gaussian fitting

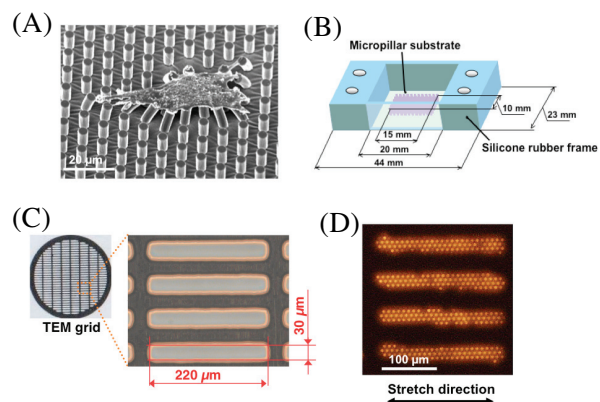


Fig. 1 Scanning electron micrograph of a substrate with a micropillar array and SMCs spread on top of the micropillars (A). Cell culture chamber with a micropillar substrate for macroscopic stretching (B). TEM grid for micropatterning of cells (C). A typical image of micropillars whose top ends have been coated with fibronectin (D).

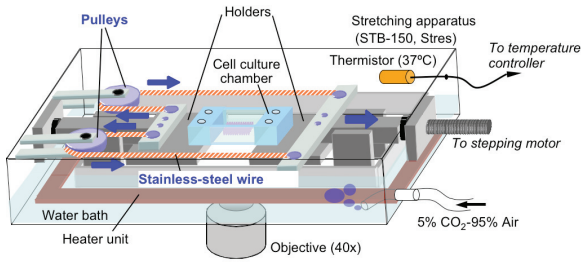


Fig. 2 Schematic representation of the main part of the apparatus used to stretch the cell culture chamber. A symmetric stretching mechanism consisting of wires and pulleys was added to the original stretching apparatus [7].

was used to determine the position of the pillars in the software. Displacement of the pillar tip from its unloaded position was used as its deflection δ . Traction forces at the pillars F were determined using the simple equation $F = k\delta$, where k is the spring constant of the micropillars. The spring constant of the pillars k was obtained from the Young's modulus of the substrate (1.6 MPa) and the pillar geometry, and was 26 nN/ μm . We also measured the strain of the substrate in the stretch direction as the whole-cell strain ϵ_{cell} . In this study, we stretched cells from $\epsilon_{\text{cell}} = 0$ to 3% three times (Cycles 1-3) and then from $\epsilon_{\text{cell}} = 0$ to 6% three times (Cycles 4-6).

3. Results and Discussion

The change in the average value of traction force at both side regions of SMCs varied from cell to cell (Fig. 3A), and was roughly classified into two types of responses: synchronous and asynchronous. In the synchronous group, the average force increased and decreased in synchronization with the applied strain ϵ_{cell} (Cell 1-4), and in the asynchronous group, the force was almost independent from ϵ_{cell} (Cell 5-8). The peak force in each cycle was larger in Cycles 4-6 than in Cycles 1-3 for the synchronous group, while in the asynchronous group the force tended to be constant among all cycles. The force in the asynchronous group looked smaller than that of the synchronous group, and it was slightly in anti-phase with the strain in some cases (Fig. 3A, arrows). SMCs looked contracted and elongated following stretch/release cycles in the synchronous and asynchronous groups, respectively (Fig. 3B and C).

We also investigated the changes in the average value of traction force at $\epsilon_{\text{cell}} = 0$, which represents the cell pretension applied to each pillar at both side regions of SMCs, and in the cell area at $\epsilon_{\text{cell}} = 0$ in both groups. A larger pretension was observed in the synchronous SMCs, and the cell area tended to decrease with the number of stretch/release cycles. In contrast, pretension was lower in the asynchronous SMCs, and the cell area increased with the number of stretch/release cycles (data not shown). The detailed mechanisms of these opposite phenomena are unclear at this stage. It has been pointed out that the Rho GTPase family is activated by mechanical stretching, and that it regulates actin dynamics which are implicated in cell contraction and elongation [8]. The activated level of Rho GTPase plays a role in determining cell contraction and elongation [9]. These findings indicate that the activation level of Rho GTPase may also affect the elongation and contraction of SMCs during the stretching/release cycles and that it switches the mechanical responses of SMCs.

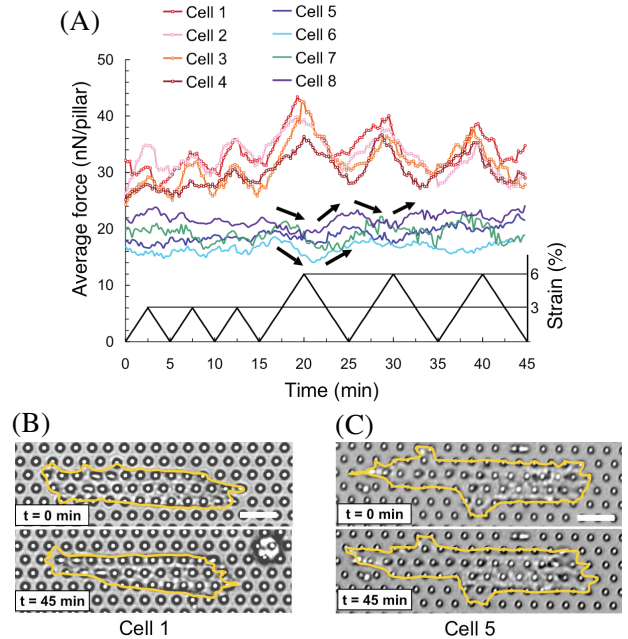


Fig. 3 Time-course changes in the average value of traction force at FAs of both side regions of SMCs (A) during stretch and release cycles, and typical images of SMCs in the synchronous and asynchronous groups (B and C, respectively) before (upper) and just after (lower) the stretch and release tests. Bars = 20 μm . Dark yellow lines in B and C represent the outlines of cells.

4. Concluding remarks

We established a novel experimental technique to measure dynamic changes in traction forces at FAs of cells during macroscopic stretching and release in their longitudinal direction, and investigated the mechanical response of SMCs. We found that SMCs showed two types of responses: the traction force changed in phase with the applied strain in some cells (synchronous group), while they were almost independent in the other cells (asynchronous group). We also found that SMCs sometimes exhibit active homeostatic responses to keep their pretension constant during macroscopic stretching, and such tensional homeostatic responses may occur concurrently with cell elongation.

Acknowledgement

Supported in part by KAKENHI from JSPS, Japan (nos. 24650257, and 24680051 to K.N., and nos. 22127008 and 22240055 to T.M.) and Tatematsu Foundation, Japan (K.N.).

References

- [1] S. Suresh, *Acta Biomater.* 3-4 (2007), 413-438.
- [2] R. Satcher et al, *Microcirc.*, 4 (1997), 439-453.
- [3] N. Wang et al, *Am. J. Physiol. Cell Physiol.* 282-3 (2002), 606-616.
- [4] J.L. Tan et al, *PNAS*, 100-4 (2003), 1484-1489.
- [5] K. Nagayama and T. Matsumoto, *Cell. Mol. Bioeng.* 4-3 (2011), 348-357.
- [6] K. Nagayama et al, *J. Biomech.* 44-15 (2011), 2699-2705.
- [7] K. Nagayama et al, *J. Biomech. Sci. Eng.* 7 (2012), 130-140.
- [8] D. Riveline et al, *J. Cell Biol.* 153-6 (2001), 1175-1186.
- [9] Y. Arakawa et al, *J. Cell Biol.* 161-2 (2003), 381-391.

Biophysical regulation of pro-inflammatory signaling under mechanical stimuli

Authors names: Shinji Deguchi

Affiliation and address: Department of Bioengineering and Robotics, Tohoku University
6-6-01 Aramaki-aoba, Sendai, Japan
Email: deguchi@bml.mech.tohoku.ac.jp

ABSTRACT

Here we investigated the effect of an imidazole-based buffer when the ionic strength was changed across a physiological range. Our results demonstrated that the use of buffers with low ionic strengths produces extracted stress fibers that are more intact with regard to structure and function. Using the extracted stress fibers, we showed a homeostatic regulation present in adherent cells. This homeostatic balance may be necessary for suppression of chronic pro-inflammatory signaling in individual cells.

1. Introduction

Stress fibers play a key role in regulation of tensional homeostasis and inflammatory signaling [1,2]. Nonmuscle myosin II (NMII), the main constituent of stress fibers, is considered to be essential to their function. Samples obtained by homogenization of cells into fragments may obscure properties specific to stress fibers. Our group has used individual stress fibers extracted from cells to overcome this problem [3,4]. Phosphate buffer solutions are generally used in the extraction procedure to wash the samples. The ionic strength of the buffers used is typically within the physiological range (i.e., ~150 mM). Ionic strength, which is a function of the concentration of all ions present, generally affects protein function and stability; however, its effect on extracted stress fibers has not been investigated in previous studies.

In our earlier studies, we prepared alternative wash buffers using imidazole [5–7]. Imidazole is a cationic buffer used within the physiological intracellular pH range. Here we investigate the effect of an imidazole-based buffer when the ionic strength was changed from 90 to 490 mM. Our results demonstrated that the use of buffers with low ionic strengths produces stress fibers that are more intact with regard to structure and function. The roles of stress fibers and focal adhesions in avoidance of chronic pro-inflammation are also discussed based on the present results.

2. Materials and method

A7r5 rat embryonic aortic smooth muscle cell lines (ATCC, CRL-1444) were cultured in DMEM (Invitrogen) supplemented with 10% FBS (JRH Biosciences) and 1% penicillin–streptomycin (Invitrogen) in a 5% CO₂ incubator at 37°C. TEA solution used for extraction of stress fibers contained 2.5 mM triethanolamine (Wako), 1 mM DTT, 1 µg/ml leupeptin, and 1 µg/ml pepstatin (Peptide Institute). Wash buffers containing 20 mM imidazole (MP Biomedicals), 2 mM EGTA (Dojindo), and 2.2 mM MgCl₂ (pMg 2.7) were adjusted to an ionic strength of 90, 100, 123, 170, 250, 330, 410, or 490 mM at pH 7.2 by the addition of KCl and HCl. The activation buffer containing 20 mM imidazole, 2 mM EGTA, 2.0 mM MgCl₂ (pMg 2.7), 1 mM ATP (Wako), and 2.0 mM CaCl₂ (pCa 4.5) was adjusted to an ionic strength of 94

mM at pH 7.1 by the addition of KCl and HCl. These different ionic strengths cannot be accurately achieved by simply adding water to the solutions. The buffers were prepared considering all the metal ions and ligands present and their equilibrium constants.

Ventral stress fibers were extracted from A7r5 cells based on a previously described method [5]. In brief, cells were washed twice with cold PBS and deroofed by repeated exposure to ice-cold TEA solution. The extracted stress fibers were incubated in wash buffer with an ionic strength of 90, 100, 123, 170, 250, 330, 410, or 490 mM at 4°C for 24 h. F-actin in the extracted stress fibers was stained with 3 nM Alexa 488–phalloidin for 1 min and observed under a microscope (IX-71; Olympus) equipped with a camera (ORCA-R2; Hamamatsu Photonics)

The extracted stress fibers were incubated in wash buffer with an ionic strength of 90, 123, 170, 250, 330, 410, or 490 mM at 4°C for 24 h. For SDS-PAGE, the extracted stress fibers and cells were solubilized in SDS sample buffer, boiled for 5 min, and fractionated on 10% polyacrylamide gels. Equal amounts of total protein (5 µg) were loaded in each lane. Gels were stained with Coomassie Brilliant Blue G-250 (CBB; Bio-Rad Laboratories). Samples were transferred onto polyvinylidene difluoride membranes (Millipore) for immunoblotting. Membranes were incubated with an antibody against non-muscle MIIA, non-muscle MIIB, smooth muscle myosin, α -actinin, fascin, α -smooth muscle actin, β -actin, myosin light chain, and MLC phosphorylated at serine 19. The primary antibodies were detected using HRP-conjugated goat anti-mouse and goat anti-rabbit secondary antibodies and enhanced chemiluminescence.

3. Results and Discussion

The extracted stress fibers were observed using phase-contrast microscopy (PM), fluorescence microscopy (FM), and EM (Fig. 1). PM revealed extracted stress fibers with a sharp and straight morphology at an ionic strength of 90 mM. Furthermore, stress fibers with this morphology were found only at ionic strengths below 250 mM, and this morphology was absent at high ionic strengths. The SF outlines became less defined as the ionic strength was increased, and at more than 410 mM they were barely observed.

Particularly straight actin filaments labeled with fluorescent phalloidin were observed by FM at an ionic strength of 90 mM. As the ionic strength increased, the fluorescent actin bundles exhibited a wavy pattern rather than a straight morphology, and appeared thicker in width. The waviness of the actin bundle was particularly prominent at an ionic strength of 490 mM. EM showed that at an ionic strength of 90 mM, isolated stress fibers displayed a tightly packed structure with several filamentous constituents bundled together. As the ionic strength increased, the bundles became looser with larger distances between the components. At the highest ionic strength examined (490 mM), the continuous arrangement of straight filamentous constituents was no longer found, but rather, loosely packed, punctuate patterns were observed along the length of the isolated stress fibers.

SDS-PAGE was performed to examine the effects of varying ionic strength on the composition of extracted stress fibers (Fig. 2). In comparison to whole cell lysates, the extracted stress fibers contained a darker band around 42 kDa, which corresponds to actin. Because samples containing equal amounts of total protein were loaded in each lane, the relative amounts of actin were higher in stress fibers than in whole cells. A distinct decrease in band intensity was observed at approximately 75 kDa in CBB-stained gels as the ionic strength increased from 90 to 490 mM. A total of 8 proteins (NMIIA, NMIIB, SMM, α -actinin, fascin, α -SMA, β -actin, and MLC) were identified by immunoblotting. Fascin, a globular F-actin cross-linking protein that is essential for filopodia formation, was only present in whole cell lysates, suggesting that the material we extracted from cells was indeed stress fibers and not actin bundle filopodia. The expression levels of all proteins, except α -actinin, were comparable regardless of the ionic strength. Two different antibodies (monoclonal and polyclonal) were used to detect α -actinin, and similar decreases with an increase in ionic strength were detected. High levels of monophosphorylated MLC (pMLC) were detected at ionic strengths greater than 330 mM, whereas it was barely detectable at ionic strengths of 170 and 250 mM.

4. Concluding remarks

We investigated the effects of varying the ionic strength of buffers on stress fibers extracted from cells. Light microscopy and EM revealed that stress fibers possessed more straight packed bundles at low ionic strengths that lost contractility completely when treated with high ionic strength buffers for a long period. These results suggest that the extracted stress fibers are more intact with regard to structure and function at low ionic strengths. The present study thus provides practical methodological information and tools for investigations regarding mechanisms of pro-inflammatory signaling.

Acknowledgments

The author would like to thank Tsubasa S. Matsui, Daiki Komatsu, Roland Kaunas, Akira C. Saito, Hitomi

Onodera, Yuka Minegishi, and Masaaki Sato for their contributions to this study. This work was supported in part by Grants-in-Aid from the Ministry of Education, Culture, Sports, Science, and Technology of Japan (Nos. 21680039 and 22650098) and JST Special Coordination Funds for Promoting Science and Technology.

References

- [1] R. Kaunas and S. Deguchi, *Cell. Mol. Bioeng.*, **4** (2010), 182-191.
- [2] S. Deguchi, et al., *Cytoskeleton*, **68** (2011), 639-651.
- [3] S. Deguchi, et al., *Mol. Cell. Biomech.*, **2** (2005), 125-134.
- [4] S. Deguchi, et al., *J. Biomech.* **39** (2006), 2603-2610.
- [5] T.S. Matsui, et al., *Biochem. Biophys. Res. Comm.* **395** (2010), 301-306.
- [6] T.S. Matsui, et al., *Interface Focus* **1** (2011), 754-766.
- [7] S. Deguchi, et al., *J. Cell. Biochem.*, **113** (2012), 824-832.

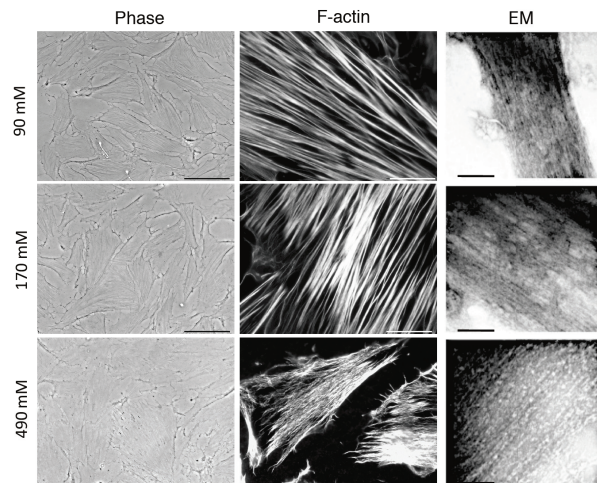


Fig. 1 The effects of changing the ionic strength of buffers on extracted stress fibers. PM (Phase), FM (F-actin), and EM images are shown. Scale bars: Phase, 50 μ m; F-actin, 20 μ m; EM, 200 nm.

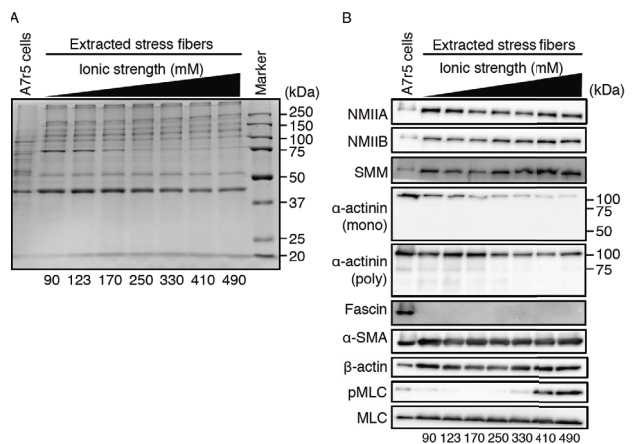


Fig. 2 Comparison of protein concentrations. (A) CBB-stained SDS-PAGE and (B) western blot analyses of whole cell lysates and extracted stress fibers.

Cyclic Stretch Recovers Ischemic Damage in Myoblasts

Takeru Naiki*, Satoko Fujii**, Kozaburo Hayashi*

*Department of Biomedical Engineering, Okayama University of Science, 1-1 Ridai-cho, Kita-ku, Okayama, Japan

**Oshu Corporation, 1-1 Nakamachi, Naka-ku, Hiroshima, Japan

tnaiki@bme.ous.ac.jp

ABSTRACT

To know the mechanisms of the muscle hypertrophy induced by Kaatsu training, the effects of hypoxia, cyclic stretch, growth hormone, and growth factors on the proliferation of cultured myoblasts were studied. The results obtained showed that the proliferation rate of myoblasts decreased soon after short-term hypoxia; however, the cyclic stretch of 10% strain increased the rate during hypoxia. On the other hand, there were no significant effects of growth hormone and growth factors. These results suggest that moderate training enhances cell proliferation during the recovery process from damages induced by hypoxia.

1. Introduction

Strength training with low load in combination with vascular occlusion, named Kaatsu training, increases muscular size and strength similarly to conventional, heavy training. Vascular occlusion which reduces muscular blood flow is induced with tourniquet cuffs installed at the proximal ends of the limbs. It has been shown that under the vascular occlusion, even low intensity (20 ~ 30% of maximum strength) training increases muscular strength and volume to the level seen after conventional heavy (over 80% of the maximum strength) training. During vascular occlusion, veins are completely collapsed. Venous occlusion is considered to induce the opening of capillaries, hypoxia, the accumulation of lactate, and acidosis in muscles. During exercise, acetylcholine and norepinephrine released from motor nerves and sympathetic nerves, respectively, contract muscle. Satellite cells are exposed to cyclic stretch. Nutrition in muscle should decrease, and cellular metabolism may change. Endoplasmic reticulum stress may increase. IGF, FGF, PDGF, and reactive oxygen species should be produced in muscle, and growth hormone may be secreted from hypophysis. After the reopening of the occluded vessels, oxidized blood flows into muscle, ischemia/reperfusion may induce cellular damages, and growth hormone should be perfused into muscle. Like these, a lot of phenomena occur during training under vascular occlusion.

However, the mechanisms of the increased muscular mass and strength by the occlusion training are not clear, although several candidates have been proposed. It has been suggested that growth hormone and several growth factors contribute to this. Although the reduction of blood flow (hypoxia and reperfusion) is also considered to contribute to the phenomena, the details of the effects are not known well. Moreover, the effects of cyclic stretch are not much studied.

The studies of training and exercise have been performed in human body. However, it is difficult to know the relationships between each factor and muscle

hypertrophy from human experimentation. Thus, we are doing in vitro cell culture experiments using to know the effects of each factor on cell proliferation without the influence of the other factors. Here, we studied the effects of hypoxia, growth hormone, several growth factors, and cyclic stretch on the proliferation rate of cultured myoblasts, which was used as a model of activated satellite cells.

2. Method

Myoblasts cell line (H9C2) was used as a model of activated satellite cells which differentiate into myotubes and myocytes. Myoblasts were cultured in culture dish (60 mm in diameter, Primaria, BD Falcon) with commonly used cell culture methods, using DMEM (D-5648, Sigma) which includes 4,500 mg/L of glucose, 10% fetal bovine serum, 100 U/mL of penicillin, and 0.1 mg/mL of streptomycin.

Growth hormone (Genotropin, Pfizer) having the concentration of 40 ng/mL was used; this concentration is the maximum level measured during Kaatsu training.

IGF (100-34, Shenandoah Biotechnology), PDGF (100-18, Shenandoah Biotechnology), and TGF- β (100-109, Shenandoah Biotechnology) having the concentrations of 2 ng/mL, 2 ng/mL, and 0.1 ng/mL, respectively, were also used. These concentrations were twice as much as ED₅₀; however, there are no data of their concentrations in muscle during Kaatsu training.

After 24 hours from seeding myoblasts on a culture dish, the number of cells in a dish was measured by using 2 mL of AlamarBlue (BUF012, Serotec) medium. Then, the culture medium was replaced by 4 mL of glucose free DMEM (D-5030, Sigma). Cells were exposed to hypoxia (2% O₂) for 1 hour in a multi-gas incubator. The glucose free medium was used to simulate a low-nutrition condition, and was put into a multi-gas incubator (hypoxia condition) for more than 24 hours before use. Then, the culture medium was replaced by 4 mL of the normal glucose included medium, and cells were put into a normoxia incubator.

At 24 hours after the onset of hypoxia, the number of cells was measured to see cell proliferation rates.

To study the effects of growth hormone and growth factors on the proliferation of myoblasts, cells were incubated with growth hormone, IGF, PDGF, or TGF- β for 72 hours. The numbers of cells were measured just before the administration, and 24, 48, and 72 hours after.

To study the cross-effects of hypoxia, growth hormone, and growth factors, the cells were first cultured in the glucose free medium and exposed to hypoxia for 1 hour. Then, the culture medium was replaced by the normal medium mixed with growth hormone, IGF, PDGF, and TGF- β , and then the cells were cultured in the normoxia condition (mixture condition). The cell numbers were measured before hypoxia, and 24, 48, and 72 hours after.

To study the effects of cyclic stretch under the hypoxia condition on the proliferation rate, myoblasts were cultured on the surface of silastic stretching chambers (Strex) which was made with a silicon elastomer (Sylgard 184). After 24 hours from seeding, the number of cells was measured. After replacing the medium by the glucose free medium, the chamber was set into a stretch machine (STB-140, Strex). It was placed in the multi-gas incubator (2% O₂), and cyclic stretch was applied to cells. The maximum strains of 10 and 18% with the minimum strain of 0% were applied to the cells at the cyclic frequency of 0.5 Hz; these strains were selected as a normal strain and an abnormal large strain, respectively. After 1 hour exposure to hypoxia and cyclic stretch, the culture medium was replaced by the normal medium. Then, the cells were cultured under a normoxia condition without cyclic stretch. The cell number was measured at 24 hours after.

In every experiment, control cells were prepared from the same root cells, seeded on the same material as that used for the experimental group, and cultured under a normoxia condition in the normal medium without cyclic stretch.

The cell number in a dish was measured by using AlamarBlue by the procedure mentioned below. The medium was replaced by the medium containing 10% of AlamarBlue. Then, the cells were incubated at 37°C for 2 hours. The medium was sampled in a cuvette. And the fluorescence intensity of the medium was measured at the excitation wavelength of 545 nm and the emission wavelength of 590 nm. This fluorescence intensity is proportional to cell number. The ratios of the intensities during 0 to 24 (I_{24}/I_0), 24 to 48 (I_{48}/I_{24}), and 48 to 72 (I_{72}/I_{48}) hours were calculated as proliferation rates. The relative proliferation rates were obtained by dividing the proliferation rates by that of each control cells to know the effects of each stimulus.

3. Results and Discussion

Hypoxia significantly decreased the proliferation rate of myoblasts during 24 hours. This result indicates that myoblasts were damaged by hypoxia and reperfusion.

There were no significant differences in proliferation rate between the control cells and the cells cultured with growth hormone, PDGF, IGF, or TGF- β .

The study of the cross-effects of hypoxia, growth hormone, and growth factors, indicated that at 24 hours the proliferation rate of the cells under the mixture condition was similar to that under the hypoxia condition. However, the proliferation rate increased between 24 and 72 hours.

The cyclic stretch of 10% strain at 0.5 Hz frequency during hypoxia significantly increased the relative proliferation rate within 24 hours (Fig. 1). On the other hand, the cyclic stretch of 18% strain increased damage.

4. Concluding remarks

The results from the present study suggest that activated satellite cells are damaged by hypoxia and reperfusion, and that the proliferation rate was increased by the recovery from the damage after more than 24 hours. Furthermore, the moderate training with 10% cyclic strain enhances cell proliferation during the recovery process.

Acknowledgements

This work was supported in part by Grant-in-Aid for Scientific Research (C) (21500641) from Japan Society for the Promotion of Science.

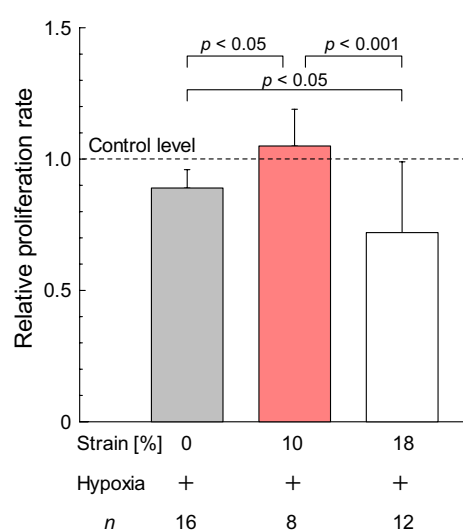


Fig. 1 Effects of cyclic stretch on the relative proliferation rate of myoblasts. ANOVA with Fisher's LSD test, Mean + S.D.

The Enhancement of C₂C₁₂ Myoblast Cell Growth on Modified Polylactide Surface Using a Highly Efficient Two-step Atmospheric Pressure Plasma Treatment Procedure

Yi-Wei Yang¹, Chih-Tung Liu¹, Guo-Chun Liao¹, Ming-Hung Chiang¹, Jane-Yii Wu² and
Jong-Shinn Wu^{1*}

¹Department of Mechanical Engineering, National Chiao Tung University, 1001 Ta-Hsueh Road, Hsinchu, Taiwan

²Department of Bioindustry Technology, Da Yeh University, Changhua, Taiwan

*E-mail: chongsin@faculty.nctu.edu.tw

ABSTRACT

In this paper, we report the development of a two-step nitrogen-based dielectric barrier discharge (DBD) plasma treatment procedure using the post-discharge region for facilitating amine functional group incorporation on polylactide (PLA) surface under atmospheric pressure condition. Treated PLA surface exhibits almost the same cell growth capability for C₂C₁₂ cells as gelatin coating method, but with a much reduced preparation time: from 10-12 hours down to 5-15 minutes. The result of ATR-FTIR and XPS analysis confirms amine functional group incorporation and shows improved N1s concentration (~10.6%), respectively.

1. Introduction

Non-thermal plasma treatment has been considered as one of the promising approaches to modify surface properties efficiently. It has been applied especially to polymers, which can not resist high temperature. The capabilities, including incorporation of functional groups, enhancement of surface energy, tailoring surface roughness and increasing wettability, have been demonstrated and widely studied [1][2]. It was shown that low-temperature plasma can be efficiently used to promote cell attachment, owing to that amine functional groups can covalently couple with biological ligands to provide receptor-ligand interaction [3][4]. However, most of these were operated in low-pressure environments, which are often costly and inconvenient in practice.

Recently, non-thermal atmospheric-pressure plasma (APP) has attracted great attention in modern science and technology development. Its advantages include: 1) low cost because of no need for expensive vacuum equipment, and 2) convenient and efficient operation under atmospheric condition. However, it was found that only low amount of amino functional group could be incorporated using atmospheric-pressure plasma [5][6], which may hinder its modification effectiveness.

In the current study, we propose a two-step atmospheric-pressure plasma treatment procedure to enhance incorporation of amine functional groups into PLA surface for facilitating cell attachment and proliferation with a much reduced preparation time. Its effectiveness is compared with that of gelatin coating method.

2. Method

In our experiment, the plasma treatments were carried out by two steps in sequence: 1) Pretreatment plasma treatment, to pretreat the surface using the N₂ DBD jet with 0.1% addition of O₂; and 2) Ammonia plasma treatment, to incorporate amine functional groups using N₂ with 5% of NH₃ plasma. In addition, a single axis moving plate was placed under the DBD to provide different plasma exposure time by controlling the number of passes. The characteristics of PLA films

before and after treatments were determined by surface energy, ATR-FTIR (BRUKER, TENSOR 27), XPS (ESCA PHI 1600) and AFM (D5000) analyses. Furthermore, we chose the C₂C₁₂ as test cells. the cell morphology, attachment and proliferation were conducted by cell culture, Inverted contrasting microscope observation (Leica, DM IL) and MTT assay, respectively.

3. Results and Discussion

Figure 1 shows the number of cells and activity of mitochondria by MTT assay. Cell attachment test shows that OD using the two-step plasma treatment is two times larger than the pure PLA sample, at the 24th hour of cell culture. Note the magnitude of OD correlates with the number of healthy cells per unit area. In the cell proliferation test, after three days, OD using the two-step plasma treatment is always much greater than that using the pure PLA. Moreover, OD using the two-step plasma treatment is always slightly higher than that of gelatin coating method during three-day period. The result of Inverted contrasting microscope observation is consistent with those of MTT assay (not shown here). Thus, we could conclude that better cell attachment and proliferation using the two-step plasma treatment could be obtained as compared to pure PLA without any treatment. In addition, the two-step plasma treatment can compete with and even better than gelatin coating method in terms of its effectiveness in cell attachment and proliferation.

ATR-FTIR measurement shows that intensity of NH₂ deformation (wavenumber: 1604) and NH stretch (wavenumber: 3200) increase after two-step plasma treatment, which confirms successful amine functional group incorporation. XPS analysis shows that N1s concentration, which represents the amount of amine functional group, can increase up to 10.6% with the proposed two-step plasma treatment that is much greater than that of pure PLA (0%). Figure 2 shows the results of AFM analysis. After two-step plasma treatment, PLA surface performs higher surface roughness (73.22 nm) as compared to that of pure PLA (0.88 nm). Figure 3 shows result of Surface energy analysis. It indicates that Polar

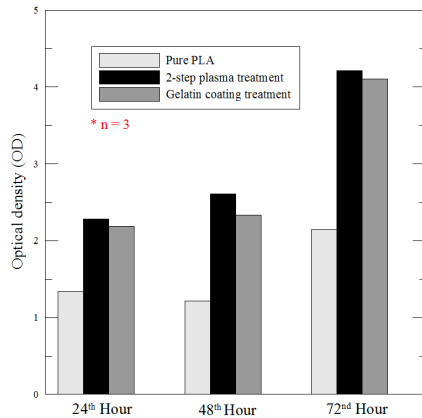


Figure 1 Optical Density (OD) of cells on pure, gelatin coated and 2-step plasma treated PLA films for a three-day test period.

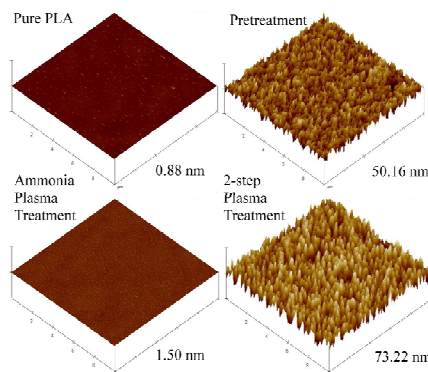


Figure 2 AFM analysis of pure and plasma treated PLA films.

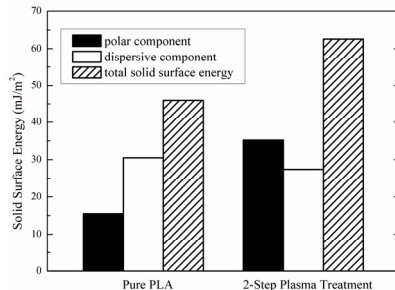


Figure 3 Surface energy analysis under pure and 2-step plasma treated PLA surface

component attributes to major increase and the total solid surface energy increases from 46 to 62.6 mJ/m² with applying two-step plasma treatment.

The most critical contribution to the enhanced cell growth on two-step plasma treated PLA should be the high amount of amine functional groups, which can covalently couple with the ligands from culture medium. Cells exhibit high affinity to a hydrophilic surface. After cells contact the surface, the integrins on cell membrane can further react with the ligands and transduce signal for cell to attach and proliferate on the surface. In addition, cells prefer to adhere on the surface having high surface energy [7], especially with a high polar component [8] and to migrate on rougher surface [9], which is beneficial to cell proliferation. These surface chemical and physical properties obtained by the two-step plasma treatment on

a PLA surface are all in favor of cell growth as we have observed in the current study. They may explain the reasons that the effectiveness of two-step plasma treatment can compete with and even better than that of gelatin coating method.

The comparison of preparation duration between the two-step plasma treatment and gelatin coating treatment is discussed next. The plasma exposure time of the former treatment equals to 8 seconds, but the realistic preparation includes setting up and removing samples on a moving stage and other necessary operations, among others. It could end up with 5-15 minutes. On the other hand, the latter treatment takes about 10 to 12 hours at least. Obviously, the preparation for the proposed two-step plasma treatment is much faster than that of gelatin coating treatment.

4. Concluding remarks

In this paper, a two-step plasma treatment procedure using the post-discharge jet region of a parallel-plate, nitrogen-based DBD is proposed. After applying the two-step plasma treatment, N1s, surface energy and surface roughness are improved very effectively to 10.6%, 62.6 mJ/m² and 73.22 nm, respectively. These modified surface properties are confirmed to be very beneficial in improving cell attachment and proliferation on PLA surface for mouse myoblast muscle cells (C₂C₁₂). In comparison with the gelatin coating method, the proposed two-step plasma treatment procedure can produce a PLA surface with almost the same (or even better) capability of cell growth for muscle cells, but with a much reduced time (5-15 minutes vs. 13-15 hours).

References

- [1] K.G. Kostov, A.L.R. dos Santos, R.Y. Honda, P.A.P. Nascente, M.E. Kayama, M.A. Algatti, *Surf. Coat. Tech.*, **204** (2010), 3064-3068.
- [2] M.L. Stee, L. Hymas, E.D. Havey, N.E. Capps, D.G. Castner, E.R. Fisher, *J. Membrane. Sci.*, **188** (2001), 97-114.
- [3] D.W. Huttmacher, T. Schantz, I. Zein, K.W. Ng, S.H. Teoh, K.C. Tan, *J. Biomedmater. Res.*, **55** (2001), 203-216.
- [4] K. Webb, V. Hlady, P.A. Tresco, *J. Biomed. Mater. Res.*, **41** (1998), 422-430.
- [5] H. Mortensen, Y. Kusano, F. Leipold, N. Rozlosnik, P. Kingshott, S. Goutianos, *Jan. J. Appl. Phys.*, **45** (2006), 8506-8511.
- [6] C.P. Klages, A. Grishin, *Plasma. Process. Polym.*, **5** (2008), 368-376.
- [7] J.M. Schakenraad, H.J. Busscher, C.R.H. Wildevuur, J. Arends, *J. Biomed. Mater. Res.*, **20** (1986), 773-784.
- [8] J. Comelles, M. Estévez, E. Martínez, J. Samitier, *Nanomed. Nanotechnol.*, **6** (2010), 44-51.
- [9] J.F. Nagle, S. Tristram-Nagle, *Biophys. Acta.*, **1469** (2000), 159-195.

Traction Force Measurement of Sheared Endothelial Cells by Using Micropillar Substrate

Toshiro Ohashi¹, Yusaku Niida², Masaaki Sato³

¹Faculty of Engineering, Hokkaido University, Kita 13, Nishi 8, Kita-ku, Sapporo, Hokkaido 0608628, Japan

²Graduate School of Engineering, Hokkaido University, Kita 13, Nishi 8, Kita-ku, Sapporo, Hokkaido 0608628, Japan

³Graduate School of Biomedical Engineering, Tohoku University, 6-6-01 Aramaki-Aoba, Aoba-ku, Sendai 9808579, Japan

ohashi@eng.hokudai.ac.jp

ABSTRACT

Vascular endothelial cells (ECs) not only demonstrate elongation and orientation but also change physiological functions in response to blood flow. Cellular traction forces are involved in the cellular mechanical environment in particular when cells attach to their substrates and migrate. It is speculated that cellular traction forces could be dynamically associated with the EC remodeling process. In this study, we have newly developed a flow-imposed device with an array of elastomeric micropillars that allows to monitor traction forces. The results suggest that changes in traction forces might be attributable to loss of intercellular junctions.

1. Introduction

Vascular endothelial cells (ECs) exposed to fluid shear stress exhibit marked elongation and orientation to the direction of flow as well as development of thick stress fibers [1]. Cellular traction forces come from contractile forces by the acto-myosin machinery are in particular generated when cells attach to their substrates and migrate. We hypothesize that cellular traction forces could be dynamically associated with the EC remodeling process. In order to measure traction forces, we have developed a newly designed flow-imposed device with arrays of elastomeric micropillars (3 μm in diameter and 10 μm in height). In this study, traction force distributions in GFP-tagged ECs in a monolayer under fluid flow are measured in a spatial and a temporal manner.

2. Method

Bovine aortic endothelial cells (BAECs) were cultured in Dulbecco's modified Eagle Medium with 10% fetal bovine serum and maintained in 5% CO₂ at 37°C. Cells were transfected with pmaxGFP Vector using Nucleofection 2 (Amaxa, USA) were plated in fibronectin coated micropillar substrate at a 25,000 cells/cm² and cultured until reaching confluence (1 - 2 days after seeding). A steady shear stress of 2 Pa was applied for 24 h to Cells using a parallel-plate flow chamber of 22 × 14 × 0.5 mm (Fig. 1).

An array of silicone micropillar was fabricated via a replica-molding using standard photolithography and softlithography techniques [2]. Briefly, A silicon master was made with a negative photoresist (SU-8 3010, Microchem, USA). Liquid PDMS (Sylgard 184, Dow Corning, USA) mixed at a 10:1 base polymer to curing agent ratio was poured onto the master and thermally cured. The surface of PDMS was made nonadhesive by a plasma treatment, followed by passivating with a fluorinated silane on this activated surface. After passivation, mixed PDMS was poured over the negative mold and thermally cured. The micropillar substrate was then peeled away from the negative mold. When cells are cultured on the micropillars, triangle meshes connecting each point of the micropillars were generated

and traction force values between the points were interpolated using a bilinear interpolation method. Each value in a cell were integrated and normalized by the cell area. Estimated values having dimensions of stress (Pa) indicate a cell traction magnitude per a cell which is independent of changes in cell area and density. Statistics were performed using one-way ANOVA followed by Tukey-Kramer post hoc test with the statistical significance set at a 5% level.

Images were captured using a CCD camera (ORCA-R2, Hamamatsu, Japan) interfaced with an inverted microscope (IX-81, Olympus, Japan) and analyzed using image analysis software (ImageJ, NIH, USA). The cell shape index (SI), defined as $4\pi A/P^2$ where A is the cell area and P is its perimeter, was used as a measure of the degree of cell elongation.

3. Results and Discussion

Figure 2 shows a representative of simultaneous measurement of traction forces and cell morphology of cells under fluid flow at 0 h. It was demonstrated that the SI of cells decreased slightly from onset of flow and cells gradually aligned to the flow direction (Fig. 3). Thus, cells on the micropillar substrate might induce cytoskeletal remodeling since the SI and cell alignment correlate to formation of stress fibers. Mean traction magnitude decreased at 4 h, however, there was a slow

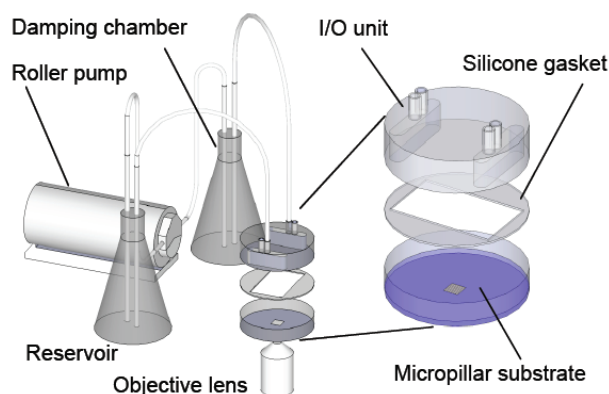


Fig. 1 Newly designed fluid-imposed device.

increase up to 24 h (Fig.4). Migration speed was doubled at 6-9 h when comparing to 0-3 h (data not shown). The decrease in traction forces suggests that shear stress regulates not only cell-substrate attachment but also cell-cell attachment. Noria et al. [3] suggested that gaps between cells were observed in a EC monolayer after an application of shear stress for 8.5 h. Taken together, the decrease in traction forces is, in part, maybe attributable to the loss of cell-cell attachment and the following increase in traction forces to the recovery of cell-cell attachment. Here, a novel approach measuring traction forces of sheared ECs was thus proposed and would contribute to further understanding of mechanism of EC remodeling.

4. Concluding remarks

In conclusion, dynamics of traction forces in sheared ECs are studied. Traction forces changed in a dynamic manner with time of the exposure and the change might be attributable to the loss of intercellular junctions.

Acknowledgements

This work was financially supported by the Grants-in-Aid for Scientific Research, Specially Promoted Research (grant No. 20001007) from the Japan Society for the Promotion of Science (JSPS).

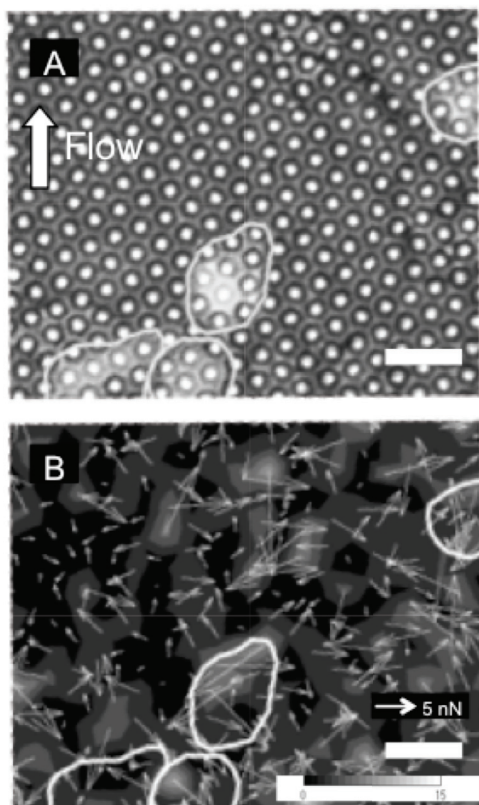


Fig. 2 (A) Merged image of GFP-tagged BAECs fluorescent image and micropillar brightfield image, and (B) corresponding traction force contour and vector taken at 0 h. Scale bar = 20 μ m.

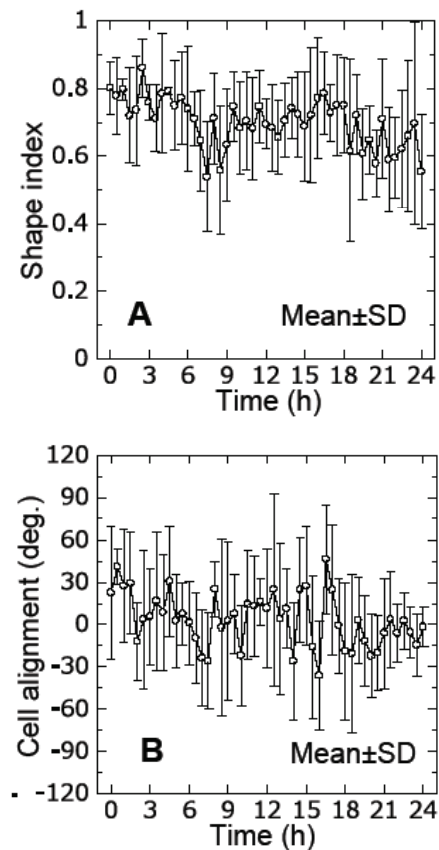


Fig. 3 Temporal changes of (A) shape index and (B) cell alignment (n=4).

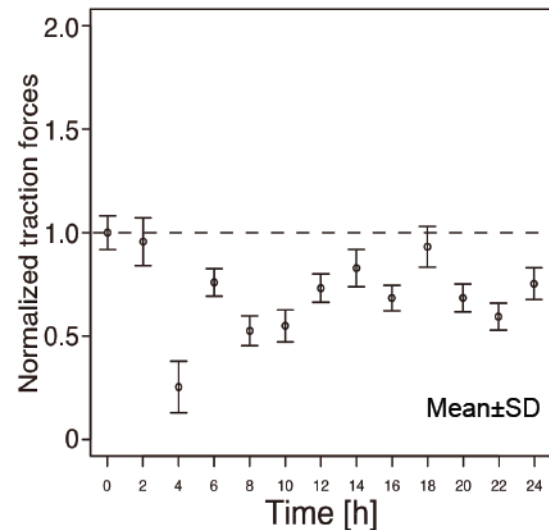


Fig. 4 Representative changes in mean traction magnitude of a BAEC in a monolayer.

References

- [1] Kataoka, N. et al., 1998, "Effect of flow direction on the morphological responses of cultured bovine aortic endothelial cells." *Med. Biol. Eng. Comp.*, **36**(1), 122-128.
- [2] Tan, J. et al., 2003, "Cells lying on a bed of microneedles: An approach to isolate mechanical force." *PNAS*, **100**(4), 1484-1489.
- [3] Noria, S. et al., 1999, "Transient and steady-state effects of shear stress on endothelial cell adherens junctions." *Circ. Res.*, **85**, 504-514.

Comprehensive Gene Expression Analysis of HeLa Cells in Response to Plasma Stimuli

Mayo Yokoyama¹, Takehiko Sato¹, and Kohei Johkura²

¹Institute of Fluid Science, Tohoku University, 2-1-1 Katahira, Aoba-ku, Sendai 980-8577

²Department of Histology and Embryology, Shinshu University School of Medicine, 3-1-1 Asahi, Matsumoto 390-8621, Japan
sato@ifs.tohoku.ac.jp

ABSTRACT

An air-water plasma system which was formed between a needle electrode and a surface of culture medium is capable of generating dissolved chemical species. Authors have clarified that the hydrogen peroxide in the plasma-treated culture medium is the key inactivation factor for HeLa cell viability. In this study, a feasibility study for a comprehensive gene analysis using a microarray was performed in the different treatment conditions to culture media and in the different comparison analyses. These results of microarray indicated that the effect of plasma-treated culture medium on the gene expressions of HeLa cells was similar to that of H₂O₂.

1. Introduction

An air-water plasma generates light, shock wave, electric field, heat, ion, and chemically reactive species [1, 2]. Those plasma stimuli have been applied to medical treatment of chronic wounds [3, 4] and low temperature sterilization [5, 6]. The mechanisms of biological responses to plasma stimuli are very complex and they have not been clarified enough yet.

Authors have focused on the effect of stable chemical species such as hydrogen peroxide in the plasma-treated culture medium on the inactivation of HeLa cell viability. It was clarified that the hydrogen oxide is the key inactivation factor for HeLa cells by verifying the cell survival ratio, morphological features of damage processes, and response to H₂O₂ decomposition by catalase [7].

In this study, to understand the biological responses in the gene expression level, the comprehensive gene expression of HeLa cells in response to plasma and

H₂O₂ stimuli was analyzed by DNA microarray.

2. Method

The HeLa cell (obtained from the Institute of Development, Aging and Cancer, Tohoku University) was incubated using a regular culture medium consisting of Minimum Essential Medium, 10% Fetal Bovine Serum, and antibiotics (Penicillin 100 u/ml; streptomycin 100 µg/ml) at 37 °C, 5 % CO₂ with a 25 cm² flask (Falcon).

The protocol for the DNA microarray analysis is shown in Fig 1. The cells were exposed to the plasma-treated culture media with the treatment time of 210 s and 40 s, or to H₂O₂-added culture media of 304 µM and 51 µM. The exposure conditions were at 37 °C, 5 % CO₂ for 1 hr (51 µM H₂O₂, Plasma 40 s) or 20 min (304 µM H₂O₂, Plasma 210 s). Total RNA was isolated by TRIzol (Invitrogen). The DNA microarray was performed by using the “Whole Human Genome Microarray Kit (Agilent Technologies)”.

The plasma flow was generated between a needle electrode and the surface of culture medium with a gap of 1.5 mm. The electrode is made of platinum, 0.3 mm in diameter. The culture medium of 1.0 ml in a microtube of 1.5 ml was set in a ground electrode. The voltage of +7.5 kV_{op} with frequency of 5 kHz and duty ratio of 4% was applied to the needle electrode for 210 s or 40 s. The power consumption was 7.1 W calculated by using the Lissajous figure.

The H₂O₂ concentration in the plasma-treated culture medium was measured by calibration with the H₂O₂ absorbance curve against a known concentration in the culture medium. By this method, we could obtain that the H₂O₂ concentration in the culture medium treated by the plasma for 210 s was 304 µM, while that by the plasma 40 s was 51µM[7].

The H₂O₂ reaction reagent (WAK- H₂O₂, Kyoritsu Chemical-Check Lab) can discolour the solution depending on the H₂O₂ concentration. We estimated that this concentration of H₂O₂ was rational and the effect of plasma radiation on the generation of H₂O₂ was sufficiently small considering the common range used in the studies of plasma medicine [8, 9, 10, 11].

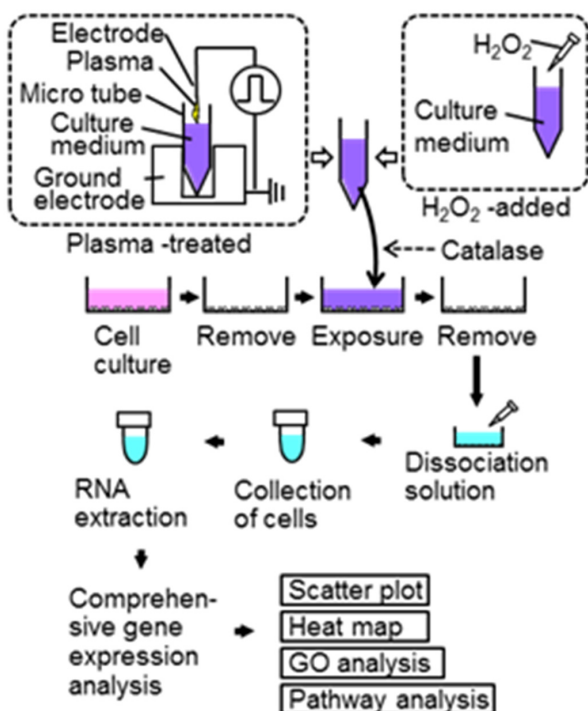


Fig. 1 Experimental procedure

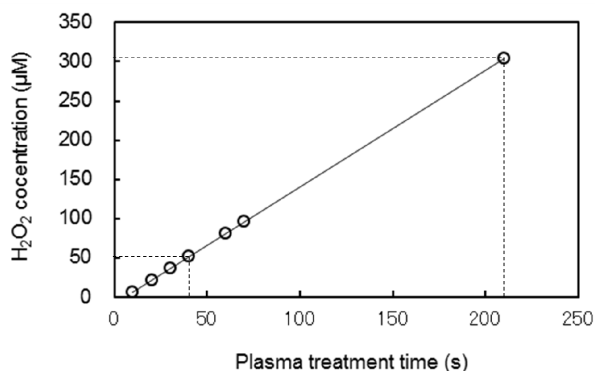


Fig. 2 The relationship between plasma treatment time and H_2O_2 concentration in the culture medium.

3. Results and Discussion

The gene expression levels were compared in two conditions of eight sets: (1) Plasma 210 s versus Control, (2) $304 \mu\text{M H}_2\text{O}_2$ versus Control, (3) Plasma 40 s versus Control, (4) $51 \mu\text{M H}_2\text{O}_2$ versus Control, (5) Plasma 210 s versus $304 \mu\text{M H}_2\text{O}_2$, (6) Plasma 210 s versus Plasma 40 s, (7) Plasma 40 s versus $51 \mu\text{M H}_2\text{O}_2$, and (8) $304 \mu\text{M H}_2\text{O}_2$ versus $51 \mu\text{M H}_2\text{O}_2$. Around 32,000 genes analyzed, the number of genes with an expression ratio ≥ 2 or ≤ 0.5 were counted in each comparison shown in Fig. 3. In the cases of 3 and 4, the numbers of genes for the expression ratio ≥ 2 were greater than 1500 and correspondingly those for the ratio ≤ 0.5 showed in the cases of 6 and 8. These results implied that the effect of plasma-treated culture medium on the gene expressions of HeLa cells was similar to that of H_2O_2 .

Figure 4 shows the scatter plot of the gene expression intensities made by a GeneSpringGX11.0.2 (Agilent Technologies). When gene expression levels in plasma-treated medium were compared with those in H_2O_2 -added medium, most of plots for high expression genes were located on the diagonal line, suggesting a comparable cellular response.

4. Conclusions

In this study, a feasibility study for a comprehensive gene analysis using a microarray was performed in the different treatment conditions to culture media and in the different comparison analyses. From these results, the effect of plasma-treated culture medium on the gene expressions of HeLa cells was similar to that of H_2O_2 .

This study was supported by the JSPS, Grant-in-Aid for Scientific Research, and by Collaborative Research Project of the IFS, Tohoku University.

References

- [1] G. E. Morfill, M. G. Kong and J. L. Zimmermann, *New J. Phys.*, **11**, 115011 (2009).
- [2] G. Fridman, G. Friedman, A. Gutsol, A. B. Shekhter, V. N. Vasilets, A. Fridman, *Plasma Process. Polym.*, **5**, 503 (2008).
- [3] J. Heinlin et al., *Acad. Dermat. Venere.*, **25**, 1 (2010).
- [4] G. Isbary et al., *Brit. J. Dermatol.*, **163**, 78 (2010).
- [5] T. Sato, T. Miyahara, A. Doi, S. Ochiai, T. Urayama

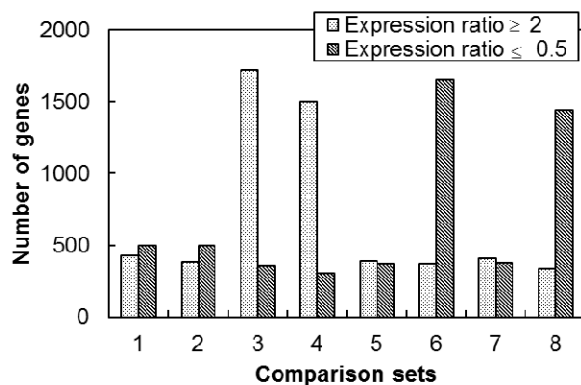


Fig. 3 Number of genes which showed different expression levels between the two conditions in each group.

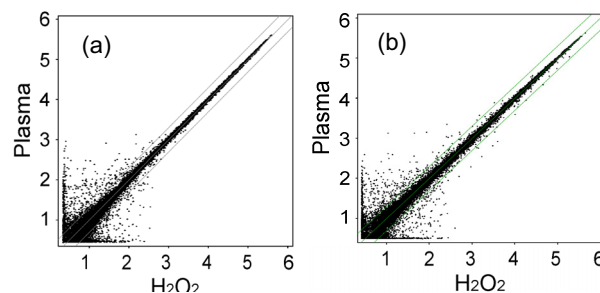


Fig. 4 Scatter plot of the expression intensities corresponding to each gene under $304 \mu\text{M H}_2\text{O}_2$ versus Plasma 210 s (a), and $51 \mu\text{M H}_2\text{O}_2$ versus Plasma 40 s (b). The values in both vertical and horizontal axes are a common logarithm (Log_{10}).

- and T. Nakatani, *Appl. Phys. Lett.*, **89**, 073902 (2006).
- [6] T. Sato, O. Furuya, K. Ikeda and T. Nakatani, *Plasma Process. Polym.*, **5**, 606. (2008).
 - [7] T. Sato, M. Yokoyama and K. Johkura, *J. Phys. D: Appl. Phys.*, **44**, 372001 (2011).
 - [8] Ikawa S, Kitano K and Hamaguchi S. *Plasma Process. Polym.*, **7**, 33 (2010).
 - [9] Dobrynin D, Fridman G, Friedman G and Fridman A. *New J. Phys.*, **11**, 115020 (2009).
 - [10] Shimizu T, Nosenko T, Morfill G, Sato T, Schmidt H-U and Urayama T *Plasma Process. Polym.*, **7**, 288 (2010).
 - [11] Miyahara T, Ochiai S and Sato T. *Europhys. Lett.*, **86**, 45001 (2009).

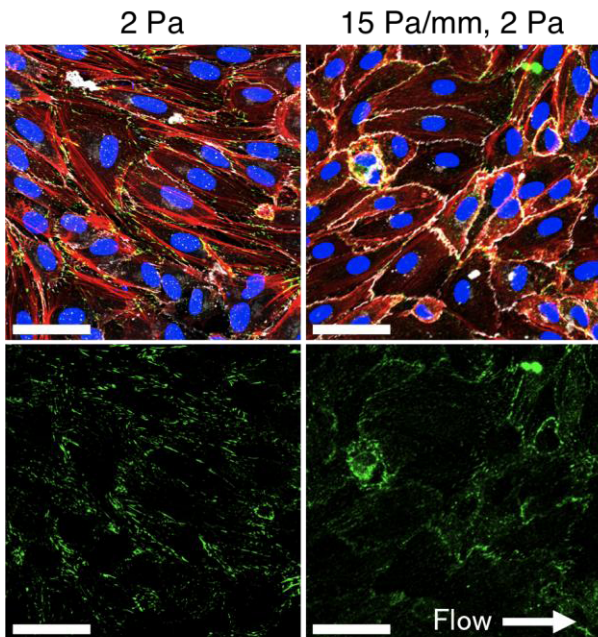


Fig. 2 Fluorescent images of ECs (blue: nucleus, white: VE-cadherin, green: paxillin, red: F-actin, bar=50 μm). Left side shows fluorescent images of ECs exposed to SS of 2 Pa. Right side shows fluorescent images of ECs exposed to SS of 2 Pa with SSG of 15 Pa/mm.

obtained by using the function of “Analyze Particles,” and information about paxillin was transferred onto a unit circle.

3. Results and Discussion

Figure 2 shows fluorescent images of ECs after 24-hour flow exposure. ECs exposed to SS without SSG were elongated and oriented in the direction of flow. Actin filaments existing along the periphery of ECs grew and became thicker, and focal adhesions were localized in the cell periphery. On closer inspection, focal adhesions were expressed in the upstream and downstream of flow direction (Fig. 3, left side). In contrast, ECs under the condition of SS with SSG were not elongated and oriented in the flow direction. Actin filaments in the periphery of cells remained thin, and the thin and short filaments were formed in the interior portion. Focal adhesions were expressed not only in the periphery but also in interior portion of cells (Fig. 3, right side).

Paxillin, a focal adhesion-associated protein, is activated by SS exposure, and disaggregation and migration of focal adhesions are encouraged by paxillin activation. When ECs, into which paxillin Y31A mutants were introduced, were exposed to SS, paxillin Y31A mutants were distributed in the interior of ECs [4]. This is similar to the distribution of paxillin under the condition of SS with SSG. Therefore, SSG has the potential to inhibit activation of paxillin. It is considered that developments of focal adhesions and actin filaments are suppressed as a result of inhibiting disaggregation and migration of focal adhesions by SSG.

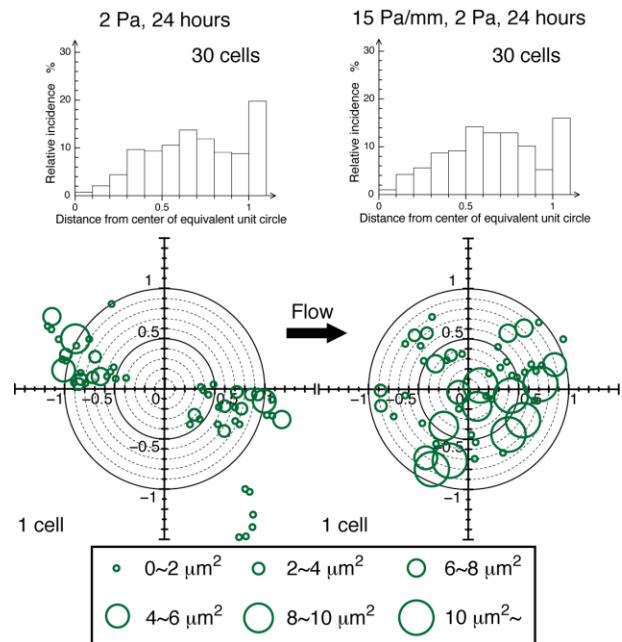


Fig. 3 Distributions of paxillin in ECs. Left side shows distribution and histogram of ECs exposed to SS of 2 Pa. Right side shows distribution and histogram of ECs exposed to SS of 2 Pa with SSG of 15 Pa/mm.

4. Summary

When ECs are exposed to fluid SS with its spatial gradient, actin filaments in the periphery of cells remained thin, and the thin and short filaments were formed in the interior portion. In addition, focal adhesions were expressed not only in the periphery but also in interior portion of cells. These results suggest that SSG suppresses formations of actin filaments and aggregation of focal adhesions, resulting in the inhibition of ECs' morphological changes in response to flow.

Acknowledgements

Authors acknowledge the support of Grants-in-Aid for Scientific Research from MEXT of Japan (No. 20001007).

References

- [1] Oshima, M., Nagare 21 (2002): 122-126.
- [2] Szymanski, M.P. et al., *Ann. Biomed. Eng.* 36 (2008): 1681-1689.
- [3] Sakamoto, N. et al., *Biochem. Biophys. Res. Commun.* (2010): 264-269.
- [4] Mattiussi, S. et al., *Cardiovas. Res.* 70 (2006): 578-588.

Molecular Dynamics Simulations of a DPPC/Cholesterol Bilayer under Equibiaxial Stretching

Taiki Shigematsu, Kenichiro Koshiyama, and Shigeo Wada

Graduate School of Engineering Science, Osaka University, Toyonaka, Osaka 560-8531, Japan

E-mail of corresponding author: koshiyama@me.es.osaka-u.ac.jp

ABSTRACT

To investigate the effects of cholesterol on the rupture of lipid bilayers at the molecular level we perform molecular dynamics (MD) simulations of DPPC bilayers including 0, 20, and 40 mol% cholesterol under unsteady equibiaxial high-speed stretching. We found that the critical areal strain, where the rupture occurs, is larger for the bilayers including cholesterol than for the pure DPPC bilayer. In the thinning bilayer, cholesterol molecules fall down and form a monolayer-like structure in the center of the “lipid” bilayer. This structure, composed of lying cholesterol molecules, may prevent the water penetration into the bilayer.

1. Introduction

Biological cell membranes play important roles in biological systems. The lipid bilayer, i.e., the fundamental structure of cellular membranes, separates the inside of a cell from the outside and acts as a matrix for membrane proteins. Under mechanical stresses, irreversible breakdown (rupture) of the bilayer sometimes occurs and interior substances leak out, followed by the cell’s death. So far, in order to understand the rupture, several experimental studies have been conducted [1][2]. However, since the rupture process of a bilayer is extremely fast, it is difficult to directly observe the rupture process at the molecular level by using experimental methods. In this paper, we perform MD simulations of bilayers including cholesterol under unsteady high-speed equibiaxial stretching [3], because it is experimentally shown that the inclusion of cholesterol affects the rupture. To understand the dynamics of the rupture process from the molecular behavior, we analyze the effects of cholesterol on the critical areal strain where the rupture occurs statistically, and the structural change of a bilayer during stretching.

2. Method

2.1. System

We constructed three systems consisting of 200 molecules, – DPPC lipids and cholesterol – with different cholesterol molar fractions: 0 mol%, 20 mol% and 40 mol%. To avoid the effects of the virtual bilayers in the z direction under periodic boundary conditions during stretching, we added 25800 water molecules to the systems. For the pure DPPC (0 mol% cholesterol) system, the thickness of the water layer was about 4 times larger than that of the bilayer. For equilibration, MD simulations of the three systems were performed for 120 ns at constant temperature and pressure of 323 K and 1 bar, respectively. The first 70 ns were considered as the stabilization stage. We extracted configurations from the trajectories of the bilayers in the rest of the calculations, to use them as the initial configurations in the stretching simulations shown below. The united atom model was used for the CH_n groups in DPPC and cholesterol molecules. For all MD calculations reported here we used the GROMACS molecular simulation codes [4].

2.2. Unsteady stretching simulation

We employed the method proposed by Koshiyama and Wada (2011) [3] on the unsteady stretching of the bilayer. In this method, box lengths l_i and coordinates of all atoms x are proportionally scaled per time step Δt from l_i to μl_i and x to μx with

$$\mu = 1 + \frac{c}{l_i} \Delta t \quad (1)$$

($i = x, y, z$), where c is the stretching speed. We set the stretching speed c to 1.0 m/s because of the computational limitation. It must be noted that this speed is extremely large compared with that of the pipette aspiration experiment, but very small when compared with that in the shockwave experiment. We used the same value of μ in the x and y directions to perform the equibiaxial stretching. On the other hand, to maintain the pressure in the z direction at a constant value, we applied Berendsen’s scaling factor [5]

$$\mu = 1 - \frac{\beta \Delta t}{3\tau_p} \{P_0 - P(t)\} \quad (2)$$

where $\tau_p = 0.5$ ps, $\beta = 4.5 \times 10^{-5} \text{ bar}^{-1}$, and $P_0 = 1.0$ bar for the scaling of the z direction.

Pore formation, which is considered as the precursor of the rupture of a bilayer in the molecular level, is a statistic phenomenon [6]. We performed unsteady stretching simulations using 10 initial configurations per system to obtain a sample average.

2.3. Analysis

We define the areal strain of the bilayer ε as the box’s areal strain on the $x - y$ plane, calculated by $(A - A_0)/A_0$, where A is the corresponding area and A_0 is the initial area. The average area during the latter 50 ns of the equilibrated MD simulation is used as the initial area A_0 .

Additionally, to analyze the configuration of cholesterol in the upper and lower layers during stretching, we estimate the z -distance between the averages of the center of mass of the cholesterol molecules in the upper and lower layers.

3. Results and discussion

Due to the stretching, the area of the DPPC/cholesterol bilayers increased. When the area exceeds a critical value, a pore forms, resulting in the rupture. The mean values and standard deviations of the

critical areal strain for the respective systems are 1.15 ± 0.08 (0 mol%), 1.40 ± 0.14 (20 mol%), and 1.33 ± 0.20 (40 mol%). The average critical areal strain for the bilayers including cholesterol is larger than that for pure DPPC bilayer. This trend is in agreement with the previous experimental study [2].

In order to understand the relationship between the rupture process and cholesterol behavior, we examine snapshots of the rupture process obtained by the unsteady stretching simulation (Fig. 1). With increasing the area of the bilayer, its thickness decreases and the configuration of cholesterol molecules becomes disordered. Before stretching, both DPPC and cholesterol molecules form the bilayer structure in the DPPC/cholesterol bilayer (Fig. 1A). However, with stretching, the bilayer structure of cholesterol disappears in the thinning lipid bilayer (Fig. 1B). After that, water molecules penetrate into the hydrophobic region of the bilayer and a water-filled pore forms, connecting upper and lower water layers (Figs. 1B and E). The pore expands with additional stretching (Figs. 1C and F), followed by the rupture of the bilayer. A similar process can be found in the case of a pure POPC bilayer rupture [3].

From the visual inspection of the rupture process (Fig. 1), we found that the bilayer structure of cholesterol disappeared with stretching. We calculated the change of the distance between the center of mass of the cholesterol molecules in the upper and lower layers (Fig. 2). The distance in the beginning of stretching (about 2 nm) is large enough to form a cholesterol bilayer structure (also see Fig. 1A). However, before the rupture occurs (around 2500 ps), it is shorter than the size of the cholesterol rigid ring structure (about 0.8 nm, see also Fig. 2 inset), indicating the fact that cholesterol molecules are coming into close contact.

In the thinning DPPC/cholesterol bilayer, cholesterol molecules fall down on the bilayer plane in the “lipid” bilayer in order to keep their rigid ring structure, and the border between the upper and lower layers of cholesterol becomes ambiguous. Thus, a monolayer-like structure composed of the lying cholesterol molecules appears in the center of the lipid bilayer. As the monolayer is hydrophobic, it may prevent the water penetration into the bilayer, which results in a delay in the pore formation and an increase in the critical areal strain.

4. Conclusion

We have performed unsteady equibiaxial high-speed stretching MD simulations on DPPC/cholesterol bilayers. We determined that the critical areal strain for the bilayer including cholesterol is larger than that for the pure DPPC bilayer. In the thinning bilayer, cholesterol molecules fall down on the bilayer plane in the “lipid” bilayer. The bilayer structure of cholesterol becomes ambiguous, and a monolayer-like structure composed of lying cholesterol molecules appears in the center of the “lipid” bilayer. This structure may prevent the water penetration into the bilayer, resulting in an increase of critical areal strain.

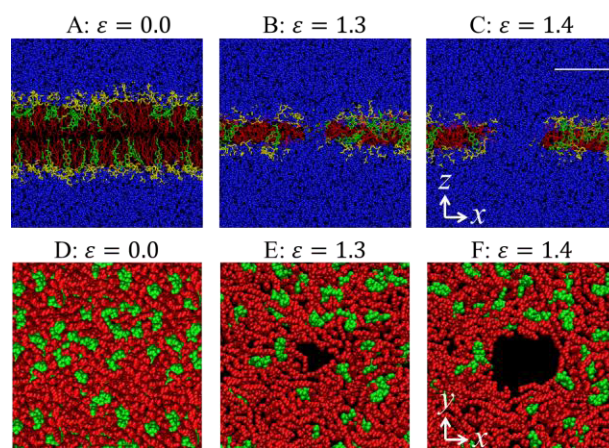


Fig. 1 Representative snapshots of the rupture process caused by unsteady stretching of a DPPC bilayer including 20 mol% cholesterol. ϵ is the areal strain. (A), (B) and (C) are side views, while (D), (E) and (F) are top views. The DPPC headgroups are shown in yellow, DPPC tails in red, cholesterol molecules in green, and water molecules in blue. DPPC headgroups and water molecules are removed from top views for clarity. The white bar in (C) corresponds to 3 nm.

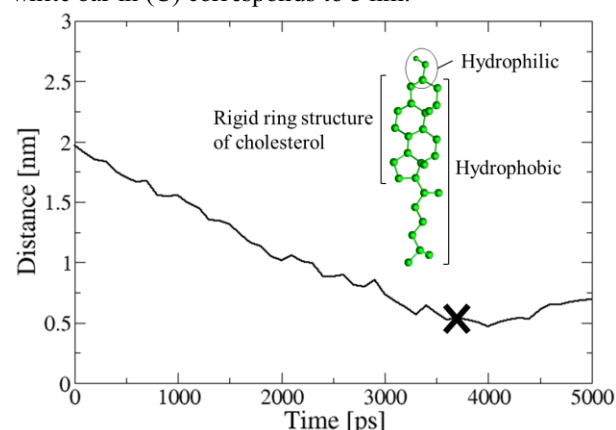


Fig. 2 The representative result of the change in the distance between the center of mass of the cholesterol molecules in the upper and lower layers. The inset shows the structure of a cholesterol molecule. The cross indicates the rupture point.

References

- [1] E. Evans and V. Heinrich, *C. R. physique.*, 4 (2003), 265-274
- [2] D. Needham and R. S. Nunn, *Biophys. J.*, 58 (1990), 997-1009
- [3] K. Koshiyama and S. Wada, *J. Biomech.*, 44 (2011), 2053-2058
- [4] B. Hess, C. Kutzner, D. van del Spoel, E. Lindahl, *J. Chem. Theory Compute.*, 4 (2008), 435-447
- [5] H. J. C. Berendsen, J. P. M. Postma, W. F. van Gunsteren, A. DiNola, and J. R. Haak, *J. Chem. Phys.*, 81 (1984), 3684-3690
- [6] K. Koshiyama, T. Yano, and T. Kodama, *PRL*, 105 (2010), 01815

JNK and P38MAPK Mediate Low Level Shear Stress-induced Migration of Human Mesenchymal Stem Cells

Lin Yuan^{1,2}, Naoya Sakamoto³, Guanbin Song², Masaaki Sato¹

1. Graduate School of Biomedical Engineering, Tohoku University, Sendai 980-8579, Japan

2. College of Bioengineering, Chongqing University, Chongqing 400044, China

3. Department of medical technology, Kawasaki University of Medical Welfare, Kawasaki 701-0193, Japan

Email: sato@bml.mech.tohoku.ac.jp

ABSTRACT

Human mesenchymal stem cells (hMSCs) are attractive candidates for cell-based tissue repair approaches and have been used as vectors for delivering therapeutic genes to sites of injury. It is believed that hMSCs are able to detect and respond to shear stress due to blood stream and interstitial fluid flow through mechanotransduction pathways after transplantation. However, information regarding hMSC migration under shear stress and its mechanism is still limited. In this study, we examined the effect of shear stress on hMSC migration and the role of mitogen-activated protein (MAP) kinases in their migration.

1. Introduction

Mesenchymal stem cells (MSCs) are primary, multipotent cells capable of differentiating to adipocytic, chondrocytic and osteocytic lineages on suitable stimulation [1]. Because of their own intrinsic properties, such as homing and immunosuppressive potency, MSCs are considered to be an attractive candidate for cell-based tissue repair and regenerative tissue engineering [2, 3]. Increasing number of studies has demonstrated that migratory ability is one of the most important factors for cell transplantation in disease treatment and tissue regeneration [4, 5]. Through intravenous, intra-arterial, or intracerebral routes of administration of MSCs, it is believed that these cells are able to sense and respond to shear stress, which generated by blood stream or interstitial fluid flow, after injection into vessels.

Several researches also have shown that shear stress can control MSC proliferation and differentiation into osteoblasts, endothelial cells or cardiomyocyte [6, 7]. However, although numerous studies have indicated that shear stress influences migratory ability in many types of cells, the effect of shear stress on MSC migration as well as its mechanism remains unknown. As a classical signaling pathway, the mitogen-activated protein kinases (MAPK), including ERK1/2, JNK and p38MAPK, have been demonstrated to control major cell functions [8]. Since it has been shown that MAPK signaling pathways take important roles in the migration of MSCs stimulated by chemical factors [9], we speculate that shear stress also utilizes the MAPK signal molecules in regulating MSCs migration.

In the present study, to make clear the responses of migration of MSCs to shear stress and the relating signaling transduction molecules, we investigate migratory ability of MSCs exposed to shear stress by wound scratch assay. Western blot analysis is also performed to examine whether ERK1/2, JNK and p38MAPK are mediate the regulation of shear stress on hMSC migration.

2. Method

Cell culture

Human MSCs (hMSCs) were cultured with Dulbecco's modified Eagle's medium (DMEM;

Invitrogen, USA) containing 10% heat-inactivated fetal bovine serum and 10 ng/ml human basic fibroblast growth factor. Cells were used from 4th to 8th generations for experiments.

Wound scratch migration assay

hMSCs grown at confluence in a cell culture dish were fluorescently labeled mitochondria by Mitotracker (Invitrogen). A linear scratch approximated 200 μm in width by a plastic cell scraper was performed in the cell monolayer. Images of the wounds were acquired 0, 1, 3, 6, and 10 h after the onset of flow by a microscope (Olympus, IX-81, Japan) with a 3CCD camera (ORCA-3CCD, Hamamatsu Photonics, Japan). Using Image J, the level of wound closure was assessed by the ratio of the closure area to the initial wound area as follows: $W_n = (1 - A_n / A_0) \times 100$ [%], where W_n represents the percentage of the wound closure; A_n represents the residual area of the wound and A_0 represents the area of the initial wound.

Flow-exposure experiment

The culture medium used for experiments was serum-free but contained Insulin Transferrin Selenium X Supplement (Invitrogen). Using a parallel flow chamber system, laminar flows of culture medium were applied in the direction vertical to the wound edges and the magnitude of shear stress (0.2–10 Pa) was controlled by changing the flow rate.

Western blot analysis

Cells were washed with ice-cold PBS and scraped immediately after exposure to laminar shear stress for 10, 30, 60, or 120 min. Protein extraction was carried out using cell lysis buffer. Following electrophoretic separation by 8% SDS-polyacrylamide gel electrophoresis, proteins were electroblotted onto polyvinylidene fluoride (PVDF) membranes and detected by corresponding antibodies.

3. Results and Discussion

In the absence of flow (control), cells reached confluence at 10 h after wound performed (Fig. 1). Under shear stress of 0.2 Pa, hMSCs closed approximately 98% of the original wound at 6 h while the cell in static condition closed only 62% of the original wound. There were no significant differences in the wound closure for 0.5 Pa and 1 Pa groups compared

with the control. In stark contrast, by the imposed shear stress of 2 Pa, migration of hMSCs was prominently inhibited. We also studied the effects of shear stress greater than 2 Pa up to 10 Pa on hMSCs migration and confirmed that higher shear stress inhibited cell migration like shear stress of 2 Pa did (data not shown). Recent evidence indicates that MSCs not only exist in bone marrow, but also reside in the medial layer of a normal healthy vessel as a subpopulation with smooth muscle cells. Thus MSCs are thought to be exposed on shear stress caused by interstitial flow in physiological conditions [10]. Coupled with our finding that low shear stress, rather than high magnitude of shear stress, acts as an accelerative condition for hMSCs migration, these results reflect the idea that promoting conditions for MSC migration are naturally present in the human body.

Using JNK or p38MAPK inhibitor-containing media for flow exposure experiments, the migratory ability of hMSCs was decreased exhaustively and shear stress did not compensate for the effect of inhibition. However, even treated with U0126 (ERK1/2 inhibitor), shear stress of 0.2 Pa still promoted hMSCs migration compared with U0126-treated control group and the significant differences in wound closure rate were apparent at 6 h after wounding (data not shown). By western blot analysis, JNK phosphorylation proceeded fast and reached a peak at 30 min in the shear stress groups, which was more than 3-fold ($p < 0.01$) higher than that in the control group. No significant difference was observed in t-JNK expression between all detected time points (Fig. 2A). p-p38 MAPK activation also increased rapidly and peaked at 30 min, which was 2.7-fold higher than that in the control group, while p38 MAPK expression remained the same (Fig.2B). These results indicate that JNK and p38MAPK play a more prominent role in shear stress-induced hMSCs migration.

4. Concluding remarks

In the present study, we investigated the responses of migration of hMSCs subjected to shear stress. Results demonstrated that lower shear stress induced hMSCs migration effectively and JNK and p38MAPK played more prominent roles in this process.

5. Acknowledgements

This study was supported in part by Grants-in-Aid for Scientific Research from the Ministry of Education, Culture, Sports, Science and Technology (MEXT) of Japan (No. 20001007), and the Fundamental Research Funds for the Central Universities (CDJXS11232243) of China.

References

- [1] Salem HK and Thiemermann C. STEM CELLS 2010; 28:585-596.
- [2] Park DH et al. STEM CELLS DEV 2009; 18:693-702.
- [3] Wang H and Chen X. FUTURE ONCOL 2008; 4:623-628.
- [4] Levesque JP et al. HANDB EXP PHARMACOL 2007; 3-36.
- [5] Chapel A et al. J GENE MED 2003; 5: 1028-1038.

- [6] Tu ML, et al. LIFE SCI 2011; 88:233-238.
- [7] Yourek G et al. REGEN MED 2010; 5:713-724.
- [8] Blüthgen N, Legewie S. ESSAYS BIOCHEM 2008; 45:95-107.
- [9] Ryu CH, et al. BIOCHEM BIOPHYS RES COMMUN 2010; 398:105-110.
- [10] Abedin M, et al. CIRC RES 2004; 95:671-676.

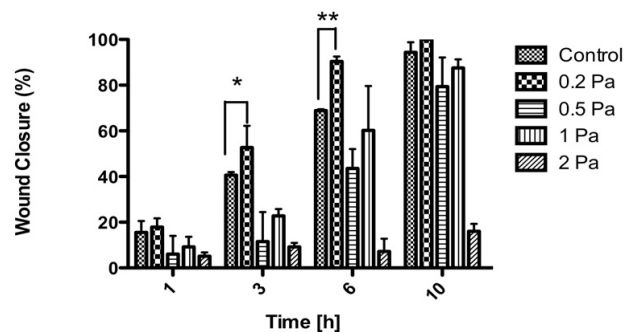
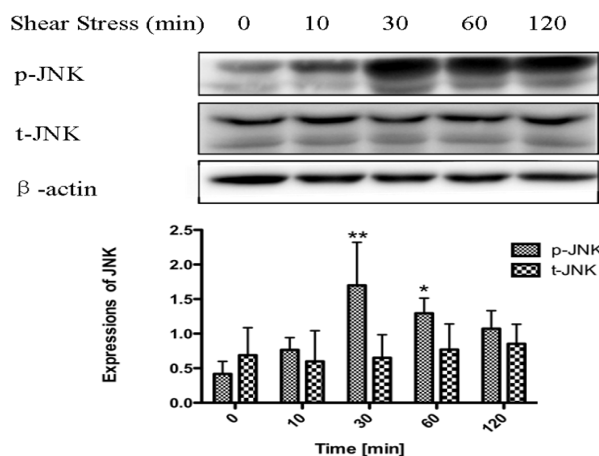


Fig. 1 The percentages of wound closure by MSCs under shear stress conditions. (mean + SD, $n=3$, * $p < 0.05$, ** $p < 0.01$).

A



B

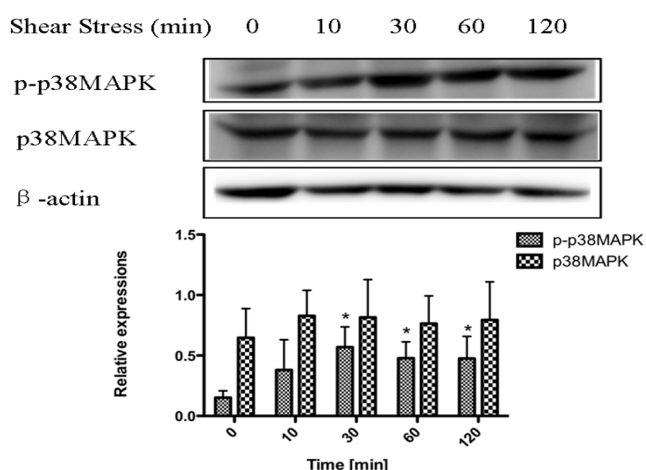


Fig. 2 Effects of shear stress on the activation of (A) p-JNK and t-JNK (B) p-p38 MAPK and p38 MAPK in hMSCs. Data are expressed as mean \pm SD. $n=3$, * $p < 0.05$, ** $p < 0.01$).

Numerical Analysis of Levitation Mechanism of Red Blood Cell in Inclined Centrifuge Microscope - Effect of Asymmetric Cell Shape on the Motion

Takashi. Oshibe¹⁾, Toshiyuki. Hayase²⁾, Kenichi. Funamoto²⁾, Atsushi. Shirai²⁾

1) Department of Bioengineering and Robotics, Graduate School of Engineering, Tohoku University,
6-6-01 Aramaki, Aoba-ku, Sendai, 980-8579.

2) Institute of Fluid Science, Tohoku University, 2-1-1 Katahira, Aoba-ku, Sendai, 980-8577.

E-mail: oshibe@reynolds.ifs.tohoku.ac.jp

ABSTRACT

In measurement of friction characteristics of red blood cells using an inclined centrifuge microscope, the cells in plasma move along a plate at a distance above the plate. In order to understand the cell motion, three-dimensional flow analyses around a rigid red blood cell model were performed with various cell shapes and angles of attack. An equilibrium state for force and moment acting on the cell was obtained at a certain angle of attack when the bottom of cell is almost flat.

1. Introduction

Studies have been extensively carried out to elucidate the complicated interactions between blood cells, plasma proteins, and glycocalyx on an endothelial surface layer of a blood vessel [1]. In order to understand the interaction mechanism, the authors measured the frictional characteristics of a red blood cell by using an inclined centrifuge microscope (Fig. 1) [2, 3]. The authors clarified the frictional characteristics of the red blood cell moving on a glass plate with/without DLC or MPC coating in plasma medium, suggesting the existence of a submicron plasma layer between the cell and the plate. Understanding the mechanism of the red blood cell motion in the inclined centrifuge microscope is important in modeling the cell motion in capillaries or in developing a new diagnostic method with the inclined centrifuge microscope, but has not been done yet.

Though the chemical interaction between the cell and the plasma may affect the cell motion, we consider the effect of fluid dynamics as the critical factor on the phenomena.

In our former study, three-dimensional numerical analyses of the flow around a red blood cell moving at a certain velocity with a given minimum distance from the plate were performed assuming the flat bottom shape and various values of the angle of attack [4]. The results indicated the existence of an equilibrium state for both the forces (lift and drag) and the moment acting on the cell at a particular angle of attack, showing a

quantitative agreement with an experimental result [2]. Considering the former study [5], the bottom shape may change the cell motion and the frictional characteristics under inclined centrifugal force.

Hence, in this study, the effect of the bottom shape of the cell on the lift, drag, and moment are investigated by three-dimensional numerical analyses, and the relationship of the frictional characteristics and the cell configuration are discussed.

2. Calculation Method

Computational conditions are shown in Fig. 2. We focused on an experimental result that a red blood cell moved on a glass plate at the mean velocity of $U = 50 \mu\text{m/s}$ in a plasma medium under a inclined centrifugal force, which is decomposed to tangential and normal forces against the plate [2, 3]. A three-dimensional configuration of the cell was generated by revolving a shape represented by Eq. (1) around the Y -axis.

(i) $0 \leq X \leq x_2$

$$Y_{\text{Top}} = (1 + \varepsilon) \left\{ y_1 + 2(y_2 - y_1) \left(\frac{X}{x_2} \right)^2 - (y_2 - y_1) \left(\frac{X}{x_2} \right)^4 \right\} - \varepsilon y_2$$

$$Y_{\text{Bottom}} = (\varepsilon - 1) Y_{\text{Top}} - \varepsilon y_2 \quad (1)$$

(ii) $x_2 \leq X \leq x_3$

$$Y_{\text{Top}} = \sqrt{R^2 - (X - x_2)^2}, \quad Y_{\text{Bottom}} = -Y_{\text{Top}}$$

We adopted the Cartesian coordinate system, which moved with the red blood cell at a velocity U . The computational domain was $L_x \times L_y \times L_z = 80 \mu\text{m} \times 54 \mu\text{m} \times 80 \mu\text{m}$. The distance between the point A and the plate was fixed at $0.09 \mu\text{m}$, and the angle of attack, α , changed in the range of $0^\circ \leq \alpha \leq 10^\circ$ around the z -directional axis passing point A. The x -directional velocity of $50 \mu\text{m/s}$ was set at the upstream and lateral boundaries.

The minimum thickness along the Y -axis was fixed as $1.0 \mu\text{m}$ at the center of the cell (Fig. 3). Asymmetric parameter, ε , with respect to the X -axis was introduced to define various shape of the cell. The case of $\varepsilon = 0$ had a biconcave shape in unloaded state, and that of $\varepsilon = 1$ had a flat bottom shape due to inclined centrifugal force.

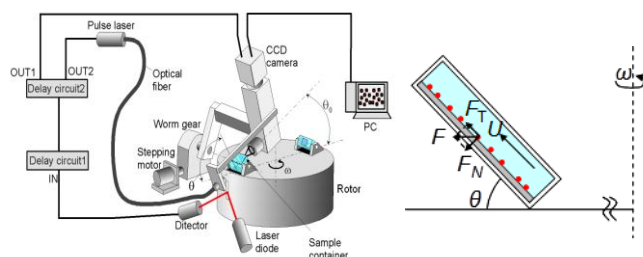


Fig. 1 Inclined centrifuge microscope

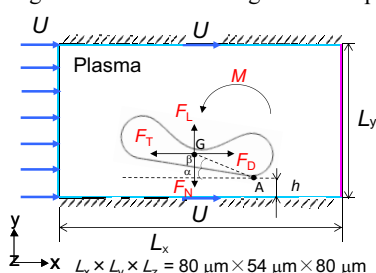


Fig. 2 Computational condition

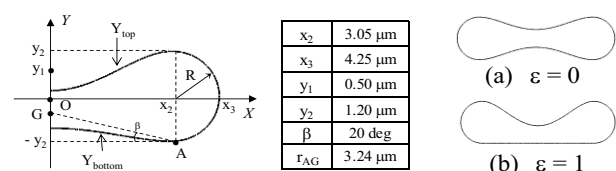


Fig. 3 Shape of red blood cell

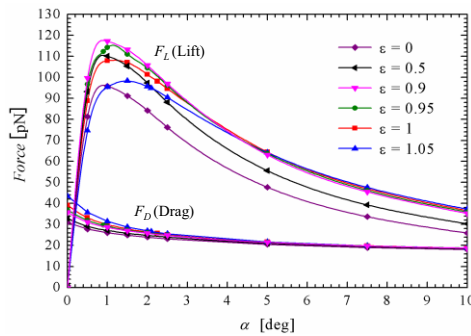
In this study, numerical analyses were performed by changing the parameter ε .

This study employed the commercial fluid dynamics software FLUENT 6.3 (ANSYS, Inc., USA), and the computational model was created by means of the preprocessing software GAMBIT 2.2 (ANSYS, Inc., USA). Computational grid sizes were $0.05 \mu\text{m}$ around the red blood cell and $2 \mu\text{m}$ in the other areas, respectively.

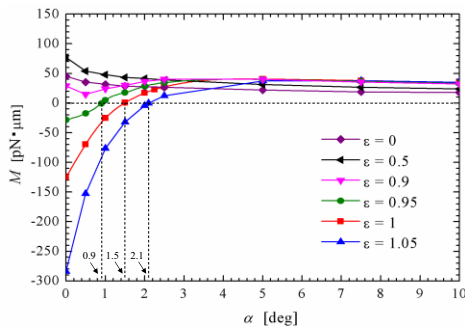
3. Results and Discussion

Figure 4 shows the lift F_L , drag F_D , and moment M , around the z -directional axis passing point A. In calculation of M , F_N and F_T are assumed to be identical to F_L and F_D respectively. The moment M , has a positive value in the range of $0 \leq \varepsilon \leq 0.9$, but it becomes zero at a certain angle of attack, α_0 , in the range of $0.95 \leq \varepsilon \leq 1.05$. Since the positive moment pushes the upstream edge of the cell to the plate, there is no equilibrium state, unless the bottom is almost flat. This finding that the moment acted in opposite directions between the case of $\varepsilon = 0$ (biconcave shape) and that of $\varepsilon = 1$ (flat shape) at $\alpha = 0^\circ$ was pointed out in our former result of two-dimensional simulation with $\alpha = 0^\circ$ [5].

The cross-sectional shape of the cell, the angle of attack, α_0 , for the balance of the moment, and the forces, F_N and F_T , with various values of ε are shown in Table 1. As increasing the value of ε , α_0 increases, meanwhile both F_N and F_T decreases. The present computational results for the friction force corresponding to F_T agree with that of the case of $F_N = 50 \text{ pN}$ in the experiment [2]. Since $F_N (= F_L)$ for the equilibrium rapidly decreases in the case of $\alpha < 1$, the frictional characteristics in experiment can be quantitatively explained by the cell



(a) Lift F_L and drag F_D



(b) Moment M

Fig. 4 Variations of lift, drag and moment with angle of attack ($h = 0.09 \mu\text{m}$, $U = 50 \mu\text{m/s}$)

Table 1 Equilibrium states for the cell shape ($h = 0.09 \mu\text{m}$, $U = 50 \mu\text{m/s}$)

ε	shape	α_0 [deg]	F_N [pN]	F_T [pN]
0		N/A	—	—
0.5		N/A	—	—
0.9		N/A	—	—
0.95		0.9	112.3	29.6
1		1.5	107.1	27.9
1.05		2.1	94.9	26.6

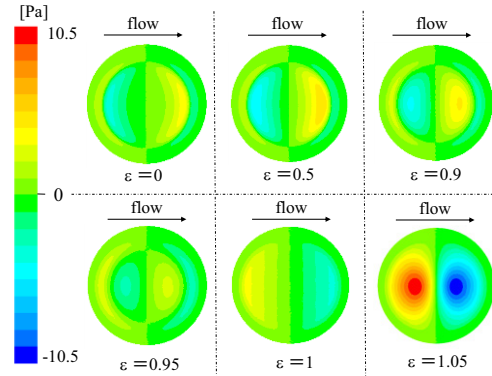


Fig. 5 Pressure distributions on bottom surface of the cell ($\alpha = 0^\circ$)

shape within the range of $0.9 < \varepsilon < 0.95$.

Distributions of pressure on the bottom surface of the red blood cell with $\alpha = 0^\circ$ are shown in Fig. 5. In comparison of the cases with equilibrium angle α_0 and the others, the distribution contrasts between the upstream side and the downstream side.

In summary, equilibrium state for force and moment acting on the cell can exist when the cell bottom shape is almost flat.

4. Conclusions

Three-dimensional analyses of the flow around a rigid red blood cell model were performed with various bottom shapes and angles of attack to understand the cell motion in an inclined centrifuge microscope. It is revealed that an equilibrium state for force and moment acting on the cell exists when the cell bottom shape is almost flat, and the frictional characteristics in the experiment may be explained for some cell shape.

5. References

- [1] Pries, A.R., et al., *Eur. J. Physiol.*, **440** (2000), 653-666.
- [2] Hayase, T. et al., *Trans. JSME* 68, No.676, B, (2002), 3386-3391, (in Japanese)
- [3] Kandori, T. et al., *J.Biomech. Eng.*, **130** (2008), 051007-1-8
- [4] Oshibe, T. et al., *Proc. 5th East Asian Pacific Student Workshop.* (2011), 82-83
- [5] Funamoto, K. et al., *JSME Int. J. Ser. C*, **46**, No.4 (2003), 1304-1311.

PS5: 6th Functionality DEsign of the COntact Dynamics: (DECO2012)

An Evaluation Method for Tangential Contact Stiffness Evaluation

Zahrul Fuadi^{1,2)*}, Toshiyuki Takagi²⁾, Hiroyuki Miki²⁾, and Koshi Adachi³⁾

¹⁾Department of Mechanical Engineering, Faculty of Engineering, Syiah Kuala University,
Jl. Syech Abdul Rauf No. 7 Banda Aceh, 23111, INDONESIA

²⁾Advanced Systems Evaluation laboratory, Institute of Fluid Science, Tohoku University,
Katahira 2-1-1, Aoba-ku, Sendai, 980-8577, JAPAN

³⁾Laboratory of Nanointerface Engineering, Division of Mechanical Engineering, Graduate School of Engineering,
Tohoku University, Aramaki-aza Aoba 6-6-1, Aoba-ku, Sendai, JAPAN

*Corresponding author: zahrulfuadi@gmail.com

ABSTRACT

The tangential contact stiffness is analyzed from the shift of certain eigenmode frequency of the system resulted from the change in the number of contact asperities and the application of normal force. As a result, it is shown that for the case of contact combination with 189 contact asperities, the corresponding eigenmode frequency shifted from 1.01 kHz at normal force of 19 N to 1.64 kHz at normal force of 148 N. This shift corresponds to the increase of the tangential contact stiffness from 34.08 MN/m at the normal force of 19 N to 67.44 MN/m at the normal force of 148 N.

1. Introduction

Topography of contact interface is one of the most important factors that determine not only the tribological but also the dynamic behavior of contacts. For example, contact topography is strongly related to generation of self-excited vibration in disc brake system [1,2]. Surface roughness has also been found to play a major role in generation of frictional sound in rubbing contact [3, 4]. Control of contact topography is therefore important for controlling the dynamic behavior of contacts.

In this paper, a novel method for estimation of the tangential contact stiffness of a contact interface with controlled contact asperities is discussed. The shift of certain eigenmode frequency of the system in contact as the result of normal force application and the change in the number of contacting asperities is analyzed and related to the quantitative value of the tangential contact stiffness. In addition to asperity controlled specimens, a group of model specimens with a specifically designed contact condition was used to describe the relationship between certain eigenmode frequency and the tangential contact stiffness. The model specimens are particularly useful in finding a clue to a real quantitative value of the tangential contact stiffness for a specific contact condition. It is expected that the proposed method can be applicable as a simple and quick method for evaluation of the tangential contact stiffness of a contact interface with controlled contact asperities.

2. Method

Two groups of specimens are prepared, denoted as block specimens and disk specimens. Block specimens and their contact characteristics are shown in Fig. 1(a). The block specimen is connected together by a built-in rod which is characterized by the ratio of diameter to length (ϕ/ℓ).

In case of the disk specimen, each of contact combination is illustrated in Fig. 1(b). The upper surface is smooth with roughness of $Ra=0.03 \mu\text{m}$ and the lower

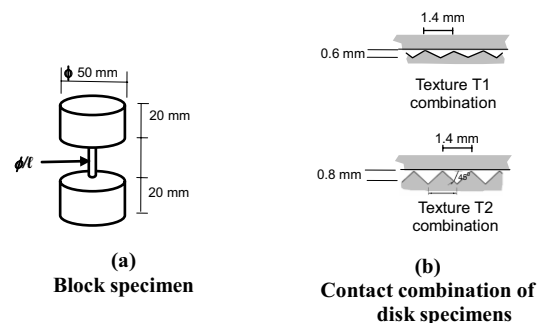


Fig. 1 Block specimen (a), and contact characteristic of disk specimens (b)

contact has textured as shown in Fig. 1(b). Both disk specimens and block specimens are 50 mm in diameter and 20 mm in thickness.

In the case of block specimens, the quantitative value of tangential contact stiffness is related to the occurrence of peak in the frequency response function (FRF) of these blocks when subjected to a small amount of impact. For the case of the disk specimens, the same method is used together with a newly proposed experimental setup shown in (Fig. 2).

3. Results

The estimated values of tangential contact stiffness, K , of block specimens and disk specimens can be summarized in Fig. 3. Those values are analyzed from the shift of peak frequencies of each system as the result of changes in contact condition. The increase of the contact stiffness values can be described using a power law given in the Figure. Here, it can be observed that the quantitative values of contact stiffness lie in the vicinity of a line illustrating the exponential increase of the contact stiffness to a theoretical maximum value, which is assumed if the contact occurs perfectly across all contact interfaces.

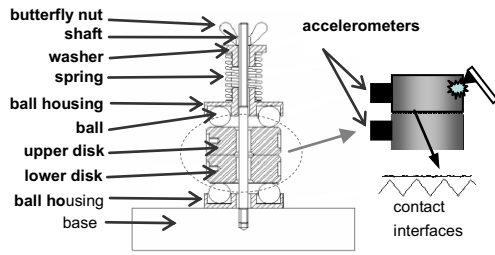


Fig.2 Experiment setup for tangential contact stiffness evaluation

Furthermore, the relationship between the tangential contact stiffness, K_T , and the peak frequency, f_p , can be described using a power relationship as follow:

$$K_T = C_1 f^{C_2}$$

where the parameters of C_1 and C_2 are constants determined experimentally.

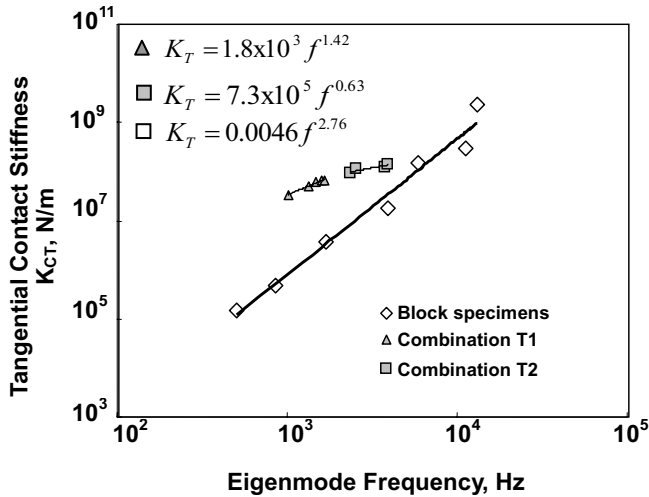


Figure 3 Relationship between tangential contact stiffness and eigenmode Frequency

4. Conclusions

The results can be concluded as follows:

1. The shift of eigenmode frequency in the frequency response function of a two-disk in contact with controlled contact asperities has been related to the tangential contact stiffness of the corresponding contact interfaces. It is found that for the each contact conditions, the shift is determined by the number of contact asperities and the normal force. For the case of contact combination I-T1 with 189 contact asperities, the corresponding eigenmode frequency shifted from 1.01 kHz at normal force of 19 N to 1.64 kHz at normal force of 148 N. This shift corresponds to the increase of the tangential contact stiffness from 34.08 MN/m at the normal force of 19 N to 67.44 MN/m at the normal force of 148 N. In the case of contact combination of I-T2 with 397 contact points, the corresponding eigenmode frequency shifted from 2.36 kHz at the normal force of 49 N to 3.9 kHz at the normal force of 153 N, which corresponds to the increase of the tangential contact stiffness from 93.91 MN/m to 140.73 MN/m.

5. References

- [1] M. Eriksson, F. Bergman, S. Jacobson. Surface characterization of brake pads after running under silent and squealing conditions. *Wear*, 232, 2, (1999), pp. 163–16
- [2] F. Bergman, M. Eriksson, S. Jacobson. Influence of disc topography on generation of brake squeal. *Wear*, 225-229, 1, (1999), pp. 621-628
- [3] B. L. Stoimenov, S. Maruyama, K. Adachi, K. Kato. The roughness effect of frequency of frictional sound. *Tribology International*, 40, 4 (2007), pp. 650-664
- [4] H. Ben Abdelounis, A. Le Bot, J. Perret-Liaudet, H. Zahouni. An experimental study of roughness noise of dry rough flat surfaces. *Wear*, 266, 1-2, (2010), pp. 650-664

Acknowledgement:

This research is supported by the Global COE Program, “World Center of Education and Research for Trans-disciplinary Flow Dynamics”, by the Ministry of Education, Culture, Sport, Science and Technology, Japan, which is gratefully acknowledged.

Tribological Behavior of Multiply-alkylated Cyclopentane Lubricated with Diamond-like Carbon Coating in the Running-in Period

Masanori Iwaki¹⁾²⁾, Takanori Takeno³⁾, Hiroyuki Miki⁴⁾ and Toshiyuki Takagi¹⁾

¹⁾ Institute of Fluid Science, Tohoku University, 2-1-1 Katahira, Aoba-ku, Sendai 980-8577, Japan

²⁾ Japan Aerospace Exploration Agency, 2-1-1 Sengen, Tsukuba 305-8505, Japan

³⁾ School of Mechanical Engineering, Tohoku University, Aramaki aza Aoba 6-3, Aoba-ku, Sendai 980-8578, Japan

⁴⁾ Center for Interdisciplinary Research, Tohoku University, Aramaki aza Aoba 6-3, Aoba-ku, Sendai 980-8578, Japan

E-mail of corresponding author: iwaki.masanori@jaxa.jp

ABSTRACT

In order to improve lubrication properties of multiply alkylated cyclopentane (MAC) oil, diamond-like carbon (DLC) coatings were deposited. Pin-on-disk friction tests in boundary lubrication regime were conducted for DLC-coated and non-coated samples in ambient air and in vacuum. There are clear differences in the formation of friction-induced surface layer formed in the contact area, which influence the tribological properties of MAC oil.

1. Introduction

Currently, Multiply-alkylated cyclopentane (MAC) is the most popular liquid lubricant for space mechanisms thanks to its excellent tribological properties in vacuum. But when a high contact pressure is applied in vacuum, it has relatively high friction coefficient in the running-in period, which produces considerable wear [1]. The authors have reported the effectiveness of diamond-like carbon (DLC) coating for this problem [2]. In this research, the tribological behavior of MAC in the running-in period was investigated in different friction conditions.

2. Method

Table 1 shows the properties of samples prepared for this research. Two types of amorphous carbon coatings (a-C and a-C II) deposited by magnetron sputtering and a hydrogenated amorphous carbon coating (a-C:H) deposited by radio frequency plasma chemical vapor deposition (RF plasma CVD) were prepared. A 440C stainless steel disk without DLC coating was also prepared for comparison. A droplet of MAC oil was put on each sample and spread uniformly over the surface using a centrifuge machine to have about 1 μg in weight.

Table 1 Properties of samples

Name	440C	a-C	a-C:H	a-C II
Material	-	DLC (a-C)	DLC (a-C:H)	DLC (a-C)
Deposition method	-	Magnetron sputtering	RF plasma CVD	Magnetron sputtering
Deposition material	-	Graphite	CH ₄ +H ₂	Graphite
Thickness, μm	-	1		2
Content of hydrogen, at. %	-	5	30	0
Interlayer	-	Gradient Cr-DLC		Cr
Substrate	440C stainless steel			15-5PH
Surface roughness	30 nm <i>R_a</i> 300 nm <i>R_z</i>			
Hardness, GPa	8.14	7.33	10.96	12.22
Elastic modulus, GPa	203	157	190	216
H/E ratio	0.038	0.047	0.058	0.057

Pin-on-disk friction tests were conducted in ambient

air and in vacuum. The mated pins are made of 440C stainless steel with a diameter of 6 mm. Detailed friction test conditions are described in Table 2. Optical observations and EPMA (Electron Probe Micro Analyzer) analysis are conducted for the wear tracks on the disks and the wear scars on the pins after the friction tests.

Table 2 Friction test conditions

Friction mode	Reciprocating slide (Pin-on-disk)
Pin diameter, mm	6
Pin material	440C stainless steel
Friction width, mm	2
Sliding speed, mm/s	2
Load, N (Maximum contact stress, GPa)	3 (0.88)
Number of reciprocating slides	10000
Test atmosphere	Air, Vacuum (below 1×10^{-5} Pa)

3. Results and Discussion

Friction behavior of the DLC-coated and non-coated samples are shown in Fig. 1 and Fig. 2. The DLC-coated samples demonstrated lower friction coefficients than 440C both in ambient air and in vacuum. In ambient air, the DLC-coated samples started with friction coefficients over 0.1 and they decreased to the range from 0.07 to 0.08 immediately, while the friction coefficient of 440C stayed around 0.1 after a temporal increase over 0.15 in the very initial stage of friction. In vacuum, the DLC-coated samples had very low friction coefficients around 0.04, but more friction cycles were needed to have the lowest friction coefficient compared with ambient air tests. The 440C sample had fluctuating friction coefficient ranging from 0.08 to 0.14 in ambient air.

Figure 3 shows the specific wear rate and the width of wear track on the disk. The wear tracks on all the DLC-coated samples were too small to distinguish from the original surface profile of the disk by surface profilometer. Those of vacuum tests are barely visible by optical microscope but those of ambient air tests are invisible. On the other hand, the specific wear rates of the pins were smaller for a-C and a-C:H and larger for a-C II compared with those of 440C (Fig. 4). This can be considered to be due to the highest hardness of a-C II among the samples.

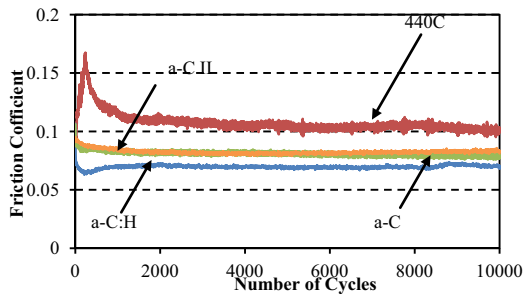


Fig. 1 Friction coefficient in ambient air

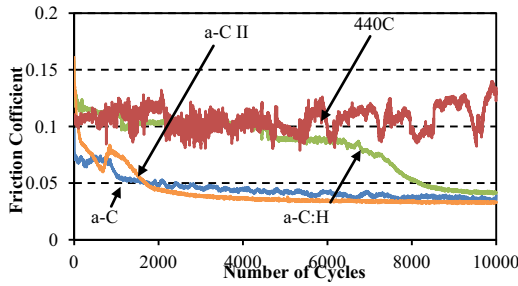


Fig. 2 Friction coefficient in vacuum

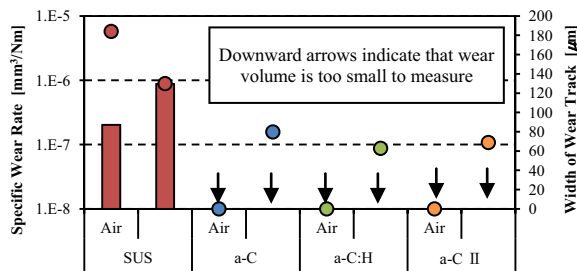


Fig. 3 Specific wear rate and width of wear track on the disk

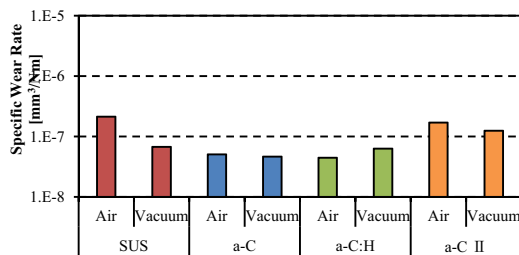


Fig. 4 Specific wear rate of the pin

Figure 5 shows the element mapping result by Electron Probe Micro Analyzer (EPMA) after removing MAC oil on the a-C II sample. Much oxygen and less carbon were observed after ambient air friction test which means that there were not any transfer film of DLC and that iron oxide film was formed. Contrarily, oxygen was not detected and clear carbon film was found in the wear scar after vacuum friction test which indicates that transfer film of DLC was formed. These results were same for other DLC samples.

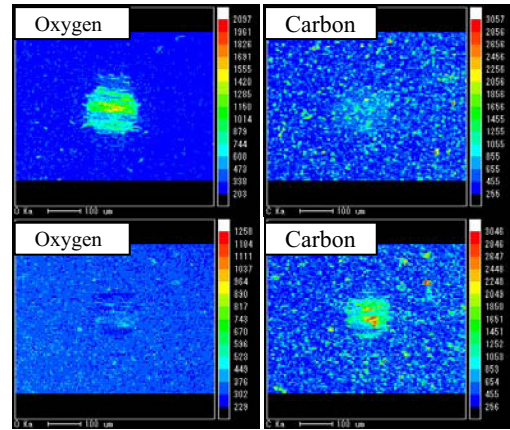


Fig. 5 EPMA element mapping of the pin for a-C II sample; after ambient air test(upper) and vacuum test(lower).

From the above results, the friction coefficient decreases as the friction-induced surface layer in the contact area forms in the running-in period (oxidized layer of iron in ambient air and transfer film of DLC in vacuum). The oxidized layer in ambient air forms faster than the transfer film of DLC in vacuum because the number of friction cycles needed to have reduced friction coefficient, while the transfer film of DLC has better lubricity than the oxidized layer because the final friction coefficient is lower in vacuum than in ambient air. In all cases, DLC-coated samples had lower friction coefficient than 440C sample. As the friction condition is boundary lubrication in this research, reducing the shear force of solid-solid contact by the application of DLC coating is very effective to reduce the friction coefficient. On the other hand, it is indicated that wear properties are related with mechanical properties of the DLC coatings. It is known that a material having a high ratio of hardness to Young's modulus is wear tolerant [3]. This is in good agreement with the result in this research. Deposition method of DLC did not affect the tribological properties in this research.

4. Concluding remarks

- Improvement of the boundary lubrication properties of MAC oil can be achieved by the application of DLC coatings.
- Reduction of friction coefficient of MAC oil lubrication with DLC coating is related with the formation of oxidized layer (in ambient air) or transfer film of DLC (in vacuum) on the contact surface. Oxidized layer forms faster than transfer film of DLC but transfer film of DLC has better tribological properties than oxidized layer.
- Wear properties are more related with mechanical properties of the DLC coatings than deposition method.

References

- [1] M. Masuko *et al.*, *J. Syn. Lub.*, **24** (2007) 217.
- [2] M. Iwaki *et al.*, 8th ICFD (2011) 650.
- [3] A. Layland *et al.*, *Wear*, **246** (2000) 1.

Effects of Substrate Bias Voltage and Target Sputtering Power on the Structural and Tribological Properties of Carbon Nitride Coatings

Pengfei Wang^{1*}, Takanori Takeno², Fontaine Julien³, Masami Aono⁴, Koshi Adachi², Hiroyuki Miki¹, Toshiyuki Takagi¹

¹ Institute of Fluid Science, Tohoku University, Katahira 2-1-1, Aoba-ku, Sendai 980-8577, Japan

² Laboratory of Nanointerface Engineering, Division of Mechanical Engineering, Tohoku University, Aoba 6-6-1, Aramaki, Aoba-ku, Sendai 980-8579, Japan

³ Laboratoire de Tribologie et Dynamique des Systèmes, UMR 5513 – CNRS/Ecole Centrale de Lyon, Bâtiment H10, 36 Avenue Guy de Collongue, Écully Cedex 69134, France

⁴ Department of Materials Science and Engineering, National Defense Academy, 1-10-20 Hashirimizu, Yokosuka, Kanagawa 239-8686, Japan

* E-mail of corresponding author: wang@wert.ifs.tohoku.ac.jp

ABSTRACT

Carbon nitride (CN_x) coatings were prepared using a CVD-PVD hybrid coating process at different substrate bias voltage and target sputtering power, i.e. -400V 200W, -400V 100W, -800V 200W, and -800V 100W. With the increase of substrate bias voltage and the decrease of target sputtering power, the deposition rate, N/C atomic ratio, hardness, and frictions of CN_x coatings decreased, while the residual stress of CN_x coatings increased. It is concluded that the substrate bias voltage and target sputtering power are effective parameters for controlling the structural and tribological properties of CN_x coatings.

1. Introduction

Excellent performances of carbon nitride (CN_x) coatings, such as low friction and high wear resistance make them good candidates for the advanced low friction mechanical systems [1]. However, those behaviors are strongly related to the deposition method of CN_x coatings. Recently, a CVD-PVD hybrid coating process, combining radio frequency plasma enhanced chemical vapor deposition (RF PECVD) and DC magnetron sputtering has been applied for the development of high performance CN_x coatings. It has been claimed that the friction behavior of CN_x coatings is highly related to the bonding structure rather than the composition of the CN_x coatings [2]. On the other hand, nitrogen ion energy is clarified to be a promising factor for tailoring the structural as well as tribological properties of the CN_x coatings [3, 4]. In the hybrid coating process, the nitrogen ion energy in the plasma can be well controlled by adjusting the substrate bias voltage and target sputtering power. Therefore, in this study, the effects of substrate bias voltage and target sputtering power on the structural and tribological properties of the CN_x coatings are investigated, with the objective to further clarify the friction mechanisms of CN_x coatings from the coating structure.

2. Experimental Procedure

CN_x coatings (~400 nm) were grown on Si (100) substrates using a hybrid coating process with the combination of RF PECVD and DC magnetron co-sputtering of the graphite target [2]. The coatings were deposited at a pressure of 1.3 Pa using a mixture of nitrogen and argon as a gas source with the N₂/Ar flow ratio of 0.1. Four combinations of substrate bias voltage and target sputtering power, such as -400V 200W, -400V 100W, -800V 200W, and -800V 100W, were employed. Thickness of CN_x coatings were measured with a surface profiler. The composition of CN_x coatings was measured by X-ray photoelectron spectroscopy. The residual stress of CN_x coatings was calculated by the bending beam method [5]. The hardness of CN_x coatings

was measured under both single stiffness mode and continuous stiffness mode for confirmation of the results. A pin-on-plate reciprocating tribometer was used for friction test. The CN_x coated Si substrates (10×20 mm) were driven to run against AISI 52100 balls (φ=6 mm) with a normal load of 1 N, a sliding speed of 3 mm/s, a stroke length of 3 mm, and a sliding period of 5000 cycles. Friction tests were performed in ambient air (23-25 °C and 30-40 %RH) and N₂ gas stream.

3. Results and Discussion

The deposition rate of CN_x coatings greatly decreased with the increase of substrate bias voltage from -400 to -800 V and the decrease of target sputtering power from

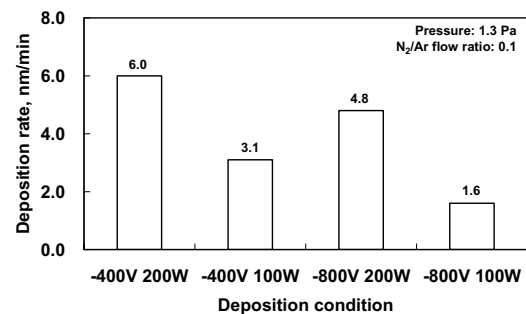


Fig. 1 Deposition rate of CN_x coatings.

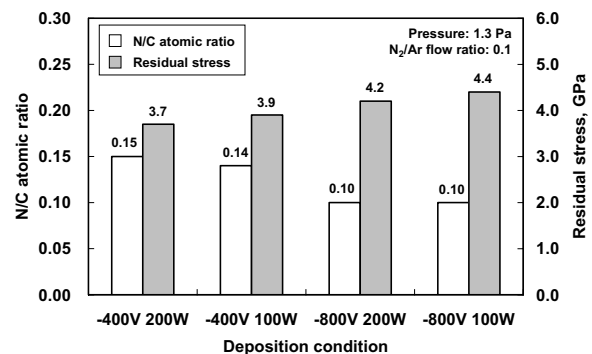


Fig. 2 N/C atomic ratio and residual stress of CN_x coatings.

200 to 100 W (Fig. 1). The lowest deposition rate of 1.6 nm/min was obtained at substrate bias voltage of -800 V and target sputtering power of 100 W (denoted as -800V 100W), which is only 27% of that at -400V 200W. As shown in Fig. 2, the N/C atomic ratio of CN_x coatings decreased from around 0.15 to 0.10 with the increase of substrate bias voltage from -400 to -800 V. Whereas, it kept almost constant with decreasing target sputtering power from 200 W to 100 W. The residual stress slightly increased with the increase of substrate bias voltage and the decrease of target sputtering power (Fig. 2). The lowest residual stress of 3.7 GPa was observed at -400V 200W. On the contrary, hardness of CN_x coatings decreased with the increase of substrate bias voltage and the decrease of target sputtering power (Fig. 3). The highest hardness of 15.0 GPa from single stiffness mode was obtained at -400V 200W. It is clarified that substrate bias voltage is more effective than target sputtering power in controlling the structural properties (N/C atomic ratio, residual stress, and hardness) of CN_x coatings. It is assumed that the adjustment of the nitrogen ion energy in the plasma by increasing substrate bias voltage and decreasing target sputtering power results in the composition and bonding structure changes of the CN_x coatings, thus causing the increase of the residual stress and decrease of the hardness.

Typical friction curves of CN_x coating (-800V 200W) sliding against AISI 52100 pin in air and N_2 gas stream are shown in Fig. 4. The frictions both in air and N_2 gas stream reached steady state after initial run-in. The average friction coefficients of CN_x coatings in air and N_2 gas stream are summarized in Fig. 5. The frictions in N_2 gas stream were higher than those in air. The frictions decreased with increasing substrate bias voltage and decreasing target sputtering power. The lowest friction coefficients of 0.11 and 0.12 were obtained in air and N_2 gas stream at -800V 100W, respectively. It is concluded that higher substrate bias voltage and lower target sputtering power are beneficial for reducing the frictions of CN_x coatings in air and N_2 gas stream. It is believed that the clarification of relationship between friction and structural properties of the CN_x coatings will help us better understand the friction mechanisms of CN_x coatings.

4. Summary

(1) Substrate bias voltage and target sputtering power are effective parameters for controlling structural and tribological properties of CN_x coatings.

(2) Higher substrate bias voltage and lower target sputtering power are beneficial for reducing the frictions of CN_x coatings in air and N_2 gas stream.

Acknowledgement

This research is supported by the Global COE Program, "World Center of Education and Research for Trans-disciplinary Flow Dynamics", by Ministry of Education, Culture, Sports, Science and Technology (MEXT) in Japan.

References

[1] P. Wang, K. Adachi, *Tribol. Online*, 6 (2011) 265-272.

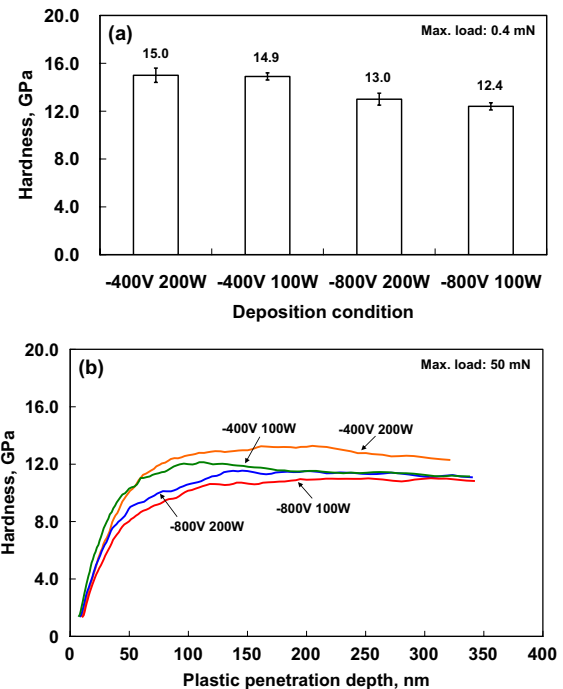


Fig. 3 Hardness of CN_x coatings measured under (a) single stiffness mode and (b) continuous stiffness mode.

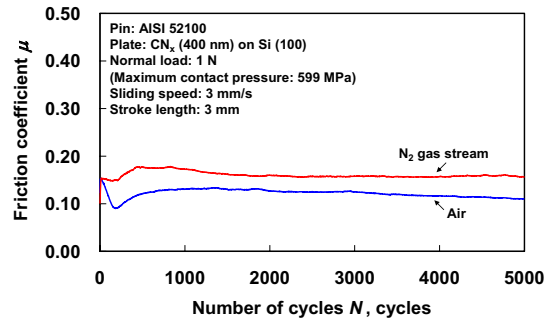


Fig. 4 Friction curves of CN_x coating (-800V 200W) sliding against AISI 52100 pin in air and N_2 gas stream.

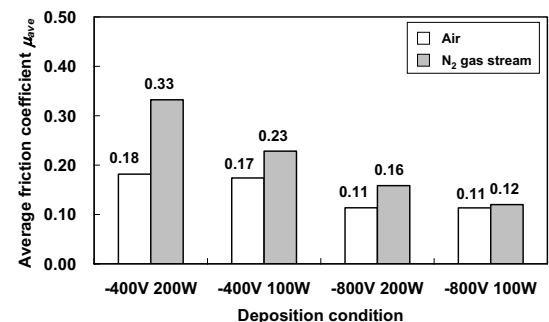


Fig. 5 Average friction coefficients of CN_x coatings sliding against AISI 52100 pins in air and N_2 gas stream.

- [2] P. Wang, T. Takeno, K. Adachi, H. Miki, T. Takagi, *Appl. Surf. Sci.*, 258 (2012) 6576-6582.
 [3] S. Wei, T. Shao, P. Ding, *Diamond Relat. Mater.*, 19 (2010) 648-653.
 [4] S. Wei, T. Shao, J. Xu, *Surf. Coat. Technol.*, 206 (2012) 3944-3948.
 [5] G. G. Stoney, *Proc. R. Soc. Lond. A*, 82 (1909) 172-175.

Towards Super-low Friction With Carbon-Based Coatings

Michel Belin¹, Hiroyuki Miki², Maria-Isabel De Barros-Bouchet¹, Julien Fontaine¹
Takanori Takeno³, Toshiyuki Takagi⁴

¹ LTDS, CNRS, Ecole Centrale de Lyon, 36 rue Guy de Collongue, 69134 Ecully cedex, France

² Center for Interdisciplinary Research, Tohoku University, Aramaki asa Aoba 6-3, Aoba-ku, Sendai, Japan

³ Graduate School of Engineering, Tohoku University, Aramaki asa Aoba 6-6, Aoba-ku, Sendai, Japan

⁴ Institute of Fluid Science, Tohoku University, 2-1-1 Katahira, Aoba-ku, Sendai, Japan

michel.belin@ec-lyon.fr

ABSTRACT

This present project is to explore the low and ultra-low friction that it is possible to get on contacts involving carbon-based thin films. Recent results reported demonstrate the surprisingly low friction values (range 10^{-2} to 10^{-3}), on thin films of microcrystalline diamond in the air, no liquid lubricant or additive being involved in. A technique has been recently developed at LTDS, called "relaxation tribometer", allows further characterization of the friction of a sliding interface with component identification "solid-type friction" and "viscous-type friction". This new project is aiming to characterize friction of microcrystalline, nanocrystalline diamond films, and various DLC.

1. Introduction

The low and ultra-low friction is identified as one of the current challenges of tribology [1,2]. Different kinds of tribosystems are expected to exhibit low friction performances. One of them is some hard coatings, and especially the carbon-based coatings under dry lubrication. Interesting results have been reported previously, obtained on CVD diamond-films. Friction coefficient values as low as 0.01 have been reached in air [3]. The authors have shown that the friction results were strongly influenced by contact conditions, especially the sliding speed. Some modelization with fluid mechanics has been achieved to describe the incidence of air flow when rubbing of very smooth surfaces. These results are very convincing, but not fully understood yet.

Starting from that point, we have set a new research program. The objective of the present project is to work on the theme of low and ultra-low friction obtained on thin films based on diamond coatings. In particular the group of H. Miki *et al.* at Tohoku University, has recently highlighted a milli-range order friction, with a contact of slightly polished microcrystalline diamond thin layers. For the other side, LTDS has setup an elaboration platform for development of thin films of nanocrystalline diamond. The complementary skills have been joined in this project to go further in the knowledge of low friction processes.

This project aims at the detailed characterization of the low friction technique called "relaxation tribometer". In particular, we will seek to quantify the two components of type "solid-type friction" independent of the speed and type "viscous-type friction" speed-dependent, identified through the use of this technique. It should be noticed that this approach has no equivalent today. Expected results should enable us to move on elucidating the phenomenon of low friction: friction coefficient in the range 10^{-2} to 10^{-4} and even lower if it happens.

2. Method

Recently, a new apparatus called "relaxation tribometer" has been developed at LTDS in order to measure the kinematic friction between two sliding surfaces [4]. The mechanical system is described by a mass-spring-damper system, based on dynamic free responses of a single degree-of-freedom mechanical oscillator. This technique has been used to carefully determine, with no need for any force measurement, the velocity-independent and velocity-dependent friction contributions, μ and ζ respectively, for a linear description of the kinematic friction, μ_k .

3. Preliminary experiments

In order to get very first results, we have performed preliminary experiments on a diamond coating surface, elaborated at Tohoku University. The diamond coating was deposited by the Hot Filament CVD method on that substrate. Deposited microcrystalline diamond film was performed machine polishing processing. The counterface was a stainless steel sphere, AISI 52100. The normal load was ranging from 50 to 300 mN. The experiments have been run in air, temperature of 25°C and humidity RH 68%.

4. Results and discussion

We present below the time-response of the loaded contact, during its evolution from the initial situation, up to the final stop, through a damped oscillating process, see Fig. 1. The normal load was set to 50 mN. In these mild conditions, the maximum Hertzian pressure was 270 MPa and no wear is expected to occur. We can observe the decay of amplitude, due to low friction value at the interface. From a qualitative point of view, we also can notice that the decay curve of the envelope is not strictly linear, giving evidence for a speed-depending contribution of friction. Data are currently under processing, for quantification of these two contributions, according to the identification technique described previously [4].

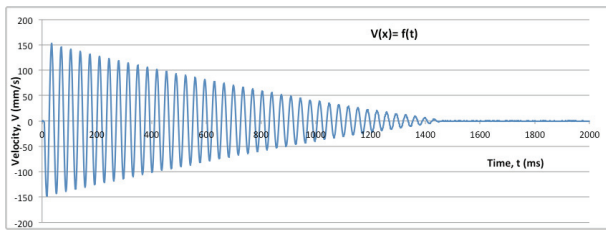


Fig. 1 Relaxation behavior of a diamond-steel contact, as operating in air. The figure shows the velocity time-response of the contact under relaxation conditions. Contact conditions: 100C6 stainless steel sphere rubbing on diamond, ambient air, normal load 50 mN.

Acknowledgments

The authors are thankful to *Institut Carnot I@L, France* for partial funding the development of the experimental technique, and to IFS, ELYT Lab. and CNRS for their interest in this new project.

References

- [1] Superlubricity, A. Erdemir & JM Martin Eds., Elsevier, (2007), ISBN: 978-0-444-52772-1.
- [2] J. Fontaine, M. Belin, T. Le Mogne, A. Grill, Trib. Int., **37** (2004), 869-877.
- [3] H. Miki, A. Tsutsui, T. Takeno, T. Takagi, Diamond and Related Materials, **24** (2012), pp. 167–170.
- [4] E. Rigaud, J. Perret-Liaudet, M. Belin, L. Joly-Pottuz, J.M. Martin, Trib. Int., **43** (2010), pp. 320–329.

Adhesion and Friction Properties of Partially Polished CVD Diamond Films on Steel Substrates

Hiroyuki Miki¹, Yosuke Nakayama², Takanori Takeno², Toshiyuki Takagi³

1) Center for Interdisciplinary Reserch, Tohoku University, Aramaki asa Aoba 6-3, Aoba-ku, Sendai, Japan

2) Graduate School of Engineering, Tohoku University, Aramaki asa Aoba 6-6, Aoba-ku, Sendai, Japan

3) Institute of Fluid Science, Tohoku University, 2-1-1 Katahira, Aoba-ku, Sendai, Japan

E-mail: miki@cir.ifs.tohoku.ac.jp

ABSTRACT

Adhesiveness and sliding characteristics of the polished polycrystalline diamond which were deposited on the steel substrate by the hot filament chemical vapor deposition method were evaluated. By using Ti intermediate layer of 2 μm film thickness, the diamond films deposited in this research have got the properties of good adhesiveness and fracture toughness.

1. Introduction

Chemical vapor deposition (CVD) diamond film has fine characteristics, such as low friction, high hardness, wear proof, and chemical stability. These characteristics are useful to a bearing and a moving part, and the CVD diamond film is expected as a novel solid lubricant.

We have reported that the polycrystalline diamond film deposited on the ceramic substrate has good friction characteristics between stainless steels [1, 2]. In this case, the diamond film has the surface shape where the deposited surface was polished properly. Although ceramic substrates, such as SiC and TiC, are usually used for diamond deposition, they have a problem of a shock resistance or a workability.

It is preferable to deposit a diamond film on a stainless steel substrate for applying. However, the big issue is present to deposit a diamond film on a stainless steel. It has low adhesiveness with a substrate, and a delamination occurs. One reason is thermal stress originating from the difference of the linear expansion coefficient between diamond and steel. And another is influence of the graphite generated between a film and a substrate by the effect of an iron catalyst.

In this paper, the method of preparing an intermediate layer between a diamond film and a stainless steel substrate was proposed. The deposited diamond has the good adhesiveness between stainless-steel substrates. The adhesiveness and sliding characteristics of the polished CVD diamond film were evaluated.

2. Experiment

The specimen prepared in this research is shown in Fig. 1. Ti intermediate layer was deposited on the surface of the stainless steel substrate (AISI440C: 20x20x4 mm) by magnetron sputtering. The surface roughness of the substrate was machined into $Ra=0.5 \mu\text{m}$. There was no difference at measured surface roughness before and after the process of intermediate layer deposition.

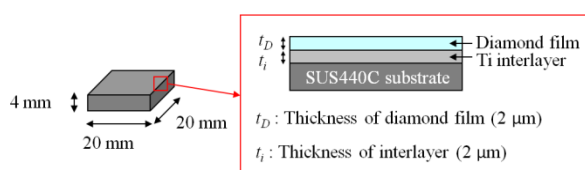


Fig.1 Schematic illustration of specimen

Table 1 Sputtering Condition for Ti interlayer

Target	Ti
Ar pressure	1.3 Pa
DC power	100 W
Thickness of the interlayer	2 μm

Table 2 Deposition condition of HFCVD

Particle size of diamond seeds	Less than 0.5 μm
Flow rate of H_2	100 ml/min
Flow rate of CH_4	2.3 ml/min
Gas pressure	11 kPa
Filament temperature	1800 $^\circ\text{C}$
Thickness of diamond film	2 μm

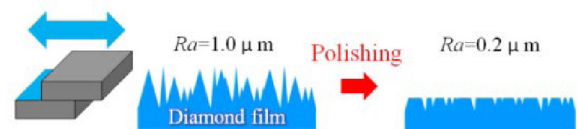


Fig.2 Simplified diagram of polishing process.

The diamond film was deposited by the Hot Filament CVD (HFCVD) method on that substrate. The deposition conditions of an intermediate layer and a diamond film are shown in Table 1 and 2, respectively.

The diamond film of 2 μm thickness was prepared in about 5 hours. Surface roughness Ra of the as-deposited diamond film is about 1.0 μm . Deposited CVD diamond films were performed machine polishing processing shown in Fig. 2 using the diamond film of the same kind. Those finished surface were controlled to

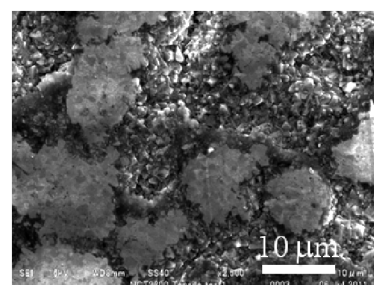


Fig.3 SEM image of polished diamond surface

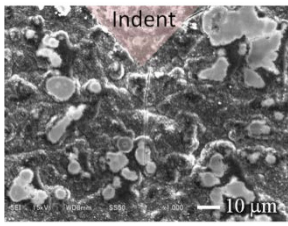


Fig.4 SEM image of indent corner (AISI440C substrate: 50 kgf)

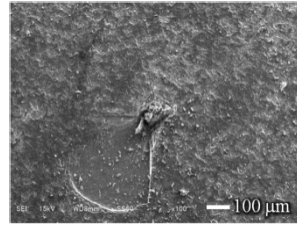


Fig.5 SEM image of indent (SiC substrate: 50 kgf)

the surface roughness $Ra=0.2 \mu\text{m}$, as shown in Fig. 3.

3. Indentation test

In order to evaluate the adhesiveness of the polished CVD diamond film prepared on the stainless steel substrate with Ti intermediate layer, the indentation test by a Vickers hardness tester was performed. The indentation test of the diamond film directly deposited on the silicon carbide substrate was done similarly. The indentation-test result of each substrate under 50 kgf load is shown in Fig.4 (AISI440C substrate) and Fig. 5 (SiC substrate).

In fig. 4, the crack length is recognized about $40 \mu\text{m}$ from the indent corner, but crack width is very small and a delamination is not observed in a neighborhood part. On the other hand, a large-scale crack and large area delamination occurred at the tested diamond on SiC substrate, which shown in Fig. 5.

In the case of AISI440C substrate, the internal stress between layers was released by an intermediate layer and the stacked layer structure and internal stress was released by the crack formation at the indent corner. It was difficult to compare adhesiveness precisely, but the diamond film got the strength to local damage and a high reliability by preparing Ti intermediate layer.

4. Ball-on-disk testing

The load dependence of the diamond film on the AISI440C substrate with Ti intermediate layer was evaluated using Ball-on-disk testing of a reciprocating motion. Test conditions are shown in Table 3.

The result of testing in each load is shown in Fig.6. Stable friction coefficient nearly 0.12 was obtained on light load conditions (1, 3N), and the friction coefficient became high in the loading condition of 5, 7N.

Table 3 Condition of reciprocal ball-on-disk test

Load	1, 3, 5, 7 N
Sliding speed v	$v=7.5\sin(\omega t)$ mm/s
Track length	15 mm
Number of laps	10,000
Ball	100Cr6 $\phi 6$ mm

Table 4 Calculated contact pressure after the friction test

Load (N)	Contact pressure (MPa)
1	10.22
3	11.04
5	2.94
7	2.23

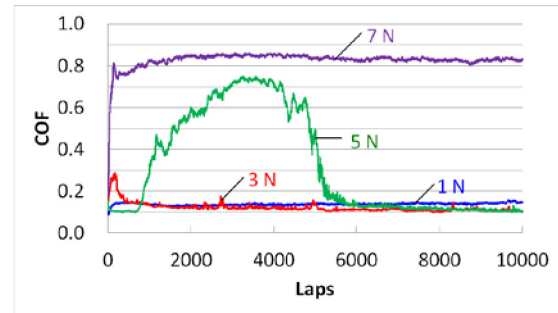


Fig.6 Applied load dependence of friction properties on polished diamond films against AISI440C pins.

Especially at the 5N load, friction coefficient temporarily increased after 700 cycles, and was recovered to around 0.12 at the time of a test terminated.

In order to clarify the load dependence of a sliding, the distribution of the iron oxide on wear traces was analyzed by Energy dispersive X-ray spectrometry. It was shown that the distribution range of iron oxide increases with the increase in loading. When the wear debris of the ball remained in the contact part, the metal to metal contact between wear debris and ball was induced. This is the dominant cause of a high friction coefficient in the conditions of load (5, 7N).

The contact pressure of the test-termination step calculated from the wear area of the ball is shown in Table 4. If wear debris does not remain on a contact surface, the maximum contact pressure which does not wear 100Cr6 ball is about 10 MPa.

5. Conclusion

By using Ti intermediate layer of $2 \mu\text{m}$ film thickness, the CVD diamond film which has good adhesiveness was made on the AISI440C substrate.

It was certified from the result of the indentation test that a diamond film is tough to local damage, and reliable. Furthermore, the boundary condition of the low wear sliding under control of the adhesion of wear debris was clarified.

Acknowledgment

This work was partially supported by the Asahi Glass Foundation in Japan, Grant-in-Aid for Scientific Research (23656113) of Japan Society for the Promotion of Science (JSPS). Authors give recognition to Mr. Takeshi Sato from Institute of Fluid Science, Tohoku University, Japan, for their technical assistance.

References

- [1] T. Takeno, et al, *Diamond and Related Materials* **14** (2005), p. 2118.
- [2] H. Miki, et al, *Diamond and Related Materials* **17** (2008), pp. 868-872.

Tribological Properties of Ag-DLC under Various Loading Conditions

Minoru GOTO¹⁾, Julien FONTAINE²⁾, Takanori TAKENO³⁾, and Hiroyuki MIKI³⁾

1) Ube National College of Technology, Japan, 2) Ecole Centrale de Lyon, France, 3) Tohoku University, Japan
mi-goto@ube-k.ac.jp

ABSTRACT

We have studied the tribological properties of silver-diamond-like carbon nanocomposite (Ag-DLC) coating against two kinds of slider materials under various loading conditions using pin-on-flat type tribometer in ambient air. The normal load dependency of friction coefficient of Ag-DLC against bearing steel was larger than that against brass. Ag-rich tribofilm was formed on the counter surface of slider both bearing steel and brass. Ag concentration in the tribofilm on the brass ball is higher than that on steel ball, which may have correlation with solubility of metals.

1. Introduction

Diamond-like carbon (DLC) coatings have been attracting a lot of researchers because of their excellent tribological characteristics such as low friction coefficient, high hardness and chemical inertness [1]. However, the DLC coatings cannot be applicable for the electric contact materials, because the DLC is lacking of electrical conductivity. In addition to that, the friction coefficient of DLC is sensitive to the loading condition during sliding.

Adding metals to DLC coatings is thus considered as a powerful method to improve electrical conductivity as well as tribological properties. Copper and silver are powerful candidates as additives because of their low electrical resistivity. In recent years, we have reported that the Cu doped DLC (Cu-DLC) showed stable friction coefficient under various loading conditions [2, 3]. This means that the load dependency of friction coefficient of Me-DLC may vary with additive metal. In this study, the friction behaviors of Ag-DLC under various loading conditions have been reported.

2. Method

A Si (100) wafer with dimensions of $8 \times 10 \times 0.6$ mm³ was used as a substrate for Ag-DLC coatings. The Si (100) substrate was ultrasonically cleaned by organic alkaline solution, and rinsed by distilled water. A drop of water on the substrate was removed by clean nitrogen blow, and then the substrate was introduced into the coating chamber of Ag-DLC. The Ag-DLC coating was deposited on a Si (100) wafer using hybrid deposition process composed of plasma enhanced chemical vapor deposition (PECVD) and DC magnetron co-sputtering of Ag target [4]. Acetylene was used as a precursor. The Ag concentration in the coating was estimated as 75 at.% by energy dispersive X-ray spectroscopy (EDS).

The tribological experiments of Ag-DLC were performed using linear reciprocating tribometer. The JIS SUJ2 bearing steel ball and JIS C2700 brass ball were used as counter materials. The diameter of the steel ball was 6 mm, and that of brass ball was 6.35 mm, respectively. The sliding length and the sliding speed were 3 mm and 2 mm/s, respectively. The normal load was applied ranging from 0.5 to 10 N, which yielded maximum Hertz contact pressure ranging from 0.5 to 1.4 GPa. After tribological experiments, the worn surfaces were observed by optical microscope (OM) and

scanning electron microscopy (SEM), and the chemical compositions of the worn surfaces have been analyzed by EDS.

3. Results and Discussion

Figure 1 shows the transition of friction coefficient until 2000 cycles between Ag-DLC and SUJ2 steel ball under various loading condition ranging from 0.5 to 10 N. The friction coefficients start at around 0.3 for all loading condition. When the normal load was 0.5 N, the friction coefficient increased gradually as the sliding cycle progress, and was reached to around 0.4 at the sliding cycles of 2000. Whereas, the friction coefficient decreased as the sliding cycle increase at the normal load of 10 N. The steady-state friction coefficient after 1000 cycles decreased from 0.4 to 0.15, as a function of the normal load. This result indicated that the friction coefficient between Ag-DLC and SUJ2 ball shows normal load dependency clearly.

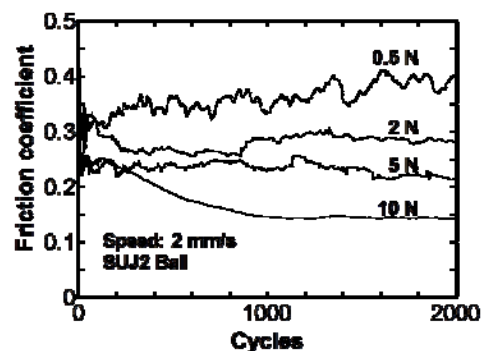


Fig. 1 Transition of friction coefficient between Ag-DLC and SUJ2 steel ball

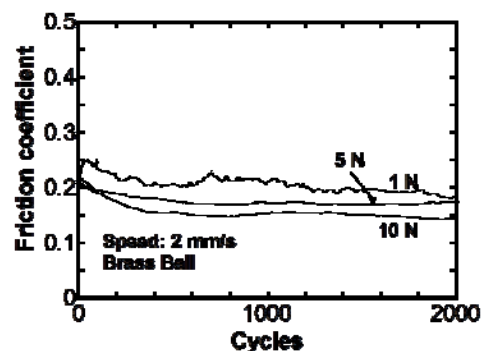
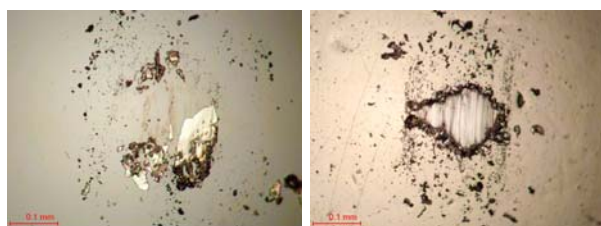


Fig. 2 Transition of friction coefficient of Ag-DLC sliding against C2700 brass ball

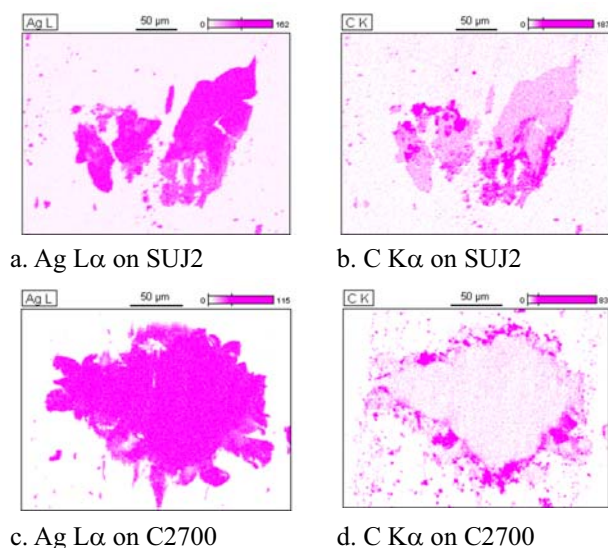
Figure 2 shows the transition of friction coefficient of Ag-DLC against C2700 brass ball. The friction coefficients start from between 0.2 and 0.25, which were slightly smaller than Ag-DLC/SUJ2 combination. The friction coefficient decreased as the sliding cycle increase for all loading conditions. The steady state friction coefficients were changed from 0.19 to 0.14 as a function of the normal load. This result indicates that the normal load dependency of the friction coefficient against C2700 ball is smaller than that against SUJ2.

The load-dependent friction behavior under the Hertz contact condition is reported for many solid lubricants, and the behavior can be explained by the Hertz contact model in which the friction coefficient depends upon elastic module and radius of curvature of slider as well as the normal load [5]. It is found that the load-dependent friction behaviors of Ag-DLC against SUJ2 and C2700 ball follow this model.

Figure 3 shows the tribofilms with metallic luster formed on a) SUJ2 ball and b) C2700 ball under the normal load of 10 N. The tribofilm evolving on SUJ2 ball has been removed partly from the ball surface, and the removed part remained on the worn track of Ag-DLC. On the other hand, the tribofilm formed closely on the C2700 surface. This means that the adhesive strength of tribofilm on the copper alloys is stronger than that on the steel.



a. SUJ2 surface b. C2700 surface
Fig. 3 Tribofilms formed on a. SUJ2 ball and C2700 ball under the normal load of 10 N.



a. Ag Lα on SUJ2 b. C Kα on SUJ2
c. Ag Lα on C2700 d. C Kα on C2700
Fig. 4 Ag Lα and C Kα images of tribofilms formed on SUJ2 ball (a and b), and C2700 ball (c and d) under the normal load of 10 N.

The adhesive strength of tribofilm is considered to have strong correlation with solubility of materials between tribofilm and slider. Figure 4 show the chemical mapping of Ag and C for two kinds of tribofilm. The purity of Ag of the tribofilm on C2700 ball is higher than that on SUJ2 ball. The solubility of Ag against Cu is significantly higher than that against steel, whereas the solubility of C against Cu is extremely lower than that against steel. The tendency of the adhesive strength of Ag-rich tribofilm on the slider surface shows good agreement with the degree of solubility of Ag against slider material.

4. Concluding remarks

The normal load dependency of friction coefficient of Ag-DLC against bearing steel was larger than that against brass. The load-dependent friction behavior has been enhanced by the increase of the elastic modules of slider, which correspond to the Hertz contact model. Ag-rich tribofilm was formed on the counter surfaces of sliders, and Ag concentration in the tribofilm on the brass ball is higher than that on steel ball. The adhesive strength of tribofilm on the copper alloys is stronger than that on the steel, which may have correlation with solubility of metals.

Acknowledgements

This work was partly supported by Grant-in-Aid for Scientific Research (A) (23246038), (B)(22360043) and (C)(23560174) of Japan Society for the Promotion of Science (JSPS). This project is performed within the framework of ELYT Lab. (France-Japan joint laboratory), as well as the GCOE program of IFS.

References

- [1] C. Donnet and A. Erdemir, "Tribology of diamond-like carbon films – fundamentals and application" 2008 Springer.
- [2] The role of tribofilm growth on the frictional behavior of copper-diamond-like carbon nanocomposite coating: M. GOTO, J. FONTAINE, S. BEC, K. ITO, T. TAKENO, M. RUET, H. MIKI, M. BELIN, T. LE MOGNE, Proc. 38th Leeds-Lyon Symposium on Tribology Sept. 6-9 2011 Lyon France.
- [3] Tribological Properties of Me-DLC Containing Ag and Cu: M. GOTO, J. FONTAINE, S. BEC, M. BELIN, T. LE MOGNE, K. ITO, T. TAKENO, and H. MIKI, Proc. Eighth International Conference on Flow Dynamics, Nov. 1-3, 2011, Sendai, Japan, pp.644-645.
- [4] T. Takeno, Y. Hoshi, H. Miki, T. Takagi, "Activation energy in metal-containing DLC films with various metals of various concentrations" Diamond and Related Materials Vol.17, 7-10 (2008) 1669-1673.
- [5] I. L. Singer, "Solid lubrication processes" I. L. Singer and H. M. Pollock (eds.), Fundamentals of Friction: Macroscopic and Microscopic Processes, (1992) 237-261.

A Method to Reduce Commutation Spark for Wear Reduction of Carbon Brush Installed in Automotive DC Motor

Ryoichi HOMBO, Naruhiko INAYOSHI, Naoki KATO
DENSO CORPORATION, 1-1, Showa-cho, Kariya-shi, Aichi 448-8661, Japan
ryoichi_honbo@denso.co.jp

ABSTRACT

Reduction of a commutation spark is an effective measure to reduce a carbon brush wear. This report presents relations between the spark and brush contact conditions. A larger spark occurs when an offset-load exists on the rear end of the brush because the electrical contact resistance between the brush and the commutator becomes extremely low at the brush-rear-end by the offset-load. Therefore, the electric current flow at the brush-rear-end becomes higher. At this time, an insufficient commutation is accelerated and it causes the larger spark. In contrast, to apply an offset-load on the front end of the brush reduces the spark.

1. Introduction

DC motors are indispensable to improve the automotive functions. Recently, 70-120 motors are installed on a luxury car and the number is increasing year by year. Normally, the motor life is determined by the brush life. If the brush wears to its limit, the motor will not rotate. To reduce brush wear is a key for competitive motor products. The main factor of the brush wear is the commutation spark. Many factors that affect the spark have been reported in previous studies, for example, influences of materials, electric circuits, conditions of use (current, sliding speed, environment), and so on [1]. In this study, characteristics of the spark under the offset-load on the brush have been investigated and a method to reduce the spark led through the investigation and a mechanism analysis is delivered.

2. Experiment

Table 1 shows experimental conditions. Both of the brush and commutator are made from 100% carbon. The offset δ shown in Fig.1 is the difference between the centers of brush and spring. In the case of $\delta = +0.2\text{mm}$, the offset-load is applied on the front end of the brush. Fig.2 shows the experimental apparatus that adopts the equivalent commutation circuit [2]. Waveforms of currents I_1 , I_2 and voltage V_1 were measured in both of the conditions 1 and 2 of Table 1 by using an oscilloscope. In the condition 1, the commutation spark is generated by an inductive voltage produced from the inductances (L). In the condition 2, each inductance was replaced with resistance (0.2Ohms) and all of the capacitances (C) were disconnected for observing only waveforms of brush contact resistance without the commutation spark.

3. Results and Discussion

The relationship between commutation current and residual current is shown in Fig.3. The residual current was measured from the waveforms recorded in the condition 1. When the brush is mechanically separated from a commutator segment, a spark occurs when the residual current is higher than the minimum arc current. The higher the residual current, the larger the spark [2]. As shown in Fig.3, the smaller the δ value, the higher the residual current. The residual current of $\delta = -0.2\text{mm}$ is approximately 2 times higher than that of $\delta = +0.2\text{mm}$

Table 1. Experimental conditions

Condition (objective)	Condition 1 (spark measurement)	Condition 2 (brush contact observation)
Offset δ , mm	-0.2, 0, +0.2	-0.2, +0.2
Commutation current I_c , A	3, 5, 7, 9	7
Inductance L , mH	0.1	-
Capacitance C , μF	1.0	-
Revolving speed of commutator, min^{-1}	7000	7000
Brush load, N	3	3

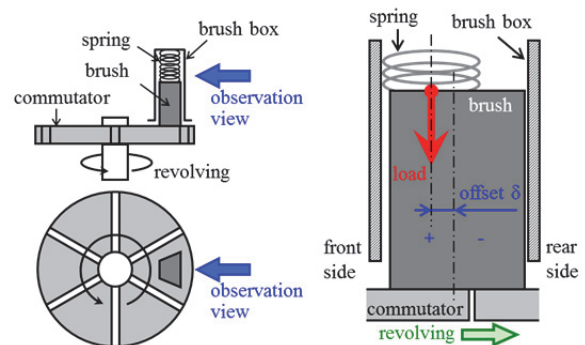


Fig. 1 Definition of offset δ

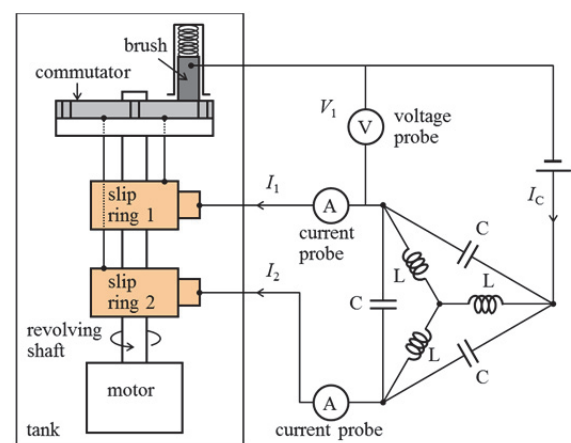


Fig. 2 Experimental apparatus

at each commutation current.

Fig.4 shows the waveforms of I_1 measured in the condition 2. Three waveforms during the commutation period (0.71ms) from each δ were drawn. At the point of

0.71ms, the brush-rear-end departs from the departing commutator segment and the electrical current becomes 0Amp. The current of $\delta = -0.2\text{mm}$ just before the departing point is quite higher than that of $\delta = +0.2\text{mm}$ and falls steeply. The high and rapid change of current induces a large inductive voltage. This behavior of current seems to cause the high residual current.

Fig.5 shows the profiles of electrical contact resistance calculated by using I_1 and V_1 measured in the condition 2. The resistance of $\delta = -0.2\text{mm}$ just before the departing point is much lower than that of $\delta = +0.2\text{mm}$.

As mentioned above, it has been found that the offset-load significantly affects the behaviors of spark. In previous studies, a lack of brush contact area (partial contact) and abnormal motions of brush (vibration, jumping, chattering, etc.) have been recognized as the major factors that cause large spark. However, the apparent brush contact areas of $\delta = -0.2\text{mm}$ and $+0.2\text{mm}$ were almost the same. And the curves of current were very smooth and irregular waveforms, such as large electrical noise and voltage ripple, caused by the abnormal motion of brush were not observed in all of the experiments. Only the differences between $\delta = -0.2\text{mm}$ and $+0.2\text{mm}$ are the profiles of current and electrical contact resistance.

For understanding above phenomenon, we provide a new model. Fig.6 shows a mechanism of high residual current occurrence in the condition of $\delta = -0.2\text{mm}$. In the case of $\delta = -0.2\text{mm}$, the distributed load of the rear end of brush seems to be larger than that of the front end because of the offset-load. Under this load distribution, the real contact area of the rear end is larger than that of the front end. Therefore, the electrical contact resistance of the rear end becomes lower than that of the front end because the electrical contact resistance varies inversely as the real contact area. Finally, the high electrical current flows at the rear end and it promotes the larger spark. In contrast, the commutation spark is reduced in the case of $\delta = +0.2\text{mm}$ by the opposite mechanism of the Fig.6.

4. Concluding remarks

Characteristics of the spark under the offset-load on brush have been investigated through the experiments using the equivalent commutation circuit. The influence and the mechanism of the offset-load on the spark have been discussed. The achievement is as follows:

- (1) A larger spark occurs when an offset-load exists on the rear end of a brush because the electrical contact resistance between the brush and the commutator becomes extremely low at the rear end of the brush and it causes a high residual current.
- (2) The spark can be reduced by applying the offset-load on the front end of the brush with the opposite mechanism of above (1).

References

- [1] R.Holm, Electric contacts, Springer-Verlag New York Inc., (1967).
- [2] R.Honbo, IEICE Trans., E89-C, 8 (2006) 1153.

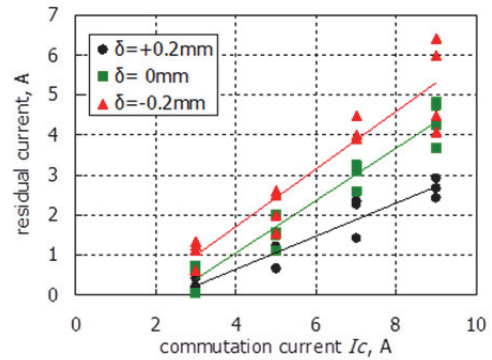


Fig. 3 Commutation current and residual current

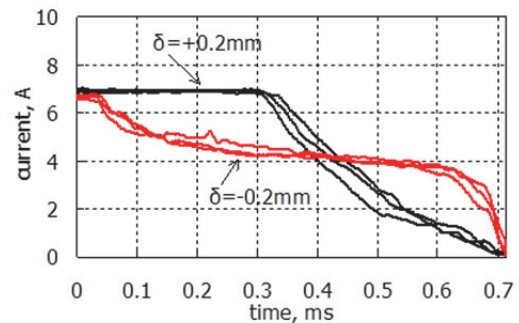


Fig. 4 Waveforms of commutation current

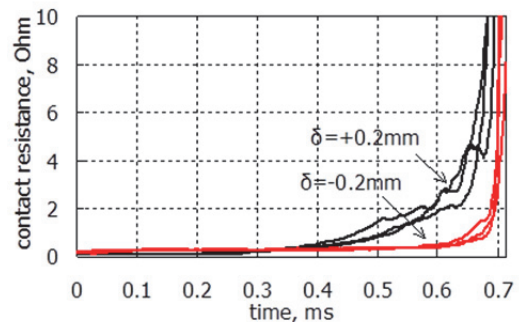


Fig. 5 Profiles of electrical contact resistance

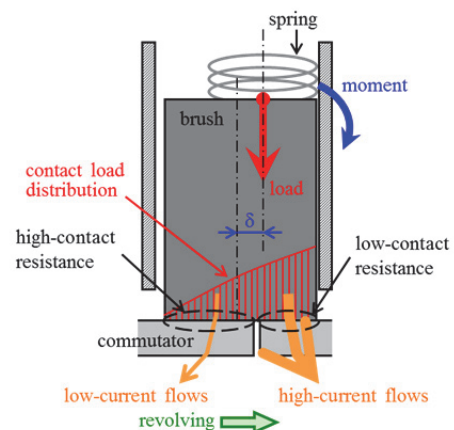


Fig. 6 Mechanism of large residual current occurrence in the condition of offset $\delta = -0.2\text{mm}$

Some Considerations on the Tribology of Solid Lubricant Coatings

Philippe KAPSA(1), Vincent FRIDRICI(1), Jiao YANG(1), Marine BERNARD(1), Dabing LUO (2)

(1) Laboratoire de Tribologie et Dynamique des Systèmes, UMR 5513 CNRS ECL ENISE, Ecole Centrale de Lyon,
Bât. H10, 36 avenue Guy de Collongue 69134 Ecully cedex, France

(2) Tribology Research Institute, Southwest Jiaotong University, 610031 Chengdu, China
Philippe.kapsa@ec-lyon.fr

ABSTRACT

Coating tribology is an old subject for tribologists but always now many problems are unsolved and research is always of interest. Numerous coatings can be used... and selecting a coating for a given application is very difficult. In most cases, a specialist thanks to its wide knowledge of coatings efficiency makes the choice. Among the coatings we can consider soft, hard, thin or thick coatings... The understanding of damage phenomena is always very important and the governing parameters have to be determined. The study of a solid lubricant coating (based on MoS₂) will help to show some damage phenomena and important parameter.

1. Introduction

In the last decade, solid lubricants have been investigated as materials with a wide variety of potential applications including contacts operating at high temperature, under reciprocating motion, under extreme contact pressures. Nowadays, with the challenge of lubricating mechanical contacts functioning at high temperature without using greases or oils, there is an increasing need for this type of lubricants.

Solid lubricants performance depends on their ability to be easily sheared when deposited in a moving interface. Their durability depends critically on its method of deposition: firm adhesion between the film and the substrate is a prerequisite for prolonged lifetime of the film.

Molybdenum disulfide (MoS₂) is one of the oldest known solid lubricants and the most widely used in industry [1]. MoS₂ can be found in many forms: powder, additive to a lubricant, resin-bonded coatings... The coating functioning temperature is limited to 450°C.

2. Behavior of a MoS₂ solid lubricant coating

The tribological properties of a MoS₂ based varnish solid lubricant coating were studied at ambient and elevated temperatures on a cylinder-on-disk alternative tribometer to determine the effects of contact temperature and pressure on the coating lifetime.

Friction tests were performed using a cylinder on flat configuration under 5 Hz reciprocating motion at various contact temperatures: ambient (20°C), 200°C and 350°C. Both the cylinder, 15 mm in length and 50 mm in diameter, and the flats were made of 304L stainless steel. Normal loads applied were: 200 N, 300 N and 400 N (corresponding respectively to a maximal Hertzian contact pressure of 140 MPa, 170 MPa and 200 MPa), until the coating was removed from the contact.

The stroke length was 5 mm. At first, a cylinder on uncoated flat test was conducted in order to determine the steel/steel friction coefficient: a value of 0.6 was obtained.

Figure 1 presents the evolution of the measured

lifetime vs the temperature for the various loads. It appears that for every applied normal load, the MoS₂ based coating shows the same behavior in terms of lifetime at different contact temperatures.

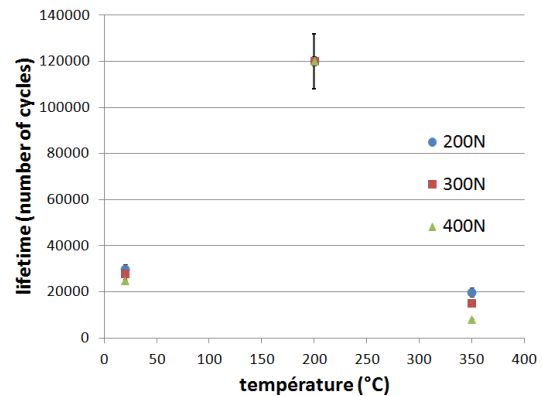


Fig 1. Calculated values of the lifetime of a MoS₂ based coating at different contact pressure and temperature

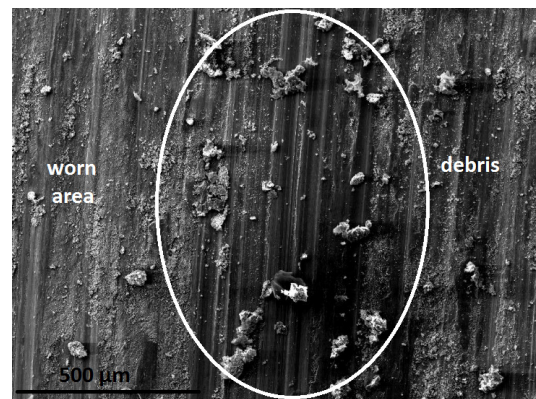


Fig 2. wears tracks micrograph (300N, 350 °C)

The observed behavior is supported by wear track SEM images. It was observed that the wear tracks at room temperature and at 200°C were quite smooth and without any debris with very few fine abrasive particles were spotted along the tracks. While at 350°C dense

debris were detected in the flat tracks (Figure 2). Those grains, which increased the abrasive effect between the coating and the cylinder, caused detachment of the coating from the surface in a short time, and a rapid increase of the friction coefficient, and thus a decrease in the lifetime.

It seems that 200°C is quite an optimum temperature for the use of a MoS₂ based varnish solid lubricant in a steel/steel contact. At this temperature, the results showed that whatever the normal load, the friction coefficient stays below the steel on steel friction coefficient value, even after a 120 000 cycles long test (≈ 6 hours). Chemical analysis of the wear track proved that the coating remains in the contact, which induces a longer lifetime.

3. Important parameters for solid lubricant coating efficiency

In this study, the method called “factorial analysis”, was introduced to quantitatively evaluate the parameters influencing the wear behavior of coatings.

Factorial design enables designers to determine simultaneously the individual and interactive effects of many factors that could affect the output results in any design. Based on the experimental results in different working conditions of fretting wear, like contact force, displacement amplitude and contact configurations, the important parameters for lifetime and friction coefficient MoS₂ based varnish coating could be discovered. Table 1 shows the controlling parameters for coating lifetime. The F -value for each factor is simply a ratio of the mean of the squared deviations to the mean of the squared errors [1]. It represents the deviation of levels for a factor. Generally speaking, it is significant if the F -value is larger than that of critical F -value. It can be used to identify whether or not the factors are significant factors affecting the coating lifetime and friction coefficient. A larger F -value means that the factor has greater significance for the coating lifetime or friction coefficient. The p -value Prob > F indicates that probability of seeing the observed F value if there is no factor effect (null hypothesis). Small probability values call for rejection of the null hypothesis. It could be observed that the contact configuration ($F = 1526.3$), displacement amplitude δ^* ($F = 501.2$) and their interaction ($F = 362.4$) are the most significant variables affecting the coating lifetime. This is because the wear behavior is subjected to the velocity accommodation mode.

Different from the results of coating durability, the most important parameters for friction coefficient is contact configuration and normal force, shown in the table 2. A larger pressure may also improve the formation of transfer films on the counterface [2] so that the friction pairs are changed to the remaining coating and transfer films accompanied by a lower friction coefficient.

Table 1. ANOVA for the coating lifetime (normal force F_n , displacement amplitude δ^* , contact configuration Con, sum of squares SS, degree of freedom df, mean squares MS).

Variance	SS ($\times 10^6$)	df	MS ($\times 10^6$)	F values	F crit	Prob>F
F_n	1.8	2	0.9	61.3	3.6	< 0
δ^*	14.4	2	7.2	501.2	3.6	< 0
Con	22.0	1	22.0	1526.3	4.4	< 0
$F_n \times \delta^*$	1.3	4	0.3	23.2	2.9	< 0
$F_n \times \text{con}$	2.2	2	1.1	77.9	3.6	< 0
$\delta^* \times \text{con}$	10.4	2	5.2	362.4	3.6	< 0
$F_n \times \delta^* \times \text{con}$	1.2	4	0.312259	21.7	2.9	< 0
Residual	0.3	18	0.01	-	-	-
Total	53.7	35	-	-	-	-

Table 2 : ANOVA for the coefficient of friction (normal force F_n , displacement amplitude δ^* , contact configuration Con, sum of squares SS, degree of freedom df, mean squares MS).

Source of variance	SS ($\times 10^{-2}$)	df	MS ($\times 10^{-2}$)	F values	F crit	Prob>F
F_n	12.5	2	6.2	229.2	3.6	< 0
δ^*	0	2	0	0.8	3.6	0.5
con	6.3	1	6.3	231.2	4.4	< 0
$F_n \times \delta^*$	0	4	0	0.3	2.9	0.9
$F_n \times \text{con}$	1.1	2	0.5	19.4	3.6	< 0
$\delta^* \times \text{con}$	0.4	2	0.2	7.8	3.6	0.004
$F_n \times \delta^* \times \text{con}$	0.2	4	0.05	1.5	2.9	0.3
Residual	0.5	18	0.0	-	-	-
Total	20.9	35	-	-	-	-

4. Concluding remarks

MoS₂ solid lubricant coatings efficiency is subjected to various changes with the tribological parameters. The temperature modifies their durability. An approach using factorial analysis can help to understand the comparative effects of various parameters.

These information can be very useful for the coating selection for an application.

References

- [1] *Delwiche and Slaughter, The little SAS book, fourth ed.* SAS Institute Inc., Cary, North Carolina, 2008, p. 259.
- [2] *POPE and PANITZ, The effects of hertzian stress and test atmosphere on the friction coefficient of MoS₂ coatings.* Surface and coatings technology, 1988. 36:p.341-350

